中国气象局气候研究开放实验室

论文汇编

第二十二卷

(2019)



LCS

气候研究开放实验室

中国气象局气候研究开放实验室

论文汇编

第二十二卷

(2019)

中国气象局气候研究开放实验室

内 容 简 介

本文集收录了2019年度中国气象局气候研究开放实验室在国内外核心期刊发表的学术论文54篇。内容涉及气候诊断、气候预测理论及方法、气候模式模拟、气候变化检测及影响评估等研究领域。

目　录

1. Extremely active tropical cyclone activities over the western North Pacific and South China Sea in summer 2018: Joint effects of decaying La Niña and intraseasonal oscillation …… Chen L J, Z S Gong, J Wu and W J Li (1)
2. Why is the East Asian summer monsoon extremely strong in 2018? —Collaborative effects of SST and snow cover anomalies …… Chen L J, Gu W, Li W J (19)
3. 影响 2018 年汛期气候的先兆信号及预测效果评估 …… 陈丽娟　顾　薇　龚振淞 等 (35)
4. 汛期我国主要雨季进程成因及预测应用进展 …… 陈丽娟　赵俊虎　顾　薇　梁　萍　彭京备 等 (47)
5. 基于最大熵模型的中国血吸虫病传播风险评估 …… 段居琦　周　骥　黄大鹏　刘绿柳 (63)
6. 基于 NCEP-GEFS 回算资料的我国极端温度变化特征研究 …… 高　丽　任宏利　郑嘉雯 等 (69)
7. 2018 年夏季海洋大气特征及对我国气候的影响 …… 顾　薇　陈丽娟 (79)
8. The spatiotemporal pattern of rainy-season precipitation in the Haihe River basin, North China …… Guo Jun, Guoyu Ren, Mingming Xiong, He Huang (88)
9. Diagnosing the spatiotemporal diversity of westerly wind events in the tropical Pacific …… Hao Xiaozhen, Hongli Ren, Wenjun Zhang, et al (107)
10. Parameter modulation of Madden-Julian Oscillation behaviors in BCC_CSM1.2: The key Role of moisture-shallow convection feedback …… Huang Kai, Ren Hongli, Liu Xiangwen, et al (121)
11. Urban Heat Island Effect and Its Cintribution to Observed Temperature Increase at Wuhan Station, Central China …… Jia Wenqian, Ren Guoyu, Suonan Kanzhuo, Zhang Panfeng, et al (147)
12. Diurnal and intra-season variation of warm-season temperature in coastal zone of Qinghai Lake …… Li Hongmei, Guoyu Ren, Wanzhi Li, et al (159)
13. Development of land surface model BCC_AVIM2.0 and its preliminary performance in LS3MIP/CMIP6 …… Weiping Li, Yanwu Zhang, Xueli Shi, et al (174)
14. More extreme marine heatwaves in the China Seas during the global warming hiatus …… Li Yan, Guoyu Ren, Qingyuan Wang, et al (193)
15. 中国地气温差时空分布及变化趋势 …… 廖要明　陈德亮　刘秋锋 (203)
16. 凤县花椒生产气候条件和灾害分析 …… 廖要明　杨文平 (214)
17. Diagnosing the leading mode of interdecadal covariability between the Indian Ocean sea surface temperature and summer precipitation in southern China …… Liu Jingpeng, Ren Hongli, Li Weijing, Jinqing Zuo (221)
18. The Major Interannual Modes of Late-Summer Precipitation over the Northern China Monsoon Region …… Liu Yang, Junhu Zhao, Po Hu, Shulin Qu, Guolin Feng (233)
19. A significant bias of T_{max} and T_{min} average temperature and its trend …… Liu Yulian, Guoyu Ren, Engyuan Kang, et al (245)
20. 2019 年春季我国主要气候异常特征及可能成因分析 …… 刘芸芸　陈丽娟 (257)
21. Impact of El Niño and Southern Oscillation on the summer precipitation over Northwest China …… Lu B, Li H Y, Wu J, et al (268)

22. ENSO Features, Dynamics, and Teleconnections to East Asian Climate as Simulated in CAMS-CSM ····· Lu B, Ren H L (276)
23. Stratospheric initial conditions provide seasonal predictability of the North Atlantic and Arctic Oscillations ····· Yu Nie, Adam Scaife, Ren Hongli, et al (296)
24. The role of extratropical air-sea interaction in the autumn subseasonal variability of the North Atlantic Oscillation ····· Nie Yu, Hongli Ren, Yang Zhang (303)
25. Seasonal predictability of winter ENSO types in operational dynamical model predictions ····· Ren Hongli, Adam A. Scaife, Nick Dunstone, et al (319)
26. The China multi-model ensemble prediction system and its application to flood-season prediction in 2018 ····· Ren Hongli, Yujie Wu, Qing Bao, Jiehua Ma, et al (341)
27. Statistical predictability of Niño indices for two types of ENSO ····· Ren Hongli, Jinqing Zuo, Yi Deng (354)
28. 动力和统计预测信息融合预测方法及我国夏季降水预测的检测 ····· 孙丞虎 崔 童 李维京 等 (376)
29. Contribution of global warming and urbanization to changes in temperature extremes in Eastern China ····· Sun Ying, Hu Ting, Zhang Xuebin, Li Chao, et al (386)
30. Diagnosing the representation and causes of the ENSO persistence barrier in CMIP5 simulations ····· Tian Ben, Hongli Ren, Feifei Jin, Malte F. Stuecker (395)
31. Urbanization Effect in Regional Temperature Series Based on a Remote Sensing Classification Scheme of Stations ····· Tysa S K, Ren G Y, Qin Y, et al (409)
32. Changes in means and extreme events of sea surface temperature in the East China Seas based on satellite data from 1982 to 2017 ····· Qingyuan Wang, Yan Li, Qingquan Li, et al (425)
33. Partition of Season Based on Multi-elements and the Decadal Change of Season Duration in China ····· Zheng Wang, Rong Zhi, Yu Wang and Guolin Feng (436)
34. Conditional nonlinear optimal perturbations of moisture triggering primary MJO initiation ····· Wei Yuntao, Mu Mu, Hongli Ren (450)
35. Modulation of ENSO on fast and slow MJO modes during boreal winter ····· Wei Yuntao, Hongli Ren (460)
36. Recent surface air temperature change over mainland China based on an urbanization-bias adjusted dataset ····· Wen Kangmin, Ren Guoyu, Li Jiao, et al (484)
37. BCC_CSM1.1气候模式年代际试验对北极涛动季节回报能力的初步评估 ····· 伍丽泉 李清泉 丁一汇 等 (499)
38. Decadal prediction skill of BCC-CSM1. 1 with different initialization strategies ····· Xin Xiaoge, Wei Min, Li Qingquan, et al (510)
39. 中国中小尺度强对流天气气候学特征 ····· 薛晓颖 任国玉 孙秀宝 等 (522)
40. Impact of daytime precipitation duration on urban heat island intensity over Beijing city ····· Yang Ping, Ren Guoyu, Hou Wei (537)
41. 华北雨季开始早晚与大气环流和海温异常的关系 ····· 于晓澄 赵俊虎 杨 柳 支 蓉 封国林 (550)

42. Interdecadal variations of the temporal and spatial distribution of summer extreme heat in China ……Naihui Zang, Junhu Zhao, Pengcheng Yan, Guolin Feng (562)
43. 10～30 d 延伸期可预报性与预报方法研究进展……章大全　郑志海　陈丽娟　张培群 (575)
44. Influence of late springtime surface sensible heat flux anomalies over the Tibetan and Iranian plateaus on the location of the South Asian High in early summer ……Haoxin Zhang, Weiping Li, Weijing Li (590)
45. Observed changes in extreme temperature over the global land based on a newly developed station daily dataset ……Zhang Panfeng, Ren Guoyu, Xu Yan, et al (601)
46. Improved assimilation of Fengyun-3 satellite-based snow cover fraction in northeastern China ……Shuai Zhang, Chunxiang Shi, Runping Shen, Jie Wu (622)
47. Comparison of Surface Air Temperature between Observation and Reanalysis Data over Eastern China for the Last 100 Years ……Zhang Siqi, Ren Guoyu, Ren Yuyu, Sun Xiubao (638)
48. Bias correction of gauge data and its effect on precipitation climatology over mainland China ……Zhang Y X, Ren Y Y, Ren G Y, et al (653)
49. MJO modulation and its ability to predict boreal summer tropical cyclone genesis over the northwest Pacific in Met Office Hadley Centre and Beijing Climate Center seasonal prediction systems ……Zhao Chongbo, Hongli Ren, Rosie Eade, et al (673)
50. 2018 年秋季我国气候异常及成因分析 ……赵俊虎　王永光 (686)
51. Relationship between Tropical Indian Ocean SSTA in Spring and Precipitation of Northeast China in Late Summer ……Zhao J H, J Zhou, K G Xiong, G L Feng (698)
52. Possible Causes of the Anomalous Characteristics of Autumn Rain in Western China in 2017 ……Jie Zhou, Junhu Zhao, Rong Zhi (713)
53. Interannual Variability of the Tropical Cyclone Landfall Frequency over the Southern and Northern Regions of East Asia in Autumn ……Xingyan Zhou, Riyu Lu (728)
54. Remote forcing of the northern tropical Atlantic SST anomalies on the western North Pacific anomalous anticyclone ……Zuo Jinqing, Li Weijing, Sun Chenghu, Ren Hongchang (738)

● FORECASTING FORUM ●

Extremely Active Tropical Cyclone Activities over the Western North Pacific and South China Sea in Summer 2018: Joint Effects of Decaying La Niña and Intraseasonal Oscillation

Lijuan CHEN[1,2*], Zhensong GONG[1], Jie WU[1], and Weijing LI[1,2]

1 *Laboratory for Climate Studies*, *National Climate Center*, *China Meteorological Administration*, *Beijing* 100081
2 *Collaborative Innovation Center on Forecast and Evaluation of Meteorological Disasters*, *Nanjing University of Information Science &Technology*, *Nanjing* 210044

(Received March 12, 2019; in final form August 5, 2019)

ABSTRACT

In summer 2018, a total of 18 tropical cyclones (TCs) formed in the western North Pacific (WNP) and South China Sea (SCS), among which 8 TCs landed in China, ranking respectively the second and the first highest since 1951. Most of these TCs travelled northwest to northward, bringing in heavy rainfall and strong winds in eastern China and Japan. The present study investigates the impacts of decaying La Niña and intraseasonal oscillation (ISO) on the extremely active TCs over the WNP and SCS in summer 2018 by use of correlation and composite analyses. It is found that the La Niña episode from October 2017 to March 2018 led to above-normal sea surface temperature (SST) over central–western Pacific, lower sea level pressure and 500-hPa geopotential height over WNP, and abnormally strong convective activities over the western Pacific in summer 2018. These preceding oceanic thermal conditions and their effects on circulation anomalies are favorable to TC genesis in summer. Detailed examination reveals that the monsoon trough was located further north and east, inducing more TCs in northern and eastern WNP; and the more eastward WNP subtropical high as well as the significant wave train with a "− + − +" height anomaly pattern over the midlatitude Eurasia–North Pacific region facilitated the northwest to northward TC tracks. Further analyses reveal that two successively active periods of Madden–Julian Oscillation (MJO) occurred in summer 2018 and the boreal summer intraseasonal oscillation (BSISO) was also active over WNP, propagating northward significantly, corresponding to the more northward TC tracks. The MJO was stagnant over the Maritime Continent to western Pacific, leading to notably enhanced convection in the lower troposphere and divergence in the upper troposphere, conducive to TC occurrences. In a word, the extremely active TC activities over the WNP and SCS in summer 2018 are closely linked with the decaying La Niña, and the MJO and BSISO; their joint effects result in increased TC occurrences and the TC tracks being shifted more northwest to northward than normal.

Key words: western North Pacific (WNP), tropical cyclone (TC), La Niña event, Madden–Julian Oscillation (MJO), boreal summer intraseasonal oscillation (BSISO)

Citation: Chen, L. J., Z. S. Gong, J. Wu, et al., 2019: Extremely active tropical cyclone activities over the western North Pacific and South China Sea in summer 2018: Joint effects of decaying La Niña and intraseasonal oscillation. *J. Meteor. Res.*, **33**(4), 609–626, doi: 10.1007/s13351-019-9009-x.

1. Introduction

The western North Pacific (WNP) is one of the regions with most frequent tropical cyclone (TC) activities. On average, about 11 TCs form in this region each summer. Tropical cyclones are often accompanied by strong winds, heavy rains, and storm surges, leading to huge economic losses and casualties. China, Japan, and the other Southeast Asian countries are greatly affected by TCs. Therefore, study on the formation and activity pattern of TCs, especially the TC occurrence frequency, moving path, intensity, and level of influence, is important for the prevention and mitigation of TC-induced disasters.

Meteorologists have long been concerned of weather and climate conditions related to TCs over the WNP

Supported by the National Key Research and Development Program of China (2018YFC1506001), National Basic Research (973) Program of China (2015CB453203), and National Natural Science Foundation of China (41275073 and 41805067).

*Corresponding author: chenlj@cma.gov.cn.

©The Chinese Meteorological Society and Springer-Verlag Berlin Heidelberg 2019

(Chen, 1965; Sadler, 1978; Chen and Ding, 1979; Ding and Reiter, 1981a, b; Wang, 1981). Further studies indicate that the TC activity in the WNP has significant intraseasonal, interannual, and interdecadal variabilities (Chen et al., 1998; Chan, 2005; Emanuel, 2005; Webster et al., 2005).

TC activity is closely associated with El Niño–Southern Oscillation (ENSO). ENSO affects TC activity through its impacts on the thermal and dynamic conditions over the WNP. Earlier studies suggested that in El Niño years, sea surface temperature (SST) over the WNP is lower than normal, sea level pressure (SLP) is higher than normal, and convection is weaker than normal; as a result, fewer TCs can form in WNP and the TC genesis positions are located to the east of their normal positions. In La Niña years, the situations are reversed (Chan, 1985; Wu and Lau, 1992; Lander, 1994). Further in-depth studies found that during different stages of the ENSO cycle, various combinations of the ENSO intensity, spatial pattern, and SST anomaly in the Indian Ocean would affect the TC genesis, TC track, TC intensity, and TC landfall in different seasons (Li C. Y., 1987; Chen et al., 1998, 2006; He et al., 1999; Chan, 2000; Wang and Chan, 2002; Kim et al., 2011; Zhan et al., 2011; Li T., 2012; Li and Zhou, 2012; Yu et al., 2016b; Xie at al., 2018). Note that results of various studies are different due to differences in data, definition, and research routines among these studies. Wang and Chan (2002) proposed that in El Niño developing years, most TCs form over the southeast quadrant of the WNP with relatively strong intensity; in La Niña developing years, TCs form largely over the northwest quadrant of the WNP with relatively weak intensity. From July to September, mean TC genesis position in strong El Niño years is further south than that in La Niña years. Xie et al. (2018) found that in the years of El Niño decaying, most of the TCs are originated in the South China Sea and move westward; in the years of La Niña decaying, TCs mostly originate over the WNP near the coastal water of China (including the Taiwan Island), and they often follow a recurvature path along the coast.

In addition, some studies suggested that the Antarctic Oscillation (AAO), Arctic sea ice, snow cover in the Tibetan Plateau, North Pacific Oscillation (NPO), SST over North Atlantic, etc., all have impacts on the interannual variability of TC activity (Wang and Fan, 2006; Fan, 2007; Wang et al., 2007; Yu et al., 2016a; Zhan et al., 2016).

The Madden–Julian Oscillation (MJO) is the most significant mode of tropical atmospheric circulation (Madden and Julian, 1971), which is characterized by eastward propagation of large-scale deep convection anomalies in the tropics. These convection anomalies initiate from the Indian Ocean, pass through Indonesia and the nearby regions, enter the western Pacific, and eventually disappear near the international dateline. TC activities and TC tracks are affected obviously by the MJO (Hu and Wang, 1992; Sobel and Maloney, 2000; Zhu et al., 2004; Huang and Chen, 2007; Kim et al., 2008; Chen and Huang, 2009; Liu G. et al., 2009; Sun et al., 2009; Pan et al., 2010; Tian et al., 2010a, b; Huang et al, 2011; Li and Zhou, 2013a, b; Liu Q. et al., 2018). Most studies conclude that the MJO would affect the atmospheric temperature, water vapor content, and sea level pressure during its eastward propagation. When the MJO is in its active phase, convection is significantly enhanced, a cyclonic vortex develops to the north of the equator at lower levels while an anticyclonic vortex develops in the upper troposphere, vertical wind shear decreases, and upper-level divergence intensifies. Such a large-scale circulation background favors the generation and development of TCs. In the westerly wind phase of the MJO, zonal convergence and meridional shear of zonal winds lead to energy transfer from low-frequency kinetic energy to high frequency kinetic energy, which subsequently intensifies high-frequency motions. As a result, more TCs are generated in this region. On the contrary, when the MJO is in the easterly wind phase over the western WNP, TC genesis is suppressed. In addition, different phases of the MJO and the quasi-biweekly oscillation (QBWO) over the WNP also affect the TC genesis, intensity, track, and landing. TCs are also under the influences of intraseasonal oscillation in the subtropics and circulation patterns over the mid–high latitude regions.

The above discussion indicates that TC activity is influenced by multiple factors. The TC genesis, track, landing, and TC-induced disasters are quite different in different years (Liu et al., 2007; Gong and Chen, 2013). TC activity can be significantly active or inactive in the summer and autumn seasons. In the summer of 2018, a total of 18 TCs formed in the WNP and South China Sea (SCS) and 8 TCs landed in China, both are much more than normal. The TC genesis frequency over the WNP and SCS in 2018 ranked the second highest since 1951, and the number of landfall TCs in China in 2018 ranked the highest since 1951. Apparently, TC activity is extremely active in summer 2018. Meanwhile, TC tracks are also complex in this season. Climatologically, the annual mean number of TCs that land along the coastal region of Zhejiang–Shanghai–Jiangsu is only 1, whereas this number rises to 4 in 2018, among which 3 landed in

Shanghai, accounting for half of the total TCs that landed in Shanghai since 1951 (including those that landed for the second time in Shanghai). Typhoons Ampil (1810), Yagi (1814), and Rumbia (1818) travelled across central–northern parts of East China and entered inland China, affecting large areas and bringing in extremely heavy precipitation along their moving paths. In particular, Typhoon Ampil went all the way north to the southeastern Inner Mongolia. It was maintained for up to 62 h over land area, which seldom occurred in history. In addition, five TCs directly landed in or influenced Japan and two TCs landed in the Korean Peninsula, incurring severe disasters there. Among the five TCs, after landing in Honshu Island, Japan, Jongdari (1812) turned west and landed in Shanghai, China. In summer 2018, TCs were crowded together, mutually restrained, and twisted, turned, or zigzagged over offshore regions, showing complicated tracks. However, among the eight TCs that landed in China, only one reached the strong typhoon intensity [Maria (1808)] and the other seven TCs remained as tropical storms or strong tropical storms. The average wind speed of the eight landfalling TCs is 26 m s^{-1} (category 10), weaker than the climatological mean value of 32.8 m s^{-1} (category 12). Although the TCs that landed in China in 2018 were weak, the TC-induced precipitation was strong, and heavy rainfall occurred over large areas such as East China, eastern North China, southern Northeast China, and South China.

In this paper, the mechanisms for the extremely active TC season of summer 2018 and the complicated TC tracks are analyzed from perspectives of ocean thermal condition, large-scale circulation, and intraseasonal oscillation. Results of the present study are expected to reveal and provide precursor signals for TC prediction and improve the capability for prevention and mitigation of TC-induced disasters.

2. Data and method

Meteorological elements such as geopotential height, horizontal winds, vertical velocity, and so on are extracted from the NCEP/NCAR monthly reanalysis data (Kalnay et al., 1996; Kistler et al., 2001). The data cover the period of 1948–2018 with a horizontal resolution of 2.5° × 2.5°. The NOAA 1.0° × 1.0° Optimum Interpolation Sea Surface Temperature dataset (OISST-V2) is used (Reynolds et al., 2002). Daily atmospheric analysis data include horizontal winds at 850 and 200 hPa are extracted from the Global/Regional Assimilation and Prediction System (GRAPES) daily analysis data with a resolution of 25 km × 25 km, together with daily outgoing longwave radiation (OLR) on a resolution of 0.01° × 0.01°. All data are interpolated to 2.5° × 2.5°grids. The Niño3.4 SST index (5°N–5°S, 120°–170°W) is produced by the U.S. Climate Prediction Center (CPC) based on ERSST v5 (Huang et al., 2017) and can be downloaded from http://origin.cpc.ncep.noaa.gov/products/analysis_monitoring/ensostuff/ONI_v5.php.

The historical information on TC occurrence frequency and genesis position is derived from the best track dataset provided by Shanghai Typhoon Institute of China Meteorological Administration (CMA) (Ying et al., 2014). The data can be downloaded from http://tcdata.typhoon.org.cn/zjljsjj_zlhq.html. In this dataset, TCs are defined as those with average wind speed of 17 m s^{-1} (category 8) or above that occur especially in the WNP and SCS, including tropical storms, strong tropical storms, typhoons, strong typhoons, and super typhoons. This best track dataset also provides the position and intensity of all TCs over the WNP (including the SCS, the Pacific Ocean to the north of the equator and to the east of 180°) since 1949 at 6-h intervals. Unless specifically stated, in this paper, the climatological mean refers to the 30-yr average over 1981–2010.

The RMM (Realtime Multi-variate MJO) index, which consists of zonal winds at 850 (U850) and 200 hPa (U200) and OLR, is used to monitor the MJO (Wheeler and Hendon, 2004). The RMM index can well represent the coupling structure of MJO between large-scale convection and circulation anomalies. The two components of the RMM index, named as RMM1 and RMM2, are used to produce a two-dimensional phase space diagram that can directly reflect the position and propagation characteristics of MJO convection in real time. This type of two-dimensional phase space diagram has been widely applied to the operational monitoring and scientific studies of MJO. To calculate the RMM index, climatic seasonal cycles (0–3 waves) and interannual variabilities (average of the previous 120 days) of U200, U850, and OLR are firstly removed from their daily values, and the meridional averages are then calculated over the tropics (15°S–15°N) and normalized by dividing their respective standard deviations. Finally, the results are projected to the first two EOF patterns to obtain the pair of RMM monitoring index. In order to ensure the consistency of results, the standard deviations and spatial modes used for normalization and projection are downloaded from http://poama.bom.gov.au/project/maproom/RMM/. In addition, the two pairs of indices defined by Lee et al. (2013), which consist of U850 and OLR and can be calculated by the similar method for RMM index and projected onto four EOF patterns, are used as monitoring in-

dex for the boreal summer intraseasonal oscillation (BSISO) (refer to http://iprc.soest.hawaii.edu/users/jylee/bsiso/).

3. Characteristics of TC activity over the WNP in summer 2018

The whole year of 2018 witnessed 29 TCs formed over the WNP and SCS, 3 more than the climatological average (26); 10 TCs landed in China, 3 more than the normal (7). The TC activity was active in summer and inactive in autumn (Fig. 1) with 18 TCs formed in summer, significantly more than the climatological mean (11). In June, July, and August, TC genesis frequency is 235%, 135%, and 156% that of the respective climatological monthly average. Eight TCs landed in China in summer 2018, more than the climatological mean (4.6). The number of TCs that landed in June, July, and August is 158%, 150%, and 206% that of the climatological mean in each corresponding month. In autumn (September–November) 2018, only 8 TCs formed, much fewer than the climatological mean (11). Among the eight TCs formed in autumn, two landed in China, similar to the climatological mean number. Statistics of TCs forming in the WNP and SCS and landing in China in summer during 1951–2018 (Fig. 2) suggests that the TC genesis frequency in summer 2018 is only smaller than that in summer 1994 (19), ranking the second highest together with that in 1967 and 1974. The number of TCs that landed in China in summer 2018 ranks the first with that in 1994, exceeding two standard deviations of its climatic value. The above results indicate that the TC activity is extremely active in summer 2018 and this abnormality could be found in every month of the summer. It is worth exploring the

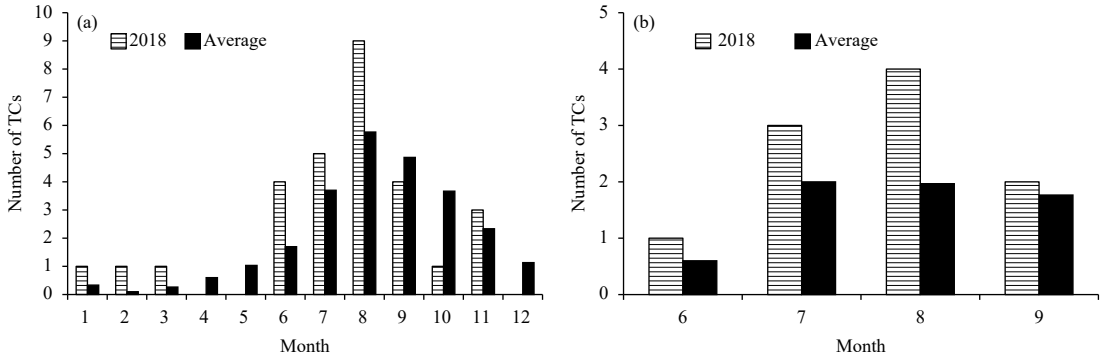

Fig. 1. Comparison of (a) the number of TCs that formed over the WNP and SCS (0°–30°N, 100°E–180°) and (b) the number of TCs that landed in China, in 2018 (column in light gray) and their climatological values (column in black).

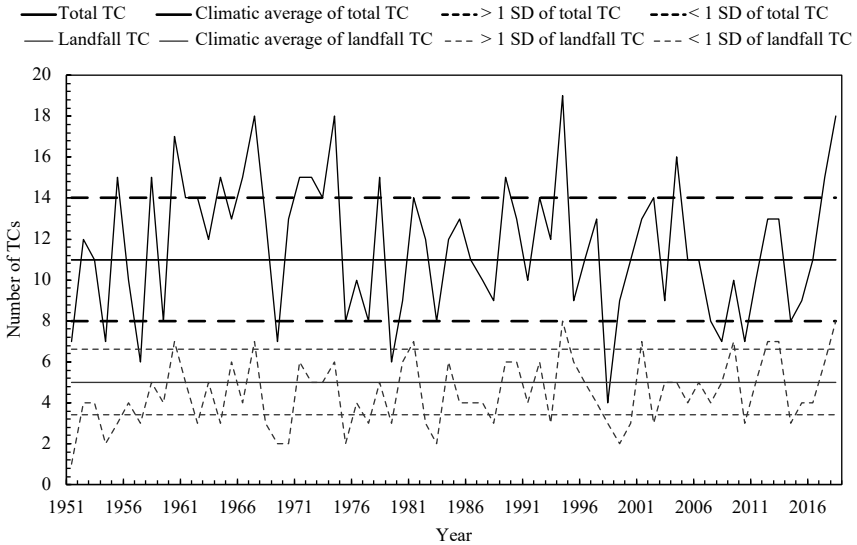

Fig. 2. Temporal evolutions of the number of TCs generated over the WNP and SCS (solid line) and landfall TCs in China (dashed line) in summer during 1951–2018. Black and gray solid lines denote the climatological mean values, and dotted lines indicate one standard deviation, for total TCs and landfall TCs, respectively.

reasons for the abnormal large number of TCs that formed over the WNP and SCS and landed in China in summer 2018.

Based on the regions of TC genesis, we chose three regions: the SCS (west of 120°E), WNP1 (120°–145°E), and WNP2 (145°E–international dateline) to perform further analysis. TC genesis frequencies over the above three regions are listed in Table 1. It is shown that over the entire year, the TC genesis frequencies in 2018 are slightly higher than the climatological values in all the three regions. But in summer, only the TC genesis frequencies in WNP1 and WNP2 are significantly higher than their climatological values by 50% and 120%, respectively. This indicates that abnormally more TCs formed in the middle–eastern WNP in summer 2018.

According to the TC track classification proposed by Tian et al. (2010b), TC tracks comprise westward-moving track, northwestward-moving track, track to the west of Japan, track for TCs landing in Japan, and track to the east of Japan. The above five types of TC track account for 27.5%, 20.1%, 20.1%, 22.8%, and 9.4% of the total TC tracks in summer. If we take the last three types of TC tracks as northward-moving recurving type, they account for 52.3% of the total TC tacks. For summer 2018, the number of TCs that follow the above five types of tracks is 2, 4, 2, 5, and 4 [Ewiniar (1804) is not counted since it formed in the SCS and landed in South China], accounting for 11.1%, 22.2%, 11.1%, 27.8%, and 22.2% of the total, respectively; and the last three types of TC tracks contribute 61.1% of the total number. That is, more TCs has followed the northwestward-moving track and the northward-moving recurving track (the large contribution tracks are those for TCs landing in Japan and the track to the east of Japan), while fewer TCs followed the westward-moving track (Fig. 3). The four TCs (1808, 1810, 1814, and 1818) that moved northwestward landed in Fujian, Zhejiang, and Shanghai, respectively (Table 2). The TC activity occurred for 5, 23, and 19 days in June, July, and August, respectively. In particular, the number of days with TC activity during July–August accounts for 68% of the total days. The four TCs that followed the northwestward track were active during 4–11 July, 18–25 July, 8–14 August, and 15–21 August. The five TCs that landed in Japan were active during 25–29 July, 3–10 August, 11–15 August, 18–24 August, and 28 August–5 September. Therefore, July–August is the period when TC impacts are concentrated in eastern China and Japan.

Table 1. Numbers of TC genesis in three regions in 2018

	SCS (West of 120°E)	120°–145°E (WNP1)	145°E–180° (WNP2)
Summer 2018	3.0	9.0	6.0
Summer (climate)	2.3	6.3	2.7
2018 total	6.0	14.0	9.0
Annual total (climate)	4.9	13.4	7.5

4. Large-scale circulation features favorable for summertime TC activities

As mentioned previously, TC activity is extremely active in summer 2018. Based on historical records shown in Fig. 2, an active (inactive) TC year is defined if the normalized TC genesis frequency in the summer of that year is one positive (negative) standard deviation larger (smaller) than its climatological value. Only the years

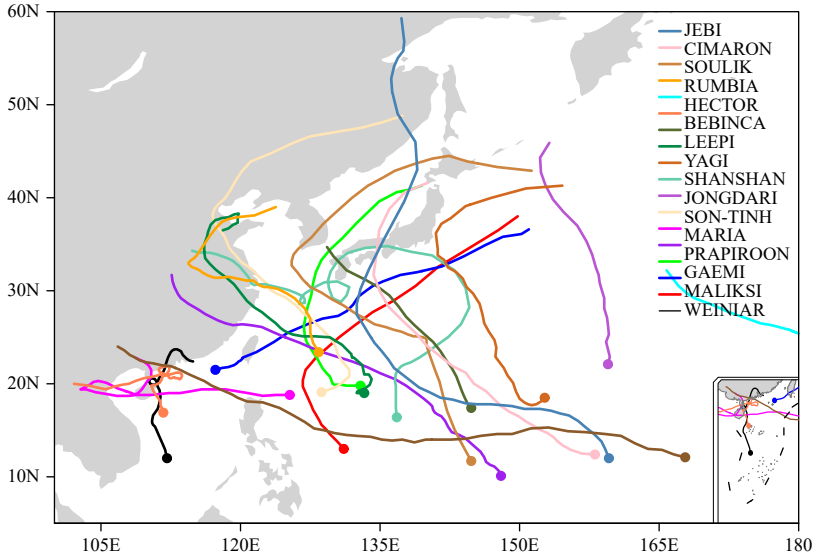

Fig. 3. Tracks of the 18 TCs formed in the WNP and SCS in summer 2018.

Table 2. Features of TCs that landed in China in summer 2018

TC number	Time of genesis	Time of landing	Position of landing	Time of extinction
1804	5 June	6–7 June	Xuwen of Guangdong, Haikou of Hainan, Yangjiang of Guangdong	9 June
1808	4 July	11 July	Lianjiang of Fujian	11 July
1809	17 July	17 July	Wanning of Hainan; Vietnam	19 July
1810	18 July	22 July	Chongming of Shanghai	25 July
1812	25 July	3 August	Jinshan of Shanghai; Onshu of Japan	3 August
1814	8 August	12 August	Wenling of Zhejiang	14 August
1816	12 August	15 August	Leizhou of Guangdong	17 August
1818	15 August	17 August	Pudong of Shanghai	21 August

after 1981 are considered because of the decadal variability of the atmospheric circulation (Li et al., 2016). Active TC years are identified to be 1981, 1989, 1992, 1994, 2002, 2004, and 2017; inactive TC years are 1983, 1998, 2007, 2008, 2010, and 2014. If the normalized TC genesis frequency in a specific year is within one standard deviation, that year is defined as a normal TC activity year. The composite large-scale circulation is obtained for active, inactive, and normal TC activity years and compared with that in 2018.

In normal TC activity years, the eastern part of the monsoon trough in the WNP is located around 140°E, the western Pacific subtropical high (WPSH) extends westward to near 130°E (Fig. 4a) with its ridge line over 25°–27°N, and a weak cyclonic circulation anomaly develops near the Philippines (Fig. 5a). In active TC years, the eastern part of the monsoon trough extends eastward till 150°E (Fig. 4c), and the western most point of WPSH withdraws to 140°E (to the east of its normal position) with a more northward ridge line at 27°–29°N. Westerly winds prevail in the low latitude of the WNP, low-level convergence is significantly stronger than normal over

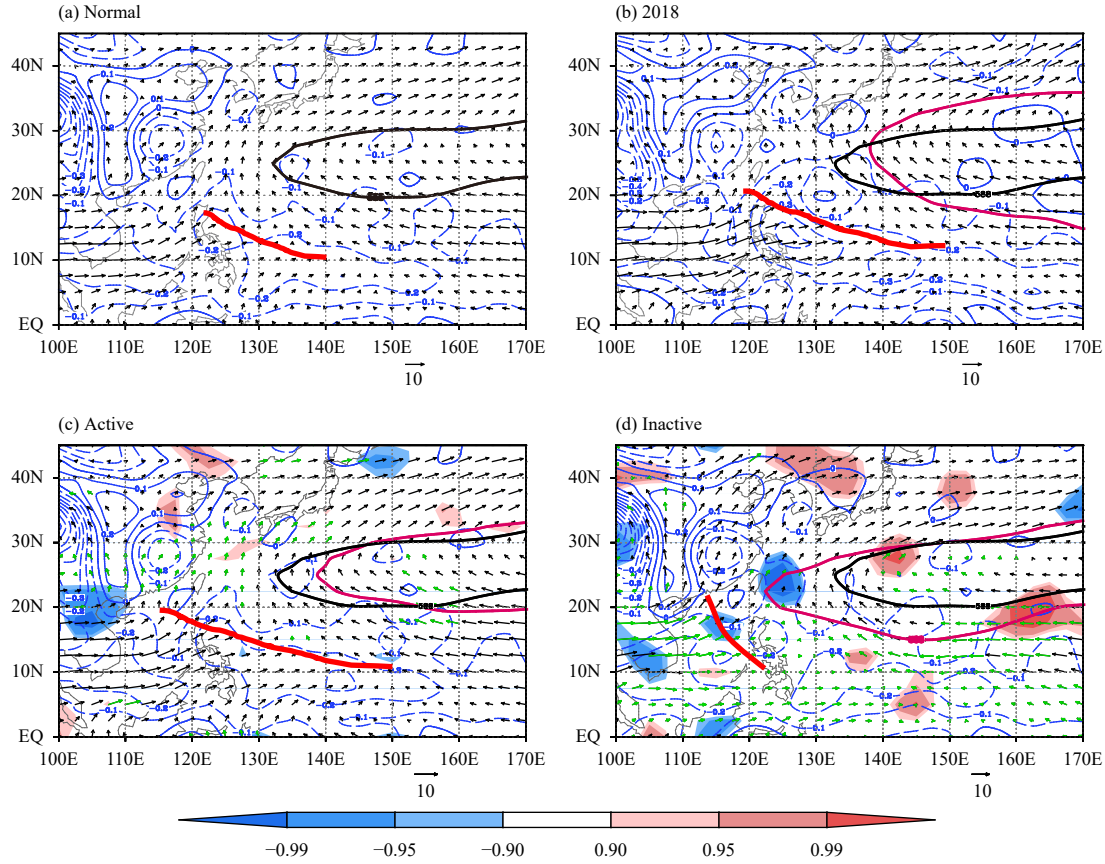

Fig. 4. Composites of 850-hPa divergence (contours; unit: 10^{-5} s^{-1}; areas shaded from light to dark indicate values significant at 0.1, 0.05, and 0.01 levels), 850-hPa winds (vectors; green arrows are for values at/above the 0.1 significance level), and 5880-gpm contour (thin red line) in summer over the WNP for (a) normal TC activity years, (b) 2018, (c) active TC activity years, and (d) inactive TC activity years. Note that the black line denotes the climatological 5880-gpm contour, which coincides with the 5880-gpm contour for normal TC activity years in (a); and the thick red line indicates the monsoon trough.

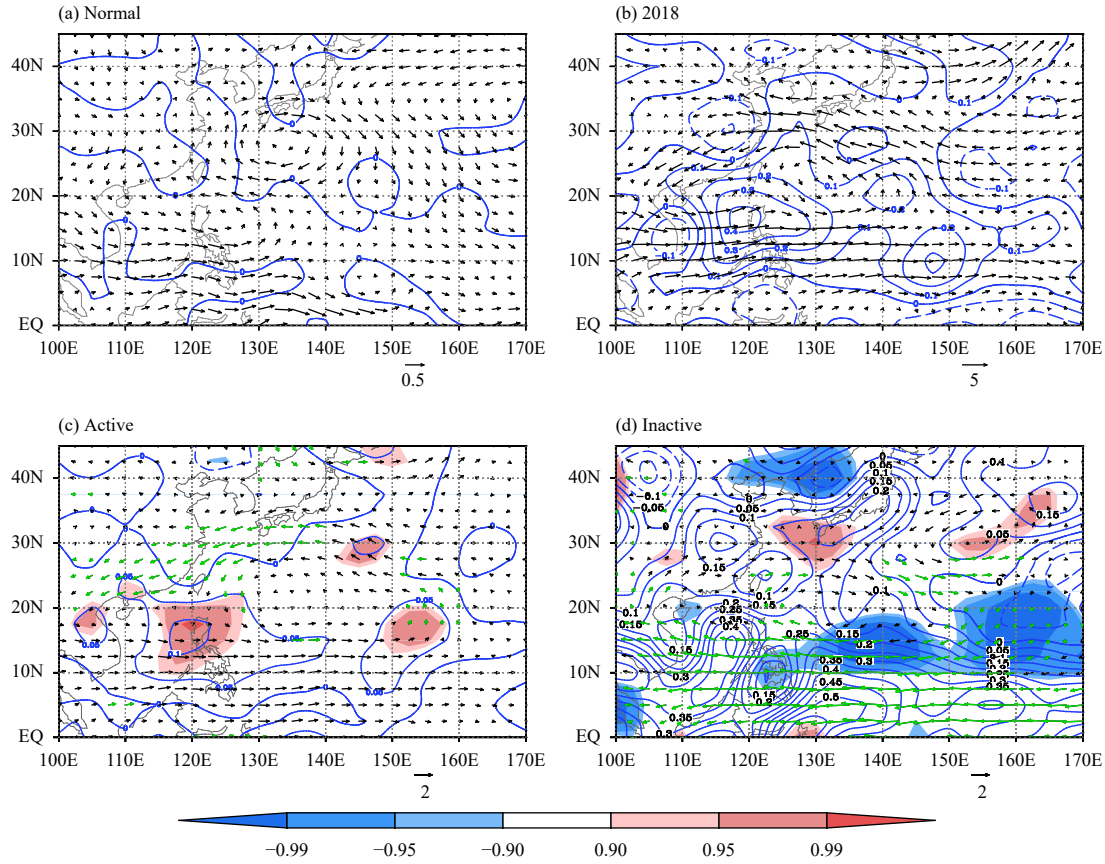

Fig. 5. Composites of 200-hPa divergence anomaly (contours; unit: 10^{-5} s^{-1}; areas shaded from light to dark indicate values significant at 0.1, 0.05, and 0.01 levels) and 850-hPa wind anomaly (vectors; green arrows indicate values significant at/above the 0.1 level) for (a) normal TC activity years, (b) 2018, (c) active TC activity years, and (d) inactive TC activity years.

the warm pool region of the western Pacific, while a large-scale cyclonic circulation anomaly develops to the east of the Philippines, corresponding to large-scale divergence at the upper levels (Fig. 5c). The low-level convergence and high-level divergence are significant at the 0.1 level, resulting in a circulation pattern favorable for the formation and development of TC (Wang et al., 2006). In inactive TC years, the eastern part of the monsoon trough only reaches near 120°E (Fig. 4d) in the South China Sea with its position shifted westward, and easterly winds that are statistically significant at the 0.1 level prevail over the low-latitude area of the western Pacific. The WPSH extends further westward to 120°E, and its ridge line is retreated southward to near 25°N. An anticyclonic circulation anomaly prevails over the Pacific Ocean to the east of the Philippines. Convection in the lower troposphere is suppressed, and divergence at the upper levels is weak (Fig. 5d). Such a circulation composite passes the significance test in most areas, and is unfavorable for the formation of TC.

In summer 2018, the eastern part of the monsoon trough reached 150°E (Fig. 4b), the WPSH extended westward and reached 140°E, and both were located to the east of their climatological positions. The WPSH ridge line was located at 29°–30°N, north of its climatological position. Westerly winds prevailed in the low-latitude area of the western Pacific, while cyclonic circulation occupied the area east of the Philippines. Convection was active in the lower troposphere, corresponding to large areas of abnormally strong divergence in the upper troposphere over the western Pacific between 5° and 35°N (Fig. 5b). This circulation pattern basically agrees well with the circulation characteristics in active TC years (Fig. 5c). Particularly, the divergence developed near the northern Philippines was statistically significant. In addition, the WPSH ridge line was located further north than the composite location for active TC years. In other words, the monsoon trough over the WNP in summer 2018 was stronger than normal and extended eastward, resulting in eastward shift of the TC genesis position; while the background circulation with convergence at low levels and divergence at upper levels was favorable for TC genesis. The above discussion explains why more TCs formed in summer 2018 and why the TC gen-

esis position was located to the east of its climatological position as shown in Table 1. Next, the SST field is further analyzed to explore the oceanic thermal background for formation of such large-scale circulation features.

5. Characteristics of TC activity over the WNP in La Niña decaying years

Tropical SST anomaly (SSTA) has pronounced impacts on atmospheric circulation in the WNP. Based on the monitoring by the National Climate Center of China, a weak eastern-type La Niña event occurred over central–eastern Pacific from October 2017 to March 2018 (Wang et al., 2018). The SSTA over the Indian Ocean gradually became weakly negative since December 2017, demonstrating a lagged response to the La Niña event. Starting from April 2018, negative SSTA over the equatorial central Pacific weakened rapidly. The Niño3.4 SST index issued by NOAA CPC was 0.1 in summer 2018, close to its normal value. Since 1981, there are 9 yr with the Niño3.4 SST index ⩽ 0.2, among which 2001, 2017, and 2018 experience more TCs in summer, while 1995, 2003, and 2014 have fewer than normal TCs, and 1986, 2005, and 2006 are normal TC years. This indicates that the summer TC activity in WNP bears no linkage to Niño3.4 SSTA. However, in summer 2018, which is a La Niña decaying year, significant SSTA occurred in tropical western–central Pacific, which may induce atmospheric circulation anomalies and lead to anomalous TC activity in WNP.

Based on the ENSO identification criteria proposed by Ren et al. (2018), decadal variability is removed and 9 La Niña events after 1981 are identified in the present study, i.e., October 1984–June 1985, May 1988–May 1989, September 1995–March 1996, July 1998–June 2000, October 2000–February 2001, August 2007–May 2008, June 2010–May 2011, August 2011–March 2012, and October 2017–March 2018. All the peaks of the above events occurred in the winter months of December and January except that during September 1995–March 1996, whose peak appeared in November. Therefore, 1985, 1989, 1996, 2000, 2001, 2008, 2011, 2012, and 2018 are identified as La Niña decaying years in the present study. Among the above 9 years, TC genesis frequency was smaller than normal in 2008 and 2011, equivalent to the multi-year average value in 1996 and 2000, and larger than normal in the remaining 5 years (Fig. 2). Anomalies of SST, sea level pressure (SLP), 500-hPa geopotential height, and vertical velocity (averaged over 5°–25°N) in the first 8 La Niña decaying years are compared with those in 2018, and the results are displayed in Fig. 6.

In the summers of La Niña decaying years, SSTA over the equatorial Pacific overall demonstrated a west warm–east cold pattern, SSTA was negative to the east of the international dateline and positive to the west of the dateline. However, the area with SSTA significant at the 0.1 level was not large and mainly located to the west of the international dateline near 150°E; in addition, SSTA was negative over the northern India Ocean, while the SSTA showed a "− + −" pattern from the tropical Atlantic to the north. Note that such an SSTA pattern failed to pass the significance test (Fig. 6a). Looking at the spatial pattern of SSTA in summer 2018, it is clear that although the Niño3.4 SST index was close to normal in the entire summer, significant positive SSTA prevailed from the area near the international dateline to its west at around 150°E with the SSTA above 0.6°C over the central warm area (Fig. 6b), which is consistent with the area of SSTA that passed the significance test in the summers of La Niña decaying years. This result suggests that the SSTA over the western Pacific in summer has more direct impacts on TC activity. In addition, the obvious negative SSTA in the northern Indian Ocean and the significant "− + −" SSTA pattern over North Atlantic are also favorable for TC activity (Yu et al., 2016a, b).

The sea level pressure is another environmental variable that reflects the degree of tropical TC activity (Li et al., 2012). The spatial pattern of SLP anomaly in the summers of La Niña decaying years shows that SLP is lower than normal from the SCS to the east of the Philippines and central Pacific, and the central area of negative SLP anomaly is located to the east of the Taiwan Island at around 140°E, where the SLP anomaly passes the significance test. Positive SLP anomaly appears in the mid- and high-latitude regions of eastern Asia (Fig. 6c). In summer 2018, SLP was distinctly lower than normal from the SCS to the east of the Philippines. The negative SLP anomaly center was located within 110°–130°E from the northern SCS to the east of Taiwan, which was further west than that in the summers of La Niña decaying years. Meanwhile, the area of negative SLP anomaly extended northwestward to the Asian continent (Fig. 6d), favorable for TC activity in northwestern Pacific.

In La Niña decaying years, 500-hPa geopotential height demonstrates a "− + − +" wave pattern from Eurasia to the midlatitude region of the northern Pacific Ocean, and the positive geopotential height anomalies to the south of Lake Baikal are statistically significant. A long wave trough appears at around 150°E to the east of Japan, while the EAP teleconnection wave train develops over the WNP with a "− + −" pattern from south to

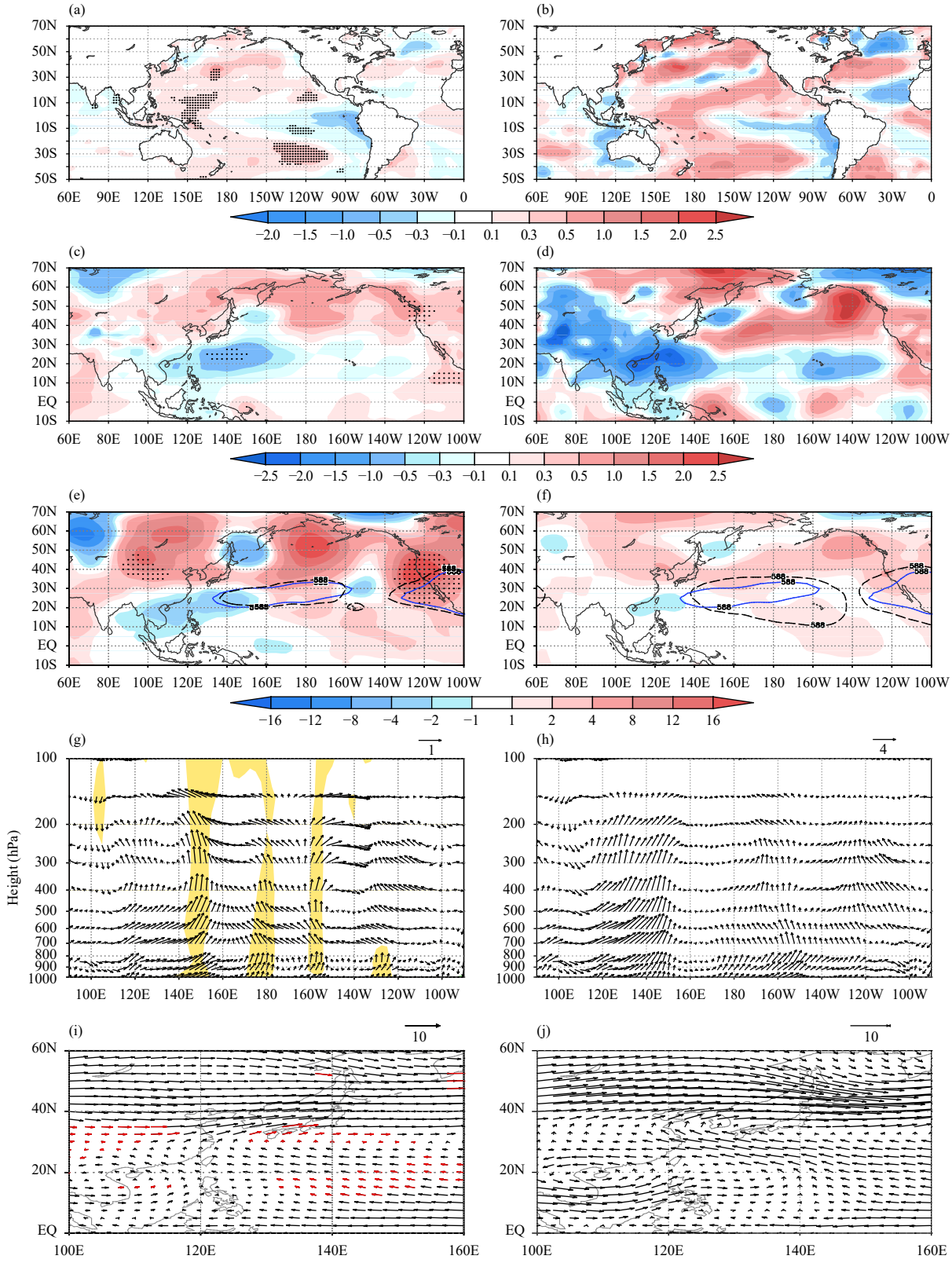

Fig. 6. Composites of (a, b) SSTA, (c, d) SLP anomaly, (e, f) 500-hPa geopotential height anomaly, (g, h) vertical and zonal (averaged over 5°–25°N) wind anomaly during June–August, and (i, j) vertically (850–300 hPa) averaged horizontal winds (vectors) during July–August, for (a, c, e, g, i) La Niña decaying years and (b, d, f, h, j) the summer of 2018. Areas marked by black dots in (a, c, e), yellow shadings in (g), and red arrows in (i) indicate values significant at/above the 0.1 level. Blue lines in (e, f) denote the climatological (1981–2010 mean) 5880-gpm contour; and black dashed lines denote that for (e) La Niña decaying years and (f) summer 2018.

north along West Pacific. However, note that this pattern is not statistically significant (Fig. 6e). Basically, in summer 2018, the 500-hPa geopotential height showed typical circulation features as those in La Niña decaying years (Fig. 6f), except that the positive anomaly center in the midlatitude Eurasia was even larger and extended southeastward from Lake Baikal to Northeast China. The positive geopotential height anomaly above Lake Baikal was coupled with the long wave trough near 150°E to the east of Japan. When the long wave trough intensified, the warm, high pressure ridge over North and Northeast China moved eastward, overlapping with the WPSH. As a result, the WPSH extended more westward, steering TCs to move westward and landed in China (Wang, 1981). In summer 2018, the circulation anomaly pattern in the midlatitude Asia (Fig. 6f) was highly favorable for the TCs to move westward and make landfall in China. Meanwhile, the WPSH abnormally shifted northward in summer 2018, subsequently the TC activity was also more northward and affected the further northward areas of China (Table 2).

In the summers of La Niña decaying years, zonally averaged convection over 5°–25°N distinctly intensifies over 110°–150°E and such intensification is statistically significant at around 150°E (Fig. 6g). Characteristics of atmospheric circulation in the middle and lower troposphere over the WNP and tropical convective activities in summer 2018 were consistent with those in La Niña decaying years, and convective activities were abnormally strong, leading to active TC activities (Fig. 6h). The comparative analysis shown in Fig. 6 suggests that although SST over the tropical central–eastern Pacific in summer 2018 was close to its climatological value, SSTA to the west of the international dateline was significant, and the atmospheric circulations over the tropical and subtropical WNP and the mid to high latitude regions were consistent with those in La Niña decaying years. These circulation characteristics were typical responses to the decaying of La Niña. In particular, the "− + − +" pattern of circulation from Eurasia to the midlatitude area of northern Pacific and the "− + −" EAP wave train in East Asia provided large-scale circulation favorable for TC genesis in northern part of the WNP. The above circulation pattern was also favorable for the northwestward movement of TCs and their ensuing impacts in northern China. Comparing wind fields averaged over 850–300 hPa in July–August between La Niña decaying years and 2018 (Figs. 6i and 6j) finds that there appear clearly steering flows for TCs to move northwestward and northward in the WNP in both cases; particularly, the steering flow for TCs to move northwestward into the Yellow Sea and East Sea along coastal China in summer 2018 is distinct, which is advantageous for TCs to land in eastern China.

Further comparison of TC tracks in the summers of La Niña decaying years and 2018 (Fig. 7) shows that in the summers of La Niña decaying years, significant positive anomalies appear over zonally extending belts in northern SCS and from east of the Taiwan Island to the international dateline with the positive center located to the east of Taiwan Island and over 20°–25°N, 140°–150°E, indicating that more TCs move through this area; and significant negative anomalies appear from central–southern of SCS to low latitude area near 170°E, where fewer TCs move over (Fig. 7a). This result is consistent with the spatial distribution of TC track density in June–November during La Niña decaying years reported by Xie et al. (2018). In La Niña decaying years, the main

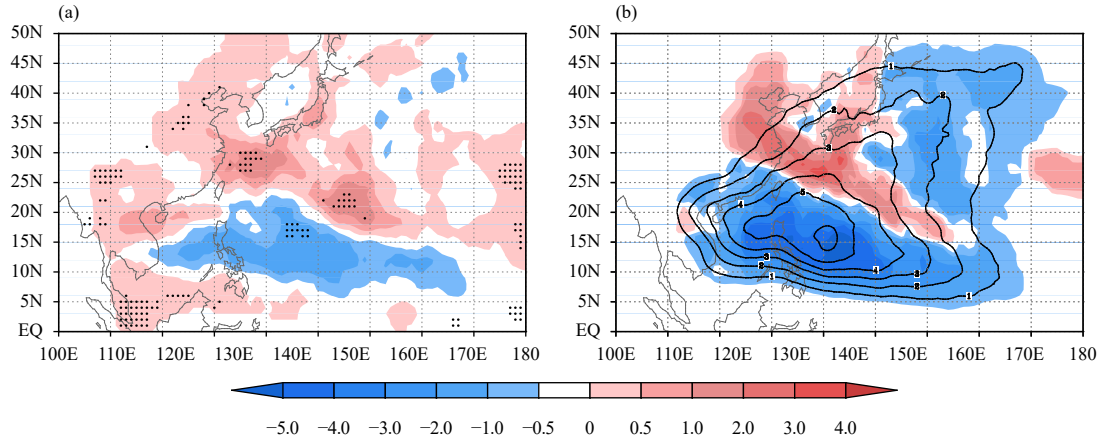

Fig. 7. (a) The difference (unit: times grid^{-1}) between the TC track frequency in La Niña decaying years and that in 1981–2010, and (b) the difference between the TC track frequency in 2018 and that in 1981–2010, averaged for June–August in the 2.5° × 2.5° grids over WNP. In (a), areas marked by black dots are for values significant at/above the 0.1 level. In (b), black contours are for 1981–2010 climatological values.

body of the monsoon trough is located over 10°–25°N, 120°–145°E, which is more northward than that in El Niño developing/decaying years and La Niña developing years. In La Niña decaying years, the WPSH weakened and retreated eastward, with the western most ridge point located at 140°E (Fig. 6e). Under the influence of easterly winds to the northeast of the monsoon trough and the steering flow on the western flank of the WPSH, most of the TCs move northwestward and/or recurve.

In summer 2018, the main body of the monsoon trough was located over 15°–25°N, 120°–150°E (Fig. 4b), which was further north and east than that in La Niña decaying years, and thus was more favorable for TCs to form in areas further north and east of WNP (Table 1). Among the 18 TCs in summer 2018, 11 formed within 10°–20°N, and 7 formed over 20°–30°N. Meanwhile, although the WPSH weakened to a certain degree, its western most ridge point reached near 140°E (Fig. 6f). Steered by the flow to the west of the WPSH, TCs were more likely to follow the northward track and then recurved in offshore areas.

Figure 7 displays TC tracks in La Niña decaying years and in summer 2018. The approach proposed by Xie et al. (2018) is used to calculate the TC tracks. The TC activity area is divided into 2.5 latitude × 2.5 longitude grids, and the TC occurrence frequency at each grid is calculated. The larger the TC occurrence frequency at a specific grid, the more TCs will pass through this grid. Spatial distribution of TC track density is obtained by this method. In Fig. 7b, positive anomalies of TC track density occurred over a northwest–southeast oriented belt extending from the north of Taiwan Island to near (15°N, 160°E), while negative anomalies occurred over the low latitude area from the SCS to near 170°E. This result indicates that the TC tracks in summer 2018 are overall similar to those in La Niña decaying years (Fig. 7a); however, the TC genesis positions and TC tracks are located further north, with the high value center located from the offshore region to the east of China and the ocean to the southeast of Japan. This feature is consistent with the results shown in Section 3 that more TCs in summer 2018 followed the northwestward-moving track and the northward-moving-recurving track (especially the track for TCs landing in Japan and the track for TCs to the east of Japan).

It is clear that the TC tracks in 2018 demonstrated general features in La Niña decaying years. However, the primary TC track in 2018 was distributed along the northwest–southeast direction, with more TCs moving northwestward and recurving to the north. These features were not completely similar to those in La Niña decaying years due to the fact that the main body of the monsoon trough shifted northward and eastward in 2018. As a result, the TC track density was significantly higher than normal over the offshore region to the east of China and the ocean to the southeast of Japan.

6. Impacts of tropical intraseasonal oscillation on TC activity in summer

In summer 2018, intraseasonal oscillation was active over the WNP. By using the amplitude of RMM index ($\sqrt{(\mathrm{RMM1})^2+(\mathrm{RMM2})^2}$) greater than 1 as the criterion (Wheeler and Hendon, 2004), two consecutive MJO active periods, 8–28 July and 2–15 August 2018, can be identified (Fig. 8). The two periods correspond to the concentration periods of TC genesis and TC activity, during which they severely affected China and Japan (Table 2). The first MJO event started at Phase 4, propagated eastward and ended at Phase 6, when convection was active over the Maritime Continent (MC) and western Pacific (WP); the second event lingered at Phase 6, when convection was stably residing over the WP.

Further analysis of the zonal (Figs. 9a, b) and meridional (Figs. 9c, d) propagations of U850 and OLR anomalies reveals the characteristics of circulation and convection anomalies corresponding to the MJO. Note that the contours in Fig. 9 indicate the anomalies that was reconstructed by the RMM index. Details can be found in Wu et al. (2016). As shown in Fig. 9, corresponding to the two MJO episodes, two distinct activities related to abnormal westerly winds can be found in the U850 field (Fig. 9a) in July and early August, respectively. In July, the eastward propagation of westerly wind anomaly was significant; in early August, however, the westerly wind anomaly largely remained over the area from the MC to WP, which promoted the transition of SSTA from negative to positive and was also favorable for the formation of Walker circulation anomaly. Low-level convergence and high-level divergence developed near the Philippines with intensified ascending motion (Tian et al., 2010a). The MJO was also reflected in convective activity, although the scale was slightly smaller than that in the circulation field (Fig. 9b). The relatively active MJO to the east of the Philippines increased the low-level convergence and mid-level moisture in this area, and thus provided favorable thermal and dynamic conditions for TC genesis. The position of TC genesis was further east than normal, which made the TCs prone to the northward moving track and recurvature (Zhao and Li, 2019). In addition, the time–latitude cross-section along 115°–130°E (Figs. 9c, d) indicates that intraseasonal convec-

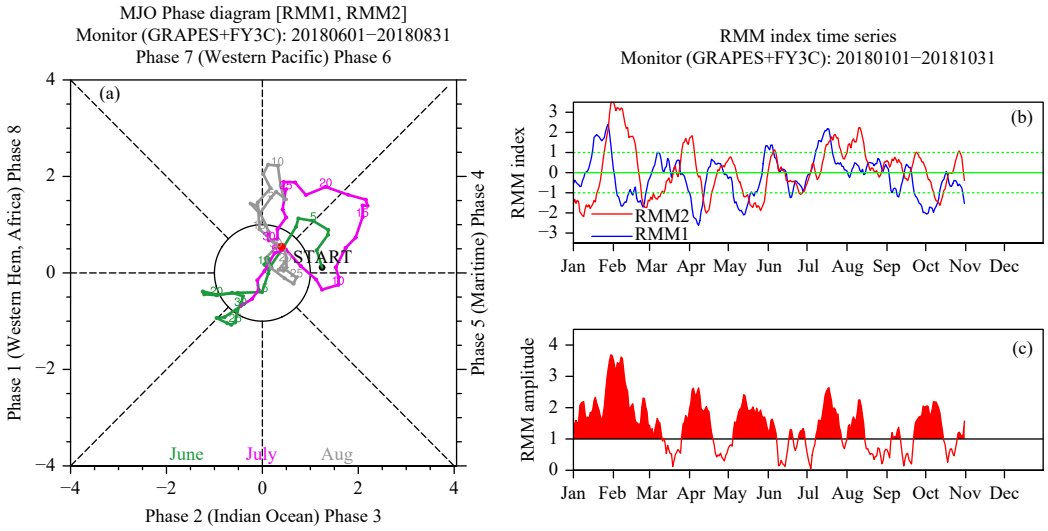

Fig. 8. (a) The RMM index phase space diagram in JJA 2018. (b) Time series of RMM1 and RMM2, and (c) amplitude of the RMM index, from January to October 2018.

tion and circulation anomalies in summer 2018 over the WP were characterized by northward propagation, which could partly be explained by the MJO impact. Convection propagated northward from the equator to 20°N near the Philippines, and triggered meridional "− + −" wave trains similar to the EAP teleconnection pattern (Huang and Li, 1987; Nitta, 1987; Huang, 1992). As a result, the WPSH shifted northward. The above circulation patterns are well reflected in the seasonal averaged 500-hPa geopotential height anomaly (Fig. 6f), which also explains why the WPSH ridge line in 2018 (see Fig. 4b) was located further north than that in La Niña decaying years. Due to the abnormal northward shift of the WPSH ridge line, TC became more active in the WNP area (Hu et al., 2005).

Wave activities of OLR in the tropics are analyzed based on zonal wavenumber–frequency spectrum decomposition following Wheeler and Kiladis (1999). Figure 10a displays characteristics of activities related to the MJO and the equatorial Kelvin waves and Rossby waves. Due to the westward dispersion of MJO energy, the dry event in late June was a precursor of the MJO convective activity in July. However, the MJO event in early August identified by the RMM index was mainly reflected in the circulation field (Fig. 9a), and the convective anomalies largely occurred to the north of the equator and were relatively weak near the equator. In addition to the slowly eastward propagating MJO, the Kelvin waves that rapidly propagated eastward and the Rossby waves that propagated westward were also active in the tropics. Figure 10b presents the time–longitude cross-section of velocity potential at 200 hPa, which can roughly reflect large-scale divergence and convergence. It is shown that the large-scale MJO signals in July and August were more significant at upper levels, and the convection-active area generally corresponded to large areas of divergence in the upper troposphere. In other words, the MJO activities in July–August further promoted convective activities in the lower troposphere and divergence in the upper troposphere over the tropical and southern subtropical regions of the WNP. The MJO effects are basically consistent with the influence of large-scale circulation in La Niña decaying years.

The number of days for MJO in various phases is calculated. According to Pan et al. (2010), when the MJO is in Phases 5–7, more TCs will generate, with the highest frequency in Phase 6, followed by that in Phase 5. The correlation coefficient between the number of days when the MJO is in Phases 5–6 and TC genesis frequency is 0.46 (for 1981–2010), which is statistically significant at the 0.01 level. In summer 2018, the number of days when the MJO was in Phases 4–6 (Table 3) was much higher than the climatological value. Particularly, the number of days when the MJO was in Phases 5–6 was almost 150% that of its normal value, indicating that the longer period of MJO staying in Phases 5–6 in summer 2018 played a vital role for the extremely active TC activities.

The boreal summer intraseasonal oscillation (BSISO), which is composed of BSISO1 and BSISO2, was also active during the summer of 2018 (Fig. 11). BSISO1 rep-

Table 3. Number of days for various MJO phases in summer 2018

MJO phase	1	2	3	4	5	6	7	8
2018	5	13	2	16	23	32	1	0
Climatological value	16.2	15.2	9.7	10.0	9.9	12.4	9.6	9.1

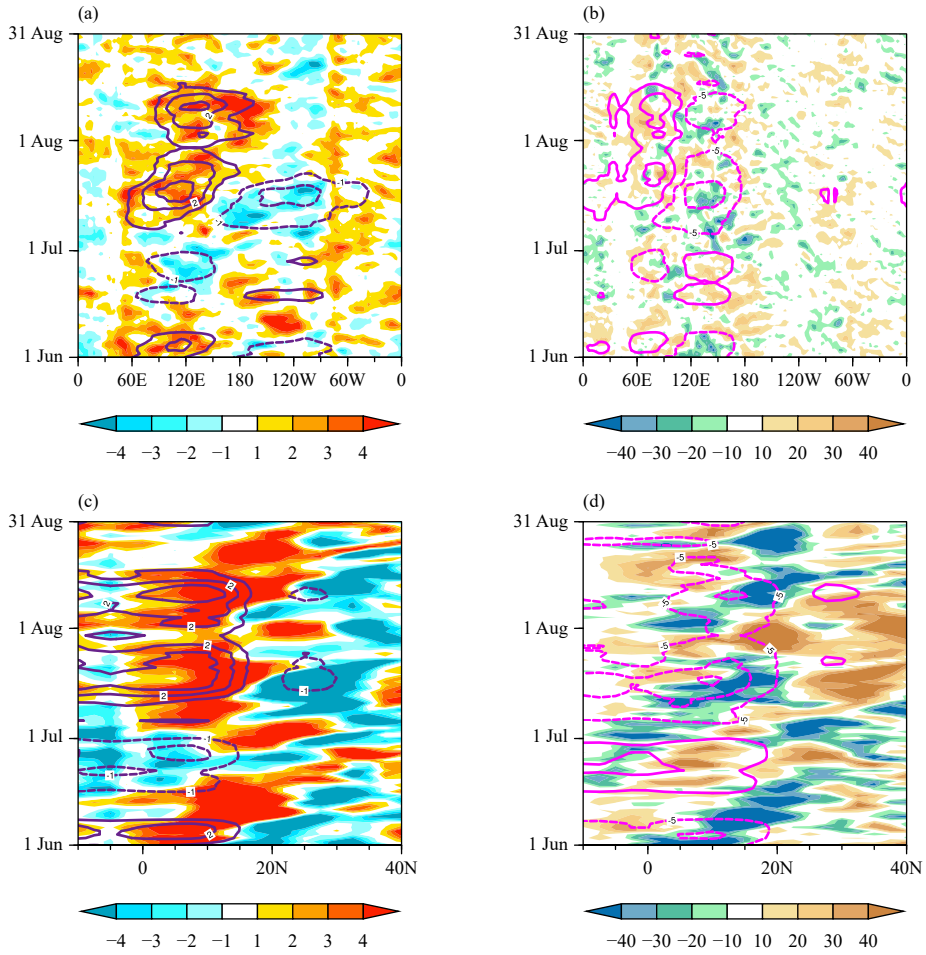

Fig. 9. (a, b) Time–longitude (averaged over 15°S –15°N) and (c, d) time–latitude (averaged over 115°–130°E) cross-sections for anomalies of (a, c) U850 (m s^{-1}) and (b, d) OLR (W m^{-2}) during June–August 2018. The shadings and contours represent the original and reconstructed anomalies by using the RMM index.

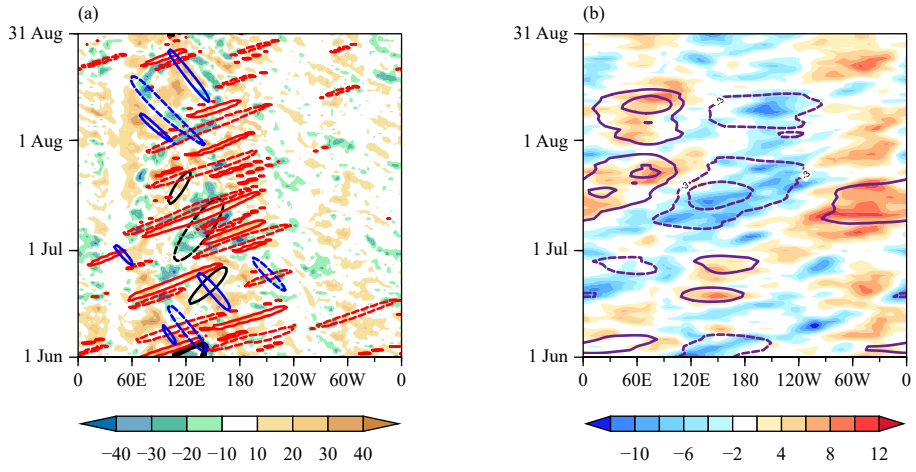

Fig. 10. Hovmöller diagram of (a) OLR (shaded; unit: W m^{-2}; averaged over 10°S–10°N) and (b) 200-hPa velocity potential (shaded; unit: 10^6 m^{-2} s^{-1}; averaged over 15°S–15°N) anomalies during June–August 2018. The MJO, Kelvin wave, and Rossby wave are shown by black, red, and blue contours in (a) respectively, and the contours in (b) represent anomalies of reconstructed RMM index.

resents the northward propagating BSISO over the Asian summer monsoon region with a 30–60-day quasi-oscillating period; and BSISO2 mainly captures the northward and northwestward propagating BSISO with peri-

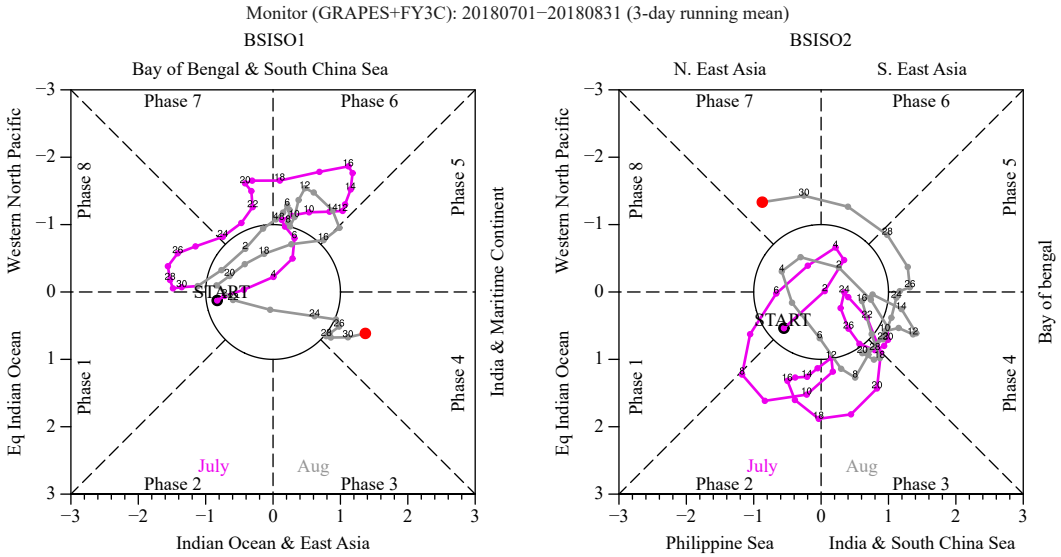

Fig. 11. Phase space diagrams of the (a) BSISO1 and (b) BSISO2 indices from July to August of 2018.

ods of both around 30 days and 10–20 days (Lee et al., 2013). Figure 11 shows that the BSISO1 mode is mainly active in Phases 6–8, while the BSISO2 mode is active in Phases 2–4. As shown in Fig. 12, during the period of concentrated TC genesis in early and middle August of 2018, abnormally active convection persisted from the SCS to the WNP. Note that although convective activities during this period were to a certain degree related to the RMM index, they were actually more consistent with convection and circulation corresponding to BSISO1. The convection anomalies slowly propagated northward instead of eastward (Fig. 9d), corresponding to the activities of BSISO1 mode in Phases 6–7. In the lower troposphere, large-scale cyclonic vorticity and water vapor anomalies persisted over the SCS and WNP, which was favorable for TC genesis in these areas. This result and the long-term statistics from climatological data can be mutually confirmed (Yoshida et al., 2014; You et al., 2019).

7. Conclusions and discussion

In summer 2018, a total of 18 tropical cyclones (TCs) formed in the western North Pacific (WNP) and South China Sea (SCS), among which 8 TCs landed in China. The number of total TCs and landfall TCs ranked the first and second highest respectively since 1951. In addition, five TCs directly landed in Japan or significantly affected Japan, and two TCs landed in the Korean Peninsula. Overall, 2018 is an extremely active TC year. Although the intensity of TCs landed in China was generally weak, precipitation induced by TCs was intense with heavy rainstorms and disastrous weather on their paths. TC genesis was concentrated in summer 2018, multiple TCs were mutually restrained, and TCs twisted, turned, or zigzagged over offshore regions, showing complicated tracks. The spatial pattern of TC track density indicates that within 120°–160°E in the WNP, more TCs occurred to the north and fewer TCs occurred to the south of 20°N. That is, positive anomalies of TC track density occurred over a northwest–southeast oriented belt extending from the north of Taiwan Island to Japan and its southeast ocean, while negative anomalies occurred over the low latitude area from the SCS to near 170°E. The present study analyzes impacts of tropical SST anomaly and ISO activity on TC genesis and TC track.

From October 2017 to March 2018, an eastern-type La Niña event occurred over the central–eastern Pacific. It is a relatively weak event and the Niño3.4 SST index was already close to its normal value in summer. However, SST was higher than normal in the central western Pacific with positive anomaly of above 0.6°C in the central area of anomaly. Atmospheric circulation in tropical and subtropical regions of the WNP demonstrated characteristics as that in La Niña decaying years. SLP was abnormally low from the SCS to the east of the Philippines; correspondingly, 500-hPa geopotential height was also abnormally low. Convective activities averaged over 5°–25°N were abnormally strong within 110°–150°E, which was favorable for the intensification and eastward extension of the monsoon trough. As a result, more TCs formed and the TC genesis position shifted further north than its normal position. Meanwhile, the "− + − +" pattern of wave trains prevailed from Asia to the midlatitude region of northern Pacific. Warm high-pressure ridge

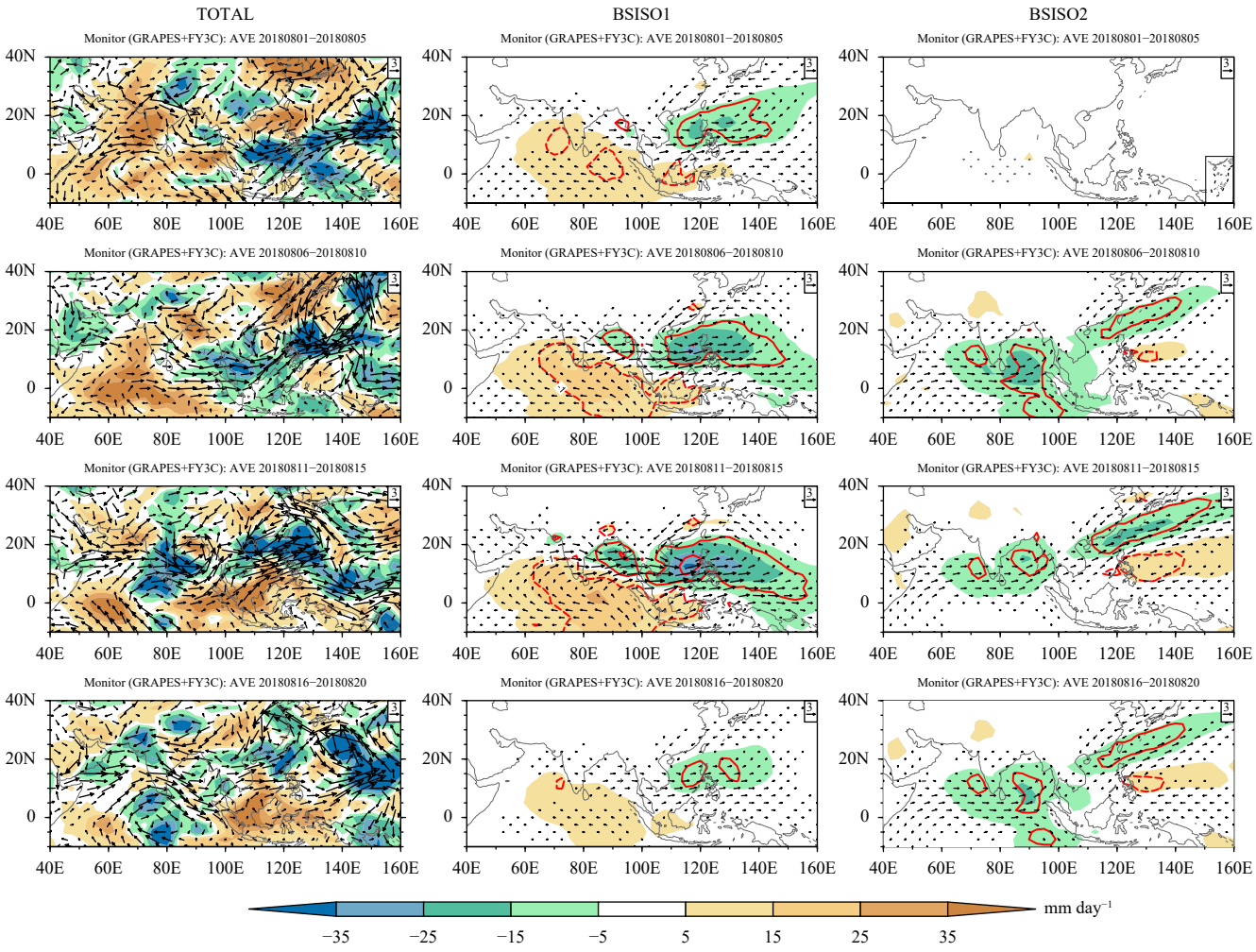

Fig. 12. Anomalies of 850-hPa wind (vectors; m s^{-1}), OLR (contours; W m^{-2}), and precipitation (shaded; mm day^{-1}) in the first four pentads of August 2018. The left column shows the original anomalies, the middle column is for the anomalies reconstructed from BSISO1, and the right column is the reconstruction from BSISO2.

dominated a large area from Lake Baikal to Northeast China. A long wave trough was located near 150°E to the east of northern Japan, which provided large-scale circulation condition for westward extension of the WPSH. This circulation pattern is also favorable for TCs to move northwestward before recurving to the north. Apparently the configuration of large-scale circulation in the tropics, subtropics, and midlatitudes was favorable for TCs to move northwestward and recurve northward.

Two consecutive MJO active periods occurred in summer 2018, which played a critical role in promoting TC activities. The number of days when the MJO was located from the MC to the WP (Phases 5–6) was almost 150% that of its normal value. Corresponding to these two MJO events, westerly wind anomalies developed, which were favorable for the formation of Walker circulation anomaly. As a result, low-level convergence, high-level divergence, and intensified ascending motion developed near the Philippines. The relatively more active MJO to the east of the Philippines in the western Pacific provided favorable dynamic condition for TC genesis, leading to much more TCs formed in the east of 120°E over WNP (Table 1). In addition, intraseasonal convection and circulation anomalies in summer 2018 over the WP were characterized by northward propagation, and the BSISO was also active. The corresponding BSISO1 mode persisted in Phase 6–7, while large-scale cyclonic vorticity and water vapor anomalies maintained from the SCS to the WNP. Such a pattern was favorable for TC genesis. Convective activities triggered the EAP teleconnection pattern, which forced the WPSH to shift northward and provided favorable large-scale conditions for TCs to move northward. In other words, the MJO and BSISO activities during July–August of 2018 promoted

low-level convective activities and upper-level divergence over tropical and southern subtropical regions of the WNP. Their impacts on large-scale circulation are consistent with the impacts in La Niña decaying years.

Therefore, TC activity in summer 2018 was under the joint influences of decaying La Niña and abnormal ISO activities. The wave trains from Asia to the midlatitude region of northern Pacific provided favorable large-scale circulation conditions for TC activity in the WNP. The mechanism for the midlatitude circulation anomalies is discussed in another paper (Chen et al., 2019). The present study provides a diagnostic base for exploring the precursor signals of TC activities and establishing predictive models.

Acknowledgments. We thank the anonymous reviewers for their constructive comments that led to improvements to this paper.

REFERENCES

Chan, J. C. L., 1985: Tropical cyclone activity in the northwest Pacific in relation to the El Niño/Southern Oscillation phenomenon. *Mon. Wea. Rev.*, **113**, 599–606, doi: 10.1175/1520-0493(1985)113<0599:TCAITN>2.0.CO;2.

Chan, J. C. L., 2000: Tropical cyclone activity over the western North Pacific associated with El Niño and La Niña events. *J. Climate*, **13** , 2960–2972, doi: 10.1175/1520-0442(2000)013<2960:TCAOTW>2.0.CO;2.

Chan, J. C. L., 2005: Interannual and interdecadal variations of tropical cyclone activity over the western North Pacific. *Meteor. Atmos. Phys.*, **89** , 143–152, doi: 10.1007/s00703-005-0126-y.

Chen, G. H., and R. H. Huang, 2009: Dynamical effects of low frequency oscillation on tropical cyclogenesis over the western North Pacific and the physical mechanisms. *Chinese J. Atmos. Sci.*, **33**, 205–214, doi: 10.3878/j.issn.1006-9895.2009.02.01. (in Chinese)

Chen, L. J., W. Gu and W. J. Li, 2019: Why is the East Asian summer monsoon extremely strong in 2018? — Collaborative effects of SST and snow cover anomalies *J. Meteor. Res.*, **33**, 593–608, doi: 10.1007/s13351-019-8200-4.

Chen, L. S., 1965: The relationship of middle–high latitude circulation pattern over Asia and typhoon track over western Pacific in late summer. *Acta Meteor. Sinica*, **35**, 476–485, doi: 10.11676/qxxb1965.055. (in Chinese)

Chen, L. S., and Y. H. Ding, 1979: *Introduction to Typhoons over West Pacific*. Science Press, Beijing, 491 pp. (in Chinese)

Chen, T. C., S. P. Weng, N. Yamazaki, et al., 1998: Interannual variation in the tropical cyclone formation over the western North Pacific. *Mon. Wea. Rev.*, **126**, 1080–1090, doi: 10.1175/1520-0493(1998)126<1080:IVITTC>2.0.CO;2.

Chen, T. C., S. Y. Wang, and M. C. Yen, 2006: Interannual variation of the tropical cyclone activity over the western North Pacific. *J. Climate*, **19**, 5709–5720, doi: 10.1175/JCLI3934.1.

Ding, Y. H., and E. R. Reiter, 1981a: Some conditions Influencing the variability of typhoon formation over the West Pacific ocean. *Arch. Meteor. Geophys. Bioclim. Ser. A*, **30**, 327–342, doi: 10.1007/BF02280644.

Ding, Y. H., and E. R. Reiter, 1981b: Large-scale circulation conditions affecting the variability in the frequency of tropical cyclones over the North Atlantic and the West Pacific. Environmental Research Paper No. 33, Colorado State University, Fort Collins, 25 pp.

Emanuel, K., 2005: Increasing destructiveness of tropical cyclones over the past 30 years. *Nature*, **436** , 686–688, doi: 10.1038/nature03906.

Fan, K., 2007: North Pacific sea ice cover, a predictor for the western North Pacific typhoon frequency? *Sci. China Ser. D Earth Sci.*, **37**, 851–856. (in Chinese)

Gong, Z. S., and L. J. Chen, 2013: Analysis of anomalous tropical cyclone activities over the western North Pacific and South China Sea in 2010. *Climatic Environ. Res.*, **18** , 342–352, doi: 10.3878/j.issn.1006-9585.2012.11063. (in Chinese)

He, M., W. L. Song, and X. F. Chen, 1999: Typhoon activity in Northwest Pacific in relation with El Niño and La Niña events. *J. Trop. Meteor.*, **5**, 153–162.

Hu, C. M., Y. H. Duan, H. Yu, et al., 2005: The diagnostic analysis of the rapid change in tropical cyclones intensity before landfall in South China. *J. Trop. Meteor.*, **21** , 377–382, doi: 10.16032/j.issn.1004-4965.2005.04.005. (in Chinese)

Hu, J., and Y. Q. Wang, 1992: Atmosphere and ocean low-frequency oscillation and their effects on tropical cyclone tracks over the northwestern Pacific. *Acta Meteor. Sinica*, **50**, 420–428, doi: 10.11676/qxxb1992.053. (in Chinese)

Huang, B. Y., P. W. Thorne, V. F. Banzon, et. al., 2017: Extended reconstructed sea surface temperature, version 5 (ERSSTv5): Upgrades, validations, and intercomparisons. *J. Climate*, **30**, 8179–8205, doi: 10.1175/JCLI-D-16-0836.1.

Huang, P., C. Chou, and R. H. Huang, 2011: Seasonal modulation of tropical intraseasonal oscillations on tropical cyclone geneses in the western North Pacific. *J. Climate*, **24** , 6339–6352, doi: 10.1175/2011JCLI4200.1.

Huang, R. H., 1992: The East Asia/Pacific pattern teleconnection of summer circulation and climate anomaly in East Asia. *Acta Meteor. Sinica*, **6**, 25–37.

Huang, R. H., and W. J. Li, 1987: Influence of the heat source anomaly over the tropical western Pacific on the subtropical high over East Asia. Proceedings of International Conference on the General Circulation of East Asia, Chengdu, 10–15 April, 40–51.

Huang, R. H., and G. H. Chen, 2007: Research on interannual variations of tracks of tropical cyclones over Northwest Pacific and their physical mechanism. *Acta Meteor. Sinica*, **65**, 683–694, doi: 10.11676/qxxb2007.064. (in Chinese)

Kalnay, E., M. Kanamitsu, R. Kistler, et al., 1996: The NCEP/NCAR 40-year reanalysis project. *Bull. Amer. Meteor. Soc.*, **77**, 437–471, doi: 10.1175/1520-0477(1996)077<0437:TNYRP>2.0.CO;2.

Kim, H.-M., P. J. Webster, and J. A. Curry, 2011: Modulation of North Pacific tropical cyclone activity by three phases of ENSO. *J. Climate*, **24**, 1839–1849, doi: 10.1175/2010JCLI3939.1.

Kim, J. H., C. H. Ho, H. S. Kim, et al., 2008: Systematic variation of summertime tropical cyclone activity in the western North Pacific in relation to the Madden–Jullian oscillation. *J. Climate*, **21**, 1171–1191, doi: 10.1175/2007JCLI1493.1.

Kistler, R., E. Kalnay, W. Collins, et al., 2001: The NCEP–NCAR 50-year reanalysis: Monthly mean CD-ROM and documentation. *Bull. Amer. Meteor. Soc.*, **82**, 247–268, doi: 10.1175/1520-0477(2001)082<0247:TNNYRM>2.3.CO;2.

Lander, M. A., 1994: An exploratory analysis of the relationship between tropical storm formation in the western North Pacific and ENSO. *Mon. Wea. Rev.*, **122** , 636–651, doi: 10.1175/1520-0493(1994)122<0636:AEAOTR>2.0.CO;2.

Lee, J. Y., B. Wang, M. C. Wheeler, et al., 2013: Real-time multivariate indices for the boreal summer intraseasonal oscillation over the Asian summer monsoon region. *Climate Dyn.*, **40**, 493–509, doi: 10.1007/s00382-012-1544-4.

Li, C. Y., 1987: A study on the influence of El Niño upon typhoon action over the western Pacific. *Acta Meteor. Sinica*, **45**, 229–236, doi: 10.11676/qxxb1987.028. (in Chinese)

Li, C. Y., J. Pan, H. Tian, et al., 2012: Typhoon activities over the western North Pacific and atmospheric intraseasonal oscillation. *Meteor. Mon.*, **38**, 1–16. (in Chinese)

Li, R. C. Y. and W. Zhou, 2012: Changes in western Pacific tropical cyclones associated with the El Niño–Southern Oscillation cycle. *J. Climate*, **25**, 5864–5878, doi: 10.1175/JCLI-D-11-00430.1.

Li, R. C. Y., and W. Zhou, 2013a: Modulation of western North Pacific tropical cyclone activity by the ISO. Part I: Genesis and intensity. *J. Climate*, **26**, 2904–2918, doi: 10.1175/JCLI-D-12-00210.1.

Li, R. C. Y., and W. Zhou, 2013b: Modulation of western North Pacific tropical cyclone activity by the ISO. Part II: Tracks and landfalls. *J. Climate*, **26**, 2919–2930, doi: 10.1175/JCLI-D-12-00211.1.

Li, T., 2012: Synoptic and climatic aspects of tropical cyclogenesis in western North Pacific. Chap. 3, *Cyclones: Formation, Triggers and Control*, K. Oouchi, and H. Fudeyasu, Eds., Nova Science Publishers, Inc., Hauppauge, 61–94.

Li, W. J., R. N. Zhang, C. H. Sun, et al., 2016: Recent research advances on the interannual–interdecadal variations of drought/flood in South China and associated causes. *J. Appl. Meteor. Sci.*, **27**, 577–591. (in Chinese)

Liu, G., Q. Y. Zhang, and S. Q. Sun, 2007: A preliminary study on activities of tropical cyclones over the western North Pacific during the summer of 2006. *Climatic Environ. Res.*, **12**, 738–750, doi: 10.3969/j.issn.1006-9585.2007.06.004. (in Chinese)

Liu, G., S. Q. Sun, Q. Y. Zhang, et al., 2009: Characteristics of the intraseasonal oscillation of intertropical convergence zone and its influence on the periodical tropical cyclogenesis. *Chinese J. Atmos. Sci.*, **33**, 879–889, doi: 10.3878/j.issn.1006-9895.2009.04.20. (in Chinese)

Liu, Q., T. Li, and W. C. Zhou, 2018: Impact of 10–60-day low-frequency steering flows on straight northward-moving typhoon tracks over the western North Pacific. *J. Meteor. Res.*, **32**, 394–409, doi: 10.1007/s13351-018-7035-8.

Madden, R. A., and P. R. Julian, 1971: Detection of a 40–50 day oscillation in the zonal wind in the tropical Pacific. *J. Atmos. Sci.*, **28** , 702–708, doi: 10.1175/1520-0469(1971)028<0702:DOADOI>2.0.CO;2.

Nitta, T., 1987: Convective activities in the tropical western Pacific and their impact on the Northern Hemisphere summer circulation. *J. Meteor. Soc. Japan*, **65**, 373–432, doi: 10.2151/jmsj1965.65.3_373.

Pan, J., C. Y. Li, and J. Song, 2010: The modulation of Madden–Julian Oscillation on typhoons in the northwestern Pacific Ocean. *Chinese J. Atmos. Sci.*, **34** , 1059–1070, doi: 10.3878/j.issn.1006-9895.2010.06.03. (in Chinese)

Ren, H.-L., B. Lu, J. H. Wan, et al., 2018: Identification standard for ENSO events and its application to climate monitoring and prediction in China. *J. Meteor. Res.*, **32** , 923–936, doi: 10.1007/s13351-018-8078-6.

Reynolds, R. W., N. A. Rayner, T. M. Smith, et al., 2002: An improved in situ and satellite SST analysis for climate. *J. Climate*, **15** , 1609–1625, doi: 10.1175/1520-0442(2002)015<1609:AIISAS>2.0.CO;2.

Sadler, J. C., 1978: Mid-season typhoon development and intensity changes and the tropical upper tropospheric trough. *Mon. Wea. Rev.*, **106**, 1137–1152, doi: 10.1175/1520-0493(1978)106<1137:MSTDAI>2.0.CO;2.

Sobel, A. H., and D. E. Maloney, 2000: Effect of ENSO and the MJO on western North Pacific tropical cyclones. *Geophys. Res. Lett.*, **27**, 1739–1742, doi: 10.1029/1999GL011043.

Sun, Z., J. Y. Mao, and G. X. Wu, 2009: Influences of intraseasonal oscillations on the clustering of tropical cyclone activities over the western North Pacific during boreal summer. *Chinese J. Atmos. Sci.*, **33**, 950–958, doi: 10.3878/j.issn.1006-9895.2009.05.06. (in Chinese)

Tian, H., C. Y. Li, and H. Yang, 2010a: Modulation of typhoon genesis over the western North Pacific by intraseasonal oscillation. *J. Trop. Meteor.*, **26**, 283–292, doi: 10.3969/j.issn.1004-4965.2010.03.004. (in Chinese)

Tian, H., C. Y. Li, and H. Yang, 2010b: Modulation of typhoon tracks over the western North Pacific by the intraseasonal oscillation. *Chinese J. Atmos. Sci.*, **34** , 559–579, doi: 10.3878/j.issn.1006-9895.2010.03.09. (in Chinese)

Wang, B., and J. C. L. Chan, 2002: How strong ENSO events affect tropical storm activity over the western North Pacific. *J. Climate*, **15**, 1643–1658, doi: 10.1175/1520-0442(2002)015<1643:HSEEAT>2.0.CO;2.

Wang, H., Y. H. Ding, and J. H. He, 2006: Influence of western North Pacific summer monsoon changes on typhoon genesis. *Acta Meteor. Sinica*, **64** , 345–356, doi: 10.11676/qxxb2006.033. (in Chinese)

Wang, H. J., and K. Fan, 2006: Relationship between the Antarctic Oscillation and typhoon frequency in the western North Pacific. *Chinese Sci. Bull.*, **51** , 2910–2914, doi: 10.3321/j.issn:0023-074X.2006.24.015. (in Chinese)

Wang, H. J., J. Q. Sun, and K. Fan, 2007: Relationships between the North Pacific Oscillation and the typhoon/hurricane frequencies. *Sci. China Ser. D Earth Sci.*, **50** , 1409–1416. (in Chinese)

Wang, Z.-L., 1981: The infuence of the westerly belt long wave trough over Asia on the western Pacific typhoon tracks. *Scientia Atmos. Sinica*, **5**, 198–206. (in Chinese)

Wang, Z. Y., Y. J. Liu, T. Ding, et al., 2018: Features and possible causes for the climate anomalies in spring 2018. *Meteor. Mon.*, **44**, 1360–1369. (in Chinese)

Webster, P. J., G. H. Holland, I. A. Curry, et al., 2005: Changes in tropical cyclone number, duration, and intensity in a warming environment. *Science*, **309**, 1844–1846, doi: 10.1126/science.1116448.

Wheeler, M., and G. N. Kiladis, 1999: Convectively coupled equa-

torial waves: Analysis of clouds and temperature in the wavenumber–frequency domain. *J. Atmos. Sci.*, **56**, 374–399, doi: 10.1175/1520-0469(1999)056<0374:CCEWAO>2.0.CO;2.

Wheeler, M. C., and H. H. Hendon, 2004: An all-season real-time multivariate MJO index: Development of an index for monitoring and prediction. *Mon. Wea. Rev.*, **132**, 1917–1932, doi: 10.1175/1520-0493(2004)132<1917:AARMMI>2.0.CO;2.

Wu, G. X., and N.-C. Lau, 1992: A GCM simulation of the relationship between tropical storm formation and ENSO. *Mon. Wea. Rev.*, **120**, 958–977, doi: 10.1175/1520-0493(1992)120<0958:AGSOTR>2.0.CO;2.

Wu, J., H.-L. Ren, C. B. Zhao, et al., 2016: Research and application of operational MJO monitoring and prediction products in Beijing Climate Center. *J. Appl. Meteor. Sci.*, **27**, 641–653, doi: 10.11898/1001-7313.20160601. (in Chinese)

Xie, P. Y., L. Tao, J. H. Li, et al., 2018: Variation of tropical cyclone track in the western North Pacific during ENSO developing and decaying years. *Chinese J. Atmos. Sci.*, **42**, 987–999, doi: 10.3878/j.issn.1006-9895.1708.17118. (in Chinese)

Ying, M., W. Zhang, H. Yu, et al., 2014: An overview of the China Meteorological Administration tropical cyclone database. *J. Atmos. Oceanic Technol.*, **31**, 287–301, doi: 10.1175/JTECH-D-12-00119.1.

Yoshida, R., Y. Kajikawa, and H. Ishikawa, 2014: Impact of boreal summer intraseasonal oscillation on environment of tropical cyclone genesis over the western North Pacific. *SOLA*, **10**, 15–18, doi: 10.2151/sola.2014-004.

You, L. J., J. Y. Gao, H. Lin, et al., 2019: Impact of the intra-seasonal oscillation on tropical cyclone genesis over the western North Pacific. *Int. J. Climatol.*, **39**, 1969–1984, doi: 10.1002/joc.5927.

Yu, J. H., T. Li, Z. M. Tan, et al., 2016a: Effects of tropical North Atlantic SST on tropical cyclone genesis in the western North Pacific. *Climate Dyn.*, **46**, 865–877, doi: 10.1007/s00382-015-2618-x.

Yu, J. H., C. Chen, T. Li, et al., 2016b: Contribution of major SSTA modes to the climate variability of tropical cyclone genesis frequency over the western North Pacific. *Quart. J. Roy. Meteor. Soc.*, **142**, 1171–1181, doi: 10.1002/qj.2722.

Zhan, R. F., Y. Q. Wang, and X. T. Lei, 2011: Contributions of ENSO and east Indian Ocean SSTA to the interannual variability of Northwest Pacific tropical cyclone frequency. *J. Climate*, **24**, 509–521, doi: 10.1175/2010JCLI3808.1.

Zhan, R. F., Y. H. Ding, L. G. Wu, et al., 2016: Role of ENSO in the interannual relationship between Tibetan Plateau winter snow cover and Northwest Pacific tropical cyclone genesis frequency. *Sci. China Earth Sci.*, **59**, 2009–2021, doi: 10.1007/s11430-015-5559-y. (in Chinese)

Zhao, C., and T. Li, 2019: Basin dependence of the MJO modulating tropical cyclone genesis. *Climate Dyn.*, **52**, 6081–6096, doi: 10.1007/s00382-018-4502-y.

Zhu, C. W., T. Nakazawa, and J. P. Li, 2004: Modulation of tropical depression/cyclone over the Indian–western Pacific oceans by Madden–Julian oscillation. *Acta Meteor. Sinica*, **62**, 42–51, doi: 10.11676/qxxb2004.005. (in Chinese)

Tech & Copy Editor: Lan YI

● FORECASTING FORUM ●

Why Is the East Asian Summer Monsoon Extremely Strong in 2018? —Collaborative Effects of SST and Snow Cover Anomalies

Lijuan CHEN[1,2], Wei GU[1*], and Weijing LI[1,2]

1 *Laboratory for Climate Studies*, *National Climate Center*, *China Meteorological Administration*, *Beijing* 100081
2 *Collaborative Innovation Center on Forecast and Evaluation of Meteorological Disasters*, *Nanjing University of Information Science &Technology*, *Nanjing* 210044

(Received December 17, 2018; in final form April 10, 2019)

ABSTRACT

In 2018, summer precipitation was above normal in North and Northwest China and below normal around the Yangtze River valley, due to an extremely strong East Asian summer monsoon (EASM). The atmospheric circulation anomalies in East Asia and key external forcing factors that influence the EASM in 2018 are explored in this paper. The results show that there existed an anomalous cyclonic circulation near the Philippines, while the western Pacific subtropical high was located more northward than its normal position. In the mid–high latitudes, a negative geopotential height anomaly center was found near the Ural Mountains, suppressing the blocking activity. Under such a circulation pattern, precipitation near the Yangtze River valley decreased because local divergence and subsidence intensified, whereas precipitation in northern China increased due to large amounts of water vapor transport by anomalously strong southerly winds. Further analyses reveal that the strong EASM circulation in 2018 might result from the joint influences of several external forcing factors. The weak La Niña event that started from October 2017, the positive North Atlantic Tripolar mode (NAT) in spring 2018, and the reduced snow cover over the Tibetan Plateau in winter 2017/18 all collaboratively contributed to formation of the cyclonic circulation anomaly near the Philippines, leading to the extremely strong EASM. Especially, the positive NAT and the reduced Tibetan snow cover may have caused the negative geopotential height anomaly near the Ural Mountains, in favor of a strong EASM. The above external factors and their reinforcing impacts on the EASM are further verified by two groups of similar historical cases.

Key words: East Asian summer monsoon, external forcing factors, La Niña, North Atlantic Tripolar mode, Indian Ocean basin mode, snow cover of the Tibetan Plateau

Citation: Chen, L. J., W. Gu, and W. J. Li, 2019: Why is the East Asian summer monsoon extremely strong in 2018? —Collaborative effects of SST and snow cover anomalies. *J. Meteor. Res.*, **33** (4), 593–608, doi: 10.1007/s13351-019-8200-4.

1. Introduction

Under the influence of the East Asian monsoon, the climate in China exhibits large interannual variability, and associated meteorological disasters occur frequently. Based on statistical analysis, the economic loss caused by various meteorological disasters accounts for about 71% of the total losses from various natural disasters in China. Among all the meteorological disasters, 80% are caused by drought and flood (Li et al., 2009; Huang et al., 2012). Since summer is the rainy season in most parts of China, it is also the season when drought and flood occur most frequently. These disasters often cause large direct or indirect damages to people's lives and economic infrastructure. For example, severe flooding disasters happened in the Yangtze River valley in summer 1998 and 2016 (Feng et al., 2000; Yuan et al., 2017), while serious meteorological drought occurred in Jianghuai and Jianghan areas in summer 2012 (Zhao et al., 2014), and a severe flooding disaster occurred over the Huaihe River basin in 2003 (Ma et al., 2011). Since the spatial variation of summer precipitation in China is mainly affected by the

Supported by the National Key Research and Development Program of China (2018YFC1506006), National Science and Technology Support Program of China (2015BAC03B04), and National Natural Science Foundation of China (41805067 and 41275073).

*Corresponding author: guwei@cma.gov.cn.

©The Chinese Meteorological Society and Springer-Verlag Berlin Heidelberg 2019

East Asian summer monsoon (EASM), it is of great scientific significance to probe the internal dynamics and external forcing factors leading to the interannual variability of the EASM, which has an important implication for disaster prevention and mitigation.

The summertime weather and climate in China are significantly affected by the EASM system, which is under the control of some external forcing factors such as sea surface temperature (SST) and land surface thermal conditions (Huang et al., 2012). Complicated interaction and combination of multiple influencing factors make the EASM and summer precipitation in China vary significantly on the interannual timescale (Chen and Zhao, 2000; Chen et al., 2013; Wang and Gu, 2016). Among all the external factors affecting summer precipitation in China, El Nino–Southern Oscillation (ENSO) is the most important one. The ENSO events also exhibit significant interannual variability, closely associated with the summer precipitation variability in China (Huang and Wu, 1989). The SST anomaly during an ENSO event may trigger an abnormal anticyclone/cyclone near the Philippines in the lower troposphere (Zhang et al., 1996; Li et al., 2017; Zhang et al., 2017). The northward propagation of the anomalous anticyclone/cyclone leads to the formation of East Asia–Pacific (EAP) teleconnection pattern and/or the Pacific–Japan (PJ) type teleconnection pattern (Huang and Li, 1987; Nitta, 1987; Wang et al., 2000; Xu et al., 2019a), which subsequently affect the EASM and summer climate in China. During this process, the local air–sea coupling in the tropical Indian Ocean and the SST anomaly over Northwest Pacific also play an important role as "capacitor," which stores and prolongs the ENSO effect into spring and summer (Xie et al., 2009, 2016). In addition, the interdecadal oscillation of the North Pacific SST, which behaves as an important interdecadal background, modulates the influence of ENSO on the EASM (Feng et al., 2014).

In addition to the SSTs in the tropical Pacific and tropical Indian Ocean, the SST in North Atlantic and the snow cover over the Tibetan Plateau may also exert significant impacts on the EASM. The North Atlantic Tripolar mode (NAT) reflects the most important interannual variability of SST over the North Atlantic region. Studies have shown that the springtime NAT may have influenced the EASM in a great manner (Gu et al., 2009; Sung et al., 2009). On the one hand, the NAT affects the blocking activity near the Ural Mountains by activating a teleconnection wave train across the mid–high latitude region of Eurasia, and thus intensifies the Meiyu front and the EASM. On the other hand, the NAT affects convective activity in the tropical western Pacific through atmospheric teleconnection in the tropics, and thus contributes to the maintaining of the abnormal anticyclone/cyclone near the Philippines (Zuo et al., 2013, 2018).

In addition to SST, some other surface thermal conditions may also influence the EASM and summer climate in China. In particular, the thermal condition over the Tibetan Plateau correlates well with the monsoon circulation over the plateau and East Asia (Ye et al., 1957; Zwiers, 1993). The extent of wintertime snow cover over the plateau and the snow melting in spring reflect the atmospheric thermal conditions over the plateau (Chen et al., 2000; Qian et al., 2003; Zhang, 2004; Zhu et al., 2007). Many previous studies have investigated the influence and mechanism of the Tibetan snow cover on the EASM. Zhang and Tao (2001) pointed out that the anomaly of wintertime snow cover over the Tibetan Plateau could maintain until spring or even summer. By changing surface albedo and soil moisture status, snow cover over large areas can greatly affect energy budget on local and regional scales, leading to significant variations of sea–land thermal difference in spring and summer, which subsequently influences the intensity of the EASM. A study by Ren et al. (2016) showed that snow cover anomalies over the Tibetan Plateau can also induce variation of the EASM intensity by triggering anticyclonic or cyclonic circulation anomalies near the Philippines. Note that such kinds of snow cover effects on atmospheric circulation are independent of ENSO effects. A recent study by Zhang et al. (2018) also pointed out that sensible heat anomalies over the Tibetan Plateau led to changes in latent heat transport to the northeast of India in summer, which may result in anomalies of the South Asian high and thus affect the intensity of the EASM.

Preliminary analyses reveal that the Asian summer monsoon system in 2018 appeared abnormally strong (Gu and Chen, 2019; Sun et al., 2019). Specifically, the Indian summer monsoon was much stronger than normal at certain stages and heavy rainfall and flooding disasters occurred in India from May to August 2018 (Sun et al., 2019); and the South China Sea summer monsoon was stronger than normal and the EASM was particularly strong in 2018 (Gu and Chen, 2019). Based on station rainfall observations in China, it is found that summer (June–August) precipitation was higher than normal in the northern and southeastern coastal areas of China but much lower than normal in the Yangtze River valley. Although previous studies have revealed different circulation patterns and external forcing factors leading to strong/weak EASM and associated precipitation anom-

alies, specific mechanisms behind the EASM anomaly are usually different for individual years. For the EASM anomaly in a certain year, it is possible that a single factor plays a leading role, or it may be the result of the joint effects of multiple factors. What is the specific mechanism for the strong EASM in 2018? This is a question that needs to be explored in particular. All in all, the current paper intends to answer the following questions. (1) What are the main characteristics of the East Asian summer circulation in 2018? (2) What are the key external factors that have exerted significant impacts on the 2018 summer circulation? (3) How do all the external factors jointly affect the EASM? Answers to these questions will provide further understanding on the mechanisms for the strong EASM in 2018 and the interannual variability of the EASM. The present study can also provide reference for future application of the precursor signals in the external forcing to more accurate seasonal climate prediction.

2. Data and method

The precipitation data used in the present study are extracted from the Daily Data of Basic Meteorological Elements of China National Ground Weather Station (V3.0) issued by the National Meteorological Information Center of China (Ren et al., 2012). This dataset covers the period of January 1951–August 2018. The atmospheric circulation data such as geopotential height and horizontal wind fields are extracted from the NCEP/NCAR reanalysis monthly data on a horizontal resolution of 2.5° × 2.5° (Kalnay et al., 1996; Kistler et al., 2001). The NOAA SST data (OISSTv2) are employed in the present study, with a horizontal resolution of 1° × 1° and the dataset starts from December 1981 (Reynolds et al., 2002) and ends in November 2018. The original snow cover data are obtained from Rutgers University in the United States (http://climate.rutgers.edu/snowcover/). Following the approach of Guo et al. (2004), the original weekly snow cover data are converted into the number of snow/snow-free days through area weighted averaging over the Tibetan Plateau, and the snow cover index over the Tibetan Plateau is obtained. The averages from 1981 to 2010 for individual fields in each dataset are taken as the corresponding climatological means. In this paper, the winter, spring, and summer means are averages from December to February, March to May, and June to August, respectively.

Three representative EASM indices defined by Shi et al. (1996), Zhang et al. (2003), and Zhu et al. (2000) are calculated in this study. The Shi index is defined as the difference of normalized sea level pressure between 110° and 160°E within the range of 20°–50°N. The Zhang index is defined as the difference in the average 850-hPa zonal wind between the eastern subtropical monsoon trough region (10°–20°N, 100°–150°E) and the East Asian subtropical region (25°–35°N, 100°–150°E). The Zhu index reflects the comprehensive east–west and north–south thermal differences over East Asia. The Niño3.4 index represents the mean SST anomaly over the Niño3.4 region (5°S–5°N, 170°–120°W). The NAT index (Marshall et al., 2001; Zuo et al., 2012) is defined as the time series corresponding to the first leading mode of the empirical orthogonal function analysis of the SST anomaly in the North Atlantic region (0°–60°N, 80°W–0°). A "negative–positive–negative" distribution of SSTA over North Atlantic from the tropics to the high latitude region reflects the feature of the NAT in its positive phase, and vice versa. In this paper, the relationship between external forcing factors and summer circulation is analyzed by composite analysis and linear regression analysis. Considering the maximum data overlapping and the interdecadal variation of the EASM, the composite/regression analyses are conducted over the period from 1982 to 2017.

3. Characteristics of the East Asian summer monsoon in 2018 and its influence on summer rainfall in China

The historical time series of the three EASM indices employed in this paper (Fig. 1) show that, for each index, the value in 2018 demonstrates an obvious positive anomaly (exceeding one standard deviation), indicating that the EASM in 2018 is much stronger than normal. Among the three indices, the index defined by Zhang et al. (2003) exceeds two standard deviations in 2018 and indicates that 2018 is the strongest EASM year since 1981 (Fig. 1b). Based on the indices defined by Shi et al. (1996) and Zhu et al. (2000), the EASM in 2018 is the 4th and 3rd strongest since 1981 (Figs. 1a, c), respectively. All the above three indices indicate that the overall intensity of the EASM is extremely large in 2018.

Summer rainfall in China shows different drought and flood distribution characteristics in various years, following different intensities of the EASM. Based on the threshold defined as 0.7 standard deviation of the EASM index proposed by Zhang et al. (2003), 11 strong EASM years (1981, 1984, 1985, 1986, 1990, 1994, 1997, 2001, 2002, 2004, and 2012) and 11 weak EASM years (1983, 1987, 1988, 1993, 1995, 1996, 1998, 2003, 2007, 2010, and 2013) are identified. Composite precipitation fields

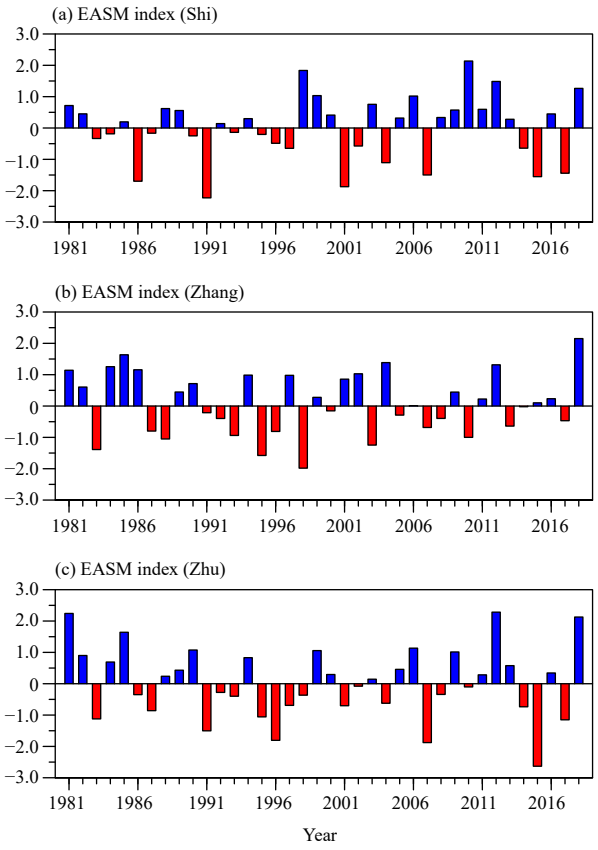

Fig. 1. Temporal evolutions of the (a) Shi, (b) Zhang, and (c) Zhu EASM indices during 1981–2018.

for the strong and weak EASM summers show that when the EASM is strong, precipitation in the middle and lower reaches of the Yangtze River is significantly lower than that in weak EASM summers, whereas precipitation in North, Northwest, Northeast, and South China is higher than that in weak EASM summers (Fig. 2a). Figure 2b shows the percentage precipitation anomaly (the percentage of precipitation anomaly relative to the climatology) in summer 2018. It can be seen that precipitation in most parts of North China, Northwest China, and South China is higher than normal while precipitation in the middle and lower reaches of the Yangtze River is obviously lower than normal (Fig. 2b). Such a distribution pattern indicates that the summer rainfall in 2018 is probably affected by the strong EASM in this year. Meanwhile, the anomalous distribution pattern of rainy days (daily precipitation ⩾ 0.1 mm) also shows that the rainy days in most areas over the middle and lower reaches of the Yangtze River are 20%–40% less than the climatological value (Fig. 2c). In contrast, for most parts of Northwest and South China, the rainy days are significantly more than normal in 2018. Such an anomalous feature of the rainy days indicates that the key circulation factors that have affected precipitation in 2018 are persistent and stable. However, for the eastern part of North China and eastern part of Huanghuai region, although the precipitation in most areas is more than normal, the rainy days are less than normal, implying that extreme precipitation may be prominent in these regions.

The historical time series of regional average summer precipitation show that summer precipitation in Northwest China (including Xinjiang and Ningxia regions, Qinghai, Gansu, and Shaanxi provinces) has reached 196 mm in 2018, which is 32% more than the climatological average over the same region and is the largest since 1981 (blue line in Fig. 3). The average precipitation in North China (including Beijing and Tianjin, and Hebei and Shanxi provinces) is 376 mm, 14% more than the climatological value (red line in Fig. 3). The average precipitation in the middle and lower reaches of the Yangtze River (including Shanghai and Hubei, Anhui, Jiangsu, Zhejiang, Jiangxi, and Hunan provinces) is 11% less than the climatological value and is also the least in the past five years (black line in Fig. 3).

The intraseasonal variation of summer precipitation in China is significant (He et al., 1995; Zhan et al., 2008;

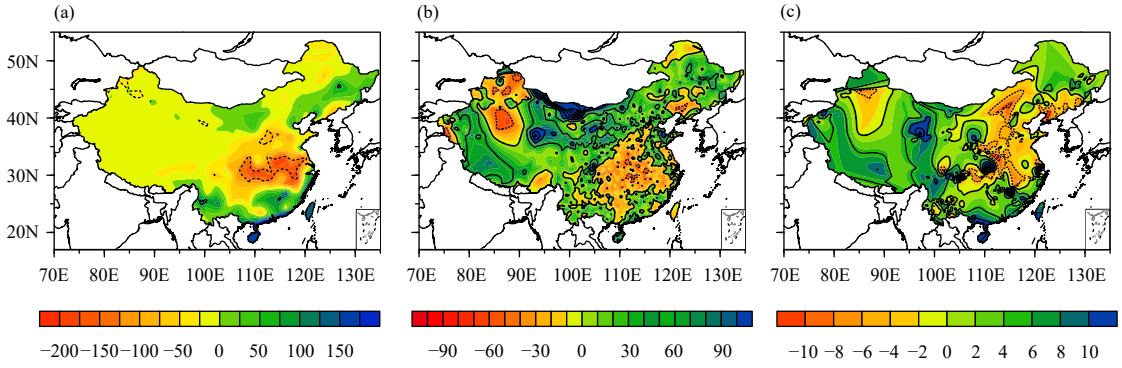

Fig. 2. (a) Difference in summer precipitation (mm) between strong and weak EASM years (thick dashed line indicates the area where the difference exceeds the significance level of 0.1). (b) Percentage precipitation anomaly (%) and (c) the anomaly of rainy days for summer 2018.

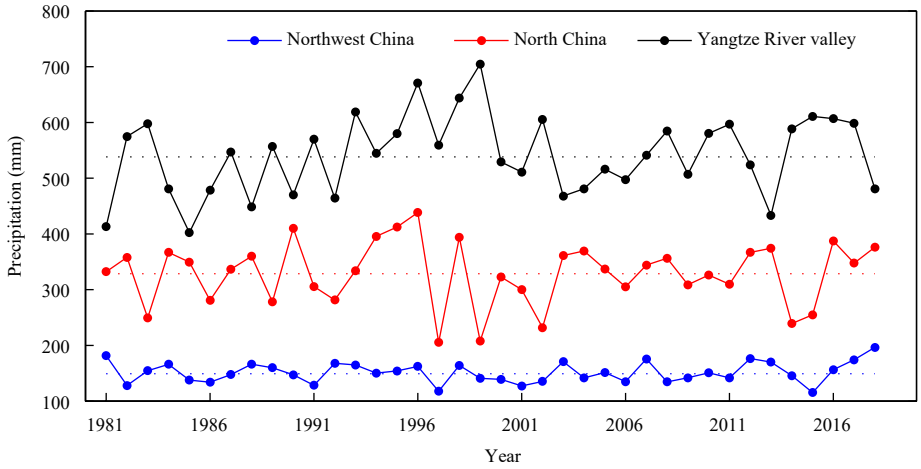

Fig. 3. Average summer precipitation (mm) in Northwest China (blue line), North China (red line), and the middle–lower reaches of Yangtze River (black line) for 1981–2018.

Zhao et al., 2011). The characteristics of precipitation anomaly in certain months in summer often exhibit large difference from overall characteristics of precipitation anomaly in the whole season (Chen et al., 2016; Yuan et al., 2017). However, in summer 2018, precipitation anomalies in June, July, and August consistently show the characteristic of "less precipitation in the middle and lower reaches of the Yangtze River and more precipitation in the northern region." This pattern indicates that during the whole summer of 2018, the anomalous atmospheric circulations are relatively persistent and stable. The above result implies that the influence of external forcing factors may have played a dominant role compared with that of internal dynamic processes of the atmosphere.

4. Characteristics of the East Asian atmospheric circulation in summer 2018

The basic cause of the East Asian monsoon is the seasonal variation of the atmospheric thermal difference between ocean and land. In summer 2018, the atmospheric thermal state over the ocean and land shows a typical feature leading to strong EASM. The thickness of the atmosphere (the difference in geopotential height between 200 and 500 hPa) is used to represent the thermal state of the atmosphere. From the perspective of climatology, a warm center of the atmosphere is located near the Tibetan Plateau in summer, and hence there is an obvious thermal difference between East Asia and the North Pacific Ocean to its east and the tropical oceans to its south (Fig. 4a). Therefore, the thermal contrast between the land area in East Asia and the adjacent oceans may cause a continental thermal low over East Asia as well as the EASM. In summer 2018, there exists an anomalous warm center in the northern–central part of East Asia (Fig. 4b), implying that the atmospheric thermal difference between the ocean and land is enhanced and the EASM is intensified correspondingly.

In summer 2018, all the key members of the East Asian atmospheric circulation system demonstrate features of a strong EASM. In the upper troposphere at 200 hPa, there exists an anomalous positive geopotential height center while an anticyclonic anomaly is located in northern East Asia (Fig. 5a). This pattern implies that the location of the East Asian subtropical upper jet stream is located fur-

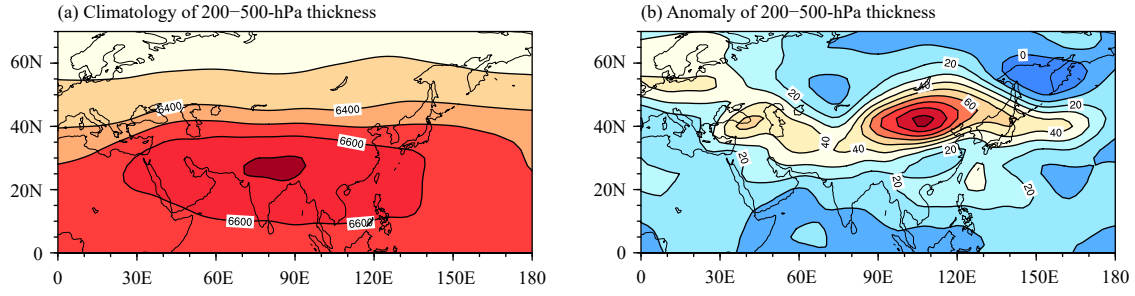

Fig. 4. Summertime geopotential height difference between 200 and 500 hPa: (a) climatological mean and (b) 2018 anomaly field (gpm).

ther north than its normal position. A positive geopotential height center is also remarkably notified at 500 hPa (Fig. 5b), accompanied by two negative centers to the north and south of the positive center respectively, forming a "negative–positive–negative" anomalous pattern along the coast of East Asia. Such a feature of circulation anomaly resembles that in the positive EAP phase (Huang, 1992; Huang et al., 2003). Affected by the above circulation anomaly, the western Pacific subtropical high (WPSH) is located further north than normal. The position index of the WPSH ridge line in summer (as in Liu et al., 2012) indicates that 2018 is the year when the WPSH has reached its northernmost position since 1981 (Fig. 6). Correspondingly, anomalous wind fields at 850 hPa (Fig. 5b) show a cyclonic anomaly located from the Taiwan Strait to the northern Philippines, and an anticyclonic anomaly situated to its north. Under the influence of such a circulation anomaly pattern, most areas to the south of the middle and lower reaches of the Yangtze River are dominated by anomalous northerly winds, suppressing the transfer of water vapor to the middle and lower reaches of the Yangtze River. The divergence of horizontal wind and that of water vapor flux increase (Figs. 5b, c), which results in stronger than normal descending motion (Fig. 5d) and less precipitation in the middle and lower reaches of the Yangtze River. For most areas in the northern part of China, the lower troposphere is under the control of southerly wind anomalies (Fig. 5b), which are conducive to the transfer of water vapor (Fig. 5c) and the intensification of ascending motion (Fig. 5d), and thereby favoring more precipitation.

In addition to the tropical and subtropical circulation systems, the atmospheric circulation in the middle and high latitudes also has important impacts on the EASM (Tao and Zhang, 1998; Wang and Gu, 2016; Xu et al., 2019b). For example, studies have pointed out that the Ural Mountains and the Okhotsk Sea are two key regions of summer atmospheric blocking activities, and establishment of the blocking situation in these two areas plays an important role in the maintenance and intensification of the Meiyu front (Tao and Zhang, 1998; Zhang and Tao, 2003). The 500-hPa geopotential height field in summer 2018 is displayed in Fig. 5b, which shows negative geopotential height centers over the regions in the vicinity of the Ural Mountains and the Okhotsk Sea, where no obvious blocking activity has occurred. Such a situation is disadvantageous for the establishment and maintenance of the Meiyu front. In contrast, it is helpful for

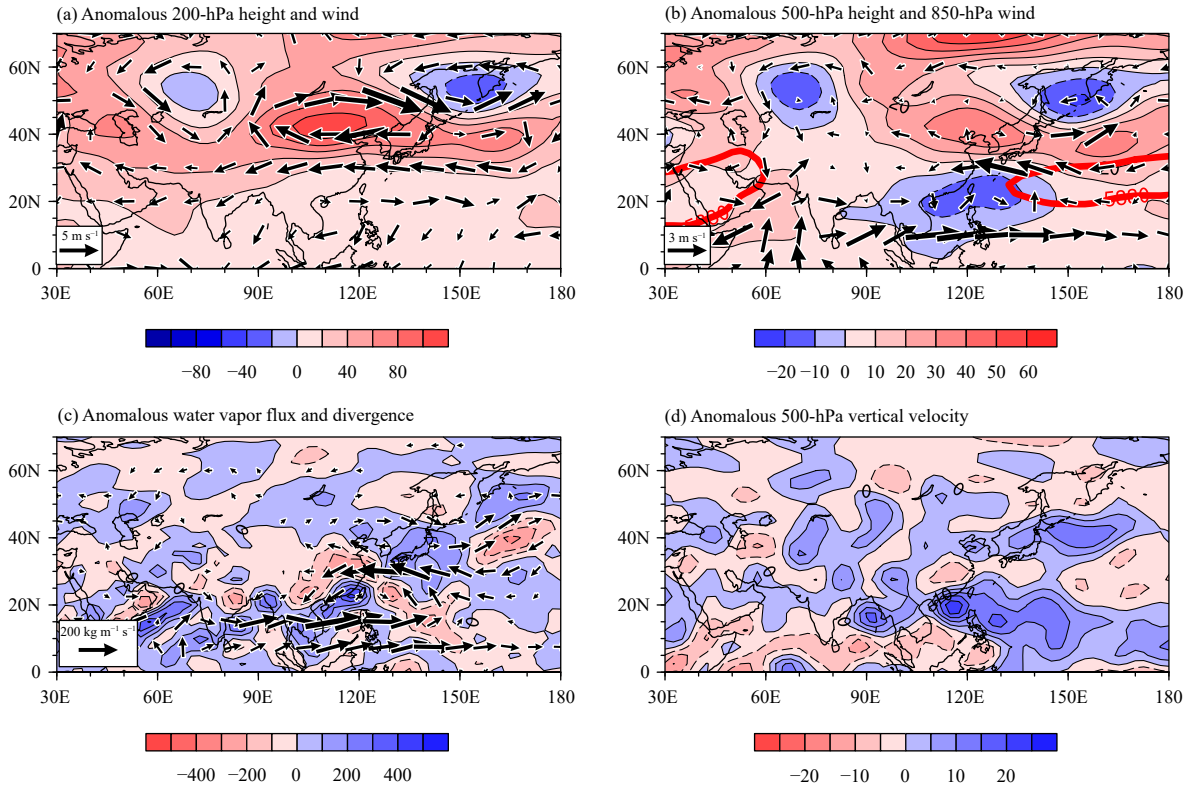

Fig. 5. Anomalous (a) geopotential height (gpm) and wind (m s^{-1}) at 200 hPa, (b) 500-hPa geopotential height (gpm) and 850-hPa wind (m s^{-1}), (c) column-integrated water vapor flux (kg m^{-1} s^{-1}) and its divergence (10^{-7} kg m^{-2} s^{-1}), and (d) 500-hPa vertical velocity (−300 Pa s^{-1}) in summer 2018. The red line in (b) represents the climatology mean 5880-gpm contour.

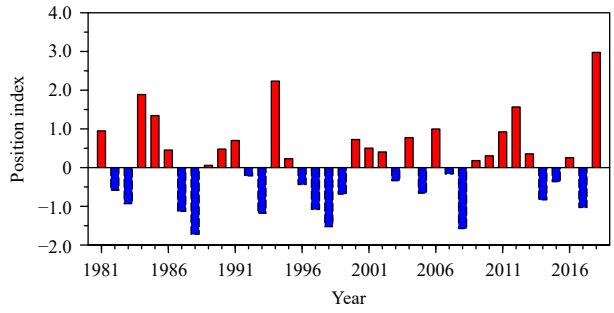

Fig. 6. North–south position index of the ridge line of the western Pacific subtropical high (WPSH) in the summers of 1981–2018.

the intensification of southerly winds over the northern part of China and thus promoting the enhancement of the EASM. To sum up, it is inferred that in addition to the East Asian subtropical jet stream and the WPSH circulation system, the atmospheric circulation anomaly over the mid–high latitudes of Eurasia also makes significant contributions to the abnormally strong EASM in 2018.

5. Collaborative impacts of external forcing factors on EASM in 2018

From autumn 2017 to spring 2018, the Niño3.4 index continued to be lower than −0.5°C, and the Southern Oscillation Index (SOI) maintained positive. A La Niña event occurred in the equatorial central eastern Pacific (Fig. 7a). According to the criterion defined by Ren et al. (2018), this is a weak La Niña event starting in October 2017 and ending in April 2018. In terms of spatial distribution of SSTA (Fig. 7b), this event is a distinct eastern type La Niña event with the cold center located near the equatorial eastern Pacific (Niño 3 region), while warm SST anomaly dominated the tropical western Pacific from winter 2017 until the subsequent summer.

Previous studies have shown that in the summer following a La Niña event, an anomalous cyclonic circulation is likely to occur near the Philippines, which is favorable for a strong EASM (Wang et al., 2000). Correspondingly, the precipitation in the middle and lower reaches of the Yangtze River would be suppressed while the precipitation in North China and South China would be enhanced (Huang and Wu, 1989; Zhang et al., 1996; Wang et al., 2000). However, the impact of ENSO event on the EASM and summer precipitation in China is not the same due to interdecadal variations (Feng et al., 2014). Under the current interdecadal background (after the 1980s), the impact of La Niña on summer precipitation in China is weaker than that before the 1980s (Gao and Wang, 2007). The monsoon index in the eight summers (1985, 1989, 1996, 2000, 2001, 2008, 2011, and 2012) that followed a La Niña event since 1981 never showed any obvious feature of a strong EASM. The EASM in all five (1989, 1996, 2000, 2001, and 2008) out

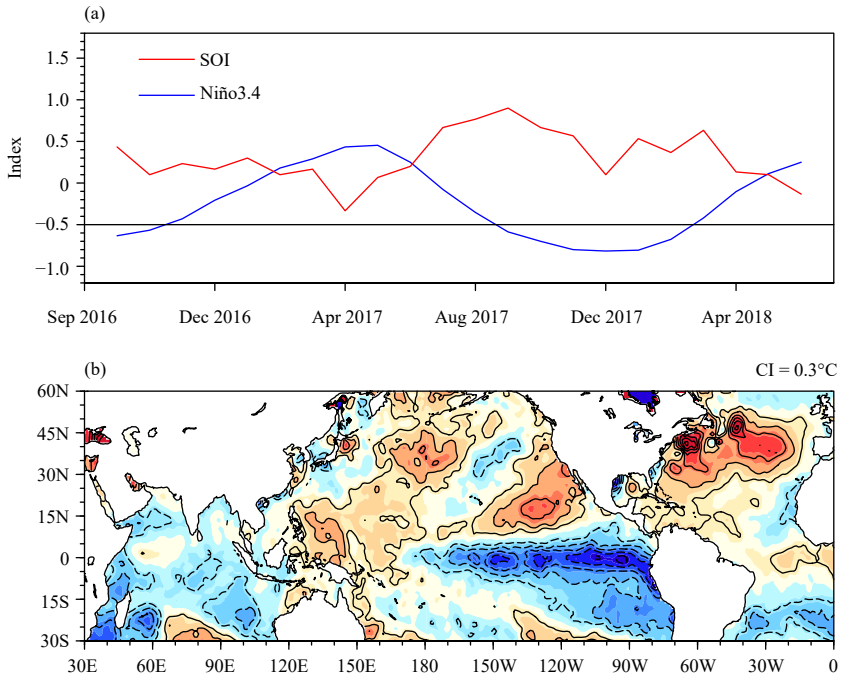

Fig. 7. (a) Evolution of the Niño3.4 index (°C) and SOI index from September 2016 to August 2018 and (b) global SST anomaly (SSTA) in the 2017/18 winter. In (b), shadings in yellow (blue) with solid (dashed) contours denote positive (negative) SSTA, and contour interval (CI) is 0.3°C.

of the above eight years is close to normal or weak (Fig. 1). Composite precipitation in the above eight summers that followed a La Niña event never showed any significant anomalous feature either (Fig. 8). Note that the composite precipitation pattern discussed above is different from that of the summer precipitation anomaly in 2018 (Fig. 2a). This indicates that the effect of the La Niña event on the EASM and summer rainfall in China has been weakened since 1981. At the same time, under the current interdecadal background, the strong EASM in 2018 may not be the result of the single factor of La Niña event. Instead, it cloud be caused by the combined influences of several external forcing factors.

In addition to the ENSO event occurring in the tropical Pacific, the tropical Indian SST, the North Atlantic SST, and the snow cover over the Tibetan Plateau are all key external forcing factors affecting the EASM (Chen Q. J. et al., 2000; Chen L. J. et al., 2013). The lead–lag correlations between the Niño3.4 index, the Indian Ocean basin wide mode (IOBW) index, the NAT index, the Tibetan Plateau snow area index, and the EASM index (Zhang et al., 2003) are calculated. The results are presented in Fig. 9. It is seen that all the above factors have significant correlation with the EASM index, although the correlation coefficient varies with different lead times. It is therefore concluded that each factor has significant influences on the EASM. However, there is a difference in the lead time of such an effect for each factor. It is worth noting that the snow cover index and the NAT index show similar relationships with the EASM index after removing the ENSO trend (figure omitted), which indicates that the impacts of the snow cover and the NAT on the EASM are independent of ENSO. Specifically, the relationship between the Niño3.4 index and the EASM index is most significant when the SST index leads about half a year, indicating the lagged effect of the wintertime ENSO mature phase on the EASM. For IOBW, it is found that the summertime SST is most significantly correlated with the EASM, indicating that the influence of the Indian Ocean on the EASM is almost instantaneous. Since the variability of summertime SST over the tropical Indian Ocean is largely attributed to its response to ENSO event, it has been revealed that the summer Indian Ocean SST mainly acts as a "capacitor" and exerts a delayed effect on the EASM, after the ENSO event (Xie et al., 2009, 2016). For the NAT, the most significantly correlated period with EASM is in spring, and the relationship between the Tibetan snow cover and the EASM is significant since winter and reaches its peak value in spring. The lead–lag correlation relationships of the above factors with the EASM are basically consistent with previous studies.

According to the period during which each factor is

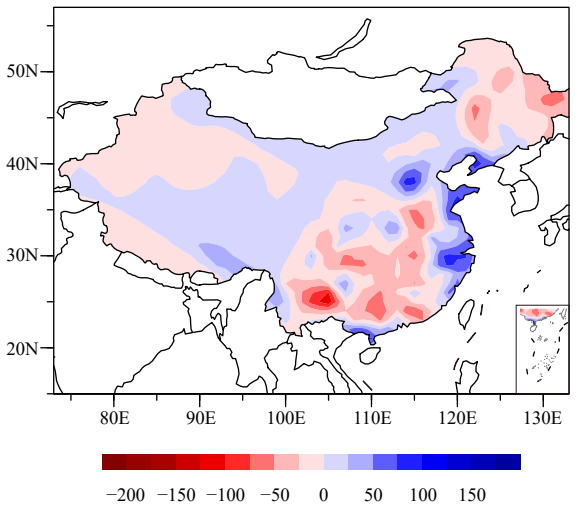

Fig. 8. Composite precipitation (mm) over eight summers that followed a La Niña event from 1981 to 2017 (no area in the figure exceeding the 0.1 significance level).

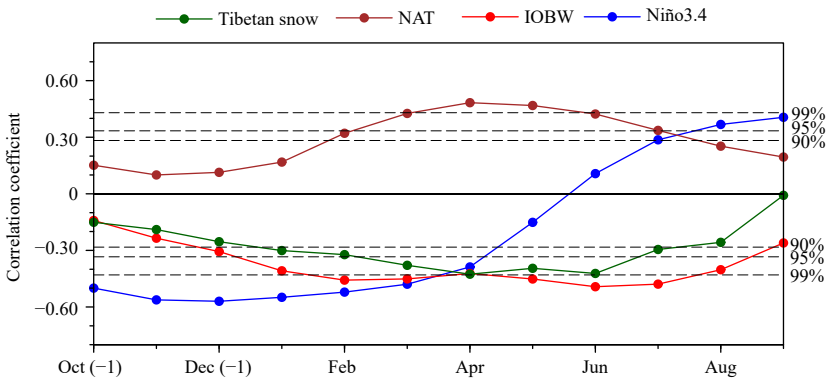

Fig. 9. Lead–lag correlation coefficients of the Niño3.4 index, IOBW index, NAT index, and Tibetan snow cover index with the EASM index (three-month sliding average is performed prior to the calculation of correlation).

significantly correlated to the EASM, the wintertime Niño3.4 index, summertime IOBW index, springtime NAT index, and wintertime Tibetan snow cover index are used to further analyze the characteristics of external forcing factors and their influences on the EASM in 2018. The historical series of the above indices show clearly that these factors in 2018 demonstrate obvious anomalous characteristics (Fig. 10). In winter, the Niño3.4 SST is significantly colder (Fig. 10a) and the Tibetan snow cover is less than normal (Fig. 10d); in spring, the NAT remains in its positive phase (Fig. 10c); in summer, the SST in the tropical Indian Ocean is colder than normal (Fig. 10b). In order to further reveal the impact of each individual factor on the EASM in 2018, the atmospheric circulation is regressed onto each external factor and the results are discussed next.

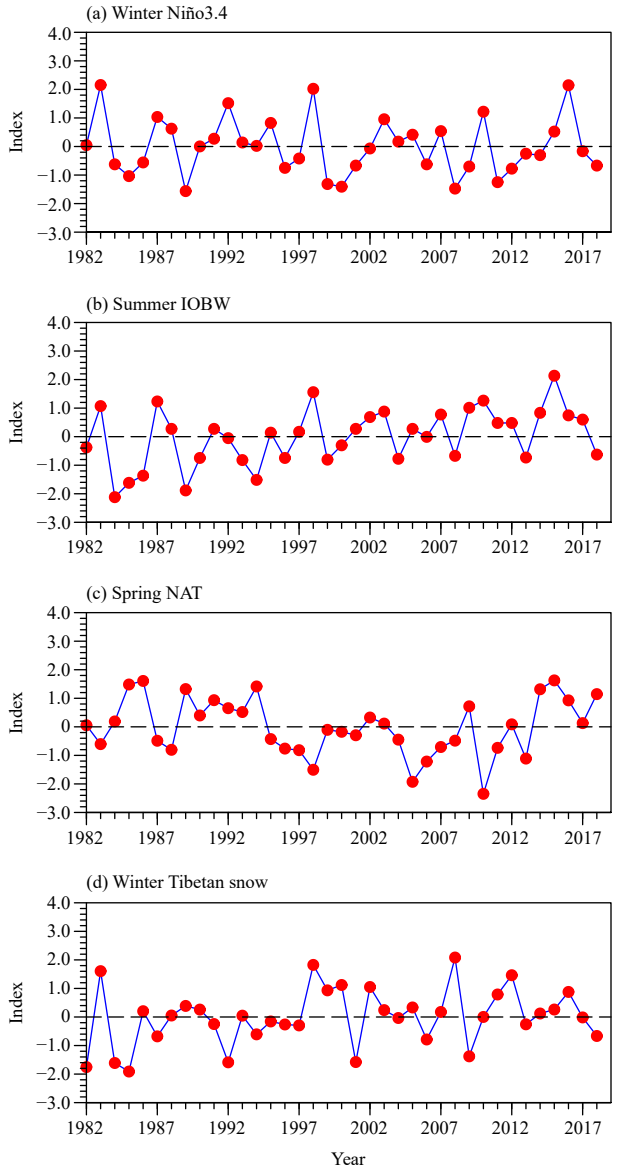

Fig. 10. Temporal evolutions of (a) the Niño3.4 index in winter, (b) the IOBW index in summer, (c) the NAT index in spring, and (d) the Tibetan snow cover index in winter during 1982–2018.

5.1 *Impacts of the tropical SST anomaly*

In the typical years with colder than normal Niño3.4 SST in winter, atmospheric circulation in the subtropical East Asia usually demonstrates significant signals of a positive EAP pattern (cyclone–anticyclone–cyclone) developing along the coastal region of East Asia at 500 hPa. The WPSH tends to be located further north and an anomalous cyclonic circulation appears near the Philippines (Fig. 11a). Such a circulation pattern reflects the main feature of a strong EASM, suggesting that the wintertime cold SST in the eastern tropical Pacific is favorable for a strong EASM. However, as shown in Fig. 11a, the significance level in the East Asian subtropical region is not very high and the corresponding geopotential height and wind anomalies are also relatively weak. The above result indicates that the influence of the La Niña event on the EASM is probably limited under the current interdecadal background.

Generally, in the summer following an ENSO event, the equatorial eastern Pacific SST usually becomes close to normal, while the anomalous anticyclone/cyclone near the Philippines can still maintain. The maintenance of the anticyclone/cyclone anomaly near the Philippines can be attributed to the IOBW, which has a strong lagged response to the ENSO event and a positive feedback with the anomalous anticyclone/cyclone in the Philippines. That is to say, the Indian Ocean SST can preserve the wintertime ENSO signal and release it in the summer. According to the composite circulation pattern in the cold IOBW summers (Fig. 11b), a positive EAP phase along the coast of East Asia and an anomalous cyclone near the Philippines are promoted by the cold Indian Ocean SST. The above impacts of the Indian Ocean on the circulation are similar to and even more significant than that of the equatorial eastern Pacific (Fig. 11a), indicating that the Indian Ocean can store the La Niña signal and "relay" it in the summer. The close relationship between the Indian Ocean SST and the summer circulation in East Asia shows that the cold IOBW in summer plays an important role in maintaining the influence of the La Niña event until summer and promoting a strong EASM.

5.2 *Impacts of the North Atlantic SST anomaly*

The NAT is the first leading mode of the North Atlantic SST and it is also the main source for the atmospheric interannual variability in North Atlantic. Previ-

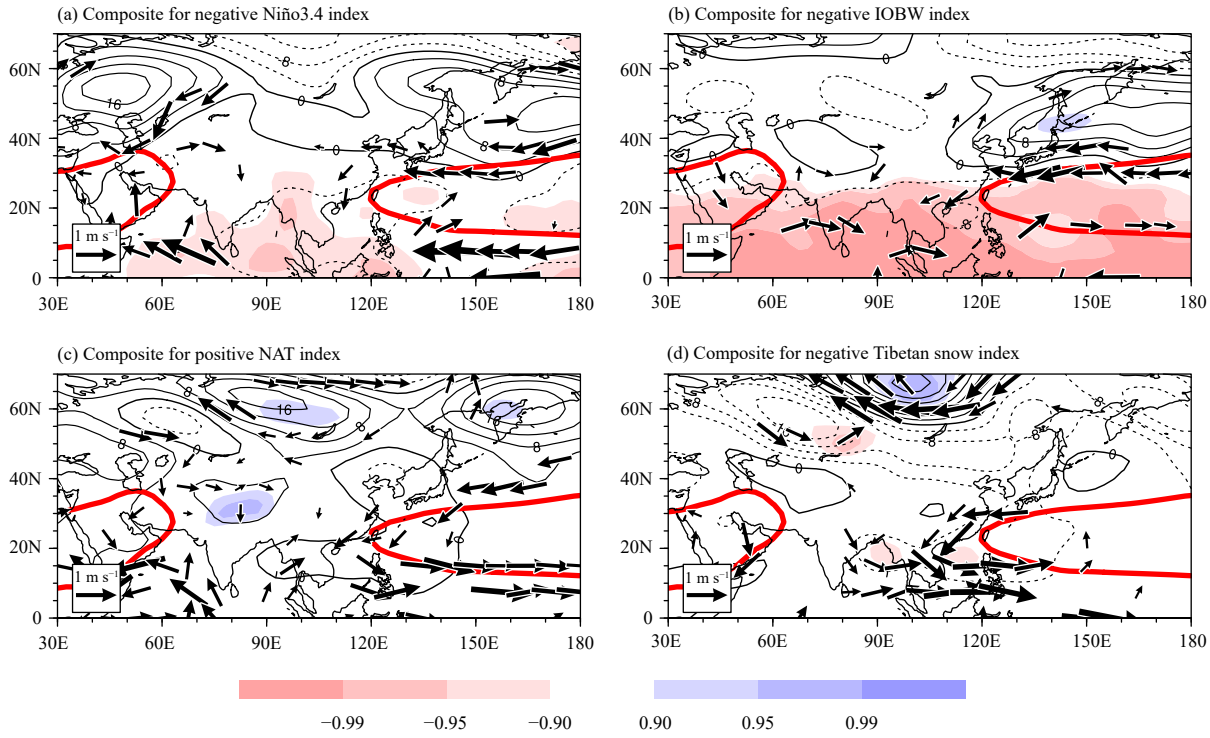

Fig. 11. Composite 500-hPa geopotential height (gpm) and 850-hPa wind (m s^{-1}) anomalies in the summers (a) following the La Niña occurrence winters with negative Niño3.4 index, (b) with negative summer IOBW index, (c) following the springs with positive NAT index, and (d) following the winters with negative winter plateau snow cover index. Dark, medium, and light shadings indicate the areas with values above the significance level of 0.01, 0.05, and 0.1, respectively; red solid lines represent the climatological mean 5870-gpm contour. Only wind vectors exceeding the 0.2 significance level are shown.

ous studies have revealed that the springtime NAT can significantly influence the EASM. It affects the EASM through triggering atmospheric teleconnection wave trains over Eurasia, which subsequently lead to circulation anomaly in the mid–high latitude area. In addition, it is found that the anomalous convective activities in the tropical Atlantic corresponding to the NAT play an important role in the anomalous cyclone/anticyclone near the Philippines (Zuo et al., 2013, 2018). The composite circulation pattern at 500 hPa in the summer following a positive springtime NAT (Fig. 11c) shows that there is a significant positive geopotential height anomaly center near the Balkhash Lake and a negative center near the Ural Mountains. This suggests that the blocking activity near the Ural Mountains is suppressed, which is not favorable for the strengthening and maintenance of the Meiyu front but is helpful for the intensification of the EASM. Meanwhile, there is an obvious anomalous cyclone located to the east of the Philippines (Fig. 11c), which has beneficial effects on the northward shift of the WPSH and a strong EASM. The anomalous circulation in summer 2018 (Fig. 5b) has shown similar features to the composite circulation pattern in positive NAT years (Fig. 11c) in the mid–high latitude regions. It is therefore deduced that the positive phase NAT probably exerts a significant influence on the circulation over the mid–high latitudes in summer 2018. Moreover, the NAT might also contribute to the anomalous cyclonic circulation around the Philippines in summer 2018.

5.3 *Influences of Tibetan Plateau snow cover*

The Tibetan Plateau plays an important role in the formation and variation of the East Asian monsoon due to its special geographical location, topographical height, and remarkable seasonal to interannual variations of thermal condition (Liu et al., 1999; Wu et al., 2018). The area of snow cover is one of the most important variables used to reflect the thermal condition on the plateau, and it is also an important external forcing signal frequently used in the diagnosis and prediction of summertime climate in China in recent years (Chen et al., 2000; Peng et al., 2005). It has been revealed that the wintertime snow cover anomaly on the Tibetan Plateau can affect the EASM either by changing the thermal difference between the plateau and the surrounding oceans (Zhang and Tao, 2001) or by contributing to the formation of the cyclone/anticyclone anomaly near the Philippines in early summer (Ren et al., 2016). The composite circula-

tion pattern during the summers that follow those winters with less snow cover on the plateau shows negative geopotential height anomalies in the subtropical region of East Asia and an anomalous cyclone near the Philippines (Fig. 11d). The above circulation pattern indicates a strong EASM, and such a snow–EASM relationship is consistent with the results found in previous studies (Zhang and Tao, 2001; Ren et al., 2016). In the 2017/18 winter, the snow cover area on the plateau was obviously smaller than normal (Fig. 10d) and the summer circulation in East Asia (Fig. 5b) also showed characteristics similar to the composite circulation pattern in less snow years (Fig. 11d). The above result indicates that the less than normal snow cover over the Tibetan Plateau in the winter of 2017/18 has also contributed to the strong EASM in the following summer of 2018.

5.4 *Combined impacts of the tropical SST, North Atlantic SST, and Tibetan snow cover on the EASM*

The above analyses have revealed that the strong EASM in summer 2018 is a result of the combined impacts of the La Niña event, the cold IOBW, the positive NAT, and the less than normal snow cover over the Tibetan Plateau. Since the variability of IOBW mainly arises from ENSO events, the influence of the IOBW on the EASM is not independent of ENSO impact. Furthermore, the correlations of the NAT index and the plateau snow cover index with the EASM index are still significant after the ENSO signal is removed, which indicates that the influences of the NAT and the snow cover on the EASM are also independent of ENSO. Therefore, when the combined effects of external factors are examined, only the La Niña event, the NAT, and the Tibetan snow cover are considered as three independent factors.

Linear regression equations for the summer circulation are established by using the Nino3.4 index, the NAT index, and the Tibetan snow cover index as predictors, respectively. The data from 1982 to 2017 are used to establish the equations. The circulation in summer 2018 is then forecasted by using the three equations and values of individual predictors in 2018, respectively. Finally, predictions of the circulation in summer 2018 based on the three equations are added to represent the combined impacts of the three predictors. The results are displayed in Fig. 12, which shows obvious negative geopotential height anomalies in the tropical western Pacific region. These negative anomalies apparently correspond to the cyclonic circulation anomaly near the Philippines. Along the coastal region of East Asia, the "cyclone–anticyclone–cyclone" distribution from south to north represents a positive phase of the EAP teleconnection pattern. In the mid–high latitude region of Eurasia, two negative geopotential height anomaly centers are located near the Ural Mountains and the Okhotsk Sea, respectively, while a positive center is found to the north of the Lake Baikal. The characteristics of the predicted circulation anomaly described above are similar to those in the observations (Fig. 5b), implying that the combined impacts of the three factors all play key roles in the East Asian circulation in summer 2018. In Fig. 12, the shadings, the red bold lines, and blue bold lines indicate the areas where the La Niña event, the NAT, and the Tibetan snow cover are significantly correlated with the 500-hPa geopotential height anomaly. It can be seen that all the three factors contribute significantly to the negative geopotential height center in the tropical western Pacific and the

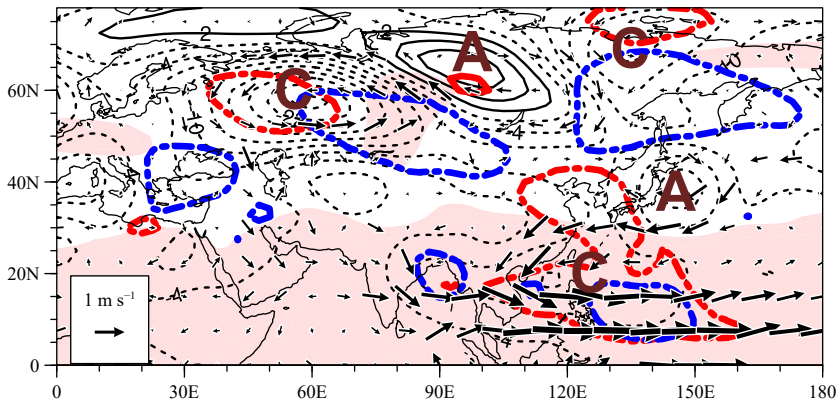

Fig. 12. Sum of the regressed values of 500-hPa geopotential height and 850-hPa wind in summer 2018 calculated according to the linear regression equations using the Niño3.4 index, the NAT index, and the Tibetan snow cover area index from 1982 to 2017, respectively. Black contours represent the 500-hPa geopotential height anomaly (gpm); vectors represent 850-hPa wind anomaly (m s^{-1}); and shadings, red thick lines, and blue thick lines indicate the areas where the correlations of the Niño3.4 index, the NAT index, and the Tibetan snow cover index with the geopotential height anomaly exceeding the significant level of 0.1. Letters A and C denote anomalous anticyclone and cyclone, respectively.

corresponding anomalous cyclone near the Philippines, while the anomalous geopotential height centers near the Ural Mountains and the Okhotsk Sea are largely related to variations of the NAT and snow cover over the Tibetan Plateau.

6. Comparative analysis of the EASM in typical years with combined influence of multiple factors

The key external forcing factors of the EASM, such as the tropical SST, the North Atlantic SST, and the Tibetan snow cover, have a complicated collaborative effect on summer climate in East Asia. Sometimes only one factor plays a dominant role, and sometimes multiple factors jointly contribute to the variation of the EASM. There are also cases in which different factors "cancel out" their impacts. The above analysis has shown clearly that in summer 2018, the tropical SST, the NAT, and the Tibetan snow cover all have reinforced their influences on the EASM circulation and these influences are consistent and collaborative; i.e., all of the three factors are favorable for a strong EASM, and they act together to have produced an extremely strong EASM in 2018.

Historical data of the three external factors since 1981 have been examined, and the EASM in 1985 is found to have features similar to that in 2018. The summer of 1985 also followed a weak La Niña event, the spring NAT was in a strong positive phase, and the wintertime Tibetan snow cover was less than normal. Correspondingly, circulation in East Asia and precipitation in China in summer 1985 are similar to their counterparts in summer 2018. The EAP pattern in its positive phase along the coast of East Asia, an anomalous cyclone near the Philippines, and a negative geopotential height center near the Ural Mountains are obvious features shown in the 500-hPa geopotential height and 850-hPa wind fields (Fig. 13a). The EASM in 1985 was also stronger than normal (Fig. 1). The main feature of precipitation in 1985 also resembled that of 2018, with negative anomalies dominating the regions around the Yangtze River valley and positive anomalies distributed mainly in North China (Fig. 14a).

Different from the situation in 1985, there are two other years with features of the external factors opposite to the case of 2018. Both the summers of 1983 and 1998 followed an El Niño event, the spring NAT in the two years was in strong negative phase, and the Tibetan snow cover in the winter was larger than normal. Correspondingly, the East Asian summer circulation and precipitation generally exhibited features opposite to that in the summers of 2018 and 1985. An anticyclone–cyclone–anticyclone circulation pattern developed along the coastal region of East Asia, corresponding to the EAP pattern in negative phase. Meanwhile, an anomalous anticyclone occurred near the Philippines and a positive geopotential height center appeared near the Ural Mountains (Figs. 13b, c). Under such a circulation circumstance, the EASM in 1983 and 1998 was much weaker than normal. According to the index defined by Zhang et al. (2003), 1998 is the weakest EASM year since 1981 (Fig. 1). In the summers of 1983 and 1998, there was more precipitation near the Yangtze River valley (Figs. 14b, c) and severe flooding disasters occurred (Li, 1999).

Comparative analysis of the EASM in typical anomalous years described above further demonstrates that ENSO event related SST anomaly, NAT, and the Tibetan snow cover all have significant influences on the EASM. Specifically, when the effects of the above factors are reinforced, their combined impact on the summer circulation and precipitation in East Asia could be highly significant.

7. Summary and discussion

According to the three representative EASM indices, the EASM in summer 2018 is found stronger than normal. Particularly, the index defined by Zhang et al. (2003) shows that 2018 is the strongest EASM year since 1981. The East Asian atmospheric circulation in summer 2018 also exhibits typical characteristics of a strong EASM. In the upper troposphere, the location of the East Asian subtropical jet is further north than normal in 2018. In the middle troposphere, the EAP in positive phase is obvious along the coastal region of East Asia and the ridge line of the WPSH is located more northward. In the lower troposphere, an anomalous cyclone occurs near the Philippines and an anomalous anticyclonic circulation appears to its north. Under the above circulation background, anomalous northerly winds occur to the south of the Yangtze River valley while southerly wind anomalies happen to the north. These circulation anomalies are favorable for the development of divergence and descending motion near the Yangtze River valley, and precipitation in this region is suppressed. For most of the northern areas of China, anomalous southerly winds are beneficial for the transfer of water vapor and more precipitation is thus induced. In addition, the features of mid–high latitude circulation also contribute to the strong EASM in 2018. Two negative geopotential height centers are located in the vicinity of the Ural

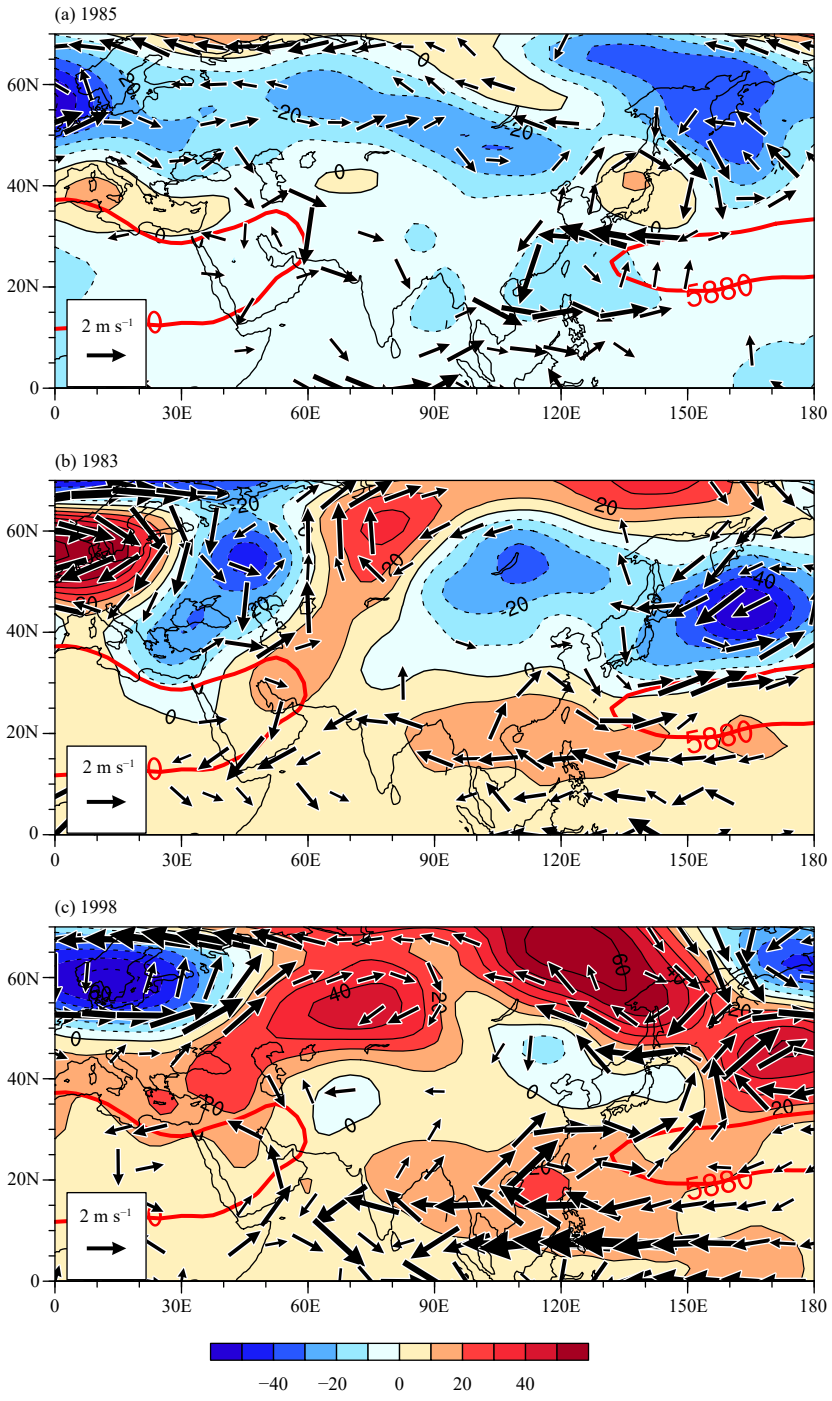

Fig. 13. 500-hPa geopotential height (gpm) and 850-hPa wind (m s^{-1}) anomalies in the summers of (a) 1985, (b) 1983, and (c) 1998. The red lines represent the climatology mean 5880-gpm contour.

Mountains and the Okhotsk Sea, respectively, and the blocking activities near the above two regions are suppressed, which weaken the Meiyu front, intensify the EASM, and promote more rainfall in the northern parts of China.

From winter 2017/18 to summer 2018, several key external forcing factors of the EASM, such as the La Niña event, the cold IOBW, the positive NAT, and the less than normal snow cover over the Tibetan Plateau all exhibit obvious anomalous features. The impacts of individual factors mentioned above are consistently favorable for the development of a strong EASM. A weak La Niña event occurred from October 2017 to April 2018, which triggered an anomalous cyclonic circulation near

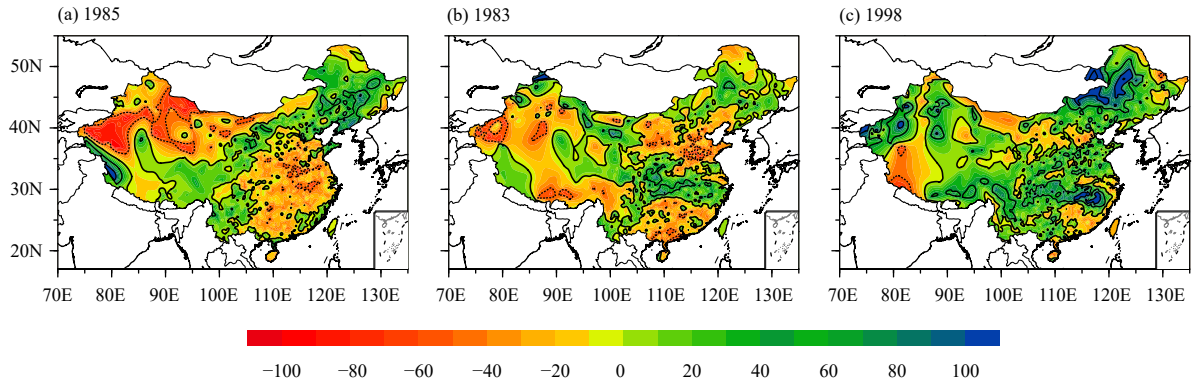

Fig. 14. Percentage precipitation anomalies (%) in the summers of (a) 1985, (b) 1983, and (c) 1998. Contour interval is 50% in each plot.

the Philippines during winter 2017. In response to the La Niña event, the IOBW entered its cold phase in the subsequent spring and summer, conducive to maintenance of the anomalous cyclone in the Philippine until summer. Meanwhile, the NAT in its positive phase in spring has weakened the blocking activities by triggering wave trains over Eurasia, resulting in a negative geopotential height center near the Ural Mountains. As a result, the Meiyu front is attenuated. The NAT in its positive phase might also contribute to the development of the cyclonic anomaly in the Philippines through remote teleconnection of the tropical atmosphere. Besides, the less than normal Tibetan snow cover in winter of 2017/18 is favorable for the strengthening of the thermal effect of the plateau in the subsequent spring and summer and further enhancement of the cyclonic anomaly in the Philippines in early summer, which further intensifies the EASM. It is concluded that the strong EASM in 2018 is closely related to the combined, reinforced, and collaborative effects of the La Niña event, the tropical Indian Ocean SST, the North Atlantic SST, and the Tibetan snow cover.

By examining the external factors that affect the EASM since 1981, it is found that the case in 1985 is similar to that in 2018, while the features in 1983 and 1998 are opposite to those in 2018. For the two groups of years with different characteristics, the East Asian summer circulation and precipitation in China exhibit opposite features. This result further demonstrates the importance of collaborative impacts of external forcing factors on the EASM, such as the tropical SST, the North Atlantic SST, and the Tibetan snow cover. With reinforced impacts of the above external factors, the anomalous feature of the EASM turns to be more remarkable. That is to say, the presence of such strong precursor signals is beneficial to improving the climate predictability and to more accurate climate prediction and better service for disaster prevention (Li, 1999; Chen et al., 2019). In the future, it is necessary to investigate the ability of dynamic climate models in simulating and predicting the combined effects of the multiple factors on the EASM and quantitatively analyze the contribution and the influencing mechanism of individual factors.

Acknowledgments. We thank the four anonymous reviewers for their constructive comments that led to improvements to this paper.

REFERENCES

Chen, L. J., Y. Yuan, M. Z. Yang, et al., 2013: A review of physical mechanisms of the global SSTA impact on the EASM. *J. Appl. Meteor. Sci.*, **24** , 521–532, doi: 10.3969/j.issn.1001-7313.2013.05.002. (in Chinese)

Chen, L. J., W. Gu, T. Ding, et al., 2016: Overview of the precursory signals of seasonal climate prediction in summer 2015. *Meteor. Mon.*, **42**, 496–506. (in Chinese)

Chen, L. J., W. Gu, Z. X. Gong, et al., 2019: Precursory signals of the 2018 summer climate in China and evaluation of the real-time prediction. *Meteor. Mon.*, **45**, 553–564. (in Chinese)

Chen, Q. J., B. Gao, W. J. Li, et al., 2000: Studies on relationships among abnormal winter snow cover over the Tibetan Plateau, Meiyu season droughts/floods in the middle–lower reaches of the Yangtze River, and atmospheric circulation patterns. *Acta Meteor. Sinica*, **58** , 582–595, doi: 10.11676/qxxb2000.060. (in Chinese)

Chen, X. F., and Z. G. Zhao, 2000: *Study on Precipitation Forecast in China During Flood Season and Associated Application*. China Meteorological Press, Beijing, 241 pp. (in Chinese)

Feng, J., L. Wang, and W. Chen, 2014: How does the East Asian summer monsoon behave in the decaying phase of El Niño during different PDO phases? *J. Climate*, **27**, 2682–2698, doi: 10.1175/JCLI-D-13-00015.1.

Feng, M., B. J. Wang, and S. Q. Xiong, 2000: Analysis on the abnormality of general circulation and sea temperature in relation to the flood water of Yangtze river in 1998. *Resour. Environ. Yangtze Basin*, **9** , 112–117, doi: 10.3969/j.issn.1004-8227.2000.01.017. (in Chinese)

Gao, H., and Y. G. Wang, 2007: On the weakening relationship

between summer precipitation in China and ENSO. *Acta Meteor. Sinica*, **65** , 131–137, doi: 10.11676/qxxb2007.013 . (in Chinese)

Gu, W., and L. J. Chen, 2019: Characteristics of atmospheric and oceanic conditions and their influence on summer climate of China in 2018. *Meteor. Mon.*, **45**, 126–134. (in Chinese)

Gu, W., C. Y. Li, X. Wang, et al., 2009: Linkage between Mei-yu precipitation and North Atlantic SST on the decadal timescale. *Adv. Atmos. Sci.*, **26** , 101–108, doi: 10.1007/s00376-009-0101-5.

Guo, Y. J., W. Li, and Q. J. Chen, 2004: An operational monitoring and diagnosing system for snow cover in the Northern Hemisphere. *Meteor. Mon.*, **30** , 24–27, doi: 10.3969/j.issn.1000-0526.2004.11.005. (in Chinese)

He, J. H., X. F. Zhi, and T. Nakazawa, 1995: Seasonal interlock of the intraseasonal variations of rainfall in East China. *J. Trop. Meteor.*, **11** , 370–374, doi: 10.16032/j.issn.1004-4965.1995.04.010. (in Chinese)

Huang, R. H., 1992: The East Asia/Pacific pattern teleconnection of summer circulation and climate anomaly in East Asia. *Acta Meteor. Sinica*, **6**, 25–37.

Huang, R. H., and W. J. Li, 1987: Influence of the heat source anomaly over the western tropical Pacific on the subtropical high over East Asia. Proc. International Conference on the General Circulation of East Asia, Chengdu, China, 40–51.

Huang, R. H., and Y. F. Wu, 1989: The influence of ENSO on the summer climate change in China and its mechanism. *Adv. Atmos. Sci.*, **6**, 21–32, doi: 10.1007/BF02656915.

Huang, R. H., W. Chen, Y. H. Ding, et al., 2003: Studies on the monsoon dynamics and the interaction between monsoon and ENSO cycle. *Chinese J. Atmos. Sci.*, **27** , 484–502, doi: 10.3878/j.issn.1006-9895.2003.04.05. (in Chinese)

Huang, R. H., J. L. Chen, L. Wang, et al., 2012: Characteristics, processes, and causes of the spatio-temporal variabilities of the East Asian monsoon system. *Adv. Atmos. Sci.*, **29** , 910–942, doi: 10.1007/s00376-012-2015-x.

Kalnay, E., M. Kanamitsu, R. Kistler, et al., 1996: The NCEP/NCAR 40-year reanalysis project. *Bull. Amer. Meteor. Soc.*, **77**, 437–472, doi: 10.1175/1520-0477(1996)077<0437:TNYRP>2.0.CO;2.

Kistler, R., E. Kalnay, W. Collins, et al., 2001: The NCEP–NCAR 50-year reanalysis: Monthly means CD-ROM and documentation. *Bull. Amer. Meteor. Soc.*, **82** , 247–268, doi: 10.1175/1520-0477(2001)082<0247:TNNYRM>2.3.CO;2.

Li, C. Y., R. H. Huang, J. F. Chou, et al., 2009: *The Study of Meteorological Disasters and Chinese Response*. China Meteorological Press, Beijing, 187 pp. (in Chinese)

Li, T., B. Wang, B. Wu, et al., 2017: Theories on formation of an anomalous anticyclone in western North Pacific during El Niño: A review. *J. Meteor. Res.*, **31**, 987–1006, doi: 10.1007/s13351-017-7147-6.

Li, W. J., 1999: General atmospheric circulation anomaly in 1998 and their impact on climate anomaly in China. *Meteor. Mon.*, **25**, 20–25, doi: 10.3969/j.issn.1000-0526.1999.04.004 . (in Chinese)

Liu, Y. M., G. X. Wu, H. Liu, et al., 1999: The effect of spatially nonuniform heating on the formation and variation of subtropical high. Part Ⅲ: Condensation heating and South Asian high and western Pacific subtropical high. *Acta Meteor. Sinica*, **57**, 525–538, doi: 10.11676/qxxb1999.051. (in Chinese)

Liu, Y. Y., W. J. Li, W. X. Ai, et al., 2012: Reconstruction and application of the monthly western North Pacific subtropical high indices. *J. Appl. Meteor. Sci.*, **23**, 414–423. (in Chinese)

Ma, Y., W. Chen, and L. Wang, 2011: A comparative study of the interannual variation of summer rainfall anomalies between the Huaihe Meiyu season and the Jiangnan Meiyu season and their climate background. *Acta Meteor. Sinica*, **69** , 334–343, doi: 10.11676/qxxb2011.028. (in Chinese)

Marshall, J., Y. Kushnir, D. Battisti, et al., 2001: North Atlantic climate variability: Phenomena, impacts and mechanisms. *Int. J. Climatol.*, **21**, 1863–1898, doi: 10.1002/joc.693.

Nitta, T., 1987: Convective activities in the tropical western Pacific and their impact on the Northern Hemisphere summer circulation. *J. Meteor. Soc. Japan*, **65**, 373–390, doi: 10.2151/jmsj1965.65.3_373.

Peng, J. B., L. T. Chen, and Q. Y. Zhang, 2005: Multi-scale variations of snow cover over QXP and tropical Pacific SST and their influences on summer rainfall in China. *Plateau Meteor.*, **24**, 366–377, doi: 10.3321/j.issn:1000-0534.2005.03.013 . (in Chinese)

Qian, Y. F., Y. Q. Zheng, Y. Zhang, et al., 2003: Responses of China's summer monsoon climate to snow anomaly over the Tibetan Plateau. *Int. J. Climatol.*, **23**, 593–613, doi: 10.1002/joc.901.

Ren, H.-C., W. J. Li, H.-L. Ren, et al., 2016: Distinct linkage between winter Tibetan Plateau snow depth and early summer Philippine Sea anomalous anticyclone. *Atmos. Sci. Lett.*, **17**, 223–229, doi: 10.1002/asl.646.

Ren, H.-L., B. Lu, J. H. Wan, et al., 2018: Identification standard for ENSO events and its application to climate monitoring and prediction in China. *J. Meteor. Res.*, **32** , 923–936, doi: 10.1007/s13351-018-8078-6.

Ren, Z. H., Y. Yu, F. L. Zou, et al., 2012: Quality detection of surface historical basic meteorological data. *J. Appl. Meteor. Sci.*, **23** , 739–747, doi: 10.3969/j.issn.1001-7313.2012.06.011. (in Chinese)

Reynolds, R. W., N. A. Rayner, T. M. Smith, et al., 2002: An improved in situ and satellite SST analysis for climate. *J. Climate*, **15** , 1609–1625, doi: 10.1175/1520-0442(2002)015<1609:AIISAS>2.0.CO;2.

Shi, N., Q. G. Zhu, and B. G. Wu, 1996: The East Asian summer monsoon in relation to summer large scale weather–climate anomaly in China for last 40 years. *Chinese J. Atmos. Sci.*, **20**, 575–583, doi: 10.3878/j.issn.1006-9895.1996.05.08 . (in Chinese)

Sun, S., D. Li, Z. Y. Wang, et al., 2019: Global major weather and climate events in 2018 and the possible causes. *Meteor. Mon.*, **45**, 533–542. (in Chinese)

Sung, M.-K., W.-T. Kwon, H.-J. Baek, et al., 2009: A possible impact of the North Atlantic Oscillation on the East Asian summer monsoon precipitation. *Geophys. Res. Lett.*, **33**, L21713, doi: 10.1029/2006GL027253.

Tao, S. Y., and Q. Y. Zhang, 1998: Response of the Asian winter and summer monsoon to ENSO events. *Chinese J. Atmos. Sci.*, **22** , 399–407, doi: 10.3878/j.issn.1006-9895.1998.04.02. (in Chinese)

Wang, B., R. G. Wu, and X. H. Fu, 2000: Pacific–East Asian teleconnection: How does ENSO affect East Asian climate? *J.*

Climate, **13** , 1517–1536, doi: 10.1175/1520-0442(2000)013<1517:PEATHD>2.0.CO;2.

Wang, L., and W. Gu, 2016: The eastern China flood of June 2015 and its causes. *Sci. Bull.*, **61** , 178–184, doi: 10.1007/s11434-015-0967-9.

Wu, G. X., Y. M. Liu, B. He, et al., 2018: Review of the impact of the Tibetan Plateau sensible heat driven air-pump on the Asian summer monsoon. *Chinese J. Atmos. Sci.*, **42**, 488–504, doi: 10.3878/j.issn.1006-9895.1801.17279. (in Chinese)

Xie, S.-P., K. M. Hu, J. Hafner, et al., 2009: Indian Ocean capacitor effect on Indo–western Pacific climate during the summer following El Niño. *J. Climate*, **22** , 730–747, doi: 10.1175/2008JCLI2544.1.

Xie, S.-P., Y. Kosaka, Y. Du, et al., 2016: Indo–western Pacific Ocean capacitor and coherent climate anomalies in post-ENSO summer: A review. *Adv. Atmos. Sci.*, **33** , 411–432, doi: 10.1007/s00376-015-5192-6.

Xu, P. Q., L. Wang, W. Chen, et al., 2019a: Structural changes in the Pacific–Japan pattern in the late 1990s. *J. Climate*, **32**, 607–621, doi: 10.1175/JCLI-D-18-0123.1.

Xu, P. Q., L. Wang, and W. Chen, 2019b: The British–Baikal corridor: A teleconnection pattern along the summertime polar front jet over Eurasia. *J. Climate*, **32**, 877–896, doi: 10.1175/JCLI-D-18-0343.1.

Ye, D. Z., S. W. Luo, and B. Z. Zhu, 1957: Wind structure and heat balance in the lower troposphere over the Tibetan Plateau and its surrounding. *Acta Meteor. Sinica*, **28** , 108–121, doi: 10.11676/qxxb1957.010. (in Chinese)

Yuan, Y., H. Gao, and Y. J. Liu, 2017: Analysis of the characteristics and causes of precipitation anomalies over eastern China in the summer of 2016. *Meteor. Mon.*, **43**, 115–121. (in Chinese)

Zhan, R. F., G. W. Sun, B. K. Zhao, et al., 2008: Quasi-biweekly oscillation of the subtropical summer monsoon rainfall over East China and its possible maintaining mechanism. *Plateau Meteor.*, **27**, 98–108. (in Chinese)

Zhang, H. X., W. P. Li, and W. J. Li, 2018: Influence of late springtime surface sensible heat flux anomalies over the Tibetan and Iranian Plateaus on the location of the South Asian high in early summer. *Adv. Atmos. Sci.*, **36** , 93–103, doi: 10.1007/s00376-018-7296-2.

Zhang, Q. Y., and S. Y. Tao, 2003: The anomalous subtropical anticyclone in western Pacific and their association with circulation over East Asia during summer. *Chinese J. Atmos. Sci.*, **27**, 369–380, doi: 10.3878/j.issn.1006-9895.2003.03.07 . (in Chinese)

Zhang, Q. Y., S. Y. Tao, and L. T. Chen, 2003: The interannual variability of East Asian summer monsoon indices and its association with the pattern of general circulation over East Asia. *Acta Meteor. Sinica*, **61** , 559–568, doi: 10.11676/qxxb2003.056. (in Chinese)

Zhang, R. H., A. Sumi, and M. Kimoto, 1996: Impact of El Niño on the East Asian monsoon: A diagnostic study of the '86/87 and '91/92 events. *J. Meteor. Soc. Japan*, **74** , 49–62, doi: 10.2151/jmsj1965.74.1_49.

Zhang, R. H., Q. Y. Min, and J. Z. Su, 2017: Impact of El Niño on atmospheric circulations over East Asia and rainfall in China: Role of the anomalous western North Pacific anticyclone. *Sci. China Earth Sci.*, **60** , 1124–1132, doi: 10.1007/s11430-016-9026-x.

Zhang, S. L., and S. Y. Tao, 2001: Influences of snow cover over the Tibetan Plateau on Asian summer monsoon. *Chinese J. Atmos. Sci.*, **25**, 372–390, doi: 10.3878/j.issn.1006-9895.2001.03.07. (in Chinese)

Zhang, Y., 2004: Research on the characteristics of the thermal parameters of the Tibetan Plateau and its climate effects. Ph.D. dissertation, Nanjing University, China, 18 pp. (in Chinese)

Zhao, C. B., T. J. Zhou, B. Li, et al., 2011: Intraseasonal oscillation of summer rainfall over eastern China simulated with a regional climate model. *Chinese J. Atmos. Sci.*, **35** , 1033–1045, doi: 10.3878/j.issn.1006-9895.2011.06.04. (in Chinese)

Zhao, J. H., R. Zhi, Q. Shen, et al., 2014: Prediction of the distribution of the 2012 summer rainfall in China and analysis of the cause for anomaly. *Chinese J. Atmos. Sci.*, **38**, 237–250, doi: 10.3878/j.issn.1006-9895.2013.12215. (in Chinese)

Zhu, C. W., J. H. He, and G. X. Wu, 2000: East Asian monsoon index and its interannual relationship with large scale thermal dynamic circulation. *Acta Meteor. Sinica*, **58**, 391–402, doi: 10.11676/qxxb2000.042. (in Chinese)

Zhu, Y. X., Y. H. Ding, and H. G. Xu, 2007: The decadal relationship between atmospheric heat source of winter and spring snow over Tibetan Plateau and rainfall in East China. *Acta Meteor. Sinica*, **65** , 946–958, doi: 10.11676/qxxb2007.089. (in Chinese)

Zuo, J. Q., W. J. Li, H.-L. Ren, et al., 2012: Change of the relationship between spring NAO and East Asian summer monsoon and its possible mechanism. *Chinese J. Geophys.*, **55** , 384–395. (in Chinese)

Zuo, J. Q., W. J. Li, C. H. Sun, et al., 2013: Impact of the North Atlantic sea surface temperature tripole on the East Asian summer monsoon. *Adv. Atmos. Sci.*, **30** , 1173–1186, doi: 10.1007/s00376-012-2125-5.

Zuo, J. Q., W. J. Li, C. H. Sun, et al., 2018: Remote forcing of the northern tropical Atlantic SST anomalies on the western North Pacific anomalous anticyclone. *Climate Dyn.*, **52**, 2837–2853, doi: 10.1007/s00382-018-4298-9.

Zwiers, F. W., 1993: Simulation of the Asian summer monsoon with the CCC GCM-1. *J. Climate*, **6**, 470–486, doi: 10.1175/1520-0442(1993)006<0469:SOTASM>2.0.CO;2.

Tech & Copy Editor: Lan YI and Qi WANG

陈丽娟,顾薇,龚振淞,等,2019. 影响 2018 年汛期气候的先兆信号及预测效果评估[J]. 气象,45(4):553-564. Chen L J,Gu W,Gong Z S,et al,2019. Precursory signals of the 2018 summer climate in China and evaluation of real-time prediction[J]. Meteor Mon,45(4):553-564(in Chinese).

影响 2018 年汛期气候的先兆信号及预测效果评估*

陈丽娟[1,2] 顾 薇[1] 龚振淞[1] 任宏利[1]

1 国家气候中心,中国气象局气候研究开放实验室,北京 100081

2 南京信息工程大学气象灾害预报预警与评估协同创新中心,南京 210044

提 要: 准确预测了 2018 年我国汛期降水"南北多,中间少,旱涝并重"的总体布局,尤其是准确预测了黄河流域降水异常偏多,而长江流域降水异常偏少的特征;对 2018 年东部地区季节内雨季进程前晚后早和夏季全国大部气温正常到偏高的预测也与实况一致;对西北太平洋和南海热带气旋生成和登陆我国的数量偏多、西北行和北上为主的移动路径、活跃程度前强后弱的预测与实况吻合。2018 年汛期气候预测重点分析了冬季达到盛期的拉尼娜事件及其衰减后热带印度洋海温偏低有利于东亚夏季风偏强的机理,还参考了国内外动力气候模式预测西太平洋副热带高压脊线偏北、菲律宾为气旋式异常环流的结果。对先兆信号影响的诊断分析以及动力模式的结果均预测东亚夏季风明显偏强,西太平洋副热带高压偏北,因此拉尼娜事件和印度洋海温对其滞后响应的偏冷特征是有利于预测汛期长江中下游地区降水明显偏少、北方地区降水偏多的重要先兆信号。

关键词: 拉尼娜事件,东亚夏季风,西太平洋副热带高压,夏季降水,评估

中图分类号: P461 **文献标志码:** A **DOI:** 10.7519/j.issn.1000-0526.2019.04.010

Precursory Signals of the 2018 Summer Climate in China and Evaluation of Real-Time Prediction

CHEN Lijuan[1,2] GU Wei[1] GONG Zhensong[1] REN Hongli[1]

1 Laboratory for Climate Studies, National Climate Centre, CMA, Beijing 100081

2 Collaborative Innovation Center on Forecast and Evaluation of Meteorological Disasters, Nanjing University of Information Science and Technology, Nanjing 210044

Abstract: In the summer (June to August) of 2018, precipitation was more than average over North China and South China, while it was less over the middle part of East China. Especially, floods were severe in the Yellow River Basin and droughts were observed in the Yangtze River Valley. The pre-flood season in South China and Meiyu season began later relatively, while the rainy season in North China began earlier. All these features were well predicted in the climate operation. The forecast also captured the anomalous features of the tropical cyclone frequency, tracks, intensity and active/inactive periods over the Northwest Pacific and South China Sea in 2018. Moreover, the forecast provided a correct prediction of the surface air temperature which was higher than average in most regions of China. Both diagnostic analyses and results from dynamic models were used to make the summer climate prediction in 2018. For the diagnostic analyses, La Niña event and the cold tropical Indian Ocean were considered to be important predictors. Under

* 国家重点基础研究发展计划(973 计划)(2015CB453203)、国家科技支撑计划项目(2015BAC03B04)及国家自然科学基金项目(41805067 和 41275073)共同资助

2019 年 2 月 11 日收稿; 2019 年 2 月 27 日收修定稿

第一作者:陈丽娟,主要从事气候异常机理诊断和短期气候预测研究. Email:chenlj@cma.gov.cn

通信作者:顾薇,主要从事气候异常机理诊断和短期气候预测研究. Email:guwei@cma.cn

the influence of the tropical SSTA, the western Pacific subtropical high (WPSH) tended to stay more northward, cyclonic circulation anomaly dominated the Philippines and the East Asian summer monsoon (EASM) was stronger than normal. Dynamic climate models from Beijing Climate Centre and abroad showed similar results of the prediction for the key members of EASM system. The results of diagnostic analyses and dynamic models all indicated that the La Niña event and the cold tropical Indian Ocean were important precursory signals for the prediction of the climate anomaly in summer 2018, which supported less rainfall in the middle and lower reaches of the Yangtze River and more in northern part of China.

Key words: La Niña event, East Asian summer monsoon (EASM), western Pacific subtropical high (WPSH), summer precipitation, evaluation

引 言

我国是世界上开展短期气候预测业务最早的国家之一(陈兴芳和赵振国,2000)。通过我国几代气象科技工作者的不懈努力,短期气候预测的业务能力、科技水平和现代化程度都迈上了一个新台阶(李维京,2012),进入了动力与统计相结合的预测方法为主导的发展阶段(贾小龙等,2013),预测结论每年都为各级政府部门部署防汛抗旱和防灾减灾工作提供决策支撑。但是短期气候预测涉及气候系统多因子在多时间尺度上复杂的相互作用(陈丽娟等,2013b),而目前国内外气象工作者对气候变异机理的认识仍不够全面和深入,各种客观预测方法仍不够完善(Wang et al,2015),因此短期气候预测仍然是一个世界性难题。在这样的背景下,及时总结短期气候预测业务和服务的成败将有助于气象工作者提高认知能力,并提出问题,进一步推动短期气候预测研究的发展。为此国家气候中心每年及时总结汛期气候预测成败的成因(陈丽娟等,2016;高辉等,2017;王永光和郑志海,2018),分析汛期气候异常的机理(Yuan et al,2017;郑志海和王永光,2018),从而提高对东亚气候变异机理的认识,总结预测方法的适用性,进一步提高短期气候预测水平和服务能力。本文首先回顾了对2018年汛期降水、汛期气温、年热带气旋、东部雨季季节进程、主要气象灾害及衍生灾害的预测效果,然后总结了发布汛期预测前重点考虑的多时间尺度先兆信号以及这些信号的应用,最后就季节气候预测的可预报性和今后需要深入研究的问题进行了讨论。

1 资 料

本文用到的降水和气温资料来自中国气象局国家气象信息中心发布的《中国国家级地面气象站基本气象要素日值数据集(V3.0)》(任芝花等,2012),资料时段为1951—2018年。大气环流资料为NCEP/NCAR逐月再分析资料中的位势高度场、水平风场等变量,资料水平分辨率为2.5°×2.5°(Kalnay et al,1996; Kistler et al,2001)。海温资料来自英国气象局哈德莱中心,数据水平分辨率为1°×1°(Rayner et al,2003)。各类数据的气候平均场均取1981—2010年平均。本文中冬季指上一年12月至当年2月平均,春季指3—5月平均,夏季指6—8月平均。

本文使用的动力气候模式数据分别来自:(1)国家气候中心BCC_CSM1.1(m)海气耦合模式,其中大气分量模式的水平分辨率为T106,垂直方向为26层(吴统文等,2013),模式气候态为1991—2010年;(2)欧洲中心的ECMWF耦合模式,模式分辨率1.5°×1.5°,气候态为1981—2010年*;(3)美国国家海洋和大气局(NOAA)的CFS V2耦合模式,模式分辨率1.0°×1.0°,气候态为1982—2010年**。

2 2018年夏季气候预测效果评估

2018年的汛期气候预测比较成功,预测东亚夏季风偏强、我国降水呈"南北多,中间少"分布、全国大部地区气温较常年偏高、生成和登陆台风较常年偏多,均与实况吻合。对汛期内主要气候事件(华南

* https://www.ecmwf.int/en/forecasts/accessing-forecasts

** http://cfs.ncep.noaa.gov/cfsv2/downloads.html

前汛期、梅雨和华北雨季等)的开始和强度趋势预测也与实况一致,3 月底发布汛期降水预测评分为 77 分,气温为 95 分,均为有汛期预测业务记录以来最好成绩。

2.1　降水

对比 2018 年汛期(6—8 月)降水量距平百分率实况及 3 月底和 5 月底发布的预报(图 1)可见,2018 年汛期预报准确把握了汛期"降水南北多,中间少,旱涝并重"的特征。3 月底发布的预测(图 1b)指出"长江中下游地区降水较常年异常偏少,偏少幅度达 20%～50%;黄河流域降水异常偏多,上中游偏多 20%～50%",对比实况(图 1a)可以看到,这次预报不仅正确给出主要旱涝区域的分布特征,而且对于这些区域旱涝程度的预测都与实况一致。此外,从实况(图 1a)来看,2018 年汛期我国北方地区多雨的特征十分突出,东北、华北和西北等北方地区平均降水量为 307.1 mm,较常年平均(263.0 mm)偏多 17%,列 1998 年之后的第二位(顾薇和陈丽娟,2019),汛期预测(图 1b 和 1c)也较好地抓住了这一特征,对华北和西北地区降水偏多程度和范围的预测与实况一致。但不足的是对东北地区的预测与实况偏差较大。在对全国七大江河的预测中,指出"黄河流域、海河流域、珠江流域要注意防范汛情",较好预测了主要流域的汛情特征,但是对辽河流域有汛情的预测与实况有偏差。在 5 月底订正预报(图 1c)中,维持"降水南北多,中间少,旱涝并重"等基本结论不变,但根据东北冷涡活动可能偏弱的特征,扩大了东北北部降水偏少的范围,并将北方多雨区和长江中下游少雨中心南移,东南沿海降水偏多范围缩小,西南地区降水范围扩大加强。这次订正对南方主要区域的预测更接近实况,但对北方多雨区的预测与实况的偏差有所加大。

2.2　气温

2018 年 3 月底发布预测指出"全国大部地区气温偏高,其中甘肃西部、青海北部、新疆大部、内蒙古西部等地偏高 1～2℃。盛夏西北地区西部、江淮、江汉、江南北部等地区高温(≥35℃)日数较常年同期偏多,可能出现阶段性高温热浪。初夏东北地区出现持续性低温的可能性小"(图 2b)。实况是 2018 年夏季全国平均气温为 21.9℃,较常年同期(20.9℃)偏高 1℃,为我国夏季平均气温有记录以来最高的一年(顾薇和陈丽娟,2019)。从空间分布特征来看,除华南南部气温较常年同期略偏低以外,全国大部分地区气温较常年同期偏高,江淮、江汉、华北、东北南部、西北大部和内蒙古大部气温偏高 1～2℃(图 2a)。根据国家气候中心监测,2018 年夏季全国平均高温日数仅次于 2017 和 2013 年,位列历史第三,江南、黄淮、西南地区东部等地 35℃以上高温日数偏多 10 d 以上。汛期的气温预测体现出全国气温偏高以及南方高温日数偏多等主要趋势特征,与实况一致,但是对北方高温的强度预计不足,尤其是北方 55 站高温突破历史极值,值得进一步诊断分析其成因。

2.3　热带气旋

对 2018 年在西北太平洋和南海地区的热带气旋(TC)活动趋势的预测是成功的,对 TC 的生成个数、登陆个数、平均强度、主要影响区域、活跃时段、路径、初终台时间等的预测均与实况比较一致(表 1)。

预测意见中指出"可能有一个台风北上登陆(在杭州湾以北地区)""台风活动路径以西北行和北行为主,对华南东部和华东沿海影响较大"。实况显示 2018 年 TC 活动路径明显偏北,有 4 个台风在中国浙江—上海—江苏一带沿海地区登陆,远远多于常年平均(1 个),其中有 3 个台风在上海登陆,为北上登陆台风个数最多的一年。夏季平均登陆 TC 强度为 26 $m \cdot s^{-1}$(10 级),比多年平均的 32.8 $m \cdot s^{-1}$(12 级)偏弱。虽然登陆 TC 强度总体偏弱,但降水强度大,给登陆地区和 TC 经过区域(华东、华北东部和东北地区南部、华南)带来强降雨影响。同时,对台风初次、末次登陆我国日期早晚趋势的预测也与实况一致,2018 年台风初次登陆我国的时间为 6 月 6 日,较常年(平均 6 月 28 日)偏早,末次登陆我国的时间为 9 月 13 日,也较常年(平均 10 月 6 日)偏早。此外,对于台风活动阶段性变化特征的预测也与实况吻合,预测意见中指出"台风活动在春末至初秋较常年同期活跃,呈现前期生成偏多、后期生成偏少的特点"。实况显示,2018 年夏季(6—8 月)西北太平洋生成 TC(18 个)和登陆中国的 TC(8 个)都明显高于常年同期平均值,其中生成 TC 频次列 1951 年以来的第二位,而登陆 TC 的频次列第一位,说明 2018 年夏季是 TC 活动异常活跃的时段。

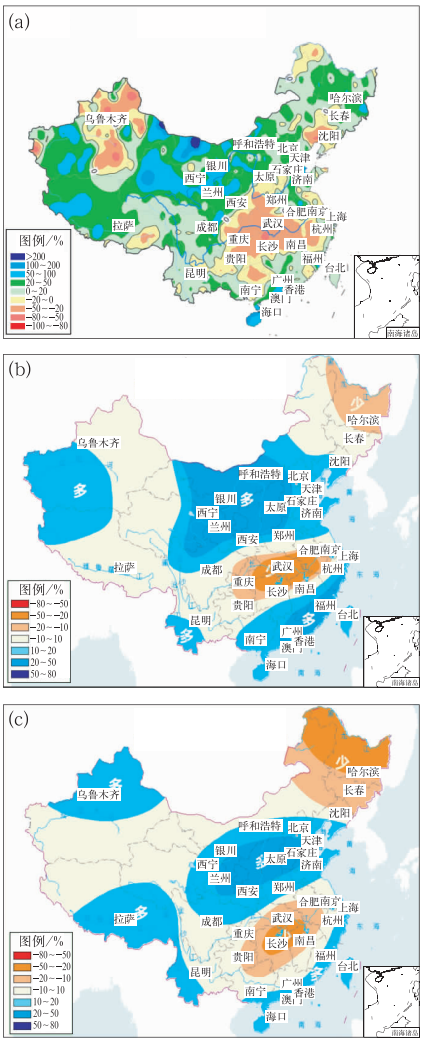

图 1 2018 年汛期(6—8 月)降水量距平百分率
(a)实况,(b)3 月底发布预报,
(c)5 月底发布预报

Fig. 1 Precipitation anomaly percentages in 2018 flood season (June—July—August)
(a) observation, summer forecast issued in (b) the end of March 2018 and (c) the end of May 2018

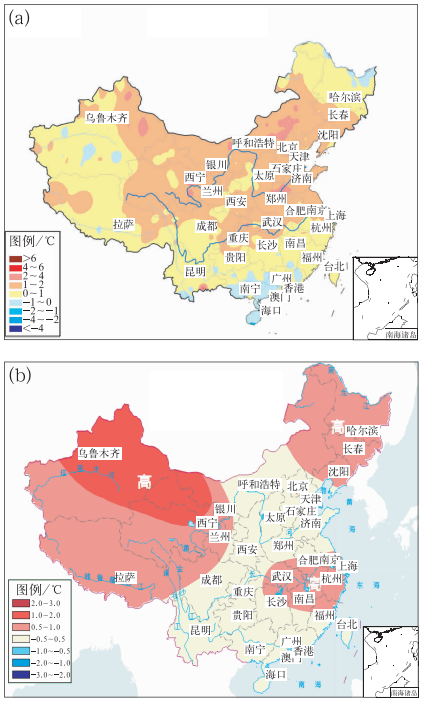

图 2 2018 年汛期(6—8 月)气温距平
(a)实况,(b)3 月底发布预报

Fig. 2 Air temperature anomaly in 2018 flood season (June—July—August)
(a) observation, (b) summer forecast issued in the end of March 2018

进入秋季(9—11 月)之后,TC 活动明显减弱,生成数量(8 个)和登陆数量(2 个)均分别低于常年同期的 10.9 和 2.4 个,体现了前期活跃后期减弱的阶段性特征(表 2)。

台风预测时主要考虑了 2017 年 10 月至 2018 年 4 月的拉尼娜事件衰减以及印度洋海温偏低对 TC 生成的影响。在这种海温背景下,西太平洋季风槽东段延伸到150°E附近,西太平洋副热带高压

表 1 2018 年热带气旋预测和实况对比

Table 1 Prediction and observation of tropical cyclone features over Northwest Pacific and South China Sea in 2018

预测对象	预测	实况	评估
生成	26～28 个	29 个(偏多)	趋势一致
登陆	7～9 个	10 个(偏多)	趋势一致
路径	西北行和北行为主	西北行和北上转向占优	趋势一致
登陆强度	偏弱	偏弱	趋势一致
影响区域	华南东部和华东沿海	华东、华北东部和东北南部、华南	趋势一致
活跃阶段	前强后弱	夏季强秋季弱	趋势一致
初台时间	偏早	6 月 6 日(偏早)	趋势一致
终台时间	偏早	9 月 13 日(偏早)	趋势一致

表 2　2018 年逐月生成 TC 数量

Table 2　Monthly numbers of TC geneses over the Northwest Pacific (0°－30°N, 100°－180°E) in 2018 and average values (1981－2010)

月份	1	2	3	4	5	6	7	8	9	10	11	12
2018	1	1	1	0	0	4	5	9	4	1	3	0
多年平均	0.3	0.1	0.3	0.6	1.0	1.7	3.7	5.8	4.9	3.7	2.3	1.1

(以下简称副高)偏北,有利于 TC 生成偏多,且以西北行和北上转向型为主,西行 TC 明显偏少(谢佩妍等,2018)。

2.4　东部雨季季节进程

我国东部地区的雨带随着夏季风进程自南向北推进。夏季风进程明显受到 ENSO 循环的影响(Zhou and Chan,2007),同时还可能受到次季节尺度大气环流(如低频振荡)的作用(李文铠等,2014;李春晖等,2016)。因此在 2018 年预测和服务时不仅考虑了不同时间尺度先兆信号的共同作用,而且还在滚动订正预测中参考临近动力气候模式的预测信息,充分考虑次季节尺度系统的特征及对夏季风进程的影响,从而较好地把握住了 2018 年汛期夏季风和各主要雨季进程早晚的总体特征(表 3)。如果单纯考虑恩索循环的影响,2017 年 10 月至 2018 年 4 月发生的拉尼娜事件有利于 2018 的夏季风进程偏早。然而在 2018 年春、夏季,热带大气低频振荡活动在 3 月下旬至 4 月上旬和 6 月上中旬都表现出阶段性活跃的特征,并分别影响了华南前汛期、南海夏季风爆发的时间,造成季节进程较常年平均滞后。在 3—5 月实时监测和预测中注意到了大气低频振荡的异常特征,并根据其影响及时订正了对气候事件开始早晚的预测,使得预测与实况更加一致。此外,对于江淮、长江中下游、江南三个区域梅雨和华北雨季季节进程早晚和雨季强度的预测也与实况基本一致(表 3)。

表 3　2018 年汛期主要气候事件的预测与实况对比

Table 3　Prediction and observation of major climate events in 2018 flood season

雨季名称	开始时间	结束时间	雨季长度	雨量	预测时间	预测强度
华南前汛期	4 月 21 日 (晚 15 d)	6 月 30 日 (晚 4 d)	70 d (短 18 d)	592 mm (少 19%)	开始偏晚	雨量偏少
江南梅雨	6 月 19 日 (晚 11 d)	7 月 13 日 (晚 5 d)	25 d (短 5 d)	249.2 mm (少 32%)	开始偏晚 结束偏早	雨量偏少
长江中下游梅雨	6 月 22 日 (晚 8 d)	7 月 13 日 (早 1 d)	21 d (短 8 d)	170.4 mm (少 39%)	开始偏晚 结束偏早	雨量偏少
江淮梅雨	6 月 28 日 (晚 7 d)	7 月 10 日 (早 5 d)	12 d (短 12 d)	172.8 mm (少 35%)	开始偏晚 结束偏早	雨量偏少
华北雨季	7 月 9 日 (早 9 d)	8 月 7 日 (早 11 d)	29 d (短 3 d)	165.6 mm (多 22%)	开始偏早 结束偏早	雨量偏多

2.5　汛期内主要气象及衍生灾害预测

国家气候中心除发布气温、降水和台风等常规气象要素的趋势预测外,还基于预测结果开展气象灾害展望和防御建议,提供有针对性的气象灾害预测结果,以便更好地为国家的防灾减灾决策服务。3 月发布的汛期主要气象灾害预测(图 3)取得了较好的服务效果。在暴雨洪涝预测中指出“黄河流域、海河流域、珠江流域、辽河流域要注意防范汛情”,实况是黄河流域 7 月下旬形成 1 号和 2 号洪峰,造成陕西洪涝灾害严重,宁夏出现汛情;珠江流域 6 月受台风活动的影响,出现局部洪涝;海河流域和辽河流域 7 月受强降水和台风活动北上的影响,出现局部洪涝(张芳和何立富,2018;张夕迪和孙军,2018)。在气象干旱预测中指出“东北北部、江淮西部、江汉南部、江南北部、西南地区东部可能有气象干旱发生”,实况是 5—6 月东北地区发生干旱,7—8 月缓解;6—7 月江南北部发生重度气象干旱,局部特旱;7—8 月江淮西部、江汉南部、西南地区东部发生中度-重度气象干旱。在高温热浪预测中指出“西北地区西部、江淮、江汉、江南北部等地可能出现阶段性高温热浪”,实况是5月江南、华南地区出现持续性高

温;6月下旬华北出现极端高温;7—8月中东部地区出现持续性高温(周晓敏和张涛,2018;张芳和何立富,2018;张夕迪和孙军,2018;王晴和张玲,2018),主要漏报了华北地区的高温,对其他区域高温情况的预测总体与实况一致。在山洪地质灾害预测中指出"西北地区中东部、华北西部、西南地区北部出现山洪地质灾害可能性大",实况显示6—8月西北地区东部和西南地区北部多次发生地质灾害,预测预警与实况吻合。

3 2018年汛期预测先兆信号及应用

2018年的汛期预测及服务能取得好效果,与发布预测前对气候系统先兆信号的全面分析以及对动力气候模式有效信息的提取密不可分。尤其是在众多信号面前,如何提取主导信号并把握各主导信号的协同作用很重要。首先对预报对象和预报因子的多时间尺度特征进行了分析,从年代际尺度、年际尺度和次季节尺度等多方面进行诊断,并在不同超前时段提供详略不同的预测信息:3月底给出汛期气候趋势展望;4月底至5月底根据亚洲夏季风的季节推进特征,对汛期气候趋势进行订正,同时提供季节内气候事件特征的趋势预测;6—8月,根据动力气候模式提供的最新预测以及夏季风推进的特点,给出季节内气候事件的开始(结束)时间及强度等详细预测信息。

3.1 年代际尺度先兆信号

预报对象和预报因子的年代际尺度特征是预报员进行气候预测时首先关注的内容。我国汛期主雨带有明显的年代际变化特征(陈丽娟等,2013a),这和北太平洋年代际涛动(Pacific decadal oscillation,PDO*)冷暖位相的变化有密切的联系。在PDO暖位相期,东亚夏季风偏弱,副高偏南,华北地区降水异常偏少,而长江中下游降水异常偏多(朱益民和杨修群,2003)。监测显示2014年9月,PDO指数由负转正,持续到2018年2月均为明显的正值(图4),说明PDO处于暖位相。而2015—2017年,我国汛期多雨区均位于南方地区,夏季风总体不强,与PDO的暖位相特征是一致的(陈丽娟等,2016;高辉等,2017;王永光和郑志海,2018)。进入2018年以来PDO指数表现出明显减小的特征,并在3月在这一汛期预测分析的关键时间节点转为负值,这种变化提示PDO暖位相的影响将减弱,不能作为主导信号,应更多地关注年际变化信号的影响。后期PDO指数的监测显示,至2018年9月,PDO指数一直较弱,在0附近波动,最大不超过0.2,证明当初的判断是正确的。

3.2 年际尺度先兆信号

继2014—2016年赤道中东太平洋发生了一次超强厄尔尼诺事件之后,2017年10月至2018年4月,赤道中东太平洋发生一次弱的东部型拉尼娜事件,并于2018年1月达到峰值。该事件强度较弱,持续时间也不长,有分析认为对我国2017/2018年冬季和2018年春季气候的影响不显著(章大全和宋文玲,2018;王遵娅等,2018)。在2018年3月国内外多数动力模式预测赤道中东太平洋海温在夏季为中性状态,那么该事件是否能成为影响我国夏季气候的主导信号呢?已有研究显示厄尔尼诺与拉尼娜事件对我国气候的影响具有明显的不对称性(Huang and Wu,1989;薛峰和刘长征,2007),而拉尼娜事件,尤其是弱拉尼娜事件对我国气候影响的不确定性更大,需要深入诊断。

为准确把握这次拉尼娜事件对我国气候的影响,进一步监测诊断了热带和副热带大气和热带印度洋海温的特征,结果表明,2017/2018年冬季和2018年3月的沃克环流显示出对拉尼娜事件的响应,冬季在热带西太平洋120°~160°E区域上升气流增强,170°E~120°W区域下沉气流也有所增强(图5a);2018年3月,沃克环流进一步增强,西太平洋上升气流区西扩至100°E,170°E以东的下沉支也明显增强。在850 hPa风场距平上,菲律宾附近为异常气旋式环流(图5b),显示了对拉尼娜事件的显著响应(Wang and Zhang,2002)。在菲律宾附近异常气旋式环流的影响下,冬季长江以南地区受到偏东北风距平的控制,降水明显偏少。此外,热带印度洋全区一致海温模态(IOBW)指数在2014年春季至2017年秋季总体表现出较强的正值,说明热带印度洋以偏暖特征为主。而进入2017年至2018年冬

* PDO指数定义和数据见 http://research.jisao.washington.edu/pdo/PDO.latest.txt。

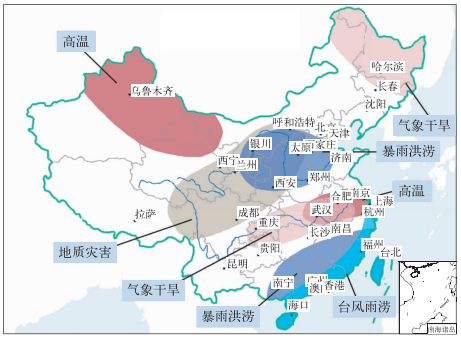

图 3　2018 年汛期(5—9 月)
主要气候灾害预测
Fig. 3　Major climate disaster prediction
in 2018 flood season (MJJAS)

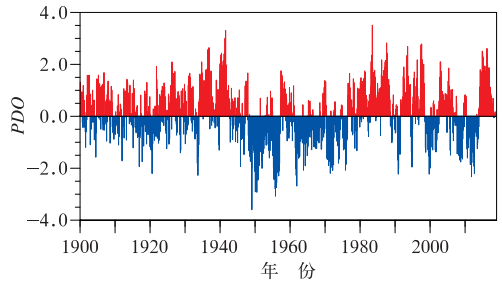

图 4　1900 年 1 月至 2018 年 9 月
PDO 指数逐月演变
Fig. 4　Monthly PDO indices from
January 1900 to September 2018

季之后，IOBW 指数明显减弱，表现出冷海温的特征(图 6)，说明印度洋海温对这次弱拉尼娜事件表现出明显的滞后响应。在 3 月分析评估了国内外动力气候模式对全球海温 2018 年春、夏季的预测，多数模式预测印度洋海温持续偏低，说明春、夏季印度洋对拉尼娜事件的这种滞后响应依然明显。偏冷的印度洋将有利于东亚夏季风偏强，从而起到对拉尼娜事件影响的“接力”作用(Xie et al，2009)。实况显示，动力模式对春、夏季印度洋海温的预测是正确的，而根据印度洋海温在春、夏季的发展趋势来考虑拉尼娜事件对东亚气候的影响显著也是成功的。事实上，近些年的研究工作深入揭示出印度洋海温对东亚夏季风的显著影响和机制(Xie et al，2009；2016)，因此在近几年的汛期预测业务当中，印度洋海温都被当做东亚夏季风的关键影响因子加以重点考虑，如 2015 和 2016 年的汛期预测都正确把握了东亚夏季风偏弱的特征，当时对春、夏季印度洋偏暖特征及其影响的考虑则是预测正确的重要原因之一(陈丽娟等，2016；袁媛等，2016；2017；Yuan et al，2017；高辉等，2017)。

2017/2018 年冬季以来印度洋冷海温的发展趋势及其对拉尼娜事件的“接力作用”说明夏季东亚地区环流和降水将会表现出对冬季拉尼娜事件/状态较典型的滞后影响。因此根据 2017/2018 年冬季以来赤道中东太平洋海温演变特征，选取 1990 年以来 Nino3.4 指数在冬季达到最低值(低于−0.5℃)，并于春夏季升温至中性状态附近的 8 个相似年(图 7a：1996、1997、2001、2006、2008、2009、2012 和 2017 年)对夏季环流和降水进行合成。结果显示，冬季拉尼娜状态有利于夏季菲律宾附近出现气旋性

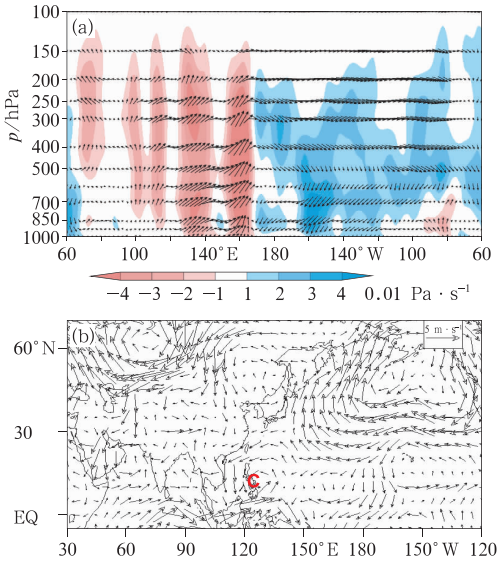

图 5　2017—2018 年冬季热带(5°S～5°N)
经向垂直风距平(a)和 850 hPa 风场距平(b)
Fig. 5　Meridional-vertical wind anomaly
averaged over (5°S—5°N) (a) and
850 wind anomaly (b) in 2017/2018 winter

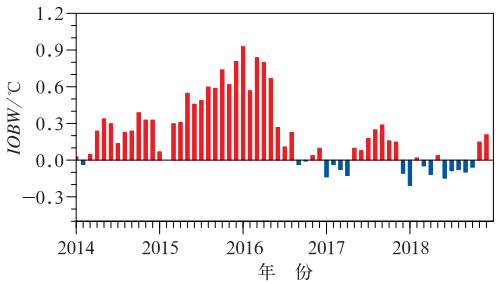

图 6　2014—2018 年热带印度洋全区一致
海温模态(IOBW)指数的逐月演变
Fig. 6　Monthly IOBW index from 2014 to 2018

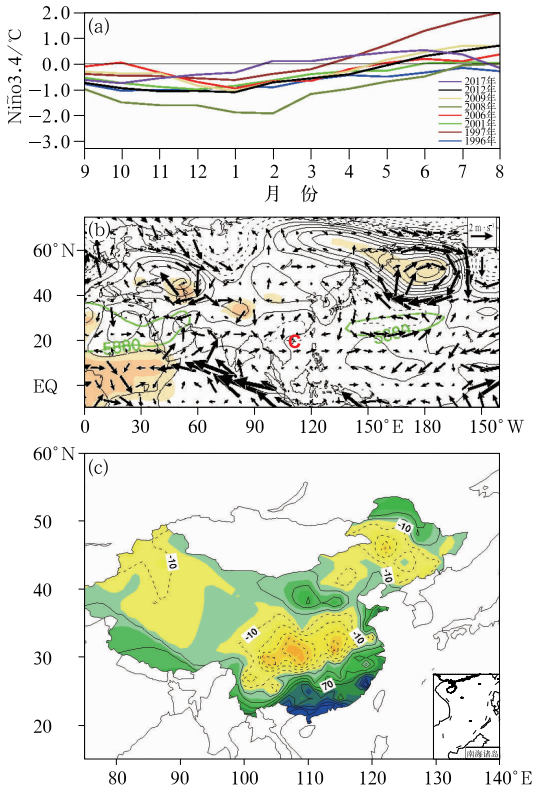

图 7 海温演变相似年的(a)Niño3.4 指数的逐月演变,夏季(b)500 hPa 高度场(等值线,间隔 3 gpm;阴影表示通过 0.10 显著性水平检验区域;绿色实线:气候平均 500 hPa 上 5880 gpm 等值线)、850 hPa 风场(矢量)和(c)降水距平的合成(单位:mm)

Fig. 7 (a) Monthly Niño3.4 index, composite maps of summer (b) 500 hPa geopotential height (contours, interval: 3 gpm; shadings: the regions exceeding the 0.10 significance level; green solid line: the climatology 5880 gpm contour at 500 hPa) and 850 hPa wind anomaly and (c) precipitation anomaly of similar years based on La Niña evolution (unit: mm)

距平环流、副高偏弱偏北、东亚夏季风偏强(图 7b),我国东部地区有南北两条多雨带,北方多雨带中心位于河套地区,南方多雨带中心位于江南南部至华南;长江 、江汉地区降水明显偏少(图 7c)。

除海温异常信号外,国家气候中心监测显示 2017/2018 年冬季的青藏高原积雪较常年偏少 0.7 个标准差,且 BCC_CSM1.1(m)模式预测春季积雪持续偏少。根据已有研究(张顺利和陶诗言,2001;陈兴芳和宋文玲,2000;竺夏英等,2013),高原积雪偏少,经过热力异常和动力异常的作用,有利于东亚夏季风偏强,长江流域易旱。高原积雪对东亚夏季风和我国降水的这种影响与拉尼娜事件的影响是一致的。监测还显示北大西洋海温三极子模态(NAT)在 2018 年 2 月以来持续正位相,可能影响到春末到夏初的欧亚中纬度环流,不利于乌拉尔山和鄂霍茨克海出现阻塞形势(Zuo et al,2013),从而不利于长江流域和江淮地区降水偏多。北大西洋三极子对东亚夏季风和我国降水的影响也与拉尼娜事件的影响是一致的。关于多因子共同影响东亚夏季风的机理将另文撰写发表。

3.3 动力气候模式的预测

除物理诊断外,还分析评估了大量国内外动力气候模式的预测结果。以国家气候中心 BCC_CSM1.1(m)的 500 hPa 环流场预测(图 8)为例,模式预测北半球中纬度欧亚大陆地区以纬向环流为主,在 60°E 以西的欧洲地区为正距平,60°E 至贝加尔湖为负距平,贝加尔湖以东至鄂霍次克海地区为正距平;东亚地区从高纬度到低纬度为北高南低型。其他国外主要业务中心(如 NCEP CFCv2、ECMWF、TCC 等)的动力模式对欧亚环流型的预测与国家气候中心类似(图略),最一致的特征都是预测东亚地区为北高南低的形势。由于西太平洋副高和菲律宾反气旋对东亚夏季风和我国汛期气候有直接的影响,对比了各模式预测的副高指数[定义见刘芸芸等(2012)]和菲律宾反气旋指数[定义见 Wang et al (2000)]。结果显示,ECMWF 模式预测夏季副高显著偏强偏西偏北,BCC_CSM1.1(m)和 CFS V2 预测夏季副高强度接近常年、位置偏东偏北。此外,

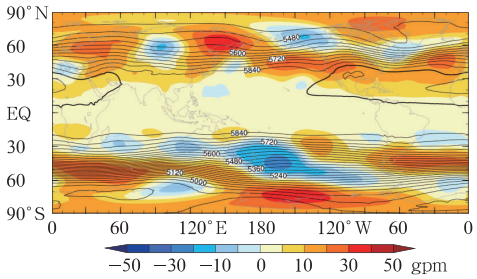

图 8 BCC_CSM1.1(m)模式 2018 年 3 月起报的 2018 年夏季 500 hPa 高度场(阴影为距平)

Fig. 8 Prediction of summer 500 hPa geopotential height anomaly by BCC_CSM1.1(m) initiated from March 2018 (Shading is anomaly)

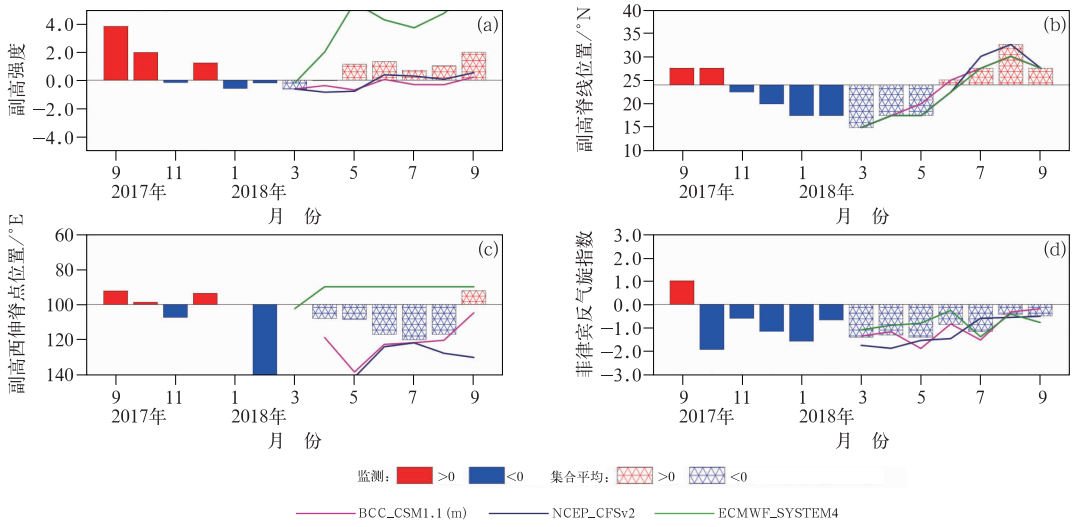

图 9　多模式 2018 年 3 月起报的逐月副高强度(a)、副高脊线南北位置(b)、副高西伸脊点位置指数(c)和菲律宾反气旋指数(d)

Fig. 9　(a) Strength index, (b) ridgeline position index, (c) westward position index of the subtropical high and (d) anticyclone index over the Philippines predicted by multi-models initiated from March 2018

三个模式均预测菲律宾反气旋指数为负值,即菲律宾附近为气旋性环流距平。三个模式集合平均的结果预测副高强度略偏强,位置偏东偏北(图 9)。实况显示,上述各动力气候模式对夏季热带和副热带主要环流型的预测效果较好,但对东北亚地区的环流预测偏差较大(顾薇和陈丽娟,2019),各动力模式一致预测鄂霍茨克海地区为正距平控制,实况在该地区则为一个明显的负距平中心,这也是导致东北地区汛期降水预测偏差大的主要原因。

国内外动力气候模式对东亚夏季降水的预测差异很大(图略),预测技巧偏低。因此主要采纳了动力模式对大尺度环流的预测信息,结合物理诊断结果,确定了东亚夏季风偏强和我国汛期降水“南北多、中间少”的布局。

4　结论和讨论

2018 年汛期准确预测了“降水南北多,中间少,旱涝并重”的总体特征,对黄河流域降水异常偏多和长江流域降水异常偏少的预测与实况吻合,但对东北地区降水趋势预测与实况有较大偏差。对 2018 年季节内雨季进程的预测与实况一致,如预测华南前汛期开始时间偏晚、雨量偏少;江南、长江中下游、江淮三个区域梅雨入梅偏晚,梅雨量明显偏少;华北雨季开始偏早、雨量偏多等,均与实况吻合。2018 年对台风生成和登陆频数偏多、登陆台风强度偏弱、台风活动路径以西北行和北上为主、台风季节内活动特征(前强后弱)的预测与实况一致,起到很好的服务效果。对夏季全国大部气温较常年偏高的总体趋势预测也与实况一致,但未能预测北方大部气温异常偏高的程度。基于要素预报,2018 年还对暴雨洪涝、气象干旱、高温热浪、山洪地质灾害等的高发区做了展望,起到了很好的气候服务效果。

在 2018 年汛期预测中,将诊断分析和国内外动力模式预测结果相结合。在分析先兆信号时,重点考虑了前冬弱拉尼娜事件及其对夏季风环流的滞后影响,虽然拉尼娜事件在春初结束,但是热带印度洋海温偏低的接力作用有利于副高脊线位置明显偏北、东亚夏季风偏强。国内外主要业务机构的动力气候模式对东亚季风环流主要成员的预测与诊断分析一致,即西太平洋副高偏北,菲律宾地区为气旋式距平环流。但是各动力模式对降水空间分布的预测差异较大,由于模式对降水预测的技巧偏低,因此主要采纳了动力模式对大尺度环流的预测结果。基于东亚夏季风偏强的预测,进一步预测我国北方大部地区降水明显偏多。因此前期拉尼娜事件和后期热

带印度洋海温偏低是2018年汛期气候趋势预测的重要先兆信号。此外,青藏高原冬季积雪偏少,北大西洋海温三极子模态正位相也对欧亚中纬度环流和副热带环流起到明显影响,对东亚夏季风偏强有明显贡献,该部分研究将另文发表。

我国汛期气候受到多时间尺度和多因子的共同作用,具有较大的变率和不确定性,需要根据预报对象的超前时间尺度,确定主导信号及其可能影响。2018年3月开始,PDO指数由正转负,此后在0值附近波动,PDO的空间分布特征不典型,其影响程度也明显减弱,不是2018年汛期预测的主导信号。除上述考虑的海温、积雪等外强迫信号外,大气低频振荡活动对季节内尺度大气演变有明显影响,2018年汛期MJO活动对东亚夏季风以及台风活动都有显著作用,该部分工作也将另文深入分析。

2018年汛期对东部主体雨带的布局预测取得成功,但也暴露出诸多科学问题,例如在海温外强迫信号较弱的背景下,如何利用大尺度环流信息客观预报我国不同区域的气候变异是我们面临的一个关键问题。2018年汛期对东北地区的预测与实况偏差明显较大,凸显了我国不同地区的气候预测存在差异,东北地区的降水异常在6月主要受东北冷涡和鄂霍茨克海阻塞高压的影响,7月主要受西太平洋副高的影响,而8月主要受西太平洋副高和东北冷涡的共同影响(丁婷和陈丽娟,2015)。2018年动力气候模式对西太平洋副高的预测技巧相对较高,而对东北冷涡和鄂霍茨克海阻塞高压的预测与实况相反,这是造成对东北地区降水预测趋势相反的重要原因。此外,2018年北上台风偏多也是东北地区降水偏多的另一个原因。对中纬度环流发展机制及预测能力的不足限制了东北地区的气候预测服务效果,无论从科学上还是服务需求上都需要加强该领域的研究。

参考文献

陈丽娟,高辉,龚振淞,等,2013a. 2012年汛期气候预测的先兆信号和应用[J]. 气象,39(9):1103-1110. Chen L J,Gao H,Gong Z S,et al,2013a. Overview of precursory signals of seasonal climate prediction and its application in summer 2012[J]. Meteor Mon,39(9):1103-1110(in Chinese).

陈丽娟,顾薇,丁婷,等,2016. 2015年汛期气候预测先兆信号的综合分析[J]. 气象,42(4):496-506. Chen L J,Gu W,Ding T,et al,2016. Overview of the precursory signals of seasonal climate prediction in summer 2015[J]. Meteor Mon,42(4):496-506(in Chinese).

陈丽娟,袁媛,杨明珠,等,2013b. 海温异常对东亚夏季风影响机理的研究进展[J]. 应用气象学报,24(5):521-532. Chen L J,Yuan Y,Yang M Z,et al,2013b. A review of physical mechanisms of the global SSTA impact on EASM[J]. J Appl Meteor Sci,24(5):521-532(in Chinese).

陈兴芳,宋文玲,2000. 欧亚和青藏高原冬春季积雪与我国夏季降水关系的分析和预测应用[J]. 高原气象,19(2):214-223. Chen X F,Song W L,2000. Analysis of relationship between snow cover on Eurasia and Qinghai-Xizang Plateau in winter and summer rainfall in China and application to prediction[J]. Plateau Meteor,19(2):214-223(in Chinese).

陈兴芳,赵振国,2000. 中国汛期降水预测研究及应用[M]. 北京:气象出版社. Chen X F,Zhao Z G,2000. Prediction and Application of Flood Season in China[M]. Beijing:China Meteorological Press(in Chinese).

丁婷,陈丽娟,2015. 东北地区夏季旱涝的环流型及动力气候模式解释应用[J]. 高原气象,34(4):1119-1130. Ding T,Chen L J,2015. Circulation pattern for summer precipitation in Northeast China and application of dynamical climate model information[J]. Plateau Meteor,34(4):1119-1130(in Chinese).

高辉,袁媛,洪洁莉,等,2017. 2016年汛期气候预测效果评述及主要先兆信号与应用[J]. 气象,43(4):486-494. Gao H,Yuan Y,Hong J L,2017. Overview of climate prediction of the summer 2016 and the precursory signals[J]. Meteor Mon,43(4):486-494(in Chinese).

顾薇,陈丽娟,2019. 2018年夏季海洋大气特征及对我国气候的影响[J]. 气象,45(1):126-134. Gu W,Chen L J,2019. Characteristics of atmospheric and oceanic condition and their influences on summer climate of China in 2018[J]. Meteor Mon,45(1):126-134(in Chinese).

贾小龙,陈丽娟,高辉,等,2013. 我国短期气候预测技术进展[J]. 应用气象学报,24(6):641-655. Jia X L,Chen L J,Gao H,et al,2013. Advances of the short-range climate prediction in China[J]. J Appl Meteor Sci,24(6):641-655(in Chinese).

李春晖,刘燕,李霞,等,2016. 热带西北太平洋10～30 d振荡对南海夏季风影响[J]. 应用气象学报,27(3):293-302. Li C H,Liu Y,Li X,et al,2016. Impact of 10－30-day oscillation intensity over the tropical Northwest Pacific Ocean on the South China Sea summer monsoon[J]. J Appl Meteor Sci,27(3):293-302(in Chinese).

李维京,2012. 现代气候业务[M]. 北京:气象出版社. Li W J,2012. Modern Climate Operation[M]. Beijing:China Meteorological Press(in Chinese).

李文铠,何金海,祁莉,等,2014. MJO对华南前汛期降水的影响及其可能机制[J]. 热带气象学报,30(5):983-989. Li W K,He J H,Qi L,et al,2014. The influence of the Madden-Julian Oscillation

on annually first rain season precipitation in South China and its possible mechanism[J]. J Trop Meteor,30(5):983-989(in Chinese).

刘芸芸,李维京,艾孜尧秀,等,2012.月尺度西太平洋副热带高压指数的重建与应用[J].应用气象学报,23(4):414-423. Liu Y Y,Li W J,Ai W X,et al,2012. Reconstruction and application of the monthly Western Pacific subtropical high indices[J]. J Appl Meteor Sci,23(4):414-423(in Chinese).

任芝花,余予,邹凤玲,等,2012.部分地面要素历史基础气象资料质量检测[J].应用气象学报,23(6):739-747. Ren Z H,Yu Y,Zou F L,et al,2012. Quality detection of surface historical basic meteorological data[J]. J Appl Meteor Sci,23(6):739-747(in Chinese).

王晴,张玲,2018. 2018 年 8 月大气环流和天气分析[J].气象,44(11):1501-1508. Wang Q,Zhang L,2018. Analysis of the August 2018 atmosphere circulation and weather[J]. Meteor Mon,44(11):1501-1508(in Chinese).

王永光,郑志海,2018. 2017 年汛期气候预测先兆信号的综合分析[J].气象,44(4):565-571. Wang Y G,Zheng Z H,2018. Precursory signal analysis of summer rainfall prediction in China in 2017[J]. Meteor Mon,44(4):565-571(in Chinese).

王遵娅,柳艳菊,丁婷,等,2018. 2018 年春季气候异常及可能成因分析[J].气象,44(10):1360-1369. Wang Z Y,Liu Y J,Ding T,et al,2018. Features and possible causes for the climate anomalies in spring 2018[J]. Meteor Mon,44(10):1360-1369(in Chinese).

吴统文,宋连春,刘向文,等,2013.国家气候中心短期气候预测模式系统业务化进展[J].应用气象学报,24(5):533-543. Wu T W,Song L C,Liu X W,et al,2013. Progress in developing the short-range operational climate prediction system of China National Climate Center[J]. J Appl Meteor Sci,24(5):533-543(in Chinese).

谢佩妍,陶丽,李俊徽,等,2018.西北太平洋热带气旋在 ENSO 发展和衰减年的路径变化[J].大气科学,42(5):987-999. Xie P Y,Tao L,Li J H,et al,2018. Variation of tropical cyclone track in the Western North Pacific during ENSO developing and decaying years[J]. Chin J Atmos Sci,42(5):987-999(in Chinese).

薛峰,刘长征,2007.中等强度 ENSO 对中国东部夏季降水的影响及其与强 ENSO 的对比分析[J].科学通报,52(23):2798-2805. Xue F,Liu C Z,2008. The influence of moderate ENSO on summer rainfall in eastern China and its comparison with strong ENSO[J]. Chin Sci Bull,53(5):791-800(in Chinese).

袁媛,高辉,贾小龙,等,2016. 2014—2016 年超强厄尔尼诺事件的气候影响[J].气象,42(5):532-539. Yuan Y,Gao H,Jia X L,et al,2016. Influences of the 2014－2016 super El Niño event on climate[J]. Meteor Mon,42(5):532-539(in Chinese).

袁媛,高辉,柳艳菊,2017. 2016 年夏季我国东部降水异常特征及成因简析[J].气象,43(1):115-121. Yuan Y,Gao H,Liu Y J,2017. Analysis of the characteristics and causes of precipitation anomalies over eastern China in the summer of 2016[J]. Meteor Mon,43(1):115-121(in Chinese).

章大全,宋文玲,2018. 2017/2018 年冬季北半球大气环流特征及对我国天气气候的影响[J].气象,44(7):969-976. Zhang D Q,Song W L,2018. Northern Hemisphere atmospheric circulation characteristics in 2017/2018 winter and its impact on weather and climate in China[J]. Meteor Mon,44(7):969-976(in Chinese).

张芳,何立富,2018. 2018 年 6 月大气环流和天气分析[J].气象,44(9):1237-1244. Zhang F,He L F,2018. Analysis of the June 2018 atmospheric circulation and weather[J]. Meteor Mon,44(9):1237-1244(in Chinese).

张顺利,陶诗言,2001.青藏高原积雪对亚洲夏季风影响的诊断及数值研究[J].大气科学,25(3):372-390. Zhang S L,Tao S Y,2001. The influences of snow cover over the Tibetan Plateau on Asian summer monsoon[J]. Chin J Atmos Sci,25(3):372-390(in Chinese).

张夕迪,孙军,2018. 2018 年 7 月大气环流和天气分析[J].气象,44(10):1370-1376. Zhang X D,Sun J,2018. Analysis of the July 2018 atmospheric circulation and weather[J]. Meteor Mon,44(10):1370-1376(in Chinese).

郑志海,王永光,2018. 2017 年夏季北半球大气环流特征及对我国天气气候的影响[J].气象,44(1):199-205. Zheng Z H,Wang Y G,2018. Northern Hemisphere atmospheric circulation characteristics in summer 2017 and its impact on weather and climate in China[J]. Meteor Mon,44(1):199-205(in Chinese).

周晓敏,张涛,2018. 2018 年 5 月大气环流和天气分析[J].气象,44(8):1110-1116. Zhou X M,Zhang T,2018,Analysis of the May 2018 atmospheric circulation and weather[J]. Meteor Mon,44(8):1110-1116(in Chinese).

竺夏英,陈丽娟,李想,2013. 2012 年冬春季高原积雪异常对亚洲夏季风的影响[J].气象,39(9):1111-1118. Zhu X Y,Chen L J,Li X,2013. Impact of Tibetan Plateau snow cover anomaly on Asian summer monsoon in 2012[J]. Meteor Mon,39(9):1111-1118(in Chinese).

朱益民,杨修群,2003.太平洋年代际振荡与中国气候变率的联系[J].气象学报,61(6):641-654. Zhu Y M,Yang X Q,2003. Relationships between Pacific decadal oscillation (PDO) and climate variabilities in China[J]. Acta Meteor Sin,61(6):641-654(in Chinese).

Huang R H,Wu Y F,1989. The influence of ENSO on the summer climate change in China and its mechanisms[J]. Adv Atmos Sci,6(1):21-32.

Kalnay E,Kanamitsu M,Kistler R,et al,1996. The NCEP/NCAR 40-year reanalysis project[J]. Bull Amer Meteor Soc,77(3):437-472.

Kistler R,Kalnay E,Collins W,et al,2001. The NCEP-NCAR 50-year reanalysis:monthly means CD-ROM and documentation[J]. Bull Amer Meteor Soc,82(2):247-268.

Rayner N A, Parker D E, Horton E B, et al, 2003. Global analyses of sea surface temperature, sea ice, and night marine air temperature since the late nineteenth century[J]. J Geophys Res Atmos, 108(D14): 4407. DOI: 10.1029/2002jd002670.

Wang B, Wu R G, Fu X H, 2000. Pacific-East Asian teleconnection: how does ENSO affect East Asian climate? [J]. J Climate, 13(9): 1517-1536.

Wang B, Zhang Q, 2002. Pacific-East Asian teleconnection. Part II: How the Philippine Sea anomalous anticyclone is established during El Niño development[J]. J Climate, 15(22): 3252-3265.

Wang H J, Fan K, Sun J Q, et al, 2015. A review of seasonal climate prediction research in China[J]. Adv Atmos Sci, 32(2): 149-168. DOI: 10.1007/s00376-014-0016-7.

Xie S P, Hu K M, Hafner J, et al, 2009. Indian Ocean capacitor effect on Indo-western Pacific climate during the summer following El Niño[J]. J Climate, 22(3): 730-747.

Xie S P, Kosaka Y, Du Y, et al, 2016. Indo-western Pacific ocean capacitor and coherent climate anomalies in post-ENSO summer: a review[J]. Adv Atmos Sci, 33(4): 411-432.

Yuan Y, Gao H, Li W J, et al, 2017. The 2016 summer floods in China and associated physical mechanisms: a comparison with 1998 [J]. J Meteor Res, 31(2): 261-277. DOI: 10.1007/s13351-017-6192-5.

Zhou W, Chan J C L, 2007. ENSO and the South China Sea summer monsoon onset[J]. Int J Clima, 27(2): 157-167.

Zuo J Q, Li W J, Sun C H, et al, 2013. Impact of the North Atlantic Sea surface temperature tripole on the East Asian summer monsoon[J]. Adv Atmos Sci, 30(4): 1173-1186.

陈丽娟,赵俊虎,顾薇,等. 汛期我国主要雨季进程成因及预测应用进展. 应用气象学报,2019,30(4):385-400.
DOI: 10.11898/1001-7313.20190401

汛期我国主要雨季进程成因及预测应用进展

陈丽娟[1)2)*] 赵俊虎[1)] 顾 薇[1)] 梁 萍[3)] 支 蓉[1)]
彭京备[4)] 赵树云[1)] 高 辉[1)] 李 想[1)] 张培群[1)]

[1)](国家气候中心 中国气象局气候研究开放实验室, 北京 100081)
[2)](南京信息工程大学气象灾害预报预警与评估协同创新中心, 南京 210044)
[3)](上海区域气候中心, 上海 200030)
[4)](中国科学院大气物理研究所, 北京 100029)

摘 要

汛期内我国中东部地区的雨季是东亚夏季风推进过程中的重要产物,主要包括华南前汛期、梅雨、华北雨季和华西秋雨等,各地雨季决定了我国中东部地区汛期的旱涝布局和旱涝演变,是我国汛期预测和服务的重点。该文回顾了4个雨季特征及影响因子方面的研究进展,在此基础上梳理物理概念预测模型。研究显示:海温异常是影响各区域雨季的重要先兆信号,但不同雨季的年际和年代际变化特征不同,海温作为外强迫信号的影响程度和时空形式也有差异。利用热带太平洋东西海温差指标能更好地解释华南前汛期降水的年际变化。而与梅雨的年际变化分量相关联的海温关键区主要分布于热带,与年代际或多年代际变化分量相联系的海温关键区则来自中高纬度。华北雨季降水的强弱不仅与ENSO循环的位相有关,更多受到ENSO演变速率的影响。而影响华西秋雨的海温关键区随着年代际背景的变化发生了改变,需要重新诊断和建模。

关键词: 雨季; 华南前汛期; 梅雨; 华北雨季; 华西秋雨

引 言

每年随着东亚夏季风的北推和南撤,我国华南、长江流域、华北地区、华西地区等相继进入降水集中期[1],分别形成当地的雨季,由于气候特色鲜明,又称为降水气候事件,先后有华南前汛期、梅雨、华北雨季、华西秋雨等。东亚夏季风的强弱与雨季的强弱往往决定着我国汛期的旱涝布局[2-3],而雨季开始和结束早晚又联结着我国汛期旱涝的次季节至季节尺度演变信息[4-7],因此,雨季起止、强度的特征和预测与多时间尺度的环流演变及外强迫因子密切相关。做好各地雨季的监测和预测既具有科学意义,又与我国的农业生产、防汛抗旱部署密切相关,还具有重要的应用价值。

在中国气象局国家气象科技创新工程项目"次季节至季节气候预测和气候系统模式"等项目的支持下,国家气候中心组织开展了针对东亚地区季节内雨季(降水气候事件)的监测诊断和预测研发。力求以机理分析和动力模式预测为基础,揭示我国汛期降水进程主要模态的年际特征和变化机理,发展主要气候事件的强度、进程的趋势预测模型。

在研发过程中遇到的首要问题是雨季自身的定义和监测。许多研究者根据自己的需求和研究目标从不同角度定义雨季的强度和起止特征,各省业务部门根据自己的地理位置、气候特征及服务需求定义雨季的监测标准,标准不统一使气象部门针对公众的服务易出现分歧。中国气象局组织国家级和省级业务部门以及科研院所的专家针对华南前汛期、梅雨、华北雨季、华西秋雨等联合开展了监测指标的

2019-02-18收到, 2019-04-26收到再改稿。
资助项目: 国家重点基础研究发展计划(2015CB453203),国家自然科学基金项目(41875093,41805067,41275073)
* 邮箱: chenlj@cma.gov.cn

研发，确定了雨季监测业务标准①-④，建立了国家级和省级业务相对统一的监测指标体系。本文主要基于该业务标准进行监测和进一步的诊断预测研究。表 1 为基于各雨季监测标准后获取的雨季基本气候特征。

根据中国雨季进程的气候特征，从南向北依次介绍华南前汛期、梅雨、华北雨季和华西秋雨的主要气候特征，以及针对雨季的监测诊断和预测研发进展，最后给出近 4 年的雨季预测在业务中的应用情况。如无特别说明，文中涉及的气候态均指 1981—2010 年平均。

表 1 汛期内我国不同雨季的主要气候特征

Table 1 Climate features of different regional rainy seasons

雨季	平均开始时间	平均结束时间	平均持续时间/d	平均强度(雨量/mm)
华南前汛期	04-06	07-04	89	733.8
江南梅雨	06-08	07-08	30	365.4
长江中下游梅雨	06-14	07-13	29	281.0
江淮梅雨	06-21	07-15	25	264.4
华北雨季	07-18	08-18	32	136.0
华西秋雨	08-31	11-01	62	202.8

1 华南前汛期

华南是我国年雨量最充沛、雨季最长的地区。受热带季风和副热带季风共同作用及台风降水影响，华南地区降水季节循环呈典型的双峰型变化特征[8]，其中第 1 个降水峰值出现在 4—6 月，该时段被称为华南前汛期，占全年降水量的近 50%，是华南地区的主汛期。4—6 月的前汛期降水按照降水性质不同分为夏季风爆发前的锋面降水和夏季风爆发后的季风降水[9-10]。

根据华南汛期监测业务规定①，国家气候中心建立了华南前汛期开始、结束、强度的实时业务监测(广东、广西、福建和海南共 261 个站点)。

华南前汛期平均入汛和出汛时间分别为 4 月 6 日和 7 月 4 日，整个前汛期平均持续 89 d(表 1)，与以往各类定义所得的结果总体一致[11-13]。华南前汛期开始和结束时间表现出明显的年际变化特征。开始日的标准方差是 18 d，最早和最晚入汛日相差超过 2 个月。前汛期结束日期的标准方差是 15 d，最早和最晚结束日相差超过 1 个月。开汛时间早晚与 3—4 月华南地区降水关系密切，开汛偏早(晚)，对应 3—4 月华南降水偏多(少)[13]。

Gu 等[14]使用前汛期入汛至出汛这一时段的华南地区 261 个站点平均降水量的累积值作为反映前汛期总降水量的指标，这一指标的历史序列显示华南前汛期降水量的年际变化非常明显，降水量最多为 1071 mm(1997 年)、最少为 430 mm(1991 年)。从降水量空间分布看，在前汛期偏涝年份华南大部地区降水量超过 800 mm，降水大值中心位于广东省，降水量超过 1600 mm；相反，在少雨年华南大部地区降水量仅为 500～600 mm，最大值不超过 1000 mm。前汛期偏涝和偏旱年降水的差异非常明显，尤其是在广东省附近相差超过600 mm。已有研究指出，华南前汛期旱涝的年际变化特征非常明显[15-16]，显著周期约为 2～4 年。马慧等[17]认为前汛期降水还表现出明显的年代际变化特征，20 世纪 50 年代前期、60 年代中期到 80 年代初为前汛期多雨期。但 1981 年以来前汛期降水量并未表现出显著(达到 0.01 显著性水平)增加或减少的线性趋势[14]，与以往研究[18-19]的结论不完全一致。

从环流特征看，华南前汛期降水的年际变化主要受到 200 hPa 青藏高原东部异常气旋及反气旋、西太平洋副热带高压(简称副高)强度和位置、以及 850 hPa 菲律宾附近异常反气旋、气旋的显著影响[14]。从气候平均 200 hPa 风场(图 1a)看，华南前汛期期间在东亚副热带地区 35°～40°N 附近为一个西风急流区，在其南侧 15°N 附近则为东风急流区，在东、西风急流之间、中印半岛上空为一个气旋式环流。从多雨年、少雨年200 hPa风场的差值合成场

①中国气象局预报与网络司. 关于印发《华南汛期监测业务规定(试行)》的通知(气预函〔2014〕2 号). 2014.

②中国气象局预报与网络司. 关于印发《梅雨监测业务规定》的通知(气预函(2014)28 号). 2014.

③中国气象局预报与网络司. 关于印发《华北雨季监测业务规定(试行)》的通知(气预函(2014)117 号). 2014.

④中国气象局预报与网络司. 关于印发《华西秋雨监测业务规定(试行)》的通知(气预函(2015)2 号). 2015.

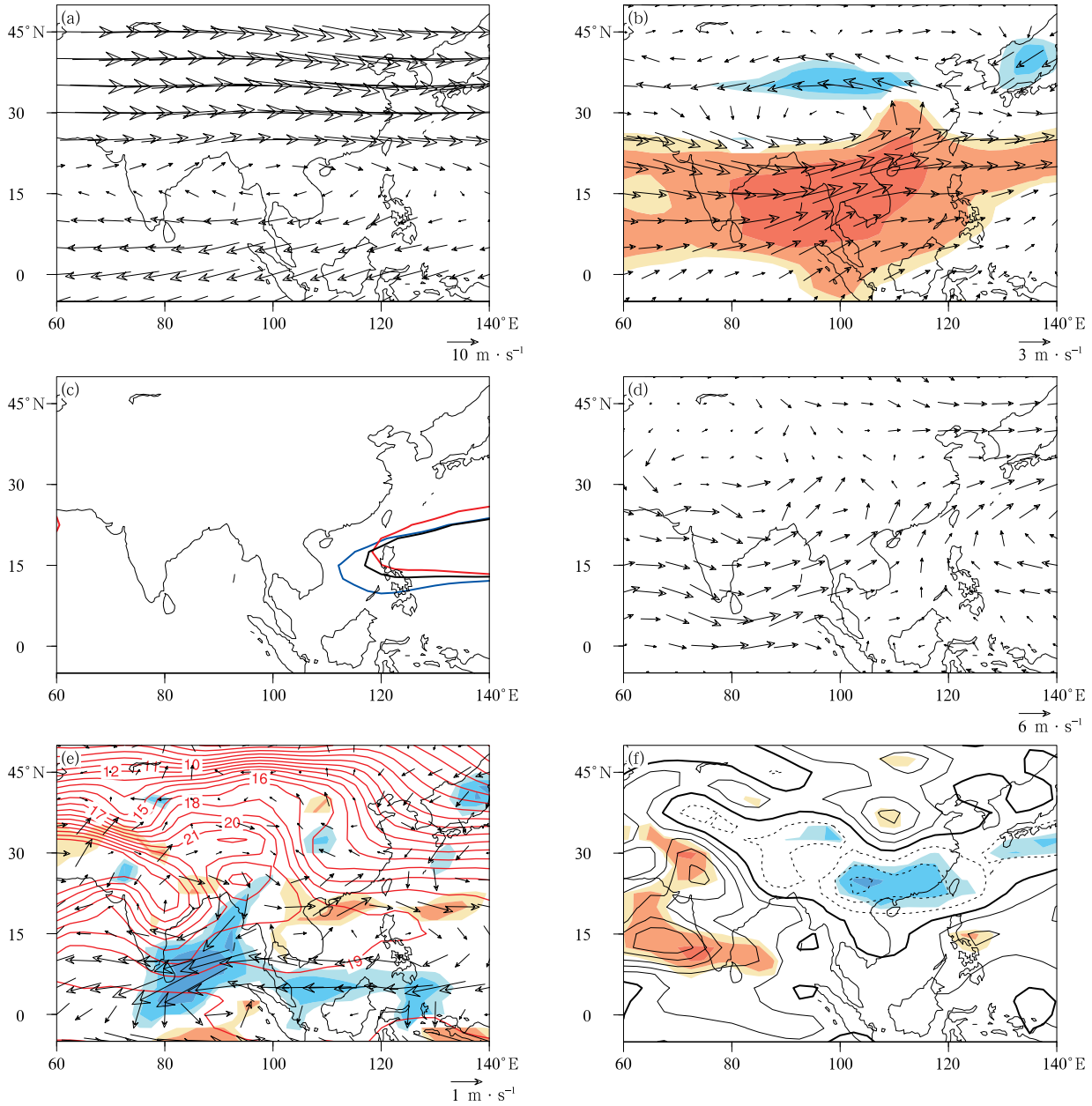

图 1　华南前汛期期间气候平均的 200 hPa 风场(a),降水偏多和偏少年 200 hPa 风场的差值合成(b),气候平均(黑色等值线)、降水偏多(蓝色等值线)和偏少(红色等值线)年 500 hPa 等压面上 5875 gpm 等值线(c),气候平均的 850 hPa 风场(d),降水偏多和偏少年 850 hPa 风场的差值合成(矢量)及气候平均 850 hPa 气温(等值线,单位:℃)(e),降水偏多和偏少年 700 hPa 对流不稳定度的差值合成(单位:10^{-5} K·Pa^{-1},等值线间隔为 2)(f)[14]

(图 1b、图 1e、图 1f 中黄色表示正相关,蓝色表示负相关,填色区浅、中、深表示达到 0.1,0.05,0.01 显著性水平)

Fig. 1　Features of pre-rainy season in South China(from Reference [14])

(a)the climatology of 200 hPa wind,(b)composite anomalies of 200 hPa wind between wet and dry years,(c)the location of the western Pacific subtropical high(indicated by 5875 gpm contour) for the climatology (the black line),wet years(the blue line),and dry years(the red line),(d)the climatology of 850 hPa wind,(e)composite anomalies of 850 hPa winds(the vector) between wet and dry years overlaid with the climatology of 850 hPa air temperature(the contour,unit:℃),(f)composite anomalies of 700 hPa convective instability between wet and dry FRS years(unit:10^{-5} K·Pa^{-1}, the interval is 2)

(the yellow and the blue denote positive and negative correlations,respectively, and the light,middle,dark shaded denote passing tests of 0.1, 0.05, 0.01 levels)

(图 1b)看,在前汛期多雨年,副热带西风急流和东风急流都明显减弱,在青藏高原东部附近存在一个异常的气旋式环流,说明中印半岛上空的反气旋也明显减弱。相应的在 500 hPa,多雨年西太平洋副高强度较常年平均偏强、位置较常年平均偏西偏南(图 1c)。在 850 hPa,多雨年在菲律宾附近存在一个异常的反气旋式环流(图 1e),这种异常形势加强了南海至华南地区的偏南风(图 1d),并从以下两个方面影响前汛期降水:一方面有利于更多的水汽从中印半岛附近输送至华南地区,从而有利于降水的增加;另一方面由于中印半岛大气温度高于南海和华南地区,这样的形势有利于暖平流输送至华南,从而增大华南地区大气的不稳定度(图 1f),有利于异常上升运动和降水的增多。覃武等[20]、苗春生等[21-22]均指出,东亚副热带西风急流和西太平洋副高等系统对前汛期降水有显著影响,与上述结论一致。伍红雨等[13]研究进一步指出,西太平洋副高对前汛期的影响不仅体现在降水量,而且对入汛时间也有明显影响,当副高偏强偏西(偏弱偏东)时,前汛期开汛偏早(晚)。

除副热带环流系统之外,已有研究还揭示出中高纬度环流系统对前汛期降水年际变化的可能影响,这些研究表明:当东北冷涡活跃[21,23]、乌拉尔山附近为异常高压[20,24]或东亚大槽加深时,华南地区北侧常常出现气旋性的低压系统[2],这种大气环流的配置有利于高纬度地区的冷空气向南侵袭[25],从而导致冷暖空气在华南地区交汇辐合,引起前汛期降水偏多。

此外,还有研究指出一些前期环流因子可能对华南前汛期降水的变异有指示意义,如徐淑爱[26]指出,冬季风对后期春季和初夏的环流影响显著,冬季风强年,初夏西太平洋副高位置偏北,西伸脊点偏东,华南及珠江三角洲前汛期降水偏少。蔡学湛等[27]的研究则显示,前期冬季西太平洋暖池附近对流活动可能会通过异常 Hadley 环流影响到前汛期的旱涝。黄先香等[28]则指出前期 1 月印度北部和 3 月西北太平洋风场异常是预测华南前汛期旱涝的前兆信号。

Gu 等[14]利用国家气候中心定义的前汛期指标研究了海温对前汛期降水的影响,结果显示:热带太平洋海温异常与前汛期降水关系密切(图 2a),是前汛期降水的重要外强迫因子之一。当热带太平洋海

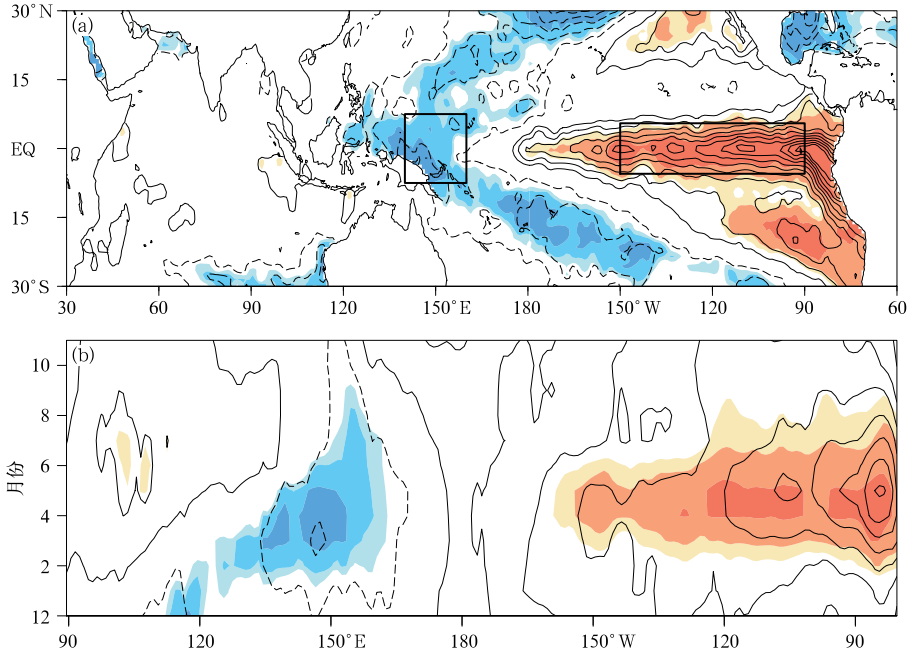

图 2 华南前汛期降水偏多、偏少年海温异常的差值合成(单位:℃,等值线间隔为 0.2)[14]
(a)春季海温,(b)逐月热带(7.5°S~7.5°N)海温(填色说明同图 1)

Fig. 2 Composite anomalies of sea surface temperature(SST) between wet and dry years of pre-rainy season in South China(unit: ℃, the interval is 0.2)(from Reference [14])
(a)SST in spring, (b)monthly tropical SST averaged over 7.5°S—7.5°N(the shaded is the same as in Fig. 1)

温东暖西冷(东冷西暖)时,前汛期降水偏多(少)。从热带海温的逐月演变特征(图 2b)看,海温与降水的这种关系从 2 月开始显著,在 4 月和 5 月达到最大,并一直持续至 6 月。根据降水与海温的显著相关区域(图 2a),将热带东太平洋(5°S～5°N,90°～150°W,右侧黑色框区域)和西太平洋(7.5°S～7.5°N,140°～160°E,左侧黑色框区域)标准化海温距平之差作为热带太平洋东西海温差指数 I_{EWC},并将该指数作为指示前汛期降水异常的重要指标。利用 I_{EWC} 对各项环流特征量进行回归分析,进一步研究热带太平洋东西海温差影响前汛期降水的可能机制,指出当热带太平洋东暖西冷时,有利于低层热带东太平洋(西太平洋)大气辐合(辐散),Walker 环流减弱(图3a);西太平洋地区附近由于对流活动受到

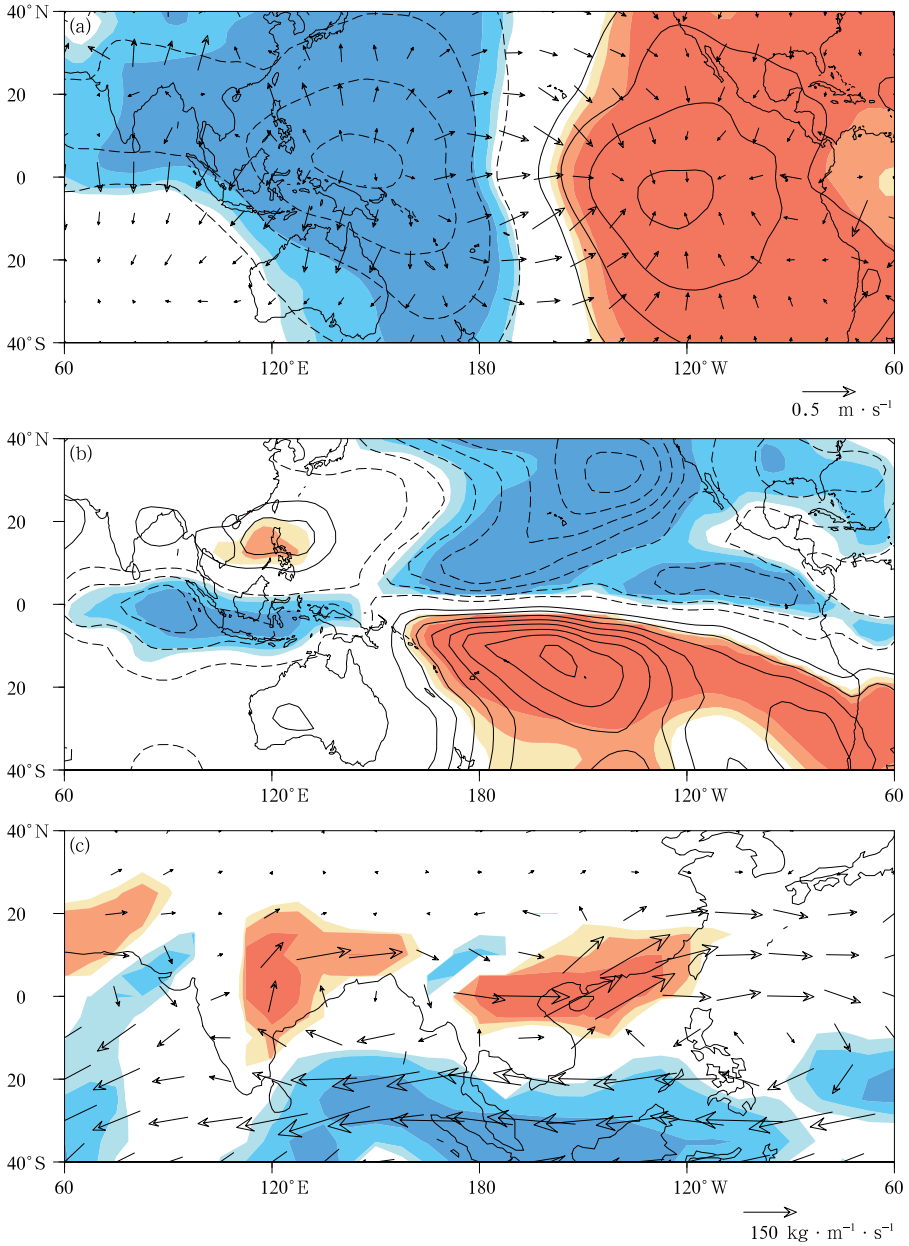

图 3　根据 1981—2015 年春季热带太平洋东西海温差指数回归的 850 hPa 速度势(等值线,单位:10^5 m^2·s^{-1})和辐散风场(矢量)(a),850 hPa 流函数(单位:10^5 m^2·s^{-1},等值线间隔为 2)(b)和整层积分的水汽通量(c)[14](填色说明同图 1)

Fig. 3　Regression of 850 hPa velocity potential(the contour, unit: 10^5 m^2·s^{-1}, the interval is 2) and divergent wind (the vector)(a), 850 hPa stream function(unit: 10^5 m^2·s^{-1}, the interval is 2)(b), and column integrated water vapor flux(c) on the normalized spring mean I_{EWC} for the period of 1981—2015(from Reference [14])(the shaded is the same as in Fig. 1)

抑制、非绝热加热减弱，因而可通过激发大气中的Rossby波使菲律宾附近出现异常的反气旋式环流(图 3b)，从而导致南海至华南地区出现异常西南风，有利于更多的暖湿气流输向华南地区(图 3c)，使降水偏多。强学民等[29]研究曾指出，西太平洋暖池海温对前汛期降水有显著影响，但 Gu 等[14]研究指出，热带太平洋东西海温差指标比单独考虑西太平洋海温能够更好地解释前汛期降水的异常变化。除热带海温之外，中高纬度海气系统对于华南前汛期降水也有显著影响，如 Li 等[30]研究指出，前汛期降水的年际变率不仅仅来源于热带海洋，同时也受到春季北大西洋中高纬度海温三极子模态的显著影响。北大西洋海温三极子对前汛期降水的影响主要是通过以下两种途径实现：一方面春季北大西洋三极子可以持续至初夏，并通过激发欧亚大陆上空的遥相关波列影响东亚中高纬度环流，从而引起前汛期降水的变化；另一方面，北大西洋三极子也可以通过西传大气遥相关影响到菲律宾附近的异常反气旋，从而导致前汛期降水的异常变化。由此可见，热带太平洋海温和北大西洋海温是华南前汛期降水年际变率的重要来源。热带海温可以通过影响西太平洋附近的对流活动，激发菲律宾附近的异常反气旋，从而影响华南地区降水，而北大西洋海温除了可以直接通过欧亚中高纬度大气遥相关波列影响前汛期降水之外，也可能通过西传的大气遥相关影响到菲律宾附近异常反气旋[31]，从而对降水产生影响(图 4)。此外，也有研究指出，孟加拉湾附近海温[2]和南海海温[13]也与前汛期降水存在显著的相关关系，但这些海温因子影响降水的机制还有待进一步研究。

在年代际尺度上，前汛期降水的变化可能也受到海温的调制作用。王彦明等[32]、章开美等[33]的研究指出，在太平洋年代际振荡(PDO)冷位相年，华南前汛期发生典型持续性暴雨过程的概率比 PDO 暖位相年大，且暴雨强度偏强，持续时间偏长。

此外，还有研究指出，积雪和极冰对华南前汛期可能产生影响，高原雪盖异常可能是通过改变海陆热力差异影响春季至初夏东亚夏季风，多雪年有利于夏季风爆发晚、前汛期降水多[34]。当南极海冰面积增大时，华南前汛期降水增加，反之亦然。海冰对前汛期的影响可能与南半球低纬度(0°～30°S)气旋活动有关[35-36]。有关各因子对华南前汛期年际和年代际变化的影响和机制还有待更多深入研究。

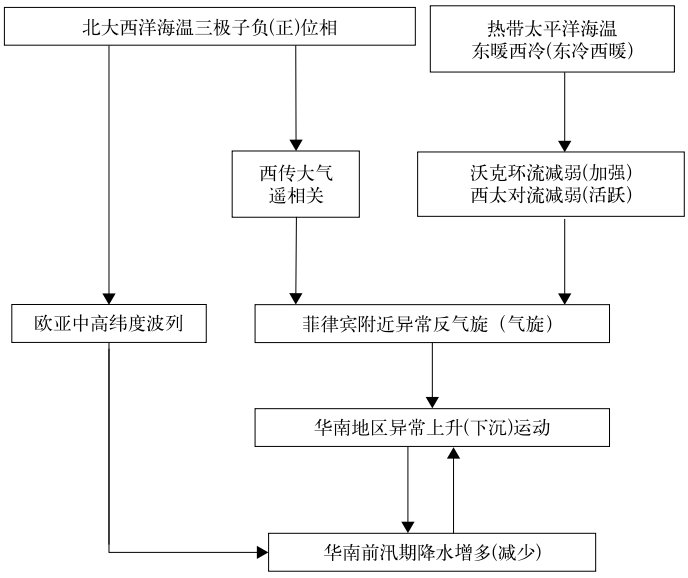

图 4 影响华南前汛期降水年际变异的关键因子物理概念图

Fig. 4 The concept map of key factors which impact annual variability of pre-rainy season in South China

2 中国梅雨

一般情况下，伴随着西太平洋副高第 1 次北跳之后，江南、长江中下游依次入梅，梅雨是东亚大气环流季节内变化的典型阶段。长期以来，有关梅雨的定义和监测标准有很大分歧，分歧的焦点在于是以天气实况为主还是以环流调整为主或二者兼顾来

划分入梅、出梅日期[37-38]。各地区标准不同,造成所得结果的可比性较差[39-44],也导致在预报服务中的不一致。2014 年 5 月中国气象局组织专家充分论证和试验性应用后,发布了中国《梅雨监测业务规定》②,新规定中以区域内各监测站的降水条件为主,西太平洋副高脊线、日平均温度、南海夏季风爆发时间等条件为辅,确定入梅、出梅、梅雨期长度、梅雨量和强度等特征,并按照气候类型将梅雨监测区域分为江南、长江中下游、江淮 3 个区域,作为国家级和相关省级气象部门开展梅雨监测预测业务的依据。该标准全面考虑了梅雨的天气要素和环流演变以及我国梅雨的空间差异特征。

根据监测规定,平均而言,江南区较长江中下游区偏早 1 周,而长江中下游区较江淮区偏早 1 周(表 1)。3 个区域梅雨入梅日存在显著的年际变化。1951—2015 年江南入梅日的标准差为 8 d,入梅最早和最晚可相差 47 d,长江中下游入梅日的标准差为 11 d,江淮入梅日的标准差为 11 d。3 个区域入梅时间在年际尺度上较一致,还存在显著的年代际变化,但是无明显长期变化趋势。3 个区域的入梅日与各自的梅雨期日数及梅雨量的相关系数均达到 0.001 显著性水平,表明入梅早晚与梅雨期的长短及梅雨量的多寡均有密切关系。入梅偏早(晚),梅雨期容易偏长(短)、同时梅雨量偏多(少)。从侧面反映了研究入梅早晚的影响系统和预测信号的重要意义[45]。

叶笃正等[46]、陶诗言等[47]很早就指出,印度西南季风爆发与东亚入梅有密切关联。文献[48-50]梳理了东亚夏季风系统的关键成员,认为东亚夏季风的异常活动可造成关键成员的偏北或偏南,从而影响到江淮流域的入梅早晚及持续时间。由于 3 个梅雨区中,一般江南入梅最早,赵俊虎等[45]利用《梅雨监测业务规定》中的入梅日期资料,以江南入梅为代表,重点研究了江南入梅早晚与同期(5—6 月)大气环流及前期海表温度变化的关系。结果表明:江南入梅偏早(晚)年,对流层高层至低层的同期大尺度环流存在明显的差异。入梅偏早(晚)年,高层南亚高压和东亚副热带西风急流(西风急流)的建立较早(晚),强度较强(弱),南亚高压北移到高原上空亦偏早(晚),西风急流北跳偏早(晚);中层中高纬度经向环流较强(弱),而西北太平洋副高第 1 次北跳偏早(晚);低层索马里越赤道气流建立较早(晚),强度较强(弱),西太平洋为反气旋(气旋)式距平环流。冬春季海表温度的异常是影响入梅早晚的重要预测信号:当冬季东太平洋海表温度为负(正)距平、澳大利亚东侧海表温度偶极子为正(负)位相、及春季北大西洋三极子处于正(负)位相时,江南入梅偏早(晚)。其中入梅前一年 12 月澳大利亚东侧海表温度偶极子和当年 3 月北大西洋三极子与江南入梅关系最为密切(图 5)。

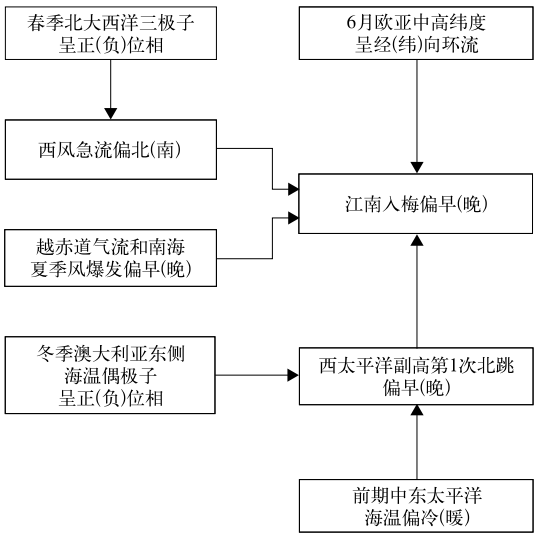

图 5　江南入梅早晚影响系统概念图[45]

Fig. 5　The concept map of impact system on Meiyu onset date over regions south of the Yangtze River(from Reference [45])

相比入梅、出梅早晚的研究,影响梅雨量异常的研究更加丰富,涉及影响梅雨的季风环流、中高纬度环流、ENSO 循环、西太平洋热力状况、雪盖、极冰等因子[49,51-58],反映出各因子对梅雨年际变化的影响。Li 等[59]研究指出,梅雨-Baiu 锋是东亚调节季风降水的主要天气系统,在多个时空尺度上表现出明显的变异性。Sampe 等[60]研究了中国梅雨-Baiu 雨带的大尺度动力学:西风急流对环境的强迫。该研究揭示了西风急流是梅雨-Baiu 的一个重要影响因素,西风急流通过引导瞬态涡流,通过对流不稳定性和绝热上升气流产生有利于对流的环境维持梅雨-Baiu 雨带。Gu 等[61]研究表明,在年代际时间尺度上冬季北大西洋三极子模态与我国梅雨量和梅雨期长度联系紧密。梅雨预测方法主要有物理统计模型

预测和气候模式预测两种方法。

梁萍等[62]对梅雨量变化的物理机制研究发现，梅雨的年代际、年际以及季节内变化的影响因子和物理机制存在差异，在实际业务中需要综合考虑多因子多尺度共同作用的结果。采用梅雨监测新规定，以长江中下游区域梅雨为代表，分析了该区域梅雨的多时间尺度变化特征，从海洋外强迫影响因子角度探讨了梅雨的可预报性来源，进一步综合海洋背景变率建立预测模型。研究显示长江梅雨呈现周期为 3～4 年、6～8 年、12～16 年、32 年、64 年的多时间尺度变化分量和长期减少趋势(图 6)。其中，3～4 年准周期变化是梅雨异常变化的主要分量。梅雨的干湿位相转变受 12～16 年的准周期变化调制，极端涝年易出现在 12～16 年准周期变化湿位相和 3～4 年变化分量峰值位相叠加的情况。长江梅雨的各准周期变化分量有不同的海洋外强迫背景，是梅雨可预报性的重要来源。与年际变化分量相关联的海温关键区主要分布于热带，而与年代际-多年代际变化分量相联系的海温关键区则来自中高纬度。3～4年准周期变化分量的海洋外强迫强信号随季

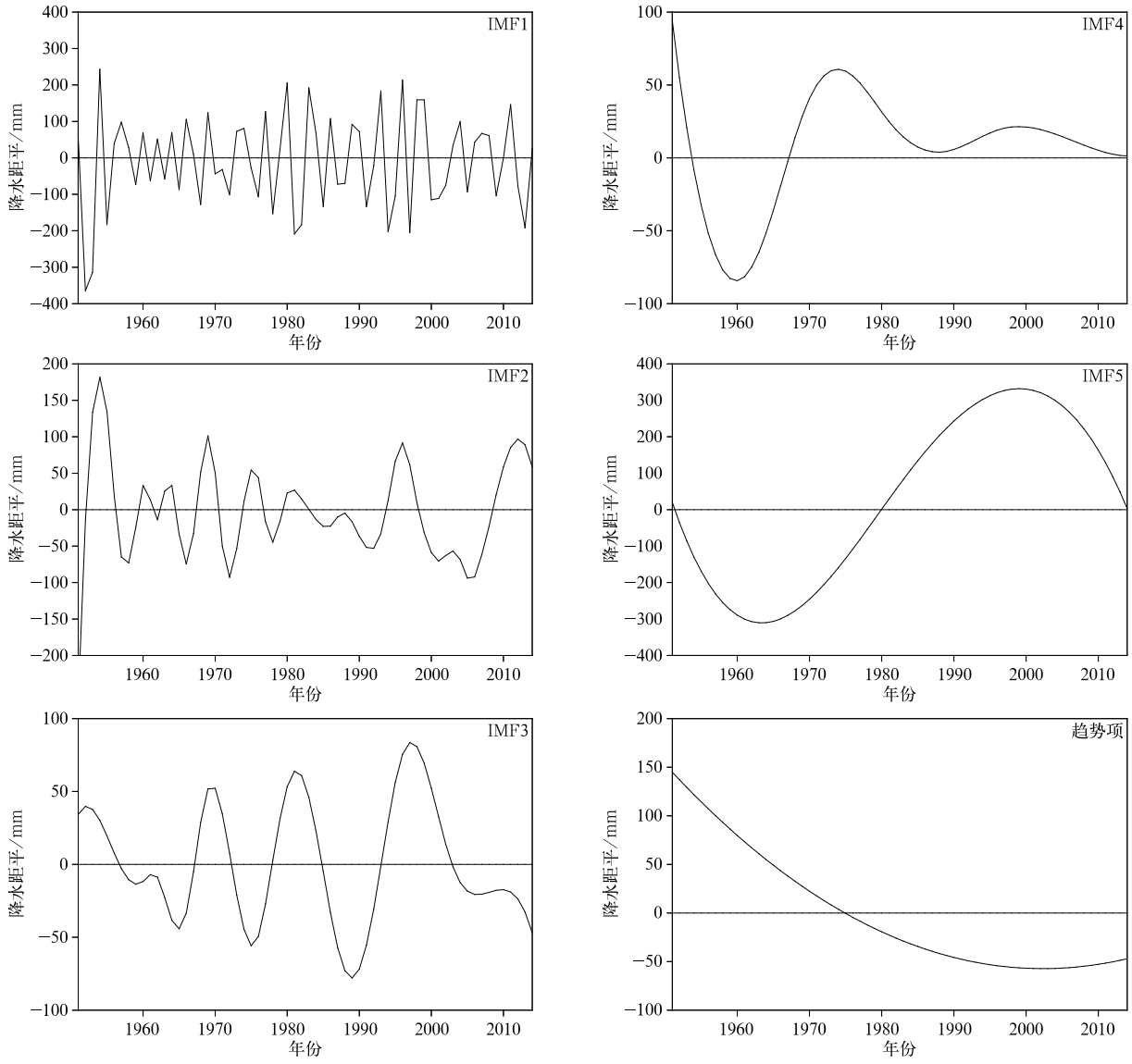

图 6 长江梅雨异常值的 5 个准周期变化分量和 1 个趋势项分量[62]

Fig. 6 Five quasi-periodic components and one trend component of anomalies of Meiyu over the Yangtze River(from Reference [62])

节变化由前冬的 ENSO 转为春末夏初的印度洋偶极子(IOD)。6～8 年和 12～16 年准周期变化分量的海洋强迫关键区主要位于太平洋,准 32 年和准 64 年周期振荡则受北太平洋多年代际变化(PDO)和北大西洋多年代际变化(AMO)的共同影响。梅雨的长期变化趋势则与全球变暖背景及以PDO为代表的年代际海洋外强迫因子相联系。

将梅雨各变化分量作为预测对象分别建模,进一步构建梅雨异常预测统计模型。各分量的预测因子和权重系数如表 2 所示。采用该模型对近 5 年梅雨预测进行独立样本检验,有较好的回报效果,验证了梅雨异常年际分量可预报性的稳定性以及基于多时间尺度分离建立梅雨预测模型的优越性。进一步还需考虑海温以外的其他外强迫信号对梅雨量多尺度异常的贡献。

Huang等[63]评估了国家气候中心大气环流模式(BCC_AGCM2.0.1)对梅雨期长江—淮河流域降水及环流的预测技巧。结果表明,BCC_AGCM2.0.1 能够合理再现长江—淮河流域梅雨的空间格局。然而,与观测相比,模式低估(高估)了暴雨和强(中、轻)降水;模式预测梅雨平均开始于 6 月初,比观测的气候平均约偏早 20 d;梅雨持续时间为 15 d,比观测时间约偏短 5 d。这表明模式对梅雨的预测还存在一定偏差。此外,Zhu 等[64]利用 MIROC_Hires 耦合模式,研究了未来变暖的情景下梅雨系统的变化,并探讨了将不均匀变暖与梅雨系统变化联系起来的可能因素。利用动力气候模式评估对梅雨的多时间尺度模拟和预测能力并在业务中应用是一个重要发展方向。

表 2　梅雨预测模型的预测因子及权重系数[62]

Table 2　Predictors and weight coefficients of Meiyu prediction model(from Reference [62])

预测分量	预测因子	权重系数
IMF1 年际增量	前冬 Niño3 区海温异常	0.865
IMF2	热带西太平洋和北太平洋海温异常	0.454
IMF3	北太平洋海温年代际变化分量	0.270
IMF4	北太平洋多年代际变化(PDO)	0.252
IMF5	北大西洋多年代际变化(AMO)	0.370
趋势项		0.393

3　华北雨季

7 月第 2～3 候,3 个区域梅雨相继结束,副高第 2 次北跳,华北雨季开始。中国气象局预报与网络司 2014 年制定了华北雨季监测标准③。监测覆盖了山西、北京、天津、河北和内蒙古的部分地区。根据该监测数据,华北雨季平均开始时间为 7 月 18 日,平均结束时间为 8 月 18 日,平均持续时间为 32 d,平均降水量为 136 mm(表 1),占华北夏季总降水量的 50%。

华北夏季降水与东亚夏季风的强度有很好的对应关系[65-67]。另外,南海夏季风爆发偏早,有利于东亚夏季风偏强,华北和东北夏季降水正常或偏多[68]。印度夏季风和华北夏季降水也有很好的正相关关系[69-71],但印度季风降水和华北季风降水的协同变化是有条件的,受到对流层中高层环半球遥相关型(CGT)波列的影响[72]。此外,还有中高纬度环流异常型[73-75]、高空急流位置[76-77]、南亚高压的东西位置、北极涛动、南极涛动、亚洲—太平洋涛动、索马里和澳大利亚越赤道气流的协同变化等也对华北夏季降水有影响[78-82]。

在外强迫信号方面,首先值得关注的是 ENSO 循环的影响[56,83-84]。但 ENSO 的类型、强度、爆发时间、结束时间、衰减过程不同,对后期夏季降水的影响也不一致[85-94]。除 ENSO 以外,还有印度洋不同模态[95]、高原积雪[96-98]、极冰[99-100]等异常也会对华北雨季强度有一定影响。

于晓澄等[101]利用国家气候中心华北雨季监测资料分析了华北雨季开始早晚的气候特征,及其与大气环流系统和关键区域海表温度的关系。结果表明:华北雨季开始时间偏早(晚),与西太平洋副热带高压第 2 次北跳偏早(晚)、东亚副热带西风急流建立偏早(晚)、东亚夏季风北进提前(滞后)等环流系统的年际变化关系密切。华北雨季开始早(晚)还与春夏季热带印度洋海表温度一致模态(IOBW)为负(正)值、赤道中东太平洋海表温度为负(正)值的相关关系显著且稳定。一般在 Niño3.4 指数和 IOBW 指数为正值时,贝加尔湖大陆高压偏强,副高偏强、

偏南，东亚夏季风偏弱，从而导致华北雨季开始偏晚。赵树云等[102]利用国家气候中心华北雨季的监测数据分析了华北雨季降水异常偏多(少)年对应的典型大气环流和 ENSO 演变特征。发现华北雨季降水异常偏多年通常发生在 El Niño 结束且当年转为 La Niña 的年份，这种情况下盛夏 500 hPa 高度场上日本海到渤海的正位势高度距平加强，热带 Walker 环流加强，均比单纯的 El Niño 衰减年更符合华北雨季降水偏多年的典型环流特征(图 7)。而华北雨季降水异常偏少年通常发生在赤道中东太平洋冷水位相结束且当年发展成 El Niño 事件的年份。因此，在业务预测过程中需要关注 ENSO 事件前期的变化速度以及未来可能的演变特征。根据已有研究成果，主要外强迫信号和关键环流系统对华北雨季降水强度年际变率影响的物理概念如图 8 所示。

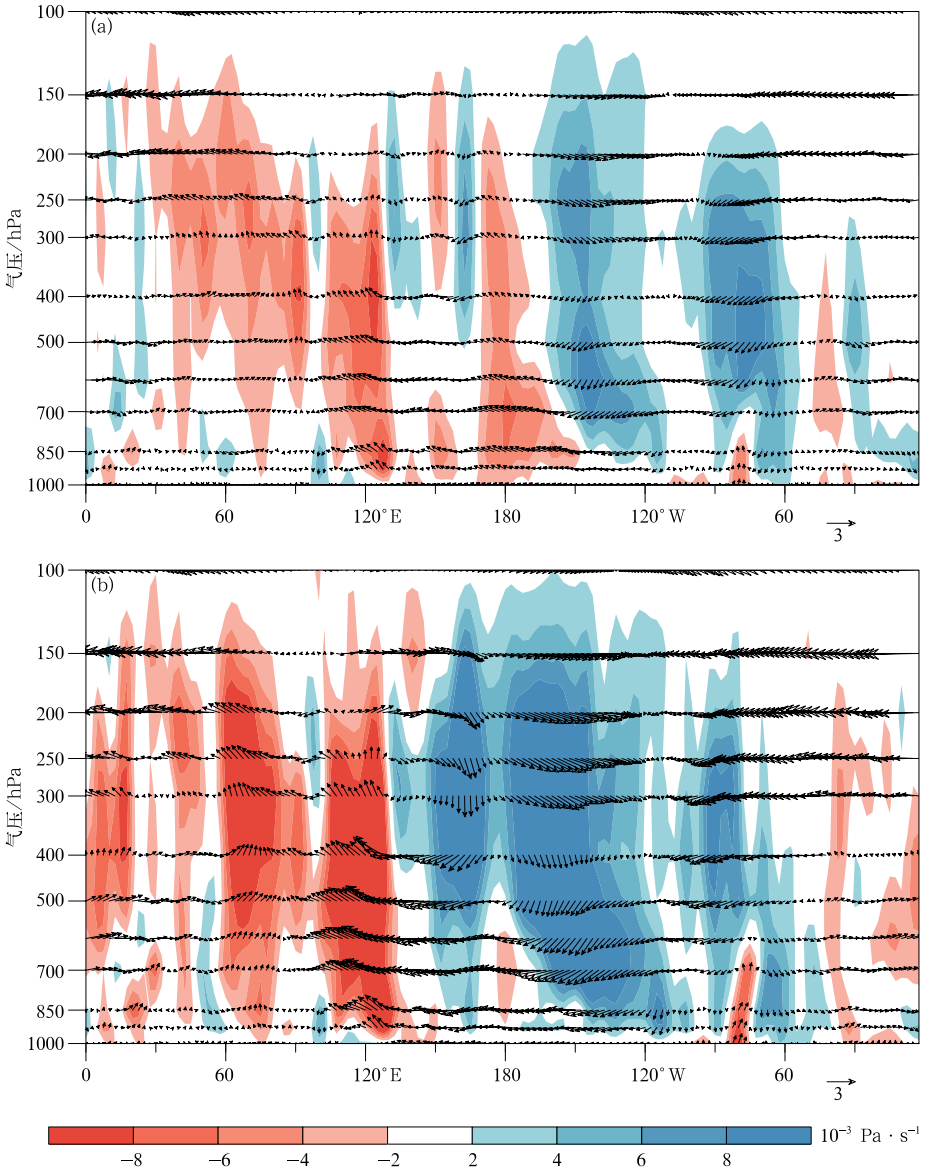

图 7 1961—2015 年 El Niño 衰减年(a)和 El Niño 转为 La Niña 年(b)合成的 7—8 月 5°S～5°N 平均垂直速度距平(填色)和纬向-垂直剖面上风场距平(矢量)[102]

Fig. 7 Zonal-vertical cross section of composites of 5°S−5°N averaged vertical velocity anomalies (the shaded) and the schematic diagram of wind fields anomalies(the vector) in Jul−Aug for El Niño decaying years(a) and years El Niño switched to La Niña(b) during 1961−2015(from Reference [102])

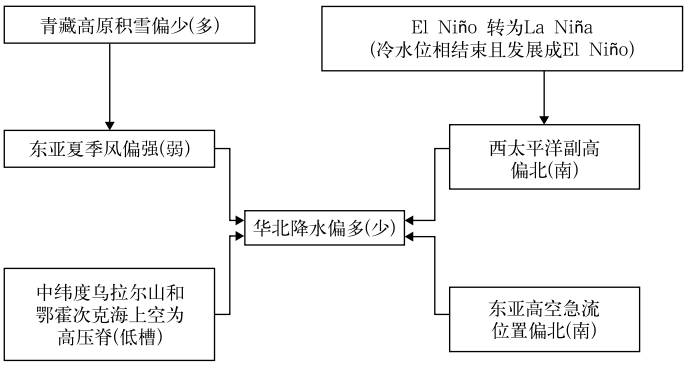

图 8　影响华北雨季降水强度年际变化的关键因子物理概念图

Fig. 8　The concept map of key factors impacting annual variability of rainy season in North China

4　华西秋雨

一般在 8 月中下旬,随着华北雨季的结束,东亚夏季风系统开始南撤,中国东部地区雨季结束,秋高气爽;然而此时西南季风及其带来的水汽输送仍然较强,同时中高纬冷空气活动开始活跃,使华西地区由于冷暖空气交汇出现仅次于夏季的降水次峰值,称为秋雨。

长期以来,华西秋雨没有统一的业务监测标准。2015 年中国气象局预报与网络司印发华西秋雨监测业务规定④,为华西秋雨的监测预测业务打下基础。根据华西秋雨的气候区域特征,监测区域分为南、北两个区,南区主要包括湖北西部、湖南西部、重庆、四川东部、贵州北部以及陕西南部部分地区;北区主要包括陕西南部大部、宁夏南部和甘肃南部。根据该标准,华西秋雨北区的平均开始时间为 9 月 8 日,结束时间为 10 月 13 日;南区则分别为 9 月 9 日和 10 月 31 日。每年以南、北两区域中秋雨开始最早区的秋雨开始日作为华西秋雨开始日,平均为 8 月 31 日,最早和最晚相差 1 个月;以秋雨结束最晚的区域结束日作为华西秋雨的结束日,平均为 11 月 1 日,最早和最晚相差近 2 个月,年际变率很大(表 1)。

华西秋雨除年际变化特征外,还存在较为显著的年代际变化特征。已有研究认为,华西秋雨总体具有准 12 年周期[103],9 月和 10 月分别有 8 年和 17 年以及 13 年的周期[104]。白虎志等[105]指出,20 世纪 60 年代到 70 年代初期、80 年代初期为华西秋雨的相对多雨期;70 年代中后期、80 年代中后期到 20 世纪末华西秋雨相对较少;21 世纪开始则又出现较明显的华西秋雨现象。对华西秋雨北区和南区的秋雨综合强度指数进行滑动 t 检验,发现 1990 年前后南、北区秋雨均发生了一次突变;此外,北区强度指数在 2000 年前后还发生了另一次突变。

华西秋雨与大气环流的配置和外强迫关系密切。徐桂玉等[106]研究发现,9—10 月 500 hPa 环流场上的类似欧亚型遥相关分布的水平结构是华西秋雨纬向型降水的基本条件;白虎志等[105]的研究指出,西太平洋副高、印缅槽、贝加尔湖低槽是华西秋雨的主要影响系统,其他研究也有类似结论[107-111]。

海洋状况,尤其是海表温度异常对环流型配置有重要作用。郑然等[112]研究表明:夏季西太平洋暖池关键区(5°S～5°N,130°～160°E)热含量偏高,其相对大气是一个异常热源,有利于中国南海—中南半岛附近形成异常气旋式环流,其偏东偏南气流有利于向华西地区输送大量中低纬度洋面上暖湿水汽,同时高层西风急流异常西伸,华西地区恰好位于急流入口右侧的辐散区,这种高、低层有利的耦合形势使得秋雨偏强,反之亦然。刘宣飞等[113-114]以及刘佳等[115]研究均表明:夏季 IOD 正位相年,秋季华西区域上空的热状况异常分布使大气对流增强,有利于华西秋雨偏强。陈忠明等[116]的研究则表明:2 月青藏高原东部地面热源状况与华西秋雨存在显著负相关关系,其机理主要是通过强迫500 hPa大气环流异常制约华西秋雨的多寡。赵佳玉等[117]研究认为,当 9—10 月 MJO 位于第 1～2 位相时,我国上空出现两槽一脊、西低东高的环流形势,华西地区冷空气活动频繁,且孟加拉湾、南海和西太平洋对华西地区水汽输送较强,有利于华西地区降水偏多;而当 9—10 月 MJO 位于第 3～8 位相,尤其是第 7 位相时,我国上空受较强西风带长波脊控制,上述 3 个海区对

华西地区的水汽输送较弱，造成华西秋雨偏弱。此外，大量研究表明 ENSO 循环对秋季降水的影响甚至比对夏季降水的影响更显著：El Niño 年我国秋季降水易出现南多北少的异常分布特征，而 La Niña 年则易出现北多南少的异常分布特征[118-122]。韩晋平[123]还探讨了北太平洋增暖对我国西北秋雨的影响。文献[124-126]研究了海温异常对我国华南秋季降水的影响。基于上述研究成果，影响华西秋雨强弱的前期外强迫信号及同期关键环流系统概念模型如图 9 所示。

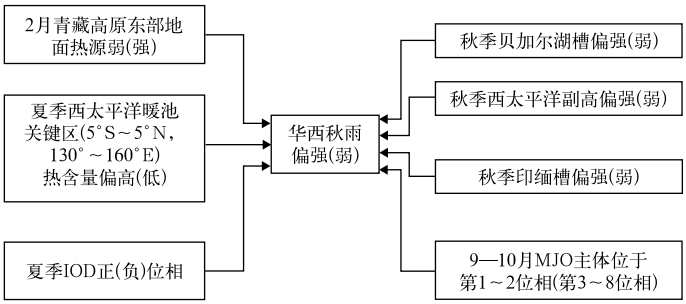

图 9 影响华西秋雨强弱的关键因子概念模型图

Fig. 9 The concept map of key factors impacting the intensity of Huaxi autumn rainfall

5 业务应用

由于预测业务和服务具有超前性，最近几年的研发工作主要是针对海温外强迫先兆信号展开，本着边研发边应用的原则，在每年 3 月底提供气候事件趋势展望，并于 4—8 月根据最新的海气演变信息分别订正华南前汛期、梅雨、华北雨季、华西秋雨等预测。表 3 为近 4 年梅雨和华北雨季的预测与实况的对比。可见气候事件开始时间的预测准确率为 75%，其中入梅日的预测准确率为 92%，明显高于华北雨季开始时间的预测。气候事件强度(雨量)的预测准确率为 81%，总体优于对开始时间的预测。雨量强弱更多地和外强迫信号的持续影响关系密切，可预报性相对较高。而气候事件的开始时间除了受海温等演变对东亚季风进程的总体影响外，还受到低频振荡和天气尺度变化的干扰，可预报性相对较低。

此外，尽管对气候事件的趋势性预测信息与实况吻合率比较高，但无法表示量级的差异，如 2015 年梅雨异常偏强而华北雨季的降水量异常偏少，旱涝并重；而 2016 年梅雨量也是异常偏强，长江流域出现区域性洪涝灾害。因此，从更好地提供防灾减灾服务角度出发，需要提供客观化的预测信息，这正是进一步努力的方向。

表 3 2015—2018 年主要气候事件实况与预测对比

Table 3 The real time prediction and observation of major climate events from 2015 to 2018

雨季	对比项	开始时间				雨量			
		2015 年	2016 年	2017 年	2018 年	2015 年	2016 年	2017 年	2018 年
江南梅雨	实况	−12 d	−14 d	−4 d	+11 d	+85%	+44%	+35%	−32%
	预测	偏早	偏早	偏晚	偏晚	偏多	偏多	偏多	偏少
长江梅雨	实况	−19 d	+5 d	+7 d	+8 d	+95%	+108%	−41%	−39%
	预测	偏早	偏晚	偏晚	偏晚	偏多	偏多	偏多	偏少
江淮梅雨	实况	+3 d	−1 d	+9 d	+7 d	+47%	+59%	−56%	−35%
	预测	偏晚	偏早	偏晚	偏晚	偏多	偏多	正常	偏少
华北雨季	实况	−3 d	−1 d	+13 d	−9 d	−52%	+19%	−28%	22%
	预测	偏晚	偏晚	偏早	偏早	偏少	略多	略多	偏多

6 展　望

已有的研发工作主要将气候事件的异常强度作为预报对象，从海温外强迫的角度挖掘前兆信号，主要从季节尺度探讨气候事件的可预报性。初步研究表明：在全球变暖的背景下，有的气候事件和影响因子之间的关系发生变化（如华西秋雨），强信号区域发生转移，需要重新诊断并建立新的预测模型。有的气候事件（如梅雨）具有显著的多时间尺度特征，需要从多尺度的角度考虑预测能力。此外，除了海温异常场外，还需要纳入积雪、极冰等其他的外强迫信号，建立多因子客观预测模型。

前期以江南入梅日期预测为代表分析了其影响系统和可能的预测信号，还需要分析各事件在季节进程中同步和非同步变异的特征和成因。如 2018 年华南前汛期开始偏早，梅雨开始均偏晚，而华北雨季开始偏早，在季节进程中并未表现一致性，预测难度大，需要从次季节尺度诊断分析并建立多尺度滚动预测模型。

下一步将继续梳理和研究汛期内气候事件在季节尺度和次季节尺度的预测信号，并评估动力气候模式是否能够反映这些可预测信号，是否可以利用多模式集合预报信息提取可预测信号并提高气候事件的客观预测能力。

参 考 文 献

[1] 王遵娅，丁一汇. 中国雨季的气候学特征. 大气科学，2008，32(1)：1-13.

[2] 吴志伟，江志红，何金海. 近 50 年华南前汛期降水、江淮梅雨、华北雨季旱涝特征对比分析. 大气科学，2006，30(3)：391-401.

[3] 李茜，魏凤英，李栋梁. 近 159 年东亚夏季风年代际变化与中国东部旱涝分布. 地理学报，2011，66(1)：25-37.

[4] 丁一汇，柳俊杰，孙颖，等. 东亚梅雨系统的天气-气候学研究. 大气科学，2007，31(6)：1082-1101.

[5] 竺夏英，何金海，吴志伟. 长江中下游入梅指数及早晚年的海气背景特征. 大气科学，2008，32(1)：113-122.

[6] Wang J，He J H，Liu X F，et al. Interannual variability of the Meiyu onset over Yangtze-Huaihe River Valley and analyses of its previous strong influence signal. *Chinese Science Bulletin*，2009，54(4)：687-695，DOI：10.1007/s11434-008-0534-8.

[7] 梁萍，丁一汇. 东亚梅雨季节内振荡的气候特征. 气象学报，2012，70(3)：418-435.

[8] 郭其蕴，沙万英. 华南前汛期降水变率的分析. 应用气象学报，1998，9(1)：9-15.

[9] 池艳珍，何金海，吴志伟. 华南前汛期不同降水时段的特征分析. 南京气象学院学报，2005，28(2)：163-171.

[10] 马玉坤，张培群，王世公，等. 华南前汛期夏季风降水开始日期的确定. 干旱气象，2015，33(2)：332-339.

[11] 林之光. 中国气候. 上海：上海科学技术出版社，1985：76-80.

[12] 强学民，杨修群. 华南前汛期开始和结束日期的划分. 地球物理学报，2008，51(5)：1333-1345.

[13] 伍红雨，杨崧，蒋兴文. 华南前汛期开始日期异常与大气环流和海温变化的关系. 气象学报，2015，73(2)：319-330.

[14] Gu Wei，Lin Wang，Hu Zeng-Zhen，et al. Interannual variations of the first rainy season precipitation over South China. *J Climate*，2018，31(2)：623-640.

[15] 吴尚森，梁建茵. 华南前汛期旱涝时空分布特征. 热带气象，1992，8(1)：87-92.

[16] 张焱，孙照渤，白莹莹，等. 近 47a 华南前汛期旱涝特征. 南京气象学院学报，2008，31(2)：176-182.

[17] 马慧，王谦谦，陈桢华. 华南前汛期降水异常的时空变化特征. 高原气象，2006，25(2)：325-329.

[18] 丁菊丽，徐志升，费建芳，等. 华南前汛期起止日期的确定及降水年际变化特征分析. 热带气象学报，2009，25(1)：59-65.

[19] 李丽平，章开美，王超，等. 近 40 年华南前汛期极端降水时空演变特征. 气候与环境研究，2010，15(4)：443-450.

[20] 覃武，孙照渤，丁宝善，等. 华南前汛期雨季开始期的降水及环流特征. 南京气象学院学报，1994，17(4)：455-461.

[21] 苗春生，吴志伟，何金海，等. 近 50 年东北冷涡异常特征及其与前汛期华南降水的关系分析. 大气科学，2006，30(6)：1249-1256.

[22] 苗春生，吴志伟，何金海. 北半球环状模（NAM）、东北冷涡与前汛期华南旱涝. 热带气象学报，2006，22(6)：593-599.

[23] 胡娅敏，翟盘茂，罗晓玲，等. 2013 年华南前汛期持续性强降水的大尺度环流与低频信号特征. 气象学报，2014，72(3)：465-477.

[24] 袁媛，任福民，王艳姣，等. 2012 年华南前汛期降水特征及环流异常分析. 气象，2012，38(10)：1247-1254.

[25] 罗艳艳，何金海，邹燕，等. 华南前汛期雨涝强、弱年的确定及其环流特征对比. 气象科学，2015，35(2)：160-166.

[26] 徐淑爱. 冬季风异常年份的环流特征及其与华南前汛期降水的关系. 热带气象，1988，4(3)：263-271.

[27] 蔡学湛，王岩，许金镜. 热带对流活动异常对华南前汛期旱涝影响的诊断分析. 热带气象学报，2002，18(2)：157-164.

[28] 黄先香，炎利军，施能. 华南前汛期旱涝影响因子和预报方法. 热带气象学报，2006，22(5)：431-438.

[29] 强学民，杨修群. 华南前汛期降水异常与太平洋海表温度异常的关系. 地球物理学报，2013，56(8)：2583-2593.

[30] Li Weijing，Ren Hongchang，Zuo Jinqing，et al. Early summer southern China rainfall variability and its oceanic drivers. *Climate Dyn*，2018，50：4691-4705.

[31] Chang Tao-Chi，Hsu Huang-Hsiung，Hong Chi-Cherng. Enhanced influences of tropical Atlantic SST on WNP-NIO atmosphere-ocean coupling since the Early 1980s. *J Climate*，2016，29(18)：6509-6525.

[32] 王彦明，高建芸，池艳珍，等. 太平洋海温场不同时间尺度背景下华南前汛期持续性暴雨的统计特征. 大气科学学报，2015，38(1)：126-131.

[33] 章开美,李丽平,项连东,等.华南前汛期极端降水气候变化特征及其与太平洋海温相关关系研究.气象与减灾研究,2015,38(1):1-7.
[34] 蔡学湛.青藏高原雪盖与东亚季风异常对华南前汛期降水的影响.应用气象学报,2001,12(3):358-367.
[35] 张爱华,吴恒强.南半球大气环流对华南前汛期降雨影响初探.气象,1997,23(8):10-15.
[36] 吴恒强,张爱华,蒋伯仁,等.华南前汛期降水与南极海冰变化的关系.南京气象学院学报,1998,21(2):266-273.
[37] 林春育.长江中下游的梅雨和预报.气象,1979,5(5):2-8.
[38] 李小泉.从整体上研究梅雨期的划分.气象,1981,7(6):9-10.
[39] 魏凤英,张京江.1885—2000年长江中下游梅雨特征量的统计分析.应用气象学报,2004,15(3):313-321.
[40] 周后福.梅雨期划分方法的再提出.成都信息工程学院学报,2005,20(4):483-487.
[41] 闵屾,钱永甫.江淮梅雨分区特征的比较研究.应用气象学报,2008,19(1):19-27.
[42] 胡娅敏,丁一汇,廖菲.江淮地区梅雨的新定义及其气候特征.大气科学,2008,32(1):101-112.
[43] 梁萍,丁一汇,何金海,等.江淮区域梅雨的划分指标研究.大气科学,2010,34(2):418-428.
[44] 李勇,金荣花,周宁芳,等.江淮梅雨季节强降雨过程特征分析.气象学报,2017,75(5):717-728.
[45] 赵俊虎,陈丽娟,熊开国.基于新监测指标的江南入梅早晚的气候特征及影响系统分析.气象学报,2018,76(5):680-698.
[46] 叶笃正,陶诗言,李麦村.在六月和十月大气环流的突变现象.气象学报,1958,16(4):249-263.
[47] 陶诗言,赵煜佳,陈晓敏.东亚的梅雨期与亚洲上空大气环流季节变化的关系.气象学报,1958,29(2):119-134.
[48] Tao S Y,Chen L X. A Review of Recent Research on the East Asian Summer Monsoon in China//Chang C P,Krishnamurti T N. Monsoon Meteorology. Oxford: Oxford University Press,1987:60-92.
[49] 陶诗言,朱文妹,赵卫.论梅雨的年际变异.大气科学,1988,12(特刊I):13-21.
[50] 徐海明,何金海,周兵.江淮入梅前后大气环流的演变特征和西太平洋副高北跳西伸的可能机制.应用气象学报,2001,12(2):150-158.
[51] 陶诗言,李吉顺,王昂生.东亚季风与我国洪涝灾害.中国减灾,1997,7(4):17-24.
[52] 黄荣辉,孙凤英.热带西太平洋暖池的热状态及其上空的对流活动对东亚夏季气候异常的影响.大气科学,1994,18(2):141-151.
[53] 刘宗秀,曹鸿兴.北极海冰对我国梅雨及气候预报的指示意义.气象,1994,20(11):21-24.
[54] 张庆云,陶诗言.夏季东亚热带和副热带季风与中国东部汛期降水.应用气象学报,1998,9(增刊I):17-23.
[55] 吴统文,钱正安.青藏高原冬春积雪异常与中国东部地区夏季降水关系的进一步分析.气象学报,2000,58(5):570-581.
[56] 黄荣辉,陈际龙,周连童,等.关于中国重大气候灾害与东亚气候系统之间关系的研究.大气科学,2003,27(4):770-787.
[57] 魏凤英,宋巧云.全球海表温度年代际尺度的空间分布及其对长江中下游梅雨的影响.气象学报,2005,63(4):477-484.
[58] 郭玲,何金海,祝从文.影响长江中下游夏季降水的前期潜在预报因子评估.大气科学,2012,36(2):337-349.
[59] Li Y N,Deng Y,Yang S,et al. Multi-scale temporospatial variability of the East Asian Meiyu-Baiu fronts: Characterization with a suite of new objective indices. *Climate Dyn*,2018,51:1659-1670.
[60] Sampe T,Xie S P. Large-scale dynamics of the Meiyu-Baiu rainband: Environmental forcing by the Westerly Jet. *J Climate*,2010,23:113-134.
[61] Gu W,Li C Y,Wang X,et al. Linkage between Mei-yu precipitation and North Atlantic SST on the decadal timescale. *Adv Atmos Sci*,2009,26(1):101-108.
[62] 梁萍,陈丽娟,丁一汇,等.长江梅雨的长期变率与海洋的关系及其可预报性研究.气象学报,2018,76(3):379-393.
[63] Huang Y,Zhang Y C,Huang A N,et al. Analysis of the simulated different-class Meiyu precipitation and associated circulation by the BCC_AGCM2.0.1. *Theor Appl Climatol*,2015,120:631-641.
[64] Zhu J,Huang D Q,Yang T. Changes of Meiyu system in the future under A1B scenario simulated by MITOC_Hires model. *Theor Appl Climatol*,2016,123:461-471.
[65] 竺可桢.东南季风与中国之雨量.地理学报,1934,1(1):1-27.
[66] 杨杰,赵俊虎,郑志海,等.华北汛期降水多因子相似订正方案与预报试验.大气科学,2012,36(1):11-22.
[67] 郝立生,丁一汇,闵锦忠.东亚夏季风变化与华北夏季降水异常的关系.高原气象,2016,35(5):1280-1289.
[68] 黄荣辉,顾雷,徐予红,等.东亚夏季风爆发和北进的年际变化特征及其与热带西太平洋热状态的关系.大气科学,2005,29(1):20-36.
[69] 孙淑清.东亚大尺度低空急流的背景场与东半球的越赤道气流.气象学报,1986,4(1):55-61.
[70] 梁平德.印度夏季风与我国华北夏季降水量.气象学报,1988,46(1):75-81.
[71] 刘芸芸,丁一汇.印度夏季风与中国华北降水的遥相关分析及数值模拟.气象学报,2008,66(5):789-799.
[72] 林大伟,布和朝鲁,谢作威.夏季中国华北与印度降水之间的关联及其成因分析.大气科学,2016,40(1):201-214.
[73] 卫捷,张庆云,陶诗言.近20年华北地区干旱期大气环流异常特征.应用气象学报,2003,14(2):140-151.
[74] Wang H J,He S P. The North China/northeastern Asia severe summer drought in 2014. *J Climate*,2015,28(17):6667-6681,DOI:10.1175/JCLI-D-15-0202.1.
[75] Xu Z,Fan K,Wang H. Decadal variation of summer precipitation over China and associated atmospheric circulation after the late 1990s. *J Climate*,2015,28:4086-4106.
[76] 陆日宇.华北汛期降水量变化中年代际和年际尺度的分离.大气科学,2002,26(5):611-24.
[77] 杜银,张耀存,谢志清.东亚副热带西风急流位置变化及其对中国东部夏季降水异常分布的影响.大气科学,2009,33(3):581-592.
[78] 龚道溢,朱锦红,王绍武.长江流域夏季降水与前期北极涛动的显著相关.科学通报,2002,47(7):546-549.
[79] 黄樱,钱永甫.南亚高压与华北夏季降水的关系.高原气象,

2003，22(6)：602-607.

[80] 范可，王会军. 有关南半球大气环流与东亚气候的关系研究的若干新进展. 大气科学，2006，30(3)：402-412.

[81] 章颖，赵平. 夏季亚洲-太平洋遥相关季节演变与大气环流和降水. 气象学报，2012，70(5)：1055-1063.

[82] 李琛，李双林. 索马里和澳大利亚越赤道气流的协同变化与我国夏季降水型. 科学通报，2016，61(13)：1453-1461.

[83] 史久恩，林学椿，周琴芳. 厄尔尼诺现象和我国夏季(6—8 月)降水、气温的关系. 气象，1983，9(4)：2-5.

[84] 林学椿，于淑秋. 厄尔尼诺与我国汛期降水. 气象学报，1993，51(4)：434-441.

[85] Yeh S W，Kug J S，Dewitte B，et al. El Niño in a changing climate. *Nature*，2009，461(7263)：511-514.

[86] 黄平，黄荣辉. El Niño 事件对其衰减阶段夏季中国降水季节内演变的影响及其机理. 大气科学学报，2010，33(5)：513-519.

[87] Feng J，Chen W，Tam C Y，et al. Different impacts of El Niño and El Niño Modoki on China rainfall in the decaying phases. *Int J Climatol*，2011，31(14)：2091-2101.

[88] 袁媛，杨辉，李崇银. 不同分布型厄尔尼诺事件及对中国次年夏季降水的可能影响. 气象学报，2012，70(3)：467-478.

[89] Yuan Y，Song Y. Impacts of different types of El Niño on the East Asian climate：Focus on ENSO cycles. *J Climate*，2012，25(21)：7702-7722.

[90] Capotondi A，Wittenberg A T，Newman M，et al. Understanding ENSO diversity. *Bull Amer Meteor Soc*，2015，96(6)：921-938.

[91] 李春晖，李霞，刘燕，等. 春季和夏季爆发型 ENSO 事件对夏季中国降水的影响. 气候与环境研究，2016，21(3)：258-268.

[92] 赵俊杰，薛峰，林万涛，等. El Niño 对东亚夏季风和夏季降水季节内变化的影响. 气候与环境研究，2016，21(6)：678-686.

[93] 陈圣劼，何金海. 两类 El Niño 不同衰减型的演变特征及其与我国夏季降水的联系. 海洋学报，2017，39(1)：11-27.

[94] 吴萍，丁一汇，柳艳菊. 厄尔尼诺事件对中国夏季水汽输送和降水分布影响的新研究. 气象学报，2017，75(3)：371-383.

[95] 杨明珠，丁一汇. 中国夏季降水对南印度洋偶极子的响应研究. 大气科学，2007，31(4)：685-694.

[96] 陈烈庭. 青藏高原冬春季异常雪盖与江南前汛期降水关系的检验和应用. 应用气象学报，1998，9(增刊 I)：2-9.

[97] 张顺利，陶诗言. 青藏高原积雪对亚洲夏季风影响的诊断及数值研究. 大气科学，2001，25(3)：372-390.

[98] 于琳琳，陈海山. 青藏高原 4 月陆面状况和地表加热异常与中国夏季降水的联系. 高原气象，2012，31(5)：1173-1182.

[99] 谢付莹，何金海. 华北夏季降水与哈得孙湾海冰的相关分析. 南京气象学院学报，2003，26(3)：308-316.

[100] Li Y，Leung L R. Potential impacts of the Arctic on interannual and interdecadal summer precipitation over China. *J Climate*，2013，26：899-917.

[101] 于晓澄，赵俊虎，杨柳，等. 华北雨季开始早晚与大气环流和海表温度异常的关系. 大气科学，2019，43(1)：107-118.

[102] 赵树云，陈丽娟，崔童. ENSO 位相转换对华北雨季降水的影响. 大气科学，2017，41(4)：857-868.

[103] 王春学，马振峰，邵鹏程，等. 我国华西秋雨的气候变化规律及其影响因子. 干旱区研究，2015，32(6)：1113-1121.

[104] 冯丽文，郭其蕴. 华西秋雨的多年变化. 地理研究，1983，2(1)：74-84.

[105] 白虎志，董文杰. 华西秋雨的气候特征及成因分析. 高原气象，2004，23(6)：884-889.

[106] 徐桂玉，林春育. 华西秋雨特征及成因探讨. 气象科学，1994，14(2)：149-154.

[107] 何敏. 我国主要秋雨区的分布及长期预报. 气象，1984，10(9)：10-13.

[108] 鲍媛媛，阿布力米提，李峰，等. 2001 年华西秋雨时空分布特点及成因分析. 应用气象学报，2003，14(2)：215-222.

[109] 谌芸，施能. 我国秋季降水、温度的时空分布变化特征及气候变化. 南京气象学院学报，2003，26(5)：622-630.

[110] 孙照渤，黄艳艳，倪东鸿. 我国秋季连阴雨的气候特征及大气环流特征. 大气科学学报，2016，39(4)：480-489.

[111] 徐金霞，闫彩霞，钟燕川，等. 北半球秋季欧亚遥相关与华西秋雨的关系. 气象科技，2017，45(3)：492-498.

[112] 郑然，刘嘉慧敏，马振峰. 夏季西太平洋暖池热含量对华西秋雨的影响及可能的物理机制. 气象学报，2017，76(5)：714-725.

[113] 刘宣飞，袁慧珍. 印度洋偶极子与中国秋季降水的关系. 南京气象学院学报，2006，29(5)：644-649.

[114] 刘宣飞，袁慧珍. ENSO 对印度洋偶极子与中国秋季降水关系的影响. 南京气象学院学报，2006，29(6)：762-768.

[115] 刘佳，马振峰，杨淑群，等. 印度洋偶极子和华西秋雨的关系. 高原气象，2015，34(4)：950-962.

[116] 陈忠明，刘富明，赵平，等. 青藏高原地表热状况与华西秋雨. 高原气象，2001，20(1)：94-99.

[117] 赵佳玉，马振峰，范广洲. 热带大气季节内振荡对华西秋雨的影响. 高原气象，2016，35(6)：1487-1497.

[118] 龚道溢，王绍武. ENSO 对中国四季降水的影响. 自然灾害学报，1998，7(4)：44-52.

[119] Zhang R H，Sumi A，Kimoto M. A diagnostic study of the impact of El Niño on the precipitation in China. *Adv Atmos Sci*，1999，16：229-241.

[120] 李耀辉，李栋梁，赵庆云，等. ENSO 对中国西北地区秋季异常降水的影响. 气候与环境研究，2000，5(2)：205-213.

[121] 谌芸，施能. 厄尔尼诺/南方涛动与我国秋季气候异常. 热带气象学报，2003，19(2)：137-146.

[122] 王春学，马振峰，王佳津，等. 华西秋雨准 4 年周期特征及其与赤道太平洋海表温度的关系. 大气科学，2015，39(3)：643-652.

[123] 韩晋平. 北太平洋增暖对我国西北秋雨的影响. 应用气象学报，2014，25(3)：257-264.

[124] Niu N，Li J P. Interannual variability of autumn precipitation over South China and its relation to atmospheric circulation and SST anomalies. *Adv Atmos Sci*，2008，25(1)：117-125.

[125] 顾薇，李维京，陈丽娟，等. 我国秋季降水的年际变化及与热带太平洋海温异常分布的关系. 气候与环境研究，2012，17(4)：467-480.

[126] Gu W，Wang L，Li W，et al. Influence of the tropical Pacific east-west thermal contrast on the autumn precipitation in South China. *Int J Climatol*，2015，35(7)：1543-1555.

Advances of Research and Application on Major Rainy Seasons in China

Chen Lijuan[1)2)] Zhao Junhu[1)] Gu Wei[1)] Liang Ping[3)] Zhi Rong[1)]
Peng Jingbei[4)] Zhao Shuyun[1)] Gao Hui[1)] Li Xiang[1)] Zhang Peiqun[1)]

[1)] (*Laboratory for Climate Studies, National Climate Center, China Meteorological Administration, Beijing* 100081)

[2)] (*Collaborative Innovation Center on Forecast and Evaluation of Meteorological Disasters, Nanjing University of Information Science & Technology, Nanjing* 210044)

[3)] (*Shanghai Regional Climate Center, Shanghai* 200030)

[4)] (*Institute of Atmospheric Physics, Chinese Academy of Sciences, Beijing* 100029)

Abstract

The pre-rainy season in South China, Meiyu, rainy season in North China and autumn rainfall in West China are important phenomena influenced by the process of the East Asian summer monsoon (EASM). These regional rainy seasons determine the distribution and evolution of drought and flood during the flood season over mid-eastern China. Therefore, the prediction of regional rainy seasons plays an important role in the meteorological service of flood season.

The research progress on characteristics and influencing factors of major rainy seasons during flood season in China are reviewed. In order to meet the demand of prediction operation, the influence and mechanism of the previous sea surface temperature (SST) and related atmosphere circulation systems on climatic events are analyzed firstly, and the statistical prediction models can be established based on that.

Recent studies show that SST anomalies (SSTAs) are important forecast signals of rainy seasons. However, the influence and spatial-temporal pattern of SST vary with the interannual and interdecadal variation characteristics of different events. For instance, the interannual variation of precipitation in the pre-rainy season in South China can be better explained using the east-west SST contrast index in the tropical Pacific. Multiple timescale variation characteristics of Meiyu over the Yangtze River correspond to different SST forcing. Key regions of SST associated with interannual variation of Meiyu over the Yangtze River are in tropics. For the interdecadal or mutli-decadal time scale of Meiyu variations, the SST in middle and high latitudes may play an important role. The intensity of rainy-season precipitation in North China is not only coincident with the ENSO phase-switching, but also influenced by the developing speed of ENSO event. The key SST region that influences autumn rain in West China has changed with the inter-decadal changing background, which requires updating impact factors and models.

These results provide strong support for the real-time prediction of climate events in recent years. During 2015—2018, the prediction accuracy of the onset date and intensity (rainfall) of Meiyu and rainy season in North China is 75% and 81%, respectively.

Key words: regional rainy seasons; pre-rainy season in South China; Meiyu; rainy season in North China; autumn rainfall in West China

基于最大熵模型的中国血吸虫病传播风险评估

段居琦[1,2] 周骥[2] 黄大鹏[1] 刘绿柳[1]

(1 国家气候中心中国气象局气候研究开放实验室,北京 100081; 2 上海市气象与健康重点实验室,上海 200135)

摘要 气候生态因子是影响媒介传播性疾病流行风险的重要环境因素。本研究根据文献调研选取影响中国血吸虫病传播风险的潜在气候生态因子,基于各潜在因子的作用大小确定影响中国血吸虫病传播风险的主导因子,发展主导气候生态因子-血吸虫病关系的最大熵模型并评价其对中国区域血吸虫病传播风险的模拟效果。结果表明:影响中国血吸虫病传播风险的气候生态因子有年降水量、最暖月平均气温、稳定通过 10 ℃持续日数和增强型植被指数(EVI),其累积贡献率为研究因子总贡献的 98.6%;最大熵模型能较好地揭示中国血吸虫病传播风险与主导气候生态因子关系,其受试者特征曲线(ROC)评价结果为"非常好"(AUC 为 0.917);模型模拟的中国血吸虫病传播中高风险区位于江苏南部、浙江北部、广西中部、广东北部、云南北部、四川中部及湖北东部、湖南东北部、安徽中部、江西北部等地。研究结果对气候环境影响下中国血吸虫传播风险评估和疾病预防宏观对策制定具有工具价值和参考意义。

关键词 血吸虫病;传播风险;气候生态因子;评估模型;最大熵模型

中图分类号: P49 **DOI**: 10.19517/j.1671-6345.20180347 **文献标识码**: A

引言

政府间气候变化专门委员会(IPCC)第 5 次评估报告[1]指出,气候变暖为与疾病有关的媒介及病原体的寄生、繁殖和传播创造了适宜条件,导致媒介传播性疾病呈现新的流行态势。血吸虫病(*Schistosomiasis*)是以钉螺为中间宿主的严重危害人类健康的媒介传播性疾病,其致病因子血吸虫及传播媒介钉螺的生长发育与气候生态因子密切相关[2-5],是气候变化健康影响评估和流行病学的重要研究对象[6]。因此,在分析血吸虫病与气候生态因素关系的基础上,构建气候生态-血吸虫病关系模型,进行中国血吸虫病传播风险分析,可以为提高气候健康影响评估能力和制定疾病预防策略提供支撑。

气候环境变化对传播性疾病影响的评估模型可分为因子决定性模型和数理统计学模型两大类[5]。因子决定性模型多根据生物学实验得出寄生虫或中间宿主的最低或最高发育阈值来预测疾病的流行范围;数理统计学模型则采用数理统计学方法,如Logistic多因素回归模型、贝叶斯空间模型等找出主要决定因子,然后应用建立的模型进行预测。在因子决定性模型研究方面,Thomas[7]应用风险图方法建立了稳定恶性疟疾非洲地区气候模型。Craig等[8]使用气候对疾病的决定性关系建立了一个恶性疟疾流行的空间模型。Zhou 等[9]分析了过去 30 年中国钉螺的潜在孳生区,并预测了 2030 年和 2050 年中国血吸虫病潜在流行区的空间分布。在统计学模型研究方面,Rogers 等[10]根据全球疟疾分布图和 IPCC 发表的气象数据,构建最佳统计模型,并预测了未来气候变化情景下全球疟疾分布,但其预测结果与 Thomas[7]应用风险图方法的研究结果存在很大差异;Jetten 等[11]以蚊类临界密度阈值的倒数表示疟疾流行潜势,模拟了当前气候及未来气候增量情景下全球各地恶性疟疾的年平均流行潜势;Yang 等[12]应用贝叶斯 Logistic 回归模型研究了江苏省气候环境敏感因子对血吸虫病传播的影响;Hales 等[13]采用 Logistic 回归模型分析了全球登革热的流行风险。

上海市气象与健康重点实验室开放基金课题"基于最大熵模型的我国血吸虫病传播潜势研究"(QXJK201405)资助

作者简介:段居琦,男,博士,高级工程师,主要从事气候影响与风险评估研究,Email:duanjq@cma.gov.cn

收稿日期:2018 年 6 月 22 日;定稿日期:2019 年 1 月 2 日

最大熵模型(Maximum Entropy Model, MaxEnt)是基于有限的已知信息对未知分布进行无偏推断的一种数学方法[14-15]。经过训练站点定义之后的最大熵模型可以估计具有同样环境变量的其他站点的物种存在概率。该理论在物种分布、入侵及病虫害流行研究中得到了较广泛应用[16-18],也有研究基于最大熵模型进行钉螺滋生地提取[19],显示了其在媒介传播性疾病传播风险评估中的潜在价值。本研究拟基于最大熵模型,阐明影响中国血吸虫病传播风险的主导气候生态因子,构建气候生态-血吸虫病传播风险的最大熵模型并评价,以为气候环境变化下中国区域血吸虫病传播风险评估和预防策略制定提供新的工具支撑和参考依据。

1　材料与方法

1.1　数据收集

本研究使用的数据主要有气候数据、MODIS卫星遥感植被数据和血吸虫病监测站点信息。气候数据来自于国家气象信息中心,为1971—2010年一个气候标准年的我国地面气候资料日值数据集中的741个气象站点记录,采用空间卷积算法,结合气象站点位置的截断高斯滤波算子作为距离权重方程[20],将日平均气温和日降水量2个气候要素插值到空间分辨率10 km×10 km网格点上,作为基础气候数据集。MODIS卫星遥感增强型植被指数(EVI)数据(2001—2010年)来自于美国NASA公开数据产品。血吸虫病监测站点信息来自于《全国血吸虫病监测方案(2011年修订版)》(图1)。

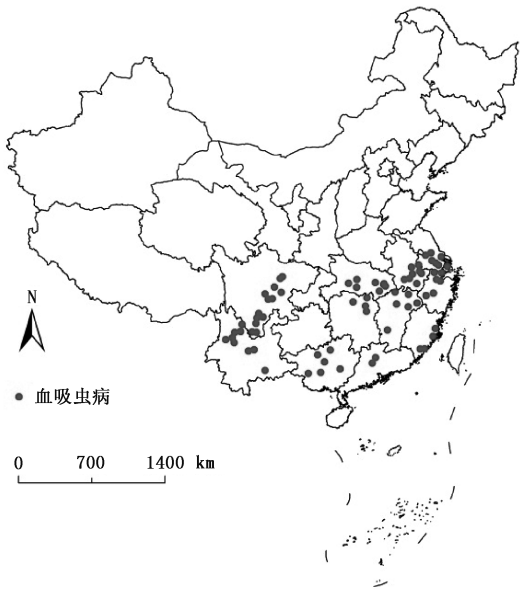

图1　中国血吸虫病监测站点信息

1.2　潜在气候生态影响因子选取

血吸虫病传播主要受中间宿主钉螺的分布和血吸虫发育的影响。参考已有研究成果和常用气候指标[2,4,5,9,21-22],从全国层次及年尺度考虑,筛选9个具有明确生物学意义的可能影响血吸虫病传播的气候生态因子,包括≥0 ℃积温、≥10 ℃积温、稳定通过10 ℃持续日数、最冷月(1月)平均气温、最暖月(7月)平均气温、最暖最冷月气温年较差、年降水量、湿润指数和增强型植被指数(EVI)。最冷月平均温度、最暖月平均温度、最冷最暖月平均温度差是从热量强度方面反映热量资源;≥0 ℃积温、≥10 ℃积温从热量累积程度方面反映热量资源;稳定通过10 ℃持续日数从持续时间方面反映热量资源;年降水量、湿润指数从绝对数量和收支平衡方面反映水分资源;增强型植被指数(EVI)反映钉螺孳生环境。各潜在气候因子计算采用1971—2000年平均值代表常态值;增强型植被指数(EVI)采用2001—2010年平均值代表常态值。

1.3　基于最大熵模型的血吸虫病传播风险评估

熵是一个系统具有的不确定度的量度,在信息论、统计物理、热力学等多学科中广为应用[23]。最大熵理论由Jaynes于1957年提出,该理论认为,在无外力作用下,事物总是在约束条件下争取最大的自由权,在已知条件下,熵最大的事物最可能接近它的真实状态[14]。最大熵统计建模就是从符合条件的概率分布中选择熵最大的分布作为最优分布,因此可以用于物种分布预测[15,23]。

最大熵模型预测血吸虫病传播风险的原理为:假设引起血吸虫病传播的环境条件未知,判断血吸虫病在某地是否发生的最合理预测就是发生与不发生各占50%。最大熵模型选择熵最大的分布作为最优分布,在已知血吸虫病发生点样本训练的基础上,估计具有同样环境变量的其他站点血吸虫病发生概率 p,取值范围为[0,1],根据发生概率 p 的大小,确定血吸虫病风险的高低[15-16]。考虑气候保证率因素[24],将传播风险进行风险等级划分,具体依据如下:受气候影响的传播风险指数分区标准结合不同气候保证率来划分,取概率<50%保证率为极低风险区,50%～80%保证率为低风险区,80%～

90%保证率为中风险区，≥90%保证率为高风险区。考虑到不同气候保证率(a)以及影响中国血吸虫病传播的4个主导因子，则某地血吸虫病传播风险等级的气候指标拟为a^4，即$0.5^4=0.06$(极低风险与低风险界限)、$0.8^4=0.41$(低风险区与中风险区界限)、$0.9^4=0.65$(中风险区与高风险区界限)。

研究选用MaxEnt模型3.3.3a版(http://www.cs.princeton.edu/~schapire/maxent/)；结合ArcGIS 9.3的空间分析功能，进行最大熵模型模拟的血吸虫病发生概率与气候生态因子关系分析。

2 结果分析

2.1 最大熵模型的适用性评价

常用的模型评价指标有总体准确性、灵敏度、特异度、Kappa统计量、TSS和AUC[25]。最大熵模型采用模型输出的受试者特征(Receiver Operating Characteristic，ROC)曲线的曲线下面积(Area Under Curve，AUC)值评估模型模拟的准确性。ROC曲线是以预测结果的每一个值作为可能的判断阈值，由此计算得到相应的灵敏度和特异度，然后以假阳性率即(1－特异度)为横坐标，以真阳性率即灵敏度(1－遗漏率)为纵坐标绘制而成。ROC曲线下面积AUC值的大小可作为模型预测准确度的衡量指标，其取值范围为[0，1][15]。AUC值越大，表示该构建模型的预测准确性越好；当AUC大于0.75时，认为构建的模型可用。AUC值的具体评估标准为：0.90～1.0(非常好)，0.80～0.90(好)，0.70～0.80(一般)，0.60～0.70(较差)，0.50～0.60(失败)[15]。ROC曲线绘制及AUC值的具体计算由最大熵模型直接输出。基于潜在气候因子构建的中国血吸虫病传播风险的最大熵模型的AUC值达0.905，表明所构建模型的预测准确性达到“非常好”的标准，可以用于中国血吸虫病传播风险研究。

2.2 影响血吸虫病传播风险的主导气候生态因子

建立统计学模型的关键过程之一是确定主导影响因子。为此，本研究根据最大熵模型迭代计算确定的潜在气候生态因子对中国血吸虫病风险影响的贡献程度，筛选影响中国血吸虫病传播的主导因子。各潜在气候生态因子对中国血吸虫病传播风险影响的重要性排序为：年降水量、最暖月平均气温、稳定通过10 ℃持续日数、增强型植被指数(EVI)、气温年较差、稳定通过10 ℃积温、最冷月平均气温、稳定通过0 ℃积温、湿润指数(表1)。根据各潜在气候生态因子对中国血吸虫病传播风险影响的贡献程度从大到小选取变量，年降水量、最暖月平均气温、稳定通过10 ℃持续日数和增强型植被指数(EVI)的累积贡献百分率达到研究因子总贡献的98.6%，可以认为这4个因子是影响中国血吸虫病传播风险的主导气候生态因子。气候生态条件呈现较大的空间差异，从水分条件来看(图2a)，年降水量为52～2203 mm，南方较多，北方较少；从热量强度条件来看(图2b)，最暖月平均气温为－0.4～30.8 ℃，除青藏高原地区外，其他地区均有较高温度时段出现；从热量累积条件来看(图2c)，稳定通过10 ℃积温为0～9108 ℃·d，青藏高原、东北地区及内蒙古等地热量累积不足，南方大部、华北及新疆等地热量累积较好；从植被生态条件看(图2d)，中国中东部大部地区植被条件较好，增强型植被指数在0～0.658，而内蒙古西部、甘肃北部、青海北部及西藏大部、新疆大部植被条件较差，增强型植被指数为－0.30～0，表示这些地区以岩石和裸土为主，或为水、雪覆盖。

表1 中国血吸虫病传播风险影响因子贡献程度

潜在影响因子	贡献百分率	累计贡献百分率
年降水量	84.6	84.6
最暖月平均气温	8.5	93.1
稳定通过10 ℃持续日数	2.8	95.9
增强型植被指数	2.7	98.6
气温年较差	0.4	99.0
稳定通过10 ℃积温	0.4	99.4
最冷月平均气温	0.3	99.7
稳定通过0 ℃积温	0.3	100
湿润指数	0.0	100

基于筛选的主导影响因子，结合最大熵模型，重新构建血吸虫病传播风险模拟模型。结果显示，基于主导气候因子的AUC值达0.917，模拟结果准确性达到非常好的标准且精度提高，表明基于筛选的主导影响因子构建的模型可用于中国血吸虫病传播潜在风险模拟。

2.3 血吸虫病传播风险及气候生态因子特征

基于最大熵模型以及影响中国血吸虫病传播风险的气候生态因子，给出了血吸虫病在待预测地区的发生概率p(图3)。受气候生态条件制约，中国南方地区血吸虫病传播风险较高，北方地区传播风险较低。血吸虫病传播的高风险区位于上海、江苏南

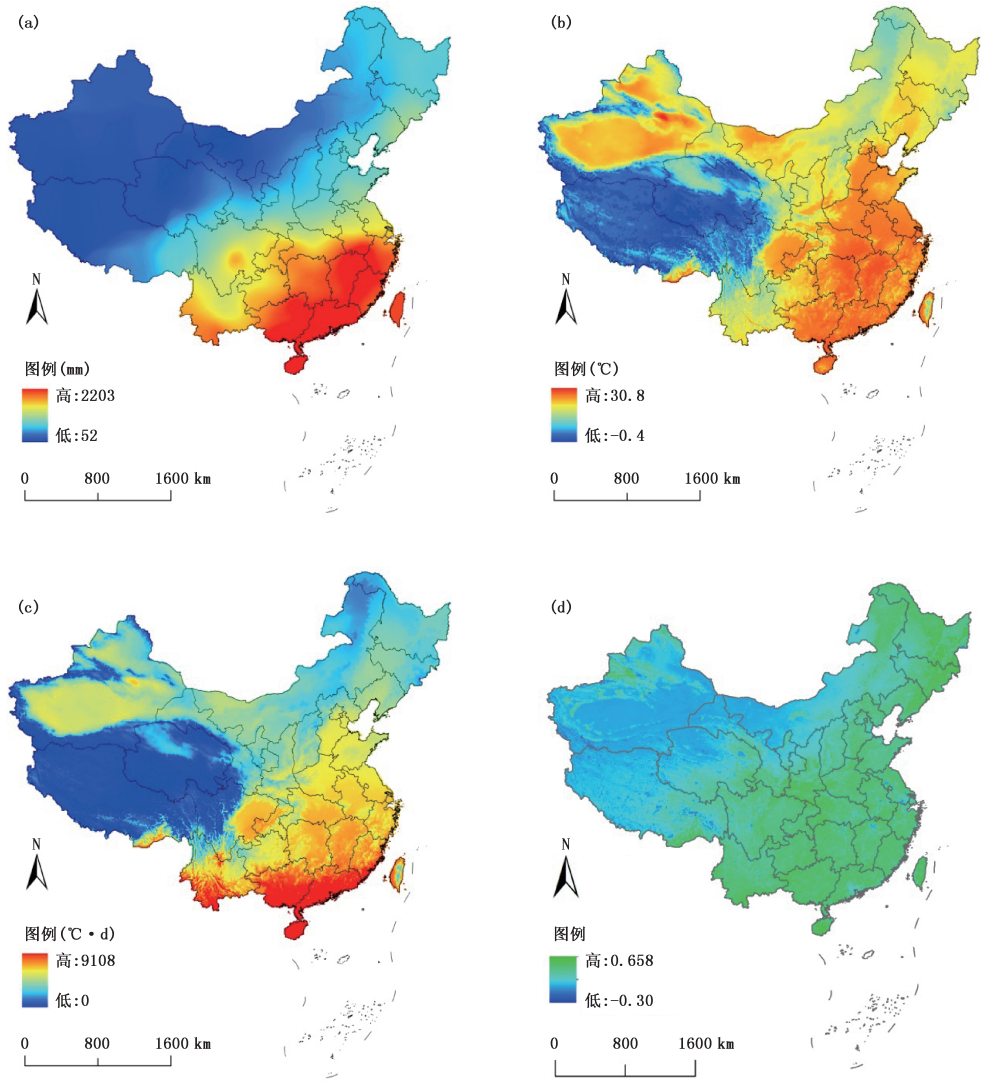

图 2　研究区域气候生态因子空间分布:(a) 年降水量,(b)最暖月平均气温,(c)稳定通过 10 ℃积温,(d)增强型植被指数

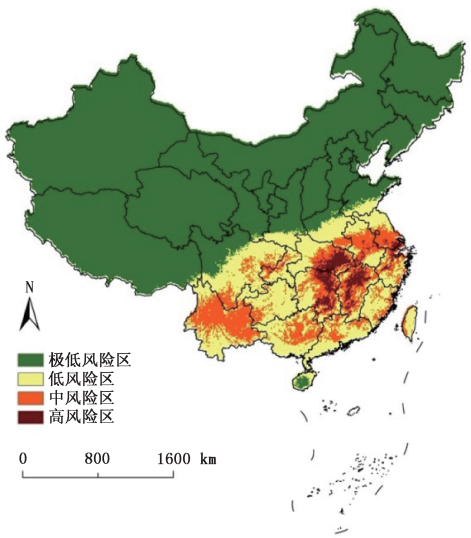

图 3　中国血吸虫病传播风险图

部、湖北东部、湖南东部、江西中北部、浙江北部等地,该地区气候因子阈值为年降水量 1095～1927 mm、最暖月平均气温 19.7～29.3 ℃、稳定通过 10 ℃持续日数 221～339 d 和增强型植被指数(EVI)为 0～0.47(表 2),主要属于北亚热带和中亚热带湿润区,冬温夏热、降水丰沛,区域内水网密布,常与江河湖泊相通,对钉螺繁殖和血吸虫病传播极为有利。中风险区位于江苏南部、安徽中部、河南南部、浙江北部、湖北东部、湖南东部、江西大部、云南北部、广西北部、广东北部、四川东部等地,该地区气候因子阈值为年降水量 996～2150 mm、最暖月平均气温 7.2～29.3 ℃、稳定通过 10 ℃持续日数 221～339 d 和增强型植被指数(EVI)为 0～0.47。低风险区主要位于江苏北部、河南中部、湖北西部、四川东部、重庆

表2 中国血吸虫病传播风险区气候环境特征

	高风险区	中风险区	低风险区	极低风险区
年降水量/mm	1095～1927	996～2150	751～2198	52～2073
最暖月平均气温/℃	19.7～29.3	7.2～29.3	3.4～28.8	−4.2～30.8
稳定通过10 ℃持续日数	221～329	3～348	0～365	0～365
增强型植被指数	0～0.47	0～0.57	0～0.64	0～0.66
主要分布区	上海、江苏南部、湖北东部、湖南东部、江西中北部、浙江北部等地。	江苏南部、安徽中部、河南南部、浙江北部、湖北东部、湖南东部、江西大部、云南北部、广西北部、广东北部、四川东部等地。	江苏北部、河南中部、湖北西部、四川东部、重庆东部、贵州东部、广西南部、广东南部、福建西部等地。	东北地区、西北地区、华北北部、青藏高原等地。

东部、贵州东部、广西南部、广东南部、福建西部等地，该地区气候生态因子阈值为年降水量751～2198 mm、最暖月平均气温3.4～28.8 ℃、稳定通过10 ℃持续日数0～365 d和增强型植被指数(EVI)为0～0.64。青藏高原和属于暖温带、中温带的广大北方地区，降水量相对较少，冬冷夏热、季节性温度变化大，不利于血吸虫病传播，为血吸虫病风险极低区。

3 结论与讨论

发展适宜的影响评估模型可为气候影响及风险定量评估提供工具支撑。不同于以生物学实验为基础确定寄生虫或中间宿主的发育阈值建立的疾病传播潜势决定性模型，确定主导气候因子是建立统计学模型的关键[5]。本研究根据最大熵模型迭代运算给出的气候生态影响因子对血吸虫病传播风险贡献大小，确定了影响中国血吸虫病传播的主导气候生态因子；通过ROC曲线的AUC值评价表明，基于主导因子-血吸虫病关系的最大熵模型能够预测血吸虫病传播范围。

研究模拟的血吸虫病传播风险分区与《中国血吸虫病地图集》[26]分布图中的未控制及传播阻断等级地区相比，高风险区的湖北东部、湖南东北部、安徽中部、江西北部等地与血吸虫病未控制区和控制区基本一致；江西中部、湖南东南部等地为血吸虫病传播阻断区或非流行区；中风险区的江苏南部、浙江北部、广西中部、广东北部、云南北部、四川中部等地与血吸虫病控制区或传播阻断区基本一致。本研究模拟的血吸虫病传播风险区范围比Zhou等[9]基于生物驱动模型模拟的血吸虫病风险区(2000年)偏北，主要为低风险区范围较大，这可能与二者选取的模拟方法、驱动因子及风险等级阈值划分方式等不同有关。

这些研究结果表明，基于主导气候生态-血吸虫病关系的最大熵模型能够较为准确地反映中国血吸虫病流行风险特征，可用于气候环境影响下中国血吸虫病传播风险评估，评估结果对血吸虫病预防宏观策略制定具有参考意义。

参考文献

[1] 张存杰，黄大鹏，刘昌义，等. IPCC第五次评估报告气候变化对人类福祉影响的新认知[J]. 气候变化研究进展，2014，10(4)：246-250.

[2] 吴刚，苏瑞平，张旭东. 长江中下游滩地植被与钉螺孳生关系的研究[J]. 生态学报，1999，19(1)：118-121.

[3] 孙乐平，周晓农，洪青标，等. 日本血吸虫幼虫在钉螺体内发育起点温度的研究[J]. 中国寄生虫学与寄生虫病杂志，2003，21(5)：303-306.

[4] 李兆芹，滕卫平，俞善贤，等. 适合钉螺、血吸虫生长发育的气候条件变化[J]. 气候变化研究进展，2007，3(2)：106-110.

[5] 杨国静，孙乐平，洪青标，等. 血吸虫病传播气候预警模型的应用与前景[J]. 中国血吸虫病防治杂志，2009，21(5)：432-436.

[6] 张庆阳，琚建华，王卫丹，等. 气候变暖对人类健康的影响[J]. 气象科技，2007，35(2)：245-248.

[7] Thomas C. Malaria: a changed climate in Africa [J]. Nature, 2004, 427: 690-691.

[8] Craig M H, Snow R W, le Sueur D. A climate-based distribution model of malaria transmission in sub-Saharan Africa [J]. Parasitology Today, 1999, 15(3): 105-111.

[9] Zhou X N, Yang G J, Yang K, et al. Potential impact of climate change on *schistosomiasis* transmission in China [J]. The American Journal of Tropical Medicine and Hygiene, 2008, 78(2): 188-194.

[10] Rogers D J, Randolph S E. The global spread of malaria in a future, warmer world [J]. Science, 2000, 289(5485): 1763-1766.

[11] Jetten J H，陈文江. 模型模拟估算全球气候变化时患疟疾的危险[J]. 国外医学：寄生虫病分册，1997，24(1)：18-19.

[12] Yang G J, Vounatsou P, Zhou X N, et al. A Bayesian-based

approach for spatio-temporal modeling of county level prevalence of Schistosoma japonicum infection in Jiangsu province, China [J]. International Journal for Parasitology, 2005, 35 (2):155-162.

[13] Hales S, de Wet N, Maindonald J, et al. Potential effect of population and climate changes on global distribution of dengue fever: an empirical model [J]. The Lancet, 2002, 360(9336): 830-834.

[14] Jaynes E T. Information theory and statistical mechanics [J]. Physic Review, 1957, 106(2): 620-630.

[15] Phillips S J, Anderson R P, Schapire R E. Maximum entropy modeling of species geographic distributions [J]. Ecological Modelling, 2006, 190(3-4): 231-259.

[16] 段居琦,周广胜. 中国水稻潜在分布及其气候特征[J]. 生态学报,2011,31 (22):6659-6668.

[17] Liu S Y, Liang X Z, Gao W, et al. Regional climate model downscaling may improve prediction of alien plant species distribution [J]. Frontiers of Earth Science, 2014, 8 (4): 457-471.

[18] 宋雄刚,王宏斌,张真,等. 应用最大熵模型模拟预测大尺度范围油松毛虫灾害[J]. 林业科学,2016,52(6):66-75.

[19] 夏聪聪,卢成芳,李思,等. 基于最大熵模型和遥感的两种钉螺孳生地提取方法的比较[J]. 中国血吸虫病防治杂志,2017,19 (1):12-23.

[20] Thornton P E, Running S W, White M A. Generating surfaces of daily meteorological variables over large regions of complex terrain [J]. Journal of Hydrology, 1997, 190(3-4): 214-251.

[21] 赵劲松,王安云,周书林,等. 青弋江江滩植被与钉螺分布关系的初步研究[J]. 中国媒介生物学及控制杂志,2013,24(3): 222-224.

[22] 李红军,郑力,雷玉平,等. 基于 EOS/MODIS 数据的 NDVI 与 EVI 比较研究[J]. 地理科学进展,2007,26(1):26-32.

[23] 邢丁亮,郝占庆. 最大熵原理及其在生态学研究中的应用[J]. 生物多样性,2011, 19 (3):295-302.

[24] 刘少军,周广胜,房世波. 中国橡胶树种植气候适宜性区划[J]. 中国农业科学,2015,48(12):2335-2345.

[25] 王运生,谢丙炎,万方浩,等. ROC 曲线分析在评价入侵物种分布模型中的应用[J]. 生物多样性,2007,15(4): 365-372.

[26] 中国疾病预防控制中心寄生虫病预防控制所. 中国血吸虫病地图集[M]. 北京:中国地图出版社,2012.

Transmission Risk Assessment of *Schistosomiasis* in China Based on Maximum Entropy Model

Duan Juqi[1,2]　Zhou Ji[2]　Huang Dapeng[1]　Liu Lyuliu[1]

(1 Laboratory for Climate Studies, National Climate Center, CMA, Beijing 100081; 2 Shanghai Key Laboratory of Meteorology and Health, Shanghai 200135)

Abstract: Climatic and ecological factors have significant impacts on vector-borne diseases. The potential climatic and ecological factors affecting transmission risk of *Schistosomiasis* in China are selected based on previous research results, and then the dominant factors are determined by contribution percentages to the transmission risk of *Schistosomiasis* in China. At last, the relation model between *Schistosomiasis* and dominant factors based on MaxEnt to model the transmission risk of *Schistosomiasis* in China is developed and its modelling results are assessed as well. The results show that the dominant climatic and ecological factors affecting the transmission risk of *Schistosomiasis* in China are annual precipitation, mean temperature of the warmest month, the number of days with temperature over 10 ℃ and enhanced vegetation index, and the accumulated contribution percentage account for 98.6% of the used potential factors. According to the Receiver Operating Characteristic (ROC) curve, Area Under Curve (AUC) is 0.917; i.e., the MaxEnt model based on dominant factors affecting *Schistosomiasis* can model the transmission risk in China "very good". The MaxEnt model results show that the medium and high transmission risk zone of *Schistosomiasis* in China are located in Southern Jiangsu, Northern Zhejiang, Central Guangxi, Northern Guangdong, Northern Yunnan, Central Sichuan and Eastern Hubei, Northeastern Hunan, Central Anhui and Northern Jiangxi, etc. In conclusion, MaxEnt can model well the transmission risk of *Schistosomiasis* in China under the impact of climatic and ecological factors, which can provide a tool to assess the impact of climate change on the transmission risk of *Schistosomiasis* in China and reference to make preventive measures.

Keywords: *Schistosomiasis*; transmission risk; climatic and ecological factors; assessment model; maximum entropy model (MaxEnt)

大气科学学报　2019 年　第 42 卷　第 1 期:58-67
“极端天气气候事件研究”专刊　http://dqkxxb.cnjournals.org

基于 NCEP-GEFS 回算资料的我国极端温度变化特征研究

高丽[①],任宏利[②*],郑嘉雯[①②③],陈权亮[③]
① 国家气象中心 中国气象局数值预报中心,北京 100081;
② 国家气候中心 中国气象局气候研究开放实验室,北京 100081;
③ 成都信息工程大学 大气科学学院/高原大气与环境四川省重点实验室,四川 成都 610225
* 联系人,E-mail:renhl@ cma.gov.cn

2018-09-11 收稿,2018-11-20 接受
国家自然科学基金资助项目(41875138);国家科技支撑计划项目(2015BAC03B01);气象预报业务关键技术发展专项(YBGJXM2018-04)

摘要　利用美国 NCEP 全球集合预报系统(GEFS)历史回算资料和中国均一化格点观测数据,分析了我国近 30 a 来极端温度变化特征,重点考察了该模式预报系统对这一变化特征的刻画性能。通过估算格点观测和模式资料中 2 m 温度的历史气候百分位,分析了我国冬夏两季极端温度的气候特征以及极端温度日数的气候分布和多年变化趋势。结果表明,我国冬季极端低温和夏季极端高温的空间分布表现出较强区域性特征:东北、华北和青藏高原区域冬季极端低温的百分位阈值对应的温度较低,而华南、西北和长江流域夏季极端高温的阈值温度则较高;近 30 a 来我国夏季平均温度和极端高温日数几乎都呈现上升趋势,冬季平均温度则在我国大部分区域呈上升趋势、西北和东北部分地区呈下降趋势,相应地冬季极端低温日数在大部分区域呈下降趋势、仅在西北、东北和华南部分地区略有上升。NCEP-GEFS 回算资料能较好地再现我国冬夏两季平均气温、冬季极端低温和夏季极端高温日数的气候趋势和年际变化,但在各区域都有不同程度的冷偏差,冬季偏差明显大于夏季,并随着预报时长的增加,冬季冷偏差逐渐增强,而夏季冷偏差则逐渐减弱。因此,本文建议采用基于百分位阈值的相对极端性定义,可自动修正模式分析场和预报场中的系统性偏差。

关键词
NCEP-GEFS;
集合预报;
极端温度;
回报;
变化特征

一般来讲,当某地的天气状态严重偏离其气候平均态时,就可以认为是不易发生的事件。在统计意义上,不容易发生的事件被称为极端事件。其定义方法很多(Beniston et al.,2007;罗亚丽,2012),利用绝对阈值对极端天气气候事件进行识别时,某一地区的极端事件在另一地区可能是正常的,气候平均的微小变化可能会对极端事件的时间和空间分布以及强度的概率分布产生巨大的影响。21 世纪初,政府间气候变化专门委员会(Intergovernmental Panel on Climate Change,IPCC)第三次与第四次评估报告(Houghton et al.,2001;Solomon et al.,2007)对极端天气给出明确定义:极端天气是指发生概率小于观测记录概率密度函数第 10 个百分位数或超过第 90 个百分位数的天气事件。

由于极端天气发生概率小、强度大、影响范围广,往往会造成严重的自然灾害和人类生命财产损失。20 世纪中后期以来,在气候变化背景下,高温热浪、低温冷害等极端温度事件频繁发生,严重影响着人民健康和社会发展。近年来,国内外学者从不同角度对极端温度进行了研究,取得了很多重要研究成果。对于我国的极端温度事件的研究,任福民和翟盘茂(1998)研究表明中国极端温度的变化趋势存在较大的季节性差异,极端最低气温在冬、秋和春季增温趋势较强,极端最高气温只有在秋季呈现显著下降趋势。翟盘茂和潘晓华(2003)研究了中国北方近 50 a 极端温度时间变化,表明中国北方夜

引用格式:高丽,任宏利,郑嘉雯,等,2019.基于 NCEP-GEFS 回算资料的我国极端温度变化特征研究[J].大气科学学报,42(1):58-67.
Gao L,Ren H L,Zheng J W,et al.,2019.Diagnosis features of extreme temperature variations in China based on the NCEP-GEFS reforecasts[J].Trans Atmos Sci,42(1):58-67.doi:10. 13878/j.cnki.dqkxxb.20180911001.(in Chinese).

间温度极端偏低的日数显著减少、白天温度偏高的日数增多。唐红玉和翟盘茂(2003)指出,1951—2002 年中国年平均最高温度北方增暖明显,江南地区呈下降趋势。刘学华等(2006)研究了中国近 40 a 极端温度分布特征和年代际差异,表明 40 a 气温极端冷指数整体呈下降趋势,极端暖指数呈上升趋势。龚志强等(2009)讨论了不同温度段对中国近 58 a 增暖的可能影响,表明中国各区域(除东南区外)温度增暖起主要作用的温度段为极端/相对高温段年发生天数的增加和极端/相对低温段年发生天数的减少,而常温段的作用相对较小,正是这种两头变化较大、中间变化较小的跷跷板现象导致了中国各区域增温。杨萍等(2010)结合季节极端温度指数分析我国近 40 a 极端温度时间变化趋势,表明冬季极端冷指数变化趋势明显、夏季极端暖指数次之、春秋季极端指数变化趋势不明显。任晨辰等(2017)分析了不同气候背景下我国冬夏两季极端气温特征。然而,极端天气研究仍是一个薄弱环节,如何描述和监测极端天气或表征极值的各种统计特征及其变化规律乃至预报问题,成为一个重要课题(Easterlling et al.,2000;Meehl et al.,2000)。

由于极端温度是小概率事件,其发展存在很大的不确定性,用单一的数值天气模式对其进行预报是不严谨的,因此引入了集合进行预报的概念。集合预报作为数值预报发展的一个重要方向,它考虑了初值及模式的不确定性,其结果反映了未来天气的多种可能状况,能为用户提供确定性预报所不能提供的信息(如预报结果的可信度等)(Palmer et al.,2000;Richardson,2000;杜钧,2002;皇甫雪官,2002;彭勇等,2012)。另外,集合预报提供的概率预报结果可以给出极端天气和气候事件在未来出现的可能性,所以集合预报对于小概率的天气事件具有更好的预报效果(van den Dool and Toth,1991;张涵斌等,2017)。

目前,由于极端温度发生样本少、且存在不连续和准确性偏低的特点,在全球大部分地区进行极端温度分析时遇到的棘手问题就是缺乏高质量且时间分辨率适合的长期气候资料。一方面,近年来基于高密度台站器测均一化处理的中国格点观测数据陆续投入了业务使用。另一方面,大量的模式模拟、特别是经过初始化的模拟(也称为回算或回报)数据在极端温度研究中尚未得到利用。为此,本文拟尝试利用国际知名的模式集合预报系统的历史回算数据对我国极端温度变化特征进行诊断分析,并与基于均一化格点观测资料的结果做比较,重点考察最近 30 a 观测到的我国极端温度变化主要特征、以及利用模式初始分析场和不同时效预报场对这一观测特征的刻画能力。本文旨在提取模式资料中的有用信息作为观测的有益补充并发现模式系统存在的不足之处,为极端温度的变化特征分析乃至预报提供参考。

1 资料及方法

1.1 模式和观测资料

本文所用模式预报资料来自于美国国家环境预报中心(National Centers for Environmental Prediction,NCEP)的全球集合预报系统(Global Ensemble Forecast System,GEFS)的历史回报 2 m 气温资料,该套资料的格点空间的水平分辨率为 1°×1°,垂直分辨率为 42 层,11 个集合成员,预报时效为 1~16 d。采用的初始条件为气候预报系统再分析(Climate Forecast System Reanalysis,CFSR)数据,初始扰动方法为重新尺度化集合转换法,模式扰动为随机全倾向扰动法,该资料的时间范围为 1985 年 12 月—2016 年 12 月共 31 a。观测 2 m 气温资料来自于国家气象信息中心提供的中国国家级地面气象站均一化气温日值 0.5°×0.5°格点数据集(V1.0),时间段取为与模式系统回报资料同一时段(1985 年 12 月—2016 年 12 月),该数据利用薄盘样条法结合三维地理空间信息进行空间插值,其数据来源包括两部分:由国家气象信息中心研制的中国国家级地面气象站均一化气温日值数据集;由 GTOPO30 数据(分辨率为 0.05°×0.05°)经过重采样生产的中国陆地 0.5°×0.5°的数字高程模型 DEM。本文将分别考察冬季(取为 Nov-Dec-Jan-Feb,NDJF)和夏季(May-Jun-July-Aug,MJJA)的极端温度特征。

2 中国极端温度气候分布及分区

2.1 冬夏两季极端温度和日数的气候分布

图 1a 和 1b 分别给出了冬季平均气候态第 10 和第 5 个百分位分布,图 1c 和 1d 分别为夏季平均气候态第 90 和第 95 个百分位分布。可以看出,冬夏两季平均温度在对应的两个百分位上的分布差异较小,为此在本文中统一选取气候态第 5 个百分位和第 95 个百分位作为定义阈值分别对我国冬季极端低温和夏季极端高温进行诊断分析。从图 1 也可看到,我国冬季极端低温和夏季极端高温的阈值分布区域性较强,因此,对于冬季极端低温和夏季极端

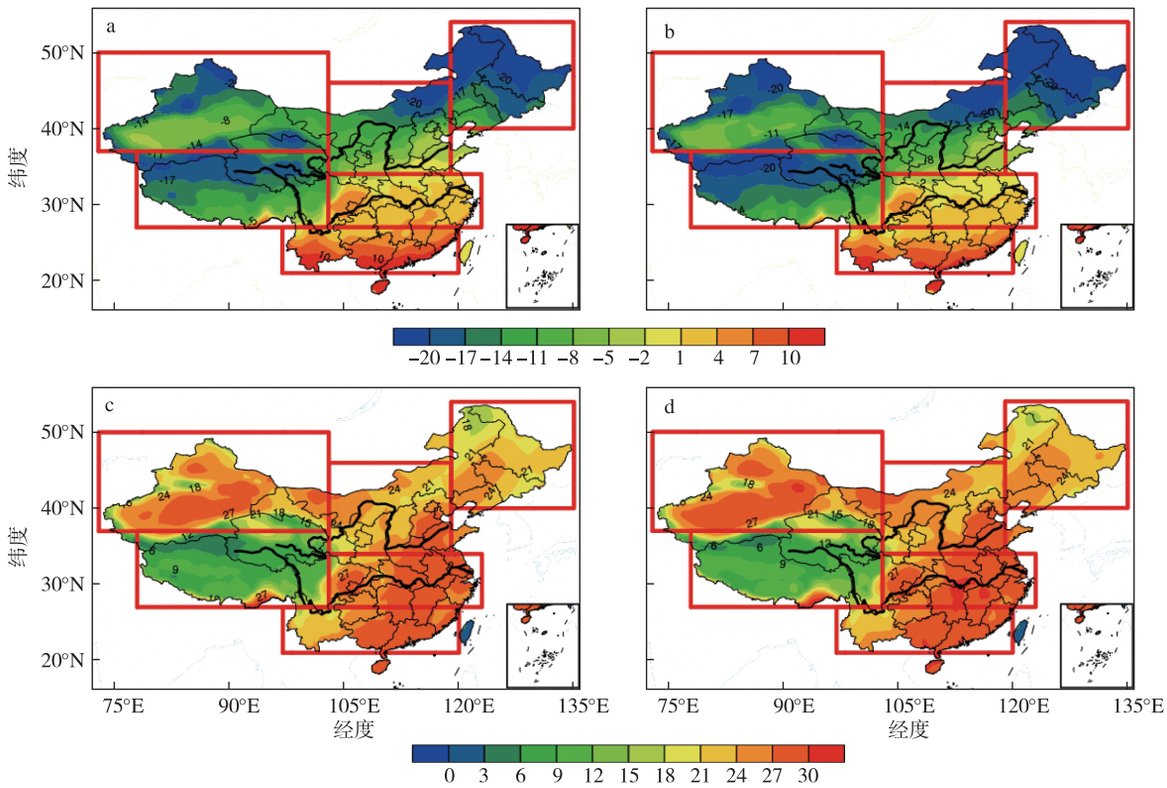

图 1　观测的我国冬季(NDJF)平均第 5 个(a)和第 10 个(b)百分位 2 m 气温以及夏季(MJJA)平均第 95 个(c)和第 90 个(d)百分位 2 m 气温的空间分布(单位:℃;其中红色方框代表 6 个区域)

Fig.1　Maps of observed winter(NDJF) mean 2 m temperature(unit:℃) at the(a) 5th percentile and(b) 10th percentile; and maps of observed summer(MJJA) mean 2 m temperature(unit:℃) at the(c) 95th percentile and(d) 90th percentile, where the six regions are included in red boxes

高温需要分区域进行研究。这里根据极端温度统计量的气候分布情况,将中国大体划分为 6 个区域,即东北、华北、西北、青藏高原、长江流域和华南。冬季极端低温阈值对应的温度值在东北、华北和青藏高原区域较低,夏季极端高温阈值对应的温度值在华南、西北和长江流域较高。由于冬季极端低温较低与夏季极端高温较高的区域更容易发生灾害性强的极端事件,本文将着重分析这两类区域。

图 2a 和 2b 分别为多年平均我国冬季极端低温和夏季极端高温发生日数分布。整体而言,由于采用了固定阈值方法来相对定义各地极端日数,全国呈现出了较为均匀的分布特征。但可以看出,我国多年平均冬季极端低温和夏季极端高温发生日数分布受地形影响很大,且在地形较高的格点附近发生的极端低温频次高于极端高温的发生频次,可能是由于计算气候百分位时采用了空间窗以增加样本,从而使山脉附近估算的气候百分位数值整体偏高,从而使统计的极端温度受地形影响较大,且地形较高的格点极端低温发生频次高于极端高温发生频次,但是其具体发生原因有待深入思考。并且,结合图 1 可以看出,冬季极端低温阈值对应的温度较低区域(东北、青藏高原和华北区域)的极端低温发生日数相对较多,夏季极端高温阈值对应的温度较高的区域(西北、长江流域和华南区域)的极端高温发生日数也较多。

2.2　冬夏两季平均温度和极端温度日数线性趋势分布

图 3a 和 3b 给出了冬季和夏季平均温度的线性趋势分布,图 3c 和 3d 为冬季极端低温和夏季极端高温发生日数(采用的阈值分别为气候态第 5 和第 95 个百分位数)的线性趋势分布。从冬季平均温度图可以看出,我国大部分区域冬季平均温度都呈上升的变化趋势,但在西北和东北的部分地区,冬季平均温度则呈现出下降趋势。对应地,从冬季极端低温发生日数分布图来看,在冬季平均温度呈下降变化趋势的西北和东北部分区域,冬季极端低温日数的变化呈上升趋势,相比之下,其余区域冬季极端低温发生日数均呈下降的变化趋势。从夏季平均温度来看,我国范围内所有区域的夏季平均温度都呈明显上升的变化趋势,就夏季极端高温日数线性趋势

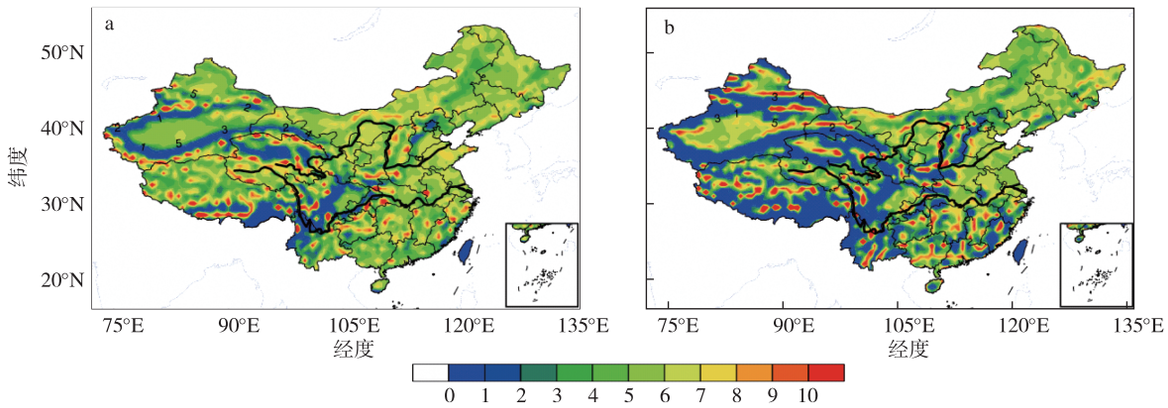

图 2　观测的多年平均冬季极端低温(a)和夏季极端高温(b)日数分布(单位:d)

Fig.2　Maps of the climatic-mean days of observed (a) winter extreme low temperature and (b) summer extreme high temperature

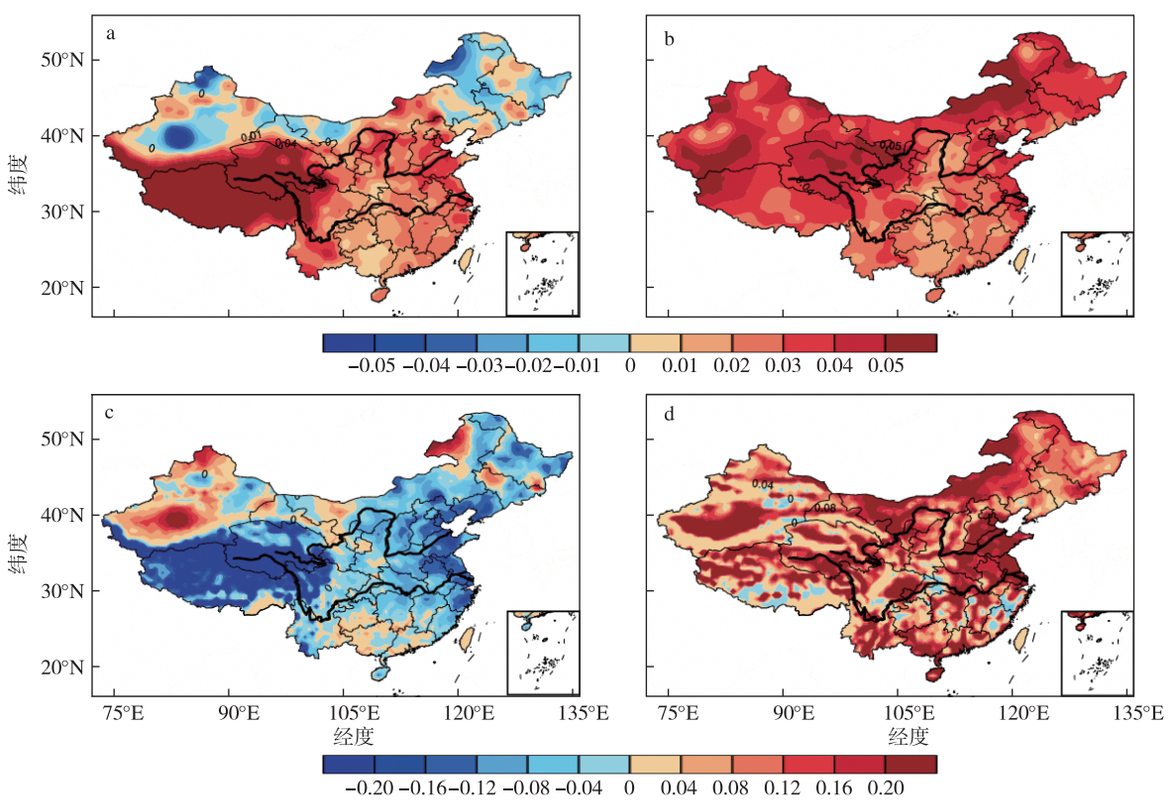

图 3　观测的冬季(a)和夏季(b)平均气温的线性趋势(单位:℃/a)分布以及冬季极端低温(c)和夏季极端高温(d)日数的线性趋势(单位:d/a)分布

Fig.3　Maps of linear trends(unit:℃/a) of observed (a) winter-mean temperature and (b) summer-mean temperature;and maps of linear trends(unit:d/a) of (c) winter extreme low temperature and (d) summer extreme high temperature

图而言,除了夏季平均温度上升趋势较不明显的小部分区域对应的夏季极端高温日数呈现较弱的下降趋势外,我国大部分地区的夏季极端高温日数分布都呈现明显上升的变化趋势。

3　基于 NCEP-GEFS 资料的中国各区域温度变化特征

3.1　冬夏两季平均温度和极端温度日数变化情况

图 4 展示了冬季极端低温阈值较低区域(东北、华北和青藏高原区域)的季节平均温度和极端低温日数(采用的阈值为气候态第 5 个百分位数)的多年变化。在理想状态下,最浅蓝色曲线应该与红色线接近或重合,即预报初始化的冬季平均温度和极端低温日数与观测保持一致,且各蓝色曲线也较为接近,即不同时效下的预报结果也呈现出一致性。但从图 4a、c、e 中可看出,不同预报时效下 NCEP-GEFS 回报的东北、华北和高原区域冬季平均 2 m 温度的变化曲线都与观测的相去甚远。红色

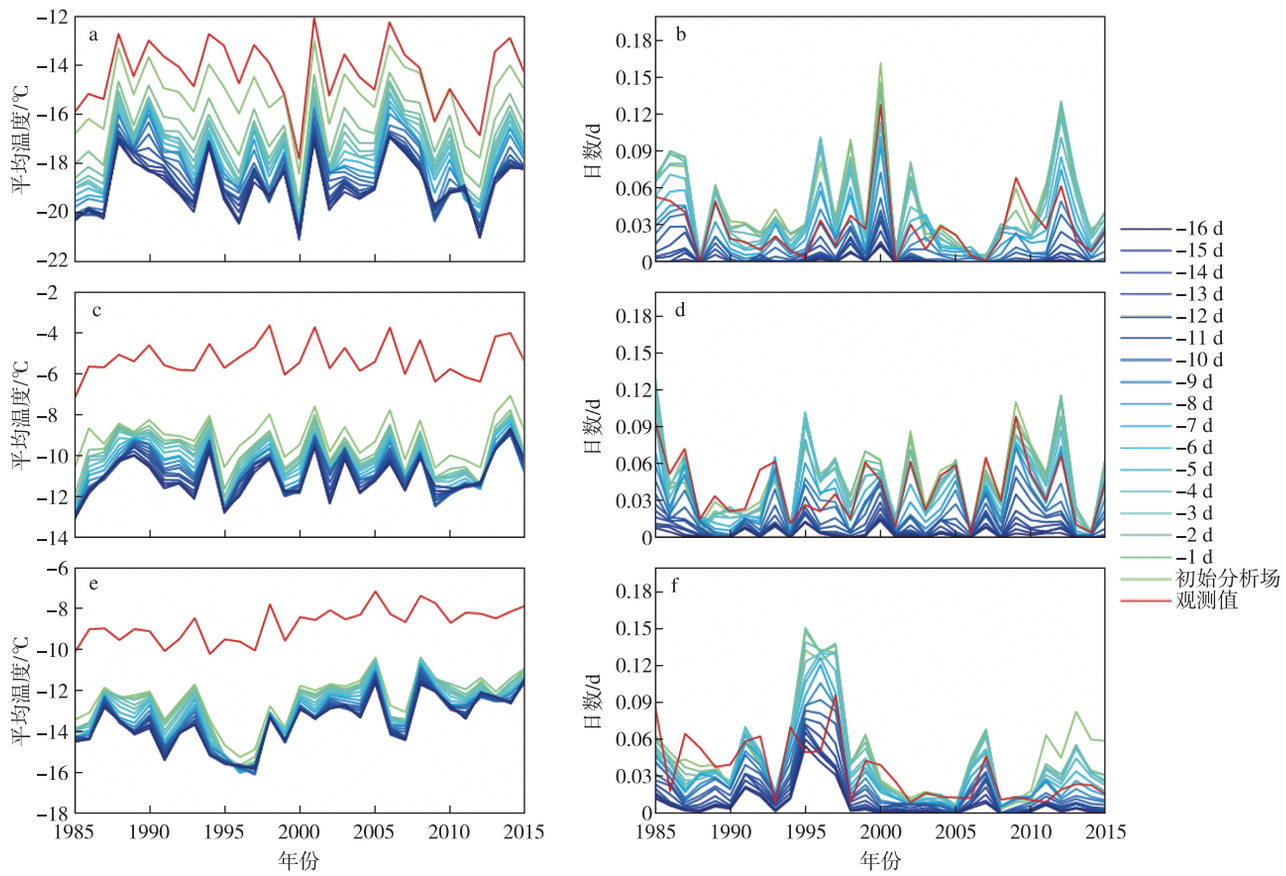

图 4　东北(a、b)、华北(c、d)及青藏高原(e、f)冬季平均温度(a、c、e)和极端低温日数(b、d、f)的多年变化(红线代表观测，蓝线由浅入深分别代表 NCEP-GEFS 初始分析场以及提前 1~16 d 的预报场)

Fig.4　Variations of (a,c,e) winter-mean temperature and (b,d,f) extreme low temperature days in (a,b) northeastern China, (c,d) northern China and (e,f) the Qinghai-Tibet Plateau, where the red lines denote observation, and the blue lines are for initial analysis and forecasts at leads of 1—16 days from dark to light blues

线均位于蓝色线上方，且蓝色线越深和红色线相差越多，即回报的冬季平均温度与观测相比有不同程度的冷偏差，并且随着预报时长的增加，对各区域冬季平均温度预报的冷偏差越强。就冬季平均温度趋势而言，东北无明显趋势，华北为弱上升趋势，而高原呈明显上升趋势，这些趋势在模式系统回报资料和观测资料中表现出了高度一致性。

对于极端低温日数，从图 4b、d、f 中可以看出，各区域整体上的趋势与冬季平均温度相反，即东北无明显的日数变化趋势，华北日数呈弱的减少，而高原则是明显下降趋势。通过对比 NCEP-GEFS 回报与观测资料的极端日数曲线，发现该模式系统的初始化结果几乎没有明显偏差，这体现出极端温度相对定义的优势，即隐含着对该模式同化系统中的冷偏差进行自动修正。但是，预报时长对于极端性的预报存在显著影响，随着预报时间的延长，极端低温发生天数明显减少，换句话说，提前做预报的时间越早，该模式对冬季极端低温的预报性能就越差。由此可见，极端温度的预报本身是很困难的，而提前 10 d 以上做预报将是难上加难，当然，这是目前模式能力的现状，可能与集合成员个数偏少也有关系。

图 5 展示了夏季极端高温 95% 阈值较高区域(长江流域、华南和西北)的季节平均温度和极端高温日数(采用的阈值为气候态第 95 个百分位数)的多年变化。从图 5a、c、e 中可看出与图 4 中类似的特征，即蓝色曲线簇和红色曲线并不重合，红色线仍位于蓝色线上方，存在系统性的冷偏差，但比图 4 中的差异性明显小一些，各区域夏季平均温度均呈现出显著的上升趋势。这些结果表明，该模式同化系统所输出的初始场虽然存在明显冷偏差，但仍能刻画出多年气候变化的大趋势和年际变化特征。进一步分析发现，各区域夏季温度随着预报时长的增加，其预报冷偏差竟然有所减弱，这是与冬季情形完全相反的，如长江流域和西北的蓝色越深的曲线与红线相差越小。

另一方面，从图 5b、d、f 中可以看出，夏季极端

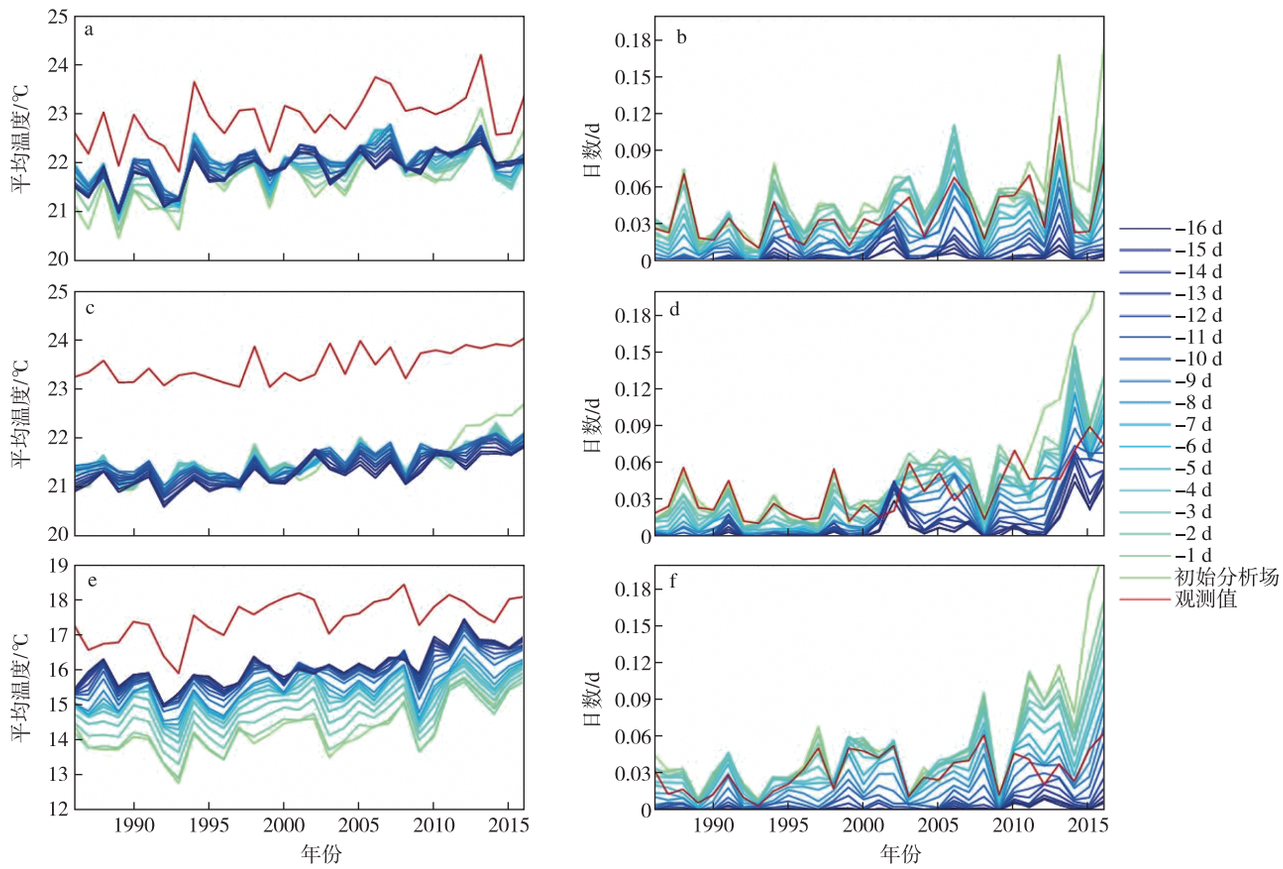

图 5　长江流域(a、b)、华南(c、d)、西北(e、f)夏季平均温度(a、c、e)和夏季极端高温日数(b、d、f)的多年变化(红线代表观测,蓝线由浅入深分别代表 NCEP-GEFS 初始分析场以及提前 1~16 d 的预报场)

Fig.5　Variations of (a,c,e) summer-mean temperature and (b,d,f) extreme high temperature days in the (a,b) Yangtze River Basin, (c,d) southern China and (e,f) northwestern China, where the red lines denote observation, and the blue lines are for initial analysis and forecasts at leads of 1—16 days from dark to light blues

高温日数的整体趋势与平均温度的趋势较为一致,即最近 30 余年二者均处于明显上升的趋势,并且可看出系统回报数据对长江流域、华南和西北区域的极端高温日数预报能较好地抓住其年际变化特征,但后两个区域在近些年的预报日数显著偏多,其原因尚不清楚。此外,与图 4 类似,该模式系统的初始场中采用相对定义的夏季极端高温日数依然没有明显偏差,但随着预报天数的增加,预报的极端高温发生日数在不同区域均明显减少。这表明,随着模式积分时间的延长,可能倾向于增加或减小温度变化的振幅,如仍用绝对极端温度阈值来定义预报中的极端高温就不适用了,因此相对的极端定义在基于该模式集合信息的极端温度预报方面更为合适。

3.2　冬夏两季温度的概率密度函数(PDF)分布

从图 6 中六个区域的温度 PDF 分布曲线可以清楚地看到,NCEP-GEFS 回报资料所展现出的我国不同区域冬季温度的 PDF 整体和峰值均位于观测 PDF 的左侧,这意味着该模式系统的初始分析和预报均表现出冷偏差,其偏冷的幅度依区域而有所不同,普遍在 5 ℃以上,长江流域的冷偏差最小。而且,模式回报得到的 PDF 形态上也有别于观测,其所跨越的值域范围要比观测的宽得多,特别是在青藏高原和华南区域该模式系统还场呈现出双峰 PDF 分布特征,这种形态上的偏差背后的原因还有待深入分析。同时也发现,随着模式系统预报时长的增加,PDF 的冷偏差倾向于逐渐加大。总体而言,NCEP-GEFS 回报对于长江流域和西北地区的 PDF 分布相对来讲与观测的最为接近,这些结果也表明,该模式系统同化出来初始温度分析场在东亚冬季真实还存在非常大的冷偏差,直接导致即便是半个月以内的集合预报也产生很大的误差。从图中还可清楚地看到,用于定义极端低温的 PDF 尾端在观测与预报之间差别明显,这说明用固定温度阈值的方式来定义极端低温或者高温,难以使模式预报达到观测极端性的标准,而图 4、5 结果充分显示出相对定义则可以剔除系统性的冷偏差。

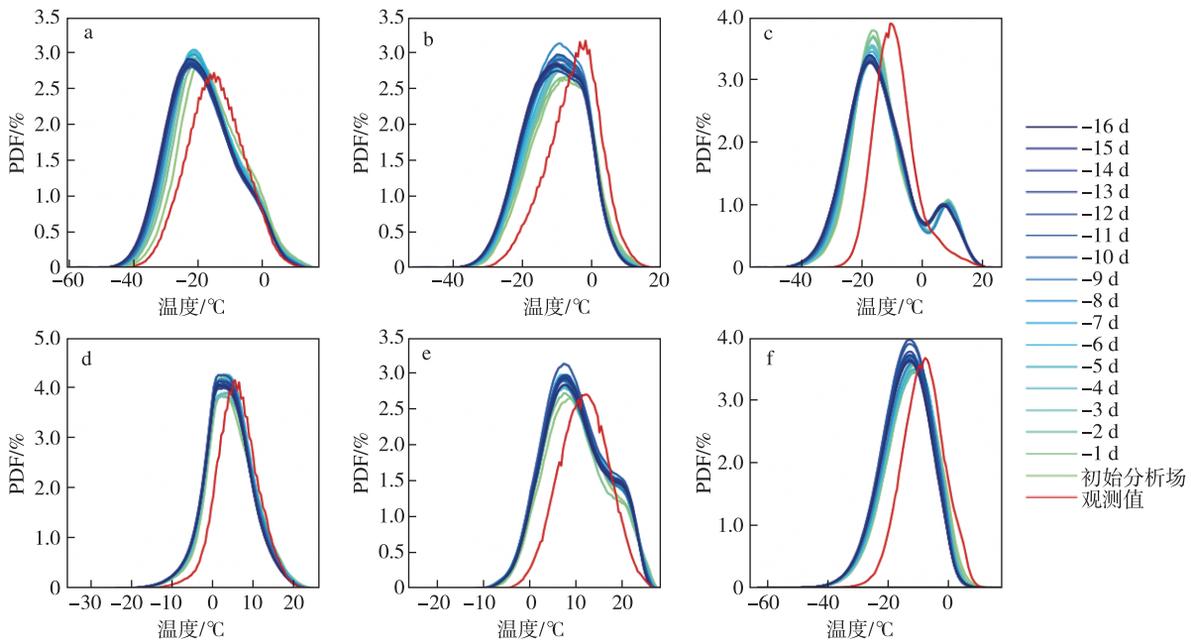

图 6　冬季温度的 PDF 分布(红线代表观测,蓝线由浅入深分别代表 NCEP-GEFS 初始分析场以及提前 1~16 d 的预报场):(a)东北;(b)华北;(c)青藏高原;(d)长江流域;(e)华南;(f)西北

Fig.6　Probabilistic density functions (PDFs) of winter temperature in (a) northeastern China, (b) northern China, (c) the Qinghai-Tibet Plateau, (d) Yangtze River Basin, (e) southern China and (f) northwestern China, where the red lines denote observation, and the blue lines are for initial analysis and forecasts at leads of 1—16 days from dark to light blues

进一步从图 7 中看到,NCEP-GEFS 对我国六个区域夏季温度 PDF 分布特征的刻画性能明显优于冬季,系统性的冷偏差显著减小,但区域依赖性比冬季复杂的多,东北和华北的模式结果与观测最为接近、呈现弱的暖偏差,其余四个区域则仍表现为冷偏差,偏冷的幅度在各区域有所不同。而且,模式回报得到的 PDF 在形态上较冬季更接近于观测,仅在高原和华南区域该模式展现出多峰 PDF 分布特征,而西北区域观测的不规则特征也未能刻画出来,这种形态偏差的成因仍不清楚,值得深入加以考察。分析也发现,随着该模式系统预报时效的延长,相比于观测的冷偏差倾向于逐渐加大。总体来看,NCEP-GEFS 对于我国南方和西北的极端高温多发区,因其自身冷偏差的影响,以某个固定温度阈值定义极端性的做法会导致模式难以报出大多数极端高温,因此需要采用气候百分位的相对定义来修正冷偏差。此外,上述结果再次表明,该模式系统所同化初始分析场与我国气温观测的 PDF 以及气候百分位特征差异明显,其在我国区域的资料同化效果并不理想,因此在使用基于 NCEP-GEFS 的分析场和再分析场资料来研究我国极端温度的识别乃至预报问题时要极为慎重。

4　结论

本文尝试利用国际知名 NCEP-GEPS 的历史回报数据和中国近年业务推广应用的均一化格点观测资料,考察了我国近 30 a 来冬夏两季平均温度和极端温度变化特征,重点关注了利用模式初始分析场和不同时效预报场对这一观测特征的刻画能力。为此,本文估算了观测和模式的温度气候百分位,分析了我国冬夏两季极端温度的气候特征以及极端温度日数的气候分布和多年变化趋势。结果显示,我国极端温度的分布具有明显的局地性,东北、华北和青藏高原区域冬季极端低温的百分位阈值所对应的温度较低,而华南、西北和长江流域夏季极端高温的百分位阈值所对应的温度较高。在不同区域温度自身百分位特征的差异明显,因此对面向极端温度预报的识别应采用具有局地性相对意义的气候百分位方法。

研究表明,近 30 a 来我国夏季平均温度和极端高温日数几乎都呈现上升趋势,冬季平均温度则在我国大部分区域呈上升趋势、西北和东北部分地区呈下降趋势,相应地冬季极端低温日数在大部分区域呈下降趋势、仅在西北、东北和华南部分地区略有上升。总体来看,NCEP-GEFS 多年历史集合回算

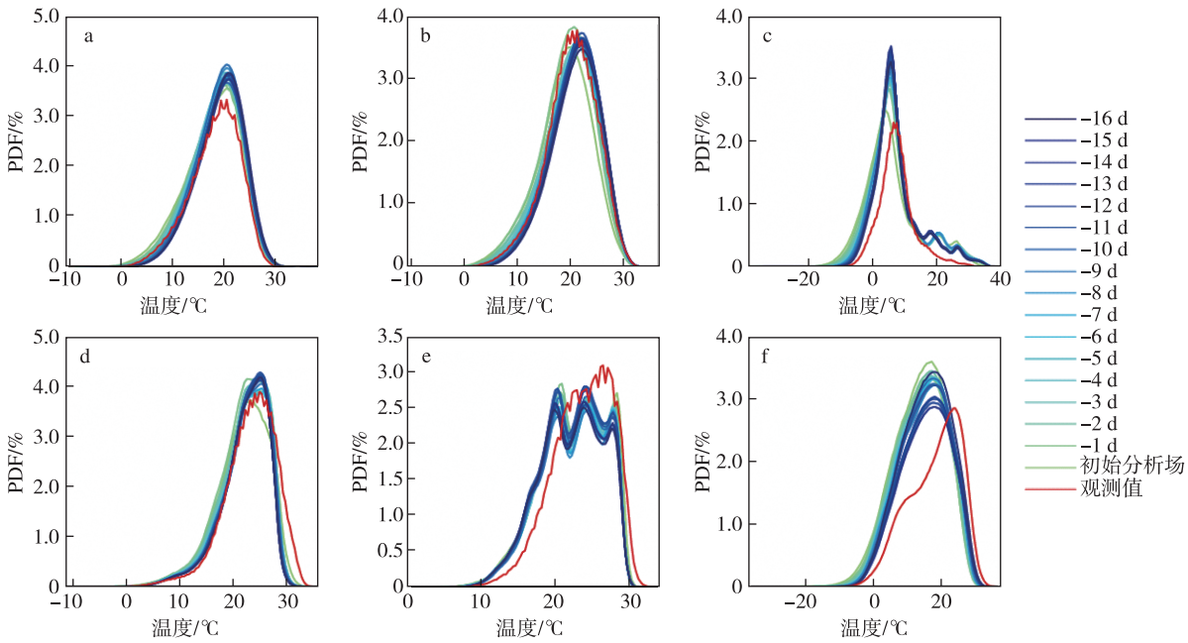

图 7　夏季温度的 PDF 分布（红线代表观测，蓝线由浅入深分别代表 NCEP-GEFS 初始分析场以及提前 1～16 d 的预报场）：（a）东北；（b）华北；（c）青藏高原；（d）长江流域；（e）华南；（f）西北

Fig.7　Probabilistic density functions (PDFs) of summer temperature in (a) northeastern China, (b) northern China, (c) the Qinghai-Tibet Plateau, (d) Yangtze River Basin, (e) southern China and (f) northwestern China, where the red lines denote observation, and the blue lines are for initial analysis and forecasts at leads of 1—16 days from dark to light blues

资料能较好地再现我国冬夏两季平均气温、冬季极端低温和夏季极端高温日数的气候趋势和年际变化，表明模式的初始化已经涵盖了气候趋势和年际变化等慢变分量。然而，模式初始分析场和预报场在各区域都有不同程度的冷偏差，冬季偏差明显大于夏季，并随着预报时长的增加，冬季冷偏差逐渐增强，而夏季冷偏差则逐渐减弱，表明在该区域的同化效果并不理想，因此在使用基于 NCEP-GEFS 的极端温度预报时要极为慎重。

此外，本文研究发现，该模式系统预报的超前量对于我国极端温度特征（包括概率密度函数分布）的刻画与观测相比仍具有明显影响，可见模式中的极端温度识别问题存在特殊性，不应是观测中极端性分析方法的简单套用。而且，随着模式积分时间的延长，模式倾向于改变温度变化的振幅，使得达到极端定义的百分位温度值振幅增加或缩小，此时用绝对极端温度定义的预报并不适用，相对的极端定义在基于该模式集合信息的预报方面具有优势。因此，本文建议采用基于百分位阈值的相对极端性定义，可以实现自动修正模式分析场和预报场中的系统性偏差。本文结论和讨论仍然较为粗浅，在今后工作中将深入加以研究。

参考文献（References）

Beniston M, Stephenson D B, Christensen O B, et al., 2007. Future extreme events in European climate: an exploration of regional climate model projections[J]. Climatic Change, 81(S1): 71-95.

杜钧，2002. 集合预报的现状和前景[J]. 应用气象学报，13(1)：16-28. Du J, 2002. Present situation and prospects of ensemble numerical prediction [J]. J Appl Meteor Sci, 13(1): 16-28. (in Chinese).

Easterling D R, Evans J L, Groisman P Y, et al., 2000. Observed variability and trends in extreme climate events: a brief review[J]. Bull Amer Meteor Soc, 81(3): 417-425.

龚志强，王晓娟，支蓉，等，2009. 中国近 58 年温度极端事件的区域特征及其与气候突变的联系[J]. 物理学报，58(6)：4342-4353. Gong Z Q, Wang X J, Zhi R, et al., 2009. Regional characteristics of temperature changes in China during the past 58 years and its probable correlation with abrupt temperature change[J]. Acta Physica Sinica, 58(6): 4342-4353. (in Chinese).

HoughtonJ T, Ding Y, Griggs D J, et al., 2001. Climate change 2001: the science of climate change[R]//Contribution of working group 1 to the third assessment report of the intergovernmental panel on climate change. Cambridge, United Kingdom and New York: Cambridge University Press.

皇甫雪官，2002. 国家气象中心集合数值预报检验评价[J]. 应用气象学报，13(1)：29-36. Huangpu X G, 2002. The verification for ensemble pre-

diction system of national meteorological center[J].J Appl Meteor Sci,13(1):29-36.(in Chinese).

刘学华,季致建,吴洪宝,等,2006.中国近 40 年极端气温和降水的分布特征及年代际差异[J].热带气象学报,22(6):618-624. Liu X H,Ji Z J,Wu H B,et al.,2006.Distributing characteristics and interdecadal difference of daily temperature and precipitation extremes in China for latest 40 years[J].J Trop Meteor,22(6):618-624.(in Chinese).

罗亚丽,2012.极端天气和气候事件的变化[J].气候变化研究进展,8(2):90-98. Luo Y L,2012.Changes in weather and climate extremes[J].Advances in Climate Change Research,8(2):90-98.(in Chinese).

Meehl G A,Karl T,Easterling D R,et al.,2000.An introduction to trends in extreme weather and climate events:observations,socioeconomic impacts,terrestrial ecological impacts,and model projections[J].Bull Amer Meteor Soc,81(3):413-416.

Palmer T N,Brankovi ć Č,Richardson D S,2010.A probability and decision-model analysis of PROVOST seasonal multi-model ensemble integrations[J].Quart J Roy Meteor Soc,126(567):2013-2033.

彭勇,王萍,徐炜,等,2012.气象集合预报的研究进展[J].南水北调与水利科技,10(4):90-96,126. Peng Y,Wang P,Xu W,et al.,2012.Review of weather ensemble prediction[J].South-to-North Water Transfers and Water Science & Technology,10(4):90-96,126.(in Chinese).

任晨辰,段明铿,智协飞,2017.不同气候背景下我国冬夏两季极端气温特征分析[J].大气科学学报,40(6):803-813. Ren C C,Duan M K,Zhi X F,2017.Characteristics of extreme surface air temperature in winter and summer over China under different climate backgrounds[J].Trans Atmos Sci,40(6):803-813.(in Chinese).

任福民,翟盘茂,1998. 1951—1990 年中国极端气温变化分析[J].大气科学,22(2):217-226. Ren F M,Zhai P M,1998.Study on changes of China's extreme temperatures during 1951—1990[J].Chin J Atmos Sci,22(2):217-226.(in Chinese).

Richardson D,2000.Skill and relative economic value of the ECMWF ensemble prediction system[J].Quart J Roy Meteor Soc,126(563):649-667.

Solomon S,Qin D,Manning M,et al.,2007.Climate change 2007:the physical science basis[R]//Contribution of working group 1 to the fourth assessment report of the intergovernmental panel on climate change.Cambridge,United Kingdom and New York:Cambridge University Press.

唐红玉,翟盘茂,2003.中国北方春季沙尘暴与北半球 500 hPa 高度场的 SVD 分析(摘要)[C]//2003 中国气象学会年会. Tang H Y,Zhai P M,2003.SVD analysis between Northern Hemisphere 500 hPa heights and spring duststorms over northern China(abstract)[C]//2003 Chinese Meteorological Society.(in Chinese).

van den Dool H M,Toth Z,1991.Why do forecasts for "near normal" often fail? [J].Wea Forecasting,6(1):76-85.

杨萍,刘伟东,王启光,等,2010.近 40 年我国极端温度变化趋势和季节特征[J].应用气象学报,21(1):29-36. Yang P,Liu W D,Wang Q G,et al.,2010.The climatic change trend and seasonal characteristics of daily temperature extremes in China for the latest 40 years[J].J Appl Meteor Sci,21(1):29-36.(in Chinese).

翟盘茂,潘晓华,2003.中国北方近 50 年温度和降水极端事件变化[J].地理学报,58(S):1-10. Zhai P M,Pan X H,2003.Change in extreme temperature and precipitation over northern China during the second half of the 20th century[J].Acta Geographica Sinica,58(S):1-10.(in Chinese).

张涵斌,智协飞,陈静,等,2017.区域集合预报扰动方法研究进展综述[J].大气科学学报,40(2):145-157. Zhang H B,Zhi X F,Chen J,et al.,2017.Achievement of perturbation methods for regional ensemble forecast[J].Trans Atmos Sci,40(2):145-157.(in Chinese).

Diagnosis features of extreme temperature variations in China based on the NCEP-GEFS reforecasts

GAO Li[1],REN Hongli[2],ZHENG Jiawen[1,2,3],CHEN Quanliang[3]

[1] *CMA Numerical Prediction Center,National Meteorological Center,Beijing* 100081,*China*;

[2] *Laboratory for Climate Studies,National Climate Center,Beijing* 100081,*China*;

[3] *College of Atmospheric Science/Plateau Atmosphere and Environment Laboratory of Sichuan Province,Chengdu University of Information Technology,Chengdu* 610225,*China*

In this study,based on the reforecast data of NCEP Global Ensemble Forecast System(GEFS) and China homogeneous grid-point observational data,features of extreme temperature variations in the past 30 years are analyzed,and the performance of the NCEP-GEFS in representing these kinds of features is thoroughly investigated. By estimating the historical climatic percentile of 2 m temperature in the observational and model data,the characteristics of extreme temperature in winter and summer,along with the spatial distribution and multi-year trend of extreme temperature days,are analyzed.The results show that some strong regional features exist in the spatial distributions of winter extreme low temperature(ELT) and summer extreme high temperature(EHT) in China,i.e.

there are relatively lower temperatures corresponding to the percentile thresholds of the winter ELT in northeastern China, northern China and the Qinghai-Tibet Plateau, with higher temperatures corresponding to the percentile thresholds of the summer EHT in southern China, northwestern China and the Yangtze River Basin. Both the summer mean temperature and EHT days throughout China show increasing trends in the past 30 years, and the winter mean temperatures are also increasing throughout most of China, yet decreasing in northwestern and northeastern China. Correspondingly, the numbers of days of the winter ELT are decreasing in most areas, and only slightly increasing in small parts of northwestern, northeastern and southern China. The NCEP-GEFS reforecasts are able to accurately reproduce the climatic trends and interannual variations of the seasonal mean temperature and extreme temperature days in the winter and summer of China, yet varying degrees of cold biases exist in the different regions. The biases in winter are significantly larger than those in summer, and as the forecast length increases, these cold biases are gradually strengthened in winter, while gradually weakened in summer. Therefore, it is suggested to adopt the relative definition of extreme temperature based on the percentile threshold, which can automatically correct these systematic biases in the model analysis and prediction products.

NCEP-GEFS; ensemble prediction; extreme temperature; reforecasts; variation features

doi:10. 13878/j.cnki.dqkxxb.20180911001

(责任编辑:刘菲)

顾薇,陈丽娟,2019. 2018 年夏季海洋大气特征及对我国气候的影响[J]. 气象,45(1):126-134. Gu W,Chen L J,2019. Characteristics of atmospheric and oceanic condition and their influences on summer climate of China in 2018[J]. Meteor Mon,45(1):126-134(in Chinese).

2018 年夏季海洋大气特征及对我国气候的影响*

顾 薇[1] 陈丽娟[1,2]

1 国家气候中心,中国气象局气候研究开放实验室,北京 100081

2 南京信息工程大学气象灾害预报预警与评估协同创新中心,南京 210044

提 要:为更好地了解 2018 年夏季(6—8 月)我国主要气候异常特征及成因,本文利用我国气象要素站点资料、再分析大气环流资料和全球海温数据分析了 2018 年夏季我国降水和气温的异常特征、东亚大气环流特征及海温对我国气候的影响。结果显示 2018 年夏季全国平均降水量较常年同期偏多 9.6%,我国中东部地区降水呈现"南北多、中间少"的分布特征,北方和华南大部降水较常年同期偏多、长江中下游降水明显偏少。降水的上述异常特征受到东亚副热带和中高纬大气环流的共同影响。2018 年夏季东亚副热带高空急流和西太平洋副热带高压位置都明显偏北,东亚沿岸由南至北为"负—正—负"的高度距平分布,呈现出"东亚—太平洋型"遥相关负位相的特征,菲律宾附近对流层低层大气维持异常的气旋式环流,东亚副热带夏季风异常偏强。同时,欧亚中高纬度大气呈现"两槽一脊"的异常高度分布特征。在副热带和中高纬大气环流的这种配置下,我国北方地区以异常偏南风为主,有利于暖湿气流的输送,降水偏多;华南地区在偏强的热带对流活动影响下,降水也总体偏多;而长江中下游地区则以明显的辐散下沉运动为主,降水偏少。从外强迫因子来看,2017 年 10 月至 2018 年 4 月发生的 La Niña 事件对东亚夏季风偏强及我国降水"南北多、中间少"的异常特征起到了重要作用。

关键词:夏季降水,东亚夏季风,菲律宾异常气旋,La Niña 事件

中图分类号:P461 **文献标志码**:A **DOI**:10.7519/j.issn.1000-0526.2019.01.011

Characteristics of Atmospheric and Oceanic Condition and Their Influences on Summer Climate of China in 2018

GU Wei[1] CHEN Lijuan[1,2]

1 Laboratory for Climate Studies, National Climate Centre, CMA, Beijing 100081

2 Collaborative Innovation Center on Forecast and Evaluation of Meteorological Disasters, Nanjing University of Information Science and Technology, Nanjing 210044

Abstract: The anomalous climate features in China during the summer (JJA) of 2018, corresponding atmospheric circulation anomalies in East Asia and possible impacts from the ocean are analyzed in this paper. The results show that in the summer (JJA) of 2018, the average precipitation in China is 9.6% more than average. The precipitation in North and South China is more than normal while the precipitation in the middle and lower reaches of Yangtze River Valley is less than average. The atmospheric circulation in summer exhibits a typical feature of strong East Asian summer monsoon. The East Asian subtropical jet and the Northwest Pacific subtropical high are both significantly more northward located than average. In the lower troposphere, a cyclonic circulation dominates the area near the Philippines. At the same time,

* 国家重点基础研究发展计划(2015CB453203)、国家科技支撑计划项目(2015BAC03B04)和国家自然科学基金项目(41805067)共同资助
2018 年 12 月 14 日收稿; 2019 年 1 月 11 日收修定稿

第一作者:顾薇,主要从事气候异常机理诊断和短期气候预测研究. Email:guwei@cma.cn

通信作者:陈丽娟,主要从事气候异常机理诊断和短期气候预测研究. Email:chenlj@cma.cn

the mid-high latitude atmospheric circulation over Eurasia mainly exhibits a zonal feature. Under the combined impacts of the subtropical and mid-high latitude circulation, the transportation of water vapor to North and Northwest China is strengthened and more precipitation is induced in these regions. The precipitation in South China is also increased because of the strengthened tropical convective activity near South China Sea. However, in the middle and lower reaches of Yangtze River Valley, anomalous divergence and subsidence is observed and less precipitation is caused. In addition, it is also revealed that the La Niña event from October 2017 to April 2018 exerted a significant impact on the East Asian summer monsoon circulation and the summer precipitation in China.

Key words: summer precipitation, East Asian summer monsoon, Philippine abnormal cyclone, La Niña event

引　言

我国地处亚澳季风区,在亚澳季风系统多个成员的协同影响下,气候复杂多变,而汛期的气候异常往往会导致严重的旱涝灾害(黄荣辉等,2006;李崇银等,2009;封国林等,2013),如 1998 年长江流域的洪涝灾害,2003 和 2007 年淮河流域的洪涝灾害等,都对人民生活造成巨大影响,给经济发展造成严重损失(李维京,1999;冯明等,2000;徐良炎,2003;高荣等,2018)。在全球变暖背景下,异常和极端的气候事件频发(Donat et al, 2016),气候异常的影响变得更大。因此,深入认识我国汛期气候异常特征及成因有助于提高气候预测准确率(王东阡等,2016;翟盘茂等,2016;袁媛等,2017;郑志海和王永光,2018),可更好地为政府和公众提供保障服务,对我国的防灾减灾部署具有重要意义。

我国夏季天气气候受多因子的影响和控制,既与东亚夏季风系统中多成员的相互协同作用有关,也与中高纬冷空气的活动密切相关(张庆云和陶诗言,1998a;1998b)。同时,东亚夏季风系统还受到海温等外强迫因子的显著影响(陈丽娟等,2013;王永光和郑志海,2018)。2017 年 10 月至 2018 年 4 月,热带中东太平洋发生了一次拉尼娜(La Niña)事件,东亚夏季风异常偏强。2018 年夏季,我国气候出现较为明显的异常特征,中东部地区降水呈现“南北多、中间少”的空间分布,我国北方和华南大部分地区降水偏多,长江中下游地区降水偏少;气温则以全国总体偏暖为主要特征。2018 年夏季我国气候受到东亚夏季风环流系统的何种影响? 2017—2018 年的 La Niña 事件对东亚夏季风环流的影响程度如何? 本文将针对上述问题开展分析和讨论,希望能够加深对 2018 年夏季气候异常成因的了解,为今后的汛期气候预测提供更多的参考和依据。

1　资料和方法

本文用到的降水和气温资料来自中国气象局国家气象信息中心发布的《中国国家级地面气象站基本气象要素日值数据集(V3.0)》(任芝花等,2012),资料时段为 1951—2018 年。各等压面的位势高度场、水平风场等大气环流资料为 NCEP/NCAR 逐日再分析资料,资料分辨率为 2.5°×2.5°(Kalnay et al, 1996; Kistler et al,2001)。海温资料为美国 NOAA 提供的最优插值全球海温数据,水平分辨率为 1°×1°(Reynolds et al, 2002),资料起始时间为 1981 年 12 月。除海温资料的气候平均值因受起始时间限制取 1982—2010 年平均以外,其余数据的气候平均值均为 1981—2010 年平均。本文中冬季指上一年 12 月至当年 2 月平均,春、夏、秋季分别为 3—5、6—8 和 9—11 月平均。

本文选用的东亚夏季风指数为:(1)张庆云等(2003)利用东亚热带季风槽区与东亚副热带地区平均 850 hPa 风场的纬向距平差定义的东亚夏季风指数。(2)祝从文等(2000)综合考虑东西和南北向热力差异所定义的季风指数。西太平洋副热带高压(以下简称副高)脊线南北位置采用刘芸芸等(2012)定义的方法计算。Niño3.4 指数为 Niño3.4 区(5°S～5°N、170°～120°W)平均海温距平。在分析海温对夏季环流的可能影响时,使用一元线性回归的方法,回归时段选 1982—2017 年。

2　2018 年夏季我国气候异常特征

2018 年夏季风季节进程总体表现为前晚后早的特征,主要气候事件的强度也是前弱后强。华南

前汛期开始时间较常年偏晚15 d,结束时间较常年偏早4 d,总降水量较常年偏少19%。我国梅雨开始时间偏晚、雨量偏少:江南梅雨开始时间较常年偏晚11 d,结束时间偏晚5 d,雨量偏少31.8%;长江中下游梅雨开始时间偏晚8 d,结束时间偏早1 d,雨量偏少39.4%;江淮梅雨开始偏晚7 d,结束偏早5 d,雨量偏少34.6%。但是华北雨季开始和结束时间均偏早,雨量较常年偏多22.0%。西南雨季开始和结束时间均接近常年,总雨量较常年偏多8.6%(表1)。

表1 2018年汛期主要气候事件的起止日期及雨量

Table 1 The start date, end date and total precipitation of major climate events in 2018

雨季名称	开始时间(常年平均)	结束时间(常年平均)	雨量(常年平均)/mm
华南前汛期	4月21日(4月6日)	6月30日(7月4日)	592(734)
江南梅雨	6月19日(6月8日)	7月13日(7月8日)	249.2(365.4)
长江中下游梅雨	6月22日(6月14日)	7月13日(7月14日)	170.4(281.0)
江淮梅雨	6月28日(6月21日)	7月10日(7月15日)	172.8(264.4)
华北雨季	7月9日(7月18日)	8月7日(8月18日)	165.6(135.7)
西南雨季	5月27日(5月26日)	10月15日(10月14日)	808.0(738.7)

注:各气候事件定义分别见预报司发文:气预函〔2013〕135号;气预函〔2014〕2,28,117号。

Note: Definations of the climate events are according to the explanation letters (Letter〔2013〕135; Letter〔2014〕2, 28 and 117) from Department to Forecasting and Networking of CMA.

2018年夏季,全国平均降水量为356.4 mm,较常年平均(325.2 mm)偏多9.6%,为1998年之后最多的一年(图1a)。从空间分布来看(图2a),我国中东部降水总体呈现"南北多、中间少"的分布特征。西北大部、华北东部、东北北部和华南南部沿海等地降水较常年同期偏多20%~50%,部分地区偏多50%以上。北方地区多雨特征最为明显,东北(黑龙江、吉林、辽宁)、华北(北京、天津、河北、陕西、内蒙古)和西北(陕西、甘肃、宁夏、青海、新疆)等地区平均降水量为307.1 mm,较常年平均(263.0 mm)偏多17%,列1998年之后的第二位,仅次于2013年(图1b)。江汉和江南大部分地区降水较常年同期偏少20%~50%(图2a)。

2018年夏季,全国平均气温为21.9℃,较常年同期(20.9℃)偏高1℃,为我国夏季平均气温有记录以来最高的一年(图1c)。从空间分布特征来看,除华南南部气温较常年同期略偏低以外,全国大部分地区气温较常年同期偏高,江淮、江汉、华北、东北南部、西北大部和内蒙古大部气温偏高1~2℃(图2b)。

3 东亚大气环流异常特征及影响

2018年夏季,在对流层上层200 hPa,东亚地区北部存在一个异常正高度中心和一个相应的反气旋式环流,在40°N以南为异常偏东风,以北为异常偏西风,即东亚副热带高空急流位置较常年同期(40°N附近)偏北(图3a)。在500 hPa高度距平场上东亚沿岸为"负—正—负"的距平分布,在30°N以南为高度场负异常中心,以北为正异常中心,即副高脊线位置较常年同期偏北(图3b)。从夏季副高脊线位置指数的年际变化(图4a)来看,2018年夏季副高脊线指数的正距平达到3个标准差,是1981年

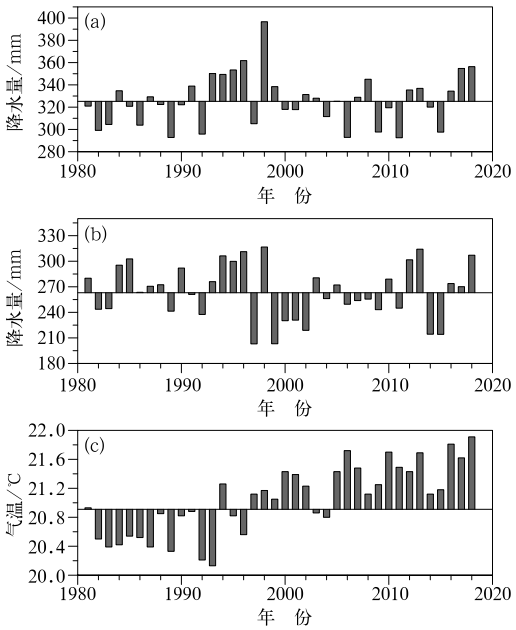

图1 1981—2018年夏季(a)全国和(b)北方地区平均降水量,(c)全国平均气温的历史序列

Fig. 1 Time series of summertime average precipitation in China (a) and in northern part of China (b), and (c) average temperature in China during 1981−2018

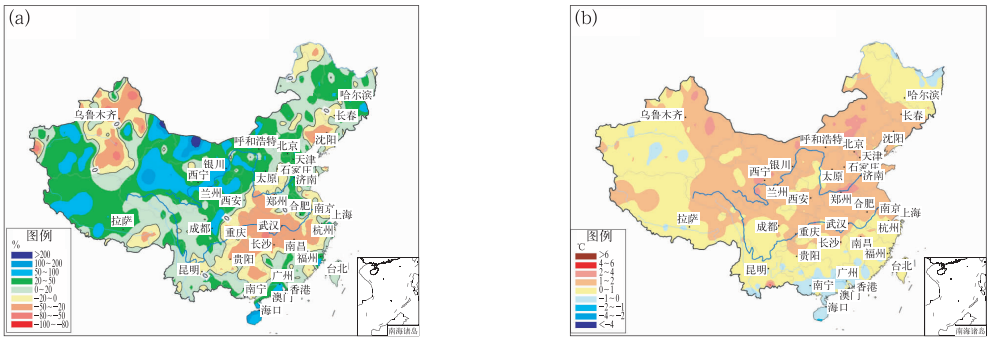

图 2　2018 年夏季全国(a)降水距平百分率和(b)气温距平分布

Fig. 2　Precipitation anomaly percentage (a) and temperature anomaly (b) in China in summer 2018

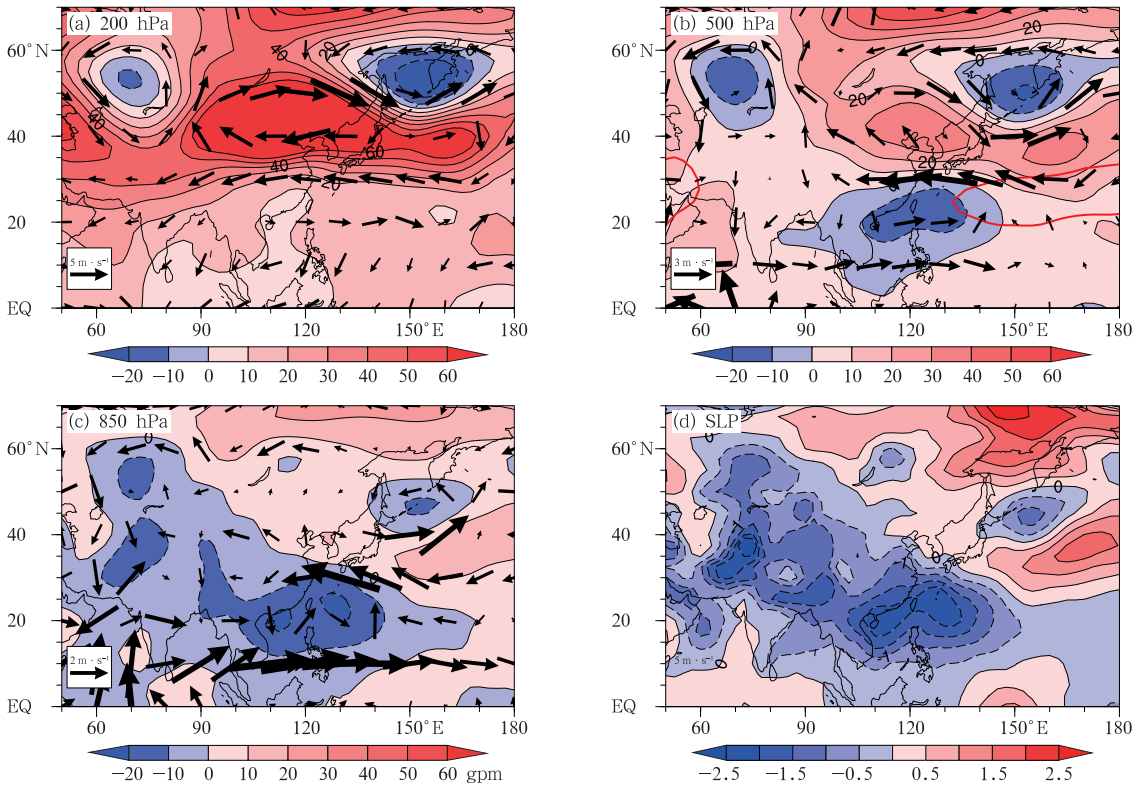

图 3　2018 年夏季(a)200 hPa、(b)500 hPa、(c)850 hPa 的高度距平(等值线和阴影,单位:gpm)和风场距平(矢量,单位:$m \cdot s^{-1}$),以及(d)海平面气压距平场(等值线和阴影,单位:hPa)

Fig. 3　(a) 200 hPa, (b) 500 hPa, (c) 850 hPa anomalous geopotential heights (contours and shadows, unit: gpm) and wind (vectors, unit: $m \cdot s^{-1}$), (d) anomalous sea level pressure (contours and shadows, unit: hPa) in summer 2018

以来最偏北的一年。850 hPa 距平风场上(图 3c)最显著的特征是菲律宾附近为异常气旋式环流,而且在东亚沿岸由南至北表现出“气旋—反气旋—气旋”的分布特征,与 500 hPa 东亚沿岸“负—正—负”的高度距平特征相对应,呈现“东亚—太平洋型”遥相关负位相的特征(黄荣辉等,2003)。从海平面气压距平场(图 3d)来看,东亚地区为异常偏低区域,即夏季大陆热低压明显偏强。总体来看,2018 年夏季对流层高、中、低层大气的异常都一致反映出东亚夏季风偏强的典型特征。

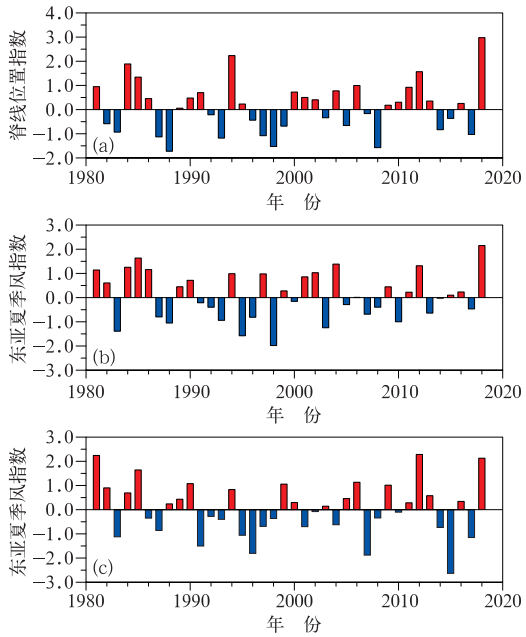

图 4 1981—2018 年(a)西太平洋副高脊线位置指数、(b)张庆云等(2003)和(c)祝从文等(2000)定义的东亚夏季风指数

Fig. 4 (a) Summertime ridge line position index of WPSH, the EASM index defined by (b) Zhang et al (2003) and (c) Zhu et al (2000) during 1981—2018

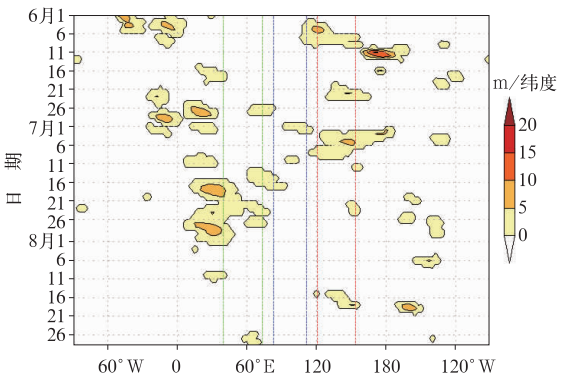

图 5 2018 年夏季欧亚中纬度阻塞高压活动指数监测图(绿色、蓝色、红色竖线所示区域分别表示乌拉尔区、贝加尔湖区和鄂霍次克海区)

Fig. 5 Blocking activity index over Eurasia in summer 2018 (The green, blue and red vertical lines represent the regions of Ural, Baikal and Okhotsk, respectively)

除了热带、副热带大气环流系统以外,2018 年夏季欧亚大陆中高纬度环流系统的异常特征也有利于东亚夏季风偏强。在 500 hPa 高度场上(图 3b),欧亚大陆地区表现为“两槽一脊”的距平分布特征,在乌拉尔山和鄂霍次克海附近分别存在负高度距平中心,而在贝加尔湖附近则为正高度距平中心。由于乌拉尔山和鄂霍次克海是夏季欧亚大陆阻塞高压最活跃的两个区域,“两槽一脊”的这种高度场异常分布特征意味着 2018 年夏季几乎没有明显的阻塞活动。从国家气候中心对中高纬度阻塞活动的监测(图 5)也可以看到,在 2018 年夏季,欧亚中高纬度地区没有异常偏强且较为持续的阻塞高压形势出现。阻塞高压偏弱有利于梅雨锋偏弱,从而使得东亚夏季风偏强(孙建华和赵思雄,2003;张庆云和陶诗言,1998a;张庆云等,2003)。因此,2018 年中高纬度阻塞高压不活跃的特征也有利于东亚夏季风偏强。

上述分析显示,无论从对流层高、中、低层大气环流,还是从热带、副热带到中高纬度大气环流都表现出东亚夏季风偏强年的典型特征。从张庆云等(2003)定义的东亚夏季风指数的年际演变(图 4b)看,2018 年东亚夏季风是 1981 年以来最强的一年。祝从文等(2000)定义的东亚夏季风指数的年际变化也显示,2018 年是 1981 年以来第三强(图 4c)。

在强东亚夏季风环流系统影响下,长江流域受到其南侧的气旋式异常环流和北侧的反气旋式异常环流的共同影响,水平风场和水汽通量的辐散形势非常明显(图 6a),有利于出现异常下沉运动。从图 6b 可以清楚地看出在 30°N 附近长江中下游地区的确出现较明显的异常下沉运动,从而使得该地区降水异常偏少。对我国 35°N 以北的大部分地区来说,低层风场以偏南风距平为主(图 3c 和图 6b),有利于暖湿气流的输送,从而有利于降水偏多。华南和南海等地处于异常低压中心(图 3d),对流活动异常活跃,上升运动明显加强(图 6b),降水偏多。同时,由于欧亚中高纬度以纬向环流特征为主,冷空气活动偏弱,有利于我国大部地区气温较常年同期偏高。

4 La Niña 事件的可能影响

根据国家气候中心对 Niño3.4 海温指数的监测(图 7a),2017 年 10 月至 2018 年 4 月,赤道中东太平洋发生了一次弱的 La Niña 事件。从海表温度距平(SSTA)的空间分布(图 7b)来看,这次 La Niña 事件表现出明显的东部型特征,冷中心位于赤道东

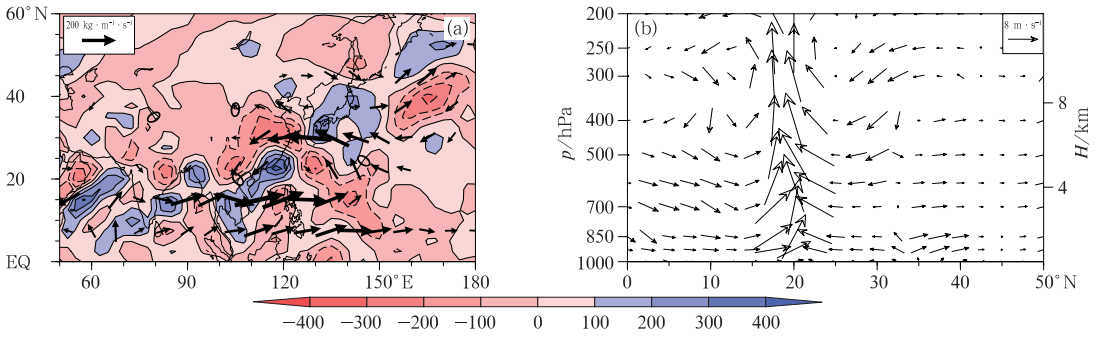

图 6　2018 年夏季(a)整层积分水汽通量距平(矢量,单位:kg·m^{-1}·s^{-1})和
散度(阴影和等值线,单位:10^{-7} kg·s^{-1}·m^{-2}),
(b) 110°～120°E 平均经向-垂直速度距平场(单位:m·s^{-1})

Fig. 6　(a) Anomalous water vapor flux (vectors, unit: kg·m^{-1}·s^{-1}) and
divergence (contours and shadow, unit: 10^{-7} kg·s^{-1}·m^{-2}),
(b) meridional-vertical wind anomaly (unit: m·s^{-1}) in 110°—120°E in summer 2018

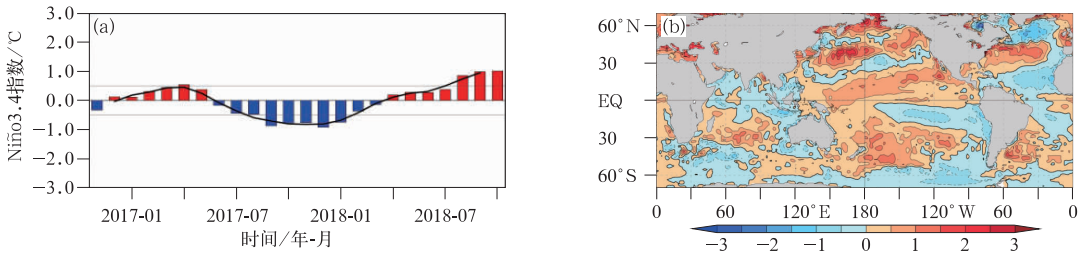

图 7　(a)2016 年 11 月至 2018 年 10 月 Niño3.4 指数和
(b)2017/2018 年冬季海表温度距平(单位:℃)

Fig. 7　(a) Monthly Niño3.4 index and (b) sea surface temperature
anomalies (unit: ℃) in the 2017/2018 winter

太平洋,西太平洋海温明显偏暖。

以往研究显示,ENSO 事件会对次年东亚夏季风和我国夏季降水产生显著影响。在 El Niño 次年,夏季风易偏弱;长江流域降水偏多;而在 La Niña 次年,东亚夏季风偏强;长江流域降水偏少(Huang and Wu,1989;陈丽娟等,2013)。当 ENSO 事件发生后,热带中东太平洋 SSTA 会通过激发大气中的异常波动使得菲律宾附近低层大气出现异常的反气旋/气旋,从而对东亚夏季风产生显著影响(Zhang et al,1996;Wang et al,2000)。图 8 显示了根据冬季 Niño3.4 指数回归的 850 hPa 速度势和水平风场。可以看到当 Niño3.4 区海温偏冷时,冬季热带东太平洋低层出现异常辐合形势,西太平洋地区则为异常辐散形势(图 8a),即沃克环流加强,热带西太平洋地区对流活动加强。热带西太平洋加强的对流活动可以在赤道两侧分别激发一个气旋式环流(Gill,1980),北侧的气旋式环流位于菲律宾附近(图 8b)。热带西太平洋地区的异常辐合形势和菲律宾附近的气旋在春季和夏季也都十分显著(图 8c～8f),说明在 La Niña 事件的影响下,西太平洋地区的对流活动异常及其所激发的菲律宾异常气旋可以从冬季一直持续至夏季。

2018 年冬、春和夏季热带和东亚副热带大气环流异常形势(图 9)与根据 Niño3.4 指数对环流的回归场(图 8)表现出相似的特征,这说明热带大气和东亚大气环流对于 2017—2018 年的弱 La Niña 事件产生了较明显的响应。在冬季和春季的850 hPa 速度势距平场(图 9a 和 9c)上可以看到,热带中东太平洋出现异常辐散运动,而热带西太平洋附近则以辐合上升运动为主,沃克环流加强。在热带

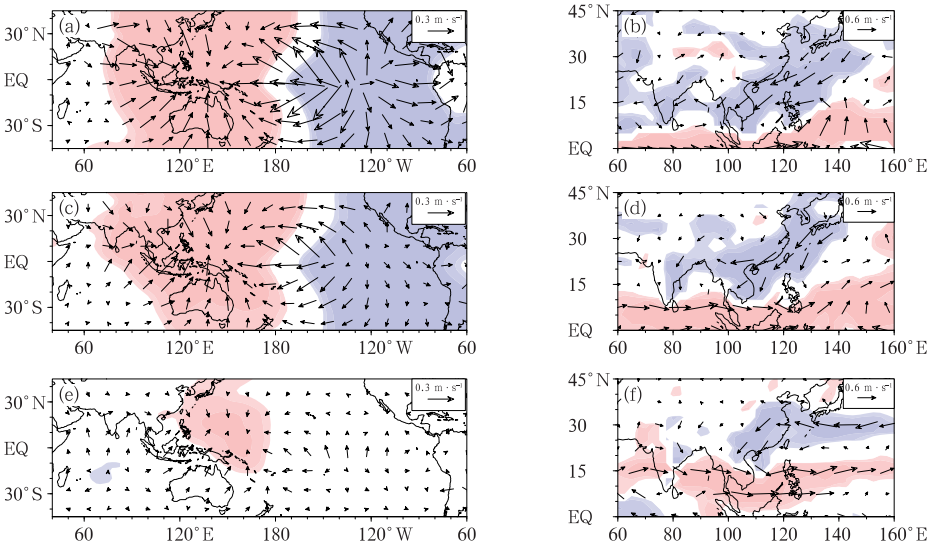

图 8 根据冬季 Niño3.4 指数回归的 850 hPa(a,b)冬季、(c,d)春季、(e,f)夏季辐散风场(a,c,e),以及水平风场(b,d,f;矢量,单位:$m \cdot s^{-1}$)

(为更好显示冷海温的作用,所得结果均反号显示;图中阴影表示通过 0.10 显著性水平的 t 检验区域)

Fig. 8 Regression of 850 hPa (a, b) winter, (c, d) spring, (e, f) summer (a, c, e) divergent wind, and (b, d, f) wind (vector, unit: $m \cdot s^{-1}$) on wintertime Niño3.4 index

(Shadow areas indicate having passed the significance test at 0.10 level)

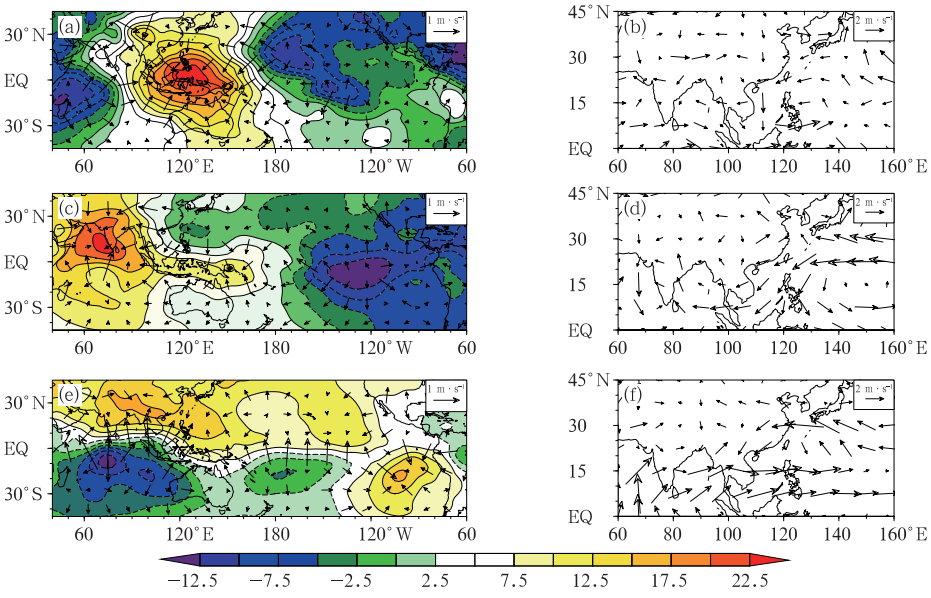

图 9 2018 年(a,b)冬季,(c,d)春季和(e,f)夏季 850 hPa 的(a,c,e)速度势(等值线和阴影,单位:$10^5\ m^2 \cdot s^{-1}$)和辐散风(矢量,单位:$m \cdot s^{-1}$),(b,d,f)水平风场(矢量,单位:$m \cdot s^{-1}$)

Fig. 9 The 850 hPa (a, b) winter, (c, d) spring, (e, f) summer velocity potential (contours and shadings, unit: $10^5\ m^2 \cdot s^{-1}$) and divergent wind (vectors, unit: $m \cdot s^{-1}$), and (b, d, f) summer 850 hPa wind (vector, unit: $m \cdot s^{-1}$) in 2018

西太平洋地区辐合上升运动加强意味着该地区的对流活动更加活跃,从而可以在菲律宾附近对流层低层大气中激发出异常的气旋式环流(图 9b 和 9d)。到了夏季,虽然热带中东太平洋的异常辐散运动减弱消失,但热带西太平洋的异常辐合运动依然持续,且位置有所北移(图 9e)。相应在 850 hPa 菲律宾地区附近,异常的气旋式环流也依然持续,位置也较冬季和春季明显北移(图 9f)。菲律宾附近的这一异常气旋式环流,有利于副高偏北、东亚夏季风偏强,从而有利于我国降水出现"南北多、中间少"的特征。由此可见,La Niña 事件是 2018 年东亚夏季风异常偏强的重要原因之一。

5　结论和讨论

2018 年夏季,全国平均降水量较常年平均偏多 9.6%,是 1998 年之后最多的一年。我国中东部地区降水总体呈现"南北多、中间少"的分布特征:北方大部分地区和华南降水较常年同期偏多,长江中下游地区较常年同期明显偏少。2018 年梅雨开始时间均较常年偏晚、雨量偏少;华北雨季开始偏早、雨量偏多。2018 年夏季全国大部气温较常年同期偏高,夏季平均气温为有历史记录以来最高的一年。

2018 年夏季对流层高、中、低层大气的异常都一致表现出东亚夏季风偏强的典型特征:东亚副热带高空急流和西太副高位置都较常年同期明显偏北,东亚沿岸由副热带至中高纬出现"负—正—负"的高度距平分布特征,菲律宾附近为异常的气旋式环流,东亚地区大陆低压加强。同时,欧亚中高纬度高度场表现出"两槽一脊"的分布特征,在乌拉尔山和鄂霍次克海附近分别存在负高度距平中心,中高纬度没有明显阻塞活动。在这种环流形势的影响下,长江流域以南为东北风距平,以北为偏南风距平,使得长江流域出现明显的异常辐散下沉运动、降水偏少。而北方大部分地区低层以偏南风为主,有利于降水偏多。华南地区由于受到热带对流活跃的影响,上升运动加强,降水偏多。同时,欧亚中高纬度大气纬向环流特征十分明显,冷空气活动偏弱,有利于我国大部地区气温较常年同期偏高。

2017 年 10 月至 2018 年 4 月赤道中东太平洋发生的 La Niña 事件对 2018 年夏季东亚大气环流产生了明显的影响,有利于东亚夏季风偏强。伴随着这次 La Niña 事件的发生,热带中东太平洋海温偏低,西太平洋海温偏高,沃克环流加强,热带西太平洋出现异常的辐合上升形势,对流活动加强,从而能够在菲律宾附近激发出一个异常的气旋式环流。热带西太平洋对流活跃的特征从冬季一直持续到夏季,相应的,菲律宾附近的异常气旋也一直持续至夏季,从而有利于副高偏北、东亚夏季风偏强。

值得注意的是,有研究表明,ENSO 事件对东亚夏季风的影响在 20 世纪 80 年代之后(高辉和王永光,2007)明显减弱,而 2017 年 10 月发生的这次 La Niña 事件强度偏弱,意味着这次弱 La Niña 事件对东亚夏季风的影响可能是有限的,即今年东亚夏季风异常偏强的特征有可能还同时受到其他因子的影响,具体影响因子和过程还有待进一步深入分析。

参考文献

陈丽娟,袁媛,杨明珠,等,2013. 海温异常对东亚夏季风影响机理的研究进展[J]. 应用气象学报,24(5):521-532. Chen L J,Yuan Y,Yang M Z,et al,2013. A review of physical mechanisms of the global SSTA impact on EASM[J]. J Appl Meteor Sci,24(5):521-532(in Chinese).

封国林,赵俊虎,支蓉,等,2013. 动力-统计客观定量化汛期降水预测研究新进展[J]. 应用气象学报,17(1):1-9. Feng G L,Zhao J H,Zhi R,et al,2013. Recent progress on the objective and quantifiable forecast of summer precipitation based on dynamical-statistical method[J]. J Appl Meteor Sci,17(1):1-9(in Chinese).

冯明,王家宝,熊守全,2000. 1998 年长江大洪水与大气环流和海温异常分析[J]. 长江流域资源与环境,9(1):112-117. Feng M,Wang J B,Xiong S Q,2000. Analysis on the abnormality of general circulation and sea temperature in relation to the flood water of Yangtze River in 1998[J]. Res Environ Yangtze Basian,9(1):112-117(in Chinese).

高辉,王永光,2007. ENSO 对中国夏季降水可预测性变化的研究[J]. 气象学报,65(1):131-137. Gao H,Wang Y G,2007. On the weakening relationship between summer precipitation in China and ENSO[J]. Acta Meteor Sinica,65(1):131-137(in Chinese).

高荣,宋连春,钟海玲,2018. 2016 年汛期中国降水极端特征及其与 1998 年对比[J]. 气象,44(5):699-703. Gao R,Song L C,Zhong H L,2018. Characteristics of extreme precipitation in China during the 2016 flood season and comparison with the 1998 situation[J]. Meteor Mon,44(5):699-703(in Chinese).

黄荣辉,蔡榕硕,陈际龙,等,2006. 我国旱涝气候灾害的年代际变化及其与东亚气候系统变化的关系[J]. 大气科学,30(5):730-743. Huang R H,Cai R S,Chen J L,et al,2006. Interdecadal variations of drought and flooding disasters in China and their association with the East Asian climate system[J]. Chinese J Atmos Sci,30(5):730-743(in Chinese).

黄荣辉,陈文,丁一汇,等,2003. 关于季风动力学以及季风与 ENSO 循环相互作用的研究[J]. 大气科学,27(4):484-502. Huang

R H,Chen W,Ding Y H,et al,2003. Studies on the monsoon dynamics and the interaction between monsoon and ENSO cycle [J]. Chinese J Atmos Sci,27(4):484-502(in Chinese).

李崇银,黄荣辉,丑纪范,等,2009.我国重大高影响天气气候灾害及对策研究[M].北京:气象出版社:187. Li C Y,Huang R H,Chou J F,et al,2009. Research on the Weather and Climate Disasters with High Impact in China and the Countermeasures [M]. Beijing:China Meteorological Press:187(in Chinese).

李维京,1999. 1998年大气环流异常及其对中国气候异常的影响[J].气象,25(4):20-25. Li W J,1999. General atmospheric circulation anomaly in 1998 and their impact on climate anomaly in China[J]. Meteor Mon,25(4):20-25(in Chinese).

刘芸芸,李维京,艾孜悦秀,等,2012.月尺度西太平洋副热带高压指数的重建与应用[J].应用气象学报,23(4):414-423. Liu Y Y,Li W J,Ai W X,et al,2012. Reconstruction and application of the monthly western Pacific subtropical high indices[J]. J Appl Meteor Sci,23(4):414-423(in Chinese).

任芝花,余予,邹凤玲,等,2012.部分地面要素历史基础气象资料质量检测[J].应用气象学报,23(6):739-747. Ren Z H,Yu Y,Zou F L,et al,2012. Quality detection of surface historical basic meteorological data[J]. J Appl Meteor Sci,23(6):739-747(in Chinese).

孙建华,赵思雄,2003. 1998年夏季长江流域梅雨期环流演变的特殊性探讨[J].气候与环境研究,8(3):291-306. Sun J H,Zhao S X,2003. A study of special circulation during Meiyu season of the Yangtze River Basin in 1998[J]. Clima Environ Res,8(3):291-306(in Chinese).

王东阡,王艳姣,崔童,等,2016. 2015年夏季气候异常特征及其成因简析[J].气象,42(1):115-121. Wang D Q,Wang Y J,Cui T,et al,2016. Analysis on climate anomalies and causations in summer 2015[J]. Meteor Mon,42(1):115-121(in Chinese).

王永光,郑志海,2018. 2017年汛期气候预测先兆信号的综合分析[J].气象,44(4):565-571. Wang Y G,Zheng Z H,2018. Precursory signal analysis of summer rainfall prediction in China in 2017[J]. Meteor Mon,44(4):565-571(in Chinese).

徐良炎,2003.淮河流域暴雨频繁洪涝严重;江南华南酷热少于伏旱发展[J].气象,29(10):62-63. Xu L Y,2003. Severe flooding in Huaihe River Valley; Intense heat and drought in Jiangnan and Huanan[J]. Meteor Mon,29(10):62-63(in Chinese).

袁媛,高辉,柳艳菊,2017. 2016年夏季我国东部降水异常特征及成因简析[J].气象,43(1):115-121. Yuan Y,Gao H,Liu Y J,2017. Analysis of the characteristics and causes of precipitation anomalies over eastern China in the summer of 2016[J]. Meteor Mon,43(1):115-121(in Chinese).

翟盘茂,余荣,郭艳君,等,2016. 2015/2016年强厄尔尼诺过程及其对全球和中国气候的主要影响[J].气象学报,74(3):309-321. Zhai P M,Yu R,Guo Y J,et al,2016. The strong El Niño in 2015/2016 and its dominant impacts on global and China's climate[J]. Acta Meteor Sinica,74(3):309-321(in Chinese).

张庆云,陶诗言,1998a.亚洲中高纬度环流对东亚夏季降水的影响[J].气象学报,56(2):199-211. Zhang Q Y,Tao S Y,1998a. Influence of Asian mid-high latitude circulation on East Asian summer rainfall[J]. Acta Meteor Sinica,56(2):199-211(in Chinese).

张庆云,陶诗言,1998b.夏季东亚热带和副热带季风与中国东部汛期降水[J].应用气象学报,9(Sl):17-23. Zhang Q Y,Tao S Y,1998b. Tropical and subtropical monsoon over East Asia and its influence of the rainfall over eastern China in summer[J]. J Appl Meteor Sci,9(Sl):17-23(in Chinese).

张庆云,陶诗言,陈烈庭,2003.东亚夏季风指数的年际变化与东亚大气环流[J].气象学报,61(5):559-568. Zhang Q Y,Tao S Y,Chen L T,2003. The inter-annual variability of East Asian summer monsoon indices and its association with the pattern of general circulation over East Asia[J]. Acta Meteor Sinica,61(5):559-568(in Chinese).

郑志海,王永光,2018. 2017年夏季北半球大气环流特征及对我国天气气候的影响[J].气象,44(1):199-205. Zheng Z H,Wang Y G,2018. Northern Hemisphere atmospheric circulation characteristics in summer 2017 and its impact on weather and climate in China[J]. Meteor Mon,44(1):199-205(in Chinese).

祝从文,何金海,吴国雄,2000.东亚季风指数及其与大尺度热力环流年际变化关系[J].气象学报,58(4):391-402. Zhu C W,He J H,Wu G X,2000. East Asian monsoon index and its inter-annual relationship with large scale thermal dynamic circulation[J]. Acta Meteor Sinica,58(4):391-402(in Chinese).

Donat M G,Lowry A L,Alexander L V,et al,2016. More extreme precipitation in the world's dry and wet regions[J]. Nature Climate Change,6(5):508-513.

Gill A E,1980. Some simple solutions for heat-induced tropical circulation[J]. Quart J Roy Meteor Soc,106(449):447-462. DOI:10.1002/qj.49710644905.

Huang R H,Wu Y F,1989. The influence of ENSO on the summer climate change in China and its mechanisms[J]. Adv Atmos Sci,6(1):21-32.

Kalney E,Kanamitsu M,Kistler R,et al,1996. The NCEP/NCAR 40 year reanalysis project[J]. Bull Amer Meteor Soc,77(3):437-471.

Kistler R,Kalnay E,Collins W,et al,2001. The NCEP/NCAR 50-year reanalysis: monthly means CD ROM and documentation [J]. Bull Amer Meteor Soc,82(2):247-268.

Reynolds R W,Rayner N A,Smith T M,et al,2002. An improved in Situ and satellite SST analysis for climate[J]. J Climate,15(13):1609-1625.

Wang B,Wu R,Fu X,2000. Pacific-East Asia teleconnection: how does ENSO affect East Asian climate[J]. J Climate,13(9):1517-1536. DOI:10.1175/1520-0442.

Zhang R H,Sumi A,Kimoto M,1996. Impact of El Nino on the East Asian monsoon: a diagnostic study of the '86/87 and '91/92 events[J]. J Meteor Soc Japan,74 (1):49-62.

hydrology

MDPI

Article

The Spatiotemporal Pattern of Rainy-Season Precipitation in the Haihe River Basin, North China

Jun Guo [1,2], Guoyu Ren [1,3,*], Mingming Xiong [2] and He Huang [2]

1 Department of Atmospheric Science, School of Environmental Studies, China University of Geosciences, Wuhan 430074, China
2 Tianjin Climate Center, Tianjin 300074, China
3 Laboratory for Climate Studies, National Climate Center, CMA, Beijing 100081, China
* Correspondence: guoyoo@cma.gov.cn

Received: 21 April 2019; Accepted: 6 May 2019; Published: 20 August 2019



Abstract: The Haihe River basin of North China is characterized by extremely low per capita water resources and a consistently long-term decreasing trend of precipitation and runoff over the last few decades. This study analyzes the climatological features of rainy season (May–September) precipitation in the Haihe River basin and its branch systems based on a high-density hourly observational dataset during 2007–2017. We show that there are two high-rainfall zones in the basin, with one along the south of the Yanshan Mountains to Taihang Mountains and another along the Tuma River in the south. Rainstorm centers exist amidst the two zones. July generally sees the highest precipitation, followed by August, and May has the lowest precipitation. The major flood season is reached between the third pentad of July and the fourth pentad of August. The precipitation is high at night but low in the daytime. In the pre-flood season before early July, rainfalls mostly arrive at 16:00–21:00 h. After entering the major flood season, the diurnal precipitation has two peaks, one at 17:00–22:00 h and the other at 0:00–7:00 h. In the post-flood season after mid-August, the most rain occurs at night, with the peak appearing at 0:00–8:00 h. The short-duration precipitation is mainly distributed in the mountainous areas, and the long-duration precipitation that contributes most to seasonal rainfalls appears in the plain areas, and the continuous precipitation mostly occurs in the windward slopes of the Taihang Mountains and the Yanshan Mountains. In addition, urbanization process around large city stations may have affected the rainy season precipitation to a certain extent in the Haihe River basin, with large and medium city stations experiencing around 10% higher precipitation than small city stations. However, this issue needs to be investigated exclusively.

Keywords: rainy season; precipitation; rainstorm; diurnal variation; urbanization; Haihe River; North China

1. Introduction

The Haihe River is the largest river in North China. Beijing, the capital of China, and Tianjin, a municipality directly under the central government, are both located in the river basin. Encompassing a total population of around 124 million, the Haihe River basin has the highest population density in the world but the lowest per capita water resources in China [1]. Intensive human intervention, excessive water resource exploitation and the severe impact of climate change in recent decades, have led to notable changes in the amount, quality and distribution of surface and underground water resources amidst the basin. The ever-increasing unbalance between supply and demand of water resources has become a key issue in the sustainable development of economy and society in the river basin. Accordingly, comprehensive knowledge on the spatial-temporal precipitation distribution

and its causes has been of great importance for understanding the dynamic variation of runoff and groundwater, and for rationally planning and effectively managing the water resources in the basin.

The Haihe River basin has a semi-humid and semi-arid continental climate. As a river in the temperate East Asian Monsoon, more than 80% of its annual precipitation occurs from May to September. Affected by the terrain of North China, the high-rainfall belt stretches from northeast to southwest, roughly along the Yanshan and Taihang Mountains. There exist three rainstorm centers in the basin, located near Tangshan, the west of Baoding, and near Jinan, respectively [2,3]. The precipitation in summer is usually concentrated in several heavy rainfall occurrences, which endows the floods in the basin with the characteristics of a high peak value, a steep peak type and a large one-time volume [4]. The climatic factors dominating the summer rainfalls are extremely complicated [5]. On the one hand, the basin is located in the northern rim of summer monsoon activities, which enables the monsoon weather systems to influence the precipitation in the flood season [6,7]; On the other hand, it is also affected by the westerly circulation system at mid-high latitudes [2,8,9]. These factors lead to uneven spatial and temporal precipitation in the basin, aggravating the difficulty and uncertainty of water resources exploitation.

Plenty of researches have been conducted on the summer rainfalls in the Haihe River basin and North China. Ren et al. (2015) reported that the annual and summer precipitation in the Haihe River basin experienced a significant downward trend in the past 50 years. Since the mid-late 1970s, the annual precipitation in North China, including the Haihe River basin, has been further declining [10–12], with the abrupt decline in the rainy season rainfall after 1979 particularly significant [11]. Liu and Ding [3,13] showed that there existed a decadal shift from high to low precipitation in North China around 1978. Hao et al. [14] found that the decreased precipitation in North China in the past 50 years was mainly due to the weakening of summer rainstorms.

With the establishment of the automatic weather station network and the accumulation of hourly precipitation data for years, attention has been paid to the fine resolution structures of precipitation [15,16]. Yu et al. [17] revealed that summer rainfalls in mainland China exhibit a remarkable spatial pattern of diurnal variations. In eastern China, for example, the peaks of precipitation mostly occur at around 17:00 and in early morning respectively. The diurnal variation of rainy season precipitation in central and eastern China shows a clear intra-seasonal evolution along with the north-south movement of the monsoon rain belt [18]. Zhou et al. [19] and Yuan et al. [20] analyzed the diurnal variation of summer rainfalls in the Huaihe River which is located between the Haihe River and the Yangtze River, concluding that there have existed two peaks, one before dawn and the other in the evening. Han et al. [21] adopted the satellite retrieved hourly precipitation data to analyze the diurnal variation of summer rainfalls in North China, and they found that the precipitation peaked late at night in the northern North China Plain, but in the morning in the central and southern parts of the plain.

Therefore, the long-term variations of precipitation and extreme rainfalls have been studied extensively in the past two decades, and the spatial-temporal precipitation distributions of summer rainfalls on different temporal scales have been examined as well. However, in-depth knowledge on diurnal precipitation variations, as well as on the more detailed spatial pattern and the relevant causes of seasonal and diurnal rainfall variations, has been far from enough considering that the adopted data in the previous works are relatively sparse in spatial distribution and coarse in temporal resolution.

In this paper, the high-density hourly precipitation observation data, which have been developed recently by the China Meteorological Administration, are used for the first time to analyze the refined spatial-temporal structure of precipitation with different durations in the Haihe River basin. The analysis reveals several novel features of precipitation in the basin, which is expected to lend support to a scientific understanding of the dynamic variations of atmospheric precipitation, surface and underground water resources in the region severely short of water.

2. Data and Methods

The Haihe River basin is located between 112–120° E and 35–43° N (Figure 1), with a total area of 318,000 square kilometers. As one of the seven largest rivers in China, its basin covers Tianjin, Beijing, most parts of the Hebei province, as well as parts of the Henan province, Shandong province, Shanxi province and Inner Mongolia. The basin is bound to the north by the east-to-west Yanshan Mountains, and to the west by the north-to-south Taihang Mountains. Inside the basin, 60% of its surface is covered by mountains and plateaus, while the other 40% is covered by plains. The basin contains nine tributaries: the Luanhe River, the Beisan River, the Yongding River, the Daqing River, the Ziya River, the Zhangwei River, the Nanyun River, the Tuhai-majia River and the lower reach of the Haihe River.

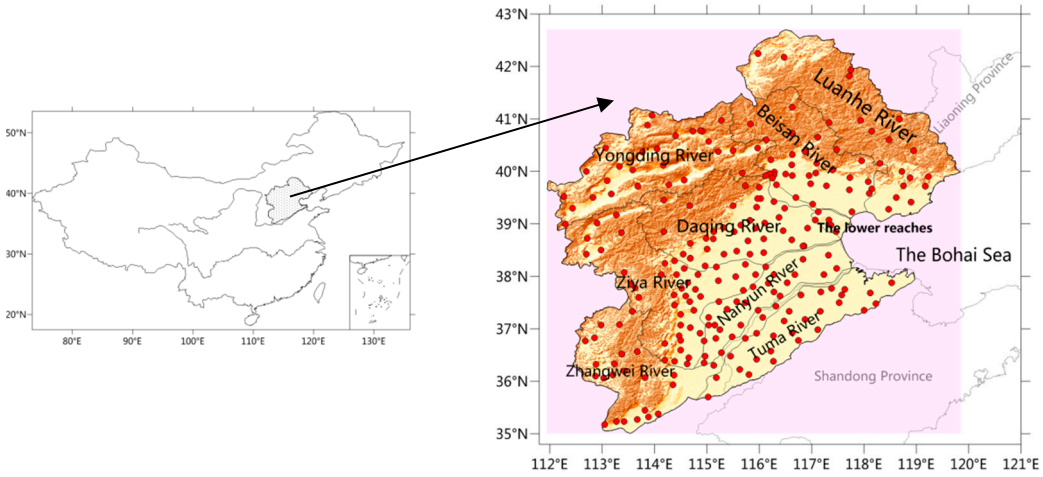

Figure 1. The geographical location and meteorological station distribution of the Haihe River basin (dots indicate locations of meteorological stations, and the purple color shows the mountains and plateaus).

The data used in this paper are the hourly precipitation observation data in the rainy season (May-September) during 2007–2017 from 249 meteorological stations in the Haihe River basin. The data are from the National Meteorological Information Center (NMIC), China Meteorological Administration (CMA). Quality control has been done for precipitation by the NMIC. A denser distribution of precipitation stations can be seen in the plain regions and the mountainous regions have relatively sparser observations (Figure 1).

In this research, a precipitation hour refers to an hour with precipitation greater than 0.1 mm. Referring to previous studies [22,23], the length of the precipitation intermittence, as the boundary between two rainfall occurrences, is set to 2 h. That is to say, when no rainfall occurs for two consecutive hours during a precipitation process, the process is judged to be terminated. In this case, discontinuous non-precipitation intervals might exist in a precipitation event. According to different durations, all of the precipitation events for any station are classified into four types in this work: short-duration precipitation (1–3 h), medium-duration precipitation (4–6 h), long-duration precipitation (6–12 h) and continuous precipitation (over 12 h).

The analysis of diurnal variation uses Beijing local time at 120° E. The intra-seasonal variation of rainfall during the rainy season is analyzed by applying the pentad mean rainfall for the period 2007–2017. Each month is thus divided into six pentads, with each of them being 5 days or six days (the last pentad of the months with 31 days) except for February that generally has three days or four days in the last pentad. A simple arithmetic average is made for the whole basin and its tributaries when calculating the areal means of precipitation amount and frequency on different time scales, by considering the relatively even distribution of the observational sites in the study region. In order to examine the possible influence of urbanization on precipitation, we classify the urban stations into

three categories: large cities with a population over 5 million, medium-sized cities with a population 0.5–2 million and small cities with a population 0.1–0.5 million. All other observational sites are regarded as rural stations.

3. Results

3.1. Warm-Season Precipitation Distribution

During 2007–2017, the rainy season precipitation averaged around 443.0 mm in the Haihe River basin. Among the tributaries, the Yongding River suffered the lowest precipitation of 337.3 mm while the Tuma River, in the south of the basin, had the highest precipitation of 486.8 mm. The average precipitation in the Luanhe River, the Beisan River and the lower reach of the Haihe River stands at around 470 mm. For other tributaries, the precipitation ranges between 400 mm and 450 mm. In spatial distribution (Figure 2), there exist two high-rainfall zones and two low-rainfall zones, with the precipitation taking on the "high-low-high-low" pattern from southeast to northwest. The precipitation in the Tuma River downstream, in the south of the basin, stays above 520 mm. The central plain receives low rainfalls of 460 mm or below, especially the Ziya River downstream where the precipitation is only 340–400 mm. The windward (south) slope of the Yanshan Mountains sees high warm-season precipitation (460–560 mm on average); in this zone, the average precipitation in the Beisan River downstream and the Luanhe River downstream stays high at 520 mm or above. When it comes to the north of the basin, the precipitation of the plateaus stays below 400 mm on average, with the lowest value hitting 270 mm. On the windward (east) slope of the Taihang Mountains, there also exists a zone with precipitation surpassing 460 mm.

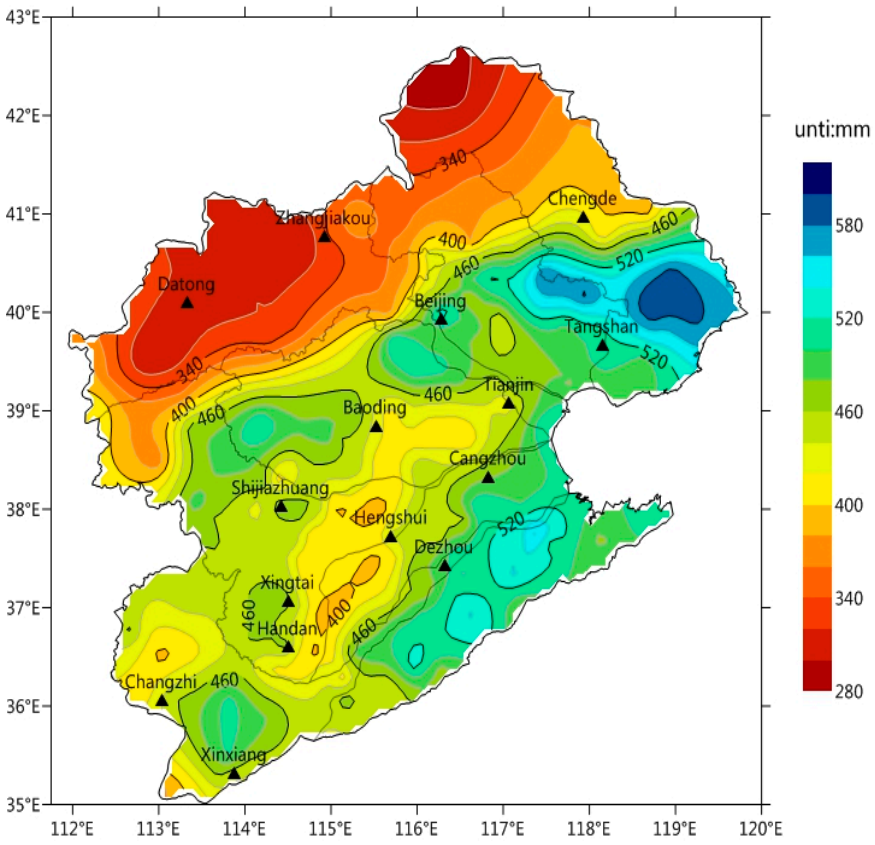

Figure 2. The spatial distribution of the rainy season total precipitation in the Haihe River basin, 2007–2014 (unit: mm).

3.2. Monthly Precipitation Pattern

Figure 3 shows the spatial distribution of the monthly average precipitation during warm-season in the Haihe River basin. A visible difference can be found for the months.

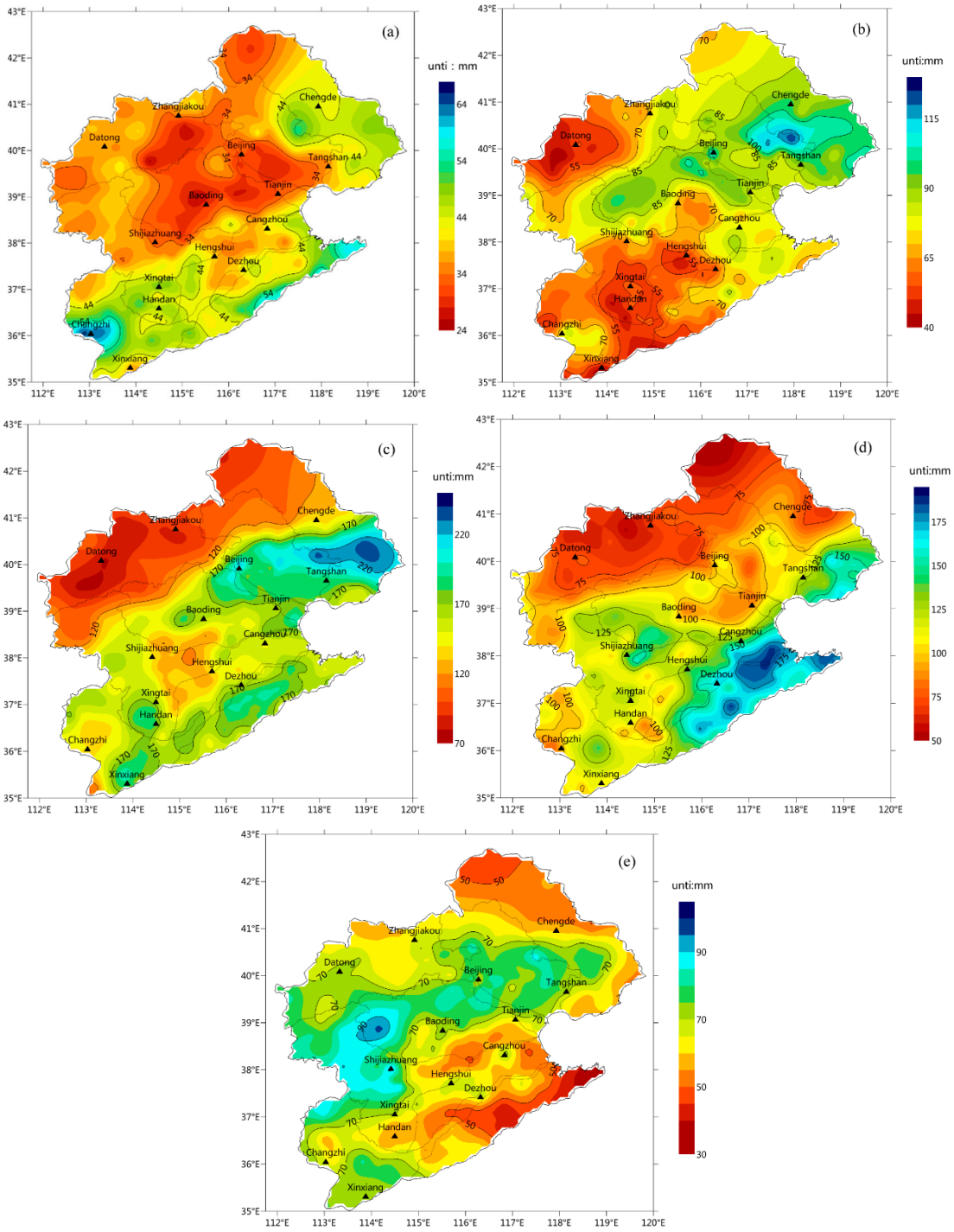

Figure 3. The spatial distribution of the monthly total precipitation in the Haihe River basin, 2007–2017 (unit: mm) ((**a**), (**b**), (**c**), (**d**) and (**e**) for May, June, July, August and September, respectively).

In May, the precipitation averages 36.8 mm, accounting for 8.3% of the total precipitation in the rainy season. During this month, the Zhangwei River and the Tuma River in the south, as well as the Luanhe River in the northeast, are covered in the high-rainfall belt, suffering an average precipitation of over 40 mm; while the Daqing River in the central basin is the zone with the lowest precipitation of

28.6 mm. In June, the average precipitation climbed to 74.9 mm, almost twice than that in May. In this month, rainfalls are high in the northeast while low in the southwest. The Luanhe River and the Beisan River in the north become the high-rainfall zones, with the average precipitation exceeding 90 mm; while the Yongding River, the Ziya River and the Zhangwei River are the low-rainfall zones, with the average precipitation ranging between 59 mm and 65 mm.

The precipitation is at 152.8 mm in July, over twice as much as in June. It accounts for 34.5% of the total precipitation in the rainy season. As for the spatial distribution, the precipitation in July indicates a "high-low-high-low" trend from south to north, similar to the pattern of the accumulative precipitation in the rainy season. The precipitation in the northern mountains and plateaus stays below 120 mm. The central plain is also covered by a low-rainfall zone in this month. When it comes to August, the precipitation edges lower at 116.2 mm, relatively high in the south while low in the north. The Tuma River, a high-rainfall zone in this month, has a level of precipitation of around 150 mm. The precipitation in the plain is estimated at 100–150 mm, and that in the mountainous area at 100 mm or below. As to September, the precipitation drops by around 80% from August. The spatial distribution is similar to that of June, except for the high-rainfall center which now moves to the northern Taihang Mountains. The Taihang Mountains and Yanshan Mountains become the high-rainfall zones while the southeastern part registers low rainfall, which is the opposite of August.

3.3. Diurnal Precipitation Variations

Figure 4 shows the diurnal variations of the average precipitation in the rainy season during 2007–2017 in the Haihe River basin. The diurnal variation curve has two peaks and a valley. The peak period takes place in the evening (17:00–21:00 h), with the hourly mean precipitation surpassing 21 mm. The maximum value, occurring at 19:00 h, is recorded at 21.9 mm. The other peak occurs at 2:00 h when the hourly mean precipitation reads 20.2 mm. The rainfall descends in the daytime (9:00–15:00 h), with the lowest precipitation occurring at noon (11:00–13:00 h). At 12:00 h, the hourly mean precipitation hits its low at 13.3 mm.

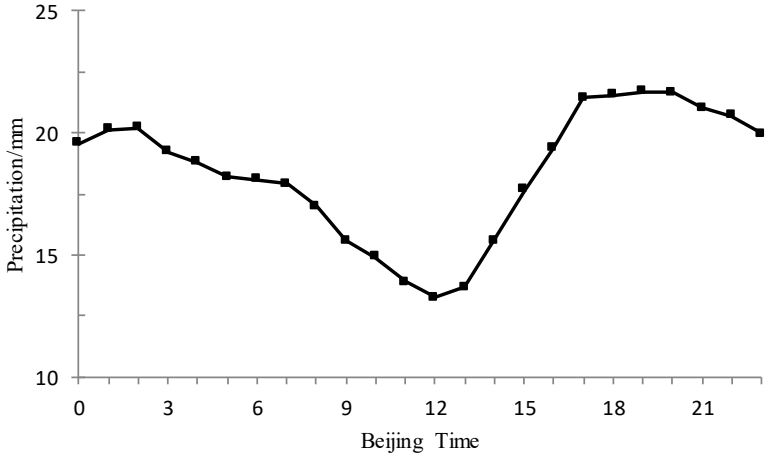

Figure 4. The diurnal variations of the basin-averaged hourly mean precipitation in the Haihe River basin.

Further analysis of the diurnal peak in each branch system shows that the occurrence periods vary greatly due to the difference in geographical location and topographic conditions (Figure 5). The precipitation in the Luanhe River, the Yongding River, the Beisan River, the Ziya River and the Zhangwei River increases during 15:00–17:00 h. The peak occurs during 21:00–23:00 h in the Beisan River, and other tributaries have the diurnal precipitation peak during 18:00–20:00 h.

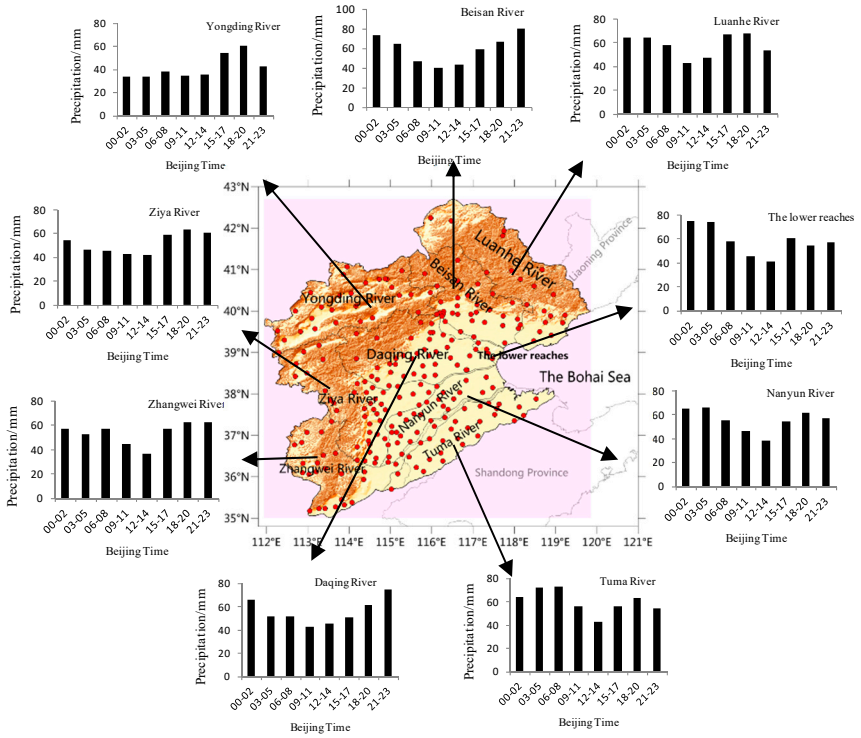

Figure 5. The diurnal variations of hourly mean precipitation for the tributaries in the Haihe River basin.

The diurnal precipitation in the lower reach of the Haihe River, the Nanyun River, and the Tuma River has two peaks, one at night and the other in the afternoon. The peak value at night is greater than that in the afternoon. Both the Nanyun River and the Tuma River reach an evening peak at 18:00–20:00 h; while the lower reach of the Haihe River encounters the afternoon peak at 15:00–17:00 h. As for night time, the peak in the lower reach of the Haihe River occurs at 0:00–2:00 h; while the peak in the Nanyun River and the Tuma River appears at 3:00–5:00 h.

3.4. The Pentad Mean Precipitation Feature

Figure 6 shows the pentad mean precipitation variations during 2007–2017 in the Haihe River basin. The pentad mean precipitation during the summer could be divided into five periods. From May to the fourth pentad of June, the hourly mean precipitation stays low at 0.1–5 mm. The diurnal precipitation, high at night but low in the daytime, mostly occurs at 16:00–20:00 h but seldom appears between 5:00–15:00 h (especially at noon) during this period. During the fifth pentad of June and the third pentad of July, the hourly mean precipitation climbs from the previous period to as high as 5–10 mm. During this period, the diurnal peak appears at 18:00–21:00 h. The major flood season of the Haihe River arrives at the period from the fourth pentad of July to the second pentad of August, or from late July to early August. In this period, the hourly mean precipitation stays high at 10–20 mm. The diurnal peak and sub-peak reach at 17:00–22:00 h and 0:00–7:00 h respectively, with the hourly mean precipitation averaging around 15 mm. Later from the third pentad of August to the second pentad of September comes the post-flood season of the study region. In this period, the hourly mean precipitation slides to 5–10 mm. The precipitation mainly occurs at night and peaks at 0:00–8:00 h. During the third pentad and the sixth pentad of September, the hourly mean precipitation further drops to 0–5 mm. The night time in this period sees most of the rainfalls. It could be concluded that fewer rainfalls come in the daytime (9:00–15:00 h) for all the five periods, although the peaks vary.

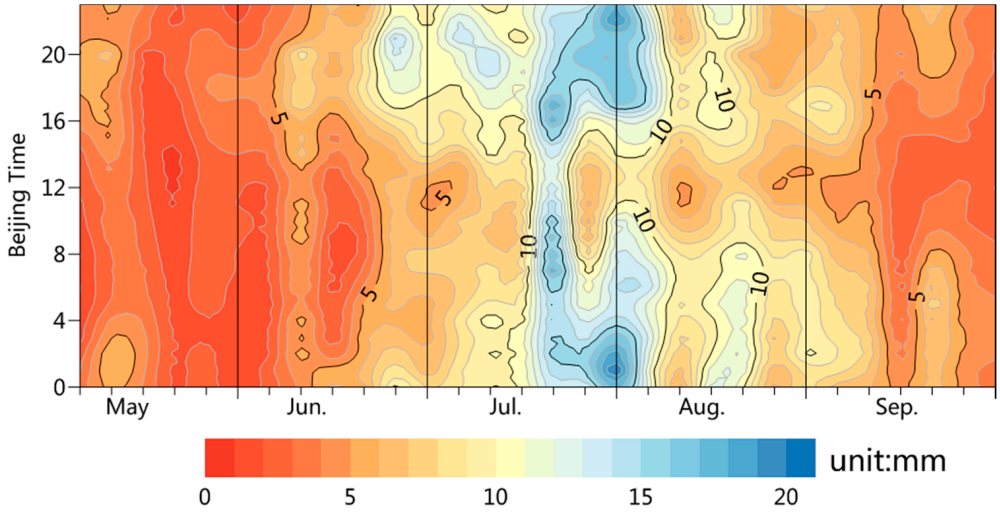

Figure 6. The pentad variations of the hourly mean precipitation in the Haihe River basin, 2007–2017.

The seasonal precipitation of each tributary is featured with a single peak in the diurnal variation. July has the highest precipitation of the rainy season, followed by August, and May witnesses the lowest precipitation. The tributaries share a similar diurnal variation pattern (Figure 7). During the first pentad of May and second pentad of July, the diurnal precipitation of each branch reaches a single peak, with most rainfall coming in the afternoon or at night. From the third pentad of July till the fourth pentad of August (major flood season), the peak of the hourly mean precipitation occurs before dawn in the Luanhe River, the Beisan River, the Nanyun River, the Zhangwei River, the Tuma River and the lower reach of the Haihe River. As for the Beisan River, the Yongding River, the Daqing River and the Ziya River in the mountainous areas, the peak appears in the afternoon or at night. The lower reach of the Haihe River, the Nanyun River and the Tuma River also witness high rainfalls for one hour in the afternoon.

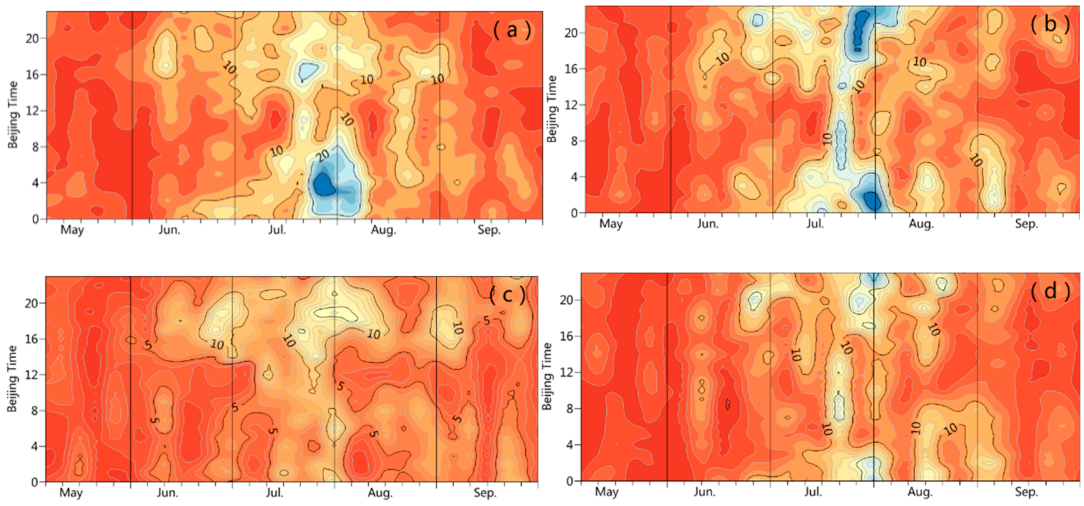

Figure 7. *Cont.*

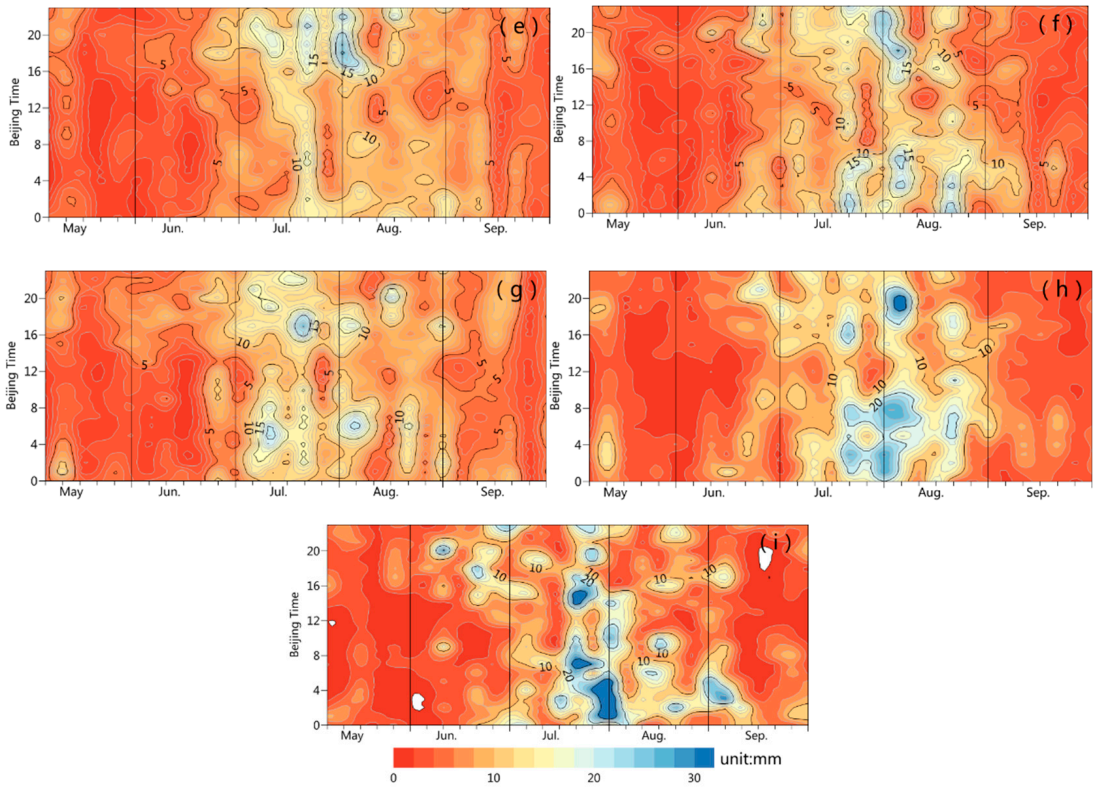

Figure 7. The pentad variations of the hourly mean precipitation for tributaries in the Haihe River basin, 2007–2017. ((**a**), Luanhe River; (**b**), Beisan River; (**c**), Yongding River; (**d**), Daqing River; (**e**), Ziya River; (**f**), Nanyun River; (**g**), Zhangwei River; (**h**), Tuma River; (**i**), low reach of Haihe River).

3.5. Duration-Based Precipitation Features

The precipitation events are classified into four types of short-duration (1–3 h), medium-duration (4–6 h), long-duration (6–12 h) and continuous precipitation (over 12 h). Figure 8 shows that the diurnal peaks of the short-duration and medium-duration precipitation appear at around 18:00 h and 22:00 h, respectively, and the peaks of the long-term duration and continuous precipitation appear before dawn.

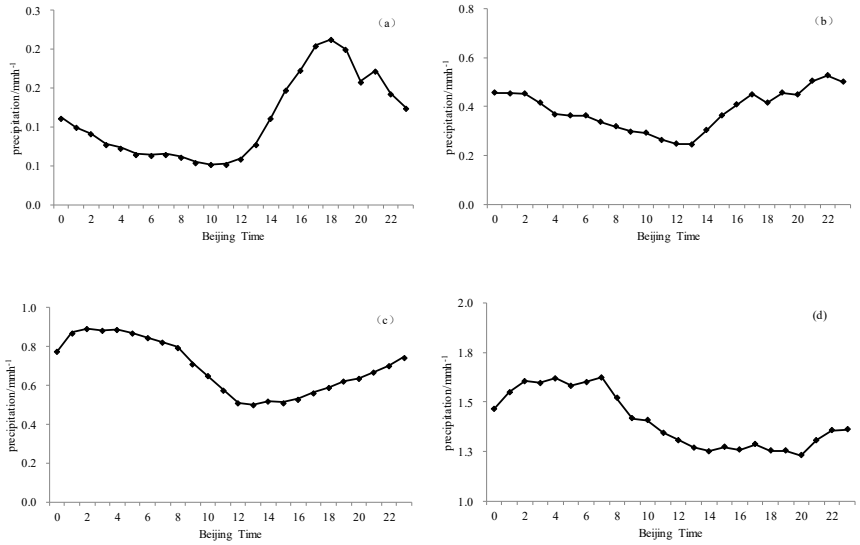

Figure 8. The diurnal variations of the different duration precipitations in the Haihe River basin, 2007–2017 ((**a**), short-duration (1–3 h) precipitation; (**b**), medium-duration (4–6 h) precipitation; (**c**), long-duration (6–12 h) precipitation; and (**d**), continuous precipitation (over 12 h) precipitation).

Figures 9–11 show the spatial distribution of the warm-season mean precipitation frequency, amount and contribution for different duration precipitation events in the Haihe River basin during 2007–2017.

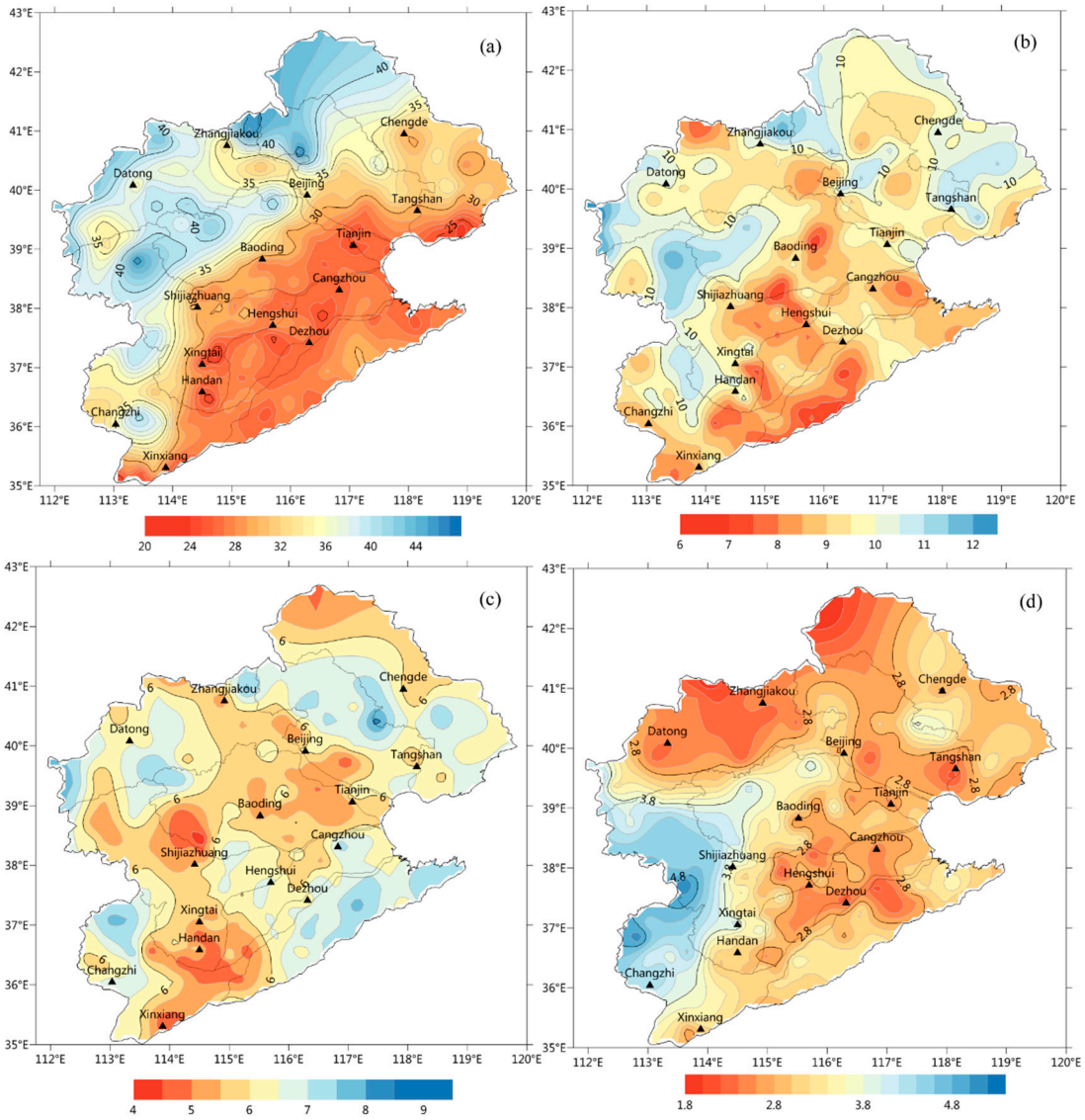

Figure 9. The precipitation frequency with different durations in the Haihe River basin, 2007–2017 (unit: hour) ((**a**), short-duration (1–3 h) precipitation; (**b**), medium-duration (4–6 h) precipitation; (**c**), long-duration (6–12 h) precipitation; and (**d**), continuous precipitation (over 12 h) precipitation).

In the whole basin, the short-duration precipitation has the highest frequency, with an average of 20 to 45 occurrences per year. The short-duration precipitation in the northwest has more occurrences than that in the plain areas. The annual occurrence of short-duration precipitation in the plain areas is below 30 times, while that in the mountainous areas generally exceeds 30 times on average. In the upper reaches of the Luanhe River and the Beisan River, most parts of the Ziya River, as well as borders between the Daqing River and the Yongding River, the warm-season mean occurrence of short-duration precipitation reaches above 40 times (Figure 9a). The probability of short-duration rainfalls in these areas is relatively large from afternoon to early evening (Figure 5). The accumulative amount of short-duration precipitation in the mountainous areas lingers even at the range of 60 to 90 mm (Figure 10a), contributing to around 30% of the total rainfalls in the rainy season (Figure 11a).

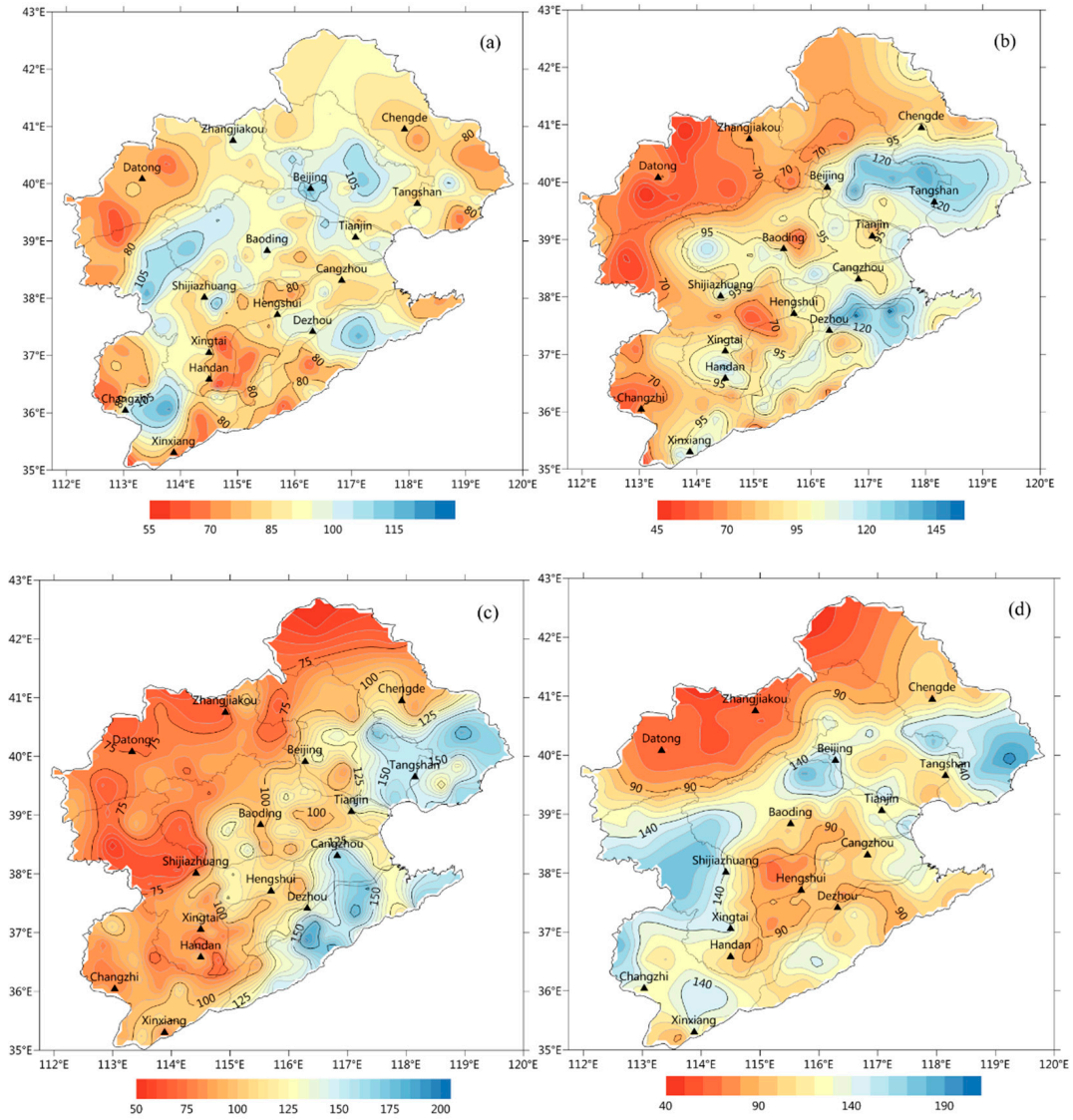

Figure 10. The precipitation amount with different durations in the Haihe River basin, 2007–2017 (unit: mm) ((**a**), short-duration (1–3 h) precipitation; (**b**), medium-duration (4–6 h) precipitation; (**c**), long-duration (6–12 h) precipitation; and (**d**), continuous precipitation (over 12 h) precipitation).

The occurrence of medium-duration precipitation during the rainy season is 6 to 12 times on average. Specifically, it happens for more than 10 times in the east of the Taihang Mountains and the lower reach of the Luanhe River, and for 8 to 10 times in other areas (Figure 9b). The medium-duration precipitation is high in the east but low in the west. The mean precipitation amount in the lower reach of the Luanhe River surpasses 120 mm, contributing around 25% to rainy season rainfalls. This corresponds to the high-value area of the precipitation frequency. Though the precipitation frequency stays high in the east of the Taihang Mountains, the accumulative precipitation amount remains low with a contribution rate below 20% (Figures 10b and 11b).

The long-duration precipitation and continuous precipitation in the Haihe River basin occur less frequently, with annual mean frequencies of 6.1 times and 3.1 times, respectively. However, the spatial distribution of the two categories is quite different. The highly-frequent occurrences of long-duration precipitation are found in the windward slope of the Yanshan Mountains, the Tuma River and parts of the Nanyun River (Figure 9c); while continuous precipitation mainly occurs in the Taihang Mountains and its eastern slope, as well as the lower reach of the Luanhe River (Figure 9d). The high-value areas of the warm-season mean precipitation amount are basically compliant with the precipitation frequency.

Specifically, the high-value areas of long-duration precipitation cover the eastern part of the basin (Figure 10c), with a contribution at around 30% (Figure 11c); those of continuous precipitation include the Taihang Mountains and the west of the Yanshan Mountains' windward slope, with a contribution rate staying above 30%.

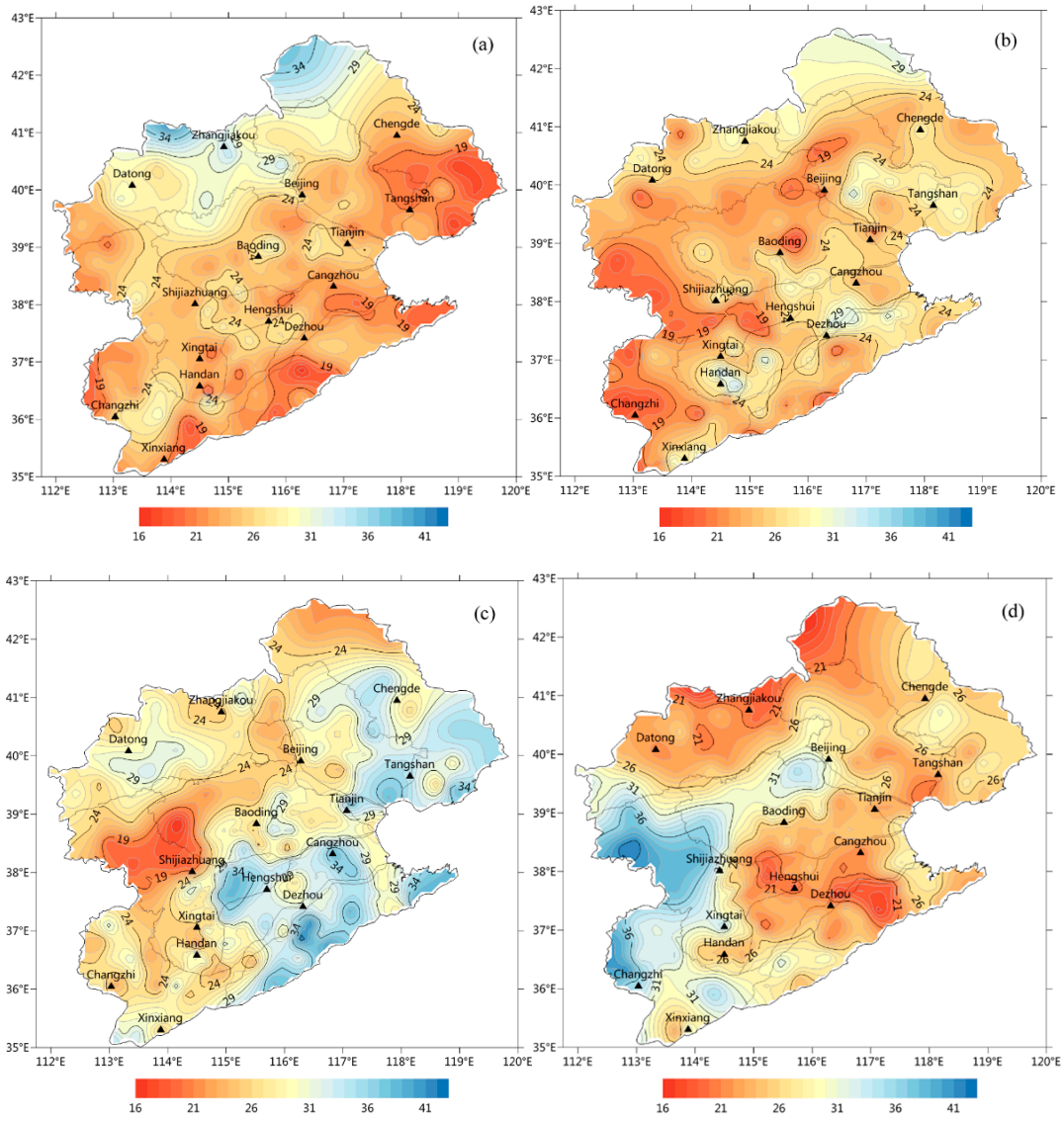

Figure 11. The precipitation contribution (to the total rainfall) with different durations in the Haihe River basin, 2007–2017 (Unit: %) ((**a**), short-duration (1–3 h) precipitation; (**b**), medium-duration (4–6 h) precipitation; (**c**), long-duration (6–12 h) precipitation; and (**d**), continuous precipitation (over 12 h) precipitation).

Above all, the short-duration precipitation contributes significantly to the total rainfalls in the northern mountainous areas (Figure 11a); while in the plain areas, the long-duration precipitation contributes more (Figure 11c). The high-value areas of continuous precipitation lie in the Taihang Mountains and its east slope. On average, the long-duration and continuous precipitation amounts contribute more to rainy season rainfalls than the short-duration precipitation, indicating that the continuous precipitation caused by the large-scale circulation of the East Asian summer monsoon has a greater impact on the precipitation in the Haihe River basin.

4. Possible Impacts from Urbanization

The basin has 10 large cities of over 5.0 million residents, 27 medium-sized cities of 0.5–2.0 million residents, as well as 21 small cities of over 0.1–0.5 million residents. All other stations are regarded as non-city stations. Due to the much larger number of the non-city stations, and also the obviously different altitudes and environments from those of the city stations, only the differences of precipitation among the different categories of cities are compared here.

Figure 12 shows that the mean precipitation in the rainy season is the lowest in the small cities, and that in the large cities is slightly higher compared with the medium-sized cities. From the perspective of the pentad mean precipitation, the three categories of cities share little difference in precipitation in May, June and September when the precipitation is low. During July and August, however, the pentad mean precipitation of large cities is larger than those of medium-sized cities and small cities, indicating that larger rainfalls are more likely to occur in large cities during the rainiest months of a year.

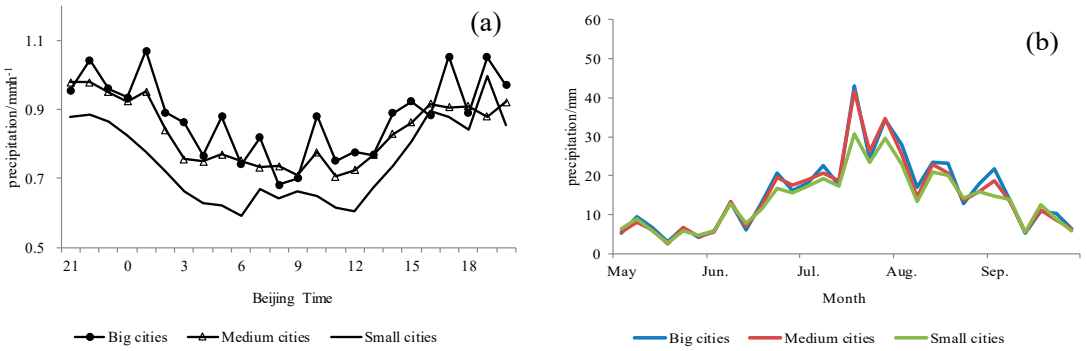

Figure 12. The diurnal precipitation variations (hourly mean precipitation) (**a**) and intra-seasonal variations (pentad mean precipitation); (**b**) for different categories of cities, 2007–2017.

Overall, the annual total precipitation during the 11 years is 49.8 mm or 12% higher at the large city stations than that at the small city stations, and 33.8 mm or 8% higher at the medium-sized city stations than that at the small city stations (Table 1). The city stations are located at approximately similar elevations, with the large city station slightly lower than the medium-sized city stations, and 300 m lower than the small city stations (Table 1). Therefore, the possible effect of altitude on the precipitation difference between large city and medium-sized city stations can be ruled out due to having almost the same altitudes, but the precipitation differences of small city stations from those of large city and medium-sized city stations would be, to some extent, affected by the altitude difference. Figure 13 shows the relationship between warm-season precipitation of all the non-city stations and their altitudes. A weak but significant negative correlation is notable and unexpected, and the decreasing rate of precipitation with altitude in the whole river basin is −7.9 mm/100 m. This relationship between precipitation and altitude could be regarded as the background lapse of rainfall in the basin. Considering this influence of altitude, however, the warm-season precipitation at large city stations (459.9 − 24.4 = 435.5 mm) is still obviously higher (6.2%) than that at the small city stations at the same altitude, and the precipitation at the medium-sized stations is marginally higher (2.5%) than that of the small city stations.

Table 1. The average altitudes and warm-season mean precipitation of the city stations in the Haihe River basin, 2007–2017.

Categories of Stations	Number of Stations	Average Altitude (m asl)	Mean Precipitation (mm)	Difference from Small City (mm)
Large city	10	34.8	459.9	49.8 (12%)
Medium-sized city	27	43.4	443.9	33.8 (8%)
Small city	19	343.8	410.1	

Note: asl-above sea level; Percentage is the proportion of the difference to precipitation of small city.

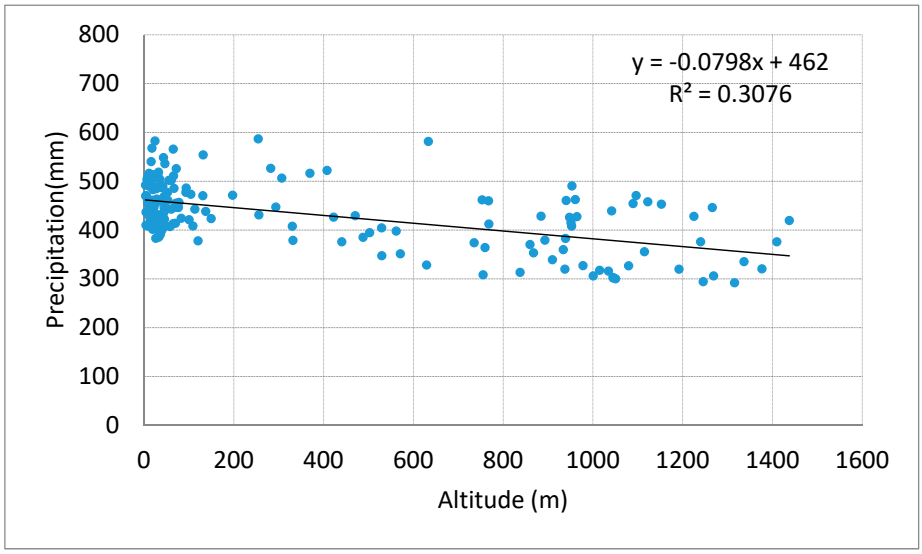

Figure 13. The relationship between warm-season precipitation of non-city stations and their altitudes in the Haihe River basin, 2007–2017.

Therefore, the warm-season precipitation at the large and medium city stations shows a notable difference from that of the small city stations, and this may have been related to the influence of urbanization on the thermal and dynamical processes of lower troposphere over the urban areas during the rainiest months of summertime.

5. Discussion

This paper has made a detailed examination of rainfall in the rainy season over the Haihe Basin, based on a high-density precipitation observational network as developed in the last decade. The work reveals a couple of interesting phenomena, and they are partially consistent with the previous analyses, but some of the phenomena are unique and worth a discussion and further investigation.

5.1. Spatial and Intra-Seasonal Variations

It could be seen that the distribution of rainy season rainfalls (Figure 2) is mainly affected by topography and prevailing winds in the Haihe River basin. In cases where easterly winds and southerly winds prevail, rainfalls are much likelier to occur on the windward slopes of the mountains due to forced uplifts by topography [24,25]. The highest-rainfall zone in the basin is found on the windward slope of the Yanshan Mountains, with the rainy season precipitation exceeding 520 mm on average. Within this zone, the average warm-season precipitation in Qinglong station has even reached 591 mm.

Regarding the summer rainfall and its intra-seasonal variation in the river basin (Figures 2 and 3), previous studies showed that they are mainly affected by the East Asian summer monsoon. The location change of the West Pacific Subtropical High (WPSH) ridge in summer directly affects the distribution of water vapor transport flux in this basin. There are three water vapor transport channels influencing the

summer rainfalls. The first one flows from the Indian Ocean and the Bay of Bengal, passing through the Indo-China Peninsula, reaching the South China Sea, turning into the southwest air stream and then reaching the Haihe River Basin; as for the second flow, the air stream in southwest of the WPSH carries water vapor from the West Pacific and the South China Sea through the southeast coast to the Haihe Basin River; the third flow originates from the mid-latitude westerlies, which transports water vapor from the west to east [14,26,27].

Before the end of June, the WPSH ridge is located at the south of 25° N, with the East Asian summer monsoon not yet extending the North China region. The Haihe River basin is jointly affected by the northwest air current as well as the southern warm and humid air current. The water vapor mainly comes from the southwest air current. In late July and early August, as the WPSH moves northwards, the air current in the southwest of the WPSH affects the basin. Overhead from the South China Sea to the West Pacific, the water vapor is transported abnormally to the west and northwest. The air current and the enhanced summer monsoon in Southeast China constitute an anticyclonic abnormal water vapor transport belt, which brings the water vapor northwards to the Haihe River basin. After mid-August, along with the weakening of the WPSH, the high ridge-line begins to retreat rapidly from north to south. With the southeast wind sweeping North China, the basin receives water vapor from the Philippine Sea and the East China Sea [28,29].

The combined influence of the WPSH and water vapor transport, and the special topography could well explain the different patterns of monthly precipitation distribution in the Haihe River basin. For example, the high precipitation in the Beisan River and the Luanhe River in June and July—mainly formed by the interaction between the prevailing southwestern—lies at the low troposphere and the windward slopes of the eastern Yanshan mountains, and the relatively high precipitation on the eastern slope of the Taihang Mountains in September is caused by the prevailing near-surface southeast currents which bring the water vapor from the East China Sea and the Yellow Sea. The small sub-centers of precipitation in the plains may be related to the urbanization effect, which will be discussed below.

5.2. Diurnal Variation of Rainy Rainfall

As is shown in Figure 5, the whole basin and all the tributaries generally see high precipitation at night and before dawn, and low precipitation in the daytime, with the lowest precipitation reached during 9:00–14:00 h. This complies with the conclusion by Yu et al. [17] that high precipitation in northern China mainly occurs at midnight and before dawn.

Precipitation in the sub-basins witness different diurnal variations, but mostly more rainfall occurs in the late afternoon and evening, as shown in Figure 5. There is a small distinction (less than half an hour) between the local time and Beijing time, and the time difference would not significantly affect the analysis results of the diurnal variation between the eastern and western sub-basins. The sub-basins with rainfall mostly in the late afternoon and evening are mainly located in mountainous areas with higher altitudes. Convection enhancement and unstable stratification caused by solar radiation in the afternoon, as well as the uplifting effect of valley wind circulation, increases the probability of rainfalls during the afternoon to evening.

On the other hand, precipitation in the plains and coastal areas mostly occurs before dawn (Figure 5), which is mainly attributed to the declination of the valley wind circulation at night and the effects of the sea-land breeze daily variation caused by differences in the sea-land thermal difference. In the latter case, from midnight to early morning, as the atmosphere over the ocean is warmer than that over the continent, the air rises in the ocean and coastal areas, causing uplifts and precipitation. Radiative cooling at the top of the cloud at night causes the boundary layer to become unstable and also promotes convection over the ocean and coastal areas. Therefore, precipitation on the sea usually occurs in the late-night hours. Due to the influence of offshore areas, the diurnal precipitation variation at coastal areas is also featured with a peak before dawn. Yin et al. [23] indicated that the spatial differences of the diurnal variation of summer rainfall in the Haihe River basin are mainly impacted by the valley circulation and the land-sea breeze circulation. In the afternoon, upward movement

occurs in the mountains in the western and northern Haihe River basin, which goes in line with the precipitation peak in this period. Meanwhile, downward movement occurs in the coastal and plain areas, resulting in the low frequency of precipitation in the afternoon.

Pentad variations of hourly mean precipitation for tributaries in the basin (Figure 7) basically go in accordance with previous studies [30]. Previous studies have also shown that thermal circulation of the valley wind is an important cause of the difference between mountainous areas and plains in terms of the diurnal precipitation variations in the Haihe River basin during the rainy season [31]. Along the Yanshan-Taihang Mountains, the precipitation peak occurs mostly in the afternoon because of the solar radiative heating and the uplifting of the air in the mountainous areas. Then the upper air moves downstream and to the southeast dragged also by the middle troposphere average air current, resulting in a substance of air and a suppression of precipitation during the afternoon. This may benefit the precipitation peak in the afternoon in the mountains and at night in the plain area [31]. After mid-August, the monsoon rain belt retreats and precipitation gradually decreases.

The short-duration and medium-duration precipitation peak at around 18:00 h and 22:00 h, respectively, and the long-term duration and continuous precipitation reach the highest level before dawn (Figure 8). These characteristics are approximately consistent with the results of previous studies [20,32] which reported that the short-duration precipitation had a diurnal peak in the evening while the long-duration and continuous precipitation peaks before dawn.

5.3. Impact of Urbanization

From the analysis on the mean precipitation with different durations and their contributions to warm-season precipitation, it could be found that high-value centers exist near large cities including Beijing, Tianjin, Shijiazhuang, Baoding, Xingtai and Handan. Previous research on the precipitation features in Beijing [33–35] showed that urban areas suffer more rainfalls and more frequent intense rainfall events than rural areas. This paper shows the generally larger rainfall at large and medium cities than at the small cities, indicating a highly possible influence of urbanization on rainfall in the summer. This is a very interesting issue and certainly deserves further investigation in the future.

The precipitation differences of large and medium-sized city stations from that of small city stations, as shown in Figure 12 and Table 1, may have been caused mainly by the development of the built-up areas or urbanization process in the larger cities. The mechanisms of the urbanization effect are clearly understood. Three aspects are important: the urban heat island (UHI) effect which causes stronger air uplifting within the urban areas by developing a UHI circulation, the enhanced surface roughness due to the high buildings, which acts as a driver to strengthen convergence of currents and to block the weather systems, and the denser air pollutants in urban areas, which may act as effective nuclei for water droplets and ice to form in clouds in the rainy season [36].

A complicated situation may arise when discussing the impact of urbanization on precipitation. Zheng and Ren [37] found that wind speed affects the precipitation capture rate of the gauge, leading to precipitation observation errors, especially for heavy rainfalls and above-grade rainfalls, in the Beijing City and the surrounding areas. Under the influence of wind speed, the precipitation might be underestimated by 7–9%. Urbanization causes not only the urban warming or the UHI effect, but also the weakening of near-surface wind speed within the urban areas, leading to an increase in the capture rate of the gauge [38]. It is possible, therefore, that the relatively higher precipitation and intense rainfall in the urban areas are induced partly by the larger capture rate of the gauge due to the weaker wind. If the under-catch effect exists, then the wind-induced bias in observations has to be adjusted before any further analysis can be made to examine the impact of urbanization on the mean and intense precipitation at urban stations of the Haihe River basin.

Therefore, the issue of urbanization effect on summer precipitation has to be better settled after the error of the gauge measurement is adjusted, and also a more sophisticated methodology is developed in the future.

6. Conclusions

This study analyzes the intra-seasonal and diurnal precipitation variations in the Haihe River basin and its branch systems, based on the hourly precipitation data in the rainy season (May–September) during 2007–2017. The following conclusions can be drawn from the analysis:

(1) The high-rainfall belt in the basin moves with the summer monsoon from south to north and then back to the south. The belt is located in the south of the Yanshan Mountains and the Tuma River. Multiple rainstorm centers are found amidst the rainy belt. Throughout the rainy season, the high-rainfall zones could be found more in the windward slope of the Yanshan Mountains and in the south of the basin.

(2) The precipitation of each branch system is featured with a single peak during the rainy season. Specifically, the precipitation keeps low before early July and strikes the bottom in May, which is marked as the pre-flood season. It peaks in July, with the major flood season coming from the third pentad of July to the fourth pentad of August. The precipitation in August ranks second, only after that in July. However, it begins to decrease after mid-August, which is named as the post-flood season.

(3) The precipitation is high at night but low during the daytime generally within the basin; still, the high-rainfall period differs among tributaries. Along with the movement of the high-rainfall belt, the precipitation in the pre-flood season (May to the third pentad of July) mostly occurs at 16:00–21:00 h. When it comes to the major flood season (the fourth pentad of July to the second pentad of August), the precipitation peaks at 17:00–22:00 h and sub-peaks at 0:00–7:00 h. In the post-flood season (the third pentad of August to September), the precipitation mostly occurs at night, with the peak occurring at 0:00–8:00 h.

(4) In the mountainous areas, the short-duration precipitation occurs most, accounting for 30% of the total rainy season rainfalls. The long-duration precipitation makes a larger contribution to the plains in the basin. The continuous precipitation is majorly encountered in the windward slopes of the Taihang Mountains and the Yanshan Mountains. From the perspective of the whole basin, the long-duration precipitation and continuous precipitation contribute more to the total rainy season rainfalls than the short-duration precipitation.

(5) Urbanization seems to have exerted a remarkable influence on local precipitation and intense rainfalls in large cities, leading to the larger warm-season mean precipitation and more frequent intense precipitation events in mid-summer and during the nighttime in large cities than in small cities. A major uncertainty in detecting the impact of urbanization may come from the possible influence of the under-catch effect of the gauge for the urban stations.

Author Contributions: Conceptualization, G.R. and J.G.; methodology, J.G. and G.R; software, J.G.; validation, G.R.; formal analysis, G.J. and H.H.; data curation, M.X.; writing—original draft preparation, J.G.; writing—review and editing, G.R.; visualization, H.H.; supervision, G.R.; funding acquisition, G.R. and J.G.

Funding: This study is supported by the National Key R&D Program of China (No. 2018YFA0606302 and No.2018YFA0605603), and the Natural Science Foundation of China (NSFC) (41575003).

Conflicts of Interest: The authors declare no conflict of interest. The funders had no role in the design of the study; in the collection, analyses, or interpretation of data; in the writing of the manuscript, or in the decision to publish the results.

References

1. Xia, J.; Liu, C.Z.; Ren, G.Y. Opportunity and Challenge of the Climate Change Impact on the Water Resource of China. *Adv. Earth Sci.* **2011**, *26*. [CrossRef]
2. Liang, P.; He, J.H.; Chen, L.X.; Li, W. Anomalous Moisture Sources for the Severe Precipitation over North China during Summer. *Plateau Meteorol.* **2007**, *26*, 460–465. (In Chinese)
3. Liu, H.W.; Ding, Y.H. The Interdecadal Variability of Summer Precipitation over North China. *J. Appl. Meteorol. Sci.* **2011**, *22*, 129–137. (In Chinese)
4. Shi, Y.S.; Yao, X.X.; Yang, X.L.; Li, Z.T. Characteristic Analysis of Unusual Summer Precipitation in North China. *Sci. Meteorol. Sin.* **2008**, *28*, 377–383. (In Chinese)

5. Yang, J.; Wang, Q.G.; Gong, Z.Q.; Guo-Lin, F. Dynamic Optimal Multi-Indexes Configuration for Estimating the Prediction Errors of Dynamical Climate Model in North China. *Acta Phys. Sin.* **2011**, *60*, 029204. (In Chinese)
6. Liu, Y.Y.; Ding, Y.H. Analysis and Numerical Simulation of the Teleconnection between Indian Summer Monsoon and Precipitation in North China. *Acta Meteorol. Sin.* **2008**, *66*, 789–799. (In Chinese)
7. Tang, X.; Qian, W.H.; Liang, P. Climate Feature of Boundary Belt for East Asian Summer Monsoon. *Plateau Meteorol.* **2006**, *25*, 375–381. (In Chinese)
8. Simmonds, I.; Bi, D.; Hope, P. Atmospheric Water Vapor Flux and Its Association with Rainfall over China in Summer. *J. Clim.* **1999**, *12*, 1353–1367. [CrossRef]
9. Tian, H.; Guo, P.W.; Lu, W.S. Characteristics of Vapor Inflow Corridors Related to Summer Rainfall in China and Impact Factors. *J. Trop. Meteorol.* **2004**, *20*, 401–408. (In Chinese)
10. Zhou, L.T. Characteristics of Interannual Variability of Summer Rainfall in North China. *Trans. Atmos. Sci.* **2009**, *32*, 412–423. (In Chinese)
11. Wang, Z.G.; Luo, Y.Z.; Liu, C.M.; Xia, J.; Zhang, M.H. Spatial and Temporal Variations of Precipitation in Haihe River Basin, China: Six Decades of Measurements. *Hydrol. Process.* **2011**, *25*, 2916–2923. [CrossRef]
12. Bao, Z.X.; Zhang, J.Y.; Wang, G.Q.; Fu, G.B.; He, R.M.; Yan, X.L.; Jin, J.L.; Liu, Y.L.; Zhang, A.J. Attribution for Decreasing Stream Flow of the Haihe River Basin, Northern China: Climate Variability or Human Activities? *J. Hydrol.* **2012**, *460–461*, 117–129. [CrossRef]
13. Liu, H.W.; Ding, Y.H. Analysis of Daily Precipitation Characteristics over North China during Rainy Seasons. *Chin. J. Atmos. Sci.* **2010**, *34*, 12–22. (In Chinese) [CrossRef]
14. Hao, L.S.; Min, J.Z.; Ding, Y.H. Analysis of Precipitation Events Changes and Causes for Rainstorm Events Reduction in North China. *Chin. J. Geophys.* **2011**, *54*, 1160–1167. (In Chinese) [CrossRef]
15. Li, J.; Yu, R.C.; Wang, J.J. Diurnal Variations of Summer Precipitation in Beijing. *Chin. Sci. Bull.* **2008**, *53*, 1933–1936. [CrossRef]
16. Yang, P.; Xiao, Z.N.; Shi, W.J. Fine-Scale Characteristics of Rainfall in Beijing Urban Area Based on a High-Density Autonomous Weather Stations (AWS) Dataset. *Chin. J. Atmos. Sci.* **2017**, *41*, 475–489. (In Chinese)
17. Yu, R.C.; Zhou, T.J.; Xiong, A.Y.; Zhu, Y.J.; Li, J.M. Diurnal Variations of Summer Precipitation over Contiguous China. *Geophys. Res. Lett.* **2007**, *34*, L01704. [CrossRef]
18. Yu, R.C.; Li, J.; Yuan, W.H.; Chen, H.M. Changes in Characteristics of Late-Summer Precipitation over Eastern China in the Past 40 Years Revealed by Hourly Precipitation Data. *J. Clim.* **2010**, *23*, 3390–3396. [CrossRef]
19. Zhou, T.J.; Yu, R.C.; Chen, H.M.; Dai, A.G.; Pan, Y. Summer Precipitation Frequency, Intensity, and Diurnal Cycle over China: A Comparison of Satellite Data with Rain Gauge Observations. *J. Clim.* **2008**, *21*, 3997–4010. [CrossRef]
20. Yuan, W.H.; Yu, R.C.; Fu, Y.F. Study of Different Diurnal Variations of Summer Long-Duration Rainfall Between the Southern and Northern Parts of the Huai River. *Chin. J. Geophys.* **2014**, *57*, 752–759. (In Chinese) [CrossRef]
21. Han, H.; Wu, H.M.; Huang, A.N. Temporal and Spatial Distributions of the Diurnal Cycle of Summer Precipitation Over North China. *Chin. J. Atmos. Sci.* **2017**, *41*, 263–274. (In Chinese) [CrossRef]
22. Yu, R.C.; Xu, Y.P.; Zhou, T.J.; Li, J. Relation between Rainfall Duration and Diurnal Variation in the Rainy Season Precipitation over Central Eastern China. *Geophys. Res. Lett.* **2007**, *34*, L13703. [CrossRef]
23. Yin, S.Q.; Gao, G.; Li, W.J.; Chen, D.L.; Hao, L.S. Long-Term Precipitation Change by Hourly Data in Haihe River Basin during 1961–2004. *Sci. China Earth Sci.* **2011**, *54*, 1576–1585. (In Chinese) [CrossRef]
24. Zheng, Z.F.; Gao, H.; Wang, Z.W.; Li, Q.C. Analysis on Spatial Distribution of Precipitation in Beijing and Its City Effect. *Plateau Meteorol.* **2014**, *33*, 522–529. (In Chinese)
25. Fan, G.Z.; Lyu, S.H. Numerical Simulation Study for the Effect of Terrain on North China Summer Precipitation. *Plateau Meteorol.* **1999**, *18*, 659–667. (In Chinese)
26. Zhu, L.; Liu, Y.X.; Zuo, H.C.; Xiang, W.G.; Gong, Q.; Yu, H.S.; Lin, N.; Cao, H.; Gu, Z.Q. Water Vapor Transport Characteristics over the Haihe River Basin. *Adv. Clim. Change Res.* **2011**, *7*, 184–188. (In Chinese)
27. Zhou, X.X.; Ding, Y.H.; Wang, P.X. Features of Moisture Transport Associated with the Precipitation over North China during July-August. *Chin. J. Atmos. Sci.* **2008**, *32*, 345–357. (In Chinese)
28. Ma, J.J.; Gao, X.Q. The Transportation Paths of Water Vapor and Its Relation to Climate Change over North China. *Plateau Meteorol.* **2008**, *25*, 893–899. (In Chinese)

29. Ye, M.; Wu, Y.P.; Zhou, J.; Wu, H.; Tu, G. Objective Quantification of the Water Vapor Path Influencing Precipitation in North China in Summer. *Acta Phys. Sin.* **2014**, *63*, 129201. (In Chinese)
30. Yu, R.C.; Li, J.; Chen, H.M.; Yuan, W.H. Progress in studies of the precipitation diurnal variation over contiguous China. *Acta Meteorol. Sin.* **2014**, *72*, 948–968. [CrossRef]
31. He, H.; Zhang, F. Diurnal Variations of Warm-Season Precipitation Over Northern China. *Mon. Weather Rev.* **2010**, *138*, 1017–1025. [CrossRef]
32. Wu, Z.H.; Chen, M.X. Climatic Analysis of Summer (JJA) Short-Period Precipitation in Beijing-Tianjin-Hebei Area. *Chin. J. Atmos. Sci.* **1993**, *17*, 268–273. (In Chinese)
33. Yang, P.; Ren, G.Y.; Hou, W.; Liu, W.D. Spatial and Diurnal Characteristics of Summer Rainfall over Beijing Municipality Based on a High-Density AWS Dataset. *Int. J. Climatol.* **2013**, *33*, 2769–2780. [CrossRef]
34. Yang, P.; Ren, G.Y.; Yan, P.C. Evidence for Strong Association of Short-Duration Intense Rainfall with Urbanization in Beijing Urban Area. *J. Clim.* **2017**. [CrossRef]
35. Zhang, L.J.; Hu, T.J.; Hu, F.; Li, L.; Xuan, C.Y. Comparison of Summer Precipitation Evolution over the Last 30 Years between Urban and Rural Region of Beijing. *Clim. Environ. Res.* **2009**, *14*, 63–68. (In Chinese)
36. Ren, G.Y.; Ren, Y.Y.; Zhan, Y.J.; Sun, X.B.; Liu, Y.J.; Chen, Y.; Wang, T. Spatial and Temporal Patterns of Precipitation Variability over Mainland China: III: Causes for Recent Trends. *Adv. Water Sci.* **2016**, *27*, 327–348. (In Chinese)
37. Zheng, Z.F.; Ren, G.Y. Effects of Gauge Under-Catch on Precipitation Observation and Long-Term Trend Estimates in Beijing Area. *Adv. Water Sci.* **2017**, *28*, 662–670. (In Chinese)
38. Ren, G.Y.; Wang, T.; Guo, J.; Hao, Z.X.; Zhan, Y.J. Characteristics of Precipitation Variations in Haihe River Basin in Modern Times. *Adv. Sci. Technol. Water Res.* **2015**, *35*, 103–110. (In Chinese) [CrossRef]



© 2019 by the authors. Licensee MDPI, Basel, Switzerland. This article is an open access article distributed under the terms and conditions of the Creative Commons Attribution (CC BY) license (http://creativecommons.org/licenses/by/4.0/).

View publication stats

Dynamics of Atmospheres and Oceans 86 (2019) 90–103

Contents lists available at ScienceDirect

Dynamics of Atmospheres and Oceans

journal homepage: www.elsevier.com/locate/dynatmoce

Diagnosing the spatiotemporal diversity of westerly wind events in the tropical Pacific

Xiaozhen Hao[a,b], Hong-Li Ren[b,c,*], Wenjun Zhang[a,**], Minghong Liu[b], Yuntao Wei[b,d,e]

[a] Nanjing University of Information Science and Technology, Nanjing, 210044, China
[b] Laboratory for Climate Studies & CMA-NJU Joint Laboratory for Climate Prediction Studies, National Climate Center, China Meteorological Administration, Beijing, 100081, China
[c] Department of Atmospheric Science, School of Environmental Studies, China University of Geoscience, Wuhan, 430074, China
[d] Key Laboratory of Ocean Circulation and Waves, Institute of Oceanology, Chinese Academy of Sciences, Qingdao, 266071, China
[e] University of Chinese Academy of Sciences, Beijing, 100049, China

ARTICLE INFO

Keywords:
Westerly wind events
Spatiotemporal diversity
Structure characteristics
Madden-Julian oscillation
Convectively coupled Kelvin waves

ABSTRACT

Westerly Wind Events (WWEs) over the tropical Pacific are characterized by their spatiotemporal diversity and classified into six types based on their different locations and durations. Various types of WWEs exhibit quite different characteristics in terms of their amplitudes. The long events with a 10–30-day duration are stronger than the short events with a 6–10-day duration, and the maximum amplitudes of the Central-Pacific (C) type and Eastern-Pacific (E) type of long events are larger than the Western-Pacific (W) type of long ones. The evolutions of these six types of WWEs are also quite different. The W-type short and long events and the C-type long events show a distinct eastward propagation, whereas the C-type short events and the E-type short and long events have no apparent propagation direction. We demonstrate that such a difference in the eastward propagation of WWEs can be significantly associated with the Madden-Julian Oscillation (MJO). The W-type events are more influenced heavily by the MJO, as indicated by their more distinct eastward propagation patterns, than the two other types of WWEs. In addition to the MJO, the convectively coupled Kelvin waves are also associated with the WWEs, especially for the short events.

1. Introduction

Westerly Wind Events (WWEs) have prominent spatiotemporal features of the zonal wind anomalies on the sub-seasonal timescales in the western-central tropical Pacific. They are primarily defined in terms of the two basic characteristics, the amplitude and duration above a certain threshold (Lengaigne et al., 2004). WWEs frequently occur over the tropical Indian Ocean and Pacific Ocean but they rarely over the Atlantic Ocean (Seiki and Takayabu, 2007a, b). WWEs could act to force substantial local and remote oceanic responses (Webster and Lukas, 1992), and play an important role in the development and maintenance of El Niño (e.g., Lau and Chan, 1988; McPhaden, 1999; Lengaigne et al., 2007). In addition, WWEs could also be commonly associated with Madden-Julian Oscillation (MJO, Madden and Julian, 1971, 1972; Chen et al., 1996), convectively coupled equatorial waves (CCEWs, Wheeler and Kiladis, 1999; Kiladis et al., 2009; Puy et al., 2016), tropical cyclones (Keen, 1982; Lian et al., 2018) and mid-latitude cold surges

* Corresponding author at: Laboratory for Climate Studies & CMA-NJU Joint Laboratory for Climate Prediction Studies, National Climate Center, China Meteorological Administration, Beijing, 100081, China.
** Corresponding author.
E-mail addresses: renhl@cma.gov.cn (H.-L. Ren), zhangwj@nuist.edu.cn (W. Zhang).

https://doi.org/10.1016/j.dynatmoce.2019.03.004
Received 20 December 2018; Received in revised form 21 March 2019; Accepted 24 March 2019
Available online 25 March 2019
0377-0265/ © 2019 Elsevier B.V. All rights reserved.

(Chu, 1988).

Large numbers of methodologies have been utilized to define and classify the WWEs in the previous studies. For example, Hartten (1996) first used the total zonal wind at 1000-hPa to define WWEs and classified WWEs based on the large-scale circulation patterns. This method can detect about 90% of the synoptic-scale WWEs in the western Pacific, but it is heavily dependent on the climatic states and dose not identify all periods where the wind anomalies are strong westerly anomalies. In contrast, Harrison and Vecchi (1997) directly made use of the anomaly to define the WWEs, by which they obtained eight more comprehensive types of WWEs with significantly different characteristics and related climatic phenomena based on the locations of the maximal westerly wind anomalies. Using this method, the regional dependence of WWEs can be well isolated, and the identified WWEs are well constrained near the peak values. The further composite analyses and model experiments in Harrison and Vecchi (1997) indicated that the region-based classification is likely more representative and reliable.

Besides the above two definitions, Puy et al. (2016) use the wind stress anomalies to define the WWEs which is consistent with the other two results. The wind stress field is actually more conducive to analyzing the oceanic response of WWEs, while the surface winds are more appropriate to analyze their essential characteristics of WWEs themselves. Puy et al. (2016) implemented the time-space integration of zonal wind stress anomalies over the wind event patch as a westerly index to intuitively infer the WWE characteristics and influences. However, this index can only reflect the cumulative features of WWEs, with no constraints on their instantaneous features. Therefore, the index-based definition of the WWEs needs to be further studied to reflect their characteristics and climatic responses more comprehensively. Indeed, the selection of definition and classification methods should be based on the purpose of research. Due to the diversity of WWEs on timescales, Kiladis et al. (1994) classified WWEs into two categories according to the duration of events i.e., the brief events with a period of 5–25 days and the sustained events with a period of 30–90 days. As the aforementioned reviewed, previous studies have indicated that the WWEs possess complex spatiotemporal characteristics. However, most of previous studies on the WWEs partially focused only on either the spatial or temporal characteristics. A systematic and comprehensive investigation of the combined spatiotemporal characteristics of the WWEs is still elusive. In this paper, we will systematically make a clear classification of the various WWEs based on both their spatial and temporal diversities, to understand them clearly.

The research on WWEs is of great significance because the WWEs are associated with many important phenomena, such as El Niño-South Oscillation (ENSO), and they play a key role in the development of El Niño events, particularly in their onset phases (e.g., Harrison, 1984; Lau and Chan, 1988; Kessler et al., 1995). WWEs can force substantial oceanic thermal and dynamical responses, both locally and remotely (Lengaigne et al., 2002). By analyzing oceanic responses to the strong WWEs that occurred in March 1997, it was found that WWEs played an important role in motivating the occurrence of the super El Niño in 1997/98 (Lengaigne et al., 2003). Also, WWEs have a significant impact on the diversity of El Niño (Chen et al., 2015). Furthermore, the intraseasonal wind and convective coupled variability is mainly controlled by the MJO over the western Pacific warm pool and therefore, MJO, as a dominant mode on the intraseasonal timescale (Zhang, 2005, 2013), may have some certain modulation effects on WWEs. Previous studies found that WWEs frequently occurred in the convection phase of MJO (Puy et al., 2016) and strong MJO also enhanced the frequency of WWEs (Seiki and Takayabu, 2007a, b). In addition, Feng and Lian (2018) found that the statistics between MJO and WWEs are heavily dependent on their definitions, such that the MJO modulation on WWEs is very weak when using the widely used definition of MJO and WWEs. Therefore, the analysis of WWEs' characteristics contributes to the deep understanding of ENSO and MJO behaviors. A greater research focus has recently been placed on the relationship between WWEs, the MJO, and ENSO, with less emphasis on a comprehensive analysis of WWE characteristics.

WWEs have complex characteristics at multiple spatiotemporal scales, reflecting the corresponding complex mechanism. Lengaigne et al. (2004) suggested that the generation of WWEs might be a result from the combination of MJO, cold surges, tropical cyclones and other mesoscale phenomena. Tropical cyclones may play an important role in generating the WWEs (Lian et al., 2018). The sporadic nature of WWEs may also root to the equatorially super clusters that propagate eastward, that is, the convectively coupled Kelvin waves (CCKWs) (Nakazawa, 1988). Baranowski et al. (2017) have revealed that the preferred occurring region of CCKWs is over the Indo-Pacific warm pool region, which just corresponds to the prevailing region of background westerly wind (Wang, 1988). The frequently convective phases of CCKWs offer a natural source of WWEs. Until now, there are still no convincing and complete theories to satisfactorily interpret mechanisms for the WWEs' generation. Therefore, we present a comprehensive analysis of the spatiotemporal characteristics in the diversity of WWEs that will provide further insights into the WWEs' generation mechanism.

The remainder of the paper is organized as follows. The data, methodology and classification criteria of WWEs are described in Section 2. The main characteristics (amplitude, duration and seasonality) of WWEs are assessed in Section 3. We present composite analysis results, including the WWEs' horizontal and vertical structures as well as the related atmospheric convection and circulation in Section 4. Section 5 tries to find some evidences that support the possibly close association of WWEs with the MJOs and CCKWs. The summary and discussions are given in Section 6.

2. Data and methods

2.1. Data

We use the daily mean 10-m wind, vertical velocity, specific humidity, and zonal wind (200–1000 hPa) data on $2.5^\circ \times 2.5^\circ$ grids for the January 1979–December 2016 period from the European Centre for Medium-Range Weather Forecasts (ECMWF) Reanalysis Interim (ERAI-Interim) to analyze the WWEs. Daily outgoing longwave radiation (OLR) data, derived by the National Oceanic and

Atmospheric Administration (NOAA) on 1°×1°grids for 1979–2016 period, are also used as a proxy for large-scale convection activity over the tropical Pacific.

2.2. Methods

2.2.1. WWEs detection and classification

The detection method of WWEs follows Harrison and Vecchi (1997) with a slight improvement. Here, we choose three types of WWEs on the equatorial regions: the Western Pacific (W) type (5 °S–5 °N, 130 °E–155 °E), the Central Pacific (C) type (5 °S–5 °N, 155 °E–180 °E), and the Eastern Pacific (E) type (5 °S–5 °N, 180 °E–150 °W). The WWEs in these three regions have significantly large variance (Figures not shown). Moreover, we have also performed a series of comparative analyses to indicate the classification clearly (Figures not shown). When all zonal wind anomalies are greater than the threshold of WWEs (i.e., 2 m/s), the maximum center of standard deviations is near the equator. In the W region, there is a center which is affected by the land mask. The other center is classified into the C and E regions, due to bigger than the W region and cross the dateline. Therefore, the WWEs over the tropical Pacific are classified by the three regions.

In this study, we first calculate the average of ERA-Interim daily mean 10-m zonal wind for 1979–2016 period and process the mean value using the Fourier decomposition and synthesis method (take the first four waves) as the climatology. The anomalies are the difference between instantaneous wind and the climatology. Then, we define a WWE of the type X as any period of 6 or more days for which the surface zonal wind anomaly, averaged over the region X through a 3-day running mean, exceeded 2 m/s (approximately one standard deviation). The center date (day (0)) of each WWE is defined as the day when the maximum value of the zonal wind anomaly, averaged over the X region, occurs. Considering that some substantial westerly wind anomalies occurred in adjacent regions at the same time, we identify the overlapping events by comparing the difference between the center dates of two adjacent events within 6 days of each other and select the one with the largest maximum values. Using this method, we identified 276 WWEs including 82 W-type events, 136 C-type events and 58 E-type events during the 1979–2016 period, corresponding to approximately 7 WWEs per year.

The durations of WWEs span multiple timescales. Many previous studies used 3 days as the threshold (e.g., Harrison and Vecchi, 1997; Chiodi et al., 2014), while we focus on the stronger WWEs with a longer duration twice as the normal threshold. Furthermore, since the frequency of WWEs is predominantly in the 6–30-day range, we focus on these durations, and divide them into two main types of events based on the threshold of 10-day where a significant change in the frequency of WWEs is observed (Figures not shown): the short (6–10 days) and the long events (10–30 days), corresponding to high frequency part and low frequency part, respectively. Due to fewer super long events with durations longer than 30 days, they are removed prior to classification. Our classification of the six WWE types for the 276 WWEs identified during the 1976–2016 period is summarized in Table 1.

2.2.2. Composite analysis method in terms of WWEs

The method of composing various events is as follows. We compute the day (0) composite fields by averaging the parameters for each X-type event on day (0). Composite days (± n) are similarly computed from each of the days (± n) using the corresponding data for the X-type events. The composite for each wind event is computed according to

$$U(x, y, t_n) = \frac{\sum_{i=1}^{N} u(x, y, t_n + \tau_i)}{N} \quad (1)$$

where τ_i is the center days for the individual event.

2.2.3. MJO events selection

In this work, the MJO events are selected based on the equatorial (5 °S-5 °N) surface zonal wind anomalies, due to focus on studying the WWEs. Although the surface zonal wind anomaly only involves the circulation signals of MJOs, it manifests as a high correlation (> 0.6) with the second component of the all-seasonal real-time multivariate MJO (RMM) index (Wheeler and Hendon, 2004) that considers both the convection and circulation (Figures not shown). Actually, Straub (2013) have proved that the excessive dependence of RMM index on the circulation. The close resemblance of surface zonal wind anomaly with RMM2 index implies that a large portion of overlapping with the selected MJO events based on either the former or the latter. To highlight the large-scale envelop of MJO, a space-time filtering technique that retains the zonal wavenumbers 1–5 and frequencies 1/96-1/30 cycles per day (Wheeler and Kiladis, 1999; Kiladis et al., 2009) have been implemented here firstly. Then, the zonal wind anomalies are normalized using their standard deviation. Spatiotemporal domains above one (below minus one) standard deviation are considered as the convective (suppressed) phases of the MJO, as illustrated in Fig. 12a in which the year of 1981 is taken as an example.

Table 1
Number of events for the different types of WWEs.

Types	W-type events	C-type events	E-type events
All (Duration ≤ 30 days)	82	128	52
Short (Duration 6–10 days)	57	56	31
Long (Duration 10–30 days)	25	72	21

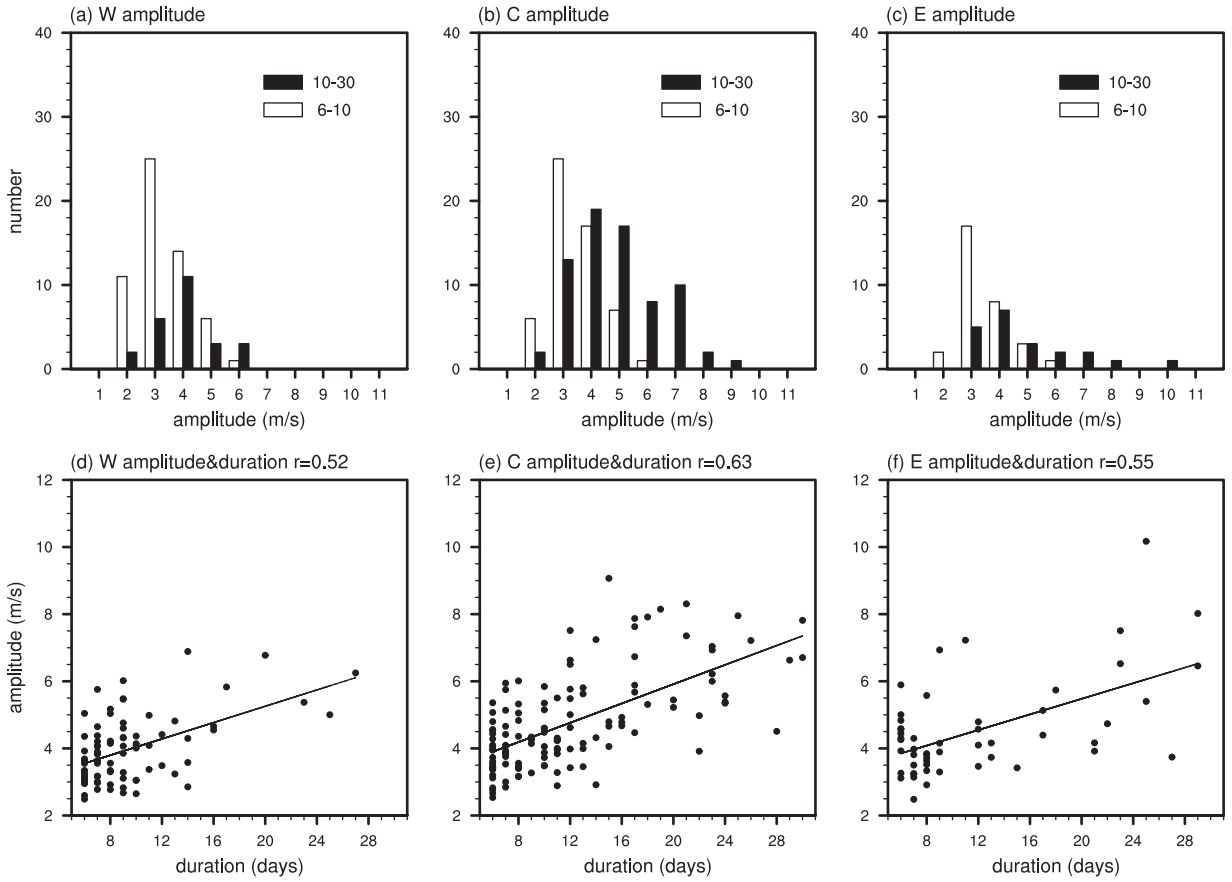

Fig. 1. Frequency number (bars) of occurrences of the short (white) and long (black) WWEs as a function of amplitude (m/s) for the (a) W, (b) C, (c) E types, respectively. (d–f) The scatter plots of the amplitude (m/s) and duration (days) of WWEs in the three regions with their correlation coefficients (r) (For interpretation of the references to colour in this figure legend, the reader is referred to the web version of this article).

3. WWEs amplitude and seasonal features

According to region and duration, we have classified six types of WWEs which indicate different features dependent on both amplitude and seasonal distributions. In this section we discuss the characteristics of amplitude and seasonal distributions of various types of WWEs. Fig. 1a–c show the amplitude distribution of every type of WWEs. In these figures, it indicates that the short events have a peak at an intensity of 3 m/s, while the long events have a larger peak at 4 m/s. The maximum values of C and E types of long events which can reach 10 m/s are greater than W-type long events only reaching 7 m/s, partially due to the frictional effect of the islands in the Maritime Continent. Fig. 1d–f illustrate that the positive correlation coefficients above 0.5 can be attained between the amplitude and duration of WWEs, which means the longer WWEs last, the stronger they are. Therefore, the amplitudes of the long WWEs are usually bigger than the short ones.

Fig. 2 provides a quantitative assessment of WWEs' seasonal distribution. The seasonal distributions for various types of WWEs are different since the generation of WWEs is modulated by many factors. The W-type long events are generally more frequent in the boreal winter, whereas the seasonal phase locking in the W-type short events is unclear (Fig. 2a). The C-type long events are also more likely to occur in the boreal winter, while the C-type short events are more likely to occur in winter and autumn (Fig. 2b). The seasonal distributions of W and C long events are affected by the background states. In the boreal winter, the position of convection over the western Pacific is biased near the equator. For the W and C short events, the amplitudes of them are weak with multiple effective factors causing their weak and complex seasonal distributions. However, the seasonality of E-type long events is not obvious, but the short events primarily occur in July. For the E-type events, the reason is not clear. In general, the population of WWEs tends to occur in the boreal winter, which is consistent with the results of Keen (1982) and Harrison and Vecchi (1997).

4. Results of composite analysis

In this section, we describe the results of our composite analysis, including the evolutions of the horizontal and vertical structure characteristics of WWEs and the atmospheric convection and circulation patterns associated with WWEs. Since the definition of WWEs used the anomalies, we firstly further analyze the total wind field of them. Seen from Fig. 3, the total wind field composites

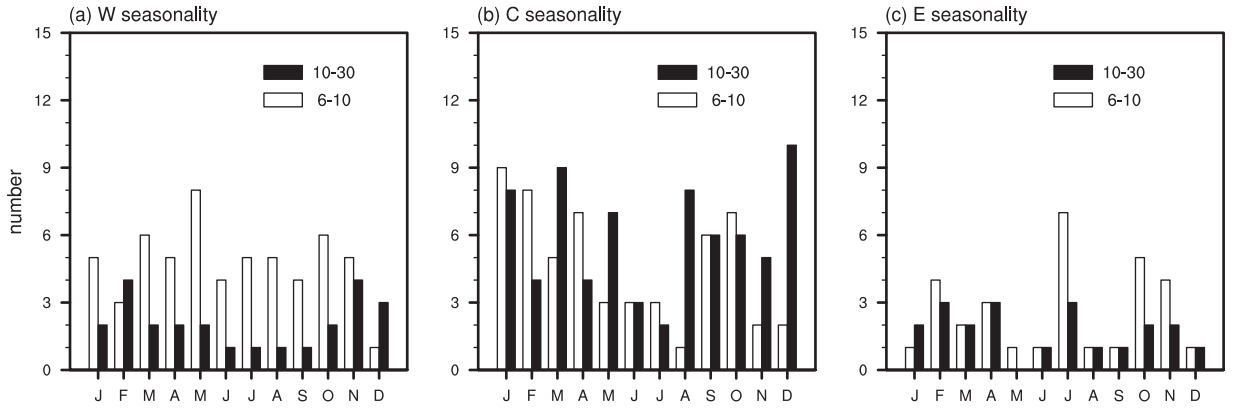

Fig. 2. Same as Fig. 1a-c, but for the seasonality changing from January to December.

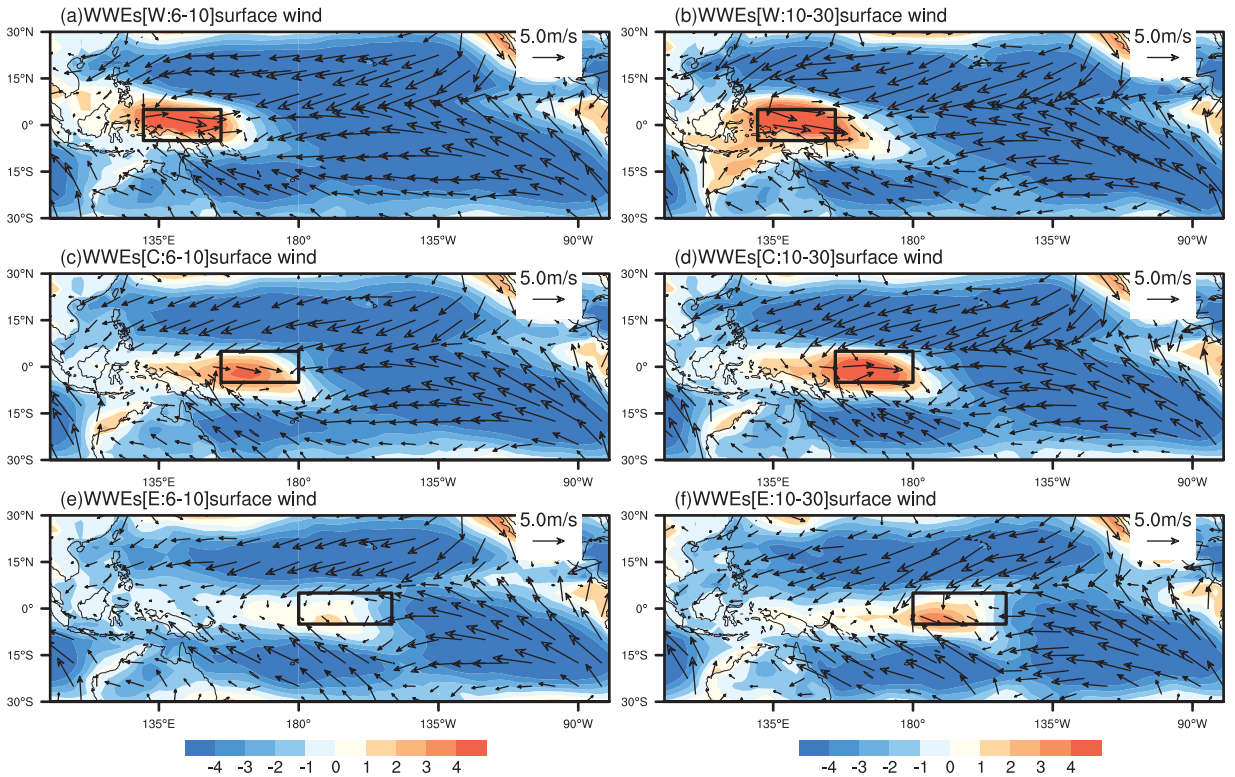

Fig. 3. Composite patterns of surface wind with vectors (m/s) and surface zonal wind with colors (m/s) for the short (left) and long WWEs (right) on day (0). The regions for the WWE classification are indicated by the black boxes, where (a, b) W-type events, (c, d) C-type events, and (e, f) E-type events.

show a westerly wind direction for each WWE type. The W- and C-type events have stronger background westerly winds than the E-type. The peak of long events is stronger than the short (Fig. 3).

4.1. Evolutions of horizontal structure characteristics

Fig. 4 shows the evolutions of surface wind anomaly field of the W-type events. We observe that the typical W-type event pattern has much stronger zonal wind anomalies than the meridional wind anomalies, with a slightly northwestward propagation throughout the lifetime, accompanied by anomalously cyclonic circulation patterns in the north of the definition domain of the W type. This result is consistent with the analysis of Harrison and Vecchi (1997). For the long event (Fig. 4b, d, and f), the anomalous circulation pattern is always strong during the whole lifetime, but for the short event (Fig. 4a, c, and e) such a pattern is only clear in the peak and decay stages. Evidently, the short event has a weaker peak intensity and smaller spatial scale than the long event.

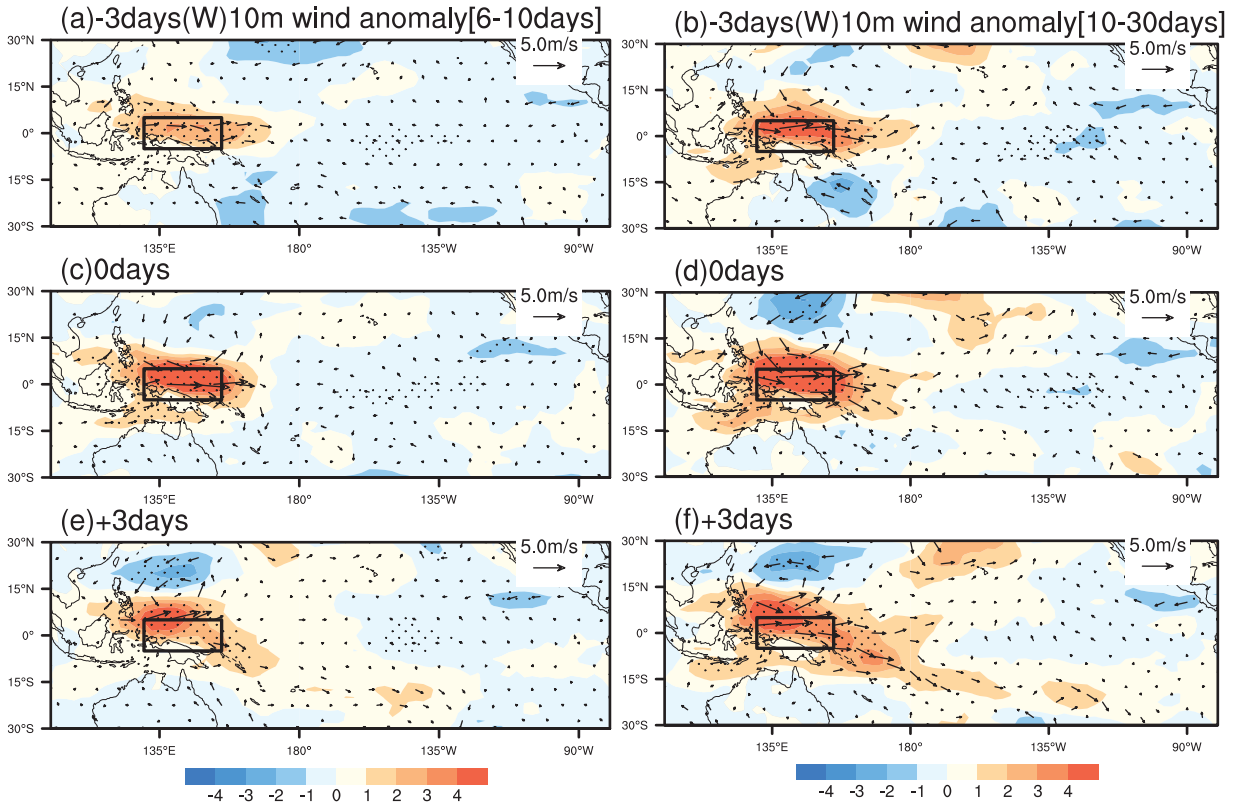

Fig. 4. Composite horizontal patterns of 10-m wind (vectors, m/s) and zonal wind anomalies (shading, m/s) associated with the W-type WWEs on (a, b) day (-3), (c, d) day (0) and (e, f) day (+3) for short events (left panels) and long events (right panels). The black boxes are same to those in Fig. 3. The dotted areas are statistically significant at the 99% confidence level of the student's *t* test.

The patterns in Fig. 5, for the C type, are overall similar to those in Fig. 4, but with an eastward displacement, showing the evolutions of anomalous surface wind field. There are no obvious anomalous cyclonic circulation patterns in the north of the C-type events domain, but a weaker pattern on both sides of the equator during the peak and decay stages of the long event. Both, the long and short events have weaker cross-equatorial wind anomalies at the center day. Compared to the short event, the long event has a larger spatial scale and larger peak intensity. Different from the W-type, the C-type long event shows a clear eastward extension during the decay stage, accompanied by an anomalous cyclonic circulation pattern in the north of the C-type region. Such a feature is not apparent for the short event.

The E-type patterns in Fig. 6 show a higher degree of similarity to those in Fig. 5 than 4, showing that a larger circulation difference exists in the E type from the W type than the C type. Here, the definition domain of the E-type events is slightly larger than those of the W- and C -type events. Both timescales of the E-type events have the anomalous cyclonic circulation patterns in the south of the domain. The cross-equatorial inflow associated with the long event is much stronger, compared to the short event. However, there are almost no zonal movements of the wind patterns associated with the E-type event.

On the whole, the E-type WWEs is clearly larger than the others. The W- and C-type events are generally accompanied by the anomalously cyclonic circulation patterns in the north of definition regions, whereas no such patterns are observed for the E-type events. For the different timescales of WWEs, the long WWEs have the larger spatial scale and peak intensity than the short ones, and the stronger associated patterns of the anomalously cyclonic circulation and cross-equatorial inflow as well. The patterns of three types of WWEs occurring in different regions are consistent with the analyses of Harrison and Vecchi (1997), but they do not analyze the differences among the various types of WWEs. To show the evolution characteristics of WWEs more clearly, Fig. 7 indicates the evolutions of amplitude for the various WWEs. Clearly, the peak values of the long events are stronger than the short, consistent with the results in Figs. 4–6. It is found that the amplitudes of the three types of short events are quite similar to each other during the evolutions, while the C- and E-type long events are much stronger than the W-type ones.

4.2. *Vertical structure characteristics*

The various WWEs have obvious baroclinic structures in the vertical direction, with the centers of positive zonal wind anomalies located between 850 and 700 hPa (Fig. 8). The relatively weak baroclinic structures of W- and C-type events are generally tilted to the east with increasing height, with the latter more pronounced than the former, while the E-type events have standard baroclinic

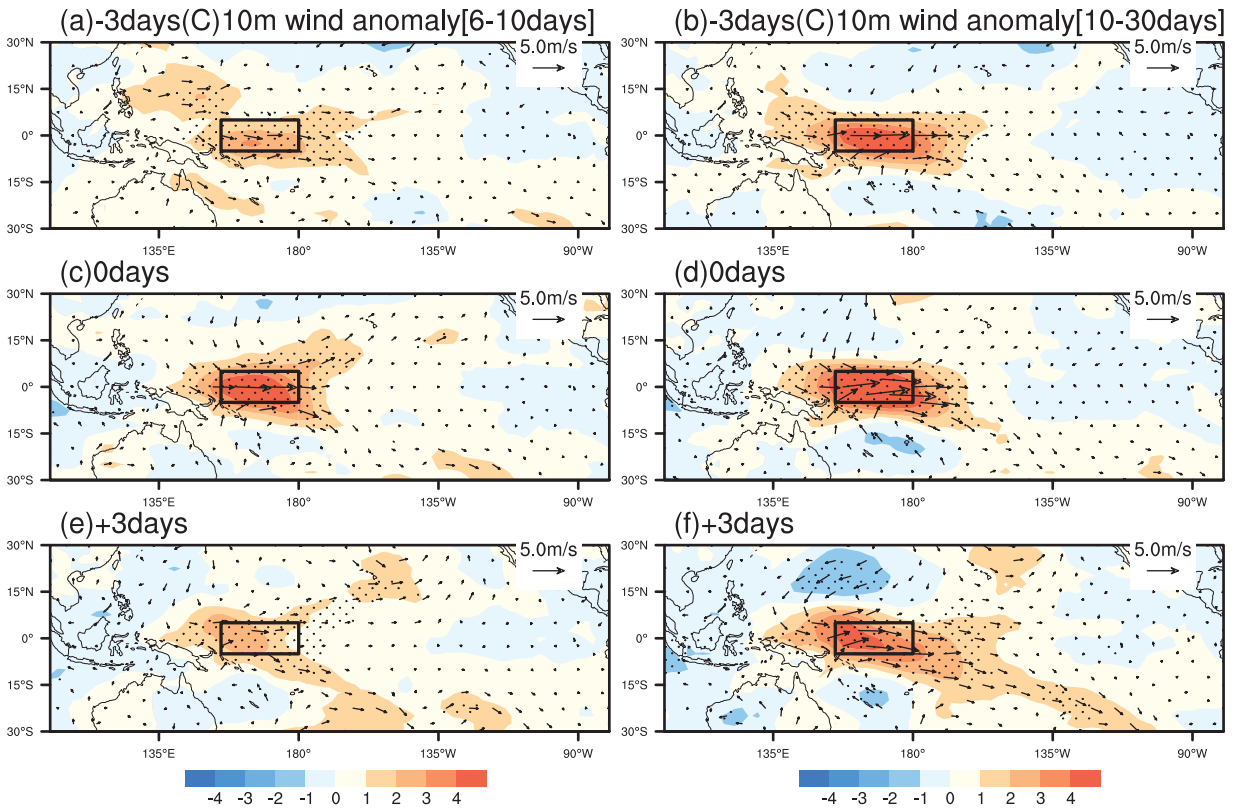

Fig. 5. Same as Fig. 4, except for the C-type WWEs.

structures without a tilt. An analysis of the different pressure levels indicated that the anomalous zonal wind structure is in phase with that of the original zonal wind at all levels for the W-type events; that is, when the original westerly wind occurs, the anomalous zonal wind is also positive. This in-phase relationship only exists in the middle and lower levels, for the C-type events (both the long and short events) and the E-type long events. For all the types of WWEs, the zonal wind anomalies of long events are stronger than those of the short (Fig. 8).

4.3. Atmospheric convection and circulation characteristics

Fig. 9 displays the composites of OLR anomalies associated with the WWEs' center dates (day(0)). All the types of WWEs are associated with a meridionally quasi-symmetric OLR pattern with respect to the equator (Puy et al., 2016). Corresponding to the OLR patterns, as shown in Fig. 10, there are the patterns of positive specific humidity anomalies due to the large-scale ascending motion over the box regions while the negative humidity anomalies with a subsidence to the west side of the regions. The relevant convection centers of the W-type events are shifted to the eastern side of the domain region (Figs. 9a and b, 10 a and b). In Fig. 11, overall, the long events generally have stronger intensities and larger spatial scales of convection than the short. For the evolutions of OLR anomalies, we found that the W-type events (both the long and short ones) and C-type long events both show evident eastward propagation during their lifetimes and particularly the eastward shift in the long events is quite distinct. However, the E-type long and short events have no obvious eastward movement (Fig. 11).

Why does a clear eastward propagation of the OLR anomalies only occurs for the W-type (both the long and short ones) and C-type long WWEs? A diagnostic from the zonal asymmetry of the specific humidity may be helpful. We see that for the W- (Fig. 10b,) and C-type (Fig. 10d) long events, the westward titled moisture shows an evidently zonal asymmetry with respect to the convective center, in which strong moist anomalies are extended to the east far whereas strong dry anomalies prevail to the west. This kind of moisture asymmetry has been used extensively to interpret the eastward propagation of the large-scale convective anomalies of the MJO (e.g., Hsu and Li, 2012; Zhao et al., 2013; Hsu et al., 2014; Li et al., 2015; Jiang et al., 2018; Wang et al., 2017, 2018). For the W-type short events (Fig. 10a), although the moisture itself is weaker than that of the long events, there is still a certain degree of zonal asymmetry of moisture and thus a weak eastward propagation (Fig. 11a). However, the dry anomalies for the C-type short event are very weak to the west (Fig. 10c), resulting in a weak eastward gradient of moisture and an invisible eastward propagation (Fig. 11b). For the E-type events, the specific humidity anomalies manifest as a dramatically eastward titled structure. Therefore, the zonal gradient surrounding the convective center becomes much weaker despite the very strong moisture anomalies, leading to standing WWEs (Fig. 11e and f). Here we can hypothesize that the different zonal propagation characteristics of the various WWEs may be due to

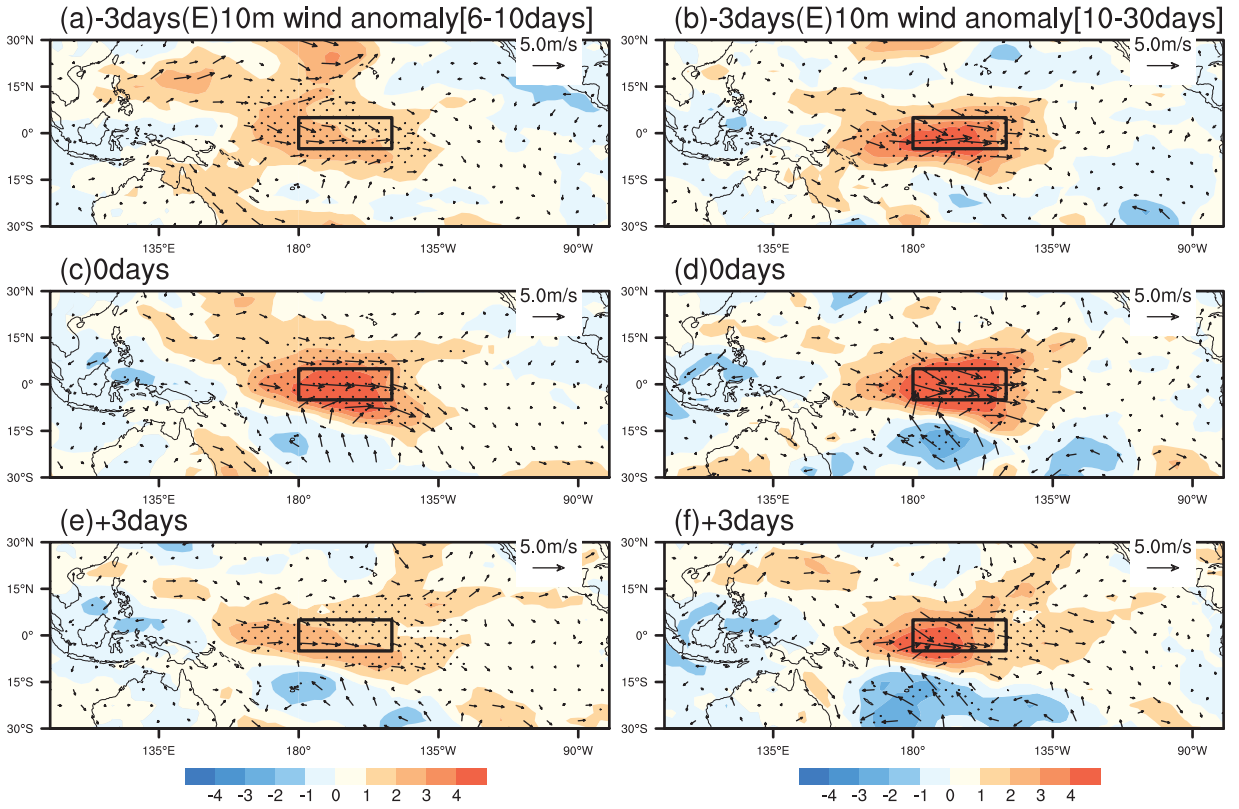

Fig. 6. Same as Fig. 4, except for the E-type WWEs.

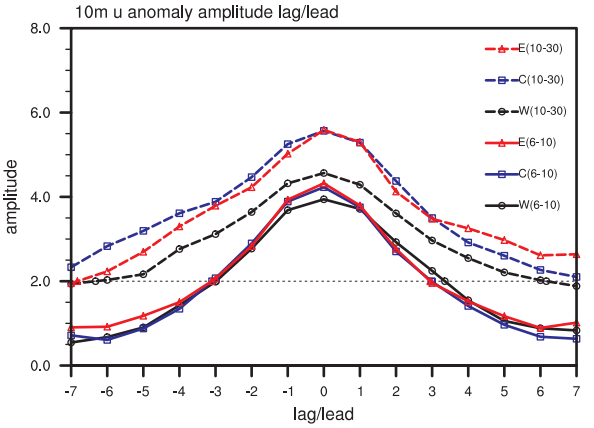

Fig. 7. Evolutions of amplitude (m/s) of the short (solid lines) and long (dashed lines) WWEs for the three different types.

modulation of the MJO which typically has a quite clear eastward propagation.

5. Relationships between WWEs and MJOs/CCKWs

In this section, we investigate the relationship between WWEs and MJOs/CCKWs to explore the possible affection of spatio-temporal diversity for WWEs.

5.1. MJOs

Previous studies suggested that the WWEs are closely related to MJO (Puy et al., 2016). The region where the W-type WWEs occur is closest to the area where MJO events occur frequently and develop rapidly, with the primary duration of the long events closer to

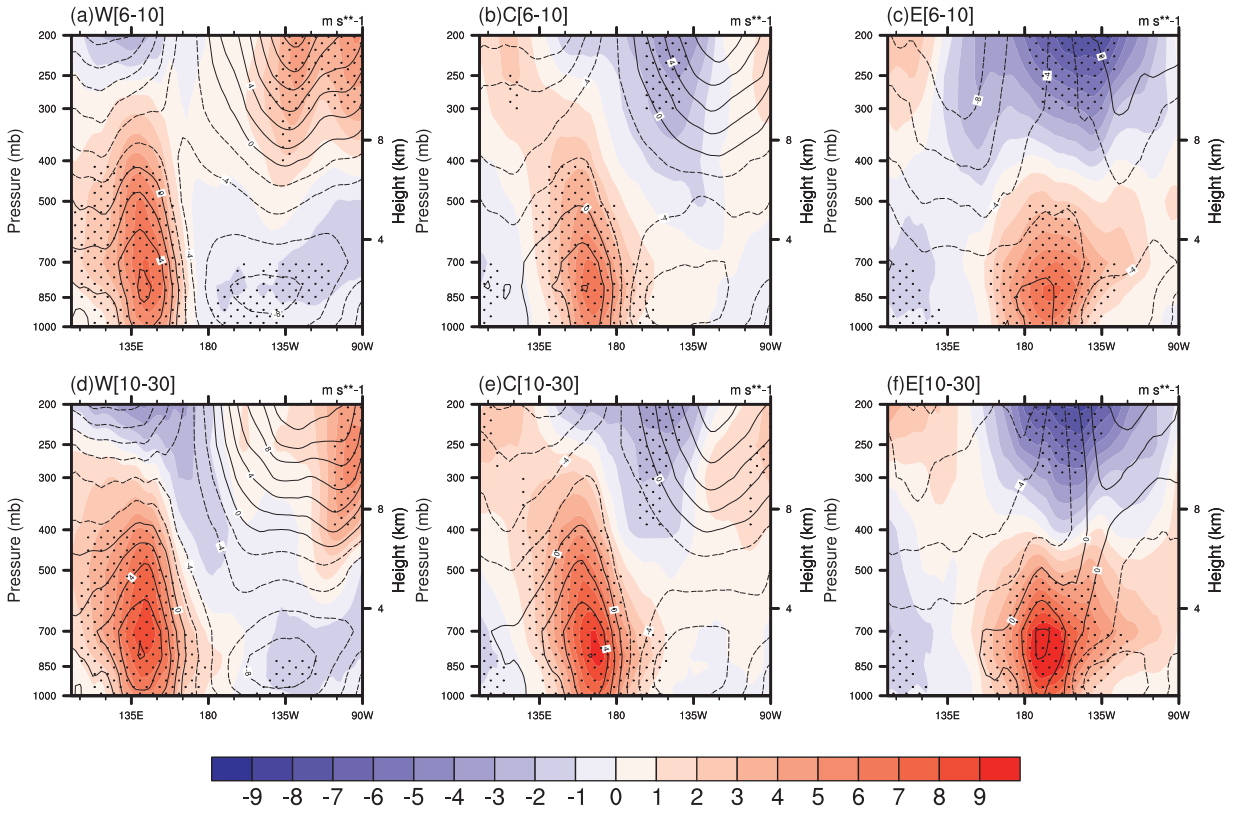

Fig. 8. Composite vertical structures of zonal wind (contours) and its corresponding anomalies (shading) for the W-type (left), C-type (middle) and E-type (right). (a–c) is for the short events and (d–f) is for the long events. The dotted parts are statistically significant exceeding at the 99% confidence level of the student's *t* test.

the typical timescale of MJO compared to the short ones. Therefore, we consider that the eastward displacements of the various WWEs are likely related to the modulation of MJO when it propagates through the prevailing regions of the WWEs. In order to confirm such a hypothesis, we analyzed the relationship between MJO and WWEs.

We counted the frequencies number of the various types of WWEs when the MJO occurred. As seen in Fig. 12b, a large percentage of the long events can be modulated by the MJO convective phase compared to the short events. More than 60% of the W-type long and short event and the C-type long events are associated with the convective MJO phases, but less than 45% of the E-type short and long events. The relationships between the WWEs and MJO are quite different for the various types of WWEs. To further represent the modulation of the MJO on the WWEs, we composite the 10-m zonal wind and wind vectors during the convective phase of the MJO for the three type of WWEs (Fig. 13). Fig. 13 shows that there are also the MJO westerly wind anomalies in the three prevailing regions of WWEs, which implies that the low-frequency MJO background state, especially the convective phases, with stronger westerly wind anomalies in the western and central definition regions. This result may serve as a supporting factor in the different modulations of the MJOs for the various WWEs. Due to the similar timescale, the long events are more strongly affected by the MJO, and we suspect that the short events are closely associate with CCKWs.

5.2. CCKWs

For further studying the generation of WWEs, we analyze the relationships between the CCKWs and various types of WWEs. Fig. 14 displays the composite Hovmöller diagrams of both surface zonal wind anomalies and CCKW-filtered (Wheeler and Kiladis, 1999; Kiladis et al., 2009) OLR anomalies associated with the W-, C-, and E-type WWEs, respectively. The CCKW filtering uses the zonal wavenumbers of 2–14 and frequencies of 1/20–1/3 cycles per day. Compared with the long WWEs (Fig. 1d–f), the short WWEs (Fig. 1a–c) possess more regions with OLR anomalies that passed the Student-*t*'s test at the 90% confidence level. This implies that the short events are generally much more closely associated with the CCKWs, possibly due to the intrinsically similar time scale between them, whereas the role of CCKWs is less important for the long events, especially the W-type WWEs. In addition, we further analyze the wavenumber-frequency spectrum of OLR anomalies associated with WWEs to confirm the relationships between the CCKWs and various types of WWEs. These results indicate that the values of short events are stronger than that of long events (Figures not shown). In general, the CCKWs are important factors for the evolution of WWEs, especially for the short events.

Based on the above analyses, we found that not only do various WWEs have different characteristics, but their relationships with

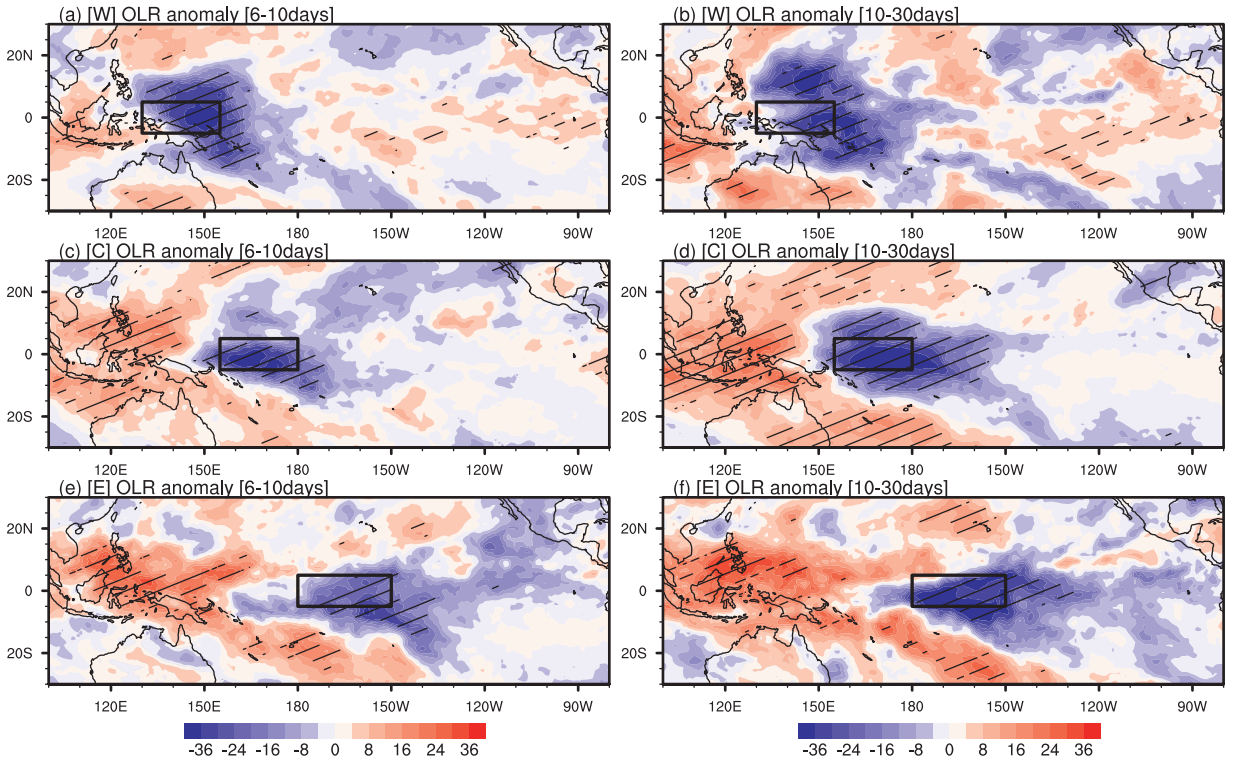

Fig. 9. Composites of OLR anomalies for all the types of WWEs: the W type (a, b), C type (c, d) and E type (e, f), where the left (right) panels are for the short (long) events. The boxes are the same as in Fig. 3. The slash parts are statistically significant exceeding at the 99% confidence level of the student's *t* test.

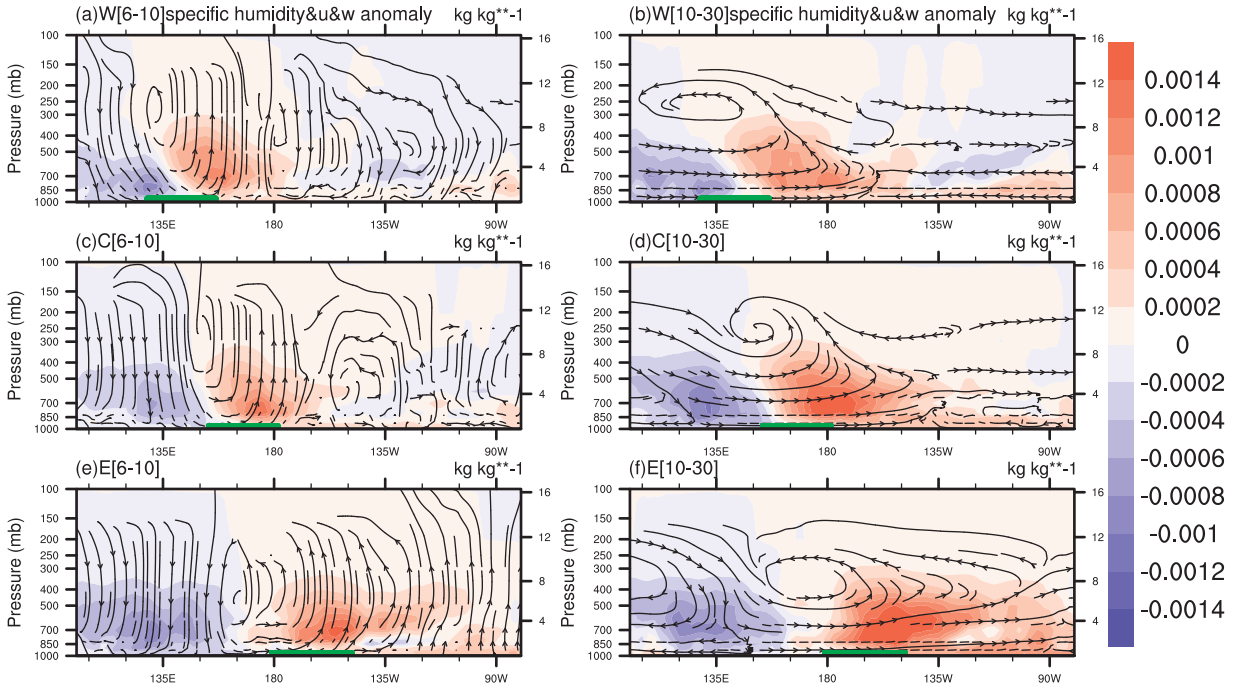

Fig. 10. Composite vertical structures of the zonal wind and specific humidity anomalies for all the types of WWEs: the W type (a, b), C type (c, d) and E type (e, f), where the left (right) panels are for the short (long) event. Shading and streamlines indicate the specific humidity and zonal-vertical flow anomalies averaged between 5 °S-5 °N. The green bars indicate the three regions. (For interpretation of the references to colour in this figure legend, the reader is referred to the web version of this article).

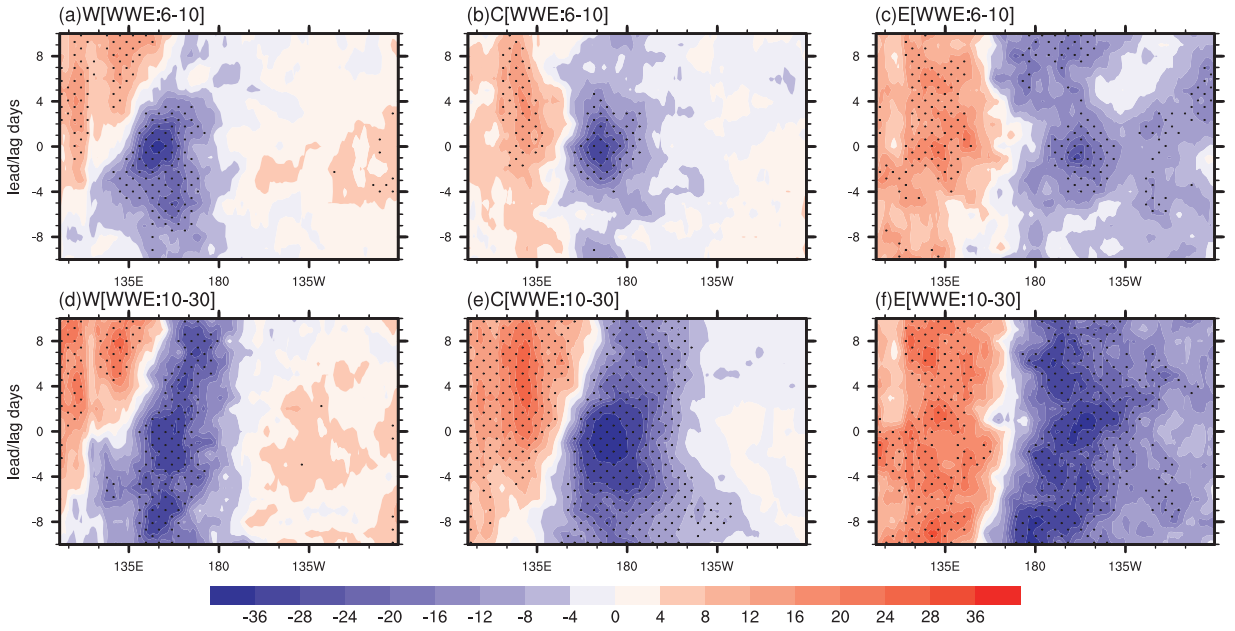

Fig. 11. Averaged 5 °S-5 °N time-longitude section of OLR anomalies for (a, d) W, (b, e) C and (c, f) E. short events (top) and long events (bottom). The section with dots is significant at a 99%. The confidence level is estimated with the student's *t*-test.

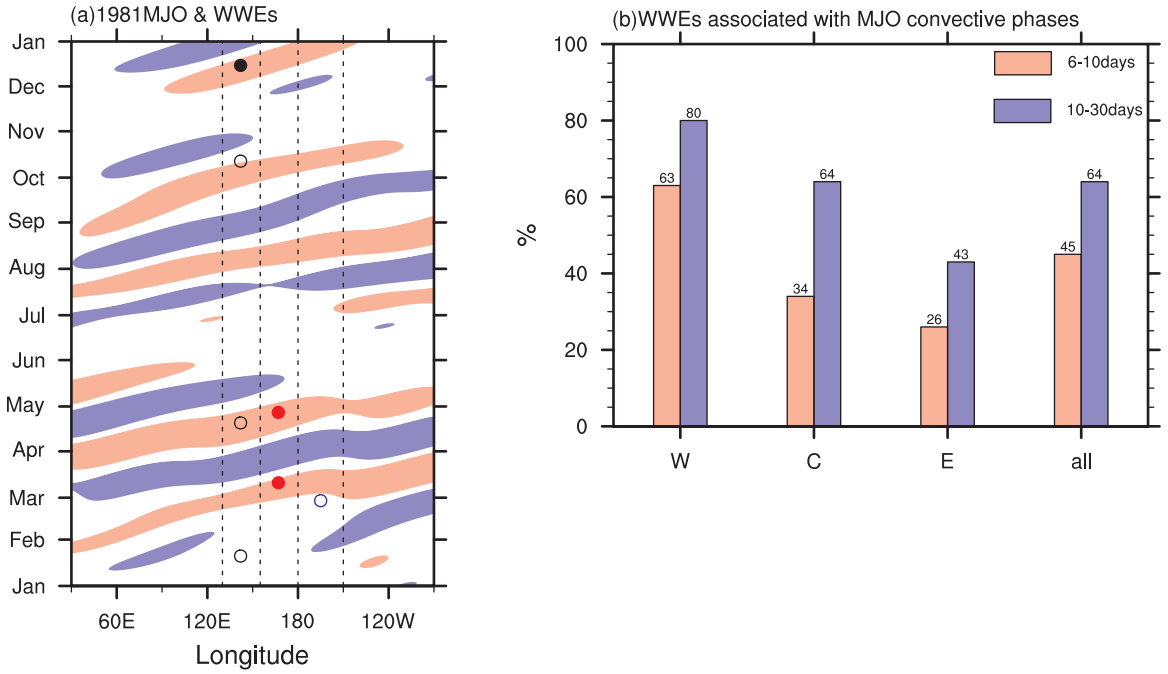

Fig. 12. (a) Time-longitude cross-section of the MJO-related surface zonal wind signal averaged over 5 °S–5 °N under the detected convective (red shading) and suppressed (blue shading) MJO phases for 1981. The black dashed lines correspond the edges of three definition regions where the WWEs occur. The black, red, and blue circles stand for the W-, C-, and E-type WWEs, with the open and solid circles denoting the short and long events, respectively. (b) Percentages of frequency number of the different types of WWEs that were embedded within the convective phases of MJO events (For interpretation of the references to colour in this figure legend, the reader is referred to the web version of this article).

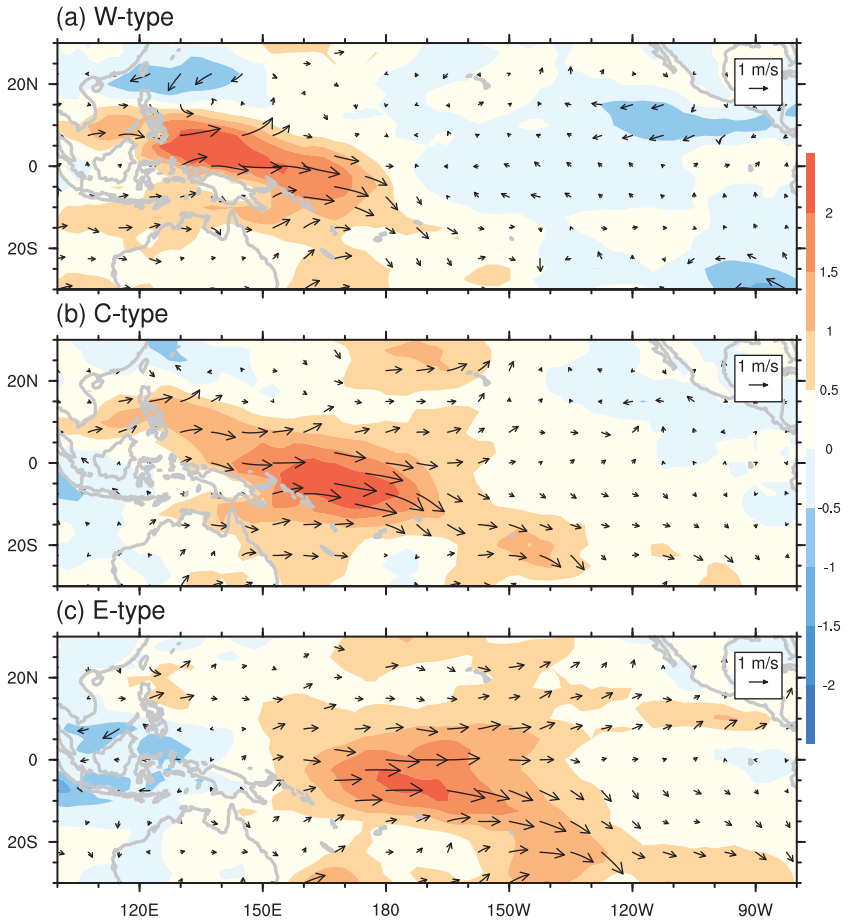

Fig. 13. (a) Composite 10-m zonal wind anomalies (shading, m/s) and 10-m winds (vectors, m/s) during the convective phase of the MJO for the W-type region. (b) and (c) are the same as (a), but for the C- and E-type regions, respectively. The contour interval is 0.5 m/s.

climate phenomena (e.g., MJO and CCKWs) are also different. Our classification of WWEs, which is based on their locations and durations, is of great significance for studying the characteristics and possible generating mechanism of WWEs.

6. Summary and discussion

In this study, we identified 276 WWEs over the tropical Pacific during the 1979–2016 period, and classified the WWEs into six types that cover three equatorial-Pacific regions where they occur frequently and have durations that span two major timescales (6–10 and 10–30 days). This detailed WWE classification is necessary since the WWEs exhibit considerable spatiotemporal variations, which makes an analysis of their characteristics and mechanisms difficult, and it allows for a more comprehensive WWE analysis.

For the amplitude of various types of WWEs, the long events are generally stronger than the short events since the duration of WWEs is positively correlated with the amplitude to some degree. Among them, the maximum amplitudes of C- and E-type long events are much stronger than the W-type long events. The seasonal distributions of various types of WWEs are effected by many various factors. The W and C long events occur more frequently in boreal winter, since the convection is near equator and the influence of MJO is stronger, in winter.

Both the spatial scale and peak intensity of the long events are larger than the short, and the correlative phenomena (anomalously cyclonic circulation and cross-equatorial inflow) of various types of events occurred in the domain regions are diverse. Various WWEs appear as vertical baroclinic structures, but the statement of them is dissimilarity in every layer. The different structural characteristics of various types of WWEs reflect the complexity of physical mechanisms. We generally cannot analyze them as a single WWE type to study the mechanisms of WWEs. A comprehensive WWE classification, such as the one we present here, is necessary to understand their mechanism better, with analyses of spatiotemporal characteristics elucidating the key factors that influence WWEs.

Our examinations of the atmospheric circulation and convection patterns related to WWEs demonstrate that the evolution of convection region associated with the W-type (both the long and short ones) events and C-type long events both indicate evident eastward propagation during their lifetimes, whereas the C-type short events and E-type (both the long and short ones) events do not. These different zonal propagation characteristics of the various WWEs are due to the different relationships between the WWEs and

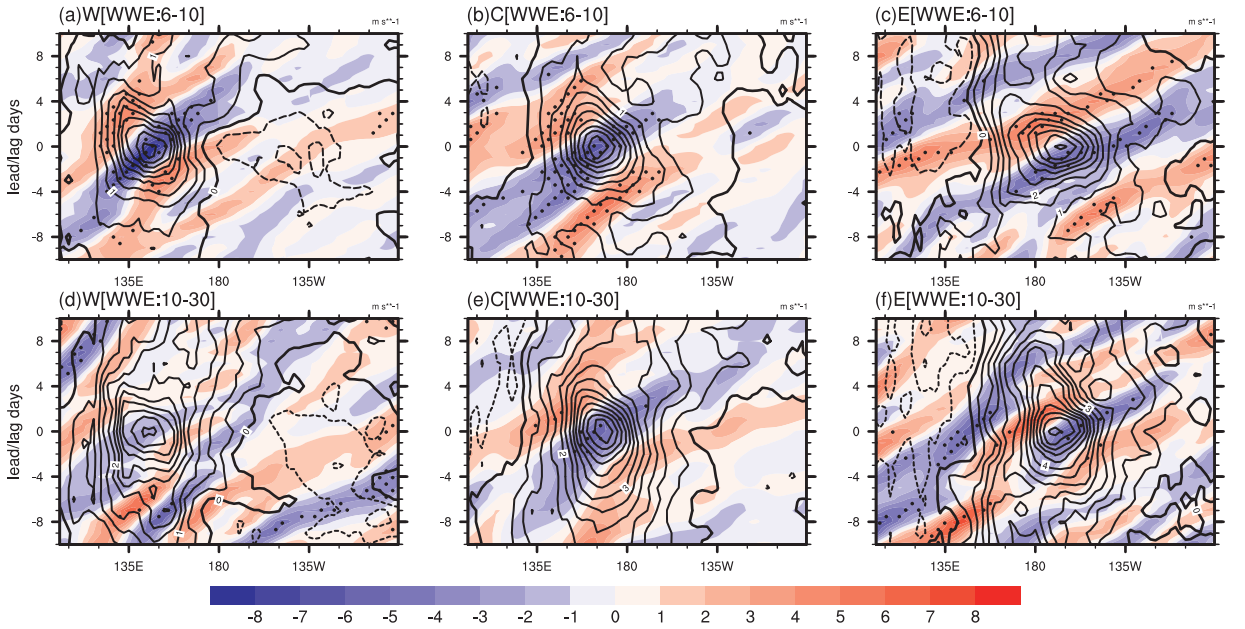

Fig. 14. Hovmöller diagrams (shading) of the lagged composite of CCKW-filtered OLR anomalies (W/m^2) associated with the W- (left panels), C- (middle panels), and E-type (right panels) WWEs, respectively. (a–c) correspond to the short events, while (d–f) represent the long events. To facilitate comparison, the composite zonal wind anomalies (m/s) are also overlaid with the westerly (easterly) shown by solid (dashed) contours. The dotted regions denote those passing the Student-t's test at the 90% confidence level.

MJO, with our research demonstrating that the W-type (both the long and short ones) events and the C-type long events are more strongly modulated by the MJO. The relationship between WWE and MJO varies considerably as functions of both the domain regions and the durations of the WWEs. Furthermore, the CCKWs also associated with the various types of WWEs, especially the short events. The related factors affect the various WWE types to different degrees result in the spatiotemporal complexity of the WWEs. Both the convection of CCKWs and MJO can lead to westerly wind generation, which can be as factors to motivate and maintain the WWEs. The modulation of MJO tend to result in the long WWEs while CCKWs tend to the short events. The degree of influence between the MJO and CCKWs can regulate the timescales of WWEs to an extent, with MJO modulation having a greater impact on the domain regions. Therefore, this spatiotemporal classification of WWEs is necessary to effectively study their mechanisms. Additionally, we find that the tropical cyclones and cross-equatorial wind anomalies influence the WWEs via analyses of their spatiotemporal characteristics. So far, some super long events which can even longer than 100days may be mainly modulated by El Niño which has lasting impacts. Studies on the spatiotemporal WWE variations deserve greater attention, highlighting the need to investigate WWE mechanisms further

Acknowledgements

This work is jointly supported by the National Key Research and Development Program on Monitoring, Early Warning and Prevention of Major Natural Disaster (2018YFC1506002), National Basic Research (973) Program of China under Grants 2015CB453203, and National Natural Science Foundation of China (41775066 and 41375062).

References

Baranowski, D.B., Flatau, M.K., Flatau, P.J., Schmidt, J.M., 2017. Multiple and spin off initiation of atmospheric convectively coupled kelvin waves. Clim. Dyn. 49 (9-10), 2991–3009. https://doi.org/10.1007/s00382-016-3487-7.

Chen, S.S., Houze Jr, R.A., Mapes, B.E., 1996. Multiscale variability of deep convection in relation to large-scale circulation in TOGA COARE. J. Atmos. Sci. 53, 1380–1409. https://doi.org/10.1175/1520-0469(1996)053<1380:MVODCI>2.0.CO;2.

Chen, D., Lian, T., Fu, C., Cane, M.A., Tang, Y., Murtugudde, R., Song, X.S., Wu, Q.Y., Zhou, L., 2015. Strong influence of westerly wind bursts on El Niño diversity. Nat. Geosci. 8 (5), 339–345. https://doi.org/10.1038/ngeo2399.

Chiodi, A., Harrison, D.E., Vecchi, C.A., 2014. Subseasonal atmospheric variability and El Niño waveguide warming: observed effects of the Madden-Julian Oscillation and westerly wind events. J. Clim. 27, 3619–3642. https://doi.org/10.1175/JCLI-D-13-00547.1.

Chu, P.-S., 1988. Extratropical forcing and the burst of equatorial westerlies in the western Pacific: a synoptic study. J. Meteorol. Soc. Jpn. 66, 549–563.

Feng, J., Lian, T., 2018. Assessing the relationship between MJO and equatorial pacific WWBs in observations and CMIP5 models. J. Clim. 31, 6394–6410. https://doi.org/10.1175/JCLI-D-17- 0526.1.

Harrison, D.E., 1984. On the appearance of sustained equatorial westerlies during the 1982 Pacific warm event. Science 225, 1099–1102. https://doi.org/10.1126/science.224.4653.1099.

Harrison, D.E., Vecchi, G.A., 1997. Westerly wind events in the tropical pacific, 1986–1995. J. Clim. 10, 3131–3156. https://doi.org/10.1175/1520-0442(1997)010<C3131:WWEITT>2.0.CO;2.

Hartten, L.M., 1996. Synoptic settings of westerly wind bursts. J. Geophys. Res. 101 (D12), 16997–17019. https://doi.org/10.1029/96JD00030.
Hsu, P.C., Li, T., 2012. Role of the boundary layer moisture asymmetry in causing the eastward propagation of the Madden-Julian oscillation. J. Clim. 25 (14), 4914–4931. https://doi.org/10.1175/JCLI-D-11-00310.1.
Hsu, P.C., Li, T., Murakami, H., 2014. Moisture asymmetry and MJO eastward propagation in an aquaplanet general circulation model. J. Clim. 27 (23), 8747–8760. https://doi.org/10.1175/JCLI-D-14-00148.1.
Jiang, Xianan, Adames, Ángel F., Zhao, Ming, Waliser, Duane, Maloney, Eric, 2018. A unified moisture mode framework for seasonality of the Madden–Julian oscillation. J. Clim. 31 (11), 4215–4224. https://doi.org/10.1175/JCLI-D-17-0671.1.
Keen, R.A., 1982. The role of cross-equatorial tropical cyclone pairs in the Southern oscillation. Mon. Weather. Rev. 110, 1405–1416. https://doi.org/10.1175/1520-0493(1982)110<1405:TROCET>2.0.CO;2.
Kessler, W.S., Mcphaden, M.J., Weickmann, K.M., 1995. Forcing of intraseasonal Kelvin waves in the equatorial Pacific. J. Geophys. Res. 100, 10613–10631. https://doi.org/10.1029/95jc00382.
Kiladis, G.N., Meehl, G.A., Weickmann, K.M., 1994. Large-scale circulation associated with westerly wind bursts and deep convection over the western equatorial Pacific. J. Geophys. Res. 99 (18) 527–18,544.
Kiladis, G.N., Wheeler, M.C., Haertel, P.T., Straub, K.H., Roundy, P.E., 2009. Convectively coupled equatorial waves. Rev. Geophys. 47 (2).
Lau, K.M., Chan, P.H., 1988. Intraseasonal and interannual variations of tropical convection: a possible link between the 40–50 day oscillation and ENSO. J. Atmos. Sci. 45, 506–521. https://doi.org/10.1175/1520-0469(1988)045<0506:iaivot>2.0.co;2.
Lengaigne, M., Boulanger, J.-P., Menkes, C., Masson, S., Madec, G., Delecluse, P., 2002. Ocean response to the March 1997 westerly wind event. J. Geophys. Res. 107, 8015. https://doi.org/10.1029/ 2001JC000841.
Lengaigne, M., Boulanger, J.-P., Menkes, C., Madec, G., Delecluse, P., Guilyardi, E., Slingo, J., 2003. The March 1997 Westerly Wind Event and the onset of the 1997/98 El Niño: understanding the atmospheric response. J. Clim. 16, 3330–3334. https://doi.org/10.1175/1520-0442(2003)016<3330:TMWWEA>2.0.CO;2.
Lengaigne, M., Boulanger, J.P., Menkes, C., Delecluse, P., Slingo, J., 2004. Westerly wind events in the tropical pacific and their influence on the coupled ocean-atmosphere system: a review. Geophys. Monogr. Ser. 147, 49–69. https://doi.org/10.1029/147GM03.
Lengaigne, M., Guilyardi, E., Boulanger, J.-P., Menkes, C., Inness, P., Cole, J., Delecluse, P., Slingo, J., 2007. Triggering of El Niño by Westerly Wind Events in a coupled general circulation model. Clim. Dyn. 23 (6), 601–620. https://doi.org/10.1007/s00382-004-0457-2.
Li, T., Zhao, C., Hsu, P.C., Nasuno, T., 2015. MJO initiation processes over the tropical Indian ocean during DYNAMO/CINDY2011. J. Clim. 28 (6), 2121–2135. https://doi.org/10.1175/JCLI-D-14-00328.1.
Lian, T., Chen, D., Tang, Y., Liu, X., Feng, J., Zhou, L., 2018. Linkage between westerly wind bursts and tropical cyclones. Geophy. Res. Lett. 45 (20), 11431–11438. https://doi.org/10.1029/2018gl079745.
Madden, R.A., Julian, P.R., 1971. Detection of a 40–50 day oscillation in the zonal wind in the Tropical Pacific. J. Atmos. Sci. 28, 702–708. https://doi.org/10.1175/1520-046 9(1971)028 <0702:DOADOI>2.0.CO;2.
Madden, R.A., Julian, P.R., 1972. Description of global-scale circulation cells in the tropics with a 40–50 day period. J. Atmos. Sci. 29, 1109–1123. https://doi.org/10.1175/1520-0469(1972)029<1109:DOGSCC>2.0.CO;2.
McPhaden, M.J., 1999. Climate oscillations-genesis and evolution of the 1997–98 El Niño. Science 283, 950–954. https://doi.org/10.1126/science.283.5404.950.
Nakazawa, T., 1988. Tropical super clusters within intraseasonal variations over the western Pacific. J. Meteorol. Soc. Jpn. 66, 823–839.
Puy, M., Vialard, J., Lengaigne, M., Guilyardi, E., 2016. Modulation of equatorial Pacific westerly/easterly wind events by the Madden–Julian Oscillation and convectively-coupled Rossby waves. Clim. Dyn. 46 (7-8), 2155–2178. https://doi.org/10.1007/s 00382-015-2695-x.
Seiki, A., Takayabu, Y.N., 2007a. Westerly wind bursts and their relationship with intraseasonal variations and ENSO. Part I: statistics. Mon. Weather Rev. 135, 3325–3345. https://doi.org/10.1175/MWR3477.1.
Seiki, A., Takayabu, Y.N., 2007b. Westerly wind bursts and their relationship with intraseasonal variations and ENSO. Part II: energetics over the Western and Central Pacific. Mon. Weather Rev. 135, 3346–3361. https://doi.org/10.1175/MWR3477.1.
Wang, B., 1988. Dynamics of tropical low-frequency waves: an analysis of the moist Kelvin wave. J. Atmos. Sci. 45, 2051–2065. https://doi.org/10.1175/1520-0469(1988)045<2051:DOTLFW>2.0.CO;2.
Wang, L., Li, T., Maloney, E., Wang, B., 2017. Fundamental causes of propagating and non-propagating MJOs in MJOTF/GASS models. J. Clim. 30, 3743–3769. https://doi.org/10.1175/JCLI-D-16-0765.1.
Wang, L., Li, T., Tomoe, N., 2018. Impact of Rossby and kelvin wave components on MJO eastward propagation. J. Clim. 31, 6913–6931. https://doi.org/10.1175/JCLI-D-17-0749.1.
Webster, P.J., Lukas, R., 1992. TOGA COARE: the coupled ocean-atmosphere response experiment. Bull. Am. Meteorol. Soc. 73, 1377–1416. https://doi.org/10.1175/1520-0477(1992)0732.0.CO;2.
Wheeler, M.C., Hendon, H.H., 2004. Anall-seasonreal-timemultivariate MJO index: development of an index for monitoring and prediction. Mon. Weather Rev. 132, 1917–1932.
Wheeler, M., Kiladis, G.N., 1999. Convectively coupled equatorial waves: analysis of clouds and temperature in the wavenumber-frequency domain. J. Atmos. Sci. 56, 374–399. https://doi.org/10.1175/1520-0469(1999)056<0374:CCEWAO>2.0.CO;2.
Zhang, C., 2005. Madden-Julian oscillation. Rev. Geophys. 43 (RG2003). https://doi.org/10.1029/2004RG000158.
Zhang, C., 2013. Madden–Julian Oscillation: bridging weather and climate. Bull. Am. Meteorol. Soc. 94 (12), 1849–1870. https://doi.org/10.1175/BAMS-D-12-00026.1.
Zhao, C., Li, T., Zhou, T., 2013. Precursor signals and processes associated with mjo initiation over the tropical Indian ocean. J. Clim. 26 (1), 291–307. https://doi.org/10.1175/JCLI-D-12-00113.1.

atmosphere

MDPI

Article

Parameter Modulation of Madden-Julian Oscillation Behaviors in BCC_CSM1.2: The Key Role of Moisture-Shallow Convection Feedback

Kai Huang [1,2,3], Hong-Li Ren [3,*], Xiangwen Liu [3], Pengfei Ren [3], Yuntao Wei [2,3,4] and Mu Mu [1,4,5]

1 State Key Laboratory of Numerical Modeling for Atmospheric Sciences and Geophysical Fluid Dynamics, Institute of Atmospheric Physics, Chinese Academy of Sciences, Beijing 100029, China; 121170022@smail.nju.edu.cn (K.H.); mumu@fudan.edu.cn (M.M.)
2 University of Chinese Academy of Sciences, Beijing 100049, China; weiyuntaowyt@163.com
3 Laboratory for Climate Studies & CMA-NJU Joint Laboratory for Climate Prediction Studies, National Climate Center, China Meteorological Administration, Beijing 100081, China; liuxiangwen_bcc@sina.com (X.L.); 18810704498@163.com (P.R.)
4 Key Laboratory of Ocean Circulation and Waves, Institute of Oceanology, Chinese Academy of Sciences, Qingdao 266071, China
5 Institute of Atmospheric Sciences & Department of Atmospheric and Oceanic Sciences, Fudan University, Shanghai 200438, China
* Correspondence: renhl@cma.gov.cn

Received: 17 March 2019; Accepted: 24 April 2019; Published: 1 May 2019



Abstract: To reveal key parameter-related physical mechanisms in simulating Madden-Julian Oscillation (MJO), seven physical parameters in the convection and cloud parameterization schemes of Beijing Climate Center Climate System Model (BCC_CSM1.2) are perturbed with Latin hypercube sampling method. A new strategy is proposed to select runs with good and poor MJO simulations among 85 generated ones. Outputs and parameter values from good and poor simulations are composited separately for comparison. Among the seven chosen parameters, a decreased value of precipitation efficiency for shallow convection, higher values of relative humidity threshold for low stable clouds and evaporation efficiency for deep convective precipitation are crucial to simulate a better MJO. Changes of the three parameters act together to suppress heavy precipitation and increase the frequency of light rainfall over the Indo-Pacific region, supplying more moisture in low and middle troposphere. As a result of a wetter lower troposphere ahead of the MJO main convection, the low-level moisture preconditioning along with the leading shallow convection tends to be enhanced, favorable for MJO's further development and eastward propagation. The MJO's further propagation across the Maritime Continent (MC) in good simulations is accompanied with more land precipitation dominated by shallow convection. Therefore, the above-mentioned three parameters are found to be crucial parameters out of the seven ones for MJO simulation, providing an inspiration for better MJO simulation and prediction with this model. This work is valuable as it highlights the key role of moisture-shallow convection feedback in the MJO dynamics.

Keywords: Madden-Julian Oscillation; moisture-convection feedback; parameter perturbation; eastward propagation; general circulation model

1. Introduction

The Madden-Julian Oscillation (MJO), named after its discoverers [1,2], is characterized by a large-scale convection ensemble initiated over India Ocean. Statistically, the MJO propagates eastward

slowly (~5 m/s) and dies after crossing the dateline, while the coupled planetary-scale baroclinic circulation still propagates throughout the whole tropical belt at a relatively faster speed [3–5]. As the dominant intraseasonal (30–90 days) signal in the tropical atmosphere [6], MJO affects the climate and weather systems over the globe such as the outbreak and withdraw of monsoon systems [3], the initiation of El Niño events [6], the genesis of tropical cyclones [7] and the evolution of extratropical circulation patterns through teleconnection [8,9].

There is a growing body of theoretical work trying to understand the essential physical mechanisms of the MJO [10]. Among the four basic theories, the first one, i.e., the convectively coupled Kelvin-Rossby wave theory was firstly proposed by Wang and Rui [11]. It emphasizes the importance of the interaction between convective heating, the low-frequency equatorial waves, and the boundary layer (BL) frictional moisture convergence. Therefore, only dynamical wave feedback is resolved in this theory [12]. The second basic theory, i.e., the moisture mode theory [13–15] regards the atmospheric humidity as the first order important variable under the weak temperature gradient approximation [10]. In this theory, the eastward propagating MJO is simulated by the so-called moisture-convection feedback [16] and moisture transport [17–20]. The third basic theory, i.e., the frictionally coupled dynamic moisture mode theory combines the above two theories by including a simplified Betts-Miller cumulus parameterization scheme, in which both the moisture-convection [21,22] and wave feedbacks [12] are resolved. The last basic theory, namely, the multiscale interaction theory includes many different schools of thinking about how mesoscale and synoptic-scale disturbances interact and contribute to the MJO dynamics. It includes the MJO skeleton model [23–28], the MJO-synoptic wave interaction model; [23,24,26,28], the multi-cloud model [29,30] and the gravity wave interference model [31–33]. Besides the aforementioned four groups of basic MJO theories, there are also two specific theories including the boreal summer intraseasonal oscillation (ISO) theory [34] and the atmosphere-ocean interaction theory [35–37].

Despite numerously conducted theoretical work trying to understand the MJO dynamics, most of the state-of-the-art climate models still suffer from different hierarchies of deficiencies of simulating realistic MJO structure and its eastward propagation [38–43]. Hung et al. [44], for example, demonstrated that only about one-third of the General Circulation Models (GCMs) from the Coupled Model Intercomparison Project phase 5 (CMIP 5) generate the spectrum peak of MJO precipitation between 30 and 70 days. Among them only one model produces the realistic eastward propagation. Jiang et al. [41] found that only one-fourth of the latest-generation GCMs could accurately simulate the systematic eastward propagation of MJO. These highlight the necessity to advance our understanding of the potential mechanisms in shaping the fundamental behaviors of the MJO, especially its smooth propagation from the Indian Ocean to the western Pacific seen in the observation statistics [2,45,46].

An important factor leading to the unrealistic MJO simulations in GCMs has been widely recognized as the uncertainty in cloud and convection parameterization schemes, which largely resolve atmospheric subgrid-scale moist and convective processes [43,47–49]. For example, by increasing the minimum value of cumulus entrainment rate of the environmental air in the Arakawa-Schubert (AS) cumulus convection parameterization scheme, the equatorial intraseasonal signals are better simulated by GCMs [50]. Wang and Schlesinger [51] demonstrated that the simulated Intraseasonal Tropical Oscillation (ITO) becomes stronger by increasing relative humidity criterion for convective heating (RH_c) in three different parameterization schemes using one GCM model. The effects of convective precipitation evaporation in unsaturated environmental air and unsaturated downdrafts are found to be essential for the amplitude of simulated MJO in GCM [52]. The role of stratiform precipitation portion in MJO simulation is investigated in Fu and Wang [53] and results show that increasing the portion of stratiform precipitation by changing the value of deep or shallow convection detrainment rate leads to a robust MJO in GCM. A robust relationship between environmental moisture and convection was also confirmed in observation [54] and models [55,56].

In this study, we seek to find out certain cloud and convection parameter perturbations leading to models' best and worst ability of simulating MJO so that the parameter-related physical processes crucial for MJO simulation could be found. Therefore, we perturb seven control parameters (such as

the moisture thresholds related to convection trigger, the low and high stable clouds, the efficiencies related to precipitation and evaporation in deep and shallow convections, and the adjustment timescale for shallow convections) in the cloud and convection parameterization schemes, using Beijing Climate Center Climate System Model (BCC_CSM1.2) with a revised Zhang and McFarlane's convection scheme (hereafter RZM) [49,57]. Therefore, a variety of model runs are generated after perturbing these parameters in order to identify parameter perturbations leading to runs with a high-skill MJO simulation (hereafter good simulations) and runs with a low-skill MJO simulation skill runs (hereafter poor simulations).

The parameter perturbation strategy and model used in this study is the same as that in Liu et al. [57], but for different purposes. Liu et al. [57] focused on the optimization of MJO simulation and prediction skills, while this study emphasizes the crucial physical mechanisms for better MJO simulation, which are modulated by values of cloud and convection parameters in this model. Besides, to objectively select the good and poor integrations, a new evaluation strategy for the MJO simulation skill is proposed in this study. Unlike Liu et al. (2018) who only select one high-skill run and one low-skill run, this study would objectively identify those good and poor simulations with the new evaluation strategy, and a composite analysis is then performed for the two groups of simulations. In this way, a robust result may be shed light on, and more importantly, the parameter-related mechanisms that are vital important to the better MJO simulations will be revealed in a robust way.

This paper is arranged as follows. Section 2 describes the data and methodology. The composite good and poor simulations of the MJO are presented in Section 3. The diagnostics of mean states are given in Section 4. Section 5 analyzes the MJO-scale cloud and moist processes, in which the key role of moisture and shallow convection feedbacks are identified and studied. Finally, the summary and discussion are given in Section 6.

2. Data and Methodology

2.1. Data

BCC_CSM1.2 model [58] is used in this study. BCC_CSM1.2 model is a climate system model including 4 components. The atmospheric component of BCC_CSM1.2 is Beijing Climate Center Atmospheric General Circulation Model (BCC_AGCM3.0), which adopts a spectral truncation of 106 waves (T106) in the horizontal and 40 layers (L40) in the vertical from surface to 0.31 hPa. Beijing Climate Center Atmosphere-Vegetation Interaction Model (BCC_AVIM2.0) [59] is used as BCC_CSM1.2's land surface component with the same horizontal resolution as BCC_AGCM3.0. The global ocean general circulation model in BCC_CSM1.2 called MOM4_L40v2 is modified from the Modular Ocean Model (MOM4) to include the ocean carbon cycle [59] with a horizontal resolution of 1/3 degrees (~30 km) and 40 vertical layers. BCC_CSM1.2 also includes the Sea Ice Simulator (SIS) [60] as its sea ice model.

The RZM scheme invoked in our work is a revised version of the original scheme of Zhang and McFarlane [48]. It is different from the original scheme in (a) the closure condition, where the original scheme only assumes that convection acts to remove the atmospheric convective available potential energy with a relaxation of 2 h while the RZM assumes that a quasi-equilibrium exists between convection and the large-scale environment in the free troposphere above the boundary layer, (b) the inclusion of a relative humidity threshold for convection triggering, which acts to suppress spurious convection when the boundary layer is dry, and (c) the allowance for the bottom of the unstable lifted layer's occurrence above the boundary layer. Details about the revision could be found in Zhang and Mu [49] and Wu et al. [61].

A series of experiments were run by perturbing the values of (1) adjustment time scale for shallow convection (τ_*shal*), (2) precipitation efficiency for shallow convection (C_0_*shal*), (3) relative humidity threshold for low stable clouds (*RH_low*), (4) relative humidity threshold for high stable clouds (*RH_high*), (5) relative humidity threshold for convection trigger (*RH_trig*), (6) precipitation efficiency for deep convection (C_0_*deep*) and (7) evaporation efficiency for deep convective precipitation

(K_e_*deep*) [57]. These parameters are perturbed with Latin Hypercube sampling (LHS) method [62] to sample points within the seven-dimensional parameter space. The Latin hypercube procedure selects pseudo-random points from the full seven-dimensional parameter space, ensuring uniform coverage across the space. Details of the experimental design could be found in Section 2.2.1 of Liu et al. [57].

Adopted from Liu et al. [57], Table 1 shows the default, maximum and minimum values of seven chosen parameters. In total, 85 perturbed points or 85 sets of different parameter values are sampled for seven parameters. The model is integrated with each set of parameters for seven years, generating 85 sets of daily outputs on grids with a horizontal resolution of 1.125° × 1.125° at 40 vertical layers. Considering that these integrations may take a few years to reach an equilibrated state after changing values of these seven parameters, we examined the time series of tropical (30° S–30° N) Surface Temperature and column-integrated (850–500 hPa) specific humidity in the 85 integrations (not shown here). Results show that most of the integrations reach an equilibrated state after 1.5–2 years of adjustment. Therefore, the last five years of each set of outputs are used for analysis.

Table 1. Description, default values and perturbed ranges of seven parameters in the model, adopted from Liu et al. [57].

Parameter	Description (units)	Default Value	Minimum	Maximum
τ_*shal*	Adjustment time scale for shallow convection (s)	1.8×10^3	0.9×10^3	9.0×10^3
C_0_*shal*	Precipitation efficiency for shallow convection (m^{-1})	0.8×10^{-4}	0.5×10^{-4}	3.0×10^{-4}
RH_low	Relative humidity threshold for low stable clouds (fraction)	0.87	0.80	0.99
RH_high	Relative humidity threshold for high stable clouds (fraction)	0.65	0.65	0.85
RH_trig	Relative humidity threshold for convection trigger (fraction)	0.60	0.60	0.85
C_0_*deep*	Precipitation efficiency for deep convection (m^{-1})	2.0×10^{-3}	1.0×10^{-3}	6.0×10^{-3}
K_e_*deep*	Evaporation efficiency for deep convective precipitation $\left(\left(\text{kg m}^{-2}\text{ s}^{-1}\right)^{-1/2}\text{ s}^{-1}\right)$	1.0×10^{-6}	0.5×10^{-6}	10.0×10^{-6}

The observational data used in this study consists of the daily outgoing longwave radiation (OLR) data from the National Oceanic and Atmospheric Administration (NOAA) polar-orbiting series of satellites [63], TRMM based precipitation observations (version 3B42 v7) [64] and the European Center for Medium-Range Weather Forecasting (ECMWF) ERA-Interim reanalysis [65] for the period of 2000–2009. All datasets and model outputs are interpolated into a 2.5° × 2.5° longitude-latitude grid and 19 vertical layers as ERA-Interim reanalysis data.

2.2. Methodology

2.2.1. Evaluation of MJO Simulation with Three Canonical Methods

Many metrics regarding MJO variability and its internal physics have been given in previous studies [41,42,44,45,55,66–69]. Jiang et al. [41] proposed two metrics to evaluate the models' ability of simulating realistic MJO. The first approach (Lag-correlation hereafter) is defined as the average value of two pattern correlation coefficients (PCCs) in each model. The equatorial (10° S–10° N) 20–100–day filtered precipitation in GCM outputs and observation are lag regressed from day -20 to 20, against the area-averaged time series of itself over India Ocean (75–85° E; 5° S–5° N) and Pacific Ocean (130–150° E; 5° S–5° N), respectively. Two regional Hovmöller plots (day −20 to 20, (60° E–180°)) are given in each

GCM and observation by averaging the regressed precipitation in meridional direction. Two PCCs are computed by regional Hovmöller plots in GCM and observation. The averaged value of these two PCCs is thus defined as the MJO simulation skill score by Lag-correlation. The other approach is based on the regional (60° E–180°) space-time power spectral analysis of precipitation or other convection related variables over an equatorial belt [70], and it is defined as the ratio of the spectral power for the eastward to westward propagation component (E/W ratio hereafter) on MJO time and space scales (period of 30–90 days, zonal wavenumber of 1–3). Another approach called "MJO tracking method" is also used to examine the MJO simulation qualities in different models in previous study [42]. It is based on the Hovmöller diagrams of filtered equatorial precipitation. A set of criteria is used to track the MJO events in model outputs. Each event's amplitude, propagation range and life span are also given by this method. Details about the MJO tracking method could be found in Zhang and Ling [71].

Three aforementioned approaches (Lag-correlation, E/W ratio and MJO tracking method) are used to examine the MJO simulation skills in 85 integrations. It is worth noting that the Lag-correlation and E/W ratio scores are computed based on the OLR data, considering that OLR is a good representation of organized convection systems and has a normal distribution. However, the MJO tracking method is still based on equatorial precipitation data because this method includes some criteria especially designed by using precipitation data like the reference longitude and the criteria used to determine the initiating and ending date of each MJO event [71]. Using OLR in MJO tracking method without changing these criteria leads to its failure to track MJO events. Therefore, we still use precipitation data in the MJO tracking method for convenience. Figure 1 shows the scores of 85 integrations given by Lag-correlation. Runs of the top 10 and bottom 10 scores are labeled in red and blue, respectively. The top (bottom) 10 is then identified as stronger (weaker) MJO runs. Compared with the result in Jiang et al. [41], the diversity of scores in our study is clearly smaller with most of them lying between 0.7 and 0.85. The E/W ratio scores computed with OLR are given along with the Lag-correlation scores in Figure 2a. Integrations identified as strong (weak) MJO simulations are scattered in red (blue). The E/W ratio scores in all 85 runs are above 1.0, indicating that the eastward propagating components of large-scale intraseasonal signals in 85 integrations are stronger than that of the westward propagation component. However, the correlation coefficient between Lag-correlation scores and E/W ratio scores is only 0.23, and the stronger MJO integrations identified by Lag-correlation scores lie in almost the same zone in E/W ratio as weaker MJO integrations. The linear fit between two scores also shows that two scores no longer corroborate each other in MJO simulation skill measurement. Considering that the Lag-correlation scores are computed with OLR data filtered only in time dimension while OLR data is filtered both in time and zonal dimension before computing E/W ratio scores, the E/W ratio in the same times scale of 30–90 days but at different wavenumbers of 1–15, and 4–15 are computed, as shown in Figure 2b,c, along with Lag-correlation scores. The regression lines in Figure 2b,c are much steeper compared with that in Figure 2a, but it is probably due to the narrower spread of E/W ratio values in the x axis. The correlation coefficient between these two scores slightly increases when including intraseasonal signals of all zonal wavenumbers. The correlation coefficient decreases to 0.13 if only a wavenumber of 4–15 spectral power is included to compute the E/W ratio.

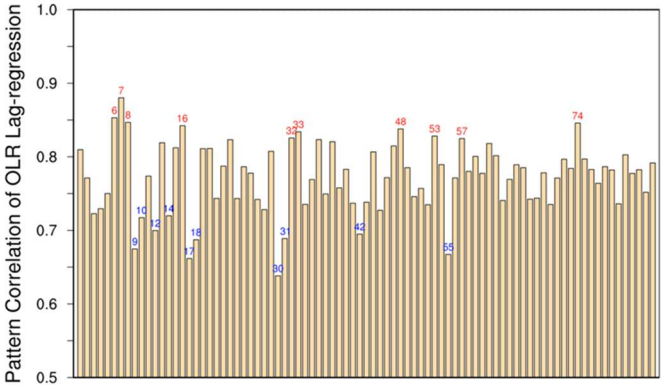

Figure 1. Scores of 85 integrations by Lag-correlation defined as the average values of two pattern correlation correlations (PCCs) in each run. The PCCs of each run are computed between the Hovmöller diagrams in it and observation, which are given by averaging equatorial (10° S–10° N; 60° E–180°) lag regressed 20-100 day filtered outgoing longwave radiation (OLR) from day −20 to 20 against the area-averaged time series of itself over India (5° S–5° N; 75° E–85° E) and Pacific (5° S–5° N; 130° E–150° E). The highest (lowest) 10 runs are labeled with their experiment identification number in red (blue).

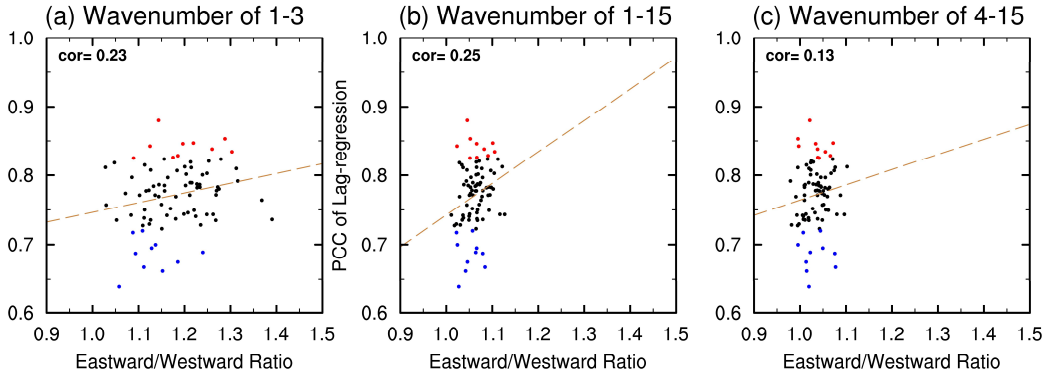

Figure 2. Scatter plot of scores by Lag-correlation (y axis) against scores by E/W ratio (x axis) of zonal wavenumber (**a**) 1–3, (**b**) 1–15, and (**c**) 4–15. The scores by Lag-correlation are the same as those in Figure 1. Scores by E/W ratio are defined as the values of dividing the spectra power in the eastward-propagating component by that in the westward-propagating component on MJO time and space scales (period of 30–90 days, zonal wavenumber of 1–3) in each run. The power spectral analysis is conducted with regional OLR (5° S–5° N; 60° E–180°) and then averaged meridionally. The 10 integrations identified by Lag-correlation as with stronger (weaker) MJO are scattered in red (blue) while the others in black. The dot line donates the linear fit by least squares means. The correlation coefficients are also displayed.

The same diagrams are done to investigate the correlation between scores given by quantities of MJO events, Lag-correlation and E/W ratio. Ling et al. [42] proposed a hypothesis after evaluating 27 GCMs that the model's ability of simulating MJO is highly related to the quantity of MJO events in model integration. The more frequent model produces MJO events, the higher MJO simulation skill the model has. Therefore, MJO tracking method is applied to get the quantity of MJO events in 85 integrations. Figure 3 presents the same scatter plots as Figure 2 but with X axis referring to the quantity of tracked MJO events in 85 integrations and Y axis referring to E/W ratio scores in Figure 3a–c, and Lag-correlation scores in Figure 3d. Among 4 correlation coefficients in scatter plots of Figure 3, the correlation coefficient between quantities of MJO events and E/W ratio is the highest, but only reaching 0.26. The low correlation coefficients in Figure 3 indicate that scores given by quantity of MJO events do not corroborate with those given by Lag-correlation, nor E/W ratio.

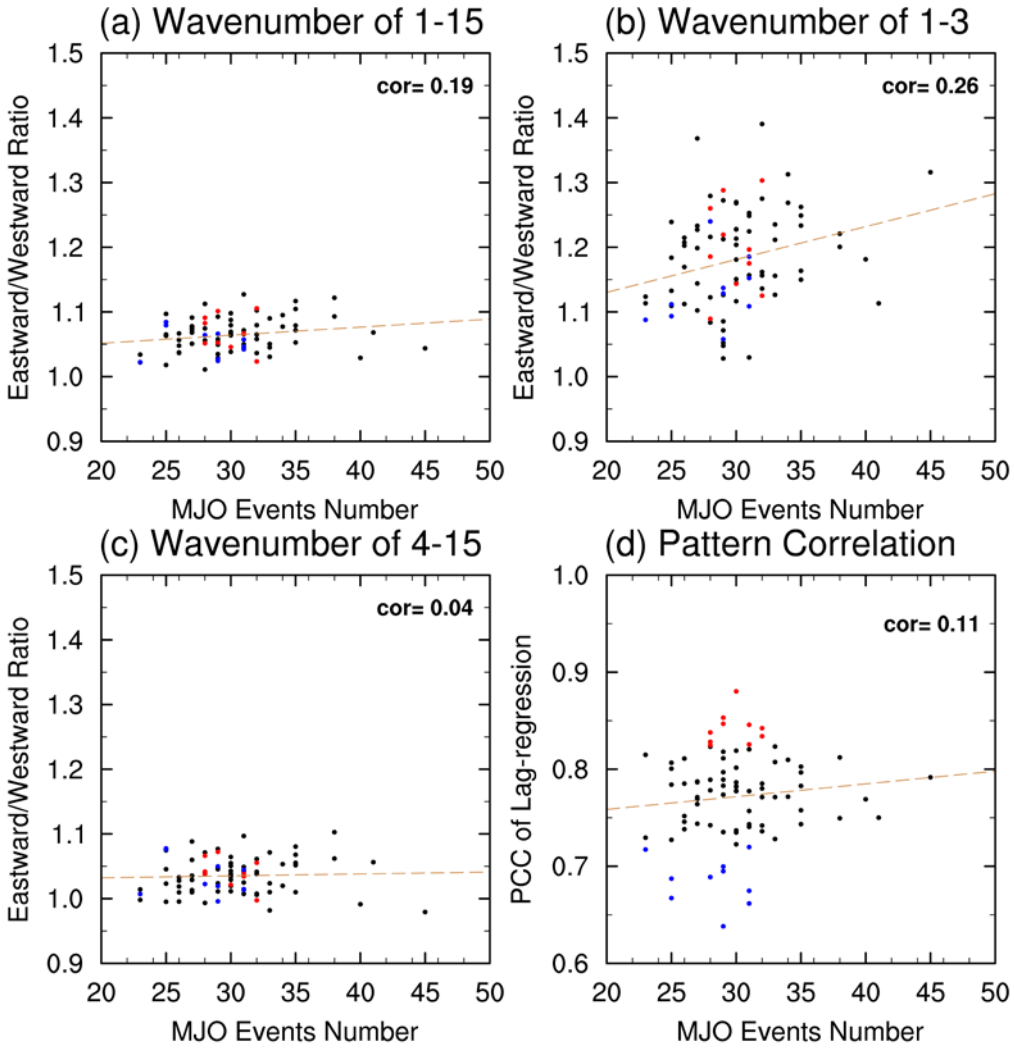

Figure 3. Same as in Figure 2 but with x axis denotes the quantity of MJO events in model integration given by MJO tracking method. y axis donates to scores by E/W ratio of wave number (**a**) 1–15, (**b**) 1–3, (**c**) 4–15 and scores by Lag-correlation in (**d**).

2.2.2. A New Strategy to Evaluate the MJO Simulation Skill

A new evaluation strategy is therefore proposed to identify integrations with good and poor MJO simulations. The contradiction in scores using the above three different canonical approaches individually makes it difficult to find out one certain integration with the highest MJO modulation skills in all respects. However, the two approaches (Lag-regression and E/W ratio) in Jiang et al. [41] are still widely used to evaluate model's MJO simulation skills. The Lag-correlation examines the propagation quality of intraseasonal signals while E/W ratio investigates whether the eastward propagation is dominant in MJO time and space scales. Therefore, a combination of Lag-regression and E/W ratio scores is used to identify good simulations and poor simulations. The new evaluation strategy consists of three steps: (i) rank 85 integrations twice, in order of Lag-correlation and E/W ratio scores respectively from high to low, (ii) divide two ranks respectively into three tiers (the top, middle and bottom tiers). Two rank's top and bottom tier sizes (hereafter tier-size) are same. (iii) identify good and poor simulations. If one integration lies in top (bottom) tier of both two ranks, this integration is thought to be good (poor) simulation.

Attempts are made to choose the appropriate tier-size during dividing two ranks into three tiers in step ii. Three rules need to be considered while choosing: (i) the quantities of selected good and poor simulations should be sufficient to do the composite analysis, (ii) the difference between the

case numbers of selected good and poor simulations is small enough to fairly compare the composite results, and (iii) the mean scores in good and poor simulations show distinct differences. Figure 4 shows the quantities of selected good and poor simulations and the difference between mean scores of these two groups according to different tier-sizes. Based on the second rule, tier-size of 10, 20 and 33 are worth considering. However, the quantities of selected good and poor simulations are too small to do the composite analysis when tier-size is under 16 and the difference between mean scores decreases rapidly when tier-size is greater than 20. Therefore, we choose 20 as the appropriate tier-size by which six good simulations (integration 1, 6, 23, 33, 38 and 48) and eight poor simulations (integration 10, 14, 18, 30, 43, 45, 55 and 70) are identified for the following analysis. Distributions of MJO scores are analyzed to investigate the validity of this new strategy. Figure 5 presents the distribution of good and poor simulations selected by this new strategy in scores of Lag-correlation and E/W ratio among 85 integrations. Uniform higher scores could be seen in good simulations compared with poor ones, especially of E/W ratio scores, indicating that such new evaluation strategy is effective in selecting high-skill and low-skill MJO simulations.

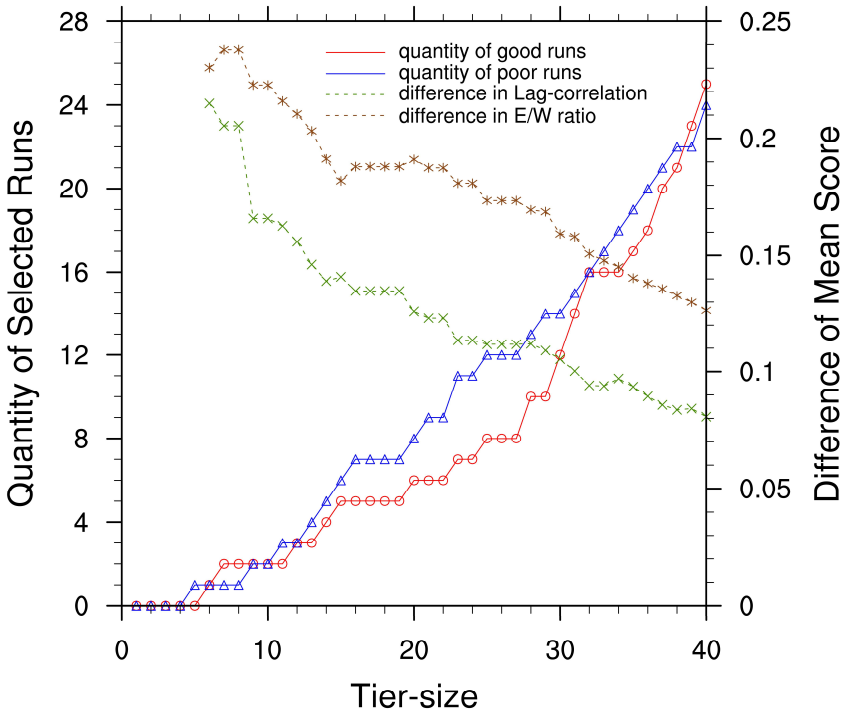

Figure 4. Quantities of selected good and poor simulations (left y-axis) and differences between mean scores of selected good and poor simulations (right y-axis) according to different values of tier-size.

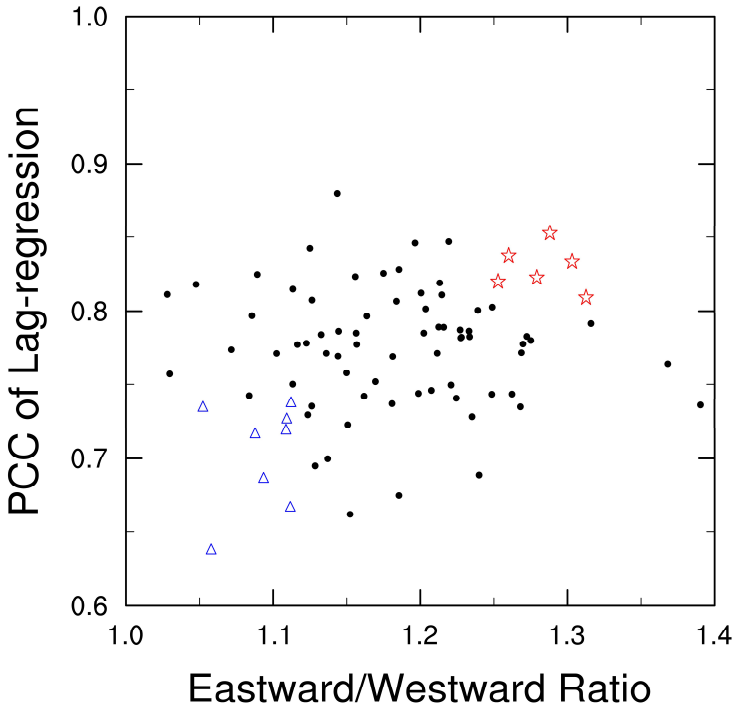

Figure 5. Scatter plots of scores by Lag-correlation (y axis) against scores by E/W ratio (x axis) with good (poor) simulations selected by the new evaluation strategy scattered in red stars (blue triangles) while the rest of 85 runs scattered in black dots.

2.2.3. Compositing Technique and Significance Test

Before the composite analysis, a linear regression technique was conducted for each group of simulation. The referenced time series is calculated as the 20–100-day, bandpass-filtered OLR anomaly averaged over the Indian Ocean (5° S–5° N; 75°–85° E) and Pacific Ocean (5° S–5° N; 130°–150° E). Then, the MJO-scale perturbations are obtained by regressing any atmospheric or oceanic parameters against this referenced time series. The composite results of the six good simulations and eight poor simulations are calculated using their associated regression patterns, respectively, in which the lags from −20 to 20 days is used to thoroughly observe the entire life cycle of the MJO. The significance test of the composite results at the 90% confidence level is based on the Student's t statistic that obeys a distribution with a degree of freedom (DOF) of N. The DOF N is 6(8) for the good (poor) simulations.

3. Composites of Good and Poor Simulations

3.1. Parameter Values

Average values of seven chosen parameters in good and poor simulations are given in Figure 6. Seven chosen parameters differ largely in their magnitudes as Table 1 shows. In order to visualize each parameter's perturbation in good and poor simulations and to compare their differences, the values of these parameters are converted to their percentiles in each parameter's changing range (maximum-minimum as in Table 1). Three parameters such as precipitation efficiency for shallow convection (C_0_*shal*), relative humidity threshold for low stable clouds (*RH_low*) and evaporation efficiency for deep convective precipitation (K_e_*deep*) exhibit significant differences between good and poor simulations. In good simulations, values of RH_low and K_e_*deep* are about twice of those in poor simulations while the value of C_0_*shal* is only about the one third of it in poor simulations.

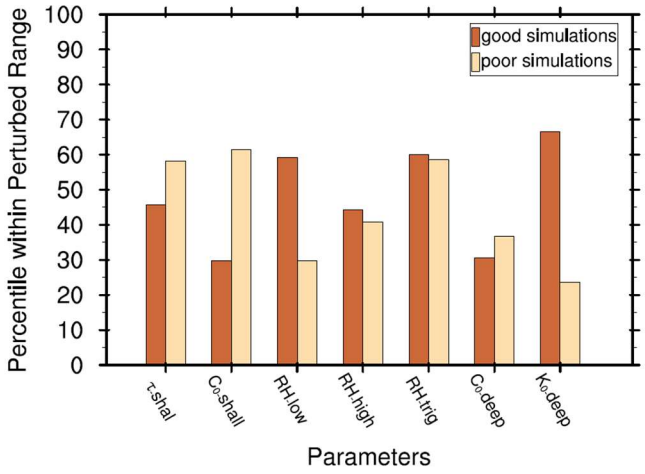

Figure 6. Average values of 7 chosen parameters in good and poor simulations in form of each parameter value's percentile within its perturbing range (maximum-minimum) as in Table 1.

Individual changes in values of the above three parameters lead to changes in cloud and convection. Increasing RH threshold for low stable clouds value leads to a reduction of low-level clouds, and this reduction results in an additional moisture accumulation beneath low stable clouds. The decrease in value of precipitation efficiency for shallow convection makes it harder for water in shallow convective clouds to convert to rain droplets. Therefore, this would decrease the shallow convective precipitation and thus humidifying the low troposphere. The sharp increase in the value of evaporation efficiency for deep convective precipitation causes a higher ratio of deep convective rain droplets evaporating while falling down. So, the deep convective precipitation declines largely due to this change. Interestingly, research shows that this change not only influences the deep convection, but also is favorable for low cloud formulation and development of shallow convection [72]. In general, the sharp contrasts between good and poor simulations in terms of these three parameter values have implied the crucial role of the lower-tropospheric moistening in supporting the better MJO simulation (e.g., Yoneyama et al. [73]; Wei et al. [74]).

3.2. Zonal Wavenumber-Frequency Spectrum

To check the characteristics of MJO along with other Convection Coupled Equatorial Waves (CCEWs), Figure 7 shows the signal-to-noise ratio of OLR anomalies computed using the space-time spectral analysis method [70]. In observation, three main CCEWs are clearly shown in Figure 7a. Westward-propagating Equatorial Rossby (ER) waves are dominant in low-frequency period of wavenumbers 3–5 while eastward-propagating Kelvin waves and MJO are also identified. The spectral band of MJO signals lies within zonal wavenumbers of 1–3 and timescales of 30–90 days, with a single peak at wavenumber of 1 and frequency of 0.15 cycles per day (period of 40 days). The timescales of Kelvin waves in observation vary between three days and 15 days with greater zonal wavenumbers of 2–8. The gap between Kelvin waves and MJO in the power spectral is distinct in observation. Figure 7b presents the composite result of spectral analysis in poor simulations. Compared with observation, the ER waves in poor simulations exhibit a new independent power center at wavenumber 6. MJO-related signals greatly shrink and are divided into two individual peaks (at wavenumber 1 and 4) with a much weaker amplitude. Kelvin waves are not well simulated in poor simulations. Kelvin waves vanish in shorter timescales and larger zonal wavenumbers. The residual part of Kelvin wave is connected with weak MJO, filling the gap between them in observation. Composite result of good simulations shows improvement in simulation of CCEWs. MJO-related signals are amplified with a center at zonal wavenumber 1 compared with poor simulations. Kelvin waves are also improved by enhancing the spectral power of its fast components with larger zonal wavenumbers. The improvement of Kelvin waves accompanied with better MJO in models is also proposed in the previous

study [75,76]. ER waves are also improved by eliminating the positive bias in zonal wavenumber 6 of westward-propagating component.

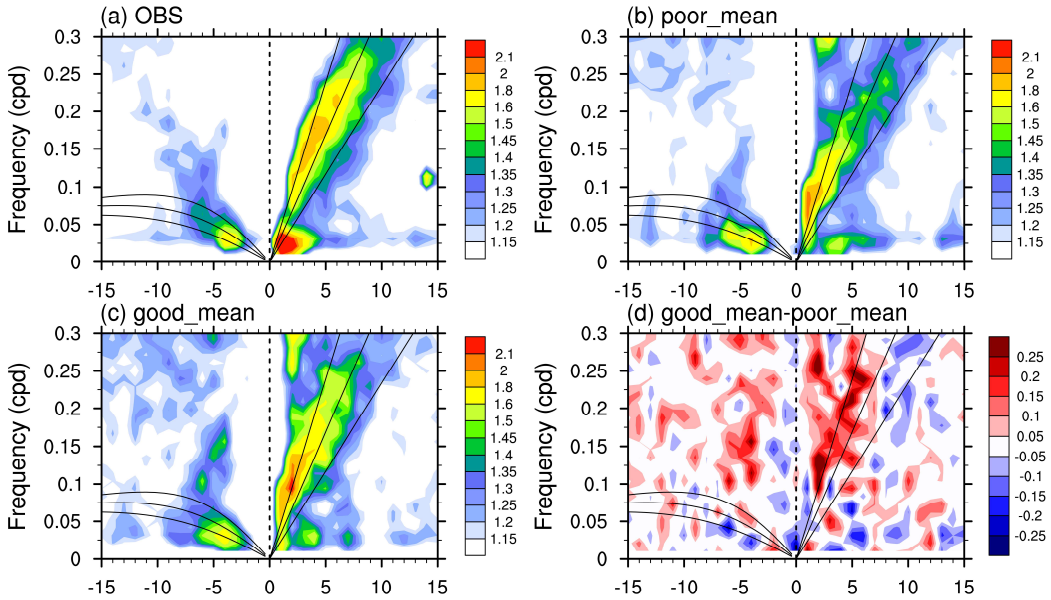

Figure 7. Boreal-winter (November–April) Signal-to-noise ratio in the wavenumber–frequency spectral domain of the 15° S–15° N symmetric components of OLR anomalies in (**a**) observation, (**b**) composite of poor simulations, (**c**) composite of good simulations and (**d**) difference between composited results of good and poor simulations.

3.3. Hovmöller diagrams

In order to investigate the propagation of intraseasonal convection systems, the boreal winter Hovmöller diagrams in observation, good and poor simulations are given in Figure 8. The equatorial (10° S–10° N), 20–100-day band-pass-filtered OLR in boreal winter is lag-regressed form day −20 to 20, against the time series of itself averaged over equatorial India Ocean (75°–85° E; 5° S–5° N) and west Pacific (130°–150° E; 5° S–5° N), respectively. The three-dimensional coefficient is then averaged in meridional direction to obtain the Hovmöller plots. In observation as Figure 8a,b show, the convection systems are initiated over Indian Ocean. Well-organized eastward propagation is produced over both India and Pacific Ocean at a speed of about 5 m/s. The barrier effect of Maritime Continent on MJO's propagation is also indicated in Figure 8b with the propagation slowed down while crossing. In poor simulations given by Figure 8c,d, the regressed coefficient exhibits a strong westward-propagating feature over India Ocean. The propagation over Pacific is relatively better with a weaker westward-propagating component, but the MJO convection dies quickly before reaching the dateline. Also, discontinuous signals are generated after day 0 over west Pacific to motivate the eastward propagation faster than observation. While in good simulations as Figure 8e,f show, the propagation of intraseasonal convection systems is improved both over India and Pacific Ocean. The westward propagations over India Ocean in poor simulations are eliminated. A new eastward-propagating convection signal occurs over Maritime Continent a few days after day 0, indicating that the intraseasonal convection initiated over India Ocean propagates further across MC in good simulations. These improvements have reached 90% confidence level. The improvement of MJO convections over Pacific Ocean is relatively weaker with a continuous signal developed at lag day −10 propagating eastward at almost the same speed in observation. The propagation range over Pacific Ocean in good simulations also gets improved with convections triggered at or even east of dateline, similar with the observational situation.

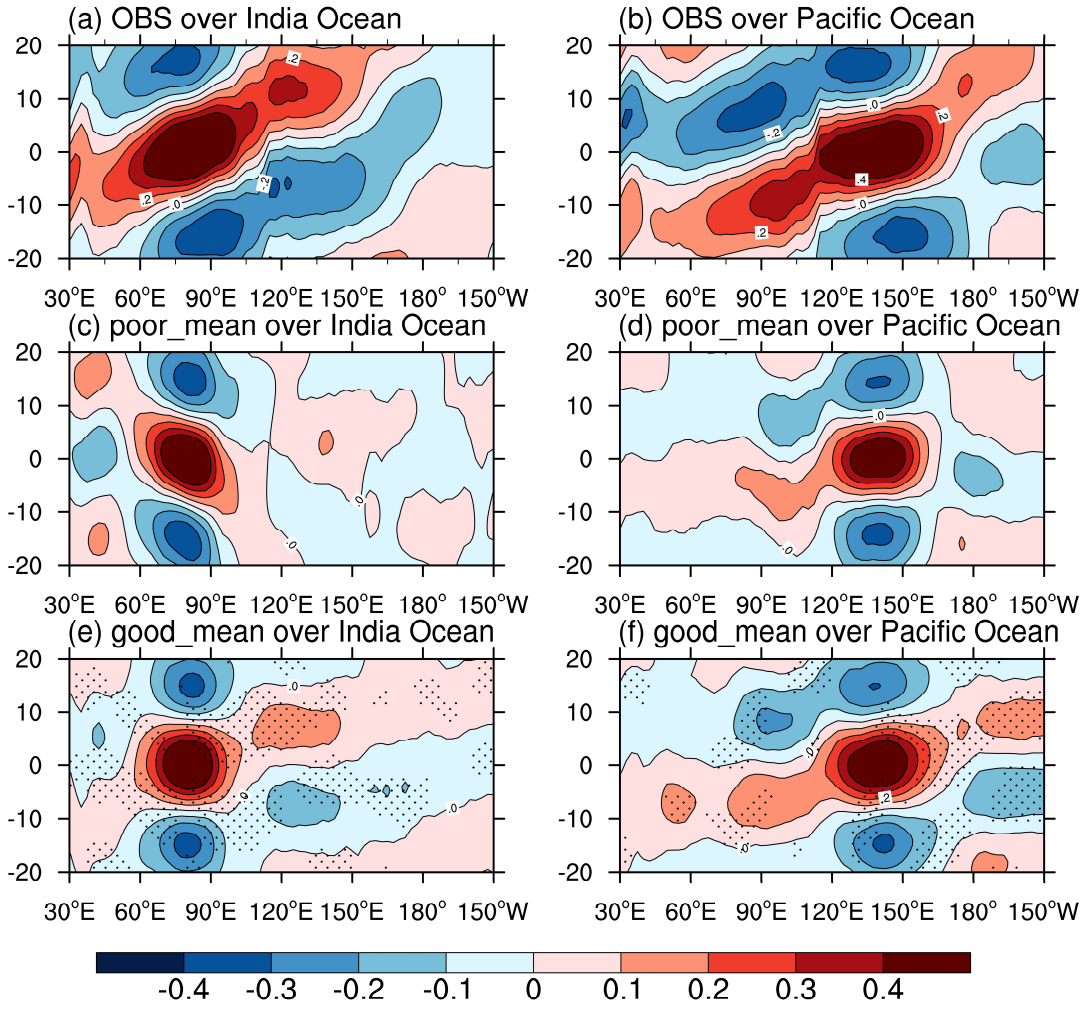

Figure 8. Boreal winter (November–April) Lag-longitude cross section of the correlation coefficient of 20–100 day filtered OLR anomalies against the area-averaged time series of itself in observation (**a** and **b**), poor simulations (**c** and **d**) and good simulations (**e** and **f**) at the reference area of equatorial India Ocean (5° S–5° N; 75°–85° E) (left column) and Pacific Ocean (5° S–5° N; 130°–150° E) right column). The regressed coefficient is averaged over 10° S–10° N. (**d**) and (**e**) are dotted where the difference between composite of good and poor simulations reach 90% confidence level.

4. Diagnostics of Climatology

4.1. Mean State

Previous studies of the MJO concluded that a reasonable mean state is necessary to simulate realistic MJOs [41,77]. Figure 9a–d show the winter-mean precipitation in the composite of poor simulations, the composite of good simulations, observation and the difference between good and poor composites, respectively. As shown in Figure 9a, poor simulations suffer from the problem of double inter-tropical convergence zone (ITCZ). Insufficient precipitation occurs over the Maritime Continent and the east boundary of the Bay of Bengal. Excessive precipitation is dominant in the South Pacific Convergence Zone (SPCZ) and southwest India Ocean. After changing the values of seven parameters, the composite pattern of climatological-mean precipitation in good simulations does not change much in the overall distribution. However, the composite of good simulations is improved by amplifying rainfall in Maritime Continent, mainly over land. The positive biases over SPCZ and south India Ocean are also amplified. In order to better examine the boreal winter mean state, the winter-mean Sea Surface Temperature (SST), u850 and integrated low-level (850–500 hPa) specific humidity in poor simulations,

good simulations, observation and the differences between good and poor simulations are given in Figure 10. Both the tropical SST and integrated specific humidity experience an overall increase in good simulations compared with poor simulations, which is consistent with the finding in previous researches that there will be more MJO events with a greater amplitude and farther propagation in a warmer and wetter world [78,79]. It is worth noting that the rise of low-level integrated specific humidity increases the meridional gradient of mean humidity. It has been proposed in Gonzalez and Jiang [80] that a steeper meridional mean humidity gradient is favorable for MJO propagation. The difference of u850 between good and poor simulations shows that the equatorial westerly over India and west Pacific gets amplified. However, the easterly south of MC is also strengthened.

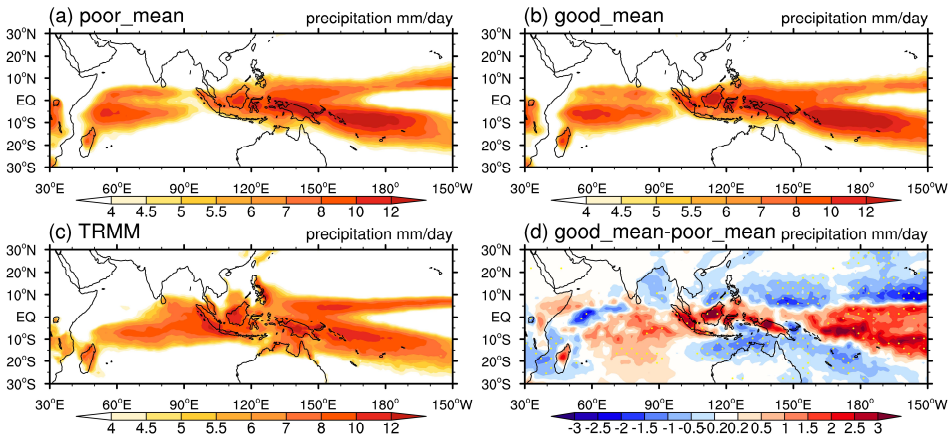

Figure 9. Winter-mean precipitation in (**a**) composite of poor simulations, (**b**) composite of good simulations, (**c**) observation and (**d**) the difference between composites of good and poor simulations with that reaching 90% confidence level dotted.

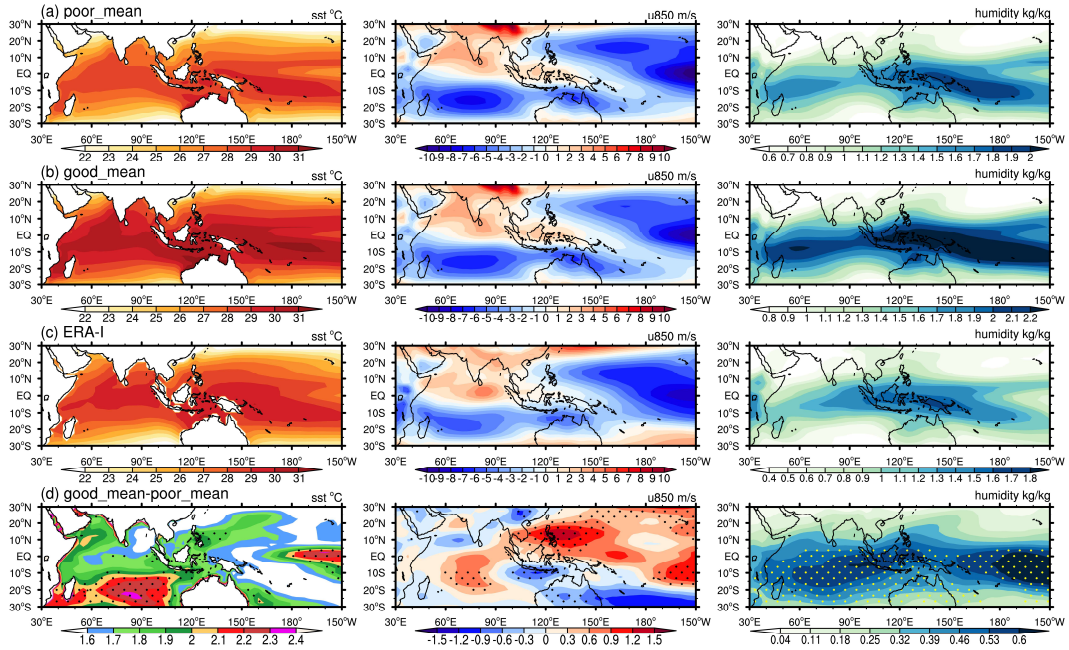

Figure 10. Boreal winter (November–April) mean state of Sea Surface Temperature (SST, left column), 850 hPa zonal wind (u850, middle column) and integrated low-level (850–500 hPa) specific humidity in (**a**) composite of poor simulations, (**b**) composite of good simulations, (**c**) observations and (**d**) the differences between composites of good and poor composites. The differences reaching 90% confidence level are dotted in (**d**).

The occurrence frequency of background precipitation is also examined because researches find out that contemporary climate models used in Phase 3 and Phase 5 of the Coupled Intercomparison Project have biases in the frequency distribution of tropical rainfall inhibiting complete formation of the tropical convective cloudiness [55,81]. The distribution of rainfall over the equatorial Indo-Pacific region (10° S–10° N; 50° E–180°) as a function of accumulated percentiles (divided by the lower 80th and upper 20th percentiles) is given in Figure 11. Light rainfall is defined with amplitude of 0.1–10 mm day^{-1}. With no precipitation accounts for almost 0% in composite results of both good and poor simulations, the percentile of light rainfall accounts for 80% in poor simulations, the same as observation although the frequency distribution varies. Composite result of the poor simulations shows large bias in the accumulated percentile distribution of rainfall less than 5 mm day^{-1} and more than 20 mm day^{-1}, which indicates an insufficient generation of extremely light precipitation (less than 5 mm day^{-1}) and excessive generation of intense precipitation in poor simulations. This bias is largely corrected in good simulations with both ends of the distribution curve closer to observation, especially for intense precipitation. Therefore, the frequency distribution of precipitation over the equatorial Indo-Pacific region is much improved by changing the values of seven parameters.

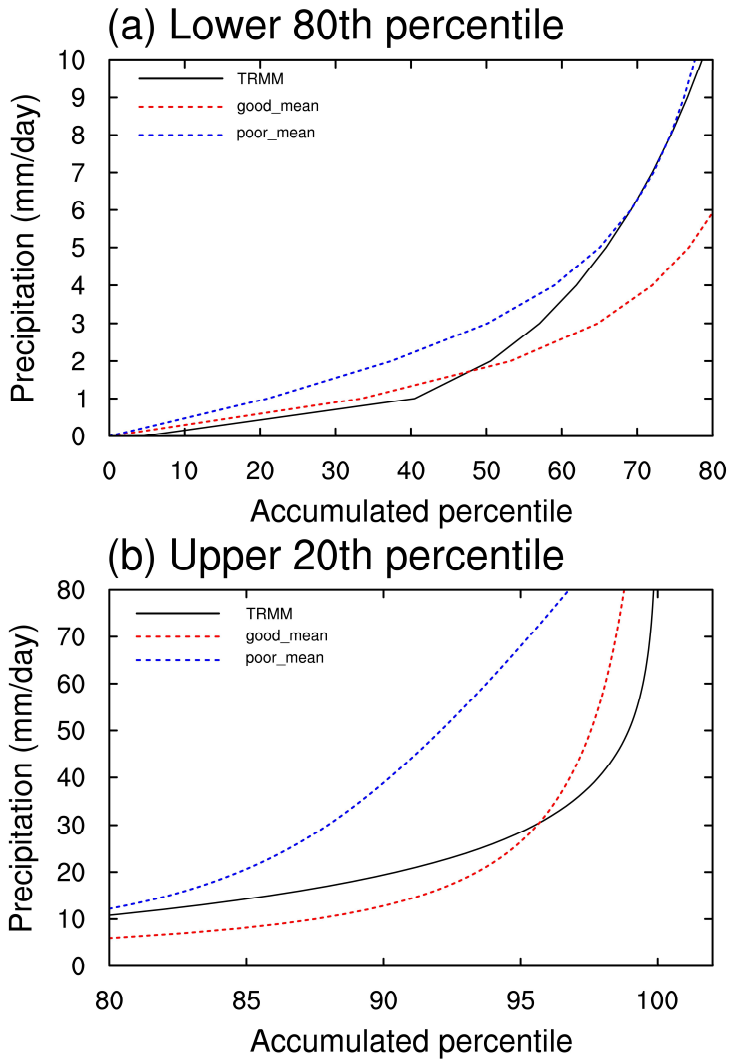

Figure 11. Histogram of precipitation (mm day^{-1}) in equatorial Indo-Pacific region (10° S–10° N; 50° E–180°) as a function of accumulated percentiles. (**a**) Lower 80th percentile and (**b**) upper 20th percentile are plotted.

4.2. Environmental Moisture Sensitivity of Convection

To examine the relationship between moisture and convection closely, composite vertical profiles of the Relative Humidity (RH) as a function of daily averaged precipitation over the Indo-Pacific region are given in Figure 12. In the observation (Figure 12a), the lower troposphere becomes more humid as the precipitation rate increases. The entire column is almost saturated when the precipitation rate is greater than 10 mm day^{-1}, which means that the heavier precipitation is suppressed until the atmosphere is almost saturated with relative humidity higher than 70%. It is similar to previous findings that more convection occurs in a more humid atmosphere [54,55]. Composite result of poor simulations in Figure 12b shows a dryer environmental atmosphere for light rainfall. Precipitation greater than 30 mm day^{-1} in poor simulations occurs with a more humid environment at levels around 350 hPa while the lower and upper troposphere are still dryer than observation. The dry bias indicates that the excessive intense precipitation as in Figure 11b consumes too much moisture in the environmental atmosphere. Therefore, most convections in poor simulations develop in a dryer atmosphere. The difference between composite results of good and poor simulations are presented in Figure 12d. The entire lower atmosphere (840–500 hPa) witnesses a moistening with a center at 600 hPa of all precipitation intensities while the humidifying center lies within light precipitation rates (0.1–10 mm day^{-1}). This is consistent with changes in rain rate frequency over the same region in Figure 10, where more frequent extremely light rainfall and less heavy precipitation could be seen in good simulations.

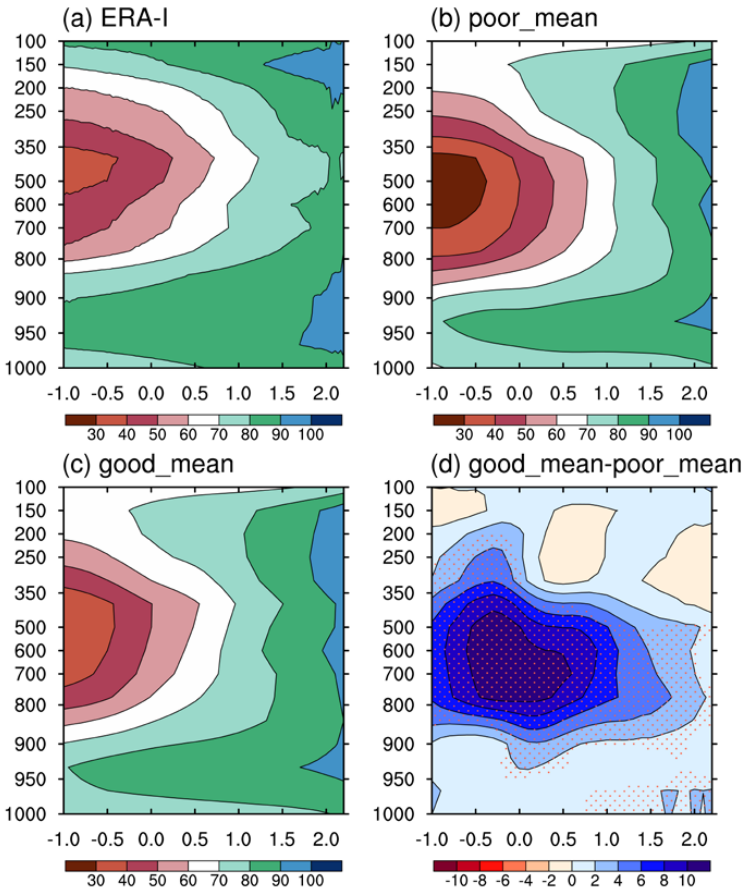

Figure 12. Composite vertical profiles of relative humidity as a function of precipitation rate over equatorial Indo-Pacific region (10° S–10° N; 50°–180° E) in (**a**) observation, (**b**) composite of poor simulations, (**c**) composite of good simulations and (**d**) the difference between composites of good and poor simulations. The differences reaching 90% confidence level are dotted. Noted that the precipitation rate on x axis is plotted on a log_{10} scale.

Difference in the moisture-convection relationship between good and poor simulations is probably due to large changes in values of three important parameters. Increasing the evaporation of deep convective precipitation is favorable for the development of shallow convection [72]. While increasing the value of RH threshold for low level stable cloud and decreasing the value of shallow convective precipitation efficiency both tend to reduce shallow convection, this reduction is compensated with the effect of humidifying low troposphere by intensifying deep convective rainfall evaporation. More shallow convection in good simulations in Figure 11 transports moisture in the low troposphere to middle level, humidifying middle troposphere and drying low troposphere. However, rigorous conversion from cloud water to shallow convective precipitation and less low cloud both lower the efficiency of low-level moisture consumption due to shallow convective precipitation, thus accumulating more moisture in low troposphere. Superimposition of all above influences results in an overall humidifying centering at middle troposphere of light precipitation.

5. Role of Moisture-Shallow Convection Feedback

5.1. Pre-Moistening Effect over the Lower-Layer Atmosphere

Profile of boreal winter regressed specific humidity at lag day 0 is diagnosed to investigate the changes in the MJO-related moisture structure. Figure 13 shows profiles of equatorial (10° S–10° N) specific humidity anomalies regressed against the 20–100 day filtered OLR time series in the reference area (5° S–5° N; 75°–85° E) in observation, good simulations, poor simulations and the difference between good and poor simulations. Result in observation given in Figure 13a shows a west-tilted structure of MJO convection system. The leading preconditioning moisture in lower troposphere and boundary layer ahead of the main convection plays an essential role in the eastward propagation of MJO (e.g., Kim et al. [77]; Hsu and Li [82]; Zhao et al. [83]; Hsu et al. [84]; Wang et al. [85]; Wei et al. [74]). Such preconditioning moisture destabilizes lower troposphere, favorable for the development of leading shallow convection. The shallow convection develops into the following deep convection of the MJO main convection system, resulting the systematic eastward propagation. Figure 13b presents the profile of regressed moisture in poor simulations. The west-titled structure in observation turns into a straight one in poor simulation centering at middle troposphere with broken weak signals ahead, which accounts for the non-propagating or even westward propagating intraseasonal convection systems as Figure 8c,d indicate. As Figure 13d presents, the difference between profiles of regressed equatorial moisture in good and poor simulations tends to compensate for the large bias in poor simulations mainly by moistening the lower troposphere and boundary layer ahead of the main convection of MJO. Therefore, the pre-moistening at low-layer troposphere is produced in good simulations, favorable for the propagation of MJO.

In order to clarify the dominant source of the pre-moistening, we use the following equation [86]:

$$\frac{\partial \langle q' \rangle}{\partial t} = -\langle \boldsymbol{V_h} \cdot \nabla_h q \rangle' - \langle \omega \frac{\partial q}{\partial p} \rangle' - \langle \frac{Q_2}{L_v} \rangle', \quad (1)$$

where $\boldsymbol{V_h} = (u, v)$ denotes the horizontal velocity vector, $\nabla_h = \left(\frac{\partial}{\partial x}, \frac{\partial}{\partial y}\right)$ is the horizontal gradient operator, Q_2 is the atmospheric apparent moisture sink, $\langle \cdot \rangle$ indicates the column integration from surface to 100 hPa. The superscript prime denotes the anomaly regressed against the area-averaged time series of 20–100 day filtered OLR in the reference area (5° S–5° N; 75°–85° E). The first term on the right-hand side of Equation (1) is the horizontal moisture advection. The second term is the large-scale adiabatic vertical motion and the third term represents the subgrid-scale evaporation and condensation. The sum of the second and third terms represents the net moistening associated with the column process. Following Yanai et al. [86], the net moistening associated with the subgrid-scale process can be approximated as the residual term between the moisture tendency and the adiabatic advective processes.

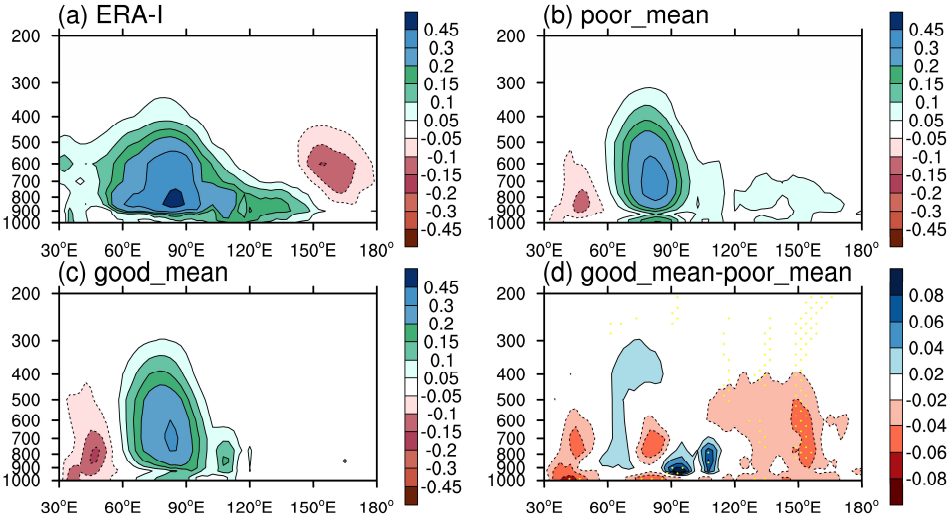

Figure 13. Longitude-height cross section of regressed specific humidity (averaged over 10° S–10° N) on lag day 0 against the area-averaged 20–100 day filtered OLR time series at the reference area (5° S–5° N; 75°–85° E) in (**a**) observation, (**b**) composite of poor simulations, (**c**) composite of good simulations and (**d**) difference between composites of good and poor simulations where the differences reaching 90% confidence level are dotted

According to Figure 13d, the enhancement of pre-moistening in good simulations is mainly over equatorial MC area (10° S–10° N; 90°–120° E) so that the column-integrated moisture budget terms are averaged over this area. Figure 14 shows the result of such budget analysis in observation, good simulations and poor simulations. Both the tendency terms in observation and composite of good simulations are positive, indicating the accumulation of moisture over this area. But the tendency term in the composite of poor simulations is negative, which accounts for the non-propagating MJO convections. In observation, the positive tendency term over pre-moistening area is mainly contributed by the meridional advection term and the column process while in good and poor simulations, the tendency term is mainly determined by the column process, which is also the most contractive term between good and poor simulations.

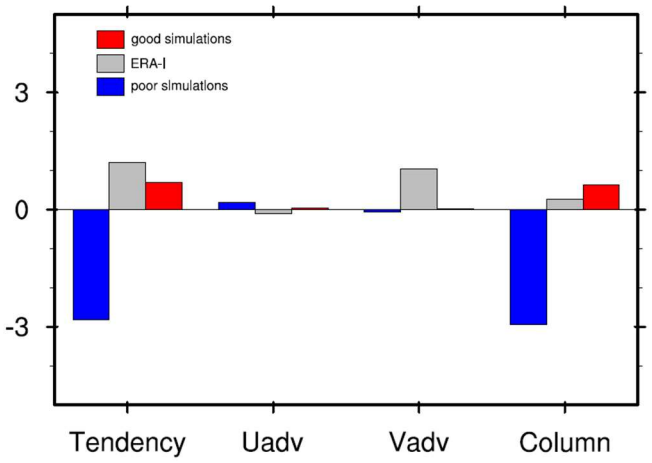

Figure 14. Results of the regressed moisture budget analysis in observation, good and poor simulations. Four terms presented are defined in Yanai et al. [86]. Each term is regressed against the time series of area-averaged 20–100 day filtered OLR in the reference area (5° S–5° N; 75°–85° E) and then vertically integrated from surface to 100 hPa. The integrated four terms are averaged in the pre-moistening area (10° S–10° N; 90°–120° E) in observation, good and poor simulations.

Therefore, to investigate the role of multi-cloud structure related with convections in pre-moistening, the Q_2 in Equation (1) is lag regressed from day −20 to 20 against the area-averaged time series of 20–100 day filtered OLR in the reference area (5° S–5° N; 75°–85° E). The four-dimensional Q_2 is then area-averaged over equatorial MC (10° S–10° N; 90°–120° E) to get the time-height cross section. Results in observation, composite of good simulations, composite of poor simulations are given in Figure 15. In observation, the low-level heating indicating the formation of low-level clouds starts since day −5, destabilizing the atmosphere column, favorable for the following development of shallow convection. Such destabilization and convection development are significantly weakened in poor simulations as the low-level heating starts since day −2 with the heating center higher than that in observation. The heating profile center remains in the low-troposphere after day 0 in observation while both shallow and deep heating sources are found in poor simulations. The difference of Q_2 profiles between good and poor simulations shows a low-level heating and middle-level cooling from day −5 to day 5, which destabilizes the atmosphere ahead of the MJO major convection, favorable for the development of leading shallow convection. The contrast between Q_2 profiles indicates a probable enhancement of leading shallow convection.

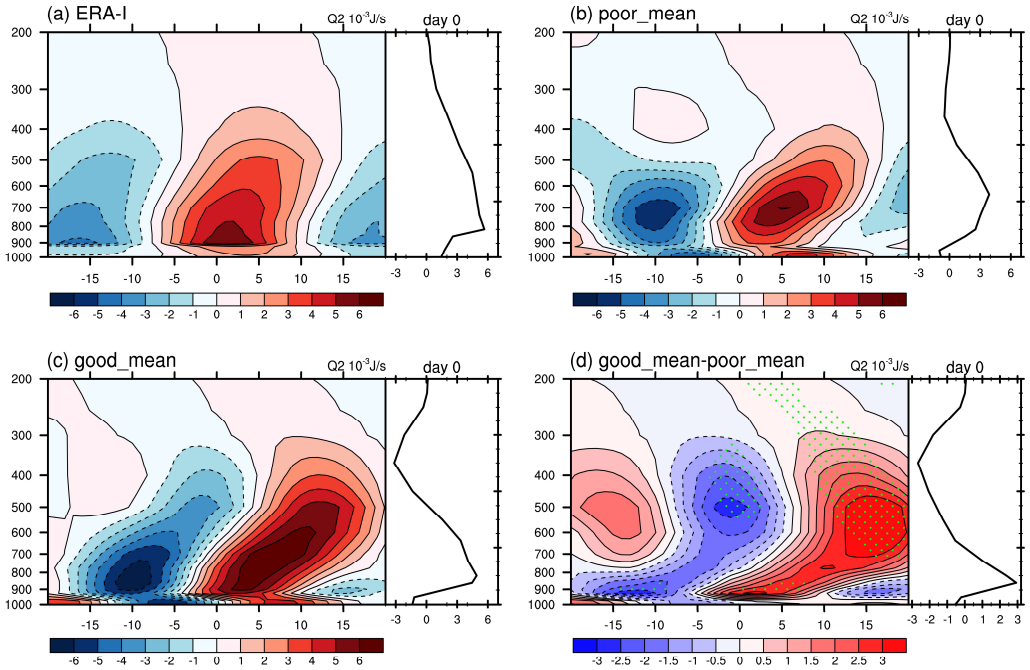

Figure 15. Time-height cross section (averaged over 10° S–10° N, 90° E–120° E) of lag regressed Q_2 from day −20 to 20 against the area-averaged 20–100 day filtered OLR time series at the reference area (5° S–5° N; 75°–85° E), along with the regressed Q_2 profile at day 0 in (**a**) observation, (**b**) composite of poor simulations, (**c**) composite of good simulations and (**d**) difference between composites of good and poor simulations where the differences reaching 90% confidence level are dotted.

5.2. Key Role of Shallow Convection Leading the Deep Convection

In order to check the enhancement of shallowing convection leading the deep convection of MJO, diagnostics of boundary layer moisture convergence (shown in Figure 16) are conducted. In observation (Figure 16a), strong moisture convergence occurs over the MC when the convective center is over the Indian ocean, indicating the existence of shallow convection leading the updrafts. This leading boundary layer moisture convergence is greatly weakened in the composite of poor simulations, while strong moisture convergence still exists in good simulations. The difference of boundary layer moisture convergence proves that the shallow convection leading MJO major convection in good simulations is indeed enhanced. The enhancement of leading boundary layer moisture convergence also indicates that the BL frictional moisture feedback [87,88] contributes to the improvement of MJO simulation.

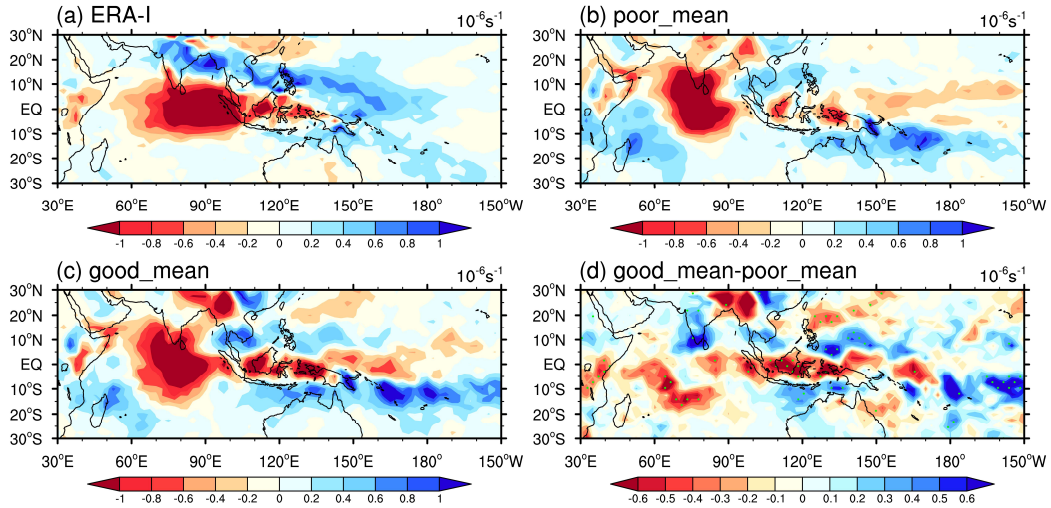

Figure 16. MJO-related boundary layer moisture convergence which is computed by regressing the vertically integrated (from surface to 700 hPa) moisture convergence against the area-averaged time series of 20–100 day filtered OLR in the reference area (5° S–5° N; 75°–85° E) in (**a**) observation, (**b**) composite of poor simulations, (**c**) composite of good simulations and (**d**) difference between the composites of good and poor simulations where the differences reaching 90% confidence level are dotted.

To better understand the role of leading shallow convection in better simulation of MJO, regressed structure of apparent heating source (Q_1) as defined in Yanai et al. [86] is given in Figure 17, along with the regressed profile of equivalent potential temperature (EPT). The regressed structure of Q_1 in observation shows that the shallow convection heating is triggered a few days before the development of the following deep convection. However, the heating of leading shallow convection vanishes in poor simulations, and the following high-level heating of deep convection is also weakened. The difference of diabatic heating between good and poor simulations shows an enhanced low-level heating caused by shallow convection from day −15. The enhanced leading shallow convection destabilizes the atmosphere column and then develops into deep convection of MJO from lag day 5 to lag day 10. The difference of regressed EPT profile at day 0 between good and poor simulations shows an increase beneath 500 hPa, producing instability for convection to develop. However, the magnitude of such increase is small compared with that of its profile in poor simulations.

Therefore, the improvement of the pre-moistening effect of MJO is probably due to the enhancement of its leading shallow convection. The deep convective precipitation in poor simulations consumes too much environmental moisture, the light precipitation thus develops in a dryer atmosphere as Figure 12a shows. As a result, the shallow convection precipitation, is insufficient in poor simulations. The shallow convection leading the major convection of MJO is also weakened in poor simulations, which is against its eastward propagation. This is remedied by enhancing the evaporation of deep convective precipitation in good simulations. Meanwhile, the weakened moisture consumption efficiency of shallow convection retains more low-level moisture in good simulations. The improvement of moisture profile in good simulations benefits from both aforementioned effects. The middle-level cooling caused by enhancing the evaporation of deep convection precipitation and the low-level heating caused by strengthening shallow convection destabilize the atmosphere column, favorable for the development of MJO convection and its further propagation.

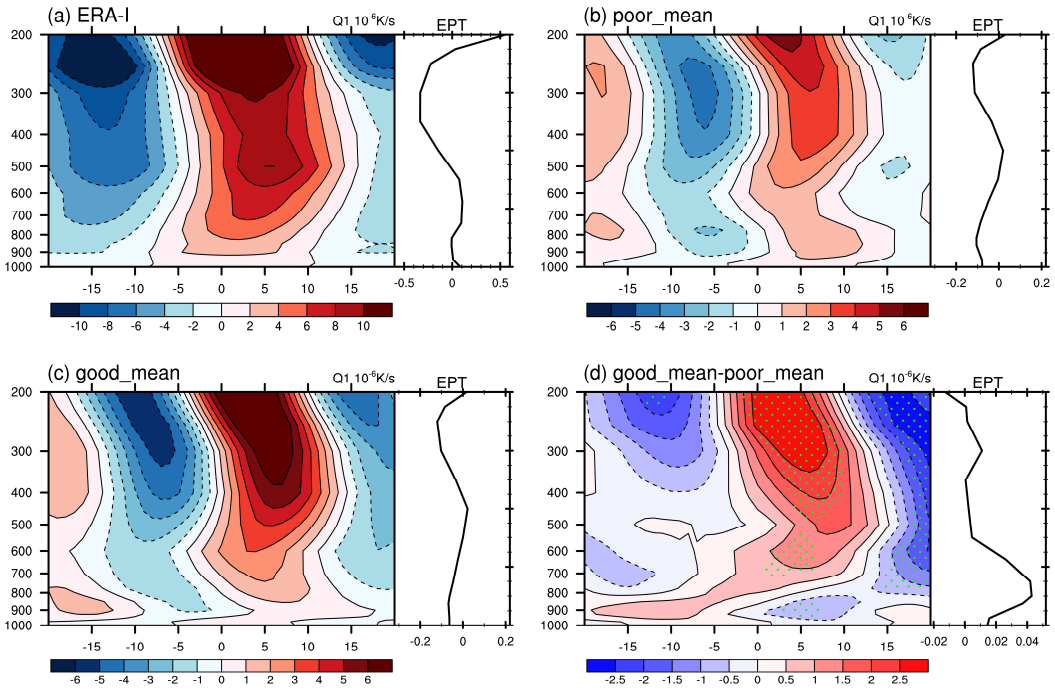

Figure 17. Time-height cross section (averaged over 10° S–10° N, 90° E–120° E) of lag regressed Q_1 from day −20 to 20 against the area-averaged 20–100 day filtered OLR time series at the reference area (5° S–5° N; 75°–85° E), along with the regressed equivalent potential temperature profile at day 0 in (**a**) observation, (**b**) composite of poor simulations, (**c**) composite of good simulations and (**d**) difference between composites of good and poor simulations where the differences reaching 90% confidence level are dotted.

6. Summary and Discussion

This study analyzed the outputs of 85 model runs produced by perturbing seven chosen parameters in the cloud and convection parameterization schemes of BCC_CSM1.2. Three canonical metrics were used individually to examine each run's ability of simulating realistic MJO. However, the scoring results of the three metrics do not corroborate each other in our study. Therefore, a new strategy combining the scores of both Lag-correlation and E/W ratio has been used to identify six good and eight poor simulations out of 85 runs. Among the seven chosen parameters as adjustment time scale for shallow convection, relative humidity threshold for high stable clouds, relative humidity threshold for convective trigger, precipitation efficiency for deep convection, precipitation efficiency for shallow convection, relative humidity threshold for low stable clouds and evaporation efficiency for deep convective precipitation, the values of last three parameters showed large differences between good and poor simulations while the rest were almost the same.

MJO exhibits a greater amplitude with an improved eastward propagation in good simulations. Other CCEWs like Kelvin waves are also improved in amplitude and space time structure as Figure 11 shows, consistent with the results of previous research [76]. MJO in poor simulations propagates with a westward speed over India Ocean. Meanwhile, its propagation range over Pacific Ocean shrinks significantly compared with that in observation. After changing values of the abovementioned seven parameters, MJO shows a systematic eastward propagation over India and Pacific Ocean.

The mean state changes along with MJO after parameter perturbation. In poor simulations, excessive precipitation exists in southwest Pacific while insufficient precipitation is produced over MC. The winter mean precipitation gets improved over MC in good simulations by amplifying land rainfalls accompanied with the improvement of MJO propagation. This is consistent to the finding in Peatman et al. [89] that land rainfall is favorable for MJO to cross MC. However, controversy still exists about this conclusion as Zhang and Ling [71] concluded that MJO crosses MC mainly through rainfall over

sea. The enhancement of land rainfall over MC, which is dominant by shallow convective precipitation, also indicates changes in the frequency distribution of rain rate. The tropical precipitation consists of too much heavy rainfall in poor simulations as Figure 11a shows. As a result, the environmental atmosphere experiences an overall dry bias in poor simulations since heavy precipitation consumes too much moisture. The dry environmental atmosphere suppresses the frequency of light rainfall. This bias gets improved in good simulations where the frequency distribution of tropical precipitation in Indo-Pacific region is closer to observation by weakening heavy precipitation and increasing the ratio of extremely light rainfall, indicating an enhancement of shallow convection.

The shallow convection leading the deep convection in MJO was enhanced by changing values of three crucial parameters as precipitation efficiency for shallow convection (C_0_*shal*), relative humidity threshold for low stable clouds (*RH_low*) and evaporation efficiency for deep convective precipitation (K_e_*deep*). *RH_low* shows greater value while values of C_0_*shal* and K_e_*deep* are smaller in good simulations. The remaining four parameter values are almost the same as those in poor simulations (Figure 6). Increasing the value of K_e_*deep* weakens the deep convection precipitation and humidifies the environmental atmosphere. As a result, shallow convection leading the MJO major convection is enhanced, which is reflected by the strengthened low-level moisture convergence ahead of the MJO major convection (as in Figure 16). The enhanced shallow convection is supposed to pump low level moisture to middle troposphere, thus humidifying middle troposphere and drying the low troposphere. However, decreasing value of C_0_*shal* and increasing value of *RH_low* both lower the low-level moisture consumption efficiency of shallow convection. The whole column of atmosphere is thus humidified with a humidification center at low troposphere. Therefore, the pre-moistening effect over lower-layer atmosphere is also strengthened along with the enhancement of leading shallow convection. Such enhancement of leading shallow convection in good simulations is the key for better simulated MJO. The low-level heating and moistening caused by enhanced shallow convection a few days before the initiation of MJO major convection destabilize the atmosphere column. The leading shallow convection therefore develops to the MJO major deep convection as Figure 17 shows, amplifying the simulated MJO convection. The leading shallow convection also improves the vertical structure of MJO moisture as indicated by Figures 13 and 14, favorable for MJO's systematic eastward propagation. Boyle et. al. [90] conducted a similar parameter perturbation experiment with CAM5, but they perturbed more parameters in not only cloud and convection parameterization schemes, but also in radiation, boundary layer and turbulence parameterizations. They showed that the MJO simulation also displayed a strong sensitivity to the parameter associated with the deep convection. They also demonstrated that by changing deep convection parameter values to suppress deep convective precipitation, MJO simulation is improved. This is consistent with the conclusion of this study. Other mechanisms such as the atmosphere-ocean interaction may also contribute to the improvement of the MJO simulation as Figure 7 shows that SST in good simulations shows an overall warming over Indian ocean which could excite more MJO events. Besides, the rise of SST in east Pacific exhibits an El Niño-like pattern, which is favorable for MJO's eastward propagation.

This work is an attempt to reveal the important parameter-related physical processes for simulating realistic MJO in BCC_CSM1.2, hoping to provide inspirations for the simulation and prediction of MJO. Three parameters were found different largely in good and poor simulations. By changing the values of these three parameters, the moisture sensitivity of convection becomes different, leading to an enhanced leading shallow convection, accounting for the improvement of MJO. However, some aspects of this research still need further study. Even integrations with relatively high-skill MJO simulations show deficiencies of simulating realistic MJO as most MJO related figures in good simulations also show considerable differences compared with observation. This is likely because we only perturbed the parameter values without changing any other components in the model, so the model's systematic deficiencies in simulating MJO [91] may not be totally compensated. However, composite results of good simulations all exhibit changes for a better simulated MJO, proving the validity of such

certain parameter perturbation. But detailed physical processes in cloud dynamics and convections determining the improvement of MJO still remains unrevealed, which needs further related studies.

Author Contributions: Conceptualization, K.H. and H.-L.R.; Data curation, X.L.; Supervision, H.-L.R. and M.M.; Validation, K.H.; Writing—original draft preparation, K.H.; Writing—review and editing, H.-L.R., P.R., and Y.W.

Funding: This work was jointly supported by the National Key Research and Development Program on monitoring, Early Warning and Prevention of Major Natural Disaster (2017YFC1502302, 2018YFC1505906), State Oceanic Administration International Cooperation Program (GASI-IPOVAI-03), China National Science Foundation project (41606019), and China Meteorological Administration Special Public Welfare Research Fund (GYHY201506013).

Acknowledgments: The authors gratefully acknowledge Fei-Fei Jin, Joshua-Xiouhua Fu, Wansuo Duan, Guodong Sun, Fei Liu, Yujie Wu and Ming Bao for their kindly discussions about this work. Constructive comments by three anonymous reviewers led to substantial improvements in the presentation. ERA-interim Reanalysis data was provided by the ECMWF from their Web site at https://www.ecmwf.int/en/forecasts/datasets/reanalysis-datasets/era-interim. Daily interpolated OLRs were obtained from NOAA/OAR/ESRL PSD, Boulder, Colorado, USA https://www.esrl.noaa.gov/psd/data/gridded/data.interp_OLR.html.

Conflicts of Interest: The authors declare no conflict of interest.

References

1. Madden, R.A.; Julian, P.R. Detection of a 40–50 day oscillation in the zonal wind in the tropical Pacific. *J. Atmos. Sci.* **1971**, *28*, 702–708. [CrossRef]
2. Madden, R.A.; Julian, P.R. Description of global-scale circulation cells in the tropics with a 40–50 day period. *J. Atmos. Sci.* **1972**, *29*, 1109–1123. [CrossRef]
3. Lau, W.K.-M.; Waliser, D.E. *Intraseasonal Variability in the Atmosphere-Ocean Climate System*; Springer Science & Business Media: Berlin, Germany, 2011.
4. Zhang, C.D. Madden-Julian oscillation. *Rev. Geophys.* **2005**, *43*, 36. [CrossRef]
5. Wei, Y.; Liu, F.; Mu, M.; Ren, H.-L. Planetary scale selection of the Madden–Julian Oscillation in an air-sea coupled dynamic moisture model. *Clim Dyn.* **2017**, *50*, 3441–3456. [CrossRef]
6. Zhang, C. Madden–Julian oscillation: Bridging Weather and Climate. *Bull. Am. Meteorol. Soc.* **2013**, *94*. [CrossRef]
7. Kim, H.-K.; Seo, K.-H. Cluster analysis of tropical cyclone tracks over the western north pacific using a self-organizing map. *J. Clim.* **2016**, *29*, 3731–3751. [CrossRef]
8. Adames, A.F.; Wallace, J.M. Three-Dimensional Structure and Evolution of the Vertical Velocity and Divergence Fields in the MJO. *J. Atmos. Sci.* **2014**, *71*, 267–287. [CrossRef]
9. Weickmann, K.M. Intraseasonal circulation and outgoing longwave radiation modes during Northern Hemisphere winter. *Mon. Weather Rev.* **1983**, *111*, 1838–1858. [CrossRef]
10. Wang, B.; Liu, F.; Chen, G. A trio-interaction theory for Madden–Julian oscillation. *Geosci. Lett.* **2016**, *3*, 34. [CrossRef]
11. Wang, B.; Rui, H. Dynamics of the coupled moist Kelvin–Rossby wave on an equatorial β-plane. *J. Atmos. Sci.* **1990**, *47*, 397–413. [CrossRef]
12. Liu, F.; Wang, B. Roles of the moisture and wave feedbacks in shaping the Madden–Julian oscillation. *J. Clim.* **2017**, *30*, 10275–10291. [CrossRef]
13. Adames, Á.F.; Kim, D. The MJO as a dispersive, convectively coupled moisture wave: Theory and observations. *J. Atmos. Sci.* **2016**, *73*, 913–941. [CrossRef]
14. Sobel, A.; Maloney, E. An idealized semi-empirical framework for modeling the Madden–Julian oscillation. *J. Atmos. Sci.* **2012**, *69*, 1691–1705. [CrossRef]
15. Sobel, A.; Maloney, E. Moisture modes and the eastward propagation of the MJO. *J. Atmos. Sci.* **2013**, *70*, 187–192. [CrossRef]
16. Woolnough, S.; Slingo, J.; Hoskins, B. The organization of tropical convection by intraseasonal sea surface temperature anomalies. *Q. J. R. Meteorol. Soc.* **2001**, *127*, 887–907. [CrossRef]
17. Andersen, J.A.; Kuang, Z. Moist static energy budget of MJO-like disturbances in the atmosphere of a zonally symmetric aquaplanet. *J. Clim.* **2012**, *25*, 2782–2804. [CrossRef]
18. Kim, D.; Kug, J.-S.; Sobel, A.H. Propagating versus nonpropagating Madden–Julian oscillation events. *J. Clim.* **2014**, *27*, 111–125. [CrossRef]

19. Maloney, E.D. The moist static energy budget of a composite tropical intraseasonal oscillation in a climate model. *J. Clim.* **2009**, *22*, 711–729. [CrossRef]
20. Maloney, E.D.; Sobel, A.H.; Hannah, W.M. Intraseasonal variability in an aquaplanet general circulation model. *J. Adv. Model. Earth Syst.* **2010**, *2*. [CrossRef]
21. Liu, F.; Wang, B. Effects of moisture feedback in a frictional coupled Kelvin–Rossby wave model and implication in the Madden–Julian oscillation dynamics. *Clim. Dyn.* **2017**, *48*, 513–522. [CrossRef]
22. Wang, B.; Chen, G. A general theoretical framework for understanding essential dynamics of Madden–Julian oscillation. *Clim. Dyn.* **2017**, *49*, 2309–2328. [CrossRef]
23. Biello, J.A.; Majda, A.J. A new multiscale model for the Madden–Julian oscillation. *J. Atmos. Sci.* **2005**, *62*, 1694–1721. [CrossRef]
24. Liu, F.; Huang, G.; Feng, L. Critical roles of convective momentum transfer in sustaining the multi-scale Madden–Julian oscillation. *Theor. Appl. Climatol.* **2012**, *108*, 471–477. [CrossRef]
25. Liu, F.; Wang, B. A frictional skeleton model for the Madden–Julian oscillation. *J. Atmos. Sci.* **2012**, *69*, 2749–2758. [CrossRef]
26. Liu, F.; Wang, B. A model for the interaction between 2-day waves and moist Kelvin waves. *J. Atmos. Sci.* **2012**, *69*, 611–625. [CrossRef]
27. Majda, A.J.; Biello, J.A. A multiscale model for tropical intraseasonal oscillations. *Proc. Natl. Acad. Sci. USA* **2004**, *101*, 4736–4741. [CrossRef] [PubMed]
28. Wang, B.; Liu, F. A model for scale interaction in the Madden–Julian oscillation. *J. Atmos. Sci.* **2011**, *68*, 2524–2536. [CrossRef]
29. Khouider, B.; Majda, A.J. A Simple multicloud parameterization for convectively coupled tropical waves. Part I: Linear analysis. *J. Atmos. Sci.* **2006**, *63*, 1308–1323. [CrossRef]
30. Khouider, B.; Majda, A.J. A simple multicloud parameterization for convectively coupled tropical waves. Part II: Nonlinear simulations. *J. Atmos. Sci.* **2007**, *64*, 381–400. [CrossRef]
31. Yang, D.; Ingersoll, A.P. Testing the hypothesis that the MJO is a mixed Rossby–gravity wave packet. *J. Atmos. Sci.* **2011**, *68*, 226–239. [CrossRef]
32. Yang, D.; Ingersoll, A.P. Triggered convection, gravity waves, and the MJO: A shallow-water model. *J. Atmos. Sci.* **2013**, *70*, 2478–2486. [CrossRef]
33. Yang, D.; Ingersoll, A.P. A theory of the MJO horizontal scale. *Geophys. Res. Lett.* **2014**, *41*, 1059–1064. [CrossRef]
34. Wang, B.; Xie, X. A Model for the boreal summer intraseasonal oscillation. *J. Atmos. Sci.* **1997**, *54*, 72–86. [CrossRef]
35. Fu, X.; Wang, B. The Boreal-Summer intraseasonal oscillations simulated in a hybrid coupled atmosphere–ocean model. *Mon. Weather Rev.* **2004**, *132*, 2628–2649. [CrossRef]
36. Liu, F.; Wang, B. An air–sea coupled skeleton model for the Madden–Julian oscillation. *J. Atmos. Sci.* **2013**, *70*, 3147–3156. [CrossRef]
37. Wang, B.; Xie, X. Coupled modes of the warm pool climate system. Part I: The role of air–sea interaction in maintaining Madden–Julian oscillation. *J. Clim.* **1998**, *11*, 2116–2135. [CrossRef]
38. Cao, G.; Zhang, G.J. Role of Vertical Structure of Convective Heating in MJO Simulation in NCAR CAM5.3. *J. Clim.* **2017**, *30*, 7423–7439. [CrossRef]
39. Fu, X.H.; Lee, J.Y.; Hsu, P.C.; Taniguchi, H.; Wang, B.; Wang, W.Q.; Weaver, S. Multi-model MJO forecasting during DYNAMO/CINDY period. *Clim. Dyn.* **2013**, *41*, 1067–1081. [CrossRef]
40. Fu, X.H.; Lee, J.Y.; Wang, B.; Wang, W.Q.; Vitart, F. Intraseasonal Forecasting of the Asian Summer Monsoon in Four Operational and Research Models. *J. Clim.* **2013**, *26*, 4186–4203. [CrossRef]
41. Jiang, X.; Waliser, D.E.; Xavier, P.K.; Petch, J.; Klingaman, N.P.; Woolnough, S.J.; Guan, B.; Bellon, G.; Crueger, T.; DeMott, C.; et al. Vertical structure and physical processes of the Madden-Julian oscillation: Exploring key model physics in climate simulations. *J. Geophys. Res. Atmos.* **2015**, *120*, 4718–4748. [CrossRef]
42. Ling, J.; Zhang, C.; Wang, S.; Li, C. A new interpretation of the ability of global models to simulate the MJO. *Geophys. Res. Lett.* **2017**, *44*, 5798–5806. [CrossRef]
43. Xavier, P.K.; Petch, J.C.; Klingaman, N.P.; Woolnough, S.J.; Jiang, X.A.; Waliser, D.E.; Caian, M.; Cole, J.; Hagos, S.M.; Hannay, C.; et al. Vertical structure and physical processes of the Madden-Julian Oscillation: Biases and uncertainties at short range. *J. Geophys. Res. Atmos.* **2015**, *120*, 4749–4763. [CrossRef] [PubMed]

44. Hung, M.-P.; Lin, J.-L.; Wang, W.; Kim, D.; Shinoda, T.; Weaver, S.J. MJO and convectively coupled equatorial waves simulated by CMIP5 climate models. *J. Clim.* **2013**, *26*, 6185–6214. [CrossRef]
45. Waliser, D.; Sperber, K.; Hendon, H.; Kim, D.; Wheeler, M.; Weickmann, K.; Zhang, C.; Donner, L.; Gottschalck, J.; Higgins, W.; et al. MJO Simulation Diagnostics. *J. Clim.* **2009**, *22*, 3006–3030.
46. Wheeler, M.C.; Hendon, H.H. An all-season real-time multivariate MJO index: development of an Index for monitoring and prediction. *Mon Weather Rev.* **2004**, *132*. [CrossRef]
47. Tiedtke, M. A Comprehensive Mass Flux Scheme for Cumulus Parameterization in Large-Scale Models. *Mon Weather Rev.* **1989**, *117*, 1779–1800. [CrossRef]
48. Zhang, G.J.; McFarlane, N.A. Sensitivity of climate simulations to the parameterization of cumulus convection in the Canadian climate centre general circulation model. *Atmos. Ocean.* **1995**, *33*, 407–446. [CrossRef]
49. Zhang, G.J.; Mu, M. Effects of modifications to the Zhang-McFarlane convection parameterization on the simulation of the tropical precipitation in the National Center for Atmospheric Research Community Climate Model, version 3. *J. Geophys. Res. Atmos.* **2005**, *110*. [CrossRef]
50. Tokioka, T.; Yamazaki, K.; Kitoh, A.; Ose, T. The equatorial 30–60 day oscillation and the Arakawa-Schubert penetrative cumulus parameterization. *J. Meteorol. Soc. Jpn. Ser. II* **1988**, *66*, 883–901. [CrossRef]
51. Wang, W.; Schlesinger, M.E. The dependence on convection parameterization of the tropical intraseasonal oscillation simulated by the UIUC 11-layer atmospheric GCM. *J. Clim.* **1999**, *12*, 1423–1457. [CrossRef]
52. Maloney, E.D.; Hartmann, D.L. The sensitivity of intraseasonal variability in the NCAR CCM3 to changes in convective parameterization. *J. Clim.* **2001**, *14*, 2015–2034. [CrossRef]
53. Fu, X.; Wang, B. Critical roles of the stratiform rainfall in sustaining the Madden–Julian oscillation: GCM experiments. *J. Clim.* **2009**, *22*, 3939–3959. [CrossRef]
54. Bretherton, C.S.; Peters, M.E.; Back, L.E. Relationships between water vapor path and precipitation over the tropical oceans. *J. Clim.* **2004**, *17*, 1517–1528. [CrossRef]
55. Kim, D.; Xavier, P.; Maloney, E.; Wheeler, M.; Waliser, D.; Sperber, K.; Hendon, H.; Zhang, C.; Neale, R.; Hwang, Y.-T. Process-oriented MJO simulation diagnostic: Moisture sensitivity of simulated convection. *J. Clim.* **2014**, *27*, 5379–5395. [CrossRef]
56. Thayer-Calder, K.; Randall, D.A. The Role of Convective Moistening in the Madden-Julian Oscillation. *J. Atmos. Sci.* **2009**, *66*, 3297–3312. [CrossRef]
57. Liu, X.; Li, W.; Wu, T.; Li, T.; Gu, W.; Bo, Z.; Yang, B.; Zhang, L.; Jie, W. Validity of parameter optimization in improving MJO simulation and prediction using the sub-seasonal to seasonal forecast model of Beijing Climate Center. *Clim Dyn.* **2018**, *52*, 3823–3843. [CrossRef]
58. Wu, T.; Song, L.; Li, W.; Wang, Z.; Zhang, H.; Xin, X.; Zhang, Y.; Zhang, L.; Li, J.; Wu, F.; et al. An overview of BCC climate system model development and application for climate change studies. *J. Meteorol. Res.* **2014**, *28*, 34–56. [CrossRef]
59. Ji, J.; Huang, M.; Li, K. Prediction of carbon exchanges between China terrestrial ecosystem and atmosphere in 21st century. *Sci. China Ser. D Earth Sci.* **2008**, *51*, 885–898. [CrossRef]
60. Winton, M. A Reformulated Three-Layer Sea Ice Model. *J. Atmos. Ocean. Technol.* **2000**, *17*, 525–531. [CrossRef]
61. Wu, T.; Yu, R.; Zhang, F.; Wang, Z.; Dong, M.; Wang, L.; Jin, X.; Chen, D.; Li, L. The Beijing Climate Center atmospheric general circulation model: description and its performance for the present-day climate. *Clim Dyn.* **2008**, *34*, 123. [CrossRef]
62. McKay, M.D. Latin hypercube sampling as a tool in uncertainty analysis of computer models. In Proceedings of the 24th Conference on Winter Simulation, Arlington, VA, USA, 13–16 December 1992; ACM Press: New York, NY, USA, 1947; pp. 557–564.
63. Liebmann, B.; Smith, C.A. Description of a Complete (Interpolated) Outgoing Longwave Radiation Dataset. *Bull. Am. Meteorol. Soc.* **1996**, *77*, 1275–1277.
64. Huffman, G.J.; Bolvin, D.T.; Nelkin, E.J.; Wolff, D.B.; Adler, R.F.; Gu, G.; Hong, Y.; Bowman, K.P.; Stocker, E.F. The TRMM Multisatellite Precipitation Analysis (TMPA): Quasi-Global, Multiyear, Combined-Sensor Precipitation Estimates at Fine Scales. *J. Hydrometeorol.* **2007**, *8*, 38–55. [CrossRef]
65. Dee, D.P.; Uppala, S.M.; Simmons, A.J.; Berrisford, P.; Poli, P.; Kobayashi, S.; Andrae, U.; Balmaseda, M.A.; Balsamo, G.; Bauer, P.; et al. The ERA-Interim reanalysis: Configuration and performance of the data assimilation system. *Q. J. R. Meteorol. Soc.* **2011**, *137*, 553–597. [CrossRef]

66. Hannah, W.M.; Maloney, E.D. The Role of Moisture-Convection Feedbacks in Simulating the Madden-Julian Oscillation. *J. Clim.* **2011**, *24*, 2754–2770. [CrossRef]
67. Hirota, N.; Ogura, T.; Tatebe, H.; Shiogama, H.; Kimoto, M.; Watanabe, M. Roles of Shallow Convective Moistening in the Eastward Propagation of the MJO in MIROC6. *J. Clim.* **2018**, *31*, 3033–3047. [CrossRef]
68. Maloney, E.D.; Wolding, B.O. Initiation of an intraseasonal oscillation in an aquaplanet general circulation model. *J. Adv. Model. Earth Syst.* **2015**, *7*, 1956–1976. [CrossRef]
69. Wolding, B.O.; Maloney, E.D. Objective Diagnostics and the Madden–Julian Oscillation. Part I: Methodology. *J. Clim.* **2015**, *28*, 4127–4140. [CrossRef]
70. Wheeler, M.; Kiladis, G.N. Convectively coupled equatorial waves: Analysis of clouds and temperature in the wavenumber-frequency domain. *J. Atmos. Sci.* **1999**, *56*, 374–399. [CrossRef]
71. Zhang, C.D.; Ling, J. Barrier Effect of the Indo-Pacific Maritime Continent on the MJO: Perspectives from Tracking MJO Precipitation. *J. Clim.* **2017**, *30*, 3439–3459. [CrossRef]
72. Zhang, Y.; Xie, S.; Covey, C.; Lucas, D.D.; Gleckler, P.; Klein, S.A.; Tannahill, J.; Doutriaux, C.; Klein, R. Regional assessment of the parameter-dependent performance of CAM4 in simulating tropical clouds. *Geophys. Res. Lett.* **2012**, *39*, L14708. [CrossRef]
73. Yoneyama, K.; Zhang, C.; Long, C.N. Tracking pulses of the Madden–Julian oscillation. *Bull. Am. Meteorol. Soc.* **2013**, *94*, 1871–1891. [CrossRef]
74. Wei, Y.; Mu, M.; Ren, H.L.; Fu, J.X. Conditional Nonlinear Optimal Perturbations of Moisture Triggering Primary MJO Initiation. *Geophys. Res. Lett.* **2019**, *46*, 3492–3501. [CrossRef]
75. Guo, Y.; Jiang, X.; Waliser, D.E. Modulation of the convectively coupled Kelvin waves over South America and the tropical Atlantic Ocean in association with the Madden–Julian oscillation. *J. Atmos. Sci.* **2014**, *71*, 1371–1388. [CrossRef]
76. Guo, Y.; Waliser, D.E.; Jiang, X. A Systematic Relationship between the Representations of Convectively Coupled Equatorial Wave Activity and the Madden–Julian Oscillation in Climate Model Simulations. *J. Clim.* **2015**, *28*, 1881–1904. [CrossRef]
77. Kim, D.; Sperber, K.; Stern, W.; Waliser, D.; Kang, I.-S.; Maloney, E.; Wang, W.; Weickmann, K.; Benedict, J.; Khairoutdinov, M. Application of MJO simulation diagnostics to climate models. *J. Clim.* **2009**, *22*, 6413–6436. [CrossRef]
78. Chang, C.W.J.; Tseng, W.L.; Hsu, H.H.; Keenlyside, N.; Tsuang, B.J. The Madden-Julian Oscillation in a warmer world. *Geophys. Res. Lett.* **2015**, *42*, 6034–6042. [CrossRef]
79. Maloney, E.D.; Adames, Á.F.; Bui, H.X. Madden–Julian oscillation changes under anthropogenic warming. *Nat. Clim. Chang.* **2019**, *9*, 26–33. [CrossRef]
80. Gonzalez, A.O.; Jiang, X. Winter mean lower tropospheric moisture over the Maritime Continent as a climate model diagnostic metric for the propagation of the Madden-Julian oscillation. *Geophys. Res. Lett.* **2017**, *44*, 2588–2596. [CrossRef]
81. Xavier, P.K. Intraseasonal Convective Moistening in CMIP3 Models. *J. Clim.* **2012**, *25*, 2569–2577. [CrossRef]
82. Hsu, P.-C.; Li, T. Role of the boundary layer moisture asymmetry in causing the eastward propagation of the Madden–Julian oscillation. *J. Clim* **2012**, *25*, 4917–4931. [CrossRef]
83. Zhao, C.; Li, T.; Zhou, T. Precursor signals and processes associated with MJO initiation over the tropical Indian Ocean. *J. Clim.* **2013**, *26*, 291–307. [CrossRef]
84. Hsu, P.-C.; Li, T.; Murakami, H. Moisture asymmetry and MJO eastward propagation in an aquaplanet general circulation model. *J. Clim.* **2014**, *27*, 8747–8760. [CrossRef]
85. Wang, L.; Li, T.; Maloney, E.; Wang, B. Fundamental Causes of Propagating and Nonpropagating MJOs in MJOTF/GASS Models. *J. Clim.* **2017**, *30*, 3743–3769. [CrossRef]
86. Yanai, M.; Esbensen, S.; Chu, J.-H. Determination of bulk properties of tropical cloud clusters from large-scale heat and moisture budgets. *J. Atmos. Sci.* **1973**, *30*, 611–627. [CrossRef]
87. Wang, B. Dynamics of tropical low-frequency waves: An analysis of the moist Kelvin wave. *J. Atmos. Sci.* **1988**, *45*, 2051–2065. [CrossRef]
88. Wang, B.; Chen, J. On the zonal-scale selection and vertical structure of equatorial intraseasonal waves. *Q. J. R. Meteorol. Soc.* **1989**, *115*, 1301–1323. [CrossRef]
89. Peatman, S.C.; Matthews, A.J.; Stevens, D.P. Propagation of the Madden–Julian Oscillation through the Maritime Continent and scale interaction with the diurnal cycle of precipitation. *Q. J. R. Meteorol. Soc.* **2014**, *140*, 814–825. [CrossRef]

90. Boyle, J.; Klein, S.; Lucas, D.; Ma, H.Y.; Tannahill, J.; Xie, S. The parametric sensitivity of CAM5's MJO. *J. Geophys. Res. Atmos.* **2015**, *120*, 1424–1444. [CrossRef]
91. Liu, X.; Wu, T.; Yang, S.; Li, T.; Jie, W.; Zhang, L.; Wang, Z.; Liang, X.; Li, Q.; Cheng, Y. MJO prediction using the sub-seasonal to seasonal forecast model of Beijing Climate Center. *Clim Dyn.* **2017**, *48*, 3283–3307. [CrossRef]



© 2019 by the authors. Licensee MDPI, Basel, Switzerland. This article is an open access article distributed under the terms and conditions of the Creative Commons Attribution (CC BY) license (http://creativecommons.org/licenses/by/4.0/).

Article ID: 1006-8775(2018)03-online-first paper

URBAN HEAT ISLAND EFFECT AND ITS CINTRIBUTION TO OBSERVED TEMPERATURE INCREASE AT WUHAN STATION, CENTRAL CHINA

JIA Wen-qian (贾文茜)[1], REN Guo-yu (任国玉)[1,2], SUONAN Kan-zhuo (索南看卓)[1] , ZHANG Pan-feng (张盼峰)[1] , WEN Kang-min (温康民)[1], REN Yong-jian (任永健)[3]

(1. Department of Atmospheric Sciences, China University of Geosciences, Wuhan 430070 China; 2. Laboratory for Climate Studies, China Meteorological Administration, National Climate Center, Beijing 100081 China; 3. Wuhan Regional Climate Center, Wuhan 430074, China)

Abstract: Based on an in-homogeneity adjusted dataset of the monthly mean temperature, minimum and maximum temperature, this paper analyzes the temporal characteristics of Urban Heat Island (UHI) intensity at Wuhan Station, and its impact on the long-term trend of surface air temperature change recorded during 1961-2015 by using an urban-rural method. Results show that UHI effect is obvious near Wuhan Station in the past 55 years, especially for minimum temperature. The strongest UHI intensity occurs in summer and the weakest in winter. For the period 1961-2004, UHI intensity undergoes a significant increase near the urban station, with the increase especially large for the period 1988-2004, but a significant decrease is registered for the last 10 years, with the decrease in minimum temperature more significant than that of maximum temperature. The annual mean urban warming and its contribution to overall warming are 0.18°C/10yr and 48.8% respectively for the period 1961-2015, with a more significant and larger urbanization effect seen in T_{min} than T_{max}. A large proportion warming, about half of the overall increase in annual mean temperature, as observed at the urban station, thus can be attributed to the rapid urbanization in the past half a century.

Key words: Wuhan; Data in-homogeneity; UHII; Urban warming; Data bias; Climate change
doi: 10.16555/j.1006-8775.2019.01.010.

1 INTRODUCTION

Climate change research is mainly based on continuous and high-quality observational records. Due to the relocation of observation sites, replacement of observation instruments and changes in the time system, however, inhomogeneities have occurred in the observational data series to varying degrees, and they can cause a significant bias in analysis of surface climate variables trends for individual stations or a small area. Furthermore, the gradually increasing Urban Heat Island (UHI) effect near the observational sites becomes the biggest systematic bias for the long-term climate change monitoring and detection in that it directly causes the trend of Surface Air Temperature (SAT) records to be overestimated in many developing regions of the world.

At present, there exists a major divergence of views in the international climatological community on the impact degree of urbanization effect on the SAT series. It is generally hold that UHI effect is small, and it had not surpassed 0.05°C in the past a hundred years on a global average, much lower than the optimal estimation of the global average annual mean SAT change of 0.8°C (e.g., Jones et al.[1]; Peterson[2]; Parker[3]; Lawrimore et al.[4]). Nevertheless, some researches for several regions have shown that the UHI effect may play a significant role in the regional SAT trend, which should be paid more consideration (e.g., Karl et al.[5]; Hansen et al.[6]; Kalnay and Cai[7]; Zhou and Dickinson[8]; Zhou et al.[9]; Ren et al.[10]).

The studies of the UHI effect on SAT records have been conducted for big cities and large regions in recent years, and interesting conclusions have been drawn thereby. For example, the investigation of UHI effect in northern China for Beijing and Shijiazhuang stations has shown that the UHI Intensity (UHII) near the observational sites is stronger at night and in winter than during the day and in summer (e.g., Xie et al.[11]; Zheng et al.[12]; Ren et al.[13]; Yang et al.[14]); Deng et al.[15] pointed out that the UHII at night in Shanghai was the

Received 2018-05-16; **Revised** 2018-06-08; **Accepted** 2018-08-08
Foundation item: National Natural Science Foundation of China (41575003); National Key R&D Program of China (2018YFA0605603)
Biography: JIA Wen-qian, M.S., primarily undertaking research on urban climate.
Corresponding author: REN Guo-yu, e-mail: guoyoo@cma.gov.cn

strongest in autumn/winter, while the UHII during the day was relatively stronger for the spring and plum rain season of early summer, and lowest in autumn. Meanwhile, studies also found that change trends of annual mean SAT observed at the meteorological stations were clearly influenced by the urban warming. For example, Huang et al.[16] showed that the annual mean SAT trend brought about by urbanization for southern coastal stations in China is higher than the background trend; Zhou et al.[9] found that the contribution of urban warming to the overall warming in the northern China region was 37.9% during 1961-2000, and it even reaches 71% at Beijing station over the same period (Chu et al.[17]); Urbanization-induced SAT trend reaches 0.19°C/10yr during 1962-2009 for Shijiazhuang station, accounting for 68% of all warming trend (Bian et al.[18]).

Wuhan, the capital city of Hubei Province, has a built-up area of approximately 400km^2 and a population of over 5millions with a rapid development and urbanization process. Wuhan city is located in the Jianghan Plain (Fig. 1), having severe heat wave and rainstorms in summer probably aggravated by urbanization effect during the past two decades. UHI effect is remarkable at Wuhan station since the 1980s, especially in winter, and the minimum temperature witnesses the highest contribution of urban warming to overall warming (e.g., Ren et al.[13]; Wu et al.[19]); Chen et al.[20] studied the UHI change trend for Wuhan station from 1960 to 2005, and found that the annual mean urban warming and contribution rate reached 0.235°C/10yr and 60.4% respectively. However, the previous researches only rely on the simple criteria to select reference stations, and the selected rural stations may have been gradually affected by UHI effect with the development of the small cities and towns themselves. There is a need to adopt a more objective method to select reference stations, and to assess whether or not the analysis results obtained by the new method are consistent with previous ones. In addition, it has been found that the temperature and sunshine hours in Wuhan decreased in recent 10 years (Cao et al.[21]), which is consistent with the global warming slowdown, and the relative humid (RH) experienced a rise in a certain degree after 2007 (Suonan et al.[22]). It is not clear whether UHI effect for Wuhan station will have some new features when the data are updated to present to include the period of climate warming slowdown.

In this paper, in-homogeneity adjustment is made for the SAT data updated to 2015. We analyze the climatological characteristics of UHI effect and the change of UHII with time near Wuhan station by using the homogeneous data from the urban station and two rural stations. Meanwhile, we estimate the urbanization effect on the long-term SAT change trend of the Wuhan station. The results of this paper are helpful for a further understanding of temporal characteristics of UHI effect, as well as nature and extent of urbanization-induced bias of SAT observation records for Wuhan station.

2 DATA AND METHODS

The monthly mean, minimum and maximum SAT data from 13 stations in Wuhan for the time period 1961-2015 and the MOD11A2 8-day LST product at 1-km spatial resolution in 0.02K unit from July 28 to August 4 in 2016 are used. The SAT are obtained from the National Meteorological Information Center of the China Meteorological Administration, which have already been quality controlled and the inhomogeneities caused by the artificial to automatic observation have been corrected. The SAT data at Caidian station missed in June, July and August in 1968 being replaced by monthly mean SAT data for 55 years.

Gallo et al.[23] used the vegetation index obtained from NOAA / AVHRR to explain the temperature difference between urban and rural areas. Ren and Ren[24] used MODIS data to select 113 SAT reference stations from 672 national reference climate stations and national basic meteorological stations of mainland China, pointing out that the method could be adopted for the adjustment study on the urbanization bias of the currently used air temperature records of surface climate stations. Compared to the other approaches used for classifying climatic stations, the remote sensing method does not rely so much on social and economic data. It is therefore feasible to use MODIS products to determine the regional boundaries of UHI-affected areas (Zhang[25]).

The remote sensing image quality is affected by the cloud cover. The Hubei area is controlled by the subtropical high in late July and the early August, and the weather condition is better. Therefore, the average LST from July 28 to August 4 in 2016 is used to determine the spatial distribution of ground surface temperature around the stations. The isothermal pattern of LST could reflect the temperature gradient from urban centers to suburbs less influenced by the UHI effect (Ren and Ren[24]). Winkler et al.[26] proposed that the boundary of the area affected by the UHI effect can be represented by the outermost closed isotherm of the annular temperature field in a city or town. In this paper, the outermost isotherm circle is 33.85°C and it can be taken as the boundary of the UHI-affected in the Wuhan city (Fig. 1).

The urban stations and the reference (rural) stations are determined according to the specific location of the station in the brightness temperature field. The stations which are located within the isotherm 33.85°C are

regarded as the urban stations. The selection of the reference stations follows the following principles: (1) outside the closed contour 33.85°C of surface temperature; (2) the distance from the boundary of built-up areas within 30km to ensure in the same large-scale circulation and climate background with the urban stations; (3) elevation difference with the urban stations less than 20m, avoiding the influence brought by height difference; (4) the micro-environment around the rural stations is open.

The determination of rural stations is particularly important for studying the urban heat island effect. We therefore chose a more objective and strict method for the reference stations selection. Relative to other approaches to classify climatological stations, the remote sensing (RS)-based method is much less dependent on social and economic data, and RS data is also relatively continuous, with high spatial comparability and objectivity.

In addition to ensuring that all historical stations are outside the outermost contour when selecting a reference station, the distance to the city station, the altitude difference, and the environment around the sites are also taken into consideration. The distance and elevation difference are limited to ensure in the same climate background with urban station, as far as possible reducing the errors of results. In addition, many natural landscapes, such as lakes, basins and hills, also affect the surface thermal structure, and may result in the closed isotherms around the stations. These have also been taken into account when determining the reference stations.

The locations of all historical observation sites for Wuhan station are located within the 33.85°C (Fig. 1), and there has been a weak but a clear urban heat island effect at the urban station (Wang et al.[27]). We therefore consider Wuhan station as a representative urban station; the rural stations of all historical observation outside the closed circle of 33.85°C are Huangpi, Hanchuan and Anlu stations. The Anlu station is too far from Wuhan station and the elevation difference from the urban station is more than 20m (Table 1), so it is not taken as a reference station, and the relocation process of Anlu station is not shown in Fig. 1. From the Google earth images (Fig. 2), the locations of remaining rural stations are at the edge of the built-up areas, with little population and few buildings. It is clear that these two stations have not yet been significantly affected by nearby settlement and the UHI effect, and they can therefore be regarded as rural stations.

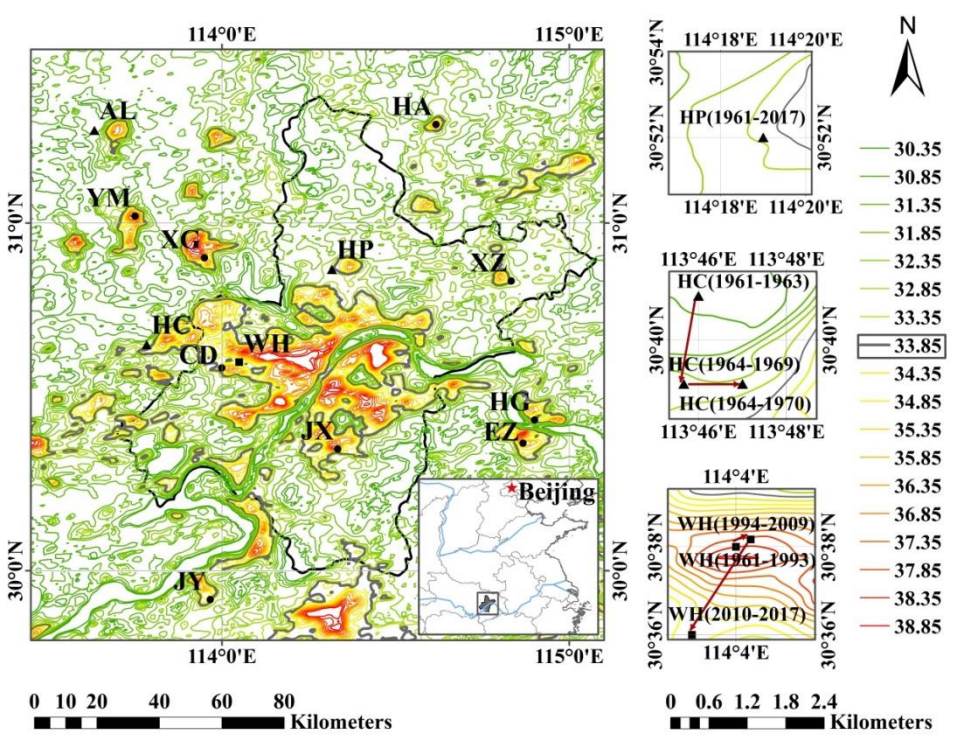

Fig. 1 The location of 13 stations and average LST isotherm distributions in Wuhan area. Abbreviations of the stations names are AL for AnLu, HA for HongAn, YM for YunMeng, XG for XiaoGan, HP for HuangPi, XZ for XinZhou, HC for HanChuan, WH for WuHan, CD for CaiDian, JX for JiangXia, HG for HuangGang, EZ for EZhou, and JY for JiaYu. The black line in the graph is the boundary of Wuhan city, and the relative position of Wuhan is shown in the illustration. The three enlarged figures on the right represent the relocation process of selected urban and rural stations, and the arrows show the relocation direction

Table 1. Information of the stations used in the study

Station name (Code)	Longitude (E)	Latitude (N)	Altitude (m.a.s.l.)	Distance from Wuhan station (m)	The time and distance of Relocations since 1961(km)
Wuhan (57494）	114.05	30.60	23.6	0	1994.4 (0.08); 2010.1 (8)
Hanchuan (57486)	113.78	30.65	27.0	26110	1964.1(6); 1970.11(3)
Huangpi (57491)	114.32	30.87	31.7	39100	
Anlu (57388)	113.63	31.27	55.5	84110	

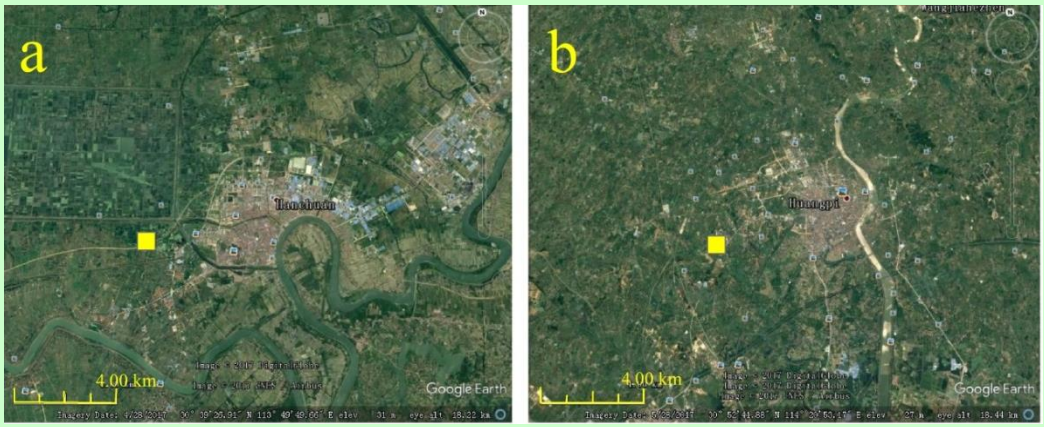

Fig. 2 Station and the surrounding landscapes as seen from Google Earth picture: (a) Hanchuan (No.57486), (b) Huangpi (No.57491)

The breakpoints of data series caused by relocations are examined for annual mean (T_{mean}), minimum (T_{min}) and maximum (T_{max}) SAT using E-P method (Easterling et al.[28, 29]). The autocorrelation problem needs to be considered in the in-homogeneity test. Annual mean SAT data series is less affected by the seasonal variability, reducing data series autocorrelation to a large extent (Cao et al.[30]). Therefore, in-homogeneity test and correction are based on the annual temperature data series in this paper.

Locations of the breakpoints could be determined based on whether or not the values of t statistics exceed the significance level. An adjustment could be made if the breakpoints could be proved to be real in reference to the metadata. The difference between the five-year average before and after the breakpoints is used as the adjustment value, and if the data is less than 5 years before and after the breakpoints, the longest time is taken to calculate the difference. Then annual adjustment values are interpolated linearly into the every month. Here, n=55, the length of the sub-series was 3 years, and the given significance level $\alpha = 0.05$.

After investigation of historical data, it is found that the relocation of Wuhan station in 2010 with a move of about 8 km has a significant impact on temperature series. The T_{mean} and T_{min} series both witnessed big breakpoints in 2010 by using moving t-test method. The breakpoints therefore for the T_{mean} and T_{min} data series are adjusted in the study. In order to ensure data uniformity, the T_{max} series also has been corrected despite the breakpoint in 2010 is undetectable. In the process of adjustment, we correct the SAT data after station moving by adding the adjustment values in order to better keep the UHI effect recorded at the original site (Wang[27])(Fig. 3).

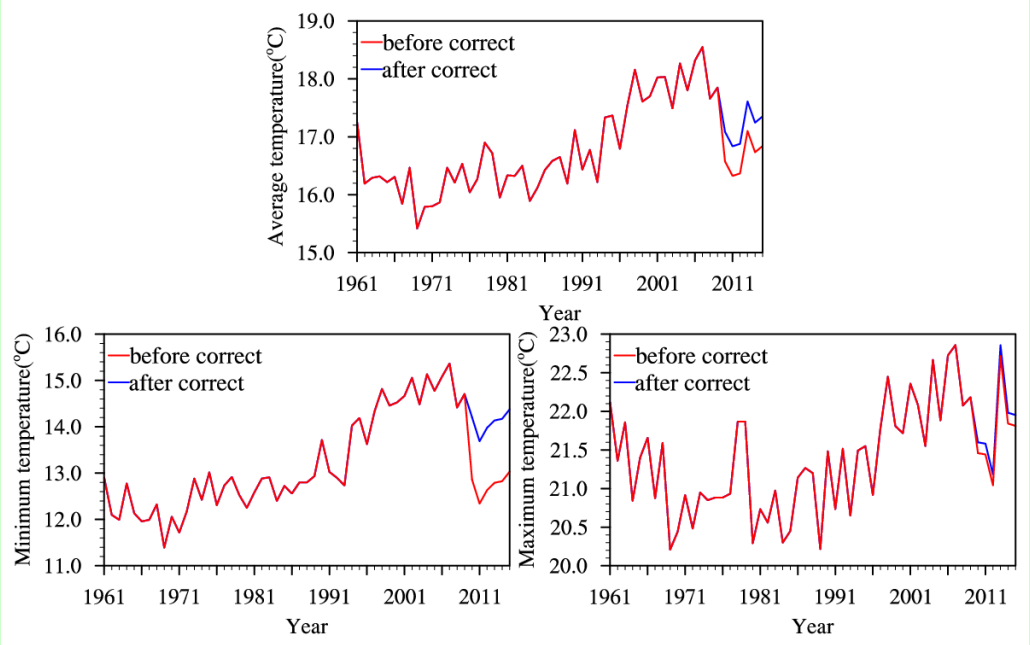

Fig. 3 Comparison of the series of annual mean, minimum and maximum temperature before and after homogenization at Wuhan station

Hanchuan station has moved for two times since 1961, but the data series has no detectable breakpoint probably because the relocation time was too early, and the data series has not been adjusted. Huangpi station has not been moved since its establishment, and this enables it to be an ideal reference station for examining the urbanization effect.

In the process of SAT data adjustment for Wuhan station, especially for the T_{mean} and the T_{min}, the corrected values are positive, indicating that T_{mean} and T_{min} originally drop sharply since 2010, which is largely due to the Wuhan station moving from the urban area to the suburbs at that time. There is a false cooling phenomenon in SAT series of Wuhan station caused by the relocation, and the warming trend of the corrected temperature series is more obvious than that of the original one (Fig. 3). The homogenization has regained the UHI effect and urban warming trend in the SAT series (Zhang et al.[31]).

UHII at Wuhan station is defined as the SAT difference between the urban and rural stations. The rural SAT or reference series is the average SAT of the two rural (reference) stations. Linear trends of the UHII series are obtained by using the least square method and the significance level of linear trend is examined by T test method. The difference of SAT linear trends between urban and rural stations is equal to the linear trend of the UHII series, and they are defined as urban warming or urbanization effect. Contribution of urbanization effect or urbanization contribution is the proportion of the statistically significant urbanization effect to the overall trend of SAT at the urban station (Ren et al.[10, 13]).

In practical calculations, the urbanization contribution may exceed 100%, probably brought by unknown local anthropogenic factors for rural stations in a few cases. In this case, it is adjusted to 100%. As indicated in the definition, if the urban warming is not statistically significant, the urbanization contribution will not be calculated and analyzed.

3 RESULTS AND DISCUSSION

3.1 *Climatological Characteristics of UHII*

Annual and seasonal mean UHII at Wuhan station for two periods of 1961-2015 and 1988-2015 are examined. As described later, UHII near Wuhan station is relatively weak before 1988, and a significant increase occurs afterward (Fig. 5).

The annual mean UHII at Wuhan station is 0.39°C for the period 1961-2015, the largest seasonal mean UHII is 0.47°C in summer, followed by 0.41°C in spring, 0.40°C in autumn, and 0.32°C in winter, but overall the seasonal difference is not significant (Table 2). The minimum temperature UHII is higher than the maximum temperature UHII, indicating that the UHII in Wuhan is stronger at night than the daytime. UHII has an obvious diurnal non-symmetry, which is consistent with most previous research results for the megacities of China (e.g.,

Zhou[32]; Xie et al.[11]; Zheng et al.[12]; Bian et al.[18]).

Table 2. Annual and seasonal mean, minimum and maximum temperature UHII for time periods 1961-2015 and 1988-2015 at Wuhan station (°C)

Period	Temperature	Spring	Summer	Autumn	Winter	Year
1961-2015	Mean	0.41	0.47	0.40	0.32	0.39
	Minimum	0.56	0.61	0.63	0.40	0.54
	Maximum	0.35	0.41	0.21	0.29	0.32
1988-2015	Mean	0.67	0.81	0.73	0.58	0.69
	Minimum	0.99	1.14	1.26	0.95	1.07
	Maximum	0.44	0.51	0.29	0.33	0.39

In the past 28 years, the seasonal feature of the mean UHII for Wuhan station is consistent with that of 1961-2015, the largest in summer and smallest in winter. The difference is that the three kinds of temperature UHII is larger during the recent period, with the minimum temperature UHII being the most obvious, almost two times the 1961-2015 period, followed by the mean temperature UHII, and the maximum temperature UHII change is the smallest. It shows that the UHII near Wuhan station has been enhanced since the late 1980s, which well corresponds to the rapid urbanization process in the city. The population and built-up areas in Wuhan had a rapid increase after the late 1980s and early 1990s, leading to an accelerating urbanization process (Xiao et al.[33]).

Whether the entire period or the recent 28 years, the seasonal mean temperature and maximum temperature UHII are the largest in summer, and the minimum temperature UHII is the strongest in fall. These features are different from the UHI effect of the metropolis in northern China in which the strongest UHII occurs in winter and the weakest in summer or spring (e.g., Bai et al.[34]; Zheng et al.[12]; Xie et al.[11]; Bian et al.[18]; Yang et al.[14]). This may be mainly due to the smaller solar elevation angle in winter (the zenith angle is larger), and the frequent temperature inversion and stable weather phenomenon controlled by the dry and cold Siberia air mass in winter in the north. Meanwhile, the humidity in lower atmosphere and cloudiness in northern China are usually less and anthropogenic heat release due to the heating is large in winter (Chen and Shi[35]). In contrast to winter, summertime in the north has a larger solar elevation angle (smaller zenith angle), and is more frequently affected by the southwest and southeast air currents, with more cloudiness and precipitation, and cooling energy consumption and artificial heat release in urban areas is smaller, leading to a generally lower UHI effect; the average wind speed in spring in the north is usually stronger, which is also against to the UHI formation and development.

Wuhan city belongs to the inland subtropical monsoon humid climate, with hundreds of lakes scattering in urban areas. In winter, the relative humidity and water vapor content of lower atmospheric are larger, and the anthropogenic heat release from urban heating is less, which may be the main reasons for the lower UHII in the cold season. In summer, the atmospheric humidity is high, with more cloudiness and precipitation, and the solar elevation angle is large (the zenith angle is small). These will not benefit the formation and development of UHI. However, the average wind speed in summer is weaker, and stable atmospheric layer and more sunny days prevail, because the city is controlled by the subtropical high in midsummer season (Wang[36]). Besides, the use of air conditioning in the summer is more common, with large anthropogenic heat release into the urban boundary layer. All of these will benefit the enhancement of the UHII in the urban areas during summertime. The weather in autumn is sunny with little cloud and the wind speed is small. In addition, the heat storage by abundant urban lakes makes boundary layer atmosphere warmer, enhancing the UHII. A higher seasonal mean UHII in autumn therefore results.

The seasonal variation feature of UHII at Wuhan station is similar to the other southern cities, such as Shanghai city and Guangzhou city, with larger UHII in autumn for mean and minimum temperature and significantly more obvious UHI phenomenon in spring and summer for maximum temperature. There is a big difference for the UHII of summer and winter for mean and minimum temperature between Wuhan station and other southern cities, however, and this may be related to the different underlying surface, geographical position and other factors (e.g., Xu et al.[37]; Deng et al.[15]; Zhou et al.[32]).

The seasonal variations of monthly mean UHII in the past 55 years and the past 28 years are similar (Fig. 4). The mean temperature UHII and minimum temperature UHII are the lowest in January, and then they gradually increase. The monthly mean temperature UHII reaches peak in July, and then slowly weakens, while the peak of minimum temperature UHII appears in September, and also higher in November for the recent 28 years. The monthly mean maximum temperature UHII has a different seasonal cycle, with the strongest in July and the

weakest in October. It is thus obvious that the difference between the maximum and minimum temperature UHII in autumn is the largest in a year.

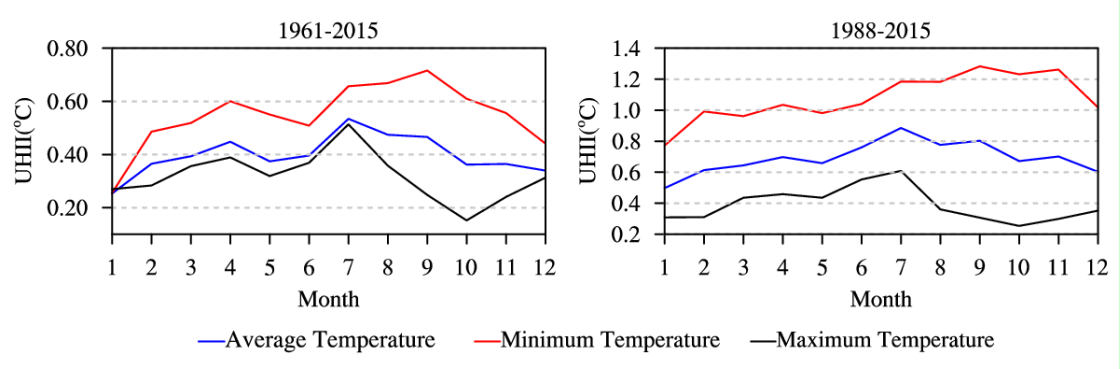

Fig. 4 Seasonal variation of monthly mean, minimum and maximum temperature UHII for time periods 1961-2015 and 1988-2015 at Wuhan station (°C)

The fact that maximum temperature UHII shows a downward trend after July can be explained by the increase in rainfall and cloudiness significantly accompanying the retreat of the subtropical high, with the suburbs and the city receiving similarly small amount of solar radiation during the daytime. The reduced anthropogenic heat release after mid-August might be another reason. In addition, large areas of lake and wetland in urban make night warmer and day cooler, with the latter offsetting the maximum temperature UHI effect to certain extent.

3.2 Urban Warming and its Contribution to Overall Warming

Fig. 5 provides the long-term change in annual mean, minimum and maximum temperature UHII at Wuhan station. Annual mean and minimum temperature UHII bears a consistent inter-annual and decadal variation, showing that UHII gradually increase since the early 1960s, especially for minimum temperature UHII as high as 33%, reaching peak around 2005 and dropping afterward. The maximum temperature UHII experiences a certain degree of decline in the 1960s, stable in the 1970s and 1980s, and a slow increase from the 1990s to 2004.

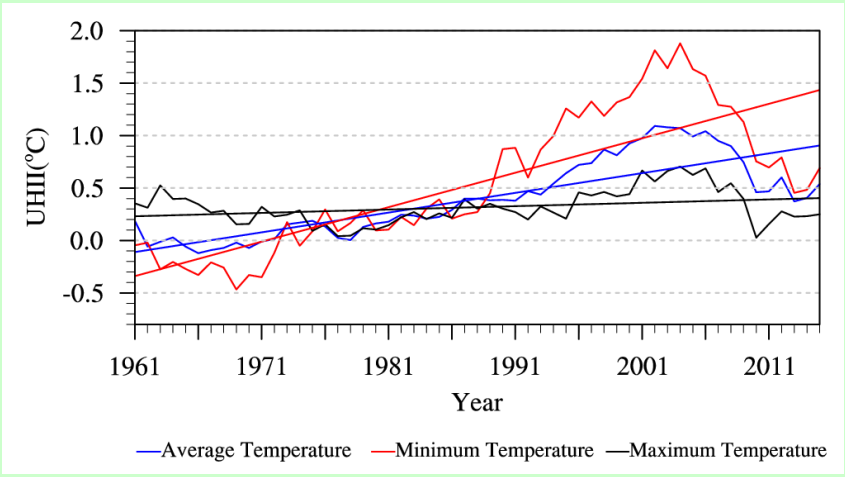

Fig. 5 Annual mean, minimum and maximum temperature UHII (polygonal lines) and their trends (straight lines) at Wuhan station

The UHII variations in the three kinds of temperatures are all characterized by lower values during the 1960s to the late 1980s, higher values after 1988. In general, the three kinds of temperatures UHII show an upward trend in the past 55 years, with an obvious rising in 1961-2004, the fastest increase (0.53°C/10yr for annual mean minimum temperature) in 1988-2004, and a decreasing in 2005-2015. Therefore, the long-term trends of UHII can be examined for four different time periods of 1961-2015, 1961-2004, 1988-2004 and 2005-2015.

Fig. 6 shows the urbanization-induced change in annual mean, minimum and maximum SAT, and the urbanization contribution to the overall warming at Wuhan station for the four periods. For the time period 1961-2015, the trend of annual mean UHII and the urbanization contribution are 0.18°C/10yr and 48.8%

respectively. A more evident urban warming and contribution occur in T_{min} than T_{max}. For the seasons, urban warming and contribution for T_{mean} are both highest in summer, followed by autumn. The largest urban warming of 0.37°C/10yr occurs in autumn T_{min}. Seasonal mean warming observed in summer T_{mean} can be entirely accounted for by the enhanced UHI effect.

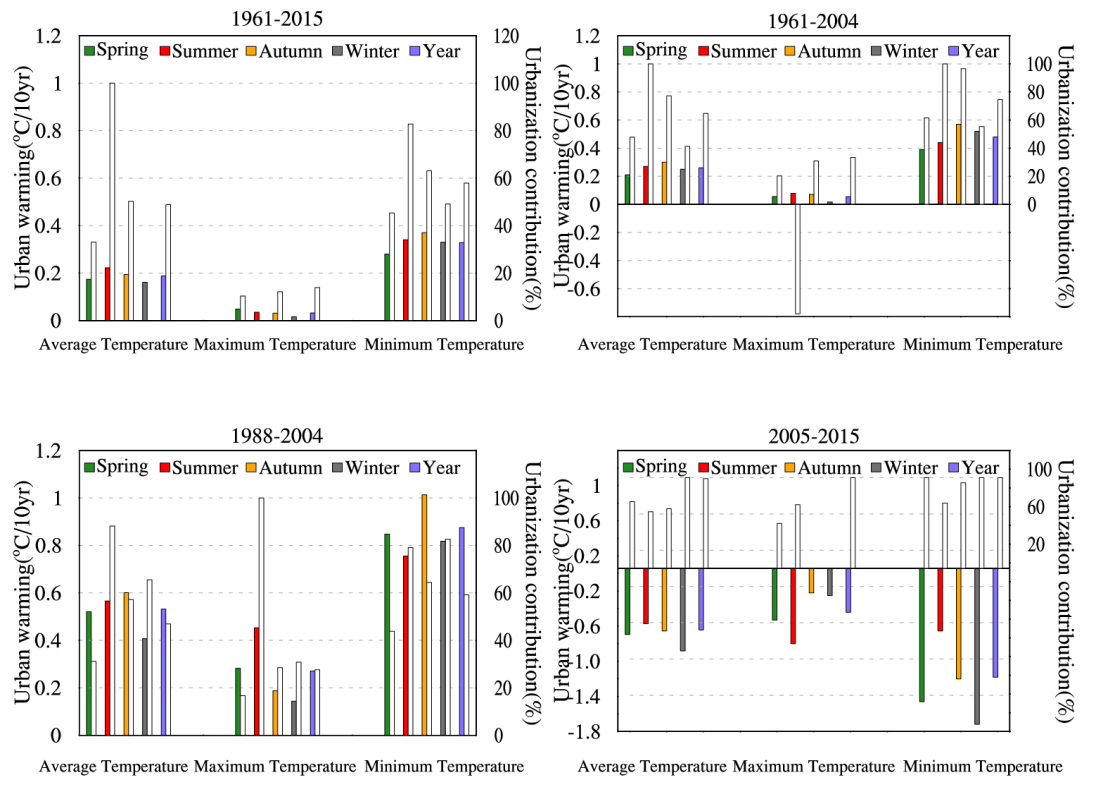

Fig 6. Urbanization effects (solid) and the urbanization contribution (blank) of seasonal and annual mean, minimum and maximum surface air temperature at Wuhan station

Seasonal mean urban warming and urbanization contribution for 1961-2004 are similar to those for the period 1961-2015, showing more evident change in summer and autumn. The difference is that contribution of urban warming in summer T_{max} is a negative value of -77.9%, implying that the background maximum SAT change during this period is characterized by a cooling trend and the urban warming is making an opposite contribution to the decrease at Wuhan station.

In comparison to periods 1961-2004 and 1961-2015, the urban warming during 1988-2004 is larger and more significant. Therefore, more significant urbanization effect at Wuhan station occurs during the late 20th century when urbanization and economic growth of China are unprecedented in history. The annual and seasonal mean, minimum and maximum temperature UHII trends are significantly greater than the other several stages, with more evident urban warming for summer and autumn T_{mean}. However, the urbanization contribution for summer T_{mean} becomes weaker relative to the periods 1961-2015 and 1961-2004. Autumn T_{min} witnesses the most significant urban warming reaching as high as 1.00°C/10yr, and the urbanization contribution as high as 65%, showing the warming observed at autumn night can be mostly accounted for by the urbanization effect.

Seasonal mean maximum temperature UHII trends and urbanization contribution during 1988-2004 are much larger than those in any other periods. This is especially true for summer, with the urbanization contribution even reaching 100%, indicating an entire contribution from the increased UHII to the positive trend of summer mean maximum temperature at the urban station (Fig. 6).

It is worth noting that the winter registers the relatively small urban warming but the quite significant urbanization contribution at Wuhan station, which is completely contrary to the results reported for the megacities of northern China (e.g., Chu and Ren[17]; Ren et al.[10]; Bian et al.[18]), where the UHII trends are the largest in winter, and the urbanization contribution to the overall seasonal warming is often smaller. This may be relative to the lower latitude, wetter and hotter climatic condition and larger proportion of wetland area in Wuhan city compared to the northern megacities. The anthropogenic heat-release difference of winter heating and summer cooling between northern and southern cities, and the different background circulation fields and multi-decadal

climate variability, would be also important to the contrary seasonality of the urbanization effects.

It is worth noting that the rural stations unaffected by urbanization effect can hardly be found in central China. The rural stations used in this paper are currently available stations that are less affected by urbanization. Therefore, there is a certain degree of urbanization impact in the rural station temperature series. As a result, urban warming and their contributions to the overall warming in different time periods as given in this work for Wuhan station could be regarded as the lowest estimates.

China has witnessed a rapid urbanization process in the past half century, especially the past 30 years. From 1978 to 2015, the urbanization rate of the country increases from 17.9% to 50.0%. This phase is also accompanied by the obvious increase in urban heat island effect around the climatic stations (Ren et al.[10]). Through calculation, the urban land and construction land increase by 58% from 1988 to 2004 in Wuhan area, with the most significant urban warming of Wuhan station as high as 0.53°C /10yr, indicating that the rapid expansion of the city is the main reason for the increase of UHI effect recorded in the SAT series.

The above three time periods (1961-2015, 1961-2004 and 1988-2004) all undergo a significantly higher urban warming for T_{min} than T_{mean} and T_{max} at Wuhan station. This indicates that the UHI effect is more obvious at night than the daytime, which is mainly due to the greater thermal admittance in the urban area than that of the suburbs, leading to a slower temperature drop in urban after sunset. The urban buildings, with many urban street canyon, generally absorb more solar radiation than the suburbs during the daytime. There are downward long-wave radiations of walls and eaves in addition to atmospheric counter-radiation, coupled with the relatively low wind speed, and the heat is not easily dissipated at night in the urban area. All of these make the nighttime UHI effect higher than daytime, and the UHI effect at night will become more obvious with the development of the city, resulting a more rapid increase in T_{min} than T_{mean} and T_{max}.

During the period from 2005 to 2015, the annual and seasonal mean, minimum and maximum temperature UHII trends are negative, indicating that the UHII for Wuhan station is weakening in the past 10 years. The descending rates of urban warming for annual and seasonal mean T_{min} are much higher than the T_{max} except for the summer. Although the UHII is weakening in the last 10 years, the urban contribution is positive and still large. This may be related to the fact that the background SAT is experiencing a decrease during the period of climate warming slowdown, and the urban station undergoes a more rapid decrease than the rural stations do (Fig. 7). The relatively slower decrease in SAT at the rural stations may be caused by the increase of built-up areas around the observational sites in recent 10 years. The rural stations may therefore have been affected by urbanization. It is highly possible that the rural stations have become unrepresentative after 2005 due to the urbanization effect in these originally suburban areas.

The annual mean T_{mean}, T_{min} and T_{max} in urban and rural stations have decreased since 2005 (Fig. 7), which is consistent with the trend of temperature changes in China. Wang[38] pointed out that the annual mean temperature shows a certain degree of downward trend from 2005-2012. The warming hiatus since about 2000 is especially obvious in North China. The temperature decrease in recent decade in both urban and rural stations may therefore be caused by large scale drivers. The fact that the temperature decrease is more significant at Wuhan station than that at the rural stations makes annual mean, minimum and maximum temperature UHII to weaken during the nearly 10 years. The reasons for the more rapid decline of temperature at the urban station need to be further studied, but it is possible that the areas around the reference or suburban stations experience a more rapid urbanization than those around the urban station.

It is notable that the relative humidity(RH) has a certain recovery recently, and the RH series is inversely related to annual mean temperature series at Wuhan station, with the correlation coefficient reaching -0.65 for 1961-2015, and the urban heat island phenomenon is always accompanied by the urban dry island (e.g., Suonan et al.[22]; Zhou et al.[39]). Rising of RH in the last 10 years therefore is not conducive to the formation and development of urban heat island around the urban station. Besides, sunshine hours have declined after 2007 in Wuhan (Suonan et al.[22]), and the winter mean wind speed near the ground surface has strengthened in the period of climate warming slowdown (Lin et al.[40]). These, in combination with the background climate cooling of eastern China and the urbanization process around the rural stations, may also account for part of the greatly weakened UHII and the large downward trend of temperature during the last decade at the urban station.

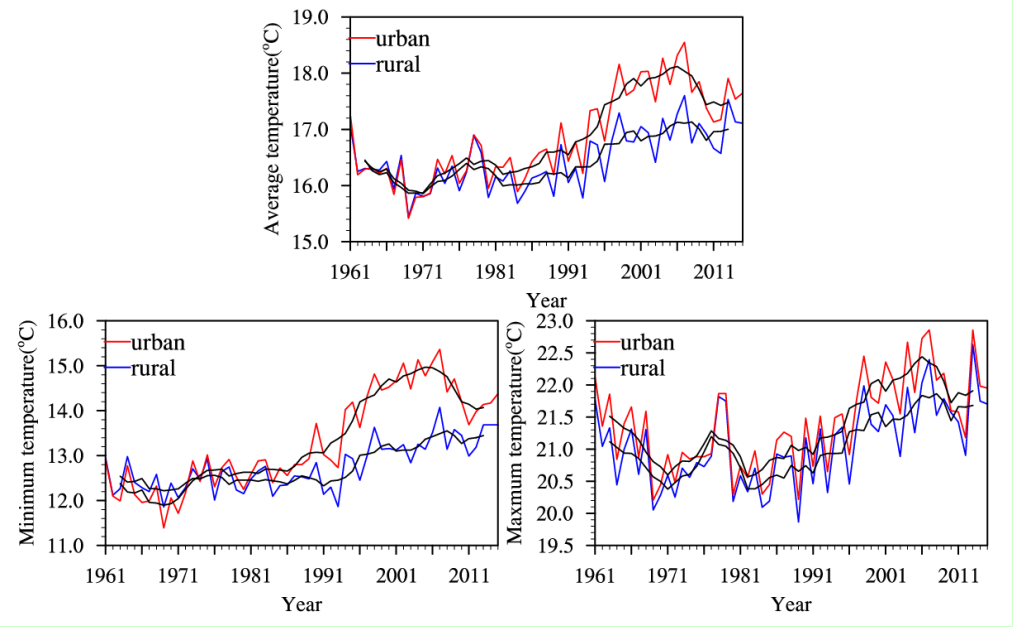

Fig. 7 Annual mean, minimum and maximum surface air temperature at Wuhan station and the two rural stations (average of two rural stations). Black solid line denotes 3 points moving average

The inhomogeneity in the observed SAT series has a significant effect on the long-term trend analysis. In this paper, the breakpoints due to the station moving are detected for the urban and rural stations. There is a sudden drop in temperature after Wuhan station moved to the suburbs in 2010, with the T_{min} difference is 1.35°C before and after the move. Historical data confirm that this decrease is not a true natural change, but an inhomogeneity error caused by the relocation (Liu et al.[41]). It makes the T_{mean} trend to drop from the 0.57°C/10yr to 0.43°C/10yr. Meanwhile, the three kinds of temperatures UHII will be weaker after 2010, especially the mean and minimum temperature UHII, if the inhomogeneity is not corrected. The effect of inhomogeneity caused by relocation on SAT series is obvious, and it is necessary to make reasonable adjustments.

Compared with previous studies on Wuhan station, we test and correct the inhomogeneities of SAT data, and use the more objective method of selecting the rural stations. The SAT data series is also updated. The conclusions are very similar to those previous works. The annual mean urbanization effect and contribution are 0.26°C/10yr and 64.7% respectively in this analysis, similar to those estimated in Ren et al.[13] (0.20°C/10yr and 64.5% for period 1961-2000), and Chen et al.[20] (0.24°C/10yr and 60.4% for period 1960-2005). The previous studies also showed that the urban warming is the highest in autumn and the second in summer, whereas the summer witnessed the largest urbanization contribution, followed by the autumn (Ren et al.[13]), which is basically the same with the results of this paper. In addition, Wang et al.[27] showed an annual mean urban warming of 0.31°C/10yr for Wuhan station for the period 1961-2010, larger than the value of 0.19°C/10yr for 1961-2015 in this paper. This difference may be mainly related to the updated data in this article, and the different rural stations applied in the two analyses.

The annual and seasonal mean urbanization effects have weakened when the data are updated to 2015, and also their seasonal distribution has a slight change with the largest urbanization effect now occurring in summer and the second largest in autumn. This may be related to the increase in anthropogenic heat release due to the recent wider use of air conditioning and refrigeration equipment in summer (Zhou[42]), as well as the compressed regulation effect of wetlands due to the rapid shrink of urban lake areas (Dan et al.[43]).

4 CONCLUSIONS

The annual mean UHII is 0.39°C for 1961-2015 at Wuhan station, and the UHI effect is more obvious during the recent 28 years, with the annual mean UHII and minimum temperature UHII reaching 0.69°C and 1.07°C respectively. The strongest monthly mean UHII appears in July, and the weakest in January.

The annual mean, minimum and maximum temperature UHII shows significant upward trends for the period 1961-2015. The annual mean urban warming and urbanization contribution are 0.18°C/10yr and 48.8% respectively, and larger and more significant urban warming and urbanization contribution are registered for T_{min}. The largest seasonal mean urban warming and urbanization contribution occur in summer.

The annual mean urban warming becomes more obvious with time, with urbanization effect reaching as high as 0.53°C/10yr for the period 1988-2004.The seasonal mean urbanization effect and urbanization contribution for the period 1988-2004 are both high in summer and autumn, with the greatest urban warming of higher than 1.00°C/10yr seen for autumn mean T_{min}.

From 2005 to 2015, the annual mean UHII for T_{mean}, T_{min} and T_{max} show evident decreasing trends. This decrease may have at least partially caused by the unrepresentativeness of the rural stations during the recent decade.

Therefore, the SAT data in Wuhan station has been significantly affected by urbanization. As an urban meteorological station, the long-term observational data of surface air temperature can be used to monitor and study urban climatology and urban climate change, but they are improper to be used in monitoring and studies of regional and global climate change without adjustment of the urbanization-induced bias, no matter if the homogenization of the data is made.

REFERENCES:

[1] JONES P D, GROISMAN P Y, COUGHLAN M. Assessment of urbanization effects in time series of surface air temperature over land[J]. Nature, 1990, 347: 171-177.
[2] PETERSON T C. Assessment of urban versus rural in situ surface temperatures in the contiguous United States: No difference found[J]. Journal of Climate, 2003, 16: 2941-2959.
[3] PARKER D E. A demonstration that large-scale warming is not urban[J]. Journal of climate, 2005, 19: 2882-2895.
[4] LAWRIMORE J H, MENNE M J, GLEASON B E. An overview of the Global Historical Climatology Network monthly mean temperature data set, version 3[J]. Journal of Geophysical Research, 2011, 116, D19121.
[5] KARL T R, DIAZ H F, KUKLA G. Urbanization: Its Detection and Effect in the United States Climate Record[J]. Journal of Climate., 1988, 1(11): 1099-1123.
[6] HANSEN J, RUEDY R, SATO M. A closer look at United States and global surface temperature change[J]. Journal of Geophysical Research Atmospheres, 2001, 106(D20): 41-49.
[7] KALNAY E, and CAI M. Impact of urbanization and land use on climate change[J]. Nature, 2003, -1(6939): 528-531.
[8] ZHOU L M, DICKINSON R E, TIAN Y H. Evidence for a significant urbanization effect on climate in China[J]. Proceedings of the National Academy of Sciences of the United States of America, 2004, 101(26): 9540-9544.
[9] ZHOU Y-Q, REN G-Y. Identifying and Correcting Urban Bias for Regional Surface Air Temperature Series of North China over Period of 1961—2000[J]. Climatic and Environmental Research, 2005, 10(4):743-753.
[10] REN G-Y, ZHOU Y-Q, CHU Z-Y. Urbanization Effects on Observed Surface Air Temperature Trends in North China[J]. Journal of Climate, 2008, 21(6):1333-1348.
[11] XIE Z, CUI J-L, CHEN D-G. The Annual, Seasonal and Monthly Characteristics of Diurnal Variation of Urban Heat Island Intensity in Beijing[J]. Climatic and Environmental Research, 2006, 11(1): 69-75.
[12] ZHENG Z-F, LIU W-D, WANG Y-C. Distributive Character of Urban Heat Island Effect in the Beijing Region[J]. Journal of Nanjing Institute of Meteorology, 2006, (05): 694-699.
[13] REN G-Y, CHU Z-Y, CHEN Z-H. Implications of temporal change in urban heat island intensity observed at Beijing and Wuhan stations[J]. Geophysical Research Letters, 2007, 34(5): 89-103.
[14] YANG P, REN G, LIU W. Spatial and Temporal Characteristics of Beijing Urban Heat Island Intensity[J]. Journal of Applied Meteorology & Climatology, 2013, 52(8):1803-1816.
[15] DENG L-T, SHU J, LI C-Y. Analysis on the Changing Characteristics of Urban Heat Island in Shanghai[J]. Journal of Tropical Meteorology, 2001, 17(3):273-280.
[16]HUANG J-Y, LIU X-N, LI Q-X. The Study Of Relationship Between HeatIsland Effect And Population In Cities Over South Of China[J]. Journal Of Tropical Meteorology, 2006, 20(6):713-722.
[17] CHU, Z-Y, REN G-Y. Effect of enhanced urban heat island magnitude on average surface air temperature series in Beijing region[J]. Journal of Meteorological Research, 2005, 63(4):534-540.
[18] BIAN T, REN G-Y, ZHANG C-H. Characteristics and change of urban climate in Shijiazhuang City, Hebei Province, China [C]. Meteorological Society annual meeting, 2012, 5: 402-408.
[19] WU Y, REN Y-J, FANG S-D. Analysis of the Urban Heat Island Effect in Wuhan and Its Influence Elements[J]. Meterology and Disaster Reduction Research, 2017, (01): 43-50.
[20] CHEN Z-H, WANG H-J, REN G-Y. Study on Asymmetric Change of Urban Heat Island Intensity in Wuhan City[J]. Advances in Climate Change Research, 2007, 05: 282-286.
[21] Cao XX. Analysis on Characteristics of Climate Change in Wuhan City form 1961-2012[D]. Central China Normal University, 2015.
[22] SUONAN K-Z, REN G-Y, JIA W-Q. Climatological Characteristics and Long-term Trend of Relative Humidity in Wuhan City. Submitted, 2017.
[23] GALLO K P, Mcnab A L, Karl T R. The use of a vegetation index for assessment of the urban heat island effect[J]. International Journal of Remote Sensing, 1993, 14(11): 2223-2230.
[24] REN Y, REN G. A Remote-Sensing Method of Selecting Reference Stations for Evaluating Urbanization Effect on Surface Air Temperature Trends[J]. Journal of Climate, 2011, 24(7): 3179-3189.
[25] ZHANG L. Urbanization effect on Extreme Temperature Change in East Asia[D]. Nanjing University Of Information Science &technology, 2014.

[26] WINKLER J A, Skaggs R H, Baker D G. Effect of Temperature Adjustments on the Minneapolis-St. Paul Urban Heat Island[J]. Journal of Applied Meteorology, 1981, 20(11): 1295-1300.
[27] WANG M, WU Y, REN Y-J. An Analysis Of The Features Of The Urban Heat Island In Wuhan And The Influence Elements[J]. Meteorology and Disaster Reduction Research, 2015, 01:43-50.
[28] EASTERLING D R, PETERSON T C. A new method for detecting undocumented discontinuities in climatological time series[J]. International Journal of Climatology, 1995a, 15(4):369–377.
[29] EASTERLING D R, PETERSON T C. The effect of artificial discontinuities on recent trends in minimum and maximum temperatures[J]. Atmospheric Research, 1995b, 37(1–3):19-26.
[30] CAO L-J, YAN Z-W. Research Progress of Homogeneity of Ground Climate Data[J]. advances in climate change reserch, 2011, 07(2):129-135.
[31] ZHANG L, REN G-Y, REN Y-Y. Effect of data homogenization on estimate of temperature trend: A case of Huairou Station in Beijing Municipality[J]. Theor Appl Climatol, 2013, 115(3-4):365-373.
[32] ZHOU S-Z, ZHANG C. heat island effect at Shanghai city[J]. Acta Geographica Sinica, 1982, 04: 372-382.
[33] XIAO J-P, FENG P, LI J-Y. Maps Testify the Development Track about the City of Wuhan During the Decade[J]. Journal of Geomatics, 2014, 39(2):59-62.
[34] BAI H-Z, REN G-Y, FANG F. Characteristics of Urban Heat Island Effect and Its Influential Factors in Lanzhou City[J]. Meteorological Science and Technology, 2005, 33(6):492-495.
[35] CHEN B, SHI G-Y. Estimation of the distribution of global anthropogenic heat flux[J]. Atmospheric and Oceanic Science Letters, 2012, 5(2): 108-112.
[36] WANG L-H. Trend Analysis of Precipitation Change in Wuhan City[J]. Water Resources and Power, 2010, 12: 4-5.
[37] XU X-D, TANG X. Introduction to Urbanization and Environmental Meteorology[M]. Meteorological Press, 2002.
[38] Wang D. Minimum temperature in China response to the warming hiatus. Nanjing University Of Information Science &technology, 2017.
[39] Zhou S-Z, Discussion of the urban-rural differences in atmospheric humidity of Shanghai area. Transactions of Oceanology and Limnoloty, 1994, 2: 13-25.
[40] LIN C, YANG K, QIN J. Observed Coherent Trends of Surface and Upper-Air Wind Speed over China since 1960[J]. Journal of Climate, 2013, 26(9):2891-2903.
[41] Liu W-B, L M, J H. Analysis of the impact of urban development on meteorological observation data in Wuhan [A]. The 33rd Annual Meeting of the Chinese Meteorological Society S10 Cities, Precipitation and Haze - The 5th Urban Meteorological Forum [C], 2016.
[42] ZHOU J, WEN Y-G. Influence of UHI intensity on annual energy consumption for heating and air-conditioning in business buildings[J]. Building Technique Development, 2012, 10:58-59.
[43] DAN Y-I, WANG H-Z, ZHANG H. Lakes evolution of central Wuhan during 2000 to 2010[J]. Acta Ecologica Sinica, 2013, 34(5):1311-1317.

Theoretical and Applied Climatology
https://doi.org/10.1007/s00704-019-02893-x

ORIGINAL PAPER

Diurnal and intra-season variation of warm-season temperature in coastal zone of Qinghai Lake

Hongmei Li[1,2] · Guoyu Ren[2,3] · Wanzhi Li[1]

Received: 19 June 2018 / Accepted: 1 May 2019
© Springer-Verlag GmbH Austria, part of Springer Nature 2019

Abstract
The Qinghai Lake is the largest saltwater lake in the Tibetan Plateau and in mainland China. Effects of the lake on surface climate of the coastal areas, however, are not well understood. This article utilizes hourly observation data of warm season from 17 automatic weather stations to analyze the diurnal and seasonal variations in air temperature in different coastal zones of the Qinghai Lake. The EOS/MODIS data was also used to analyze the surface temperature differences between the lake and its surrounding areas. The results show a few unique characteristics of the plateau lake: (1) based on the satellite data, lake surface temperature is lower than its surrounding areas (4.9~25.1 °C and 12.2~35.6 °C respectively) in the daytime, while it is obviously higher than that in the surrounding areas (1.9~10.5 °C and − 13.1~6.3 °C respectively) at the nighttime. Daily mean water surface temperature is higher than that in the surrounding areas, which is 7.8~17.9 °C and − 2.6~17.9 °C respectively; (2) based on data of meteorological stations, coastal zones closer to the shoreline have a higher air temperature during the warm season largely due to the much warmer nighttime near the shoreline than those in deep inland zones. For the on-shore, near-shore, and far-shore zones, mean daytime air temperature is 8.7~9.6 °C, 9.5~11.1 °C, and 10.0~10.7 °C, respectively, and the mean nighttime air temperature is 2.9~4.1 °C, 1.3~12.3 °C, and − 0.2~0.4 °C respectively. The hourly mean diurnal temperature range (DTR) increases with distance to the shoreline, which is 8.6 °C, 10.9 °C, and 12.3 °C in the on-shore, near-shore, and far-shore zones respectively; (3) differences between maximum and minimum 5-day mean daily maximum (minimum) air temperature during the warm season are 20.3 °C (23.3 °C), 21.7 °C (25.6 °C), and 22.6 °C (26.7 °C) for the on-shore, near-shore, and far-shore zones, respectively, indicating an asymmetrical effect on daytime and nighttime air temperature in the on-shore zone; (4) daily maximum air temperature of the on-shore zone is lower before early October, but it is slightly higher afterward and occurs later; (5) daily minimum air temperature of the on-shore zone is on average higher than that of the far-shore zone, especially after the mid-September, and it also appears later in autumn than in summer.

1 Introduction

Located in the northeastern part of the Tibetan Plateau (TP), Qinghai Lake (QL) is the largest saltwater lake in the high plateau and China, and probably in any of the world high plateaus, with an average lake level altitude 3200 m. Currently, it has a surface area of 4450 km^2, an average depth of 21 m, a maximum depth of 33 m, and a volume of 1050 × 10^9 m^3. The QL basin is surrounded by mountains, with the Datong Mountains in the north, the Riyue Mountains in the east, the Qinghai South Mountains in the south, and the Amuniniku Mountains in the west (Editorial Board of Ecological Environment Protection and Restoration in Qinghai Lake Basin 2008). The terrain within the lake basin is varied, and there are obvious spatial differences in vegetation cover. The major types of vegetation include temperate coniferous forests, plateau and valley shrubs, alpine shrubs, sand shrubs, temperate grasslands, alpine grasslands, alpine meadows, swamp meadows, and alpine rocky slope vegetation (Chen and Peng 1993).

The QL and its surrounding regions have a temperate, semi-arid plateau climate, with a cold winter, warm summer, and meager precipitation. The surface area of the QL is in a

✉ Guoyu Ren
guoyoo@cma.gov.cn

[1] Qinghai Climate Center, Xining 810001, China

[2] Department of Atmospheric Science, School of Environmental Science, China University of Geosciences (CUG), Wuhan 430074, China

[3] Laboratory for Climate Studies, National Climate Center, China Meteorological Administration (CMA), Beijing 100081, China

Published online: 18 May 2019

medium size in view of the global lakes (Crosman and Horel 2010), but the largest in China and East Asia, producing a benefiting condition for a lake climate effect. The vast lake water surface should particularly affect the air temperature of surrounding regions during the warm season, a phenomenon which is worth investigation. The climatic effects of the major lakes of the world have already been extensively explored, especially with regard to North America's Great Lakes (Scott and Huff 1997; Kunkel et al. 1998; Ackerman et al. 2013; Lofgren et al. 2011). There have also been many investigations into the Caspian Sea and Aral Sea of Central Asia (Small et al. 2001; Tursun and Kasim 2002; Guo et al. 2011; Chen et al. 2012), including observational research and numerical simulation analysis. These researches have found that inland lakes with large surface areas have an observable regulatory effect on the climate of the surrounding regions (Scott and Huff 1996; Vincent and Mekis 2006). They decrease spring and summer temperatures, increase autumn and winter temperatures, and buffer the diurnal and seasonal temperature variations. A reduction in diurnal temperature range, for example, is especially conspicuous from April to August in the Great Lakes Region (Eichenlaub 1979; Bates et al. 1993; Angel and Isard 1998). At the same time, lakes also increase precipitation on their windward shores during autumn and winter, especially snowfall (Niziol 1987; Chang and Braham 1991; Kristovich 2009; Barthold and Kristovich 2011).

In recent years, a few groups have used numerical simulation methods to study the lake-land breeze phenomenon. Among these are relatively early research that used lake-land breeze numerical models on the Great Lakes (Moroz 1967; Alpert and Neumann 1983; Ballentine 1982; Maddukuri 1982) and the recent research focused on major lakes in mainland China (e.g. Chen et al. 1994; Lv et al. 2008; You et al. 2016a). Research on the QL lake effect has been concentrated on the characteristics of local circulation and the atmospheric boundary layer, the lake-land breeze, and local precipitation processes (Chen et al. 1995; Lv et al. 2007; Liu et al. 2013; Tang et al. 2016). Existing researches on the climatic effects of lakes using actual meteorological observation data in the Dianshan Lake, Taihu Lake and the Poyang Lake have yielded a few results (Zhang and Wu 1988; Peng et al. 2010; Yang et al. 2013; Cao et al. 2015), but no observational research on the QL climatic effects is referable.

The domestic researches generally reported the similar influence of large inland lakes on nearby surface climate with those shown in other countries, with a cooling effect during summer or warm seasons, and warming effect during the winter or cold seasons. However, the investigations into the Boyang Lake and Taihu Lake in the mid- to lower reaches of the Yangtze River exhibited a different lake effect during summer, in spite of the fact that they did consistently showed a warming effect during winter season (Lin 1985; Lu and Wei 1990; Wang and Fu 1991; Wang 1993; Wan et al. 1994; Ren et al. 2017). The reasons for the difference may result from the datasets and models use, and also may be related to the significant decline of solar radiation in the areas during summer (Ren et al. 2005).

The QL is an exceptionally high-altitude saltwater lake situated in inland mid-latitude. On the one hand, the water surface area of the Qinghai Lake is much larger than other lakes in China, its average depth of water reaches more than two times of other inland lakes in the country, and thus, it may exert a larger effect on the surrounding climates; on the other hand, the westerly circulation above the lake is strong and there is a higher background wind speed in the QH lake region during warm season, which may weaken the climatic effect of the lake in some extent. However, the current research is significantly lacking on the climatic effects of the QH Lake under the influence of various factors, and the level of scientific knowledge on this topic is quite low.

Due to the complexity and diversity of the QL basin surfaces and the relatively big differences in the climatic conditions and climate change of different terrains (Qi and Guo 2007; Li et al. 2008; Chen et al. 2011; You et al. 2016b), the use of modeling techniques alone is somewhat limited and may lead to significant uncertainty. An investigation of temporal and spatial pattern of the climatic effect of the mid-latitude inland plateau lake using observational data of surface meteorological stations is badly needed.

This article utilizes hourly observation data from 17 automatic weather stations around the QL for 6-year observations from 2009 to 2014 to analyze the effects of the lake on the average seasonal and diurnal temperature variations during the warm season. Our analysis overcomes the problems of observational data insufficiency and the poor representativeness of the data in previous investigations, and the reliability of the analysis would be higher. The results would help in deepening our understanding of climatic effects of the huge plateau lake and could also provide scientific information for the future implementation of ecological protection measures in the lake basin.

2 Data and methods

2.1 Data

Data on hourly air temperatures, including hourly mean temperature, maximum and minimum air temperature, and the near-surface wind direction were collected from 17 Automatic Weather Stations (AWS) around the QL from 2009 to 2014. The data have been quality controlled in the Information Center of Qinghai Met Bureau. The locations of the AWSs are displayed in Fig. 1.

The satellite land surface temperature data of MYD11A2 from 2009 to 2014 is provided by the US NASA Data Center (https://earthdata.nasa.gov/search?q=MYD11A2), and the dataset used in this study have been adjusted for cloud effect

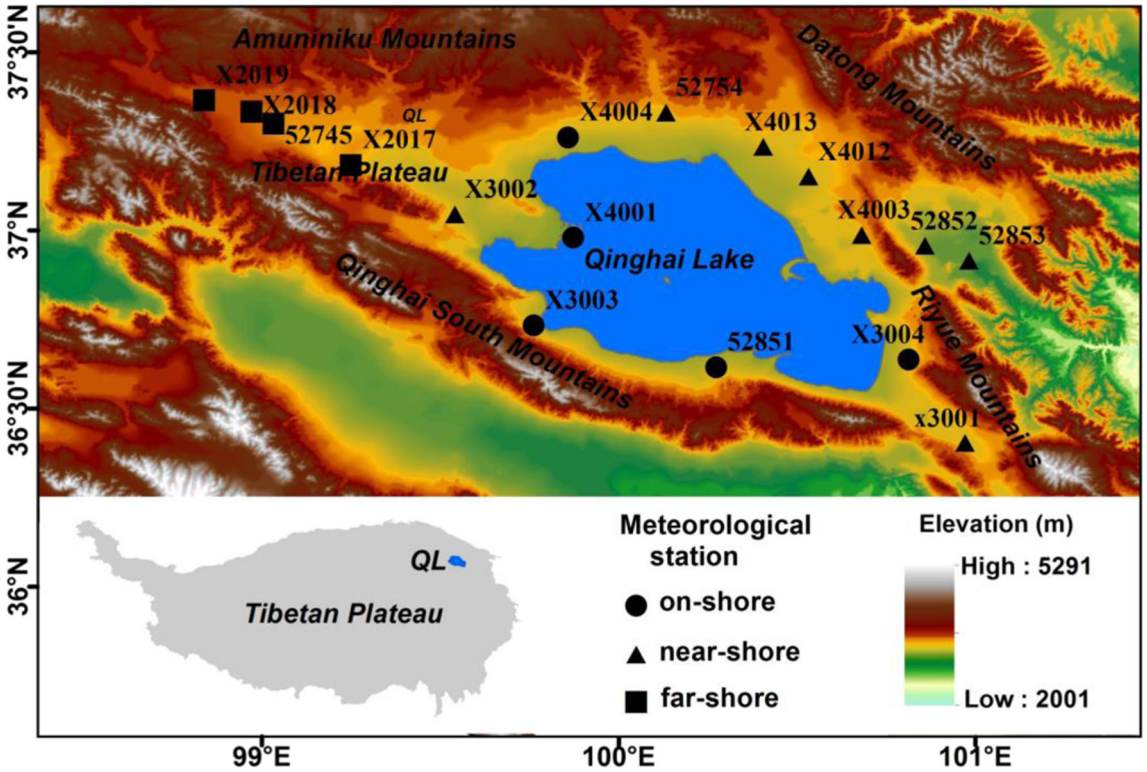

Fig. 1 Distribution of different categories of meteorological stations surrounding the Qinghai Lake (QL)

(Wan et al. 2015). The spatial resolution is 1 km × 1 km, and the time resolution is 8d. The EOS/MODIS Aqua satellite has two transit times per day above the QL, with one around 2: 00 am Beijing time, representing the night land surface temperature, and the other around 13:00 pm Beijing time, representing the land surface temperature during the day. The average land surface temperature of the QL and its surrounding areas was calculated according to the arithmetic mean of two temperature observations during the daytime and nighttime.

The satellite NDVI data come from the MOD13Q1 product, available on the NASA website (http://lpdaac.usgs.gov/dataset_discovery/modis/modis_products_table/mod13q1) in the United States, and its spatial resolution is 250 m × 250 m, and the time resolution is 16d.

The data of beginning to freeze and complete ablation in the Qinghai Lake come from the MOD09GQ product on the NASALPDA, and its spatial resolution is 250 m × 250 m and the time resolution is 1d.

2.2 Methods

Based on the linear distance from the shoreline, the meteorological stations were divided into three categories: those within 10 km were defined as representing the lakeside or on-shore zone, those within 10–30 km the near-shore zone, and those within 30–105 km the far-shore zone (Table 1). Using the meteorological stations in the far-shore zone as reference sites, the temperature difference between the on-shore and near-shore zones and the reference sites were calculated to indicate the climatic effect of the lake. Table 1 also shows that the average latitude of each of the weather stations in the on-shore, near-shore, and far-shore zones is 36.85°, 37.01°, and 37.29°, respectively, and their average altitudes are 3234 m, 3223 m, and 3408 m respectively. The surface air temperature difference caused by latitudinal and altitude factors would be not large and thus, the method would be effective for analyzing the effects of the lake on the surface air temperature.

The threshold method has been used to determine the beginning and ending dates of lake water freezing and ablating. This method is able to directly distinguish ice and water by using different characteristics of reflectivity and surface temperature (Wei and Ye 2010). Freezing and ablating time was based on the records of 2009–2014. The average dates for the QL to start freezing and to completely freeze over was calculated. It was thus determined that 10th of December to 13th of April of the following year is the climatologically freezing period or cold season, while 14th of April to 9th of December is the climatologically thawing season or warm season.

The 5-day average temperature was calculated starting from the 21st 5-day interval (11–15th of April) and ending on the 68th 5-day interval (6–10th of December), and this way, the averages of every 5 (or 6) days within a month of warm season were obtained.

The temperature is monitored every minute. The hourly mean temperature is the average of the past 60 min. The daily

Table 1 Information of the weather stations used in the study

Zone	Station #	Longitude	Latitude	Altitude	NDVI value	Distance from lake shore (km)
On-shore zone	X4001	99.87°	36.98°	3201 m	–	0.00
	X3003	99.76°	36.73°	3205 m	0.71	1.65
	52851	100.27°	36.62°	3241 m	0.67	2.20
	X4004	99.86°	37.26°	3229 m	0.59	4.18
	X3004	100.81°	36.64°	3296 m	0.62	7.48
	Average		36.85	3234 m	0.65	3.10
Near-shore zone	X4013	100.41°	37.24°	3266 m	0.67	12.98
	X3002	99.54°	37.05°	3241 m	0.72	13.11
	52754	100.13°	37.33°	3302 m	0.59	14.08
	52853	100.98°	36.92°	3010 m	0.72	26.40
	X4003	100.68°	36.99°	3280 m	0.41	16.94
	X4012	100.53°	37.15°	3265 m	0.5	17.60
	52852	100.86°	36.96°	3140 m	0.76	18.50
	X3001	100.97°	36.40°	3283 m	0.62	29.34
	Average		36.99	3223 m	0.62	18.62
Far-shore zone	X2017	99.25°	37.18°	3335 m	0.59	55.00
	52745	99.03°	37.30°	3417 m	0.57	75.92
	X2018	98.97°	37.33°	3421 m	0.58	84.73
	X2019	98.84°	37.36°	3459 m	0.56	102.36
	Average		37.29	3408 m	0.58	79.50

maximum (minimum) temperature is the maximum (minimum) values of the minutely temperature in the past 1440 min (24 h × 60 min), which is utilized in analyzing the spatial pattern of daily maximum temperature, minimum temperature and diurnal temperature range (DTR) during warm period (Fig. 3), and also the intra-seasonal variation of pentad (5-day or 6-day) mean maximum and minimum temperature (Fig. 9). The daily maximum (minimum) hourly mean temperature is the maximum (minimum) values of hourly mean temperature over the past 24 h, which is used in describing the diurnal variation of temperature (Fig. 4). The average maximum (minimum) temperature in the warm season is the average of the daily maximum (minimum) temperatures derived from minutely temperature from April 14 to December 9, while the pentad maximum (minimum) temperature is the average of the daily maximum (minimum) temperatures derived from minutely temperature for every 5 days (or 6 days). Obviously, the average maximum (minimum) temperature for a given period of time as used in this paper is lower (higher) than the traditional maximum (minimum) value. For temporal variation within a day, Beijing time is used consistently; the time difference between Beijing time and the Qinghai Lake local time is about 1.2 h.

The EOS/MODIS NDVI values of each site are synthesized according to the MVC (maximum value composites) method in every month, and the maximum monthly NDVI value is defined as the annual value. The average annual NDVI value from 2009 to 2014 represents the vegetation cover.

3 Results and discussion

3.1 Spatial distribution of temperature

The spatial characteristics of the land surface temperature and the surface air temperature are shown in Fig. 2. During the warm season, the satellite surface temperature of the lake water is obviously higher than that of the surrounding land (Fig. 2a). The lake and land surface temperature has obvious diurnal variation, with the lake surface temperature lower than the surrounding land surface temperature in the daytime (Fig. 2b), but higher than the surrounding land surface temperature during the nighttime (Fig. 2c). The surface air temperature observed from the AWSs has the similar spatial variations, with the higher average air temperature in the warm season found in zone closer to the lake (Fig. 2d). The distribution of daytime and nighttime air temperatures is opposite. On-shore zone witnesses a lower average air temperature in the daytime (Fig. 2e), and a higher average air temperature in the nighttime (Fig. 2f). Similarly, the air temperature observed from the meteorological stations also shows that, the closer to the lake, the higher the average air temperature in the warm season (Fig. 2d). The distribution of daytime and nighttime air temperatures is opposite, with the sites closer to the lake recording a lower temperature in the daytime (Fig. 2e) and a higher temperature in the nighttime (Fig. 2f).

Comparing the observations by satellite and automatic stations, both show that the temperature is lower during the

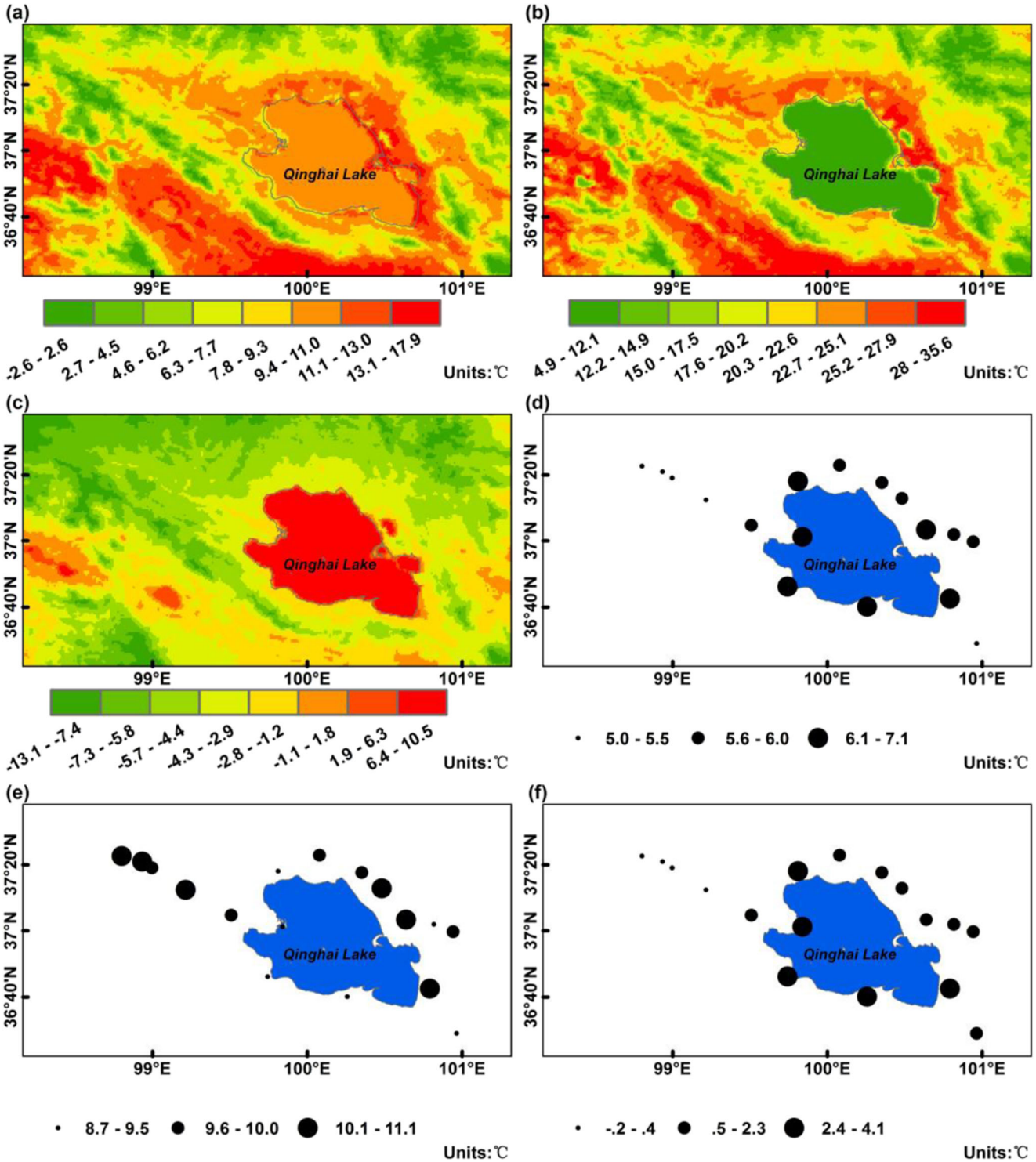

Fig. 2 Distribution of warm-season mean land surface temperature (**a**), daytime mean land surface temperature (**b**), and nighttime mean land surface temperature (**c**) based on satellite data from 2009 to 2014, and warm-season mean air temperature (**d**), daytime mean air temperature (**e**), and nighttime mean air temperature (**f**) based on data of meteorological stations from 2009 to 2014 (unit: °C)

daytime and higher at night near the lake. However, the former is land surface temperature and the latter is surface air temperature, a small difference exists between them, with the data of satellite higher than those of automatic stations. The average land surface temperature during daytime, nighttime and daily mean is 4.9~25.1 °C, 1.9~10.5 °C, and 7.8~17.9 °C respectively in the lake surface, and it is 12.2~35.6 °C, −13.1~6.3 °C, and −2.6~17.9 °C respectively in the surrounding land. The average air temperature in the daytime, nighttime and daily mean is 8.7~9.6 °C, 2.9~4.1 °C, and 6.3~6.7 °C

respectively in the on-shore zone, but it is 9.5~11.16 °C, 1.3~2.3 °C, and 5.4~6.5 °C respectively in the near-shore zone, and 10.0~10.7 °C, − 0.2~0.4 °C, and 5.0~5.5 °C in respectively the far-shore zone.

Our analysis was focused on surface air temperature as observed from the meteorological stations. It is interesting to note that the warm-season mean air temperature of the on-shore zone is relatively higher, ranging between 5.8 and 6.5 °C, and the mean temperature of the near-shore zone ranges between 5.0 and 5.7 °C. Probably due to the combined effects of the distance from the lake water and the vegetation coverage, the warm-season mean air temperature of the far-shore zone is the lowest, on average between 4.4 and 4.9 °C (Fig. 3a).

The on-shore zone is warmer than other costal zones in terms of warm-season average temperature (Table 2), though the average maximum air temperature in this zone is still lower, and this is unexpected because the phenomenon is opposite those found for the lakes of low-elevation regions during the summer season. The research results on large deep-water lakes of low-altitude areas show that the lakes in the summer have a cold effect along the coastal zone (e.g., Scott and Huff 1997; Small et al. 2001). The larger the area and the deeper the lake water, the more obvious the cooling effect of summertime (e.g., Lu and Wei 1990; Wang 1993; Scott and Huff 1996).

The difference from the previous studies, as shown in this study, cannot be explained by the definition of the warm season (14th of April to 9th of December) used in this analysis, which includes a few months out of the climatologically defined summer (JJA), because the phenomenon of higher air temperature near the lake also appears in summer or even in mid-summer (Fig. 8). It might not have been caused by the difference of the observational elevations either because there is very similar average elevations of the stations between the on-shore zone and the near-shore zone, with the former even 11 m higher than the latter (3234 m:3223 m) (Tables 1 and 2).

The influence of the lake water might have been the best explanation for the difference of the temperature between the different coastal zones. It is plausible that the huge plateau lake is exerting a unique influence on the surface air

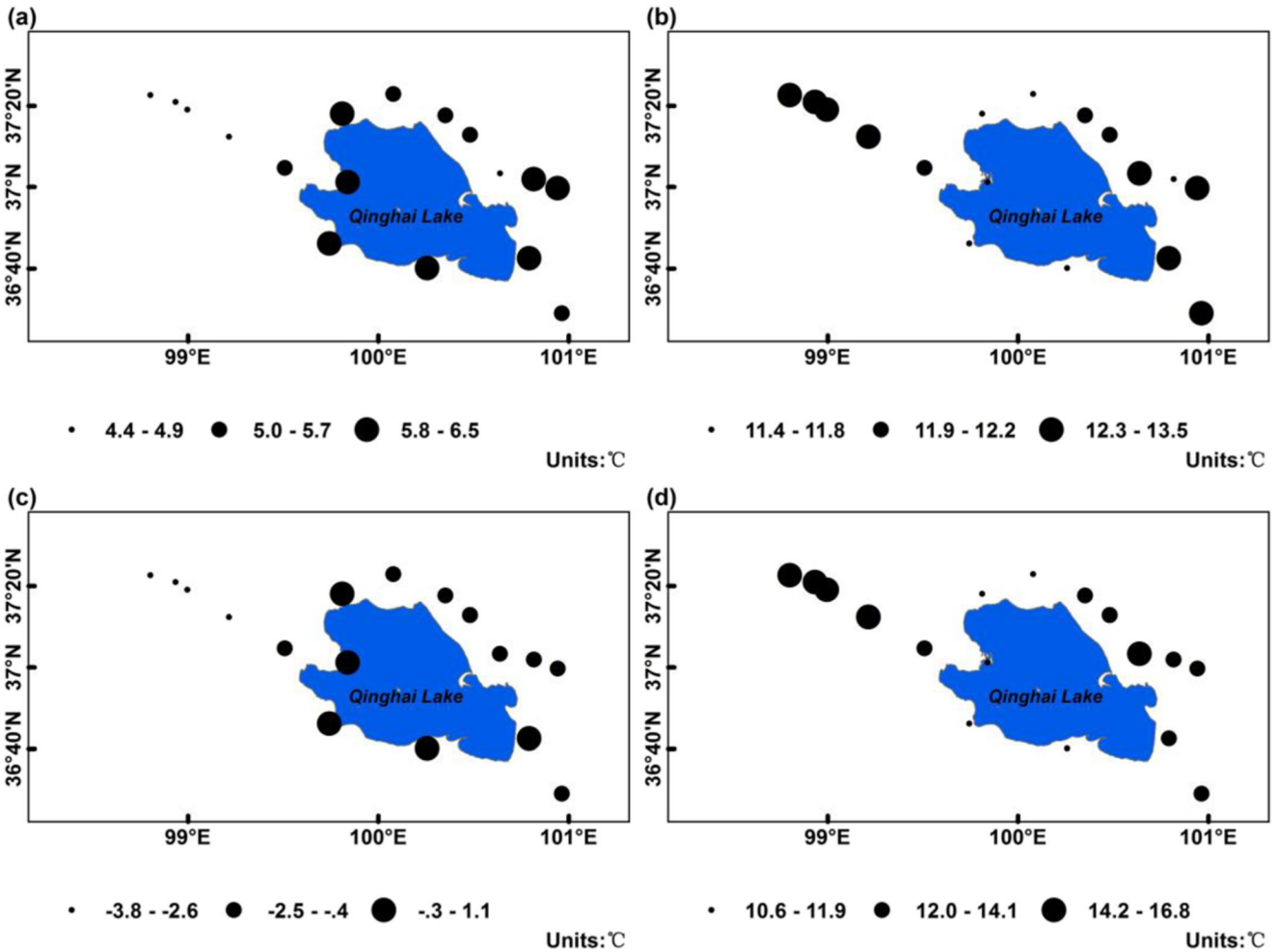

Fig. 3 Distribution of warm-season mean air temperature (**a**), mean maximum air temperature (**b**), mean minimum air temperature (**c**), and the mean diurnal temperature range (DTR) (**d**),based on observational data of meteorological stations from 2009 to 2014 in the Qinghai Lake region (unit: °C)

Table 2 Average geographical and climatic parameters for the on-shore zone, near-shore zone, and far-shore zone of the Qinghai Lake during warm season

Zone	Altitude	Latitude	Longitude	Average temperature in warm season	Average maximum temperature in warm season	Average minimum temperature in warm season	NDVI value
On-shore zone	3234 m	36.85°	100.11°	6.21 °C	11.9 °C	0.74 °C	0.67
Near-shore zone	3223 m	37.01°	100.51°	5.51 °C	12.4 °C	− 1.20 °C	0.62
Far-shore zone	3408 m	37.29°	99.02°	4.85 °C	12.3 °C	− 2.54 °C	0.58

temperature of the costal land areas due to the colder atmosphere and stronger wind of the near-surface layer which is effectively chilling the inland surface air, especially during daytime when the stronger turbulent flow in boundary layer cause a larger downward transfer of momentum and a stronger near-surface wind.

It is also possible that, in the high plateau region, the lake water is with higher salinity, and its specific heat capacity is smaller than that of fresh water, absorbing more heat during the daytime and the temperature increases faster. Though the lake is located in the low temperature area, the lake water temperature is not too lower than surrounding land during the daytime. At night, the infrared radiation emitted into the atmosphere from the surface is strong due to the thinner atmospheric layer and less water vapor, and the air temperature in the on-shore zone is obviously higher, causing the daily and season mean temperature to be obviously higher than that of the near-shore and far-shore zones.

Certainly, the causes of the higher average air temperature in on-shore zone than that in the other costal zones need to be further investigated in the future.

From the warm-season mean maximum and minimum temperatures of each weather station, it can be seen that, the closer to the shore, the lower the mean maximum temperature (Fig. 3b) and the higher the mean minimum temperature (Fig. 3c). The effects cause the DTR of the on-shore zone to be the lowest, about 10.6 to 11.9 °C. The mean DTR of the near-shore zone is about 12.0 to 14.5 °C, and the largest mean DTR of 14.6 to 16.8 °C occurs in the far-shore zone (Fig. 3d). Therefore, the warming effect of the lake in the on-shore zone seems to dominantly occur during nighttime, and the daytime sees a similarly cooling effect of lake to those found in other regions.

3.2 Diurnal temperature variation

Figure 4 shows diurnal air temperature variation of warm season for the three zone averages and the individual sites of the zones in the QL region. The QL has a clear effect on the surface air temperatures of the nearby observational sites. The closer the sites are to the shoreline, the higher the nighttime hourly mean temperature, the lower the afternoon hourly mean temperature, and the smaller the diurnal temperature variation. These are typical diurnal characteristics resulting from the general lake effect. However, it is also clear that the hourly mean temperature of the on-shore zone at nighttime is much higher than that of the near-shore zone and far-shore zone, and the daytime mean temperature differences among the zones is very small, indicating that the warmer warm-season climate near the shoreline dominantly results from the obviously higher nighttime temperature. Although the lake does somehow cool the on-shore zone during daytime, the cooling effect is rather weaker than those found surrounding the large likes of other regions.

Lakes have a greater heat capacity, and the diurnal temperature variation at the surface of the lake and in locations nearby is generally smaller. During the daytime, especially in the afternoon, the on-shore site temperature rises more slowly and the maximum temperature is lower, and in the evening the temperature drops more slowly and the minimum temperature is higher, causing diurnal temperature range to be noticeably smaller than that of the far-shore zone. The day-to-night conversion of lake-land wind circulation is likely also one of the direct causes of the smaller diurnal temperature fluctuations in the on-shore and near-shore zones.

Taking July as an example, we calculated the average hourly wind direction frequency and drawn the monthly mean wind rose diagram for the period 2009–2014. The meteorological stations 52754, 52851, 52852, and X4001 are located respectively in the north, south, east, and west sides of the QL. Figures 5 and 6 show the distribution of wind direction frequency at different time of a day at stations 52754 (north) and 52851 (south). The wind direction in the north and south shores of the lake had obvious changes, which was the manifestation of the lake-land breeze. At station 52754, the north wind is dominant at nighttime, which is land breeze from the land southward to the lake, and the south wind is dominant during daytime, which is the lake breeze from the lake northward to the land. Similarly, there are also wind direction shifts at stations 52853 and X4001, and the lake-land breeze is obviously notable. It can also be found that the land breeze during nighttime is more obvious than the lake breeze during daytime. Take station 52754 (north) as an example, the northerly wind (land breeze) is dominant, and the maximum wind direction frequency is 37.8%; meanwhile, the frequency of other wind directions is very low at night; while during the

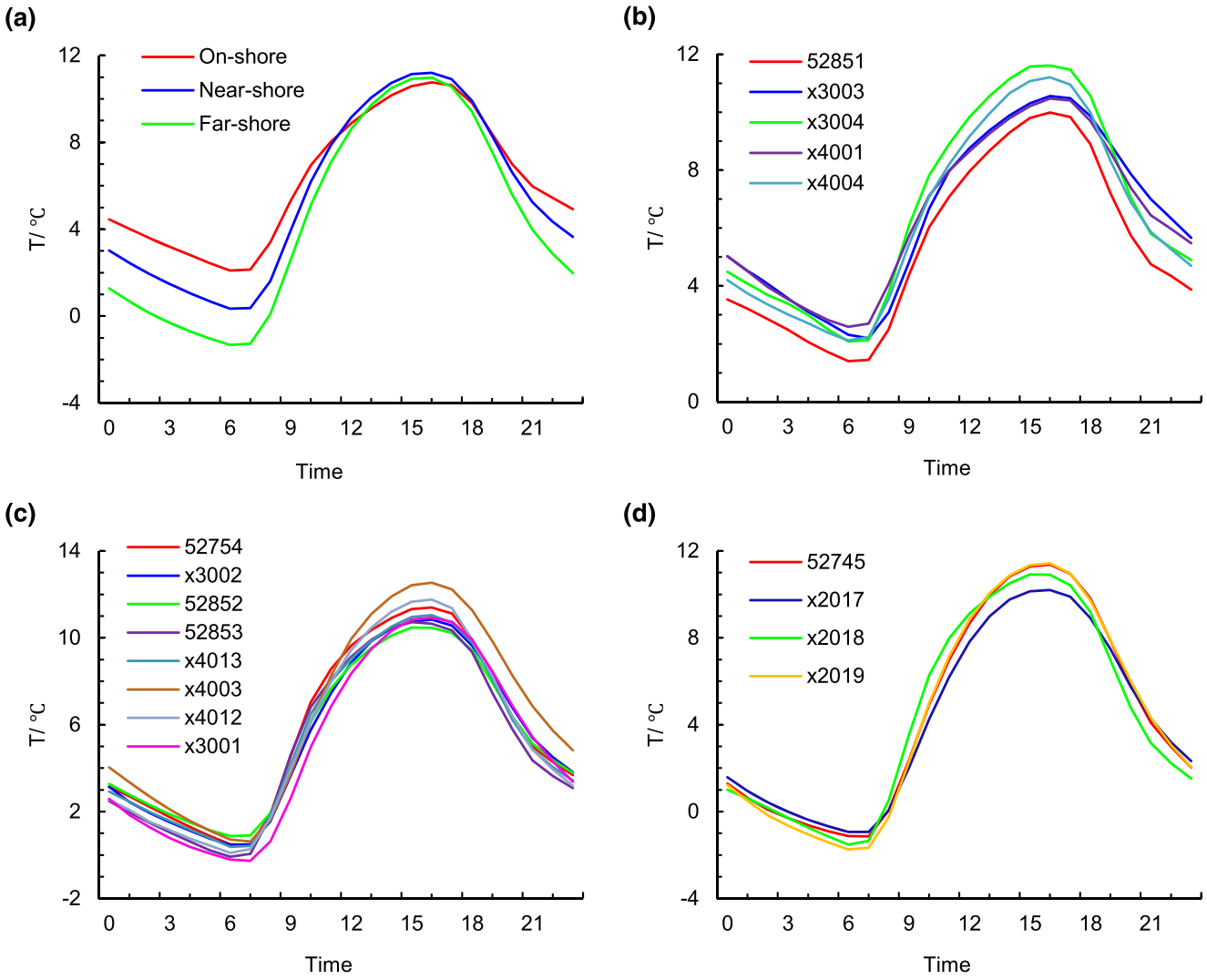

Fig. 4 Average warm-season diurnal temperature variation for the on-shore, near-shore, and far-shore zones (**a**), and individual stations of the on-shore (**b**), near-shore (**c**), and far-shore zones (**d**), in the Qinghai Lake region

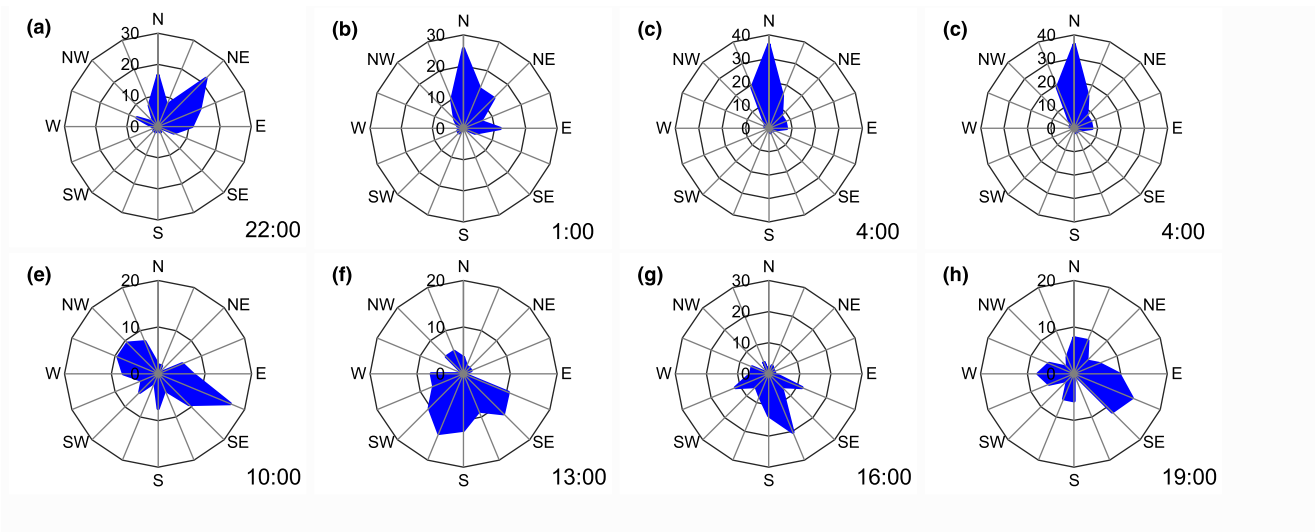

Fig. 5 The distribution of mean near-surface wind direction frequency at different time (Beijing time) in July from 2009 to 2014 at station 52754 (unit: %)

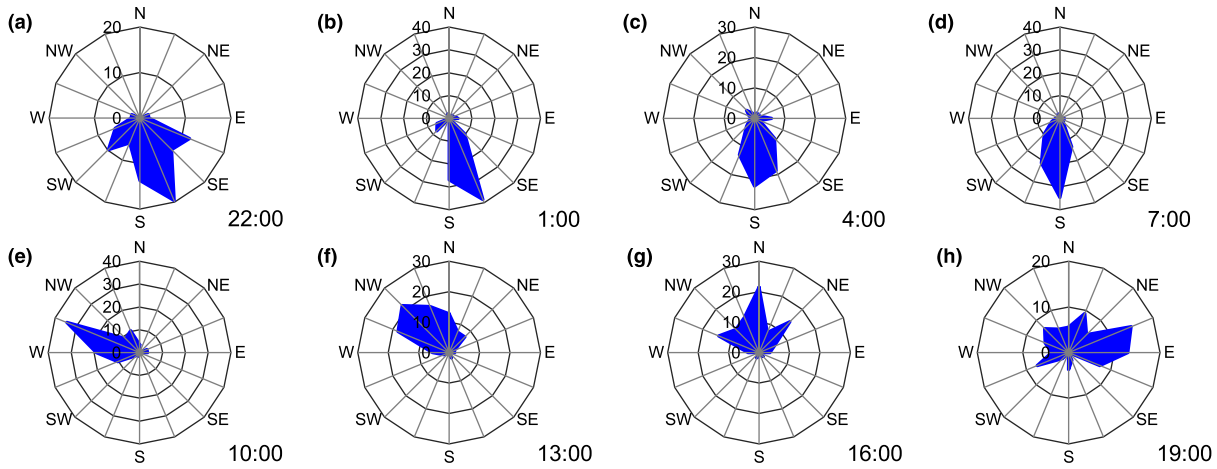

Fig. 6 The distribution of mean near-surface wind direction frequency at different time (Beijing time) in July from 2009 to 2014 at station 52851 (unit: %)

daytime, although the southerly wind (lake breeze) is dominant, the maximum wind frequency is only 20.3%, and the frequency of other wind directions is relatively higher.

This may be because the mid-tropospheric high-speed westerly currents are closer to the surface on the plateau, and the near-surface wind speed would be much larger, leading to a generally non-benefiting background circulation field for the formation and development of the daytime lake breeze due to the downward transfer of momentum by the turbulence. At nighttime, however, the stronger surface cooling due to the upward long-wave radiation from the surface results in the formation of a temperature inversion layer, which may have effectively prevented the upper westerly momentum from downward transportation, and thus benefited the development of the land breeze within a thin boundary layer. This suggested mechanism could be further investigated in further research by using a numerical model.

In zones with varying distances from the lake shoreline, diurnal temperature variations display different characteristics for specific sites. Temperature variations at the sites of the on-shore zone are mostly slower and smaller. The smallest hourly mean DTR among all the weather stations of the zone is 7.9 °C, while the greatest DTR is 9.5 °C. In analyzing the diurnal temperature fluctuations in all of the weather stations of the on-shore zone, it is evident that the lake exerts a clear effect on diurnal temperature variations. Located from the nearest to the furthest distance from the lake shoreline, the hourly mean DTR of the 5 on-shore zone weather stations X4001, X3003, 52851, X4004, and X3004 are 7.9 °C, 8.4 °C, 8.6 °C, 9.1 °C, and 9.5 °C respectively (Fig. 4b).

The smallest diurnal fluctuation in temperature among all the weather stations of the near-shore zone is 9.6 °C, while the greatest is 11.9 °C. Located from the nearest to the furthest distance from the lake shoreline, the near-shore zone weather stations X4013, X3002, X4012, 52754, X4003, 52852, 52853, and X3001 register the DTR values of 10.7 °C, 10.4 °C, 11.7 °C, 10.9 °C, 11.9 °C, 9.6 °C, 10.8 °C, and 11.2 °C respectively. It is possible that, apart from the lake effect, the state of vegetation cover at the sites also had an effect on the temperature of the near-shore zone. NDVI can represent vegetation cover, and the high NDVI value indicates high vegetation coverage. At stations 52852 and 52853, which had a relatively high NDVI values (0.76 and 0.72 respectively), witness smaller DTR, whereas station X4003, which was relatively lacking in vegetation cover (NDVI value was 0.41), had a larger DTR (Fig. 4c). However, the possible influences from vegetation around the stations need to be investigated in the future.

The far-shore zone (Fig.4d) is mostly distributed to the northwest of the QL; it is in the alluvial plains between the Qinghai South Mountains and the Amuniniku Mountains. Located from nearest to furthest distance from the shoreline, the meteorological stations X2017, 52745, X2018, and X2019 have DTRs of 11.1 °C, 12.5 °C, 12.4 °C, and 13.2 °C respectively. It can be seen that the diurnal temperature variations was large in the far-shore than that in the on-shore and near-shore areas, and the regulating effect of water on air temperature is obviously weakened with distance from the shoreline.

Figure 7 shows the relationship of warm-season mean maximum temperature, minimum temperature and diurnal temperature range of all the stations with the straight-line distances of the AWSs from the shoreline. It can be seen that, within 30 km (i.e., within the on-shore and near-shore zones), the lake had a clear effect on the mean maximum and minimum temperatures. The maximum temperature and DTR sharply increase and the minimum temperature rapidly decrease with the distance from the shoreline in the two zones. In the far-shore zone, which is approximately 50 km or more from the shoreline, however, the lake effect is not as conspicuous. The fluctuations in diurnal temperature are more subject to the lake

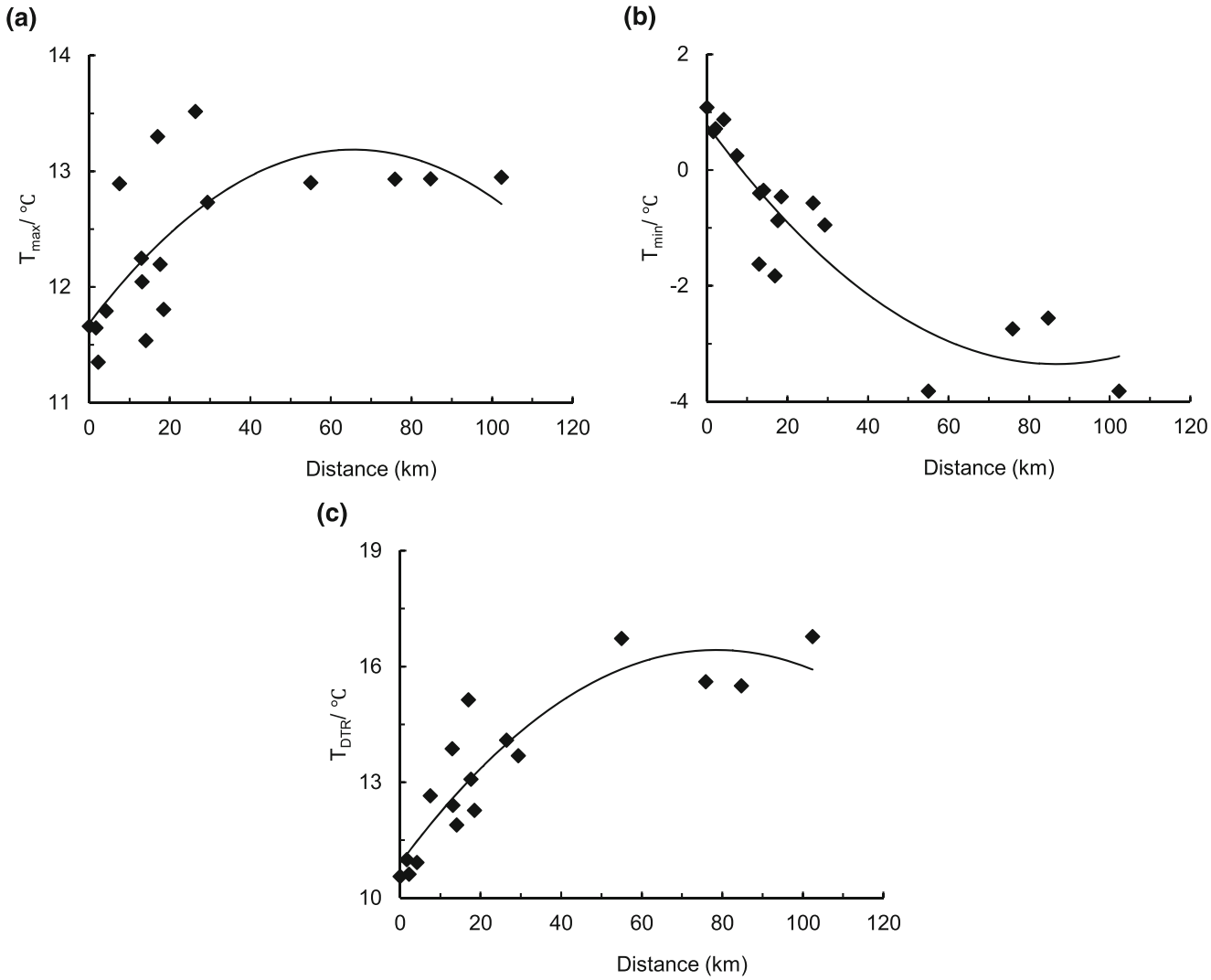

Fig. 7 The relationship between mean maximum temperature (**a**), mean minimum temperature (**b**), and mean diurnal temperature range (**c**) of the observational stations and their straight-line distance from the shoreline in the warm season

effect within about 50 km of the shoreline, while the lake effect on DTR is inconspicuous for most sites of the far-shore zone.

Table 3 shows that, when the daily average maximum and minimum temperatures and diurnal temperature range are fitted to a curve, they form a half-parabola pattern. The fitted equation passes the test with a significance level of 0.01. It is thus evident that, within a certain distance, the lake exerts a significant effect on the maximum and minimum temperatures, and the DTR, but after exceeding a certain distance, the lake effect gradually disappears.

3.3 Intra-seasonal temperature variation

For the on-shore, near-shore and far-shore zones, the intra-seasonal cycles of the 5-day average temperatures all represent a single-peak variation type, with the maximum value occurring at the 42nd 5-day interval (26th–31st of July) and the

Table 3 Fitted equations for the daily mean maximum temperature, minimum temperature, and diurnal temperature range versus distance from the lake shoreline

Meteorological element	Fitted curve	R^2	Significance level
Maximum temperature	$Y = -0.000\,X^2 + 0.046\,X + 11.686$	0.492	**
Minimum temperature	$y = 0.001\,X^2 - 0.095\,X + 0.784$	0.827	**
DTR	$y = -0.001\,X^2 + 0.141\,X + 10.897$	0.822	**

Y represents the temperature and X represents the distance from the lake shoreline. Double asterisk represents passing the test of 0.01 significance level

minimum value at the 68th 5-day interval (6th–10th of December) (Fig. 8). During the warm season, the 5-day average temperature ranges (maximum–minimum) for the on-shore, near-shore, and far-shore zones are respectively 19.7 °C, 22.1 °C, and 22.9 °C. From Fig. 7a, it can be seen that the difference of the 5-day average temperatures of the on-shore and near-shore zones from the far-shore zone are all positive, indicating that, compared to the far-shore zone, the average temperatures of the on-shore and near-shore zones are always higher during the warm season. The temperature difference between the on-shore zone and far-shore zone slowly rises from the 36th 5-day interval (26th–30th of June) to the 52nd 5-day interval (16th–20th of September), but only by about 1.0 °C. From the 53rd 5-day interval (21th–25th of September), however, the difference rises rapidly peaking at around 4.0 °C near the end of the warm season. The temperature decrease for the on-shore zone is therefore particularly slow after mid-September when it is clearly subject to the

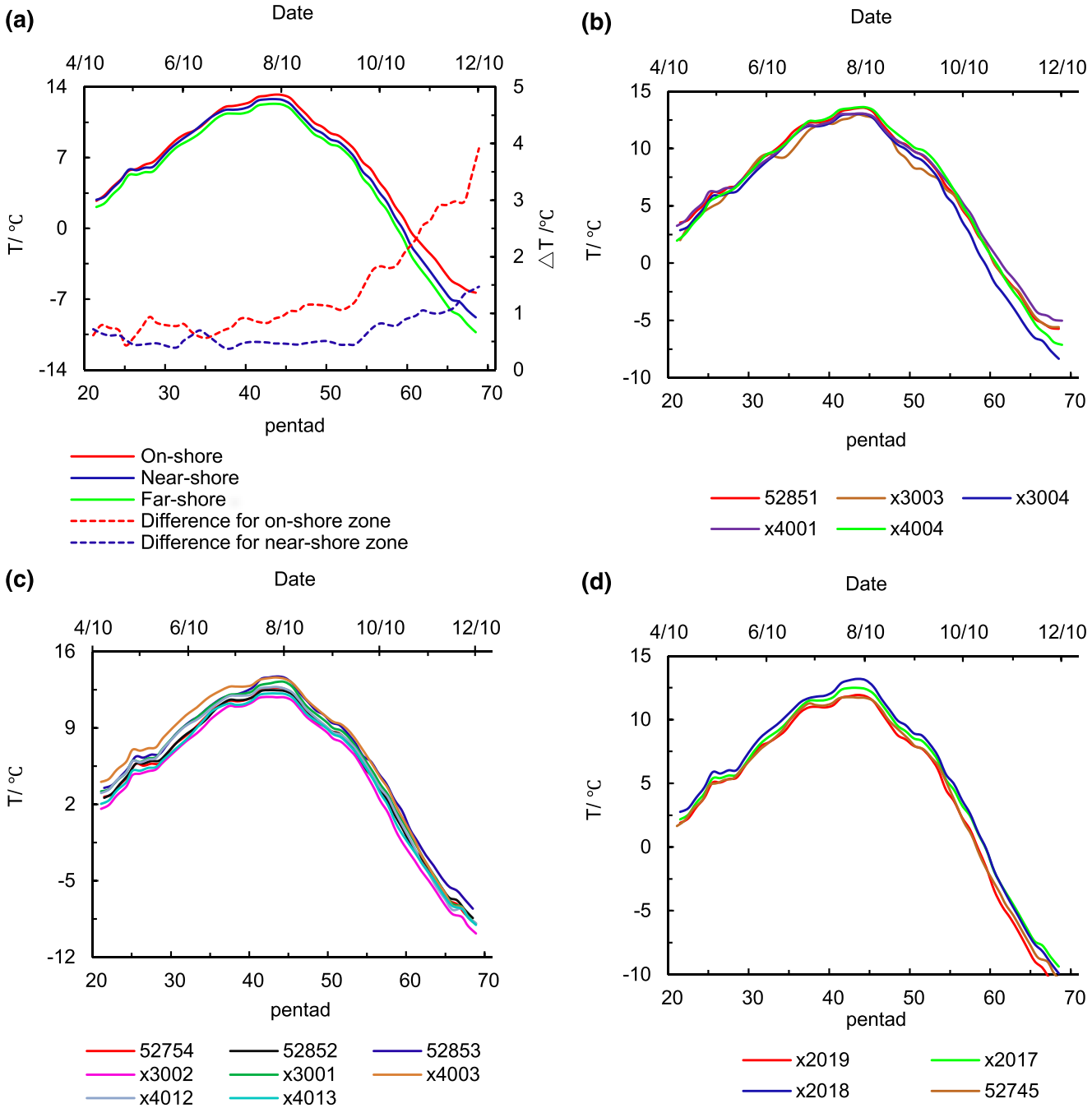

Fig. 8 Five-day average temperatures for different zones and the differences of 5-day average temperature of the on-shore zone and near-shore zone from the far-shore zone (**a**), and the 5-day average temperature variations for individual stations for the on-shore zone (**b**), near-shore zone (**c**), and far-shore zone (**d**)

buffering effects of the lake water, whereas the regulatory effect of the lake on the near-shore zone starts to become prominent beginning in mid-October.

It is obvious that the 5-day average temperature for the on-shore zone always remains at a relatively higher value than that of the near-shore or far-shore zones during the warm season, a result well consistent with the abovementioned seasonal mean temperature spatial pattern (Fig. 3 and Table 2). The temperature difference of the on-shore zone from the far-shore zone is especially large after the late September, with the largest difference found in the end of the warm season (Fig. 8a), indicating that the most remarkable lake effect occurs in late autumn and early winter. The larger lake effect may be because the deep lake usually stores heat in summer and releases it in autumn and winter. It is also likely that the development of inversion layer and the more frequent calm weathers at night in the transitional season benefit the lake-land surface air temperature contrast.

As observed with the diurnal temperature change, the closer the site of the on-shore zone is to the lake, the smaller the fluctuations in the 5-day average temperature will be. For example, the closest station to the lake shoreline(X4001) had a 5-day average temperature range of 18.3 °C during the warm season, while the station furthest from the lake shoreline in the on-shore zone(X3004) has a 5-day average temperature range of 21.6 °C (Fig. 8b).

In the near-shore zone, apart from being subject to the lake effect, vegetation cover likely has an additional influence on seasonal temperature variations. The temperature rise is inhibited by the vegetation transpiration and soil evaporation during daytime. The soil moisture can also reduce the decreasing rate of air temperature during nighttime. These can all result in a reduced diurnal air temperature variation. For example, although the station nearest to the lake shoreline (X4013) has a moderate NDVI value of 0.67, the 5-day average temperature range is relatively small at 21.6 °C because it is relatively close to the lake. Station 52852 has a high NDVI value of 0.76, and it has the smallest 5-day average temperature range at 21.3 °C (Fig. 8c).

For the far-shore sites, the 5-day average temperature ranges (maximum–minimum) at stations X2017, 52745, X2018, and X2019 are 22.3 °C, 22.6 °C, 23.3 °C, and 23.4 °C respectively. It can be seen that, compared to the on-shore and the near-shore area, the 5-day average temperature ranges at the far-shore stations increase greatly with the disappearance of the lake regulation (Fig. 8d).

Figure 9 shows the average 5-day maximum temperatures of various zones and the differences of the on-shore and near-shore zones from the far-shore zone (Fig. 9a), along with the diurnal time (Beijing time, h) when the average 5-day maximum temperature occurs and the differences of the occurrence time of the on-shore and near-shore zones from the far-shore zone (Fig. 9b). The intra-season 5-day average maximum temperature ranges in the on-shore, near-shore, and far-shore zones are 20.3 °C, 21.7 °C, and 22.6 °C respectively. Compared to the sites far away from the lake shoreline, the 5-day average maximum temperature of the on-shore zone is always smaller than that of the other zones before early October. After early October, the 5-day average maximum temperature in the on-shore zone is slightly higher than that

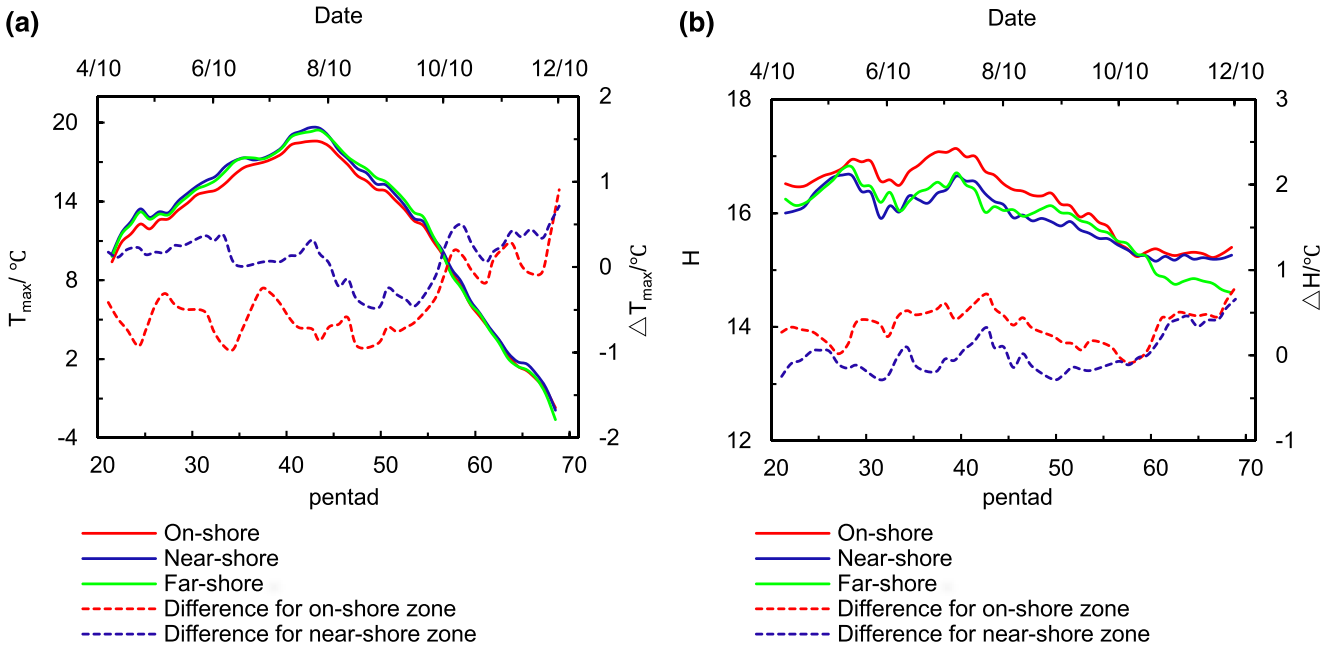

Fig. 9 Five-day average maximum temperatures for different zones and the differences of 5-day average maximum temperature of the on-shore zone and near-shore zone from the far-shore zone (**a**), and the diurnal time at which the 5-day average maximum temperature occurs (Beijing time) and the difference of the occurrence time of the on-shore zone and near-shore zone from the far-shore zone (**b**)

of the far-shore district and the 5-day average maximum temperature of the near-shore zone is almost the same with that of the far-shore zone.

As the lake water can absorb a great deal of solar radiation heat between April and September, the daily maximum temperature of the on-shore zone rises relatively more slowly than that of the other zones due to the lower lake surface temperature and the warmer inland surface, and the 5-day average maximum temperature is correspondingly lower. By early October, the inland surface temperature has begun to drop, but the lake water still keeps warmer, and the on-shore maximum temperature is relatively higher due to the lake effect. The maximum temperature of the on-shore zone drops relatively more slowly as well (Fig. 9a).

Compared to the far-shore zone, the daily maximum temperature occurs relatively later in the on-shore zone, particularly from late May to late August and also after the beginning of October, with the delayed occurrence time of about 1 h. The occurrence time of the daily maximum temperature for the near-shore zone is also generally later than that of the far-shore zone, but the difference is very small (Fig. 9b). Due to the regulatory effect the lake on the nearby air temperature, the occurrence time of the daily maximum temperature for the lake surface and the on-shore zone is obviously delayed during summer and autumn, displaying a typical feature of lake and oceanic climate.

The 5-day average minimum temperature ranges of the warm season for the on-shore, near-shore, and far-shore zones are 23.3 °C, 25.6 °C, and 26.7 °C respectively. Figure 10a shows that the 5-day average minimum temperature for the on-shore and near-shore zones is generally higher than that of the far-shore zone. Starting from the middle of September, the minimum temperature for the on-shore zone is clearly higher than that of the far-shore zone, while the near-shore zone sees a narrowing difference from the far-shore zone probably due to the effects of other factors like vegetation withering. Compared to the far-shore zone, the occurrence time of the daily minimum temperature is a little later for the on-shore and near-shore zones, but the delay is smaller than that of the daily maximum temperature, especially for the period before September (Fig. 10b). After September, the difference of the occurrence time of the minimum air temperature becomes larger, probably because of the increased surface thermal contrast between the lake and the inland area.

4 Conclusions

Using the satellite data of land surface temperature and vegetation coverage and the hourly observation data from meteorological stations situated around the Qinghai Lake, the spatial contrast of land surface temperature in Qinghai Lake and its surrounding and the seasonal and diurnal variations in air temperature of the coastal zones during warm season were analyzed. The following conclusions were drawn:

1. During the warm season, lake water surface temperature derived from remote sensing was lower than that in the surrounding land areas in the daytime, while it was obviously higher than that in the surrounding land areas at

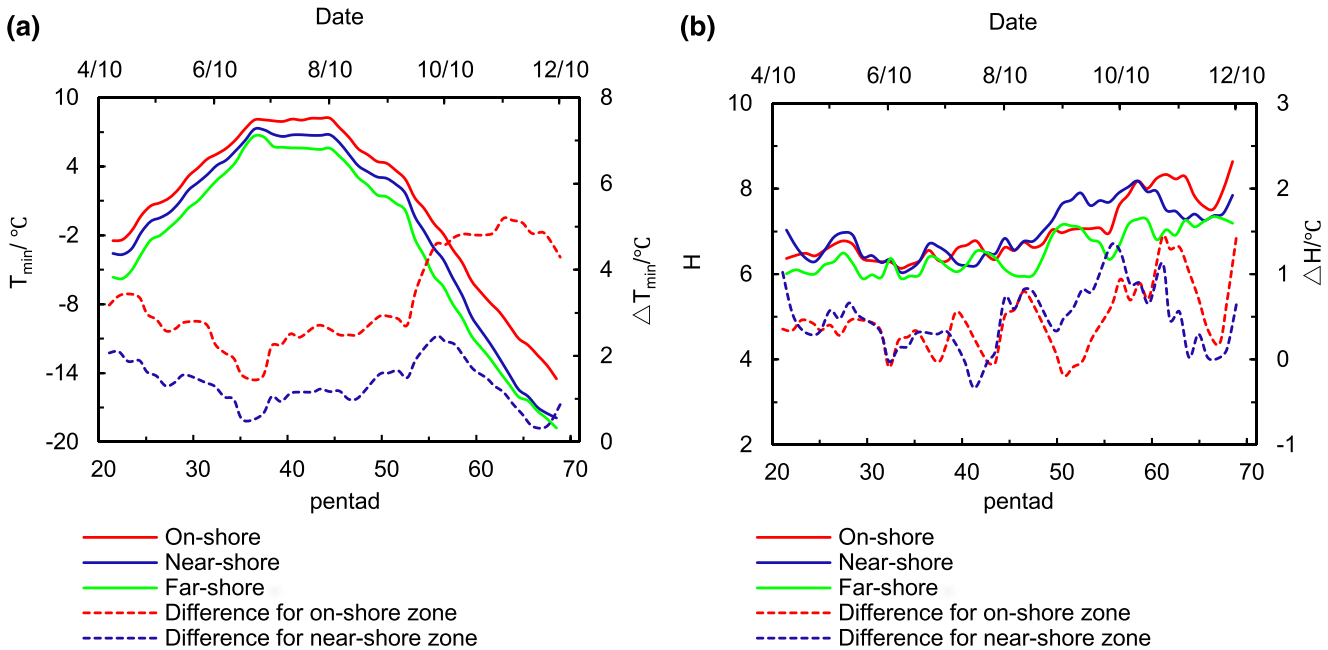

Fig. 10 Five-day average minimum temperatures for different zones and the differences of 5-day average minimum temperature of the on-shore zone and near-shore zone from the far-shore zone (**a**), and the diurnal time at which the 5-day average minimum temperature occurs and the difference of the occurrence time of the on-shore zone and near-shore zone from the far-shore zone (**b**)

nighttime. The daily mean the lake water surface temperature was higher than that in the surrounding areas.

2. The sites closer to the shoreline experience higher average air temperature and smaller diurnal temperature variations. This results from a slight cooling of 0.26 °C during daytime and a much larger warming of 3.17 °C during the nighttime in the on-shore zone as compared to the far-shore zone. The diurnal temperature ranges of the on-shore, near-shore, and far-shore zones are 8.7 °C, 10.9 °C, and 12.3 °C respectively.
3. The 5-day average temperature ranges of the warm season for the on-shore, near-shore, and far-shore zones are 19.7 °C, 22.1 °C, and 22.9 °C respectively. Compared to the far-shore zone, the 5-day average temperature for the on-shore and near-shore zones is generally higher during the whole warm season.
4. The 5-day average maximum temperature ranges of the warm season for the on-shore, near-shore, and far-shore zones are 20.3 °C, 21.7 °C, and 22.6 °C respectively. The 5-day average maximum temperature for the on-shore zone is always lower than that of the far-shore zone before early October, but it is slightly higher after early October probably due to the frequent invasion of cold air in autumn. The occurrence time of the diurnal maximum temperature is delayed in the on-shore zone, especially after early October.
5. The 5-day average minimum temperature ranges of the warm season for the on-shore, near-shore, and far-shore zones are 23.3 °C, 25.6 °C, and 26.7 °C respectively. The minimum temperatures for the on-shore and near-shore zones are generally higher than that of the far-shore zone. The occurrence time of the diurnal minimum temperature is generally later in the on-shore and near-shore zones than that of the far-shore zone.

Therefore, the effect of the QH Lake on surface air temperature is unique in diurnal variation of warm season compared to those of inland big lakes in the lower altitude, with the obviously asymmetrical effect. The lake effect on night-time air temperature in the on-shore zone is much higher than that of daytime. The mechanism for this asymmetrical effect needs to be further investigated in future studies. The thinner and leaner plateau atmosphere which allows a stronger daytime downward radiation and a larger absorption of heat in lake water, the stronger near-surface wind speed during daytime due to the combined influence of daytime turbulent mixing and unusual altitude, and the huge water body and heat capacity as the largest lake in mainland China, however, may have been the main reasons for the distinctive characters as found in this analysis.

Funding information This study is financed by the National Key R&D Program (No: 2018YFA0605603, 2016YFC0501903) and the Natural Science Foundation of China (NSFC) (No: 41575003).

References

Ackerman SA, Heidinger A, Foster MJ, Maddux B (2013) Satellite regional cloud climatology over the Great Lakes. Remote Sens 5(12): 6223–6240

Alpert P, Neumann J (1983) A simulation of Lake Michigan's winter land breeze on 7 November 1978. Mon Wea Rev 111(9):1873–1881

Angel JR, Isard SA (1998) The frequency and intensity of Great Lakes cyclones. J Clim 11(1):61–71

Ballentine RJ (1982) Numerical simulation of land-breeze-induced snow bands along the western shore of Lake Michigan. Mon Wea Rev 110(11):1544–1553

Barthold FE, Kristovich DAR (2011) Observations of the cross-lake cloud and snow evolution in a lake-effect snow event. Mon Wea Rev 139(8):2386–2398

Bates GT, Giorgi F, Hostetler SW (1993) Toward the simulation of the effects of the Great Lakes on regional climate. Mon Wea Rev 121(5):1373–1387

Cao JH, Liu XM, Li GP, Zou HB (2015) Analysis of the phenomenon of lake-land breeze in Poyang Lake area. Plat Meteorol 34(2):426–435

Chang SS, Braham RR (1991) Observational study of a convective internal boundary layer over Lake Michigan. J Atmos Sci 48(20):2265–2279

Chen GC, Peng M (1993) Types and distribution of vegetation in Qinghai Lake region. Acta Phytoecologica Geobotanica Sinica 17(1):71–81

Chen WL, Chen J, Chen YN, Peng JY (1994) A numerical simulation of the effect of vegetation with the lake breeze. J Nanjing Inst Meteorol 17(1):64–72

Chen WL, Sun WG, Zhou JN, Chen J (1995) A numerical study of Qinghai Lake lake land breeze. J Lake Sci 7(4):289–296

Chen L, Chen KL, Liu BK, Hou GL, Cao SK, Han YL, Yang L, Wu YP (2011) Characteristics of climate variation in Qinghai Lake basin during the recent 50 years. J Arid Meteorol 29(4):483–487

Chen QC, Xia ZQ, Guo LD, Wang JC (2012) Characteristics of temperature variation in lake zones of Central Asia. J Hohai Univ (Nat Sci) 40(1):88–94

Crosman ET, Horel JD (2010) Sea and lake breezes: a review of numerical studies. Bound-Layer Meteorol 137(1):1–29

Editorial Board of Ecological Environment Protection and Restoration in Qinghai Lake Basin (2008) Ecological environment protection and restoration in Qinghai Lake Basin, Qinghai People's Publishing House. Xining

Eichenlaub VL (1979) Weather and climate of the Great Lakes region. University of Notre Dame Press, p 335

Guo LD, Xia ZQ, Wang ZJ (2011) Comparisons of hydrological variations and environmental effects between Aral Sea and Lake Balkhash. Adv Water Sci 22(6):764–770

Kristovich DAR (2009) Climate sensitivity of Great Lakes–generated weather systems. Climatology, variability, and change in the Midwest. Indiana University Press, 236–250

Kunkel KE, Changnon SA, Croley TE, Quinn FH (1998) Transposed climates for study of water supply variability on the Laurentian Great Lakes. Clim Chang 38(4):387–404

Li XY, Xu HY, Ma YJ, Wang JH, Sun YL (2008) Land use/cover change in the Qinghai Lake watershed. J Nat Resour 23(2):285–296

Lin ZG (1985) The climate of the middle and lower reaches of the Yangtze River and the possible climatic effects of the Three Gorges Reservoir. Meteorology 11(12):24–28

Liu X, Long X, Zhang WY, Zhang BK, Tian M (2013) Numerical simulation research into atmospheric characteristics influenced by Qinghai Lake in the process of local snowfall. J Lanzhou Uni (Nat Sci) 49(3):347–353

Lofgren BM, Hunter TS, Wilbarger J (2011) Effects of using air temperature as a proxy for potential evapotranspiration in climate change

scenarios of Great Lakes basin hydrology. J Great Lakes Res 37: 744–752
Lu HB, Wei GL (1990) Analysis of air temperature effect of Taihu Lake. Oceanol Et Limnol Sinica 43(3):80–87
Lv YQ, Yang XY, Ma YM (2007) Numerical simulation of summer circulation and atmospheric boundary layer characteristics over Qinghai Lake. Plat Meteorol 26(4):686–692
Lv YQ, Ma YM, Li MS, Yang XY (2008) Numerical simulation of typical atmospheric boundary layer characteristics over Lake Namco Region, Tibetan Plateau in summer. Plat Meteorol 27(4): 733–740
Maddukuri CS (1982) A numerical simulation of an observed lake breeze over southern Lake Ontario. Boundary-Layer Meteorol 23(3):369–387
Moroz WJ (1967) A lake breeze on the eastern shore of Lake Michigan: observations and model. J Atmos Sci 24(4):337–355
Niziol TA (1987) Operational forecasting of lake effect snowfall in western and Central New York. Weather Forecast 2(4):310–321
Peng HQ, Qian PD, Zhu LY (2010) Local microclimate characteristics near Taihu Lake. J Meteorol Environ 26(1):27–31
Qi WL, Guo LY (2007) Climate and its variation in the Qinghai Lake Basin ecological environment impact analysis. Prataculture& Animal Husbandry 7:33–43
Ren GY, Guo J, Xu MZ, Chu ZY, Zhang L, Zou XK, Li QX, Liu XN (2005) Climate changes of China's mainland over the past half century. Acta Meteorol Sinica 63(6):942–956
Ren X, Wang YW, Zhang Z, Yang YC, Hu C, Kang HQ (2017) Simulation studies for Lake Taihu effect on surrounding cities thermal environment. Acta Meteorol Sinica 75(4):645–660
Scott RW, Huff FA (1996) Impacts of the Great Lakes on regional climate conditions. J Great Lakes Res 22(4):845–863
Scott RW, Huff FA (1997) Lake effects on climatic conditions in the Great Lakes Basin. SWS Contract report 617
Small EE, Sloan LC, Nychka D (2001) Changes in surface air temperature caused by desiccation of the Aral Sea. J Clim 14(3):284–299
Tang Y, Huang AN, Tian LR, Sun H, Qi PD, Shen PF (2016) Numerical study on summer local climatic effect over Taihu Lake. J Meteorol Sci 36(5):647–654
Tursun LASO, Kasim APIZ (2002) Study on the shift of Aral Sea and its effects on environment. J Xinjiang Uni (Nat Sci) 19(4):492–494
Vincent L, Mekis E (2006) Changes in daily and extreme temperature and precipitation indices for Canada over the twentieth century. Atmosphere-Ocean 44(2):177–193
Wan JS, Lv DM, Liu FJ (1994) Summer temperature field and its temperature effect in Poyang Lake. Quart J Appl Meteorol 5(3):374–379
Wan Z, Hook S, Hulley G (2015) MYD11A2 MODIS/aqua land surface temperature/emissivity 8-day L3 global 1km SIN grid V006 [data set], NASA EOSDIS LP DAAC
Wang H (1993) A preliminary study about the different climatic effects of deep and shallow water body. J Nanjing Uni (Nat Sci) 29(3):517–522
Wang H, Fu BP (1991) The effects of water body on temperature. Scientia Meteorol Sinica 11(3):233–243
Wei QF, Ye QH (2010) Review of lake ice monitoring by remote sensing. Prog Geogr 29(7):803–810
Yang JB, Liu HN, Fei S, Zhang N, Jiang WM (2013) The impact of urbanization on the urban heat island in Suzhou under the influence of Taihu lake-land breeze. J Meteorol Sci 33(5):473–484
You Y, Guo JX, Chen YZ, Shen XF, Jin LJ, Zhong ZHH (2016a) Observation experiment and simulation evaluation of influence of non-frozen water body on air temperature. Plat Meteorol 35(2):495–506
You QL, Min JZ, Kang SC (2016b) Rapid warming in the Tibetan Plateau from observations and CMIP5 models in recent decades. Int J Climatol 36(6):2660–2670
Zhang XB, Wu SF (1988) Influence on local climate in Dianshan Lake. Trans Oceanol Limnol 4:26–32

Publisher's note Springer Nature remains neutral with regard to jurisdictional claims in published maps and institutional affiliations.

Development of Land Surface Model BCC_AVIM2.0 and Its Preliminary Performance in LS3MIP/CMIP6

Weiping LI[1,2*], Yanwu ZHANG[1,2], Xueli SHI[1,2], Wenyan ZHOU[1,2], Anning HUANG[2,3], Mingquan MU[4], Bo QIU[2,3,5], and Jinjun JI[6]

1 *Laboratory for Climate Studies*, *National Climate Center*, *China Meteorological Administration (CMA)*, *Beijing* 100081, *China*
2 *CMA–NJU Joint Laboratory for Climate Prediction Studies*, *Nanjing University (NJU)*, *Nanjing* 210023, *China*
3 *Department of Atmospheric Sciences*, *Nanjing University*, *Nanjing* 210023, *China*
4 *Department of Earth System Science*, *University of California*, *Irvine*, *Irvine*, *CA* 92697-3100, *USA*
5 *Jiangsu Provincial Key Laboratory of Geographic Information Science and Technology*, *International Institute for Earth System Science*, *Nanjing University*, *Nanjing* 210023, *China*
6 *Institute of Atmospheric Physics*, *Chinese Academy of Sciences*, *Beijing* 100029, *China*

(Received March 18, 2019; in final form May 7, 2019)

ABSTRACT

The improvements and validation of several parameterization schemes in the second version of the Beijing Climate Center Atmosphere–Vegetation Interaction Model (BCC_AVIM2.0) are introduced in this study. The main updates include a replacement of the water-only lake module by the common land model lake module (CoLM-lake) with a more realistic snow–ice–water–soil framework, a parameterization scheme for rice paddies added in the vegetation module, renewed parameterizations of snow cover fraction and snow surface albedo to accommodate the varied snow aging effect during different stages of a snow season, a revised parameterization to calculate the threshold temperature to initiate freeze (thaw) of soil water (ice) rather than being fixed at 0°C in BCC_AVIM1.0, a prognostic phenology scheme for vegetation growth instead of empirically prescribed dates for leaf onset/fall, and a renewed scheme to depict solar radiation transfer through the vegetation canopy. The above updates have been implemented in BCC_AVIM2.0 to serve as the land component of the BCC Climate System Model (BCC_CSM). Preliminary results of BCC_AVIM in the ongoing Land Surface, Snow, and Soil Moisture Model Intercomparison Project (LS3MIP) of the Coupled Model Intercomparison Project Phase 6 (CMIP6) show that the overall performance of BCC_AVIM2.0 is better than that of BCC_AVIM1.0 in the simulation of surface energy budgets at the seasonal timescale. Comparing the simulations of annual global land average before and after the updates in BCC_AVIM2.0 reveals that the bias of net surface radiation is reduced from −12.0 to −11.7 W m^{-2} and the root mean square error (RMSE) is reduced from 20.6 to 19.0 W m^{-2}; the bias and RMSE of latent heat flux are reduced from 2.3 to −0.1 W m^{-2} and from 15.4 to 14.3 W m^{-2}, respectively; the bias of sensible heat flux is increased from 2.5 to 5.1 W m^{-2} but the RMSE is reduced from 18.4 to 17.0 W m^{-2}.

Key words: BCC_AVIM2.0, LS3MIP, CMIP6, surface radiation, sensible heat flux, latent heat flux

Citation: Li, W. P., Y. W. Zhang, X. L. Shi, et al., 2019: Development of land surface model BCC_AVIM2.0 and its preliminary performance in LS3MIP/CMIP6. *J. Meteor. Res.*, **33**(5), 851–869, doi: 10.1007/s13351-019-9016-y.

1. Introduction

A land surface model (LSM) is an important tool to simulate the variations of earth surface conditions and to investigate the physical processes involved in land–atmosphere interactions. A variety of LSMs has been developed in the past decades, depicting various processes of land surface evaporation, snow cover, soil water freeze/thaw, vegetation growth, terrestrial carbon cycle, and so on (Sellers et al., 1996; Sun et al., 1999; Dai et al., 2003; Xue et al., 2003; Li et al., 2010; Bonan et al., 2011; Lawrence et al., 2011; Luo et al., 2017). Endeavors have been made at the Beijing Climate Center (BCC), China Meteorological Administration in recent

Supported by the National Key Research and Development Program of China (2017YFA0604300, 2016YFA0602100, and 2016YFA0602602) and National Natural Science Foundation of China (41275075 and 91437219).

*Corresponding author: liwp@cma.gov.cn.

©The Chinese Meteorological Society and Springer-Verlag Berlin Heidelberg 2019

years to develop a climate system model (CSM) with an integrated LSM to simulate the physical as well as biogeophysical processes of land surfaces.

The first version of the BCC Atmosphere–Vegetation Interaction Model (BCC_AVIM1.0) was based on the AVIM developed by Ji (1995) and Ji et al. (2008), which included three sub-modules simulating biogeophysical, ecophysiological, and soil carbon–nitrogen dynamical processes, and a modified biogeophysical framework with 10 soil layers and up to 5 snow layers [almost the same as that in the NCAR Community Land Model (CLM; Oleson et al., 2004)]. In BCC_AVIM1.0, the terrestrial carbon cycle was realized via a series of biochemical and physiological processes related to the photosynthesis and respiration of vegetation. There was a seasonally varying allocation of carbohydrates to leaves, stems, and roots as a function of the prognostic leaf area index (LAI). Carbon loss due to turnover and mortality of vegetation tissues and carbon dioxide release into the atmosphere from soil respiration was also taken into account. Plant litter on the ground surface and in the soil was theoretically divided into eight terrestrial carbon pools according to the timescale of carbon decomposition of each pool and the transfers between different pools based on the works of Parton et al. (1988) and Cao and Woodward (1998). BCC_AVIM1.0 has served as the land component of the BCC Climate System Model (BCC_CSM) and performed well in both operational seasonal climate prediction (Wu et al., 2014) and experiments of the Coupled Model Intercomparison Project Phase 5 (CMIP5; Arora et al., 2013; Su et al., 2013; Todd-Brown et al., 2013; Wu et al., 2013; Bao et al., 2014; Friedlingstein et al., 2014).

Like other current LSMs, BCC_AVIM1.0 has many deficiencies in its physical and biogeophysical parameterizations and consequent biases in its simulations. For example, BCC_AVIM1.0 underestimated the snow cover fraction of the Eurasian continent in winter (Xia and Wang, 2015). It produced earlier start and end dates for thaw (freeze) of soil ice (liquid water) over the Tibetan Plateau compared with the observations due to the unrealistic threshold temperature (i.e., 0°C) to initiate thaw (freeze) of soil ice (water) (Xia et al., 2011). Moreover, BCC_AVIM1.0 produced overestimation of land surface albedo (Zhou et al., 2018) and delayed vegetation phenology during the growing season. The aforementioned and other deficiencies of BCC_AVIM1.0 has motivated us to improve the parameterization schemes of relevant land surface processes.

After completion of the CMIP5 experiments, attempts were made to improve the parameterization schemes in BCC_AVIM1.0 related to snow cover, soil freeze/thaw processes, rice paddies, lakes with real depths in a snow–ice–water–soil framework, solar radiation transfer through vegetation canopies, and a prognostic phenology based on the carbon budget of a plant functional type (PFT). The above updates were implemented in BCC_AVIM2.0 and coupled to BCC_CSM2.0 for use in the ongoing CMIP6 project. This work gives a brief introduction to BCC_AVIM2.0 and its preliminary performance in the Land Surface, Snow and Soil Moisture Model Intercomparison Project (LS3MIP; van den Hurk et al., 2016).

The remainder of this paper is organized as follows. Section 2 describes the data and method that we have employed to evaluate BCC_AVIM. The updates of parameterizations in BCC_AVIM2.0 are presented in Section 3. Section 4 displays the performance of BCC_AVIM2.0 in LS3MIP. Finally, conclusions are given in Section 5.

2. Data and methods to evaluate BCC_AVIM

The observation datasets used in this study to validate the simulations of BCC_AVIM include: (1) site observations at Col de Porte, France (Morin et al., 2012), (2) site observations in Shouxian County of Anhui Province, China, (3) surface water temperature of the Great Lakes in North America on the daily analysis (on an approximately 1-km horizontal resolution) from NOAA satellite observations for 1995–2006 (ftp://coastwatch.glerl.noaa.gov/glsea), (4) LAI data derived from the Advanced Very High Resolution Radiometer (AVHRR) covering 1982 to 2010 (Myneni et al., 1997), (5) surface turbulent heat and carbon fluxes from the Global Biosphere–Atmosphere Flux (GBAF) dataset (upscaled from FLUXNET and satellite observations) spanning 1982 to 2008 (Jung et al., 2009, 2011), (6) above ground biomass from pantropical biomass (Avitabile et al., 2016) and the global biomass carbon dataset covering 1990 to 2010 (Saatchi et al., 2011), and (7) the surface radiation budget from the Cloud and Earth Radiant Energy System (CERES) from 2000 to 2010 (Kato et al., 2013).

In addition to the above observation datasets, the atmospheric forcing data at a specific site or at the global scale used to drive the LSM are also needed to evaluate the model simulations. The atmospheric forcing to drive BCC_AVIM2.0 in this study for the Great Lakes region and the entire globe is the Princeton global forcing dataset (Sheffield et al., 2006), which was developed for land surface and other terrestrial models, and for analyzing changes in near-surface climate. The dataset was based

on 6-hourly surface climate data from the NCEP–NCAR reanalysis and was corrected for biases at diurnal, daily, and monthly timescales by using a variety of observation datasets. The data used in this study are on a 1-degree spatial resolution and a 3-h time step, and cover the period from 1948 to 2014. The Princeton global forcing dataset is among several options of atmospheric forcing for the ongoing LS3MIP of CMIP6.

BCC_AVIM2.0 was run offline at a crop field site in Shouxian County of Anhui Province, China for evaluation of surface heat fluxes over rice paddies, in Col de Porte, France for evaluation of snow albedo, around the Great Lakes region of North America for evaluation of lake surface temperature, and over the globe for evaluation of vegetation phenology.

In addition to the traditional validation of a LSM at a specific site, benchmarking has been widely used to assess the ability of climate models to capture the spatial and temporal variability of observations during the historical period. For the carbon cycle and terrestrial ecosystems, the design and development of an open-source community platform has been an important goal as part of the International Land Model Benchmarking (ILAMB) project. The ILAMB package was designed and developed as a diagnostic system that enables users to specify the models, benchmarks, and scoring metrics used to tailor the large amount of results to specific model intercomparison projects. The ILAMB scoring system used information from three different aspects of climate, including the climate mean spatial pattern, the seasonal cycle, and the amplitude of interannual variability. A stable version of the ILAMB package was released in 2015 during the American Geophysical Union fall meeting (Mu et al., 2016; Mu and ILAMB team, 2019). The ILAMB package was used to evaluate the preliminary performance of BCC_AVIM2.0 in simulating global land surface energy budgets and their seasonal evolutions.

3. Updates of parameterization schemes in BCC_AVIM2.0

3.1 *The lake with variable depth in a snow–ice–water–soil framework*

As a specific nonvegetated underlying water body, a lake has been explicitly described in most LSMs to simulate thermal transfer within the water body and energy exchange between the lake surface and the overlying atmosphere, and related biogeochemical effects (Subin et al., 2012). With the increase of model horizontal resolution, the lake cover percentage in a model grid cell becomes larger and the climate impacts of lakes become more prominent, and more complicated and realistic processes describing the lake–atmosphere interactions need to be considered.

The lake module in BCC_AVIM1.0 is similar to that of NCAR CLM. It has 10 prescribed layers of water and a fixed depth of 50 m (Oleson et al., 2004); snow cover accumulation over the lake surface is much simplified and the soil beneath the lake water body is not considered. In BCC_AVIM2.0, we implemented the lake module of the Common Land Model (CoLM) of Dai et al. (2003) on the basis of previous works (Zeng et al., 2002; Subin et al., 2012). The main physical processes in the CoLM-lake module include the freeze/thaw at the surface of a lake body, snow accumulation over the frozen surface, eddy diffusion, heat exchange between the atmosphere and the lake surface, and heat exchange between the bottom water and the underlying soil layer.

In the CoLM-lake module, the lake surface roughness lengths for momentum (z_{0m}), heat (z_{0h}), and water vapor (z_{0q}) under unfrozen conditions are parameterized as follows (Dai et al., 2018):

$$z_{0m} = \max\left(\frac{0.1\nu}{u_*},\ C\frac{{u_*}^2}{g}\right) \geqslant 10^{-5}\text{m}, \tag{1}$$

$$z_{0h} = z_{0m}\exp\left\{-\frac{0.4}{0.713}\left(4\sqrt{R_0}-3.2\right)\right\} \geqslant 10^{-5}\text{m}, \tag{2}$$

$$z_{0q} = z_{0m}\exp\left\{-\frac{0.4}{0.66}\left(4\sqrt{R_0}-4.2\right)\right\} \geqslant 10^{-5}\text{m}, \tag{3}$$

where u_* is the surface friction velocity (m s^{-1}), g = 9.8 m s^{-2} is the acceleration of gravity, and ν is the kinematic viscosity. In Eqs. (2) and (3), $R_0 = \max\left(\frac{z_{0m}u^*}{\nu},\ 0.1\right)$ is the near-surface atmospheric roughness Reynolds number. The kinematic viscosity ν is calculated as:

$$\nu = \nu_0\left(\frac{T_g}{T_0}\right)^{1.5}\frac{P_0}{P_{ref}}, \tag{4}$$

in which $\nu_0 = 1.51 \times 10^{-5}$ m^2 s^{-1}, $T_0 = 293.15$ K, $P_0 = 1.013 \times 10^5$ Pa, and P_{ref} is the air pressure at the atmospheric reference height. The effective Charnock coefficient C in Eq. (1) is calculated as:

$$C = C_{min} + (C_{max} - C_{min})\exp[-\min(A, B)], \tag{5}$$

$$A = \left(\frac{F\cdot g}{u^2}\right)^{1/3}/f_c, \tag{6}$$

$$B = \varepsilon\frac{\sqrt{d\cdot g}}{u}, \tag{7}$$

where the maximum and minimum values of C are assumed to be C_{max} = 0.11 and C_{min} = 0.01, respectively; A and B represent restrictions from the wind-driving-waves length scale (F) and the lake depth (d), respectively; u (m s^{-1}) is near surface atmospheric wind; and F depends on lake depth, which is assumed to be a constant of 100 for lakes shallower than 4 m and a constant 25 times the lake depth for those deeper than 4 m. The constant f_c = 22; and ε is set to 1 for the time being and is adjustable based on the availability of data. More technical details can be found in the studies about CoLM-lake (Dai et al., 2018; Huang et al., 2019).

Offline simulations were conducted to compare the CoLM-lake of real depths in BCC_AVIM2.0 with the original water-only lake module of a fixed depth of 50 m in BCC_AVIM1.0. Figure 1 displays lake surface temperatures over the Great Lakes region in North America. Satellite observations show that the main body surface temperatures of the five lakes in January are above 0°C (Fig. 1a). The surface temperature of the northernmost Lake Superior ranges from 2 to 3°C; Lake Michigan to the south is relatively warmer, with surface temperature between 3 and 4°C; the surface temperature in the central part of Lake Huron and most of Lake Ontario is above 3°C; and the surface temperature of the southernmost yet shallowest Lake Erie is colder than 3°C. It is common to the five lakes that the central part of each lake is warmer than its outer parts in January, the margins of each lake freeze in winter, and the coverage of the frozen surface experiences interannual variability. In the simulation of BCC_AVIM1.0 (Fig. 1b), the surface temperatures of all five lakes are underestimated by as much as 6–8°C, e.g., Lake Superior, parts of Lake Michigan, and Lake Huron to the north of 44°N are colder than −6°C; temperatures increase southward of 44°N, yet the southern ends of Lake Michigan and Lake Erie are still colder than 2°C. In contrast, the surface temperature simulated by CoLM-lake in BCC_AVIM2.0 is much closer to the observations in both magnitude and spatial pattern, especially over Lake Ontario and the southern part of Lake Michigan (Fig. 1c). Lake Huron is approximately 1°C colder than the observations but the northernmost Lake Superior and the southernmost Lake Erie are approximately 2–3°C colder than the observations. The overall simulation of BCC_AVIM2.0 in January is statistically much better than that of BCC_AVIM1.0, with the spatial correlation coefficient between simulated and observed surface temperatures over the Great Lakes region being 0.21 for BCC_AVIM1.0 and 0.65 for BCC_AVIM2.0, and the root mean square error (RMSE) remarkably reduced from 10.3°C for BCC_AVIM1.0 to 1.8°C for

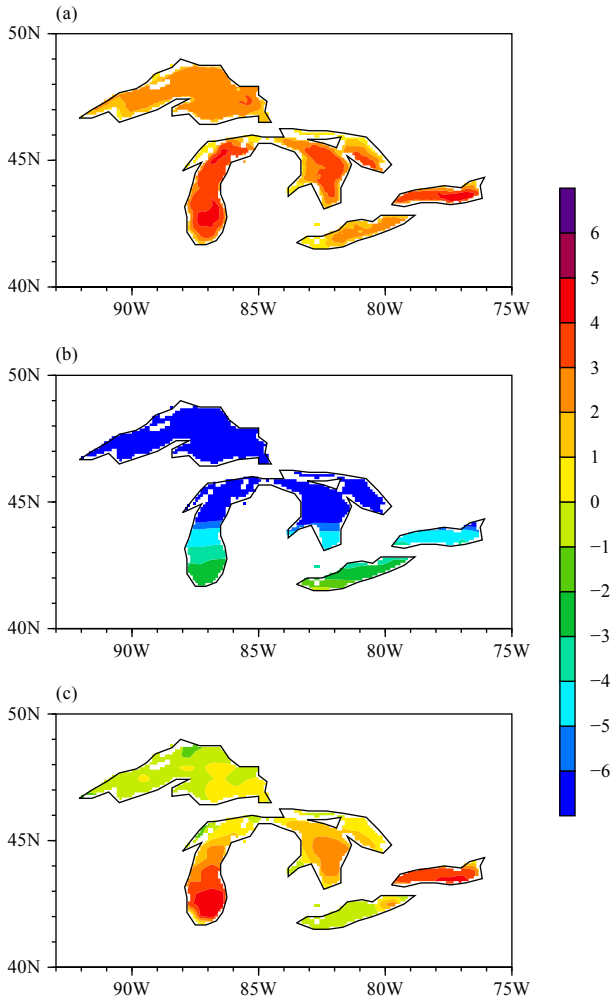

Fig. 1. January mean lake surface temperature over the Great Lakes region in North America derived from (a) AVHRR/NOAA satellite observation averaged for 1995–2006, (b) simulation of BCC_AVIM1.0, and (c) simulation of CoLM-Lake with real lake depths in BCC_AVIM2.0.

BCC_AVIM2.0. The January cold bias in BCC_AVIM1.0 is possibly due to the quick freezing of surface water without considering the insulation of snow cover, and the alleviation of this cold bias in the lake surface temperature simulation of BCC_AVIM2.0 is partly due to the larger heat capacity of the entire water–soil system of CoLM-lake in BCC_AVIM2.0 than that from the water-only lake module in BCC_AVIM1.0.

The remarkable feature in observed lake surface temperature in July is the gradient distribution either within a specific lake or among different lakes (Fig. 2a). The northernmost Lake Superior is the coldest and the southernmost Lake Erie is the warmest. The northern part of Lake Superior is as cold as 9°C, and the southwestern part of the lake body becomes increasingly warmer as it becomes shallower. The surface temperature of Lake

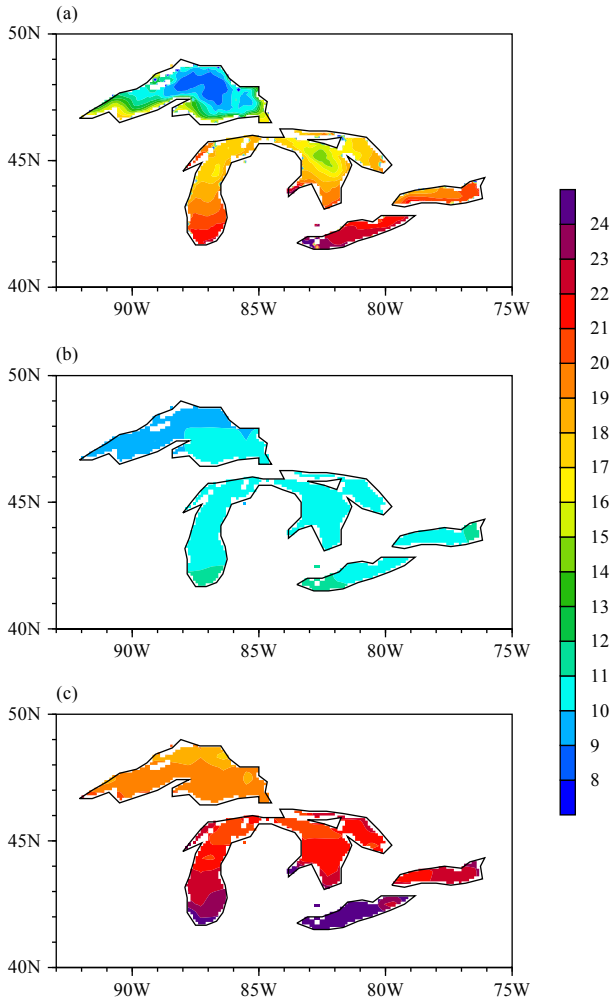

Fig. 2. As in Fig. 1, but for July.

Michigan increases from approximately 17°C in the northern part to above 21°C in the southern end. The north central region of Lake Huron is approximately 14°C, and the southern end of Lake Huron and most of Lake Ontario are approximately 19°C, almost as warm as their counterpart of Lake Michigan located in the same latitudinal belt. The latitudinal gradient in surface temperature of Lake Erie is also obvious, ranging from 20°C in the northeastern part to 23°C in the southwestern end. Compared with the aforementioned observations, BCC_AVIM1.0 produces uniformly colder surface temperatures in the five lakes, except for the northern part of Lake Superior; the cold bias is approximately 6°C (16°C vs. 10°C) in northern Lake Michigan and approximately 9°C (20°C vs. 11°C) in southern Lake Michigan; and the cold bias in the BCC_AVIM1.0 simulation can be as large as 12°C (23°C vs. 11°C) in southern Lake Eire (Fig. 2b). The performance of BCC_AVIM2.0 (Fig. 2c) is much better than that of BCC_AVIM1.0. The overall spatial distribution of lake surface temperature is similar to observations but the magnitude is generally higher and the warm biases are larger at higher latitudes. The surface temperature of northern Lake Superior is approximately 8°C higher than that in the observations; the warm bias is approximately 6°C in northern Lake Huron; and the warm bias reduces to approximately 3°C in southern Lake Michigan. The summertime cold bias of surface temperature in BCC_AVIM1.0 simulation is associated with the strong heat diffusion from surface to deeper water layers; in contrast, the warm bias in BCC_AVIM2.0 is due to the relatively weak heat diffusion between vertical layers in the CoLM-lake module of BCC_AVIM2.0. Statistically, CoLM-lake in BCC_AVIM2.0 performs better than the lake module in BCC_AVIM1.0 in July, with the spatial correlation coefficient between the observed lake surface temperature and that simulated by BCC_AVIM1.0 over the Great Lakes region being 0.61 and that by BCC_AVIM2.0 being 0.75, and the RMSE reduced from 7.4°C for BCC_AVIM1.0 to 6.4°C for BCC_AVIM2.0.

3.2 *Rice paddies*

The interactions between agricultural land and overlying atmosphere play an important role, especially in paddy rice fields in eastern and southeastern parts of Asia, where surface latent heat flux (LHFX) values are relatively large. Using only one PFT to represent crop in BCC_AVIM1.0 undoubtedly underestimates surface evaporation over rice paddies where the ground is covered by water. A new scheme for rice paddy fields was developed in BCC_AVIM2.0 to incorporate the addition of surface water above soil, which is distinct from dry farmland; the energy flux stored in surface water is important to the energy balance and affects climate via heat and water fluxes at the canopy and water surface. The essential difference in the calculation of LHFX between this study and the original crop scheme in BCC_AVIM1.0 lies in that there is no limit in the evaporation from a rice paddy assumed to be a water body in BCC_AVIM2.0. The evaporation from rice paddies in BCC_AVIM2.0 comprises two parts: E_v from the rice canopy and E_w from the ground water body; and they are calculated as:

$$E_v = -\rho_{atm}\frac{\left(q_s - q_{sat}^{T_v}\right)}{r_{total}}, \tag{8}$$

$$E_w = -\rho_{atm}\frac{(q_s - q_w)}{r_{aw}}, \tag{9}$$

where ρ_{atm} is the density of air (kg m^{-3}); q_s is the specific humidity of canopy air at the zero-plane displacement

height (kg kg^{-1}); $q_{\rm sat}^{T_{\rm v}}$ is the saturation water vapor specific humidity at the vegetation temperature $T_{\rm v}$; $q_{\rm w}$ is the specific humidity at the ground water surface (kg kg^{-1}); $r_{\rm total}$ is the total resistance to water vapor transfer from the canopy to the canopy air, which includes contributions from the leaf boundary layer and leaf stomatal resistance; and $r_{\rm aw}$ is the aerodynamic resistance (s m^{-1}) to water vapor transfer between the ground water body and the canopy air. In addition to the aforementioned modification to ground surface evaporation, rice phenology is empirically prescribed according to planting dates to simulate two growing seasons of rice in central China rather than one growing season for crop in BCC_AVIM1.0. On the other hand, the technical details about the surface sensible heat flux (SHFX) over rice paddies are quite similar to those over vegetated surfaces in CLM (Oleson et al., 2004).

Figure 3 shows the seasonal evolution of daily mean SHFX and LHFX at a field station in Shouxian County of Anhui Province, China. In the observation, SHFX remains below 30 W m^{-2} almost year-round, except in June when it increases to above 60 W m^{-2}. Surface LHFX is dominant during most of the year and is more than 30 W m^{-2} from March to November; two peaks of more than 130 W m^{-2} appear in Mayand July corresponding to the double growing seasons of rice in the midlatitudes of China. It is observed that the new scheme (Rice) in BCC_AVIM2.0 has simulated the seasonal variations of SHFX and LHFX more accurately than the old scheme (Crop) in BCC_AVIM1.0, both in magnitude and in the temporal evolution. Two peaks of LHFX simulated by the Rice scheme in May and July are associated with the growing seasons of rice and the consequent strong evapotranspiration; the dip in LHFX in June and the peak in SHFX around that period correspond to the harvest of rice and subsequent restricted evapotranspiration. Quantitatively, the RMSEs of SHFX simulation using the Crop and Rice schemes are 45.95 and 19.09 W m^{-2} respectively, and the RMSE of corresponding LHFX simulation is remarkably reduced from 46.10 to 16.83 W m^{-2}. The improvements in the Rice scheme are due to increased evaporation from the water surface over rice paddies and the two growing seasons compared with relatively less evaporation over dry farmland and only one growing season in the old Crop scheme.

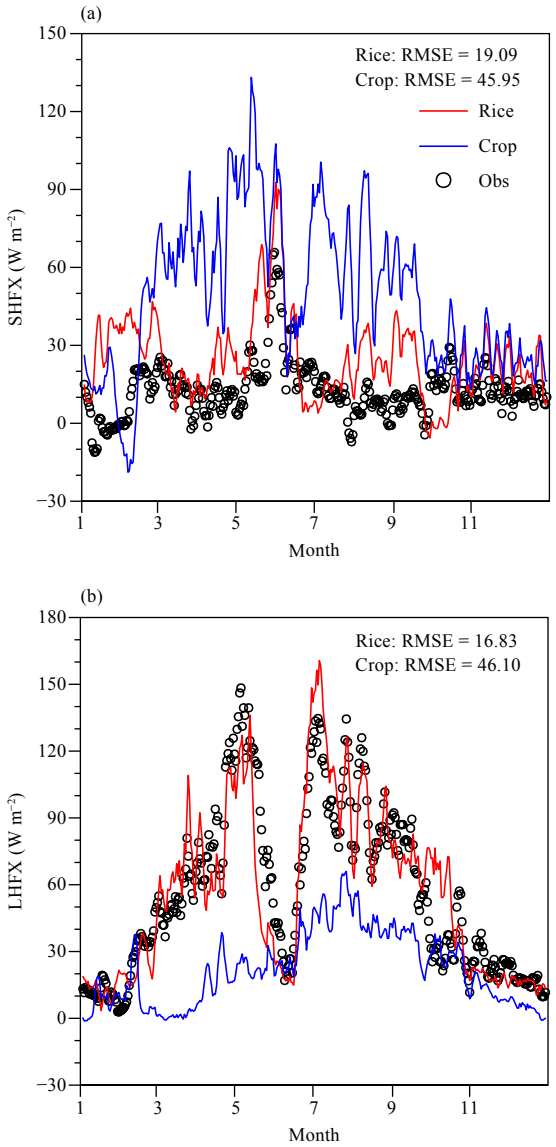

Fig. 3. Temporal evolution of (a) sensible heat flux (SHFX) and (b) latent heat flux (LHFX). Black circles: observations; blue curve: crop scheme in BCC_AVIM1.0; red curve: rice scheme in BCC_AVIM2.0.

3.3 *Snow cover fraction*

Snow cover fraction (SCF) is the percentage of a model grid cell covered by snow. SCF is usually parameterized by the roughness length of the land surface and snow depth or snow water equivalence. SCF is generally underestimated in some LSMs in winter (Li et al., 2009; Xia and Wang, 2015), and the negative bias of SCF could be partly alleviated by using improved schemes (Niu and Yang, 2007). Meanwhile, SCF is overestimated in the regions with fluctuating topography such as southern Europe and in the areas around the Tibetan Plateau and the Mongolian Plateau (Li et al., 2009). An obvious defect in the previous SCF schemes is that the soil roughness length is assumed to be a global constant, although it should be location dependent (Yang et al., 1997). Considering the heterogeneous land surface and inhomogeneous precipitation, LSMs should take into account the subgrid variability of topography in a model grid cell to decrease the magnitude of SCF (Roesch et al., 2001).

The SCF in BCC_AVIM2.0 is parameterized as:

$$F_{\mathrm{sno}} = \tanh\left(\frac{h_{\mathrm{sno}}}{2.5z_0}\right).\left(\frac{h_{\mathrm{sno}}}{h_{\mathrm{sno}}+\varepsilon+0.0002\sigma_z}\right)^a, \quad (10)$$

where h_{sno} is the snow depth (m); z_0 is the roughness length of bare soil; σ_z (m) is the spatial variability of subgrid topography (i.e., the standard deviation of topographic height from the regional mean) in a grid cell of an LSM; ε is a minute constant (10^{-5}) to avoid division by zero for totally flat and snow-free grid boxes; and the power exponent a is an adjustable constant smaller than 1 according to the spatial resolution of the model grid cell.

3.4 *Snow aging and snow surface albedo*

In current empirical parameterizations for snow surface albedo (SA), snow surface temperature is considered as an important and sometimes even the only dominant factor, and the distinct characteristics of snow aging at different stages of a snow season are neglected. However, analysis of observation data indicates that it is necessary to consider the different reduction rates of snow albedo in the accumulating and melting stages of a snow season. Snow albedo decreases more rapidly in the melting period than in the previous accumulating period (Aoki et al., 2003; Chen et al., 2014). Snow albedo in the melting stage of a snow season might be overestimated by previous schemes using a set of unified parameters throughout the entire snow season, which partly explains why the melting rate is weakened and the final ablation of the snow cover is delayed in BCC_AVIM1.0. The diffuse albedos of snow at different spectral bands are parameterized as those in Biosphere–Atmosphere Transfer Scheme (BATS; Dickinson et al., 1993):

$$\alpha_{\mathrm{diff,vis}} = (1.0 - C_{\mathrm{vis}} \cdot F_{\mathrm{age}})\alpha_{\mathrm{diff,vis0}}, \quad (11)$$

$$\alpha_{\mathrm{diff,nir}} = (1.0 - C_{\mathrm{nir}} \cdot F_{\mathrm{age}})\alpha_{\mathrm{diff,nir0}}, \quad (12)$$

where $\alpha_{\mathrm{diff,vis}}$ and $\alpha_{\mathrm{diff,nir}}$ are the diffuse albedos of snow at visible and near infrared wave bands, respectively; C_{vis} and C_{nir} are empirical constants that depict the albedo reduction with time; F_{age} is a snow aging parameter related to snow surface temperature and impurities; and $\alpha_{\mathrm{diff,vis0}}$ and $\alpha_{\mathrm{diff,nir0}}$ are the albedos of freshly fallen snow at visible and near infrared bands, respectively. The direct beam albedo of snow is the sum of the above diffuse albedo and the correction associated with solar zenith angle (Dickinson et al., 1993; Oleson et al., 2004).

In BCC_AVIM1.0, C_{vis} and C_{nir} are assumed to be constant (0.2 and 0.5 respectively) throughout the entire snow season, which weakens the snow aging effect during the melting stage and therefore overestimates snow albedo at that time. To better represent the reduction of snow albedo with elapsed time after a snowfall event, two sets of C_{vis} and C_{nir} are used before and after mid March to simply mimic the different snow aging effects for the accumulating and melting stages of a snow season in the Northern Hemisphere (NH) in BCC_AVIM2.0. The values of C_{vis} and C_{nir} are assumed to be 0.2 and 0.5 respectively for the snow accumulation period before mid March, and 0.3 and 0.65 for the snow melting stage afterwards. This revised scheme can partly alleviate the overestimation of snow albedo during boreal spring in BCC_AVIM1.0 as it keeps the SA of the previous accumulating period unchanged, thus shortening the snow season length by approximately 5 days, closer to the observations (Fig. 4).

3.5 *Threshold temperature to initiate freeze/thaw of soil water/ice*

Liquid water freezes when the soil temperature decreases to 0°C in BCC_AVIM1.0, and the soil temperature will remain at 0°C until all the liquid water has frozen. However, liquid water can coexist with ice in the real world when the soil temperature is below 0°C. The relationship between soil water content and soil temperature is determined by the inherent characteristics of soil hydraulics and the thermodynamic equilibrium between soil water potential and soil temperature. Therefore, the method to calculate the soil freeze/thaw critical temperature used by Li and Sun (2008) was adopted in BCC_AVIM2.0 to replace the unreasonable assumption used in BCC_AVIM1.0.

Soil water potential remains in equilibrium with the vapor pressure over soil ice when freezing occurs. Combining the relationship between soil water matrix potential ψ (mm) and soil temperature $\psi(T)$ with the relationship between soil water matrix potential ψ (mm) and soil liquid water content $\psi(\theta_{\mathrm{liq}})$, the expression for the functional relation between the freeze/thaw threshold temperature of soil water (T_{thre}) and the soil liquid water content can be derived as:

$$T_{\mathrm{thre}} = \frac{10^3 L_{\mathrm{f}} \cdot T_{\mathrm{frz}}}{10^3 L_{\mathrm{f}} - \psi_{\mathrm{sat}}\left(\frac{\theta_{\mathrm{liq}}}{\theta_{\mathrm{sat}}}\right)^{-b} \cdot \mathrm{g}}, \quad (13)$$

where L_{f} is the latent heat of fusion (J kg^{-1}); T_{frz} is the freezing point of pure water (K); ψ_{sat} is the saturated soil matrix potential (mm), which is usually negative; θ_{sat} and θ_{liq} are soil porosity and the partial volume of liquid water, respectively; b is the Clapp–Hornberger parameter; and g is the gravitational acceleration (m s^{-2}). The threshold temperature gradually rises as liquid water con-

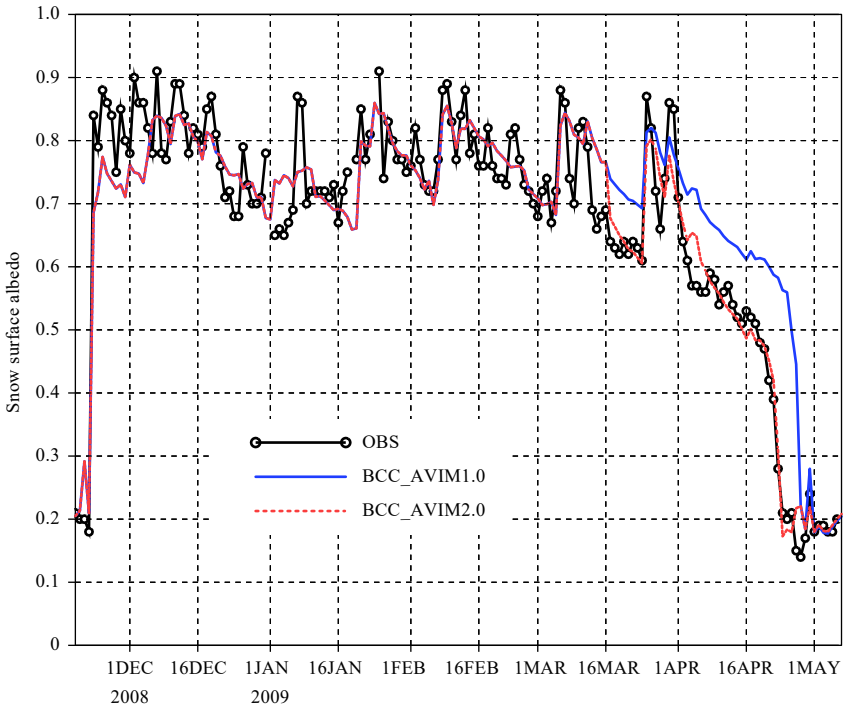

Fig. 4. Temporal evolution of snow surface albedo (SA) averaged over the 2008–09 snow season at the Col de Porte site in France. The black line with circles denotes observation (OBS), and the blue (red) curve denotes BCC_AVIM1.0 (BCC_AVIM2.0) simulation.

tent increases but is always below the freezing point of pure water T_{frz}. It can be deduced from Eq. (13) that under the same condition of soil liquid water content, the freeze/thaw threshold temperature for coarse sandy soil is higher than that for other kinds of soil with smaller soil particle size and relatively larger porosity. The absolute value of the saturated soil water potential of clayey soil is greater than that of sandy soil with the same liquid water content; the second term (with negative value) in the denominator is larger in magnitude for clayey soil, and the final value of T_{thre} is thus smaller for clayey soil. The underlying reason is that sandy soil has macropores that can be easily drained and the assembled water can easily freeze; therefore T_{thre} for sandy soil is higher than T_{thre} for clayey soil with a similar soil water content.

Validation of different parameterization schemes to simulate the seasonal freeze/thaw of soil water/ice shows that the temporal evolution of soil temperature is closer to observations by using Eq. (13) to initiate thaw in spring and freeze in autumn. After the melting of the seasonal frozen layer, the seasonal warming of soil temperature is delayed and is closer to observations compared with the old scheme (Xia et al., 2011). Considering that the T_{thre} to initiate thawing of soil ice is usually higher than that for the freezing of soil liquid water, for the sake of simplicity and for the time being, 0.5°C is added to T_{thre} to initiate thawing of soil ice in BCC_AVIM2.0.

Soil organic matter serves as an insulator for heat transfer through soil layers, and the soil solid heat capacity of organic matter is larger than that of mineral (Lawrence and Slater, 2008), both of which delay soil freeze/thaw processes. These factors will be considered in the future version of BCC_AVIM.

3.6 *Prognostic phenology of vegetation*

The phenology of a PFT in BCC_AVIM1.0 is empirically prescribed to ensure that the simulated seasonal evolution of LAI is in phase with the climatology derived from satellite observations (Ji, 1995). In other words, there is no interannual variation in leaf expansion and leaf fall dates for a PFT in BCC_AVIM1.0. To capture the interannual variation and long term trend in vegetation phenology, a prognostic phenology scheme based on the work of Arora and Boer (2005) is implemented in BCC_AVIM2.0. The phenology for deciduous ecosystems consists of four stages: the rapid expansion period of LAI indicating the start of a growing season, the normal growth period, the leaf fall period, and a dormant season without leaves. The herbaceous biomes experience three phonological stages during their growth in a year, which are the same as the first three phenology stages of the deciduous forests. Unlike deciduous forests, herbaceous ecosystems maintain leaves as long as the environmental and physiological conditions are met. The

evergreen forests are always in a normal growth state. Maintenance respiration is separately calculated for leaves, stems, and roots, depending on the separate biomasses and a temperature dependent Q_{10} factor. Growth respiration for each biomass pool (leaf, stem, and root) is assumed to be a fixed percentage (25%) of the residual of gross primary productivity (GPP) minus maintenance respiration.

Allocation to and from the three vegetation biomass pools (leaf, stem, and root) leads to dynamic vegetation that in turn produces litter fall and ultimately transfers to soil organic carbon (SOC). The allocation of carbon to the three vegetation biomass pools depends on the light availability, water stress, and phenology stages of the canopy, and follows the formulations of Arora and Boer (2005). Most carbon assimilated in photosynthesis is allocated to the leaves during the leaf onset stage, carbon is allocated to the three vegetation carbon pools during the normal growth stage, and allocation to leaves stops during the leaf fall stage. The allocation of carbon to the vegetation biomass pools is constrained by the adverse effects of limited availability of light and water. Accordingly, the allocation in roots can help address the limited availability of water, whereas investments in stems tend to increase canopy access to light.

The carbon allocation process is constrained by two conditions. First, for the cold deciduous trees, almost all carbon is allocated to the leaves during leaf onset in order to maximize photosynthetic carbon gain. The second condition is to assure that the plant structure is preserved, which implies that sufficient root and stem biomass must be built up in advance to support the leaf biomass. The allocation of carbohydrates produced by photosynthesis to different biomass pools (leaf, stem, and root) is parameterized as follows:

$$\alpha_{\text{stem}} = \frac{\varepsilon_{\text{stem}} + \omega(1-L)}{1+\omega(2-L-W)}, \tag{14}$$

$$\alpha_{\text{root}} = \frac{\varepsilon_{\text{root}} + \omega(1-W)}{1+\omega(2-L-W)}, \tag{15}$$

$$\alpha_{\text{leaf}} = \frac{\varepsilon_{\text{leaf}}}{1+\omega(2-L-W)} = 1-\alpha_{\text{stem}}-\alpha_{\text{root}}, \tag{16}$$

where ω, $\varepsilon_{\text{leaf}}$, $\varepsilon_{\text{stem}}$, and $\varepsilon_{\text{root}}$ are PFT-dependent constants for the sake of simplicity, and the parameters L and W are associated with LAI and soil moisture conditions respectively, as given by:

$$L = e^{-K\cdot\text{LAI}}, \tag{17}$$

$$W = \sum_{i=1}^{n} W_i \cdot \text{Root}f_i, \tag{18}$$

where K is a PFT-dependent light extinction coefficient, W_i is the soil wetness, and Rootf_i is the fraction of root distribution in the ith soil layer. It can be deduced from Eq. (16) that under the same soil moisture condition (W), a larger L is associated with a larger α_{leaf}. The philosophy is that more carbohydrates are allocated to the canopy to increase LAI at the beginning of a growing season when LAI is small and the parameter L is relatively large, which favors photosynthesis and canopy growth and thus the increase of LAI.

The litter fall from leaves, stems, and roots is estimated as a function of temperature, water stress, and turnover rates. The turnover timescale for leaves is biome-dependent and varies from 0.75 yr for savanna to 2 yr for evergreen forests (Foley et al., 1996). The turnover rates for stems vary from 2.5 yr for savanna to 50 yr for evergreen forests (Malhi et al., 2004), and for root turnover the rates are between 1 and 8 yr for different PFTs.

The timing of the LAI peak in a year depends on the seasonal evolution of photosynthesis of a specific PFT, which strongly influences the seasonal variation of turbulent heat exchanges between the land surface and the atmosphere. Figure 5 displays the geographical distribution of the climate mean calendar month when LAI reaches its annual maximum. The LAI peak timing derived from AVHRR data clearly displays the seasonal evolution of vegetation growth along the latitude belts, especially in the middle to high latitudes of the NH with four distinctive seasons (Fig. 5a). In North America, the earliest LAI peak occurs in the southern Great Plains of the US in May, LAI in northwestern US reaches its maximum in June, large areas spanning from central Canada northwestward to Alaska see maximum LAI in July, and most of the other parts of North America experience peak LAI in August, except that Mexico and the southeastern US see LAI peaks in September or October. In the Southern Hemisphere (SH), the timing of peak LAI is slightly heterogeneous. The central Amazon basin at approximately 10°S experiences its LAI peak in July, whereas the Conco basin at similar latitudes in Africa experiences peak LAI in November; the Brazilian Plateau to the southeast of the Amazon basin and most parts of the South African continent see peak LAI in February to March; and the southern end of South America to the south of 35°S see peak LAI in November.

The empirical phenology scheme in BCC_AVIM1.0 simulates an almost uniform timing of peak LAI: August in the NH and February in the SH, one month after the height of summer in both hemispheres, except for several regions at approximately 30°N (e.g., western and cen-

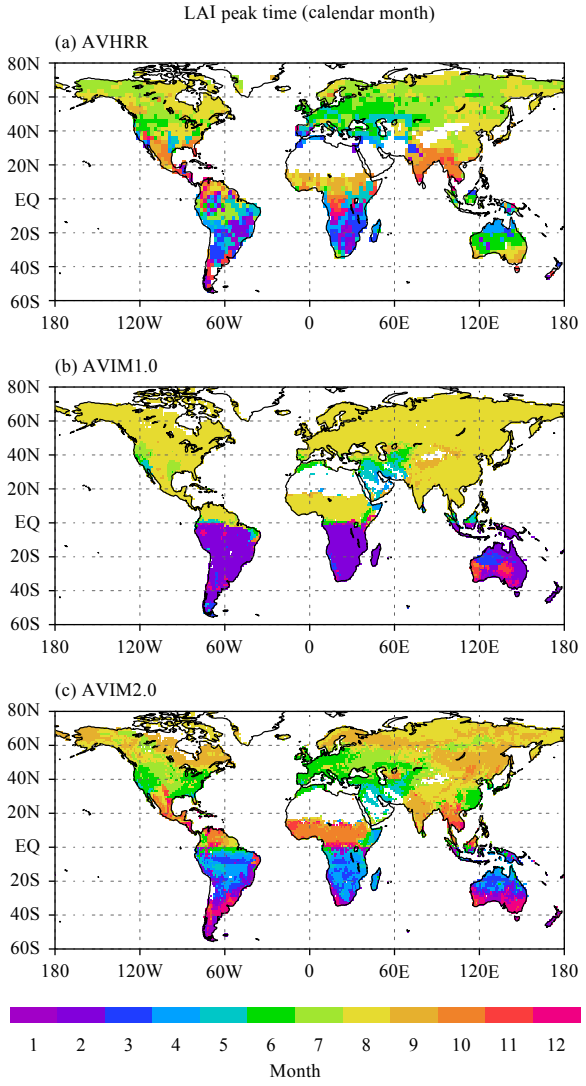

Fig. 5. The timing of LAI peaks (month). (a) AVHRR, (b) BCC_AVIM1.0, and (c) BCC_AVIM2.0.

tral part of the southern US, western Asia) with peak LAI in June–July, and in November in southern Australia (Fig. 5b). In contrast, BCC_AVIM2.0 performs better in simulating the geographical LAI peak timing, especially in the NH (Fig. 5c). The details of BCC_AVIM2.0 simulation in different continents are presented next.

In the North American continent, LAI reaches a maximum in June in the western and eastern parts of the US, while central US and central Canada see peak LAI in July, and most of the other parts of the North American continent from Alaska to eastern Canada experience the LAI peak in August to September. Generally, the timing of peak LAI in the BCC_AVIM2.0 simulation is approximately one month earlier than in the AVHRR data in the central and eastern US but one month later than in the AVHRR data in other parts of the North American continent to the north of approximately 50°N.

In the Eurasian continent, regions to the south of 60°N and to the west of 30°E see peak LAI in June, which is consistent with the AVHRR observations. Most of the midlatitude regions from 30°E to 90°E experience peak LAI in July, and the other parts of the Eurasian continent to the north of 40°N see peak LAI in August to September, one or two months later than in the AVHRR data. In contrast, the timing of peak LAI in the BCC_AVIM2.0 simulation is approximately one month earlier than in AVHRR observations in the southeastern parts of Asia; for example, eastern China experiences peak LAI in June–July, central and eastern India sees peak LAI in September.

In the SH, the timing of the LAI peak in April–May in the central Amazon basin is approximately two months earlier than in the observations. The LAI peak in January to February in the Brazilian Plateau is close to observations but the area coverage at approximately 40°S in South America with peak LAI in November expands more northward than in observations. In the South African continent, tropical forests in the Congo basin see peak LAI in December to January, and most of the other parts see LAI peaks in March to April, approximately one month later than in observations (Figs. 5a, c).

The improvement in vegetation phenology produces better simulation of LAI at the seasonal timescale. In the AVHRR observations, there are three latitudinal belts of LAI maxima associated with three integrated belts of the earth's ecosystem. The northernmost belt corresponds to the boreal mixed forests in high latitudes of the NH. The central belt is related to the temperate zone forests in southeastern US and southeastern China, and the third belt is associated with tropical forests in the Amazon basin in South America, the Congo basin in central Africa, and the Maritime Continent in Southeast Asia (Figs. 6a1, b1). The LAI of tropical rainforests remains above 4 throughout the year. Boreal forests experience remarkable seasonal variation: LAI is less than 2 in boreal winter (December, January, and February, i.e., DJF) and can be more than 4 in boreal summer (June, July, and August, i.e., JJA). Both BCC_AVIM1.0 and BCC_AVIM2.0 capture the general pattern of LAI distribution in both seasons, although BCC_AVIM1.0 overestimates LAI in most parts of the summer hemisphere, i.e., positive biases in the NH in JJA and in the SH in DJF, except for patchy negative biases in central North America and central Europe in JJA (Figs. 6a2, b2). The above LAI biases in the BCC_AVIM1.0 simulation correspond to the unrealistic phenology in BCC_AVIM1.0 dis-

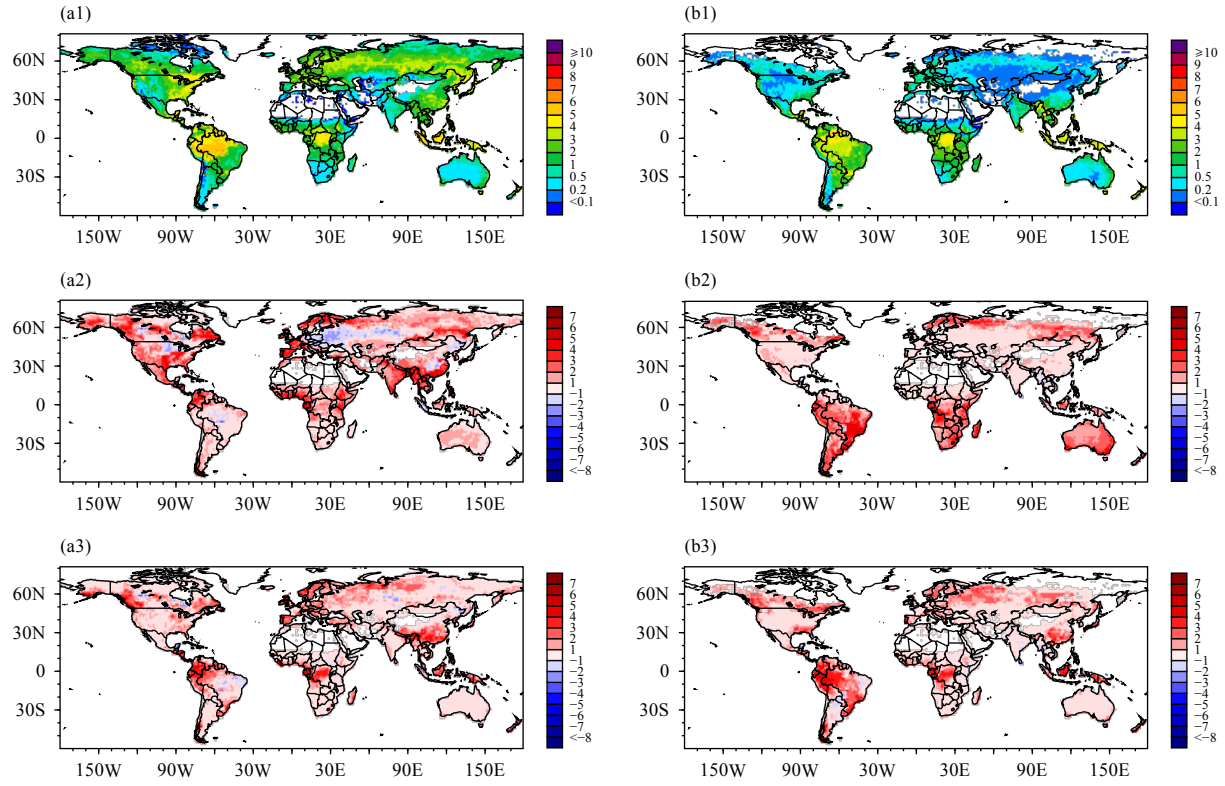

Fig. 6. Distributions of multi-year (1982–2008) seasonal mean LAI in (a1–a3) boreal summer (June, July, and August) and (b1–b3) boreal winter (December, January, Feburary). (a1, b1) AVHRR observations; (a2, b2) BCC_AVIM1.0 minus AVHRR; and (a3, b3) BCC_AVIM2.0 minus AVHRR.

played in Fig. 5b and consequent GPP simulation biases (figure omitted). In contrast, LAI biases in the BCC_AVIM2.0 simulation are reduced to some extent (Figs. 6a3, b3), except for the overestimations of LAI in the northwestern Amazon basin, western central Africa, and southeastern mainland China in both JJA and DJF, which might be due to the too-large maximum rate of carboxylation prescribed for tropical and subtropical forests in BCC_AVIM2.0 and the consequent overestimation of GPP in the aforementioned regions, issues that need to be addressed by more sensitivity experiments in the future.

3.7 *Solar radiation transfer within the vegetation canopy*

The two-stream scheme for calculating solar radiation transfer within a vegetation canopy in BCC_AVIM1.0 was originally developed by Dickinson (1983) and is widely used in LSMs. The four-stream radiation transfer module used in BCC_AVIM2.0 is based on the atmospheric radiation transfer theory (Liou, 1992), and it analytically solves a basic radiation transfer equation for the canopy, each parameter of which has its own geometry as well as specific leaf and canopy optical characteristics. The upward/downward radiation fluxes and canopy albedo calculated by the four-stream module are related to several factors such as the diffuse phase function, the area extinction coefficient, leaf reflectivity and transmissivity, LAI, and solar angle. Offline simulations show that the albedo of a vegetation canopy calculated by the four-stream module is lower than that calculated by the previous two-stream scheme. When coupled with the LSM BCC_AVIM2.0, the four-stream radiation transfer scheme produces lower albedos in mid–high latitudes but slightly higher albedos in most tropical dry land regions, which are closer to the observations (Zhou et al., 2018).

4. Performance of BCC_AVIM2.0 in LS3MIP/CMIP6

The main purpose of LS3MIP is to provide a comprehensive assessment of land surface processes and associated feedbacks on climate variability and climate change and to diagnose systematic biases in the land component of current CSMs (van den Hurk et al., 2016). Two sets of experiments are designed for LS3MIP: the first addresses systematic biases of land surfaces in the offline mode and the second addresses land feedbacks attributed to snow cover and soil moisture in an integrated framework. LS3MIP has proposed several sets of atmospheric

forcing data to drive LSMs in offline mode. The results of historical experiments with BCC_AVIM1.0 and BCC_AVIM2.0 driven by the Princeton global forcing dataset (Sheffield et al., 2006) are analyzed in this section under the framework of ILAMB (Mu et al., 2016), which focuses on land surface energy budgets and terrestrial carbon cycles at the seasonal timescale, especially the summer and winter seasons.

4.1 *Net surface radiation*

According to the CERES data (Kato et al., 2013), the seasonal variation of net surface radiation (NSR; including both shortwave and longwave) strongly depends on the seasonal evolution of solar radiation, which peaks in summer and reaches its minimum in winter in both hemispheres. The tropics sees relatively strong year-round net radiation (Figs. 7a1, b1). Taking the summertime NH as an example (Fig. 7a1), the magnitude of NSR is above 90 W m^{-2} almost everywhere except in the Sahara desert in northern Africa, the Arabian Peninsula, and the Taklimakan desert in northwestern China. Most parts of mid- and high-latitude areas in the NH see more than 120 W m^{-2} of NSR; the southeastern part of the US even experiences more than 150 W m^{-2} of NSR in JJA. Generally, BCC_AVIM2.0 has reasonably captured the geographical distribution and seasonal evolution of NSR (figure omitted), although the simulation biases are obvious in both summer and winter, especially in the SH (Figs. 7a2, b2). During the boreal JJA, negative biases of NSR in southern US and in the Sahel region are mainly associated with negative net longwave radiation biases (Figs. 7a2, a4). Patchy positive biases in the northern Eurasian

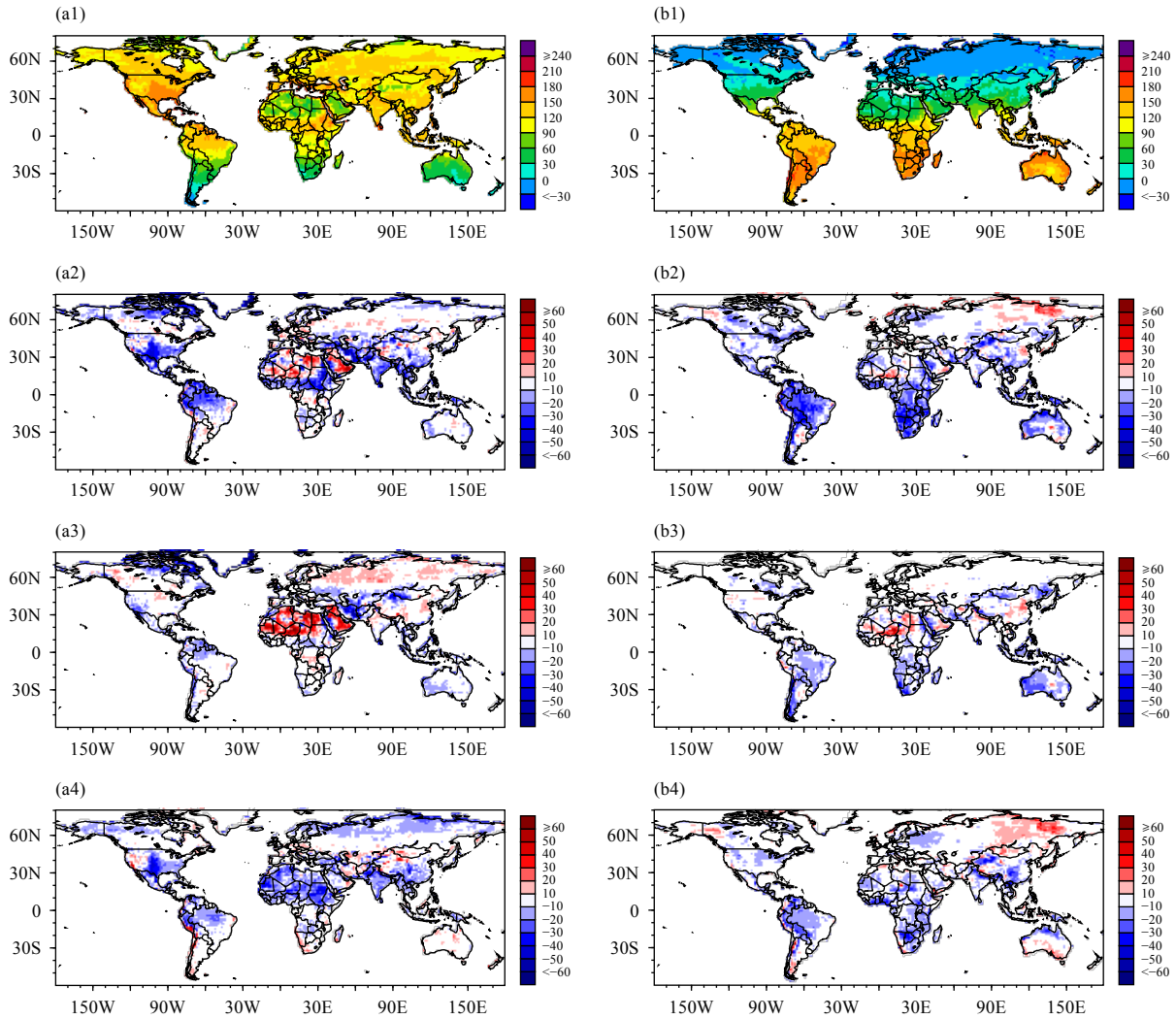

Fig. 7. Distributions of multi-year (2000–09) seasonal mean net surface radiation (NSR; W m^{-2}) in (a1–a4) boreal summer and (b1–b4) boreal winter. (a1, b1) CERES (net radiation); (a2, b2) BCC_AVIM2.0 minus CERES (net radiation); (a3, b3) BCC_AVIM2.0 minus CERES (shortwave); (a4, b4) BCC_AVIM2.0 minus CERES (longwave).

continent, the Sahara desert of North Africa, and the Arabian Peninsula are associated with overestimation of net solar radiation in the above areas (Figs. 7a2, a3). The aforementioned underestimation (overestimation) of net shortwave radiation results from larger (smaller) SA simulation in relevant regions (figure omitted). In contrast to the above shortwave radiation-dominant cases, overestimation of NSR in the northeast part of the Eurasian continent in DJF is due to the positive net longwave radiation bias in the BCC_AVIM2.0 simulation in that area (Figs. 7b2, b4). Underestimations of DJF net shortwave radiation in BCC_AVIM2.0 simulations in the SH are responsible for the negative NSR biases, and negative biases of net longwave radiation in the southern American and southern African continents may have also made some contributions (Figs. 7b2–b4). The aforementioned systematic biases indicate that there is much room to improve BCC_AVIM2.0 to reasonably simulate the surface energy budget.

4.2 *LHFX*

Land surface evaporation includes three parts: soil surface evaporation, evaporation from canopy intercepted precipitation, and vegetation transpiration through leaf pores (Lawrence et al., 2007). In addition to wind speed, the availability of net surface energy, soil water, and canopy-intercepted precipitation are among those factors that influence land evaporation. The LHFX magnitudes in the tropical areas remain more than 80 W m^{-2} year-round, and the NH experiences maximum LHFX in JJA, whereas LHFX peaks in DJF in the SH (Figs. 8a1, b1). There is an obvious northeastward gradient of LHFX in the Eurasian continent in JJA and DJF. In JJA, the magnitude of LHFX decreases from more than 80 W m^{-2} in western Europe to approximately 60–80 W m^{-2} in the central part and less than 60 W m^{-2} in the northeastern part of the Eurasian continent. LHFX can be more than 80 W m^{-2} in eastern Asia and as high as 100 W m^{-2} in southern Asia (Fig. 8a1). In DJF, most parts of the NH to the north of 50°N experience surface freezing, and the LHFX values in these regions are thus below 5 W m^{-2}. In contrast, LHFX in the subtropical areas in South America and the African continent reach peaks as high as 100 W m^{-2} (Fig. 8b1). BCC_AVIM2.0 has captured the overall geographical distribution and seasonal evolution of LHFX, except for some magnitude difference from the GBAF observations (Figs. 8a2, b2). The systematic biases of the BCC_AVIM2.0 simulation in JJA are obvious. There are approximately 20-W m^{-2} underestimations of LHFX in eastern US, tropical South America,

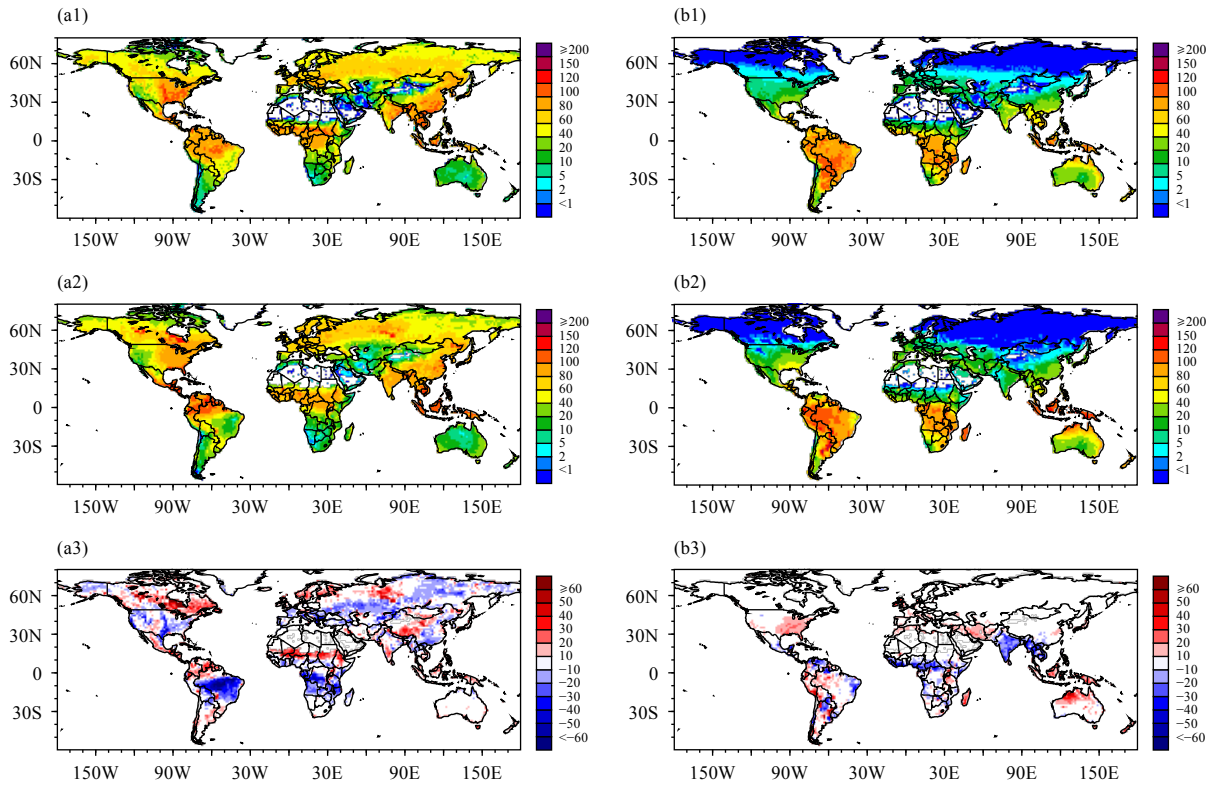

Fig. 8. Distributions of multi-year (1982–2008) seasonal mean seasonal mean LHFX (W m^{-2}) in (a1–a3) boreal summer and (b1–b3) boreal winter. (a1, b1) GBAF observation, (a2, b2) BCC_AVIM2.0 simulation, and (a3, b3) BCC_AVIM2.0 minus GBAF.

tropical Africa, and southeastern China. In contrast, approximately 20-W m^{-2} overestimations of LHFX exist in semiarid regions in the NH such as northern Canada, northern Sahel, the Tibetan Plateau, and the Mongolian plateau (Fig. 8a3). In DJF, the LHFX underestimations in tropical South America, tropical Africa, and South Asia are approximately 10–20 W m^{-2} (Fig. 8b3). The aforementioned underestimations in LHFX simulation in both JJA and DJF can be attributed to the negative biases in NSR shown in Figs. 7a2, b2, which indicates the dominance of available energy on land surface evaporation.

4.3 *SHFX*

The surface SHFX indicates the land surface thermal status and directly affects the overlying atmospheric circulation. Generally, lower surface pressure and near surface cyclonic circulation usually occurs over warmer surfaces with relatively high SHFX, and vice versa. The seasonal variation of SHFX is remarkable in high latitudes to the north of 50°N. Taking the latitude belt of approximately 60°N as an example, SHFX reaches more than 40 W m^{-2} in JJA and decreases to less than 10 W m^{-2} and even below zero in DJF, which means that the land surface in high-latitude NH is a heat sink in boreal winter. This heat sink in DJF can extend southward to 50°N in North America and the Eurasian continent to the west of 90°E (Figs. 9a1, b1). BCC_AVIM2.0 can simulate the overall geographical distribution of SHFX, except for the more southward expansion (approximately 40°N) of low SHFX coverage in North America and the northern Eurasian continent to the west of 110°E during DJF (Fig. 9b2). In JJA, there are approximately 20-W m^{-2} overestimations of SHFX in the BCC_AVIM2.0 simulation in dry lands, such as the central part of North America, the Brazilian Plateau, the Arabian Peninsula, and the midlatitude belt from west Asia to Mongolian Plateau (Fig. 9a3). The positive biases of SHFX in the central part of North America and the Brazilian Plateau coincide with the underestimation of LHFX in these regions, which is a common deficiency in the simulation of arid and semiarid land surface processes (Wang et al., 2017; Zhang et al., 2017). In DJF, there are approximately 10–20-W m^{-2} positive biases to the north of 60°N and negative biases in the midlatitudes of the NH between 30°N and 60°N (Fig. 9b3). The overestimation of SHFX by BCC_AVIM2.0 in the northeastern part of the Eurasian continent in DJF is probably due to the underestimation of SCF there in winter (figure omitted).

4.4 *Comparison between simulations of BCC_AVIM1.0 and BCC_AVIM2.0*

The simulations of BCC_AVIM1.0 and BCC_AVIM2.0

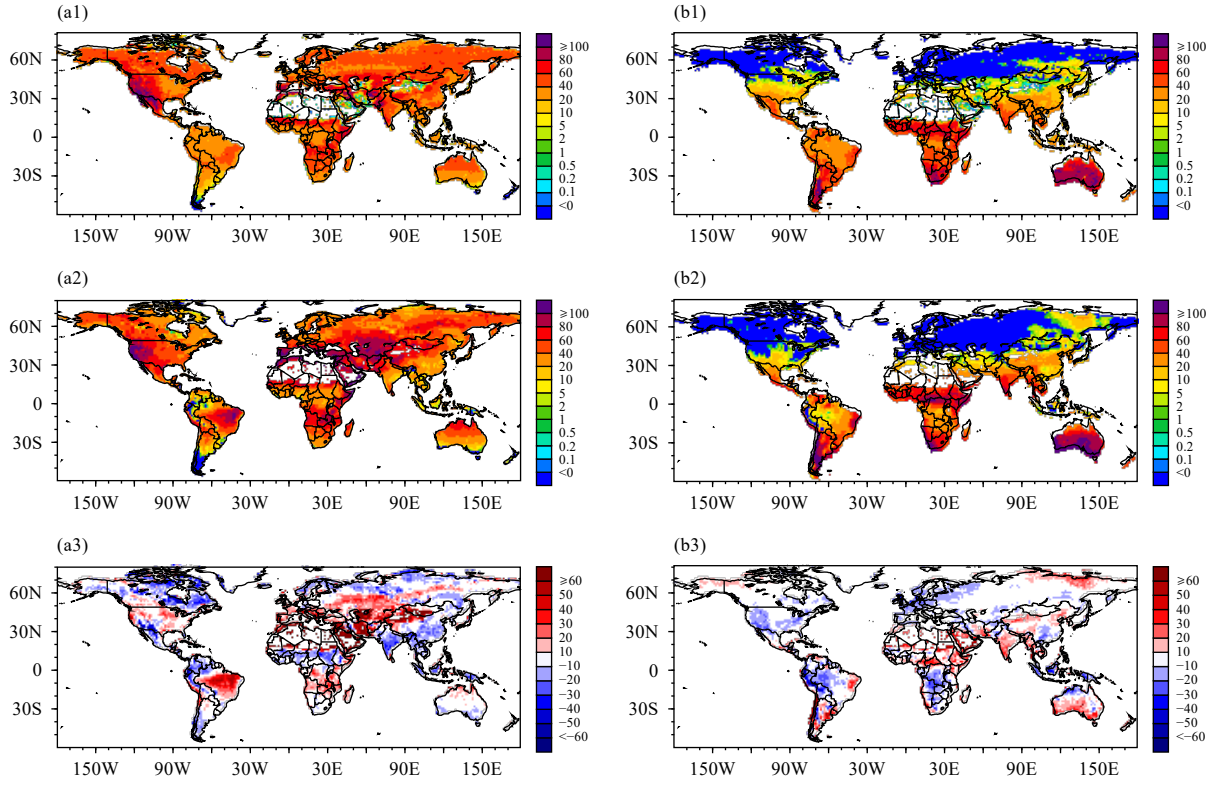

Fig. 9. As in Fig. 8, but for SHFX (W m^{-2}).

are compared in this section to check the overall impacts of the updates in parameterizations described in Section 3. The climatological annual cycles of regional averaged solar and surface fluxes (NSR, SHFX, and LHFX) and LAI are examined and analyzed, over the main body of the Eurasian continent (40°–70°N, 0°–140°E) and the South African continent (0°–35°S, 10°–40°E). These two domains are chosen as examples to represent the NH and SH, respectively.

Figure 10 shows the annual cycle for the Eurasian continent. NSR peaks in June in CERES observations, and both BCC_AVIM1.0 and BCC_AVIM2.0 simulations captured the seasonal cycle, except that the simulated NSRs are less than the observations by approximately 5–15 W m^{-2} from February to November. BCC_AVIM2.0 values are larger than BCC_AVIM1.0 and closer to CERES from June to October but BCC_AVIM1.0 performs better from February to May, although the difference between the two simulations is within 5 W m^{-2} (Fig. 10a). The underestimation of NSR in both simulations is due to more reflected shortwave radiation and more emitted longwave radiation than those in the observations (figure omitted); the contribution of longwave radiation is larger than that of shortwave radiation from March to October, especially in boreal spring. SHFX in BCC_AVIM1.0 is approximately 5 W m^{-2} smaller than GBAF observations from January to April, and SHFX in BCC_AVIM2.0 is smaller than GBAF by approximately 5–10 W m^{-2} from January to May. SHFXs in BCC_AVIM1.0 and BCC_AVIM2.0 are close to each other from June to December; they are nearly 7 W m^{-2} larger than GBAF from June to August but approximately 5 W m^{-2} smaller than GBAF from October to December (Fig. 10b). LHFX in BCC_AVIM2.0 is approximately 5 W m^{-2} larger than BCC_AVIM1.0 and is closer to GBAF from May to August (Fig. 10c). Further investigation indicates that this improvement in LHFX in BCC_AVIM2.0 is due to more transpiration through vegetation (figure omitted). LAI is larger in BCC_AVIM1.0 than in the AVHRR data by approximately 1 all year round, and the bias of LAI in BCC_AVIM1.0 can be as large as 2 in August when LAI peaks in BCC_AVIM1.0 (Fig. 5b). BCC_AVIM2.0 is better than BCC_AVIM1.0 in both the magnitude and phase of the seasonal evolution of LAI (Fig. 10d). In short, the seasonal cycle is better in BCC_AVIM2.0 due to the better representation of vegetation phenology.

The situation in the South African continent is shown in Fig. 11. NSR reaches a maximum of approximately 165 W m^{-2} in January and a minimum of approximately 75 W m^{-2} in July in CERES. Both BCC_AVIM1.0 and

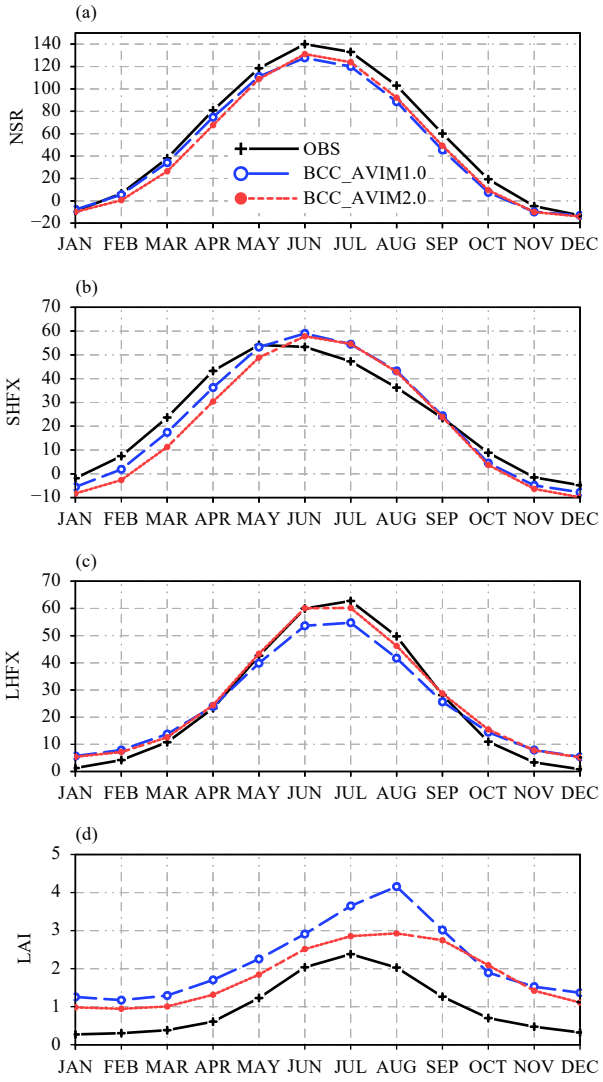

Fig. 10. Annual cycle of regional averaged (a) NSR, (b) SHFX, (c) LHFX, and (d) LAI over the main part of the Eurasian continent (40°–70°N, 0–140°E). Unit is W m^{-2} for energy fluxes in (a–c).

BCC_AVIM2.0 capture this seasonal evolution with year-round negative biases in both simulations. BCC_AVIM1.0 underestimates NSR by approximately 40 W m^{-2} in January and approximately 10 W m^{-2} in July. BCC_AVIM2.0 reduces this negative bias by approximately 5 W m^{-2} from February to September. The underestimation of NSR for the South African continent is due to more reflected shortwave radiation and more outgoing longwave radiation from the surface in both simulations (figure omitted). SHFX reaches a minimum (about 40 W m^{-2}) in June and a maximum (about 67 W m^{-2}) in October according to GBAF. BCC_AVIM1.0 underestimates SHFX by approximately 7 W m^{-2} from October to the following April, whereas SHFX in BCC_AVIM2.0 is larger than in BCC_AVIM1.0 year-round and closer to GBAF from October to the following April (Fig. 11b).

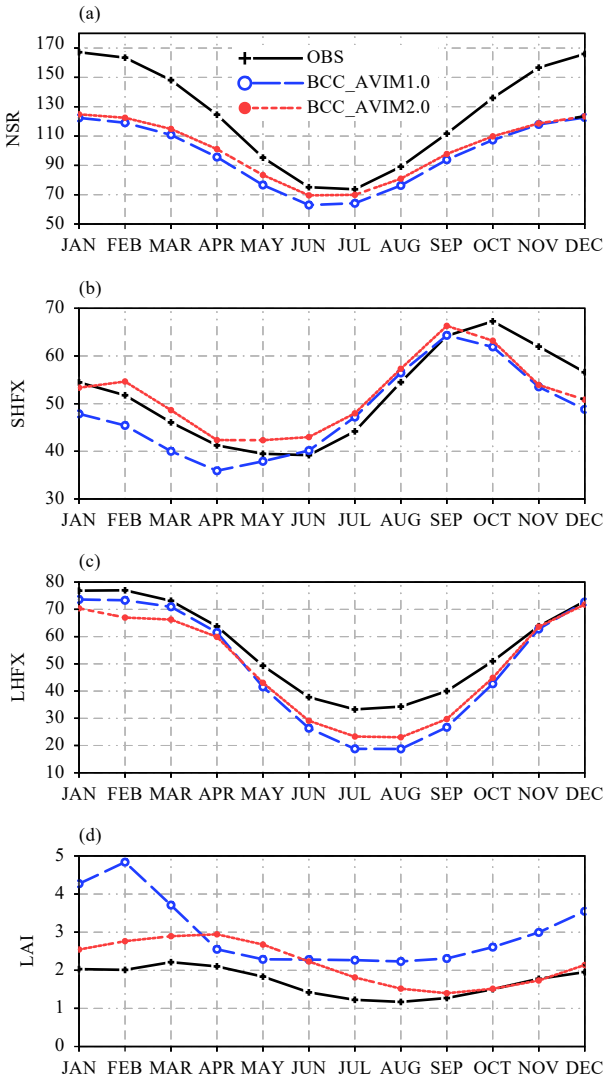

Fig. 11. As in Fig. 10, but over the South African continent (0–35°S, 10°–40°E). Unit is W m^{-2} for energy fluxes in (a–c).

However, this alleviation of negative SHFX bias in BCC_AVIM1.0 is at the cost of underestimation of LHFX by BCC_AVIM2.0 from January to April (Fig. 11c). The slight improvement in BCC_AVIM2.0 simulation of LHFX from May to October is associated with the better simulation of NSR during that period (Fig. 11a). LAI from AVHRR reaches a peak of approximately 2 in March. BCC_AVIM1.0 overestimates LAI by approximately 1 all year round, with a maximum near 5 in February; whereas BCC_AVIM2.0 captures the seasonal cycle of LAI evolution quite well, except for positive biases of approximately 0.5–1.0 from January to August (Fig. 11d). The maximum of LAI in the BCC_AVIM2.0 simulation from February to April is coincident with the LAI peak time over the South African continent shown in Fig. 5c. This indicates the advantage of the updated phenology scheme in BCC_AVIM2.0.

Statistics of the annual global land average of the aforementioned variables displayed in Table 1 also indicate improvements of BCC_AVIM2.0 simulations after the updates of the parameterizations. The global mean bias of NSR is reduced from −12.0 to −11.7 W m^{-2}, and the RMSE drops from 20.6 to 19.0 W m^{-2}. The bias of LHFX is reduced from 2.3 to −0.1 W m^{-2} and the RMSE is reduced from 15.4 to 14.3 W m^{-2}. One exception is that the global mean SHFX bias is increased from 2.5 to 5.1 W m^{-2}, whereas the RMSE is reduced from 18.4 to 17.0 W m^{-2}. The bias of LAI is reduced from 0.89 to 0.75, and the RMSE is reduced from 1.46 to 1.27.

The overall performance of BCC_AVIM1.0 and BCC_AVIM2.0 in simulating the global annual climatology of surface energy budgets, LAI, and variables associated with terrestrial carbon cycle is displayed in the Taylor diagram in Fig. 12. Both models perform well in simulating 9 variables with higher than 0.6 spatial correlations with the relevant observations [except for net ecosystem exchange (NEE) in the BCC_AVIM1.0 simulation], and 13 out of 18 standardized deviations fall approximately into the 0.5–1.5 range compared with the reference variability. Concerning spatial correlation, BCC_AVIM2.0 performs better than BCC_AVIM1.0 in simulating NEE, LAI, net surface radiation (NSR), SA, and SHFX, whereas BCC_AVIM1.0 performs slightly better in simulating GPP and respiration of ecosystem (RECO). It is noted that the two red circles representing the simulation performances of RECO and LAI in BCC_AVIM2.0 are very close to each other in Fig. 12. With respect to standardized deviation, which indicates the spatial variability of each variable, BCC_AVIM2.0 performs better than BCC_AVIM1.0 and closer to the thick reference circular arc in the simulation of GPP, RECO, tropical biomass, NSR, and SA.

5. Conclusions and discussion

This paper has documented the updates in several land surfaces related parameterization schemes in the second version of the Beijing Climate Center Atmosphere–Ve-

Table 1. Bias and RMSE values (in brackets) of annual global land averaged simulations of BCC_AVIM1.0 and BCC_AVIM2.0. The observations for NSR are from CERES (W m^{-2}), LHFX and SHFX data are from GBAF (W m^{-2}), and LAI is from AVHRR (unitless)

	BCC_AVIM1.0	BCC_AVIM2.0
NSR	−12.0 (20.6)	−11.7 (19.0)
LHFX	2.3 (15.4)	−0.1 (14.3)
SHFX	2.5 (18.4)	5.1 (17.0)
LAI	0.89 (1.46)	0.75 (1.27)

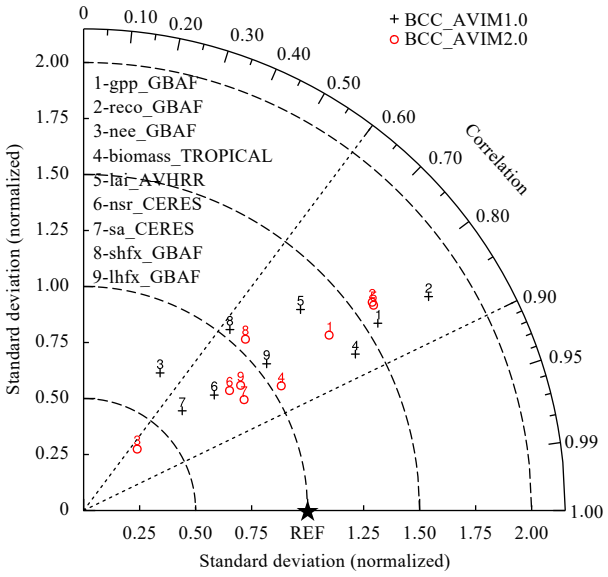

Fig. 12. Taylor diagram for the global annual climatology of gross primary productivity (gpp), respiration of ecosystem (reco), net ecosystem exchange of CO_2 (nee), biomass, leaf area index (lai), land net surface radiation (nsr), surface albedo (sa), surface sensible heat flux (shfx), and surface latent heat flux (lhfx). The upper case suffix after each variable indicates the source of observation. The radial coordinate shows the standard deviation of the spatial pattern, normalized by the observed standard deviation. The azimuthal variable shows the correlation of the modeled spatial pattern with the observed spatial pattern. Analysis is for the entire globe (except that biomass is for tropical areas). The BCC_AVIM2.0 and BCC_AVIM1.0 simulations are averaged over the same period as that for the relevant reference dataset. Crosses are for BCC_AVIM1.0 and circles for BCC_AVIM2.0.

getation Interaction Model (BCC_AVIM2.0). The updated parameterizations include those for lakes of variable depth in the framework of snow–ice–water–soil, evapotranspiration over rice paddies, snow cover fraction and snow surface albedo, threshold temperature to initiate freeze (thaw) of soil water (ice), prognostic vegetation phenology, and solar radiation transfer through the vegetation canopy. The performance of BCC_AVIM2.0 after the implementation of the revised parameterizations is evaluated with available observations.

The BCC_AVIM2.0 simulation of surface temperature of the Great Lakes region in North America is much improved, with lower RMSE and higher spatial correlation coefficients with observations, especially in wintertime. The cold bias in the BCC_AVIM1.0 simulation in January is possibly due to the relatively quick freezing of surface water without considering the insulation of snow cover. The alleviation of this cold bias in the simulation of BCC_AVIM2.0 is possibly due to the more efficient heat exchange in the vertical layers and larger heat capacity of the entire water–soil system of CoLM-lake in BCC_AVIM2.0 than in the water-only lake module in BCC_AVIM1.0.

Increased LHFX and reduced SHFX over rice paddies are closer to the observations in BCC_AVIM2.0 than in BCC_AVIM1.0. The increase of LHFX is due to enhanced ground water evaporation, and the decrease of SHFX is attributed to the redistribution of available NSR budget. It is inferred that the improvement in the seasonal evolutions of surface heat fluxes results from the revised rice phenology with two growing seasons in a year, which is closer to the midlatitude situation in China.

The two-stage snow albedo scheme in BCC_AVIM2.0 captures the different snow aging effects at the accumulation and melting periods of a snow season and decreases the overestimation of snow albedo during the snow melting period. This alleviates delay of final ablation of snow cover in boreal spring in the BCC_AVIM1.0 simulation, leading to improved simulation results.

The prognostic phenology scheme in BCC_AVIM2.0 can quite well reproduce the diversity of global timing of the LAI peak, especially the seasonal northeastward movement of the peak timing of vegetation growth in the Eurasian continent. Better simulation of LAI peak timing is favorable for the improvement in simulating land surface heat fluxes and land–atmosphere interactions. Therefore, it is beneficial to the simulation of the overlying atmospheric circulation, which will be validated in the future by running the coupled BCC_CSM with BCC_AVIM2.0 as its land component model.

Preliminary results of BCC_AVIM2.0 in the ongoing LS3MIP of CMIP6 show that it can reasonably capture the geographic distribution and seasonal evolution of surface energy fluxes. The overall performance of BCC_AVIM2.0 in simulation of the land surface energy budgets and terrestrial carbon cycle is better than that of BCC_AVIM1.0 in terms of geographical distribution and standardized deviations. The annual global land averaged biases and RMSEs of NSR, LHFX, and LAI are reduced after the updates of the parameterization schemes in BCC_AVIM2.0. The global mean RMSE of SHFX is also reduced whereas the bias of SHFX is increased.

The positive biases of SHFX in central North America and the Brazilian Plateau in the BCC_AVIM2.0 simulation in JJA are coincident with the underestimation of LHFX in these regions. The above overestimation of SHFX and underestimation of LHFX are associated with the positive biases in the surface temperature and the surface outgoing longwave radiation and thus the negative bias in NSR over these semiarid regions, which involves complicated interactions between surface energy budgets and the water cycle. This is an interesting topic that deserves further investigation.

Since there are uncertainties among different observational datasets and various atmospheric forcings to drive LSMs, it is necessary to employ alternative atmospheric forcings to run BCC_AVIM2.0 and evaluate the simulations against multi-source observations, which will provide new insights into land surface processes and enhance the understanding of the mechanisms involved in land–atmosphere interactions.

Acknowledgments. The authors thank Professor Shufen Sun of the Institute of Atmospheric Physics, Chinese Academy of Sciences for his constant support to the development of BCC_AVIM. We also thank the two reviewers for their valuable suggestions to improve the manuscript.

REFERENCES

Aoki, T., A. Hachikubo, and M. Hori, 2003: Effects of snow physical parameters on shortwave broadband albedos. *J. Geophys. Res. Atmos.*, **108**, 4616, doi: 10.1029/2003JD003506.

Arora, V. K., and G. J. Boer, 2005: A parameterization of leaf phenology for the terrestrial ecosystem component of climate models. *Glob. Change Biol.*, **11**, 39–59, doi: 10.1111/j.1365-2486.2004.00890.x.

Arora, V. K., G. J. Boer, P. Friedlingstein, et al., 2013: Carbon–concentration and carbon–climate feedbacks in CMIP5 earth system models. *J. Climate*, **26**, 5289–5314, doi: 10.1175/JCLI-D-12-00494.1.

Avitabile, V., M. Herold, G. B. M. Heuvelink, et al., 2016: An integrated pan-tropical biomass map using multiple reference datasets. *Glob. Change Biol.*, **22**, 1406–1420, doi: 10.1111/gcb.13139.

Bao, Y., Y. H. Gao, S. H. Lyu, et al., 2014: Evaluation of CMIP5 earth system models in reproducing leaf area index and vegetation cover over the Tibetan Plateau. *J. Meteor. Res.*, **28**, 1041–1060, doi: 10.1007/s13351-014-4023-5.

Bonan, G. B., P. J. Lawrence, K. W. Oleson, et al., 2011: Improving canopy processes in the community land model version 4 (CLM4) using global flux fields empirically inferred from fluxnet data. *J. Geophys. Res. Biogeosci.*, **116**, G02014, doi: 10.1029/2010JG001593.

Cao, M. K., and F. I. Woodward, 1998: Net primary and ecosystem production and carbon stocks of terrestrial ecosystems and their responses to climate change. *Glob. Change Biol.*, **4**, 185–198, doi: 10.1046/j.1365-2486.1998.00125.x.

Chen, A. J., W. P. Li, W. J. Li, et al., 2014: An observational study of snow aging and the seasonal variation of snow albedo by using data from Col de Porte, France. *Chinese Sci. Bull.*, **59**, 4881–4889, doi: 10.1007/s11434-014-0429-9.

Dai, Y. J., X. B. Zeng, R. E. Dickinson, et al., 2003: The Common Land Model. *Bull. Amer. Meteor. Soc.*, **84**, 1013–1024, doi: 10.1175/BAMS-84-8-1013.

Dai, Y. J., N. Wei, A. J. Huang, et al., 2018: The lake scheme of the common land model and its performance evaluation. *Chinese Sci. Bull.*, **63**, 3002–3021, doi: 10.1360/N972018-00609. (in Chinese)

Dickinson, R. E., 1983: Land surface processes and climate–surface albedos and energy balance. *Adv. Geophys.*, **25**, 305–353, doi: 10.1016/S0065-2687(08)60176-4.

Dickinson, R. E., A. Henderson-Sellers, and P. J. Kennedy, 1993: Biosphere–Atmosphere Transfer Scheme (BATS) Version 1e as Coupled to the NCAR Community Climate Model. NCAR Technical Note NCAR/TN-387+STR, National Center for Atmospheric Research, Boulder, CO, USA, 72 pp.

Foley, J. A., I. C. Prentice, N. Ramankutty, et al., 1996: An integrated biosphere model of land surface processes, terrestrial carbon balance, and vegetation dynamics. *Glob. Biogeochem. Cycles*, **10**, 603–628, doi: 10.1029/96GB02692.

Friedlingstein, P., M. Meinshausen, V. K. Arora, et al., 2014: Uncertainties in CMIP5 climate projections due to carbon cycle feedbacks. *J. Climate*, **27**, 511–526, doi: 10.1175/JCLI-D-12-00579.1.

Huang, A. N., Lazhu, J. B. Wang, et al., 2019: Evaluating and improving the performance of three 1-D lake models in a large deep lake of the central Tibetan Plateau. *J. Geophys. Res. Atmos.*, **124**, 3143–3167, doi: 10.1029/2018JD029610.

Ji, J. J., 1995: A climate–vegetation interaction model: Simulating physical and biological processes at the surface. *J. Biogeogr.*, **22**, 2063–2069.

Ji, J. J., M. Huang, and K. Li, 2008: Prediction of carbon exchange between China terrestrial ecosystem and atmosphere in 21st century. *Sci. China Ser. D Earth Sci.*, **51**, 885–898.

Jung, M., M. Reichstein, and A. Bondeau, 2009: Towards global empirical upscaling of FLUXNET eddy covariance observations: Validation of a model tree ensemble approach using a biosphere model. *Biogeosciences*, **6**, 2001–2013, doi: 10.5194/bg-6-2001-2009.

Jung, M., M. Reichstein, H. A. Margolis, et al., 2011: Global patterns of land–atmosphere fluxes of carbon dioxide, latent heat, and sensible heat derived from eddy covariance, satellite, and meteorological observations. *J. Geophys. Res. Biogeosci.*, **116**, G00J07, doi: 10.1029/2010JG001566.

Kato, S., N. G. Loeb, F. G. Rose, et al., 2013: Surface irradiances consistent with CERES-derived top-of-atmosphere shortwave and longwave irradiances. *J. Climate*, **26**, 2719–2740, doi: 10.1175/JCLI-D-12-00436.1.

Lawrence, D. M., and A. G. Slater, 2008: Incorporating organic soil into a global climate model. *Climate Dyn.*, **30**, 145–160, doi: 10.1007/s00382-007-0278-1.

Lawrence, D. M., P. E. Thornton, K. W. Oleson, et al., 2007: The partitioning of evapotranspiration into transpiration, soil evaporation, and canopy evaporation in a GCM: Impacts on land–atmosphere interaction. *J. Hydrometeor.*, **8**, 862–880, doi: 10.1175/JHM596.1.

Lawrence, D. M., K. W. Oleson, M. G. Flanner, et al., 2011: Parameterization improvements and functional and structural advances in version 4 of the community land model. *J. Adv. Model. Earth Syst.*, **3**, M03001, doi: 10.1029/2011MS00045.

Li, Q., and S. F. Sun, 2008: Development of the universal and simplified soil model coupling heat and water transport. *Sci. China Ser. D Earth Sci.*, **51**, 88–102, doi: 10.1007/s11430-007-0153-2.

Li, Q., S. F. Sun, and Y. K. Xue, 2010: Analyses and development of a hierarchy of frozen soil models for cold region study. *J. Geophys. Res. Atmos.*, **115**, D03107, doi: 10.1029/2009JD012530.

Li, W. P., X. Liu, S. P. Nie, et al., 2009: Comparative studies of snow cover parameterization schemes used in climate models. *Adv. Earth Sci.*, **24**, 512–522, doi: 10.11867/j.issn.1001-8166.2009.05.0512. (in Chinese)

Liou, K. N., 1992: *Radiation and Cloud Processes in the Atmo-*

sphere: Theory, Observation and Modeling. Oxford University Press, London, 487 pp.

Luo, S. Q., X. W. Fang, S. H. Lyu, et al., 2017: Improving CLM4.5 simulations of land–atmosphere exchange during freeze–thaw processes on the Tibetan Plateau. *J. Meteor. Res.*, **31**, 916–930, doi: 10.1007/s13351-017-6063-0.

Malhi, Y., T. R. Baker, O. L. Phillips, et al., 2004: The above-ground coarse wood productivity of 104 neotropical forest-plots. *Glob. Change Biol.*, **10**, 563–591, doi: 10.1111/j.1529-8817.2003.00778.x.

Morin, S., Y. Lejeune, B. Lesaffre, et al., 2012: An 18-yr long (1993–2011) snow and meteorological dataset from a mid-altitude mountain site (Col de Porte, France, 1325 m alt.) for driving and evaluating snowpack models. *Earth Syst. Sci. Data*, **4**, 13–21, doi: 10.5194/essd-4-13-2012.

Mu, M. Q., F. Hoffman, D. Lawrence, et al., 2016: International Land Model Benchmarking (ILAMB) Package v001.00. Sponsored by the US DOE Office of Science (SC), Biological and Environmental Research (BER), doi: 10.18139/ILAMB.v001.00/1251597. Available at https://www.bgc-feedbacks.org/software/10.18139/ILAMB.v001.00/.

Mu, M. Q., and ILAMB team, 2019: Design and development of a community benchmark system for land surface models. Proc. International Workshop on Weather and Climate Variability and Their Mechanism, 7–9 August, Beijing, China, 337–356.

Myneni, R. B., R. Ramakrishna, R. Nemani, et al., 1997: Estimation of global leaf area index and absorbed Par using radiative transfer models. *IEEE Trans. Geosci. Remote Sens.*, **35**, 1380–1393, doi: 10.1109/36.649788.

Niu, G.-Y., and Z.-L. Yang, 2007: An observation-based formulation of snow cover fraction and its evaluation over large North American river basins. *J. Geophys. Res. Atmos.*, **112**, D21101, doi: 10.1029/2007JD008674.

Oleson, K. W., Y. J. Dai, G. Bonan, et al., 2004: Technical Description of the Community Land Model (CLM). NCAR Technical Note NCAR/TN-461+STR. National Center for Atmospheric Research, Boulder, CO, USA, 173 pp.

Parton, W. J., J. W. B. Stewart, and C. V. Cole, 1988: Dynamics of C, N, P and S in grassland soils: A model. *Biogeochemistry*, **5**, 109–131, doi: 10.1007/BF02180320.

Roesch, A., M. Wild, H. Gilgen, et al., 2001: A new snow cover fraction parametrization for the ECHAM4 GCM. *Climate Dyn.*, **17**, 933–946, doi: 10.1007/s003820100153.

Saatchi, S. S., N. L. Harris, S. Brown, et al., 2011: Benchmark map of forest carbon stocks in tropical regions across three continents. *Proc. Natl. Acad. Sci. USA*, **108**, 9899–9904, doi: 10.1073/pnas.1019576108.

Sellers, P. J., D. A. Randall, G. J. Collatz, et al., 1996: A revised land surface parameterization (SiB2) for atmospheric GCMs. Part I: Model formulation. *J. Climate*, **9** , 676–705, doi: 10.1175/1520-0442(1996)009<0676:ARLSPF>2.0.CO;2.

Sheffield, J., G. Goteti, and E. F. Wood, 2006: Development of a 50-year high-resolution global dataset of meteorological forcings for land surface modeling. *J. Climate*, **19**, 3088–3111, doi: 10.1175/JCLI3790.1.

Su, F. G., X. L. Duan, D. L. Chen, et al., 2013: Evaluation of the global climate models in the CMIP5 over the Tibetan Plateau. *J. Climate*, **26**, 3187–3208, doi: 10.1175/JCLI-D-12-00321.1.

Subin, Z. M., W. J. Riley, and D. Mironov, 2012: An improved lake model for climate simulations: Model structure, evaluation, and sensitivity analyses in CESM1. *J. Adv. Model. Earth Syst.*, **4**, M02001, doi: 10.1029/2011MS000072.

Sun, S. F., J. M. Jin, and Y. K. Xue, 1999: A simple snow–atmosphere–soil transfer model. *J. Geophys. Res. Atmos.*, **104**, 19,587–19,597, doi: 10.1029/1999JD900305.

Todd-Brown, K. E. O., J. T. Randerson, W. M. Post, et al., 2013: Causes of variation in soil carbon simulations from CMIP5 earth system models and comparison with observations. *Biogeosciences*, **10** , 1717–1736, doi: 10.5194/bg-10-1717-2013.

van den Hurk, B., H. Kim, G. Krinner, et al., 2016: LS3MIP (v1.0) contribution to CMIP6: The land surface, snow and soil moisture model intercomparison project—Aims, setup and expected outcome. *Geosci. Model Dev.*, **9** , 2809–2832, doi: 10.5194/gmd-9-2809-2016.

Wang, C., Z. G. Wei, Z. C. Li, et al., 2017: Testing and improving the performance of the Common Land Model: A case study for the Gobi landscape. *J. Meteor. Res.*, **31** , 625–632, doi: 10.1007/s13351-017-6080-z.

Wu, T. W., L. C. Song, W. P. Li, et al., 2013: Global carbon budgets simulated by the Beijing Climate Center climate system model for the last century. *J. Geophys. Res. Atmos.*, **118**, 4326–4347, doi: 10.1002/jgrd.50320.

Wu, T. W., L. C. Song, W. P. Li, et al., 2014: An overview of BCC climate system model development and application for climate change studies. *J. Meteor. Res.*, **28** , 34–56, doi: 10.1007/s13351-014-3041-7.

Xia, K., and B. Wang, 2015: Evaluation and projection of snow cover fraction over Eurasia. *Climatic Environ. Res.*, **20** , 41–52, doi: 10.3878/j.issn.1006-9585.2014.13126. (in Chinese)

Xia, K., Y. Luo, and W. P. Li, 2011: Simulation of freezing and melting of soil on the northeast Tibetan Plateau. *Chinese Sci. Bull.*, **56**, 2145–2155, doi: 10.1007/s11434-011-4542-8.

Xue, Y. K., S. F. Sun, D. S. Kahan, et al., 2003: Impact of parameterizations in snow physics and interface processes on the simulation of snow cover and runoff at several cold region sites. *J. Geophy. Res. Atmos.*, **108** , 8859, doi: 10.1029/2002JD003174.

Yang, Z.-L., R. E. Dickinson, A. Robock, et al., 1997: Validation of the snow submodel of the biosphere–atmosphere transfer scheme with Russian snow cover and meteorological observational data. *J. Climate*, **10** , 353–373, doi: 10.1175/1520-0442(1997)010<0353:VOTSSO>2.0.CO;2.

Zeng, X. B., M. Shaikh, Y. J. Dai, et al., 2002: Coupling of the common land model to the NCAR community climate model. *J. Climate*, **15** , 1832–1854, doi: 10.1175/1520-0442(2002)015<1832:COTCLM>2.0.CO;2.

Zhang, G., G. S. Zhou, and F. Chen, 2017: Analysis of parameter sensitivity on surface heat exchange in the Noah land surface model at a temperate desert steppe site in China. *J. Meteor. Res.*, **31**, 1167–1182, doi: 10.1007/s13351-017-7050-1.

Zhou, W. Y., Y. Luo, W. P. Li, et al., 2018: Comparative studies of different radiation schemes within vegetation in a land model. *Chinese Sci. Bull.*, **63** , 2772–2784, doi: 10.1360/N972018-00398. (in Chinese)

Tech & Copy Editor: Lan YI

Environmental Research Letters

LETTER

More extreme marine heatwaves in the China Seas during the global warming hiatus

Yan Li[1,2], Guoyu Ren[2,3], Qingyuan Wang[4,6] and Qinglong You[5]

[1] National Marine Data and Information Service, Tianjin, 300171, People's Republic of China
[2] Department of Atmospheric Science, School of Environmental Studies, China University of Geosciences, Wuhan, 430074, People's Republic of China
[3] Laboratory for Climate Studies, National Climate Center, China Meteorological Administration, Beijing, 100081, People's Republic of China
[4] Tianjin Meteorological Observatory, Tianjin, 300074, People's Republic of China
[5] Fudan University, Shanghai, 200433, People's Republic of China
[6] Author to whom any correspondence should be addressed.

E-mail: wqyjx417@163.com

Keywords: marine heatwave, sea surface temperature, global warming hiatus, China seas

OPEN ACCESS

RECEIVED
27 January 2019

REVISED
10 June 2019

ACCEPTED FOR PUBLICATION
11 June 2019

PUBLISHED
4 October 2019

Original content from this work may be used under the terms of the Creative Commons Attribution 3.0 licence.

Any further distribution of this work must maintain attribution to the author(s) and the title of the work, journal citation and DOI.

Abstract

Based on the satellite-derived global daily sea surface temperature (SST) data set with high resolution (0.25° by 0.25°), we analyzed changes in annual mean SST and extreme SSTs over the China Seas since 1982. Results show that the annual mean SST in the China Seas has experienced a remarkable declining trend during the global warming hiatus (1998–2013), which was dominated by the striking cooling of SST in boreal winter. Despite annual mean SST experienced warming hiatus after 1998, the regional averaged SST for 1998–2013 was still 0.5 °C above that for 1982–1997. The statistical distributions show that there are not only significant warmer climate shift in annual mean SSTs but also in annual extreme hot SSTs and cold SSTs. These changes can increase the likelihood of extreme oceanic warming events, known as marine heatwaves (MHWs). Further analyses reveal that, from 1982 to present, the MHW frequency increases at a rate of 1.13 events per decade, 2.5 times the global mean rate. For the period 1998–2013, the MHWs in the China Sea has never decreased in both of the frequency and intensity but has already become more frequent, longer duration and more intense than those metrics of MHWs during 1982–1997.

1. Introduction

Despite the continued increase of atmospheric greenhouse gases concentrations, the global surface mean temperature (GMST) has exhibited an unexpected shift from rapid to flat warming at 1998 and ending around 2014 (Medhaug *et al* 2017). This phenomenon was called the 'global warming hiatus', 'warming pause' or 'slowdown' (Meehl *et al* 2013, Trenberth *et al* 2014, Lewandowsky *et al* 2015) and has been ascribed to various possible causes: internal climate variability, reduced solar energy output, heat uptake in deep ocean, and strong shifts to La Niña states (Kosaka and Xie 2013, Trenberth *et al* 2014, Guan *et al* 2015). Several studies have attributed the warming hiatus to the 60-year-quasi-periodic natural climate variability —Pacific decadal oscillation (PDO) (Tollefson 2014). Though, there are still debates on the global warming hiatus, it is virtually certain that the warming hiatus were more noticeable in regional scales at the Northern Hemisphere (NH): for example, mainland China and Eurasian continents (Duan and Xiao 2015, Guan *et al* 2015, Li *et al* 2015, Garfinkel *et al* 2017, Sun *et al* 2017, Xie *et al* 2017, Shen *et al* 2018). Compared to the studies on the terrestrial warming hiatus, less focus has been given to warming hiatus at marginal seas.

Since the turn of the 21st century, special attention has been paid to extreme meteorological, hydrological, and oceanographic events such as heatwaves, cold snaps, storms, floods and tropical cyclones, which often trigger complex and, in some cases, catastrophic consequences (IPCC 2013, Oliver *et al* 2017, Herring *et al* 2019). Notable extreme ocean warm events or marine heatwaves (MHWs) have been observed in

© 2019 The Author(s). Published by IOP Publishing Ltd

recent years (Hobday *et al* 2016, Oliver *et al* 2017, 2018), including events in the northern Mediterranean (Garrabou *et al* 2009), offshore of western Australia (Benthuysen *et al* 2018), in the northwest Atlantic (Chen *et al* 2014), and in the Tasman Sea (Oliver *et al* 2017), etc. MHWs are characterized as regions of large-scale and persistent at least five consecutive extreme hot days (EHDs) when daily SST exceeds a seasonally varying threshold (Hobday *et al* 2016). MHWs can be classified by multiple characteristics, such as intensity, frequency, duration, and timing similar to their terrestrial counterpart. MHWs with long duration and high intensity can cause serious marine ecological disasters and economic losses (Thomson *et al* 2015, Caputi *et al* 2016, Wernberg *et al* 2016, Frölicher and Laufkötter 2018), and are worthy of further attention.

The China Seas are one of the largest shelf seas of the world (its area is more than twice the size of the North Sea), with rich marine ecosystems and fishing grounds. As a warming hotspot where the warming rate has been considerably faster than the global average, the China Seas are more vulnerable, suffering from more frequent, longer lasting and stronger hot extremes (Belkin 2009, Wu *et al* 2012, Oliver *et al* 2018). Given the slowdown of GMST, it remains unclear what changes of annual or seasonal mean SSTs and extreme SSTs have occurred in this region and whether they are, and how if so, affected by the warming hiatus. After a wave of scientific publications and public debate, with GMSTs setting new records again after 2014 (World Meteorological Organization (WMO) 2019), it is time to take stock of what can be learned from the warming hiatus in the China Seas.

In this paper, we analyze the changes of annual mean SST and extreme warm SST events in the China Seas in the past decades, with an emphasis on the context of global warming hiatus. Data sets and methods are described in sections 2 and 3. Results are presented in section 4. Discussion on the causation and ecological impact of MHWs is given in section 5, and conclusions are shown in section 6.

2. Study region and data sets

2.1. Study region

The China Seas, including the Bohai Sea, the Yellow Sea, the East China Sea, the South China Sea, are bounded by mainland China, the Ryukyu (Nansei) Islands and the Korean Peninsula. The study region also covers a vicinity of the China Seas to show a better perspective for the analyzed SST variability, for example, the SST variability in the Kuroshio in the East China Sea. Thus, we approximated the area at (15°–45°N, 105°–130°E) (figure 1).

2.2. Data

The NOAA daily Optimum Interpolation (OI) SST v2 with high resolution (0.25° by 0.25°) in length (1982–2018) (OISST v2, Banzon *et al* 2016) was used to detect the warming hiatus at the China Seas. For comparison purposes, we also used other three global gridded monthly mean SST data sets with a horizontal resolution of 1° by 1° in the same period as OISST v2. The monthly mean SST data sets are from the Hadley Centre Sea Ice and SST data set (HadISST, Rayner *et al* 2003), the Centennial Observation-Based Estimates of SST version 2 (COBE SST2, Hirahara *et al* 2012) and the International Comprehensive Ocean-Atmosphere Data Set-SST section (ICOADS SST, Woodruff *et al* 2011). Due to the high spatial and temporal resolutions, OISST v2 is recommended for evaluating water extremes. The suitability of the database to identify extreme events was previously confirmed in literature (Lima and Wethey 2012, Oliver *et al* 2017, Benthuysen *et al* 2018). Statistical analyses of extreme SSTs and MHWs in our study were both based on this data set.

3. Methods

3.1. Extreme SSTs and marine heat wave (MHW)

In our study, the 90th (10th) percentile SST in each year (referred to as 90th (10th) SST) is used for the annual threshold of extreme hot (cold) SSTs, rather than the 95th (5th) or 99th (1th), so as to allow for the robust detection by applying a greater number of extreme SSTs. Daily SST anomalies are calculated to remove the seasonal cycle. This is achieved by subtracting from the SST of a certain day (e.g. January 1, 1982) the mean temperature of that day (January 1) over the climatic period 1983–2012.

We used the definition of Hobday *et al* to identify and quantify marine heatwaves (MHWs). In this definition, a MHW is defined as a discrete prolonged anomalously warm water event at a particular location. Specifically, 'discrete' implies the MHW is an identifiable event with clear start and end dates and 'prolonged' means it persists at least five consecutive EHDs. Here, the marine EHD was a day when daily temperature was above a defined threshold. The threshold was taken to be the seasonally varying 90th percentile climatology, following the recommendation of Hobday *et al* (2016). The climatological threshold and the mean were calculated for each calendar day of the year using daily temperature values across all years and within an 11-day window centered on the day, and were then smoothed using a 31-day moving window. The use of a seasonally-varying threshold allows for the detection of summer MHW as well as winter warm spells, both of which can have ecological impacts. This definition has been implemented in Python (available from https://github.com/ecjoliver/marineHeatWaves, also see Hobday *et al* 2016).

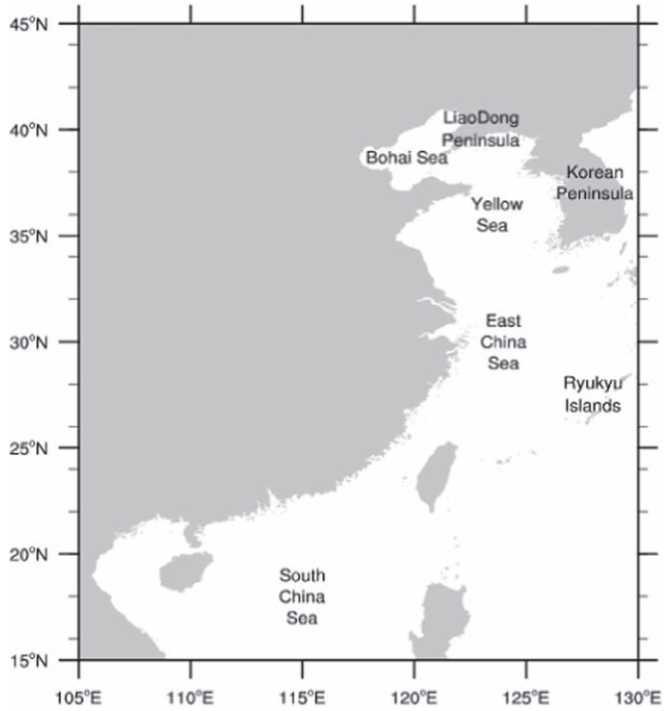

Figure 1. The location of the Bohai Sea, the Yellow Sea, the East China Sea, the South China Sea and the adjacent seas.

In our study, daily SSTs were spatially averaged over the China Seas (15°–45°N, 105°–130°E) to generate a regional daily SST time series covering 1982–2017. The MHW definition was then applied to the SST time series to detect all the MHWs in the China Seas. Following Oliver *et al* (2018), the implication of spatially averaging SSTs and then performing the MHW calculation, as opposed to detecting MHWs directly from the pixel-based data, can smooth away some of the high-frequency variability and thereby slightly increase average MHW duration at the expense of annual frequency. Annual statistics were then calculated including the frequency of events (i.e., the number of discrete events occurring in each year), mean annual duration and mean annual cumulative intensity. Here, 'duration' was the time between the event's start and end dates, 'maximum intensity' was the maximum temperature anomaly (measured relative to the climatological, seasonally-varying mean) over the duration of the event, and 'cumulative intensity' was the integrated temperature anomaly over the duration of the event, where units were °C days (more details in the table 2 of Hobday *et al* 2016).

3.2. Statistical methods

We used a nonparametric Kendall's tau based Sen's slope estimator (Sen 1968) to calculate trends, since the method does not assume a distribution for the residuals and thus is insensitive to the effect of outliers in the series, and it has been widely used in the studies of hydrological and extreme climate change. The significance of the Sen's slope was judged by using Mann-Kendall test method. A trend was considered to be statistically significant if it was significant at the 5% level ($p < 0.05$).

4. Results

4.1. Warming hiatus in the China Seas

The annual mean SSTA time series from four independent SST datasets are shown in figure 2(a). As a regional average, all of the four SSTA time series agree well during 1982–2013. Based on the observational evidence, SST over the China Seas switched from a previously accelerated warming period to a recent warming hiatus since 1998. There was a decreasing tendency in the accelerated warming period and an increasing tendency in the warming hiatus in the four accumulated SSTA series (figure 2(b)). We detected a significant temporal breakpoint at 1997/1998 in the four time series in the satellite era from 1982 to 2013 (figure 2(b)). Because of the shortness of the hiatus period, significance testing of the trends has limited relevance. Still, over the 16-year period from 1998 to 2013, decreases in ICOADS R2.5 SST, HadISST1, COBE SST2 and OISST are all significant at the 5% level (Mann–Kendall test), with the respective rates of −0.26, −0.24, −0.32, −0.37 °C per decade. Therefore, there was a remarkable shift in 1998 and the warming hiatus indeed existed in the China Seas. Moreover, during the warming hiatus, the annual mean SST over the China Seas experienced notable cooling. This remarkable hiatus phenomenon at the China Seas has shifted synchronously with the warming hiatus of GMST and mainland China (Trenberth *et al* 2014,

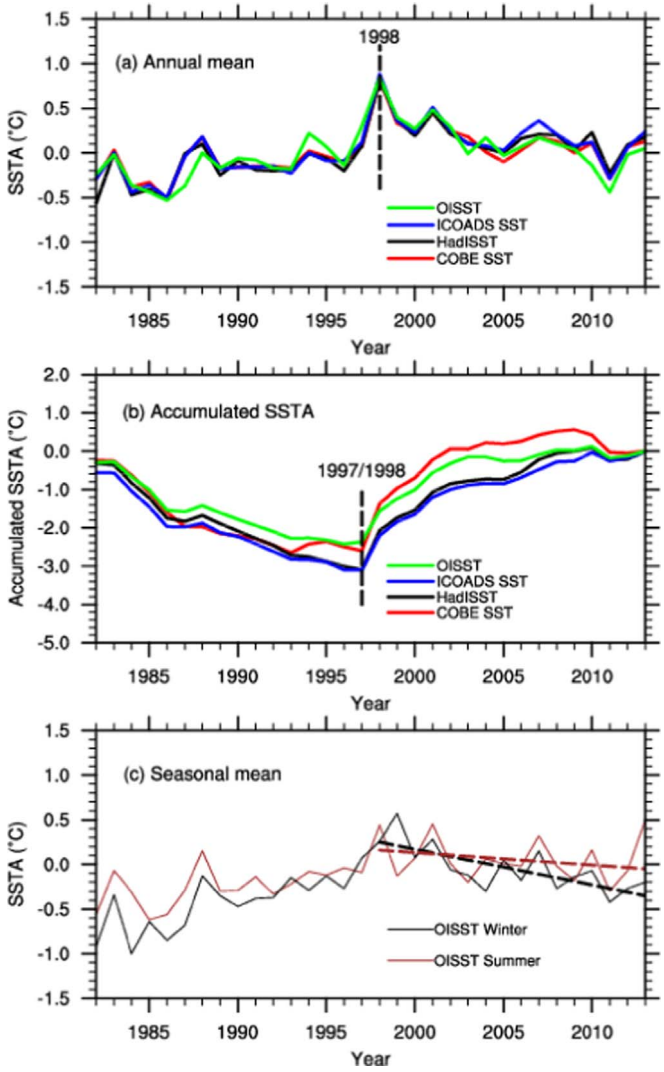

Figure 2. (a) Time series of the regional averaged annual mean SST anomalies (SSTAs) in the China Seas (15°–45°N, 105°–130°E) from COBE SST (red), HadISST1 (black), ICOADS R2.5 SST (blue) and OISST v2 (green) for period 1982–2013. (b) The same as (a), but for long-term variation of the accumulated anomalies. The black dashed line refers to their corresponding climate-jump year. (c) Time series of the regional averaged seasonal mean SSTAs in summer (brown line) and winter (black line) from OISST v2 during 1982–2013. The brown and black dashed lines are the linear trends based on the least squares estimator for 1998–2013 in summer and winter respectively. Anomalies are relative to the average of 1983–2012.

Duan and Xiao 2015, Xie *et al* 2017). Since 1998, the PDO switch from warm phase to the cool phase. The previously accelerated warming period in the China Seas was in the period when PDO was in the strong positive phase. The recent warming hiatus after 1998 was basically consistent with the period when PDO entered into its negative phase (figure omitted). Studies found that the PDO were suggested to influence the East Asian winter monsoon (EAWM) and deepening of East Asian trough (EAT), especially for the interdecadal variability (Ding *et al* 2014, Wang and Chen 2014, Xie *et al* 2017), which suggested the possible connections between the enhanced EAWM during the warming hiatus with the negative phase of PDO.

In our study, we find that the cooling tendency is not homogeneous or asymmetric in seasonal scale. Seasonally, the winter SSTA has experienced a significant cooling trend since 1998, while there is a slightly decreasing (trend very close to zero) in summer (figure 2(c)). Because the four SST gridded datasets displayed similar results, we just show the seasonal SST anomalies series during 1982–2013 from OISST v2. Previous studies reported that the most hiatus in global or regional warming was a seasonal phenomenon, prevalent in boreal winter (Cohen *et al* 2012, Trenberth *et al* 2014, Sun *et al* 2017). Figure 2(c) indicates that the annual mean SST decrease in the China Seas is also primarily from the contribution of cooling in boreal winter rather than in summer. The cooling of the winter SST during 1998–2013 is probably related to the combined influence from the recent strengthening of EAWM, weakening of Arctic oscillation (AO) and deepening of EAT (You *et al* 2013, Ding *et al* 2014, Sun *et al* 2017).

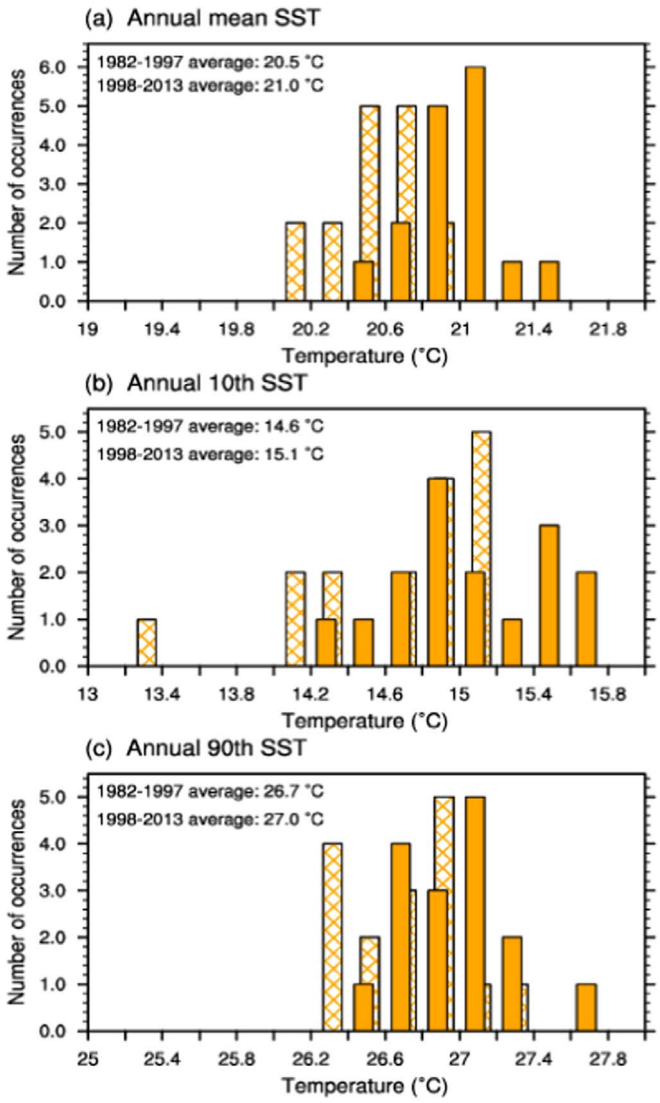

Figure 3. The regional averaged annual mean SST (a), 10th SST (b) and 90th SST (c) histograms for two periods: 1982–1997 (hatched bars) and 1998–2013 (orange bars).

4.2. Changes in extreme SST and MHWs

The statistical occurrences of the regional averaged annual mean SST, annual 10th SST and 90th SST at the 16-year periods are displayed in figure 3 for 1982–1997 (hatched bars) and 1998–2013 (orange bar). Although annual mean SST experienced a warming hiatus after 1998, the average SST for 1998–2013 (21.0 °C) is still 0.5 °C above that for 1982–1997 (20.5 °C) (figure 3(a)). All of these SST metrics appear to have remarkably shifted upward a warmer climate during the hiatus. The mean increase is higher for the 10th SST as it has shifted by 0.5 °C (from 14.6 °C to 15.1 °C) (figure 3(b)), compared to the shifting of the 90th SST by 0.3 °C (figure 3(c)).

The mean warming during 1998 to 2013 was also accompanied by changes in temperature extremes. The statistical occurrences of the regional average daily SST anomalies in 1982–1997 and 1998–2013 are illustrated in figure 4. Warm SSTAs (exceeding 90th percentile) that occurred around 2% of the total SSTAs during the period 1982–1997, occurred over 15% of the total SSTAs during the period 1998–2013 (figures 4(a), (b)). There are more frequent occurrences of warm SSTAs surpassing the threshold during warming hiatus. Compared to the significantly decreasing of cold SSTAs (below 10th percentile), the warm SSTAs experienced a general increase, and even the very hot SSTAs (exceeding 99th percentile) in annual and seasonal scales have occurred. Specially, the very cold SSTAs (below 1th percentile) disappeared in winter and summer and warm SSTAs have become common in winter after 1998 (figures 4(d), (f)). A more pointed and higher peak indicates the temperature closely around the mean value in winter and summer (figures 4(c), (e)), but the occurrences become more dispersed with the increase of warm events (figures 4(d), (f)).

As illustrated in figure 4, the hot regional average daily SST anomalies have greatly increased during 1998–2013. It indicated that more MHWs probably

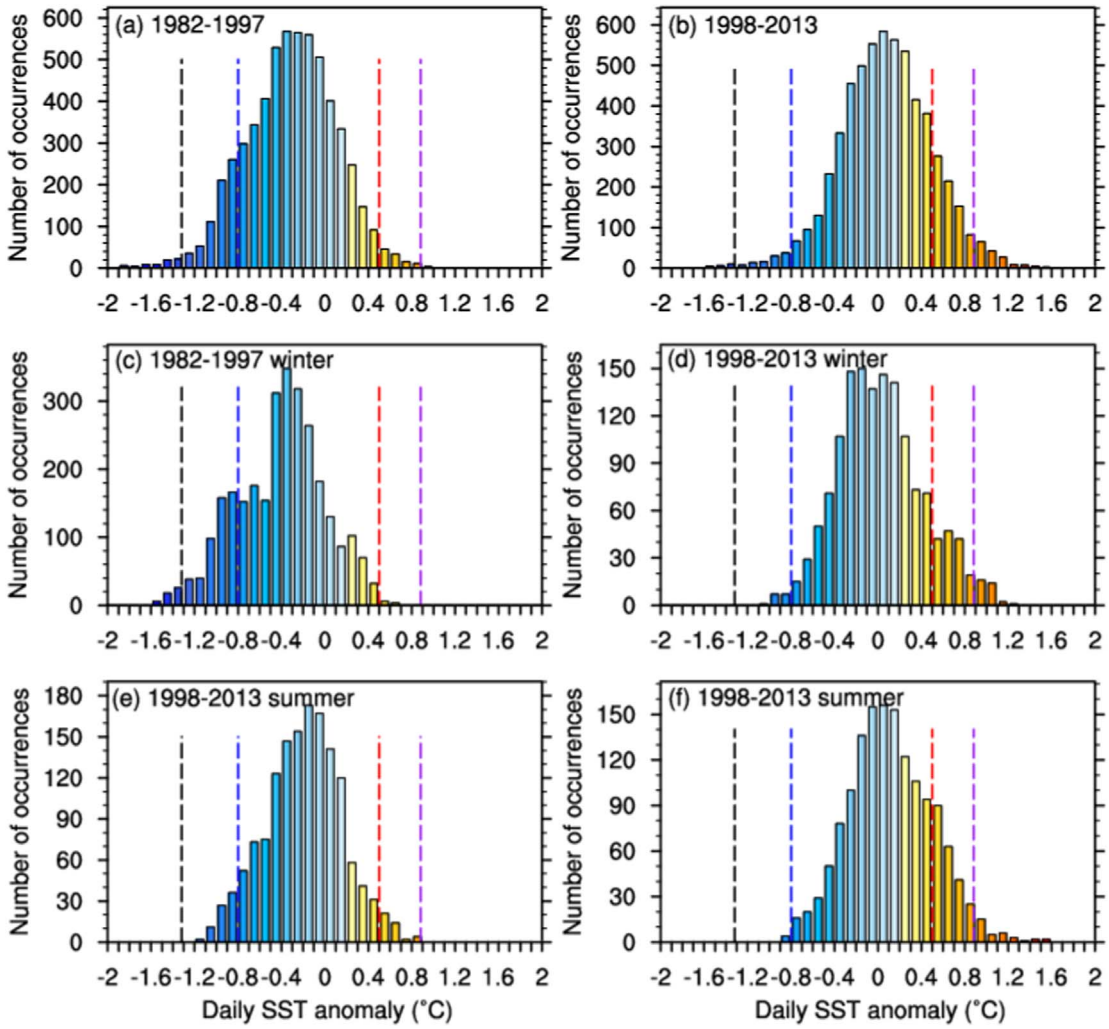

Figure 4. The daily mean SSTAs histograms for 1982–1997 (left) and 1998–2013 (right) for the whole year (a), (b), winter (c), (d) and summer (e), (f). The red and purple dashed line represents the 90th percentile and 99th percentile of climatological period (1983–2012). The blue and black dashed line represents the 10th percentile and 1th percentile of the climatological period 1983–2012.

occurred over the later period. Referring to Hobday *et al* (2016) (see Methods), we examined changes of regional average MHW with frequency, duration, and cumulative intensity during 1982–2013 (figure 5). An obvious ascending trend can be observed in all of the three metrics. As a regional average, annual mean MHW frequency significantly increased from about 0.5 events per year during 1982–1997 to 3.4 events per year during 1998–2013 (5.8 times increased). The regional averaged time series also showed general increases in MHW duration from about 4.8 EHDs to 11.8 EHDs (1.75 times increased), and cumulative intensity from 3.0 °C days to 9.8 °C days (2.27 times increased). It shows that, on average, not only was there no decrease in the frequency of MHWs over the China Seas during the global warming hiatus but the MHWs had already become more long-lasting, frequent and intense than those before 1997. Moreover, MHWs frequency in the China Seas increased significantly with a trend of 1.13 events per decade ($p < 0.01$), 2.5 times the global average rate (0.45 events per decade, Oliver *et al* 2018) in the same period of 1982–2016.

Three better-known MHW regions, Western Australia, the Mediterranean Sea and northwest Atlantic, have experienced 59, 70 and 67 MHWs during 1982–2014 (Hobday *et al* 2016). During the same period, a total of 65 events were also identified in the China Seas. Results suggest that, as a part of western boundary current extension region, the China Seas probably are also the high-risk region suffering from more frequent, longer lasting and stronger MHWs in the past decades. The latest studies show that, from 1925 to 2016, global average marine heatwave frequency and duration increased by 34% and 17% which largely is explained by increases in mean ocean temperatures (Frölicher *et al* 2018, Oliver *et al* 2018). Consistent with the previous works, the regional annual mean SST and mean MHW frequency, duration and the cumulative intensity over the China Seas are strongly correlated ($r_a = 0.83$; $r_b = 0.70$; $r_c = 0.72$, $p < 0.01$), with the highest correlation

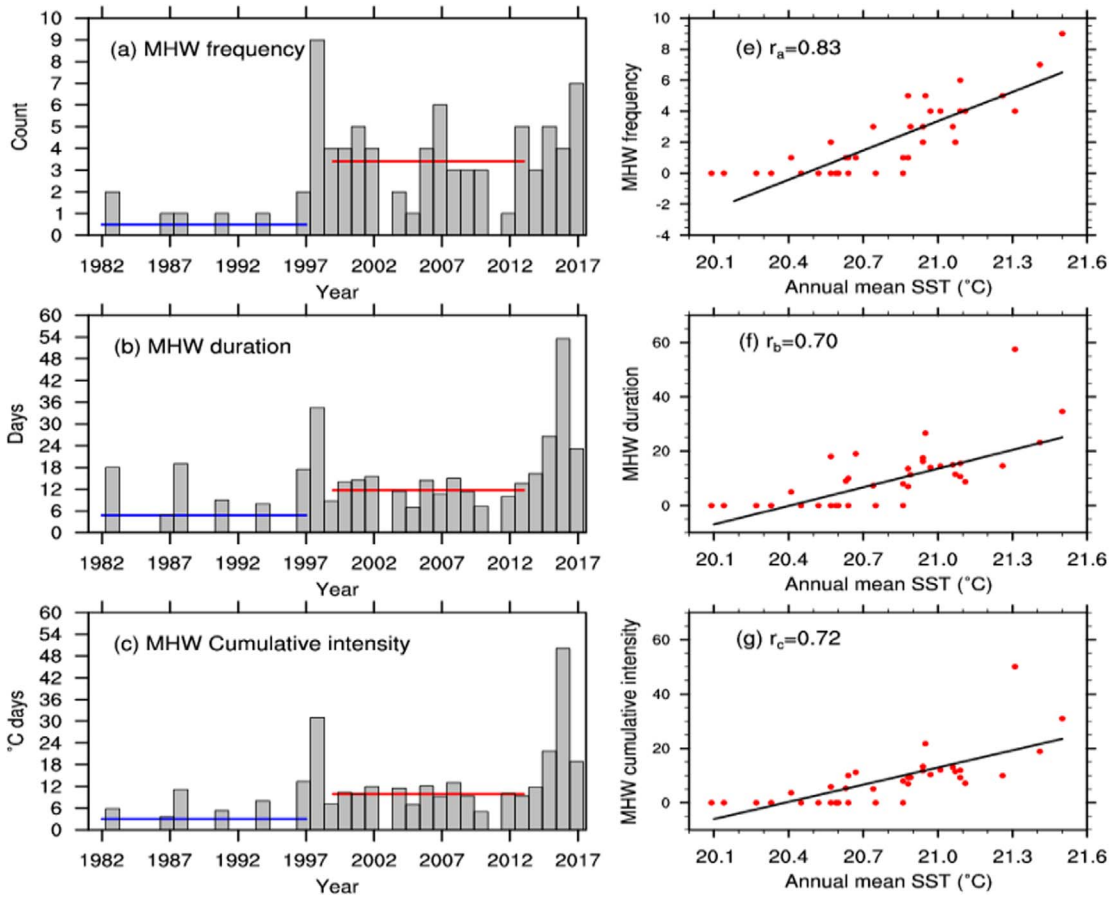

Figure 5. Regional averaged annual mean MHW frequency (a), duration (b) and cumulative intensity (c), and scatter plots of annual mean SST and MHW frequency (e), duration (f), and cumulative intensity (g), over the China Seas during 1982–2017. Red lines show the mean value over 1998–2013, blue lines show the mean value over 1982–1997, and black lines show the best-fit linear curve.

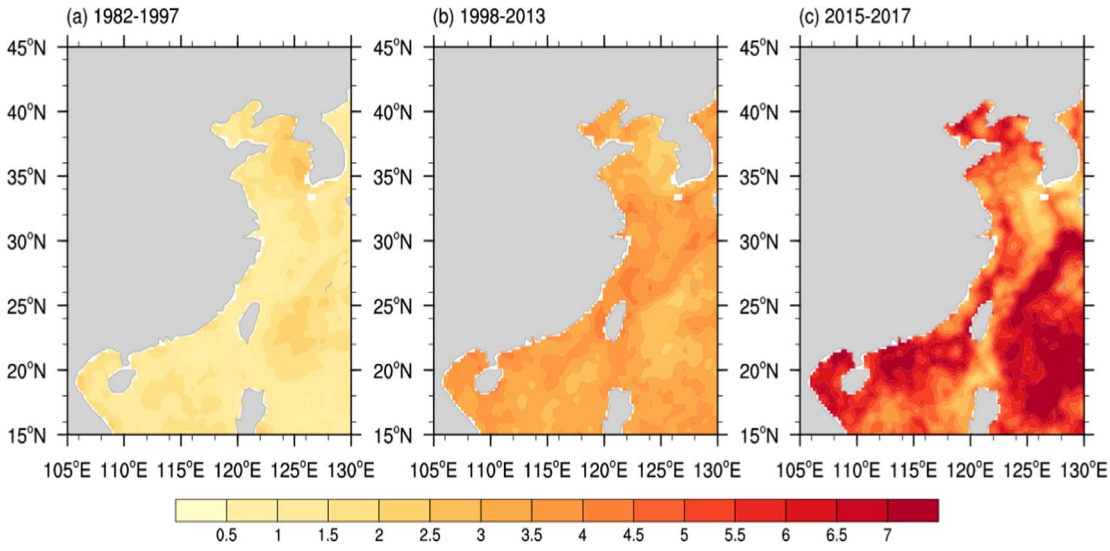

Figure 6. Annual mean MHWs frequency during the period of 1982–1997 (a), 1998–2013 (b) and 2015–2017 (c) in the China Seas.

found between SST and MHW frequency (figures 5(e)–(g)).

Spatial distributions of annual mean MHWs over different periods are shown in figure 6. The annual mean occurrences of MHWs ranged from about 0 to 2 events, depending on location (figure 6(a)). During 1998–2013, MHW frequency increased considerably across the whole China Seas (figure 6(b)), reaching 2 to 3 events on average. The larger increase occurred in

the coastal areas of the China Seas and along the Kuroshio Current axis.

5. Discussion

While the characteristics, mechanisms and impacts of terrestrial heatwaves have been well explored, MHWs over the China Seas are generally understudied. In this work, we analyze the spatial and temporal pattern of the change in means and extreme events of SST in the China Seas. Analysis shows a significant increase in MHWs in the China Seas during 1998–2013. The increase is basically consistent with those reported for other oceanic regions. A recent study confirmed that an extreme strong and prolonged El Niño occurred during 2015–2016 and it probably ended the global warming hiatus (Hu and Fedorov 2017). Despite the warming hiatus, the globally mean temperatures of most years since 1998 were the warmest on record as the long-term warming trend continues; the frequency and intensity of both terrestrial and oceanic extreme events are also increasing globally (Herring *et al* 2019, World Meteorological Organization WMO (2019)). The more occurrences of extreme hot SSTAs are related to both rising mean temperatures and climate variability; the former would be the dominant driver of the increasing frequency of MHWs over most of the global ocean (Oliver 2019). In the China Seas, the regional mean SSTs 20.5 °C for 1982–1997, but 21.0 °C, for 1998–2013 following with 2015–2017, with the value of 21.2 °C. The regional mean SSTs were continuously rising in the three periods, though there was a warming hiatus during 1998–2013. The warm-side toward shift in mean temperature could be causing the increased MHWs.

Meanwhile, these events could be also influenced by additional processes. In this discussion, given the atmospheric priming of the MHW, we preliminarily analyzed the possible relationship between the warming and the large-scale atmosphere circulation modes. The Western North Pacific Subtropical High (WNPSH) indices of area and intensity have notably increased during 1982–2013, and the western edge of the WNPSH ridge has experienced a westward expansion (figure is omitted). The strengthening and westward extension of the WNPSH could cause strong descending motion and have contributed considerably to the surface warming in the study region. Thus, warming SST observed during 1982–2013 is probably related to the influence from the recent changes in the WNPSH. Meanwhile, it is also found that 500-hPa geopotential height (HGT500) exhibited a significant enhancing trend around Lake Baikal, which implies that the Baikal Ridge has been intensifying during the past decades (figure omitted). Influenced by this circulation pattern, the East China Seas was behind the deepened East Asian trough and before the enhanced Baikal Ridge, and therefore the descending movement and the northwesterly in the upper level were prevailing, which brought clear skies and more surface net solar radiation, was favorable for the abnormal hot and dry extremes (Wang *et al* 2017).

Besides, MHWs can also be affected by low-frequency oceanic modes, including the PDO, ENSO, and Indian Ocean dipole (IOD) (Benthuysen *et al* 2018, Oliver *et al* 2018, Tan and Cai 2018). However, there remain complex physical mechanisms between changes of large-scale atmospheric and oceanic systems and MHWs. These physical mechanisms are complicated by local processes, including the Yangtze River discharge, Kuroshio Current, Taiwan Warm Current, etc. (Wu *et al* 2012, Cai *et al* 2017, Pei *et al* 2017). Determining these causal factors, including anthropogenic forcing and natural variability modes, is still an area of ongoing research.

Spatially, in the period 2015–2017, much more MHWs occurred annually in the western China Seas, almost 2–4 more events annually than those occurred in the period before 2014 (figure 6(c)). Studies point out that MHWs will very likely become more common and more intense under future global warming (Frölicher *et al* 2018, Oliver *et al* 2018). Whatever the underlying causes are, the observed and expected increase of MHWs in the China Seas would exert a non-negligible impact on the marine ecosystem. Recently, the observed MHWs in the China Seas, especially in the western China Seas and the Yellow Sea have caused huge economic losses through impacts on fisheries and aquaculture. The 'Zhangzi Island scallops event in 2017' and 'Sea cucumber mortality event in 2018' are the two well-known marine fishery disasters. In July and August 2017, exceptionally warm SSTAs occurred at the northern Yellow Sea, with the temperature anomalies >1.0 °C covering approximately 5.8×10^5 km^2 (figure 7(a)). The northern Yellow Sea 2017 MHW lasted for 60 days from 30th June to 28th August (figure 7(b)). The date of the peak was 20th July with a maximum daily SSTA of 2.93 °C (figure 7(c)). The cumulative intensity of the event was up to 115 °C days. This local MHW was unprecedented as the longest event on record in this region, and it probably exceeded the marine ecosystem tolerance limits. This MHW event was considered as one of the most important factors leading to the mass emaciation and mortality of filter/suspension-feeding scallops (*Patinopecten yessoensis*) in Zhangzi Island (39.05°N, 122.75°E) in the 'Zhangzi Island scallops event in 2017'.

The impacts of these MHWs can be compared and contrasted with other major events that have occurred abroad recently. For example, the Tasman Sea 2015/16 MHW appeared to be restricted to sessile, sedentary or cultured species in the shallow coastal near-shore environment including outbreaks of disease in commercially viable species (Oliver *et al* 2017). The Alaskan Sea 2016 MHW favored some phytoplankton species, leading to harmful algal blooms, shellfish

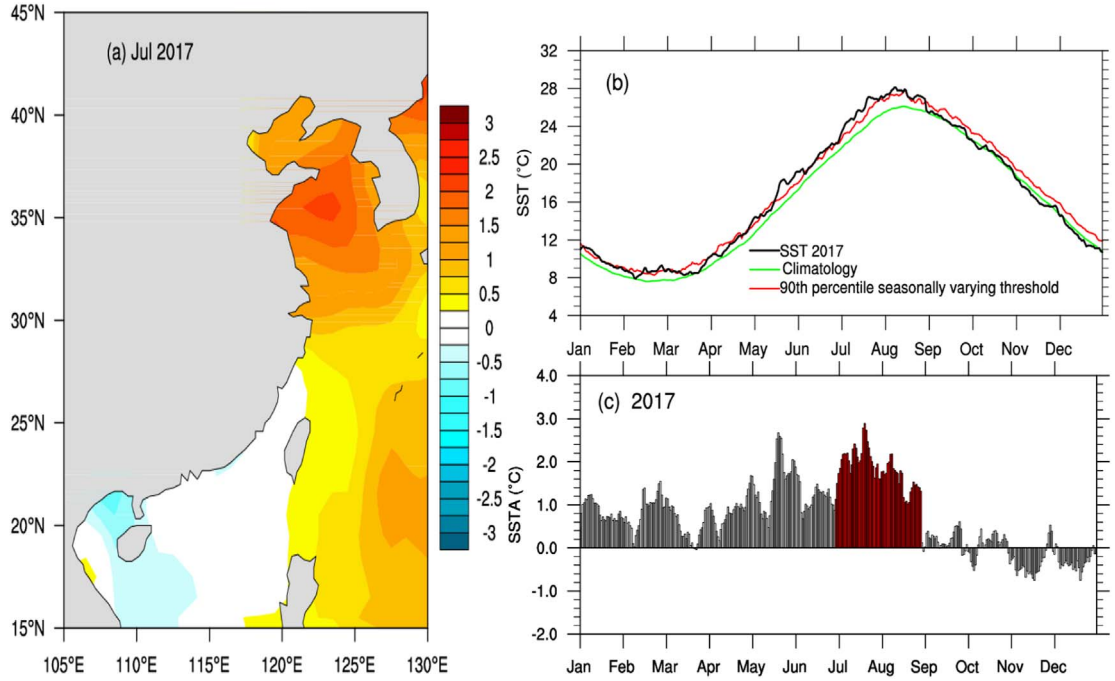

Figure 7. Pattern of monthly mean SST anomalies (SSTAs) from NOAA OISST v2 in July 2017 (a); domain-averaged SST time series for the northern Yellow Sea (30°–40°N, 117°–128°E), the 90th percentile seasonally varying threshold (red), and the climatology (green) (b); domain-averaged SST anomalies for the northern Yellow Sea (30°–40°N, 117°–128°E) (bar), with the red shaded regions indicating the northern Yellow Sea 2017 MHW detected using the definition of Hobday *et al* (2016) (c).

poisoning events and mortality events in seabirds (Walsh *et al* 2018). The examples described above indicate that a range of organisms and ecosystems can be impacted by MHWs. Considering the emerging risks from MHWs, we emphasize the importance of planning for strategies in the context of increased and intense MHWs in the China Seas. It is necessary and essential to take a more proactive approach to reduce the negative consequences of MHWs on food production from aquaculture and other marine ecosystems, such as setting up an early warning system and a seasonal prediction system.

6. Conclusions

We analyze the characteristics of the change in SST and MHWs in the China Seas, by using four global gridded SST data sets. One of the key findings of the analysis is that there is a remarkable warming shift in 1998 over the China Seas, which is consistent with change in GMST. During 1998–2013, the annual mean SST exhibits a declining tendency in the China Seas, with the rates at the range of $-0.37 \sim -0.24$ °C per decade. The annual mean SST declining after 1998 was mainly controlled by the remarkable cooling in boreal winter.

Importantly, despite the recent warming hiatus in the China Seas, the regional average annual mean SST for 1998–2013 is unexpectedly 0.5 °C above that for 1982–1997. The statistical distributions manifest that warm SSTAs and very hot SSTAs increased as the China Seas' mean climate shifts towards warmer during 1998–2013. Further analysis in this study finds that, not only there is no decrease in MHWs over the China Seas during the global warming hiatus, but actually they have become more frequent, intensive and longer during 1998–2013 compared to those during 1982–1997. In terms of spatial distribution, more frequent MHWs occurred in the coastal areas of the China Seas and along the Kuroshio Current axis during the warming hiatus, with the increase reaching two to three events annually.

Further investigation is needed to understand the underlying causes and the possible impacts of the observed increase in MHWs. In particular, we emphasize the importance of adaptation for local people to reduce the negative consequences of MHWs on fisheries, aquaculture and marine ecosystems.

Acknowledgments

This study was supported by the program of National Natural Science Foundation of China (41706020) and the National Key Research and Development Program of China (2017YFC1404700; 2018YFA0605603).

ORCID iDs

Qinglong You https://orcid.org/0000-0002-9480-8638

References

Banzon V, Smith T M, Chin T M, Liu C and Hankins W 2016 A long-term record of blended satellite and *in situ* sea-surface temperature for climate monitoring, modeling and environmental studies *Earth Syst. Sci. Data* **8** 165–76

Belkin I M 2009 Rapid warming of large marine ecosystem *Prog. Oceanogr.* **81** 207–13

Benthuysen J, Oliver E C J, Feng M and Marshall A G 2018 Extreme marine warming across Tropical Australia during austral summer 2015–2016 *J. Geophys. Res.* **123** 1301–26

Cai R S, Tan H J and Kontoyiannis H 2017 Robust surface warming in offshore China Seas and its relationship to the East Asian Monsoon wind field and ocean forcing on interdecadal time scales *J. Clim.* **30** 8987–9905

Caputi N *et al* 2016 Management adaptation of invertebrate fisheries to an extreme marine heat wave event at global warming hot spot *Ecol. Evol.* **6** 3583–93

Chen K, Gawarkiewicz G G, Lentz S J and Bane J M 2014 Diagnosing the warming of the Northeastern US Coastal Ocean in 2012: a linkage between the atmospheric jet stream variability and ocean response *J. Geophys. Res.* **119** 218–27

Cohen J L, Furtado J C, Barlow M, Alexeev A and Cherry J E 2012 Asymmetric seasonal temperature trends *Geophys. Res. Lett.* **39** L04705

Ding Y *et al* 2014 Interdecadal variability of the East Asian winter monsoon and its possible links to global climate change *J. Meteor. Res.* **28** 693–713

Duan A and Xiao Z 2015 Does the climate warming hiatus exist over the Tibetan Plateau? *Sci. Rep.* **5** 13711

Frölicher T L, Fischer E M and Gruber N 2018 Marine heatwaves under global warming *Nature* **560** 360–4

Frölicher T L and Laufkötter C 2018 Emerging risks from marine heat waves *Nat. Commun.* **9** 650

Garfinkel C L, Son S W, Song K, Aquila V and Oman L D 2017 Stratospheric variability contributed to and sustained the recent hiatus in Eurasian winter warming *Geophys. Res. Lett.* **44** 374–82

Garrabou J *et al* 2009 Mass mortality in Northwestern Mediterranean rocky benthic communities: effects of the 2003 heat wave *Glob. Change Biol.* **15** 1090–103

Guan X, Huang J, Guo R and Lin P 2015 The role of dynamically induced variability in the recent warming trend slowdown over the Northern Hemisphere *Sci. Rep.* **5** 12669

Herring S C, Christidis N, Hoell A, Hoerling M P and Stott P A 2019 Eds Explaining extreme events of 2017 from a climate perspective *Bull. Amer. Meter. Soc.* **100** S1–117

Hirahara S, Ishii M and Fukuda Y 2012 Centennial-scale sea surface temperature analysis and its uncertainty *J. Clim.* **27** 57–75

Hobday A J *et al* 2016 A hierarchical approach to defining marine heatwaves *Prog. Oceanogr.* **141** 227–38

Hu S and Fedorov A V 2017 The extreme El Niño of 2015–2016 and the end of global warming hiatus *Geophys. Res. Lett.* **44** 3816–24

IPCC 2013 Climate change 2013: the physical science basis *Contribution of Working Group I to the Fifth Assessment Report of the Intergovernmental Panel on Climate Change.* (Cambridge: Cambridge University Press) p 1535

Kosaka Y and Xie S P 2013 Recent global-warming hiatus tied to equatorial Pacific surface cooling *Nature* **501** 403–7

Lewandowsky S, Risbey J S and Oreskes N 2015 On the definition and identifiability of the alleged 'hiatus' in global warming *Sci. Rep.* **5** 16784

Li Q *et al* 2015 China experiencing the recent warming hiatus *Geophys. Res. Lett.* **42** 889–98

Lima F P and Wethey D S 2012 Three decades of high-resolution coastal sea surface temperature reveal more than warming *Nat. Commun.* **3** 704

Medhaug I *et al* 2017 Reconciling controversies about the 'global warming hiatus' *Nature* **545** 41–7

Meehl G A, Hu A, Arblaster J M, Fasullo J and Trenberth K E 2013 Externally forced and internally generated decadal climate variability associated with the Interdecadal Pacific Oscillation *J. Clim.* **26** 7298–310

Oliver E C J *et al* 2017 The unprecedented 2015/16 Tasman Sea marine heatwave *Nat. Commun.* **8** 16101

Oliver E C J *et al* 2018 Longer and more frequent marine heatwaves over the past century *Nat. Commun.* **9** 1324

Oliver E C 2019 Mean warming not variability drives marine heatwave trends *Clim. Dyn.* **53** 1653–9

Pei Y H, Liu X H and He H L 2017 Interpreting the sea surface temperature warming trend in the Yellow Sea and East China Sea *Sci. China Earth Sci.* **60** 1558–68

Rayner N A, Parker D E, Horton E B, Folland C K, Alexander L V, Rowell D, Kent E C and Kaplan A 2003 Global analyses of sea surface temperature, sea ice, and night marine air temperature since the late nineteenth century *J. Geophys. Res.* **108** 4407

Sen P K 1968 Estimates of regression coefficient based on Kendall's tau *J. Am. Stat. Assoc.* **63** 1379–89

Shen X J, Liu B and Lu X 2018 Weak cooling of cold extremes versus continued warming of hot extremes in China during the recent global surface warming hiatus *J. Geophy. Res. Atmos.* **123** 4073–87

Sun X B, Ren G Y, Ren Y Y, Liu Y L and Xue X Y 2017 A remarkable climate warming hiatus over Northeast China since 1998 *Theor. Appl. Climatol.* **9** 1–16

Sun Y *et al* 2014 Rapid increase in the risk of extreme summer heat in Eastern China *Nat. Clim. Change* **4** 1082–5

Tan H and Cai R 2018 What caused the record-breaking warming in East China Seas during August 2016? *Atmos. Sci. Lett.* **19** e853

Thomson J, Burkholder D D, Heithaus M, Fourqureen J, Fraser M, Statton J C and Kendrick G 2015 Extreme temperature, foundation species, and abrupt ecosystem change: an example from an iconic seagrass ecosystem *Glob. Change Biol.* **21** 1463–74

Tollefson J 2014 Climate change: the case of the missing heat *Nature* **505** 276–8

Trenberth K E, Fasullo J T, Branstator G and Phiilips A S 2014 Seasonal aspects of the recent pause in surface warming *Nat. Clim. Change* **4** 911–6

Walsh J E *et al* 2018 The high latitude marine heat wave of 2016 and its impacts on Alaska *Bull. Amer. Meteor. Soc.* **99** S39–43

Wang L and Chen W 2014 The East Asian winter monsoon: re-amplification in the mid-2000 s *Chinese Sci. Bull.* **59** 430–6

Wang S X, Yuan X and Li Y 2017 Does a strong El Niño imply a higher predictability of extreme drought? *Sci. Rep.* **7** 40741

Wernberg T *et al* 2016 Climate-drive regime shift of a temperature marine ecosystem *Science* **353** 169–72

Woodruff S D *et al* 2011 ICOADS Release 2.5: extensions and enhancements to the surface marine meteorological archive *Int. J. Climatol.* **31** 951–67

World Meteorological Organization (WMO) 2019 *WMO Statement on the State of the Global Climate in 2018.* (Switzerland) p 44

Wu L X, Cai W and Zhang L 2012 Enhanced warming over the global subtropical western boundary currents *Nat. Clim. Change* **2** 161–6

Xie Y, Huang J and Liu Y 2017 From accelerated warming to warming hiatus in China *Inter. J. Climatolo.* **37** 1758–73

You Q L, Ren G Y, Fraedrich K, Kang S, Ren Y Y and Wang P L 2013 Winter temperature extremes in China and their possible causes *Int. J. Climatol.* **33** 1444–55

第 15 卷 第 4 期
2019 年 7 月

气 候 变 化 研 究 进 展
CLIMATE CHANGE RESEARCH

Vol. 15 No. 4
July 2019

DOI: 10.12006/j.issn.1673-1719.2018.199
廖要明，陈德亮，刘秋锋．中国地气温差时空分布及变化趋势 [J]. 气候变化研究进展，2019, 15 (4): 374-384
Liao Y M, Chen D, Liu Q F. The spatiotemporal characteristics and long-term trends of surface-air temperatures difference in China [J]. Climate Change Research, 2019, 15 (4): 374-384

中国地气温差时空分布及变化趋势

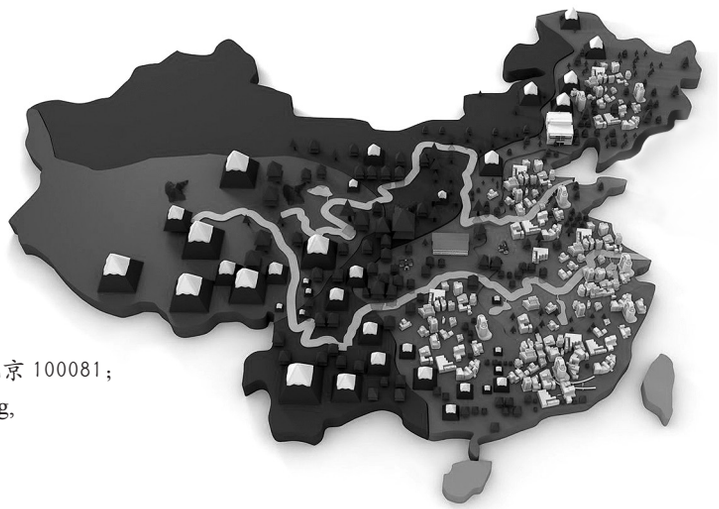

廖要明[1]，陈德亮[2]，刘秋锋[1]

1 国家气候中心 中国气象局气候研究开放实验室，北京 100081；
2 Department of Earth Sciences, University of Gothenburg, Gothenburg 40530, Sweden

摘 要：利用中国 825 个气象站点 1961—2016 年的逐日地表温度和气温观测资料，系统分析了中国地区地气温差（地表温度减气温）的时空分布以及变化趋势。结果表明，中国多年平均的年地气温差西部大部地区及华南部分地区在 2.5 ℃以上，而中东部大部地区在 2.5 ℃以下。其中春、夏季全国各地地气温差均为正值，且总体呈经向型分布，西高东低；秋、冬季中国各地地气温差总体呈纬向型分布，南高北低，尤其是冬季北方部分地区为负值。年内，中国区域平均各月地气温差均为正值，其中 1 月份和 12 月份相对较小，6—8 月份（夏季）相对较大。不同地区地气温差的年内分布特征有所不同，西藏地区地气温差年平均值为全国最大，最大值出现在雨季来临前的 5 月份；东北、华北、黄淮、西北及内蒙古地区最大值均出现在雨季来临前的 6 月份；江淮、江汉、江南、华南地区地气温差最大值均出现在雨季过后的 7 月份或 8 月份；西南地区年内各月地气温差变化相对较小，在雨季之前的 5 月和雨季之后的 8 月出现 2 次峰值，呈双峰型分布。1961—2016 年，中国区域平均地气温差 4 月和 4—10 月上升趋势较明显，而 7 月和 10 月变化趋势不明显或略有上升趋势。空间分布上，东北、西北及内蒙古、西藏西部等地平均地气温差有增加趋势，而中东部地区有减小趋势。

关键词：地气温差；时空分布；气候变化；中国

引 言

中国幅员辽阔，南北从热带经亚热带到温带延伸约 50 个纬度[1]，东临世界最大的海洋——太平洋，西有全球最高的高原——青藏高原，地形、地貌极其复杂。因此，中国具有多种类型的下垫面，既有戈壁、沙漠的典型干旱区，黄土高原和草原的半干旱区，又有季风湿润区，还有青藏高原区，这些全球具有一定代表性和典型性的下垫面的能量和水分循环特性的差异对于全球气候和水文的变化，特别是对气候灾害的发生有严重影响[2-4]。地表感热通量是低层大气的重要能量来源，也是地面热量平衡的重要分量，在陆气相互作用过程中，感热通量对于陆面和大气边界层热力交换起着极为重要的作用，其水平分布的不均匀必然会引起陆面对大气加热的差异，从而影响季风环流

收稿日期：2018-12-28；**修回日期**：2019-02-20
资助项目：国家重点研发计划项目（2018YFA0606304）；公益性行业（气象）科研专项（GYHY201506001）
作者简介：廖要明，男，高级工程师，lymzxr@cma.gov.cn

www.climatechange.cn

的建立和维持[5-11]。地气温差是地表感热通量的主要贡献项，不少学者利用地温、气温和地面附近风场等要素的观测资料计算地表感热通量[12-15]。地气温差的变化基本反映了地表感热通量的变化特征[16-18]，对大气环流、天气变化、农业生产和生态环境有重要影响。研究中国地气温差的时空分布及气候变化特征，可以更好地掌握中国的地表感热通量分布及变化特征，对于了解中国气候变化的内在机制和短期气候预测都具有重要意义。同时，地气温差对长江中下游地区夏季降水有一定的指示意义[19-20]，也是衡量土壤荒漠化程度和进程的重要指标[21]；地气温差对农作物的种子发芽、出苗以及光合作用等有直接影响，对作物病虫害的发生、发展，土壤微生物的活动也有不同程度的影响，对农作物的正常生长发育有着十分重要的作用[22]。

近年来，我国对地气温差的研究分析主要集中在中国的西北地区、青藏高原或者个别省份，甚至个别气象站点。范丽军等[16]、符睿等[23]分析了西北干旱区地气温差的时空变化特征；周连童等[19]分析了我国西北干旱、半干旱区春季和夏季地气温差的年代际变化特征及其与夏季降水的联系；王澄海等[24]分析了东亚夏季风建立前青藏高原地气温差变化特征；杨智等[25]研究发现云南省地气温差在夏季最大，其次为秋季和春季，冬季最小，且有逐年缓慢上升趋势；陈超等[26]、王超等[27]分别利用阿拉善左旗气象站和敦煌双墩子戈壁试验站资料，分析了当地地气温差的变化规律。而我国幅员辽阔，地形复杂，具有多种典型的下垫面，气候类型多种多样。因此，很有必要对中国全国范围的地气温差时空分布和气候变化特征等进行系统、全面分析。虽然温李明等[28]对我国东西部地区地气温差的年代际变化特征及其差异进行了一些研究，但研究站点有限（218 个），研究区域主要集中在中国的西北部和东南部，对中国的代表性不够。本文将利用中国 825 个站点 1961—2016 年共 56 年的逐日地表温度和平均气温观测资料，系统地分析中国各地全年及各个季节地气温差的时空分布及其变化趋势。

1　资料与方法

由于我国部分气象站点不同时具有地表温度和气温观测资料，且 20 世纪 50 年代观测站点较少，资料缺测比较严重。所以本文选择 1961—2016 年作为研究时段，选择该时段同时具有 25 年以上逐日地表温度和气温观测资料的 825 个站点（其中中国香港、澳门和台湾资料缺）作为研究站点。将某气象观测站的地表温度与气温的差值定义为该站的地气温差，即 T_s-T_a，其中 T_s 表示地表温度，即 0 cm 地温，T_a 表示气温，为离地面 1.5 m 高度处的空气温度。把中国划分为东北、华北、西北、黄淮、江淮、江汉、江南、华南、西南、西藏和内蒙古共 11 个区域[29]，中国各区域及 825 个气象观测站点的空间分布见图 1。把一年划分为春季（3—5 月）、夏季（6—8 月）、秋季（9—11 月）、冬季（12 月至次年 2 月）4 个季节。

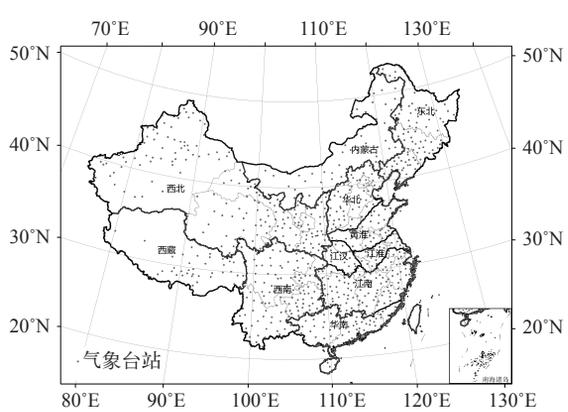

图 1 研究站点分布及中国气候分区图

Fig. 1 Distribution of stations and climate zones in China

我国气象观测站点在 2005 年以后开始普遍采用自动站取代人工观测，由于自动站地表温度的观测规范与人工观测不同，会造成冬季地面有积雪时自动站观测地表温度比人工观测偏高。这是由于当人工观测地表温度时，如果温度表被雪埋住，按照《地面气象观测规范》规定必须将温度表从雪中取出，水平安装在未被破坏的雪面上，感应部分和表身埋入雪中一半，再进行读数[30]，所以人工观测的地表温度实际上就是雪面温度。而在使用自动站观测时，由于铂电阻地面温度传

感器被积雪埋住时仍按正常观测，所以自动站观测的地表温度是雪下温度，这两个观测数据之间存在差异，造成了有积雪时，自动站观测地表温度比人工观测的记录偏高。为排除 2005 年以后冬季降雪自动观测站点地表温度因观测手段改变所带来的影响，本文在分析年及四季多年平均值时未使用 2000 年以后的数据，仅使用 1961—2000 年的数据；在分析中国地区地气温差的年代际气候变化特征时，舍弃较冷的几个月，只统计 1961—2016 年 4 月（代表春季）、7 月（代表夏季）、10 月（代表秋季）及 4—10 月的数据。文中利用最小二乘法 [31] 估计各站点 1961—2016 年不同季节地气温差的线性变化趋势。

2 结果分析

2.1 空间分布特征

由中国 1961—2000 年平均的年（图 2）及四季（图 3）地气温差空间分布可以看出：(1) 中国西部大部地区及华南部分地区年平均地气温差在 2.5 ℃以上，其中西藏大部、青海西部、云南南部、海南大部等地在 3.5 ℃以上，西藏南部、海南西部的部分地区达 4.0 ℃以上；而中国中东部大部地区年平均地气温差在 2.5 ℃以下，其中东北、华北东部以及山东西部、江苏东南部、湖南北部、湖北西南部、重庆、四川东部、新疆东北部等地在 2.0 ℃以下，黑龙江大部、吉林东部等地在 1.5 ℃以下。我国地气温差的这种西高东低的空间分布格局，与东、西气候和地表特征差异密切相关：西部地区太阳辐射强烈，植被覆盖稀疏，土壤干燥，地表感热加热强；中东部地区则是全球强季风区，降水丰富，土壤湿润，植被茂密，地表感热加热相对较弱。(2) 春、夏季，中国各地平均地气温差均为正值，总体呈经向型分布，东部偏低、西部偏高，这种分布格局与中国地势等值线西高东低的分布型基本吻合，可能与山脉的抬高加热作用有关，西部多山脉，海拔相对较高，相当于将太阳辐射的吸收面抬高了，从而可以吸收更多的太阳辐射，产生更强的热力对流 [32]，地气温差

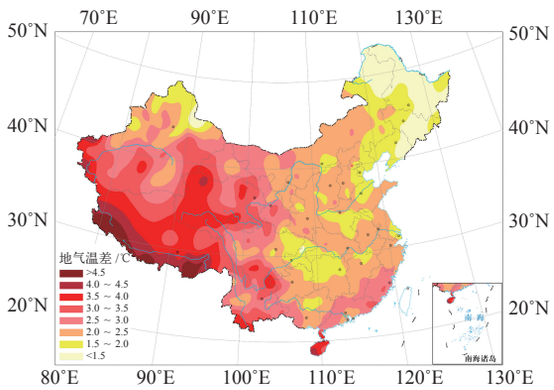

图 2 中国年平均地气温差分布

Fig. 2 Distribution of annual mean surface-air temperature difference in China

增大。春季地气温差高值中心位于西藏、青海、新疆西南部、四川南部、海南等地，地气温差在 4.0 ℃以上，低值中心位于西南东部、江南西部、华南北部、东北北部和东部等地，地气温差在 2.0 ℃以下；夏季地气温差高值中心位于西藏西部、青海西部、新疆、甘肃西部等地，地气温差在 5.0 ℃以上，低值区主要出现在四川盆地、江苏东南部、广东中南部、辽宁东部等地的部分地区，地气温差在 3.0 ℃以下。(3) 秋、冬季，由于太阳直射点向南半球偏移，中国各地地气温差总体呈纬向型分布，南方地区偏高、北方地区偏低。秋季高值区主要位于华南以及西藏、青海南部、云南南部等地的部分地区，地气温差在 3.0 ~ 4.0 ℃，局部地区在 4.0 ℃以上；冬季高值区主要位于西藏东南部、云南南部、四川南部、雷州半岛、海南等地，地气温差在 2.0 ~ 3.0 ℃，局部地区在 3.0 ℃以上。秋、冬季节，我国广大北方地区地气温差均相对较低，尤其是冬季，东北、华北以及内蒙古中东部、新疆等地地气温差出现负值，主要是由于这些地区冬季地表多为冰雪覆盖，反照率大，地表获得的太阳有效辐射较小，同时浅层土壤为冻土，还需要吸收地表的大量热量，因而造成地表温度低于气温，地气温差为负值。

2.2 时间分布特征

由中国地区 825 个站点 1961—2000 年逐日地表温度和气温资料计算得到的中国平均地表温度、

www.climatechange.cn

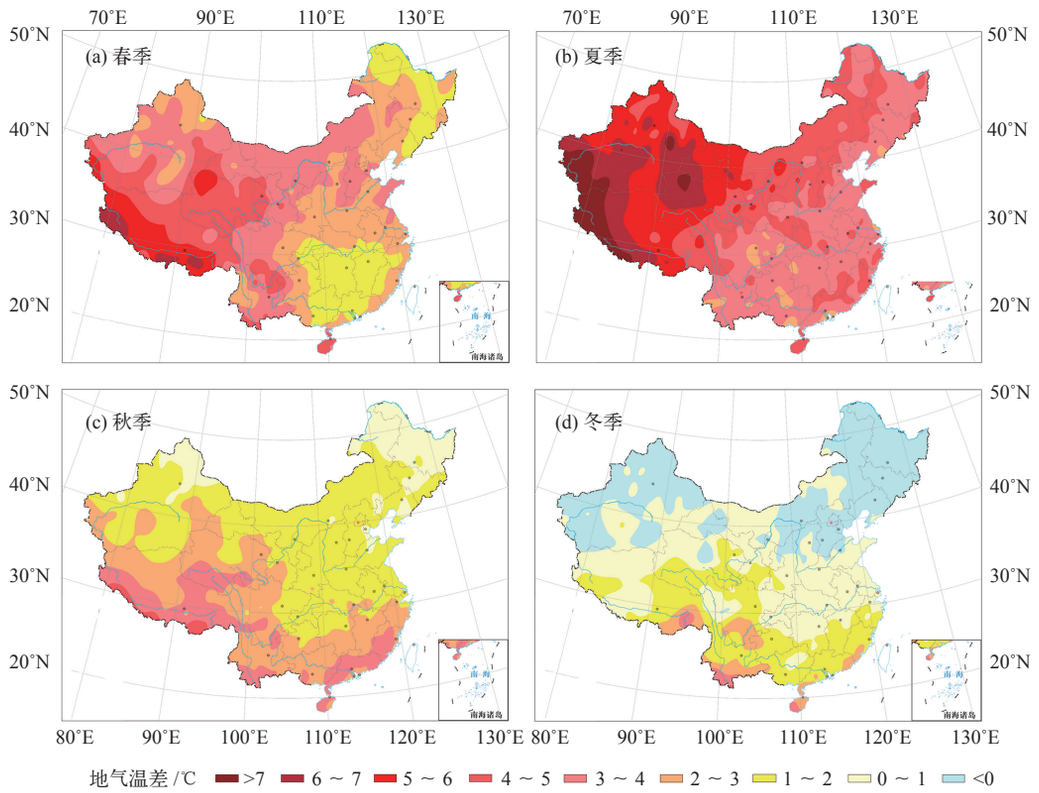

图 3　中国春 (a)、夏 (b)、秋 (c)、冬 (d) 季平均地气温差分布

Fig. 3　Distribution of seasonal mean surface-air temperature difference of spring (a), summer (b), autumn (c) and winter (d) in China

气温和地气温差年内 1—12 月的变化图（图 4）可以看出，3 条曲线基本上都呈上凸的抛物线型。中国平均地表温度和气温的最小值均出现在 1 月份，分别为 −2.2 ℃和 −2.6 ℃，从 1 月份开始中国平均地表温度和气温逐步上升，到 7 月份达到最大值，分别为 28.0 ℃和 23.8 ℃，7 月份以后又逐渐减小。中国区域平均地气温差年内 12 个月均为正值，其中 1 月份和 12 月份相对较小，分别为 0.4 ℃和 0.3 ℃；6、7 和 8 月（夏季），中国区域平均地气温差相对较大，分别为 4.0 ℃、4.2 ℃和 4.0 ℃。

地气温差的年内变化主要取决于太阳辐射量、下垫面温湿状况和当地的盛行天气形势等，中国不同地区由于地理环境和下垫面状况等的差异，地气温差的年内分布特征有所不同。从表 1 可以看出：(1) 东北地区年平均地气温差相对最小，只有 1.5 ℃，年内 1 月份和 12 月份平均地温明显低于气温，地气温差在 −1.0 ℃左右，2 月份和 11 月份平均地温和气温相差不大，地气温差接近 0 ℃，

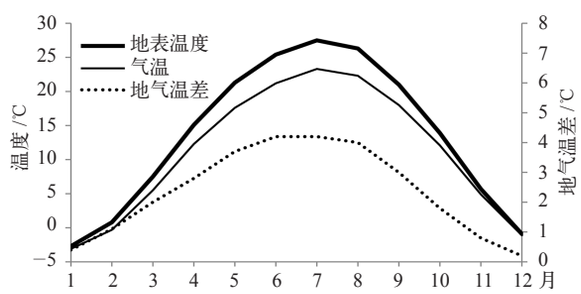

图 4　中国平均地表温度、气温和地气温差年内变化

Fig. 4　Intra-annual change of national mean surface temperature, air temperature and surface-air temperature difference in China

其余月份地气温差均在 0.5 ℃以上，最大值出现在雨季来临前的 6 月份，为 3.8 ℃。(2) 华北和内蒙古地区年平均地气温差均为 2.0 ℃，年内 1 月份和 12 月份平均地温低于气温，华北地区地气温差在 −0.5 ℃左右，内蒙古地区在 −1.0 ℃左右，11 月份两地平均地温和气温相当，地气温差接近 0 ℃，其余月份均 >0 ℃，最大值均出现在雨季来临前的 6 月份，分别为 4.5 ℃和 4.8 ℃。(3) 黄淮和西北地区年平均地气温差分别为 2.1 ℃和 2.6 ℃，

年内 1 月份、11 月份和 12 月份地气温差接近 0 ℃，其余月份均在 0.5 ℃以上，最大值也均出现在雨季来临前的 6 月份，分别为 4.1 ℃和 5.4 ℃。(4) 江淮、江汉、江南地区年平均地气温差相差不大，分别为 2.1 ℃、2.3 ℃和 2.2 ℃，年内各月平均地气温差均 >0 ℃，最小值均出现在 12 月或 1 月，最大值均出现在雨季过后的 7、8 月份。(5) 西南和华南地区年平均地气温差分别为 2.6 ℃和 2.7 ℃，年内各月平均地气温差均在 1.4 ℃以上，月际间的变化幅度较其他地区相对较小，其中华南地区平均地气温差最大值出现在雨季过后的 7 月份，西南地区出现在雨季过后的 8 月份，且西南地区地气温差年内分布呈双峰型，即 5 月和 8 月出现两个峰值，这可能与西南地区 6—7 月降水充沛有关，加之下垫面植被茂盛，这段时间地气交换以潜热为主，地表通过潜热的方式向大气输送的热量较感热要大，因此地气温差在 6—7 月略有下降 [33]。(6) 青藏高原作为北半球同纬度地区的一个强大热源，其热力作用强化了亚洲季风，并影响中国的降水 [5]。因此，西藏地区年平均地气温差较全国其他地区明显偏大，达 4.0 ℃，年内各月平均地气温差除 1 月份和 12 月份在 2.0 ℃以下外，其余月份均在 2.0 ℃以上，其中最小值出现在 12 月份，为 1.0 ℃，最大值出现在雨季来临之前的 5 月份，达 6.5 ℃。中国各地地气温差的这种年内分布特征，特别是北方地区最大值基本出现在雨季来临前的一个月，南方地区出现在雨季之后的一个月，与各地太阳辐射的年内分布特征非常相似 [34]。

2.3 变化趋势

1961—2016 年，中国区域平均 4 月、7 月、10 月以及 4—10 月平均地表温度和气温总体均有增加趋势，且地表温度较气温增加幅度相对更大，所以地气温差总体也有增加趋势（图 5）。(1) 4 月，中国平均地表温度、气温和地气温差总体均呈增加趋势，地表温度和气温的最小值出现在 2010 年，分别为 14.0 ℃和 11.1 ℃，最大值出现在 1998 年，分别为 18.2 ℃和 15.4 ℃；4 月，中国区域平均地气温差在 2.2 ～ 3.6 ℃，年代际变化特征明显，其中 1961—2003 年，中国 4 月平均地气温差基本在 2.2 ～ 3.0 ℃，最小值（2.2 ℃）出现在 1969 年，2003 年以后大部分年份中国区域平均地气温差在 3.0 ℃以上，最大值（3.6 ℃）出现在 2011 年。(2) 7 月，中国区域平均地表温度、气温和地气温差总体呈略微增加的变化趋势，其中 20 世纪 60 年代到 90 年代初，地表温度和气温略有

表 1 中国及其 11 个区域 1—12 月和全年平均地气温差

Table 1 Average monthly and annual surface-air temperature difference in China and its 11 regions

℃

地区	1 月	2 月	3 月	4 月	5 月	6 月	7 月	8 月	9 月	10 月	11 月	12 月	全年
东北	−1.1	0.0	1.5	1.9	2.9	3.8	3.6	3.3	2.3	0.7	−0.2	−0.9	1.5
华北	−0.4	0.6	1.9	3.0	4.1	4.5	3.9	3.5	2.6	1.1	0.0	−0.5	2.0
黄淮	0.4	1.0	1.9	2.9	3.9	4.1	3.4	3.6	2.7	1.5	0.3	0.0	2.1
西北	−0.1	0.8	2.0	3.4	4.7	5.4	5.3	4.6	3.1	1.5	0.2	−0.4	2.6
江淮	0.6	1.1	1.6	2.3	3.2	3.5	3.6	4.1	2.9	1.8	0.7	0.3	2.1
江汉	0.7	1.2	1.5	2.3	2.8	3.6	4.2	4.4	3.0	1.9	0.9	0.5	2.3
江南	1.0	1.1	1.3	1.7	2.3	2.8	4.2	4.2	3.2	2.3	1.3	1.0	2.2
华南	1.8	1.9	2.0	2.2	3.0	3.1	3.8	3.7	3.5	3.2	2.3	2.0	2.7
西南	1.5	1.9	2.4	2.9	3.3	3.0	3.5	3.7	3.0	2.3	1.8	1.4	2.6
西藏	1.2	2.6	3.8	5.4	6.5	6.4	5.6	5.2	4.5	3.7	2.2	1.0	4.0
内蒙古	−0.8	0.2	1.9	3.0	4.2	4.8	4.4	3.8	2.6	1.0	−0.2	−0.9	2.0
全国	0.4	1.1	1.8	2.7	3.6	4.0	4.2	4.0	3.0	1.8	0.8	0.3	2.3

www.climatechange.cn

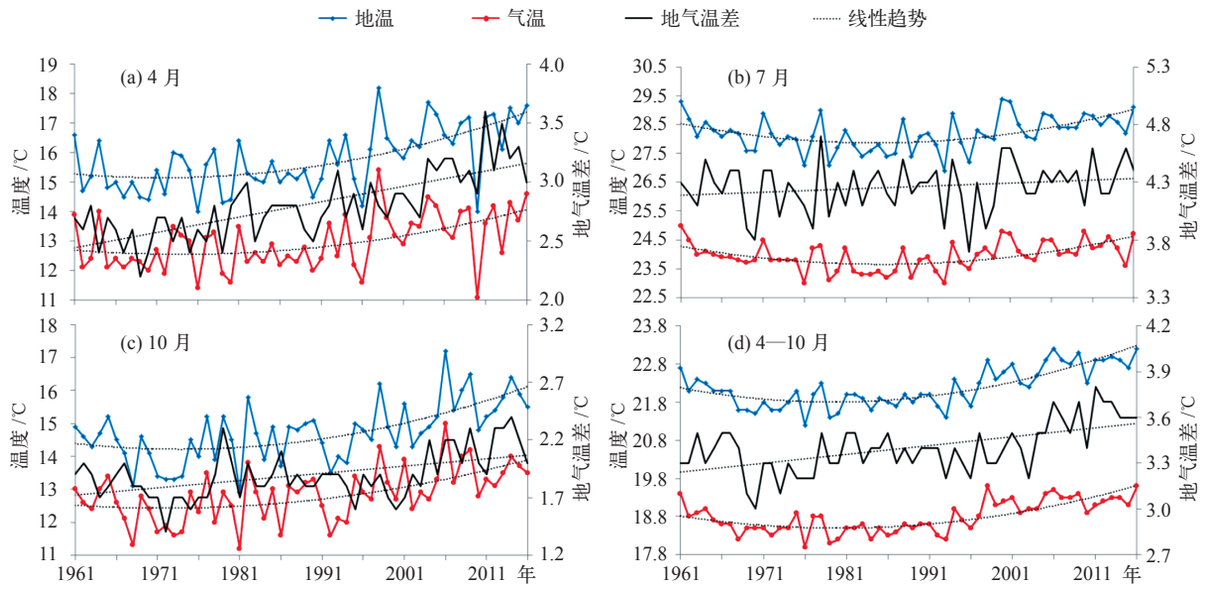

图 5　1961—2016 年 4 月 (a)、7 月 (b)、10 月 (c) 及 4—10 月 (d) 中国平均地温、气温和地气温差历年变化

Fig. 5　Changes of monthly mean surface temperature, air temperature and surface-air temperature difference of April (a), July (b), October (c) and from April to October (d) in China from 1961 to 2016

下降趋势，1994 年以后略有上升趋势；7 月，中国平均地气温差相对较大，在 3.7 ～ 4.7 ℃，最小值出现在 1996 年，最大值出现在 1978 年。(3) 20 世纪 60 年代至 80 年代初，中国 10 月平均地表温度和气温基本都呈下降趋势，最小值出现在 1981 年，分别为 12.9 ℃和 11.2 ℃，但从 1982 年开始出现上升趋势，最大值出现在 2006 年，分别为 17.2 ℃和 15.0 ℃；10 月，中国区域平均地气温差相对较小，在 1.4 ～ 2.4 ℃，最小值出现在 1972 年，最大值出现在 2014 年，长期变化趋势不明显，但 2004 年以来有明显的增大趋势，大部分年份平均地气温差在 2.0 ℃以上。(4) 20 世纪 60 年代至 70 年代后期，中国 4—10 月平均地表温度和气温总体都呈下降趋势，最小值出现在 1976 年，分别为 21.2 ℃和 18.0 ℃，但从 20 世纪 80 年代开始出现上升趋势，最大值出现在 2016 年，分别为 23.2 ℃和 19.6 ℃；4—10 月，中国平均地气温差在 3.0 ～ 3.8 ℃，总体呈上升趋势，特别是 2006 年以来中国平均地气温差相对较大，大部分年份 ≥3.6 ℃。

图 6 给出 1961—2016 年中国 4 月、7 月、10 月和 4—10 月的平均地气温差线性变化趋势空间分布，可以看出：(1) 4 月平均地气温差线性变化趋势，除广东东部、福建南部、浙江东部、四川盆地等地为负值外，全国其余大部分地区为正值，其中西北大部、黄淮、江淮、江汉、东北大部以及西藏中西部、内蒙古、云南东部和北部、海南大部等地在 0.1 ～ 0.3 ℃/10a，部分地区超过 0.3 ℃/10a，增大趋势较明显。(2) 7 月平均地气温差线性变化趋势，>0.1 ℃/10a 的区域往北往西收缩，主要位于西北大部及西藏西部、内蒙古、黑龙江大部、吉林等地；而中东部 <−0.1 ℃/10a 的区域明显扩大，浙江东北部、江苏东南部、上海、湖北南部、湖南北部、福建东南部、广东东部和河北中部等地的部分地区 <−0.2 ℃/10a。(3) 10 月，地气温差线性变化趋势除新疆南部、西藏西部、青海大部、甘肃中部和西部、内蒙古西部和东北部、黑龙江西北部等地 >0.1 ℃/10a，河北中南部、天津、广东中部、福建南部等地 < −0.1 ℃/10a 外，全国其余大部地区在 −0.1 ～ 0.1 ℃/10a。(4) 4—10 月，除西北大部、东北大部及内蒙古大部、西藏西部等地地气温差线性变化趋势在 0.1 ～ 0.3 ℃/10a，局部地区超过 0.3 ℃/10a 外，中国其余大部地区地气温差线性变化趋势在 0.1 ℃/10a 以下，其中中东

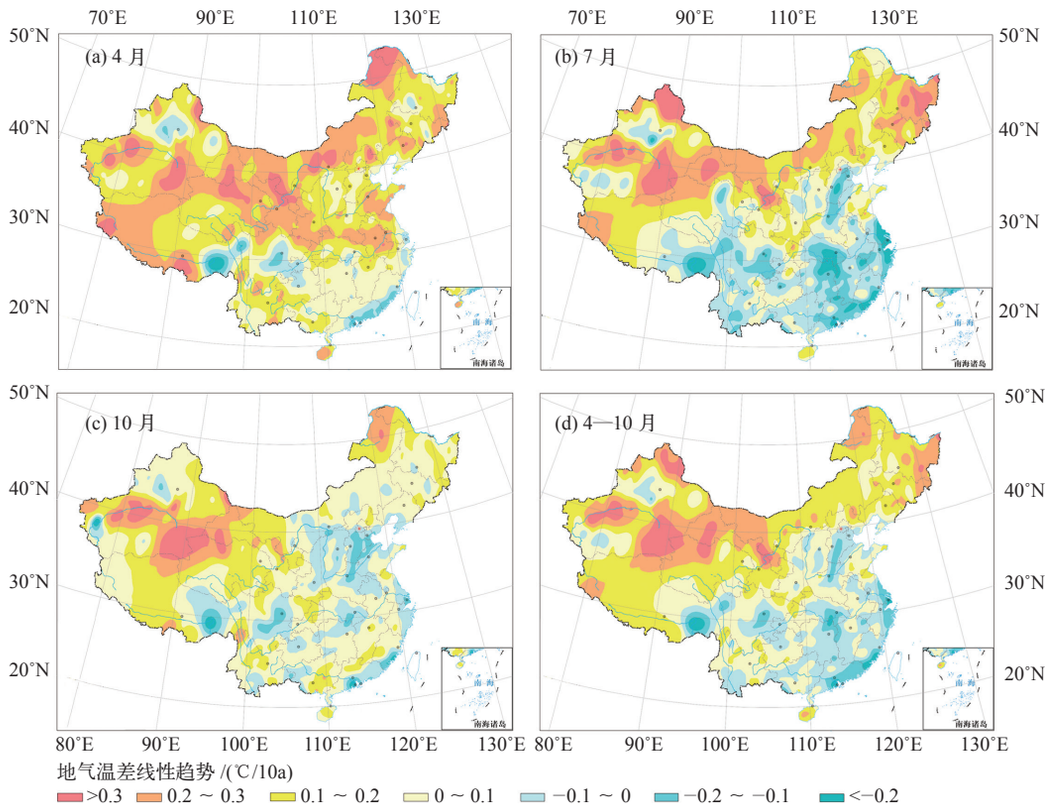

图 6 1961—2016 年中国 4 月 (a)、7 月 (b)、10 月 (c) 及 4—10 月 (d) 平均地气温差线性变化趋势分布

Fig. 6 Linear trend of monthly mean surface-air temperature difference of April (a), July (b), October (c) and from April to October (d) in China during 1961−2016

部大部地区为负值，地气温差呈减小趋势，河北中部、江苏东南部、浙江东部、湖北中南部、广东东部等地减小趋势在 −0.2 ~ −0.1 ℃/10a，局部地区 <−0.2 ℃/10a。

从 1961—2016 年全国及中国不同区域 4—10 月平均地气温差的年代际平均和线性变化趋势（表 2）来看，(1) 全国平均地气温差总体呈上升趋势，线性变化趋势为 0.06 ℃/10a，其中 20 世纪 60 年代、70 年代和 90 年代平均地气温差相对较小，均为 3.3 ℃，2011—2016 年平均最大，为 3.7 ℃。(2) 东北、西北、内蒙古地区的平均地气温差有明显的上升趋势，线性变化趋势在 0.15 ℃/10a 左右，其中内蒙古地区上升趋势相对最为明显，达 0.16 ℃/10a，东北和西北地区线性变化趋势分别为 0.14 ℃/10a 和 0.15 ℃/10a；西北地区平均地气温差阶段性上升特征明显，其中 20 世纪 60 年代和 70 年代平均地气温差均为 3.9 ℃，80 年代和 90 年代分别为 4.1 ℃和 4.2 ℃，21 世纪以来升高明显，前 10 年和 2011—2016 年平均地气温差分别达 4.4 ℃和 4.6 ℃。(3) 华北、黄淮、江淮、西南和西藏地区平均地气温差变化趋势不明显，年代际之间平均地气温差变化较小，其中华北地区在 3.2 ~ 3.5 ℃之间，黄淮地区在 2.9 ~ 3.3 ℃之间，江淮地区在 2.9 ~ 3.2 ℃之间，西南地区在 3.0 ~ 3.3 ℃之间，西藏地区在 5.3 ~ 5.7 ℃之间。(4) 地处南方的江汉、江南、华南地区平均地气温差有下降趋势，线性变化趋势均≤−0.05 ℃/10a，分别为 −0.07 ℃/10a、−0.05 ℃/10a、−0.09 ℃/10a。

3 结论与讨论

(1) 中国多年平均的年地气温差，西部大部地区及华南部分地区在 2.5 ℃以上，而中东部大部地区在 2.5 ℃以下。其中春、夏季全国各地地气温差均为正值，总体呈经向型分布，西高东低，且与中国地势等值线分布基本吻合，这可能与山脉的抬

www.climatechange.cn

表 2 中国及其 11 个区域 4—10 月地气温差年代际平均及线性变化趋势

Table 2 Inter-decadal mean surface-air temperature difference and linear trend from April to October in China and its 11 regions

地区	地气温差年代际均值 /℃						线性倾向率 /(℃/10a)
	1961—1970 年	1971—1980 年	1981—1990 年	1991—2000 年	2001—2010 年	2011—2016 年	
东北	2.7	2.6	2.7	2.7	3.1	3.5	0.14
华北	3.3	3.3	3.3	3.2	3.2	3.5	0.00
黄淮	3.0	3.1	3.3	3.2	2.9	3.3	0.00
西北	3.9	3.9	4.1	4.2	4.4	4.6	0.15
江淮	3.2	3.1	3.0	2.9	3.0	3.2	−0.02
江汉	3.3	3.3	3.1	3.0	3.0	3.1	−0.07
江南	3.1	2.9	3.0	2.9	2.9	2.9	−0.05
华南	3.4	3.2	3.2	3.0	3.0	3.0	−0.09
西南	3.1	3.2	3.1	3.0	3.3	3.3	0.02
西藏	5.4	5.4	5.3	5.3	5.5	5.7	0.04
内蒙古	3.3	3.3	3.5	3.5	3.9	4.1	0.16
全国	3.3	3.3	3.4	3.3	3.5	3.7	0.06

高加热作用有关；秋、冬季中国各地地气温差总体呈纬向型分布，南高北低，尤其是冬季北方部分地区地气温差为负值，与这些地区冬季地表多为冰雪覆盖、反照率大，同时浅层土壤为冻土，还需要吸收地表的大量热量有关。周连童等 [10,19,35] 分析指出，西北地区地气温差以及感热对我国夏季降水有着明显的影响。那么，我国不同区域地气温差的这种分布特征是否也会对各地的夏季或全年的降水产生明显的影响也是今后需要进一步研究分析的问题。

(2) 年内各月，中国多年平均地气温差均为正值，其中 1 月份和 12 月份相对较小，6—8 月份（夏季）相对较大。中国不同地区由于地理环境和下垫面热力状况等的差异，地气温差的年内分布特征有所不同，东北、华北和内蒙古地区在 1 月份和 12 月份均为负，2 月和 11 月接近 0 ℃，黄淮和西北地区在 1 月、11 月和 12 月份均接近 0 ℃，上述地区其余月份平均地气温差均在 0.5 ℃以上，最大值也均出现在雨季来临前的 6 月份；西藏地区地气温差年平均值为全国最大，年内地气温差最小值出现在 12 月份，最大值出现在雨季来临前的 5 月份；江淮、江汉、江南、华南地区地气温差最小值出现在 12 月份或 1 月份，最大值均出现在雨季过后的 7 月份或 8 月份；西南地区年内各月地气温差变化相对较小，在雨季之前的 5 月份和雨季之后的 8 月份出现 2 次峰值，呈双峰型分布。我国各地地气温差的这种年内变化特征与各地太阳辐射的年内分布特征非常相似，这与 Song 等 [36] 有关地气温差的变化受太阳辐射影响最为显著的研究成果是一致的。其中西北地区、西南地区和西藏地区等地地气温差的这种年内变化规律，与前人的研究结果也是基本一致的。

(3) 1961—2016 年，中国区域平均地气温差 4 月和 4—10 月上升趋势较明显，而 7 月和 10 月变化趋势不明显或略有上升趋势。空间分布上，东北、西北及内蒙古、西藏西部等地平均地气温差有增加趋势，而中东部地区有减小趋势。4—10 月，全国平均地气温差线性变化趋势为 0.06 ℃/10a，但是不同地区变化趋势又有所不同，其中东北、西北及内蒙古大部和西藏西部地区平均地气温差线性变化趋势 >0.10 ℃/10a，内蒙古地区平均达 0.16 ℃/10a；华北、黄淮、江淮、西南和西藏大部地区平均地气温差变化趋势不明显；南方的江汉、江南和华南地区平均地气温差均有下降趋势，线

性变化趋势均≤−0.05 ℃/10a。地气温差的变化是由地温和气温的变化共同决定的，在不同的季节，地温和气温对地气温差年代际变化的贡献程度也不同。同时，因为地温和气温的变化受到诸多因素的影响，并且二者之间也存在着复杂的相互作用和联系，所以关于地气温差年代际变化的机理问题有待进一步的研究分析。■

参考文献

[1] 郑景云 , 卞娟娟 , 葛全胜 , 等 . 1981—2010 年中国气候区划 [J]. 科学通报 , 2013, 58: 3088-3099. Zheng J Y, Bian J J, Ge Q S, *et al*. The climate regionalization in China for 1981−2010 [J]. Chinese Science Bulletin, 2013, 58: 3088-3099 (in Chinese)

[2] 张强 , 胡隐樵 . 绿洲地理特征及其气候效应 [J]. 地球科学进展 , 2002, 17 (4): 477-486. Zhang Q, Hu Y Q. The geographical features and climatic effects of oasis [J]. Advance in Earth Science, 2002, 17 (4): 477-486 (in Chinese)

[3] 张强 , 胡隐樵 , 曹晓彦 , 等 . 论西北干旱气候的若干问题 [J]. 中国沙漠 , 2000, 20 (4): 357-362. Zhang Q, Hu Y Q, Cao X Y, *et al*. On some problems of arid climate system of Northwest China [J]. Journal of Desert Research, 2000, 20 (4): 357-362 (in Chinese)

[4] 张强 , 黄荣辉 , 王胜 , 等 . 西北干旱区陆—气相互作用试验 (NWC-ALIEX) 及其研究进展 [J]. 地球科学进展 , 2005, 20 (4): 427-441. Zhang Q, Huang R H, Wang S，*et al*. NWC-ALIEX and its research advances [J]. Advance in Earth Science, 2005, 20 (4): 427-441 (in Chinese)

[5] 叶笃正 , 高由禧 . 青藏高原气象学 [M]. 北京 : 气象出版社 , 1979: 1-278. Ye D Z, Gao Y X. The meteorology of Tibet Plateau [M]. Beijing: China Meteorological Press, 1979: 1-278 (in Chinese)

[6] 周连童 . 欧亚大陆干旱、半干旱区春夏季感热通量的时空变化特征 [J]. 大气科学学报 , 2010, 33 (3): 299-306. Zhou L T. Characteristics of temporal and spatial variability of sensible heat flux in the arid and semi-arid region of Eurasia [J]. Transactions of Atmospheric Sciences, 2010, 33 (3): 299-306 (in Chinese)

[7] 沈学顺 , 木本昌秀 . 春季欧亚大陆地表气温变化特征的气候意义 [J]. 大气科学 , 2007, 31 (1): 19-27. Shen X S, Masahide K. Studies of the interannual variability of springtime Eurasian surface air temperature [J]. Chinese Journal of Atmospheric Science, 2007, 31 (1): 19-27 (in Chinese)

[8] 周长春 , 高晓清 , 陈文 , 等 . 中亚感热异常对我国西北温度、降水的影响 [J]. 高原气象 , 2009, 28 (2): 395-401. Zhou C C, Gao X Q, Chen W, *et al*. The impact of sensible heat flux anomaly over Central Asia on temperature and precipitation in Northwest China [J]. Plateau Meteorology, 2009, 28 (2): 395-401 (in Chinese)

[9] 高荣 , 董文杰 , 韦志刚 . 西北干旱区感热异常对中国夏季降水影响的模拟 [J]. 高原气象 , 2008, 27 (2): 320-324. Gao R, Dong W J, Wei Z G. Numerical simulation of the impact of abnormity of sensible heat flux in northwest arid zone on precipitation in China [J]. Plateau Meteorology, 2008, 27 (2): 320-324 (in Chinese)

[10] Zhou L T, Huang R H. The interdecadal variability of summer rainfall in Northwest China and its possible causes [J]. International Journal of Climatology, 2010, 30 (4): 549-557

[11] Zhou L T, Hang R H. Regional differences in surface sensible and latent heat fluxes in China [J]. Theoretical and Applied Climatology, 2014, 116: 625-637

[12] Kalnay E, Kanamitsu M, Kistler R, *et al*. The NCEP/NCAR 40-year reanalysis project [J]. Bulletin of the American Meteorological Society, 1996, 77 (3): 437-471

[13] 周连童 . 比较 NCEP/NCAR 和 ERA-40 再分析资料与观测资料计算得到的感热资料的差异 [J]. 气候与环境研究 , 2009, 14 (1): 9-20. Zhou L T. A comparison of NCEP/NCAR, EAR-40 reanalysis and observational data of sensible heat in Northwest China [J]. Climatic and Environmental Research, 2009, 14 (1): 9-20 (in Chinese)

[14] 李玉梅 , 彭玉麟 , 简茂球 , 等 . 中国南方地表感热通量的时空变化 [J]. 热带气象学报 , 2014, 30 (6): 1027-1036. Li Y M, Peng Y L, Jian M Q, *et al*. Spatio-temporal variation of sensible heat flux over southern China [J]. Journal of Tropical Meteorology, 2014, 30 (6): 1027-1036 (in Chinese)

[15] Zhou L T, Huang R H. An assessment of the quality of surface sensible heat flux derived from reanalysis data through comparison with station observations in Northwest China [J]. Advances in Atmospheric Sciences, 2010, 27 (3): 500-512

[16] 范丽军 , 韦志刚 , 董文杰 . 西北干旱地区地气温差的时空特征分析 [J]. 高原气象 , 2004, 23 (3): 360-367. Fan L J，Wen Z G，Dong W J. The characteristic of temporal and spatial distribution of the differences between ground and air temperature in the arid region of Northwest China [J]. Plateau Meteorology, 2004, 23 (3): 360-367 (in Chinese)

[17] 张文纲 , 李述训 , 吴通华 , 等 . 青藏高原地气温差变化分析 [J]. 地理学报 , 2006, 61 (9): 900-910. Zhang W G, Li S X, Wu T H, *et al*. Changes of the differences between ground and air temperature over the Qinghai-Xizang Plateau [J]. Acta Geographica Sinica, 2006, 61 (9): 900-910 (in Chinese)

[18] Zhou L T, Wu R G, Huang R H. Variability of surface sensible heat flux over Northwest China [J]. Atmospheric and Oceanic Science Letters, 2010, 3 (2): 75-80

[19] 周连童 , 黄荣辉 . 中国西北干旱、半干旱区春季地气温差的年际变化特征及其对华北夏季降水年代际变化的影响 [J]. 气候与环境研究 , 2006, 11 (1): 1-13. Zhou L T，Huang R H. Characteristics of interdecadal variability of the difference between surface temperature and surface air temperature in spring in arid and semi-arid region of Northwest China and its impact on summer precipitation in North China [J]. Climatic and Environmental Research, 2006, 11 (1): 1-13 (in Chinese)

[20] 刘颖 , 徐祥德 , 施晓晖 . 春季地气温差与长江中下游夏季旱涝异常的相关 [J]. 气象科技 , 2009, 37 (3): 301-305. Liu Y, Xu X D, Shi X H. Distribution of differences between ground and air temperature in

www.climatechange.cn

spring and its impact on precipitation in mid-lower reaches of Yangtze River [J]. Meteorological Science and Technology, 2009, 37 (3): 301-305 (in Chinese)

[21] 艾丽坤 , 郭维栋 . 从地—气温差的长期变化检测中国北部土壤荒漠化 [J]. 地理学报 , 2003, 58 (S): 108-116. Ai L K, Guo W D. The desertification over North China through comparing the long-time variation of air temperature and 0 cm soil temperature [J]. Acta Geographica Sinica, 2003, 58 (S): 108-116 (in Chinese)

[22] 顾欣 , 张艳梅 , 黄大卫 . 近 50 年来黔东南地区浅层地气温差的时空特征分析 [J]. 中国农业气象 , 2012, 33 (1): 71-77. Gu X, Zhang Y M, Huang D W. Temporal and spatial characteristics of soil-air temperature difference (T_s-T_a) in southeast Guizhou last 50 years [J]. Chinese Journal of Agrometeorology, 2012, 33 (1): 71-77 (in Chinese)

[23] 符睿 , 韦志刚 , 文军 , 等 . 西北干旱地区地气温差季节和年际变化特征的分析 [J]. 高原气象 , 2008, 27 (4): 844-851. Fu R, Wei Z G, Wen J, *et al*. Analyses on characteristic of seasonal and interannual variation of difference between surface and air temperature (T_s-T_a) in arid region in Northwest China [J]. Plateau Meteorology, 2008, 27 (4): 844-851 (in Chinese)

[24] 王澄海 , 崔洋 . 东亚夏季风建立前青藏高原地气温差变化特征 [J]. 气候与环境研究 , 2011, 16 (5): 586-596. Wang C H, Cui Y. Characteristics of the difference of temperature between surface and atmosphere over the Tibetan Plateau in the early stage of East Asian summer monsoon onset [J]. Climatic and Environmental Research, 2011, 16 (5): 586-596 (in Chinese)

[25] 杨智 , 刘志刚 , 李娟 . 云南省地气温差时空变化特征分析 [J]. 云南大学学报 : 自然科学版 , 2010, 32 (S1): 289-293. Yang Z, Liu Z G, Li J. The characteristic of temporal and spatial distribution of the differences between ground and air temperature in Yunnan [J]. Journal of Yunnan University: Natural Sciences Edition, 2010, 32 (S1): 289-293 (in Chinese)

[26] 陈超 , 周广胜 . 1961—2010 年阿拉善左旗气温和地温的变化特征分析 [J]. 自然资源学报 , 2014, 29 (1): 91-103. Chen C, Zhou G S. Characteristics of air temperature and ground temperature in Alxa left Banner from 1961 to 2010 [J]. Journal of natural resources, 2014, 29 (1): 91-103 (in Chinese)

[27] 王超 , 韦志刚 , 李振朝 , 等 . 敦煌戈壁地区地气温差变化特征分析 [J]. 干旱区资源与环境 , 2011, 25 (11): 72-78. Wang C, Wei Z G, Li Z C, *et al*. The variation characteristics of difference between surface and air temperature in Dunhuang Gobi [J]. Journal of Arid Land Resources and Environment, 2011, 25 (11): 72-78 (in Chinese)

[28] 温李明 , 周连童 , 黄荣辉 , 等 . 我国东西部地区地气温差的年代际变化特征 [J]. 气候与环境研究 , 2014, 19 (5): 636-648. Wen L M, Zhou L T, Huang R H, *et al*. Characteristics of interdecadal variability in the difference between surface temperature and surface air temperature in Southeast and Northwest China [J]. Climatic and Environmental Research, 2014, 19 (5): 636-648 (in Chinese)

[29] 中国气象局 . 中国气象地理区划手册 [M]. 北京 : 气象出版社 , 2006: 1-72. China Meteorological Administration. Atlas of China disastrous weather and climate [M]. Beijing: China Meteorological Press, 2006: 1-72 (in Chinese)

[30] 中国气象局 . 地面气象观测规范 [M]. 北京 : 气象出版社 , 2003: 1-72. China Meteorological Administration. Specification for surface meteorological observation [M]. Beijing: China Meteorological Press, 2003: 1-72 (in Chinese)

[31] 魏淑秋 . 农业气象统计 [M]. 福州 : 福建科学技术出版社 , 1985: 1-377. Wei S Q. Agricultural meteorology statistics [M]. Fuzhou: Fujian Science and Technology Press, 1985: 1-377 (in Chinese)

[32] 丁一汇 . 高等天气学 [M]. 北京 : 气象出版社 , 2005: 1-217. Ding Y H. Advanced synoptic meteorology [M]. Beijing: China Meteorological Press, 2005: 1-217 (in Chinese)

[33] 杨智 , 刘劲松 , 朱以维 , 等 . 云贵高原西部大理地区近地层湍流特征分析 [J]. 大气科学学报 , 2010, 33 (1): 117-124. Yang Z, Liu J S, Zhu Y W, *et al*. Analyses of turbulence characteristics in the surface layer at Dali of the western Yunnan-Guizhou plateau [J]. Transaction of Atmospheric Sciences, 2010, 33 (1): 117-124 (in Chinese)

[34] 张家诚 . 中国气候丛书 : 中国气候总论 [M]. 北京 : 气象出版社 , 1991: 1-477. Zhang J C. A series of climate for China: climate of China [M]. Beijing: China Meteorological Press, 1991: 1-477 (in Chinese)

[35] 周连童 , 黄荣辉 . 中国西北干旱、半干旱区感热的年际变化特征及其与中国夏季降水的关系 [J]. 大气科学 , 2008, 32 (6): 1276-1288. Zhou L T, Huang R H. Interdecadal variability of sensible heat in arid and semi-arid regions of Northwest China and its relation to summer precipitation in China [J]. Chinese Journal of Atmospheric Sciences, 2008, 32 (6): 1276-1288 (in Chinese)

[36] Song J Y, Wang Z H, Myint S W, *et al*. The hysteresis effect on surface-air temperature relationship and its implications to urban planning [J]. Landscape and Urban Planning, 2017, 167: 198-211

The spatiotemporal characteristics and long-term trends of surface-air temperatures difference in China

LIAO Yao-Ming[1], CHEN Deliang[2], LIU Qiu-Feng[1]

1 *Laboratory for Climate Studies, National Climate Center, China Meteorological Administration, Beijing* 100081*, China*;
2 *Department of Earth Sciences, University of Gothenburg, Gothenburg* 40530*, Sweden*

Abstract: In this study, we analyzed the temporal and spatial distributions and long-term linear trend of surface-air temperatures difference (ΔT) in China. The values of ΔT were calculated based on the daily surface and air temperature measured at 825 weather stations from 1961 to 2016. The results showed that the annual ΔT was above 2.5 ℃ in most of western China and parts of South China, while below 2.5 ℃ in most of central and eastern China. In spring and summer, the ΔT was positive and generally distributed meridionally, high in western China and low in eastern China. In autumn and winter, the ΔT was generally distributed zonally, high in southern China and low in northern China. Especially in some areas of northern China, ΔT was negative in winter. The average monthly ΔT in China was positive, but it was relatively low in winter (January and December) and high in summer. The intra-annual distribution characteristics of ΔT varied across regions. The annual ΔT in Tibet was the highest in China with the maximum in May prior the rainy season. The regional average ΔT in the Northeast China, North China, Huanghuai region, Northwest China and Inner Mongolia reached the peak in June before the arrival of the rainy season. The maximum ΔT appeared in July or August after the rainy season in Yangtze-Huaihe region, Jianghan, south of the Yangtze River and South China. The monthly ΔT in Southwest China had smaller change and had two peaks respectively in May before the rainy season and August after the rainy season. From 1961 to 2016, the countrywide mean ΔT displayed an upward linear trend in April and from April to October, while there was no significant linear trend in July and October. The ΔT had an increasing trend in Northeast China, Northwest China, Inner Mongolia, and western Tibet, while a decreasing trend was identified in central and eastern China.

Keywords: Surface-air temperature difference; Spatiotemporal distribution; Climate change; China

中国农学通报 2019,35(23):84-90
Chinese Agricultural Science Bulletin

凤县花椒生产气候条件和灾害分析

廖要明[1],杨文平[2]
([1]中国气象局气候研究开放实验室/国家气候中心,北京 100081;[2]陕西省凤县气象局,陕西凤县 721700)

摘 要:为实现对花椒生产的气候生态适应性定量评估,从花椒生长气候影响条件和主要气象灾害2个方面构建花椒生产的气候影响评价指标体系,在此基础上,根据凤县1961—2018年长序列的逐日气温、降水和日照等气候资料,对凤县花椒生产的气候条件和主要气象灾害进行系统分析。结果表明,1961—2018年凤县所有年份的年平均气温、降水量和日照时数均处于花椒种植的适宜范围,其中年平均气温、日照时数和降水量分别有89.7%、87.9%和77.6%的年份处于最适范围。凤县花椒生长季≥0℃积温、开花至果实着色期≥0℃积温、果实膨大生长期平均气温和果实着色期气温日较差所有年份均处于适宜范围,其中开花至果实着色期≥0℃积温和果实着色期气温日较差所有年份均处于最适范围;果实着色期平均气温和开花至果实膨大生长期降水量也有75%以上的年份处于适宜范围,其中65%以上年份处于最适范围;果实膨大至着色期相对湿度条件相对较差,处于适宜和最适范围的年份分别为65.5%和24.1%。总体来说,凤县花椒生长季气候条件适宜,有利于花椒产量和品质的提高。凤县花椒生产过程中主要的气象灾害有干旱、低温冷冻害和连阴雨等,但是1961—2018年这些灾害均有减轻的变化趋势。

关键词:花椒;气候条件;气候灾害;评价指标;凤县
中图分类号:S162.3 **文献标志码:**A **论文编号:**casb19030104

Analysis of Climate Condition and Disaster for Chinese Prickly Ash Production in Fengxian County

Liao Yaoming[1], Yang Wenping[2]
([1]*Laboratory for Climate Studies, China Meteorological Administration/ National Climate Center*, Beijing 100081;
[2]*Meteorological Bureau of Fengxian County*, Fengxian Shaanxi 721700)

Abstract: The paper aims to quantitative assessment of climatic and ecological adaptability of Chinese prickly ash production in Fengxian county. The assessement index system of climatic impact for Chinese prickly ash production was constructed from the aspects of climatic impact conditions and main climate disasters. Based on the assessement index system, climate conditions and disasters of Chinese prickly ash production in Fengxian county of Shaanxi Province was analyzed with daily temperature, precipitation and sunshine hours history data from 1961 to 2018. The results showed that from 1961 to 2018, the annual temperature, precipitation and sunshine hours of all yeas in Fengxian county were in the suitable range for Chinese prickly ash cultivation, especially with 89.7% years of annual temperature, 87.9% years of annual sunshine hours and 77.6% years of annual precipitation are in the optimum range. All the years with accumulated temperature above 0℃ during growing season and from flowering to fruit coloring period, average temperature during fruit enlargement growth period, average diurnal temperature range during fruit cloring period in Fengxian county were in the suitable range, and all the years with accumulated temperature above 0℃ from flowering to fruit coloring period and average diurnal temperature range during fruit coloring period were in the optimum range. Average temperature

基金项目:国家重点研发计划项目"京津冀超大城市和城市群的气候变化影响和适应研究"(2018YFA0606304);国家重点研发计划项目"小麦生产系统对气候变化的响应机制及其适应性栽培途径"(2017YFD0300201);公益性行业(气象)科研专项"干旱气象科学研究——我国北方干旱致灾过程及机理"(GYHY201506001)。

第一作者简介:廖要明,男,1972年出生,湖南邵阳人,高级工程师,博士,主要从事气候与气候变化对农业生产的影响以及气象灾害风险评估等研究。通信地址:100081 北京市海淀区中关村南大街46号 中国气象局国家气候中心,Tel:010-58991595,E-mail:lymzxr@cma.gov.cn。

收稿日期:2019-03-25,**修回日期:**2019-05-28。

during fruit coloring period and precipitation from flowering to fruit enlargement were in the suitable range for more than 75% of the years, of which more than 65% were in the optimum range. Compared with other climate conditions, the relative humidity from fruit enlargement growth to coloring stage were relatively poor, with 65.5% and 24.1% years in suitable and optimum range respectively. Generally speaking, the climate conditions in Fengxian county during the growing season of Chinese prickly ash were suitable, which was conducive to the improvement of yield and quality of Chinese prickly ash. The main climate disasters for production of Chinese prickly ash in Fengxian county included drought, freezing damage at low temperature and continuous rain. But these disasters had a mitigating trend from 1961 to 2018.

Keywords: Chinese prickly ash; climate condition; climate disaster; assessement index; Fengxian county

0 引言

花椒为芸香科花椒属落叶灌木或小乔木。花椒果实是中国八大调味品之一，具有极高的食用价值，同时还具有较高的药用价值。花椒具有速生、早实、实用性强、易栽培、好管理等特点，是山区群众脱贫致富奔小康的经济树种。同时由于花椒树根系发达，固土能力强，也是保护水土、防止水土流失的生态树种。花椒是集经济效益和生态效益于一体的理想造林树种[1-5]。

凤县隶属于陕西省宝鸡市，位于陕西省西南部，地处秦岭腹地，嘉陵江源头。凤县花椒具有1800多年的人工栽培历史，由于独特的自然气候条件，所产的大红袍花椒品质优良闻名全国，堪称花椒之极品，被人们誉之为“凤椒”。千百年来，“凤椒”以粒大、肉厚、色泽鲜红、形具似双耳、麻味悠久、清香浓郁而享誉全国，素有“香飘十里”之美誉，被誉为“花椒之王”。凤县花椒栽植面积超过3万hm^2，年产值超过5亿元，农民来自花椒产业的人均纯收入达7000余元，占全县农民人均纯收入的60%以上。凤县大红袍花椒和凤县先后获“国家地理标志保护产品”和“中国花椒之乡”等荣誉称号[6-9]。2018年底，全国气候与气候变化标准化技术委员会从凤县的气候条件、生态环境条件以及花椒品质等多个方面综合考虑，评定凤县花椒符合国家气候标志优质农产品标准，并授予国家气候标志。所以，系统构建花椒气候条件评价指标，分析凤县花椒生产的主要气候条件、气象灾害以及气候变化特征，可为当地及国内其他花椒产区的花椒生产和合理布局提供科学依据。

1 资料与方法

1.1 资料

陕西省凤县逐日降水量、平均气温、最高气温、最低气温和日照时数等气候资料来自国家气象信息中心。利用陕西省凤县1961—2018年逐日气候资料以及当地花椒生产的物候期资料[9]，结合花椒生产气候条件影响评价指标，统计凤县花椒生产各相关评价指标在适宜和最适范围出现的频率，进行当地花椒生产的气候条件分析；根据凤县花椒生产的主要气象灾害，结合花椒灾害气候评价指标，分析当地花椒生产的主要气象灾害及其变化特征。

1.2 花椒气候影响评估指标的确定

1.2.1 花椒生长气候评价指标 花椒属阳性喜温和树种，在年平均气温8~16℃的地方都可栽培，当年平均气温10~14℃时，花椒生长发育良好，结实正常，色味俱佳，成熟充分，可获得较高产量，其中最适的年平均气温为11~13℃[10-16]。花椒树耐旱性强，对水分的需求量并不是很大，年降水量400 mm以上，且分布比较均匀即可正常生长发育和结实，最适的年降水量为500~800 mm。如果降水过少，容易发生干旱灾害，造成花椒落花落果，影响产量；降水过多，土壤过于湿润，不利于花椒的生长，积水或冲淤造成土壤板结，可使椒树死亡[17-19]。花椒属于比较喜光的树种，要求年日照时数在1200 h以上，最适宜的范围为1500 h以上。充足的日照，一方面会使紫外线增多，有利于花椒着色，提高品质；另一方面会使光合产物增多，有利于椒果果肉增厚，提高产量[20-22]。

花椒的整个生育期主要包括发芽抽稍期、开花坐果期、果实膨大生长期、果实着色期、果实成熟采收期和越冬期，花椒的产量和品质与各时期的气候条件密切相关。其中气温是影响花椒生长发育和品质形成的重要气候因子，花椒生育期≥0℃积温一般要求在2000℃·d以上，最好在4100~5000℃·d，其中开花至果实着色期在1950℃·d以上时，生长发育良好，结实正常，色味俱佳，成熟充分，可获得高产优质。花椒不同生育期对温度的要求不同，其中在花椒果实膨大生长期，平均气温17~20℃最为适宜，低于15℃或高于30℃都会抑制果实的生长；果实着色成熟期是是花椒色泽、油腺、香气发育积累的过程，影响花椒品质的关键生育期，一般要求平均气温在18~24℃，最适宜温度为22~24℃，气温日较差应当在7.8℃以上，最好在8.5℃以

上[23-26]。花椒生长发育和产量、品质的形成，还与生育期间的降水密切相关，特别是开花至果实膨大生长期，花椒处于营养生长和生殖生长的并进期，椒树既要长叶生枝，又要开花结果，对水分的需求异常敏感。该时期降水量一般应该在70~180 mm，最适宜的降水量范围为80~150 mm，水分过多或过少都会影响花椒的正常生长发育和产量形成。相对湿度反映了空气的干湿状况，对作物的生长发育及收获、病虫害的发生等都有重要的影响。特别是花椒果实膨大至着色成熟期，是花椒品质形成的关键时期，空气相对湿度的大小对花椒品质形成影响很大。空气相对湿度较小(60%~70%)，多太阳散射光，有利于芳香油和麻味素的积累；而如果空气湿度过大(>75%)，降水过多，光照不足，会造成花椒色泽变淡，品质欠佳[27-30]。表1列出了影响花椒生长的主要气候指标及其适宜范围。

表1 花椒生长气候适宜性指标及范围

指标	适宜范围	最适范围
年平均气温/℃	10~14	11~13
年降水量/mm	≥400	500~800
年日照时数/h	≥1200	≥1500
生长季≥0℃积温/℃·d	≥2000	4100~5000
开花至果实着色期≥0℃积温/℃·d	≥1900	≥1950
果实膨大生长期平均气温/℃	15~21	17~20
果实着色期平均气温/℃	18~24	22~24
果实着色期气温日较差/℃	≥7.8	≥8.5
开花至果实膨大生长期降水量/mm	70~180	80~150
果实膨大至着色期相对湿度/%	60~75	60~70

1.2.2 花椒生长气象灾害指标 凤县花椒生产过程中最主要的气象灾害有干旱、春季低温冻害和连阴雨。干旱可造成花椒大量落花、落果，但降水过多又会使花椒树根系处于无氧呼吸状态而使椒树生长不良甚至死亡。由于3—7月是凤县花椒的主要生长季节，也是干旱的多发季，所以用3—7月的干旱日数来评价干旱灾害。凤县花椒春季冻害发生时间主要在3月下旬—4月中旬，往往造成花椒嫩芽和花器官冻伤甚至冻死，从而引起花椒减产，通常可以用日最低气温≤2℃的天数和极端最低气温作为低温灾害的评价指标[16,31-32]。花椒属比较耐旱树种，连阴雨天气往往造成土壤过多的积水，影响根系的透气性，严重时可使椒树死亡，还会引起病害增多，降低花椒的产量和品质。相关研究表明，花椒成熟采摘期降水量≥150 mm会造成花椒的成熟延迟，连续3天以上日降水量≥5 mm会对花椒采摘晾晒产生影响。所以以花椒成熟采摘期降水量≥150 mm、连续3天以上日降水量≥5 mm及最长连续降水日数作为连阴雨灾害的评价指标[19,24]。

2 结果与分析

2.1 气候条件分析

凤县属暖温带半湿润山地气候，常年(1981—2010年，下同)平均气温11.7℃，最暖年平均气温为12.8℃(2006年)，最冷年为10.7℃(1976年、1984年)，均处于花椒种植的适宜温度范围(10~14℃)。1961—2018年，凤县年平均气温总体呈升高趋势，线性升高速率为0.21℃/10年；58年中，凤县有52年平均气温处于花椒生长发育最适的温度范围11~13℃，占总年数的89.7%(图1)。

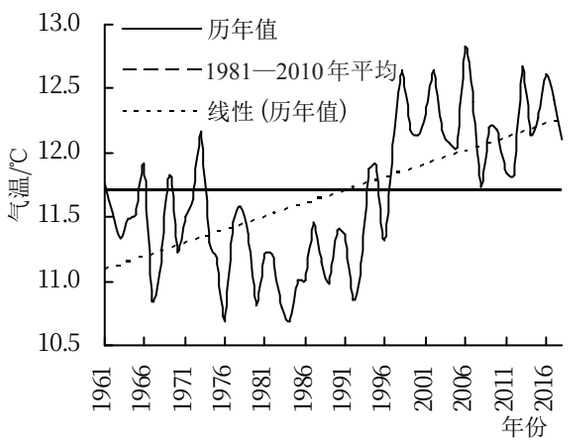

图1 1961—2018年凤县年平均气温历年变化

凤县常年平均年降水量636.7 mm，最多年达972.4 mm(1981年)，最少年只有400.2 mm(2002年)，最多年是最少年的2倍多，但均处于花椒生长发育的适宜年降水量范围。1961—2018年，凤县年降水量有略微增加的趋势，增加速率为1.62 mm/10年；58年中，凤县年降水量有45年处于花椒生长发育最适宜范围(500~800 mm)，占总年数的77.6%(图2)。

凤县常年日照时数为1614.3 h，平均每天日照时间4.4 h；但年际间变化较大，最多年日照时数有2076.2 h(1977年)，最少年只有1391.2 h(1989年)，最多年比最少年多将近700 h，但都处于花椒生长发育的适宜年日照时数范围。1961—2018年，凤县年日照时数在花椒生长发育最适的日照时数范围(≥1500 h)的有51年，占总年数的87.9%，但有明显的减少趋势，减少速率达57.5 h/10年(图3)。

凤县花椒生长季≥0℃的活动积温常年平均为4140.8℃·d，1992年最少，为3834.1℃·d，2002年最多，

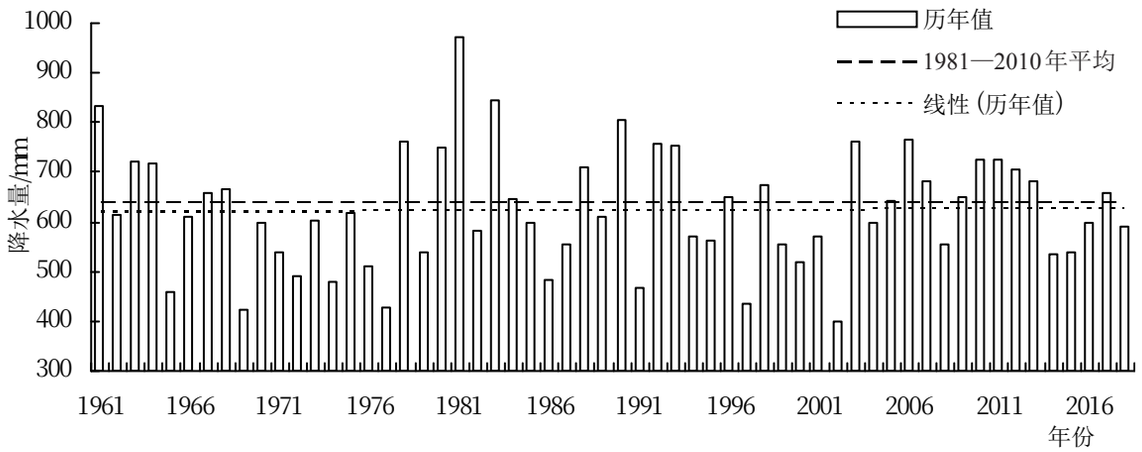

图2 1961—2018年凤县年降水量历年变化

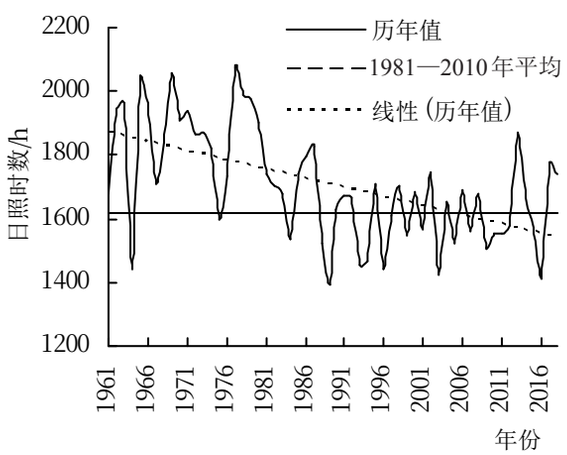

图3 1961—2018年凤县年日照时数历年变化

达4587.6℃·d,均处于花椒适宜生长发育的积温范围。1961—2018年,凤县花椒生长季≥0℃的活动积温呈显著的增多趋势,增多速率达54.3℃·d/10年,其中有37年在4100~5000℃·d,处于花椒生长发育最适的积温范围,占总年数的63.8%,特别是1997年以来,连续22年≥0℃活动积温均处于花椒生长发育的最适范围(图略)。4月下旬—8月上旬是凤县花椒开花至果实着色期,该时期凤县≥0℃的活动积温在2000~2400℃·d,常年平均为2215.2℃·d,均处于花椒生长发育最适的积温范围内。

5月中旬—6月上旬,凤县花椒处于果实膨大期。1961—2018年,凤县花椒果实膨大生长期平均气温均在16℃以上,其中处于最适温度范围17~20℃的年份有51年,占总年数的87.9%,并且该时期凤县平均气温有略微升高的趋势,对当地的花椒生产有利。果实着色成熟期是花椒品质形成的关键时期,气温适宜,气温日较差大,有利于芳香油和麻味素的积累,凤县花椒果实着色期一般在7月中旬—8月上旬。1961—2018年,凤县花椒果实着色期平均气温均在18℃以上,其中处于最适温度范围22~24℃的年份有42年,占总年数的72.4%。凤县花椒着色期气温日较差常年平均为11.7℃,远超最适的下限范围;1961—2018年,凤县花椒果实着色期气温日较差9.3~15.2℃,处于最适的气温日较差范围内。

4月下旬—6月上旬,凤县花椒处于开花至果实膨大生长期,该时期凤县常年平均降水量为99.3 mm,处于最适的降水量范围。1961—2018年,凤县花椒开花至果实膨大生长期降水量有增多趋势,其中在70~180 mm的年份有45年,占总年数的77.6%;处于最适降水量80~150 mm的有39年,占总年数的67.2%。

5月中旬—8月上旬,凤县花椒处于果实膨大至着色成熟期,该时期相对湿度常年平均为73.8%,较最适范围(60%~70%)偏高,但也处于适宜范围(60%~75%)内;1961—2018年,凤县花椒果实膨大至着色成熟期平均相对湿度有增大的趋势,其中在60%~75%的年份有38年,占总年数的65.5%。

表2详细列出了1961—2018年凤县花椒气候适宜性条件的线性变化趋势及不同适宜程度出现年数的百分率。总体来说,凤县气候条件非常适宜花椒的生长,大部分指标所有年份均处于适宜范围,其中最适宜的年份在70%以上。

2.2 灾害性天气气候条件分析

2.2.1 干旱 凤县年平均中旱及以上干旱日数为45.1天,主要集中在3—7月,正好也是花椒的主要生长季节,其中5月干旱日数最多,达7.8天,1月和2月基本没有中度及以上干旱发生(图4)。3—7月,凤县中度及以上干旱发生日数平均为29.1天,占全年干旱日数

表2 1961—2018年凤县花椒气候适宜性气候条件线性变化趋势及不同适宜程度出现年数占比

指标	线性趋势	适宜占比/%	最适占比/%
年平均气温	0.21℃/10年	100	89.7
年降水量	1.62 mm/10年	100	77.6
年日照时数	57.5 h/10年	100	87.9
生长季≥0℃积温	54.3℃·d/10年	100	63.8
开花至果实着色期≥0℃积温	10.1℃·d/10年	100	100
果实膨大生长期平均气温	0.04℃/10年	100	87.9
果实着色期平均气温	0.11℃/10年	86.2	72.4
果实着色期气温日较差	-0.03℃/10年	100	100
开花至果实膨大生长期降水量	2.11 mm/10年	77.6	67.2
果实膨大至着色期相对湿度	0.32%/10年	65.5	24.1

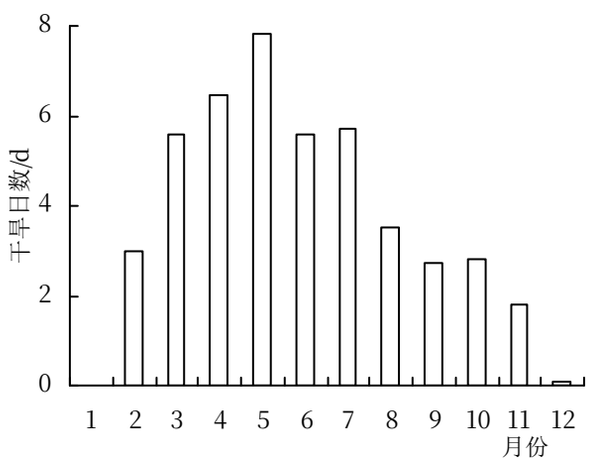

图4 凤县常年各月中旱及以上干旱日数

的64.5%。4—5月是凤县花椒的需水关键期，同时也是干旱的多发期，平均每月中度及以上干旱日数在6~8天，需要积极防范干旱对花椒生产的不利影响。

1961—2018年，凤县3—7月中旱及以上干旱日数总体呈减少趋势，减少速率为4.4天/10年。其中干旱日数最多的年份达111天（2001年），年干旱日数在60天以上的有10年，在30~60天的有14年（图5）。

2.2.2 低温冷冻害 凤县地处秦岭腹地，位于亚热带与温带的分界线，气温多变，低温冷冻害是影响该地区花椒生产最主要的气象灾害之一，其中春季低温往往造成花椒嫩芽和花器官冻伤甚至冻死，从而引起花椒减产。春季低温冷冻害发生时间主要在3月下旬—4月中旬，该时期凤县常年日最低气温≤2℃的日数为5.4天，最多年有12天（1962年、1987年和1990年）。1961—2018年，凤县日最低气温≤2℃的低温日数和极端最低气温分别有减少和上升的趋势（图6），减少和上升速率为0.54天/10年和0.36℃/10年，低温日数减少、极端最低气温上升，低温灾害有减轻的趋势，对当地的花椒生产有利。

2.2.3 连阴雨 1961—2018年，凤县花椒成熟采摘期降

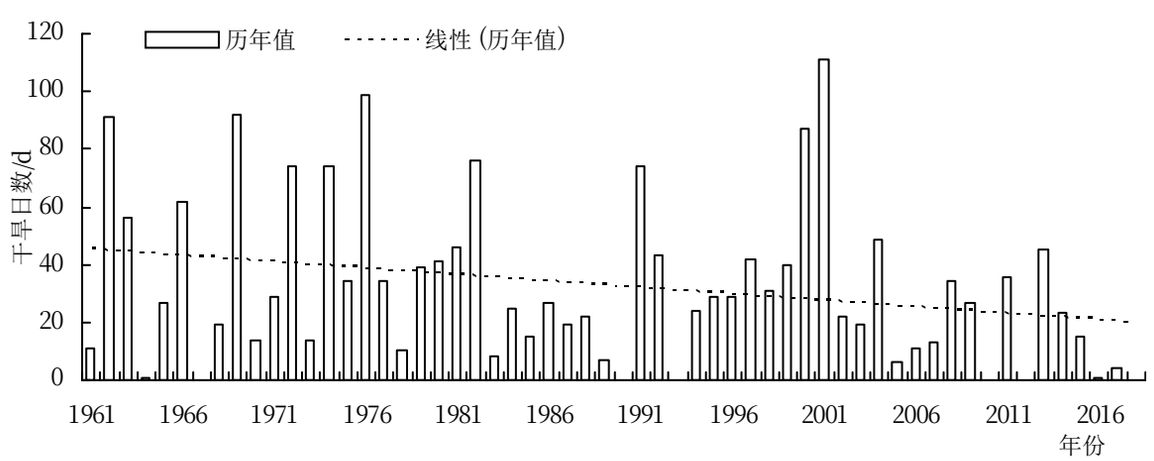

图5 1961—2018年凤县3—7月中旱及以上干旱日数历年变化

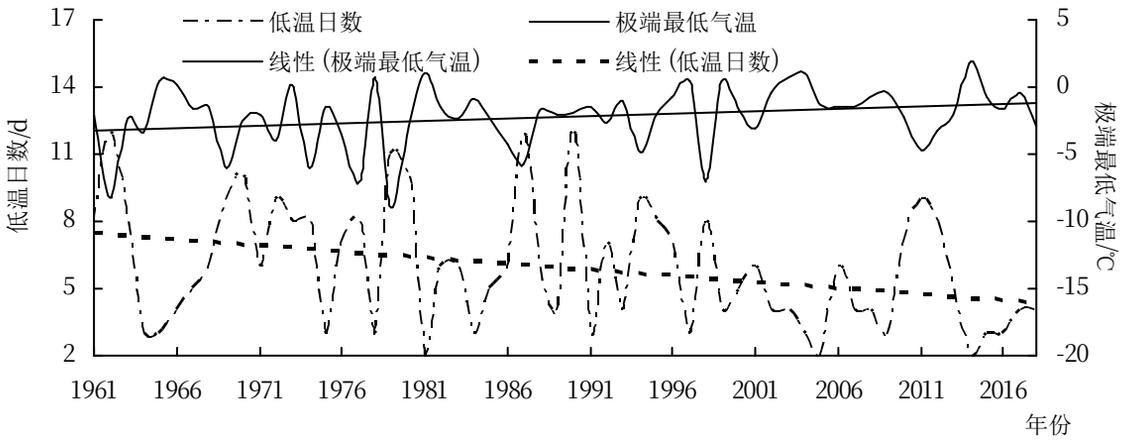

图6 1961—2018年凤县3月下旬—4月中旬低温日数和极端最低气温历年变化

水量≥150 mm的年数有20年,日降水量≥5 mm连续3天及以上的年数有21年,分别占总年数的34.5%和36.2%;最长连续降水日数常年平均为5.3天,最多年达14天,最少年只有2天(图7)。其中1981年降水量最多,达494.1 mm,远超过150 mm的标准,最长连续降水日数达14天,日降水量≥5 mm连续天数达8天,均为历史同期最长,持续连阴雨天气严重影响花椒的成熟采摘,也对花椒品质造成较大影响。1961—2018年,凤县花椒成熟采摘期降水量和日降水量≥5 mm持续日数以及最长连续降水日数均有减少的趋势,说明连阴雨灾害的风险有降低趋势。

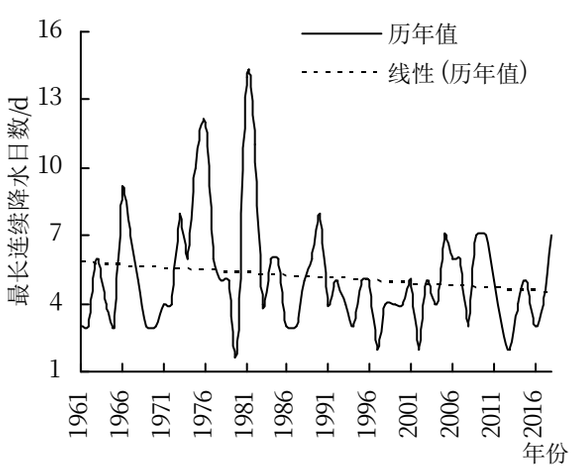

图7 1961—2018年凤县花椒成熟采摘期最长连续降水日数历年变化

3 结论

(1)凤县气候条件非常适宜花椒的种植。1961—2018年,凤县所有年份年平均气温、降水量和日照时数均处于花椒种植的适宜范围,其中年气温和日照时数分别有89.7%和87.9%的年份为最适范围,降水量有77.6%的年份处于最适范围。凤县应当根据当地山区地形地貌复杂多变、海拔高差较大的特点,结合花椒的生理生态适应性,建立优质花椒生产产业基地,以提高花椒质量和效益为核心,加强新建椒园管理,进一步提高凤县花椒的产量和质量。

(2)1961—2018年,凤县花椒生长季≥0℃积温、开花至果实着色期≥0℃积温、果实膨大生长期平均气温和果实着色期气温日较差所有年份均处于适宜范围,其中开花至果实着色期≥0℃积温和果实着色期气温日较差所有年份均处于最适范围;果实着色期平均气温和开花至果实膨大生长期降水量也有75%以上的年份处于适宜范围,其中65%以上年份处于最适范围;果实膨大至着色期相对湿度条件相对较差,处于适宜和最适范围的年份分别为65.5%和24.1%。总体来说,花椒生长季凤县气候条件适宜,有利于花椒产量和品质的提高,当地应当合理利用和保护农业气候资源,在充分考虑各地气候资源、气候承载力和生态系统功能的基础上,优化产业布局,充分挖掘独特的气候优势。

(3)凤县花椒生产过程中主要的气象灾害有干旱、低温冷冻害和连阴雨等,但是1961—2018年这些灾害均有减轻的趋势。当地政府应当针对不同的气象灾害,研究制定科学的防护措施,降低灾害对花椒生产的不利影响,加强气象灾害的监测、预测和风险评估,提高花椒生产应对气候变化的能力,实现凤县优质花椒生产的可持续发展。

4 讨论

花椒是国内重要的特色农产品,具有很高的经济价值和药用价值。笔者综合大量文献调研,系统构建了花椒生产的气候生态适宜性评价指标体系,对于国

内花椒生产和合理布局有重要意义。凤县地处秦岭腹地、嘉陵江源头，是秦岭绿色屏障的重要组成部分，同时也是重要的优质花椒产地，分析花椒生产的气候优势可以为当地花椒生产提供科学依据。

由于凤县长序列气象观测资料只有凤县国家基本站，自动气象观测站虽然较多，但资料序列长度较短。笔者只是基于凤县国家基本站一个站点的分析结果，可以为当地的花椒生产和布局提供参考。但凤县地势从北向南、自东向西倾斜，山谷台地纵横交错，各地气候差异较大。为了更好地指导花椒生产，将来可以借助区域气候模式等更精细化的气候资料，对当地花椒生产的气候生态适宜性做进一步研究。

参考文献

[1] 蒲淑芬,原双进,马建兴.花椒丰产栽培技术[M].西安:陕西科技出版社,2002:1-10.

[2] 陈旅,杨途熙,魏安智,等.花椒研究概况[J].中国调味品,2016,41(10):149-156.

[3] 肖正春,张卫民.花椒的主要品种及其开发利用[J].中国野生植物资源,2016,35(1):60-63.

[4] 叶友恩.花椒干旱造林研究[J].甘肃林业科技,2008,33(1):62-64.

[5] 原野.陕西花椒产业发展现状及对策[J].陕西林业科技,2018,46(1):74-76.

[6] 刘谆.凤县花椒产业发展成效和策略[J].陕西林业科技,2015(2):55-57,62.

[7] 景海斌,张开慧,尚婧.凤县花椒栽培现状及发展前景探究[J].山西农经,2017(4):53-54.

[8] 张开慧,尚婧,景海斌.凤县大红袍花椒产业发展存在的问题及对策[J].农业科技与信息,2017(10):11,13.

[9] 郑瑞华.凤县花椒年周期管理工作要点[J].陕西林业科技,2013(4):103-105.

[10] 狄彩霞,王正银.影响花椒产量和品质的因素[J].中国农学通报,2004,20(3):179-181,189.

[11] 雷莉萍,韦娜,杨文莉.大红袍花椒适宜气候条件与高产栽培技术[J].陕西气象,2007 (6):31-33.

[12] 王广玉.甘肃省花椒生产中的气象因素影响分析及相应技术措施推广[J].甘肃科技,2015,31(22):148-151.

[13] 刘丽,张燕,孙畅,等.甘肃武都花椒生长气象条件分析及气候适应性区划研究[J].中国农学通报,2017,33(19):126-132.

[14] 任三学.陇南花椒生产的气候土壤条件和建议[J].甘肃农业科技,1990(1):18.

[15] 李霞.气象因素对临夏花椒生产的影响及相关技术的推广[J].中国林业产业,2017(4):304.

[16] 李小卫,贺文丽,张西玲.韩城大红袍花椒冻害分析及预防[J].陕西气象,2005(6):28-30.

[17] 任三学.陇南花椒种植气候条件分析[J].甘肃气象,1991(4):38-39.

[18] 张甫宪.汉源花椒与气候[J].农业科技通讯,1990(11):13.

[19] 李小卫.韩城花椒气候资源分析与气候区划[J].陕西气象,2013(6):28-30.

[20] 程敏,高阳华,杨世琦,等.重庆市花椒气候生态区划研究[J].西南师范大学学报:自然科学版,2016,41(6):53-59.

[21] 张福平,廖宇.文县种植花椒的气候条件分析[J].现代农业科技,2013(4):260.

[22] 吴宗兴,彭树松,刘治富.阿坝州大红袍花椒分布区气候简析[J].林业科技开发,1997(4):53-54.

[23] 余优森,任三学.陇南花椒品质气象条件和气候区划[J].中国农业气象,1995,16(6):32-34.

[24] 李小卫.花椒农业气象服务技术[J].现代农业科技,2013(18):239,241.

[25] 李智杰,孙德祥,邓振义,等.不同产地花椒多指标综合排序及环境因子影响分析[J].西北林学院学报,2006,21(5):74-77.

[26] 孙玉莲,边学军,韦伯龙,等.甘肃临夏地区花椒生态气候适应性分析与产量动态气候模型[J].西南农业学报,2014,27(2):846-851.

[27] 余优森,任三学.花椒果实膨大生长与品质的气象条件[J].气象,1994,20(7):50-54.

[28] 赵洁,孙恩虹,杨宝钢,等.吴滩"彬哥"花椒气候品质认证指标体系研究[J].江西农业,2017(14):65.

[29] 李三明,李恒茂.花椒生长与气象条件[J].陕西气象,2002(增刊):25-26.

[30] 肖志强,李小军,焦素慧,等.陇南山区特色农业气候适宜性区划研究[J].现代农业科技,2017(21):215-216,219.

[31] 解锋,张宏辉,康克功,等.凤县花椒冻害机理的研究及防御措施[J].陕西农业科学,2007(2):22,147.

[32] 李建军,聂义军.凤县花椒霜冻特点及御防[J].陕西气象,2009(2):32-35.

Theoretical and Applied Climatology (2019) 135:1295–1306
https://doi.org/10.1007/s00704-018-2430-8

ORIGINAL PAPER

Diagnosing the leading mode of interdecadal covariability between the Indian Ocean sea surface temperature and summer precipitation in southern China

Jingpeng Liu[1,2,3] · Hong-Li Ren[3,4] · Weijing Li[3] · Jinqing Zuo[3]

Received: 16 October 2017 / Accepted: 14 February 2018 / Published online: 7 March 2018
© Springer-Verlag GmbH Austria, part of Springer Nature 2018

Abstract
Precipitation in southern China during boreal summer (June to August) shows a substantial interdecadal variability on the timescale longer than 8 years. In this study, based on the analysis of singular value decomposition, we diagnose the leading mode of interdecadal covariability between the observational precipitation in southern China and the sea surface temperature (SST) in the Indian Ocean. Results indicate that there exist a remarkable southern China zonal dipole (SCZD) pattern of interdecadal variability of summer precipitation and an interdecadal Indian Ocean basin mode (ID-IOBM) of SST. It is found that the SCZD is evidently covaried with the ID-IOBM, which may induce anomalous inter-hemispheric vertical circulation and atmospheric Kelvin waves. During the warm phase of the ID-IOBM, an enhanced lower-level convergence and upper-level divergence exist over the tropical Indian Ocean, which is a typical Gill-Matsuno-type response to the SST warming. Meanwhile, the accompanied upper-level outflow anomalies further converge over the Indo-China peninsula, resulting in a lower-level anticyclone that contributes to reduction of the eastward moisture transport from the Bay of Bengal to the west part of southern China. In addition, the Kelvin wave-like pattern, as a response of the warm ID-IOBM phase, further induces the lower-level anticyclonic anomaly over the South China Sea–Philippines. Such an anticyclonic circulation is favorable for more water vapor transport from the East China Sea into the east part of southern China. Therefore, the joint effects of the anomalous inter-hemispheric vertical circulation and the Kelvin wave-like pattern associated with the ID-IOBM may eventually play a key role in generating the SCZD pattern.

1 Introduction

Southern China is one of the most populated agricultural regions in the world. The economy and the whole society in general are quite vulnerable to the variability in summer precipitation. Southern China summer precipitation (SCSP) exhibits variability on a broad range of timescales. Large interannual variability often causes precipitation to vary from year to year (e.g., Fu et al. 2017; Yuan et al. 2017), while the interdecadal variability always brings about persistent droughts and floods, which have great impacts on the societal and economic development (Liu et al. 2011). Thereby, studying the interdecadal variability of SCSP and understanding the underlying mechanisms are of great importance.

On the interdecadal timescale, many people have focused on summer precipitation over eastern and southern China in the recent two decades (Huang et al. 1999; Huang et al. 2006; Ding et al. 2008; Ding et al. 2009; Huang et al. 2011; Si and Ding 2016; Yang et al. 2017). Previous studies showed that there are two dominant meridional modes of interdecadal variability of summer precipitation in eastern China during the period of 1951–2004 (e.g., Ding et al. 2008; Huang et al. 2011). One is the meridional tripole pattern, with more precipitation over the middle and lower reaches of the Yangtze River but less precipitation over South and North China, and the other is the meridional

✉ Hong-Li Ren
renhl@cma.gov.cn

[1] Chinese Academy of Meteorological Sciences, Beijing 100081, China

[2] University of Chinese Academy of Sciences, Beijing 100049, China

[3] Laboratory for Climate Studies and CMA-NJU Joint Laboratory for Climate Prediction Studies, National Climate Center, CMA, Beijing 100081, China

[4] Department of Atmospheric Science, School of Environmental Studies, China University of Geoscience, Wuhan 430074, China

dipole pattern, which is usually referred to as the "southern flooding and northern drought" pattern (Ding et al. 2008; Huang et al. 2011; Yang et al. 2017). A further study of Ding et al. (2009) indicated that these two dominant modes could be attributed to the combined effects of abrupt increase in winter–spring snow cover over the Tibetan Plateau since around 1977 and significant interdecadal warming of SST in the tropical central and eastern Pacific Ocean that occurred in the mid-1960s, the late 1970s, and the early 1990s. Since the middle of the twentieth century, summer precipitation over eastern China has experienced three decadal variations, which occurred in the mid and late 1970s, early 1990s, and late 1990s, respectively (Xu et al. 2015). The abrupt shift of summer precipitation pattern over eastern China in the late 1970s is associated with the weakening of the East Asian summer monsoon (Wang 2001; Huang et al. 2006; Huang et al. 2011). In the early 1990s, summer precipitation over South China increased remarkably (Kwon et al. 2007; Ding et al. 2008), which could possibly be caused by the warming of the tropical Indian Ocean (IO) SST in summer and the increase in snow cover over the Tibetan Plateau in winter and spring (Wu et al. 2010). In the late 1990s, the decadal variation of summer precipitation over eastern China was probably associated with the shift of the Pacific Decadal Oscillation (PDO) from positive to negative phase.

The PDO is well known as the leading mode of decadal variability of Pacific SST (Mantua et al. 1997). Previous studies have revealed the impacts of the PDO on summer precipitation in China (Zhu and Yang 2003; Chan and Zhou 2005; Zhu et al. 2011; Qian and Zhou 2014; Yu et al. 2015). Qian and Zhou (2014) found that the drought index in North China is significantly negatively correlated with the PDO index during 1900–2010. Zhu et al. (2011) attributed the increased precipitation in the Huang-Huai River region and decreased precipitation in the Yangtze River region in the late 1990s to the phase shift of the PDO from warm to cold around 1999. Wu and Mao (2017) found that the wintertime PDO contributed to the interdecadal variability of South China monsoon rainfall in early summer via atmospheric and oceanic teleconnections during 1926–2013. Several recent studies also showed that the PDO contributed to the decadal variability of the meridional dipole pattern of summer precipitation in eastern China (Si and Ding 2016; Yang et al. 2017).

In addition, SST in the North Atlantic may also affect precipitation over eastern China on decadal timescale (Lu et al. 2006; Wang et al. 2009; Si and Ding 2016). The positive phase of Atlantic Multidecadal Oscillation (AMO) can lead to strengthened East Asian summer monsoon (Lu et al. 2006; Wang et al. 2009). Li et al. (2008) found that anomalous southerly winds in southeastern China are favorable for abnormally high precipitation in this region in the positive phase of AMO. The mid-high-latitude precipitation in eastern China is also sensitive to the North Atlantic SST forcing. The abrupt decrease in North China precipitation in the 1960s was proposed to be connected to the cooling of extra-tropical North Atlantic Ocean based on an AGCM simulation (Liu and Chiang 2012). Si and Ding (2016) revealed that AMO might lead to the decadal variability of East China summer precipitation by causing negative (positive) precipitation anomalies over the Yangtze River valley (Huanghe-Huaihe River valley) through a stationary circumglobal baroclinic wave train. Most of the previous studies by far have focused on the decadal variability of summer precipitation over the whole southern and eastern China. However, there has been relatively limited research focusing on precipitation variability in the west part of southern China (Cao et al. 2014). Thereby, it is quite important to focus on the interdecadal variability of precipitation in southern China by considering the summer precipitation over both the west and east parts of southern China, and to further discuss the primary features of the interdecadal variability of summer precipitation and the associated mechanisms.

Furthermore, AMO and PDO have been regarded as the two principal drivers for the interdecadal variability of summer precipitation over East China. However, some studies also emphasized the role of the IO in the interdecadal variability of SCSP (Wu et al. 2010; Zhang et al. 2016). Zhang et al. (2016) revealed that the South IO SST influenced the interdecadal changes of the East Asian summer monsoon, which was featured by a decrease in the late 1970s and an increase in the early 1990s of SCSP. An interdecadal cooling in the South IO could trigger anomalous vertical overturning circulation, which led to abnormal descending motion and a lower-level anticyclonic anomaly over the South China Sea–Philippines. Such a pattern of circulation anomaly would result in additional moist air transport into southern China and subsequent precipitation increase there. Wu et al. (2010) revealed that the equatorial IO SST had increased since the early 1990s, which led to the development of an anomalous lower-level anticyclone over the South China Sea and the Philippines, and as a result, the SCSP increased. So far, the impacts of PDO and AMO on summer precipitation in eastern and southern China have been well studied, whereas the impacts of the IO on southern China have been less investigated. Particularly, little study has been conducted to explore the characteristic responses of SCSP to the IO SST forcing and the associated mechanisms behind. Thus, the present study is focused on the interdecadal variability characteristics of SCSP and their connections with the IO SST.

The rest of this paper is organized as follows. Section 2 describes the datasets and methods used in this study. Section 3 investigates the leading mode of the interdecadal covariability between SCSP and IO SST. Section 4 describes the possible mechanisms through which SST anomalies in the IO can be physically connected with SCSP. Finally, the summary and discussion are presented in Section 5.

2 Datasets and methods

2.1 Datasets

In this study, 114 years of monthly precipitation data (1901–2014) are used to examine the interdecadal variability of summer (June to August, JJA) precipitation in southern China. The monthly precipitation data include monthly mean precipitation from the Climatic Research Unit (CRU, New et al. 2000) with a spatial resolution of 0.5° × 0.5° and monthly precipitation in China provided by National Meteorological Information Center of China Meteorological Administration on a grid of 5° × 5° for the period of 1901–2014 (NMIC, Li et al. 2012). Monthly mean sea surface temperature is provided by the Hadley Centre of the UK Met Office (HadISST, Rayner et al. 2003) for the period of 1847–2014. Monthly mean atmospheric fields are extracted from the NOAA-CIRES twentieth Century Reanalysis products (20CR, Compo et al. 2011) for the period of 1851–2014. The spatial resolutions of the HadISST datasets and the 20CR datasets are 2° × 2° and 1° × 1°, respectively. As SST observations in the tropical ocean are very sparse before 1920 (Dai 2013), analyses of the present study are focused on the period of 1920–2014.

2.2 Methods

2.2.1 Extracting interdecadal signal

Linear trends are removed first from all the data. Variabilities on the timescales shorter than 11 years are then filtered out using the Lanczos filter method (Duchon 1979). The anomalies relative to the climatology for the period of 1920–2014 are calculated. The anomalous precipitation and SST are normalized before analysis.

2.2.2 Significance tests

The significance test uses the Monte Carlo method (Livezey and Chen 1983). Considering time series A and B, the original time series A is randomly rearranged to obtain a new time series at each grid point. The correlation between this new atmospheric time series and time series B is then calculated. This progress is repeated for 1000 times and a distribution of correlation values at each grid point is finally obtained. The quoted significance level of the correlation between time series A and B indicates the percentage of randomized correlation coefficients that exceed the value being tested. The significance of regression coefficient is tested in the same way.

2.2.3 Singular value decomposition

The singular value decomposition (SVD) method (Bretherton et al. 1992) is used to identify major linear covariation modes between interdecadal variability of SCSP and SST anomalies in the IO. SVD is an algebraic technique to decompose arbitrary matrices in orthogonal matrices. It is easy to perform and requires no user-supplied parameters. To identify statistically significant modes from random noise, experiments with Gaussian-distributed random data are repeated 100 times, and variance contribution rates of the singular values at a significance level of 95% are obtained via the Monte Carlo method (Shen and Lau 1995).

3 Interdecadal covariation of SCSP with IO SST

First of all, the SVD analysis is implemented to reveal the spatially and temporally covariated mode between interdecadal SCSP and IO SST. Figure 1 shows the climatology and standard deviation of SCSP based on the original CRU precipitation data. It can be found that climatological summer precipitation is mainly distributed to the south of 30° N, where there are also relatively high values of standard deviation. The climatological precipitation gradually decreases from south to north, with values ranging between 5 and 10 mm day^{-1}.

For the interdecadal variability, the ratio of the interdecadal variance to the total variance of summer precipitation (Fig. 1(b)) is also calculated using spectrum analysis method (Thomson 1982). The ratio is as high as 40% in the west and east parts of southern China, which indicates the important role of the interdecadal variability in these areas. In contrast, the ratio in the Yangtze River basin is less than 20%, indicating that the interannual variation of summer precipitation is probably dominant there. Given the climatology of summer precipitation and the high ratio of its interdecadal variability to total variability, the region of southern China over the area (20° N–30° N, 99° E–120° E) is selected for the present study (see the black rectangle box in Fig. 2(a)).

In the SVD analysis, the left field is the normalized interdecadal SCSP, and the right field is the normalized IO SST anomalies (30° S–25° N, 40° E–105° E). The precipitation and SST are normalized by their area-averaged standard deviation. Results show that the first pair of SVD modes exceeds the noise level (not shown) and explains 61.3% of the total covariance. It is significantly larger than, and separated from, other SVD modes. Thereby, analyses will be focused on the first pair of SVD modes in the following sections.

As shown in Fig. 2(a), the first SVD mode of interdecadal SCSP displays an apparent zonal dipole pattern, which is termed as the southern China zonal dipole (SCZD) hereafter. The positive center with values larger than 0.6 is mainly

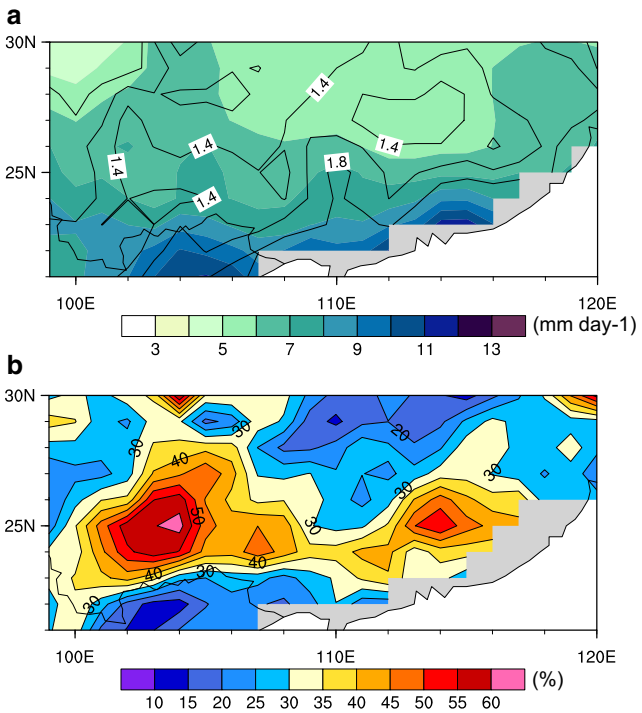

Fig. 1 (a) Climatological mean of summer precipitation (shading; mm day^{-1}) and corresponding standard deviations (contour; mm) based on the original CRU precipitation data for the period of 1920–2014, and (b) the ratio of interdecadal variance to total variance of precipitation (%) using CRU precipitation data. All plots were generated using NCL

located in the east part of southern China (ESC, 25° N–30° N, 110° E–120° E), and the negative center with values less than − 0.5 is mainly located in the west part of southern China (WSC, 25° N–30° N, 99° E–108° E). Thus, the positive phase of SCZD is characterized by increased (decreased) precipitation anomalies in the ESC (WSC), and vice versa. Such a spatial pattern is different from the well-known meridional dipole or tripole pattern in East China (Ding et al. 2008). The question is, what is the mechanism responsible for the SCZD?

The associated simultaneous SST field exhibits a basin-wide monopole pattern in the IO as shown in Fig. 2(b). This pattern is consistent with that revealed in the study by Dong et al. (2016), who showed that a basin-wide SST anomaly pattern was the dominant mode of IO decadal variability. The basin-wide monopole pattern revealed in the present study is similar to the conventional Indian Ocean basin mode (IOBM) defined on the interannual timescale (Yang et al. 2007; Yang et al. 2009; Zhu et al. 2015). Given this resemblance, the interdecadal basin-wide mode of Indian Ocean SST is termed as ID-IOBM. The warm (cold) phase of ID-IOBM is characterized by the warming (cooling) in the entire IO.

The correlation coefficient between the time series of SCZD (Fig. 2(c)) and ID-IOBM (Fig. 2(d)) is 0.79, which is significant at the 99% confidence level, suggesting that the interdecadal basin-wide mode in the IO is closely associated with the SCZD. When the ID-IOBM is in positive phase with above-normal SST over the entire IO, summer precipitation tends to be abundant in the ESC and deficient in the WSC.

To further confirm the SVD results, the NMIC data is used to calculate the average precipitation in the ESC and WSC (denoted by right and left green rectangle boxes in Fig. 2(a)). The difference between the normalized average precipitation in the ESC and WSC is defined as the SCZD index (the green line in Fig. 2(c)). The correlation coefficient between the SCZD index and Pre_TS1 is 0.87, which is significant at the 99% confidence level, indicating that the SCZD mode is robust in observational precipitation data. Meanwhile, the average SST anomaly in the IO is also calculated, which is defined as the ID-IOBM index (the black line in Fig. 2(d)). The correlation coefficient between the ID-IOBM index and the SST_TS1 is 0.99 (significant at the 99% confidence level).

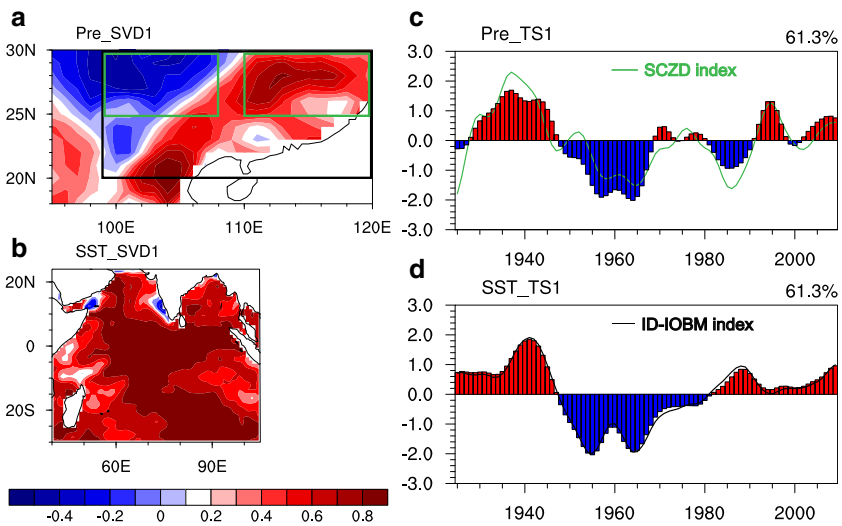

Fig. 2 First leading modes of SVD for JJA 11-year low-pass filtered CRU precipitation anomalies in southern China (a), SST anomalies in the IO (b) for the period of 1925–2009, and normalized time series of first SVD modes (c, d, bars). The green line in (c) denotes the SCZD index. The black line in (d) denotes the ID-IOBM index. The black rectangle box in (a) denotes the region of southern China. The left (right) green rectangle box in (a) denotes the region of west (east) part of southern China. All plots were generated using NCL

Moreover, the SCZD index and ID-IOBM index are significantly correlated with the correlation coefficient of 0.69. Hereafter, these two indices are used for further analyses.

Previous studies have demonstrated that the interdecadal variation of precipitation is always accompanied by atmospheric circulation variability (Zhu 2011; Xu et al. 2015). Therefore, summer atmospheric circulation patterns associated with the SCZD index are examined in the present study, and the upper-level and lower-level circulation patterns associated with the ID-IOBM index are investigated to verify the interdecadal connection between the SCZD and ID-IOBM.

The lower-level circulation anomalies associated with the SCZD index and the ID-IOBM index are shown in Fig. 3(c, d), respectively. In Fig. 3c, easterly wind anomalies prevail over the entire tropical IO and the Maritime Continent area, while an anomalous anticyclone exists over the Indo-China peninsula. At the west flank of the anticyclone are the significant easterlies, which may suppress moisture transport from the Bay of Bengal (BOB) to southern China. Figure 3(c) also shows a Pacific–Japan (PJ) wave-like pattern over East Asia. Moreover, an obvious anticyclonic anomaly is located over the tropical western North Pacific Ocean. To the north of the anticyclonic anomaly, there is a cyclonic anomaly appearing over southeastern China, which is favorable for the enhanced moisture transport from the East China Sea to southern China. Such a wave-like pattern resembles the PJ pattern initially defined on the interannual or intraseasonal timescales (Nitta 1987; Huang and Sun 1992). A recent study revealed that the interdecadal PJ pattern could be driven by negative convective heating anomalies over the tropical western North Pacific (Wu et al. 2016). They showed that the anomalous meridional circulation centers are distributed along 120° E, which was consistent with the result in the present study. Figure 3(d) shows that the PJ-like pattern is also visible over East Asia in the lower-level circulation anomalies associated with the ID-IOBM, indicating that such a circulation pattern is likely induced by the latter. The link between the PJ-like pattern and the ID-IOBM will be further discussed in Section 4.

The stream function pattern regressed against the SCZD index at 200 hPa is shown in Fig. 3(a). The most distinct signal in this field is the wave-like pattern along the Asian Westerly Jet Stream (AWJS), where two positive centers are located over west-central Asia and East China, respectively, and one negative center is located over Northwest China. Kuang et al. (2007) argued that the AWJS could act as the waveguide, and the Rossby wave energy propagated along the waveguide to downstream regions (Ambrizzi et al. 1995). The positive center over eastern China is favorable for upper-level divergence and accompanying ascending motion. Considering the upper-level circulation anomalies associated with the ID-IOBM, the most significant feature is the Rossby wave-like pattern along the AWJS at 200 hPa (Fig. 3(b)), which is similar to the wave-like pattern shown in Fig. 3(a). To verify this, we calculate the spatial correlation coefficient between regressed 200-hPa stream function patterns against the SCZD index and the ID-IOBM index, which is 0.92. Meanwhile, the spatial correlation coefficient between regressed 850-hPa wind patterns against the two indices reaches 0.93 (see Table 1), which validate the hypothesis to some degree that the ID-IOBM may be the main factor that leads to the SCZD.

In summary, the lower-level anomalous anticyclone over Indo-China peninsula may have an impact on the SCZD via suppressing the moisture transport from the BOB to southern China. Moreover, the anomalous cyclone over eastern China is favorable for more westward moist air transport from the ocean into southern China. Indeed, such lower-level circulation anomalies are closely connected with the ID-IOBM.

4 Possible mechanisms of interdecadal covariability between SCSP and IO SST

To further investigate the possible influence of the ID-IOBM on the SCZD and associated physical processes, regression and correlation analyses are performed in the present study. The results are shown in terms of a positive phase of the SCZD and a warm phase of the ID-IOBM, which also apply to a negative phase of SCZD and a cold phase of the ID-IOBM.

Figure 4(a) shows the regressed pattern of SST anomalies and wind anomalies at 850 hPa against the ID-IOBM index. It is clear that the entire IO experiences an apparent warming in the warm phase of the ID-IOBM. According to the study of Xie et al. (2009), such a warming pattern tends to trigger a Kelvin wave-like pattern, which subsequently induces northeasterly surface wind anomalies. The resultant subtropical divergence and suppressed deep convection favor to form an anomalous anticyclonic pattern in the northwest Pacific. In Fig. 4(a), it can be seen that an anomalous anticyclone is located over the South China Sea and to the east of the Philippines. To the north of the anticyclone, there is an anomalous cyclonic pattern appearing over southeastern China. To verify the existence of such a PJ-like pattern, we calculate the wave activity fluxes (Takaya and Nakamura 1997) associated with the ID-IOBM index for the lower troposphere. It is found in Fig. 4(b) that the poleward energy transport from the subtropical northwestern Pacific to East Asia is evident at 850 hPa, which is a typical property of the conventional PJ pattern, consistent with the results showed by Wu et al. (2016). To investigate the mechanism responsible for the PJ-like pattern, we show precipitation anomalies associated with the ID-IOBM in Fig. 4(c). As noted by Kosaka and Nakamura (2006), the anomalous convective heating to the east of the Philippines would induce the conventional PJ pattern, where the perturbation associated with the convective heating is able to propagate into the mid-latitudes in the form of Rossby waves in the lower troposphere. As shown in Fig. 4(c), a suppressed

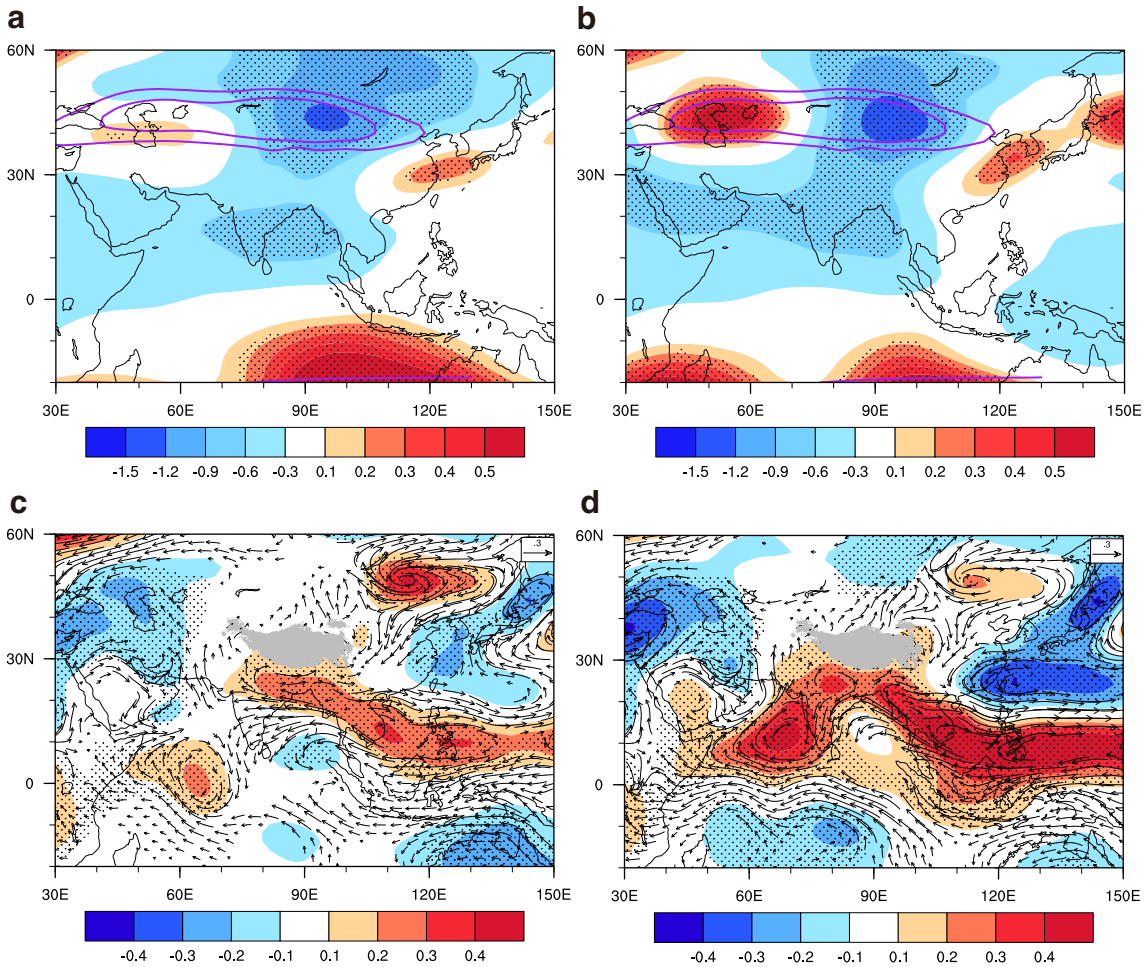

Fig. 3 Stream function (shading; 10^6 m^2 s^{-1}) at 200 hPa regressed against the SCZD index and the ID-IOBM index (a, b), and stream function (shading; 10^6 m^2 s^{-1}) and wind field (vectors; m s^{-1}) anomalies at 850 hPa in JJA (c, d). Purple contours in (a) and (b) denote the climatological means of 20 and 25 m s^{-1} zonal wind isoline at 200 hPa. Black dots denote areas significant at the 95% confidence level. All plots were generated using NCL

heating pattern that corresponds to the negative precipitation anomalies is located to the east of the Philippines, which may contribute to generation of the PJ-like pattern through the poleward propagation of perturbation as Rossby waves. Meanwhile, as we can see in Fig. 4(c), an enhanced precipitation center is located over southeastern China, which is probably associated with the abnormal cyclone center of the PJ-like pattern. Such a cyclonic circulation contributes to the increased westward moisture transport and subsequent moisture convergence in the east part of southern China. Therefore, the PJ-like pattern might be connected with the ID-IOBM through its Kelvin wave-like response pattern. Evidently, the cyclonic anomaly over southeastern China associated with the PJ-like pattern is favorable for higher than normal moisture transport into southern China.

Furthermore, Fig. 5 shows the regressed divergent wind and velocity potential against the SCZD index and the ID-IOBM index. Anomalous easterlies associated with the Kelvin wave are found over the entire tropical IO and the Maritime Continent region. The anomalous easterlies and northeasterlies from the BOB converge at the central tropical IO. A notable lower-level convergence and upper-level divergence in association with the ID-IOBM can be found over the central tropical IO (Fig. 5(b, d)). At the upper levels, outflows

Table 1 Spatial correlations between the patterns regressed against the SCZD index and the ID-IOBM index, respectively

200 hPa divergent wind	200 hPa stream function	850 hPa divergent wind	850 hPa stream function	850 hPa wind	Water vapor flux/ corresponding divergence
0.85	0.92	0.84	0.71	0.93	0.80/0.82

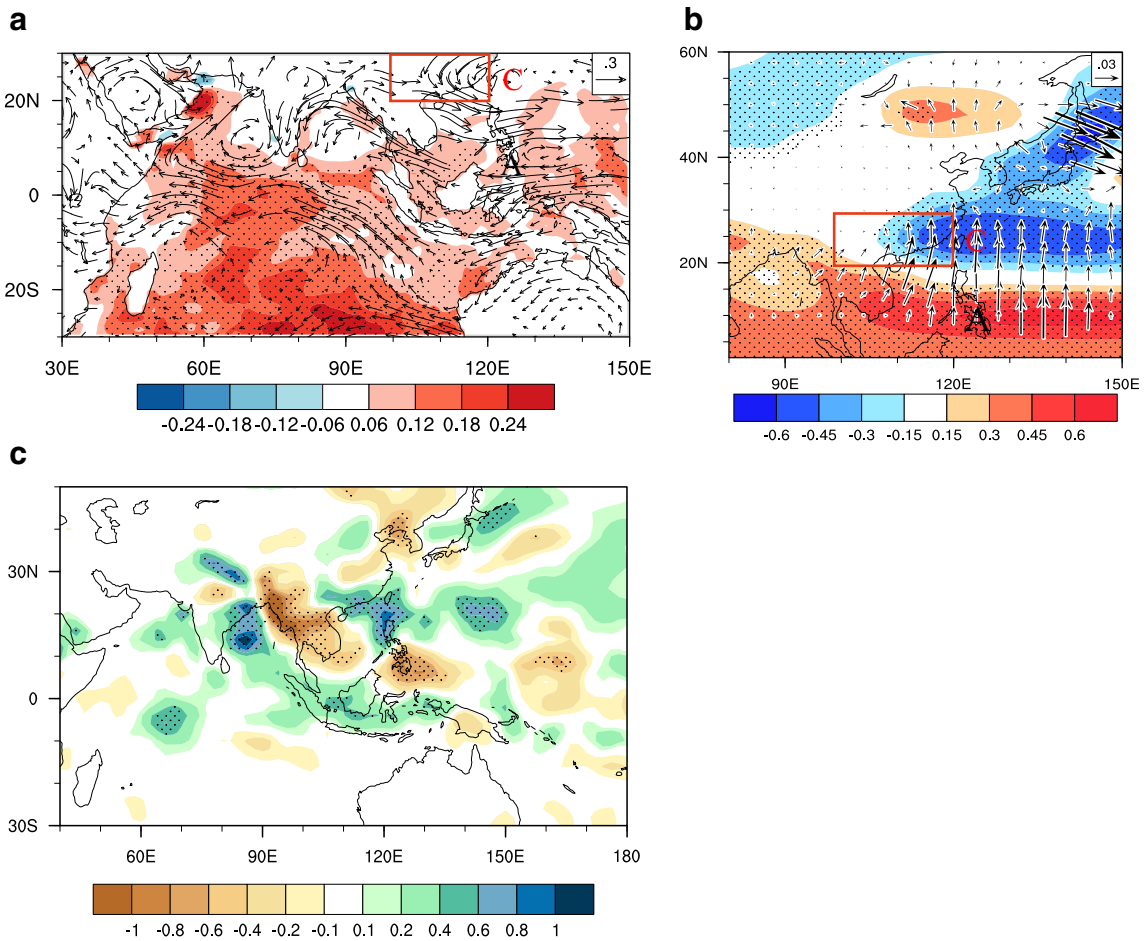

Fig. 4 (a) Regressions of SST anomalies (shading; °C) and wind anomalies (vectors; m s^{-1}) against the ID-IOBM index at 850 hPa in JJA for the period of 1925–2009. (b) Same as (a) but for stream function (shading; 10^{-6} m^2 s^{-1}) and wave activity flux (vectors; 10^{-6} m^2 s^{-2}). (c) Same as (a) but for precipitation (shading; 10^{-2} Pa s^{-1}). Black dots denote areas significant at the 95% confidence level. The rectangular box indicates southern China. "A" and "C" denote anticyclone and cyclone, respectively. All plots were generated using NCL

from the central tropical IO converge over the Indo-China peninsula, corresponding to a regional descending motion. Accompanying with such a descending motion, an anomalous anticyclone appears at 850 hPa over the Indo-China peninsula while abnormal easterlies occur in the northern BOB, both of which behave to decrease the moisture transport from the BOB to southern China (Fig. 3(c, d)). Thus, such an inter-hemispheric anomalous vertical circulation emerging between the central tropical IO and the Indo-China peninsula is likely responsible for forming the SCZD by reducing the moisture transport from the BOB to the west part of southern China. Figure 5 shows that the regressed divergent wind patterns associated with the ID-IOBM index exhibit patterns that are highly similar to those associated with the SCZD index. The spatial correlation coefficient between the divergent wind patterns regressed against the ID-IOBM index and the SCZD index is 0.85 at 200 hPa. Meanwhile, the spatial correlation coefficient between the divergent wind patterns regressed against the two indices is 0.84 at 850 hPa (see Table 1), indicating that the anomalous inter-hemispheric vertical circulation induced by the ID-IOBM in its warm phase may be an important factor that leads to the SCZD pattern.

To further verify the linkage between the inter-hemispheric vertical circulation and the lower-level PJ-like pattern on the SCZD, Fig. 6 shows the vertical and zonal wind patterns associated with the SCZD index and the ID-IOBM index, respectively. The descending motions over the west part of southern China are associated with the vertical circulation, which corresponds to the lower-level moisture divergence. Such a divergence is in favor of decreased precipitation in the west part of southern China. Meanwhile, the ascending motions over the east part of southern China are associated with the PJ-like pattern, which contributes to the increased precipitation there.

Figure 7 further gives patterns of the vertically integrated moisture flux anomaly and its divergence regressed against the two indices, respectively. We can see that the convergence is centered over the ESC and the divergence over the WSC.

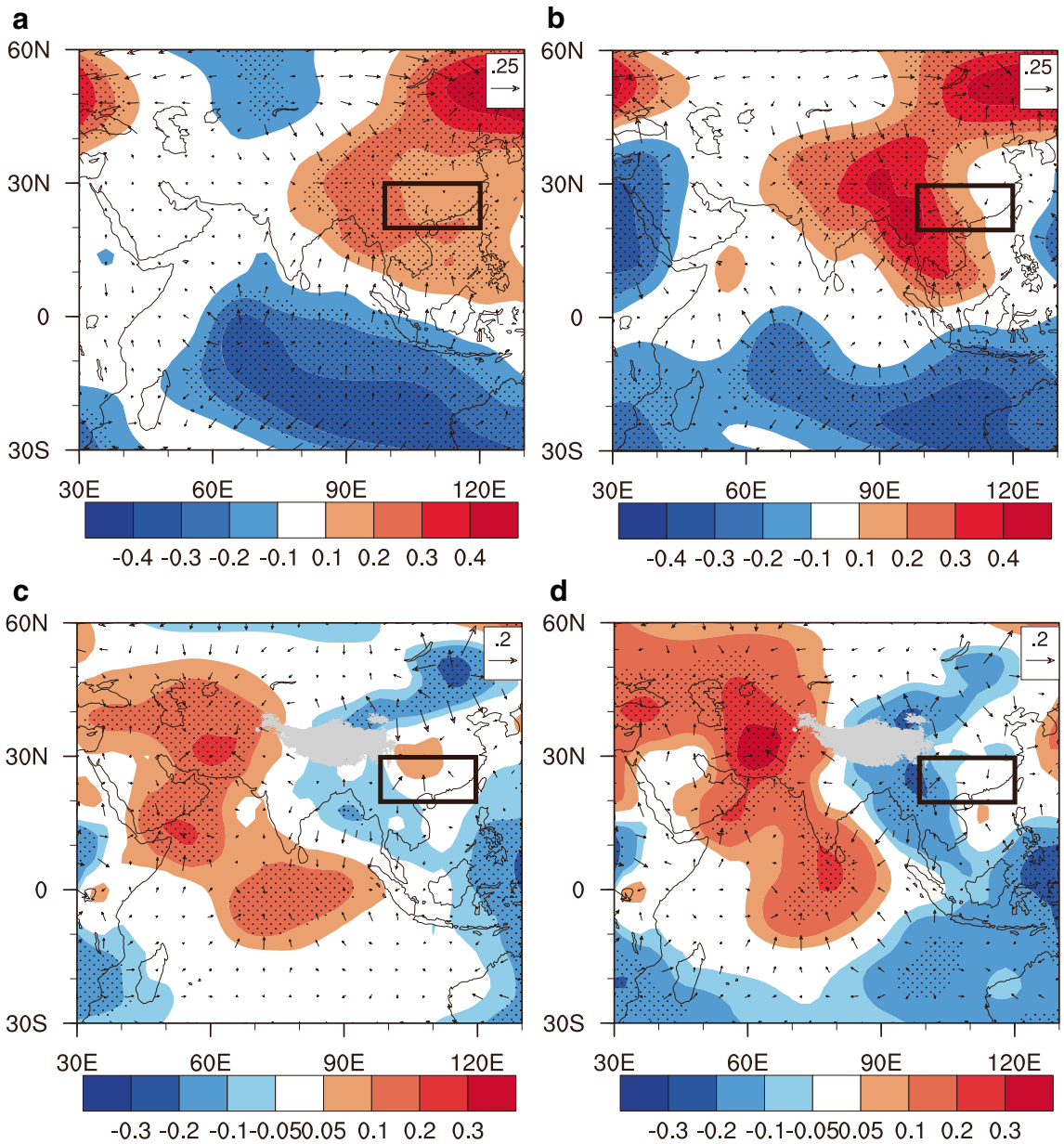

Fig. 5 Regressed divergent winds (vectors; m s^{-1}) and velocity potentials (shading; 10^6 m^2 s^{-1}) at 200 hPa (a, b) and 850 hPa (c, d) against the SCZD index (a, c) and the ID-IOBM index (b, d). The rectangular box indicates southern China. Black dots denote areas significant at the 95% confidence level. All plots were generated using NCL

Both the anomalous descending motion and corresponding lower-level divergence contribute to a decreased transport of moisture into the WSC and thus are unfavorable for precipitation there. The enhanced moisture flux from the East China Sea can transport additional moisture into the ESC and is favorable for precipitation increase there. The spatial correlation coefficients between the vertically integrated moisture flux and its divergence patterns regressed against the two indices are 0.80 and 0.82, respectively, indicating that the SCZD is well covariated with the ID-IOBM.

The SCZD is significantly related to the ID-IOBM through two ways: the inter-hemispheric vertical circulation and the lower-level Kevin wave-like pattern. The divergence at lower level associated with the descending branch of the vertical circulation could impact the SCZD through reducing the moisture transport into the WSC. The lower-level Kelvin wave-like pattern could mainly impact on the SCZD through enhancing the moisture supply to the ESC.

5 Summary and discussion

In this study, we focus on diagnosing the leading mode of the interdecadal covariability between the SCSP and the IO SST

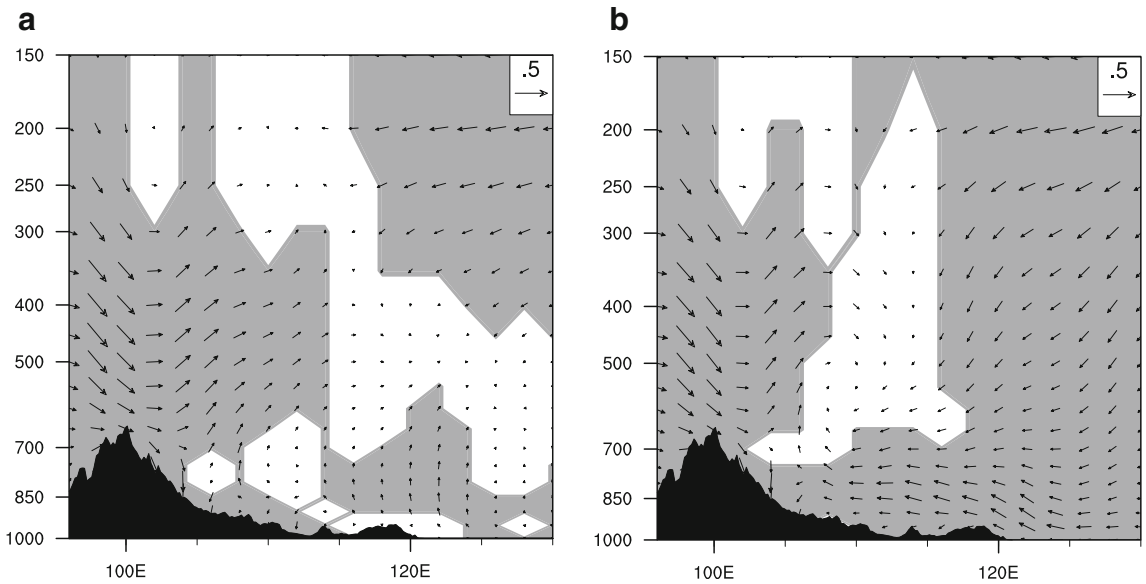

Fig. 6 Patterns of vertical velocity (hPa day^{-1}) and zonal wind (m s^{-1}) averaged between 25° N and 30° N regressed against the SCZD index (a) and the ID-IOBM index (b) (shading indicates the areas significant at the 90% confidence level). All plots were generated using NCL

through conducting the SVD analysis of the precipitation and SST data. We found a remarkable zonal dipole mode of interdecadal SCSP termed the SCZD, and an ID-IOBM. This leading mode, as represented by the first pair of SVD modes derived from 11-year low-frequency-pass filtered summer precipitation and simultaneous SST anomalies, had an increased (decreased) precipitation in the ESC (WSC) and a basin-wide warming in the IO. Our diagnosis results showed that the SCZD had a positive covariation with the ID-IOBM in summer and the dynamical processes linking the SCZD to the ID-IOBM were then examined.

Figure 8 shows the schematic diagram of the physical picture of the key anomalous circulation patterns associated with the SCZD in response to the ID-IOBM. The SCZD is related to the ID-IOBM which may induce the anomalous interhemispheric vertical circulation and the Kelvin wave-like pattern. During the warm phase of the ID-IOBM, an enhanced lower-level convergence and upper-level divergence occur over the tropical IO, which is a typical Gill-Matsuno-type response to the warm phase of the ID-IOBM. The corresponding upper-level outflow anomalies from the tropical IO converge over the Indo-China peninsula, corresponding to a

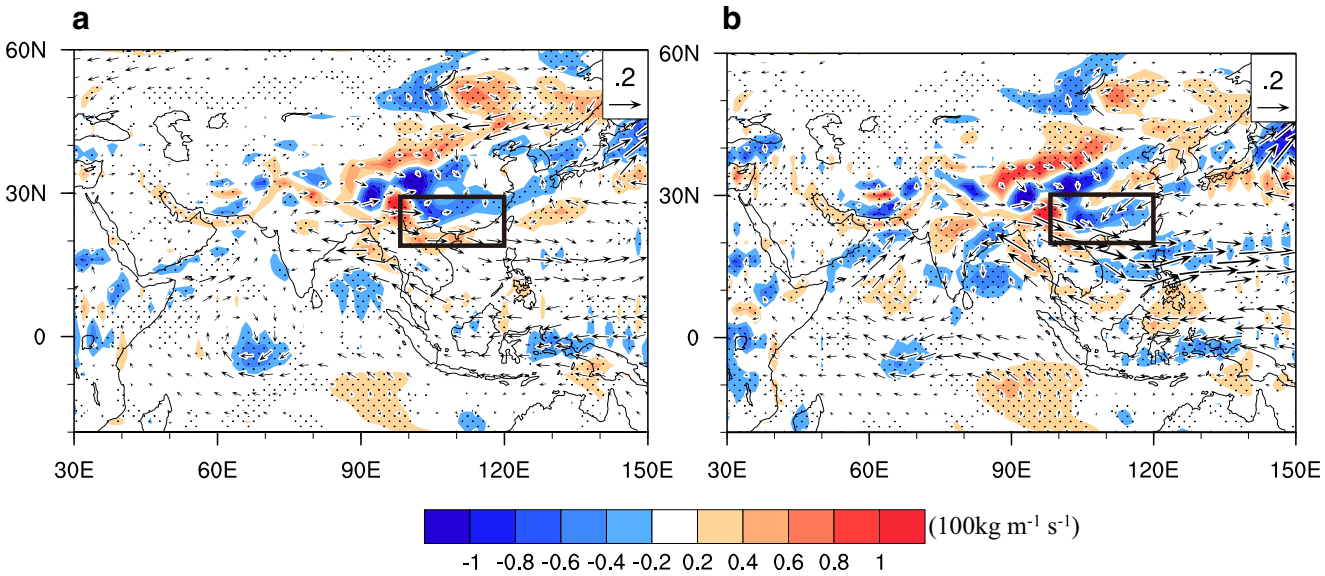

Fig. 7 Regression of vertically integrated (from the surface to 300 hPa) water vapor flux (vector; 100 kg m^{-1} s^{-1}) against the SCZD index (a) and the ID-IOBM index (b), and corresponding divergence in JJA (shading; 100 kg m^{-2} s^{-1} dots indicate areas significant at the 95% confidence level). The rectangular box indicates southern China. All plots were generated using NCL

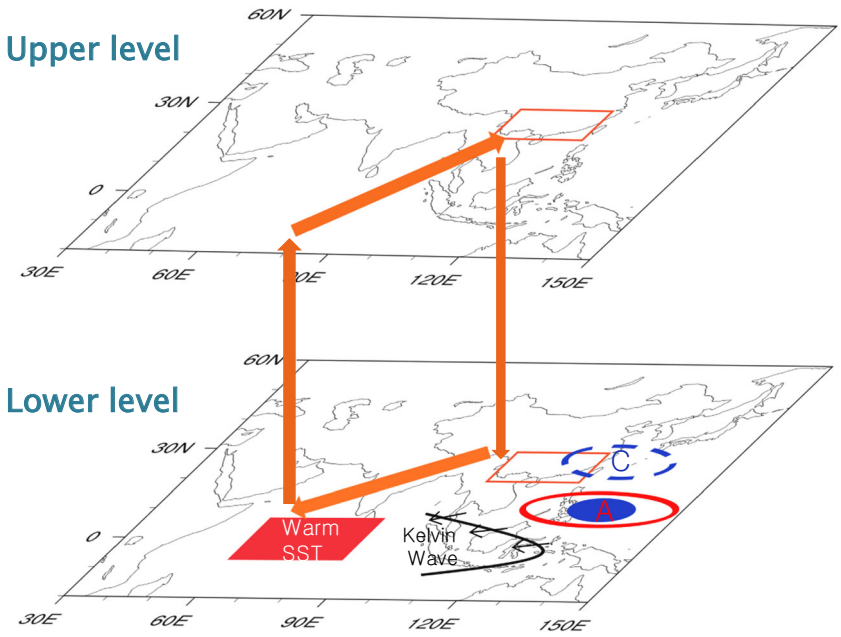

Fig. 8 Schematic diagram of the response of atmospheric circulation to SST anomalies in the IO. The red rectangle box denotes anomalous SST in the IO. The blue round box denotes negative convective heating. The brown rectangle box denotes southern China. The brown vectors denote the abnormal inter-hemispheric vertical circulation. Black curve and vectors denote Kelvin wave and corresponding divergence around the South China Sea and the Philippines in lower level. "A" and "C" denote abnormal anticyclone and cyclone, respectively. This plot was generated using NCL and licensed Microsoft PowerPoint

lower-level anomalous anticyclone that contributes to the reduction of the eastward moisture transport from the BOB into the west part of southern China. Meanwhile, the ID-IOBM in its warm phase tends to form the Kelvin wave-like pattern over the equatorial western Pacific, which acts to induce northeasterly surface wind anomalies. The resultant subtropical divergence and suppressed deep convection lead to an anomalous anticyclonic pattern to the east of the Philippines. The anomalous anticyclone in turn tends to suppress the precipitation, where such a suppressed pattern to the east of the Philippines can further lead to the PJ-like pattern. Meanwhile, the enhanced precipitation center is located over southeastern China, which is probably associated with the anomalous cyclone center of the PJ-like pattern. Such a cyclone contributes to the increased westward moisture transport which converges into the east part of southern China. Therefore, the above-normal moisture transport associated with the Kevin wave-like pattern is favorable for the increased precipitation in the east part of southern China. Besides, the suppressed moisture transport associated with the inter-hemispheric vertical circulation in the west part of southern China brings about the decreased precipitation there. The joint effects of the anomalous inter-hemispheric vertical circulation and the Kevin wave-like pattern associated with the ID-IOBM may eventually lead to the formation of the SCZD pattern.

It is well-known that some mid-high-latitude circulation factors can influence the SCSP. Figure 3(a) shows clearly that a Rossby wave-like pattern exists over the middle latitudes, which may have impacts on the SCZD through an upper-level divergence and an anomalous ascending motion over southeastern China. The active centers of the wave-like pattern are the same as the interdecadal circumglobal teleconnection pattern over the Asian continent, which is linked to the AMO (Lin et al. 2016). Thus, the mechanisms for such a wave-like pattern may be related to upstream factors, which are beyond the scope of this study and would be considered in the future.

In Fig. 2(c), it is interesting to note that the positive phase of SCZD has become active after the 2000s, which may indicate that summer precipitation in the WSC tends to become subnormal during the 2000s. This is consistent with the fact that frequency of severe droughts increased in Southwest China in the last decade. Record-breaking droughts hit Southwest China in the summer of 2006 (Peng et al. 2007), the autumn of 2009 (Wang et al. 2015) and the late summer of 2011 (Wang et al. 2015). Thus, this study will help us improve our understanding of the interdecadal modulation of severe droughts in Southwest China.

Although the possible impacts of ID-IOBM on the interdecadal variability of SCSP have been revealed in this diagnostic paper, the corresponding mechanisms of such an interdecadal covariability still need to be further verified by numerical experiments, which will be addressed in future study.

Funding information The authors are grateful to the anonymous reviewers for their insightful comments, which helped improve the quality of this paper. We also acknowledge the supports from the National Key Research Program and Development of China (No. 2017YFC1502302) and the National (Key) Basic Research and Development (973) Program of China (Nos. 2013CB430203 and 2010CB950404).

References

Ambrizzi T, Hoskins BJ, Hsu H (1995) Rossby wave propagation and teleconnection patterns in the austral winter. J Atmos Sci 52:3661–3672. https://doi.org/10.1175/1520-0469(1995)052<3661:RWPATP>2.0.CO;2

Bretherton CS, Smith C, Wallace JM (1992) An intercomparison of methods for finding coupled patterns in climate data. J Clim 5:

541–560. https://doi.org/10.1175/1520-0442(1992)005<0541:AIOMFF>2.0.CO;2
Cao J, Yao P, Wang L (2014) Summer rainfall variability in low-latitude highlands of China and subtropical Indian Ocean dipole. J Clim 27:880–892. https://doi.org/10.1175/JCLI-D-13-00121.1
Chan JCL, Zhou W (2005) PDO, ENSO and the early summer monsoon rainfall over south China. Geophys Res Lett 32:L08810. https://doi.org/10.1029/2004GL022015
Compo GP, Whitaker JS, Sardeshmukh PD (2011) The twentieth century reanalysis project. Quart J Roy Meteor Soc 137:1–28. https://doi.org/10.1002/qj.776
Dai A (2013) The influence of the inter-decadal Pacific oscillation on US precipitation during 1923–2010. Climate Dyn 41:633–646. https://doi.org/10.1007/s00382-012-1446-5
Ding Y, Wang Z, Sun Y (2008) Inter-decadal variation of the summer precipitation in East China and its association with decreasing Asian summer monsoon part I: observed evidences. Int J Climatol 28:1139–1161. https://doi.org/10.1002/joc.1615
Ding Y, Sun Y, Wang Z (2009) Inter-decadal variation of the summer precipitation in China and its association with decreasing Asian summer monsoon part II: possible causes. Int J Climatol 29:1926–1944. https://doi.org/10.1002/joc.1759
Dong L, Zhou T, Dai A (2016) The footprint of the inter-decadal Pacific oscillation in Indian Ocean sea surface temperatures. Sci Rep 6:21251. https://doi.org/10.1038/srep21251
Duchon CE (1979) Lanczos filtering in one and two dimensions. J Appl Meteorol 18:1016–1022. https://doi.org/10.1175/1520-0450(1979)018<1016:LFIOAT>2.0.CO;2
Fu YF, Pan X, Yang YJ, Chen F, Liu P (2017) Climatological characteristics of summer precipitation over East Asia measured by TRMM PR: a review. J Meteor Res 31:142–159. https://doi.org/10.1007/s13351-017-6156-9
Huang R, Sun F (1992) Impacts of the tropical western Pacific on the East Asian summer monsoon. J Meteor Soc Japan 70:243–256. https://doi.org/10.2151/jmsj1965.70.1B_243
Huang R, Xu Y, Zhou L (1999) The interdecadal variation of summer precipitations in China and the drought trend in north China. Plateau Meteor 18:465–476 (in Chinese)
Huang R, Cai RS, Chen JL, Lian-Tong AZ (2006) Interdecadal variations of drought and flooding disasters in China and their association with the East Asian climate system. Chinese J Atmos Sci 30:730–743 (in Chinese)
Huang R, Chen J, Liu Y (2011) Interdecadal variation of the leading modes of summertime precipitation anomalies over Eastern China and its association with water vapor transport over East Asia. Chinese J Atmos Sci 35:589–606 (in Chinese)
Kuang X, Zhang Y, Liu J (2007) Seasonal variations of the East Asian subtropical westerly jet and the thermal mechanism. J Meteor Res 21:192–203
Kosaka Y, Nakamura H (2006) Structure and dynamics of the summertime Pacific-Japan teleconnection pattern. Q J R Meteorol Soc 132:2009–2030. https://doi.org/10.1256/qj.05.204
Kwon MH, Jhun JG, Ha KJ (2007) Decadal change in East Asian summer monsoon circulation in the mid-1990s. Geophys Res Lett 34:L21706. https://doi.org/10.1029/2007GL031977
Li Q, Peng J, Shen Y (2012) Development of China homogenized monthly precipitation dataset during 1900–2009. J Geogr Sci 22:579–593. https://doi.org/10.1007/s11442-012-0948-8
Li SL, Perlwitz J, Quan X, Hoerling MP (2008) Modelling the influence of North Atlantic multidecadal warmth on the Indian summer rainfall. Geophys Res Lett 35:L05804. https://doi.org/10.1029/2007GL032901
Lin JS, Wu B, Zhou TJ (2016) Is the interdecadal circumglobal teleconnection pattern excited by the Atlantic multidecadal Oscillation? Atmospheric and Oceanic Science Letters 9(6):451–457. https://doi.org/10.1080/16742834.2016.1233800
Liu Y, Huang G, Huang R (2011) Inter-decadal variability of summer rainfall in Eastern China detected by the Lepage test. Theor Appl Climatol 106:481–488. https://doi.org/10.1007/s00704-011-0442-8
Liu Y, Chiang J (2012) Coordinated abrupt weakening of the Eurasian and North African monsoons in the 1960s and links to extratropical North Atlantic cooling. J Clim 25:3532–3548. https://doi.org/10.1175/JCLI-D-11-00219.1
Livezey R, Chen W (1983) Statistical field significance and its determination by Monte Carlo techniques. Mon Wea Rev 111:46–59. https://doi.org/10.1175/1520-0493(1983)111<0046:SFSAID>2.0.CO;2
Lu R, Dong B, Ding H (2006) Impact of the Atlantic Multidecadal Oscillation on the Asian summer monsoon. Geophys Res Lett 33:L24701. https://doi.org/10.1029/2006GL027655
Mantua NJ, Hare SR, Zhang Y, Wallace JM, Francis RC (1997) A Pacific interdecadal climate oscillation with impacts on salmon production. Bull Amer Meteor Soc 78:1069–1079. https://doi.org/10.1175/1520-0477(1997)078,1069:APICOW.2.0.CO;2
New M, Hulme M, Jones P (2000) Representing twentieth-century space-time climate variability. Part II: development of 1901–96 monthly grids of terrestrial surface climate. J Clim 13:2217–2238. https://doi.org/10.1175/1520-0442(2000)013<2217:RTCSTC>2.0.CO;2
Nitta T (1987) Convective activities in the tropical western Pacific and their impact on the northern hemisphere summer circulation. J Meteor Soc Japan 65:373–390. https://doi.org/10.2151/jmsj1965.65.3_373
Peng J, Zhang Y, Bueh C (2007) On the characteristics and possible causes of a severe drought and heat wave in the Sichuan-Chongqing region in 2006. Climatic Environ Res 12:464–474 (in Chinese)
Qian C, Zhou T (2014) Multidecadal variability of north China aridity and its relationship to PDO during 1900–2010. J Clim 27:1210–1222. https://doi.org/10.1175/JCLI-D-13-00235.1
Rayner N, Parker D, Horton E (2003) Global analyses of sea surface temperature, sea ice, and night marine air temperature since the late nineteenth century. J Geophys Res 108:1063–1082. https://doi.org/10.1029/2002JD002670
Shen S, Lau K (1995) Biennial oscillation associated with the East Asian summer monsoon and tropical sea surface temperatures. J Meteor Soc Japan 73:105–124. https://doi.org/10.2151/jmsj1965.73.1_105
Si D, Ding Y (2016) Oceanic forcings of the interdecadal variability in East Asian summer rainfall. J Clim 29:7633–7649. https://doi.org/10.1175/JCLI-D-15-0792.1
Takaya K, Nakamura H (1997) A formulation of a wave-activity flux for stationary Rossby waves on a zonally varying basic flow. Geophys Res Lett 24:2985–2988. https://doi.org/10.1029/97GL03094
Thomson D (1982) Spectrum estimation and harmonic analysis. Proc IEEEs 70:1055–1096. https://doi.org/10.1109/PROC.1982.12433
Wang H (2001) The weakening of the Asian monsoon circulation after the end of 1970's. Adv Atmos Sci 18:376–386. https://doi.org/10.1007/BF02919316
Wang L, Chen W, Zhou W (2015) Understanding and detecting super-extreme droughts in Southwest China through an integrated approach and index. Quart J Roy Meteor Soc 142:529–535. https://doi.org/10.1002/qj.2593
Wang Y, Li S, Luo D (2009) Seasonal response of Asian monsoonal climate to the Atlantic Multidecadal Oscillation. J Geophys Res 11:356–360. https://doi.org/10.1029/2008JD010929
Wu B, Zhou T, Li T (2016) Impacts of the Pacific–Japan and circumglobal teleconnection patterns on the interdecadal variability of the East Asian summer monsoon. J Clim 29:3253–3271. https://doi.org/10.1175/JCLI-D-15-0105.1
Wu R, Wen Z, Yang S (2010) An interdecadal change in southern China summer rainfall around 1992/93. J Clim 23:2389–2403. https://doi.org/10.1175/2009JCLI3336.1

Wu X, Mao J (2017) Interdecadal variability of early summer monsoon rainfall over South China in association with the Pacific Decadal Oscillation. Int J Climatol 37:706–721. https://doi.org/10.1002/joc.4734

Xie S, Hu K, Hafner J (2009) Indian Ocean capacitor effect on Indo-western Pacific climate during the summer following El Niño. J Clim 22:730–747. https://doi.org/10.1175/2008JCLI2544.1

Xu Z, Fan K, Wang H (2015) Decadal variation of summer precipitation over China and associated atmospheric circulation after the late 1990s. J Clim 28:4086–4106. https://doi.org/10.1175/JCLI-D-14-00464.1

Yang J, Liu Q, Xie S (2007) Impact of the Indian Ocean SST basin mode on the Asian summer monsoon. Geophys Res Lett 34:155–164. https://doi.org/10.1029/2006GL028571

Yang J, Liu Q, Liu Z (2009) Basin mode of Indian Ocean sea surface temperature and Northern Hemisphere circumglobal teleconnection. Geophys Res Lett 36:L19705. https://doi.org/10.1029/2009GL039559

Yang Q, Ma Z, Fan X (2017) Decadal modulation of precipitation patterns over East China by sea surface temperature anomalies. J Clim 30:7017–7033. https://doi.org/10.1175/JCLI-D-16-0793.1

Yu L, Furevik T, Ottera OH, Gao Y (2015) Modulation of the Pacific Decadal Oscillation on the summer precipitation over East China: a comparison of observations to 600-years control run of Bergen climate model. Clim Dyn 44:475–494. https://doi.org/10.1007/s00382-014-2141-5

Yuan Y, Gao H, Li WJ, Liu YJ, Chen LJ, Zhou B, Ding YH (2017) The 2016 summer floods in China and associated physical mechanisms: a comparison with 1998. J Meteor Res 31:261–277. https://doi.org/10.1007/s13351-017-6192-5

Zhang H, Wen Z, Wu R, Chen Z, Guo Y (2016) Inter-decadal changes in the East Asian summer monsoon and associations with sea surface temperature anomaly in the South Indian Ocean. Climate Dyn 48:1–15. https://doi.org/10.1007/s00382-016-3131-6

Zhu J, Huang B, Kumar A, Kinter JL III (2015) Seasonality in predictive skill and predictable patterns of tropical Indian Ocean SST. J Clim 28:7962–7984. https://doi.org/10.1175/JCLI-D-15-0067.1

Zhu Y, Yang X (2003) Relationships between Pacific decadal oscillation (PDO) and climate variabilities in China. Acta Meteor Sin 61:641–654 (in Chinese)

Zhu Y, Wang H, Zhou W, Ma J (2011) Recent changes in the summer precipitation pattern in East China and the background circulation. Climate Dyn 36:1463–1473. https://doi.org/10.1007/s00382-010-0852-9

Check for updates

The Major Interannual Modes of Late-Summer Precipitation Over the Northern China Monsoon Region

Liu Yang[1,2,†], Jun-hu Zhao[2,†*], Po Hu[1,2], Shu-lin Qu[1], and Guo-lin Feng[1,2,3,*]

[1]*College of Atmospheric Science, Lanzhou University, Lanzhou 730000, People's Republic of China*
[2]*Laboratory for Climate Studies, National Climate Center, China Meteorological Administration, Beijing 100081, People's Republic of China*
[3]*Department of Physical Science and Technology, Yangzhou University, Yangzhou 225000, People's Republic of China*

[Original manuscript received 28 March 2019; accepted 10 July 2019]

ABSTRACT *Summer precipitation in the northern China monsoon region (NCMR; 35°–55°N, 108°–135°E) shows significant intraseasonal variability. The early-summer (June) and late-summer (July–August) precipitation patterns show clear differences in their formation mechanisms and the systems that affect them. We used empirical orthogonal function (EOF) analysis to investigate the two leading modes of July–August precipitation over the NCMR and their associated atmospheric circulation anomalies using linear regression. The results show that the first (EOF1) and second (EOF2) modes correspond to a pan-NCMR precipitation variation pattern and a precipitation oscillation pattern between North China (NC) and Northeast China (NEC), respectively. These two modes account for 22.1% and 10.1% of the total variance, respectively. The associated principal components (PCs) both have significant interannual variability with a period of 2–4 years. In addition, PC1 has significant interdecadal variability with a period of 20–30 years. Further analysis suggests that EOF1 and EOF2 clearly have a different relationship with the summer monsoon circulation system. In the positive phase of PC1, the East Asian subtropical westerly jet stream (EAWJS) shows a northward trend with higher intensity than normal the blocking high at mid- to high latitudes is inactive; and the western Pacific subtropical high (WPSH) is located to the north of its normal position. The NCMR is controlled by stronger southerly winds, which cause the convergence of water vapour, favouring more precipitation in this region and vice versa. In the positive phase of PC2, the EAWJS swings to the south of Lake Baikal. Significant positive height anomalies exist from western NC to NEC. Significant negative height anomalies occur to the subtropical northwestern Pacific. This indicates that the cold vortex in Northeast China is inactive, the WPSH tends to be weaker and located to the south of its normal position, and NEC (NC) is dominated by anomalous northeasterly (southeasterly) winds. The convergence (divergence) of water vapour in NC (NEC) favours more (less) precipitation in NC (NEC) and vice versa. Therefore, EOF1 is related to the large-scale circulation anomalies over East Asia and the northwest Pacific in July and August, whereas EOF2 is more closely related to the anomalies in the regional circulation over the NCMR and the subtropical northwestern Pacific.*

RÉSUMÉ *[Traduit par la rédaction] Les précipitations estivales qui tombent sur la région de mousson du nord de la Chine (35° à 55° N, 108° à 135° E) présentent une variabilité intrasaisonnière notable. Les régimes de précipitations du début (juin) et de la fin (juillet-août) de l'été montrent de nettes différences quant à leurs mécanismes de formation et aux systèmes qui les régissent. Nous appliquons des fonctions orthogonales empiriques (FOE) pour analyser les deux principaux modes de précipitations en juillet-août dans la région de mousson et étudions les anomalies de circulation atmosphérique connexes à l'aide de régression linéaire. Les résultats indiquent que les premier (FOE 1) et deuxième (FOE 2) modes correspondent respectivement à des variations des précipitations régionales et à une oscillation dans les précipitations entre le nord de la Chine et le nord-est de la Chine. Ces deux modes expliquent respectivement 22,1% et 10,1% de la variance totale. Les composantes principales associées présentent toutes deux une variabilité d'une période de 2 à 4 ans. De plus, la première composante principale montre une variabilité notable d'une période de 20 à 30 ans. Une analyse poussée laisse penser que les fonctions 1 et 2 possèdent avec le système de circulation de la mousson d'été une relation qui diffère nettement. Dans la phase positive de la 1re composante principale, le courant-jet subtropical d'ouest révèle sur l'Asie orientale une tendance vers le nord et une intensité supérieure à la normale, le régime de blocage anticyclonique dans les latitudes moyennes à hautes est inactif et l'anticyclone subtropical du Pacifique Ouest se situe au nord de sa position normale. La région de mousson est sous l'influence de forts vents du sud qui causent une convergence de la vapeur d'eau et favorisent une augmentation des précipitations dans cette région et vice versa. Dans la phase positive de la 2e composante, le courant-jet se déplace vers le sud du lac Baïkal. Il existe des anomalies positives de hauteur notables, du nord-ouest*

[†]Jun-hu Zhao contributed equally to this paper. Liu Yang and Jun-hu Zhao are the lead authors.
*Corresponding authors' emails: zhaojh@cma.gov.cn, fenggl@cma.gov.cn

au nord-est de la Chine. Des anomalies négatives de hauteur notables se produisent dans le nord-ouest du Pacifique subtropical. Cette situation indique que le vortex froid dans le nord-est de la Chine est inactif, que l'anticyclone subtropical du Pacifique Ouest est de moindre intensité et se situe au sud de sa position normale, et que des vents anormaux du nord-est (du sud-est) dominent sur le nord-est (nord) de la Chine. La convergence (divergence) de la vapeur d'eau sur le nord (nord-est) de la Chine favorise (défavorise) les précipitations dans le nord (nord-est) de la Chine et vice versa. Par conséquent, la 1re FOE est liée aux anomalies de circulation à grande échelle sur l'Asie orientale et le Pacifique du Nord-Ouest en juillet et août, tandis que la 2e FOE est plus étroitement associée aux anomalies de la circulation régionale sur la région de mousson du nord de la Chine et le Pacifique du Nord-Ouest subtropical.

KEYWORDS North China; Northeast China; atmospheric circulation; East Asia summer monsoon; precipitation

1 Introduction

The northern China monsoon region (NCMR) includes both North China (NC) and Northeast China (NEC). Because of its location on the northern edge of the East Asian summer monsoon (EASM) region, the weather and climate in this region are affected not only by the tropical and subtropical monsoon circulation systems but also mid- to high-latitude circulations and the polar climate system, which results in considerable variability in the climate (Shi and Zhu, 1996; Lian et al., 2003; Gao et al., 2014). The EASM has large interannual variability that causes severe climate events, such as summer floods and droughts, in the NCMR (Zhang et al., 2003b; Li and Zeng, 2005; Guo and Zhang, 2016). The frequency of droughts and floods has increased significantly in the NCMR since the late 1970s as a result of global climate change (Sun et al., 2000; Lu, 2002), causing great losses in the local area. The excessively heavy rainfall in the Songhuajiang–Nenjiang river valley in 1998 (Li, 1999; Zhang et al., 2003a), heavy rainfall over the Beijing area in July 2012 (Sun et al., 2013), and torrential rainfall in July 2016 in NC (Quan and He, 2016) all caused enormous amounts of damage. The accurate prediction of drought and flood anomalies is, therefore, important for agricultural production and disaster prevention and mitigation. Also, studying the mechanism of precipitation anomalies over the NCMR under the effects of global warming is of great scientific value.

In many previous studies, the NCMR was divided into NC and NEC when analyzing summer rainfall in this region. Li (1992) reported that precipitation in NC has an interannual variability with a period of 2–4 years and an interdecadal variability with a period of 16 years, and the interannual variability is closely related to the quasi-biennial oscillation in the equatorial stratosphere at 30–50 hPa. Lu (2002) showed that interdecadal and interannual time scales are dominant in the rainfall over NC during the rainy season. These studies also analyzed the associated atmospheric circulation anomalies on different time scales. Some previous studies have shown that the western Pacific subtropical high (WPSH), the blocking high, the East Asian westerly jet stream (EAWJS), the continental subtropical high, and the EASM have important roles in the interannual variability of summer rainfall in NC (Zhang et al., 2003b; Huang et al., 2008; Dong et al., 2017; Zhao et al., 2018). For example, Zhang et al. (2003a) showed that more precipitation occurs over NC when the Okhotsk blocking high is inactive, the EASM is strong, and the WPSH is located to the north of its normal position and vice versa. The south–north location of the EAWJS is considered to be closely related to precipitation over NC (Zhang, 2005).

The trend of increasing drought events in NC has been noticeable since the late 1970s (Huang et al., 1999; Li et al., 2003; Chen et al., 2004; Ma and Fu, 2006; Guo et al., 2012). Huang et al. (1999) considered that decreased precipitation over NC is related to warming of the sea surface temperature in the middle and eastern equatorial Pacific. Chen et al. (2004) indicated that decreased summer precipitation over NC since the 1970s is closely related to warming of the Indian Ocean. Other studies have suggested that decreased summer precipitation over NC is closely related to weakening of the EASM (Dai et al., 2003; Ding et al., 2008). Lin et al. (2017) showed that the impact of the Indian early summer monsoon on precipitation over NC has weakened since the late 1970s. The precipitation over NC is closely related to the Pacific Decadal Oscillation on an interdecadal time scale. Ma (2007) noted that drought events in NC always corresponded to the warm phase of the Pacific Decadal Oscillation after the mid- to late 1970s. Feng et al. (2014) showed that the different El Niño–EASM relationships are caused by the influence of the Pacific Decadal Oscillation on the decaying speed of El Niño. Based on the interannual and interdecadal variability of summer precipitation over NC, Guo et al. (2012) established a time scale decomposition statistical downscaling model to predict precipitation over NC, and the results showed that the forecast improved.

The location of NEC is at the northern margin of the EASM region. Summer precipitation over NEC is affected by multiple factors including the high-latitude blocking high (Yao and Dong, 2000; Feng et al., 2013), the EASM (Shi and Zhu, 1996; Lian et al., 2003), the NEC cold vortex (NECV; He et al., 2007; Zhao et al., 2015), and the WPSH (Sun et al., 2000; Shen et al., 2011). In addition, abnormalities in these factors affect the establishment time and northward speed of the EASM, causing it to be early or late and strong or weak, resulting in more or less precipitation in NEC (Lian et al., 2003; Sun et al., 2017). He et al. (2007) found that the NECV is an important weather system at mid- and high latitudes in East Asia. Frequent NECV activity has a significant "climate effect" that influences not only the weather

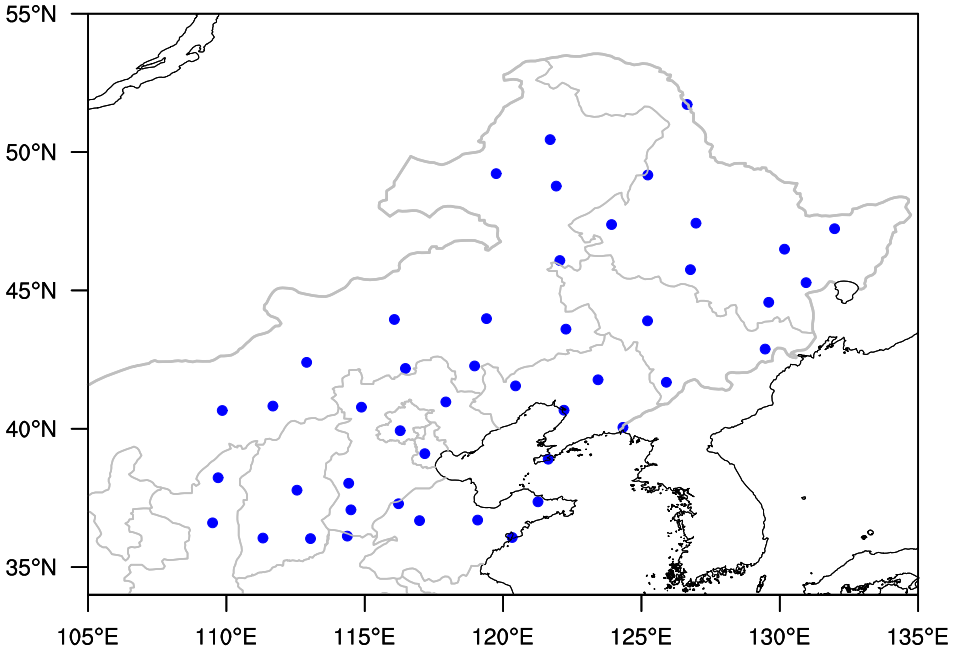

Fig. 1 Spatial distribution of the 46 stations over the northern China monsoon region (NCMR).

and climate in NEC but also the Meiyu rainfall in East Asia. Summer precipitation over NEC has obvious interannual and interdecadal variabilities (Sun et al., 2000). The variation of summer precipitation over NEC during 1909–1997 shows significant cycles of 2–4, 11, and 22 years. Gong et al. (2005) investigated the causes and development of the interannual and interdecadal variabilities of summer precipitation over NEC. They suggested that the stronger the EASM, the more precipitation there is over NEC at both interdecadal and interannual time scales. Summer precipitation over NEC decreased significantly from the 1960s to the early 1980s on an interdecadal time scale then began to increase until the end of the twentieth century. The Pacific Decadal Oscillation has a modulating effect on this decadal variation in precipitation and the associated circulation (Zhu and Yang, 2003).

There are also obvious intraseasonal characteristics of summer precipitation over NEC. The precipitation anomalies over NEC in early and late summer are affected by different circulation systems. Early-summer precipitation is mainly influenced by the activity of the NECV, whereas precipitation in late summer is mainly influenced by the EAWJS, the WPSH, the southerly wind over NEC, and the mid-latitude blocking high over northeast Asia (Shen et al., 2011; Sun et al., 2017; Zhao et al., 2018).

Previous studies on precipitation over the NCMR have looked at NC and NEC separately. However, the major circulation systems affecting summer precipitation over those two regions are very similar. Most of the earlier studies did not consider the intraseasonal variation in summer precipitation over the NCMR. Shen et al. (2011) and Zhao et al. (2018) showed that precipitation over NC and NEC has significant intraseasonal characteristics and that the circulation systems are clearly different in June and July–August. Precipitation over the NCMR is concentrated mainly in the July–August period. Therefore, based on previous studies, this study aimed to investigate the major modes of July–August precipitation over the NCMR and to determine the differences and similarities between the associated circulation anomalies.

The remainder of the paper is organized as follows. Section 2 introduces the data and methods, and Section 3 presents the major modes of July–August precipitation over the NCMR. Section 4 explores the circulation systems affecting the two major modes. Section 5 focuses on the differences between the atmospheric circulations associated with the first empirical orthogonal function mode (EOF1) and the second EOF mode (EOF2). Section 6 provides a summary and discussion.

2 Data and methodology

a *Data*

The main datasets used in this study are the following.

- Monthly average precipitation data for 160 stations from the China Meteorological Administration for the 1951–2017 period. A total of 46 stations are located in the NCMR (35°–55°N, 108°–135°E; Fig. 1).
- Monthly mean atmospheric reanalysis data from the National Centers for Environmental Prediction/National Center for Atmospheric Research for 1951−2017 (Kalnay et al., 1996), with a horizontal resolution of 2.5° × 2.5°. The variables include monthly geopotential height (h), horizontal wind (u, v), and specific humidity.
- The EASM index is defined as the area-averaged 850 hPa meridional wind (V_{850}) within and area bounded by 20°–

40°N and 110°–125°E (Huijun, 2002). The area index, intensity index, westward-extending ridge index, and ridge line index of the WPSH are from the National Climate Center of the China Meteorological Administration.

b *Methodology*

This study investigated the major modes of July–August precipitation over the NCMR using EOF analysis (Jolliffe, 2003), which is a statistical method for meteorological elements. The basic principle is the decomposition of spatially varying meteorological element fields into space function and time function parts (Wei, 2007). The power spectrum method is used to analyze the period of the first two EOF modes of July–August precipitation over the NCMR from 1951 to 2017. Correlation analysis and linear regression analysis are used to show relationships between the atmospheric circulation, water vapour transport, and July–August precipitation over the NCMR. We used a Student's *t*-test to check the significance of the correlation and regression analyses.

3 Two major modes of July–August precipitation over the NCMR

Before studying the major modes, the climatic characteristics of monthly precipitation over the NCMR from June to August are analyzed. In June, the precipitation in most areas is less than 80 mm, except for the southeastern part of NEC (Fig. 2a), and the average precipitation is only 69.7 mm. However, the spatial distribution of the precipitation in July is significantly different from that in June. The precipitation over almost the entire region is greater than 100 mm, and the average precipitation is 125.4 mm, which is nearly twice that in June. Furthermore, the precipitation centre, where precipitation exceeds 120 mm, covers a large area from NC to NEC (Fig. 2b). This pattern of the spatial distribution of precipitation in July may be a result of the seasonal northward shift of the EASM and other circulation systems. The spatial characteristics of precipitation in August are similar to those in July. And precipitation in August is larger than in June and smaller than in July (Fig. 2c). The July–August precipitation in the NCMR accounts for more than 70% of the total annual summer precipitation (Fig. 2e). The standard deviations of precipitation in most areas in the July–August period is more than 30 mm (Fig. 2f), which indicates that the precipitation in the July–August period in the NCMR is not only plentiful but also has large interannual variations.

The PC variation characteristics of the major modes can be obtained through EOF analysis of the July–August precipitation over the NCMR during the 1951–2017 period. To reflect the spatial patterns of July–August precipitation relative to climatology, the EOF analysis does not use monthly precipitation fields directly but rather uses the monthly precipitation anomaly percentage fields. The first two leading EOF modes account for 22.1% and 10.1% of the total variance, respectively. The cumulative explanatory variance of the first 10 modes is 71.2%, which shows that the convergence of the EOF analysis is very slow, reflecting the diversity and complexity of the spatial patterns of July–August precipitation over the NCMR.

The first two leading modes and corresponding normalized principal components (PCs) are shown in Fig. 3. A pan-NCMR precipitation variation pattern is shown by EOF1 (Fig. 3a), and the associated PC1 has significant interannual variability with a period of 2–4 years and interdecadal variability with a 25-year period through power spectrum analysis (Fig. 4a). Before the 1980s, PC1 has a positive phase and turns to a clearly negative phase from the start of the twenty-first century, which is consistent with the interdecadal variations in the intensity of the EASM (Zhang et al., 2003b; Ding et al., 2008). A precipitation oscillation pattern between NC and NEC is described by EOF2 (Fig. 3b), and the associated PC2 also has a clear period of 2–4 years (Fig. 4b).

4 Atmospheric circulation anomalies associated with the two major modes of the NCMR July–August precipitation

We asked the following questions. Are these two leading EOF modes physically meaningful? How are they associated with the low, middle, and high atmospheric circulations and water vapour transport anomalies? What are the physically consequential impact factors for each PC? These questions are addressed for each mode in the following sections.

a *Atmospheric Circulation and Water Vapour Transport Anomalies Associated with EOF1*

Figure 5 shows the atmospheric circulation anomalies associated with EOF1. As a representative of the upper atmosphere circulation, the 200 hPa *U* wind fields clearly reflect the EAWJS anomalies. Figure 5a shows that positive anomalous westerly winds occur over NC and NEC, and the anomalous centre lies in the northern part of the NCMR. By contrast, negative anomalies are present in southern East Asia (25°–35°N, 80°–140°E) with the centre located between the lower reaches of the Yangtze River and the islands of Japan. This indicates that the position of the EAWJS is farther north than normal in the positive phase of PC1. To quantitatively describe the interannual relationship between the position and intensity of the EAWJS and PC1, the position index of the EAWJS is defined as the regional average (100°–140°E) latitude where the 200 hPa *U* wind speed is at a maximum, and the intensity index of the EAWJS is defined as the regional average (100°–140°E) *U* wind speed (Zhao et al., 2018). The position index can be used to measure the position of the EAWJS axis. The correlation coefficients between PC1 and the position index and between PC1 and the intensity index of the EAWJS are 0.25 and 0.13 (Table 1), respectively. Therefore, EOF1 corresponds well with the strength and location of the EAWJS. The key region of westerly winds is over eastern Inner Mongolia. The westerly intensity index

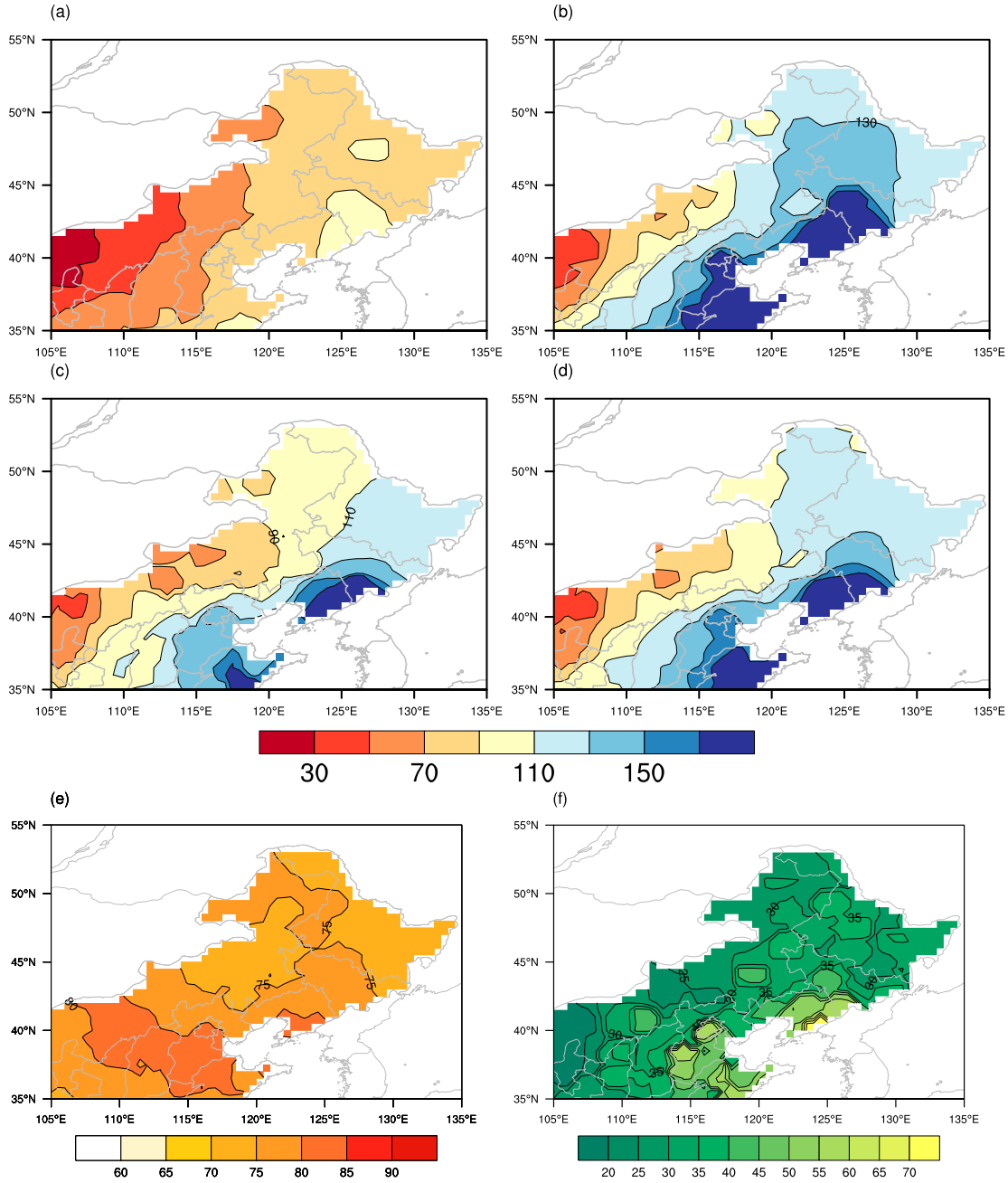

Fig. 2 The spatial distribution of precipitation (mm) in (a) June, (b) July, (c) August, and (d) July and August (average value), respectively. (e) July–August (JA) precipitation as a percentage of total summer (June, July, and August (JJA)) precipitation. (f) The standard deviation (mm) of JA precipitation over the NCMR for the 1951–2017 period.

over eastern Inner Mongolia (EIMW) is defined as the average U wind over 40°–50°N, 110°–130°E. The correlation coefficient between the EIMW index and PC1 is 0.76 (>99.9% confidence level). This implies that the interannual impact of the EIMW on the EOF1 of July–August precipitation over the NCMR is important.

Figure 5b shows that the atmospheric circulation anomalies at 500 hPa associated with EOF1 have the following main characteristics. Corresponding to the positive phase of EOF1, the region from western Lake Balkhash to Lake Baikal (40°–50°N, 90°–110°E) is covered with a negative anomaly with a positive anomaly from the East China Sea to the southern Korean Peninsula (32.5°–37.5°N, 120°–135°E). The configuration of the circulation field shows that the intensity and location of the Lake Baikal blocking high and the WPSH are closely related to July–August precipitation over the NCMR. To show the detailed features of the relationship between PC1 and these circulation systems, we defined the southwestern Lake Baikal high (SWLBH) index as the area-averaged 500 hPa geopotential height (H_{500}) within the area bounded by 40°–50°N and 90°–

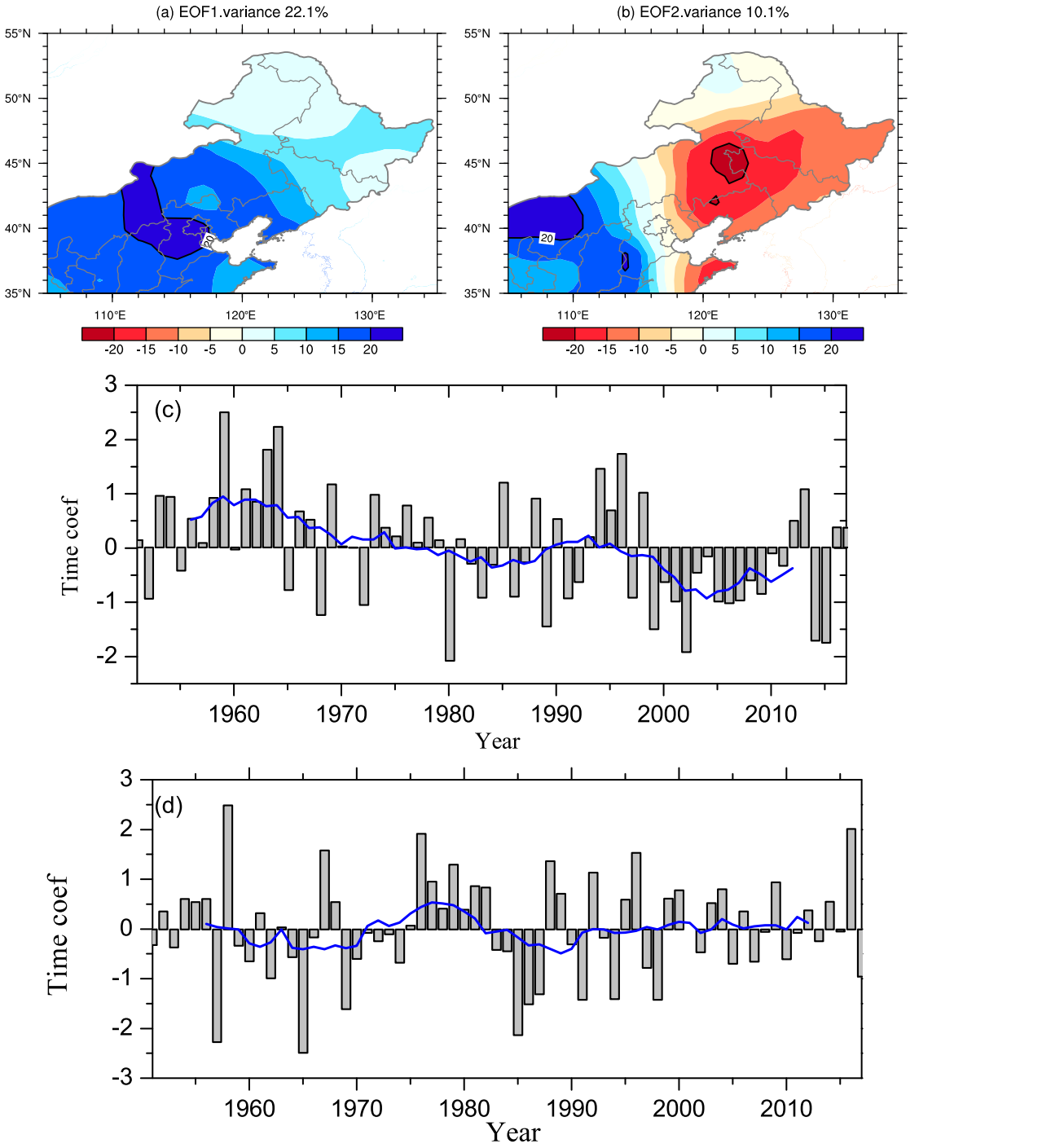

Fig. 3 The first two leading EOF modes of JA precipitation over the NCMR: (a) EOF1 and (b) EOF2 (mm, contour interval 5 mm); (c) and (d) normalized time series (bars) and the 11-year running mean (curve) for PC1 and PC2, respectively.

110°E. The correlation coefficient between the SWLBH index and the Lake Baikal blocking high index defined by Zhao (1999) is 0.87 (exceeding the 99% confidence level), which indicates that the SWLBH can reflect the strength of the blocking high over Lake Baikal. This SWLBH index was in a negative phase before the mid-1970s but changed to a positive phase after the mid-1970s (figure not shown). The frequency of occurrence of the SWLBH was low before the mid-1970s but was active after the mid-1970s. The correlation coefficient between the SWLBH index and PC1 is 0.51 (Table 1, exceeding the 99.9% confidence level). This implies that the impact of the SWLBH on EOF1 of the July–August precipitation over the NCMR is considerable. The area index, intensity index, the ridge line index of the WPSH, and the westward-extending ridge index are closely associated with PC1, with correlation coefficients of −0.27, −0.26, 0.20, and 0.15, respectively. This

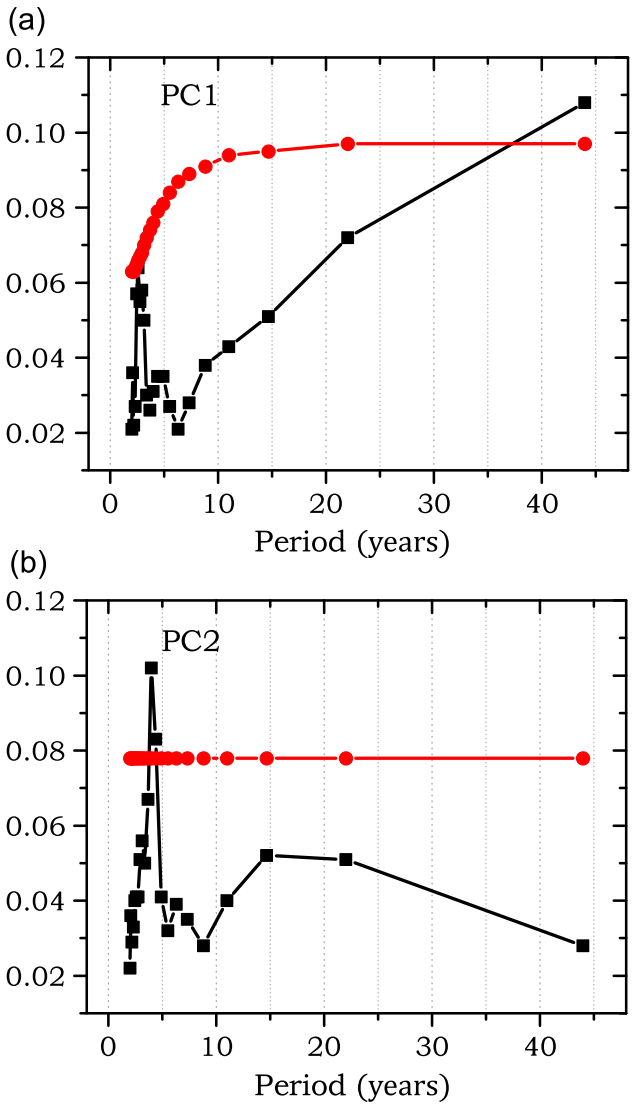

Fig. 4 Power spectrum analysis for the first two principal components (PCs) of JA precipitation over the NCMR during the 1951–2017 period. (a) PC1 and (b) PC2. The black line indicates the power spectral density. The red line indicates the 90% confidence level. The *x*-axis is the period (years).

shows that more precipitation is favoured over the NCMR when the WPSH is weaker and located to the north of its normal position.

The other significant region associated closely with PC1 is located on the Korean Peninsula (32.5°–37.5°N, 120°–135°E). We define the Korean Peninsula high (KPH) index as the area-averaged H_{500} within the area bounded by 32.5°–37.5°N, 120°–135°E. The correlation coefficients between the KPH index and the intensity index and ridge line index of the WPSH are 0.33 and 0.46, respectively, exceeding the 95% and 99% confidence levels, respectively. When the WPSH is located to the north of its normal position, a high-volume system is easily formed from the eastern China Sea to the southern Korean Peninsula. The correlation coefficient between the KPH index and PC1 is 0.22 (Table 1). This implies that the impact of the SWLBH on the EOF1 of July–August precipitation over the NCMR is greater than the impact at either the WPSH and KPH. This high-volume system is favourable for the transport of water vapour from the western Pacific Ocean to the NCMR.

Corresponding to the positive phase of PC1, the 850 hPa wind fields have the following main characteristics: a cyclonic (anticyclonic) wind anomaly controlling a large area south of Lake Baikal (the southern Korean Peninsula, the islands of Japan, and the surrounding ocean) and strong anomalous southerly winds over East Asia, extending into the NCMR (Fig. 5c). This indicates that the stronger the EASM, the more precipitation falls over the NCMR. We used the EASM strength index defined by Huijun (2002) to quantitatively analyze the relationship between the EASM and PC1. The correlation coefficient between the EASM index and PC1 was 0.58 (Table 1), which exceeds the 99.9% confidence level. This further confirms that a stronger EASM favours greater precipitation over the NCMR.

The water vapour transport anomalies associated with typical anomalous July–August precipitation patterns over the NCMR can be estimated by regressing the vertically integrated moisture flux anomalies on the corresponding PCs of the precipitation EOF modes. Figures 5d and 5e show the water vapour transport and divergence anomalies of the vertically integrated water vapour transport associated with PC1. A strong convergence of the tropical and subtropical water vapour transport associated with a positive PC1 is found over East Asia. The warmer tropical water vapour flows northeastward along eastern China before meeting cold air from higher latitudes. The anomalous tropical water vapour transport has two branches, one from the South China Sea and the other from the northwest Pacific. The warm water vapour and the cold air eventually converge over the NCMR, accompanied by an upward movement from the lower troposphere to the upper layer in this area (Fig. 5f). These circulation configurations favour more precipitation over the NCMR.

b *Atmospheric Circulation and Water Vapour Transport Characteristics Associated with EOF2*

Figure 6 shows the atmospheric circulation and water vapour transport characteristics associated with PC2. There is more precipitation in NC and less precipitation in NEC in the positive phase of PC2. Compared with the 200 hPa *U* wind fields associated with PC1, the significant positive anomalous westerly winds move westward to southern Lake Baikal and the positive anomaly centre tends to be weaker (Fig. 6a). The correlation coefficients between the intensity and position of the EAWJS and PC2 are −0.12 and 0.16, respectively (Table 1), that is, more precipitation is favoured in NC and less precipitation in NEC when the EAWJS is located farther to the west and north than average.

Figure 6b shows the 500 hPa geopotential height fields associated with the positive phase of PC2. East China is dominated by positive anomalies, with a significant positive anomaly centre situated in NC and western NEC. The

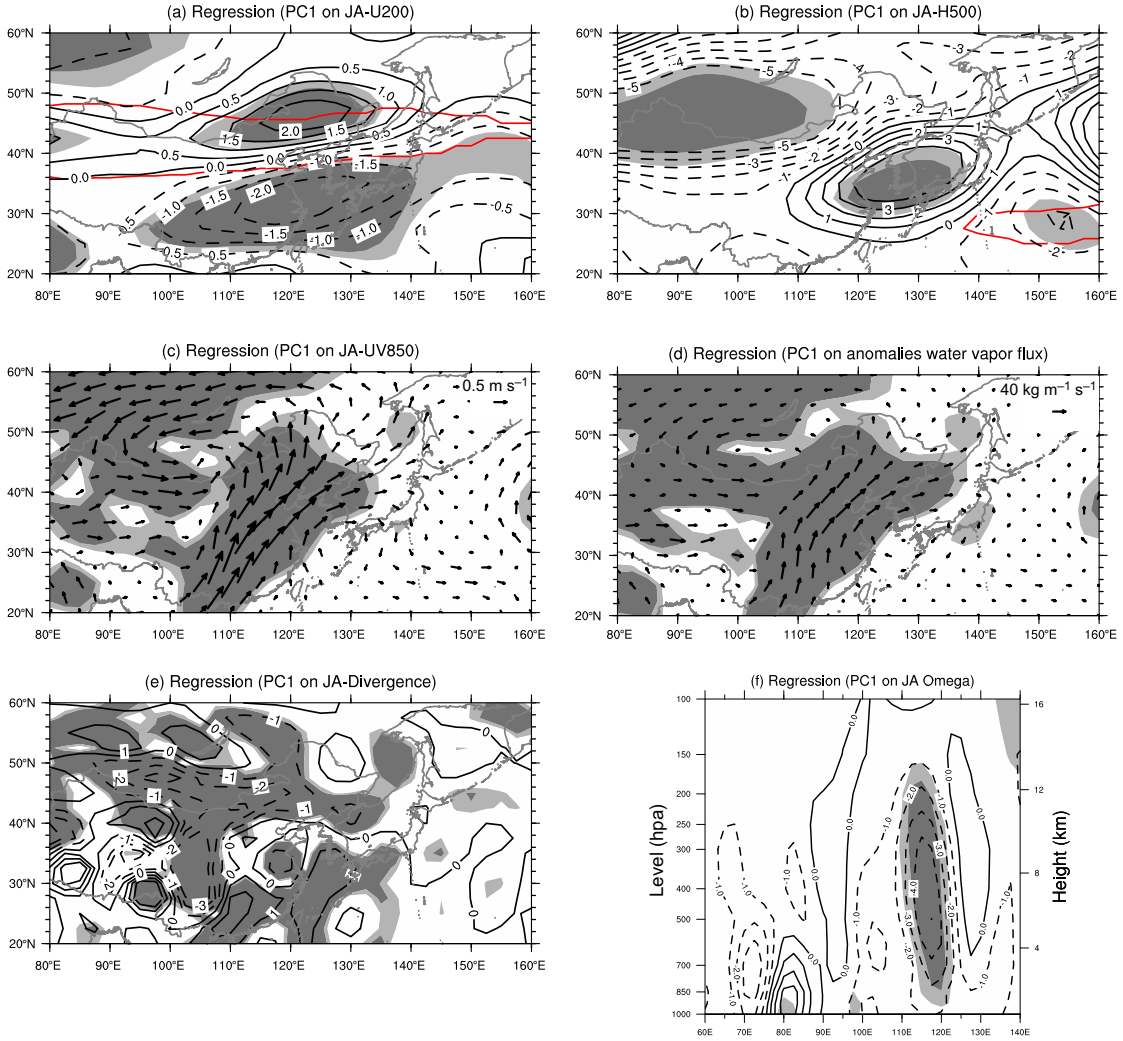

Fig. 5 Regression maps of (a) 200 hPa zonal wind (black lines, m s^{-1}), (b) 500 hPa geopotential height (black lines, gpm), (c) 850 hPa wind (m s^{-1}), (d) vertically integrated water vapour transport from the surface to 300 hPa (kg m^{-1} s^{-1}), (e) divergence anomalies of vertically integrated water vapour transport from the surface to 300 hPa (kg m^{-1} s^{-1}), and (f) longitude cross-sections of omega averaged over 35°–55°N (hPa s^{-1}) on the normalized PC1 of JA precipitation over the NCMR during the 1951–2017 period. The red lines in (a) and (b) indicate the climate mean (1981–2010 average) of the 20 m s^{-1} contour of the 200 hPa zonal wind and the 5880 gpm contour of 500 hPa geopotential height, respectively. Solid (dashed) contours indicate positive (negative) values, and light and dark shading indicate the 95% and 99% confidence levels, respectively.

TABLE 1. Correlation coefficients between the two principal component (PC) time series and indices of key circulation systems; * and ** indicate the 95% and 99% confidence levels, respectively.

Index	PC1	PC2
Position index of the EAWJS	0.25*	0.16
Intensity index of the EAWJS	0.13	−0.12
EIMW index	0.76**	—
SWLBH index	−0.51**	0.11
Area index of the WPSH	−0.27*	−0.01
Intensity index of the WPSH	−0.26*	0.01
Ridge line index of the WPSH	0.20	−0.09
Westward-extending ridge of the WPSH	0.15	0.04
KPH index	0.22	0.05
NCMRH index	—	0.29*
EASM index	0.58**	−0.13

western Pacific to the southeast of the islands of Japan is dominated by significant negative anomalies. This indicates that the 500 hPa geopotential height field anomalies over the NCMR and the WPSH are closely related to EOF2. To quantitatively investigate the relationship between the most significant region and PC2, we defined the NCMR high (NCMRH) index as the area-averaged H_{500} within the area bounded by 40°–47.5°N, 117.5°–122.5°E. The correlation coefficient between the NCMRH index and the NECV (Zhao et al., 2015) is −0.91. This indicates that the NCMRH is a good reflection of the strength of the NECV. The NCMRH index was positive before the mid-1970s and negative after the mid-1990s (figure not shown). It also shows that the NECV was active before the mid-1970s but inactive after the mid-1990s. The correlation coefficient between the NCMRH index and PC2 is 0.29, significant at the 99% confidence level. In addition, the correlation coefficients between the area index, the intensity index, the ridge line index of the WPSH, and the west-extending ridge index and PC2 were −0.01, 0.01, −0.09, and 0.04 (Table 1), respectively, and the

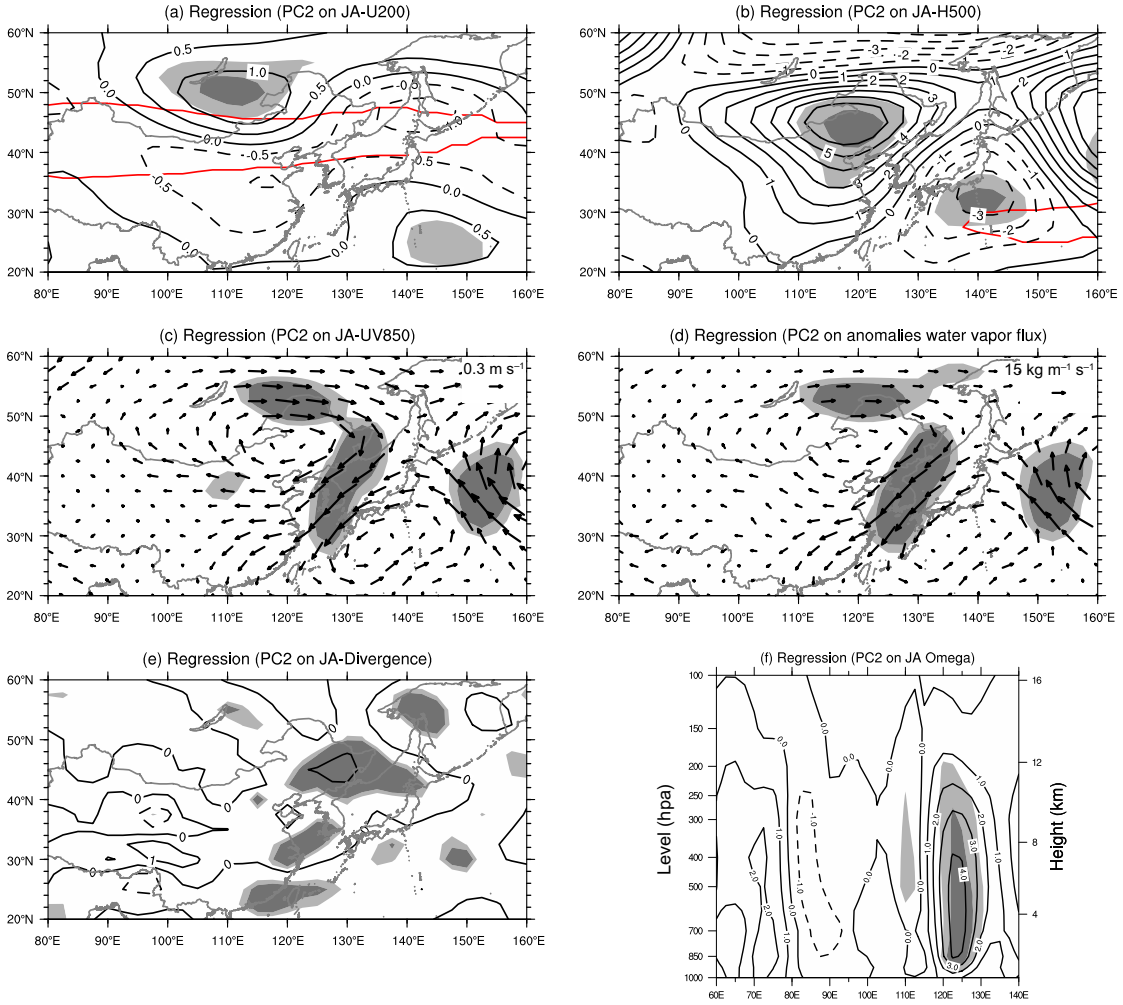

Fig. 6 Regression maps of (a) 200 hPa zonal wind (black lines, m s^{-1}), (b) 500 hPa geopotential height (black lines, gpm), (c) 850 hPa wind (m s^{-1}), (d) vertically integrated water vapour transport from the surface to 300 hPa (kg m^{-1} s^{-1}), (e) divergence anomalies of vertically integrated water vapour transport from the surface to 300 hPa (kg m^{-1} s^{-1}), and (f) longitude cross-sections of omega averaged over 35°–55°N latitude (hPa s^{-1}) on the normalized PC2 of JA precipitation over the NCMR during the 1951–2017 period. The red lines in (a) and (b) indicate the climate mean (1981–2010 average) of the 20 m s^{-1} contour of the 200 hPa zonal wind and the 5880 gpm contour of 500 hPa geopotential height respectively. Solid (dashed) contours: positive (negative) values; light and dark shading indicate the 95% and 99% confidence levels, respectively.

correlation coefficient between the KPH and PC2 was 0.05, indicating that the correlations between the intensity and position of the WPSH and EOF2 were weaker. This reflects the complexity of the EASM systems associated with EOF2.

The 850 hPa wind field associated with PC2 is almost the opposite to that associated with PC1. The region from southeastern Lake Baikal to the NCMR is controlled by an anticyclonic anomaly, whereas the northwest Pacific subtropical area is controlled by a cyclonic anomaly. In addition, southeasterly wind anomalies prevail in NC and northeasterly wind anomalies prevail in NEC (Fig. 6c). The correlation coefficient between PC2 and the July–August EASM index is −0.13 (Table 1), which is not significant at the 95% confidence level.

Figure 6d shows the water vapour transport associated with PC2. Associated with a positive PC2, a strong convergence of the subtropical water vapour transport from the seas around the Korean Peninsula and the islands of Japan is found over NC. The transport of water vapour is a result of anticyclonic circulation from the islands of Japan to NC, rather than the EASM. Northeasterly wind anomalies control the area of NEC, which cause weak water vapour transport and less precipitation.

Figure 6e shows the divergence anomalies of the vertically integrated water vapour transport associated with PC2. It can be seen that the water vapour flux divergence in most parts of the NCMR is insignificant except for a small area in southeastern NEC. Exceptional vertical movement is important in the formation of precipitation. Figure 6f shows a vertical cross-section of the vertical velocity over the NCMR. There is significant ascending motion over NC and a weak descending motion over NEC. Anomalous ascending (descending) motion results in increasing (decreasing) precipitation over NC (NEC). Therefore, it can be concluded that the vertical motion may have a greater influence on the distribution of precipitation over the NCMR than the water vapour divergence anomalies.

TABLE 2. Typical years of PC1 and PC2.

Index	Year
PC1 ≥ 1 (10 years)	1959, 1961, 1963, 1964, 1969, 1985, 1994, 1996, 1998, 2013
PC1≤-1 (11 years)	1968, 1972, 1980, 1989, 1999, 2001, 2002, 2005, 2006, 2014, 2015
PC2 ≥ 1 (8 years)	1958, 1967, 1976, 1979, 1988, 1992, 1996, 2016
PC2≤-1 (9 years)	1957, 1965, 1969, 1985, 1986, 1987, 1991, 1994, 1998

5 Difference in associated atmospheric circulation between EOF1 and EOF2

According to our analysis, there are clear differences in the characteristics of the atmospheric circulation associated with EOF1 and EOF2. Therefore, normalized PC1 and PC2 greater than 1 and less than −1 were selected to represent the typical positive and negative phases of EOF1 and EOF2, respectively. Using this method, the typical positive (negative) phase of EOF1 occurs in 10 (11) years and the typical positive (negative) phase of EOF2 occurs in 8 (9) years during the 1951–2017 period (Table 2).

Figure 7a presents the different distributions of the 500 hPa geopotential height anomalies between the typical positive phases of PC1 and PC2. The most significant negative difference occurs at mid- to high latitudes from the southern Ural Mountains to the NCMR and the subtropical regions from the equator northward to 30°N. A significant positive difference occurs over the islands of Japan. This distribution of high anomalies favours the transport of water vapour to the NCMR and higher levels of precipitation over NC and NEC. In terms of the distribution of the anomaly difference of the 850 hPa wind fields, a cyclonic (anticyclonic) wind anomaly controls the NCMR (the ocean south of the islands of Japan), and the NCMR presents significant southerly wind anomalies (Fig. 7c). This shows that a strong EASM in July–August favours precipitation in NC and NEC and vice versa.

We analyzed the difference in the 500 hPa geopotential height between the typical negative phases of PC1 and PC2. The most significant positive difference occurs from east of central Mongolia to NEC, whereas a significant negative difference occurs in the south of Japan (Fig. 7b). There are anomalous 850 hPa southeast winds over NC, but anomalous northeasterly winds over NEC (Fig. 7d). These differences show that the anticyclonic anomaly over the NCMR and the cyclonic anomaly over the south of Japan favour strengthening (weakening) of water vapour transport to NC (NEC) and vice versa. We conclude that EOF1 is related to the large-scale circulation over East Asia and the northwest Pacific, whereas EOF2 is more closely related to the regional circulation anomaly over the NCMR and the islands of Japan.

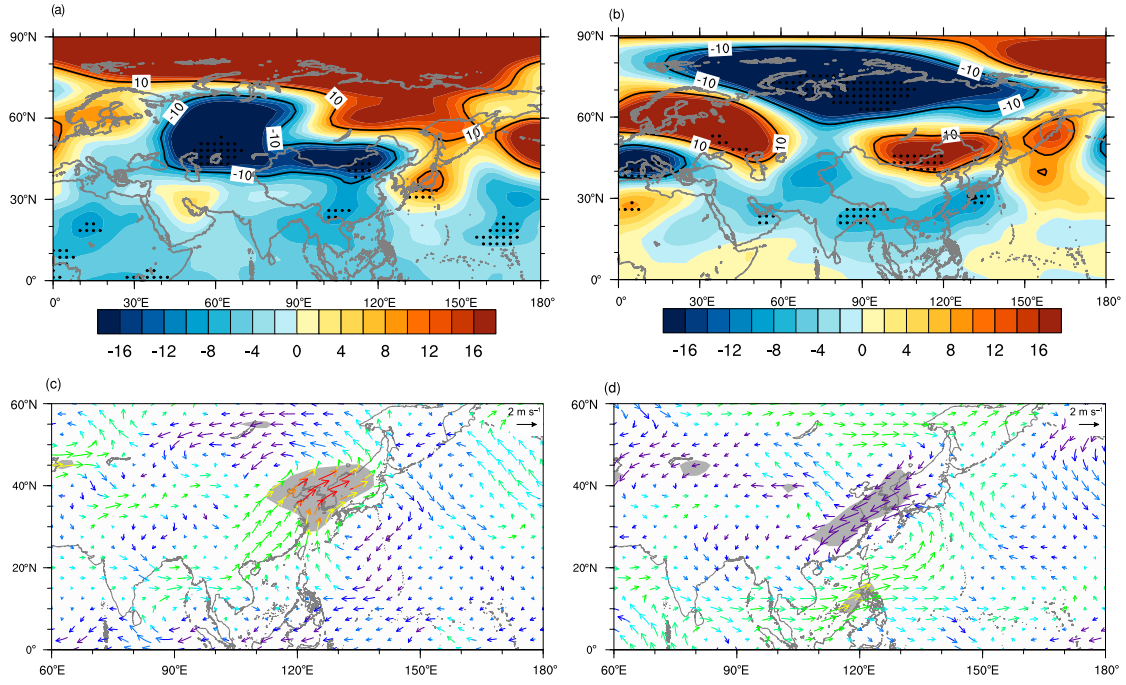

Fig. 7 The difference distributions of JA (a) and (b) 500 hPa geopotential height anomaly and (c) and (d) 850 hPa wind anomaly between EOF1 and EOF2 of JA precipitation over the NCMR during the 1951–2017 period. (a) and (c) Difference between the typical positive phase years of PC1 and PC2. (b) and (d) Difference between the typical negative phase years of PC1 and PC2. The black lines indicate 10 gpm. The black dots in (a) and (b) and the shaded areas in (c) and (d) denote statistical significance at the 95% confidence level.

6 Summary and discussion

We investigated the two major modes of late-summer precipitation over the NCMR using recent 67-year observational datasets and EOF analysis and explored the characteristics of the associated atmospheric circulation through linear regression and correlation analysis; EOF1 and EOF2 reflect a pan-NCMR July–August precipitation variation pattern and a July–August precipitation oscillation pattern between NC and NEC, respectively. These two modes account for 22.1% and 10.1% of the total variance, respectively. Both associated PCs have significant interannual variability with a period of 2–4 years; PC1 also has a significant interdecadal variability with a period of 20–30 years.

Further analysis suggests that there are obvious differences in the associated atmospheric circulation anomalies between the two major modes of July–August precipitation in the NCMR. During the July–August period over East Asia and the northwest Pacific, EOF1 is related to the large-scale circulation anomalies, whereas EOF2 is more closely related to the anomalies of the regional circulation over the NCMR and the islands of Japan. In the positive (negative) phase of PC1, the EAWJS shows a northward (southward) trend with a higher (lower) intensity than normal; the blocking high in the mid- to high latitudes is inactive (active); the WPSH is located to the north (south) of its normal position; and the NCMR is controlled by southerly (northerly) winds, which then cause the convergence (divergence) of water vapour, favouring more (less) precipitation in this region. In the positive phase of PC2, the EAWJS swings to the south of Lake Baikal; there are significant positive height anomalies from western NC to NEC; and significant negative height anomalies exist in the south of Japan, indicating that the cold vortex is inactive, that the WPSH tends to be weaker and located south of its normal position, and that NC (NEC) is dominated by northeasterly (southeasterly) wind anomalies. The convergence (divergence) of water vapour in NC (NEC) favours more (less) precipitation in NC (NEC).

This work analyzed the spatial and temporal characteristics of July–August precipitation over the NCMR and its associated atmospheric circulation characteristics. Our conclusions may be helpful for short-term predictions of July–August droughts and floods in the NCMR. The climate of the NCMR is very complex and is affected by the atmospheric circulation in both tropical and extra-tropical regions as a result of its special location in the mid- to high latitudes of East Asia and on the northern edge of the EASM region. The forecasting skills of the climate model are not entirely satisfactory over the NCMR; therefore, it is difficult to predict the climate in this region. Sea surface temperature anomalies are the main signals in climate prediction, but global warming has led to an interdecadal change in the relationship between these signals and the regional climate (Huijun, 2002; Gao et al., 2006; Han et al., 2018). This makes it harder to predict precipitation in the NCMR. Thus, more research on the instability of the influence of the main sea surface temperature modes on summer droughts and floods over the NCMR will help improve climate prediction. These scientific problems will be studied further in subsequent research.

Disclosure statement

No potential conflict of interest was reported by the authors.

Funding

This work was jointly supported by the National Key Research and Development Program of China [grant number 2017YFC1502303] and the National Natural Science Foundations of China [grant numbers 41875093, 41530531, 41505061, 41705074, and 41675092].

References

Chen, L. X., Zhou, X. J., Li, W. L., Luo, T. F., & Zhu, W. Q. (2004). Characteristics of the climate change and its formation mechanism in China in last 80 years [in Chinese]. *Acta Meteorologica Sinica*, *62*(5), 634–646. doi:10.3321/j.issn:0577-6619.2004.05.010

Dai, X. G., Wang, P., & Chou, J. F. (2003). Multiscale characteristics of the rainy season rainfall and interdecadal decaying of summer monsoon in north China. *Chinese Science Bulletin*, *48*(24), 2730–2734. doi:10.1360/03wd0199

Ding, Y., Wang, Z., & Sun, Y. (2008). Inter-decadal variation of the summer precipitation in East China and its association with decreasing Asian summer monsoon. Part I: Observed evidences. *International Journal of Climatology*, *28*(9), 1139–1161. doi:10.1002/joc.1615

Dong, X., Lin, R. P., & Fan, F. X. (2017). Comparison of the two modes of the western Pacific subtropical high between early and late summer. *Atmospheric Science Letters*, *18*(4), 153–160. doi:10.1002/asl.737

Feng, G., Sun, S., Zhao, J., & Zheng, Z. (2013). Analysis of stable components for extended-range (10–30 days) weather forecast: A case study of continuous overcast-rainy process in early 2009 over the mid-lower reaches of the Yangtze River. *Science China Earth Sciences*, *56*(9), 1576–1587. doi:10.1007/s11430-012-4527-8

Feng, J., Wang, L., & Chen, W. (2014). How does the East Asian summer monsoon behave in the decaying phase of El Niño during different PDO phases? *Journal of Climate*, *27*(7), 2682–2698. doi:10.1175/JCLI-D-13-00015.1

Gao, H., Wang, Y., & He, J. (2006). Weakening significance of ENSO as a predictor of summer precipitation in China. *Geophysical Research Letters*, *33*(9), 9807. doi:10.1029/2005gl025511

Gao, Z., Hu, Z. Z., Zhu, J., Song, Y., Zhang, R. H., Xiao, Z., & Jha, B. (2014). Variability of summer rainfall in northeast China and its connection with spring rainfall variability in the Huang-Huai region and Indian Ocean SST. *Journal of Climate*, *27*(18), 7086–7101. doi:10.1175/JCLI-D-14-00217.1

Gong, Q., Wang, P. X., Wang, H. Y., & Li, L. P. (2005). Constitutes and formation cause of inter-decadal and inter-annual variations of summer rainfall anomalies in northeast China [in Chinese]. *Journal of Nanjing Institute of Meteorology*, *28*(2), 233–240. doi:10.3969/j.issn.1674-7097.2005.02.012

Guo, H., & Zhang, Q. Y. (2016). The dominant modes of precipitation anomalies over eastern China during the northern China rainy season and the possible causes [in Chinese]. *Chinese Journal of Atmospheric Sciences*, *40*(5), 946–964. doi:10.3878/j.issn.1006-9895.1510.15218

Guo, Y., Li, J., & Li, Y. (2012). A time-scale decomposition approach to statistically downscale summer rainfall over north China. *Journal of Climate*, *25*(2), 572–591. doi:10.1175/jcli-d-11-00014.1

Han, T., He, S., Wang, H., & Hao, X. (2018). Enhanced influence of early-spring tropical Indian ocean SST on the following early-summer precipitation over northeast China. *Climate Dynamics*, *51*(11-12), 4065–4076. doi:10.1007/s00382-017-3669-y

He, J., Wu, Z., Jiang, Z., Miao, C., & Han, G. (2007). "Climate effect" of the northeast cold vortex and its influences on Meiyu. *Chinese Science Bulletin*, *52*(5), 671–679. doi:10.1007/s11434-007-0053-z

Huang, R. H., Gu, L., Chen, J. L., & Huang, G. (2008). Recent progress in studies of the temporal-spatial variations of the East Asian monsoon system and their impacts on climate anomalies in China [in Chinese]. *Chinese Journal of Atmospheric Sciences*, *32*(4), 691–719.

Huang, R. H., Xu, Y. H., & Zhou, L. T. (1999). The interdecadal variations of summer precipitation in China and the drought trend in north China [in Chinese]. *Plateau Meteorology*, *18*(4), 465–476. doi:10.3321/j.issn:1000-0534.1999.04.001

Huijun, W. (2002). The instability of the East Asian summer monsoon–ENSO relations. *Advances in Atmospheric Sciences*, *19*(1), 1–11. doi:10.1007/s00376-002-0029-5

Jolliffe, I. T. (2003). A cautionary note on artificial examples of EOFs. *Journal of Climate*, *16*(7), 1084–1086. doi:10.1175/1520-0442(2003)0162.0.CO;2

Kalnay, E., Kanamitsu, M., Kistler, R., Collins, W., Deaven, D., Gandin, L., … Reynolds, R. (1996). The NCEP/NCAR 40-year reanalysis project. *Bulletin of the American Meteorological Society*, *77*(3), 437–471. doi:10.1175/1520-0477(1996)077<0437:TNYRP>2.0.CO;2

Li, C. Y. (1992). An analytical study on the precipitation in the flood period over Huabei area [in Chinese]. *Acta Meteorologica Sinica*, *50*(1), 41–49. doi:10.11676/qxxb1992.005

Li, J. P., & Zeng, Q. C. (2005). A new monsoon index, its interannual variability and relation with monsoon precipitation [in Chinese]. *Climatic and Environmental Research*, *10*(3), 351–365. doi:10.3969/j.issn.1006-9585.2005.03.009

Li, W. J. (1999). General atmospheric circulation anomaly in 1998 and their impact on climate anomaly in China [in Chinese]. *Meteorological Monthly*, *25*(4), 20–25. doi:10.3969/j.issn.1000-0526.1999.04.004

Li, W. J., Zhao, Z. G., Li, X., & Sun, L. H. (2003). The drought characteristics analysis in north China and its causes of formation [in Chinese]. *Arid Meteorology*, *21*(4), 1–5. doi:1006-7639(2003)-04-0001-05

Lian, Y., Shen, B. Z., Gao, Z. T., An, G., & Tang, X. T. (2003). The study of the on-set criterion and the date of Asian summer monsoon in northeast China and its main characteristic analysis [in Chinese]. *Acta Meteorologica Sinica*, *61*(5), 548–559.

Lin, Z., Lu, R., & Wu, R. (2017). Weakened impact of the Indian early summer monsoon on north China rainfall around the late 1970s: Role of basic-state change. *Journal of Climate*, *30*(19), 7991–8005. doi:10.1175/jcli-d-17-0036.1

Lu, R. (2002). Separation of interannual and interdecadal variations of rainfall in north China [in Chinese]. *Chinese Journal of Atmospheric Sciences*, *26*(5), 611–624. doi:10.3878/j.issn.1006-9895.2002.05.03

Ma, Z. G. (2007). The interdecadal trend and shift of dry/wet over the central part of north China and their relationship to the Pacific Decadal Oscillation (PDO). *Chinese Science Bulletin*, *52*(15), 2130–2139. doi:10.1007/s11434-007-0284-z

Ma, Z. G., & Fu, C. B. (2006). Some evidence of drying trend over northern China from 1951 to 2004. *Chinese Science Bulletin*, *51*(23), 2913–2925. doi:10.1007/s11434-006-2159-0

Quan, W. Q., & He, L. F. (2016). Analysis of the July 2016 atmospheric circulation and weather [in Chinese]. *Meteorological Monthly*, *42*(10), 1283–1288. doi:10.7519/j.issn.1000-0526.2016.10.014

Shen, B., Lin, Z., Lu, R., & Lian, Y. (2011). Circulation anomalies associated with interannual variation of early- and late-summer precipitation in northeast China. *Science China Earth Sciences*, *54*(7), 1095–1104. doi:10.1007/s11430-011-4173-6

Shi, N., & Zhu, Q. (1996). An abrupt change in the intensity of the East Asian summer monsoon index and its relationship with temperature and precipitation over East China. *International Journal of Climatology*, *16*(7), 757–764. doi:10.1002/(SICI)1097-0088(199607)16:7<757::AID-JOC50>3.0.CO;2-5

Sun, J. H., Zhao, S. X., Fu, S. M., Wang, H. J., & Zheng, L. L. (2013). Multi-scale characteristics of record heavy rainfall over Beijing area on July 21, 2012 [in Chinese]. *Chinese Journal of Atmospheric Sciences*, *37*(3), 705–718. doi:10.3878/j.issn.1006-9895.2013.12202

Sun, L., An, G., Ding, L., & Shen, B. Z. (2000). A climatic analysis of summer precipitation features and anomaly in northeast China [in Chinese]. *Acta Meteorologica Sinica*, *58*(1), 70–82. doi:10.3321/j.issn:0577-6619.2000.01.007

Sun, L., Shen, B., Sui, B., & Huang, B. (2017). The influences of East Asian Monsoon on summer precipitation in northeast China. *Climate Dynamics*, *48*(5-6), 1647–1659. doi:10.1007/s00382-016-3165-9

Wei, F. Y. (2007). *Statistical diagnosis and prediction technology of modern climate* (pp. 105–125). Beijing: Meteorological Press.

Yao, X. P., & Dong, M. (2000). Research on the features of summer rainfall in northeast China [in Chinese]. *Journal of Applied Meteorological Science*, *11*(3), 297–303. doi:10.3969/j.issn.1001-7313.2000.03.006

Zhang, Q. Y., Tao, S. Y., & Chen, L. T. (2003b). The inter-annual variability of East Asian summer monsoon indices and its association with the pattern of general circulation over East Asia [in Chinese]. *Acta Meteorologica Sinica*, *61*(5), 559–568. doi:10.3321/j.issn:0577-6619.2003.05.005

Zhang, Q. Y., Wei, J., & Tao, S. Y. (2003a). A study of excessively heavy rainfall in the Songhuajiang-Nenjiang River valley in 1998 [in Chinese]. *Chinese Journal of Atmospheric Sciences*, *25*(4), 567–576. doi:10.3878/j.issn.1006-9895.2001.04.13

Zhang, Y. (2005). Relationship between the simulated East Asian westerly jet biases and seasonal evolution of rainbelt over eastern China. *Chinese Science Bulletin*, *50*(14), 1503. doi:10.1360/982004-361

Zhao, J. H., Yang, L., & Feng, G. L. (2018). Circulation system configuration characteristics of four rainfall patterns in summer over the East China. *Theoretical and Applied Climatology*, *131*(3-4), 1211–1219. doi:10.1007/s00704-017-2047-3

Zhao, J. H., Yang, L., Hou, W., Liu, G., & Zeng, Y. X. (2015). Extra-seasonal prediction of summer 500-hPa height field in the area of cold vortices over East Asia with a dynamical-statistical method. *Chinese Physics B*, *24*(5), 059202. doi:10.1088/1674-1056/24/5/059202

Zhao, J. H., Zhou, J., Yang, L., Hou, W., & Feng, G. L. (2018). Inter-annual and inter-decadal variability of early- and late-summer precipitation over northeast China and their background circulation. *International Journal of Climatology*, *38*(6), 2880–2888. doi:10.1002/joc.5470

Zhao, Z. G. (1999). *Drought/flood and environment field of summer in China* (pp. 68–72 [in Chinese]). Beijing: China Meteorological Press.

Zhu, Y. M., & Yang, X. Q. (2003). Relationships between Pacific Decadal Oscillation (PDO) and climate variabilities in China [in Chinese]. *Acta Meteorologica Sinica*, *61*(6), 641–654. doi:10.3321/j.issn:0577-6619.2003.06.001

A Significant Bias of T_{max} and T_{min} Average Temperature and Its Trend

YULIAN LIU

Department of Atmospheric Science, School of Environmental Science, China University of Geosciences, Wuhan, and Heilongjiang Climate Center, Harbin, China

GUOYU REN

Department of Atmospheric Science, School of Environmental Science, China University of Geosciences, Wuhan, and Laboratory for Climate Studies, National Climate Center, China Meteorological Administration, Beijing, China

ENGYUAN KANG

Harbin Meteorological Bureau, Harbin, China

XIUBAO SUN

Laboratory for Climate Studies, National Climate Center, China Meteorological Administration, Beijing, China

(Manuscript received 12 January 2019, in final form 28 May 2019)

ABSTRACT

The systematic bias of the estimated average temperature using daily T_{max} and T_{min} records relative to the standard average temperature of four time-equidistant observations and its effect on the estimated trend of long-term temperature change have not been well understood. This paper attempts to evaluate the systematic bias across mainland China using the daily data of national observational stations. The results revealed that the positive bias of annual mean temperature was large, reaching 0.58°C nationally on average; regional average bias was lowest in the northwest arid region and highest in the Qinghai–Tibetan Plateau; the bias was low in spring and summer and high in autumn and winter, reaching its lowest point in mid- and late May and highest point in early November. Furthermore, the bias showed a significant upward trend in the past 50 years, with a rising rate of 0.021°C $(10\ yr)^{-1}$, accounting for about 12% of the overall warming as estimated from the data of the observational network; the largest positive trend bias was found in the northwest arid region, while the east monsoon region experienced the smallest change; the most remarkable increase of the bias occurred after early 1990s. These results indicate that the customarily applied method to calculate daily and monthly mean temperature using T_{max} and T_{min} significantly overestimates the climatological mean and the long-term trend of surface air temperature in mainland China.

1. Introduction

Temperature is an indicator of thermal state that characterizes a warm or cold climatic condition and is one of the basic climatic variables. Accurately estimating daily mean temperature, however, is affected by the observations and the statistical methods used for calculating average temperature. To understand the possible effect of current observational practices and statistical methods on daily and monthly mean temperature estimates, therefore, has important significance for both climatological and climate change research (Brooks 1921; Edwards 1982; Tang and Ding 2007).

Currently, the T_{max} and T_{min} are more frequently shared in the international exchange data, and usually the daily mean temperature can be obtained by averaging the maximum and minimum temperatures (i.e., the max–min average method). Furthermore, several datasets of global land historical temperature primarily use the max–min average method to calculate the daily and monthly mean temperatures (Lawrimore et al. 2011; Jones et al. 2012; Morice et al. 2012; Sun et al. 2018). According to the *Specifications for Surface Meteorological Observation (2003)* of the China Meteorological Administration

Corresponding author: G. Ren, guoyoo@cma.gov.cn

DOI: 10.1175/JAMC-D-19-0001.1

© 2019 American Meteorological Society. For information regarding reuse of this content and general copyright information, consult the AMS Copyright Policy (www.ametsoc.org/PUBSReuseLicenses).

(CMA 2003), however, it is stipulated that the daily mean temperature of the national meteorological stations be calculated based on the average of 4 temperatures recorded at 0200, 0800, 1400, and 2000 Beijing time. This 4-time-observation average is the most frequently used average temperature in the national meteorological service and the scientific research works conducted in China (Tang and Ren 2005; Ren 2008; Li and Yan 2009; Cao et al. 2013).

In the studies conducted by Brooks (1921), Miller (1976), and Edwards (1982), it is shown that the annual and seasonal mean temperatures obtained using the max–min average method are generally higher than the mean temperatures estimated based on records at regular intervals like the 4-time-observation method. Additionally, Tang and Ren (2005) and Tang and Ding (2007) compared the monthly and annual mean temperature obtained from the max–min average method versus the temperature obtained from averaging four regular observations for eastern China and concluded that the difference in the temperature anomaly series and the rate of temperature increase was not significant. Moreover, Tang and Ren (2005) and Tang and Ding (2007) found that, when a large enough number of stations are used, the two methods were interchangeable. However, the research in China only used the observation data from a limited number of stations and focused on the influence of the estimation of temperature trends in the previous works; the systematic analysis of the error as calculated by using the max–min average method is lacking.

Some works have been focused on data homogenization and uncertainties (e.g., Thompson et al. 2008; Ren 2008; Jones and Stott 2011; Kennedy et al. 2011). Considering the inhomogeneities and uncertainties, however, the previous studies found, by using the monthly and annual mean temperature as an indicator, that global and regional climates had been in a significant warming trend (IPCC 2013; Carrasco 2013; Osborn and Jones 2014; Kothawale et al. 2010, 2016). This warming is characterized by an asymmetry between the maximum and minimum temperatures (Karl et al. 1993; Qian and Lin 2004; Rehman and Al-Hadhrami2012; Samba and Nganga 2014; Chen et al. 2007). The following problems remained, however: 1) what is the difference between the temperatures obtained from the max–min average method and from the average of 4-time-observation per day at equal intervals? 2) How does this difference (i.e., temperature bias), if it exists, vary spatially and seasonally? Finally, 3) how much does the bias affect the estimation for the trend of long-term temperature change? Currently, our understanding of these issues is insufficient both in China and around the world.

This study focuses on the three questions by taking China as an example. Using the observation data of daily and hourly temperature of the national reference climate and basic meteorological station network, the temperature bias in different regions and seasons, and its effect on the estimate of long-term change of temperature, was analyzed. The analysis results will provide new insights into the systematic errors of surface air temperature and its change as calculated from the max–min average method for studies of climatological and climate change.

2. Data and methods

a. Data collection

The daily data were from the National Meteorological Information Center, CMA. The Daily Dataset of China's Surface Climatic Data, version 3.0 (V3.0), contained the daily temperature data [the daily mean (4-time observations), daily maximum, and daily minimum records] of the Chinese national reference climate and basic meteorological stations since 1 January 1951. To ensure the accuracy of the observation records at stations and to avoid the analysis bias caused by the short-term absence of measurements at individual stations, only data from stations with complete records and consecutive observations were retained. Thus this study applied data of 719 stations with complete records ranging from 1964 to 2013. The data were quality controlled but not homogenized for possible inhomogeneities induced by relocation and instrumentation.

To examine the effect of homogenization on temperature bias and its trends, the homogenized data from monthly mean temperature based on 4-time observations (Li et al. 2004) and the maximum and minimum temperature data from the same 719 stations were also used [the China Homogenized Historical Temperature Dataset (CHHTD-V1.0)] to evaluate the difference of the results by using the two datasets. The distribution of the annual and monthly mean temperature biases were analyzed using both the raw and the homogenized data.

b. Methodology

To understand the long-term trend of temperature change, the correlation coefficient (i.e., trend coefficient) between temperature and time sequence of observational years was calculated according to the method outlined in Von Storch and Zwiers (2003) and Shi et al. (2003). The trend coefficients defined in this way are dimensionless and vary between $[-1, 1]$. This minimizes the effect of variance of meteorological variables and the unit on the numerical values of linear regression coefficients,

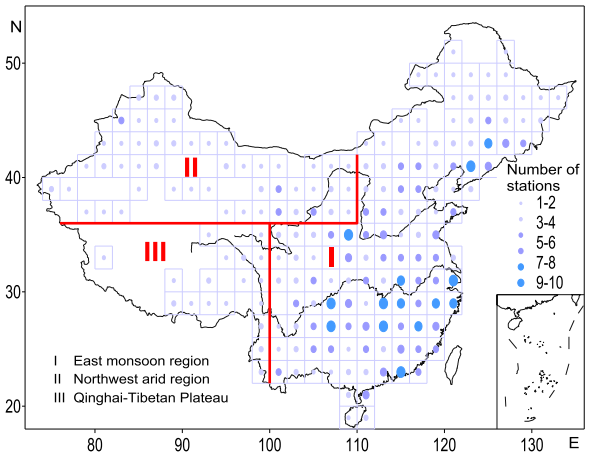

FIG. 1. Distribution of longitude–latitude boxes of 2.0° × 2.0° with observational stations, and the boundaries of three subregions. The values in the boxes are the numbers of stations. The three subregions: east monsoon region (region 1), northwest arid region (region 2), and the Qinghai–Tibetan Plateau (region 3).

and thus makes it easily comparable across geographical locations and suitable for studying the spatial characteristics of long-term trends of large-scale temperature change.

There were more stations distributed in the east than in the west. If regional average is calculated by simple arithmetic mean of all the sites with equal weights, then the data from the eastern region will outweigh that from the western region. To avoid this imbalance, the method by Jones and Hulme (1996) was utilized. According to this method, the average regional climatic time series are calculated by using an area-weighted average procedure.

The whole study region was divided into longitude–latitude boxes of 2.0° × 2.0°. A total 196 effective boxes with more than one station in each throughout mainland China was produced (Fig. 1). When calculating the national or regional average series, the arithmetic mean of the temperature recorded by the stations in each box was calculated first to obtain box averages; the cosine of the center latitude of each box was used as the weight coefficient and the regional average time series was then calculated by using the area-weighted average method.

The study region is divided into three subregions referring to G. Y. Ren et al. (2016): the east monsoon region (region 1), the northwest arid region (region 2), and the Qinghai–Tibetan Plateau (region 3). For the temperature analysis and the convenience of calculation, the boundaries of the three subregions were further simplified on basis of the previous studies (Ding et al. 2013; G. Y. Ren et al. 2016) (Fig. 1).

c. Statistical analysis

Following equation was used to calculate the temperature bias of the max–min average from the 4-time observation average:

$$T_d = T_{\mathrm{mn}} - T_4, \tag{1}$$

where T_d is the temperature bias, T_{mn} is the average temperature calculated using the max–min average method, and T_4 is the average temperature obtained using the 4-time observations at 0200, 0800, 1400, and 2000 Beijing time; T_{dh} was defined as T_d based on the homogenized temperature data.

To address whether T_4 could be used as a criterion or reference temperature for evaluating the temperature bias, we compared the 24-h observation data (T_{24}) of 3 stations located in northern China (from east to west): Jixi, Beijing, and Urumqi stations. The deviation of T_4 relative to T_{24} (Table 1) was calculated. T_{24} is the daily mean temperature of 24-h observations (hourly means). The months January, April, July, and October were used as representatives for winter, spring, summer, and autumn, respectively.

The mean temperature values for T_4 and T_{24} were calculated for 2017; there were certain differences in these values. Namely, T_4 values of Beijing and Urumqi stations were lower than T_{24} with an accuracy of 10^{-2}°C (−0.043° and −0.077°C, respectively). The T_4 of Jixi station was higher than T_{24} with an accuracy of 10^{-3}°C (0.001°C). The T_4 of Beijing station was higher than T_{24} in spring with accuracy of 10^{-1}°C, but lower than T_{24} in other seasons, particularly in winter. The T_4 of Jixi station was lower than T_{24} in summer, but higher than T_{24} in other seasons. The T_4 of Urumqi station was higher than T_{24} in winter and lower than T_{24} in other seasons. However, the biases of T_4 relative to T_{24} were small overall, and the average annual mean absolute difference was well below 0.04°C, one magnitude of power lower than T_d as seen below. Therefore, the bias of the T_{mn} can be evaluated using T_4 as a benchmark. The reason for the applicability of the T_4 as standard to assess the uncertainty of T_{mn} will further discussed below.

The analysis period was from 1964 to 2013. The seasonal division was made using the definition of meteorological season. Winter included December of the previous year, and January and February; spring included March, April, and May; summer included June, July, and August; and autumn included September, October, and November. The seasonal mean temperature was calculated as the average of the 3 monthly mean temperatures in the season. The annual mean temperature was calculated as the average across the 12 months. Decadal means were also calculated, where

TABLE 1. Comparison of average difference between T_4 and T_{24} at three meteorological stations of northern China (Jixi, Beijing, Urumqi) in 2017.

Station	Latitude (°N)	Longitude (°E)	Altitude (m)	January (°C)	April (°C)	July (°C)	October (°C)	Annual (°C)
Jixi	45.3	130.92	272.5	0.000	0.074	−0.011	0.039	0.001
Beijing	39.8	116.47	31.3	−0.143	0.126	−0.019	−0.039	−0.043
Urumqi	43.78	87.65	935	0.020	−0.118	−0.137	−0.072	−0.077
Average				−0.041	0.027	−0.056	−0.024	−0.040

the first 10 years for decadal means ranged from 1964 to 1973, and the fifth decade ranged from 2004 to 2013.

The significance of linear trend in the analysis was examined by the correlation coefficient using the two tailed *t*-test method. Under the assumption that the correlation coefficient $p = 0$ is established, the probability density function of the correlation coefficient r is the density function of the t distribution, and the statistic

$$t = \text{sqrt}(n-2)r/\text{sqrt}(1-r^2) \quad (2)$$

follows a t distribution with a degree of freedom (d.f.) $n - 2$. Given a significance level α, and if $t \geq t_\alpha$, the correlation coefficient is considered significant. The linear trend of α over 0.05 (0.01) significance level was expressed as $p \leq 0.05$ (0.01).

3. Results

a. National and regional average T_d

The analysis results for annual and seasonal mean T_d for the country and different regions are shown in Table 2. The T_d values were positive in every season of every region of mainland China. The national average annual mean T_d was 0.58°C. The average T_d was the highest in region 3 (0.85°C), and the lowest in region 2 (0.47°C). In all seasons, the average T_d values in region 3 were the highest, with the maximum value in autumn (1.07°C). In spring and summer, the T_d values of region 2 were the lowest (0.21° and 0.27°C, respectively). The annual and seasonal mean T_d values of region 1 were close to the national averages. The values of autumn and winter were relatively high, while the spring and summer were lower.

b. Spatial distribution of T_d

T_d values were positive in most parts of the country, indicating a universally higher average of the T_{mn} than that of T_4 (Fig. 2). The areas with a high T_d value were located in the eastern part of the Qinghai–Tibetan Plateau (region 3) and the Sichuan basin and the Yunnan–Guizhou Plateaus, where T_d was greater than 1.00°C. The highest values were found at Malcolm of Sichuan (1.85°C) and Mengla of Yunnan (1.62°C). The T_d values of regions 2 and 1 were relatively low (less than 0.4°C). Only two stations in the whole study region showed a small negative T_d (i.e., the T_{mn} is lower than that of T_4). They were Shiquanhe station in Tibet (−0.09°C) and Kumux station in Xinjiang (−0.04°C).

All national average seasonal mean T_d values were positive for each season, with the lowest value in the spring (0.43°C) followed by the summer (0.46°C) (Fig. 3). The autumn mean T_d value was the highest (0.74°C), followed by the winter (0.71°C). In the areas south of 30°N in mainland China, T_d was positive for all seasons. The areas with high seasonal mean values were found in the eastern part of the Qinghai–Tibetan Plateau (region 3), where the autumn and winter mean T_d was higher than those of other seasons (2.21° and 2.01°C, respectively), indicating a very large bias of seasonal mean T_{mn}. There were no negative T_d values in the winter for the whole country; negative T_d values only appeared in western Tibet in the autumn (−0.20°C), and in western Tibet and northern China in the spring and summer (−0.44° and −0.37°C, respectively).

c. Seasonal variation of T_d

Figure 4 shows the within-year variations in daily mean T_d averaged for 30 years of 1981–2010 in mainland China and the three subregions. The daily mean T_d series, starting from 1 January, experienced a decrease–increase–decrease variation within a year (Fig. 4). In late January, the T_d value in region 3 was noticeably lower, while the T_d values in region 1 and 2 did not notably decrease. The T_d values of region 1 and 2 rapidly decreased in

TABLE 2. Regional average annual and seasonal mean T_d for mainland China and the three subregions (1981–2010) (unit: °C).

	East monsoon region (region 1)	Northwest arid region (region 2)	Qinghai–Tibetan Plateau (region 3)	Mainland China
Spring	0.46	0.27	0.61	0.43
Summer	0.49	0.21	0.85	0.46
Autumn	0.69	0.71	1.07	0.74
Winter	0.68	0.69	0.88	0.71
Year	0.58	0.47	0.85	0.58

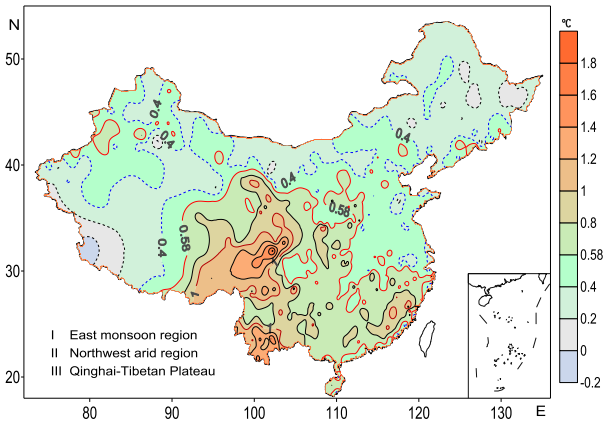

FIG. 2. The spatial distribution of annual mean T_d in mainland China (1981–2010) (red line = 0. 58; blue line = 0.40; brown = 1.00) (unit: °C).

mid-February and this decrease continued through mid- and late May. The T_d value of region 3 stopped decreasing in late February to early March, when it began to slightly increase. This increase continued through late September when there was another noticeable decline. The T_d values of region 1 and 2 rose at the beginning of June, peaked in early November, and then decreased. The T_d of region 2 declined relatively quickly from April to May, showing a large fluctuation in the bias of T_{mn}. The T_d of region 3 also showed a large fluctuation in February and December.

It is also notable from Fig. 4 that the differences of daily mean T_d among the three subregions were generally small during winter, but large during spring and early summer. The largest difference appeared between region 2 and region 3 from late April to early June, reaching 0.70°C, and the smallest difference was seen between region 1 and region 2 during wintertime. In addition, a larger variability of daily mean T_d was obvious in region 2 during period of mid- to late April.

d. The long-term change of T_d

From 1964 to 2013, both annual mean T_{mn} and T_4 in mainland China showed a significant upward trend, as shown in Fig. 5. The temperature increase rate of annual mean T_{mn} is 0.318°C $(10\,\text{yr})^{-1}$ (d.f. = 48, t = 8.167, p = 0.001), and the annual mean T_4 increase at a rate of 0.297°C $(10\,\text{yr})^{-1}$ (d.f. = 48, t = 8.167, p = 0.001).

It is also clear from Fig. 5 that all annual mean T_d values were positive from 1964 to 2013 and exhibited a significant upward trend with a rising rate of 0.021°C $(10\,\text{yr})^{-1}$ (d.f. = 48, t = 9.653, p = 0.001). Since the beginning of the twenty-first century, this increase has become more notable and the annual mean T_d was

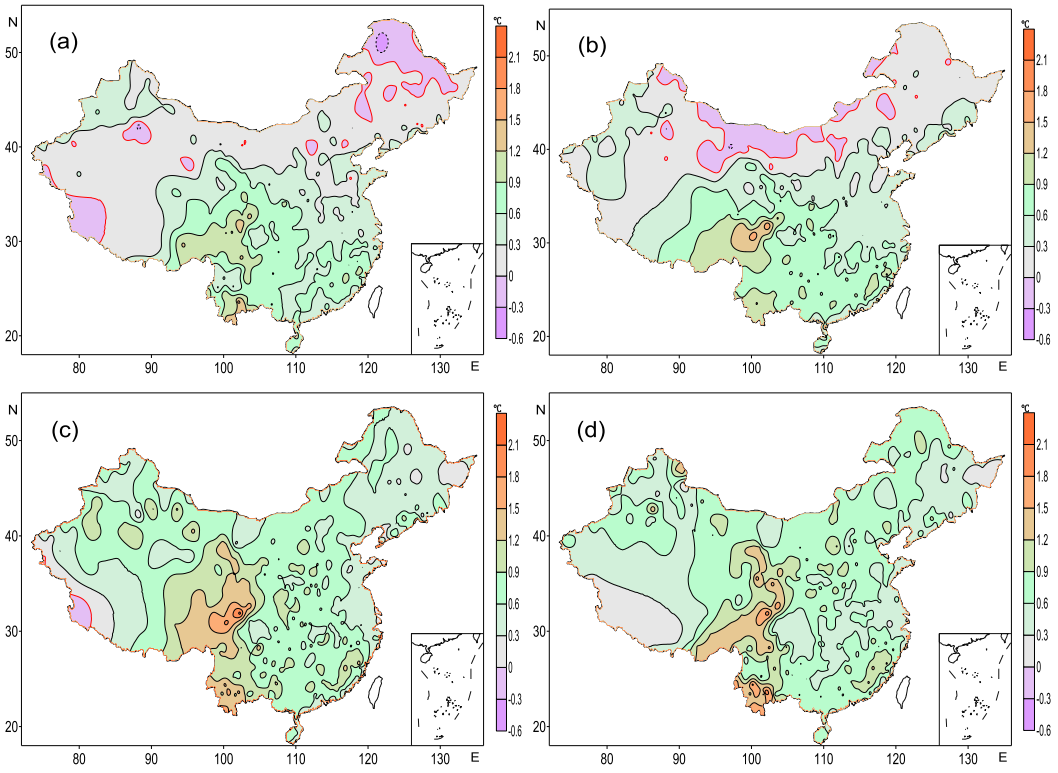

FIG. 3. Spatial distribution of seasonal mean T_d in mainland China (1981–2010): (a) spring, (b) summer, (c) autumn, and (d) winter (unit: °C).

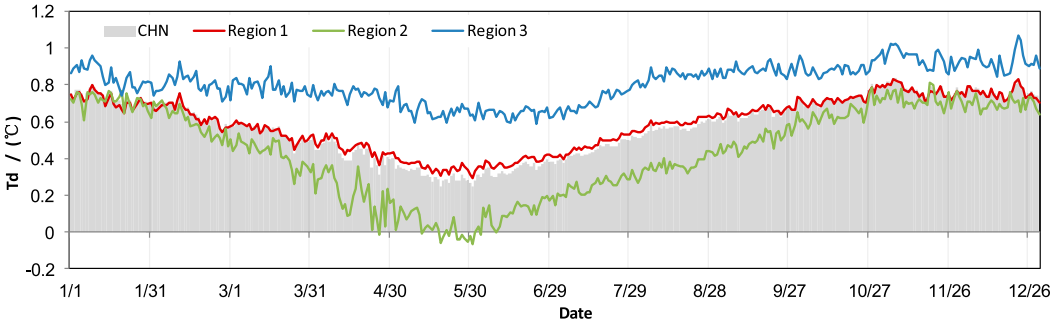

FIG. 4. The seasonal variation of daily mean T_d in mainland China and the three subregions (1981–2010): 1/1 denotes 1 Jan and 12/26 denotes 26 Dec. CHN: mainland China. Region 1: east monsoon region; region 2: northwest arid region; region 3: Qinghai–Tibetan Plateau.

higher than the average from 1981 to 2010. After 2008, however, the T_d underwent a slight decrease, but it rose again in 2013 with a historical maximum value (0.63°C) registered.

The annual mean T_d values of all 3 subregions were positive and exhibited significant upward trends from 1964 to 2013 (Fig. 6). The most apparent increase appeared in the twenty-first century, when all T_d values were above the 30-year average. The highest rising rate was in region 2 [0.027°C $(10\,\text{yr})^{-1}$, d.f. = 48, t = 8.810, p = 0.001], followed by region 3 [0.022°C $(10\,\text{yr})^{-1}$, d.f. = 48, t = 5.259, p = 0.001]. In contrast, the rising rate of T_d in region 1 was lower [0.018°C $(10\,\text{yr})^{-1}$, d.f. = 48, t = 9.097, p = 0.001].

Figure 7 shows that, for each season, the T_d value of region 3 was the highest, and the seasonal mean values were 0.61°, 0.85°, 1.07°, and 0.88°C for spring, summer, autumn, and winter, respectively (Fig. 7). In the summer, the T_d value of region 3 was 0.64°C higher than region 2, and 0.36°C higher than region 1. All of the seasonal mean T_d values in the three subregions and in the country as a whole showed upward trends during 1964–2013, with the most obvious increases generally occurring after 2000. In the autumn, the T_d value of region 3 was 0.36°C higher than region 2, and 0.39°C higher than region 1. The possible causes for the accelerated increase in more recent years needs to be further examined, but it may have been related to the more widespread urbanization, which will result in a greater increase in $T_{\min}$ in the north and in $T_{\max}$ in the south (Ren and Zhou 2014), or the alleviated air pollution (Wang and Yang 2014; Lowsen and Conway 2016), which leads to a more rapid increase in $T_{\max}$.

The linear trend and significance test results of seasonal mean T_d in different subregions and in mainland China on a whole are shown in Table 3. There was a significant increasing trend in annual and seasonal mean T_d for the 3 regions and for mainland China as a whole, except for winter for region 1, region 2, and the whole region (Table 3). The maximum linear increasing trend was found for summer in region 1 and region 2, whereas in region 3, it appeared in spring. In view of annual mean temperature, the increasing bias shown in Table 3 accounts for about 12% of the overall

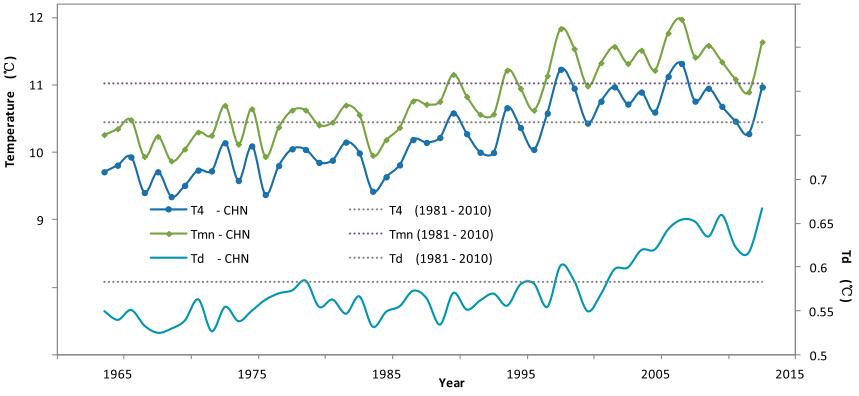

FIG. 5. Change in national average annual mean T_4, T_{mn}, and T_d values in mainland China during 1964–2013 (unit: °C). CHN: mainland China.

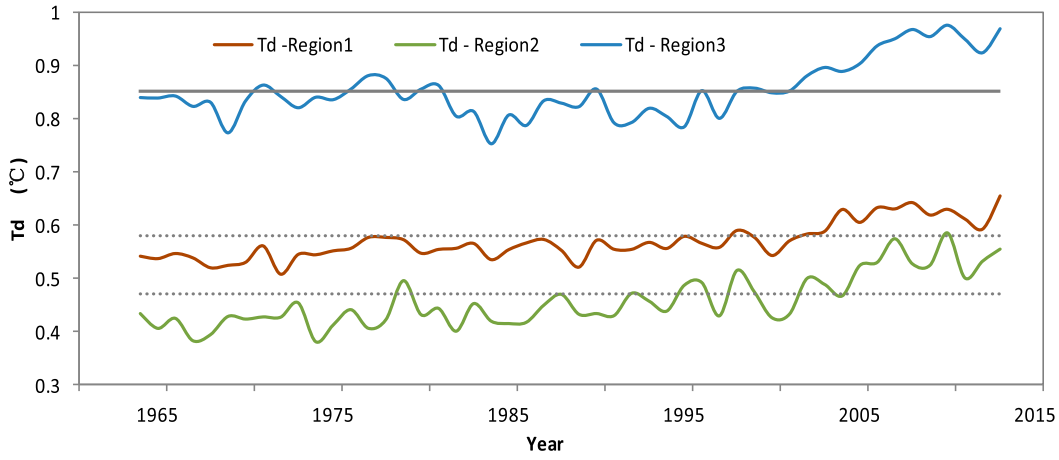

FIG. 6. Change in regional average annual mean T_d values in different subregions of mainland China during 1964–2013 (unit: °C). Region 1: east monsoon region; region 2: northwest arid region; region 3: Qinghai–Tibetan Plateau.

warming as estimated from the data of the national observational network.

4. Discussion

Previous studies pointed out that the daily and monthly mean temperature values obtained from the max–min average method show some differences from the "real" average temperature (Brooks 1921; Miller 1976; Edwards 1982; Tang and Ren 2005; Tang and Ding 2007). Therefore, there is certain bias of the daily and monthly mean temperature as calculated from the daily T_{max} and T_{min} records. In this study, the magnitude and detailed spatial–temporal pattern of the bias, and in particular the trend of its long-term change, were analyzed with the mainland China as an example.

The analysis revealed that the daily mean temperature value obtained from the max–min average method was warmer than the standard 4-time observation average. The national average annual mean T_d reached 0.58°C, with the Qinghai–Tibetan Plateau (region 3) as large as 0.85°C. The average T_d of autumn and winter were even higher. The analysis results also showed that the annual and seasonal mean T_d values exhibited a significant upward trend from 1964 to 2013, with the rate of increase in mainland China average annual mean T_d reaching 0.021°C $(10\,\text{yr})^{-1}$. The trends of increase in three subregion average annual and seasonal mean T_d was also significant, with the exception for winter.

Overall, the T_{mn} average values were higher than the T_4 or T_{24}. This is because the former only has two observational points in a day, before sunrise and in the afternoon (at about 0600 and 1400 Beijing time near 120°E in spring and autumn, respectively). The two observational points are separated by only 8 h, with the records of 0200 and 2000 Beijing time in the T_4 absent (Fig. 8). They are therefore more affected by the daytime surface heat condition and especially the impact of the hottest afternoon period, but they escape in a larger extent from the effects of ground thermal conditions of nighttime when the surface air is colder than the daytime.

In the eastern part of northeast China and western China, the daily T_{max} and T_{min} occur slightly earlier or later than those in Beijing. In western China, the T_{max} and T_{min} occur 3 h later at most than those in Beijing. The interval between the occurrence of the T_{max} and T_{min} does not increase. Therefore, the T_{mn} values still have large biases in terms of daily mean temperature in these regions far away from the meridian of 120°E. The impact of time difference between east and west of the country on T_4 and T_{24} would be minor, because the four times of observations are made with an equal interval (6 and 1 h) in a day.

Additionally, climatic conditions of the observational stations may have an effect on the T_d value (Fig. 9). The other factors that could affect the T_d value include humidity, wind speed, elevation, and precipitation days (Fig. 9). Precipitation day refers to the day with precipitation greater than or equal to 0.1 mm from 0800 to 0800 Beijing time. Clearly, the annual mean T_d values show a positive correlation with relative humidity (r = 0.30), elevation (r = 0.32), and precipitation days (r = 0.53). The T_d values exhibit a significant negative correlation with the average wind speed (r = −0.51). In regions with higher relative humidity and more precipitation days, the T_d values were larger. The T_d values were also large in the high-elevation areas, and in regions that had a small annual mean wind speed.

The T_d values were larger in areas with high humidity and more precipitation days. This is likely related to the abundance of atmospheric moisture in these areas and a

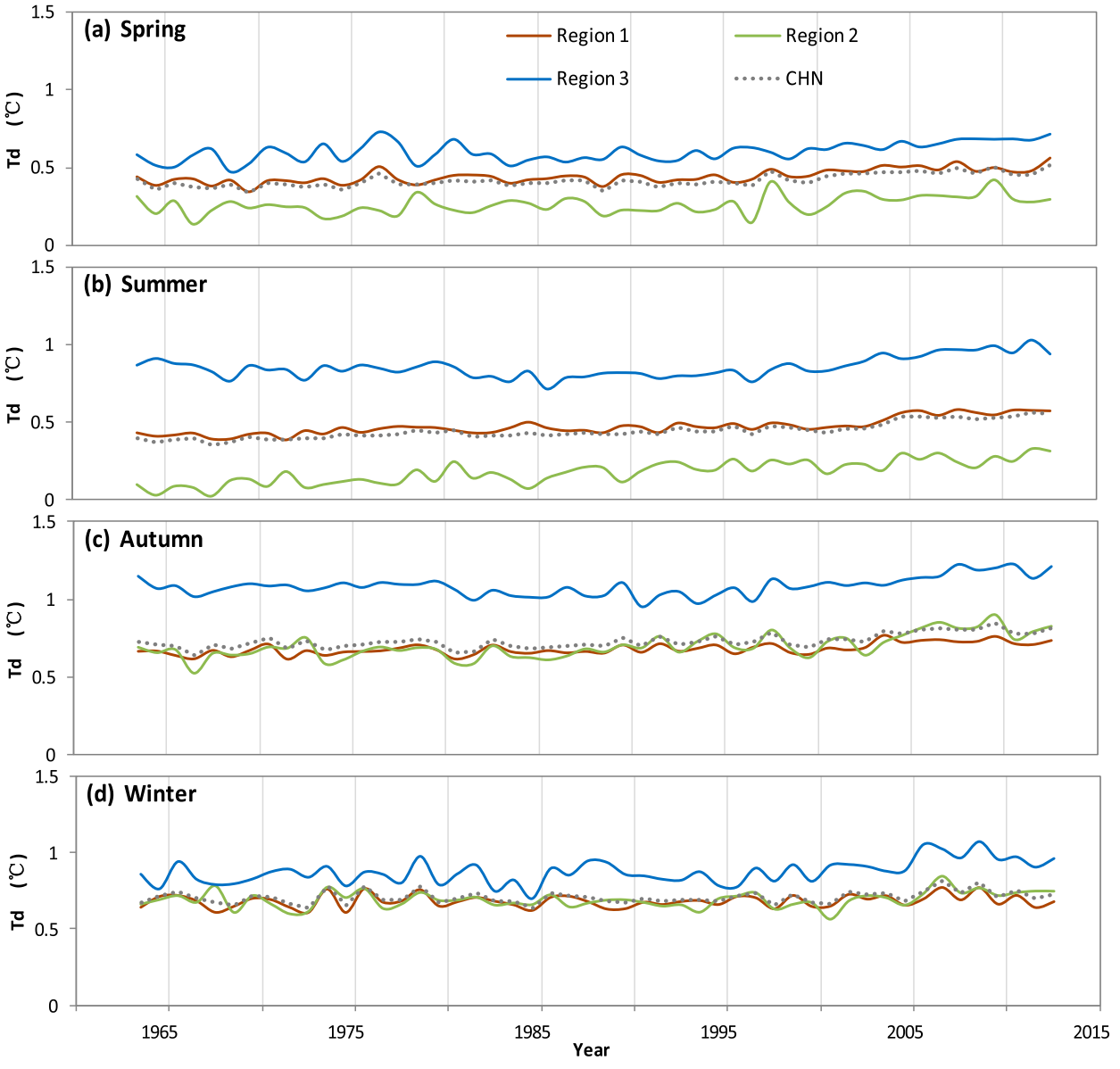

FIG. 7. Change in seasonal mean T_d values in mainland China and the different subregions during 1964–2013: (a) spring, (b) summer, (c) autumn, and (d) winter) (unit: °C). Region 1: east monsoon region; region 2: northwest arid region; region 3: Qinghai–Tibetan Plateau.

high cloudiness. Higher atmospheric relative humidity and cloudiness at the coldest stage of the early morning can cause the minimum temperature to be higher due to the trapping effect of the longwave radiation from the surface, leading to a greater T_d value. Particularly, in South China, southwest China, the eastern Qinghai–Tibetan Plateau, and in other areas with high humidity and a high number of precipitation days, the night rain rate is usually high (Yu et al. 2007; Duan et al. 2013). This is conducive to raising the minimum temperature in the early morning and at the same time does not significantly reduce the afternoon maximum temperature, increasing the T_d value. The T_d values showed a negative correlation with the annual mean wind speed, possibly because near-surface turbulence and convection are stronger when daytime wind speed is high, which helps the heat to be diffused. This is unfavorable to the afternoon maximum temperature rise and causes the max–min average values to be low.

The T_d value is generally large in a high-elevation area, but the correlation with elevation is not significant and the reasons for this need to be investigated further. One possible reason may be that the humidity and cloudiness of high-elevation areas are also high; cloudiness is high when the surface air reaches its lowest

TABLE 3. Linear trends and significance test results of annual and seasonal mean biases (T_d) in mainland China and the three subregions (1964–2013). Asterisk (*) indicates significant at $p = 0.05$ level. CHN: mainland China.

Linear trend [°C (10 yr)$^{-1}$]	East monsoon region	Northwest arid region	Qinghai–Tibetan Plateau	CHN
Spring	0.022*	0.018*	0.022*	0.021*
Summer	0.029*	0.044*	0.021*	0.032*
Autumn	0.017*	0.035*	0.017*	0.021*
Winter	0.005	0.008	0.027*	0.008
Year	0.018*	0.027*	0.022*	0.021*

temperature in early morning but sunshine is sufficient in the afternoon, resulting in a significantly higher T_{mn} value. This is especially true in eastern parts of the Qinghai–Tibetan Plateau (Yu et al. 2007; G. Y. Ren et al. 2016). However, the western Qinghai–Tibetan Plateau has fewer precipitation days and a drier climate, and this may be one of the reasons why the correlation of T_d with elevation is not significant in mainland China on a whole.

From 1964 to 2013, there was a significant upward trend in the national and regional average annual and seasonal mean T_d, which may be related to the "asymmetric" change of the diurnal temperature. In most regions of mainland China, T_{max} and T_{min} rose in the past half-century, but T_{min} rose much faster than T_{max} (Zhai and Ren 1997; Ren and Zhou 2014), which may have caused the T_d value to rise continuously relative to the trends of the standard T_4 or T_{24}. A recent study applying hourly mean temperature data also showed that, since the early 1970s, the most rapid surface air temperature rise in a day occurs around sunrise and early morning, especially between 0600 and 1400; temperature rise slows in the afternoon and most of the night (Y. Y. Ren et al. 2016). Therefore, the minimum temperature, and the maximum temperatures in less extent, occurs at time when the most rapid warming is experienced in a day, resulting in a significant increase in annual and seasonal mean T_d over time. Moreover, the cause of the asymmetry in diurnal temperature change may be related to the effects of urbanization and the effect of aerosols around the observational grounds of the stations (Ren and Zhou 2014; Y. Y. Ren et al. 2016).

Although the data used in this paper were quality controlled, they were not processed for homogenization. The inhomogeneities of the observational data were likely caused by the relocation of stations and the change of instruments. T_d values thus may be affected by the inhomogeneities of data. To understand this effect, the difference between the homogenized data from 719 stations and the results of this study were calculated and analyzed. The homogenized temperature data were developed by Cao et al. (2016). The inhomogeneities in individual station series were detected by using a penalized maximum t test (PMT) that accounted for the first-order autocorrelation. Detailed metadata information was applied to validate the breakpoints caused by changes in the observational sites and instruments. The quartile-matching (QM) method was applied to adjust the discontinuities caused by the nonclimate changes.

The difference between the annual mean T_{dh} (bias of T_{mn} as calculated based on homogenized data) and T_d as given above is shown in Fig. 10. The differences were positive in 2013 only and negative in all previous years. In general, homogenization of data reduced T_d, but the change was in the accuracy range of 0.01°C. This indicates that the bias of the homogenized data is slightly lower, but the difference is very small, showing a negligible effect of homogenized data on the estimate of the bias of average T_{mn}. In view of the long-term trend of the bias, however, the data homogenization increased T_d trend (d.f. = 48, $t = 8.026$, $p = 0.001$), indicating that the present analysis actually underestimated the increasing trend of the temperature bias of T_{mn}. If the homogenized data are used, therefore, the rate of the increased T_d with time will become larger.

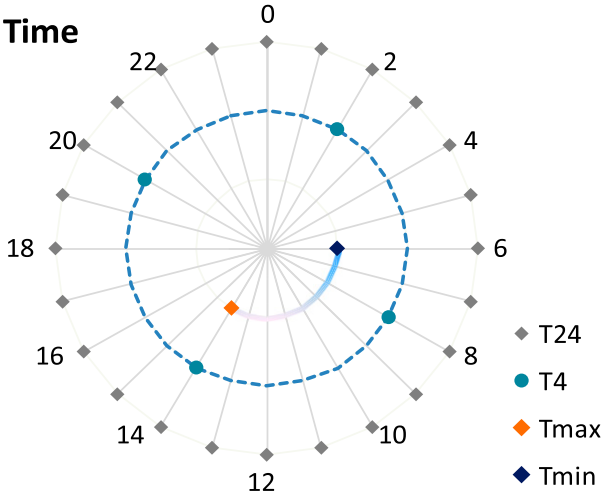

FIG. 8. A schematic diagram of distribution of observational points in the day for the maximum and minimum temperature (T_{max}, T_{min}), 4-time fixed intervals (T_4), and 24-time fixed intervals (T_{24}).

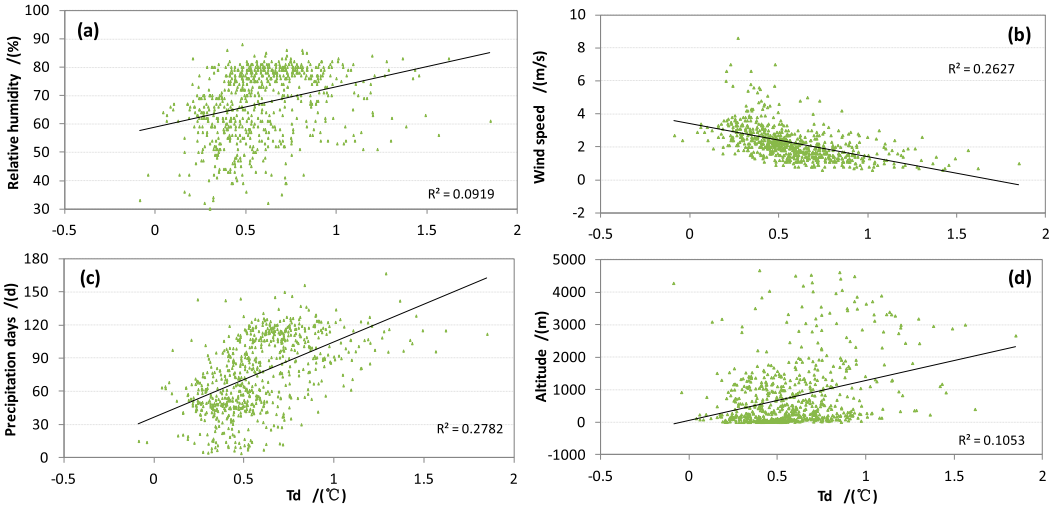

FIG. 9. Relationship of annual mean T_d with meteorological variables: (a) relative humidity, (b) wind speed, and (c) precipitation days; and geographical variable (d) altitude, in mainland China.

The results of this paper are of significance for understanding the uncertainties in studies of climatology and climate change. In climatological studies and climate prediction, the use of T_{mn} generally causes a higher daily and monthly mean temperature than T_{24} or T_4 in mainland China, and probably in other subcontinental regions of the world. In some regions of the country, the bias even reaches 1.00°C in certain seasons. This requires a careful consideration or adjustment when more accurate analysis and prediction are needed.

In monitoring and studies of climate change, the annual and seasonal mean temperature is usually calculated and analyzed by using the max–min average method due to the difficulty in acquiring 4-time equal interval observation data, let alone the 24-times-a-day observations. It was found in this study, however, that annual and seasonal mean T_d has a significant increasing trend over time, and if the homogenized temperature data series is used, the upward trend will be greater. This shows that the average warming trend in mainland China, and probably in other large regions of the world, is generally overestimated by using daily and monthly mean temperature data as calculated from daily T_{max} and T_{min} records. If the homogenized temperature data are used, the overestimate will be a little larger.

These findings are novel and have practical significance. In China, it was a usual practice to use the daily and monthly mean temperature as calculated from 4 records at 0200, 0800, 1400, and 2000 Beijing time to analyze the long-term change in surface air temperature. However, the method was changed in analyzing change trends of temperature over time periods longer than the last 50–60 years. The long data series include the early instrumental records with different observational time in a day, which had been found to result in data inhomogeneities. In this case, a suggestion was made to use the max–min average method to avoid the possible breakpoints in data series (Tang and Ren 2005; Cao et al. 2013; Ren et al. 2017). It is obvious from this analysis that the max–min average method diminishes the effect of inhomogeneities

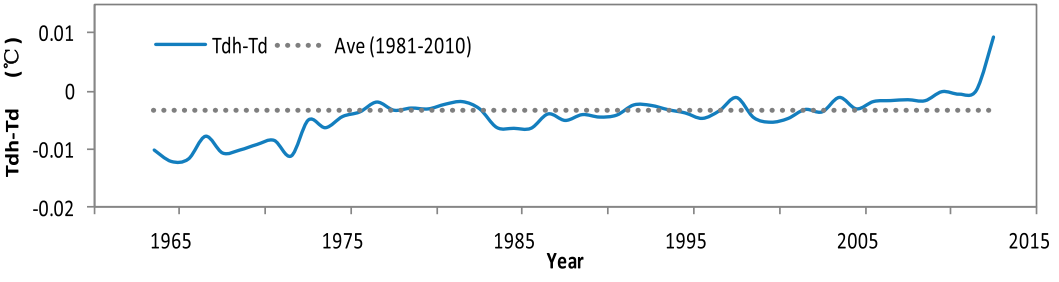

FIG. 10. Effect of data homogenization on temperature bias of the max–min average (T_d) as estimated based on the same observational station network in mainland China. Shown in the figure is the difference of country-averaged annual mean biases of the max–min average temperature between homogenized and nonhomogenized data.

on data series in some extents, but it at the same time significantly overestimates the warming trend of the past decades in mainland China. This overestimate becomes even more serious when homogenized data of the max–min average method based monthly mean temperature are applied.

Most of the previous studies of global land surface air temperature change also utilized the data of daily and monthly mean temperature as estimated by T_{max} and T_{min} (i.e., the max–min average method) (Lawrimore et al. 2011; Jones et al. 2012; Sun et al. 2018). It is unclear whether or not, or in what extents, the global land analyses based on monthly mean data, which mostly applied the daily mean temperature of T_{max} and T_{min} (or T_{mn}), have overestimated the past temperature increasing trends. However, the case from mainland China that has a diverse climate types and a vast territory indicates a need to further address this issue in future studies.

If this issue is nonignorable in global land, or the large deviations in the average temperatures and linear trends as calculated using the max–min average method exist in the current global land surface air temperature datasets, then there is an urgent need to adjust the daily and monthly observational data and the estimations of temperature trends based on them, and also to revise the data submission agreement by World Meteorological Organization (WMO) for the future operation and research of climate and climate change.

5. Conclusions

The bias of the average temperature estimated (T_d) using daily T_{max} and T_{min} records, including its temporal and spatial variation were analyzed using daily temperature data from 719 stations in mainland China. The following conclusions were drawn:

1) Starting in January, the daily mean T_d experienced a decrease in January, an increase after June, and a decrease once again after November. Generally, the T_d value was relatively large in autumn and winter, with the largest value occurring in early November, and it was relatively low in spring and summer.
2) T_d was positive in most areas, with larger values in the eastern part of the Qinghai–Tibetan Plateau, the Sichuan basin and the Yunnan–Guizhou Plateau (>1.0°C). The lowest T_d values were found in northwest and northeast China (0°–0.4°C).
3) There was a significant upward trend of annual mean T_d over time [0.021°C (10 yr)$^{-1}$]. The three subregions were all showed a significant increase. The highest rising rate of annual mean T_d was in northwest arid region [0.027°C (10 yr)$^{-1}$].
4) The T_d value of each season in the areas south of 30°N was positive. Negative values appeared only in western Tibet in autumn and in northern China in spring and summer. The increase of the seasonal mean T_d was generally largest in the summer.
5) With the homogenized data, the T_d values were lower, but the trend of T_d increased more significant over time. The analysis of the long-term surface air temperature change by using the monthly mean homogenized temperature data thus result in a further overestimate of warming trend.

Overall, the present analysis indicates that the previously applied method to calculate daily and monthly mean temperature using T_{max} and T_{min} significantly overestimates not only the climatological mean of the national stations and mainland China on a whole, but also the upward trends of surface air temperature at most of the stations and in the country. In particular, because the data of monthly mean temperature as calculated using T_{max} and T_{min} have been widely used in studies of long-term change in global land and regional average surface air temperature, the biases as revealed in this work should be carefully considered in future studies.

Acknowledgments. This work was supported by the Ministry of Science and Technology (MOST) National Key R&D Program (2018YFA0605603), the Natural Science Foundation of China (NSFC) (41575003, 41771067) and the Provincial Science Foundation of Heilongjiang (LH2019D013).

REFERENCES

Brooks, C., 1921: True mean temperature. *Mon. Wea. Rev.*, **49**, 226–229, https://doi.org/10.1175/1520-0493(1921)49<226:TMT>2.0.CO;2.

Cao, L. J., P. Zhao, Z. W. Yan, P. Jones, Y. N. Zhu, Y. Yu, and G. L. Tang, 2013: Instrumental temperature series in eastern and central China back to the nineteenth century. *J. Geophys. Res.*, **118**, 8197–8207, https://doi.org/10.1002/jgrd.50615.

——, Y. N. Zhu, G. L. Tang, F. Yuan, and Z. Yan, 2016: Climatic warming in China according to a homogenized data set from 2419 stations. *Int. J. Climatol.*, **36**, 4384–4392, https://doi.org/10.1002/joc.4639.

Carrasco, J. F., 2013: Decadal changes in the near-surface air temperature in the western side of the Antarctic Peninsula. *Atmos. Climate Sci.*, **3**, 275–281, https://doi.org/10.4236/acs.2013.33029.

Chen, Z. H., H. J. Wang, and G. Y. Ren, 2007: Asymmetrical change of urban heat island intensity in Wuhan, China. *Adv. Climate Chang. Res.*, **3**, 282–286.

CMA, 2003: *Specifications for Surface Meteorological Observations*. China Meteorological Press, 151 pp.

Ding, Y. H., S. W. Wang, J. Y. Zheng, H. J. Wang, and X. Q. Yang, Eds., 2013: *Climate in China*. Science Press, 557 pp.

Duan, C. F., W. Cao, and Q. L. Miao, 2013: Spatial distribution characteristics of summer night rain in China. *Ziran Ziyuan Xuebao*, **28**, 1935–1944.

Edwards, H. B., 1982: Measurement of true mean temperature for determination of climatic trends. *J. Appl. Meteor.*, **21**, 1763–1766, https://doi.org/10.1175/1520-0450(1982)021<1763:MOTMTF>2.0.CO;2.

IPCC, 2013: *Climate Change 2013: The Physical Science Basis*. Cambridge University Press, 1535 pp., https://doi.org/10.1017/CBO9781107415324.

Jones, G. S., and P. A. Stott, 2011: Sensitivity of attribution of near surface temperature warming to the choice of observational dataset. *Geophys. Res. Lett.*, **38**, L21702, https://doi.org/10.1029/2011GL049324.

Jones, P. D., and M. Hulme, 1996: Calculating regional climatic time series for temperature and precipitation: Methods and illustrations. *Int. J. Climatol.*, **16**, 361–377, https://doi.org/10.1002/(SICI)1097-0088(199604)16:4<361::AID-JOC53>3.0.CO;2-F.

——, D. H. Lister, and T. J. Osborn, 2012: Hemispheric and large-scale land-surface air temperature variations: An extensive revision and an update to 2010. *J. Geophys. Res.*, **117**, D05127, https://doi.org/10.1029/2011JD017139.

Karl, T. R., P. D. Jones, and R. W. Knight, 1993: A new perspective on recent global warming: Asymmetric trends of daily maximum and minimum temperature. *Bull. Amer. Meteor. Soc.*, **74**, 1007–1021, https://doi.org/10.1175/1520-0477(1993)074<1007:ANPORG>2.0.CO;2.

Kennedy, J. J., N. A. Rayner, R. O. Smith, M. Saunby, and D. E. Parker, 2011: Reassessing biases and other uncertainties in sea-surface temperature observations measured in situ since 1850: 2. Biases and homogenisation. *J. Geophys. Res.*, **116**, D14104, https://doi.org/10.1029/2010JD015220.

Kothawale, D. R., A. A. Munot, and K. K. Krishna, 2010: Surface air temperature variability over India during 1901–2007, and its association with ENSO. *Climate Res.*, **42**, 89–104, https://doi.org/10.3354/cr00857.

——, N. R. Deshpande, and R. K. Kolli, 2016: Long term temperature trends at major, medium, small cities and hill stations in India during the period 1901-2013. *Amer. J. Climate Change*, **5**, 383–398, https://doi.org/10.4236/ajcc.2016.53029.

Lawrimore, J. H., M. J. Menne, B. E. Gleason, C. N. Williams, D. B. Wuertz, R. S. Vose, and J. Rennie, 2011: An overview of the Global Historical Climatology Network monthly mean temperature dataset, version 3. *J. Geophys. Res.*, **116**, D19121, https://doi.org/10.1029/2011JD016187.

Li, Q. X., X. N. Liu, H. Z. Zhang, T. C. Peterson, and D. R. Easterling, 2004: Detecting and adjusting temporal inhomogeneity in Chinese mean surface air temperature data. *Adv. Atmos. Sci.*, **21**, 260–268, https://doi.org/10.1007/BF02915712.

Li, Z., and Z. W. Yan, 2009: Homogenized daily mean/maximum/minimum temperature series for China from 1960-2008. *Atmos. Ocean. Sci. Lett.*, **2**, 237–243, https://doi.org/10.1080/16742834.2009.11446802.

Lowsen, D. H., and G. A. Conway, 2016: Air pollution in major Chinese cities: Some progress, but much more to do. *J. Environ. Prot.*, **7**, 2081–2094, https://doi.org/10.4236/jep.2016.713162.

Miller, A. A., 1976: *Climatology*. 9th ed. Methuen & COLTD, 318 pp.

Morice, C. P., J. J. Kennedy, N. A. Rayner, and P. D. Jones, 2012: Quantifying uncertainties in global and regional temperature change using an ensemble of observational estimates: The HadCRUT4 data set. *J. Geophys. Res.*, **117**, D08101, https://doi.org/10.1029/2011JD017187.

Osborn, T. J., and P. D. Jones, 2014: The CRUTEM4 land-surface air temperature data set: Construction, previous versions and dissemination via Google Earth. *Earth Syst. Sci. Data*, **6**, 61–68, https://doi.org/10.5194/essd-6-61-2014.

Qian, W., and X. Lin, 2004: Regional trends in recent temperature indices in China. *Climate Res.*, **27** (5), 119–134, https://doi.org/10.3354/cr027119.

Rehman, S., and L. M. Al-Hadhrami, 2012: Extreme temperature trends on the west coast of Saudi Arabia. *Atmos. Climate Sci.*, **2**, 351–361, https://doi.org/10.4236/acs.2012.23031.

Ren, G. Y., 2008: History, current state and uncertainty of studies of climate change attribution. *Diqiu Kexue Jinzhan*, **23**, 1084–1091.

——, and Y. Q. Zhou, 2014: Urbanization effect on trends of extreme temperature indices of national stations over mainland China, 1961–2008. *J. Climate*, **27**, 2340–2360, https://doi.org/10.1175/JCLI-D-13-00393.1.

——, Y. J. Liu, and X. B. Sun, 2016: Spatial and temporal patterns of precipitation variability over mainland China—III: Causes for recent trends. *Adv. Water Sci.*, **27**, 327–348, https://doi.org/10.14042/j.cnki.32.1309.2016.03.001.

——, Y. H. Ding, and G. L. Tang, 2017: An overview of mainland China temperature change research. *J. Meteor. Res.*, **31**, 3–16, https://doi.org/10.1007/s13351-017-6195-2.

Ren, Y. Y., D. Parker, and G. Y. Ren, 2016: Tempo-spatial characteristics of sub-daily temperature trends in mainland China. *Climate Dyn.*, **46**, 2737–2748, https://doi.org/10.1007/s00382-015-2726-7.

Samba, G., and D. Nganga, 2014: Minimum and maximum temperature trends in Congo-Brazzaville: 1932-2010. *Atmos. Climate Sci.*, **4**, 404–430, https://doi.org/10.4236/acs.2014.43040.

Shi, N., X. X. Huang, and Y. Yang, 2003: Temporal and spatial characteristics of global precipitation annual precipitation field trends from 1948 to 2000. *Chin. J. Atmos. Sci.*, **27**, 971–982.

Sun, X. B., G. Y. Ren, Y. Y. Ren, Y. H. Fang, Y. L. Liu, X. Y. Xue, and P. F. Zhang, 2018: A remarkable climate warming hiatus over northeast China since 1998. *Theor. Appl. Climatol.*, **133**, 579–594, https://doi.org/10.1007/s00704-017-2205-7.

Tang, G. L., and G. Y. Ren, 2005: Reanalysis of surface air temperature change of the last 100 Years over China. *Climatic Environ. Res.*, **10**, 791–798.

——, and Y. H. Ding, 2007: Impacts of the average air temperature derived from maximum and minimum temperatures on annual mean air temperatures series of China. *J. Appl. Meteor. Sci.*, **18**, 187–192.

Thompson, D. W. J., J. J. Kennedy, J. M. Wallace, and P. D. Jones, 2008: A large discontinuity in the mid-twentieth century in observed global mean surface temperature. *Nature*, **453**, 646–649, https://doi.org/10.1038/nature06982.

Von Storch, H., and F. W. Zwiers, 2003: *Statistical Analysis in Climate Research*. Cambridge University Press, 484 pp.

Wang, Y. W., and Y. H. Yang, 2014: China's dimming and brightening: Evidence, causes and hydrological implications. *Ann. Geophys.*, **32**, 41–55, https://doi.org/10.5194/angeo-32-41-2014.

Yu, R., T. Zhou, and A. Xiong, 2007: Diurnal variations of summer precipitation over contiguous China. *Geophys. Res. Lett.*, **34**, 223–234, https://doi.org/10.1029/2006GL028129.

Zhai, P. M., and F. M. Ren, 1997: On changes of China's maximum and minimum temperatures in the recent 40 years (in Chinese). *Acta Meteor. Sin.*, **55**, 418–429.

刘芸芸,陈丽娟,2019. 2019年春季我国主要气候异常特征及可能成因分析[J]. 气象,45(10):1483-1493. Liu Y Y, Chen L J, 2019. Features and possible causes for the spring climate anomalies in 2019[J]. Meteor Mon, 45(10):1483-1493(in Chinese).

2019年春季我国主要气候异常特征及可能成因分析*

刘芸芸[1,2] 陈丽娟[1,2]

1 国家气候中心,中国气象局气候研究开放实验室,北京 100081

2 南京信息工程大学气象灾害预报预警与评估协同创新中心,南京 210044

提 要: 2019年春季(3—5月),全国平均气温为11.5℃,为1961年以来历史同期第四位;全国平均降水量为148.7 mm,接近常年同期,但旱涝分布差异显著。东北、西北地区东部和华南降水显著偏多,而黄淮、江淮及云南大部降水异常偏少,其中云南地区降水量为历史同期最少。气温偏高和降水空间分布不均导致旱涝灾害并存。季内气候变化显著,表现出东亚冬季风环流向夏季风环流转换期的特征。春季(尤其是3—4月)全国大部地区气温偏高受到中纬度环流型的明显影响,乌拉尔山及其以北地区为负高度距平中心,而乌拉尔山以东到贝加尔湖地区为大范围正高度距平,这种异常环流形势非常有利于我国气温整体偏高。另一方面,低伟度大气环流则表现出对热带海温异常的明显响应,西太平洋副热带高压(简称西太副高)异常偏强、偏西及偏南,这基本决定了我国春季降水异常的空间分布型,其强度和位置不仅能够直接影响南方降水分布,同时通过与中高纬异常环流的相互作用,共同影响我国北方降水异常格局。进一步分析热带海温外强迫的影响显示,在El Niño衰减年的春季,热带印度洋海温的增暖对西太副高持续偏强偏西起到更重要的作用;而El Niño事件本身对西太副高强度的影响在春季逐渐减弱,对西太副高南北位置的影响增强。

关键词: 2019,春季气候异常,西太平洋副热带高压,El Niño,印度洋海温

中图分类号: P461 **文献标志码:** A **DOI:** 10.7519/j.issn.1000-0526.2019.10.015

Features and Possible Causes for the Spring Climate Anomalies in 2019

LIU Yunyun[1,2] CHEN Lijuan[1,2]

1 Laboratory for Climate Studies, National Climate Centre, CMA, Beijing 100081

2 Collaborative Innovation Center on Forecast and Evaluation of Meteorological Disasters, Nanjing University of Information Science and Technology, Nanjing 210044

Abstract: In spring 2019 (March—April—May, MAM), the average temperature in China is 11.5℃, ranking the fourth in the same period since 1961. The average precipitation in China is 148.7 mm (near normal), with profound spatial differences. The precipitation is more than normal over Northeast China, east part of Northwest China and South China, but less than normal over Huanghuai, Jianghuai and most of Yunnan Province in MAM 2019. The MAM precipitation in Yunnan is the least since 1961. High temperature and uneven spatial distribution of precipitation lead to the coexistence of drought and flood disasters in MAM 2019. The sub-seasonal climate variability in spring 2019 is significant, showing the characteristics of the transition period from East Asian winter monsoon circulation to summer monsoon circulation. The high temperature in most China in spring (especially in March and April) is obviously affected by the mid-latitude circulation anomalies pattern. The Ural Mountains and to their north regions are the

* 国家重点研发计划(2018YFC1505806、2018YFC1506006)和国家自然科学基金项目(41275073)共同资助

2019年7月12日收稿; 2019年9月9日收修定稿

第一作者:刘芸芸,主要从事短期气候预测研究. Email:liuyuny@cma.gov.cn

通信作者:陈丽娟,主要从事短期气候预测研究. Email:chenlj@cma.gov.cn

center of negative height anomaly, while the areas east of Ural Mountains to Lake Baikal are the center of positive height anomaly. Such an anomalous circulation pattern is very helpful to the overall high temperature in China. The atmospheric circulation systems present an obvious response to the tropical SST anomalies in MAM 2019. The western North Pacific subtropical high (WPSH) is strong, westward and southward extending, which basically determines the spatial pattern of spring precipitation anomaly in China. The intensity and location of WPSH not only directly control the pattern of precipitation anomaly in southern China, but also affect the distribution of precipitation over northern China through the interaction of circulation anomalies in mid-high latitudes. Further analysis on the influence of tropical SST forcing shows that the warming of tropical Indian Ocean SST plays a more important role in the sustained strengthening and westward trend of WPSH in the El Niño decaying spring. The influence of the El Niño event on the intensity of WPSH gradually weakens in spring, and the effect on the north-south position of WPSH becomes more obvious.

Key words: 2019, climatic anomaly in MAM, western North Pacific subtropical high, El Niño, Indian Ocean SST

引 言

春季是东亚冬季风环流向夏季风环流的转换期,控制我国大陆的冬季冷高压逐渐被热低压所替代,高压则慢慢占据了海洋。此时,中高纬冷空气势力和热带暖湿气流激烈交绥,造成大气层结很不稳定,并进一步引起天气气候的变化,甚至带来一些极端天气气候事件。此外,华南前汛期、江南春雨(Tian and Yasunari, 1998; 詹丰兴等,2013)以及南海夏季风的爆发(Tao and Chen, 1987)等气候事件都在春季发生,从而造成春季复杂多变的区域气候特征。已有研究表明,我国春季气候具有显著的年际变化(袁媛等,2014;邵勰等,2015;2016;龚志强等,2017;王遵娅等,2018),而此时大多数地区正值农作物播种和生长期,因此春季的气候异常将对农业生产和人民生活造成重要的影响,有效地理解春季气候异常并做好预报服务有利于防灾减灾。

中国春季气候异常往往同时受中高纬和低纬大气环流系统的共同影响(尹姗等,2013;王遵娅等,2018),而大气环流异常又与海洋和陆面等外强迫因子密切相关,如热带海温(陈丽娟等,2013;詹丰兴等,2013;袁媛等,2014;龚志强等,2017)、欧亚-青藏高原积雪(Wu and Kirtman, 2007;左志燕和张人禾,2012;陈红等,2017;Chen et al, 2019)、北极海冰(Wu et al, 2016)等。海洋由于其面积广且热容量大,尤其受到关注(Liu et al, 2013;2015;2019;顾薇和陈丽娟,2019)。研究表明,El Niño 盛期,华南春季降水显著偏多(Zhang and Sumi, 2002; 詹丰兴等,2013),同时也与北太平洋上的环流异常有密切联系(王林等,2011)。El Niño 期间,华北当年和来年春季降水往往偏多(王群英和龚道溢,1999)。另外,前期冬季印度洋海温与中国华北春季降水也有显著关系(顾伟宗等,2006)。

2018年9月开始,热带中东太平洋上发生了一次新的 El Niño 事件,并于秋末冬初到达盛期,全球多地气候特征和极端天气气候事件表现出对此次事件的响应,如澳大利亚持续高温、美国中西部严重洪涝、中国南方持续连阴雨等。2019年春季,El Niño 事件持续发展,热带印度洋海温也持续偏暖,在这样的海温异常配置下,春季我国气候表现出气温大范围偏高和降水空间差异大的分布特征,旱涝灾害并存。本文将全面介绍2019年春季我国的主要气候特征,并从大气环流和海温外强迫的角度重点分析造成2019年春季我国降水异常的可能成因。

1 资料与方法

本文所用的资料包括:(1)国家气候中心提供的1951—2019年全国160站的逐月气温和降水资料;(2)国家气象信息中心整编的全国2400站的逐日气温和降水资料(任芝花等,2012)。(3)美国国家环境预报中心(NCEP)和美国国家大气研究中心(NCAR)发布的1951—2019年的大气环流再分析资料(Kalnay et al, 1996),要素包括位势高度场、风场、比温等,空间分辨率为2.5°×2.5°;(4)美国国家海洋大气管理局(NOAA)发布的扩展重建的逐月海温资料(ERSSTv5; Huang et al, 2017),空间分

辨率为 2°×2°。文中春季指北半球春季(3—5 月平均),所有变量的气候态(常年)均为 1981—2010 年的平均,距平场去除的都是气候态的平均。热带海温指数 Niño3.4 为(5°S～5°N、120°～170°W)区域平均的海表温度距平,热带印度洋海盆一致模(IOBM)指数为(20°S～20°N、40°～110°E)区域平均的海表温度距平(Chambers et al, 1999)。

2　2019 年春季中国气候异常特征

春季全国平均气温为 11.5℃,较常年同期(10.4℃)偏高 1.1℃,为 1961 年以来历史同期第四位(图 1)。与常年同期相比,我国东北、华北大部、黄淮及西北大部地区气温偏高 1～2℃,局地偏高 2℃以上;仅青海南部局部地区气温较常年同期偏低 0.5～1℃(图 2a)。从逐月的气温距平分布可以看到,季节内的气温分布差异很大(图 2b,2c,2d)。3 月,我国北方大部及江淮、江南大部气温偏高 1～4℃,而青藏大部地区气温偏低 1～2℃,呈现"西低东高"的分布。4 月,除东北南部、华北东部气温略偏低外,全国其余大部地区气温接近常年到偏高 1～4℃。5 月,我国气温偏高的范围明显缩小,全国月平均气温由前期3—4月的显著偏暖转为接近气候平均值;5 月气温偏高的地区主要集中在东北、华北、黄淮和西南南部,其余地区气温接近常年到偏低,其中从西北地区到华中地区,以及江南西部和华南大部的气温均较常年明显偏低,西北大部和西南地区东部气温偏低 1～2℃。由于 3—4 月全国气温偏高的贡献,使得春季平均气温总体仍明显偏高,但季内表现出前期偏暖后期转冷的变化特征,这与中纬度环流的季内调整密切相关。

春季全国平均降水量为 148.7 mm,较常年同期(143.7 mm)偏多 3.5%(图 3)。旱涝空间分布差异显著(图 4a),其空间型接近于经验正交模态分解的第二模态(EOF2)特征(龚志强等,2017)。东北大

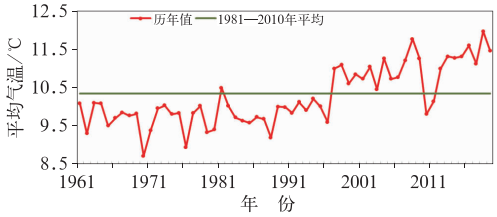

图 1　1961—2019 年春季全国平均气温历年变化

Fig. 1　Time series of air temperature averaged from March to May (MAM mean) in China during 1961－2019

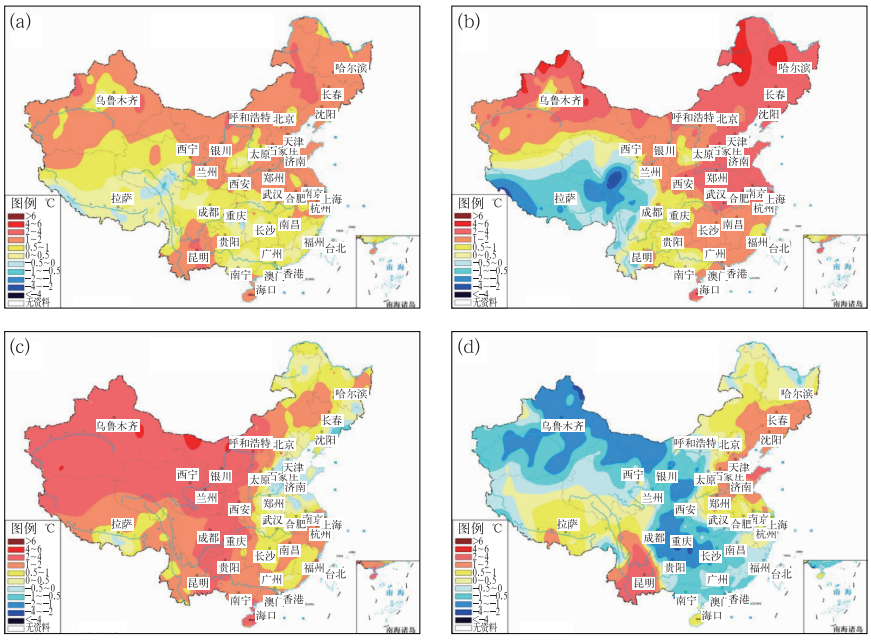

图 2　2019 年春季(a)和 3 月(b)、4 月(c)、5 月(d)的全国平均气温距平分布

Fig. 2　Distribution of air temperature anomaly over China in (a) MAM, (b) March, (c) April, and (d) May 2019

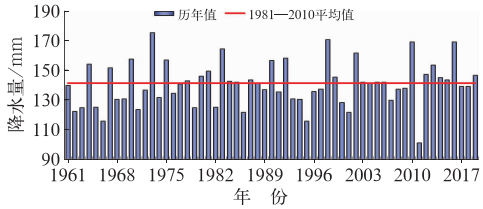

图 3 1961—2019 年春季全国平均降水量历年变化

Fig. 3 Time series of MAM mean rainfall in China during 1961－2019

部、西北地区中东部、华南东部及新疆中西部等地降水量较常年同期偏多 20%至 2 倍，局地偏多 2 倍以上；而黄淮、江淮、江汉北部及西南地区南部降水量较常年同期偏少 20%～80%，局地偏少 80%以上，其中云南降水量为 1961 年以来历史同期最少值。从逐月的降水分布来看，北方旱涝转换明显：3 月北方大部分地区降水偏少(图 4b)，4 月西北和华北大部降水偏多(图 4c)，5 月西北和东北大部降水偏多(图 4d)；与季内变率较大的北方地区不同，南方地区“东多西少”的降水异常特征稳定维持，云南降水持续偏少，而江南南部和华南的降水持续偏多，这与热带海温持续的强迫影响有关(Wu et al，2003；Hu et al，2012)。

气温总体偏高和降水空间分布不均导致我国春季旱涝灾害并重。一方面，我国南方春季共出现 12 次区域性暴雨天气过程，长江中下游及华南等地持续遭受暴雨洪涝灾害。持续的降水过程也导致今年华南前汛期的开始较常年同期明显偏早(3 月 9 日开始，较常年同期偏早 28 d)。另一方面，由于高温少雨，东北地区 3—4 月干旱发展，5 月随着降水的增多干旱缓解；黄淮和华北南部在 3 和 5 月都出现了中至重度气象干旱；而西南中南部气象干旱在春季持续发展(图 5)。以云南为例，4—5 月云南降水量 59.5 mm，为 1961 年以来历史同期最少，气温较常年同期偏高 2.1℃，为历史同期最高；持续的高温少雨导致云南大部发生严重春旱，气象干旱范围和强度为近 20 年同期最强。

从上面的分析可以看到，无论是气温还是降水，春季气候季内变化都非常显著，这也是春季作为东亚冬季风环流向夏季风环流的转换期所特有的表现。但是气候异常中也有稳定维持的特征，尤其是南方降水“东多西少”的空间型贯穿春季，下面将主要针对春季中相对持续的异常特征作进一步的成因分析。

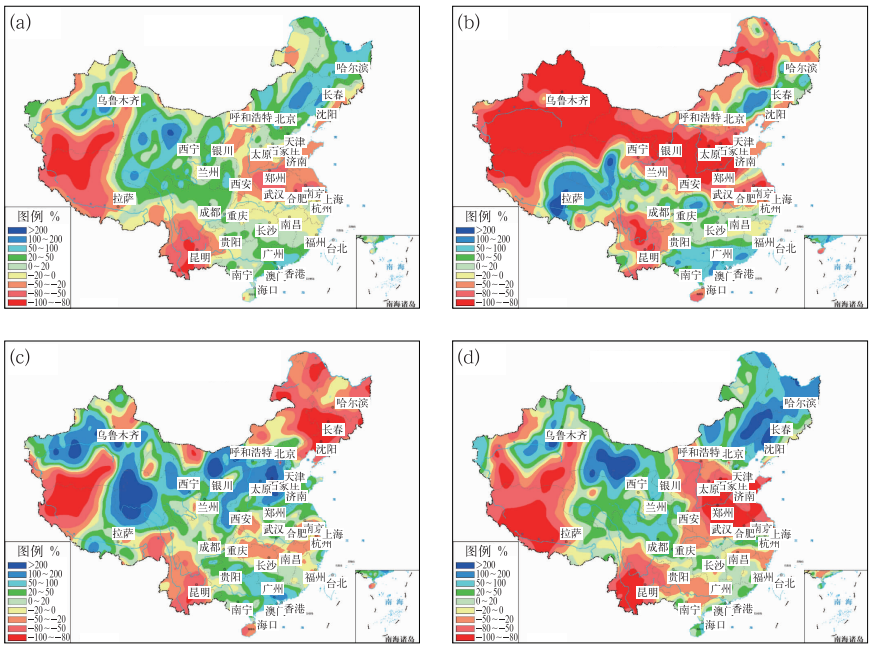

图 4 2019 年春季(a)、3 月(b)、4 月(c)和 5 月(d)的全国降水距平百分率分布

Fig. 4 Distribution of rainfall anomaly percentage over China in (a) MAM, (b) March, (c) April, and (d) May 2019

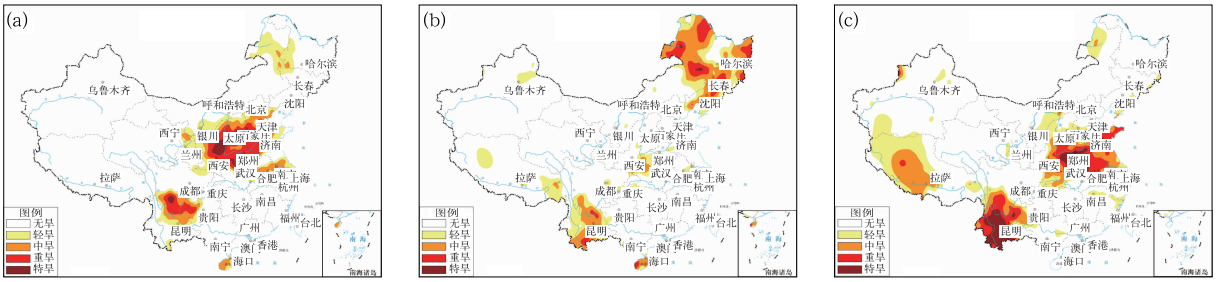

图 5　2019 年 3 月 31 日(a)、4 月 30 日(b)和 5 月 31 日(c)的全国气象干旱综合监测

Fig. 5　Distribution of meteorological drought over China on (a) 31 March, (b) 30 April and (c) 31 May 2019

3　2019 年春季气候异常的可能成因

3.1　大气环流异常特征

从 500 hPa 位势高度距平场分布(图 6a)可以看到,欧亚中高纬为较平直的纬向型环流,乌拉尔山以北存在一个负高度距平中心,乌拉尔山以东到贝加尔湖地区为显著的正高度距平,同时中国大陆地区上空也是较强的正高度距平,从而不利于来自高纬的冷空气南下影响我国。这样的异常环流形势在春季前期(3—4 月)尤为显著(图略)。春季全国平均气温与 500 hPa 位势高度场的相关分布(图 6b)进一步说明,当乌拉尔山及其以北地区出现负高度距

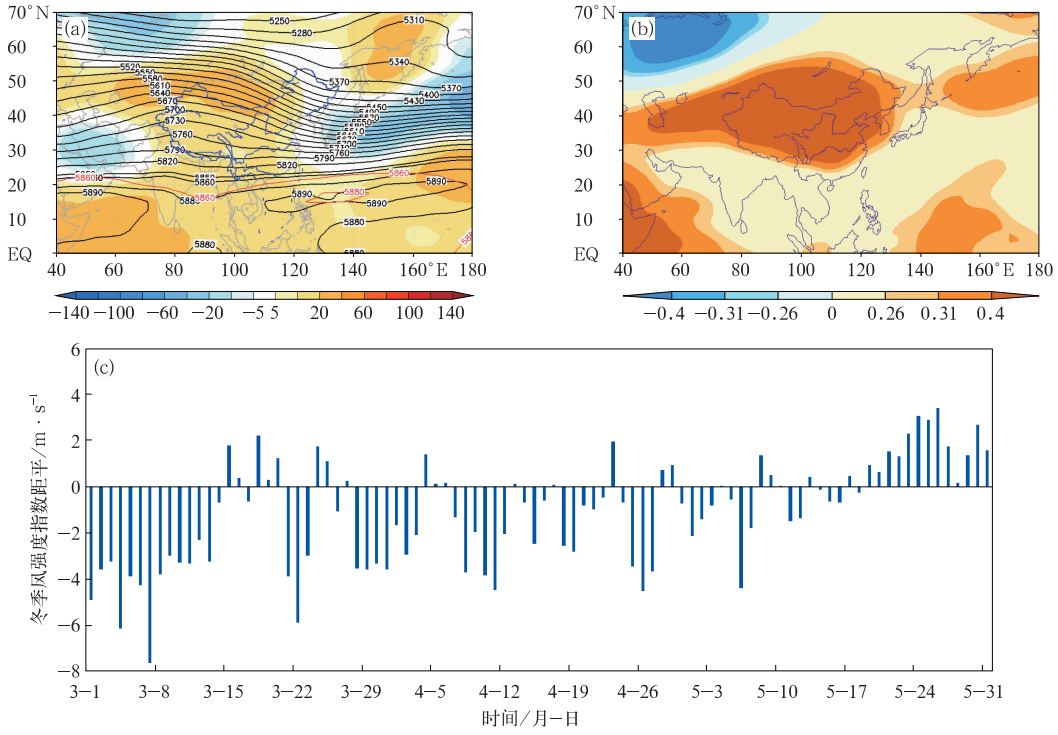

图 6　2019 年春季(a)500 hPa 高度(等值线)及距平场(阴影)分布(单位:gpm),(b)全国平均气温距平与 500 hPa 高度距平场的相关分布(浅中深阴影分别表示超过 0.1、0.05 和 0.01 显著性水平的区域),(c)东亚冬季风强度指数距平的逐日变化

Fig. 6　(a) The 500 hPa geopotential height (contour) and anomalies (shaded) (unit: gpm); (b) correlation between the averaged MAM temperature anomay in China and 500 hPa geopotential height anomalies (Light, medium and dark shadings indicate the areas with values above the significance level of 0.1, 0.05, and 0.01, respectively); (c) the daily East Asian winter monsoon intensity index in MAM 2019

平中心，并且从乌拉尔山以东到贝加尔湖地区为大范围正高度距平的异常环流形势时，非常有利于我国气温整体偏高。而东亚冬季风强度指数(Chen et al，2000)的逐日监测也显示(图 6c)，受中高纬异常环流形势的影响，2019 年 3 月以来东亚冬季风强度显著偏弱，对应 3—4 月全国气温大范围偏高(图 3b 和 3c)，而 5 月中旬之后冬季风强度转强，则对应 5 月气温偏高的范围较前期明显缩小(图 3d)。

春季环流的另一个特点是东亚地区自北向南为典型的“＋－＋”的异常环流型分布(图 6a)，春季内各月也基本维持“＋－＋”的分布特征(图略)，尤其在副热带地区的环流稳定维持正距平，其中西太平洋副热带高压(以下简称西太副高)较气候态偏大、偏强、偏西，总体偏南(图 7)，对我国南方“东多西少”的降水异常分布有重要贡献。对流层低层环流场上(图 8)，日本以南洋面上为显著的气旋性异常环流，其西侧的偏北风距平与来自偏南偏强的西太副高西侧的偏南风距平在我国东南沿海汇合，有利于江南南部和华南地区降水偏多。孟加拉湾存在显著的反气旋性异常环流，在其南侧的赤道印度洋以北区域为弱的偏东风距平，对应印度西南夏季风偏弱，输送到我国西南南部地区的水汽明显减弱，对应该地区为显著的水汽辐散(图 9)，从而导致云南大部地区春季降水异常偏少。而中高纬地区，贝加尔湖和鄂霍次克海两个高度正距平之间存在一个相对低值区(图 6a)，东北冷涡阶段性活跃，对应低层风场上也是显著的气旋性环流(图 8)，有利于东北地区降水偏多。可见，春季虽然存在季节内变率，但是副热带环流系统的稳定以及春季前期(3—4 月)欧亚中高纬度环流异常的持续对春季气候异常特征起到主要贡献。

进一步计算了西太副高指数(刘芸芸等，2012)与我国春季降水的同期相关(图 10)可见，西太副高脊线与我国华南降水表现为显著负相关关系，与江淮和黄淮大部为显著正相关关系(图 10c)，即副高脊线偏南时，有利于我国华南地区春季降水偏多，而江淮、黄淮降水偏少。这与 2019 年春季我国东部地区降水异常的空间分布特征非常相近。副高面积、强度及西伸脊点由于其自身具有高相关性(刘芸芸等，2012)，它们与春季降水的相关分布也较为一致，主要在我国东北、西北地区中东部、新疆北部和华南东部为正相关，而与西南南部地区为负相关(图 10a，10b 和 10d)，即西太副高偏大、偏强和偏西时，有利于我国东北、西北中东部、新疆北部和华南东部降水偏多，而云南大部降水偏少。这样的降水分布型与 2019 年春季降水异常分布实况(图 4a)非常吻合，也进一步证实 2019 年春季西太副高异常偏强、偏西及偏南的特征，基本决定了我国春季降水异

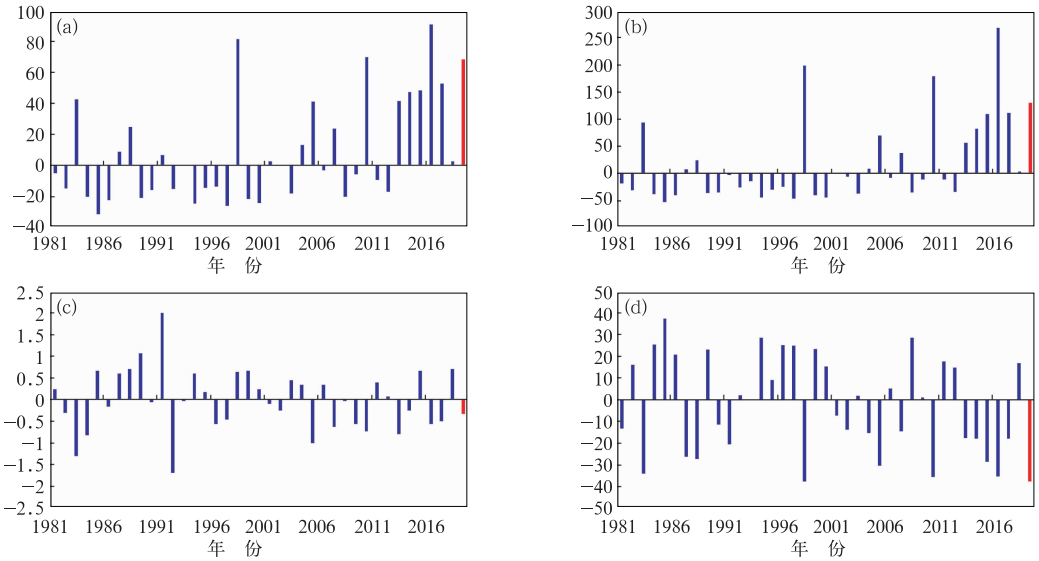

图 7 1981—2019 年春季西太副高指数的历年变化，包括面积指数(a)，强度指数(b)，脊线指数(c)，西伸脊点(d)
(红色柱状为 2019 年春季)

Fig. 7 Time series of MAM WPSH indices during 1981－2019, including (a) area index, (b) intensity index, (c) ridgeline index, and (d) westernmost point.
(Red bars indicate the indices in MAM 2019)

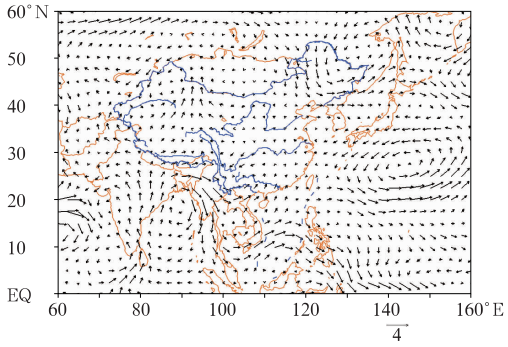

图 8　2019 年春季 850 hPa 距平风场(单位:m·s^{-1})

Fig. 8　Distribution of 850 hPa horizontal wind anomaly (unit: m·s^{-1}) in MAM 2019

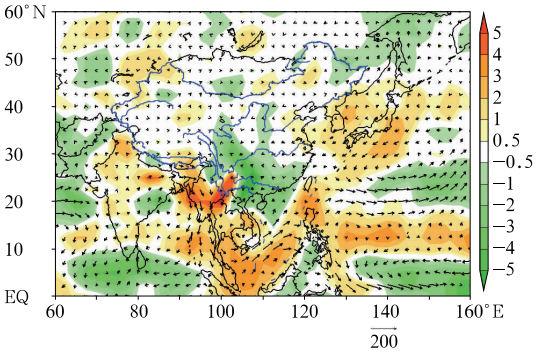

图 9　2019 年春季对流层整层积分的水汽输送距平(箭头,单位:kg·s^{-1}·m^{-1})及其散度场(阴影,单位:10^{-5} kg·m^{-2}·s^{-1})

Fig. 9　Vertically integrated moisture transport anomalies (vector, unit: kg·s^{-1}·m^{-1}) and associated divergence anomalies (shaded area, unit: 10^{-5} kg·m^{-2}·s^{-1}) in MAM 2019

常的分布型。这也从一定程度上说明,西太副高作为东亚夏季风系统中的重要成员之一,其强度和位置不仅能够直接影响南方降水分布,同时也通过与中高纬异常环流系统的配置,进一步影响我国北方降水异常的格局。

3.2　可能的外强迫因子

是什么原因导致今年春季西太副高出现偏强偏西及偏南的特征呢?有研究指出,来自海洋的外强迫往往通过海气相互作用(陈丽娟等,2013)和大气波动的传播等方式引起大气环流异常并进一步导致气候异常(Matsuno,1966;Gill,1980)。图 11 为 2019 年春季海表温度距平的分布及关键海区海温指数的逐月演变。可以看到,自 2018 年 9 月以来,Niño3.4 指数持续超过0.5 ℃,至2019年1月已达

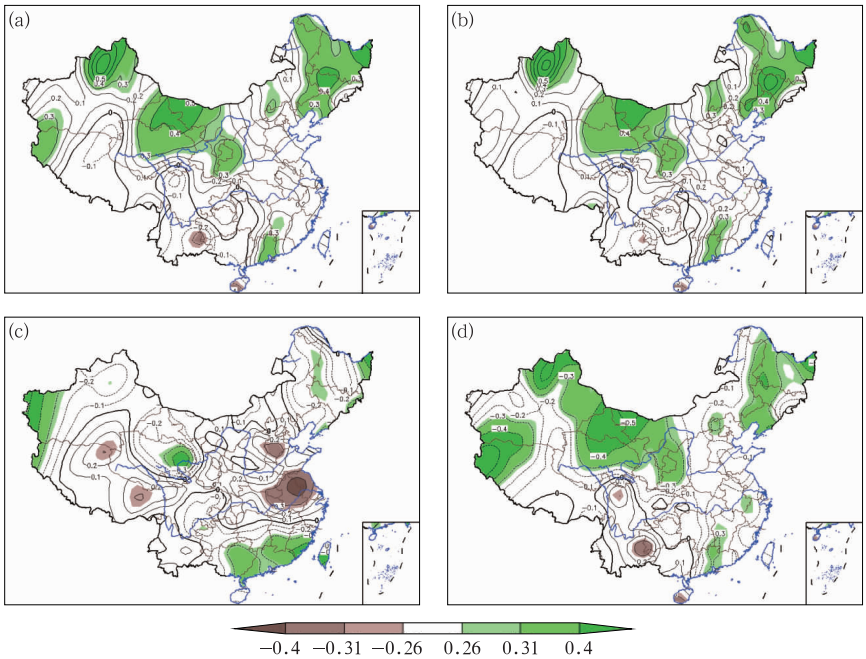

图 10　我国春季降水异常分别与西太副高面积指数(a)、强度指数(b)、脊线指数(c)和西伸脊点(d)的相关(浅中深阴影分别表示超过 0.1、0.05 和 0.01 的显著性水平的区域)

Fig. 10　Correlation distributions of the MAM precipitation anomalies with (a) area index, (b) intensity index, (c) ridgeline index, and (d) westernmost point of WPSH (Light, medium and dark shadings indicate the areas with values above the significance level of 0.1, 0.05, and 0.01, respectively)

到一次 El Niño 事件标准，并于秋末冬初达到峰值（图 11b）。2019 年春季 Niño3.4 指数开始减小，表现出 El Niño 衰减年的特征。由于赤道中东太平洋海温异常偏暖，西太平洋暖池及海洋性大陆地区海温相对偏低（图 11a），使得春季热带西太平洋暖池区域对流受到一定的抑制，有利于热带对流辐合带（ITCZ）位置相对偏南（Chan 2000；Chia and Ropelewski，2002；Wang and Chan，2002）。西北太平洋地区（110°～150°E 平均）对外长波辐射（OLR）距平的纬度-时间剖面图显示，从 2019 年 3 月以来，对流活跃区基本在 12°N 以南，对应西太副高的脊线位置则稳定维持在 14°～17°N（图 12）。由于缺少季节性北推的动力和热力条件，导致西太副高位置变化不大，由冬季的相对气候态异常偏北转为春季相对气候态偏南的特征。从春季西太副高脊线指数与前期逐月的关键海区海温指数的相关系数演变可以更加直观地看到，春季副高脊线与 3—5 月的 Niño3.4 指数相关关系最为显著，超过 0.05 显著性水平（图 13b）。也就是说，当春季赤道中东太平洋海温异常偏暖时，相对应的西太暖池偏冷，对流不活跃，西太副高位置容易偏南，从而易导致我国南方降水出现东多西少的异常空间型。

与此同时，春季热带印度洋海温也持续偏暖（图 11a），IOBM 指数（Chambers et al，1999）自 2018 年 11 月开始转为正距平（图 11b）。有研究表明，热带印度洋海温偏暖（偏冷）通常滞后于 El Niño（La Niña）事件大约 3～4 个月（Lau and Nath，2003；Yang et al，2007），印度洋暖海温的发展通过

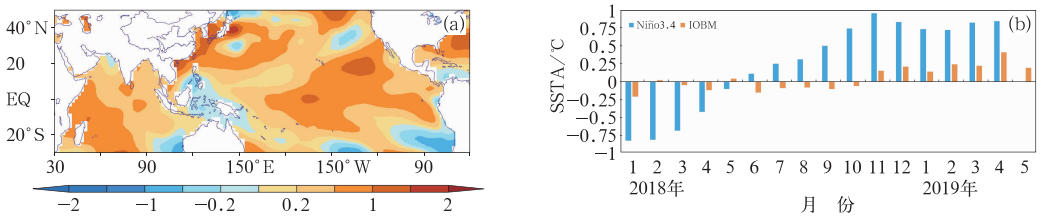

图 11 2019 年春季全球海温距平场分布（a，单位：℃）和 Niño3.4 与 IOBM 海温指数的逐月变化（b）

Fig. 11 (a) Distribution of the global sea surface temperature anomaly (unit: ℃), (b) time series of the monthly Nino3.4 and IOBM indices in MAM 2019

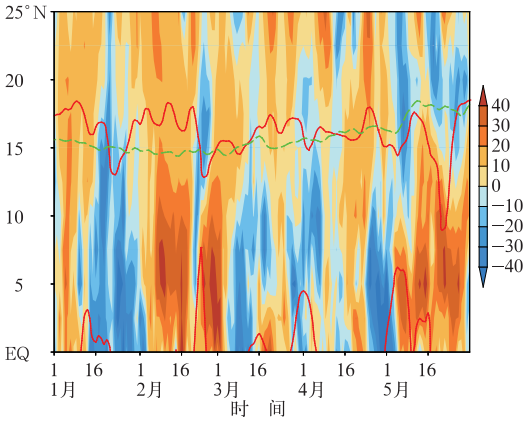

图 12 2019 年 1—5 月西北太平洋地区（110°～150°E）对外长波辐射距平（阴影，单位：W·m^{-2}）和西太副高脊线（10°N 以北的红实线，绿色虚线为气候平均值）的纬度-时间剖面图

Fig. 12 Latitude-time section of OLR anomaly (shaded area, unit: W·m^{-2}) and WPSH ridgeline (red line: north of 10°N; green dashed line: climatic mean) from January to May 2019

Matsuno-Gill 响应（Matsuno，1966；Gill，1980）激发 Kelvin 波，在孟加拉湾和南海分别产生异常的反气旋环流，该反气旋环流有利于西太副高的加强西伸（Yuan et al，2012）。2019 年春季的低纬度大气环流系统表现出对热带海温异常的显著响应，孟加拉湾和南海地区均存在较为明显的反气旋性异常环流（图 8），有利于西太副高在春季持续偏强偏西。春季西太副高强度指数与前期逐月热带海温指数的相关也可以看到，随着时间的演变，春季 3—5 月 IOBM 指数与副高强度指数的正相关关系最为显著，超过 0.01 的显著性水平（图 13a）。由于副高强度和西伸脊点本身具有高相关性（刘芸芸等，2012），副高的西伸脊点指数与热带海温指数的相关与前者类似（图略）。即春季热带印度洋海盆整体偏暖时，西太副高容易偏强偏西。同时也注意到，相比热带印度洋海温异常，赤道中东太平洋的暖海温异常对西太副高强度的影响在逐渐减弱，表明在 El Niño 衰减年的春季，热带印度洋海温的增暖对西太副高

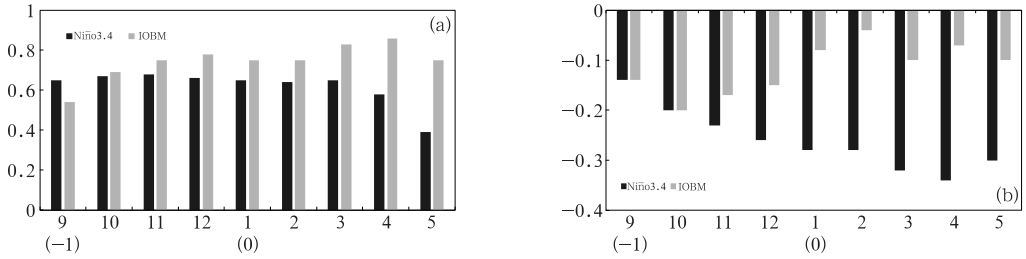

图 13　1981—2019 年春季西太副高强度指数(a)和脊线指数(b)分别与 Niño3.4 指数、IOBM 指数的线性相关

(相关系数 0.31 达到 0.05 显著性水平;横坐标中的(−1)表示超前一年,(0)表示同一年)

Fig. 13　Correlation coefficients between the MAM WPSH indices and tropical monthly SST indices during 1981−2019

(Correlation coefficients exceeding 0.31 reach the significant level of 0.05; (−1) in the x axis indicates one year in advance, and (0) indicates the same year)

持续偏强偏西起到更加重要的作用。这与先前的研究结果也是一致的(Xie et al, 2009; Liu et al, 2013;袁媛等,2014;He and Zhou, 2015)。

4　结论和讨论

本文利用中国站点降水和气温资料、NCEP/NCAR 再分析资料和观测的海温资料,总结了 2019 年春季(3—5 月)我国主要气候异常特征,并分析了导致我国降水区域差异显著的可能成因。主要结论如下:

2019 年春季,全国平均气温为 11.5℃,为 1961 年以来历史同期第四位;全国平均降水量为 148.7 mm,接近常年同期,但旱涝空间的差异显著。东北、西北地区东部和华南降水显著偏多,而黄淮、江淮及西南地区南部降水却异常偏少,其中云南地区降水量为历史同期最少。气温偏高和降水空间分布不均导致旱涝灾害并重。季内气候变化显著,这是春季作为东亚冬季风环流向夏季风环流的转换期所特有的表现。春季(尤其是 3—4 月)全国大部地区气温偏高受到中纬度乌拉尔山至贝加尔湖环流型的明显影响。

低纬度大气环流表现出对热带海温异常的显著响应,西太副高异常偏强、偏西及偏南的特征基本决定了我国春季降水异常的分布型,其强度和位置不仅能够直接影响南方降水东多西少的分布,同时也通过与中高纬异常环流系统间的相互作用影响我国北方降水异常的格局。进一步分析热带海温外强迫的影响显示,在 El Niño 衰减年的春季,热带印度洋海温的增暖对西太副高持续偏强偏西起到更加重要的作用,而 El Niño 事件对西太副高强度的影响在春季逐渐减弱,更多地表现出对西太副高南北位置的影响。

另外,还有研究指出,ENSO 事件还对我国云南春季降水具有显著影响(杨亚力等,2011),El Niño 年孟加拉湾出现明显的反气旋式环流异常,使得对云南地区的水汽输送减弱,导致云南大部地区春季降水偏少。这与 2019 春季的大气环流异常特征非常吻合,也从一定程度上说明 2019 年春季大气环流对 El Niño 事件的响应是显著的。

参考文献

陈红,2017. 欧亚大陆积雪对我国春季气候可预报性的影响[J]. 大气科学,41 (4):727-738. Chen H,2017. Impacts of Eurasian snow condition on spring climate predictability over China by a global climate model[J]. Chin J Atmos Sci,41(4):727-738(in Chinese).

陈丽娟,袁媛,杨明珠,等,2013. 海温异常对东亚夏季风影响机理的研究进展[J]. 应用气象学报,24(5):521-532. Chen L J,Yuan Y,Yang M Z,et al,2013. A review of physical mechanisms of the global SSTA impact on EASM[J]. J Appl Meteor Sci,24(5):521-532(in Chinese).

龚志强,宋文玲,王东阡,等,2017. 2017 年春季我国主要气候特征及其成因分析[J]. 气象,43(10):1296-1301. Gong Z Q,Song W L,Wang D Q,et al,2017. Features and causes for the climate anomalies in spring 2017[J]. Meteor Mon,43(10):1296-1301(in Chinese).

顾薇,陈丽娟,2019. 2018 年夏季海洋大气特征及对我国气候的影响[J]. 气象,45(1):126-134. Gu W,Chen L J,2019. Characteristics of atmospheric and oceanic condition and their influences on summer climate of China in 2018[J]. Meteor Mon,45(1):126-

134(in Chinese).

顾伟宗,陈海山,孙照渤,2006.华北春季降水机理及其与前期印度洋海温的关系[J].南京气象学院学报,29(4):484-490. Gu W Z, Chen H S, Sun Z B, 2006. Spring precipitation in North China and its relation to SST of Indian Ocean in the preceding winter [J]. J Nanjing Institute Meteor, 29(4): 484-490(in Chinese).

刘芸芸,李维京,艾婉秀,等,2012.月尺度西太平洋副热带高压指数的重建与应用[J].应用气象学报,23(4):414-423. Liu Y Y, Li W J, Ai W X, et al, 2012. Reconstruction and application of the monthly western North Pacific subtropical high indices[J]. J Appl Meteor Sci, 23(4): 414-423(in Chinese).

邵勰,柳艳菊,李多,等,2015.2015年春季我国主要气候特征及其成因分析[J].气象,41(10):1292-1297. Shao X, Liu Y J, Li D, et al, 2015. Main characteristics and possible causes for the climate in China in spring 2015[J]. Meteor Mon, 41(10): 1292-1297(in Chinese).

邵勰,柳艳菊,孙丞虎,等,2016.2016年春季我国主要气候特征及其成因分析[J].气象,42(10):1278-1282. Shao X, Liu Y J, Sun C H et al, 2016. Main characteristics and possible causes for the climate in China during the spring of 2016[J]. Meteor Mon, 42(10): 1278-1282(in Chinese).

任芝花,余予,邹凤玲,等.2012.部分地面要素历史基础气象资料质量检测[J].应用气象学报,23(6):739-747. Ren Z H, Yu Y, Zou F L, et al, 2012. Quality detection of surface historical basic meteorological data[J]. J Appl Meteor Sci, 23(6): 739-747(in Chinese).

王林,陈文,冯瑞权,等,2011.北太平洋涛动的季节演变及其与我国冬春气候异常的联系[J].大气科学,35(3):393-402. Wang L, Chen W, Fong S, et al, 2011. The seasonal march of the North Pacific Oscillation and its association with the interannual variations of China's climate in boreal winter and spring[J]. Chin J Atmos Sci, 35(3): 393-402(in Chinese).

王群英,龚道溢,1999.华北降水资源的变化及其与厄尔尼诺的关系[J].自然资源科学,14(2):103-108. Wang Q Y, Gong D Y, 1999. Variation of rainfall over North China and its possible connection to El Niño[J]. J Natrual Res, 14(2): 103-108(in Chinese).

王遵娅,柳艳菊,丁婷,等,2018.2018年春季气候异常及可能成因分析[J].气象,44(10):1360-1369. Wang Z Y, Liu Y J, Ding T, et al, 2018. Features and possible causes for the climate anomalies in spring 2018[J]. Meteor Mon, 44(10): 1360-1369(in Chinese).

杨亚力,杜岩,陈海山,等,2011.ENSO事件对云南及临近地区春末初夏降水的影响[J].大气科学,35(4):729-738. Yang Y L, Du Y, Chen H S, et al, 2011. Influence of ENSO event on rainfall anomaly over Yunnan Province and its neighboring regions during late spring-early summer[J]. Chin J Atmos Sci, 35(4): 729-738(in Chinese).

袁媛,柳艳菊,王艳姣,等,2014.2014年春季我国主要气候特征及成因简析[J].气象,40(10):1279-1285. Yuan Y, Liu Y J, Wang Y J, et al, 2014. Main characteristics and possible causes for the climate anomalies in spring 2014[J]. Meteor Mon, 40(10): 1279-1285(in Chinese).

尹姗,冯娟,李建平,2013.前冬北半球环状模对春季中国东部北方地区极端低温的影响[J].气象学报,71(1):96-108. Yin S, Feng J, Li J P, 2013. Influences of the preceding winter Northern Hemisphere annular mode on the spring extreme low temperature events in the north of eastern China[J]. Acta Meteor Sin, 71(1): 96-108(in Chinese).

詹丰兴,刘芸芸,何金海,2013.江南春季降水的准两年振荡及其与热带海温异常的关系[J].地理科学,33(8):1006-1013. Zhan F X, Liu Y Y, He J H, 2013. Tropospheric biennial oscillation of the precipitation over Jiangnan area in China in MAM and its relationship with the tropical SST anomaly[J]. Sci Geographica Sin, 33(8): 1006-1013(in Chinese).

左志燕,张人禾,2012.中国春季降水异常及其与热带太平洋海面温度和欧亚大陆积雪的联系.大气科学,36(1):185-194. Zuo Z Y, Zhang R H, 2012. The anomalies of spring rainfall in eastern China and its relation with tropical Pacific SST and Eurasian snow[J]. Chin J Atmos Sci, 36(1): 185-194(in Chinese).

Chambers D P, Tapley B D, Stewart R H, 1999. Anomalous warming in the Indian Ocean coincident with El Niño[J]. J Geophys Res, 104: 3035-3047.

Chan J C L, 2000. Tropical cyclone activity over the western North Pacific associated with El Niño and La Niña events[J]. J Climate, 13: 2960-2972.

Chen L J, Gu W, Li W J, 2019. Why is the East Asian summer monsoon extremely strong in 2018? ——collaborative effects of SST and snow cover anomalies[J]. J Meteor Res, 33(4): 593-608.

Chen W, Graf H-F, Huang R H, 2000. The interannual variability of East Asian winter monsoon and its relation to the summer monsoon[J]. Adv Atmos Sci, 17(1): 48-60.

Chia H H, Ropelewski C F, 2002. The interannual variability in the genesis location of tropical cyclones in the Northwest Pacific [J]. J Climate, 15: 2934-2944.

Gill A E, 1980. Some simple solutions for heat-induced tropical circulation[J]. Quart J Roy Meteor Soc, 106(449): 447-462.

He C, Zhou T J, 2015. Decadal change of the connection between summer western North Pacific Subtropical High and tropical SST in the early 1990s[J]. Atmos Sci Lett, 16 (3): 253-259.

Hu Z-Z, Kumar A, Jha B, Wang W, Huang B H, Huang B Y, 2012. An analysis of warm pool and cold tongue El Niños: Air-sea coupling processes, global influences, and recent trends[J]. Clim Dyn, 38: 2017-2035.

Huang B, Thorne P W, Banzon V F, et al, 2017 Extended Reconstructed Sea Surface Temperature version 5 (ERSSTv5), Upgrades, validations, and intercomparisons [J]. J Climate, 30: 8179-8205.

Kalnay E, Kanamitsu M, Kistler R, et al, 1996. The NCEP/NCAR 40-Year Reanalysis Project[J]. Bull Amer Meteor Soc, 77: 437-472.

Lau N C, Nath M J, 2003. Atmosphere-ocean variations in the Indo-Pacific sector during ENSO episodes[J]. J Climate, 16(1): 3-20.

Liu Y Y, Ding Y H, Gao H, et al, 2013. Tropospheric biennial oscillation of the western Pacific subtropical high and its relationships with the tropical SST and atmospheric circulation anomalies[J]. Chin Sci Bull, 58, 3664-3672.

Liu Y Y, Hu Z-Z, Kumar A, Peng P, Collins D and Jha B, 2015. Tropospheric biennial oscillation of summer monsoon rainfall over East Asia and its association with ENSO[J]. Clim Dyn, 45 (7-8), 1747-1759.

Liu Y Y, Liang P, Sun Ying, 2019. The Asian Summer Monsoon: Characteristics, Variability, Teleconnections and Projection[M]. Amsterdam: Elsevier, 237pp.

Matsuno T, 1966. Quasi-geostrophic motions in the equatorial area [J]. J Meteor Soc Japan, 44(1): 25-43.

Tao S Y, Chen L X, 1987. A review of recent research on the East Asian summer monsoon in China[M]// Chang C P, Krishnamurti T N, Monsoon Meteorology, Oxford: Oxford University Press.

Tian S F, Yasunari T, 1998. Climatological aspect and mechanism of spring persistent rains over central China[J]. J Meteor Soc Japan, 76(1): 57-71.

Wang B, Chan J C L, 2002. How strong ENSO events affect tropical storm activity over the western North Pacific[J]. J Climate, 15: 1643-1658.

Wu R, Hu Z Z, Kirtman B P, 2003. Evolution of ENSO-related rainfall anomalies in East Asia[J]. J Climate, 16(22), 3742-3758.

Wu R G, Kirtman B P, 2007. Observed relationship of spring and summer East Asian rainfall with winter and spring Eurasian snow[J]. J Climate, 20(7): 1285-1304.

Wu Z W, Li X X, Li Y J, 2016. Potential Influence of Arctic Sea Ice to the interannual variation of East Asian spring precipita-tion. J Climate, 29: 2797-2813.

Xie S P, Hu K, Hafner J, et al, 2009. Indian Ocean capacitor effect on Indo-western Pacific climate during the summer following El Niño[J]. J Climate, 22(3): 730-747.

Yang S, Ding X, Zheng D, et al, 2007. Time-frequency characteristics of the relationships between tropical Indo-Pacific SSTs[J]. Adv Atmos Sci, 24(3): 343-359.

Yuan Y, Yang S, Zhang Z Q, 2012. Different evolutions of the Philippine Sea anticyclone between Eastern and Central Pacific ElNiño: Effects of Indian Ocean SST[J]. J Climate, 25(22): 7867-7883.

Zhang R H, Sumi A, 2002. Moisture circulation over East Asia during El Niño episode in the northern winter, spring and autumn [J]. J Meteor Soc Japan, 80: 213-227.

新书架

《气象科技论文写作与编辑要领》

王银平 著

该书是作者从事气象科技期刊编辑工作二十多年的经验积累与智慧结晶。书中,作者理论联系实际,以科技期刊编辑人的独特视角,指明了科技论文的写作要领、编辑要领与作者因素,剖析了提升科技期刊影响力和竞争力的编辑因素以及编辑与作者的关系,同时分析了未来我国科技期刊可持续发展可能面临的问题及相应对策,说理深入浅出,论述通俗易懂,指导实用性强。书中相关要领、观点或结论,对致力于科技论文写作的研究人员、业务技术人员和管理人员,从事科技期刊出版工作的编辑人员,以及大气科学或相关专业学生都有参考价值。

16 开　定价:55.00 元

《气温变化的不确定性分析与应用》

华维 等 著

该书从气候变化不确定性的基本概念出发,较为全面地阐述了气温变化观测数据的不确定性理论、关键科学问题及实际应用。全书分为 5 章,包括气温变化观测数据不确定性研究现状及意义、气温变化观测数据的不确定性源分析、我国及相关区域气温变化的不确定性评估、不确定性对极端冷暖年排序的影响、不确定性在历史气温场重建中的应用等方面的研究成果。本书内容丰富、资料翔实、文图并茂,可供气象、水文、资源、环境及其相关领域科技工作者参考,也可作为大气科学类研究生课程的教科书或本科高年级学生专业选修课的教学参考书。

16 开　定价:39.00 元

《气候变化与建筑节能》

李明财 著

该书从建筑运行及设计对气象的需求入手,系统介绍了气候变化对建筑能耗、节能设计气象参数及建筑气候区划等多方面影响,指出要充分考虑其影响,提出和制订适应气候变化的建筑节能对策。本书可供气象、建筑热环境及暖能空调等专业人员开展建筑节能工作参考使用。

16 开　定价:65.00 元

气象出版社网址:http://www.qxcbs.com, E-mail:qxcbs@cma.gov.cn

联系电话:010-68408042(发行部), 010-68407021(读者服务部)

传真:010-62176428

Received: 8 May 2019 | Revised: 16 June 2019 | Accepted: 18 June 2019

DOI: 10.1002/asl.928

RESEARCH ARTICLE

Atmospheric Science Letters RMetS

Impact of El Niño and Southern Oscillation on the summer precipitation over Northwest China

Bo Lu[1,2] | **Haiyan Li**[3] | **Jie Wu**[3] | **Taixi Zhang**[3] | **Jing Liu**[3] | **Bao Liu**[3] | **Ying Chen**[3] | **Jiazila Baishan**[3]

[1]Laboratory for Climate Studies, China Meteorological Administration, Beijing, China

[2]CMA-NJU Joint Laboratory for Climate Prediction Studies, Institute for Climate and Global Change Research, School of Atmospheric Sciences, Nanjing University, Nanjing, China

[3]Xinjiang Climate Center, Xinjiang Meteorological Bureau, Urumqi, China

Correspondence
Bo Lu, Laboratory for Climate Studies, China Meteorological Administration, No. 46 Zhongguancun Nandajie, Beijing 100081, China.
Email: bolu@cma.gov.cn

Funding information
National Key Research and Development Program of China, Grant/Award Number: 2018YFC1506002, 2016YFA0602104 and 2017YFC1502302; National Natural Science Foundation of China, Grant/Award Number: 41605116; Key Research Program of Xinjiang Meteorological Bureau, Grant/Award Number: ZD201802

Abstract

Using the reanalysis data and local weather station data, the relationship between El Niño and Southern Oscillation (ENSO) and the summer precipitation over Northwest China (SPNWC) is investigated. A pronounced rainfall response is observed in post-ENSO summer, especially over North Xinjiang and Yili River valley. A possible mechanism is proposed for such a seasonal lagged impact. El Niño could induce Indian Ocean warming that persists into boreal spring and summer although El Niño itself has dissipated. The warmer Indian Ocean sea surface temperature (SST) would heat the tropospheric atmosphere and elevate the tropical geopotential height at the upper level. As a result, the South Asian High (SAH) exhibits a southward extension due to the increasing geopotential height in its southern flank. A southward displacement of subtropical jet is evident associated with such SAH shift, which further induces a barotropic low pressure anomaly over central Asia. Meanwhile, associated with the southward displacement of subtropical jet, the water vapor from tropical Indian Ocean tends to transport across Iranian Plateau and bring wet and warm air into central Asia. The resultant convergence of water vapor with cold and dry air from high latitude leads to the observed rainfall anomaly to the south and east of Balkhash Lake, explaining the lagged relationship between ENSO and SPNWC. Our results have potential applications on the seasonal prediction of SPNWC.

KEYWORDS

ENSO, impact, mechanism, Northwest China, summer precipitation

1 | INTRODUCTION

Northwest China is located in the inland of Eurasian continent, which is far away from the oceans. Owing to the lack of precipitation, Northwest China is featured as the arid-semiarid region. However, the interannual variation of the precipitation is pronounced in this region, especially during the boreal summer. For example, during the summer in 2016, heavy rainfall took place in the Xinjiang province over Northwest China, resulting in the severe road damages and civilian casualties. Recent studies have shown the increasing trend of such extreme precipitation since recent decades (Jiang *et al.,* 2005; Chen *et al.,* 2011). The economic and social loss could be reduced if skillful seasonal prediction can be provided. However, compared with the remarkable progresses in understanding the monsoonal climate over East China (e.g., reviewed by Ding and Chan, 2005), less attention is paid to the

This is an open access article under the terms of the Creative Commons Attribution License, which permits use, distribution and reproduction in any medium, provided the original work is properly cited.
© 2019 The Authors. *Atmospheric Science Letters* published by John Wiley & Sons Ltd on behalf of the Royal Meteorological Society.

dynamics and predictability of the precipitation over Northwest China.

Previous studies have shown that the teleconnection patterns, such as the Silk Road pattern and Europe–China pattern are responsible for the July precipitation variations in Northwest China (Chen and Huang, 2012). The meridional teleconnection in central Asia can affect the summer rainfall over Tarim Basin in Northwest China by exciting the favorable water vapor transport (Huang *et al.,* 2015). Significant correlation is discovered between the middle-upper tropospheric temperature and the summer rainfall over Tarim Basin (Zhao *et al.,* 2014a; 2014b). In addition, the meridional displacement of subtropical westerly jet (Yang and Zhang, 2008; Zhao *et al.,* 2014a; 2014b), the anomalous cyclone over central Asia (Yang and Zhang, 2007), previous thermal anomaly over Tibetan Plateau (Zhao *et al.,* 2016) and the variation of South Asian High (SAH) (Wang *et al.,* 2017) are also suggested to be the controlling factors for the summer precipitation in Northwest China. These findings mainly focus on the internal atmospheric variations, teleconnections and the local land-atmosphere interactions.

El Niño and Southern Oscillation (ENSO) is the strongest climate fluctuation on interannual timescale, which can induce remote climate impacts by stimulating teleconnections (Trenberth *et al.,* 1998). Extensive studies have pointed out the control of ENSO on the East Asian monsoon (e.g., Fu and Teng, 1988; Huang and Wu, 1989; Zhang *et al.,* 2016), in which the strengthening of northwestern Pacific subtropical high during the El Niño decaying summer plays a key role (Wang *et al.,* 2000; Stuecker *et al.,* 2015; Xie *et al.,* 2016; Li *et al.,* 2017; Zhang *et al.,* 2017). Northwest China lies in the "westerly dominated regime" (Huang *et al.,* 2015), which is different from East China that controlled by monsoon circulations. However, recent evidences have shown that the summer temperature and precipitation in Northwest China is also correlated with tropical SST anomalies (Yang *et al.,* 2010; Li *et al.,* 2018). In this study, the observations, reanalysis data, and the results from Atmospheric Model Intercomparison Project (AMIP) are analyzed to investigate the possible relationship between the Northwestern China summer precipitation and ENSO. In addition, a possible physical mechanism is proposed.

2 | DATA AND METHODOLOGY

This study utilizes HadISST (Hadley Center Global Sea Surface Temperature data set; Rayner *et al.,* 2006) for the observed monthly mean SST, with horizontal grid resolutions of 1° × 1° since 1870. Hadley Center/Climatic Research Unit CRU_ts4.02 is adopted to obtain the high resolution (0.5° × 0.5°) land precipitation since 1901 (Harris *et al.,* 2014), which is verified by the station precipitation data in Xinjiang province, Northwest China since 1961. Reanalysis-1 (National Centers for Environmental Prediction–National Center for Atmospheric Research reanalysis data; Kalnay *et al.,* 1996) is used to retrieve the fields of horizontal wind, geopotential height and humidity since 1948. A common period after 1961 is analyzed for the observational data.

As an effort to confirm the atmospheric response to ocean forcings, the Atmospheric Models Intercomparison Project (AMIP) experiment output of 22 climate models that participate in Coupled Models Intercomparison Project phase 5 (CMIP5) are analyzed in this paper (Table S1). These experiments are imposed with historical sea surface temperature (SST; Taylor *et al.,* 2012), and the common overlay period from 1979 to 2008 is analyzed.

To focus on the interannual variability of SST, circulation and precipitation, the linear trend derived from the linear regression is removed. This is necessary, especially when studying the SST in tropical Indian Ocean, which exhibits a remarkable increasing trend (Du and Xie, 2008).

3 | RESULTS

The correlation of the summer precipitation with ENSO in previous winter is given in Figure 1. A significant correlation is evident to the south and east of Balkhash Lake (Figure 1a). Especially in North Xinjiang over Northwest China, the correlation coefficient reaches 0.5, which is comparable with the summer rainfall response to ENSO in East China (Zhang *et al.,* 2016). This result is further confirmed by the observational weather station data. As demonstrated in Figure 1c, the summer precipitation is tightly correlated with previous Niño3.4 anomalies at the stations located around Alatao Mountain, Yili River valley and the northern periphery of the Tienshan Mountains, which is consistent with the findings using CRU reconstructions. It is also noted that the precipitation over other parts of Northwest China, such as Tarim Basin, is unaffected by previous ENSO. It implies the different mechanisms of summer rainfall formation between the southern and northern sides of Tienshan Mountain.

It is interesting that the concurrent response of North Xinjiang precipitation to ENSO is weak, with the insignificant correlation of 0.2 (Figure 1e). The robust relationship occurs in post-ENSO spring and summer. In this paper, only the summer (from June to August) precipitation is studied given the fact that the climatological mean and interannual variation is largest over Northwest China in boreal summer. Such a lagged response in post-ENSO summer is worthy of investigation since equatorial SST anomalies has disappeared then (black curve in Figure 1e). The mechanism of this two-season lagged response remains unclear. Similar lagged correlation exists for ENSO-East Asian summer monsoon relationship, which has been extensively studied

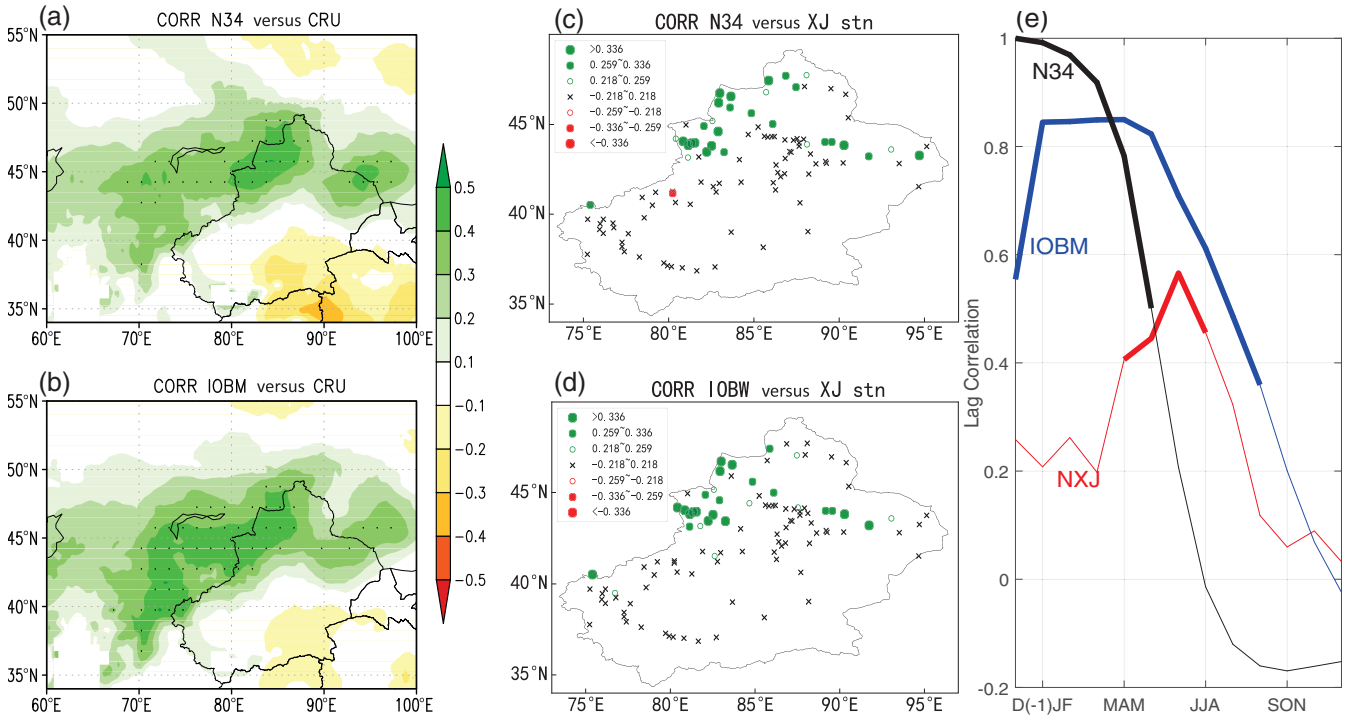

FIGURE 1 The correlation patterns of summer (June to August) precipitation (left panel for CRU precipitation; median panel for station precipitation in Xinjiang Province over Northwest China) against Niño3.4 anomalies during previous winter (November to January; a, c) and IOBM anomalies during current spring (March to May; b, d). The large solid circle, median solid circle and small open circle in (c, d) represent the significant correlation at 99, 95 and 90% confidence levels, respectively. (e) The lag correlations of the Niño3.4 anomalies (black curve), IOBM anomalies (blue curve) and summer precipitation over North Xinjiang (red curve) against Niño3.4 anomalies during previous winter, with 3-month running average applied. The thick curves in indicate the significant correlations at 99% confidence level based on the student *t* test

(Fu and Teng, 1988; Huang and Wu, 1989; Zhang *et al.,* 2016). As demonstrated in Figure 1e, the Indian Ocean Basin Mode SST (defined as the averaged SST within 40°–110°E; 20°S–20°N) anomaly develops after the mature phase of ENSO and persists into the following spring and summer. Xie et al. (2009) proposed that this Indian Ocean SST anomaly acts as a capacitor that prolongs the impact of fast decaying ENSO SST and further induces the anomalous anticyclone over northwestern Pacific. Figure 1b shows that the summer precipitation over North Xinjiang is also related to with the IOBM during boreal spring. The correlation pattern generally resembles that with ENSO during previous winter (Figure 1b), which is also verified by the station data (Figure 1d). This statistical result is not surprising, given the fact that IOBM in post-ENSO spring is highly correlated with ENSO in its mature phase (Figure 1e). Figure 2 further demonstrates the regression pattern of SST anomalies against the summer precipitation over North Xinjiang. During previous winter, the most remarkable SST anomaly is observed over the equatorial central to eastern Pacific (Figure 2a), which resembles the spatial pattern of ENSO. As ENSO decays, the correlation over the equatorial eastern Pacific drops in boreal spring and summer (Figure 2b and (c)). However, the consistent correlation is evident over Indo-western Pacific Ocean (Figure 2b,c), indicating the capacity effect of Indian Ocean that prolongs the influence of ENSO on the summer climate over North Xinjiang. Thus, it is necessary to investigate the mechanism of how IOBM affects the summer precipitation over Northwest China (SPNWC).

In the subtropical upper troposphere, the westerly jet is an important atmospheric circulation pattern (contours in Figure 3) which is closely related to the summer precipitation distribution in central (Schiemann *et al.,* 2009) and East Asia (Lu, 2004). Figure 3 shows the difference of the composite zonal wind anomalies at 200 hPa between the positive and negative IOBM years. Here, the positive (negative) IOBM years is defined when the detrended IOBM index exceeding 0.5 (−0.5) *SD*. In the observation, the positive (negative) wind anomalies are evident to the south (north) of the climatologic jet core. This pattern indicates the pronounced southward (northward) shift with the Indian Ocean warming (cooling). This result is further examined by the AMIP experiments. With the historical Indian Ocean SST forcing, the ensemble mean of 22 AMIP models is able to produce this jet shift, although the amplitude is underestimated due to intermodal cancelation (Figure S1). Previous studies have shown that this meridional shift of jet axis,

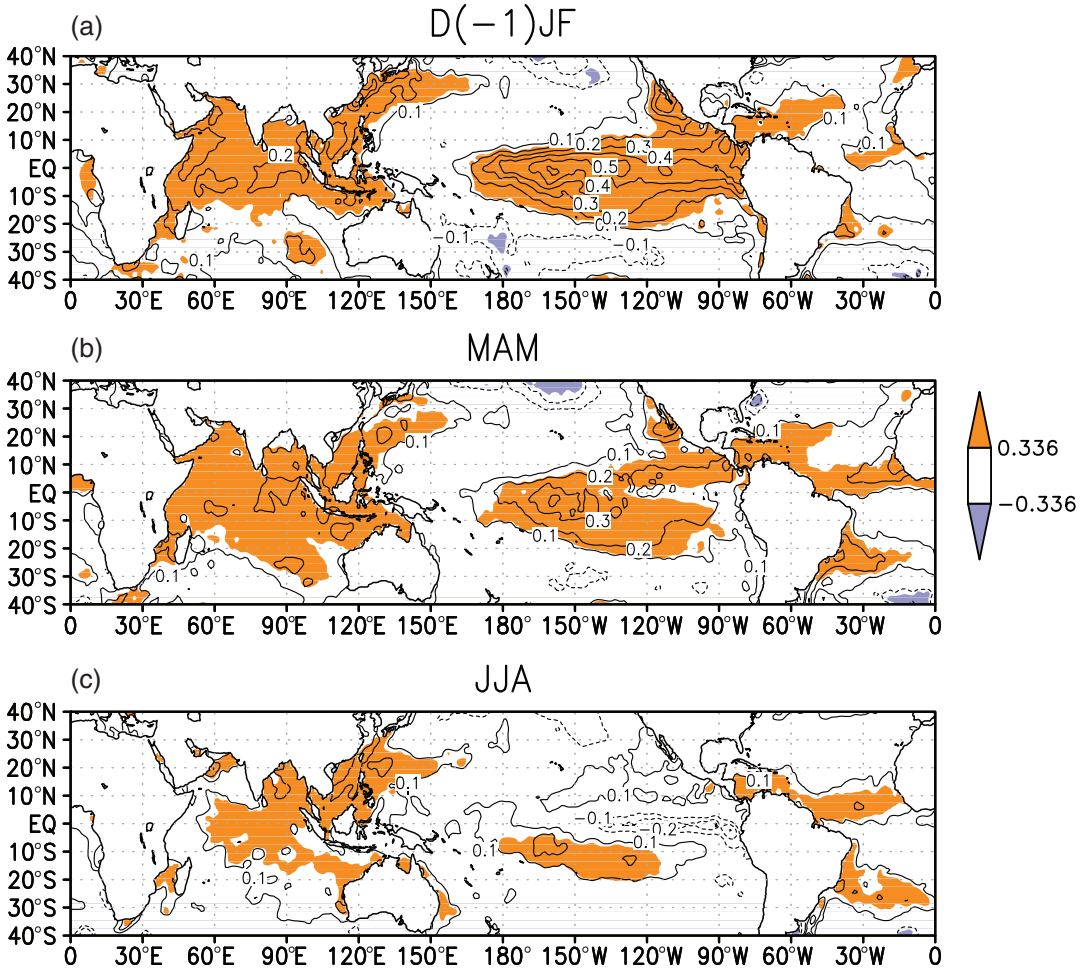

FIGURE 2 The regression patterns of SST anomalies against the summer rainfall over North Xinjiang in D(−1)JF (a), MAM (b) and JJA (c). The shadings indicate the regions with significant correlations at 99% confidence level

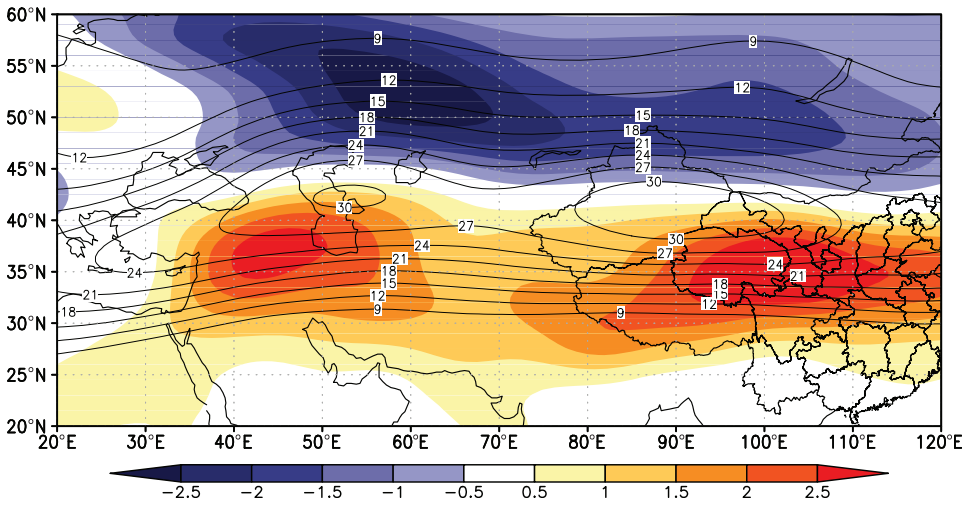

FIGURE 3 The summer (June to August) climatologic zonal wind (contour; unit: m/s) and the composite differences of its anomalies between the positive and negative IOBM years (shading; unit: m/s) at 200 hPa in the observation

rather than the variation of jet strength, is the leading mode of the interannual jet variation (Lin and Lu, 2005; Zhao *et al.,* 2014a; 2014b). The location of the westerly jet, especially the active center over Caspian Sea, is critical to the SPNWC (Zhao *et al.,* 2014a; 2014b). Figure 4 demonstrates the regression pattern of circulation and water vapor transport against the normalized Jet location index (defined as the difference between the averaged 200 hPa zonal wind within

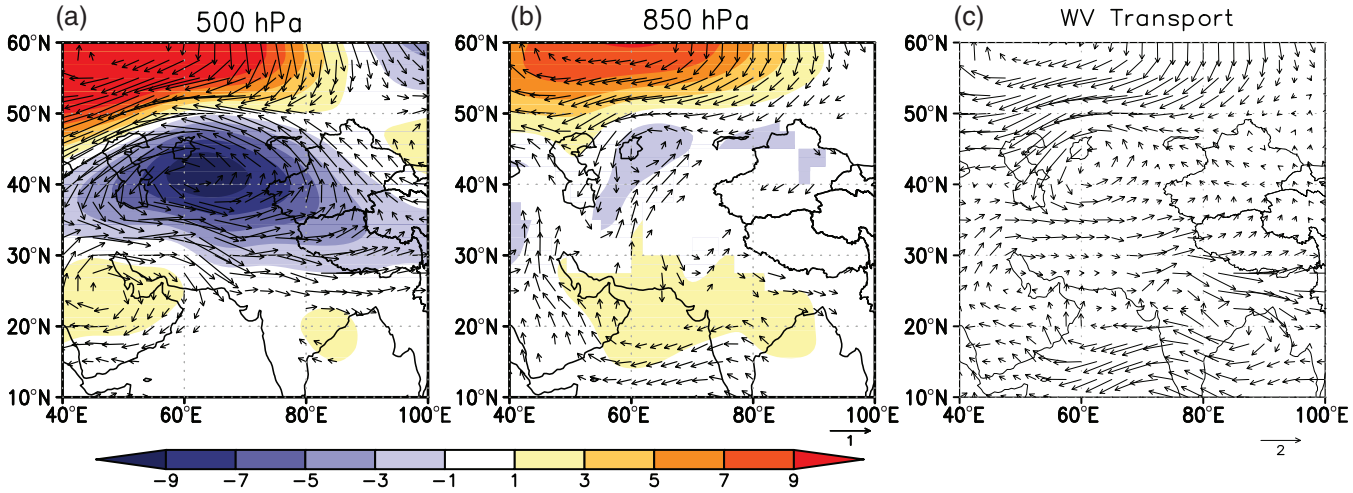

FIGURE 4 The regression patterns of horizontal wind (vector; unit: m/s) and geopotential height anomalies (shading; unit: gpm) at 500 hPa (a) and 850 hPa (b) against the normalized Jet Position Index during boreal summer. (c) The regression of vertical integrated water vapor transport against the normalized Jet Position Index during boreal summer (surface to 300 hPa; unit: 10^4g/[s m])

40°–80°E; 30°–42.5°N and 40°–80°E; 42.5°–55°N). The southward shift of the jet over Caspian Sea would stimulate a cyclonic circulation at 500 hPa (Figure 4a), which is a well-known key circulation pattern favorable for the summer precipitation over North Xinjiang. In the lower troposphere, the anomalous warm and wet air from the Indian Ocean transports across the Iranian Plateau and meets with the cold air from high latitude around the Balkhash Lake (Figure 4b). The vertical integrated water vapor transport also demonstrates the moisture convergence around the Balkhash Lake

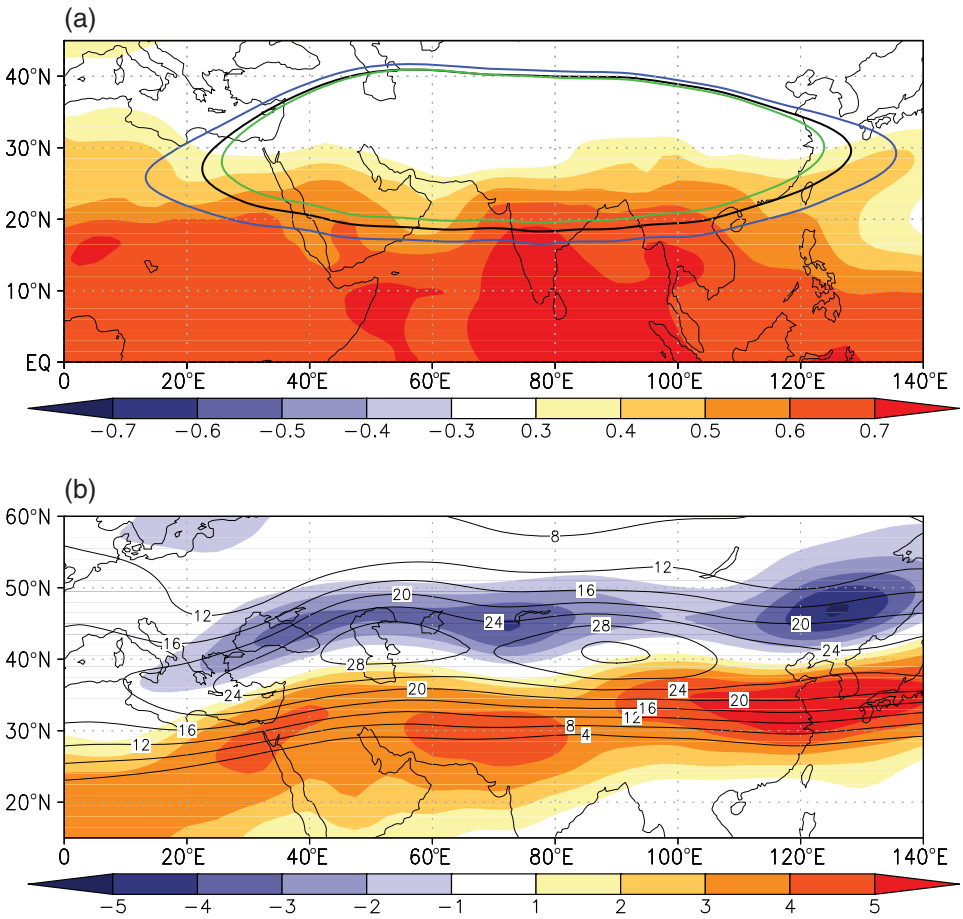

FIGURE 5 (a) The correlation patterns between IOBM and the summer tropospheric (1,000–100 hPa) temperature anomalies (shading), and the climatologic (black contour) and the composites of SAH during the positive (blue contour) and negative (green contour) IOBM years in the observation. Note that SAH is indicated by the 100 hPa 16,720 gpm geopotential height here. (b) The climatologic (contour) and the composite differences of zonal wind anomalies at 200 hPa between the years with southward and northward displacement of SAH (shading) in the observation

(Figure 4c). This moisture convergence is confirmed by replacing the NCEP reanalysis with ERA-interim reanalysis (Figure S2; Dee *et al.,* 2011). The above mentioned circulation features associated with the jet shift resembles the general circulation characteristics for the abundant summer rainfall over north Xinjiang (Yang and Zhang, 2007).

It has been shown that the meridional shift of subtropical westerly jet is statistically connected with ENSO-induced Indian Ocean SST anomalies, which can further induce favorable circulation patterns for SPNWC. However, what is the physical mechanism behind the IOBM-jet location relationship still remains unclear. Figure 5 (shading) demonstrates the correlation patterns between the IOBM and the summer tropospheric (1,000–100 hPa) temperature anomalies. The significant correlation is evident, indicating the pronounced tropospheric heating with surface Indian Ocean warming. Huang *et al*. (2011) suggests that such tropospheric heating is caused by the changes in the equivalent potential temperature in the atmospheric boundary layer associated with Indian Ocean warming, which could elevates the geopotential height at the upper troposphere to the south of the SAH (SAH). As a result, the SAH exhibits a southward extension during the warming phase of Indian Ocean (contours in Figure 5a). Using the ensemble mean of 22 AMIP models, the tropospheric warming and southward shift of SAH can also be reproduced (Figure S3a), indicating the robustness of the mechanism proposed by Huang *et al*. (2011). Since SAH is the dominant circulation system over Asian continent, its southward extension could lead to the southward displacement of the subtropical jet (Lin and Lu, 2005). As shown in Figure 5b, the observed southward jet shift is associated with southward extension of SAH, which is well reproduced with the AMIP experiments (Figure S3b). Above all, we show that SAH connects the Indian Ocean SST and subtropical jet via the tropospheric heating and the consistent meridional displacement at the upper troposphere.

4 | SUMMARY AND DISCUSSION

In this article, the response of Northwest China precipitation during post-ENSO summer is studied. Both the reconstructed and station observation data show that the pronounced response occurred to the south and east of Balkhash Lake, with significant correlations in North Xinjiang and Yili River valley. This result is different from previous findings. Yang *et al*. (2010) studied the relations between the summer rainfall over North Xinjiang and SST anomalies. They argued that the summer rainfall over North Xinjiang is uncorrelated with ENSO. Here, we show the significant correlation between the Nino3.4 anomalies in D(−1)JF and JJA rainfall over North Xinjiang.

A possible mechanism for such seasonal lagged response is also proposed. First, the ENSO-induced tropical Indian Ocean SST anomalies persist into post-ENSO spring and summer. Second, the local tropospheric atmosphere is heated by the Indian Ocean warming, which further elevates the geopotential height at the upper troposphere. Third, the SAH exhibits a southward extension due to the increased geopotential height in its southern flank, resulting in the southward displacement of upper level circulations, such as the subtropical westerly jet. Fourth, associated with the southward shift of subtropical jet, a barotropic response of anomalous cyclonic circulation is evident over central Asia at 500 hPa. Meanwhile, the warm and wet air from the tropical Indian Ocean transports into central Asian and converges with the cold air near Balkhash Lake. This circulation configuration is favorable for the precipitation over North Xinjiang. The above mechanism is examined by using the ensemble simulation of 22 AMIP models.

Previous studies have proposed that the relationship between ENSO and East Asia summer monsoon is unstable in different periods (e.g., Wang, 2002). We also investigate whether such interdecadal variation exists regarding the impact of ENSO on Northwest China precipitation. The preliminary results show that this relationship is generally stable during 1961–2018 (Figure S4). In addition, the impacts of different El Niño flavors are compared. Similar results are obtained for two types of El Niño, in terms of their lagged impacts on the summer rainfall over Northwestern Xinjiang (figures not shown). This study could shed some light on the seasonal prediction of summer rainfall over Northwest China.

ACKNOWLEDGEMENTS

The study was supported by the National Key Research and Development Program of China (2018YFC1506002, 2016YFA0602104 and 2017YFC1502302), Key Research Program of Xinjiang Meteorological Bureau (ZD201802), and National Natural Science Foundation of China (41605116).

CONFLICT OF INTEREST

The authors declare no conflict of interest.

ORCID

Bo Lu https://orcid.org/0000-0002-4063-3035

REFERENCES

Chen, G. and Huang, R. (2012) Excitation mechanisms of the teleconnection patterns affecting the July precipitation in Northwest China. *Journal of Climate*, 25, 7834–7851.

Chen, F., Huang, W., Jin, L., Chen, J. and Wang, J. (2011) Spatiotemporal precipitation variations in the arid Central Asia in the context of global warming. *Science China Earth Sciences*, 54(12), 1812–1821.

Dee, D.P., Uppala, S.M., Simmons, A.J., Berrisford, P., Poli, P., Kobayashi, S., Andrae, U., Balmaseda, M.A., Balsamo, G., Bauer, P., Bechtold, P., Beljaars, A.C.M., van de Berg, L., Bidlot, J., Bormann, N., Delsol, C., Dragani, R., Fuentes, M., Geer, A.J., Haimberger, L., Healy, S.B., Hersbach, H., Hólm, E.V., Isaksen, L., Kållberg, P., Köhler, M., Matricardi, M., McNally, A. P., Monge-Sanz, B.M., Morcrette, J.J., Park, B.K., Peubey, C., de Rosnay, P., Tavolato, C., Thépaut, J.N. and Vitart, F. (2011) The ERA-interim reanalysis: configuration and performance of the data assimilation system. *Quarterly Journal of the Royal Meteorological Society*, 137, 553–597.

Ding, Y.H. and Chan, J.C.L. (2005) The east Asian summer monsoon: an overview. *Meteorology and Atmospheric Physics*, 89, 117–142.

Du, Y. and Xie, S.P. (2008) Role of atmospheric adjustments in the tropical Indian Ocean warming during the 20th century in climate models. *Geophysical Research Letters*, 35, L08712.

Fu, C. and Teng, X. (1988) The relationship between ENSO and climate anomaly in China during the summer time. *Science Atmospheric Sinica*, 12, 133–141 in Chinese.

Harris, I., Jones, P.D., Osborn, T.J. and Lister, D.H. (2014) Updated high–resolution grids of monthly climatic observations–the CRU TS3.10 dataset. *International Journal of Climatology*, 34(3), 623–642.

Huang, R. and Wu, Y. (1989) The influence of ENSO on the summer climate change in China and its mechanism. *Advances in Atmospheric Sciences*, 6, 21–32.

Huang, G., Qu, X. and Hu, K.M. (2011) The impact of the tropical Indian Ocean on South Asian high in boreal summer. *Advances in Atmospheric Sciences*, 28, 421–432.

Huang, W., Chen, J., Zhang, X., Feng, S. and Chen, F. (2015) Definition of the core zone of the "westerlies-dominated climatic regime", and its controlling factors during the instrumental period. *Science China Earth Sciences*, 58, 676–684.

Jiang, F., Zhu, C., Mu, G.J., Hu, R.J. and Meng, Q. (2005) Magnification of flood disasters and its relation to regional precipitation and local human activities since the 1980s in Xinjiang, northwestern China. *Nature Hazards*, 36, 307–330.

Kalnay, E., Kanamitsu, M., Kistler, R., Collins, W., Deaven, D., Gandin, L., Iredell, M., Saha, S., White, G., Woollen, J., Zhu, Y., Leetmaa, A., Reynolds, R., Chelliah, M., Ebisuzaki, W., Higgins, W., Janowiak, J., Mo, K.C., Ropelewski, C., Wang, J., Jenne, R. and Joseph, D. (1996) The NCEP/NCAR 40-year reanalysis project. *Bulletin of the American Meteorological Society*, 77, 437–471.

Li, T., Wang, B., Wu, B., , Zhou T., Chang C.P., Zhang R. (2017) Theories on formation of an anomalous anticyclone in Western North Pacific during El Niño: a review. *Journal of Meteorological Research*, 31, 987–1006.

Li, C.F., Lu, R.Y., Bett, P.E., Scaife, A.A. and Martin, N. (2018) Skillful seasonal forecasts of summer surface air temperature in western China by Global Seasonal Forecast System version 5. *Advances in Atmospheric Sciences*, 35, 955–964.

Lin, Z.D. and Lu, R.Y. (2005) Interannual meridional displacement of the East Asian upper-tropospheric jet stream in summer. *Advances in Atmospheric Sciences*, 22, 199–211.

Lu, R.Y. (2004) Associations among the components of the East Asian summer monsoon system in the meridional direction. *Journal of the Meteorological Society of Japan*, 82, 155–165.

Rayner, N.A., Brohan, P., Parker, D.E., Folland, C.K., Kennedy, J.J., Vanicek, M., Ansell, T.J. and Tett, S.F.B. (2006) Improved analyses of changes and uncertainties in sea surface temperature measured in situ since the mid-nineteenth century: the HadSST2 dataset. *Journal of Climate*, 19, 446–469.

Schiemann, R., Lüthi, D. and Schär, C. (2009) Seasonality and interannual variability of the westerly jet in the Tibetan Plateau region. *Journal of Climate*, 22(11), 2940–2957.

Stuecker, M.F., Jin, F.-F., Timmermann, A. and McGregor, S. (2015) Combination mode dynamics of the anomalous Northwest Pacific anticyclone. *Journal of Climate*, 28, 1093–1111.

Taylor, K.E., Stouffer, R.J. and Meehl, G.A. (2012) An overview of CMIP5 and the experiment design. *Bulletin of the American Meteorological Society*, 93, 485–498.

Trenberth, K.E., Branstator, G.W., Karoly, D., Kumar, A., Lau, N.C. and Ropelewski, C. (1998) Progress during TOGA in understanding and modeling global teleconnections associated with tropical sea surface temperatures. *Journal of Geophysical Research: Oceans*, 103, 14291–14324.

Wang, H.J. (2002) Instability of the East Asian summer monsoon-ENSO relations. *Advances in Atmospheric Sciences*, 19, 1–11.

Wang, B., Wu, R.G. and Fu, X.H. (2000) Pacific–East Asian teleconnection: how does ENSO affect East Asian climate. *Journal of Climate*, 13, 1517–1536.

Wang, Q., Zhao, Y., Chen, F., Yang, Q. and Huang, A. (2017) Characteristics of different patterns of South Asia high and their relationships with summer precipitation in Xinjiang. *Plateau Meteorology*, 3, 1209–1220 in Chinese.

Xie, S.P., Hu, K., Hafner, J., Tokinaga, H., Du, Y., Huang, G. and Sampe, T. (2009) Indian Ocean capacitor effect on Indo–western Pacific climate during the summer following El Niño. *Journal of Climate*, 22, 730–747.

Xie, S.P., Kosaka, Y., Du, Y., Hu, K., Chowdary, J.S. and Huang, G. (2016) Indo-western Pacific Ocean capacitor and coherent climate anomalies in post-ENSO summer: a review. *Advances in Atmospheric Sciences*, 33(4), 411–432.

Yang, L.M. and Zhang, Q. (2007) Circulation characteristics of interannual and interdecandal anomalies of summer rainfall in northern Xinjiang. *Chinese Journal of Geophysics*, 50(2), 412–419 in Chinese.

Yang, L. and Zhang, Q. (2008) Interannual variation of summer precipitation in Xinjiang and Asian subtropical westerly jet stream. *Journal of Applied Meteorological Science*, 19, 171–179 in Chinese.

Yang, L., Yang, T., Zhao, L. and Wang, M.Z. (2010) Relationship between summer precipitation in Northern Xinjiang and sea surface temperature anomalies. *Journal of Desert Research*, 30(5), 1215–1220 in Chinese.

Zhang, W., Jin, F.F., Stuecker, M.F., Wittenberg, A.T., Timmermann, A., Ren, H.L., Kug, J.S., Cai, W. and Cane, M. (2016) Unraveling El Niño's impact on the East Asian Monsoon

and Yangtze River summer flooding. *Geophysical Research Letters*, 43, 11375–11382.

Zhang, R., Min, Q. and Su, J. (2017) Impact of El Niño on atmospheric circulations over East Asia and rainfall in China: role of the anomalous western North Pacific anticyclone. *Science China Earth Sciences*, 60, 1124–1132.

Zhao, Y., Huang, A., Zhou, Y., Huang, D., Yang, Q., Ma, Y., Li, M. and Wei, G. (2014a) Impact of the middle and upper tropospheric cooling over Central Asia on the summer rainfall in the Tarim Basin, China. *Journal of Climate*, 27(12), 4721–4732.

Zhao, Y., Wang, M.Z., Huang, A.N., Li, H.J., Huo, W. and Yang, Q. (2014b) Relationships between the West Asian subtropical westerly jet and summer precipitation in northern Xinjiang. *Theoretical and Applied Climatology*, 116(3–4), 403–411.

Zhao, Y., Huang, A., Wang, Q. and Yang, Q. (2016) The relation between thermal anomaly contrast over the Tibetan Plateau and its surrounding areas in May and summer rainfall in northern Xinjiang. *Climatic and Environmental Research*, 21(6), 653–662 in Chinese.

SUPPORTING INFORMATION

Additional supporting information may be found online in the Supporting Information section at the end of this article.

How to cite this article: Lu B, Li H, Wu J, *et al.* Impact of El Niño and Southern Oscillation on the summer precipitation over Northwest China. *Atmos Sci Lett*. 2019;20:e928. https://doi.org/10.1002/asl.928

ENSO Features, Dynamics, and Teleconnections to East Asian Climate as Simulated in CAMS-CSM

Bo LU[1,2] and Hong-Li REN[1,3*]

1 *Laboratory for Climate Studies & China Meteorological Administration–Nanjing University Joint Laboratory for Climate Prediction Studies, National Climate Center, China Meteorological Administration, Beijing* 100081
2 *Xinjiang Climate Center, Urumqi* 830002
3 *Department of Atmospheric Science, School of Environmental Studies, China University of Geoscience, Wuhan* 430074

(Received June 15, 2018; in final form November 19, 2018)

ABSTRACT

This study evaluates the performance of CAMS-CSM (the climate system model of the Chinese Academy of Meteorological Sciences) in simulating the features, dynamics, and teleconnections to East Asian climate of the El Niño–Southern Oscillation (ENSO). In general, fundamental features of ENSO, such as its dominant patterns and phase-locking features, are reproduced well. The two types of El Niño are also represented, in terms of their spatial distributions and mutual independency. However, the skewed feature is missed in the model and the simulation of ENSO is extremely strong, which is found—based on Bjerknes index assessment—to be caused by underestimation of the shortwave damping effect. Besides, the modeled ENSO exhibits a regular oscillation with a period shorter than observed. By utilizing the Wyrtki index, it is suggested that this periodicity bias results from an overly quick phase transition induced by feedback from the thermocline and zonal advection. In addition to internal dynamics of ENSO, its external precursors—such as the North Pacific Oscillation with its accompanying seasonal footprinting mechanism, and the Indian Ocean Dipole with its 1-yr lead correlation with ENSO—are reproduced well by the model. Furthermore, with respect to the impacts of ENSO on the East Asian summer monsoon, although the anomalous Philippine anticyclone is reproduced in the post-El Niño summer, it exhibits an eastward shift compared with observation; and as a consequence, the observed flooding of the Yangtze River basin is poorly represented, with unrealistic air–sea interaction over the South China Sea being the likely physical origin of this bias. The response of wintertime lower-tropospheric circulation to ENSO is simulated well, in spite of an underestimation of temperature anomalies in central China. This study highlights the dynamic processes that are key for the simulation of ENSO, which could shed some light on improving this model in the future.

Key words: model evaluation, ENSO, dynamics, teleconnection, CAMS-CSM

Citation: Lu, B., and H.-L. Ren, 2019: ENSO features, dynamics, and teleconnections to East Asian climate as simulated in CAMS-CSM. *J. Meteor. Res.*, **33**(1), 46–65, doi: 10.1007/s13351-019-8101-6.

1. Introduction

El Niño–Southern Oscillation (ENSO) is the most dominant climatic fluctuation on the interannual timescale. It is characterized by large-scale sea surface temperature (SST) anomalies over the central to eastern Pacific, associated with changes of thermal condition in the upper ocean and convective anomalies in the atmosphere. Since Bjerknes (1969), great progress has been made in understanding the dynamics of ENSO (e.g., Wyrtki, 1985; Suarez and Schopf, 1988; Battisti and Hirst, 1989; Neelin, 1991; Li, 1997). ENSO is well-recognized as resulting from ocean–atmosphere interactions over the tropical Pacific, and theories have been proposed to explain its formation and development. For example, Jin (1997a, b) proposed a recharge oscillator framework, which highlights the importance of changes of upper-ocean heat content in the phase transition of ENSO.

Supported by the National Key Research and Development Program of China (2018YFC1506002, 2017YFC1502302, and 2016YFA0602104), Key Research Program of Xinjiang Meteorological Bureau (ZD201802), China Meteorological Administration Special Public Welfare Research Fund (GYHY201506013), and National Natural Science Foundation of China (41205058, 41375062, 41405080, 41505065, 41606019, and 41605116).

*Corresponding author: renhl@cma.gov.cn.

©The Chinese Meteorological Society and Springer-Verlag Berlin Heidelberg 2019

In spite of the advanced theoretical understanding of ENSO, accurately simulating ENSO with coupled global circulation models (CGCMs) remains challenging. For instance, Guilyardi (2006) showed that the simulated ENSO often exhibits large spread in amplitude among those CGCMs that participated in the Coupled Model Intercomparison Project phase 3 (CMIP3). Although this diversity in amplitude has been reduced in CMIP5, the biases in ENSO periodicity are still large (Bellenger et al., 2014; Lu et al., 2018). The modeled oscillation is often too regular (AchutaRao and Sperber, 2006), as compared to the broad spectrum ranging from 2 to 7 yr found in observation. Besides, the asymmetry (Bellenger et al., 2014) and seasonal phase-locking feature (Guilyardi et al., 2009) of ENSO are often poorly simulated by CGCMs.

The biases in ENSO behaviors originate from the poor representation of key physical processes in ENSO dynamics. For example, Bellenger et al. (2014) showed that current CGCMs generally underestimate ENSO-induced surface wind, which results in a weakened thermocline and zonal advective feedbacks. In addition, due to biases in the modeled relationship between shortwave radiation and SST, the heat-flux-induced SST damping is also underestimated, which has been demonstrated in models for both CMIP3 (Lloyd et al., 2009) and CMIP5 (Bellenger et al., 2014) models. The errors in the modeled long-term mean state in the tropical Pacific Ocean can also be a source of bias in the modeled behaviors of ENSO (van Oldenborgh et al., 2005; Guilyardi, 2006). Since the physics of ENSO is complex, its modeled behaviors might be good due to error compensations (Kim S. T. et al., 2014b). Thus, it is necessary to evaluate the modeled physics of ENSO in detail.

Based on the linear framework of the recharge/discharge oscillator (Jin, 1997a), Jin et al. (2006) proposed the Bjerknes stability index (BJ-index), which measures the growth rate of ENSO and captures the effects of thermocline feedback, zonal advective feedback, Ekman feedback, thermal damping, and dynamical damping comprehensively. Many studies have shown that the BJ-index provides a basis for a better understanding of the biases in the modeled amplitude of ENSO (e.g., Kim and Jin, 2011; Kim S. T. et al., 2014a). Recently, Lu et al. (2018) formulated the Wyrtki index to capture the periodicity of ENSO, which describes the thermocline and zonal advective feedbacks multiplied by the efficiency of the discharge–recharge process of the equatorial oceanic heat content driven by ENSO wind stress anomalies. The diversity of the simulated periodicity of ENSO in CMIP5 models can be explained well by this index (Lu et al., 2018). In this paper, the simulation of ENSO by a coupled climate model, CAMS-CSM (the climate system model of the Chinese Academy of Meteorological Sciences), is evaluated. In particular, the dynamical origin of the biases in ENSO behaviors is investigated by adopting the BJ-index and Wyrtki Index.

As the strongest climate phenomenon on the interannual timescale, ENSO can induce remote climate impacts by stimulating teleconnections. A number of studies have shown that El Niño might weaken the East Asian winter monsoon (EAWM) by suppressing convection over the northwestern Pacific (Li, 1990; Zhang et al., 1996). In addition, the relationship between ENSO and the East Asian summer monsoon (EASM) relationship has been extensively studied. In the decaying summer of two super-strong El Niño events, in 1982/83 and 1997/98, destructive flooding occurred in the Yangtze River basin. A number of hypotheses have been proposed to explain this well-known ENSO–EASM relationship (Wang et al., 2000; Xie et al., 2009, 2016; Stuecker et al., 2015; Zhang et al., 2016). Models with a better representation of ENSO-induced teleconnections are capable of better predicting the East Asian climate (Li et al., 2016; Lu et al., 2017; Liu et al., 2018). Thus, a realistic simulation of ENSO itself is insufficient for East Asian climate simulation, although successful ENSO simulation is often necessary for a reasonable simulation of ENSO teleconnections (Gong et al., 2014, 2015, 2018). In this paper, the modeled impacts of ENSO on East Asian climate in CAMS-CSM are also assessed.

The remainder of the paper is organized as follows. The observational dataset and a description of CAMS-CSM are given in Section 2. The simulated mean state of the tropical Pacific and the modeled behaviors of ENSO are presented in Section 3. ENSO's dynamics and the origin of the simulated ENSO biases are investigated in Section 4. Section 5 documents the simulated influence of ENSO teleconnections on East Asian climate. Finally, a summary and discussion are provided in Section 6.

2. Data and methodology

This study utilizes Hadley Centre Global Sea Surface Temperature dataset (HadISST; Rayner et al., 2006) for the observed monthly mean SST, Climate Prediction Center Merged Analysis of Precipitation (CMAP; Xie and Arkin, 1997) for the observed precipitation, Hadley Centre/Climatic Research Unit version 4.6 (HadCRUT-4.6; Morice et al., 2012) for the observed surface air tem-

perature, and Wave and Anemometer-based Sea-surface Wind dataset (WASWind ; Tokinaga and Xie, 2011) for the observed surface wind over ocean. Their horizontal grid resolutions are 1° × 1°, 2.5° × 2.5°, 5° × 5°, and 4° × 4°, respectively. A common period after 1979 is analyzed for the observational data. Reanalysis-1 (NCEP–NCAR reanalysis data; Kalnay et al., 1996) is used to retrieve the horizontal wind, geopotential height, and surface heat flux. The horizontal grid resolution of the atmospheric reanalysis data is 2.5° × 2.5°, and a common period of 1979–2016 is analyzed to be consistent with the observational data. Global Ocean Data Assimilation System (GODAS) data (Behringer et al., 1998) are used to represent the objective estimations of the monthly 3-D current and temperature reanalysis data in ocean, as well as the momentum at sea surface since 1980. GODAS reanalysis data contain 40 vertical levels, with a horizontal resolution of 1° × 1/3°.

CAMS-CSM is composed of an atmospheric model (ECHAM5), oceanic model [Modular Ocean Model, version 4 (MOM4); Griffies et al., 2004], sea-ice model (SIS), and land-surface model (CoLM). The resolution of CAMS-ECHAM is T106, with 31 vertical levels from the surface to 10 hPa. The oceanic component, MOM4, uses a tripolar grid (Murray, 1996), with a zonal resolution of 1° globally. The meridional resolution is 1/3° within 10°S–10°N, which changes to 1° from 30°S (N) to the poles. There are 50 vertical layers in CAMS-MOM. For more detailed information about the model design, please refer to Rong et al. (2018).

In this paper, the historical simulation of CAMS-CSM is evaluated. CAMS-CSM is initialized at the quasi-equilibrium state derived from the control experiment. Then, the historical simulation is performed under the historical forcings of ozone, solar forcing, greenhouse gases, and anthropogenic aerosol from 1900–2013. The atmospheric output is available during the whole simulation period, while the three-dimensional oceanic output is only available from 1980–2013.

3. Modeled features of ENSO

It has been reported that the behaviors of ENSO are sensitive to the mean state of the tropical Pacific, such as the mean thermocline depth (Zebiak and Cane, 1987; Timmermann et al., 1999; Fedorov and Philander, 2001), mean trade wind (Fedorov and Philander, 2001; Zheng et al., 2008), and zonal SST gradient (Knutson et al., 1997; Fedorov and Philander, 2001). Thus, the simulated mean state in CAMS-CSM is firstly assessed. Figures 1a and 1b compare the annual mean SST and surface wind patterns between observation and simulation. Generally, CAMS-CSM captures the fundamental features of the mean state over the tropical Pacific, including the prevailing easterly trade wind and the "warm pool (WP)–cold tongue (CT)" distribution of SST. However, some biases still exist. For example, the trade wind over

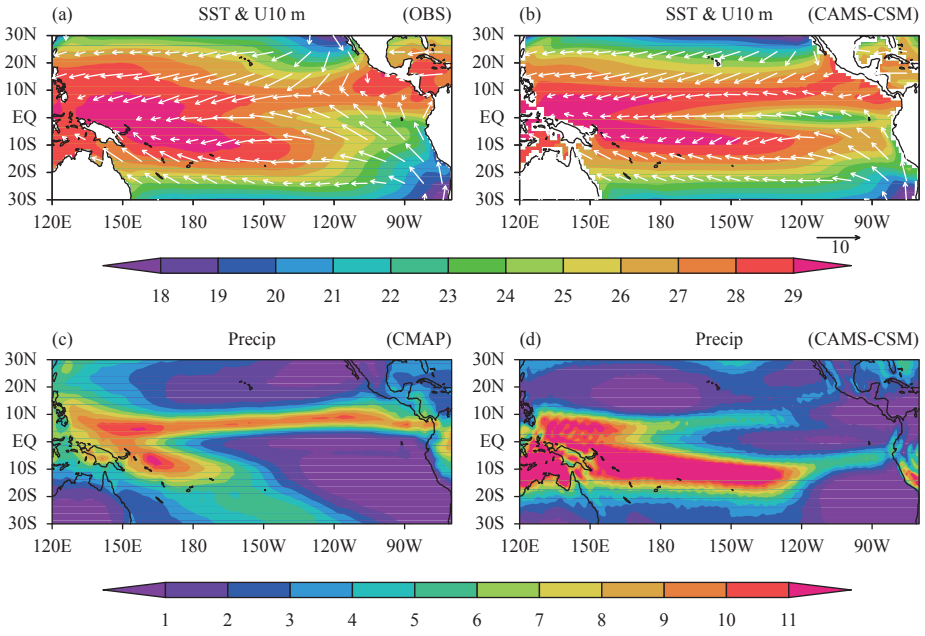

Fig. 1. Climatological annual mean (a, b) SST (color shaded; °C) overlapped with surface wind (vectors; m s^{-1}) and (c, d) precipitation (mm day^{-1}) from (a, c) observation and (b, d) CAMS-CSM.

the southeastern Pacific is underestimated by the model. As a result, the SST in the southeastern Pacific is warmer than observed. Meanwhile, the WP in the Southern Hemisphere exhibits an eastward extension. Associated with this SST mean-state bias, excessive precipitation is evident in the South Pacific Convergence Zone (Figs. 1c, d). This so-called "double ITCZ (Intertropical Convergence Zone) problem" is suffered by most state-of-the-art CGCMs (Lin, 2007; Hwang and Frierson, 2013). In addition, compared with observation, an excessive westward extension of the modeled equatorial Pacific CT is evident. This so-called CT bias is another common error in many CGCMs (Misra et al., 2008; Li and Xie, 2014), which can have impacts on the simulation of ENSO (Vannière et al., 2013).

Mean thermocline depth is an important indicator of the strength of thermocline feedback (Fedorov and Philander, 2001). Figure 2 demonstrates the mean thermocline depth (indicated by the 20°C isotherm) and equatorial zonal wind stress along 120°E–80°W. The modeled climatological thermocline is slightly shallower in the central to western Pacific, which is consistent with the westward extension of the simulated CT. It implies that the modeled thermocline is less tilted than observed. The simulated easterly wind stress is slightly weaker in the central to eastern Pacific.

To obtain the principal modes of SST variability over the tropical Pacific, empirical orthogonal function (EOF) analysis is performed. As shown in Fig. 3a, the leading EOF mode indicates the CT El Niño, which is characterized by a strong anomalous warming along the equatorial central to eastern Pacific. The simulated leading EOF mode is similar to that observed in terms of the SST spatial distribution, except the overly strong anomalous warming (Fig. 3b). As shown in Fig. 3c, the observed second EOF mode indicates the WP El Niño, which is characterized by an anomalous warming in the central tropical Pacific and cooling in the eastern tropical Pacific (Ashok et al., 2007; Weng et al., 2007). Such WP El Niño events have occurred more frequently since 2000, which can be attributed to the La Niña-like interdecadal SST mean state (Chung and Li, 2013). Associated with this distinct SST pattern, the climatic impact of WP El Niño is very different to that of conventional (CT) El Niño (Weng et al., 2009). Here, it is demonstrated that CAMS-CSM generally captures the observed features of WP El Niño (Fig. 3d). Anomalous warming extending from the subtropical northeastern Pacific to the central Pacific is simulated well (Yu et al., 2010), with anomalous cooling in the eastern Pacific. It should be noted, however, that the modeled equatorial warming shows a westward extension, with an unrealistic warming to the west of 150°E. In addition, the explained variance of the modeled second EOF mode is 7%, which is much smaller than the observed.

Ham and Kug (2012) showed that the Niño3 and Niño4 indices are significantly correlated with each other in most CMIP3 models, implying the existence of one single type of El Niño rather than two types in CMIP3 simulations. Such a performance is slightly improved in CMIP5 models, in that the two types of El Niño are simulated with greater independence compared with CMIP3 (Kug et al., 2012). Here, the dependence between the two types of El Niño is examined for CAM-CSM. Following Ham and Kug (2012), the modified Niño3 (SST averaged over 5°S–5°N, 170°–110°W) and Niño4 (SST aver-

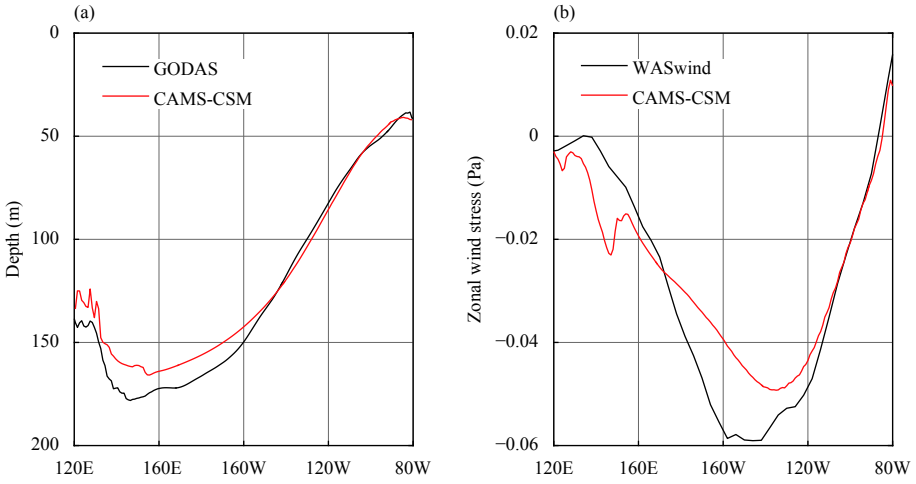

Fig. 2. The mean (a) thermocline depth (indicated by the 20°C isotherm) and (b) equatorial (5°S–5°N average) zonal wind stress along 120°E–80°W in observation (black curve) and the CAMS-CSM simulation (red curve).

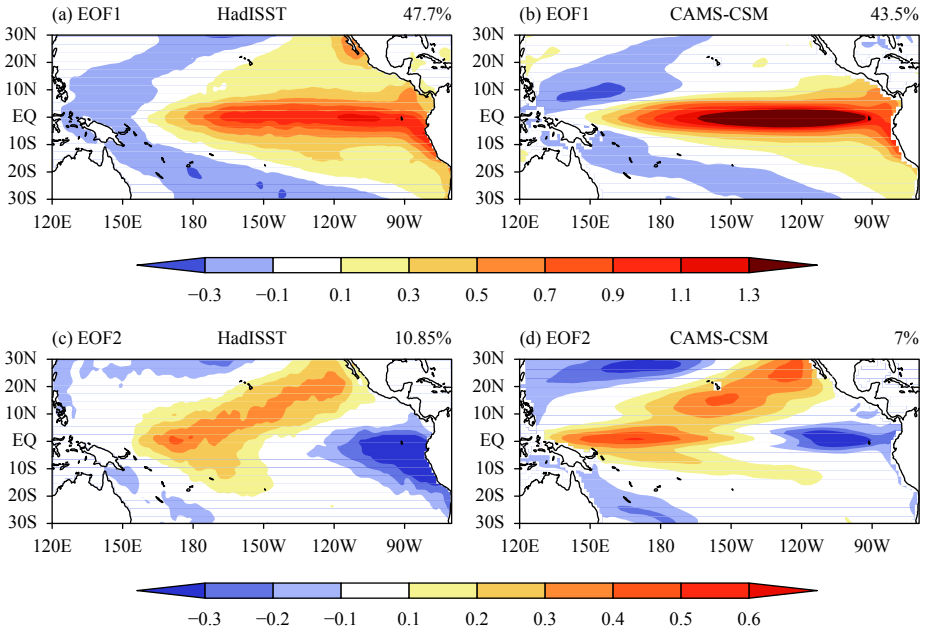

Fig. 3. Spatial patterns of the (a, b) first and (c, d) second EOF modes of SST anomalies in the tropical Pacific in (a, c) observation and (b, d) the CAMS-CSM simulation.

aged over 5°S–5°N, 140°E–170°W) indices are adopted to indicate the CT El Niño and WP El Niño, respectively. As demonstrated in Fig. 4a, the magnitude of the modified Niño3 index is not linearly proportional to the modified Niño4 index, implying the potential existence of two types of El Niño in observation. In the CAMS-CSM simulations (Fig. 4b), the CT El Niño events and WP Niño events depart from the one-to-one line. In other words, the independence between CT El Niño and WP El Niño can be simulated to some degree. Unlike the El Niño cases, CT La Niña events and WP La Niña events gather along the one-to-one line (Fig. 4c), which implies that the flavors of La Niña events are not so clear as those for El Niño. In the model simulation, the observed relations between CT La Niña and WP La Niña events are reproduced but with greater dependency (Fig. 4d). Kug et al. (2009, 2011) suggested that La Niña events are harder to separate into two types because of the similarity in SST patterns. Here, we show that this asymmetric characteristic between El Niño and La Niña events is captured well by CAM-CSM. However, it is noted that, although the model captures the spatial patterns and mutual independence of the two types of El Niño events, more evaluations should be performed regarding their distinct dynamics, which is beyond the scope of this study.

The evolutions of El Niño and La Niña events are assessed in Fig. 5. The seasonal phase-locking feature is successfully captured by CAMS-CSM. Similar to observed, the modeled El Niño and La Niña events develop during boreal summer, and mature in boreal winter. This may due to the realistic seasonally dependent coupled instability (Li, 1997) in CAMS-CSM. In observation (Fig. 5b), most El Niño events turn to a La Niña event in the following winter (Chen M. C. et al., 2016), and few El Niño events persist for more than 2 yr (Chen and Li, 2017), while La Niña is often re-intensified in the second year (Fig. 5d). This evolutionary asymmetry is caused by the asymmetric wind response in the western Pacific and the asymmetric cloud–radiation–SST and evaporation–SST feedbacks in different phases of ENSO (Chen M. C. et al., 2016). Although CAMS-CSM simulates the phase transition for El Niño (Fig. 5a), the re-intensification of La Niña is poorly simulated. As demonstrated in Fig. 5c, most modeled La Niña events turn into El Niño events in the following winter, indicating a failure to simulate the observed evolutionary asymmetry. It is also clear that the simulated El Niño and La Niña events are generally stronger than those observed. Figure 6a demonstrates the standard deviation of Niño3.4 SST anomalies. It is clear that the overestimation of ENSO amplitude is pronounced in each calendar month. In addition, this bias in amplitude exists for both types of El Niño, since the standard deviation of the modified Niño3 and Niño4 anomalies are both overestimated (Figs. 6b, c). Observationally, El Niño events are usually stronger than La Niña events. The skewness of the observed Niño3.4 SST anomaly is 0.4. However, this asymmetry is poorly represented in the simulation. The modeled El Niño and La

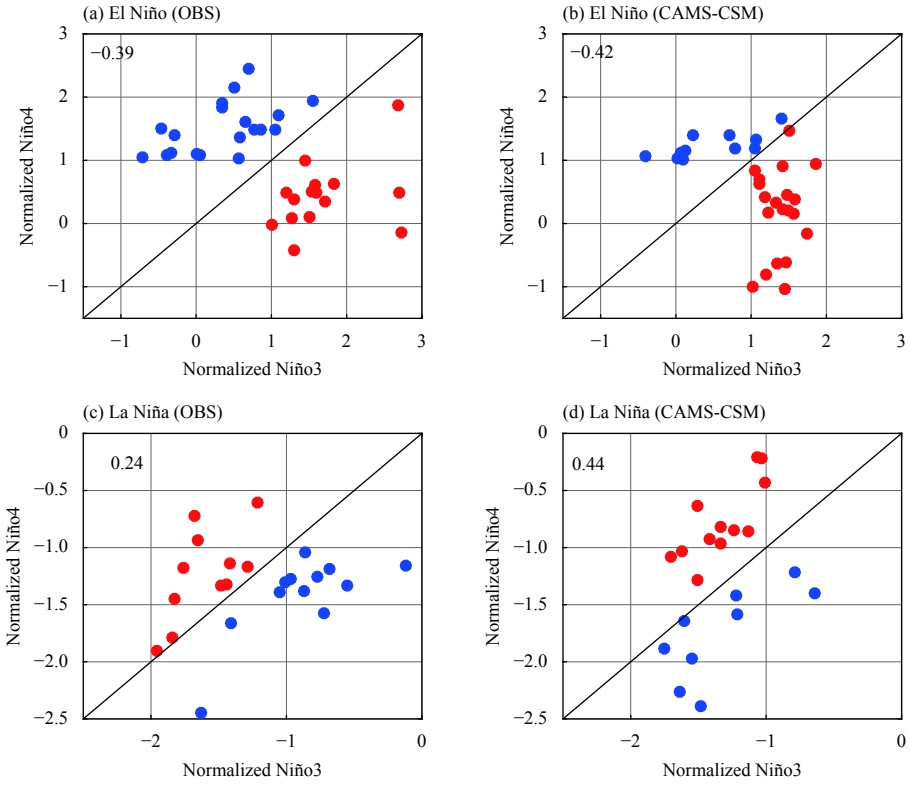

Fig. 4. Scatterplots between the normalized modified Niño3 and Niño4 indices in boreal winter (December–February) during (a, b) El Niño events and (c, d) La Niña events from (a, c) observation and (b, d) the CAMS-CSM simulation. Note that the red (blue) dots denote the CT (WP) El Niño and La Niña. The correlation coefficients are also given. The definition of the modified Niño3 index is the seasonal mean SST anomalies averaged over 5°S–5°N, 170°–110°W, while that of Niño4 is over 5°S–5°N, 140°E–170°W.

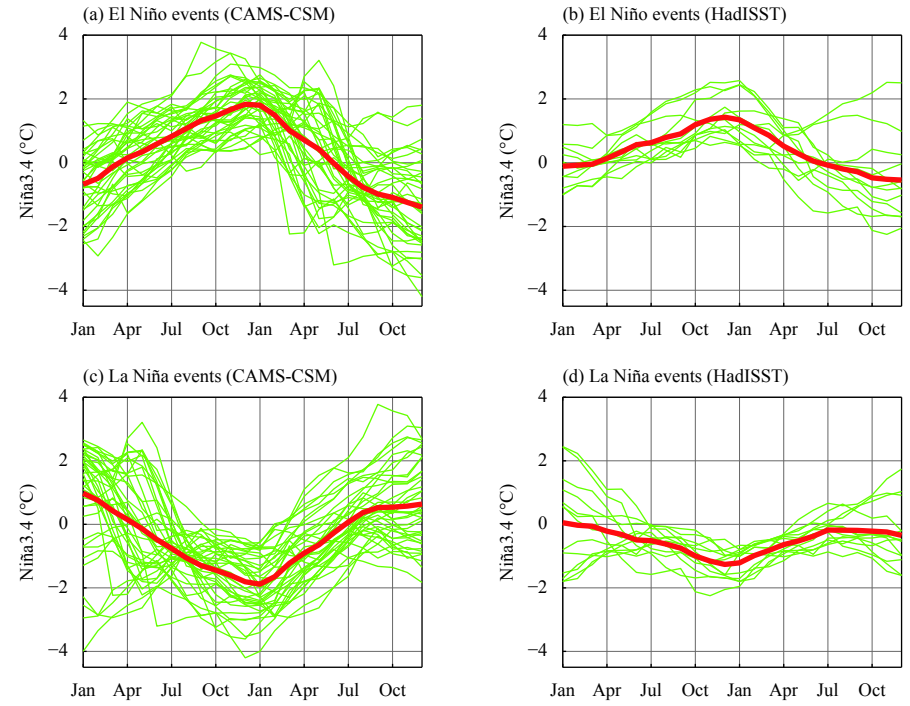

Fig. 5. Evolution of Niño3.4 anomalies during (a, b) El Niño and (c, d) La Niña events from (a, c) the CAMS-CSM simulation and (b, d) observation. The composites are indicated by the thick red curves. Here, the events with an absolute peak value exceeding 0.5°C are selected.

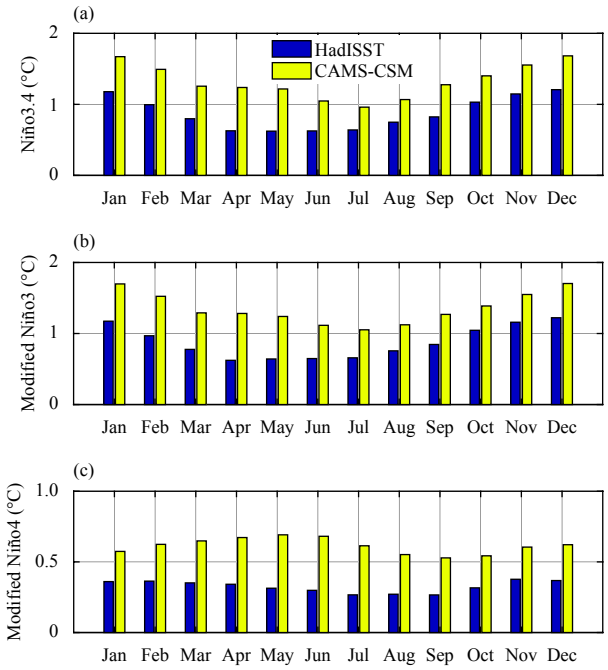

Fig. 6. Standard deviation of SST anomalies (°C) averaged within the (a) Niño3.4 region (5°S–5°N, 170°–120°W), (b) modified Niño3 region (5°S–5°N, 170°–110°W), and (c) modified Niño4 region (5°S–5°N, 140°E–170°W), in each calendar month, in observation (blue bars) and the CAMS-CSM simulation (yellow bars).

Niña events have comparable amplitude, and the skewness of the modeled Niño3.4 SST anomaly is –0.1. ENSO's periodicity is further evaluated in Fig. 7. The observed spectrum exhibits a broad band from 2–7 yr. The modeled spectrum, however, shows a strong peak every 2.8 yr, implying ENSO in CAMS-CSM tends to be more frequent and regular in terms of its oscillation pattern, with a shorter period compared to observed.

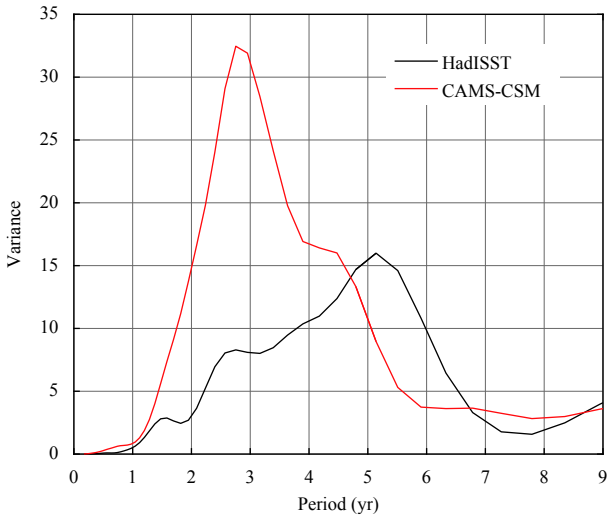

Fig. 7. Spectra of Niño3.4 anomalies in observation (black curve) and the CAMS-CSM simulation (red curve).

4. ENSO dynamics in CAMS-CSM

4.1 *Amplitude bias and its physical origin*

To improve the model, it is necessary to understand the physical origins of the errors in simulating the behaviors of ENSO. It has been shown that CAMS-CSM overestimates the amplitude of ENSO (Figs. 5, 6). The BJ-index, proposed by Jin et al. (2006), provides a powerful dynamical estimation of ENSO's growth rate (Kim and Jin, 2011; Kim S. T. et al., 2014a), and thus it is adopted here to diagnose the origin of this amplitude bias in CAMS-CSM. Based on the recharge–discharge framework, the BJ-index can be formulated as follows:

$$I_{\mathrm{BJ}} = \frac{R-\varepsilon}{2} \approx \frac{R}{2}, \tag{1}$$

$$R = \mu_a\beta_u < -\frac{\partial \overline{T}}{\partial x} > + \mu_a\beta_h a_h < \frac{H(\overline{w})\overline{w}}{H_{\mathrm{m}}} > + \mu_a\beta_w < H(\overline{w})\frac{\partial \overline{T}}{\partial z} > - (a_1\frac{<\Delta\overline{u}>}{L_x} + a_2\frac{<\Delta\overline{v}>}{L_y}) - \alpha_{\mathrm{s}}, \tag{2}$$

where T denotes ocean temperature averaged over the mixed layer; u, v, and w represent the zonal, meridional, and vertical ocean current, respectively; L_x and L_y are the zonal and meridional extents of the Pacific; H_{m} is the mixed-layer depth, which is fixed at 50 m for simplicity; a_1 (a_2) is derived by regressing the SST anomalies at zonal (meridional) boundaries against the area-averaged SST anomalies; $H(x)$ is a step function, which only considers regions with upward vertical advection; the sign "< >" denotes the average of quantities over the eastern Pacific (5°S–5°N, 170°–80°W); and the overbars represent the climatological mean state. For more details about the formulation of the BJ-index, readers are referred to Jin et al. (2006).

To obtain the BJ-index in Eq. (2), several balance relationships are applied. The parameter μ_a indicates the strength of the wind stress response to ENSO SST forcing; β_u measures the wind-driven zonal current anomalies; β_h represents the response of the thermocline slope to the surface wind stress anomalies; β_w measures the wind-driven upwelling anomalies; α_s indicates the surface heat flux changes in response to ENSO SST forcing; and a_h denotes the relationship between the subsurface temperature anomaly and thermocline depth anomaly. As demonstrated in Fig. 8, these balance relationships hold relatively well for both the GODAS reanalysis data and the CAMS-CSM simulation, which ensures the robust-

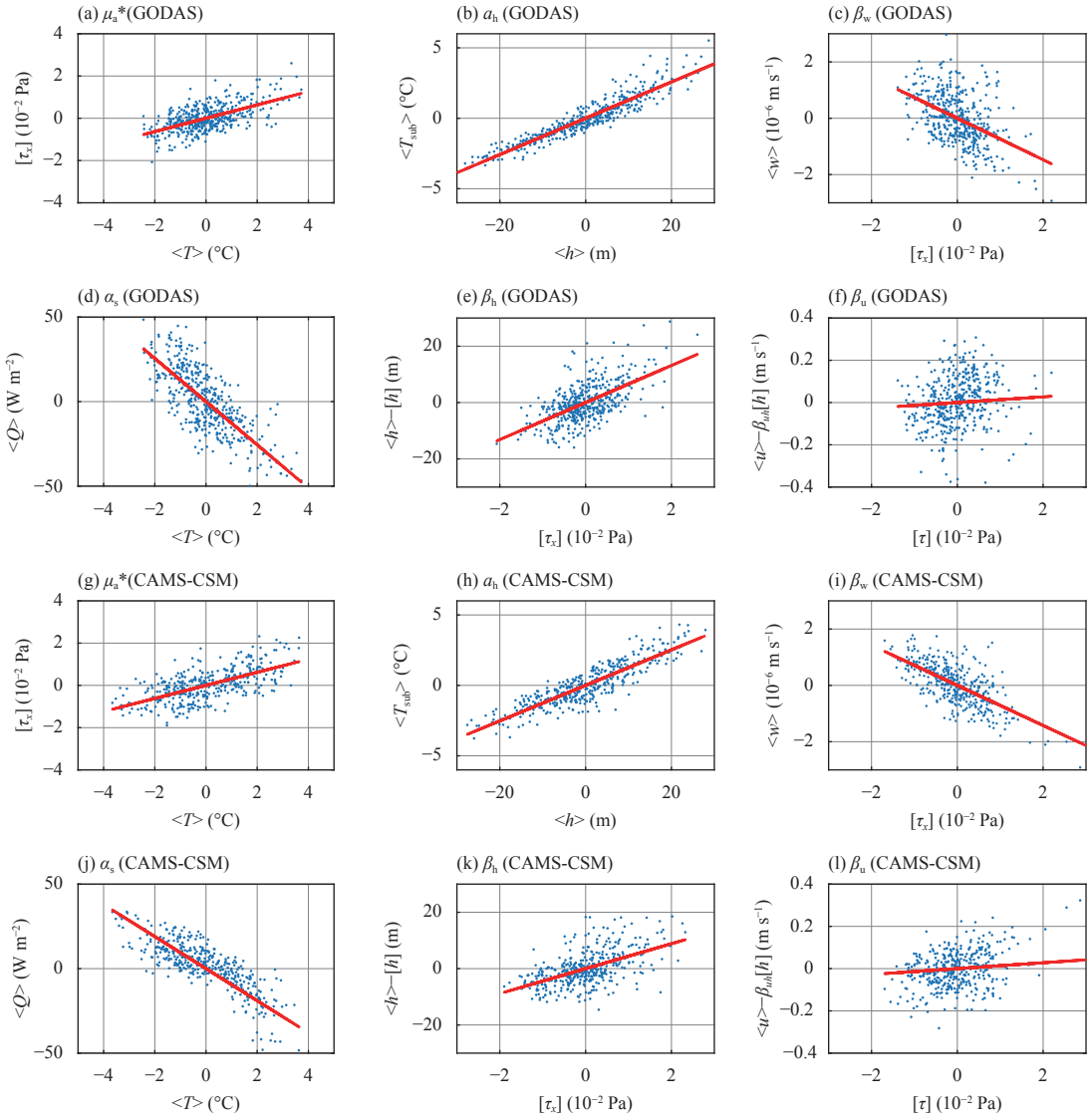

Fig. 8. Scatterplots of (a, g) $[\tau_x] = \mu^*{}_a < T >$, (b, h) $< T_{\rm sub} >= a_h < h >$, (c, i) $< w >= -\beta_w[\tau_x]$, (d, j) $< Q >= -\alpha_s < T >$, (e, k) $< h > -[h] = \beta_h[\tau_x]$, and (f, l) $< u > -\beta_{uh}[h] = \beta_u[\tau]$, in (a–f) observation and (g–l) the CAMS-CSM simulation. The linear fitting lines are indicated by the red straight lines. Please refer to Jin et al. (2006) for more details about these balance equations.

ness of the BJ-index in representing ENSO's growth rate.

In Eq. (2), the BJ-index consists of three positive feedbacks (zonal advective feedback: $\mu_a\beta_u < -\dfrac{\partial \overline{T}}{\partial x} >$; thermocline feedback: $\mu_a\beta_h a_h < \dfrac{H(\overline{w})\overline{w}}{H_{\rm m}} >$; and Ekman feedback: $\mu_a\beta_w < H(\overline{w})\dfrac{\partial \overline{T}}{\partial z} >$) and two negative feedbacks (mean advection damping: $-(a_1\dfrac{<\Delta\overline{u}>}{L_x} + a_2\dfrac{<\Delta\overline{v}>}{L_y})$; and thermal damping: $-\alpha_{\rm s}$). Figure 9 compares each contributing processes of the BJ-index in the GODAS reanalysis data and the CAMS-CSM simulation. Clearly, the thermocline feedback is the dominant term among all three feedbacks. CAMS-CSM tends to produce a weaker thermocline feedback than observed (Fig. 9). This underestimation of thermocline feedback can be attributed to three physical processes. First, the wind stress response to ENSO SST forcing (μ_a) is too weak in the CAMS-CSM simulation. Figure 10 demonstrates the regression patterns of precipitation and surface wind onto Niño3.4 anomalies. It can be seen that the ENSO-induced atmospheric convection is fairly weak in the CAMS-CSM simulation and, as a consequence, the westerly wind response over the central to western Pacific is underestimated. Second, the thermocline response to surface wind stress is also weak in CAMS-CSM. As shown in Fig. 11a, the westerly wind stress tends to lift the thermocline in the western Pacific and deepen the thermocline in the eastern Pacific. However,

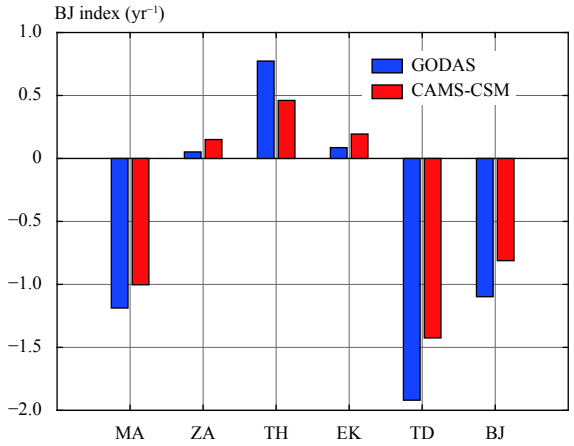

Fig. 9. The BJ-index (BJ) and its five contributing terms (MA: mean advective damping, ZA: zonal advective feedback, TH: thermocline feedback, EK: Ekman feedback, and TD: thermal damping) in observation (blue bars) and the CAMS-CSM simulation (red bars). The calculation of the BJ-index is given in Eqs. (1) and (2).

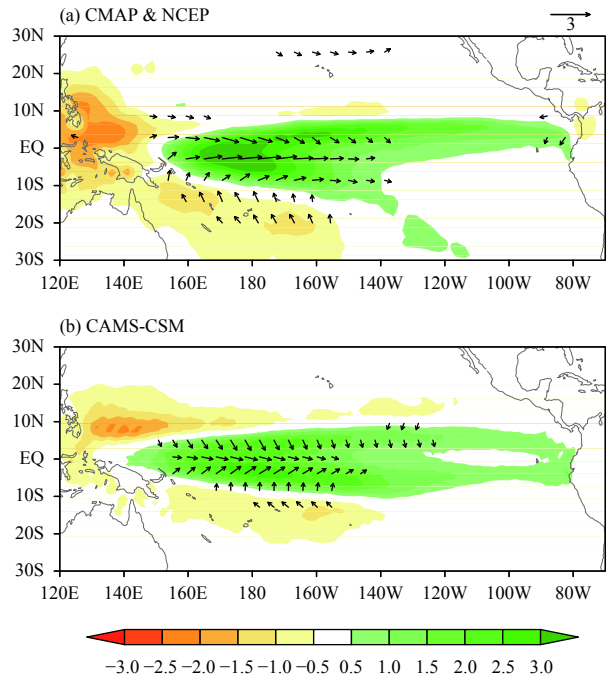

Fig. 10. Regression patterns of the anomalous precipitation (color shaded; mm day^{-1} °C^{-1}) and surface wind (vectors; m s^{-1} °C^{-1}) against Niño3.4 anomalies in (a) observation and (b) the CAMS-CSM simulation.

the simulated thermocline changes are weaker than observed (Fig. 11b), which gives rise to parameter β_h being smaller. Third, the modeled mean upwelling in the central to eastern Pacific (4.2×10^{-6} m s^{-1}) is also slightly weaker than observed (4.6×10^{-6} m s^{-1}). Above all, in the simulation by CAMS-CSM, the ENSO-SST-induced weak westerly wind stress can further induce weak subsurface temperature changes, which are then brought to

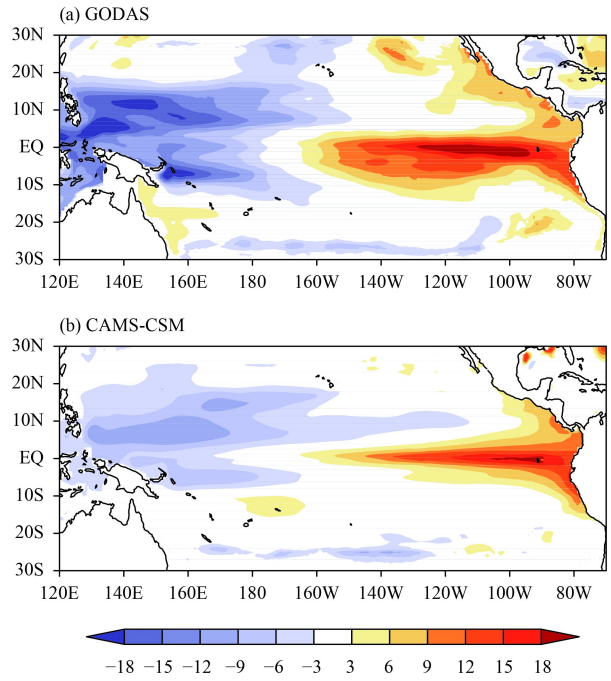

Fig. 11. Regression patterns of anomalous thermocline depth (m Pa^{-1}) against the surface wind stress anomalies along the equator (5°S–5°N, 140°–80°W) in (a) observation and (b) the CAMS-CSM simulation.

the mixed layer by the weak mean upwelling. As a result, the modeled thermocline feedback is weaker than observed.

Despite the underestimation of thermocline feedback, the modeled amplitude of ENSO is still larger than observed. As shown in Fig. 9, the overestimation of negative heat flux damping is remarkable, which overwhelms the underestimated thermocline feedback. The surface heat flux can be divided into four components: shortwave radiation flux, longwave radiation flux, latent heat flux, and sensible heat flux. As shown in Fig. 12, both the shortwave radiation and latent heat fluxes are quite important in ENSO dynamics, which is consistent with previous studies (Lloyd et al., 2011, 2012). The El Niño-induced reduction in shortwave radiation is remarkably underestimated by CAMS-CSM (Fig. 12). The modeled negative shortwave radiation feedback is only one third of the observed value. This underestimation of shortwave feedback prevails in many CGCMs (Sun et al., 2009; Lloyd et al., 2012; Chen L. et al., 2013; Chen and Yu, 2014). Previous studies have pointed out that an excessive equatorial CT is a key factor causing this bias (Chen and Yu, 2014; Chen et al., 2016b). Those models with a more excessive CT will produce a westward shift of the convective response to ENSO, which leads to the underestimated shortwave feedback over the central to eastern Pacific (Chen L. et al., 2013). Here, we show that

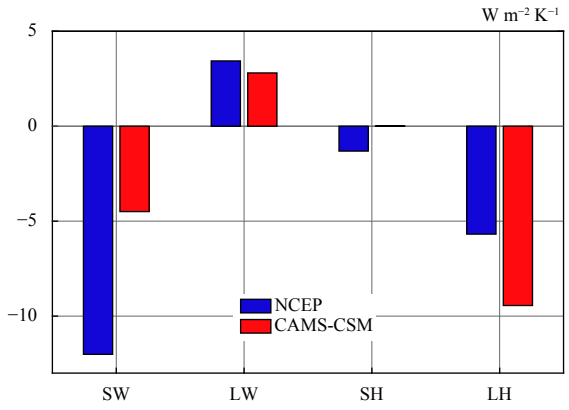

Fig. 12. Regression of anomalous shortwave radiation (SW), longwave radiation (LW), sensible heat flux (SH), and latent heat flux (LH) against the SST anomaly in the Niño3.4 region in observation (blue bars) and the CAMS-CSM simulation (red bars).

CAMS-CSM also suffers from this common bias in CGCMs. Figure 13 demonstrates the regression patterns of shortwave radiation flux against Niño3.4 anomalies. A pronounced reduction in shortwave radiation is evident from 160°E to 100°W in observation, which cools the El Niño-related SST anomalies. However, the modeled shortwave reduction is much weaker than observed. In addition, its zonal position displaces in the western Pacific, which cannot reduce the El Niño SST warming in the central to eastern Pacific. Based on a previous argument (Chen L. et al., 2013, 2016b; Chen and Yu, 2014), this westward shift of the atmospheric response is consistent with the excessive CT in CAMS-CSM (Fig. 1). In addition, the shortwave radiation even slightly increases in the equatorial eastern Pacific (Fig. 13b). This implies that the modeled atmosphere in the eastern Pacific is quite stable, such that higher SSTs destabilize the boundary layer and prevent the formation of stratiform cloud (Philander et al., 1996). This positive cloud–radiation–SST feedback seems to be dominant over the eastern Pacific in CAMS-CSM, which could further increase the downward shortwave radiation and intensify the growth rate of El Niño.

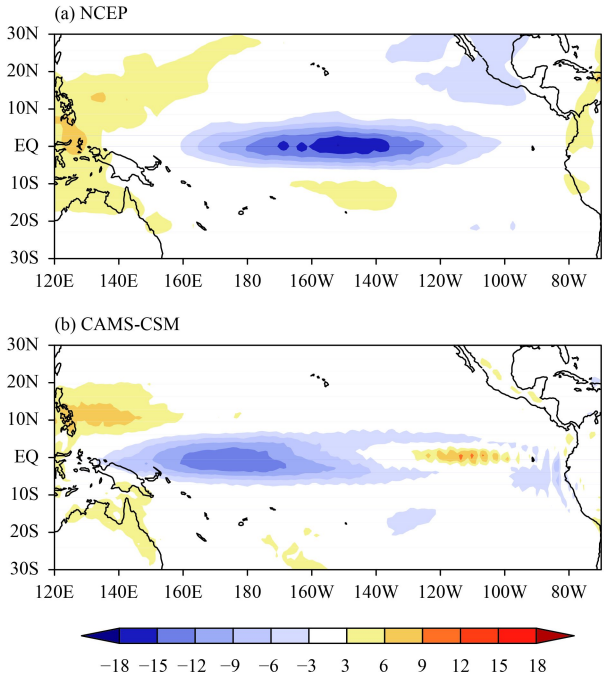

Fig. 13. Regression patterns of anomalous shortwave radiation flux (W m^{-2} °C^{-1}) against the Niño3.4 index in (a) observation and (b) the CAMS-CSM simulation.

As shown in Fig. 9, the gross effect, as indicated by the BJ-index, is negative in observation, which is consistent with the theory that ENSO is a damped oscillation triggered by stochastic forcing (e.g. Kleeman and Moore, 1997; Kirtman and Schopf, 1998). In the simulation by CAMS-CSM, the BJ-index is also negative but the absolute value is smaller. This implies that the modeled ENSO is a less damped mode, which explains the overestimation of ENSO's amplitude (Fig. 6). Here, we show that the BJ-index is useful in diagnosing the physical origin of the bias in ENSO's amplitude, especially when error compensation occurs. For CAMS-CSM, the weak negative shortwave radiation feedback overwhelms the weak thermocline feedback, giving rise to a stronger modeled ENSO.

4.2 *Periodicity bias and its physical origin*

Realistically simulating ENSO's periodicity remains a challenging issue in current CGCMs (Bellenger et al., 2014; Lu and Ren, 2016). For CAMS-CSM, the modeled ENSO oscillates regularly with a period of 2.8 yr, which is shorter than observed. Here, the so-called Wyrtki index, proposed by Lu et al. (2018), is adopted to estimate the physical origin of this periodicity bias. Similar to the BJ-index, the Wyrtki index is also derived from the linear recharge–discharge framework:

$$\frac{\mathrm{d}<T>}{\mathrm{d}t} = R<T> + F[h], \tag{3}$$

$$\frac{\mathrm{d}[h]}{\mathrm{d}t} = -\varepsilon[h] - B<T>, \tag{4}$$

where T denotes SST; h represents thermocline depth; the sign "< >" denotes the average of quantities over the eastern Pacific (5°S–5°N, 170°–80°W); and the sign "[ ]" denotes the average of quantities over the entire equatorial Pacific domain (5°S–5°N, 140°E–80°W); R indicates the damping rate of eastern Pacific SST, and is often referred to as the Bjerknes instability index (Jin et al.,

2006); ε denotes the damping rate of thermocline depth due to the energy leak at the western boundary and mixing; F represents the impact of the discharged or recharged state of the ocean heat content on SST; and B indicates the efficiency of the discharging or recharging of the equatorial heat content driven by the equatorial wind stress curl anomalies induced by the anomalies of ENSO SST. The noise forcing and nonlinear terms are omitted here for brevity. This simple linear framework is capable of representing the linear low-frequency dynamics of ENSO's growth rate (Jin et al., 2006) and frequency (Lu et al., 2018). The Wyrtki index can be formulated as:

$$I_{\text{Wyrtki}} = \frac{4\pi}{\sqrt{4B \cdot F - (R+\varepsilon)^2}} \approx \frac{2\pi}{\sqrt{B \cdot F}}. \quad (5)$$

The simulated parameter B is 3.9×10^{-7} m (s K)$^{-1}$, which is quite close to the observed value of 4.3×10^{-7} m (s K)$^{-1}$. However, the modeled parameter F is 1.3×10^{-8} K (s m)$^{-1}$, which is much larger than the observed value of 8.3×10^{-9} K (s m)$^{-1}$. As a result, the modeled Wyrtki index is 2.8 yr, which is slightly shorter than the observed Wyrtki index of 3.4 yr. In other words, the phase transition of ENSO induced by the thermocline and zonal advective feedbacks is quicker than observed, which contributes to the shorter period of ENSO in CAMS-CSM.

4.3 *Triggers for ENSO in CAMS-CSM*

In addition to the internal dynamics of ENSO as discussed above, assessing the external forcings for ENSO is also very important, given the fact that ENSO is a damped oscillation mode (Fig. 14) and can be triggered by several precursors, such as North Pacific Oscillation (NPO; Vimont et al., 2001; Alexander et al., 2010), the Indian Ocean Dipole (IOD; Izumo et al., 2010), Arctic Oscillation in spring (Chen S. F. et al., 2014), an anomalous EAWM (Li, 1990, 1996), thermocline changes in the western Pacific (Chen et al., 2016a), and the consecutive occurrence of westerly wind bursts (Chen et al., 2017). We begin by evaluating the precursor of NPO during the previous winter.

As shown in Fig. 14a, the sea level pressure (SLP) changes (negative minus positive) in North Pacific might reduce the trade winds, which in turn may induce footprint-like SST anomalies in the subtropics via latent heat flux changes. This footprint signal persists throughout the spring and potentially affects the tropical Pacific throughout the following year (Figs. 14c, e, f; Vimont et al., 2001). This so-called "seasonal footprinting mechanism" is reproduced well by CAMS-CSM, in terms of the seasonal evolution of SST and surface wind (Fig. 14). In fact, the SLP anomalies in North Pacific (10°–25°N, 175°–145°W) during the previous winter are significantly correlated with ENSO (Fig. 15a). CAMS-CSM tends to simulate a similar NPO–ENSO relationship as observed (Fig. 15b), implying a realistic seasonal footprinting mechanism in this model.

Izumo et al. (2010) pointed out that the IOD is another precursor of El Niño, at a lead time of 14 months. Figure 16 compares the lead–lag correlations between the IOD [averaged from September to October of Year (0)] and the Niño3.4 index in observation [1980–2016, following Izumo et al. (2010)] and in the CAMS-CSM simulation, separately. A significant positive correlation is evident in Year (0). The El Niño condition is often accompanied by a positive IOD phase, with a strengthening of the easterly winds off Sumatra in summer, which may in turn aid the development of El Niño (Annamalai et al., 2005; Luo et al., 2010). This covariability of ENSO and the IOD is simulated well by the CAMS-CSM, with a positive correlation (0.6) in Year (0) (Fig. 16). In addition, a significant negative correlation is clear one year after the IOD peak. In other words, a positive (negative) IOD phase leads the ENSO peak by around 14 months. This relationship has been applied in an ENSO prediction model with reliable skill (Izumo et al., 2010). As shown in Fig. 16b, such a relation of the prior IOD signal with ENSO is also captured by CAMS-CSM.

5. Impact of ENSO on East Asian climate

ENSO teleconnections are of great interest from the perspective of East Asian climate. The EASM (Chen et al., 1992; Zhang et al., 1996; Wang et al., 2000; Li et al., 2017) and EAWM (Li, 1990) are both influenced by ENSO. Realistically simulating ENSO teleconnections has the potential to enable skillful seasonal predictions in East Asia (Li et al., 2016; Lu et al., 2017; Liu et al., 2018). Figure 17 demonstrates the anomalous patterns of precipitation, 850-hPa horizontal wind, and SST during the boreal summer following strong El Niño events. The Indo-western Pacific capacitor effect is evident in observation (Xie et al., 2016). The SST warming and easterly wind anomalies are pronounced over the Indo-western Pacific, which stimulates an anomalous anticyclone (AAC) over the northwestern Pacific. As a result of the increased water vapor transport, summer rainfall is enhanced over the Yangtze River valley. As shown in Fig. 17d, the SST warming over the Indo-western Pacific is simulated by CAMS-CSM during post-El Niño summer. However, the AAC exhibits an eastward displacement compared with observation (Fig. 17b) and, as a con-

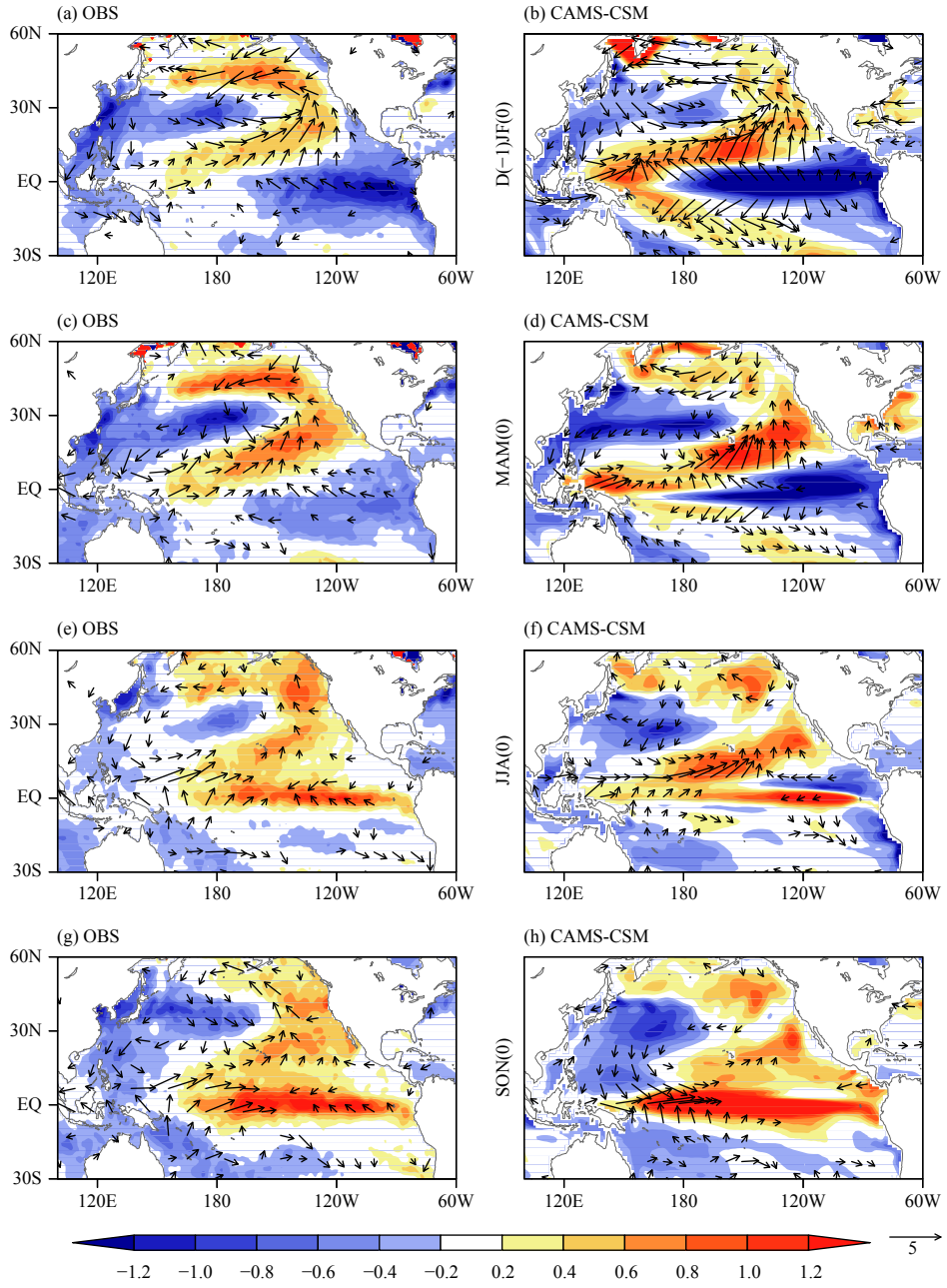

Fig. 14. Seasonal composites of negative-minus-positive SLP index cases for SST (color shaded; °C) and 10-m winds (arrows; m s^{-1}) in observation (left-hand panels) and the CAMS-CSM simulation (right-hand panels).

sequence, the rainfall band shows a southeastward shift following the position of the AAC. In other words, the observed flooding in the Yangtze River valley in post-El Niño summer is poorly presented by CAMS-CSM.

The cause of the eastward-displaced AAC in the model is key for understanding the unrealistic ENSO–EASM relationship in CAMS-CSM. In observation, the convection activity is weakened from the tropical northwestern Pacific to the South China Sea (SCS), which is associated with the location of the observed AAC. However, the simulated convection is enhanced over the SCS, which induces the eastward displacement of the modeled AAC. Note that the underlying SST is warming in both observation and the CAMS-CSM simulation. Thus, the observed precipitation over the SCS is uncoupled with local SST warming. In fact, the correlation between the observed SST and local precipitation over the SCS is –0.47 during boreal summer (Fig. 18a), while the correlation between SCS SST and surface shortwave radiation is 0.37 (Fig. 18c). This implies that SCS SST is passively modulated by the atmospheric heat flux, which is consistent with previous studies (e.g., Wang et al., 2006).

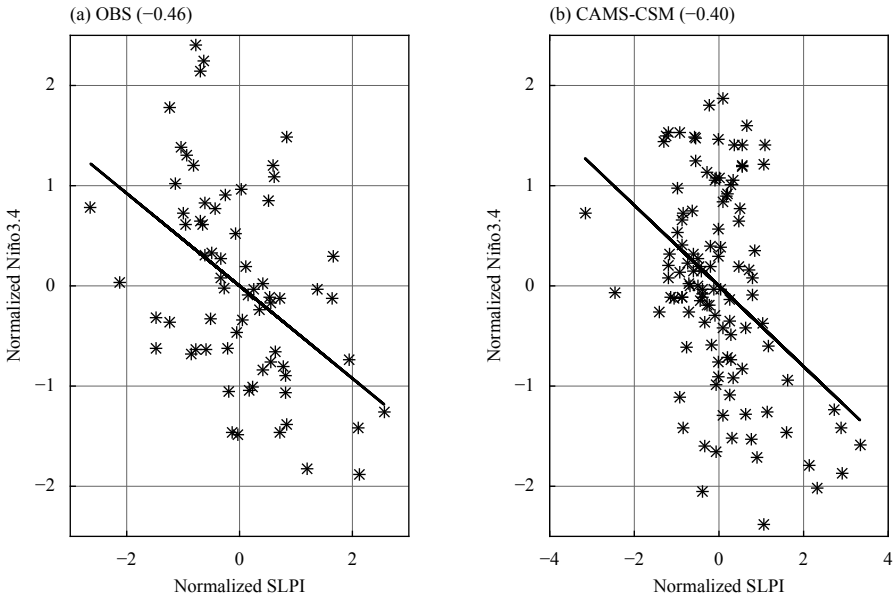

Fig. 15. Scatterplots between the normalized Niño3.4 index averaged during November (0) to January (1) and the normalized SLP index averaged during November (–1) to March (0) from (a) observation and (b) the CAMS-CSM simulation. The correlation coefficients are given in parentheses on top of each panel.

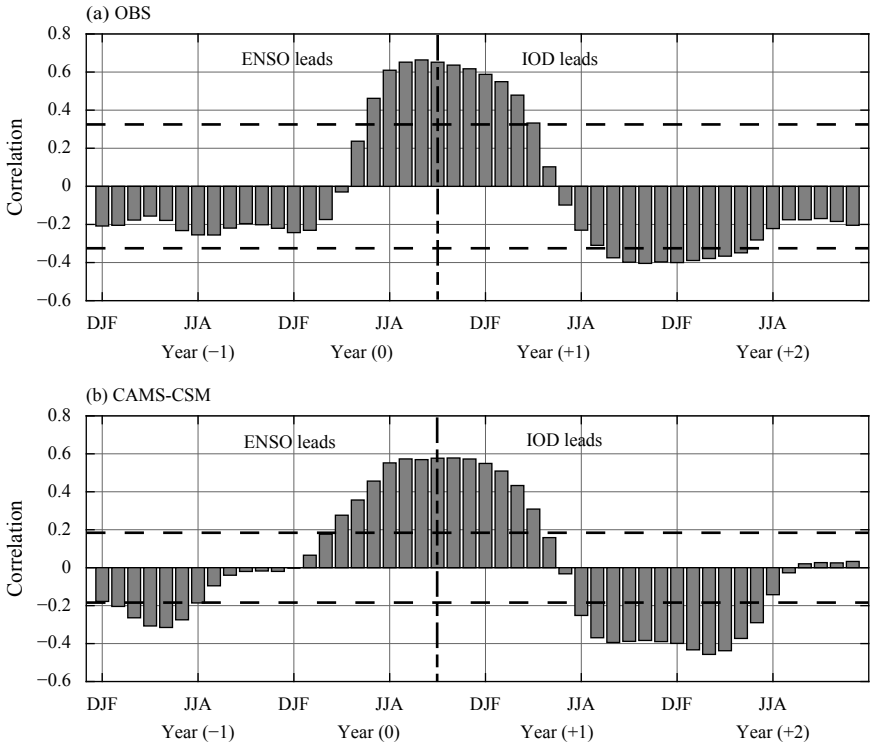

Fig. 16. Lag-correlation between the IOD [averaged from September to November of Year (0)] and the Niño3.4 index (three-month running average applied) in (a) observation and (b) the CAMS-CSM simulation. The dashed lines indicate the 95% confidence level. The vertical dashed lines denote the September–October–November in Year (0) for a co-occurring IOD.

However, in CAMS-CSM, the air–sea interaction is unrealistically strong over the SCS. As shown in Fig. 18b, the modeled precipitation over the SCS is positively correlated with local SST (Fig. 18b), which explains the simulated biases in SCS precipitation and the shift in the location of the AAC in post-El Niño summer.

Although the EAWM is mainly influenced by mid–high-latitude climatic modes (Gong et al., 2001; Wu et

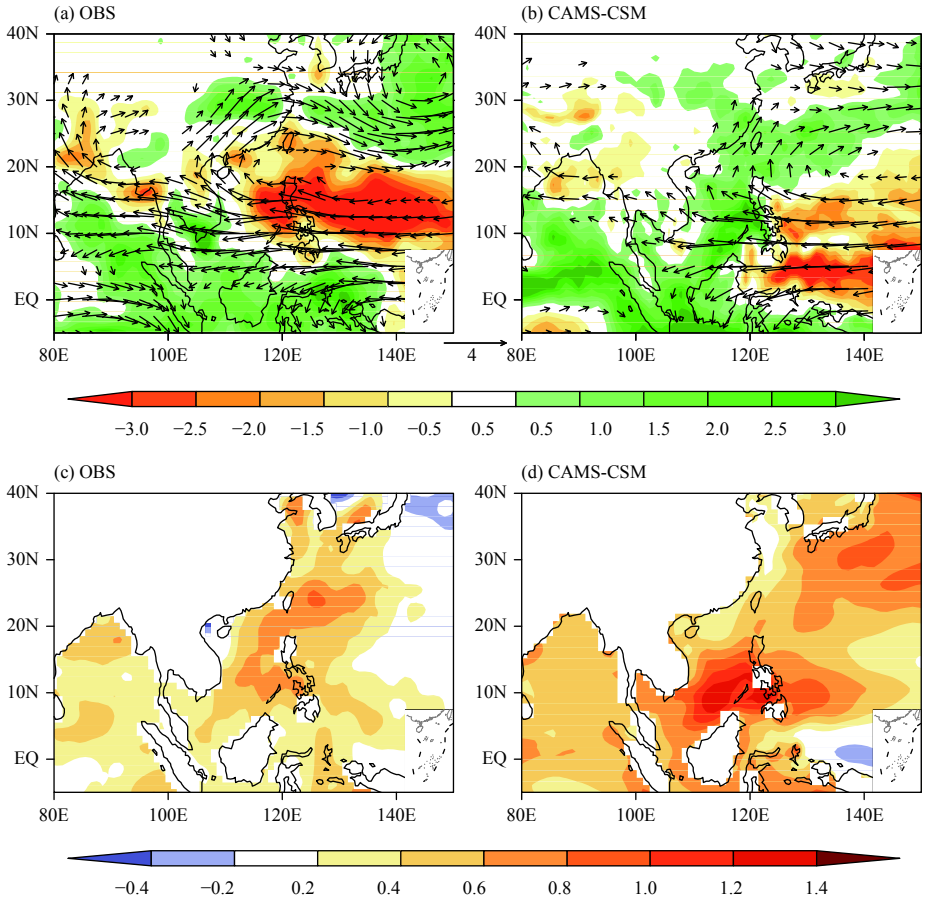

Fig. 17. Composite patterns of the (a, b) anomalous precipitation (color shaded; mm day^{-1}) overlapped with horizontal wind at 850 hPa (vectors; m s^{-1}) and (c) SST (°C) during boreal summer in the decaying year of strong El Niño events from (a, c) observation (1982/83, 1997/98, and 2015/16) and (b, d) the CAMS-CSM simulation. A modeled strong El Niño event is defined as occurring when the value of the November–December–January mean Niño3.4 index exceeds 1.5 times its standard deviation.

al., 2006), ENSO can also modulate the strength of the EAWM (Li, 1990; Zhang et al., 1996). Recent studies suggest that ENSO can influence the tropical component of the EAWM, while its extratropical component is affected by midlatitude factors (Liu et al., 2012; Chen Z. et al., 2014). A combined effect of Arctic Oscillation and ENSO on the EAWM has also been discovered (Chen W. et al., 2013). Figure 19 demonstrates the running correlation of the Niño3.4 index with two EAWM indices, designed by Li and Yang (2010) and Shi (1996), respectively. The former EAWM index is defined by the zonal wind at 200hPa, while the latter is defined by the SLP. Negative correlation is evident in both observation and in the CAMS-CSM simulation, which exhibits pronounced interdecadal variation. Extensive studies have shown that this interdecadal modulation is caused by Pacific Decadal Oscillation (Wang et al., 2008; Kim J. W. et al., 2014; Wang and Lu, 2016), Atlantic Multidecadal Oscillation (Li and Bates, 2007; Jiang et al., 2014), and their combination (He and Wang, 2013). As shown in Fig. 19a, the ENSO-induced change in the EAWM in the upper troposphere is pronounced after 1995, which is overestimated by CAMS-CSM, with significant correlation during a large portion of the simulation period. For the low-level EAWM (Fig. 19b), its correlation with ENSO exhibits interdecadal changes, which is captured well by CAMS-CSM. Figure 20 shows the differences in winter surface air temperature and horizontal wind at 850 hPa between El Niño and La Niña years. Observationally, a southwesterly wind anomaly is evident over southeastern China, which is consistent with previous studies (Chen et al., 2000). This southwesterly wind anomaly brings warm air from the SCS and prevents the southward movement of cold air from the mid to high latitudes. As a result, the surface air temperature over China tends to be warmer in El Niño years than La Niña years. In the CAMS-CSM simulation, the southwesterly wind anomaly is stronger than observed, which is consistent with the overestimation of the ENSO–EAWM relationship (Fig. 19). However, this modeled southwesterly wind an-

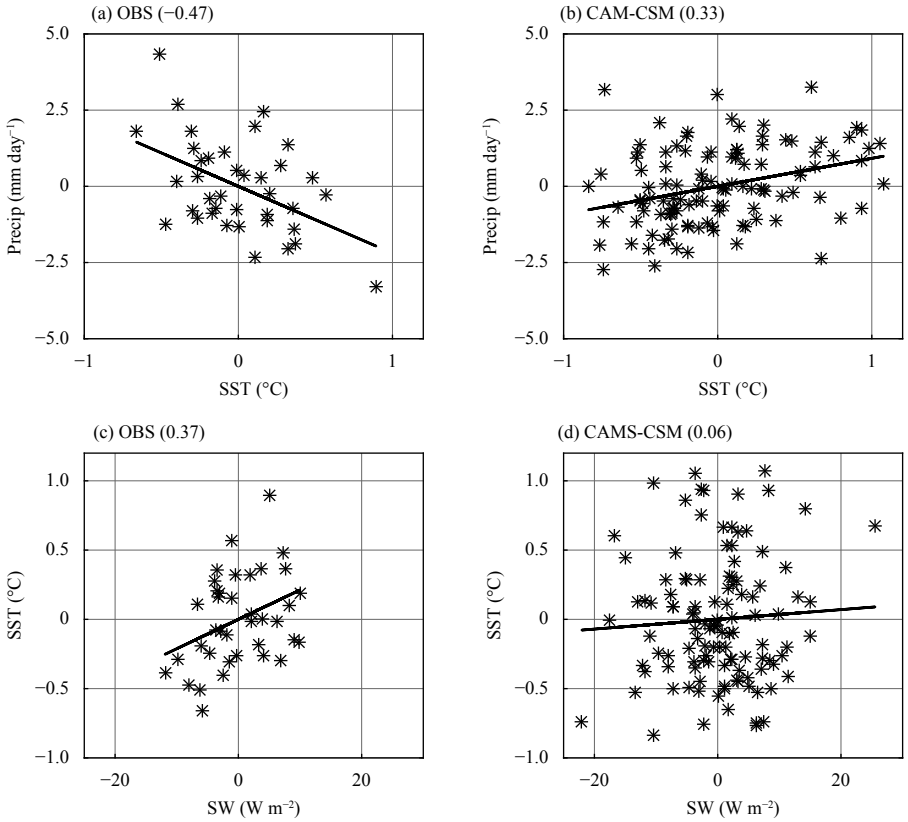

Fig. 18. Scatterplots of (a, b) local precipitation against the local SST anomaly and (c, d) the local SST anomaly against local shortwave radiation, over the South China Sea (8°–22°N, 110°–120°E), during boreal summer in (a, c) observation and (b, d) the CAMS-CSM simulation. Linear fitting lines are indicated by the straight lines. Correlation coefficients are given in parentheses on top of each panel.

omaly is located along coastal regions of China, implying an eastward shift of the modeled AAC over the northwestern Pacific. Thus, an eastward-located western North Pacific anticyclone is a common bias in both summer (Fig. 17) and winter (Fig. 20). Consequently, the simulated warming is remarkable only in southern and eastern China, with an underestimation of observed warming in central China. It should be noted that the EAWM can also affect ENSO (Li, 1990, 1996) and its teleconnections in the extratropics (Ma et al., 2018), which needs to be evaluated for CAMS-CSM in the future.

6. Summary and discussion

This study evaluates the performance of ENSO in the historical simulation of CAMS-CSM. The mean state of the tropical Pacific, ENSO's properties and dynamics, as well as its impact on East Asian climate, are assessed in detail. Furthermore, the physical origins of model biases are discussed. The main conclusions can be summarized as follows:

(1) In general, the mean state of the tropical Pacific is simulated well by CAMS-CSM, including the prevailing easterly trade winds, CT and WP. However, the well-known double ITCZ problem and CT bias still exist, which are common errors in most CGCMs (Li and Xie, 2014). CAMS-CSM captures the two types of El Niño well, with realistic spatial patterns and independence. The annual cycle and phase-locking features of ENSO are also reproduced; however, ENSO's amplitude is overestimated in each calendar month. Observationally, ENSO is skewed to a positive phase. However, El Niño and La Niña events tend to have similar amplitude in CAMS-CSM. The observed ENSO spectrum is broad (2–7 yr), while the modeled ENSO spectrum exhibits a sharp peak at around 2.8 yr.

(2) The dynamics of ENSO in CAMS-CSM are examined in terms of the BJ-index and Wyrtki index. It is found that biases of positive thermocline feedback and negative heat flux feedback are dominant in CAMS-CSM. The thermocline feedback is underestimated by CAMS-CSM, which is contributed by an underestimation of ENSO-induced westerly wind and the thermocline changes in response to surface wind stress. This weakened thermocline feedback is overwhelmed by the

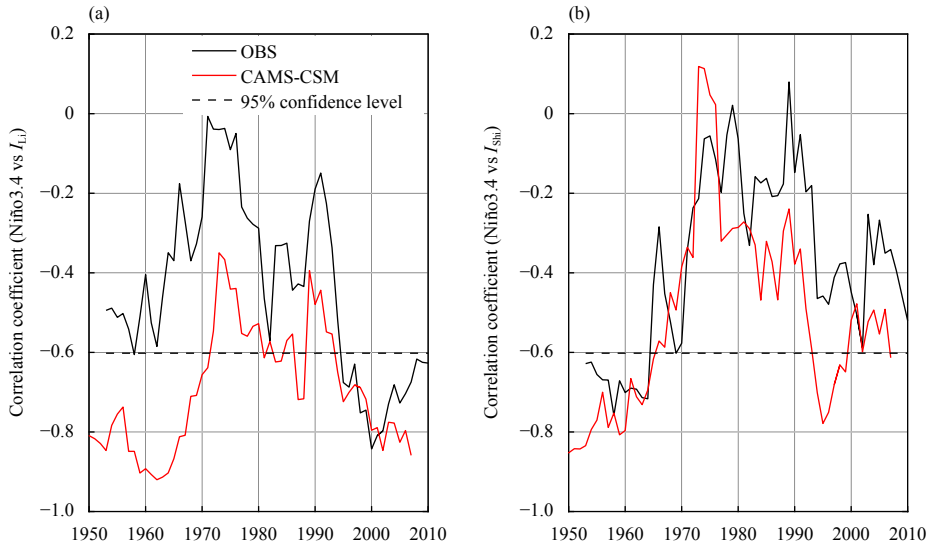

Fig. 19. The 11-yr moving correlations between wintertime Niño3.4 anomalies and the EAWM indices designed by (a) Li and Yang (2010) and (b) Shi (1996) in observation (black curves) and the CAMS-CSM simulation (red curves). The horizontal dashed line denotes the 95% confidence level.

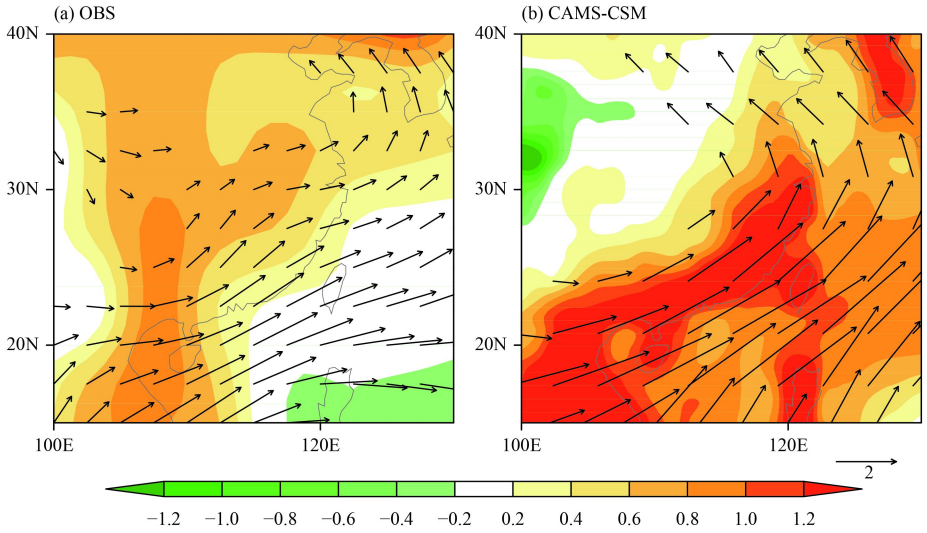

Fig. 20. Differences in wintertime anomalous surface air temperature (color shaded; °C) and horizontal wind at 850 hPa (vectors; m s^{-1}) between El Niño years and La Niña years in (a) observation and (b) the CAMS-CSM simulation.

biases of heat flux damping. The modeled ENSO-induced shortwave reduction is one third of that observed. As a result, the modeled ENSO is more easily stimulated, as indicated by the gross BJ-index. This explains the overestimation of ENSO's amplitude in CAMS-CSM. In addition, the simulated periodicity bias is estimated by the Wyrtki index. It is found that the phase transition induced by the thermocline and zonal advective feedbacks is too quick, which explains the relatively shorter period in CAMS-CSM. The triggers of ENSO, such as the seasonal footprinting mechanism and IOD, are captured well by CAM-CSM.

(3) The relationship between ENSO and the East Asian monsoon is further assessed. During post-El Niño summer, the northwestern Pacific AAC is reproduced by CAMS-CSM. However, the modeled AAC exhibits eastward displacement, such that water vapor cannot be transported to the Yangtze River valley and the observed flooding in this region in post-El Niño summer is poorly simulated. It is further demonstrated that the eastward displacement of the modeled AAC is caused by an unrealistic enhancement of convection over the SCS. Observationally, the SCS SST is a passive response to surface heat flux, and is negatively correlated with local pre-

cipitation. However, the modeled air–sea coupling is too strong over the SCS, which leads to an unrealistic positive correlation between precipitation and local SST. For the EAWM, CAMS-CSM reproduces the observed negative correlation between wintertime lower-tropospheric circulation and ENSO. However, the response of surface air temperature in the central China is weaker than observed.

This study shows that a stronger thermocline feedback and stronger heat flux damping is needed to give a better representation of ENSO dynamics. Improving the convective scheme could be a way to develop the model in the future. For example, modifying the cumulus entrainment may provide a more realistic response of convection to ENSO (Watanabe et al., 2011), which may in turn give a better representation of ENSO's properties (Lu et al., 2017). In addition, the triggering conditions of convection over the SCS need to be improved, such that a better relationship between ENSO and the EASM can be obtained.

Acknowledgments. We would like to thank the editors and reviewers for their valuable comments.

REFERENCES

AchutaRao, K., and K. R. Sperber, 2006: ENSO simulation in coupled ocean–atmosphere models: Are the current models better? *Climate Dyn.*, **27** , 1–15, doi: 10.1007/s00382-006-0119-7.

Alexander, M. A., D. J. Vimont, P. Chang, et al., 2010: The impact of extratropical atmospheric variability on ENSO: Testing the seasonal footprinting mechanism using coupled model experiments. *J. Climate*, **23** , 2885–2901, doi: 10.1175/2010JCLI3205.1.

Annamalai, H., S.-P. Xie, J.-P. McCreary, et al., 2005: Impact of Indian Ocean sea surface temperature on developing El Niño. *J. Climate*, **18**, 302–319, doi: 10.1175/JCLI-3268.1.

Ashok, K., S. K. Behera, S. A. Rao, et al., 2007: El Niño Modoki and its possible teleconnection. *J. Geophys. Res. Oceans*, **112**, C11007, doi: 10.1029/2006JC003798.

Battisti, D. S., and A. C. Hirst, 1989: Interannual variability in a tropical atmosphere–ocean model: Influence of the basic state, ocean geometry and nonlinearity. *J. Atmos. Sci.*, **46**, 1687–1712, doi: 10.1175/1520-0469(1989)046<1687:IVIATA>2.0.CO;2.

Behringer, D. W., M. Ji, and A. Leetmaa, 1998: An improved coupled model for ENSO prediction and implications for ocean initialization. Part I: The ocean data assimilation system. *Mon. Wea. Rev.*, **126** , 1013–1021, doi: 10.1175/1520-0493(1998)126<1013:AICMFE>2.0.CO;2.

Bellenger, H., E. Guilyardi, J. Leloup, et al., 2014: ENSO representation in climate models: From CMIP3 to CMIP5. *Climate Dyn.*, **42**, 1999–2018, doi: 10.1007/s00382-013-1783-z.

Bjerknes, J., 1969: Atmospheric teleconnections from the equatorial Pacific. *Mon. Wea. Rev.*, **97** , 163–172, doi: 10.1175/1520-0493(1969)097<0163:ATFTEP>2.3.CO;2.

Chen, L., and Y. Q. Yu, 2014: Preliminary evaluations of ENSO-related cloud and water vapor feedbacks in FGOALS. *Flexible Global Ocean–Atmosphere–Land System Model: A Modeling Tool for the Climate Change Research Community*, T. J. Zhou, Y. Q. Yu, Y. M. Liu, et al., Eds., Springer, Berlin, 189–197, doi: 10.1007/978-3-642-41801-3_23.

Chen, L., Y. Q. Yu, and D.-Z. Sun, 2013: Cloud and water vapor feedbacks to the El Niño warming: Are they still biased in CMIP5 models? *J. Climate*, **26**, 4947–4961, doi: 10.1175/JCLI-D-12-00575.1.

Chen, L., T. Li, S. K. Behera, et al., 2016a: Distinctive precursory air–sea signals between regular and super El Niños. *Adv. Atmos. Sci.*, **33**, 996–1004, doi: 10.1007/s00376-016-5250-8.

Chen, L., Y. Q. Yu, and W. P. Zheng, 2016b: Improved ENSO simulation from climate system model FGOALS-g1.0 to FGOALS-g2. *Climate Dyn.*, **47** , 2617–2634, doi: 10.1007/s00382-016-2988-8.

Chen, L., T. Li, B. Wang, et al., 2017: Formation mechanism for 2015/16 super El Niño. *Sci. Rep.*, **7** , 2975, doi: 10.1038/s41598-017-02926-3.

Chen, L. X., M. Dong, and Y. N. Shao, 1992: The characteristics of interannual variations on the East-Asian monsoon. *J. Meteor. Soc. Japan*, **70** , 397–421, doi: 10.2151/jmsj1965.70.1B_397.

Chen, M. C., and T. Li, 2018: Why 1986 El Niño and 2005 La Niña evolved different from a typical El Niño and La Niña. *Climate Dyn.*, **51** , 4309–4327, doi: 10.1007/s00382-017-3852-1.

Chen, M. C., T. Li, X. Y. Shen, et al., 2016: Relative roles of dynamic and thermodynamic processes in causing evolution asymmetry between El Niño and La Niña. *J. Climate*, **29**, 2201–2220, doi: 10.1175/JCLI-D-15-0547.1.

Chen, S. F., B. Yu, and W. Chen, 2014: An analysis on the physical process of the influence of AO on ENSO. *Climate Dyn.*, **42**, 973–989, doi: 10.1007/s00382-012-1654-z.

Chen, W., H.-F. Graf, and R.-H. Huang, 2000: The interannual variability of East Asian winter monsoon and its relation to the summer monsoon. *Adv. Atmos. Sci.*, **17** , 48–60, doi: 10.1007/s00376-000-0042-5.

Chen, W., X. Q. Lan, L. Wang, et al., 2013: The combined effects of the ENSO and the Arctic Oscillation on the winter climate anomalies in East Asia. *Chinese Sci. Bull.*, **58** , 1355–1362, doi: 10.1007/s11434-012-5654-5.

Chen, Z., R. G. Wu, and W. Chen, 2014: Distinguishing interannual variations of the northern and southern modes of the East Asian winter monsoon. *J. Climate*, **27** , 835–851, doi: 10.1175/JCLI-D-13-00314.1.

Chung, P. H., and T. Li, 2013: Interdecadal relationship between the mean state and El Niño types. *J. Climate*, **26** , 361–379, doi: 10.1175/JCLI-D-12-00106.1.

Fedorov, A. V., and S. G. Philander, 2001: A stability analysis of tropical ocean–atmosphere interactions: Bridging measurements and theory for El Niño. *J. Climate*, **14**, 3086–3101, doi: 10.1175/1520-0442(2001)014<3086:ASAOTO>2.0.CO;2.

Gong, D. Y., S. W. Wang, and J. H. Zhu, 2001: East Asian winter monsoon and Arctic oscillation. *Geophys. Res. Lett.*, **28**, 2073–2076, doi: 10.1029/2000GL012311.

Gong, H. N., L. Wang, W. Chen, et al., 2014: The climatology

and interannual variability of the East Asian winter monsoon in CMIP5 models. *J. Climate*, **27**, 1659–1678, doi: 10.1175/JCLI-D-13-00039.1.

Gong, H. N., L. Wang, W. Chen, et al., 2015: Diverse influences of ENSO on the East Asian–western Pacific winter climate tied to different ENSO properties in CMIP5 models. *J. Climate*, **28**, 2187–2202, doi: 10.1175/JCLI-D-14-00405.1.

Gong, H. N., L. Wang, W. Chen, et al., 2018: Diversity of the Pacific–Japan pattern among CMIP5 models: Role of SST anomalies and atmospheric mean flow. *J. Climate*, **31**, 6857–6877, doi: 10.1175/JCLI-D-17-0541.1.

Griffies, S. M., M. J. Harrison, R. C. Pacanowski, et al., 2004: A Technical Guide to MOM4. GFDL Ocean Group Technical Report No. 5, NOAA/Geophysical Fluid Dynamics Laboratory, Princeton, NJ, 339 pp.

Guilyardi, E., 2006: El Niño-mean state-seasonal cycle interactions in a multi-model ensemble. *Climate Dyn.*, **26**, 329–348, doi: 10.1007/s00382-005-0084-6.

Guilyardi, E., A. Wittenberg, A. Fedorov, et al., 2009: Understanding El Niño in ocean–atmosphere general circulation models: Progress and challenges. *Bull. Amer. Meteor. Soc.*, **90**, 325–340, doi: 10.1175/2008BAMS2387.1.

Ham, Y. G., and J. S. Kug, 2012: How well do current climate models simulate two types of El Niño? *Climate Dyn.*, **39**, 383–398, doi: 10.1007/s00382-011-1157-3.

He, S. P., and H. J. Wang, 2013: Oscillating relationship between the East Asian winter monsoon and ENSO. *J. Climate*, **26**, 9819–9838, doi: 10.1175/JCLI-D-13-00174.1.

Hwang, Y.-T., and D. M. W. Frierson, 2013: Link between the double-intertropical convergence zone problem and cloud biases over the Southern Ocean. *Proc. Natl. Acad. Sci. USA*, **110**, 4935–4940, doi: 10.1073/pnas.1213302110.

Izumo, T., J. Vialard, M. Lengaigne, et al., 2010: Influence of the state of the Indian Ocean Dipole on the following year's El Niño. *Nat. Geosci.*, **3**, 168–172, doi: 10.1038/ngeo760.

Jiang, Z. H., H. Yang, Z. Y. Liu, et al., 2014: Assessing the influence of regional SST modes on the winter temperature in China: The effect of tropical Pacific and Atlantic. *J. Climate*, **27**, 868–879, doi: 10.1175/JCLI-D-12-00847.1.

Jin, F.-F., 1997a: An equatorial ocean recharge paradigm for ENSO. Part I: Conceptual model. *J. Atmos. Sci.*, **54**, 811–829, doi: 10.1175/1520-0469(1997)054<0811:AEORPF>2.0.CO;2.

Jin, F.-F., 1997b: An equatorial ocean recharge paradigm for ENSO. Part II: A stripped-down coupled model. *J. Atmos. Sci.*, **54**, 830–847, doi: 10.1175/1520-0469(1997)054<0830:AEORPF>2.0.CO;2.

Jin, F.-F., S. T. Kim, and L. Bejarano, 2006: A coupled-stability index for ENSO. *Geophys. Res. Lett.*, **33**, L23708, doi: 10.1029/2006GL027221.

Kalnay, E., M. Kanamitsu, R. Kistler, et al., 1996: The NCEP/NCAR 40-year reanalysis project. *Bull. Amer. Meteor. Soc.*, **77**, 437–472, doi: 10.1175/1520-0477(1996)077<0437:TNYRP>2.0.CO;2.

Kim, J. W., S. W. Yeh, and E. C. Chang, 2014: Combined effect of El Niño–Southern Oscillation and Pacific decadal oscillation on the East Asian winter monsoon. *Climate Dyn.*, **42**, 957–971, doi: 10.1007/s00382-013-1730-z.

Kim, S.-T., and F.-F. Jin, 2011: An ENSO stability analysis. Part II: Results from the twentieth and twenty-first century simulations of the CMIP3 models. *Climate Dyn.*, **36**, 1609–1627, doi: 10.1007/s00382-010-0872-5.

Kim, S. T., W. J. Cai, F.-F. Jin, et al., 2014a: ENSO stability in coupled climate models and its association with mean state. *Climate Dyn.*, **42**, 3313–3321, doi: 10.1007/s00382-013-1833-6.

Kim, S. T., W. J. Cai, F.-F. Jin, et al., 2014b: Response of El Niño sea surface temperature variability to greenhouse warming. *Nat. Climate Change*, **4**, 786–790, doi: 10.1038/nclimate2326.

Kirtman, B. P., and P. S. Schopf, 1998: Decadal variability in ENSO predictability and prediction. *J. Climate*, **11**, 2804–2822, doi: 10.1175/1520-0442(1998)011<2804:DVIEPA>2.0.CO;2.

Kleeman, R., and A. M. Moore, 1997: A theory for the limitation of ENSO predictability due to stochastic atmospheric transients. *J. Atmos. Sci.*, **54**, 753–767, doi: 10.1175/1520-0469(1997)054<0753:ATFTLO>2.0.CO;2.

Knutson, T. R., S. Manabe, and D. F. Gu, 1997: Simulated ENSO in a global coupled ocean–atmosphere model: Multidecadal amplitude modulation and CO_2 sensitivity. *J. Climate*, **10**, 138–161, doi: 10.1175/1520-0442(1997)010<0138:SEIAGC>2.0.CO;2.

Kug, J. S., and Y. G. Ham, 2011: Are there two types of La Nina? *Geophys. Res. Lett.*, **38**, L16704, doi: 10.1029/2011GL048237.

Kug, J. S., F. F. Jin, and S. I. An, 2009: Two types of El Niño events: Cold tongue El Niño and warm pool El Niño. *J. Climate*, **22**, 1499–1515, doi: 10.1175/2008JCLI2624.1.

Kug, J. S., Y. G. Ham, J. Y. Lee, et al., 2012: Improved simulation of two types of El Niño in CMIP5 models. *Environ. Res. Lett.*, **7**, 039502, doi: 10.1088/1748-9326/7/3/039502.

Li, C. F., A. A. Scaife, R. Y. Lu, et al., 2016: Skillful seasonal prediction of Yangtze River valley summer rainfall. *Environ. Res. Lett.*, **11**, 094002, doi: 10.1088/1748-9326/11/9/094002.

Li, C. Y., 1990: Interaction between anomalous winter monsoon in East Asia and El Niño events. *Adv. Atmos. Sci.*, **7**, 36–46, doi: 10.1007/BF02919166.

Li, C. Y., 1996: A further study on interaction between anomalous winter monsoon in East Asia and El Nino. *J. Meteor. Res.*, **10**, 309–320.

Li, G. and S.-P. Xie, 2014: Tropical biases in CMIP5 multimodel ensemble: The excessive equatorial pacific cold tongue and double ITCZ problems. *J. Climate*, **27**, 1765–1780, doi: 10.1175/JCLI-D-13-00337.1.

Li, S. L., and G. T. Bates, 2007: Influence of the Atlantic multidecadal oscillation on the winter climate of East China. *Adv. Atmos. Sci.*, **24**, 126–135, doi: 10.1007/s00376-007-0126-6.

Li, T., B. Wang, B. Wu, et al., 2017: Theories on formation of an anomalous anticyclone in western North Pacific during El Niño: A review. *J. Meteor. Res.*, **31**, 987–1006, doi: 10.1007/s13351-017-7147-6.

Li, T. M., 1997: Phase transition of the El Niño–Southern Oscillation: A stationary SST mode. *J. Atmos. Sci.*, **54**, 2872–2887, doi: 10.1175/1520-0469(1997)054<2872:PTOTEN>2.0.CO;2.

Li, Y. Q., and S. Yang, 2010: A dynamical index for the East Asian winter monsoon. *J. Climate*, **23**, 4255–4262, doi: 10.1175/2010JCLI3375.1.

Lin, J.-L., 2007: The double-ITCZ problem in IPCC AR4 coupled GCMs: Ocean–atmosphere feedback analysis. *J. Climate*, **20**, 4497–4525, doi: 10.1175/JCLI4272.1.

Liu, G., L.-R. Ji, S.-Q. Sun, et al., 2012: Low- and mid-high latitude components of the East Asian winter monsoon and their reflecting variations in winter climate over eastern China. *Atmos. Ocean. Sci. Lett.*, **5**, 195–200, doi: 10.1080/16742834.2012.11446985.

Liu, Y., H.-L. Ren, A. A. Scaife, et al., 2018: Evaluation and statistical downscaling of East Asian summer monsoon forecasting in BCC and MOHC seasonal prediction systems. *Quart. J. Roy. Meteor. Soc.*, doi: 10.1002/qj.3405.

Lloyd, J., E. Guilyardi, H. Weller, et al., 2009: The role of atmosphere feedbacks during ENSO in the CMIP3 models. *Atmos. Sci. Lett.*, **10**, 170–176, doi: 10.1002/asl.227.

Lloyd, J., E. Guilyardi, and H. Weller, 2011: The role of atmosphere feedbacks during ENSO in the CMIP3 models. Part II: Using AMIP runs to understand the heat flux feedback mechanisms. *Climate Dyn.*, **37**, 1271–1292, doi: 10.1007/s00382-010-0895-y.

Lloyd, J., E. Guilyardi, and H. Weller, 2012: The role of atmosphere feedbacks during ENSO in the CMIP3 models. Part III: The shortwave flux feedback. *J. Climate*, **25**, 4275–4293, doi: 10.1175/JCLI-D-11-00178.1.

Lu, B., and H.-L. Ren, 2016: Improving ENSO periodicity simulation by adjusting cumulus entrainment in BCC_CSMs. *Dyn. Atmos. Oceans*, **76**, 127–140, doi: 10.1016/j.dynatmoce.2016.10.005.

Lu, B., A. A. Scaife, N. Dunstone, et al., 2017: Skillful seasonal predictions of winter precipitation over southern China. *Environ. Res. Lett.*, **12**, 074021, doi: 10.1088/1748-9326/aa739a.

Lu, B., F.-F. Jin, and H.-L. Ren, 2018: A coupled dynamic index for ENSO periodicity. *J. Climate*, **31**, 2361–2376, doi: 10.1175/JCLI-D-17-0466.1.

Luo, J.-J., R. C. Zhang, S. K. Behera, et al., 2010: Interaction between El Niño and extreme Indian Ocean dipole. *J. Climate*, **23**, 726–742, doi: 10.1175/2009JCLI3104.1.

Ma, T. J., W. Chen, D. Nath, et al., 2018: East Asian winter monsoon impacts the ENSO-related teleconnections and North American seasonal air temperature prediction. *Sci. Rep.*, **8**, 6547, doi: 10.1038/s41598-018-24552-3.

Misra, V., L. Marx, M. Brunke, et al., 2008: The equatorial Pacific cold tongue bias in a coupled climate model. *J. Climate*, **21**, 5852–5869, doi: 10.1175/2008JCLI2205.1.

Morice, C. P., J. J. Kennedy, N. A. Rayner, et al., 2012: Quantifying uncertainties in global and regional temperature change using an ensemble of observational estimates: The HadCRUT4 data set. *J. Geophys. Res. Atmos.*, **117**, D08101, doi: 10.1029/2011JD017187.

Murray, R. J., 1996: Explicit generation of orthogonal grids for ocean models. *J. Comput. Phys.*, **126**, 251–273, doi: 10.1006/jcph.1996.0136.

Neelin, J. D., 1991: The slow sea surface temperature mode and the fast-wave limit: Analytic theory for tropical interannual oscillations and experiments in a hybrid coupled model. *J. Atmos. Sci.*, **48**, 584–606, doi: 10.1175/1520-0469(1991)048<0584:TSSSTM>2.0.CO;2.

Philander, S. G. H., D. Gu, G. Lambert, et al., 1996: Why the ITCZ is mostly north of the equator. *J. Climate*, **9**, 2958–2972, doi: 10.1175/1520-0442(1996)009<2958:WTIIMN>2.0.CO;2.

Rayner, N. A., P. Brohan, D. E. Parker, et al., 2006: Improved analyses of changes and uncertainties in sea surface temperature measured in situ since the mid-nineteenth century: The HadSST2 dataset. *J. Climate*, **19**, 446–469, doi: 10.1175/JCLI3637.1.

Rong, X. Y., J. Li, H. M. Chen, et al., 2018: The CAMS climate system model and a basic evaluation of its climatology and climate variability simulation. *J. Meteor. Res.*, **32**, 839–861, doi: 10.1007/s13351-018-8058-x.

Shi, N., 1996: Features of the East Asian winter monsoon intensity on multiple time scale in recent 40 years and their relation to climate. *Quart. J. Appl. Meteor.*, **7**, 175–182. (in Chinese)

Stuecker, M. F., F.-F. Jin, A. Timmermann, et al, 2015: Combination mode dynamics of the anomalous northwest Pacific anticyclone. *J. Climate*, **28**, 1093–1111, doi: 10.1175/JCLI-D-14-00225.1.

Suarez, M. J., and P. S. Schopf, 1988: A delayed action oscillator for ENSO. *J. Atmos. Sci.*, **45**, 3283–3287, doi: 10.1175/1520-0469(1988)045<3283:ADAOFE>2.0.CO;2.

Sun, D. Z., Y. Q. Yu, and T. Zhang, 2009: Tropical water vapor and cloud feedbacks in climate models: A further assessment using coupled simulations. *J. Climate*, **22**, 1287–1304, doi: 10.1175/2008JCLI2267.1.

Timmermann, A., J. Oberhuber, A. Bacher, et al., 1999: Increased El Niño frequency in a climate model forced by future greenhouse warming. *Nature*, **398**, 694–697, doi: 10.1038/19505.

Tokinaga, H., and S.-P. Xie, 2011: Wave- and anemometer-based sea surface wind (WASWind) for climate change analysis. *J. Climate*, **24**, 267–285, doi: 10.1175/2010JCLI3789.1.

van Oldenborgh, G. J., S. Y. Philip, and M. Collins, 2005: El Niño in a changing climate: A multi-model study. *Ocean Sci.*, **1**, 81–95, doi: 10.5194/os-1-81-2005.

Vannière, B., E. Guilyardi, G. Madec, et al., 2013: Using seasonal hindcasts to understand the origin of the equatorial cold tongue bias in CGCMs and its impact on ENSO. *Climate Dyn.*, **40**, 963–981, doi: 10.1007/s00382-012-1429-6.

Vimont, D. J., D. S. Battisti, and A. C. Hirst, 2001: Footprinting: A seasonal connection between the tropics and mid-latitudes. *Geophys. Res. Lett.*, **28**, 3923–3926, doi: 10.1029/2001GL013435.

Wang, B., R. G. Wu, and X. H. Fu, 2000: Pacific–East Asian teleconnection: How does ENSO affect East Asian climate? *J. Climate*, **13**, 1517–1536, doi: 10.1175/1520-0442(2000)013<1517:PEATHD>2.0.CO;2.

Wang, C. Z., W. Q. Wang, D. X. Wang, et al., 2006: Interannual variability of the South China Sea associated with El Niño. *J. Geophys. Res. Oceans*, **111**, C03023, doi: 10.1029/2005JC003333.

Wang, L., and M.-M. Lu, 2016: The East Asian winter monsoon. *The Global Monsoon System: Research and Forecast*, 3rd Ed. C. P. Chang, H. C. Kuo, N. C. Lau, et al., Eds., World Scientific, Singapore, 51–61, doi: 10.1142/9789813200913_0005.

Wang, L., W. Chen, and R. H. Huang, 2008: Interdecadal modulation of PDO on the impact of ENSO on the East Asian winter monsoon. *Geophys. Res. Lett.*, **35**, L20702, doi: 10.1029/2008GL035287.

Watanabe, M., M. Chikira, Y. Imada, et al., 2011: Convective control of ENSO simulated in MIROC. *J. Climate*, **24**, 543–562, doi: 10.1175/2010JCLI3878.1.

Weng, H., K. Ashok, S. K. Behera, et al., 2007: Impacts of recent

El Niño Modoki on dry/wet conditions in the Pacific rim during boreal summer. *Climate Dyn.*, **29** , 113–129, doi: 10.1007/s00382-007-0234-0.

Weng, H., S. K. Behera, and T. Yamagata, 2009: Anomalous winter climate conditions in the Pacific rim during recent El Niño Modoki and El Niño events. *Climate Dyn.*, **32**, 663–674, doi: 10.1007/s00382-008-0394-6.

Wu, B. Y., R. Zhang, and R. D'Arrigo, 2006: Distinct modes of the East Asian winter monsoon. *Mon. Wea. Rev.*, **134**, 2165–2179, doi: 10.1175/MWR3150.1.

Wyrtki, K., 1985: Water displacements in the Pacific and the genesis of El Niño cycles. *J. Geophys. Res. Oceans*, **90**, 7129–7132, doi: 10.1029/JC090iC04p07129.

Xie, P. P., and P. A. Arkin, 1997: Global precipitation: A 17-year monthly analysis based on gauge observations, satellite estimates, and numerical model outputs. *Bull. Amer. Meteor. Soc.*, **78**, 2539–2558, doi: 10.1175/1520-0477(1997)078<2539:GPAYMA>2.0.CO;2.

Xie, S.-P., K. M. Hu, J. Hafner, et al., 2009: Indian Ocean capacitor effect on Indo-western Pacific climate during the summer following El Niño. *J. Climate*, **22** , 730–747, doi: 10.1175/2008JCLI2544.1.

Xie, S.-P., Y. Kosaka, Y. Du, et al., 2016: Indo-western Pacific Ocean capacitor and coherent climate anomalies in post-ENSO summer: A review. *Adv. Atmos. Sci.*, **33** , 411–432, doi: 10.1007/s00376-015-5192-6.

Yu, J.-Y., H.-Y. Kao, and T. Lee, 2010: Subtropics-related interannual sea surface temperature variability in the central equatorial Pacific. *J. Climate*, **23** , 2869–2884, doi: 10.1175/2010JCLI3171.1.

Zebiak, S. E., and M. A. Cane, 1987: A model El Niño–Southern Oscillation. *Mon. Wea. Rev.*, **115** , 2262–2278, doi: 10.1175/1520-0493(1987)115<2262:AMENO>2.0.CO;2.

Zhang, R., A. Sumi, and M. Kimoto, 1996: Impact of El Niño on the East Asian monsoon: A diagnostic study of the '86/87 and '91/92 events. *J. Meteor. Soc. Japan*, **74**, 49–62, doi: 10.2151/jmsj1965.74.1_49.

Zhang, W. J., F.-F. Jin, M. F. Stuecker, et al., 2016: Unraveling El Niño's impact on the East Asian monsoon and Yangtze River summer flooding. *Geophys. Res. Lett.*, **43**, 11375–11382, doi: 10.1002/2016GL071190.

Zheng, W., P. Braconnot, E. Guilyardi, et al., 2008: ENSO at 6ka and 21ka from ocean–atmosphere coupled model simulations. *Climate Dyn.*, **30**, 745–762, doi: 10.1007/s00382-007-0320-3.

Tech & Copy Editor: Zhirong CHEN

Environmental Research Letters

LETTER

Stratospheric initial conditions provide seasonal predictability of the North Atlantic and Arctic Oscillations

Yu Nie[1], Adam A Scaife[2,3], Hong-Li Ren[1,4], Ruth E Comer[2], Martin B Andrews[2], Philip Davis[2] and Nicola Martin[2]

[1] Laboratory for Climate Studies, CMA-NJU Joint Laboratory for Climate Prediction Studies, National Climate Center, China Meteorological Administration, Beijing, People's Republic of China
[2] Met Office Hadley Centre, Exeter, United Kingdom
[3] College of Engineering, Mathematics and Physical Sciences, University of Exeter, Exeter, United Kingdom
[4] Department of Atmospheric Science, School of Environmental Studies, China University of Geoscience, Wuhan, People's Republic of China

E-mail: nieyu@cma.gov.cn

Keywords: seasonal prediction, stratosphere, NAO/AO, GloSea5

OPEN ACCESS

RECEIVED
22 October 2018

REVISED
15 January 2019

ACCEPTED FOR PUBLICATION
31 January 2019

PUBLISHED
6 March 2019

Original content from this work may be used under the terms of the Creative Commons Attribution 3.0 licence.

Any further distribution of this work must maintain attribution to the author(s) and the title of the work, journal citation and DOI.

Abstract

The North Atlantic Oscillation (NAO), the regional manifestation of the Arctic Oscillation (AO), dominates winter climate variability in Europe and North America. Skilful seasonal forecasting of the winter NAO/AO has been demonstrated recently by dynamical prediction systems. However, the role of initial conditions in this predictability remains unknown. Using a latest generation seasonal forecasting system and reanalysis data, we show that the initial upper stratospheric zonal wind anomaly contributes to winter NAO/AO predictability through downward propagation of initial conditions. An initial polar westerly/easterly anomaly in the upper stratosphere propagates down to the troposphere in early winter, favoring a poleward/equatorward shift of the tropospheric mid-latitude jet. This tropospheric anomaly persists well into the late winter and induces the positive/negative phase of NAO/AO in the troposphere. Our results imply that good representation of stratospheric initial condition and stratosphere-troposphere coupling in models is important for winter climate prediction.

1. Introduction

The North Atlantic Oscillation (NAO), the regional manifestation of the Arctic Oscillation (AO), dominates atmospheric variability in the North Atlantic winter circulation, and is typically described by the Sea Level Pressure (SLP) difference between the Arctic and Atlantic subtropics (Hurrell 1995, Vallis *et al* 2004). This annular pattern exhibits an equivalent barotropic dipolar structure, extending from the surface to the stratosphere in late winter. Variations of the NAO/AO are linked to the temperature and precipitation anomalies across Europe and North America (Hurrell *et al* 2013). Given these widespread impacts on surface climate, skillful seasonal prediction of the winter NAO/AO is of great importance.

As an internal mode of the atmospheric variability, the NAO/AO variability is often considered to be primarily maintained by eddy-mean flow interactions (Robinson 2000, Lorenz and Hartmann 2003, Barnes and Hartmann 2010, Zhang *et al* 2012). However, on monthly to seasonal time scales, a portion of the wintertime NAO/AO variability can be driven by external forcing besides the internal processes (Deser *et al* 2007), thus permitting more predictability of the NAO/AO on longer time scales (Smith *et al* 2012). Several possible sources of seasonal NAO/AO predictability have been proposed, including remote influence of tropical rainfall (Scaife *et al* 2017), autumnal Sea Surface Temperature (SST) anomaly over North Atlantic (Czaja and Frankignoul 2002, Deser *et al* 2004, Magnusdottir *et al* 2004), cryospheric forcings over Arctic and Eurasia (Cohen *et al* 2014), stratospheric forcings (Kidston *et al* 2015, Scaife *et al* 2016) and solar variability (Ineson *et al* 2011).

High-level NAO/AO prediction skill of dynamical prediction systems has been noted recently by several studies (Riddle *et al* 2013, Kang *et al* 2014,

© 2019 The Author(s). Published by IOP Publishing Ltd

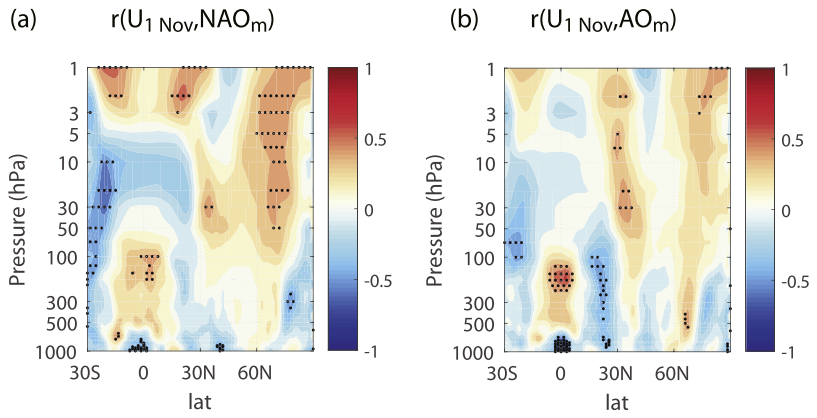

Figure 1. (a) Correlation between the initial zonal wind anomaly on 1 November and the predicted surface NAO index during DJF. (b) As in (a) but for the correlation between initial wind anomaly and the predicted AO index. Values significant at $\alpha = 0.05$ confidence level using one-tailed test are highlighted with black dots.

Scaife *et al* 2014, Dunstone *et al* 2016). For example, the forecast skill (as measured by the anomaly correlation coefficient, ACC) of DJF-mean NAO is 0.62 for 1993–2012 in Metoffice seasonal hindcasts (Scaife *et al* 2014) and even exceeding 0.8 for 1997–2011 in multi-model hindcasts (Athanasiadis *et al* 2016). However, not all winters are equally well predicted and although a large proportion of the extratropical forecast signals can be explained by their connections with tropical rainfall (e.g. Scaife *et al* 2017) there is other predictable variance that remains unexplained. Here, we show that the stratospheric initial conditions play a role in winter NAO/AO predictions. Moreover, we will show that the stratospheric initial conditions are an important source of skill.

2. Data and method

We analyze hindcasts of monthly-mean SLP, and zonal velocity from 1000 to 1 hPa from the Global Seasonal forecast System 5 (GloSea5) (MacLachlan *et al* 2014). The climate model at the core of this forecast system is the Hadley Centre Global Environmental Model version 3 (HadGEM3). It has atmospheric resolution of 0.83° longitude by 0.55° latitude (about 60 km at mid-latitudes), and 85 atmospheric levels with an upper boundary near the mesopause. The ocean resolution is 0.25° with 75 levels. The research ensemble described by MacLachlan *et al* (2014) is supplemented with recent operational hindcast to give a combined ensemble of 45 members per year for each winter during 1994–2012. The ensemble forecasts are initialized with observational estimate of the state of the climate system on three start dates centered on 1 November (25 October, 1 November, and 9 November). SLP and zonal velocity from ERA-Interim (Dee *et al* 2011) are used for validation. The robustness of the results is also checked using JRA-55 reanalysis (Kobayashi *et al* 2015).

In this study, the winter NAO index is computed as the SLP difference between Azores (38°*N*, 27°*W*) and Iceland (65°*N*, 20°*W*) averaged during DJF (December–February). The principal component-based definition is also used to guarantee the robustness of the results (Hurrell *et al* 2013). The AO index is defined by projection onto the leading empirical orthogonal function pattern of the SLP anomalies over 20°*N*–90°*N* of the observational reanalysis. To investigate the role of stratospheric initial conditions in the NAO/AO predictability, an initial wind index U_i is also obtained by averaging the initial zonal wind anomaly in the upper stratosphere where the positive correlation with the predicted winter NAO/AO index is strongest. Here, the initial zonal wind anomaly is calculated as the difference between the zonal wind on the initial date from the observational reanalysis and its daily climatology. The explaining variance of predicted NAO/AO by initial wind anomaly is given by squaring the correlation coefficient between U_i and NAO/AO index (a coefficient of determination). The evolution of the signals in winds is represented by the monthly-mean zonal wind anomaly which is computed as the difference between the 45-member ensemble mean zonal wind at each month and its 19-year climatological value.

3. Results

3.1. Upper stratospheric circulation: a source of winter NAO/AO predictability

To understand the role of initial atmospheric conditions in predicting the winter NAO, figure 1(a) shows the correlation between the initial zonally-averaged zonal wind anomaly on 1 November from the observational reanalysis and the 45-member ensemble mean predicted NAO index for the winter mean (DJF). A significant positive correlation is found in the polar upper stratosphere with further positive correlation at lower latitudes, implying that the initial stratospheric

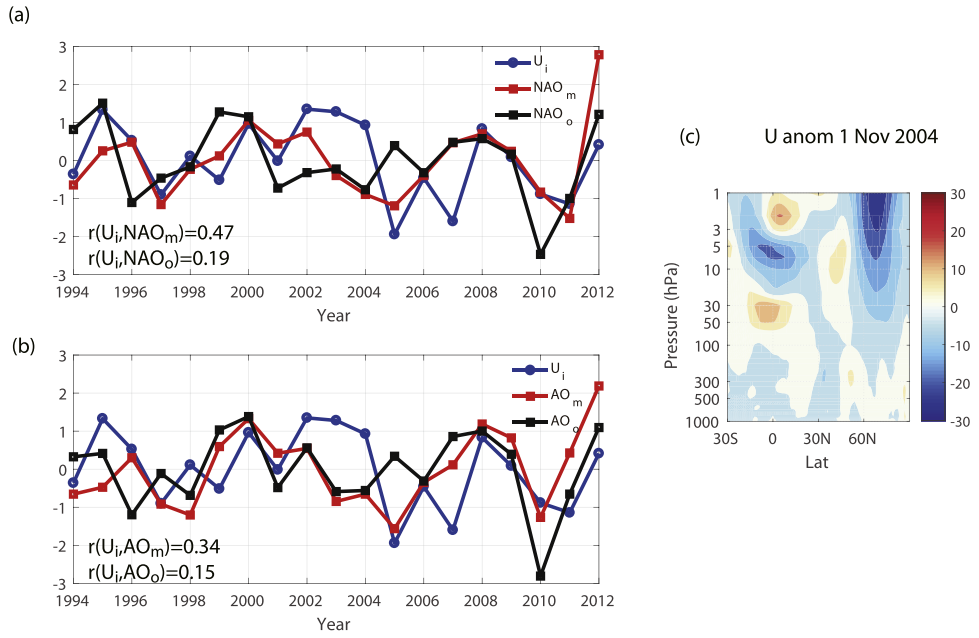

Figure 2. (a) Predicted ensemble mean winter standardized NAO index (red line) and U_i index (blue line). The NAO index in observational reanalysis (black line) is shown for comparison. (b) As in (a) but for AO index and U_i index. The labeled year corresponds to the January of each DJF season (e.g. 2005 forecast verifies in DJF 2004/2005). (c) The zonal wind anomaly on 1 November 2004 in the observational reanalysis, with positive/negative value denoting westerly/easterly anomaly.

conditions may play a role in subsequent winter NAO predictions. For comparison, the correlation between the initial wind anomaly and the ensemble mean predicted DJF AO index is displayed in figure 1(b). The correlation shows a similar spatial structure to figure 1(a), suggesting that the stratospheric initial conditions also play a role in AO predictions. Note, there is a similar but weaker pattern in observational reanalysis (not shown). This is to be expected given that the NAO/AO in observational reanalysis is in but one realization and contains unpredictable NAO/AO variability which is removed from our ensemble mean. Figure 1 suggests that the initial upper stratospheric zonal wind anomalies may exert a significant influence on the model predicted winter NAO/AO.

To represent the variation of initial stratospheric zonal wind anomalies, a stratospheric zonal wind index U_i is defined by averaging the zonal-mean zonal wind anomaly on 1 November over (60°N–90°N, 1–5 hPa) where the positive correlation with the predicted winter NAO/AO index is strongest in figure 1. Figure 2(a) shows the time series of standardized U_i as well as the standardized DJF NAO indices in ensemble mean forecasts and observational reanalysis. The correlation between the initial zonal wind index and the predicted NAO index is 0.47, which is significant at the $\alpha = 0.05$ level by Student's t-test. This implies that around 22% of the predicted NAO variability could come from the initial stratospheric zonal wind anomaly, and suggests that initial atmospheric conditions are important for seasonal prediction as in Stockdale *et al* (2015). The correlation between U_i and the single DJF NAO in observational reanalysis is 0.19, which is well within the range of ensemble member correlations. Similar correlation analysis is also applied to the AO. As shown in figure 2(b), the correlation coefficient between U_i and the predicted ensemble-mean AO index is around 0.34, implying that approximately 12% of the variance in the seasonal forecast of the AO can be explained by the stratospheric initial conditions.

It is interesting to note the 2004/2005 winter, for which the forecast NAO anomaly was previously noted for its difference from the observed NAO anomaly and that implied by predicted tropical rainfall (Scaife *et al* 2017). For this unusual winter, the initial zonal wind index U_i reached its lowest value during 1994–2012. Given the relationship seen in the other years, this negative value of U_i is linked to the unusually negative phase of the NAO predicted by the model ensemble mean, implying that the initial strong easterly wind anomaly gave rise to the negative phase of the NAO predicted for this winter. Figure 2(c) further shows the spatial pattern of the zonal wind anomaly on 1 November 2004. The strong easterly anomaly in the upper-stratospheric polar region suggests a weakening of the polar night jet at the start of the forecast. This anomalous signal persists in the November-mean (not shown), explaining the predicted negative phase of the NAO in 2004/2005 winter by the exceptional easterly anomaly of the upper stratospheric wind on the initial date. Although the observed 2004/2005 winter NAO is opposite to the ensemble mean predicted NAO, it is still within the range of the ensemble spread. There may not be an error in the model forecast for this winter, it is just that the ensemble mean was shifted down by the stratospheric initial

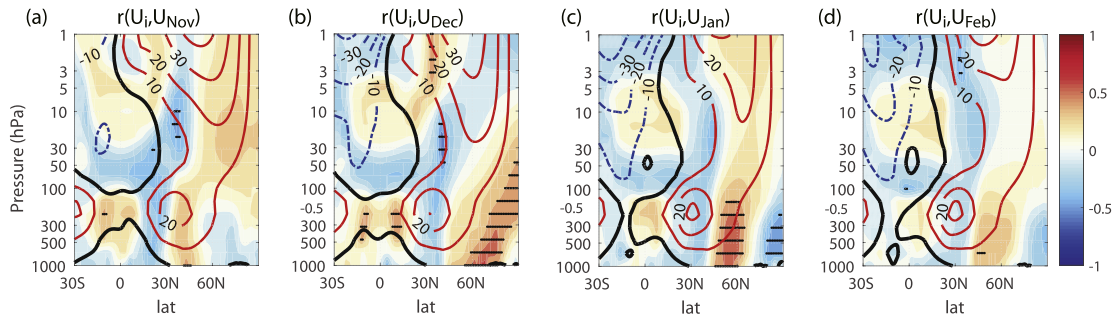

Figure 3. Correlation between initial wind index U_i and the monthly-mean zonal wind anomaly for (a) November, (b) December, (c) January and (d) February, compared with climatological mean states (solid contours with an interval of 10 ms^{-1}; zero values in black thick lines). Values significant at $\alpha = 0.05$ confidence level using one-tailed test are highlighted with black dots.

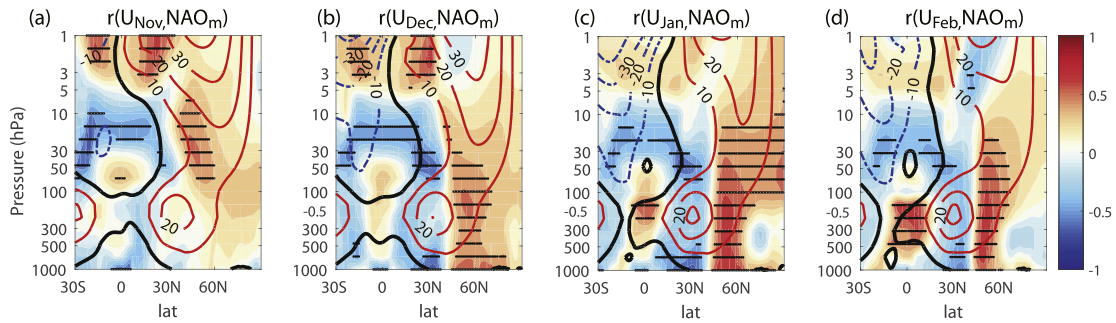

Figure 4. As in figure 3 but for the correlation between the predicted DJF NAO index and the monthly-mean zonal wind anomaly at (a) November, (b) December, (c) January and (d) February.

conditions whereas the observations happened to be higher, presumably due to internal unpredictable variability. It is also noteworthy to point out that the 2006/2007 winter, which is the year exhibiting second lowest value of U_i during 1994–2012, shows a positive phase of NAO prediction. The predicted NAO index is opposite to the NAO suggested by the stratospheric initial condition but is consistent with the observed value. As suggested by Scaife *et al* (2017), the positive phase of NAO this year can be well explained by the tropical rainfall (their figure 12). The above case studies further suggest that the initial stratospheric zonal wind anomaly may provide an additional seasonal predictability source to the NAO besides tropical rainfall.

3.2. Space-time evolution of the stratospheric signal

To explore the connection between the initial zonal wind anomaly in the stratosphere and the predicted winter NAO/AO, figure 3 shows the correlation between the initial wind index U_i and the model predicted zonal-mean zonal wind anomaly from November to February relative to the climatological mean states. The zonal wind climatology in all months shows a strong polar night jet in the stratosphere and two tropospheric jets: subtropical jet and extra-tropical jet. As shown in figure 3(a), the largest positive correlation between U_i and November zonal wind anomaly is found in the polar lower stratosphere, suggesting a strengthening of the polar night jet in November. This stratospheric anomaly then extends down to the troposphere in December. As shown in figure 3(b), the strongest positive correlation is located around 60°*N*, suggesting a poleward shift of the tropospheric extra-tropical jet. This anomaly in the extra-tropical jet persists well into late winter as illustrated in figures 3(c)–(d), consistent with the positive phase of the predicted NAO/AO. This downward propagation of upper stratospheric zonal wind perturbation to the troposphere is consistent with similar signals in many other observation and modeling studies (Kodera *et al* 1990, Kodera 1995, Baldwin and Dunkerton 1999).

To further quantify the relative contribution of the initial stratospheric zonal wind anomaly to winter ensemble mean NAO prediction, figure 4 shows the correlation between the predicted DJF-mean NAO index and the predicted zonal-mean zonal wind anomaly from November to February compared to the climatological mean states. By doing so, the evolution of the signals in winds accompanying the DJF-mean NAO can be clearly shown and compared with the wind evolution induced by the stratospheric initial conditions. In November, as shown in figure 4(a), a strong positive correlation is found in the stratosphere, suggesting a strengthening of the polar night jet before positive NAO. In December (figure 4(b)), the correlation exhibits a dipolar structure in the

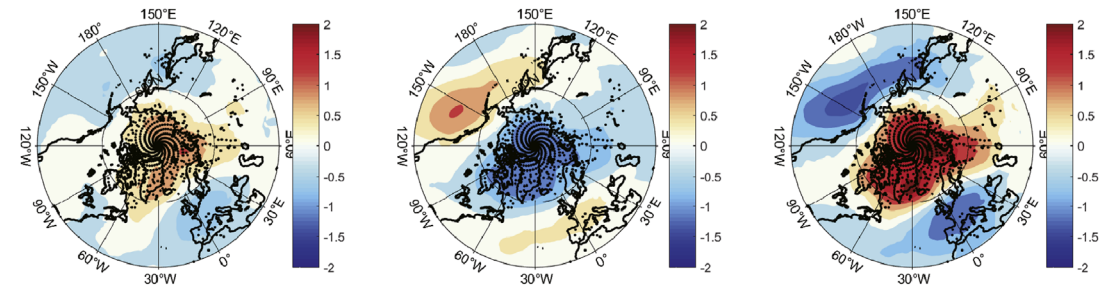

Figure 5. Composites of the DJF-mean SLP anomalies (hPa) with initial (a) easterly anomalies and (b) westerly anomalies. (c) Composites of the DJF-mean SLP difference (hPa) between initial easterly and westerly wind anomaly cases. Values significant at $\alpha = 0.05$ confidence level are highlighted with black dots.

troposphere, with positive correlation at high latitude and negative correlation at low latitude, thus indicating a poleward displacement of the midlatitude jet with positive phase of the NAO. This dipolar pattern of correlation persists into January and February and becomes stronger, as shown in figures 4(c)–(d). Comparison between figures 3 and 4 illustrates that the spatial and time evolution of the zonal wind anomaly induced by the initial upper stratospheric conditions is similar to the zonal wind evolution accompanying the predicted NAO. This further demonstrates that the downward propagation of initial stratospheric wind perturbations plays a role in the prediction of the winter NAO and demonstrates that the influence on the NAO is likely mediated by the zonal wind anomalies (figure 4). The conclusions for the NAO also hold for the AO (results not shown).

3.3. Impact on surface climate

The impact of the initial upper stratospheric zonal wind anomaly on the surface climate is examined through composite analysis. Figures 5(a) and (b) present the composite DJF-mean SLP anomalies with initial easterly and westerly anomalies in the stratosphere. By definition, the easterly (westerly) phase of U_i refers to years when U_i is below (above) -0.5 ($+0.5$) standard deviations. As shown in figure 5(a), for the initial easterly case, the winter SLP increases in the Arctic region and decreases at mid-latitudes in both the Atlantic and Pacific basins corresponding to a negative NAO and AO. For the initial westerly case, as shown in figure 5(b), the composite DJF SLP anomalies display opposite spatial pattern which represents positive phase of NAO/AO. The composite of SLP difference between initial easterly phase and westerly phase displays a stronger negative phase of NAO/AO as shown in figure 5(c). The above results illustrate that the initial upper-stratospheric easterly/westerly anomaly induces a negative/positive phase of the NAO and AO. Very similar patterns are seen in observed surface climate response to stratospheric variability (Gerber *et al* 2012, Kidston *et al* 2015).

4. Conclusions and discussion

Using a dynamical seasonal forecast system and reanalysis data, the role of the initial stratospheric conditions on the predictability of winter NAO/AO is investigated. We find that:

- The upper stratospheric zonal wind anomaly on the initial date plays a role in the winter prediction of the NAO/AO. Around 22% of the 19-year period winter NAO variability can be explained by the initial upper stratospheric zonal wind anomaly in November.
- An initial westerly anomaly in the stratospheric pole in November propagates downward to the troposphere in December, inducing a poleward shift of the tropospheric mid-latitude jet. Then the anomalous poleward jet shift persists well into January and February, which finally results in the positive phase of NAO/AO. The reverse happens for easterly initial anomalies.
- The resulting surface response resembles the NAO and AO in SLP and has an amplitude of 1–2 hPa.

As a source of predictability, tropical rainfall may make the leading contribution to the winter NAO/AO predictability (Scaife *et al* 2017). However, stratospheric initial condition can explain a significant additional part of the predicted variability. This study further proposes that the initial stratospheric zonal wind anomaly plays a role that can even dominate in some years (e.g. winter 2004/2005). An upper stratospheric easterly anomaly in November leads to a negative anomaly in the predicted winter NAO/AO in the model and vice versa. A role for initial atmospheric conditions in NAO/AO predictions was also found by Stockdale *et al* (2015) using an 8-year period but the source was not identified and we suggest it may be located in the stratosphere. The important role played by the stratospheric initial conditions in our model in the winter NAO/AO predictability is also consistent with a very recent modeling study by

O'Reilly *et al* (2018), in which the influence of the initial conditions in the tropical stratosphere is emphasized. The influence of stratospheric conditions in November on the subsequent winter NAO/AO is evident in observations as well during some particular years (e.g. extreme 2009/2010 winter) as suggested by Wang and Chen (2010) and Fereday *et al* (2012). The mechanism for initial stratospheric conditions affecting the tropospheric NAO/AO appears to be very similar to downward propagating signals in other contexts such as sudden stratospheric warming (Baldwin and Dunkerton 2001, Kuroda 2008, Marshall and Scaife 2010) and quasi-biennial oscillation (Marshall and Scaife 2009, Taguchi 2018). As these events appear to be important for seasonal prediction of the NAO/AO (Mukougawa *et al* 2009, Sigmond *et al* 2013, Scaife *et al* 2016), it may also be fruitful to further examine these events in hindcasts. Finally, since the stratospheric initial conditions are important for the winter NAO/AO prediction, improving initial conditions and the representation of stratosphere–troposphere coupling in climate models may further enhance winter prediction skill.

Acknowledgments

We thank the two anonymous reviewers for their constructive suggestions, which help improve the quality of the manuscript. This work is supported by the National Key Research and Development Program on monitoring, Early Warning and Prevention of Major Natural Disaster (2017YFC1502302), NSF of China under grant 41705043, and the UK-China Research & Innovation Partnership Fund through the Met Office Climate Science for Service Partnership (CSSP) China as part of the Newton Fund. This work was done while the lead author was visiting Adam A Scaife at the Met Office Hadley Center.

ORCID iDs

Yu Nie https://orcid.org/0000-0001-7019-0442
Martin B Andrews https://orcid.org/0000-0003-3145-2264

References

Athanasiadis P J, Bellucci A, Scaife A A, Hermanson L, Materia S, Sanna A, Borrelli A, MacLachlan C and Gualdi S 2016 A multisystem view of wintertime NAO seasonal predictions *J. Clim.* **30** 1461–75

Baldwin M P and Dunkerton T J 1999 Propagation of the Arctic Oscillation from the stratosphere to the troposphere *J. Geophys. Res.—Atmos.* **104** 30937–46

Baldwin M P and Dunkerton T J 2001 Stratospheric harbingers of anomalous weather regimes *Science* **294** 581–4

Barnes E and Hartmann D 2010 Dynamical feedbacks and the persistence of the NAO *J. Atmos. Sci.* **67** 851–65

Cohen J *et al* 2014 Recent Arctic amplification and extreme mid-latitude weather *Nat. Geosci.* **7** 627–37

Czaja A and Frankignoul C 2002 Observed impact of Atlantic SST anomalies on the North Atlantic Oscillation *J. Clim.* **15** 606–23

Dee D, Uppala S, Simmons A, Berrisford P, Poli P, Kobayashi S, Andrae U, Balmaseda M, Balsamo G and Bauer P 2011 The ERA-Interim reanalysis: configuration and performance of the data assimilation system *Quart. J. R. Meteor. Soc.* **137** 553–97

Deser C, Magnusdottir G, Saravanan R and Phillips A 2004 The effects of North Atlantic SST and sea ice anomalies on the winter circulation in CCM3: II. Direct and indirect components of the response *J. Clim.* **17** 877–89

Deser C, Tomas R A and Peng S 2007 The transient atmospheric circulation response to North Atlantic sst and sea ice anomalies *J. Clim.* **20** 4751–67

Dunstone N, Smith D, Scaife A, Hermanson L, Eade R, Robinson N, Andrews M and Knight J 2016 Skilful predictions of the winter North Atlantic Oscillation one year ahead *Nat. Geosci.* **9** 809–14

Fereday D R, Maidens A, Arribas A, Scaife A A and Knight J R 2012 Seasonal forecasts of Northern Hemisphere Winter 2009/10 *Environ. Res. Lett.* **7** 034031

Gerber E P *et al* 2012 Assessing and understanding the impact of stratospheric dynamics and variability on the Earth system *Bull. Am. Meteor. Soc.* **93** 845–59

Hurrell J W 1995 Decadal trends in the North Atlantic Oscillation: regional temperatures and precipitation *Science* **269** 676–9

Hurrell J W, Kushnir Y, Ottersen G and Visbeck M 2013 An overview of the North Atlantic Oscillation *The North Atlantic Oscillation: Climatic Significance and Environmental Impact* ed J W Hurrell, Y Kushnir, G Ottersen and M Visbeck (New York: Wiley) pp 1–35

Ineson S, Scaife A A, Knight J R, Manners J C, Dunstone N J, Gray L J and Haigh J D 2011 Solar forcing of winter climate variability in the northern hemisphere *Nat. Geosci.* **4** 753–7

Kang D, Lee M-I, Im J, Kim D, Kim H-M, Kang H-S, Schubert S D, Arribas A and MacLachlan C 2014 Prediction of the Arctic Oscillation in boreal winter by dynamical seasonal forecasting systems *Geophys. Res. Lett.* **41** 3577–85

Kidston J, Scaife A A, Hardiman S C, Mitchell D M, Butchart N, Baldwin M P and Gray L J 2015 Stratospheric influence on tropospheric jet streams, storm tracks and surface weather *Nat. Geosci.* **8** 433–40

Kobayashi S *et al* 2015 The JRA-55 reanalysis: general specifications and basic characteristics *J. Meteor. Soc. Japan* **93** 5–48

Kodera K 1995 On the origin and nature of the interannual variability of the winter stratospheric circulation in the Northern Hemisphere *J. Geophys. Res.—Atmos.* **100** 14077–87

Kodera K, Yamazaki K, Chiba M and Shibata K 1990 Downward propagation of upper stratospheric mean zonal wind perturbation to the troposphere *Geophys. Res. Lett.* **17** 1263–6

Kuroda Y 2008 Role of the stratosphere on the predictability of medium-range weather forecast: a case study of winter 2003–2004 *Geophys. Res. Lett.* **35** L19701

Lorenz D and Hartmann D 2003 Eddy-zonal flow feedback in the Northern Hemisphere winter *J. Clim.* **16** 1212–27

MacLachlan C *et al* 2014 Global seasonal forecast system version 5 (GloSea5): a high-resolution seasonal forecast system *Quart. J. R. Meteor. Soc.* **141** 1072–84

Magnusdottir G, Deser C and Saravanan R 2004 The effects of North Atlantic sst and sea ice anomalies on the winter circulation in CCM3: I. Main features and storm track characteristics of the response *J. Clim.* **17** 857–76

Marshall A G and Scaife A A 2010 Improved predictability of stratospheric sudden warming events in an atmospheric general circulation model with enhanced stratospheric resolution *J. Geophys. Res.—Atmos.* **115** D16114

Marshall A G and Scaife A A 2009 Impact of the QBO on surface winter climate *J. Geophys. Res.—Atmos.* **114** D18110

Mukougawa H, Hirooka T and Kuroda Y 2009 Influence of stratospheric circulation on the predictability of the tropospheric northern annular mode *Geophys. Res. Lett.* **36** L08814

O'Reilly C H, Weisheimer A, Woollings T, Gray L J and MacLeod D 2018 The importance of stratospheric initial conditions for winter North Atlantic Oscillation predictability and implications for the signal-to-noise paradox *Q. J. R. Meteorol. Soc.* **145** 1–17
Riddle E, Butler A, Furtado J, Cohen J and Kumar A 2013 CFSv2 ensemble prediction of the wintertime Arctic Oscillation *Clim. Dyn.* **41** 1099–116
Robinson W A 2000 A baroclinic mechanism for the eddy feedback on the zonal index *J. Atmos. Sci.* **57** 415–22
Scaife A A *et al* 2014 Skillful long-range prediction of European and North American winters *Geophys. Res. Lett.* **41** 2514–9
Scaife A A *et al* 2017 Tropical rainfall, rossby waves and regional winter climate predictions *Quart. J. R. Meteor. Soc.* **143** 1–11
Scaife A A *et al* 2016 Seasonal winter forecasts and the stratosphere *Atmos. Sci. Lett.* **17** 51–6
Sigmond M, Scinocca J F, Kharin V V and Shepherd T G 2013 Enhanced seasonal forecast skill following stratospheric sudden warmings *Nat. Geosci.* **6** 98
Smith D M, Adam A S and Ben P K 2012 What is the current state of scientific knowledge with regard to seasonal and decadal forecasting? *Environ. Res. Lett.* **7** 015602
Stockdale T N, Molteni F and Ferranti L 2015 Atmospheric initial conditions and the predictability of the Arctic Oscillation *Geophys. Res. Lett.* **42** 1173–9
Taguchi M 2018 Seasonal winter forecasts of the northern stratosphere and troposphere: results from jma seasonal hindcast experiments *J. Atmos. Sci.* **75** 827–40
Vallis G, Gerber E, Kushner P and Cash B 2004 A mechanism and simple dynamical model of the North Atlantic Oscillation and annular modes *J. Atmos. Sci.* **61** 264–80
Wang L and Chen W 2010 Downward Arctic Oscillation signal associated with moderate weak stratospheric polar vortex and the cold December 2009 *Geophys. Res. Lett.* **37** L09707
Zhang Y, Yang X-Q, Nie Y and Chen G 2012 Annular mode-like variation in a multilayer quasigeostrophic model *J. Atmos. Sci.* **69** 2940–58

The Role of Extratropical Air–Sea Interaction in the Autumn Subseasonal Variability of the North Atlantic Oscillation

YU NIE

Laboratory for Climate Studies and China Meteorological Administration–Nanjing University Joint Laboratory for Climate Prediction Studies, National Climate Center, China Meteorological Administration, Beijing, China

HONG-LI REN

Laboratory for Climate Studies and China Meteorological Administration–Nanjing University Joint Laboratory for Climate Prediction Studies, National Climate Center, China Meteorological Administration, Beijing, and Department of Atmospheric Science, School of Environmental Studies, China University of Geoscience, Wuhan, China

YANG ZHANG

China Meteorological Administration–Nanjing University Joint Laboratory for Climate Prediction Studies, Institute for Climate and Global Change Research, School of Atmospheric Science, Nanjing University, Nanjing, China

(Manuscript received 22 January 2019, in final form 9 August 2019)

ABSTRACT

Considerable progress has been made in understanding the internal eddy–mean flow feedback in the subseasonal variability of the North Atlantic Oscillation (NAO) during winter. Using daily atmospheric and oceanic reanalysis data, this study highlights the role of extratropical air–sea interaction in the NAO variability during autumn when the daily sea surface temperature (SST) variability is more active and eddy–mean flow interactions are still relevant. Our analysis shows that a horseshoe-like SST tripolar pattern in the North Atlantic Ocean, marked by a cold anomaly in the Gulf Stream and two warm anomalies to the south of the Gulf Stream and off the western coast of northern Europe, can induce a quasi-barotropic NAO-like atmospheric response through eddy-mediated processes. An initial southwest–northeast tripolar geopotential anomaly in the North Atlantic forces this horseshoe-like SST anomaly tripole. Then the SST anomalies, through surface heat flux exchange, alter the spatial patterns of the lower-tropospheric temperature and thus baroclinicity anomalies, which are manifested as the midlatitude baroclinicity shifted poleward and reduced baroclinicity poleward of 70°N. In response to such changes of the lower-level baroclinicity, anomalous synoptic eddy generation, eddy kinetic energy, and eddy momentum forcing in the midlatitudes all shift poleward. Meanwhile, the 10–30-day low-frequency anticyclonic wave activities in the high latitudes decrease significantly. We illustrate that both the latitudinal displacement of midlatitude synoptic eddy activities and intensity variation of high-latitude low-frequency wave activities contribute to inducing the NAO-like anomalies.

1. Introduction

As the dominant mode of the subseasonal atmospheric variability in the North Atlantic Ocean, the North Atlantic Oscillation (NAO) describes the oscillation of the sea level pressure (SLP) between the Arctic and Atlantic subtropics (Hurrell 1995). The variation of NAO anomalies is often accompanied by changes in storminess, wind speeds, surface air temperature, and precipitation across the North Atlantic as well as over Europe and eastern America (Hurrell et al. 2013). Observational studies have suggested that persistence of the NAO is primarily maintained by the nonlinear positive feedback between the synoptic eddy forcing and the mean flow anomalies (Feldstein and Lee 1998; Feldstein 2003; Vallis and Gerber 2008; Barnes and Hartmann 2010), and phase transition of the NAO is often associated with wave-breaking processes (Benedict et al. 2004; Strong and Magnusdottir 2008; Woollings et al. 2008).

Besides internal eddy–mean flow feedback and wave-breaking processes, extratropical air–sea interactions may also play a role in the subseasonal variability of NAO

Corresponding author: Hong-Li Ren, renhl@cma.gov.cn

DOI: 10.1175/JCLI-D-19-0060.1

© 2019 American Meteorological Society. For information regarding reuse of this content and general copyright information, consult the AMS Copyright Policy (www.ametsoc.org/PUBSReuseLicenses).

(Lau 1997; Kushnir et al. 2002). Many previous studies have suggested that the extratropical air–sea interactions in the North Atlantic are dominated by the atmospheric driving effect (Cayan 1992; Deser and Timlin 1997; Deser et al. 2010). The positive NAO anomalies, via Ekman heat transport and surface turbulent heat fluxes, can drive significant tripolar sea surface temperature (SST) anomaly pattern (Frankignoul and Hasselmann 1977; Czaja and Frankignoul 2002) marked by zonally oriented cold anomalies in the subpolar and subtropical North Atlantic, and warm anomalies in the midlatitudes. However, it remains elusive how the underlying SST anomalies affect the atmospheric variability in the North Atlantic, especially on the subseasonal time scale. Because of the large heat capacity of the well-mixed layer of upper ocean, an oceanic thermal signal can persist for months, which allows for a persistent thermal forcing of the overlying atmosphere (e.g., impact of North Atlantic SST anomalies on the NAO; Czaja and Frankignoul 2002). Modeling studies have suggested that the SST anomaly with strong meridional gradient in the oceanic frontal zones can affect the eddy-driven jet and annular mode variability (Rodwell et al. 1999; Nakamura et al. 2008; Sampe et al. 2013; O'Reilly et al. 2017) through either the surface energy fluxes and Ekman currents (Frankignoul 1985; Minobe et al. 2008, 2010) or the eddy-mediated processes (Deser et al. 2004; Ferreira and Frankignoul 2005). However, the numerical studies show diverse atmospheric response to the given SST anomalies, probably due to different experiment designs, initial atmospheric conditions, background states (Peng et al. 1997; Brayshaw et al. 2008), or even different eddy–mean flow interactions (Kushnir et al. 2002). Suffering from the length of available observational high-frequency data, the impact of the SST on the overlying atmosphere lacks observational evidence. Using weekly atmospheric and oceanic reanalysis data, Ciasto and Thompson (2004) have first argued that the SST anomalies over the Gulf Stream region may play an important role in exciting the winter NAO-like atmospheric response on the subseasonal time scale. Wills et al. (2016) further used daily-mean reanalysis data and supported the results of Ciasto and Thompson (2004) by showing that the poleward and upward advection of anomalous warm air from the Gulf Stream SST front are the key processes in generating the winter NAO anomalies.

Many of these observational and modeling studies on extratropical air–sea interactions have focused primarily on the winter season when the atmosphere driving effect on the SST variability is most vigorous and midlatitude eddy–mean flow interactions are strongest. Less is known about the pattern of air–sea interaction during the rest of the year. In particular, during the transition season (e.g., autumn), the daily SST variability is more active than that in winter (Deser et al. 2010). Meanwhile, the atmospheric internal variability is reduced but the eddy–mean flow interactions are still relevant (Peixoto and Oort 1992). As suggested by Kushnir et al. (2002), the knowledge of the SST in autumn is most likely to help in extended-range prediction. Thus, examining the physical processes on how the daily SST variation over North Atlantic in autumn influences the overlying atmospheric circulation is of great importance for understanding the NAO variability as well as enhancing the skill of extended-range climate prediction.

Using daily atmospheric and oceanic reanalysis data, this study highlights the role of extratropical air–sea interaction in the subseasonal variability of the NAO during autumn. We show that a particular horseshoe-like SST pattern can give rise to a significant NAO-like atmospheric response through the eddy-mediated processes. The structure of this paper is assigned as below. Section 2 is a description of the dataset and diagnostic method. The characteristics of the climatological SST variability and eddy statistics are reviewed in section 3. The observed SST–NAO interactions on the subseasonal time scale during autumn are investigated in section 4. The detailed processes through which the daily SST anomalies affect the NAO during autumn are elucidated in section 5. A summary and discussion of the results are presented in section 6.

2. Data and diagnostic method

In this study, the atmospheric data consist of 35 years (1982–2016) of 1.5° × 1.5° latitude–longitude gridded daily (1200 UTC) wind, temperature, geopotential height at constant pressure levels, 10-m wind components and surface heat fluxes from the ERA-Interim dataset produced by European Centre for Medium-Range Weather Forecasts (Dee et al. 2011). The daily SST data with a horizontal resolution of 1° × 1° from the NOAA Optimum Interpolation (OI) SST, version 2 (V2), dataset (Reynolds et al. 2002) are also employed. The ocean surface current data are from the NCEP Global Ocean Data Assimilation System (GODAS). Mixed layer depth data are estimated from the Ocean Mixed Layer Depth Climatology Dataset (De Boyer Montegut et al. 2004). The surface heat fluxes from the Woods Hole Oceanographic Institution

Objectively Analyzed Air–Sea Fluxes (OAFlux) dataset (Yu and Weller 2007) are also tested to guarantee the robustness of the results.

To analyze the subseasonal variability of both the atmosphere and ocean, daily anomaly data of all fields are used throughout this paper by removing the mean seasonal cycle, which is defined as the annual average plus the first four Fourier harmonics of the daily climatology. To investigate the roles of synoptic and low-frequency eddies, the anomalous fields are split into high- and low-frequency components, representing variability on time scales less than and greater than 10 days, respectively. This frequency division uses a 10-day-cutoff Lanczos filter with 41 weights (Hamming 1989) applied to the eddy component of the wind and temperature of all seasons over 35 years. The September–November (SON) and December–February (DJF) fields are retained after such a filtering was performed on the entire period.

The spatial pattern of NAO in this work is represented by the leading empirical orthogonal function (EOF) of the monthly-mean geopotential height at 1000 hPa (Z1000) for the North Atlantic sector (90°W–40°E, 20°–90°N) as in the method used in Barnes and Hartmann (2010). The results in this work are insensitive to the definition of NAO pattern based on different lower-tropospheric circulation variables (e.g., SLP or zonal wind). For the EOF analysis, the data fields are properly weighted to account for the decrease of area toward the North Pole (North et al. 1982). The daily NAO indices are calculated by projecting the daily Z1000 anomalies onto the NAO pattern.

To investigate the two-way interaction between the ocean and atmosphere, two SST indices are generated by projecting the daily SST anomalies onto the two typical NAO-associated SST anomaly patterns, with one preceding the NAO peak by 20 days and the other following the NAO peak by 3 days. The interactions are thus investigated through conducting the lead–lag regressions and composites of key atmospheric and oceanic fields against these SST indices. For the composite analysis, the robust positive phase of SST index is defined as the period when the normalized SST index is greater than one. In this study, the SST and NAO indices are always centered on the SON period, whereas the lagged regressions and composites are based on 11 August–20 December.

The baroclinicity in this study is represented by the maximum Eady growth rate at 850 hPa σ_{BI}, which is calculated as in Hoskins and Valdes (1990): $\sigma_{\mathrm{BI}} = 0.31(f/N)(\partial \mathbf{U}/\partial z)$, where f is the Coriolis parameter, N is the Brunt–Väisälä frequency, $\mathbf{U}$ is the horizontal wind velocity, and z is the geometric height. To examine the evolution of the anomalous wave activities associated with the underlying SST anomaly, the transient $\mathbf{E}$ vectors in Hoskins et al. (1983) and the local finite-amplitude wave activity (LWA) diagnostics as in Huang and Nakamura (2016) and Chen et al. (2015) are also employed in this study. The transient $\mathbf{E}$ vector, which is computed as $\mathbf{E} = (v'^2 - u'^2, -u'v')$, corresponds to the horizontal components of the high-frequency $\mathbf{E}$ vector defined by Hoskins et al. (1983). The vector may be interpreted as an effective momentum flux by synoptic eddies, and its horizontal divergence can force the background zonal flow. The LWA measures the waviness of a dynamical field (300-hPa potential vorticity in this study) and gives the longitudinal distribution of the finite-amplitude wave activity. It is an objective diagnostic of midlatitude atmospheric blocking and can capture well the features of the blocking high (Chen et al. 2015; Nakamura and Huang 2018). In this study, we detect blocking if the LWA is unusually larger than its climatological median value at each longitude and is persistent for at least 5 days as in Martineau et al. (2017).

3. Climatology of SST variability and eddy statistics

Before analyzing the subseasonal air–sea interactions over the North Atlantic, some key aspects of the climatological SST fields and eddy statistics are reviewed in this section. Figure 1a shows the climatology and the standard deviation of the daily SST field in the North Atlantic during autumn. The SSTs have their largest horizontal gradients in the Gulf Stream region. As noted extensively in previous studies, the standard deviation of midlatitude SSTs often peaks in the oceanic front region with largest horizontal temperature gradients (Deser et al. 2010). Indeed, the largest daily SST variability in the North Atlantic is located in the Gulf Stream SST front region as in Wills et al. (2016). The winter distribution of SST fields is shown in Fig. 1b for comparison. It is shown that the daily variability of SST is more active in autumn than winter, which is consistent with Deser et al. (2010).

The climatological distributions of the 10-day high-frequency eddy heat flux and eddy kinetic energy (EKE), and the 10-day low-frequency eddy heat fluxes are displayed in the second and third rows of Fig. 1, respectively. The high-frequency eddies are most active along the Gulf Stream SST front with strong horizontal temperature gradient. The low-frequency eddies are more active in the higher latitudes, peaking to the east of Greenland. Comparison of the eddy heat fluxes between autumn and winter further shows that the eddy activities are more vigorous in winter. The above analyses

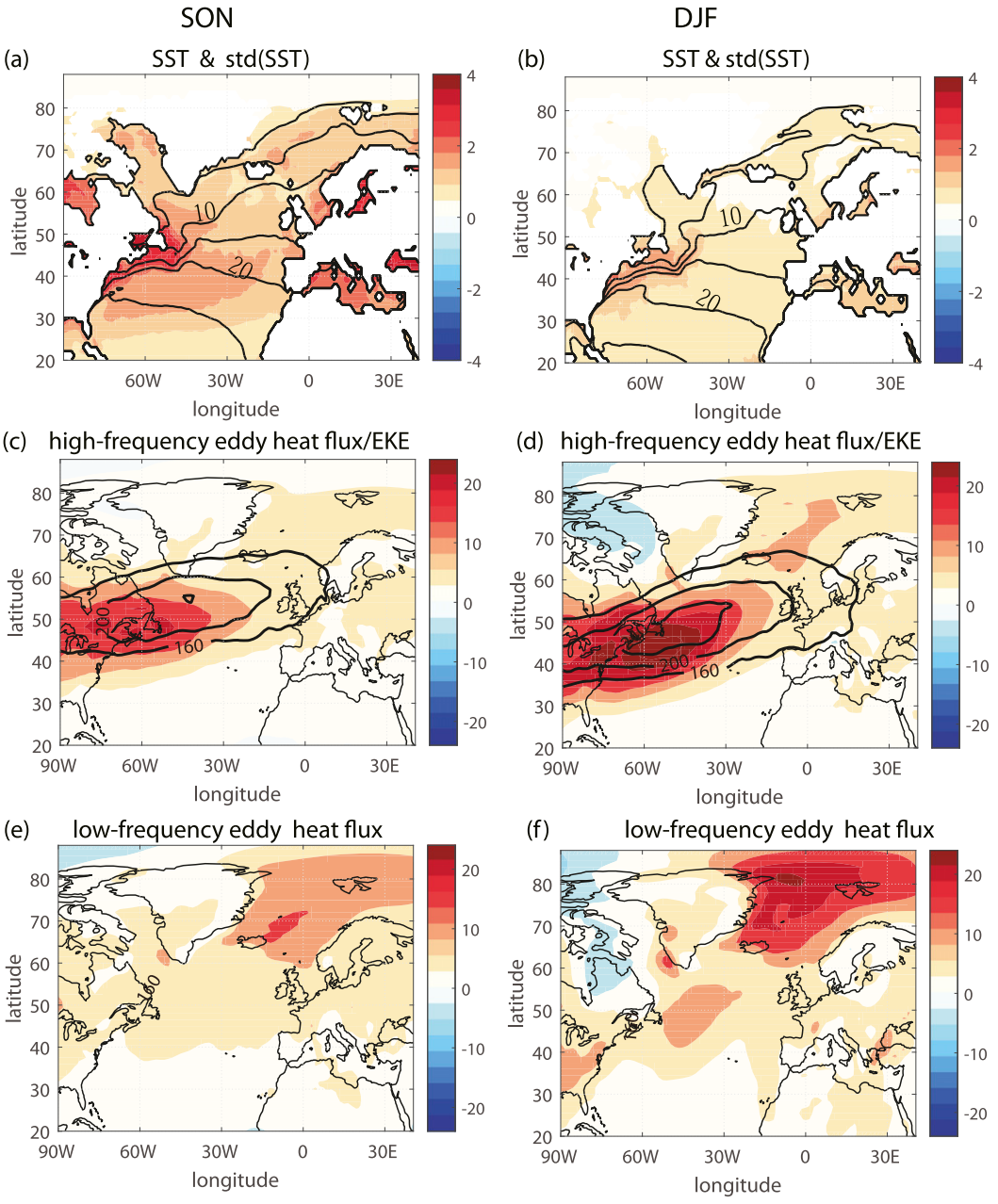

FIG. 1. (a),(b) Climatology (contour intervals of 5 K) and standard deviation of the daily SST (shading, with interval of 0.5 K) in the North Atlantic and climatologies of the (c),(d) 10-day high-frequency 850-hPa eddy heat flux (shading, with interval of 5 m s^{-1} K) and eddy kinetic energy at 300 hPa (contours; m^2 s^{-2}) and (e),(f) 10-day low-frequency eddy heat flux for (left) SON and (right) DJF.

illustrate that both the daily SST variability and eddy activities are active during autumn.

4. Observed NAO–SST relationship on the subseasonal time scale

In this section, the observed characteristics of the extratropical air–sea interaction associated with the subseasonal NAO variability in autumn are examined. We first investigate the SST pattern driven by the NAO variability. Figures 2a–f show the lagged regression patterns of SST/Z1000 anomaly with respect to the daily NAO index in autumn. The NAO pattern at lag 0 (Fig. 2c) manifests a seesaw-like change of geopotential height anomalies between the subpolar and subtropical Atlantic regions. Following the peak of NAO, the SST

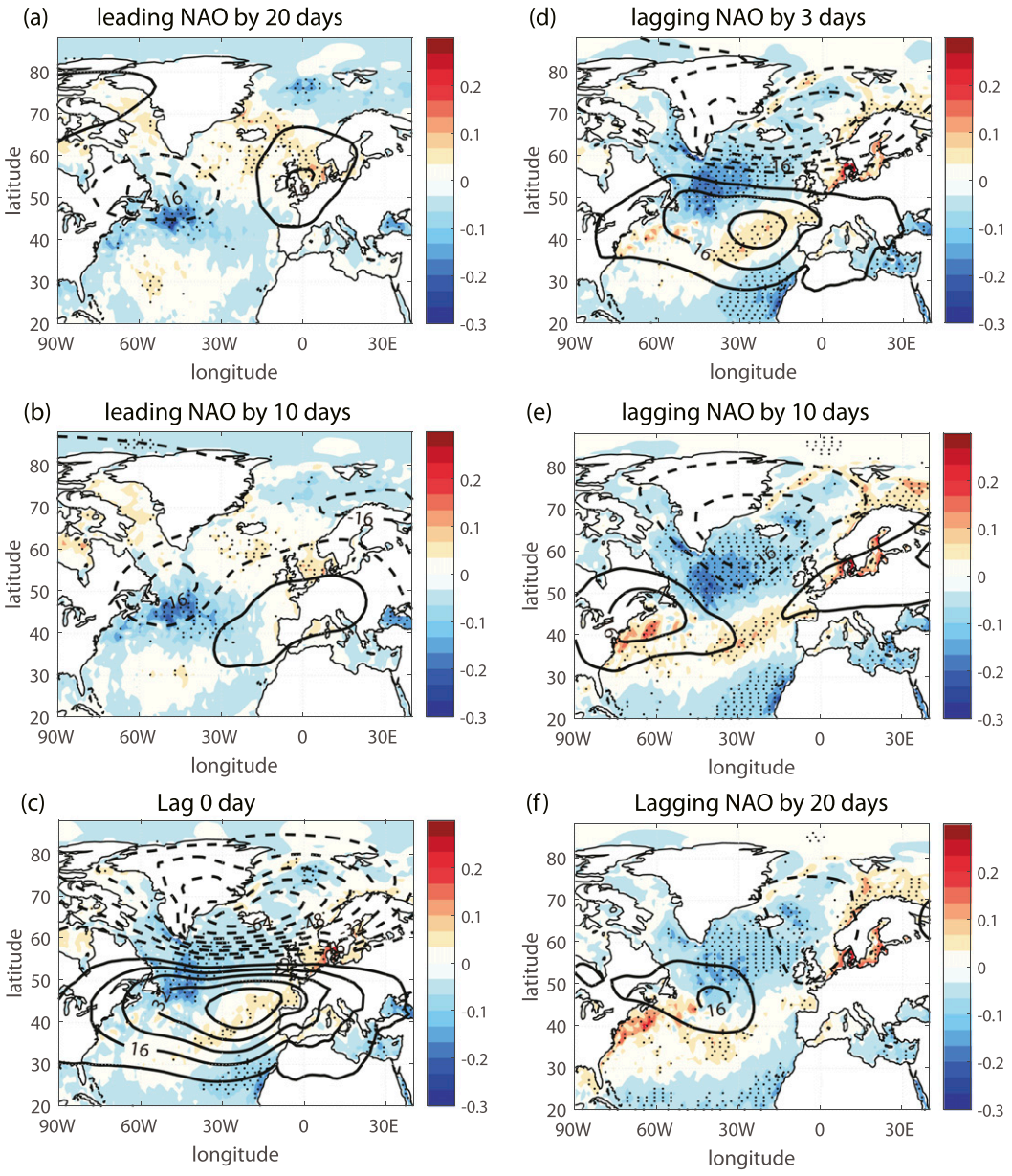

FIG. 2. Lagged regressions of Z1000 (contour intervals of 8 m) and SST (shading, with interval of 0.05 K) onto the normalized daily NAO index in autumn. Values that are significant at the 95% confidence level using a two-tailed *t* test are highlighted with black dots.

anomaly pattern shows tripolar zonal bands (Figs. 2d–f) marked by a cold anomaly in the subpolar North Atlantic, a warm anomaly in the midlatitudes, and a cold subtropical anomaly between the equator and 30°N as in Czaja and Frankignoul (2002), indicating a strong driving effect of NAO on the tripolar SST anomalies over North Atlantic.

Then the SST pattern that could affect the NAO variability is examined through the regression analyses when the SST anomalies lead the NAO index, as displayed in Figs. 2a and 2b. It is clear that the SST anomalies preceding the peak of NAO show a weak and more localized tripolar pattern, with cold anomalies in the Gulf Stream area, and warm anomalies off the western coast of northern Europe and to the south of Gulf Stream region, respectively. This tripolar SST pattern is similar to the North Atlantic SST horseshoe (NAH) pattern (Czaja and Frankignoul 2002), but with the subtropical anomaly displaced to the west. The above lead–lag regression analyses reveal that the

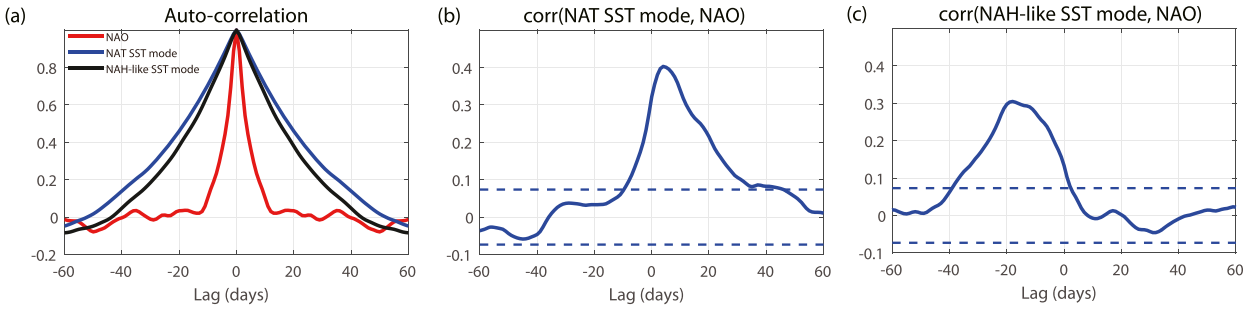

FIG. 3. (a) Autocorrelation of the NAO and two SST indices, and (b),(c) their lagged correlations in autumn. Negative or positive lags denote that SST leads or lags NAO, respectively. The dashed lines denote the corresponding values of 95% significance level, which are estimated from the autocorrelations of each time series.

anomalous SST pattern that may induce the NAO anomalies is spatially different from the SST pattern directly forced by the NAO during autumn (spatial correlation is weak).

To quantitatively represent the SST variability associated with the NAO during autumn, two SST indices are obtained by projecting the daily SST anomaly onto the typical SST pattern following the NAO peak by 3 days (Fig. 2d) and preceding the NAO peak by 20 days (Fig. 2a), respectively. In the following analyses, the zonally tripolar SST pattern in Fig. 2d refers to North Atlantic tripolar (NAT) SST mode, which represents the typical SST pattern driven by the NAO. The localized SST pattern in Fig. 2a is denoted as North Atlantic horseshoe-like (NAH-like) SST mode, which represents the SST pattern prior to the peak of NAO anomaly. The *e*-folding decorrelation time scales of the NAO index and the two SST indices are further examined in Fig. 3a. During autumn, the typical time scale of NAO is 9 days, which is consistent with Feldstein (2000). The time scale of SST anomalies for either of the two indices is around 30 days because of large thermal inertia of the ocean.

The interactions between the NAO and two modes of SST anomalies in autumn are further investigated by calculating the lead–lag correlation between the NAO index and the two SST indices. As shown in Fig. 3b, the correlation is largest when the NAT SST mode lags the NAO by 3 days, suggesting an apparent driving effect of NAO anomaly on the NAT SST mode. At negative lags, when the NAT SST mode leads the NAO, the positive correlation is relatively weak, showing little feedback of the NAT SST mode to the NAO anomaly. For the NAH-like SST mode, as shown in Fig. 3c, the significant correlation reaches its maximum (0.3) when the SST anomalies lead the NAO by around 10–20 days, consistent with a significant delayed response of NAO to the NAH-like SST mode. This correlation analysis further validates the different roles of the NAT and NAH-like SST modes in the NAO variability during autumn.

5. Atmospheric response to the NAH-like SST mode

The atmospheric response to the NAH-like SST mode in autumn is investigated in this section. The temporal evolution of the composite SST and Z1000 anomalies for the positive NAH-like SST index is shown in the left panels of Fig. 4. By construction, the SST anomalies peak at lag 0 and decay slowly with increment of lag. At negative lags (i.e., the atmosphere leading the NAH-like SST mode), the Z1000 anomalies manifest a southwest–northeast tripolar pattern, with a negative height anomaly located northeast of the cold anomaly in the Gulf Stream SST front region and positive anomalies to its northeast and southwest. As indicated in previous studies (Deser and Timlin 1997; Magnusdottir et al. 2004), such Z1000 anomalies at negative lags are consistent with the atmospheric forcing of the SST field, which could be triggered by some remote tropical or extratropical disturbances (e.g., Cassou 2008; Scaife et al. 2017).

At positive lags, when the Z1000 anomalies lag the SST index, the Z1000 evolves to a dipolar structure resembling the NAO pattern located farther eastward, with negative anomalies to the east of Greenland and positive anomalies south of it. Note that the magnitude of the geopotential height anomalies at lag +20 day is roughly 30% of the maximum NAO variability (magnitude of geopotential height anomalies at the NAO peak day). The response of upper-level geopotential height (Z300) is further displayed in the right panels of Fig. 4 for comparison. The Z300 response shows similar structures to the Z1000 at large positive lags, indicating that eddy-mediated processes may play a role in generating such quasi-barotropic atmospheric response (Deser et al. 2004; Ring and Plumb 2007, 2008; Nie et al. 2016). The detailed processes through which the

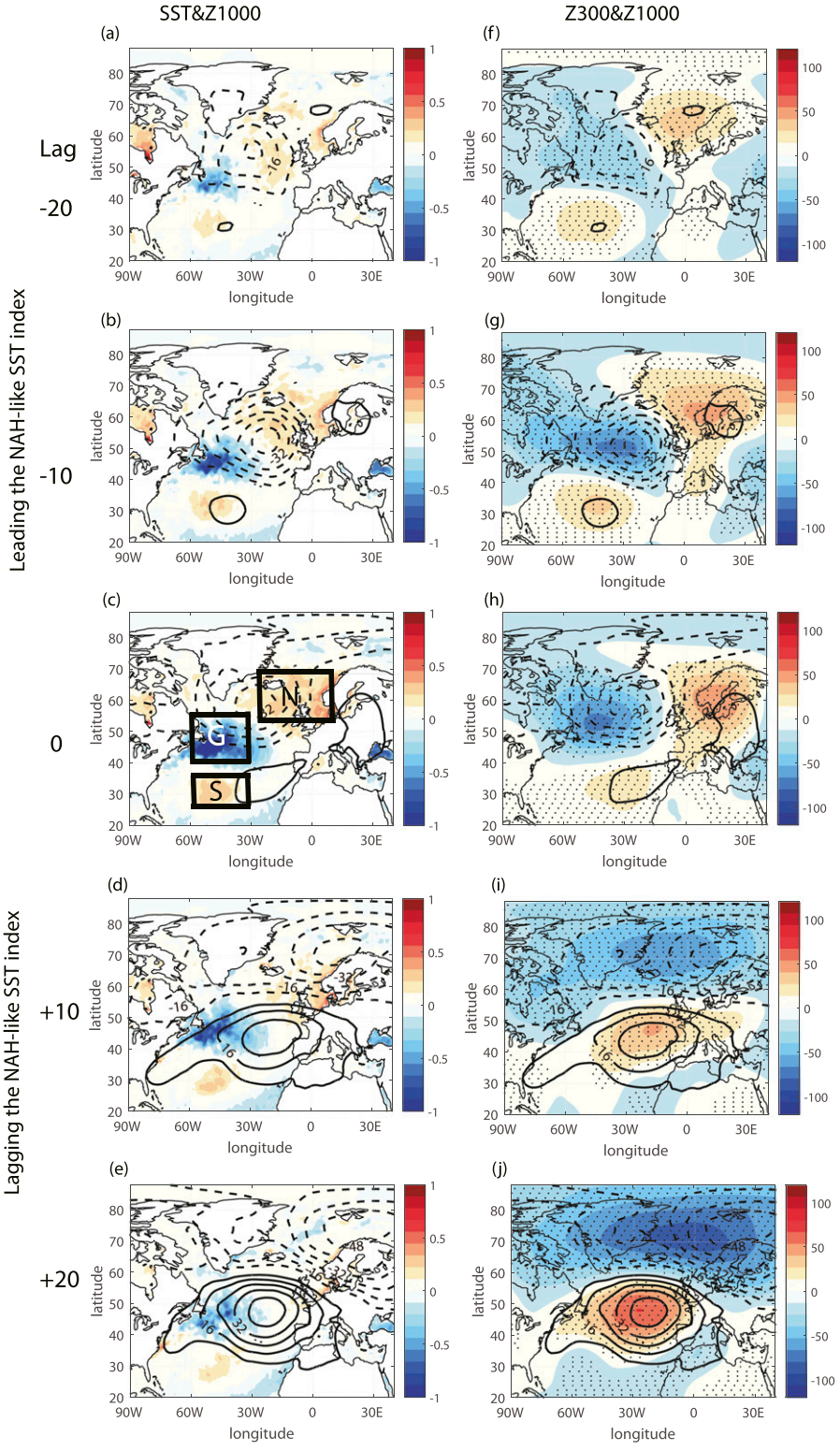

FIG. 4. (a)–(e) Composites of Z1000 (contour intervals of 8 m) and SST (shading, with interval of 0.05 K) anomalies for the positive phase of the normalized NAH-like SST mode index in autumn, with negative or positive lags denoting that Z1000/SST anomalies are leading or lagging NAT-like SST index, respectively. (f)–(j) as in (a)–(e) but for Z1000 (contour interval of 8 m) and Z300 (shading, with interval of 16 m). Values that are significant at the 95% confidence level are highlighted with black dots. The black-outlined boxes in (c) denote three key SST regions, including the areas off the western coast of northern Europe (label N; 55°–70°N, 20°W–10°E), the Gulf Stream region (label G; 40°–55°N, 60°–30°W), and to the south of the Gulf Stream region (label S; 25°–35°N, 60°–30°W).

atmosphere responds to the NAH-like SST anomalies are analyzed in the following sections by conducting lagged composite analyses.

a. *Response of the surface heat flux and lower-tropospheric temperature*

Figure 5 shows the lagged composites of the spatial patterns of the dominant components in the heat budget of the ocean surface (i.e., sensible heat flux, latent heat flux, radiative flux) and the SST tendency with respect to the NAH-like SST index. The surface turbulent heat flux anomalies, especially the latent heat flux, as shown in Figs. 5a–e, change their spatial patterns from driving the SST anomalies at negative lags to dissipating the SST anomalies at positive lags. Prior to the peak of SST anomalies, both the surface sensible and latent heat fluxes exhibit tripolar structures, with a downward heat flux above the warm SST anomalies. This indicates the warming effect of the atmospheric circulation anomalies on the local SST pattern (positive SST tendency shown in Figs. 5k,l). However, following the peak of SST anomalies, the surface heat fluxes show opposite spatial structures, with the largest upward heat flux above the warm SST anomalies, dissipating the SST anomalies (negative SST tendency shown in Figs. 5n,o) and thus heating the atmosphere. The radiative flux anomalies, dominated by the longwave component (Figs. 5f–j), show a spatial pattern similar to those of the surface heat fluxes, but with much weaker magnitude, suggesting its minor role in affecting the atmosphere, which is consistent with the previous study of Cayan (1992). The Ekman heat transport, which is mainly induced by the surface wind anomaly, always acts to drive the SST anomaly (results thus not shown). The above results show that the NAH-like SST anomaly affects the lower troposphere mainly through the surface heat flux.

How the surface heat flux anomalies affect the lower-tropospheric temperature and thus baroclinicity is further examined in Fig. 6. The left panels of Fig. 6 show the composite pattern of the tropospheric 2-m temperature against NAH-like SST index. In addition to the surface heat flux exchange, the variations of surface air temperature are affected by the atmospheric dynamical processes in the boundary layer. As shown in Figs. 6a–e, the variations of 2-m temperature south of 60°N are generally consistent with those of the SST anomalies, reflecting the adjustment of the surface air temperature anomalies through the surface heat flux. At negative lags, as shown in Figs. 6a and 6b, the surface air temperature displays warm anomalies above the warm SST anomalies, which is consistent with the positive surface heat flux from atmosphere to the ocean in Figs. 5a and 5b, and implies a warming effect of the atmosphere on the SST anomalies. However, at positive lags, the surface air temperature south of 60°N over the North Atlantic displays an opposite-sign spatial pattern to the surface turbulent heat fluxes in Figs. 5d and 5e, suggesting a possible governing effect of the SST anomalies on the overlying atmosphere through the surface heat flux exchange. The high-latitude cold surface air temperature anomalies to the southeast of Greenland at positive lags are primarily affected by a northeastward cold air advection (figures not shown).

The response of the lower-tropospheric baroclinicity (i.e., 850-hPa Eady growth rate) in the right panels of Fig. 6 shows a consistent pattern with the surface air temperature anomalies. Prior to the peak of SST anomalies, the baroclinicity shows a tripolar pattern. Following the variation of NAH-like SST mode, the significant change of baroclinicity moves eastward, with a reduced temperature contrast over subtropics and Arctic but an enhanced contrast between the two regions. As suggested by Nie et al. (2016) and Xiao et al. (2016), such lower-tropospheric baroclinicity anomalies can evidently affect the eddy activities through either the eddy generation or the eddy dissipation and wave breaking, which may further give rise to the upper-tropospheric atmospheric circulation anomalies related to the NAO.

b. *Response of the atmospheric eddy activities*

As suggested by previous studies (e.g., Seo et al. 2017), the formation of the quasi-barotropic atmospheric response could be facilitated by two possible eddy-mediated processes: synoptic eddy feedback in midlatitude (Ren et al. 2009, 2011) and low-frequency dynamics involving wave breaking and blocking in high latitudes (Woollings et al. 2008, 2010). In this section, both the responses of the synoptic eddy activities and the low-frequency wave breaking/blocking are examined through the lagged composite analyses when the NAH-like SST anomaly leads the atmosphere.

1) ROLES OF THE SYNOPTIC EDDIES

The response of the synoptic eddy activities to the NAH-like SST mode is investigated in Fig. 7. As shown in Figs. 7a and 7b, the composite synoptic eddy heat flux in the lower troposphere shows a significant dipolar structure at lag +20 days, implying that the SST anomalies could induce the poleward shift of the generation zone for the synoptic eddies. The response of the synoptic eddy kinetic energy at 300 hPa, which often manifests the storm-track activities, is then displayed in Figs. 7c and 7d. The synoptic EKE exhibits a stronger poleward displacement at 10°W–40°E, consistent with the synoptic eddy heat flux shift but moving farther

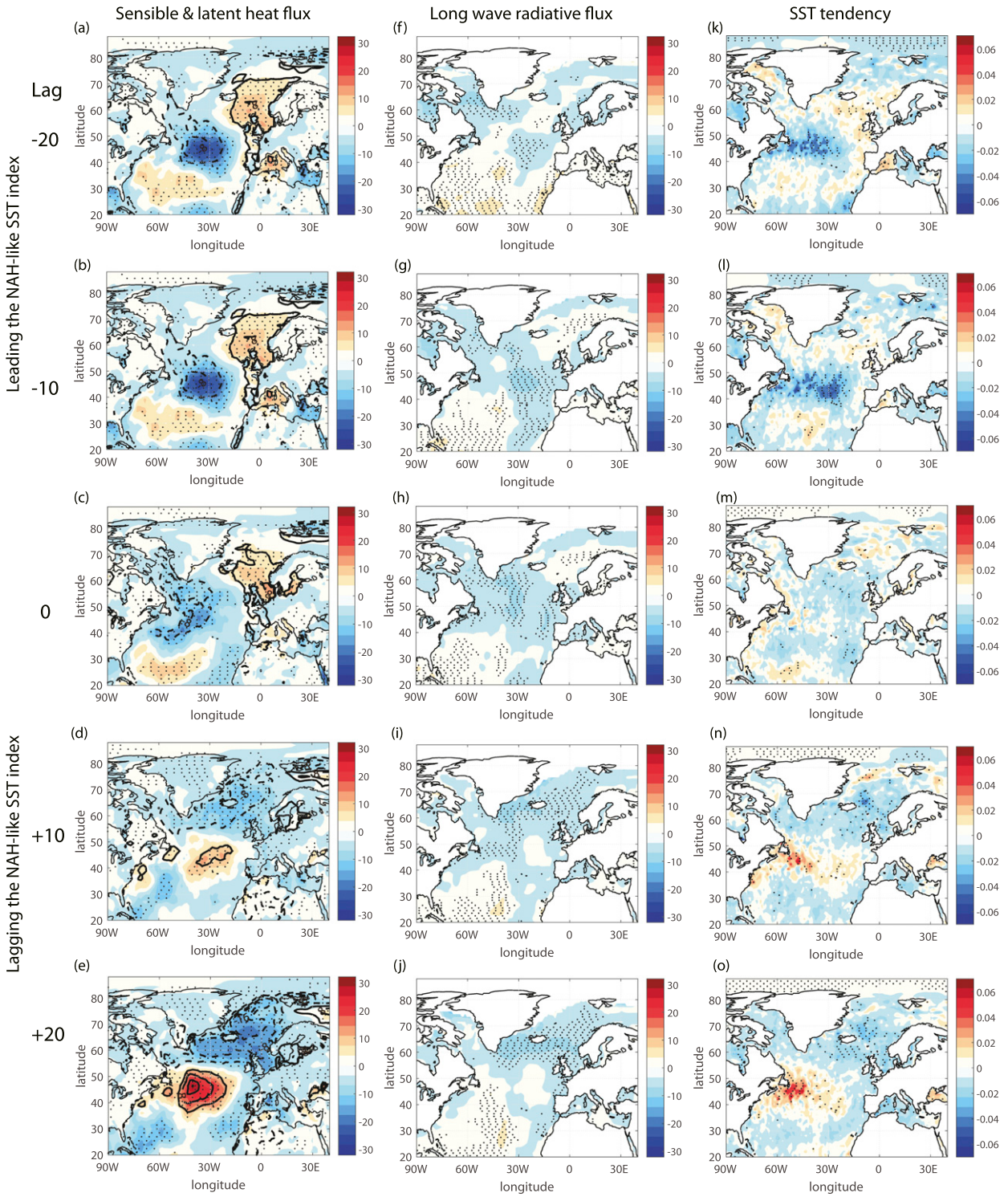

FIG. 5. As in Fig. 4, but for the composites of (a)–(e) sensible (contour intervals of 4 W m^{-2}) and latent (shading, with interval of 4 W m^{-2}) heat fluxes, (f)–(j) longwave radiative flux (shading, with interval of 4 W m^{-2}), and (k)–(o) SST tendency (shading, with interval of 0.01 K day^{-1}). The sign is defined as positive in the downward direction for heat and radiative fluxes.

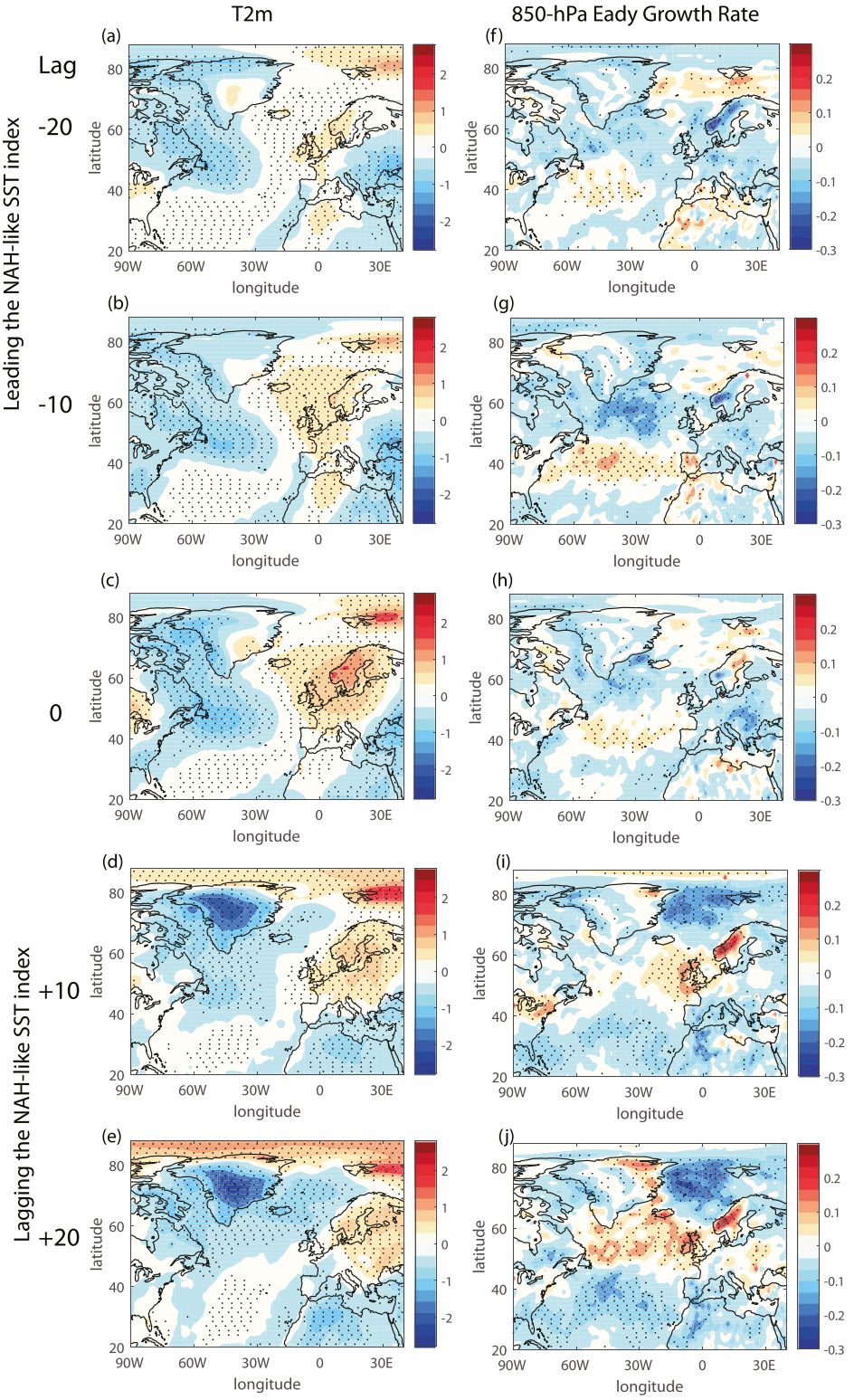

FIG. 6. As in Fig. 4, but for the composites of (a)–(e) surface air temperature (shading, with interval of 0.4 K) and (f)–(j) 850-hPa Eady growth rate (shading, with interval of 0.05 day^{-1}).

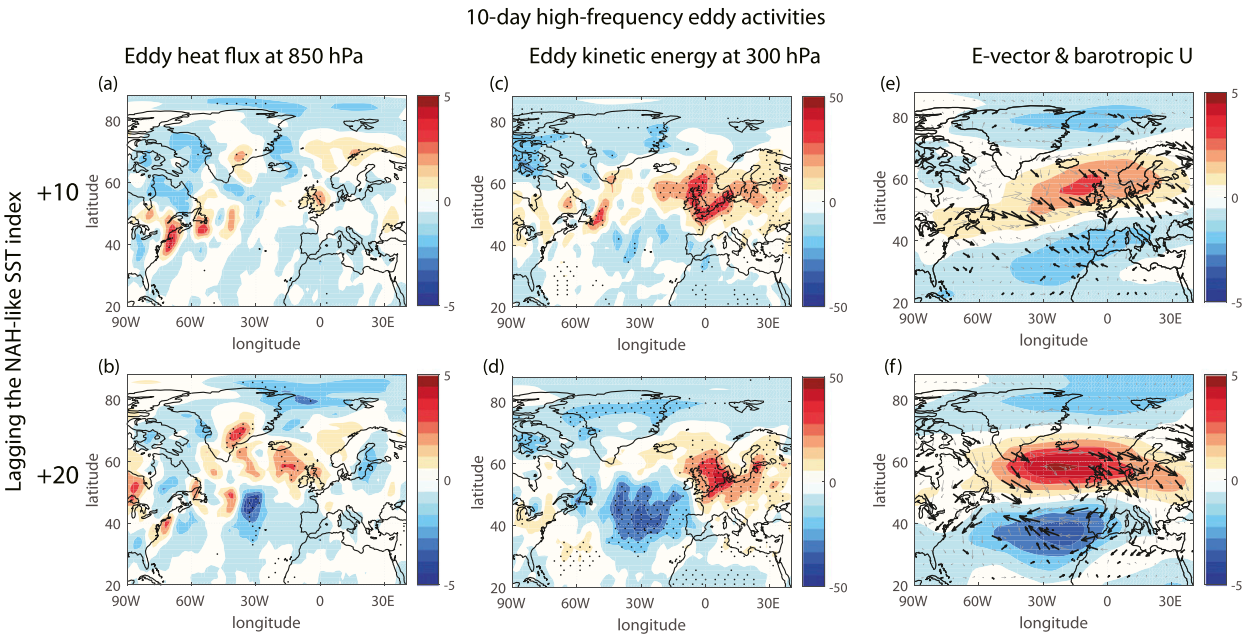

FIG. 7. Composites of anomalous 10-day high-frequency (a),(b) eddy meridional heat flux at 850 hPa (shading, with interval of 1 ms^{-1} K), (c),(d) eddy kinetic energy at 300 hPa (shading, with interval of 10 $m^2 s^{-2}$), and (e),(f) transient **E**-vector fluxes at 300 hPa (gray arrows, with significant fluxes at the 80% confidence level overplotted with black; $m^2 s^{-2}$) and 1000–100-hPa vertically averaged zonal wind (shading, with interval of 1 ms^{-1}) for the normalized NAH-like SST index in autumn when the atmospheric anomalies lag NAH-like SST index by (top) 10 and (bottom) 20 days. Values that are significant at the 95% confidence level are highlighted with black dots.

eastward. The response is strongest when the SST leads by 20 days. The horizontal wave propagation properties and the associated barotropic zonal wind are further displayed in Figs. 7e and 7f. Given that the synoptic **E** vector can be interpreted as an effective momentum flux by synoptic eddies, and its horizontal divergence can force the background zonal flow, we composite the horizontal **E** vectors and the vertically averaged zonal wind for the positive phase of NAH-like SST index. The composite wind shows a clear poleward shift of the jet. This can be understood because the **E** vector exhibits evident anomalous divergence where the zonal wind is stronger and convergence where the zonal wind is weaker, which implies a strong synoptic eddy momentum forcing on the zonal flow. The above analyses illustrate that in response to the positive phase of NAH-like SST mode, the synoptic eddy heat flux, eddy kinetic energy, and eddy momentum forcing all shift poleward, which further result in the poleward shift of the barotropic zonal wind and thus favor a positive phase of NAO anomalies.

2) ROLES OF LOW-FREQUENCY ANTICYCLONIC WAVE ACTIVITIES

The responses of the low-frequency eddy activities and atmospheric blocking to the NAH-like SST mode are examined in Fig. 8. The low-frequency eddy activity is represented by the 10-to-30-day meridional eddy heat flux, and the atmospheric blocking is diagnosed through the frequency of unusually large and persistent anticyclonic local finite-amplitude wave activities (Nakamura and Zhu 2010; Huang and Nakamura 2016; Martineau et al. 2017; Nakamura and Huang 2018). Figures 8a and 8b display the response of the low-frequency eddy heat flux. The low-frequency eddy heat flux in the lower troposphere shows a significant reduction in western northern Europe, suggesting a suppression of the low-frequency eddy generation in the high latitudes. Figures 8c and 8d then display the composite patterns of the unusually large and persistent anticyclonic LWA frequency at 300 hPa for the NAH-like SST index. The anticyclonic wave activity frequency shows a strong reduction to the southeast of Greenland, in agreement with the reduction of the low-frequency eddy heat flux in the lower troposphere. The connection between the NAO and persistent anticyclonic wave activities around southern Greenland has been demonstrated extensively as a Greenland blocking regime (Cheng and Wallace 1993; Vautard 1990; Kimoto and Ghil 1993), which suggests that a positive NAO phase can be considered as a basic, unblocked situation and a negative NAO often describes a period with frequent Greenland blocking. The large simultaneous correlation between the daily NAO index and Greenland blocking frequency

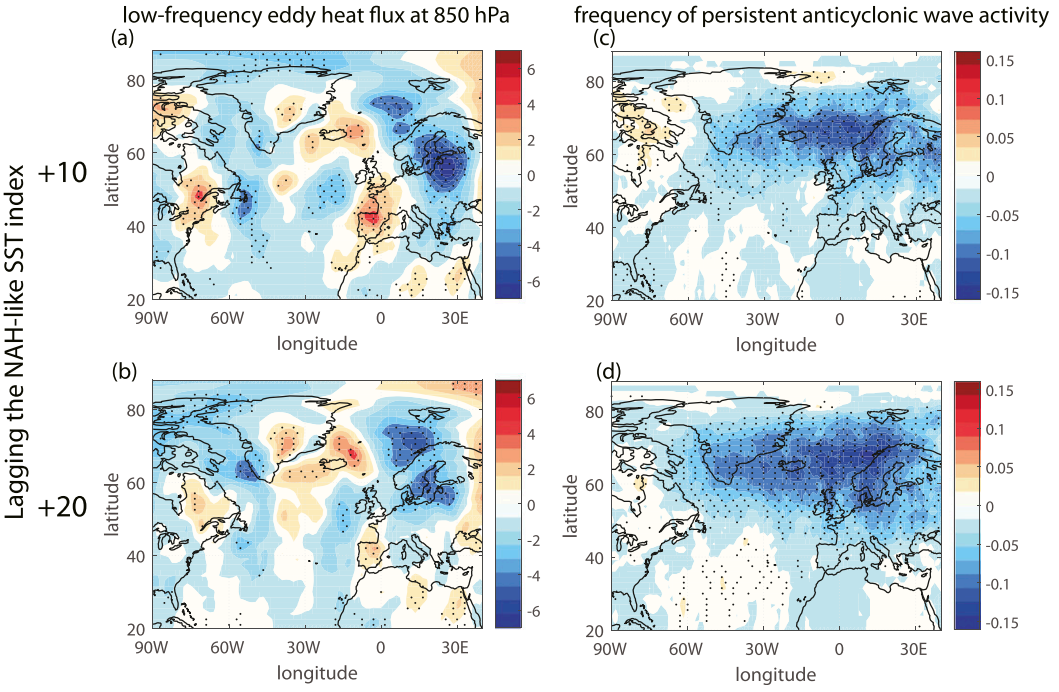

FIG. 8. As in Fig. 7, but for the composites of (a),(b) 10-day low-frequency eddy heat flux at 850 hPa (shading, with interval of 1 m s^{-1} K) and (c),(d) the frequency of unusually large and persistent anticyclonic wave activities at 300 hPa (shading, with interval of 0.02).

shown in Woollings et al. (2008) further confirms the clear contribution of the changes in Greenland blocking occurrence to the NAO anomalies. Following these above arguments, our study further shows that the NAH-like SST anomaly pattern, through altering the low-frequency anticyclonic wave activity in the high latitude of North Atlantic, can give rise to an NAO-like atmospheric circulation anomaly during autumn.

6. Atmospheric response to the variation of SST anomalies in three key regions

The above analyses have suggested that the tripolar NAH-like SST mode has a significant impact on the overlying atmosphere, particularly on the subsequent NAO-like anomalies. To further validate these results, we define three SST indices by area-averaging the SST anomalies near each center of the NAH-like SST mode, including the areas off the western coast of northern Europe (N box; 55°–70°N, 20°W–10°E), the Gulf Stream region (G box; 40°–55°N, 60°–30°W), and to the south of the Gulf Stream region (S box, 25°–35°N, 60°–30°W) as denoted in the black-outlined boxes of Fig. 4c. The forcing and response to the SST anomalies in these different boxes are delineated through composite analyses of the lower-level and upper-level geopotential height anomalies during the typical positive phase of each SST index. Prior to the peak of N-box SST anomalies by 10 days, as shown in Fig. 9a, there is a tripolar southwest–northeast geopotential height anomaly structure in North Atlantic, with largest positive anomalies located to the east of Greenland and negative anomalies to the south of Greenland, which is consistent with the atmospheric circulation pattern preceding the NAH-like SST anomalies (Fig. 4g). This suggests that the atmospheric forcing on the N-box SST anomaly is in agreement with the atmospheric forcing on the NAH-like SST anomaly. By contrast, the atmospheric forcings on the G box and S box shown in Figs. 9b and 9c are relatively local. Following the peak of SST anomalies by 20 days, as shown in Fig. 9d, the geopotential height anomalies in response to N-box SST anomalies are characterized by a positive phase of NAO-like structure, which is also consistent with the circulation anomaly response to NAH-like SST anomaly shown in Fig. 4j. This suggests that the dipolar height anomalies in response to NAH-like SST anomalies is mainly contributed by the atmospheric response to the N-box SST anomalies. The atmospheric responses to the G-box and S-box SST anomalies are relatively weak and mainly confined in the lower troposphere (Figs. 9e,f). We also carry out the composites of the surface heat fluxes and eddy activities against the SST indices of these three regions. It is found that the N-box SST anomalies are

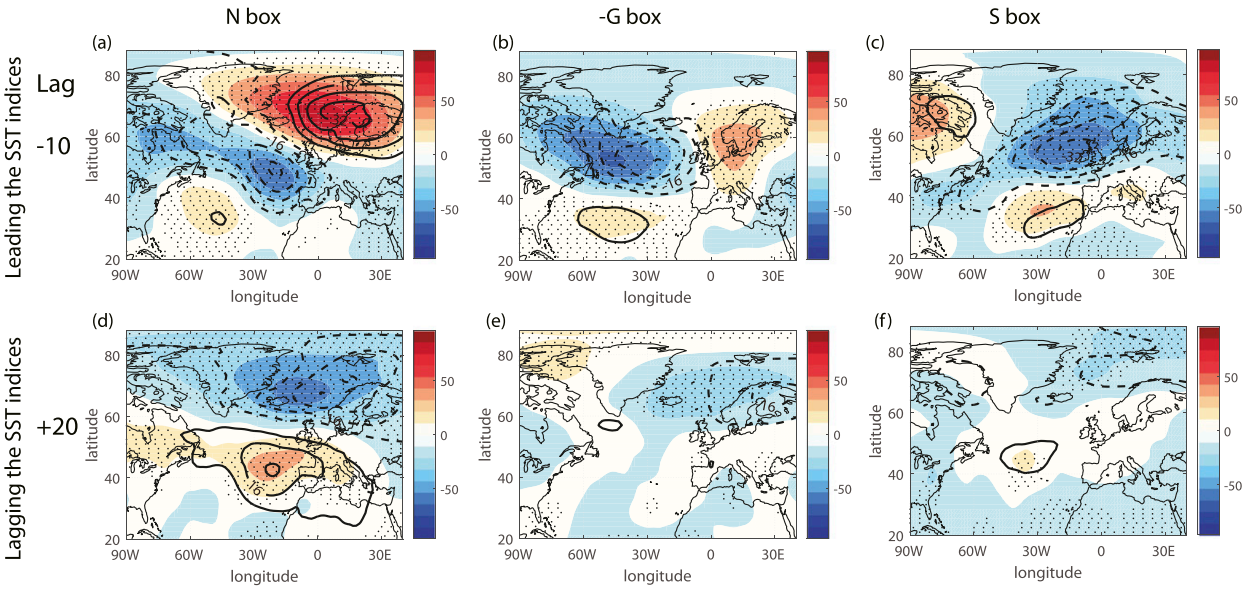

FIG. 9. Composites of Z1000 (contour intervals of 8 m) and Z300 (shading, with interval of 16 m) anomalies with normalized SST index for the (a),(d) N box, (b),(e) −G box, and (c),(f) S box when the atmosphere leads the SST indices by (top) 10 and (bottom) 20 days. For ease of comparison, the SST index in the G box is multiplied by −1.

most efficient in affecting the surface heat fluxes. Meanwhile, the response of low-frequency eddies is also strongest to the N-box SST anomalies (figures not shown), probably because the climatological low-frequency eddies peak in the higher latitudes. Therefore, the above analyses imply that the SST anomalies in the higher latitudes might be more efficient in shaping the low-frequency eddies and further affect the full-tropospheric NAO pattern, whereas the SST anomalies in the middle latitudes can only affect the lower-tropospheric circulation.

7. Summary and discussion

Many progresses have been made over the past years in understanding the subseasonal variability of winter NAO with a focus on the internal eddy–mean flow interaction. This study highlights the role of extratropical air–sea interactions in the NAO variability during the transition season (autumn) when the daily SST variability is stronger. More importantly, using daily atmospheric and oceanic reanalysis data, our study illustrates the physical processes through which the daily SST variation over North Atlantic affects the NAO during autumn.

On the subseasonal time scale, the NAO anomalies in autumn can significantly force a zonally tripolar SST anomalies in the North Atlantic but with little feedback from this anomalous SST pattern. However, a distinct and localized SST anomaly preceding the NAO anomalies by 10–20 days could induce a significant and moderate NAO-like atmospheric response. This SST anomaly, marked by a cold anomaly in the Gulf Stream region and warm anomalies off the western coast of northern Europe and to the south of the Gulf Stream area (Fig. 4c), is implied to be a potential candidate for predicting the subseasonal variability of the NAO.

An initial southwest–northeast tripolar geopotential anomaly in the North Atlantic forces this localized tripolar SST anomaly. Then the SST anomaly pattern acts to alter the spatial patterns of the lower-tropospheric temperature and baroclinicity anomalies through surface heat flux exchange (Fig. 5). Changes in the lower-tropospheric baroclinicity further induce the poleward shift of synoptic eddy generation in the midlatitude and strong decrease of the low-frequency eddy generation and anticyclonic wave activity in the high latitude. On the one hand, the poleward shift of the synoptic eddy generation modulates the poleward shift of the transient eddy kinetic energy and eddy momentum forcing, which further results in the poleward shift of the barotropic zonal wind thus contributing to the positive phase of NAO (Fig. 7). This is consistent with transient eddy feedback playing an important role in the atmospheric response to the underlying SST anomalies in previous studies (Peng and Whitaker 1999; Magnusdottir et al. 2004; Deser et al. 2007; Sampe et al. 2010; Ren et al. 2009; Seo et al. 2017). On the other hand, the reduction of low-frequency high-latitude blocking also contributes to the positive phase of NAO (Fig. 8), which supports Woollings et al. (2008) that a positive NAO is envisaged as being a description of periods in which the high-latitude North Atlantic blocking is infrequent and can be considered as an unblocked situation.

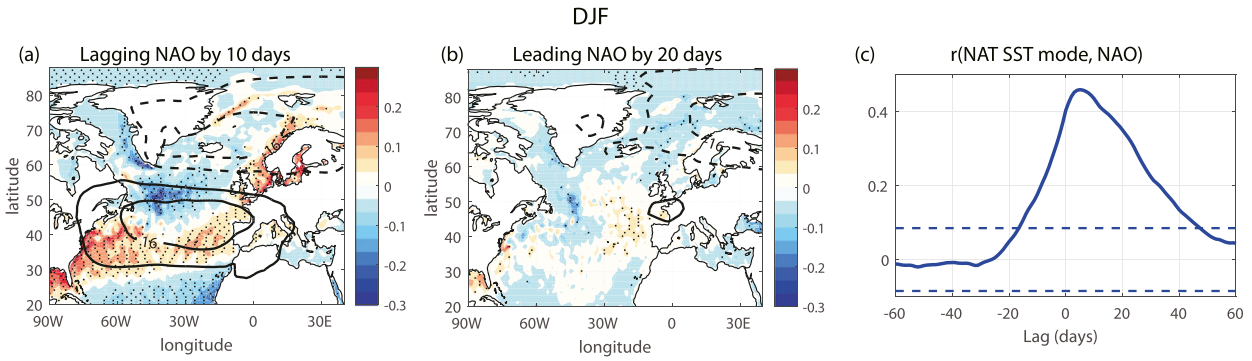

FIG. A1. Lagged regression of Z1000 (contour interval of 8 m) and SST (shading, with interval of 0.05 K) onto the normalized daily NAO index in winter, with Z1000/SST anomalies (a) lagging NAO index by 10 days and (b) leading NAO index by 20 days. Also shown is the (c) cross correlation between the NAO index and NAT SST index during winter. Negative lags denote that the SST index leads the NAO index.

Furthermore, we show that the SST anomalies in the higher latitudes might be more efficient in shaping the low-frequency eddies and anticyclonic blocking, which could further affect the barotropic NAO-like pattern (Fig. 9). In contrast, the direct impact of the SST anomaly in the middle latitudes is relatively shallow with the atmospheric response confined in the lower troposphere. This probably can be explained from the thermodynamic viewpoint that the surface heat flux into the atmosphere accompanied with the midlatitude SST anomalies are quickly balanced by the strong horizontal wind in the lower troposphere above the front region (Hoskins and Karoly 1981).

Our study contributes to a growing body of observational evidence that extratropical SST anomalies are capable of significantly influencing the large-scale atmospheric circulation on the subseasonal time scale during autumn (Xiao et al. 2016; Wills et al. 2016), which supports previous modeling studies (Rodwell et al. 1999; Nakamura et al. 2008; Sampe et al. 2013; O'Reilly et al. 2017). The impact of the SST anomalies on the overlying atmospheric circulation in winter is much weaker as a result of the less active daily SST variability. Air–sea interaction over North Atlantic during winter is dominated by the stronger atmospheric driving effect (see the appendix for details). Note that this study mainly addresses the role of extratropical SST anomalies in affecting the lower-tropospheric NAO variability. The upper-tropospheric NAO variability is different because of some remote influences from the tropical SST anomalies or the stratosphere (e.g., Cassou 2008; Scaife et al. 2017), and thus deserves further studies. Our work also demonstrates that the barotropic NAO-like response to the extratropical SST anomalies can be attributed to two eddy-mediated processes: the synoptic eddy feedbacks and high-latitude blocking variation. However, the relative importance of these two processes is difficult to evaluate simply from the statistical diagnostic analysis. Future works will be conducted to quantify these processes by setting up numerical experiments in an idealized air–sea coupled model, and further examine the impact of high-latitude SST anomalies on the formation of low-frequency eddies and the NAO persistence.

Acknowledgments. We thank Fei-Fei Jin, Adam Scaife, and Nick Dunstone for valuable discussions and the three anonymous reviewers for their constructive suggestions, which helped to improve the quality of the paper. This work is supported by NSF of China under Grants 41705043, 41775066, and 41675055.

APPENDIX

Winter Subseasonal Air–Sea Interaction in the North Atlantic

The winter subseasonal air–sea interaction over the North Atlantic is briefly discussed through the lagged SST–NAO regression analyses. Here, the SST and NAO indices are centered on the DJF period, whereas the lagged regressions are based on 11 November–20 March from lag −20 days to lag +20 days. Figures A1a and A1b display the regressions of SST anomalies against winter daily NAO index when SST anomalies lag the NAO by 10 days and lead the NAO by 20 days, respectively. As shown in Fig. A1a, the SST anomalies following the NAO peak display an NAT spatial pattern, which is similar to that in autumn but with stronger amplitude. This indicates a stronger atmospheric driving effect on the SST anomalies. The SST anomalies preceding the NAO (Fig. A1b) exhibit a similar spatial pattern to those following the NAO (Fig. A1a) but with much weaker amplitudes, suggesting an evidently weaker impact of this SST pattern onto the atmospheric circulation. To further

quantify the relationship between the NAT SST anomaly pattern and NAO, Fig. A1c further shows the lagged correlation between the NAT index and NAO index during winter. The largest correlation between the NAO index and NAT SST index appears when the NAO leads by 3–10 days, implying the strong driving effect of NAO on the underlying NAT SST anomaly pattern in winter. In contrast, no significant positive correlations are observed when the SST index leads NAO, showing little feedback of SST anomalies on the NAO. These results illustrate that the winter air–sea interaction is dominated by stronger atmospheric driving effect, which supports the results of Deser and Timlin (1997) and Ciasto and Thompson (2004).

REFERENCES

Barnes, E., and D. Hartmann, 2010: Dynamical feedbacks and the persistence of the NAO. *J. Atmos. Sci.*, **67**, 851–865, https://doi.org/10.1175/2009JAS3193.1.

Benedict, J. J., S. Lee, and S. B. Feldstein, 2004: Synoptic view of the North Atlantic Oscillation. *J. Atmos. Sci.*, **61**, 121–144, https://doi.org/10.1175/1520-0469(2004)061<0121:SVOTNA>2.0.CO;2.

Brayshaw, D. J., B. Hoskins, and M. Blackburn, 2008: The storm-track response to idealized SST perturbations in an aqua-planet GCM. *J. Atmos. Sci.*, **65**, 2842–2860, https://doi.org/10.1175/2008JAS2657.1.

Cassou, C., 2008: Intraseasonal interaction between the Madden–Julian oscillation and the North Atlantic oscillation. *Nature*, **455**, 523, https://doi.org/10.1038/nature07286.

Cayan, D. R., 1992: Latent and sensible heat flux anomalies over the northern oceans: Driving the sea surface temperature. *J. Phys. Oceanogr.*, **22**, 859–881, https://doi.org/10.1175/1520-0485(1992)022<0859:LASHFA>2.0.CO;2.

Chen, G., J. Lu, D. A. Burrows, and L. R. Leung, 2015: Local finite-amplitude wave activity as an objective diagnostic of midlatitude extreme weather. *Geophys. Res. Lett.*, **42**, 10 952–10 960, https://doi.org/10.1002/2015GL066959.

Cheng, X., and J. M. Wallace, 1993: Cluster analysis of the Northern Hemisphere wintertime 500-hPa height field: Spatial patterns. *J. Atmos. Sci.*, **50**, 2674–2696, https://doi.org/10.1175/1520-0469(1993)050<2674:CAOTNH>2.0.CO;2.

Ciasto, L. M., and D. W. J. Thompson, 2004: North Atlantic atmosphere–ocean interaction on intraseasonal time scales. *J. Climate*, **17**, 1617–1621, https://doi.org/10.1175/1520-0442(2004)017<1617:NAAIOI>2.0.CO;2.

Czaja, A., and C. Frankignoul, 2002: Observed Impact of Atlantic SST anomalies on the North Atlantic Oscillation. *J. Climate*, **15**, 606–623, https://doi.org/10.1175/1520-0442(2002)015<0606:OIOASA>2.0.CO;2.

De Boyer Montegut, C., G. Madec, A. S. Fischer, A. Lazar, and D. Iudicone, 2004: Mixed layer depth over the global ocean: An examination of profile data and a profile-based climatology. *J. Geophys. Res.*, **109**, C12003, https://doi.org/10.1029/2004JC002378.

Dee, D., and Coauthors, 2011: The ERA-Interim reanalysis: Configuration and performance of the data assimilation system. *Quart. J. Roy. Meteor. Soc.*, **137**, 553–597, https://doi.org/10.1002/qj.828.

Deser, C., and M. S. Timlin, 1997: Atmosphere–ocean interaction on weekly timescales in the North Atlantic and Pacific. *J. Climate*, **10**, 393–408, https://doi.org/10.1175/1520-0442(1997)010<0393:AOIOWT>2.0.CO;2.

——, G. Magnusdottir, R. Saravanan, and A. Phillips, 2004: The effects of North Atlantic SST and sea ice anomalies on the winter circulation in CCM3. Part II: Direct and indirect components of the response. *J. Climate*, **17**, 877–889, https://doi.org/10.1175/1520-0442(2004)017<0877:TEONAS>2.0.CO;2.

——, R. A. Tomas, and S. Peng, 2007: The transient atmospheric circulation response to North Atlantic SST and sea ice anomalies. *J. Climate*, **20**, 4751–4767, https://doi.org/10.1175/JCLI4278.1.

——, M. A. Alexander, S.-P. Xie, and A. S. Phillips, 2010: Sea surface temperature variability: Patterns and mechanisms. *Annu. Rev. Mar. Sci.*, **2**, 115–143, https://doi.org/10.1146/annurev-marine-120408-151453.

Feldstein, S. B., 2000: The timescale, power spectra, and climate noise properties of teleconnection patterns. *J. Climate*, **13**, 4430–4440, https://doi.org/10.1175/1520-0442(2000)013<4430:TTPSAC>2.0.CO;2.

——, 2003: The dynamics of NAO teleconnection pattern growth and decay. *Quart. J. Roy. Meteor. Soc.*, **129**, 901–924, https://doi.org/10.1256/qj.02.76.

——, and S. Lee, 1998: Is the atmospheric zonal index driven by an eddy feedback? *J. Atmos. Sci.*, **55**, 3077–3086, https://doi.org/10.1175/1520-0469(1998)055<3077:ITAZID>2.0.CO;2.

Ferreira, D., and C. Frankignoul, 2005: The transient atmospheric response to midlatitude SST anomalies. *J. Climate*, **18**, 1049–1067, https://doi.org/10.1175/JCLI-3313.1.

Frankignoul, C., 1985: Sea surface temperature anomalies, planetary waves, and air–sea feedback in the middle latitudes. *Rev. Geophys.*, **23**, 357–390, https://doi.org/10.1029/RG023i004p00357.

——, and K. Hasselmann, 1977: Stochastic climate models. Part II: Application to sea-surface temperature anomalies and thermocline variability. *Tellus*, **29**, 289–305, https://doi.org/10.3402/tellusa.v29i4.11362.

Hamming, R. W., 1989: *Digital Filters*. Dover, 284 pp.

Hoskins, B. J., and D. J. Karoly, 1981: The steady linear response of a spherical atmosphere to thermal and orographic forcing. *J. Atmos. Sci.*, **38**, 1179–1196, https://doi.org/10.1175/1520-0469(1981)038<1179:TSLROA>2.0.CO;2.

——, and P. J. Valdes, 1990: On the existence of storm-tracks. *J. Atmos. Sci.*, **47**, 1854–1864, https://doi.org/10.1175/1520-0469(1990)047<1854:OTEOST>2.0.CO;2.

——, I. N. James, and G. H. White, 1983: The shape, propagation and mean-flow interaction of large-scale weather systems. *J. Atmos. Sci.*, **40**, 1595–1612, https://doi.org/10.1175/1520-0469(1983)040<1595:TSPAMF>2.0.CO;2.

Huang, C. S. Y., and N. Nakamura, 2016: Local finite-amplitude wave activity as a diagnostic of anomalous weather events. *J. Atmos. Sci.*, **73**, 211–229, https://doi.org/10.1175/JAS-D-15-0194.1.

Hurrell, J. W., 1995: Decadal trends in the North Atlantic Oscillation: Regional temperatures and precipitation. *Science*, **269**, 676–679, https://doi.org/10.1126/science.269.5224.676.

——, Y. Kushnir, G. Ottersen, and M. Visbeck, 2013: An overview of the North Atlantic Oscillation. *The North Atlantic Oscillation: Climatic Significance and Environmental Impact, Geophys. Monogr.*, Vol. 134, Amer. Geophys. Union, 1–36, https://doi.org/10.1029/134GM01.

Kimoto, M., and M. Ghil, 1993: Multiple flow regimes in the Northern Hemisphere winter. Part I: Methodology and hemispheric regimes. *J. Atmos. Sci.*, **50**, 2625–2644, https://doi.org/10.1175/1520-0469(1993)050<2625:MFRITN>2.0.CO;2.

Kushnir, Y., W. A. Robinson, I. Blade, N. M. J. Hall, S. Peng, and R. Sutton, 2002: Atmospheric GCM response to extratropical

SST anomalies: Synthesis and evaluation. *J. Climate*, **15**, 2233–2256, https://doi.org/10.1175/1520-0442(2002)015<2233:AGRTES>2.0.CO;2.

Lau, N.-C., 1997: Interactions between global SST anomalies and the midlatitude atmospheric circulation. *Bull. Amer. Meteor. Soc.*, **78**, 21–34, https://doi.org/10.1175/1520-0477(1997)078<0021:IBGSAA>2.0.CO;2.

Magnusdottir, G., C. Deser, and R. Saravanan, 2004: The effects of North Atlantic SST and sea ice anomalies on the winter circulation in CCM3. Part I: Main features and storm track characteristics of the response. *J. Climate*, **17**, 857–876, https://doi.org/10.1175/1520-0442(2004)017<0857:TEONAS>2.0.CO;2.

Martineau, P., G. Chen, and D. A. Burrows, 2017: Wave events: Climatology, trends, and relationship to Northern Hemisphere winter blocking and weather extremes. *J. Climate*, **30**, 5675–5697, https://doi.org/10.1175/JCLI-D-16-0692.1.

Minobe, S., A. Kuwano-Yoshida, N. Komori, S.-P. Xie, and R. J. Small, 2008: Influence of the Gulf Stream on the troposphere. *Nature*, **452**, 206–209, https://doi.org/10.1038/nature06690.

——, M. Miyashita, A. Kuwano-Yoshida, H. Tokinaga, and S.-P. Xie, 2010: Atmospheric response to the Gulf Stream: Seasonal variations. *J. Climate*, **23**, 3699–3719, https://doi.org/10.1175/2010JCLI3359.1.

Nakamura, H., T. Sampe, A. Goto, W. Ohfuchi, and S.-P. Xie, 2008: On the importance of midlatitude oceanic frontal zones for the mean state and dominant variability in the tropospheric circulation. *Geophys. Res. Lett.*, **35**, L15709, https://doi.org/10.1029/2008GL034010.

Nakamura, N., and D. Zhu, 2010: Finite-amplitude wave activity and diffusive flux of potential vorticity in eddy–mean flow interaction. *J. Atmos. Sci.*, **67**, 2701–2716, https://doi.org/10.1175/2010JAS3432.1.

——, and C. S. Y. Huang, 2018: Atmospheric blocking as a traffic jam in the jet stream. *Science*, **361**, 42–47, https://doi.org/10.1126/science.aat0721.

Nie, Y., Y. Zhang, G. Chen, and X.-Q. Yang, 2016: delineating the barotropic and baroclinic mechanisms in the midlatitude eddy-driven jet response to lower-tropospheric thermal forcing. *J. Atmos. Sci.*, **73**, 429–448, https://doi.org/10.1175/JAS-D-15-0090.1.

North, G., F. Moeng, T. Bell, and R. Cahalan, 1982: The latitude dependence of the variance of zonally averaged quantities. *Mon. Wea. Rev.*, **110**, 319–326, https://doi.org/10.1175/1520-0493(1982)110<0319:TLDOTV>2.0.CO;2.

O'Reilly, C. H., S. Minobe, A. Kuwano-Yoshida, and T. Woollings, 2017: The Gulf Stream influence on wintertime North Atlantic jet variability. *Quart. J. Roy. Meteor. Soc.*, **143**, 173–183, https://doi.org/10.1002/qj.2907.

Peixoto, J. P., and A. H. Oort, 1992: *Physics of Climate*. American Institute of Physics, 520 pp.

Peng, S., and J. S. Whitaker, 1999: Mechanisms determining the atmospheric response to midlatitude SST anomalies. *J. Climate*, **12**, 1393–1408, https://doi.org/10.1175/1520-0442(1999)012<1393:MDTART>2.0.CO;2.

——, W. A. Robinson, and M. P. Hoerling, 1997: The modeled atmospheric response to midlatitude SST anomalies and its dependence on background circulation states. *J. Climate*, **10**, 971–987, https://doi.org/10.1175/1520-0442(1997)010<0971:TMARTM>2.0.CO;2.

Ren, H.-L., F.-F. Jin, J.-S. Kug, J.-X. Zhao, and J. Park, 2009: A kinematic mechanism for positive feedback between synoptic eddies and NAO. *Geophys. Res. Lett.*, **36**, L11709, https://doi.org/10.1029/2009GL037294.

——, ——, ——, and L. Gao, 2011: Transformed eddy-PV flux and positive synoptic eddy feedback onto low-frequency flow. *Climate Dyn.*, **36**, 2357–2370, https://doi.org/10.1007/s00382-010-0913-0.

Reynolds, R. W., N. A. Rayner, T. M. Smith, D. C. Stokes, and W. Wang, 2002: An improved in situ and satellite SST analysis for climate. *J. Climate*, **15**, 1609–1625, https://doi.org/10.1175/1520-0442(2002)015<1609:AIISAS>2.0.CO;2.

Ring, M., and R. Plumb, 2007: Forced annular mode patterns in a simple atmospheric general circulation model. *J. Atmos. Sci.*, **64**, 3611–3626, https://doi.org/10.1175/JAS4031.1.

——, and ——, 2008: The response of a simplified GCM to axisymmetric forcings: Applicability of the fluctuation-dissipation theorem. *J. Atmos. Sci.*, **65**, 3880–3898, https://doi.org/10.1175/2008JAS2773.1.

Rodwell, M. J., D. P. Rowell, and C. K. Folland, 1999: Oceanic forcing of the wintertime North Atlantic Oscillation and European climate. *Nature*, **398**, 320–323, https://doi.org/10.1038/18648.

Sampe, T., H. Nakamura, A. Goto, and W. Ohfuchi, 2010: Significance of a midlatitude SST frontal zone in the formation of a storm track and an eddy-driven westerly jet. *J. Climate*, **23**, 1793–1814, https://doi.org/10.1175/2009JCLI3163.1.

——, ——, and ——, 2013: Potential influence of a midlatitude oceanic frontal zone on the annular variability in the extratropical atmosphere as revealed by aqua-planet experiments. *J. Meteor. Soc. Japan*, **91A**, 243–267, https://doi.org/10.2151/jmsj.2013-A09.

Scaife, A. A., and Coauthors, 2017: Tropical rainfall, Rossby waves and regional winter climate predictions. *Quart. J. Roy. Meteor. Soc.*, **143**, 1–11, https://doi.org/10.1002/qj.2910.

Seo, H., Y.-O. Kwon, T. M. Joyce, and C. C. Ummenhofer, 2017: On the predominant nonlinear response of the extratropical atmosphere to meridional shifts of the Gulf Stream. *J. Climate*, **30**, 9679–9702, https://doi.org/10.1175/JCLI-D-16-0707.1.

Strong, C., and G. Magnusdottir, 2008: Tropospheric Rossby wave breaking and the NAO/NAM. *J. Atmos. Sci.*, **65**, 2861–2876, https://doi.org/10.1175/2008JAS2632.1.

Vallis, G., and E. Gerber, 2008: Local and hemispheric dynamics of the North Atlantic Oscillation, annular patterns and the zonal index. *Dyn. Atmos. Oceans*, **44**, 184–212, https://doi.org/10.1016/j.dynatmoce.2007.04.003.

Vautard, R., 1990: Multiple weather regimes over the North Atlantic: Analysis of precursors and successors. *Mon. Wea. Rev.*, **118**, 2056–2081, https://doi.org/10.1175/1520-0493(1990)118<2056:MWROTN>2.0.CO;2.

Wills, S. M., D. W. J. Thompson, and L. M. Ciasto, 2016: On the observed relationships between variability in Gulf Stream sea surface temperatures and the atmospheric circulation over the North Atlantic. *J. Climate*, **29**, 3719–3730, https://doi.org/10.1175/JCLI-D-15-0820.1.

Woollings, T., B. Hoskins, M. Blackburn, and P. Berrisford, 2008: A new Rossby wave-breaking interpretation of the North Atlantic Oscillation. *J. Atmos. Sci.*, **65**, 609–626, https://doi.org/10.1175/2007JAS2347.1.

——, A. Hannachi, and B. Hoskins, 2010: Variability of the North Atlantic eddy-driven jet stream. *Quart. J. Roy. Meteor. Soc.*, **136**, 856–868, https://doi.org/10.1002/qj.625.

Xiao, B., Y. Zhang, X.-Q. Yang, and Y. Nie, 2016: On the role of extratropical air–sea interaction in the persistence of the southern annular mode. *Geophys. Res. Lett.*, **43**, 8806–8814, https://doi.org/10.1002/2016GL070255.

Yu, L., and R. A. Weller, 2007: Objectively analyzed air–sea heat fluxes for the global ice-free oceans (1981–2005). *Bull. Amer. Meteor. Soc.*, **88**, 527–540, https://doi.org/10.1175/BAMS-88-4-527.

Climate Dynamics (2019) 52:3869–3890
https://doi.org/10.1007/s00382-018-4366-1

Seasonal predictability of winter ENSO types in operational dynamical model predictions

Hong-Li Ren[1,2] · Adam A. Scaife[3,4] · Nick Dunstone[3] · Ben Tian[1] · Ying Liu[1] · Sarah Ineson[3] · June-Yi Lee[5] · Doug Smith[3] · Changzheng Liu[1] · Vikki Thompson[3] · Michael Vellinga[3] · Craig MacLachlan[3]

Received: 2 February 2018 / Accepted: 11 July 2018 / Published online: 25 July 2018
© The Author(s) 2018

Abstract
The El Niño-Southern Oscillation (ENSO) events of recent decades have been divided into the two different types based on their spatial patterns, the Eastern Pacific (EP) type and Central Pacific (CP) type. Their most significant difference is the distinguished zonal center locations of sea surface temperature (SST) anomalies in the equatorial Pacific. In this study, based on six operational climate models, we evaluate predictability of the two types of ENSO events in winter to examine whether dynamical predictions can distinguish between the two spatial patterns at lead time of 1 month and tell us more than simply whether an event is on the way. We show that winter EP and CP El Niño and La Niña events can only be distinguished in a minority of these models at 1-month lead, and the EP type tends to has a more realistic zonal positions of SST pattern centers than the CP type. Compared to the SST patterns, the differences between the two types are less apparent in precipitation especially for the two La Niña types in the models. Examinations of the extratropical teleconnections to the two ENSO types show that some of the models can reproduce the differences between EP and CP teleconnections. Evaluations of model predictions show that the EP El Niño event has the same level hit rate with the CP El Niño and the CP La Niña event has much higher hit rate than the EP La Niña. While the multi-model ensemble increases Niño index prediction skill, it does not help to improve forecast skill of center longitude index of the SST patterns and distinguish the two types of ENSO events. Although ENSO skill is very high at this lead time, the rapid loss of the initialized information on the different ENSO types in most of the models severely limits the predictability of the two types of winter ENSO events and more research is needed to improve the performance of climate models in forecasting the two ENSO types.

Keywords Two types of winter ENSO events · Predictability · Dynamical model · Evaluation

1 Introduction

The El Niño Southern Oscillation (ENSO) phenomenon has been well known to play a key role in influencing global climate (e.g., Rasmusson and Carpenter 1982; Mason and Goddard 2001; Davey et al. 2014; Zhang et al. 1996). Now, the ENSO events in recent decades are often divided into two different types in terms of their spatial patterns. One is the canonical type of ENSO which has its sea surface temperature (SST) anomaly center over the equatorial Eastern Pacific (EP). The other one is a non-canonical type of ENSO, in additional to the canonical type, which has its major SST anomalies centered over the central Pacific (CP) regions. This non-canonical type is becoming more frequent since the late 1970s (Larkin and Harrison 2005a, b; Ashok et al. 2007; Kao and Yu 2009; Kug et al. 2009; Ren et al. 2013) and may become more frequent under a warming

✉ Hong-Li Ren
renhl@cma.gov.cn

1 Laboratory for Climate Studies and CMA-NJU Joint Laboratory for Climate Prediction Studies, National Climate Center, China Meteorological Administration, 46 Zhongguancun, Haidian District, Beijing 100081, China

2 Department of Atmospheric Science, School of Environmental Studies, China University of Geoscience, Wuhan 430074, China

3 Met Office Hadley Centre, Exeter, UK

4 College of Engineering, Mathematics and Physical Sciences, Exeter University, Exeter, UK

5 Research Center for Climate Sciences, Pusan National University, Busan, South Korea

climate (Yeh et al. 2009). For this non-canonical type, there have been various nomenclatures and definitions in the literature, including the dateline El Niño (Larkin and Harrison 2005a, b), El Niño Modoki (Ashok et al. 2007), central Pacific ENSO (Kao and Yu 2009; Yeh et al. 2009; Yu et al. 2011), and WP El Niño/ENSO (Kug et al. 2009; Ren and Jin 2011, 2013). In this study, we will adopt the terminology of the EP and CP ENSO for describing the two types.

Many previous studies revealed that the CP type of El Niño has significantly different global climate impacts from the EP El Niño through tropical-extratropical teleconnections (e.g., Weng et al. 2007, 2009; Kim et al. 2009; Feng et al. 2010; Feng and Li 2011; Zhang et al. 2011, 2012; Yuan and Yang 2012) as these two types of El Niño are accompanied with distinct tropical atmospheric circulations. La Niña events, the negative phase of ENSO events, are usually less distinguishable in terms of the two types (Kug and Ham 2011). However, they were also divided into the two types in some studies (Ashok and Yamagata 2009; Yuan and Yan 2013), particularly if the decadal background is eliminated since 1980 (Ren et al. 2013). Indeed, the value of distinguishing the two types for either El Niño or La Niña events is clearest from their distinct global and regional climate impacts rather than their different SST patterns (Zhang et al. 2015). From this point of view, both types of El Niño and La Niña events will be focused on in this study.

Due to the significant impacts of ENSO on global climate, in recent 30 years, many international efforts were made towards ENSO prediction, and progress were made in improving skill levels of ENSO prediction (Latif et al. 1998; Jin et al. 2008; Barnston et al. 2012). A great many approaches were developed to predict ENSO, including statistical models, simplified air-sea coupled models, and fully coupled global climate models (GCMs) (e.g., Cane et al. 1986; Zebiak and Cane 1987; Chen et al. 1995, 2004; Kang and Kug 2000; Kirtman 2003; Luo et al. 2005, 2008; Zheng et al. 2006; Ham et al. 2009; Cheng et al. 2010; Izumo et al. 2010; Zhu et al. 2012, 2017; Ren et al. 2014; Liu and Ren 2017). Dynamical prediction based on fully coupled ocean–atmosphere GCMs has become a powerful tool for ENSO prediction as a result of large improvements in understanding ENSO, climate modeling, and ocean data assimilation. Here we test whether predicting the two ENSO types using the dynamical coupled GCMs is now possible given that they have already been shown to predict the canonical ENSO.

Previous studies have shown that most current coupled GCMs still have difficulty in reproducing the distinct SST anomaly patterns of two ENSO types due to model biases and other deficiencies (Yu and Kim 2010; Ham and Kug 2012). This presents a challenge to the dynamical prediction of the two ENSO types based on current GCMs. In comparison with the studies on prediction of the canonical ENSO, relatively little effort has been made to assess skill of the dynamical models in predicting the two types. In recent years, a few studies have used initialized hindcasts of some operational GCMs to do this. Hendon et al. (2009) and Lim et al. (2009) first attempted to predict differences between autumn modoki and canonical El Niños in the POAMA coupled seasonal forecast model of Australian Bureau of Meteorology (BoM) but the predictive lead time is limited to less than one season. Along this line, Jeong et al. (2012) found the lead time could be extended to 4 months for winter in the multi-model ensemble (MME) mean sense utilizing the hindcast data of the MME suite in the Asia–Pacific Economic Cooperation Climate Center (APCC), and Jeong et al. (2015) showed the predictability was subject to an apparent inter-decadal change. Yang and Jiang (2014) further showed the seasonal dependence of prediction skill of the two ENSO types for related SST anomalies and climate impacts in the Climate Forecast System version 2 (CFSv2) of National Centers for Environmental Prediction (NCEP). Zhu et al. (2015) examined prediction skill of the two types in the ECMWF prediction systems and found that the EP ENSO has higher skill than the CP. It has also been suggested that CP events may be more difficult to predict due to their smaller amplitude (Imada et al. 2015) and hence smaller signal to noise ratio. These studies overall indicate better performance for the EP ENSO than CP ENSO predictions though they are to some degree dependent on the principal components of tropical Pacific SST anomalies and the associated indices based on empirical orthogonal functions (EOFs) analysis, which are also unable to discriminate the asymmetry between El Niño and La Niña.

In this study, we will further examine the model predictability of these two types of ENSO by directly focusing on the El Niño and La Niña events that are well defined in the literature, based on initialized hindcasts from a group of current operational seasonal forecast systems. We aim to carry out a comprehensive event-based ENSO prediction evaluation and reveal whether dynamical predictions can distinguish the spatial differences between the two types of events and their teleconnections at seasonal lead times. This paper is organized as follows. Data and method are described in Sect. 2. Comparisons of prediction skill and patterns of SST anomalies, precipitation responses, and teleconnections are given in Sects. 3, 4, and 5, respectively. We show event-based skill of predictions of different ENSO types in Sect. 6 and attempts using the MME method in Sect. 7. Summary and discussion are given in Sect. 8.

2 Data and method

2.1 Hindcast datasets from six operational seasonal forecast systems

In this study, we use hindcast data of wintertime (December-January-February, DJF) initialized in November, collected from six operational prediction systems referred to as CFSv2, BCCv2, P24A, ECMWF4, G5GC2, and DPS3, respectively, and defined below. All of the models are fully coupled climate models that provide real-time operational predictions accompanying with hindcast datasets to evaluate and then calibrate these models.

CFSv2 is the Climate Forecast System version 2 from the NCEP, which is the upgraded version of CFSv1 (Saha et al. 2006) and has been used in operation since 2011. In CFSv2, there are substantial changes made from CFSv1, showing some significant advances in operational predictions (Saha et al. 2014). CFSv2 hindcast is a set of 9-month reforecasts initialized from every fifth day with four times of that day as totally 24 ensemble members, spanning the period of 1982−2010. To elongate the dataset, the real-time forecasts of 2011 are added. Initial conditions for the atmospheric and oceanic models are from the NCEP CFS Reanalysis (Saha et al. 2010).

BCCv2 is the second generation of climate forecasting system in Beijing Climate Center of China Meteorological Administration (BCC/CMA), a operational system from 2016. BCCv2 is based on the BCC Climate System Model version 1.1 m (BCC_CSM1.1 m) (Wu et al. 2013). Its atmospheric component is the BCC AGCM2.2 with a T106 horizontal resolution and 26 vertical levels (Wu et al. 2010), and its land component is the BCC Atmosphere and Vegetation Interaction Model version 1.0. The ocean component of BCCv2 is the Geophysical Fluid Dynamics Laboratory Modular Ocean Model version 4 and the sea ice component is the Sea Ice Simulator. BCCv2 hindcast is initiated from the 1st day of each month during 1991−2014 with a 13-mon integration. The atmospheric initial values are initialized from the four-time daily NCEP Reanalysis I and the oceanic initial values from variables of the NCEP Global Oceanic Data Assimilation System, using a nudging scheme of 3-D atmospheric fields and ocean temperature. Each hindcast includes 24 ensemble members by combining different atmospheric and oceanic initial conditions.

P24A is the operational seasonal prediction model in BoM (P24A) including BAMv3.0d (T47L17) and ACOM2 (0.5°–1.5°lat × 2°lon L25) (Lim et al. 2012), participating in the Asia–Pacific Economic Cooperation Climate Center/Climate Prediction and its Application to Society (APCC/CliPAS) (Wang et al. 2009; Lee et al. 2010). POAMA stands for Predictive Ocean Atmosphere Model for Australia. POAMA is the Bureau of Meteorology's dynamical (physics based) climate model used for multi-week to seasonal through to inter-annual climate outlooks. It is a state of the art long-range forecast system using ocean, atmosphere, ice, and land data observations to initiate outlooks up to 9 months ahead. The P24A hindcast we use here is initialized on the 1st day of every month from 1981 to 2010, 30 years in total.

ECMWF4 is the European Centre for Medium-Range Weather Forecasts (ECMWF) System 4. ECMWF4 utilizes the ECMWF atmosphere model, with a higher resolution and a higher atmosphere top, and more ensemble members than the previous system (Molteni et al. 2011). The ECMWF4 hindcast is a set of 7-month seasonal reforecasts including 15 member ensembles, initialized on the 1st day of every month during 1981−2010, 30 years in total. More details of this system can be referred to http://www.ecmwf.int/products/forecasts/seasonal/documentation/system4.

G5GC2 is the Met Office global seasonal forecast system 5 (GloSea5) (MacLachlan et al. 2015). Its hindcasts used here were run in research mode over 1992–2011, using a 24 member ensemble. DPS3 is the Met Office decadal climate prediction system 3 (DePreSys3) (Dunstone et al. 2016). The DPS3 hindcasts used in this paper cover the period 1981–2014. DPS3 and G5GC2 use the same climate model but differ in the way in which they are initialized. G5GC2 is initialized directly from atmospheric fields of ECMWF ERA-Interim reanalysis data and its forced hindcast ocean reanalysis (GloSea5 Ocean and Sea Ice Analysis) that are coupled together on the first forecast time step (see MacLachlan et al. 2015 for details). Whereas DPS3 is via weakly coupled data assimilation, where analyzed monthly ocean temperature, salinity, and sea-ice concentration and reanalysis winds and temperatures are continuously nudged into the coupled model (see Smith et al. 2007; Knight et al. 2014, and Dunstone et al. 2016 for details). Forecasts are then branched off this assimilation run. In both G5GC2 and DPS3 the underpinning climate model is the Met Office global coupled model 2.0 (GC2). In this configuration the vertical resolution is 85 levels in the atmosphere (with a top at 85 km) and 75 levels in the ocean (with a 1 m top level). The ocean horizontal resolution is 0.25° on a tri-polar grid and in the atmosphere a horizontal resolution of N216 (60 km in mid-latitudes) is used. This model has been shown to have good representation of the modes of climate variability, including ENSO (Williams et al. 2015). Both G5GC2 and DPS3 use random seeds to drive a stochastic physics scheme in order to generate forecast ensemble members. We put the brief description of all the models into Table 1.

Anomalies of all hindcast variables are obtained by removing their own climate mean of the whole period of hindcast data used here. Winter means are used

Table 1 Description of the six models

System short names	Institutes (model names)	AGCM (resolution)	OGCM (resolution)	Ensemble number	Data periods
CFSv2	NCEP (NCEP CFSv2)	GFS (T126L64)	MOM4 (1/4° Eq. L40)	24	1982–2011
BCCv2	BCC (BCC_CSM1.1 m)	BCC_AGCM2.2 (T106L26)	MOM4 (1/3°–1°lat × 1°lon L40)	24	1991–2014
P24A	BoM (POAMA)	BAMv3.0d (T47L17)	ACOM2 (0.5°–1.5°lat × 2°lon L25)	10	1981–2010
ECMWF4	ECMWF (ECMWF System4)	IFS cycle 36r4 (T255L91)	NEMO (1/3°–1° L42)	15	1981–2010
G5GC2	Met Office (HadGEM3-GC2)	MetUM-GA3(N216L85)	NEMO-GO3 (0.25° L75)	24	1992–2011
DPS3	Met Office (HadGEM3-GC2)	MetUM-GA3(N216L85)	NEMO-GO3 (0.25° L75)	40	1981–2014

throughout the paper and constructed by averaging data for December–January–February (DJF).

2.2 Observational reanalyses

In this study, to verify the model hindcasts, we use the following observations: for SST we use HadISST (Rayner et al. 2003), for mean sea level pressure (MSLP) we use HadSLP2 (Allan and Ansell 2006), and for precipitation we use the Global Precipitation Climatology Project (GPCP) version 2.2 (Adler et al. 2003). Although the GPCP is limited to the satellite era (1979-onwards), it provides global coverage over the oceans which gauge-based datasets cannot provide. Observational anomalies in this paper are calculated from the climatology defined by the data during the period of 1981–2010.

Traditional Niño3.4, Niño3 and Niño4 indices of SST anomalies are used, which are defined as SST anomaly averages over the Niño3.4 region (5°S–5°N, 170°–120°W), Niño3 region (5°S–5°N, 150°–90°W), and Niño4 region (5°S–5°N, 160°E–150°W), respectively. To quantify the two types of ENSO, we choose the Niño Warm-Pool index (denoted as WPI) and Niño Cold-Tongue index (denoted as CTI) that were proposed by Ren and Jin (2011) for representing the CP and EP ENSO types, respectively, based on a nonlinear transformation of Niño3 and Niño4 indices; i.e., $\mathrm{WPI} = \mathrm{Niño4} - \alpha\mathrm{Niño3}$ and $\mathrm{CTI} = \mathrm{Niño3} - \alpha\mathrm{Niño4}$, where $\alpha = 0.4$ when $\mathrm{Niño3}^*\mathrm{Niño4} > 0$; otherwise, $\alpha = 0$.

2.3 Evaluation methods

In this study, we carry out an evaluation through the event-based method. That is, we focus on the patterns of the two ENSO types based on composites of historical events. To define the El Niño or La Niña events, we refer to the definition of Yeh et al. (2009), namely contrasting differences between Niño3 and Niño4 indices either exceeding 0.5 °C. We identify historical events which are mainly consistent with the literature (e.g., Kao and Yu 2009; Kim et al. 2009; Kug et al. 2009; McPhaden et al. 2011; Xiang et al. 2013) that has been well recognized. Note that the classification for La Niña events is still controversial. Here we directly refer to the previous study (Zhang et al. 2015). The winters for the different types of winter-mean ENSO indices are listed in Table 2.

Composite patterns for observation are calculated by averaging the anomalous fields that correspond to the different types of events. For the model hindcasts, composite patterns are calculated in terms of the observed events for the different types, where the predicted ENSO events can be identified using ensemble means of these models with the available data periods for the same years as in the observations. In this study, we remove the linear trend from all of the data before doing analyses.

3 Comparisons of patterns of SST anomalies

First of all, as a reference, Fig. 1 presents skill of ENSO prediction based on winter Niño indices in the models. It is clearly seen that Niño3.4 index has the highest skill score

Table 2 Events of two types of El Niño and La Niña from 1981/82 to 2014/15 winters

Types	Winters	Numbers
EP El Niño	1982/83, 1986/87, 1991/92, 1997/98, 2006/07	5
CP El Niño	1987/88, 1994/95, 2002/03, 2004/05, 2009/10, 2014/15	6
EP La Niña	1984/85, 1995/96, 1999/00, 2005/06, 2007/08	5
CP La Niña	1983/84, 1988/89, 1998/99, 2000/01, 2008/09, 2010/11, 2011/12	7

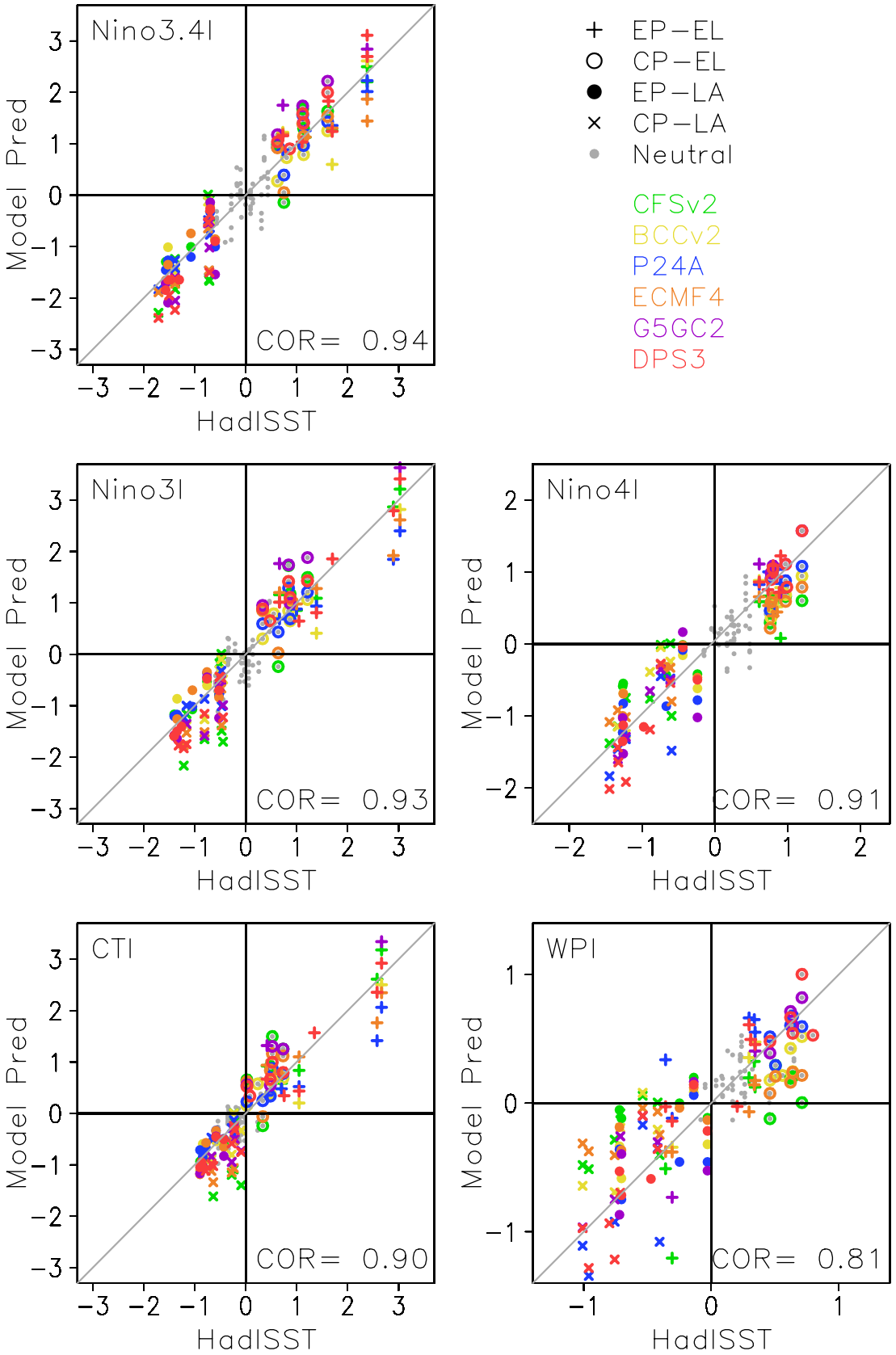

Fig. 1 Scatter maps of the HadISST (x-axis) and model predictions (y-axis) for DJF-mean Niño3.4 index, Niño3 index, Niño4 index, CTI, and WPI. Each symbol denotes one DJF mean. CORs are correlation coefficients for all of value pairs and colors are for different models

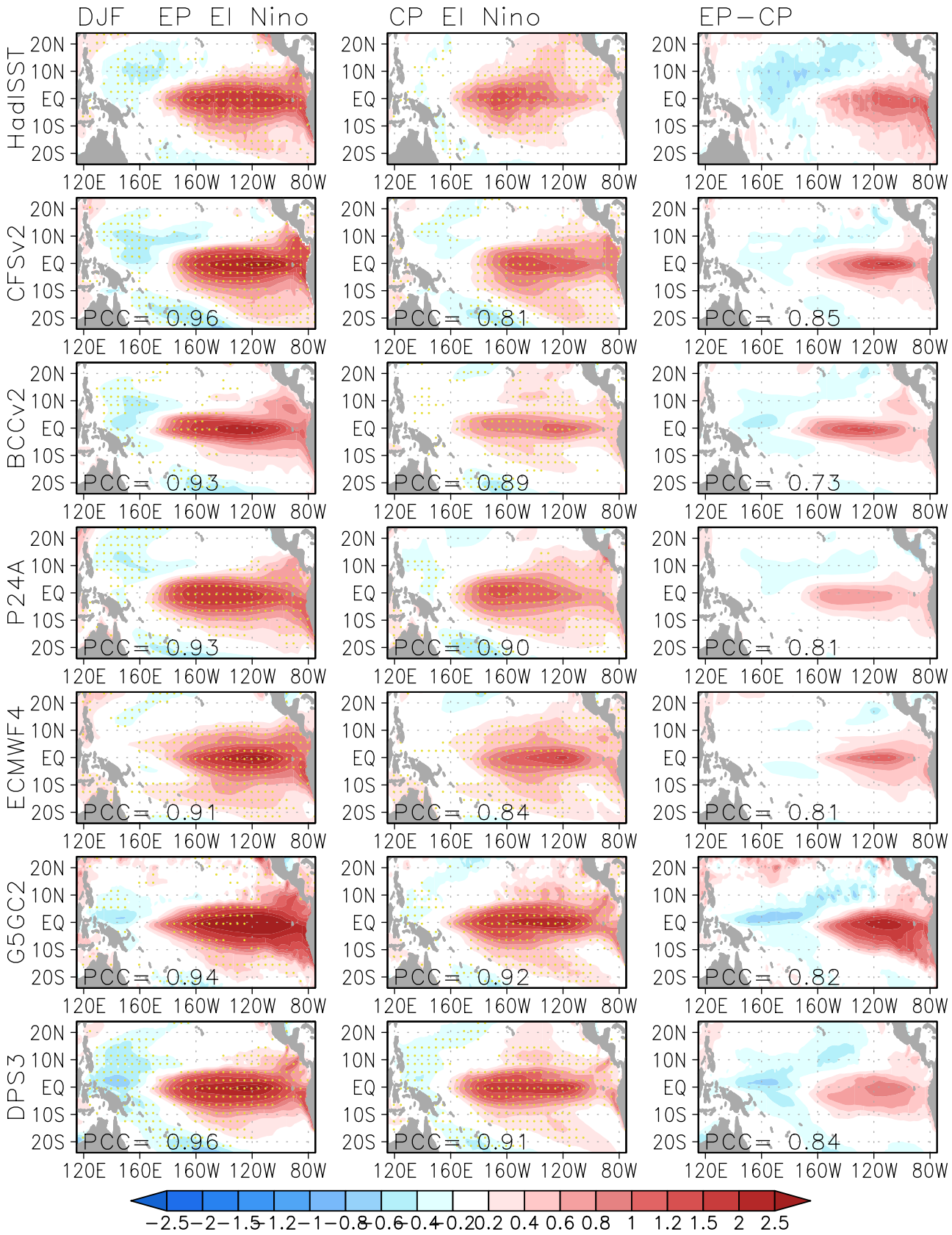
DJF EP El Nino
CP El Nino
EP−CP
HadISST
CFSv2
BCCv2
P24A
ECMWF4
G5GC2
DPS3
20N
10N
EQ
10S
20S
120E 160E 160W 120W 80W
PCC= 0.96
PCC= 0.81
PCC= 0.85
PCC= 0.93
PCC= 0.89
PCC= 0.73
PCC= 0.93
PCC= 0.90
PCC= 0.81
PCC= 0.91
PCC= 0.84
PCC= 0.81
PCC= 0.94
PCC= 0.92
PCC= 0.82
PCC= 0.96
PCC= 0.91
PCC= 0.84
−2.5 −2 −1.5 −1.2 −1 −0.8 −0.6 −0.4 −0.2 0.2 0.4 0.6 0.8 1 1.2 1.5 2 2.5

◂**Fig. 2** Composite patterns of SST anomalies (unit: ºC) for the EP-type (left panels) and CP-type (middle panels) El Niño events as well as their differences (right panels) based on the observation (top three panels) and model hindcasts (below panels). Black numbers in panels are pattern correlation coefficients (PCCs) between the model patterns and the corresponding observation pattern. Yellow dots denote the *t*-test significance at the 95% confidence level

with a correlation coefficient of 0.94 between observations and predictions at 1 month lead. All the model forecasts are highly consistent with the observed El Niño, Neutral, and La Niña phases, and a similar situation is found for the EP cases, with slightly reduced correlations of 0.93 and 0.90 for Niño3 index and CTI, respectively. As a comparison, the skill score in WPI for the CP type is relatively lower (correlation is 0.81) and the spread across models is clearly larger. Meanwhile, Niño4 index is also highly predictable (correlation is 0.91), which is sometimes used to represent the CP type. These results confirm previous studies in which the indices for representing the two types are usually well predicted, particularly within a few months lead. The composite spatial patterns of SST anomalies of the EP and CP El Niño events (Table 2) over the equatorial Pacific in observations and the six different models are shown in Fig. 2. A distinct difference between the EP and CP events is shown in the observations. The EP events are stronger, with the largest anomalies occurring between 160°W and the eastern boundary, and extending southwards along the Peruvian coastline. In contrast, the CP events show the centers of equatorial SST anomalies between 170 and 150°W. The EP-CP difference plot shows the EP events have greater warming in the south-east but are generally cooler north of the equator and in the west.

All of the models assessed show stronger EP than CP events, agreeing well with the observations, where the pattern correlation coefficients (PCCs) are generally above 0.9 and 0.80 for the EP and CP types, respectively, as shown in Fig. 2. However, some do not show as much separation between the two types as several of the model composites for the CP type show maximum SST anomalies to the east of the observed maximum. In the models the CP events also tend to show overestimated warming along the Peruvian coast although we note that the modeled EP events remain stronger in this region. The differences between EP and CP events in the western Pacific are also generally poorly represented in the models, with several showing underestimated relative cooling, presumably due to the well-known westward extension bias of ENSO anomalies (e.g., Ham and Kug 2015). Among the models, DPS3 best represents the observed differences of the two ENSO types, CFSv2 also performs well but shifts CP events too far east, and G5GC2 overstates the differences with greater anomalies during EP events although this may be due to relatively smaller sample size of its hindcast still including the large 1997/98 event.

Figure 3 shows the La Niña composite SST anomalies. In observations the difference between the two event types is less distinct than that for El Niño events. The CP events are slightly stronger in the central Pacific, and weaker in the eastern equatorial Pacific, also showing a greater cooling anomaly than EP events in the southeast tropical Pacific. The difference between the EP and CP events is also less distinct in the models, compared to the two El Niño types. As seen in Fig. 3, although the PCCs are still above 0.9 and 0.80 for the two types, those for the EP-CP differences are all below 0.70. Meanwhile, although a majority of the models correctly show stronger CP La Niña events, two of the models, BCCv2 and G5GC2, do not. Two models, CFSv2 and DPS3, show the cooling anomaly extending into the southeast tropical Pacific in CP events, as seen in observations. As with the El Niño composites, several of the models have maximum anomalies in the CP events eastward of the observed position.

Generally, the models predict the differences between EP and CP events in El Niño better than in La Niña. The observations show smaller anomaly differences between the EP and CP La Nina events than in El Niño conditions. DPS3 best simulates the observed differences between the EP and CP events, though all models capture some of the characteristics. Figure 4 collectively contrasts the central positions of the SST anomaly patterns shown in Figs. 2 and 3 for the EP and CP event composites by directly identifying the center longitude index (CLI) that is defined as the center longitude where the amplitude of equatorial-mean (5°S−5°N) SST anomaly reaches maximum. In observations the SST centers of the CP ENSO types are steadily located west of 160ºW and those of the EP types are east of 145ºW. The longitudinal separation of the two types of La Niña events is evidently less than that between the two types of El Niño events.

In Fig. 4, almost all of the models have relatively realistic longitudinal center positions for the EP type in both El Niño and La Niña conditions except that P24A shows a strong westward shift. However, for the CP type only DPS3 and P24A have positions close to those observed, with the other models showing a clear eastward displacement, where DPS3 does the best job. This conclusion would be much clearer in Fig. 5 when we extract the main longitudinal center positions of the two types. It is quite clearly seen in Fig. 5 that the canonical center longitudes of EP and CP El Niño events can only be distinguished by 2−3 models, and this is slightly less true for La Niña events where four out of six models are unable to distinguish the canonical center positions between the two types of La Niña events.

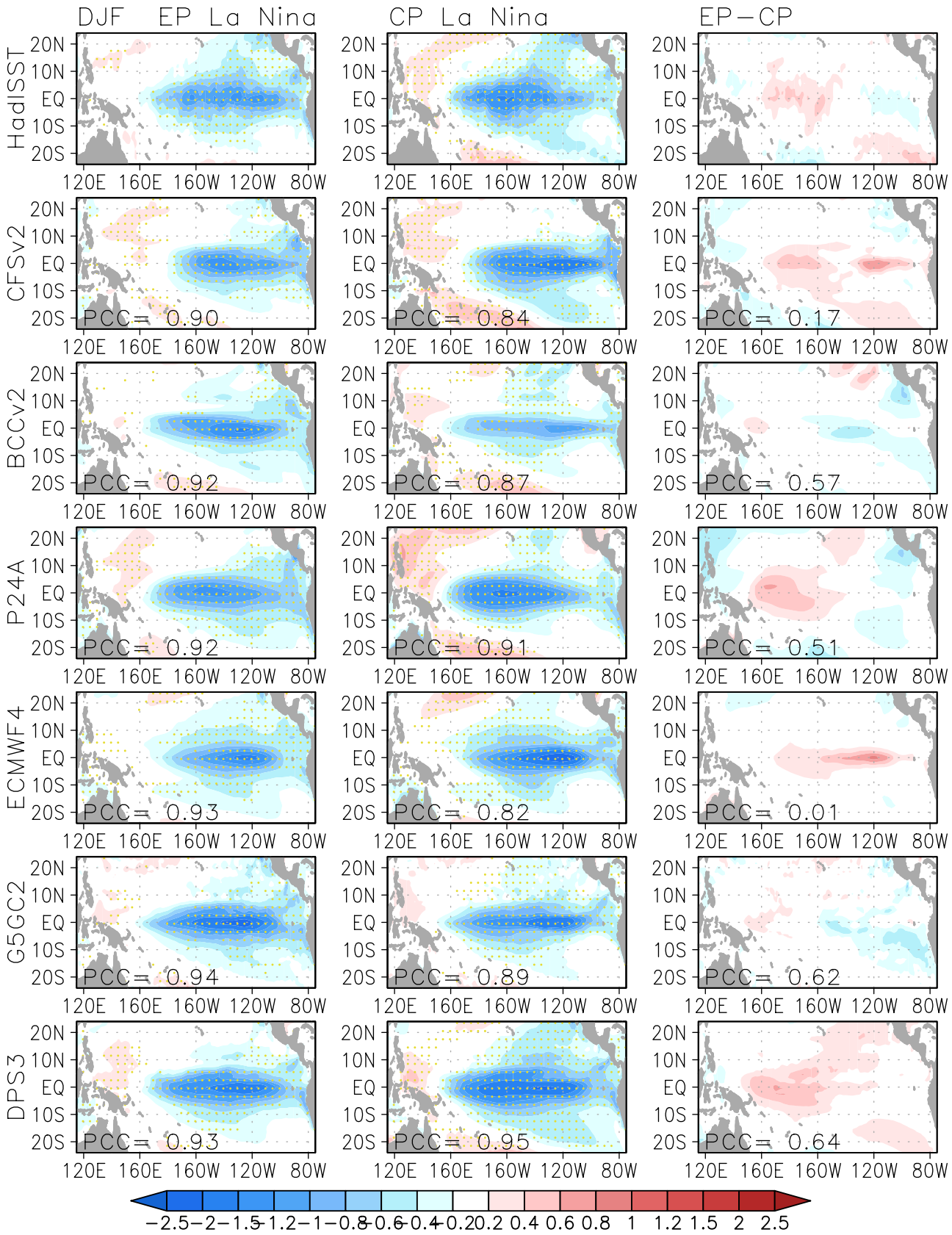

Fig. 3 The same to Fig. 2, but for the two types of La Niña events

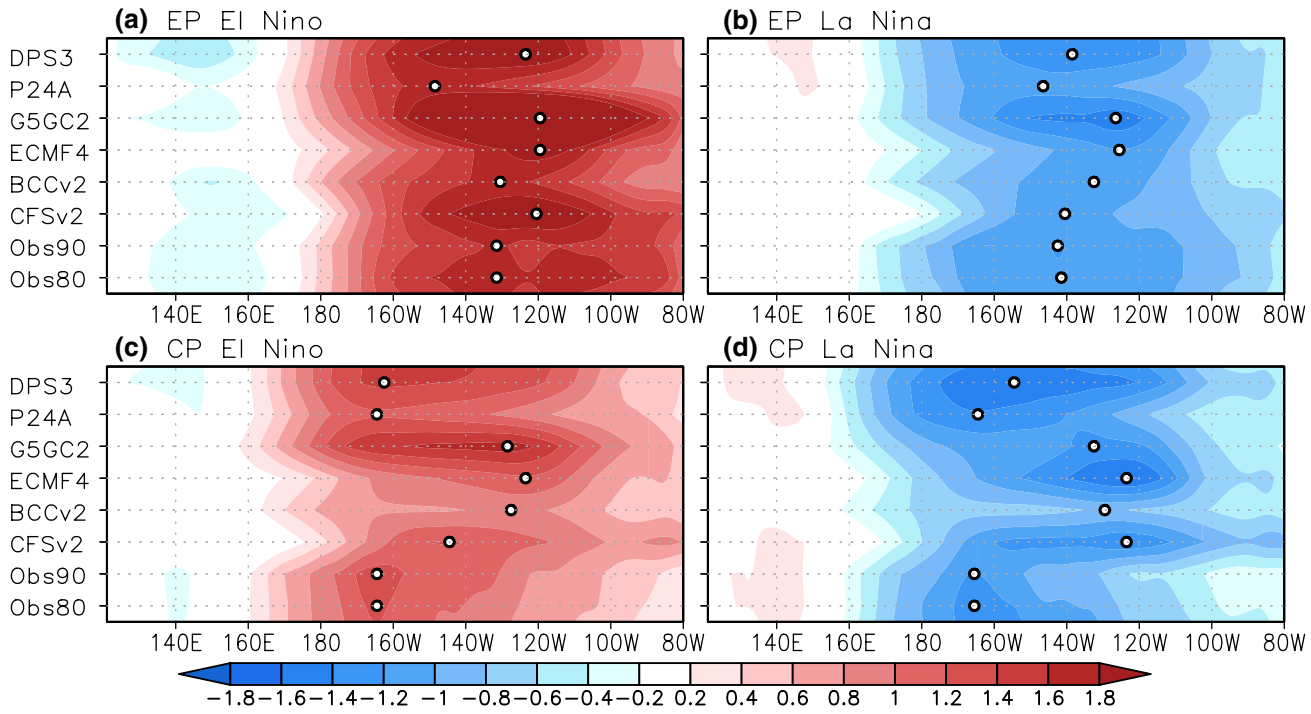

Fig. 4 Equatorial mean (5°S−5°N) of SST composite patterns of observation and predictions for different ENSO types (**a**–**d**), where Obs80 and Obs90 denote the HadISST results of 1980–2014 and 1990–2014 periods, respectively

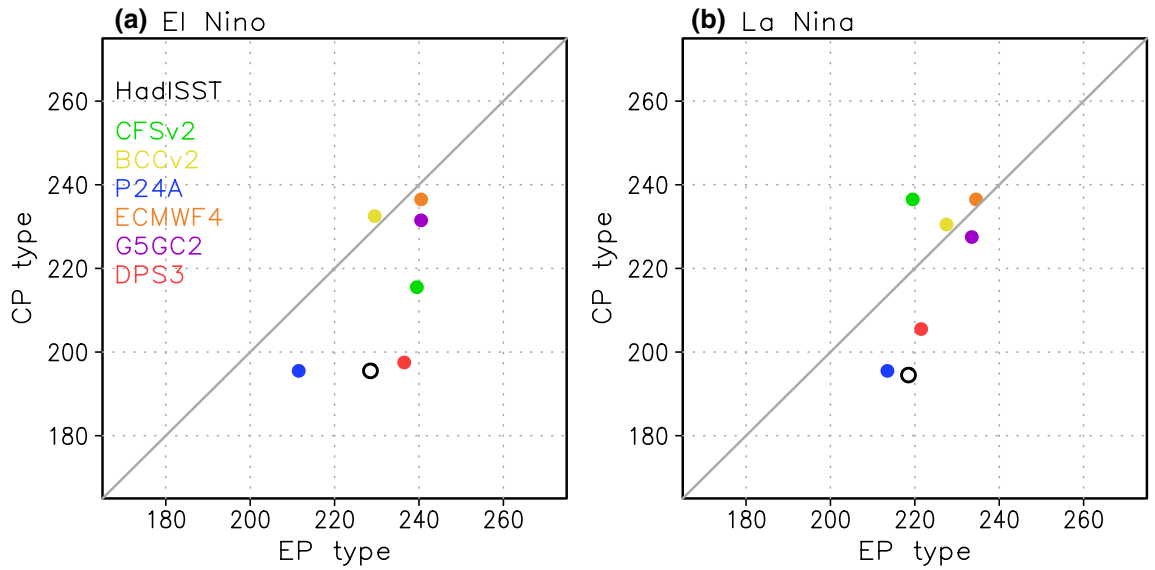

Fig. 5 Scatter maps between SST anomaly center longitudes (viz. LPIs shown in Fig. 4) of two types of El Niño (**a**) and La Niña (**b**). Colored dots denote the model results. Black circles are for the HadISST results during 1980–2014 period. Unit of the two axes is ºE

4 Patterns of precipitation responses

Figure 6 shows precipitation anomalies for the composites of EP and CP El Niño events for observations and model hindcasts. The observations show during EP events the precipitation is enhanced along the equatorial region from 160°E to 80°W, with the SPCZ displaced to the north and east of its climatological position and the ITCZ, which lies to the north of the equator, displaced strongly southward,

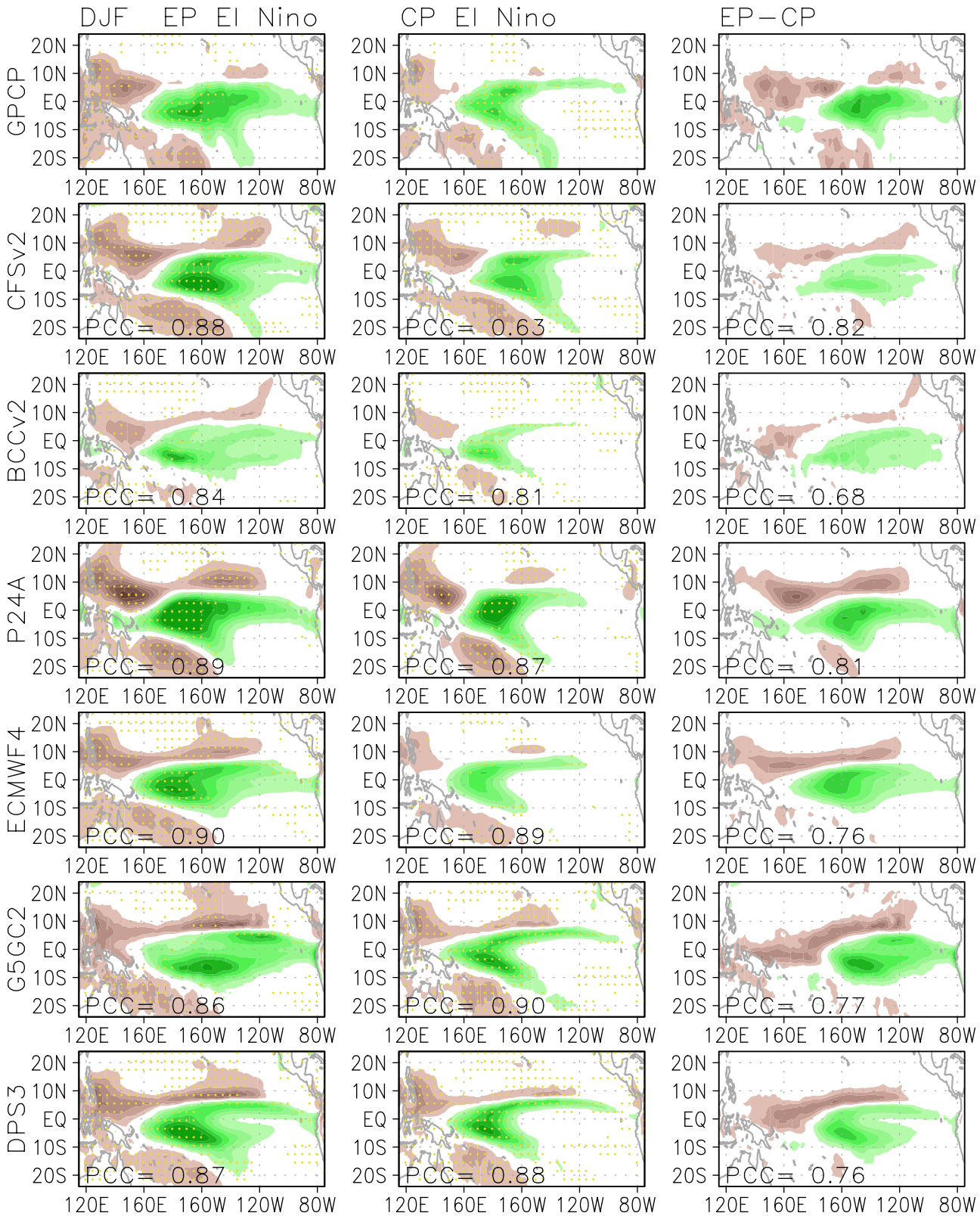
DJF EP El Nino
CP El Nino
EP−CP
GPCP
CFSv2
BCCv2
P24A
ECMWF4
G5GC2
DPS3
20N
10N
EQ
10S
20S
120E 160E 160W 120W 80W
PCC= 0.88
PCC= 0.63
PCC= 0.82
PCC= 0.84
PCC= 0.81
PCC= 0.68
PCC= 0.89
PCC= 0.87
PCC= 0.81
PCC= 0.90
PCC= 0.89
PCC= 0.76
PCC= 0.86
PCC= 0.90
PCC= 0.77
PCC= 0.87
PCC= 0.88
PCC= 0.76
−7 −6 −5 −4 −3 −2 −1 1 2 3 4 5 6 7

◂**Fig. 6** Composite patterns of precipitation anomalies (unit: mm/day) for the EP-type (left panels) and CP-type (middle panels) El Niño events as well as their differences (right panels) based on the observation (top three panels) and model hindcasts (below panels). Black numbers in panels are PCCs between the model patterns and the corresponding observation pattern. Yellow dots denote the *t*-test significance at the 95% confidence level

resulting in a largely zonal feature along the equator. Precipitation tends to be weaker than normal over northern Australia, maritime Southeast Asia, and the Philippines. The pattern during CP events has a quite different spatial structure. That is, enhanced precipitation largely occurs between 160°E and 160°W, with anomalies of less than 1 mm/day to the east of 160°W, and the SPCZ and ITCZ are distinct features with the SPCZ extending southwestwards from the equator and shifted less strongly to the east and the ITCZ displaced less strongly southward. This leads to a difference map showing stronger precipitation along the equatorial region in EP events, with weaker bands either side.

Many of the models show the rainfall differences between the EP and CP events well (Fig. 6, lower panels). The precipitation anomalies are generally greater in the models than seen in observations except BCCv2. The plots of the differences between EP and CP events show stronger equatorial precipitation anomalies in EP events with a band of weaker precipitation to the north. P24A most clearly shows less precipitation to the south in EP events although there are traces of this in other models. DPS3 is less successful at capturing the zonal nature of the EP pattern in the eastern Pacific than some other models, with the enhanced precipitation lying mainly to the north of the equator. This bias is also apparent, to a lesser extent in G5GC2 and CFSv2.

As was shown for SSTs, for La Niña conditions the difference between precipitation patterns of the EP and CP events is not as clear as for El Niño conditions. Figure 7 shows maps of the spatial precipitation patterns. The observations show very similar patterns in EP and CP events with negative precipitation anomalies around the equator and positive anomalies on the western coasts. The CP events show greater decreases of precipitation east of 150ºE. The inter-model spread is large in capturing the precipitation response to the two La Niña types. P24A shows larger anomalies than observed, but BCCv2 shows weaker anomalies. In DPS3 and G5GC2 the negative anomalies extend too far east north of the equator, and in BCCv2 the anomalies do not extend far enough east. Despite these differences in the anomaly patterns, the differences between the EP and CP events are similar between the models, showing a greater decrease in precipitation in the CP events in agreement with observations. Clearly, the models have a less capability of reproducing the difference between the two La Niña types than that between the two El Niño ones, as shown by the PCCs in the right panels of Figs. 6 and 7.

Further, Fig. 8 collectedly shows contrast of the center positions of the precipitation anomaly patterns shown in Figs. 6 and 7 for the EP and CP event composites by identifying their center longitude index (CLI), same as to that of the SST anomaly but with the equatorial-mean (5°S−5°N) precipitation anomaly reaching its maximum. The observed rainfall centers of the CP El Niño types are steadily located west of around 180 and around east of 160ºW for the EP types, whereas those of the EP and CP La Niña types are almost undistinguishable in terms of their longitudinal positions. The ability of the models to distinguish the canonical rainfall pattern centers between the two types is significantly lower than that in distinguishing the SST pattern centers.

5 Patterns of teleconnections

ENSO teleconnections provide a potential predictability source of extratropical climate prediction skill on seasonal (e.g., Jia et al. 2012; Jeong et al. 2012; Lee and Ha 2015; Scaife et al. 2017a) and perhaps longer interannual timescales. However, it is difficult from observational records to decide whether these influences are variable from one event to another (e.g., Greatbatch et al. 2004; Toniazzo and Scaife 2006), or simply the same in all events but masked in some cases by other climate variability so that long records are required to extract stable teleconnections (Brönnimann et al. 2007). Ensemble hindcasts used in this study provide the opportunity to decide between these two possibilities and potentially identify robust teleconnection patterns by using the ensembles to minimize unpredictable internal variability.

Figure 9 shows teleconnections to EP and CP El Niño events in observational analysis and a number of hindcast sets. All models successfully generate the Pacific teleconnection pattern during EP events with high pressure in the tropical west Pacific and low pressure over the Aleutians in North Pacific. Similar signatures to the observed pattern are also reproduced in the southern hemisphere with a sequence of high–low–high pressure features terminating off the tip of South America. Atlantic patterns are weaker but DPS3 and G5GC2 show high pressure close to northwest Europe in a pattern similar to that identified in the strongest El Niño events (Toniazzo and Scaife 2006) and which occurs when stratospheric polar vortex is undisturbed (Bell et al. 2009; Ineson and Scaife 2009).

In CP events the Pacific teleconnections are similar in pattern but weaker in amplitude, as expected given the generally lower amplitude of CP events (Fig. 2). However, the Atlantic response is much clearer in CP events with a negative NAO like response in the observational composite. This pattern dominates the overall Atlantic response to

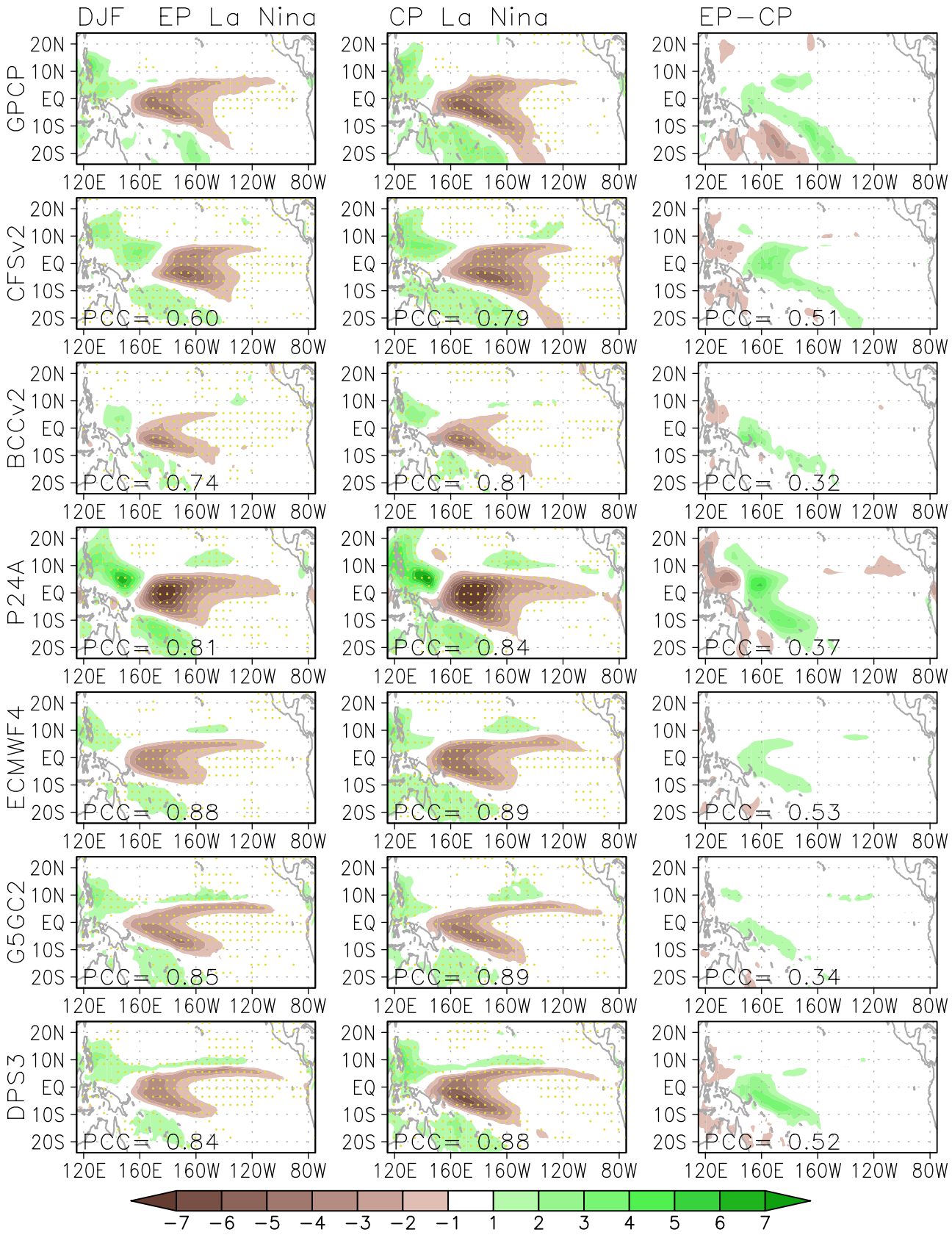

Fig. 7 The same to Fig. 5, but for the two types of La Niña events

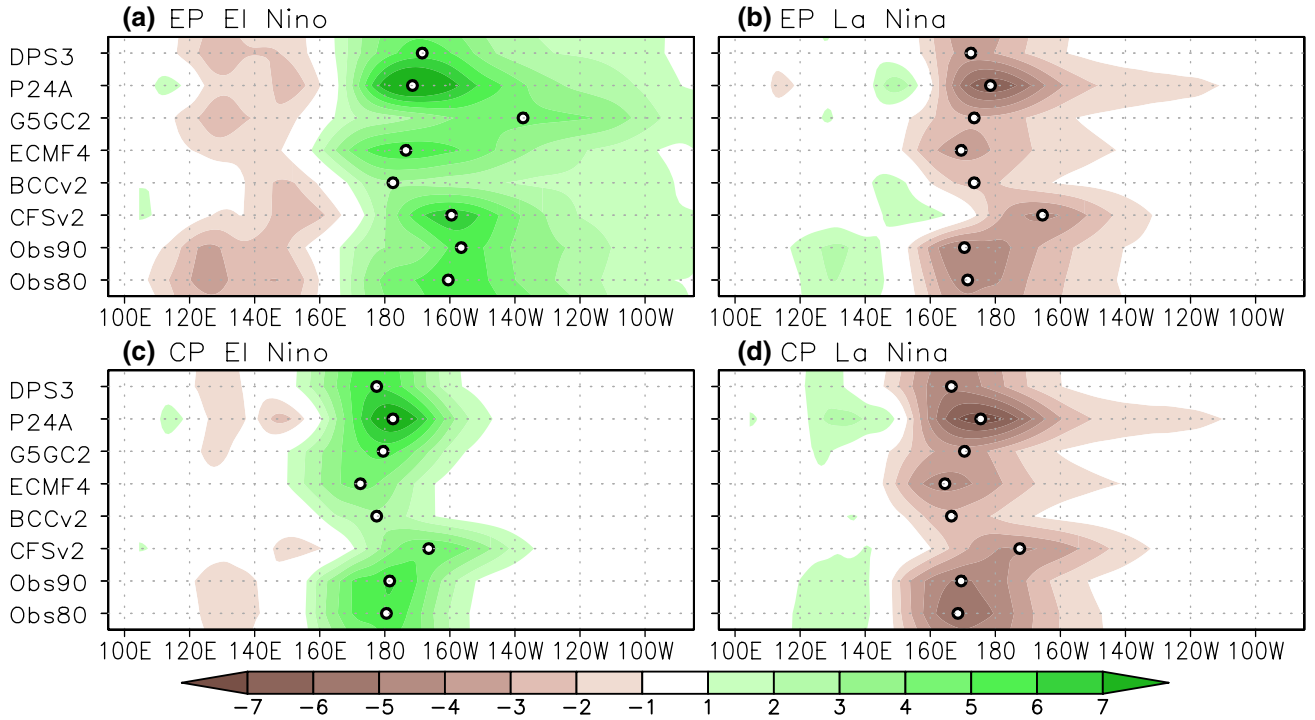

Fig. 8 The same to Fig. 4, but for the equatorial-mean precipitation composites, where Obs80 and Obs90 denote the GPCP results of 1980–2014 and 1990–2014 periods, respectively

ENSO as has been noted in many studies (e.g., Brönnimann 2007; Fereday et al. 2008; Cagnazzo and Manzini 2009; Butler et al. 2016). Observational studies have also found that this negative NAO response comes mainly from the moderate ENSO events (Toniazzo and Scaife 2006), but studies during the reanalysis period have obtained controversial results regarding whether this response is associated more closely with CP (Graf and Zanchettin 2012) or EP (Sung et al. 2014) events, highlighting the problems of sampling relatively short records. A recent paper examining the response in CMIP5 models supports the association of CP events with the negative NAO response (Calvo et al. 2015). Some of our models shown here simulate a similar negative NAO response to our observed composite (BCCv2, G5GC2, DPS3) while others produce part of the response (P24A, CFSv2). The ECMWF model does not appear to reproduce the observed response to CP events and this model also has the weakest teleconnection over the North Pacific.

Figure 10 shows the SLP composites from La Niña events for the observations and model hindcasts. As was seen in the SST and precipitation composites (Fig. 2, 3, 6, and 7) the difference between EP and CP events is less pronounced in La Niña events than El Niño events. This is particularly true in the tropics where there is little difference between the SLP responses in EP and CP La Niña events. In the extratropics there are some distinct differences consistent between the EP and CP events. The Aleutian Low weakens in both event types, but the weakening is greater in CP events. Although this also occurs in observations it appears more pronounced in the models. The location of the Aleutian Low shifts consistently in the models with CP showing greater increase in SLP further to the west.

In the observations the North Atlantic shows strong differences between the EP and CP La Niña events, with CP events again showing a strong (positive) NAO signal. Only BCCv2 simulate this positive NAO pattern well, whereas P24A shows a more positive NAO signal in EP events. CFSv2 and G5GC2 show much weaker differences between the event types over the North Atlantic than observed, while DPS3 does better. In the southern hemisphere the models capture the observed differences between the event types well. The CP events show stronger anomalies, with a strong negative center in the southeast Pacific. All the models show this negative anomaly, although P24A shows a stronger anomaly in EP events. In addition, the North Pacific shows only weak differences between the two event types in spite of the differences in the intensity and geophysical positions of the main circulation centers. Still, over the North Pacific the models tend to capture the EP associated circulation patterns better than the CP ones and the EP-CP differences and the fact that differences are small in the Pacific but large over the Atlantic is consistent with a tropical Atlantic pathway for the teleconnections to the north Atlantic (e.g. Toniazzo and Scaife 2006; Scaife et al. 2017a).

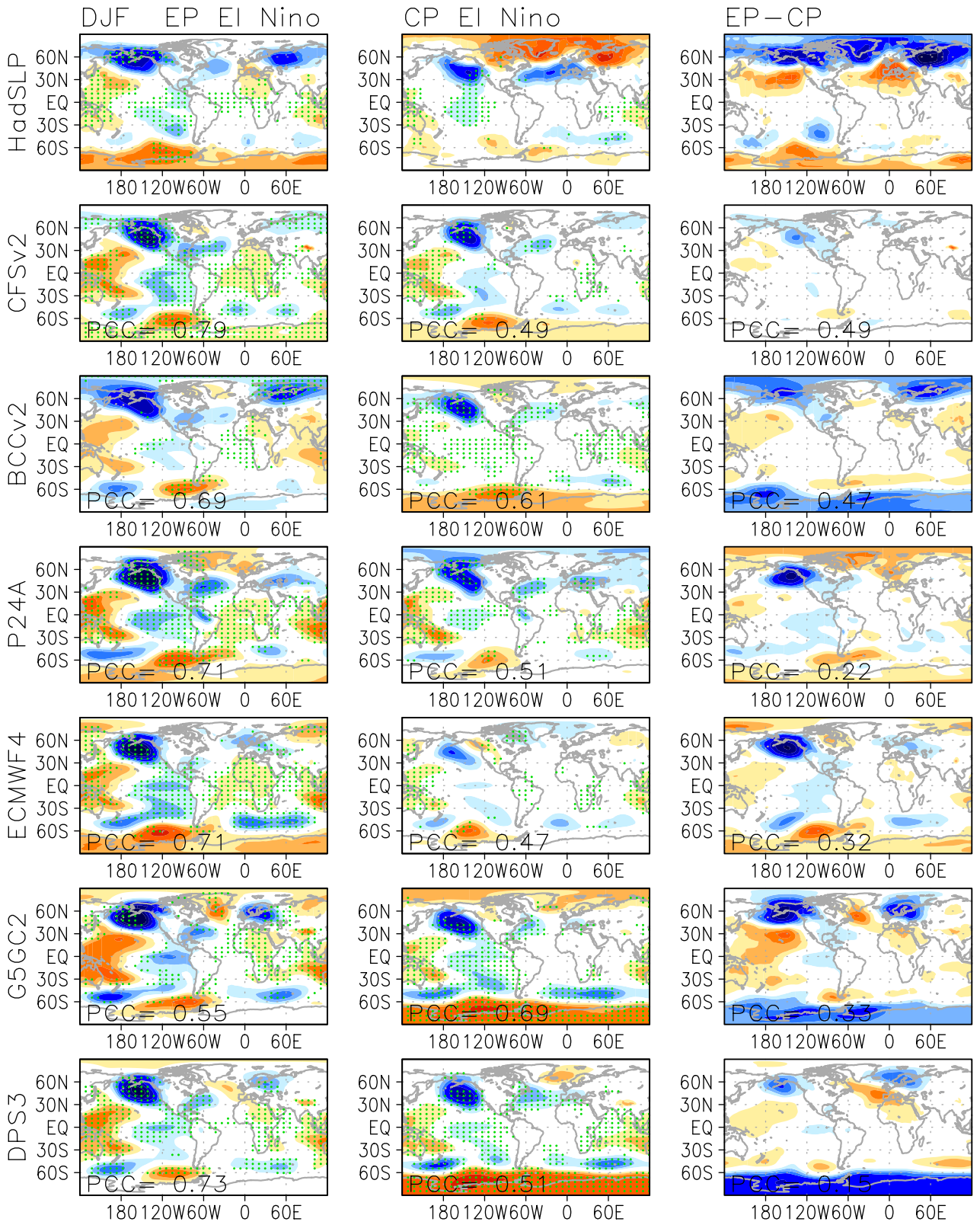
DJF EP El Nino
CP El Nino
EP−CP
HadSLP
CFSv2
BCCv2
P24A
ECMWF4
G5GC2
DPS3
60N
30N
EQ
30S
60S
180 120W 60W 0 60E
PCC= 0.79
PCC= 0.49
PCC= 0.49
PCC= 0.69
PCC= 0.61
PCC= 0.47
PCC= 0.71
PCC= 0.51
PCC= 0.22
PCC= 0.71
PCC= 0.47
PCC= 0.32
PCC= 0.55
PCC= 0.69
PCC= 0.33
PCC= 0.73
PCC= 0.51
PCC= 0.15
−5 −4 −3 −2 −1.5 −1 −0.5 0.5 1 1.5 2 3 4 5

◂**Fig. 9** Composite patterns of SLP anomalies (Unit: hPa) for the EP-type (left panels) and CP-type (middle panels) El Niño events as well as their differences (right panels) based on the observation (top three panels) and model hindcasts (below panels). Black numbers in panels are PCCs between the model patterns and the corresponding observation pattern. Green dots denote the *t*-test significance at the 95% confidence level

In this Section, we can see that the model hindcasts have helped us identify the robust teleconnection patterns by using the ensemble data at the shortest lead. Our examination of the extratropical teleconnections to the two ENSO types show that some of the models can reproduce the differences between EP and CP teleconnections. Therefore, through this study we can find out that the ENSO teleconnection is definitely variable with the different ENSO types and phases changing, which provides a good reference for climate prediction.

6 Prediction skill of different types of ENSO events

To simply illustrate the main information of evaluation of the event-based canonical patterns, we collect all the PCC skill scores between the observed and forecasted patterns of SST, precipitation, and SLP anomalies, into Fig. 11. It can be clearly seen that, if PCC can measure to some degree the capability of the models in predicting the two types of ENSO events, these models overall give slightly higher skill for the EP than the CP SST patterns for both El Niño and La Niña events, and this is less true for the precipitation patterns. However, such high PCCs do not definitely bring us the high skill that the models distinguish the two types in terms of the EP−CP differences in their canonical SST patterns. It is also clearly seen that the global teleconnection patterns for the CP La Niña and EP La Niña are not always well represented by the models, and that particularly the EP−CP differences are difficult to represent, though some regional circulation patterns can be predicted in different sectors.

We now investigate the prediction skill of the forecast systems in predicting the two types of ENSO events during winter and test whether the year-to-year forecast categories match those observed. Table 3 lists the observed frequencies when the forecast is for either an EP or CP target event for El Niño and La Niña. Here the predicted ENSO events are identified by the same standard as observed using ensemble means of each model and the observed frequencies have been accumulated for all the model forecasts.

As seen in Table 3, importantly, when an El Niño or La Niña event is forecast to occur, there are no incidences of the opposite event occurring (the lower-left and upper-right corners of Table 3 are blank). The skill of differentiating between the sub-types (EP or CP) is more of a challenge for the dynamical model systems, even from this relatively short lead time. Indeed, only half probability can be observed when any given type of El Niño event is forecasted, as shown by the highest numbers along the diagonal of Table 3. Neutral events are particularly well forecast (successful in ~ 70% of cases), with a small tendency for the models to misclassify CP La Niña events as neutral.

The most successful predictions are apparent for the CP La Niña type with over 90% of those forecasts correctly predicted. However, as discussed in the previouspart, the models tend to under represent the frequency of CP La Niña events and hence there are only eleven such events predicted to occur. This lower sample size means that our models are less confident about the skill of this CP La Niña category, but also suggests that when the model does forecast a CP La Niña, the dynamical conditions are such that it is very likely to be observed, compared to Table 2. An opposite situation could be used to partially explain why the EP La Niña type has the lowest hit rate with a highest sample size. Possible reason is worthy of being further examined. While many of the differences between the prediction skill of different ENSO types are unlikely to be significant, we conclude that the models can discriminate between ENSO types to a reasonable degree at this lead time as the most likely type occurs more often than any other type in all five phases. Given the different extratropical teleconnections noted above, this could also be useful in real time predictions where the details of the ENSO type can be important (e.g., Scaife et al. 2017b).

7 MME prediction of detailed SST patterns

Based on the analyses of the predictability of the canonical patterns and the observed events, we further extend the verification of the prediction for the two ENSO types from the traditional domain-averaged SST anomaly indices to the identified zonal positions of the SST anomaly center of those observed events. With the datasets used in Table 3, we can generate the center longitude indices (CLIs) for the observed and predicted events in terms of the types. Figure 12a first shows the results of verifications of the CLI forecasts by all the models. The EP ENSO events have higher prediction skill than the CP events at 1 month lead. The MME mean forecasts of either all the models or the two "best" models (P24A and DPS3 that generally discriminate the CP type from EP type of canonical patterns) have similar skills, as shown in Fig. 12b, c, and more skillful compared to Fig. 12a, which are likely due to the much smaller sample size. Further, we show the forecast of only DPS3 in Fig. 12d, e, which has relatively satisfactory skill in spite of the apparent errors occurring during the first four events after 2000. As we can see, although the MME mean method does improve prediction skills of their Niño indices to

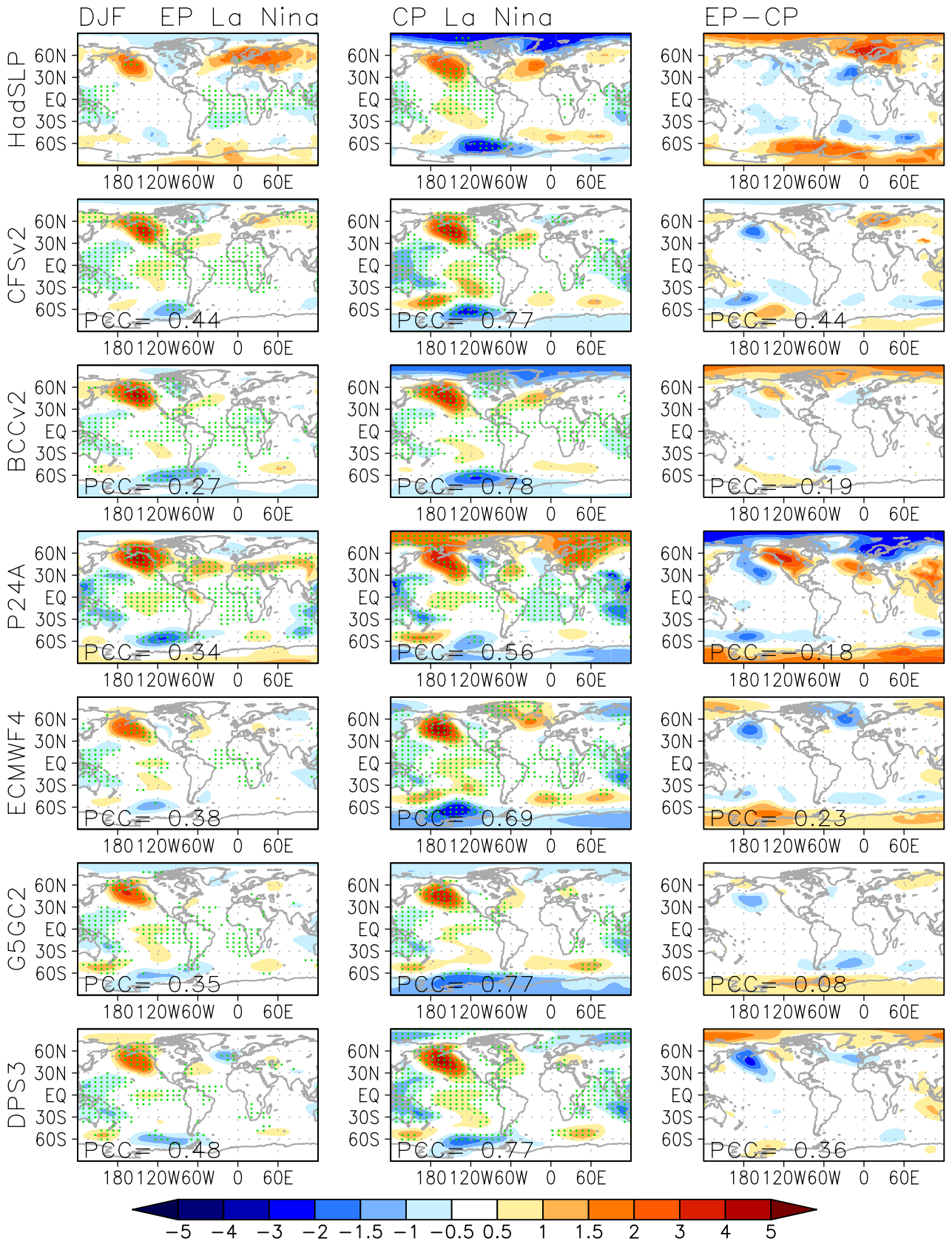

Fig. 10 The same to Fig. 9, but for the two types of La Niña events

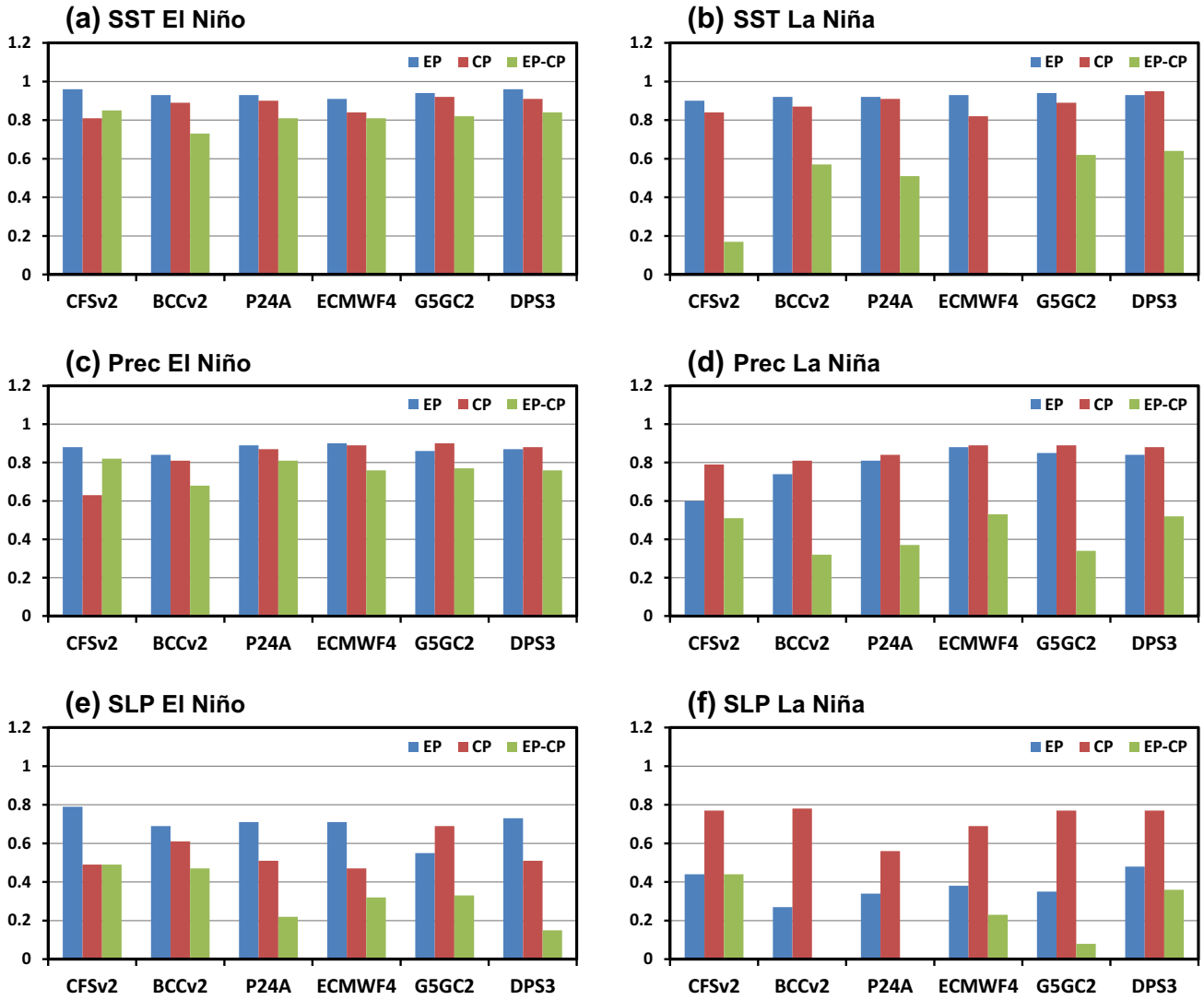

Fig. 11 PCCs between the observed patterns and model forecasted patterns for the EP type (blue), CP type (red), and their differences (green), which are collected from **a** El Niño SST anomaly patterns in Fig. 2, **b** La Niña SST anomaly patterns in Fig. 3, **c** El Niño precipitation anomaly patterns in Fig. 6, **d** La Niña precipitation anomaly patterns in Fig. 7, **e** El Niño SLP anomaly patterns in Fig. 9, and **f** La Niña SLP anomaly patterns in Fig. 10, respectively

some degree (not shown here, but demonstrated in many previous literatures), distinguishing the center positions of the SST anomaly patterns for the two types would not been expected to realize by the MME mean because most of the models are still difficult to identify the separated centers between the two types. Thus, the MME method has no evident contributions to distinguishing the two types in terms of their center positions, compared to the better models.

8 Summary and discussions

Different types of ENSO events coexist under the current climate conditions and have significantly distinct remote effects. A few previous studies have focused on the prediction assessments for the two ENSO types using single models (e.g., Hendon et al. 2009; Yang and Jiang 2014;

Table 3 Contingency table showing the skill of the seasonal forecast systems in predicting the correct type of ENSO

All the models		Predicted ENSO types				
		EP El Niño (39)	CP El Niño (16)	Neutral (48)	EP La Niña (48)	CP La Niña (11)
Observation types	EP El Niño	49%	31%			
	CP El Niño	41%	50%	8%		
	Neutral	10%	19%	69%	17%	
	EP La Niña			8%	46%	9%
	CP La Niña			15%	37%	91%

Tabulated are the percentage of events that are observed to occur given the model forecast of a particular EP or CP type for both El Niño and La Niña. The number of forecasts for each type made by all the models is quoted in brackets

Imada et al. 2015). The current study provides a multi-model evaluation for the two types of ENSO events for the SST anomalies, rainfall patterns, and teleconnections, based on six coupled GCMs from different operational centers. Compared to the EOF/indices-based studies (Jeong et al. 2012, 2015), we presented an event-based 1-month-lead predictability evaluation for the two types of ENSO in terms of the El Niño and La Niña events.

It is suggested that a comprehensive evaluation of ENSO predictability for the two types should be based on both continuous and event-based approaches. Our results show that EP and CP El Niño events during winter can be distinguished only in 2−3 of our 6 models even at this short lead time, and this is slightly less true for La Niña events, and the EP type tends to has a more realistic zonal positions of SST pattern centers than the CP type. Compared to the SST patterns, the precipitation patterns have smaller differences between the two types especially for La Niña events. The models can reproduce the separation of events for precipitation in some cases, but often show off-equatorial maxima. For teleconnections in the extratropics to the two ENSO types, we can find out that they are definitely variable with the different ENSO types and phases changing. We confirmed that our EP events, which sample several strong El Niño events, can drive strong Atlantic wave-trains while our composite of CP events produce a negative NAO response, consistent with

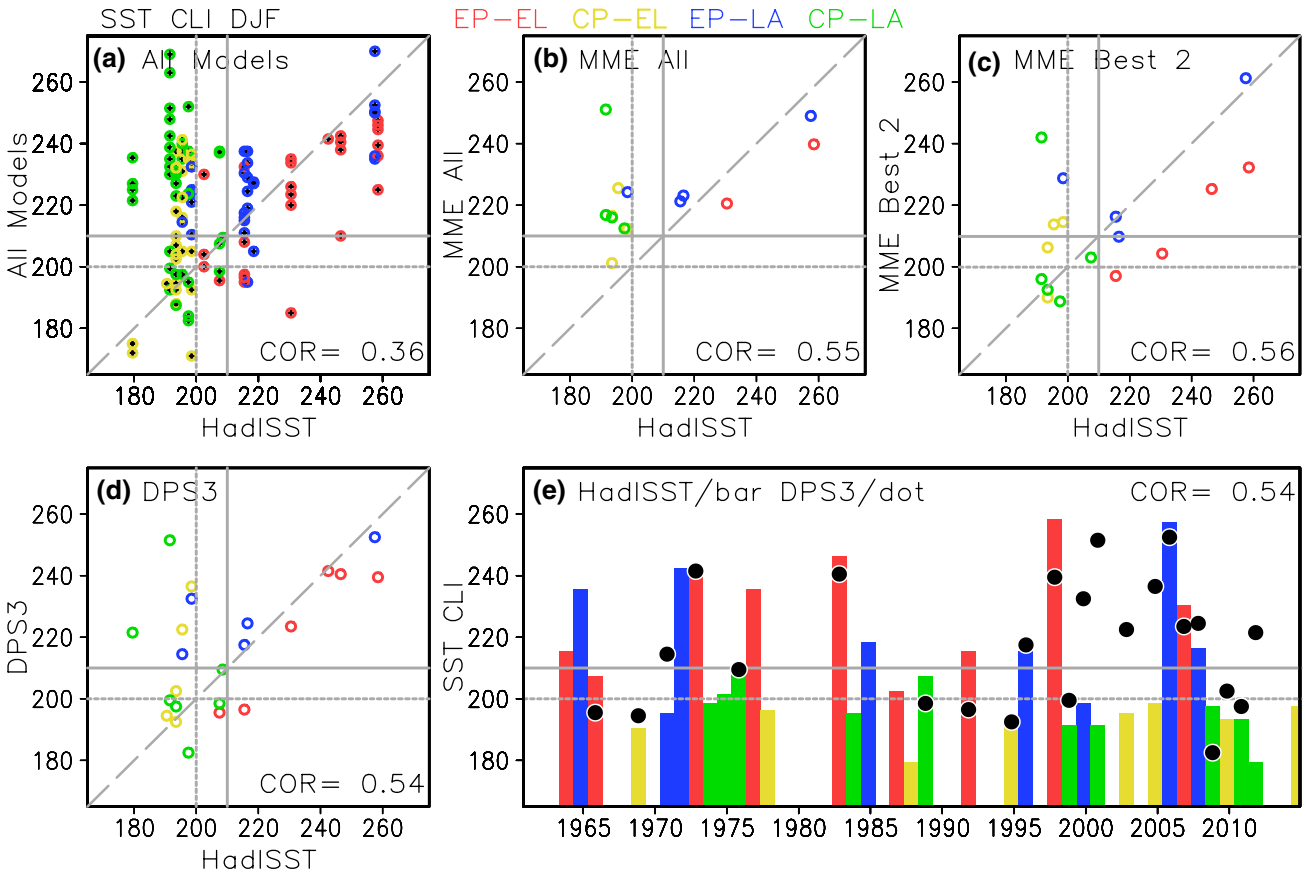

Fig. 12 Scatter plots of the observed CLIs (HadISST, x-axis) and the model forecasted CLIs (y-axis) of **a** all models, **b** MME mean of all models, **c** MME mean of the P24A and DPS3, **d** the DPS3 and **e** the bar (HadISST)–dot (DPS3) plot in which the symbols and bars are for the events of the EP El Niño (red), CP El Niño (yellow), EP La Niña (blue), and CP La Niña (green)

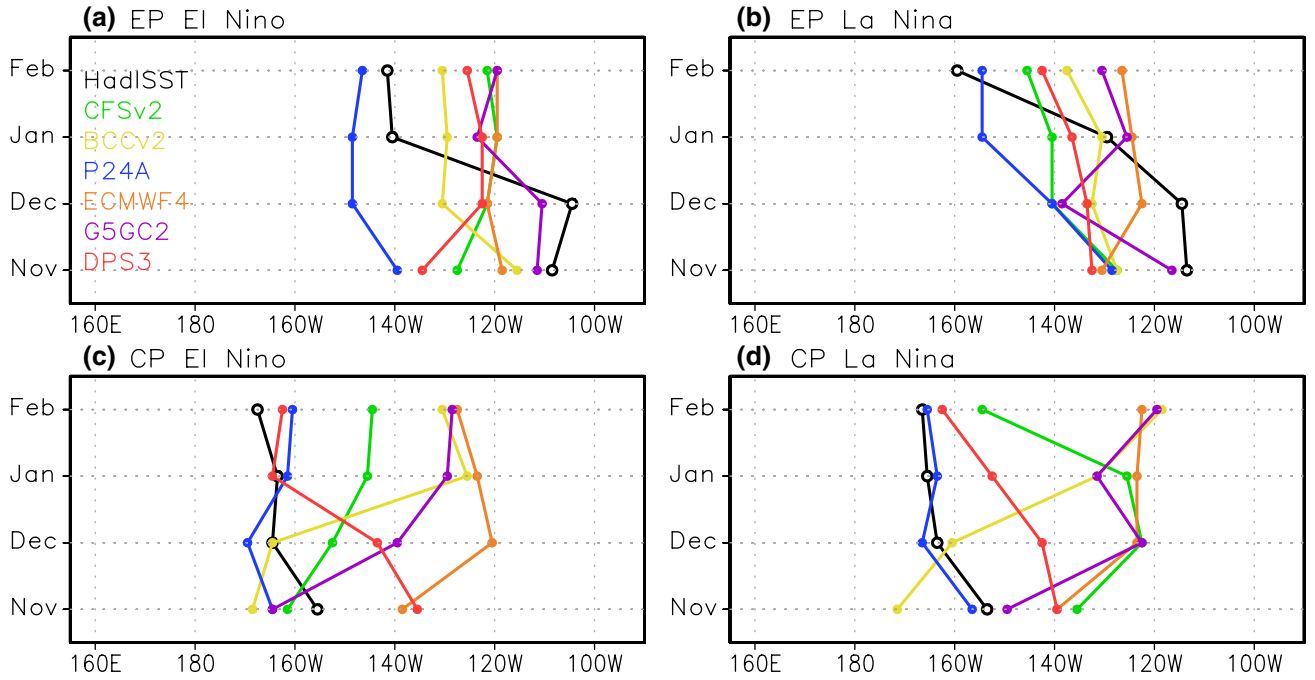

Fig. 13 Evolutions of the composite center longitudes of the HadISST (1980–2014) and the initialized (Nov) and forecasted (Dec–Jan–Feb) SST anomaly patterns (solid lines) using the events of the EP El Niño (**a**), EP La Niña (**b**), CP El Niño (**c**), and CP La Niña (**d**)

the observed CP composite in this study. However, why the extratropical teleconnections show such large differences from quite similar tropical precipitation patterns between the two La Niña types, is still an open question. Our results show that some of the models can reproduce the differences between the observed canonical teleconnections patterns at 1-month lead.

This study examined predictability of the two ENSO types in dynamical predictions near their peak in the wintertime, at seasonal lead time. It would be interesting in future work to determine the longest lead time that the main differences between the two types of ENSO events can be reasonably predicted as shown for some single models (e.g., Hendon et al. 2009; Yang and Jiang 2014). Our results also showed that EP ENSO indices are overall better predicted than CP ENSO indices in the six models, which is consistent with previous studies (e.g., Yang and Jiang 2014; Imada et al. 2015). Further, the event-based evaluations of model predictions show that the EP El Niño event has the same level hit rate with the CP El Niño and the CP La Niña event has much higher hit rate than the EP La Niña. Explanation of this interesting result will require further study but may well be related to amplitude. However, this result is still controversial as Kim et al. (2009) concluded that EP events are less predictable than CP events based on analysis of relative persistence of the traditional SST indices, and Ren et al. (2016) found that the CP type has a much weaker and more delayed persistence barrier than the EP type. Moreover, it would also be interesting to examine the dynamical processes and mechanisms for the generation and maintenance of the two ENSO types in the models.

We found that the MME mean of the models is not able to improve forecast skill of center longitude index of the SST patterns and distinguish the two ENSO types, though prediction skill of the Niño indices can be increased. In this case, we should note that the MME mean has no evident contribution to prediction of the zonal positions of SST anomaly centers between the two ENSO types. This is because only a few coupled GCMs in the model group are able to distinguish the longitudinal differences between the two types of events. Moreover, La Niña events are less well separated in terms of the two types in both the observation and most model predictions. Nevertheless, we note here that at least some dynamical models are able to predict more than the average ENSO spatial pattern, at least at short lead time. Recent studies showed that the analogue-based correction of the CFSv2 and BCCv2 can significantly improve the dynamical ENSO predictions in terms of the two types (Ren et al. 2017; Liu and Ren 2017), providing an alternative way to make prediction of the two ENSO types better than original dynamical model predictions.

Finally, we come back to a key question why the majority of these operational models have difficulty in predicting the center positions of winter SST anomaly patterns between the different ENSO types only at one month lead? Fig. 13

presents the evolution of the center positions of the composite SST patterns of different models with lead time for each ENSO type. Although the maximum SSTs are initially anchored near to the observations as a result of initialization of the models, this information is quickly lost during the following few months in most of the models. Particularly, such a quick dissipation of initial distinctions generally occurs more in the CP types of El Niño and La Niña than the EP ones. For example, G5GC2 almost has the best initialized center positions of the SST anomaly patterns in the different types but are visible to usually evolve into quite different ways compared to the observations. On one hand, this suggests that the initialization processes of subsurface ocean rather than the SST only could be quite important for the models to capture the initial signals of the ENSO types. On the other hand, this result indicates that, except the model initialization, model performance including drift and the ability to represent ENSO types may be the key aspect that limit the predictability of the winter two types of ENSO events. Therefore, more efforts are required to improve the performance of the climate models in distinguishing the two types of ENSO and additional investigation of thermocline and current anomalies may provide important information in explaining why some models fails to predict the ENSO types.

Acknowledgements This work is jointly supported by National Key R&D Program of China (2017YFC1502302), China Meteorological Special Project (GYHY201506013), and National Natural Science Foundation of China (Grants 41606019 and 41405080). The contributors (AAS, ND, VT, SI, DS, MV, CM) are supported by the UK-China Research & Innovation Partnership Fund through the Met Office Climate Science for Service Partnership (CSSP) China as part of the Newton Fund. The authors are grateful to three anonymous reviewers for their insightful comments to improve the quality of the paper.

Open Access This article is distributed under the terms of the Creative Commons Attribution 4.0 International License (http://creativecommons.org/licenses/by/4.0/), which permits unrestricted use, distribution, and reproduction in any medium, provided you give appropriate credit to the original author(s) and the source, provide a link to the Creative Commons license, and indicate if changes were made.

References

Adler RF, Huffman GJ, Chang A, Ferraro R, Xie P, Janowiak J, Rudolf B, Schneider U, Curtis S, Bolvin D, Gruber A, Susskind J, Arkin P (2003) The version 2 global precipitation climatology project (GPCP) monthly precipitation analysis (1979–present). J Hydrometeorol 4:1147–1167

Allan RJ, Ansell TJ (2006) A new globally complete monthly historical mean sea level pressure data set (HadSLP2). J Clim 19:1850–2004 5816–5842.

Ashok H, Yamagata T (2009) Climate change: the El Niño with a difference. Nature 461:481–484. https://doi.org/10.1038/461481a

Ashok K, Behera SK, Rao SA, Weng H, Yamagata T (2007) El Niño Modoki and its possible teleconnection. J Geophys Res 112:C11007. https://doi.org/10.1029/2006JC003798

Barnston AG, Tippett MK, L'Heureux ML et al (2012) Skill of real-time seasonal ENSO model predictions during 2002–11: is our capability increasing? Bull Am Meteorol Soc 93(5):631–651

Bell CJ, Gray LJ, Charlton-Perez AJ, Joshi MM, Scaife AA (2009) Stratospheric communication of El Niño teleconnections to European winter. J Clim 22(15):4083–4096

Brönnimann S (2007) The impact of El Niño-Southern Oscillation on European climate. Rev Geophys 45:RG3003. https://doi.org/10.1029/2006RG000199

Brönnimann S, Xoplaki E, Casty C, Pauling A, Luterbacher J (2007) ENSO influence on Europe during the last centuries. Clim Dyn 28:181–197. https://doi.org/10.1007/s00382-006-0175-z

Butler AH et al (2016) The Climate historical forecast project: do stratosphere-resolving models make better seasonal climate predictions in boreal winter? Quart J Roy Met Soc 142:1413–1427

Cagnazzo C, Manzini E (2009) Impact of the stratosphere on the winter tropospheric teleconnections between ENSO and the North Atlantic and European region. J Clim 22(5):1223–1238. https://doi.org/10.1175/2008JCLI2549.1

Calvo N, Iza M, Hurwitz MM, Manzini E, Peña-Ortiz C, Butler AH, Cagnazzo C, Ineson S, Garfinkel CI (2017) Northern hemisphere stratospheric pathway of different El Niño flavors in CMIP5 models. J Clim. https://doi.org/10.1175/JCLI-D-16-0132.1

Cane MA, Zebiak SE, Dolan SC (1986) Experimental forecasts of El Niño. Nature 321:827–832

Chen D, Zebiak SE, Busalacchi AJ et al (1995) An improved procedure for El Niño forecasting: Implications for predictability. Science 269:1699–1702

Chen D, Cane MA, Kaplan A et al (2004) Predictability of El Niño over the past 148 years. Nature 428:733–736. https://doi.org/10.1038/nature02439

Cheng YJ, Tang YM, Zhou XB et al (2010) Further analysis of singular vector and ENSO predictability in the Lamont model—part I: singular vector and the control factors. Clim Dyn 35:807–826

Davey MK, Brookshaw A, Ineson S (2014) The probability of the impact of ENSO on precipitation and near-surface temperature. Clim Risk Manag 1:5–24. https://doi.org/10.1016/j.crm.2013.12.002

Dunstone N, Smith D, Scaife AA et al (2016) Skilfulpredictions of the winter North Atlantic Oscillation one year ahead. Nat GeoSci 9:809–814

Feng J, Li J (2011) Influence of El Niño Modoki on spring rainfall over south China. J Geophys Res 116:D13102. https://doi.org/10.1029/2010JD015160

Feng J, Wang L, Chen W, Fong SK, Leong KC (2010) Different impacts of two types of Pacific Ocean warming on Southeast Asian rainfall during boreal winter. J Geophys Res 115:D24122. https://doi.org/10.1029/2010JD014761

Fereday DR, Knight JR, Scaife AA, Folland CK, Philipp A (2008) Cluster analysis of North Atlantic–European circulation types and links with tropical Pacific Sea surface temperatures. J Clim 21:3687–3703

Graf H-F, Zanchettin D (2012) Central Pacific El Niño, the "subtropical bridge," and Eurasian climate. J Geophys Res 117(D1):D01102. https://doi.org/10.1029/2011JD016493

Greatbatch RJ, Lu J, Peterson KA (2004) Nonstationary impact of ENSO on Euro-Atlantic winter climate. Geophys Res Lett 31:L02208. https://doi.org/10.1029/2003GL018542

Ham Y-G, Kug J-S (2012) How well do current climate models simulate two types of El Niño? Clim Dyn 39:383–398. https://doi.org/10.1007/s00382-011-1157-3

Ham Y-G, Kug J-S (2015) Improvement of ENSO simulation based on intermodel diversity. J Climate 28(3):998–1015
Ham Y-G, Kug J-S, Kang I-S (2009) Optimal initial perturbations for El Niño ensemble prediction with ensemble Kalman filter. Clim Dyn 33(7):959–973. https://doi.org/10.1007/s00382-009-0582
Hendon HH, Lim E, Wang G, Alves O, Hudson D (2009) Prospects for predicting two flavors of El Niño. Geophys Res Lett 36:L19713. https://doi.org/10.1029/2009GL040100
Imada Y, Tatabe H, Ishii M, Chikamoto Y, Mori M, Arai M, Watanabe M, Kimoto M (2015) Predictability of two types of El Niño assessed using an extended seasonal prediction system by MIROC. Mon Wea Rev 143:4597–4617
Ineson S, Scaife AA (2009) The role of the stratosphere in the European climate response to El Niño. Nat Geosci 2:32–36. https://doi.org/10.1038/ngeo381
Izumo T, Vialard J, Lengaigne M et al (2010) Influence of the state of the Indian Ocean Dipole on the following year's El Niño. Nat Geosci 3(3):168–172. https://doi.org/10.1038/ngeo760
Jeong H-I, Lee DY, Ashok K, Ahn J-B, Lee J-Y, Luo J-J, Schemm J-KE, Hendon HH, Braganza K, Ham Y-G (2012) Assessment of the APCC couple MME suite in predicting the distinctive climate impacts of two flavors of ENSO during boreal winter. Clim Dyn 39:475–493. https://doi.org/10.1007/s00382-012-1359-3
Jeong H-I, Ahn J-B, Lee J-Y, Alessandri A, Hendon HH (2015) Interdecadal change of interannual variability and predictability of two types of ENSO. Clim Dyn 44:1073–1091. https://doi.org/10.1007/s00382-014-2127-3
Jia X, Lin H, Lee J-Y, Wang B (2012) Season-dependent forecast skill of the dominant atmospheric circulation patterns over the Pacific-North American region. J Climate 25:7248–7265
Jin EK, Kinter JL, Wang B et al (2008) Current status of ENSO prediction skill in coupled ocean–atmosphere models. Clim Dyn 31(6):647–664
Kang I-S, Kug J–S (2000) An El-Niño prediction system using an intermediate ocean and a statistical atmosphere. Geophys Res Lett 15:1167–1170
Kao HY, Yu JY (2009) Contrasting eastern-Pacific and central-Pacific types of El Niño. J Clim 22:615–632. https://doi.org/10.1175/2008JCLI2309.1
Kim, H-M., PJ, Webster, Curry JA (2009) Impact of shifting patterns of Pacific Ocean warming on north Atlantic tropical cyclones. Science 325:77–80. https://doi.org/10.1126/science.1174062
Kirtman PB (2003) The COLA anomaly coupled model: Ensemble ENSO prediction. Mon Wea Rev 131:2324–2341
Knight JR, Andrews MB, Smith DM, Arribas A, Colman AW, Dunstone NJ, Eade R, Hermanson L, MacLachlan C, Peterson KA, Scaife AA, Williams A (2014) Predictions of climate several years ahead using an improved decadal prediction system. J Clim 27:7550–7567. https://doi.org/10.1175/JCLI-D-14-00069.1
Kug J-S, Ham Y-G (2011) Are there two types of La Niña? Geophys Res Lett 38:L16704. https://doi.org/10.1029/2011GL048237
Kug J-S, Jin F-F, An S-I (2009) Two types of El Niño events: Cold tongue El Niño and warm pool El Niño. J Clim 22:1499–1515. https://doi.org/10.1175/2008JCLI2624.1
Larkin NK, Harrison DE (2005a) On the definition of El Niño and associated seasonal average U.S. weather anomalies. Geophys Res Lett 32:L13705. https://doi.org/10.1029/2005GL022738
Larkin NK, Harrison DE (2005b) Global seasonal temperature and precipitation anomalies during El Niño autumn and winter. Geophys Res Lett 32:L16705. https://doi.org/10.1029/2005GL022860
Latif M, Anderson D, Barnett T et al (1998) A review of the predictability and prediction of ENSO. J Geophys Res 103:14375–14393
Lee J-Y, Ha K-J (2015) Understanding of interdecadal changes in variability and predictability of the Northern Hemisphere summer tropical-extratropical teleconnection. J Clim 28:8634–8647
Lee J-Y, Wang B, Kang I-S, Shukla J, Kumar A, Kug J-S, Schemm J, Juo J-J, Yamagata T, Fu X, Alves O, Stern B, Rosati T, Park CK (2010) How are seasonal prediction skills related to models performance on mean state and annual cycle? Clim Dyn 35: 267–283
Lim EP, Hendon HH, Hudson D, Wang G, Alves O (2009) Dynamical forecast of inter–El Niño variations of tropical SST and Australian spring rainfall. Mon Wea Rev 137:3796–3810. https://doi.org/10.1175/2009MWR2904.1
Liu Y, Ren H-L (2017) Improving ENSO prediction in CFSv2 with an analogue-based correction method. Inter J Clim 37(15):5035–5046. https://doi.org/10.1002/joc.5142
Luo J-J, Masson S, Behera S et al (2005) Seasonal climate predictability in a coupled OAGCM using a different approach for ensemble forecasts. J Clim 18:4474–4497
Luo J-J, Masson S, Behera SK et al (2008) Extended ENSO predictions using a fully coupled ocean-atmosphere model. J Clim 21(1):84–93
MacLachlan C, Arribas A, Peterson KA, Maidens A, Fereday D, Scaife AA, Gordon M, Vellinga M, Williams A, Comer RE, Camp. J, Xavier P, Madec G (2015) Global seasonal forecast system version 5 (GloSea5): a high resolution seasonal forecast system. Q J R Meteorol Soc 141(689):1072–1084. https://doi.org/10.1002/qj.2396
Mason SJ, Goddard L (2001) Probabilistic precipitation anomalies associated with ENSO. Bull Am Meteorol Soc 82:619–638
McPhaden MJ, Lee T, McClurg D (2011) El Niño and its relationship to changing background conditions in the tropical Pacific Ocean. Geophys Res Lett 38:L15709
Molteni F, Stockdale T, Balmaseda M, Balsamo G, Buizza R, Ferranti L, Magnusson L, Mogensen K, Palmer T, Vitart F (2011) The new ECMWF seasonal forecast system (System 4). ECMWF Technical Memorandum 656
Rasmusson EM, Carpenter TH (1982) Variations in tropical sea surface temperature and surface wind fields associated with the Southern Oscillation/El Niño. Mon Weather Rev 110:354–384
Rayner NA, Parker DE, Horton EB, Folland CK, Alexander LV, Rowell DP, Kent EC, Kaplan A (2003) Global analyses of sea surface temperature, sea ice, and night marine air temperature since the late nineteenth century. J Geophys Res 108(D14):4407. https://doi.org/10.1029/2002JD002670
Ren H-L, Jin F-F (2011) Niño indices for two types of ENSO. Geophys Res Lett 38:L04704. https://doi.org/10.1029/2010GL046031
Ren H-L, Jin F-F (2013) Recharge oscillator mechanisms in two types of ENSO. J Clim 26(17):6506–6523
Ren H-L, Jin F-F, Stuecker MF, Xie R (2013) ENSO regime change since the late 1970s as manifested by two types of ENSO. J Meteor Soc Jpn 91(6):835–842
Ren H-L, Liu Y, Jin F-F, Yan Y-P, Liu X-W (2014) Application of the analogue-based correction of errors method in ENSO prediction. Atmos Oceanic Sci Lett 7(2):157–161. https://doi.org/10.3878/j.issn.1674-2834.13.0080
Ren H-L, Jin F-F, Tian B et al (2016) Distinct persistence barriers in two types of ENSO. Geophys Res Lett 43:10973–10979
Ren H-L, Jin F-F, Song L, Lu B, Tian B, Zuo J, Liu Y, Wu J, Zhao C, Nie Y, Zhang P, Ba J, Wu Y, Wan J, Yan Y, Zhou F (2017) Prediction of primary climate variability modes in Beijing Climate Center. J Meteorol Res 31(1):204–223. https://doi.org/10.1007/s13351-017-6097-3
Saha S et al (2006) The NCEP climate forecast system. J Clim 19:3483–3517. https://doi.org/10.1175/JCLI3812.1
Saha S et al (2010) The NCEP climate forecast system reanalysis. Bull Am Meteorol Soc 91:1015–1057. https://doi.org/10.1175/2010BAMS3001.1
Saha S et al (2014) The NCEP climate forecast system version 2. J Clim 27:2185–2208. https://doi.org/10.1175/JCLI-D-12-00823.1

Scaife AA et al (2017a) Tropical rainfall, rossby waves and regional winter climate predictions. Quart J R Met Soc 143:1–11. https://doi.org/10.1002/qj.2910

Scaife AA et al (2017b) Predictability of European winter 2015/16. Atmos Sci Let 18:38–44

Smith DM, Cusack S, Colman AW, Folland CK, Harris GR, Murphy JM (2007) Improved surface temperature prediction for the coming decade from a global climate model. Science 317:796–799. https://doi.org/10.1126/science.1139540

Sung M-K, Kim B-M, An S-I (2014) Altered atmospheric responses to eastern Pacific and central Pacific El Niños over the North Atlantic region due to stratospheric interference. Clim Dyn 42(1–2):159–170

Toniazzo T, Scaife AA (2006) The influence of ENSO on winter North Atlantic climate. Geophys Res Lett 33:L24704. https://doi.org/10.1029/2006GL027881

Wang B, Lee J-Y et al (2009) Advance and prospectus of seasonal prediction: assessment of the APCC/CliPAS 14-model ensemble retrospective seasonal prediction (1980–2004). Clim Dyn 33:93–117

Weng H, Ashok K, Behera S, Rao AS, Yamagata T (2007) Impacts of recent El Niño Modoki on dry/wet conditions in the Pacific Rim during boreal summer. Clim Dyn 29:113–129. https://doi.org/10.1007/s00382-007-0234-0

Weng H, Behera SK, Yamagata T (2009) Anomalous winter climate conditions in the Pacific Rim during recent El Niño Modoki and El Niño events. Clim Dyn 32:663–674

Williams KD, Harris CM et al (2015) The Met Office global coupled model 2.0 (GC2) configuration. Geosci Model Dev 8:1509–1524

Wu TW et al (2010) The Beijing Climate Center atmospheric general circulation model: description and its performance for the present-day climate. Clim Dyn 34:123–147

Wu TW et al (2013) Global carbon budgets simulated by the Beijing Climate Center climate system model for the last century. J Geophys Res 118:4326–4347

Xiang B, Wang B, Li T (2013) A new paradigm for predominance of standing Central Pacific Warming after the late 1990s. Clim Dyn 41:327–340

Yang S, Jiang X (2014) Prediction of eastern and central Pacific ENSO events and their impacts on East Asian climate by the NCEP climate forecast system. J Clim 27:4451–4472. https://doi.org/10.1175/JCLI-D-13-00471.1

Yeh SW, Kug JS, Dewitte B, Kwon MH, Kirtman BP, Jin F-F (2009) El Niño in a changing climate. Nature 461:511–514

Yu J-Y, Kim ST (2010) Identification of central-Pacific and eastern-Pacific types of ENSO in CMIP3 models. Geophys Res Lett 37:L15705. https://doi.org/10.1029/2010GL044082

Yu J-Y, Kao H-Y, Lee T et al (2011) Subsurface ocean temperature indices for Central-Pacific and Eastern-Pacific types of El Niño and La Niña. events. Theor Appl Climatol 103(3):337–344

Yuan Y, Yan H-M (2013) Different types of La Niña events and different responses of the tropical atmosphere. Chin Sci Bull 58:406–415. https://doi.org/10.1007/s11434-012-5423-5

Yuan Y, Yang S (2012) Impacts of different types of El Niño on the East Asian climate: Focus on ENSO cycles. J Clim 25:7702–7722. https://doi.org/10.1175/JCLI-D-11-00576.1

Zebiak SE, Cane MA (1987) A model El Niño-Southern Oscillation. Mon Weather Rev 115:2262–2278

Zhang R, Sumi A, Kimoto M (1996) Impact of El Niño on the East Asia monsoon: a diagnostic study of the '86/87 and '91/92 events. J Meteorol Soc Jpn 74:49–62

Zhang W, Jin F-F, Li J, Ren H-L (2011) Contrasting impacts of two-type El Niño over the western north Pacific during boreal autumn. J Meteorol Soc Jpn 89(5):563–569

Zhang W, Jin F-F, Ren H-L, Li J, Zhao J-X (2012) Differences in teleconnection over the North Pacific and rainfall shift over the USA associated with two types of El Niño during boreal autumn. J Meteorol Soc Jpn 90(4):535–552

Zhang W, Wang L, Xiang B, Qi L, He J (2015) Impacts of two types of La Niña on the NAO during boreal winter. Clim Dyn 44:1351–1366

Zheng F, Zhu J, Zhang R-H et al (2006) Ensemble hindcasts of SST anomalies in the tropical Pacific using an intermediate coupled model. Geophys Res Lett 33:L19604

Zhu J, Huang B, Marx L, Kinter JL III, Balmaseda MA, Zhang R-H, Hu Z-Z (2012) Ensemble ENSO hindcasts initialized from multiple ocean analyses. Geophys Res Lett 39:L09602. https://doi.org/10.1029/2012GL051503

Zhu J, Huang B, Cash B, Kinter JL, Manganello J, Barimalala R, Altshuler E, Vitart F, Molteni F, Towers P (2015) ENSO prediction in project minerva: sensitivity to atmospheric horizontal resolution and ensemble size. J Clim 28:2080–2095. https://doi.org/10.1175/JCLI-D-14-00302.1

Zhu J, Kumar A, Wang W, Hu Z-Z, Huang B, Balmaseda MA (2017) Importance of convective parameterization in ENSO predictions. Geophys Res Lett 44(12):6334–6342. https://doi.org/10.1002/2017GL073669

The China Multi-Model Ensemble Prediction System and Its Application to Flood-Season Prediction in 2018

Hong-Li REN[1*], Yujie WU[1], Qing BAO[2], Jiehua MA[3], Changzheng LIU[1], Jianghua WAN[1], Qiaoping LI[4], Xiaofei WU[5], Ying LIU[1], Ben TIAN[1], Joshua-Xiouhua FU[6], and Jianqi SUN[3]

1 *Laboratory for Climate Studies &China Meteorological Administration–Nanjing University Joint Laboratory for Climate Prediction Studies, National Climate Center, China Meteorological Administration, Beijing* 100081
2 *State Key Laboratory of Numerical Modeling for Atmospheric Sciences and Geophysical Fluid Dynamics, Institute of Atmospheric Physics, Chinese Academy of Sciences, Beijing* 100029
3 *Nansen–Zhu International Research Centre, Institute of Atmospheric Physics, Chinese Academy of Sciences, Beijing* 100029
4 *National Climate Center, China Meteorological Administration, Beijing* 100081
5 *School of Atmospheric Sciences/Plateau Atmosphere and Environment Key Laboratory of Sichuan Province, Chengdu University of Information Technology, Chengdu*, 610225
6 *Institute of Atmospheric Sciences, Fudan University, Shanghai* 200433

(Received October 29, 2018; in final form February 27, 2019)

ABSTRACT

Multi-model ensemble prediction is an effective approach for improving the prediction skill short-term climate prediction and evaluating related uncertainties. Based on a combination of localized operation outputs of Chinese climate models and imported forecast data of some international operational models, the National Climate Center of the China Meteorological Administration has established the China multi-model ensemble prediction system version 1.0 (CMMEv1.0) for monthly–seasonal prediction of primary climate variability modes and climate elements. We verified the real-time forecasts of CMMEv1.0 for the 2018 flood season (June–August) starting from March 2018 and evaluated the 1991–2016 hindcasts of CMMEv1.0. The results show that CMMEv1.0 has a significantly high prediction skill for global sea surface temperature (SST) anomalies, especially for the El Niño–Southern Oscillation (ENSO) in the tropical central–eastern Pacific. Additionally, its prediction skill for the North Atlantic SST triple (NAST) mode is high, but is relatively low for the Indian Ocean Dipole (IOD) mode. Moreover, CMMEv1.0 has high skills in predicting the western Pacific subtropical high (WPSH) and East Asian summer monsoon (EASM) in the June–July–August (JJA) season. The JJA air temperature in the CMMEv1.0 is predicted with a fairly high skill in most regions of China, while the JJA precipitation exhibits some skills only in northwestern and eastern China. For real-time forecasts in March–August 2018, CMMEv1.0 has accurately predicted the ENSO phase transition from cold to neutral in the tropical central–eastern Pacific and captures evolutions of the NAST and IOD indices in general. The system has also captured the main features of the summer WPSH and EASM indices in 2018, except that the predicted EASM is slightly weaker than the observed. Furthermore, CMMEv1.0 has also successfully predicted warmer air temperatures in northern China and captured the primary rainbelt over northern China, except that it predicted much more precipitation in the middle and lower reaches of the Yangtze River than observation.

Key words: multi-model ensemble, China multi-model ensemble prediction system (CMME), real-time forecast, skill assessment

Citation: Ren, H.-L., Y. J. Wu, Q. Bao, et al., 2019: The China multi-model ensemble prediction system and its application to flood-season prediction in 2018. *J. Meteor. Res.*, **33**(3), 540–552, doi: 10.1007/s13351-019-8154-6.

1. Introduction

Climate anomalies affect social and economic development worldwide. Accurate predictions of climate anomalies are imperative for preventing and mitigating climate associated disasters. Despite the tremendous societal

Supported by the National Key Research and Development Program of China (2017YFC1502306, 2017YFC1502302, and 2018YFC1506004) and China Meteorological Administration Special Project for Developing Key Techniques for Operational Meteorological Forecast (YBGJXM201805).

*Corresponding author: renhl@cma.gov.cn.

©The Chinese Meteorological Society and Springer-Verlag Berlin Heidelberg 2019

demand, short-term climate prediction spanning from 10 days to a few seasons is always a hot but difficult issue in both scientific and technical senses. In particular, China is located in the East Asian monsoon region where the climate variation is dominated by complex spatiotemporal climate variability with multi-scale interactions, which gives rise to a great challenge for the operational short-term climate prediction in China. Therefore, it is considerably important to carry out operational short-term climate prediction in China, and to improve the prediction skill by keeping abreast with the advancements in climate prediction research and practice around the world.

At present, dynamical prediction using numerical climate models is one of the most important approaches for short-term climate prediction, and it has been widely used in operational predictions of global climate and climate variability (e.g., Saha et al., 2006, 2014; Weisheimer et al., 2009; Wang et al., 2015; Ren et al., 2017). Dynamical prediction methodology has been developing over the past three decades from the two-tier approach proposed by Bengtsson et al. (1993) in the early 1990s for seasonal forecasting, which has a physical basis under slowly varying forcing of the lower boundary (ocean, land use, etc.), to the one-tier approach that uses coupled general circulation models (GCMs) or climate system models to effectively describe the interactions among various components in the climate system, which has been available since approximately 2000 (Latif et al., 2001; Davey et al., 2002; Schneider et al., 2003). Although climate scientists have made great progress in dynamical prediction, the skills of model-based prediction remain limited, and difficulties arise mainly from uncertainties of the initial conditions and model parameterizations of unresolved sub-grid processes.

One of the widely used methods for overcoming these difficulties is multi-model ensemble (MME) prediction proposed by Krishnamurti et al. (1999) and Palmer et al. (2000). The MME method has been designed to quantify the uncertainties in climate predictions and is considered as an effective way to improving climate prediction skill (Peng et al., 2002; Doblas-Reyes et al., 2005; Hagedorn et al., 2005; Kirtman and Min, 2009; Lavers et al., 2009). For a single-model, the method used to construct ensemble prediction members can be realized by perturbing either the initial conditions or model parameterization schemes. The single-model ensemble prediction constructed by the initial condition perturbation has been widely used in operational weather and climate prediction worldwide; however, the multi-initial-condition ensemble prediction system generally has the problem of insufficient spread among ensemble members (Buizza et al., 1998). In fact, compared with weather forecast, climate prediction may be more sensitive to model errors, especially the model uncertainties caused by parameterization schemes of sub-grid physical processes. Teixeira and Reynolds (2008) suggested that the single-model ensemble prediction using the initial condition perturbation and the MME approach can better reflect and measure the uncertainties of dynamical climate prediction.

In recent years, several major research and operational centers, such as the ECMWF, the Asia–Pacific Economic Cooperation Climate Center (APCC), the International Research Institute for Climate and Society (IRI), and the NCEP have developed their own MME prediction systems, in which the MME method has been implemented and employed for dynamical seasonal climate prediction. It has been confirmed that MME prediction is usually superior to predictions made by any single model (Wang et al., 2009; Becker et al., 2014; Min et al., 2014). To fill the blank in the field of operational MME prediction in China and make full use of the achievements in model development and dynamical climate prediction by Chinese scientists, the National Climate Center (NCC) of the China Meteorological Administration (CMA) has devoted considerable efforts to developing an MME prediction system to produce improved and well-validated monthly–seasonal forecasting of climate and climate variability modes, such as the western Pacific subtropical high (WPSH), El Niño–Southern Oscillation (ENSO), as well as climate state variables of temperature, precipitation, and so on for research and operational purposes, based on a combination of several domestic operational climate models and imported prediction data. Recently, the China multi-model ensemble prediction system version 1.0 (CMMEv1.0) was established and applied to real-time climate prediction at the NCC/CMA.

In this paper, we present the recent progress in the development of the CMMEv1.0 system, including an introduction to its technical framework, model setup, key methods, some of the main products, and its application to the 2018 flood season (June–August) prediction started from March 2018, as well as verification of related prediction skills. The reminder of this paper is organized as follows. Section 2 introduces the technical framework and model setup. Section 3 describes data and methods. Section 4 shows the real-time forecasts for the 2018 flood season and related prediction skills. Summary and discussions are provided in Section 5.

2. Construction of the CMMEv1.0 system

Based on several domestic operationally-run climate

models and internationally imported prediction data, the NCC/CMA has established CMMEv1.0 for monthly–seasonal forecasting. Figure 1 shows its technical framework. As shown, the CMMEv1.0 consists of several modules, such as data collection, model initialization, time integration, post-processing, and the product output. Currently, CMMEv1.0 includes four domestic climate models and two imported prediction datasets. The domestic climate models are BCC-CSM1.1m from NCC/CMA (Wu et al., 2014), FGOALS-f2 from the State Key Laboratory of Numerical Modeling for Atmospheric Sciences and Geophysical Fluid Dynamics (LASG) of Institute of Atmospheric Physics (IAP) of Chinese Academy of Sciences (CAS) (Bao et al., 2019), FGOALS-s2 from LASG/IAP/CAS (Bao et al., 2013), and NZC-PCCSM4 from the Nansen–Zhu International Research Centre (NZC) of IAP/CAS (Ma and Wang, 2014). The imported prediction data are from ECMWF-SYSTEM4 (ECMWF-S4) (Molteni et al., 2011) and the NCEP Climate Forecast System version 2 (NCEP-CFSv2) (Saha et al., 2014).

Table 1 lists detailed information on these models in CMMEv1.0. The atmospheric component of BCC-CSM1.1m has a T106 horizontal resolution and 26 vertical levels; the horizontal resolution of the land component is the same as the atmospheric component; the oceanic component has a resolution of 1.0° latitude × 1.0° longitude × 40 vertical levels and has the same resolution as the sea ice component. The atmospheric component of FGOALS-f2 is FAMIL with a 1.0° × 1.0° horizontal resolution and 32 vertical levels; the land component is CLM4.0 (Oleson et al., 2010); the oceanic component of FGOALS-f2 is POP2, which uses two displaced-pole grids centered at Greenland, at a nominal 1° (gx1v6) horizontal resolution and 60 vertical levels; the horizontal resolution of the sea ice component CICE4 (Holland et al., 2012), is the same as the oceanic component. The atmospheric component of FGOALS-s2 is SAMIL2 version 2.4.7, which is a spectral model with a R42 horizontal resolution (approximately 1.66° × 2.81°) and 26 vertical levels; the land component is CLM3.0 (Oleson et al., 2004); the horizontal resolution of the oceanic component (LICOM2, Liu et al., 2004) is increased in the tropics (from 1.0° × 1.0° to 0.5° × 0.5°) with 30 vertical levels; the sea ice component is CSIM5 (Briegleb et al., 2004) and has the same horizontal resolution as the oceanic component. The atmospheric component (CAM4) of NZC-PCCSM4 has a 2.5° × 1.9° horizontal resolution and 26 vertical levels; the horizontal resolution of the land component (CLM4, Lawrence et al., 2011) is the same as that of CAM4; the oceanic component is a mixed-layer model (SOM) with a resolution of 1.0° × 1.0°; the horizontal resolution of the sea ice component CICE4 used is the same as the oceanic component.

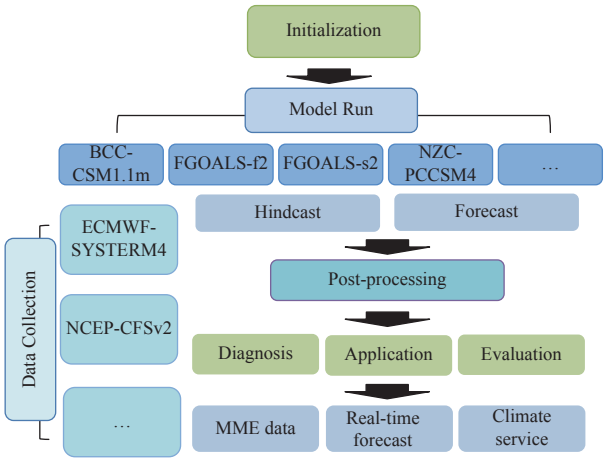

Fig. 1. Framework of the China multi-model ensemble prediction system version 1.0 (CMMEv1.0).

These models use the nudging method to assimilate atmospheric and oceanic reanalysis data for initialization. The atmospheric assimilation data include the meridional and zonal winds, air temperature, and geopotential height from the Japanese 55-yr reanalysis (JRA55, Kobayashi et al., 2015) for FGOALS-f2, FGOALS-s2, and NZC-PCCSM4, and from the NCEP-I reanalysis for BCC-CSM1.1m. The oceanic assimilation data of the four models are the 3D ocean temperature from the NCEP Global Ocean Data Assimilation System (GODAS, Behringer and Xue, 2004). The initial condition perturbation is used to generate ensemble members for each model. The number of ensemble members of BCC-CSM1.1m, FGOALS-f2, FGOALS-s2, and NZC-PCCSM4 are 24, 35, 4, and 8, respectively. The real-time

Table 1. Descriptions of the climate prediction models in CMMEv1.0

	Model	Institute	Atmospheric resolution	Oceanic resolution	Ensemble member	Forecast lead month
M1	FGOALS-f2	IAP	1.0°×1.0°, L32	1.0°×1.0°, L60	35	6
M2	FGOALS-s2	IAP	R42, L26	0.5°×0.5°–1.0°×1.0°, L30	4	6
M3	BCC-CSM1.1m	BCC	T106, L26	1.0°×1.0°, L40	24	13
M4	NZC-PCCSM4	IAP	2.5°×1.9°, L26	1.0°×1.0°	8	6
M5	ECMWF-S4	ECMWF	TL255, L91	1.0°×1.0°, L42	15	7
M6	NCEP-CFSv2	NCEP	T126, L64	1.0°×1.0°, L40	4	9

Note: The initial condition perturbation is used to generate ensemble members for each model.

forecasts begin on the 20th and 21st days of each month for FGOALS-f2, FGOALS-s2, and NZC-PCCSM4 and on the 1st day of each month for BCC-CSM1.1m. Recently, CMMEv1.0 has generated a monthly mean hindcast dataset for the period of 1991–2016 and a real-time forecast dataset since 2017. All of the model outputs were interpolated into a unified horizontal resolution of 1.0° × 1.0°.

3. Data and methods

The prediction skill (temporal correlation coefficient, TCC) of CMMEv1.0 is calculated based on the monthly mean hindcast for the period of 1991–2016. To verify the prediction performance, the anomalies of prediction are derived by subtracting the hindcast climatology from the original prediction data for each model in CMMEv1.0, where the model climatology is calculated by using the monthly hindcast data during 1991–2010 as a function of the initial calendar month and lead month, and observational climatology is obtained for the same period. All of the observational SST indices are calculated by using the Optimum Interpolation SST version 2 (OISSTv2) (Reynolds et al., 2007). The atmospheric verification data are computed by using NCEP–I reanalysis data for air temperature, 500-hPa geopotential height, and 850-hPa zonal wind (Kalnay et al., 1996) and the NOAA Climate Prediction Center (CPC) Merged Analysis of Precipitation (CMAP, Xie and Arkin, 1997). The summer (June–July–August, JJA) average surface (2 m) air temperature and precipitation for China are from the daily climate data of Chinese stations for global exchange (V3.0).

CMMEv1.0 has carried out the real-time forecasts for the 2018 flood season (June–August) based on the outputs of FGOALS-f2, FGOALS-s2, and NZC-PCCSM4 starting on 20 and 21 February, BCC-CSM1.1m starting on 1 March, ECMWF-S4 starting on 10 March, and NCEP-CFSv2 starting on 18 March 2018. In this paper, we show the monthly mean predictions during March–August and the JJA average predictions in 2018, including the global SST, ENSO, Indian Ocean Dipole (IOD), North Atlantic SST triple (NAST), WPSH, East Asian summer monsoon (EASM), surface air temperature (SAT), and precipitation. Table 2 shows definitions of the indices used for ENSO, IOD, NAST, WPSH, and EASM predictions.

4. CMMEv1.0 prediction and verification

4.1 *Prediction of global SST*

First, Figs. 2a–f show the TCC skill of the CMMEv1.0 hindcast for the global SST anomalies (SSTAs) beginning from March. CMMEv1.0 exhibits significantly high prediction skills over most of the ocean region, especially in the mid and low latitudes. In Figs. 2g–l and 2m–r, there is a good similarity between the real-time SSTA forecasts from March 2018 and their corresponding observations, in which CMMEv1.0 has accurately predicted the gradual warm-up of the cold SSTAs in the tropical central–eastern Pacific. During springtime, pattern correlation coefficients (PCCs) of global SSTAs are high (0.60 for March, 0.57 for April, and 0.42 for May), and CMMEv1.0 successfully reproduced the weakening of the cold SSTAs in the eastern Indian Ocean and the pattern of the NAST but with a relatively weaker intensity than observation. During summertime, the PCCs are relatively low, and the predicted SSTAs are overall

Table 2. Definitions of the different indices used in the prediction

Index	Definition	Reference
Niño3.4	(5°S–5°N, 170°E–120°W) regional mean SSTA	Internationally used
Niño4	(5°S–5°N, 160°E–150°W) regional mean SSTA	Internationally used
Niño3	(5°S–5°N, 150°–90°W) regional mean SSTA	Internationally used
N_{CP}	Niño4 − α×Niño3, when Niño3×Niño4 > 0，α = 0.4; otherwise α = 0	Ren and Jin (2011)
N_{EP}	Niño3 − α×Niño4, when Niño3×Niño4 > 0，α = 0.4; otherwise α = 0	Ren and Jin (2011)
IOD	Difference between (10°S–10°N, 50°–70°E) and (10°S–0°, 90°–110°E) regional mean SSTA	Saji et al. (1999)
NAST	[SSTA]A − ([SSTA]S + [SSTA]T), [SSTA]A: (34°–44°N, 72°–62°W) mean SSTA; [SSTA]S: (44°–56°N, 40°–24°W) mean SSTA; [SSTA]T: (0°–18°N, 46°–24°W) mean SSTA	Zuo et al. (2013)
Area of WPSH	Over 110°E–180° and north of 10°N, the total area of all ⩾ 588-dagpm contours in 500-hPa geopotential height field	Liu et al. (2012)
Intensity of WPSH	Over 110°E–180° and north of 10°N, sum of the product of the area of ⩾ 588-dagpm contours in 500-hPa geopotential height field and the grid point height minus 587 dagpm	Liu et al. (2012)
Western ridge point of WPSH	Over 90°E–180°, the longitude of the 588-dagpm westernmost point. If there is no 588-dagpm contour in a certain month, it is replaced by the historical maximum value of the month for 1991–2016	Liu et al. (2012)
EASM	Difference between (10°–20°N, 100°–150°E) and (25°–35°N, 100°–150°E) regional mean 850-hPa zonal wind	Zhang et al. (2003)

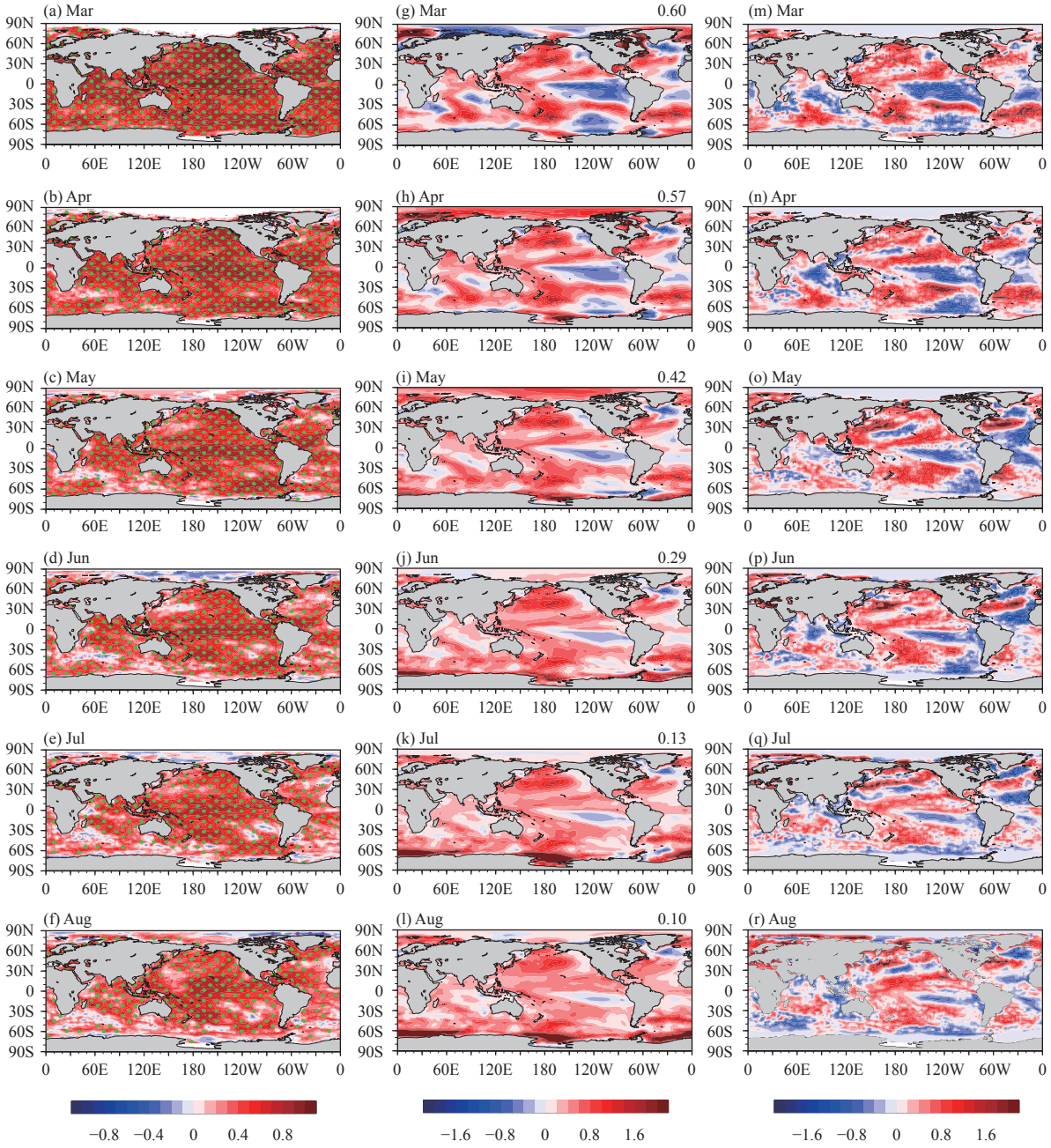

Fig. 2. (a–f) TCC skills for the global monthly (March–August) mean SSTA predicted by CMMEv1.0 initiated in March over 1991–2016; and monthly mean of the global SSTA (°C) for March–August 2018 (g–l) predicted by CMMEv1.0 and (m–r) derived from OISSTv2. The dotted areas in (a–f) are statistically significant at the 95% confidence level with a Student *t*-test. The numbers at the top right of (g–l) are the pattern correlation coefficients between monthly mean predictions and observations of the global SSTA.

warmer than observation, especially in North Atlantic and the Southern Ocean.

4.2 *Prediction of ENSO*

ENSO is a dominant mode of interannual variability with remarkable climate impacts worldwide (e.g., Li, 1990; Zhang et al., 1996; Wang et al., 2000; Chen, 2002; Zhang et al., 2011, 2012; Ren et al., 2018). Accurate and reasonable prediction of ENSO is considered as one of the primary indicators for the performance of climate prediction (e.g., Jiang et al., 2013a; Ren et al., 2017). Figure 3 shows the TCC skills for Niño3.4, Niño4, Niño3, N_{CP}, and N_{EP} indices (Ren and Jin, 2011, 2013) from March to August and JJA season over 1991–2016. As shown in Figs. 3a–e, the five ENSO indices are significantly skillful and the scores of the MME for both

Niño3.4 and Niño4 indices are larger than 0.8 at the six-month leadtime, which is more skillful than any single model. We further compare the real-time forecasts of CMMEv1.0 and the corresponding observations for these indices in Fig. 3. For Niño3.4 index, the CMMEv1.0 prediction accurately captured the trend of the ENSO transition from cold phase to neutral phase and then the warm phase during spring–summer of 2018, and the MME prediction almost coincides with observation (Fig. 3f).

There are still some major differences in the predictions among the different models. The forecast by FGOALS-f2 is closest to observation. NZC-PCCSM4 has predicted gradual warming of SSTA, which is similar to that of NCEP-CFS2, whereas ECMWF-S4 predicts relatively rapid warming. BCC-CSM1.1m predicts that the Niño3.4 index would more rapidly warm up and exceed 0.5 in summer, likely representing an El Niño event. The forecast by FGOALS-s2 is quite different from the others and is characterized by changing SSTAs with an initial increase and then a decrease. Both predictions of the Niño4 and Niño3 indices are consistent with that of the Niño3.4 index; i.e., the MME forecast is similar to observation despite some differences among the models. The above results further indicate the superiority of MME prediction to single model prediction.

As is known, the impacts of EP (Eastern Pacific)-type and CP (Central Pacific)-type El Niño on the climate are quite different from each other (e.g., Weng et al., 2007, 2009; Zhang et al., 2011, 2012). In the development summer of El Niño, the influence of CP-type El Niño on East Asian precipitation is more significant than that of EP-type El Niño (Yuan and Yang, 2012; Ren et al., 2018). Thus, in addition, we predicted evolutions of the EP- and CP-type ENSO indices (N_{EP} and N_{CP}) using CMMEv1.0. The skills of the spring–summer predictions that start in March for both N_{EP} and N_{CP} indices are larger than 0.6. The real-time forecast of CMMEv1.0 has shown no CP-type El Niño signal occurring in the 2018 flood season, which is consistent with observations. It has been known that the EP (CP) type of ENSO features a spring (summer) persistence barrier (Ren et al., 2016) and thus, is subject to the spring (summer) prediction barrier (Ren et al., 2019b), which could be indicated by the different timings of the maximum decline speeds of the TCC scores in Fig. 3. Our MME predictions show that the EP-type ENSO has a higher prediction skill than the CP-type in terms of their indices, although the dynamic models still have difficulties in distinguishing the two types in terms of their SSTA center positions (Ren et al., 2019a), which could be statistically corrected (Liu and Ren, 2017). Indeed, the difficulty of the dynamic models in predicting the two ENSO types is still formidable and further research is needed.

4.3 *Prediction of IOD and NAST*

Both the IOD and NAST play important roles in influencing global and local climate variations (Birkett et al., 1999; Ashok et al., 2001; Li S. L. et al., 2003; Saji and Yamagata, 2003; Yang et al., 2007; Jia et al., 2011; Gitau et al., 2015; Tan et al., 2017; Lu et al., 2018). Figures 4a, c show the prediction skills, real-time forecasts, and related observations of the IOD index, respectively. As Fig. 4a shows, the TCC scores for IOD beginning from March are limited. This is presumably due to its winter prediction barrier, where model prediction of the IOD is usually subject to a significant decline in skill from January to March; the causes for this remain unclear (Wajsowicz, 2005; Luo et al., 2007; Feng et al., 2014). The results from CMMEv1.0 indicate that the simulation and prediction of IOD in the current climate models need to be improved further. For the real-time forecast, the six ensemble model members predict a near-normal IOD state in spring and a weak positive anomaly in summer, which are consistent with observations; however, the predicted intensity is significantly weakened.

Figure 4b shows that CMMEv1.0 has a higher prediction skill for NAST than for IOD. In March–June, the TCC scores for NAST are all larger than or close to 0.6 and then become lower in July–August, whereas in the JJA season the prediction skill is close to 0.6. As seen in Fig. 4d shows, the predictions of CMMEv1.0 for NAST and those of other models are very close to each other except in March, and their MME mean prediction is quite consistent with observations except for weaker positive anomalies of NAST.

4.4 *Prediction of WPSH and EASM*

The WPSH is one of the most important circulation patterns affecting the East Asian weather and climate. The variations of its area, intensity, and location have important impacts on the flood season in China (Wu et al., 2002). Accurate prediction of these characteristics of the WPSH can provide important reference information for predicting the transition and variation of summer rainbelts in China. Figures 5a–c show the prediction skills for the area index, the intensity index, and the western ridge point index of the WPSH (Liu et al., 2012), respectively. It is shown that the WPSH area, intensity, and western ridge point in CMMEv1.0 are significantly skillful, especially for the JJA season. For the 2018 flood season, real-time forecasts of the WPSH indices by CMMEv1.0 models (except for ECMWF-S4), as shown in

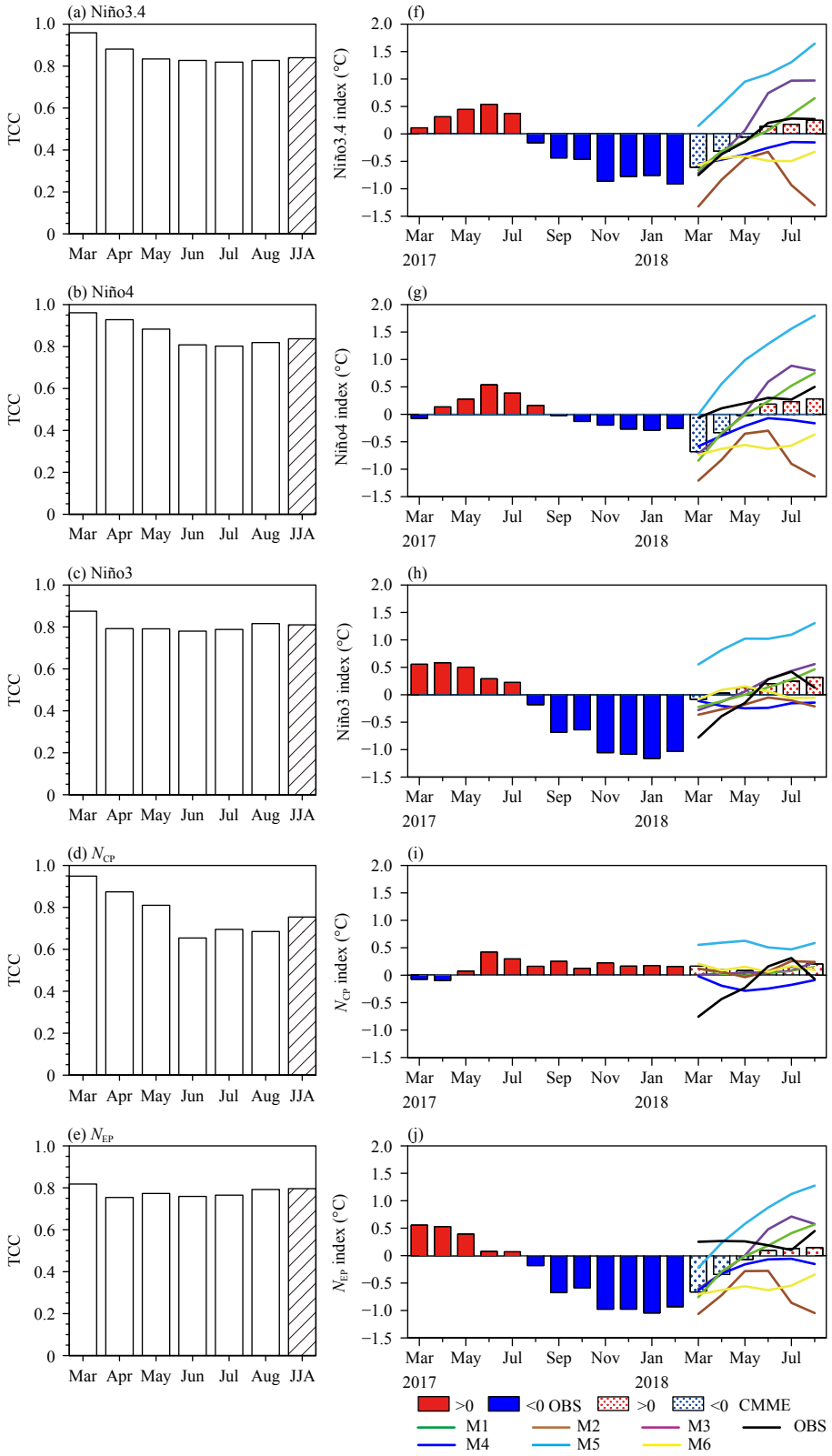

Fig. 3. Left panels: TCC prediction skills for (a) Niño3.4, (b) Niño4, (c) Niño3, (d) N_{CP}, and (e) N_{EP} indices from monthly (March–August; hollow bars) and seasonal (JJA; hatched bars) mean predictions by CMMEv1.0 initiated in March over 1991–2016. Right panels: monthly evolutions of (f) Niño3.4, (g) Niño4, (h) Niño3, (i) N_{CP}, and (j) N_{EP} indices (°C) derived from OISSTv2 for March 2017–August 2018 (OBS; denoted by red/blue bars before March 2018 and by the thick black line after March 2018) and from CMMEv1.0 for March–August 2018 (forecast; denoted by red/blue hatched bars for the ensemble mean and by color lines for individual models M1–M6).

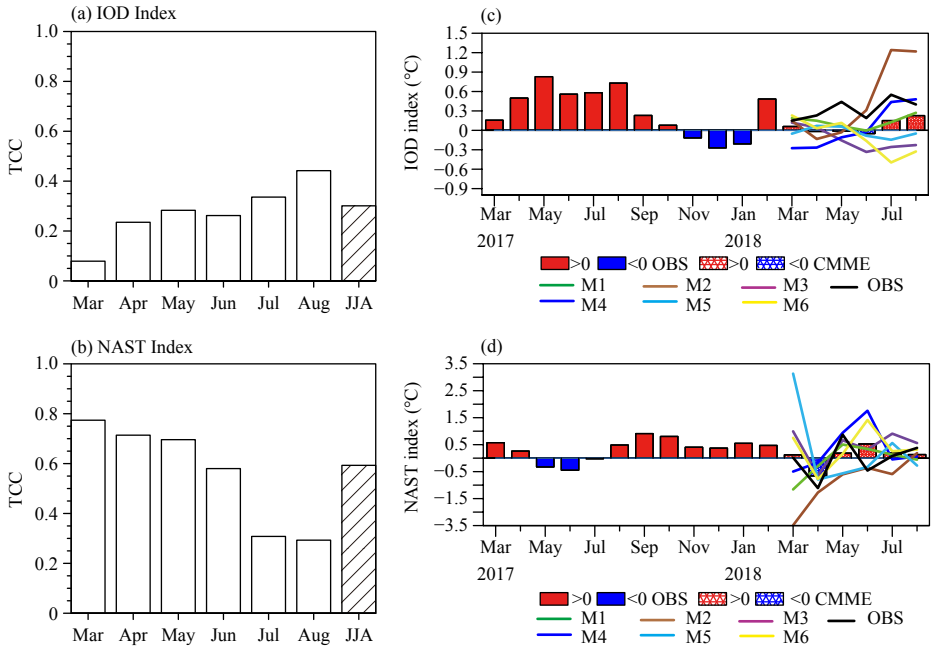

Fig. 4. Left panels: TCC prediction skills for (a) IOD and (b) NAST indices for monthly (March–August; hollow bars) and seasonal (JJA; hatched bars) mean predictions by the CMMEv1.0 initiated in March over 1991–2016. Right panels: monthly evolutions of (c) IOD and (d) NAST indices (°C) derived from OISSTv2 for March 2017–August 2018 (OBS; denoted by red/blue bars before March 2018 and by the thick black line after March 2018) and from CMMEv1.0 for March–August 2018 (forecast; denoted by red/blue hatched bars for the ensemble mean and by color lines for individual models M1–M6).

Figs. 5e–g, are quite consistent with observations. Forecast results also reveal that both the area and intensity of the WPSH in the summer of 2018 tend to be near normal and the western ridge point is significantly eastward.

The EASM is considerably important for the global atmospheric circulation systems. Precipitation in most regions of China, especially eastern China, is strongly affected by the intensity of the EASM, and the EASM index is significantly correlated with precipitation in central and eastern China (Jiang et al., 2013a). Successful EASM prediction will definitely help to forecast precipitation anomalies in China. Previous studies have indicated that dynamic prediction can capture the main spatial pattern and features of the EASM-related precipitation and large-scale circulation several months in advance (e.g., Yang et al., 2008; Jiang et al., 2013a). As Fig. 5d shows, CMMEv1.0 has a quite high prediction skill for the EASM intensity index (Zhang et al., 2003) in JJA season. During summer 2018, the observed EASM is stronger than climatology, and the predictions of each model and MME in CMMEv1.0 are similar to the observations but tend to be slightly weaker (Fig. 5h).

4.5 *Prediction of surface air temperature and precipitation in China*

Figure 6 presents the prediction skill, the 2018 real-time forecasts of CMME v1.0, and related observations for the JJA SAT and precipitation anomalies in China. Clearly, Fig. 6a shows that the summer SAT prediction in most areas of China is skillful in CMMEv1.0 at the three-month leadtime, though TCCs are relatively low for the Huang–Huai area and small parts of western China. Comparison of Fig. 6b and 6c reveals that the real-time SAT forecast for summer 2018 is quite consistent with observation; i.e., the SAT in most regions of China is warmer than climatology with relatively larger anomalies in northern China and smaller anomalies in central and southern China; however, the predicted intensity is slightly weaker than the observation in most regions.

In contrast to SAT, the CMMEv1.0 has limited TCC skills for predicting summer precipitation in China for a leadtime of three months. As Fig. 6d shows, there are no significant skills in most regions of China except northwestern and eastern China. Comparison of the real-time forecast and observation for precipitation anomalies in summer 2018, as shown in Figs. 6e, f, indicates an overall good performance of CMMEv1.0. Observations show that the main rainbelt in the 2018 flood season exhibits a "positive–negative–positive" distribution in the north–south direction; i.e., precipitation in the northern and southern China is more than climatology but less than climatology over the Yangtze River basin. This rainfall

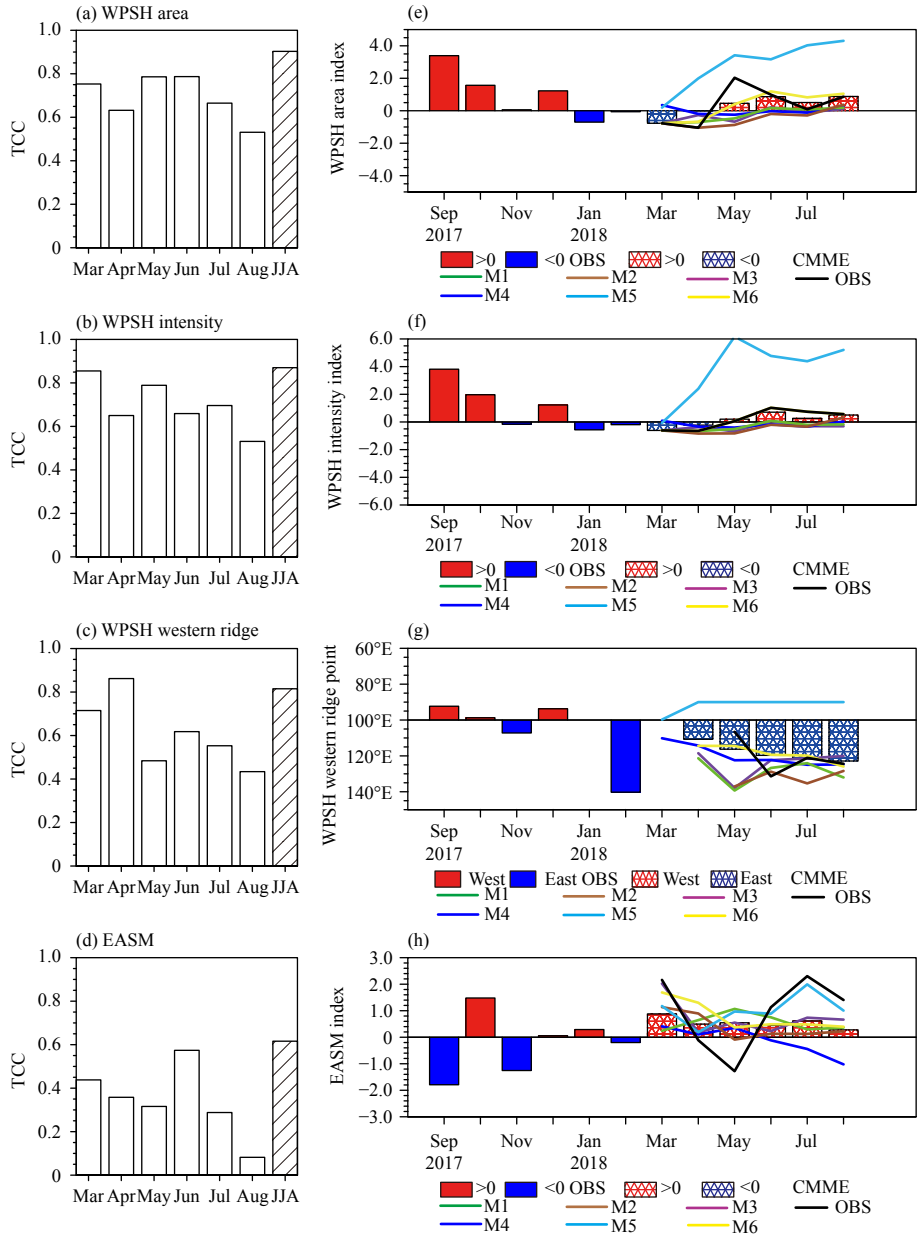

Fig. 5. Left panels: TCC prediction skills for (a) WPSH area (b) WPSH intensity, (c) western ridge point, and (d) EASM indices for monthly (March–August; hollow bars) and seasonal (JJA; hatched bars) mean predictions by the CMMEv1.0 initiated in March over 1991–2016. Right panels: monthly evolutions of the indices of (e) WPSH area, (f) WPSH intensity, (g) western ridge point, and (h) EASM derived from NCEP-I for September 2017–August 2018 (OBS; denoted by red/blue bars before March 2018 and by the thick black line after March 2018) and from CMMEv1.0 for March–August 2018 (forecast; denoted by red/blue hatched bars for ensemble mean and by color lines for individual models M1–M6).

anomaly pattern in summer 2018 has been well captured by the CMMEv1.0 prediction; however, the latter shows much more precipitation in the middle and lower reaches of the Yangtze River than the observation.

5. Summary and discussion

The multi-model ensemble (MME) prediction has become one of the most popular and useful approaches for short-term climate prediction and for development of current climate models towards a higher spatiotemporal resolution, more complicated physical processes, and seamless dynamical prediction. A number of previous studies have demonstrated that MME mean prediction is not only theoretically superior to single model prediction but can also significantly reduce the impact of systematic

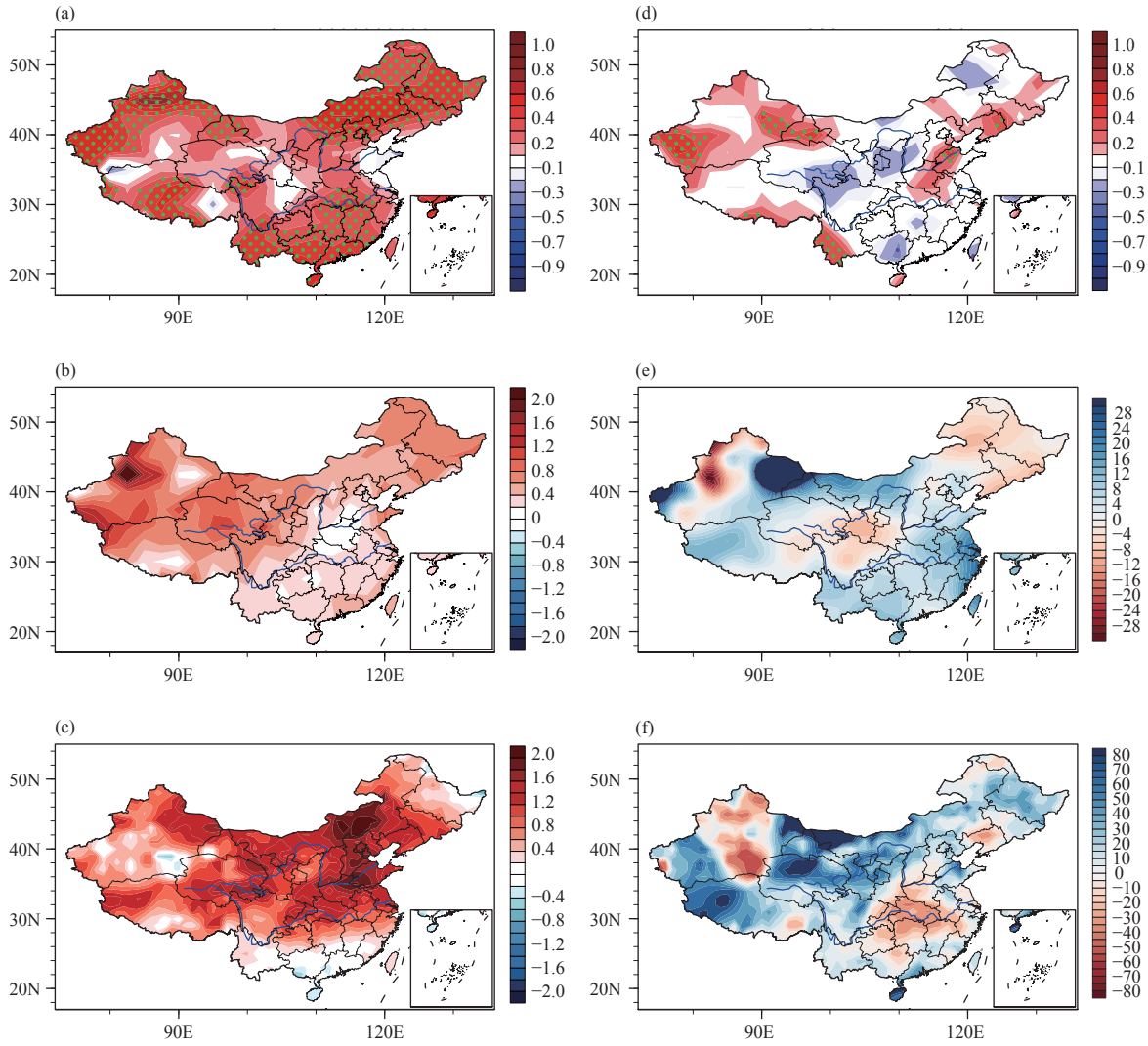

Fig. 6. TCC prediction skills for seasonal (JJA) mean predictions of (a) SAT and (d) precipitation in China by CMMEv1.0 initiated in March over 1991–2016; and the seasonal mean of (b, c) SAT (°C) and (e, f) precipitation anomaly (%) for JJA 2018 (b, e) predicted by CMMEv1.0 initiated in March 2018 and (c, f) derived from OISSTv2. The dotted area in (a, d) denotes the statistical significant values at the 95% confidence level with the Student *t*-test.

model errors on climate prediction. Because of the highly complex climate conditions in East Asia mixed with the uncertainties of the model itself and its initial values, short-term climate prediction based on a single model can no longer meet the increasing demands of climate services. Therefore, it is necessary to develop an operational MME climate prediction system and improve the prediction skill, particularly for East Asia and China.

Based on some advanced domestic and international climate models, the NCC/CMA has designed a unified initialization and post-processing framework and established CMMEv1.0, which has thus far been particularly used for monthly–seasonal climate forecasting. The CMMEv1.0 carries out its operational applications to predicting some primary modes of climate variability (such as the ENSO, IOD, NAST, WPSH, and EASM) and climate elements (SAT and precipitation). According to the evaluation of the 1991–2016 hindcast, CMMEv1.0 skillfully predicts global SSTA, especially for ENSO in terms of its various indices including the types. Our results show that TCC scores for both Niño3.4 and Niño4 indices are larger than 0.8 at the six-month leadtime, and the other El Niño indices and the NAST index are also accurately predicted by CMMEv1.0, whereas the accuracy of the IOD index starting from March is relatively low. The prediction skills for the area, intensity, and western ridge point of WPSH, and the intensity of EASM, especially in the boreal summer, are high. Moreover, CMMEv1.0 exhibits significant high skill for summer SAT for most regions of China for a three-

month leadtime; however, it is only skillful for summer precipitation in Northwest and East China.

We have also produced real-time forecasts using CMMEv1.0 of the climate variability modes and climate elements for the 2018 flood season (June–August) starting from March 2018. Our results show that CMMEv1.0 has accurately captured the transition of ENSO from cold phase to neutral and warm phases and the weak positive anomalies of NAST. Due to the winter prediction barrier, the predicted IOD is weaker than observed in summer 2018. The WPSH is observed to be near-normal in intensity and eastward in summer 2018, which has been successfully captured by CMMEv1.0; however, the EASM is slightly weaker in the prediction than in the observation. CMMEv1.0 has also accurately predicted the spatial distribution of warmer temperatures in most parts of China. The main rainbelts in North China and southern coastal China in summer 2018 are well captured; however, CMMEv1.0 has shown much more precipitation in the middle and lower reaches of the Yangtze River than observation.

The analysis and evaluation results reported in this paper indicate that the MME mean predictions from CMMEv1.0 are more accurate than predictions of any single model. Overall, CMMEv1.0 can skillfully predict global SST anomalies (especially in the equatorial central and eastern Pacific), the WPSH area and intensity, and the EASM intensity. However, many aspects of CMMEv1.0 still need further improvement, such as its relatively lower performance for IOD prediction. Jiang et al. (2013b) mentioned that the CFSv2 has a low prediction skill for IOD, which is related to the annul cycle of IOD, the systematic errors of the Indian Ocean simulations, and the model biases in the IOD response to ENSO (Li T. et al., 2003; Fischer et al., 2005; Shi et al., 2012). Because of the relatively low ability of climate models to simulate and predict the East Asian climate, precipitation prediction remains challenging. Therefore, the MME mean shows limited improvement in precipitation prediction. Presently, the performance of CMMEv1.0 for predicting precipitation still cannot sufficiently meet the demands of operational climate prediction, and methods for improving its prediction skill need to be explored further. One option for consideration is to take advantage of the empirical correction of the prediction error, statistical downscaling, and other advanced methods for extracting predictable information and reducing model prediction error (e.g., Ren and Chou, 2006, 2007; Kug et al., 2008). Overall, research and development on the MME prediction system are still at an initial stage in China, and it is necessary to make full use of achievements in both domestic and international research in the field of MME prediction to improve the level of short-term climate prediction in China.

Acknowledgments. The authors are grateful to the three anonymous reviewers for their insightful comments, which have helped improve the quality of the paper.

REFERENCES

Ashok, K., Z. Y. Guan, and T. Yamagata, 2001: Impact of the Indian Ocean dipole on the relationship between the Indian monsoon rainfall and ENSO. *Geophys. Res. Lett.*, **28**, 4499–4502, doi: 10.1029/2001GL013294.

Bao, Q., P. F. Lin, T. J. Zhou, et al., 2013: The flexible global ocean–atmosphere–land system model, spectral version 2: FGOALS-s2. *Adv. Atmos. Sci.*, **30**, 561–576, doi: 10.1007/s00376-012-2113-9.

Bao, Q., X. F. Wu, J. X. Li, et al., 2019: Outlook for El Niño and the Indian Ocean Dipole in autumn–winter 2018–2019. *Chinese Sci. Bull.*, **64**, 73–78, doi: 10.1360/N972018-00913. (in Chinese)

Becker, E., H. van den Dool, and Q. Zhang, 2014: Predictability and forecast skill in NMME. *J. Climate*, **27**, 5891–5906, doi: 10.1175/JCLI-D-13-00597.1.

Behringer, D. W., and Y. Xue, 2004: Evaluation of the Global Ocean Data Assimilation System at NCEP: The Pacific Ocean. Proceedings of the Eighth Symposium on Integrated Observing and Assimilation System for Atmosphere, Ocean, and Land Surface, AMS 84th Annual Meeting, Seattle, Washington, USA, 11–15.

Bengtsson, L., U. Schlese, E. Roeckner, et al., 1993: A two-tiered approach to long-range climate forecasting. *Science*, **261**, 1026–1029, doi: 10.1126/science.261.5124.1026.

Birkett, C., R. Murtugudde, and T. Allan, 1999: Indian Ocean climate event brings floods to East Africa's lakes and the Sudd Marsh. *Geophys. Res. Lett.*, **26**, 1031–1034, doi: 10.1029/1999GL900165.

Briegleb, B. P., C. M. Bitz, E. C. Hunke, et al., 2004: Scientific Description of the Sea Ice Component in the Community Climate System Model, Version 3. NCAR Tech Note NCAR/TN-463+ STR, NCAR, Boulder, CO, USA, 70 pp.

Buizza, R., T. Petroliagis, T. Palmer, et al., 1998: Impact of model resolution and ensemble size on the performance of an ensemble prediction system. *Quart. J. Roy. Meteor. Soc.*, **124**, 1935–1960, doi: 10.1002/qj.49712455008.

Chen, W., 2002: Impacts of El Niño and La Niña on the cycle of the East Asian winter and summer monsoon. *Chinese J. Atmos. Sci.*, **26**, 595–610. (in Chinese)

Davey, M., M. Huddleston, K. Sperber, et al., 2002: STOIC: A study of coupled model climatology and variability in tropical ocean regions. *Climate Dyn.*, **18**, 403–420, doi: 10.1007/s00382-001-0188-6.

Doblas-Reyes, F. J., R. Hagedorn, and T. N. Palmer, 2005: The rationale behind the success of multi-model ensembles in seasonal forecasting—II. Calibration and combination. *Tellus A Dyn. Meteor. Oceanogr.*, **57**, 234–252, doi: 10.3402/tellusa.v57i3.14658.

Feng, R., W. S. Duan, and M. Mu, 2014: The "winter predictability barrier" for IOD events and its error growth dynamics: Results from a fully coupled GCM. *J. Geophys. Res. Oceans*, **119**, 8688–8708, doi: 10.1002/2014JC010473.

Fischer, A. S., P. Terray, E. Guilyardi, et al., 2005: Two independent triggers for the Indian Ocean dipole/zonal mode in a coupled GCM. *J. Climate*, **18**, 3428–3449, doi: 10.1175/JCLI3478.1.

Gitau, W., P. Camberlin, L. Ogallo, et al., 2015: Oceanic and atmospheric linkages with short rainfall season intraseasonal statistics over equatorial Eastern Africa and their predictive potential. *Int. J. Climatol.*, **35**, 23829–2399, doi: 10.1002/joc.4131.

Hagedorn, R., F. J. Doblas-Reyes, and T. N. Palmer, 2005: The rationale behind the success of multi-model ensembles in seasonal forecasting—I. Basic concept. *Tellus A Dyn. Meteor. Oceanogr.*, **57**, 219–233, doi: 10.3402/tellusa.v57i3.14657.

Holland, M. M., D. A. Bailey, B. P. Briegleb, et al., 2012: Improved sea ice shortwave radiation physics in CCSM4: The impact of melt ponds and aerosols on Arctic Sea ice. *J. Climate*, **25**, 1413–1430, doi: 10.1175/JCLI-D-11-00078.1.

Jia, X. L., L. J. Chen, Z. S. Gong, et al., 2011: Anomalies of ocean and atmospheric circulation in 2010 and their impacts on climate in China. *Meteor. Mon.*, **37**, 446–453. (in Chinese)

Jiang, X. W., S. Yang, Y. Q. Li, et al., 2013a: Seasonal-to-interannual prediction of the Asian summer monsoon in the NCEP climate forecast system version 2. *J. Climate*, **26**, 3708–3727, doi: 10.1175/JCLI-D-12-00437.1.

Jiang, X. W., S. Yang, J. P. Li, et al., 2013b: Variability of the Indian Ocean SST and its possible impact on summer western North Pacific anticyclone in the NCEP climate forecast system. *Climate Dyn.*, **41**, 2199–2212, doi: 10.1007/s00382-013-1934-2.

Kalnay, W., M. Kanamitsu, R. Kistler, et al., 1996: The NCEP/NCAR 40-year reanalysis project. *Bull. Amer. Meteor. Soc.*, **77**, 437–472, doi: 10.1175/1520-0477(1996)077<0437:TNYRP>2.0.CO;2.

Kirtman, B. P., and D. Min, 2009: Multimodel ensemble ENSO prediction with CCSM and CFS. *Mon. Wea. Rev.*, **137**, 2908–2930, doi: 10.1175/2009MWR2672.1.

Kobayashi, S., Y. Ota, Y. Harada, et al., 2015: The JRA-55 reanalysis: General specifications and basic characteristics. *J. Meteor. Soc. Japan*, **93**, 5–48.

Krishnamurti, T. N., C. M. Kishtawal, T. E. LaRow, et al., 1999: Improved weather and seasonal climate forecasts from multimodel superensemble. *Science*, **285**, 1548–1550, doi: 10.1126/science.285.5433.1548.

Kug, J. S., J. Y. Lee, and I. S. Kang, 2008: Systematic error correction of dynamical seasonal prediction of sea surface temperature using a stepwise pattern project method. *Mon. Wea. Rev.*, **136**, 3501–3512, doi: 10.1175/2008MWR2272.1.

Latif, M., K. Sperber, J. Arblaster, et al., 2001: ENSIP: The El Nino simulation intercomparison project. *Climate Dyn.*, **18**, 255–276, doi: 10.1007/s003820100174.

Lavers, D., L. F. Luo, and E. F. Wood, 2009: A multiple model assessment of seasonal climate forecast skill for applications. *Geophys. Res. Lett.*, **36**, L23711, doi: 10.1029/2009GL041365.

Lawrence, D. M., K. W. Oleson, M. G. Flanner, et al., 2011: Parameterization improvements and functional and structural advances in version 4 of the Community Land Model. *J. Adv. Model. Earth Syst.*, **3**, M03001, doi: 10.1029/2011MS00045.

Li, C. Y., 1990: Interaction between anomalous winter monsoon in East Asia and El Nino events. *Adv. Atmos. Sci.*, **7**, 36–46, doi: 10.1007/BF02919166.

Li, S. L., W. A. Robinson, and S. L. Peng, 2003: Influence of the North Atlantic SST tripole on northwest African rainfall. *J. Geophys. Res. Atmos.*, **108**, 4594, doi: 10.1029/2002JD003130.

Li, T., B. Wang, C. P. Chang, et al., 2003: A theory for the Indian Ocean dipole–zonal mode. *J. Atmos. Sci.*, **60**, 2119–2135, doi: 10.1175/1520-0469(2003)060<2119:ATFTIO>2.0.CO;2.

Liu, H. L., Y. Q. Yu, W. Li, et al., 2004: *Manual for LASG/IAP Climate System Ocean Model* (*LICOM1.0*). Science Press, Beijing, 128 pp. (in Chinese).

Liu, Y., and H.-L. Ren, 2017: Improving ENSO prediction in CFSv2 with an analogue-based correction method. *Int. J. Climatol.*, **37**, 5035–5046, doi: 10.1002/joc.5142.

Liu, Y. Y., W. J. Li, W. X. Ai, et al., 2012: Reconstruction and application of the monthly western Pacific subtropical high indices. *J. Appl. Meteor. Sci.*, **23**, 414–423, doi: 10.3969/j.issn.1001-7313.2012.04.004. (in Chinese)

Lu, B., H.-L. Ren, R. Eade, et al., 2018: Indian Ocean SST modes and their impacts as simulated in BCC_CSM1.1(m) and HadGEM3. *Adv. Atmos. Sci.*, **35**, 1035–1048, doi: 10.1007/s00376-018-7279-3.

Luo, J. J., S. Masson, S. Behera, et al., 2007: Experimental forecasts of the Indian Ocean dipole using a coupled OAGCM. *J. Climate*, **20**, 2178–2190, doi: 10.1175/JCLI4132.1.

Ma, J. H., and H. J. Wang, 2014: Design and testing of a global climate prediction system based on a coupled climate model. *Sci. China Earth Sci.*, **57**, 2417–2427, doi: 10.1007/s11430-014-4875-7.

Min, Y. M., V. N. Kryjov, and S. M. Oh, 2014: Assessment of APCC multimodel ensemble prediction in seasonal climate forecasting: Retrospective (1983–2003) and real-time forecasts (2008–2013). *J. Geophys. Res. Atmos.*, **119**, 12132–12150, doi: 10.1002/2014JD022230.

Molteni, F., T. Stockdale, M. Alonso-Balmaseda, et al., 2011: The New ECMWF Seasonal Forecast System (System 4). ECMWF Technical Memorandum 656, ECMWF, Reading, UK, 49 pp, doi: 10.21957/4nery093i.

Oleson, K. W., Y. Dai, G. Bonan, et al., 2004: Technical Description of the Community Land Model (CLM). NCAR/TN-461+STR, NCAR, Boulder, CO, USA, 173 pp, doi: 10.5065/D6N877R0.

Oleson, K. W., D. M. Lawrence, G. B. Bonan, et al., 2010: Technical Description of Version 4.0 of the Community Land Model (CLM). NCAR Technical Note NCAR/TN-478+STR, NCAR, Boulder, CO, USA, 257 pp, doi: 10.5065/D6FB50WZ.

Palmer, T. N., Č. Branković, and D. S. Richardson, 2000: A probability and decision-model analysis of PROVOST seasonal multi-model ensemble integrations. *Quart. J. Roy. Meteor. Soc.*, **126**, 2013–2033, doi: 10.1002/qj.49712656703.

Peng, P. T., A. Kumar, H. van den Dool, et al., 2002: An analysis of multimodel ensemble predictions for seasonal climate anomalies. *J. Geophys. Res. Atmos.*, **107**, 4710, doi: 10.1029/2002JD002712.

Ren, H. L., and J. F. Chou, 2006: Analogue correction method of errors by combining statistical and dynamical methods. *Acta Meteor. Sinica.*, **20**, 367–373.

Ren, H. L., and J. F. Chou, 2007: Strategy and methodology of dynamical analogue prediction. *Sci. China Earth Sci.*, **50**, 1589–1599, doi: 10.1007/s11430-007-0109-6.

Ren, H.-L., and F.-F. Jin, 2011: Niño indices for two types of ENSO. *Geophys. Res. Lett.*, **38**, L04704, doi: 10.1029/2010GL046031.

Ren, H.-L., and F.-F. Jin, 2013: Recharge oscillator mechanisms in two types of ENSO. *J. Climate*, **26**, 6506–6523, doi: 10.1175/JCLI-D-12-00601.1.

Ren, H.-L., F.-F. Jin, B. Tian, et al., 2016: Distinct persistence barriers in two types of ENSO. *Geophys. Res. Lett.*, **43**, 10973–10979, doi: 10.1002/2016GL071015.

Ren, H.-L., F.-F. Jin, L. C. Song, et al., 2017: Prediction of primary climate variability modes at the Beijing Climate Center. *J. Meteor. Res.*, **31**, 204–223, doi: 10.1007/s13351-017-6097-3.

Ren, H.-L., B. Lu, J. H. Wan, et al., 2018: Identification standard for ENSO events and its application to climate monitoring

and prediction in China. *J. Meteor. Res.*, **32**, 923–936, doi: 10.1007/s13351-018-8078-6.

Ren, H.-L., A. A. Scaife, N. Dunstone, et al., 2019a: Seasonal predictability of winter ENSO types in operational dynamical model predictions. *Climate Dyn.*, 3869–3890, doi: 10.1007/s00382-018-4366-1.

Ren, H.-L., J. Q. Zuo, and Y. Deng, 2019b: Statistical predictability of Niño indices for two types of ENSO. *Climate Dyn.*, 5361–5382, doi: 10.1007/s00382-018-4453-3.

Reynolds, R. W., T. M. Smith, C. Y. Liu, et al., 2007: Daily high-resolution-blended analyses for sea surface temperature. *J. Climate*, **20**, 5473–5496, doi: 10.1175/2007JCLI1824.1.

Saha, S., S. Nadiga, C. Thiaw, et al., 2006: The NCEP climate forecast system. *J. Climate*, **19**, 3483–3517, doi: 10.1175/JCLI3812.1.

Saha, S., S. Moorthi, X. R. Wu, et al., 2014: The NCEP climate forecast system version 2. *J. Climate*, **27**, 2185–2208, doi: 10.1175/JCLI-D-12-00823.1.

Saji, N. H., and T. Yamagata, 2003: Possible impacts of Indian Ocean dipole mode events on global climate. *Climate Res.*, **25**, 151–169, doi: 10.3354/cr025151.

Saji, N. H., B. N. Goswami, P. N. Vinayachandran, et al., 1999: A dipole mode in the tropical Indian Ocean. *Nature*, **401**, 360–363, doi: 10.1038/43854.

Schneider, E. K., B. P. Kirtman, D. G. DeWitt, et al., 2003: Retrospective ENSO forecasts: Sensitivity to atmospheric model and ocean resolution. *Mon. Wea. Rev.*, **131**, 3038–3060, doi: 10.1175/1520-0493(2003)131<3038:REFSTA>2.0.CO;2.

Shi, L., H. H. Hendon, O. Alves, et al., 2012: How predictable is the Indian Ocean dipole? *Mon. Wea. Rev.*, **140**, 3867–3884, doi: 10.1175/MWR-D-12-00001.1.

Tan, G. R., H.-L. Ren, H. S. Chen, et al., 2017: Detecting primary precursors of January surface air temperature anomalies in China. *J. Meteor. Res.*, **31**, 1096–1108, doi: 10.1007/s13351-017-7013-6.

Teixeira, J., and C. A. Reynolds, 2008: Stochastic nature of physical parameterizations in ensemble prediction: A stochastic convection approach. *Mon. Wea. Rev.*, **136**, 483–496, doi: 10.1175/2007MWR1870.1.

Wajsowicz, R. C., 2005: Potential predictability of tropical Indian Ocean SST anomalies. *Geophys. Res. Lett.*, **32**, L24702, doi: 10.1029/2005GL024169.

Wang, B., R. G. Wu, and X. H. Fu, 2000: Pacific–East Asian teleconnection: How does ENSO affect east Asian climate? *J. Climate*, **13**, 1517–1536, doi: 10.1175/1520-0442(2000)013<1517:PEATHD>2.0.CO;2.

Wang, B., J.-Y. Lee, I.-S. Kang, et al., 2009: Advance and prospectus of seasonal prediction: Assessment of the APCC/CliPAS 14-model ensemble retrospective seasonal prediction (1980–2004). *Climate Dyn.*, **33**, 93–117, doi: 10.1007/s00382-008-0460-0.

Wang, H. J., K. Fan, J. Q. Sun, et al., 2015: A review of seasonal climate prediction research in China. *Adv. Atmos. Sci.*, **32**, 149–168, doi: 10.1007/s00376-014-0016-7.

Weisheimer, A., F. J. Doblas-Reyes, T. N. Palmer, et al., 2009: ENSEMBLES: A new multi-model ensemble for seasonal-to-annual predictions—Skill and progress beyond DEMETER in forecasting tropical Pacific SSTs. *Geophys. Res. Lett.*, **36**, L21711, doi: 10.1029/2009GL040896.

Weng, H. Y., K. Ashok, S. K. Behera, et al., 2007: Impacts of recent El Niño Modoki on dry/wet conditions in the Pacific Rim during boreal summer. *Climate Dyn.*, **29**, 113–129, doi: 10.1007/s00382-007-0234-0.

Weng, H. Y., S. K. Behera, and T. Yamagata, 2009: Anomalous winter climate conditions in the Pacific Rim during recent El Niño Modoki and El Niño events. *Climate Dyn.*, **32**, 663–674, doi: 10.1007/s00382-008-0394-6.

Wu, G. X., J. F. Chou, Y. M. Liu, et al., 2002: *Dynamics of the Formation and Variation of Subtropical Anticyclones*. Science Press, Beijing, 314 pp. (in Chinese)

Wu, T. W., L. C. Song, W. P. Li, et al., 2014: An overview of BCC climate system model development and application for climate change studies. *J. Meteor. Res.*, **28**, 34–56, doi: 10.1007/s13351-014-3041-7.

Xie, P. P., and P. A. Arkin, 1997: Global precipitation: A 17-year monthly analysis based on gauge observations, satellite estimates, and numerical model outputs. *Bull. Amer. Meteor. Soc.*, **78**, 2539–2558, doi: 10.1175/1520-0477(1997)078<2539:GPAYMA>2.0.CO;2.

Yang, S., Z, Q. Zhang, V. E. Kousky, et al., 2008: Simulations and seasonal prediction of the Asian summer monsoon in the NCEP Climate Forecast System. *J. Climate*, **21**, 3755–3775, doi: 10.1175/2008JCLI1961.1.

Yang, X., Z. Y. Guan, and B. L. Zhu, 2007: Role of Indian Ocean dipole events in the influence of ENSO on the summer rainfall and temperature in China. *J. Nanjing Inst. Meteor.*, **30**, 170–177, doi: 10.3969/j.issn.1674-7097.2007.02.004. (in Chinese)

Yuan, Y., and S. Yang, 2012: Impacts of different types of El Niño on the East Asian climate: Focus on ENSO cycles. *J. Climate*, **25**, 7702–7722, doi: 10.1175/JCLI-D-11-00576.1.

Zhang, Q. Y., S. Y. Tao, and L. T. Chen, 2003: The interannual variability of East Asian summer monsoon indices and its association with the pattern of general circulation over East Asia. *Acta Meteor. Sinica*, **61**, 559–568, doi: 10.11676/qxxb2003.056. (in Chinese)

Zhang, R. H., A. Sumi, and M. Kimoto, 1996: Impact of El Niño on the East Asian monsoon: A diagnostic study of the '86/87 and '91/92 events. *J. Meteor. Soc. Japan*, **74**, 49–62, doi: 10.2151/jmsj1965.74.1_49.

Zhang, W. J., F.-F. Jin, J. P. Li, et al., 2011: Contrasting impacts of two-type El Niño over the western North Pacific during boreal autumn. *J. Meteor. Soc. Japan*, **89**, 563–569, doi: 10.2151/jmsj.2011-510.

Zhang, W. J., F.-F. Jin, H.-L. Ren, et al., 2012: Differences in teleconnection over the North Pacific and rainfall shift over the USA associated with two types of El Niño during boreal autumn. *J. Meteor. Soc. Japan*, **90**, 535–552, doi: 10.2151/jmsj.2012-407.

Zuo, J. Q., W. J. Li, C. H. Sun, et al., 2013: Impact of the North Atlantic sea surface temperature tripole on the East Asian summer monsoon. *Adv. Atmos. Sci.*, **30**, 1173–1186, doi: 10.1007/s00376-012-2125-5.

Tech & Copy Editor: Hongqun ZHANG

Climate Dynamics (2019) 52:5361–5382
https://doi.org/10.1007/s00382-018-4453-3

Statistical predictability of Niño indices for two types of ENSO

Hong-Li Ren[1,2] · **Jinqing Zuo**[1,3] · **Yi Deng**[4]

Received: 4 June 2018 / Accepted: 17 September 2018 / Published online: 29 September 2018
© The Author(s) 2018

Abstract
The El Niño-Southern Oscillation (ENSO) has been shown to manifest as primarily two types, the eastern Pacific (EP) type and central Pacific (CP) type, in terms of the zonal positions of the sea surface temperature (SST) anomalies. This study focuses on examining the predictability of the two types of ENSO by developing statistical models for their corresponding Niño indices, which have their own distinct key precursors. The results show that the statistical predictability of the Niño indices representing the two types of ENSO primarily originates from the preceding variations in the equatorial Pacific upper-ocean heat content and the surface zonal wind stress, which intrinsically reflect the zonally uniform and contrasted thermocline patterns, respectively. The traditional Niño3 and Niño4 indices are more predictive than the Niño indices of the EP and CP ENSO types; however, all the indices are subject to predictability barriers with different timings and intensities, which might be weakened by introducing additional external precursors. The EP ENSO indices have overall higher skills than the CP indices, in which the statistical model has much higher skill scores than persistence forecast for the EP ones while it does less for the CP ones. We demonstrate that the precursors outside the tropical Pacific, e.g., the Indian Ocean Dipole, North Pacific oscillation, North American dipole, and Southern Hemispheric SST modes, except the northern tropical Atlantic SST, as suggested in previous studies, only make limited contributions to improving the prediction skills of the two ENSO types at specific initial months and leads compared to a benchmark model built using the equatorial Pacific heat content and zonal wind stress indices. This is primarily because these precursors have already transferred most of their signals into the variation of the two indices in the benchmark model. We further show that conditionally adding the northern tropical Atlantic SST precursor to the benchmark could provide considerable additional prediction skill scores for both types of ENSO and weaken the intensity of the ENSO predictability barriers that occur during boreal spring−summer.

Keywords Two types of ENSO · Statistical predictability · Niño indices · Precursors

1 Introduction

The El Niño-Southern Oscillation (ENSO) dominates interannual climate variability in the tropics and has a remarkable impact on the global climate (e.g., Rasmusson and Carpenter 1982; Brönnimann 2007; Zhang et al. 2017). Over the past three decades, much attention has been given to predicting ENSO and such predictions of the ENSO signal have laid a strong foundation for short-term climate predictions. Previous studies focusing on improving ENSO predictions have made significant progress. Overall, the predictive skill for ENSO has been high when using the Niño3.4 sea surface temperature (SST) anomaly index to represent the ENSO phenomenon (Latif et al. 1998; Jin et al. 2008; Luo et al. 2008; Ren et al. 2017); this skill, however, is always relatively lower in real-time forecasts than in hindcasts and varies during epochs with considerable uncertainties (Barnston

✉ Jinqing Zuo
zuojq@cma.gov.cn; jqzuo425@126.com

[1] Laboratory for Climate Studies and CMA-NJU Joint Laboratory for Climate Prediction Studies, National Climate Center, China Meteorological Administration, Beijing 100081, China

[2] Department of Atmospheric Science, School of Environmental Studies, China University of Geoscience, Wuhan 430074, China

[3] Collaborative Innovation Center on Forecast and Evaluation of Meteorological Disasters, Nanjing University of Information Science and Technology, Nanjing 210044, China

[4] School of Earth and Atmospheric Sciences, Georgia Institute of Technology, Atlanta, GA, USA

et al. 2012). The recent experiences in predicting 2014–2016 super El Niño event have challenged current capability of international ENSO prediction and given enlightenments for further researches on prediction (Mu and Ren 2017).

Many methods and techniques are being continuously developed to understand atmospheric and oceanic processes key to the formation of ENSO-related SST anomalies and to improve ENSO predictions as a result of progress with respect to ENSO dynamics, climate modeling, and oceanic data assimilation (e.g., Sun et al. 2006; Deng et al. 2012; Park et al. 2012). In general, models for predicting ENSO include simplified dynamical atmosphere–ocean coupled models, fully coupled global climate models, and climate system models, as well as physics-based statistical models (e.g., Zebiak and Cane 1987; Chen et al. 1995; Kang and Kug 2000; Kirtman 2003; Luo et al. 2005; Izumo et al. 2010; Zhang and Gao 2016). All these types of models are used in the monthly routine ENSO forecasting issued jointly by the CPC/NCEP (the Climate Prediction Center/National Centers for Environmental Prediction) and the IRI (the International Research Institute for Climate and Society).

Accompanying the increased understanding of ENSO dynamics, several intermediate atmosphere–ocean coupled models were designed to predict ENSO; such models usually involve simplified atmosphere–ocean coupling and physics with coarse resolutions (Cane et al. 1986; Zebiak and Cane 1987; Chen et al. 1995; Kang and Kug 2000; Zhang et al. 2003) and, being thought to efficiently capture the major dynamics and key physics of ENSO, are still used in operation (Barnston et al. 1999, 2012). Moreover, fully coupled climate models have been widely used to produce ENSO forecasts and have made great progress (Latif et al. 1998; Jin et al. 2008); however, it is always an issue how to accurately initialize these complicated coupled models (Luo et al. 2008; Kirtman and Min 2009). The multi-model ensemble has been proved to be an effective method to improve ENSO predictions (Wang et al. 2009; Kirtman et al. 2014). Meanwhile, due to model deficiencies, post-calibration of ENSO predictions is required via the development of empirical/statistical correction methods for model forecasts (Kug et al. 2008; Ren et al. 2014; Wang et al. 2017; Liu and Ren 2017).

Because current dynamical models are unrealistic to some degree when depicting ENSO dynamics, statistical ENSO prediction is still an alternative with advantages, such as directly reflecting the intrinsic processes, and external factors that control the variations of ENSO are worthy of being used in operations with a real-time prediction skill comparable to that of dynamical models (Barnston et al. 2012). Many statistical models have been developed and used for ENSO prediction (Xue et al. 2000; Clarke and Van Gorder 2001, 2003; Ruiz et al. 2005; Drosdowsky 2006; Lima et al. 2009; Izumo et al. 2010; Boschat et al. 2013; Tseng et al. 2017). In addition to the initial values of the SST anomaly, the equatorial Pacific warm water volume (WWV) and the surface zonal wind stress (ZWS), which together control the intrinsic dynamics of ENSO, have been widely proved to be effective indicators and the key precursors of the Niño SST indices representing the variations of ENSO (Clarke 2014). The WWV precursor represents the zonally quasi-uniform mode of the tropical Pacific thermocline depth variations, with its peak occurring several months prior to that of the central–eastern Pacific SST anomalies due to the discharge–recharge process of the upper-ocean heat content (Jin 1997a, b; Clarke et al. 2007). The ZWS precursor reflects the contribution of the equatorial zonal wind anomaly, which is phase-locked with the seasonal cycle over the Indo–Pacific areas, to the growth of the SST anomaly in the central–eastern Pacific (Clarke 2014). Other precursors that are located outside the tropical Pacific have also been, or can potentially be, used in ENSO statistical predictions by transferring their signals into ENSO preconditions. Such precursors primarily include the Indian Ocean Dipole (IOD) (Izumo et al. 2010), the North Pacific oscillation (NPO) (Chang et al. 2007; Park et al. 2013), the tropical Atlantic SST anomalies (Ham et al. 2013a, b), and the Southern Hemispheric SST modes (Terray 2011; Boschat et al. 2013). However, further effort is needed to examine the relative roles of these external factors by involving them in "benchmark" statistical prediction models that have previously been established using both the WWV and ZWS precursors.

Despite its considerable successes, ENSO prediction is still a challenging issue with considerable uncertainties, particularly because ENSO behaviors have become increasingly diverse and therefore difficult to predict since around the year 2000 (Barnston et al. 2012). The major factor that caused the decrease in the prediction skill is related to ENSO diversity. A large amount of evidence indicates the coexistence of two flavors/types of ENSO events, the eastern Pacific (EP) type and central Pacific (CP) type, in terms of the zonal positions of their equatorial SST anomaly center, which was likely first noted by Fu et al. (1986). Many studies have revealed that the CP type has become more frequent since the 1980s (Larkin and Harrison 2005a, b; Ashok et al. 2007; Kao and Yu 2009; Kug et al. 2009; Ren and Jin 2011) and will likely become more frequent in a changed climate (Yeh et al. 2009). The EP and CP types of ENSO, also called the cold-tongue (CT) and warm-pool (WP) types, correspond to two coupled ENSO modes (Bejarano and Jin 2008; Ren et al. 2013; Wang and Ren 2017; Xie and Jin 2018). Because the impact of the CP-type ENSO on the climate worldwide is distinctly different from that of the EP type (e.g., Weng et al. 2007; Kim et al. 2009; Hegyi and Deng 2012; Zhang et al. 2011, 2012; Hegyi et al. 2014; Wang and Wang 2014), large amounts of attention have been given to examining

the typical features and mechanisms of the two ENSO types (Yeh et al. 2014, and references therein); however, less attention has been given to their predictability.

Recent studies have assessed the performance of dynamical models in predicting the two ENSO types (Hendon et al. 2009; Lim et al. 2009; Jeong et al. 2012, 2015; Yang and Jiang 2014; Imada et al. 2015; Zhu et al. 2015; Ren et al. 2017). These studies show that the EP type has a relatively higher prediction skill than the CP type, even though the latter tends to possess a better persistence or weaker persistence barrier than the former in terms of the Niño indices (Kim et al. 2009; Ren et al. 2016a). It remains unclear whether the CP type is dynamically less predictable than the EP type because current models are not capable of sufficiently reproducing the observed differences in the two ENSO types (Yu and Kim 2010; Ham and Kug 2012). Using an analogue-based correction method for reducing model prediction errors which can be diagnosed from hindcasts at historical analogue states (Ren et al. 2014), forecast skills of the Niño indices representing the two ENSO types can be significantly improved in the CFSv2 predictions (Liu and Ren 2017).

Studies of the statistical predictability of the two ENSO types are necessary, in addition to those based on dynamical models, because many studies have revealed the physical mechanisms for motivation and maintenance of the two ENSO types. Both the equatorial Pacific thermocline and the zonal wind variations play important roles in motivating and maintaining the two ENSO types (Ashok et al. 2007; Ren and Jin 2013), and the recharge oscillator mechanism proposed by Jin (1997a, b) occurs in both ENSO types (Ren and Jin 2013), suggesting that both the WWV and ZWS precursors are expected to be applicable to statistical predictions of the two types of Niño indices. Moreover, some external motivators outside the tropical Pacific could be potential precursors of the two ENSO types (e.g., Boschat et al. 2013; Xie et al. 2013). For example, atmospheric signals from the Pacific subtropics and extratropics tend to trigger the CP El Niño via the seasonal footprinting mechanism (Yu et al. 2010) and the SST anomalies in the northern tropical Atlantic also favor the CP type (Ham et al. 2013a). Conversely, the equatorial Atlantic SST anomalies tend to enhance the EP type (Ham et al. 2013b; Keenlyside et al. 2013). Recently, a North American dipole (NAD) mode was shown to serve as a unique precursor of a CP El Niño (Ding et al. 2017). Until now, it is still lack of comprehensive examining of statistical predictability of the two ENSO types and hence developing specifically effective statistical models for their respective Niño indices. It also remains unclear whether and to how large a degree these predictors can contribute to the statistical predictability in terms of the two ENSO types because some of these precursors are not generally suitable to ENSO prediction but are strongly locked to the seasonal cycle.

In this study, we focus on the development of statistical prediction models for the different Niño indices that represent the two types of ENSO and examine the statistical predictability of these two types. To do this, we quantitatively demonstrate the relative importance of the key precursors that have been suggested in previous studies with different definitions and then set up an advanced statistical model with relatively high prediction skill for the respective Niño indices of the two ENSO types. Following the introduction, the data and methods are introduced in Sect. 2. The benchmark models for statistically predicting the different Niño indices are set up in Sect. 3. The statistical predictabilities of the two ENSO types are examined in Sect. 4 by incorporating the external precursors into the benchmark models. The establishment and evaluations of the eventual statistical prediction models for the Niño indices of the two ENSO types are given in Sect. 5. A discussion and summary are given in Sect. 6.

2 Data and methods

Traditional Niño3.4, Niño3, and Niño4 indices are calculated as SST anomalies averaged over the Niño3.4 (5°S–5°N, 170°–120°W), Niño3 (5°S–5°N, 150°–90°W), and Niño4 (5°S–5°N, 160°E–150°W) regions, respectively. The Niño warm-pool index (WPI) and the Niño cold-tongue index (CTI) proposed by Ren and Jin (2011) are used in this study to represent the CP and EP types of ENSO, respectively. We also use the El Niño Modoki index (EMI) of Ashok et al. (2007) for comparison. In this study, the EP-type ENSO indices include both the CTI and the Niño3 index, and the CP-type indices include the WPI, EMI as well as the Niño4 index. Definitions of these SST-based indices are given in Table 1. All indices are calculated using monthly optimum interpolation SST (OISST) data from the National Oceanic and Atmospheric Administration (Reynolds et al. 2002), which have a horizontal resolution of 1° × 1°.

We use the monthly potential temperature and the zonal momentum flux (zonal wind stress) from the NCEP Global Ocean Data Assimilation System (Behringer and Xue 2004; Huang et al. 2008). These datasets have a horizontal resolution of 0.333° in latitude and 1.0° in longitude. The WWV is represented by the 20 °C isotherm depth. Monthly global atmospheric circulation data are derived from the NCEP/National Center for Atmospheric Research Reanalysis data, which have a horizontal resolution of 2.5° × 2.5° (Kalnay et al. 1996). The study is conducted during the period of 1982–2016, when all these datasets were available. Monthly anomalies are calculated relative to the climatology of the entire period, and a 3-month running average is applied to the data to reduce the noise. Linear trends were removed prior to the analysis.

Table 1 Definitions of the Niño indices and their precursors from the tropical Indian and Atlantic oceans and the extratropics

Indices	Definitions	References
Niño3	SST(15°–90°W, 5°S–5°N)	Trenberth and Stepaniak (2001)
Niño4	SST(160°E–150°W, 5°S–5°N)	
Niño3.4	SST(170°–120°W, 5°S–5°N)	
CTI	Niño3 –αNiño4	Ren and Jin (2011)
WPI	Niño4–αNiño3	
EMI	SST(165°E–140°W, 10°S–10°N)–SST(110°–70°W, 15°S–5°N)/2–SST(125°–145°E, 10°S–20°N)/2	Ashok et al. (2007)
IOD	SST(50°–70°E, 10°S–10°N)–SST(90°–110°E, 10°S–EQ)	Saji et al. (1999)
NTA	SST(EQ–15°N, 90°W–20°E)	Ham et al. (2013)
SIOD	SST(30°–50°S, 35°–75°E)–SST(15°–48°S, 80°–120°E)	Terray (2011); Boschat et al. (2013)
SAOD	SST(30°–50°S, 50°W–20°E)–SST(10°–30°S, 50°W–20°E)	
NAD	SLP(9°–29°N, 58°–93°W)–SLP(53°–68°N, 43°–77°W)	Ding et al. (2017)
NPO	SLP(50°–71°N, 175°–120°W)–SLP(8°–26°N, 179°E–139°W)	

Note that $\alpha = 0.4$ when Niño3 × Niño4 > 0, and otherwise, $\alpha = 0$

SST and SLP denote the sea surface temperature and sea level pressure, respectively

The prediction skills of the Niño indices are evaluated using the temporal correlation coefficients (TCCs) between the observations and the predictions. Both the leave-one-out cross validation and the independent validation are used to assess the statistical predictabilities of the Niño indices. For the independent validation, the prediction is performed during the period of 1997–2016 using observations for the period from 1982 to the target year. Because the skill scores obtained from the cross validation are very similar to those obtained from the independent validation, we only show the results of the cross validation. The statistical significance of the regression coefficient and the correlation coefficient is assessed using a two-tailed Student's t test, and the difference between two correlation coefficients is tested using the Steiger's z test (Meng et al. 1992).

3 Benchmark models using the equatorial Pacific heat content and zonal wind stress

3.1 Relationships of the Niño indices with the heat content and zonal wind stress

In previous statistical models that did not consider the two ENSO types, the equatorial Pacific upper-ocean heat content (i.e., the WWV) and the ZWS precursors have been widely used. Due to their importance in the ENSO evolution, Figs. 1 and 2 examine the lead–lag correlations of different Niño indices with the equatorial (5°S–5°N) WWV and ZWS anomalies, respectively. It is clearly seen in Fig. 1 that significant WWV signals appear in nearly the entire equatorial Pacific prior to the SST peak, and in particular, the zonally quasi-uniform WWV signal leads the SST peak by more than half a year for all the Niño indices. It is noteworthy that the WWV signal associated with the EP-type indices (Fig. 1a–b) is centered more eastward compared to that for the CP-type indices (Fig. 1d–f). Moreover, the lag relationships of the WPI and EMI with the equatorial Pacific WWV anomalies are obviously weaker compared to those for the other Niño indices.

In Fig. 2, the most significant positive ZWS anomalies are observed over the equatorial central–western Pacific leading the SST peak by up to 10 months for all the Niño indices. In addition, note that remarkably negative ZWS anomaly signals appear in the equatorial eastern Pacific prior to the CP ENSO peak, whereas prior to the EP ENSO peak, there are much weaker signals there as well as apparent signals in the equatorial eastern Indian Ocean. Overall, the lead time of the ZWS signal with respect to the SST signal is relatively shorter than that of the WWV signal for both the EP and CP ENSO indices, and the lag correlation of the Niño3.4 index with both the WWV and ZWS precursors is relatively high compared to the other Niño indices.

3.2 Benchmark models and prediction skills for different Niño indices

In this study, we first build benchmark models that use only the initial values of the Niño indices and the equatorial Pacific WWV and ZWS as precursors. Here, we give a multi-element linear regression equation to represent the benchmark model:

$$\text{Niño}(t) = \alpha\text{Niño}(t) + \beta\text{WWV}(t) + \gamma\text{ZWS}(t), \quad (1)$$

where α, β, and γ are parameters that change with calendar month and lead month, and can be obtained by applying a

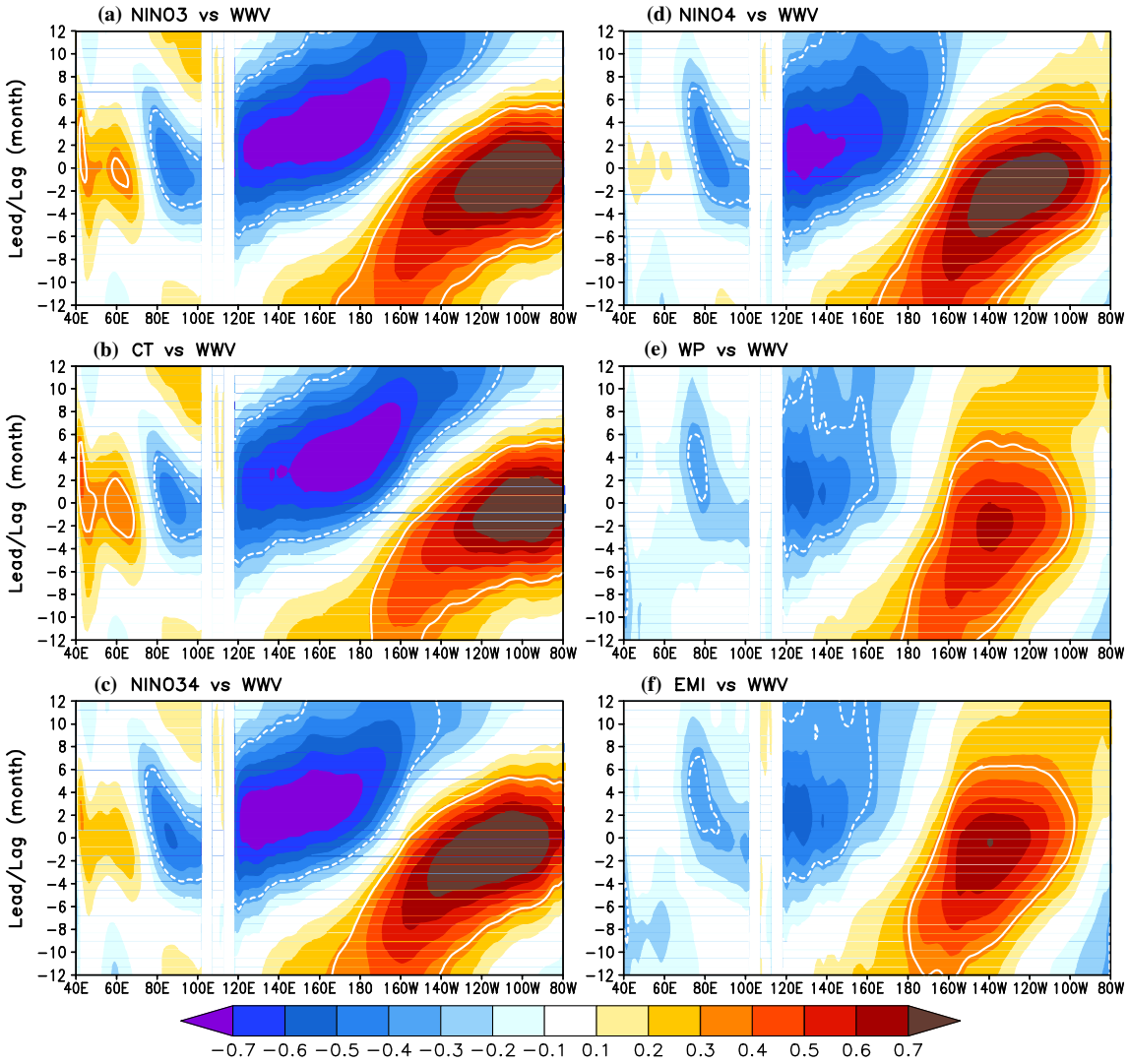

Fig. 1 Lead–lag correlations between the **a** Niño3, **b** CT, **c** Niño3.4, **d** Niño4, **e** WP, and **f** EMI indices and the equatorial (5°S–5°N) mean depth of the 20 °C isotherm (WWV) for all months combined during the period of 1982–2016. White contours indicate significance at 95% confidence level. Lead times with negative values indicate that the WWV is leading

linear fit to the observations, t denotes the target month for the prediction, and τ denotes the initial month.

For the model of each Niño index, the definitions of the WWV and ZWS indices refer to the correlation domains shown in Figs. 1 and 2. Table 2 lists the spatial domains used to define the WWV and ZWS indices as precursors for the different Niño indices, which are generally grouped for the EP and CP ENSO types. According to the results shown in Fig. 2, the ZWS anomalies in both the equatorial central–western and eastern Pacific are combined to define the precursors in the models of the CP ENSO indices, whereas only those in the equatorial central–western Pacific are used to define the precursors of the EP ENSO indices. Additional attempts were made to define the WWV and ZWS indices by changing the zonal range of the domains, and for each Niño index, we have chosen the domains that offer the best prediction of that Niño index. Note that the definition of the WWV index for the CP type is slightly different from that for the EP type, while the definitions of the ZWS index differ significantly for the two types.

As Clarke and Van Gorder (2003) revealed, the westerly (easterly) wind anomalies, which are phase-locked to the seasonal cycle, usually propagate from the equatorial eastern Indian Ocean into the western Pacific with the development of an El Niño (La Niña) event. They demonstrated that a space–time integration of the Indo–Pacific ZWS signal could improve the prediction skill of the Niño3.4 index for some leads in the range of 10–15 months. However, we did not find an apparent improvement in the prediction of the Niño indices for leads in the range of 0–11 months

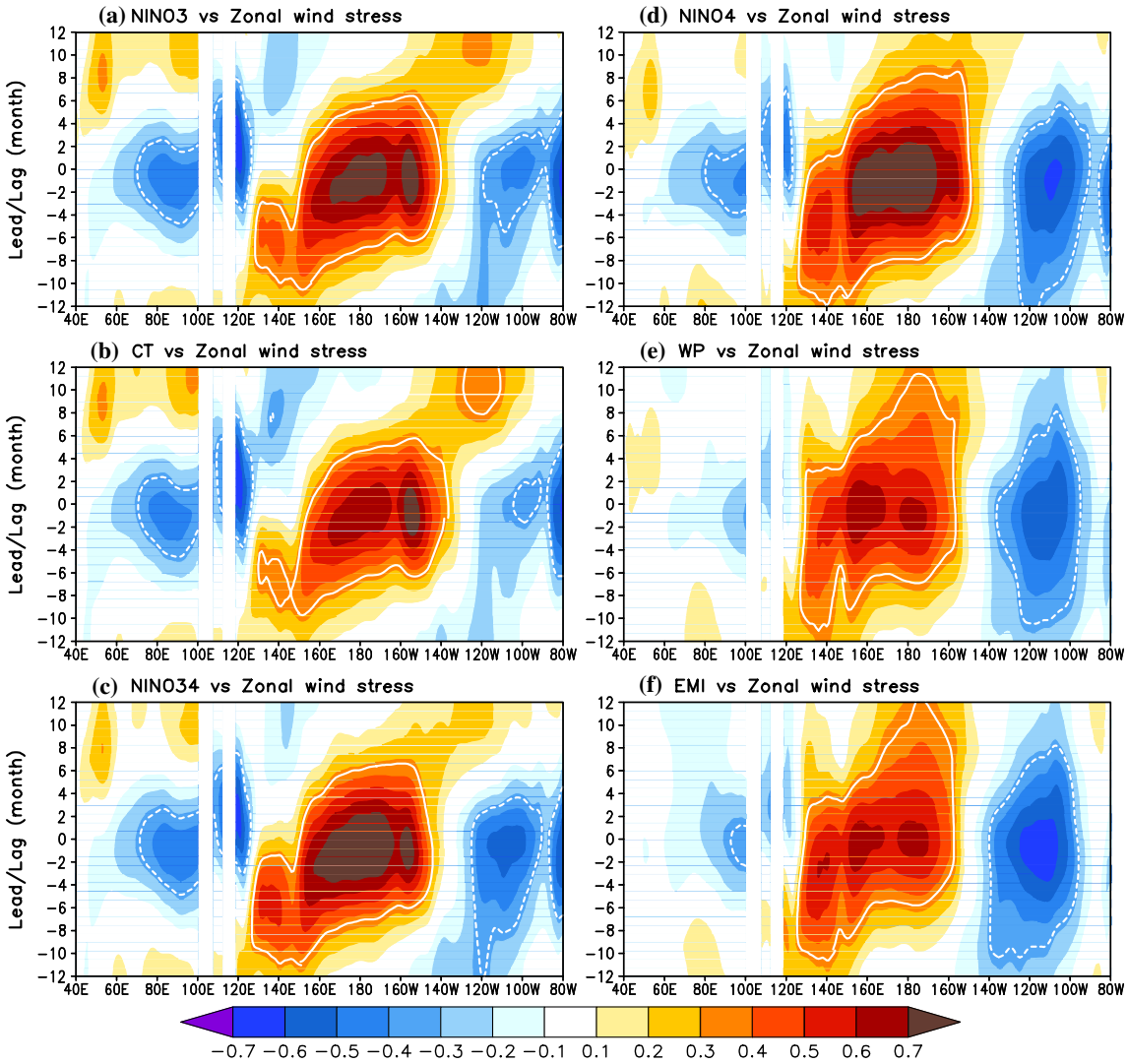

Fig. 2 The same as Fig. 1, but for correlations with the equatorial (5°S–5°N) zonal wind stress (ZWS) anomalies

Table 2 Domains used to calculate the WWV and ZWS precursors for each Niño index

	WWV	ZWS
Niño3, CTI and Niño3.4	130°E–80°W, 5°S–5°N	130°E–150°W, 5°S–5°N
Niño4, WPI and EMI	130°E–100°W, 5°S–5°N	(125°E–160°W, 5°S–5°N)–(125°W–100°W, 5°S–5°N)

using a scheme involving both the equatorial Indian and Pacific ZWS signals compared to our scheme, which considers only the equatorial Pacific ZWS (figures omitted). This result reflects the fact that both the EP and CP ENSO indices have major correlations with the simultaneous or short-lead ZWS signals in the equatorial Indian Ocean (Fig. 2). Therefore, only the equatorial Pacific ZWS signals are used in our benchmark models.

To evaluate the prediction skill of the benchmark model, the cross-validated TCC skill scores of the Niño indices predicted by the benchmark model and their differences relative to the persistence forecast for all the months combined during the period of 1982–2016 are computed, as shown in Fig. 3. It is indicated that the skill scores of the benchmark model feature a gradual decline with increasing lead months for all the Niño indices (Fig. 3a). Compared to the

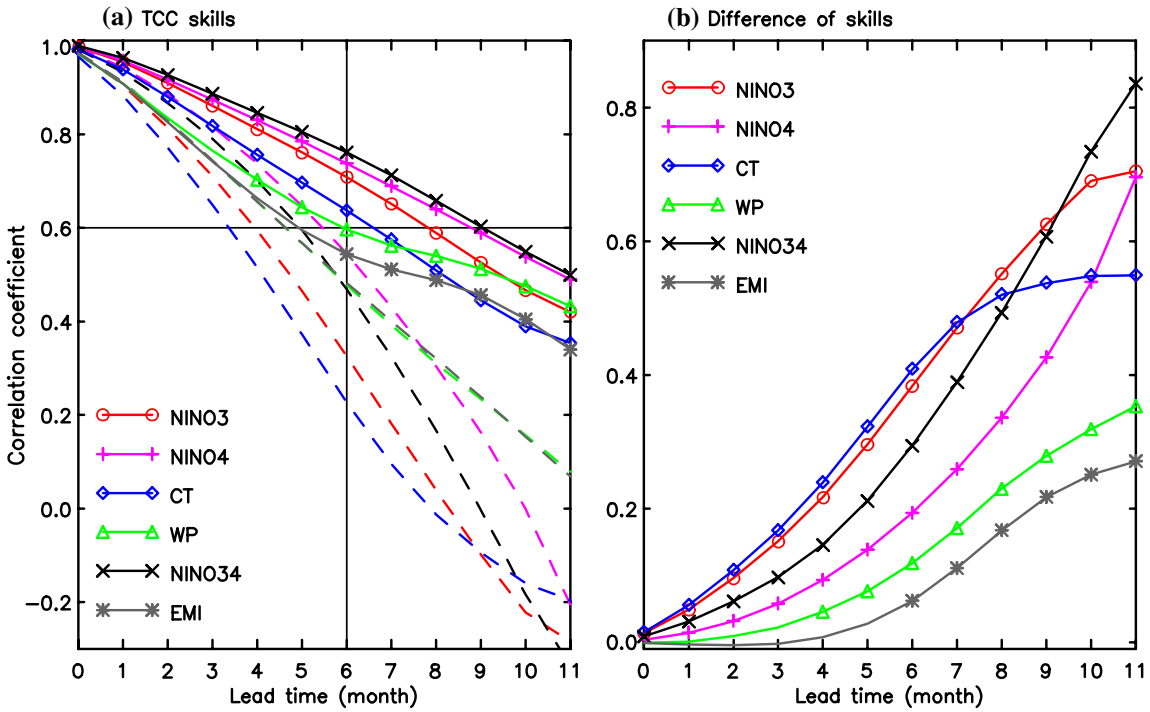

Fig. 3 **a** Cross-validated correlation skill scores (solid line) of the Niño indices predicted by the benchmark model and **b** their differences relative to the persistence forecast (dashed line in panel **a**) for all months combined during the period of 1982–2016. Markers indicate that the difference is significant at the 95% confidence level

skill scores of persistence forecast, the WWV and ZWS precursors can significantly contribute to the skills of the CTI and the Niño3, Niño4 and Niño3.4 indices for leads of 1–11 months (Fig. 3b). For the EMI (WPI), its skill in the benchmark model is much higher than that of the persistence forecast for leads longer than 6 (4) months. Note that the Niño3.4 index has the highest skill and that the Niño4 index has a slightly higher skill than the Niño3 index. Moreover, both the CTI and the WPI, defined as a transformation of the Niño3 and Niño4 indices (Ren and Jin 2011), show relatively lower skills compared to the latter two, respectively. This may be due to their definitions, which use the differences of the two domain-averaged Niño indices, and is consistent with the results shown in Figs. 1 and 2, where the correlations for the Niño3 and Niño4 indices are for the most part higher than those for the CTI and WPI.

We further examine the dependence of the skills of the benchmark models on the target calendar months, as shown in Fig. 4. The cross-validated skill scores (see the contours) of the three Niño indices that are usually used to represent the traditional or EP ENSO are higher during boreal autumn and winter but much lower during spring and summer (Fig. 4a–c), whereas those of the CP ENSO indices appear to be higher during winter and spring but lower during late summer and autumn (Fig. 4d–f). This is one of the most significant features in the differences of the statistical predictability between the two ENSO types. In Fig. 4c, the skill pattern of the Niño3.4 index is similar to those in previous studies (e.g., Barnston et al. 2012). It is clear that the predictions of the CTI and the Niño3 and Niño3.4 indices have a higher skill score for most of the target and lead months, except the target months of January−April with short leads, compared to those of the persistence forecast. However, the predictions of the CP-type indices are less skillful in the benchmark model than those of the EP-type indices for some of the target and lead months. In particular, the EMI only has superior skill scores in the boreal autumn and winter with long leads in the model, compared to the persistence forecast.

Figure 4 indicates that the WWV and ZWS precursors in the benchmark models can significantly contribute to the prediction skills of most of the Niño indices with leads longer than ~ 1 (6) month(s) for target months during the period of June–December (January–February). A useful skill score (of more than 0.6) can be obtained across the spring predictability barrier (SPB) where the prediction skills decline most rapidly. The SPB is closely related to the persistence barrier of ENSO, which usually occurs in late spring to early summer (Ren et al. 2016a), as shown in Fig. 5. In the study of Ren et al., the persistence barrier is quantitatively shown to be distinct for the EP and CP types of ENSO; the persistence barrier tends to occur in

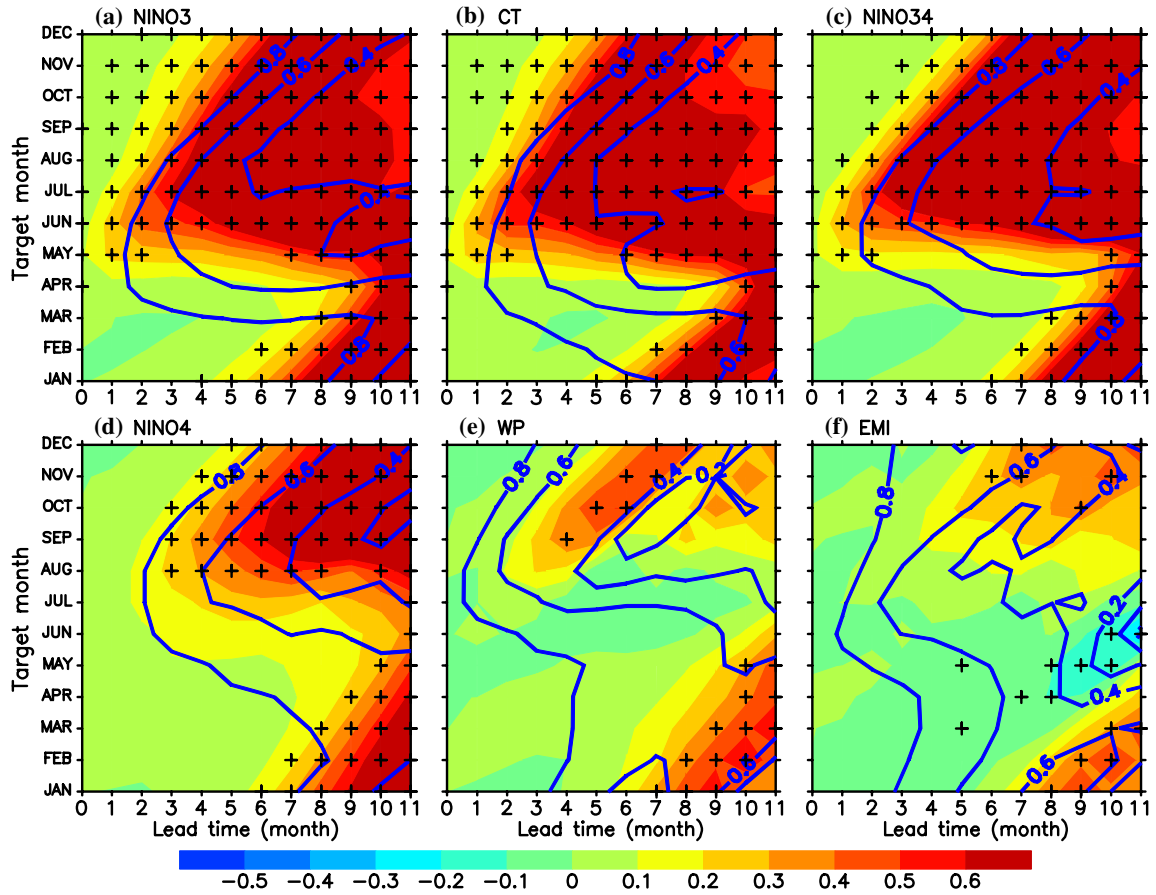

Fig. 4 Cross-validated correlation skill scores (contours) as a function of target calendar month (*y* axis) and lead month (*x* axis) for the benchmark model and their differences (shading) relative to the persistence forecast for the **a** Niño3, **b** CT, **c** Niño3.4, **d** Niño4, **e** WP, and **f** EMI indices during the period of 1982–2016. Crosses indicate that the difference is significant at the 95% confidence level

late spring with a stronger intensity for the EP type and in summer with a weaker intensity for the CP type (see the shading in Fig. 6). Based on Fig. 4, similar conclusions can be obtained for the SPB. Here, we can examine the timings and intensity of the SPB by identifying the maximum decline rate of the prediction skills using a method similar to the definition of the ENSO persistence barrier (Ren et al. 2016a). It is shown that the SPB of the EP type appears to be earlier and stronger compared to that of the CP type (see the contours in Fig. 6). In fact, the predictability barrier of the EP type typically occurs during boreal spring, whereas that of the CP type tends to be more visible during boreal summer. It is also clear that the evident skill superiority provided by the WWV and ZWS precursors, compared to the persistence forecast, primarily occurs during the SPB and afterwards. However, the prediction skills for the CP ENSO indices have much less skill superiority, partly due to their own better persistence (Ren et al. 2016a). Indeed, involving new precursors outside the tropical Pacific is likely a potential way to further improve the CP ENSO prediction.

4 Predictability from other precursors in the tropics and extratropics

4.1 Contributions to the prediction skills of Niño indices

Previous studies have demonstrated that there are several external signals from outside the tropical Pacific that can lead the ENSO peak (Ding et al. 2017 and references therein). Impacts of these external signals on the prediction skills of the Niño indices are examined here. The examined precursors include the IOD in Sept–Oct–Nov (SON), the northern tropical Atlantic (NTA) SST anomalies in Feb–Mar–Apr (FMA), the southern Indian Ocean Dipole (SIOD) in FMA, the southern Atlantic Ocean Dipole (SAOD) in FMA, and the NAD and NPO in Nov–Dec–Jan (NDJ), which have been demonstrated to have an important impact on the ENSO variability (Izumo et al. 2010; Boschat et al. 2013; Ham et al. 2013a, b; Ding et al. 2017). Definitions of these precursors are given in Table 1, where the IOD, NTA, SIOD, and SAOD indices are defined using

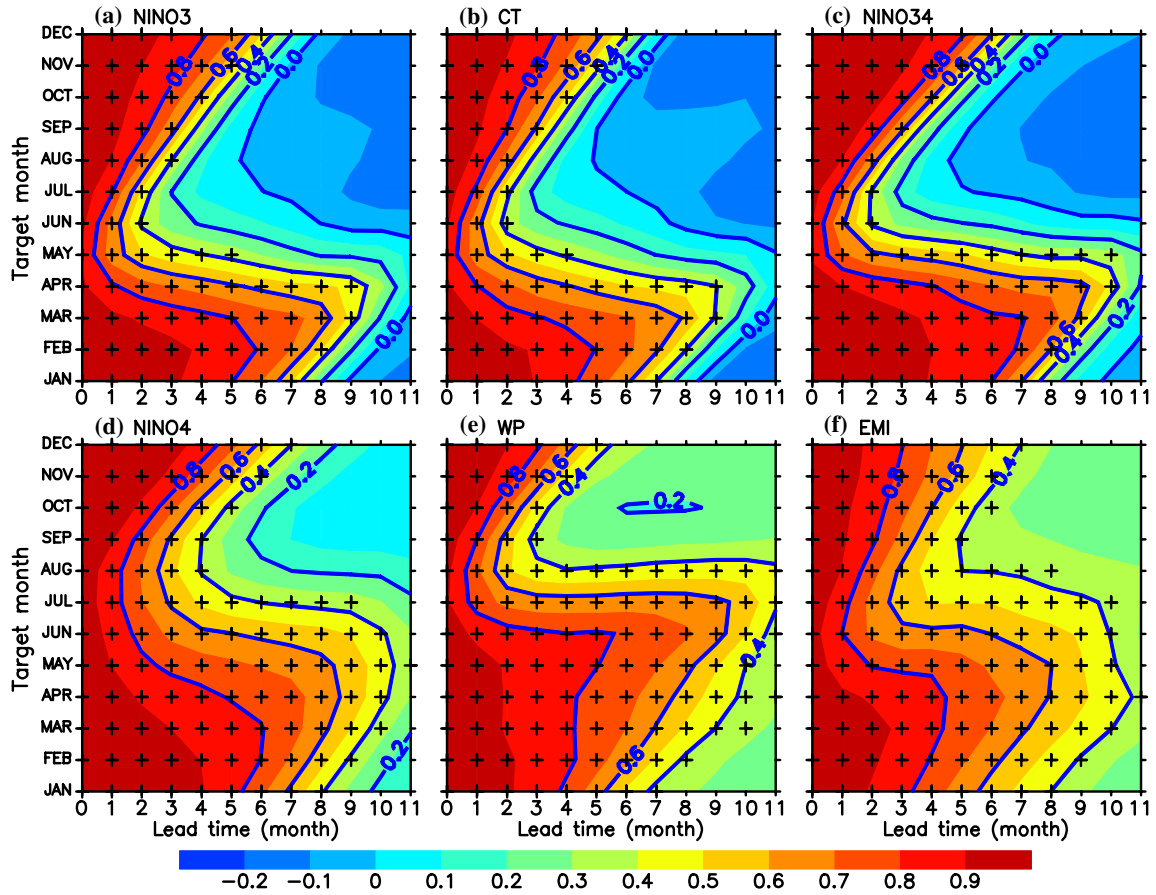

Fig. 5 Autocorrelations of the **a** Niño3, **b** CT, **c** Niño3.4, **d** Niño4, **e** WP, and **f** EMI indices during the period of 1982–2016. Crosses indicate significance at the 95% confidence level

SST anomalies while the NAD and NPO indices are defined using sea level pressure (SLP) anomalies.

These selected precursors have distinct ways to affect ENSO, as referred to these aforementioned papers. The IOD related signal in SON can influence the sequent winter ENSO in phase and the second sequent winter ENSO out of phase through exciting the surface westerly wind anomalies over the western Pacific and then the ocean dynamics (Izumo et al. 2010). The NTA SST cooling in FMA contributes to the CP warming at the sequent winter via the air-sea interaction over the tropical Pacific (Ham et al. 2013a). The NAD in NDJ, as an atmospheric signal, can induce SST anomalies in the NTA and then subsequently influence the development of the CP El Niño (Ding et al. 2017). The NPO-related atmospheric signals from the Pacific subtropics and extratropics tend to trigger the CP El Niño via the seasonal footprinting mechanism (Chang et al. 2007; Park et al. 2013). The SIOD and SAOD in FMA both can affect ENSO development by modulating the southeast trades over the South Pacific in spring (Terray 2011; Boschat et al. 2013).

To investigate the impact of precursors from outside the tropical Pacific on the prediction skills of the Niño indices, the benchmark skill score is first obtained from a benchmark model built with the WWV and ZWS precursors and then the TCC skill scores are calculated for each Niño index by individually adding other precursor (e.g., IOD) to the benchmark model. Figure 7 shows the lag correlations of the Niño indices with the aforementioned precursors at a given season from which the impacts of Niño3.4 SST signal in the previous Dec–Jan–Feb (DJF) season have been linearly removed by using a regression, and Fig. 8 displays cross-validated TCC skill scores for the Niño indices predicted by individually adding these precursors into the benchmark model and their differences relative to the benchmark skills. Note that the IOD and other precursors are used at all initial months as predictors in the statistical models and not just locked to certain seasons as discussed previously.

Figure 7a demonstrates that the Niño3.4 index has a significant in-phase relationship with the SON IOD index for short lags but an out-of-phase relationship for long lags, with a maximum correlation at a lag of ~ 15 months. This agrees well with Izumo et al. (2010), who revealed that a negative (positive) phase of the SON IOD leads the El Niño (La Niña) peak by approximately 14 months. Similar results

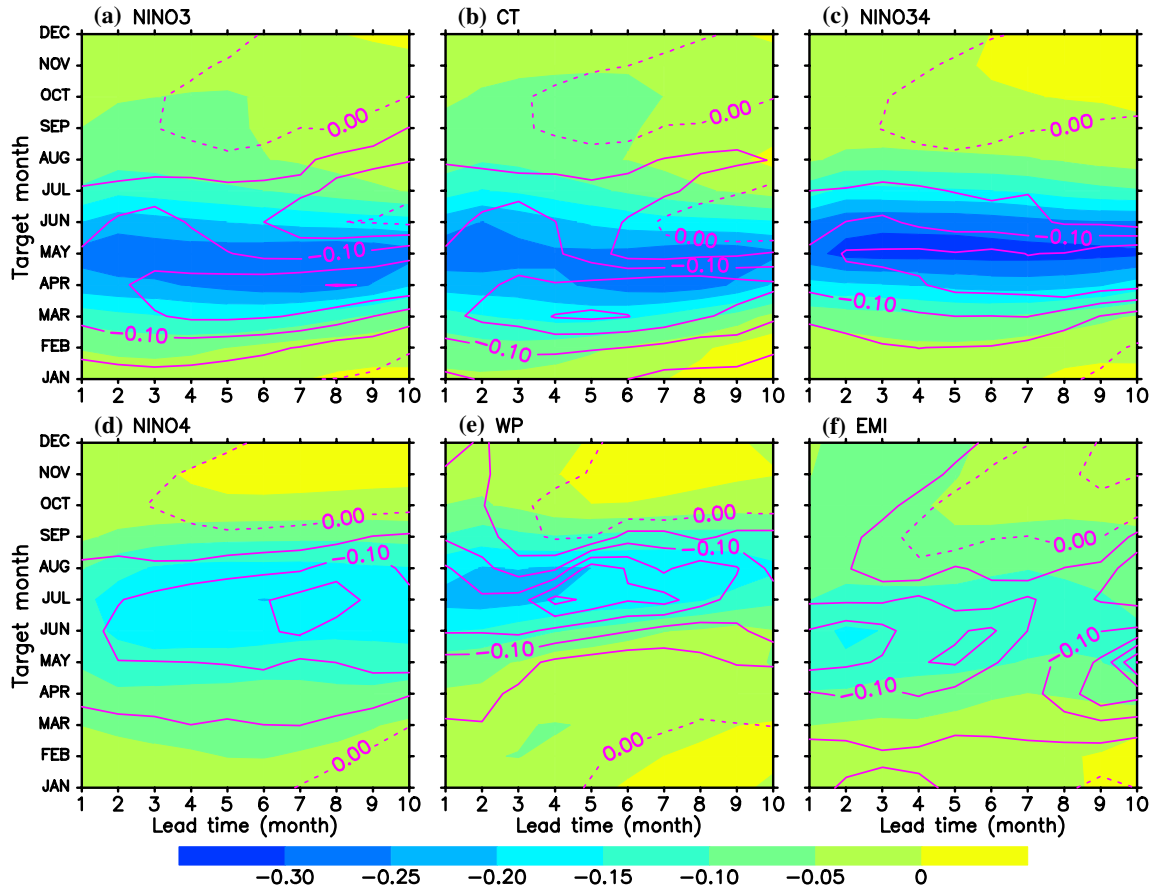

Fig. 6 Decline rate of the autocorrelations (shading) and cross-validated correlation skill scores for the benchmark model (contours) of the **a** Niño3, **b** CT, **c** Niño3.4, **d** Niño4, **e** WP, and **f** EMI indices during the period of 1982–2016. Contours with negative values are solid

of a lag relationship are obtained for the CTI and the Niño3 and Niño4 indices; however, a relatively weak and still significant correlation is found between the WPI and the SON IOD index. As expected, the TCC skill scores of the Niño indices, except WPI, are improved by introducing the IOD signal when the predictions are initiated during the boreal autumn and this limited improvement is not significant and is only visible after 4–5 forecast months (Fig. 8a–e).

The NTA SST anomalies during the boreal spring (FMA) could be a candidate predictor of the CP ENSO (Ham et al. 2013a, b). This is supported by Fig. 7b, which indicates that the NTA index in FMA has a significant and negative correlation with both the WPI and the Niño4 index in the following months, with a maximum correlation for a lead of ~ 10 months. Consistently, significant improvements are observed in the boreal autumn–winter predictions of WPI when starting from January–February (Fig. 8i), while similar but relatively weak improvements are found for the Niño4 index (Fig. 8h). Conversely, the correlations of the NTA index in FMA with the CTI and the Niño3 index in the following months are relatively weak (Fig. 7b); therefore, the impact of the former on the skill scores of the two EP ENSO indices is also weak (Fig. 8f, g). However, note that the NTA precursor during the late summer−early autumn can significantly improve the predictions of the EP ENSO indices, as well as the Niño3.4 index, as opposed to the CP ENSO indices, as seen in Fig. 8f, g, j. Such a distinct impact of the boreal spring and summer−autumn NTA SST anomalies on the two types of ENSO may be related to the seasonal evolutions of the mean state (Rodríguez-Fonseca et al. 2009; Ham et al. 2013a, b), which requires further examination but lies beyond the scope of the present study.

The subtropical dipole-like SST variability in the southern Indian and Atlantic oceans may provide another source of predictability for ENSO during recent decades (Terray 2011; Boschat et al. 2013). Here, we define the SST-based SIOD and SAOD indices, where the spatial domains are determined following Terray (2011) and Boschat et al. (2013). The SIOD index in FMA is significantly and positively correlated with the CTI and the Niño3 and Niño3.4 indices when the former leads over a range of 1–14 months (Fig. 7c), and similar correlation patterns are observed for the SAOD index in FMA with even higher correlations (Fig. 7d). Both the SIOD and SAOD indices in FMA have

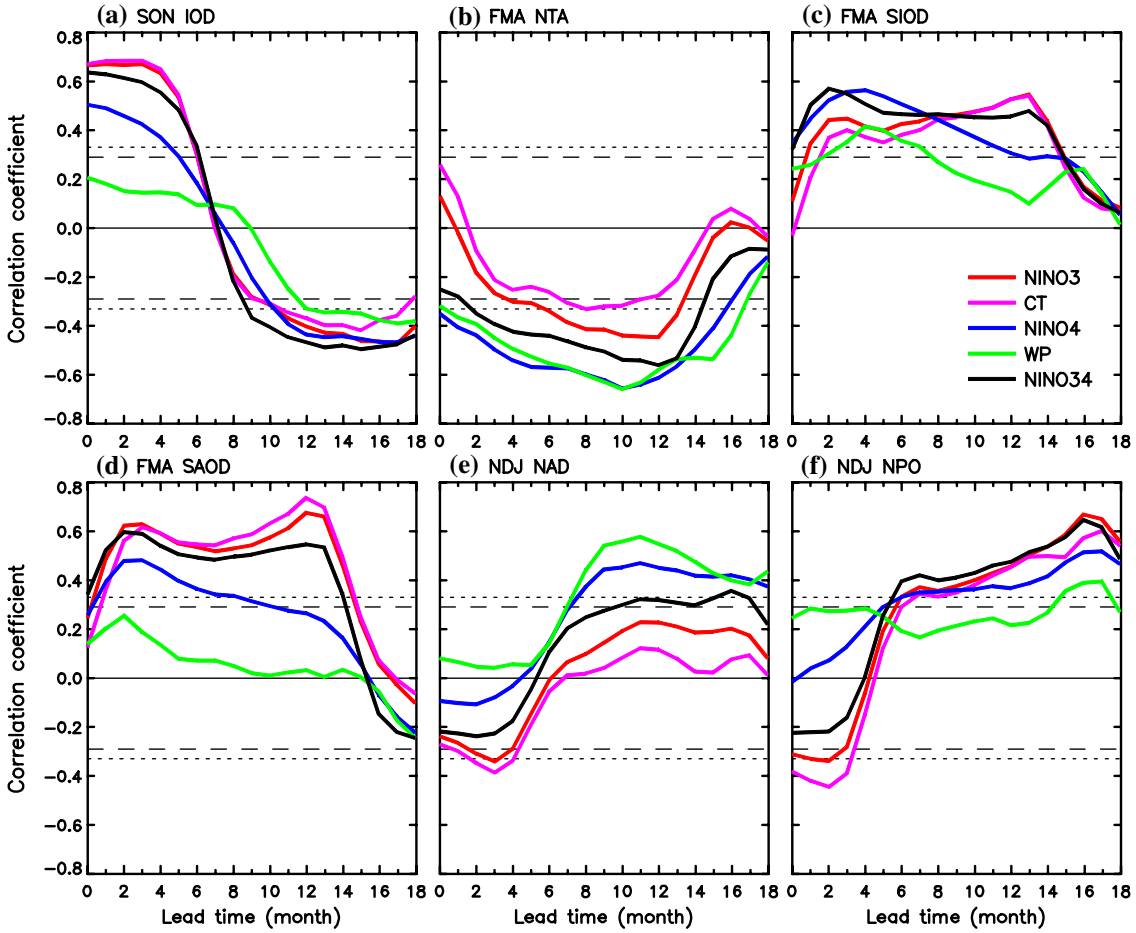

Fig. 7 Lag correlations of the Niño indices with the **a** IOD in Sep–Oct–Nov (SON), **b** NTA in Feb–Mar–Apr (FMA), **c** SIOD in FMA, **d** SAOD in FMA, **e** NAD in Nov–Dec–Jan (NDJ), and **f** NPO in NDJ after excluding the Niño3.4 SST signal in the previous Dec–Jan–Feb (DJF) season during the period of 1982–2016. The dotted (dashed) line indicates significance at the 95% (90%) confidence level. The lead time indicates that the Niño indices are lagged

the highest positive correlations with the Niño4 index for a lead of approximately 3 months and then decrease gradually with increasing lead time. Much weaker lag correlations are seen for the WPI. However, no significant improvement can be observed in the prediction skills of any of the Niño indices when adding either the SIOD or SAOD precursor to the benchmark model (Fig. 8k–t).

Both the boreal winter NAD and NPO in the extratropical Northern Hemisphere play roles in influencing the ENSO variability in the following winter (Ding et al. 2017). As indicated in Fig. 7e, the NAD index in NDJ has a significant in-phase relationship with both the WPI and the Niño4 index for a lead of approximately 8 months or longer but a very weak relationship with both the CTI and the Niño3 index. This is consistent with Ding et al. (2017), who revealed that the NAD signal is more closely related to the CP ENSO than to the EP ENSO. Consistently, the NAD precursor in early winter can increase the prediction skills of the WPI and the Niño4 index in the following autumn−early winter seasons, even though a significant improvement is only observed when the NAD leads the WPI by approximately 10 months (Fig. 8w–s). Similarly, the NPO index in NDJ has a significant in-phase relationship with all the Niño indices except WPI for a lead of approximately 6 months or longer (Fig. 7f); however, no significant improvement is obtained in the prediction of any of the Niño indices when adding the NPO precursor to the benchmark model (Fig. 8a–e).

4.2 Dependence on the equatorial Pacific WWV and ZWS indices

According to the recharge oscillator mechanism (Jin 1997a, b), the evolutions of the two types of ENSO are intimately related to the equatorial Pacific WWV and ZWS anomalies (Ren and Jin 2013). Even though the physical processes responsible for the linkage of the IOD, NTA SST anomalies,

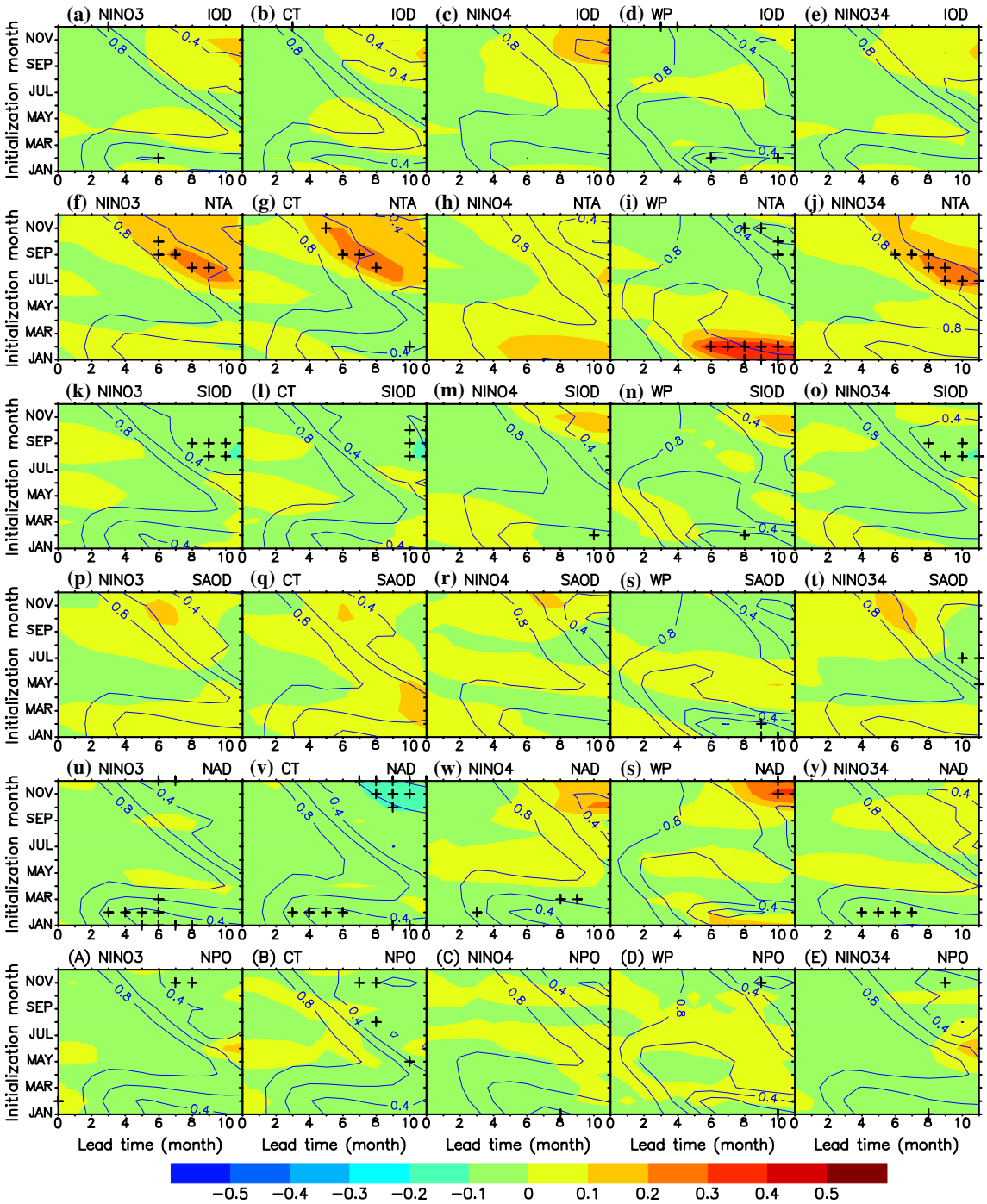

Fig. 8 Cross-validated correlation skill scores (contours) for the **a** Niño3, **b** CT, **c** Niño4, **d** WP, and **e** Niño3.4 indices predicted when adding the IOD precursor to the benchmark model and their differences (shading) relative to the benchmark skill scores during the period of 1982–2016. Crosses indicate that the difference is significant at the 95% confidence level. **f**–**y** and **a**–**e** are the same as **a**–**f** but for the NTA, SIOD, SAOD, NAD, and NPO precursors, respectively

and extratropical precursors to the two types of ENSO are different, all these ENSO precursors have signatures in the equatorial Pacific WWV and/or ZWS (e.g., Izumo et al. 2010; Terray 2011; Boschat et al. 2013; Ham et al. 2013a, b; Ding et al. 2017).

To examine whether the impacts of the aforementioned precursors on the prediction skills of the Niño indices are related to the WWV and/or ZWS anomalies that might be remotely initialized by affecting the equatorial Pacific atmosphere–ocean conditions, we perform two sensitivity

experiments. That is, we exclude either the ZWS or WWV precursor from the benchmark model and then recalculate the prediction skills of the Niño indices by individually adding other precursors into this new benchmark model. Figures 9 and 10 show the corresponding cross-validated TCC skill scores of the Niño indices and their differences relative to the benchmark skill scores.

A comparison of Fig. 9 with Fig. 8 indicates that the improvement in the prediction skills of the Niño4 index and the WPI caused by the use of the NTA and NAD precursors becomes more obvious when the ZWS precursor is excluded from the benchmark model. In particular, the NTA precursor in January–April can significantly improve the prediction skill of the WPI in the following autumn–winter seasons and

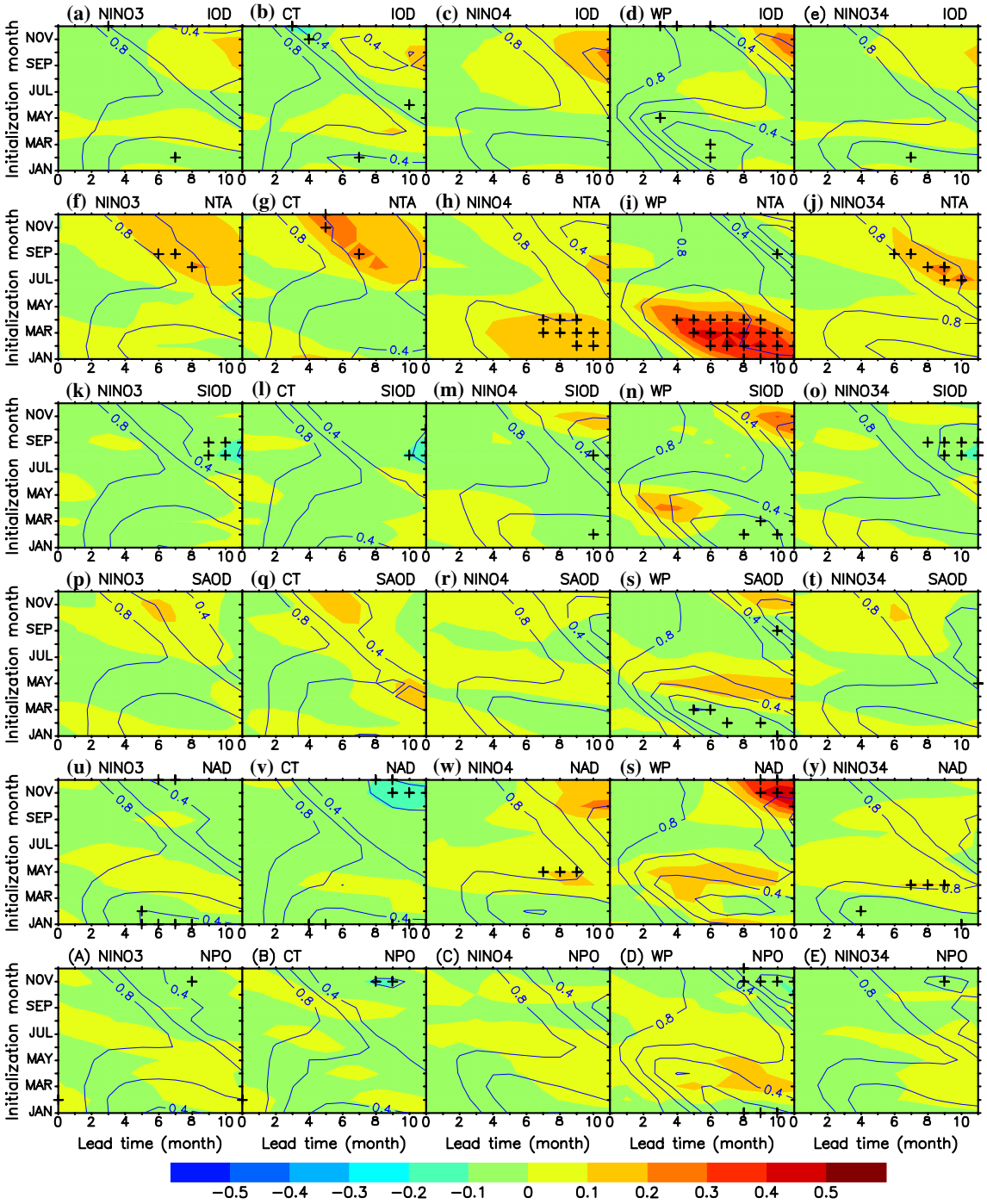

Fig. 9 The same as Fig. 8, but for the skill scores excluding the ZWS precursor from the benchmark model

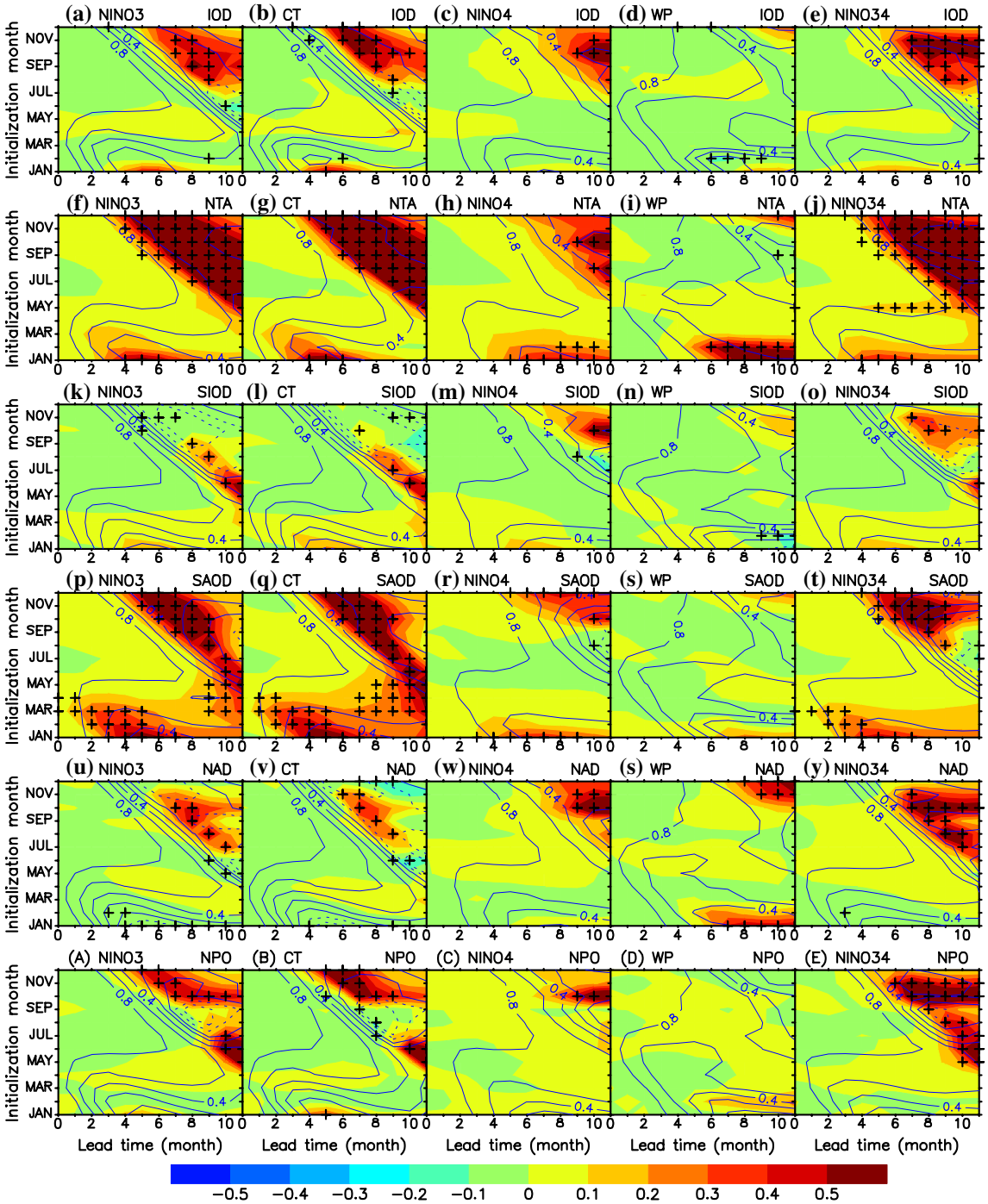

Fig. 10 The same as Fig. 8, but for the skill scores excluding the WWV precursor from the benchmark model

that in late summer−autumn can significantly contribute to improvement of prediction of the two EP ENSO indices during the next spring when excluding the ZWS precursor from the benchmark model (Fig. 9i). However, the improvement in predicting the Niño indices by other precursors based on a benchmark model excluding the ZWS signal is similar to that in the benchmark model including both the WWV and ZWS signals. This clearly suggests that the NTA SST and NAD act to inject remote signals into the equatorial Pacific ZWS anomalies that tend to initialize the CP ENSO, and the NTA SST also contribute to improving predictions of the EP ENSO in the following spring, whereas the information from other precursors is weakly involved in the ZWS signals.

Conversely, the comparison of Fig. 10 with Fig. 8 shows a pronounced improvement in the prediction skills of the Niño indices except WPI caused by the use of the IOD, NTA, SAOD, and NPO precursors across the SPB domain when the WWV precursor is excluded from the benchmark model; such an improvement is also seen for the SIOD and NAD precursors but covers much smaller domains. For the WPI, the improvement in the prediction skills in the autumn–winter seasons caused by the use of the NAD precursor in the previous winter becomes significant and more pronounced (Figs. 8s, 10s) and the improvement caused by the use of the NTA precursor in the previous winter becomes slightly higher in this case (Figs. 8h, 10h). These results indicate that the influences of most of the external precursors on ENSO are realized via the initialization of the WWV anomalies for the Niño indices. In other words, external precursors do not increase the ENSO prediction skill unless they introduce extra effective signals into the benchmark model in which both the WWV and ZWS precursors are included.

These results suggest that the ENSO precursors from outside the tropical Pacific that are focused on in this study all have an impact on the prediction skills of the Niño indices. The pronounced impacts of the IOD, SAOD, and NPO anomalies primarily occur across the SPB only when excluding the WWV precursor from the benchmark model. Conversely, the NTA SST and NAD anomalies during the winter–spring seasons have a significant impact on the prediction skills of the Niño4 index and the WPI during the following autumn–winter seasons, which becomes more significant when excluding either the WWV or ZWS precursor from the benchmark model. Note that the NTA SST anomalies also have a pronounced impact on the prediction skills of the CTI and the Niño3 and Niño3.4 indices across the SPB, which can only be detected when excluding the WWV precursor from the benchmark model. Based on Figs. 8, 9 and 10, it can be inferred that the NTA SST anomalies in the previous winter−spring seasons supply extra signals compared to the WWV and ZWS for the following autumn−winter generation of both types of ENSO.

To support the above conclusions, Fig. 11 further shows the correlations of the SON IOD, NDJ SAOD, FMA NTA, and NDJ NAD indices with the WWV and ZWS indices from which the impacts of Niño3.4 SST signal in the previous DJF season have been linearly removed. These precursors (i.e., IOD, SAOD, NTA, and NAD) at the corresponding specific seasons are chosen according to the results shown in Figs. 8, 9 and 10. That is, the impact of the IOD in SON and SAOD in NDJ on the prediction skills of the Niño3 index and the CTI primarily depends on the equatorial Pacific WWV anomalies, while the impact of the NTA SST in FMA and NAD in NDJ on the prediction skills of the Niño4 index and the WPI is related to both the equatorial Pacific WWV and ZWS anomalies.

As seen in Fig. 11a, b, both the IOD index in SON and the SAOD index in NDJ are highly correlated with the WWV index when the former two lead by approximately 2–3 months or longer; however, their correlations with the ZWS index are relatively weak when they lead by 3–12 months. Conversely, the NTA index in FMA has a significant correlation with the ZWS (WWV) index in the following 0–12 (3–8) months, even though the lag correlations for the WWV index are somewhat weaker than those for the ZWS index over a lag time range of 3–8 months (Fig. 11c). The correlations of the NAD index in NDJ with the WWV index are comparable to those of the ZWS index in the following months and become significant when the former leads the latter two by approximately 6 months or longer (Fig. 11d). These consistent results confirm our conclusions regarding the relationship of the precursors from outside the tropical Pacific with the equatorial Pacific WWV and ZWS anomalies and therefore explain their effects on the prediction skills of the Niño indices.

5 Establishment and evaluations of models for the two ENSO types

The analysis has demonstrated that the NTA SST during the middle winter−early spring (late summer−early autumn) can significantly improve the predictions of the WP (EP) ENSO indices in the following months, while the other precursors from outside the tropical Pacific that are focused on in this study have limited contributions to improving the prediction skills of both types of ENSO relative to the benchmark model built with the equatorial Pacific WWV and ZWS precursors. We further attempt to improve the statistical prediction skills of the Niño indices for the two types of ENSO by conditionally introducing the NTA precursor into the benchmark model as follows:

$$\text{Niño}(t) = \alpha\text{Niño}(t) + \beta\text{WWV}(t) + \gamma\text{ZWS}(t) + \delta\text{NTA}(t). \quad (2)$$

Here, δ is a new parameter corresponding to the new term relative to Eq. (1). In the equation, the NTA precursor to be added to the benchmark model depends on the initial calendar months for the EP and CP ENSO indices. For the EP-type (CP-type) indices, including the CTI and Niño3 (WPI and Niño4) indices, the NTA precursor is added to the benchmark model for the initial months from July to December (from January to June), while for the Niño3.4 index the NTA precursor is added for all the initial months.

Figure 12 presents the cross-validated TCC skill scores of the Niño indices predicted when conditionally adding the NTA precursor to the benchmark model and their differences relative to the benchmark skills for all the months combined. The TCC skill scores are higher than 0.6 for

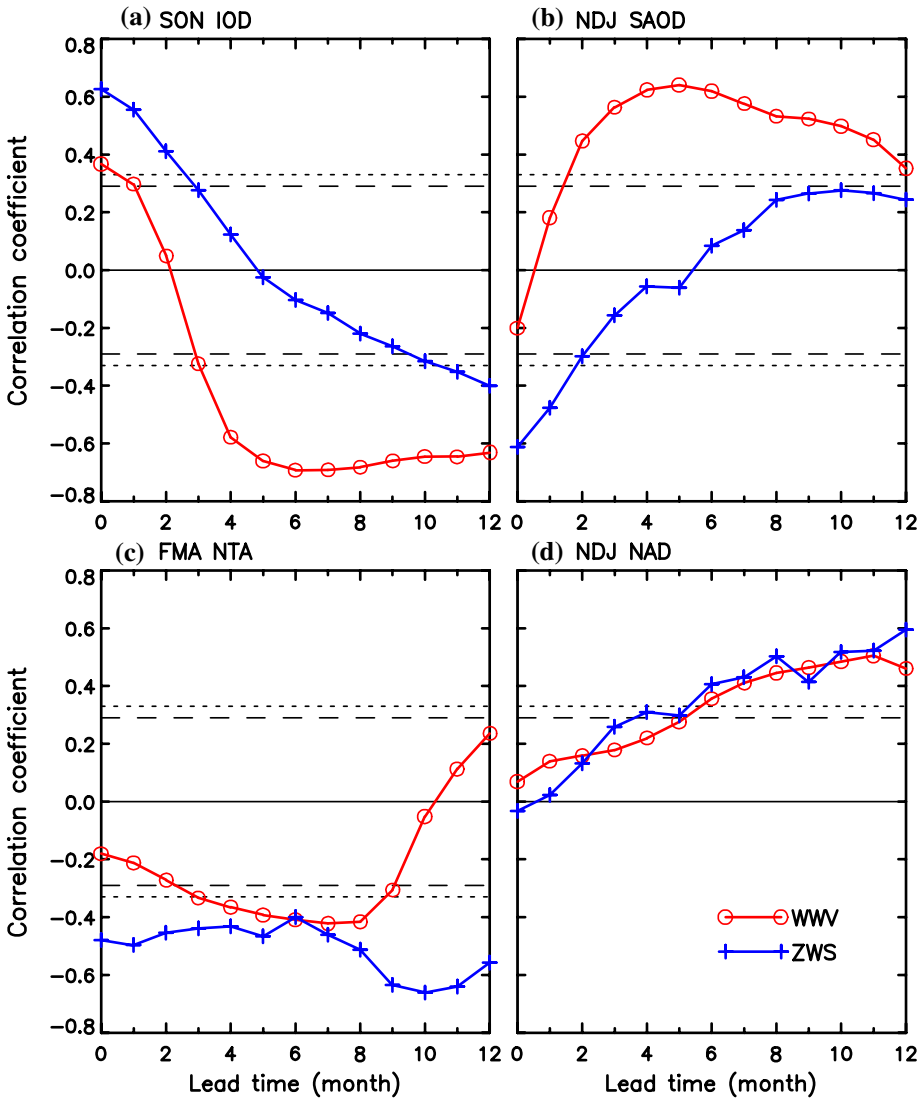

Fig. 11 Lag correlations of the WWV and ZWS indices with the **a** SON IOD, **b** NDJ SAOD, **c** FMA NTA, and **d** NDJ NAD indices after excluding the Niño3.4 SST signal in the previous DJF season during the period of 1982–2016. The dotted (dashed) line indicates significance at the 95% (90%) confidence level. The lead time indicates that the WWV and ZWS indices are lagged

all the Niño indices for a lead of 6 months (Fig. 12a), and significant improvements are observed for most leads in the range of 3–11 months when conditionally adding the NTA precursor to the benchmark model (Fig. 12b). The Niño3.4 and Niño4 indices have the highest TCC skill scores compared to the other Niño indices for leads in the range of 0–11 months, with values of 0.79 and 0.77 for a lead of 6 months, respectively. Conversely, the WPI and EMI have the lowest skill scores for leads shorter than 7 months, with values of 0.63 and 0.61 for a lead of 6 months, respectively. For the Niño3 index and the WPI (CTI), the TCC skill score is still higher than 0.6 for a lead of 8 (7) months. In short, these results suggest that the prediction skills of both the EP-type and CP-type indices of ENSO can be further improved by conditionally considering the NTA SST signal in a statistical model that includes the equatorial Pacific WWV and ZWS precursors.

We further demonstrate that the improvement in the prediction skills depends on the initial/target months, as shown in Fig. 13. It is clear that the skill scores at nearly all the target and lead months increased after conditionally introducing the NTA precursor to the benchmark model and that all the apparent skill score increases appear over the domains where the benchmark skill scores are relatively low. The patterns of the skill increments are different for the EP and CP ENSO types due to the conditionally involved NTA SST precursors. Further, it is found that introducing the NTA precursor to the benchmark model weakened the intensity of the predictability barriers of the Niño indices for either type of ENSO compared to the benchmark model, as seen by comparing Fig. 14 with Fig. 6, where the maxima of the decline rate of the skill scores is weakened along the barriers of the predictability.

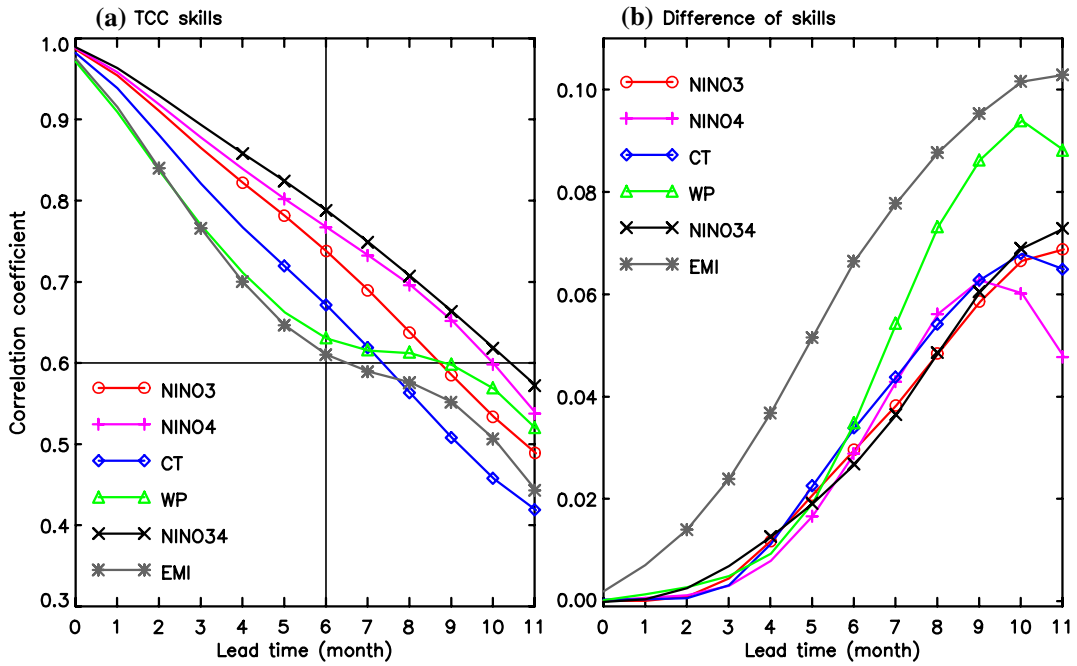

Fig. 12 The same as Fig. 3, but for **a** the skill scores when conditionally adding the NTA precursor to the benchmark model and **b** their improvements relative to the benchmark skills

6 Summary and discussions

The two observed types of ENSO, as a manifestation of the diversity of ENSO, have drawn much attention in recent decades. Due to their distinct impacts on global climate, research concerning the prediction and predictability of the two ENSO types has become increasingly important. Real-time operational prediction of the two types of ENSO has been routinely performed since the 2014–2016 El Niño event (Ren et al. 2016b). However, as mentioned in the introduction, the current generation of climate models has a limited ability to reproduce the typical observed features of the two ENSO types; therefore, it is difficult to distinguish between them in most operational dynamical forecasting systems. In this study, we examined the predictability of the two types of ENSO by building up statistical models that include both the equatorial Pacific WWV and ZWS precursors as a benchmark version and attempted to involve several external precursors from outside the tropical Pacific to further improve the statistical models.

Our results show that the preceding variations of the equatorial Pacific WWV and ZWS, which represent the ENSO-related zonally uniform and contrasted thermocline variability patterns, respectively, contribute to the main statistical predictability of the Niño indices that are used to represent ENSO in terms of the two types. Note that the ZWS precursor has been distinctly defined in the models for the EP and CP ENSO indices. The benchmark statistical model has a higher skill score for both the EP and CP ENSO indices than the persistence forecast, and the improvement in skill score is more pronounced for the EP type than that for the CP type. As a comparison, both the traditional Niño3 and Niño4 indices, which combine signals from both types, are relatively more statistically predictable than the Niño indices that individually represent the two ENSO types. Moreover, the prediction skill scores of the EP ENSO indices in the benchmark model are higher during boreal autumn and winter but much lower during spring and summer, whereas those of the CP ENSO indices appear to be higher during winter and spring but lower during late summer and autumn. The evident skill superiority provided by the WWV and ZWS precursors, compared to the persistence forecast, primarily occurs during the predictability barrier and afterwards.

We further examined the impacts of the precursors from the tropical Indian and Atlantic oceans, as well as the extratropics, including the IOD, NTA SST, SIOD, SAOD, NAD, and NPO, which could be considered to be ENSO predictor candidates as revealed in previous studies (e.g., Izumo et al. 2010; Boschat et al. 2013; Ham et al. 2013a; Ding et al. 2017), on the prediction skills of the Niño indices. The results show that all the external precursors that are focused on in this study, except the NTA SST, only make limited contributions to improving the prediction skills of the two ENSO types at specific initial months and leads, compared to a benchmark model built using both the WWV and ZWS precursors. It is found that the NTA SST anomalies can

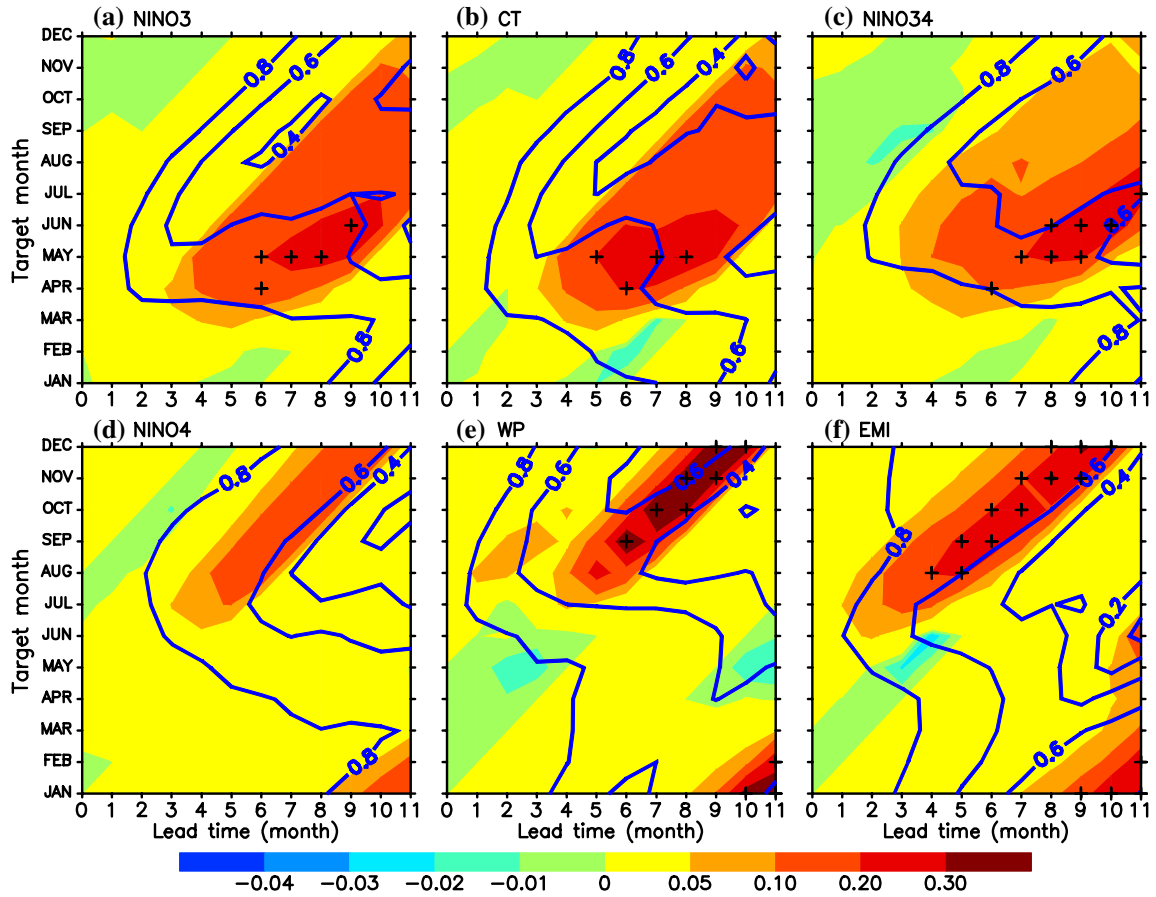

Fig. 13 The same as Fig. 4, but for the skill scores when conditionally adding the NTA precursor to the benchmark model (contours) and their differences relative to the benchmark skills (shading)

reliably provide significant increases in the prediction skill scores for the different types of Niño indices relative to the benchmark skill score. We further demonstrate that the signals of some ENSO precursors, such as the IOD, SIOD, SAOD, NAD, and NPO, which are known to predict ENSO at specific initial or target months, have been already transferred most of their signals into variations in the equatorial Pacific WWV and ZWS anomalies. Note that these external precursors are used at all initial/target months as predictors in the statistical models in this study, as opposed to being locked to certain seasons as mentioned in previous studies. If focusing on the ENSO prediction at some specific initial/target month, it is possible to use these particular external precursors to set up the statistical models. Indeed, for operational use, relatively general statistical models that involve stably effective, highly independent, and high-performance precursors are needed.

Finally, we configured a new statistical model for the Niño indices of the two ENSO types by conditionally adding the NTA precursor to the benchmark model. It is demonstrated that the Niño3.4 index has the highest prediction skill, compared to the other Niño indices. The statistical predictabilities of the Niño indices representing the two types of ENSO are very different; this is the Niño indices of EP ENSO (i.e., the Niño3 index and CTI) have an overall higher prediction skill than those of CP ENSO (i.e., WPI and EMI). However, such skills usually differ between different initial months and are subject to different predictability barrier properties, such as timing and intensity. The different Niño indices tend to have similar predictability barriers, and the EP ENSO indices show a stronger barrier than the CP ENSO indices but with similar timing. Introducing the NTA precursor tends to weaken the intensity of the barriers for both ENSO types, compared to that of the benchmark model.

Moreover, our results also showed that features in the statistical predictability and prediction skill of the Niño3.4 index are more similar with those of the Niño3 index and CTI, compared to the Niño4 index and WPI, indicating that the Niño3.4 index more reflects the variation in the EP ENSO type than the CP type. To further apply our results to real forecast, we suggest that the Niño3 index can be preferentially used for EP ENSO predictions and that WPI is still preferential for CP ENSO predictions because the

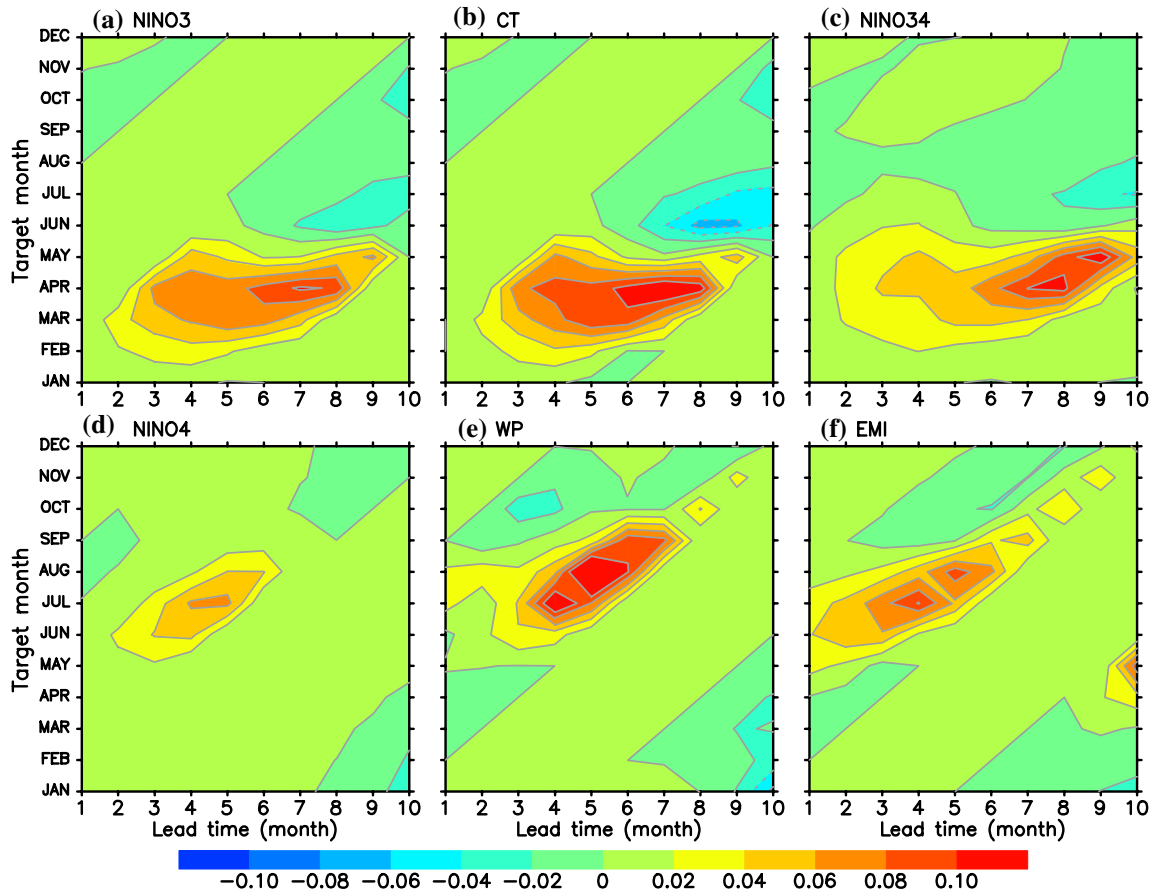

Fig. 14 Difference in the decline rate of the cross-validated correlation skill scores between the scheme conditionally adding the NTA precursor and the benchmark model (former minus latter) for the **a** Niño3, **b** CT, **c** Niño3.4, **d** Niño4, **e** WP, and **f** EMI indices during the period of 1982–2016

Niño3 index is highly correlated with CTI and has a higher prediction skill.

A statistical model is still a good method to predict the two ENSO types by simply inputting a few easily calculated indices that are available in real time. This is an advantage of statistical model compared to climate models whose prediction performance usually degrades as they are operated in real time. In future, more studies need to be conducted to better predict the two types of ENSO and studies concerning their predictability and prediction methodology also need to be developed.

Acknowledgements This work is jointly supported by National Key Research and Development Program of China (2017YFC1502302), China Meteorological Special Project (GYHY201506013), and the 973 Program of China (2013CB430203). Yi Deng is supported by the National Science Foundation Climate and Large-Scale Dynamics (CLD) program through Grants AGS-1354402 and AGS-1445956.

Open Access This article is distributed under the terms of the Creative Commons Attribution 4.0 International License (http://creativecommons.org/licenses/by/4.0/), which permits unrestricted use, distribution, and reproduction in any medium, provided you give appropriate credit to the original author(s) and the source, provide a link to the Creative Commons license, and indicate if changes were made.

References

Ashok K, Behera SK, Rao SA, Weng H, Yamagata T (2007) El Niño Modoki and its possible teleconnection. J Geophys Res 112:C11007. https://doi.org/10.1029/2006JC003798

Barnston AG, Glantz M, He Y (1999) Predictive skill of statistical and dynamical climate models in SST forecasts during the 1997–98 El Niño and the 1998 La Niña onset. Bull Am Meteor Soc 80:217–243. https://doi.org/10.1175/1520-0477(1999)080%3C0217:PSOSAD%3E2.0.CO;2

Barnston AG, Tippett MK, L'Heureux ML, Li S, Dewitt DG (2012) Skill of real-time seasonal ENSO model predictions during 2002–11: Is our capability increasing? Bull Am Meteor Soc 93:631–651. https://doi.org/10.1175/BAMS-D-11-00111.1

Behringer DW, Xue Y (2004) Evaluation of the global ocean data assimilation system at NCEP: The Pacific Ocean. Eighth Symposium on integrated observing and assimilation systems for atmosphere, oceans, and land surface, AMS 84th Annual Meeting. Washington State Convention and Trade Center, Seattle, Washington, pp 11–15

Bejarano L, Jin F-F (2008) Coexistence of equatorial coupled modes of ENSO. J Clim 21:3051–3067. https://doi.org/10.1175/2007JCLI1679.1

Boschat G, Terray P, Masson S (2013) Extratropical forcing of ENSO. Geophys Res Lett 40:1605–1611. https://doi.org/10.1002/grl.50229

Brönnimann S (2007) The impact of El Niño–southern oscillation on European climate. Rev Geophys 45:RG3003. https://doi.org/10.1029/2006RG000199

Cane MA, Zebiak SE, Dolan SC (1986) Experimental forecasts of El Niño. Nature 321:827–832

Chang P, Zhang L, Saravanan R, Vimont DJ, Chiang JCH, Ji L, Seidel H, Tippett MK (2007) Pacific meridional mode and El Niño—southern oscillation. Geophys Res Lett 34:L16608. https://doi.org/10.1029/2007GL030302

Chen D, Zebiak SE, Busalacchi AJ, Cane MA (1995) An improved procedure for El Niño forecasting: implications for predictability. Science 269:1699–1702. https://doi.org/10.1126/science.269.5231.1699

Clarke AJ (2014) El Niño physics and El Niño predictability. Ann Rev Mar Sci 6:79–99. https://doi.org/10.1146/annurev-marine-010213-135026

Clarke AJ, Van Gorder S (2001) ENSO prediction using an ENSO trigger and a proxy for western equatorial Pacific warm pool movement. Geophys Res Lett 28:579–582. https://doi.org/10.1029/2000GL012201

Clarke AJ, Van Gorder S (2003) Improving El Niño prediction using a space-time integration of Indo-Pacific winds and equatorial Pacific upper ocean heat content. Geophys Res Lett 30:1399. https://doi.org/10.1029/2002GL016673

Clarke AJ, Van Gorder S, Colantuono G (2007) Wind stress curl and ENSO discharge/recharge in the equatorial Pacific. J Phys Oceanogr 37:1077–1091. https://doi.org/10.1175/JPO3035.1

Deng Y, Park T, Cai M (2012) Process-based decomposition of the global surface temperature response to El Niño in boreal winter. J Atmos Sci 69:1706–1712. https://doi.org/10.1175/JAS-D-12-023.1

Ding R, Li J, Tseng Y, Sun C, Zheng F (2017) Linking a sea level pressure anomaly dipole over North America to the central Pacific El Niño. Clim Dyn 49:1321–1339. https://doi.org/10.1007/s00382-016-3389-8

Drosdowsky W (2006) Statistical prediction of ENSO (Niño 3) using sub-surface temperature data. Geophys Res Lett 33:L03710. https://doi.org/10.1029/2005GL024866

Fu C, Diaz HF, Fletcher JO (1986) Characteristics of the response of sea surface temperature in the central Pacific associated with warm episodes of the southern oscillation. Mon Weather Rev 114:1716–1739. https://doi.org/10.1175/1520-0493(1986)114%3C1716:COTROS%3E2.0.CO;2

Ham Y-G, Kug J-S (2012) How well do current climate models simulate two types of El Niño? Clim Dyn 39:383–398. https://doi.org/10.1007/s00382-011-1157-3

Ham Y-G, Kug J-S, Park J-Y, Jin F-F (2013a) Sea surface temperature in the north tropical Atlantic as a trigger for El Niño/Southern Oscillation events. Nat Geosci 6:112–116. https://doi.org/10.1038/ngeo1686

Ham Y-G, Kug J-S, Park J-Y (2013b) Two distinct roles of Atlantic SSTs in ENSO variability: north tropical Atlantic SST and Atlantic Niño. Geophys Res Lett 40:1–6. https://doi.org/10.1002/grl.50729

Hegyi B, Deng Y (2012) A dynamical fingerprint of tropical Pacific sea surface temperatures in the decadal-scale variability of the cool-season Arctic precipitation. J Geophys Res 116:D20121. https://doi.org/10.1029/2011JD016001

Hegyi B, Deng Y, Black RX, Zhou R (2014) Initial transient response of the winter polar stratospheric vortex to idealized equatorial pacific sea surface temperature anomalies in the NCAR WACCM. J Clim 27:2699–2713. https://doi.org/10.1175/JCLI-D-13-00289.1

Hendon HH, Lim E, Wang G, Alves O, Hudson D (2009) Prospects for predicting two flavors of El Niño. Geophys Res Lett 36:L19713. https://doi.org/10.1029/2009GL040100

Huang B, Xue Y, Behringer DW (2008) Impacts of Argo salinity in NCEP global ocean data assimilation system: the tropical Indian ocean. J Geophys Res 113:C08002. https://doi.org/10.1029/2007JC004388

Imada Y, Tatabe H, Ishii M, Chikamoto Y, Mori M, Arai M, Watanabe M, Kimoto M (2015) Predictability of two types of El Niño assessed using an extended seasonal prediction system by MIROC. Mon Weather Rev 143:4597–4617. https://doi.org/10.1175/MWR-D-15-0007.1

Izumo T, Vialard J, Lengaigne M et al (2010) Influence of the state of the Indian Ocean dipole on the following year's El Niño. Nat Geosci 3:168–172. https://doi.org/10.1038/ngeo760

Jeong H-I et al (2012) Assessment of the APCC couple MME suite in predicting the distinctive climate impacts of two flavors of ENSO during boreal winter. Clim Dyn 39:475–493. https://doi.org/10.1007/s00382-012-1359-3

Jeong H-I, Ahn J-B, Lee J-Y, Alessandri A, Hendon HH (2015) Interdecadal change of interannual variability and predictability of two types of ENSO. Clim Dyn 44:1073–1091. https://doi.org/10.1007/s00382-014-2127-3

Jin F-F (1997a) An equatorial ocean recharge paradigm for ENSO. Part I: conceptual model. J Atmos Sci 54:811–829. https://doi.org/10.1175/1520-0469(1997)054%3C0811:AEORPF%3E2.0.CO;2

Jin F-F (1997b) An equatorial ocean recharge paradigm for ENSO. Part II: a stripped-down coupled model. J Atmos Sci 54:830–847. https://doi.org/10.1175/1520-0469(1997)054%3C0830:AEORPF%3E2.0.CO;2

Jin EK et al (2008) Current status of ENSO prediction skill in coupled ocean–atmosphere models. Clim Dyn 31:647–664. https://doi.org/10.1007/s00382-008-0397-3

Kalnay E et al (1996) The NCEP/NCAR 40-year reanalysis project. Bull Am Meteor Soc 77:437–472. https://doi.org/10.1175/1520-0477(1996)077,0437:TNYRP.2.0.CO;2

Kang I-S, Kug J-S (2000) An El-Niño prediction system using an intermediate ocean and a statistical atmosphere. Geophys Res Lett 15:1167–1170

Kao H-Y Yu J-Y (2009) Contrasting eastern-Pacific and central-Pacific types of El Niño. J Clim 22:615–632. https://doi.org/10.1175/2008JCLI2309.1

Keenlyside NS, Ding H, Latif M (2013) Potential of equatorial Atlantic variability to enhance El Niño prediction. Geophys Res Lett 40:2278–2283. https://doi.org/10.1002/grl.50362

Kim H-M, Webster PJ, Curry JA (2009) Impact of shifting patterns of Pacific Ocean warming on north Atlantic tropical cyclones. Science 325:77–80. https://doi.org/10.1126/science.1174062

Kirtman PB (2003) The COLA anomaly coupled model: Ensemble ENSO prediction. Mon Weather Rev 131:2324–2341. https://doi.org/10.1175/1520-0493(2003)131%3C2324:TCACME%3E2.0.CO;2

Kirtman PB, Min D (2009) Multimodel ensemble ENSO prediction with CCSM and CFS. Mon Weather Rev 137:2908–2930. https://doi.org/10.1175/2009MWR2672.1

Kirtman BP et al (2014) The North American MultiModel Ensemble (NMME): Phase-1, seasonal-to-interannual prediction; phase-2, toward developing intraseasonal prediction. Bull Am Meteor Soc 95:585–601. https://doi.org/10.1175/BAMS-D-12-00050.1

Kug J-S, Lee J-Y, Kang I-S (2008) Systematic error correction of dynamical seasonal prediction of sea surface temperature using a stepwise pattern project method. Mon Weather Rev 136:3501–3512. https://doi.org/10.1175/2008MWR2272.1

Kug J-S, Jin F-F, An S-I (2009) Two types of El Niño events: cold tongue El Niño and warm pool El Niño. J Clim 22:1499–1515. https://doi.org/10.1175/2008JCLI2624.1

Larkin NK, Harrison DE (2005a) On the definition of El Niño and associated seasonal average U.S. weather anomalies. Geophys Res Lett 32:L13705. https://doi.org/10.1029/2005GL022738

Larkin NK, Harrison DE (2005b) Global seasonal temperature and precipitation anomalies during El Niño autumn and winter. Geophys Res Lett 32:L16705. https://doi.org/10.1029/2005GL022860

Latif M et al (1998) A review of the predictability and prediction of ENSO. J Geophys Res 103:14375 – 14393. https://doi.org/10.1029/97JC03413

Lim EP, Hendon HH, Hudson D, Wang G, Alves O (2009) Dynamical forecast of inter–El Niño variations of tropical SST and Australian spring rainfall. Mon Weather Rev 137:3796–3810. https://doi.org/10.1175/2009MWR2904.1

Lima CHR, Lall U, Jebara T, Barnston AG (2009) Statistical prediction of ENSO from subsurface sea temperature using a nonlinear dimensionality reduction. J Clim 22:4501–4519. https://doi.org/10.1175/2009JCLI2524.1

Liu Y, Ren H-L (2017) Improving ENSO prediction in CFSv2 with an analogue-based correction method. Int J Clim 37:5035–5046. https://doi.org/10.1002/joc.5142

Luo J-J, Masson S, Behera S, Shingu S, Yamagata T (2005) Seasonal climate predictability in a coupled OAGCM using a different approach for ensemble forecasts. J Clim 18:4474–4497. https://doi.org/10.1175/JCLI3526.1

Luo J-J, Masson S, Behera S, Yamagata T (2008) Extended ENSO predictions using a fully coupled ocean-atmosphere model. J Clim 21:84–93. https://doi.org/10.1175/2007JCLI1412.1

Meng X-L, Rosenthal R, Rubin DB (1992) Comparing correlated correlation coefficients. Psychol Bull 111:172–175. https://doi.org/10.1037/0033-2909.111.1.172

Mu M, Ren H-L (2017) Enlightenment from researches and predictions of 2014–2016 super El Niño event. Sci China Earth Sci 60:1569–1571. https://doi.org/10.1007/s11430-017-9094-5

Park T, Deng Y, Cai M (2012) Feedback attribution of the El Niño-Southern oscillation-related atmospheric and surface temperature anomalies. J Geophys Res 117:D23101. https://doi.org/10.1029/2012JD018468

Park J-Y, Yeh S-W, Kug J-S, Yoon J (2013) Favorable connections between seasonal footprinting mechanism and El Niño. Clim Dyn 40:1169–1181. https://doi.org/10.1007/s00382-012-1477-y

Rasmusson EM, Carpenter TH (1982) Variations in tropical sea surface temperature and surface wind fields associated with the southern oscillation/El Niño. Mon Weather Rev 110:354–384. https://doi.org/10.1175/1520-0493(1982)110%3C0354:VITSST%3E2.0.CO;2

Ren H-L, Jin F-F (2011) Niño indices for two types of ENSO. Geophys Res Lett 38:L04704. https://doi.org/10.1029/2010GL046031

Ren H-L, Jin F-F (2013) Recharge oscillator mechanisms in two types of ENSO. J Clim 26:6506–6523. https://doi.org/10.1175/JCLI-D-12-00601.1

Ren H-L, Jin F-F, Stuecker MF, Xie R (2013) ENSO regime change since the late 1970s as manifested by two types of ENSO. J Meteor Soc Japan 91:835–842

Ren H-L, Liu Y, Jin F-F, Yan Y-P, Liu X-W (2014) Application of the analogue-based correction of errors method in ENSO prediction. Atmos Ocean Sci Lett 7:157–161. https://doi.org/10.3878/j.issn.1674-2834.13.0080

Ren H-L, Jin F-F, Tian B, Scaife AA (2016a) Distinct persistence barriers in two types of ENSO. Geophys Res Lett 43:10973–10979. https://doi.org/10.1002/2016GL071015

Ren H-L, Liu Y, Zuo J, Lu B, Tian B, Jin F-F, Wan J (2016b) The new generation of ENSO prediction system in Beijing Climate Centre and its predictions for the 2014/2016 super El Niño event. Meteorol Mon 42:521–531 **(in Chinese)**

Ren H-L et al (2017) Prediction of primary climate variability modes in Beijing Climate Center. J Meteor Res 31:204–223. https://doi.org/10.1007/s13351-017-6097-3

Reynolds RW, Rayner NA, Smith TM, Stokes DC, Wang W (2002) An improved in situ and satellite SST analysis for climate. J Clim 15:1609–1625. https://doi.org/10.1175/1520-0442(2002)015%3C1609:AIISAS%3E2.0.CO;2

Rodríguez-Fonseca B, Polo I, García-Serrano J, Losada T, Mohino E, Mechoso CR, Kucharski F (2009) Are Atlantic Niños enhancing Pacific ENSO events in recent decades? Geophys Res Lett 36:L20705. https://doi.org/10.1029/2009GL040048

Ruiz JE, Cordery I, Sharma A (2005) Integrating ocean subsurface temperatures in statistical ENSO forecasts. J Clim 18:3571–3586. https://doi.org/10.1175/JCLI3477.1

Sun C, Li W, Ren H-L, Zhang P, Wang D (2006) A dynamic-analogue error correction model for ENSO prediction and its initial hindcast verification. Chin J Atmos Sci 30:965–976 **(in Chinese)**

Terray P (2011) Southern hemisphere extra-tropical forcing: a new paradigm for El Niño-southern oscillation. Clim Dyn 36:2171–2199. https://doi.org/10.1007/s00382-010-0825-z

Tseng Y-H, Hu Z-Z, Ding R, Chen H-C (2017) An ENSO prediction approach based on ocean conditions and ocean–atmosphere coupling. Clim Dyn 48:2025–2044. https://doi.org/10.1007/s00382-016-3188-2

Wang R, Ren H-L (2017) The linkage between two ENSO types/modes and the interdecadal changes of ENSO around the year 2000. Atmos Ocean Sci Lett 10:168–174. https://doi.org/10.1080/16742834.2016.1258952

Wang X, Wang C (2014) Different impacts of various El Niño events on the Indian Ocean Dipole. Clim Dyn 42:991–1005. https://doi.org/10.1007/s00382-013-1711-2

Wang B et al (2009) Advance and prospectus of seasonal prediction: assessment of the APCC/CliPAS 14-model ensemble retrospective seasonal prediction (1980–2004). Clim Dyn 33:93–117. https://doi.org/10.1007/s00382-008-0460-0

Wang L, Ren H-L, Chen Q, Tian B, Liu Y (2017) Statistical correction of ENSO prediction in BCC_CSM1.1 m based on a stepwise pattern projection method. Meteorol Mon 43:294–304. (in Chinese)

Weng H, Ashok K, Behera S, Rao AS, Yamagata T (2007) Impacts of recent El Niño Modoki on dry/wet conditions in the Pacific Rim during boreal summer. Clim Dyn 29:113–129. https://doi.org/10.1007/s00382-007-0234-0

Xie R, Jin F-F (2018) Two leading ENSO modes and El Niño types in the Zebiak–Cane model. J Clim 31:1943–1962. https://doi.org/10.1175/JCLI-D-17-0469.1

Xie R, Huang F, Ren H (2013) Subtropical air-sea interaction and the development of central Pacific El Niño. J Ocean Univ China 12:260–271. https://doi.org/10.1007/s11802-013-2143-7

Xue Y, Leetmaa A, Ji M (2000) ENSO prediction with Markov models: the impact of sea level. J Clim 13:849–871. https://

doi.org/10.1175/1520-0442(2000)013%3C0849:EPWMMT%3E2.0.CO;2

Yang S, Jiang X (2014) Prediction of eastern and central Pacific ENSO events and their impacts on east Asian climate by the NCEP climate forecast system. J Clim 27:4451–4472. https://doi.org/10.1175/JCLI-D-13-00471.1

Yeh S-W, Kug J-S, An S-I (2014) Recent progress on two types of El Niño: observations, dynamics, and future changes. Asia Pac J Atmos Sci 50:69–81. https://doi.org/10.1007/s13143-014-0028-3 2014.

Yeh S-W, Kug JS, Dewitte B, Kwon M-H, Kirtman BP, Jin F-F (2009) El Niño in a changing climate. Nature 461:511–514. https://doi.org/10.1038/nature08316

Yu J-Y, Kim ST (2010) Identification of central-Pacific and eastern-Pacific types of ENSO in CMIP3 models. Geophys Res Lett 37:L15705. https://doi.org/10.1029/2010GL044082

Yu J-Y, Kao H-Y, Lee T (2010) Subtropics-related interannual sea surface temperature variability in the equatorial central Pacific. J Clim 23:2869 – 2884. https://doi.org/10.1175/2010JCLI3171.1

Zebiak SE, Cane MA (1987) A model El Niño-Southern Oscillation. Mon Weather Rev 115:2262–2278

Zhang R-H, Gao C (2016) The IOCAS intermediate coupled model (IOCAS ICM) and its real-time predictions of the 2015–2016 El Niño event. Sci Bull 61:1061–1070. https://doi.org/10.1007/s11434-016-1064-4

Zhang R-H, Zebiak SE, Kleeman R, Keenlyside N (2003) A new intermediate coupled model for El Niño simulation and prediction. Geophys Res Lett 30:2012. https://doi.org/10.1029/2003GL018010

Zhang W, Jin F-F, Li J, Ren H-L (2011) Contrasting impacts of two-type El Niño over the western north Pacific during boreal autumn. J Meteor Soc Jpn 89:563–569

Zhang W, Jin F-F, Ren H-L, Li J, Zhao J-X (2012) Differences in teleconnection over the North Pacific and rainfall shift over the USA associated with two types of El Niño during boreal autumn. J Meteor Soc Jpn 90:535–552

Zhang RH, Min Q, Su JZ (2017) Impact of El Niño on atmospheric circulations over east Asia and rainfall in China: role of the anomalous western North Pacific anticyclone. Sci China Earth Sci 60:1124–1132. https://doi.org/10.1007/s11430-016-9026-x

Zhu J et al (2015) ENSO prediction in project minerva: sensitivity to atmospheric horizontal resolution and ensemble size. J Clim 28:2080–2095. https://doi.org/10.1175/JCLI-D-14-00302.1

孙丞虎，崔童，李维京等. 2019. 动力和统计预测信息融合预测方法及对我国夏季降水预测的检验. 地球物理学报，62(11)：4110-4119，doi：10.6038/cjg2019M0646.

Sun C H, Cui T, Li W J, et al. 2019. A merging method for dynamic model and statistical predictions and evaluation of summer precipitation prediction skill in China. *Chinese J. Geophys.* (in Chinese), 62(11): 4110-4119, doi: 10.6038/cjg2019M0646.

动力和统计预测信息融合预测方法及对我国夏季降水预测的检验

孙丞虎[1,2]，崔童[3*]，李维京[3,2*]，左金清[3,2]

1 中国气象科学研究院灾害天气国家重点实验室及气候与气候变化研究所，北京 100081

2 南京信息工程大学气象灾害预报预警与评估协同创新中心，南京 210044

3 国家气候中心气候研究开放实验室，北京 100081

摘要 短期气候预测中如何将气候模式和统计方法的预测结果科学、客观的集成起来，一直是非常重要的问题. 本文针对动力模式和统计方法预测结果相结合的问题，引入资料同化中信息融合的思想，采用最优内插同化方法，实现了动力模式和统计季节降水预测结果的融合. 检验表明，对 1982—2015 年我国夏季降水百分率的回报，融合预测结果与观测的平均空间相关系数可达 0.44，分别较统计预测和 CFSv2 模式统计降尺度订正的技巧提高了 0.1 左右，而均方根误差较两者可以降低 5%～20%. 可见，该方法可以进一步提升对我国夏季降水的预测技巧，具有显著的业务应用价值.

关键词 中国夏季降水；统计预测；动力模式预测；融合

doi：10.6038/cjg2019M0646 **中图分类号** P456 **收稿日期** 2018-11-16，2019-01-26 收修定稿

A merging method for dynamic model and statistical predictions and evaluation of summer precipitation prediction skill in China

SUN ChengHu[1,2], CUI Tong[3*], LI WeiJing[3,2*], ZUO JinQing[3,2]

1 *State Key Laboratory of Severe Weather and Institute of Climate System, Chinese Academy of Meteorological Sciences, Beijing* 100081, *China*

2 *Collaborative Innovation Center on Forecast and Evaluation of Meteorological Disasters, Nanjing University of Information Science & Technology, Nanjing* 210044, *China*

3 *Laboratory for Climate Studies, National Climate Center, Beijing* 100081, *China*

Abstract How to make an objective combination for the predictions from climate dynamic model and statistical method is an important issue in the short-term climate prediction area. To resolve this problem, we use the optimum interpolation assimilation method to merge the predictions of summer precipitation percentage anomalies in China from CFSv2 model and statistical method. The verification of prediction skill indicates that during 1982—2015 periods, the spatial correlation coefficient of merging predictions with the observations is as highly as 0.44, which is

基金项目 “十三五”国家重点研发计划项目(2016YFA0601501)，公益性行业专项(GYHY201406018)，Basic Scientific Research and Operation Foundation of CAMS (2018Z006, 2018KJ029, 2018KJ030)，国家重点基础研究发展计划 973 项目(2013CB430203)共同资助.

第一作者简介 孙丞虎，主要从事气候与气候变化研究. E-mail：sunch@cma.gov.cn

***通讯作者** 崔童，主要从事气候监测预测研究. E-mail：cuitong@cma.gov.cn

higher than the skill of statistical prediction method and the downscaling of CFSv2 model about 0.1. Moreover, the root mean square error of merging predictions is also reduced by 5%～20% than that of statistical method and CFSv2 model downscaling. Our results indicate that this new prediction method can further improve the prediction skill of summer precipitation in China and has the potential application values.

Keywords China summer precipitation; Statistic prediction; Dynamic mode prediction; Merging

0　引言

我国夏季降水变率受东亚季风活动显著影响(Huang et al. 2004),改进降水的季节预测能力一直是国内外学者为之不懈努力研究的热点问题. 近年来,国内外在夏季降水统计预测方法上已有长足的发展(范可等,2007;Wu et al.,2009,2013,2015;Yim et al.,2014,2015;朱蒙等,2014;庞轶舒,2014;Xing et al.,2016;阮成卿和李建平,2016). 如,范可等(2007)通过预测长江中下游夏季降水的年际增幅,实现了对该区域夏季降水距平百分率的预测,这种方法在1997—2006年回报中平均均方根误差仅有18%. Wu 等(2013,2015)将多种预测因子进行MEOF分解,再利用空间模态与相应的时间系数序列构建Markov预测模型,结果发现对东亚北方地区降水有较好的预测技巧. 朱蒙等(2014)根据欧亚大陆土壤温度和全球海表温度与中国东部夏季降水的关系,将不同关键区的欧亚大陆土壤温度和海表温度作为预测因子对中国东部夏季降水进行预测也发现具有一定的预测技巧.

为了利用气候模式开展夏季降水预测,不少研究分析了模式的模拟、预测能力. 如 Wang 等(2004)对11个AGCM模式分析后发现,模式对北半球夏季降水异常的模拟预测能力较差,尤其是对东亚5°N—30°N之间夏季风年际变率缺乏预报技巧. 对美国国家环境预报中心的气候预测系统模式CFSv1和v2(Saha et al.,2006,2014)的预测技巧分析也表明,模式对亚洲地区大尺度季风环流的模拟偏弱,对季节时间尺度和流域空间尺度的降水预报能力尚待完善(Yang et al.,2008;Kim et al.,2012;Luo et al.,2013). 鉴于当前的先进气候模式仍存在较大的偏差,难以对夏季风的平均强度和季节变率做出准确预测的问题(Wang et al.,2008),人们先后发展了多种动力-统计相结合的模式预测结果订正方法,如多元回归、CCA、SVD等统计方法,它们以前期海温等热力强迫预测因子结合模式误差的系统性订正来改进降水预测技巧,取得了不错的效果(Barnston and Smith,1996;Ting and Wang,1997;Feddersen et al.,1999;Liu,2003;Kang et al.,2003;任宏利和丑纪范,2005;Chen and Lin,2006;Kug et al.,2008;Chen 等,2012;Sun and Chen,2012;李维京等,2013;Heo et al.,2014). 值得注意的是,在进行动力和统计结合时,一种新思路是基于气候变量的规律,利用模式大尺度环流的预测信息和预测变量相关的前期观测信息,采用年际增量的方法或场耦合等预测方法建立预测模型(Fan 等,2012;Liu and Fan,2014;Dai et al.,2018). 这种方法最早应用于东亚夏季风的预测,继而推广到季节降水、气温等方面表现出较高的技巧.

但是,伴随着统计预测方法以及动力模式预测方法的蓬勃发展,如何将多种预测方法、模式的预测结果科学、客观地进行集成,提供最有价值的预测结果给气候预测人员参考,成为一个新的问题(Krishnamurti et al.,1999; Krishnamurti and Kumar,2012;Stephenson et al.,2005;王会军等,2012;Wang et al.,2015). 故在多模式集成预测领域,相继发展了包括简单集成、权重集成及贝叶斯最优集成在内的多种集成方法(Krishnamurti et al.,1999;Yun et al.,2003;Kug et al.,2008;Stephenson et al.,2005;Rodrigues et al.,2018). 但是,需要指出的是对于某一地点的预测,上述集成方法对某一种预测结果的集成权重实际上主要取决于其历史预测技巧的高低(即误差的时间传播特征),并未兼顾考虑误差的空间分布形态(即误差的空间传播特征),以及利用该点附近有技巧的预测信息来改善预测技巧,而这恰好是资料同化方法所能兼顾考虑的(Kalnay,2002). 鉴于此,本文将引入资料同化中信息融合的方法,综合考虑预测误差的时间和空间传播特征,将动力模式与统计方法的预报结果进行信息融合获取最优预测结果,以期提高我国夏季降水的预测技巧.

1 资料和方法

本文使用的资料包括:1982—2015 年中国 160 站月平均降水量资料、GPCP V2.2 月平均降水资料、NCEP/NCAR 再分析资料的 500 hPa 高度场、200 hPa 风场资料及 ERSST v3 全球月平均海表温度资料. 对于美国 CFSv2 模式资料,同刘颖等(2013)类似我们选取了 1982—2015 年历年 3 月起报的夏季降水历史预报资料建立交叉预测检验数据集. 其中,1982—2010 为历史回报数据,2011—2015 年的资料由于 CFSv2 进入了实时预测阶段采用实时预测的结果,对 2011 年的资料因实时下载数据缺失故该年份不参与本文计算. 对于 CFSv2 模式起报时间,从起报月的 0、6、12 和 18 UTC 开始积分,积分时间为 9 个月. 本研究中我们对不同起报时间的积分结果进行了集合平均,取其中的 6—8 月资料进行研究使用.

本文在进行统计预测和模式预测结果融合时,使用了最优内插同化方法(Gandin,1965;Daley,1991; Kalnay,2002). 我们将动力模式预测结果视为同化中的"背景场",统计模型预测结果视做同化中的"观测值",以便利用该方法开展融合预测. 本文中"真值"是实况观测的夏季降水距平百分率资料. 基于上述假设, 动力预测和统计预测结果形成的融合预测可以表达为

$$\boldsymbol{Yp} = \boldsymbol{Xd} + \boldsymbol{W} \cdot (\boldsymbol{Xe} - \boldsymbol{Xd}),$$

其中,$\boldsymbol{Yp}$ 为融合预测结果,$\boldsymbol{Xd}$ 表示动力模式预测结果,$\boldsymbol{Xe}$ 表示统计模型预测结果,$\boldsymbol{W}$ 为最优权重系数矩阵.

当假定统计预测的误差和动力模式预测的误差均"无偏"且不相关,考虑融合预报误差极小化条件,对最优权重系数矩阵 $\boldsymbol{W}$ 有

$$\boldsymbol{W} = \boldsymbol{B} \cdot (\boldsymbol{R} + \boldsymbol{B})^{-1},$$

其中,$\boldsymbol{B}$ 表示动力模式预测结果的误差协方差阵,$\boldsymbol{R}$ 表示统计预测结果的误差协方差阵,它们可以利用历史上的"真值"即观测资料对统计模型、动力模式回报的结果进行误差统计来获得. 在计算出各自的误差协方差矩阵之后,即可求取最优权重系数矩阵 $\boldsymbol{W}$. 最优内插同化方法的主要优势是利用了统计预测资料和模式预测资料提供的先验信息,通过最小方差估计确定权重函数,得到统计意义上的"最优预测值",从而实现对统计和动力模式预测结果的最优集成.

2 结果分析

2.1 统计预测模型及预测技巧检验

本文中,我们采用了庞轶舒(2014)和 庞轶舒等(2014)发展的方法建立我国夏季降水距平百分率的统计预测模型,步骤如下:首先,对我国夏季降水距平百分率场进行 EOF 分解获取主要模态,进而计算这些主要模态与前期海温、大气环流因子(即 500 hPa 位势高度场以及 200 hPa 纬向风场)的相关关系,寻找关键区作为预测因子,再利用多元回归方程建立对降水距平百分率的预测方程. 图 1 给出了我国夏季降水距平百分率的前 4 个 EOF 模态,它们可以解释总方差变化的 41%. 其中,EOF1 的解释方差为 14.9%,表现为我国中东部地区以长江为界"南北反向"的异常分布特征;EOF2 的解释方差为 10.5%,呈现为河套、华南沿海地区与江淮—黄淮地区反向变化的分布特征;EOF3 解释方差约 8.6%,表现为我国中东部地区由北向南"－＋－"三极子型分布特征;对于 EOF4 其解释方差为 7.0%,呈现黄河、长江之间同西北东部—内蒙古中部、华南大部之间反向变化的分布特征. 经进一步分析,发现上述 EOF 的时间系数表现为显著的年际变化特征(图 2).

按照庞轶舒(2014)和 庞轶舒等(2014)的办法,我们将依次选取海洋、大气中的前期预测因子建立各 PC 系数的预报方程. 需要指出的是,由于前期预测因子的选取对预测结果有重要影响,所以在预测建模前我们逐一对因子进行组合试验,取预测技巧最高者入选(图略). 下面给出关键因子的选取结果:从前冬(12—2 月平均)海温与夏季降水 PC1 的相关场来看(图 3a),赤道中东太平洋以及印度洋存在显著相关,这实际反映了 ENSO 及响应产生的印度洋一致偏暖模态的影响(Yang and Lau, 1998;Kawamura, 1998;Zhang,2000;Yang et al.,2007),故选取图中方框内区域作为海温预测因子的关键区. 对于大气因子,我们计算了前冬 200 hPa 纬向风与 PC1 的相关系数(图 3b),并选取图中位于北大西洋和北美大陆方框内区域作为关键区. 进一步以上述海温和 200 hPa 纬向风场关键区为预测因子,与 PC1 建立多元回归方程,并且采用交叉检验办法分析预测技巧. 结果表明,对于 PC1 的预测技巧,其在 1982—2015 年的平均时间相关系数(即 TCC)为0.64,通过了 99%的显著性检验(图略). 对于 PC2 而言,从前冬海温与 PC2 的相关场来看(图 4a),赤道中东太平

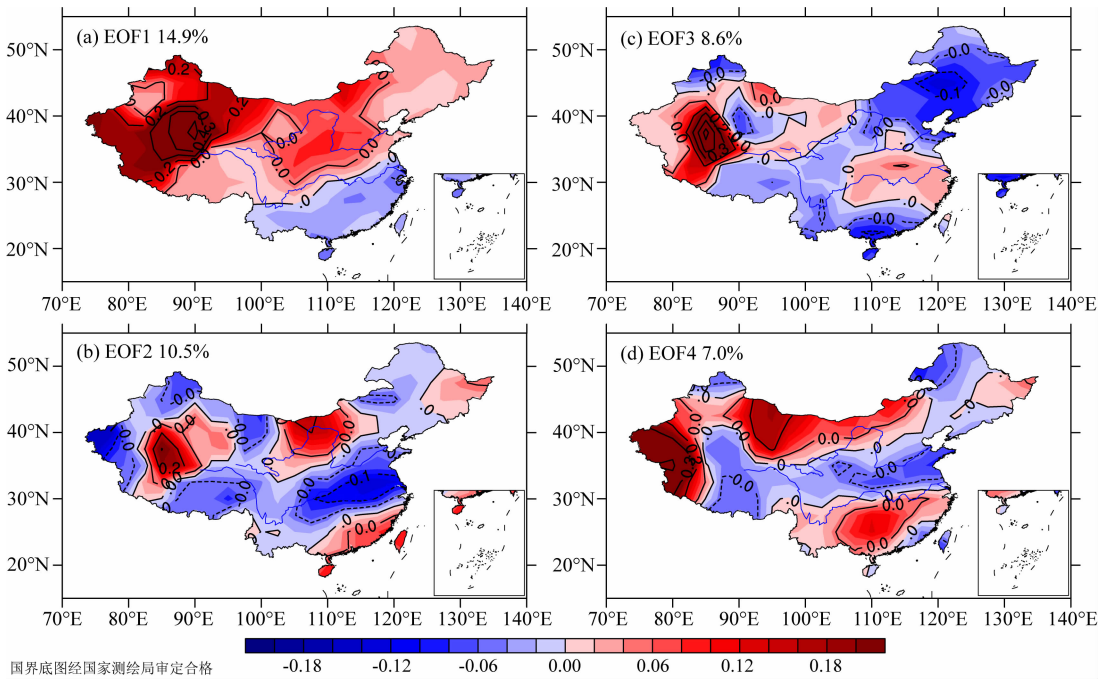

图 1　1982—2015 年我国夏季降水距平百分率场前 4 个 EOF 的空间分布：(a) EOF1；(b) EOF2；(c) EOF3；(d) EOF4

Fig. 1　Spatial structure of the four leading EOF modes of summer precipitation percentage anomalies in China during 1982—2015: (a) EOF1; (b) EOF2; (c) EOF3; (d) EOF4

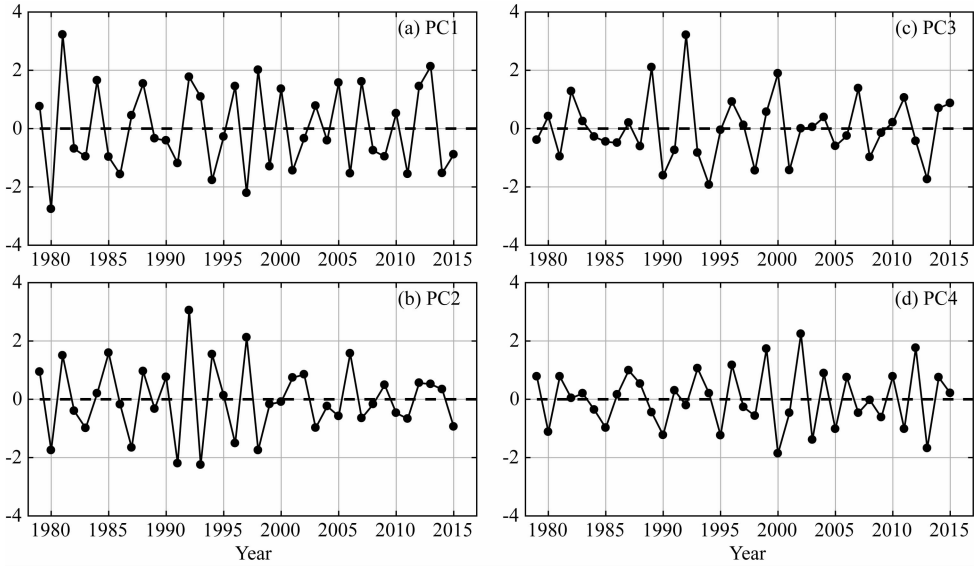

图 2　1982—2015 年我国夏季降水距平百分率场前 4 个 EOF 的 PC 系数曲线：(a) PC1；(b) PC2；(c) PC3；(d) PC4

Fig. 2　PC time series of the four leading EOF modes of summer precipitation percentage anomalies in China during 1982—2015: (a) PC1; (b) PC2; (c) PC3; (d) PC4

洋及澳大利亚东部太平洋与 PC2 存在显著相关，选取图中方框内区域作为关键区；同理求出前冬 200 hPa 纬向风与 PC2 的相关场(图 4b)，选取热带印度洋和热带东太平洋图中方框内区域作为关键区，同样利用上述 4 个关键区建立 PC2 的多元回归方程，并且采用交叉检验方法分析预测技巧，结果显示其平均预测 TCC 为 0.44，通过 99%的显著性检验(图略).

对于 PC3，从前冬海温与 PC3 的相关场来看(图 5a)，孟加拉湾、南海、南印度洋等区域海表温度与 PC3 存在显著相关，选取图中方框内区域作为关键区，进一步求出前冬 500 hPa 位势高度场与 PC3 的相关场(图 5b)，选取东亚大陆南部图中方框内区域作为关键区，也可建立 PC3 的多元回归方程，并且采用交叉检验方法检验其技巧. 结果表明，对于 PC3

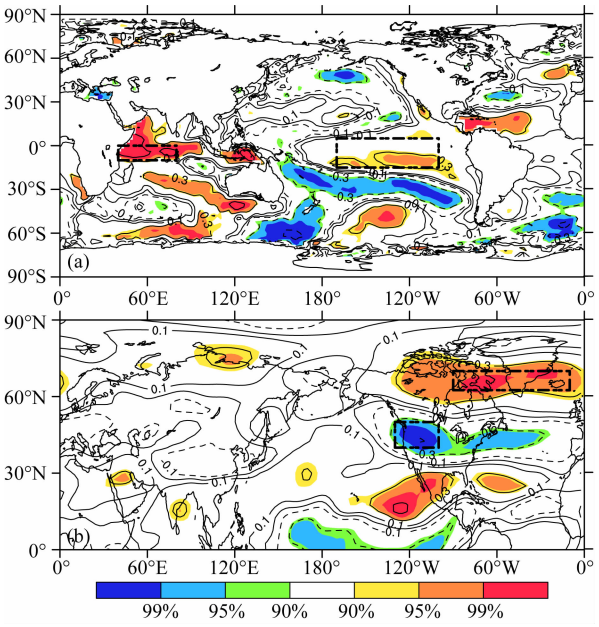

图 3 前冬海表温度(a)、前冬 200 hPa 纬向风(b)与我国夏季降水 PC1 的相关分布图,阴影表示 90%～99%显著性检验,方框表示关键区

Fig. 3 The correlation coefficients of PC1 with SST (a) and U200 (b) in previous DJF season. The shaded areas correspond to 90%～ 99% confidence levels, and the boxes represent the key regions

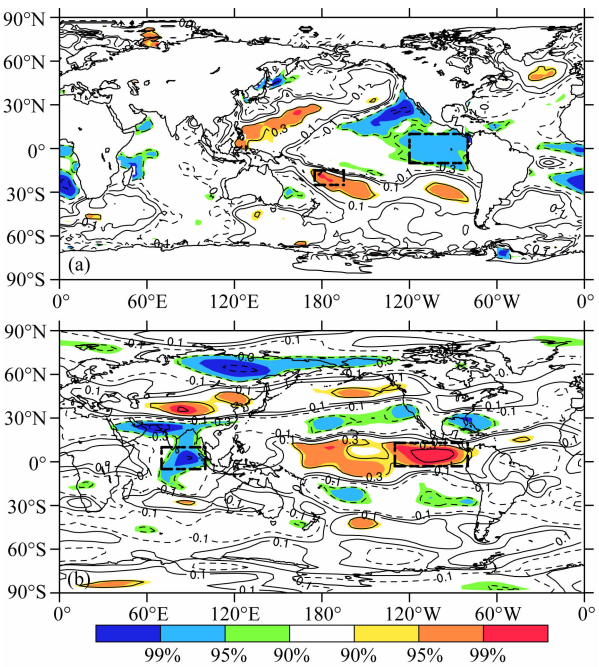

图 4 前冬海表温度(a)、前冬 200 hPa 纬向风(b)与夏季我国降水 PC2 的相关系数分布图,阴影表示 90%～99%显著性检验,方框表示关键区

Fig. 4 The correlation coefficients of PC2 with SST (a) and U200 (b) in previous DJF season. The shaded areas correspond to 90%～ 99% confidence levels, and the boxes represent the key regions

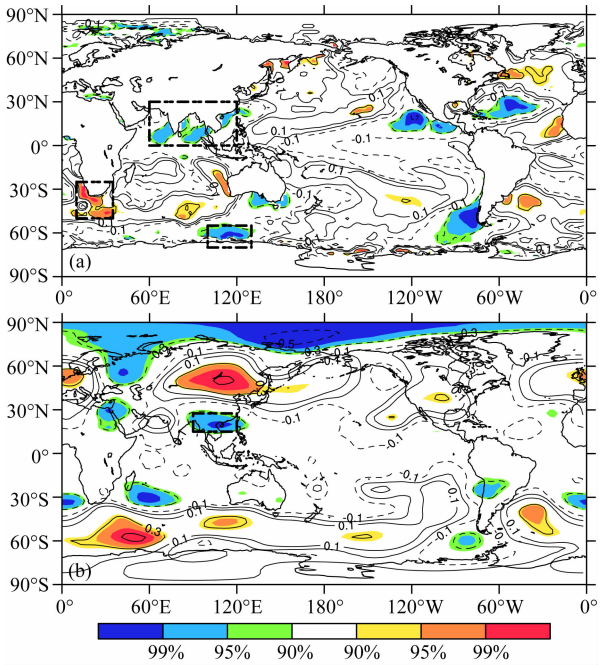

图 5 前冬海表温度(a)、前冬 500 hPa 高度场(b)与夏季我国降水 PC3 的相关分布图,阴影表示 90%～99%显著性检验,方框表示关键区

Fig. 5 The correlation coefficients of PC3 with SST (a) and H500 (b) in previous DJF season. The shaded areas correspond to 90%～99% confidence levels and the boxes represent the key regions

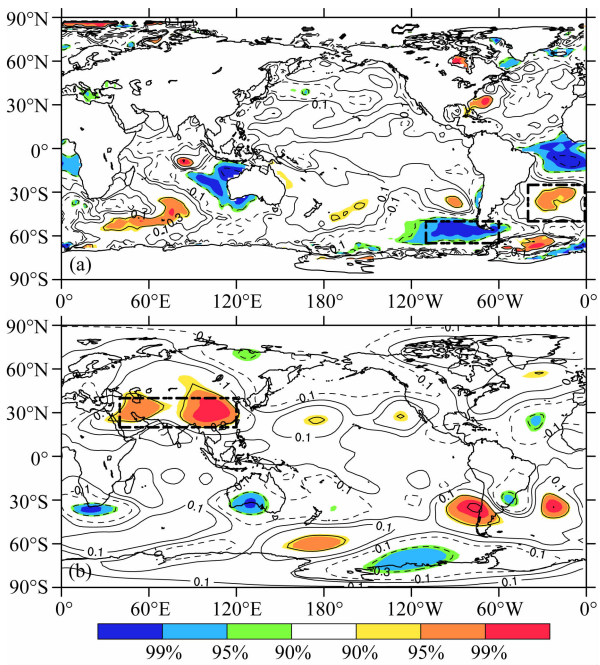

图 6 前冬海表温度(a)、前冬 500 hPa 高度场(b)与夏季我国降水 PC4 的相关分布图,阴影表示 90%～99%显著性检验,方框表示关键区

Fig. 6 The correlation coefficients of PC4 with SST (a) and H500 (b) in previous DJF season. The shaded areas correspond to 90%～99% confidence levels and the boxes represent the key regions

的预测技巧，平均 TCC 为 0.46，通过了 99%的显著性检验(图略). 对于 PC4，南大西洋中部、以及东南太平洋海表温度与 PC4 存在显著相关(图 6a)，选取图中方框内区域作为关键区，同理求出前冬 500 hPa 位势高度与 PC4 的相关场(图 6b)，并选取亚洲大陆南部图中方框内区域作为关键区. 利用上述 3 个关键区建立 PC4 的多元回归方程，并采用交叉检验方法检验其技巧. 结果表明，对于 PC4 的预测技巧，其平均 TCC 为 0.49，可以通过 99%的显著性检验.

我们进一步利用预测的前 4 个夏季降水 PC 系数及基于这些 PC 系数重建的降水距平百分率场，建立我国夏季降水总场变化的预测模型. 回报技巧检验表明：我国中东部大部分地区降水预测与观测实况的相关系数可以通过 95%显著性检验，其中黄淮、江南、华南、西南东部、东北南部和西北北部等区域的预测技巧较高(图 7). 此外，从预测与观测间空间相关系数的历年变化来看(图 8a)，表现为明显的年际差异，最低为−0.49(1987 年)，最高为 0.82(1997 年).

由此可见，以前冬关键环流与海温作为预测因子所建立的夏季降水距平百分率预测模型具有一定的预测技巧，我们将进一步利用其开展和 CFSv2 模式预测信息的融合试验.

2.2　CFSv2 模式的统计降尺度订正及预测技巧检验

考虑到最优内插同化中，模式背景场误差应具有无偏特征，而前人的分析表明 CFSv2 模式对东亚夏季降水的预测技巧较低. 因此，在开始进行统计预测和模式预测结果融合之前，我们依照刘颖等(2013)的工作，同样选取了 CFSv2 模式的夏季 H500 环流预报场和前一年秋、冬季海表面温度观测场作为预测因子，使用场信息耦合型方法建立统计降尺度订正预测模型，以减小 CFSv2 模式直接预测降水的误差，使其具有和统计预测模型相当的预测技巧.

图 8b 给出了 CFSv2 统计降尺度订正模型对 1982—2015 年中国夏季降水回报的交叉检验结果，我们可以发现其较 CFSv2 模式的原始预测技巧显著提高，其多年平均空间距平相关系数(PCC)由 0.03提高到 0.31(表 1). 原始 CFSv2 模式的预测结果与观测间的 PCC 系数仅有 6 年可以通过 99%显著性水平，而降尺度订正后的预测结果有 22 年都通过了 99% 显著性检验，且有 13 年的预测 PCC 系数超过 0.4.

从预测与观测的时间相关系数(TCC)的空间分布看，原始 CFSv2 模式的预测结果仅在黄淮地区、华北南部等地的 TCC 相关系数超过 0.2(图 9a)，而 CFSv2 模式统计降尺度订正的 TCC 在我国中东大

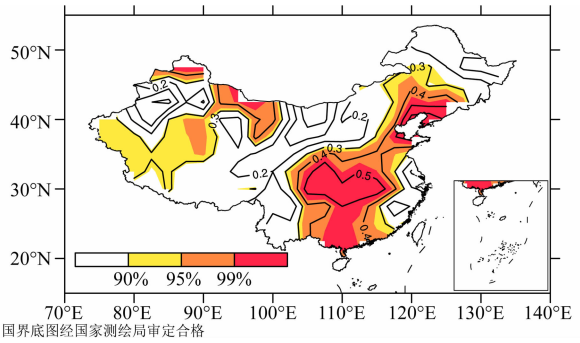

图 7　1982—2015 年统计模型降水预测结果与观测的时间相关系数空间分布，阴影表示 90%～99%显著性水平

Fig. 7　The correlation coefficients of observed summer precipitation percentage anomalies with statistical predictions during 1982—2015. The shaded areas correspond to 90%～99% confidence levels

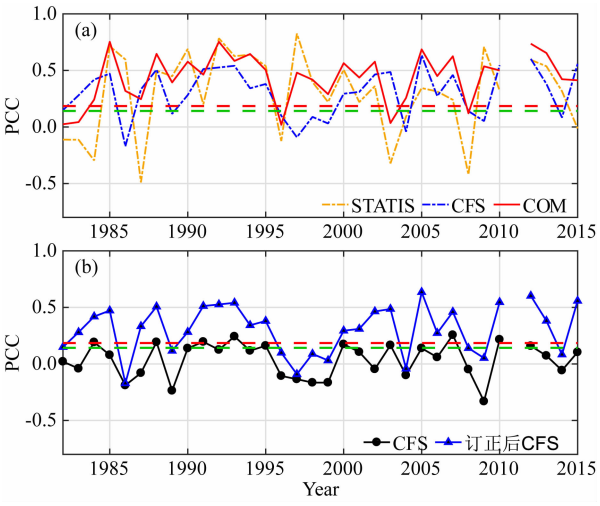

图 8　(a) 1982—2015 年统计预测模型(黄虚线)、CFSv2 统计降尺度订正(蓝虚线)及融合(红实线)降水预测的结果与观测之间的空间相关系数；(b) 统计降尺度订正前(黑线)和订正后(蓝线)CFSv2 模式预测结果与观测之间的空间相关系数，绿、红虚线分别为 95%和 99%显著性水平

Fig. 8　(a) The spatial correlation coefficients of observed summer precipitation with statistical predictions (yellow dot line), CFSv2 statistical downscaling (blue dot line) and merging predictions (red line); (b) the spatial correlation coefficients of original CFSv2 model predictions (black line) as well as the CFSv2 model statistical downscaling results (blue line) with the observations during 1982—2015. The green and red dashed lines correspond to the 95% and 99% confidence levels, respectively

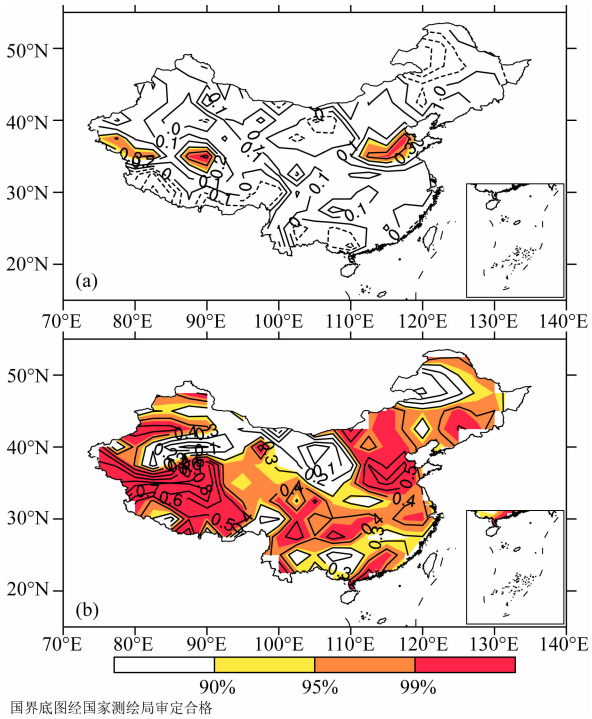

图 9 1982—2015 年原始 CFSv2(a)和 CFSv2 统计降尺度订正(b)预测结果与观测的时间相关系数空间分布，阴影表示 90%～99%显著性水平

Fig. 9 The correlation coefficients of observed summer precipitation with (a) original CFSv2 predictions, (b) CFSv2 statistical downscaling predictions during 1982—2015. The shaded areas correspond to 90%～99% confidence levels

部地区超过 0.2(图 9b)，其中在华北、黄淮大部、西南中部、青藏高原地区等地可达 0.4～0.6. 可见，经过降尺度订正后 CFSv2 模式对我国夏季降水的预测技巧显著提升.

2.3 CFSv2 模式与统计预测结果的融合

为了分析模式预测偏差对融合预测效果的影响，我们首先给出了原始 CFSv2 模式与统计预测结果进行融合预测的技巧检验结果. 结果表明(表 1)，当以原始 CFSv2 模式结果为背景场，使用其与统计预测结果进行融合时，在 1982—2015 年间对中国夏季降水的回报结果与观测的多年平均空间距平相关系数(PCC)仅为 0.26，介于原始 CFSv2 模式及统计模型各自技巧之间(原始 CFSv2 模式为 0.03，统计模型为 0.30)，预测技巧提升并不明显. 这表明，当两种预测模型对中国夏季降水的预测技巧差异过大，尤其是动力模式预测水平远远低于统计模型时，二者融合后总体预测误差并不会达到极小化. 因此，在开展预测信息融合时偏差订正是必要的(Kalnay, 2002).

那么，当统计模型和动力模式预测技巧水平相当时，融合之后的预测结果能否有所改进？为此，我们采用统计降尺度订正后的 CFSv2 模式结果与统计预测结果进行融合，同样以订正后的 CFSv2 模式结果为背景场. 结果表明(表 1)，其对 1982—2015 年间中国夏季降水的回报技巧显著提升，其多年平均空间距平相关系数(PCC)达到 0.44，较统计模型和 CFSv2 模式统计降尺度订正的技巧也均有提升. 进一步分析还发现(图 8a)，在 CFSv2 模式统计降尺度订正预测与统计模型预测结果差异较大的年份(如 1986 年)，融合预测的 PCC 多介于两者之间，而在两者预测技巧差异较小的年份(如 2012 年)，融合预测的 PCC 则会超过两者.

表 1 1982—2015 年平均的统计模型、原始 CFSv2、CFSv2 统计降尺度订正以及融合预测结果与观测夏季降水距平百分率间的空间相关系数

Table 1 The mean spatial correlation coefficients of observed summer precipitation with statistical predictions, original CFSv2, CFSv2 statistical downscaling and merging predictions during 1982—2015

预测技巧	统计模型	原始 CFSv2	CFSv2 统计降尺度订正	原始 CFSv2 与统计预测融合	CFSv2 统计降尺度订正与统计预测融合
平均空间相关系数	0.3	0.03	0.31	0.26	0.44

从融合预测结果与观测之间时间相关系数(TCC)的空间分布来看(图 10)，预测技巧较高的区域有华北、黄淮、东北南部、江南大部地区、华南以及高原地区等地，并且大部分地区通过了 95%的信度检验. 这些区域基本上是 CFSv2 模式统计降尺度订正与统计模型各自预测技巧都偏高区域的叠加，实现了有效融合. 而在内蒙古西部及东北部、西北地区东部、黑龙江大部、云南大部、新疆中南部等地，因 CFSv2 模式统计降尺度订正与统计模型各自预测技巧都偏低，导致了融合结果在上述地区的预测技巧提升不明显.

进一步，我们通过比较融合预测结果的均方根误差(rmse)与 CFSv2 模式统计降尺度订正和统计模型预测均方根误差之间的差异来说明融合预测相对于前两者的优势. 这里定义均方根误差(rmse)的降低百分率：

$$Drmse = [(R_a - R_{com})/R_a],$$

其中，R_a 表示 CFSv2 模式统计降尺度订正预测的 rmse 或统计模型的 rmse，R_{com} 表示融合预测的

rmse. 图 11a，b 分别为融合预测与 CFSv2 模式统计降尺度订正和统计预测模型间 *D*rmse 的空间分布，正值表示融合预测结果的 rmse 减少，负值表示融合结果的 rmse 增大. 可以看出，融合预测比 CFSv2 模式统计降尺度订正的结果在我国大部分地区误差减少(图 11a)，

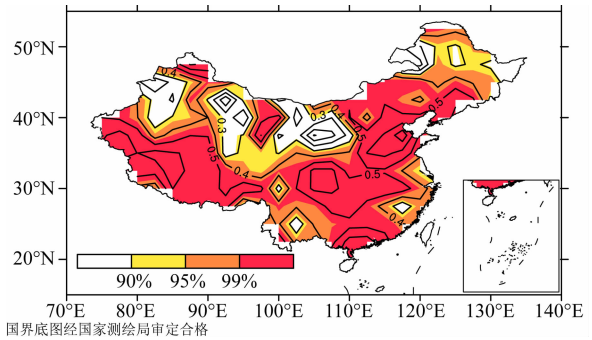

图 10　1982—2015 年 CFSv2 统计降尺度订正与统计预测的融合结果同夏季降水观测之间时间相关系数的空间分布，阴影表示 90%～99%显著性水平

Fig. 10　The correlation coefficients of observed summer precipitation with the merging predictions of statistical model and CFSv2 statistical downscaling during 1982—2015. The shaded areas correspond to 90%～99% confidence levels

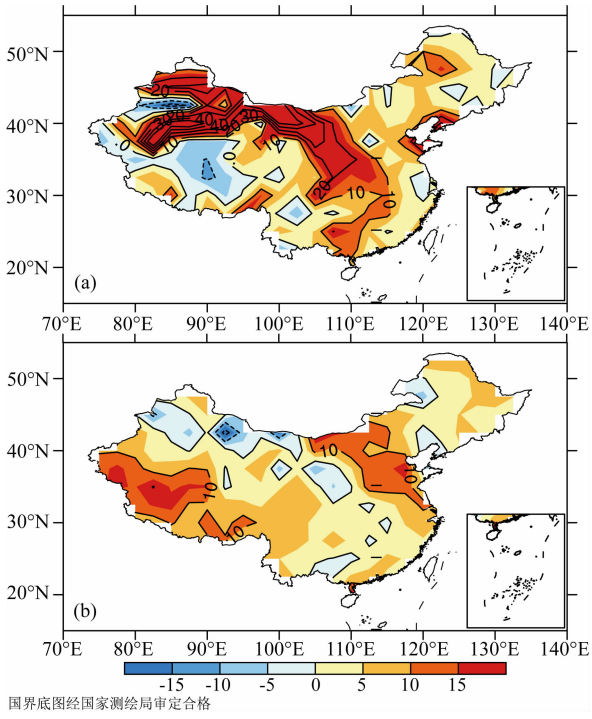

图 11　1982—2015 年融合夏季降水预测与(a)CFSv2 统计降尺度订正和(b)统计模型预测的 *D*rmse(%)

Fig. 11　The *D*rmse (%) of merging summer precipitation predictions with (a) CFSv2 statistical downscaling and (b) statistical model predictions during 1982—2015

其中在西北地区东部、西南东北部、华中东部、华南西部、东北南部、内蒙古西部、新疆大部地区 rmse 降低 5%～15%，部分地区降低 20%以上. 另外，融合预测相对于统计模型预测在我国大部分地区 rmse 也明显降低，其中在华北大部、黄淮、江淮东部、内蒙古中部、西南西部、东北北部等地误差降低 5%～10%，局部地区降低 10%以上(图 11b).

此外，为了分析最优权重系数的重要作用，我们做了一组控制实验. 假定反映 CFSv2 模式预测和统计预测场两者关系的误差协方差不随时间、空间位置而改变，即权重系数为相等权重. 结果表明，这种“等权重”融合预测的多年平均空间距平相关系数(PCC)会下降到 0.27(图略). 同时，从预测结果与观测之间的 TCC 空间分布来看(图略)，在西北大部、西藏南部、内蒙古中部、东北北部、华北西部、福建、广东、广西等地预测技巧均明显降低. 可见，最优权重系数在融合预测方法中对提高预测技巧确有重要作用.

综上，利用最优内插同化方法将统计预测结果和动力预测结果进行融合，将不失为一种行之有效地提升我国夏季降水预测准确率的新方法，其初步实现了动力模式与统计方法预测结果的客观集成，进一步提高预测技巧.

3　结论

(1)以前冬海温和关键区环流场作为预测因子，建立了我国夏季降水距平百分率的统计预测模型. 对 1982—2015 年交叉回报检验的结果表明，预测与观测之间的多年平均的空间相关系数为 0.30. 从时间相关系数的空间分布看，在我国西北北部、东北南部、黄淮、江汉、西南东部和华南等地预测技巧较高.

(2)选取 CFSv2 动力模式预测的当年夏季 500 hPa 高度场和前一年秋、冬季海表温度观测场作为预测因子，使用场信息耦合型方法建立了 CFSv2 模式统计降尺度订正夏季降水预测模型. 交叉回报检验结果表明，订正后夏季降水预测与观测的多年平均空间相关系数可由订正前的 0.03 提高到 0.31.

(3)基于上述统计预测模型和 CFSv2 模式统计降尺度订正预测的结果，采用最优内插同化方法发展了动力和统计预测信息的融合方案. 回报检验表明，融合预测与观测的多年平均空间相关系数可达 0.44，且均方根误差较统计预测模型和 CFSv2 模式统计降尺度订正预测的结果也降低了 5%～20%，

可以进一步提升对我国夏季降水的预测技巧,具有一定的业务应用价值.

虽然,本文基于最优内插同化方法开展了统计方法和 CFSv2 模式动力预测信息的融合试验,初步实现了动力和统计预测结果的有机结合,但是如何进一步利用国内外多种先进预测模式、模型的预测结果,深入发展多模式、多预测模型结果的融合预测方法,值得我们进一步进行探索.

致谢 作者衷心感谢聂肃平、沈艳和王润博士提供的有益讨论和帮助.

References

Barnston A G, Smith T M. 1996. Specification and prediction of global surface temperature and precipitation from global SST using CCA. *Journal of Climate*, 9(11): 2660-2697.

Chen H, Lin Z H. 2006. A correction method suitable for dynamical seasonal prediction. *Advances in Atmospheric Sciences*, 23(3): 425-430.

Chen H P, Sun J Q, Wang H J. 2012. A statistical downscaling model for forecasting summer rainfall in China from DEMETER hindcast datasets. *Weather and Forecasting*, 27(3): 608-628, doi: 10.1175/WAF-D-11-00079.1.

Dai H X, Fan K, Tian B Q. 2018. A hybrid downscaling model for winter temperature over northeast China. *International Journal of Climatology*, 38(S1): e349-e363.

Daley R. 1991. Atmospheric Data Analysis. Cambridge: Cambridge University Press.

Fan K, Liu Y, Chen H P. 2012. Improving the prediction of the East Asian summer monsoon: new approaches. *Weather and Forecasting*, 27(4): 1017-1030, doi: 10.1175/WAF-d-11-000921.

Feddersen H, Navarra A, Ward M N. 1999. Reduction of model systematic error by statistical correction for dynamical seasonal predictions. *Journal of Climate*, 12(7): 1974-1989.

Gandin L S. 1965. Objective analysis of meteorological fields: U.S. Dept. Commerce and National Science Foundation (Washington, DC.), 242.

Heo K Y, Ha K J, Yun K S, et al. 2014. Methods for uncertainty assessment of climate models and model predictions over East Asia. *International Journal of Climatology*, 34(2): 377-390.

Huang R H, Huang G, Wei Z G. 2004. Climate variations of the summer monsoon over China. // Chang C P ed. East Asian Monsoon. World Scientific Publishing Co. Pte Ltd., 213-270.

Kalnay E. 2002. Atmospheric Modeling, Data Assimilation and Predictability. Cambridge, UK: Cambridge University Press.

Kang I S, Lee J Y, Park C K. 2003. Potential predictability of summer mean precipitation in a dynamical seasonal prediction system with systematic error correction. *Journal of Climate*, 17(4): 834-844.

Kawamura R. 1998. A possible mechanism of the Asian summer monsoon-ENSO coupling. *Journal of the Meteorological Society of Japan. Ser. II*, 76(6): 1009-1027.

Kim H M, Webster P J, Curry J A. 2012. Asian summer monsoon prediction in ECMWF System 4 and NCEP CFSv2 retrospective seasonal forecasts. *Climate Dynamics*, 39(12): 2975-2991.

Krishnamurti T N, Kishtawal C M, LaRow T E, et al. 1999. Improved weather and seasonal climate forecasts from multimodel superensemble. *Science*, 285(5433): 1548-1550.

Krishnamurti T N, Kumar V. 2012. Improved seasonal precipitation forecasts for the Asian monsoon using 16 atmosphere-ocean coupled models. Part II: Anomaly. *Journal of Climate*, 25(1): 65-88.

Kug J S, Lee J Y, Kang I S, et al. 2008. Optimal multi-model ensemble method in seasonal climate prediction. *Asian-Pacific Journal of the Atmospheric Sciences*, 44: 233-247.

Li W J, Zheng Z H, Sun C H. 2013. Improvements to dynamical analogue climate prediction method in China. *Chinese Journal of Atmospheric Sciences* (in Chinese), 37(2): 341-350.

Liu Y, Fan K, Zhang Y. 2013. A statistical downscaling model for summer rainfall over China stations based on the Climate Forecast System. *Chinese Journal of Atmospheric Sciences* (in Chinese), 37(6): 1287-1296, doi: 10.3878/j.issn.1006-9895.2012.

Liu Y, Fan K. 2014. An application of hybrid downscaling model to forecast summer precipitation at stations in China. *Atmospheric Research*, 143: 17-30, doi: 10.1016/j.atmosres.2014.01.024.

Liu Y Q. 2003. Prediction of monthly-seasonal precipitation using coupled SVD patterns between soil moisture and subsequent precipitation. *Geophysical Research Letter*, 30(15): 1827, doi: 10.1029/2003GL017709.

Luo L F, Tang W, Lin Z H, et al. 2013. Evaluation of summer temperature and precipitation predictions from NCEP CFSv2 retrospective forecast over China. *Climate Dynamics*, 41(7-8): 2213-2230.

Pang Y S. 2014. The stability analysis of EOF modes of summer rainfall in China and statistical downscaling forecast [Master's thesis] (in Chinese). Beijing: Chinese Academy of Meteorological Sciences.

Pang Y S, Zhu C W, Liu K. 2014. Analysis of stability of EOF modes in summer rainfall anomalies in China. *Chinese Journal of Atmospheric Sciences* (in Chinese), 38(6): 1137-1146.

Ren H L, Chou J F. 2005. Analogue correction method of errors by combining statistical and dynamical methods. *Acta Meteorologica Sinica* (in Chinese), 63(6): 988-993.

Rodrigues L R L, Doblas-Reyes F J, Coelho C A S. 2018. Calibration and combination of monthly near-surface temperature and precipitation predictions over Europe. *Climate Dynamics*, doi: 10.1007/s00382-018-4140-4.

Ruan C Q, Li J P. 2016. An improvement in a time-scale decomposition statistical downscaling prediction model for summer rainfall over North China. *Chinese Journal of Atmospheric Sciences* (in Chinese), 40(1): 215-226, doi: 10.3878/j.issn.1006-9895.1503.14317.

Saha S, Nadiga S, Thiaw C, et al. 2006. The NCEP climate forecast system. *Journal of Climate*, 19(15): 3483-3517.

Saha S, Moorthi S, Wu X R, et al. 2014. The NCEP climate forecast system version 2. *Journal of Climate*, 27(6): 2185-2208.

Stephenson D B, Coelho C A S, Doblas-Reyes F J, et al. 2005. Forecast assimilation: a unified framework for the combination of multi-model weather and climate predictions. *Tellus A*, 57(3): 253-264.

Sun J Q, Chen H P. 2012. A statistical downscaling scheme to improve global precipitation forecasting. *Meteorology and Atmospheric Physics*, 117(3-4): 87-102, doi: 10.1007/s00703-012-0195-7.

Ting M F, Wang H. 1997. Summertime U. S. precipitation variability and its relation to pacific sea surface temperature. *Journal of Climate*, 10(8): 1853-1873.

Wang B, Kang I S, Lee J Y. 2004. Ensemble simulations of Asian Australian monsoon variability by 11 AGCMs. *Journal of Climate*, 17(4): 803-818.

Wang B, Lee J Y, Kang I S, et al. 2008. How accurately do coupled climate models predict the leading modes of Asian-Australian monsoon interannual variability? *Climate Dynamics*, 30(6): 605-619. doi: 10.1007/s00382-007-0310-5.

Wang H J, Fan K, Lang X M, et al. 2012. Advances in Climate Prediction Theory and Technique of China (in Chinese). Beijing: Meteorological Press, 147-159.

Wang H J, Fan K, Sun J Q, et al. 2015. A review of seasonal climate prediction research in China. *Advances in Atmospheric Sciences*, 32(2): 149-168.

Wu Q Y, Yan Y, Chen D K. 2013. A linear Markov model for East Asian monsoon seasonal forecast. *Journal of Climate*, 26(14): 5183-5195.

Wu Q Y, Yan Y, Chen D K. 2015. Seasonal prediction of East Asian monsoon precipitation: skill sensitivity to various climate variabilities. *International Journal of Climatology*, 36(1): 324-333.

Wu Z W, Wang B, Li J P, et al. 2009. An empirical seasonal prediction model of the East Asian summer monsoon using ENSO and NAO. *Journal of Geophysical Research: Atmospheres*, 114(D18): D18120, doi: 10.1029/2009JD011733.

Xing, W, Wang B, Yim S Y. 2016. Long-lead seasonal prediction of China summer rainfall using an EOF-PLS regression-based methodology. *Climate Dynamics*, 29(5): 1783-1796.

Yang J L, Liu Q Y, Xie S P, et al. 2007. Impact of the Indian Ocean SST basin mode on the Asian summer monsoon. *Geophysical Research Letter*, 34(2): L02708, doi: 10.1029/2006GL028571.

Yang S, Lau K M. 1998. Influences of sea surface temperature and ground wetness on Asian summer monsoon. *Journal of Climate*, 11(12): 3230-3246.

Yang S, Zhang Z Q, Kousky V E, et al. 2008. Simulations and seasonal prediction of the asian summer monsoon in the NCEP climate forecast system. *Journal of Climate*, 21(15): 3755-2775.

Yim S Y, Wang B, Xing W. 2014. Prediction of early summer rainfall over South China by a physical-empirical model. *Climate Dynamics*, 43(7-8): 1883-1891.

Yim S Y, Wang B, Xing W, et al. 2015. Prediction of Meiyu rainfall in Taiwan by multi-lead physical-empirical models. *Climate Dynamics*, 44(11-12): 3033-3042, doi: 10.1007/s00382-014-2340-0.

Yun W T, Stefanova L, Krishnamurti T N. 2003. Improvement of the multimodel superensemble technique for seasonal forecasts. *Journal of Climate*, 16(22): 3834-3840.

Zhang R H. 2000. Features of the East Asian monsoon during El Niño episode. CLIVAR Exchanges, 5(2): 21-22.

Zhu M, Chen H S, Jiang W, et al. 2014. A preliminary test of the summer rainfall prediction in China based on the land surface thermal factors. *Acta Meteorologica Sinica* (in Chinese), 72(6): 1135-1142.

附中文参考文献

范可，王会军，Choi Y J. 2007. 一个长江中下游夏季降水的物理统计预测模型. 科学通报，52(24)：2900-2905.

李维京，郑志海，孙丞虎. 2013. 近年来我国短期气候预测中动力相似预测方法研究与应用进展. 大气科学，37(2)：341-350.

刘颖，范可，张颖. 2013. 基于CFS模式的中国站点夏季降水统计降尺度预测. 大气科学，37(6)：1287-1296，doi：10.3878/j.issn.1006-9895.2012.

庞轶舒. 2014. 中国夏季降水模态时间稳定性和统计降尺度预测研究[硕士论文]. 北京：中国气象科学研究院.

庞轶舒，祝从文，刘凯. 2014. 中国夏季降水异常EOF模态的时间稳定性分析. 大气科学，38(6)：1137-1146.

任宏利，丑纪范. 2005. 统计-动力相结合的相似误差订正法. 气象学报，63(6)：988-993

阮成卿，李建平. 2016. 华北汛期降水分离时间尺度降尺度预测模型的改进. 大气科学，40(1)：215-226，doi：10.3878/j.issn.1006-9895.1503.14317.

王会军，范可，郎咸梅等. 2012. 我国短期气候预测的新理论、新方法和新技术. 北京：气象出版社，147-159.

朱蒙，陈海山，蒋薇等. 2014. 陆面热力因子应用于中国夏季降水预测的初步试验. 气象学报，72(6)：1135-1142.

（本文编辑　胡素芳）

Geophysical Research Letters

RESEARCH LETTER
10.1029/2019GL084281

Contribution of Global warming and Urbanization to Changes in Temperature Extremes in Eastern China

Ying Sun[1,2], Ting Hu[1], Xuebin Zhang[3], Chao Li[4], Chunhui Lu[1], Guoyu Ren[1,5], and Zhihong Jiang[2]

[1]National Climate Center, Laboratory for Climate Studies, China Meteorological Administration, Beijing, China, [2]Collaborative Innovation Center on Forecast and Evaluation of Meteorological Disasters, Nanjing University of Information Science & Technology, Nanjing, China, [3]Climate Research Division, Environment and Climate Change Canada, Toronto, Ontario, Canada, [4]State Key Laboratory of Estuarine and Coastal Research, Key Laboratory of Geographic Information Science (Ministry of Education), School of Geographic Sciences, East China Normal University, Shanghai, China, [5]Department of Atmospheric Science, School of Environmental Studies, China University of Geosciences, Wuhan, China

Key Points:
- Global warming and urbanization exert important influences on both warm and cold days and nights in Eastern China
- Both anthropogenic and urban signals are detected in nighttime extreme temperatures while only the former is detected in daytime extremes
- The effect of urbanization is estimated to have contributed as much as one third of the observed warming in nighttime temperature extremes

Supporting Information:
- Supporting Information S1

Correspondence to:
Y. Sun,
sunying@cma.gov.cn

Citation:
Sun, Y., Hu, T., Zhang, X., Li, C., Lu, C., Ren, G., & Jiang, Z. (2019). Contribution of global warming and urbanization to changes in temperature extremes in Eastern China. *Geophysical Research Letters*, *46*. https://doi.org/10.1029/2019GL084281

Received 27 JUN 2019
Accepted 21 SEP 2019
Accepted article online 22 OCT 2019

©2019. The Authors.
This is an open access article under the terms of the Creative Commons Attribution License, which permits use, distribution and reproduction in any medium, provided the original work is properly cited.

Abstract The anthropogenic-induced global warming and local urbanization exert important influences on temperature extremes in Eastern China. Here we use China station observations and climate models to investigate their effects on the warm and cold days and nights simultaneously. We quantified the contribution from these two factors based on an optimal fingerprinting method. We find that both anthropogenic and urbanization signals can be clearly detected and separated from each other in the nighttime temperature extremes. The effect of urbanization may explain as much as one third of the observed changes in cold and warm nights while the urbanization signal is weak in the daytime extremes. The results are robust against sampling uncertainty in the estimate of urbanization signal, but uncertainty due to collinearity between the urbanization signal and global warming is difficult to assess.

Plain Language Summary Understanding the causes behind changes in temperature extremes is of significance for reliably projecting future climate change. Previous studies have separately shown that global warming and the urbanization effects are the two important drivers for the increase of warm extremes and decrease of cold extremes in Eastern China. In this study, we consider these two factors simultaneously using an optimal fingerprinting method. We find that climate models can well reproduce the observed changes in extreme temperature when the urbanization effects are included. Both global warming and urbanization have contributed to changes in nighttime temperature extremes, with global warming contributing slightly more. On the other hand, changes in daytime temperature extremes seem to be predominantly due to global warming.

1. Introduction

Eastern China is the most populous and economically developed region in China and is significantly impacted by weather and climate extremes. For example, the summer of 2013 was the historically hottest at the time, and the heat and accompanying drought resulted in 59 billion RMB damage (Hou et al., 2014). Observations have shown that Eastern China has experienced an increase in extreme high-temperature events and a decrease in extreme low-temperature events since the mid-twentieth century (Lu et al., 2016; Wang et al., 2012; Yin et al., 2017; You et al., 2011). In particular, the past 10 years have witnessed frequent record-breaking high temperatures along with serious heat waves. It is projected that what was a rare heat wave in the historical record will become a usual event in the coming decades even under a median Representative Concentration Pathway (RCP)4.5 emission scenarios (Sun et al., 2014, 2018).

There are at least two major drivers contributing to the observed mean temperature-warming trend in China. One third of the observed mean temperature increase of 1.44 °C during the period 1961–2013, or about 0.49 °C, can be accounted for by the effect of urbanization that occurred since the middle 1980s (Sun et al., 2016). External forcing to the climate system, including large-scale anthropogenic influences, that is, human emissions of greenhouse gases and aerosols (referred to as anthropogenic forcing hereafter), and

natural external forcing including solar and volcanic activities can explain most of the remaining warming (Sun et al., 2016). As temperature extremes are ultimately related to mean temperatures, it follows that these two drivers must have also influenced extreme temperatures.

Previous studies have investigated the contributions to changes in extreme temperatures by individual drivers separately (Zhang et al., 2006). In a series of studies, Lu et al. (2016, 2018), Yin et al. (2017), Yin and Sun (2018) and Dong et al. (2018) found that the anthropogenic forcings exert clear detectable influence on intensity, frequency, and duration of temperature extremes represented by various temperature indices in China. The effect of urbanization, however, was not considered in these studies. As both anthropogenic forcing and urbanization cause regional warming in China, the regression approach that scales the regional temperature response to anthropogenic forcing to best match the observations, without explicitly considering the urbanization effect, could attribute at least some warming that is due to urbanization as a result of anthropogenic forcing.

Effects of urbanization on temperature extremes have been estimated by computing the difference in indices of temperature extremes between urban stations and rural stations (Zhang et al., 2011; Zhou & Ren, 2011). For this purpose, different methods have been used to estimate regional averages of extreme temperature indices for urban and rural areas by classifying observing sites into urban and rural stations (Ren et al., 2008, 2015; Ren & Zhou, 2014; Yang et al., 2011, 2017). Ren and Zhou (2014) used criteria including the population, station history, and the built-up size of the area to identify a fixed set of urban stations and rural stations. In their approach, a station is classified either as an urban station or as a rural station. The entire historical records for the urban stations are used to estimate averages of urban regions while those for rural stations are used to estimate rural averages. Because most of observing sites were established in inhabited regions, economic development of China has gradually urbanized what used to be rural areas. As a result, there is not a clear division between urban sites and rural sites. A rural site may have been urbanized to some degree; and thus, the differences between urban and rural sites may underestimate the urbanization effect. Yang et al. (2017) used the concept of dynamical classification of Yang et al. (2011) according to nighttime light data. In their approach, a station is considered as an urban station if the mean nighttime light values exceed a certain threshold and the urban land ratio is greater than 0.2 within a 7-km circular buffer area during 1978–2013. Regional averages for urban and rural areas are estimated based on variable set of stations each year. This approach makes an implicit underlying assumption that climate change and variability in the region is completely homogeneous in space and time such that the evolution of rural (or urban) areas does not result in any tangible differences in the rural and urban time series. As a result, this approach could potentially attribute some aspect of differences resulting from spatial and temporal variability of temperature extremes as an urbanization effect. Since the different approaches employed by Ren and Zhou (2014) and Yang et al. (2017) result in different sets of urban and rural stations, the regional mean series from these two sets of stations could differ. As a consequence, the effect of urbanization so identified would also differ. It should also be noted that sampling uncertainty in the estimates of urbanization effect, which can be quite large, was not evaluated in either approaches.

While it is straightforward to compute the difference series between rural and urban stations or between rural and urban and rural combined stations using the fixed-stations method of Ren and Zhou (2014) or variable-station method of Yang et al. (2011), there is not a simple interpretation for the difference series and, thus, the effect of urbanization estimated by these methods. This is because it is difficult to characterize the spatial representativeness of stations for urban and rural regions and to quantify the effect of sampling uncertainty in both space and time. Recognizing the difficulties in estimating the magnitude of urbanization effect on temperature and the fact that both urbanization and large-scale anthropogenic forcing contribute to temperature change, Sun et al. (2016) proposed a different method that estimates the effect of urbanization and large-scale anthropogenic forcing in tandem. This approach assumes that the pattern of the urbanization effect can be accurately estimated using the difference series and that models can simulate spatial and temporal patterns of anthropogenically forced temperature response correctly. The magnitudes of the effects of urbanization and anthropogenic forcings are estimated simultaneously from the observations and simulated responses to external forcings using an optimal fingerprint method. Here we use the Sun et al. (2016) method to attribute the observed changes in temperature extremes in Eastern China to urbanization and external forcings.

2. Data and Methods

2.1. Indices of Temperature Extremes

We consider four indices representing moderately extreme warm and cold temperature events. They are annual percentage of days when daily minimum temperature is greater than its ninetieth percentile (TN90p) or less than its tenth percentile (TN10p), as well as annual percentage of days when daily maximum temperature is greater than its ninetieth percentile (TX90p) or less than its tenth percentile (TX10p). These four indices have been used widely as they represent extreme events relative to daily temperature climatology (Zhang et al., 2011). Additionally, they have higher signal to noise ratio when compared with annual absolute extreme temperatures because many more daily observations are involved in their calculation.

2.2. Observational Data

We use the homogenized daily maximum and daily minimum temperatures at 2,419 stations in China to compute the temperature indices. These station data are provided by China National Meteorological Information Center (Xu et al., 2013). As historical simulations from the climate models end in 2012 (see below), and as station coverage was poor prior to the late 1950s, we use the time period 1958–2012 in this study. For more data information, please refer to supporting information.

We use the ETCCDI software (available from RClimDex/FClimdex software package at http://etccdi.pacificclimate.org/software.shtml) to compute these indices to avoid data inhomogeneity caused by the use of a base period (Zhang et al., 2005). Regional averages of the observation series are obtained based on the station data. This involves three steps: 1) estimate station anomalies by removing the 1961–1990 mean from individual station series and 2) average station anomalies within $5° \times 5°$ grid boxes to obtain gridded anomalies. In total, there are 22 grid boxes used in the study. 3) Compute regional averages from the gridded values.

2.3. Indices From Climate Model Simulations

The same indices are also computed from daily outputs of simulations by the climate models participating in the Couple Model Intercomparison Project Phase 5 (CMIP5, Taylor et al., 2012). Indices computed by Sillmann, Kharin, Zhang, et al. (2013) and Sillmann, Kharin, Zwiers, et al. (2013) for historical and RCP experiments are used. These include one run for each climate model. Indices for other members of ALL forcing runs, for NAT forcing runs, or for control simulations were not used in Sillmann, Kharin, Zhang, et al. (2013) and Sillmann, Kharin, Zwiers, et al. (2013), they are computed separately using the code that generated the indices by Sillmann, Kharin, Zhang, et al. (2013). Historical ALL forcing simulations that end in 2005 were extended to 2012 using corresponding RCP4.5 runs. The model data used in the study are the same as those used in Lu et al. (2016). They include simulations driven by 1) historical anthropogenic and natural forcings (ALL) and the RCP4.5 forcing scenario, 2) the natural forcing only (NAT), and 3) the preindustrial experiments (CTL). The ALL experiments include 96 simulations from 21 models. The time period for these indices is 1958–2012. CTL simulations by 28 models are used to estimate internal climate variability. Model simulations are on different grids and are interpolated onto $5° \times 5°$ grid boxes that are consistent with the observations.

2.4. Estimate of Urbanization Signal Pattern

To determine the urban signal pattern (URB), we estimate regional averages for the urban and rural stations separately using the method described in section 2.2. Among all 1,641 stations in Eastern China (Supporting Information Figure S1), 86 stations are determined to be rural according to Ren and Zhou (2014). The remaining stations are regarded as urban stations in this paper. The URB signal is estimated by fitting a logistic sigmoid function to the difference between urban and rural series because the urbanization signal is expected to be a positive and monotonic increasing function. This signal pattern T_{URB} is finally used as the signal in the optimal fingerprinting approach described below.

2.5. Detection Method

To simultaneously detect the effects of anthropogenic forcing and urbanization on these temperature extreme indices in Eastern China, we use the optimal fingerprinting method based on a total least square method (Allen & Stott, 2003; Ribes et al., 2013; Sun et al., 2016). We regress the observational data onto the patterns of model simulated ALL response as well as the URB signal pattern such that

$$T_{OBS} = \beta_{ALL}(T_{ALL} - \nu_{ALL}) + \beta_{URB}(T_{URB} - \nu_{URB}) + \epsilon.$$

where T_{OBS} is a vector of observed temperature anomalies, T_{ALL} and T_{URB} are signal patterns for ALL and URB, ν_{ALL} and ν_{URB} are noise in the ALL and URB signal patterns, and β_{ALL} and β_{URB} are scaling factors (the regression coefficients). The ν_{ALL} is assumed to have the same form of model-simulated variability, with its variance inversely proportional to the number of model simulations used in the estimation of variability. It is not straightforward to estimate ν_{URB}. To ease the estimation of the scaling factors, we assume that there is effectively no uncertainty in the URB signal in the regression. This is done by assuming the variance to be equivalent to that of the average series from 1,000 model simulations. We, subsequently, separately consider the effect of sampling uncertainty in URB signal by conducting the detection and attribution analysis using each of the 1,000 bootstrap variations of the URB signal. As is generally considered in detection and attribution analyses (Allen & Stott, 2003; Ribes et al., 2013), a signal pattern is detected if its corresponding scaling factor is significantly greater than 0 at the 5% significance level. If in addition, this 90% confidence interval (CI) of the scaling factor also includes 1, it may be possible to attribute the observed changes to the signals if other plausible causes of the observed changes can be ruled out. The best estimates of the scaling factors adjust the ALL and URB signals to best match the observations, thereby enabling the estimation of the magnitude of ALL and URB signals in the observations simultaneously.

3. Results

3.1. Observed Changes in Warm and Cold Nights, the Urbanization Effects

The station map (Supporting Information Figure S1) in Eastern China shows a clear decrease of extreme cold days and nights (TX10p and TN10p) and an increase of extreme warm days and nights (TX90p and TN90p) in most stations, with smaller changes in daytime extremes (TX10p and TX90p) than in nighttime extremes (TN10p and TN90p). The upper portion of panels in Figure 1 shows the time series of eastern China averages for urban (black) and rural (yellow) stations, along with their difference (red) for the period 1958–2012. Changes in these series are consistent with median trends of individual station series. For the daytime extremes, the linear trends for the urban and rural stations are −0.54% per decade and −0.45% per decade for TX10p, 0.96% per decade and 0.95% per decade for TX90p, respectively. The linear trends in the difference series (red lines) of TX10p and TX90p are small, with a linear trend of −0.09% per decade for TX10p and 0.01% per decade for TX90p, respectively. For the nighttime extremes, the linear trends in the urban and rural series are −1.62% per decade and −1.1%/ per decade for TN10p and 2.06% per decade and 1.24% per decade for TN90p, respectively. The linear trends in the urban and rural difference series are quite large, at −0.52% per decade for TN10p and 0.82% per decade for TN90p, respectively. The urbanization effects can be clearly seen in the trends of the nighttime extremes. If the effect of urbanization is defined according to previous studies (e.g., Ren & Zhou, 2014) as the ratio between the difference in the trends of the urban and rural series and trends in the urban series, urbanization can explain the observed changes in nighttime extremes by 30% to 40%. These are larger than the estimates of urbanization effect on the same extremes for the whole country, which are between 18% and 28% according to Ren and Zhou (2014). The higher values in our estimates for Eastern China are reasonable, reflecting the fact that Eastern China has urbanized more strongly than the rest of the country because of more rapid and wider-spread development.

The lower portion of each panel in Figure 1 shows the sigmoid fit to the difference series. The sigmoid function fits the evolution of the urbanization effect well. The trends computed from the fitted curves and from the original series are of very similar values. Note that the urbanization signal in the daytime extremes is very small and flat, without any clear trends, in both the fitted curves and the original series. To estimate sampling uncertainty in the urban-rural difference series and corresponding sigmoid fits, we used a bootstrap procedure outlined in Sun et al. (2016). Here we divided Eastern China into 22 5° × 5° grid boxes and computed difference series between urban and rural stations within each grid box for the four indices separately. We then sampled, with replacement, these grid box values to form 22 boxes to compute regional mean values. These regional means were then fitted to logistic curves. This procedure was repeated 1,000 times. The gray shading in the lower portion of Figure 1 shows the 5th to the 95th percentiles of the fit. It appears that the sampling error in the estimate of urbanization effect can be large.

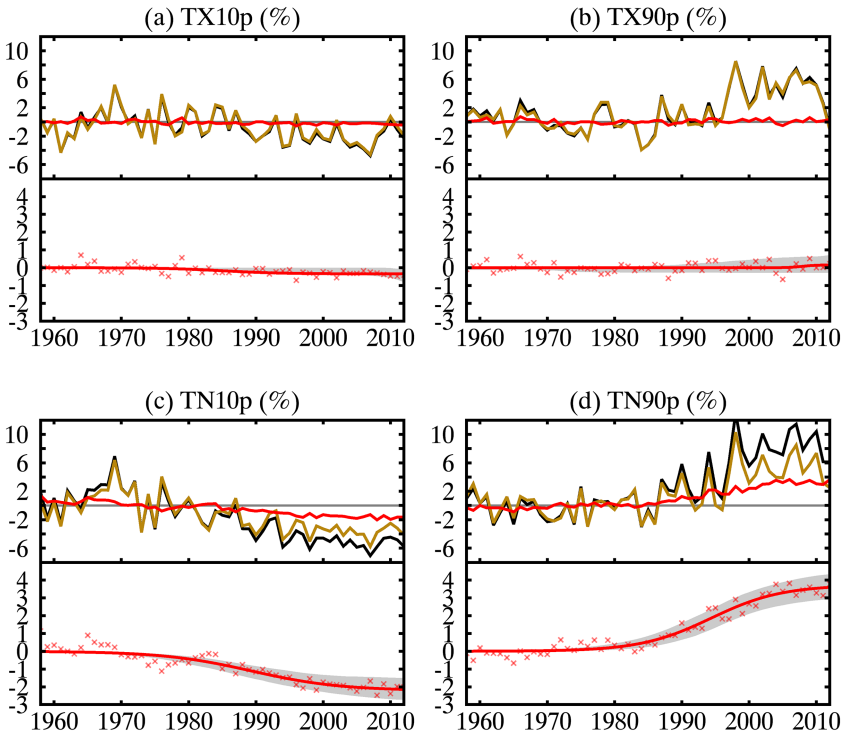

Figure 1. Upper portion of each panel: Time series of regional mean extreme temperature indices in Eastern China. Black and yellow lines are for urban and rural stations, respectively, while red line shows the difference between them. Lower portion of each panel: Difference between regional mean extreme temperature series of urban and rural stations. Red lines show sigmoid fits that are used as URB signal pattern in the detection and attribution analyses. The gray shading areas represent the 5th and 95th percentile ranges (gray areas) of the URB signal, estimated from the 1,000 bootstrap samples.

3.2. Comparison Between Observations and Simulations

Figure 2 displays the nonoverlapping 3-year mean series of the indices from the observations and simulations. The simulations under the ALL forcing generally reproduce the observed decrease in cold extremes and increase in warm extremes. For the daytime extremes, the simulations match the observations well with observations almost always at the center of the simulations. The URB signal is weak. For the nighttime extremes, the observed series are within the range of simulations but at the outer edge of simulations, indicating that while simulations are broadly consistent with observations, models tend to underestimate the observed decrease in cold nights and observed increase in warm nights. If the urbanization effect is removed from the observation, the match between the observations and simulations improves substantially.

3.3. Results From Detection and Attribution Analyses

Results from the two-signal detection and attribution analyses, by regressing observations onto the ALL and URB signals, are presented in Figure 3. For the daytime extremes, ALL is clearly detected with the fifth percent lower bound of the scaling factors above 0 while the URB signal is not detected. This means that external forcing has clearly affected these daytime extremes. The lack of detection of URB signal in daytime extremes can mean either a) effect of urbanization on daytime extremes is weak or b) the signal pattern constructed from the urban and rural differences is too weak to constrain the regression. As shown in Figure 2, simulations under ALL forcing track the observations well. It thus can be argued that the urbanization effect on daytime extremes may indeed be small, which would need to be verified by other studies that consider urbanization effect at a process level. For the nighttime extremes, both the ALL and URB signals are detected and they can also be separated from each other. This means that the effect of external forcing on these extremes can be identified with the consideration of the urbanization effect and vice versa. The best estimates of the scaling factors for ALL and URB signals are 0.83 (90% CI: 0.40–1.26) and 1.09 (90% CI: 0.26–1.92) for TN10p. They are 0.63 (90% CI: 0.16–1.12) and 1.23 (90% CI: 0.07–2.40) for TN90p, respectively. The fact

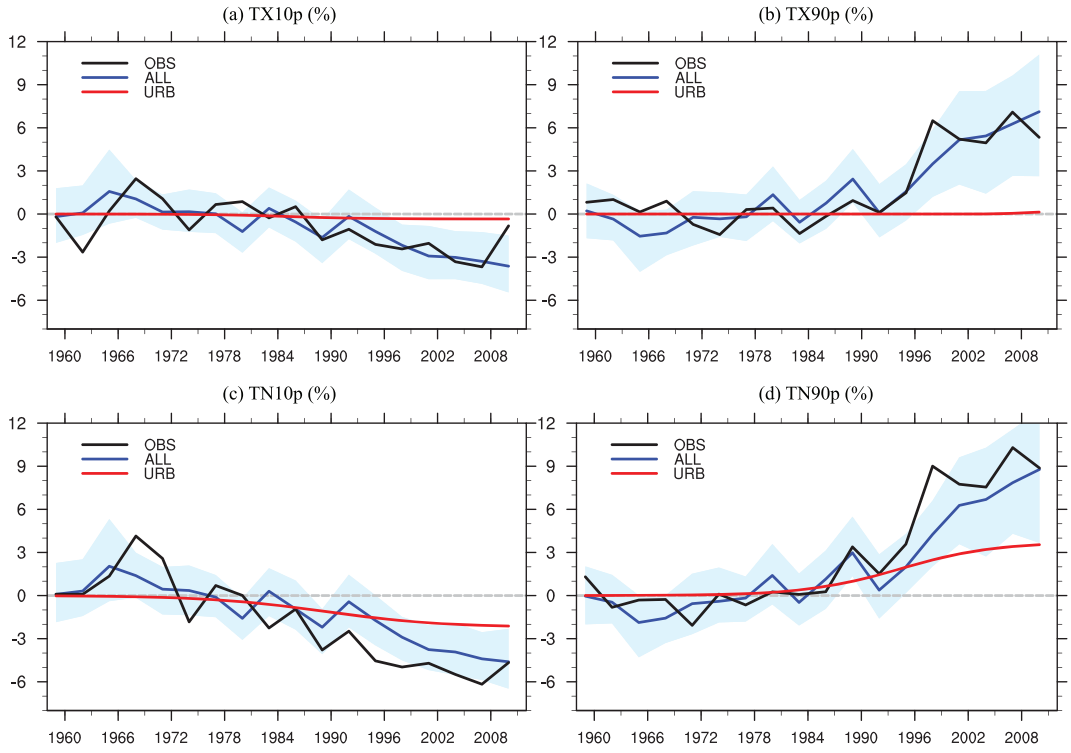

Figure 2. Regional mean 3-year nonoverlapping series for four extreme temperature indices from the observations (OBS), model simulated responses to all forcings (ALL), and the signal pattern for urbanization effect (URB). The URB is based on the sigmoid fits in Figure 1. Blue shading shows spread of the model-simulated responses to ALL forcings.

that the scaling factors for ALL are smaller than 1 from the two-signal analysis indicates that the models may still overestimate the observed changes in nighttime extremes even after the urbanization effect has been taken into account. Christidis et al. (2011) and Zwiers et al. (2011) found CMIP3 models tend to overestimate the most observed warming of nighttime extremes though this effect was less obvious in

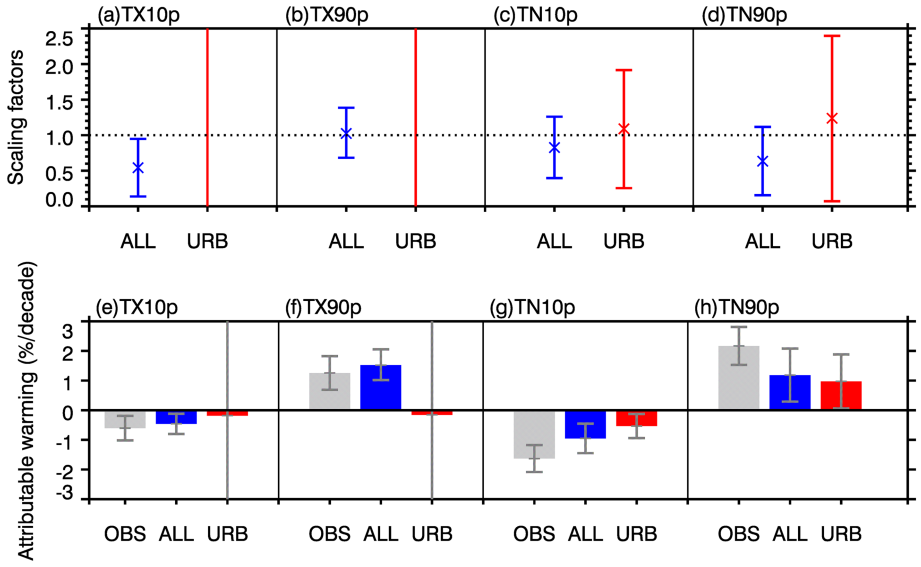

Figure 3. (a–d) Best estimates of scaling factors and their 5–95% confidence intervals for ALL and URB in two-signal analyses for the four temperature indices. (e–h) Observed trends for the extreme temperature indices and attributable changes, along with their 5–95% confidence intervals.

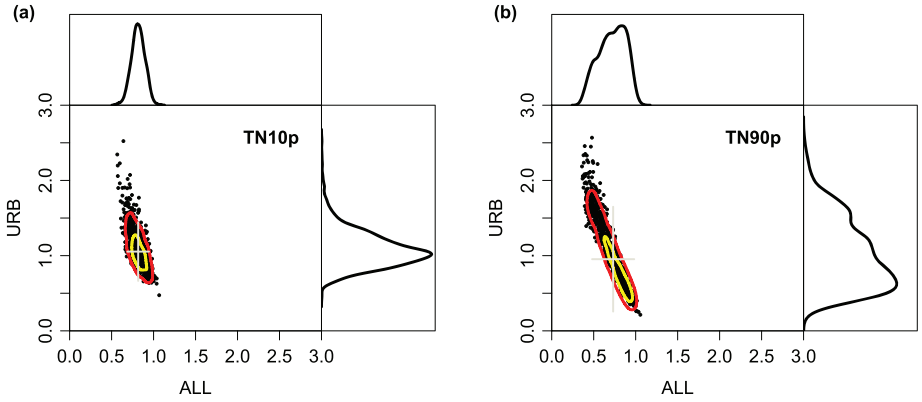

Figure 4. Scatter plots of ALL and URB scaling factors for TN10p (left) and TN90p (right) based on the 1,000 bootstrap samples of the URB signal. The joint 90% and 50% confidence regions are encircled by red and yellow curves, respectively. The gray lines represent 90% marginal confidence intervals. The marginal densities of the scaling factors are plotted on the top of (for ALL) or to the right of (for URB) the scatter plots.

CMIP5 models (Sillmann, Kharin, Zhang, et al., 2013). Morak et al. (2013) found similar results with HadGEM1 simulations. Both cloud and land processes in the models may have played a role but the exact cause of this is unclear.

We compute the attributable warming as the product between the linear trends in the noise-reduced model-simulated signals and the corresponding scaling factors. For the nighttime extremes, the observed trends, the estimated contributions from ALL, and URB for TN10p are −1.63% per decade (90% CI: −1.18% to −2.08%), −0.95% per decade (90% CI: −0.46% to −1.45%), and −0.53% per decade (90% CI: −0.13% to −0.94%), respectively. The corresponding values for TN90p are 2.17% per decade (90% CI: 1.53% to 2.81%), 1.18% per decade (90% CI: 0.29% to 2.08%), and 0.97% per decade (90% CI: 0.06% to 1.88%), respectively. This indicates that the urbanization effect explains about 33% and 45% of observed changes in TN10p and TN90p, respectively, assuming that other factors that might have affected trends are negligible. These are slightly higher than the estimates directly obtained from the difference series between urban (or urban and rural stations combined) and rural stations. Note however that these best estimates and confidence intervals are still subject to additional sampling uncertainty in the estimation of the URB signal, as we will see in the following subsection.

3.4. Robustness of Detection Results to Sampling Uncertainty

Figure 1 shows that the estimate of urbanization effect during the later decades may be subject to relatively large sampling uncertainty for the nighttime extremes. To examine the influence of this sampling uncertainty on detection and attribution analyses, we used each of the 1,000 bootstrapped estimates of the URB pattern in the two-signal detection and attribution analyses. For TN10p, the ALL and URB signals are detected 992 and 953 times. Both ALL and URB are simultaneously detected 948 times. For TN90p, the ALL and URB signals are detected 903 and 644 times with both signals simultaneously detected 547 times. Therefore, detection of the urbanization and global warming effects and their separation are both robust for nighttime temperature extremes, albeit more so for cold nights than warm nights.

Figure 4 displays scatter plots of the best estimate of ALL and URB scaling factors from the 1,000 bootstrap samples, along with their 90% and 50% confidence regions, as well as their marginal densities, for TN10p and TN90p (It should be pointed out that those are best estimates from each bootstrap sample, and they have their own confidence regions; the overall uncertainty shall be wider than illustrated by these confidence regions), respectively. Most of the best estimates of scaling factors fall in a well-defined region. The uncertainty range for ALL scaling factor is quite small, indicating relatively small influence due to sampling error in the URB signal estimate. The median values of the ALL and URB scaling factors for TN10p are 0.83 and 1.05, respectively, and those for TN90p are 0.73 and 0.95. As the median URB scaling is close to 1, it is reasonable to scale the estimated ALL signal down. Sampling uncertainty in the URB signal estimate likely contributed to the relatively small value of ALL scaling factor at 0.63

that was reported in section 3.3; nevertheless, ALL does still need to be scaled down to match the observations. Given these considerations, we conclude that urbanization effect on nighttime extreme temperature indices is substantial and may explain as much as one third of the observed warming in these indices. The strongest urbanization in China took place at the time of strongest warming in the global mean temperature, resulting in a strong collinearity between URB and ALL signals. This collinearity must have introduced additional uncertainty in our estimation. Nevertheless, given the considerations discussed above, uncertainty due to collinearity between the two signals should not qualitatively alter our above conclusion.

4. Conclusions

Previous studies have identified the anthropogenic forcing and urbanization as important factors contributing to the observed changes in moderate temperature extremes in Eastern China. These studies only consider one factor at a time, without taking the effect of the other factor into account. As the effects of urbanization and external forcing including the greenhouse gases and aerosols on temperature extremes are highly collinear, it can be difficult to know to what extent these estimates are affected by not considering the other factor. Here, we consider both effects in tandem by regressing the observations onto these two factors simultaneously. We find that the influence of anthropogenic forcing is clearly detected in the daytime extremes but changes in the size of the urbanization effect seem to be small. We also found that both external forcing and urbanization have played an important role in the observed changes in nighttime extremes. Simulations fit better with observations when the urbanization effect is considered, although the models tend to overestimate changes in these extremes even after accounting for urbanization. The urbanization effect on nighttime extremes is large, explaining perhaps as much as one third of the observed warming in these extremes. The results seem to be robust against sampling uncertainty in the estimate of urbanization effect. As the increase in nighttime extreme temperatures can exert serious impacts on human health, the added warming due to the continued urbanization in regions that are less urbanized today should be considered.

Acknowledgments
We thank Francis Zwiers and two anonymous reviewers for their very constructive comments. We acknowledge the Program for Climate Model Diagnosis and Intercomparison and the Working Group on Coupled Modeling of the World Climate Research Programme (WCRP) for their roles in making the WCRP CMIP multimodel data sets available. We thank the China National Meteorological Information Center for archiving the observational data (available at http://data.cma.cn/). This study was supported by the National Key R&D Program of China (2018YFC1507702), the National Science Foundation of China (41675074), and Climate Change Project (CCSF201905).

References

Allen, M. R., & Stott, P. A. (2003). Estimating signal amplitudes in optimal fingerprinting. Part I: Theory. *Climate Dynamics*, *21*, 477–491. https://doi.org/10.1007/s00382-003-0313-9

Christidis, N., Stott, P. A., & Brown, S. J. (2011). The role of human activity in the recent warming of extremely warm daytime temperatures. *Journal of Climate*, *24*, 1922–1930.

Dong, S.-Y., Sun, Y., Aguilar, E., Zhang, X.-B., Peterson, T. C., Song, L.-C., & Zhang, Y.-X. (2018). Observed changes in temperature extremes over Asia and their attribution. *Climate Dynamics*, *51*, 339–353. https://doi.org/10.1007/s00382-017-3927-z

Hou, W., Chen, Y., Li, Y., Wang, Y., Wang, Z., Zhu, X., & Zhao, L. (2014). Climatic characteristics over China in 2013. *Meteorological Monthly*, *40*, 491–501.

Lu, C.-H., Sun, Y., Wan, H., Zhang, X.-B., & Yin, H. (2016). Anthropogenic influence on the frequency of extreme temperatures in China. *Geophysical Research Letters*, *43*, 6511–6518. https://doi.org/10.1002/2016GL069296

Lu, C.-H., Sun, Y., & Zhang, X.-B. (2018). Multimodel detection and attribution of changes in warm and cold spell durations. *Environmental Research Letters*, *13*, 074013. https://doi.org/10.1088/1748-9326/aacb3e

Morak, S., Hegerl, G. C., & Christidis, N. (2013). Detectable changes in the frequency of temperature extremes. *Journal of Climate*, *26*, 1561–1574.

Ren, G.-Y., Li, J., Ren, Y.-Y., Chu, Z.-Y., Zhang, A.-Y., Zhou, Y.-Q., et al. (2015). An integrated procedure to determine a reference station network for evaluating and adjusting urban bias in surface air temperature data. *Journal of Applied Meteorology and Climatology*, *54*, 1248–1266. https://doi.org/10.1175/JAMC-D-14-0295.1

Ren, G.-Y., & Zhou, Y.-Q. (2014). Urbanization effect on trends of extreme temperature indices of national stations over mainland China,1961-2008. *Journal of Climate*, *27*, 2340–2360. https://doi.org/10.1175/JCLI-D-13-00393.1

Ren, G.-Y., Zhou, Y.-Q., Chu, Z.-Y., Zhou, J.-X., Zhang, A.-Y., Guo, J., & Liu, X.-F. (2008). Urbanization effects on observed surface air temperature trends in North China. *Journal of Climate*, *21*, 1333–1348. https://doi.org/10.1175/2007JCLI1348.1

Ribes, A., Planton, S., & Terry, L. (2013). Application of regularised optimal fingerprinting to attribution. Part I: Method, properties and idealised analysis. *Climate Dynamics*, *41*, 2817–2836. https://doi.org/10.1007/s00382-013-1735-7

Sillmann, J., Kharin, V. V., Zhang, X.-B., Zwiers, F. W., & Bronaugh, D. (2013). Climate extremes indices in the CMIP5 multimodel ensemble: Part 1, model evaluation in the present climate. *Journal of Geophysical Research: Atmospheres*, *118*, 1716–1733. https://doi.org/10.1002/jgrd.50203

Sillmann, J., Kharin, V. V., Zwiers, F. W., Zhang, X. B., & Bronaugh, D. (2013). Climate extremes indices in the CMIP5 multimodel ensemble: Part 2, future climate projection. *Journal of Geophysical Research: Atmospheres*, *118*, 2473–2493. https://doi.org/10.1002/jgrd.50188

Sun, Y., Hu, T., & Zhang, X. B. (2018). Substantial increase in heat wave risks in China in a future warmer world. *Earth's Future*, *6*(11), 1528–1538. https://doi.org/10.1029/2018EF000963

Sun, Y., Zhang, X., Zwiers, F. W., Song, L., Wan, H., Hu, T., & Ren, G. Y. (2014). Rapid increase in the risk of extreme summer heat in Eastern China. *Nature Climate Change*, *4*, 1082–1085. https://doi.org/10.1038/nclimate2410

Sun, Y., Zhang, X.-B., Ren, G.-Y., Zwiers, F. W., & Hu, T. (2016). Contribution of urbanization to warming in China. *Nature Climate Change*, *6*, 706–709. https://doi.org/10.1038/nclimate2956

Taylor, K. E., Stouffer, R. J., & Meehl, G. A. (2012). An overview of CMIP5 and the experiment design. *Bulletin of the American Meteorological Society*, *93*, 485–498. https://doi.org/10.1175/BAMS-D-11-00094.1

Wang, H.-J., Sun, J. Q., Chen, H. P., Zhu, Y. L., Zhang, Y., Jiang, D. B., et al. (2012). Extreme climate in China: Facts, simulation and projection. *Meteorologische Zeitschrift*, *21*(3), 279–304. https://doi.org/10.1127/0941-2948/2012/0330

Xu, W.-H., Li, Q.-X., Wang, X.-L., Su, Y., Cao, L.-J., & Feng, Y. (2013). Homogenization of Chinese daily surface air temperatures and analysis of trends in the extreme temperature indices. *Journal of Geophysical Research: Atmospheres*, *118*, 9708–9720. https://doi.org/10.1002/jgrd.50791

Yang, X.-C., Hou, Y.-L., & Chen, B.-D. (2011). Observed surface warming induced by urbanization in east China. *Journal of Geophysical Research*, *116*, D14113. https://doi.org/10.1029/2010JD015452

Yang, X. C., Ruby Leung, L., Zhao, N., Zhao, C., Qian, Y., Hu, K., et al. (2017). Contribution of urbanization to the increase of extreme heat events in an urban agglomeration in east China. *Geophysical Research Letters*, *44*, 6940–6950. https://doi.org/10.1002/2017GL074084

Yin, H., & Sun, Y. (2018). Detection of anthropogenic influence on fixed threshold indices of extreme temperature. *Journal of Climate*, *31*(16), 6341–6352. https://doi.org/10.1175/JCLI-D-17-0853.1

Yin, H., Sun, Y., Wan, H., Zhang, X.-B., & Lu, C.-H. (2017). Detection of anthropogenic influences on the intensity of extreme temperatures in China. *International Journal of Climatology*, *37*, 1229–1237. https://doi.org/10.1002/joc.4771

You, Q. L., Kang, S., Aguilar, E., Pepin, N., Flügel, W. A., Yan, Y., et al. (2011). Changes in daily climate extremes in China and their connection to the large scale atmospheric circulation during 1961–2003. *Climate Dynamics*, *36*(11-12), 2399–2417. https://doi.org/10.1007/s00382-009-0735-0

Zhang, X. B., Alexander, L., Hegerl, G. C., Jones, P., Tank, A. K., Peterson, T. C., et al. (2011). Indices for monitoring changes in extremes based on daily temperature and precipitation data. *Wiley Interdisciplinary Reviews: Climate Change*, *2*(6), 851–870. https://doi.org/10.1002/wcc.147

Zhang, X.-B., Hegerl, G. C., Zwiers, F. W., & Kenyon, J. (2005). Avoiding inhomogeneity in percentile-based indices of temperature extremes. *Journal of Climate*, *18*, 1641–1651. https://doi.org/10.1175/JCLI3366.1

Zhang, X.-B., Zwiers, F. W., & Stott, P. A. (2006). Multimodel multisignal climate change detection at regional scale. *Journal of Climate*, *19*, 4294–4307. https://doi.org/10.1175/jcli3851.1

Zhou, Y.-Q., & Ren, G.-Y. (2011). Change in extreme temperature events frequency over mainland China during 1961–2008. *Climate Research*, *50*, 125–139. https://doi.org/10.3354/cr01053

Zwiers, F. W., Zhang, X.-B., & Feng, Y. (2011). Anthropogenic influence on long return period daily temperature extremes at regional scales. *Journal of Climate*, *24*(3), 881–892. https://doi.org/10.1175/2010JCLI3908.1

Climate Dynamics (2019) 53:2147–2160
https://doi.org/10.1007/s00382-019-04810-4

Diagnosing the representation and causes of the ENSO persistence barrier in CMIP5 simulations

Ben Tian[1] · Hong-Li Ren[1,2] · Fei-Fei Jin[3] · Malte F. Stuecker[4,5]

Received: 25 September 2018 / Accepted: 8 May 2019 / Published online: 14 May 2019
© Springer-Verlag GmbH Germany, part of Springer Nature 2019

Abstract
In this study, the persistence barrier (PB) of the El Niño–Southern Oscillation (ENSO) phenomenon is investigated using reanalysis data and historical simulations of the Coupled Model Intercomparison Project Phase 5 (CMIP5) models. Both the timing and intensity of the ENSO PB can be quantified using the maximum gradient of autocorrelation decline of Niño sea surface temperature (SST) anomaly indices. Most of the CMIP5 models were found to reasonably reproduce the observed timing of the ENSO PB that typically occurs during the boreal late spring to early summer, and underestimated the PB intensity compared to observations. Furthermore, the PB properties of the Eastern Pacific (EP) ENSO indices were much better represented by the models than those of the Central Pacific (CP) ENSO indices, probably because CP ENSO events are more challenging to simulate than their counterparts. Approximately half of the models can satisfyingly reflect the intensity and timing of PB for indices of EP ENSO and their distinctions from those of the CP ENSO, with a larger uncertainty for the modeled PB timing than intensity. Further diagnosis has revealed the relationship between the ENSO PB intensity and the factors associated with the tropical Pacific background state. The PB intensity exhibits a stronger relationship with the seasonality of the SST amplitude in CP, compared to the SST amplitude, and the strength of seasonal synchronization of EP SST anomalies is highly correlated with the PB intensity. These results suggest that the seasonality of tropical SST variability may fundamentally contribute to the ENSO PB.

Keywords ENSO · Persistence barrier · CMIP5 simulations

1 Introduction

The El Niño–Southern Oscillation (ENSO) is the dominant mode of interannual climate variability and has attracted considerable attention due to its large impacts on global climate (e.g., Rasmusson and Carpenter 1982; Timmermann et al. 2018). Significant progress has been made in understanding and predicting ENSO, and ENSO could now be well predicted 6 months in advance, and probably longer (Barnston et al. 2012; Jin et al. 2008; Latif et al. 1994; Ren et al. 2014; Timmermann et al. 2018; Zhu et al. 2012). Nevertheless, the accuracy of ENSO predictions decreases abruptly for forecasts made before and during boreal spring. This so-called ENSO spring predictability barrier is at least partially caused by seasonal transitions in the monsoon circulation (Webster and Yang 1992), ocean–atmosphere coupling strength variation (Chen et al. 2015; Hu et al. 2011; Larson and Kirtman 2016; Webster 1995; Zebiak and Cane 1987), seasonal change in the signal-to-noise ratio (Barnett et al. 1994; Torrence and Webster 1998; Zheng and Zhu 2010), initial errors of certain specific patterns (Duan et al. 2009; Mu et al. 2007; Tian and Duan 2016b), model biases (Lopez and Kirtman 2015; Zheng and Zhu 2010), seasonality of ocean surface–subsurface connection (Zhu et al. 2015), and westerly wind burst activity (WWB) (Chen

✉ Hong-Li Ren
renhl@cma.gov.cn

1 Laboratory for Climate Studies, CMA-NJU Joint Laboratory for Climate Prediction Studies, National Climate Center, China Meteorological Administration, Beijing 100081, China

2 Department of Atmospheric Science, School of Environmental Studies, China University of Geoscience, Wuhan 430074, China

3 Department of Atmospheric Sciences, University of Hawaii, Honolulu 96822, USA

4 Center for Climate Physics, Institute for Basic Science (IBS), Busan, Republic of Korea

5 Pusan National University, Busan, Republic of Korea

et al. 2015; Larson and Kirtman 2016; Lopez and Kirtman 2015). Importantly, the degree of ENSO seasonal synchronization in the annual cycle seems to affect the spring predictability barrier of ENSO (Levine and McPhaden 2015) and is thought to determine the strength of the ENSO persistence drop-off (Torrence and Webster 1998). The ENSO persistence barrier (PB), which is commonly considered a natural and observable ENSO property, refers to the rapid decline in persistence (lagged autocorrelations) across boreal spring, irrespective of which starting time is chosen. Considering the similarity of basic characteristics between the two phenomena, it is reasonable to hypothesize that the spring predictability barrier in models, including the Coupled Model Intercomparison Project Phase 5 (CMIP5) models, is closely related to the observed ENSO PB; meanwhile, the former may potentially be reduced using improved model initializations (Chen et al. 1995; Mu et al. 2007). Therefore, improving our understanding of the ENSO PB should allow us to identify important dynamical mechanisms that affect operational ENSO predictions.

Previous efforts investigating the ENSO persistence and predictability barrier were mostly conducted using observations and models of limited complexity (e.g., Levine and McPhaden 2015; Mu et al. 2007; Torrence and Webster 1998). In addition, recent findings using the CCSM4 model might be model-dependent (Larson and Kirtman 2016). Therefore, there is ongoing debate regarding the cause of the spring predictability barrier. Moreover, some of the research on the ENSO PB lacks quantitative descriptions. Recently, Ren et al. (2016) proposed measuring the intensity of the ENSO PB using the largest gradient of the autocorrelation decline of Niño indices of the sea surface temperature (SST) anomaly and demonstrated distinct PB features in terms of the two ENSO types (Ashok et al. 2007; Kao and Yu 2009; Kug et al. 2009). Here we combine the aforementioned measures of ENSO PB occurrence timing and intensity to assess PB features within a large group of coupled general circulation models (CGCMs). Exploring the ENSO PB phenomenon and its causes is feasible using this approach due to large number of models contributing to CMIP5. It was previously assumed that the simulation performance of the ENSO PB may be related to the seasonal synchronization of ENSO in these models (Torrence and Webster 1998). Therefore, an improved understanding of the ENSO PB may also enable future model improvement. It is important to note that many of the current generation of climate models fail to simulate the Central Pacific (CP) ENSO events realistically (Ham and Kug 2012; Kim and Yu 2012). Therefore, we use various ENSO indices to explore PBs in distinct SST anomaly (SSTA) regions, which characterize SST variability associated with Eastern Pacific (EP) and CP ENSO, respectively.

The observational data and utilized models are introduced in Sect. 2, together with definitions related to the ENSO SST indices and PB metrics. The models used in this paper are separated into two groups as described in Sect. 3. The ENSO PB features in 38 CGCMs are then investigated and compared with the observations. Next, the relationships between the PB intensity and several features of the tropical Pacific background state are explored. Potential factors that additionally may influence the PB intensity are discussed in Sect. 4. A summary is provided in Sect. 5.

2 Data

Monthly data from 38 CMIP5 models (Taylor et al. 2012) is utilized (see Table 1). Realizing that ENSO PB could experience decadal variability just like other properties of ENSO such as the amplitude and period, we analyze the historical simulations (also referred to as twentieth century simulations) and focus on the most recent 30 years of those experiments (1976–2005), a period of reliable contemporary observations to compare to. Ice and sea surface temperature (HadISST, Rayner 2003) data is obtained for the same time period. The observed ENSO PB characteristics are virtually identical to HadISST when using Extended Reconstructed Sea Surface Temperature V3b (ERSST) monthly data from NCEI/NOAA for our analysis (Smith et al. 2008). We also use two sets of surface wind stress monthly data from NCEP/NCAR Reanalysis 1 between 1976 and 2005 (Kalnay et al.

Table 1 The 38 CMIP5 models (18 models that simulate ENSO PB better are in italics, please see text for details) used in this manuscript

No.	Model abbreviated	No.	Model abbreviated
1	Access1-0	20	GISS-E2-H
2	Access1-3	*21*	*GISS-E2-R*
3	BCC-CSM1-1	*22*	*HadCM3*
4	*BCC-CSM1-1-m*	23	HadGEM2-AO
5	*CanCM4*	24	HadGEM2-CC
6	*CanESM2*	25	HadGEM2-ES
7	*CCSM4*	26	INMCM4
8	*CESM1-BGC*	27	IPSL-CM5A-LR
9	*CESM1-CAM5*	28	*IPSL-CM5A-MR*
10	CMCC-CESM	*29*	*IPSL-CM5B-LR*
11	*CMCC-CM*	30	MIROC5
12	CMCC-CMS	*31*	*MIROC-ESM-CHEM*
13	*CNRM-CM5*	*32*	MIROC-ESM
14	CSIRO-Mk3-6-0	33	MPI-ESM-LR
15	*FGOALS-g2*	34	MPI-ESM-MR
16	FIO-ESM	35	MPI-ESM-P
17	*GFDL-CM3*	36	MRI-CGCM3
18	*GFDL-ESM2G*	*37*	*NorESM1-ME*
19	*GFDL-ESM2M*	38	NorESM1-M

1996) and between 1980 and 2005 from the NCEP-DOE Reanalysis 2 (Kanamitsu et al. 2002).

The Niño3.4, Niño3, and Niño4 indices (defined as SSTA averages over the respective regions) are adopted as measures for ENSO-associated SST anomalies. The Cold-Tongue and Warm-Pool (NiñoCT and NiñoWP, respectively) Niño indices defined by Ren and Jin (2011) are used together with the El Niño Modoki index proposed by Ashok et al. (2007). These different ENSO indices are used to investigate PBs in distinct SSTA regions associated with the two ENSO types. In addition to the aforementioned Niño indices, we utilize the first two SSTA empirical orthogonal functions (EOFs) in the tropical Pacific (30°S–30°N, 110°E–70°W), and their corresponding principal components: Niño-PC1 and Niño-PC2, which provides an additional measure for EP and CP ENSO. All indices are calculated for the 1976–2005 period with the 30-year climatologies and linear trends removed from the SST data. In observation, Niño3, Niño3.4, NiñoCT and Niño-PC1 usually depict EP ENSO better.

3 ENSO PB in CMIP5 model outputs

3.1 Simulated PB characteristics

The PB is a clear observable feature of the Niño3.4 index. ENSO persistence represented by the autocorrelation of the Niño3.4 index is shown in Fig. 1a. The autocorrelations decline with increasing lag months and exhibit a strong seasonal dependency. Then the autocorrelation decline rate for given ENSO index is expressed by the centered difference of the autocorrelation, i.e., $G_j^i = \left(C_{j+1}^i - C_{j-1}^i\right)/2$. Here i is the initial calendar month, j is the lag month and C_j^i is the

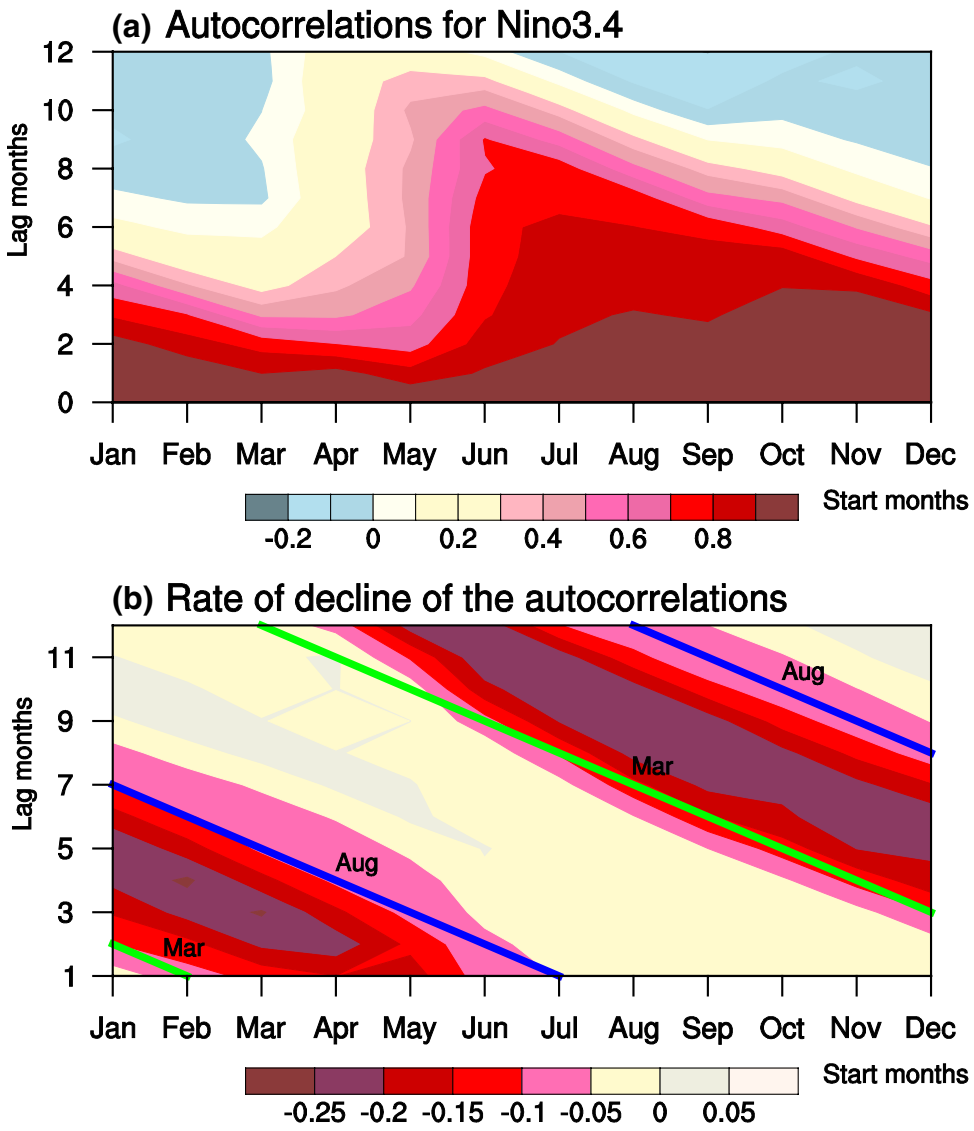

Fig. 1 **a** Autocorrelations as a function of initial calendar month and lag month for Niño3.4 index (from HadISST), and **b** decline rate of autocorrelations (month^{-1}) as a function of initial calendar month and lag month for the Niño3.4 index where green and blue lines denote target months of March and August, respectively, in the lag month domain

autocorrelation of the ENSO index for a given start and lag month (see Fig. 1a). Thus, the G_j^i value that results from the centered difference of C_j^i reflects the autocorrelation decline rate for given ENSO index. The maximum decline rate of autocorrelation (nearly all the autocorrelation decline gradients are negative and absolute values reflect the decline rapidity) for the Niño3.4 index (Fig. 1b) occurs primarily in boreal spring and summer, viz., from March to August and is centered around June. In contrast, a weaker loss of persistence is observed for the other target calendar months, which is consistent with previous studies (e.g., Yu and Kao 2007; Ren et al. 2016). Note that decline rate of autocorrelations for the Niño3.4 index could be shown as a function of initial calendar month and lag month as in Fig. 1b, and can also be transformed into Fig. 2 where it is expressed as a function of target calendar month and lag month. So in general, Figs. 1b and 2 present similar information but from different viewpoints. Specifically, PB intensity and timing could be more distinct quantitatively among varied models when they are related to target calendar month. As shown in Fig. 2, the majority of the 38 models reasonably reproduce the observed ENSO PB features, such as PB intensity and PB timing; however, some models show a weaker Niño3.4 PB intensity. To further quantify these characteristics, the 12-lag-month mean (average over the Y-axis in Fig. 2) of the decline rates of the Niño3.4 autocorrelation is plotted as a function of target calendar month (Fig. 3). The 38 models are then classified into two groups based on the following two criteria: (1) whether the two largest Niño3.4 autocorrelation decline rates in Fig. 3 are situated between the target months of April and July as observed, and (2) whether this maximum decline rate reaches a similar value (a value less than -0.15 month^{-1}) as seen in the observations (Fig. 3). The models that satisfy both of these conditions are then included in group A (marked by italics in Table 1: 18 models), and the remainder is placed in group B. Meanwhile, based on the observed ENSO PB pattern (from HADISST) in Fig. 2, the simulations of two groups of models are presented in a Taylor diagram (Fig. 4). Indeed, there is a great contrast between models in group B and the two observational data sets. The subsequent analysis will be conducted following this group classification.

The Niño indices describing the different ENSO types (i.e., EP and CP) exhibit different PB magnitudes in observations (Ren et al. 2016). For each ENSO metric, the PB intensity (PBI) index, which is dependent on the start month, is defined by summing up the rates of autocorrelation decline from March to August within the first 12 lag months, i.e., $\mathrm{PBI}^i = -\sum_{k=\mathrm{Mar}}^{\mathrm{Aug}} G_k^i$, *where* $G_j^i = \left(C_{j+1}^i - C_{j-1}^i\right)/2$ (Ren et al. 2016). Here i is the initial calendar month, j is the lag month and C_j^i is the autocorrelation of the ENSO index for a given start and lag month. The mean of all PBI index values for 12 initial months of a given Niño index is used to characterize the PB intensity of this Niño index and is termed mPBI. Notice the definition of PBI (as well as mPBI) in Ren et al. (2016) corresponds to generally positive values for PBI, which could help better describe the decline rapidity. In Fig. 5, the PBI index is given as a function of the initial calendar month and only four Niño indices are shown to represent our main points (For ENSO PB of other Niño indices, one could refer to Fig. 6 of a comprehensive collection). In the observations, EP ENSO has a significantly stronger PB than CP ENSO, with Niño3.4 having the largest PBI (Fig. 5). The observed Niño4 index exhibits the strongest PB among those CP ENSO indices, potentially because it captures some EP ENSO variability (Niño3.4 and Niño4 are not orthogonal). To examine the modeled PB intensity, we compared the PBI for different Niño indices between models in terms of the two aforementioned groups and show their composites in Fig. 5. Both the observations and model composites exhibit a similar PB intensity for these ENSO indices; the EP ENSO indices (the left row in Fig. 5) have significantly larger PBIs than the CP ENSO indices, although this is less evident for the models in group B.

As mentioned earlier, the group classifications are based on the model representations of Niño3.4 autocorrelation decline; however, model simulations of all EP ENSO indices in group A, rather than those in group B, have a more similar PB to the parallel observations (Fig. 6). Meanwhile, it is noted that the two model groups perform equally in terms of PB intensity simulation of CP ENSO indices and the PBI indices remain somewhat stronger in group A, compared to the group B models (Fig. 6).

The PB timing for these ENSO indices is another focus of our comparison in addition to the PB intensity. For a given start month, the time when the most rapid autocorrelation decline arises represents the occurrence of ENSO PB for that month, and the mean of all PB occurrence time for the 12 initial months is utilized to represent the PB timing for a given Niño index. In Fig. 7, the PB timing for the 38 models is presented along with relevant observations. As indicated by Ren et al. (2016), the PB in observations generally occurs in boreal late spring-early summer for EP ENSO and in boreal summer for the CP ENSO. Compared to the EP ENSO indices, the observed PB timing is clearly delayed for the CP ENSO indices (the right row in Fig. 7), which can be generally represented by the CMIP5 models but with a large inter-model spread. Compared to the PB intensity in Fig. 5, the PB occurrence time in these models exhibits no clear structure, especially for the CP ENSO indices; however, the group mean does not significantly deviate from the observed features due to the inter-model offset. This conspicuous divergence as well as the departure from the observed ENSO PB timing reflects the unrealistic representation of CP ENSO (including the second EOF of tropical Pacific SSTA) in

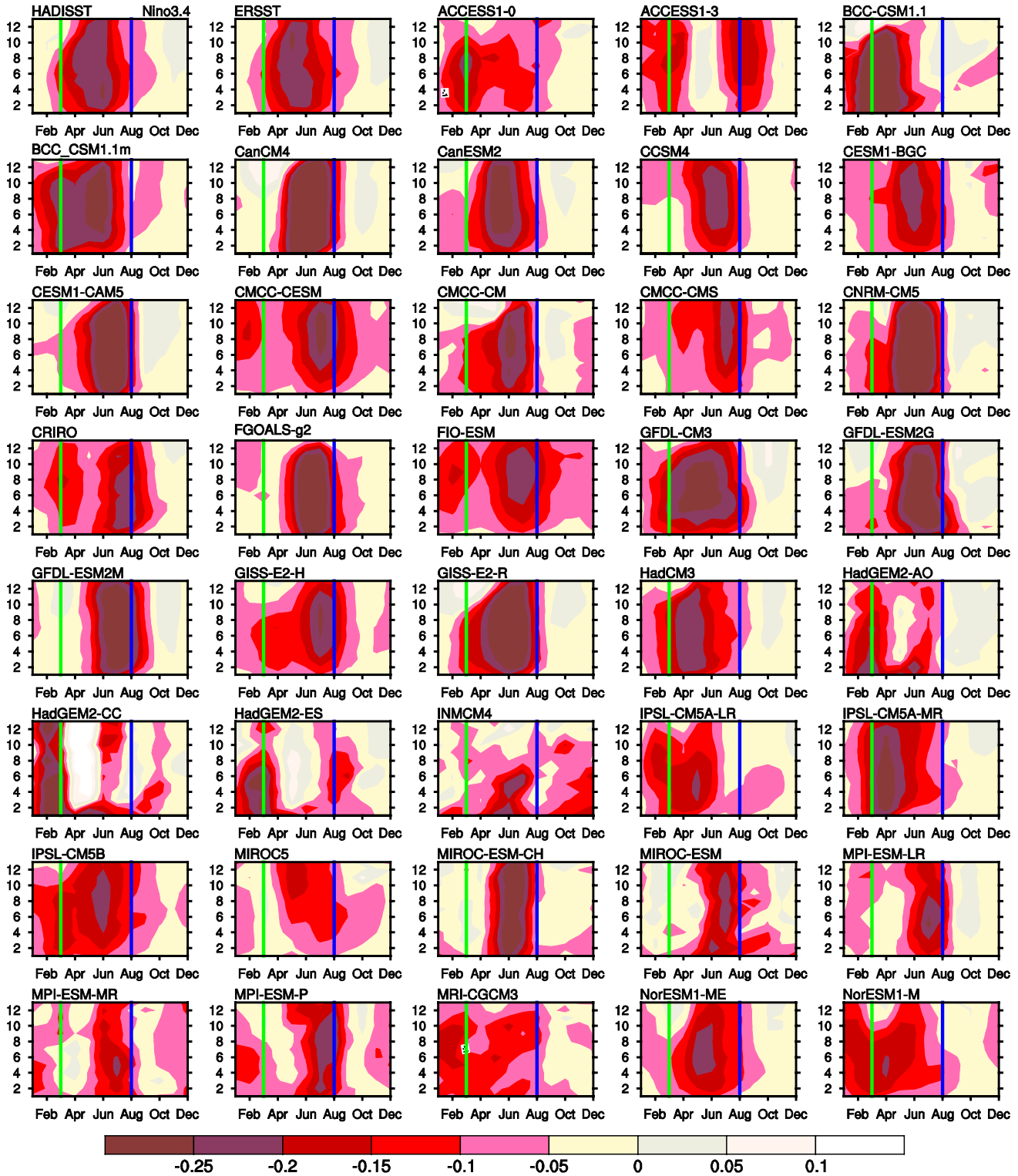

Fig. 2 Decline rates of autocorrelations (month^{-1}) as a function of target calendar month and lag month for the Niño3.4 index among observations (HadISST and ERSST) and the CMIP5 models. Green and blue lines demonstrate the decline rates of autocorrelation targeting March and August with all the lag months, respectively. Model names are defined in Table 1

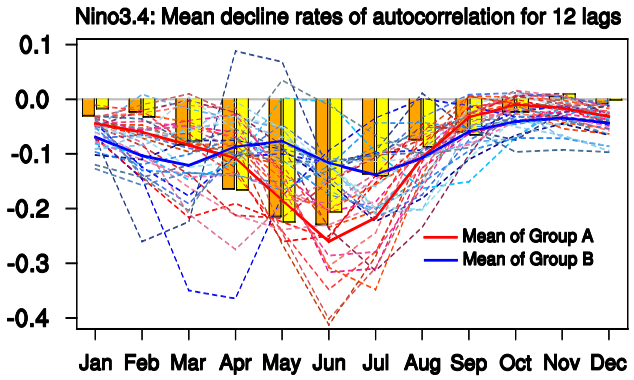

Fig. 3 The average autocorrelation decline rates (month^{-1}) for all 12 lag months as a function of target calendar month for the Niño3.4 index among HADISST (orange bars), ERSST (yellow bars), and CMIP5 model output (dashed lines). The two CMIP5 group means (please see Sect. 3.1 for model classification) highlight the ENSO PB as seen in Fig. 2

current models (see Fig. 6 for other Niño indices). For both the observations and the ensemble mean of group A, the EP ENSO indices generally show a PB occurring in May–June, while the PB timing for the CP ENSO indices occurs about one or 2 months later in June–July. This characteristic is less clear for the ensemble mean of the group B models, which tends to be generally around May–June (Fig. 6). At present, most of the models still have problems simulating CP ENSO realistically, especially its center location and SST anomaly amplitude (Ham and Kug 2012; Kim and Yu 2012). What we find here further suggests that the simulated PB of EP ENSO rather than CP ENSO could potentially be utilized to distinguish the performance between different models. In this regard, an unrealistic representation of CP ENSO may limit the prediction of CP ENSO as well and thus it may be not suitable to explore whether EP or CP ENSO is more predictable within current models, which will be further discussed in Sect. 5.

3.2 ENSO PBI and its causes

In this section, several aspects of the model background state that may relate to the ENSO PB intensity bias are investigated. It is evident that both in observations and model simulations, the PBs of the EP ENSO indices are much more pronounced compared to those of the CP ENSO indices (e.g., Fig. 6). Given the weaker strength of CP ENSO compared to EP ENSO (Ashok et al. 2007; Kao and Yu 2009; Kug et al. 2009), the obvious question here is whether the PB intensity of a given ENSO index is positively correlated to the amplitude of that index. Here, the standard deviation (STD) is utilized to characterize the amplitude of a certain ENSO index. Here, we focus on the PB intensity of Niño3.4 index only, which is the most commonly used index for monitoring and predicting ENSO.

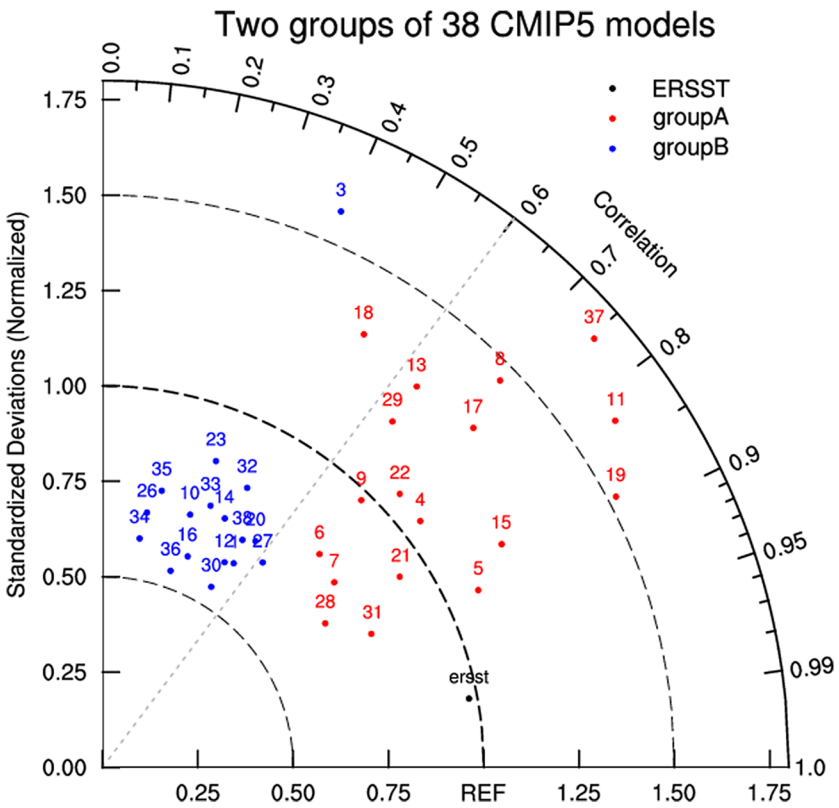

Fig. 4 Taylor diagram comparing the two groups of CMIP5 model simulations (blue and red dots) and ERSST with the observed ENSO PB pattern (from HADISST) in Fig. 2. Group A consists of 18 models and group B of 20 models. The model numbers are the same as in Table 1. Note that three models in group B are not seen in the diagram as they exhibit negative correlations with the observations

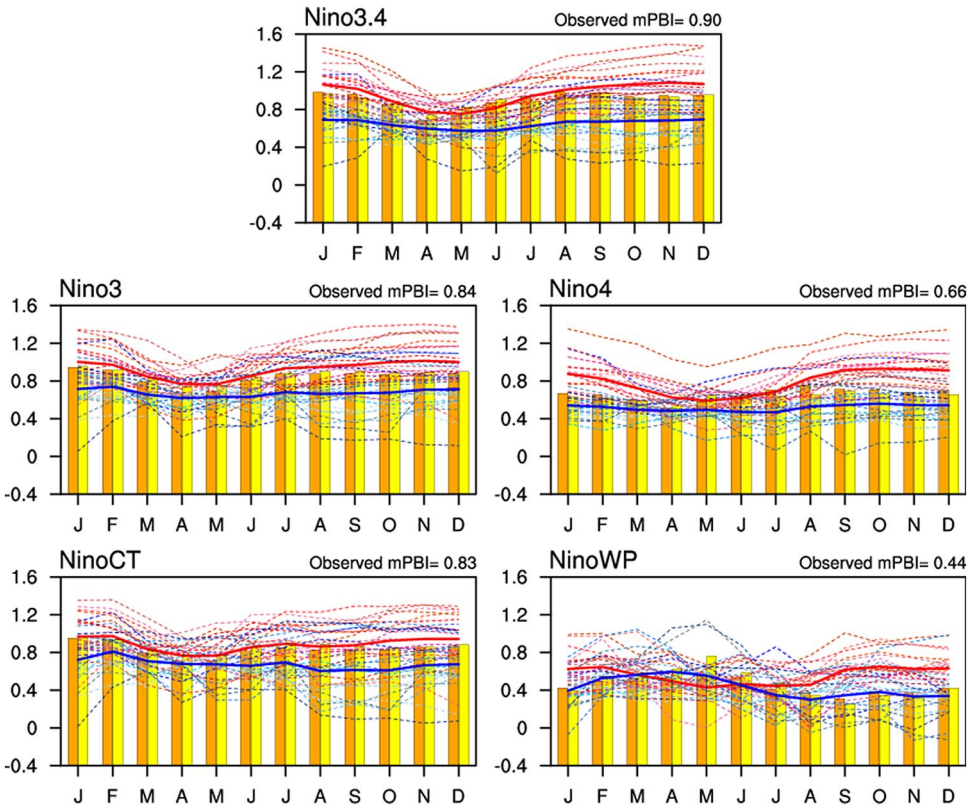

Fig. 5 PBI indices of varied ENSO Niño indices as a function of initial calendar month (month^{-1}), where mPBI denotes the annual mean PBI index of 12 initial calendar months. Observed mPBI in each panel is obtained from HadISST. Orange and yellow bars indicate HadISST and ERSST results, respectively, and red and blue dashed lines indicate models from group A and B, respectively. Solid lines indicate each group's ensemble mean

We calculate 40 STDs for each grid point using the Pacific SSTA observations and 38 model simulations (a sequence with a sample size of 40) with the 30-year climatologies and linear trends removed (see Fig. 8 for an illustration). These 40 STD fields are then used to obtain correlations with Niño3.4 PBI with those 40 samples. Hereinafter, Niño3.4 PBI is expressed by mPBI of the same index. As shown in Figs. 8 and 9, some positive correlations can be seen in the tropical central–eastern Pacific, but these are only statistically significant at the 95% confidence level between SSTA STD and PBI of Niño3.4 in boreal winter (Fig. 9b). We also find that the correlation between amplitude and PBI of the ENSO Niño3.4 is generally only moderate (Fig. 9c, d). Therefore, the amplitude of a certain Niño SST index is only a modest indicator of the PBI of the same index but may not be the key factor.

Previous studies have emphasized the importance of the annual cycle in the tropical Pacific for explaining the ENSO persistence/predictability barrier, and both observational and theoretical evidence have been given to support this hypothesis (e.g., Torrence and Webster 1998; Mu et al. 2007; Levine and McPhaden 2015; Larson and Kirtman 2016). For instance, Webster (1995) explained that the PB occurs during boreal spring when the signal-to-noise ratio in the air–sea coupled system is lowest and the near-equatorial circulation is most easily perturbed by external influences. Therefore, we hypothesize that the seasonality of SSTA amplitude in the tropical Pacific rather than the SSTA amplitude may play a more important role in influencing ENSO PB intensity. Here, we first explore the relationship between ENSO PB intensity and the seasonality of the SSTA amplitude. The seasonality of the Pacific SSTA STD is defined as follows: $\mathrm{SI}_{STD} = \mathrm{Max}\left(STD_{12-month}\right) - \mathrm{Min}\left(STD_{12-month}\right)$, where $STD_{12-month}$ represents the monthly standard deviation of SSTA evolution, comprising the 12 values of the 12 calendar months at each grid point for both the observations and models. In this sample of 40, the correlation patterns between SI_{STD} of Pacific SSTA and PBI of Niño3.4 is shown in Fig. 10a. As hypothesized, the ENSO PBI appears to be closely related to the seasonality of SSTA amplitude in the tropical central Pacific which is the common area for the ENSO indices shown in Fig. 10b, c. That is, the stronger seasonality of SSTA amplitude corresponds to an enhanced Niño3.4 PB intensity (Fig. 10d).

Furthermore, it was also suggested that the strength of the PB seems to depend on the degree of ENSO seasonal synchronization (Torrence and Webster 1998), and the latter one may play a key role in the spring predictability barrier of ENSO (Levine and McPhaden 2015). Thus, we further explore whether the PB intensity is associated with the ENSO seasonal synchronization. The ratio between winter (November–January) and spring (March–May) average Niño-3 SST anomalies standard deviations is adopted (Bellenger et al. 2014), which is a measure of the

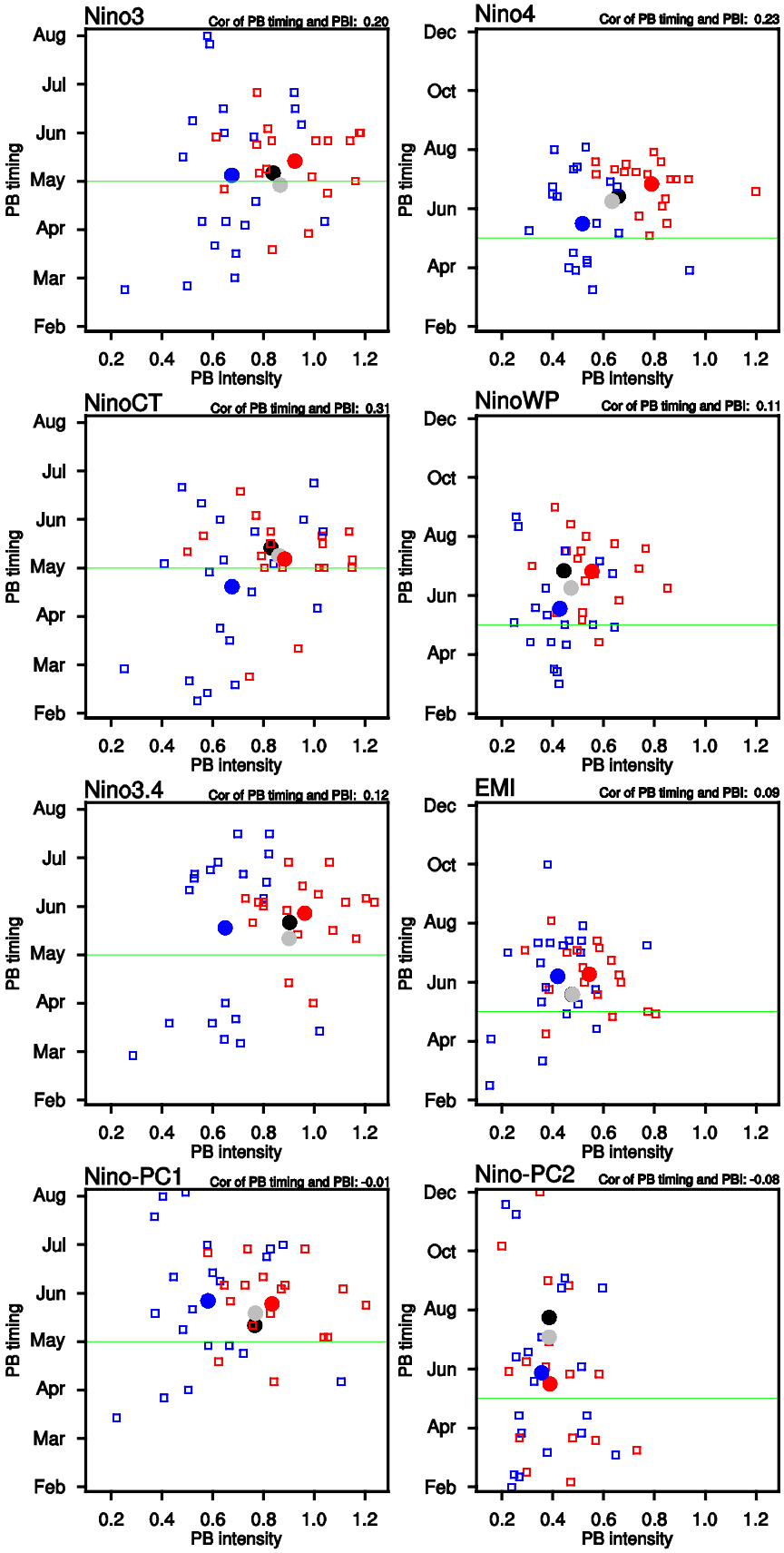

Fig. 6 Scatterplots of ENSO PBI and PB timing for HadISST (black solid circle), ERSST (gray solid circle), mean of CMIP5 model group A (red solid circle), and mean of CMIP5 model group B (blue solid circle). For a given model (red and blue squares indicate models from group A and B respectively), PBI is expressed by mPBI of each Niño index. For a given month, the time when the most rapid autocorrelation decline arises represents the occurrence of ENSO PB for that start month, and PB timing is the average of PB occurrence time for 12 initial calendar months. Green line in each panel indicates the month of May as the PB timing, and correlations between ENSO PB timing and PBI are shown on top right of each panel

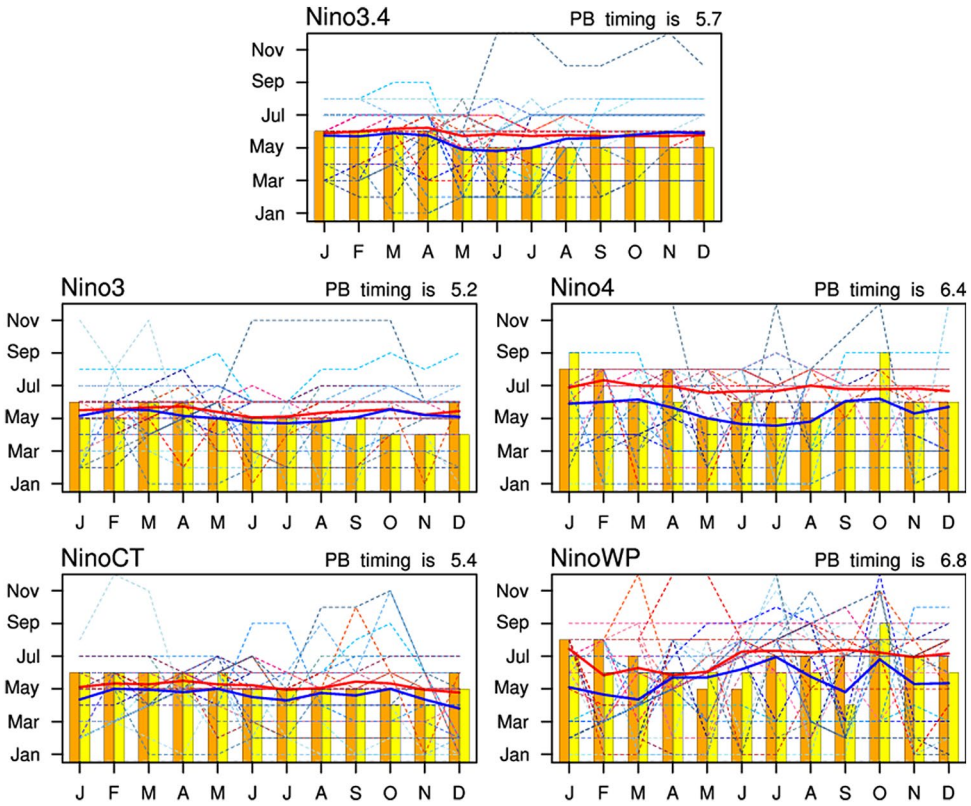

Fig. 7 PB occurrence time for various ENSO indices as a function of the 12 initial calendar months. PB timing is the mean of all PB occurrence time for the 12 initial months and the value (e.g., 1 equals Jan., 2 equals Feb. and so forth) on the top right corner of each panel is obtained from HadISST. Orange and yellow bars indicate HadISST and ERSST results, respectively. Red and blue dashed lines indicate models from group A and B, respectively, with a solid line showing each group's ensemble mean

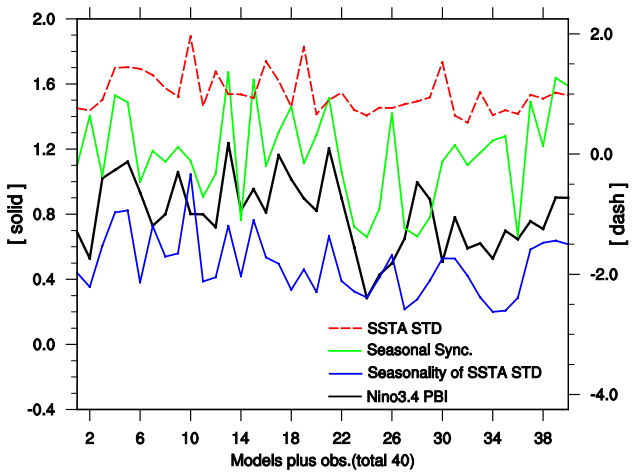

Fig. 8 Schematic diagram of PBIs of Niño3.4 (month^{-1}), SSTA standard deviations (K) of a grid (0°, 160°W), seasonality of SSTA standard deviations (K) of a grid (0°, 160°W), and SST seasonal synchronization strength (dimensionless) of a grid (0°, 120°W) for 40 samples (numbers 1–38 indicate results from the 38 CMIP5 models and numbers 39–40 the two observational data sets, constituting 40 elements in each sequence). The order of models (i.e., from 1 to 38 in each sequence) is the same as in Table 1. Various sequences with a sample size of 40 (like sequences shown here) will be adopted in subsequent correlation analysis

ENSO seasonal synchronization character. Unlike the terminology "phase-locking" used in Bellenger et al. (2014), seasonal synchronization is adopted as it mainly presents the distribution of variance with respect to the annual cycle and better reflects amplitude modulation. This ratio can also be calculated for each grid point individually for the tropical Pacific, referred to as SST seasonal synchronization strength. Statistically significant positive correlations between the PBI and strength of the SST seasonal synchronization can be seen in the tropical eastern Pacific (Fig. 11a). Similarly, in Fig. 11d, the correlation coefficient between the ENSO seasonal synchronization strength and Niño3.4 PBI is relatively high with a correlation of 0.65, denoting significance at the 99% confidence level. These results confirm a close connection between the SST seasonal synchronization and PB intensity of ENSO, as suggested by Torrence and Webster (1998), and provide a reference for understanding model simulations of ENSO persistence. We also find that SST seasonal synchronization is strongest in the eastern Pacific in observations (not shown). This feature can be generally captured by models from group A, however not by the models of group B. Considering the high relevance of the Niño PBI to seasonal synchronization in this area, it may explain why the ENSO PB is stronger in the group A compared to the group B models for a given ENSO index (Figs. 5 and 6).

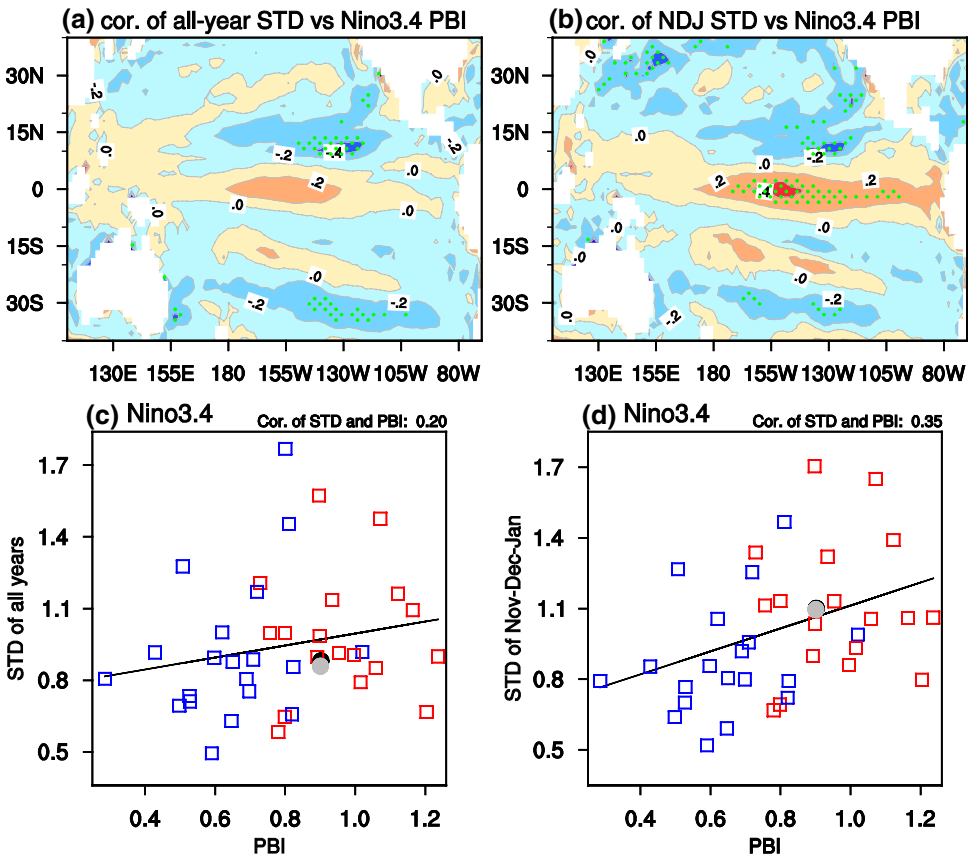

Fig. 9 Correlation patterns between the standard deviation (STD) of SST anomalies and the Niño3.4 index PBI for 40 samples (two observational data sets and 38 climate models) for the **a** long term mean and **b** ENSO mature phase (Nov–Dec–Jan) mean. Green stippling denotes statistical significance at the 95% confidence level. Scatterplots of Niño3.4 PBI and the STD (their correlations are shown on the top right corner of each panel) of the **c** long term mean, and **d** Nov–Dec–Jan mean for the same data (black/gray solid circles indicate HadISST/ERSST, and red/blue squares indicates models from group A/B)

4 Discussion

Thus far, we have assessed the representations of the ENSO PB intensity for multiple Niño indices in CMIP5 model simulations and emphasized the close relationship between it and the tropical Pacific annual cycle (e.g., seasonal synchronization of ENSO). The region that exhibits the strongest relationship between SST seasonal synchronization and PB intensity is located in the eastern Pacific, where SST seasonal synchronization is most pronounced. According to CMIP3 model results, the zonal SST gradient and related zonal wind contribute to the seasonal synchronization of ENSO (Ham et al. 2012). The surface wind stress, which exhibits a strongly seasonally modulated response to Niño3.4 SSTA mainly over the equatorial central Pacific, is an important factor in the seasonal synchronization of ENSO (Ham et al. 2012; Harrison and Vecchi 1999; Stuecker et al. 2013). This implies that the close relationship between ENSO PBI and SSTA that is shown in Fig. 10 may also be seen in atmospheric variables. Thus, we explore the relationship between ENSO PB intensity and the zonal wind stress magnitude seasonality, for which the latter is defined in the same way as the seasonality of SSTA STD. As expected, the region that exhibits the closest relationship is quite similar to the SSTA-related patterns in Fig. 10 with a slightly southward shift towards the location where the strongest air–sea coupling occurs (Ham et al. 2012; Lloyd et al. 2009). Indeed, a weaker relationship is evident between Niño3.4 PBI and the seasonality of surface zonal stress strength among models, with a correlation coefficient of 0.4 that is statistically significant at the 95% confidence level (figure not shown). Thus, the coupling between the mean surface zonal wind and local SST enables the close relationship between ENSO PB intensity and SST seasonality in the tropical central Pacific (Fig. 10), and may even change the way that ENSO seasonal synchronization affects ENSO PB intensity.

One may realize that the two ENSO types are thought to involve different processes but the PB intensity of the two ENSO types is found to closely relate to similar causes. Thus, it is difficult to explain why EP ENSO exhibit a larger PB intensity compared to CP ENSO in this study. The PB of the CP ENSO indices may be more susceptible to the extratropical seasonally varying forcing (e.g., Yu et al. 2010). This stochastic forcing originates from the north Pacific and then influences the tropical central Pacific with a maximum effect in boreal winter according to the Seasonal Footprinting mechanism (Chang et al. 2007; Chiang and Vimont 2004; Vimont et al. 2003). Considering that the tropical central Pacific is the common area where the PB intensity of various Niño indices

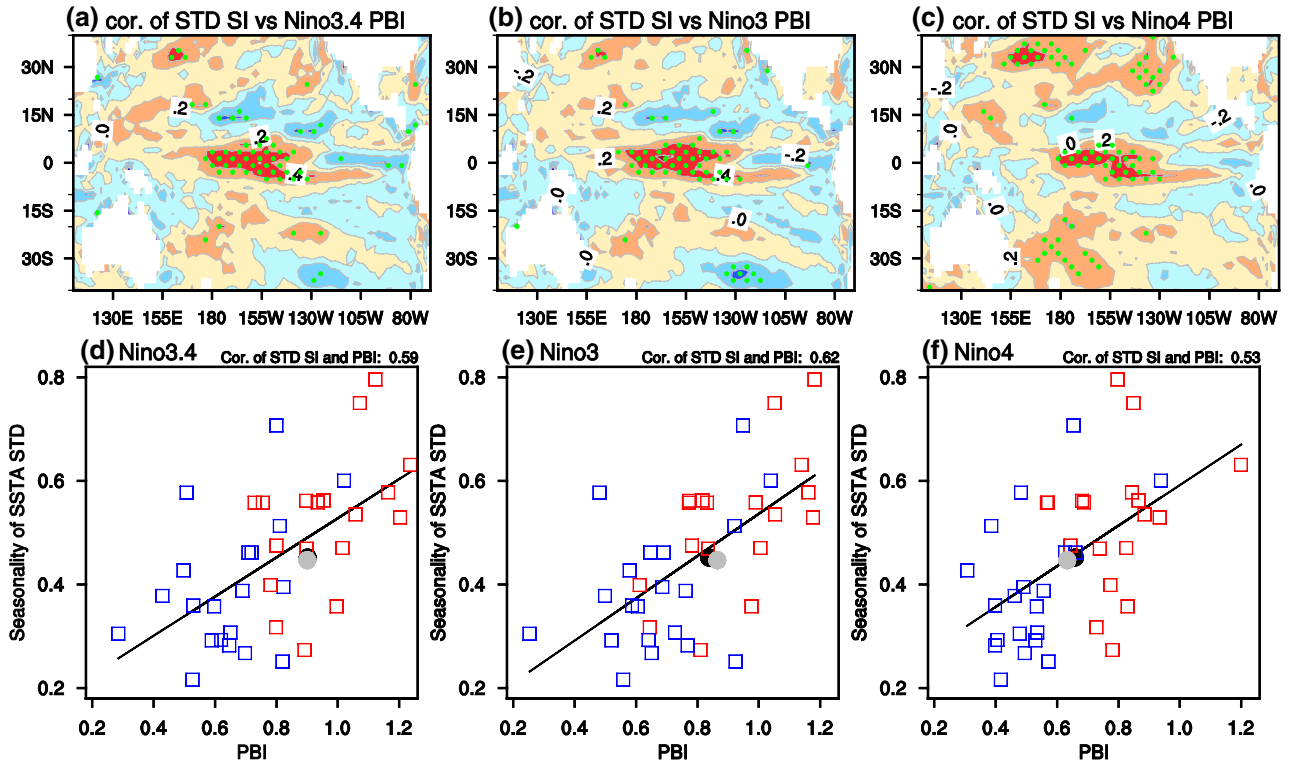

Fig. 10 Correlation patterns between seasonality of SST anomaly standard deviation and the PBI of **a** Niño3.4, **b** Niño3, and **c** Niño4 index for 40 samples (two observational data sets and 38 climate models). Green stippling denotes statistical significance at the 95% confidence level. Scatterplots of ENSO PBI for **d** Niño3.4, **e** Niño3, and **f** Niño4 and the regional mean (5°S–5°N, 180°–145°W) seasonality of SSTA STD (their correlations are shown on the top right corner of each panel) for the same data (black/gray solid circles indicate HadISST/ERSST, and red/blue squares indicate models from group A/B)

is related to the seasonality of SSTA amplitude, the role of this extratropical process may not result in the PB difference between the two ENSO types directly. As discussed in previous studies (e.g., McPhaden 2012; Yu and Kao 2007), the subsurface ocean temperature over the equatorial Pacific represents a major source for the following SST development in tropical eastern Pacific (EP ENSO events) but with much less effectiveness of thermocline feedbacks in governing the evolution of CP ENSO SST. The equatorial Pacific heat content (also known as warm water volume) anomalies, which exhibit a boreal winter PB that is not further addressed in this study, usually lead the eastern equatorial Pacific SST anomalies by several months (McPhaden 2012; Yu and Kao 2007). Thus, it is reasonable to hypothesize that differing thermocline feedback strength between EP and CP ENSO events might result in a contrast between the PBs of two types of ENSO.

5 Conclusions

Here, we investigated the PB phenomenon for a variety of ENSO indices by comparing historical simulations from 38 CMIP5 models with the observations. Utilizing a metric of ENSO PBI proposed by Ren et al. (2016), we found that most of the models reasonably reproduced the observed ENSO PB characteristics. Moreover, approximately half of the models also realistically simulated a distinct PBI between CP and EP ENSO indices. The observed PB timing for the ENSO indices can be represented to a lesser degree by the CMIP5 models with a large inter-model spread. Therefore, some indications for distinguishing the two different ENSO types are found in the PB characteristics as simulated by current CMIP5 models.

The relationships between ENSO PBI and several potential physical causes were investigated next. We found a weak relationship between ENSO amplitude and the PBI for various ENSO indices. Instead, the intensity of the PB for different ENSO indices is closely related to the seasonality of the climatological SST amplitude. Furthermore, the intensity of seasonal synchronization of Niño3 SST anomalies to the annual cycle is associated with the ENSO PB intensity. Specifically, the seasonality of the zonal wind stress strength, which constitutes one important part of the tropical coupled system, is thought to influence both the seasonal synchronization of ENSO and the seasonal variation of tropical SSTs. This result provides further evidence that the seasonality

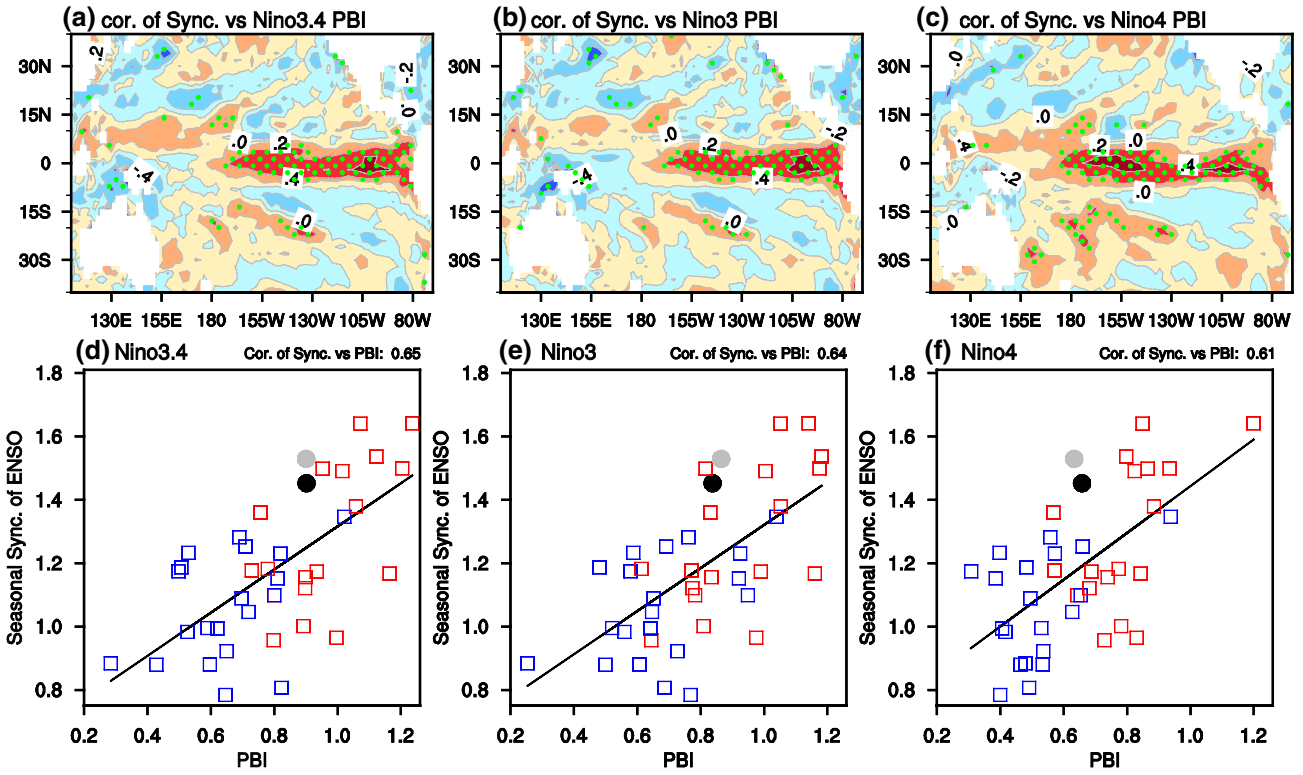

Fig. 11 Correlation patterns between the strength of SST seasonal synchronization (see text for details) and the PBI of **a** Niño3.4, **b** Niño3 and **c** Niño4 index for 40 samples (two observational data sets and 38 climate models). Green stippling denotes statistical significance at the 95% confidence level. Scatterplots of ENSO PBI of **d** Niño3.4, **e** Niño3, **f** Niño4 and the strength of ENSO seasonal synchronization (note that their correlations are shown on the top right corner of each panel) for 40 samples (black/gray solid circle indicates HadISST/ERSST, and red/blue squares indicate models from group A/B)

of the tropical Pacific background state is a crucial factor in controlling the ENSO PB. Hence, a better reproduction of ENSO seasonal synchronization might in turn result in a more realistic representation of the ENSO PB in models. Here, only the physical mechanisms related to the ENSO PB intensity were explored, and potential factors controlling the ENSO PB timing difference across models are beyond the scope of this study and may be the subject of future work.

Around half of the CMIP5 models are able to capture the observed discrepancy in PB intensity between the two ENSO types by reproducing a larger PB intensity for EP ENSO than CP ENSO. This suggests that CP ENSO may possess a higher upper limit of predictability in comparison to EP ENSO and could be more predictable by simply setting up autoregression statistical models of the indices. However, it proves difficult to compare the predictability of the two different ENSO types within dynamical prediction models. On one hand, the results here are based on the latest 30 years of CMIP5 historical simulations as well as parallel observations, thus the potential influence of decadal variability (and associated shift in ENSO predictability) on the PB characteristics of the two ENSO types are not considered (McPhaden 2012; Zhu et al. 2015). On the other hand, simulating and predicting CP ENSO, in contrast to EP ENSO, remains a large challenge. Considerable model drift seems to limit the ability to simulate/predict CP ENSO and the differences between the two types of ENSO (Duan et al. 2014; Hendon et al. 2009; Tian and Duan 2016a). Therefore, an improved understanding of the mechanisms responsible for the two different ENSO types and reduction of model mean state and seasonal cycle biases might open the gates for a more conclusive study of the processes that are responsible for the different PB characteristics, and lead to a more appropriate analysis of predictability of two types of ENSO.

Acknowledgements This work was jointly supported by the National Key Research and Development Program on monitoring, Early Warning and Prevention of Major Natural Disaster (2018YFC1506000), the China National Science Foundation project (41606019 and 41706016), the China Scholarship Council (CSC) State Scholarship Fund, and the Institute for Basic Science (Project code IBS-R028-D1).

References

Ashok K, Behera SK, Rao SA, Weng H, Yamagata T (2007) El Niño Modoki and its possible teleconnection. J Geophys Res. https://doi.org/10.1029/2006JC003798

Barnett TP et al (1994) Forecasting global ENSO-related climate anomalies. Tellus A 46:381–397

Barnston AG, Tippett MK, L'Heureux ML, Li S, DeWitt DG (2012) Skill of real-time seasonal ENSO model predictions during 2002–11: is our capability increasing? B Am Meteorol Soc 93:631–651. https://doi.org/10.1175/bams-d-11-00111.1

Bellenger H, Guilyardi E, Leloup J, Lengaigne M, Vialard J (2014) ENSO representation in climate models: from CMIP3 to CMIP5. Clim Dyn 42:1999–2018. https://doi.org/10.1007/s00382-013-1783-z

Chang P et al (2007) Pacific meridional mode and El Niño–Southern Oscillation. Geophys Res Lett 34:130–144. https://doi.org/10.1029/2007gl030302

Chen D, Zebiak SE, Busalacchi AJ, Cane MA (1995) An improved procedure for El Nino forecasting: implications for predictability. Science 269:1699–1702

Chen D et al (2015) Strong influence of westerly wind bursts on El Niño diversity. Nat Geosci 8:339–345. https://doi.org/10.1038/ngeo2399

Chiang JCH, Vimont DJ (2004) Analogous Pacific and Atlantic meridional modes of tropical atmosphere–ocean variability. J Clim 17:4143–4158

Duan W, Liu X, Zhu K, Mu M (2009) Exploring the initial errors that cause a significant "spring predictability barrier" for El Niño events. J Geophys Res 114:C04022. https://doi.org/10.1029/2008jc004925

Duan W, Tian B, Xu H (2014) Simulations of two types of El Niño events by an optimal forcing vector approach. Clim Dyn 43:1677–1692. https://doi.org/10.1007/s00382-013-1993-4

Ham Y-G, Kug J-S (2012) How well do current climate models simulate two types of El Nino? Clim Dyn 39:383–398. https://doi.org/10.1007/s00382-011-1157-3

Ham Y-G, Kug J-S, Kim D, Kim Y-H, Kim D-H (2012) What controls phase-locking of ENSO to boreal winter in coupled GCMs? Clim Dyn 40:1551–1568. https://doi.org/10.1007/s00382-012-1420-2

Harrison DE, Vecchi GA (1999) On the termination of El Niño. Geophys Res Lett 26:1593–1596. https://doi.org/10.1029/1999gl900316

Hendon HH, Lim E, Wang G, Alves O, Hudson D (2009) Prospects for predicting two flavors of El Niño. Geophys Res Lett. https://doi.org/10.1029/2009gl040100

Hu Z-Z, Kumar A, Jha B, Wang W, Huang B, Huang B (2011) An analysis of warm pool and cold tongue El Niños: air–sea coupling processes, global influences, and recent trends. Clim Dyn 38:2017–2035. https://doi.org/10.1007/s00382-011-1224-9

Jin EK et al (2008) Current status of ENSO prediction skill in coupled ocean–atmosphere models. Clim Dyn 31:647–664. https://doi.org/10.1007/s00382-008-0397-3

Kalnay E et al (1996) The NCEP/NCAR 40-year reanalysis project B. Am Meteorol Soc 77:437–471

Kanamitsu M, Ebisuzaki W, Woollen J, Yang S, Hnilo JJ, Fiorino M, Potter GL (2002) NCEP-DOE AMIP-II Reanalysis (R-2) B. Am Meteorol Soc 83:1631–1643. https://doi.org/10.1175/bams-83-11

Kao H-Y, Yu J-Y (2009) Contrasting Eastern-Pacific and Central-Pacific types of ENSO. J Clim 22(3):615–632. https://doi.org/10.1175/2008JCLI2309.1

Kim ST, Yu J-Y (2012) The two types of ENSO in CMIP5 models. Geophys Res Lett 39:221–228. https://doi.org/10.1029/2012gl052006

Kug J-S, Jin F-F, An SI (2009) Two types of El Niño events: cold tongue El Niño and warm pool El Niño. J Clim 22(6):1499–1515. https://doi.org/10.1175/2008JCLI2624.1

Larson SM, Kirtman BP (2016) Drivers of coupled model ENSO error dynamics and the spring predictability barrier. Clim Dyn 48:3631–3644. https://doi.org/10.1007/s00382-016-3290-5

Latif M et al (1994) A review of ENSO prediction studies. Clim Dyn 9:167–179

Levine AFZ, McPhaden MJ (2015) The annual cycle in ENSO growth rate as a cause of the spring predictability barrier. Geophys Res Lett 42:5034–5041. https://doi.org/10.1002/2015gl064309

Lloyd J, Guilyardi E, Weller H, Slingo J (2009) The role of atmosphere feedbacks during ENSO in the CMIP3 models. Atmos Sci Lett 10:170–176. https://doi.org/10.1002/asl.227

Lopez H, Kirtman BP (2015) WWBs, ENSO predictability, the spring barrier and extreme events. J Geophys Res Atmos 119:10114–10138. https://doi.org/10.1002/2014jd021908

McPhaden MJ (2012) A 21st century shift in the relationship between ENSO SST and warm water volume anomalies. Geophys Res Lett. https://doi.org/10.1029/2012gl051826

Mu M, Xu H, Duan W (2007) A kind of initial errors related to "spring predictability barrier" for El Niño events in Zebiak-Cane model. Geophys Res Lett 34:L03709. https://doi.org/10.1029/2006gl027412

Rasmusson EM, Carpenter TH (1982) Variations in tropical sea surface temperature and surface wind fields associated with the Southern Oscillation/El Nino. Mon Weather Rev 110:354–384

Rayner NA (2003) Global analyses of sea surface temperature, sea ice, and night marine air temperature since the late nineteenth century. J Geophys Res 108:1063–1082. https://doi.org/10.1029/2002jd002670

Ren HL, Jin FF (2011) Nino indices for two types of ENSO. Geophys Res Lett 38:L04704. https://doi.org/10.1029/2010gl046031

Ren HL, Liu Y, Jin FF, Yan YP, Liu XW (2014) Application of the analogue-based correction of errors method in ENSO prediction. Atmos Ocean Sci Lett 7:157–161. https://doi.org/10.3878/j.issn.1674-2834.13.0080

Ren H-L, Jin F-F, Tian B, Scaife AA (2016) Distinct persistence barriers in two types of ENSO. Geophys Res Lett 43:10973–10979. https://doi.org/10.1002/2016gl071015

Smith TM, Reynolds RW, Peterson TC, Lawrimore J (2008) Improvements to NOAA's historical merged land–ocean surface temperature analysis (1880–2006). J Clim 21:2283–2296. https://doi.org/10.1175/2007jcli2100.1

Stuecker MF, Timmermann A, Jin FF, McGregor S, Ren HL (2013) A combination mode of the annual cycle and the El Nino/Southern Oscillation. Nat Geosci 6:540–544. https://doi.org/10.1038/NGEO1826

Taylor KE, Stouffer RJ, Meehl GA (2012) An overview of CMIP5 and the experiment design. B Am Meteorol Soc 93:485–498. https://doi.org/10.1175/bams-d-11-00094.1

Tian B, Duan W (2016a) Comparison of constant and time-variant optimal forcing approaches in El Niño simulations by using the Zebiak-Cane model. Adv Atmos Sci 33:685–694. https://doi.org/10.1007/s00376-015-5174-8

Tian B, Duan W (2016b) Comparison of the initial errors most likely to cause a spring predictability barrier for two types of El Niño events. Clim Dyn 47:779–792. https://doi.org/10.1007/s00382-015-2870-0

Timmermann A et al (2018) El Nino-Southern Oscillation complexity. Nature 559:535–545. https://doi.org/10.1038/s41586-018-0252-6

Torrence C, Webster PJ (1998) The annual cycle of persistence in the El Nino/Southern Oscillation. Q J R Meteorol Soc 124:1985–2004

Vimont DJ, Wallace JM, Battisti DS (2003) The seasonal footprinting mechanism in the Pacific: implications for ENSO. J Clim 16:2668–2675

Webster PJ (1995) The annual cycle and the predictability of the tropical coupled ocean-atmosphere system. Meteorol Atmos Phys 56:33–55

Webster PJ, Yang S (1992) Monsoon and ENSO: selectively interactive systems. Q J R Meteorol Soc 118:877–926

Yu J-Y, Kao H-Y (2007) Decadal changes of ENSO persistence barrier in SST and ocean heat content indices: 1958–2001. J Geophys Res Atmos 112:125–138. https://doi.org/10.1029/2006jd007654

Yu J-Y, Kao H-Y, Lee T (2010) Subtropics-related interannual sea surface temperature variability in the central equatorial pacific. J Clim 23:2869–2884. https://doi.org/10.1175/2010jcli3171.1

Zebiak SE, Cane MA (1987) A model El Nino-Southern oscillation. Mon Weather Rev 115:2262–2278

Zheng F, Zhu J (2010) Spring predictability barrier of ENSO events from the perspective of an ensemble prediction system. Glob Planet Change 72:108–117. https://doi.org/10.1016/j.gloplacha.2010.01.021

Zhu J, Huang B, Marx L, Kinter JL, Balmaseda MA, Zhang R-H, Hu Z-Z (2012) Ensemble ENSO hindcasts initialized from multiple ocean analyses. Geophys Res Lett 39:L09602. https://doi.org/10.1029/2012gl051503

Zhu JS, Kumar A, Huang BH (2015) The relationship between thermocline depth and SST anomalies in the eastern equatorial Pacific: seasonality and decadal variations. Geophys Res Lett 42:4507–4515. https://doi.org/10.1002/2015GL064220

Publisher's Note Springer Nature remains neutral with regard to jurisdictional claims in published maps and institutional affiliations.

JGR Atmospheres

RESEARCH ARTICLE
10.1029/2019JD030948

Urbanization Effect in Regional Temperature Series Based on a Remote Sensing Classification Scheme of Stations

Suonam Kealdrup Tysa[1], Guoyu Ren[1,2], Yun Qin[1], Panfeng Zhang[1], Yuyu Ren[2], Wenqian Jia[1], and Kangmin Wen[1]

[1]Department of Atmospheric Science, School of Environmental Studies, China University of Geosciences, Wuhan, China, [2]Laboratory for Climate Studies, National Climate Center, China Meteorological Administration, Beijing, China

Key Points:
- A new method to determine urbanization level around stations is presented, which shows the applicability to classify stations for assessing urbanization effect
- Also provided is the further evidence that the urbanization has significantly contributed to the observed warming trendsover the last decades in mainland China
- Urbanization effect shows notable difference for different data sets of national stations and for different timeperiods of 1960–2015 and 1980–2015

Supporting Information:
- Supporting Information S1

Correspondence to:
G. Ren,
guoyoo@cma.gov.cn

Citation:
Tysa, S. K., Ren, G., Qin, Y., Zhang, P., Ren, Y., Jia, W., & Wen, K. (2019). Urbanization effect in regional temperature series based on a remote sensing classification scheme of stations. *Journal of Geophysical Research: Atmospheres*, *124*, 10,646–10,661. https://doi.org/10.1029/2019JD030948

Received 4 MAY 2019
Accepted 30 AUG 2019
Accepted article online 11 OCT 2019
Published online 21 OCT 2019

©2019. American Geophysical Union. All Rights Reserved.

Abstract Quantifying the urbanization effect on station and regional surface air temperature (SAT) trends is a prerequisite for monitoring and detecting long-term climate change. Based on the data set of satellite visible spectral remote sensing, a new method is developed to determine the urbanization level around observational sites on varied spatial scales and to classify the sites into different categories of stations (U1, U2, ..., U6) with U1 the least and U6 the largest affected by urbanization. Urbanization effect on SAT anomaly series of urban and national stations are then evaluated for the periods of 1980–2015 and 1960–2015. Results show that the percentage of built-up area in different circumferences of the observational sites can be considered as a good indicator of comprehensive urbanization level of station and can be used to classify stations and to determine reference stations; the largest increase in annual mean SAT (T_{mean}) during 1980–2015 occurred at U6 stations, and U1 stations registered the weakest annual mean warming. The urbanization level is significantly positively correlated to the linear trends of annual mean T_{mean} and minimum SAT (T_{min}) and significantly negatively correlated to the diurnal temperature range (DTR) change. The data sets of the national reference climate station network and basic meteorological station network show large urbanization effect and contribution, with the annual mean urbanization contributions reaching 28.7% and 25.8% for the periods 1960–2015 and 1980–2015, respectively. For all the national stations (2,286 in total), the urbanization contributions are 17.1% and 14.6% for the two same periods, respectively.

1. Introduction

Urbanization can alter local environments via a series of physical processes, resulting in local environmental stresses (Cardelino & Chameides, 1990; Intergovernmental Panel on Climate Change, 2013) and, at the same time, affecting the trends of surface climate observations of urban stations (Rai et al., 2012; Ren et al., 2007, 2015). In mainland China, for example, the climate warmed significantly over the past half century (Committee of Chinese National Assessment, 2016), but the increasing temperature trends have been overestimated due to the effect of urbanization, which is probably one of the most important systematic biases in surface air temperature (SAT) series of urban stations with different urbanization levels.

In the previous studies, long-term trends of SAT in local and regional scales have been found to be associated with the urbanization level in a large extent in mainland China (He et al., 2007; Hua et al., 2008; Li et al., 2018; Ren et al., 2005, 2008; Yang et al., 2013; Zhang et al., 2010; Zhou et al., 2004). It is necessary to evaluate the bias of urbanization effect to the data sets, because the data had been extensively used by researchers in their analyses of regional (Ren et al., 2005, 2012) and global (Hansen et al., 2010; Jones et al., 2008; Lawrimore et al., 2011) climate change. Sun et al. (2016) reported that the linear trend in the observed annual mean temperature of all the national stations in mainland China is 1.44 °C over the period 1961–2013, of which 0.49 °C (0.12–0.86 °C) or about one third can be attributed to urbanization. Ren et al. (2015) showed that the contribution of the urbanization effect to the SAT warming is at least 24.9% for the national stations of mainland China during the period 1961–2004, approximately consistent with that reported by Zhang et al. (2010).

Most of the related researches have estimated the urban warming in a large-scale temperature series based on the comparison of urban and rural/reference (Hinkel & Nelson, 2007; Mete et al., 1997; Ren & Ren, 2011; Wen et al., 2019), which is a widely used method and generally regarded as the most robust way to examine the urban biases (Brohan et al., 2006; Hartmann et al., 2013). Different urbanization indicators

have been adopted to classify stations with different urbanization levels and to select representative reference stations as benchmark. The most frequently applied indicators include population (total population, urban resident population, and population density) in the urban areas where the stations are located (Chu & Ren, 2005; Jones et al., 1990; Portman, 1993; Zhou & Ren, 2005), remote sensing nighttime light level (Hansen et al., 1999; Owen et al., 1998; Peterson et al., 1999), satellite remote sensing surface temperature (Gallo et al., 1993; Ren & Ren, 2011), and satellite remote sensing visible spectral data (Gallo et al., 1999; Gallo et al., 2002; Hansen et al., 2001; Kalnay & Cai, 2003; Yang et al., 2013). The difference in the methods and data set used by the various researchers is one of the main causes of the different estimates obtained for urbanization effects and contributions.

Land use/land cover (LULC) derived from the satellite remote sensing visible spectral data could be used to reflect the urbanization process around the observational stations intuitively. The LULC data have higher spatial resolution and wide coverage and thus have a good potential to be applied in classifying stations and selecting reference stations. Previous researches have separated different categories of stations based on urban land use around the observational sites to evaluate SAT trends due to urbanization in mainland China (He et al., 2013; Wang & Ge, 2012; X. Yang et al., 2011; Yang, Shi, et al., 2011; Yang, Wu, et al., 2013).

X. Yang et al. (2011), Yang, Shi, et al. (2011) used satellite remote sensing visible spectral data to evaluate the observational environment of six meteorological stations in Anhui Province, China, and the method showed a good applicability to surveying and selecting of representative meteorological stations. They also applied the data to classify the observational sites of Hefei City, China, into urban and rural stations according to the percentage of urban land use area in a buffer area around the stations, showing a good relationship between the annual mean temperature (annual mean minimum temperature) and the percentage urban land use area in the buffer areas. They further analyzed the urbanization effects on SAT changes for the urban stations and all national stations during 1970–2008, showing a large and significant urbanization-induced warming at the urban stations as well as the national stations during the period (X. Yang et al., 2011; Yang, Shi, et al., 2011).

Wang and Ge (2012) applied the satellite remote sensing data set but took the urbanization rate around the stations into consideration. They classified the national stations of China into three categories with different urbanization levels according to urban land use change around the stations, taking the stations with weak urbanization process as reference stations to evaluate the urbanization effect on temperature trends of other categories of urban stations. The analysis showed large urbanization contribution of 41% for the stations with high urbanization rate and an urbanization contribution of 20% for all the national stations in mainland China during 1980–2009.

He et al. (2013) applied the change in proportion of urban area as an indicator of urbanization rate around the stations and related the urbanization rate to annual mean SAT trends observed at the national stations in the Beijing-Tianjin-Hebei area, North China. They found a significant positive correlation between the urbanization rates and the SAT trends at all stations and an increase of 10% in urban area around the stations approximately contributed to the 0.13 °C rise in annual mean SAT in addition to regional warming. They showed an urbanization contribution of 44.1% to the overall warming trend as observed at the national stations during 1978–2008.

Urbanization effect on SAT series can be related to the influences of human activity on different spatial scales (Gallo & Xian, 2016; Ren et al., 2015; Stewart & Oke, 2012). At least three spatial scales would be important: the mesoscale from the whole city, the local scale of the size of a park and functional district, and the microscale of buildings nearby a station (Peterson, 2003; Ren et al., 2015). Gallo et al. (1996) noted that the effect of LULC is more significant at 10-km radius around the stations by examining the impact of urbanization on observed diurnal temperature range (DTR). The above-mentioned studies applied remote sensing visible spectral data generally considered the influence of local or microscale LULC but did not consider the possible simultaneous influence at microscale and mesoscale.

The works of Wang and Ge (2012) and He et al. (2013) have an advantage over the earlier remote sensing data based studies in taking the rate of urbanization around the stations into consideration in classifying stations or selecting reference stations, but at the same time, the methods also limit the analysis period to the shorter aft-satellite era, which only lasts three to four decades. On the other hand, it is unnecessary to address the rate of urbanization around the observational site for selecting rural or reference station if only the

present observational environment of a station is good enough because the observational environments around almost all of the "bad" stations have been gradually worsened since their establishments (Ren et al., 2015). A "good" station which is good at present must also be good in the past, given that the station experienced no relocation.

In this study, a new methodology is developed based on the satellite remote sensing visible spectral data, and the percentage/relative area of urban land use on multispatial scales around an observational site at present was used as an indicator of urbanization level to classify the observational stations in mainland China. Six different urbanization levels including the weakest degree of urbanization are identified for the national stations. Urbanization effects on, and contributions to, the overall trends of annual and seasonal mean SAT series of urban stations for the period 1980–2015, and of two different national station networks for the periods 1980–2015 and 1960–2015, are quantitatively assessed.

2. Data and Methods

2.1. Data

The monthly SAT data set of "China National Surface Meteorological Station Homogenization Temperature Monthly Dataset (V1.0)," which includes 2,419 stations with a record length of 66 years (i.e., 1950–2015), has been homogenized in the National Meteorological Information Center, China Meteorological Administration (Cao et al., 2016). The data set includes the records of monthly mean SAT, monthly mean maximum SAT, and monthly mean minimum SAT. It can be divided into three sub–data sets: the national Reference Climate Network (RCN), the national Basic Meteorological Network (BMN), and the national Ordinary Meteorological Network (OMN). The RCN and BMN (RCN + BMN), about 825 stations totally, have been most frequently applied in analyses and monitoring of climate change in China, but recently, a few of groups have also begun to use all the stations from the three sub–data sets (RCN + BMN + OMN).

In this study, 2,286 stations from the RCN + BMN + OMN are used, considering the problem of missing data by discarding the temperature series with missing monthly records of more than 3 months in any year of the period 1960–2015. A total of four types of temperature indicators are analyzed, including mean SAT (T_{mean}), maximum SAT (T_{max}), minimum SAT (T_{min}), and DTR.

The LULC data set of mainland China in 2015 was provided by the Resources and Environmental Sciences Data Center, Chinese Academy of Sciences (Xu et al., 2018). The spatial resolution of the data set is 1.0 km × 1.0 km, which is based on the Landsat 8 remote sensing images and generated by artificial visual interpretation. The Resources and Environmental Sciences Data Center data have undergone a unified quality control and an integrated check. Compositions of land use classes in the data set include cultivated land, forestry land, grass land, water area, urban, rural and residential land, and unused land. The numbers 51 and 53 in classification system are used as urban land use in this paper, including the built-up areas of large, medium and small cities, the county capitals and towns, and other construction land (factories and mines, large industrial areas, oil fields, salt fields, quarries, as well as traffic roads, airports, and special land use; Xu et al., 2018).

2.2. Methods

2.2.1. Selection of Urbanization Indicator

In order to estimate the effects of urbanization of different levels on temperature trends at varied spatial scales from microscale (0–10 km) to mesoscale (more than 10 km but less than 100 km), the percentage of urban land use area around the observational sites is calculated in different buffer circles with the stations as the centers of them. This is done with an assumption that the larger proportion of built-up areas around the observational sites at any spatial scales within a maximum circumference will exert an impact on SAT records.

First, we determine study extent of urban land use around stations, that is, the maximum spatial scale for the urban land use impact on SAT records of stations. For each of the stations, 20 circles with radius of 1, 2, 3, ..., 20 km (1-km increment) and stations as the centers are determined, which are defined as buffer circles. Second, the urban land use categories are extracted, and the percentages of urban land use (PULU) in 2015 are calculated for each of the buffer circles, and a total 20 PULU values are produced for each station.

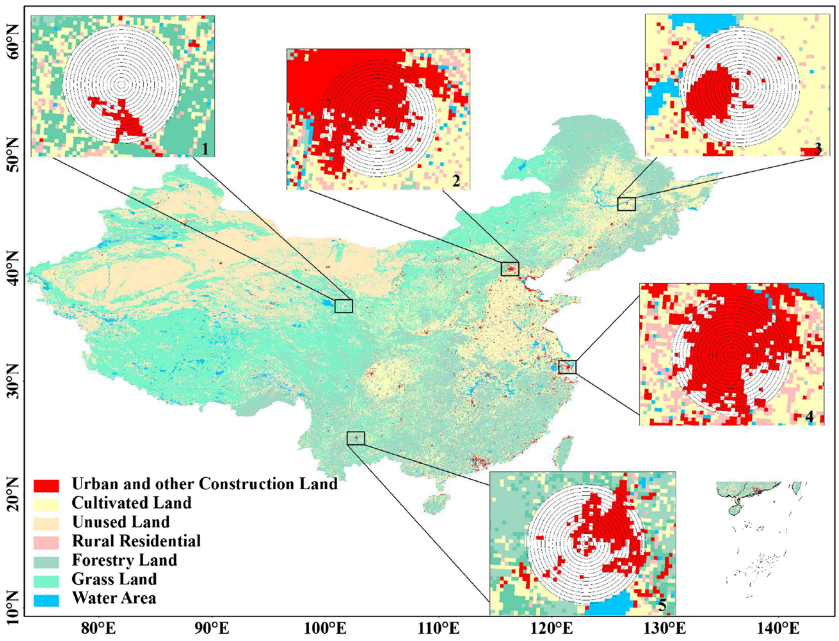

Figure 1. Visualization of land use/land cover in mainland China in 2015 and urban land use in 16 buffer circles around five representative meteorological sites (only the urban land use in buffer circles is shown; 1: Xining; 2: Peking; 3: Harbin; 4: Shanghai; 5: Kunming).

Finally, the Pearson's correlation coefficients between the annual T_{mean} trend series and 20 PULU values in all buffer circles of the total 2,286 stations are calculated (Supporting Information, Figure S1).

The results showed that all the correlation coefficients are above the 99.9% confidence level in each buffer circle with radii less than 20 km. The largest correlation coefficient is found when the radius of buffer circle is 4 km, and then the correlations gradually decrease with an increase of the radius. However, a slight upward trend is observed when the radius is larger than 16 km. The possible reason for this is that, when the radius of buffer circle is larger than 16 km, it may have already reached the distance to the neighboring city/town, especially in case that a denser observational network of 2,286 stations are utilized.

However, the largest spatial scale affected by urbanization is just within the mesoscale extent, which is approximately comparable to those found by applying change rate of urban land areas rather than PULU in the buffer circles (He et al., 2013; Wang & Ge, 2012). In this study, therefore, urban land use information in 16-km buffer circles around the station can be extracted to analyze the urban impact on SAT series. Different from all previous studies (He et al., 2013; Wang & Ge, 2012; Yang, Hou, et al., 2011; Yang, Shi, et al., 2011; Yang et al., 2013), however, we consider PULU values themselves, rather than the change rate of urban land areas, in each of 1- to 16-km radius buffer circles (Figure 1), which means that the possible impact of urban land use on SAT series of observation sites in varied spatial extents from microscale to mesoscale are all examined.

2.2.2. Classification of Urbanization Level

Based on the maximum of PULU values (MPULU) in all 16 buffer circles around stations, the 2,286 national stations are divided into 11 groups. The first group is defined as the MPULU ranges from 0% to 5% in all of the 1–16 km radius buffer circles, indicating that PULU in all buffer circles are less than 5%, or within the range of 0–5% for the stations in this group. The second group of stations has a MPULU value between 5% and 15% in the 16 buffer circles, and the 11th group of stations registers a MPULU value between 95% and 100%.

The MPULU usually appears in the fourth buffer circle (3–4 km) for all the 11 groups of stations (Figure S2), which can explain the above-mentioned finding that PULU has the highest correlation with the annual T_{mean} trends series in the 4-km radius buffer circle (Figure S1). This is also consistent with the fact that most of the stations are located within or near the medium-sized and small cities of the country, and the level of urbanization effect on the temperature change at the observational sites will be closely related to their distance from the urban centers (Ren et al., 2015).

In addition to the MPULU around station, the average of each PULU value at all spatial scales also needs to be considered. Therefore, the second step of classification of urbanization level for the above stations of 11 groups is to calculate the area-weighted average of the PULU (APULU) in the 16 buffer circles around stations for each of the groups, by using the inverse function distance weighting method:

$$APULU = \frac{\sum_{r=1}^{16} \frac{1}{r+c} \cdot PULU(r)}{\sum_{r=1}^{16} \frac{1}{r+c}}, \quad (1)$$

where r stands for the radius of buffer circle, $PULU(r)$ for the percentage of urban land use in r-km radius buffer circle, and c for a constant. The purpose of adding the constant c is to avoid the distance of the sample being too small as to infinite of the inverse function. Here, c is set to 5.

Though the urbanization level should have a positive correlation with the annual mean T_{mean} trend, the annual mean T_{mean} trends of the 11 groups do not increase linearly (Figure S3). The annual mean T_{mean} trends of the stations in the fourth, sixth, and ninth groups are somehow lower than the neighboring groups (as showed by the orange area in Figure S3), for example, but these lower trend values well correspond to the similarly lower APULU, indicating a good correspondence between the two variables. The classification of urbanization level thus not only calculates the MPULU in the 16 buffer circles as conducted in the first step but also considers the mean state of PULU values in all scales around the station. Around such stations as those in the fourth, sixth, and ninth groups, the PULU only has an abnormally large value in 1-km radius of buffer circle (Figure S2).

Therefore, certain groups as classified only by the range of the MPULU values have obviously lower APULU values and also the corresponding smaller temperature trends. Based on the APULU values, the 11 groups are regrouped into six categories (units), including U1, U2, U3, U4, U5, and U6, in order of increasing urbanization levels (Figure S4). The stations in ninth group are thus classified as U4 stations (yellow bar as shown in Figure S4) due to mean APULU values in all scales around these stations are close to the values around the stations of fifth and sixth groups (19.17%). The six categories of stations will be used to analyze the effects of varied urbanization levels on long-term trends of temperature.

Table S1 shows the six categories of stations differently affected by urbanization processes. It is assumed that the first category of stations (U1) with APULU less than 1% is hardly affected by urbanization, and they can be taken as reference stations. The relative warming of stations in other categories to that of reference stations can generally represent the urbanization effect. The stations in other categories have been affected by low (U2), lower (U3), medium (U4), higher (U5), and high (U6) urbanization levels, respectively, and they are termed as urban stations. It is very likely that the actual temperature anomaly series of the stations in U1 have still been affected by urbanization though in a much less extent.

2.2.3. Selection of Reference Stations

The specific criteria for selecting reference station in the RCN + BMN + OMN data set in mainland China are used in previous studies (Ren et al., 2015; Zhang et al., 2010), which had to be of sufficient length in data series and good continuity in the observations, higher stability and less relocation of observational sites, and, most importantly, an immunity to the urbanization influences. These criteria have been referred to determine the reference stations in this study.

The following specific steps are set for selecting reference stations: First, we choose stations in U1 with the beginning of record no later than 1960, the number of relocation less than three times after 1960 and horizontal distance of relocation less than 5 km, the difference between the elevation of the candidate reference station and the arithmetic mean elevation of other stations in same grid box is less than 40 m. A total of 128 U1 stations are selected, and this category of reference stations is regarded as U1 reference stations (green points as shown in Figure 2a; green grids in Figures 2b and 2c), and each green grid box has a maximum of two U1 reference stations. It can be seen, however, that there is no U1 reference station in some of the grid boxes of eastern region, in particular, in North China Plain and Northeast China Plain, due to the highly urbanization around the stations.

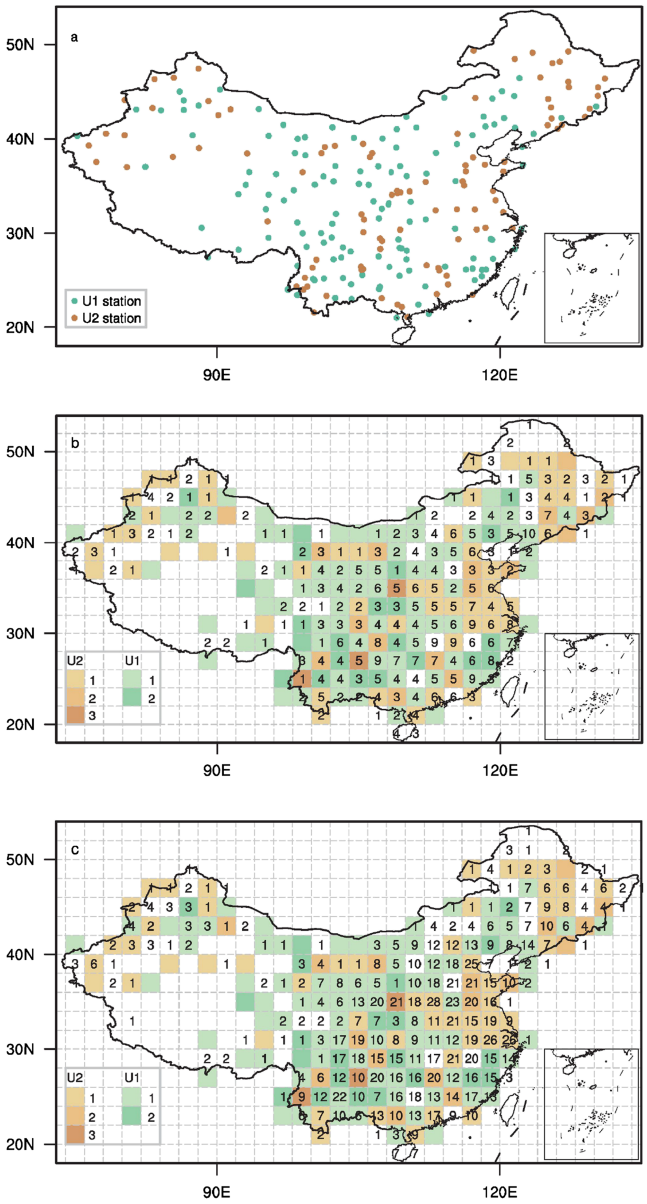

Figure 2. (a) Distribution of reference stations (green marks stand for U1 reference station; brown marks for U2 reference station), and number of reference and urban stations in grid boxes at a spatial resolution of 2° × 2° in mainland China (b: RCN + BMN data set; c: RCN + BMN + OMN data set; color grid boxes stand for the number of reference station in the grid, number for the number of urban station in the grid).

Based on the fact that the MPULU range 5–15% and the APULU is 3.36% around the U2 stations, respectively, stations in U2 category have potential applicability as reference stations in highly urbanization area of the plains. Therefore, in order to obtain enough reference stations to fill the blank boxes in eastern China, we use the same selecting criteria to filter the U2 stations for the remaining empty grids. This category of reference stations is regarded as U2 reference stations (brown points as shown in Figure 2a; brown grids in Figures 2b and 2c). The number of U2 stations and boxes are 101 and 72, respectively. The total reference stations (U1 + U2) are thus 228, and the total boxes with reference stations are 175. The reference station network including two categories of reference stations is utilized in this study to estimate urbanization effect and contribution in the SAT series of "urban stations" with different urbanization levels from 1980 to 2015, and of the national stations of the RCN + BMN + OMN and RCN + BMN data sets during different periods.

The "urban stations," which are all the stations in addition to the reference stations in the data set, will be assessed for the urbanization effect contained in their temperature series for period 1980–2015. Therefore, the target stations have excluded the reference stations for the assessment of urban stations. Also assessed for urbanization effect are the two complete data sets of the national stations (RCN + BMN + OMN and RCN + BMN) for periods 1980–2015 and 1960–2015. In this later assessment, however, the reference stations have not been excluded from the target stations so that the actual effects of urbanization on the usually used temperature data series can be determined, as practiced in the previous studies (Ren et al., 2008; Ren & Zhou 2014).

In order to ensure comparability between different urbanization effects, all results with different urbanization levels were based on the grids that have U3–U6 stations referring to the common practice as done in estimating regional averaged temperature series.

2.2.4. Statistical Methods

In this study, annual mean values are the average of 12 monthly mean values, and seasonal mean values are the average of 3 months in any of the seasons, which are divided according to climatological seasons of spring (March, April, and May), summer (June, July, and August), autumn (September, October, and November), and winter (December, January, and February).

The whole study area is divided into grid boxes with a spatial resolution of 2° × 2°, and at least one station is selected in each grid so that the reference series and "urban station" series of the grid can be established. Arithmetic average series of each of the reference and target stations are made to obtain the respective mean temperature anomaly series for the grid box. Temperature anomaly is calculated relative to the average of climatological reference period 1981–2010. The linear trend of difference of the urban station (national station) and reference station mean temperature series for the grid is defined as urbanization effect. If the urbanization effect is significant statistically on the grid, the urbanization contribution, which is defined as percent proportion of urbanization effect to the overall trend, will be calculated. The calculation method of the urbanization effect can be expressed as

$$\Delta T_{U-R} = T_U - T_R, \tag{2}$$

where is the linear trend of SAT series of urban station (national station) and is the linear trend of SAT series of reference station. Urbanization contribution is expressed as

$$C_U = \left| {}^{\Delta T_{U-R}}\!/_{T_U} \right| \cdot 100\%. \tag{3}$$

The detailed introduction about the calculation of urbanization effect and contribution for individual stations and grid boxes could be found in Chu and Ren et al. (2005), Ren et al. (2008), and Ren & Zhou (2014).

The linear trend of the temperature anomaly series is estimated using the ordinary least squares method. The serial correlation of the monthly mean SAT should not significantly affect the trend estimate, and it is not processed before the calculation of the trends (Von Storch & Navarra, 1999). The statistical significance of the linear trend of the temperature anomaly series is judged using the Student's *t*-test. The trend of temperature (temperature difference) series is considered statistically significant when a confidence level is equal to or higher than 99%.

3. Results

3.1. Distribution of Stations and Their Temperature Trends

The stations with the urbanization above median level (U4) are mainly distributed in East and North China (Figure 3), with the U6 stations totally distributed in North China and the coastal zone, and U5 stations dominantly located in eastern parts of the country. However, middle and western parts of China own more stations with lower urbanization levels. As the urbanization level increases, the average trends of annual mean T_{mean} of various categories at different latitudes gradually shift to the right of the *x*-axis (right panels of Figure 3), ranging from 0.298 to 0.425 °C per decade (−0.28 to 0.79 °C per decade for extreme value), which confirm the simultaneous variation of the urbanization levels and the trends of annual mean SAT series.

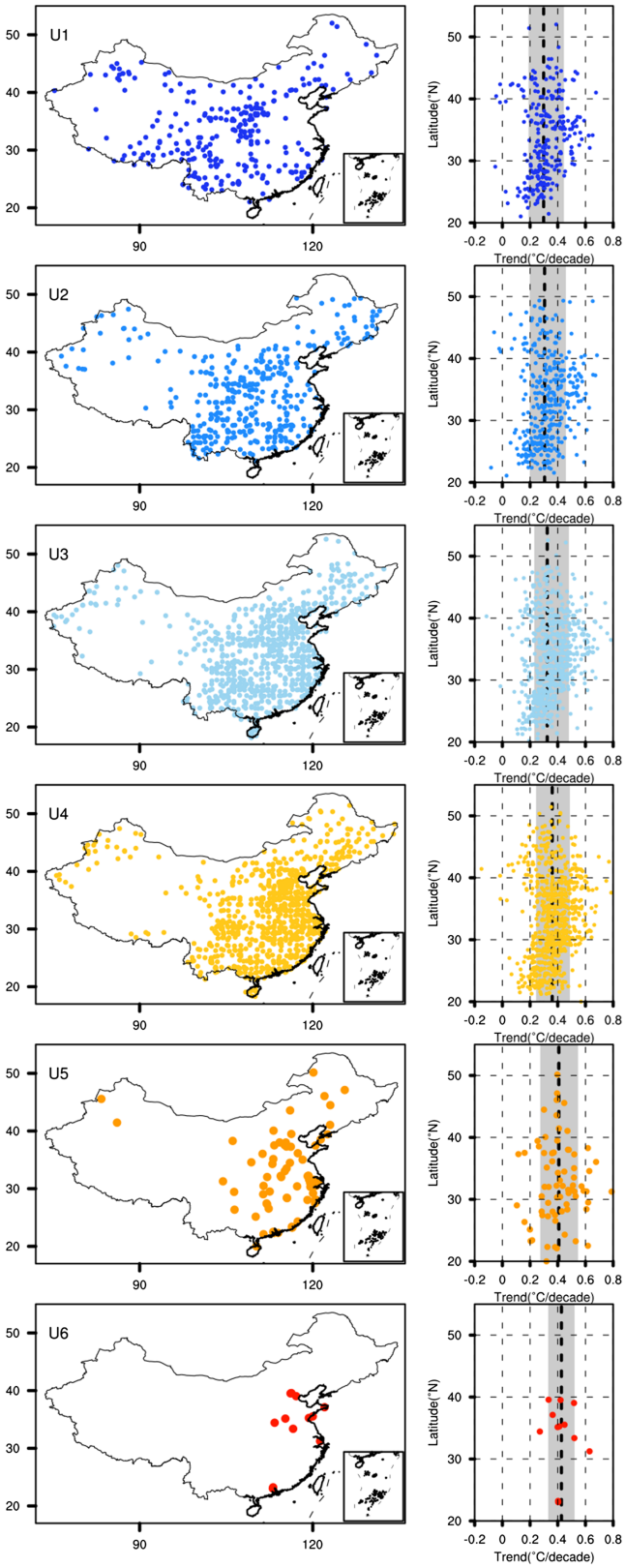

Figure 3. Spatial distribution of stations and average annual mean T_{mean} trends of various categories (U1–U6) during the period 1980–2015 (black dashed lines on the right panels stand for the average values of the temperature trends, and the width of the gray areas for a standard deviation).

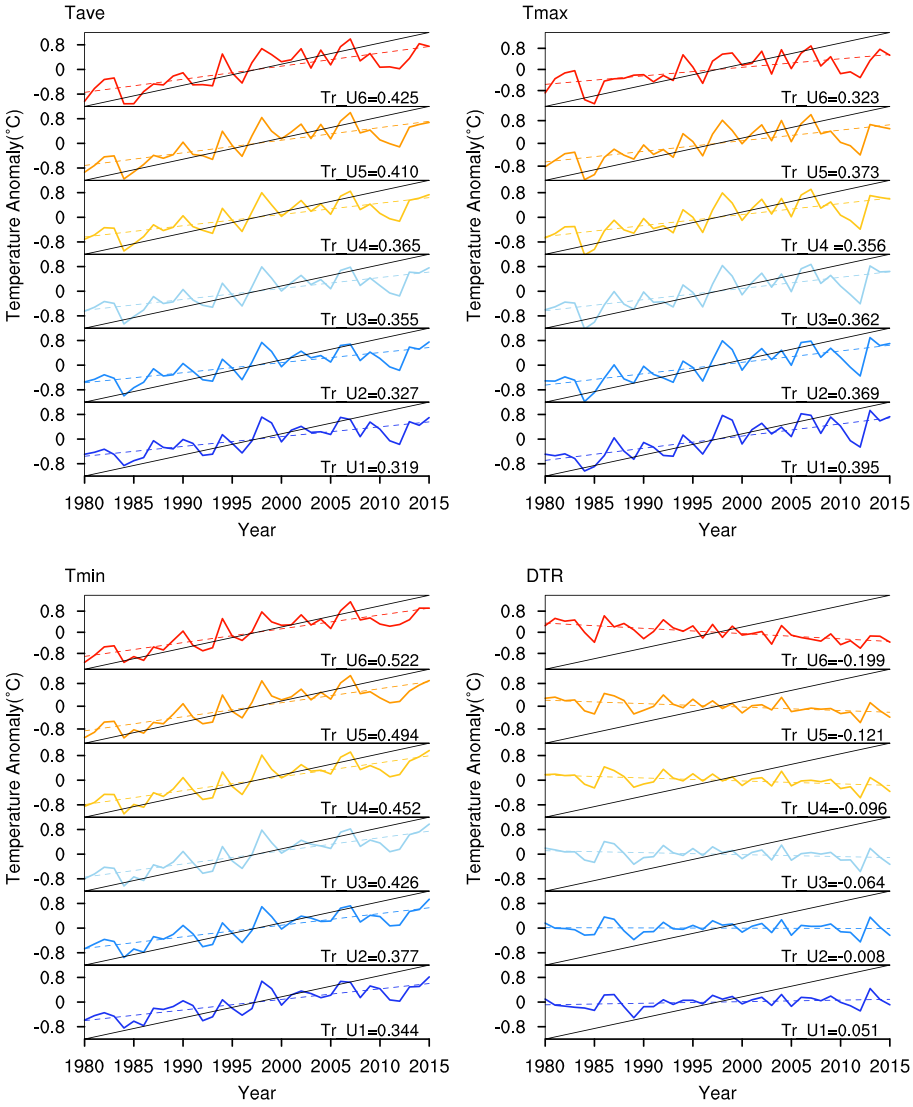

Figure 4. Regional average annual mean surface air temperature (DTR) anomalies for different categories of stations in mainland China during 1980–2015 (the values stand for average linear trend of series [unit: °C per decade]). DTR = diurnal temperature range.

3.2. Temperature Trends for Stations with Different Urbanization Levels

Changes in regional average annual mean SAT of the different categories of stations in the past 36 years are all positive (Figure 4). Annual mean T_{min} and T_{mean} increases are large and highly significant, and the increase rates are proportional to the urbanization levels. The maximum trend in annual mean T_{mean} occurs at the stations affected by the highest urbanization level (U6) in mainland China, which has an annual mean linear trend of 0.425 °C per decade during the period 1980–2015. As the urbanization level increases, annual mean T_{min} trends at stations in each category change from 0.344 °C per decade for U1 stations to 0.522 °C per decade for U6 stations. Though annual mean T_{max} trend is negatively correlated with the urbanization level probably due to the increased effect of aerosols at the higher urbanization level stations during daytime (e.g., Wang & Dickinson, 2013; Zhang et al., 2012), the trend differences between the stations in each category are very small.

For U1 stations, annual mean T_{max} increases faster than other categories of stations, and annual mean T_{min} rises more slowly, but the difference between the two trends is small so that annual mean DTR only slightly increases (Figure 4). As the urbanization level increases, annual mean T_{min} increase more obvious than

Table 1
Urbanization Effect (Unit: °C per decade) on, and Urbanization Contribution (Unit: %) to, the Annual Mean Surface Air Temperature (DTR) Trends for Varied Categories of Urban Stations (U3–U6) in Mainland China During 1980–2015

SAT		U3	U4	U5	U6
T_{mean}	A	0.036*	0.046*	0.091*	0.106*
	B	10.3	12.8	22.2	25.0
T_{min}	A	0.082*	0.108*	0.151*	0.178*
	B	19.3	24.0	30.5	34.2
T_{max}	A	−0.033	−0.039	−0.021	−0.072*
	B	N/A	N/A	N/A	22.1
DTR	A	−0.115*	−0.147*	−0.172*	−0.250*
	B	100	100	100	100

Note. "A" denotes urbanization effect (°C per decade); "B" denotes urbanization contribution (%); "N/A" indicates that the urbanization effect did not pass significance of the confidence level 99%. DTR = diurnal temperature range.
*Significance at the confidence level 99%.

annual mean T_{max}, and the annual mean DTR is significantly reduced. It shows that the annual mean T_{max} and T_{min} increases at the urban stations (U2–U6 stations) are becoming asymmetry, and urbanization level is negatively correlated to the DTR trend.

Of the four seasons, seasonal mean SAT increases most in spring, followed by winter and autumn, and summer temperature change is the smallest. With the increase of urbanization level, the amplified warming occurs most obviously in winter, spring, and autumn (Figure S5). In particular, the difference of average (median) trends between U1 and U6 is large for seasonal mean T_{min}, reaching more than 0.200 °C per decade.

The seasonal mean DTR trends for U1 stations are positive in all seasons (Figure S5). However, the average (median) DTR trends for urban stations are negative except for U2–U5 for spring. Although the increase of DTR happens in most categories of stations with the decrease of urbanization level, the U6 stations with the highest level of urbanization witnesses a negative trend of DTR in spring, due to the largest increase in T_{min} and the almost same change of T_{max} to that of U1 in this season. The seasonal mean DTR are more sensitive to urbanization level in cold season. From U1 to U6, not only the DTR trends change from positive to negative gradually, but the absolute values of the differences between the urban stations and U1 stations also increase, and the maximum difference of average (median) trends even reaches more than 0.400 °C per decade for autumn, with the trend of U6 stations far below those other categories of stations, probably due to the much lower increasing rate of seasonal mean T_{max} than other categories of stations (Figure S5).

3.3. Urbanization Effect for Urban Stations

The urbanization effects on, and contributions to, annual/seasonal mean SAT and DTR change during 1980–2015 gradually strengthen for different groups of urban stations (U3–U6) with the increase of urbanization levels (Table 1; Figure S6). U2 stations are not included in the figure and the table because they have already been taken as reference stations for some of the grid boxes.

Urbanization effects are positive for annual mean T_{min} and T_{mean} for all categories of urban stations during 1980–2015. For annual mean T_{min}, which witnesses a maximum urbanization effect of 0.178 °C per decade for the urban stations with the highest urbanization level (U6), average urbanization contribution is 34.2% (Table 1). The average contributions of annual mean T_{mean} range from 10.3% to 25.0% for urban stations with different urbanization levels. The decrease of annual mean T_{max} difference series is much less than that on the increase of annual T_{min} difference series for urban stations, with effects of urbanization on T_{max} trends range from −0.033 °C per decade for U3 stations to −0.072 °C per decade for U6 stations (Table 1). Therefore, the annual mean DTR difference series have highly significant decline trend. As the urbanization level increases, the urbanization effect on the DTR trends of the urban stations gradually increases, with a maximum urbanization effect of −0.250 °C per decade for U6 stations. Urbanization contributions to the annual and seasonal mean DTR trends reach 100% for all of the urban stations.

The annual mean T_{mean} and T_{min} are more affected by urbanization as mentioned above. On the seasonal scale, the average (median) urbanization effects are more significant on winter, spring, and autumn for urban stations, all reaching more than 0.150 °C per decade for T_{min} (Figure S6). Urbanization contributions to seasonal mean T_{min} trends for U6 are all above 36.0% in cold seasons, and the urbanization contribution to seasonal mean T_{mean} trend for U6 stations also reaches 30.4% in winter (Table S2). The urbanization contributions to seasonal mean T_{max} trends are mainly reflected in the winter, with winter maximum value at 30.8%.

As urbanization level increases, the significant decrease of seasonal mean DTR difference series happens, especially in cold seasons. For example, the average (median) urbanization effects in autumn mean DTR change are −0.100 °C per decade for U3 stations and −0.348 °C per decade for U6 stations (Figure S6). However, though the U3 stations have a low urbanization level, while the contributions in each of the seasons are close or equal to 100%, it may relate to the study region, the grids with U3–U6 were selected to

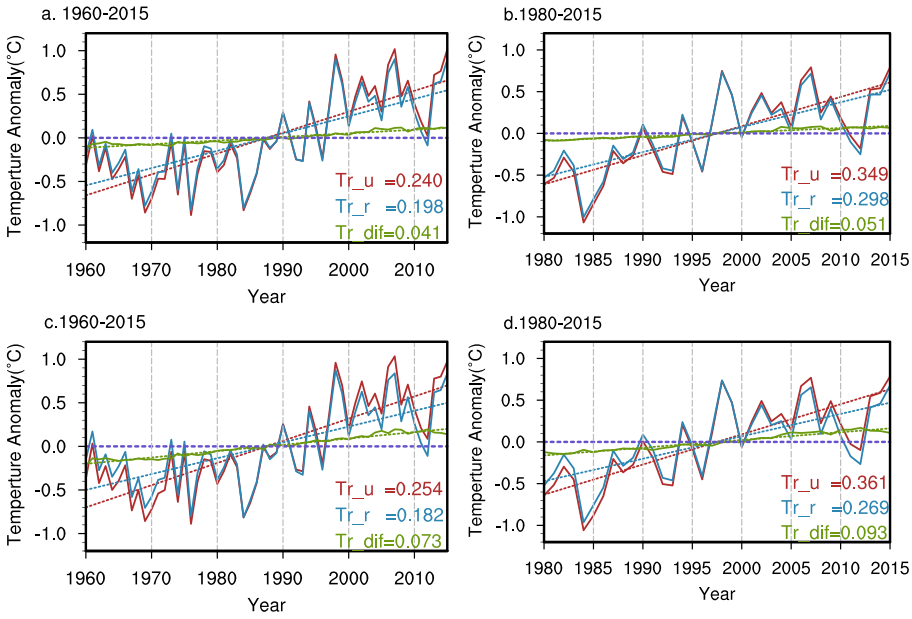

Figure 5. Annual mean T_{mean} anomalies of the stations of RCN + BMN + OMN (a, b) and RCN + BMN (c, d), reference stations, and the differences between national stations and reference stations, during 1960–2015 (a, c) and 1980–2015 (b, d) in mainland China (red lines stand for national stations series, blue lines for reference stations series, and green lines for the difference series; values are the linear trends of the series [unit: °C per decade]).

calculate urbanization effect and contribution, which are mainly distributed in the east of China, the most developed region.

3.4. Urbanization Effect for National Stations

Figure 5 shows annual mean T_{mean} anomalies of the stations of RCN + BMN + OMN (a, b) and RCN + BMN (c, d), the reference stations, and the national stations minus reference stations differences during 1960–2015 (a, c) and 1980–2015 (b, d). The four annual mean T_{mean} difference series all exhibit a statistically significant positive trend, the urbanization effect on the annual mean T_{mean} trend reaches 0.041 °C per decade, and the urbanization contribution is 17.1% in the data series of RCN + BMN + OMN but is 0.073 °C per decade and 28.7% in the data series of RCN + BMN, respectively, during the period 1960–2015 (Figures 5a, 5c, and 6a). In the last three decades, the annual mean urbanization effect reaches 0.051 °C per decade, and the urbanization contribution is 14.6% in RCN + BMN + OMN, but 0.093 °C per decade and 25.8% in RCN + BMN, respectively (Figures 5b, 5d, and 6b). The results of evaluation using the same reference station network show that the urbanization contributions to the annual mean T_{mean} trends in the two data sets differs by 11.6% and 11.2% for the different time periods 1960–2015 and 1980–2015, respectively.

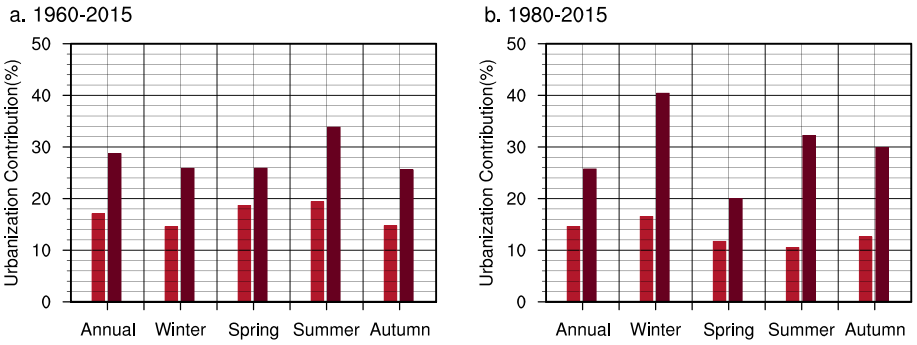

Figure 6. Urbanization contribution to the annual and seasonal mean T_{mean} trends of the national stations of RCN + BMN + OMN (red) and RCN + BMN (purple) for the periods 1960–2015 (a) and 1980–2015 (b).

The urbanization effects on the seasonal mean T_{mean} trends in the data set of RCN + BMN are also larger than those in the data set of RCN + BMN + OMN for the two periods (Figure S7 and Table S3). The range of urbanization effects in the two data sets is 0.032 to 0.087 °C per decade on the seasonal scale during the period 1960–2015. Urbanization effects are largest in winter for both of the RCN + BMN + OMN and RCN + BMN stations for the past 56 years, reaching 0.044 and 0.087 °C per decade, respectively. The smaller seasonal mean urbanization effects occur in summer and autumn (Figure S7). The seasonal characteristic of urbanization effects on the seasonal mean T_{mean} trends is identical in the two time period, but the values are lager for the past 36 years (Figure S7 and Table S3). However, the seasonal characteristic of urbanization contributions to the overall T_{mean} trends shows the difference in two time periods. The highest contribution occurs in warm season for the period 1960–2015, being 19.4% for RCN + BMN + OMN and 33.9% for RCN + BMN in summer; but the largest seasonal mean urbanization contributions, 16.6% and 40.4% for the two data sets, respectively, occur in winter in the period 1980–2015 (Figure 6).

The difference of urbanization effects and contributions in the same temperature data set between the two study periods is notable. After 1980, urbanization is developing more rapidly in mainland China, which has been reflected in the different urbanization effects of the T_{mean} series. At the same time the background change and natural variability of the annual mean T_{mean} series during the last three decades are also larger than those in the longer time period, so the annual mean urbanization contributions in both of the two data sets are generally reduced after 1980 (Figure 6). However, the urbanization contribution just increase greatly in winter, and it may be related to climate warming hiatus.

On the other hand, the different results also appear in two data sets over the same period. The main reason why urbanization effect and contribution are larger in the data series of RCN + BMN than RCN + BMN + OMN is obvious. The stations of RCN + BMN are mostly located in urban areas or margin of big and medium-sized cities because of the historical and unique socioeconomic conditions, which require the weather and climate observations to be near the urban areas as much as possible (Ren et al., 2008, 2015). In case of OMN stations, which accounts for more than two third of the RCN + BMN + OMN stations, the observations are generally made in or near the county capitals which are mostly small cities or towns. In addition, most of the stations in RCN + BMN have been moved for at least one time from urban to suburban areas due to the rapid urbanization process, as compared to the stations of OMN, and the adjustment to the breakpoints of the temperature series or the data inhomogeneity mainly due to relocations would in certain extent recover the urbanization effect that was ever weakened in its original data series (Hansen et al., 1999; Ren et al., 2015; Zhang et al., 2014).

4. Discussion

4.1. Classification Method of Urbanization Level

Compared with the previous studies which used the change of urban land use around the stations to analyze the effect of urbanization on temperature series (Yang, Hou, et al., 2011; Yang, Shi, et al., 2011; Wang & Ge, 2012; He et al., 2007), the method to determine the urbanization level around observational sites developed in this study has taken a comprehensive consideration of both microscale and mesoscale effects of urban land use around the observational sites and also has solved the problem of limited analysis period due to the shorter aft-satellite era for usage of change rate of urban land coverage. We also applied a bigger data set, which is almost three times of the previous data sets in terms of observational stations, for the classification of land use around each of the stations.

Based on the analysis of correlation between the annual mean SAT trends and 20 PULU data in all buffer circles of 2,286 stations, we selected urban land use within buffer less than 16-km radius to assess the effect of urbanization on SAT changes. However, the areas of urban land use around these stations are sometimes larger than 16-km radius buffer circle, for example, in case of Beijing or Shanghai cities (Figure 1). We only considered the average status of area of the urban land use around all stations in mainland China, but for stations that still have urban land use in a buffer circle radius greater than 16 km, this may influence the classification results of these stations. Additionally, the selected reference stations (U1) may have been affected in certain extent by the urbanization, though the effect would be substantially small compared to those of the urban stations. At the same time, not all grid boxes have U1 stations as reference, and about 41% grids used

U2 as the reference stations when estimating urbanization effect in the data sets. Therefore, the evaluation results of urbanization effect with U2 as the reference stations would be underestimated compared with those with U1 as the reference stations. As a result, the urbanization effect and contribution as shown in this paper should be regarded as conservative. Another potential source of uncertainties would be the homogenization of the data. Because the stations moved usually from the urban areas to the suburban areas, the urbanization effect on the data series will be restored after homogenization by using the generally applied methodologies (Ren et al., 2015; Zhang et al., 2014). However, the land use data are still for the current observational sites, leading to a mismatch sometimes between the urban warming rates and the PULU around the observational grounds. Although this would have a small impact on the determination of their correlations, reference stations, and urban stations, the urban indicator should be further completed to consider the exact positions of the historical observational sites. This issue should be emphasized especially when the samples (stations) for use are insufficient. However, the above uncertainties can be reduced when the method is applied in less developed regions or in regions where enough stations are available for selecting reference observational data series.

Overall, the method took relative area of urban land use around the meteorological observational site at varied spatial scales as indicator of urbanization to analyze urbanization effect on, and contribution to, the trend of temperature data series at urban and national stations, showing analysis results comparable to those by using other sophisticated procedures as described below. Therefore, it has a good potential to be applied in the future for the studies of urbanization effect in the long-term SAT data series in regional and global land scales.

4.2. Compared with Other Analyses in Mainland China

Compared with the results of Sun et al. (2016) based on the RCN + BMN + OMN data set, the conclusion in this study is slightly smaller than theirs that showed a one-third urbanization contribution to the linear trend of annual mean SAT in the past 50 years (Table S4). This may be related to the different methods used to attribute the locally anthropogenic forcing to SAT change. Sun et al. (2016) applied the optimal fingerprinting approach to evaluate anthropogenic influences including urban warming by examining if an observed SAT change is significantly larger than that expected from internal variability and if the observed SAT trend is consistent with that simulated by climate models, while this study used the urban minus rural method to directly assess the urbanization effect. The two procedures have their own advantages and disadvantages, and the results derived from them would be different. However, our analysis might have produced an underestimate of the urbanization effect because the selected reference stations might have been affected by urbanization in a less extent, and the result in our analysis should be regarded as a conservative estimate.

It is therefore noteworthy that, due to the remnants of urbanization effect in the data series of the reference stations used in this study, the urbanization effect and contribution at the stations other than reference stations given in this paper should be regarded as the lowest estimates, and the real values would be higher than the results.

For the analyzing results by using the RCN + BMN data set, no result based on the optimal fingerprinting approach is available for time being. As for the studies by using the urban minus rural method, the selected reference stations are various due to the varied procedures used for determining the rural observational sites, and the inconsistency of study period may also lead to slightly different results. However, the result in this study is approximately consistent with the previous ones when the homogenized RCN + BMN data set were used (Table S4). Majority of the results stayed between 20% and 30% in the past 50 years or so, but all the estimates should be lower than the true values. As there was no any previous study which had used the same method to analyze urbanization effect and contribution in the SAT series of the different data sets in mainland China, however, there is no analysis result available to be strictly compared with here.

Figure S8 presents the growing condition of the urban land use in the buffer circle of 16-km radius around two meteorological stations without any relocation during 1980–2015, which are located in the typical medium-sized cities of Beijing-Tianjin-Hebei region and the Pearl River Delta, respectively. There were significant urban land expansions around the two stations since early 1990s, and PULU in 16-km radius buffer circles are close to or exceeded 50% in 2015, which shows that the impacts of urbanization on the

observational environment are evident at the observational sites. Other urban stations in mainland China also experience similar change in land cover around the observational grounds during the past decades in varied extents.

Figure S9 shows the averaged PULU within 8-km radius buffer circle around the 2,419 observational stations during 1980–2015. The 8-km buffer radius is selected to show some consideration for the majority of small cities in the data set. The PULU at a local scale around all stations in RCN + BMN + OMN data set for each of the buffer circles in 1980, 1990, 1995, 2000, 2005, 2010, and 2015 were calculated. The annual average values of all the stations for all buffer circles show the remarkable increase of PULU around stations since the early 1980s, from 4% in 1980 to 10% in 2015 (Figure S9). However, the results also show that the urbanization process around the observational sites was nonlinear during the period 1980–2015, with the more strong urbanization processes found during 2000–2005 and 2010–2015, respectively. After 2010, the increase of the average PULU becomes very strong.

Therefore, on one hand, under the background of the large-scale climate change and variability, urbanization development in the whole time periods of 1980–2015 and 1960–2015 may have strengthened the urban heat intensity around the observational stations, leading to a consistent SAT rising in addition to the global and regional warming. On the other hand, the urbanization effect in different periods may have been different for individual and regional SAT series due to the nonlinear characteristics of urban land use variation. Moreover, we should give attention not only to the regional average SAT series caused by urbanization in the different data set and periods but also to the unbalanced spatial pattern of the urbanization effect in the country.

5. Conclusions

This study presented a new satellite-based methodology to classify the observational stations in mainland China and shows the analysis results of urbanization effect and contribution in the annual and seasonal mean SAT series of urban stations and different categories of national stations for varied periods over mainland China, based on the new methodology. The following conclusions can be drawn:

The percentage of built-up area in different buffer circles around the observational sites can be considered as a good indicator for the comprehensive urbanization level of a station and can be used to classify stations and also to select reference temperature stations for assessing the urbanization effect on the SAT data series of urban and national stations.

Correlation coefficients between the annual mean SAT trends of 1980–2015 and the PULU in each of the buffer circles with radius from 1 to 16 km are all highly significant (≥99.9% confidence level) for the 2,286 stations in mainland China. The highest correlation was found when the radius of buffer circle was 4 km. The urbanization indicator in this study considers the effect of urban land use around the observational sites at both microscale and mesoscale.

All stations are classified as six categories, or U1, U2, U3, U4, U5, and U6, respectively, in order of increasing urbanization levels. The largest increase in annual mean SAT occurred at the stations affected by urbanization of the highest level (U6) during 1980–2015, and the U1 stations registered the smallest annual mean SAT trends. Winter, spring, and autumn mean SAT had a larger warming rate and are more sensitive to the urbanization level.

During the period of 1980–2015, urbanization contribution to annual mean surface SAT trends ranges from 10.3% to 25.0% for urban stations (U3–U6); urbanization effect and contribution are larger and more significant in the annual mean minimum SAT series, with a maximum urbanization effect and contribution of 0.178 °C per decade and 34.2% for U6 stations; urbanization led to a nonsignificant negative impact on annual mean maximum SAT trends, and a highly significant decline of annual mean DTR trends. The urbanization contribution to the downward trends of annual mean DTR reaches 100% for all urbanization level of stations (U3–U6).

The assessment of national stations using U1 and U2 stations as reference shows significant but different urbanization effects in the annual mean SAT trends. Larger urbanization effect and contribution for the national reference climate and basic meteorological station networks (RCN + BMN) than those on all the national stations (RCN + BMN + OMN) for both 1960–2015 and 1980–2015 are found. During the two

periods, the urbanization contributions are 28.7% and 25.8%, respectively, for annual mean SAT trends of RCN + BMN, and they are 17.1% and 14.6% for all the national stations.

Acknowledgments
The land use/land cover data set of mainland China is provided by the Resources and Environmental Sciences Data Center (RESDC), Chinese Academy of Sciences (CAS) (www.resdc.cn/data.aspx?DATAID=184). The monthly surface air temperature data set is provided by the National Meteorological Information Center (NMIC), China Meteorological Administration (CMA) (http://data.cma.cn/data/detail/dataCode/A.0029.0004.html). This work is supported by the National Key R&D Program (2018YFA0605603) and the Natural Science Foundation of China (NSFC; 41575003).

References

Brohan, P., Kennedy, J. J., Harris, I., Tett, S. F. B., & Jones, P. D. (2006). Uncertainty estimates in regional and global observed temperature changes: A new dataset from 1850. *Journal of Geophysical Research*, *111*, D12106. https://doi.org/10.1029/2005JD006548

Cao, L. J., Zhu, Y. N., Tang, G. L., Yuan, F., & Yan, Z. W. (2016). Climatic warming in China according to a homogenized data set from 2419 stations. *International Journal of Climatology*, *36*(13), 4384–4392. https://doi.org/10.1002/joc.4639

Cardelino, C. A., & Chameides, W. L. (1990). Natural hydrocarbons, urbanization, and urban ozone. *Journal of Geophysical Research*, *95*, 13971. https://doi.org/10.1029/JD095iD09p13971

Chu, Z. Y., & Ren, G. Y. (2005). Effect of enhanced urban heat island magnitude on average surface air temperature series in Beijing region. *Acta Meteorologica Sinica*, *63*, 534–540. In Chinese

Committee of Chinese National Assessment (2016). *Report on Climate Change Third China's National Assessment Report on Climate Change*, Beijing: China Science Press. (In Chinese)

Gallo, K., & Xian, G. (2016). Changes in satellite-derived impervious surface area at US historical climatology network stations. *ISPRS Journal of Photogrammetry and Remote Sensing*, *120*, 77–83, 83. https://doi.org/10.1016/j.isprsjprs.2016.08.006

Gallo, K. P., Adegoke, J. O., Owen, T. W., & Elvidge, C. D. (2002). Satellite-based detection of global urban heat-island temperature influence. *Journal of Geophysical Research*, *107*(D24), 4776. https://doi.org/10.1029/2002JD002588

Gallo, K. P., Easterling, D. R., & Peterson, T. C. (1996). The influence of land use/land cover on climatological values of the diurnal temperature range. *Journal of Climate*, *9*(11), 2941–2944. https://doi.org/10.1175/1520-0442(1996)009<2941:TIOLUC>2.0.CO;2

Gallo, K. P., McNab, A. L., Karl, T. R., Brown, J. F., Hood, J. J., & Tarpley, J. D. (1993). The use of a vegetation index for assessment of the urban heat island effect. *Journal of Applied Meteorology*, *32*, 899–908. https://doi.org/10.1080/01431169308954031

Gallo, K. P., Owen, T. W., Easterling, D. R., & Jamason, P. F. (1999). Temperature trends of the U.S. Historical Climatology Network based on satellite-designated land use/land cover. *Journal of Climate*, *12*(5), 1344–1348. https://doi.org/10.1175/1520-0442(1999)012<1344:TTOTUS>2.0.CO;2

Hansen, J., Ruedy, R., Glascoe, J., & Sato, M. (1999). GISS analysis of surface temperature change. *Journal of Geophysical Research*, *104*(D24), 30,997–31,022. https://doi.org/10.1029/1999JD900835

Hansen, J., Ruedy, R., Sato, M., Imhoff, M., Lawrence, W., Easterling, D., et al. (2001). A closer look at United States and global surface temperature change. *Journal of Geophysical Research*, *106*(D20), 23,947–23,963. https://doi.org/10.1029/2001JD000354

Hansen, J., Ruedy, R., Sato, M., & Lo, K. (2010). Global surface temperature change. *Reviews of Geophysics*, *48*, RG4004. https://doi.org/10.1029/2010RG000345

Hartmann, D. L., Klein Tank, A. M. G., Rusticucci, M., Alexander, L. V., Brönimann, S., Charabi, Y., et al. (2013). Observations: Atmosphere and surface. In T. F. Stocker et al. (Eds.), *Climate change 2013: The physical science basis. Contribution of Working Group I to the Fifth Assessment Report of the Intergovernmental Panel on Climate Change* (Chap. 2, pp. 31–39). Cambridge, United Kingdom, and New York: Cambridge University Press.

He, J., Liu, J., Zhuang, D., Zhang, W., & Liu, M. (2007). Assessing the effect of land use/land cover change on the change of urban heat island intensity. *Theoretical and Applied Climatology*, *90*, 217–226. https://doi.org/10.1007/s00704-006-0273-1

He, Y. T., Jia, G. S., Hu, Y. Y., & Zhou, Z. J. (2013). Detecting urban warming signals in climate records. *Advances in Atmospheric Sciences*, *30*, 1143–1153. https://doi.org/10.1007/s00376-012-2135-3

Hinkel, K. M., & Nelson, F. E. (2007). Anthropogenic heat island at Barrow, Alaska, during winter: 2001–2005. *Journal of Geophysical Research*, *112*, D06118. https://doi.org/10.1029/2006JD007837

Hua, L. J., Ma, Z. G., & Guo, W. D. (2008). The impact of urbanizationon air temperature across China. *Theoretical and Applied Climatology*, *93*(3-4), 179–194. https://doi.org/10.1007/s00704-007-0339-8

Intergovernmental Panel on Climate Change (2013). Summary for policymakers. In T. F. Stocker, D. Qin, G. K. Plattner, M. Tignor, S. K. Allen, J. Boschung, A. Nauels, Y. Xia, V. Bex, & P. M. Midgley (Eds.), *Climate change 2013: The physical science basis. Contribution of Working Group I to the Fifth Assessment Report of the Intergovernmental Panel on Climate Change*. Cambridge: Cambridge University Press.

Jones, P. D., Lister, D. H., & Li, Q. (2008). Urbanization effects in large-scale temperature records, with an emphasis on China. *Journal of Geophysical Research*, *113*, D16122. https://doi.org/10.1029/2008JD009916

Jones, P. D., Ya, P., Groisman, M. C., Plummer, N., Wang, W. C., & Karl, T. R. (1990). Assessment of urbanization effects in time series of surface air temperature over land. *Nature*, *347*(6289), 169–172. https://doi.org/10.1038/347169a0

Kalnay, E., & Cai, M. (2003). Impact of urbanization and land-use change on climate. *Nature*, *423*(6939), 528–531. https://doi.org/10.1038/nature01675

Lawrimore, J. H., Menne, M. J.,Gleason, B. E., Williams, C. N., Wuertz, D. B., Vose, R. S., & Rennie, J. (2011). An overview of the global historical climatology network monthly mean temperature data set, version 3. *Journal of Geophysical Research Atmospheres*, *116*, D19121. https://doi.org/10.1029/2011JD016187

Li, Y., Wang, L., & Zhou, H. (2018). Urbanization effects on changes in the observed air temperatures during 1977–2014 in China. *International Journal of Climatology*, *39*(1), 251–265. https://doi.org/10.1002/joc.5802

Mete, T., Karaca, M., & Yenigün, O. (1997). Annual and seasonal air temperature trend patterns of climate change and urbanization effects in relation to air pollutants in Turkey. *Journal of Geophysical Research*, *102*(D2), 1909–1919. https://doi.org/10.1029/96JD02108

Owen, T. W., Gallo, K. P., Elvidge, C. D., & Baugh, K. E. (1998). Using DMSP-OLS light frequency data to categorize urban environments associated with US climate observing stations. *International Journal of Remote Sensing*, *19*(17), 3451–3456. https://doi.org/10.1080/014311698214127

Peterson, T. C. (2003). Assessment of urban versus rural in situ surface temperatures in the contiguous United States: No difference found. *Journal of Climate*, *16*, 2941–2959. https://doi.org/10.1175/1520-0442(2003)0162.0.CO;2

Peterson, T. C., Gallo, K. P., Lawrimore, J., Owen, T. W., & Huang, A. (1999). Global rural temperature trends. *Geophysical Research Letters*, *26*, 329–332. https://doi.org/10.1029/1998gl900322

Portman, D. A. (1993). Identifying and correcting urban bias in regional time series: Surface temperature in China's northern plains. *Journal of Climate*, *6*(12), 2298–2308. https://doi.org/10.1175/1520-0442(1993)006<2298:IACUBI>2.0.CO;2

Rai, A., Joshi, M. K., & Pandey, A. C. (2012). Variations in diurnal temperature range over India: Under global warming scenario. *Journal of Geophysical Research*, *117*, D02114. https://doi.org/10.1029/2011JD016697

Ren, G. Y., Xu, M. Z., Chu, Z. Y., Guo, J., Li, X. Q., Liu, X. N., et al. (2005). Climate changes of China mainland over the past half century. *Climatic and Environmental Research*, *63*, 942–956. (In Chinese)

Ren, G. Y., Chu, Z. Y., Chen, Z., & Ren, Y. Y. (2007). Implications of temporal change in urban heat island intensity observed at Beijing and Wuhan stations. *Geophysical Research Letters*, *34*, L05711. https://doi.org/10.1029/2006GL027927

Ren, G. Y., Zhou, Y. Q., Chu, Z. Y., Zhou, J. X., Zhang, A. Y., Guo, J., & Liu, X. F. (2008). Urbanization effects on observed surface air temperature trends in North China. *Journal of Climate*, *21*, 1333–1348. https://doi.org/10.1175/2007JCLI1348.1

Ren, G. Y., Ding, Y. H., Zhao, Z. C., Zheng, J. Y., Wu, T. W., Tang, G. L., & Xu, Y. (2012). Progess in studies of climate change in China. *Advances in Atmospheric Sciences*, *29*, 958–977.

Ren, G. Y., & Zhou, Y. Q. (2014). Urbanization effect on trends of extreme temperature indices of national stations over Mainland China, 1961–2008. *Journal of Climate*, *27*, 2340–2360. https://doi.org/10.1175/JCLI-D-13-00393.1

Ren, G. Y., Li, J., Ren, Y. Y., Chu, Z. Y., Zhang, A. Y., Zhou, Y. Q., et al. (2015). An integrated procedure to determine a reference station network for evaluating and adjusting urban bias in surface air temperature data. *Journal of Applied Meteorology and Climatology*, *54*, 1248–1266. https://doi.org/10.1175/JAMC-D-14-0295.1

Ren, Y. Y., & Ren, G. Y. (2011). A remote-sensing method of selecting reference stations for evaluating urbanization effect on surface air temperature trends. *Journal of Climate*, *24*, 3179–3189. https://doi.org/10.1175/2010JCLI3658.1

Stewart, I. D., & Oke, T. R. (2012). Local climate zones for urban temperature studies. *Bulletin of the American Meteorological Society*, *93*(12), 1879–1900. https://doi.org/10.1175/BAMS-D-11-00019.1

Sun, Y., Zhang, X. B., Ren, G. Y., Zwiers, F. W., & Hu, T. (2016). Contribution of urbanization to warming in China. *Nature Climate Change*, *6*(7), 706–709. https://doi.org/10.1038/nclimate2956

Von Storchn, H., & Navarra, H. A. (1999). *Analysis of climate variability—Applications of statistical techniques*, (pp. 15–18). Berlin Heidelberg: Springer-Verlag. https://doi.org/10.1016/S1364-6826(97)87052-6

Wang, F., & Ge, Q. S. (2012). Estimating urban heat island effect in China from 1980 to 2009 based on satellite land use changes. *China Science Bulletion*, *57*(14), 1708–1715. https://doi.org/10.1007/s11434-012-4999-0

Wang, K., & Dickinson, R. E. (2013). Contribution of solar radiation to decadal temperature variability over land. *Proceedings of the National Academy of Sciences*, *110*(37), 14,877–14,882. https://doi.org/10.1073/pnas.1311433110

Wen, K. M., Ren, G. Y., Li, J., Zhang, A. Y., Ren, Y. Y., Sun, X. B., & Zhou, Y. Q. (2019). Recent surface air temperature change over mainland China based on an urbanization-bias adjusted dataset. *Journal of Climate*, *32*(10), 2691–2705. https://doi.org/10.1175/JCLI-D-18-0395.1

Xu, X. L., Liu, J. Y., Zhang, S. W., Li, R. D., Yan, C. Z., & Wu, S. X.. (2018). China multiple periods of land use land cover remote sensing monitoring dataset. Chinese Academy of Sciences, Resources and Environment Science Data Center Data Registration and Publication System (http://www.resdc.cn/DOI), https://doi.org/10.12078/2018070201

Yang, X., Hou, Y., & Chen, B. (2011). Observed surface warming induced by urbanization in east China. *Journal of Geophysical Research*, *116*, D14113. https://doi.org/10.1029/2010JD015452

Yang, Y. J., Shi, T., Tang, W. A., Wu, B. W., Xun, S. P., & Zhang, H. Q. (2011). Study of observational environment of meteorological station based on remote sensing: Cases in six stations of Anhui province. *Remote Sensing Technology and Application*, *26*, 791–797. (In Chinese)

Yang, Y. J., Wu, B. W., Shi, C. E., Zhou, J. H., Li, Y. B., Tang, W. A., et al. (2013). Impacts of urbanization and station-relocation on surface air temperature series in Anhui Province. *Pure and Applied Geophysics*, *170*(11), 1969–1983. https://doi.org/10.1007/s00024-012-0619-9

Zhang, A. Y., Ren, G. Y., Zhou, J. X., Chu, Z. Y., Ren, Y. Y., & Tang, G. L. (2010). Urbanization effect on surface air temperature trends over China. *Acta Meteorologica Sinica*, *68*, 957–966. (In Chinese)

Zhang, H., Wang, Z. L., Wang, Z. Z., Liu, Q., Gong, S., Zhang, X., et al. (2012). Simulation of direct radiative forcing of aerosols and their effects on East Asian climate using an interactive AGCM-aerosol coupled system. *Climate Dynamics*, *38*(7-8), 1675–1693. https://doi.org/10.1007/s00382-011-1131-0

Zhang, L., Ren, G. Y., Ren, Y. Y., Zhang, A. Y., Chu, Z. Y., & Zhou, Y. Q. (2014). Effect of data homogenization on estimate of temperature trend: A case of Huairou station in Beijing Municipality. *Theoretical and Applied Climatology*, *115*(3-4), 365–373. https://doi.org/10.1007/s00704-013-0894-0

Zhou, L. M., Dickinson, R. E., Tian, Y. H., Fang, J. Y., Li, Q. X., Kaufman, R. K., et al. (2004). Evidence for a significant urbanization effect on climate in China. *Proceedings of the National Academy of Sciences*, *101*(26), 9540–9544. https://doi.org/10.1073/pnas.0400357101

Zhou, Y. Q., & Ren, G. Y. (2005). Identifying and correcting urban bias for regional surface air temperature series of north China over period of 1961–2000. *Climatic Environment Research*, *21*(1), 95–102. https://doi.org/10.1007/s10409-004-0010-x

atmosphere

MDPI

Article

Changes in Means and Extreme Events of Sea Surface Temperature in the East China Seas Based on Satellite Data from 1982 to 2017

Qingyuan Wang [1], Yan Li [2], Qingquan Li [3,4,*], Yiwei Liu [1] and Ya-nan Wang [1]

1 Tianjin Meteorological Observatory, Tianjin 300074, China; wqyjx417@163.com (Q.W.); liuyiwei1983@aliyun.com (Y.L.); wang_ya_nan05@126.com (Y.-n.W.)
2 National Marine Data and Information Service, Tianjin 300171, China; ly_nmdis@163.com
3 Laboratory for Climate Studies, National Climate Center, China Meteorological Administration, Beijing 100081, China
4 Collaborative Innovation Center on Forecast and Evaluation of Meteorological Disasters (CIC-FEMD), Nanjing University of Information Science & Technology, Nanjing 210044, China
* Correspondence: liqq@cma.gov.cn

Received: 7 January 2019; Accepted: 5 March 2019; Published: 14 March 2019



Abstract: Marginal seas are fundamental to humans for their importance in mariculture resources and commerce. Based on the NOAA 0.25 degree daily Optimum Interpolation (OI) sea surface temperature (SST) data set, spatiotemporal changes in mean and extreme SST in the East China Seas (ECSs) were examined for from 1982 to 2017. As a regional average, the annual mean SST has notably increased at a rate of 0.21 ± 0.08 °C per decade. The warming SST during 1982–2017 is probably related to the influence from a recent strengthening and westward extension of the WPSH. There are also notable warming trends in annual minimum and maximum SST. Spatially, the rapid warming of annual mean SSTs are located in the vicinity of the Yangtze Estuary, exceeding 0.2 °C per decade and part of the ECS-Kuroshio. This pattern may be largely affected by the spatial changes of minimum SST. Rapid warming of maximum SST can be found across the region, from the northern East China Sea (ECS) to the Bohai Sea. Since 1982, extreme hot days (EHDs) have undergone an obvious increasing trend, at a rate of 15.2 days per decade. Conversely, extreme cold days (ECDs) have been decreasing. Notably, the largest increase of EHDs appears in the western ECS and the Bohai Sea, which both have rich marine ecosystems. The trend of EHDs has a significant relationship to mean SST, suggesting that there will be a further increase in EHDs under continued warming in the ECSs. These findings emphasize the importance and urgency of strategies which should be planned for the adaptation and mitigation of specific types of extreme hot events in this region.

Keywords: sea surface temperature (SST); extreme hot days (EHDs); extreme cold days (ECDs); warming

1. Introduction

Sea surface temperature (SST) is considered to be one of the most important indicators in quantifying climate change [1]. A rapid warming is expected to have a large impact on regional marine biodiversity, both at the ecosystem level and at the population level [2]. The Fifth Assessment Report of the Intergovernmental Panel on Climate Change affirmed that our warming of the climate system is unequivocal and its extremes are also changing [3]. To better adapt to climate warming and decision-making, an improved and detailed understanding of regional climate changes is required.

Part of the Northwest Pacific Ocean, the Bohai Sea, Yellow Sea, and East China Sea (ECSs) is located at one of the largest continental shelves in the world, with a large number of estuaries, gulfs, freshwater inputs, and maricultures. There have been much literature focused on the SST

variability over the China Seas [4–8]. They found that the mean warming in the China Seas has been considerably faster than the global average. In addition, the ECSs are vulnerable to climate change, especially changes in climate extremes [4,6,9]. However, the previous studies covering the China Seas typically used reconstructed or reanalyzed monthly mean SST data sets. The detailed extreme hot and cold SST changes and their relationship with changes in SST annual ranges (ARs) remain unknown, owing to the lower spatial and temporal resolution of data sets. At present, extreme water temperature events can cause shifts in species ranges, local extinctions, and economic loss on aquaculture and seafood industries [9–11]. For instance, the rapid warming of the ECSs has been linked to frequent occurrences of harmful algae blooms and northward shifts of marine fishes [12]. A Chinese Marine Disaster Bulletin from 2012 [13] indicated that severely harmful algae occurred at the coast of the southern ECS, causing a direct economic loss of two billion RMB. Changes in the SST at shorter than seasonal scales and variations in the frequency of SST extreme events in sub-region scales should be taken into account when planning for strategies to mitigate these changes. Thus, the present study adds some new insights into understanding the inter-annual variations of annual mean, annual minimum, annual maximum SSTs, and AR averaged of the ECSs and spatial distribution of trends in the ECSs from 1982 to 2017. Meanwhile, extreme hot and cold events are also detected in detail during the study period. Finally, we will discuss the possible preliminary impacts on marine fisheries. The information through our work will improve the understanding of the hydrography and climate trends in this region and benefit fisheries and marine biological research.

The remainder of the paper is organized as follows. Following the introduction, Section 2 briefly introduces the study region, data sources, and methods. Section 3 describes the changes of mean SST and extreme SST. Changes in extreme events are conducted in the following section. A summary and discussion are given in Section 5.

2. Study Region, Data Source and Methods

2.1. Study Region

The study region including the Bohai Sea, the Yellow Sea, and the East China Sea (ECS) is bounded by China, the Ryukyu (Nansei) Islands, Kyushu, and the Korean Peninsula (Figure 1). The study region also covered a vicinity area in order to show a better perspective for the SST variability, such as the SST variability in the ECS-Kuroshio. Thus, we approximated the study region in a range of 116–132° E and 22–42° N.

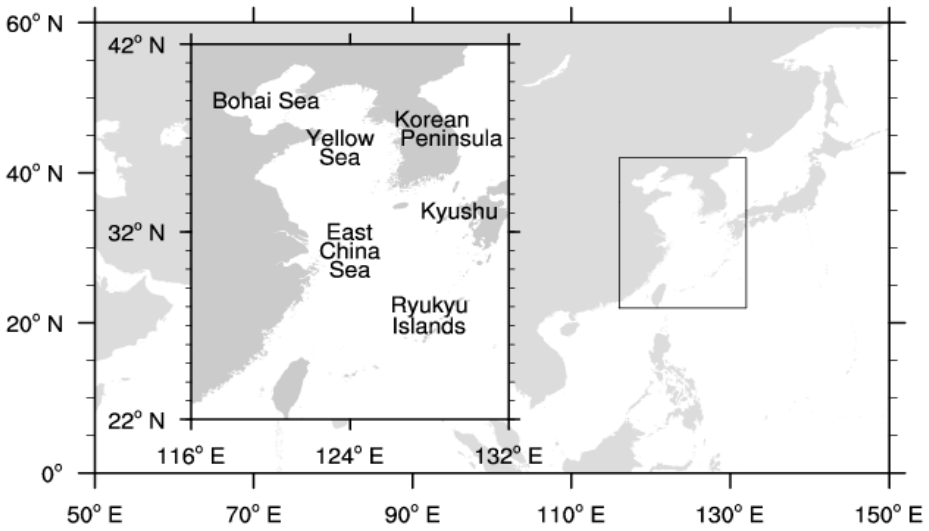

Figure 1. Map showing the geographical location of the study region, including the Bohai Sea, the Yellow Sea, the East China Sea, and adjacent seas.

2.2. Data Source

A daily SST data set was acquired from the NOAA National Climatic Data Center (NCDC), available at https://www.ncdc.noaa.gov/oisst with a high spatial resolution of 0.25° × 0.25° from 1982–2017 [14]. This data set is derived from the Optimum Interpolation (OI) SST Analysis Product, referred herein as OISST v2, which uses SST data from an advanced very high-resolution radiometer infrared satellite from the Pathfinder satellite combined with buoy data, ship data, and sea ice data SST data sets. In order to apply the correction for bias in OISST, the satellite data have been classified into daytime and nighttime bins and corrected separately using the patterns of 15 days averaged by in situ SSTs using NOAA's OI algorithm. The bias-corrected daytime and nighttime satellite SST, ship, and buoy SSTs are merged based on noise-to-signal ratio maps for each data type, which have averaged weights of 15.1, 15.1, 1.0, and 15.1, respectively. Therefore, it can be interpreted as the bulk SST at about 0.5 m depth [15].

In this paper, we use the Taylor diagram to provide a statistical summary of how well the OISST v2 represents the 19 stations-based observations along the coastal ECSs. In order to do the comparison and evaluation, OISST v2 has been interpolated to the stations' locations. The correlation and standard deviation on the annual basis are computed and shown in a Taylor diagram (Figure 2). As seen in Figure 2, OISST v2 are clustered around the reference values (REF), except for 4 points (points 3, 13, 14, and 18). Most of them have positive correlations with observations in the range of 0.5~0.9. A total of 79% of these points has a lower standard deviation and smaller root mean square error, which suggests that OISST and in situ water temperatures in the coast area of China agree reasonably well. Additional analysis (not shown here) indicated that there is no statistically significant trend in the differences between the long-term water temperature records. OISST is currently the longest satellite data record that can be used to study long-term SST variability. This data set has been widely used in scientific researches [16–19]. The suitability of the data base to identify extreme events was previously shown in work of Lima and Wethdy and Liao et al. [16,20].

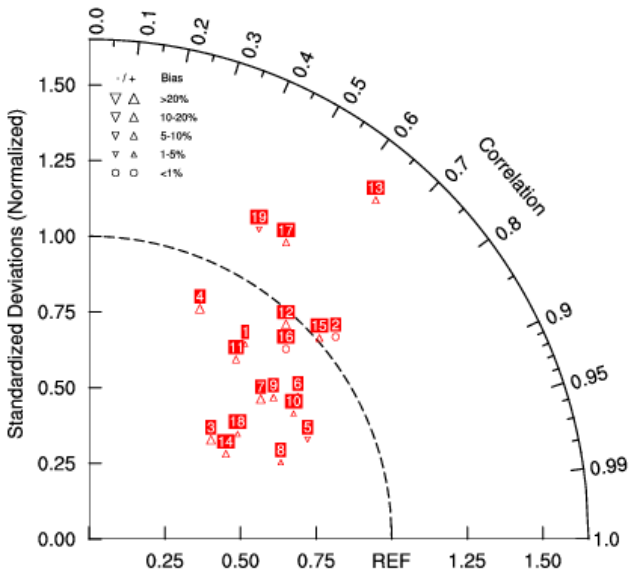

Figure 2. Taylor diagram of the annual mean SSTs from OISST v2 compared with 19 stations-based observations, REF stands for reference values of SST observations. The radial distance from the origin is proportional to the standard deviation ratio. The triangles and circle denote the bias between OISST and stations-based observations.

2.3. Annual Frequency of Extremely Cold and Hot Days

Extreme days were carried out for each pixel as follows: daily SST anomalies were calculated to remove the seasonal cycle. This was achieved by subtracting from the SST of a certain day (e.g.,

January 1, 1982) the mean temperature of that day (January 1) of the climatic baseline period of 1982–2011 [17,21]. Therefore, an extreme day can occur at any time of the year. An EHD (or ECD) is defined as a day with its SST anomaly above (or below for ECDs) the 90th (or 10th for ECDs) percentile of standardized anomaly of the climatic baseline period. Then, the number of EHDs (or ECDs) was calculated as the number of days per year with extremely high (low for ECDs) SST anomalies.

2.4. Testing for Significance of Correlations and Trends

When test the significance of correlation between two time series and the significance of the presence of trends in a time series, an important question requires consideration: how large sample correlations and sample trends need to be, even if the stochastic processes, which generate the series, are not correlated at all and exhibit no trends. Firstly, we have to make an assumption, namely the processes X and Y share no correlation, or segments of length L of the process have no trend. Standard procedures are available in the literature, namely p values for correlations and Mann–Kendall for trends [22,23] when there are "no correlations" between the underlying processes and trends can hardly appear in limited segments of an infinite stationary time series.

In the case of correlations, the assumption is that the underlying processes are stationary (free of systematic trends) and serially independent, that is, X_t and X_{t+1} for any t are independent. In the case of trends, the assumption is the independence of X'_t. However, in geophysical cases, these assumptions are not satisfied—the result is that the null hypotheses are more often falsely rejected (i.e., in cases where there are no correlations or no trends [22] than stipulated by the significance level (normally 5%).

A practical remedy for avoiding such errors is to deal with normalized series (mean = 0, standard deviation = 1) X'_t (and Y'_t) as follows:

(1) "detrend" the time series before testing for correlations between two time series X_t and Y_t. Firstly, determining the linear fit f_t^X and f_t^Y, and then do the hypothesis testing with $X'_t = X_t - f_t^X$ and $Y'_t = Y_t - f_t^Y$

(2) "prewhiten" the time series, by first determining the sample autocorrelation $\alpha = 1/L\sum_t X_t X_{t+1}$ of the time series X_t of length L, and forming a series $X'_t = X_t - \alpha X_t$, and then testing for the null hypothesis of no trend.

For both cases, the standard routines are applied. If the null hypothesis is rejected at the stipulated significance level of 5%, then the sample trend f_t^X, or the sample correlation $1/L\sum_t X_t X_{t+1}$, is considered "significant".

3. Annual SST Changes

Figure 3 shows the time series of regional averaged annual mean SST, maximum SST and minimum SST anomalies in the ECS from 1982 to 2017, as well as AR SST, which was defined as the difference between the annual maximum SST and minimum SST. The annual mean SST increased at a rate of 0.21 ± 0.08 °C per decade, significant at the 95% level ($p < 0.05$) (Figure 3a). The warming trend is higher than the global average SST warming rate of 0.15 ± 0.03 °C per decade from 1982 to 2017. Moreover, we found that the largest annual mean SST anomaly appeared in 1998, followed by the second largest SST anomaly in 2016. Both of the 1997/1998 and 2015/2016 El Niño events are by far the strongest El Niño events since the beginning of the 20th century [24,25]. The SST peaks were probably caused by the low-frequency El Niño/Southern Oscillation (ENSO) variabilities [26,27]. When ENSO is closely related to the East Asian Monsoon [28,29], it can lead to weaker than normal East Asian Winter Monsoon (EAWM) and a stronger west Pacific subtropical high (WPSH) [8,30–32], and also favors an abnormally high SST in the marginal seas.

The general warming may have been mainly caused by anthropogenic increase in atmospheric CO_2 concentration [33], and partly by the urbanization effect around the observational stations. In this subsection, however, we further analyzed the possible relationship between the warming and the large-scale atmosphere circulation modes. As shown in Figure 4a–c, the WPSH indices of

area and intensity notably increased during 1982–2017, in contrast to the westward extension index, which notably decreased with the longitude of the western edge of the WPSH ridge decreasing. The strengthening and westward extension of the WPSH could have caused strong descending motion and contributed considerably to the surface warming in study region. It is clear that the EAWM index shifted through several phases during 1982–2017 (Figure 4d). The EAWM index decreased during 1982–1997 and increased notably after 1998. During this whole period, there was no significant tendency for the EAWM index. Thus, an increasing SST during 1982–2017 is probably related to the influence from the recent strengthening and westward extension of the WPSH.

To better examine changes in the minimum and maximum SST over time, statistical distribution of the annual mean SST at two 18-year periods were calculated; one covering 1982–1999, and the other one covering 2000–2017 (Figure omitted). A shift in the annual mean SST was noticeable. The mean SST shifted by 0.35 °C, from 20.62 °C to 20.97 °C. Slight changes in mean climate can cause disproportionally larger changes in the intensity and frequency of extremes [34,35]. During this study period, the increasing rate of the annual minimum SST anomalies is 0.21 ± 0.18 °C per decade, significant at the 95% level ($p < 0.05$) (Figure 3b). The annual maximum SST increased at a rate of 0.20 ± 0.13 °C per decade, significant at the 95% level ($p < 0.05$) (Figure 3c). However, during the studied period, regional averaged AR SST showed an insignificant decreasing range trend of −0.02 ± 0.02 °C per decade (Figure 3d), which may due to the similar warming amplitudes of annual maximum and minimum SST.

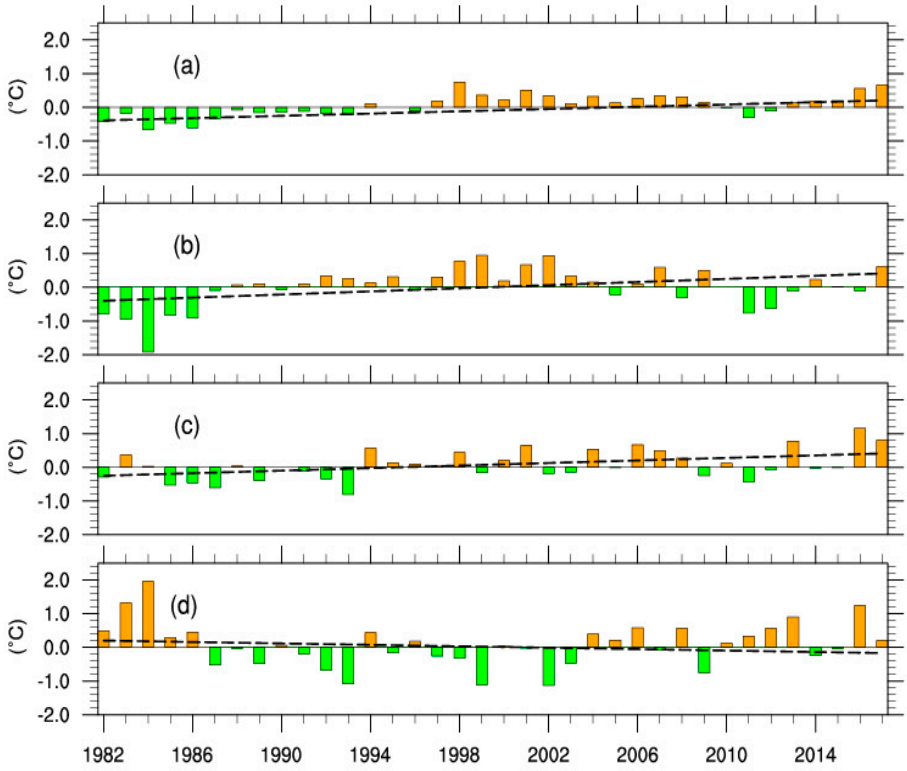

Figure 3. Time series of the regional averaged annual mean SST (**a**), annual minimum SST (**b**), annual maximum SST (**c**) anomalies and AR SST (**d**) in the ECSs from 1982–2017 (Units: °C, 1982–2011 base period). The black dashed lines are the linear trend lines based on the least squares estimator.

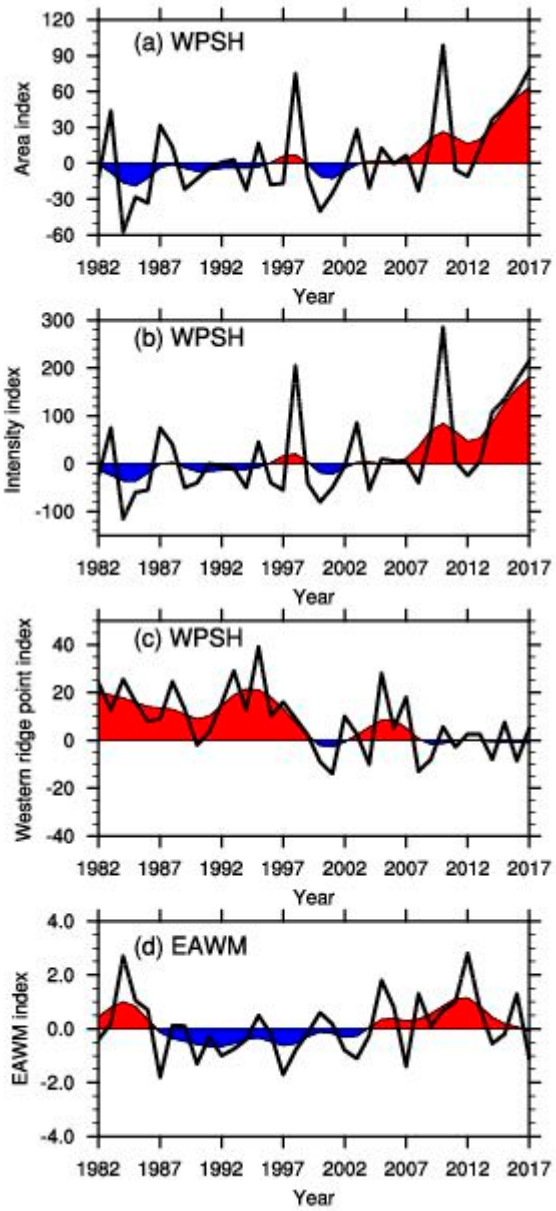

Figure 4. Time series of summer mean (black lines) and 9 year running mean (shaded lines) indices from 1982–2017 of the west Pacific subtropical high (WPSH): area (**a**), intensity (**b**), westward extension (**c**), and time series of the East Asia winter monsoon Index (**d**). Data are all from the Chinese National Climate Center (CNCC).

Spatially, the significant high warming rates of the annual mean SST appear in the western ECS and part of the ECS-Kuroshio, exceeding 0.2 °C per decade (Figure 5a). In them, warming rates of the Yangtze River estuary are especially large, up to 0.4 °C per decade. The rapid warming in the western ECS coincides with the previous findings [7,8]. Studies pointed that the stream temperature in the vicinity of the Yangtze Estuary had increased by ~2 °C since 1986, thereby contributing to the extremely rapid warming observed in the western ECS [4,36]. However, the other significant warming at the ECS-Kuroshio has not been captured using the coarse SST grid dataset in the previous studies. There are weak cooling trends occurs in the west of the Korea Island in Figure 5a which were not clearly shown in the previous studies and needs a further investigation.

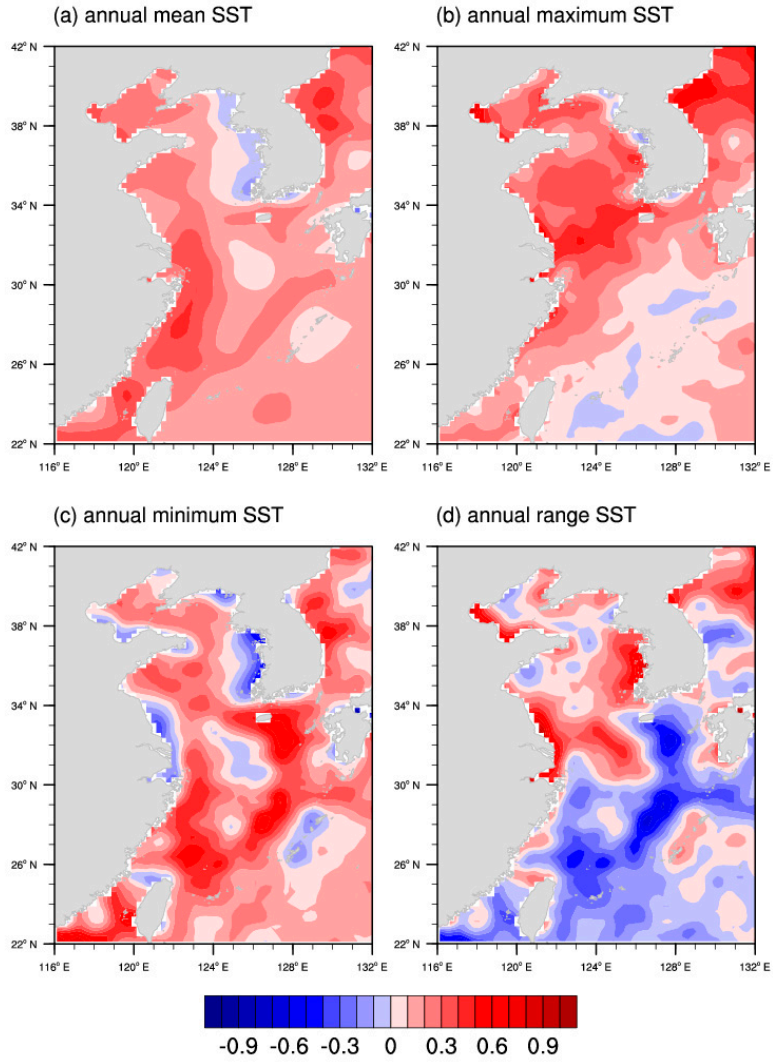

Figure 5. Linear trends spatial distribution of (**a**) annual mean SST, (**b**) annual maximum SST, (**c**) annual minimum SST, (**d**) AR SST in the ECSs (Units: °C per decade).

We also estimate the trends distribution of annual minimum and maximum SST in the study region (Figure 5b,c). Comparing to the rapid warming of minimum SST in the range of the ECS-Kuroshio and the Yangtze River estuary, the maximum SST shows clear increasing in the most part from the northern ECS to the Bohai Sea. The inter-annual SST variability in the ECSs is not only associated with large-scale climate oscillations in the Pacific (for instance, Pacific Decadal Oscillation, North Pacific Oscillation, East Asia Monsoon, ENSO, etc.) but also affect by many local processes, including the Yangtze River discharge, Kuroshio, and East Asian Monsoon, etc. The complex local processes may lead to regional differences in trends. Wu et al. [6] related the phenomenon of high SST increasing trend along the western Pacific marginal seas to the poleward shift and the intensification of the Kuroshio. In boreal winters, weakening northeasterly winds after 1982 would strengthen the northward advection of the Kuroshio and its cross-shelf currents into the ECS, due to a strong southward upper Ekman drift [31]. It is actually coincident with the finding that a rapid warming of annual minimum SST in the range of the ECS-Kuroshio. As shown in Figure 5d, there is an out-of-phase change on both sides of 30° N (Figure 5d). The AR SST is notably weakened in the band of the ECS-Kuroshio, with the decreasing center located at (127–128° E, 28-30° N). The decrease of the AR SST is associated with a rapid warming of the minimum SST and the slow warming of the maximum SST. AR SSTs in the Bohai Sea and the Yellow Sea are increasing, except some much small areas.

4. Changes in the Extreme Events and Their Relationship with Mean SST

In this section, we examine the changes of extreme SSTs based on the daily OISST v2. Figure 6 exhibits the time series of regional averaged annual EHDs and ECDs in the study region. The number of annual EHDs significantly increased, at a rate of 15.2 days per decade (significant at the 95% level, $p < 0.05$). In contrast, the number of annual ECDs remarkably decreased, at a rate of 10.5 days per decade (significant at the 95% level, $p < 0.05$). Annual EHDs and ECDs are positively (0.80) and negatively (-0.92) correlated with annual mean SST, respectively. In general, the increase of EHDs is accompanied by a decrease of ECDs ($r = -0.76$, $p < 0.01$). Therefore, the region with higher warming rates tends to have more EHDs and less ECDs. Spatially, significant increases in the frequency of EHDs were observed over the western ECS and the Bohai Sea (near shore areas even exceeding 20 days per decade), in association with a decrease in the frequency of ECDs simultaneously in Figure 7. This high rate is consistent with a rapid warming of annual mean SST in the western ECS. Lima and Wethey [17] studied trends of coastal warm and cold days in the world's coastlines from 1982 to 2010 using OISST v2. They detected an increase in EHDs on the range of 10~20 days per decade and the decrease in ECDs on the range of 5~15 days per decade in the coastline of the China Seas, consistent with our finding of the rapid increase of EHDs in the coastal areas.

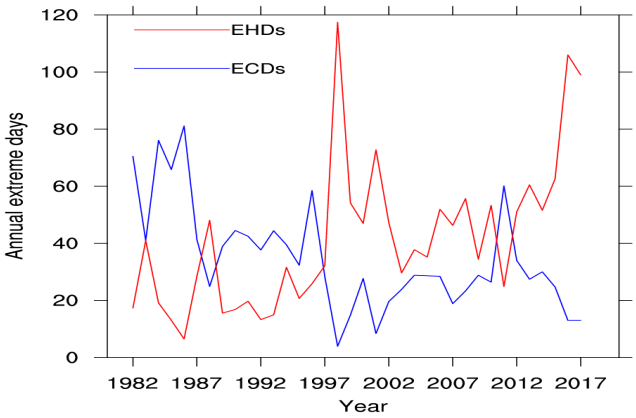

Figure 6. Regional averaged annual EHDs (red line) and ECDs (blue line) from 1982 to 2017 in the study region (units: days).

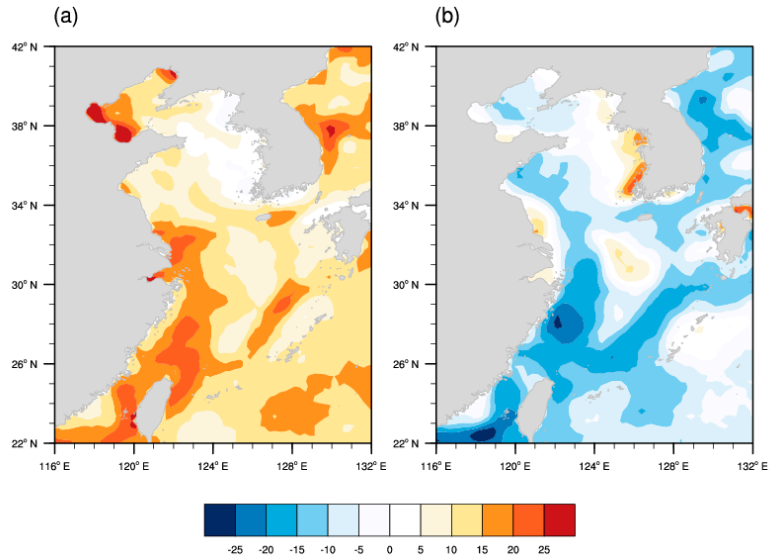

Figure 7. Linear trends of the annual EHDs (**a**) and annual ECDs (**b**) during 1982–2017 (Units: days per decade).

5. Summary and Discussions

Our main goal in this paper was to characterize the changes in mean and extreme SST in the ECSs. For this purpose, we used the NOAA OISST v2, which has high spatial and temporal resolutions. The analysis of SST variability in the ECSs successfully lead to a better understanding of this marine environment, including climate related hydrographic and ecosystem trends. The main findings of the present study can be summarized as follows:

(1) As a regional average, annual mean SSTA over the ECSs is subject to more notable warming trend, with a rate of 0.21 $\pm$ 0.08 °C per decade which is higher than the global mean trend based on the same data set during 1982–2017. The most significant warming was observed at the western ECS and the Bohai Sea. The warming SST during 1982–2017 is probably related to the influence from the recent strengthening and westward extension of the WPSH.

(2) Our results indicate that there are significant warming tendencies in annual minimum SST and maximum SST. Compared to the rapid warming of maximum SST from the northern ECS to the Bohai Sea, the rapid warming of minimum SST mainly covers the western ECS and part of the ECS-Kuroshio. AR SST shows an out-of-phase change on both sides of 30° N during 1982–2017.

(3) Rapid decreases in EHDs and increases in ECDs were detected in the ECSs from 1982 to 2017, at a rate of 15.2 days per decade and 10.5 days per decade, respectively. Spatially, the notable increases in the frequency of EHDs were observed in almost all of the ECSs, especially in the Bohai Sea and the western ECS, exceeding 20 days per decade.

Significantly higher SSTs above average in some area are implicated in dramatic changes to the physical, chemical and biological state of the marine environment. It is worth noting that our analysis indicates that the warming trend in the ECSs is greater than the trend of the global averaged SST. This finding is consistent with previous results based on different SST data sets [6,8]. The increase in SST makes the abundance of warm water species and the decrease of warm-temperate species in the Yangtze Estuary area [37–39]. Also, it can cause latitudinal shifts in species distributions [39]. Moreover, exposure and vulnerability to extreme events can destroy marine fishery assets and infrastructure. For instances, extreme higher water temperature can lead to abnormal metabolism of scallop, a cold-water species [40]. In the boreal summer of 2017, Zhangzi Island (122.7° E and 39° N) of the Yellow Sea had experienced more than 40 EHDs, with the maximum daily SST anomaly of 4.12 °C. Under such conditions, scallop could not absorb nutrients normally, resulting in malnutrition, bacterial infection and eventually inducing widespread mortality of scallops in this area.

Currently, the frequency and intensity of extreme events are increasing globally as a consequence of anthropogenic and natural climate change influence [3,33]. The latest research points out that the human-induced global warming has never stopped and the human influence is dominant in long-term warming [41]. In the present study, we found the likelihood of extreme hot events increases from 1982 to 2017 in the ECSs, especially in the sub-regions of the Bohai Sea and the western ECS. Given the continued global warming, there will be more frequency and intense extreme hot events in the study region. Given the information mentioned above, contemporary warming events are possibly superimposed onto the warming trends, increasing the risk of extreme SST events on marine ecosystem. Thus, better targeted strategies should be designed for an adaptation and mitigation against specific types of hot extremes as early as possible.

Author Contributions: Conceptualization, Q.W. and Y.L.; Methodology, Y.L. and Y.W.; Data analysis and discussion of the results, Q.W., Y.L. and Q.L.; Writing-Original Draft Preparation, Y.L., Y.L.; Writing-Review & Editing, Q.W.; Visualization, Q.L.; Supervision, Q.L.; Funding Acquisition, Q.L.

Funding: This research was funded by the Strategic Priority Research Program of Chinese Academy of Sciences (Grant No. XDA20100304) and the National Key Research Program of China (2016YFA0602200, 2012CB955203, 2013CB430202).

Conflicts of Interest: The authors declare no conflict of interest.

References

1. Bojinski, S.; Verstraete, M.; Peterson, T.C.; Simmons, A.; Zemp, M. The concept of essential climate variables in support of climate research, applications, and policy. *Bull. Am. Meteorol. Soc.* **2014**, *95*, 1431–1443. [CrossRef]
2. Giménez, L. Exploring mechanisms linking temperature increase and larval phenology: The importance of variance effects. *J. Exp. Mar. Biol. Ecol.* **2011**, *400*, 227–235. [CrossRef]
3. IPCC. Climate change 2013: The physical science basis. In *Contribution of Working Group I to the Fifth Assessment Report of the Intergovernmental Panel on Climate Change*; Stocker, T.F., Qin, D., Plattner, G.-K., Tignor, M., Allen, S.K., Boschung, J., Nauels, A., Xia, Y., Bex, V., Midgley, P.M., Eds.; Cambridge University Press: Cambridge, UK, 2003; p. 1535.
4. Belkin, I.M. Rapid warming of large marine ecosystem. *Prog. Oceanogr.* **2009**, *81*, 207–213. [CrossRef]
5. Belkin, I.M.; Lee, M.-A. Long-term variability of sea surface temperature in Taiwan Strait. *Clim. Chang.* **2014**, *124*, 821–834. [CrossRef]
6. Wu, L.X.; Cai, W.; Zhang, L. Enhanced warming over the global subtropical western boundary currents. *Nat. Clim. Chang.* **2012**, *2*, 161–166. [CrossRef]
7. Liu, Q.Y.; Zhang, Q. Analysis on long-term change of sea surface temperature in the China Seas. *J. Ocean Univ. China* **2013**, *12*, 295–300. [CrossRef]
8. Bao, B.; Ren, G.Y. Climatological characteristics and long-term change of SST over the marginal seas of China. *Cont. Shelf Res.* **2014**, *77*, 96–106. [CrossRef]
9. Oliver, E.C.; Benthuysen, J.A.; Bindoff, N.L.; Hobday, A.J.; Holbrook, N.J.; Mundy, C.; Perkins-Kirkpatrick, S.E. The unprecedented 2015/16 Tasman Sea marine heatwave. *Nat. Commun.* **2017**, *8*, 16101. [CrossRef]
10. Wernberg, T.; Bennett, S.; Babcock, R.C.; de Bettignies, T.; Cure, K.; Depczynski, M.; Dufois, F.; Fromont, J.; Fulton, C.J.; Hovey, R.K.; et al. Climate-drive regime shift of a temperature marine ecosystem. *Science* **2016**, *353*, 169–172. [CrossRef]
11. Frölicher, T.L.; Laufkötter, C. Emerging risks from marine heat waves. *Nat. Commun.* **2018**, *9*, 650. [CrossRef]
12. Cai, R.S.; Tan, H.J.; Qi, Q.H. Impacts of and adaptation to inter-decadal marine climate change in coastal China seas. *Int. J. Clim.* **2016**, *36*, 3770–3780. [CrossRef]
13. State Oceanic Administration. *Bulletin of Marine Disaster of China*; State Oceanic Administration: Beijing, China, 2013.
14. Banzon, V.; Smith, T.M.; Chin, T.M.; Liu, C.; Hankins, W. A long-term record of blended satellite and in situ sea-surface temperature for climate monitoring, modeling and environmental studies. *Earth Syst. Sci. Data* **2016**, *8*, 165–176. [CrossRef]
15. Reynolds, R.W.; Smith, T.M.; Liu, C.; Chelton, D.B.; Casey, K.S.; Schlax, M.G. Daily high-resolutionblended analyses for sea surface temperature. *J. Climate* **2007**, *20*, 5473–5496. [CrossRef]
16. Knapp, K.R.; Ansari, S.; Bain, C.L.; Bourassa, M.A.; Dickinson, M.J.; Funk, C.; Helms, C.N.; Hennon, C.C.; Holmes, C.D.; Huffman, G.J.; et al. Globally gridded satellite observations for climate studies. *Bull. Am. Meteorol. Soc.* **2011**, *92*, 893–907. [CrossRef]
17. Lima, F.P.; Wethey, D.S. Three decades of high-resolution coastal sea surface temperatures reveal more than warming. *Nat. Commun.* **2012**, *3*, 704. [CrossRef]
18. Park, K.A.; Lee, E.Y.; Chang, E.; Hong, S. Spatial and temporal variability of sea surface temperature and warming trends in the Yellow Sea. *J. Mar. Syst.* **2015**, *143*, 24–38. [CrossRef]
19. Benthuysen, J.A.; Oliver, E.C.; Feng, M.; Marshall, A.G. Extreme marine warming across Tropical Australia during austral summer 2015–2016. *J. Geophys. Res.* **2018**, *123*, 1301–1326. [CrossRef]
20. Liao, E.H.; Lu, F.; Yan, X.H.; Jiang, Y.; Kidwell, A.N. The coastal ocean response to the global warming acceleration and hiatus. *Sci. Rep.* **2015**, *5*, 16630. [CrossRef]
21. Costoya, X.; Decastro, M.; Gómezgesteira, M.; Santos, F. Changes in sea surface temperature seasonality in the Bay of Biscay over the last decades (1982–2014). *J. Mar. Syst.* **2015**, *150*, 91–101. [CrossRef]
22. Kulkarni, A.; Storch, H.V. Monte Carlo experiments on the effect of serial correlation on the Mann-Kendall-test of trends. *Meteorol. Z.* **1995**, *4*, 82–85. [CrossRef]
23. Von Storch, H.; Zwiers, F.W. *Statistical Analysis in Climate Research*; Cambridge University Press: London, UK, 1999.

24. Wolter, K.; Timlin, M.S. El Niño/Southern Oscillation behavior since 1871 as diagnosed in an extended multivariate ENSO index. *Int. J. Clim.* **2001**, *31*, 1074–1087. [CrossRef]
25. Hu, S.; Fedorov, A.V. The extreme El Niño of 2015–2016 and the end of global warming hiatus. *Geophys. Res. Lett.* **2017**, *44*, 3816–3824. [CrossRef]
26. Song, D.H.; Yu, H.M.; Bao, X.W. Analysis of the interannual variability of the eastern China Seas and its adjacent seas surface temperature. *Period. Ocean Univ. China* **2007**, *37*, 21–28, (In Chinese with English Abstract).
27. Pei, Y.H.; Zhang, R.H.; Zhang, X.; Jiang, L.; Wei, Y. Variability of sea surface height in the South China Sea and its relationship to Pacific oscillations. *Acta. Oceanol. Sin.* **2015**, *34*, 80–92. [CrossRef]
28. Zhang, Q.Y.; Tao, S.Y.; Chen, L.T. The inter-annual variability of East Asian summer monsoon and its association with pattern of general circulation over East Asia. *Act. Meteorol. Sin.* **2003**, *61*, 559–568, (In Chinese with English Abstract).
29. Zhang, R.H.; Li, Q. Impact of sea temperature variability of tropical oceans on East Asian Monsoon. *Meteorol. Mon.* **2004**, *30*, 22–26, (In Chinese with English Abstract).
30. Pei, Y.H.; Liu, X.H.; He, H.I. Interpreting the sea surface temperature warming trend in the Yellow Sea and East China Sea. *Sci. China Earth Sci.* **2017**, *60*, 1558–1568. [CrossRef]
31. Cai, R.S.; Tan, H.J.; Kontoyiannis, H. Robust surface warming in offshore China Seas and its relationship to the East Asian Monsoon wind field and ocean forcing on interdecadal time scales. *J. Clim.* **2017**, *30*, 8987–9905. [CrossRef]
32. Zhao, S.; Chang, F.M.; Li, T.G.; Zhuang, L.H.; Xiong, Z.F.; Xu, Y. Seasonal and Inter-Annual Anomalies of Sea Surface Temperature Offshore Northeastern Taiwan and Its Implication to Historical Climate Reconstructions. *Earth Sci.* **2018**, *43*, 851–861, (In Chinese with English Abstract).
33. World Meteorological Organization (WMO). *WMO Statement on the State of the Global Climate in 2017*; World Meteorological Organization: Geneva, Switzerland, 2018; p. 35.
34. Perkins, S.E.; Alexander, L.V. On the measurement of heat waves. *J. Clim.* **2013**, *26*, 4500–4517. [CrossRef]
35. Perkins, S.E.; Alexander, L.V.; Nairn, J.R. Increasing frequency, intensity and duration of observed global heatwaves and warm spells. *Geophys. Res. Lett.* **2012**, *39*, 20714. [CrossRef]
36. Zhou, X.Y.; Hu, D.B.; Wang, C.Z. Seasonal and interannual SST variations in the Changjiang Estuary. *Period. Ocean Univ. China* **2005**, *35*, 357–362, (In Chinese with English Abstract).
37. Li, Y.; Xu, Z.L.; Gao, Q. Effects of global warming on Sagitta crassa and Sagitta enflata in the Changjiang Estuary during different years. *Acta Ecol. Sin.* **2009**, *29*, 4773–4780, (In Chinese with English Abstract).
38. Ma, Z.L.; Xu, Z.L.; Zhou, J. Effect of global warming on the distribution of Lucifer intermedius and L. hanseni (Decapoda) in the Changjiang estuary. *Prog. Nat. Sci.* **2009**, *19*, 1389–1395, (In Chinese with English Abstract). [CrossRef]
39. Xu, Z.L. Ecological characters of Euchaeta Concinna (Copepod) in the East China Sea. *Oceanol. Limnol. Sin.* **2006**, *32*, 97–104, (In Chinese with English Abstract).
40. Liu, C. *The Effect of Temperature on the Fitness Characters of Bottom Sowed Yesso Scallop*; University of Chinese Academy of Sciences: Shenzhen, China, 2016.
41. Medhaug, I.; Stolpe, M.B.; Fischer, E.M.; Knutti, R. Reconciling controversies about the 'global warming hiatus'. *Nature* **2017**, *545*, 41–47. [CrossRef]



© 2019 by the authors. Licensee MDPI, Basel, Switzerland. This article is an open access article distributed under the terms and conditions of the Creative Commons Attribution (CC BY) license (http://creativecommons.org/licenses/by/4.0/).

Article ID: 1006-8775(2019) 03-0385-14

PARTITION OF SEASON BASED ON MULTIELEMENTS AND THE DECADAL CHANGE OF SEASON DURATION IN CHINA

WANG Zheng (王 正)[1], ZHI Rong (支 蓉)[2], WANG Yu (王 瑜)[1], FENG Guo-lin (封国林)[1,2]
(1. College of Atmospheric Sciences, Lanzhou University, Lanzhou 730000 China; 2. Laboratory for Climate Studies, National Climate Center, China Meteorological Administration, Beijing 100081 China)

Abstract: Using the multielements similarity measurement method and 1950-2017 NCEP/NCAR gridded daily reanalysis datasets, we analyzed season duration in China during 1950-2016, and we defined the element with maximum absolute sensitivity as the key impact element at each point using the sensitivity analysis method. The decadal change of season duration and its key impact element before and after 1980 were studied. The results indicated obvious meridional and zonal differences in the distribution of season duration for the 67-year average, and that the key impact element has the same distribution characteristics as season duration. In addition, complementary relationships were found between the durations of spring and summer, autumn and winter, and the cold and warm seasons. Among them, the complementary relationship between the durations of spring and summer was strongest and the regions of complementarity were numerous. The complementary regions of autumn and winter durations were found mainly in western China. In the cold and warm seasons, the complementary regions were widespread and the complementary relationship was generally weak. Comparison of the periods before and after 1980 revealed an east-west difference in the interdecadal variation of season duration. Interdecadal variation in spring and summer was found concentrated in northern and western regions, while that in autumn and winter was concentrated in the western region. Areas of significant interdecadal variation of the key elements were found concentrated in northern and western regions, corresponding well to the areas of significant interdecadal variation of season duration.

Key words: multielements similarity measurement method; season duration; key impact element; decadal change
CLC number: P467 **Document code:** A
doi: 10.16555/j.1006-8775.2019.03.010

1 INTRODUCTION

Increasing concentrations of greenhouse gases in the atmosphere and rising global temperature have prompted increasing attention from the academia, the public, and governments on environmental problems related to global climate change (Qin [1]). The Fifth Assessment Report of the IPCC claims that evidence of the warming of the climate system is irrefutable. Global combined land and ocean temperature data show an increase of approximately 0.85℃ during 1980 –2012, which is considered the warmest period since the Industrial Revolution (IPCC5 [2]). The Second National Assessment Report on Climate Change states that annual mean ground temperature in China increased by 1.38℃ during 1960 –2009, which is much lower in the Northern Hemisphere (Second National Assessment Report on Climate Change[3]). Since the late 1970s, the main areas of warming in China have been in the northwest, northeast, and northern China (Shi et al. [4]). Global climate change has had an important impact on the interdecadal change of the seasons in China (Gong et al.[5]; Zhang et al.[6]; Shen et al. [7]). Therefore, studying season duration in China could clarify its spatial characteristics, elucidate its sensitivity to meteorological elements, and reveal its interdecadal variation, which will help determine the impact of global climate change on the characteristics of the seasons in China. This will be beneficial for improving societal adaptability to global climate change, and for achieving sustainable and harmonious socioeconomic and environmental development (Lu et al. [8]).

Seasons can be distinguished based on astronomical, phenological, climatological, and meteorological classification systems (Zeng et al. [9]). In meteorological research, the study of seasons focuses primarily on two considerations: atmospheric circulations and meteorological elements. Each perspective has its specific rationality and limitations. Dividing seasons using atmospheric circulations can better explain the dynamic mechanism and abrupt change of each season, but this method is specific to individual regions and the outcome is not very accurate. Dividing seasons using meteorological elements can produce results for each region that are more accurate, but they can be difficult to

Received 2018-01-09; **Revised** 2019-05-06; **Accepted** 2019-08-15
Foundation item: National Key Research and Development Program of China (2017YFC1502306); National Natural Science Foundation of China Project (41575082)
Biography: WANG Zheng, Ph. D., primarily undertaking research on seasonal division and climate change.
Corresponding author: ZHI Rong, e-mail: z_rongphy@126.com

(C)1994-2019 China Academic Journal Electronic Publishing House. All rights reserved. http://www.cnki.net

explain in terms of theory and dynamic mechanisms. In addition, the influence of the climate system on season duration is a complex, highly nonlinear, scale-free, multilevel, and forced dissipative system (Guo et al.[10]; Hao et al.[11]), the variation of which is a nonstationary process (Gong et al.[5]; Li et al.[12]). Thus, existing methods for dividing seasons have certain limitations in terms of comprehensive and accurate assessment of the response of climate change to global warming (Zhang et al.[13]).

Many studies have been undertaken regarding the division of seasons in China. Previous studies based on atmospheric circulations (e.g., Zhu[14]; Tu et al.[15]; Ye et al.[16]; Zhang et al.[17]; Yuan et al.[18]; Fan et al.[19]) have focused mainly on monsoons and other large-scale circulations and their division standards have tended to be qualitative. Earlier studies based on meteorological elements (e.g., Zhang[20]; Zhu[21]; Zhang et al.[22]; Liao et al.[23]) have used a single element or multiple elements. Such studies have tended to focus on the seasonal variation of certain meteorological elements, e.g., temperature, from which they might have artificially derived some quantitative division standards. Thus, these methods might be incapable of comprehensively revealing the main characteristics of seasonal variation, and generalizations alone cannot predict climatic change scientifically (Liu et al.[24]).

By considering the shortcomings of both approaches, Zeng et al., Zhang et al. and Xue et al. have all proposed adopting the similarity measurement method for the division of seasons to obtain results that are more objective and quantitative[9, 25, 26]. Based on the similarity measurement method, Sun et al. and Hou et al. suggested a new approach to the division of seasons using multielements to structure the climate fields[27, 28], which makes the division more accurate and comprehensive. However, the sensitivity of season duration to meteorological elements in China has not been studied previously, and related studies on the interdecadal variation of regional seasonal characteristics are lacking. In this study, we divided the seasons during 1950–2016 in Chinese mainland using NCEP/NCAR gridded daily reanalysis datasets and the multielements similarity measurement method. Moreover, we also investigated the sensitivity of season duration to the meteorological elements. In addition, we analyzed the interdecadal variation of season duration in China and its key impact element. The results provide a unique picture of climate change characteristics in China from the prospective of season duration.

2 DATA AND METHODS

2.1 *Data*

To investigate season duration in Chinese mainland and its key impacting element, we used 1950 –2017 NCEP/NCAR gridded (2.5°×2.5°) daily reanalysis surface datasets of temperature (T), relative humidity (R_H), pressure (P), zonal wind (U), and meridional wind (V). In this study, data acquired on February 29 of leap years were removed so that each year comprised of 365 days and 73 pentads.

2.2 *Regional division*

According to our research needs and China's Physical Geography (1995), China was divided into eight areas, as shown in Fig. 1. Area 1 covered northeast China (42°–54° N, 110°–135° E), including Heilongjiang, Jilin, Liaoning and the northeastern parts of Inner Mongolia, and it incorporated 55 and 35 grid points within and near China, respectively. Area 2 encompassed northern China (34°–42° N, 110°–128° E), including Hebei, Shandong, eastern Shanxi, Beijing, and Tianjin, and it included 21 and 17 grid points within and near China, respectively. Area 3 was central China (27°–34° N, 110°–123° E), including Jiangsu, Zhejiang, Anhui, Henan, Hubei, and some adjacent regions, and it included 18 and 15 grid points within and near China, respectively. Area 4 covered southern China (18°–27° N, 110°–123° E), including Guangdong, eastern Guangxi, the annexes, southwestern Jiangxi, southern Hunan, Hainan, and Taiwan, and it incorporated 18 and 12 grid points within and near China, respectively. Area 5 encompassed eastern parts of northwest China (37°–45° N, 95°–110° E), including the middle part of Inner Mongolia, western and northern Shaanxi, Ningxia, and northern Gansu, and it covered 18 grid points in China. Area 6 included western parts of northwest China(37°–49°N, 73°–97°E), including Xinjiang, and it encompassed 40 and 31 grid points within and near China, respectively. Area 7 covered southwest China (22°–37° N, 97°–110° E), including Yunnan, Guizhou, western Guangxi, Sichuan, Chongqing, western Hunan, and southern Shaanxi, and it included 30 and 29 grid points within and near China, respectively. Area 8 was Tibet (27°–37° N, 78°–97° E), including southwestern Tibet and Qinghai, and it incorporated 28 and 25 grid points within and near China, respectively.

2.3 *Method used for season division*

The multielements similarity measurement method, adopted in this study to divide seasons, was implemented as follows. (1) Five days were taken as a pentad and 365-day daily mean data of the five climate elements were obtained to form 73-pentad pentad mean datasets, from which we constructed a climate state function F(θ, λ, p, t) of time t at (θ, λ, p, t),

$$F(t)=(P, T, R_H, U, V) \quad (1)$$

where P, T, R_H, U and V represent pressure, temperature, relative humidity, zonal wind, and meridional wind, respectively. $F(t)$ is a vector field formed by the five climate elements that vary with time. (2) Based on the similarity measurement method, we recorded the mean fields of January (winter) and July (summer) as F_W and F_S, respectively. Eliminating the mean of the two fields, $F^*=(F_W+F_S)/2$, we obtained the typical fields of winter and summer, F_W' and F_S', respectively. (3) At every pentad, we eliminated F^* to obtain the deviation of pentad mean

(C)1994-2019 China Academic Journal Electronic Publishing House. All rights reserved. http://www.cnki.net

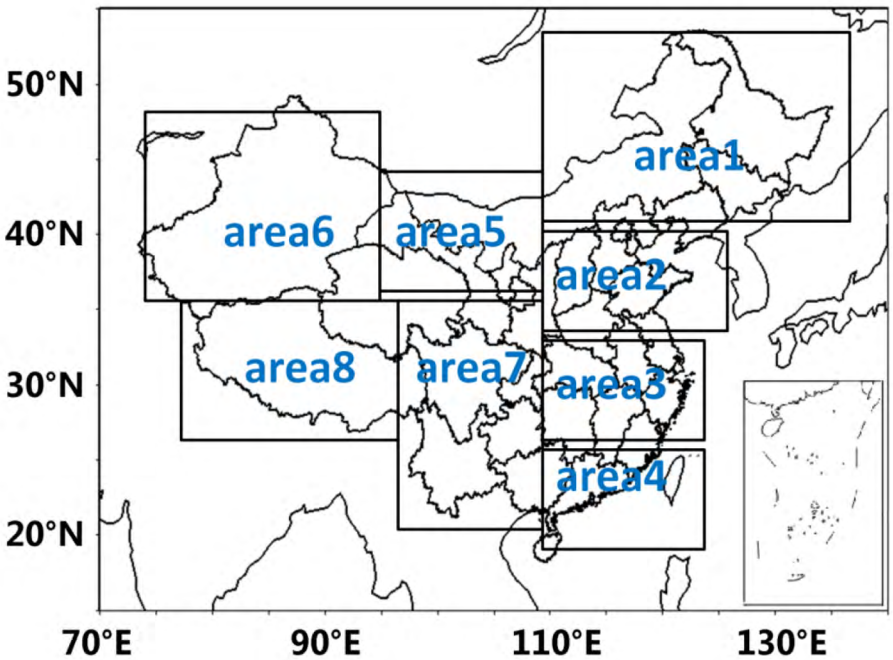

Figure 1. Division of study regions in China.

typical field $F'(t)$, $F'(t)=F(t)-F^*$. (4) Finally, we calculated the similarity coefficient $R(t)$ between $F'(t)$ and F'_W (or F'_S) of each pentad:

$$R(t)=(F'(t), F'_W)/[\,\|F'(t)\|\cdot\|F'_W\|\,]. \quad (2)$$

In Equation (2), each variable on the right is a vector, so the inner product and norm are those of the vector. Here, F'_W and F'_S are two opposite vectors, so only F'_W or F'_S need to be used to calculate $R(t)$. Here, $R(t)$ characterizes the similarity between the climate anomaly field and the typical field of winter (or summer) in each pentad. When the similarity is above/below a certain threshold, we can consider the season to have changed.

According to the projection angle of $R(t)$, $\theta=\arccos R_w(t)$; therefore, the following criteria for season division are derived, following Xue et al.[26]:

$$\begin{cases} 0\leqslant\theta\leqslant\pi/4 & \text{(winter)} \\ 3\pi/4\leqslant\theta\leqslant\pi & \text{(summer)} \\ \pi/4<\theta<3\pi/4 & \text{(spring or autumn)} \end{cases}$$

2.4 *The complementarity index*

We examined the complementary relationship between the lengths of two seasons in China. The complementarity index is used in economics to measure the degree of coincidence between the export products of one country and the import products of another country. Based on the complementarity index proposed by the economist Drysdale[29], we made a simple modification to the calculation to obtain an index that could express the complementarity relationship between the durations of two seasons:

$$C_{ab}=-k\cdot[LT_a-\overline{LT_a}/\overline{LT_a}]\cdot[LT_b-\overline{LT_b}/\overline{LT_b}] \quad (3)$$

where C_{ab} represents the complementarity of season duration between season a and season b; LT_a and LT_b represent the duration of season a and season b at grid points, respectively; $\overline{LT_a}$ and $\overline{LT_b}$ represent the average duration of season a and season b in China, respectively; k is a constant. If C_{ab} is positive, it means that the durations of seasons a and b are complementary, and the larger the value of C_{ab}, the stronger the complementarity. If C_{ab} is negative, it means that the durations of seasons a and b do not have complementarity.

2.5 *Sensitivity analysis*

Sensitivity analysis is an effective method with which to understand and evaluate a model, i.e., by keeping other elements the same, the effects caused by a change of one parameter can be analyzed (Yi et al. [30]). Sensitivity analysis was adopted to determine the key impact element of regional season duration, which might help explain the derived changes of season duration. Sensitivity of season duration (SD) to meteorological element (X) can be obtained using partial derivatives, i.e., $\partial SD/\partial X$. Because of the different dimensions and scales of different elements, we first needed to nondimensionalize the variable (McCuen[31]):

$$S=\frac{\partial SD}{\partial X}\cdot\frac{|X|}{SD} \quad (4)$$

A simple and effective method for calculating the relative sensitivity coefficient is to use an approximate solution of the finite difference of the Taylor series expansion (Hupet and Vanclooster [32]; Lenhart and Eckhardt[33]):

$$S=\frac{\Delta SD}{\Delta X}\cdot\frac{|X|}{SD} \quad (5)$$

(C)1994-2019 China Academic Journal Electronic Publishing House. All rights reserved. http://www.cnki.net

where ΔX is the change of a meteorological element, and ΔSD is the change of season duration caused by ΔX. The greater the absolute value of S, the higher the sensitivity of season duration (SD) to X, and the greater the impact of X on season duration (SD). The relative sensitivity coefficient is dimensionless; therefore, it is convenient for comparing the impacts of different meteorological elements on season duration (Yi et al. [30]).

In this study, each time we changed one meteorological element with value μ and kept the other elements the same, we calculated SD and S. By comparing the absolute value S of different meteorological elements, we defined the meteorological element with the greatest absolute value S as the key impact element. Normally, the value of μ is not constant and it should be adjusted. Based on many experiments, we choose a value of μ= 20% in this study (Goyal [34]). To illustrate the sensitivity of season duration to meteorological elements, certain figures in this paper use different colors to represent different meteorological elements, and circles and triangles are used to reflect positive and negative values of the sensitivity of the key elements, respectively. A positive value indicates that the key element has positive effect on season duration, and an increase of that element would lead to an increase of season duration, and vice versa.

3 SPATIAL DISTRIBUTION OF SEASON DURATION IN CHINA AND KEY IMPACT ELEMENTS

3.1 *Season duration*

Most previous related studies (e.g., Zhang et al. [13]; Xue et al. [26]; Huang et al. [35]) have focused mainly on the time of the onset of specific seasons and thus regional season duration has not been studied extensively. Here, we analyze the spatial distribution of season division in Chinese mainland during 1950–2016 (Fig. 2) using the multielements similarity measurement method. In the Liaodong Peninsula and the north, southwest, and eastern parts of northwest China, spring duration is above 17 pentads (Fig. 2a) and much longer than in other regions of the country. Areas in which spring has an obviously shorter duration (<10 pentads) are distributed mainly in southern China, northern parts of northeast China, western parts of the Tibet Plateau, and Xinjiang. Spring duration shows obvious north-south and east-west differences. Similar differences exist in summer (Fig. 2b) but with a converse distribution of areas with longer and shorter duration. The duration of summer on the Liaodong Peninsula, in northern China, and in eastern parts of northwest and southwest China is much shorter (<20 pentads) than in other areas, whereas summer duration is above 27 pentads in southern China, on the Tibet Plateau, and in Xinjiang. Comparison of Fig. 2a and 2b reveals an opposite relationship between the duration of spring and summer in most regions of China. It means that in a region where spring duration is long, summer duration will be short, and vice versa.

The definitions of warm and cold seasons are slightly different for different regions (Lin et al. [36]; Lin et al. [37]; Shi et al. [38]). Shi et al. defined the sum of normal spring and summer as the warm season, and the sum of

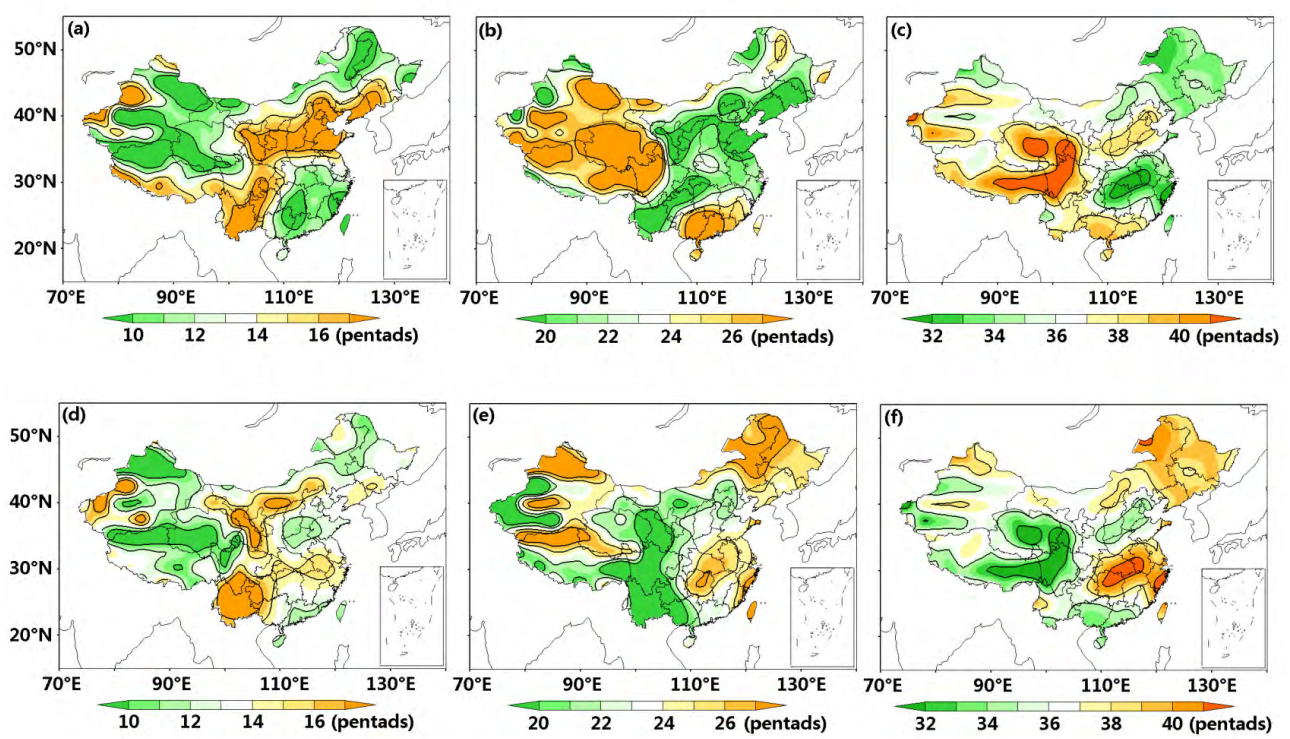

Figure 2. Spatial distribution of 1950–2016 mean season duration in China: (a) spring, (b) summer, (c) warm season, (d) autumn, (e) winter, and (f) cold season.

(C)1994-2019 China Academic Journal Electronic Publishing House. All rights reserved. http://www.cnki.net

normal autumn and winter seasons as the cold season in east China [38]. Other earlier studies have also roughly defined the warm and cold seasons as extending from March to August and from September to February, respectively. However, few studies have focused on the durations of warm and cold seasons defined using an objective division method. The spatial distributions of the duration of the warm and cold seasons in China during 1950 –2016, defined using the similarity measurement method, are shown in Fig. 2c and 2f, respectively. As the results are averages of many years, the durations of the warm and cold seasons are reasonably fixed, which leads to almost opposite spatial distributions of duration between the two seasons. The spatial distribution of warm season duration shows obvious zonal differences, i.e., shorter in eastern areas and longer in the west. The distribution features are obviously opposite for the cold season. Furthermore, the duration distribution also presents obvious meridional differences in east China, reflecting a short-long-short-long pattern in warm season duration from north to south, but a long-short-long-short pattern in cold season duration. These differences are likely due to both the different dominant elements affecting season duration in each region and the seasonal variation characteristics of meteorological elements.

3.2 *Interseasonal complementarity index in China*

We also calculated the complementarity index between spring and summer durations, between autumn and winter durations, and between warm and cold season durations. Except for some regions (i.e., middle and lower reaches of the Yangtze River, northern parts of northeast China, and southeastern parts of Tibet), the complementarity of season durations in spring and summer is significant (Fig. 3). The regions with strong complementarity of season duration in autumn and winter are concentrated mainly in western regions (i.e., west of 110° E), including western Xinjiang, northern Tibet, southwest China, and eastern parts of northwest China, while there is no complementarity in eastern regions. The spatial distribution characteristics of complementarity are consistent with the spatial distribution characteristics of season duration shown in Fig. 2, indicating that the complementarity coefficient can well reflect the complementary characteristics of the seasons. Because of the complementarity illustrated in Fig. 3a and 3b, the duration of the warm (cold) season shown in Fig. 2 varies slightly in most parts of China. The regions with longer and shorter (shorter and longer) seasons in Fig. 2c (2f) correspond well with those without complementarity in Fig. 3a (3b). Because the sum of the durations of the cold and warm seasons is reasonably constant, complementarity between the cold and warm seasons exists throughout the entire country, although it is generally weak. The regions with longer and shorter (shorter and longer) warm (cold) seasons correspond well with those with strong complementarity in Fig. 3c. Evident complementarity of season duration exists between spring and summer, autumn and winter, and the cold and warm seasons and, to a certain extent, it can explain the spatial distribution characteristics of season duration.

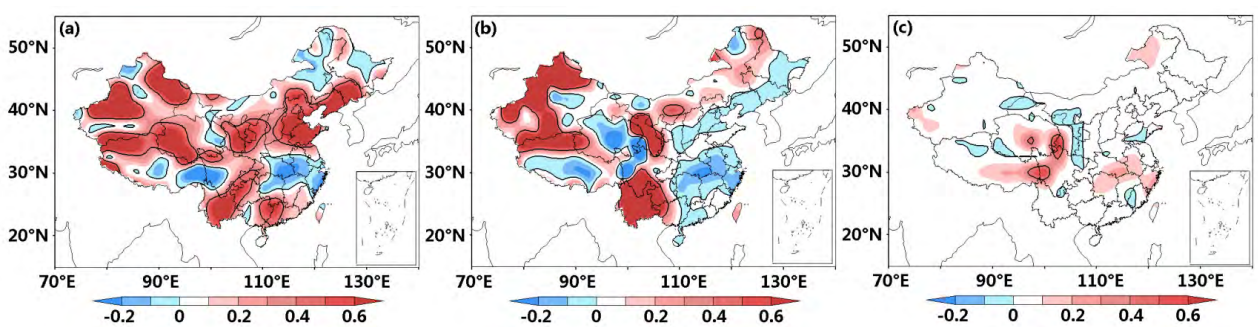

Figure 3. Spatial distribution of complementary index between two seasons. (a) Complementary index between spring and summer; (b) between autumn and winter; (c) between warm and cold seasons. Black solid line indicates significant complementarity.

3.3 *Key impact elements*

We investigated the sensitivity coefficient of season duration to meteorological elements, and we defined the one with the maximum absolute value as the key impact element. The results are presented in Fig. 4. In accordance with the definition of regions in section 2.2, the first two main elements affecting season duration are listed in Table 1.

The main element affecting spring duration in China is pressure (Fig. 4a), while other elements have relatively small impact. The impact of each element on spring duration is largely positive, indicating that an increase of any element would lead to an extension of the duration of spring. Regionally (Table 1), the second major element affecting spring duration in the eastern region is temperature, while the second major element affecting spring duration in western region is meridional wind. Among all regions, spring duration in northeast China is affected mostly by pressure; conversely, spring duration in northern China is affected least by pressure and influenced more by temperature and relative humidity.

Throughout the entire country, summer duration is affected greatly by relative humidity and pressure, while the influence of meridional wind is relatively small and

(C)1994-2019 China Academic Journal Electronic Publishing House. All rights reserved. http://www.cnki.net

confined mainly to central China. The effects of air pressure and meridional wind on summer duration are both negative, while the effect of relative humidity is positive. In regions other than northern China and central China (Table 1), the effects of air pressure and relative humidity are reasonably strong. In northern China, the influence of relative humidity on summer duration is the greatest. In central China, the influence of relative humidity on summer duration is the smallest, but the influence of meridional wind is enhanced.

Figure 4c shows that autumn duration in northwest China and Tibet is affected mainly by relative humidity and temperature; the effect of temperature is positive, while that of relative humidity is negative. Autumn duration in east and southwest China is affected mainly by pressure, and the effect of pressure in east China is negative. In addition, the influence of relative humidity is reasonably strong in all regions except central and south China (Table 1).

The main characteristics of the distributions of the key elements affecting winter duration (Fig. 4d) are that winter duration in Tibet is affected mainly by relative humidity, while that in other areas is affected mainly by pressure. In northern China, winter duration is also affected by temperature. The effects of relative humidity and air pressure are mainly positive, while the effect of temperature is mainly negative. Winter duration in southern China is affected mostly by pressure; thus, winter duration would increase as pressure increases.

In conclusion, there are obvious regional differences in the spatial distributions of the key elements affecting season duration in China. In summer, autumn, and winter, regional differences are obvious and the key impact elements exhibit evident differences between eastern and western China, consistent with the regional differences of season duration. Eastern China is characterized as a monsoon area; thus, the key impact element on season duration has a clear meridional distribution. Western China encompasses the monsoon marginal zone, westerly climate zone, and plateau climate zone; thus, the climate is more complex. In addition, the underlying surface condition has clear regional differences, and there is greater variety in the key elements that affect season duration in this area. Therefore, the spatial distribution is reasonably scattered, and the sign of the sensitivity of season duration to the key impact element is different in the western region. Furthermore, to a certain extent, the distribution of the key elements affecting season duration shown in Fig. 4 corresponds to the spatial distributions of season duration shown in Fig. 2. If we consider the seasonal variation of meteorological elements and the distributions of the key elements concurrently, we can infer the season duration in each region. The distributions of the key elements affecting season duration can explain, to a certain extent, the spatial distribution of season duration.

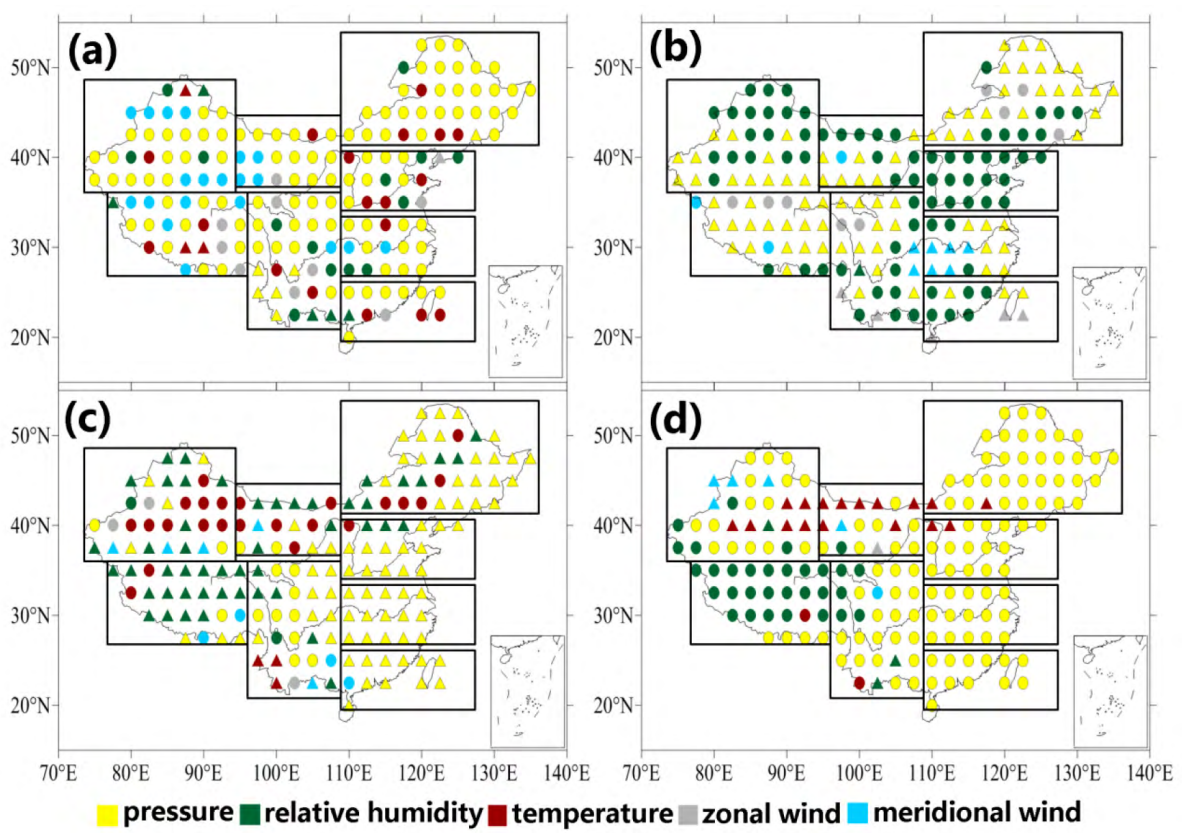

Figure 4. Spatial distribution of key impact elements on season duration: (a) spring, (b) summer, (c) autumn, and (d) winter. Circles (triangles) indicate that sensitivity coefficient is positive (negative).

(C)1994-2019 China Academic Journal Electronic Publishing House. All rights reserved. http://www.cnki.net

Table 1. Percentage of the first two main elements affecting the duration of the four seasons in China. P: barometric pressure, R: relative humidity, T: temperature, U: zonal wind, and V: meridional wind. Positive (negative) values mean positive (negative) sensitivity.

		Spring	Summer	Autumn	Winter
Area 1	1st	+P(82.86%)	−P(65.71%)	−P(62.86%)	+P(94.29%)
	2nd	+T(11.43%)	+R(22.86%)	−R(22.86%)	−T(5.71%)
Area 2	1st	+P(41.18%)	+R(100%)	−P(76.47%)	+P(88.24%)
	2nd	+T,+R(23.53%)	0	−R(17.65%)	−T(11.76%)
Area 3	1st	+P(66.67%)	−P(46.67%)	−P(100%)	+P(100%)
	2nd	+R,+V(13.33%)	−V(33.33%)	0	0
Area 4	1st	+P(58.33%)	+R(50%)	−P(91.67%)	+P(100%)
	2nd	+T(25%)	−P,−U(25%)	+V(8.33%)	0
Area 5	1st	+P(66.67%)	+R(50%)	+T(33.33%)	+P(44.44%)
	2nd	+V(22.22%)	−P(44.44%)	−R(33.33%)	−T(38.89%)
Area 6	1st	+P(58.06%)	+R(58.06%)	−R(32.26%)	+P(48.39%)
	2nd	+V(22.58%)	-P(41.94%)	+T(29.03%)	−T(19.35%)
Area 7	1st	+P(41.38%)	−P(41.38%)	+P(31.03%)	+P(68.97%)
	2nd	+R(13.79%)	+R(34.48%)	−P(27.59%)	+R(17.24%)
Area 8	1st	+P(44%)	−P(68%)	−R(68%)	+R(80%)
	2nd	+V(24%)	+R,+U(12%)	−P(12%)	+P(16%)

4 INTERDECADAL CHANGE OF SEASON DURATION AND ASSOCIATED KEY IMPACT ELEMENTS

4.1 *Change of season duration*

To analyze the decadal change of season duration, we used anomaly histograms of season duration in China over the past 67 years (Fig. 5). The 9-point smoothing curves shown in Fig. 5 reveal obvious interdecadal variation in season duration during the late 1970s and early 1980s.

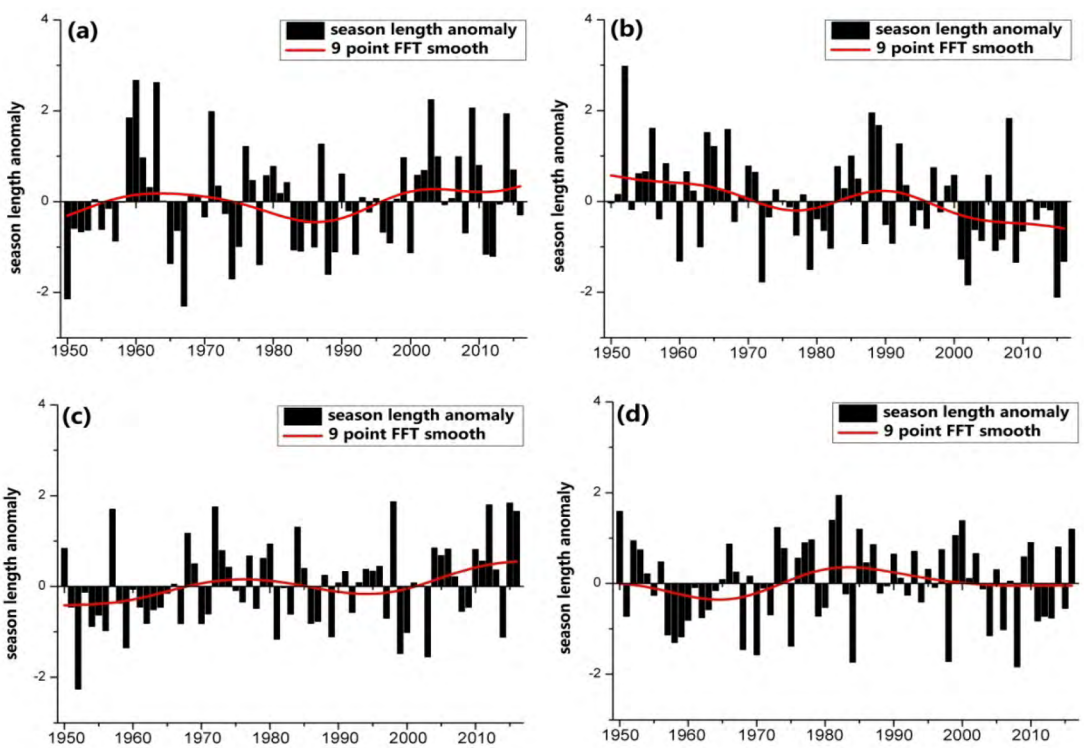

Figure 5. Annual variation of season duration in China during 1950−2016: (a) spring, (b) summer, (c) autumn, and (d) winter. Red curve is the 9-point FFT smooth curve.

(C)1994-2019 China Academic Journal Electronic Publishing House. All rights reserved. http://www.cnki.net

Following previous research (e.g., IPCC [2]; Shi et al. [39]; Zhao et al. [40]; He et al. [41]; Gong et al. [42]), we compared the season durations of the two periods of 1950–1980 (period 1) and 1981–2016 (period 2). The differences of season duration between the two periods are presented in Fig. 6. Fig. 6a shows that the change of spring duration shows obvious meridional differences after 1980, i.e., spring duration in the eastern region increases, while that in the western region decreases. The increased high-value areas include northern parts of northeast China, eastern parts of northern China, eastern parts of northwest China, and South China. The decreased high-value areas cover almost the entire western region. The change of spring duration in each of the above areas is greater than two pentads. The meridional differences are the same(Fig. 6b) but the pattern is the opposite. Summer duration increases in the eastern region and decreases in the western region. In southern and eastern Tibet, summer duration increases most. In northern parts of northeast China, northern China, and eastern parts of northwest China, summer duration decreases most. The change of summer duration in each of the above areas is greater than two pentads. The changes of spring and summer durations after 1980 show obvious differences between areas to the west and east of 105° E (Fig. 6a and 6b, respectively). This difference in distribution corresponds well with the regional differences of the key impact elements, and it suggests the regional differences of duration changes might be related to the regional key impact elements. There is a reasonable complementary relationship between the changes of spring duration and summer duration. It means that in a region where spring duration increases, summer duration might decrease correspondingly, and vice versa. Because of this complementary relationship, changes in the duration of the warm season in most areas of China are reasonably small (Fig. 6c); however, overall, the warm season duration is shortened.

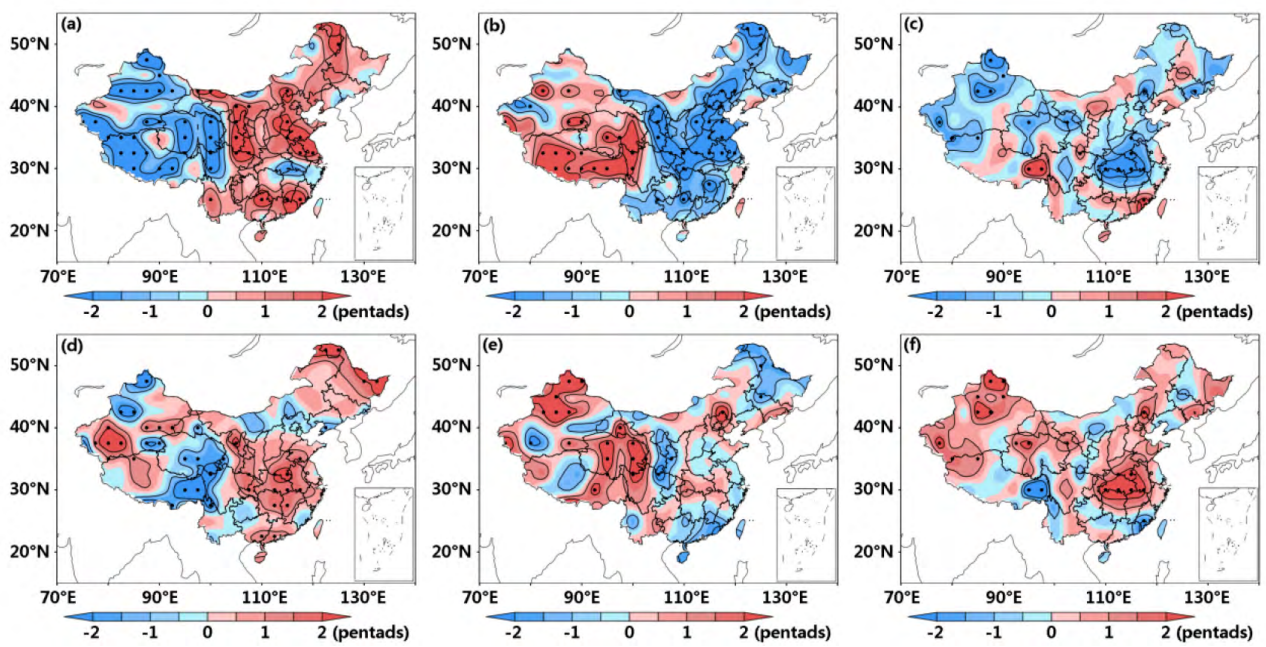

Figure 6. Difference (period 2 minus period 1) of season duration between 1950–1980 (period 1) and 1981–2016 (period 2): (a) spring, (b) summer, (c) warm season, (d) autumn, (e) winter, and (f) cold season. Shading indicates area of significant change.

Although the changes of autumn and winter durations have meridional differences, they occur mainly in western parts and are smaller than in spring and summer. The areas of significant increase in autumn duration are northern parts of northeast and central China and some western parts of northwest China. The areas of significant decrease in autumn duration are eastern Tibet and some western parts of northwest China. Overall, autumn duration is decreased in the west and increased in the east. The areas of significant increase in winter duration are eastern Tibet and northern Xinjiang. Thus, winter duration is increased in the west and decreased in the east. Furthermore, although the cold season duration (Fig. 6f) is increased, its change is reasonably small in most parts of China.

From the above, we know that the interdecadal variation between spring and summer durations is different to that between autumn and winter durations. Furthermore, the meridional differences of the interdecadal variation are obvious. The interdecadal variation in spring and summer is concentrated in northern and western regions. In autumn and winter, the interdecadal variation does not show obvious meridional differences, and it occurs mainly in northern and western regions. The regions of significant interdecadal change in our study are like those found in other research (e.g.,

(C)1994-2019 China Academic Journal Electronic Publishing House. All rights reserved. http://www.cnki.net

Zhou et al.[43]). In addition, the interdecadal variations of cold and warm season durations are different. Overall, the warm season duration China decreased and the cold season duration increased. Because the sum of the cold and warm season durations is reasonably fixed, the areas of significant change in cold and warm season durations are similar, i.e., concentrated mainly in the area of the middle and lower reaches of the Yangtze River and northern Xinjiang. Sections 3.1 and 3.3 highlighted that the distributions of season duration are related closely both to the distributions of the key elements and to the changes of the meteorological elements. Without considering the interdecadal variations of the meteorological elements, the interdecadal variations of the key elements affecting season duration will have greater impact on the variation of season duration. The interdecadal variations of the key elements affecting season duration are discussed in the following paragraphs.

4.2 *Changes of key impact elements*

To further explore the interdecadal variation of season duration in different regions, we determined the differences of the key impact elements before and after 1980 (Fig. 7). We also calculated the changing percentage (period 2 minus period 1) of five elements affecting

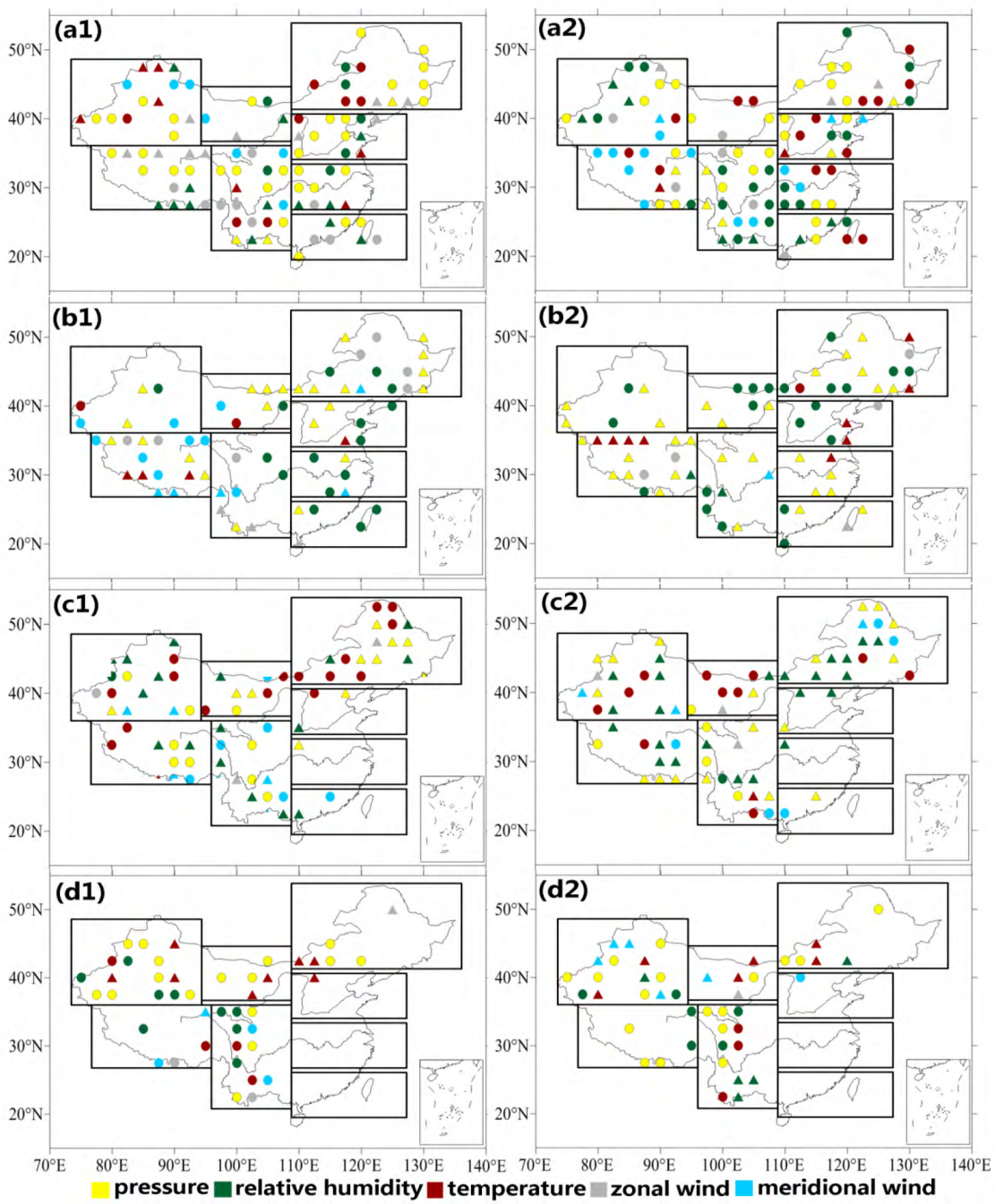

Figure 7. Distributions of the key elements affecting season duration before 1980: (a1) spring, (b1) summer, (c1) autumn, and (d1) winter and after 1980: (a2) spring, (b2) summer, (c2) autumn, and (d2) winter. Circles (triangles) indicate that sensitivity coefficient is positive (negative).

(C)1994-2019 China Academic Journal Electronic Publishing House. All rights reserved. http://www.cnki.net

season duration in each region.

The key elements affecting the durations of spring and summer in China changed markedly between the two periods and the regions affected are distributed throughout the country (Fig. 7). The key elements affecting the durations of autumn and winter in China are mainly in the western region, while the key element affecting autumn is mainly in the northeastern region. For ease of comparison of the changes of the key elements in the two periods, Table 2 shows the change percentage of first key element between the two periods in each of the eight regions. The regions in which the key elements changed markedly are distributed reasonably widely in spring and summer, whereas they are concentrated mainly

Table 2. Percentage changes of the elements affecting season duration in China before 1980 (1950–1980) and after 1980 (1981–2011). P: barometric pressure, R: relative humidity, T: temperature, U: zonal wind, and V: meridional wind. Positive and negative values are sensitivity coefficients. Black (red) bold values indicate a change that is >10% (>20%).

	Element	D value			
		Spring	Summer	Autumn	Winter
Area 1	P	–2.86%	5.71%	0.00%	0.00%
	R	2.86%	5.71%	**–11.43%**	–2.86%
	T	0.00%	–2.86%	**–14.29%**	0.00%
	U	–2.86%	–8.57%	2.86%	2.86%
	V	0.00%	2.86%	2.86%	0.00%
Area 2	P	**–17.65%**	**11.76%**	0.00%	0.00%
	R	5.88%	0.00%	–5.88%	0.00%
	T	**11.76%**	–5.88%	–5.88%	5.88%
	U	**11.76%**	5.88%	0.00%	0.00%
	V	**–11.76%**	0.00%	0.00%	5.88%
Area 3	P	**–13.33%**	**–20.00%**	6.67%	0.00%
	R	**26.67%**	**–20.00%**	–6.67%	0.00%
	T	**20.00%**	–6.67%	0.00%	0.00%
	U	–6.67%	0.00%	0.00%	0.00%
	V	**13.33%**	6.67%	0.00%	0.00%
Area 4	P	–8.33%	–8.33%	–8.33%	0.00%
	R	8.33%	–8.33%	8.33%	0.00%
	T	**16.67%**	0.00%	0.00%	0.00%
	U	**–16.67%**	0.00%	0.00%	0.00%
	V	0.00%	0.00%	0.00%	0.00%
Area 5	P	5.56%	5.56%	5.56%	**–11.11%**
	R	0.00%	**16.67%**	0.00%	0.00%
	T	**11.11%**	–5.56%	5.56%	0.00%
	U	**11.11%**	0.00%	–5.56%	–5.56%
	V	–5.56%	–5.56%	–5.56%	–5.56%
Area 6	P	–3.23%	–6.45%	**–16.13%**	–3.23%
	R	0.00%	3.23%	–3.23%	–9.68%
	T	**12.90%**	–3.23%	0.00%	0.00%
	U	3.23%	0.00%	–3.23%	0.00%
	V	–9.68%	–6.45%	0.00%	**–12.90%**
Area 7	P	–6.90%	–6.90%	**–10.34%**	3.45%
	R	**20.69%**	0.00%	6.90%	**–17.24%**
	T	–3.45%	0.00%	0.00%	3.45%
	U	–6.90%	6.90%	0.00%	–3.45%
	V	–3.45%	–3.45%	–3.45%	–6.90%
Area 8	P	**–12.00%**	**–16.00%**	**–20.00%**	**12.00%**
	R	**20.00%**	0.00%	–8.00%	4.00%
	T	4.00%	**12.00%**	0.00%	–4.00%
	U	**12.00%**	0.00%	0.00%	–4.00%
	V	**24.00%**	**–12.00%**	–4.00%	0.00%

(C)1994-2019 China Academic Journal Electronic Publishing House. All rights reserved. http://www.cnki.net

in the western region in autumn and winter. There is reasonable correspondence between the regions with large variation of the key elements and those with significant variation of season duration (section 4.1), indicating that the interdecadal variation of the key elements could explain for, to a certain extent, the interdecadal variation of season duration.

It can be seen from Fig. 7a1, 7a2, and Table 2 that spring is the season in which the key elements change most. In all areas except northeast China, the key elements vary considerably, especially in central China, southwest China, and Tibet. Moreover, the range of the positive influence of temperature in the northern region widens, the area of positive influence of relative humidity in the southern region expands, and the influence of meridional wind in Tibet gradually increases. These changes might be attributable to increased sensitivity of global warming to winter end time and summer start time (i.e., spring duration can be calculated using winter end time and summer start time) in the north, which leads to greater influence of temperature over a wider range in spring. In southern China and Tibet, the increasing sensitivity of duration to relative humidity and meridional wind, respectively, is attributable to the decrease of precipitation and the reduction of meridional wind speed in spring (Zuo et al. [44]; Yao et al. [45]).

In summer, the regions in which the key elements change markedly are northern China, central China, eastern parts of northwest China, and Tibet (Table 2), and the region with significant change in the key elements is central China. It can be seen from Fig. 7b1 and 7b2 that the range of influence of relative humidity increases in the north and decreases in the south, which might be related both to the warming and drying of the north in summer and to increased precipitation in southern coastal areas in summer (Ren et al. [46]; Han et al. [47]; Jin et al. [48]; Liu et al. [49]; Zhang et al. [50]).

The regions in which the key elements change markedly in autumn are northeast China, western parts of northwest China, southwest China, and Tibet (Table 2), and the region with significant change in the key elements is Tibet. The effect of relative humidity on autumn duration in northeast China (Fig. 7c1, 7c2) is enhanced, which might be attributable to the decrease of autumn precipitation in this region (Liu et al. [51]). The change of the effect of pressure in Tibet and its surrounding areas might be related to the increase of high pressure after 1978 (Zhang et al.[52]). In winter, the changes of the key elements are concentrated mainly in the west; however, the changes are not significant and there are no obvious trends.

In summary, between the two periods, the changes of the key elements are concentrated mainly in the north and west, consistent with the results of previous studies (Shi et al. [4]; Zhou et al. [43]). The changes of the key elements in southern areas are mainly in spring and summer. The changes of the key elements in Tibet are reasonably large in all four seasons, consistent with the current interdecadal climate change on the Qinghai-Tibet Plateau (Lu et al.[8]; Jin et al.[48]; Liu et al.[49]; Peng[53]).

5 CONCLUSIONS AND DISCUSSION

In this study, we investigated season duration in China and we considered certain key impact elements during 1950–2016 using daily NCEP/NCAR reanalysis datasets. We also explored their interdecadal changes. The findings can be summarized as follows.

(1) Season duration in various regions of China shows obvious meridional and zonal differences, as well as close relationships with certain key impact elements. In most regions, the high-value (low-value) areas of spring duration correspond well with the low-value (high-value) areas of summer duration, especially in autumn and winter. The spatial distribution of warm season duration shows obvious zonal differences, i.e., shorter in the east and longer in the west; the spatial distribution of cold season duration shows the converse. The duration distribution presents obvious meridional differences in eastern China, reflecting a short-long-short-long pattern from north to south in the warm season, but a long-short-long-short pattern from north to south in the cold season.

(2) There are complementary relationships between spring and summer durations, between autumn and winter durations, and between cold and warm season durations, which can explain, to a certain extent, the spatial distribution characteristics of the durations of these seasons. The complementary relationship between spring and summer durations is the best and the regions of complementarity are widespread. The complementary regions of autumn and winter durations are concentrated mainly in the western region. The complementary regions of cold and warm season durations are widespread but their relationships are weak.

(3) There are obvious regional differences in the spatial distributions of the key elements affecting season duration in China. The regional differences found in summer, autumn, and winter are reasonably obvious and reflected mainly in east-west and north-south directions. To a certain extent, the spatial distributions of the key elements affecting season duration correspond to the spatial distributions of season durations.

(4) The interdecadal variation between spring and summer durations is markedly different to that between autumn and winter durations. The meridional differences of the interdecadal variation in spring and summer are obvious and concentrated in northern and western regions, whereas there are no obvious meridional differences in autumn and winter.

(5) The areas of significant interdecadal variation of the key elements are concentrated in northern and western regions, and they correspond well with the areas of significant interdecadal variation of season duration. Regions in which the key elements changed greatly are

(C)1994-2019 China Academic Journal Electronic Publishing House. All rights reserved. http://www.cnki.net

reasonably widespread in spring and summer but concentrated mainly in the western region in autumn and winter.

There were two principal reasons for choosing the multielements method for this study. The first was that the method adopted produces a measure of similarity, reflecting the seasonal changes of the meteorological elements. When there are more elements, each element influences the result and the result is reasonably stable. When there are fewer elements, the effect of a single element increases; thus, the fluctuation of the division results increases and the accuracy decreases. The second reason was that the regional differences and the elements affecting the seasonal variations are not the same. For example, the differences in temperature and humidity between seasons are large in the north but small in the south, while the change of air pressure on the Qinghai-Tibet Plateau is obvious. Therefore, we used the similarity measure method and we selected the five basic meteorological variables that could best reflect the meteorological state in the process of season division. To better consider the dynamic effects in seasonal division, we also conducted an experiment only using zonal and meridional winds to divide the four seasons in China. Fig. 8 shows the corresponding season duration distributions of the two methods. The season durations of summer and winter obtained by the two methods have reasonable spatial similarity. The multielement partitioning method reflects the seasonal partitioning characteristics in the dynamic sense, because it already contains the wind element, which also demonstrates the effectiveness of the seasonal partitioning method. However, there are certain differences between the two methods in the western region and in northern China. This also shows that using temperature and relative humidity for seasonal division can also reflect, to a certain extent, the thermodynamic characteristics.

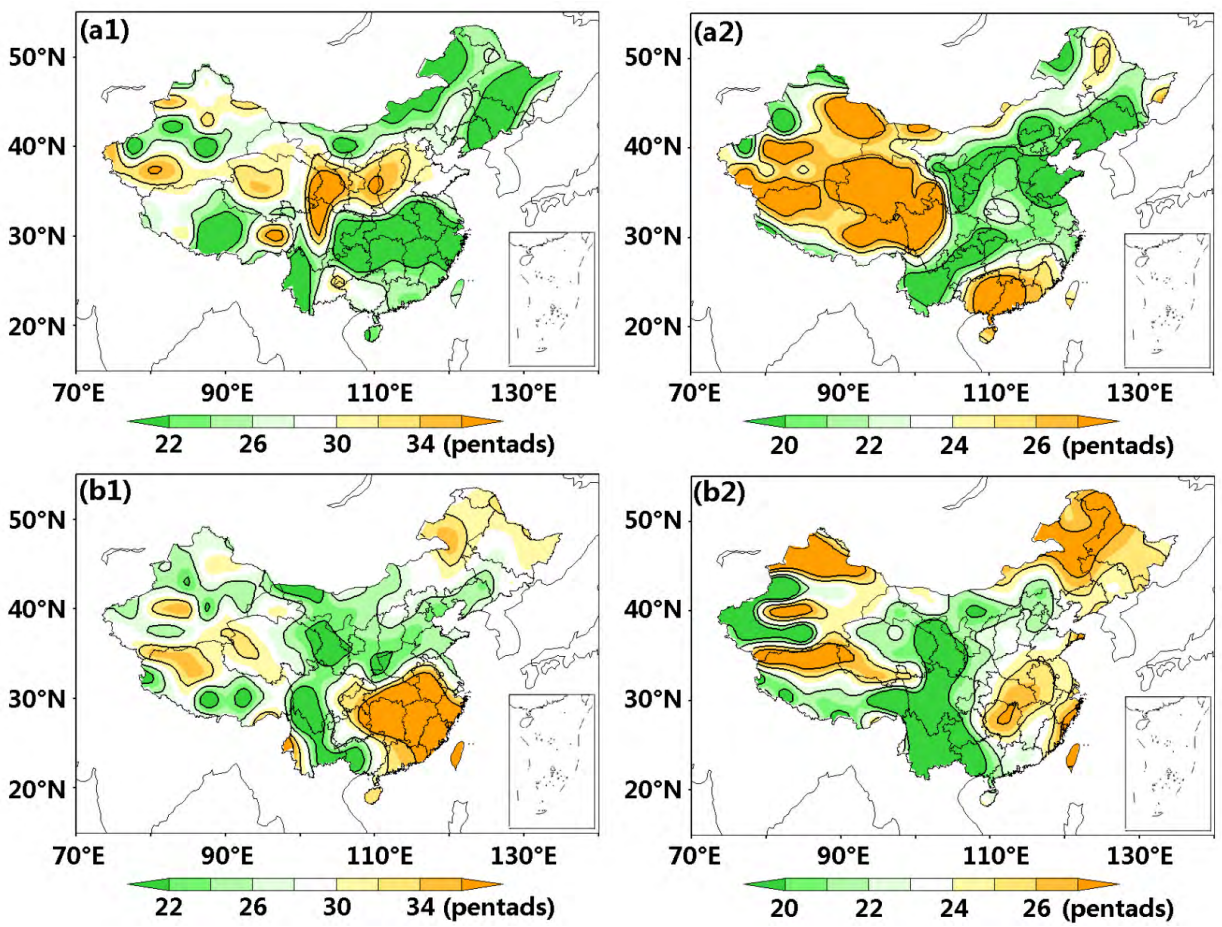

Figure 8. A comparison of season durations determined by (left) wind elements and (right) multielements similarity methods: (a1, a2) summer and (b1, b2) winter.

The results of season division obtained in this study are not the same as derived using traditional seasonal division methods. This is because our method focuses on the change of the atmospheric state, i.e., when changing from one stable atmospheric state to another.

We also investigated the interdecadal variation of season duration in China and its key impact elements. Such study can help elucidate the effects of global climate change on human life and provide important scientific support for studying regional climate change adaptation.

(C)1994-2019 China Academic Journal Electronic Publishing House. All rights reserved. http://www.cnki.net

The interdecadal variation of season duration varies in different parts of China and the corresponding changes in regional meteorological elements are also different. Furthermore, the impact caused by each meteorological element varies over time, which could have even more influence on season duration in the relevant region than the key element itself. Further investigation is needed to understand the impact of such influence.

Acknowledgement: We thank James Buxton MSc from Liwen Bianji, Edanz Group China, for editing the English text of this manuscript.

REFERENCES:

[1] QIN Da-he. Latest progress on climate change research [J]. Sci Technol Rev, 2008, 26(7), 3-3.

[2] IPCC. Climate Change 2013: The Physical Science Basis, Contribution of Working Group I to the Fifth Assessment Report of the Intergovernmental Panel on Climate Change [R]. Stocker T F (eds), Cambridge: Cambridge University Press, 2013: 1535.

[3] Committee on China's National Assessment Report on Climate Change. Second National Assessment Report on Climate Change [M]. Beijing: Science Press, 2011.

[4] SHI Neng, CHEN Jia-qi, TU Qi-pu. 4-phase climate change features in the last 100 years over China [J]. Acta Meteor Sin, 1995, 56(3): 257-271.

[5] GONG Zhi-qiang, FENG Guo-lin, DONG Wen-jie, et al. The research of dynamic structure abrupt change of nonlinear time series [J]. Acta Phys Sin, 2006, 55 (6): 3180-3187 (in Chinese).

[6] ZHANG Shi-xuan, ZHANG Lu, SUN Shu-peng, et al. Changes of the seasons in mainland China under global warming [J]. Plat Meteor, 2011, 30 (3): 659-667 (in Chinese).

[7] SHEN Bai-zhu, ZHANG Shi-xuan, YANG Han-wei, et al. Analysis of characteristics of a sharp turn from drought to flood in the middle and lower reaches of the Yangtze River in spring and summer in 2011 [J]. Acta Phys Sin, 2012, 61(10): 530-540 (in Chinese).

[8] LU Ai-gang, HE Yuan-qing, ZHANG Zhong-lin, et al. Regional sensitivity analysis of the response of Chinese mainland to global warming [J]. J Glaciol Geocryol, 2005, 27(6): 827-832 (in Chinese).

[9] ZENG Qing-cun, ZHANG Bang-lin. On the seasons of general atmospheric circulation and their abrupt changes, Part Ⅰ: general concept and method [J]. Atmos Sci, 1992, 16(6): 641-648.

[10] GUO Yan-juan, YANG Xiu-qun. Temporal and spatial characteristics of interannual and interdecadal variations in the global ocean-atmosphere system [J]. Meteor Sci, 2002, 22(2): 127-138.

[11] HAO Cheng-yuan, WU Shao-hong, LI Shuang-cheng. Measurement of climate complexity using permutation entropy [J]. Geographical Res, 2007, 26(1): 46-52.

[12] LI Jian-ping, CHOU Ji-fan. Advances in nonlinear atmospheric dynamics [J]. Chin J Atmos Sci, 2003, 27 (4): 653-673.

[13] ZHANG Shi-xuan, ZHI Rong, FENG Guo-lin, et al. The Relationship between the onset date of preceding winter and following summer rainfall in eastern China [J]. Chin J Atmos Sci, 2012, 36(3): 564-578.

[14] ZHU Ke-zhen. Southeast monsoon and rainfall in China [J]. Acta Geographica Sinica, 1934, 1: 1-28 (in Chinese).

[15] TU Chang-wang, HUANG Shi-song. The advance and retreat of the summer monsoon [J]. J Meteor, 1944, 18 (1-4): 82-92.

[16] YE Du-zheng, ZHU Bao-zhen. On the arrival of east transitional season from changes in atmospheric circulation [J]. Acta Meteor Sinica, 1955, 26(1-2): 71-87 (in Chinese).

[17] ZHANG Qing-yun, TAO Shi-yan. Influence of Asian mid-high latitude circulation on East Asian summer rainfall [J]. Acta Meteorologica Sinica, 1998, 56 (2): 199-211 (in Chinese).

[18] YUAN Xu, LIU Xuan-fei. Onset-withdrawal dates of autumn persistent rains over western China and the associated autumn to winter evolution of the atmospheric circulation [J]. Acta Meteor Sinica, 2013, 71(5): 913-924 (in Chinese).

[19] FAN Wen-xuan, WANG Jing-yue, WANG Wei-guo, et al. Temporal-spatial structural switch and evolution characteristics of the residual circulation in the different seasons [J]. Acta Meteor Sinica, 2014, 72(3): 542-553 (in Chinese).

[20] ZHANG Bao-kun. Distribution of the four seasons in China [J]. Acta Geographica Sinica, 1934, 1: 1-18 (in Chinese).

[21] ZHU Bing-hai. Climate in China [M]. Beijing: Science Press, 1962: 254-262.

[22] ZHANG Jia-cheng, LIN Zhi-guang. Climate in China [M]. Shanghai: Shanghai Scientific and Technical Publishers, 1985: 55-63.

[23] LIAO Qi-long, WANG Yong. Division of the season in China and analysis of its variation characteristics [C]// Chinese Meteorological Society 2007 Annual Conference on Climate Change. Guangzhou, 2007: 693-701.

[24] LIU Kuang-nan, WU Hong-xun. A preliminary study on the determination of natural synoptic summer season over Asiatic natural synoptic region and the prevailing weather process in this season [J]. Acta Meteor Sinica, 1956, 27 (3): 219-242 (in Chinese).

[25] ZHANG Bang-lin, ZENG Qing-cun. A Study on the seasons of general atmospheric circulation and their abrupt changes, Part Ⅱ: Case study of particular year [J]. Atmos Sci, 1998, 22(2): 130-136.

[26] XUE Feng, LIN Yi-hua, ZENG Qing-cun. On the seasonal division of atmospheric general circulation and its abrupt change, Part Ⅲ: Climatology [J]. Atmos Sci, 2002, 26(3): 307-314.

[27] SUN Shu-peng, ZHANG Lu, HOU Wei, et al. A non-linear similarity method for season division in China [J]. Acta Physica Sinica, 2011, 60(2): 803-809 (in Chinese).

[28] HOU Wei, SUN Shu-peng, ZHANG Shi-xuan, et al. Season division and its temporal and spatial variation features of general atmospheric circulation in East Asia [J]. Acta Physica Sinica, 2011, 60(10): 781-789 (in Chinese).

[29] DRYSDALE P. Japan, Australia and New Zealand: the prospects for western integration [J]. Economic Record, 1967, 45(111): 321-342.

(C)1994-2019 China Academic Journal Electronic Publishing House. All rights reserved. http://www.cnki.net

[30] YI Yun-he, WU Shao-hong, DAI Er-fu. Determining elements in potential evapotranspiration changes over China in the period 1971-2008 [J]. Chin Sci Bull, 2010, 55(22): 2226-2234.
[31] MCCUEN R H. A sensitivity and error analysis of procedures used for estimating evaporation [J]. Water Resour Bull, 1974, 10(3): 486-497.
[32] HUPET F, VANCLOOSTER M. Effect of the sampling frequency of meteorological variables on the estimation of the reference evapotranspiration [J]. J Hydrol, 2001, 243(3-4): 192-204.
[33] LENHART T, ECKHARDT K, FOHRER N, et al. Comparison of two different approaches of sensitivity analysis [J]. Phys Chem Earth, 2002, 27(9): 645-654.
[34] GOYAL R K. Sensitivity of evapotranspiration to global warming: a case study of arid zone of Rajasthan (India) [J]. Agric Water Management, 2004, 69(1): 1-11.
[35] HUANG Jiao-wen, HE Jin-hai, XU Hai-ming, et al. Relationship between the seasonal transition of east Asian monsoon circulation and Asia pacific thermal field and possible mechanisms [J]. J Trop Meteor, 2016, 32 (6): 817-830 (in Chinese).
[36] LIN Zhen-yao, WU Xiang-ding, TIAN Guo-liang. A preliminary analysis of atmospheric turbidity and extinction property in the Xizang Plateau during the warm season [J]. Acta Geographica Sinica, 1984, 3: 298-306 (in Chinese).
[37] LIN Xiang, QIAN Wei-hong. Trends on the daily mean air temperature and its anomalous strength in China for the warm season in the last 40 years [J]. Acta Geographica Sinica, 2003, 58(z1): 21-30 (in Chinese).
[38] SHI Xiao-hui, XU De-xiang, XIE Lian. Climate change characteristics of aerosol "influence region" in warm season in East China [J]. Sci in China (D): Geosci, 2008, 38(4): 519-528.
[39] SHI N, ZHU Q G. An abrupt change in the intensity of the East Asian summer monsoon index and its relationship with temperature and precipitation over East China [J]. Int J Climatol, 2015, 16(7): 757-764.
[40] ZHAO Jun-hu, FENG Guo-lin. Reconstruction of conceptual prediction model for the three rainfall patterns in the summer of eastern China under global warming [J]. Sci China: Earth Sci, 2014, 57 (12): 3047-3061.
[41] HE W P, WANG L, JIANG Y D, et al. An improved method for nonlinear parameter estimation: a case study of the Rössler model [J]. Theor Appl Climatol, 2016, 125 (3-4): 521-528.
[42] GONG Zhi-qiang, LI Shang-feng, HU Po, et al. Dynamic-analogue correction of the decadal change of East Asian summer precipitation in the late 1990s [J]. Acta Meteor Sinica, 2016, 30(3): 341-355 (in Chinese).
[43] ZHOU Zi-kang, TANG Yan-bing, YU Lian-gen, et al. Response of China climate to global warming[J]. Bull Sci Technol, 1997, 13(2): 69-74.
[44] ZUO Zhi-yan, ZHANG Ren-he, WU Bing-yi. The interdecadal variation characteristics of spring precipitation in the south of China during the period of 1979-2004 and its relationship with the snow cover of Eurasia continent [J]. Sci in China: Geosci, 2011, 41(11): 1688-1696.
[45] YAO Hui-ru, LI Dong-liang. The interannual variation of wind speed in the Tibetan Plateau in spring and its response to global warming during 1971 -2012 [J]. Acta Meteor Sin, 2016, 74(1): 60-75 (in Chinese).
[46] REN Guo-yu, WU Hong, CHEN Zheng-hong. Spatial patterns of change trend in rainfall of China [J]. Quart J Appl Meteor, 2000, 11(3): 322-330.
[47] HAN Yan-feng, JIANG Zhi-hong, WANG Ji, et al. Temporal and spatial characteristics of summer rainfall in northeast China [J]. Meteor Sci Technol, 2005, 33 (2): 136-141.
[48] JIN Li-ya, FU Jiao-lan, CHEN Fa-hu. Spatial differences of precipitation over northwest China during the last 44 years and its response to global warming [J]. J Geograph Sci, 2005, 25(5): 567-572.
[49] LIU Hai-wen, DING Yi-hui. The interdecadal variability of summer precipitation over north China [J]. J Appl Meteor, 2011, 22(2): 129-137.
[50] ZHANG Shu-jie, ZHANG Yu-shu, CHEN Peng-shi, et al. Change characteristics of humid index and dry/wet climate boundary in northeast China [J]. Agric Res Arid Areas, 2011, 29(3): 226-232.
[51] LIU Dan-dan, LIANG Feng, WANG Wan-zhao, et al. Spatial and temporal variations of precipitation in northeast China from 1901 to 2010 based on GPCC data [J]. Research of Soil and Water Conservation, 2017, 24(2): 124-131.
[52] ZHANG Qiong, QIAN Yong-fu, ZHANG Xue-hong. Interannual and interdecadal variations of the South Asia High [J]. Chin J Atmos Sci, 2000, 24(1): 67-78.
[53] PENG Hua. A discussion on the effect of Tibet Plateau swelling on the climate in China [J]. Geograp Res, 1989, 8(3): 85-94.

Citation: WANG Zheng, ZHI Rong, WANG Yu, et al. Partition of season based on multi-elements and the decadal change of season duration in China [J]. J Trop Meteor, 2019, 25(3): 385-398.

(C)1994-2019 China Academic Journal Electronic Publishing House. All rights reserved. http://www.cnki.net

Geophysical Research Letters

RESEARCH LETTER
10.1029/2018GL081755

Special Section:
Bridging Weather and Climate: Subseasonal-to-Seasonal (S2S) Prediction

Conditional Nonlinear Optimal Perturbations of Moisture Triggering Primary MJO Initiation

Yuntao Wei[1,2,3], Mu Mu[1,4], Hong-Li Ren[3], and Joshua-Xiouhua Fu[3,4]

[1]Key Laboratory of Ocean Circulation and Waves, Institute of Oceanology, Chinese Academy of Sciences, Qingdao, China, [2]College of Earth and Planetary Sciences, University of Chinese Academy of Sciences, Beijing, China, [3]Laboratory for Climate Studies and CMA-NJU Joint Laboratory for Climate Prediction Studies, National Climate Center, China Meteorological Administration, Beijing, China, [4]Institute of Atmospheric Sciences and Department of Atmospheric and Oceanic Sciences, Fudan University, Shanghai, China

Abstract The Madden-Julian Oscillation (MJO) is a dominant intraseasonal variability originating in the tropics and influencing global weather and climate. Despite this dominance, we still lack reliable precursor signals triggering nonlinear initiation of primary MJO events. Here for the first time, we deal with this question from the point of view of nonlinearity, with successful implementation of conditional nonlinear optimal perturbation (CNOP). Our results show that relative to random perturbations, CNOPs of moisture have the most potential to trigger the strongest primary MJO events more than 15–20 days in advance from the given non-MJO reference states. The CNOPs manifest as a moist equator and aggregate in the lower troposphere, with stronger signals over the western Indian Ocean than over the eastern one. These CNOPs can also capture the observational moist precursor conditions of primary MJO events. This work also implies the necessity of utilizing nonlinear optimal moist initialization in subseasonal predictions.

Plain Language Summary As a dominant intraseasonal (20–90 days) variability prevailing in the tropics, the Madden-Julian Oscillation (MJO) casts significant impacts on global weather and climate. However, we still lack reliable precursor signals for MJOs initiating over the western Indian Ocean, especially for primary events, that is, those without an immediately preceding MJO event. Here for the first time, we deal with this topic from the point of view of nonlinearity, with the successful implementation of conditional nonlinear optimal perturbation (CNOP). In particular, we find that our CNOPs can identify the optimal precursors of primary MJO initiation. We examined four non-MJO reference states, selected based on both circulation- and convection-based MJO indices. Although different reference states produce different CNOPs, all tend to manifest as a moist equator and aggregate in the lower troposphere, with stronger signals over the western Indian Ocean than over the eastern Indian Ocean. These CNOP-type moist precursor conditions are also found preceding the onset of observed primary events. We find that, relative to random perturbations, CNOPs of moisture have the most potential to trigger the strongest MJO event more than 15–20 days in advance. This work implies the necessity of utilizing nonlinear optimal moist initialization to improve subseasonal (15–60 days) predictions.

Key Points:
- We first investigate the initiation of primary MJO events from the point of view of nonlinearity
- CNOPs of moisture have the most potential to trigger the strongest primary MJO initiation more than 15–20 days in advance
- CNOPs of moisture can also capture the observational precursor conditions of primary MJO events

Supporting Information:
- Supporting Information S1

Correspondence to:
M. Mu and H.-L. Ren,
mumu@fudan.edu.cn;
renhl@cma.gov.cn

Citation:
Wei, Y., Mu, M., Ren, H.-L., & Fu, J.-X. (2019). Conditional nonlinear optimal perturbations of moisture triggering primary MJO initiation. *Geophysical Research Letters*, *46*, 3492–3501. https://doi.org/10.1029/2018GL081755

Received 20 DEC 2018
Accepted 30 JAN 2019
Accepted article online 5 FEB 2019
Published online 22 MAR 2019

©2019. American Geophysical Union. All Rights Reserved.

1. Introduction

A remarkable feature of tropical mesoscale cloud clusters is their tendency to be organized as slowly eastward propagating (~5 m/s) convective envelops at a planetary scale (Nakazawa, 1988). This phenomenon is known as the Madden-Julian Oscillation (MJO; Madden & Julian, 1971, 1972). Widely recognized as the dominant intraseasonal (20–90 days) variability prevailing over the tropics (Zhang, 2005), the MJO can cast significant impacts not only on tropical systems but also on a variety of climate phenomena across different spatial and temporal scales. These phenomena include (1) modulating the occurrence of extreme weather (Ren et al., 2018; Ren & Ren, 2017; Xavier et al., 2014), (2) affecting the onsets and breaks of global monsoon systems (Wang, Liu, et al., 2017; Zhou & Chan, 2010), (3) interacting with the extratropics by exciting Rossby wave train and teleconnection (Henderson et al., 2017; Jones et al., 2004), and (4) contributing to the life cycle of El Niño events (McPhaden, 1999). The successful prediction of the MJO, which bridges weather and climate (Zhang, 2013), is thus invaluable for saving and improving human lives around the world.

The MJO has intrigued scientific communities since it was first documented. Over the past four decades of scientific pursuit, the MJO has become well understood as an equatorially trapped, unstably initiating,

planetary-scale circulation system (Li & Zhou, 2009; Wei et al., 2017), coupled with a multiscale convective complex (Majda & Biello, 2004), moving eastward slowly with a rearward-tilted (Kiladis et al., 2009), mixed Kelvin-Rossby wave structure (Chen & Wang, 2018a; Wang et al., 2018; Wang & Chen, 2016). In spite of significant progress in simulating and predicting the MJO, there are still numerous long-standing, fundamental, yet unresolved scientific questions about the MJO. One of the most challenging and least studied among these is the identification of the optimal precursors that trigger the initiation of large-scale, organized, eastward propagating, deep convection of the MJO over the western Indian Ocean (Ling et al., 2017). Building on previous works, two major schools of thought have developed as follows. The first school considers the triggering of MJO initiation to arise exclusively from tropical dynamic and thermodynamic processes, including regeneration from upstream circumnavigating Kelvin waves (Lau & Peng, 1987; Sakaeda & Roundy, 2015, 2016; Zhang et al., 2017); the recharge of moist static energy through localized nonlinear interaction among radiation, convection, and evaporation (Bladé & Hartmann, 1993; Kemball-Cook & Weare, 2001; Maloney & Wolding, 2015); air-sea interactions (Fu & Wang, 2004; Li et al., 2008; Rydbeck & Jensen, 2017; Rydbeck et al., 2017; Webber et al., 2010, 2012); and downstream Rossby wave dynamic effects (Li et al., 2015; Wang et al., 2005; Zhao et al., 2013). The second school emphasizes the critical role of tropical-extratropical interaction (Hsu et al., 1990; Ray et al., 2009; Ray & Zhang, 2010).

A consensus on the essential mechanisms for MJO initiation has not yet been reached. One possible reason for the lack of agreement is the intrinsic diversity and sporadic nature of the MJO. Each MJO event can be classified as either primary, that is, with no immediately preceding MJO event, or successive, that is, immediately following a preceding event (Matthews, 2008). Unlike the smooth variation of the real-time multivariate MJO (RMM) index (Wheeler & Hendon, 2004) throughout both the initiation and development in successive MJO events, a fast, localized growth of the composite RMM index always occurs prior to the eastward propagation of primary events (e.g., Figure 4 in Ling et al., 2013, and Figure 6 in Straub, 2013). A new MJO is then triggered after sufficient predestabilization, possibly by the advective moistening processes associated with equatorial wave dynamics (Zhao et al., 2013) and/or three-way interaction among radiation, evaporation, and convection (Bladé & Hartmann, 1993). This kind of sudden initiation from non-MJO states strongly suggests that some nonlinear processes play important roles. Thus, the linearized theoretical framework has previously experienced difficulty in simulating MJO initiation that occurs without a strong predecessor signal (e.g., Adames & Kim, 2016; Wang & Chen, 2016; Wang, Wei, et al., 2017; Wei et al., 2017). This may be a result of linear models' omission of key components of MJO initiation and amplification that have not yet been identified. However, nonlinear processes are perhaps critical to primary MJO initiation and linear models should not be expected to perform well under these circumstances. Consequently, a new nonlinear framework methodology is urgently needed to study the initiation of MJO events, especially that of primary MJO events.

This study aims to demonstrate that primary MJO events can be triggered in a process of nonlinear optimal moist initialization. Roles of moist processes have been shown to be essential in initiating (e.g., Li et al., 2015; Zhao et al., 2013) and maintaining the MJO (e.g., Adames & Kim, 2016; Hsu & Li, 2012; Sobel & Maloney, 2012, 2013) and also in improving subseasonal to seasonal prediction (e.g., Ham et al., 2012; Ren et al., 2016). Our efforts will be devoted to mathematically identifying moist optimal precursors that trigger primary MJO initiation in a coupled global climate model (CGCM). Benefiting from this advanced CGCM, we have developed a new nonlinear framework methodology to study the initiation of the MJO. In this work, the key accomplishment is the successful implementation and application of "conditional nonlinear optimal perturbation" (CNOP), a technique proposed by Mu et al. (2003).

In section 2, we introduce the data and model used in this paper. Section 3 describes a new nonlinear methodological framework for studying primary MJO initiation. The results are provided in section 4, and the final section gives a brief summary and discussion of this research.

2. Data and Model

2.1. Data

To measure convective activity, we use the daily mean outgoing longwave radiation (OLR) interpolated from the National Oceanic and Atmospheric Administration's Advanced Very High Resolution Radiometer satellite (Liebmann & Smith, 1996). The daily mean winds and specific humidity are from the reanalysis project of the National Centers for Environmental Prediction/the National Center for Atmospheric Research

(Kalnay et al., 1996). The time period analyzed herein is from 1979 to 2013. All data sets have been interpolated to horizontal resolution of 2.5° × 2.5° before analysis. For simplicity, we refer to them as "observations" throughout this paper.

2.2. The Hybrid CGCM

The model used in this study is a hybrid CGCM (Fu & Wang, 2004). The atmospheric component is the standard T42 version of the ECHAM-4 model (Roeckner et al., 1996), which resolves 19 vertical layers extending from the surface to 10 hPa. The oceanic component is a tropical upper ocean model of intermediate complexity (Fu & Wang, 2001). The ECHAM-4 model was coupled with the ocean model once per day by exchanging surface heat fluxes, surface wind stress, and sea surface temperature over the tropical global ocean without heat flux corrections. A 30-year free run was carried out and is analyzed below. The CGCM shows substantial capability in simulating the first two combined empirical orthogonal function (EOF) modes (Wheeler & Hendon, 2004), the nonlinear features of the MJO (Majda & Stechmann, 2011), and the primary MJO events (Matthews, 2008); for further details please see supporting information Text S1 and Figures S1–S3.

3. A New Methodological Framework for Studying Primary MJO Initiation

After some unsuccessful attempts to derive suitable linear solutions, we have directly chosen the nonlinear method, that is, CNOP (Appendix A). Using a CNOP framework, we constructed MJO initiation as a unified nonlinear optimization problem. We first identified eight non-MJO reference states (NMRSs; Appendix B), half of which were randomly chosen for examination in this study. Each NMRS has a 42-day duration, with very weak (<1) index values for both the OLR-based MJO index (OMI; Kiladis et al., 2014) and the RMM index. Neither convection nor circulation displays an organized, large-scale, eastward propagating MJO signal. It is noteworthy that this kind of convective initiation from non-MJO to MJO event, if any, must be primary (Ling et al., 2013; Straub, 2013).

To find optimal precursors mathematically, an indicator must be constructed in advance to (i) clearly distinguish non-MJO and MJO events and (ii) measure the strength of the triggered MJO events. Taking advantage of the 42-day power spectra of convection and circulation, an indicator can be formulated as follows:

$$I = \sum_{i=1}^{3} \frac{\rho_i}{\pi_i} \iint_{\Omega_{\mathrm{MJO}}} P_i(\omega, k) \mathrm{d}\omega \mathrm{d}k, \tag{1}$$

where i(=1, 2, 3) denotes OLR, 850-hPa zonal wind (U850) and coherence square between them, respectively. $\rho_i \in [0, 1]$ is the weight coefficient. Here we take $\rho_1 = \rho_2 = \rho_3 = 1/3$, which guarantees a more precise definition of MJO initiation that further considers the tight coupling between circulation and convection. $P_i(\omega, k)$ is power variance at frequency ω and wavenumber k. $(\omega, k) \in \Omega_{\mathrm{MJO}} = [1/100, 1/20] \times [0, 3]$, which outlines the spatiotemporal range of the eastward propagating MJO signal. To satisfy the additivity requirement, prenormalization is necessary. π_i is the standard deviation of the total power spectrum in Ω_{MJO}. Remarkably, under the "perfect model" assumption, I is totally controlled by the initial conditions of each individual NMRS.

To identify the optimal moist precursors, we let q_0 be the initial specific humidity of the prechosen reference state and q_0' be a finite-amplitude disturbance of q_0, that is, $\|q_0'\| \leq \delta$. We term "ctr" and "per" as the respective numerical integrations initiated from q_0 and from $q_0 + q_0'$. Contributions of initial moist perturbations to the MJO can be derived as follows:

$$J = J(q_0') = I_{\mathrm{per}}(q_0' + q_0) - I_{\mathrm{ctr}}(q_0) \tag{2}$$

From equation (2), a stronger MJO event must correspond to a larger value of J. Thus, searching for the optimal moist precursor $\widetilde{q_0'}$ that triggers the strongest primary MJO initiation can be generalized as the following unified nonlinear optimization problem:

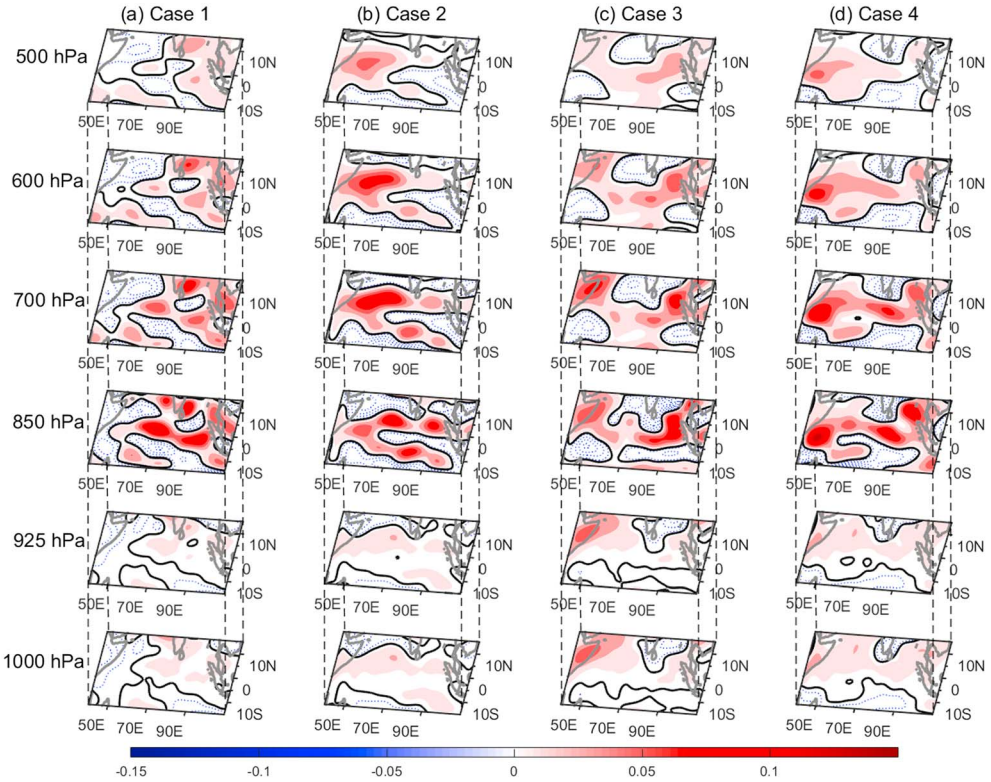

Figure 1. Three-dimensional structure of conditional nonlinear optimal perturbation (in grams per kilogram) in cases 1 to 4, from left to right. The six subplots in each column represent different pressure levels, that is, 500, 600, 700, 850, 925, and 1,000 hPa, from top to bottom. The wet anomaly is represented as red shading. The dry anomaly is shown by blue dotted contours at intervals of 0.02 g/kg. The thick black contour denotes the zero value. The *x* axis is longitude (in degrees), and the *y* axis is latitude (in degrees).

$$J(\widetilde{q_0'}) = \max_{\|q_0'\| \le \delta} J(q_0') \tag{3}$$

Equation (3) tells us that the moist optimal precursor should be the global optimal point in the feasible region $\{q_0' | \|q_0'\| \le \delta\}$, that is, CNOP.

Upon obtaining the CNOP of each given NMRS, we performed three reforecasts: The first run ("Control run") began with unperturbed initial conditions, the second run ("CNOP run") had CNOP-perturbed initial conditions, and the third run ("RP run") was initialized with random perturbations. To facilitate comparison, we scale any random perturbations to have the same norm as the CNOPs. The role of CNOP in triggering primary MJO initiation was then revealed by comparing the three runs.

4. Results

4.1. CNOPs and Observational Evidence

In this section, we first discuss the three-dimensional (3-D) structures of the CNOPs in all four cases. To demonstrate the ability of CNOPs to capture the "true" precursor conditions of primary MJO initiation, we then search for these signals in observational data.

In general, the 3-D distributions of CNOPs (Figure 1) show that different NMRSs produced different CNOPs, which implies that different MJO events should have distinctive preceding optimal growing initial perturbations. Despite the different patterns overall, all CNOPs tend to be wet along the equatorial Indian Ocean but dry away from the equator. The strongest signals aggregate over the lower troposphere, with stronger perturbations in the equatorial western Indian Ocean (WIO) than in eastern Indian Ocean (EIO). To search for these signals from observations, we calculated the Hovmöller diagrams of the equatorially averaged (10°S

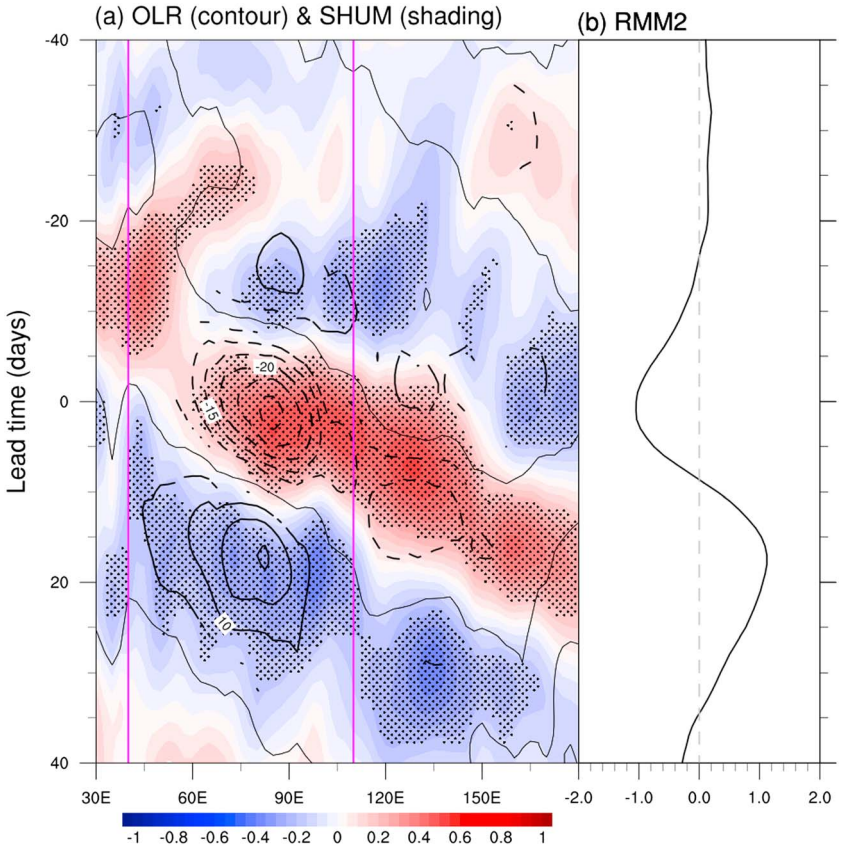

Figure 2. (a) Composite Hovmöller diagrams of equatorially averaged (10°S to 10°N), 20- to 90-day bandpass-filtered OLR (contour in watts per square meter) and 850-hPa specific humidity (shading in grams per kilogram) anomalies using the 23 observed primary MJO events. The solid (dashed) contour is from 5 (−5) W/m^2 at intervals of 5 W/m^2. The thin black contour denotes the zero values. The two magenta lines outline the zonal region for calculating the conditional nonlinear optimal perturbations. The dotted area and contours represent results passing Student's *t* test at the 95% confidence level. The *x* axis is longitude (in degrees), while the *y* axis is lead time (in days). (b) Composite RMM2 index of observed primary Madden-Julian Oscillation events. The *x* axis is RMM2, while the *y* axis is lead time (in days). OLR = outgoing longwave radiation; RMM = real-time multivariate MJO; SHUM = specific humidity.

to 10°N), 20- to 90-day bandpass-filtered OLR and 850-hPa specific humidity (q850) anomalies in each observed primary MJO event. We further examined any anomalous moisture preceding the onset of each MJO event.

The results showed that 23 of 49 events are clearly preconditioned by a moisture anomaly. The composite of these 23 events (Figure 2) shows that preceding the onset of large-scale, eastward propagating, deep convection, a significant moisture signal originates from the EIO and moves toward the WIO. Since day −10, this moisture signal tends to be reflected near eastern Africa. Then it continuously moves eastward and triggers primary MJO initiation at day −5. In addition, there also exists a small, localized, narrow, and suppressed convection over the EIO at day −15, which may also play a role in initiating the MJO through a midtropospheric, cooling-induced, predestabilization effect (Matthews, 2008). The horizontal structure of q850 and the vertical distribution of specific humidity have been also diagnosed (Figures S4 and S5). Together, the above findings demonstrate the existence, well captured by the CNOPs, of significant moisture anomalies aggregating in the lower troposphere over eastern Africa and the WIO.

4.2. CNOPs Triggering Primary MJO Initiation

Despite displaying distinctive 3-D structures, all the CNOPs tend to trigger a similar spatiotemporal variance pattern, especially over Ω_{MJO}. This pattern is illustrated by the composite zonal wavenumber-frequency spectra of both convection (OLR) and circulation (U850) in Figure 3. As expected, both the Control run

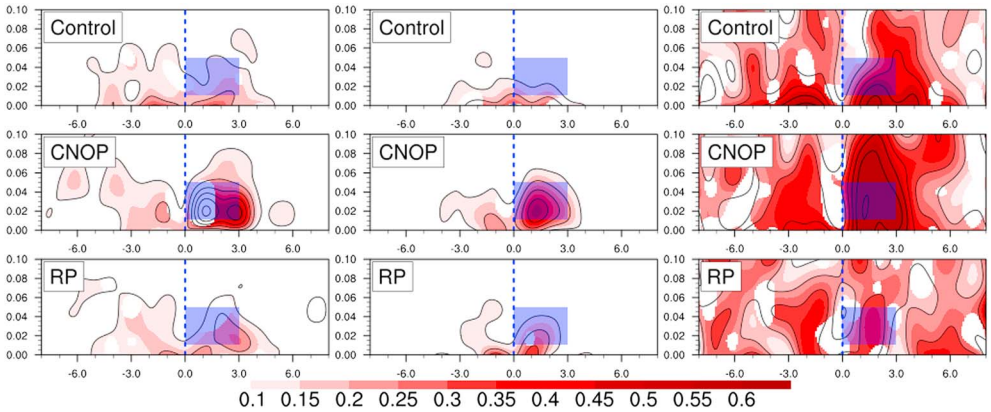

Figure 3. Composite zonal wavenumber-frequency spectrum of OLR (left column), U850 (middle column), and coherence square between them (right column) in the Control run (first row), the CNOP run (second row), and the RP run (third row). The *x* axis is zonal wavenumber ($2\pi/40{,}000$ km), and the *y* axis is frequency (cycles per day). The blue shading denotes Ω_{MJO}, which outlines the wavenumber and frequency ranges of eastward propagating MJO signals. The red shading denotes the results passing the Student's *t*-test at the 95% confidence level. to keep color legend consistent, the OLR spectrum has been multiplied by 0.02. Contour starts from 0.1 at intervals of 0.1. OLR = outgoing longwave radiation; CNOP = conditional nonlinear optimal perturbation; RP = random perturbation.

and RP run show very weak power spectral variance, and the westward signal is comparable with the eastward one. However, when the nonlinear optimal moist initialization with the CNOPs is included, the variances of convection and circulation associated with the eastward propagating MJO increase intensely, leaving a largely reduced westward signal. In a further difference from the Control and RP runs, the CNOP run's Ω_{MJO} shows a strong variance of the coherence square between OLR and U850, which implies that strong coupling between convection and circulation has been also triggered by the CNOPs.

To demonstrate the triggering of primary MJO initiation, we also investigated the phase diagram of the RMM index (Figure S6). The results show that, in contrast to the RMM index's small growth in the Control and RP runs, the CNOP run's RMM index increased quickly and crossed the unit circle after 15–20 days of development, which is a typical initiation of primary MJO events (Ling et al., 2013; Straub, 2013).

The triggering of primary MJO initiation can be observed more clearly from the time-longitude sections of OLR and U850 (Figures 4a–4c). During the first 10 days, the perturbations in the three runs show very

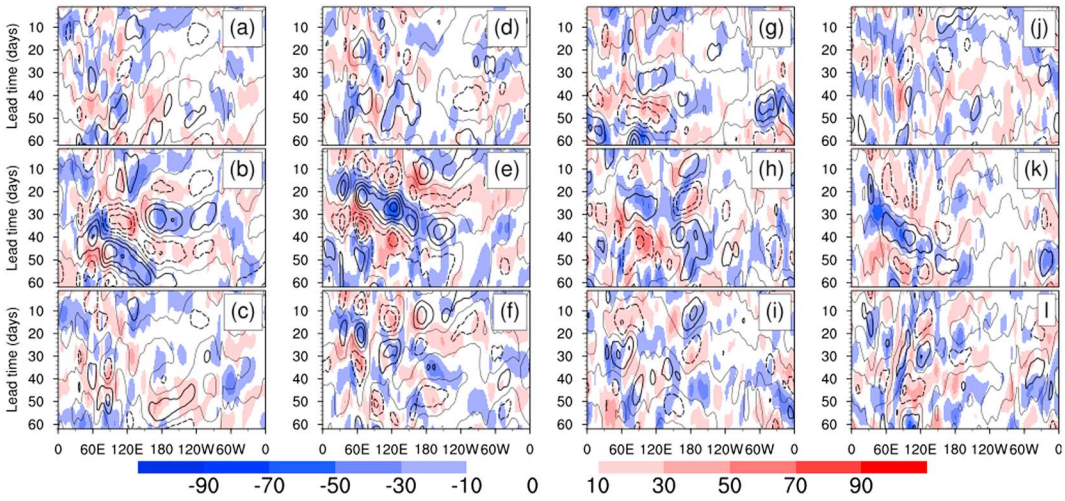

Figure 4. Hovmöller diagrams of equatorially averaged (10°S to 10°N) 20- to 90-day bandpass-filtered outgoing longwave radiation (shading) and U850 (contour) anomalies in the Control run (first row), the conditional nonlinear optimal perturbation run (second row), and the random perturbation run (third row). Solid (dashed) contours denote westerly (easterly) wind anomalies at intervals of 2 m/s. The thin black contour shows the zero values. Panels (a)–(c) are case 1, (d)–(f) case 2, (g)–(i) case 3, and (j)–(l) case 4. To fully represent the life cycle of triggered Madden-Julian Oscillation events, the time shown has been extended to day 62.

similar patterns. After days 10 to 15, the results start to diverge. The differences increase with lead time. After days 25 to 30, an organized, large-scale, slowly eastward propagating, convectively coupled, primary MJO event is triggered only in the CNOP run. In contrast, for the Control run and RP run, as implicated by their small index evolutions, there are only very weak and unorganized anomalies. This distinction with respect to random perturbations demonstrates the power of nonlinear fast growth of the CNOPs in triggering the strongest primary MJO event from a given NMRS. A strong, new, primary MJO event is also triggered by the CNOPs in other NMRSs (Figures 4d–4l), although the initiation time, strength, duration, and phase speed are somewhat different, reflecting MJO diversity and dependence on basic flow (Lorenz, 1965).

5. Conclusions and Discussion

A newly developed nonlinear methodological framework was applied to identify the optimal precursors triggering primary MJO initiation. This framework mathematically identified optimal precursors from the four prechosen NMRSs using a hybrid CGCM that can accurately simulate observed primary MJO events and a novel concept of CNOP. In this new framework, searching for the optimal precursors of primary MJO initiation can be generalized as solving for optimal solutions, that is, CNOPs, of a unified constraint nonlinear optimization problem.

Our results show that although different CNOPs have been found in different NMRSs, they tended to manifest as a moist equator and aggregate over the lower troposphere, with stronger signals in the WIO than in the EIO. Preceding the initiation of observed primary MJO events, we found significant lower-tropospheric moisture signals moving toward the equatorial WIO, implying the key role of moisture-convection feedback while demonstrating the true-to-life quality of the CNOPs. The GCM reforecast experiments show that CNOPs have the most potential to initiate the strongest primary MJO events from any given NMRSs, while random perturbations only induce a non-MJO or weak-MJO initiation.

CNOPs trigger a new primary MJO event after a development of more than 15–20 days, which may imply that we can predict the onset of primary MJO initiation more than 15–20 days in advance, if the CNOPs are implemented in the initial conditions. Comparing the linear and nonlinear evolutions of CNOPs, we found that nonlinear growth is always dominant on the 20- to 90-day intraseasonal timescale (see Text S2, Figure S7, and Table S1). This finding may suggest the necessity of utilizing nonlinear optimal moisture initialization in subseasonal (15- to 60-day timescale) prediction.

Under the conditions of limited computational resources and as a preliminary application of this new methodological framework, we examined only humidity field with limited vertical levels and four NMRSs. In addition, we eschewed the problem of identifying the dominant physical processes that control the nonlinear growth of CNOPs. These issues deserve in-depth study, which will be part of our future work.

Appendix A

We write the evolution equations for the state vector U, which may represent wind, specific humidity, temperature, etc., as follows

$$\begin{cases} \dfrac{\partial U}{\partial t} = F(U,P) \\ U|_{t=0} = U_0 \end{cases}, \tag{A1}$$

where U_0 is the initial state, P is model parameter that is independent with time t, and F is a nonlinear differential operator. Assuming that equation (A1) is well defined, the solution to equation (A1) for the state vector U at time τ is given by

$$U(\tau) = M_\tau(P)(U_0). \tag{A2}$$

Here $M_\tau(P)$ is the propagator of equation (A1) with the parameter P and "propagates" the initial value U_0 to the time τ in the future. Now we consider the situation in which there exist both initial perturbation u_0 and parameter perturbation p' in equation (A2). Then we have

$$U(\tau) + u(u_0, p'; \tau) = M_\tau(P + p')(U_0 + u_0), \tag{A3}$$

where $u(u_0, p'; \tau)$ is the departure from the reference state $U(\tau)$ caused by the combined error mode (u_0, p'). A nonlinear optimization problem is defined as follows.

$$J(u_0; p') = \left\| M_\tau(P + p')(U_0 + u_0) - M_\tau(P)(U_0) \right\|, \tag{A4}$$

and

$$J(u_{0\delta}; p'_\sigma) = \max_{u_0 \in C_\delta, p' \in C_\sigma} J(u_0; p'). \tag{A5}$$

Here $u_0 \in C_\delta$ and $p' \in C_\sigma$ are, respectively, the constraint conditions of the initial perturbation and parameter perturbations, where C_δ and C_σ are closed and δ and σ distinguish the constraints of initial perturbation and parameter perturbation. The optimal combination mode of initial perturbation and parameter perturbation, that is, $(u_{0\delta}; p'_\sigma)$, of the constrained maximization problem (A5) is called the CNOP (Mu et al., 2010).

In this work, we consider the perfect model assumption, that is, $p' = 0$. In this case, the optimization problem is reduced to

$$J_{u_0}(u^I_{0\delta}) = \max_{u_0 \in C_\delta} \| M_\tau(P)(U_0 + u_0) - M_\tau(P)(U_0) \|. \tag{A6}$$

The initial perturbation $u^I_{0\delta}$ satisfying equation (A6) is just the CNOP defined in Mu et al. (2003).

Appendix B

The NMRSs have been selected based on both the RMM and OMI indices. First, the RMM amplitude is calculated. To facilitate selection, we use a 5-day running mean to remove high-frequency variability. Second, we identify day 0 when the amplitude reaches its minimum. Third, the amplitudes from day 0 to day 31 should be smaller than a prescribed threshold of one standard deviation. In some scenarios, however, the convection may be still active, albeit with a weak RMM index (Straub, 2013). Thus, the 5-day running mean OMI is also examined to adjust the weak event selected by the RMM index. To be specific, we have removed those events that continuously maintain a high-amplitude (>1) OMI lasting for more than 10 days. In the present article, we focus solely on the extended boreal winter from 15 October to 15 May

Appendix C

To improve computational efficiency, an EOF-based strategy is carried out to reduce the model dimensionality. We assume that the role of low-frequency basic state (> 90 days) is minor in triggering the large-scale, deep convection initiation on intraseasonal time scales (20 to 90 days). The variance of the 90-day highpass-filtered specific humidity prefers the Indo-Pacific region and aggregates over the lower atmosphere (500–1,000 hPa). Considering that MJO events are often initiated over the equatorial Indian Ocean (Matthews, 2008), we choose that precise region for the extraction of possible precursor signals, in particular the lower-level, equatorially symmetric Indian Ocean from 15°S to 15°N, from 40° to 110°E, tiered vertically at 1,000, 925, 850, 700, 600, and 500 hPa. The EOF results demonstrate that the first 50 PCs can explain more than 80% of the total variance. Most of them can pass the North test (North et al., 1982) and thus are well separated. Any initial perturbation can be expanded orthogonally by the first 50 EOF modes

$$q'_0 \approx q'_0(\lambda'_0) = \sum_{i=1}^{50} \lambda_0^{i\prime} e_i, \tag{C1}$$

where $\lambda_0^{i\prime}$ is the initial time coefficient disturbance corresponding to the ith EOF mode e_i.

Acknowledgments
The authors gratefully acknowledge Fei-Fei Jin, Fei Liu, and Wansuo Duan for their kind discussions about this work. Constructive comments by three anonymous reviewers led to substantial improvements in the presentation. This work was jointly supported by the National Basic Research (973) Program of China under grant 2015CB453203, the China National Science Foundation under grants 41775066, 41375062 and 41875064, the NSFC Innovative Group under grant 41421005, and the NSFC-Shandong Joint Fund for Marine Science Research Centers under grant U1406401. NCEP Reanalysis data were provided by the NOAA/OAR/ESRL PSD, Boulder, Colorado, USA, from their Web site at https://www.esrl.noaa.gov/psd/. Daily interpolated OLRs were obtained from NOAA/OAR/ESRL PSD, Boulder, Colorado, USA, https://www.esrl.noaa.gov/psd/.

References

Adames, Á. F., & Kim, D. (2016). The MJO as a dispersive, convectively coupled moisture wave: Theory and observations. *Journal of the Atmospheric Sciences*, *73*(3), 913–941. https://doi.org/10.1175/JAS-D-15-0170.1

Bladé, I., & Hartmann, D. L. (1993). Tropical intraseasonal oscillations in a simple nonlinear model. *Journal of the Atmospheric Sciences*, *50*(17), 2922–2939. https://doi.org/10.1175/1520-0469(1993)050<2922:TIOIAS>2.0.CO;2

Chen, G., & Wang, B. (2018a). Dynamic moisture mode versus moisture mode in MJO dynamics: Importance of the wave feedback and boundary layer convergence feedback. *Climate Dynamics*. https://doi.org/10.1007/s00382-018-4433-7

Chen, G., & Wang, B. (2018b). Does the MJO have a westward group velocity? *Journal of Climate*, *31*(6), 2435–2443. https://doi.org/10.1175/JCLI-D-17-0446.1

Fu, X., & Wang, B. (2001). A coupled study of the seasonal cycle of the Pacific cold tongue. Part I: Simulation and sensitivity experiments. *Journal of Climate*, *14*(5), 765–779. https://doi.org/10.1175/1520-0442(2001)014<0765:ACMSOT>2.0.CO;2

Fu, X., & Wang, B. (2004). Difference of boreal-summer intraseasonal oscillations simulated in an atmosphere-ocean coupled model and an atmosphere-only model. *Journal of Climate*, *17*(6), 1263–1271. https://doi.org/10.1175/1520-0442(2004)017<1263:DOBSIO>2.0.CO;2

Fu, X., Wang, W., Ren, H.-L., Jia, X., & Shinoda, T. (2018). Three different downstream fates of the boreal-summer MJOs on their passages over the maritime continent. *Climate Dynamics*, *51*(5-6), 1841–1862. https://doi.org/10.1007/s00382-017-3985-2

Ham, Y. G., Schubert, S., & Chang, Y. (2012). Optimal initial perturbations for ensemble prediction of the Madden-Julian Oscillation during boreal winter. *Journal of Climate*, *25*(14), 4932–4945. https://doi.org/10.1175/JCLI-D-11-00344.1

Henderson, S. A., Maloney, E. D., & Son, S. W. (2017). Madden-Julian Oscillation Pacific teleconnections: The impacts of the basic state and MJO representation in general circulation models. *Journal of Climate*, *30*(12), 4567–4587. https://doi.org/10.1175/JCLI-D-16-0789.1

Hsu, H.-H., Hoskins, B. J., & Jin, F.-F. (1990). The 1985/86 intraseasonal oscillation and the role of the extratropics. *Journal of the Atmospheric Sciences*, *47*(7), 823–839. https://doi.org/10.1175/1520-0469(1990)047<0823:TIOATR>2.0.CO;2

Hsu, P.-C., & Li, T. (2012). Role of boundary layer moisture asymmetry in causing the eastward propagation of the Madden-Julian Oscillation. *Journal of Climate*, *25*(14), 4914–4931. https://doi.org/10.1175/JCLI-D-11-00310.1

Jones, C., Waliser, D. E., Lau, K.-M., & Stern, W. (2004). The Madden-Julian Oscillation and its impact on Northern Hemisphere weather predictability. *Monthly Weather Review*, *132*(6), 1462–1471. https://doi.org/10.1175/1520-0493(2004)132<1462:TMOAII>2.0.CO;2

Kalnay, E., Kanamitsu, M., Kistler, R., Collins, W., Deaven, D., Gandin, L., et al. (1996). The NCEP/NCAR 40-Year Reanalysis Project. *Bulletin of the American Meteorological Society*, *77*(3), 437–471. https://www.jstor.org/stable/26232740

Kemball-Cook, S. R., & Weare, B. C. (2001). The onset of convection in the Madden-Julian Oscillation. *Journal of Climate*, *14*(5), 780–793. https://doi.org/10.1175/1520-0442(2001)014<0780:TOOCIT>2.0.CO;2

Kiladis, G. N., Dias, J., Straub, K. H., Wheeler, M. C., Tulich, S. N., Kikuchi, K., et al. (2014). A comparison of OLR and circulation-based indices for tracking the MJO. *Monthly Weather Review*, *142*(5), 1697–1715. https://doi.org/10.1175/MWR-D-13-00301.1

Kiladis, G. N., Wheeler, M. C., Haertel, P. T., Straub, K. H., & Roundy, P. E. (2009). Convectively coupled equatorial waves. *Reviews of Geophysics*, *47*, RG2003. https://doi.org/10.1029/2008RG000266

Lau, K.-M., & Peng, L. (1987). Origin of low frequency (intraseasonal) oscillations in the tropical atmosphere. Part I: Basic theory. *Journal of the Atmospheric Sciences*, *47*(12), 1443–1462.

Li, T., Tam, F., Fu, X., Zhou, T.-J., & Zhu, W.-J. (2008). Causes of the intraseasonal SST variability in the Tropical Indian Ocean. *Atmospheric and Oceanic Science Letters*, *1*(1), 18–23. https://doi.org/10.1080/16742834.2008.11446758

Li, T., Zhao, C., Hsu, P.-C., & Nasuno, T. (2015). MJO initiation processes over the tropical Indian Ocean during DYNAMO/CINDY2011. *Journal of Climate*, *28*(6), 2121–2135. https://doi.org/10.1175/JCLI-D-14-00328.1

Li, T., & Zhou, C. (2009). Planetary scale selection of the Madden-Julian Oscillation. *Journal of the Atmospheric Sciences*, *66*(8), 2429–2443. https://doi.org/10.1175/2009JAS2968.1

Liebmann, B., & Smith, C. (1996). Description of a complete (interpolated) outgoing longwave radiation dataset. *Bulletin of the American Meteorological Society*, *77*, 1275–1277. https://www.jstor.org/stable/26233278

Ling, J., Li, C., Li, T., Jia, X., Khouider, B., Maloney, E. D., et al. (2017). Challenges and opportunities in MJO studies. *Bulletin of the American Meteorological Society*, *98*(2), ES53–ES56. https://doi.org/10.1175/BAMS-D-16-0283.1

Ling, J., Zhang, C., & Bechtold, P. (2013). Large-scale distinctions between MJO and non-MJO convective initiation over the tropical Indian ocean. *Journal of the Atmospheric Sciences*, *70*(9), 2696–2712. https://doi.org/10.1175/JAS-D-13-029.1

Lorenz, E. N. (1965). A study of the predictability of a 28-variable atmospheric model. *Tellus*, *17*(3), 321–333.

Madden, R. A., & Julian, P. R. (1971). Detection of a 40-50 day oscillation in the zonal wind in the tropical Pacific. *Journal of the Atmospheric Sciences*, *28*(5), 702–708. https://doi.org/10.1175/1520-0469(1971)028<0702:DOADOI>2.0.CO;2

Madden, R. A., & Julian, P. R. (1972). Description of global-scale circulation cells in the tropics with a 40-50 day period. *Journal of the Atmospheric Sciences*, *29*(6), 1109–1123. https://doi.org/10.1175/1520-0469(1972)029<1109:DOGSCC>2.0.CO;2

Majda, A. J., & Biello, J. A. (2004). A multiscale model for tropical intraseasonal oscillations. *Proceedings of the National Academy of Sciences*, *101*(14), 4736–4741. https://doi.org/10.1073/pnas.0401034101

Majda, A. J., & Stechmann, S. N. (2011). Nonlinear dynamics and regional variations in the MJO skeleton. *Journal of the Atmospheric Sciences*, *68*(12), 3053–3071. https://doi.org/10.1175/JAS-D-11-053.1

Maloney, E. D., & Wolding, B. O. (2015). Initiation of an intraseasonal oscillation in an aquaplanet general circulation model. *Journal of Advances in Modeling Earth Systems*, *7*, 1956–1976. https://doi.org/10.1002/2015MS000495

Matthews, A. J. (2008). Primary and successive events in the Madden-Julian Oscillation. *Quarterly Journal of the Royal Meteorological Society*, *134*(631), 439–453. https://doi.org/10.1002/qj.224

McPhaden, M. J. (1999). The genesis and evolution of the 1997-98 El Niño. *Science*, *283*(5404), 950–954. https://doi.org/10.1126/science.283.5404.950

Mu, M., Duan, W. S., & Wang, B. (2003). Conditional nonlinear optimal perturbation and its applications. *Nonlinear Processes in Geophysics*, *10*(6), 493–501. https://doi.org/10.5194/npg-10-493-2003

Mu, M., Duan, W. S., Wang, Q., & Zhang, R. (2010). An extension of conditional nonlinear optimal perturbation approach and its applications. *Nonlinear Processes in Geophysics*, *17*(2), 211–220. https://doi.org/10.5194/npg-17-211-2010

Nakazawa, T. (1988). Tropical super clusters within intraseasonal variations over the western Pacific. *Journal of the Meteorological Society of Japan*, *66*(6), 823–839.

North, G. R., Bell, T. L., Cahalan, R. F., & Moeng, F. J. (1982). Sampling errors in the estimation of empirical orthogonal functions. *Monthly Weather Review*, *110*(7), 699–706. https://doi.org/10.1175/1520-0493(1982)110<0699:SEITEO>2.0.CO;2

Ray, P., & Zhang, C. (2010). A case study of the mechanics of extratropical influences on the initiation of the Madden-Julian Oscillation. *Journal of the Atmospheric Sciences*, *67*(2), 515–528. https://doi.org/10.1175/2009JAS3059.1

Ray, P., Zhang, C., Dudhia, J., & Chen, S. S. (2009). A numerical case study on the initiation of the Madden-Julian Oscillation. *Journal of the Atmospheric Sciences*, *66*(2), 310–331. https://doi.org/10.1175/2008JAS2701.1

Ren, H.-L., & Ren, P. (2017). Impact of Madden–Julian Oscillation upon winter extreme rainfall in southern China: Observations and predictability in CFSv2. *Atmosphere*, *8*(12), 192. https://doi.org/10.3390/atmos8100192

Ren, H.-L., Wu, J., Zhao, C., Cheng, Y., & Liu, X. (2016). MJO ensemble prediction in BCC-CSM1.1(m) using different initialization schemes. *Atmospheric and Oceanic Science Letters*, *9*(1), 60–65.

Ren, P., Ren, H.-L., Fu, X., Wu, J., & Du, L. (2018). Impact of boreal summer Intraseasonal oscillation on rainfall extremes in southeastern China and its predictability in CFSv2. *Journal of Geophysical Research: Atmospheres*, *123*, 4423–4442. https://doi.org/10.1029/2017JD028043

Roeckner, E., Arpe, K., Bentsson, L., Christoph, M., Claussen, M., Dümenil, L., et al. (1996). The atmospheric general circulation model ECHAM-4: Model description and simulation of present-day climate. *Comptes Rendus Des Séances De La Société De Biologie Et De Ses Filiales*, *151*(2), 361–363.

Roundy, P. E., & Frank, W. M. (2004). Applications of a multiple linear regression model to the analysis of relationships between eastward- and westward-moving intraseasonal modes. *Journal of the Atmospheric Sciences*, *61*(24), 3041–3048. https://doi.org/10.1175/JAS-3349.1

Roundy, P. E., & Frank, W. M. (2004b). Effects of low-frequency wave interactions on intraseasonal oscillations. *Journal of the Atmospheric Sciences*, *61*(24), 3025–3040.

Rydbeck, A. V., & Jensen, T. G. (2017). Oceanic impetus for convective onset of the Madden-Julian Oscillation in the western Indian Ocean. *Journal of Climate*, *30*, 4299–4316.

Rydbeck, A. V., Jensen, T. G., & Nyadjro, E. S. (2017). Intraseasonal sea surface warming in the western Indian Ocean by oceanic equatorial Rossby waves. *Geophysical Research Letters*, *44*, 4224–4232. https://doi.org/10.1002/2017GL073331

Sakaeda, N., & Roundy, P. E. (2015). The development of upper-tropospheric wind over the western hemisphere in association with MJO convective initiation. *Journal of the Atmospheric Sciences*, *72*(8), 3138–3160. https://doi.org/10.1175/JAS-D-14-0293.1

Sakaeda, N., & Roundy, P. E. (2016). The development of upper-tropospheric geopotential anomaly in the western hemisphere during MJO convective initiations. *Quarterly Journal of the Royal Meteorological Society*, *142*(695), 942–956. https://doi.org/10.1002/qj.2696

Sobel, A., & Maloney, E. D. (2012). An idealized semi-empirical framework for modeling the Madden-Julian Oscillation. *Journal of the Atmospheric Sciences*, *69*(5), 1691–1705. https://doi.org/10.1175/JAS-D-11-0118.1

Sobel, A., & Maloney, E. D. (2013). Moisture modes and the eastward propagation of the MJO. *Journal of the Atmospheric Sciences*, *70*(1), 187–192. https://doi.org/10.1175/JAS-D-12-0189.1

Straub, K. H. (2013). MJO initiation in the real-time multivariate MJO index. *Journal of Climate*, *26*(4), 1130–1151. https://doi.org/10.1175/JCLI-D-12-00074.1

Wang, B., & Chen, G. (2016). A general theoretical framework for understanding essential dynamics of Madden-Julian Oscillation. *Climate Dynamics*, *49*, 2309–2328.

Wang, B., Lee, S.-S., Waliser, D. E., Zhang, C., Sobel, A., Maloney, E. D., et al. (2018). Dynamics-oriented diagnostics for the Madden-Julian Oscillation. *Journal of Climate*, *31*, 3117–3135.

Wang, B., Webster, P. J., & Teng, H. (2005). Antecedents and self-induction of active-break south Asian monsoon unraveled by satellites. *Geophysical Research Letters*, *32*, L04704. https://doi.org/10.1029/2004GL020996

Wang, H., Liu, F., Wang, B., & Li, T. (2017). Effects of intraseasonal oscillation on South China Sea summer monsoon onset. *Climate Dynamics*, *51*(7-8), 2543–2558. https://doi.org/10.1007/s00382-017-4027-9

Wang, H., Wei, Y., & Liu, F. (2017). Effect of spatial variation of convective adjustment time on the Madden-Julian Oscillation: A theoretical model analysis. *Atmosphere*, *8*(12), 204. https://doi.org/10.3390/atmos8100204

Webber, B., Matthews, A., & Heywood, K. (2010). A dynamical ocean feedback mechanism for the Madden-Julian Oscillation. *Quarterly Journal of the Royal Meteorological Society*, *136*, 740–754.

Webber, B., Matthews, A., Heywood, K., & Stevens, D. (2012). Ocean Rossby waves as a triggering mechanism for primary Madden-Julian events. *Quarterly Journal of the Royal Meteorological Society*, *138*(663), 514–527. https://doi.org/10.1002/qj.936

Wei, Y., Liu, F., Ren, H.-L., & Mu, M. (2017). Planetary scale selection of the Madden–Julian Oscillation in an air-sea coupled dynamic moisture model. *Climate Dynamics*, *50*, 3441–3456.

Wheeler, M. C., & Hendon, H. H. (2004). An all-season real-time multivaritae MJO index: Development of an index for monitoring and prediction. *Monthly Weather Review*, *132*(8), 1917–1932. https://doi.org/10.1175/1520-0493(2004)132<1917:AARMMI>2.0.CO;2

Wheeler, M. C., & Kiladis, G. N. (1999). Convectively coupled equatorial waves: Analysis of clouds and temperature in the wavenumber–frequency domain. *Journal of the Atmospheric Sciences*, *56*(3), 374–399. https://doi.org/10.1175/1520-0469(1999)056<0374:CCEWAO>2.0.CO;2

Xavier, P., Rahmat, R., Cheong, W., & Wallace, E. (2014). Influence of Madden-Julian Oscillation on Southeast Asia rainfall extremes: Observations and predictability. *Geophysical Research Letters*, *41*, 4406–4412. https://doi.org/10.1002/2014GL060241

Zhang, C. (2005). Madden-Julian oscillation. *Reviews of Geophysics*, *43*, RG2003. https://doi.org/10.1029/2004RG000158

Zhang, C. (2013). Madden-Julian Oscillation: Bridging weather and climate. *Bulletin of the American Meteorological Society*, *94*(12), 1849–1870. https://doi.org/10.1175/BAMS-D-12-00026.1

Zhang, C., & Ling, J. (2017). Barrier effect of the Indo-Pacific maritime continent on the MJO: Perspectives from tracking MJO precipitation. *Journal of Climate*, *30*(9), 3439–3459. https://doi.org/10.1175/JCLI-D-16-0614.1

Zhang, F., Taraphdar, S., & Wang, S. (2017). The role of global circumnavigating mode in the MJO initiation and propagation. *Journal of Geophysical Research: Atmospheres*, *122*, 5837–5856. https://doi.org/10.1002/2016JD025665

Zhao, C., Li, T., & Zhou, T. (2013). Precursor signals and processes associated with MJO initiation over the tropical Indian Ocean*. *Journal of Climate*, *26*(1), 291–307. https://doi.org/10.1175/JCLI-D-12-00113.1

Zhou, W., & Chan, J. (2010). Intraseasonal oscillation and the South China Sea summer monsoon onset. *International Journal of Climatology*, *25*(12), 1585–1609.

Modulation of ENSO on Fast and Slow MJO Modes during Boreal Winter

YUNTAO WEI

Laboratory for Climate Studies and China Meteorological Administration–Nanjing University Joint Laboratory for Climate Prediction Studies, National Climate Center, China Meteorological Administration, Beijing, and Key Laboratory of Ocean Circulation and Waves, Institute of Oceanology, Chinese Academy of Sciences, Qingdao, and University of Chinese Academy of Sciences, Beijing, China

HONG-LI REN

Laboratory for Climate Studies and China Meteorological Administration–Nanjing University Joint Laboratory for Climate Prediction Studies, National Climate Center, China Meteorological Administration, Beijing, China

(Manuscript received 8 January 2019, in final form 12 June 2019)

ABSTRACT

This study investigates modulation of El Niño–Southern Oscillation (ENSO) on the Madden–Julian oscillation (MJO) propagation during boreal winter. Results show that the spatiotemporal evolution of MJO manifests as a fast equatorially symmetric propagation from the Indian Ocean to the equatorial western Pacific (EWP) during El Niño, whereas the MJO during La Niña is very slow and tends to frequently ''detour'' via the southern Maritime Continent (MC). The westward group velocity of the MJO is also more significant during El Niño. Based on the dynamics-oriented diagnostics, it is found that, during El Niño, the much stronger leading suppressed convection over the EWP excites a significant front Walker cell, which further triggers a larger Kelvin wave easterly wind anomaly and premoistening and heating effects to the east. However, the equatorial Rossby wave to the west tends to decouple with the MJO convection. Both effects can result in fast MJO propagation. The opposite holds during La Niña. A column-integrated moisture budget analysis reveals that the sea surface temperature anomaly driving both the eastward and equatorward gradients of the low-frequency moisture anomaly during El Niño, as opposed to the westward and poleward gradients during La Niña, induces moist advection over the equatorial eastern MC–EWP region due to the intraseasonal wind anomaly and therefore enhances the zonal asymmetry of the moisture tendency, supporting fast propagation. The role of nonlinear advection by synoptic-scale Kelvin waves is also nonnegligible in distinguishing fast and slow MJO modes. This study emphasizes the crucial roles of dynamical wave feedback and moisture–convection feedback in modulating the MJO propagation by ENSO.

1. Introduction

The Madden–Julian oscillation (MJO) (Madden and Julian 1971, 1972) is the dominant mode of tropical intraseasonal variability (20–100 days) (Zhang 2005) and exerts significant impacts on the global weather and climate (Zhang 2013), including tropical cyclones (Maloney and Hartmann 2000), westerly wind events (Hao et al. 2019), convectively coupled equatorial waves (Roundy 2008; Kiladis et al. 2009), extreme rainfall (Ren and Ren 2017; Ren et al. 2018), monsoons (Lau and Chan 1986a; Lorenz and Hartmann 2006), and El Niño–Southern Oscillation (ENSO) (McPhaden 1999; Hendon et al. 2007). Over the past several decades, even though large progress has been frequently reported with respect to understanding the dynamics and physics of the MJO (e.g., Madden and Julian 1994; Zhang 2005; Lau and Waliser 2012; Li 2014; DeMott et al. 2015; Wang et al. 2016), most state-of-the-art general circulation models (GCMs) still struggle to satisfactorily simulate some fundamental characteristics of the MJO, especially its systematic eastward propagation from the Indian Ocean (IO) to the equatorial western Pacific (EWP) (e.g., Kim et al. 2009; Neena et al. 2014; Jiang et al. 2015; Ahn et al. 2017). This strongly suggests the necessity of advancing our understanding of the MJO propagation mechanism.

Of the numerous theories, three representative kinds have been widely used to explain the eastward propagation of the MJO. The first theory emphasizes the first-order importance of the tropical atmospheric humidity

Corresponding author: Hong-Li Ren, renhl@cma.gov.cn

DOI: 10.1175/JCLI-D-19-0013.1

© 2019 American Meteorological Society. For information regarding reuse of this content and general copyright information, consult the AMS Copyright Policy (www.ametsoc.org/PUBSReuseLicenses).

under the weak temperature gradient approximation (Sobel et al. 2001), that is, the ''moisture mode'' theory (Sobel and Maloney 2012, 2013; Adames and Kim 2016). Based on diagnostic results from GCMs (Maloney 2009; Andersen and Kuang 2012), reanalysis (Kiranmayi and Maloney 2011), and observations (Sobel et al. 2014), the intraseasonal variation of the anomalous moisture is assumed to be determined by a linear combination of the frictionally driven boundary layer (BL) moisture convergence, the horizontal moisture advection, and the net moistening of evaporation and precipitation. This theory can appropriately simulate not only the eastward propagation phase speed but also the westward-moving group velocity of the MJO, both of which arise primarily from the meridional advection of the low-frequency background moisture due to the MJO-related wind anomalies (Adames and Kim 2016).

The second theory highlights the key role of dynamical wave feedbacks, such as the frictionally coupled Kelvin–Rossby wave theory (Wang 1988; Wang and Rui 1990). In this theory, the moisture tendency is neglected. This means that the diabatic precipitation heating is directly parameterized as a function of the moisture convergence, which is essentially a Kuo-type cumulus scheme (Kuo 1965). Therefore, unlike the so-called moisture mode theory, which retains the two-way interaction of moisture and convection, this theory can only resolve the wave feedback, regardless of the key role of moisture–convection feedback (Wang et al. 2016; Liu and Wang 2017b). The simulated eastward propagation of the MJO is completely determined by the dynamical wave feedbacks, which involve both the equatorially eastward-propagating Kelvin waves and westward-moving Rossby waves. For example, the easterly wind anomaly of a Kelvin wave can drive large-scale moisture convergence and therefore destabilization to the east of the convective center, contributing to the further eastward propagation of the MJO. This mechanism associated with Kelvin wave dynamics appears to be agreed upon (e.g., Wang et al. 2017; Chen and Wang 2018a). However, there are still contrasting views concerning the impact of Rossby wave, one of which (called the ''drag effect''), as derived from observational diagnostics (Wang and Lee 2017; Chen and Wang 2018a), aquaplanet GCM experiments (Kang et al. 2013), and theoretical studies (Wang and Chen 2016; Wang et al. 2016), suggests that the tight coupling of the equatorially westward-propagating Rossby waves will naturally slow down the eastward-propagating phase speed of the MJO. However, the other view (called the ''acceleration effect'') argues that a stronger Rossby wave to the west can enhance the east–west zonal asymmetry of the moisture tendency and therefore favors eastward propagation (e.g., Hsu and Li 2012; Wang et al. 2017, 2018b).

The third theory, namely the frictionally coupled dynamic moisture mode theory (Wang and Chen 2016; Liu and Wang 2017a), has been put forward as a coupling of the first two theories. The eastward propagation of the MJO can be well reproduced by the three-way interaction among convective heating, moisture, and wave–BL dynamics. In fact, Liu and Wang (2017b) have pointed out that both dynamical wave feedback and moisture–convection feedback are essential to shape the MJO. They showed that the former is helpful to slow down the eastward propagation and increase the growth rate of the planetary waves, while the latter is responsible for producing dispersive MJO modes. On the basis of previous work, in this study, we try to explain the distinctive propagation characteristics of the MJO under different ENSO background states by examining both dynamical wave feedback and moisture–convection feedback.

Studies of the modulation of the ENSO on the MJO can be traced back to Lau and Chan (1986b), who revealed that El Niño might reduce the frequency of the MJO via the air–sea interactions. Subsequently, a large number of studies tried to understand the MJO variation under ENSO (e.g., Weickmann 1991; Li and Smith 1995; Slingo et al. 1999; Zhang and Gottschalck 2002; Hendon et al. 2007; Moon et al. 2011; Pillai and Chowdary 2016; Wu and Song 2018). Even though some uncertainties still exist, the preferred finding may be summarized as follows: the MJO intensity should vary with the different ENSO phases. Typically, the MJO activity over the EWP is enhanced in the developing phase of El Niño and reduced in and after the mature and decaying phases. Recently, with the recognition of non-canonical-type El Niño events in the 1990s, namely El Niño Modoki (Ashok et al. 2007), central Pacific (CP) El Niño (Kao and Yu 2009), or the warm-pool ENSO (Kug et al. 2009; Ren and Jin 2011), the above findings have been argued to only be true during canonical eastern Pacific (EP) El Niño years (Yuan et al. 2015; Chen et al. 2016). However, the MJO activity is always enhanced during CP El Niño years regardless of the phase (Wang et al. 2018a; Hsu and Xiao 2017).

As seen from the above studies, a large amount of effort has been made to explore the modulations of the ENSO on the MJO intensity. However, there are only a few studies mentioning variations in the MJO propagation under the ENSO background state. For example, Pohl and Matthews (2007) found significantly shorter (longer) lifetimes of the MJO during warm (cold) conditions in the EP, consistent with Gray (1988) and Goulet and Duvel (2000). Therefore, they concluded that the phase speed of the MJO is significantly higher during El Niño years. In an observational analysis combined with a theoretical validation, Liu et al. (2016)

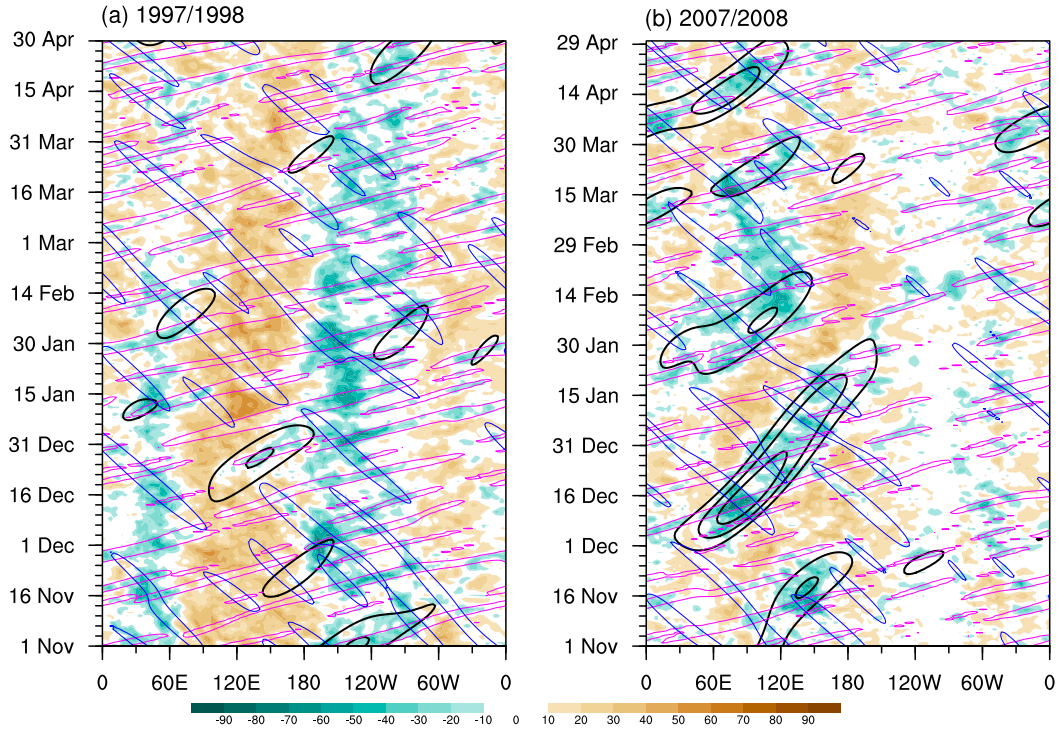

FIG. 1. Hovmöller diagrams of equatorial (15°S–15°N) OLR anomalies ($W m^{-2}$) during the (a) 1997/98 and (b) 2007/08 boreal winters. The thick black contours denote the MJO-filtered OLR anomalies. The contours are drawn from $-8 W m^{-2}$ with intervals of $-10 W m^{-2}$. The thin magenta (blue) contours of $-5 W m^{-2}$ represent the equatorial Kelvin wave (Rossby wave) filtered OLR anomalies.

demonstrated that the boreal summer intraseasonal oscillation over the western North Pacific is dominated by a relatively high-frequency (low-frequency) oscillation during El Niño (La Niña) summers. More recently, Suematsu and Miura (2018) showed that the low-frequency (LF; period > 60 days) basic-state sea surface temperature (SST) anomaly pattern has a robust connection with the eastward propagation of the MJO. Composites of the LF SST anomalies showed contrasting patterns for the eastward propagating MJO from the IO to the EWP and those short-lived, stagnant, and convective events, which were associated with positive and negative SST anomalies over the EWP, respectively.

Enlightened by these studies, we conjecture that the MJO propagation tends to be faster during El Niño years and slower during La Niña years. As an example, Figs. 1a and 1b provide a comparison of time–longitude sections of the equatorial (15°S–15°N), MJO-filtered (Wheeler and Kiladis 1999; Kiladis et al. 2009) outgoing longwave radiation (OLR) anomalies during the 1997/98 El Niño and 2007/08 La Niña winters, respectively. We can see that the eastward propagation of the MJO convection is very fast during the entire winter season of 1997/98. Meanwhile, during the boreal winter of 2007/08, especially prior to around 30 January, the eastward movement is very slow, even though the convection becomes fast again after early February. How does the complexity of the ENSO (Timmermann et al. 2018) modulate the phase speed of the MJO? How do the moisture–convection feedback and the dynamical wave feedback work under different ENSO background states? These questions are the primary focus of this study. The rest of this paper is arranged as follows. In section 2, we introduce the data and methodology. The basic characteristics under different ENSO background states are shown in section 3. In section 4, we explore the mechanisms through which the ENSO modulates the fast and slow MJO modes. Section 5 discusses possible roles of other LF variabilities over the Indo-Pacific warm pool, tropical–extratropical interactions, and dynamically and thermodynamically intraseasonal air–sea interactions in modulating the MJO eastward propagation. A summary and concluding remarks are given in section 6.

2. Data and methodology

a. Data

The daily Advanced Very High Resolution Radiometer (AVHRR) interpolated OLR data from the National Oceanic and Atmospheric Administration

(NOAA) satellite (Liebmann and Smith 1996) are used as an indicator of the convective activity. The daily atmospheric reanalysis data are from the European Centre for Medium-Range Weather Forecasts (ECMWF) interim reanalysis (ERA-Interim, hereinafter ERA-I; Dee et al. 2011). The three-dimensional fields consist of the zonal and meridional winds (u and v), the vertical pressure velocity (ω), the specific humidity (q), and the geopotential (ϕ) at 19 levels from the surface to 10 hPa. The all-season real-time multivariate MJO (RMM) index of Wheeler and Hendon (2004) is also used here. We identify the El Niño and La Niña events via the monthly global 2° × 2° Extended Reconstructed SST version 5 (ERSSTv5) (Huang et al. 2017), which incorporates a new release of the International Comprehensive Ocean–Atmosphere Dataset 3.0 (Freeman et al. 2017), a decade of near-surface data from Argo floats, and a new estimate of centennial sea ice from the Hadley Centre Sea Ice and Sea Surface Temperature dataset version 2 (Titchner and Rayner 2014). Huang et al. (2017) showed that, compared to the ERSST version 4 (Huang et al. 2015, 2016), this newest version of the SST dataset has improved the magnitudes of El Niño and La Niña events. Both the NOAA OLR and the ERA-I data have a horizontal resolution of 2.5° × 2.5°. The 37-yr data from 1980 to 2016 are analyzed in this study, and we focus on the boreal winter from November to April when both the MJO and ENSO peak.

b. Methodology

1) Data processing

The daily (monthly) anomalies were obtained by removing the daily (monthly) climatology and the first three harmonics from 1980 to 2016. A 20–100-day bandpass filtering using the Lanczos filter (Duchon 1979) with 201 weights was further performed on the daily anomalies to extract variations on the intraseasonal time scale. The daily synoptic-scale high-frequency (HF) activity and LF basic state were obtained using a 20-day high-pass and a 100-day low-pass filtering, respectively. In Fig. 1, to highlight the eastward propagation of the wave envelope associated with the large-scale MJO signals, we performed a zonal wavenumber–frequency filtering (Wheeler and Kiladis 1999). The retained range is 1–5 for zonal wavenumber and 1/100–1/20 cpd for the frequency. A filtering with a broad frequency range can adequately simulate the fast (slow) eastward propagation during El Niño (La Niña) winters. Following Wheeler and Kiladis (1999), the equatorial Kelvin wave was derived based on a period of 3–20 days and wavenumbers 2–14, while the equatorial Rossby wave was based on a period of 10–40 days and wavenumbers 2–10.

2) Selection of El Niño and La Niña events

Following the definition of the NOAA Climate Prediction Center, we chose the warm and cold periods based on a threshold of ±0.5°C for the Oceanic Niño Index (ONI), which is calculated as the 3-month running mean of the ERSSTv5 anomalies in the Niño-3.4 region (120°–170°W, 5°N–5°S). The El Niño (La Niña) events were identified as the periods above (below) normal SSTs when the threshold was met for a minimum of five consecutive overlapping seasons. In this way, a total of 8 La Niña (1984/85, 1988/89, 1995/96, 1999/00, 2000/01, 2007/08, 2010/11, and 2011/12), and 10 El Niño (1982/83, 1986/87, 1991/92, 1994/95, 1997/98, 2002/03, 2004/05, 2006/07, 2009/10, and 2015/16) years were selected.

To distinguish the EP and CP El Niño events, we used the cold tongue index (CTI) and the warm pool index (WPI), which were proposed by Ren and Jin (2011). These two indices are calculated as follows:

$$\begin{cases} \mathrm{CTI} = N_3 - \alpha N_4, \\ \mathrm{WPI} = N_4 - \alpha N_3, \end{cases} \quad \alpha = \begin{cases} 2/5, & N_4 N_3 > 0 \\ 0, & \text{otherwise} \end{cases}. \tag{1}$$

Here, N_3 and N_4 denote the Niño-3 and Niño-4 indices, which are defined as the ERSSTv5 anomalies over the regions 150°–90°W, 5°S–5°N and 160°E–150°W, 5°S–5°N, respectively. For specified El Niño events selected by the ONI, when the CTI was larger than the WPI, we regarded it as an EP-type event; otherwise, we regarded it a CP-type event (Ren et al. 2018). Motivated by the significant influence of the contrasting intensities of the different types of El Niño events on the background states of the wind, temperature, and moisture (e.g., Latif et al. 2015; Rao and Ren 2016; Geng et al. 2017) and therefore the different propagation characteristics of the MJO, in this study we also partitioned the EP-type El Niño events into super and regular El Niño cases. Because the amplitude of EP El Niño events is generally stronger than that of CP El Niño events (Kug et al. 2009), we used a Niño-3.4 index warmer than 2.5°C to select the super El Niño events. In the end, we selected three super El Niño years (1982/83, 1997/98, and 2015/16), three regular EP El Niño years (1986/87, 1991/92, and 2006/07), and four CP El Niño years (1994/95, 2002/03, 2004/05, and 2009/10), which is consistent with previous studies (e.g., Kug et al. 2009; Ren et al. 2019).

3) Compositing technique

In this subsection, we explain the methodology used to select the existing MJO events. To observe the entire life cycle of the MJO, a lagged composite technique was introduced.

The second component of the RMM (i.e., the RMM2 index) was used here to identify the possible convection peaks occurring over the IO. This is because the dominant spatial pattern of convection associated with the negative RMM2 displays a seesaw structure over the Indo-Pacific warm pool, in which enhanced convection is located in the IO, while suppressed convection prevails over the WP (Wheeler and Hendon 2004). We first selected possible MJO events based on the following procedure: 1) we identified the "day 0" (or MJO phase 2) when the RMM2 index reached a local minimum smaller than one negative standard deviation; 2) after day 0, the RMM amplitude should increase above 1.0 and remain high for at least 7 days; and 3) subsequently, the RMM index should progress through at least two phases, that is, reach the MJO phase 4, in the counterclockwise direction. The first two steps guarantee that it is a realistic MJO initiation (Straub 2013; Kiladis et al. 2014), and we do not require that the RMM amplitude be larger than 1.0 preceding phase 2; in this way, both the primary and successive events (Matthews 2008; Wei et al. 2019) are included here. The third step implies that IO-initiated MJO events should, at the very least, propagate into the western Maritime Continent (MC); therefore, both the propagating and nonpropagating MJO cases (Kim et al. 2014; Feng et al. 2015) were considered here. Finally, the Hovmöller diagram of the meridionally (10°S–10°N) averaged, 20–100-day, bandpass-filtered OLR anomaly overlaid by the MJO-filtered, wave-envelope pattern was also examined. This was motivated by the fact that the RMM index may exaggerate the role of the upper-level circulation signals (Straub 2013). More specifically, we observed if the OLR anomaly showed an organized (the convective center evolved continuously for at least 10 days following day 0), large-scale (maximal zonal range $> 50°$), and eastward-propagating (phase speed $> 2.0\,\mathrm{m\,s^{-1}}$) pattern. We also tested the sensitivity of our results to some key parameters by modulating the duration of high (>1) RMM amplitude since day 0 ranging from 7 to 9 days, propagating phases ranging from 2 to 3, and maximal zonal distances ranging from 50° to 60°. As a consequence, the total number of MJO events only varied from 29 to 37 under the ENSO background state. Nevertheless, the composite results remain unchanged whether using 29 or 37 cases.

Once the events were isolated, we obtained the composite 91-day (from −45 days to 45 days) time series $\overline{S} = \overline{S}(x, t_0 - \tau)$ associated with any meteorological field S with any dimensionality, where t_0 is the composite lag 0, and τ is the time lag ranging from −45 days to 45 days. To test the significance, we used the following statistic that obeys the Student's t distribution with a degree of freedom (DOF) of $N - 1$:

$$T = \frac{\mu}{\sqrt{\sigma^2}}\sqrt{N-1}, \tag{2}$$

where μ and σ^2 are the population mean and variance, respectively. Using the sampling technique, the T statistic can be evaluated as follows:

$$\hat{T} = \frac{\hat{\mu}}{\sqrt{\hat{\sigma}^2}}\sqrt{n-1}, \tag{3}$$

where $\hat{\mu}$ and $\hat{\sigma}^2$ denote the sample mean and variance, respectively, and n is the DOF, that is, the total number of MJO cases. The sample mean $\hat{\mu}$ is significant when the $\hat{T}$ value is larger than the threshold at the 90% confidence level.

4) Evaluating the MJO phase speed

To quantitatively examine the modulation of the ENSO on the eastward propagation speed of the MJO, we developed a new algorithm to objectively calculate the phase speed. The methodology is introduced step by step as follows.

Step 1: For a given time (from −30 days to 30 days)–longitude (30°E–180°) pattern of the composite equatorial (15°S–5°N) OLR anomalies, we first identified the longitudinal location of the OLR minimum at lag 0 and stored the result as (x_0, t_0). However, there may be multiple equatorial minima at lag 0. Under such scenarios, we only considered those that finally evolved into a large-scale, eastward propagating MJO signal.

Step 2: We drew two reference lines passing through the point (x_0, t_0) with a slope of $v_{\min} = 2\,\mathrm{m\,s^{-1}}$ and $v_{\max} = 10\,\mathrm{m\,s^{-1}}$, respectively. The longitudinal locations of the OLR minimum at lags 1 and −1 are chosen from

$$\{x | x_0 + v_{\min}\,dt \le x \le x_0 + v_{\max}\,dt\} \tag{4}$$

and

$$\{x | x_0 - v_{\max}\,dt \le x \le x_0 - v_{\min}\,dt\}, \tag{5}$$

respectively, where $dt = 1$ day. A tacit assumption is that a reasonable MJO phase speed should range from 2.0 to $10.0\,\mathrm{m\,s^{-1}}$ (Ling et al. 2013; Zhang and Ling 2017). The results were stored as (x_1, t_1) and (x_{-1}, t_{-1}), respectively.

Step 3: Step 2 was repeated but the referenced point (x_0, t_0) was updated to (x_{-i}, t_{-i}) $(i = 1, \ldots, 9)$ for negative time lags and to (x_j, t_j) $(j = 1, \ldots, 19)$ for positive time lags. Then, the next newly tracked

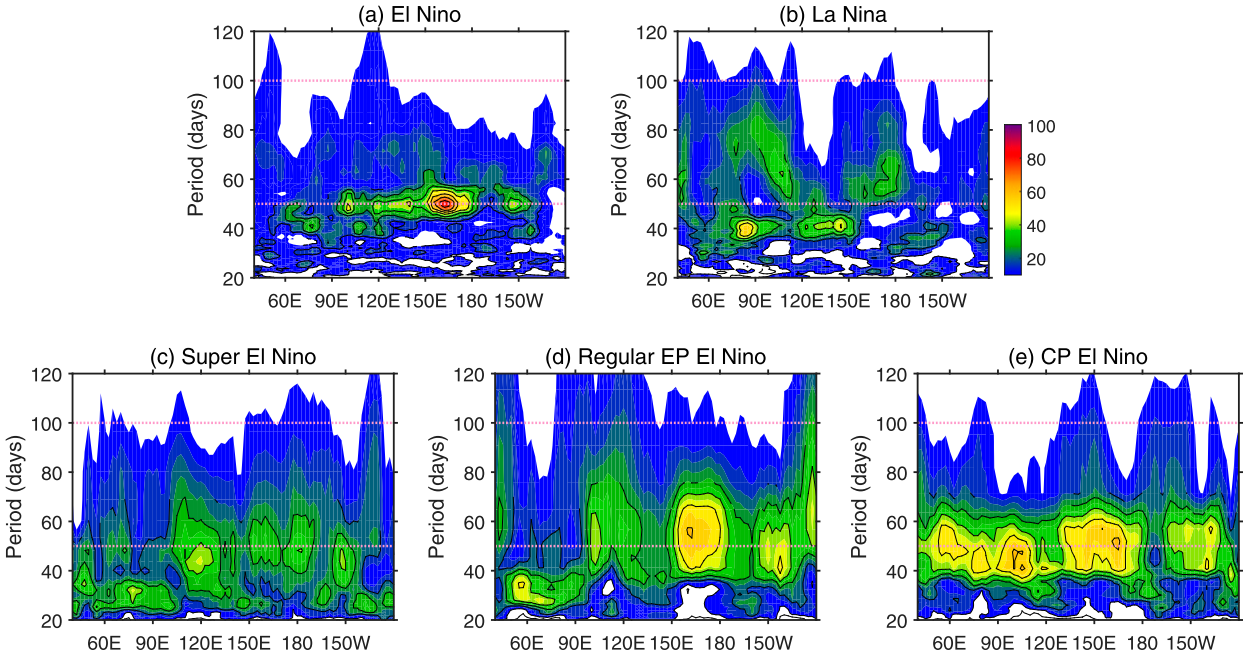

FIG. 2. Longitudinal distributions of the power spectral variance of the equatorially (10°S–10°N) averaged OLR anomalies ($W m^{-2}$) during (a) El Niño, (b) La Niña, (c) super El Niño, (d) regular EP El Niño, and (e) CP El Niño conditions. The black contour outlines those anomalies passing the Student's *t* test at the 90% confidence level. The two horizontal dashed lines indicate periods of 50 and 100 days. The horizontal axis indicates the longitude (°), while the vertical axis indicates the period (days).

points of the OLR minimum at lags of $j + 1$ and $i + 1$ were respectively chosen from

$$\{x|x_j + v_{\min}\,dt \le x \le x_j + v_{\max}\,dt\} \tag{6}$$

and

$$\{x|x_{-i} - v_{\max}\,dt \le x \le x_{-i} - v_{\min}\,dt\}. \tag{7}$$

Step 4: The phase speed of this space–time field was evaluated as the regression coefficient of X (in meters) versus T (in seconds), where $X = (x_{-10}, \ldots, x_0, \ldots, x_{20})$, and $T = (t_{-10}, \ldots, t_0, \ldots, t_{20})$.

We also carried out a series of sensitivity experiments with continuously varying parameter values for $v_{\min}$ and $v_{\max}$. The results showed that the evaluated phase speed remains unchanged when specifying any combination of $v_{\min}$ and $v_{\max}$ from the following sets:

$$\{v_{\min}|0.2 \le v_{\min} \le 3.0\}, \tag{8}$$

$$\{v_{\max}|9.6 \le v_{\max} \le 12.6\}. \tag{9}$$

When choosing the values of these two parameters beyond sets (8) and (9), the evaluated phase speed becomes unrealistic. For example, the MJO propagation speed is overestimated when using a value of $v_{\min}$ larger than $3.0\,m\,s^{-1}$ or a value of $v_{\max}$ larger than $12.6\,m\,s^{-1}$. Conversely, the phase speed is underestimated with a parameter value of $v_{\min}$ smaller than $0.2\,m\,s^{-1}$ or a value of $v_{\max}$ smaller than $9.6\,m\,s^{-1}$. Zhang and Ling (2017) also showed that the propagation speed of MJO can exist in the range of 2.0–10.0 $m\,s^{-1}$, which is just contained within the sets (8) and (9).

3. Modulation of ENSO on the MJO

a. Power spectrum analysis

Figures 2a and 2b show the longitudinal distribution (40°E–120°W) of the power spectrum of the daily, equatorial (10°S–10°N) OLR anomaly for the 10 El Niño and 8 La Niña winters during the period of 1980–2016. The data connection method is the same as that used by Liu et al. (2016). The significance of the power spectra was obtained by comparing the power spectral variance of the input time series with that of the background red noise at the significance level of 0.1. It is interesting to note that the MJO in the IO during El Niño winters is dominated by a much weaker HF oscillation with a significant spectral peak of 40 days. However, over the IO during La Niña winters, the MJO spectrum variance is very strong and exhibits a significant double-peak spectrum with both a 40-day HF oscillation and an 80-day LF oscillation, which implies that the La Niña background state may breed two types of intraseasonal

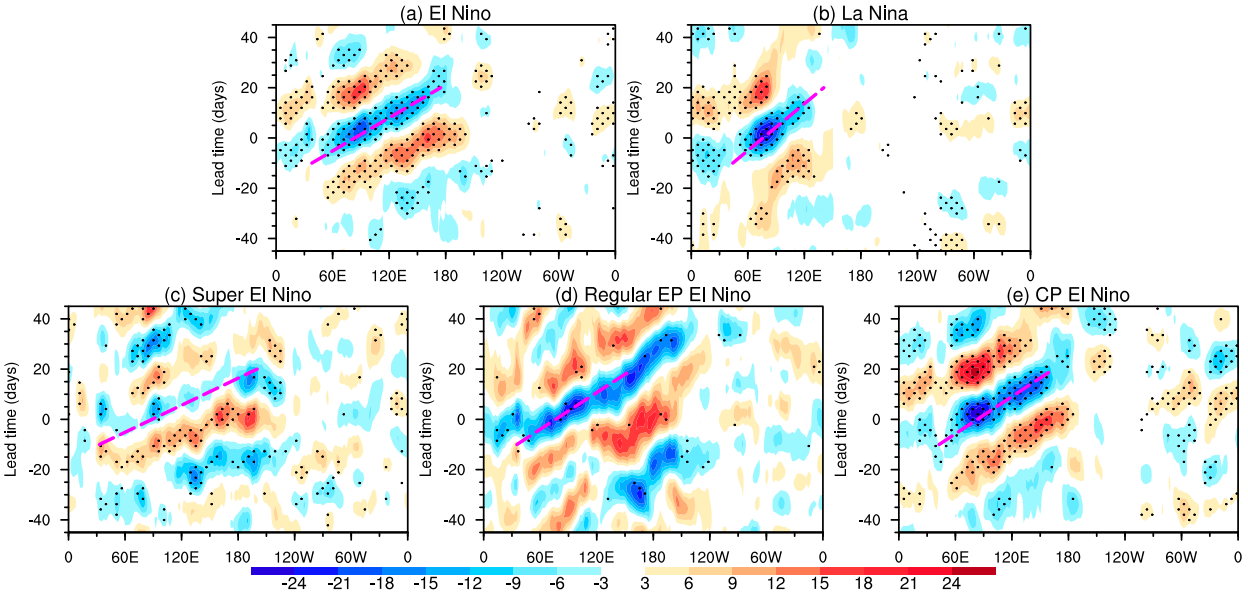

FIG. 3. Lagged composites of the equatorial (15°S–5°N) OLR anomalies (W m^{-2}) for the (a) 10 El Niño, (b) 8 La Niña, (c) 3 Super El Niño, (d) 3 regular EP El Niño, and 4 CP El Niño winters. The blue (red) shading with interval of 3 W m^{-2} indicates the enhanced (suppressed) convection. The dotted area represents those anomalies passing the two-tailed Student's *t* test at the confidence level of 90%. The dashed magenta lines show the regression lines for the tracked longitude locations. The evaluated phase speed of the enhanced convection is 5.8 m s^{-1} for El Niño, 4.1 m s^{-1} for La Niña, 7.1 m s^{-1} for super El Niño, 5.3 m s^{-1} for regular EP El Niño, and 5.2 m s^{-1} for CP El Niño winters.

modes characterized by distinctive frequencies (e.g., Saji et al. 2006; Izumo et al. 2010). The spatial distribution of the 20–100-day variance over the Indo-Pacific region was also examined (figure not shown), and it was found that the MJO intensity of El Niño winters over the IO is weaker than that of La Niña winters, consistent with Wu and Song (2018) and Li and Mao (2019).

Over the MC–Pacific region, as seen in Figs. 2a and 2b, the frequency distribution of the spectrum in El Niño is much narrower than that in La Niña. For example, the former displays a very regular and much stronger HF oscillation with a period of 50 days, whereas in the latter, the oscillating period displays a mixture with the variance peak occurring at 40–60 days over the MC and 60–70 days over the western CP. In addition, the El Niño condition also displays a 50-day oscillation at 150°W, which indicates that the MJO may propagate farther east during the warm phase of the ENSO cycle. This spectral analysis may imply that the MJO eastward propagation should be faster in the warm phase and slower in the cold phase of the ENSO cycle (Gray 1988; Goulet and Duvel 2000; Pohl and Matthews 2007).

Previous studies have demonstrated that the MJO intensity in the Indo-Pacific warm pool undergoes a strong sensitivity to the diversity of the El Niño (e.g., Hsu and Xiao 2017; Wang et al. 2018a). Is this still true for the main periodicity of the MJO? To answer this question, we calculated the power spectrum for the four CP El Niño, three super El Niño, and three regular EP El Niño winters during the period from 1980 to 2016 (Figs. 2c–e). As can be seen, over the IO–MC region, the variance in the 20–100-day frequency range is very strong during the CP El Niño events (Fig. 2e). For the EP El Niño events, however, the variance is very weak, especially for the super El Niño events (Fig. 2a), whereas over the equatorial Pacific both the regular EP and CP El Niño conditions support strong MJO activity. More interestingly, the predominate period of the winter MJO over the IO also displays a clear difference with 30 days in EP El Niño and 45 days in CP El Niño. Over the MC and equatorial Pacific, the spectrum of the super El Niño events exhibits a broad frequency ranging from 22 to 80 days and the EP El Niño events also exhibit a broad-frequency oscillation (35–80 days). For CP El Niño, the oscillation is very regular with a narrow period range of 40–60 days.

b. Hovmöller diagrams

Figures 3a and 3b shows the propagation patterns of the composite meridionally averaged (15°S–5°N) OLR anomalies during the El Niño and La Niña winters, respectively. As expected from Fig. 2a, the MJO over the IO during the warm phase of the ENSO cycle (Fig. 3a) is weak while quickly propagating toward the east

($\sim$5.8 m s^{-1}). In the cold phase of the ENSO cycle (Fig. 3b), however, the MJO moves eastward slowly ($\sim$4.1 m s^{-1}) with a much stronger amplitude, especially over the IO. Over the EWP, both the enhanced and suppressed phases of the MJO are slightly stronger during El Niño, implying that a warm (cold) ENSO event may support the propagating (nonpropagating) MJO events (Kim et al. 2014; Feng et al. 2015; Wang et al. 2017; Zhang and Ling 2017; Fu et al. 2018). Representations of the MJO properties in Figs. 3a and 3b, including the phase speed, amplitude, and propagation, are similar to those shown in Fig. 4 of Yadav and Straus (2017) and in Fig. 4 of Henderson and Maloney (2018), even though they primarily focus on the North Atlantic Oscillation and the high-latitude blocking response to the MJO, respectively. Our results, together with previous studies (e.g., Pohl and Matthews 2007; Henderson and Maloney 2018; Suematsu and Miura 2018), strongly suggest that the LF SST anomalies exert a fundamental influence on the eastward propagation speed of the boreal winter MJO. In addition, the dispersive property is also modulated by the ENSO cycle; as seen here: the eastward propagation pattern of the OLR anomalies displays a clear westward group velocity (Adames and Kim 2016; Chen and Wang 2018b) during the El Niño winters (Fig. 3a), whereas during the La Niña winters (Fig. 3b) the westward dispersion is weak.

To further examine the modulation of the different types of El Niño background states on the MJO propagation, the composite equatorial (15°S–5°N) OLR anomalies during the CP, regular EP, and super El Niño events were also investigated (Figs. 3c–e). As demonstrated in previous studies (e.g., Yuan et al. 2015; Chen et al. 2015) and implied in Figs. 2c–e, the much stronger convective anomalies of the MJO during the CP El Niño winter (Fig. 3e) can propagate farther eastward. In the EP El Niño winters, especially the super El Niño winters (Fig. 3c), however, the MJO is much weaker. With the small number of MJO samples occurring under EP El Niño conditions, especially under regular EP El Niño conditions, the dotted areas that can pass the Student's t significance test, even at the 90% confidence level, in the composite results are very sparse. Regardless, the strong evolution of the dry phase from day −20 to day 0 is still significant. In addition, the phase speed of the MJO also manifests diversity. In regular EP (CP) El Niño events, the evaluated speed is approximately 5.3 (5.2) m s^{-1}. The fastest propagation occurs during super El Niño ($\sim$7.1 m s^{-1}). It is interesting to observe that the westward group velocity is primarily contributed to by the EP El Niño background state (Fig. 3d); however, the group velocity is nearly zero during CP El Niño.

c. *Evolution patterns of MJO convection and circulation*

Before studying the mechanism of the ENSO modulating the fast and slow MJO modes, we first examine the evolution patterns of the MJO convection and circulation under the El Niño and La Niña winters (Fig. 4). There are four primary differences that can be observed from the contrasting evolutions: 1) the propagation speed of the MJO is much faster in El Niño winters than in La Niña winters, especially the eastward progression of the enhanced phases from day −5 to day 15; 2) the overall amplitude of the suppressed convections over the equatorial western CP during El Niño is well organized and stronger than that during La Niña; 3) as a major response to the more strongly suppressed convection over the equatorial western CP, the coupled equatorial easterly wind anomalies are also stronger in El Niño winters; and 4) the convective phase of the MJO tends to have a meridionally symmetric structure with respect to the equator and can smoothly propagate across the MC along the equator during El Niño winters, whereas the MJO evolution during La Niña winters tends to support a "detour" (Kim et al. 2017) via the southern MC.

Can these differences in shape, especially the leading suppressed convection and the associated easterly wind anomalies over the western CP, contribute to the fast and slow MJO propagation modes? We try to answer this question in the following section.

4. How does the ENSO modulate the fast and slow MJO modes?

In this section, we try to unravel the mechanism through which the ENSO modulates the propagation speed of the MJO. First, the aforementioned dynamical wave feedback is examined based on a dynamics-oriented diagnostic proposed by Wang et al. (2018), including the coupling between the equatorial waves and MJO convection, and the vertical structures of the MJO associated circulation, moisture, and precipitation heating. Second, to evaluate the moisture–convection feedback, a column-integrated moisture budget analysis from the surface to 100 hPa is performed for El Niño and La Niña winters, respectively.

a. *Dynamical wave feedback*

We start with the diagnosis of the horizontal structures of the MJO circulation in the lower troposphere. Figure 5 shows the composite 850-hPa wind anomaly overlaid with its zonal component at lag 0 for the fast MJO mode during El Niño and for the slow mode during La Niña. A clear zonal asymmetry can be observed in this figure in terms of the MJO circulation between the fast and slow MJO

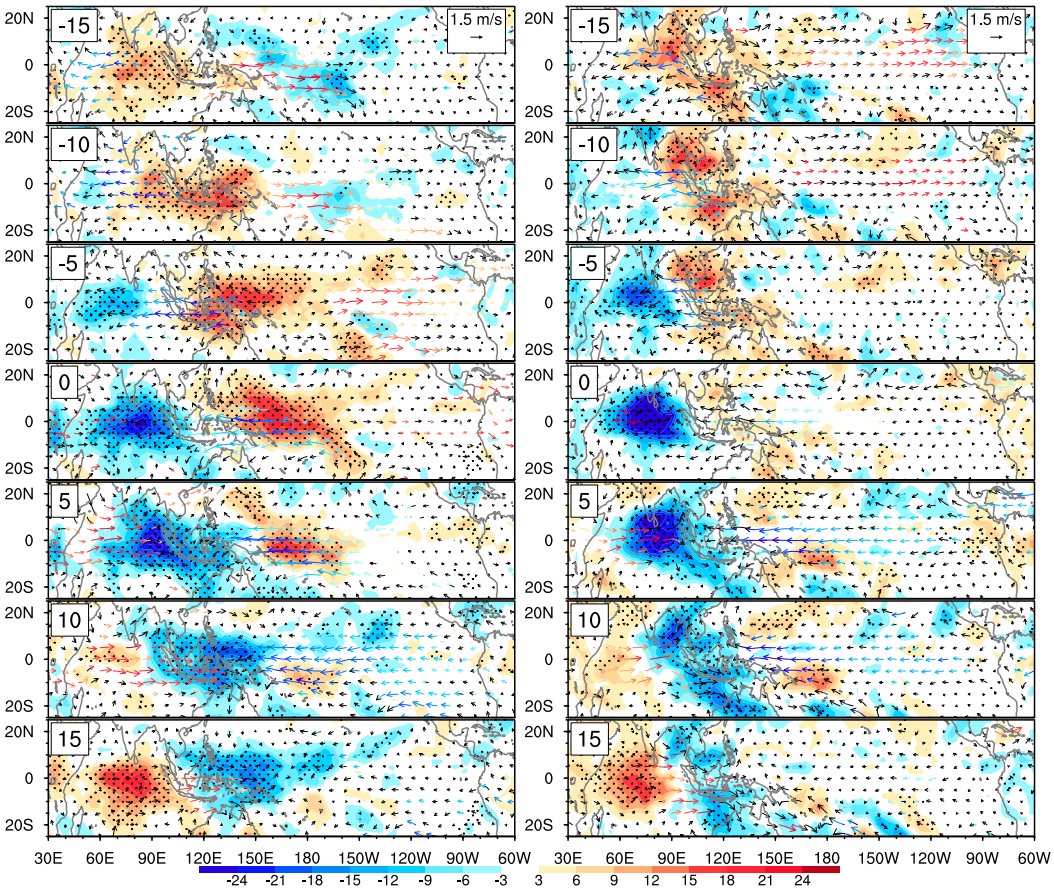

FIG. 4. Evolution patterns of the composite OLR (W m^{-2}; shading) and 850-hPa wind (m s^{-1}; vectors) anomalies from day −15 to day 15 every 5 days during (a) El Niño and (b) La Niña winters. The contour interval is 3 W m^{-2}. The dotted areas, as well as the color vectors, denote those anomalies passing the two-tailed Student's *t* test at the 90% confidence level.

modes. First, for the fast MJO mode (Fig. 5a), the organized easterly wind anomaly over the EWP is very strong and even reaches an amplitude of 6.0 m s^{-1}, whereas it is much weaker (~2.5 m s^{-1}) and nonorganized in the slow MJO mode (Fig. 5b), suggesting that the relatively stronger easterly Kelvin wind anomaly located over the EWP may favor a faster eastward propagation of the MJO (Chen and Wang 2018a). Second, to the west of the convective center, the zonal range of the westerly wind anomaly in the fast MJO mode is much larger than that in the slow mode. However, in the slow mode, the equatorial westerly wind anomaly is fairly localized and only appears over the western-central IO. In addition, the maximal equatorial westerly wind anomaly is located closer to the convective center for the slow mode. These evident contrasts may imply that the equatorial Rossby wave has a weak coupling with the MJO during El Niño; therefore, it can move farther toward the west, which is well reflected in the significantly widespread westerly wind anomalies over Africa and the EP. In the La Niña condition, conversely, the Rossby wave may have a tight coupling with the MJO as can be seen from the very limited westward propagation of the equatorial westerly wind anomaly. One could argue that the equatorially westerly wind anomaly for the fast MJO mode may be a dry Kelvin wave response to the strong negative convection over the EWP; however, its much wider longitudinal range may offer evidence that it is also rooted, possibly more so, in the moist Rossby wave response to the positive convection over the IO.

To further explain of the above dynamical wave feedback, Fig. 6 shows the composite 850-hPa geopotential anomalies at lag 0 for the fast and slow MJO modes. As we can see in Fig. 6a, the geopotential anomaly for the fast MJO mode displays a well-defined zonal wavenumber-1 structure. It is interesting to see that the two low pressure centers (~30°S and 40°N) to the west are located very far from the convective center, which confirms that the Rossby wave gyres have a weak coupling with the fast MJO mode during the El Niño condition. For the slow mode during La Niña (Fig. 6b), the negative geopotential

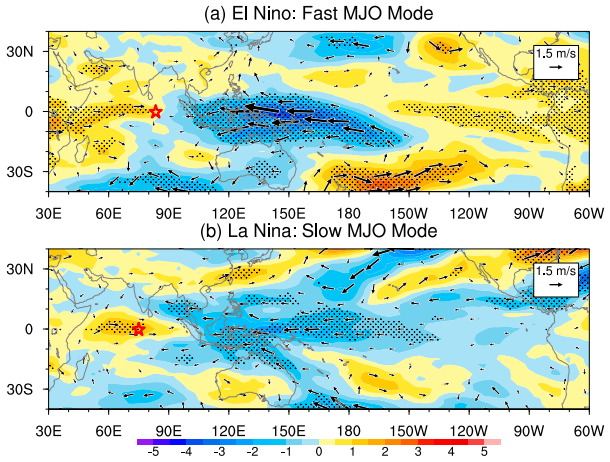

FIG. 5. Horizontal structures of the composite lower-tropospheric (850 hPa) wind ($m\,s^{-1}$; vector) anomalies and their zonal components ($m\,s^{-1}$; shading) at lag 0 during (a) El Niño and (b) La Niña winters. The yellow (blue) shading shows the westerly (easterly) wind anomaly, and the contour interval is $0.5\,m\,s^{-1}$. The dotted areas denote those anomalies passing the two-tailed Student's t test at the 90% confidence level. The red stars mark the deep convective center of the MJO.

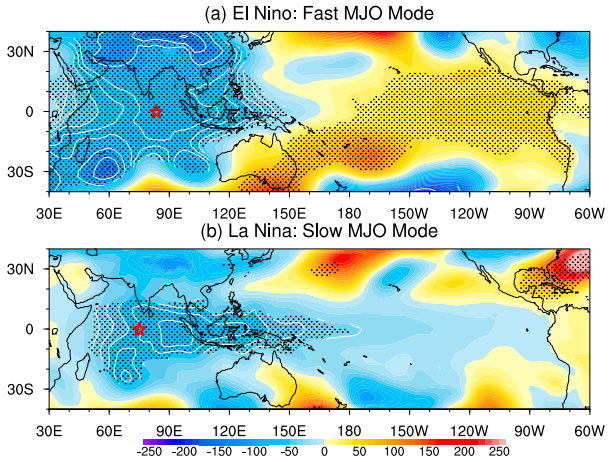

FIG. 6. As in Fig. 5, but for the geopotential anomaly (gpm).

anomaly penetrates into the entire equatorial region (10°S–10°N). In addition, it can be clearly seen that the two off-equatorial Rossby wave gyres are well coupled with the convective center. This implies that a tight coupling of the westward-moving Rossby wave may effectively drag on the MJO convection, therefore clearly slowing the eastward propagation (Kang et al. 2013; Wang et al. 2018b).

In particular, the circulation response of the slow MJO mode manifests as a clearer Gill-like response (Gill 1980) and a narrower meridional scale (see the negative geopotential anomalies over 40°–150°E), whereas for the fast MJO mode, the meridional scale of the anomalous circulation is much larger. For the steady atmospheric response to the idealized equatorial diabatic heating, the Kelvin wave exists to the east, while to the west two Rossby gyres straddle the north and south sides of the equator. Close to the equator, the easterly Kelvin (westerly Rossby) wave leads (trails) the convective center. Because of the 3 times larger eastward-propagating phase speed of the Kelvin wave ($\sim 15\,m\,s^{-1}$) compared to the westward-moving Rossby wave ($\sim 5\,m\,s^{-1}$), the ratio of the zonal extent between the easterly equatorial Kelvin wind and the westerly Rossby wind is just 3.0 (Gill 1980). Based on this discussion and following Wang and Chen (2016), a shape parameter for the MJO can be defined as the ratio of the zonal extent of the equatorial easterly "Kelvin" (below −0.2 in terms of the normalized value) versus the westerly "Rossby" (above 0.2 in terms of the normalized value) averaged between 5°S and 5°N. We find that the slow MJO mode has a more Gill-like response with a shape parameter of 1.7, which is much larger than that of the fast MJO mode (0.5). This suggests a dramatic dependence of the MJO's eastward propagation speed on the structure of the MJO itself (Wang and Chen 2016; Wang et al. 2016; Wang and Lee 2017; Wang et al. 2018).

Moreover, the propagation speed of the MJO acts to interactively influence the structure of itself. For example, the fast MJO mode corresponds to a small shape parameter, primarily due to the Doppler effect induced by the fast moving diabatic heating. Conversely, the more standing-like heating source of the slow MJO mode just excites a more Gill-like response with a larger shape parameter. These arguments imply that the MJO may be regarded as a structure-propagation nexus (Wang et al. 2019).

To represent the intensity of the equatorial waves, we also calculated the ratio of the maximum equatorial Rossby westerly and Kelvin easterly wind anomalies, namely, the so-called *westerly intensity index* proposed by Wang and Chen (2016). The results showed that the westerly intensity index is 0.73 for the slow MJO mode during La Niña but only 0.48 for the fast MJO mode during El Niño. This further proves that a stronger Kelvin wave component versus Rossby wave component is associated with a faster propagation of the MJO.

The above discussion focused on the horizontal structures of the MJO; however, some more interesting phenomena can be detected when examining the vertical distributions. Accordingly, we further investigated the vertical structures of the MJO-associated circulation, moisture, and atmospheric apparent moisture sink Q_2 anomalies (Fig. 7). The Q_2, which represents the precipitation heating to some extent, is estimated from the residual between the moisture tendency and the adiabatic advection processes (Yanai et al. 1973). As we can see in Figs. 7a and 7b, for the fast MJO mode during the El Niño winters, there is an obviously stronger

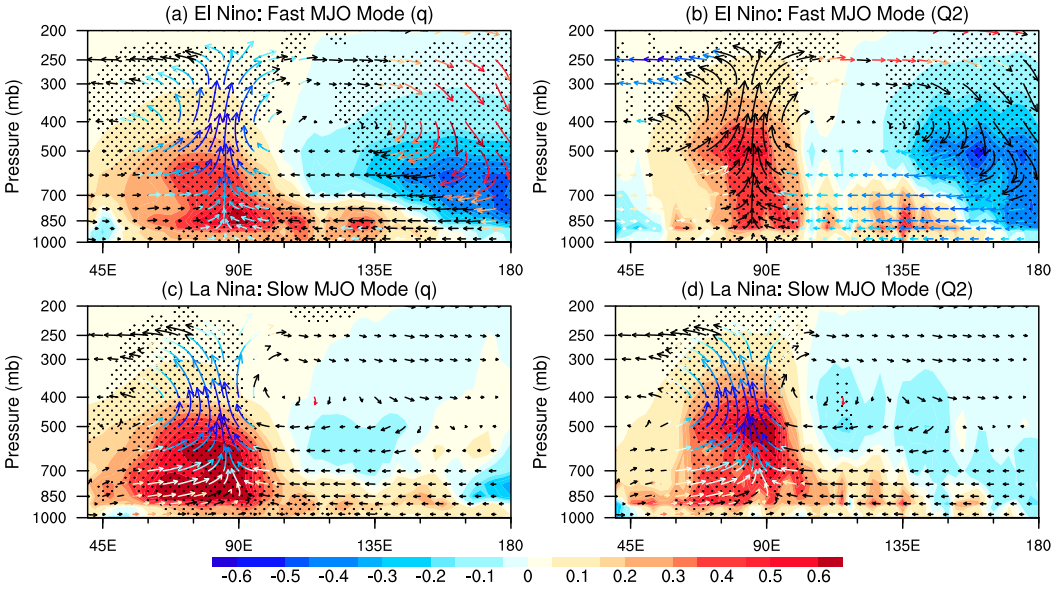

FIG. 7. Composite vertical structures of the equatorial (10°S–5°N) specific humidity (g kg^{-1}; shading) and (u, $\omega \times 300$) (vector) anomalies at lag 0 during (a) El Niño and (c) La Niña winters. To clearly reflect the updraft and downdraft, the vertical pressure velocity ω has been amplified by a factor of 300. The contour interval is 0.05 g kg^{-1}. The dotted areas, as well as the color vectors, denote those anomalies passing the Student's t test at the 90% confidence level. (b),(d) As in (a) and (c), respectively, but for the precipitation heating (shading) and vertical circulation (vector). The significance test for the vectors in (a) and (c) is based on the vertical pressure velocity anomaly and for those in (b) and (d) on the zonal wind anomaly.

east–west zonal circulation cell leading a strong updraft over the IO. Chen and Wang (2018a) called this the "front Walker cell" (FWC), and it serves as a new mechanism to understand the eastward propagation of the MJO. The strong leading suppressed convection over the EWP supports a stronger downdraft there. Meanwhile, mass continuity drives a stronger easterly wind anomaly associated with the Kelvin wave, which initiates an extended premoistening perturbation to the east (120°–150°E). The corresponding lower-level precipitation heating anomalies are also significantly stronger and even extend upward above 700 hPa, suggesting massive energetic congestus clouds developing to the east of the deep convection. The congestus convection further predestabilizes the lower-level atmosphere likely via moistening and heating due to the subgrid-scale processes of entrainment and condensation, respectively, and therefore speeds up the eastward propagation.

Conversely, for the slow MJO mode during the La Niña winters (Figs. 7c,d), the leading suppressed convection over the EWP is much weaker and nonorganized (refer to Fig. 4), resulting in a weaker subsidence and therefore a weaker FWC. These weaker easterly Kelvin wind anomalies only produce regionally confined BL moistening, and these weaker shallow congestus clouds tend to trigger a relatively weaker lower-level predestabilization effect and therefore a slower eastward propagation of the MJO. These details confirm the critical role of the leading suppressed convection in contributing to the eastward MJO propagation (Kim et al. 2014; Chen and Wang 2018a), and significantly support the distinct responses of the MJO propagation during different ENSO phases.

b. *Moisture budget analysis*

Before performing a budget analysis, we should first examine the variations of the LF background states in the different types of El Niño and La Niña events (Fig. 8). For the El Niño background state characterized by a warm SST anomaly over the equatorial EP (Figs. 8a,f,k), there are strong westerly wind and positive moisture anomalies over the central EP as well as a negative moisture anomaly off the equator. When the MJO convection is located over the eastern IO (see day 0 in Figs. 4 and 5), the intraseasonal easterly wind anomaly prevails over the MC–EWP region. The eastward gradient of the LF background moisture may induce positive zonal advection due to the easterly wind anomaly (Liu and Wang 2016). Meanwhile, both the strong negative meridional gradient of the specific humidity over the MC–EWP region along 4°N and the positive moisture gradient along 7°S may also produce a net moistening effect due to the intraseasonal southerly and northerly wind anomalies, respectively (Kim et al.

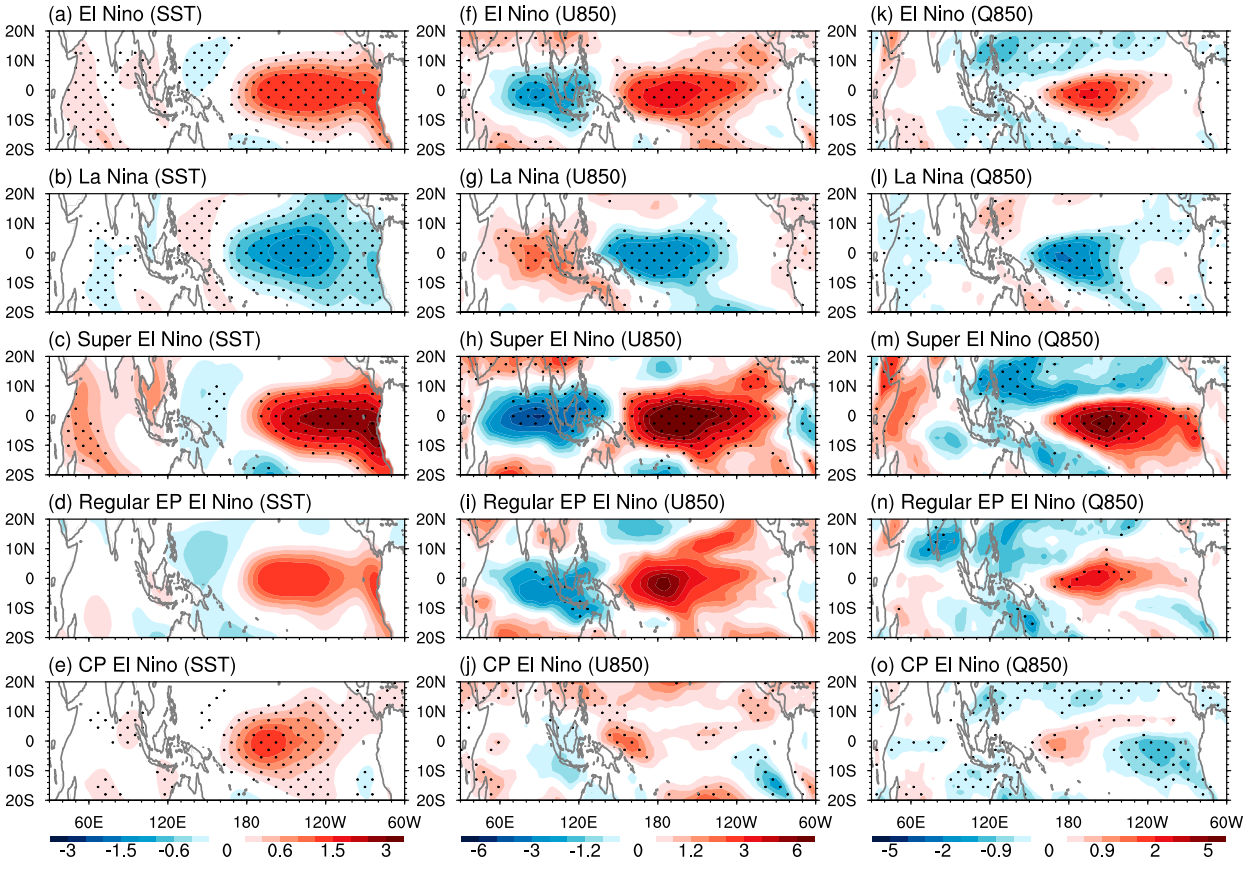

FIG. 8. (left) Composite monthly SST anomaly (°C) for the (a) 10 El Niño, (b) 8 La Niña, (c) 3 super El Niño, (d) 3 regular EP El Niño, and (e) 4 CP El Niño winters. (center),(right) As in the left panels, but for the 100-day, low-pass-filtered, lower-tropospheric (850 hPa) (f)–(j) zonal wind ($m\,s^{-1}$) and (k)–(o) specific humidity ($g\,kg^{-1}$) anomalies. The dotted areas denote those anomalies passing the Student's *t* test at the 90% confidence level.

2014; Wang et al. 2017). This scenario is also true for the super (Figs. 8c,h,m), regular EP (Figs. 8d,i,n), and CP El Niño (Figs. 8e,j,o) conditions, in which the moistening effect may decrease progressively due to the weakening atmospheric response to the decreasing LF SST anomaly. During the La Niña winters (Figs. 8b,g,l), however, the central-EP displays nearly opposite patterns including the LF background easterly wind anomaly and a poleward meridional and westward moisture gradient anomalies, all of which may cause a net drying tendency over the MC–EWP region. This suggests that the zonal gradient of LF SST from the eastern to western hemisphere may serve as a new indication of the MJO propagation speed. We prove the above qualitative descriptions in the following.

The moisture or moist static energy budget analysis has been widely recognized as a powerful tool to understand both the eastward propagation of the winter MJO (e.g., Maloney 2009; Hsu and Li 2012; Kim et al. 2014, 2017; Jiang 2017) and the northward propagation of the boreal summer intraseasonal oscillation (e.g., Adames et al. 2016; Jiang et al. 2018). Here to quantitatively prove the dependence of the fast and slow eastward propagations of the MJO on the horizontal advection-induced net moistening over the EWP, a column-integrated moisture budget is further analyzed.

Figures 9a and 9b show the spatial distributions of the composite column-integrated (from the surface to 100 hPa) specific humidity and its temporal tendency anomalies at lag 0 for the fast MJO mode during El Niño winters and the slow mode during La Niña winters, respectively. We can see that there is a strong net moistening over the equatorial eastern MC–EWP region, the Bay of Bengal, and the southern MC, and a strong net drying in the equatorial western Indian Ocean (WIO) and the northwestern Pacific for the fast MJO mode during El Niño (Fig. 9a). Conversely, for the slow MJO mode during La Niña (Fig. 9b), both the positive moisture tendency over the equatorial eastern MC–EWP and the negative tendency over the equatorial WIO and the northwestern Pacific are fairly weak. Therefore, along the equator, the zonal asymmetry of the moisture

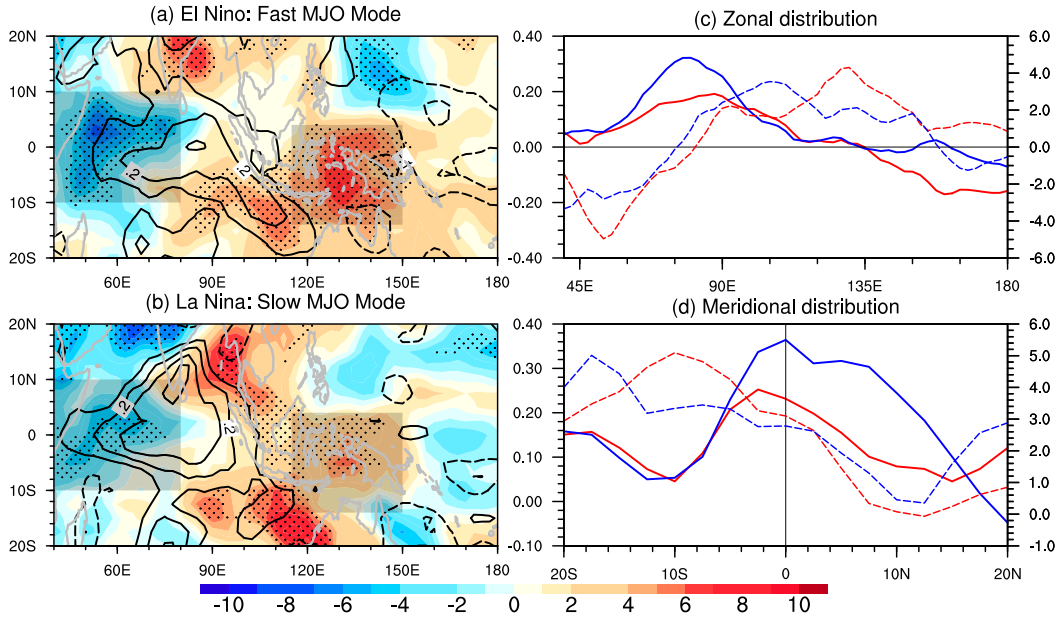

FIG. 9. (a) Spatial distribution of the composite column-integrated specific humidity (q; contour; g kg^{-1}) and its temporal tendency (q_t; shading; 1×10^{-10} g kg^{-1} s^{-1}) anomalies for the fast MJO mode during El Niño. The contour interval is 0.1 g kg^{-1} and the zero contours are omitted. The dotted areas denote those anomalies passing the Student's t test at the 90% confidence level. The two gray rectangles denote the west (WBOX; 10°S–10°N, 40°–80°E) and east (EBOX; 4°S–14°N, 115°–150°E) boxes used for the budget analysis. (b) As in (a), but for the slow MJO mode during La Niña. (c) Zonal distributions of q (solid) and q_t (dashed) over 10°S–10°N for El Niño (red) and La Niña (blue). The left (right) axis indicates q (q_t). (d) As in (c), but for the meridional distribution over 60°–90°E (100°–140°E) associated with q (q_t).

tendency for the fast MJO mode during El Niño is stronger than that for the slow mode during La Niña (refer to the dashed lines shown in Fig. 9c). This suggests that a strong (weak) zonal asymmetry of the moisture tendency should support a fast (slow) eastward propagation of the MJO (Hsu and Li 2012; Hsu et al. 2014; Wang et al. 2017, 2018b). As seen in Figs. 9a and 9b, the positive anomalies of the moisture tendency over the southern MC in the slow MJO mode are much stronger than those in the fast mode (refer to the dashed lines shown in Fig. 9d), implying that the "detour" feature of the MJO (Kim et al. 2017) tends to be more frequent during La Niña conditions.

In addition, the moisture anomaly itself, which serves as a good indicator of the MJO intensity (Sobel and Maloney 2012, 2013; Adames and Kim 2016), is weaker for the fast MJO mode in El Niño than for the slow mode in La Niña (refer to the solid lines shown in Figs. 9c and 9d). Two implications may shed light on this interesting phenomenon. First, using only the moisture advection may be insufficient to satisfactorily explain the unstable MJO growth. Second, a weaker moisture anomaly during El Niño implies that a moisture tendency of the same size or larger can propagate a weaker moisture anomaly eastward more quickly. In summary, we can make the conjecture that a stronger zonal asymmetry of the moisture tendency does not necessarily result in a larger growth of the MJO, but instead can contribute to a faster eastward propagation. The theoretical study of Adames and Kim (2016) also showed that it is the eastward propagation rather than the selection of the planetary-scale instability that results from the moisture advection. The following analysis demonstrates that such a zonal asymmetry is largely determined by the horizontal advection, especially its meridional component, associated with the ENSO background variations.

To examine the dominant source of the zonal asymmetry of the moisture tendency, we use the following equation (Yanai et al. 1973):

$$\frac{\partial q'}{\partial t} = -\langle \mathbf{V}_h \cdot \nabla_h q \rangle' - \left\langle \omega \frac{\partial q}{\partial p} \right\rangle' - \left\langle \frac{Q_2}{L_v} \right\rangle', \qquad (10)$$

where $\mathbf{V}_h = (u, v)$ denotes the horizontal velocity vector, $\nabla_h = [(\partial/\partial x), (\partial/\partial y)]$ is the horizontal gradient operator, Q_2 is the atmospheric apparent moisture sink, $\langle \cdot \rangle$ indicates column integration from the surface to 100 hPa, and the prime symbol denotes the anomaly at the 20–100-day intraseasonal time scale. The first term on the right-hand side of (10) is the horizontal moisture advection. The sum of the second and third terms represents the net

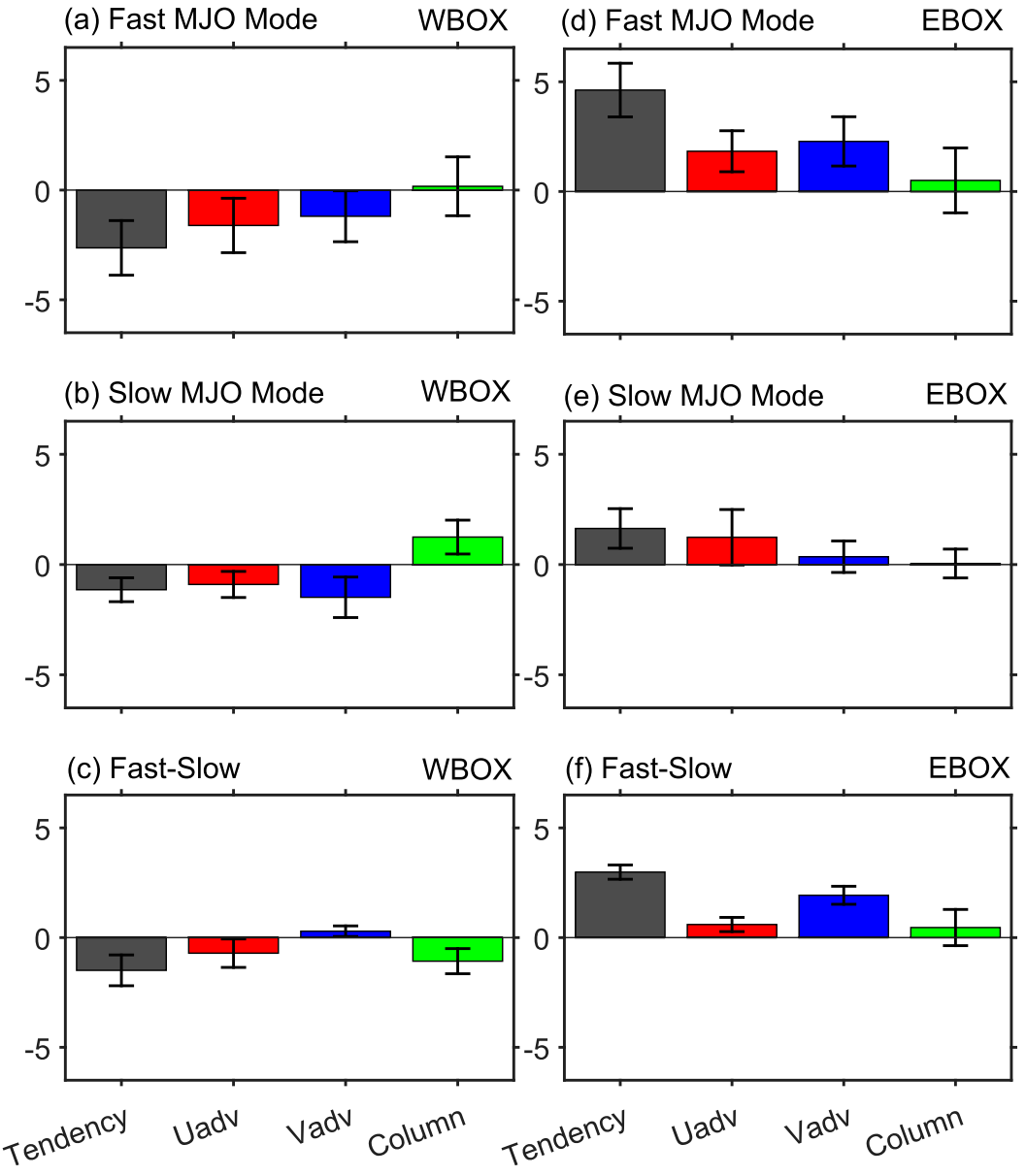

FIG. 10. The west box (WBOX; 10°S–10°N, 40°–80°E)-averaged moisture tendency (black bar), zonal advection (red bar), meridional advection (blue bar), and net moistening associated with column processes (green bar) for (a) the fast MJO mode during El Niño and (b) the slow MJO mode during La Niña. (c) The difference between the fast and slow MJO modes. (d)–(f) As in (a)–(c), but for the east box (EBOX; 4°S–14°N, 115°–150°E). The error bars denote the uncertainty range of composite results generated based on the standard deviation of sampling members.

moistening associated with the column processes, including the large-scale adiabatic vertical motion and the subgrid-scale evaporation and condensation. Following Yanai et al. (1973), the net moistening associated with the subgrid-scale processes can be approximated as the residual term between the moisture tendency and the adiabatic advective processes.

According to the descriptions of Fig. 9, the most significant difference associated with the zonal asymmetry in terms of the moisture tendency between the fast and slow MJO modes is primarily reflected in the net drying over the equatorial IO and the net moistening over the equatorial eastern MC–EWP region. Therefore, two boxes (refer to the gray rectangles shown in Fig. 9) are specified here: a west box (WBOX: 10°S–10°N, 40°–80°E) and an east box (EBOX: 15°S–5°N, 115°–150°E). Figure 10 shows the composite column-integrated total moisture budget results averaged in WBOX and

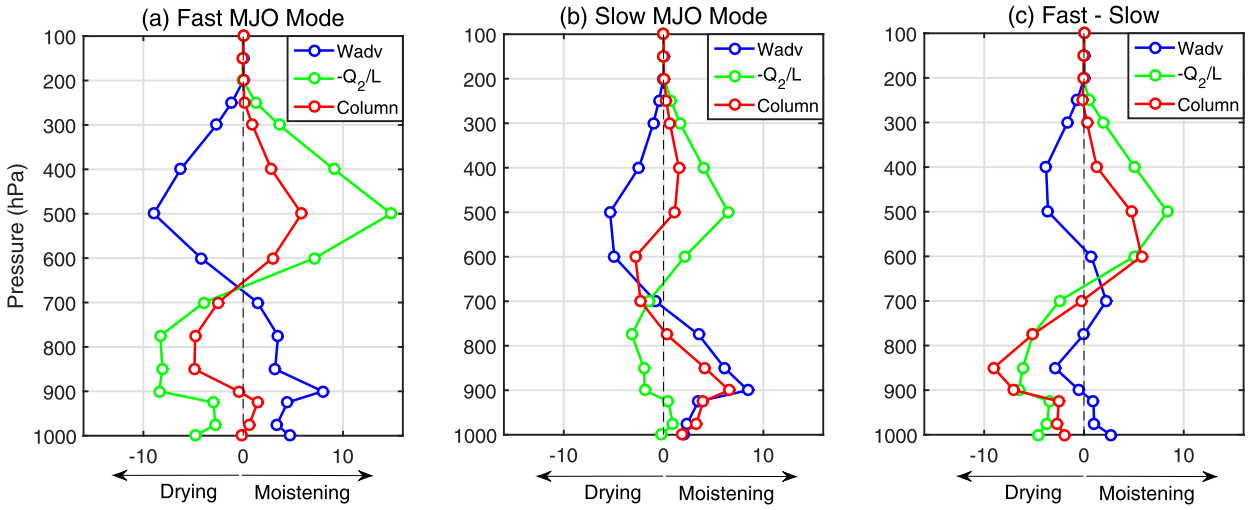

FIG. 11. (a) Composite vertical profiles of the east box (EBOX; 4°S–14°N, 115°–150°E)-averaged vertical moisture advection (Wadv; blue), the subgrid-scale moistening effect associated with the atmospheric apparent moisture sink Q_2 (green), and the column processes (red) for the fast MJO mode during El Niño. (b) As in (a), but for the slow MJO mode during La Niña. (c) The difference between the fast and slow MJO modes. The positive values on the x axis denote moistening, while the negative values denote drying; both have units of 10^{-10} g kg^{-1} s^{-1}. The y axis indicates the pressure level (hPa).

EBOX at the intraseasonal time scale (20–100 days) for the fast and slow MJO modes and the difference between them. To represent the uncertainty range of composite results, the error bars generated based on the standard deviation of sampling members are also drawn. To make the results under different amplitude MJO events comparable, each budget term was normalized by the domain-averaged (10°S–15°N, 50°–110°E) moisture anomaly. For the fast MJO mode, as seen in Figs. 10a and 10d, both the zonal and meridional advection contribute to the net drying over WBOX (i.e., over the IO) and to the net moistening over EBOX (i.e., equatorial eastern MC–EWP). For the slow MJO mode (Figs. 10b,e), even though the role of the horizontal advection is qualitatively similar to that for the fast mode, their amplitudes are very weak, especially the zonal component over WBOX and the meridional component over EBOX. From the plot of the differences in the horizontal advection between the fast and slow MJO modes (Figs. 9c,f), we can see that the dominant process distinguishing these two MJO modes is the meridional moisture advection over EBOX. The zonal moisture advection also enhances the net drying over WBOX and the net moistening over EBOX, therefore contributing to the zonal asymmetry of the moisture tendency and the fast eastward propagation of the MJO.

Revisiting Fig. 10f, we find that the column processes play a comparable role as to zonal advection in contributing to the net moistening over EBOX. To examine the role of the column processes, Fig. 11 shows the composite vertical profiles of the EBOX-averaged vertical advection $-Q_2/L_v$ and the net effect of the column processes for the fast and slow MJO modes and the differences between them. As seen from the results for the fast MJO (Fig. 11a), both the vertical advection and $-Q_2/L_v$ manifest as a vertical diploe structure, in which the node is found at 700 hPa. Above this node, the atmosphere shows a net moistening, while below it drying dominates. Because the amplitude of $-Q_2/L_v$ is generally stronger than that of vertical advection, both the net drying and the net moistening are contributed to by the latter, consistent with previous studies (e.g., Hung and Sui 2018). In the slow mode (Fig. 11b), however, all the budget terms are very weak, especially $-Q_2/L_v$, below 700 hPa. Therefore, with respect to the difference between the fast and slow modes (Fig. 11c), the net moistening effect of the column processes displays a very similar distribution to $-Q_2/L_v$. In summary, the moistening effect of the column processes shown in Fig. 10f is primarily located above 700 hPa and contributed to by $-Q_2/L_v$. However, below 700 hPa, the column processes primarily offer a net heating effect, therefore further destabilizing the column and supporting a fast eastward propagation. As seen in Fig. 7b, this heating effect is largely contributed to by the strong congestus clouds below 700 hPa during El Niño.

To quantitatively distinguish the modulation of the ENSO on the fast and slow MJO modes, following Wang et al. (2017), we decomposed each variable P (u, v, or q) into three time scales: the HF synoptic scale P^*

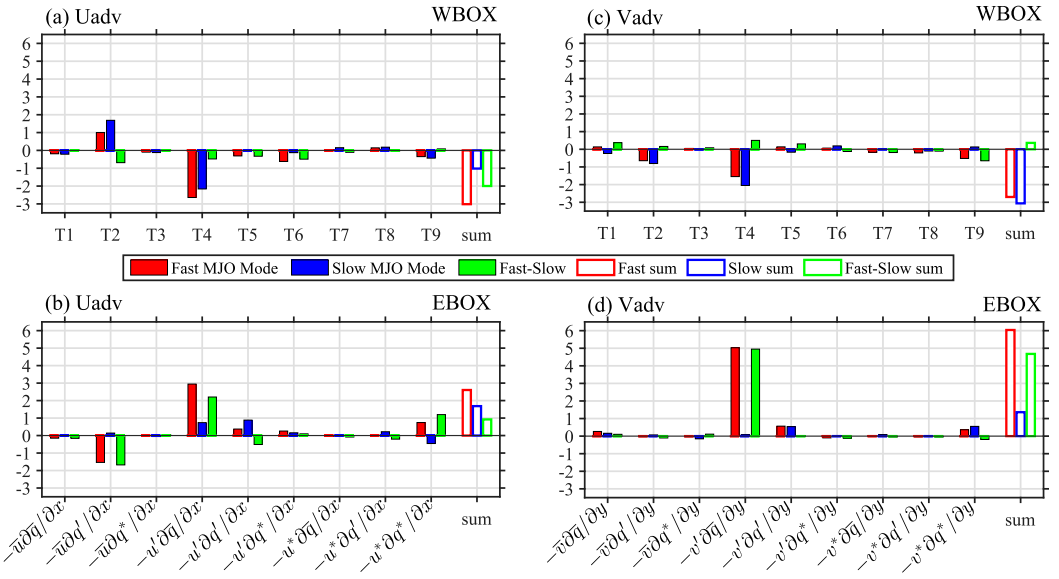

FIG. 12. Scale decomposition of the (left) zonal advection and (right) meridional advection. (a),(c) The west box (WBOX; 10°S–10°N, 40°–80°E)-averaged nine advection terms (T1–T9) for the fast MJO modes during El Niño (red bars), the slow MJO modes during La Niña (blue bars), and their difference (green bars). (b),(d) As in (a) and (c), but for the east box (EBOX; 4°S–14°N, 115°–150°E).

(<20 days), the intraseasonal time scale P' (20–100 days), and the LF background scale $\overline{P}$ (>100 days); accordingly, both the zonal and meridional advections can be divided into nine terms as follows:

$$\underbrace{-(\overline{u}\overline{q}_x)'}_{\text{T1}}\ \underbrace{-(\overline{u}q'_x)'}_{\text{T2}}\ \underbrace{-(\overline{u}q^*_x)'}_{\text{T3}}\ \underbrace{-(u'\overline{q}_x)'}_{\text{T4}}\ \underbrace{-(u'q'_x)'}_{\text{T5}}\ \underbrace{-(u'q^*_x)'}_{\text{T6}}\ \underbrace{-(u^*\overline{q}_x)'}_{\text{T7}}\ \underbrace{-(u^*q'_x)'}_{\text{T8}}\ \underbrace{-(u^*q^*_x)'}_{\text{T9}}, \tag{11}$$

$$\underbrace{-(\overline{v}\overline{q}_y)'}_{\text{T1}}\ \underbrace{-(\overline{v}q'_y)'}_{\text{T2}}\ \underbrace{-(\overline{v}q^*_y)'}_{\text{T3}}\ \underbrace{-(v'\overline{q}_y)'}_{\text{T4}}\ \underbrace{-(v'q'_y)'}_{\text{T5}}\ \underbrace{-(v'q^*_y)'}_{\text{T6}}\ \underbrace{-(v^*\overline{q}_y)'}_{\text{T7}}\ \underbrace{-(v^*q'_y)'}_{\text{T8}}\ \underbrace{-(v^*q^*_y)'}_{\text{T9}}, \tag{12}$$

For ease of writing, we call the nine terms T1, T2, . . . , T9 from left to right in (11) and (12), respectively. As in the case of (10), each term in (11) and (12) is filtered to the intraseasonal (20–100-day) time scale prior to the budget analysis.

The time-scale decomposition results over the aforementioned two boxes (WBOX and EBOX) are shown in Fig. 12. Seen in Figs. 12a and 12c, the net drying associated with both the zonal and meridional advection over IO is largely contributed to by the linear zonal advections T2 and T4. This budget result holds for both the fast MJO mode during El Niño and the slow mode during La Niña, which confirms the previous studies to some extent (e.g., Maloney 2009; Andersen and Kuang 2012; Adames and Kim 2016). Influences of ENSO on the MJO can be detected from T2 and T4 (refer to the green bars in Figs. 12a and 12c) in the zonal component, which are respectively modulated by the LF winds and the moisture gradient anomalies associated with the ENSO background state variations, even though the amplitudes are relatively weaker. In addition, the nonlinear advection, including T5 and T6 of the zonal advection and T9 of the meridional advection, also plays a role in making the IO drier for the fast MJO mode. Over EBOX (i.e., over the equatorial eastern MC–EWP region), the difference between the fast MJO mode of El Niño and slow mode of La Niña has reached its maximum. For example, for the fast mode during the warm phase of ENSO cycle, the amplitude of the linear zonal advection term T4 is more than 3 times larger than that for the slow mode (Fig. 10b), leaving a net moistening effect of T4 to distinguish the two MJO modes. For the meridional components (Fig. 10f), in the fast MJO mode during El Niño, the linear advection term T4 contributes nearly all of the total net moistening over the equatorial eastern MC–EWP region. During La Niña, however, all the budget terms become very small or even

negative. Because the magnitude of the meridional component is generally larger than that of the zonal component (see Figs. 10f and 12d), the modulation of the ENSO on the fast and slow MJO modes during the boreal winter is primarily rooted in the linear meridional advection term T4, that is, the moisture advection of the ENSO-related LF moisture anomaly by the MJO-scale meridional wind.

Another interesting phenomenon seen in Fig. 12b is that the ENSO background state variation also has a nonnegligible modulating effect on the nonlinear HF zonal advection term T9, which can be further detected in Fig. 1. As can be seen, the activity of the convectively coupled Kelvin waves (CCKWs) over MC–EWP in the 1997/98 El Niño is much stronger than that in the 2007/08 La Niña, which led to a much faster ($\sim$5.8 m s^{-1}) MJO event initiating on 13 December 1997 and a much slower ($\sim$3.0 m s^{-1}) MJO event initiated on 23 November 2007, respectively. This case study offers some evidence that supports the key role of the strong nonlinear upscale moisture feedback of CCKW on the fast MJO mode during El Niño. Conversely, La Niña winter corresponds to a slow MJO mode as a result of the weak upscale moisture feedback of the CCKWs. Note that our results here are somewhat similar to those of Guo et al. (2015), who showed that the reliability of GCMs in simulating the systematic eastward propagation of the MJO always corresponds to a well-simulated CCKW.

The above moisture budget analyses suggests that the modulation of the ENSO on the fast and slow MJO modes is primarily manifested as a net moistening over the equatorial eastern MC–EWP region, which then enhances the zonal asymmetry of the moisture tendency and therefore leads to a faster eastward propagation of the MJO during El Niño than during La Niña. As suggested by Fig. 8, the dominant physical processes associated with this net moistening effect have been diagnosed as the linearly horizontal advection (both meridional and zonal) of the LF background moisture anomaly by the intraseasonal (20–100 days) wind anomalies. The nonlinear advection by the HF zonal winds also plays a role in speeding up the east propagation of the MJO during El Niño conditions. The budget analysis results also imply the close relationship between the eastward propagation of the MJO and the background state variations (e.g., Kim et al. 2009; Jiang et al. 2015; Liu et al. 2016; Gonzalez and Jiang 2017; Ling et al. 2017).

5. Discussion of other factors in modulating the eastward MJO propagation

From section 4, the modulation effect of the ENSO on the fast and slow MJO modes can be ultimately rooted in the influences of LF (>100 days) circulation and convection. In this section, we discuss the possible roles of 1) other LF variabilities including the Indian Ocean dipole (IOD; Saji et al. 1999) and the quasi-biennial oscillation (QBO; Baldwin et al. 2001), 2) the tropical–extratropical interaction, and 3) the dynamically and thermodynamically intraseasonal air–sea interactions in modulating the eastward propagation of the MJO.

a. IOD

Several previous studies have focused on the year-to-year variability of the MJO under the IOD-related LF background state. For example, Shinoda and Han (2005) found that the interannual variation of the intraseasonal variability in the central and eastern equatorial IO is highly correlated with the large-scale zonal SST gradient of the IOD. Motivated by a hypothesis proposed by Saji et al. (2006), Izumo et al. (2010) proved that there exist two types of MJO modes: a higher-frequency mode with a period of 30–50 days and a lower-frequency mode with a period of 55–100 days, which show equatorially symmetric and asymmetric structures, respectively. Modulated by the changes in the background atmospheric circulation after an IOD, the HF MJO modes propagate eastward faster than the LF modes. Wilson et al. (2013) further demonstrated that the MJO becomes weaker and faster during the positive IOD condition, and the opposite is true during the negative IOD condition. However, because many of the SST anomalies associated with the IOD could be produced remotely by the ENSO in the tropical Pacific (Baquero-Bernal et al. 2002; Shinoda et al. 2004), it is interesting and necessary to distinguish the relative contributions of ENSO and the IOD to the MJO propagation, which is an important part of our ongoing and future research.

b. QBO

Despite being a leading mode of the interannual variability in the tropical stratosphere, the impacts of the QBO, which feature the changing of flow direction of the zonal mean zonal wind at 50 hPa every other year (Baldwin et al. 2001), on the MJO have not been well documented until very recently (e.g., Liu et al. 2014; Yoo and Son 2016; Marshall et al. 2017; Sun et al. 2019). In summary, it has been found that the composite OLR anomaly shows a larger negative value and a slower eastward propagation with a prolonged period of active convection in the QBO easterly (QBOE) phase than in the QBO westerly (QBOW) phase (e.g., Nishimoto and Yoden 2017; Son et al. 2017). The reasons for the fast eastward propagation of the MJO under QBOW conditions may result from two mechanisms: 1) the deep convection of the MJO itself in the QBOW phase is

weaker, possibly leading to a much faster phase speed of the planetary-scale Kelvin waves (Chang 1977) and therefore the MJO (Seo and Kumar 2008; Son et al. 2017); and 2) the dry convection preceding the eastward propagation of deep convection under QBOW conditions is generally stronger than that under QBOE conditions, especially over the MC–EWP region (see Fig. 3 of Zhang and Zhang 2018). According to our findings in this study, the much stronger leading suppressed convection may speed up the eastward propagation of the MJO with a weaker intensity.

c. *Tropical–extratropical interaction*

Our findings indicate that ENSO modulation of the MJO propagation is indirectly caused by enhancing of the leading suppressed convection rather than by accelerating the process of deep convective clouds. However, it remains unclear what causes this leading suppressed convection. Yong and Mao (2016) suggested that the anomalous descending motion associated with suppressed convection is dynamically forced by an anomalous convergence. This convergent wind anomaly results from changes in the subtropical circulation structure forced by extratropical disturbances associated with the equatorward advection of positive potential vorticity. Chen and Wang (2018a) showed that for the successive MJO cases (Matthews 2008), the anomaly comes from the eastward propagation of the preceding dry MJO phases, while for the primary cases it is brought about by a two-way interaction between the tropical heating of the MJO and the associated tropical–extratropical teleconnection, which evolves and forms an anomalous cyclone over the western North Pacific that generates upper-level convergence.

d. *Intraseasonal air–sea interaction*

The intraseasonal air–sea interaction has been shown to play a key role in the MJO dynamics [see the review of DeMott et al. (2015)]. During El Niño winters, the prevailing background westerly wind anomalies against the easterly wind of the MJO over the EWP region may lead to a net warming due to the reduced surface latent heat flux or the entrainment feedback beneath the mixed layer base. In addition, the strong leading suppressed convection over the EWP may also bring in more insolation and therefore warm the oceans directly. During La Niña winters, however, the amplified winds associated with the easterly wind of the MJO and the background easterly wind of ENSO cool the oceans via enhanced wind–evaporation–entrainment–SST feedback (Wang and Xie 1998; Li et al. 2008; Wei et al. 2018). The weak leading suppressed convection over the EWP may also induce cooling via the cloud–radiation–SST feedback (Wang et al. 1995; Liu and Wang 2013). Therefore, the intraseasonal warm (cool) SST anomalies over the EWP may also feed back to the atmosphere and support the fast (slow) MJO modes.

In addition to the above thermodynamical air–sea interactions, the oceanic responses to the atmospheric forcing may also cause a dynamic feedback to the MJO propagation. Han (2005) revealed that the observed 90-day spectral peak of the SST in the equatorial IO could be explained as a result of a selective response to the 90-day winds rather than to the 30–60-day winds. This implies that oceanic feedback is more important for the lower-frequency MJO modes (Saji et al. 2006; Izumo et al. 2010) because, at lower frequencies, both the Rossby and Kelvin waves of low-order baroclinic modes have longer wavelengths, which are more effectively excited by large-scale winds (Han 2005). A quantitative investigation concerning the roles of intraseasonal air–sea interaction in contributing to different propagations of the MJO, both dynamical and thermodynamical, requires a detailed observational diagnostic analysis and an auxiliary numerical modeling study.

6. Summary and concluding remarks

Using the observations and ECMWF reanalysis data since the 1980s, this study investigated the modulation of the ENSO on the fast and slow MJO modes during boreal winter. The main conclusions are summarized as follows.

The power spectrum analysis showed that the MJO variability during El Niño winters is very uniform along the entire Indo-Pacific region and is dominated by a relatively HF oscillation with a significant spectral peak of 40–50 days. However, during La Niña winters, the spectrum is very broad and is only visible over the IO and MC, and, more interesting, the MJO variability displays a double-peak spectrum with both a 40-day HF oscillation and an 80-day low-frequency oscillation. The diversity of El Niño events also evidently results in a modulation on the MJO periodicity. For example, over the IO, the period of the MJO manifests a clear difference between 30 days in EP El Niño winters and 45 days in CP El Niño winters.

The eastward propagation speed of the MJO varies strongly for different ENSO background states. For example, the evaluated phase speeds using an objective algorithm are 5.8 and 4.1 $m\,s^{-1}$ for the fast MJO mode during El Niño and the slow one during La Niña, respectively. In addition, the phase speed and intensity of the fast MJO mode tends to vary as a function of the El Niño amplitude, where the strongest super El Niño produces the fastest propagation ($\sim$7.1 $m\,s^{-1}$) and the

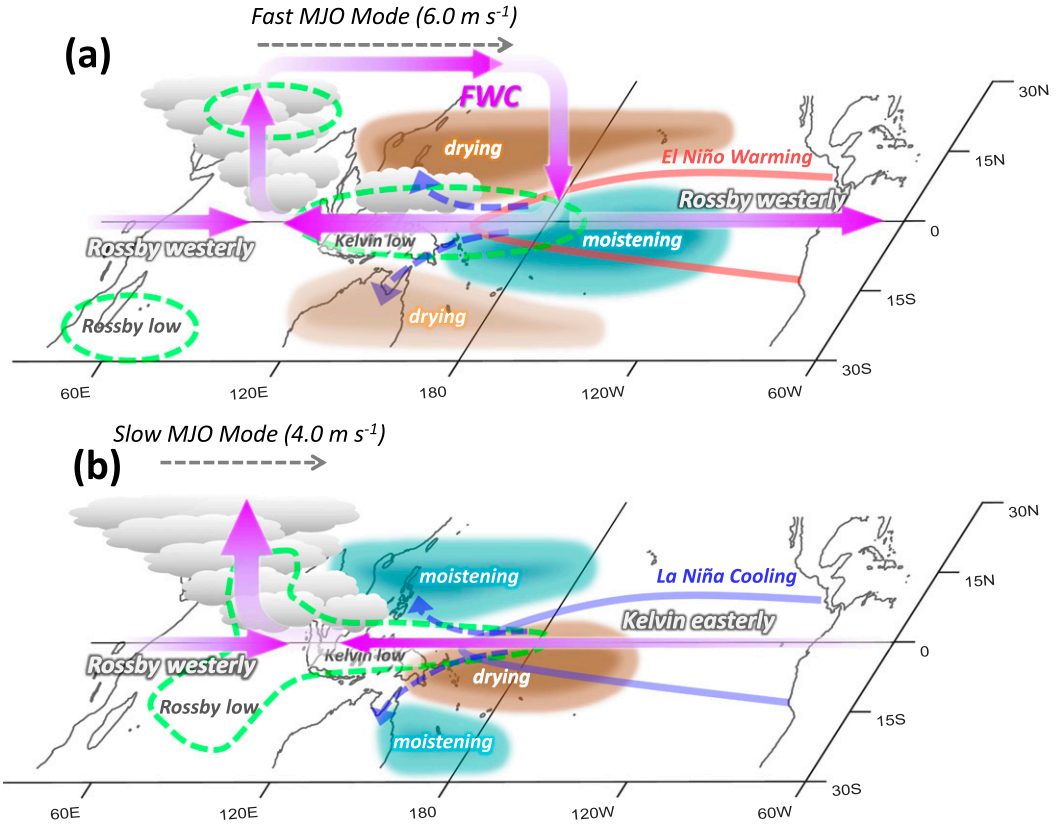

FIG. 13. Schematic diagrams illustrating the mechanisms for how the ENSO modulates the (a) fast (~6.0 m s^{-1}) and (b) slow (~4.0 m s^{-1}) MJO modes during boreal winter. The cloud cluster denotes the MJO deep convection, while the preceding nonprecipitable cloud over the MC–EWP represents the net heating effect of shallow congestus clouds below 700 hPa. The FWC (purple ellipse), intraseasonal easterly and northerly wind anomalies (dashed blue arrows) and moisture anomalies (turquoise shading stands for moistening, brown shading for drying), and Kelvin–Rossby low pressure centers (green dashed ellipse) are overlaid. Along the equator, the eastward (westward) arrow indicates the westerly Rossby (easterly Kelvin) wave wind anomaly. For all the symbols, thicker lines or deeper color shadings indicate greater strengths. The thick red (blue) line outlining the central-eastern equatorial Pacific denotes the warming (cooling) associated with the El Niño (La Niña) background state. The dashed black arrows at the top of the diagrams denote the eastward propagation of the MJO circulation–convection coupled system.

weakest MJO, while regular EP and CP El Niño winters only generate a moderate phase speed but a somewhat stronger MJO. The dispersive feature of the MJO is also evidently modulated by the ENSO background state. Even though the westward group velocity is visible during La Niña, it is considerably weaker than during El Niño. The significantly westward dispersion of the MJO wave energy during the warm phase of the ENSO is primarily contributed by the EP-type El Niño events.

The fast MJO mode during El Niño winters can propagate smoothly across the MC into the EWP, and the corresponding evolution pattern manifests an obvious meridional symmetry with respect to the equator. However, the La Niña condition tends to support an MJO "detour" via the southern MC. The horizontal distribution of the large-scale convection of the MJO indicates that that the overall amplitude of the leading suppressed convection over the EWP for the fast MJO mode is much stronger than that for the slow MJO mode.

The mechanisms by which the different ENSO background states modulate the fast and slow MJO modes are illustrated schematically in Fig. 13. From a dynamical point of view (e.g., Wang and Rui 1990; Kang et al. 2013; Wang and Chen 2016; Liu and Wang 2017b; Wang et al. 2017, 2018; Wang et al. 2018), as we can see from Fig. 13a, during the El Niño winters the leading suppressed convection over the EWP is much stronger, therefore generating a large zonal pressure gradient over the Indo-Pacific warm pool and lower-level Kelvin easterly wind anomalies. Due to mass continuity, a strong FWC (Chen and Wang 2018a) is excited to initiate an extended premoistening to the east of the deep convection. The premoistening-induced shallow congestus

clouds (below 700 hPa) can destabilize the lower troposphere to the east and contribute to the fast eastward propagation (refer to Fig. 11). However, the two off-equatorial Rossby wave low pressure centers tend to decouple from the major convection, which is reflected in the distant location of the maximal equatorial westerly from the convective center and the widespread westerly to the west covering Africa and the EP. This weak coupling reduces the ''drag effect'' of the westward-moving Rossby wave and therefore generates a faster MJO mode. For La Niña winter (Fig. 12b), because both the leading suppressed convection and the FWC are very weak, the easterly wind anomaly of Kelvin wave over the EWP becomes very small. In addition, the two low pressure centers of the Rossby wave to the west are tightly coupled to the major convection, which can be seen from the small localized equatorial westerly wind anomaly over the IO and the closer location of the maximal westerly to the convective center. In summary, unlike the fast MJO mode during El Niño, the La Niña condition, which supports the slow eastward propagation of the MJO, generates a more Gill-like circulation response to the diabatic heating. This implies the dramatic dependence of the eastward propagation speed of the MJO on its own structure (e.g., Wang and Chen 2016; Wang et al. 2016; Wang and Lee 2017; Wang et al. 2018).

When focusing on the moisture–convection feedback (e.g., Sobel and Maloney 2012, 2013; Adames and Kim 2016; Jiang et al. 2018), the column-integrated moisture budget analysis showed that the modulation of the ENSO on the fast and slow MJO modes is primarily manifested as a net moistening over the equatorial eastern MC–EWP region, which can further enhance the zonal asymmetry of the moisture tendency and therefore lead to a faster eastward propagation (e.g., Hsu and Li 2012; Hsu et al. 2014; Wang et al. 2017). This net moistening is predominated by the horizontal advection, especially its meridional component. The scale decomposition revealed that the ENSO modulates the MJO propagation primarily by changing both the longitudinal and latitudinal gradients of the LF (>100 days) background moisture anomaly (refer to Figs. 8 and 12). The role of the nonlinear zonal moisture advection by the HF (<20 days) transients, possibly by the CCKWs, was also demonstrated to be nonnegligibly important in contributing to the net moistening over the equatorial eastern MC–EWP region.

This observational diagnostic analysis requires an in-depth validation from both an intercomparison of GCM modeling studies and a theoretical modeling work. As a first step, we have utilized a long-term run from a hybrid coupled GCM (HcGCM), that is, the fourth generation of ECHAM GCM (Roeckner et al. 1996) coupled with a mixed layer oceanic model (Fu and Wang 2001), to validate the observed findings represented in this study (figure not shown). The results showed that this HcGCM could well reproduce the fast MJO mode ($\sim$6.2 m s^{-1}) during El Niño and slow MJO mode ($\sim$3.7 m s^{-1}) during La Niña. In addition, the much stronger (weaker) leading suppressed convection and Kelvin wave easterly over the MC–EWP region for the fast (slow) MJO mode are also well simulated. These results show that the modulation of ENSO on the fast and slow MJO modes during boreal winter and the underlying mechanisms are also well captured and validated by the HcGCM.

The mechanisms proposed in this paper involve equatorial wave dynamics, moisture–convection feedback, diabatic precipitation heating, and the intraseasonal air–sea interaction. In future work, we plan to further 1) validate our conclusions by evaluating MJO simulations from the multimodel comparison project developed by the Working Group on Numerical Experimentation (WGNE) MJO Task Force and the GEWEX Atmosphere System Studies (Petch et al. 2011; Jiang et al. 2015; Wang et al. 2018) and 2) utilize the theoretical model developed by Wei et al. (2018), which can adequately consider these mechanisms, to validate the results presented in this paper.

Acknowledgments. This work was jointly supported by the National Key Research and Development Program on Monitoring, Early Warning and Prevention of Major Natural Disaster (2018YFC1506004), the National Basic Research (973) Program of China under Grant 2015CB453203, the China National Science Foundation under Grants 41775066 and 41375062, the NSFC Innovative Group Grant 41421005, and the NSFC-Shandong Joint Fund for Marine Science Research Centers U1406401. Daily interpolated OLRs were obtained from NOAA/OAR/ESRL PSD, Boulder, Colorado, https://www.esrl.noaa.gov/psd/.

REFERENCES

Adames, Á. F., and D. Kim, 2016: The MJO as a dispersive, convectively coupled moisture wave: Theory and observations. *J. Atmos. Sci.*, **73**, 913–941, https://doi.org/10.1175/JAS-D-15-0170.1.

——, J. M. Wallace, and J. M. Monteiro, 2016: Seasonality of the structure and propagation characteristics of the MJO. *J. Atmos. Sci.*, **73**, 3511–3526, https://doi.org/10.1175/JAS-D-15-0232.1.

Ahn, M.-S., D. Kim, K. R. Sperber, I.-S. Kang, E. Maloney, D. Waliser, and H. Hendon, 2017: MJO simulation in CMIP5 climate models: MJO skill metrics and process-oriented diagnosis. *Climate Dyn.*, **49**, 4023–4045, https://doi.org/10.1007/s00382-017-3558-4.

Andersen, J. A., and Z. Kuang, 2012: Moist static energy budget of MJO-like disturbances in the atmosphere of a zonally

symmetric aquaplanet. *J. Climate*, **25**, 2782–2804, https://doi.org/10.1175/JCLI-D-11-00168.1.

Ashok, K., S. Behera, S. Rao, H. Weng, and T. Yamagata, 2007: El Niño Modoki and its possible teleconnection. *J. Geophys. Res.*, **112**, C11007, https://doi.org/10.1029/2006JC003798.

Baldwin, M. P., and Coauthors, 2001: The quasi-biennial oscillation. *Rev. Geophys.*, **39**, 179–229, https://doi.org/10.1029/1999RG000073.

Baquero-Bernal, A., M. Latif, and S. Legutke, 2002: On dipolelike variability of sea surface temperature in the tropical Indian Ocean. *J. Climate*, **15**, 1358–1368, https://doi.org/10.1175/1520-0442(2002)015<1358:ODVOSS>2.0.CO;2.

Chang, C. P., 1977: Viscous internal gravity waves and low-frequency oscillations in the tropics. *J. Atmos. Sci.*, **34**, 901–910, https://doi.org/10.1175/1520-0469(1977)034<0901:VIGWAL>2.0.CO;2.

Chen, G., and B. Wang, 2018a: Effects of enhanced front Walker cell on the eastward propagation of the MJO. *J. Climate*, **31**, 7719–7738, https://doi.org/10.1175/JCLI-D-17-0383.1.

——, and ——, 2018b: Does the MJO have a westward group velocity? *J. Climate*, **31**, 2435–2443, https://doi.org/10.1175/JCLI-D-17-0446.1.

Chen, X., C. Li, and Y. Tan, 2015: The influences of El Niño on MJO over the equatorial Pacific. *J. Ocean Univ. China*, **14**, 1–8, https://doi.org/10.1007/S11802-015-2381-Y.

——, J. Ling, and C. Li, 2016: Evolution of the Madden–Julian oscillation in two types of El Niño. *J. Climate*, **29**, 1919–1934, https://doi.org/10.1175/JCLI-D-15-0486.1.

Dee, D., and Coauthors, 2011: The ERA-Interim reanalysis: Configuration and performance of the data assimilation system. *Quart. J. Roy. Meteor. Soc.*, **137**, 553–597, https://doi.org/10.1002/qj.828.

DeMott, C. A., N. P. Klingaman, and S. J. Woolnough, 2015: Atmosphere–ocean coupled processes in the Madden-Julian oscillation. *Rev. Geophys.*, **53**, 1099–1154, https://doi.org/10.1002/2014RG000478.

Duchon, C. E., 1979: Lanczos filtering in one and two dimensions. *J. Appl. Meteor.*, **18**, 1016–1022, https://doi.org/10.1175/1520-0450(1979)018<1016:LFIOAT>2.0.CO;2.

Feng, J., T. Li, and W. Zhu, 2015: Propagating and nonpropagating MJO events over the Maritime Continent. *J. Climate*, **28**, 8430–8449, https://doi.org/10.1175/JCLI-D-15-0085.1.

Freeman, E., and Coauthors, 2017: ICOADS release 3.0: A major update to the historical marine climate record. *Int. J. Climatol.*, **37**, 2211–2232, https://doi.org/10.1002/joc.4775.

Fu, X., and B. Wang, 2001: A coupled modeling study of the seasonal cycle of the Pacific cold tongue. Part I: Simulation and sensitivity experiments. *J. Climate*, **14**, 765–779, https://doi.org/10.1175/1520-0442(2001)014<0765:ACMSOT>2.0.CO;2.

——, W. Wang, H.-L. Ren, X. Jia, and T. Shinoda, 2018: Three different downstream fates of the boreal-summer MJOs on their passages over the Maritime Continent. *Climate Dyn.*, **51**, 1841–1862, https://doi.org/10.1007/s00382-017-3985-2.

Geng, X., W. Zhang, M. F. Stuecker, and F. F. Jin, 2017: Strong subseasonal wintertime cooling over East Asia and northern Europe associated with super El Niño events. *Sci. Rep.*, **7**, 3770, https://doi.org/10.1038/s41598-017-03977-2.

Gill, A. E., 1980: Some simple solutions for heat-induced tropical circulation. *Quart. J. Roy. Meteor. Soc.*, **106**, 447–462, https://doi.org/10.1002/qj.49710644905.

Gonzalez, A. O., and X. Jiang, 2017: Winter mean lower tropospheric moisture over the Maritime Continent as a climate model diagnostic metric for the propagation of the Madden-Julian oscillation. *Geophys. Res. Lett.*, **44**, 2588–2596, https://doi.org/10.1002/2016GL072430.

Goulet, L., and J.-P. Duvel, 2000: A new approach to detect and characterize intermittent atmospheric oscillations: Application to the intraseasonal oscillation. *J. Atmos. Sci.*, **57**, 2397–2416, https://doi.org/10.1175/1520-0469(2000)057<2397:ANATDA>2.0.CO;2.

Gray, B. M., 1988: Seasonal frequency variation in the 40–50 day oscillation. *J. Climatol.*, **8**, 511–519, https://doi.org/10.1002/joc.3370080507.

Guo, Y., D. E. Waliser, and X. Jiang, 2015: A systematic relationship between the representations of convectively coupled equatorial wave activity and the Madden–Julian oscillation in climate model simulations. *J. Climate*, **28**, 1881–1904, https://doi.org/10.1175/JCLI-D-14-00485.1.

Han, W., 2005: Origins and dynamics of the 90-day and 30–60-day variations in the equatorial Indian Ocean. *J. Phys. Oceanogr.*, **35**, 708–728, https://doi.org/10.1175/JPO2725.1.

Hao, X., H.-L. Ren, W. Zhang, M. Liu, and Y. Wei, 2019: Diagnosing the spatiotemporal diversity of westerly wind events in the tropical Pacific. *Dyn. Atmos. Oceans*, **86**, 90–103, https://doi.org/10.1016/j.dynatmoce.2019.03.004.

Henderson, S. A., and E. D. Maloney, 2018: The impact of the Madden-Julian oscillation on high-latitude winter blocking during El Niño–Southern Oscillation events. *J. Climate*, **31**, 5293–5318, https://doi.org/10.1175/JCLI-D-17-0721.1.

Hendon, H. H., M. C. Wheeler, and C. Zhang, 2007: Seasonal dependence of the MJO–ENSO relationship. *J. Climate*, **20**, 531–543, https://doi.org/10.1175/JCLI4003.1.

Hsu, P.-C., and T. Li, 2012: Role of the boundary layer moisture asymmetry in causing the eastward propagation of the Madden–Julian oscillation. *J. Climate*, **25**, 4914–4931, https://doi.org/10.1175/JCLI-D-11-00310.1.

——, and T. Xiao, 2017: Differences in the initiation and development of the Madden–Julian oscillation over the Indian Ocean associated with two types of El Niño. *J. Climate*, **30**, 1397–1415, https://doi.org/10.1175/JCLI-D-16-0336.1.

——, T. Li, and H. Murakami, 2014: Moisture asymmetry and MJO eastward propagation in an aquaplanet general circulation model. *J. Climate*, **27**, 8747–8760, https://doi.org/10.1175/JCLI-D-14-00148.1.

Huang, B., and Coauthors, 2015: Extended reconstructed sea surface temperature version 4 (ERSST. v4). Part I: Upgrades and intercomparisons. *J. Climate*, **28**, 911–930, https://doi.org/10.1175/JCLI-D-14-00006.1.

——, and Coauthors, 2016: Further exploring and quantifying uncertainties for extended reconstructed sea surface temperature (ERSST) version 4 (v4). *J. Climate*, **29**, 3119–3142, https://doi.org/10.1175/JCLI-D-15-0430.1.

——, and Coauthors, 2017: Extended reconstructed sea surface temperature, version 5 (ERSSTv5): Upgrades, validations, and intercomparisons. *J. Climate*, **30**, 8179–8205, https://doi.org/10.1175/JCLI-D-16-0836.1.

Hung, C.-S., and C.-H. Sui, 2018: A diagnostic study of the evolution of the MJO from Indian Ocean to Maritime Continent: Wave dynamics versus advective moistening processes. *J. Climate*, **31**, 4095–4115, https://doi.org/10.1175/JCLI-D-17-0139.1.

Izumo, T., and Coauthors, 2010: Low and high frequency Madden–Julian oscillations in austral summer: Interannual variations. *Climate Dyn.*, **35**, 669–683, https://doi.org/10.1007/s00382-009-0655-z.

Jiang, X., 2017: Key processes for the eastward propagation of the Madden–Julian oscillation based on multimodel simulations.

J. Geophys. Res. Atmos., **122**, 755–770, https://doi.org/10.1002/2016JD025955.

——, and Coauthors, 2015: Vertical structure and physical processes of the Madden–Julian oscillation: Exploring key model physics in climate simulations. *J. Geophys. Res.*, **120**, 4718–4748, https://doi.org/10.1002/2014JD022375.

——, Á. F. Adames, M. Zhao, and E. Maloney, 2018: A unified moisture mode framework for seasonality of the Madden–Julian oscillation. *J. Climate*, **31**, 4215–4224, https://doi.org/10.1175/JCLI-D-17-0671.1.

Kang, I.-S., F. Liu, M.-S. Ahn, Y.-M. Yang, and B. Wang, 2013: The role of SST structure in convectively coupled Kelvin–Rossby waves and its implications for MJO formation. *J. Climate*, **26**, 5915–5930, https://doi.org/10.1175/JCLI-D-12-00303.1.

Kao, H.-Y., and J.-Y. Yu, 2009: Contrasting eastern-Pacific and central-Pacific types of ENSO. *J. Climate*, **22**, 615–632, https://doi.org/10.1175/2008JCLI2309.1.

Kiladis, G. N., M. C. Wheeler, P. T. Haertel, K. H. Straub, and P. E. Roundy, 2009: Convectively coupled equatorial waves. *Rev. Geophys.*, **47**, RG2003, https://doi.org/10.1029/2008RG000266.

——, and Coauthors, 2014: A comparison of OLR and circulation-based indices for tracking the MJO. *Mon. Wea. Rev.*, **142**, 1697–1715, https://doi.org/10.1175/MWR-D-13-00301.1.

Kim, D., and Coauthors, 2009: Application of MJO simulation diagnostics to climate models. *J. Climate*, **22**, 6413–6436, https://doi.org/10.1175/2009JCLI3063.1.

——, J.-S. Kug, and A. H. Sobel, 2014: Propagating versus non-propagating Madden–Julian oscillation events. *J. Climate*, **27**, 111–125, https://doi.org/10.1175/JCLI-D-13-00084.1.

——, H. Kim, and M. I. Lee, 2017: Why does the MJO detour the Maritime Continent during austral summer? *Geophys. Res. Lett.*, **44**, 2579–2587, https://doi.org/10.1002/2017GL072643.

Kiranmayi, L., and E. D. Maloney, 2011: Intraseasonal moist static energy budget in reanalysis data. *J. Geophys. Res.*, **116**, D21117, https://doi.org/10.1029/2011JD016031.

Kug, J.-S., F.-F. Jin, and S.-I. An, 2009: Two types of El Niño events: Cold tongue El Niño and warm pool El Niño. *J. Climate*, **22**, 1499–1515, https://doi.org/10.1175/2008JCLI2624.1.

Kuo, H. L., 1965: On formation and intensification of tropical cyclones through latent heat release by cumulus convection. *J. Atmos. Sci.*, **22**, 40–63, https://doi.org/10.1175/1520-0469(1965)022<0040:OFAIOT>2.0.CO;2.

Latif, M., V. A. Semenov, and W. Park, 2015: Super El Niños in response to global warming in a climate model. *Climatic Change*, **132**, 489–500, https://doi.org/10.1007/s10584-015-1439-6.

Lau, K.-M., and P. Chan, 1986a: Aspects of the 40–50 day oscillation during the northern summer as inferred from outgoing longwave radiation. *Mon. Wea. Rev.*, **114**, 1354–1367, https://doi.org/10.1175/1520-0493(1986)114<1354:AOTDOD>2.0.CO;2.

——, and ——, 1986b: The 40–50 day oscillation and the El Niño/Southern Oscillation: A new perspective. *Bull. Amer. Meteor. Soc.*, **67**, 533–534, https://doi.org/10.1175/1520-0477(1986)067<0533:TDOATE>2.0.CO;2.

——, and D. E. Waliser, 2012: *Intraseasonal Variability in the Atmosphere–Ocean Climate System*. 2nd ed. Springer, 613 pp.

Li, C., and I. Smith, 1995: Numerical simulation of the tropical intraseasonal oscillation and the effect of warm SST. *Acta Meteor. Sin.*, **9**, 1–12.

Li, J., and J. Mao, 2019: Factors controlling the interannual variation of 30-60-day boreal summer intraseasonal oscillation over the Asian summer monsoon region. *Climate Dyn.*, **52**, 1651–1672, https://doi.org/10.1007/s00382-018-4216-1.

Li, T., 2014: Recent advance in understanding the dynamics of the Madden–Julian Oscillation. *J. Meteor. Res.*, **28**, 1–33, https://doi.org/10.1007/S13351-014-3087-6.

——, F. Tam, X. Fu, T. Zhou, and W. Zhu, 2008: Causes of the intraseasonal SST variability in the tropical Indian Ocean. *Atmos. Oceanic Sci. Lett.*, **1**, 18–23, https://doi.org/10.1080/16742834.2008.11446758.

Liebmann, B., and C. A. Smith, 1996: Description of a complete (interpolated) outgoing longwave radiation dataset. *Bull. Amer. Meteor. Soc.*, **77**, 1275–1277.

Ling, J., C. Zhang, and P. Bechtold, 2013: Large-scale distinctions between MJO and non-MJO convective initiation over the tropical Indian Ocean. *J. Atmos. Sci.*, **70**, 2696–2712, https://doi.org/10.1175/JAS-D-13-029.1.

——, ——, S. Wang, and C. Li, 2017: A new interpretation of the ability of global models to simulate the MJO. *Geophys. Res. Lett.*, **44**, 5798–5806, https://doi.org/10.1002/2017GL073891.

Liu, C., B. Tian, K.-F. Li, G. L. Manney, N. J. Livesey Y. L. Yung, and D. E. Waliser, 2014: Northern Hemisphere mid-winter vortex-displacement and vortex-split stratospheric sudden warmings: Influence of the Madden–Julian oscillation and quasi-biennial oscillation. *J. Geophys. Res.*, **119**, 12 599–12 620, https://doi.org/10.1002/2014JD021876.

Liu, F., and B. Wang, 2013: An air–sea coupled skeleton model for the Madden–Julian Oscillation. *J. Atmos. Sci.*, **70**, 3147–3156, https://doi.org/10.1175/JAS-D-12-0348.1.

——, and ——, 2016: Role of horizontal advection of seasonal-mean moisture in in Madden–Julian oscillation: A theoretical model analysis. *J. Climate*, **29**, 6277–6293, https://doi.org/10.1175/JCLI-D-16-0078.1.

——, and ——, 2017a: Effects of moisture feedback in a frictional coupled Kelvin-Rossby wave model and implication in the Madden–Julian oscillation dynamics. *Climate Dyn.*, **48**, 513–522, https://doi.org/10.1007/s00382-016-3090-y.

——, and ——, 2017b: Roles of the moisture and wave feedbacks in shaping the Madden–Julian oscillation. *J. Climate*, **30**, 10 275–10 291, https://doi.org/10.1175/JCLI-D-17-0003.1.

——, T. Li, H. Wang, L. Deng, and Y. Zhang, 2016: Modulation of boreal summer intraseasonal oscillations over the western North Pacific by ENSO. *J. Climate*, **29**, 7189–7201, https://doi.org/10.1175/JCLI-D-15-0831.1.

Lorenz, D. J., and D. L. Hartmann, 2006: The effect of the MJO on the North American monsoon. *J. Climate*, **19**, 333–343, https://doi.org/10.1175/JCLI3684.1.

Madden, R. A., and P. R. Julian, 1971: Detection of a 40–50 day oscillation in the zonal wind in the tropical Pacific. *J. Atmos. Sci.*, **28**, 702–708, https://doi.org/10.1175/1520-0469(1971)028<0702:DOADOI>2.0.CO;2.

——, and ——, 1972: Description of global-scale circulation cells in the tropics with a 40–50 day period. *J. Atmos. Sci.*, **29**, 1109–1123, https://doi.org/10.1175/1520-0469(1972)029<1109:DOGSCC>2.0.CO;2.

——, and ——, 1994: Observations of the 40–50-day tropical oscillation—A review. *Mon. Wea. Rev.*, **122**, 814–837, https://doi.org/10.1175/1520-0493(1994)122<0814:OOTDTO>2.0.CO;2.

Maloney, E. D., 2009: The moist static energy budget of a composite tropical intraseasonal oscillation in a climate model. *J. Climate*, **22**, 711–729, https://doi.org/10.1175/2008JCLI2542.1.

——, and D. L. Hartmann, 2000: Modulation of hurricane activity in the Gulf of Mexico by the Madden–Julian oscillation. *Science*, **287**, 2002–2004, https://doi.org/10.1126/science.287.5460.2002.

Marshall, A. G., H. H. Hendon, S. W. Son, and Y. Lim, 2017: Impact of the quasi-biennial oscillation on predictability of the

Madden–Julian oscillation. *Climate Dyn.*, **49**, 1365–1377, https://doi.org/10.1007/s00382-016-3392-0.

Matthews, A. J., 2008: Primary and successive events in the Madden–Julian Oscillation. *Quart. J. Roy. Meteor. Soc.*, **134**, 439–453, https://doi.org/10.1002/qj.224.

McPhaden, M. J., 1999: Genesis and evolution of the 1997-98 El Niño. *Science*, **283**, 950–954, https://doi.org/10.1126/science.283.5404.950.

Moon, J.-Y., B. Wang, and K.-J. Ha, 2011: ENSO regulation of MJO teleconnection. *Climate Dyn.*, **37**, 1133–1149, https://doi.org/10.1007/s00382-010-0902-3.

Neena, J. M., J. Y. Lee, D. Waliser, B. Wang, and X. Jiang, 2014: Predictability of the Madden–Julian oscillation in the Intraseasonal Variability Hindcast Experiment (ISVHE). *J. Climate*, **27**, 4531–4543, https://doi.org/10.1175/JCLI-D-13-00624.1.

Nishimoto, E., and S. Yoden, 2017: Influence of the stratospheric quasi-biennial oscillation on the Madden–Julian oscillation during austral summer. *J. Atmos. Sci.*, **74**, 1105–1125, https://doi.org/10.1175/JAS-D-16-0205.1.

Petch, J., D. Waliser, X. Jiang, P. Xavier, and S. Woolnough, 2011: A global model intercomparison of the physical processes associated with the Madden–Julian oscillation. *GEWEX News*, No. 21, International GEWEX Project Office, Silver Spring, MD, 3–5.

Pillai, P. A., and J. S. Chowdary, 2016: Indian summer monsoon intra-seasonal oscillation associated with the developing and decaying phase of El Niño. *Int. J. Climatol.*, **36**, 1846–1862, https://doi.org/10.1002/joc.4464.

Pohl, B., and A. J. Matthews, 2007: Observed changes in the lifetime and amplitude of the Madden–Julian oscillation associated with interannual ENSO sea surface temperature anomalies. *J. Climate*, **20**, 2659–2674, https://doi.org/10.1175/JCLI4230.1.

Rao, J., and R. Ren, 2016: Asymmetry and nonlinearity of the influence of ENSO on the northern winter stratosphere: 1. Observations. *J. Geophys. Res. Atmos.*, **121**, 9000–9016, https://doi.org/10.1002/2015JD024520.

Ren, H.-L., and F.-F. Jin, 2011: Niño indices for two types of ENSO. *Geophys. Res. Lett.*, **38**, L04704, https://doi.org/10.1029/2010GL046031.

——, and P. Ren, 2017: Impact of Madden–Julian oscillation upon winter extreme rainfall in southern China: Observations and predictability in CFSv2. *Atmosphere*, **8**, 192, https://doi.org/10.3390/atmos8100192.

——, and Coauthors, 2019: Seasonal predictability of winter ENSO types in operational dynamical model predictions. *Climate Dyn.*, **52**, 3869–3890, https://doi.org/10.1007/S00382-018-4366-1.

Ren, P., H.-L. Ren, X. Fu, J. Wu, and L. Du, 2018: Impact of boreal summer intraseasonal oscillation on rainfall extremes in southeastern China and its predictability in CFSv2. *J. Geophys. Res. Atmos.*, **123**, 4423–4442, https://doi.org/10.1029/2017JD028043.

Roeckner, E., and Coauthors, 1996: The atmospheric general circulation model ECHAM-4: Model description and simulation of present-day climate. Max Planck Institute for Meteorology Rep. 218, 90 pp.

Roundy, P. E., 2008: Analysis of convectively coupled Kelvin waves in the Indian Ocean MJO. *J. Atmos. Sci.*, **65**, 1342–1359, https://doi.org/10.1175/2007JAS2345.1.

Saji, N. H., B. N. Goswami, P. N. Vinayachandran, and T. Yamagata, 1999: A dipole mode in the tropical Indian Ocean. *Nature*, **401**, 360–363, https://doi.org/10.1038/43854.

——, S. P. Xie, and C. Y. Tam, 2006: Satellite observations of intense intraseasonal cooling events in the tropical south Indian Ocean. *Geophys. Res. Lett.*, **33**, L14704, https://doi.org/10.1029/2006GL026525.

Seo, K. H., and A. Kumar, 2008: The onset and life span of the Madden–Julian oscillation. *Theor. Appl. Climatol.*, **94**, 13–24, https://doi.org/10.1007/s00704-007-0340-2.

Shinoda, T., and W. Han, 2005: Influence of the Indian Ocean dipole on atmospheric subseasonal variability. *J. Climate*, **18**, 3891–3909, https://doi.org/10.1175/JCLI3510.1.

——, M. A. Alexander, and H. H. Hendon, 2004: Remote response of the Indian Ocean to interannual SST variations in the tropical Pacific. *J. Climate*, **17**, 362–372, https://doi.org/10.1175/1520-0442(2004)017<0362:RROTIO>2.0.CO;2.

Slingo, J., D. Rowell, K. Sperber, and F. Nortley, 1999: On the predictability of the interannual behaviour of the Madden–Julian oscillation and its relationship with El Niño. *Quart. J. Roy. Meteor. Soc.*, **125**, 583–609, https://doi.org/10.1002/qj.49712555411.

Sobel, A., and E. Maloney, 2012: An idealized semi-empirical framework for modeling the Madden–Julian oscillation. *J. Atmos. Sci.*, **69**, 1691–1705, https://doi.org/10.1175/JAS-D-11-0118.1.

——, and ——, 2013: Moisture modes and the eastward propagation of the MJO. *J. Atmos. Sci.*, **70**, 187–192, https://doi.org/10.1175/JAS-D-12-0189.1.

——, J. Nilsson, and L. M. Polvani, 2001: The weak temperature gradient approximation and balanced tropical moisture waves. *J. Atmos. Sci.*, **58**, 3650–3665, https://doi.org/10.1175/1520-0469(2001)058<3650:TWTGAA>2.0.CO;2.

——, S. Wang, and D. Kim, 2014: Moist static energy budget of the MJO during DYNAMO. *J. Atmos. Sci.*, **71**, 4276–4291, https://doi.org/10.1175/JAS-D-14-0052.1.

Son, S. W., and Coauthors, 2017: Stratospheric control of the Madden–Julian oscillation. *J. Climate*, **30**, 1909–1922, https://doi.org/10.1175/JCLI-D-16-0620.1.

Straub, K. H., 2013: MJO initiation in the real-time multivariate MJO index. *J. Climate*, **26**, 1130–1151, https://doi.org/10.1175/JCLI-D-12-00074.1.

Suematsu, T., and H. Miura, 2018: Zonal SST differences as a potential environmental factor supporting the longevity of the Madden–Julian oscillation. *J. Climate*, **31**, 7549–7564, https://doi.org/10.1175/JCLI-D-17-0822.1.

Sun, L., H. Wang, and F. Liu, 2019: Combined effect of the QBO and ENSO on the MJO. *Atmos. Oceanic Sci. Lett.*, **12**, 170–176, https://doi.org/10.1080/16742834.2019.1588064.

Timmermann, A., and Coauthors, 2018: El Niño–Southern Oscillation complexity. *Nature*, **559**, 535–545, https://doi.org/10.1038/s41586-018-0252-6.

Titchner, H. A., and N. A. Rayner, 2014: The Met Office Hadley Centre sea ice and sea surface temperature data set, version 2: 1. Sea ice concentrations. *J. Geophys. Res.*, **119**, 2864–2889, https://doi.org/10.1002/2013JD020316.

Wang, B., 1988: Dynamics of tropical low-frequency waves: An analysis of the moist Kelvin wave. *J. Atmos. Sci.*, **45**, 2051–2065, https://doi.org/10.1175/1520-0469(1988)045<2051:DOTLFW>2.0.CO;2.

——, and H. Rui, 1990: Dynamics of the coupled moist Kelvin–Rossby wave on an equatorial β-plane. *J. Atmos. Sci.*, **47**, 397–413, https://doi.org/10.1175/1520-0469(1990)047<0397:DOTCMK>2.0.CO;2.

——, and X. Xie, 1998: Coupled modes of the warm pool climate system. Part I: The role of air–sea interaction in maintaining Madden–Julian oscillation. *J. Climate*, **11**, 2116–2135, https://doi.org/10.1175/1520-0442-11.8.2116.

——, and G. Chen, 2016: A general theoretical framework for understanding essential dynamics of Madden–Julian oscillation.

Climate Dyn., **49**, 2309–2238, https://doi.org/10.1007/s00382-016-3448-1.

——, and S.-S. Lee, 2017: MJO propagation shaped by zonal asymmetric structures: Results from 24 GCM simulations. *J. Climate*, **30**, 7933–7952, https://doi.org/10.1175/JCLI-D-16-0873.1.

——, T. Li, and P. Chang, 1995: An intermediate model of the tropical Pacific Ocean. *J. Phys. Oceanogr.*, **25**, 1599–1616, https://doi.org/10.1175/1520-0485(1995)025<1599:AIMOTT>2.0.CO;2.

——, F. Liu, and G. Chen, 2016: A trio-interaction theory for Madden–Julian oscillation. *Geosci. Lett.*, **3**, 34, https://doi.org/10.1186/s40562-016-0066-z.

——, and Coauthors, 2018: Dynamics-oriented diagnostics for the Madden–Julian oscillation. *J. Climate*, **31**, 3117–3135, https://doi.org/10.1175/JCLI-D-17-0332.1.

——, G. Chen, and F. Liu, 2019: Diversity of the Madden–Julian oscillation. *Sci. Adv.*, **5**, eaax0220,https://doi.org/10.1126/SCIADV.AAX0220.

Wang, L., T. Li, E. Maloney, and B. Wang, 2017: Fundamental causes of propagating and nonpropagating MJOs in MJOTF/GASS models. *J. Climate*, **30**, 3743–3769, https://doi.org/10.1175/JCLI-D-16-0765.1.

——, ——, L. Chen, S. K. Behera, and T. Nasuno, 2018a: Modulation of the MJO intensity over the equatorial western Pacific by two types of El Niño. *Climate Dyn.*, **51**, 687–700, https://doi.org/10.1007/s00382-017-3949-6.

——, ——, and T. Nasuno, 2018b: Impact of Rossby and Kelvin wave components on MJO eastward propagation. *J. Climate*, **31**, 6913–6931, https://doi.org/10.1175/JCLI-D-17-0749.1.

Wei, Y., F. Liu, H.-L. Ren, and M. Mu, 2018: Planetary-scale selection of the Madden–Julian oscillation in an air–sea coupled dynamical moisture model. *Climate Dyn.*, **50**, 3441–3456, https://doi.org/10.1007/s00382-017-3816-5.

——, M. Mu, H.-L. Ren, and J.-X. Fu, 2019: Conditional nonlinear optimal perturbations of moisture triggering primary MJO initiation. *Geophys. Res. Lett.*, **46**, 3492–3501, https://doi.org/10.1029/2018GL081755.

Weickmann, K., 1991: El Niño/Southern Oscillation and Madden–Julian (30–60 day) oscillations during 1981–1982. *J. Geophys. Res.*, **96**, 3187–3195, https://doi.org/10.1029/90JD01832.

Wheeler, M., and G. N. Kiladis, 1999: Convectively coupled equatorial waves: Analysis of clouds and temperature in the wavenumber–frequency domain. *J. Atmos. Sci.*, **56**, 374–399, https://doi.org/10.1175/1520-0469(1999)056<0374:CCEWAO>2.0.CO;2.

——, and H. H. Hendon, 2004: An all-season real-time multivariate MJO index: Development of an index for monitoring and prediction. *Mon. Wea. Rev.*, **132**, 1917–1932, https://doi.org/10.1175/1520-0493(2004)132<1917:AARMMI>2.0.CO;2.

Wilson, E. A., A. L. Gordon, and D. Kim, 2013: Observations of the Madden–Julian oscillation during Indian Ocean dipole events. *J. Geophys. Res. Atmos.*, **118**, 2588–2599, https://doi.org/10.1002/JGRD.50241.

Wu, R., and L. Song, 2018: Spatiotemporal change of intraseasonal oscillation intensity over the tropical Indo-Pacific Ocean associated with El Niño and La Niña events. *Climate Dyn.*, **50**, 1221–1242, https://doi.org/10.1007/s00382-017-3675-0.

Yadav, P., and D. M. Straus, 2017: Circulation response to fast and slow MJO episodes. *Mon. Wea. Rev.*, **145**, 1577–1596, https://doi.org/10.1175/MWR-D-16-0352.1.

Yanai, M., S. Esbensen, and J.-H. Chu, 1973: Determination of bulk properties of tropical cloud cluster from large-scale heat and moisture budgets. *J. Atmos. Sci.*, **30**, 611–627, https://doi.org/10.1175/1520-0469(1973)030<0611:DOBPOT>2.0.CO;2.

Yong, Y., and J. Mao, 2016: Mechanistic analysis of the suppressed convective anomaly precursor associated with the initiation of primary MJO events over the tropical Indian Ocean. *Climate Dyn.*, **46**, 779–795, https://doi.org/10.1007/s00382-015-2612-3.

Yoo, C., and S. W. Son, 2016: Modulation of the boreal wintertime Madden–Julian oscillation by the stratospheric quasi-biennial oscillation. *Geophys. Res. Lett.*, **43**, 1392–1398, https://doi.org/10.1002/2016GL067762.

Yuan, Y., C. Li, and J. Ling, 2015: Different MJO activities between EP El Niño and CP El Niño (in Chinese). *Sci. Sin. Terr.*, **45**, 318–334.

Zhang, C., 2005: Madden–Julian Oscillation. *Rev. Geophys.*, **43**, RG2003, https://doi.org/10.1029/2004RG000158.

——, 2013: Madden–Julian oscillation: Bridging weather and climate. *Bull. Amer. Meteor. Soc.*, **94**, 1849–1870, https://doi.org/10.1175/BAMS-D-12-00026.1.

——, and J. Gottschalck, 2002: SST anomalies of ENSO and the Madden–Julian oscillation in the equatorial Pacific. *J. Climate*, **15**, 2429–2445, https://doi.org/10.1175/1520-0442(2002)015<2429:SAOEAT>2.0.CO;2.

——, and J. Ling, 2017: Barrier effect of the Indo-Pacific Maritime Continent on the MJO: Perspectives from tracking MJO precipitation. *J. Climate*, **30**, 3439–3459, https://doi.org/10.1175/JCLI-D-16-0614.1.

——, and B. Zhang, 2018: QBO–MJO connection. *J. Geophys. Res.*, **123**, 2957–2967, https://doi.org/10.1002/2017JD028171.

Recent Surface Air Temperature Change over Mainland China Based on an Urbanization-Bias Adjusted Dataset

KANGMIN WEN,[a] GUOYU REN,[a,b] JIAO LI,[c] AIYING ZHANG,[d] YUYU REN,[b] XIUBAO SUN,[a,b,e] AND YAQING ZHOU[f]

[a] *Department of Atmospheric Science, School of Environmental Studies, China University of Geosciences, Wuhan, China*
[b] *Laboratory for Climate Studies, National Climate Center, China Meteorological Administration, Beijing, China*
[c] *Tieling Meteorological Bureau, Liaoning Province, Tieling, China*
[d] *Beijing Meteorological Bureau, Beijing, China*
[e] *College of Atmospheric Science, Nanjing University of Information Science and Technology, Nanjing, China*
[f] *Jinzhong Meteorological Bureau of Shanxi Province, Jinzhong, China*

(Manuscript received 20 June 2018, in final form 16 February 2019)

ABSTRACT

A dataset from 763 national Reference Climate and Basic Meteorological Stations (RCBMS) was used to analyze surface air temperature (SAT) change in mainland China. The monthly historical observational records had been adjusted for urbanization bias existing in the data series of size-varied urban stations, after they were corrected for data inhomogeneities mainly caused by relocation and instrumentation. The standard procedures for creating area-averaged temperature time series and for calculating linear trend were used. Analyses were made for annual and seasonal mean temperature. Annual mean SAT in mainland China as a whole rose by 1.24°C for the last 55 years, with a warming rate of 0.23°C decade^{-1}. This was close to the warming of 1.09°C observed in global mean land SAT over the period 1951–2010. Compared to the SAT before correction, after-corrected data showed that the urbanization bias had caused an overestimate of the annual warming rate of more than 19.6% during 1961–2015. The winter, autumn, spring, and summer mean warming rates were 0.28°, 0.23°, 0.23°, and 0.15°C decade^{-1}, respectively. The spatial patterns of the annual and seasonal mean SAT trends also exhibited an obvious difference from those of the previous analyses. The largest contrast was a weak warming area appearing in central parts of mainland China, which included a small part of southwestern North China, the northwestern Yangtze River, and the eastern part of Southwest China. The annual mean warming trends in Northeast and North China obviously decreased compared to the previous analyses, which caused a relatively more significant cooling in Northeast China after 1998 under the background of global warming slowdown.

1. Introduction

One of the core issues of contemporary climate change research is global and subcontinental surface air temperature (SAT) change. In mainland China, the climate observational network is not dense enough in some remote areas and data gaps are a serious problem prior to 1951, and there is a large uncertainty in estimating changes and long-term trends for SAT over the past 100 years. Hence, in order to better understand the detailed temporal and spatial structure in modern SAT change in mainland China, many researchers have turned to analyze the high-quality and high-density observational network records of recent decades.

Researchers had used varieties of methods to analyze the SAT change over mainland China since the late of 1980s, but most of these works did not consider the inhomogeneities in SAT data (Qiao and Qin 1990; Zhao et al. 1990; Chen et al. 1991; Lin et al. 1995; Chen and Zhu 1998; Zhai and Ren 1999; Qian and Lin 2004; Wang et al. 2004; Huang et al. 2005; Qian and Qin 2005). Since 2005, homogenized datasets obtained by various methods were used to analyze the land SAT changes over mainland China. Thus, the discontinuities in historical observational data, such as instrumentation and relocation of stations, had been corrected to some extent.

Ren et al. (2005a,b) analyzed spatial and temporal characteristics of annual- and seasonal-mean SAT changes during 1951–2004 by using monthly mean SAT data from 740 national Reference Climate and Basic

Corresponding author: Guoyu Ren, guoyoo@cma.gov.cn

DOI: 10.1175/JCLI-D-18-0395.1

© 2019 American Meteorological Society. For information regarding reuse of this content and general copyright information, consult the AMS Copyright Policy (www.ametsoc.org/PUBSReuseLicenses).

Meteorological Stations (RCBMS, or national stations) across mainland China, for example, and they found that the annual-mean SAT increased with a rate of 0.25°C decade^{-1} up to 2004, and the warming across the country mainly appeared after the mid-1980s. Tang et al. (2005) compared the SAT change of eastern China with that of western China during 1951–2002, showing that the spring and winter mean SAT of eastern China increased more significantly than those in western China, but the summer and autumn warming of eastern China were not as obvious as that of western China. Cao et al. (2016) analyzed annual- and seasonal-mean SAT variations in mainland China during 1960–2014 by utilizing a homogenized dataset of 2400 stations. They found that the annual-mean maximum SAT increased with a rate of 0.22°C decade^{-1} and the annual-mean SAT increased with a rate of 0.38°C decade^{-1}, which were significantly larger than the rates estimated by the previous analyses (Ren et al. 2005a,b; Ding and Ren 2008).

Ren et al. (2016) studied the temporal and spatial variations of SAT during 1973–2011 in mainland China by utilizing an hourly temperature dataset. They concluded that the annual-mean SAT of the whole country increased rapidly at night until 1992, with rapid warming often occurred around midnight. However, rapid warming during the daytime happened after 1992, with the strongest warming appeared in the later afternoon. Li et al. (2015) and Sun et al. (2017a) found the phenomenon of warming slowdown over mainland China, in particular even a cooling trend in Northeast China, after 1998. In Northeast China, the cooling trend was the most remarkable in the cold season including winter and spring (Sun et al. 2017a).

On regional and subcontinental scales, however, urbanization, including the strengthened urban heat island (UHI) effect, has been confirmed to exert significant impacts on the estimated trends at many meteorological stations and the regional-averaged SAT series, including those studies for mainland China.

Zhou et al. (2004) estimated warming of mean surface temperature of 0.05°C decade^{-1} attributable to urbanization based on analysis of impacts of land-use changes on surface temperature in southeast China, where rapid urbanization has occurred. Ren et al. (2005c, 2008) pointed out that the increasing of annual mean SAT induced by urbanization for national stations reaches 0.44°C during 1961–2000 in North China, which experienced the most remarkable warming in the country, with an increasing rate of SAT reached 0.11°C decade^{-1}, accounting for 38% of the total warming trend as recorded by these stations. Tang et al. (2008) analyzed the effect of urbanization to the SAT changes during 1961–2004 in southwest China, and found that the warming rates of town and city stations, and national stations on a whole, were greater than those at rural stations. In annual mean SAT records of national stations, urban warming trend was estimated as 0.05°C decade^{-1}, and its contribution to overall annual mean SAT trend was 45.3%. Hua et al. (2008) investigated the variations of annual and seasonal mean SAT during 1961–2000 in mainland China due to urbanization. They found that there was a positive correlation between urban population and the rate of urban warming. The northern stations showed a stronger urban warming than the southern stations. According to the metadata of specific locations of the stations and the population of residential areas near observational sites, Zhou and Ren (2009) classified the stations in northern China into five categories to examine the urbanization effect retained in the observed SAT records. They showed that all of the categories underwent a warming in terms of average SAT and minimum SAT, with the national stations and all categories of urban stations experiencing larger increase in annual mean SAT than that of the rural stations.

Yang et al. (2011) pointed out that UHI effects contributed 24.2% to regional average warming trends over eastern China, and the strongest effect of urbanization on annual mean SAT trends occurred over the metropolis and large city stations, with corresponding contributions to total warming were 44.0% and 35.0%, respectively, during 1981–2007. Wang and Ge (2012) reported that the urbanization effect was 0.09°C decade^{-1} and accounted for 20.0% of the total warming over mainland China. He et al. (2013) found that the warming caused by urbanization contributed to about 44.1% of the total increasing rate during 1978–2008 in the plain area of North China. Sun et al. (2017b) suggested that the urbanization effects on the SAT trends in varied periods and regions and the unevenly and sparsely distributed data in the early years might have posed the greatest problems in the present estimates of global and regional average SAT change over the last century.

The first attempt to examine the effect of urbanization in mainland China on a whole was carried out by Zhang et al. (2010) by using a homogenized dataset and a reference station network as reported in Ren et al. (2015). They confirmed that the urbanization effect contained in the warming trend of annual mean SAT of the national stations during 1961–2004 for mainland China was at least 0.08°C decade^{-1}. This impact was highly significant statistically, and the contribution of urbanization exceeded 27.3%. Ren et al. (2015) reported a comprehensive procedure for determining reference stations for evaluating urbanization effects recorded at urban stations, and estimated the urbanization effect and contribution in the

SAT data series of the Chinese national stations. They showed a highly significant urbanization effect of 0.07°C decade^{-1} and an urbanization contribution of 24.9% for the national stations of the country during the time period 1961–2004, which compared well to the results previously reported by Zhang et al. (2010).

The urbanization effect contained in the extreme temperature indices series of national stations was assessed by Ren and Zhou (2014) by utilizing the reference network data that were developed by Ren et al. (2015) and used in Zhang et al. (2010), showing that urbanization effects on the long-term trends of annual and seasonal mean minimum SAT (Tmin), average SAT (Tavg), diurnal temperature range (DTR), and the extreme SAT indices commonly used internationally were larger in mainland China during 1961–2008. In particular, the urbanization effects on the downward trend of DTR and the upward trend of Tmin were highly significant, with the urbanization contribution for annual mean DTR trend exceeding 32% over mainland China. This suggests that the urbanization effect not only exists to a great extent in the mean SAT trends on the subcontinental scale but also is not ignorable in the time series of the extreme temperature indices. Sun et al. (2016) made an attribution analysis on the basis of a dataset of 2400 stations and found that 1/3 of the overall increase of annual mean SAT in mainland China during the half century was attributable to the urbanization effect.

Therefore, the regional average SAT trends in mainland China obtained by previous studies, mostly based on the dataset of the RCBMS (Ren et al. 2008, 2012), contained great bias due to the urbanization effect. Although there existed a divergence among the estimates of the urbanization effect, the majority of the previous works, especially of those based on more sophisticated and objective procedures to select reference stations (e.g., Ren et al. 2008, 2015; Zhang et al. 2010; Yang et al. 2011; Wang and Ge 2012; He et al. 2013), were in favor of an urbanization contribution around 20.0% for annual-mean SAT trends of the RCBMS for the last half century for the country.

Hence, urbanization effect have exerted significant impacts on SAT records and the estimated trends at most of the RCBMS as well as on the regionally averaged SAT series in mainland China, and it is now desirable to quantify the urbanization biases and more importantly to remove them from the homogenized RCBMS dataset before it is used for studying the regional average SAT change. The obtained urbanization-bias adjusted dataset will play its due role in promoting studies of climate change detection and attribution and climate model validation, and also in conducting studies of regional climate change impact and vulnerability assessment.

Recently, Wen et al. (2019) developed a method for correcting the urbanization biases in monthly mean SAT dataset of the urban stations network, and made an effort to adjust the urbanization biases for each national station in mainland China. An urbanization-bias adjusted dataset has been finally constructed. In this study, we utilize the urbanization-bias adjusted dataset to analyze the SAT change in mainland China, so as to obtain a better understanding of SAT changes over mainland China over the past decades.

2. Data and methods

a. Data sources

An urbanization-bias adjusted monthly SAT dataset of 763 national stations during 1961–2015 was used here to analyze SAT change in mainland China. The data were adjusted for urbanization bias of different categories of urban stations by applying a new adjusted method (Wen et al. 2019), after it had been homogenized by the National Meteorological Information Center (Li 2011; Cao et al. 2016).

The data source for urbanization bias correction is the homogenized monthly mean SAT dataset, which is from the National Meteorological Information Center (NMIC), China Meteorological Administration (CMA). It consists of a total of about 2400 meteorological stations, with 34.4% of observation sites coming from RCBMS (national stations), and 65.6% from ordinary weather stations. In the field of climate change monitoring and research in mainland China, the mostly frequently applied SAT data were from RCBMS datasets (Ren et al. 2008, 2012). Therefore, the urbanization biases corrections were made to the monthly temperature data of RCBMS (Wen et al. 2019).

Considering the lack of temperature data before 1961 and after 2015, the time range from 1961 to 2015 was selected. It was stipulated that the missing rate of data could not exceed 2% during the period 1961–2015, and there are 763 RCBMS that meet the criterion (Fig. 1a). For the missing values (less than 2% in the target stations), the monthly mean values of the 10 years (5 years before and 5 years after the missing years respectively) were used to fill up the gaps. This guarantees that the filled monthly mean values fall within the decadal averages.

b. Reference stations for mainland China

A key to assess and adjust the urbanization bias is the development of a surface air temperature dataset of

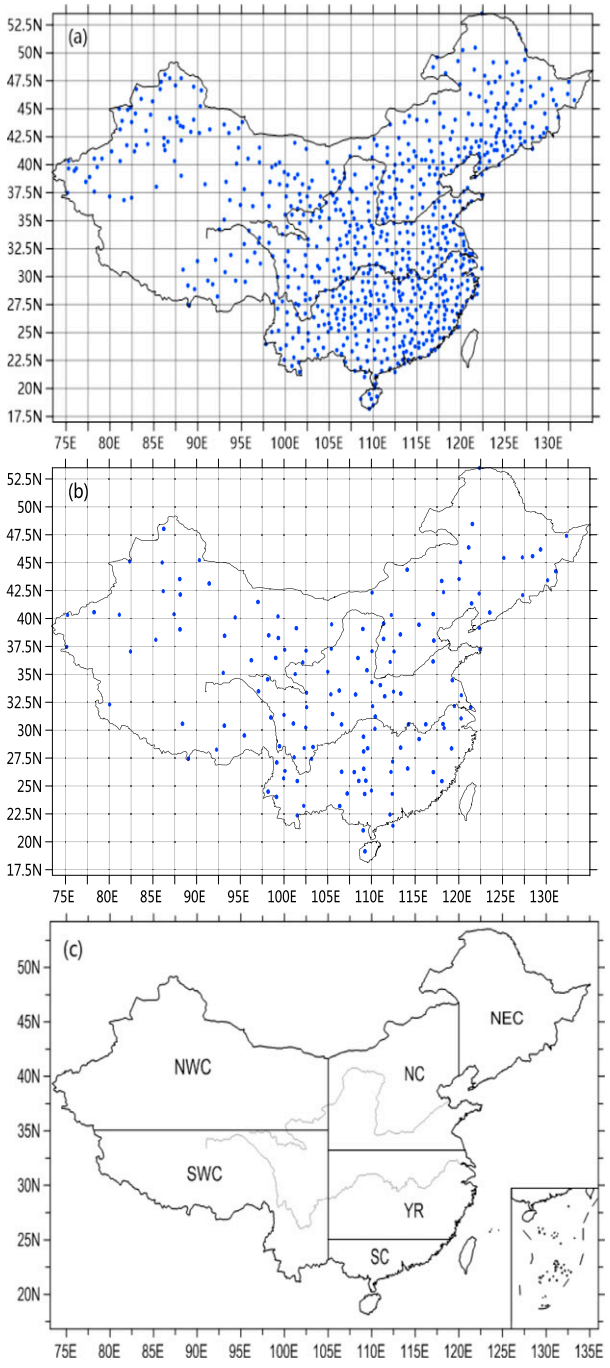

FIG. 1. (a) Distribution of 763 national stations and (b) 143 reference stations distributed in the grid of 2.5° latitude × 2.5° longitude in mainland China, and (c) boundaries of the divided six subregions. NEC, NC, NWC, SWC, YR, and SC represent Northeast China, North China, Northwest China, Southwest China, the middle to lower Yangtze River valley, and South China, respectively.

reference stations (rural stations). The reference stations network developed in previous studies (Ren et al. 2010, 2015; Zhang et al. 2010) was used to adjust the urbanization biases in RCBMS data in this work. According to Ren et al. (2010, 2015), the reference stations were selected from 2400 observational stations (RCBMS and ordinary weather stations) across the country. The criteria and steps used for selecting the reference stations were as follows:

1) Candidate reference stations had records of more than 50 years, with the beginning of record being no later than 1961, and without any missing records. In all, 1330 stations met these criteria.
2) Furthermore, 332 stations were selected from the 1330 candidate stations with the consideration that the permanent population of the settlements near the stations was less than 20 000 in 2000, but less than 70 000 in plain areas of eastern China.
3) The number of relocations had to be less than 3 after 1961, and the horizontal distances for the relocations were less than 5 km in plains and plateau areas. After this round of selection, 245 stations were remained.
4) The circumambient environment of the 245 stations was examined to guarantee the relative proportion of the built-up area within the circular of 2-km radius less than 33.0%. Only 148 stations were kept after this round of selection.
5) Five stations were discarded because they were too close to others. Finally, 143 stations were kept as the reference stations (Fig. 1b).

Based on the data of the reference stations, previous analyses (Zhang et al. 2010; Ren et al. 2015) assessed the urbanization effect (urbanization bias) and contribution in the monthly mean SAT data series of the RCBMS data. Referring to the methods in Ren et al. (2015), we updated the calculation urbanization biases for the 684 national stations in mainland China for the period 1961–2015. Figure 2 shows the spatial distribution of urbanization biases on basis of stations. The areas with large urbanization biases were distributed in northern and eastern China, including North China, parts of central China, the northern parts of Northeast China, East China, and parts of the Qinghai-Tibetan Plateau, with the values ranging from 0.10° to 0.30°C decade^{-1}. The negative urbanization biases appeared in parts of Northwest China and the western and the southern Qinghai-Tibetan Plateau, probably due to the effect of oasis expansion in the urban areas of the arid and semiarid regions (Zhang et al. 2010; Ren et al. 2015). A few of the national stations located in south of Northeast China, South China coastal areas, and central China also showed small negative urbanization bias.

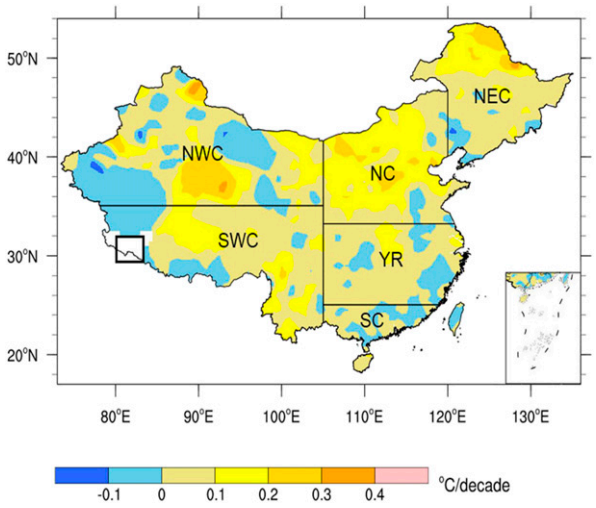

FIG. 2. Distribution of urbanization biases for 684 national stations in mainland China. A black box indicates lack of data.

c. *Reference stations and series for target stations*

Among all of the reference stations, there were 79 national stations and 64 ordinary stations. The 79 national stations of the reference stations network did not need adjustment for urbanization bias. In addition, Xisha station, which is located in the South China Sea near Hainan Province, was not considered for adjustment because there were no proper reference stations within 300 km. Finally, data of total 684 national stations or RCBMSs were corrected for urbanization biases. To compare urban–rural differences on a subcontinental scale like that of mainland China, we must take the large-scale patterns of climate change into consideration. In addition, we had to take into account the density and distribution of the reference stations in order to ensure that each target station could still have at least one reference station in the areas where reference stations were distributed relatively sparsely. Therefore, we stipulated that the reference stations chosen could not exceed 300 km from their target stations; that is, the reference stations had to be within the large circles of 300-km radius with the target stations as centers.

In establishing the specific reference stations for each target station, we referred to the method developed for testing the spatial consistency of climate records in data quality control (Karl and Williams 1987; Mitchell and Jones 2005; Li 2011). A station within a circle with a fixed radius centered on an urban station was used as a reference observational site for the urban station. The distance between two stations was calculated by using the following formula [Eq. (1)]:

$$d(A_1, A_2) = R\cos^{-1}[\sin\varphi_1\sin\varphi_2 + \cos\varphi_1\cos\varphi_2\cos(\theta_1 - \theta_2)], \quad (1)$$

where θ_1 and φ_1 are the longitude and latitude of station A_1, θ_2 and φ_2 are the longitude and latitude of station A_2, and R is the radius of Earth (6371 km).

To obtain reference stations for arbitrary target stations in the northeast, central, and western regions of the Qinghai-Tibetan Plateau where the reference stations are distributed more sparsely, we adopted a method of iterative correction that first adjusted the target stations from east to west for each longitudes, and the target stations after correcting urbanization bias then could also serve as reference stations.

After stipulating the distance between the target stations and the reference stations and selecting the candidate reference stations of any target stations, a further consideration was made as to whether the interannual and interdecadal SAT variability of the candidate reference stations were consistent with the target stations, or whether they were located in the same zones of climate variability. Therefore, the correlation coefficient of the annual mean temperature at the two stations after removing the linear trend was used as an indicator of the variability similarity. The series that removed linear trend mainly reflected the variability of SAT on interannual and interdecadal scales. The linear trend was obtained by one-dimensional linear regression analysis. If the correlation coefficients of the detrended annual mean temperature series between each target station and the nearby candidate reference stations passed a $p = 0.005$ significance level test, then the candidate reference stations were selected as the final reference stations for the target station. To adjust the urbanization bias of RCBMS data, it was important to construct a reference series for each of the target stations. Studies (e.g., Yu et al. 2012) found that, for the interpolation of missing SAT data at any station, the interpolated values calculated by the four neighboring stations with the highest correlation were highly accurate. Other studies (e.g., Jiang et al. 2008) showed that, in the correction of the inhomogeneity of precipitation data series in mainland China, the reference series could be constructed by using the data of three stations with the highest correlation coefficients among the closest 20 stations. Referring to these methods, and taking into account that an excessive number of reference stations involved in the calculation will lead to significant error, we stipulated that, when the number of reference stations of a target station is more than four, four stations with the highest correlation coefficients with the target station annual mean temperature were taken as the final reference stations, but the

TABLE 1. Number of stations with different adjusted temperature magnitude and their percentages.

Adjusted temperatures (°C decade^{-1})	−0.3 to −0.2	−0.2 to −0.1	−0.1 to 0	0 to 0.1	0.1 to 0.2	0.2 to 0.3	0.3 to 0.4	0.4 to 0.5
No. of stations	1	15	187	289	139	48	4	1
Percentage (%)	0.15	2.19	27.34	42.25	20.32	7.02	0.58	0.15
Cumulative percentage (%)	—	2.34	29.68	71.93	92.25	99.27	99.85	100

candidate reference stations were all retained when there were fewer than four.

To obtain the reference series of monthly mean SAT for each target station, the weighted averages of monthly mean SATs of all reference stations of the target station were calculated by using the squares of correlation coefficients of monthly mean SAT series between the reference stations and the target station as the weights. The formula for calculating the reference series for each target station is [Eq. (2)]

$$T = \frac{\sum_{i=1}^{m} (C_i^2 \times T_i)}{\sum_{i=1}^{m} (C_i^2)}, \tag{2}$$

where T is the monthly mean SAT of reference series, i = 1, 2, ..., m (m is the number of reference stations), C_i denotes the correlation coefficient of monthly mean SAT series between reference station i and the target station, and T_i is the monthly mean SAT of reference station i.

d. Method of adjustment

Based on the method of linear correction (Zhou and Ren 2005; Zhang 2009), urbanization bias at the target station was adjusted by using the linear trend difference of SAT between the target station and the reference series as the total correction. The procedure was based on two assumptions: 1) the linear trend of the established reference series of a target station represented the regional background temperature trends, and 2) the effect of urbanization on the trend of the target station mean SAT series was linear; that is, the effect was similar in different years and decades. The urbanization bias in SAT series of the target station was actually removed on the annual basis.

The correcting method is to add the yearly correction (X/n, with X = total correction, and n = length of the data series) from the second-last year to the first year of the data series year by year for the target station, with the recorded value of the last year (2015) kept unchanged [Eq. (3)]:

$$T_i' = T_i + (\Delta T_{u-r}/10)(k - i), \tag{3}$$

where T_i' is the temperature corrected in year i, T_i is the temperature in year i before correction, ΔT_{u-r} is the urbanization bias during the study period (°C decade^{-1}), and k is the ending year of the temperature series. The corrected series put the temperature data in the last year and the coming years as the fixed values, and thus would have a better extensibility.

Table 1 showed the number of stations with different adjusted temperature magnitudes and their percentages. The adjusted temperature magnitudes of −0.10° to −0.05°, −0.05° to 0°, 0° to 0.05°, 0.05° to 0.10°, 0.10° to 0.15°, and 0.15° to 0.20°C decade^{-1} accounted for larger proportion, and possessed a total number of 615 stations, accounting for 89.91% of all the national stations adjusted. There were 80 national stations that did not need to be adjusted for urbanization biases. Figure 3 shows the variation for number of stations with different adjusted temperature magnitudes. The number of stations increased after the temperature magnitude of 0°C decade^{-1}, and the maximum number of stations (226) was reached between 0° and 0.05°C decade^{-1}. With the increase of the absolute values of the adjusted temperature magnitudes, the numbers of stations gradually reduced.

e. Method of trend analysis

Based on the adjusted monthly mean temperature data, we reanalyzed the long-term changes in annual and seasonal mean SAT over mainland China for the period

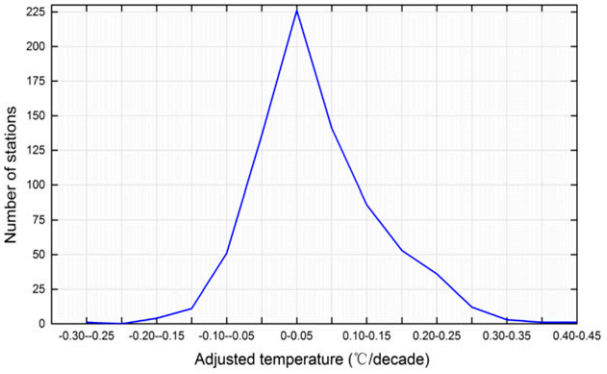

FIG. 3. Variations for number of stations with different adjusted temperature magnitude.

1961–2015. We defined the spring as March to May, summer as June to August, autumn as September to November, and winter as last year's December and the current year's January and February. The region-averaged annual and seasonal mean SAT anomalies for mainland China and six subregions were analyzed, and the spatial patterns of linear trends for annual- and seasonal-mean SAT were examined. We focused on the long-term trends of annual- and seasonal-mean SAT for each of the subregions and mainland China on a whole.

The six subregions were divided based on a comprehensive judgment of the spatial differences of natural geography, climate condition, and convenience of usage (Xu et al. 2011; Zhang et al. 2010), referring to previous works (Xu et al. 2011; Zhang et al. 2010). They are Northeast China (NEC), North China (NC), Northwest China (NWC), Southwest China (SWC), the middle to lower Yangtze River valley (YR), and South China (SC), respectively (Fig. 1c).

The methods to construct the regional average SAT anomaly series were as follows:

1) First, calculate the monthly, seasonal, and annual temperature anomalies of each year for each of the stations, which were the departures from the normal climate period from 1971 to 2000.
2) To calculate the grid average monthly, seasonal, and annual anomalies of each year for all the 2.5° × 2.5° latitude and longitude grids over mainland China, simply arithmetically average all records of the stations within each of the grids (Figs. 1a,b).
3) Finally, to obtain the regional averaged monthly, seasonal, and annual mean SAT anomalies series over mainland China, calculate the average values of all grids by using the grids area weighting method (Jones and Hulme 1996). The formula for calculating the area weighted average of all grids is [Eq. (4)] is

$$Y_k = \frac{\sum_{i=1}^{m} (\cos\theta_i) \times Y_{ik}}{\sum_{i=1}^{m} (\cos\theta_i)}, \tag{4}$$

where Y_k means the regional average of year k, $i = 1, 2, \ldots, m$ (m is the number of grids), Y_{ik} means the average of grid i for year k, and θ_i means the center latitude of grid i.

The spatial distributions of the linear trends for annual and four seasons mean SAT over mainland China were analyzed by drawing isopleth of the trend values. The significance of the linear trend of temperature was examined by using correlation coefficient test method, with a trend considered to be statistically significant when $\alpha < 0.05$.

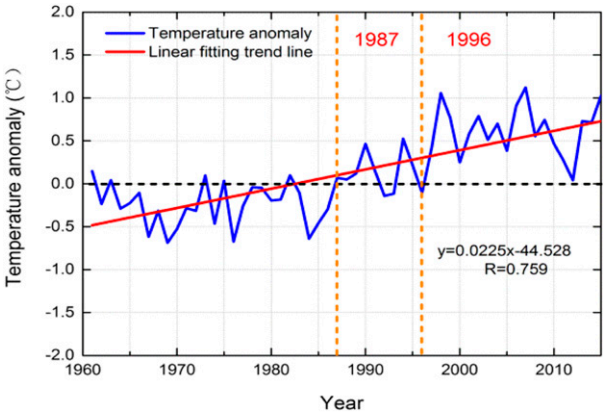

FIG. 4. Annual mean SAT anomalies in mainland China during 1961–2015.

Temperature trends were examined for statistical significance using the two-tailed Student's t test. A trend is considered statistically significant if it is significant at the 95% ($p < 0.05$) confidence level. The possible influence of serial correlation on trend estimate was not considered because the data series are long enough (Bayazit and Önöz 2007).

3. Results

a. *Time series of SAT anomalies*

Figure 4 shows the variation of annual mean SAT anomaly during 1961–2015 for mainland China. Annual-mean SAT increased at a rate of 0.23°C decade^{-1}, and the trend is statistically significant ($p < 0.05$). The lowest annual-mean SAT anomaly was −0.69°C in 1969. The anomalies before 1987 were mostly negative, with positive temperature anomalies only in 1961, 1963, 1973, 1975, and 1982; since 1987, however, the temperature has risen sharply, reaching the highest positive anomaly of 1.12°C in 2007. There were 26 years with positive temperature anomalies after 1987. The difference of annual mean SAT between the first 5 years in the 1960s and the last 5 years studied (2011–15) reached 0.67°C. The first decade of the twenty-first century was the warmest decade, and 2007 was the warmest year, in mainland China over the past 55 years.

The seasonal mean SAT anomalies all showed the rising trends in mainland China over the past 55 years, but the warming rates were different (Fig. 5). In the period analyzed, the winter, autumn, spring, and summer mean SAT rose by 1.56°, 1.28°, 1.24°, and 0.84°C respectively. Therefore, the rising rate of winter mean SAT was 0.28°C decade^{-1}, which was the largest among the four

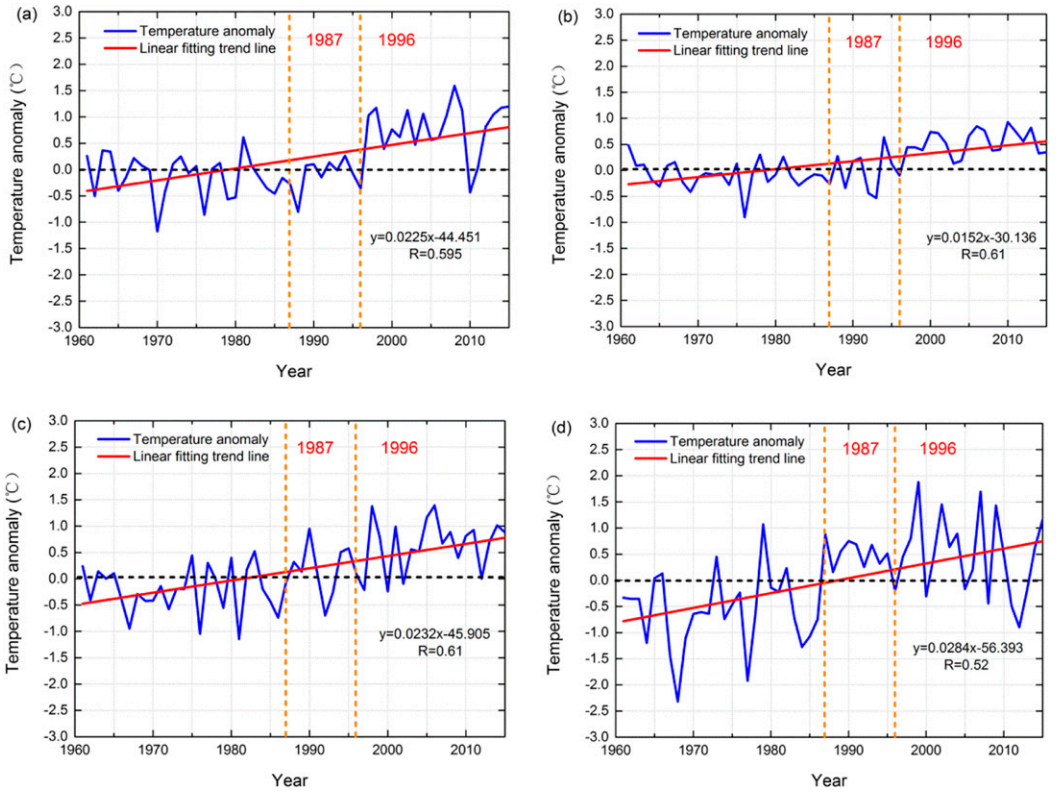

FIG. 5. Seasonal mean SAT anomalies in mainland China during 1961–2015: (a) spring, (b) summer, (c) autumn, and (d) winter.

seasons, and autumn, spring, and summer mean warming rates were 0.23°, 0.23°, and 0.15°C decade^{-1}, respectively.

The spring mean SAT was the lowest in 1970, with a negative anomaly of −1.17°C, and it reached a peak in 2008. The summer mean SAT showed the lowest value in 1976 and a peak in 2010. The warmest autumn occurred in 2006, with an anomaly of 1.40°C, and the coldest autumn was in 1981, with an anomaly of −1.15°C. The lowest winter mean SAT was found in 1968, and the anomaly was as low as −2.32°C. The highest winter mean SAT, 1.88°C higher than normal, appeared in 1999.

For spring, summer, and autumn, the fluctuation ranges and linear trends of seasonal mean temperature were generally small, and the most stable temperatures occurred after about the mid-1990s. Spring and summer mean temperature began to increase in the mid- to late 1990s, much later than for autumn and winter, which witnessed obvious warming in the mid-1980s. Winter mean temperature also saw a greater interannual and decadal variability than any other season.

b. *Monthly mean trends and decadal variations*

Figure 6 presents the monthly mean SAT trends in mainland China over 1961–2015. The fastest warming occurred in February at a rate of 0.48°C decade^{-1}. March, November, and April also registered higher trends of 0.28°, 0.27°, and 0.24°C decade^{-1}. Smaller warming trends of 0.14° and 0.15°C decade^{-1} appeared in July and May, and the smallest warming occurred in

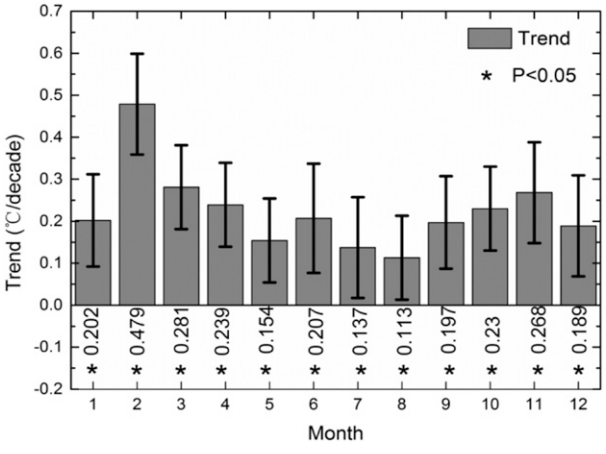

FIG. 6. Trends of monthly mean SAT in mainland China during 1961–2015. Numbers indicate the rates of change. Error bars indicate 2 times the standard deviation. Statistically significant ($p <$ 0.05) trends are marked with asterisks.

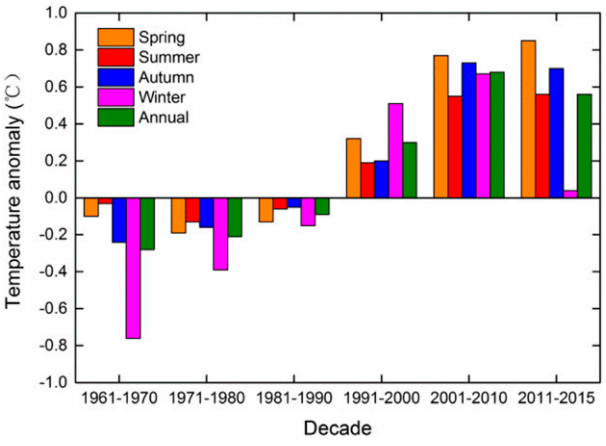

FIG. 7. Decadal averages of annual and seasonal mean SAT anomalies in mainland China.

TABLE 2. Trends of annual and seasonal mean SAT for six climate regions in mainland China during 1961–2015 (unit: °C decade^{-1}). NEC, NC, NWC, SWC, YR, and SC represent Northeast China, North China, Northwest China, Southwest China, the middle to lower Yangtze River valley, and South China respectively. An asterisk denotes that the trend is statistically significant at the 0.05 ($p < 0.05$) level.

Region	Temperature trend				
	Annual	Spring	Summer	Autumn	Winter
Mainland China	0.23*	0.23*	0.15*	0.23*	0.28*
NEC	0.27*	0.26*	0.22*	0.28*	0.32*
NC	0.21*	0.26*	0.09*	0.18*	0.29*
NWC	0.29*	0.26*	0.24*	0.33*	0.33*
SWC	0.22*	0.18*	0.18*	0.22*	0.30*
YR	0.14*	0.22*	−0.01	0.15*	0.20*
SC	0.16*	0.15*	0.11*	0.19*	0.20*

August at a rate of 0.11°C decade^{-1}. The trends of all months were statistically significant at the 95% confidence level. The monthly results are consistent with the seasonal features in mainland China obtained in this paper.

As can be seen from Fig. 7, the spring mean SAT in mainland China decreased before the 1970s, and gradually increased from the 1980s. The lowest temperature occurred in the 1970s with −0.19°C. The summer mean SAT decreased slightly before the 1970s and then increased generally after the 1970s. The autumn mean SAT got warm gradually from the 1960s onward. For the winter mean SAT, it warmed gradually before the beginning of the twenty-first century, and got slightly colder in the last 5 years. The annual mean SAT showed a warming trend before the beginning of the twenty-first century and a cooling trend afterward, and it was colder than normal between the 1960s and 1980s, with decadal mean temperature anomalies of −0.28°, −0.21°, and −0.09°C respectively.

c. *Time series of regional average temperature*

The SAT trends for six climate regions and mainland China during 1961–2015 are given in Table 2. In general, the annual mean SATs of the regions all showed warming trends. The lowest increasing trend appeared in the Yangtze River region with a trend of 0.14°C decade^{-1}, and higher warming trends appeared in Northwest, Northeast, Southwest, and North China, with the increasing trends of 0.29°, 0.27°, 0.22°, and 0.21°C decade^{-1}, respectively.

Seasonal mean SAT also exhibited the warming trends in each of the regions except for summer of the Yangtze River. The lowest spring warming was seen in South China. For summer, the Yangtze River showed a weak cooling with the trend of −0.01°C decade^{-1}, but Northwest, Northeast, and Southwest China experienced significant warming. The lowest autumn mean SAT increase occurred in the Yangtze River, and the highest autumn increasing trend occurred in Northwest China. For winter, the smallest warming was seen in the Yangtze River and South China, and the largest warming appeared in Northwest China, but all the regions except Yangtze River witnessed the largest increases in SAT among all of the seasons. In summary, the warming was the largest in winter, and the regions of Southwest, Northwest, North, and Northeast China all showed larger and significant warming in four seasons. Annual and seasonal mean SAT trends of each region were significant except for summer of the Yangtze River.

The SAT anomalies variations for each of the climate regions are presented in Fig. 8. The larger warming was in Northeast, North, Northwest, and Southwest China. Northwest China had little change before the mid-1980s but a tremendous warming after the mid-1980s. An obvious fluctuation was found in Northeast China in the past 55 years, with a slight cooling trend in 1960s, and a fast warming after the mid-1980s. The other regions showed variations similar to Northwest and Northeast China, with the warming trends not so obvious before the mid-1980s, but a rapid warming since then.

d. *Spatial characteristics of temperature change*

Figure 9 exhibits the spatial distribution of trends for annual mean SAT during 1961–2015 in mainland China. In the 55 years, annual-mean SAT increased at a rate of 0.30°–0.40°C decade^{-1} in regions of northern and central Northeast China, northern North China, eastern, northern, and southwestern Northwest China, and northern Southwest China. Annual mean SAT rose at a rate of 0.20°–0.30°C decade^{-1} in southern, eastern, and midnorthern Northeast China, midnorthern and southeastern North China, the eastern Yangtze River basin,

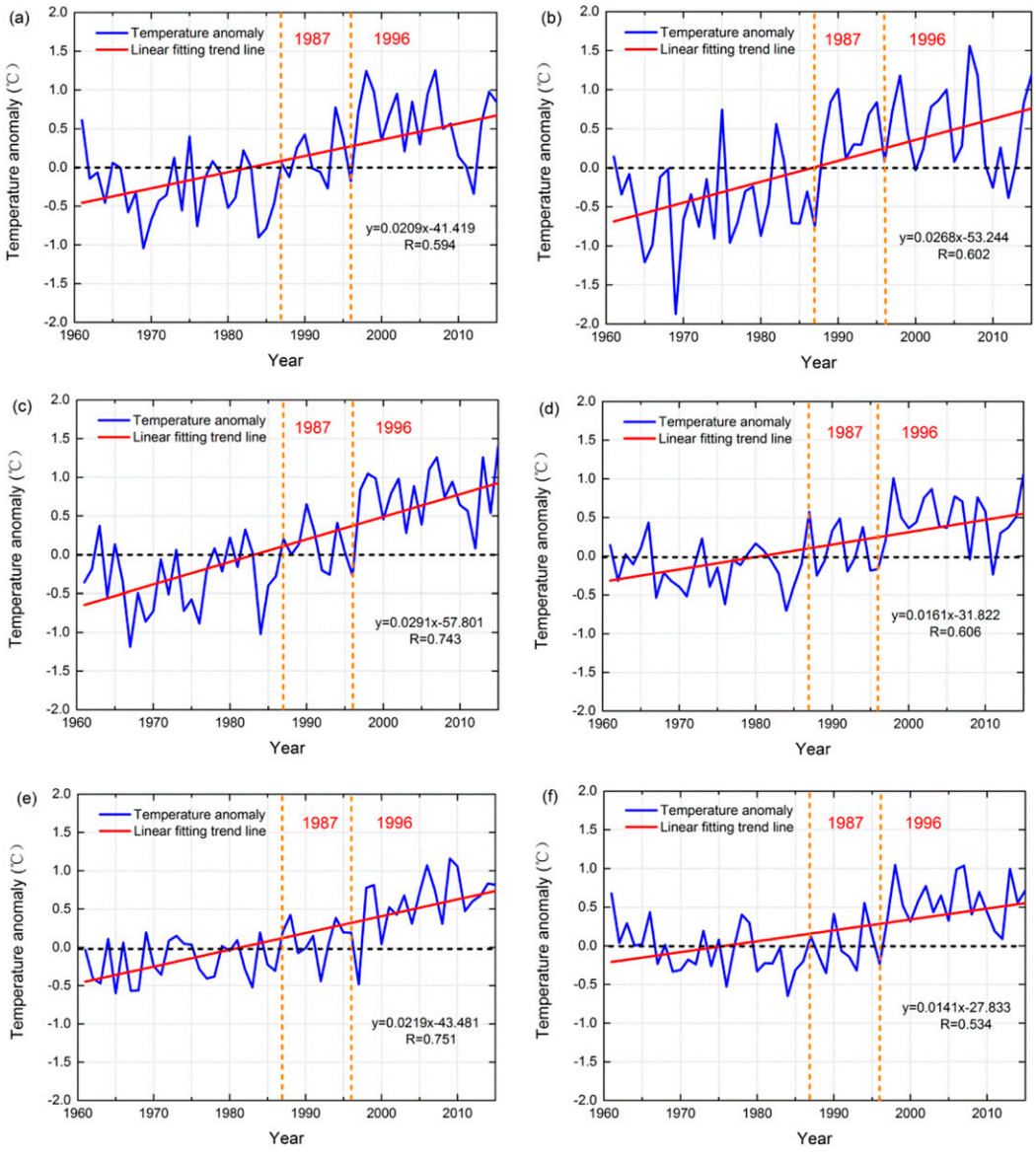

FIG. 8. Regional average annual mean SAT anomalies during 1961–2015: (a) North China, (b) Northeast China, (c) Northwest China, (d) South China, (e) Southwest China, and (f) the middle to lower Yangtze River valley.

and central Southwest and Northwest China. The weakest warming appeared in central parts of mainland China, including a little part of southwestern North China, the northwestern Yangtze River, and the eastern part of the Southwest China.

The spatial patterns of seasonal mean SAT trends in mainland China are shown in Fig. 10. The most obvious characteristic is the contrast of the remarkable winter warming and the weaker summer temperature trends, with the summer mean SAT even decreasing in northern parts of the Yangtze River region and southern North China in the 55 years. Spring mean SAT also slightly increased at a rate up to 0.20°C decade^{-1} in most parts of South China, the western and southern Yangtze River basin, eastern Southwest China, central North China, southern Northeast China, and a little part of central Northwest China. Large increases in spring mean SAT were found in western Northeast China, a small part of northern and southeastern North China, the northeastern Yangtze River region, and a small part of northeastern Northwest China, with a rate of 0.30°–0.40°C decade^{-1}.

Summer mean SAT increased at a smaller rate of 0°–0.20°C decade^{-1} in South China, the eastern and

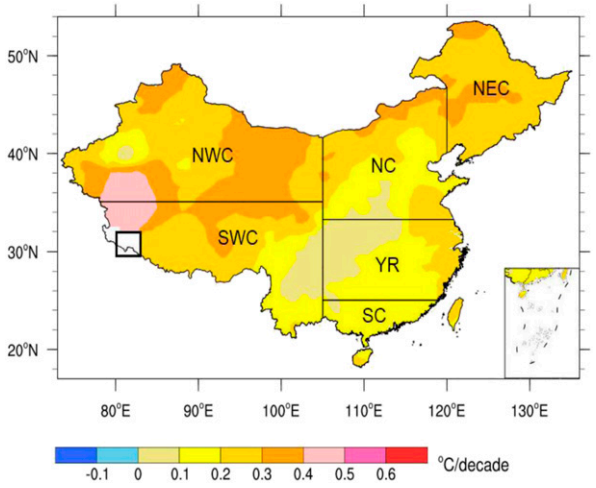

FIG. 9. Trends of annual mean SAT in mainland China during 1961–2015. A black box represents lack of data.

southwestern Yangtze River region, eastern Southwest China, central and southeastern North China, and part of central Northwest China. A remarkable increase in summer mean SAT was observed in most of Northwest, Southwest, Northeast, and northern North China with a rate at least 0.20°C decade^{-1}. A decrease of summer mean SAT appeared in the central, western, and northern Yangtze River basin and in central and southwestern North China.

In most parts of the upper and middle Yangtze River basin, western and central South China, parts of eastern Southwest China, and most of North China, autumn mean SAT increased at a rate of 0°–0.20°C decade^{-1}, registering the smallest warming in the country. The larger and significant increase in autumn mean SAT appeared in southeastern, southwestern, and northern Northwest China and in central Northeast China, ranging from 0.30° to 0.40°C decade^{-1}. The largest increase in autumn mean SAT occurred in western Southwest China and a little part of southwestern and northwestern Northwest China with a rate at least 0.40°C decade^{-1}.

Winter witnessed the largest increase in seasonal mean SAT. The most significant increase appeared in a belt extending from the northernmost part of Northeast China to the southernmost part of Southwest China, showing large trends of 0.40°–0.50°C decade^{-1}. In most other regions, the winter mean SAT trends of 0°–0.40°C decade^{-1} could be observed, with the smallest warming in parts of western Yangtze River, southeastern Southwest China, and western South China.

4. Discussion

This work made a first attempt to analyze the SAT change over mainland China by using the urbanization-bias

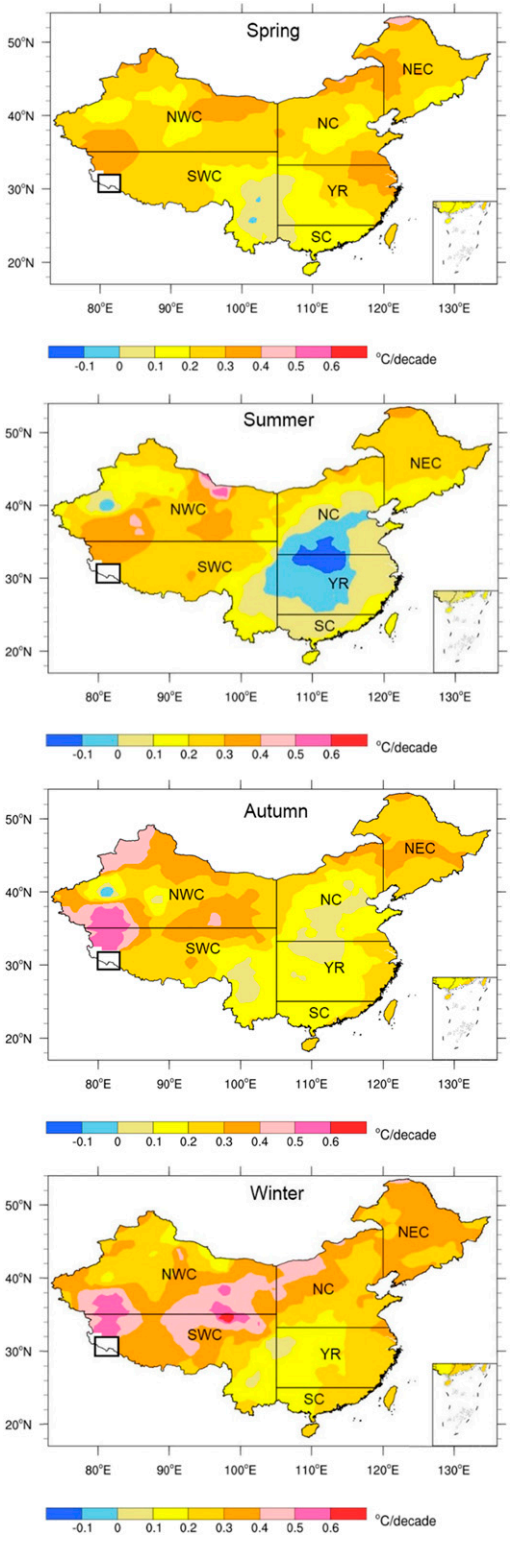

FIG. 10. Trends of seasonal mean SAT in mainland China during 1961–2015. A black box represents lack of data.

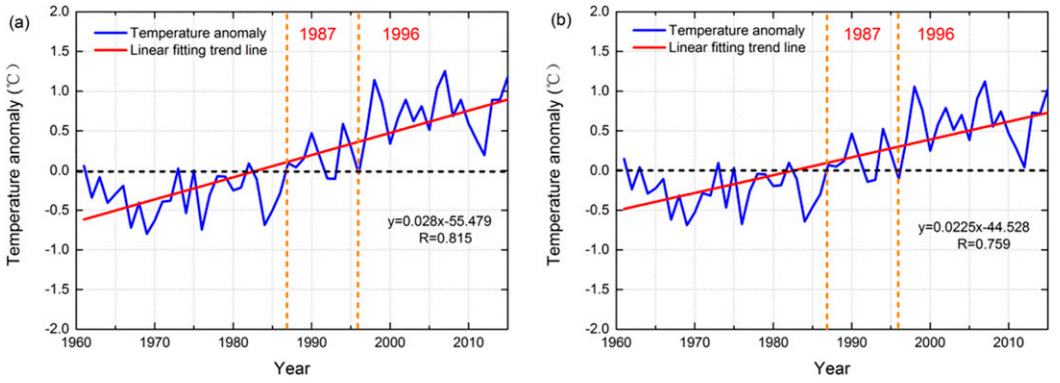

FIG. 11. Country averaged annual mean SAT anomalies (a) before and (b) after urbanization bias adjustment in mainland China during 1961–2015.

adjusted dataset. From the annual mean SAT anomaly curves for the before and after adjustment data (Fig. 11), two obvious characteristics could be found: 1) the trend after adjustment was reduced compared to that before adjustment, and 2) the annual mean SAT anomaly curve became more flattened in years after 1998.

The period after 1998 is referred to as the warming hiatus, or slowdown of climate warming (Trenberth and Fasullo 2013; Sun et al. 2017a,b). There is a weak upward trend before data adjustment during the period in mainland China, but the trend is almost 0 after the urbanization bias was corrected. For the whole period analyzed, the urbanization bias had caused an overestimate of the annual warming rate of more than 19.6%, a little smaller than, but close to, the contribution of 27.3% estimated in Zhang et al. (2010) for the period 1961–2004 using the same homogenized data of the national stations. In this study, when considering the period 1961–2013, the warming trend of SAT in mainland China is 0.22°C decade^{-1}, and the SAT increase for the whole period is 1.16°C. This is a little higher than the deurbanized value of 0.95°C (over all warming 1.44°C) during the period 1961–2013 reported in Sun et al. (2016). For period 1961–2010 in this study, the warming trend of SAT in mainland China is 0.24°C decade^{-1}, and the SAT increased by 1.19°C for the 50 years, which is close to the warming of 1.09°C observed in global mean land SAT over the period 1951–2010. The higher warming rate in this study may be because the estimate in Sun et al. (2016) used a dataset of a larger observational station network that included more rural stations, and also the urbanization contribution as given by them were larger than that estimated in this paper.

By applying a homogenized daily SAT dataset of the national stations, Ren et al. (2015) found that annual mean SAT increased at rates of 0.31°C decade^{-1} in mainland China during 1961–2008, when the data were not corrected for urbanization bias, but this was reduced to 0.24°C decade^{-1} if a correction was applied to the country-averaged SAT data series. The increasing trend of annual mean SAT reduced by 22.6% after the data series were adjusted. This is very close to the 19.6% urbanization bias obtained for period 1961–2015 in this paper.

In an earlier study, Ren et al. (2005a) used a monthly mean temperature dataset, which had been adjusted for inhomogeneity, to analyze SAT change during 1951–2001 in mainland China. Here we made a comparison of the present work with the previous analysis, by ending the urbanization-bias adjusted data in 2001. In Ren et al. (2005a), there were only two warm years before the mid-1980s (1973 and 1982) but 13 warm years after the mid-1980s, and the warmest year occurred in 1998 with a country average annual mean temperature anomaly of 1.13°C. When we used the adjustment data, more warm years (6 years) were found before 1987, but the number of warm years after 1987 was reduced to 12, and the annual mean SAT anomaly of the warmest year in 1998 was now 1.06°C.

Winter has been the season that has experienced the most rapid warming in mainland China. After the mid-1980s, there were 14 warm winters, and the maximum anomaly was 1.93°C in 1999, when the data without adjustment of the urbanization bias were applied (Ren et al. 2005a). After the urbanization bias adjustment, there were 13 warm winters, with the maximum anomaly in 1999 reduced to 1.88°C.

The spatial patterns of the annual and seasonal mean SAT trends also exhibited obvious differences from those of the previous analyses. The largest contrast was an increased extent of the weak warming area appearing in central parts of mainland China, which included the

southwestern part of North China, the western part of the Yangtze River region, and the eastern part of Southwest China. The weak warming of the Sichuan basin and its neighboring regions may have been related to the combined influence of landform and pollutants emission. The regions are located to the east of the Tibetan Plateau, and the near-surface wind speed is very small when the westerly in mid- and lower troposphere bypass the Tibetan Plateau, forming one static wind area, which make the aerosols not easy to spread. Hence, the annual mean SAT in the regions increased weakly or even decreased at a few stations. However, the weak warming area presently extended to include the southern part of the Loess Plateau and the southwestern part of the North China Plain, and this may have been caused by the larger adjustments of the urbanization biases due to the more apparently unrepresentative observational settings in the flat regions.

In eastern part of Southwest China, the annual mean SAT showed a weak increasing trend, which is different from previous studies that reported a decreasing trend, despite that the cooling was not significant (Zhang and Fang 1988; Song 1994; Chen et al. 1991; Ren et al. 2005b). This may due to the warming trend after the mid-1990s in this region (Ren et al. 2005b) and the data series were extended to 2015 in this paper to catch the warming stage well.

Compared to the results of the only homogenized data (Ren et al. 2005b), the warming trends of annual mean SAT in Northeast China and North China obviously decreased, which caused a relatively more significant cooling in Northeast China after 1998 under the background of the global warming slowdown. Both the global warming hiatus after 1998 and the urbanization bias adjustment are important for the difference. The region is a relatively more significant cooling area in the Northern Hemisphere after 1998 (Sun et al. 2017a), and the urbanization effect on the SAT trends is generally larger (Zhang et al. 2010). Therefore, the urbanization-bias adjusted data series showed less warming during the 55 years.

In the middle and lower reaches of the Yangtze River and the Huaihe River basin, summer mean SAT showed a weak decreased trend (Ren et al. 2005b); after the adjustment, the weak cooling area extended to southwestern and central North China region. The southwestern North China region is located in the Qinling Mountains and the Loess Plateau, and the weak cooling may have been caused mainly by the rugged terrain, which resulted in a less development and urbanization bias; also, the urbanization effects in the central part of North China region were stronger, with the summer mean SAT trends shifting from positive to negative after the adjusted data were used.

In the western part of Southwest China, both national stations and reference stations were lacking. Actually there is only one reference station (Shiquanhe station) in the area, and it is also located in a small town, which may have been affected itself by urbanization. Therefore, the robustness of the adjustment in this area might be lower, and further work is needed when more data are available.

Using the urbanization-bias adjusted monthly mean SAT dataset of 763 RCBMS to analyze the long-term SAT change, a more real spatial and temporal pattern could be obtained, with the overestimated warming bias in the country on a whole reduced to a large extent and the more coherent spatial characteristics of the SAT change obtained. The new urbanization bias adjusted monthly mean SAT dataset could be applied in monitoring, detection, and attribution of large-scale climate change. There will also be some practical value in areas including climate model validation, impact assessments, and vulnerability studies of regional climate change.

However, there are still some issues that need to be solved in the studies of SAT change in mainland China. One major issue would be related to the representativeness of the reference stations when urbanization bias is assessed and corrected. The reference stations, as a baseline to adjust urbanization bias, are actually not located in real rural areas, and they are being increasingly affected by urbanization processes in the small cities and towns in the country. Considering this deficiency, the adjustments made in this work have to be regarded as conservative, and there are still residual biases of the urbanization effect in the adjusted temperature data series. It is also noteworthy that the absence of observational data in vast regions of the Qinghai-Tibetan Plateau and the Taklimakan Desert may have brought considerable uncertainty to estimates of long-term SAT changes and the adjustment of urbanization biases in western China. These should be gradually solved in future work.

5. Conclusions

In this paper, the SAT changes in mainland China during 1961–2015 were analyzed by using the urbanization-bias adjusted dataset of 763 national stations. The following conclusions can be drawn:

1) Annual mean SAT increased significantly at a rate of 0.23°C decade^{-1} in mainland China. The rising rate of winter mean SAT reached 0.28°C decade^{-1}, and the autumn, spring, and summer mean warming rates were 0.23°, 0.23°, and 0.15°C decade^{-1} respectively.
2) The annual mean SAT values in different regions all showed significant increasing trends. The smallest warming appeared in the Yangtze River region,

with a rate of 0.14°C decade^{-1}, and the largest warming appeared in Northwest China, reaching 0.29°C decade^{-1}. Summer mean SAT in the Yangtze River region exhibited a weak cooling trend.

3) The fastest warming occurred in February at a rate of 0.48°C decade^{-1}, followed by March, November, and April (0.28°, 0.27°, and 0.24°C decade^{-1} respectively). July and May witnessed slower warming trends (0.14° and 0.15°C decade^{-1}), and the slowest warming occurred in August (0.11°C decade^{-1}).
4) For annual mean SAT, weaker warming areas with rends of 0°–0.10°C decade^{-1} appeared in central parts of mainland China. Parts of the weaker warming areas, including southern North China, a little part of eastern Southwest China, and the northwestern Yangtze River region, were characterized by a cooling in summer.

Acknowledgments. This work was supported by the Chinese Ministry of Science and Technology (MOST) National Key Research and Development Program (Fund 2018YFA0605603) and the Natural Science Foundation of China (NSFC) (Fund 41575003).

REFERENCES

Bayazit, M., and B. Önöz, 2007: To prewhiten or not to prewhiten in trend analysis. *Hydrol. Sci. J.*, **52**, 611–624, https://doi.org/10.1623/hysj.52.4.611.

Cao, L. J., Y. N. Zhu, G. L. Tang, Y. Yuan, and Z. W. Yan, 2016: Climatic warming in China according to a homogenized data set from 2419 stations. *Int. J. Climatol.*, **36**, 4384–4392, https://doi.org/10.1002/joc.4639.

Chen, L. X., and W. Q. Zhu, 1998: Study on climate change of China over the past 45 years. *Acta Meteor. Sin.*, **56**, 257–271.

——, Y. N. Shao, Q. F. Zhang, Z. H. Ren, and G. S. Tian, 1991: Preliminary analysis of climatic change during the last 39 years in China (in Chinese). *J. Appl. Meteor. Sci.*, **2**, 164–174.

Ding, Y. H., and G. Y. Ren, 2008: *Introduction to Climate Change Science of China* (in Chinese). China Meteorological Press, 281 pp.

He, Y. T., G. S. Jia, Y. H. Hu, and Z. J. Zhou, 2013: Detecting urban warming signals in climate records. *Adv. Atmos. Sci.*, **30**, 1143–1153, https://doi.org/10.1007/s00376-012-2135-3.

Hua, L. J., Z. G. Ma, and W. D. Guo, 2008: The impact of urbanization on air temperature across China. *Theor. Appl. Climatol.*, **93**, 179–194, https://doi.org/10.1007/s00704-007-0339-8.

Huang, M., G. B. Peng, L. M. Leslie, X. M. Shao, and W. Y. Sha, 2005: Seasonal and regional temperature changes in China over the 50 year period 1951–2000. *Meteor. Atmos. Phys.*, **89**, 105–115, https://doi.org/10.1007/s00703-005-0124-0.

Jiang, Z. H., Q. Huang, and Q. X. Li, 2008: Study of precipitation series homogeneous adjustment and their correction over China in the last 50 years (in Chinese). *Climatic Environ. Res.*, **13**, 67–74.

Jones P. D., and M. Hulme, 1996: Calculating regional climatic time series for temperature and precipitation: Methods and illustrations. *Int. J. Climatol.*, **16**, 361–377, https://doi.org/10.1002/(SICI)1097-0088(199604)16:4<361::AID-JOC53>3.0.CO;2-F.

Karl, T. R., and C. N. Williams, 1987: An approach to adjusting climatological time series for discontinuous inhomogeneities. *J. Climate Appl. Meteor.*, **26**, 1744–1763, https://doi.org/10.1175/1520-0450(1987)026<1744:AATACT>2.0.CO;2.

Li, Q. X., 2011: *Introductory Study of Historic Climate Data Homogeneity*. China Meteorological Press, 115 pp.

——, and Coauthors, 2015: China experiencing the recent warming hiatus. *Geophys. Res. Lett.*, **42**, 889–898, https://doi.org/10.1002/2014GL062773.

Lin, X. C., S. Q. Yu, and G. L. Tang, 1995: Temperature series of the past 100 years for China (in Chinese). *Atmos. Sci.*, **19**, 525–534.

Mitchell, T. D., and P. D. Jones, 2005: An improved method of constructing a database of monthly climate observations and associated high-resolution grids. *Int. J. Climatol.*, **25**, 693–712, https://doi.org/10.1002/joc.1181.

Qian, W. H., and X. Lin, 2004: Regional trends in recent temperature indices in China. *Climate Res.*, **27**, 119–134, https://doi.org/10.3354/cr027119.

——, and A. Qin, 2005: Spatial-temporal characteristics of temperature variation in China. *Meteor. Atmos. Phys.*, **93**, 1–16, https://doi.org/10.1007/s00703-005-0163-6.

Qiao, S. X., and J. Qin, 1990: The diagnoses of the effect from the urbanization of a county town on temperature (in Chinese). *Meteor. Mon.*, **16**, 17–20, https://doi.org/10.7519/j.issn.1000-0526.1990.11.003.

Ren, G. Y., and Y. Q. Zhou, 2014: Urbanization effect on trends of extreme temperature indices of national stations over mainland China, 1961–2008. *J. Climate*, **27**, 2340–2360, https://doi.org/10.1175/JCLI-D-13-00393.1.

——, J. Guo, M. Z. Xu, Z. Y. Chu, L. Zhang, X. K. Zou, Q. X. Li, and X. N. Liu, 2005a: Climate changes of China's mainland over the past half century (in Chinese). *Acta Meteor. Sin.*, **63**, 942–956.

——, M. Z. Xu, Z. Y. Chu, J. Guo, Q. X. Li, X. N. Liu, and Y. Wang, 2005b: Changes of surface air temperature in China during 1951–2004 (in Chinese). *Climatic Environ. Res.*, **10**, 717–727.

——, and Coauthors, 2005c: Recent progresses in studies of regional temperature changes in China (in Chinese). *Climatic Environ. Res.*, **10**, 701–716.

——, Y. Q. Zhou, Z. Y. Chu, J. X. Zhou, A. Y. Zhang, J. Guo, and X. F. Liu, 2008: Urbanization effects on observed surface air temperature trends in North China. *J. Climate*, **21**, 1333–1348, https://doi.org/10.1175/2007JCLI1348.1.

——, A. Y. Zhang, Z. Y. Chu, J. X. Zhou, Y. Y. Ren, and Y. Q. Zhou, 2010: Principles and procedure for selecting reference surface air temperature stations in China (in Chinese). *Meteor. Sci. Technol.*, **38**, 78–85.

——, Y. H. Ding, Z. C. Zhao, J. Y. Zheng, T. W. Wu, G. L. Tang, and Y. Xu, 2012: Recent progress in studies of climate change in China. *Adv. Atmos. Sci.*, **29**, 958–977, https://doi.org/10.1007/s00376-012-1200-2.

——, and Coauthors, 2015: An integrated procedure to determine a reference station network for evaluating and adjusting urban bias in surface air temperature data. *J. Appl. Meteor. Climatol.*, **54**, 1248–1266, https://doi.org/10.1175/JAMC-D-14-0295.1.

Ren, Y. Y., D. Parker, G. Y. Ren, and R. Dunn, 2016: Tempo-spatial characteristics of sub-daily temperature trends in mainland China. *Climate Dyn.*, **46**, 2737–2748, https://doi.org/10.1007/s00382-015-2726-7.

Song, L. C., 1994: Characteristics of temperature in spatial and temporal variation in China during recent 40 years (in Chinese). *J. Appl. Meteor. Sci.*, **5**, 119–124.

Sun, X. B., G. Y. Ren, Y. Y. Ren, Y. H. Fang, Y. L. Liu, X. Y. Xue, and P. F. Zhang, 2017a: A remarkable climate warming hiatus over Northeast China since 1998. *Theor. Appl. Climatol.*, **133**, 579–594, https://doi.org/10.1007/s00704-017-2205-7.

——, ——, W. H. Xu, Q. Li, and Y. Ren, 2017b: Global land-surface air temperature change based on the new CMA GLSAT data set. *Sci. Bull.*, **62**, 236–238, https://doi.org/10.1016/j.scib.2017.01.017.

Sun, Y., X. B. Zhang, G. Y. Ren, F. W. Zwiers, and T. Hu, 2016: Contribution of urbanization to warming in China. *Nat. Climate Change*, **6**, 706–709, https://doi.org/10.1038/nclimate2956.

Tang, G. L., G. Y. Ren, and J. X. Zhou, 2008: Change of urban heat island intensity and its effect on surface mean air temperature records in Southwest China (in Chinese). *J. Appl. Meteor. Sci.*, **19**, 722–730.

Tang, H. Y., P. M. Zhai, and Z. Y. Wang, 2005: On change in mean maximum temperature, minimum temperature, and diurnal range in China during 1951–2002 (in Chinese). *Climatic Environ. Res.*, **10**, 728–735.

Trenberth, K. E., and J. T. Fasullo, 2013: An apparent hiatus in global warming? *Earth's Future*, **1**, 19–32, https://doi.org/10.1002/2013EF000165.

Wang, F., and Q. S. Ge, 2012: Estimation of urbanization bias in observed surface temperature change in China from 1980 to 2009 using satellite land-use data. *Chin. Sci. Bull.*, **57**, 1708–1715, https://doi.org/10.1007/s11434-012-4999-0.

Wang, Z. Y., Y. H. Ding, J. H. He, and J. Yu, 2004: An updated analysis of the climate change in China in recent 50 years (in Chinese). *Acta Meteor. Sin.*, **62**, 228–236, https://doi.org/10.11676/qxxb2004.023.

Wen, K. M., G. Y. Ren, J. Li, Y. Y. Ren, X. B. Sun, and Y. Q. Zhou, 2019: Adjustment of urbanization bias in surface air temperature over mainland China (in Chinese). *Adv. Geogr. Sci.*, in press.

Xu, X., Y. G. Du, J. P. Tang, and Y. Wang, 2011: Variations of temperature and precipitation extremes in recent two decades over China. *Atmos. Res.*, **101**, 143–154, https://doi.org/10.1016/j.atmosres.2011.02.003.

Yang, X. C., Y. L. Hou, and B. D. Chen, 2011: Observed surface warming induced by urbanization in east China. *J. Geophys. Res.*, **116**, D14113, https://doi.org/10.1029/2010JD015452.

Yu, Y., J. Li, Z. H. Ren, and Coauthors, 2012: Application of standardized method in estimating missing daily mean air temperature (in Chinese). *Meteor. Mon.*, **38**, 1135–1139.

Zhai, P. M., and F. M. Ren, 1999: On changes of China's maximum and minimum temperature in 1951–1990. *Acta Meteor. Sin.*, **13**, 278–290.

Zhang, A. Y., 2009: Detection and correction of urbanization bias to national station data series of surface air temperature (in Chinese). M.S. thesis, Chinese Academy of Meteorological Sciences, 60 pp.

——, G. Y. Ren, J. X. Zhou, Z. Y. Chu, Y. Y. Ren, and G. L. Tang, 2010: Urbanization effect on surface air temperature trends over China (in Chinese). *Acta Meteor. Sin.*, **68**, 957–966.

Zhang L. S., and X. Q. Fang, 1988: Regional differentiation of the temperature fluctuation process in China (in Chinese). *J. Beijing Normal Univ.*, **3**, 78–85.

Zhao, Z. C., G. C. Xu, and K. L. Wang, 1990: Effect of urbanization on climate change (in Chinese). *Meteor. Sci. Technol.*, **1**, 71–76, https://doi.org/10.19517/j.1671-6345.1990.01.012.

Zhou, L. M., R. E. Dickinson, Y. H. Tian, J. Y. Fang, Q. Li, R. K. Kaufmann, C. J. Tucker, and R. B. Myneni, 2004: Evidence for a significant urbanization effect on climate in China. *Proc. Natl. Acad. Sci. USA*, **101**, 9540–9544, https://doi.org/10.1073/pnas.0400357101.

Zhou, Y. Q., and G. Y. Ren, 2005: Identifying and correcting urbanization bias for regional surface air temperature series of north China over period of 1961–2000 (in Chinese). *Climatic Environ Res*, **10**, 743–753.

——, and ——, 2009: The effect of urbanization on maximum, minimum temperatures, and daily temperature range in north China (in Chinese). *Plateau Meteor.*, **28**, 1158–1166.

第 15 卷 第 1 期
2019 年 1 月
气 候 变 化 研 究 进 展
CLIMATE CHANGE RESEARCH
Vol. 15 No. 1
January 2019

doi:10.12006/j.issn.1673-1719.2018.004
伍丽泉，李清泉，丁一汇，等. BCC_CSM1.1 气候模式年代际试验对北极涛动季节回报能力的初步评估 [J]. 气候变化研究进展，2019, 15 (1): 1-11
Wu L Q, Li Q Q, Ding Y H, *et al*. Preliminary assessment on the seasonal hindcast skill of the Arctic Oscillation with decadal experiment by BCC_CSM1.1 climate model [J]. Climate Change Research, 2019, 15 (1): 1-11

BCC_CSM1.1 气候模式年代际试验对北极涛动季节回报能力的初步评估

伍丽泉[1,2]，李清泉[1,2]，丁一汇[2]，王黎娟[1]，辛晓歌[2]，魏 敏[3]

1 南京信息工程大学气象灾害教育部重点实验室／气候与环境变化国际合作联合实验室／气象灾害预报预警与评估协同创新中心，南京 210044；
2 国家气候中心 中国气象局气候研究开放实验室，北京 100081；
3 中国气象局国家气象信息中心，北京 100081

摘 要：本文基于国家气候中心气候系统模式 BCC_CSM1.1 自 1960—2004 年每年起报的年代际预测试验结果，初步评估了该模式对北极涛动（AO）的预报技巧。同时，把该模式年代际预测结果与历史试验模拟比较，分析了气候模式初始化对年代际试验预测季节尺度 AO 及其年际变化的贡献。结果表明，年代际试验和历史试验均能反映出 AO 模态是北半球中高纬大气变率第一模态的特征，其中年代际预测试验回报的 AO 模态与观测的空间相关系数高于历史试验。两组试验基本能再现 AO 指数冬季最强、夏季最弱的特征。与历史试验相比，年代际预测试验回报月和冬季 AO 指数与观测的相关系数更高，特别是年代际试验与观测的月 AO 指数相关系数达到了 0.1 的显著性水平。年代际试验回报月、春季 AO 指数的变化周期更接近观测结果。因此，年代际试验中初始状态使用海温资料进行初始化，在一定程度上可以提高 AO 的回报能力。

关键词：BCC_CSM1.1；气候模式；年代际；北极涛动（AO）；季节回报

引 言

近百年来北半球显著增温，其中气候变暖最明显的是北极，其增暖是全球平均增暖的 2 倍以上 [1]。北极涛动（AO）是北半球热带外行星尺度大气变率的首要模态，即北极地区与中纬度大气质量呈跷跷板变化 [2]。AO 的活动中心覆盖了整个极区，与欧亚大陆的地表气温的耦合作用较强 [2]，对中纬度风暴强度、高纬度阻塞形势和寒潮爆发均有调制作用 [3]。AO 对中国冬季气候以及极端天气事件有重要影响，也是反映气候变化的强信号。一方面 AO 与冬季东亚气温有密切联系，当 AO 为正位相时，极区冷空气对中国北方地区影响不大，我国大部偏暖 [4-5]。另一方面，AO 指数极端异常时，会显著影响中国冬季最高、最低气温 [6]。龚道溢等 [4] 指出，年代际尺度上 AO 对冬季气温、降水均有显著影响。此外，AO 还会对东亚地区其他季节的气候产生影响 [7-8]。因此，将 AO 作为研究对象，有助于理解中纬度地区（包括中国）的气候变化机制。

耦合模式是描述气候系统中各圈层相互作用和人类活动造成影响的客观工具，也是研究 AO

收稿日期：2018-01-12；**修回日期**：2018-04-13
资助项目：国家自然科学基金项目（41790471）；国家重点基础研究发展计划（2016YFA0602200，2012CB955203，2013CB430202）
作者简介：伍丽泉，女，硕士研究生；王黎娟（通信作者），女，教授，wljfw@163.com

现象和预测其变率的有效工具。气候模式能否真实再现 AO 模态及其气候影响，是其能否开展 AO 机制研究的必要基础。同时，AO 作为北半球热带外大气低频变化第一模态，是评估模式模拟性能的重要内容之一。基于国际耦合模式比较计划的历史模拟试验研究表明，气候模式能够模拟出 AO 模态的主要特征，但对 AO 分布在北大西洋和北太平洋活动中心强度的模拟存在明显的偏差，夸大了后者的强度，甚至强于前者 [9-13]。已有的研究表明，气候模式季节预测系统对冬季 AO 的时空特征及其气候异常具有较高的预报技巧 [14-15]。冬季，AO 的季节预测能为欧亚区域气候预测提供有用的信息，从而拓展新的气候服务。然而，政府制定规划往往需要时间尺度比季节更长的预测。Dunstone 等 [16] 使用英国气象局的年代际气候预测系统，提前一年预测出北大西洋涛动（NAO）的时空特征。NAO 与 AO 有很多相似之处，甚至有学者认为 NAO 是 AO 在北大西洋的局地表现 [17]。

为了更好地评估和改进气候模式，国际耦合模式比较计划第五阶段（CMIP5）增加了耦合模式的年代际预测试验，其输出结果有利于预估未来气候变化 [18]。以往的研究多是利用历史试验的结果评估模式对 AO 模拟效果 [11-13]。本文利用中国气象局国家气候中心参加 CMIP5 的气候系统模式 BCC_CSM1.1 年代际试验输出结果，评估该模式对 AO 回报能力，并利用气候模式年代际试验第 1 年的预测结果探索季节尺度 AO 及其年际变化的可预报性。此外，本文还采用了该模式历史试验的结果，以便了解模式初始化对 AO 回报能力的影响，为未来的气候预估以及模式发展完善提供依据。

1 模式、资料和方法

1.1 BCC_CSM1.1 模式

BCC_CSM1.1 模式是全球气候耦合模式，包含大气、海洋、陆面、海冰模式分量。其中大气模式为 BCC_AGCM2.1，水平分辨率约 2.8°×2.8°，垂直方向有 26 层 [19]。海洋模式为 MOM4_L40，水平分辨率 1°，经向上热带地区加密为（1/3）°，垂直分为 40 层 [20]。陆面模式为 BCC_AVIM1.0，是大气、植被、土壤互相作用的模式。海冰模式 SIS 水平分辨率也为 1°×1°，垂直方向包含 1 层积雪和 2 层海冰。耦合模式的详细情况可以参见文献 [21]。

1.2 资料

BCC_CSM1.1 模式开展的 CMIP5 试验具体介绍可参见文献 [22]。其中，历史试验是以工业革命前控制试验为基础，取不同初始场在 1850—2012 年进行积分，仅考虑了外强迫的影响，没有考虑初始化方案。年代际预测试验的初始化使用了美国简单海洋资料同化（SODA）的全球月平均海温再分析资料 [23]。初始化方案是将模拟的海温向 SODA 海温资料逼近，恢复时间是 1 d。年代际试验将 BCC_CSM1.1 模式在观测外强迫资料的驱动下对 1960—2004 年期间的每年起始进行 10 年的模拟，共 3 个样本。年代际和历史试验所采用的强迫场由 CMIP5 统一提供，包括温室气体、气溶胶、臭氧、太阳常数和碳排放 [22]。

为评估模式回报性能，使用 1961—2005 年的 HadSLP2(r) 的海平面气压（SLP）资料 [24]，其水平分辨率是 5.0°×5.0°。为便于讨论，在与模式结果相对比时，将该资料简称为观测资料。由于观测资料与模式资料水平分辨率不同，故使用双线性插值将其统一插值到水平分辨率为 2.5°×2.5° 的规则网格上。

1.3 方法

本文定义 AO 为北半球热带外（20°N 以北）逐月海平面气压（SLP）距平场面积加权后进行经验正交函数（EOF）分解得到的第一模态 [25]。参考美国国家气候预报中心（CPC）关于 AO 指数的计算方法，把逐月 SLP 距平场投影到 AO 模态并进行标准化处理得到 AO 指数。在 EOF 分解前，随纬度变化对 SLP 距平场做面积加权。将 AO 模态表示为 SLP 距平场对 AO 指数的回归系数，以便比较其振幅强度。

www.climatechange.cn

由于初始化导致年代际预测中产生了系统误差，即模式气候态与观测相比存在偏移，这将影响对模式回报能力评估[26-29]。因此本文采用世界气候研究计划（WCRP）推荐的方法，通过对回报结果计算距平去除气候偏移[28-29]。BCC_CSM1.1 模式年代际预测试验的起报时间为 1960—2004 年每年的 9 月 1 日、11 月 1 日、次年 1 月 1 日，每年 3 个样本，每个样本积分 10 年。例如，试验从 1960 年起报时，3 个样本分别从 1960 年 9 月 1 日和 11 月 1 日、1961 年 1 月 1 日起报。根据 CMIP5 试验统一规定，BCC 模式 3 个样本统一存储 1961 年 1 月至 1970 年 12 月的回报结果。试验从其他年份起报时，以此类推。为避免随机初值的影响，采用年代际和历史试验中 3 个不同起始时刻样本，集合平均之后的结果。根据预测时效对回报数据重新排列，选取预测起始时刻之后第 1 年的输出结果，作为提前 1 年的预测结果。将每年起报、提前 1 年的预测结果连接起来，构成 1961 年 1 月—2005 年 12 月的长序列。定义前一年 12 月至当年 2 月为当年的冬季。由于没有 1960 年 12 月的输出结果，因此舍弃了 1961 年冬季。第一个冬季（DJF）取为 1961 年 12 月—1962 年 2 月，春季（MAM）、夏季（JJA）和秋季（SON）依次为 3—5 月、6—8 月、9—11 月。每个季节有 44 年的数据。为了与各个季节相对应，逐月的回报序列是 1961 年 12 月—2005 年 11 月。此外，还采用相关分析、谱分析、滑动 *T* 检验以及 EOF 分析等统计方法。

2　结果分析

2.1　AO 的基本模态

AO 模态是评估气候模式回报能力的重要内容之一。对观测、年代际和历史试验逐月北半球热带外 SLP 距平场进行 EOF 分析得到第一模态（EOF1，图 1）。由图 1(a) 可以看到，观测的 AO 模态共有 3 个活动中心。图 1(a) 中观测的负极区覆盖整个北极，呈偶极结构，一极位于格陵兰岛东南部，另一极则偏向于欧亚大陆，位于乌拉尔山脉附近，强度达 −1.5 hPa。一个正极区中心在北大西洋，并向欧洲延伸；另一正极区则分布在北太平洋地区，强度为 1 hPa 以上，但比北大西洋的活动中心强度弱，整体呈现环状模的结构特征。观测的 AO 模态与 Thompson 等[2-3]得到结果一致。年代际（图 1b）和历史试验（图 1c）均能基本再现北极地区与观测范围和强度相当的负极区，也对环状模有一定的预报技巧。两组试验回报的北太平洋正距平中心均强于北大西洋地区。但年代际试验回报的北大西洋正中心强于历史试验，而北太平洋正中心比历史试验弱。因此，进行初始化的年代际试验在一定程度上能够改变 AO 中高纬度正活动中心的强度，与观测更加接近。模式与观测的偏差不受 AO 定义方式的影响，例如使用 1000 hPa 位势高度计算得到的 AO 模态（图略）也有正距平中心强度的偏差。以往的一些研究[9-10]也发现气候模式往往夸大冬季 AO 模态中位于北太平洋的正值区，且强度强于北大西洋的活动中心。Gong 等[13]认为这种误差是由于模式高估了实际 AO 与北太平洋 SLP 主导模态（NPM）之间的微弱联系造成，这一偏差可以通过线性回归去除 AO 指数中 NPM 变率进行订正。但这种偏差订正仅是统计方法，并没有改善气候模式。

BCC_CSM1.1 模式的年代际和历史试验均能反映出 AO 模态是北半球中高纬大气年际变率的第一模态。观测 AO 模态的解释方差为 20.8%，年代际和历史试验的 AO 解释方差都比观测偏高，但与历史试验（25.0%）相比，年代际试验结果（23.8%）更接近观测。另外，计算年代际试验 AO 空间模态与观测的空间相关系数为 0.84，也略高于历史试验 AO 模态与观测的空间相关系数（0.81），二者均达到 0.05 的显著性水平。

综上所述，对于北半球热带外 SLP 距平场 EOF1 的模拟，与历史试验比较，年代际试验与观测更接近。

2.2　AO 指数的基本特征

图 2 是观测与年代际和历史试验模拟的四季 AO 指数。很明显，模式与观测一致，AO 指数在

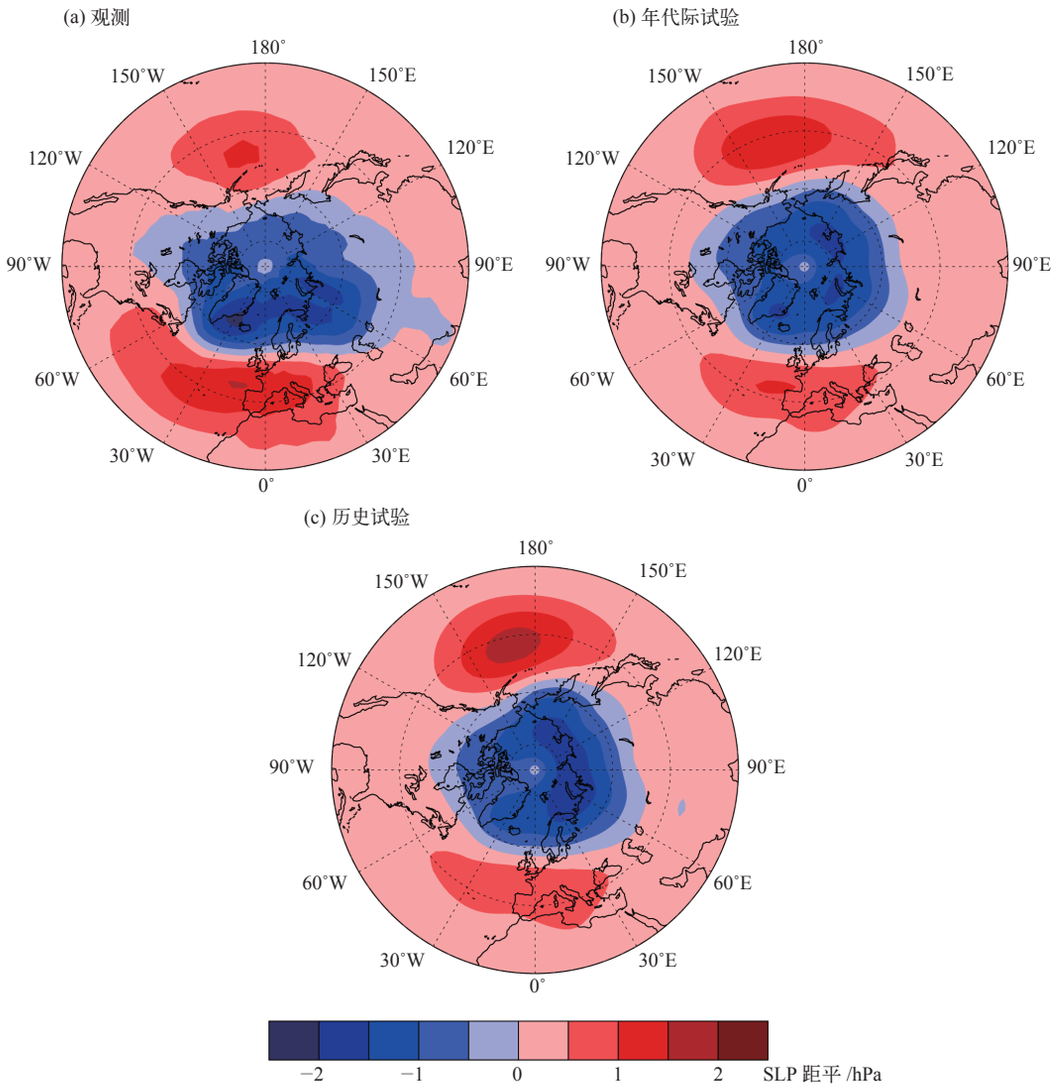

图 1 1962—2005 年北半球热带外 SLP 距平的 EOF 分解第一模态

Fig. 1 The leading EOF mode of extra-tropical SLP (sea level pressure) anomalies in the Northern Hemisphere during 1962−2005 in observation (a), decadal experiment (b) and historical experiment (c)

冬季最强，其次是春季和秋季，夏季最弱。且观测显示，1962—2005 年冬季 AO 指数有明显增强趋势，且在 20 世纪 80 年代中期有从负位相向正位相的显著年代际转换（图 2a）。进一步对 AO 指数进行滑动 T 检验（图 3），发现观测的冬季 AO 指数在 1986 年出现年代际突变（图 3a），并且观测的秋季 AO 指数在 1994 年有从正位相向负位相的年代际突变（图 3d），但是年代际和历史试验都没能再现冬季和秋季 AO 指数的这个观测特征（图 2 和图 3）。朱献等 [30] 也指出 28 个 CMIP5 模式的历史试验都没能模拟出冬季 AO 指数从负位相向正位相的年代际转变特征。

表 1 给出了观测及年代际和历史试验模拟的四季标准化 AO 指数的线性趋势。观测的冬、春、夏季 AO 指数呈上升趋势，只有冬季 AO 指数通过了 0.05 的显著性检验；历史试验模拟的冬季 AO 指数亦呈上升趋势（0.14 $(10a)^{-1}$），但比观测结果弱；年代际试验回报的冬季 AO 指数与观测趋势相反。年代际试验和历史试验回报的春、夏季 AO 指数呈明显上升趋势，且比观测强。观测的秋季 AO 指数趋势为 0，而年代际试验回报和历史试验模拟的上升趋势明显。

www.climatechange.cn

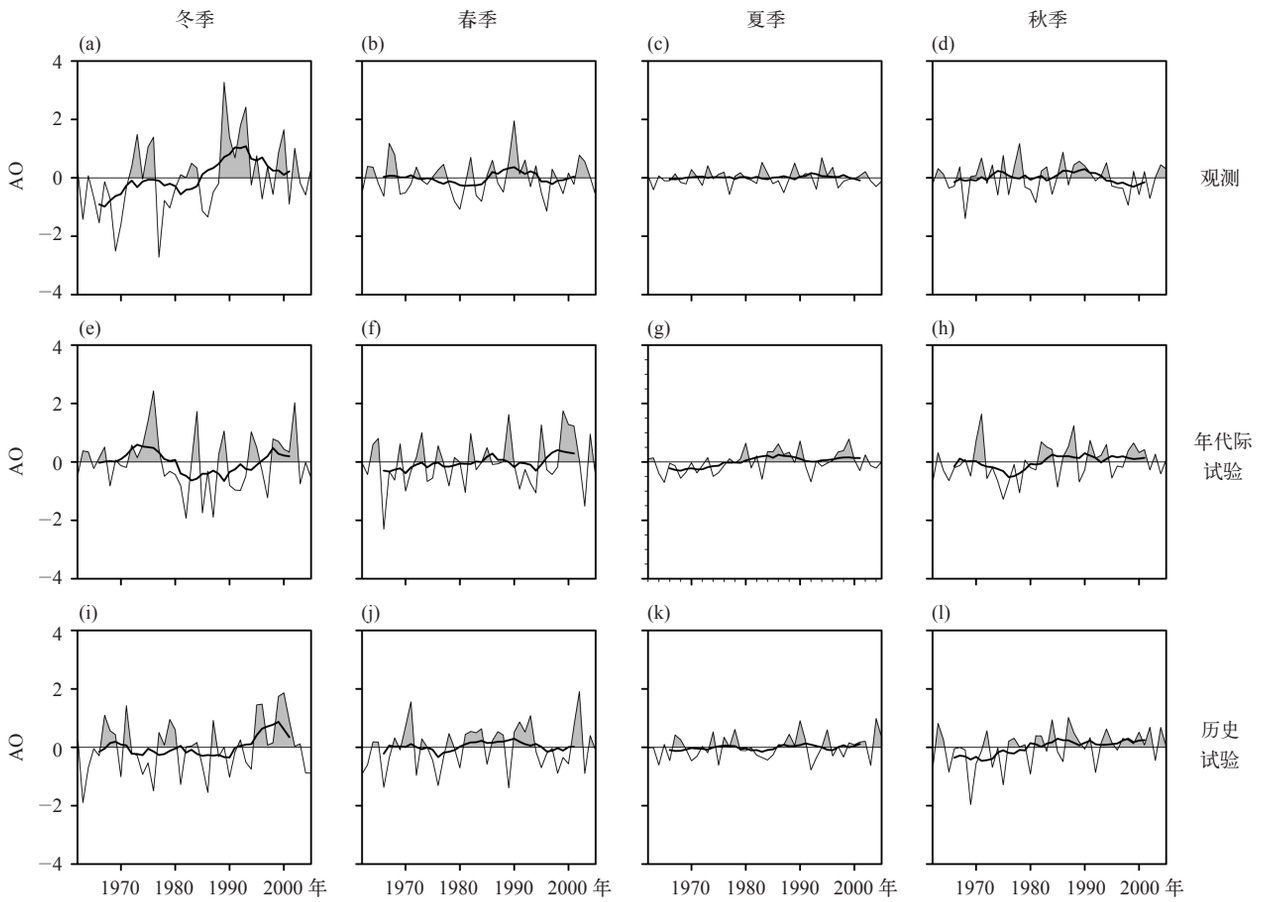

注：黑实线为 9 年滑动平均曲线。

图 2　1962—2005 年四季 AO 指数时间序列

Fig. 2　Seasonal AO indices during 1962−2005 in observation (a−d), decadal experiment (e−h) and historical experiment (i−l) (The four columns from left to right mean winter, spring, summer and autumn. The black lines indicate 9-year running means)

表 1　1962—2005 年观测、年代际和历史试验的四季 AO 指数的线性趋势

Table 1　Linear trend of seasonal AO indices during 1962−2005 in observation, decadal experiment and historical experiment

$(10a)^{-1}$

时段	观测	年代际试验	历史试验
冬季	0.25**	−0.10	0.14
春季	0.01	0.14	0.12
夏季	0.03	0.25**	0.14
秋季	−0.00	0.17	0.25**

注：** 表示通过 0.05 的显著性检验。

为进一步分析年代际和历史试验对月和四季 AO 指数年际变率的回报能力，分别计算了模拟与观测 AO 指数的相关系数（表 2）。由表 2 可见，年代际试验回报的月 AO 指数与观测的相关系数（去趋势前、后均为 0.08）通过了 0.1 的显著性检验，明显高于历史试验的月 AO 指数与观测的相关系数（去趋势前、后分别为 −0.01 和 −0.02）。AO 在冬季信号最强，而在其他 3 个季节较弱。对于冬季 AO 指数，年代际试验模拟与观测的相关系数在去趋势前、后分别为 0.20 和 0.23，也明显好于历史试验的结果（去趋势前、后分别为 0.03 和 −0.04）。因此，年代际试验对月、冬季 AO 指数有一定预报技巧。年代际和历史试验模拟春季、夏季和秋季的 AO 指数都不理想，与观测 AO 指数甚至在夏季出现负相关关系。但在秋季，年代际试验结果好于历史试验结果，年代际试验回报的 AO 指数与观测的相关系数为正相关（0.07），而历史试验为负相关（−0.14）。表 2 分别计算了回报与观测的已去除线性趋势的 AO 指数的相关

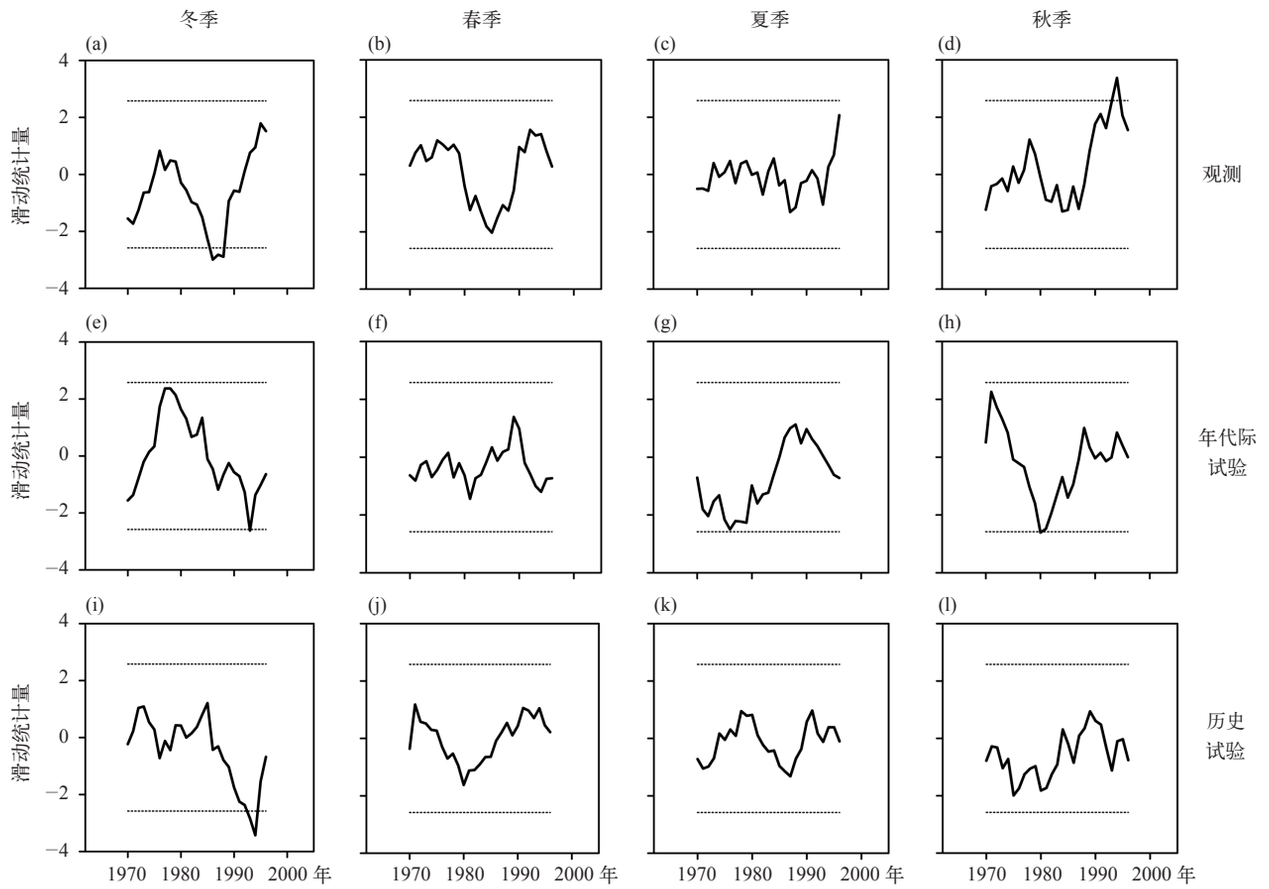

注：黑虚线为 0.05 显著性水平临界值。

图 3 1962—2005 年四季 AO 指数滑动 *T* 检验

Fig. 3 The moving *T*-test of seasonal AO indices during 1962−2005 in observation (a−d), decadal experiment (e−h) and historical experiment (i−l) (The four columns from left to right mean winter, spring, summer and autumn. The black bashed lines show significant at the 0.05 level)

表 2 1962—2005 年年代际和历史试验模拟的月及四季 AO 指数与观测的相关系数

Table 2 Correlation coefficients of monthly and seasonal AO indices during 1962−2005 between decadal experiment and historical experiments and observations

时段	年代际试验原始序列	年代际试验去趋势后	历史试验原始序列	历史试验去趋势后
月	0.08*	0.08*	−0.01	−0.02
冬季	0.20	0.23	0.03	−0.04
春季	0.01	0.01	0.07	0.07
夏季	−0.18	−0.20	−0.12	−0.13
秋季	0.07	0.08	−0.14	−0.15

注：* 表示通过 0.1 的显著性检验。

系数，以避免线性趋势的影响。结果发现，除了历史试验的冬季 AO 指数与观测的相关系数在去趋势前、后由正值（0.03）变为负值（−0.04）外，其他相关系数没有明显变化。

此外，表 3 给出了观测和回报的不同季节 AO 指数的相关系数。结果发现，观测的 AO 指数，除了春 − 夏为负相关（−0.10），其他季节均呈正相关。其中，观测的 AO 指数冬 − 夏、秋 − 冬有

www.climatechange.cn

表 3 1962—2005 年观测和模拟的不同季节 AO 指数的相关系数

Table 3 Correlation coefficients between different seasonal AO indices during 1962−2005 from observation and simulations

时段	观测	年代际试验	历史试验
冬－春	0.23	0.18	0.01
冬－夏	0.36**	−0.05	−0.06
秋－冬	0.33**	−0.06	0.32**
春－夏	−0.10	0.17	0.05
秋－春	0.08	0.33**	−0.08
夏－秋	0.14	0.14	0.29**

注：** 表示通过 0.05 的显著性检验。

显著相关性，相关系数分别是 0.36 和 0.33。只有历史试验对 AO 指数秋－冬的持续性有一定的模拟能力，相关系数为 0.32，通过 0.05 的显著性检验。与观测结果比较，年代际试验回报抓住了 AO 指数冬－春、秋－春，以及夏－秋的正相关关系，且明显好于历史试验模拟结果。Sun 等 [14] 的研究也表明，在当前的数值模式中，海表面温度（SST），特别是热带太平洋 SST 的变率是季节气候预测的主要因子。在本研究中，与模式历史试验相比，年代际预测试验考虑了海洋初始化，海洋初值更接近于观测结果，模式预测的海温也更加接近观测。因此，年代际预测有助于改进 AO 的预测，进而提高 AO 不同季节间关系的预测能力。

2.3　AO 指数的变率

表 4 给出了观测及年代际试验回报和历史试验模拟的四季 AO 指数的方差。由表 4 可见，观测中冬季 AO 指数变率最强，春、秋季次之，夏季最弱。年代际试验和历史试验都能抓住这个特征，但模式回报的冬季变率强度比观测弱，其他季节模拟的变率均比观测强。因此，BCC_CSM1.1 模式低估了冬季 AO 指数的变化、高估了其他季节的变化。与历史试验相比，年代际试验改进了模式对冬季和夏季 AO 变率的模拟能力，回报与观测的 AO 指数方差比分别增加 5% 和减少 43%，但春季和秋季没有改善。

表 4 1962—2005 年观测、年代际和历史试验的四季 AO 指数方差

Table 4 Variance of seasonal AO indices during 1962−2005 from observation, decadal experiment and historical experiment

时段	观测	年代际试验	历史试验
冬季	1.44	0.88 (61%)	0.81 (56%)
春季	0.37	0.71 (192%)	0.54 (146%)
夏季	0.07	0.13 (186%)	0.16 (229%)
秋季	0.27	0.36 (134%)	0.36 (134%)

注：括号内的百分数表示模拟与观测的方差百分比。

为了考察不同试验对 AO 周期性变率的再现能力，计算了观测和模拟的月及四季 AO 指数功率谱（图 4 和图 5）。在功率谱计算前，AO 指数均已去除线性趋势。如图 4 所示，观测的月 AO

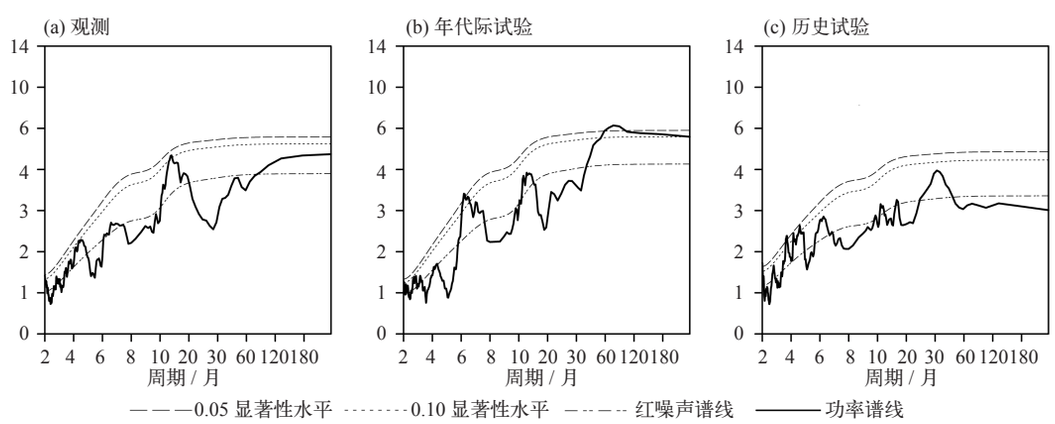

图 4 1962—2005 年月 AO 指数的功率谱

Fig. 4 Smoothed power spectra for monthly AO index during 1962−2005 derived from observation (a), decadal experiment (b) and historical experiment (c)

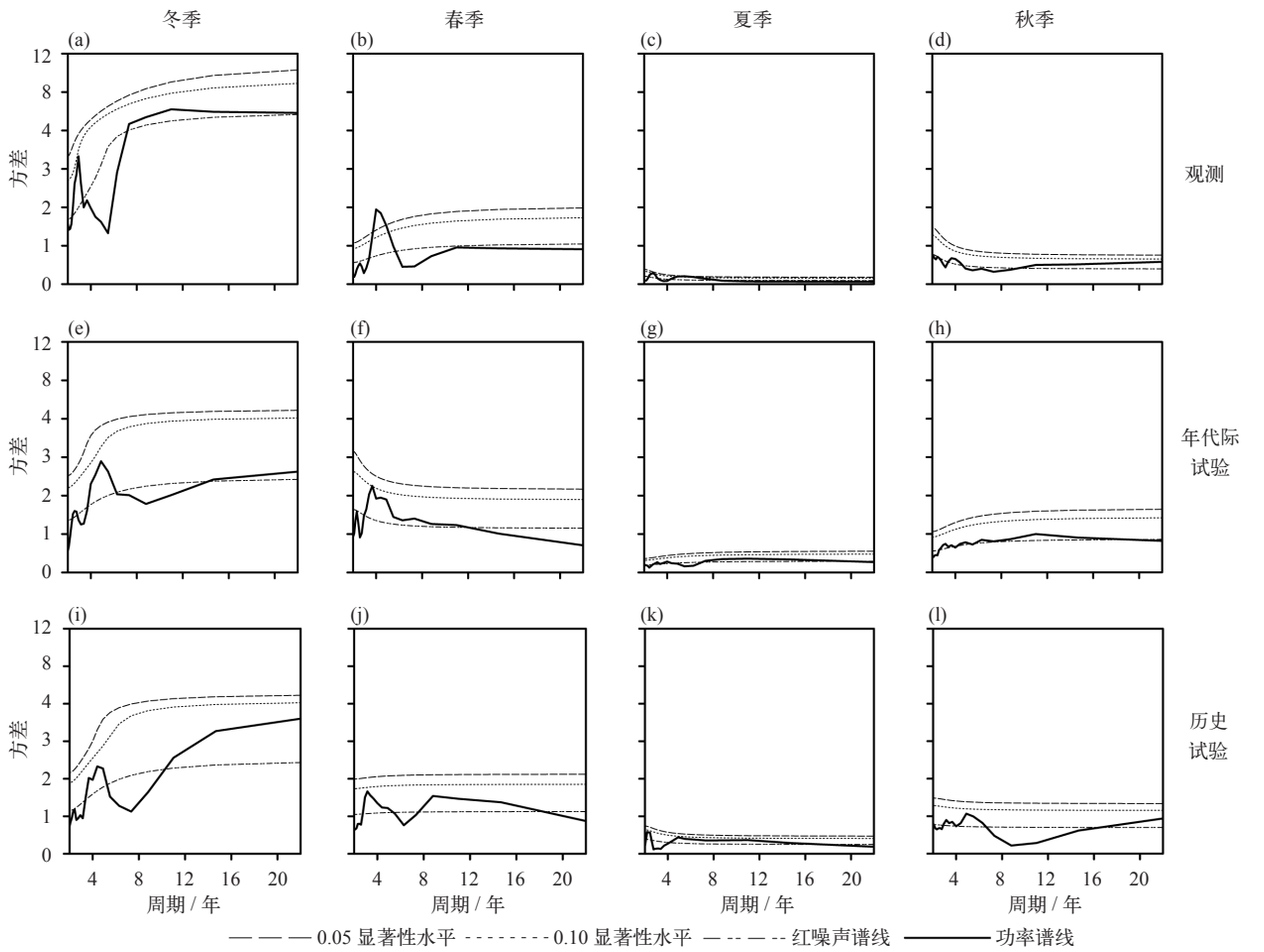

图 5 1962—2005 年四季 AO 指数的功率谱

Fig. 5 Smoothed power spectra for seasonal AO indices during 1962−2005 derived from observation (a−d), decadal experiment (e−h) and historical experiment (i−l)

指数的 2 个峰值周期分别为 13 个月和 5 个月，均通过了 0.1 的显著性水平。这与左金清等 [31] 给出的峰值周期为 12 个月和 6 个月一致。这意味着 AO 指数具有半年和 1 年左右的短周期振荡。年代际和历史试验基本再现了观测 AO 的半年周期变化，但是仅年代际试验对 1 年周期有一定表现能力，只通过了红噪声信度检验。各个季节 AO 指数的功率谱分析如图 5 所示。观测的冬季 AO 指数有 2 ～ 3 年的短周期变化，在年代际尺度上有 11 年的变化周期，通过红噪声信度检验。模拟结果均呈现 4 ～ 5 年的短周期，无明显长周期变化。观测的春季 AO 指数有明显的 4 ～ 5 年短周期，无长周期振荡特征。两组试验能抓住春季 AO 指数短周期变化特征，但历史试验出现虚假的 9 ～ 10 年长振荡周期。夏季，观测和模拟的 AO 指数没有明显周期特征。秋季，历史试验能大致反映观测的 AO 指数 4 年左右的短周期，年代际试验则呈现出观测 AO 指数的 11 年长周期。总的来看，年代际试验对 AO 周期变化的回报能力比历史试验模拟能力好。

3 结论与讨论

本文利用中国气象局国家气候中心 BCC_CSM1.1 模式参加 CMIP5 计划的年代际试验和历史试验结果以及 HadSLP2(r) 的海平面气压资料，着重评估了该模式年代际试验对 AO 模态和指数的回报能力，并分析了模式初始化对年代际预测

www.climatechange.cn

的影响，主要结论如下。

(1) 年代际试验和历史试验都能在北半球热带外模拟出 AO，AO 空间模态与观测的空间相关系数均达到 0.05 的显著性水平，年代际试验（0.84）略好于历史试验（0.81）；观测 AO 模态能解释 SLP 变化总方差的 20.8%，与历史试验（25.0%）相比，年代际试验结果（23.8%）更接近观测。

(2) 两组试验都能抓住观测 AO 指数在冬季最强、春季和秋季次之、夏季最弱的特征，但模拟的 AO 指数冬季偏强，其他季节偏弱。观测的冬季和秋季 AO 指数分别在 1986 年和 1994 年发生了年代际突变，并且观测的冬季 AO 指数呈现显著的上升趋势，但是年代际和历史试验都没能很好地再现这些观测特征。年代际试验与观测的月 AO 指数相关系数明显高于历史试验的月 AO 指数与观测的相关系数。年代际试验与观测的冬季 AO 指数相关系数也明显好于历史试验的结果。因此，年代际试验对月、冬季 AO 指数有一定预报技巧。

(3) 观测的 AO 指数，除了春－夏为负相关，其他不同季节均呈正相关。其中，观测的 AO 指数冬－夏、秋－冬有显著相关性，相关系数分别为 0.36 和 0.33。年代际试验回报抓住了 AO 指数冬－春、秋－春和夏－秋的正相关关系，且明显好于历史试验模拟结果。两个试验都低估了冬季 AO 指数的变率、高估了其他季节的变率。与历史试验相比，年代际试验对冬季和夏季 AO 指数变率的回报能力较好，但春季和秋季没有改善。

(4) 观测的月 AO 指数具有半年和 1 年左右的周期振荡，年代际和历史试验基本再现了观测 AO 的半年周期变化，但是仅年代际试验对 1 年周期有一定再现能力。两组试验抓住了春季观测 AO 指数 4 ～ 5 年周期的年际变化，但没能抓住冬季观测 AO 指数 2 ～ 3 年周期的年际变化和 AO 年周期的年代际变化。秋季，历史试验能大致反映观测的 AO 指数 4 年左右的短周期，年代际试验则呈现出观测 AO 指数的 11 年长周期。

综上所述，与历史试验结果相比，年代际试验使用 SODA 的海温再分析资料进行初始化，在一定程度上改进了 AO 模态以及 AO 指数的年际和年代际变率的回报能力。历史试验仅考虑了外强迫的影响，没有考虑初始化方案；年代际试验考虑了海洋初始化，将模拟的海温向观测海温资料逼近，有更为准确的海洋初值。Jadin[32] 指出，AO 的外部生成机制可以用北太平洋 SST 偶极子的年际变化对平稳行星波的热激发来解释。本文的研究也表明，由于采用了海洋初始化方案，在观测的海温强迫下，年代际试验对 AO 变率的预报技巧较历史试验有所提高。但仍存在不足之处，如 BCC_CSM1.1 模式模拟的 AO 模态正距平在北太平洋均强于北大西洋地区。年代际预测试验采用的海洋初始化方案对 AO 模态和变率的预报技巧有所提高，但对 AO 长期趋势预测没有贡献。为此，在未来的年代际预测试验中，将通过改进海洋初始化方案以及引入大气的初始化，进一步提高气候模式对 AO 的预测技巧。■

参考文献

[1] Cohen J, Screen J A, Furtado J C, *et al*. Recent Arctic amplification and extreme mid-latitude weather [J]. Nature Geoscience, 2014, 7 (9): 627-637

[2] Thompson D W J, Wallace J M. The Arctic Oscillation signature in the wintertime geopotential height and temperature fields [J]. Geophysical Research Letters, 1998, 25 (9): 1297-1300

[3] Thompson D W, Wallace J M. Regional climate impacts of the Northern Hemisphere annular mode [J]. Science, 2001, 293: 85-89

[4] 龚道溢 , 王绍武 . 近百年北极涛动对中国冬季气候的影响 [J]. 地理学报 , 2003, 58 (4): 559-568

[5] 梁苏洁 , 丁一汇 , 赵南 , 等 . 近 50 年中国大陆冬季气温和区域环流的年代际变化研究 [J]. 大气科学 , 2014, 38 (5): 974-992

[6] 所玲玲 , 黄嘉佑 , 谭本馗 . 北极涛动对我国冬季同期极端气温的影响研究 [J]. 热带气象学报 , 2008, 24 (2): 163-168

[7] 琚建华 , 吕俊梅 , 任菊章 . 北极涛动年代际变化对华北地区干旱化的影响 [J]. 高原气象 , 2006, 25 (1): 74-81

[8] He S P, Gao Y Q, Li F, *et al*. Impact of Arctic Oscillation on the East Asian climate: a review[J]. Earth-Science Reviews, 2017, 164: 48-62

[9] Miller R L, Schmidt G A, Shindell D T. Forced annular variations in the 20th century Intergovernmental Panel on Climate Change Fourth Assessment Report models [J]. Journal of Geophysical Research Atmospheres, 2006, 111, D18101

[10] 辛晓歌 , 周天军 , 宇如聪 . 气候系统模式对北极涛动的模拟 [J]. 地球物理学报 , 2008, 51 (2): 337-351

[11] Cattiaux J, Cassou C. Opposite CMIP3/CMIP5 trends in the wintertime

Northern Annular Mode explained by combined local sea ice and remote tropical influences [J]. Geophysical Research Letters, 2013, 40 (14): 3682-3687

[12] Zuo J Q, Li W J, Ren H L. Representation of the Arctic Oscillation in the CMIP5 models [J]. Advances in Climate Change Research, 2013, 4 (4): 242-249

[13] Gong H N, Wang L, Chen W, *et al*. Biases of the wintertime Arctic Oscillation in CMIP5 models[J]. Environmental Research Letters, 2017, 12, 014001

[14] Sun J, Ahn J. Dynamical seasonal predictability of the Arctic Oscillation using a CGCM [J]. International Journal of Climatology, 2015, 35 (7): 1342-1353

[15] Stockdale T N, Molteni F, Ferranti L. Atmospheric initial conditions and the predictability of the Arctic Oscillation [J]. Geophysical Research Letters, 2015, 42 (4): 1173-1179

[16] Dunstone N, Smith D, Scaife A, *et al*. Skilful predictions of the winter North Atlantic Oscillation one year ahead [J]. Nature Geoscience, 2016, 9 (11): 809-814

[17] Ambaum M, Hoskins B J, Stephenson D B. Arctic Oscillation or North Atlantic Oscillation? [J]. Journal of Climate , 2001, 14 (16): 3495-3507

[18] Taylor K E, Stouffer R J, Meehl G A. An overview of CMIP5 and the experiment design [J]. Bulletin of the American Meteorological Society, 2012, 93 (4): 485-498

[19] Wu T W, Yu R C, Zhang F, *et al*. The Beijing Climate Center atmospheric general circulation model: description and its performance for the present day climate [J]. Climate Dynamics, 2010, 34 (1): 123-147

[20] LI Q Q, Tan J, Wang L N, *et al*. Simulation of the natural distribution of carbon and nutrients in the ocean based on the global ocean carbon cycle model MOM4_L40 [J]. Chinese Journal of Geophysics, 2015, 58 (1): 1-19

[21] Wu T W, Li W P, Ji J J, *et al*. Global carbon budgets simulated by the Beijing Climate Center climate system model for the last century [J]. Journal of Geophysical Research Atmospheres, 2013, 118 (10): 4326-4347

[22] 辛晓歌 , 吴统文 , 张洁 . BCC 气候系统模式开展的 CMIP5 试验介绍 [J]. 气候变化研究进展 , 2012, 8 (5): 378-382

[23] Carton J A, Giese B S. A reanalysis of ocean climate using Simple Ocean Data Assimilation (SODA) [J]. Monthly Weather Review, 2008, 136: 2999-3017

[24] Allan R, Ansell T. A new globally complete monthly historical gridded mean sea level pressure dataset (HadSLP2): 1850−2004 [J]. Journal of Climate, 2006, 19: 5816-5842

[25] Thompson D W J, Wallace J M. Annular modes in the extratropical circulation. Part I month-to-month variability [J]. Journal of Climate, 2000, 13: 1000-1016

[26] García-Serrano J, Doblas-Reyes F J. On the assessment of near-surface global temperature and North Atlantic multi-decadal variability in the ensembles decadal hindcast [J]. Climate Dynamics, 2012, 39: 2025-2040

[27] Goddard L, Kumar A, Solomon A, *et al*. A verification framework for interannual-to-decadal predictions experiments [J]. Climate Dynamics, 2013, 40: 245-272

[28] Wei M, Li Q Q, Xin X G, *et al*. Improved decadal climate prediction in the North Atlantic using EnOI-assimilated initial condition [J]. Science Bulletin, 2017, 62: 1142-1147

[29] Xin X G, Gao F, Wei M, *et al*. Decadal prediction skill of BCC-CSM1.1 model in East Asia [J]. International journal of Climatology, 2018, 38: 584-592

[30] 朱献 , 董文杰 , 郭彦 . CMIP3 及 CMIP5 模式对冬季和春季北极涛动变率模拟的比较 [J]. 气候变化研究进展 , 2013, 9 (3): 165-172

[31] 左金清 , 李维京 , 任宏利 . CMIP5 模式对北极涛动的模拟评估 [J]. 气候变化研究进展 , 2013, 9 (3): 157-164

[32] Jadin E A. Arctic Oscillation and interannual variations of the sea surface temperature in the Atlantic and Pacific [J]. Russian Meteorology and Hydrology, 2001, 18: 28-40

www.climatechange.cn

Preliminary assessment on the seasonal hindcast skill of the Arctic Oscillation with decadal experiment by BCC_CSM1.1 climate model

WU Li-Quan[1, 2], LI Qing-Quan[1, 2], DING Yi-Hui[2], WANG Li-Juan[1], XIN Xiao-Ge[2], WEI Min[3]

1 *Key Laboratory of Meteorological Disaster, Ministry of Education/Joint International Research Laboratory of Climate and Environment Change/Collaborative Innovation Center on Forecast and Evaluation of Meteorological Disasters, Nanjing University of Information Science &Technology (NUIST), Nanjing* 210044*, China*; 2 *Laboratory for Climate Studies, National Climate Center, China Meteorological Administration, Beijing* 100081*, China*; 3 *National Meteorological Information Center, China Meteorological Administration, Beijing* 100081*, China*

Abstract: This study assesses projection skill of Arctic Oscillation (AO) in initialized decadal experiment with the Beijing Climate Center Climate System Model (BCC_CSM1.1). As compared with the observations and uninitialized historical experiment, the contribution of climate model initialization to predict the seasonal scale AO and its interannual variations is estimated. Results show that the spatial correlation coefficient of AO mode, which depicts the dominant mode of the extra-tropical atmospheric variability, simulated by the decadal experiment is higher than that in the historical experiment. The two groups of experiments can basically reproduce the characteristics of the strongest winter AO index and the weakest summer index. Compared with historical experiment, the correlation coefficient of the monthly and winter AO index is higher in the decadal experiment. In particular, the correlation coefficient of the monthly AO index between the decadal simulations and the observation reached 0.1 significant level. Furthermore, the periodicity of the monthly and spring AO index are achieved only in the decadal experiment. Hence, the hindcast skill of AO is robust when the initial state is initialized by sea surface temperature data.

Keywords: BCC_CSM1.1; Climate model; Decadal; Arctic Oscillation (AO); Seasonal hindcast

Decadal Prediction Skill of BCC-CSM1.1 with Different Initialization Strategies

Xiaoge XIN

Laboratory for Climate Studies, National Climate Center, China Meteorological Administration, China

Min WEI

National Meteorological Information Center, China Meteorological Administration, China
Ministry of Education Key Laboratory for Earth System Modeling, Department of Earth System Science, and Joint Center for Global Change Studies (JCGCS), Tsinghua University, China

Qingquan LI

Laboratory for Climate Studies, National Climate Center, China Meteorological Administration, China
Collaborative Innovation Center on Forecast and Evaluation of Meteorological Disasters, Nanjing University of Information Science and Technology, China

Wei ZHOU

State Key Laboratory of Tropical Oceanography, South China Sea Institute of Oceanology, Chinese Academy of Sciences, China

Yong LUO

Ministry of Education Key Laboratory for Earth System Modeling, Department of Earth System Science, and Joint Center for Global Change Studies (JCGCS), Tsinghua University, China

and

Zongci ZHAO

Ministry of Education Key Laboratory for Earth System Modeling, Department of Earth System Science, and Joint Center for Global Change Studies (JCGCS), Tsinghua University, China

(Manuscript received 19 July 2018, in final form 18 March 2019)

Abstract

Two sets of decadal prediction experiments were performed with Beijing Climate Center climate system model version 1.1 (BCC-CSM1.1) with different initialization strategies. One experiment is relaxing modeled ocean temperature to the Simple Ocean Data Assimilation (SODA) reanalysis data (SODAInit). In the other (EnOI_HadInit) experiment, the modeled ocean temperature were relaxed toward the assimilated ocean data, which were generated by assimilating sea surface temperature (SST) of the Hadley Centre Sea Ice and Sea Surface Tempera-

Corresponding author: Qingquan Li, Beijing Climate Center, Zhongguancun Nandajie No.46, Haidian District, Beijing, 100081, China
E-mail: liqq@cma.gov.cn
J-stage Advance Published Date: 1 April 2019

©The Author(s) 2019. This is an open access article published by the Meteorological Society of Japan under a Creative Commons Attribution 4.0 International (CC BY 4.0) license (https://creativecommons.org/licenses/by/4.0).

ture (HadISST) data to the ocean model of BCC-CSM1.1 using Ensemble Optimum Interpolation (EnOI) method. Comparisons between EnOI_HadInit and SODAInit hindcasts show that EnOI_HadInit is more skillful in predicting SST over the North Pacific, the southern Indian Ocean, and the North Atlantic. Improved prediction skill is also found for surface air temperature (SAT) over South Europe, North Africa, and Greenland, which is associated with the skillful prediction of the Atlantic multi-decadal oscillation in EnOI_HadInit. EnOI_HadInit and SODAInit are both skillful in predicting East Asian SAT, which is related to their skillful predictions of the tropical western Pacific SST. The result indicates that assimilated data generated by the ocean model of BCC-CSM1.1 with EnOI assimilation provide better initial conditions than SODA reanalysis data for the decadal predictions of BCC-CSM1.1.

Keywords decadal prediction; initialization; BCC-CSM; Ensemble Optimum Interpolation

Citation Xin, X., M. Wei, Q. Li, W. Zhou, Y. Luo, and Z. Zhao, 2019: Decadal prediction skill of BCC-CSM1.1 with different initialization strategies. *J. Meteor. Soc. Japan*, **97**, 000–000, doi:10.2151/jmsj.2019-043.

1. Introduction

Decadal climate predictions are of particular scientific interest in recent years, because of their potential impacts on economy and social development. Initial condition and external forcing are both important for decadal predictions with climate models (Smith et al. 2007; Keenlyside et al. 2008). The role of initialization was seen as a better representation of the internal variability. Initialized climate prediction is an important component of Coupled Model Intercomparison project phases 5 (CMIP5) (Taylor et al. 2012). Multi-model mean ensemble of CMIP5 showed that the enhancement in skill due to the initialization is robust for global mean temperature and the Atlantic multi-decadal oscillation (AMO) (IPCC 2013). Increased skill for sea surface temperature (SST) was found for some models in the North Atlantic, the Indian Ocean, and the North Pacific (Wu and Zhou 2012; Doblas-Reyes et al. 2013; Ham et al. 2014). However, Beijing Climate Center climate system model version 1.1 (BCC-CSM1.1) for CMIP5 had poor decadal prediction skill in the North Pacific and the North Atlantic (Gao et al. 2012; Han et al. 2017), and needs further improvement.

The Pacific and Atlantic climate variability is an important driver of climate variability over the continents (e.g., Zhou et al. 2008; Si and Ding 2016). Skillful prediction arising from the initialization was found for surface air temperature (SAT) over America, northern Eurasia (Keenlyside et al. 2008; Doblas-Reyes et al. 2013), East Asia (Xin et al. 2018), and for precipitation in Africa (Gaetani and Mohino 2013). However, the decadal prediction skill was still poor. Improving the decadal predictions skill of climate models was considered to be a grand scientific challenge of CMIP6 (Eyring et al. 2016).

Skill of decadal climate prediction depends greatly on the accurate estimation of initial climate states. Modeling groups used different initialization techniques in decadal predictions of CMIP5 (Meehl et al. 2014). Most of the models used full-filed initialization to restore oceanic temperature to observation-based ocean reanalysis, including BCC-CSM1.1, CFSv2-2011, CMCC-CM, EC-Earth, FGOALS-s2, FGOALS-g2, and HadCM3. There are also models restoring the modeled ocean temperature to the assimilated ocean data using offline assimilation in the ocean model (CanCM4, CNRM-CM5). Models including CCSM4, GFDL-CM2.1, and GEOS-5 used assimilation in the coupled prediction system. Due to the large computation cost of the coupled assimilation in decadal predictions, full-field initialization with reanalysis ocean data or assimilated ocean data are commonly used for climate models. Bellucci (2013) found a strong predictive skill dependency on the ocean data assimilation product used to constrain the oceanic initial conditions.

Our recent study assimilated the HadISST in the ocean model of BCC-CSM1.1 via the Ensemble Optimum Interpolation (EnOI) method, and generated better prediction skill in the North Atlantic than using Simple Ocean Data Assimilation (SODA) reanalysis in the initialization (Wei et al. 2017). The possible improvement for the prediction skill over the globe needs further investigation, especially for the SST in the Pacific and Indian oceans and SAT over the land. This is the main aim of this paper. Our results will provide reference for the initialization strategy adopted by BCC-CSM model in Decadal Climate Prediction Comparison (DCPP) of CMIP6 (Boer et al. 2016).

The paper is organized as follows. Data and methods used in this study are presented in Section 2. Global SST prediction skills are described in Section 3. Section 4 explores the prediction skills of SAT over the land. The conclusions of this paper are presented in Section 5.

2. Model, experiments, data and methodology

2.1 Model

The model used in this study is BCC-CSM1.1 developed by Beijing Climate Center, which participated in CMIP5 and carried out most of the experiments (Xin et al. 2013). The atmospheric component of BCC-CSM1.1 is BCC_AGCM2.1 with T42 resolution (about 280 km) in the horizontal and 26 vertical layers (Wu et al. 2010). The oceanic component is the Modular Ocean Model version 4 (MOM4) with the tripolar grid of 1° × 1/3° horizontal resolution and 40 vertical levels, which is named MOM4_L40 (Griffies et al. 2005; Li et al. 2015). More detailed descriptions about BCC-CSM1.1 can be found in Wu et al. (2013).

2.2 Experiments and data

Two sets of decadal prediction experiments were carried out with BCC-CSM1.1. The experimental names, ocean initiation, and integration time are listed in Table 1. Each experiment consists of 45 hindcasts, initialized annually for the period of 1961–2005 and integrated for ten years. In both experiments, the modeled oceanic temperature is nudged to observation-based ocean data, with the restoring timescale of one day. The difference between these two experiments is the initialization strategy of the ocean condition. One experiment is to restore the modeled sea temperature to the SODA reanalysis data (Cartchion and Giese 2008), hereafter called SODAInit. The other experiment is to restore the modeled sea temperature to the EnOI-assimilated data (ASSIM), generated by assimilating the Hadley Centre Sea Ice and SST data set (HadISST) data (Rayner et al. 2003) to MOM4_L40 model using the EnOI method, hereafter called EnOI_HadInit.

In the EnOI assimilation, the background error covariance is kept unchanged throughout the assimilation cycle, which is estimated from a prescribed static ensemble. The procedure for the assimilation is as follows. First, a control simulation is run with the MOM4_L40 model forced by daily NCEP/NCAR reanalysis (Kalnay et al. 1996). This control run is used to generate the static ensembles. Then the EnOI method is used to assimilate the HadISST data to the MOM4_L40 model, with the time window of one month. The generated data is named ASSIM. As indicated in Wei et al. (2017), the ASSIM data are more coordinated with the ocean of BCC-CSM1.1 model than the SODA reanalysis.

The CMIP5 historical simulation of BCC-CSM1.1 with no initialization is also used for comparison (Xin et al. 2013), hereafter called NoInit (Table 1). All experiments including SODAInit, EnOI_HadInit, and NoInit were forced by the identical external forcing, including greenhouse gases, solar irradiation, volcanic activity, ozone, and aerosols. Each experiment consists of three ensemble members. The results shown in this study are the ensemble means.

2.3 Data and methodology

The observation data used to validate the prediction skill are as follows. The SAT data are from Global Historical Climatology Network–Climate Anomaly Monitoring System (GHCN-CAMS) dataset (Fan and van del Dool 2008). The precipitation data are from Climatic Research Unit Time-Series Version 3.23 (CRU-TS3.23) dataset (University of East Anglia Climatic Research Unit et al. 2015). The SST data are from the Extended Reconstructed Sea Surface Temperature (ERSST) Version 4 (ERSST V4) dataset (Huang et al. 2016).

The reason why we use ERSST in the validation is that this dataset is independent from the SODA data and HadISST data used in the initialization. In fact, the SST of ERSST is close to that of the HadISST

Table 1. Experimental design for SODAInit, EnOI_HadInit and NoInit.

Experiment name	Ocean initialization	Years	Ensemble size
SODAInit	Full-field initialization. Relaxing toward SODA reanalysis data.	Annual forecasts for ten years, staring at 1961, 1962, …, 2005	3
EnOI_HadInit	Full-filed initialization. Offline assimilation of HadISST with EnOI method in the ocean model of BCC-CSM1.1.	Annual forecasts for ten years, staring at 1961, 1962, …, 2005	3
NoInit	No	1850–2005	3

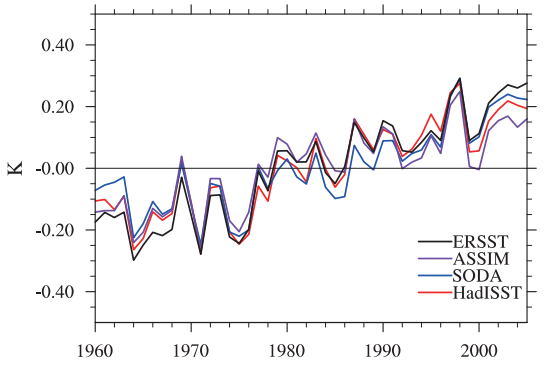

Fig. 1. Global annual mean SST anomalies (K) with respect to the 1960–2005 climatology for HadISST dataset, ERSST dataset, SODA reanalysis, and the EnOI-assimilated data (ASSIM) generated in this study.

(Fig.1). The correlation coefficient between the global (70°S–60°N) mean SST anomalies from 1960 to 2005 is 0.98. In the EnOI-assimilation, we use SST from the HadISST but not the SODA reanalysis. This may be unequal for the two sets of decadal prediction in this study. Therefore, we compare the interannual anomalies of the global mean SST for the HadISST, ASSIM and SODA datasets. The time series from the three different datasets are similar (Fig. 1). The correlation coefficient between SODA and HadISST (ERSST) is 0.95. The SST from the ASSIM data also shows great resemblance with that from the HadISST and ERSST, with the correlation coefficients both at 0.96, indicating the effectiveness of the assimilation. We infer that the different SST dataset used in the assimilation may not introduce much difference for the interannual variability of the output data, since they are all observation-based data. However, the ASSIM data shows some difference from the SODA data, and the correlation coefficient between the global mean SST anomalies of the two datasets is 0.90. This may be attributed to the different scheme and model version used in the assimilation processes.

Full-field initialization leads to initial shocks in decadal predictions (García-Serrano and Doblas-Reyes 2012), so we compare the anomalies in the analysis. For the NoInit and observed, anomalies are relative to their respective climatology. The anomalies of decadal predictions are defined with respect to the climatology of the ensemble mean and lead time, as used in earlier studies (García-Serrano and Doblas-Reyes 2012; Wei et al. 2017; Xin et al. 2018). We will focus on the 4-yr average forecast periods (14, 2–5, 3–6, 4–7, 5–8, 6–9) of the decadal hindcasts. A 4-yr running mean is also applied to the observed and NoInit anomalies in order to equivalently compare with the decadal hindcasts (García-Serrano and Doblas-Reyes 2012; Goddard et al. 2012; Kim et al. 2012; Gaetani and Mohino 2013).

Root-mean-square error (RMSE) and anomaly correlation coefficient (ACC) relative to the observations are two metrics we used to estimate the prediction skill of the decadal hindcasts. To study the role of the ocean initialization on the internal climate variability, the linear trend was removed in observation and simulation data at each grid before calculating ACC. In the student's t test of ACC, the effective sample size (N_e) was calculated after removing the auto-correlation (Bretherton et al. 1999).

$$N_e = N(1-r_1r_2)/(1+r_1r_2),$$

where N is the sample size and r_1 and r_2 are the lag^{-1} autocorrelations of the two time series.

3. Prediction skill of SST

3.1 SST over the globe

The skill improvement due to the initialization is assessed by the ratio of the RMSEs between the decadal hindcast and NoInit for the forecast years of 2–5. As shown in Figs. 2a, b, both EnOI_HadInit and SODAIinit have less RMSE than the NoInit over the tropical western Pacific, North Pacific, and tropical Atlantic Ocean. The EnOI_HadInit experiment shows a smaller RMSE ratio over tropical western Pacific, central North Pacific, Northeast Atlantic, and the southern Indian Ocean than the SODAInit (Fig. 2c), indicating a higher prediction skill for EnOI_HadInit. It is noted that there are larger RMSEs in the EnOI_HadInit and SODAInit hindcasts than the NoInit over parts of the North Atlantic and Indian Oceans (Figs. 2a, b), indicating that the error in the variance of the SST anomalies could hardly be reduced through the initialization in these regions. Such a phenomenon also appears in some other models, such as the FGOALS-S2 (Wu et al. 2015). The reason for this phenomenon may partly be related to the small number of the ensembles.

The detection of significant ACC after removing the linear trend suggests the predictive skill beyond the global warming signal. EnOI_HadInit (Fig. 3a) hindcast displays a significant ACC in the tropical western Pacific Ocean, North Pacific Ocean, southern Indian Ocean, and extratropics of the North Atlantic Ocean for the forecast years 2–5. While in the hindcast of SODAInit (Fig. 3b), significant ACC mainly exists in

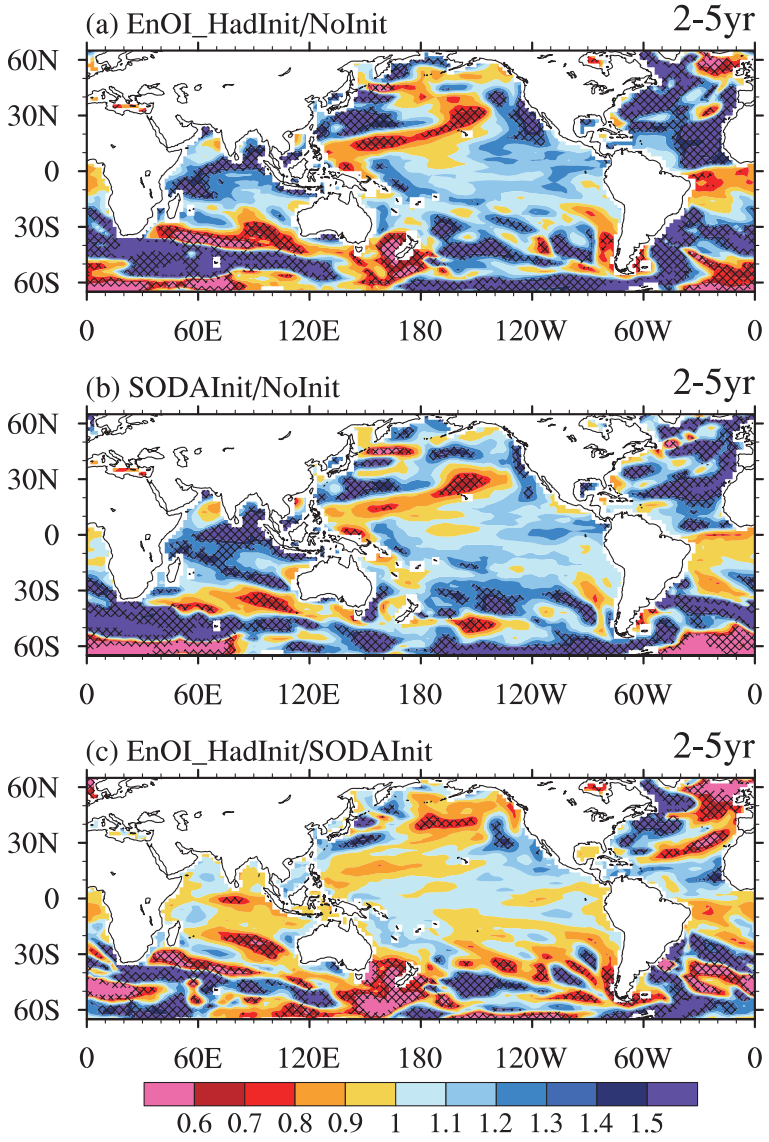

Fig. 2. Ratios of SST RMSEs between ENOI_HadInit and NoInit (a), between SODAInit and NoInit (c), and between EnOI_HadInit and SODAInit for the forecast years 2–5. Hatched area identifies the region where the ratio is statistically significantly above or below 1 with 90 % confidence level using a two-sided F-test.

the tropical western Pacific Ocean and tropical Atlantic Ocean. The NoInit shows a significant ACC only in the tropical Atlantic Ocean (Fig. 3c). Consequently, it is concluded that the ocean initiation scheme of SODA mainly improves the prediction skill in the tropical western Pacific Ocean compared to no initialization of ocean state (NoInit). Meanwhile, the initialization with EnOI-assimilated data further improves the prediction skill of SST over the North Pacific Ocean, southern Indian Ocean, and the extratropics of the North Atlantic Ocean.

3.2 SST indices

Based on the map of significant ACC of SST predicted by EnOI_HadInit, four domains are selected to make further analysis of prediction skill over the forecast time. The chosen regions and their SST indices are: (i) the tropical western Pacific (125–150°E, 15°S–15°N), its SST index is denoted by the area averaged SST anomalies (TWP index); (ii) the North

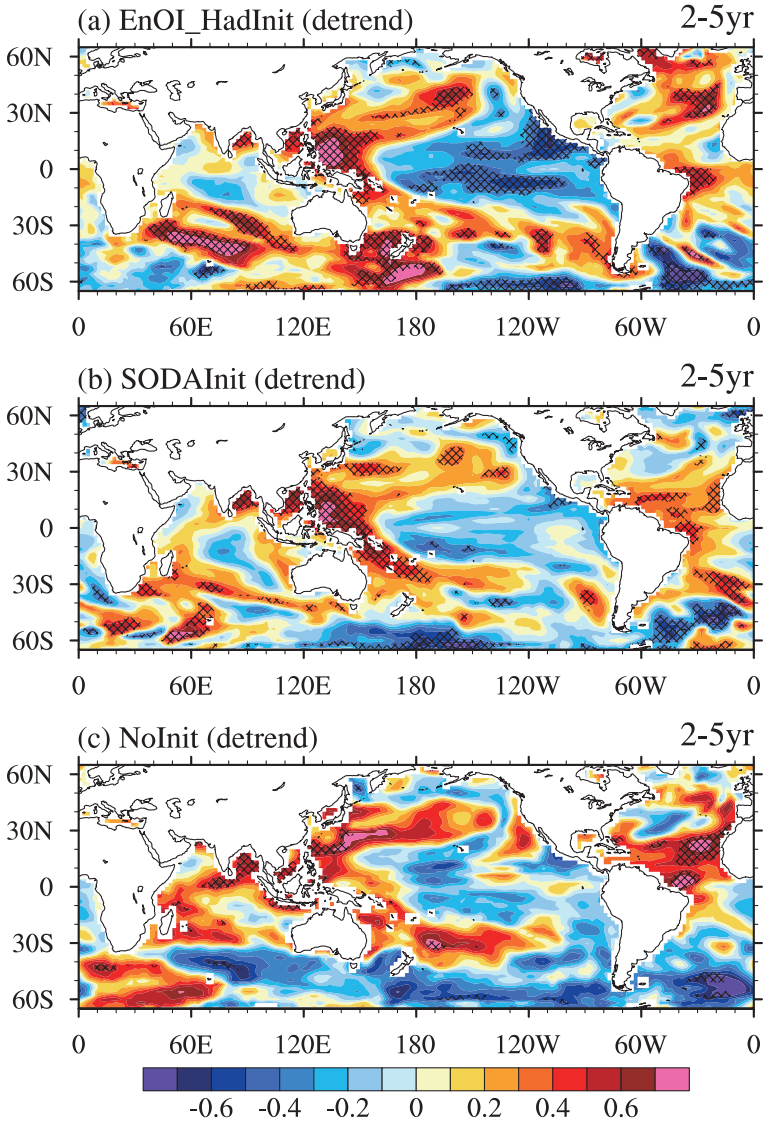

Fig. 3. ACC skills of SST hindcast by EnOI_HadInit (a), SODAInit (b), and NoInit (c) for the forecast years 2–5 with respect to the observation. Hatched area identifies the region where the ACC is above the 90 % confidence level.

Pacific region (180–210°E, 30–50°N), SST index is the area averaged SST anomalies (NP index); (iii) the southern Indian Ocean Dipole (SIOD) index, defined as the difference of SST anomalies averaged over (45–75°E, 45–30°S) and (80–100°E, 25–15°S); and (iv) the North Atlantic sector, denoted by AMO index, which is the SST anomalies in the North Atlantic (80–0°W, 0–60°N) relative to the global-mean SST (60°S–60°N).

ACCs of the SST indices between the hindcasts and the observed values are calculated in these four regions at different forecast time periods (1–4, 2–5, 3–6, 4–7, 5–8, 6–9). Figure 4a shows that both EnOI_HadInit and SODAInit have significant ACCs for TWP SST index over all forecast time periods from 1–4 to 6–9; but the former displays the relatively higher prediction skills in the forecast years of 1–4 and 2–5.

Figure 4b shows that over the North Pacific region, the ACCs of NP index from the EnOI_HadInit are much higher than the ACCs from the SODAInit, and the former pass the 10 % significant level while the

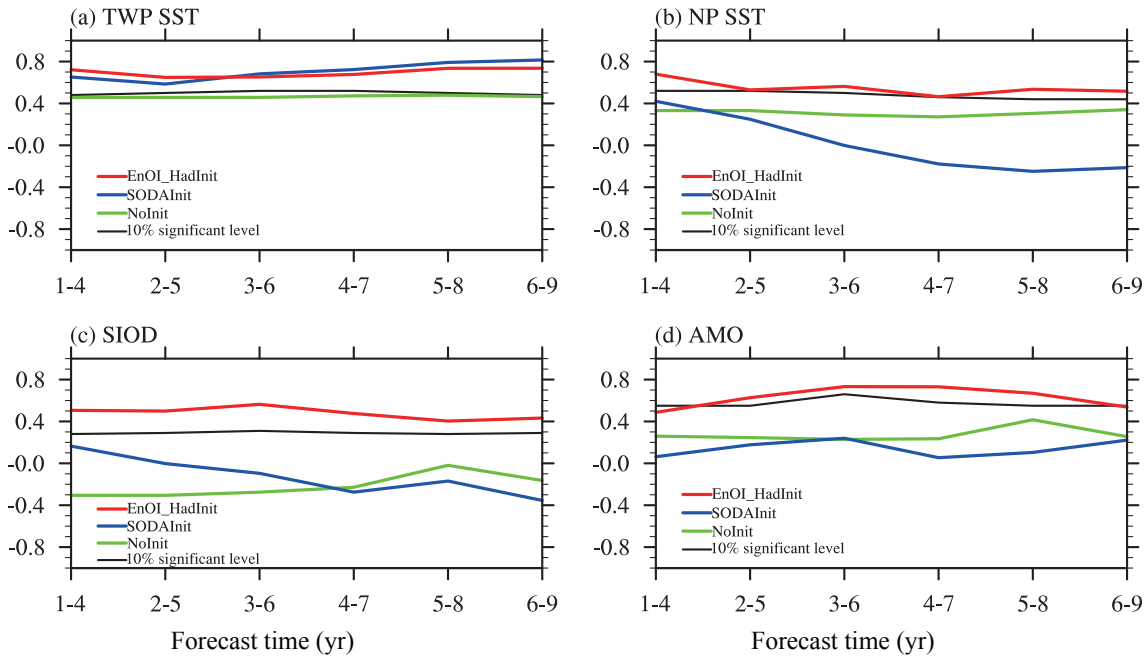

Fig. 4. ACCs between the hindcasts and the observation for TWP SST (a), NP SST (b), SIOD (c), and AMO (d) indices along the forecast time for 4-year averages.

latter do not for all forecast time periods. Furthermore, the ACC values of SIOD exceed 0.4 over all forecast time periods from 1−4 to 6−9 in EnOI_HadInit hindcast, which is much higher than the SODAInit and NoInit equivalents (Fig. 4c). The improved forecast skill up to 9-year ahead over the Indian Ocean by EnOI_HadInit is consistent with the simulation result from GEOS-5 model, in which the EnOI initialization scheme was also adapted (Ham et al. 2014).

Figure 4d shows that the AMO can be well predicted by EnOI_HadInit for forecast time periods ranging from 2−5 up to 6−9 years, with ACC above the 10 % significance level. However, the ACCs of AMO predicted by SODAInit and NoInit are much lower than those from EnOI_HadInit. The better prediction skill for AMO is consistent with the more skillful prediction of Atlantic meridional overturning circulation by EnOI_HadInit, which is documented by Wei et al. (2017).

It is concluded that using assimilated ocean data in the initialization improves the prediction skill for North Pacific SST, the SIOD, and AMO up to 6−9 years ahead for BCC-CSM1.1. The improved skill for some of these SST indices was reported in previous studies (Wu and Zhou 2012; Doblas-Reyes et al. 2013; Ham et al. 2014).

4. Prediction skill of SAT

4.1 Surface air temperature

The prediction skill of SAT over the land is explored. Figure 5 shows the ACCs beteeen the hindcasts and the observed SAT for the forecast years 2-5, as well as the difference between them. Southern Europe and North Africa, East Asia, and Greenland stand out as the areas featuring high skills in the EnOI_HadInit hindcast (Fig. 5a). The prediction skill of EnOI_HadInit over southern Europe and Greenland is higher than that of SODAInit (Figs. 5b, c). EnOI_HadInit and SODAInit are both skillful in predicting SAT over East Asia (Figs. 5a, b).

Figure 6 shows the area averaged SAT time series predicted by the decadal hindcasts for the forecast years 2−5 over the selected regions, including South Europe and North Africa (10−50°E, 15−55°N), East Asia (100−120°E, 25−40°N), and Greenland (300−340°E, 60−80°N). The higher coefficient (0.55) between the predicted SAT by EnOI_HadInit and observed SAT in the south Europe and North Africa indicates that EnOI_HadInit is able to predict more realistic SATs in these two regions than SODAInit (Fig. 6a). The time evolution of East Asian SAT predicted by EnOI_HadInit is similar with SODAInit, with the

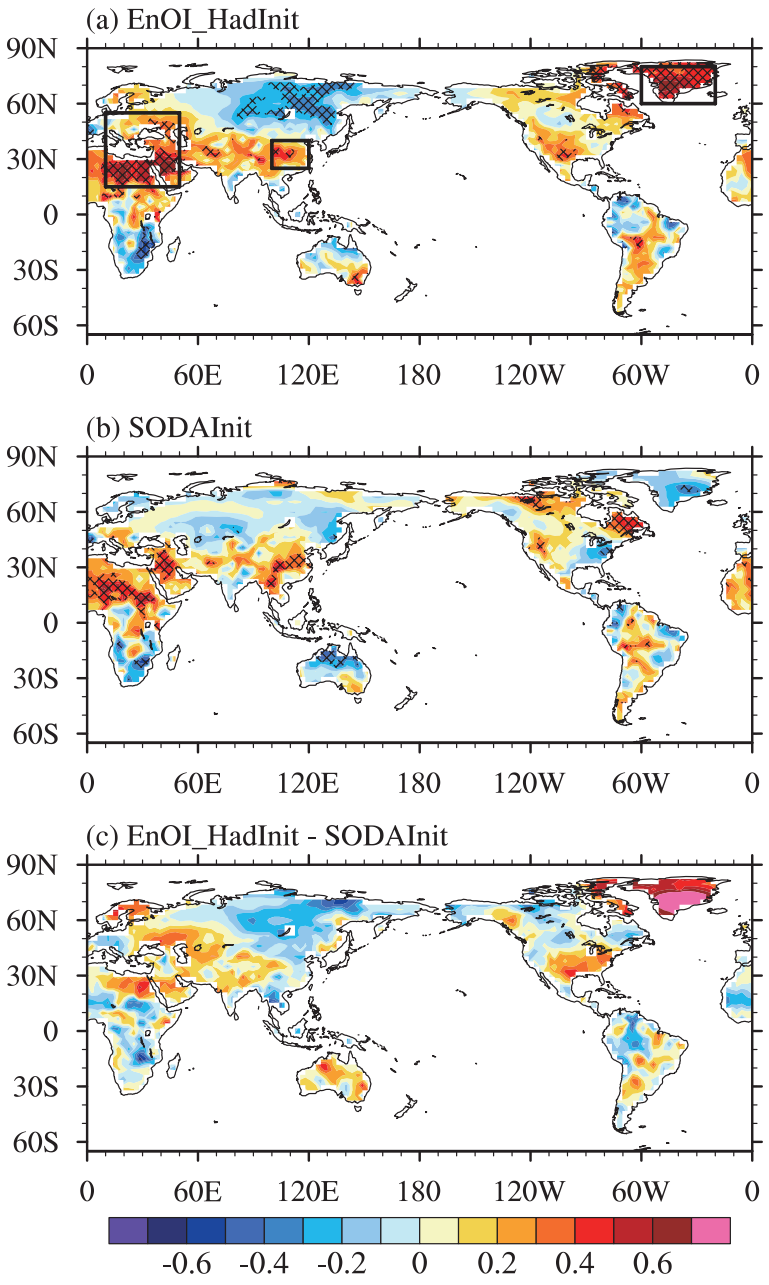

Fig. 5. ACC skills of SAT hindcast by EnOI_HadInit (a), SODAInit (b), and the difference between them (c) for the forecast years 2–5. Hatched area identifies the region where the ACC is above the 90 % confidence level.

same ACC value 0.41 (Fig. 6b). Over Greenland, the predicted SAT by EnOI_HadInit is more consistent with the observation than SODAInit and NoInit (Fig. 6c).

4.2 Relationship between AMO and SAT

The AMO was found to influence the climate of the surrounding continents (Knight et al. 2006). The skillful prediction of the AMO has the potential impacts on the prediction skill of regional climate. We attempted to further investigate where the prediction skill of SAT is related to the AMO in the decadal hindcasts with BCC-CSM1.1.

As shown in Fig. 7a, the predicted SAT by EnOI_

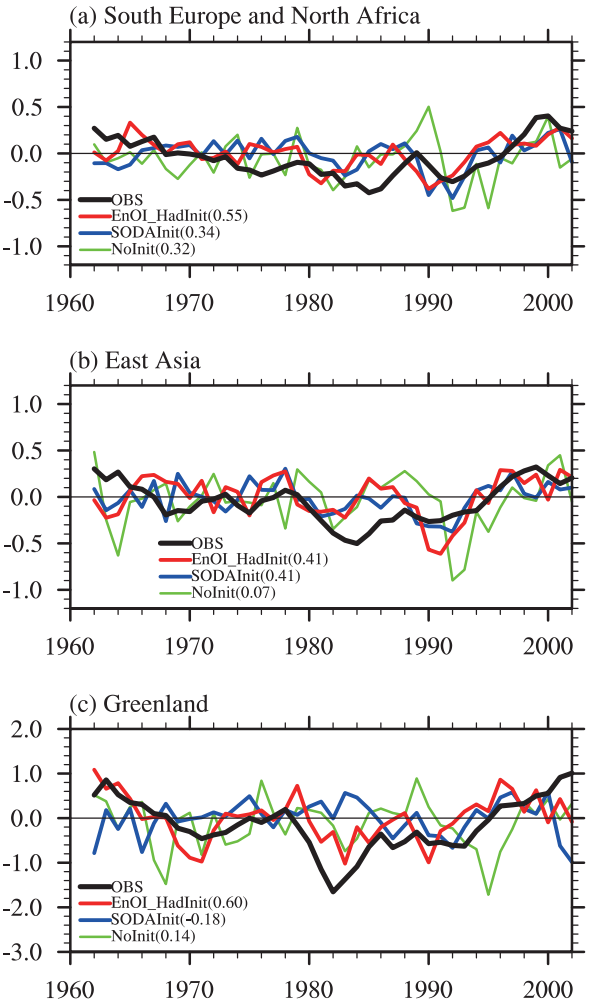

Fig. 6. Time series of SAT averaged over Europe and North Africa (a), East Asia (b), and Greenland (c) in decadal hindcasts for the forecast years 2–5. The value in the bracket indicates correlation coefficient between the hindcast and observation.

HadInit is closely correlated to the AMO index over South Europe and North Africa and Greenland. This is consistent with the observation (Fig. 7c). Therefore, we argue that the higher prediction skills of EnOI_HadInit in these three regions are related to its skillful prediction in the AMO. It is noted that the SODAInit also reproduces the robust correlation between the AMO and the SAT in Greenland. However, SODAInit has poor skill in the hindcast of the AMO (Fig. 7b). This may explain why there is little ACC skill for the Greenland SAT in SODIAInit (Figs. 5c, 6c).

4.3 Relationship between East Asian SAT and SST indices

The observed East Asian climate is influenced by the Pacific SST and the AMO (Zhou et al. 2008; Si and Ding 2016). Since East Asian SAT could be well predicted by both EnOI_HadInit and SODAInit, we expect to explore its relationship with these SST indices in the decadal hindcasts for the forecast years 2–5.

As shown in Table 2, the observed East Asian SAT is positively correlated with the TWP, NP, and AMO indices significantly, and negatively correlated with SIOD index significantly. EnOI_HadInit and SODAInit both reproduce the significant positive correlation between East Asian SAT and TWP SST, although they both overestimate the correlation coefficients. The atmospheric process linking the TWP SST with the East Asian SAT in the SODAInit prediction was revealed by Xin et al. (2018).

The relationship between East Asian SAT and other SST indices including NP, SIOD and AMO indices could not be reproduced by EnOI_HadInit and SODAInit hindcasts. So it is inferred that the prediction skill of East Asian SAT mainly arises from the oceanic forcing from the TWP in EnOI_HadInit and SODAInit hindcasts. The physical processes linking East Asian climate with SST in the North Pacific, SIOD, and the AMO need further improvement in climate models. This will favor further improvement in the forecast skill over East Asia in decadal predictions.

5. Conclusions

We assessed and compared the prediction skills of two sets of decadal prediction experiments (SODAInit and EnOI_HadInit) carried out with BCC-CSM1.1. SODAInit and EnOI_HadInit differ in the ocean initialization scheme and the observed sea temperature data used in the initialization. SODAInit used the SODA reanalysis data, while the EnOI_HadInit used the assimilated ocean data generated by assimilating HadISST to the ocean model of BCC-CSM1.1 using the EnOI method. We found that EnOI_HadInit is more skillful in predicting the SST over the North Pacific, the North Atlantic, and southern Indian Ocean than SODAInit. The SIOD and AMO indices are well predicted by EnOI_HadInit over forecast time periods ranging from 2–5 up to 6–9 years.

The EnOI_HadInit has better prediction skills for SAT over South Europe, North Africa, and Greenland than the SODAInit, which is related to its skillful prediction of the AMO. In addition, EnOI_HadInit and SODAInit are both skillful in predicting the East Asian SAT. This is related to the skillful prediction

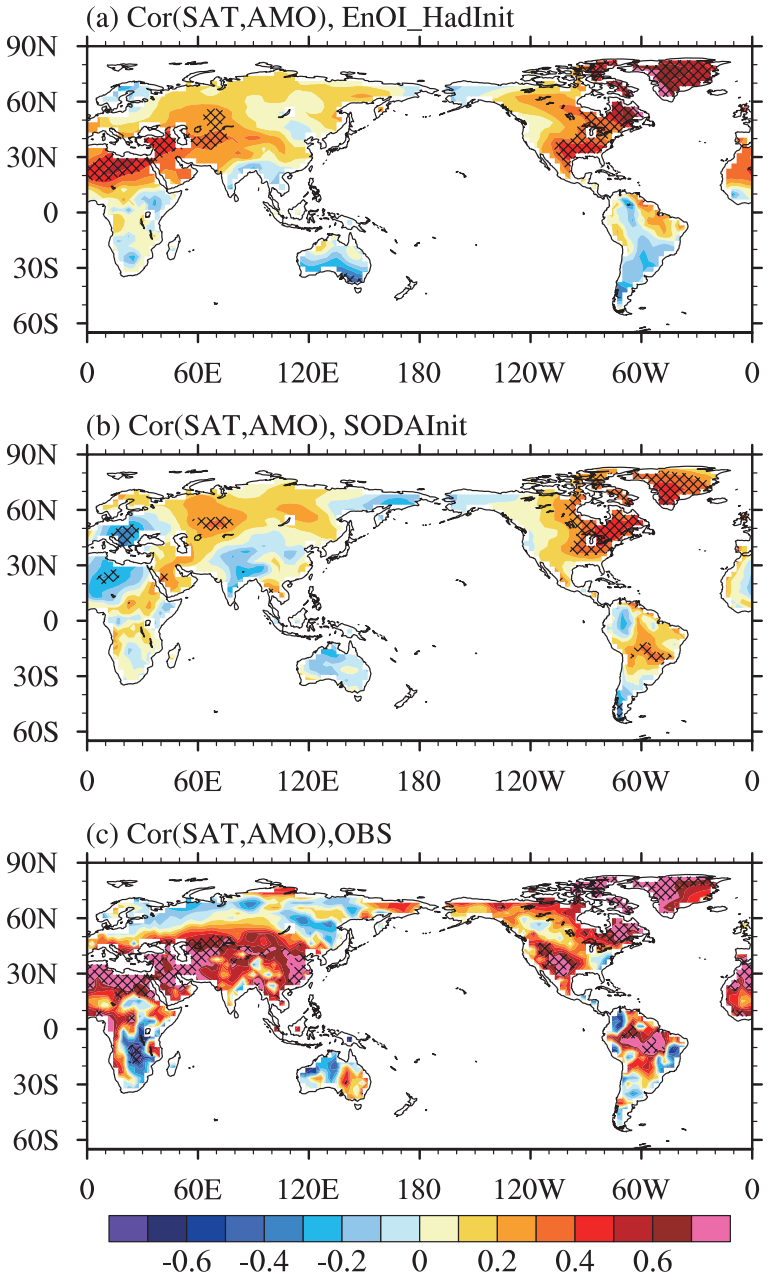

Fig. 7. Correlation between SAT and AMO index hindcast by EnOI_HadInit (a), SODAInit (b), and observation (c) for the forecast years 2−5. Hatched area identifies the region where the ACC is above the 90 % confidence level.

of the TWP SST. The observed close relationship between East Asian SAT and North Pacific SST, SIOD, and AMO indices could not be reproduced by the decadal hindcasts and needs further improvement.

These increased skills in SST and SAT predicted by EnOI_HadInit confirm that the assimilated data generated by the ocean model of BCC-CSM1.1 with EnOI assimilation can provide better initial conditions than SODA reanalysis data for the decadal predictions of BCC-CSM1.1. It indicates that appropriately constraining the initial states of the model through assimilation strategy is crucial for decadal predictions. Wu et al. (2018) constructed a decadal prediction system with EnOI and incremental analysis update

Table 2. Correlation coefficients between East Asian (100–120°E, 25–40°N) SAT time series with tropical western Pacific (TWP) SST, North Pacific (NP) SST, southern Indian Ocean Dipole (SIOD), and Atlantic multi-decadal oscillation (AMO) indices hindcast by EnOI_HadInit and SODAInit for the forecast years 2–5, as well as in the observation. All data are detrended before the calculation. Bold values are above the 90 % confidence level.

Experiment name	TWP SST	NP SST	SIOD	AMO
EnOI_HadInit	0.72	0.33	−0.15	0.14
SODAInit	0.61	0.37	−0.25	0.02
OBS	0.41	0.56	−0.42	0.79

scheme, which was verified to be skillful in the prediction of SST anomalies in midlatitude North Pacific, North Atlantic, and the key areas of ENSO. Further development based on EnOI needs to be done in the decadal prediction systems of BCC-CSM. The assimilation of the ocean salinity will also be considered in the new decadal prediction systems of BCC-CSM.

Acknowledgments

This work was jointly supported by the National Program on Key Basic Research Project of China (2016YFA0602100, 2016YFA0602200, 2016YFE 0102404, 2012CB955203, and 2013CB430202), and Tsinghua University Initiative Scientific Research Program (20131089357).

References

Bellucci, A., S. Gualdi, S. Masina, A. Storto, E. Scoccimarro, C. Cagnazzo, P. Fogli, E. Manzini, and A. Navarra, 2013: Decadal climate predictions with a coupled OAGCM initialized with oceanic reanalyses. *Climate Dyn.*, **40**, 1483–1497.

Boer, G. J., D. M. Smith, C. Cassou, F. Doblas-Reyes, G. Danabasoglu, B. Kirtman, Y. Kushnir, M. Kimoto, G. A. Meehl, R. Msadek, W. A. Mueller, K. E. Taylor, F. Zwiers, M. Rixen, Y. Ruprich-Robert, and R. Eade, 2016: The Decadal Climate Prediction Project (DCPP) contribution to CMIP6. *Geosci. Model. Dev.*, **9**, 3751–3777.

Bretherton, C. S., M. Widmann, V. P. Dymnikov, J. M. Wallace, and I. Bladé, 1999: The effective number of spatial degrees of freedom of a time-varying field. *J. Climate*, **12**, 1990–2009.

Carton, J. A., and B. S., Giese, 2008: A reanalysis of ocean climate using Simple Ocean Data Assimilation (SODA). *Mon. Wea. Rev.*, **136**, 2999–3017.

Doblas-Reyes, F. J., I. Andreu-Burillo, Y. Chikamoto, J. García-Serrano, V. Guemas, M. Kimoto, T. Mochizuki, L. R. L. Rodrigues, and G. J. van Oldenborgh, 2013: Initialized near-term regional climate change prediction. *Nat. Commun.*, **4**, 1715, doi:10.1038/ncomms 2704.

Eyring, V., S. Bony, G. A. Meehl, C. A. Senior, B. Stevens, R. J. Stouffer, and K. E. Taylor, 2016: Overview of the Coupled Model Intercomparison Project Phase 6 (CMIP6) experimental design and organization. *Geosci. Model. Dev.*, **9**, 1937–1958.

Fan, Y., and H. van den Dool, 2008: A global monthly land surface air temperature analysis for 1948-present. *J. Geophys. Res.*, **113**, D01103, doi: 10.1029/2007JD 008470.

Gao, F., X. Xin, and T. Wu, 2012: A study of the prediction of regional and global temperature on decadal time scale with BCC_CSM1.1 model. *Chinese J. Atmos. Sci.*, **36**, 1165–1179 (in Chinese with English abstract).

Gaetani, M., and E. Mohino, 2013: Decadal prediction of the Sahelian precipitation in CMIP5 simulation. *J. Climate*, **26**, 7708–7719.

García-Serrano, J., and F. J. Doblas-Reyes, 2012: On the assessment of near-surface global temperature and North Atlantic multi-decadal variability in the ENSEMBLES decadal hindcast. *Climate Dyn.*, **39**, 2025–2040.

Goddard, L., A. Kumar, A. Solomon, D. Smith, G. Boer, P. Gonzalez, V. Kharin, W. Merryfield, C. Deser, S. J. Mason, B. P. Kirtman, R. Msadek, R. Sutton, E. Hawkins, T. Fricker, G. Hegerl, C. A. T. Ferro, D. B. Stephenson, G. A. Meehl, T. Stockdale, R. Burgman, A. M. Greene, Y. Kushnir, M. Newman, J. Carton, I. Fukumori, and T. Delworth, 2012: A verification framework for interannual-to-decadal predictions experiments. *Climate Dyn.*, **40**, 245–272.

Griffies, S. M., A. Gnanadesikan, K. W. Dixon, J. P. Dunne, R. Gerdes, M. J. Harrison, A. Rosati, J. L. Russell, B. L. Samuels, M. J. Spelman, M. Winton, and R. Zhang, 2005: Formulation of an ocean model for global climate simulations. *Ocean Sci.*, **1**, 45–79.

Ham, Y.-G., M. M. Rienecker, M. J. Suarez, Y. Vikhliaev, B. Zhao, J. Marshak, G. Vernieres, and S. D. Schubert, 2014: Decadal prediction skill in the GEOS-5 forecast system. *Climate Dyn.*, **42**, 1–20.

Han, Z. Y., B. Wu, and X. G. Xin, 2017: Decadal prediction skill of the global sea surface temperature in the BCC-CSM1.1 climate model. *Adv. Earth Sci.*, **32**, 382−395 (in Chinese with English abstract).

Huang, B., P. W. Thorne, T. M. Smith, W. Liu, J. Lawrimore, V. F. Banzon, H.-M. Zhang, T. C. Peterson, and M. Menne, 2016: Further exploring and quantifying uncertainties for Extended Reconstructed Sea Surface Temperature (ERSST) version 4 (v4). *J. Climate*, **29**, 3119–3142

IPCC, 2013: *Climate Change 2013: The Physical Science Basis. Contribution of Working Group I to the Fifth Assessment Report of the Intergovernmental Panel on Climate Change*. Stocker, T. F., D. Qin, G.-K. Plattner,

M. M. B. Tignor, S. K. Allen, J. Boschung, A. Nauels, Y. Xia, V.Bex, and P. M. Midgley (eds.), Cambridge University Press, 1523 pp.

Kalnay, E., M. Kanamitsu, R. Kistler, W. Collins, D. Deaven, L. Gandin, M. Iredell, S. Saha, G. White, J. Woollen, Y. Zhu, M. Chelliah, W. Ebisuzaki, W. Higgins, J. Janowiak, K. C. Mo, C. Ropelewski, J. Wang, A. Leetmaa, R. Reynolds, Roy Jenne, and D. Joseph, 1996: The NCEP/NCAR 40-Year Reanalysis Project. *Bull. Amer. Meteor. Soc.*, **77**, 437–470.

Keenlyside, N. S., M. Latif, J. Jungclaus, L. Kornblueh, and E. Roeckner, 2008: Advancing decadal-scale climate prediction in the North Atlantic sector. *Nature*, **453**, 84–88.

Kim, H.-M., P. J. Webster, and J. A. Curry, 2012: Evaluation of short-term climate change prediction in multi-model CMIP5 decadal hindcasts. *Geophys. Res. Lett.*, **39**, L10701, doi:10.1029/2012GL051644.

Knight, J. R., C. K. Folland, and A. A. Scaife, 2006: Climate impacts of the Atlantic Multidecadal Oscillation. *Geophys. Res. Lett.*, **33**, L17706, doi:10.1029/2006GL026242.

Li, Q.-Q., J. Tan, L.-N. Wang, M. Wei, and Q.-G. Zhao, 2015: Simulation of the natural distribution of carbon and nutrients in the ocean based on the global ocean carbon cycle model MOM4_L40. *Chinese J. Geophys.*, **58**, 1–19.

Meehl, G. A., L. Goddard, G. Boer, R. Burgman, G. Branstator, C. Cassou, S. Corti, G. Danabasoglu, F. Doblas-Reyes, E. Hawkins, A. Karspeck, M. Kimoto, A. Kumar, D. Matei, J. Mignot, R. Msadek, A. Navarra, H. Pohlmann, M. Rienecker, T. Rosati, E. Schneider, D. Smith, R. Sutton, H. Teng, G. J. van Oldenborgh, G. Vecchi, and S. Yeager, 2014: Decadal climate prediction: An update from the trenches. *Bull. Amer. Meteor. Soc.*, **95**, 243–267.

Rayner, N. A., D. E. Parker, E. B. Horton, C. K. Folland, L. V. Alexander, D. P. Rowell, E. C. Kent, and A. Kaplan, 2003: Global analyses of sea surface temperature, sea ice, and night marine air temperature since the late nineteenth century. *J. Geophys. Res.*, **108**, 4407, doi:10.1029/2002JD002670.

Si, D., and Y. H. Ding, 2016: Oceanic forcings of the interdecadal variability in East Asian summer rainfall. *J. Climate*, **29**, 7633–7649.

Smith, D. M., S. Cusack, A. W. Colman, C. K. Folland, G. R. Harris, and J. M. Murphy, 2007: Improved surface temperature prediction for the coming decade from a global climate model. *Science*, **317**, 796–799.

Taylor, K. E., R. J. Stouffer, and G. A. Meehl, 2012: An overview of CMIP5 and the experiment design. *Bull. Amer. Meteor. Soc.*, **93**, 485–498.

University of East Anglia Climatic Research Unit, Harris, I., and Jones, P. D., 2015: *CRU TS3.23: Climatic Research Unit (CRU) Time-Series (TS) Version 3.23 of High Resolution Gridded Data of Month-by-month Variation in Climate (Jan. 1901–Dec. 2014*). Centre for Environmental Data Analysis, 09 November 2015, doi:10.5285/4c7fdfa6-f176-4c58-acee-683d5e9d2ed5.

Wei, M., Q. Li, X. Xin, W. Zhou, Z. Han, Y. Luo, and Z. Zhao, 2017: Improved decadal climate prediction in the North Atlantic using EnOI-assimilated initial condition. *Sci. Bull.*, **62**, 1142–1147.

Wu, B., and T. J. Zhou, 2012: Prediction of decadal variability of sea surface temperature by a coupled global climate model FGOALS_gl developed in LASG/IAP. *Chinese Sci. Bull.*, **57**, 2453–2459.

Wu, B., X. Chen, F. Song, Y. Sun, and T. Zhou, 2015: Initialized decadal predictions by LASG/IAP climate system model FGOALS-s2: Evaluations of strengths and weaknesses. *Adv. Meteor.*, **6**, 904826, doi:10.1155/2015/904826.

Wu, B., T. Zhou, and F. Zheng, 2018: EnOI-IAU initialization scheme designed for decadal climate prediction system IAP-DecPreS. *J. Adv. Model. Earth Syst.*, **10**, 342–356.

Wu, T., R. Yu, F. Zhang, Z. Wang, M. Dong, L. Wang, X. Jin, D. Chen, and L. Li, 2010: The Beijing Climate Center for atmospheric general circulation model: Description and its performance for the present-day climate. *Climate Dyn.*, **34**, 123–147.

Wu, T., W. Li, J. Ji, X. Xin, L. Li, Z. Wang, Y. Zhang, J. Li, F. Zhang, M. Wei, X. Shi, F. Wu, L. Zhang, M. Chu, W. Jie, Y. Liu, F. Wang, X. Liu, Q. Li, M. Dong, X. Liang, Y. Gao, and J. Zhang, 2013: Global carbon budgets simulated by the Beijing Climate Center Climate System Model for the last century. *J. Geophys. Res.*, **118**, 4326–4347.

Xin, X.-G., T.-W. Wu, and J. Zhang, 2013: Introduction of CMIP5 experiments carried out with the climate system models of Beijing Climate Center. *Adv. Climate Change Res.*, **4**, 41–49.

Xin, X., F. Gao, M. Wei, T. Wu, Y. Fang, and J. Zhang, 2018: Decadal prediction skill of BCC-CSM1.1 model in East Asia. *Int. J. Climatol.*, **38**, 584–592.

Zhou, T., R. Yu, H. Li, and B. Wang, 2008: Ocean forcing to changes in global monsoon precipitation over the recent half-century. *J. Climate*, **21**, 3833–3852.

薛晓颖, 任国玉, 孙秀宝, 等. 2019. 中国中小尺度强对流天气气候学特征 [J]. 气候与环境研究, 24 (2): 199−213. Xue Xiaoying, Ren Guoyu, Sun Xiubao, et al. 2019. Climatological characteristics of meso-scale and micro-scale strong convective weather events in China [J]. Climatic and Environmental Research (in Chinese), 24 (2): 199−213, doi:10.3878/j.issn.1006-9585.2018.17148.

中国中小尺度强对流天气气候学特征

薛晓颖[1, 2, 3]　任国玉[2, 4]　孙秀宝[4, 5]　任玉玉[4]　余予[6]

1 中国气象科学研究院，北京 100081
2 中国地质大学（武汉）环境学院，武汉 430074
3 辽宁省营口市气象局，辽宁营口 115000
4 国家气候中心中国气象局气候研究开放实验室，北京 100081
5 南京信息工程大学大气科学学院，南京 210044
6 中国气象局国家气象信息中心，北京 100081

摘　要　中小尺度强对流天气具有极强的破坏力，了解其气候学特征对于预测、预报和影响评价都具有实际意义。利用 1961～2015 年的 2332 个高密度逐月国家级气象站观测资料，分析了中国大陆 3 种常见中小尺度强对流天气（雷暴、闪电、冰雹）在年、季、月尺度上发生日数的时间变化规律和空间分布特征。结果表明：全国年平均雷暴、闪电和冰雹发生频率分别为 39.23 d/a、20.56 d/a 和 1.07 d/a；雷暴和闪电主要发生在夏季 3 个月，雷暴日数 7 月最多，闪电日数 8 月最多；冰雹主要发生每年 5～9 月，6 月发生频率最高；雷暴和闪电的高发区分布基本一致，主要集中在华南和西南，青藏高原也是雷暴的高发区域之一；冰雹的高发区主要集中在青藏高原、内蒙古高原东部以及中西部山地，而东南沿海地区发生频率则较低。进一步分析发现，我国雷暴和冰雹出现频率随海拔高度增加而明显增加，冰雹和海拔高度有更好的对应关系，二者增加速率分别为 2.87 d/500 m 和 1.80 d/500 m，表明地势高度对这两种强对流天气形成和发展具有重要影响。

关键词　中小尺度强对流　雷暴　闪电　冰雹　地形　气候学特征
文章编码　1006-9585（2019）02-0199-16　　**中图分类号**　P445　　**文献标识码**　A
doi:10.3878/j.issn.1006-9585.2018.17148

Climatological Characteristics of Meso-scale and Micro-scale Strong Convective Weather Events in China

XUE Xiaoying[1, 2, 3], REN Guoyu[2, 4], SUN Xiubao[4, 5], REN Yuyu[4], and YU Yu[6]

1 *Chinese Academy of Meteorological Sciences*, *Beijing* 100081
2 *Department of Atmospheric Science, School of Environmental Studies, China University of Geosciences*, *Wuhan* 430074
3 *Yingkou Meteorological Bureau, Yingkou*, *Liaoning Province* 115000
4 *Laboratory for Climate Studies, National Climate Center*, *China Meteorological Administration, Beijing* 100081
5 *College of Atmospheric Science, Nanjing University of Information Science and Technology*, *Nanjing* 210044
6 *National Meteorological Information Center, China Meteorological Administration*, *Beijing* 100081

Abstract Meso-scale and micro-scale strong convective weather events usually contain a great destructive power. Understanding climatological characteristics of strong convective weather events is of great importance for forecast,

收稿日期　2017-10-19；**网络预出版日期** 2018-02-11
作者简介　薛晓颖，女，1988 年出生，博士研究生，主要从事气候变化研究。E-mail:xuexiaoying@camscma.cn。
通讯作者　任国玉，E-mail: guoyoo@cma.gov.cn
资助项目　国家自然科学基金项目 41575003，国家公益性行业（气象）科研专项 GYHY201206012
Funded by　National Natural Science Foundation of china (Grant 41575003), the Ministry of Science and Technology of China (Grant GYHY201206012)

prediction and impact assessment of convective weather. In this paper, a newly developed dataset of meso-scale and micro-scale strong convective weather events in China that includes observations at 2332 national weather stations for the period of 1961–2015 is used to reanalyze the climatological characteristics of strong convective weather events (thunderstorms, lightnings, hails) on annual, seasonal, and monthly scales in China. The results show that the occurrence frequencies of thunderstorm, lightning, and hail are 39.23 d/a, 20.56 d/a, and 1.07 d/a, respectively. Thunderstorms and lightnings mainly occur in the summer, while most of the thunderstorms occur in July and most of lightnings occur in August. Hails mainly occurr between May and September, and the highest frequency occurs in June. Areas with high frequency of thunderstorms are similar to those with high frequency of lightnings, which are mainly located in southern and southwestern China and the Qinghai–Tibet Plateau. The occurrence frequency of hail is closely related to topography, and areas with high frequency of hail are mainly distributed in the Qinghai–Tibet Plateau, the eastern part of Inner Mongolia and the mountainous areas of central and western China, while the southeastern coastal areas have lower frequency than other areas. In addition, hail and thunderstorm increase significantly with elevation, especially hail, and the increase rates are 2.87 d/500 m and 1.80 d/500 m, respectively. It is found that elevation has important influences on the formation and development of these two types of strong convective weather.

Keywords Meso-scale and micro-scale strong convective weather event, Thunderstorm, Lightning, Hail, Topography, Climatological characteristics

1 引言

中小尺度强对流天气是多种灾害性天气的统称，而其中最受人们关注的 3 种强对流天气分别是雷暴、闪电和冰雹。中小尺度强对流天气是一种复杂的大气现象，其特有的复杂性、局地性和突发性都增加了预报的难度（俞小鼎等，2012；Zhang et al.，2017）。强对流天气通常与其他极端天气现象相伴而生，雷暴、闪电和冰雹一般伴随着极端强降水过程（陈思蓉等，2009）。这种伴随性天气发生的特点，使中小尺度强对流天气具有了更强的破坏力，更容易造成社会经济损失（符琳等，2011）。因此，分析中小尺度强对流天气的时空分布特征，对加深气象灾害规律的理解及预防有着重要的科学意义。

在全球尺度上，Dai（2001）运用 1975～1997 年全球约 15000 个站的实测资料研究雷暴的日变化特征，发现雷暴存在海陆差异，大部分陆地上雷暴主要出现在傍晚，而海洋上则出现在午后。Brooks et al.（2003）使用再分析资料分析欧洲超强雷暴，发现欧洲南部是全球可能孕育超强雷暴环境最佳的地区。Christian et al.（2003）利用光学瞬态检测器研究全球闪电频率和分布，发现全球每年约有 14 亿次闪电发生，陆地闪电发生平均概率是海洋的 10 倍，北半球夏季闪电发生较多，北大西洋和西太平洋闪电发生频次比热带东太平洋和印度洋多。Sioutas et al.（2009）分析希腊北部冰雹空间分布，发现高海拔地区和靠近高山的区域冰雹发生较多。

对于中国大陆，雷暴、冰雹等中小尺度强对流天气的气候学特征很早就受到了普遍关注。例如，张敏锋和冯霞（1998）利用中国 104 个台站 30 年的雷暴资料，分析了中国雷暴天气气候学分布特征，发现我国 30 年平均的雷暴日空间分布可大致分为 4 个区域：东南及华南高值区，高原及邻近地区的次高值区，华北、华中及西北东部的次低值区和西北地区的雷暴最低值区。郄秀书等（2014）系统回顾了我国学者针对闪电气象学和气候学的研究进展，总结了对应于不同类型强对流天气的闪电活动特征、闪电活动与雷暴的联系，闪电资料同化方法及其在强对流天气中的预警预报作用等。Zhang et al.（2017）利用 1961～2010 年 580 个观测站的雷暴资料，分析了我国雷暴的空间分布特征，发现华南地区是雷暴发生频次最多地区、青藏高原东部和东南部是次大值区。

在更小的区域尺度上，徐桂玉和杨修群（2001）使用我国南方 62 个气象观测站 1971～1995 年雷暴日数资料研究发现，南方雷暴分布总趋势自南向北递减，多雷暴带与主要山地分布密切相关，东南沿海地区雷暴比内陆要少。李照荣等（2005）研究西北地区雷暴活动的差别发现，总的特征是高原和山区雷暴发生频率更高，河谷、盆地和沙漠雷暴少，并且雷暴夏季最强，而春、秋次之，冬季几乎无雷暴发生。以上研究结果在其他区域范围的研究中也得到了证实（秦丽等，2006；李韬光等，2015；黄武斌等，2016）。

综上，国内目前研究已经开始关注不同地区中

小尺度强对流天气的气候学特征。已有的研究提高了人们对中小尺度强对流天气的气候学分布、季节性和周期性等方面的认知，但在气候学特征研究方面，仍存在以下 3 方面的不足：第一，对于区域尺度的分析较多，而把全国作为一个整体的研究较少，这样就造成了对于全国整体的中小尺度强对流天气气候学特征认识不足；第二，已有的针对全国的研究，选用较为稀疏或不完善的观测站网资料，空间分辨率不高，且观测站密度东部明显大于西部，这样就造成全国尺度中小尺度强对流天气气候学特征研究代表性不充分的问题；第三，已有研究更多关注于雷暴、闪电或冰雹单一的强对流天气现象，利用长时间高分辨率数据对于 3 种中小尺度强对流天气进行综合分析研究，还是非常欠缺的。造成上述不足的主要原因是，过去缺少更新到现在的全国高密度、高质量台站观测资料。

本文利用中国气象局国家气象信息中心最新发布的全国 2425 个高密度台站观测资料，综合分析中国大陆 3 种中小尺度强对流天气的气候学特征，包括年、月、季节尺度的时间演化特征，以及不同区域之间发生频率的空间差异。本文结果对中小尺度强对流天气的监测、预报和影响评价，都具有重要的参考价值。

2 资料和方法

2.1 资料

雷暴、闪电和冰雹资料来源于国家气象信息中心最新发布的《中国地面强对流天气数据集》（赵煜飞和余予，2015）中的逐月数据。全部台站约为 2425 个，其中包括国家基本、基准和一般站。资料长度起始年为 1954 年，雷暴和闪电资料截止于 2013 年，冰雹资料截止于 2015 年。图 1a 表明，观测站点数在 1954 年不足 500 个，之后快速增长，1961 年以后台站数超过 2000 个，并且之后基本保持不变。

数据基本来源于地面气象观测数据文件，月值由日值统计得到，若 1 月中出现 7 d 及以上缺测，则该月日数为缺测。年值由月值统计得到，若一年中各月日数有 1 个及以上缺测时，则年日数为缺测。

在数据集制作过程中，主要应用内部一致性方法，对雷暴、闪电和冰雹的日值数据进行质量控制。参与质量控制的相关要素为日云状、日最大风速和日降水量。具体质控方案如下：（1）若某日出现雷暴现象，且未出现积雨云，日最大风速小于 5.4 m/s，则该现象数据视为可疑；（2）若某日出现闪电现象，且未出现积雨云，日最大风速小于 5.4 m/s，则该现象数据视为可疑；（3）若某日出现冰雹现象，且未出现积雨云，日降水量等于 0.0 mm，则该现象数据视为可疑。月值质控基于日值统计给出，若 1 月中出现 1 d 及以上可疑数据，则月值记录为可疑数据。年值质控基于月值统计给出，若 1 年中出现 1 月及以上可疑数据，则年值记录为可疑数据。最终质控结果显示，各项要素数据的实有率均在 98%以上，数据的正确率均接近 100%（赵煜飞和余予，2015）。本文在数据处理时，剔除了数据集中标记的所有可疑数据。

2.2 中小尺度强对流天气现象

雷暴指积雨云云中、云间或云地之间产生的放电现象，表现为闪电并有雷声，有时亦可只闻雷声而不见闪电。闪电指积雨云云中、云间或云地之间产生放电时伴随的光芒，但不闻雷声。冰雹指坚硬的球状、锥状或形状不规则的固态降水，大小差异大，大的直径可达到数十毫米，常伴随雷暴出现。当某日台站观测出现了雷暴（闪电、冰雹）现象，则记为 1 个雷暴（闪电、冰雹）日（赵煜飞和余予，2015）。

2.3 台站选取

因为数据集在 1961 年以后台站数稳定超过 2000 个，所以选取雷暴、闪电的研究时段为 1961～2013 年，冰雹的研究时段为 1961～2015 年。根据上述台站记录不一致的情况及后续研究的需要，依据以下 3 条标准对台站进行筛选：（1）台站观测记录大于或等于 35 年；（2）台站每年观测记录大于或等于 3 个月；（3）1981～2010 年台站观测记录大于或等于 20 年。根据以上 3 条标准，筛选后观测台站共有 2332 个。图 1b 为筛选后观测台站的空间分布情况，台站空间上基本覆盖了除台湾外的全国范围，其中东北、西北和青藏高原台站相对较稀疏，其他地区台站覆盖率相对较高。

2.4 方法说明

全国平均，采用的是全国所有站的算术平均。具体计算方法是：计算每个月所有站的平均值，缺测时不参与计算，然后再计算研究时段内所有月份的平均值，最后根据各月的平均值获得年或季节的平均值。季节划分采用气象季节划分的方法，即

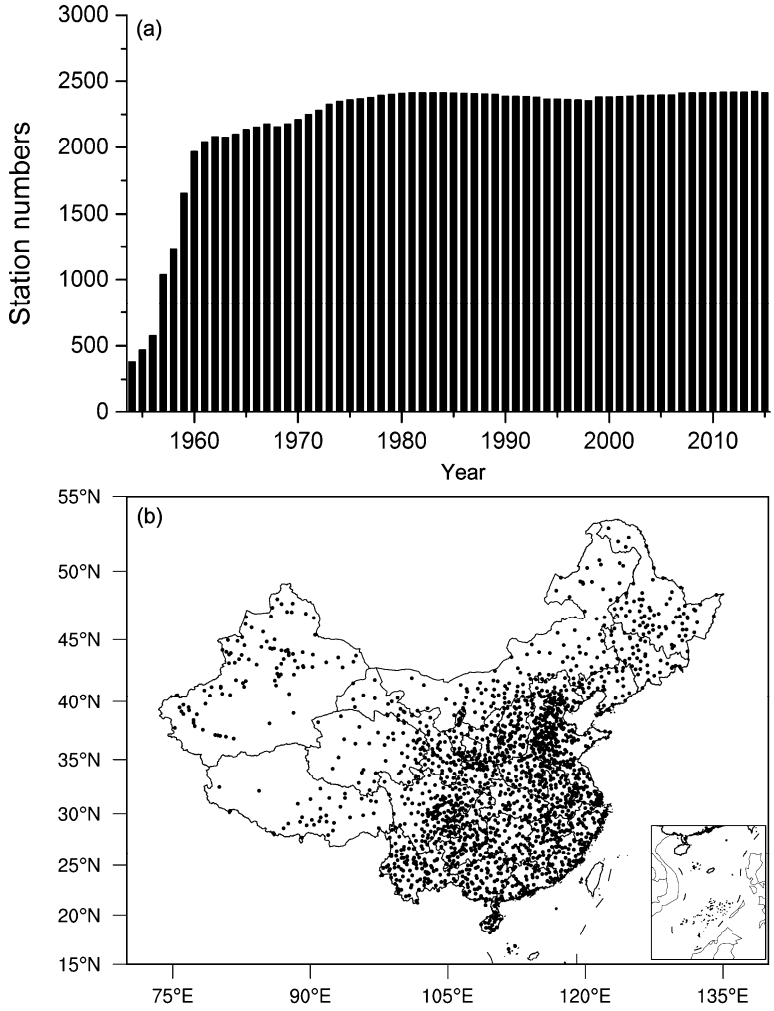

图 1 （a）1954 年以来中国观测台站数随时间的变化和（b）筛选后 2332 个台站位置的空间分布

Fig. 1 (a) Temporal change in the numbers of stations in China since 1954 and (b) spatial distribution of the selected 2330 stations

上年 12 月至当年 2 月为冬季，3～5 月为春季，6～8 月为夏季，9～11 月为秋季。

3 结果

3.1 雷暴日数气候学特征

图 2a 为全国平均的各月平均雷暴日数年际变化，图 2b 为全国平均年内各月平均雷暴发生日数。我国雷暴发生日数主要分布在 2～11 月，夏季（6～8 月）是雷暴发生的高频期，雷暴日数占全年雷暴总日数的 62.31%，其中 7 月是雷暴日数最多的月份，次多月份为 8 月。1961～2013 年，全国平均雷暴日数在波动中变化，但整体呈减少趋势。2000 年代以前全国夏季雷暴发生频率在 7 月最大可以达到 13 d，1980 年代以前夏季雷暴发生频率保持在每月 12 d 以上。由此可见，我国雷暴主要发生在夏季，以 7 月发生日数最多，近 50 年来虽然雷暴的季节性高频期并没有太大变化，但雷暴发生日数逐渐趋于减少。

图 3a 为雷暴日数多年平均值的空间分布情况。全国年平均雷暴为 39.23 d/a，年平均雷暴日数随着纬度的增加而明显减少。在长江流域附近，年平均雷暴日数为 40～50 d，两广和海南为 70～120 d，其他地区为 50～70 d。华南和西南地区是高雷暴中心，海南岛是全国雷暴发生日数最多的地区。东南部丘陵地带年平均雷暴日数高于同纬度平原地区，同时内陆比沿海地区雷暴发生频次高。

中国雷暴次大值区包含青藏高原东南部和云贵高原，前者年平均雷暴日数明显大于同纬度的其他地区，一般为 40～110 d，云贵高原南部为 100～

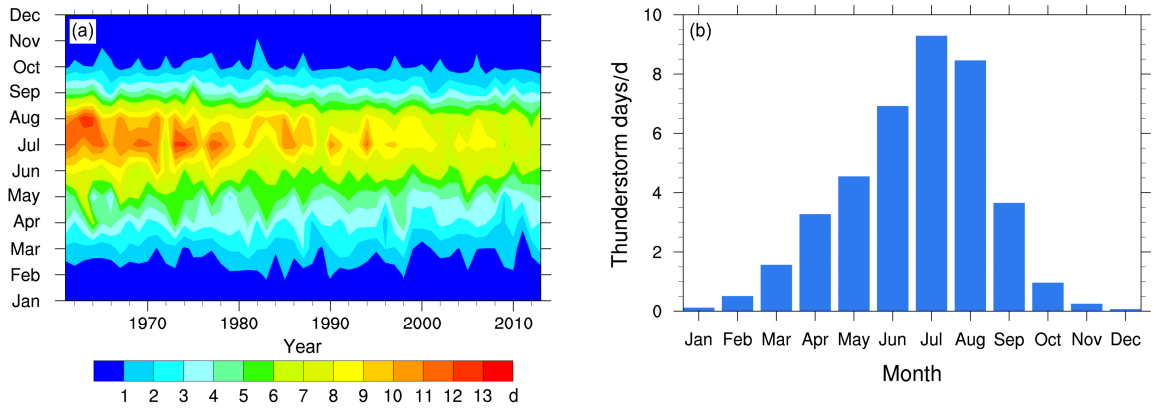

图 2 1961～2013 年（a）全国平均各月雷暴日数年际变化（横坐标为年份，纵坐标为月份，填色为每年各月的雷暴日数全国平均值），以及（b）全国平均年内各月雷暴发生日数

Fig. 2 (a) Inter-annual variation of monthly mean thunderstorm days in China during 1961−2013 (*X*-axis indicates the year, *Y*-axis indicates the month and various colors indicate monthly mean numbers of thunderstorms averaged in China), and (b) average values of monthly mean thunderstorm days in China during 1961−2013

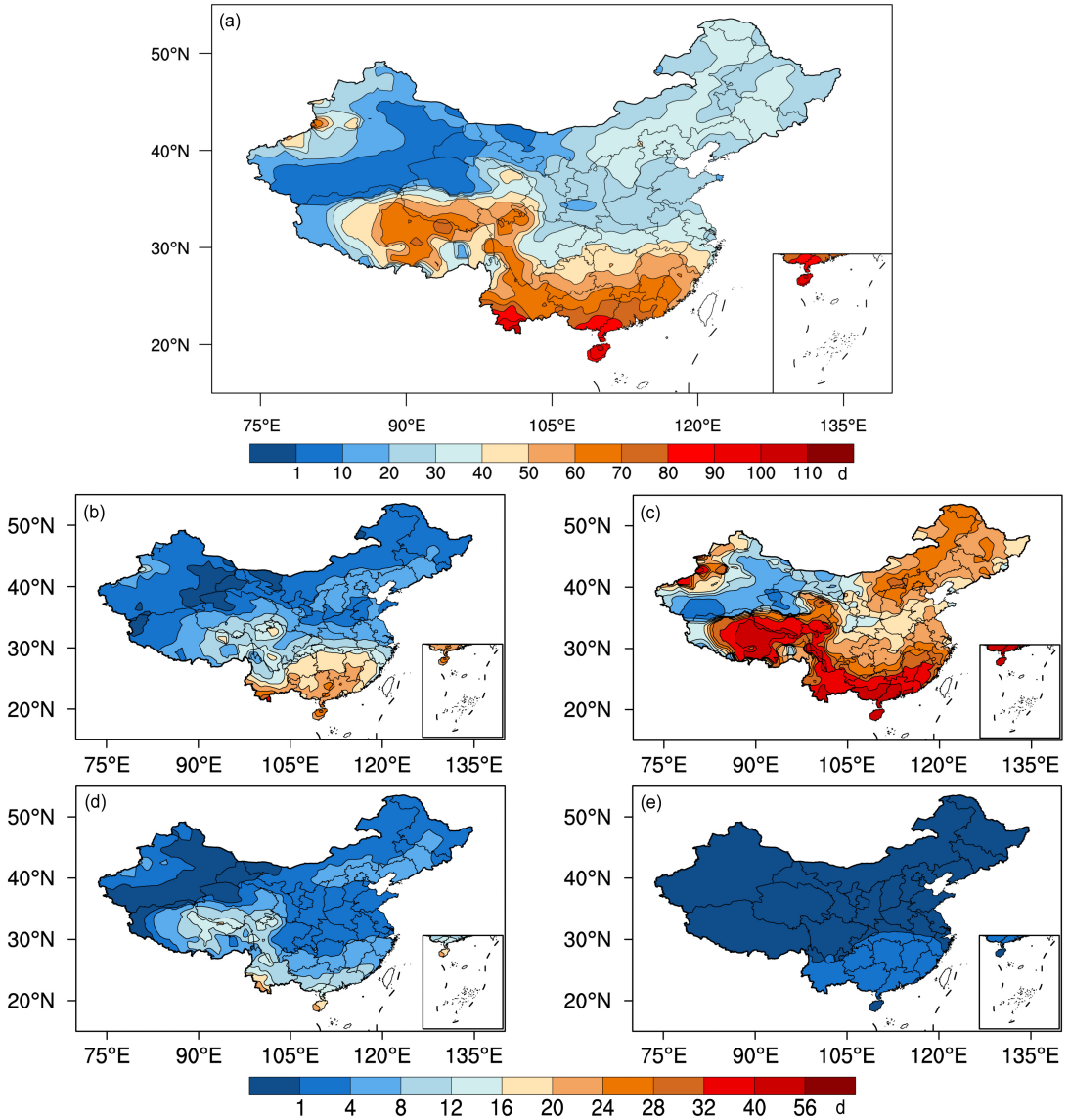

图 3 1961～2013 年中国年平均和季节平均雷暴日数空间分布：（a）年；（b）春季；（c）夏季；（d）秋季；（e）冬季

Fig. 3 Spatial distributions of annual and seasonal mean numbers of thunderstorm days in China during 1961−2013: (a) Annual; (b) spring; (c) summer; (d) autumn; (e) winter

110 d。年平均雷暴日数水平梯度大，等值线极为密集。青藏高原中东部和四川西部雷暴日数一般为60～90 d，雅鲁藏布江中下游区域雷暴日数较少。

长江以北的华北和东北地区，年平均雷暴日数随纬度的变化不明显，一般在 20～40 d，其中黄河流域中下游为 20 d 左右，是个相对低值区；内蒙古东部地区相对较高，年平均雷暴日在 35 d 以上。

西北干燥区为全国年平均雷暴日的最低值区。这个区域下垫面主要是沙漠和戈壁，年平均雷暴日在 30 d 以下，尤其是甘肃的北部、内蒙的西部以及新疆东部等地区，年平均雷暴日数在 10 d 以下。

图 3b、3c、3d、3e 为各个季节平均雷暴日数空间分布。全国四季平均雷暴日数分别为春季 9.28 d，夏季 24.49 d，秋季 4.81 d，冬季 0.68 d。四季雷暴发生日数的高低值分布和全年分布特征相类似，但量级大小不同。春季雷暴主要发生在华南、西南和青藏高原东部，且表现为纬度越低则发生日数越多；夏季发生区遍及全国，而高发区同样集中在华南、西南和青藏高原，但青藏高原高发区范围已经由春季的高原东部扩展到几乎整个高原；秋季雷暴发生频次空间分布和春季类似，但次数低于春季；冬季全国大部分地区不再有雷暴出现，仅在华南和西南仍有少量雷暴发生，最大日数均在 5 d 以下。

图 4 给出年平均雷暴日数的各年代平均的分布情况。各年代大值区的分布情况变化不大，即两广、海南、云南的南部、青藏高原中东部和四川的西部。然而，几乎所有地区年平均雷暴日数在早期 3 个年代偏多，此后不断减少；雷暴日数大值区范围随时间不断缩小更为明显。

因此，我国雷暴主要发生在夏季、年和四季平均雷暴日数有着不同的空间分布特征，但是大值区分布范围较为固定，主要在华南、西南和青藏高原，并且纬度越低雷暴发生日数越多；年平均雷暴日数的年际和年代际变化，都表现出了随时间不断减少现象，雷暴高发区域范围也在缩小。

3.2 闪电日数气候学特征

图 5a 为全国平均的各月平均闪电日数的年际变化，图 5b 为全国平均年内各月平均闪电发生日数。我国闪电日数在 3～11 月均有发生，并且夏季（6～8 月）是闪电发生的高频期，夏季发生闪电日数占全年闪电总日数的 65.59%，其中 8 月是闪电日数最多的月份，次多月份是 7 月。从 1961～2013 年，全国平均各月闪电的发生日数在明显减少，尤其是在 1990 年代以后，1970 年代以前全国夏季闪电发生频率在 8 月最大可以达到 10 d 以上，2000 年代以后夏季闪电减少到了每月 1～3 d。由此可见，我国闪电主要发生在夏季，并且 8 月发生最多，虽然近 50 年闪电的季节性高频期没有太大变化，但闪电发生日数明显在减少。

图 6a 为闪电日数多年平均值的空间分布情况。全国年平均闪电为 20.56 d/a，闪电均值有类似于雷暴的空间分布。在长江流域附近，年平均闪电日数为 15～25 d/a，闪电日数随着纬度的增加而减少，但是递减幅度弱于雷暴。两广和海南为 50～100 d/a，其他地区为 25～50 d/a。华南和云南是闪电发生日数最多的地区，这也与雷暴的高发区相重合。

中国闪电次大值区包含云南的南部、四川的西部以及西藏的边缘部分地区，为 35～80 d/a。闪电与雷暴空间分布相比有很明显的不同，尤其是在青藏高原的中东部，雷暴显示出高发，而闪电并没有显示出高发。

长江以北的华北和东北地区，年平均闪电日数和雷暴一样随纬度的变化不明显，在 5～30 d/a，其中黄河流域中下游一般为 5 d/a 左右，是个发生相对低值区。

西北干燥区为全国年平均闪电日数的最低值区，年平均闪电日数低于 30 d，尤其是甘肃的西北部、青海的西部和新疆的东南部，闪电每年发生日数在 5 d 以下。

图 6 b、6c、6d、6e 为各个季节平均闪电日数的空间分布。全国四季闪电日数分别为春季 3.40 d，夏季 13.52 d，秋季 3.49 d，冬季 0.19 d。春季、夏季、秋季闪电发生日数的高低值分布类似于年的分布，高值区都在华南、广西的南部、云南的南部以及四川的西部，冬季闪电主要发生在云南的南部。

图 7 为年平均闪电日数的各年代分布情况。各年代大值基本分布在华南南部、广西的南部、云南的南部及四川的西部。1960 年代至 1990 年代闪电日数偏多，之后不断减少，尤其从 1990 年代以后这种变化更加明显，并且大值区范围也变得越来越小，2010 年之后全国闪电发生日数趋于一致。

因此，闪电发生在每年 3～11 月，同样主要发生在 6～8 月。年平均闪电日数的空间分布和雷暴类似。春季、夏季、秋季闪电有类似于年的分布，冬季闪电主要发生在云南的南部。年平均闪电日数的年际和年代际变化，都表现出了近 50 年闪电发

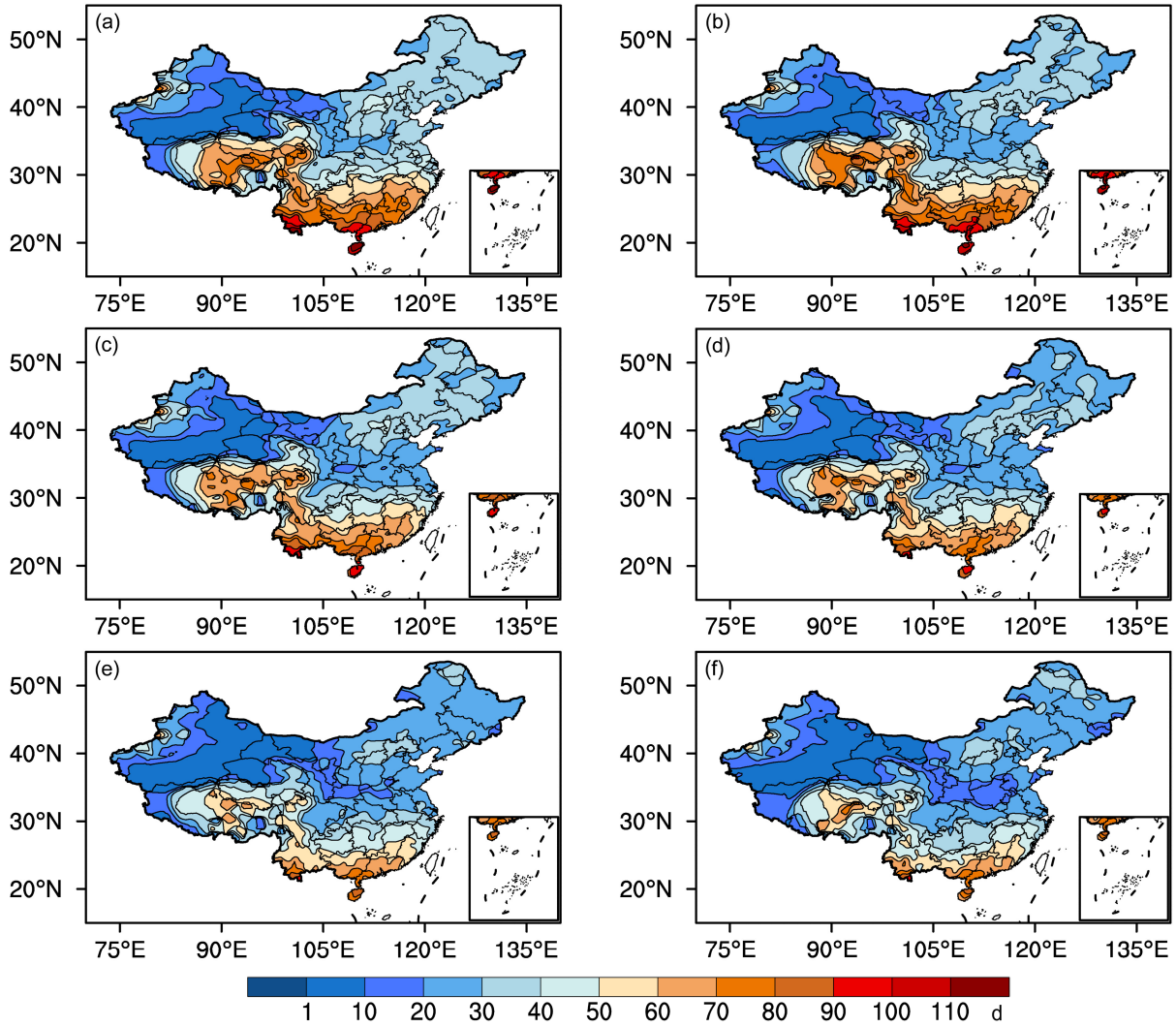

图 4 不同年代（时期）平均的中国年平均雷暴日数空间分布：（a）1961～1970 年；（b）1971～1980 年；（c）1981～1990 年；（d）1991～2000 年；（e）2001～2010 年；（f）2011～2013 年

Fig. 4 Interdecadal variation of annual mean thunderstorm days in China: (a) 1961−1970; (b) 1971−1980; (c) 1981−1990; (d) 1991−2000; (e) 2001−2010; (f) 2011−2013

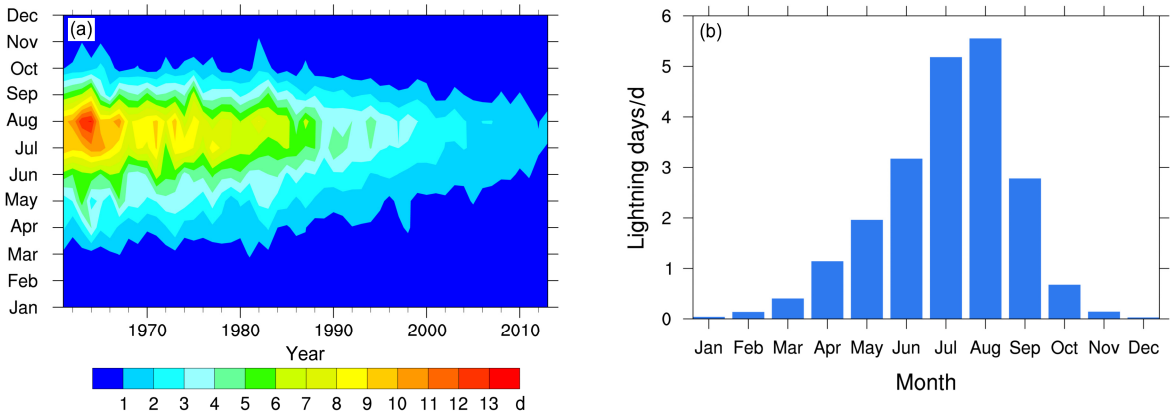

图 5 同图 2，但为闪电日数

Fig. 5 Same as Fig. 2, but for lightning days

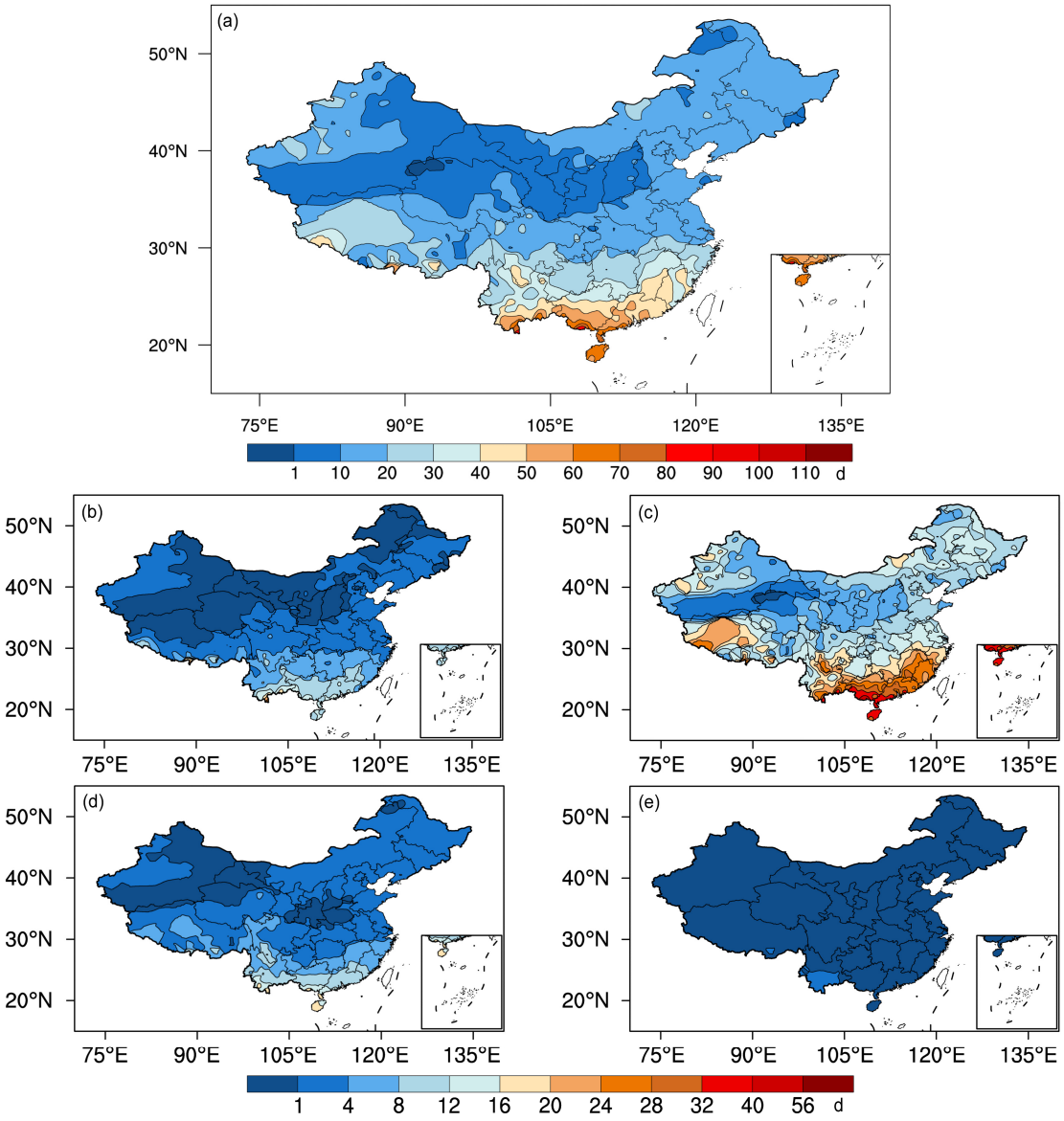

图 6 同图 3，但为闪电日数

Fig. 6 Same as Fig. 3, but for lightning days

生日数在随时间减少，并且在 2000 年代以后全国发生闪电日数趋于一致。

3.3 冰雹日数气候学特征

图 8a 为全国平均的各月平均冰雹日数年际变化，图 8b 为全国平均年内各月平均冰雹发生日数。全国 2～11 月均有冰雹发生，但主要发生在 5～9 月，占全年冰雹总日数的 76.65%，其中 6 月是冰雹日数最多的月份，5 月和 9 月是冰雹发生的次多月。研究时期内，在 2000 年代以前冰雹发生日数在波动中几乎没有变化，但是 2000 年代以后冰雹发生日数明显减少，在 1990 年代以前冰雹发生频率在 6 月份最大可达到 0.35 d 以上，但是到 2000 年以后全国冰雹平均每年发生不足 0.15 d。由此可见，我国冰雹主要发生在 5～9 月，近 50 年发生日数在 2000 年代以前变化不大，但是 2000 年代以后明显减少。

图 9a 为冰雹日数多年平均值的空间分布情况。全国年平均发生冰雹日数为 1.07 d。年平均发生冰雹日数同雷暴、闪电相比有很大差异。长江流域以南，除西南地区很少有冰雹发生，在此区域中年平均冰雹日数一般都在 1 d/a 以下，是全国冰雹的低值区。

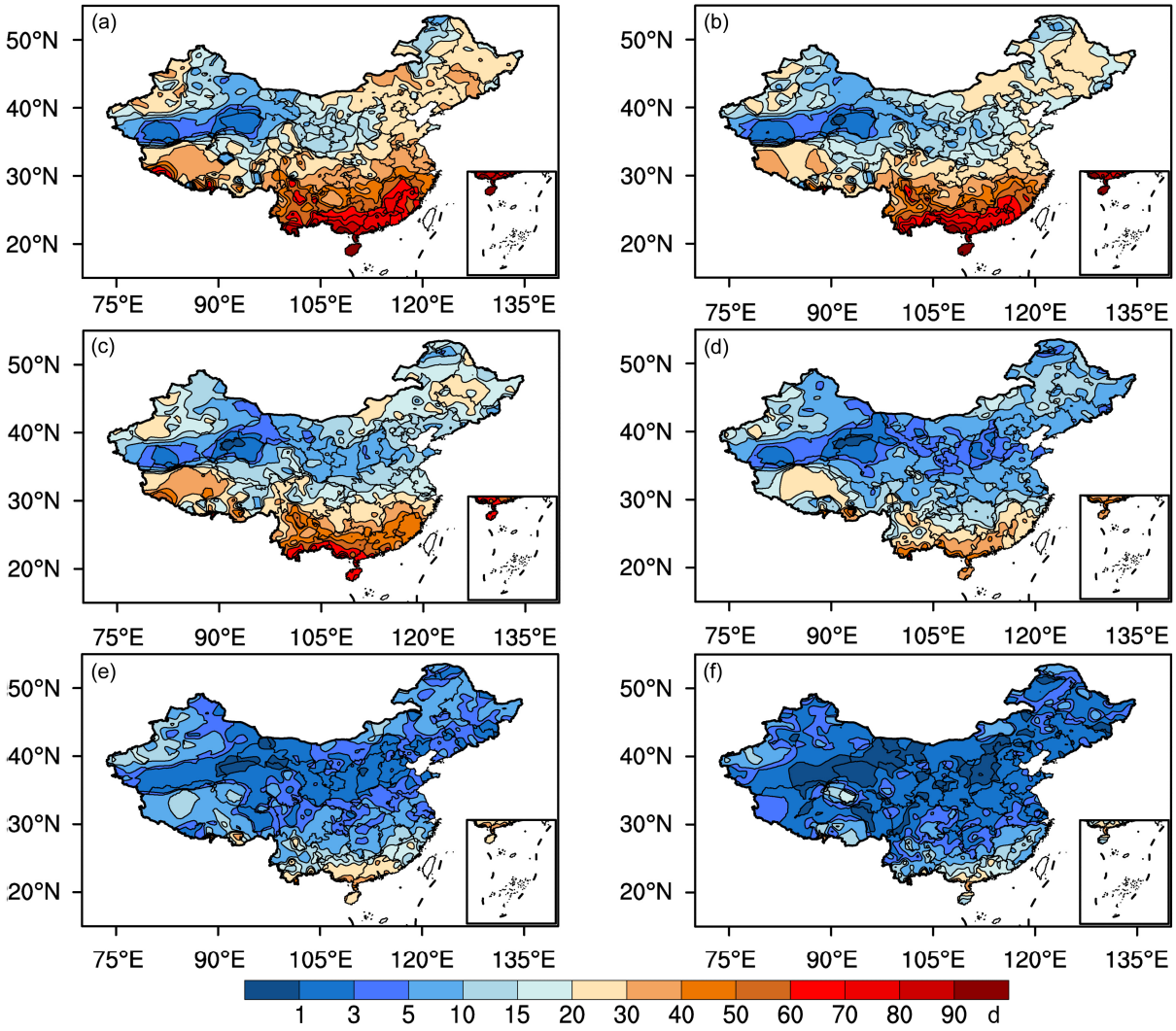

图 7 同图 4，但为闪电日数

Fig.7 Same as Fig. 4, but for lightning days

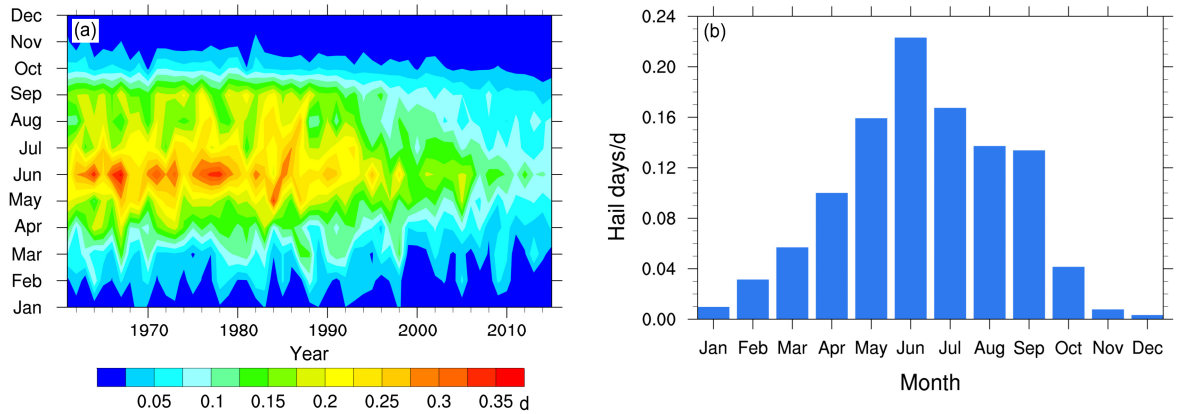

图 8 同图 2，但为冰雹日数，且研究时段为 1961～2015 年

Fig. 8 Same as Fig. 2, but for hail days and the period is from 1961 to 2015

中国冰雹的高发区集中在青藏高原及高原周边地区，这些区域也是中国地势最高的区域，在高原中部有一个明显的大值中心，最多每年可发生冰雹 24 d 以上，除了这个大值中心冰雹高发区域内一般每年发生冰雹都在 1～8 d。

长江以北的华北和东北地区是全国冰雹发生的次高值区域，在东北大部分地区、内蒙古东部冰雹每年发生 1～4 d，其他地区每年发生冰雹在 1 d 以下，但多年平均都会有冰雹发生。

西北干旱区同样也是全国冰雹较少发生的地区之一，除了新疆的西部以及青藏高原的周边地区每年发生冰雹在 1～4 d，其他地区基本没有冰雹发生。

图 9b、9c、9d、9e 为各季节全国冰雹发生日数均值的空间分布。全国四季冰雹分别为春季 0.31 d/a，夏季 0.53 d/a，秋季 0.18 d/a，冬季 0.04 d/a。春季冰雹只发生在新疆极少地区和青藏高原的东北部，每年发生日数为 1 d 以上；夏季冰雹发生区域扩大，冰雹大值区在青藏高原可达 3 d/a 以上，中心最大可达 15 d/a 以上，但大值区中心和春季相比西南移。秋季冰雹大值区和夏季类似，频率明显比夏季小但大于春季，大值中心在 7 d/a 以下。冬季全国基本没有冰雹出现。由此可见，我国冰雹主要集中发生在青藏高原地区，这主要受地形的局地

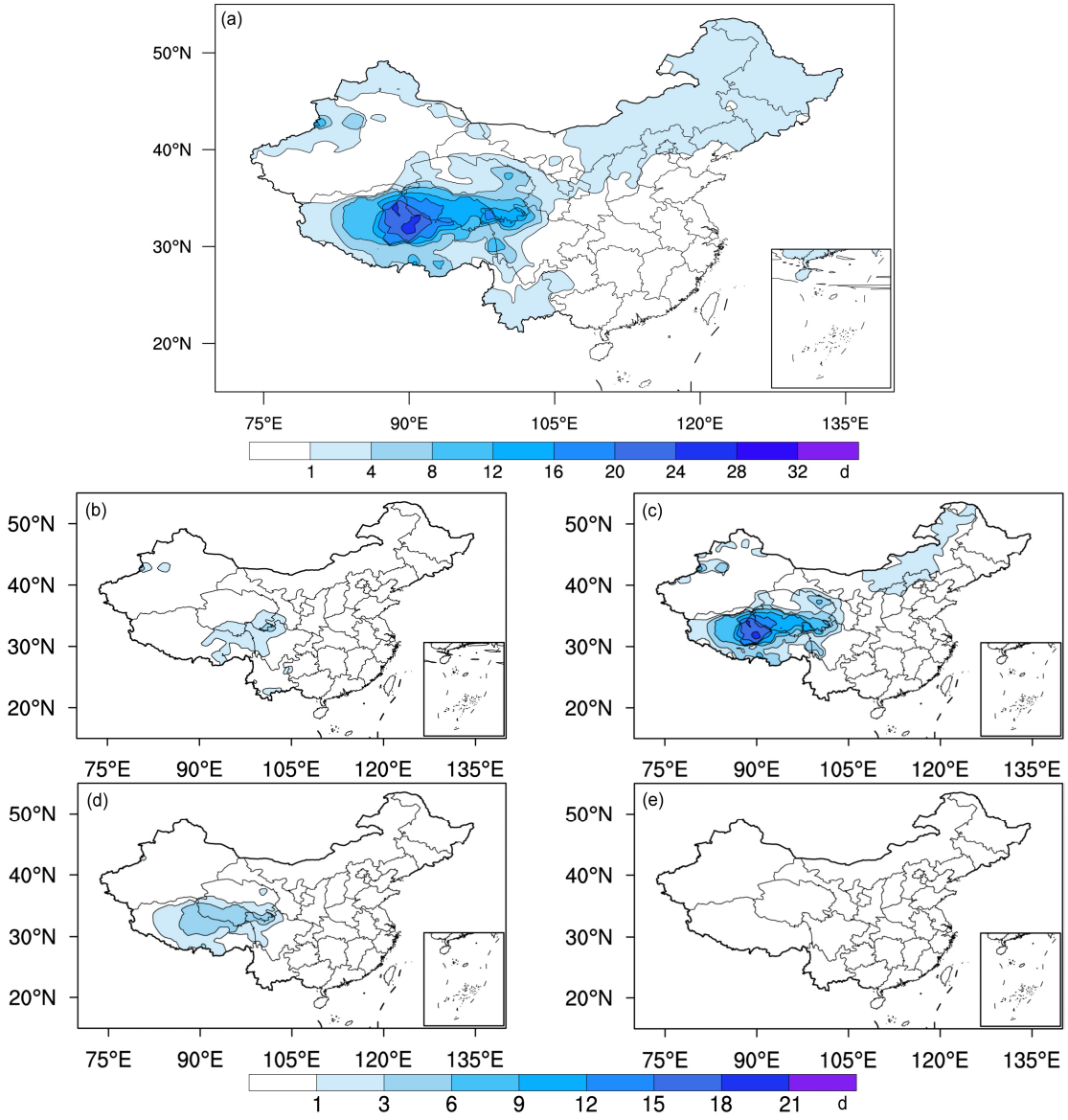

图 9 同图 3，但为冰雹日数，且研究时段为 1961～2015 年

Fig. 9 Same as Fig. 3, but for hail days and the period is from 1961 to 2015

条件影响，复杂的地形使得边界层内各物理量水平分布不均匀，容易触发易产生冰雹的不稳定条件。冰雹均值分布的大值区在年、春季、夏季和秋季均在青藏高原有个大值区，且春季大值区位置在高原东部，夏秋季节高值区域扩大并且高值中心变化到高原中部。

图 10 为冰雹日数各年代分布情况。年代之间差异显示各年代空间分布变化不大，大值区都在青藏高原地区，但是发生的范围越来越小，尤其是从 2000 年代以后，华北和东北基本没有冰雹发生了，青藏高原虽然仍有冰雹发生，但是日数明显减少。

因此，冰雹主要发生在每年 5～9 月，年和四季的冰雹日数有着不同的空间分布特征，但年、春季、夏季和秋季均在青藏高原表现出一个大值区，平均冰雹日数的年际变化和冰雹日数均值的年代际变化，都表现出了冰雹发生日数近 50 年在 2000 年代以前变化不大，但是 2000 年代以后明显减少。

4 讨论

对我国不同地区中小尺度强对流天气的气候学特征，已经开展了一些分析。徐桂玉和杨修群（2001）研究我国南方地区雷暴地理分布特征，发现雷暴频数是从南向北递减，高发区主要分布在东南和华南区域，其次是青藏高原地区，这与本文获得的雷暴频率空间分布特点基本相致。Zhang et al.（2017）、张芳华和高辉（2008）分析发现，全国冰雹主要发生在晚春到初秋，这与本文发现的冰雹发生在 2～11 月结果也基本相一致，但全国平均最高发生频率是在 6 月。本文分析发现青藏高原和华北北部是冰雹的高发区，

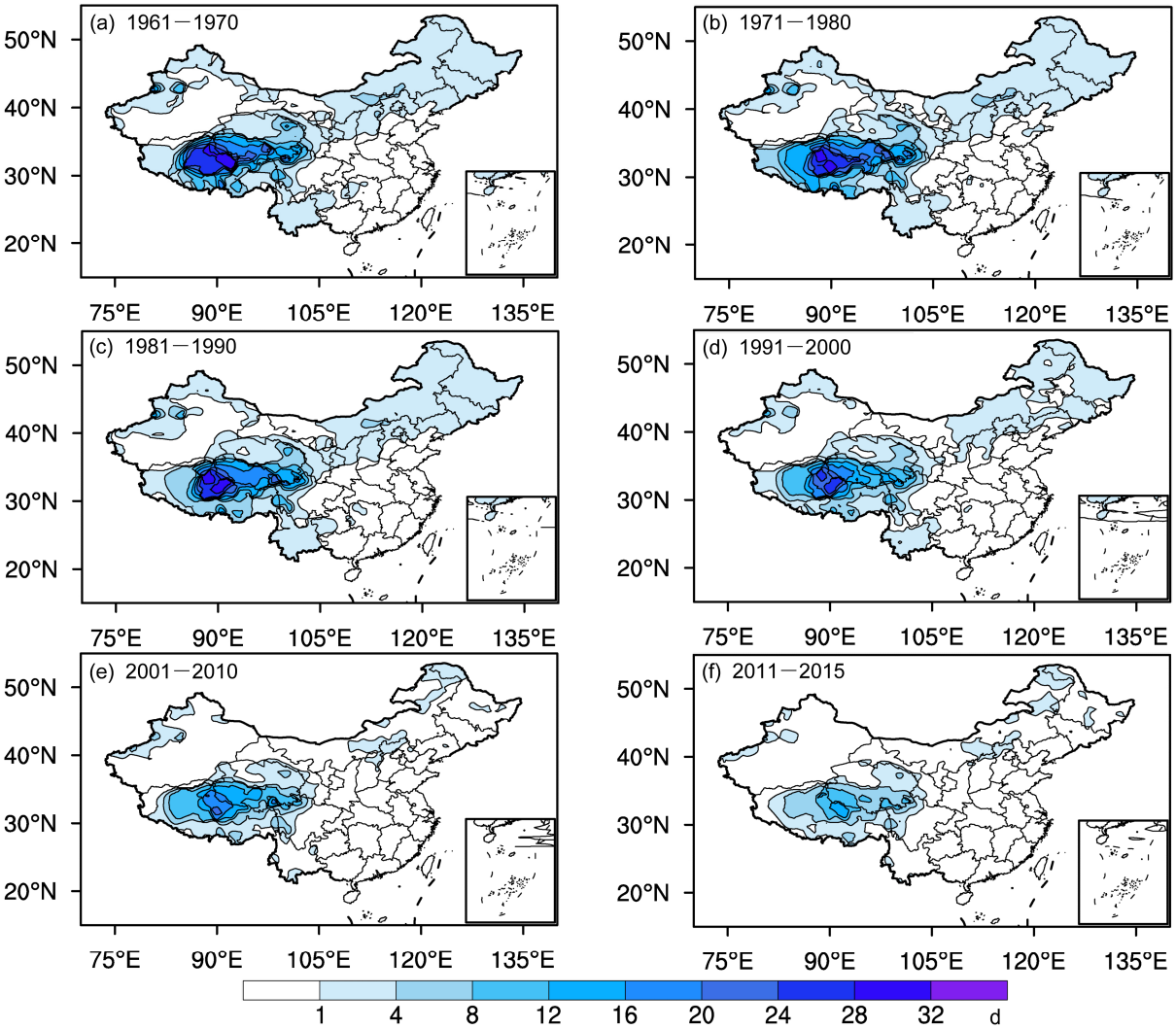

图 10 同图 4，但为冰雹日数，且研究时段为 1961～2015 年

Fig. 10 Same as Fig. 4, but for hail days and the period is from 1961 to 2015

这与先前研究指出的冰雹空间分布结论大体一致（张芳华和高辉，2008；Zhang et al.，2017），但不同于早期研究结论，本文还发现东北地区也是冰雹天气的另外一个主要发生区。

总体上看，先前针对部分地区和个别极端天气事件的分析结果，与本文利用更新资料对大尺度多种极端天气事件的分析结果，基本一致。在相同区域内，与前人研究相比出现的空间分布和季节性差异，可能主要和所用资料密度、质量和观测记录长度不同有关，区域平均方法不同也会造成分析结果的差异。本文采用所有国家级台站长序列观测资料，资料质量得到较严格的检验和控制，区域平均方法也得到改进，因此其结果具有更高的可信度。

对于 3 种中小尺度强对流天气现象形成原因，已有成熟的解释（俞小鼎等，2012；孙继松和陶祖钰，2012）。3 种强对流天气发生频率之间的联系，也是值得关注的一个问题。雷暴、闪电、冰雹都与强风暴系统有着密切的关系，尤其雷暴和闪电常常伴随性发生。图 11 给出全国 2332 个站点年平均雷暴和闪电发生次数的对应关系和拟合曲线，可以看出，雷暴和闪电有着很好的对应关系，闪电频数随雷暴频数的变化不是简单的线性关系，而是呈近似指数关系，雷暴发生次数越多的站点闪电发生次数越多，且随着雷暴频数增加，闪电频数上升更快，决定系数达到了 0.65。但是，雷暴和冰雹、闪电和冰雹发生频数之间并不存在明显的关系，相关性不好。这可能与冰雹的局地性，更依赖于海拔高度有关。

雷暴和冰雹都在青藏高原地区表现出一个大值区，但是闪电没有。为了探讨 3 种强对流天气和海拔高度的关系，选取了青藏高原及其周边地区（25°N～40°N，80°E～105°E），在此区域内包含 309 个观测站点，海拔高度最低为 292.8 m，最高为 4800 m。图 12 为青藏高原及其周边地区年平均雷暴、闪电、冰雹发生次数和海拔高度的关系，图 12a 显示雷暴随着海拔高度的增加总体呈现出在波动中增加的趋势，平均每上升 500 m 雷暴天数增加 2.87 d，1000～1500 m 年平均雷暴天数最少为 30.84 d，4500 m 以上年平均雷暴天数最多为 61.37 d。而图 12b 闪电随着海拔高度的增加总体在波动中呈现微弱的减少趋势，平均每上升 500 m 闪电天数减少 0.26 d，在 3000～3500 m 平均年闪电天数最少为 13.95 d，而在 500 m 以下、1500～2000 m、3500～4000 m 平均年闪电天数较多在 20 天以上。图 12c 显示冰雹随着海拔高度的变化表现出了极为明显的上升趋势，这表明冰雹和海拔高度有特别好的对应关系，平均每上升 500 m 冰雹天数增加 1.80 d，1500 m 以下平均年冰雹天数较少为 1 d 以下，逐渐增加到 4500 m 以上年平均为 19.67 d。同时在 3000 m 以下冰雹随海拔高度增加，但是增加不明显，而 3000 m 以上冰雹发生次数随着海拔高度增加强烈增加。

通过年代之间发生频率的比较，发现全国雷暴、闪电和冰雹均在 1960 年代至 1980 年代发生日

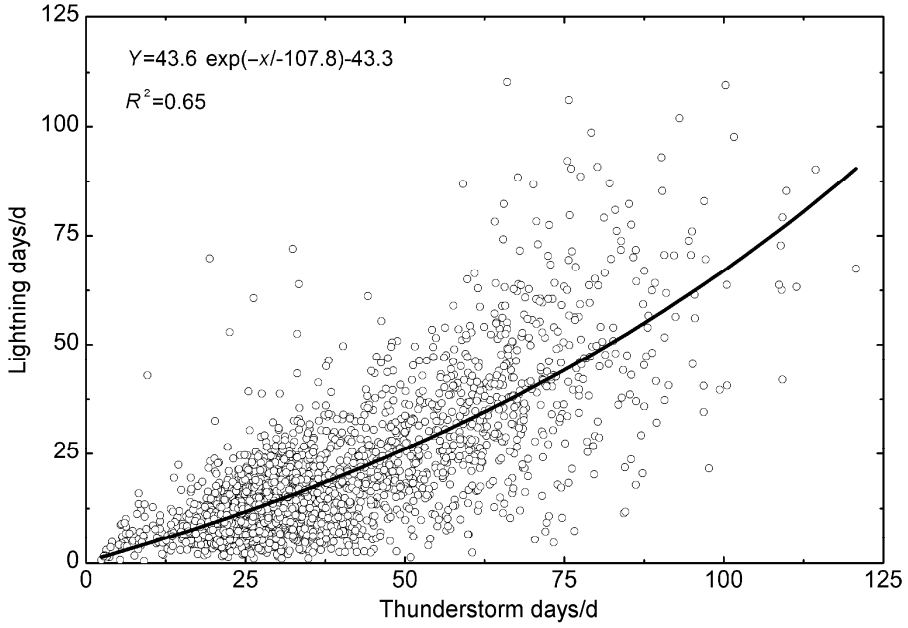

图 11　1961～2013 年我国台站年平均雷暴和闪电发生日数的对应关系（圆圈）和二者的拟合曲线（黑色曲线）

Fig. 11　The correlation between annual average days of thunderstorm and lightning (circles) and their fitting curve (black line)

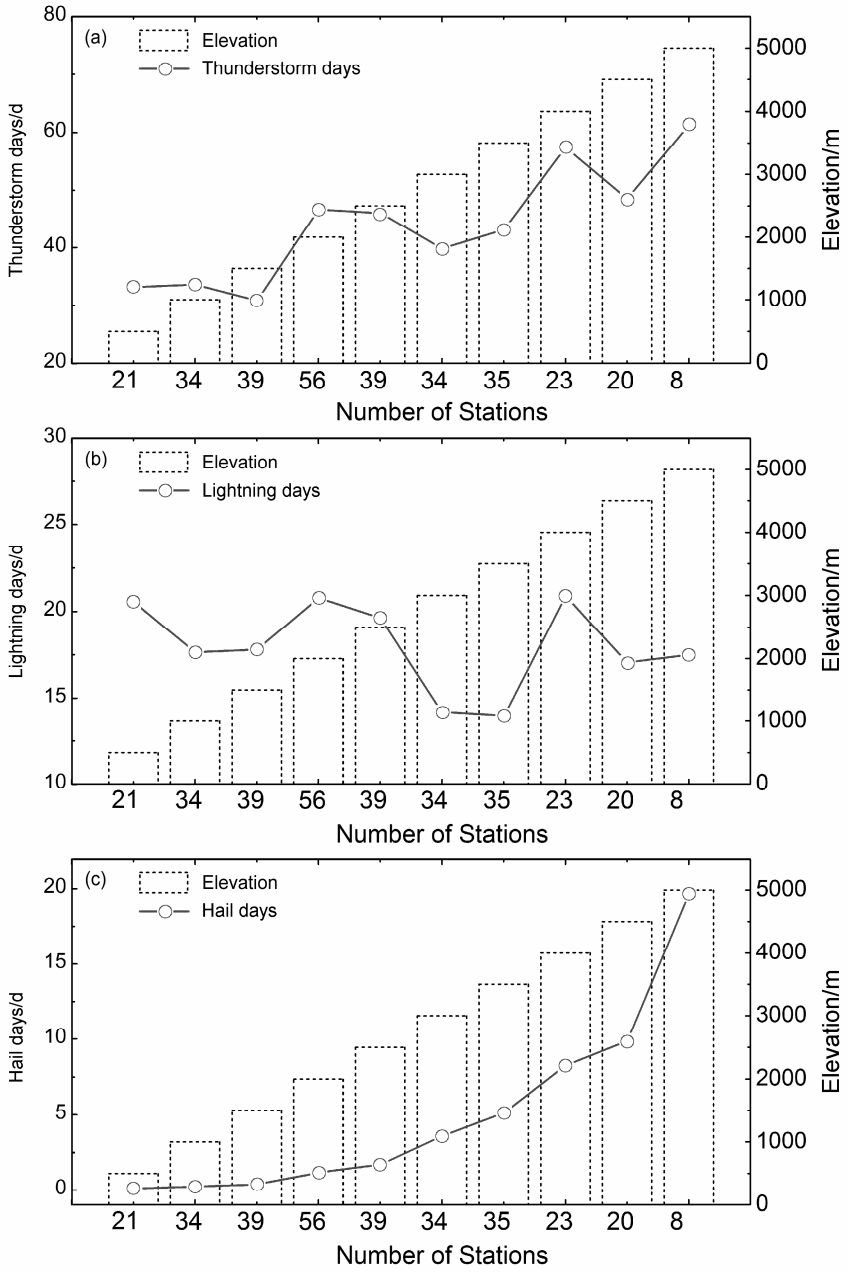

图 12 青藏高原及其周边地区（25°N～40°N，80°E～105°E）（a）雷暴、（b）闪电、（c）冰雹天数随海拔高度的变化

Fig. 12 Changes in the days of (a) thunderstorms, (b) lightning, and (c) hail with elevation in the Qinghai–Tibet Plateau and its surrounding areas (25°N–40°N, 80°E–105°E)

数偏多，而在 1990 年代之后明显减少。总体上，这些变化与早期针对部分地区和个别极端事件的研究结论也相一致（张敏锋和冯霞，1998；徐桂玉和杨修群，2001；张芳华和高辉，2008；余蓉等，2012；Zhang et al.，2017）。对于 3 种中小尺度强对流天气事件减少的原因，目前还没有很好的解释。观测研究表明，我国相对降水指标和极端强降水事件在近 60 年出现增加趋势（翟盘茂等，2007；任国玉等，2015，2016），但全国范围极端强降水事件频率和累计降水量增多，可能和多种区域性和局地性自然、人为因素有关，也可能和降水观测资料的系统偏差有一定联系（任国玉等，2016）。中小尺度强对流天气中雷暴、闪电和冰雹一般情况下伴随着极端强降水事件，但本文分析得到的 3 种极端天气现象普遍减少减弱的结论，和先前有关短历时极端强降水事件频率有所增加的结论并不一致。

本文研究初步显示，雷暴、闪电和冰雹在年代际变化上表现出减少和减弱趋势，特别是 1990 年代以后 3 种强对流天气事件频数的减少现象更加突出。这一现象在前人研究中已有总结（任国玉等，2010）。对于中小尺度强对流天气现象年代际减少的原因，前人也已有一些初步分析（张敏锋和冯霞，1998；陈思蓉等，2009；符琳等，2011；Zhang et al.，2017）。张敏锋和冯霞（1998）指出雷暴气候变化异常是个很复杂的非线性过程，只有在充分理解日地关系、雷暴气候和大气环流变化关系、雷暴起电及放电物理过程的基础上，才能对这种长期变化机制有更为客观的认识与理解，并指出温度变化与雷暴变化之间可能存在着某种联系。Zhang et al.（2017）认为，过去 50 年中小尺度强对流天气急剧减少，与全球气候快速变暖、社会经济快速发展、城市化以及人口增长有关，同时指出雷暴的减少、减弱可能和亚洲夏季风减弱有关，但是相关性并不意味着因果关系。此外，大气水汽输送和动力条件的减弱也被认为可能引起了雷暴、闪电和冰雹减少的原因（余蓉等，2012）。而大气动力条件变化可能和普遍增加的气溶胶含量有关（陈思宇等，2012）。陈思蓉等（2009）认为影响雷暴发生的因子十分复杂，应该对于空间进行分型，在不同环流情况、不同地形条件下考虑影响雷暴长期变化趋势的原因。符琳等（2011）认为 20 世纪 70 年代末局地垂直温度场结构的变化是我国北方冰雹减少的主要原因。总体来说，目前的研究还不能确定我国中小尺度强对流事件频数快速减少的确切物理机制。对于本文报告的全国范围雷暴、闪电和冰雹频数年代际明显减少的事实和原因，还有待未来开展进一步研究。

同先前的研究比较，本文应用了更新的观测记录和更密集的台站资料，结果应该具有更高的可信度。然而，本文分析仍旧存在两方面的不确定性。一是全国台站的空间分布仍然不均匀，目前台站主要分布在中国东部、西部青藏高原和新疆的台站相对稀疏，这种东西部台站分布的不均匀会给平均结果带来一定程度的不确定性；二是天气现象的观测方法具有主观性，目前使用的数据都是人为观测，以观测员听到雷声或看到闪电为准，看到或听到则记录为一个雷暴或闪电日数，这势必造成漏记等情况存在，这也会为最终的分析结果带来一定程度的不确定性。今后需要加强对上述不确定性的系统评估。

5 结论

通过分析近 50 年中国 2332 个台站中小尺度强对流天气的气候学特征，获得以下主要结论：

（1）我国雷暴在每年 2～11 月均有发生，但主要发生在夏季。全国年平均雷暴日数为 39.23 d，其中全国春季平均为 9.28 d，夏季为 24.49 d，秋季为 4.81 d，冬季只有 0.68 d。华南、西南和青藏高原是雷暴高频中心；甘肃北部、内蒙古西部以及新疆东部是雷暴低值区。年以及春季、夏季、秋季在青藏高原中东部和四川西部均有个大值区，冬季雷暴仅发生在华南和西南地区。

（2）闪电发生在每年 3～11 月，同样主要发生在夏季。全国年平均闪电日数为 20.56 d，其中全国春季平均 3.40 d，夏季 13.52 d，秋季 3.49 d，冬季 0.19 d。年平均闪电日数的空间分布和雷暴类似，主要区别在于闪电在青藏高原不存在大值区。春季、夏季、秋季闪电有类似于年的分布，冬季闪电主要发生在云南的南部。

（3）冰雹发生在每年 2～11 月，但主要发生在 5～9 月。全国年平均冰雹日数为 1.07 d，其中全国春季平均为 0.31 d，夏季为 0.53 d，秋季为 1.90 d，冬季仅有 0.04 d。我国冰雹集中发生在内陆山地和高原地区，东南部沿海地区发生较少，年、春季、夏季和秋季均在青藏高原有大值分布区。

（4）上述 3 种中小尺度强对流天气事件，其年际变化和年代际变化均表现出减少和减弱趋势，1990 年代以后，这 3 种强对流天气事件的减少现象更加突出。

（5）雷暴和冰雹随着海拔高度的增加而明显增加，雷暴增加趋势可达 2.87 d/500 m，闪电则随着海拔高度的变化有微弱的减少趋势（−0.26 d/500 m），冰雹对海拔高度具有更高的敏感性，并且具有很好的对应关系，增加趋势为 1.80 d/500 m。

参考文献（References）

Brooks H E, Lee J W, Craven J P. 2003. The spatial distribution of severe thunderstorm and tornado environments from global reanalysis data [J]. Atmospheric Research, 67–68: 73–94, doi:10.1016/S0169-8095(03)00045-0.

陈思蓉, 朱伟军, 周兵. 2009. 中国雷暴气候分布特征及变化趋势 [J]. 大气科学学报, 32 (5): 703–710. Chen Sirong, Zhu Weijun, Zhou Bing. 2009. Climate characteristic and variation tendency of thunderstorm in China [J]. Transactions of Atmospheric Sciences (in Chinese), 32 (5): 703–710.

陈思宇, 黄建平, 付强, 等. 2012. 气溶胶对我国中东部地区秋季降水的影响 [J]. 热带气象学报, 28 (3): 339–347. Chen Siyu, Huang Jianping,

Fu Qiang, et al. 2012. Effects of aerosols on autumn precipitation over mid-eastern China[J]. Journal of Tropical Meteorology (in Chinese), 28 (3): 339–347, doi:10.3969/j.issn.1004-4965.2012.03.006.

Christian H J, Blakeslee R J, Boccippio D J, et al. 2003. Global frequency and distribution of lightning as observed from space by the optical transient detector [J]. J. Geophys. Res., 108 (D1): 4005, doi:10.1029/2002JD002347.

Dai A G. 2001. Global precipitation and thunderstorm frequencies. Part II: Diurnal variations [J]. J. Climate, 14 (6): 1112–1128, doi:10.1175/1520-0442(2001)014<1112:GPATFP>2.0.CO;2.

符琳, 李维京, 张培群, 等. 2011. 近 50 年我国冰雹年代际变化及北方冰雹趋势的成因分析 [J]. 气象, 37 (6): 669–676. Fu Lin, Li Weijing, Zhang Peiqun, et al. 2011. Inter-decadal change of hail events over China and causation analysis in northern China in recent 50 years [J]. Meteorological Monthly (in Chinese), 37 (6): 669–676, doi:10.7519/j.issn.1000-0526.2011.6.003.

黄武斌, 王研峰, 黄玉霞, 等. 2016. 1974～2013 年甘肃省冰雹气候时空变化特征 [J]. 气象与环境学报, 32 (1): 103–107. Huang Wubin, Wang Yanfeng, Huang Yuxia, et al. 2016. Spatial and temporal climatic characteristics of hail from 1974 to 2013 in Gansu Province [J]. Journal of Meteorology and Environment (in Chinese), 32 (1): 103–107, doi:10.11927/j.issn.1673-503X.2016.01.015.

李韬光, 张红雨, 柳琼, 等. 2015. 1981～2013 年山西地区冰雹气候特征分析 [J]. 气象与环境学报, 31 (5): 165–170. Li Taoguang, Zhang Hongyu, Liu Qiong, et al. 2015. Climate characteristics of hail in Shanxi Province from 1981 to 2013 [J]. Journal of Meteorology and Environment (in Chinese), 31 (5): 165–170.

李照荣, 康凤琴, 马胜萍. 2005. 西北地区雷暴气候特征分析 [J]. 灾害学, 20 (2): 83–88. Li Zhaorong, Kang Fengqin, Ma Shengping. 2005. Analysis on climatic characteristics of thunderstorm in Northwest China [J]. Journal of Catastrophology (in Chinese), 20 (2): 83–88, doi:10.3969/j.issn.1000-811X.2005.02.018.

郄秀书, 刘冬霞, 孙竹玲. 2014. 闪电气象学研究进展 [J]. 气象学报, 72 (5): 1054–1068. Qie Xiushu, Liu Dongxia, Sun Zhuling. 2014. Recent advances in research of lightning meteorology [J]. Acta Meteorologica Sinica (in Chinese), 72 (5): 1054–1068, doi:10.11676/qxxb2014.048.

秦丽, 李耀东, 高守亭. 2006. 北京地区雷暴大风的天气—气候学特征研究 [J]. 气候与环境研究, 11 (6): 754–762. Qin Li, Li Yaodong, Gao Shouting. 2006. The synoptic and climatic characteristic studies of thunderstorm winds in Beijing [J]. Climatic and Environmental Research (in Chinese), 11 (6): 754–762, doi:10.3878/j.issn.1006-9585.2006.06.10.

任国玉, 封国林, 严中伟. 2010. 中国极端气候变化观测研究回顾与展望 [J]. 气候与环境研究, 15 (4): 337–353. Ren Guoyu, Feng Guolin, Yan Zhongwei. 2010. Progresses in observation studies of climate extremes and changes in mainland China [J]. Climatic and Environmental Research (in Chinese), 15 (4): 337–353, doi:10.3878/j.issn.1006-9585.2010.04.01.

任国玉, 任玉玉, 战云健, 等. 2015. 中国大陆降水时空变异规律——Ⅱ. 现代变化趋势 [J]. 水科学进展, 26 (4): 451–465. Ren Guoyu, Ren Yuyu, Zhan Yunjian, et al. 2015. Spatial and temporal patterns of precipitation variability over mainland China: II: Recent trends [J]. Advances in Water Science (in Chinese), 26 (4): 451–465, doi:10.14042/j.cnki.32.1309.2015.04.001.

任国玉, 柳艳菊, 孙秀宝, 等. 2016. 中国大陆降水时空变异规律——Ⅲ. 趋势变化原因 [J]. 水科学进展, 27 (3): 327–348. Ren Guoyu, Liu Yanju, Sun Xiubao, et al. 2016. Spatial and temporal patterns of precipitation variability over mainland China: Ⅲ: Causes for recent trends [J]. Advances in Water Science (in Chinese), 27 (3): 327–348, doi:10.14042/j.cnki.32.1309.2016.03.001.

Sioutas M, Meaden T, Webb J D C. 2009. Hail frequency, distribution and intensity in northern Greece [J]. Atmospheric Research, 93 (1–3): 526–533, doi:10.1016/j.atmosres.2008.09.023.

孙继松, 陶祖钰. 2012. 强对流天气分析与预报中的若干基本问题 [J]. 气象, 38 (2): 164–173. Sun Jisong, Tao Zuyu. 2012. Some essential issues connected with severe convective weather analysis and forecast [J]. Meteorological Monthly (in Chinese), 38 (2): 164–173, doi:10.7519/j.issn.1000-0526.2012.2.004.

徐桂玉, 杨修群. 2001. 我国南方雷暴的气候特征研究 [J]. 气象科学, 21 (3): 299–307. Xu Guiyu, Yang Xiuqun. 2001. Climatic features of thunderstorms in the South China[J]. Scientia Meteorologica Sinica (in Chinese), 21 (3): 299–307, doi:10.3969/j.issn.1009-0827.2001.03.006.

余蓉, 张小玲, 李国平, 等. 2012. 1971～2000 年我国东部地区雷暴、冰雹、雷暴大风发生频率的变化 [J]. 气象, 38 (10): 1207–1216. Yu Rong, Zhang Xiaoling, Li Guoping, et al. 2012. Analysis of frequency variation of thunderstorm, hail, and gale wind in eastern China from 1971 to 2000 [J]. Meteorological Monthly (in Chinese), 38 (10): 1207–1216, doi:10.7519/j.issn.1000-0526.2012.10.006.

俞小鼎, 周小刚, 王秀明. 2012. 雷暴与强对流临近天气预报技术进展 [J]. 气象学报, 70 (3): 311–337. Yu Xiaoding, Zhou Xiaogang, Wang Xiuming. 2012. The advances in the nowcasting techniques on thunderstorms and severe convection [J]. Acta Meteorologica Sinica (in Chinese), 70 (3): 311–337, doi:10.11676/qxxb2012.030.

翟盘茂, 王萃萃, 李威. 2007. 极端降水事件变化的观测研究[J]. 气候变化研究进展, 3(3): 144–148. Zhai Panmao, Wang Cuicui, Li Wei. 2007. A review on study of change in precipitation extremes [J]. Advances in Climate Change Research (in Chinese), 3 (3): 144–148, doi:10.3969/j.issn.1673-1719.2007.03.004.

张芳华, 高辉. 2008. 中国冰雹日数的时空分布特征 [J]. 南京气象学院学报, 31 (5): 687–693. Zhang Fanghua, Gao Hui. 2008. Temproal and spatial features of hail days in China [J]. Journal of Nanjing Institute of Meteorology (in Chinese), 31 (5): 687–693, doi:10.3969/j.issn.1674-7097.2008.05.011.

张敏锋, 冯霞. 1998. 我国雷暴天气的气候特征 [J]. 热带气象学报, 14 (2): 156–162. Zhang Minfeng, Feng Xia. 1998. A study on climatic features and anomalies of the thunderstorm in China [J]. Journal of Tropical Meteorology (in Chinese), 14 (2): 156–162.

Zhang Q H, Ni X, Zhang F Q. 2017. Decreasing trend in severe weather occurrence over China during the past 50 years [J]. Scientific Reports, 7: 42310, doi:10.1038/srep42310.

赵煜飞, 余予. 2015. 中国地面强对流天气数据集 [DB]. 国家气象信息中心, http://10.1.64.154/mdms/jsp_index.index?d=http://10.1.64.154/mdms/jsp_metadata.index?id=194 [2016-11-02]. Zhao Yufei, Yu Yu. 2015. Chinese Strong Convective Weather Data Set (in Chinese) [DB]. National Meteorological Information Center, http://10.1.64.154/mdms/jsp_index.index?d=http://10.1.64.154/mdms/jsp_metadata.index?id=194 [2016-11-02].

View publication stats

Urban Climate 28 (2019) 100463

Contents lists available at ScienceDirect

Urban Climate

journal homepage: www.elsevier.com/locate/uclim

Impact of daytime precipitation duration on urban heat island intensity over Beijing city

Ping Yang[a,b,c], Guoyu Ren[d,*], Wei Hou[e]

[a] China Metrological Administration (CMA) Training Center, Beijing, China
[b] Department of Atmospheric Science, School of Environmental Studies, China University of Geosciences, Wuhan, China
[c] Institute of Urban Meteorology CMA, Beijing, China
[d] Laboratory for Climate Studies, National Climate Center, CMA, Beijing, China
[e] National Climate Center, CMA, Beijing, China

ARTICLE INFO

Keywords:
Daytime
Precipitation
Duration
UHI
Diurnal variation
Beijing city

ABSTRACT

This study used the daytime hourly precipitation records and divided them into four types of duration to examine the impact of different daytime precipitation conditions on Urban Heat Island Intensity (UHII) over Beijing city. Results show that the magnitude differences of UHII are in close relation with the length of Continuous Precipitation Hours of Daytime (CPHD). The longer the CPHD, the less obvious the average UHI. When continuous precipitation events dominate the daytime, the diurnal variation pattern of UHII will be changed greatly. There are generally two (strong and weak) stable stages of UHII in no-rainy condition, while it disappears completely in the longest continuous daytime precipitation conditions. However, the diurnal cycles of UHII differences between each of the rainy daytimes and no-rain daytimes appear similar, with all of the dual peaks of the UHII differences occurring around sunrise (0600-0700 LST) and sunset (2000 LST), and the minimum of the UHII differences appearing stably from 1100 to 1500 LST.

1. Introduction

The previous studies have confirmed that urbanization has significant impacts on local to regional climate through land use and land cover transformations at the surface (Landsberg, 1981; Oke, 1988). Radical change in land use and land cover modifies the energy balance and boundary layer properties significantly, and is capable of inducing some unique climatic phenomena in cities, such as urban heat island (UHI) (Arnfield, 2003), urban rain island (Yang et al., 2017a) and urban dryness island (Yang et al., 2017b).Besides the influence of urbanization, the local climate phenomena surely depends on the geography and background atmospheric circulation. For example, land cover and availability of soil moisture make a significant contribution to the eventual positive or negative sign of the UHI (Georgescu et al., 2011). Recent work has specified the footprint effect of the built environment for surface temperature UHI of 32 cities across China based on MODIS land surface temperature data (Zhou et al., 2015).

As an important factor, weather condition is also strongly related to UHI effect. High pressure system in summer can restrain the development of a boundary layer, being conducive to UHI (Craig and Bornstein, 2002; Stewart and Oke, 2012). The steady weather system such as bright, calm, unclouded condition can help in developing strong UHI effect, while unstable weather will reduce the UHI effect (Landsberg, 1981; Oke, 1988). A number of studies have revealed significant correlation between UHII and cloudiness or

* Corresponding author.
E-mail address: guoyoo@cma.gov.cn (G. Ren).

https://doi.org/10.1016/j.uclim.2019.100463
Received 13 August 2017; Received in revised form 31 December 2018; Accepted 5 April 2019
2212-0955/ © 2019 Elsevier B.V. All rights reserved.

solar radiation (Kim and Baik, 2002; Petralli et al., 2009; Arnds et al., 2017). It has also been demonstrated that UHII tends to be stronger at night, while becomes negative under moist conditions and larger thermal admittances by rural areas (Tereshchenko and Filonov, 2001; Yang et al., 2013c). Aerosols are another impact factor for UHII, because the presence of aerosols in urban environment could acts as clouds in the thermal equilibrium of urban boundary, and also affect the development of clouds and precipitation (Diem and Brown, 2004; Shimadera et al., 2015).

Precipitation is closely related to many other weather conditions including air temperature and atmospheric humidity. Continuous attentions have been paid to the possible linkage between UHI and precipitation over the last decades.

Previous studies have demonstrated that UHI effect has a significant impact on mesoscale circulation, resulting in abnormal convection and precipitation over urban areas (Changnon, 1979; Huff, 1986; Han et al., 2014; Zhong et al., 2015). Researches indicated that larger roughness in urban areas can enhance convection and precipitation (e.g. Thielen et al., 2000), while other researchers reported that the larger roughness could increase the convergence on the windward side of city (e.g. Rozoff et al., 2003). Recent simulation results appear to explain the physical mechanism behind observed increases of precipitation within the highly populated metropolitan area (Magaña et al., 2003; Benson-Lira et al., 2016).

However, most of previous studies on relationship between UHI and precipitation were focused on the UHI impact on precipitation event (e.g. Changnon et al., 1991; Aws et al., 2017; Yang et al., 2017a; Wang et al., 2019), and fewer works were made to examine the impact of precipitation on UHII. Some analyses have concluded that the UHII reduced with an increase in precipitation amount (Guo et al., 2009; Wang et al., 2009; Liu, 2014), but another analysis shows that the UHII will be reinforced in the region with higher annual precipitation (Zhao et al., 2014). In spite of the previous works, the roles of precipitation in modifying detailed pattern of UHII over urban areas still need further investigation.

Beijing is a mega city of mainland China, with > 15 million populations settling in the built-up areas. Due to the large and rapid change of urban environment, more intense UHI and precipitation in urban areas over Beijing have been observed in previous observational researches (Li et al., 2008; Miao et al., 2010; Song et al., 2014; Yang et al., 2017c). The strongest UHII generally appeared within or around the 4th Ring Road in Beijing City, in accordance to Beijing's major transportation system with a multi Ring-Road network (Yang et al., 2013c), and short-duration intense precipitation events dominate summer precipitation in urban regions of Beijing (Yang et al., 2013b, 2017c). The previous works on UHII and urban precipitation are independently conducted, and the association between them, in particular, the possible influence of daytime precipitation on UHII pattern, has not yet exclusively examined. The reason for the lack of thus studies may be because of the lack of denser and high-quality observational data in urban areas, which is a necessity for investigating the relations between UHI and precipitation events in a finer spatial and temporal scale.

The purpose of this paper is to examine how the UHII changes under different daytime precipitation conditions in Beijing urban areas. The UHII contrast between the no-rainy case and each of the rainy cases are analyzed by using hourly observational data of Automatic Weather Stations (AWS). It is well known that daytime solar radiation is one of the most important elements which could change the energy and water balances in urban surface, affecting the potency of diurnal UHII critically. Thus, the main emphasis of our research in this paper is to examine the possible impact of varied duration daytime precipitation (from 0400 LST to 2000 LST) on UHII. The analysis results would be helpful to further separate the driving force on UHI and to understand the formation mechanism of UHI.

2. Study area, data and methods

2.1. Study area

Beijing, a high-density mega city covering about 1.6 million square kilometers, is at the northern end of the North China Plain and in the south to the Yanshan Mountains. The flat southeast area occupies about 38% of Beijing, the elevations of which are roughly ranging from 20 m ASL (above sea level) to 80 m ASL. The northwest is mainly mountainous areas. Climatologically, Beijing has a typical monsoon-driven semi-humid to humid continental climate , which is hot and humid in summer and cold and dry in winter. The rainy days and precipitation amount in Beijing are mainly concentrated in summer (Jun-Jul-Aug), contributing to about two thirds of its annual total precipitation (Yang et al., 2017c).

With accelerating urban expansion, population in Beijing City undergoes a rapid growth and over half of the population settled in the urban areas. A multi Ring-Road (RR) system of transportation (including 4th, 5th and 6th RRs, Fig. 1) has been built in the urban regions so far (Yang et al., 2013c). The zones inside different RRs could represent different levels of urbanization with varied densities of city population and buildings as well. In this paper, stations located inside the 6th RR in Beijing are considered as the urban sites (Fig. 1).

2.2. Observational data

In this study, the observed hourly surface air temperature (1.5 m) and precipitation amount data from 65 stations in urban area of Beijing for time period 2007–2015 are obtained from the Meteorological Information Center, Beijing Meteorological Bureau (MIC/BMB). The data have been preliminarily quality-controlled by the MIC, and the possibly wrong records have been taken out by applying a regionally climatological extreme value method.

In order to increase the reliability of the analysis, the data are checked and quality-controlled once again using the methods by Yang et al. (2011) and Yang and Liu (2013). The incredible stations with unrepresentative observational environment have been taken out of the dataset, and the methods of threshold values and manual identification are applied in checking. Based on the

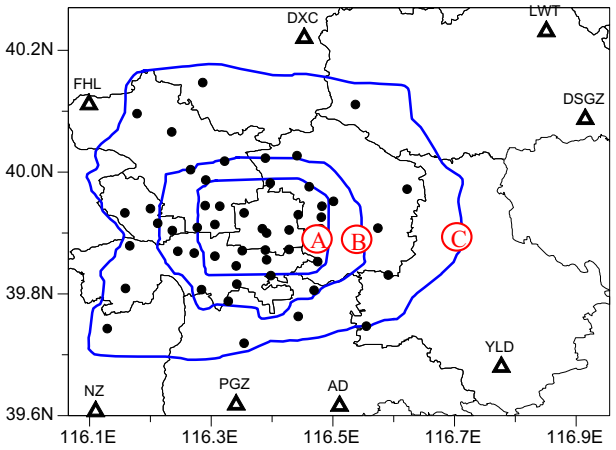

Fig. 1. Stations used in the Beijing urban region as outlined by the 6th Ring Road (blue solid circles, line A-C respectively represents 4th RR, 5th RR and 6th RR) and the 8 rural stations outside of the 6th Ring Road (Abbreviations of the station names are FHL for Feng Huang Ling, YLD for Yong Le Dian, PGZ for Pang Ge Zhuang, AD for An Ding, NZ for Nan Zhao, DSGZ for Da Sun Ge Zhuang, and LWT for Long Wan Tun , DXC for Dong Xin Cheng). (For interpretation of the references to colour in this figure legend, the reader is referred to the web version of this article.)

observational records and the climatological features in Beijing, different seasons have been given different threshold values for quality control both for temperature and precipitation data. If the hourly records exceed 100 mm (summer), 65 mm (spring and autumn), 30 mm (winter) respectively, for example, they were considered as suspicious, and they will be removed if proved wrong further by comparing the records of the adjacent stations. The method of temperature thresholds is more complex relatively. They are based on the temperature information of 20 national stations of Beijing for the past 30 years. The extreme temperature value of each month have been calculated and floating thresholds also be considered (Yang et al., 2011). For minimizing the influence of missing records on the analysis, only those sites with missing values < 3% of the total records for the 9 years are chosen for use. Additional detailed description of the methodology and quality control techniques used are accounted in details by Yang et al. (2011) and Yang and Liu (2013).

After the quality control of the data, 51 observational stations inside 6th RR are selected for use (Fig. 1) eventually, which are considered as urban observational sites. Eight reference stations surrounding the urban areas are also used in order to calculate the UHII of those urban stations. The heights of the reference stations are almost the same as those in urban areas (Table 1). Due to the importance of the selection of the reference stations, the 8 reference stations are selected by referring to a remote-sensing method as detailed in Ren and Ren (2011) and Yang et al. (2013c), which is according to a strictly defined standard, and has been confirmed objective and valid in representing rural areas in previous works (Ren and Ren, 2011; Yang et al., 2013c, 2017a).

2.3. Analysis methods

In the paper, UHII is estimated by calculating the temperature difference between urban and rural sites at varied time scales of hour, month, season and year. The rural temperature (T_r) is the mean temperature values of the 8 reference stations, while the urban temperature (T_u) is the temperature of anyone of 51 urban stations inside 6th Ring Road, or the mean values of all urban stations inside any specific urban areas. So, UHII ($\Delta T_{u\text{-}r}$) can be calculated using Eq. (1)

$$\text{UHII} = \Delta T_{u-r} = T_u - T_r \quad (1)$$

Term Continuous Precipitation Hours of Daytime (CPHD) is applied in this study, and it is defined as the number of hours from the beginning to end of any continuous precipitation event within the periods between 0400LST and 2000 LST separately for each station

Table 1
Basic information of eight reference stations.

Abbrev. (name)	Lon. (E)/Lat. (N)	Elevation (m)	Elevation difference from urban areas (m)
FHL (Fenghuangling)	116.10°/40.11°	73.0	24.6
YLD (YongleDian)	116.78°/39.68°	17.0	−31.4
PGZ (Panggezhuang)	116.34°/39.62°	34.0	−14.4
AD (Anding)	116.51°/39.62°	24.0	−24.4
NZ (Nanzhao)	116.11°/39.61°	34.0	−14.4
DXC (Dongxincheng)	116.45°/40.22°	49.0	−0.6
DSGZ (Dasungezhuang)	116.92°/40.09°	35.0	−13.4
LWT (Longwantun)	116.85°/40.23°	52.0	3.6
Average	116.51°/39.90°	31.8	−8.8

of the 51 observational sites. The hourly precipitation here is defined as rain record with > 0.1 mm precipitation amount accumulated during an hour. It is further assumed that the continuous precipitation of daytime is the precipitation event that has continuous durations without any intermittence within a given period from 0400 to 2000 LST. The reason why the period of daytime precipitation is applied as an indicator is that the sunshine during daytime is one of the key factors for forming UHI phenomenon, and the sunlight-related force might be separated from those related to urban canopy geometry and anthropogenic heat release in the formation of UHII pattern, if more cases of influence of daytime precipitation on UHII could be investigated. Time period 0400LST to 2000 LST is used because the sunrise is usually around 04:30 LST and sunset around 19:30 LST in Beijing during Summer Solstice, and it thus contains the complete daytime in any months.

In order to examine the impact of varied precipitation event duration in daytime on UHII over Beijing, CPHD is further divided into four different categories, which are respectively 0 h, 0–3 h, 3–6 h and > 6 h. In order to compare the differences between no-rainy case and each of the rainy cases, we also calculate UHII differences between them as following on basis of stations and regional average:

$$\Delta UHII = |UHII_{each\ rainy\ case} - UHII_{no-rainy\ case}| \quad (2)$$

There may be more than one CPHD processes in a day, especially during summertime (June to August) when > 70% of annual total precipitation will occur in Beijing region. In this case, in order to make the analysis of UHI under different precipitation duration ranges more significant, only the event with the longest duration in a day was considered in the following calculation.

3. Results

3.1. Characteristics of UHII and precipitation

The spatial distribution of annual mean values of UHII in the urban regions (inside the 6th RR) is shown in Fig. 2. It is obvious that the UHII spatial distribution is consistent of the divergent expansion of built-up areas and transportation system, conforming to the dense distribution of urban populations. The maximum UHII value (2.07 °C) appears at Si Hui Qiao (SHQ, 39.91°N, 116.48°E), northeastern part inside the 4th RR. The only station with negative UHII (−0.25 °C) is Dao Xiang Hu (DXH, 40.10°N, 116.18°E) in the northwest of the built-up areas. Previous researches have indicated that, DXH station, though inside the 6th RR, is surrounded by less buildings and a small lake nearby, which may be the reason that a negative UHII was observed (Yang et al., 2013c).

Fig. 3 shows the annual (Fig. 3a) and seasonal (Fig. 3b) mean diurnal UHII variations in urban areas over Beijing. The annual mean diurnal UHII curve contains two relatively stable stages separated by two swiftly changing stages. One stable stage is characterized by the strong UHII lasting from late evening (2100 LST) to early morning (0600 LST), and another by the weak UHII lasting from 1100 LST to 1600 LST. The rest two stages change swiftly by a drop-off (0600–1100 LST) and a surge-up (1600–2100 LST) respectively. In other inland cities, similarly stable high nocturnal UHII and weak midday UHII have also been reported (e.g. Memon et al., 2011).

Among different seasons, a common diurnal variation pattern can be found. Moreover, the length of strong stable stage in autumn (2000–0700 LST) and winter (2000–0800 LST) is a little longer than that in spring (0900–0600 LST) and summer (0900–0500 LST). Besides, for the strong stable stage, the UHII in autumn and winter are also larger than that in spring and summer. However, the stable weak stages of four seasons have relatively apparent differences. The stable weak stage in summer keeps the longest (0900–1800 LST), with the mean UHII (0.50 °C) of which is higher than that of other seasons. In spring, the length of stable weak stage (1000–1700 LST) is a little shorter than that in summer, and the mean UHII is weaker (0.36 °C) apparently. The stable weak stages in autumn and winter are similar in lengths (1200–1600 LST) and mean values of UHII (0.25 °C in autumn and 0.34 °C in winter). It is interesting to note that though the UHII at nighttime in summer is weaker than that in other seasons, the UHII during the

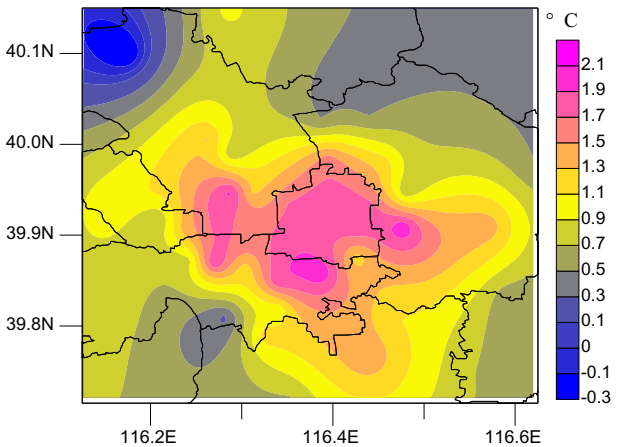

Fig. 2. Spatial distributions of annual mean values of UHII in Beijing urban area during 2007–2015.

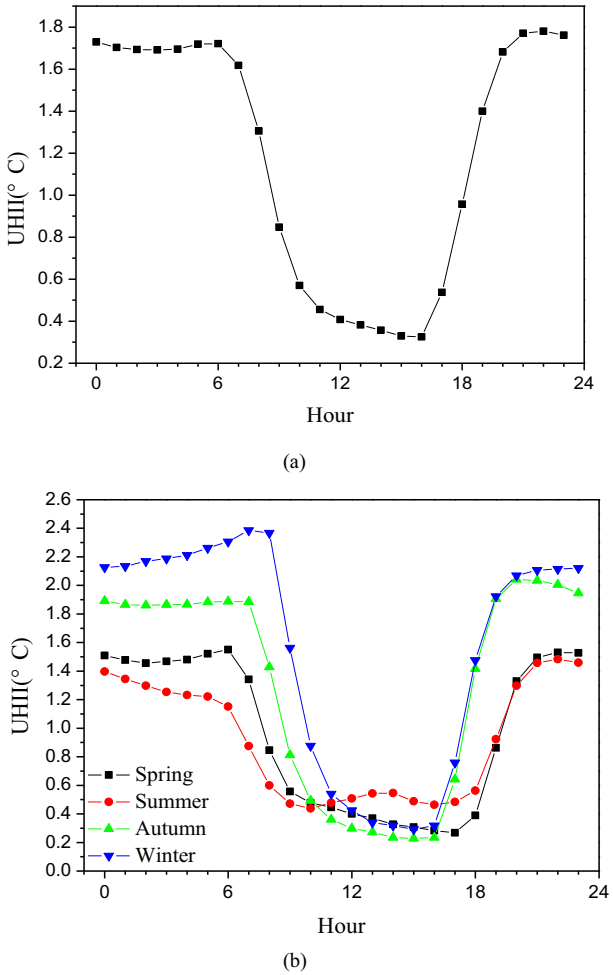

Fig. 3. Spatial distributions of UHII in (a) spring (b) summer (c) autumn (d) winter in Beijing urban area during 2007–2015.

daytime in summer is the strongest among the seasons. Similar conclusions also have been reported by Lee and Baik (2010) and Yang et al. (2013b). Roth (2007) has stated that, when rural surface is wet or saturated, thermal admittance will be increased. Thus, the daily surface temperature range will become relatively small and rural cooling during summer daytime will increase the corresponding UHII. It is also possible that the more extensive application of air conditioning in the urban areas in recent years has exaggerated the UHI effect of daytime during summer (Ren and Zhou, 2014).

The spatial distribution of annual mean occurrence times of different CPHD events during 2007–2015 is shown in Fig. 4. It is evident that the distributions of different daytime precipitation processes are rather different from each other. For no-rainy case, the lowest frequencies mainly prevail in urban center, while sites with the highest frequencies are located in the southwest to the central area. The precipitation events with 0 h $<$ CPHD $\leq$ 3 h mostly occur in the urban center, and they occur less frequently in the western and southern parts to the urban center. For the case of 3 h $<$ CPHD $\leq$ 6 h, the northern sites captures the highest frequencies of the precipitation events, while the fewest times come from the southeastern part of the urban areas. Meanwhile, the urban center is not characterized by the high and low centers. A more concentrated distribution in the urban center is seen for the precipitation events with CPHD $>$ 6 h. It is therefore clear that the short duration of precipitation events (0 h $<$ CPHD $\leq$ 3 h) and the long duration of precipitation events (CPHD $>$ 6 h) are the most basic precipitation mode over the urban center in Beijing, which is approximately in consistence to the previous study (Yang et al., 2013a).

Table 2 illustrates the significant differences among four seasons. For no-rainy days, the largest annual mean times is 85.29 in urban areas in winter, followed by 79.20 in spring, 74.86 in autumn, and 62.32 in summer. For the events of 0 h $<$ CPHD $\leq$ 3 h and 3 h $<$ CPHD $\leq$ 6 h, the annual mean frequencies of CPHD in whole urban areas achieve the largest values in summer. All of the times of precipitation events with CPHD $>$ 6 h are low, being $<$ 5 times. In comparison, the frequencies of CPHD $>$ 6 h precipitation events are the most in autumn.

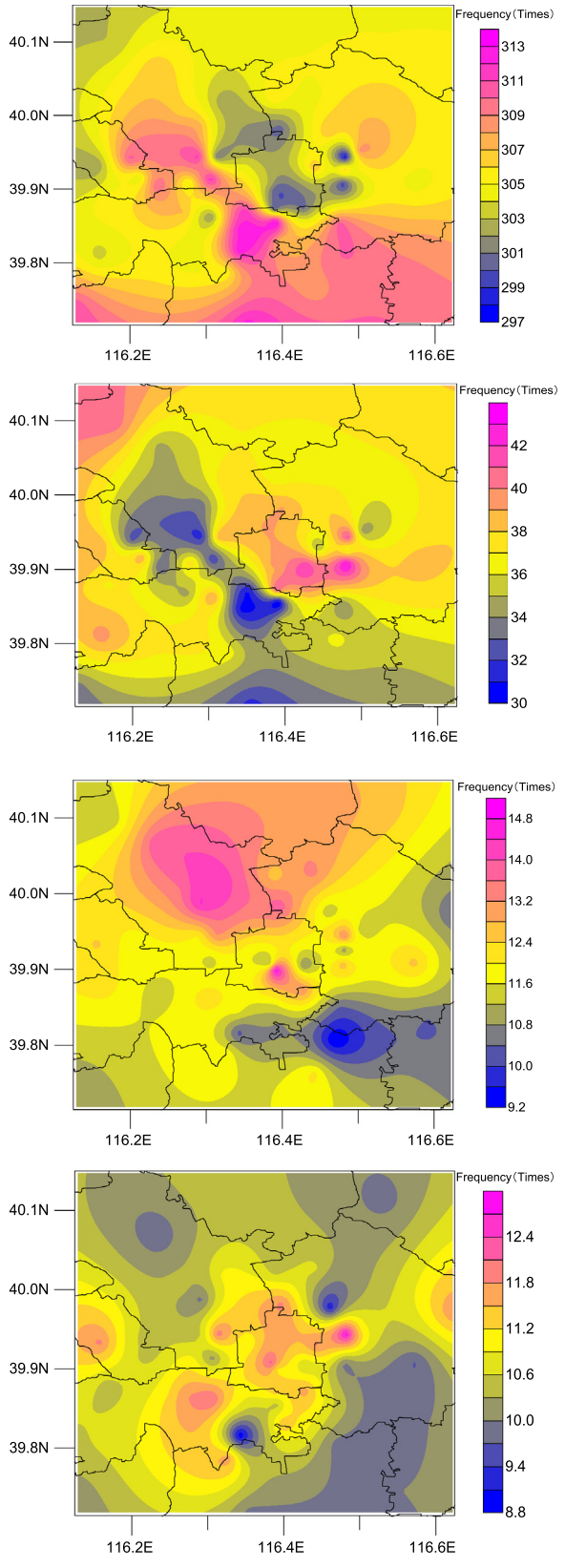

Fig. 4. Spatial distributions of frequency of CPHD with different precipitation duration ranges during 2007–2015. (a) CPHD = 0 h, (b) 0 h < CPHD ≤ 3 h, (c) 3 h < CPHD ≤ 6 h, (d) CPHD > 6 h. Unit: times.

Table 2
Seasonal mean frequency of CPHD in four different precipitation duration ranges over the urban areas of Beijing.

Unit (times)	CPHD = 0 h	0 h < CPHD ≤ 3 h	3 h < CPHD ≤ 6 h	CPHD > 6 h
Spring	79.20	8.49	2.28	2.03
Summer	62.32	18.09	6.13	3.69
Autumn	74.86	7.26	2.85	4.28
Winter	85.29	2.03	0.54	0.62

3.2. The impact of CPHD on UHII

Spatial distributions of average UHII in above four different ranges of CPHD in urban areas of Beijing during 2007–2015 are shown in Fig. 5. The spatial distributions reveal diverse features in different precipitation duration conditions. When there is no precipitation in daytime (Fig. 5a), the spatial pattern is similar to the distribution of annual mean UHII of Beijing city. This exhibits some regional differences in the effect of urbanization on surface air temperature with higher UHII in central urban area. Besides, the mean value of UHII (1.30 °C) over the whole urban areas on no-rainy days is a little higher than that on all days through whole year (1.18 °C). This is easy to understand and the similar conclusions have been found in previous researches (e.g. Hu et al., 2016). Nevertheless, noticeable discrepancies are observed in the UHII isotherm distributions in other three CPHD events (Fig. 5b–c). In the case of 0 h < CPHD ≤ 3 h (Fig. 5b), a triply weak warm cores are found in urban center and in eastern and western parts of the city near the urban center. The mean values of the warm cores are obviously lower than those in no precipitation case. For the two other precipitation duration ranges (Fig. 5c–d), the spatial differences are less significant, compared to the cases with no or less-rainy cases. Especially for the longest precipitation duration range (CPHD > 6 h), the UHII over the whole urban area is almost unable to detect.

Table 3 gives the means, maximum, minimum and range values of UHII over the urban areas in the four CPHD cases. It illustrates the significant differences among the cases. Generally speaking, the larger the CPHD, the lower the means of UHII are. In addition, the spatial difference is also closely related to the length of CPHD. It can also be seen that, the larger the CPHD is, the lower the range values of UHII are. Although the mean values of UHII warm cores are obviously lower in long duration precipitation condition than those in no precipitation, however, the UHII spatial pattern is relatively unchanged (Fig. 5), despite the average distributions of different rain events exhibit an explicit spatial difference. The higher UHII is always located in the urban centers. This may be related to the fact that, although the distributions of varied duration precipitation events are limited to a smaller extent, the cloud covers are distributed spatially broadly and consistently, leading to the uniform decline of UHII across the city.

Fig. 6 shows the diurnal variations of UHIIs in different precipitation duration ranges in Beijing city during 2007–2015. For the case of no-rainy days, the diurnal variation exhibits a typical pattern that many previous researches have shown (e.g. Lee and Baik, 2010; Yang et al., 2013c). The UHII sharply increase in the evening and decrease in the morning. Two stable stages of diurnal mean UHII could be obviously observed, a pattern similar to that shown in Fig. 4a. Compared to the case of no-rainy days, the diurnal variations of UHII with each of the rainy conditions present some different and interesting characters. Firstly, the longer the length of CPHD is, the lower the UHII will be. The diurnal character is in accordance with its spatial feature shown in Fig. 5. Secondly, the stable strong and weak stages of UHII are not apparent when the CPHD is no > 6 h, and will disappear completely when it surpasses 6 h. It means that, when precipitation events dominate the daytime, the diurnal pattern of UHII will change greatly. Thirdly, the curves of diurnal variation for two cases (3 h < CPHD ≤ 6 h and CPHD > 6 h) indicate that the UHII with serious rainy daytime (CPHD > 6 h) could be close to or a little higher than that with less rainy daytime (3 h < CPHD ≤ 6 h) for a few moments (from 1600 to1800 LST) during the whole day. The phenomenon could not be easily explained, but may be related to the fewer samples of the CPHD > 6 h case.

The diurnal variations of seasonal mean values of UHII in different CPHD cases in Beijing city during 2007–2015 is shown in Fig. 7. All cases show clear diurnal variations in the seasonal mean UHII, with higher nighttime UHII values and lower values at noontime in different seasons. In addition, under different CPHD conditions, the mean UHII present similar diurnal variations for different seasons. For instance, stable strong or weak stages could not be found in diurnal curves of all seasons for the conditions of CPHD > 6 h, but they exist in other cases more or less. In no-rainy case, the stable strong and weak stages are longer and in deeper contrast in winter and autumn than those in spring and summer. In the case of CPHD > 6 h, the peaks of hourly UHII in different seasons all occur at midnight time with small difference. The difference of maximum (0.93 °C in spring) and minimum (0.79 °C in autumn) value is only 0.14 °C. It is notable that, under the condition of long continuous rain, the character of stronger UHI in autumn won't be kept. In addition, it is also interesting to note that the UHII varied apparently during the nighttime among the varied CPHD conditions, while the UHII differences are not so clear under different precipitation conditions during noontimes.

The average annual cycles of UHII under different precipitation conditions for 2007–2015 in urban areas of Beijing are shown in Fig. 8. The UHII has prominent seasonal characteristics. During the wet or windy season (from March to August), corresponding to spring and summer, monthly mean UHII values are lower apparently. The UHII is best developed in no-rainy case and comparably lower in each of the rainy cases. For the precipitation case of 0 h < CPHD ≤ 3 h, all of the monthly mean UHII values are lower than those of no-rainy case. In addition, the season with stronger UHII in the case of 0 h < CPHD ≤ 3 h is mostly from September to February, with the peak in December and the valley in June. Contrary to the case with no or less-rainy cases, the UHII under heavier precipitation cases of 3 h < CPHD ≤ 6 h and CPHD > 6 h has a different monthly variation. Dry seasons including winter and autumn often have higher values of UHII, but Fig. 8 shows that sometimes the UHII in wet or windy season can also reach a relatively

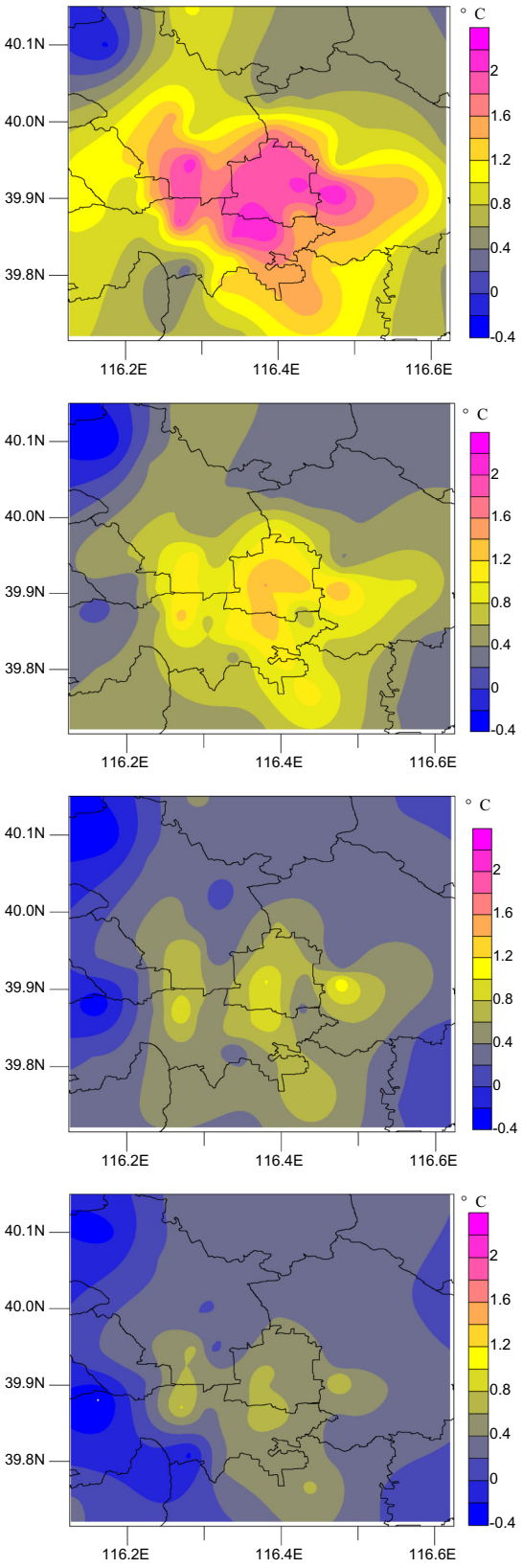

Fig. 5. Spatial distributions of UHII under different precipitation duration ranges in Beijing urban area during 2007–2015. (a) CPHD = 0 h (b) 0 h < CPHD ≤ 3 h (c) 3 h < CPHD ≤ 6 h (d) CPHD > 6 h.

Table 3
Means, maximum, minimum and range values of UHII over the urban areas of Beijing in four different precipitation duration ranges (Unit: ˚C).

	Mean	Maximum	Minimum	Range(Max-Min)
CPHD = 0 h	1.30	2.25	−0.23	2.48
0 h < CPHD ≤ 3 h	0.72	1.43	−0.38	1.81
3 h < CPHD ≤ 6 h	0.45	1.17	−0.34	1.51
CPHD > 6 h	0.36	0.84	−0.42	1.26

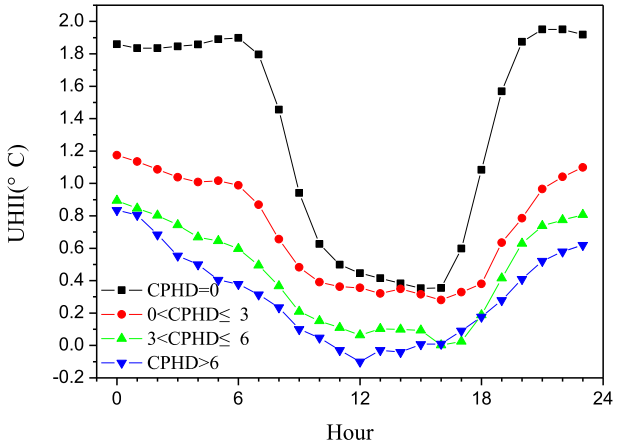

Fig. 6. Diurnal variations of UHIIs in different precipitation duration ranges in Beijing urban area during 2007–2015.

higher level. Taking the precipitation duration range of CPHD > 6 h as an example, the three lowest values of monthly mean UHII occur in July, March and April, while the UHII in May (0.36 ˚C) and June (0.31 ˚C) is not so weak, which even exceeds the monthly mean value (0.30 ˚C).

In order to examine their differences during different time scales, the differences of UHII in different time scale between each of the precipitation duration cases and no-rainy days have been calculated respectively, and they are shown in Figs. 9 and 10.

The lowest UHII difference in precipitation duration case of CPHD > 6 h can be found in April, May and June, and that for the case of 3 h < CPHD ≤ 6 h has a similar seasonal variation. For the case of 0 h < CPHD ≤ 3 h, however, the low ΔUHII is also found in November in addition to the similar weak periods as those in the above cases. The values of ΔUHII stay roughly at moderate levels in wet season from July to October.

In view of the diurnal variations, it is apparent that the patterns of ΔUHII in each rainy cases appears very similar (Fig. 10). The dual peak of UHII differences between each rainy case and no rainy case is close to sunrise (0600–0700 LST) and sunset (2000 LST). The minimum of ΔUHII remain stable from 1100 to 1500 LST, the period which has large solar radiation of a day. However, the differences of ΔUHII among the rainy conditions are significant. The hourly mean ΔUHII with weakest rainy condition (0 h < CPHD ≤ 3 h) have the lowest value in all of the day. The difference of hourly mean ΔUHII between the heavier (3 h < CPHD ≤ 6 h) and the heaviest (CPHD > 6 h) cases is not so prominent, however, especially for the sharply increasing and decreasing hours.

4. Discussion

Many studies of urban climatology were conducted for Beijing City, and some basic features of the UHI have been evidenced (Xu et al., 2006a,b; Liu et al., 2009; Wang et al., 2011; Yang et al., 2013b). In our previous work, we have examined the detailed temporal and spatial structure of the UHII in Beijing urban areas inside the 6th RR, using the observational hourly data from 2007 to 2010 (Yang et al., 2013c). Due to the restrictions on the length of data, the previous study was concentrated merely on the general characters of UHII over Beijing urban areas. Five years later, when we do further examination of the UHII in the city in different conditions of daytime precipitation using an updated dataset, we are able to find a few of additional interesting phenomena.

It is well known that frequencies of the hourly precipitation with different types vary widely in even small urban areas, which are closely related to the surface energy and water balance. There is no doubt that the occurrence times of no-rainy days are the smallest in urban center or inside 4th RR. However, the spatial patterns of precipitation are specific for each of the different precipitation duration conditions. The spatial distribution of precipitation with 0 h < CPHD ≤ 3 h is different from that under no-rainy case with the highest values inside 4th RR. More frequencies of precipitation is not always close to the urban center, however, and this is especially true for the case of 3 h < CPHD ≤ 6 h. It seems that, when we get deep into smaller space-time scale, more complicated characters have been demonstrated, which may be due to complex structure of underlying surface and the resulting modification of surface energy balance.

A detailed spatial pattern of UHII under different types of daytime precipitation duration in the urban areas over Beijing has been

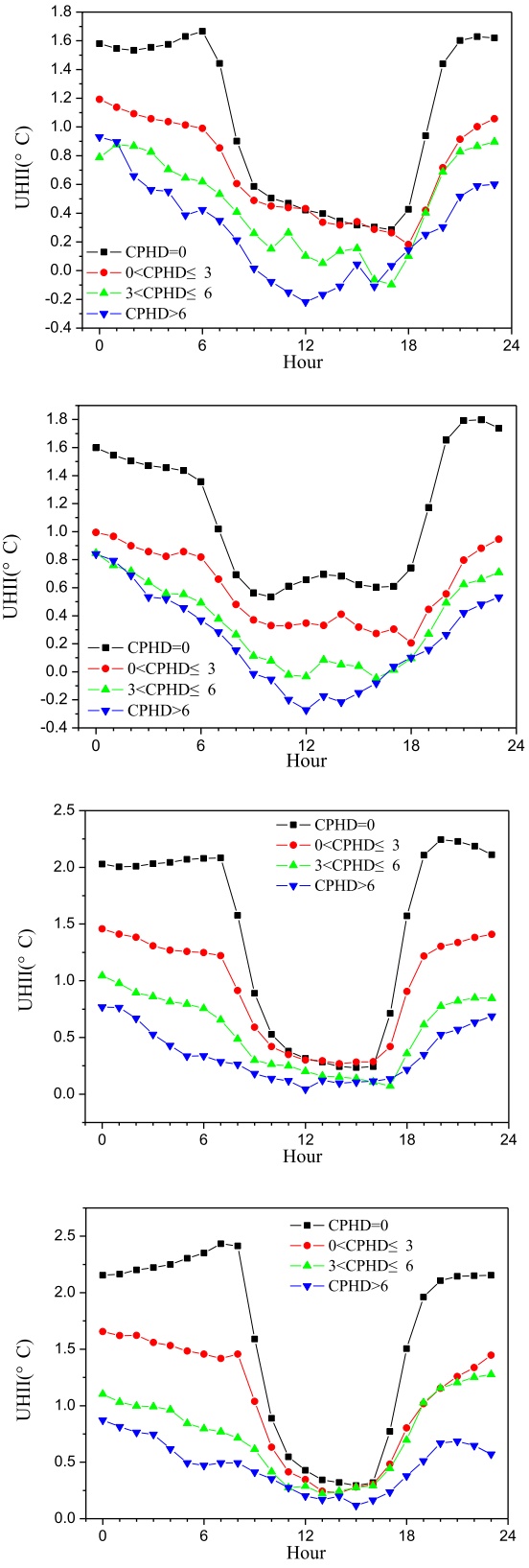

Fig. 7. Diurnal variations of seasonal mean values of UHII in different precipitation duration ranges in Beijing urban area during 2007–2015. (a) spring (b) summer (c) autumn (d) winter.

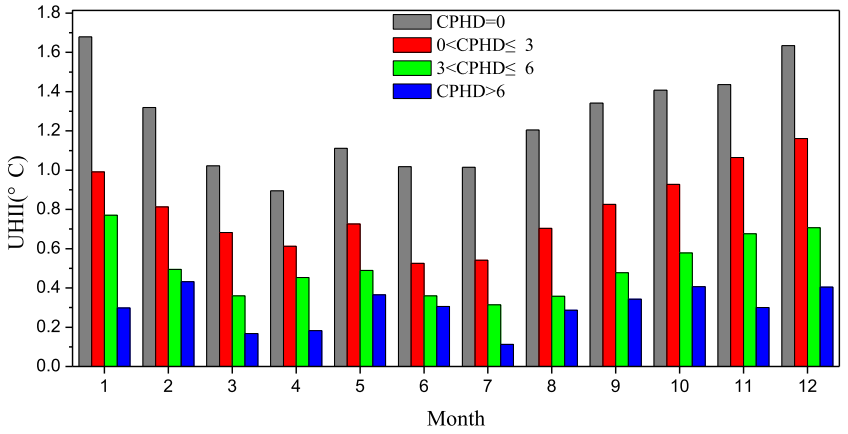

Fig. 8. Monthly mean value of UHIIs in different precipitation duration ranges in Beijing urban area during 2007–2015.

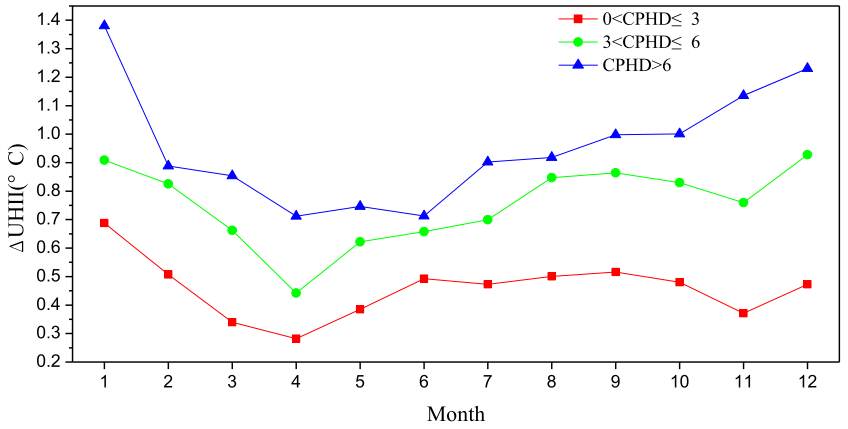

Fig. 9. Monthly variations of UHII difference between each of the precipitation duration ranges and no rainy day.

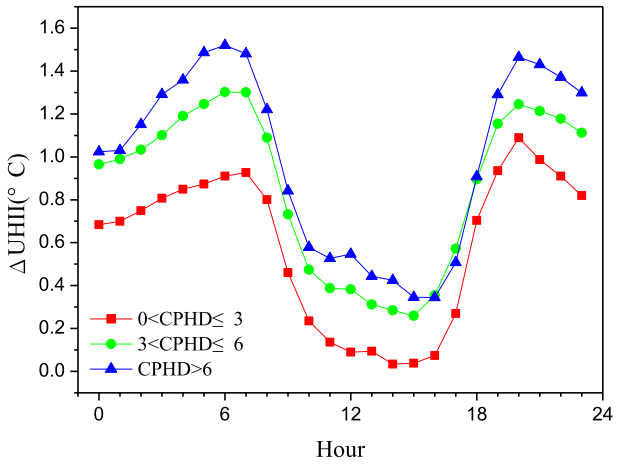

Fig. 10. Diurnal variations of UHII difference between each of the precipitation duration ranges and no rainy day.

revealed in this work. This is also the main emphasis of the analysis. It is well known that UHI is closely related to the structure, coverage, fabric, and metabolism of built-rise area, which leads to the substantial modification of surface energy and water balance (Oke, 1988). During the daytime, the multi-reflections of sunlight among high-up buildings apparently increase the absorptivity of heat in urban canopy (Ren, 2015). The reflection of urban canopy decreases, and the absorption of solar short-wave radiation and trapped heat within the urban surface therefore increase. The heat is released by long-wave radiation into sky in nighttime. The

increasing (decreasing) sensible (latent) heat flux due to the decreased soil moisture and vegetation cover is another important feature of surface energy and water balance in urban areas. Previous observations also revealed that there is difference of solar radiation and surface energy balance between city and its suburban counties (Chow and Shao, 1987).

Because of the importance of daytime solar radiation in formation and development of the UHI, we restrict the precipitation span between sunrise (0400 LST) and sunset (2000 LST), corresponding to the longest daytime on the Summer Solstice. In case of daytime precipitation, the direct solar radiation reaching at the surface is reduced to nil due to the influence of cloudiness. It is thus helpful to further recognize the contribution of direct solar radiation change to the UHI effect by examining the UHII under different durations of daytime precipitation. In daytime, when the precipitation is infrequent, the high UHII center of urban areas can still be found easily. That may be because, under weak rainy condition, the cloudiness and weather condition are not changed significantly, and the UHII is not much different from that of no-rainy condition. The heat absorbed and stored at the urban surfaces in daytime is not decreased evidently. On the contrary, under the long continuous rainy conditions, heat absorbed and stored at urban surfaces may be reduced largely owing to the lack of incoming short wave radiation, as well as the evaporation of the captured rain water at concrete surfaces. Moreover, because of the relatively high cloudiness and humidity in rainy cases, nocturnal long-wave radiative cooling is also limited. The abundant soil moisture in rural areas generally enables the rural thermal admittance to increase. Hence, the difference in thermal admittance between urban and rural areas is decreased under apparently rainy conditions, leading to a weaker UHII in the urban areas. The heavier of the rainy degree is, the more apparent the difference between rainy and no rainy cases is.

Some of previous studies on UHI and precipitation were focused on the UHI impact on precipitation event (e.g. Changnon et al., 1991; Aws et al., 2017; Yang et al., 2017c), and fewer works were turned to the opposite or the impact of precipitation on UHI. One analysis has concluded that the UHII of Beijing City reduced with an increase in precipitation levels (Liu, 2014). Although the conclusion is consistent with that reported in this paper, it was drawn based on of the limited data collected from only one station of Beijing with hourly data in only one year of 2012, and obviously needed a confirmation from a more sophisticated investigation. Our results indicated that varied precipitation durations of daytime can reduce the intensity of UHI in different extents, and this impact is more significant during nighttime. At night, the longwave radiation from the ground surface and high-rise building walls, which has been absorbed and stored in these materials during fine daytime, is emitted upward and absorbed by the near-surface atmosphere, increasing the surface air temperature and the UHII in the urban areas. If the daytime precipitation occurs continuously or frequently, the heat received and stored in the surface materials and the emission of the longwave radiation during nighttime will decreased apparently, leading to reduced surface air temperature and the UHII in the urban areas. This indicates that the solar radiation received at the urban canopy layer during daytime might have played a dominant role in the formation and variations of the UHI in Beijing City for each of the seasons.

It is found, however, that the frequency of long-duration precipitation events in winter is small. The insufficient samples may bring to some uncertainties especially for winter. The UHII spatial and temporal patterns in precipitation case with CPHD > 6 h obviously need further investigation. It is also noted that the longer period of the high-density observations, in combination with the usage of other observational data like cloudiness retrieved from satellites or radars, would greatly strengthen reliability of the analysis results.

5. Conclusions

In this study, the impacts of urban daytime precipitation on UHII are examined by using an hourly observational data from a high-density Automatic Weather Station (AWS) network in Beijing. The following conclusions are drawn from the analysis:

(1) The detailed spatial distribution of precipitation over Beijing urban areas show that the short duration precipitation events (0 h < CPHD ≤ 3 h) and long duration precipitation events (CPHD > 6 h) both tend to more frequently occur over the urban center of Beijing City.
(2) The spatial differences of UHII under different precipitation duration ranges are closely related to the length of CPHD during daytime. The longer the CPHD is, the less obvious the regional differences of UHII are and the smaller the UHII in the urban areas is.
(3) When continuous precipitation dominates the daytime, the diurnal variation pattern of UHII will be changed greatly. The stable strong and weak stages of UHII under no-rainy condition will be not so apparent when the CPHD is larger than 0 h and < 6 h, and they will disappear completely when the CPHD surpasses 6 h.
(4) For different types of daytime precipitation duration, the seasonal cycles of differences between each of the precipitation duration ranges and no rainy case is not similar. In the cased of 3 h < CPHD ≤ 6 h and CPHD > 6 h, the lowest UHII difference can be found in April, May and June; In the cases of 0 h < CPHD ≤ 3 h, the low ΔUHII also occurs in November in addition to the same low-value months as those in other rainy conditions.
(5) The diurnal variations of the differences between each of the rainy conditions and no-rainy case appeared very similar. All of them had a dual peaks close to sunrise (0600–0700 LST) and sunset (2000 LST), while the minimum value remains stable from 1100 to 1500 LST. For the sharply increasing and decreasing hours, the differences of the hourly mean ΔUHII between the longer (3 h < CPHD ≤ 6 h) and the longest (CPHD > 6 h) cases is very small.

Acknowledgements

The study is supported by the National Natural Science Foundation of China (Grant No. 41775078 , 41575003 and 41675092),

the Ministry of Science and Technology of China (Grant No. 2018YFA0605603).

References

Arnds, D., Bohner, J., Bechtel, B., 2017. Spatio-temporal variance and meteorological drivers of the urban heat island in a European city. Theor. Appl. Climatol. 128, 43–61. https://doi.org/10.1007/s00704-015-1687-4.

Arnfield, A.J., 2003. Two decades of urban climate research: a review of turbulence, exchanges of energy and water, and the urban heat island. Int. J. Climatol. 23 (1), 1–26.

Aws, A.A., Ashok, K.M., Abdul, A.K., 2017. Urban and peri-urban precipitation and air temperature trends in mega cities of the world using multiple trend analysis methods. Theor Appl. Climatol. 1–16.

Benson-Lira, V., Georgescu, M., Kaplan, S., Vivoni, E.R., 2016. Loss of a lake system in a megacity: the impact of urban expansion on seasonal meteorology in Mexico City. J. Geophys. Res. 121 (7), 3079–3099.

Changnon, S.A., 1979. Rainfall changes in summer caused by St. Louis. Science 205, 402–404. https://doi.org/10.1126/science.205.4404.402.

Changnon, S.A., Shealy, R.T., Scott, R.W., 1991. Precipitation changes in fall, winter and spring caused by St. Louis. J. Appl. Meteorol. 30, 126–134. https://doi.org/10.1175/1520-0450(1991)030<0126:PCIFWA>2.0.CO;2.

Chow, S.D., Shao, J.M., 1987. Shanghai urban influence on solar radiation. Acta Geo. Sini. 42, 319–327.

Craig, K.J., Bornstein, R.D., 2002. Mm5 Simulations of Urban Induced Convective Precipitation Over Atlanta. Fourth Symp on the Urban Environment, Norfolk, VA. Amer. Meteor. Soc.. pp. 5–6.

Diem, J.E., Brown, D.P., 2004. Anthropogenic impacts on summer precipitation in Central Arizona. U.S.A. Prof. Geogr. 55, 343–355. https://doi.org/10.1111/0033-0124.5503011.

Georgescu, M., Moustaoui, M., Mahalov, A., Dudhia, J., 2011. An alternative explanation of the semiarid urban area oasis effect. J. Geophys. Res. 116, D24113. https://doi.org/10.1029/2011JD016720.

Guo, Jun, Li, Mingcai, Liu, Deyi, 2009. Effects of urbanization on air temperature of Tianjin in recent 40 years. Ecol. Environ. Sci. 18 (1), 29–34.

Han, J.Y., Baik, J.J., Lee, H., 2014. Urban impacts on precipitation. Asia-Pac. J. Atmos. Sci. 50, 17–30. https://doi.org/10.1007/s13143-014-0016-7.

Hu, X.M., Xue, M., Klein, P.M., 2016. Analysis of urban effects in Oklahoma City using a dense surface observing network. J. Appl. Meteorol. Climatol. 55, 723–741.

Huff, F.A., 1986. Urban hydrometeorology review. Bull. Amer. Meteor. Soc. 67, 703–712.

Kim, Y.H., Baik, J.J., 2002. Maximum urban heat island intensity in Seoul. J. Appl. Meteorol. 41, 651–659.

Landsberg, H.E., 1981. The Urban Climate. Academic Press, New York (275pp).

Lee, S.H., Baik, J.J., 2010. Statistical and dynamical characteristics of the urban heat island intensity in Seoul. Theor Appl Climat. 100, 227–237. https://doi.org/10.1007/s00704-009-0247-1.

Li, X.R., Hu, F., Shu, W.J., Liang, B.L., 2008. Characteristics of urban heat island effect and its meteorological influencing factors over Beijing in autumn. Clim. Environ. Res. 13 (3), 291–299.

Liu, B., 2014. Temporal and Spatial Distribution Characteristics and Factor Analysis of Beijing Heat Island. Master's Thesis. Nanjing University of Information Science and Technology. Pp75.

Liu, W.D., You, H.L., Dou, J.X., 2009. Urban-rural humidity and temperature differences in the Beijing area. Theor. Appl. Climatol. 96, 201–207.

Magaña, V., Pérez, J., Méndez, M., 2003. Diagnosis and prognosis of extreme precipitation events in the Mexico city Basin. Geofis. Int. 42 (2), 247–260.

Memon, R.A., Leung, D.Y.C., Liu, C.H., Leung, M.K.H., 2011. Urban heat island and its effect on the cooling and heating demands in urban and suburban areas of Hong Kong. Theor. Appl. Climatol. 103, 441–450. https://doi.org/10.1007/s00704-010- 0310-y.

Miao, S.G., Chen, F., Li, Q.C., Fan, S.Y., 2010. Impacts of urban processes and urbanization on summer precipitation: a case study of heavy rainfall in Beijing on 1 august 2006. J. Appl. Meteorol. Climatol. 50, 506–825. https://doi.org/10.1175/2010JAMC2513.1.

Oke, T.R., 1988. The urban energy balance. Prog. Phys. Geogr. 12, 471–508.

Petralli, M., Massetti, L., Orlandini, S., 2009. Solar radiation exposure of shielded air temperature sensors and measurement error evaluation in an urban environment: a preliminary study in Florence, Italy. Adv. Sci. Res. 3, 9–12.

Ren, G.Y., 2015. Urbanization as a major driver of urban climate change. Adv. Clim. Chang. Res. 6, 1–6. https://doi.org/10.1016/j.accre.2015.08.003.

Ren, Y.Y., Ren, G.Y., 2011. A remote-sensing method of selecting reference stations for evaluating urbanization effect on surface air temperature trends. J. Clim. 24, 3179–3189. https://doi.org/10.1175/2010JCLI3658.1.

Ren, G.Y., Zhou, Y.Q., 2014. Urbanization effects on trends of extreme temperature indices of national stations over mainland China, 1961-2008. J. Clim. 27, 2340–2360. https://doi.org/10.1175/JCLI-D-13-00393.1.

Roth, M., 2007. Review of urban climate research in (sub) tropical regions. Int. J. Climatol. 27, 1859–1873. https://doi.org/10.1002/joc.1591.

Rozoff, C.M., Cotton, W.R., Adegoke, J.O., 2003. Simulation of St. Louis, Missouri, land use impacts on thunderstorms. J. Appl. Meteorol. 42, 716–738.

Shimadera, H., Konodo, A., Shrestha, K.L., Kitaoka, K., Inoue, Y., 2015. Numerical evaluation of the impact of urbanization on summertime precipitation in Osaka. Japan. Adv. Aeteorol. 2015, 379361.

Song, X.M., Zhang, J.Y., AghaKouchak, A., Liu, C.S., 2014. Rapid urbanization and changes in spatiotemporal characteristics of precipitation in Beijing metropolitan area. J. Geophys. Res. Atmos. 119. https://doi.org/10.1002/2014JD022084.

Stewart, I.D., Oke, T.R., 2012. Local Climate Zones for urban temperature studies. Bull. Am. Meteorol. Soc. https://doi.org/10.1175/BAMS- D-11-00019.1.

Tereshchenko, I.E., Filonov, A.E., 2001. Air temperature fluctuations in Guadalajara, Mexico, from 1926 to 1994 in relation to urban growth. Int. J. Climatol. 21, 483–494.

Thielen, J., Wobrock, W., Gadian, A., Mestayer, P.G., Creutin, J.D., 2000. The possible influence of urban surfaces on rainfall development: a sensitivity study in 2D in the meso-γ-scale. Atmos. Res. 54, 15–39.

Wang, J.P., Sun, J.S., Wang, S.G., 2011. Impact of basin terrain urban Heat Island effect on precipitation in surrounding region of Xi'an. J. Arid Meteorol. 29 (2), 168–173.

Wang, Q.C., Guo, L.P, Zhang, S.H., 2019. Urban heat island effect under different meteorological conditions over Langfang Hebei province. J. Meteorol. Environ. 25 (6), 44–48.

Xu, X.D., Ding, G.A., Bian, L.G., 2006a. Beijing city air pollution observation experiment. J. Appl. Meteorol Sci. 17 (6), 815–828.

Xu, Z., Zhang, L., Ruan, B., 2006b. Analysis on the spatiotemporal distribution of precipitation in the Beijing region. Arid Land Geogr. 29 (2), 186–192.

Yang, P., Liu, W.D., 2013. Evaluating the quality of meteorological data measured at automatic weather stations in Beijing during 1998-2010. Adv. Meteorol. Sci. Technol. 3, 27–34.

Yang, P., Liu, W.D., Zhong, J.Q., Yang, J., 2011. Evaluating the quality of temperature measured at automatic weather stations in Beijing. J. Appl. Meteorol. Sci. 22, 706–715.

Yang, P., Ren, G.Y., Hou, W., Liu, W.D., 2013b. Spatial and diurnal characteristics of summer rainfall over Beijing municipality based on a high-density AWS dataset. Int. J. Climatol. 33, 2769–2780. https://doi.org/10.1002/joc.3622.

Yang, P., Ren, G.Y., Liu, W.D., 2013c. Spatial and temporal characteristics of Beijing urban heat island intensity. J. Appl. Meteorol. Climatol. 52, 1803–1816. https://doi.org/10.1175/JAMC-D-12-0125.1.

Yang, P., Ren, G.Y., Yan, P.C., 2017a. Evidence for a strong association of short-duration intense rainfall with urbanization in the Beijing urban area. J. Clim. 30, 5851–5870. https://doi.org/10.1175/JCLI-D-16-0671.1.

Yang, P., Ren, G.Y., Hou, W., 2017b. Temporal-spatial patterns of relative humidity and the urban dryness island effect in Beijing city. J. Appl. Meteorol. Climatol. https://doi.org/10.1175/JAMC-D-16-0338.1.

Yang, P., Xiao, Z.N., Shi, W.J., 2017c. Fine-scale characteristics of rainfall in Beijing urban area based on a high-density AWS dataset. Chin. J. Atmos. Sci. 41 (3), 475–489.

Zhao, Lei, Lee, Xuhui, Smith, Ronald B., Oleson, Keith, 2014. Strong contributions of local background climate to urban heat islands. Nature 511 (10), 216–219. https://doi.org/10.1038/nature13462.

Zhong, S., Qian, Y., Zhao, C., Leung, R., Yang, X.Q., 2015. A case study of urbanization impact on summer precipitation in the greater Beijing metropoliatan area. urban heat island versus aerosol effects. J. Geophys. Res. Atmos. 120, 10903–10914. https://doi.org/10.1002/2015JD023753.

Zhou, Decheng, Zhao, Shuqing, Zhang, Liangxia, Sun, Ge, Liu, Yongqiang, 2015. The footprint of urban heat island effect in China. Sci. Rep. 5, srep11160. https://doi.org/10.1038/srep11160.

View publication stats

于晓澄, 赵俊虎, 杨柳, 等. 2019. 华北雨季开始早晚与大气环流和海表温度异常的关系 [J]. 大气科学, 43 (1): 107−118. Yu Xiaocheng, Zhao Junhu, Yang Liu, et al. 2019. The relationship between the onset date of the rainy season in North China and the atmospheric circulation and SST [J]. Chinese Journal of Atmospheric Sciences (in Chinese), 43 (1): 107−118, doi:10.3878/j.issn.1006-9895.1801.17242.

华北雨季开始早晚与大气环流和海表温度异常的关系

于晓澄[1, 2] 赵俊虎[2] 杨柳[1] 支蓉[2] 封国林[1, 2]

1 兰州大学大气科学学院，兰州 730000
2 国家气候中心中国气象局气候研究开放实验室，北京 100081

摘 要 本文利用国家气候中心的 1961～2016 年华北雨季监测资料、美国国家环境预报中心/大气研究中心（NCEP/NCAR）的大气再分析资料、NOAA 海表温度资料，分析了华北雨季开始早晚的气候特征，然后利用合成分析、回归分析等方法，研究了华北雨季开始早晚与大气环流系统和关键区域海表温度的关系。结果表明，56 a 来华北雨季开始最早在 7 月 6 日，最晚在 8 月 10 日，1961～2016 年华北雨季开始平均日期是 7 月 18 日。华北雨季开始时间具有显著的年际变化，但雨季发生早晚的长期变化趋势不太明显。华北雨季开始早晚与西太平洋副热带高压（简称副高）、东亚副热带西风急流、东亚夏季风等环流系统的活动关系密切，当对流层高层副热带西风急流建立偏早偏强，中层西太平洋副高第二次北跳偏早，低层东亚夏季风北进提前时，华北雨季开始偏早，反之华北雨季开始偏晚。华北雨季开始早晚与春、夏季热带印度洋、赤道中东太平洋海表温度关系显著且稳定，当 Niño3.4 指数和热带印度洋全区海表温度一致模态（IOBW）为正值时，贝加尔湖大陆高压偏强，副高偏强偏南，东亚夏季风偏弱，导致华北雨季开始偏晚；当海表温度指数为负值时，则华北雨季开始偏早。

关键词 华北雨季开始 大气环流 赤道东太平洋 印度洋海表温度
文章编号 1006-9895(2019)01-0107-12 **中图分类号** P461 **文献标识码** A
doi:10.3878/j.issn.1006-9895.1801.17242

The Relationship between the Onset Date of the Rainy Season in North China and the Atmospheric Circulation and SST

YU Xiaocheng[1, 2], ZHAO Junhu[2], YANG Liu[1], ZHI Rong[2], and FENG Guolin[1, 2]

1 *College of Atmospheric Sciences, Lanzhou University, Lanzhou* 730000
2 *Laboratory for Climate Studies, National Climate Center, China Meteorological Administration, Beijing* 100081

Abstract Using atmospheric data of NCEP / NCAR re-analysis, NOAA Sea Surface Temperature (SST) data, and monitoring data of the rainy season in North China from 1961-2016, the climatic characteristics of the onset date of rainy season in North China (OSDRS_NC) is analyzed. Through synthetic analysis and regression analysis, the relationship between OSDRS_NC and the atmospheric circulation system as well as SST anomalies (SSTA) is analyzed. The results show that the mean OSDRS_NC was July 18 in the past 56 years. The earliest OSDRS_NC was July 6, and the latest was

收稿日期 2017-09-20；**网络预出版日期** 2018-01-31
作者简介 于晓澄，女，1994 年出生，硕士，主要从事短期气候预测研究。E-mail: 437865922@qq.com
通讯作者 赵俊虎，E-mail: zhaojh@cma.gov.cn
资助项目 国家重点研发计划项目 2017YFC1502303、2018YFA0606301，国家自然科学基金项目 41875093、41530531、41505061
Funded by National Key Research and Development Program of China (Grants 2017YFC1502303, 2018YFA0606301), National Natural Science Foundation of China (Grants 41875093, 41530531, 41505061)

August 10. The OSDRS_NC shows significant inter-annual variation, and its long-term variation trend is not obvious. The OSDRS_NC is closely linked to the activities of the western Pacific subtropical high (WPSH), the East Asian westerly jet stream (EAWJS) and the East Asian summer monsoon (EASM). When the establishment of the EAWJS, the second northward jump of the WPSH, and the northward movement of the EASM are earlier than normal, the OSDRS_NC is earlier than normal, and vice versa. The relationship between the OSDRS_NC and the SST over the Tropical Indian Ocean and the equatorial central and eastern Pacific is significant and stable in the spring and summer. When the Niño3.4 index and the Indian Ocean Basin-wide Warming (IOBW) display positive (negative) anomalies, the WPSH enhances (weakens) and shifts to the south, the Lake Baikal high enhances (weakens) and the EASM weakens (enhances). These anomalies lead to late (early) onset of the rainy season in North China.

Keywords Rainy season onset in North China, Atmospheric circulation, Equatorial East Pacific SST, Indian Ocean SST

1 引言

华北雨季指的是每年 7 月中下旬至 8 月中上旬在中国华北地区出现的以持续多雨为主要特征的气候现象，雨季的长短和雨量多寡，都与夏季风雨带的进退、移动和停滞有关（竺可桢，1934；赵汉光，1994；施能等，1996；张庆云等，2003），雨季平均降水量一般达到夏季总降水量的 50%（赵振国，1999）。华北雨季是东亚夏季风季节性北推过程中的重要阶段，这一时期中国东部雨带主要徘徊在淮河以北，并往往伴随着持续性暴雨、洪涝灾害的发生，给国家和人民的生命财产等带来巨大损失。因此，揭示华北雨季的变化规律及其异常成因，具有重要的科学意义，对防灾、减灾也具有十分重要的指导意义。

过去几十年，国内外气象学者对华北地区的天气和气候开展了大量的研究。但这些研究多数是针对华北夏季的旱涝，而对华北雨季的研究较少。例如张庆云（1999）通过分析 1880 年以来华北地区的降水变化，发现 1883～1997 年华北地区降水存在丰沛或偏少的年代际变化。张利平等（2008）分析发现，华北地区降水存在明显的季节变化、准 2 a 震荡和准 19 a 周期变化特征，且具有明显的阶段性。郭彦和李建平（2012）研究指出华北汛期（7～8 月）降水具有年际变率和年代际变率，并以华北汛期降水为例，利用分离时间尺度的统计降尺度模型开展了预测研究。丁一汇和刘芸芸（2008）提到与华北雨季相关的两个系统是印度夏季风系统和西北太平洋夏季风系统，印度夏季风强（弱）时，华北地区容易出现降水偏多（少）的天气，华北地区降水偏多（少）时，印度夏季风偏强（弱）的机率却低一些。华北地区降水还间接受到热带太平洋海表温度、印度洋海表温度、北大西洋海表温度、南海海表温度等因素的影响。吴志伟等（2006）发现华北雨季降水年代际变化显著，与西太平洋暖池、大西洋西部和北太平洋的海表温度有着显著的相关关系。陈文等（2006）研究发现，我国华北地区的降水异常跟热带中、东太平洋海表温度变化显著相关，并且从比较长的时间尺度来看，华北地区的降水从 1965 年左右开始减少，特别是大约 1976 年后有显著的减少，而与这种异常现象显著关联的海表温度异常关键区包括太平洋、印度洋以及热带和南大西洋。

此外，张天宇等（2007）研究了华北雨季降水集中度和集中期的时空变化特征，发现华北东部地区的降水较西部更为集中，且华北地区雨季集中期和雨季降水量与东亚夏季风具有较好的正相关关系，华北北部地区为集中期与东亚夏季风的显著相关区。闵锦忠等（2016）指出在华北雨季开始前后，最显著的变化特征是蒙古低压的建立和西伯利亚地区、菲律宾海环流的变化。近来，赵树云等（2017）利用国家气候中心发布的华北雨季新监测标准，分析了 ENSO 位相转换对华北雨季降水的影响，发现华北雨季降水异常偏多年通常发生在 El Niño 结束且当年转为 La Niña 的年份，而华北雨季降水异常偏少年通常发生在赤道中东太平洋冷水位相结束且当年发展成 El Niño 事件的年份。

综上可见，大气环流的变化和海表温度异常对华北地区降水有重要影响，以往大部分关于华北降水的研究主要是聚焦到华北夏季降水的年际、年代际变化及其影响系统，而对于华北雨季开始早晚的研究极少。由于华北夏季降水主要集中在华北雨季，而雨季开始早晚年际差异较大，会给防汛和抗旱工作带来较大的影响。雨季开始早晚的年际变化，对华北雨季降水量也有一定影响，那么雨季开始早晚与大气环流的是否密切相关？与海表温度异常是否存在显著关系？是否与华北地区旱涝变

化，华北暴雨的发生频率有关？这都是需要进一步研究的科学问题。总之，对华北雨季开始早晚进行深入研究，有很大的科学价值。同时国家气候中心 2014 年发布了新的华北雨季开始日期的监测业务规定，那么在新的雨季开始划分标准下，雨季开始早晚的异常与环流、海表温度的关系如何？基于此，本文利用 1961～2016 年华北雨季检测资料，重点分析了近 56 a 来华北雨季的气候变化特征，及影响华北雨季开始早晚的关键环流系统，以及关键海表温度因子与华北雨季开始早晚的关系，以期对华北雨季预测提供科学依据。

2 资料和方法

所用资料包括：美国国家环境预报中心和国家大气研究中心（NCEP/NCAR）发布的全球日和月平均高度场（*H*）、风场（*U*、*V* 分量）再分析资料，水平空间分辨率为 2.5°×2.5°，垂直方向从 1000～10 hPa 共 17 层等压面（Kalnay et al., 1996）；美国国家海洋和大气管理局（NOAA）的全球 2°×2° 月平均海表温度重建资料（Reynolds et al.，2002），中国气象局国家气候中心（NCC）提供的 Niño1.2、Niño3.4、印度洋全区海表温度一致模态（IOBW）指数，时段均为 1961 年 1 月至 2016 年 12 月。

华北雨季是按照国家气候中心监测指标来确定，华北雨季监测区主要包括北京、天津、河北（京津冀）、山西、内蒙古共 236 站（图 1）。确定区域雨季开始、结束和长度的主要依据是区域内各监测站的降水条件，华北雨季典型环流形势等为辅助条件，具体方法如下：

（1）单站雨季开始日期：自 7 月初开始，若监测区内某站任意连续 5 天累计降水量≥35（25）毫米，并且 5 天内至少出现一次日降水量≥10 毫米的雨日，则将首个≥10 毫米的雨日定义为该站雨季开始日期。

（2）单站雨季结束日期：雨季开始后，若监测区内某站截止某日时，向前连续 10 天中逐日 5 天滑动累计降水量≤35（25）毫米，则将此日定为雨季结束日期。

（3）区域雨季起讫日期：某区域内，截止某日雨季已开始（结束）的累计站点比率（即累计达标站点数与区域总站数的比率）达到相应开始（结束）的比率阈值时（累计站点比率见表 1），则将该日确定为该区域雨季的开始（结束）日期。

表 1 区域雨季开始（结束）累计站点比率

Table 1 The cumulative regional site ratio on rainy season beginning (end) date

	累计站点比率		
	京津冀	山 西	内蒙古
开始	70%	60%	60%
结束	60%	60%	50%

（4）华北雨季起讫日期：以京津冀、山西、内蒙古三个区域中，最早进入雨季区域的日期作为华北雨季的开始日期；上述三个区域中，最晚结束雨季区域的日期作为华北雨季的结束日期。

关于华北雨季开始、结束和雨量的其他业务规范请参考中国气象局预报与网络司 2014 年发布的《华北雨季监测业务规定》[①]，这里不再赘述。

3 华北雨季开始早晚气候特征

图 2 为 1961～2016 年华北雨季开始日期（Onset data of the rainy season in North China，简称 OSDRS_NC）距平的年际变化、线性趋势以及 9 a 滑动平均。由图 2 可见，OSDRS_NC 存在明显的年际变化，表 2 为 1961～2016 年的华北雨季开始日期，也体现了华北雨季近 56 a 以来的年际特征，1961～2016 年华北雨季开始时间集中在 7、8 月，其中从 7 月中下旬开始的有 54 a，其次是 8 月上旬（2 a），开始最早的有 5 a，发生在 7 月 6 日（1963、1964、1973、1977、1981、1988、1994、1999 和 2000 年），开始最晚的只有一年，发生在 8 月 10 日（1980 年），最早与最晚相差 35 天。1961～2017 年华北雨季开始平均日期是 7 月 18 日，标准差为 8 天。为研究华北雨季开始早晚的影响系统，采用雨季开始偏早和偏晚 10 天及以上的标准来划分华北雨季开始异常偏早晚年，得到偏早年共 12 年（1962、1963、1964、1973、1977、1981、1988、1994、1999、2000、2012、2013 年），偏晚年共 8 年（ 1965、1980、1983、1987、2002、2007、2010、2014 年）。对这 20 个异常年进行合成典型场分析，研究影响华北雨季开始偏早晚异常的环流系统。

从图 2 OSDRS_NC 的 9 a 平滑曲线看出其存在显著的年代际变化：20 世纪 60 年代一直到 80 年代

① 中国气象局预报与网络司. 2014. 关于印发《华北雨季监测业务规定》的通知, 气预函 (2014)117 号 [R].

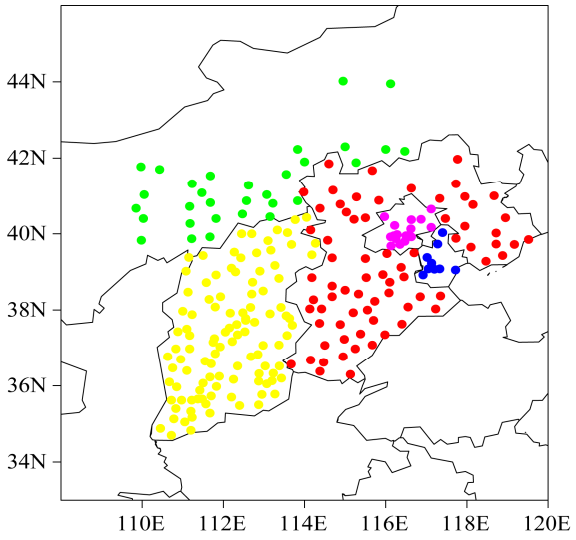

图 1 华北雨季监测站点空间分布示意图（紫点为北京监测区站点，蓝点为天津监测区站点，红点为河北监测区站点，黄点为山西监测区站点，绿点为内蒙古监测区站点）

Fig. 1 Schematic diagram of the division of the monitoring area and spatial distribution of the rainy season monitoring stations in North China (purple spots are stations in Beijing, blue spots are stations in Tianjin, red spots are stations in Hebei, yellow spots are stations in Shanxi, green spots are stations in Inner Mongolia)

初，偏早偏晚变化不明显，在正常附近波动，从 80 年代中期一直到 90 年代以偏早为主，从 21 世纪初以来以偏晚为主。对 1961～2016 年 OSDRS_NC 进行小波功率谱分析表明（图略），近 56 a 来 OSDRS_NC 存在显著的 4 年周期。线性趋势直线说明近 56 a 来 OSDRS_NC 呈现不太明显的偏晚的长期变化趋势。

4 影响华北雨季开始早晚与环流系统的关系

华北雨季受东亚夏季风环流系统向北推进的影响，首先从环流形势的角度出发，分析 OSDRS_NC 与高层到低层大气环流系统的关系。图 3 给出了 OSDRS_NC 与 7 月对流层各层大气环流场的相关系数分布。由 OSDRS_NC 与高层（200 hPa）纬向风场（U）的相关分布（图 3a）可见，华北北部至东北呈显著的负相关，长江至日本一带呈显著的正相关。7 月东亚副热带西风急流（西风急流）主体基本在 40°N 及其以北地区。图 4 给出了华北雨季开始偏早年和偏晚年东亚（110°～140°E 平均）上空 200 hPa 纬向风的时间—纬度剖面图。偏早年

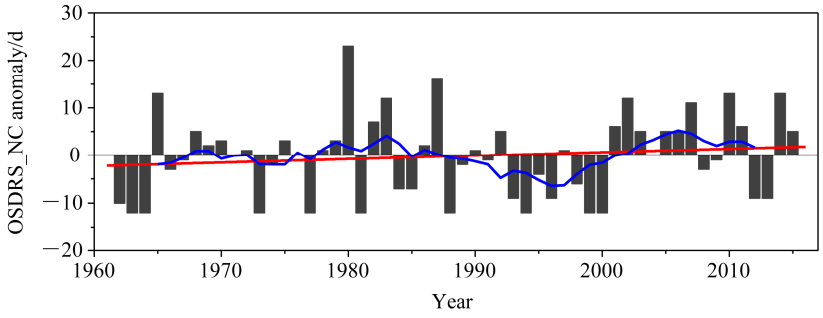

图 2 1961～2016 年华北雨季开始日期（OSDRS_NC）距平序列图，直线表示线性趋势，曲线表示 9 a 滑动平均

Fig. 2 Anomaly sequence chart of onset dates of the rainy season in North China (OSDRS_NC) from 1961 to 2016, where the straight line represents the linear trend and the curve represents the 9-year running average

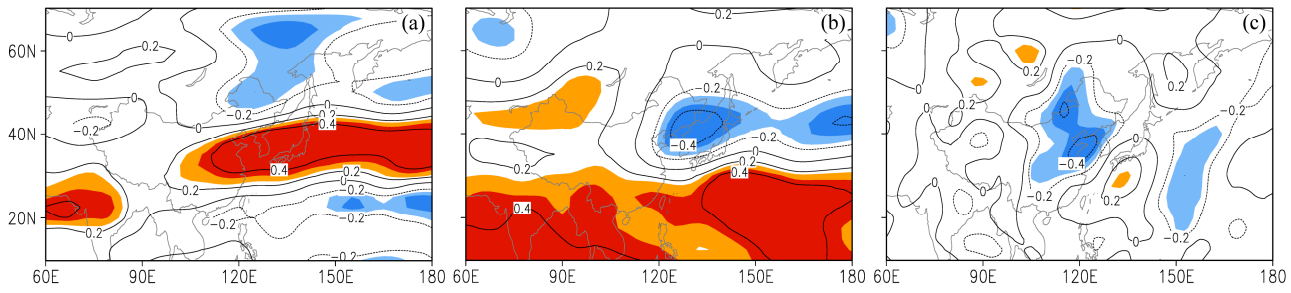

图 3 1961～2016 年华北雨季开始时间与 7 月各层环流场的相关分布：（a）200 hPa 纬向风场；（b）500 hPa 高度场；（c）850 hPa 经向风场。浅、深阴影区分别表示置信水平达到 95%和 99%

Fig. 3 Correlation maps between OSDRS_NC and (a) 200 hPa zonal wind, (b) 500 hPa geopotential height, (c) 850 hPa meridional wind during 1961–2016. The light and dark shadings indicate values at the 95% and 99% confidence levels, respectively

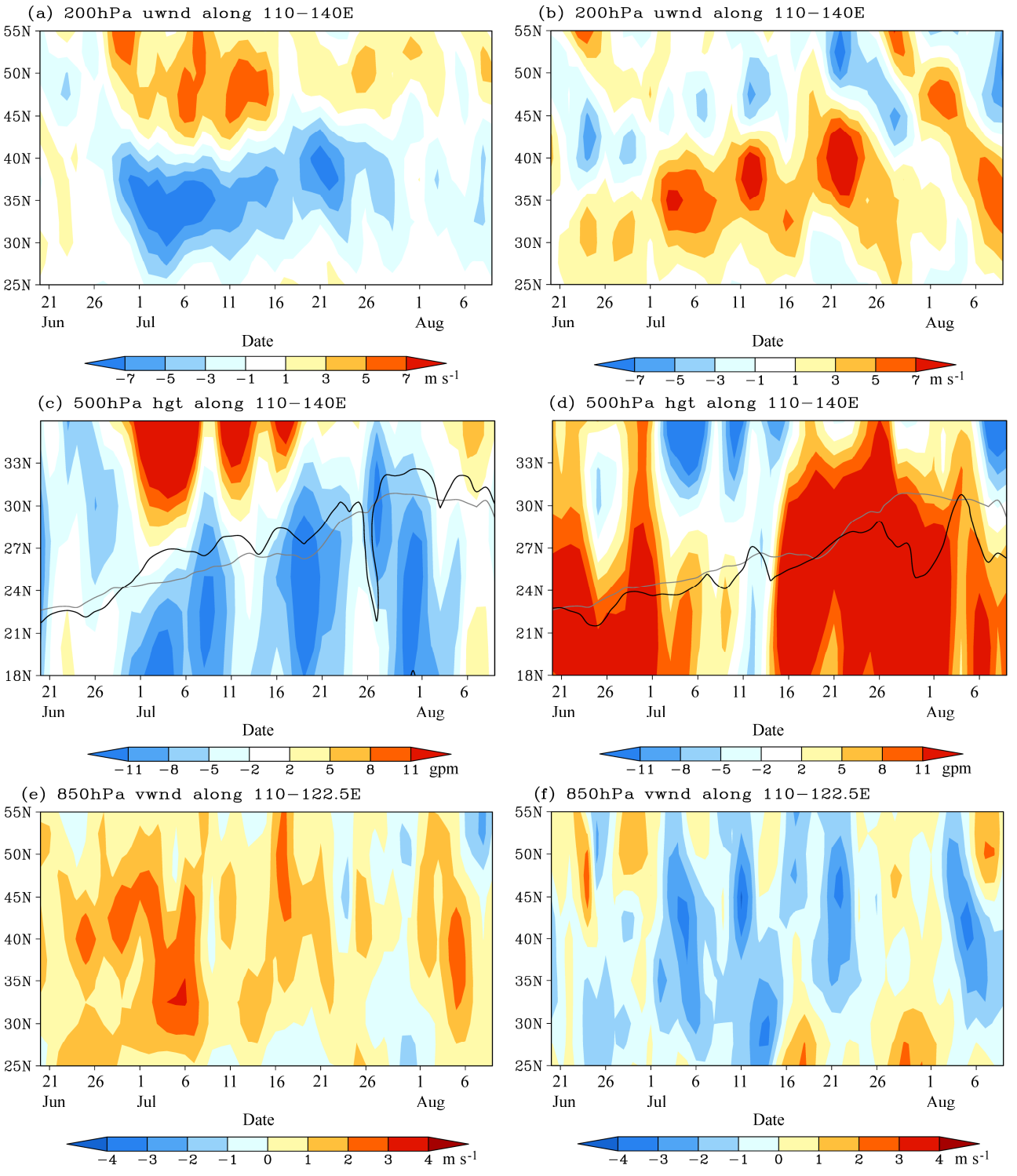

图 4 华北雨季开始偏早年（左列）和偏晚年（右列）各层环流场的时间—纬度剖面：（a、b）东亚 110°～140°E 平均的 200 hPa 纬向风（单位：m s^{-1}）；（c、d）东亚 110°～140°E 平均的 500 hPa 高度场（单位：gpm）；（e、f）沿 110°～122.5°E 平均的 850 hPa 经向风场（单位：m s^{-1}）。虚线表示气候平均副高脊线，实线表示异常年平均副高脊线

Fig. 4 Time–latitude cross sections of (a, b) zonal wind (units: m s^{-1}) at 200 hPa and (c, d) geopotential height (units: gpm) at 500 hPa averaged over 110°–140°E. (e, f) Time–latitude cross sections of meridional wind at 850 hPa (units: m s^{-1}) averaged over 110°–122.5°E. (a, c, e) are for early OSDRS_NC years, (b, d, f) are for late OSDRS_NC years. The dotted line represents the climatological mean subtropical high ridge line, and the solid line represents the mean subtropical high ridge line in anomalous years

（图 4a），在 6 月下旬至 8 月中旬，40°N 以北为正距平，以南为负距平，表明西风急流北跳偏早；而在偏晚年（图 4b），在 6 月下旬至 7 月中旬，40°N 以北为负距平，以南为正距平，7 月下旬 40°N 以北转为正距平，表明西风急流北跳偏晚。图 5a 对比了 1961～2016 年西风急流位置变化与华北雨季开始早晚的年际变化，其中西风急流位置指数为 200 hPa 的 *U* 风场所在区域内最大风速所在纬度的区域平均（卫玮和黄卓禹，2012）。两者的相关系数为－0.33，置信水平达到 95%，从图中可以看出西风急流位置变化与华北雨季开始早晚基本一致，当西风急流位置偏北，距平值为正时，56 a 华北雨季开始时间基本偏早，距平值负，这种同步在 20 世纪 90 年代之后更加明显，即 6 月下旬至 7 月西风急流偏北（南），有利于华北雨季开始偏早（晚）。

西太平洋副热带高压（简称副高）的南北移动可以直接影响华北雨季的开始早晚和雨季长度（张庆云和陶诗言，2000；赵俊虎等，2012，2014；Ye et al, 2014, 2015）。图 3b 给出了 OSDRS_NC 与 7 月 500 hPa 高度场的相关系数分布图。雨季开始与 7 月 500 hPa 高度场在副热带地区呈显著正相关，与东北地区高度场呈显著负相关，表明副高偏强偏北、东北冷涡活跃时，华北雨季开始偏早，反之则偏晚。图 5b 进一步给出了 1961～2016 年华北雨季开始早晚与副热带高压第二次北跳（候）时间的年际变化，两者相关系数为 0.36，置信水平达到 99%，可清楚地看到，两者变化是基本一致的，当副高第二次北跳偏晚，距平值为正时，对应华北雨季开始偏晚，距平值为正，尤其是到 20 世纪 90 年代以来，变化更加同步。表 2 给出了 1961～2016 年副热带高压第 2 次北跳时间，对比华北雨季开始日期，进一步验证了两者的显著关系。图 4c、d 对比了 500 hPa 高度场（110°～140°E 平均）偏早年和偏晚年的时间－纬度剖面图。偏早年（图 4c），副高脊线在 6 月末有一次明显的北跳，7 月初脊线达到 27°N 以北，并一直较气候平均偏北，而偏晚年（图 4d）基本与偏早年相反，副高脊线一直较气候平均偏南，在 7 月下旬才达到 27°N。由此可见，华北雨季开始偏早晚与副高的北跳早晚有关，副高北跳偏早（晚）有利于华北雨季开始偏早（晚）。

低层环流系统可以直接反应越赤道气流、东亚夏季风爆发早晚及其强弱、及水汽的辐合辐散等。图 3c 是 OSDRS_NC 与 7 月 850 hPa *V* 风场的相关系数分布。由图可见，雨季开始日期与长江至华北地区的 *V* 风场呈显著的负相关，表明 7 月东亚季风偏强时，有利于水汽向北方输送，进而有利于华北

表 2　1961～2016 年华北雨季开始时间（日）与西太平洋副热带高压（简称副高）第二次北跳时间（候）

Table 2　Onset dates of the rainy season in North China and the time (pentad) of second northward jump of the WPSH (western Pacific subtropical high)　from 1961 to 2016

年份	华北雨季开始日期	副高第二次北跳	年份	华北雨季开始日期	副高第二次北跳	年份	华北雨季开始日期	副高第二次北跳
1961	7 月 18 日	6 月第 5 候	1980	8 月 10 日	9 月第 2 候	1999	7 月 6 日	7 月第 5 候
1962	7 月 8 日	7 月第 5 候	1981	7 月 6 日	7 月第 2 候	2000	7 月 6 日	7 月第 4 候
1963	7 月 6 日	7 月第 3 候	1982	7 月 25 日	7 月第 6 候	2001	7 月 24 日	7 月第 1 候
1964	7 月 6 日	7 月第 4 候	1983	7 月 30 日	8 月第 1 候	2002	7 月 30 日	7 月第 5 候
1965	7 月 31 日	8 月第 3 候	1984	7 月 11 日	6 月第 5 候	2003	7 月 23 日	8 月第 4 候
1966	7 月 15 日	7 月第 3 候	1985	7 月 11 日	7 月第 5 候	2004	7 月 18 日	7 月第 4 候
1967	7 月 17 日	7 月第 4 候	1986	7 月 20 日	8 月第 6 候	2005	7 月 23 日	8 月第 2 候
1968	7 月 23 日	8 月第 2 候	1987	8 月 3 日	8 月第 2 候	2006	7 月 23 日	7 月第 6 候
1969	7 月 20 日	7 月第 4 候	1988	7 月 6 日	7 月第 6 候	2007	7 月 29 日	7 月第 6 候
1970	7 月 21 日	7 月第 5 候	1989	7 月 16 日	7 月第 3 候	2008	7 月 15 日	7 月第 5 候
1971	7 月 18 日	7 月第 1 候	1990	7 月 19 日	7 月第 4 候	2009	7 月 17 日	7 月第 2 候
1972	7 月 19 日	7 月第 2 候	1991	7 月 17 日	7 月第 4 候	2010	7 月 31 日	7 月第 4 候
1973	7 月 6 日	7 月第 2 候	1992	7 月 23 日	7 月第 5 候	2011	7 月 24 日	8 月第 4 候
1974	7 月 16 日	7 月第 5 候	1993	7 月 9 日	8 月第 5 候	2012	7 月 9 日	7 月第 4 候
1975	7 月 21 日	7 月第 1 候	1994	7 月 6 日	7 月第 1 候	2013	7 月 9 日	7 月第 2 候
1976	7 月 18 日	7 月第 4 候	1995	7 月 14 日	7 月第 5 候	2014	7 月 31 日	7 月第 4 候
1977	7 月 6 日	7 月第 4 候	1996	7 月 9 日	7 月第 4 候	2015	7 月 23 日	7 月第 6 候
1978	7 月 19 日	7 月第 2 候	1997	7 月 19 日	8 月第 4 候	2016	7 月 18 日	7 月第 6 候
1979	7 月 21 日	7 月第 5 候	1998	7 月 12 日	9 月第 3 候			

降水。图 5 给出了 1961～2016 年 7 月东亚夏季风强度指数与华北雨季开始早晚的年际变化，其中东亚夏季风指数使用王会军定义（Wang, 2002），根据图 3b 的相关显著区域，选取（30°～50°N，110°～125°E）为异常风速平均区域，两者相关系数－0.31，置信水平达到 95%，两者变化基本一致，当夏季风偏强时，华北雨季开始偏早，在 20 世纪 90 年代以后这种同步变化更加明显。图 4e、f 对比了华北雨季开始偏早、晚异常年 850 hPa *V* 风场的时间—纬度剖面图。偏早年，6 月下旬至 7 月下旬，中国东部地区从南至北（25°～50°N）多为南风距平，说明夏季风爆发偏早、偏强，有利于水汽向华北地区输送，有利于华北雨季开始偏早。偏晚年则正好相反，中国东部呈北风距平，表明东亚夏季风爆发偏晚、偏弱，不利于水汽向华北地区输送，导致华北雨季开始偏晚。

综上可见，华北雨季开始早晚是东亚大气环流系统从南向北推进快慢的结果，具体而言，从对流层高层到低层，与 6 月下旬至 7 月上旬，西风急流北跳偏早、副高第二次北跳偏早和东亚夏季风向北推进的较快，有利于华北雨季开始偏早，偏晚年则相反，而且这种环流配置建立早晚、强度与华北雨季开始早晚的异常在 20 世纪 90 年代后同步变化明显增加。

5 华北雨季开始早晚与前期至同期海表温度（SST）的关系

ENSO 对中国降水有重大影响，是导致亚洲季

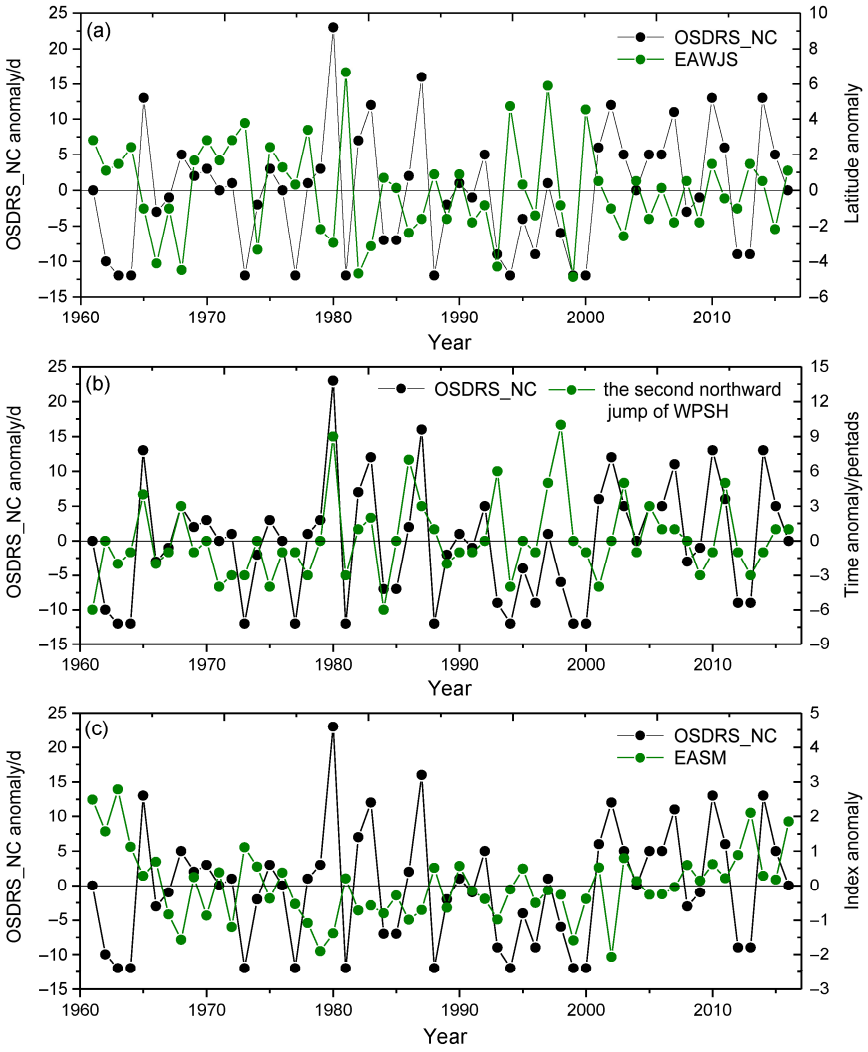

图 5 1961～2016 年华北雨季开始时间与（a）副热带西风急流位置（纬度）、（b）副高第二次北跳时间（候）、（c）东亚夏季风强度指数距平的年际变化

Fig. 5 Interannual variability of the onset date of the rainy-season in North China and that of (a) the latitude of the EAWJS (East Asian westerly jet stream), (b) the time of the second northward jump of WPSH (the western Pacific subtropical high), and (c) the intensity index of EASM (East Asian summer monsoon) from 1961 to 2016

风异常和我国旱涝发生的关键因素，郝立生和丁一汇（2012）指出在 ENSO 事件发展阶段，华北降水偏少，多干旱。同时印度洋海表温度也在影响华北地区降水，华北地区夏季降水的减少，是由于热带印度洋海表温度升高造成的（郝立生，2011），而且 ENSO 与中国夏季降水之间的年际变化关系存在变化，在不同年代背景下，其对中国夏季降水的影响有不同的表现（宗海锋等，2010），黄荣辉等（1999）分析华北地区干旱化发现，赤道中、东太平洋海表温度的升高与降低，对华北地区干旱化趋势有很大影响。同时也有研究发现，Niño3 区海表温度与印度季风的关系是变化的（Webster et al., 1998）。

分析 1961～2016 年 NCRSSD 与前冬（上一年 12 月至当年 2 月）、春季（3～5 月）和夏季（6～7 月）的 SST 场相关系数分布（图 6），在前冬 SST 相关场上，热带印度洋和赤道东太平洋出现显著正相关区（图 6a），但显著区域比较小；到 3～5 月，春季 SST 相关场上（图 6b），热带印度洋显著正相关区域强度大小基本不变，但赤道中东太平洋显著正相关区域范围变大，中心最大值达到 99%的置信水平，在太平洋北部出现了显著负相关区；在夏季 SST 相关场上（图 6c），热带印度洋仍呈显著的正相关，最大显著区域出现在北印度洋，相关区域较春季变大，强度变强，中心最大值达到 99%的置信水平，在印度洋中心区域也出现了一个显著相关区，中心最大值通过 99%的置信水平，春季出现在太平洋北部的显著负相关区在夏季消失，太平洋的显著正相关区域变大，强度增强。表明春季 El Niño 发展，春夏季印度洋偏暖时，华北雨季开始偏晚；反之则偏早。

由此可见，与 OSDRS_NC 有关的显著关键海表温度区域为赤道中东太平洋和热带印度洋。为了进一步了解赤道太平洋海表温度和印度洋海表温

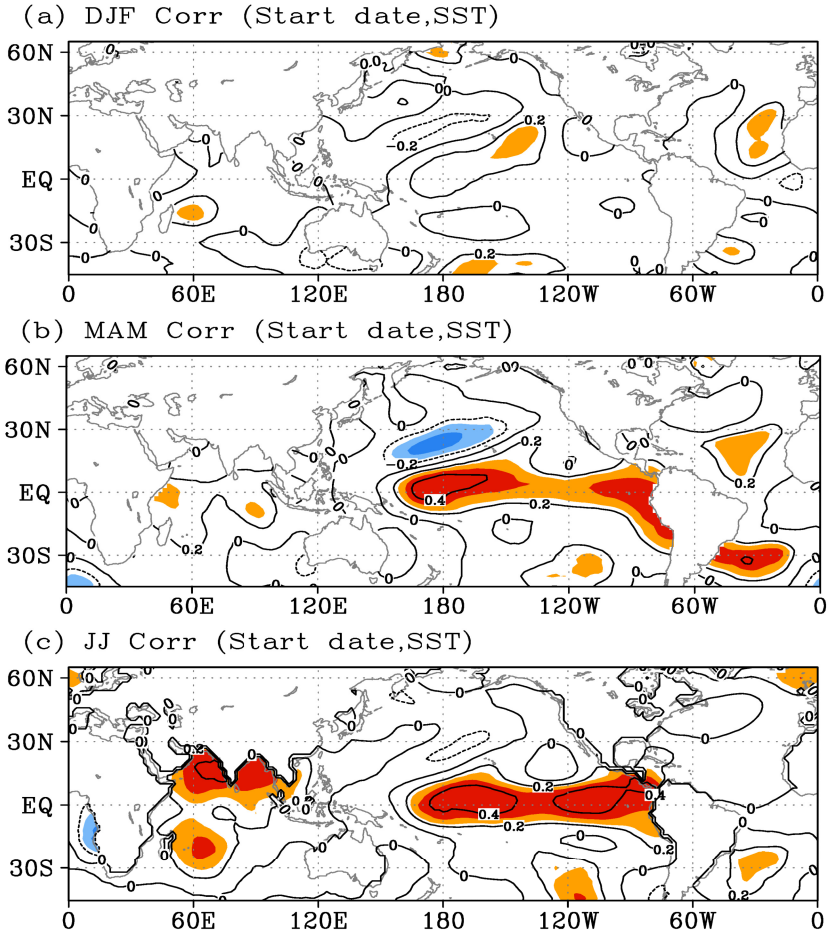

图 6　1961～2016 年华北雨季开始日期与海表温度的相关系数分布：（a）冬季；（b）春季；（c）6～7 月。浅、深阴影区分别表示置信水平达到 95%和 99%

Fig. 6　Correlation maps between OSDRS_NC and SST (Sea Surface Temperature) in the (a) winter, (b) spring, and (c) June and July during 1961–2016. The light and dark shadings indicate values at the 95% and 99% confidence levels, respectively

度异常与 OSDRS_NC 的关系，选取 Niño3.4 指数、Niño1.2 指数和热带印度洋全区一致海表温度模态指数（IOBW），分析 SST 逐月指数与华北雨季开始时间的相关系数变化（图 7）。由图 7 可见，三个 SST 指数与 OSDRS_NC 一直是正相关，相关系数从 1 月到 6 月逐渐升高，相关显著月份集中在 4～6 月，达到了 95%的置信水平，其中 Niño1.2 指数与 OSDRS_NC 相关最大月份为 4 月，Niño3.4 指数、IOBW 指数与 OSDRS_NC 相关最大月份均为 6 月，Niño3.4 指数在 6 月的相关系数接近 0.5，达到了 99%的置信水平。

进一步检验关键区 SST 与 OSDRS_NC 的相关关系是否发生年代际转变，分别计算三个指数（4 月 Niño1.2 指数、6 月 Niño3.4 指数和 IOBW 指数）与 OSDRS_NC 的 21 年滑动相关（图 8）。Niño1.2

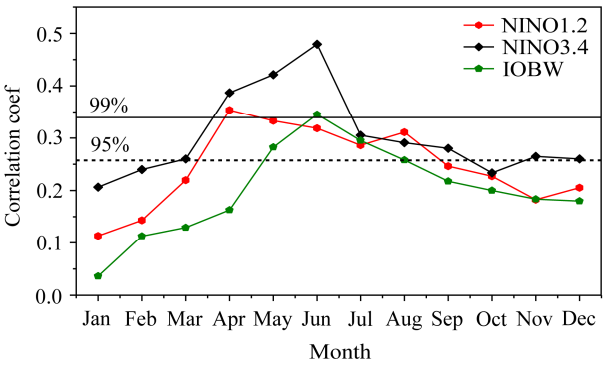

图 7 1961～2016 年华北雨季开始日期与关键区域海表温度指数的逐月相关系数。虚（实）线表示置信水平达到 95%（99%）

Fig. 7 Correlation coefficients between the OSDRS_NC and monthly SST [Niño1.2, Niño3.4, and IOBW (Indian Ocean Basin-wide Warming)] indexes from 1961–2016. The dashed and solid lines indicate values at the 95% and 99% confidence levels, respectively

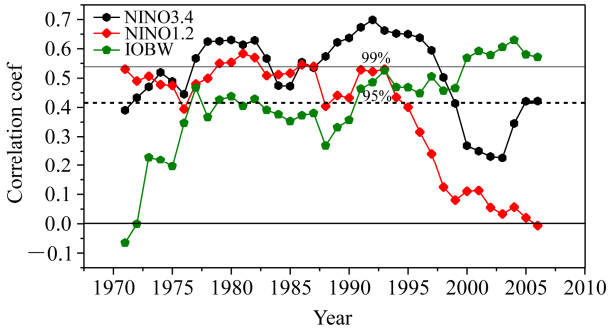

图 8 华北雨季开始时间与海表温度指数相关最大月份的 21 年滑动相关，虚（实）线表示置信水平达到 95%（99%）

Fig. 8 21-year sliding window correlations between the OSDRS_NC and the SST indexes in the months the correlation coefficients are largest. The dashed and solid lines indicate values at the 95% and 99% confidence levels, respectively

指数与 OSDRS_NC 的相关系数在 1995 年之前呈显著的正相关关系，之后相关系数逐步下降；Niño3.4 指数与 OSDRS_NC 的相关系数在 2000 年之前呈显著的正相关关系，2000 年之后相关系数略有下降；IOBW 指数与 OSDRS_NC 的相关系数在 1972 年之前呈负相关，之后转为正相关，且相关关系一直增强，20 世纪 90 年代之后呈显著的正相关关系。以上分析说明，6 月 Niño3.4 和 IOBW 对 OSDRS_NC 的影响相对显著和稳定。

用 6 月的 IOBW 指数和 Niño3.4 指数分别回归 7 月大气环流（图 9）首先，从 IOBW 回归的 7 月 500 hPa 高度场（图 9a）可见，热带至副热带 30°N 以南地区、贝加尔湖及其周边地区为显著的正高度场，表明副高偏强偏南，大陆高压偏强；从 IOBW 回归的 7 月 850 hPa 经向风场（图 9c）可见，黄淮、华北、东北地区为显著的北风距平。即 6 月 IOBW 指数为正时，大陆高压偏强，副高偏强偏南，东亚夏季风偏弱，导致华北雨季开始偏晚。

从 6 月的 Niño3.4 指数回归的 7 月 500 hPa 高度场（图 9b）可见，在日本岛东南面的西太平洋为显著正值区，朝鲜半岛至鄂霍次克海为显著负值区；在 6 月的 Niño3.4 指数回归的 7 月 850 hPa 风场上（图 9d），我国华北和东北为负值区。表明当 6 月 Niño3.4 指数为正时，7 月副高偏强、偏南，东亚夏季风偏弱，导致华北雨季开始偏晚，指数为负时则相反。

6 结论与讨论

华北地处东亚大陆和太平洋交界处，华北雨季受到热带和副热带多个系统的综合影响，华北雨季开始偏早晚的成因复杂。本文利用国家气候中心对 1961～2016 年华北雨季开始日期的监测资料、NCEP/NCAR 再分析资料，NOAA 海表温度资料等，采用中国气象局对华北雨季监测的业务规定，分析了 1961~2016 年华北雨季开始早晚的气候特征，以及影响华北雨季开始偏早晚的关键环流系统和海表温度异常强迫作用，得到的主要结论如下：

（1）华北雨季开始时间具有显著的年际变化特征，雨季开始最早出现在 7 月 6 日（9 a），最晚出现在 8 月 10 日（1 a），雨季开始集中在 7、8 月，1961～2016 年华北雨季开始时间平均在 7 月 18 日，呈现不太明显的偏晚的长期变化趋势。

（2）华北雨季开始早、晚与副热带西风急流、

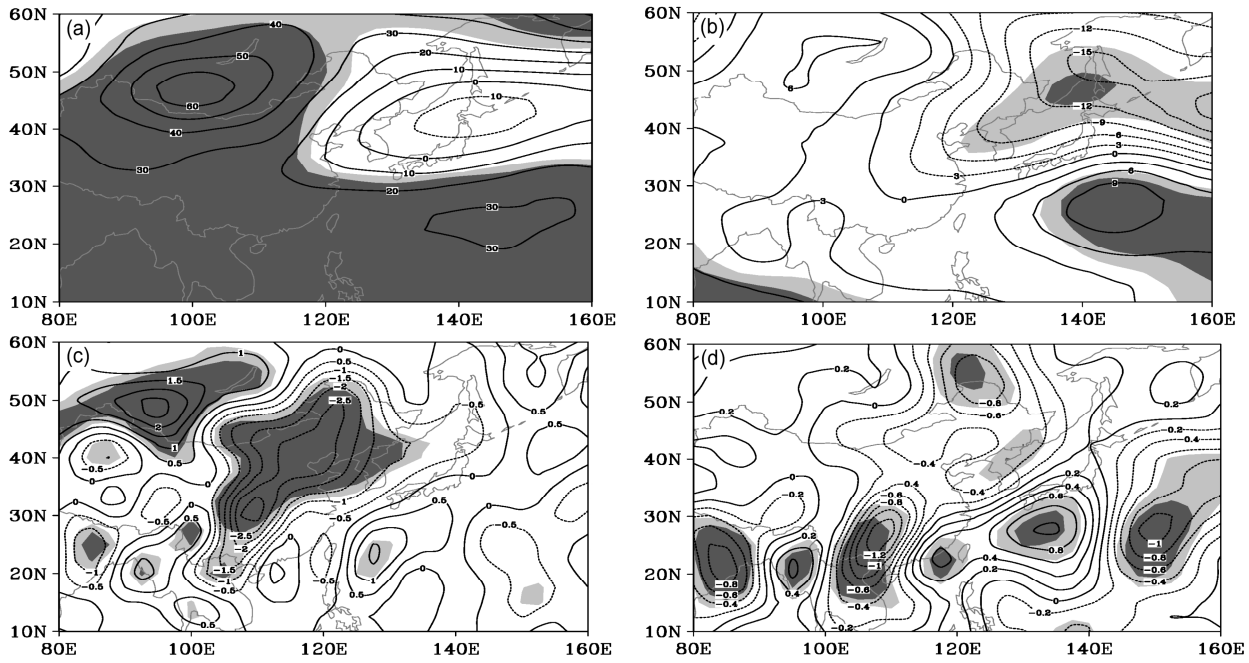

图 9　1961～2016 年 6 月 IOBW 指数（左列）和 Niño3.4 指数（右列）回归的 7 月（a、b）500 hPa 高度场和（c、d）850 hPa 经向风场。浅、深阴影区分别表示置信水平达到 95%和 99%

Fig. 9　(a, b) Geopotential height at 500 hPa (units: gpm) and (c, d) horizontal wind at 850 hPa (units: m s^{-1}) in July linearly regressed onto (a, c) IOBW and (b, d) Niño3.4 indexes in June. The light and darkshadings indicate values at the 95% and 99% confidence levels, respectively

副热带高压、和东亚夏季风等各层环流系统的演变有关，当高层西风急流建立较早，强度较强，中层副高第二次北跳偏早，低层东亚夏季风向我国北方推进偏早时，有利于水汽向北输送，导致华北雨季开始偏早；若上述环流系统演变特征相反，华北雨季开始将会偏晚；

（3）华北雨季开始早晚与全球海表温度场存在两个主要相关区域，即赤道中东太平洋区域和热带印度洋，春、夏季赤道中东太平洋与华北雨季开始早晚呈显著的正相关，夏季热带印度洋海表温度与华北雨季开始早晚呈显著的正相关，且 Niño3.4 指数和IOBW指数与华北雨季开始日期的相关系数较稳定，没发生显著的年代际变化；

（4）Niño3.4 与 IOBW 与华北雨季相关最大月份均为 6 月，当 6 月 Niño3.4 和 IOBW 指数为正值时，7 月副高偏强、偏南，东亚夏季风偏弱，不利于水汽向华北地区输送，导致华北雨季开始偏晚；当两个指数为负值时，东亚环流系统则呈相反的特点，导致华北雨季开始偏早。

本研究通过观测资料的诊断分析，研究了影响华北雨季的关键环流系统配置和前期海表温度信号，还需要通过数值试验进一步阐述相关结论的物理机制。此外，我们将继续开展华北雨季降水量的影响系统和预测信号研究，给华北雨季预测提供一些依据。

参考文献（References）

陈文, 康丽华, 王玎. 2006. 我国夏季降水与全球海表温度的耦合关系分析 [J]. 气候与环境研究, 11 (3): 259–269. Chen Wen, Kang Lihua, Wang Ding. 2006. The coupling relationship between summer rainfall in China and global sea surface temperature [J]. Climatic and Environmental Research (in Chinese), 11 (3): 259–269, doi:10.3969/j.issn.1006-9585.2006.03.002.

丁一汇, 刘芸芸. 2008. 亚洲－太平洋季风区的遥相关研究 [J]. 气象学报, 66 (5): 670–682. Ding Yihui, Liu Yunyun. 2008. A study of the teleconnection in the Asian–Pacific monsoon region [J]. Acta Meteor. Sinica (in Chinese), 66 (5): 670–682, doi:10.3321/j.issn:0577-6619.2008.05.002.

郭彦, 李建平. 2012. 一种分离时间尺度的统计降尺度模型的建立和应用——以华北汛期降水为例 [J]. 大气科学, 36 (2): 385–396. Guo Yan, Li Jianping. 2012. A time-scale decomposition statistical downscaling model: Case study of North China rainfall in rainy season [J]. Chinese Journal of Atmospheric Sciences (in Chinese), 36 (2): 385–396, doi:10.3878/j.issn.1006-9895.2011.11045.

郝立生. 2011. 华北降水时空变化及降水量减少影响因子研究 [D]. 南京信息工程大学博士学位论文. Hao Lisheng. 2011. Spatial–temporal variation of the precipitation in North China and the impact factors of

precipitation reduction [D]. Ph. D. dissertation (in Chinese), Nanjing University of Information Science & Technology.

郝立生, 丁一汇. 2012. 华北降水变化研究进展 [J]. 地理科学进展, 31 (5): 593–601. Hao Lisheng, Ding Yihui. 2012. Progress of precipitation research in North China [J]. Progress in Geography (in Chinese), 31 (5): 593–601, doi:10.11820/dlkxjz.2012.05.007.

黄荣辉, 徐予红, 周连童. 1999. 我国夏季降水的年代际变化及华北干旱化趋势 [J]. 高原气象, 18 (4): 465–476. Huang Ronghui, Xu Yuhong, Zhou Liantong. 1999. The interdecadal variation of summer precipitations in China and the drought trend in North China [J]. Plateau Meteorology (in Chinese), 18 (4): 465–476, doi:10.3321/j.issn:1000-0534.1999.04.001.

Kalnay E, Kanamitsu M, Kistler R, et al. 1996. The NCEP/NCAR 40-year reanalysis project [J]. Bull. Amer. Meteor. Soc., 77 (3): 437–472, doi:10.1175/1520-0477(1996)077<0437:TNYRP>2.0.CO;2.

闵锦忠, 赵悦晨, 郝立生. 2016. 华北雨季监测及对应环流变化特征 [J]. 干旱区地理, 39 (3): 539–547. Min Jinzhong, Zhao Yuechen, Hao Lisheng. 2016. Monitoring of rainy season and characteristics of corresponding circulation changes in North China [J]. Arid Land Geography (in Chinese), 39 (3): 539–547.

Reynolds R W, Rayner N A, Smith T M, et al. 2002. An improved in situ and satellite SST analysis for climate [J]. J. Climate, 15 (13): 1609–1625, doi:10.1175/1520-0442(2002)015<1609:AIISAS>2.0.CO;2.

施能, 朱乾根, 吴彬贵. 1996. 近 40 年东亚夏季风及我国夏季大尺度天气气候异常 [J]. 大气科学, 20 (5): 575–583. Shi Neng, Zhu Qian'gen, Wu Bingui. 1996. The East Asian summer monsoon in relation to summer large scale weather–climate anomaly in China for last 40 years [J]. Chinese Journal of Atmospheric Sciences (in Chinese), 20 (5): 575–583, doi:10.3878/j.issn.1006-9895.1996.05.08.

卫玮, 黄卓禹. 2012. 夏季东亚高空西风急流气候特征分析 [J]. 沙漠与绿洲气象, 6 (4): 21–26. Wei Wei, Huang Zhuoyu. 2012. Climatic characteristics of East Asian summer high-altitude westerly jet [J]. Desert and Oasis Meteorology (in Chinese), 6 (4): 21–26, doi:10.3969/j.issn.1002-0799.2012.04.005.

吴志伟, 江志红, 何金海. 2006. 近 50 年华南前汛期降水、江淮梅雨和华北雨季旱涝特征对比分析 [J]. 大气科学, 30 (3): 391–401. Wu Zhiwei, Jiang Zhihong, He Jinhai. 2006. The comparison analysis of flood and drought features among the first flood period in South China, Meiyu period in the Yangtze River and the Huaihe River valleys and rainy season in North China in the last 50 years [J]. Chinese Journal of Atmospheric Sciences (in Chinese), 30 (3): 391–401, doi:10.3878/j.issn.1006-9895.2006.03.03.

Wang H J. 2002. The instability of the East Asian summer monsoon−ENSO relations [J]. Adv. Atmos. Sci., 19 (1): 1–11, doi:10.1007/s00376-002-0029-5.

Webster P J, Magaña V O, Palmer T N, et al. 1998. Monsoons: Processes, predictability, and the prospects for prediction [J]. J. Geophys. Res., 103 (C7): 14451–14510, doi:10.1029/97JC02719.

Ye T S, Zhi R, Zhao J H, et al. 2014. The two annual northward jumps of the West Pacific subtropical high and their relationship with summer rainfall in eastern China under global warming [J]. Chin. Phys. B, 23 (6): 069203, doi:10.1088/1674-1056/23/6/069203.

Ye T S, Shen Q, Wang K, et al. 2015. Interdecadal change of the northward jump time of the western Pacific subtropical high in association with the Pacific decadal oscillation [J]. J. Meteor. Res., 29 (1): 59–71, doi:10.1007/s13351-014-4040-4.

张利平, 夏军, 胡志芳. 2008. 华北地区降水多时间尺度演变特征 [J]. 气候变化研究进展, 4 (3): 140–144. Zhang Liping, Xia Jun, Hu Zhifang. 2008. Precipitation change and drought−flood evolution in North China [J]. Advances in Climate Change Research (in Chinese), 4(3): 140–144, doi:10.3969/j.issn.1673-1719.2008.03.002.

张庆云. 1999. 1880 年以来华北降水及水资源的变化 [J]. 高原气象, 18 (4): 486–495. Zhang Qingyun. 1999. The variations of the precipitation and water resources in North China since 1880 [J]. Plateau Meteorology (in Chinese), 18 (4): 486–495, doi:10.3321/j.issn:1000-0534.1999.04.003.

张庆云, 陶诗言. 2000. 夏季西太平洋副热带高压北跳及异常的研究 [J]. 气象学报, 57 (5): 539–548. Zhang Qingyun, Tao Shiyan. 2000. The study of the sudden northward jump of the subtropical high over the western Pacific [J]. Acta Meteor. Sinica (in Chinese), 57 (5): 539–548, doi:10.11676/qxxb1999.052.

张庆云, 陶诗言, 陈烈庭. 2003. 东亚夏季风指数的年际变化与东亚大气环流 [J]. 气象学报, 61 (5): 559–568. Zhang Qingyun, Tao Shiyan, Chen Lieting. 2003. The inter-annual variability of East Asian summer monsoon indices and its association with the pattern of general circulation over East Asia [J]. Acta Meteor. Sinica (in Chinese), 61 (5): 559–568, doi:10.11676/qxxb2003.056.

张天宇, 程炳岩, 王记芳, 等. 2007. 华北雨季降水集中度和集中期的时空变化特征 [J]. 高原气象, 26 (4): 843–853. Zhang Tianyu, Cheng Bingyan, Wang Jifang, et al. 2007. Temporal and spatial change characteristics of precipitation-concentration degree (PCD) and precipitation-concentration period (PCP) over North China in rainy reason [J]. Plateau Meteorology (in Chinese), 26 (4): 843–853.

赵汉光. 1994. 华北的雨季 [J]. 气象, 20 (6): 3–8. Zhao Hanguang. 1994. Rainy season in North China [J]. Meteorological Monthly (in Chinese), 20 (6): 3–8.

赵俊虎, 封国林, 杨杰, 等. 2012. 夏季西太平洋副热带高压的不同类型与中国汛期大尺度旱涝的分布 [J]. 气象学报, 70 (5): 1021–1031. Zhao Junhu, Feng Guolin, Yang Jie, et al. 2012. Analysis of the distribution of large-scale drought/flood of summer in China under different types of western Pacific subtropical high [J]. Acta Meteor. Sinica (in Chinese), 70 (5): 1021–1031, doi:10.11676/qxxb2012.085.

赵俊虎, 支蓉, 申茜, 等. 2014. 2012 年我国夏季降水预测与异常成因分析 [J]. 大气科学, 38 (2): 237–250. Zhao Junhu, Zhi Rong, Shen Qian, et al. 2014. Prediction of the distribution of the 2012 summer rainfall in China and analysis of the cause for anomaly [J]. Chinese Journal of Atmospheric Sciences (in Chinese), 38 (2): 237–250, doi:10.3878/j.issn.1006-9895.2013.12215.

赵树云, 陈丽娟, 崔童. 2017. ENSO 位相转换对华北雨季降水的影响 [J]. 大气科学, 41 (4): 857–868. Zhao Shuyun, Chen Lijuan, Cui Tong. 2017. Effects of ENSO phase-switching on rainy-season precipitation in North China [J]. Chinese Journal of Atmospheric Sciences (in Chinese), 41 (4): 857–868, doi:10.3878/j.issn.1006-9895.1701.16226.

赵振国. 1999. 中国夏季旱涝及环境场 [M]. 北京: 气象出版社, 68–72. Zhao Zhenguo. 1999. Drought/Flood and Environment Field of Summer

in China (in Chinese) [M]. Beijing: China Meteorological Press, 68–72.

竺可桢. 1934. 东南季风与中国之雨量 [J]. 地理学报, (1): 1–27. Chu C. 1934. The enigma of southeast monsoon in China [J]. Acta Geographica Sinica (in Chinese), (1): 1–27, doi:10.11821/xb193401001.

宗海锋, 陈烈庭, 张庆云. 2010. ENSO 与中国夏季降水年际变化关系的不稳定性特征 [J]. 大气科学, 34 (1): 184–192. Zong Haifeng, Chen Lieting, Zhang Qingyun. 2010. The instability of the interannual relationship between ENSO and the summer rainfall in China [J]. Chinese Journal of Atmospheric Sciences (in Chinese), 34(1): 184–192, doi:10.3878/j.issn.1006-9895.2010.01.17.

Check for updates

Interdecadal Variations of the Temporal and Spatial Distribution of Summer Extreme Heat in China

Naihui Zang[1,2], Junhu Zhao[2,*], Pengcheng Yan[3], and Guolin Feng[1,4,*]

[1]*College of Atmospheric Sciences, Lanzhou University, Lanzhou 730000, People's Republic of China*
[2]*Laboratory for Climate Studies, National Climate Center, China Meteorological Administration, Beijing 100081, People's Republic of China*
[3]*Key Laboratory of Arid Climatic Change and Reducing Disaster of Gansu Province / Key Open Laboratory of Arid Climatic Change and Reducing Disaster of China Meteorological Administration, Institute of Arid Meteorology, China Meteorological Administration, Lanzhou 730020, People's Republic of China*
[4]*College of Physical Science and Technology, Yangzhou University, Yangzhou 225002, People's Republic of China*

[Original manuscript received 10 June 2019; accepted 7 September 2019]

ABSTRACT *This study reveals the spatial and temporal variations of summer extreme heat (EH) distribution in China under the background of anthropogenic climate change. Using data from 1542 meteorological stations in China during the 1961–2018 period, both the interannual and interdecadal variations of the frequency and intensity of EH are analyzed. Variations in the temporal and spatial distribution of EH in summer, which is categorized into early summer and midsummer, are determined through empirical orthogonal function (EOF) analysis. The results show that summer EH in China has the following characteristics in terms of time of occurrence and variation of spatial distribution on both intraseasonal and interdecadal time scales. Since 2000, the range and intensity of EH has increased in May, especially during the 2010s with an obvious early onset. The spatial distribution of EH in summer features an intraseasonal variation. In the Huanghuai region, EH mainly occurs in early summer (June), while in the Jiangnan and Jianghuai regions it occurs in midsummer (July–August). Since 2010, the frequency and intensity of EH has decreased in early summer but increased in conventional summer (June–August) with significant intraseasonal variation. The variation trend of the frequency and intensity of EH in North China, Huanghuai region, and Jianghuai region in both early summer and midsummer are consistent with the trend across the entire country, indicating that these regions are positive contributors to EH variation throughout the country.*

RÉSUMÉ *[Traduit par la rédaction] Cette étude révèle les variations spatiales et temporelles de la répartition de la chaleur extrême estivale en Chine dans le contexte des changements climatiques anthropiques. Nous analysons les variations interannuelles et interdécennales de la fréquence et de l'intensité des canicules estivales à l'aide de données relevées en Chine entre 1961 et 2018, et issues de 1542 stations météorologiques. Nous déterminons la variation des répartitions temporelle et spatiale des chaleurs extrêmes estivales, selon qu'elles sont hâtives ou tardives, au moyen de fonctions orthogonales empiriques (FOE). Les résultats montrent qu'en Chine les canicules estivales présentent les caractéristiques suivantes selon la période d'occurrence et la variation de la répartition spatiale aux échelles intrasaisonnières et interdécennales. Depuis 2000, l'étendue et l'intensité des chaleurs extrêmes ont augmenté en mai, surtout au cours des années 2010, qui montrent un début hâtif évident. La répartition spatiale des canicules estivales présente une variation intrasaisonnière. Dans la région de Huanghuai, les chaleurs extrêmes se produisent principalement au début de l'été (juin), tandis que dans les régions du Jiangnan et du Jianghuai, elles surviennent au milieu de l'été (juillet-août). Depuis 2010, la fréquence et l'intensité des canicules ont diminué au début de l'été, mais ont augmenté en plein été (juin à août) et montrent des variations intrasaisonnières importantes. La tendance de la variation de la fréquence et de l'intensité des chaleurs extrêmes dans le nord de la Chine, la région de Huanghuai et la région du Jianghuai au début et au milieu de l'été correspond à la tendance dans tout le pays, et indique que ces régions contribuent de façon positive à la variation des chaleurs extrêmes partout au pays.*

KEYWORDS extreme heat; temporal and spatial variation; early summer and midsummer; interdecadal variation; climate change and China

*Corresponding authors' emails: zhaojh@cma.gov.cn, fenggl@cma.gov.cn

1 Introduction

Against the backdrop of anthropogenic climate change, the frequency, intensity, and range of extreme heat (EH) events on a global scale show a robust increasing trend (Fischer & Knutti, 2015; Karmalkar & Bradley, 2017; King, Karoly, & Henley, 2017; Luterbacher, Dietrich, Xoplaki, Grosjean, & Wanner, 2004; Vincent & Mekis, 2006). According to the special report on climate change from the Intergovernmental Panel on Climate Change (Allen, Dube, Solecki, & Aragón-Durand, 2018), as of 2017, human activities have led to an increase of 1.0°C (±0.2°C) in the average global surface temperature relative to pre-industrial levels, which is higher than the warming of 0.87°C (±0.12°C) from pre-industrial levels to the 2006–2015 period. Most of the surface warming trend is larger than the global average. These EH events are serious threats to the natural environment and development of human society. For example, both the EH in Europe in 2003 and the EH in Moscow in 2010 caused more than 10,000 deaths and led to serious economic losses (Coumou & Rahmstorf, 2012; Dole et al., 2011; Luterbacher et al., 2004). In the United States in 2012 (Ye, Yin, Chen, Zheng, & Wu, 2013), southern China in 2013, and some parts of North China and Northeast China in 2018, the number of EH days and maximum temperatures in summer exceeded any in the historical record (Peng, Liu, & Sun, 2016). Currently, about 30% of the world's population is exposed to high temperatures for at least 20 days in a year, which increases the risk of human illness and death (Im, Pal, & Eltahir, 2017; Mora et al., 2017).

The severe impacts and threats of EH on the economy and the environment have caused widespread concern in all sectors of society. Easterling et al. (1997, 2000) and Beniston et al. (2007) have defined EH events from various perspectives, such as extreme temperature and the wide range of temperature anomalies, and have noted that variation of the daily maximum temperature results in a decrease in the diurnal temperature range and an increase in the average temperature. Casati and de Elia (2014) used the non-stationary model for Generalized Extreme Value distribution to analyze the trend in extreme temperatures. Since the 1990s, a large number of researchers have studied the characteristics of the variation and regional differences in EH in China. Although the frequency and intensity of EH in most parts of China show staged changes, over the past 50 years the overall trend is still increasing, with an average annual temperature increase of 1.1°C. Since the 1990s, the frequency and intensity of EH events in China have increased significantly (Ding et al., 2007; Qin, Ding, Su, Wang, & Ren, 2005; Xu, Lu, Mao, & Chen, 2019; Ye et al., 2013). Feng, Hou, Zhi, Yang, and Zhang (2012) used non-linear dynamic methods to study massive and continuous extreme events. They found that the occurrence of EH events in China is increasing and that the turning points of the EH events differed between regions. Tang, Zhai, and Wang (2005) pointed out that from the 1950s to the beginning of the 2000s, the change in annual average maximum temperature in northern China was significantly higher than in the south, and the Jiangnan region was a cooling zone. Wang, Ren, and Yan (2013) have shown that the areas with high intensity and frequency of EH events in China are located mainly in the northwest and southeast regions. Before the 1990s, the frequency of EH events showed a decreasing trend, and then significantly increased from the late 1990s to the 2000s. Shen, You, Wang, and Kong (2018) analyzed the temporal and spatial variation of EH events and found that after 1998, high-intensity EH waves appeared frequently in South China. Previous studies selected partial areas of eastern China, or a single province or city, and representative stations to conduct research on EH events in China. For example, Chen and Lu (2014, 2015) studied EH events in Northeast and North China and analyzed the EH difference caused by topography in each sub-area. Yuan, Ding, Gao, and Li (2018) found that EH events in southern China show two different spatial distribution patterns in summer: Jianghuai type and Jiangnan type.

Extreme weather and climate events show significant spatial and temporal differences (Alexander et al., 2006; Turner & Gyakum, 2010; Wang, Feng, & Vincent, 2014). Research has shown the EH variation in various regions of China has strong interdecadal characteristics, but the selection of study area and study period has a great influence on the results (Sun, Wang, & Yuan, 2011). Previous studies of EH events in China have mainly focused on the spatial and temporal characteristics of conventional summer (June–August), and not enough attention has been paid to the intraseasonal characteristics of EH in various regions of China. However, the northward progress of the summer rain belt in eastern China, a typical monsoon region, is affected by summer monsoon activity and, therefore, has obvious periodic characteristics (Gong, Feng, & Fang, 2015; Hu, Shen, Wang, & Feng, 2016; Lian, Shen, Gao, An, & Tang, 2003). This results in obvious intraseasonal variation of EH in eastern China (Zhang, Li, Li, Shang, & Zheng, 2016). In addition, southwest China, which is affected by the Indian low, shows obvious seasonal variation of EH (Wang, 1962). Therefore, it is necessary to systematically study the variation of summer EH in China on both intraseasonal and interdecadal time scales.

In this study, EH days are defined based on the standard of the National Meteorological Administration to study the variation of the frequency and intensity of EH in China from May to September over the past 58 years (Shi, Ding, & Cui, 2009; Tao & Zhang, 2019). Based on interannual changes, conventional summer (June–August) is divided into two periods, early summer (June) and midsummer (July–August), to provide a systematic analysis of the variation of the frequency and intensity of summer EH in China.

2 Data and methods

a *Data*

For our study, observed daily surface air temperature data from 1 January 1951 to 31 August 2018 for 2374 stations

were provided by the National Weather Information Center of the China Meteorological Administration. To ensure the completeness and continuity of the time series, the stations with the highest temperature (T_{max}) missing for more than one day were excluded. Finally, T_{max} data from the May–September period for 1542 sites from 1961 to 2018 were selected. The spatial distribution of the 1542 selected stations is shown in Fig. 1. Station density in the eastern region is high, and station density in the western region, especially the Qinghai–Tibet Plateau, is low. Therefore, the following analysis mainly involves areas with high site density.

b *Methods*

An EH day is an effective indicator of EH events. In general, when the maximum daily temperature is greater than or equal to a certain threshold temperature (such as 30°, 32°, or 35°C), the day is defined as an EH day. Sherwood and Huber (2010) showed that humans maintain a core body temperature near 37°C that varies slightly among individuals but does not adapt to the local climate. It is generally considered that human skin temperature should be below 35°C. When skin temperature exceeds this threshold, the human body is uncomfortable. The Chinese Meteorological Department also defines 35°C as the EH threshold, and an EH day is determined to have occurred when the maximum temperature of the day is greater than or equal to 35°C (Ding, Qian, & Yan, 2010; Shi et al., 2009; Sun et al., 2011). To further study the differences in EH distribution in different regions, this fixed threshold is used to define an EH day in this study. In addition, based on this definition, this study further defines the intensity of EH events, which is expressed as the difference between the highest daily temperature and the EH threshold temperature: the greater the difference, the stronger the intensity of the EH event. Using the frequency and intensity of EH, the temporal and spatial variations of summer EH are studied in different decades. To further determine intraseasonal differences in EH, which include both interdecadal variations and variations in the temporal and spatial distribution, empirical orthogonal function (EOF) analysis of the EH day anomalies in both early summer and midsummer during the 1961–2018 period was performed for each of the 1542 stations in China. The climatology used in this study is the 1981–2010 average.

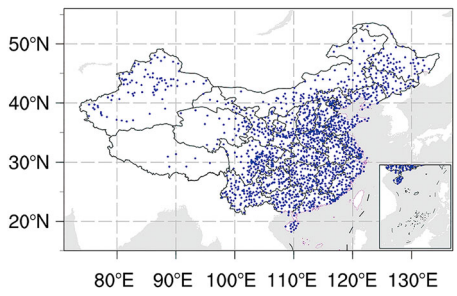

Fig. 1 Spatial distribution of the 1542 sites in China.

3 Results and analysis

a *Temporal and spatial distribution characteristics of the frequency of extreme high temperatures during various periods in China*

Figure 2 shows the standardized anomalous, linear trend and the nine-year running mean of the total number of EH days in China during conventional summer (June–August) and May–September from 1961 to 2018, all of which show significant interdecadal increases except for May and September. From the late 1960s to the end of the 1990s, negative anomalies dominated. Since the start of the twenty-first century, positive anomalies have been observed. Previous studies have shown that the trend in the frequency of EH in most parts of northern China from the 1950s to the 1990s is less obvious than the trend after the 1990s (Chen & Lu, 2014; Ma, Fu, Ren, & Yang, 2003; Ye et al., 2013), and in most parts of southern China there is no trend or a weakly decreasing trend before the 1990s (Tang et al., 2005; Wang et al., 2013). Therefore, to further study the variation of EH on intraseasonal and interdecadal time scales, a decade-by-decade statistical analysis of EH is given in the following.

1 MONTHLY CHARACTERISTICS OF EH STATIONS AND EH DAYS IN VARIOUS DECADES

Figure 3 shows the annual average of stations with a record of EH (AAN) in each period from May to September from 1961 to 2018 (Fig. 3a) and the annual average of the total number of EH days (AAD) in each period from May to September from 1961 to 2018 (Fig. 3b). It can be seen that the AAN and AAD have both intermonthly and interdecadal variations.

In each decade, the trend for AAN per month increased at first and then decreased, reaching a peak in July in all six decades. The trend for the AAD per month is very similar to the trend for the stations. The decadal average of AAN increases from 31% (May) to 75% (June) compared with the AAD in July. However, the decadal average of AAD only increases from 11% (May) to 41% (June) compared with the AAD in July. The trend for AAN for May to July increases faster than the trend for the AAD, which means that the range of EH in June is larger, but the duration is short.

In each month, the variations in AAN and the AAD had an interdecadal decreasing trend at first followed by an increasing trend. At the end of the 1960s, the AAN and AAD decreased gradually in all months. In the 1990s, the weakening trend slowed and, in some months, began to increase. Since the start of the twenty-first century, AAN and AAD have increased in the five months (May–September), and this increase is more robust. This trend is more pronounced in July and August and is consistent with the previous conclusions of Ding et al. (2007) and Wang et al. (2013).

In May, the highest AAN and the highest AAD, with 418 stations and 1275 days, respectively, occurred in the 2010s. The AAN increased by 47% compared with the 2000s (284 stations). At the same time, the AAD increased by 77% compared with the 2000s (721 days). The data show that since the

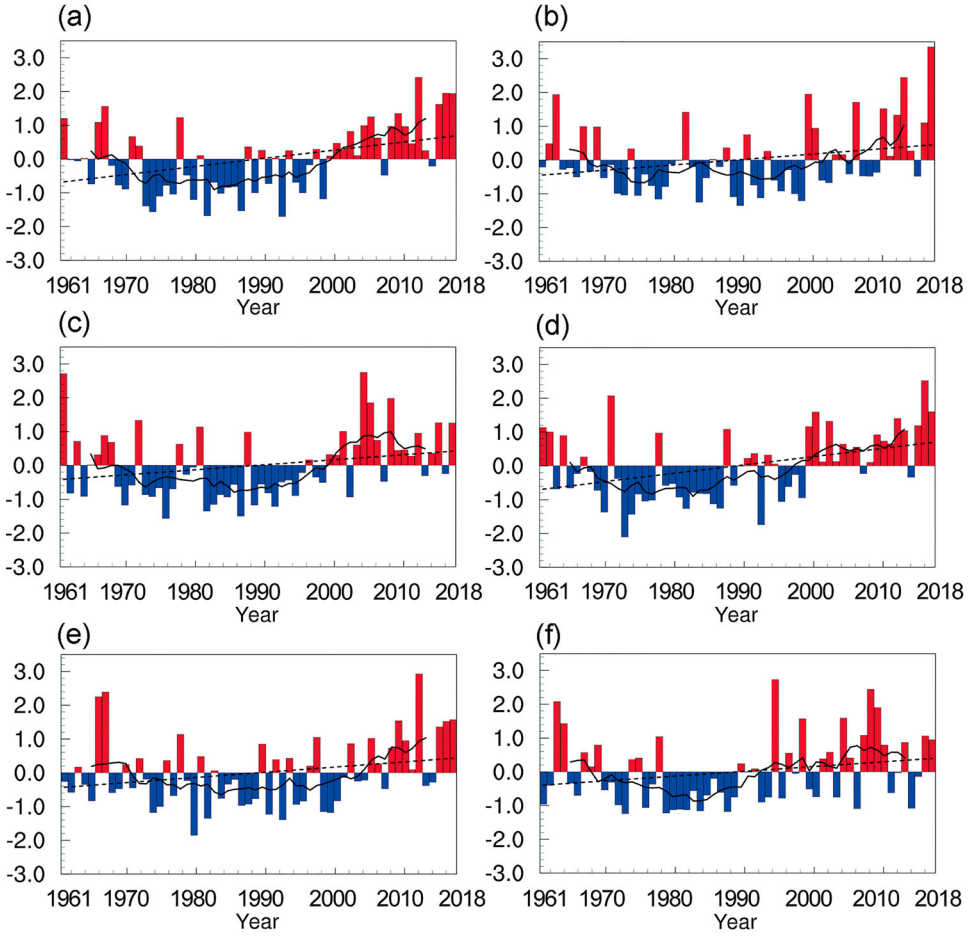

Fig. 2 Standardized anomalies (histogram), linear trend (dashed line), and nine-year running mean (solid line) of the total number of EH days in conventional summer (June–August) and May–September for 1961–2018. (a) Conventional summer, (b) May, (c) June, (d) July, (e) August, and (f) September. The linear trends for conventional summer, June, July, and August are statistically significant at the 90% confidence level, but the trends for May and September are not.

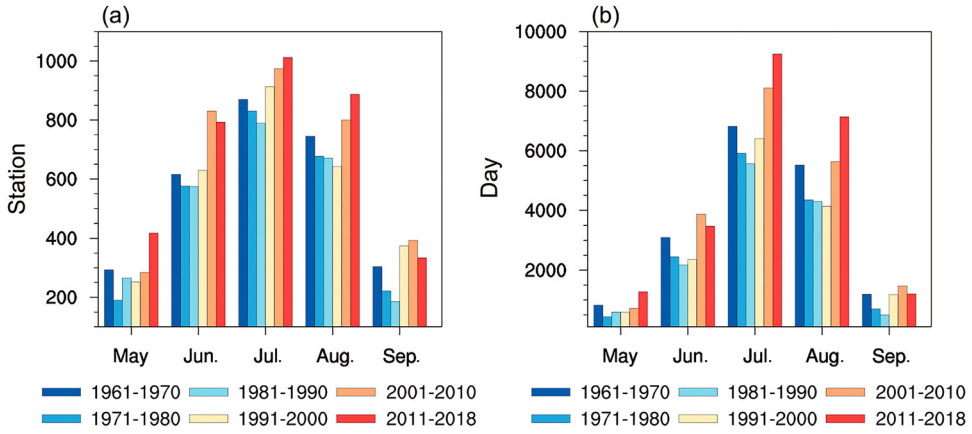

Fig. 3 (a) Annual average of stations with a record of EH (AAN) in each decade from May to September for 1961–2018 in China. (b) Annual average of the total number of EH days (AAD) in each decade from May to September for 1961–2018 in China.

beginning of the twenty-first century, the range, frequency, and intensity (not shown) of EH have all increased. In particular, since the 2010s, the range and intensity have increased significantly, which indicates early onset of EH.

In June, the highest AAN (830 stations) and AAD (3868 days) occurred in the 2000s, with an increase of nearly one-third and two-thirds, respectively, from the 1990s. In the 2010s, the AAN and the AAD decreased by 4% and 10%,

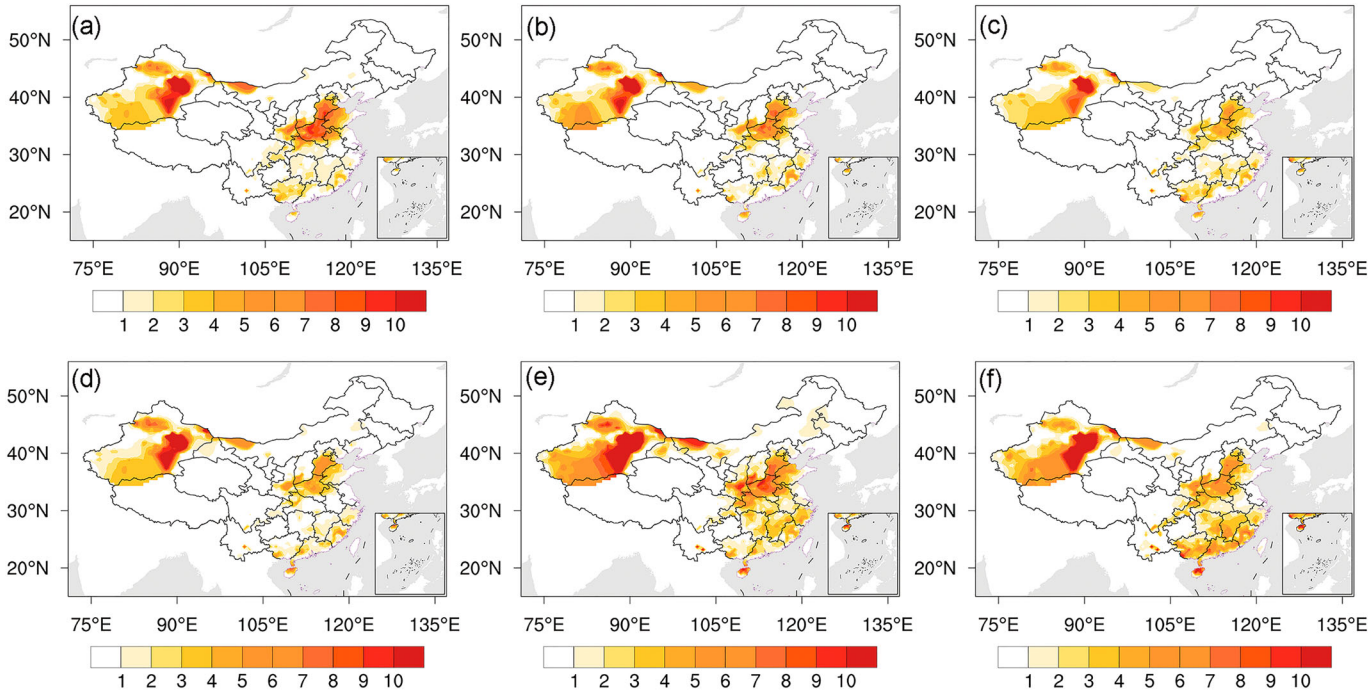

Fig. 4 Spatial distribution of the annual average of the number of EH days in June in each decade from 1961 to 2018 in China (days per year). (a) 1961–1970, (b) 1971–1980, (c) 1981–1990, (d) 1991–2000, (e) 2001–2010, and (f) 2011–2018.

respectively. However, in the 2010s, the AAN and the AAD in conventional summer increased by 3% and 12%, respectively, compared with the 2000s, indicating that the frequency and intensity of EH decreased in early summer (June). The values of frequency and intensity for summer EH tend to be concentrated in midsummer (July–August) after 2010.

In July and August, both the highest AAN (1012 and 887 stations, respectively) and highest AAD (9250 and 7134 days, respectively) occurred in the 2010s. Both the increased rates of the AAN and AAD in July (4% and 14%), compared with the 2000s, are lower than in August (10% and 27%). However, as of June, both the highest AAN (393 stations) and the highest AAD (1469 days) in September occurred in the 2000s and decreased by 15% and 18%, respectively, in the 2010s. The decrease in September indicates that both the higher values of frequency and intensity of summer EH tend to be concentrated in midsummer after 2010 and increased faster in August.

2 SPATIAL DISTRIBUTION CHARACTERISTICS OF EXTREME HIGH TEMPERATURE DAYS IN EACH DECADE

In June, EH days in China are mainly concentrated in the west of Northwest China, the Huanghuai region (the area between the lower Yellow River and the Huai River), and the Jiangnan region (the area between South China and south of the Yangtze River), while the number of EH days in the Jianghuai region (the area from north of the Yangtze River to the Huai River) is small. In eastern China, the frequency of EH shows a staggered distribution from north to south (Fig. 4).

The number of EH days in June from 1961 to 2018 showed a decadal decreasing trend at first followed by an increasing trend. Compared with the 1960s, the number of EH days in the Huanghuai region decreased significantly in the 1970s and decreased further in the 1980s, but there was little change in the 1990s. However, in the west of Northwest China and south of the Yangtze River, the change in the number of EH days is not obvious from the 1960s to the 1990s. In the 2000s, the number of EH days in both eastern China and the west of Northwest China increased significantly, especially in the west of Northwest China and the Huanghuai region. In the 2010s, the number of EH days decreased slightly in the Huanghuai region but increased in areas from South China to the Jiangnan region.

In July, the average range of EH days in China increases (Fig. 5). The EH days are mainly concentrated in the west of Northwest China and southeastern China. The high-value area of EH days in the east is located in the south of Jiangnan region. According to the difference in the number of EH days between decades (not shown), compared with the 1960s, the number of EH days in the Huanghuai and Jiangnan regions decreased significantly in the 1970s and decreased further in the 1980s. However, in South China and the west of Northwest China, the change in the number of EH days is not obvious from the 1960s to the 1980s (Wang et al., 2013; Ye et al., 2013). In the 1990s, the number of EH days increased significantly north of the middle and lower Yangtze River, especially in the Huanghuai and North China regions but decreased slightly in the South China region. In the 2000s, the number of EH days increased significantly south of the middle and lower Yangtze River. In the 2010s, the number and range of EH days in the west of

Northwest China and the Jianghuai and Huanghuai regions increased further.

Both the regional and interdecadal variations of the average number of EH days in August resemble those in July, and the interdecadal variations of EH in different regions are similar. However, both the range and number of EH days in August (Fig. 5) were smaller than those in July, and the spatial distribution of EH days north of the Yangtze River was relatively stable from the 1980s to the 2000s.

In summary, the main areas where EH occurs in June and from July to August are located in the west of Northwest China and Southeast China. In all three months there is an interdecadal decreasing trend at first followed by an increasing trend, which is consistent with the interdecadal trend of the stations with EH and number of EH days in Fig. 3. However, in eastern China, there are significant spatial differences in the number of EH days in June and the period from July to August. In June, EH occurs mainly in the Huanghuai region and the area from South China to the Jiangnan region, while the occurrence of EH in the Jianghuai region is less frequent, so the spatial distribution of the number of EH days in eastern China is not continuous. This is mainly because the Meiyu rains occur in June in the Jianghuai region (Tao, Zhao, & Chen, 1958). During this period, it is unlikely that an EH event would occur when there is frequent heavy precipitation. In the period from July to August, the main rainbelt in eastern China is pushed north (Gong et al., 2015; Hu et al., 2016; Lian et al., 2003), and the areas from South China to the Jianghuai region are affected by the western Pacific subtropical high (Lin, Bi, & He, 2005; Zhang et al., 2005; Zhang et al., 2016). The western Pacific subtropical high extends westward and strengthens, resulting in an increase in the number of EH days in the middle and lower Yangtze region (Peng et al., 2016) and even in Northeast China (Tao & Zhang, 2019). The mid-high-latitude circulation system and the activities in the Pacific Northwest also play an important role in EH in midsummer in the Jianghuai region (Yuan et al., 2018).

In addition, from the 1960s to the 1990s, the interdecadal trends of the spatial distribution of EH events in China in June and from July to August are almost the same. However, entering the twenty-first century, the number of EH days in June increased significantly in the Huanghuai region, while the significant increase in July and August is located in the area from South China to the Jiangnan region. In the 2010s, the number of EH days in the North China, Huanghuai, and Jianghuai regions decreased in June but increased in the period from July to August. Furthermore, the variation trends in the regions of North China, Huanghuai, and Jianghuai in both early and midsummer are consistent with the trend of EH days over all China in the 2010s (Fig. 3). This indicates that these three regions make a positive contribution to the change in EH throughout the country in the summer. The variation also reflects the obvious intraseasonal differences in the spatial distribution of EH in June and from July to August.

The number of EH days in June and from July to August are significantly different in the interdecadal spatial distribution in various regions. Therefore, it is not appropriate or accurate to consider the period from June to August as a whole when studying EH, as has been done in previous studies.

b *Temporal and spatial distribution characteristics of EH intensity in China*

The average EH intensity in China in June has obvious interdecadal characteristics (Fig. 6). The area with the highest EH intensity is mainly concentrated in Northwest China and the Huanghuai region. The highest intensity is located in the west of northwestern China. Both the trends of intensity and range of EH decreased at first and then increased. Compared with the 1960s, the EH intensity gradually weakened in the 1970s and 1980s and began to increase in the 1990s. In the 2000s, the EH intensity increased significantly, and the range expanded. In the 2010s, the EH intensity and range have continued to increase.

The EH intensity in July (Fig. 7) was mainly distributed in the west of Northwest China. The intensity centres for all decades are located in the west of Northwest China and south of the Yangtze River. Compared with the 1960s, the EH intensity in the 1970s and 1980s continued to weaken and reached a minimum and remained unchanged in the 1990s. However, compared with the 1960s, the EH intensity in the west of Northwest China increased in the 1970s, at the same time the EH intensity decreased in June of the same decade. Furthermore, during the period from the 1970s to the 1990s, the EH intensity in northwestern China was not significant. In the twenty-first century, the EH intensity increased significantly, especially in northwestern China and the area from South China to the Jiangnan region. In the 2010s, the EH intensity in the west of Northwest China and in the Huanghuai and Jiangnan regions experienced a further increase, and the range of high-intensity areas also increased. This is consistent with the prediction of Christidis, Stott, and Brown (2011) that future EH intensity would strengthen. The spatial distribution of EH intensity in August (Fig. 7) was similar to that in July, but both the range and intensity were smaller than in July.

In summary, the EH intensity in China from June to August is distributed mostly in the northwest and southeast regions, and the interdecadal trend of EH intensity is similar for all three months. Moreover, in the same month, the spatial distribution of the EH frequency (Figs 4 and 5) is consistent with the spatial distribution of EH intensity. These conclusions are consistent with the findings of Wang et al. (2013) who found that the highest EH intensity and frequency in China occur mainly in northwestern and southeastern China. Owing to factors such as topography and precipitation, the interdecadal variation of EH in the west of Northwest China is relatively stable (Sun et al., 2011). In eastern China, which has a typical monsoon climate, the central values of EH intensity from June to August resemble the central values of EH frequency in each month, with large climate variability (Wang, 2001; Sun et al., 2011). Therefore, based on the difference in the frequency and intensity of EH,

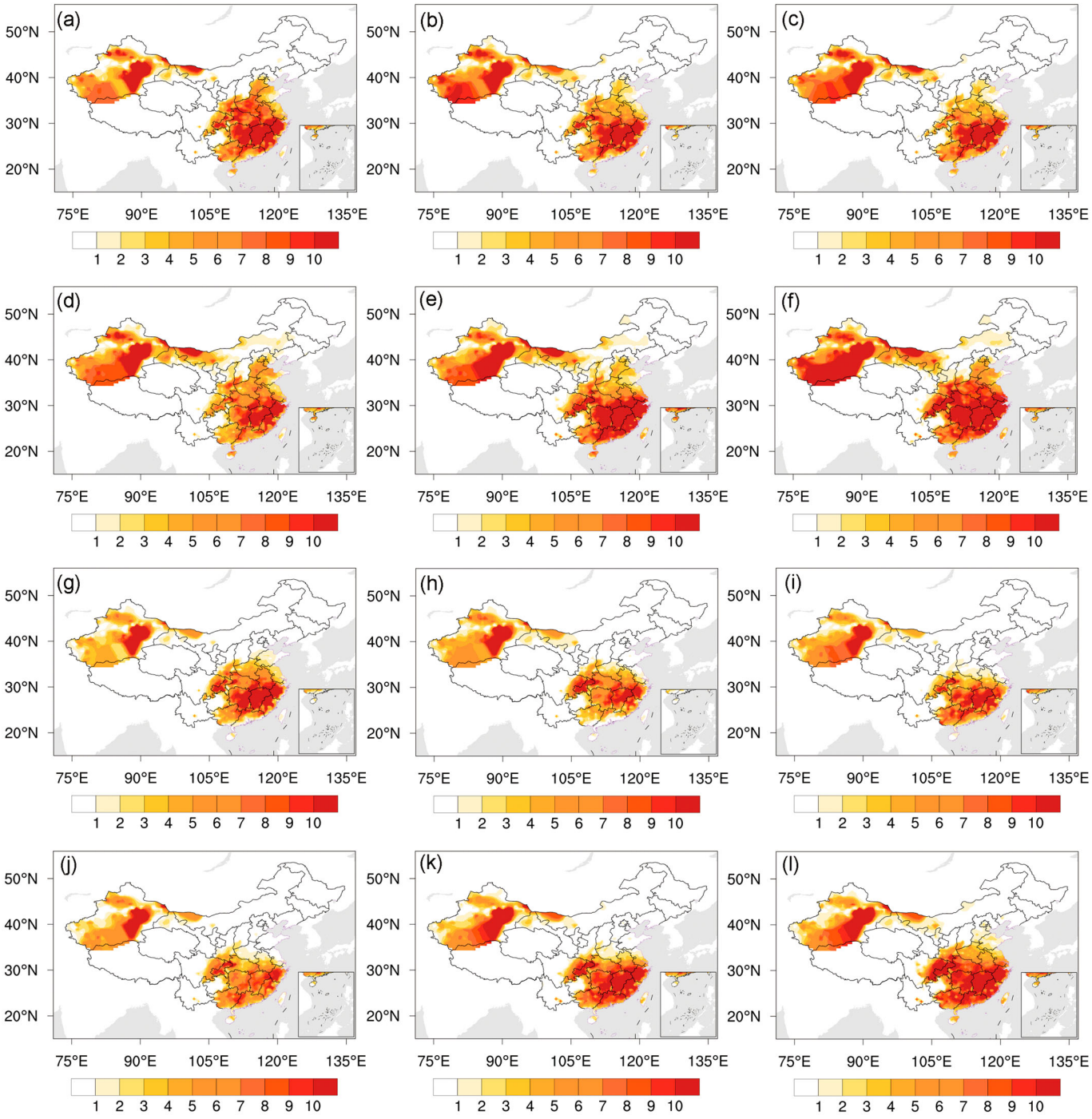

Fig. 5 As in Fig. 4, but for (a) to (f) July and (g) to (l) August. (a) and (g) 1961–1970, (b) and (h) 1971–1980, (c) and (i) 1981–1990, (d) and (j) 1991–2000, (e) and (k) 2001–2010, and (f) and (l) 2011–2018.

this study divided conventional summer into early summer (June) and midsummer (July–August) for systematic analysis.

c *Temporal and spatial distribution characteristics of summer EH days in China*

The spatial and temporal distributions of EH frequency and intensity in early summer and midsummer are significantly different. The results of the EOF analysis of EH day anomalies in both early summer and midsummer follow.

1 TEMPORAL AND SPATIAL DISTRIBUTION CHARACTERISTICS OF EH DAYS IN EARLY SUMMER

Figure 8 shows the spatial patterns of the first three leading EOF modes and the time series of the corresponding principal components (PC) in early summer (Fig. 8). The first leading

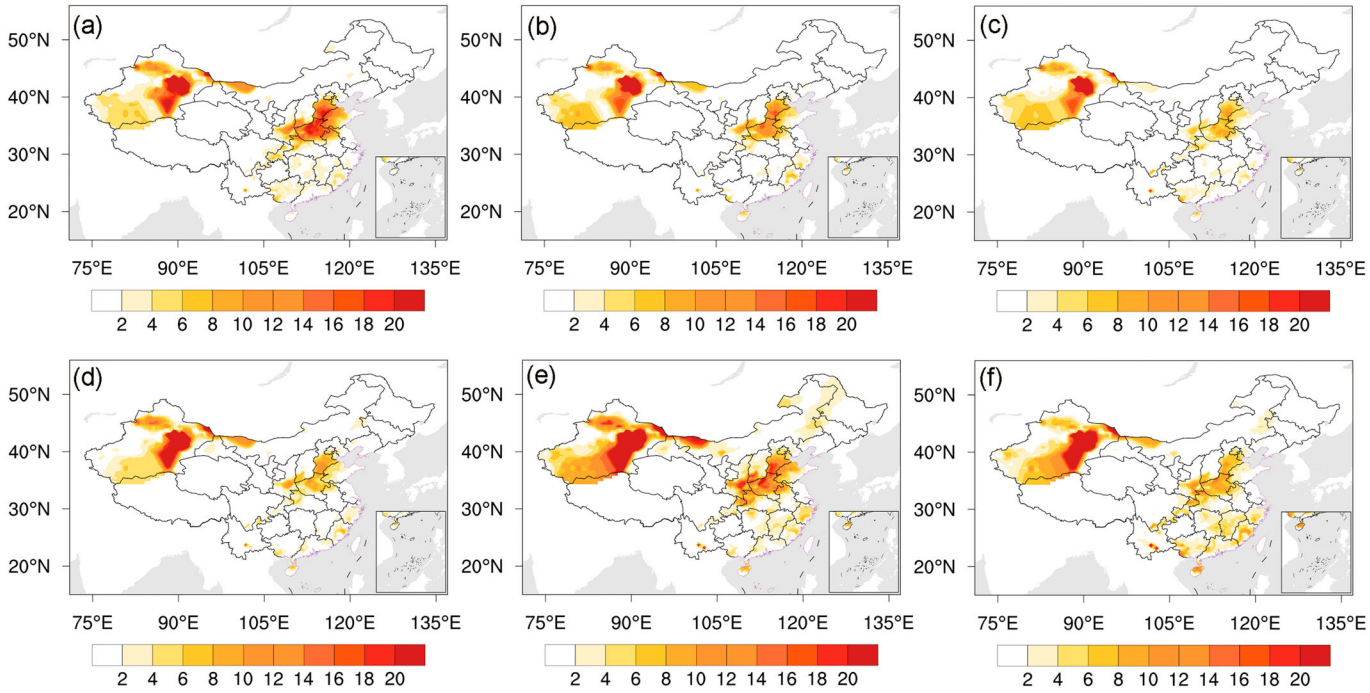

Fig. 6 Spatial distribution of EH intensity in June in each decade from 1961 to 2018 in China (°C per year). (a) 1961–1970, (b) 1971–1980, (c) 1981–1990, (d) 1991–2000, (e) 2001–2010, and (f) 2011–2018.

EOF mode (EOF1) explains about 26.76% of the total variance. The EOF1 of EH day anomalies in early summer (Fig. 8a) is characterized by warming in the Yellow–Huai River basin. The warm centre is located in the Huanghuai region. However, Northeast, Southwest, and South China (each showing negative in Fig. 8a) experienced cooling.

In early summer, the time coefficient of EOF1 and the nine-year running mean show significant interdecadal variations with two interdecadal transitions (Fig. 8b). In the 1960s, there were more occurrences of EH days, and the first interdecadal change occurred in the 1970s. There were fewer occurrences of EH days from the 1970s to the late 1990s. At the beginning of the 2000s, the second interdecadal change occurred. The amplitude increased, turning from negative to positive values and reaching a maximum in 2005, and then decreased.

In Figs 8c and 8d, the second leading mode (EOF2) and the time series of the corresponding PC are shown, respectively. The EOF2 features a north–south dipole in EH day anomalies over eastern China and explains 19.17% of the total variance. The warm centre is located in southern China. The Huanghuai region and Northeast China have negative values.

The time coefficient of EOF2 in early summer and the nine-year running mean show an interdecadal change from negative to positive. In the 1990s, there was an interdecadal transition, and the EH days showed a reversal in the spatial distribution between north of the Yangtze River and south of the Yangtze River. Since the 2000s, the nine-year running mean shows an obvious increase, and the number of EH days in the Jiangnan–South China region has gradually increased.

The third mode (EOF3) is mostly characterized by a north–south dipole in the EH day anomalies over China, with warming north of the Yellow River (Fig. 8e); however, it explains only 6.18% of the total variance. The values in the Huanghuai and Jiangnan regions are negative, and the centre of the low values is located in the Huanghuai region. In early summer, the time coefficient of EOF3 and the nine-year running mean (Fig. 8f) are basically consistent with the change in EOF2, but the positive value of the amplitude was larger than for EOF2 from the late 1990s to 2000s.

In the Jianghuai region in early summer there is no significant positive or negative change in the anomaly fields of the three modes, reflecting the stable temperature change in the Jianghuai region in early summer.

2 TEMPORAL AND SPATIAL DISTRIBUTION CHARACTERISTICS OF EH DAYS IN MIDSUMMER

Figure 9 presents the EOF analysis for midsummer. The first leading EOF mode explains about 38.75% of the total variance. The first leading mode (EOF1) of the EH day anomalies in midsummer reflects the strength of the EH days over southeastern China (Fig. 9a). The warm centre is located mainly in the area from Jianghuai to Jiangnan. This centre is almost identical to the maximum centre of the frequency and intensity distribution of summer heatwaves in China over the past 50 years noted by Ye et al. (2013) and Yuan et al. (2018). Negative values are mainly located in Northeast and Northwest China. Compared with EOF1 for early summer, the warm centre in midsummer moved to the southeast, capturing the characteristics of the increasing number of EH days after the

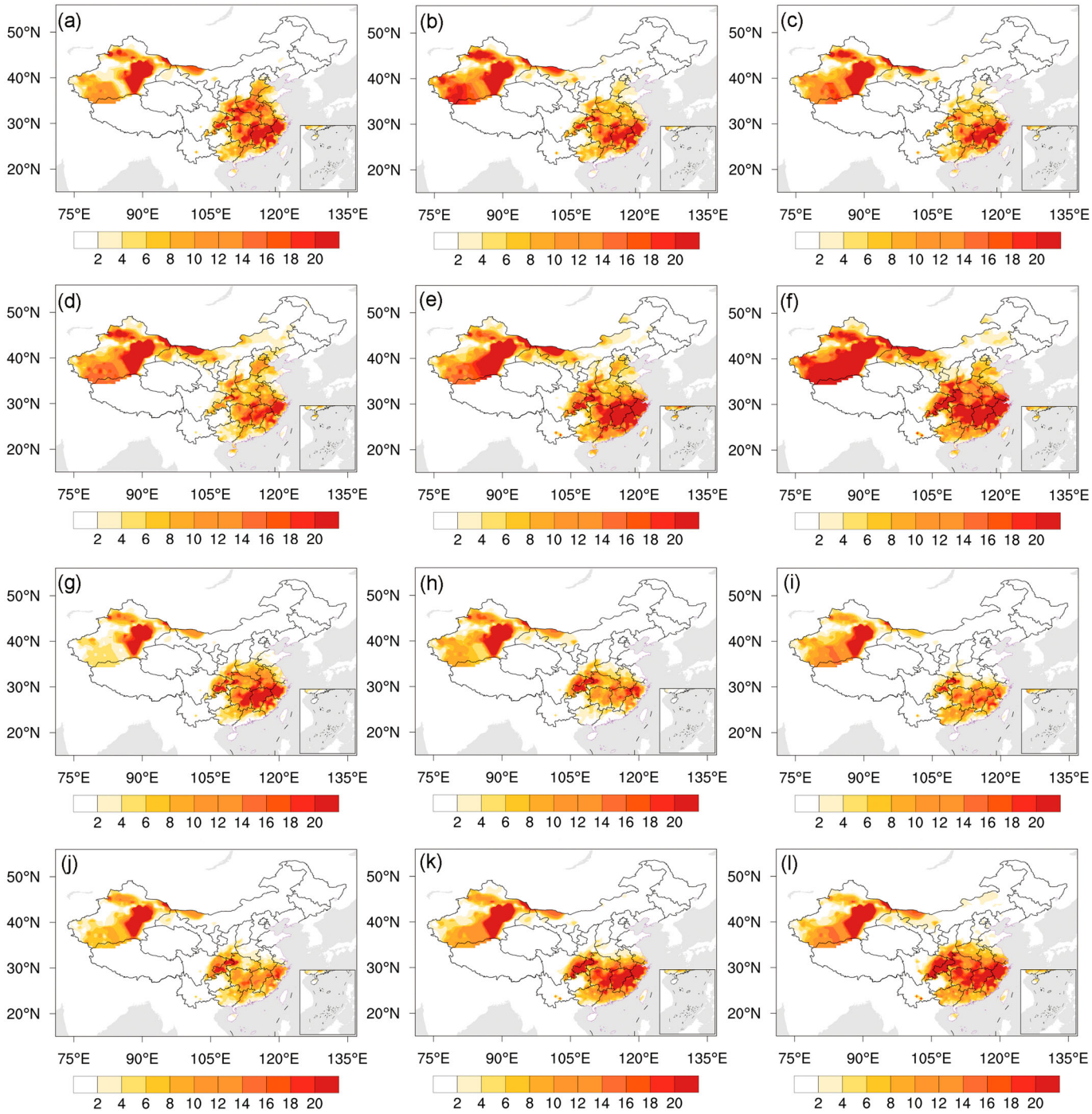

Fig. 7 As in Fig. 6, but for (a) to (f) July and (g) to (l) August. (a) and (g) 1961–1970, (b) and (h) 1971–1980, (c) and (i) 1981–1990 (d) and (j) 1991–2000, (e) and (k) 2001–2010, and (f) and (l) 2011–2018.

end of the Meiyu rains in the Jianghuai region. Both the time coefficient and the nine-year running mean of EOF1 in midsummer (Fig. 9b) resemble those in early summer, but the linear growth trend in midsummer is obvious. Entering the 2010s, the EH day anomalies increase notably.

The second mode (EOF2) is basically characterized by an inverse variation in temperature between the areas south and north of the Yangtze River (Fig. 9c) and explains 14.07% of the total variance. The warm centre is located in South China, which is basically consistent with the Jiangnan-type EH proposed by Yuan et al. (2018). The area north of the Yangtze River has a cold centre. Compared with EOF2 of early summer, both the positive-value zone and the warmer centre range are smaller, and the negative zone is farther south. The time coefficient of the summer EOF2 and the nine-year running mean (Fig. 9d) have obvious interdecadal

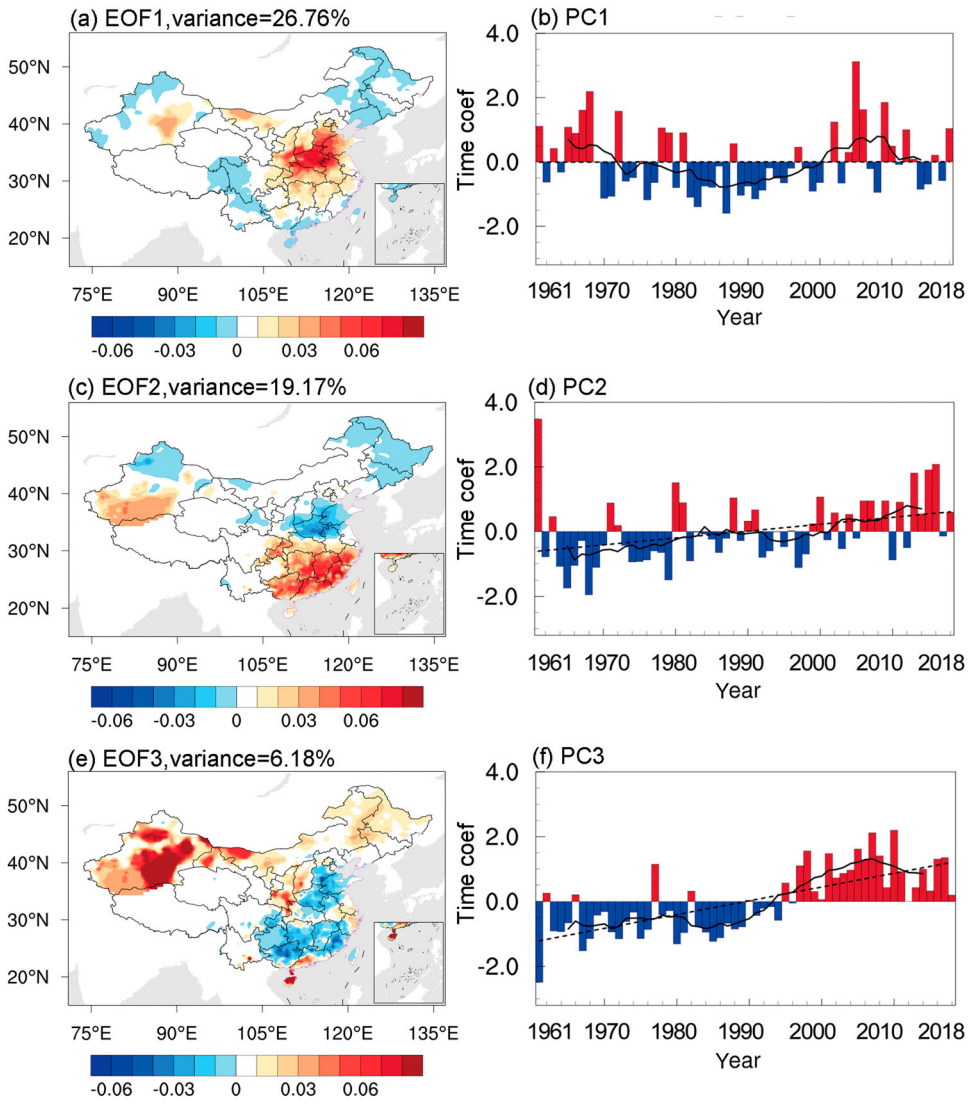

Fig. 8 (a) and (b) EOF1, (c) and (d) EOF2, and (e) and (f) EOF3 of the anomaly of the number of EH days in early summer for the 1961–2018 period in China: (a), (c), and (e) the spatial patterns of the first three leading EOF modes, respectively; (b), (d), and (f) the standardized time series (histogram), linear trend (dashed line), and nine-year running mean (solid line), respectively, of the corresponding principal components.

changes with three interdecadal transitions. The first change occurred in the late 1970s, and the other two changes occurred in the early 1990s and the late 1990s. At the beginning of the 2000s, the trend again became positive.

In the third mode (EOF3), the spatial characteristics of the midsummer EOF3 in the Huanghuai–Jiangnan region (Fig. 9e) are quite different from those of early summer, but it explains only 9.02% of the total variance. In midsummer, EOF3 captures the characteristics that the variation of EH in the Jianghuai region is similar to that in the Jiangnan region. The time coefficient and the nine-year running mean of the summer EOF3 (Fig. 9f) are also similar to those in early summer.

3 CORRELATION ANALYSIS OF EXTREME HEAT IN EARLY SUMMER AND MIDSUMMER

To analyze the difference in EH days between early summer and midsummer, the correlation coefficients of the three modal time coefficients in the anomaly field are calculated (Fig. 10), which are 0.27, 0.01, and 0.62 for EOF1, EOF2, and EOF3, respectively. The first and second modes are not statistically significant at the 95% confidence level according to a Student's *t*-test, but the third mode is. When the EOF analysis range is reduced to southeastern China (20°–42.5°N, 110°–123°E), the correlation coefficients of the time coefficients of each mode are 0.17, −0.01, and 0.15, respectively (not shown). None of the three modes are statistically significant at the 95% confidence level according to a Student's *t*-test. Therefore, the correlation between early summer and midsummer is not significant, and there is no direct correlation between the two.

4 Discussion and conclusions

In this study, we selected daily maximum temperature data from 1542 stations from 1 May 1961 to 30 September 2018

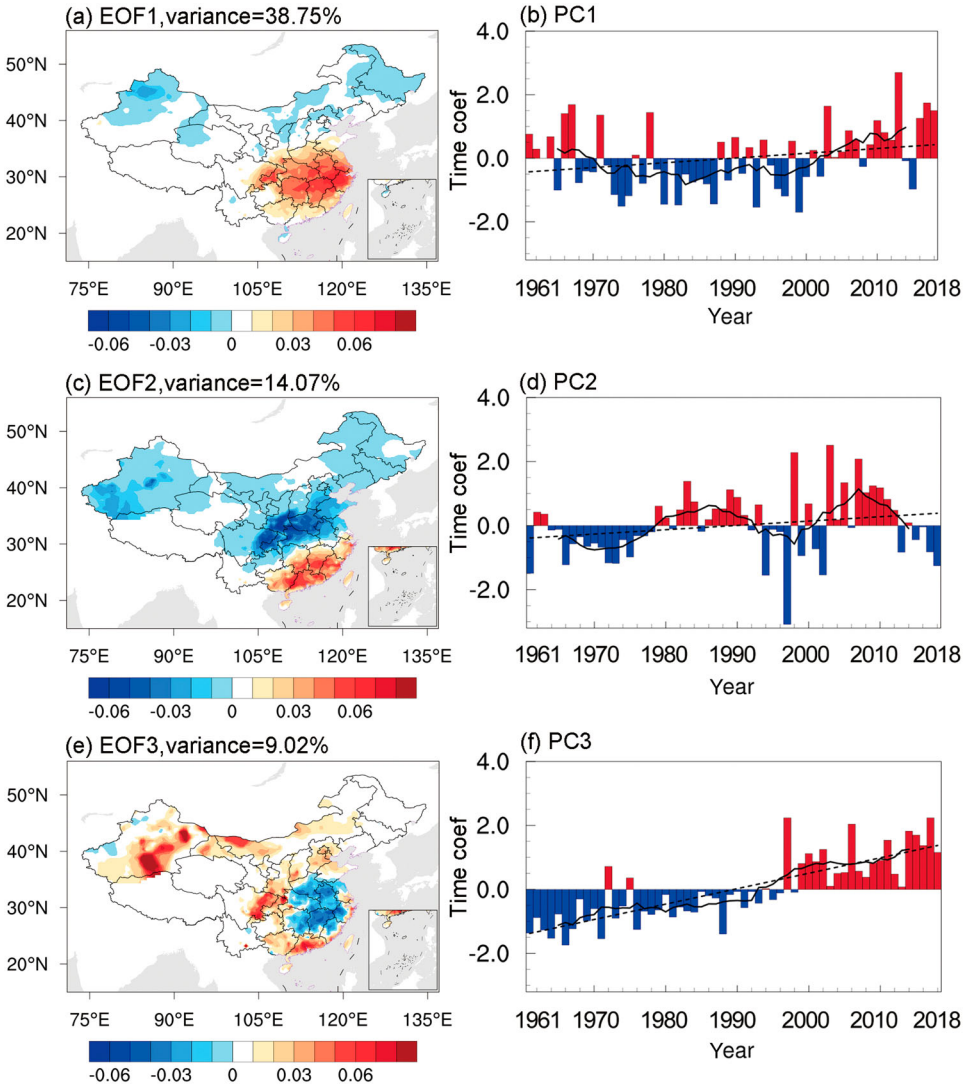

Fig. 9 As in Fig. 8, but for midsummer.

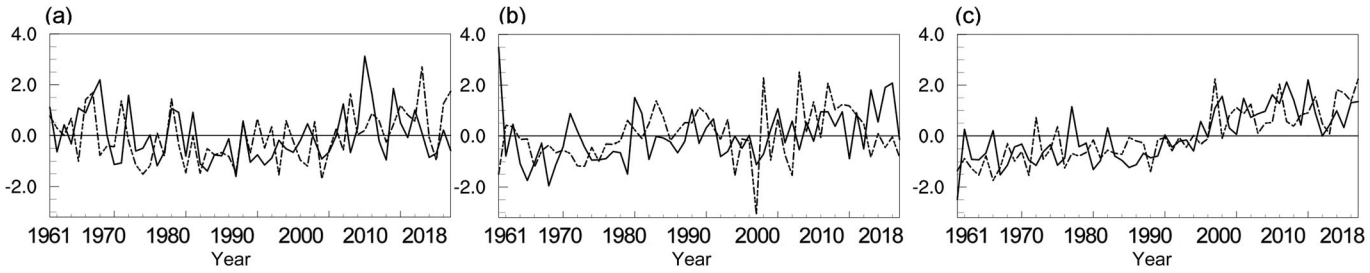

Fig. 10 Correlation coefficients between the modal time coefficients of early summer (solid line) and midsummer (dashed line): (a) mode 1, (b) mode 2, and (c) mode 3.

and focused on the analysis of the highest temperature data in summer from June to August. The temporal and spatial variations of EH frequency and intensity are studied between early summer and midsummer. Our conclusions follow.

(i) After 2010, EH shows a trend of early onset, and the frequency of EH increases significantly in May. Compared with the 1970s, there are twice as many sites where EH events occur earlier after 2010, reaching their highest value since the 1960s.

(ii) The frequency and intensity of EH in summer display an increasing trend. The frequency and intensity of EH events in early summer in the 2010s are weaker than those in the 2001–2010 period. However, the frequency and intensity of EH events in midsummer are significant, which means that EH occurs in summer more frequently than in midsummer.

(iii) Owing to the influence of Meiyu rains in the lower Yangtze region, the spatial distribution of EH in China has an obvious seasonal variation. In early summer, EH mainly occurs in the Huanghuai region, while in midsummer EH occurs mainly in the Jianghuai to Jiangnan region.

(iv) Since 2000, there have been significant intraseasonal differences in the interdecadal spatial distribution of EH in eastern China. In the early summer, after 2010, the number of EH days north of the Yangtze River changed from increasing to decreasing, and EH in southern China increased significantly. However, in midsummer, the warm centre moved from south of the Yangtze River to north of the river after 2010.

(v) Since 2010, the number of EH days in North China, as well as in the Huanghuai, and Jianghuai regions, have decreased in early summer and increased in midsummer, which is consistent with the value for the entire summer in the same period. The spatial distribution changes in these areas are more obvious than in other regions. It is clear that the North China, Huanghuai, and Jianghuai regions are positive contributors to summer EH.

It should be noted that this study is based on the analysis of the frequency and intensity of EH in China on the interdecadal scale. We found that the variation of EH in China is different in early summer and midsummer. The contrast in precipitation among the various regions results in the difference in the spatial distribution of EH days. In future, we need to conduct more in-depth research on the characteristics of interdecadal variations of summer EH events in various regions of China and comprehensively study the intraseasonal variation characteristics of EH waves in different regions under climate change.

Acknowledgements

We are grateful to the two anonymous reviewers and the editors for their comments and suggestions that have enabled us to greatly improve this manuscript. We would like to acknowledge those who shared their data and prespectives for the success of the present study. We thank Xiaoyue Liu from Lanzhou University and Zan Wang from Xuzhou Medical University for their valuable suggestions.

Disclosure statement

No potential conflict of interest was reported by the authors.

Funding

This study was jointly supported by the National Key Research and Development Program of China [grant numbers 2017YFC1502303 and 2018YFA0606301]; the National Natural Science Foundation of China (NSFC) [grant number 41875093] and [grant number 41530531]; and Yangzhou University High-end Talent Support Program.

References

Alexander, L. V., Zhang, X., Peterson, T. C., Caesar, J., Gleason, B., Tank, A. M. G. K., … Vazquez-Aguirre, J. L. (2006). Global observed changes in daily climate extremes of temperature and precipitation. *Journal of Geophysical Research-Atmospheres*, *111*(D5), D05109. doi:10.1029/2005jd006290

Allen, M. R., Dube, O. P., Solecki, W., & Aragón-Durand, F. (2018). *Special Report: Global warming of 1.5°C*. Retrieved from https://www.ipcc.ch/sr15/

Beniston, M., Stephenson, D. B., Christensen, O. B., Ferro, C. A. T., Frei, C., Goyette, S., … Woth, K. (2007). Future extreme events in European climate: An exploration of regional climate model projections. *Climatic Change*, *81*, 71–95. doi:10.1007/s10584-006-9226-z

Casati, B., & de Elía, R. (2014). Temperature extremes from Canadian regional climate model (CRCM) climate change projections. *Atmosphere-Ocean*, *52*(3), 191–210. doi:10.1080/07055900.2014.886179

Chen, R. D., & Lu, R. Y. (2014). Dry tropical nights and wet extreme heat in Beijing: Atypical configurations between high temperature and humidity. *Monthly Weather Review*, *142*(5), 1792–1802. doi:10.1175/Mwr-D-13-00289.1

Chen, R. D., & Lu, R. Y. (2015). Comparisons of the circulation anomalies associated with extreme heat in different regions of Eastern China. *Journal of Climate*, *28*(14), 5830–5844. doi:10.1175/Jcli-D-14-00818.1

Christidis, N., Stott, P. A., & Brown, S. J. (2011). The role of human activity in the recent warming of extremely warm daytime temperatures. *Journal of Climate*, *24*(7), 1922–1930. doi:10.1175/2011jcli4150.1

Coumou, D., & Rahmstorf, S. (2012). A decade of weather extremes. *Nature Climate Change*, *2*(7), 491–496. doi:10.1038/Nclimate1452

Ding, T., Qian, W. H., & Yan, Z. W. (2010). Changes in hot days and heat waves in China during 1961-2007. *International Journal of Climatology*, *30*(10), 1452–1462. doi:10.1002/joc.1989

Ding, Y. H., Ren, G. Y., Zhao, Z. C., Xu, Y., Luo, Y., Li, Q. P., & Zhang, J. (2007). Detection, causes and projection of climate change over China: An overview of recent progress. *Advances in Atmospheric Sciences*, *24*(6), 954–971. doi:10.1007/s00376-007-0954-4

Dole, R., Hoerling, M., Perlwitz, J., Eischeid, J., Pegion, P., Zhang, T., … Murray, D. (2011). Was there a basis for anticipating the 2010 Russian heat wave? *Geophysical Research Letters*, *38*, L06702. doi:10.1029/2010gl046582

Easterling, D. R., Evans, J. L., Groisman, P. Y., Karl, T. R., Kunkel, K. E., & Ambenje, P. (2000). Observed variability and trends in extreme climate events: A brief review. *Bulletin of the American Meteorological Society*, *81*(3), 417–425. doi:10.1175/1520-0477(2000)081<0417:Ovatie>2.3.Co;2

Easterling, D. R., Horton, B., Jones, P. D., Peterson, T. C., Karl, T. R., Parker, D. E., … Folland, C. K. (1997). Maximum and minimum temperature trends for the globe. *Science*, *277*(5324), 364–367. doi:10.1126/science.277.5324.364

Feng, G. L., Hou, W., Zhi, R., Yang, P., & Zhang, D. Q. (2012). *Detection, diagnosis and predictability research of extreme climate events* [in Chinese]. Beijing, People's Republic of China: Science Press.

Fischer, E. M., & Knutti, R. (2015). Anthropogenic contribution to global occurrence of heavy-precipitation and high-temperature extremes. *Nature Climate Change*, *5*(6), 560–564. doi:10.1038/nclimate2617

Gong, Z. Q., Feng, T. C., & Fang, Y. H. (2015). Objective identification research on cold vortex and mid-summer rainy periods in Northeast China. *Chinese Physics B*, *24*(4), 049204. doi:10.1088/1674-1056/24/4/049204

Hu, P., Shen, H. Y., Wang, X. J., & Feng, G. L. (2016). A study on characteristics of precipitation and circulation pattern in early summer, midsummer and conventional summer in northeast Asia. *Chinese Journal of Atmospheric Sciences* [in Chinese], *42*(1), 109–123. doi:10.3878/j.issn.1006-9895.1706.16290

Im, E. S., Pal, J. S., & Eltahir, E. A. B. (2017). Deadly heat waves projected in the densely populated agricultural regions of South Asia. *Science Advances*, *3*(8), E1603322. doi:10.1126/sciadv.1603322

Karmalkar, A. V., & Bradley, R. S. (2017). Consequences of global warming of 1.5 degrees C and 2 degrees C for regional temperature and precipitation changes in the contiguous United States. *Plos One*, *12*(1), E0168697. doi:10.1371/journal.pone.0168697

King, A. D., Karoly, D. J., & Henley, B. J. (2017). Australian climate extremes at 1.5 degrees C and 2 degrees C of global warming. *Nature Climate Change*, *7*(6), 412–416. doi:10.1038/Nclimate3296

Lian, Y., Shen, B. Z., Gao, C. T., An, G., & Tang, X. L. (2003). The study of the on-set criterion and the date of East Asian summer monsoon in Northeast China and its main characteristic analysis. *Acta Meteorologica Sinica* [in Chinese], *61*(05), 548–558.

Lin, J., Bi, B. G., & He, J. H. (2005). Physical mechanism responsible for western Pacific subtropical high variation and hot wave in southern China in July 2003. *Chinese Journal of Atmospheric Sciences* [in Chinese], *29*(4), 594–599.

Luterbacher, J., Dietrich, D., Xoplaki, E., Grosjean, M., & Wanner, H. (2004). European seasonal and annual temperature variability, trends, and extremes since 1500. *Science*, *303*(5663), 1499–1503. doi:10.1126/science.1093877

Ma, Z. G., Fu, C. B., Ren, X. B., & Yang, C. (2003). Trend of annual extreme temperature and its relationship to regional warming in northern China. *Acta Geographica Sinica* [in Chinese], *S1*, 11–20.

Mora, C., Dousset, B., Caldwell, I. R., Powell, F. E., Geronimo, R. C., Bielecki, C. R., … Trauernicht, C. (2017). Global risk of deadly heat. *Nature Climate Change*, *7*(7), 501–506. doi:10.1038/Nclimate3322

Peng, J. B., Liu, G., & Sun, S. Q. (2016). An analysis on the formation of the heat wave in southern China and its relation to the anomalous western Pacific subtropical high in the summer of 2013. *Chinese Journal of Atmospheric Sciences* [in Chinese], *40*(05), 897–906.

Qin, D. H., Ding, Y. H., Su, J. L., Wang, J. W., & Ren, S. W. (2005). Assessment of climate and environment changes in China (1): climate and environment changes in Chinese and their project. *Advances in Climate Change Research* [in Chinese], *1*(1), 4–9.

Shen, H. J., You, Q. L., Wang, P. L., & Kong, L. (2018). Analysis on heat waves variation features in China during 1961–2014. *Journal of the Meteorological Sciences* [in Chinese], *38*(1), 28–36.

Sherwood, S. C., & Huber, M. (2010). An adaptability limit to climate change due to heat stress. *Proceedings of the National Academy of Sciences of the United States of America*, *107*(21), 9552–9555. doi:10.1073/pnas.0913352107

Shi, J., Ding, Y. H., & Cui, L. L. (2009). Climatic characteristics of extreme maximum temperature in East China and its causes. *Chinese Journal of Atmospheric Sciences* [in Chinese], *33*(2), 347–358.

Sun, J. Q., Wang, H. J., & Yuan, W. (2011). Decadal variability of the extreme hot event in China and its association with atmospheric circulations. *Climatic and Environmental Research* [in Chinese], *16*(2), 199–208.

Tang, H. Y., Zhai, P. M., & Wang, Z. Y. (2005). On change in mean maximum temperature, minimum temperature and diurnal range in China during 1951-2002. *Climatic and Environmental Research* [in Chinese], *10*(4), 728–735.

Tao, P., & Zhang, Y. (2019). Large-scale circulation features associated with the heat wave over Northeast China in summer 2018. *Atmospheric and Oceanic Science Letters*, *12*(4), 254–260. doi:10.1080/16742834.2019.1610326

Tao, S. Y., Zhao, Y. J., & Chen, X. M. (1958). The relationship between May-Yu in Far east and the behaviour of circulation over Asia. *Acta Meteorologica Sinica* [in Chinese], *29*(2), 119–134.

Turner, J. K., & Gyakum, J. R. (2010). Trends in Canadian surface temperature variability in the context of climate change. *Atmosphere-Ocean*, *48*(3), 147–162. doi:10.3137/AO1102.2010

Vincent, L. A., & Mekis, E. (2006). Changes in daily and extreme temperature and precipitation indices for Canada over the twentieth century. *Atmosphere-Ocean*, *44*(2), 177–193. doi:10.3137/ao.440205

Wang, H. J. (2001). The weakening of the Asian monsoon circulation after the end of 1970s. *Advances in Atmospheric Sciences*, *18*(3), 376–386. doi:10.1007/BF02919316

Wang, S. W. (1962). Years of changes in East Asian atmospheric activity centers and climate vibration in China. *Acta Meteorologica Sinica* [in Chinese], *32*(1), 19–36.

Wang, X. L. L., Feng, Y., & Vincent, L. A. (2014). Observed changes in one-in-20 year extremes of Canadian surface air temperatures. *Atmosphere-Ocean*, *52*(3), 222–231. doi:10.1080/07055900.2013.818526

Wang, Y. J., Ren, F. M., & Yan, F. (2013). Study on temporal and spatial variations of regional continual high temperature event in China. *Scientia Geographica Sinica* [in Chinese], *33*(3), 314–321. doi:10.13249/j.cnki.sgs.2013.03.014

Xu, K., Lu, R., Mao, J., & Chen, R. (2019). Circulation anomalies in the mid-high latitudes responsible for the extremely hot summer of 2018 over northeast Asia. *Atmospheric and Oceanic Science Letters*, *12*(4), 231–237. doi:10.1080/16742834.2019.1617626

Ye, D. X., Yin, J. F., Chen, Z. H., Zheng, Y. F., & Wu, R. J. (2013). Spatiotemporal change characteristics of summer heatwaves in China in 1961–2010. *Advances in Climate Change Research* [in Chinese], *9*(1), 15–20.

Yuan, Y., Ding, T., Gao, H., & Li, W. J. (2018). Major modes of midsummer air temperature in southern China and their relationship with sea surface temperature anomalies. *Chinese Journal of Atmospheric Sciences* [in Chinese], *42*(6), 1245–1262.

Zhang, S. Y., Zhang, H. D., Xu, X. D., Zhang, D. K., Liao, Y. M., & Song, Y. L. (2005). Climatic character and cause analysis of summer high temperature in main cities of East China. *Plateau Meteorology* [in Chinese], *24*(5), 829–835.

Zhang, Y. H., Li, Y., Li, D. S., Shang, K. Z., & Zheng, F. K. (2016). Study on the space distribution and circulation pattern of extreme high temperature over eastern China in summer. *Plateau Meteorology* [in Chinese], *35*(02), 469–483.

章大全,郑志海,陈丽娟,等. 10～30 d 延伸期可预报性与预报方法研究进展. 应用气象学报,2019,30(4):416-430.
DOI: 10.11898/1001-7313.20190403

10～30 d 延伸期可预报性与预报方法研究进展

章大全 郑志海* 陈丽娟 张培群
(国家气候中心 中国气象局气候研究开放实验室, 北京 100081)

摘 要

10～30 d 延伸期的可预报性既依赖于初始条件,也与缓变的下垫面有关,寻找延伸期时段内可预报性较高的低频特征,识别延伸期的可预报性来源及影响的物理机制是提高延伸期预报水平的关键。近年延伸期可预报性来源、热带大气季节内振荡监测预测和影响等领域的研究取得较大进展,提出和应用了动力统计相结合以及大气低频信号释用等新的延伸期预报方法。对延伸期可预报性来源及其与初值和外强迫异常的关系分析表明,海气相互作用能提高亚洲和西太平洋区域延伸期时段大气环流和要素的可预报性。热带大气季节内振荡、平流层爆发性增温以及各种次季节尺度的海气、陆气耦合作用和大气响应均为延伸期预报提供了重要的可预报性来源。由于数值模式延伸期时段的预报性能与实际业务需求还存在一定距离,基于动力统计相结合和物理统计的延伸期预报方法被广泛应用于业务预报,表现出一定的预报技巧。

关键词: 延伸期预报; 可预报性; 季节内振荡

引 言

10～30 d 延伸期(简称延伸期)预报填补了中期天气预报和短期气候预测之间的缝隙,在防灾减灾决策服务中起着重要作用,一直是科学研究和业务预报关注的重点和难点。世界气象组织(World Meteorological Organization, WMO)下属的世界天气研究计划(World Weather Research Programme, WWRP)和世界气候研究计划(World Climate Research Programme, WCRP)于 2013 年联合发起了次季节到季节(Sub-seasonal to Seasonal, S2S)预测计划[1],目前已经完成项目第 1 阶段的主要研究任务,并开始为期 5 年的第 2 阶段计划研究。欧洲中期天气预报中心(European Centre for Mediumrange Weather Forecasts, ECMWF)在其发布的"2025 路线图"中提出,在 10 年内将高影响天气事件的有效预报时效提升至 2 周,大尺度环流形势及转折的预报时效提升至超前 4 周[2]。美国国家科学院(National Academy of Sciences, NAS)发布了未来 2 周至 12 个月的预测研究计划[3],目标是在 10 年内将次季节至季节尺度预测应用的广度和深度提升至目前天气预报的水平。美国国家海洋大气局(National Oceanic and Atmospheric Administration, NOAA)计划在已有的北美多模式集合预报系统(North American Multi-Model Ensemble, NMME)基础上发展次季节到年际尺度的预报系统,并提供未来 3～4 周的预报服务[4]。中国气象局在印发的"全面推进气象现代化行动计划(2018—2020 年)"和"智能网格预报行动计划(2018—2020 年)"中,明确提出将气象要素和重要天气过程的延伸期预报列为重点任务和着力攻关的关键核心技术之一。

延伸期预报比逐日天气预报的时效更长,大气初始信息的贡献持续衰减;较以月和季节为代表的短期气候预测的时效更短,海温、积雪、土壤湿度等下垫面信号的作用还显现得不够充分,这使得延伸期的可预报性与天气预报和短期气候预测的可预报

2019-02-18 收到, 2019-04-26 收到再改稿。
资助项目: 国家重点研究发展计划专项(2017YFC1502303),国家重点基础研究发展计划(2015CB453203),国家自然科学基金项目(41605078, 41875101, 41730964)
* 通信作者, 邮箱: zhengzh@cma.gov.cn

性存在显著不同,它的可预报信号既来自于初始条件,也与下垫面条件有关[5]。大量研究表明:该预报时段存在一些潜在的可预报源,如热带低频振荡(Madden-Julian Oscillation, MJO)和北半球夏季大气季节内振荡(Boreal Summer Intra-seasonal Oscillation, BSISO)[6-8]、热带海洋大气相互作用、平流层和对流层相互作用[9-11]、土壤湿度[12]、积雪和海冰[13-14]以及热带-热带外遥相关等,都为该时段的预报提供了科学基础。同时,大量的数值模式和预报方法被广泛应用,旨在提高延伸期时段的预报技巧。

1　延伸期的可预报性来源

初始条件、边界条件的误差和数值模式中的各种近似导致预报结果不可避免地存在不确定性,这种不确定性与预报时效密切相关,一直是天气和气候可预报性研究的重要内容之一[15-20]。根据预报时效的不同,大气可预报性通常可分为两类:第 1 类与初值有关,强调初始条件的重要性,逐日的天气预报属于该类,依赖于初值信息记忆的逐日天气可预报上限约为 2～3 周[21-22];第 2 类与边值有关,强调边界条件的作用,它依赖于大气系统对边界条件的响应。气候系统中一些缓慢变化的下垫面异常(如海温、积雪、土壤湿度等)特征能提供持续时间更长的信息,这些缓变信号对大气系统有重要作用,是短期气候(月到季节尺度)预测的基础。

延伸期预报处于天气预报和短期气候预测之间,其可预报性来源既与初值有关,也与下垫面的异常密切相关。在这一时间尺度,虽然大气初始信息的贡献在不断衰减,但它仍然对延伸期时段的大气环流演变有着重要影响。首先,大气的可预报性不是固定不变的,它与初始条件所处的状态有关,如初始条件靠近于天气型转换时,可预报时效往往较短;而处于稳定的环流型时,可预报时效相对较长。但很难识别哪类初值在延伸期的潜在可预报性更高[23]。其次,不同尺度的波具有不同的预报时效,天气尺度的不稳定性和慢变的行星尺度的波非线性相互作用后可能产生不同的可预报性特征,如热带大气低频振荡、平流层和对流层的相互作用等具有较长生命周期的气候现象,是延伸期预报的重要可预报性来源[24-25]。此外,对不同区域而言,可预报性对初始条件的依赖性也有所不同[26-28],并导致我国不同地区可预报性的差异[29-30]。

海气相互作用,尤其是热带海温,是延伸期预报的重要信息源,它对大气低频流型的建立和维持均有影响。以厄尔尼诺和南方涛动(El Niño-Southern Oscillation, ENSO)为代表的热带太平洋海气耦合现象对全球气候有重要影响[31],是已知的季节到年际气候变率最重要的可预报源[32-33],它通过大气环流以遥相关形式影响东亚季风系统,尤其是 ENSO 的位相和强度与东亚地区的气候密切相关。对 2015/2016 年超强 El Niño 事件背景下我国月预测的技巧差异分析表明:在 El Niño 发展位相,降水预报和环流预报技巧较高且稳定,而在 El Niño 衰减位相,月预报技巧总体偏低[34]。进一步分析表明:亚洲-太平洋涛动(Asian-Pacific Oscillation, APO)[35]可能是造成这种差别的重要影响因素,即当 El Niño 和 APO 对西北太平洋环流的影响不一致时,将直接影响东亚环流的可预报性高低以及动力模式的预报技巧。除热带太平洋的影响外,其他海区的海温对区域大气低频流型同样有着重要影响。对欧亚尤其是东亚地区而言,印度洋和大西洋海温异常有着明显的影响,如印度洋热力状况的改变会通过海气相互作用影响到东亚地区的天气气候异常,它也是东亚等地环流异常的信号来源之一[36]。而作为重要桥梁联系春季北大西洋涛动(North Atlantic Oscillation, NAO)和东亚夏季风的北大西洋海温,也与欧亚中高纬度环流异常密切相关[37],数值试验结果也证实了北大西洋海温与东亚环流异常的联系[38]。海气相互作用不仅在热带地区对延伸期预报有贡献,Wang 等[39]在完美模式的假定下,将其中一个集合预报成员作为实际观测,而将其他成员作为预报,即不考虑模式误差影响的情况下,发现海气耦合过程对北半球热带外地区的延伸期潜在可预报性也有重要贡献。

延伸期的可预报性既依赖于大气初始条件,也依赖于下垫面异常,因此,大气环流模式和耦合模式(主要是海气耦合)是目前延伸期预报的主要工具。二者的优劣目前尚无定论,一方面,耦合模式在反映下垫面异常的演变特征及其与大气的相互作用方面具有优势,尤其是在大气初始信息快速衰减后;另一方面,除了大气环流模式本身的误差外,海气耦合模式还会由于海洋模式本身以及海气耦合过程的缺陷使误差增加,即海气耦合模式增加了可预报的信息源,同时也引入了新的误差。因此,增加的可预报信

号和新增的误差之间的相对贡献大小是海气耦合模式较之大气环流模式是否更有优势的关键。鉴于此，国际上主要的业务预报中心在延伸期动力模式预报方案的选择上存在明显不同，如美国气候预报中心(Climate Prediction Center，CPC)采用耦合模式[40]，日本东京气候中心(Tokyo Climate Center，TCC)和中国气象局国家气候中心则采用大气环流模式，海温异常给定为初始海温异常的持续，而 ECMWF 采用了不同的方案，前 10 d 采用分辨率较高的大气模式，10 d 则采用降低分辨率后的耦合模式[41]。各家模式采用的不同延伸期预报方案表明：不同的动力模式中海气相互作用的贡献与误差增加之间的相对大小表现并不一致，因而对初始条件和海气相互作用在延伸期预报中的贡献认识也存在差异。对热带季节内低频信号尤其是 MJO 在触发、传播和消亡过程中大气内部动力和海气相互作用的贡献已有大量研究工作，但在北半球中高纬度地区，大气初值和海气相互作用的贡献需进一步研究。近年来，一些研究讨论了延伸期预报中大气初值与下垫面异常的贡献，如 Reichler 等[42-43]利用完美模式方法比较了大气初值、陆面以及海洋异常对热带地区月平均预测的作用，发现当 ENSO 现象较弱时，初值对东半球的影响最强，3 周以后边界强迫是热带可预报性的主要因子；DeMott 等[44]通过比较不同版本的海气耦合模式与大气模式，证明了耦合模式对季节内振荡具有更高模拟能力；Fu 等[45-46]通过分析初始条件对季节内预测技巧的影响和海气相互作用对季风季节内振荡的贡献，表明海气相互作用能显著提高整个亚洲-西太平洋区域的可预报性，耦合模式对季风季节内振荡的预报时效较大气环流模式能延长 1 周。汪栩加等[47]利用中国气象局国家气候中心大气环流模式，设计 4 组不同大气初值与海温的配置关系构成对比试验，分析了大气初值与海温边值对延伸期预报的相对贡献。初始条件记忆和海气相互作用在不同时段、不同区域的相对作用存在明显差异。初始条件的影响随着预报时效延长，衰减速度在不同时段和区域也不相同。同时，慢变的海表温度影响不同区域的大气环流所需要的时间也存在明显的区域差异。对比大气初值、海温边值均采用观测值(IOBO 方案)及大气初值采用观测值、海温边值采用气候值(IOBC 方案)两种方案结果(图 1)可知，海温异常最先影响的是海气相互作用显著的低纬度地区，且从低层到高层逐渐呈现。第 3 候以后，海温异常对大气环流的影响逐渐扩展到中高纬度地区，但影响的范围和程度均小于低纬度地区，低纬度海洋上的影响仍然最为明显。

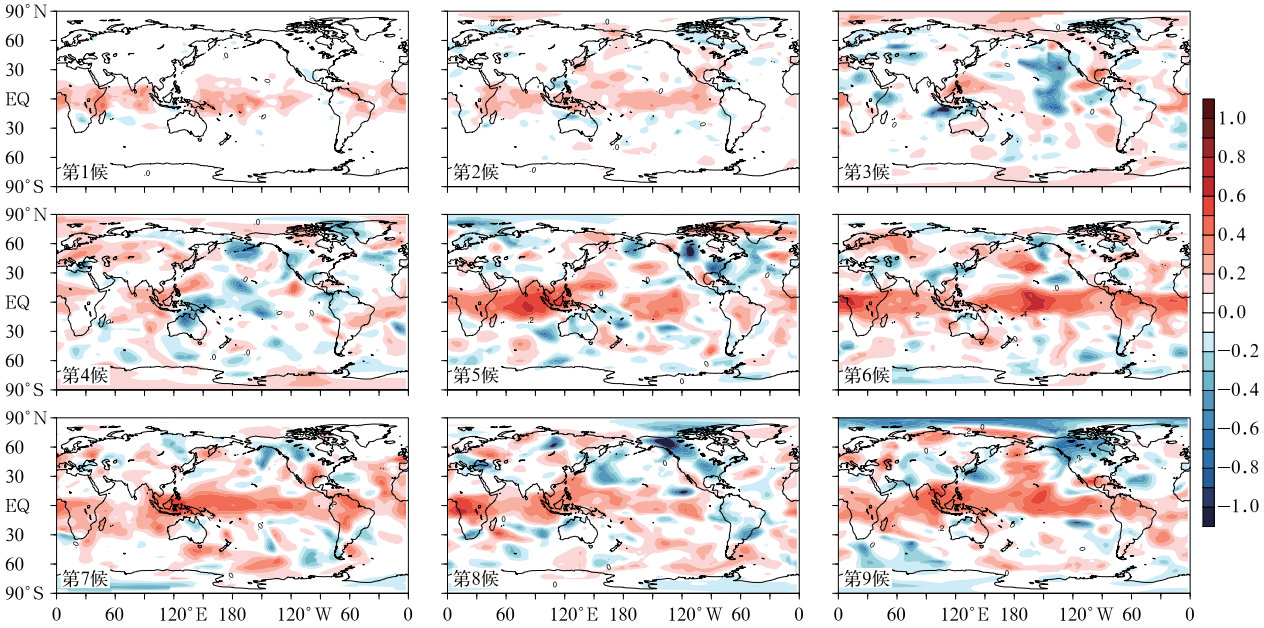

图 1 1991—2000 年 IOBO 方案与 IOBC 方案 500 hPa 高度场逐候 MSSS 评分分布[47]

Fig. 1 MSSS of pentad mean 500 hPa geopotential height between scheme IOBO and scheme IOBC from 1991 to 2000(from Reference [47])

2　延伸期预报相关的次季节气候现象及预报技巧

根据非线性可预报性理论,逐日天气预报存在2周左右的可预报性上限[16,48],但这并不意味着延伸期大气运动没有可预报的分量[49]。首先,大气运动的可预报性与其时空尺度有关,如局地雷暴、冰雹、龙卷等强对流天气的可预报性上限为小时量级,天气尺度系统的可预报时效通常在2周以内,而一些行星尺度的大气活动中心(如副热带高压、极涡等)的特征时间尺度则远长于天气尺度。其次,许多长生命周期的气候现象,如平流层爆发性增温、大气遥相关等,以及大气中存在的准双周、10～30 d和30～60 d等多种时间尺度的季节内振荡[50],均为延伸期预报提供了重要的可预报信号来源。此外,一些大气外强迫系统,如海温、积雪和海冰、土壤湿度等具有较长时间尺度的记忆性特征,逐周到月时间尺度上的海气、陆气耦合作用及大气响应也是延伸期可预报性的重要来源。近年来,对延伸期可预报信号源及相关气候现象的研究已取得一定成果,特别是对MJO等具有低频振荡特征的次季节尺度现象的监测预测取得了较大进展。

2.1　MJO

MJO作为热带大气季节内变率的主模态,不但对热带区域气候影响显著,对中高纬度次季节气候变率也有重要影响,因而被认为是次季节尺度最重要的可预报性来源[51]。基于信噪比等指标的检验评估结果显示,数值模式中MJO的实时多变量(Real-time Multivariate, RMM)指数[52]潜在可预报时效为35～45 d,且可预报上限与MJO的位相以及强度有关[53-54]。近期参加S2S预测计划的各家模式对MJO的RMM指数预报技巧上限为10～38 d,其中美国地球物理流体力学实验室(Geophysical Fluid Dynamics Laboratory, GFDL)和日本东京大学全球对流解析模式(Nonhydrostatic Icosahedral Atmospheric Model, NICAM)对冬季MJO的预报技巧时效可达4周[55],英国气象局(United Kingdom Met Office, UKMO)模式[56]、中国北京气候中心气候系统模式(Beijing Climate Center Climate System Model, BCC_CSM)[57]和美国耦合混合网格模式(atmospheric Flow-following Icosahedral Model coupled with the icosahedral-grid version of the Hybrid Coordinate Ocean Model, FIM-iHYCOM)[58]预报技巧时效在3周左右。

MJO有显著的季节变化,冬季MJO主要表现为自西向东传播,而夏季在印度季风区以北传和东北传播分量为主,西太平洋-东亚区域以北传和西北传播分量为主。针对这一特征,Lee等[59]采用与MJO指数相似的方法定义了东亚季风区BSISO指数。BSISO指数根据定义分为BSISO1和BSISO2指数,分别代表周期为30～60 d和10～30 d的振荡。大气季节内变率预报试验(Intraseasonal Variability Hindcast Experiment, ISVHE)[60]结果表明:强BSISO事件的可预报上限和预报技巧时效可达6周和3周,与冬季MJO的可预报性相当。S2S计划模式数据[1]分析结果显示:目前数值模式对BSISO1指数逐日预报技巧上限约为3周,BSISO2指数上限约为2周,但不同强度和位相状态下的BSISO指数预报技巧差异较大,如ECMWF模式对强BSISO事件第6、第7位相的预报技巧可达30 d左右[61]。

强MJO信号可以改变热带及副热带地区大尺度环流形势,并对热带气旋活动[62]、南海季风爆发[63]、季节进程以及降水等要素的时空分布[64]产生重要影响。BSISO在不同位相的演变也会影响到东亚夏季风进程[65]。吴捷等[66]基于国内外研究成果,发展了MJO实时监测预测方法,建立了ISV/MJO监测预测业务系统(ISV/MJO Monitoring and Prediction System, IMPRESS),投入实时业务运行,其监测预测和影响信息有效地支撑了延伸期-月预测业务。2016年6—7月受超强厄尔尼诺事件的影响,西北太平洋为异常反气旋性环流,长江流域降水异常偏多。2016年8月有较强的MJO东传至西太平洋并持续长达25 d,激发了异常活跃的热带气旋活动,从而导致西太平洋副热带高压断裂,西北太平洋为异常气旋性环流控制,水汽输送条件转差,我国长江流域降水由前期异常偏多转为偏少[67]。2018年春夏季发生3次显著的热带低频振荡活动,分别影响了华南前汛期、南海夏季风的爆发时间,造成了季节进程的滞后,而一般在拉尼娜事件发生后,有利于亚洲夏季风季节进程提前[68],MJO的活动对次季节尺度的雨季进程起到调制作用。次季节尺度气候现象监测预测业务系统的建设,使预报员能及时获取相关预报和可能的影响信息,从而获得较高技巧的季节内预测和服务效果[69-70]。

2.2 ENSO

ENSO不仅是年际尺度海气系统中最强信号，在次季节到季节尺度预测中也十分重要。首先，热带太平洋海温的持续性和转折特征为次季节尺度可预报性提供了重要来源。ENSO事件的空间型变化[71]可能影响到次季节到季节尺度气候特征[72-73]。2018年秋季发生一次弱的El Niño事件，季节内El Niño状态由中部型向东部型发展，热带印度洋海温偶极子正位相持续，秋季后期El Niño影响增强，东亚副热带大气环流也发生明显的季节内响应，西太平洋副热带高压由前期的偏强偏北转为偏强偏南，加上欧亚中高纬环流异常的季节内调整，二者共同导致了我国南方地区降水由初秋的东少西多转变为秋末的东多西少的季节内变化特征[74]。

其次，不同ENSO背景下MJO具有不同的发生发展特征[75]，与MJO相联系的西风爆发也与ENSO有着密切联系[76-77]。在El Niño期间，MJO强度减弱，且结构趋于正压性。积云对流加热反馈是热带大气季节内振荡(Intra-seasonal Oscillation，ISO)的主要动力学机制，ENSO能通过海表温度异常和对流加热对MJO的传播及其影响产生作用[78]。不同分布型El Niño事件的盛期和衰减位相，MJO活动特征也存在显著差异。与传统东部型El Niño盛期MJO明显减弱不同，中部型El Niño盛期至次年春季，热带中西太平洋MJO强度再次加强，从热带印度洋向赤道中东太平洋持续东传的特征更为显著[72]。ENSO与MJO的相互作用关系为延伸期预报提供了重要的时间窗口，当与之联系的遥相关较强且对气象要素异常的影响较为显著时，可以利用这种关系提升延伸期预报技巧[79]。

2.3 平流层与对流层相互作用

平流层与对流层相互作用是次季节尺度另一可预报性来源[10]，研究表明：在平流层爆发性增温(Stratospheric Sudden Warming，SSW)事件中，在平流层下传信号的影响下，对流层大气往往呈现出长达数周的持续性环流异常[80-81]，特别是北半球环状模(Northern Hemisphere Annular Mode，NAM)在SSW事件发生后通常处于负位相，北极地区海平面气压偏高，欧亚北部和北美地区的低温事件发生频次上升[82]。研究显示，这些时段的延伸期预报往往具有更高的预报技巧。需要指出的是，尽管SSW事件对对流层的作用在统计上是显著的，但并非所有SSW事件信号都能够下传并影响对流层大气[83]，同时SSW事件的可预报性与极涡的空间结构有关，分裂型的SSW事件的可预报性通常低于移动型[84]。

多家模式预报的评估结果表明：SSW事件的预报时效上限通常约为10 d，但不同强度等级SSW事件的可预报时效存在较大差异，部分SSW事件的可预报时效可达20 d[85-88]。目前还不清楚这些可预报性分析结果仅仅是反映了模式系统的预报技巧，还是SSW事件自身的潜在可预报性。因此，还需要结合不同模式系统对这些结果作进一步诊断分析，以提升对SSW事件可预报性的认识。

2017年12月—2018年2月我国气温变化呈现出前冬暖、隆冬和后冬偏冷的阶段性特征[89]。这种季节内变化特征与2018年2月中旬北半球极地平流层发生的SSW事件有密切关系。北极地区的平流层中上层气温在短时间内快速升高了20℃左右，突发性升温造成极区平流层大气环流发生了强烈变化，位势高度升高，纬向西风转变为东风，平流层环流异常伴随着北极涛动信号下传到对流层，从而对低层大气和东亚天气气候产生重要影响。2018年2月下旬—3月中旬北极涛动指数持续异常负位相，500 hPa东亚大槽加深西移，我国东北和华北北部等地气温持续偏低。预报员及时监测到SSW事件，并根据动力气候模式的预测和监测诊断信息，预测到2月下旬—3月中旬的强冷空气活动和对我国的影响，取得较好的预测服务效果。

2.4 土壤湿度

土壤湿度记忆可达数周，可通过改变蒸发和表面能量收支影响区域的气温和降水变率[90-91]。已有研究指出，考虑陆面初值对延伸期要素预报技巧具有改进作用[92]。对比大气和陆面初值对模式延伸期要素预报技巧的贡献结果显示：大气初值信号在预报的前2周占主导地位，但在预报第3～4周，两种信号对预报技巧的贡献可达到同一量级。不同区域陆面初值信息对模式要素预报技巧的影响也有显著差异，如在湿润和干旱地区的过渡带，考虑土壤湿度初值对气温预报技巧的提升最为明显[93]。对2003年欧洲和2010年俄罗斯西部夏季高温热浪的分析结果显示，区域土壤湿度异常对大尺度环流异常的维持起重要作用[94-95]。大气对土壤湿度偏低异常信号的响应表现为低层为热低压，对流层中上层为反气旋式高压脊。2003年夏季，该正反馈机制加强了欧洲上空的反气旋式环流异常，并进一步造成

地表气温以及土壤湿度的异常。另一方面,同期降水的缺乏和与之相关的土壤湿度偏低,削弱了潜热冷却作用,放大了高温热浪事件的极端性。陆气耦合模式数值试验结果表明,土壤湿度异常和大气的相互作用显著增加了高温热浪的持续日数[96]。

2.5　积　雪

积雪是气候系统中的另一个缓变分量,大范围积雪的辐射和热力效应可对次季节到季节尺度的气候异常产生重要影响[97]。分析积雪信号对全球大气环流模式(Community Atmosphere Model Version3, CAM3)冬半年次季节气温预测技巧影响的结果表明,考虑积雪深度初值可以有效改进模式对北半球中纬度地区气温的预报能力[98]。Orsolini 等[99]利用 ECMWF 模式对秋冬季积雪的气候效应进行分析,结果显示:在预报前 15 d,大范围雪盖导致欧亚和北美的地表气温下降,而在预报 30 d 的时间尺度上,雪盖引起西伯利亚高压加强西伸,北极变暖而欧亚中高纬度地区变冷。这种由积雪造成的"暖北极-冷大陆"变化使模式预报的地表气温和实况更为接近。研究发现,欧亚积雪异常偏多有利于北大西洋涛动负位相的建立和维持[100]。

青藏高原积雪是东亚气候重要的陆面影响因子,其变化的时间尺度长于大气而比海洋短。高原冬春积雪由于其较高的反照率,能降低冬春高原的地表温度,减少地表向大气的感热和潜热输送,削弱青藏高原的热源作用;而在积雪融化时又会吸收大量潜热,同时融雪使土壤湿度增大,土壤热容量上升,造成地表能量平衡和水分交换异常,因此,不同的物理过程对东亚季风的影响也有所不同[101]。另一方面,我国东部降水从春季到夏季是逐渐推进的过程,在季风推进过程中降水性质也存在锋面降水和季风降水的变化,而青藏高原积雪异常对东亚地区的环流影响也存在季节内差异。冬春转换季节青藏高原积雪对数值模式延伸期预报技巧影响的分析显示,在青藏高原积雪显著影响的青藏高原地区、贝加尔湖地区和北太平洋地区,青藏高原积雪异常年动力模式的预报技巧明显高于正常年份。随着预报时效的延长,预报技巧在青藏高原积雪偏多年衰减最慢,其次为积雪偏少年,而在积雪正常年衰减最快。结果表明:青藏高原积雪的异常对延伸期预报技巧有重要贡献,即其为东亚地区延伸期预报的潜在可预报源[102]。

2.6　热带-热带外遥相关

大气遥相关是短期气候预测的重要因子之一。已有研究工作大多集中在季节尺度大气遥相关的形成机理及其气候影响,而部分大气遥相关模态还存在次季节尺度变率[103-104],如热带和中纬度次季节尺度相互作用和遥相关是热带和热带外环流以及天气气候异常的重要影响因子。季节内遥相关也被认为是尚未得到充分研究和利用的次季节可预报性来源[105],然而季节内遥相关机理的复杂性和多样性以及相关概念模型研究的缺乏,阻碍了这种潜在可预报性向实际预报技巧的转化。

总体而言,目前对延伸期可预报信号源及相关气候现象的研究已取得一定成果,特别是对 MJO 等次季节尺度现象的研究和预测取得了较大进展,但对延伸期可预报信号源与天气气候异常的联系及其物理机制的研究还相对薄弱,在充分利用和实现延伸期潜在可预报性方面还有许多物理过程和方法问题需要解决。在可预报信号源影响比较显著的时间窗口,延伸期环流和要素的预报技巧可能相对较高,但是目前对于延伸期较强可预报性时段的成因和判定方法还不清楚。尽管如此,一些次季节尺度强信号的监测和预测能力的提升(如 MJO, SSW 等)在业务中获得广泛应用,推动了服务效果的提高。

3　延伸期预报方法和预报技巧

20 世纪 80 年代在 Miyakoda 等[106]利用大气环流模式对 1977 年 1 月的阻塞高压成功预测后,全球各大预报中心相继利用数值模式开展延伸期预报试验。美国国家气象中心开展了 1986/1987 年冬春每月 30 d 的逐日数值预报试验[107]。Deque 等[108]利用法国 T42 全球模式预报了月平均500 hPa 高度场。ECMWF 开展了 1985 年 4 月—1989 年 1 月逐月的延伸期预报[109]。加拿大、日本也进行了类似的试验[110-111]。各数值预报中心对大气环流模式的检验评估显示,模式对第 1 周或前 10 d 环流形势的预报能力决定了后面预报效果的优劣。丑纪范等[25]指出,仅依赖初值信息的大气环流模式的有技巧预报主要位于前 10 d,10 d 后模式预报技巧迅速下降。近年来,尽管数值模式性能有了很大提升,但 10 d

以上的预报技巧改善并不明显。

针对依赖初值信息的大气模式的可预报性上限问题,考虑海温等外强迫的耦合模式逐步成为改进延伸期预报技巧的重要研究方向。UKMO的数值试验结果[112]表明:在考虑海洋外强迫影响后,模式对热带大气环流的预报技巧在不同预报时效上均有提升,对中高纬度环流形势的预报技巧在30 d及以上时间尺度提升较为显著,而对10 d以内预报技巧的改善不明显。月平均环流预报中由海表面温度产生的预报技巧与由初值产生的预报技巧差异相当[113]。在大气环流对海温外强迫信号的响应时间研究方面,数值试验结果显示:大气对海温强迫信号响应的时间约为10 d,实时海温对10 d以内的预报结果影响较小,但对月时间尺度的影响十分明显[114-115],特别是当预报时效超过3周时,在热带地区下边界强迫是可预报性的主要来源。

目前国际上主要业务预报中心延伸期预报已由大气环流模式逐步过渡到耦合模式,如美国CPC业务预报模式(Climate Forecast System version 2, CFSv2),即为包括大气、海洋、海冰、陆面模式的全耦合气候系统模式,逐日滚动发布未来4周的环流和要素距平预报,每个时次的预报包含16个集合样本。CPC还提供未来6～10 d和8～14 d的气候趋势概率预报产品,包括气温偏高(低)、降水偏多(少)和接近正常的发生概率,采用的主要预报方法包括对各种动力和统计客观方法预报结果的综合集成。ECMWF延伸期预报业务中采用了两种预报方案:一种是将中期预报进行延伸,并在预报开始的10 d之后考虑海气耦合作用;另一种延伸期预报和季节预报类似,直接采用全耦合方案,并给出未来4周逐周平均的要素预报[116]。加拿大环境和气候变化中心(Environment and Climate Change Canada, ECCC)的全球集合预报系统每周四提供至未来32 d的预报结果,并处理为第5～11天、第12～18天、第19～25天和第26～32天以及30 d(月)平均的预报产品。日本气象厅(Japanese Meteorological Agency, JMA)的延伸期预报也称月预报,模式集合预报提供未来第1周和第2周、第3周、第4周以及28 d平均的预报结果。模式每周三提供1次预报结果,产品形式包括不同高度层环流场、降水、气温以及海表温度异常的预报。中国气象局国家气候中心第2代月动力延伸预测模式系统(Dynamic Extended Range Forecast operational system version 2.0, DERF2.0)基于大气环流谱模式建立,提供未来40 d逐旬和月平均环流形势和要素的预报[117],2014年开始在第2代气候系统模式的基础上研发了BCC_CSM1.2模式用于延伸期预报,并提交了模式回算数据参加国际S2S预测计划。此外,中国气象局国家气候中心每旬第1天滚动发布未来10～30 d延伸期预报产品,产品内容包括延伸期气候趋势和强降水、强降温等重要天气过程预报。总体而言,与主要发达国家相比,我国延伸期预报业务还处于起步阶段,产品形式相对单一,现有数值模式集合预报系统还无法满足延伸期预报业务的需求。

3.1 数值模式延伸期预报技巧

在延伸期降水、气温等要素的预报对象方面,目前国际主流数值预报中心的预报产品形式大多以逐周平均的距平异常为主。逐周预报一方面考虑到逐日天气预报的理论上限[118],另一方面通过平均滤除了逐日天气噪音,提升了气候信号的可预报性[119-120]。对ECMWF、美国CFSv2和日本TCC模式延伸期逐周降水集合预报性能评估结果显示,除了太平洋、大西洋的热带辐合带(Intertropical Convergence Zone, ITCZ)以及海洋性大陆区域,各模式对延伸期降水的预报技巧在第2～4周均明显衰减。其中ECMWF模式对延伸期降水的预报能力明显高于其他两家,尤其是未来第3～4周[121]。对比分析CFSv2模式对大气环流和气象要素的延伸期预报能力发现[122],模式对500 hPa高度场的预报技巧最高,850 hPa纬向风场次之,降水最低,同时模式对延伸期气候要素的预报技巧与MJO特别是BSISO的强度密切相关。而将降水等气候要素分解为一系列正交的空间模态后,其中许多分量也都具有显著的预报技巧[123-124]。ECCC月预报系统的评估结果显示,模式对中国东部的气温和500 hPa位势高度预报技巧可达4周,降水的预报技巧相对较低,仅约5～11 d,同时模式对东亚地区气候要素次季节变率的预报技巧受到MJO和ENSO的共同影响[125]。大量研究结果表明:模式对延伸期第3～4周的有技巧预报仍局限在热带地区,部分高层变量如位势高度场[126],以及某些气候因子[127],而对中纬度陆地上的延伸期时段气温和降水等气候要素的预报技巧的影响几乎可以忽略不计。

中国气象局国家气候中心第2代月动力延伸模式对月平均环流及气温和降水具有一定预测能力,但对延伸期时段环流和要素以及强降水、强降温等

重要天气过程的预测技巧相对较低[128-129]。评估结果显示:模式对延伸期逐候降水空间相关系数大于0.1的预报约能持续 2～3 候,即约 10～15 d,之后技巧迅速下降。模式对东亚和南亚地区延伸期降水的预报技巧较低,仅能持续不到 2 候,技巧相对较高的区域主要位于在热带太平洋和大西洋地区。

3.2　动力统计相结合的延伸期预报方法

由于直接利用数值模式结果进行延伸期预报与实际业务需求还存在一定距离,因此,基于动力模式有效预测信息和物理统计方法的动力统计相结合预测方案在业务中发挥着重要作用。陈丽娟等[130]针对传统的统计降尺度方法中预报因子和预报对象之间统计关系稳定性较差这一问题,利用简化的大气动力学方程组推导局地月平均降水距平和大气环流场之间的关系[131],构建了一种新的月降水降尺度预测模型。该降尺度模型既有明确的动力学意义,又充分利用了历史气候数据,实现了动力和统计的有机结合。任宏利等[132]提出了一种能有效减少月平均和逐日大气环流预报误差的动力相似集合预报方法[133],该方法在模式积分过程中通过提取大气环流历史相似信息,对模式误差进行参数化处理,形成多个时变的相似强迫量来扰动生成预报的集合成员,从而实现了动力模式与统计经验的内在结合。

近年来,从延伸期可预报性的角度,中国气象局国家气候中心发展了一系列基于数值模式可预报分量的误差订正和集合预报方法[134-137]。对数值模式的可预报分量和随机分量分别采用不同的集合预报方案,通过在各个模式可预报分量误差订正的基础上,从考虑模式不确定性的角度进行集合,随机分量部分则直接采用预报量的气候概率分布,以避免模式误差对随机分量概率分布的影响(图 2)。预报检验结果表明:该方法对环流形势预报技巧有一定提高,对不同空间尺度的波也有不同尺度的改进,显示出潜在的业务应用前景[138]。章大全等[139]利用要素历史观测和模式回报数据的概率密度分布特征,采用非参数百分位映射法订正了 DERF2.0 模式月平均温度预报,有效降低了模式预报的均方根误差,同时对温度距平分布预报也有不同程度改善。

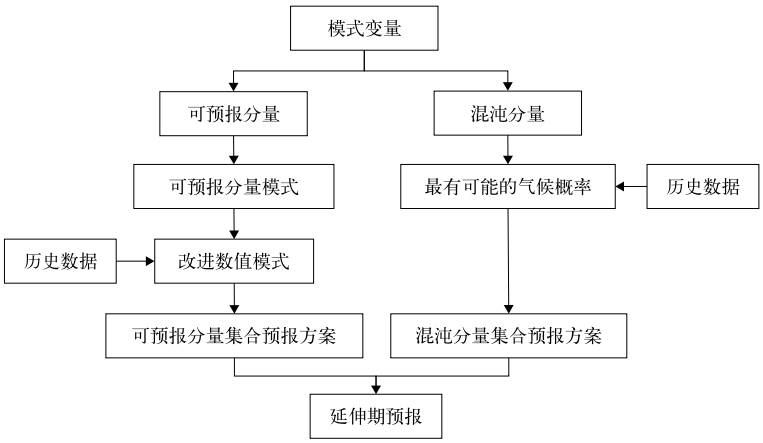

图 2　基于可预报分量的延伸期数值模式集合预报方法原理

Fig. 2　Scheme of extended-range numerical ensemble forecast based on predictable components

3.3　基于物理统计的延伸期预报方法

基于延伸期时段存在一些可预报的信号源,如热带的大气低频变率(特别是 MJO)、大气韵律周期关系等,近年来一些基于物理统计的延伸期预报方法得到广泛应用,取得了较好的预报效果[140-141]。如中国气象局国家气候中心发展的 IMPRESS1.0 版本,提供了基于 MJO 降尺度模型的我国未来 6 候的平均气温和降水异常预报[66];上海市气候中心利用大气低频振荡及其传播与延伸期降水、气温之间的关系,基于低频天气图等方法开发了月内重要天气过程与气候趋势预测系统(Monthly/extended-range Anomaly and Process Forecast System, MAPFS)[142-144];福建省气候中心根据热带 ISO 制作了华南持续性暴雨过程的延伸期预报[145];西北区域气候中心[146]根据大气的准周期运动规律,提出用 150 d 韵律方法对月内过程进行预报;钱维宏等[147]提出任何一个大气变量的瞬时观测场都可以物理分解成逐日气候分量、行星尺度瞬变扰动分量和天气尺度瞬变扰动分量,而极

端天气事件的预报可用瞬变涡扰动法，为延伸期极端天气气候事件的预报提供了新的思路。

除了上述利用大气低频信号、韵律周期关系或者物理量分解的预测方法之外，还有一些基于线性或非线性方法建模的延伸期预报方法，如中国气象局国家气候中心和美国夏威夷大学合作研发的非滤波时空投影(Spatial-Temporal Projection Models，STPM)方法。该方法利用奇异值分解建立起预报量与前期因子的关系，并用长期历史数据对模型进行训练，并将前期环流场投影到预报因子上得到随时间演变的预报量，有效提取和利用了观测数据中的低频分量和历史信息，被广泛应用于强降水[148]、热带对流活动[149]、南海夏季风爆发[150]和热带气旋[151]等的延伸期预报中。陈丽娟等[152]基于非线性时空序列预测理论，利用局域近似法对延伸期逐候纬向平均高度场进行预测，发现非线性时空序列预测方法对纬向平均高度距平场的预报优于持续性预报和模式动力延伸预报，体现了一定的改进延伸期环流预报的能力。杨秋明[153-154]通过提取气候要素和大尺度环流的低频主成分分量，分别构建了扩展复数自回归模型(Extended Complex Autoregressive model，ECAR)和主成分复数回归模型(Principal Component-Complex Autoregressive model，PC-CAR)以及多变量时滞回归模型(Multivariate Lagged Regressive model，MLR)等预报模型，对夏季长江下游低频降水、气温和高温天气进行预测试验，显示出较好的预测效果和应用前景。

上述方法模型和预测系统极大支撑了延伸期预报业务和服务，尤其是在一些重大气象保障活动中发挥了决策作用。中国气象局国家气候中心综合IMPRESS系统对MJO指数的监测和预测信息，重建的延伸期时段候平均气温和降水异常预测，以及延伸期逐日变温过程概率预测结果，对首届中国国际进口博览会期间上海地区气温偏高、中后期有明显降温过程并伴有降水的天气形势进行成功预测，取得了良好的服务效果。在上海市气候中心开展的梅雨相关延伸期预报业务中，利用关键区低频信号建立的回归模型，较好预报出梅雨区延伸期降水的峰值出现时段和逐候降水量增加或减少的演变，同时对逐候降水量异常也有一定的预报能力[155]。

4 小 结

延伸期预报填补了传统中短期天气预报和短期气候预测之间的空隙，是构建无缝隙预报体系的必然要求，对防御重大气象灾害、服务国民经济具有重要意义。本文从延伸期的可预报性及其来源、预报的主要方法几个方面回顾了延伸期预报的相关科研和业务实践情况，重点分析了近年来可预报性研究进展和应用，以及预报水平现状。整体而言，延伸期预报作为当前科研和业务服务的重点和难点，需要解决的科学问题、方法以及业务标准规范仍然很多，概括起来主要有以下几个方面：

1) 延伸期时段的预报和检验对象及方法问题。根据大气可预报性及非线性误差增长理论，逐日确定性天气预报的可预报性上限一般为2周左右。直接借鉴月、季尺度短期气候预测的做法，针对延伸期时段要素平均值及其距平进行预报，可能在预测结果的针对性和指导意义上存在局限性。延伸期时段重要天气过程(包括持续性异常天气事件特别是极端天气事件)的准确预报[156]是延伸期预报的核心问题，如何针对预报对象制定兼顾科学性和实用性的预测对象和检验标准，是首先需要解决的问题。目前国外主流数值预报中心普遍将延伸期逐周平均的气象要素和环流距平作为预报对象，并对逐周技巧进行评估。这种处理方式比较简单，但不适合过程预测及服务，需要研究针对用户服务需求的更好的方案。

2) 针对MJO等低纬度地区的大气季节内低频振荡已有大量研究工作，然而中高纬度地区低频振荡的活动规律和传播特征以及与我国气象要素之间的联系还缺乏深入研究。如何综合考虑低纬度和中高纬度的低频信息，建立与要素预报的物理联系仍然是难点。此外，如何充分利用模式对次季节尺度主要气候现象的预测能力，有效改进我国延伸期时段要素特别是重要天气过程的预测，也值得深入研究。

3) 已有研究表明：延伸期时段的大尺度环流形势以及重要天气过程的有效预报时效和预报技巧与大气的初始状态、海温等外强迫信号密切相关，而目前对不同海温及大气初始条件下影响我国天气气候的关键环流系统以及主要的极端天气气候事件延伸期时段的可预报性研究还相对较少。充分利用海温等外强迫信号在延伸期时段的预报技巧及其大气响应特征，提取耦合数值模式有效预报信息改进延伸期预报，可能是改进延伸期预报的途径之一。

延伸期预报目前还处于研究和业务试用阶段，

数值模式预报的发展被认为是从根本上解决天气气候预测问题的途径，但目前数值模式的预报时效和性能还远不能满足延伸期业务的需求。对数值模式延伸期预报中大气初值和下垫面异常的贡献研究表明，海气、陆气等耦合作用能够提升延伸期时段大气环流和要素的可预报性。此外，许多次季节尺度气候现象，如 MJO、平流层爆发性增温以及大气遥相关等，都为延伸期预报提供了重要的可预报信号来源。但对延伸期可预报信号源与天气气候异常的联系及其物理机制的研究还相对薄弱，在充分挖掘延伸期潜在可预报性，改进延伸期环流和要素的预报技巧方面，还有许多物理过程和关键技术问题需要解决。因此，深入研究大气季节内振荡以及海气、陆气相互作用机理，不断完善和改进气候系统耦合模式的物理过程和参数化方案，将潜在可预报性转化为实际的预报技巧，提升数值模式延伸期时段的预报预测性能方面仍需进行大量探索。

参 考 文 献

[1] Vitart F, Ardilouze C, Bonet A, et al. The subseasonal to seasonal (S2S) prediction project database. *Mon Wea Rev*, 2017, 99(1): 163-173.

[2] ECWMF. A Roadmap to 2025: The Strength of a Common Goal. Reading: ECWMF, 2016: 1-10.

[3] Black J, Johnson N C, Baxter S, et al. The prediction and forecast skill of northern hemisphere teleconnection patterns for lead times of 3－4 weeks. *Mon Wea Rev*, 2017, 145(7): 2855-2877.

[4] Zhu Y, Zhou X, Peña M, et al. Impact of sea surface temperature forcing on weeks 3 and 4 forecast skill in the NCEP global ensemble forecasting system. *Wea Forecasting*, 2017, 32(6): 2159-2174.

[5] Vitart F. Monthly forecasting at ECMWF. *Mon Wea Rev*, 2004, 132(12): 2761-2779.

[6] Waliser D, Weickmann K, Dole R, et al. The Experimental MJO Prediction Project. *Bull Amer Meteor Soc*, 2006, 87(4): 425-431.

[7] 贾小龙，陈丽娟，高辉，等. 我国短期气候预测技术进展. 应用气象学报，2013，24(6)：641-655.

[8] 任宏利，吴捷，赵崇博，等. MJO 预报研究进展. 应用气象学报，2015，26(6)：658-668.

[9] Baldwin M P, Dunkerton T J. Propagation of the Arctic Oscillation from the stratosphere to the troposphere. *J Geophys Res*, 1999, 104(D24): 30937-30946.

[10] Baldwin M P, Stephenson D B, Thompson D W, et al. Stratospheric memory and skill of extended-range weather forecast. *Science*, 2003, 301(5633): 636-640.

[11] Polvani L M, Kushner P J. Tropospheric response to stratospheric perturbations in a relatively simple general circulation model. *Geophy Res Lett*, 2002, 29(7): 1-4.

[12] Koster R D, Suarez M J. Impact of land surface initialization on seasonal precipitation and temperature prediction. *J Hydrometeorol*, 2003, 4(2): 408-423.

[13] Cohen J, Entekhabi D. Eurasian snow cover variability and Northern Hemisphere climate variability. *Geophy Res Lett*, 1999, 26(3): 345-348.

[14] Holland M M, Blanchard-Wrigglesworth E, Kay J, et al. Initial-value predictability of Antarctic ice in the Community Climate System Model 3. *Geophys Res Lett*, 2013, 40(10): 2121-2124.

[15] Thompson P D. Uncertainty of initial state as a factor in the predictability of large-scale atmospheric flow patterns. *Tellus*, 1957, 9(3): 275-295.

[16] Lorenz E N. Deterministic nonperiodic flow. *J Atmos Sci*, 1963, 20(2): 130-141.

[17] 丑纪范. 长期数值天气预报. 北京：气象出版社，1986.

[18] 李崇银. 气候变化及可预报性（CLIVAR）——气候研究的国际新计划. 气候与环境研究，1996，1(1)：87-95.

[19] 穆穆，李建平，丑纪范，等. 气候系统可预报性理论研究. 气候与环境研究，2002，7(2)：227-235.

[20] Li J, Ding R. Temporal-spatial distribution of atmospheric predictability limit by local dynamical analogs. *Mon Wea Rev*, 2011, 139(10): 3265-3283.

[21] Molteni F, Buzzia R, Palmer T N, et al. The ECMWF ensemble prediction system: Methodology and validation. *Q J Roy Meteor Soc*, 1996, 122(52): 73-119.

[22] 丁瑞强，李建平. 天气可预报性的时空分布. 气象学报，2009，67(3)：343-354.

[23] Kalnay E. 大气模式、资料同化和可预报性. 蒲朝霞，杨福全，邓北胜，等译. 北京：气象出版社，2005.

[24] 丑纪范. 大气科学中的非线性与复杂性. 北京：气象出版社，2002.

[25] 丑纪范，郑志海，孙树鹏. 10—30 d 延伸期数值天气预报的策略思考——直面混沌. 气象科学，2010，30(5)：569-573.

[26] Reichler T J, Roads J O. The role of boundary and initial conditions for dynamical seasonal predictability. *Nonlinear Proc Geoph*, 2003, 10(3): 211-232.

[27] 郑志海，任宏利，黄建平. 基于季节气候可预报分量的相似误差订正方法和数值实验. 物理学报，2009，58(10)：7359-7367.

[28] 郑志海，封国林，丑纪范，等. 数值预报中自由度的压缩及误差相似性规律. 应用气象学报，2010，21(2)：139-148.

[29] 刘景鹏，陈丽娟，李维京，等. 月尺度气温可预报性对资料长度的依赖及可信度. 应用气象学报，2015，26(2)：151-159.

[30] Liu J, Li W, Chen L, et al. Estimation of the monthly precipitation predictability limit in China using the nonlinear local Lyapunov exponent. *J Meteor Res*, 2016, 30(1): 93-102.

[31] Sarachik E S, Cane M A. The El Niño-Southern Oscillation Phenomenon. Cambridge: Cambridge University Press, 2010.

[32] 张人禾，周广庆，巢纪平. ENSO 动力学与预测. 大气科学，2003，27(4)：674-688.

[33] 王会军，孙建奇，郎咸梅，等. 几年来我国气候年际变异和短期气候预测研究的一些新成果. 大气科学，2008，32(4)：806-814.

[34] 陈丽娟,李想,李维京,等. 2015/2016年超强El Niño事件背景下我国月预测技巧差异分析. 大气科学学报,2016,39(6):756-765.

[35] Zhao P,Zhu Y N,Zhang R H. An Asian-Pacific teleconnection in summer tropospheric temperature and associated Asian climate variability. *Climate Dyn*,2007,29(2-3):293-303.

[36] 晏红明,肖子牛. 印度洋海温异常对亚洲季风区天气气候影响的数值模拟研究. 热带气象学报,2000,16(1):18-27.

[37] Zuo J,Li W,Sun C,et al. Impact of the North Atlantic sea surface temperature tripole on the East Asian summer monsoon. *Adv Atmos Sci*,2013,30(4):1173-1186.

[38] 杨修群,谢倩,黄士松. 大西洋海温异常对东亚夏季大气环流影响的数值试验. 气象学报,1992,50(3):349-354.

[39] Wang X,Zheng Z,Feng G. Effects of air-sea interaction on extended-range prediction of geopotential height at 500 hPa over the northern extratropical region. *Theor Appl Climatol*,2018,132(1-2):31-40.

[40] Saha S,Moorthi S,Wu X,et al. The NCEP Climate Forecast System version 2. *J Climate*,2014,27(6):2185-2208.

[41] Vitart F,Molteni F. Dynamical extended-range prediction of early monsoon rainfall over India. *Mon Wea Rev*,2009,137(4):1480-1492.

[42] Reichler T J,Roads J O. Long-range predictability in the tropics. Part I:Monthly averages. *J Climate*,2005,18(5):619-633.

[43] Reichler T J,Roads J O. Long-range predictability in the tropics. Part II:30—60-day variability. *J Climate*,2005,18(5):634-650.

[44] DeMott C A,Stan C,Randall D A,et al. Intraseasonal variability in coupled GCMs:The roles of ocean feedbacks and model physics. *J Climate*,2014,7(13):4970-4995.

[45] Fu X,Wang B,Waliser D E,et al. Impact of atmosphere-ocean coupling on the predictability of monsoon intraseasonal oscillations. *J Atmos Sci*,2007,64(1):157-174.

[46] Fu X,Wang B,Lee J Y,et al. Sensitivity of dynamical intraseasonal prediction skills to different initial conditions. *Mon Wea Rev*,2011,139(8):2572-2592.

[47] 汪栩加,郑志海,封国林,等. 延伸期预报中大气初值与海温边值的相对作用. 气象学报,2017,75(1):111-122.

[48] Charney J G,Shukla J. Predictability of Monsoons// Monsoon Dynamics. Cambridge:Cambridge University Press,1981:99-109.

[49] Zhu H,Wheeler M C,Sobel A H,et al. Seamless precipitation prediction skill in the tropics and extratropics from a global model. *Mon Wea Rev*,2014,142(4):1556-1569.

[50] Zhang C. Madden-Julian oscillation:Bridging weather and climate. *Bull Amer Meteor Soc*,2013,94(12):1849-1870.

[51] Robertson A W,Kumar A,Pena M,et al. Improving and promoting subseasonal to seasonal prediction. *Bull Amer Meteor Soc*,2015,96(3):ES49-ES53.

[52] Wheeler M,Hendon H H. An all-season real-time multivariate MJO index:Development of the index for monitoring and prediction in Australia. *Mon Wea Rev*,2004,132(8):1917-1932.

[53] Neena J M,Lee J Y,Waliser B,et al. Predictability of the Madden-Julian oscillation in the Intraseasonal Variability Hindcast Experiment (ISVHE). *J Climate*,2014,27(27):4531-4543.

[54] Wu J,Ren H L,Zuo J Q,et al. MJO prediction skill,predictability,and teleconnection impacts in the Beijing Climate Center Atmospheric General Circulation Model. *Dynam Atmos Oceans*,2016,75(9):78-90.

[55] Miyakawa T,Satoh M,Miura H,et al. Madden-Julian oscillation prediction skill of a new generation global model demonstrated using a supercomputer. *Nature Communications*,2014,5:3769.

[56] MacLachlan C,Arribas A,Peterson K A,et al. Global Seasonal forecast system version 5 (GloSea5):A high-resolution seasonal forecast system. *Q J Roy Meteor Soc*,2015,141(689):1072-1084.

[57] Liu X,Wu T,Yang S,et al. MJO prediction using the sub-seasonal to seasonal forecast model of Beijing Climate Center. *Climate Dyn*,2017,48(9-10):3283-3307.

[58] Green B W,Sun S,Bleck R,et al. Evaluation of MJO predictive skill in multiphysics and multimodel global ensembles. *Mon Wea Rev*,2017,145(7):2555-2574.

[59] Lee J Y,Wang B,Wheeler M C,et al. Real-time multivariate indices for the boreal summer intra-seasonal oscillation over the Asian summer monsoon region. *Climate Dyn*,2013,40(1-2):493-509.

[60] Lee S S,Wang B,Waliser D,et al. Predictability and prediction skill of the boreal summer intra-seasonal oscillation in the Intra-seasonal Variability Hindcast Experiment. *Climate Dyn*,2015,45(7-8):2123-2135.

[61] Jie W,Vitart F,Wu T,et al. Simulations of the Asian summer monsoon in the sub-seasonal to seasonal prediction project (S2S) database. *Q J Roy Meteor Soc*,2017,143(706):2282-2295.

[62] Liebmann B,Hendon H H,Glick J D. The relationship between the tropical cyclones of the western Pacific and Indian Oceans and the Madden-Julian Oscillation. *J Meteor Soc Japan*,1994,72(3):401-412.

[63] Zhou W,Chan J C. Intraseasonal oscillations and the South China Sea summer monsoon onset. *Int J Climatol*,2005,25(12):1585-1609.

[64] 李崇银,潘静,宋洁. MJO研究新进展. 大气科学,2013,37(2):229-252.

[65] Ren P,Ren H,Fu X,et al. Impact of boreal summer intraseasonal oscillation on rainfall extremes in southeastern China and its predictability in CFSv2. *J Geophys Res*,2018,123(9):4423-4442.

[66] 吴捷,任宏利,赵崇博,等. 国家气候中心MJO监测预测业务产品研发与应用. 应用气象学报,2016,27(6):641-653.

[67] 袁媛,高辉,柳艳菊. 2016年夏季我国东部降水异常特征及其成因简析. 气象,2017,43(1):115-121.

[68] Zhou W,Chan J C L. ENSO and South China Sea summer

monsoon onset. *Int J Climatol*，2007，27(2)：157-167.

[69] 高辉，袁媛，洪洁莉，等. 2016 年汛期气候预测效果评述及主要先兆信号与应用. 气象，2017，43(4)：486-494.

[70] 陈丽娟，顾薇，龚振淞，等. 影响 2018 年汛期气候的先兆信号和预测效果评估. 气象，2019，45(4)：553-564.

[71] Ashok K，Behera S K，Rao S A，et al. El Niño Modoki and its possible teleconnection. *J Geophys Res*，2007，112：C11007.

[72] 袁媛，李崇银，凌健. 不同分布型 El Niño 期间 MJO 活动的差异. 中国科学(地球科学)，2015，45(3)：318-334.

[73] 陈丽娟，顾薇，丁婷，等. 2015 年汛期气候预测先兆信号的综合分析. 气象，2016，42(4)：496-506.

[74] 赵俊虎，王永光. 2018 年秋季我国气候异常及成因分析. 气象，2019，45(4)：565-576.

[75] Yoo J H，Robertson A W，Kang I S. Analysis of intraseasonal and interannual variability of the Asian summer monsoon using a hidden Markov model. *J Climate*，2010，23(20)：5498-5515.

[76] Kessler W S，McPhaden M J，Weickmann K M. Forcing of intraseasonal Kelvin waves in the equatorial Pacific. *J Geophys Res*，1995，100(C6)：10613-10631.

[77] Vitart F，Balmaseda M A，Ferranti L，et al. Westerly wind events and the 1997/98 El-Niño event in the ECMWF seasonal forecasting system. *J Climate*，2003，16(19)：3153-3170.

[78] Riddle E E，Stoner M，Johnson N，et al. The impact of the MJO on clusters of wintertime circulation anomalies over the North American region. *Climate Dyn*，2013，40(7-8)：1749-1766.

[79] Johnson N C，Collins D C，Feldstein S B，et al. Skillful wintertime North American temperature forecasts out to 4 weeks based on the state of ENSO and MJO. *Wea Forecasting*，2014，29(1)：23-38.

[80] Thompson D W J，Baldwin M P，Wallace J M. Stratospheric connection to Northern Hemisphere winter-time weather：Implications for prediction. *J Climate*，2002，15(12)：1421-1428.

[81] Lehtonen I，Karpechko A Y. Observed and modeled tropospheric cold anomalies associated with sudden stratospheric warmings. *J Geophys Res*，2016，121(4)：1591-1610.

[82] Kolstad E W，Breiteig T，Scaife A A. The association between stratospheric weak polar vortex events and cold air outbreaks in the Northern Hemisphere. *Q J Roy Meteor Soc*，2010，136(649)：886-893.

[83] Karpechko A Y，Hitchcock P，Peters D H W，et al. Predictability of downward propagation of major sudden stratospheric warmings. *Q J Roy Meteor Soc*，2017，143(704)：1459-1470.

[84] Taguchi M. Predictability of major stratospheric sudden warmings：Analysis results from JMA operational 1-month ensemble predictions from 2001/02 to 2012/13. *J Atmos Sci*，2015，73(2)：789-806.

[85] Marshall A G，Scaife A A. Improved predictability of stratospheric sudden warming in an atmospheric general circulation model with enhanced stratospheric resolution. *J Geophys Res*，2010，115：D16114.

[86] Tripathi O P，Charlton-Perez A，Sigmond M，et al. Enhanced long-range forecast skill in boreal winter following stratospheric strong vortex conditions. *Environ Res Lett*，2015，10：104007.

[87] Tripathi O P，Baldwin M，Charlton-Perez A，et al. Examining the predictability of the stratospheric sudden warming of January 2013 using multiple NWP systems. *Mon Wea Rev*，2016，144(5)：1935-1960.

[88] Karpechko A Y. Predictability of sudden stratospheric warmings in the ECMWF extended-range forecast system. *Mon Wea Rev*，2018，146(4)：1063-1075.

[89] 章大全，宋文玲. 2017/2018 年冬季北半球大气环流特征及对我国天气气候的影响. 气象，2018，44(7)：969-976.

[90] Vinnikov K Y，Yeserkepova I B. Soil moisture：Empirical data and model results. *J Climate*，1991，4(1)：66-79.

[91] Entin J K，Robock A，Vinnikov K Y，et al. Temporal and spatial scales of observed soil moisture variations in the extratropics. *J Geophys Res*，2000，105(D9)：11865-11877.

[92] Koster R D，Suarez M J，Liu P，et al. Realistic initialization of land surface states：Impacts of subseasonal forecast skill. *J Hydrometeor*，2004，5(6)：1049-1063.

[93] Koster R D，Mahanama S P P，Yamada T J，et al. The second phase of the Global Land-Atmosphere Coupling Experiment：Soil moisture contribution to subseasonal forecast skill. *J Hydrometeor*，2011，12(5)：805-822.

[94] Seneviratne S I，Corti T，Davin E L，et al. Investigating soil moisture-climate interactions in a changing climate：A review. *Earth-Sci Rev*，2010，99(3-4)：125-161.

[95] Seo E，Lee M，Jeong J，et al. Impact of soil moisture initialization on boreal summer subseasonal forecasts：Mid-latitude surface air temperature and heat wave events. *Climate Dyn*，2018，52(3-4)：1695-1709.

[96] Fischer E M，Seneviratne S I，Vidale P L，et al. Soil moisture-atmosphere interactions during 2003 European summer heat wave. *J Climate*，2007，20(20)：5081-5099.

[97] Yang F，Kumar A，Wang H M，et al. Snow-albedo feedback and seasonal climate variability over North America. *J Climate*，2001，14(22)：4245-4248.

[98] Jeong J H，Linderholm H W，Woo S H，et al. Impacts of snow initialization on subseasonal forecasts of surface air temperature for the cold season. *J Climate*，2013，26(6)：1956-1972.

[99] Orsolini Y J，Senan R，Balsamo G，et al. Impact of snow initialization on sub-seasonal forecasts. *Climate Dyn*，2013，41(7-8)：1969-1982.

[100] Orsolini Y J，Senan R，Vitart F，et al. Influence of the Eurasian snow on the negative North Atlantic Oscillation in subseasonal forecasts of the cold winter 2009/2010. *Climate Dyn*，2016，47(3-4)：1325-1334.

[101] 段安民，肖志祥，吴国雄，等. 青藏高原冬春积雪影响亚洲夏季风的研究进展. 气候与环境科学，2014，7(3)：94-101.

[102] 韩世茹,郑志海,周须文,等.青藏高原积雪深度对延伸期预报技巧的影响.大气科学,2019,43(1):119-130.

[103] Frederiksen J S,Lin H. Tropical-extratropical interactions of intraseasonal oscillations. *J Atmos Sci*,2013,70(10):3180-3197.

[104] Wang J,Wen Z,Wu R,et al. The mechanism of growth of the low-frequency East Asia-Pacific teleconnection and the triggering role of tropical intraseasonal oscillation. *Climate Dyn*,2016,46(11-12):3965-3977.

[105] Stan C,Straus D M,Frederiksen J S,et al. Review of tropical-extratropical teleconnections on intraseasonal time scales. *Rev Geophys*,2017,55(4):902-937.

[106] Miyakoda K,Gordon T,Carerly R,et al. Simulation of a blocking event in January 1977. *Mon Wea Rev*,1983,111(4):846-869.

[107] Tracton M S,Mo K,Chen W,et al. Dynamical extended range forecasting (DERF) at the National Meteorological Center. *Mon Wea Rev*,1989,117(7):1604-1635.

[108] Deque M,Royer J F. The skill of extended-range extratropical winter dynamical forecasts. *J Climate*,1992,5(11):1346-1356.

[109] Palmer T N. Extended-range atmospheric prediction and the Lorenz model. *Bull Amer Meteor Soc*,1993,74(1):49-65.

[110] Boer G J. Dynamical Extended Range Forecasting at the Canadian Climate Centre. Reading:ECMWF,1988:135-152.

[111] Yamada S,Maeda S,Nakamura K. Time Lagged Ensemble Forecast Experiments in the Extended Range the JMA Global Prediction Model// WMO Training Workshop. Diagnosis and Prediction of Monthly and Seasonal Atmospheric Variations. Geneva:WMO,1991:231-234.

[112] Owen J A,Palmer T N. The Impact of El Niño on an ensemble of extended-range forecasts. *Mon Wea Rev*,1987,115(9):2103-2117.

[113] Mo K C,Kalnay E. Impact of sea surface temperature anomalies on the skill of monthly forecasts. *Mon Wea Rev*,1991,119(12):2771-2793.

[114] 骆美霞,张道民.实时海温对动力延伸(月)预报影响的数值试验研究.应用气象学报,2002,13(6):727-733.

[115] 王秋良,张立凤,关吉平.不同海温强迫的月动力延伸集合预报试验.气候与环境研究,2013,18(4):517-523.

[116] Vitart F. Evolution of ECMWF sub-seasonal forecast skill scores. *Q J Roy Meteor Soc*,2014,140(683):1889-1899.

[117] 吴统文,宋连春,刘向文,等.国家气候中心短期气候预测模式系统业务化进展.应用气象学报,2013,24(5):533-543.

[118] Lorenz E N. Climate Predictability// The Physical Basis of Climate and Climate Modeling. GARP Publication Series. Geneva:WMO,1975:133-136.

[119] Palmer T N,Anderson D L T. The prospects for seasonal forecasting-A review paper. *Q J Roy Meteor Soc*,1994,120(518):755-793.

[120] Mason S,Goddard L,Graham N E,et al. The IRI seasonal climate prediction system and the 1997/98 El Niño event. *Bull Amer Meteor Soc*,1999,80(9):1853-1873.

[121] Li S,Robertson A W. Evaluation of submonthly precipitation forecast skill from global ensemble prediction systems. *Mon Wea Rev*,2015,143(7):2871-2889.

[122] Liu R F,Wang W. Multi-week prediction of South-East Asia rainfall variability during boreal summer in CFSv2. *Climate Dyn*,2015,45(1-2):493-509.

[123] DelSole T,Trenary L. Predictability of week 3-4 average temperature and precipitation over the Contiguous United States. *J Climate*,2017,30(10):3499-3512.

[124] DelSole T,Tippett M K. Laplacian eigenfunctions for climate analysis. *J Climate*,2015,28(18):7420-7436.

[125] Liang P,Lin H. Sub-seasonal prediction over East Asia during boreal summer using the ECCC monthly forecasting system. *Climate Dyn*,2018,50(3-4):1007-1022.

[126] Pegion K,Sardeshmukh P D. Prospects for improving subseasonal predictions. *Mon Wea Rev*,2011,139(11):3648-3666.

[127] Wang W,Hung M P,Weaver S J,et al. MJO prediction in the NCEP Climate Forecast System version 2. *Climate Dyn*,2014,42(9-10):2509-2520.

[128] 何慧根,李巧萍,吴统文,等.月动力延伸预测模式业务系统DERF2.0对中国气温和降水的预测性能评估.大气科学,2014,38(5):950-964.

[129] 白慧,黄晨然,李忠燕.DERF2.0模式对贵州延伸期、月预测质量对比分析.中低纬山地气象,2018,42(5):1-5.

[130] 陈丽娟,李维京,张培群,等.降尺度技术在月降水预报中的应用.应用气象学报,2003,14(6):648-655.

[131] 李维京,陈丽娟.动力延伸预报产品释用方法的研究.气象学报,1999,57(3):338-344.

[132] 任宏利,张培群,李维京,等.提高月预报业务水平的动力相似集合方法.气象学报,2014,72(4):723-730.

[133] 李维京,郑志海,孙丞虎.近年来我国短期气候预测中动力相似预测方法研究与应用进展.大气科学,2013,37(2):341-350.

[134] 丑纪范.天气和气候的可预报性.气象科技进展,2011,1(2):11-14.

[135] 王阔,封国林,孙树鹏,等.基于2008年1月南方低温雨雪冰冻事件10～30天延伸期稳定分量的研究.物理学报,2012,61(10):1-10.

[136] 王启光,丑纪范,封国林.数值模式延伸期可预报分量提取及预报技术研究.中国科学(地球科学),2014,44(2):343-354.

[137] Zheng Z,Hu Z,L Heureux M. Predictable components of ENSO evolution in real-time multi-model predictions. *Scientific Reports*,2016,6:35909.

[138] 郑志海,黄建平,封国林,等.延伸期可预报分量的预报方案和策略.中国科学(地球科学),2013,43(4):594-605.

[139] 章大全,陈丽娟.基于DERF2.0的月平均温度概率订正预报.大气科学,2016,40(5):1022-1032.

[140] 金荣花,马杰,毕宝贵.10～30 d延伸期预报研究进展的业

务现状.沙漠与绿洲气象,2010,4(2):1-5.

[141] 何金海,梁萍,孙国武.延伸期预报的思考及其应用研究进展.气象科技进展,2013,3(1):11-17.

[142] 梁萍,何金海,穆海振.MJO 在延伸期预报中的应用进展.气象科技进展,2013,3(1):31-38.

[143] 孙国武,李震坤,信飞,等.延伸期天气过程预报的一种新方法——低频天气图.大气科学,2013,37(4):945-954.

[144] 陈伯民,梁萍,信飞,等.延伸期过程预报预测技术及应用.气象科技进展,2017,7(6):82-91.

[145] 高建芸,陈彩珠,周信禹,等.2010 年福建前汛期典型持续性暴雨过程的低频特征分析.气象科技进展,2013,3(1):39-45.

[146] 林纾,惠志红,郭俊琴,等.150 天韵律方法月内过程预测系统简介及应用检验.气象科技进展,2013,3(5):48-51.

[147] 钱维宏.瞬变涡扰动法在极端天气事件预报中的应用.气象科技进展,2012,2(5):44-48.

[148] Hsu P-C, Li T, You L, et al. A spatial-temporal projection method for 10－30-day forecast of heavy rainfall in Southern China. *Climate Dyn*, 2015, 44(5-6): 1227-1244.

[149] Zhu Z, Li T, Hsu P-C, et al. A spatial-temporal projection model for extended-range forecast in the tropics. *Climate Dyn*, 2015, 45(3-4): 1085-1098.

[150] Zhu Z, Li T. Empirical prediction of the onset dates of South China Sea summer monsoon. *Climate Dyn*, 2017, 48(5-6): 1633-1645.

[151] Zhu Z, Li T, Bai L, et al. Extended-range forecast for the temporal distribution of clustering tropical cyclogenesis over the western North Pacific. *Theor Appl Climatol*, 2017, 130(3-4): 865-877.

[152] 陈丽娟,陈伯民,李维京,等.T63 模式月动力延伸预报高度场的改进实验.应用气象学报,2005,16(增刊 I):92-96.

[153] 杨秋明.基于 20～30 d 振荡的长江下游地区夏季低频降水延伸期预报方法研究.气象学报,2014,72(3):494-507.

[154] 杨秋明.长江下游夏季低频温度和高温天气的延伸期预报研究.地球科学进展,2018,33(4):385-395.

[155] 梁萍,丁一汇.基于季节内振荡的延伸预报试验.大气科学,2012,36(1):102-116.

[156] 杜良敏,柯宗建.一种适用于延伸期过程事件预报的检验方法.应用气象学报,2013,24(6):686-694.

Advances on the Predictability and Prediction Methods of 10—30 d Extended Range Forecast

Zhang Daquan Zheng Zhihai Chen Lijuan Zhang Peiqun

(*Laboratory for Climate Studies, National Climate Center, China Meteorological Administration, Beijing* 100081)

Abstract

The 10—30 d extended range forecast (ERF) fills the gap between traditional weather forecast and short-term climate prediction, and it plays an important role in the decision making of disaster prevention and mitigation. Therefore, ERF becomes one hot topic in both scientific research and predictive operations. The research progress and operational status of ERF are reviewed from three aspects, the source of predictability, sub-seasonal climate phenomenon and operational predictions. The research achievements on predictability of ERF and its applications are specially emphasized, and some new forecasting methods of ERF in recent years are summarized. At last, key scientific issues and technical problems are raised and some thoughts and possible ways enhancing the predictive skills of ERF are proposed.

ERF exceeds time limits of traditional daily weather forecast, largely beyond the atmospheric memory of initial conditions, while it is too short to consider the variability of the ocean, which makes it difficult to beat persistence. Fortunately, recent years, some research work indicates the existence of some important sources of predictability at this time range, such as Madden-Julian oscillation (MJO), ENSO, soil moisture, snow cover and sea ice, stratosphere-troposphere interaction, ocean conditions, tropics-extratropics teleconnections, etc. Verification results of numerical model indicate that upper bounds of the prediction skill can be extended to 4 weeks. However, the complexity and diversity of mechanisms associated with the connection between source of predictability and climate variables prevent the potential predictability from being transformed into realized forecast skill. The effective forecast of most climate variables of numerical model is still limited within 2 weeks.

Although the direct application of numerical dynamical model output in ERF is unsatisfactory, some research institutes and operational centers still conduct a series of scientific research and propose some practical methods. According to utilization of numerical model data, those forecast methods can be divided into two categories, i. e., statistical methods and the combination of both statistical and dynamical methods. Based on dynamical forecast model, Beijing Climate Center develops several methods, including Dynamical-Analogue Ensemble Forecasting (DAEF), statistical downscaling, ensemble forecast of ERF based on predictable components and probabilistic calibration of model biases. On the other side, based on predictable signals of extended range, such as low frequency variation of atmosphere, MJO and periodic relationship, some statistical forecast methods are proposed, which show considerable predictive skill and good prospects of application.

Key words: extended range forecast; predictability; intra-seasonal oscillation

ADVANCES IN ATMOSPHERIC SCIENCES, VOL. 36, JANUARY 2019, 93–103

• **Original Paper** •

Influence of Late Springtime Surface Sensible Heat Flux Anomalies over the Tibetan and Iranian Plateaus on the Location of the South Asian High in Early Summer

Haoxin ZHANG[1,2,3], Weiping LI[*1], and Weijing LI[1,3]

[1]*Laboratory for Climate Studies, China Meteorological Administration, Beijing* 100081*, China*

[2]*University of Chinese Academy of Sciences, Beijing* 100049*, China*

[3]*Collaborative Innovation Center on Forecast and Evaluation of Meteorological Disasters, Nanjing University of Information Science and Technology, Nanjing* 210044*, China*

(Received 28 November 2017; revised 9 July 2018; accepted 19 July 2018)

ABSTRACT

Variation in the location of the South Asian High (SAH) in early boreal summer is strongly influenced by elevated surface heating from the Tibetan Plateau (TP) and the Iranian Plateau (IP). Based on observational and ERA-Interim data, diagnostic analyses reveal that the interannual northwestward–southeastward (NW–SE) shift of the SAH in June is more closely correlated with the synergistic effect of concurrent surface thermal anomalies over the TP and IP than with each single surface thermal anomaly over either plateau from the preceding May. Concurrent surface thermal anomalies over these two plateaus in May are characterized by a negative correlation between sensible heat flux over most parts of the TP (TPSH) and IP (IPSH). This anomaly pattern can persist till June and influences the NW–SE shift of the SAH in June through the release of latent heat (LH) over northeastern India. When the IPSH is stronger (weaker) and the TPSH is weaker (stronger) than normal in May, an anomalous cyclone (anticyclone) appears over northern India at 850 hPa, which is accompanied by the ascent (descent) of air and anomalous convergence (divergence) of moisture flux in May and June. Therefore, the LH release over northeastern India is strengthened (weakened) and the vertical gradient of apparent heat source is decreased (increased) in the upper troposphere, which is responsible for the northwestward (southeastward) shift of the SAH in June.

Key words: Tibetan Plateau, Iranian Plateau, surface sensible heat flux, latent heat of condensation, South Asian High

Citation: Zhang, H. X., W. P. Li, and W. J. Li, 2019: Influence of late springtime surface sensible heat flux anomalies over the Tibetan and Iranian plateaus on the location of the South Asian High in early summer. *Adv. Atmos. Sci.*, **36**(1), 93–103, https://doi.org/10.1007/s00376-018-7296-2.

1. Introduction

In the middle of the 1950s, Ye et al. (1957) studied surface thermal conditions on the Tibetan Plateau (TP) and its impact on general atmospheric circulation over East Asia. With the increasing availability of observational data and the improvement of research methods during the past decades, more studies have revealed the thermal effects of the TP influences on summer rainfall in China by modulating the Bay of Bengal (BOB) summer monsoon and the East Asian summer monsoon (EASM) (Zhang and Wu, 1998, 1999; Zhang and Qian, 2002; Duan and Wu, 2005; Liang et al., 2005; Wang et al., 2014). The magnitude of sensible heat flux (SH) over the Iranian Plateau (IP) is larger than that of the TP, although the area and altitude of the IP is smaller than the TP. It has been revealed that SH over the TP (TPSH) is persistently decreasing (Duan and Wu, 2008, 2009; Cui and Wang, 2009; Yang et al., 2011; Duan et al., 2013), while SH over the IP (IPSH) is persistently increasing, in spring and summer during the last three decades, and both experienced a reversed anomaly at the decadal time scale around the end of the 20th century (Zhang et al., 2017). More studies have demonstrated that the thermal effect of the IP is another factor responsible for anomalies in the general atmospheric circulation over East Asia; specifically, the synergistic thermal effects of the TP and IP are crucial in modulating the onset and seasonal evolution of the Asian summer monsoon (Wu et al., 2012, 2015; Liu et al., 2017b). Against the background of global warming and the synergistic effect of concurrent IP and TP thermal anomalies, the general atmospheric circulation over Asia has been an interesting topic.

The South Asian High (SAH) is the strongest and most stable atmospheric circulation system in the upper troposphere during boreal summer, and its formation and evolution are closely related to the seasonal enhancement of tropical convection near the Philippines (Liu et al., 2013, 2017a) and the diabatic heating of the TP (Flohn, 1957; Gao et al.,

* Corresponding author: Weiping LI
Email: liwp@cma.gov.cn

© Institute of Atmospheric Physics/Chinese Academy of Sciences, and Science Press and Springer-Verlag GmbH Germany, part of Springer Nature 2019

1982). Recent studies have also revealed the importance of the thermal effect from the IP to atmospheric circulation during boreal summer. The difference in the thermal conditions of these two plateaus can cause anomalies in air temperature in the upper-level troposphere, resulting in the east–west oscillation of the summertime SAH at an interannual time scale. The SAH located to the west is called the "Iranian mode", when the IP is warmer than normal; and the eastward located SAH is called the "Tibetan mode", when the TP is warmer than normal, also named the "warm-preference property" of the SAH (Qian et al., 2002a, 2002b; Wu et al., 2004). In addition, compared to the diabatic heating of the plateaus, the latent heat (LH) of condensation associated with monsoon rainfall is larger in quantity and can heat the upper-level troposphere directly; therefore, LH plays a more important role in strengthening the SAH. Zhang et al. (2016) noted positive feedback between condensation heating associated with the EASM precipitation and the SAH variability: higher condensation associated with a stronger EASM heats the eastern flank of the summertime SAH; then, geopotential heights on the western flank of the SAH are elevated by a westward propagating Rossby wave; and finally, the whole SAH is strengthened. As two subsystems of the Asian summer monsoon, the negative correlation between the Indian summer monsoon (ISM) rainfall and EASM rainfall could cause a northwest–southeast (NW–SE) shift of the summer SAH on an interannual time scale (Wei et al., 2015). In addition to the land–sea thermal contrast, the thermal effect of the IP and TP on the generation and evolution of the ISM and EASM should not be neglected. A higher TPSH in late spring can strengthen the intensity of the EASM (Duan and Wu, 2003; Duan et al., 2003) and bring forward the onset of the ISM by suppressing air convection over northeastern India (Zhang et al., 2015); and a higher IPSH mainly contributes to a strengthening of the ISM (Wu et al., 2012), and vice versa. Considering the effects of IPSH and TPSH on the onset and intensity of the Asian summer monsoon, as well as the close connection between these two plateaus, analysis of concurrent SH anomalies over the IP and TP and the effect on subsequent Asian summer monsoons and the SAH is necessary.

Variation in the location of the SAH at the interannual time scale greatly affects summer weather and climate in China and South Asia. Undoubtedly, the climate condition—especially the thermal situations of high elevations like the IP and TP—also influence the location of the SAH. From the viewpoint of the climate mean, the core of the SAH in May is located over the Indochina Peninsula (Liu et al., 2017a). It then moves northward and westward with the evolution of the seasons, reaching its northernmost position in August, which is coincident with the seasonal continental warming, especially over the IP and TP, and then retreats southeastward in boreal autumn. Generally speaking, SH always outweighs LH over the IP; while over the TP, SH peaks in May and outweighs LH except for June to September (Zhang et al., 2017). The effect of SH, especially TPSH, on atmospheric circulation, is weakened after the onset of the Asian summer monsoon, when LH from condensation accompanying monsoon rainfall gradually becomes a dominant factor. Besides, the relationship between late springtime SH and the early summer SAH deserves further investigation in a prediction sense. Different from separately analyzing the isolated thermal effects of the TP and IP in previous studies, we explore the combined impact of late springtime SH anomalies over the TP and IP on the early summertime SAH, the aim being to provide a reference for summer climate prediction in China.

The rest of this paper is structured as follows: Section 2 briefly describes the data and methods used. In section 3, we present the interannual variation of the SAH in June and the anomalous atmospheric circulation during the same period. The dominant feature of concurrent SH anomalies over the IP and TP in late spring and its relationship with the interannual variation of the SAH is discussed in section 4. In section 5, we explore the possible mechanisms causing the concurrent SH anomalies over the IP and TP in boreal late spring that affect the early summertime SAH. And finally, conclusions and a discussion are presented in section 6.

2. Data and methods

2.1. *Data*

The data used in this study include monthly mean geopotential height, surface sensible heat flux and 6-h means for air temperature, zonal and meridional wind speeds, vertical velocities and specific humidity from the European Center for Medium-Range Weather Forecasts interim reanalysis (ERA-Interim), which has a horizontal resolution of $1.5^\circ \times 1.5^\circ$ and 37 vertical levels. The monthly mean precipitation data are from the Global Precipitation Climatology Project (GPCP) dataset, which has a $2.5^\circ \times 2.5^\circ$ horizontal resolution. All the data are from 1979 to 2014.

2.2. *Methods*

Statistical methods, such as empirical orthogonal function (EOF), singular value decomposition (SVD), correlation, and composite analyses, are used in this study. The area for the IP is represented by 101 grids (in ERA-Interim), with terrain height more than 300 m in the region (25.5°–40.5°N, 49.5°–70.5°E). The TP is represented by 116 grids (in ERA-Interim), with a terrain height higher than 3000 m over the domain (25.5°–40.5°N, 75°–105°E), which is similar to the definition from Zhang et al. (2017). The core of the SAH is defined by a 12500-gpm isoline at 200 hPa; its ridgeline is located where zonal wind speeds u equal 0 m s^{-1} and $\partial u/\partial y > 0$, according to Liu and Wu (2004), and the center of the SAH is defined as the point where geopotential height is maximal at 200 hPa. Considering the relatively short time series of the data (36 years), we focus on the relationship between SH anomalies over the TP and IP and variations of the SAH, on the interannual time scale. All indexes defined in this study, which characterize variations in the SAH and SH over the two plateaus, are high-pass filtered over nine years.

The apparent heat source (Q_1), apparent moisture sink (Q_2) and their vertical integrations in an air column, $\langle Q_1 \rangle$

and $\langle Q_2 \rangle$, are calculated based on the 6-h mean datasets from ERA-Interim and follow the formulas from Yanai et al. (1973):

$$Q_1 = C_p \left[\frac{\partial T}{\partial t} + \boldsymbol{V} \cdot \nabla T + \left(\frac{p}{p_0} \right)^{\kappa} \omega \frac{\partial \theta}{\partial p} \right] ; \quad (1)$$

$$Q_2 = -L \left[\frac{\partial q}{\partial t} + \boldsymbol{V} \cdot \nabla q + \omega \frac{\partial q}{\partial p} \right] ; \quad (2)$$

$$\langle Q_1 \rangle = \frac{1}{g} \int_{p_t}^{p_s} Q_1 dp ; \quad (3)$$

$$\langle Q_2 \rangle = \frac{1}{g} \int_{p_t}^{p_s} Q_2 dp . \quad (4)$$

Here, T is air temperature; θ is potential temperature; q is specific humidity; $\boldsymbol{V}$ is the orizontal wind vector, ω is vertical velocity in pressure coordinates, $p_0 = 1000$ hPa, $\kappa = R/C_p$, R and C_p are the gas constant and specific heat at a constant pressure for dry air, respectively; L is the latent heat of condensation; and p_s and p_t are the pressures at the surface and the top layer (i.e., 1 hPa), respectively. It can be deduced that the latent heat of condensation is the primary contributor to atmospheric heat sources when the quantity of $\langle Q_2 \rangle$ is similar to $\langle Q_1 \rangle$.

3. Interannual variation of the SAH in early summer

3.1. *Definition of the SAH index and its interannual variation in June*

The climatological ridgeline of the SAH in June (i.e., the zonal dashed green curves in Fig. 1) lies over the subtropical Asian continent between 18°N and 30°N, and the center of the SAH (i.e., the cross point of the dashed green lines in Fig. 1) is located to the south of the Himalaya. The spatial patterns of the geopotential height anomalies at 200 hPa in early boreal summer can be mainly classified into two modes according to the climatological ridgeline and location of the center of the SAH: geopotential height anomalies that are generally uniformly positive or negative within the SAH domain (EOF1, figure not shown), and geopotential height anomalies in the northwestern part of the SAH that are opposite to those in the southeastern part of the SAH (EOF2, Fig. 1a). The spatial pattern of EOF2 displays a northwest–southeast (NW–SE) shift of the SAH at the interannual time scale, which is associated with a negative correlation between the ISM rainfall and EASM rainfall and has received much attention (Wei et al., 2015). In this study, we focus on EOF2 of the SAH and its relationship with the thermal conditions of the IP and TP in late spring.

To better describe the NW–SE shift of the SAH, we define an SAH index based on the spatial pattern of the EOF2 shown in Fig. 1. The SAH index is the difference in standardized area-averaged 200-hPa geopotential height ["Nor" in Eq. (5) represents standardization and "Z200" represents 200-hPa geopotential height] between the northwest region and the southeast region of the SAH core (dashed black boxes in Fig. 1). We define the June SAH index accordingly to accurately describe the NW–SE shift in the SAH based on its climate mean location as follows:

$$\mathrm{SAH6_{NW-SE}} = \mathrm{Nor[Z200_{NW}]} - \mathrm{Nor[Z200_{SE}]} . \quad (5)$$

$\mathrm{Z200_{NW}}$ represents the regional mean of 200-hPa geopotential height covering 25.5°N–31.5°N and 63°E–90°E, and $\mathrm{Z200_{SE}}$ represents the regional mean of 200-hPa geopotential height covering 17°N–23°N and 93°E–120°E. The temporal evolution of $\mathrm{SAH6_{NW-SE}}$ is closely related to the second principal component (PC2) of the SAH EOF2 in June, with a correlation coefficient as high as 0.88, statistically significant at the 99.9% confidence level. The advantage of the SAH index defined in this study is that it can exhibit the NW–SE shift of the SAH quite well (Fig. 1b) but is not dependent on the domain size that contains the SAH, which is a weakness in the EOF analysis.

The interannual variation of the SAH location ($\mathrm{SAH6_{NW-SE}}$) is shown in Fig. 1b. During 1979–2014, 12 years with a standardized $\mathrm{SAH6_{NW-SE}}$ above 0.5 are selected to represent the northwestward-located SAH (abbrevi-

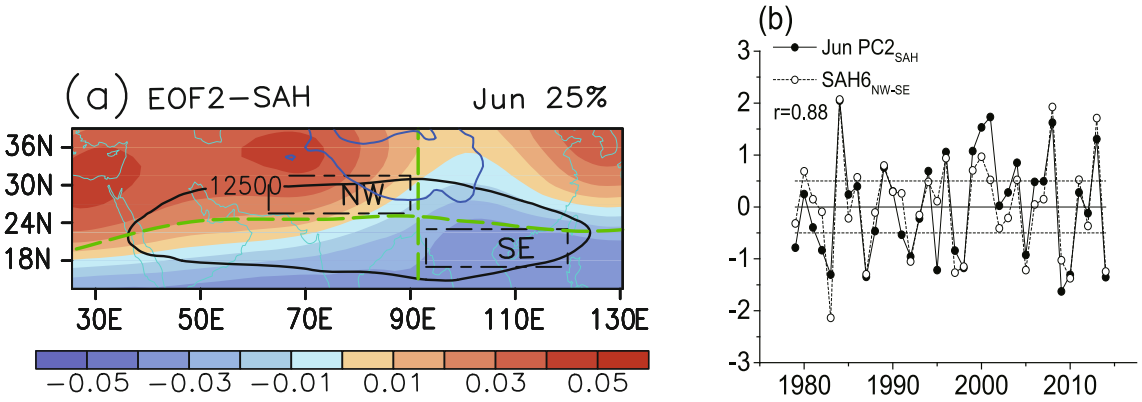

Fig. 1. (a) Second EOF mode for 200-hPa geopotential height (Z200) in June (shaded), in which the climatological core of the SAH (Z200) from 1979 to 2014 is shown by the black contour 12 500 gpm. The dashed black boxes indicate the NW and SE regions of the SAH from which the SAH index is calculated. The horizontal dashed green curve indicates the ridge line of the SAH, and the cross point of the dashed green lines indicate the center of the SAH (the maximum of Z200). Blue curve in (a) represents the Tibetan Plateau. (b) Time series of EOF2 (PC2) for Z200 and $\mathrm{SAH6_{NW-SE}}$.

ated to NW-SAH hereafter) cases, and nine years with standardized $SAH6_{NW-SE}$ values below −0.5 are chosen for the southeastward-located SAH (abbreviated to SE-SAH hereafter) cases.

3.2. *Relationships between SAH variation and the anomalies of atmospheric circulation in Asian monsoon regions*

As the strongest atmospheric general circulation system in the upper troposphere during boreal summer, the SAH covers most Asian summer monsoon regions. The variation in the SAH is closely associated with the anomalous atmospheric circulation spanning West to East Asia during the same period. Composite analysis is utilized to examine the dominant features in atmospheric circulation anomalies at 200 hPa, 500 hPa and 850 hPa.

In the NW-SAH cases in June (Figs. 2a, c and e), a positive anomaly center of geopotential height at 200 hPa overlying between the border of the IP and the TP contributes to the northwestward shift in the SAH (Fig. 2a). At 500 hPa, as seen in Fig. 2c, a negative anomaly center in geopotential heights and an anomalous cyclone over the Indian subcontinent contributes to the strengthening of lower-level air convection. Positive anomalies in geopotential heights are found over the IP, TP and Northeast Asia, which could cause northward movement in the western Pacific subtropical high (WPSH) in the mid-troposphere (figure not shown). The ISM is stronger, and there is an anomalous southwesterly flow toward India and a cyclonic wind shear at 850 hPa over the northern Indian subcontinent, resulting in an anomalous convergence in total column moisture flux, implying a positive anomaly in precipitation and LH release. At the same time, an anomalous anticyclone and the divergence of total column moisture flux occur over the western Pacific Ocean to the south of Japan. In addition, anomalous southerly winds at 850 hPa over eastern China bring an increase in water vapor from the South China Sea, which is consistent with the anomalous convergence of total column moisture flux over the Yangtze–Huaihe river basin (Fig. 2e). When the location of the SAH is located to the southeast in June (SE-SAH cases), the anomalous circulation patterns at all levels and vertical integrated moisture flux show almost contrary features with that in the NW-SAH cases (Figs. 2b, d and f); both the ISM and EASM are weaker, and the location of the WPSH moves southward. Weakened air convection over the northern Indian subcontinent and the Yangtze–Huaihe river basin, with anomalous divergence in total column moisture flux, are responsible for the decrease in rainfall over these regions (figure not shown).

4. Relationship between May SH anomalies over the IP and TP and the SAH in early summer

It is well-known that land–sea thermal contrast is the primary driving force of Asian monsoon. In this section, we first investigate the thermal conditions over the IP and TP before the onset of Asian summer monsoon season. Seasonal variations in both TPSH and IPSH are remarkable, and SH anomalies over these two plateaus are closely related to each other (Liu et al., 2017b; Zhang et al., 2017). The contribution of the first SVD mode from TPSH and IPSH ($SVD1_{IPTP-SH}$) to the total variance exceeds 35% in each month from March to May; the contribution of $SVD1_{IPTP-SH}$ is 48% in May, which is much more than the contribution percentage from other SVD modes in May. Besides, $SVD1_{IPTP-SH}$ in May is significantly correlated with the location shift of the SAH, which is the focus of our study. The correlation coefficient between May $SVD1_{IPTP-SH}$ and $SAH6_{NW-SE}$ is 0.54, which is statistically significant at the 99.9% confidence level; this indicates that variations in the SAH during June are closely related to SH anomalies over the IP and TP from the previous May. In addition, the correlation coefficient between March (April) $SVD1_{IPTP-SH}$ and $SAH6_{NW-SE}$ is only 0.01 (0.24). The relatively small quantity of SH over the IP and TP and the weak persistence of the SH anomaly in March and April may be responsible for the low correlations between the early springtime SH anomaly and the SAH in summer. Therefore, concurrent anomalies of TPSH and IPSH in May and the early summer SAH are the main focuses in the following sections.

The relationship between springtime SH anomalies over the IP or TP and summertime SAH variations is explored separately before we analyze the synergistic impact of springtime SH anomalies over both plateaus on the variation of the SAH in the following summer. A partial correlation analysis is employed to eliminate signals from SH anomalies over the IP (TP) when analyzing correlations between SH anomalies over the TP (IP) and the NW–SE shift of the SAH. It should be noted that the PC1 of SH over the TP has a remarkable trend, which is related to the strengthening trend of the SAH's intensity (figure not shown). This paper focuses on the correlation between the SAH and SH over the IP and TP at the interannual time scale, and therefore the EOF1 of SH is not discussed here. The partial correlation coefficients between the PC2 of SH over the TP (May, eliminated signals from PC1 or PC2 of SH over the IP), PC2 of SH over the IP (May, eliminated signals from PC2 of SH over the TP) and $SAH6_{NW-SE}$ are 0.33, 0.53 and 0.42, respectively, all of which are statistically significant at the 95% confidence level. However, all these partial correlation coefficients are smaller than the correlation coefficient (0.54) between May $SVD1_{IPTP-SH}$ and $SAH6_{NW-SE}$. This implies that the synergistic impact of May SH anomalies over the IP and TP on SAH variations in June is more remarkable than the impact of May SH anomalies over each single plateau. In addition, the interannual variations of $SVD1_{IPTP-SH}$ in May and $SAH6_{NW-SE}$ are not always consistent with each other (Fig. 3b), which implies that factors besides the elevated thermal effect on these two plateaus may also have some influence on the variation in location of the SAH.

The spatial pattern of the May $SVD1_{IPTP-SH}$ shows that the TPSH anomaly is generally negatively correlated with the IPSH anomaly (Fig. 3a), especially in the northern IP (north of 32°N) and south-central TP (south of 34°N).

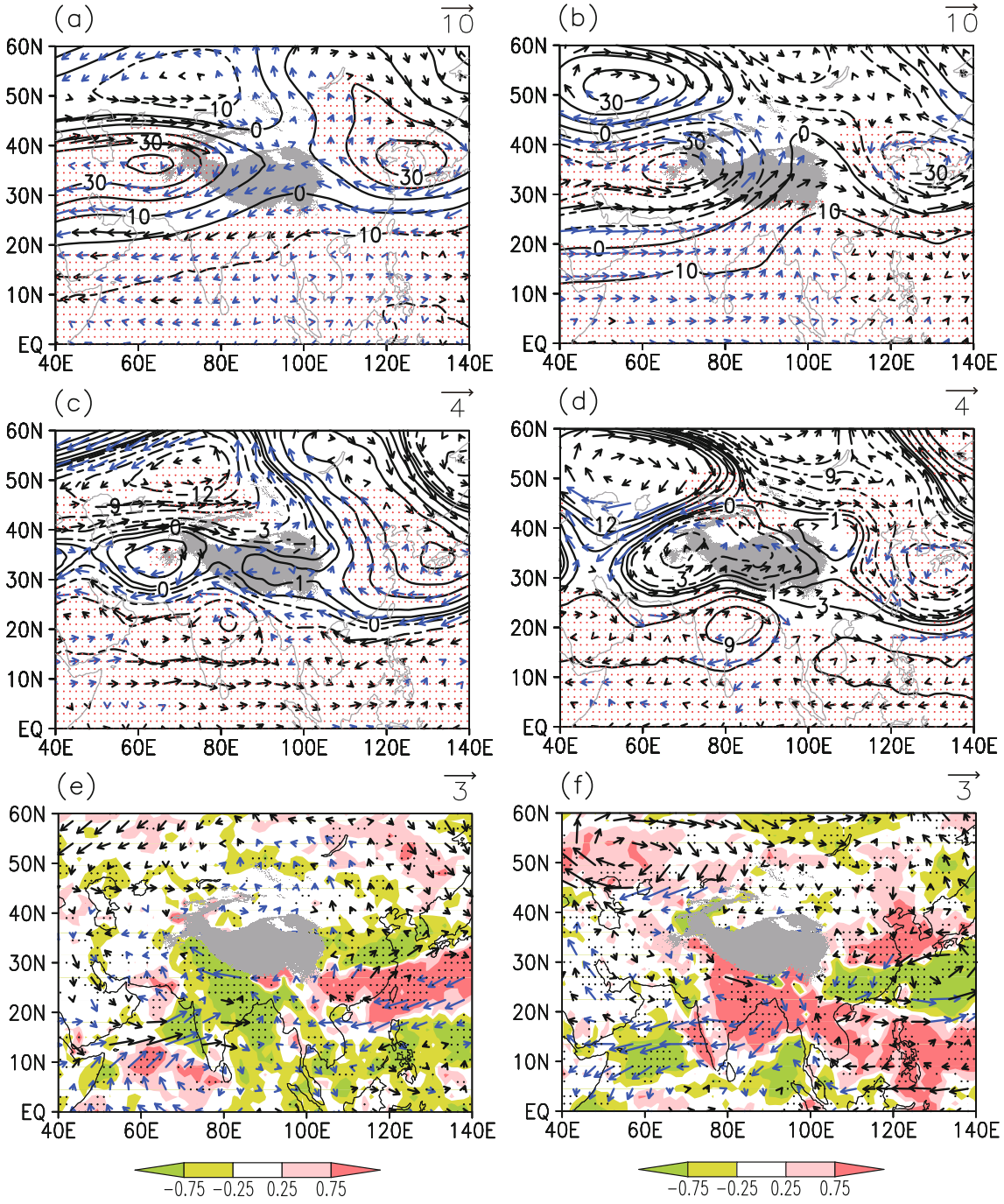

Fig. 2. June anomaly composites of geopotential height (contour; units: gpm) and horizontal wind (vector; units: m s^{-1}) at (a, b) 200hPa, (c, d) 500hPa and (e, f) anomaly composites of horizontal wind (vector; units: m s^{-1}) at 850hPa and divergence of vertical integrated moisture flux (shaded; unit: 10^{-5} s^{-1}) for years with a standardized $SAH6_{NW-SE}$ (a, c, e) higher than 0.5 or (b, d, f) lower than −0.5. Stippled areas and blue vectors indicate where relevant anomalies are statistically significant above the 90% confidence level. Grey shading in each panel represents the Tibetan Plateau.

In years with positive $SVD1_{IPTP-SH}$ in May, IPSH is primarily stronger, while TPSH is weaker than normal (Fig. 3c), and the opposite is true for negative $SVD1_{IPTP-SH}$ in May. Therefore, the significant positive correlation between May $SVD1_{IPTP-SH}$ and $SAH6_{NW-SE}$ indicates that the SAH in June is northwestward-located (southeastward-located) when IPSH is higher (lower) and TPSH is lower (higher) than normal in May. This relationship can also be demonstrated by composite analysis based on $SVD1_{IPTP-SH}$ in May. The 12500-gpm isoline at 200 hPa in June is obviously northwestward-located (southeastward-located) during years with an $SVD1_{IPTP-SH}$ above 0.5 (below −0.5).

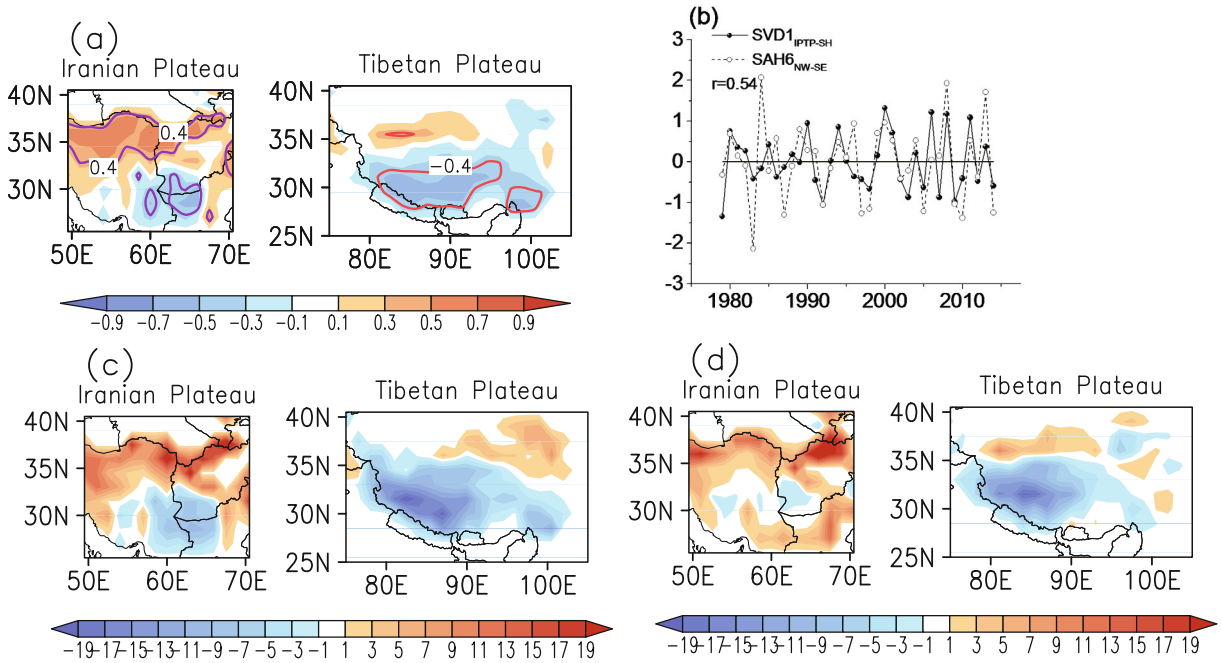

Fig. 3. (a) The first mode of the SVD analysis of the surface sensible heat fluxes over the IP and TP ($SVD1_{IPTP-SH}$) in May, in which areas encircled by contours indicate correlations significant at the 99% confidence level. (b) Temporal evolution of the standardized time series for May $SVD1_{IPTP-SH}$ and $SAH6_{NW-SE}$. (c, d) Composite difference in surface sensible heat fluxes (units: W m^{-2}) over the IP and TP in May (c) and June (d) between years with a standardized May $SVD1_{IPTP-SH}$ higher than 0.5 and lower than −0.5.

However, the composite for the SAH in July based on May $SVD1_{IPTP-SH}$ does not exhibit any obvious deviation from its climatological state; there is only a slight westward shrinkage (eastward extension) at the eastern edge of the SAH during strong (weak) May $SVD1_{IPTP-SH}$ years (figure not shown). It can be inferred that, with increasing rainfall in monsoon regions after the onset of the Asian summer monsoon, the thermal effect from SH anomalies over the two plateaus on the SAH is weakened, while LH from condensation accompanying Asian monsoon rainfall gradually becomes a dominant factor of influencing the variation of the SAH. The above analyses show that the negative correlation between TPSH and IPSH in May is closely related to the NW–SE shift of the SAH in June but has a weak relationship with the SAH in July.

Composite analysis based on the May $SVD1_{IPTP-SH}$ time series shows that the SH anomaly over the IP and TP in May can persist till June (Figs. 3c and d). This surface thermal "memory" may be the result of soil enthalpy "memory" (Hu and Feng, 2004) and the feedback mechanism between IPSH and TPSH (Liu et al., 2017b).

5. Mechanisms explaining how concurrent SH anomalies over the TP and IP in late spring influence SAH variation in early summer

The previous results reported in section 4 show a close relationship between IPSH and TPSH in May and the location of the SAH in June. In this section, we focus on the persistent anomalies of IPSH and TPSH from May to June and discuss how they affect the distribution of vorticity and modify the location of the SAH.

Composite analysis shows that, in the years with positive anomalies of $SVD1_{IPTP-SH}$ in May, IPSH is stronger and TPSH is weaker than normal (Fig. 3c). The stronger IPSH strengthens low-level air ascending motion around most parts of the IP and over the western TP below 200 hPa (Fig. 4c). An anomalous cyclone is located over the south of the IP and, accordingly, southwesterly flow to India brings more moisture to northern India and a cyclonic wind shear exists over northern India and the northern BOB at 850 hPa (Fig. 4a). The greater convergence of moisture flux and anomalous upward movement over the southwest TP is possibly responsible for the higher rainfall and lower SH over that region. A somewhat contrary situation is true for the composite with negative anomalies of May $SVD1_{IPTP-SH}$ (Figs. 4b and d).

Since the anomalies of SH over the IP and TP in June are similar to those in May (Figs. 3c and d), composite anomalous atmospheric circulation similar to that in May is expected in June. There is an anomalous cyclone at 850 hPa between 15°N and 30°N spanning from West Asia, northern India, to the northern BOB (Fig. 5a), and the strengthened Somali jet contributes to anomalous southwesterly winds over the western Indian subcontinent, carrying more water vapor from the Indian Ocean to eastern India and the northern BOB. This anomalous low-level circulation is responsible for the convergence of total column moisture flux over the eastern

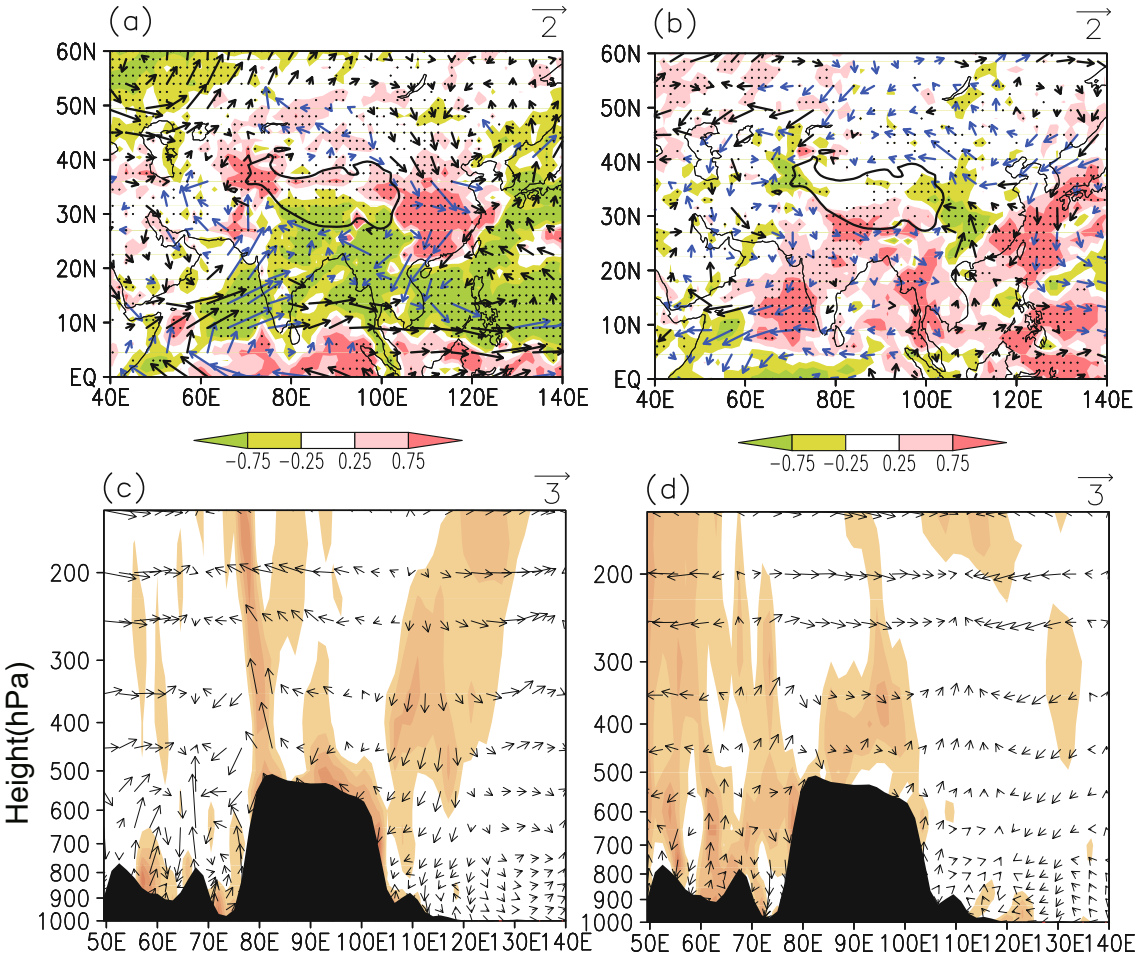

Fig. 4. (a, b) May anomaly composites of horizontal winds (vector; units: m s^{-1}, blue vectors indicate wind anomalies are significant above the 90% confidence level) at 850 hPa and divergence of total column moisture flux (shaded; units: 10^{-5} s^{-1}, stippled areas indicate moisture flux anomalies are significant above the 95% confidence level). (c, d) May anomaly composites of zonal-vertical motion along the 31.5°N cross section (units: m s^{-1} for u and −100 Pa s^{-1} for ω, color shadings indicate anomalies are significant above the 95% confidence level). Composites are calculated for years with a standardized May $SVD1_{IPTP-SH}$ (a, c) higher than 0.5 or (b, d) lower than −0.5. Thick black curve in (a, b) represents the Tibetan Plateau and black shading in (c, d) represents the topography profile along 31.5°N.

India subcontinent and northern BOB, as well as the anomalous ascending motion over northern India from the IP to the western TP (Fig. 5c). Of note is that the anomalous descending motion over the eastern TP is accompanied by moisture divergence, meaning the weaker TPSH during May leads to less rainfall in the eastern TP in June due to its weakened heat pump effect. Over East Asia, an anomalous southerly flow and anticyclone to the east of Taiwan carry more water vapor to eastern China from the South China Sea and western Pacific. These two vapor flows merge over the Yangtze–Huaihe river basin, resulting in an anomalous convergence of total column moisture flux there (Fig. 5a). In years with lower $SVD1_{IPTP-SH}$ values in May (Figs. 5b and d), an anomalous anticyclone and divergence in total column moisture flux exists over northeastern India and the northern BOB, which implies that the ISM in June is weakened; the anomalous cyclone over Northeast Asia and northerly winds weaken the monsoon over East China to the north of the Yangtze River valley in June (Fig. 5b). As for vertical motion, there is anomalous descent over a wide region from the western IP to northeastern India and the Yangtze River valley (Fig. 5d).

To verify the influence of concurrent SH anomalies over the IP and TP on the aforementioned anomalous atmospheric circulation and NW–SE shift of the SAH, the vertical vorticity equation (Wu and Liu, 1998; Liu et al., 2001, 2013) is used to investigate the vorticity generation and diabatic heating:

$$\frac{\partial \zeta}{\partial t} + \boldsymbol{V}\cdot\nabla\zeta + \beta v = -(f+\zeta)\nabla\cdot\boldsymbol{V} + \frac{f+\zeta}{\theta_z}\frac{\partial Q_1}{\partial z} + \frac{1}{\theta_z}\left(\frac{\partial u}{\partial z}\frac{\partial Q_1}{\partial y} - \frac{\partial v}{\partial z}\frac{\partial Q_1}{\partial x}\right). \quad (6)$$

Here, ζ is vertical vorticity, u is zonal wind, v is meridional wind, f is geostrophic parameter and β is the meridional gradient of f, θ_z is the vertical gradient of θ. Other variables in Eq. (6) are consistent with preceding definitions.

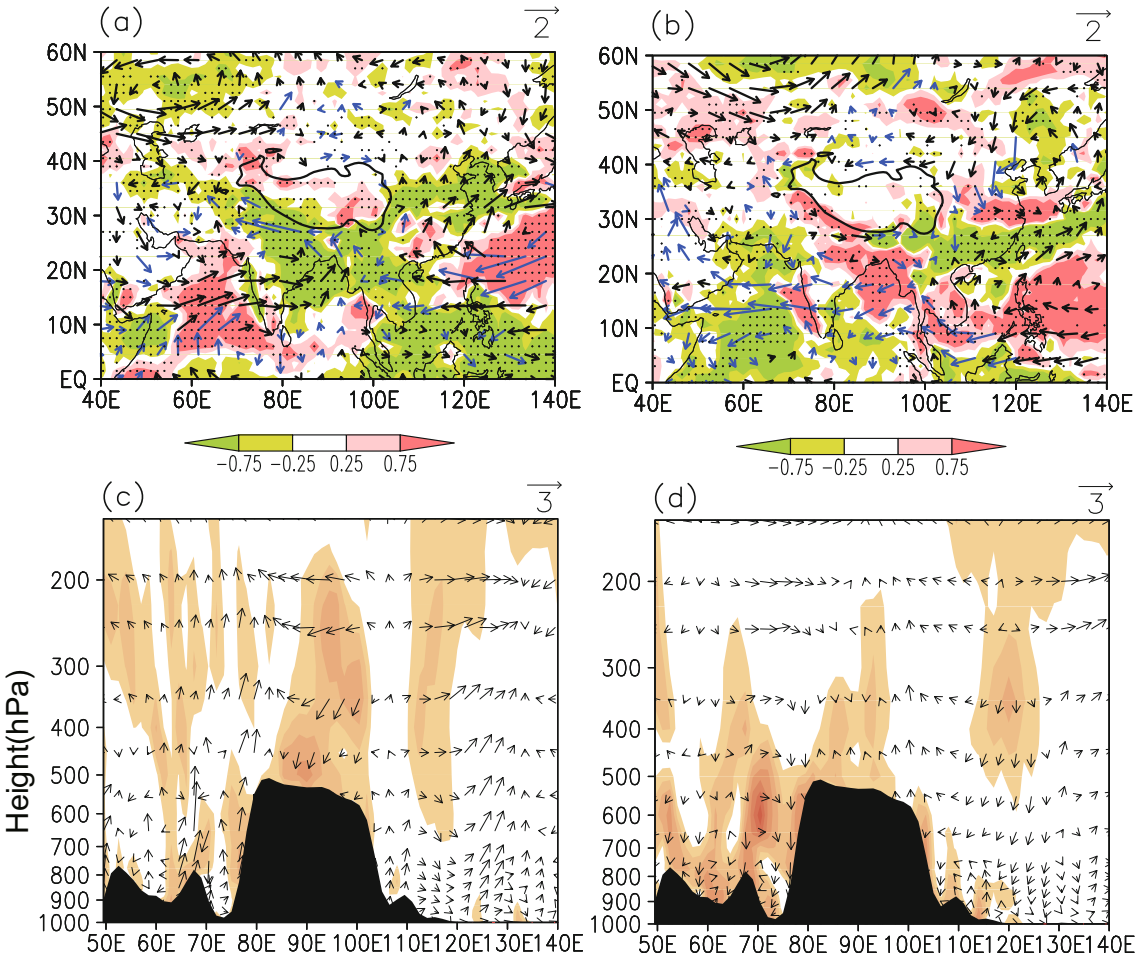

Fig. 5. As in Fig. 4 but for the June anomaly composite according to the May $\mathrm{SVD1}_{\mathrm{IPTP-SH}}$.

On the right-hand side of Eq. (6), the latter two terms represent the effects of the vertical and horizontal gradients of diabatic heating. Because the magnitude of $[(f+\zeta)/\theta_z](\partial Q_1/\partial z)$ $(10^{-10}\ \mathrm{s}^{-2})$ is one order of magnitude larger than that of $(1/\theta_z)[(\partial u/\partial z)(\partial Q_1/\partial y)-(\partial v/\partial z)(\partial Q_1/\partial x)]$ $(10^{-11}\ \mathrm{s}^{-2})$, the vorticity generated from diabatic heating can be represented by $[(f+\zeta)/\theta_z](\partial Q_1/\partial z)$, which is the vertical shear of apparent heat source. For other terms in the equation, the advection term $\boldsymbol{V}\cdot\nabla\zeta$ on the left-hand side is balanced by the vorticity divergence term $-(f+\zeta)\nabla\cdot\boldsymbol{V}$ on the right-hand side, and $\partial\zeta/\partial t$ is neglected when the monthly mean is the major concern. Therefore, Eq. (6) can be simplified as

$$\beta v \propto \frac{f+\zeta}{\theta_z}\frac{\partial Q_1}{\partial z}\ . \tag{7}$$

That is to say, in a steady state, southerly flow is associated with a positive vertical gradient of Q_1, and vice versa. When IPSH is stronger in May, which means the upward heat diffusion above the ground surface and low-level Q_1 is intensified, considering the surface heat diffusion is almost zero (Wu et al., 2007), the near-surface (800 hPa) vertical gradient of Q_1 $[(f+\zeta)/\theta_z](\partial Q_1/\partial z)$ is strengthened over a wide region from the IP to northern India (Fig. 6a), which is responsible for the anomalous southerly over that region in May (Fig. 4a). Similarly, when stronger IPSH in June generates larger low-level Q_1, there is an anomalous positive gradient of Q_1 $[(f+\zeta)/\theta_z](\partial Q_1/\partial z)$ at 800 hPa over most regions from the IP to northern India (Fig. 6b), which is responsible for the anomalous low-level southerly over the Arabian Sea and total moisture convergence over northern India and the southwestern TP (Fig. 5a). Furthermore, more convergence of moisture flux in northern India is coincident with more ISM rainfall in June and generates stronger Q_1 in the mid-troposphere, which is associated with LH release over northern India (Fig. 6c). The negative anomaly of the vertical gradient of Q_1 above 400 hPa over northern India and the southwestern TP is responsible for the anomalous northerly over that region and the stronger anticyclone at 200 hPa (Fig. 2a) to the west of the intensified heating center (Liu et al., 2001), and hence the northwestward shift of the SAH in June.

In order to validate the conjecture about the aforementioned relationships among ISM rainfall, atmospheric circulation, and surface heating, the correlation coefficients of May $\mathrm{SVD1}_{\mathrm{IPTP-SH}}$ with $\langle Q_1\rangle$ and $\langle Q_2\rangle$ in June are calculated. Both are significantly positive in northern and eastern India and negative over the tropical Indian Ocean, and their spatial distributions are quite similar (Fig. 7). The remarkable consistency between the distribution of $\langle Q_1\rangle$ and $\langle Q_2\rangle$ in June

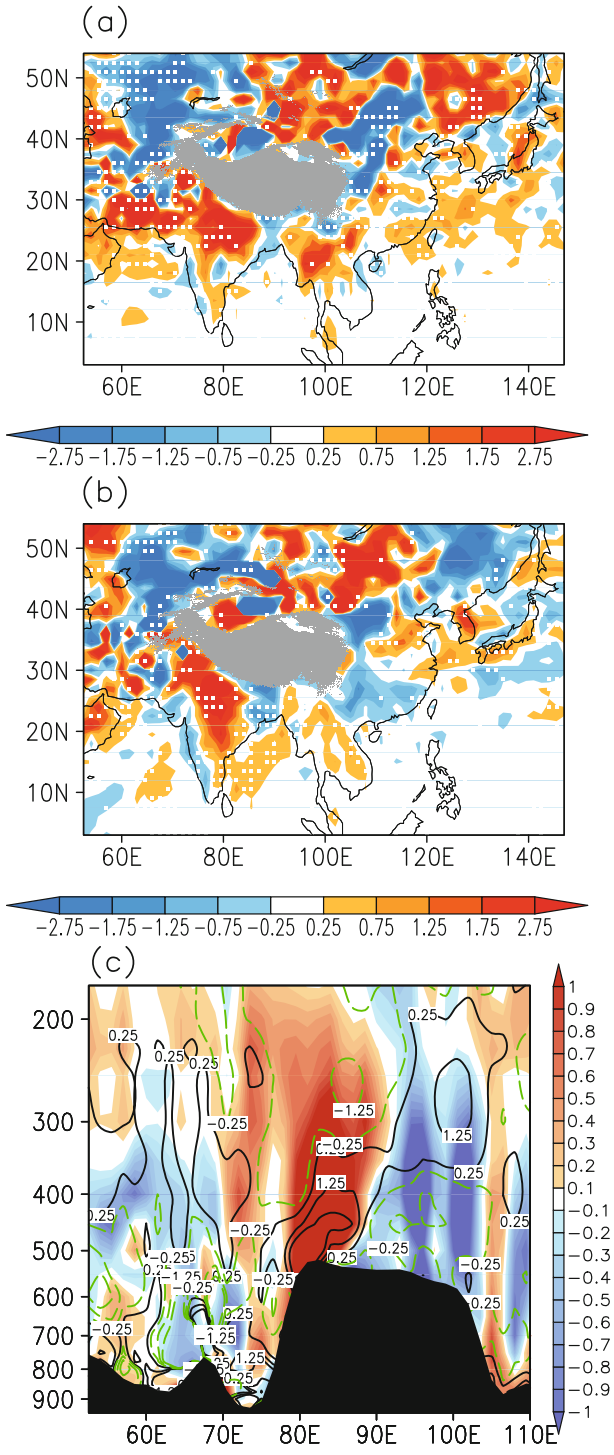

Fig. 6. Composite differences in $[(f+\zeta)/\theta_z](\partial Q_1/\partial z)$ at 800 hPa (units: 10^{-10} s^{-2}) in (a) May and (b) June, and (c) differences in the pressure-longitude cross section of Q1 (shaded; units: 10^{-10} s^{-2} W m^{-2}) and $[(f+\zeta)/\theta_z](\partial Q_1/\partial z)$ (contours; units: 10^{-10} s^{-2}) along 31.5°N in June between years with a May $\mathrm{SVD1}_{\mathrm{IPTP-SH}}$ higher than 0.5 and lower than −0.5. Stipples in (a, b) indicate differences are significant above the 95% confidence level. Grey shading in (a, b) represents the Tibetan Plateau, black shading in (c) represents the topography profile along 31.5°N.

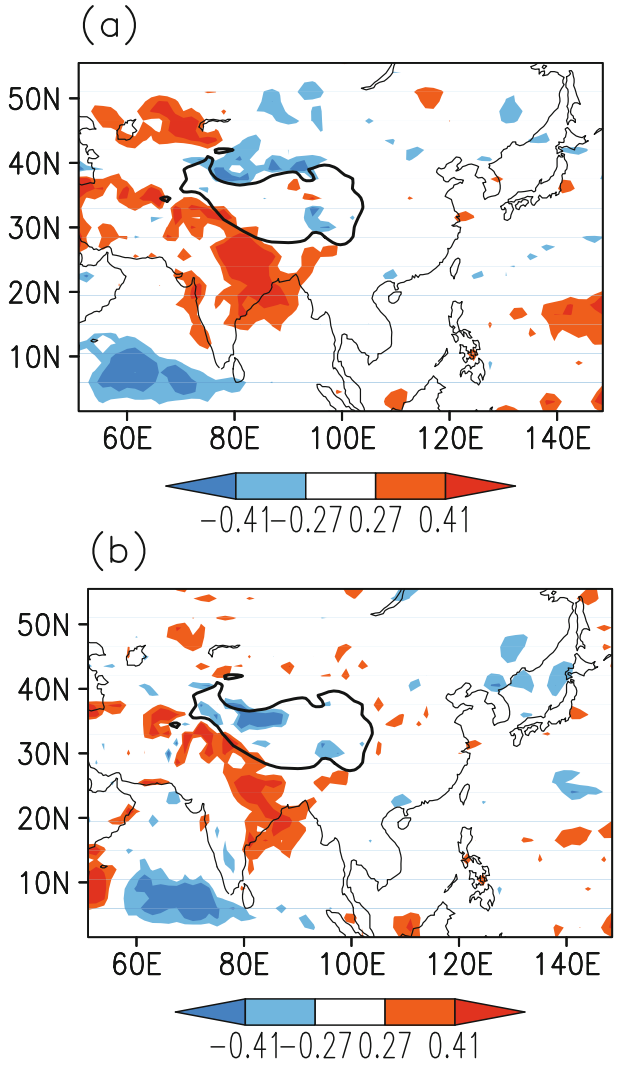

Fig. 7. Spatial distributions of correlation coefficients between (a) May $\mathrm{SVD1}_{\mathrm{IPTP-SH}}$ and June $\langle Q_1 \rangle$, (b) May $\mathrm{SVD1}_{\mathrm{IPTP-SH}}$ and June $\langle Q_2 \rangle$. Light and heavy shadings indicate correlations are significant at the 90% and 99% confidence level respectively. Thick black curve represents the Tibetan Plateau.

implies that the intensified release of LH is the primary component in atmospheric heat source over northeastern India, which is associated with anomalous low-level circulation and is traced back to the surface thermal anomaly in May. From the above analysis, anomalies in atmospheric heat source associated with ISM rainfall in June may be a link between concurrent SH anomalies over the IP and TP in May and the NW–SE shift of the SAH in June.

6. Conclusions and discussion

Based on ERA-Interim data of atmospheric variables and GPCP precipitation data, the synergistic effect of concurrent SH anomalies over the TP and IP in boreal late spring on the variation in location of the SAH is investigated. The main results can be summarized as follows:

The concurrent late springtime surface thermal anomaly over the TP and IP, which is characterized by a negative correlation between TPSH and IPSH in May and persistence till June, is closely related to the variation of the SAH in June. This synergistic effect of concurrent late springtime thermal anomalies over the two plateaus is more efficient in affecting the variation of the SAH than each single surface thermal anomaly over either the TP or IP. By modulating the intensity of the ISM and air convection over northern India in May and June, the concurrent thermal contrast between the TP and IP in May causes an anomalous release in LH over northern India, which changes the vertical distribution of atmospheric heat source. Finally, an anomalous anticyclone in the upper troposphere over northwestern India results in a NW–SE shift of the SAH in June. When IPSH is stronger (weaker) and TPSH is weaker (stronger) than normal in May and persists till June, there is an anomalous cyclonic (anticyclonic) circulation over the IP and northern India at low levels. Consistent with the strengthened (weakened) low level cross-equatorial southerly flow over the western equatorial Indian Ocean and the Indian subcontinent, synergistic concurrent thermal anomalies over the two plateaus strengthen (weaken) the ISM in June. At the same time, the weaker (stronger) TP thermal effect strengthens (weakens) atmospheric convection over northeastern India. Under the composite surface thermal conditions of both the IP and TP, the release of LH over northern India is strengthened (weakened), the decreased (increased) vertical gradient of Q_1 above 400 hPa generates an anomalous anticyclone (cyclone) on the western side of the anomalous heating center, and therefore the SAH in June shifts northwestward (southeastward).

Whether concurrent SH anomalies over the IP and TP in May lead to the NW–SE shift of the SAH in July is still inconclusive. Although feedback between atmospheric circulation in June and the release of LH associated with precipitation is, to some extent, responsible for the NW–SE shift of the SAH in July, the July composite for the SAH based on May $\mathrm{SVD1}_{\mathrm{IPTP-SH}}$ does not exhibit any obvious deviation from its climatological state (figure not shown). This is partly due to the time-limited "memory" of the spring surface thermal anomaly over the IP and TP. Furthermore, the atmospheric circulation and associated rainfall is much stronger in July, as the Asian monsoon reaches its mature stage, which outweighs the surface thermal anomaly in the previous spring.

There are other issues regarding the variation in the SAH and Asian summer monsoon worth exploring, in addition to thermal anomalies over the TP and IP. Compared with land surface heating, forcing from the oceans also modulates the Asian summer monsoon; for example, ISM rainfall is significantly correlated with Indian Ocean sea surface temperature and moisture flux in the preceding winter and spring (Li et al., 2001). The EASM is also greatly affected by ENSO (Lau and Nath, 2006). It seems that, in years when the concurrent thermal effect of the IP and TP and the NW–SE shift of the SAH are not in-phase, oceanic forcing plays a dominant role in the variation of the SAH. Therefore, comprehensively considering the effects of land and ocean forcing will improve our understanding regarding variations in the SAH and summer rainfall in Asia. Further investigation through numerical simulations would give us new insights into the relationship between springtime thermal anomalies over the IP and TP and subsequent summertime variations in the SAH and the Asian monsoon.

Acknowledgements. This work was supported by the National Natural Science Foundation of China (Grant Nos. 91437219, 41275075 and 41175005) and the National Basic Research Program of China (Grant No. 2013CB430203).

REFERENCES

Cui, Y., and C. H. Wang, 2009: Comparison of sensible and latent heat fluxes during the transition season over the western Tibetan Plateau from reanalysis datasets. *Progress in Natural Science*, **19**(6), 719–726, https://doi.org/10.1016/j.pnsc.2008.11.001.

Duan, A. M., and G. X. Wu, 2003: The main spatial heating patterns over the Tibetan Plateau in July and the corresponding distributions of circulation and precipitation over Eastern Asia. *Acta Meteorologica Sinica*, **61**(4), 447–456, https://doi.org/10.3321/j.issn:0577-6619.2003.04.006. (in Chinese with English abstract)

Duan, A. M., and G. X. Wu, 2005: Role of the Tibetan Plateau thermal forcing in the summer climate patterns over subtropical Asia. *Climate Dyn.*, **24**(7–8), 793–807, https://doi.org/10.1007/s00382-004-0488-8.

Duan, A. M., and G. X. Wu, 2008: Weakening trend in the atmospheric heat source over the Tibetan plateau during recent decades. Part I: Observations. *J. Climate*, **21**(13), 3149–3164, https://doi.org/10.1175/2007JCLI1912.1.

Duan, A. M., and G. X. Wu, 2009: Weakening trend in the atmospheric heat Source over the Tibetan plateau during recent decades. Part II: Connection with climate warming. *J. Climate*, **22**(15), 4197–4212, https://doi.org/10.1175/2009JCLI2699.1.

Duan, A. M., Y. M. Liu, and G. X. Wu, 2003: The April to June Tibetan plateau thermal condition and anomalies of the summer precipitation and general atmospheric circulation over East Asia. *Science in China* (*Series D*), **33**(10), 997–1004, https://doi.org/10.3969/j.issn.1674-7240.2003.10.011. (in Chinese)

Duan, A. M., M. R. Wang, Y. H. Lei, and Y. F. Cui, 2013: Trends in summer rainfall over China associated with the Tibetan plateau sensible heat source during 1980–2008. *J. Climate*, **26**(1), 261–275, https://doi.org/10.1175/JCLI-D-11-00669.1.

Flohn, H., 1957: Large-scale aspects of the "summer monsoon" in South and East Asia. *J. Meteor. Soc. Japan*, **75**, 180–186.

Gao, Y. X., C. Li, F. M. Yuan, X. H. Yang, and X. C. Yong, 1982: Influences of land-sea and topography distributions on temperature fields in July. *Plateau Meteorology*, **1**(4), 46–59. (in Chinese with English abstract)

Hu, Q., and S. Feng, 2004: A role of the soil enthalpy in land memory. *J. Climate*, **17**(18), 3633–3643, https://doi.org/10.1175/1520-0442(2004)017<3633:AROTSE>2.0.CO;2.

Lau, N. C., and M. J. Nath, 2006: ENSO modulation of the interannual and intraseasonal variability of the East Asian Monsoon—A model study. *J. Climate*, **19**(18), 4508–4530, https://doi.org/10.1175/JCLI3878.1.

Li, T., Y. S. Zhang, C. P. Chang, and B. Wang, 2001: On the relationship between Indian Ocean sea surface temperature and Asian Summer Monsoon. *Geophys. Res. Lett.*, **28**(14), 2843–2846, https://doi.org/10.1029/2000GL011847.

Liang, X. Y., Y. M. Liu, and G. X. Wu, 2005: Effect of Tibetan plateau on the site of onset and intensity of the Asian summer monsoon. *Acta Meteorologica Sinica*, **63**(5), 799–805, https://doi.org/10.11676/qxxb2005.076. (in Chinese with English abstract)

Liu, B. Q., C. W. Zhu, and Y Yuan, 2017a: Two interannual dominant modes of the South Asian High in May and their linkage to the tropical SST anomalies. *Climate Dyn.*, **49**, 2705–2720, https://doi.org/10.1007/s00382-016-3490-z.

Liu, B. Q., G. X. Wu, J. Y. Mao, and J. H. He, 2013: Genesis of the South Asian high and its impact on the Asian summer monsoon onset. *J. Climate*, **26**(9), 2976–2991, https://doi.org/10.1175/JCLI-D-12-00286.1.

Liu, Y. M., and G. X. Wu, 2004: Progress in the study on the formation of the summertime subtropical anticyclone. *Adv. Atmos. Sci.*, **21**, 322–342, https://doi.org/10.1007/BF02915562.

Liu, Y. M., G. X. Wu, H. Liu, and P. Liu, 2001: Condensation heating of the Asian summer monsoon and the subtropical anticyclone in the Eastern Hemisphere. *Climate Dyn.*, **17**(4), 327–338, https://doi.org/10.1007/s003820000117.

Liu, Y. M., Z. Q. Wang, H. F. Zhuo, and G. X. Wu, 2017b: Two types of summertime heating over Asian large-scale orography and excitation of potential-vorticity forcing II. Sensible heating over Tibetan-Iranian Plateau. *Science China Earth Sciences*, **60**(4), 733–744, https://doi.org/10.1007/s11430-016-9016-3.

Qian, Y. F., Q. Zhang, and X. H. Zhang, 2002b: The South Asian high and its effects on China's Mid-summer climate abnormality. *Journal of Nanjing University* (*Natural Science*), **38**(3), 295–307, https://doi.org/10.3321/j.issn:0469-5097.2002.03.004. (in Chinese with English abstract)

Qian, Y. F., Q. Zhang, Y. H. Yao, and X. H. Zhang, 2002a: Seasonal variation and heat preference of the South Asia high. *Adv. Atmos. Sci.*, **19**(5), 821–836, https://doi.org/10.1007/s00376-002-0047-3.

Wang, Z. Q., A. M. Duan, and G. X. Wu, 2014: Time-lagged impact of spring sensible heat over the Tibetan Plateau on the summer rainfall anomaly in East China: Case studies using the WRF model. *Climate Dyn.*, **42**, 2885–2898, https://doi.org/10.1007/s00382-013-1800-2.

Wei, W., R. H. Zhang, M. Wen, B. J. Kim, and J. C. Nam, 2015: Interannual variation of the South Asian high and its relation with Indian and East Asian summer monsoon rainfall. *J. Climate*, **28**(7), 2623–2634, https://doi.org/10.1175/JCLI-D-14-00454.1.

Wu, G. X., and H. Liu, 1998: Vertical vorticity development owing to down-sliding at slantwise isentropic surface. *Dyn. Atmos. Oceans*, **27**, 715–743.

Wu, G. X., J. Y. Mao, A. M. Duan, and Q. Zhang, 2004: Recent progress in the study on the impacts of Tibetan Plateau on Asian summer climate. *Acta Meteorologica Sinica*, **62**(5), 528–540, https://doi.org/10.3321/j.issn:0577-6619.2004.05.002. (in Chinese with English abstract)

Wu, G. X., Y. M. Liu, B. He, Q. Bao, A. M. Duan, and F. F. Jin, 2012: Thermal Controls on the Asian Summer Monsoon. *Scientific Reports*, **2**, 404, https://doi.org/10.1038/srep00404.

Wu, G. X., and Coauthors, 2007: The influence of mechanical and thermal forcing by the Tibetan plateau on Asian climate. *Journal of Hydrometeorology*, **8**, 770–789, https://doi.org/10.1175/JHM609.1.

Wu, G. X., and Coauthors, 2015: Tibetan plateau climate dynamics: Recent research progress and outlook. *National Science Review*, **2**(1), 100–116, https://doi.org/10.1093/nsr/nwu045.

Yanai, M., S. Esbensen, and J. H. Chu, 1973: Determination of bulk properties of tropical cloud clusters from large-scale heat and moisture budgets. *J. Atmos. Sci.*, **30**(4), 611–627, https://doi.org/10.1175/1520-0469(1973)030<0611:DOBPOT>2.0.CO;2.

Yang, K., X. F. Guo, and B. Y. Wu, 2011: Recent trends in surface sensible heat flux on the Tibetan Plateau. *Science China Earth Sciences*, **54**(1), 19–28, https://doi.org/10.1007/s11430-010-4036-6.

Ye, D. Z., S. W. Luo, and B. Z. Zhu, 1957: The wind structure and heat balance in the lower troposphere over Tibetan plateau and its surrounding. *Acta Meteorologica Sinica*, **28**(2), 108–121, https://doi.org/10.11676/qxxb1957.010. (in Chinese with English abstract)

Zhang, H. X., W. J. Li, and W. P. Li, 2017: Spatial and temporal distribution characteristics of surface heat fluxes over both Tibetan Plateau and Iranian Plateau in boreal spring and summer and their relationships. *Acta Meteorologica Sinica*, **75**(2), 260–274, https://doi.org/10.11676/qxxb2017.002. (in Chinese with English abstract)

Zhang, P. F., Y. M. Liu, and B. He, 2016: Impact of East Asian summer monsoon on the interannual variation of South Asian high. *J. Climate*, **29**(1), 159–173, https://doi.org/10.1175/JCLI-D-15-0118.1.

Zhang, Y., and Y. F. Qian, 2002: Thermal effect of surface heat source over the Tibetan plateau on the onset of Asian summer monsoon. *Journal of Nanjing Institute of Meteorology*, **25**(3), 298–306, https://doi.org/10.3969/j.issn.1674-7097.2002.03.002. (in Chinese with English abstract)

Zhang, Y. S., and G. X. Wu, 1998: Diagnostic investigations of mechanism of onset of Asian summer monsoon and abrupt seasonal transitions over northern hemisphere Part I. *Acta Meteorologica Sinica*, **56**(5), 513–528, https://doi.org/10.11676/qxxb1998.047. (in Chinese with English abstract)

Zhang, Y. S., and G. X. Wu, 1999: Diagnostic investigations on the mechanism of the onset of Asian summer monsoon and abrupt seasonal transitions over the northern hemisphere Part: II the role of surface sensible heating over Tibetan plateau and surrounding regions. *Acta Meteorologica Sinica*, **57**(1), 56–73, https://doi.org/10.11676/qxxb1999.005. (in Chinese with English abstract)

Zhang, Y. Y., Z. X. Li, and B. Q. Liu, 2015: Interannual variability of surface sensible heating over the Tibetan plateau in boreal spring and its influence on the onset time of the Indian summer monsoon. *Chinese Journal of Atmospheric Sciences*, **39**(6), 1059–1072, https://doi.org/10.3878/j.issn.1006-9895.1410.14226. (in Chinese with English abstract)

Observed Changes in Extreme Temperature over the Global Land Based on a Newly Developed Station Daily Dataset

PANFENG ZHANG,[a] GUOYU REN,[a,b] YAN XU,[c] XIAOLAN L. WANG,[d] YUN QIN,[a] XIUBAO SUN,[a,b,e] AND YUYU REN[b]

[a] *Department of Atmospheric Science, School of Environmental Studies, China University of Geosciences, Wuhan, China*
[b] *Laboratory for Climate Studies, National Climate Center, China Meteorological Administration, Beijing, China*
[c] *National Meteorological Information Center, China Meteorological Administration, Beijing, China*
[d] *Climate Research Division, Atmospheric Science and Technology Directorate, Science and Technology Branch, Environment Canada, Toronto, Ontario, Canada*
[e] *South China Sea Institute of Oceanology, Chinese Academy of Sciences, Guangzhou, China*

(Manuscript received 30 October 2018, in final form 31 August 2019)

ABSTRACT

This paper presents an analysis of changes in global land extreme temperature indices (1951–2015) based on the new global land surface daily air temperature dataset recently developed by the China Meteorological Administration (CMA). The linear trends of the gridpoint time series and global land mean time series were calculated by using a Mann–Kendall method that accounts for the lag-1 autocorrelation in the time series of annual extreme temperature indices. The results, which are generally consistent with previous studies, showed that the global land average annual and seasonal mean extreme temperature indices series all experienced significant long-term changes associated with warming, with cold threshold indices (frost days, icing days, cold nights, and cold days) decreasing, warm threshold indices (summer days, tropical nights, and warm days) increasing, and all absolute indices (TXx, TXn, TNx, and TNn) also increasing, over the last 65 years. The extreme temperature indices series based on daily minimum temperatures generally had a stronger and more significant trend than those based on daily maximum temperatures. The strongest warming occurred after the mid-1970s, and a few extreme temperature indices showed no significant trend over the period from 1951 to the mid-1970s. Most parts of the global land experienced significant warming trends over the period 1951–2015 as a whole, and the largest trends appeared in mid- to high latitudes of the Eurasian continent.

1. Introduction

Global mean surface temperature has increased over the last 100 years (Cubasch et al. 2013; Jones et al. 2012; Sun et al. 2017b). A changing climate may lead to changes in the frequency, intensity, duration, and timing of weather and climate extremes and can probably result in unprecedented weather-related disasters. If exposure and vulnerability remain unchanged, extreme weather and climatic events will have direct negative impact on natural and human systems (Handmer et al. 2012; Seneviratne et al. 2012). During the period of 1980–2010, the global annual economic losses caused by extreme weather and climatic events have ranged from a few billion U.S. dollars to more than $200 billion (in 2010 dollars), with the highest value in 2005 (Handmer et al. 2012). A better understanding of long-term change of extreme climate thus cannot only contribute to climate change detection, attribution and projection, but can also improve management of extreme-climate-related disaster risk.

During the last two decades, great progress was made in the studies of both global and regional long-term changes in extremes, thanks to the efforts of the joint Expert Team on Climate Change Detection and Indices (ETCCDI) of the WMO Commission for Climatology (CCL) and World Climate Research Programme (WCRP) Climate Variability and Predictability (CLIVAR) project, which organized a series of regional workshops to develop, calculate and analyze a suite of extreme climate indices (Frich et al. 2002; Peterson et al. 2002; Easterling et al. 2003; Aguilar et al. 2005; Vincent et al. 2005, 2011; Peterson 2005; Zhang et al. 2005a; Klein Tank et al. 2006; New et al. 2006;

Corresponding author: G. Y. Ren, guoyoo@cma.gov.cn

DOI: 10.1175/JCLI-D-18-0733.1

© 2019 American Meteorological Society. For information regarding reuse of this content and general copyright information, consult the AMS Copyright Policy (www.ametsoc.org/PUBSReuseLicenses).

TABLE 1. Summary of data sources used in GLSDT-V1.0. Shown in the table are the priority grade (1 for first priority and 4 for least priority) of each dataset when included in GLSTD-V1.0, the number of total stations contained in each of the datasets, and the number of unique stations that each data source provides for GLSTD-V1.0.

Source	Priority	Name/country	No. of total stations	No. of unique stations
Global	2	GHCND (Menne et al. 2012a,b)	30 519	24 127
	3	GSOD[a]	28 514	9630
	4	CPC[b]	11 267	3390
Regional	1	ECA&D (Klein Tank et al. 2002)	2872	2811
Country	1	Mainland of China (Cao et al. 2016)	2419	2419
	1	Russia	223	88
	1	Australia (Trewin 2001)	103	72
	1	South Korea	76	70
	1	Vietnam	22	22

[a] ftp://ftp.ncdc.noaa.gov/pub/data/gsod.
[b] https://www.cpc.ncep.noaa.gov/.

Alexander et al. 2006; Peterson and Manton 2008; Donat et al. 2013a). A total of 27 core indices (including 16 extreme temperature indices) and the corresponding calculation procedures (e.g., RClimDex and FClimDex) were formulated (X. Zhang et al. 2011), which were also widely used for studies of regional extreme temperature change (Yan et al. 2002; Klein Tank and Können 2003; Zhai and Pan 2003; Vincent and Mekis 2006; Brown et al. 2010; Zhou and Ren 2011; Xu et al. 2013; Sharma and Babel 2014; Fonseca et al. 2016; Sun et al. 2017a; Jayawardena et al. 2018).

Extreme climate datasets, for example, the Met Office Hadley Centre climate extremes datasets HadEX (Alexander et al. 2006) and HadEX2 (Donat et al. 2013a), and the Global Historical Climatology Network–Daily datasets HadGHCND (Caesar et al. 2006; Donat et al. 2013b) and GHCNDEX (Donat et al. 2013b), were developed to facilitate the analyses of global extreme climate change. Most of the daily temperature datasets were sourced from the European Climate Assessment dataset, the Global Historical Climatology Network–Daily dataset, and a series of regional workshops on extreme climate and covered a period from 1951 to recent years. Generally, the results of the analyses based on these datasets showed widespread and significant changes in the temperature extremes associated with climate warming, with those indices derived from daily minimum temperature exhibiting larger and more significant trends over the past decades (Alexander et al. 2006; Caesar et al. 2006; Donat et al. 2013a,b).

A new global land surface daily temperature dataset was recently developed by National Meteorological Information Center of the China Meteorological Administration (CMA), under the framework of the national research project of public welfare supported by the Ministry of Science and Technology of China (Ren et al. 2014; Xu et al. 2014). This work was based on the CMA Global Land Surface Daily Temperature (GLSDT-V1.0) dataset, which was an integrated international and national dataset with a good observational coverage in some regions especially in East Asia, permitting a new analysis of the global change of the main extreme temperature indices over the period 1951–2015.

The rest of this paper is organized as follows: the data and methods are first described in section 2. In particular, the data quality control, the homogeneity test procedures, extreme temperature indices and their calculation, and the methods of gridding, area weight averaging, trend estimate, and significance test are introduced in this section. The results are then presented in section 3. The discussion and conclusions are offered in sections 4 and 5, respectively.

2. Data and methods

a. Data sources and data integration

This study was based on the GLSDT-V1.0 (Ren et al. 2014; Xu et al. 2014) and China Homogenized Historical Temperature Dataset (CHHTD-V1.0) developed by the National Meteorological Information Center, CMA (Cao et al. 2016).

GLSDT-V1.0 is an integrated daily temperature dataset that is from three global sources [Global Historical Climatology Network–Daily (GHCND), Global Surface Summary of the Day (GSOD), and Climate Prediction Center (CPC)], one regional source [European Climate Assessment and Dataset (ECA&D)], and five national sources (mainland of China, Russia, Australia, South Korea, and Vietnam). All the data in the GLSDT-V1.0 global sources and regional sources are open access, and the data in national sources are collected through bilateral exchanges with relevant countries (Table 1).

The integration of multiple data sources mainly includes the following steps:

1) Data standardization. The datasets come from different sources, with station naming rules, data units, precisions, missing values codes, observational time system, and data formats being different. Therefore, it is necessary to standardize the data from various sources first. The processing steps are as follows:
   (i) Unified station identification code. Referring to the station naming rules of GHCND (Menne et al. 2012a,b) data products, the first 2 digits are national codes, the middle digit is the data source identifier (if it is a WMO station number, the logo is "W"), and the last 8 digits retain the original station code of each source. If the station code is less than 8 digits, "0" was added to front as prefix.
   (ii) Unified data units. Fahrenheit degrees were converted to Celsius degrees (°C).
   (iii) Unified data precision. The precision of the original daily temperature data is generally 0.1°C, but the temperature data of the United States are mostly stored in whole Fahrenheit degrees, which is equivalent to a precision of 0.56°C; most of the Canada data have a precision of 0.5°C, and many of the Mexican records have a precision of 1°C (Zhang et al. 2009; Peterson et al. 2008). The precision is lower than the standard of 0.1°C recommended by World Meteorological Organization (WMO 2008), which would affect the estimation of the trends and means of the four relative threshold indices (TN10p, TN90p, TX10p, TX90p) because the quantile estimator may be related to data resolution (Zhang et al. 2009; Peterson et al. 2008). Therefore, we added a small uniform random number from the interval (−0.5, 0.5) to each daily temperature series (T_{max} and T_{min}) and then rounded it to the nearest 0.1°C when computing the four relative threshold indices, following the proposal by Zhang et al. (2009). Other indices analyzed in this study were calculated by using the original daily temperature series that had not been processed by adding any random numbers because the calculation of these indices does not need to estimate the quantile.
   (iv) Shifting Chinese data backward by 1 day. The data of China's ground-based manual meteorological stations are observed at 2000–2000 Beijing time (BT) before around year 2003. In line with global data, the time system of China's stations was converted to 0000–0000 BT. For example, the daily maximum and minimum temperature from 2000 BT 2 January to 2000 BT 3 January is taken as the daily maximum and minimum temperature of 3 January because the daily maximum temperature always appears around 1300–1600 BT, and the daily minimum temperature always appears around 0600–0900 BT. This practice can be problematic in some special cases (about 1%). For example, suppose that the temperature began to drop sharply after 2000 BT 3 January, which caused the daily minimum temperature on 3 January to probably appear between 2000 and 2400 BT instead of around 0600–0900 BT. Currently, there is no better way to solve this problem.
   (v) Unified data formats. In each station's data file, from left to right are the station number, date, climate element (maximum and minimum temperature), and quality control code, respectively.
   (vi) Unified missing values code. The missing values code of a climate element (maximum temperature and minimum temperature), longitude and latitude, and elevation are marked as −999.9.
2) Checking and integration of the repetitive stations. The data from different sources may contain duplicated stations. The stations will be regarded as duplicated ones on the condition that the WMO station codes are the same, or the latitude and longitude are exactly the same (the precision of latitude and longitude used in this study is 0.01°), or the latitude and longitude are close (difference of longitude and/or latitude between the stations of two data sources is less than 0.50°) and at least 60% records of the two source series during the study period are identical.

It is necessary to make further analysis for the duplicated stations to decide which stations should be retained. The stations with the longer series were retained. If the series length is same, then the stations series with the higher priority were retained. The priority of data was assigned based on the data sources, the frequency of updates, and the length of time series (see Table 1). The integrity and quality of data product released by the national meteorological agencies of China, South Korea, Australia, Russia, and Vietnam are relatively high, so these data products have the highest priority.

The dataset of CHHTD-V1.0 (Cao et al. 2016) had undergone a rigorous quality control and had been homogenized through the software RHtestsV3 (Wang and Feng 2010). The dataset has the best coverage of homogeneous daily temperature data in the mainland of China. Therefore, in order to make the best use of the existing homogeneous dataset, we replaced the part of

the dataset for the mainland of China in the GLSDT-V1.0 with the CHHTD-V1.0.

We also used the dataset of stratospheric aerosol optical depth at 550 nm (Sato et al. 1993) that is available online (https://data.giss.nasa.gov/modelforce/strataer/). This dataset starts in 1850 and ends in July 2012. Considering the time period in this study, we only use the data between January 1951 and December 2011.

b. Data quality control

The dataset GLSDT-V1.0 had undergone a quality control when it was developed in 2014. After the two datasets of GLSDT v1.0 and CHHTD-V1.0 (Cao et al. 2016) were integrated to one, we conducted a new quality control that was mainly based on the module embedded in the software RClimDex (Zhang and Feng 2004). This work was performed following the 6-step checks below:

1) Whether the latitude and longitude values of the stations are out of bounds. The longitude and latitude values of each station should be limited between −180° and 180°, −90° and 90°, respectively.
2) Whether the records are repetitive. The data of different months for the same station were checked for repetition. For example, the daily maximum temperature records for the whole years of 1959 and 1979 are the same at station AG000060590, and these two years data were replaced by missing values.
3) Whether the dates are repetitive. The results show that there are not any repetitive dates.
4) The climatological limit value of the temperature. Because the highest temperature and the lowest temperature reported for the globe in literature (Cerveny et al. 2007) were 57.8° and −89.4°C, respectively, the daily temperature values that fall outside of this range (from −89.4° to 57.8°C) were regarded as missing values.
5) The internal consistency. Daily minimum and maximum temperatures were set to missing values if the daily minimum temperature is larger than the daily maximum temperature.
6) The climate extreme value. The maximum range of daily minimum (or maximum) temperature was defined as five standard deviations (std) of the reference period (1961–90) mean value, that is, [mean ± 5 × std]. Daily temperatures that were found falling outside of this range were replaced by missing values. It is possible that an extremely small portion of these outliers could be a true climatic extreme that was excluded, and this treatment may have made the extreme temperature indices change of certain stations or grid boxes less extreme.

Finally, stations that have no more than 15 days of missing values in a year and no more than 15 years of missing values during the reference period 1961–90 were retained. Totally, there are 12 295 such stations, which were selected for use in the following analysis.

c. Data homogeneity

Homogenization is a more complicated problem when compared with the problems of data quality. The inhomogeneity of data series can be caused by the changes of nonclimatic factors (e.g., observing procedures and practice, station relocation, and observing times), which will make the estimate of trend of climate change unreliable. There is not always a coherent approach to cope with the problem of inhomogeneity (Peterson et al. 1998). A number of global or regional homogeneous monthly datasets had been developed (Menne and Williams 2009; Lawrimore et al. 2011; Jones et al. 2012; Vincent et al. 2012; Xu et al. 2018). However, only a few homogenized regional daily temperature datasets have been developed (Vincent et al. 2002; Wijngaard et al. 2003; Brunet et al. 2006; Li and Yan 2009; Trewin 2013; Xu et al. 2013; Cao et al. 2016) because of the difficulty caused by the largely spatiotemporal variability of daily temperature (Vincent et al. 2012) and the sensitivity of daily temperature to topography and local environment (Trewin and Trevitt 1996).

In this study, although the datasets of the mainland of China and Australia had been homogenized (Cao et al. 2016; Trewin 2001), the data in other regions have not been adjusted for homogeneity. To avoid erroneous trend estimates caused by the nonclimatic factors as much as possible, however, we used the penalized maximal F test method of RHtestsV4 software (Wang 2008a,b; Wang and Feng 2013) to test the homogeneity of all the station data series without a reference series. If step changes of data series were detected, they would be excluded. Because of the lack of metadata, and also since some of these step changes detected may sometimes reflect true climatic shifts, a high confidence threshold of 99.99% was adopted, which means that only the most substantial inhomogeneities would be detected and excluded. This would be a reasonable approach that was also applied for other large datasets such as ECA&D (Klein Tank et al. 2002) and HadEX (Alexander et al. 2006). In total, 1074 out of the 12 295 stations were identified as inhomogeneous at the high confidence level and were thus excluded from our subsequent analysis. Given that the daily maximum/minimum temperature of GSOD dataset may be calculated from incomplete days and most of the GSOD stations located in the areas where the daily temperature records are already well covered by other datasets, we finally excluded most of GSOD stations, except for the 64 stations in Africa and South America where the station

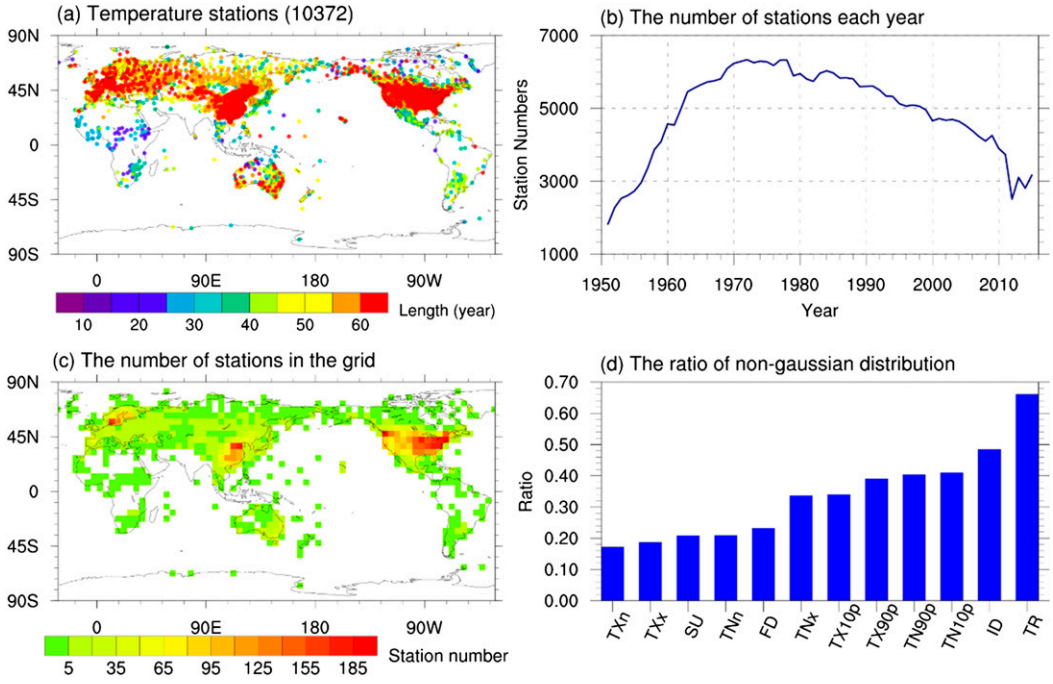

FIG. 1. (a) Locations of temperature stations used in this study. The colors represent the length of time series of stations. The number in parentheses indicates the total number of stations. (b) The number of stations each year. (c) The number of stations in the grid. (d) The station ratio of non-Gaussian distribution for each of the 12 extreme temperature indices.

coverage was sparse. Therefore, the new dataset of GLSDT-V1.0 thus contains in total 10 372 stations for use in this study. The stations are shown in Fig. 1a, the yearly counts of stations with data in Fig. 1b, and the number of stations in each grid point with at least one station in Fig. 1c.

Figures 1a and 1c show the uneven distribution of the stations across the continents. The densest observations are seen in three regions: Europe, East Asia, and the United States. Blank areas and sparser observations are visible in Africa, West Asia, South Asia, Southeast Asia, and South America. The yearly count of stations is characterized by a low value in the early 1950s, a high level of over 6000 stations during 1961–95, and a decline after the mid-1990s (Fig. 1b). The recent decline in data coverage mainly occurs in Europe, Asia, Africa, and Canada (Figs. 2a–d). Compared with other datasets including HadEX2 (Donat et al. 2013a) and GHCNDEX (Donat et al. 2013b), more available temperature stations were added in this research, especially in East Asia. The temperature stations included only in this research but not in GHCNDEX and HadEX2 are shown in Figs. 2f and 2h. The largest increase in number of stations in GLSDT can be seen in Asia, but other continents also witness increase in varied extents in the data coverage. It should be noted that the HadEX2 dataset only incorporated the United States and Australia subsets of the stations with homogeneous data series, and this is the main reason why GLSDT has more stations in these regions compared to HadEX2. Overall, this research applies more stations in East Asia, Europe, and South America compared to the GHCNDEX; and in East Asia, the United States, and continents of the Southern Hemisphere compared to HadEX2.

d. Extreme temperature indices

To make comparisons with previous studies, 12 extreme temperature indices recommended by ETCCDI were used. Four indices [the warm spell duration index (WSDI), cold spell duration index (CSDI), growing season length (GSL), and daily temperature range (DTR)] included in the recommendation of ETCCDI were also calculated but not analyzed in this paper. The 27 ETCCDI indices are defined by the intensity, frequency, and duration of abnormal temperature events. (Detailed definitions and calculation of these indices are described at http://etccdi.pacificclimate.org/list_27_indices.shtml.)

We developed a new procedure, based on the functions of R language package climdex.pcic (Bronaugh 2015), to batch calculate the extreme indices for multistations, which was different from the climdex.pcic package that can only be used to calculate a single station

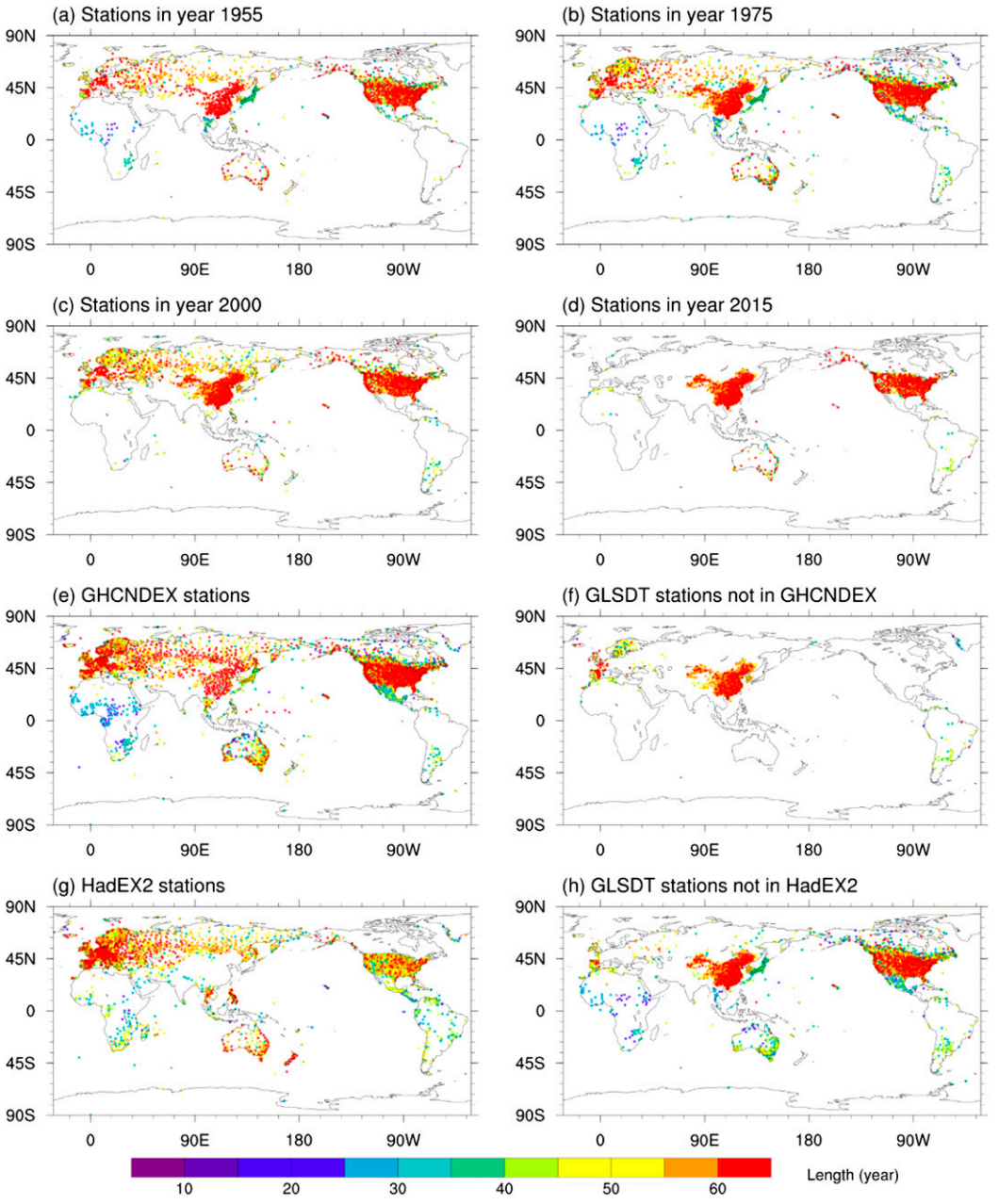

FIG. 2. (a)–(d) The stations distribution in the years 1955, 1975, 2000, and 2015. (e)–(h) The stations of GHCNDEX and HadEX2 (Donat et al. 2013a,b), and the corresponding temperature stations that are included only in GLSDT dataset but not in GHCNDEX and HadEX2, respectively. All the selected stations have at least 15 years of nonmissing data during the reference period 1961–90. The station record length refers to the length of nonmissing data from 1951 to 2015.

one time. It should be pointed out that, when calculating the four relative threshold indices (TN10p, TX10p, TN90p, and TX90p) by the definitions, there are artificial inhomogeneities at the beginning and end of the reference period, which make these indices unsuitable for monitoring and detecting long-term change; these can be effectively eliminated by using a bootstrap resampling procedure (Zhang et al. 2005b). The climdex.pcic package (Bronaugh 2015) also adopted this bootstrap resampling method (Zhang et al. 2005b) in its algorithm for calculating the four relative threshold indices, which was also used by other researchers (Sillmann et al. 2013).

The time period of 1961–90 was considered as the climate reference period in this study. Regarding the

calculation of the monthly indices, the number of missing values should be no more than 3 days in a month. For the calculation of the annual indices, not only the number of missing days should be no more than 3 days in a month, but also the number of missing days should be no more than 15 days in a year. The units of the four relative threshold indices (TN10p, TX10p, TN90p, and TX90p) were converted into days for better understanding.

e. *Analysis methods*

As the elevations of stations are variable and the spatial distribution of stations is uneven at different regions, it is unreliable to calculate the global average series through simple arithmetic average of the station data. Hence, the station temperature indices were first calculated for daily time series, and then the station indices values in the grids of 5° × 5° latitude–longitude were averaged to obtain the grid indices values. The grid area-weighted average method developed by Jones and Hulme (1996) was used to calculate the global average extreme temperature indices series.

First, the annual/seasonal anomaly series relative to the reference period were calculated based on stations indices.

Second, we divided Earth's surface into 5° × 5° latitude–longitude grids as mentioned above and averaged all the available station anomaly series within a grid box to get the grid anomaly series. The numbers and distribution of the grids with values varies among the different extreme temperature indices, but the blank grids are mostly distributed in Africa, Antarctic, and northern South America.

Finally, the global land average anomaly series was calculated using the gridbox area-weighted average method, with the weights being the cosines of the latitude of center of each grid with value (Jones and Hulme 1996). The global land average time series were calculated using only those gridcell series with at least 90% of data during 1951–2015.

Ordinary least squares (OLS) is widely used in the calculation of trends due to its simplicity and intelligibility. As OLS method is based on the hypothesis that the data have a Gaussian distribution, it is not robust to estimate trends when the data are not Gaussian distributed or there are outliers at the bound. Hence, the Shapiro–Wilk normality test (Royston 1982) was used to examine if the data series of a station comes from Gaussian distribution. The results showed that most of the indices violate the Gaussian assumption in varied extents (Fig. 1d). Additionally, serial correlation could increase the rejection rate of trend significant test (i.e., more significant trend would be obtained), which made the result unreliable (Von Storch and Navarra 1999). We calculated the partial autocorrelations of annual mean extremes indices series for each grid points for different lag (lag = 1, 2, . . . , 12). As a result, we found that few partial autocorrelations for lag $>$ 1 are significant at the 5% level. Therefore, the linear trend of a gridbox average mean anomaly time series was calculated using a modified Theil–Sen estimator (Sen 1968) that diminished the effect of lag-1 autocorrelation using an iterative prewhitening process (Zhang et al. 2000; Wang and Swail 2001), and the Mann–Kendall test (Mann 1945; Kendall 1955) was used to test the significance of trend at the 5% level. It was determined that, when the trends of gridcell series were estimated, the length of the time series should not be less than 40 years and the last year of the time series should not be earlier than 2000; otherwise the grid trend was set as missing values.

However, if a gridcell series of four absolute threshold indices [number of frost days (FD), number of summer days (SU), number of icing days (ID), and number of tropical nights (TR)] is all zero values, that is, no extreme events occurred in the entire time series, the trend of this gridcell series would still be calculated, but a cross mark would be added on the grid cell, which indicated that the trend estimate of this gridcell series was not being robust in statistics (Frei and Schär 2001). In addition to zero values, there is another situation in which the extreme events occurred every day of the year, that is, the saturated values (365/366). For example, summer days and/or tropical nights of some stations near the equator may have saturated values (365/366) in almost all years. We found that none of the stations have all saturated values in the entire time series, and only a few stations (3–5) whose ratio of saturated values to record length exceeds 90%. So, the situation of saturated values would not be taken into account in this study.

In addition to the whole time period of 1951–2015, we also calculated and analyzed the trends of the extreme temperature indices for two subperiods of 1951–75 and 1976–2015 according to the change characteristics of these indices. Climatic seasons were applied to analyze the long-term change in seasonal mean extreme temperature indices. March, April, and May (MAM) were considered spring (autumn in Southern Hemisphere); June, July, and August (JJA) were considered summer (winter in Southern Hemisphere); September, October, and November (SON) were considered autumn (spring in Southern Hemisphere); and December, January,

TABLE 2. Trend estimates for 12 global extreme temperature indices over the periods 1951–75, 1976–2015, and 1951–2015. Trends of at least 5% significance are shown in bold. The units of cold nights (TN10p), cold days (TX10p), warm nights (TN90p), and warm days (TX90p) were converted to days.

Index	Trend			
	1951–75	1976–2015	1951–2015	Units
Frost days (FD)	−0.83	**−2.31**	**−1.96**	days decade^{-1}
Summer days (SU)	−0.21	**2.95**	**1.76**	days decade^{-1}
Icing days (ID)	−0.50	−0.83	**−0.96**	days decade^{-1}
Tropical nights (TR)	0.00	**2.03**	**1.27**	days decade^{-1}
Maximum T_{max} (TXx)	−0.08	**0.25**	**0.13**	°C decade^{-1}
Maximum T_{min} (TNx)	−0.01	**0.27**	**0.19**	°C decade^{-1}
Minimum T_{min} (TXn)	0.07	**0.40**	**0.28**	°C decade^{-1}
Minimum T_{min} (TNn)	0.05	**0.52**	**0.40**	°C decade^{-1}
Cold nights (TN10p)	−0.97	**−3.64**	**−4.01**	days decade^{-1}
Cold days (TX10p)	−0.45	**−3.41**	**−2.85**	days decade^{-1}
Warm nights (TN90p)	0.13	**8.31**	**5.34**	days decade^{-1}
Warm days (TX90p)	−1.75	**6.07**	**3.95**	days decade^{-1}

and February (DJF) were considered winter (summer in Southern Hemisphere).

3. Results

For all the indices, the global land average anomaly series shows a significant (at the 5% level) warming trend during the period 1951–2015. However, the change mainly occurred during the period 1976–2015. For most of the indices, the trend magnitude over the period 1951–76 is small and not significant statistically (Table 2). This temporal characteristic is consistent with the global land mean surface air temperature change as reported in previous works (Lawrimore et al. 2011; Jones et al. 2012). It should be also noted that the results are not strictly ''global land average'' because of the substantial spatial gap in some regions.

In the rest of this section, we mainly analyzed the absolute threshold indices (FD, SU, ID, and TR), relative threshold indices (TN10p, TX10p, TN90p, and TX90p), and extreme value indices (TXx, TNx, TXn, and TNn) to keep the length of this article within the limit (see Table 2 for descriptions of these indices).

a. Absolute threshold indices

Figure 3 shows the spatial distribution of trend and the global land average anomaly series for the four absolute threshold indices for the period 1951–2015.

In the perspective of spatial distributions of trends, the frequency of frost days was decreasing in most parts of the world, with Europe and Asia decreasing more than the other regions and North America and Australia decreasing modestly (Fig. 3a). However, the frequency of the frost days of a few grid boxes in southern Europe, North America, and the southern part of South America were increasing, although the upward trends were mostly insignificant. The frequency of summer days was increasing in most parts of the global land, and the midlatitude zone of the Northern and Southern Hemispheres is the most obvious area for warming in summer; in eastern and central North America, however, the frequency of summer days was decreasing (Fig. 3b). The frequency of icing days was decreasing in the most regions of the world, but the eastern, central, and southern parts of the United States witnessed an increasing trend (Fig. 3c). The frequency of tropical nights was also increasing in the most parts of the world, despite a decreasing trend that could be seen in a small part of the central United States (Fig. 3d).

The global land average of frost days decreased over the entire study period, with the most rapid decline occurring after the mid-1970s during which the anomaly value of the index was mainly negative. Frost days were relatively lower in 1990, 1998, 2007, and 2015, and the lowest values occurred in 2015 (Fig. 3a). The change pattern of icing days is similar to that of frost days, but the latter has a greater trend in most parts of the world (Table 2). Before the mid-1970s, there was almost no obvious trend in summer days, but the global average index series increased rapidly since the mid-1970s. Since the mid-1970s, except for the obvious negative anomalies in 1983–85 and 1992–93, all the other years registered positive anomalies, with the highest positive values appearing in the last decade. The lowest level occurred in 1992–93, when the stratospheric aerosol optical depth was at its peak due to the influence of the eruption of the Mount

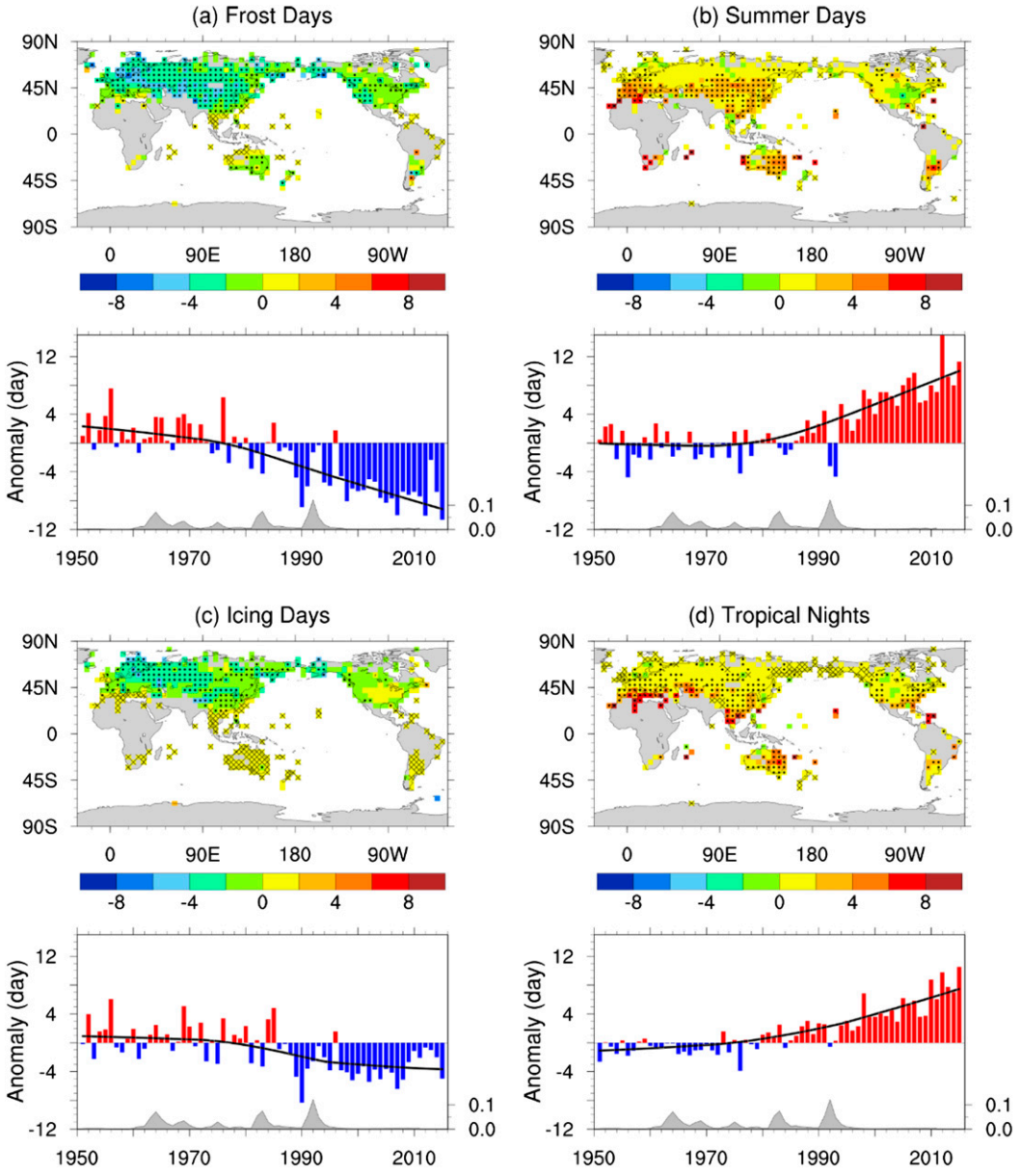

FIG. 3. Trends distribution of grid average annual extreme temperature indices (day decade^{-1}) and global land average time series of annual anomalies relative to the reference period (1961–90) average (day) over 1951–2015 for (a) frost days (FD), (b) summer days (SU), (c) icing days (ID), and (d) tropical nights (TR). Trends were calculated only for the grid boxes that have at least 40 years of data during the study period and the last year of the data does not occur before 2000. The global average time series were calculated using only the gridcell series that have at least 90% of data during 1951–2015. Stippling indicates the gridcell trends are significant at the 5% level. Cross marks indicate the gridcell series with only zero values, i.e., no extreme events occurred in the entire time series. The black smooth curves on the bar chart were obtained by using the locally weighted scatter smoothing (LOWESS) method (Cleveland 1979). Gray shading presents the time evolution of global average aerosol optical depth series at 550 nm (Sato et al. 1993).

Pinatubo volcano in 1991. When the stratospheric aerosol optical depths were relatively high, the summer days were usually fewer. The change of tropical nights is similar to summer days, but the trend magnitude of the former is generally greater.

Therefore, all of the four absolute threshold indices indicate warming trends during the study period 1951–2015 (i.e., frost days and icing days decreased, and summer days and tropical nights increased), but the warming of these indices mainly occurred after the mid-1970s. No

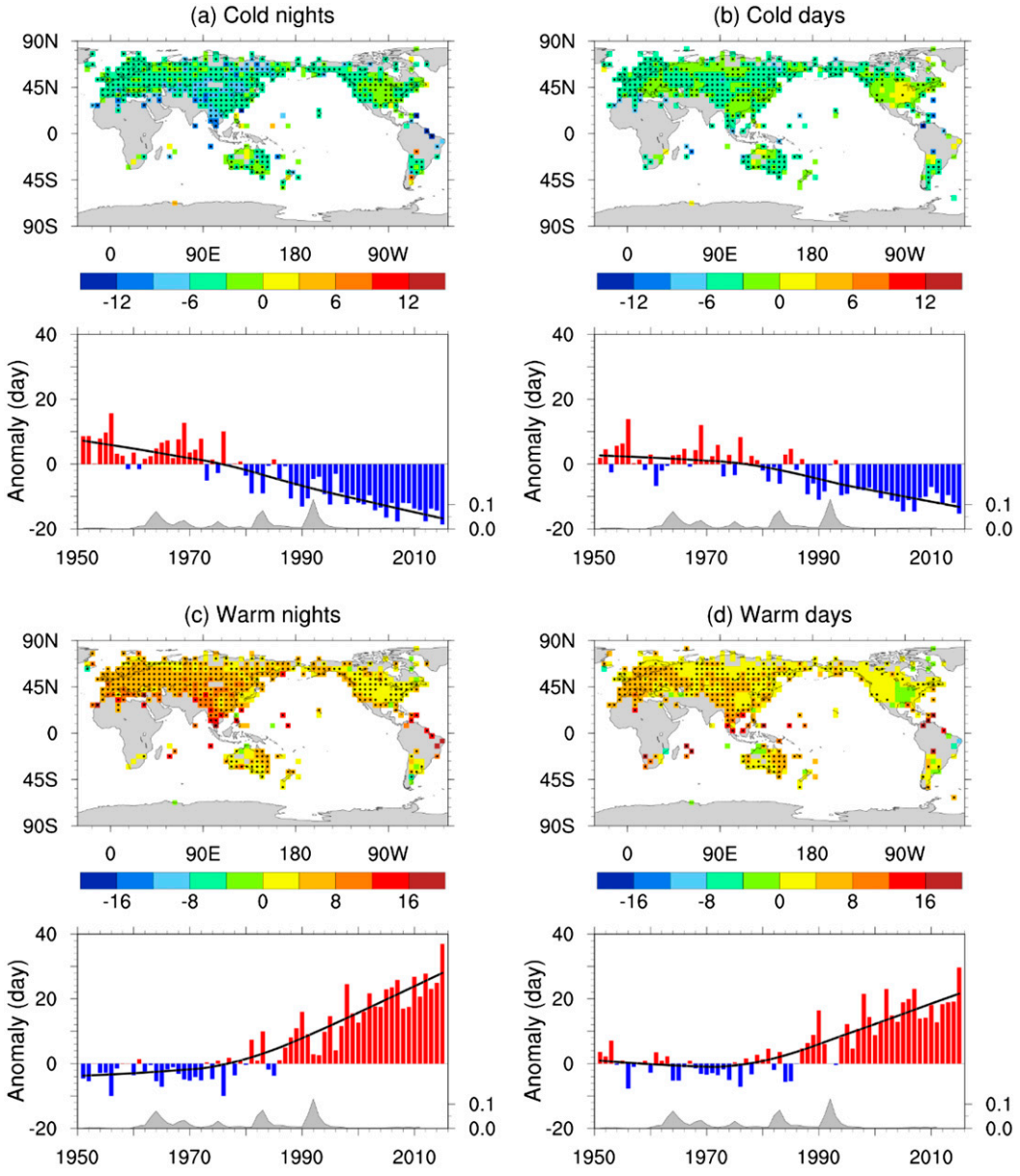

FIG. 4. As in Fig. 3, but for relative threshold indices: (a) cold nights (TN10p), (b) cold days (TX10p), (c) warm nights (TN90p), and (d) warm days (TX90p). The units of these indices were converted to days.

statistically significant change occurred for these indices before the mid-1970s.

b. Relative threshold indices

Figure 4 presents the linear trends patterns and global land average series of four relative threshold indices (cold nights, cold days, warm nights, and warm days). In view of the spatial distributions of the trends, cold nights and warm nights showed a good spatial consistency. Except for a few grid boxes, the regions of the continents experienced a warming trend, that is, the cold nights were decreasing and warm nights were increasing in frequency, cold nights decreased more in Eurasia than other continents, and similarly, warm nights also increased more in Eurasia than other continents.

At the same time, cold days showed a decreasing trend and warm days showed an increasing trend in the most parts of the continents. However, the central and southern parts of the United States presented a spatial inconsistency with the rest of world. In these areas, the cold days were increasing and warm days were decreasing in frequency, forming the so-called warming

hole (Pan et al. 2004), although the trends of these areas were not significant statistically. Similarly, the magnitude of trends in these indices was larger in Eurasia than in the other continents including North America.

Global land average extreme cold indices (cold days and cold nights) were decreasing in frequency, extreme warm indices (warm days and warm nights) were increasing in frequency, and the change magnitude of extreme cold indices was smaller than that of the extreme warm indices. It was notable that, before the mid-1970s, the extreme cold indices and extreme warm indices were relatively stationary and the trends were also not significant statistically (Table 2). However, these indices changed quickly, and the trends were also statistically significant after the mid-1970s (Table 2). The last year (2015) of the study period was the year with the highest frequency of extreme warm events and the lowest frequency of extreme cold events in the last 65 years.

c. *Extreme value indices*

As shown in Fig. 5, the four extreme value indices (TXx, TNx, TXn, and TNn) show a warming trend in most parts of the world, but the trends of the indices related to the daily maximum temperature (TXx and TXn) are spatially more variable than the indices related to daily minimum temperature (TNx and TNn). A cooling trend of TXx could be seen once again in eastern United States. Although the trends of TXn in central and southern United States are negative, they are not significant at the 0.05 level. The cold extreme events (TXn and TNn) experienced a larger warming trend in mid- and high-latitude regions of Northern Hemisphere than in other regions.

The global land average time series of four extreme value indices did not change significantly before the mid-1970s (Table 2), but experienced a rapid increase after the mid-1970s, which is consistent with the changes in the other extreme temperature indices.

d. *Seasonal changes*

In this section, we present the seasonal analysis results for only the cold nights (TN10p; Fig. 6) and warm days (TX90p; Fig. 7) because of the limited length of the paper.

All seasons have warmed during the study period 1951–2015 in terms of changes in the two indices. The frequency of cold nights was decreasing, the frequency of warm days was increasing, and the linear trends of the two indices are significant statistically (Figs. 6 and 7 and Table 3). However, there was a shift near the middle of 1970s. Before that time, almost all seasons (except for the cold nights in MAM) changed slowly, and the trend was found to be insignificant statistically; after the mid-1970s, the changes were faster, and the trends were found to be significant statistically. The cold nights in MAM exhibited a faster decreasing trend before the mid-1970s than during the later period, indicating an earlier warming of nighttime in boreal spring. At the same time, warm days had a small decreasing trend in all seasons before the mid-1970s, showing that there was a tendency to become cooler during the daytime, although it was not significant statistically.

The signal of the Mount Pinatubo volcano eruption in 1991 seemed strong in the global land annual anomaly series of warm days in JJA and SON, but was not so obvious in other seasons (Fig. 7). The boreal autumn and summer signal of the eruption was also notable, to a less extent, in the annual anomaly series of cold nights in 1992–93.

In view of spatial distribution, cold nights (Fig. 6) in Asia (especially in DJF) have decreased more than those in any other regions, while the decrease was relatively small in the United States, where it even witnessed an increasing trend in DJF (Fig. 6d), though the trend are not significant statistically. This is consistent with that reported in Alexander et al. (2006) for cold nights.

In MAM, warm days have increased more in Asia and Europe than in the other regions, while in JJA, the daytime warming mainly occurred in southern Europe and northern Africa, central and Southeast Asia, and Australia. The frequency of warm days decreased in the central and southern part of the United States in all the four seasons, with the decrease being most remarkable in JJA. An area with little change in warm days can be seen in eastern China in summertime.

4. Discussion

a. *Comparison with previous studies*

Overall, our findings in this paper are similar to the previous analyses investigating global land changes in temperature extremes (Easterling 2000; Frich et al. 2002; Alexander et al. 2006; Caesar et al. 2006; Donat et al. 2013a,b). The trends of the HadGHCND and GHCNDEX datasets over the periods 1951–2011 were reported in Donat et al. (2013b). For the sake of comparison, we also calculated the trend of each index over the period 1951–2011, as shown in Table 4. In general, the change magnitude of the extreme cold indices is greater than the change magnitude of the extreme warm indices in all of these datasets. For extreme value indices and relative threshold indices, the linear trends estimated in this study show substantial similarity to those estimated

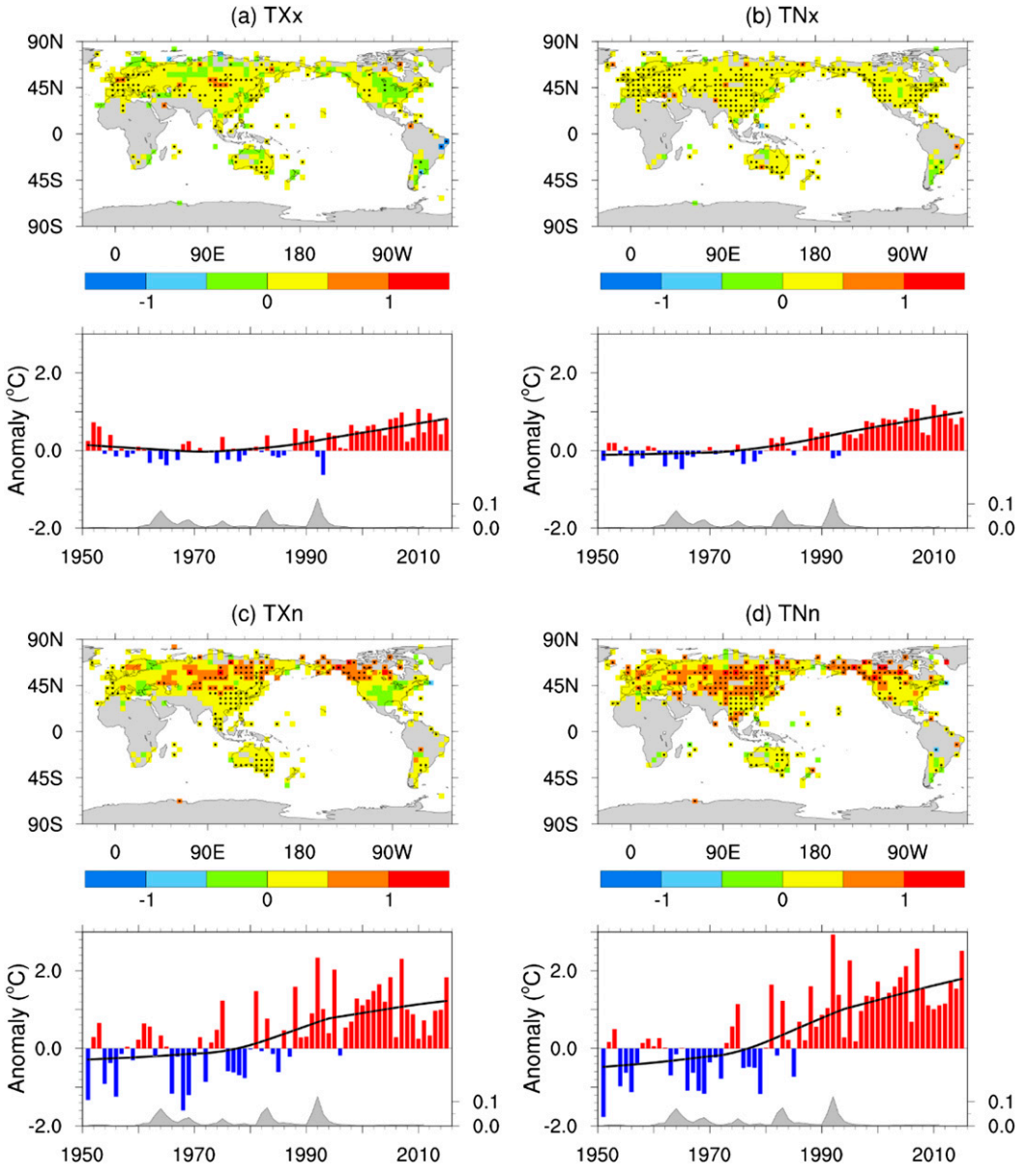

FIG. 5. As in Fig. 3, but for indices (a) maximum T_{max} (TXx), (b) maximum T_{min} (TNx), (c) minimum T_{max} (TXn), and (d) minimum T_{min} (TNn).

in the previous studies, with most of our estimates of trend values for relative threshold indices standing between those based on the HadGHCND (Caesar et al. 2006; Donat et al. 2013b) and GHCNDEX (Donat et al. 2013b) datasets.

There are some minor differences of trends among the three datasets, most probably due to the fact that 1) the different criteria had been used for choosing stations and the resulting different data coverage in the continents, 2) the different methods had been used to create grid averages from station data, or 3) the extreme temperature indices had been calculated from stations and then gridded (GHCNDEX) or from gridded daily data to calculate grid indices series (HadGHCND) (X. Zhang et al. 2011). In this research, the temperature indices series were first calculated from station daily time series, and then the station indices values were averaged to obtain the gridded fields. The differences in the calculation order also may affect the results in certain extent and their interpretation (X. Zhang et al. 2011; Avila et al. 2015). Dunn et al. (2014) investigated the uncertainties in global gridded datasets of climate

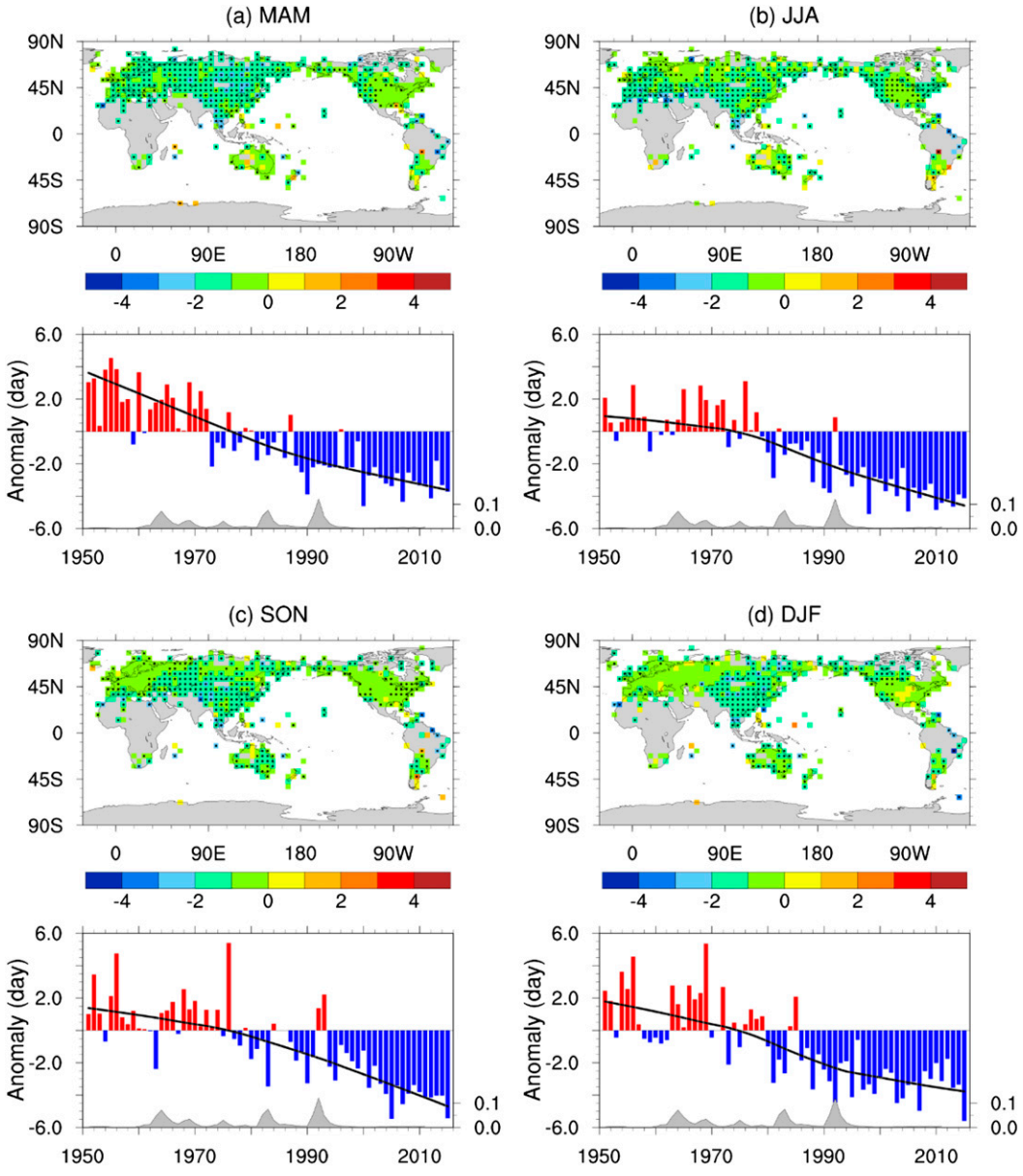

FIG. 6. As in Fig. 4a, but for the seasonal results of cold nights (TN10p): (a) March–May, (b) June–August, (c) September–November, and (d) December–February.

extremes and found that the global land time series of the indices were only slightly affected by "parametric uncertainty" (the changes of parameters within the analytical framework), but were largely affected by "structural uncertainty" (the changes of overall analytical framework). The structural uncertainty can be estimated by having multiple independent teams analyze the same dataset using distinct methods (Hartmann et al. 2013). The trend 1.59 days decade^{-1} of summer days in this study is significantly greater than the trend of GHCNDEX and HadGHCND, which may be caused by structural uncertainty because a similar trend 1.29 days decade^{-1} of summer days can be obtained by calculated the GHCNDEX dataset using the same procedures used in this study.

Some extreme events (frost days, summer days, icing days, and tropical nights) may never occur in certain regions. For example, frost days and icing days occur rarely in low-latitude regions, and summer days and tropical nights occur rarely in high latitudes and high-elevation regions. Therefore, if the grid series of four absolute threshold indices is all zero values, that

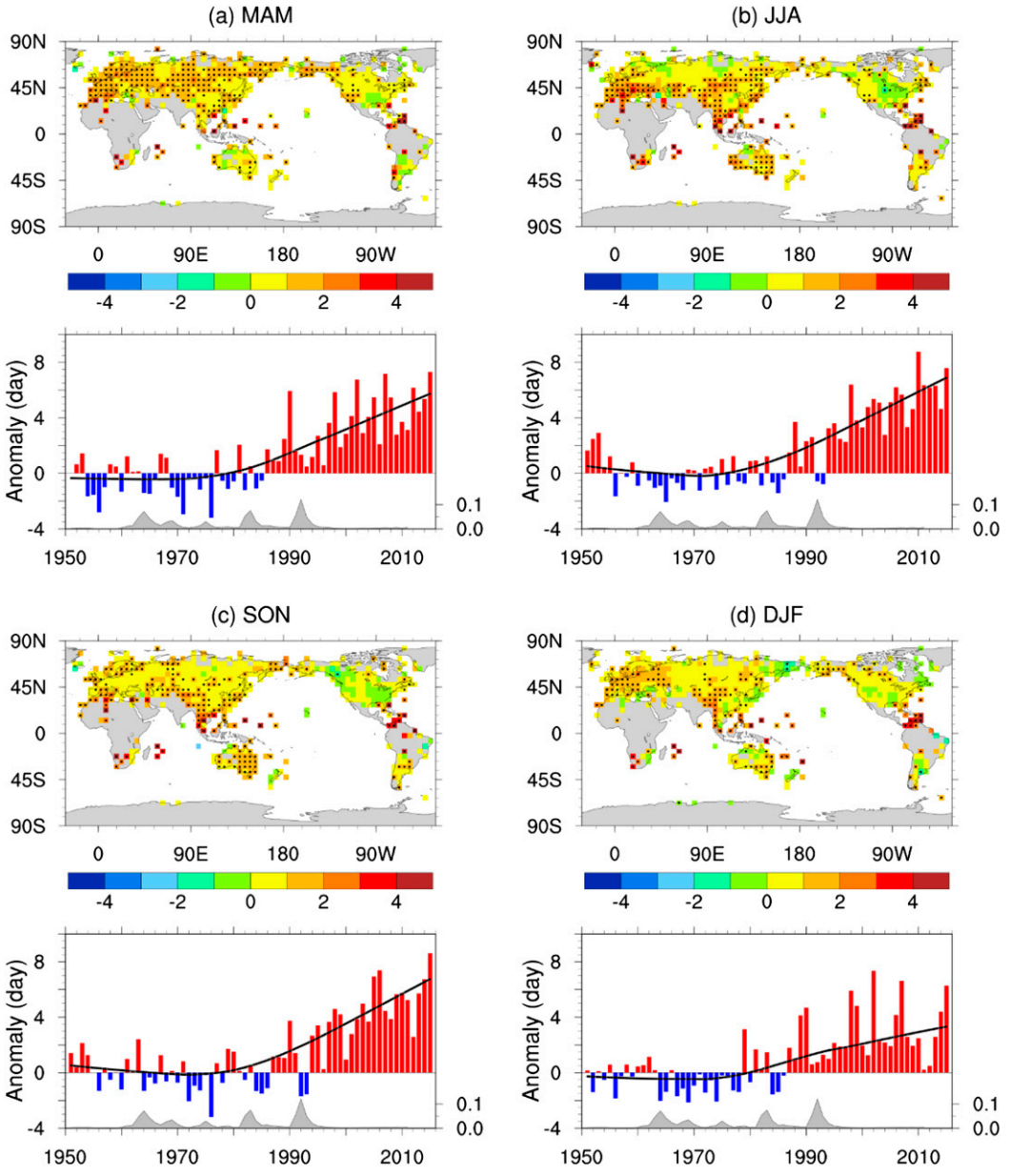

FIG. 7. As in Fig. 4d, but for the seasonal results of warm days (TX90p): (a) March–May, (b) June–August, (c) September–November, and (d) December–February.

is, no extreme events occurred in the entire time periods, the trend of this grid cell would still be calculated, but a cross mark would be added on the grid cell, which indicated that the trend estimate of this grid series was not being robust statistically (Frei and Schär 2001). In this study, the global land average time series of the four absolute threshold indices were calculated using all the gridcell series (including all zero values series) that have at least 90% data during 1951–2015, which results in a more consistent global land averaged trend with previous works (e.g., GHCNDEX and HadGHCND), but a generally significantly larger trend of global land averaged series can be obtained when a more rigorous restriction (lower tolerance for the number of zero values in the indices series) were applied in the spatial average estimate of trend. The latter procedure would reduce the size of the sampling area (fewer grid boxes being sampled for this purpose) and narrows the extents calculated. Further experiments are needed to understand which procedure is more robust in statistics and spatial representativeness.

TABLE 3. Linear trends in temperature extremes indices during 1951–75, 1976–2015, and 1951–2015. The units of cold nights (TN10p), cold days (TX10p), warm nights (TN90p), and warm days (TX90p) were converted to days. Trends of at least 5% significance are shown in bold.

Index		Trend			
		1951–75	1976–2015	1951–2015	Units
Cold nights (TN10p)	MAM	−1.40	**−0.84**	**−1.18**	days decade^{-1}
	JJA	0.14	**−0.89**	**−0.97**	days decade^{-1}
	SON	−0.32	**−1.19**	**−1.03**	days decade^{-1}
	DJF	−0.29	**−0.92**	**−0.98**	days decade^{-1}
Warm days (TX90p)	MAM	−0.20	**1.70**	**1.03**	days decade^{-1}
	JJA	−0.49	**2.00**	**1.11**	days decade^{-1}
	SON	**−0.70**	**1.93**	**1.10**	days decade^{-1}
	DJF	−0.39	**1.07**	**0.69**	days decade^{-1}

This paper made a preliminary seasonal analysis for cold nights and warm days, but the range of change magnitude of seasonal results of this study differ significantly from the study of Alexander et al. (2006). For example, the value of the cold nights time series in this study varies from −6 to 6, but the study of Alexander et al. (2006) is from −20 to 20. In this study, cold nights and warm days were first calculated on basis of monthly percentages, then the monthly percentages were converted to monthly days, and at last, the monthly values (days) were summed to obtain the seasonal and annual values (days). The annual values (days) are the sum of four seasonal values (days). Consequently, the range of change magnitude of annual cold night and warm day series should be greater than the seasonal ones. In Alexander et al. (2006); however, the magnitudes of annual and seasonal change of the two indices series are similar. This difference may also be related to the different grid coverage, and the procedures on how the anomalies were calculated and how the data were averaged.

b. *"Warming hole" in the United States*

Over the past 65 years, most regions of the world have experienced warming trends, but the central and southeastern part of the United States experienced no significant change or a slight cooling trend, characterized by an increase in cold extremes indices and a decrease in warm extremes indices especially for those related to the daily maximum temperature. The seasonal trends of warm days (Fig. 7) showed that the cooling mainly appeared in the daytime during boreal summer and autumn (i.e., JJA and SON), but in the other two seasons (MAM and DJF), only a few grid boxes experienced a cooling trend in these areas and all of the trends were not statistically significant.

Folland et al. (2001) found that central United States showed a cooling trend over the period 1976–2000 for the summer season. Pan et al. (2004) named this cooling

TABLE 4. Trend estimates for global average series of 12 extreme temperature indices over the periods 1951–2011. Trends of at least 5% significance are shown in bold. To compare with HadGHCND (Caesar et al. 2006; Donat et al. 2013b) and GHCNDEX (Donat et al. 2013b), the units of cold nights (TN10p), cold days (TX10p), warm nights (TN90p), and warm days (TX90p) were not converted to days here.

Index	Decadal trend: 1951–2011			
	GHCNDEX	HadGHCND	GLSDT	Unit
Frost day (FD)	**−1.80**	**−1.72**	**−1.95**	days decade^{-1}
Summer day (SU)	**0.47**	0.54	**1.59**	days decade^{-1}
Icing days (ID)	**−1.23**	**−1.18**	**−1.09**	days decade^{-1}
Tropical night (TR)	**0.91**	**1.05**	**1.13**	days decade^{-1}
Maximum T_{max} (TXx)	**0.11**	**0.10**	**0.12**	°C decade^{-1}
Maximum T_{min} (TNx)	**0.12**	**0.17**	**0.19**	°C decade^{-1}
Minimum T_{min} (TXn)	**0.28**	**0.27**	**0.29**	°C decade^{-1}
Minimum T_{min} (TNn)	**0.45**	**0.39**	**0.40**	°C decade^{-1}
Cold night (TN10p)	**−1.09**	**−1.26**	**−1.09**	% decade^{-1}
Cold day (TX10p)	**−0.67**	**−0.86**	**−0.76**	% decade^{-1}
Warm night (TN90p)	**1.17**	**1.79**	**1.33**	% decade^{-1}
Warm day (TX90p)	**0.80**	**1.14**	**0.95**	% decade^{-1}

area in summer as ''warming hole'' and argued that the changes in low-level atmospheric circulation might have supplied more soil moisture in summer, which would increase the summer evapotranspiration and repress the daily maximum temperatures. Kunkel et al. (2006) found that central United States temperature and North Atlantic sea surface temperatures are positively correlated, and central United States temperature and central equatorial Pacific sea surface temperature are negatively correlated. The long-term cooling in the North Atlantic and warming in the central equatorial Pacific were thus regarded as the main reason for the summer cooling in the central and eastern United States. Leibensperger et al. (2012) found that radiative forcing of U.S. anthropogenic aerosols caused the daily maximum temperature of summer and autumn in the central United States to decline in the period 1970–90. The cooling effect of anthropogenic aerosol reduced surface evaporation, which reduced the precipitation on the east coast of the United States, but increased the air moisture flowing northward from the Gulf of Mexico that would increase the cloud cover and precipitation in the central United States (Leibensperger et al. 2012).

Our analysis results showed that the cooling of the United States mainly appeared in the daytime of boreal summer and autumn supports the claim that the weakening daytime solar radiation, or the interaction between solar radiation and soil moisture, may have played an important role in forming the cooling area in the last 65 years. The declining solar radiation may have been caused by the increasing cloudiness rather than increasing aerosol concentration, because aerosol emission in the region had been controlled to a large degree (Li et al. 2011). A smaller cooling area or no significant change area is also visible in eastern China during boreal summer, and it may have been caused by the daytime weakening of solar radiation most probably related to the combined effect of increasing aerosol emission and cloudiness, with the rising aerosol concentration playing a larger role in northern part of the region (Qian et al. 2003; Zhang et al. 2007; Ding and Ren 2008; Li et al. 2011).

c. *Influence of stratospheric aerosol*

Earth's radiation balance was affected by aerosols that absorb upward terrestrial thermal radiation and reflect sunlight to space. The stratospheric aerosol optical depth is one of the principle parameters affecting the Earth surface climate (Lacis et al. 1992; Sato et al. 1993). Figures 3–7 show that the stratospheric aerosol optical depth might have an important impact on interannual variability of the extreme temperature indices. When the stratospheric aerosol optical depth reached a peak, the frequency of cold extreme events would increase, and the frequency of warm extreme events would decrease, especially for the daytime extremes of boreal summer and autumn. A good example is the abnormally low level of annual and summer daytime warm event frequency in 1992–93 following the Mount Pinatubo volcano eruption in 1991 (Figs. 3–7).

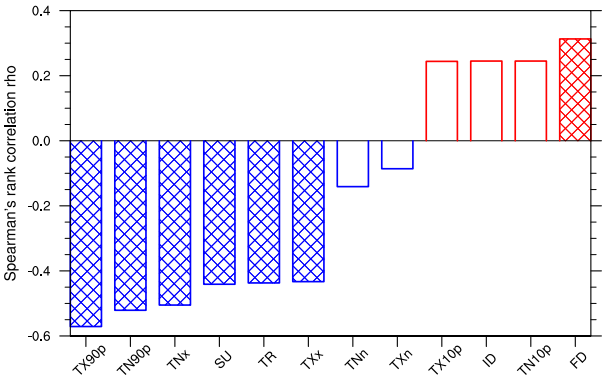

FIG. 8. The Spearman's rank correlation (rho) between extreme temperature indices and stratospheric aerosol optical depth at 550 nm. Correlations (rho) of at least 5% significance are filled with grid lines.

We calculated the Spearman's rank correlation (rho) (Best and Roberts 1975; Hollander and Wofle 1973) between global land average extreme indices and the stratospheric aerosol optical depth after removing the linear trends. As shown in Fig. 8, it can be clearly seen that the stratospheric aerosol optical depths were positively correlated with cold extreme threshold indices (TN10p, ID, TX10p, and FD) and were negatively correlated with warm extreme threshold indices (TX90p, TN90p, SU, and TR), and the absolute magnitude of correlation coefficient with warm extremes indices (TX90p, TN90p, SU, and TR) are larger and are more significant statistically. The higher the stratospheric aerosol optical depth, the cooler the daytime surface air during warm seasons of Northern Hemisphere. The indices associated with temperature extreme values (TNx, TXx, TNn, and TXn) were all negatively correlated with stratospheric aerosol optical depth regardless it is warm indices or cold indices, and the indices of TNx and TXx (warm indices) have a more significant negative correlation with aerosol optical depth than the indices of TNn and TXn (cold indices). The reason for the association is that more stratospheric aerosols would absorb and reflect more solar radiation in stratosphere, leading to less radiation received in the surface and an abnormally cooling condition during daytime. Of course, the interannual to decadal variability is the result of the interaction of many factors including stratospheric aerosols.

d. Uncertainty of trend estimates

In this study, the homogeneity test was conducted by using RHtestsV4 (Wang 2008a,b; Wang and Feng 2013) software and the station series identified as inhomogeneous were discarded. It is inevitable to exclude some potential natural climate shifts because there is no further analysis for these step changes due to the lack of metadata and the observations from densely stations. To avoid this ''false exclusion'' as much as possible, a higher confidence threshold 99.99% was used for homogeneity testing. Meanwhile, this method was designed to detect only step changes (sudden shifts in the mean) in the data series but not to detect gradual temperature changes, including those related to urbanization effects and gradual changes in the local observing environment.

It is well known that the urban heat island effect can cause the urban surface air temperature to be higher than the suburb or rural areas. Meanwhile, a large number of stations are located in or near urban areas, despite the urban areas only accounting for a small portion (<1%) of the global land. As a result, if these observations of temperature at urban stations are used to analyze mean temperature and extreme temperature change, the warming trends can be overestimated not only for individual stations and grid boxes but also for the regional average series (Ren 2015).

Urbanization effects differ from region to region due to the different speed of urban development and the specifically designed locations of the observational sites in different countries. It is possible that, in developed areas, the urban infrastructure of well-established cities did not expand in the last decades. Although the stations located in a city center observed a warmer climate than those located in rural stations, the trend for the decades might be similar, because the influences on urban temperature have not changed over this period (Peterson 2003; Jones et al. 2008; Ren 2015). However, in developing areas, such as the mainland of China and western Asian countries, the urbanization effect on temperature trends might not be negligible due to the rapid urban development (Zhou et al. 2004; Ren et al. 2008; Zhou and Ren 2011; Li and Huang 2013; Ren and Zhou 2014; Sun et al. 2016). It is unclear for the time being to what extents the urbanization processes had affected the estimated trends of the global land average annual and seasonal mean extreme temperature indices as reported in this paper. An attempt could be made to tackle this issue in the future.

On a regional scale, however, there had been a couple of studies examining the urbanization effect on extreme temperature trends (Zhou and Ren 2009, 2011; L. Zhang et al. 2011; Ren and Zhou 2014). Zhou and Ren (2011) found that urbanization effect on long-term trends of the T_{min}-related extreme temperature indices of national stations in North China was rather large and statistically highly significant for the period 1961–2008, and the urbanization contributions for the regional average annual series of frost days, tropical nights, cold nights, and warm nights reached 45%, 64%, 44%, and 48% respectively. Taking mainland of China as a whole, the urbanization also has a statistically significant effect on the above-mentioned four extreme temperature indices series of national stations during the same time period, and the urbanization accounts for more than 10%, 38%, 17%, and 26% of the overall trends, respectively (Ren and Zhou 2014).

Therefore, it is possible that the global land average annual and seasonal extreme temperature indices series over the last 65 years contain some degree of urbanization effects, in particular in developing regions. However, the urbanization may have little effects for the other regions when compared to those found for the mainland of China, mainly due to the relatively slow development of urban areas in the regions outside East Asia in the last 65 years.

Another major uncertainty source is the data gaps in different periods in Africa, India, and South America. The number of available temperature stations reached the maximum in the late 1970s and started to decline since then, as shown in Figs. 1a and 1c. Furthermore, these data gaps were changing over time, leading to a temporal change in the spatial coverage of observations. These would make the accurate assessment and robust detection of extreme temperature change in these regions particularly difficult, and also result in another systematic bias in the estimate of the global land average extreme temperature indices trends. This bias needs to be investigated in the following works. It is generally deemed, however, that the bias in the global land average annual mean surface air temperature series due to the data coverage is small compared to the overall trends estimated for various time periods of the last century (Hansen et al. 2006; Lawrimore et al. 2011; Jones et al. 2012).

However, the effect of the daily temperature data coverage and its change with time, in particular in Africa, southern parts of Asia, Arctic regions, and South America, on trend estimates of global land average extreme temperature indices still needs to be examined. As there are not any daily temperature data in most grid boxes in Africa and South America, all the extreme temperature indices series could not be calculated. Before the influence of data coverage on the estimated trends of extreme temperature indices is addressed, it is reasonable to assume that the current global land

analysis results, including those reported in this paper, heavily reflect the long-term changes of average extreme temperature indices of Northern Hemispheric continents, especially those of the data-dense Europe, East Asia, and North America.

5. Conclusions

In this paper, we presented a new analysis of global land extreme temperature indices changes based on an integrated global land surface daily temperature dataset (GLSDT-V1.0) recently developed by the National Meteorological Information Center, CMA. Our main conclusions are as follows:

1) The global land average annual and seasonal mean extreme temperature indices all experienced significant long-term changes over the period 1951–2015, with cold threshold indices (frost days, icing days, cold days, and cold nights) decreasing and warm threshold indices (summer days, tropical nights, warm days and warm nights) increasing. The extreme temperature indices based on daily minimum temperature generally had a stronger and more significant trend than those based on daily maximum temperature.
2) The most significant warming in most extreme temperature indices occurred after the mid-1970s, and before the mid-1970s the global land average indices series generally showed no significant change. Most parts of the global land experienced significant warming trends over the period 1951–2015 as a whole, and the largest trends appeared in mid- to high latitudes of the Eurasian continent.
3) The seasonal analysis showed that, during the period of 1951–2015, the global land average annual and seasonal frequency of cold nights and warm days experienced similarly large and significant changes, with the seasonal cold nights decreasing at rates from -0.97 to -1.18 days decade^{-1}, and the seasonal warm days increasing at rates from 0.69 to 1.11 days decade^{-1}. The most significant seasonal trends of the two extreme indices occurred in the period of 1976–2015, and the pre-1976 seasonal changes were generally small and statistically insignificant.
4) Most parts of the world experienced warming during the period 1951–2015. However, in the summer and autumn of central and southeastern United States, the indices calculated from the daily maximum temperature did not experience the warming trend, resulting in the so-called warming hole. The warm-season daytime cooling phenomenon also appeared in eastern China to a lesser extent.
5) In most of the T_{max}-based and warm extreme temperature indices series, the signal of volcano eruptions was notable, with the influence of the 1991 Pinatubo eruption on the extreme temperature indices particularly clear for warm days, cold days, and summer days in the boreal summer and autumn in 1992–93.

Acknowledgments. This study is supported by the National Key R&D Program of China (2018YFA0605603) and the Natural Science Foundation of China (NSFC) (41575003). The authors thank Yang Feng, Kangmin Wen, Xiaoying Xue, Xiaoming Liu, and two anonymous reviewers for their comments and suggestions that greatly improved the manuscript.

REFERENCES

Aguilar, E., and Coauthors, 2005: Changes in precipitation and temperature extremes in Central America and northern South America, 1961–2003. *J. Geophys. Res.*, **110**, D23107, https://doi.org/10.1029/2005JD006119.

Alexander, L. V., and Coauthors, 2006: Global observed changes in daily climate extremes of temperature and precipitation. *J. Geophys. Res.*, **111**, D05109, https://doi.org/10.1029/2005JD006290.

Avila, F. B., S. Dong, K. P. Menang, J. Rajczak, M. Renom, M. G. Donat, and L. V. Alexander, 2015: Systematic investigation of gridding-related scaling effects on annual statistics of daily temperature and precipitation maxima: A case study for south-east Australia. *Wea. Climate Extremes*, **9**, 6–16, https://doi.org/10.1016/j.wace.2015.06.003.

Best, D. J., and D. E. Roberts, 1975: Algorithm AS 89: The upper tail probabilities of Spearman's rho. *Appl. Stat.*, **24**, 377, https://doi.org/10.2307/2347111.

Bronaugh, D., 2015: climdex.pcic: PCIC Implementation of Climdex Routines, version 1.1-6. R package, https://CRAN.R-project.org/package=climdex.pcic.

Brown, P. J., R. S. Bradley, and F. T. Keimig, 2010: Changes in extreme climate indices for the northeastern United States, 1870–2005. *J. Climate*, **23**, 6555–6572, https://doi.org/10.1175/2010JCLI3363.1.

Brunet, M., and Coauthors, 2006: The development of a new dataset of Spanish Daily Adjusted Temperature Series (SDATS) (1850–2003). *Int. J. Climatol.*, **26**, 1777–1802, https://doi.org/10.1002/joc.1338.

Caesar, J., L. Alexander, and R. Vose, 2006: Large-scale changes in observed daily maximum and minimum temperatures: Creation and analysis of a new gridded data set. *J. Geophys. Res.*, **111**, D05101, https://doi.org/10.1029/2005JD006280.

Cao, L., Y. Zhu, G. Tang, F. Yuan, and Z. Yan, 2016: Climatic warming in China according to a homogenized data set from 2419 stations. *Int. J. Climatol.*, **36**, 4384–4392, https://doi.org/10.1002/joc.4639.

Cerveny, R. S., J. Lawrimore, R. Edwards, and C. Landsea, 2007: Extreme weather records: Compilation, adjudication, and publication. *Bull. Amer. Meteor. Soc.*, **88**, 853–860, https://doi.org/10.1175/BAMS-88-6-853.

Cleveland, W. S., 1979: Robust locally weighted regression and smoothing scatterplots. *J. Amer. Stat. Assoc.*, **74**, 829–836, https://doi.org/10.1080/01621459.1979.10481038.

Cubasch, U., D. Wuebbles, D. Chen, M. C. Facchini, D. Frame, N. Mahowald, and J.-G. Winther, 2013: Introduction. *Climate*

Change 2013: The Physical Science Basis, T. F. Stocker et al., Eds., Cambridge University Press, 119–158.

Ding, Y. H., and G. Y. Ren, 2008: *Introduction of China Climate Change Science*. China Meteorological Press, 281 pp.

Donat, M. G., and Coauthors, 2013a: Updated analyses of temperature and precipitation extreme indices since the beginning of the twentieth century: The HadEX2 dataset. *J. Geophys. Res. Atmos.*, **118**, 2098–2118, https://doi.org/10.1002/jgrd.50150.

——, L. V. Alexander, H. Yang, I. Durre, R. Vose, and J. Caesar, 2013b: Global land-based datasets for monitoring climatic extremes. *Bull. Amer. Meteor. Soc.*, **94**, 997–1006, https://doi.org/10.1175/BAMS-D-12-00109.1.

Dunn, R. J. H., M. G. Donat, and L. V. Alexander, 2014: Investigating uncertainties in global gridded datasets of climate extremes. *Climate Past*, **10**, 2171–2199, https://doi.org/10.5194/cp-10-2171-2014.

Easterling, D. R., 2000: Climate extremes: Observations, modeling, and impacts. *Science*, **289**, 2068–2074, https://doi.org/10.1126/science.289.5487.2068.

——, L. V. Alexander, A. Mokssit, and V. Detemmerman, 2003: CCI/CLIVAR Workshop to Develop Priority Climate Indices. *Bull. Amer. Meteor. Soc.*, **84**, 1403–1407, https://doi.org/10.1175/BAMS-84-10-1409.

Folland, C. K., T. R. Karl, and J. R. Christy, 2001: Observed climate variability and change. *Climate Change 2001: The Scientific Basis*, J. H. Houghton et al., Eds., Cambridge University Press, 99–181.

Fonseca, D., M. J. Carvalho, M. Marta-Almeida, P. Melo-Gonçalves, and A. Rocha, 2016: Recent trends of extreme temperature indices for the Iberian Peninsula. *Phys. Chem. Earth Parts ABC*, **94**, 66–76, https://doi.org/10.1016/j.pce.2015.12.005.

Frei, C., and C. Schär, 2001: Detection probability of trends in rare events: theory and application to heavy precipitation in the Alpine region. *J. Climate*, **14**, 1568–1584, https://doi.org/10.1175/1520-0442(2001)014<1568:DPOTIR>2.0.CO;2.

Frich, P., L. Alexander, P. Della-Marta, B. Gleason, M. Haylock, A. Klein Tank, and T. Peterson, 2002: Observed coherent changes in climatic extremes during the second half of the twentieth century. *Climate Res.*, **19**, 193–212, https://doi.org/10.3354/cr019193.

Handmer, J. Y., and Coauthors, 2012: Changes in impacts of climate extremes: Human systems and ecosystems. *Managing the Risks of Extreme Events and Disasters to Advance Climate Change Adaptation*, C. B. Field et al., Eds., Cambridge University Press, 231–290, https://www.ipcc.ch/site/assets/uploads/2018/03/SREX-Chap4_FINAL-1.pdf.

Hansen, J., M. Sato, R. Ruedy, K. Lo, D. W. Lea, and M. Medina-Elizade, 2006: Global temperature change. *Proc. Natl. Acad. Sci. USA*, **103**, 14 288–14 293, https://doi.org/10.1073/pnas.0606291103.

Hartmann, D. L., and Coauthors, 2013: Observations: Atmosphere and surface. *Climate Change 2013: The Physical Science Basis*, T. F. Stocker et al., Eds., Cambridge University Press, 159–218.

Hollander, M., and D. A. Wofle, 1973: *Nonparametric Statistical Methods*. John Wiley & Sons, 185–194 pp.

Jayawardena, I. M. S. P., D. W. T. T. Darshika, and H. M. R. C. Herath, 2018: Recent trends in climate extreme indices over Sri Lanka. *Amer. J. Climate Change*, **07**, 586–599, https://doi.org/10.4236/ajcc.2018.74036.

Jones, P. D., and M. Hulme, 1996: Calculating regional climatic time series for temperature and precipitation: Methods and illustrations. *Int. J. Climatol.*, **16**, 361–377, https://doi.org/10.1002/(SICI)1097-0088(199604)16:4<361::AID-JOC53>3.0.CO;2-F.

——, D. H. Lister, and Q. Li, 2008: Urbanization effects in large-scale temperature records, with an emphasis on China. *J. Geophys. Res.*, **113**, D16122, https://doi.org/10.1029/2008JD009916.

——, ——, T. J. Osborn, C. Harpham, M. Salmon, and C. P. Morice, 2012: Hemispheric and large-scale land-surface air temperature variations: An extensive revision and an update to 2010. *J. Geophys. Res.*, **117**, D05127, https://doi.org/10.1029/2011jd017139.

Kendall, M. G., 1955: *Rank Correlation Methods*. Charles Griffin, 196 pp.

Klein Tank, A. M. G., and G. P. Können, 2003: Trends in indices of daily temperature and precipitation extremes in Europe, 1946–99. *J. Climate*, **16**, 3665–3680, https://doi.org/10.1175/1520-0442(2003)016<3665:TIIODT>2.0.CO;2.

——, and Coauthors, 2002: Daily dataset of 20th-century surface air temperature and precipitation series for the European Climate Assessment: European temperature and precipitation series. *Int. J. Climatol.*, **22**, 1441–1453, https://doi.org/10.1002/joc.773.

——, and Coauthors, 2006: Changes in daily temperature and precipitation extremes in central and south Asia. *J. Geophys. Res.*, **111**, D16105, https://doi.org/10.1029/2005JD006316.

Kunkel, K. E., X.-Z. Liang, J. Zhu, and Y. Lin, 2006: Can CGCMs simulate the twentieth-century ''warming hole'' in the central United States? *J. Climate*, **19**, 4137–4153, https://doi.org/10.1175/JCLI3848.1.

Lacis, A., J. Hansen, and M. Sato, 1992: Climate forcing by stratospheric aerosols. *Geophys. Res. Lett.*, **19**, 1607–1610, https://doi.org/10.1029/92GL01620.

Lawrimore, J. H., M. J. Menne, B. E. Gleason, C. N. Williams, D. B. Wuertz, R. S. Vose, and J. Rennie, 2011: An overview of the Global Historical Climatology Network monthly mean temperature data set, version 3. *J. Geophys. Res.*, **116**, D19121, https://doi.org/10.1029/2011JD016187.

Leibensperger, E. M., and Coauthors, 2012: Climatic effects of 1950–2050 changes in US anthropogenic aerosols—Part 2: Climate response. *Atmos. Chem. Phys.*, **12**, 3349–3362, https://doi.org/10.5194/acp-12-3349-2012.

Li, Q., and J. Huang, 2013: Effects of urbanization on extreme warmest night temperatures during summer near Bohai. *Acta Meteor. Sin.*, **27**, 808–818, https://doi.org/10.1007/s13351-013-0602-0.

Li, Z., and Z. Yan, 2009: Homogenized daily mean/maximum/minimum temperature series for China from 1960-2008. *Atmos. Ocean. Sci. Lett.*, **2**, 237–243, https://doi.org/10.1080/16742834.2009.11446802.

——, F. Niu, J. Fan, Y. Liu, D. Rosenfeld, and Y. Ding, 2011: Long-term impacts of aerosols on the vertical development of clouds and precipitation. *Nat. Geosci.*, **4**, 888–894, https://doi.org/10.1038/ngeo1313.

Mann, H. B., 1945: Nonparametric tests against trend. *Econ. Soc.*, **13**, 245–259, https://doi.org/10.2307/1907187.

Menne, M. J., and C. N. Williams, 2009: Homogenization of temperature series via pairwise comparisons. *J. Climate*, **22**, 1700–1717, https://doi.org/10.1175/2008JCLI2263.1.

——, and Coauthors, 2012a: Global Historical Climatology Network–Daily (GHCN-Daily), version 3.12. NOAA National Climatic Data Center, accessed 13 August 2014, https://doi.org/10.7289/V5D21VHZ.

——, I. Durre, R. S. Vose, B. E. Gleason, and T. G. Houston, 2012b: An overview of the Global Historical Climatology Network–Daily database. *J. Atmos. Oceanic Technol.*, **29**, 897–910, https://doi.org/10.1175/JTECH-D-11-00103.1.

New, M., and Coauthors, 2006: Evidence of trends in daily climate extremes over southern and west Africa. *J. Geophys. Res.*, **111**, D14102, https://doi.org/10.1029/2005JD006289.

Pan, Z. T., R. W. Arritt, E. S. Takle, W. J. Gutowski, C. J. Anderson, and M. Segal, 2004: Altered hydrologic feedback in a warming climate introduces a "warming hole." *Geophys. Res. Lett.*, **31**, L17109, https://doi.org/10.1029/2004GL020528.

Peterson, T. C., 2003: Assessment of urban versus rural in situ surface temperatures in the contiguous United States: No difference found. *J. Climate*, **16**, 2941–2959, https://doi.org/10.1175/1520-0442(2003)016<2941:AOUVRI>2.0.CO;2.

——, 2005: Climate change indices. *WMO Bull.*, **54**, 83–86.

——, and M. J. Manton, 2008: Monitoring changes in climate extremes—A tale of international collaboration. *Bull. Amer. Meteor. Soc.*, **89**, 1266–1271, https://doi.org/10.1175/2008BAMS2501.1.

——, and Coauthors, 1998: Homogeneity adjustments of in situ atmospheric climate data: A review. *Int. J. Climatol.*, **18**, 1493–1517, https://doi.org/10.1002/(SICI)1097-0088(19981115)18:13<1493::AID-JOC329>3.0.CO;2-T.

——, and Coauthors, 2002: Recent changes in climate extremes in the Caribbean region. *J. Geophys. Res.*, **107**, 4601, https://doi.org/10.1029/2002JD002251.

——, X. Zhang, M. Brunet-India, and J. L. Vázquez-Aguirre, 2008: Changes in North American extremes derived from daily weather data. *J. Geophys. Res.*, **113**, https://doi.org/10.1029/2007JD009453.

Qian, Y., L. Ruby Leung, S. J. Ghan, and F. Giorgi, 2003: Regional climate effects of aerosols over China: Modeling and observation. *Tellus*, **55B**, 914–934, https://doi.org/10.1046/j.1435-6935.2003.00070.x.

Ren, G., 2015: Urbanization as a major driver of urban climate change. *Adv. Climate Change Res.*, **6**, 1–6, https://doi.org/10.1016/j.accre.2015.08.003.

——, and Y. Zhou, 2014: Urbanization effect on trends of extreme temperature indices of national stations over Mainland China, 1961–2008. *J. Climate*, **27**, 2340–2360, https://doi.org/10.1175/JCLI-D-13-00393.1.

——, ——, Z. Chu, J. Zhou, A. Zhang, J. Guo, and X. Liu, 2008: Urbanization effects on observed surface air temperature trends in north China. *J. Climate*, **21**, 1333–1348, https://doi.org/10.1175/2007JCLI1348.1.

——, Y. Ren, Q. Li, and W. Xu, 2014: An overview on global land surface air temperature change. *Diqiu Kexue Jinzhan*, **29**, 934–946, https://doi.org/doi:10.11867/j.issn.1001-8166.2014.08.0934.

Royston, P., 1982: Algorithm AS 181: The W test for normality. *Appl. Stat.*, **31**, 176–180, https://doi.org/10.2307/2347986.

Sato, M., J. E. Hansen, M. P. McCormick, and J. B. Pollack, 1993: Stratospheric aerosol optical depths, 1850–1990. *J. Geophys. Res.*, **98**, 22 987–22 994, https://doi.org/10.1029/93JD02553.

Sen, P. K., 1968: Estimates of the regression coefficient based on Kendall's tau. *J. Amer. Stat. Assoc.*, **63**, 1379–1389, https://doi.org/10.1080/01621459.1968.10480934.

Seneviratne, S. I., and Coauthors, 2012: Changes in impacts of climate extremes and their impacts on the natural physical environment. *Managing the Risks of Extreme Events and Disasters to Advance Climate Change Adaptation*, C. B. Field et al., Eds., Cambridge University Press, 109–230.

Sharma, D., and M. S. Babel, 2014: Trends in extreme rainfall and temperature indices in the western Thailand. *Int. J. Climatol.*, **34**, 2393–2407, https://doi.org/10.1002/joc.3846.

Sillmann, J., V. V. Kharin, X. Zhang, F. W. Zwiers, and D. Bronaugh, 2013: Climate extremes indices in the CMIP5 multimodel ensemble: Part 1. Model evaluation in the present climate. *J. Geophys. Res.*, **118**, 1716–1733, https://doi.org/10.1002/jgrd.50203.

Sun, X., G. Ren, A. B. Shrestha, Y.-Y. Ren, Q.-L. You, Y.-J. Zhan, Y. Xu, and R. Rajbhandari, 2017a: Changes in extreme temperature events over the Hindu Kush Himalaya during 1961–2015. *Adv. Climate Change Res.*, **8**, 157–165, https://doi.org/10.1016/j.accre.2017.07.001.

——, ——, W. Xu, Q. Li, and Y. Ren, 2017b: Global land-surface air temperature change based on the new CMA GLSAT data set. *Sci. Bull.*, **62**, 236–238, https://doi.org/10.1016/j.scib.2017.01.017.

Sun, Y., X. Zhang, G. Ren, F. W. Zwiers, and T. Hu, 2016: Contribution of urbanization to warming in China. *Nat. Climate Change*, **6**, 706–709, https://doi.org/10.1038/NCLIMATE2956.

Trewin, B. C., 2001: Extreme temperature events in Australia. Ph.D. thesis, University of Melbourne, 417 pp.

——, 2013: A daily homogenized temperature data set for Australia. *Int. J. Climatol.*, **33**, 1510–1529, https://doi.org/10.1002/joc.3530.

——, and A. C. F. Trevitt, 1996: The development of composite temperature records. *Int. J. Climatol.*, **16**, 1227–1242, https://doi.org/10.1002/(SICI)1097-0088(199611)16:11<1227::AID-JOC82>3.0.CO;2-P.

Vincent, L. A., and É. Mekis, 2006: Changes in daily and extreme temperature and precipitation indices for Canada over the twentieth century. *Atmos.–Ocean*, **44**, 177–193, https://doi.org/10.3137/ao.440205.

——, X. Zhang, B. R. Bonsal, and W. D. Hogg, 2002: Homogenization of daily temperatures over Canada. *J. Climate*, **15**, 1322–1334, https://doi.org/10.1175/1520-0442(2002)015<1322:HODTOC>2.0.CO;2.

——, and Coauthors, 2005: Observed trends in indices of daily temperature extremes in South America 1960–2000. *J. Climate*, **18**, 5011–5023, https://doi.org/10.1175/JCLI3589.1.

——, and Coauthors, 2011: Observed trends in indices of daily and extreme temperature and precipitation for the countries of the western Indian Ocean, 1961–2008. *J. Geophys. Res.*, **116**, D10108, https://doi.org/10.1029/2010JD015303.

——, X. L. Wang, E. J. Milewska, H. Wan, F. Yang, and V. Swail, 2012: A second generation of homogenized Canadian monthly surface air temperature for climate trend analysis. *J. Geophys. Res.*, **117**, D18110, https://doi.org/10.1029/2012JD017859.

Von Storch, H., and A. Navarra, Eds., 1999: Misuses of statistical analysis in climate research. *Analysis of Climate Variability—Applications of Statistical Techniques*. Springer-Verlag, 11–26.

Wang, X. L., 2008a: Penalized maximal F test for detecting undocumented mean shift without trend change. *J. Atmos. Oceanic Technol.*, **25**, 368–384, https://doi.org/10.1175/2007JTECHA982.1.

——, 2008b: Accounting for autocorrelation in detecting mean shifts in climate data series using the penalized maximal t or F test. *J. Appl. Meteor. Climatol.*, **47**, 2423–2444, https://doi.org/10.1175/2008JAMC1741.1.

——, and V. R. Swail, 2001: Changes of extreme wave heights in Northern Hemisphere oceans and related atmospheric circulation regimes. *J. Climate*, **14**, 2204–2221, https://doi.org/10.1175/1520-0442(2001)014<2204:COEWHI>2.0.CO;2.

——, and Y. Feng, 2010: RHtests V3 User Manual. Climate Research Division, Atmospheric Science and Technology Directorate. Science and Technology Branch, Environment Canada, 27 pp., http://etccdi.pacificclimate.org/RHtest/RHtestsV3_UserManual.doc.

——, and ——, 2013: RHtests V4 User Manual. Climate Research Division, Atmospheric Science and Technology Directorate.

Science and Technology Branch, Environment Canada, 29 pp., http://etccdi.pacificclimate.org/RHtest/RHtestsV4_UserManual_20July2013.pdf.

Wijngaard, J. B., A. Tank, and G. P. Konnen, 2003: Homogeneity of 20th century European daily temperature and precipitation series. *Int. J. Climatol.*, **23**, 679–692, https://doi.org/10.1002/joc.906.

WMO, 2008: *Guide to Meteorological Instruments and Methods of Observation*. 7th ed. WMO 8, 33 pp.

Xu, W., Q. Li, X. L. Wang, S. Yang, L. Cao, and Y. Feng, 2013: Homogenization of Chinese daily surface air temperatures and analysis of trends in the extreme temperature indices. *J. Geophys. Res. Atmos.*, **118**, 9708–9720, https://doi.org/10.1002/jgrd.50791.

——, and Coauthors, 2018: A new integrated and homogenized global monthly land surface air temperature dataset for the period since 1900. *Climate Dyn.*, **50**, 2513–2536, https://doi.org/10.1007/s00382-017-3755-1.

Xu, Y., W. Xu, and Q. Li, 2014: Report on the development and evaluation of global land daily temperature and precipitation data sets. National Meteorological Information Center of China Meteorological Administration, 21 pp.

Yan, Z., and Coauthors, 2002: Trends of extreme temperatures in Europe and China based on daily observations. *Climatic Change*, **53**, 355–392, https://doi.org/10.1023/A:1014939413284.

Zhai, P., and X. Pan, 2003: Trends in temperature extremes during 1951–1999 in China. *Geophys. Res. Lett.*, **30**, 1913, https://doi.org/10.1029/2003GL018004.

Zhang, L., G. Ren, J. Liu, Y. Zhou, Y. Ren, A. Zhang, and Y. Feng, 2011: Urban effect on trends of extreme temperature indices at Beijing Meteorological Station. *Chin. J. Geophys.*, **54**, 1150–1159.

Zhang, X., and Y. Feng, 2004: RClimDex User Manual. Climate Research Branch, Environment Canada, 23 pp.

——, L. A. Vincent, W. D. Hogg, and A. Niitsoo, 2000: Temperature and precipitation trends in Canada during the 20th century. *Atmos.–Ocean*, **38**, 395–429, https://doi.org/10.1080/07055900.2000.9649654.

——, G. Hegerl, F. W. Zwiers, and J. Kenyon, 2005b: Avoiding inhomogeneity in percentile-based indices of temperature extremes. *J. Climate*, **18**, 1641–1651, https://doi.org/10.1175/JCLI3366.1.

——, and Coauthors, 2005a: Trends in Middle East climate extreme indices from 1950 to 2003. *J. Geophys. Res.*, **110**, D22104, https://doi.org/10.1029/2005JD006181.

——, F. W. Zwiers, G. C. Hegerl, F. H. Lambert, N. P. Gillett, S. Solomon, P. A. Stott, and T. Nozawa, 2007: Detection of human influence on twentieth-century precipitation trends. *Nature*, **448**, 461–465, https://doi.org/10.1038/nature06025.

——, ——, and G. Hegerl, 2009: The influences of data precision on the calculation of temperature percentile indices. *Int. J. Climatol.*, **29**, 321–327, https://doi.org/10.1002/joc.1738.

——, L. Alexander, G. C. Hegerl, P. Jones, A. K. Tank, T. C. Peterson, B. Trewin, and F. W. Zwiers, 2011: Indices for monitoring changes in extremes based on daily temperature and precipitation data. *Wiley Interdiscip. Rev.: Climate Change*, **2**, 851–870, https://doi.org/10.1002/wcc.147.

Zhou, L., R. E. Dickinson, Y. Tian, J. Fang, Q. Li, R. K. Kaufmann, C. J. Tucker, and R. B. Myneni, 2004: Evidence for a significant urbanization effect on climate in China. *Proc. Natl. Acad. Sci. USA*, **101**, 9540–9544, https://doi.org/10.1073/pnas.0400357101.

Zhou, Y., and G. Ren, 2009: The Effect of urbanization on maximum, minimum temperatures and daily temperature range in North China. *Plateau Meteor.*, **28**, 1158–1994.

——, and ——, 2011: Change in extreme temperature event frequency over mainland China, 1961–2008. *Climate Res.*, **50**, 125–139, https://doi.org/10.3354/cr01053.

Improved Assimilation of Fengyun-3 Satellite-Based Snow Cover Fraction in Northeastern China

Shuai ZHANG[1], Chunxiang SHI[1,2*], Runping SHEN[1], and Jie WU[3]

1 *School of Geographic Sciences*, *Nanjing University of Information Science & Technology*, *Nanjing* 210044
2 *National Meteorological Information Center*, *China Meteorological Administration*, *Beijing* 100081
3 *Laboratory for Climate Studies*, *National Climate Center*, *China Meteorological Administration*, *Beijing* 100081

(Received December 26, 2018; in final form May 29, 2019)

ABSTRACT

Assimilation of snow cover is an important method to improve the accuracy of snow simulation. However, the effects of snow assimilation are poor because satellite observed snow cover data contain erroneous information, such as cloud contamination. In this paper, an improved approach is proposed to reduce the effects of observational errors during assimilation of snow cover fraction acquired by the Fengyun-3 (FY-3) satellite in northeastern China. A snow depth constraint was imposed on quality control of a snow depth product from a microwave radiation imager. The assimilation experiments were carried out before and after quality control (denoted as SCFDA and SCFDA_WSD, respectively). The snow cover fraction results were evaluated against the Moderate Resolution Imaging Spectroradiometer (MODIS) snow cover products. When assimilating the snow cover fraction with the snow depth constraint (i.e., SCFDA_WSD), substantially larger improvement was obtained than that without such a constraint/quality control (SCFDA), and the deviation and root mean square error of the snow cover fraction were significantly reduced. The assimilation performance was also evaluated against in-situ snow depth observations. The SCFDA_WSD also showed greater improvements during the snow accumulation and snowmelt periods than the SCFDA. The SCFDA_WSD improvements in woodland and shrubland were the most obvious. At different altitudes, the effects of the SCFDA_WSD were basically equivalent, and the deeper the snow depth was, the better the effect. In addition, the SCFDA_WSD method was found in close agreement with the observations during a sudden snowfall event.

Key words: snow cover assimilation, FY-3 satellite-based snow products, snow cover fraction

Citation: Zhang, S., C. X. Shi, R. P. Shen, et al., 2019: Improved assimilation of Fengyun-3 satellite-based snow cover fraction in northeastern China. *J. Meteor. Res.*, **33**(5), 960–975, doi: 10.1007/s13351-019-8205-z.

1. Introduction

Snow serves as an essential component of climate because of its unique characteristics of high albedo, low roughness, and large thermal conductivity. Snow influences soil moisture and temperature, changes the quantity of sensible and latent heat fluxes from the ground to the atmosphere as water vapor, and influences radiation flux (Qian et al., 2003; Hu et al., 2010; Gao et al., 2011). A preliminary climate feedback study on snow cover of the Tibetan Plateau found that snow exerts a positive radiative forcing on the climate (Xiao and Che, 2015). An abnormal distribution of snow in winter will lead to an anomalous circulation response of the East Asian winter monsoon (Chen et al., 2003). Attention should be paid to the effects of snow on both weather and climate (Xu and Wu, 2012a, b; Zuo and Zhang, 2012; Li and Wang, 2013; Zhang R. N. et al., 2015; Zhang et al., 2016; Yang F. et al., 2017; Yang K. et al., 2017).

Various snow-related products mainly originate from ground measurements, satellite remote sensing, and land surface models. Ground measurements have the characteristics of a long time series, but contain uncertainties in spatial representativeness, especially in areas with complex terrain. Satellite remote sensing has global coverage and plays an important role in estimating snow cover.

Supported by the National Natural Science Foundation of China (91437220), National Key Research and Development Program of China (2018YFC1506601), and China Meteorological Administration Special Public Welfare Research Fund (GYHY201506002).

*Corresponding author: shicx@cma.gov.cn.

©The Chinese Meteorological Society and Springer-Verlag Berlin Heidelberg 2019

The snow cover fraction estimates from satellite-based snow observations have been made by visible and near-infrared sensors, including the sensors onboard the Fengyun-3 (FY-3) meteorological satellites. Snow products are considered to be reliable under cloud-free conditions (Hall et al., 2002), and snow mass can be estimated by observations of passive and active microwaves (Stevenson, 2006). However, retrieval algorithms have errors due to an insufficient understanding of the radiation transfer mechanism, and the retrieval algorithms used with satellite remote sensing also have large uncertainties (Bai et al., 2011).

Land surface models represent the interactions and feedback between physical, biological, and chemical processes (Sellers et al., 1997; Pitman, 2003; Yang, 2004) and provide a way to obtain more accurate and spatially continuous snow products. However, a land surface model contains errors caused by forcing data, model dynamic structure, and parameterization. Hence, satellite snow observations are incorporated into land surface models via assimilation. An optimization algorithm is used to fuse the model simulation and observation data to obtain the optimal estimation of snow physical parameters, and the optimal estimation is used as the initial field at the next step and improves the snow simulation (Che, 2006).

In recent years, various techniques have been developed to assimilate observations into land surface models (Liu and Gupta, 2007; Crow and Reichle, 2008; Reichle, 2008; Xia et al., 2019), including the widely used ensemble Kalman filter (EnKF; Evensen, 1994). A number of studies have been carried out on assimilation of snow observations/products (Reichle et al., 2002; De Lannoy et al., 2012; Yatheendradas et al., 2012) with the goal of improving snow state simulations (Su et al., 2008; Yatheendradas et al., 2012; Wang et al., 2016; Xu and Shu, 2016; Toure et al., 2018), estimating accurately the amount of runoff produced by snow (Clark et al., 2006; Zhang et al., 2014; Stigter et al., 2017), improving the forecasting of seasonal temperatures (Lin et al., 2016), and estimating the effects of drought (Kumar et al., 2014; Kumar, 2015).

The snow assimilation result is largely influenced by the observation quality. To improve the effects of snow assimilation, many scientists have used data quality control (Kumar et al., 2015; Stigter et al., 2017) and bias correction (Mocko et al., 2012; Dziubanski and Franz, 2016) on observations. In the process of assimilating the snow cover fraction, snow fusion products and cloud removal algorithms are often utilized to improve the assimilation effects. For example, Liu et al. (2013) assimilated satellite-based snow-depth and snow-cover products with the goal of improving snow forecasting in Alaska, and used an EnKF assimilation approach to assimilate the standard Moderate Resolution Imaging Spectroradiometer (MODIS) data; however, by assimilating the standard MODIS data, the snow cover fraction was found to have little effect on the snow and streamflow predictions. Nonetheless, bias-corrected snow depth (SD) estimates from global snow products and the interpreted snow cover fractions can be useful to improve snow and streamflow predictions, and the most consistent improvements have resulted from reduced cloud coverage and improved snow mapping accuracy. While visible-based snow products are severely affected by cloud and weather factors (Hall et al., 2002), microwave radiation imager products are less affected by relevant factors (Stevenson, 2006). Thus, in the present study, to reduce the effects of erroneous observations caused by cloud cover during the snow cover fraction assimilation process, an improved approach is proposed—an SD product quality control is added for assimilation of the snow cover fraction in northeastern China. The influences of the quality control on snow cover fraction assimilation are analyzed and discussed in this study.

The present study used NASA's Land Information System, China Meteorological Administration (CMA) Land Data Assimilation System (CLDAS) meteorological forcing, and the Noah 3.6 model (Chen et al., 1996, 1997; Chen and Dudhia, 2001; Chen, 2005). Assimilation experiments were conducted by using the FY-3 snow cover fraction data from 2011 to 2014. To avoid the use of erroneous information from snow cover fraction observations, the FY-3 SD data were used to control the quality of the snow cover fraction data to improve the assimilation result. Then, the assimilation performance was evaluated by using the MODIS snow-cover products and in-situ SD observations.

In this paper, the study domain and datasets are presented in Section 2. The model, methods, and experimental design are provided in Section 3. The results from the data assimilation experiments against the MODIS snow cover fraction and in-situ SD measurements are evaluated in Section 4. Finally, the conclusions, discussion, and future work are given in Section 5.

2. Study domain and datasets

2.1 *Study domain*

Northeastern China features a temperate monsoon climate that becomes increasingly cold from south to north and lies in the middle temperate and cold temperate zones. Northeastern China is also one of China's stable snow-covered areas. Snow cover increases rapidly in late

November, with a large amount of snow cover from November to the end of February, which generally peaks in January. The snow begins to melt in the middle of March, which continues until June (Li and Mi, 1983).

2.2 *Data*

The snow cover fraction datasets used for the assimilation in the present study were from the FY-3 product and are derived from different optical remote sensing platforms by using visible light, an infrared scanning radiometer, and a high-resolution spectral imager. In addition, FY-3 SD data were used to constrain the FY-3 snow cover fraction for quality control. Daily observations of the snow cover fraction from MODIS with 0.05° climate model grid (CMG) cells were used to evaluate the snow cover fraction. The study domain included 117 SD stations (Fig. 1) to evaluate the SD results produced by the Noah model during the study period (from 1 September 2011 to 1 September 2014).

2.2.1 *FY-3 snow cover fraction observations*

FY-3 observations of the snow cover fraction were used for the snow cover fraction assimilation in the present study. The FY-3 Multi-Sensor Synergy (MULSS) snow product fuses two results from different optical remote sensing platforms for visible light, an infrared scanning radiometer, and a high-resolution spectral imager. The FY-3 snow cover fraction data are collected globally on a daily basis. The spatial resolution of the snow cover product is 1 km; this product was mapped to 0.05° CMG cells for use in the snow cover fraction assimilation experiments in this study. Examination of the data shows that the FY-3 snow cover fraction accuracy is higher than 90% (Zhang Y. H. et al., 2015; Wu et al., 2018; Zhang et al., 2018).

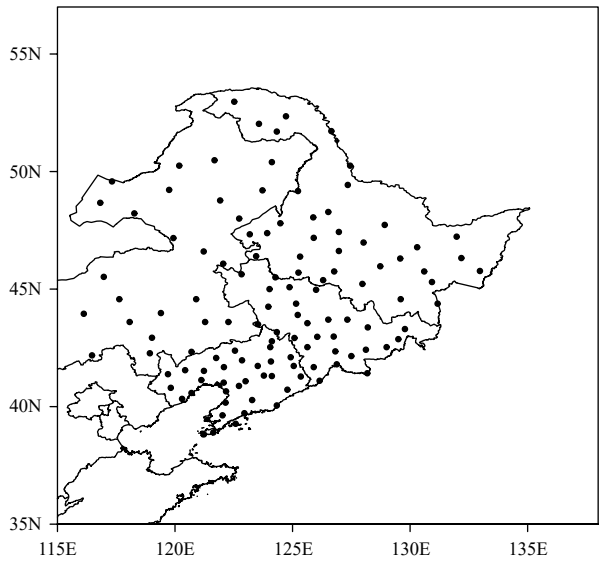

Fig. 1. Study domain covering the Heilongjiang, Jilin, and Liaoning provinces along with the eastern Inner Mongolia Autonomous Region. Black dots represent the snow depth (SD) observation sites.

2.2.2 *FY-3 SD observations*

FY-3 SD data were used to constrain the FY-3 snow cover fraction. The daily products include daily snow water equivalent and SD products for both the Northern and Southern Hemispheres. The microwave radiation imager's correlated channel brightness data were used on a 25-km resolution with azimuth projections of both the Northern and Southern Hemispheres for daily readings (http://satellite.nsmc.org.cn/PortalSite/default.aspx). The FY-3 SD data algorithm is a semiempirical inversion algorithm for snow parameters in China (Jiang et al., 2014). In the research of Liu et al. (2018), the overall accuracy of the FY-3 algorithm was the highest of all the tested algorithms. The accuracy of the SD products is better than 10 cm (Wu et al., 2018).

2.3 *Evaluation datasets*

2.3.1 *MODIS snow cover fraction product*

The snow cover fraction results were evaluated against the MODIS snow cover fraction (MOD10C1) remote-sensing observations. This dataset was generated from snow cover data from the normalized difference snow index in the MOD10A1 dataset. MOD10A1 observations on a 500-m resolution were mapped to 0.05° CMG cells, binned by observation type (e.g., snow, snow-free land, and cloud), and tallied. Snow and cloud cover percentages were generated by computing the ratios of the numbers of snow or cloud observations to the total number of land observations that were mapped into each CMG cell (http://nsidc.org/data). MODIS snow products have an accuracy of approximately 90% without the effects of snow conditions or surface cover types (Hall and Riggs, 2007). Simultaneously, the quality of MODIS snow products in China has been widely verified. The accuracy of MOD10A1 in the northern part of Xinjiang, Northwest China is very high under the clear sky view; the overall accuracy of the MODIS snow cover mapping algorithm is as high as 98.5%, and the snow accuracy reaches 98.2% (Zhang et al., 2008).

2.3.2 *SD station observation*

SD station observations for evaluating snow simulations from the land surface model were provided by the National Meteorological Information Center of China. These SD data are manually observed and reliable. A total of 117 sites with stable data quality were selected in northeastern China in the present study (Fig. 1). These

stations were located in cropland (30.8%), grassland (38.4%), forest (7.7%), woodland (2.7%), shrubland (6.8%), and mixed land (13.6%). Daily SD data from these sites collected from 2011 to 2014 were used in this study. The SD data were converted from centimeter into meter during the evaluation process. The in-situ observations were preprocessed, reliable site observations were selected, and missing records were deleted.

3. Noah model, methods, and experimental design

3.1 *Noah model*

The NCEP of the United States developed, optimized, and improved the Noah land surface model. The Noah model depicts the exchange of water in the snow–vegetation–soil mixing layer and simulates the snow accumulation, sublimation, melting, and associated heat transfer, in which aging, freezing, compacting, and dynamic SD, as well as density change processes, are considered. The model can output snow water equivalent (SWE), SD, and snow density and can be used to calculate snow cover fraction based on the region's empirical ablation curve. Noah versions 3.3–3.6 adopt a snow cover fraction parameterization scheme (Koren et al., 1999) that emphasizes the relationship between the snow coverage rate and SWE. Many scholars have further studied and evaluated this model (e.g., Zhang et al., 2016). The relationships between the snow cover fraction, SWE, and SD were calculated by using Eqs. (1) and (2):

$$\mathrm{RSNOW} = \mathrm{SNEQV}/\mathrm{SNUP}, \tag{1}$$

$$\mathrm{SNCOVR} = 1.0 - [\exp(-\mathrm{SALP}\times\mathrm{RSNOW}) - \mathrm{RSNOW}\times\exp(-\mathrm{SALP})], \tag{2}$$

where SNCOVR is snow cover, SNEQV is SWE, SNUP is the SD threshold when the snow cover fraction equals 1, RSNOW is the ratio of SNEQV to SNUP, and SALP is an adjustable coefficient.

The Noah 3.6 land surface model is taken as the model operator for snow cover fraction assimilation, and SD and SWE are state variables of the land surface model. EnKF is used to assimilate the FY-3 snow cover fraction products into the Noah land surface model, and the state variables of the model are updated. The snow cover ablation curve describes the relationship between snow cover and SD in Noah 3.3–3.6, and is used as an observation operator in the snow cover fraction assimilation by use of Eqs. (1) and (2).

3.2 *Methods*

3.2.1 *EnKF*

In the present study, the Noah 3.6 model was driven by CLDAS-2.0 forcing, and the EnKF (Evensen, 2003) method was used to assimilate the FY-3 snow cover fraction product. Downward shortwave radiation (SW) and precipitation (PRCP) are subject to multiplicative perturbations with a mean of 1 and standard deviations of 0.1 (SW) and 0.5 (PRCP), respectively. Zero-mean additive perturbations are applied to air temperature (T) and longwave radiation (LW) with standard deviations of 0.5 K (T) and 15 W m^{-2} (LW), respectively. The Noah model prognostic variables for SWE and SD are subject to multiplicative perturbations with mean = 1 and standard deviation = 0.01. A total of 25 members and the perturbation method in Table 1 were used for the EnKF runs following the methods of De Lannoy et al. (2012), with an assumption that the disturbance of these variables obeys the normal distribution. The standard deviation of the snow cover fraction in snow cover fraction assimilation was set to 0.1, which was identified according to Su et al. (2008) and Andreadis and Lettenmaier (2006).

3.2.2 *Quality control with the FY-3 SD product*

Without quality control on the snow cover products, erroneous observations may be assimilated, and erroneous results would be produced. Therefore, quality control of snow cover products is very important. The scatter plots of averaged monthly snow cover fraction and SD, based on the FY-3 0.05° daily snow cover fraction and 0.25° SD data from November 2013 to April 2014, are shown in Figs. 2a, c, which reveal some problems as follows: (1) in some grid cells, the snow cover fraction was small (nearly 0), but the SD was very large; and (2) the SD was 0 in some grid cells, but the snow cover fraction was 1.

The above situations in Figs. 2a, c are unreasonable. Therefore, it is necessary to use SD data to control the quality of remote sensing snow cover products. Figure 3 is a flow chart of the process used for FY-3 snow cover fraction quality control. The following unreasonable

Table 1. Ensemble perturbation method used in the snow cover assimilation. SCF denotes snow cover fraction

Variable		Perturbation method	Standard deviation
Model states	SWE	Multiplicative	0.01 (–)
	SD	Multiplicative	0.01 (–)
Forcing	SW	Multiplicative	0.1 (–)
	LW	Additive	15 W m^{-2}
	PRCP	Multiplicative	0.5 (–)
	T	Additive	0.5 K
Observation	SCF	Multiplicative	0.1

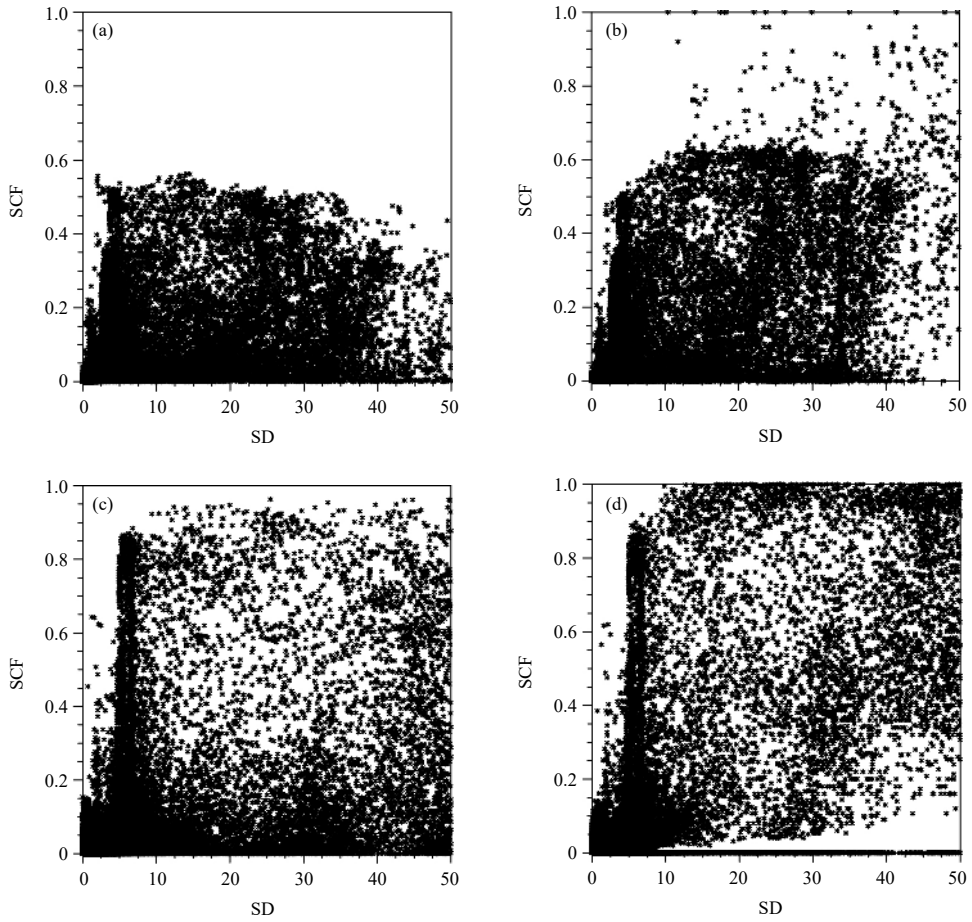

Fig. 2. Scatter plots of snow cover fraction (SCF) and snow depth (SD) from the FY-3 0.05° daily SCF and 0.25° SD (cm) products (a, b) for November 2013–April 2014 and (c, d) in February 2014. (a, c) SCFDA and (b, d) SCFDA_WSD.

snow cover fractions must be assigned default values (−9999.0) to avoid assimilating these unreasonable values into the model: (1) when the snow cover fraction of the grid is 100% but the SD is less than 1 cm, and (2) when the snow cover fraction of the grid is less than 30% but the SD is greater than 10 cm. In Fig. 3, SCF is the original FY-3 snow cover fraction, SCF′ is the processed (quality controlled) FY-3 snow cover fraction, SD is the FY-3 SD, and undef stands for missing value, which is set to −9999.0 in this study.

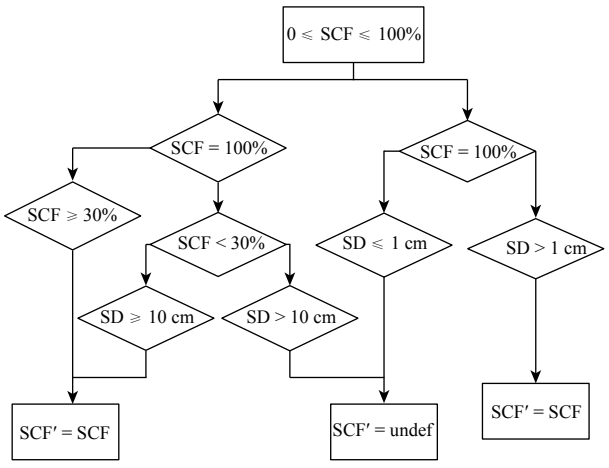

Fig. 3. Flow chart of FY-3 snow cover fraction (SCF) quality control.

3.3 *Experimental setup and evaluation indices*

To illustrate the effects of the quality control on the snow cover fraction assimilation, a series of experiments were carried out by using the FY-3 snow cover fraction, which was assimilated into the Noah model. The CLDAS-V2.0 (CMA Land Data Assimilation System version 2) forcing data were obtained from the National Meteorological Information Center of China, and the Noah 3.6 model was run from arbitrary initial conditions for 21 yr by cycling the CLDAS forcing data from 1 January 2008 to 31 December 2014, with three repetitions for the spin-up. The meteorological forcing analyses with hourly products covering the region of Asia (0°–65°N, 60°–160°E) have a spatial resolution of

0.0625° × 0.0625°, and these forcing data have a good effect on snow simulation in winter (Shi et al., 2018). The Noah 3.6 land surface model was run from 1 January 2008, and began to carry out the FY-3 snow cover fraction assimilation experiments from 1 November 2011. Model runs were carried out at 6.25 km and hourly resolutions. The grid data were processed at the model resolution (0.0625°).

In the FY-3 snow cover assimilation experiment, the surface parameters were first input into the land surface model, and the Noah model was driven by CLDAS-2.0 forcing data to obtain stable initial conditions; then, the snow cover simulation was started. Snow cover fraction products were assimilated at a daily frequency. The snow cover fraction product was assimilated at 1330 local solar time to be close to the overpass time of *FY-3B*. The snow cover fraction was quality controlled from a microwave radiation imager SD product before assimilation, and then EnKF was used to assimilate snow cover products to update the SD and water equivalent in the Noah model, and the assimilation results of snow variables were then examined. Figure 4 shows a flow chart of FY-3 snow cover fraction assimilation.

The FY-3 snow cover fraction assimilation was carried out, and the improved effects of the assimilation were verified against the MODIS remote-sensing satellite products. The SD results were compared with the SD station observations. This paper used the BIAS, root mean square error (RMSE), and correlation coefficient (R) as evaluation indices as follows:

$$\mathrm{BIAS} = N^{-1}\sum_{i=1}^{N}[X_\mathrm{m}(i) - X_\mathrm{o}(i)], \tag{3}$$

$$\mathrm{RMSE} = \sqrt{N^{-1}\sum_{i=1}^{N}[X_\mathrm{m}(i) - X_\mathrm{o}(i)]^2}, \tag{4}$$

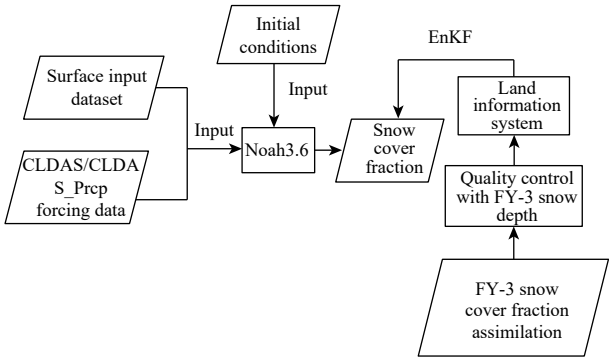

Fig. 4. Flow chart of FY-3 snow cover fraction assimilation.

$$R = \frac{\sum_{i=1}^{N}[X_\mathrm{m}(i) - N^{-1}\sum_{i=1}^{N}X_\mathrm{m}(i)][X_\mathrm{o}(i) - N^{-1}\sum_{i=1}^{N}X_\mathrm{o}(i)]}{\sqrt{\sum_{i=1}^{N}[X_\mathrm{m}(i) - N^{-1}\sum_{i=1}^{N}X_\mathrm{m}(i)]^2}\sqrt{\sum_{i=1}^{N}[X_\mathrm{o}(i) - N^{-1}\sum_{i=1}^{N}X_\mathrm{o}(i)]^2}}, \tag{5}$$

where X_o represents the observation, X_m represents the model value, and N is the total number of observations.

4. Results

4.1 *Quality control of snow cover products*

Scatter plots of monthly average snow cover fraction and snow depth are drawn based on the FY-3 0.05° daily snow cover fraction and 0.25° daily SD products from November 2013 to April 2014 (Figs. 2b, d). The number of irrational points was greatly reduced compared to that before quality control (snow cover fraction is 0, so SD is high). Before quality control, because the snow cover fraction of many points equaled 0, the monthly average snow cover fraction was small (basically below 0.5), which led to an average monthly snow cover fraction of 0 and an average monthly SD above 50 cm. After quality control, such points were reduced, with a less "thick" graphic showing reduced points of SCF = 0 and large SD; these points accounted for only 0.3% of all grid points. Because of the quality control, fewer irrational snow grids were taken into the assimilation.

Figures 5a and 5b show the BIAS histogram of the SD from November 2013 to April 2014 before and after quality control. Clearly, the BIAS in Fig. 5a is mainly concentrated between −0.06 and 0.02 m, whereas the BIAS in Fig. 5b is mainly concentrated between −0.02 and 0.02 m; the large BIAS values are reduced, and the histogram distribution in Fig. 5b is closer to the normal distribution. It is believed that considerable erroneous snow data points with snow cover fraction of 0 and SD of large values were eliminated during the quality control process.

4.2 *Assimilation of FY-3 snow cover fraction with quality control*

4.2.1 *Evaluation against SCF observations*

The FY-3 snow cover fraction assimilation results were evaluated and analyzed by using the MODIS snow cover fraction product. The FY-3 snow cover fraction assimilations with and without quality control (proposed in this paper) are denoted here as SCFDA_WSD and SCFDA, respectively.

Figure 6 shows distributions of the average snow cover fraction in northeastern China during the snow accu-

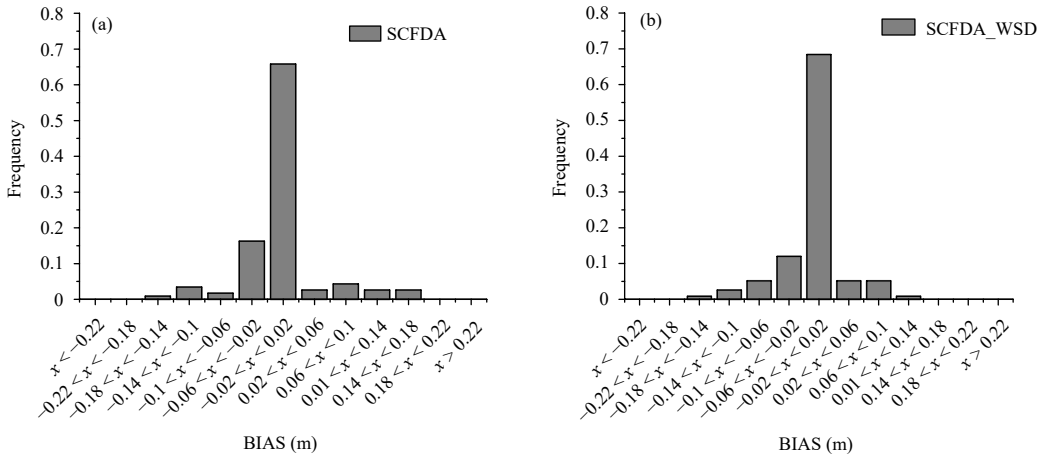

Fig. 5. BIAS histogram of SD output from November 2013 to April 2014. (a) SCFDA and (b) SCFDA_WSD.

mulation period (NDJ: November, December, and January) and the snowmelt period (FMA: February, March, and April) from November 2013 to April 2014. The MODIS snow cover fraction (Figs. 6a, d) shows that the snow cover in northeastern China was mainly concentrated in the western part of the Greater Khingan Mountains in Inner Mongolia and the eastern part of Heilongjiang Province. The snow cover fraction values were mostly within 40%–60%. It was lower in the snowmelt period than in the snow accumulation period. SCFDA_WSD in Figs. 6c, f reduces the snow cover overestimations in Heilongjiang and Jilin provinces. The

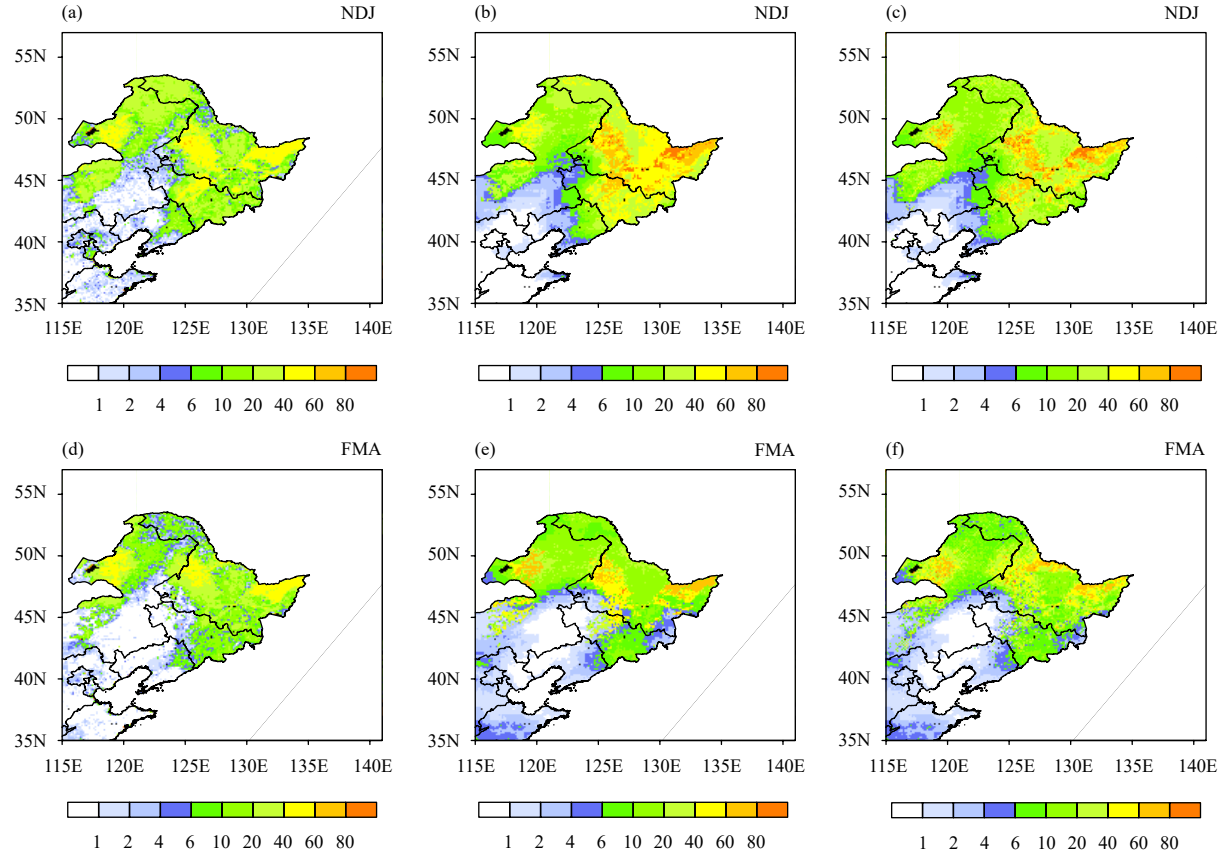

Fig. 6. Distributions of the average snow cover fraction (%) during the (a, b, c) snow accumulation period (NDJ: November, December, and January) and (d, e, f) snowmelt period (FMA: February, March, and April) in northeastern China. (a, d) MODIS observations, (b, e) SCFDA, and (c, f) SCFDA_WSD.

magnitude and spatial distribution of SCFDA_WSD were more consistent with the observations than those of SCFDA in Figs. 6b, e.

The BIAS and RMSE of the SCFDA snow cover fraction were large in northeastern China, and the improvement achieved by SCFDA in northeastern China (BIAS in Figs. 7a, b and RMSE in Figs. 8a, d) was insignificant. It is believed that erroneous snow information was assimilated, resulting in too much snow. In addition, the SCFDA_WSD result was significantly improved in northeastern China (see BIAS in Figs. 7c, d and RMSE in Figs. 8b, e), with reduced snow cover fraction in the overestimated areas and significantly decreased BIAS and RMSE. Compared with SCFDA, the BIAS of snow cover in SCFDA_WSD decreased from 0.0905 to 0.0806 (a decrease by 9.3%) and the RMSE decreased from 0.1782 to 0.1692 (a decrease of 5%). Compared with the Open Loop simulation (Figs. 8c, f), the RMSE of SCFDA_WSD decreased by 23%. When assimilating the snow cover fraction with an SD constraint (SCFDA_WSD), snow cover fraction estimates showed a substantially larger improvement than those produced by assimilating the snow cover fraction without quality control (SCFDA). The erroneous snow information in the FY-3 snow cover fraction was reduced with the FY-3 SD constraint.

Figure 9 shows the time series of the correlation coefficient (R) in Northeast China from December to March 2011–14. Compared with SCFDA, the R values of SCFDA_WSD are significantly improved during these periods. Especially after February, the improvement in R is obvious. Figure 9 shows that SCFDA_WSD has a significantly larger improvement than SCFDA.

4.2.2 *Evaluation against SD observations*

The SD simulation results were evaluated against the station SD data. Figure 10a shows the time series of the average SD of the selected in-situ SD measurements (117 points) in northeastern China from November 2013 to April 2014. In some grids, the assimilated snow cover fraction may be inconsistent with the actual fraction at some stations, resulting in an abnormal SD. The SD BIAS in SCFDA_WSD was reduced more significantly

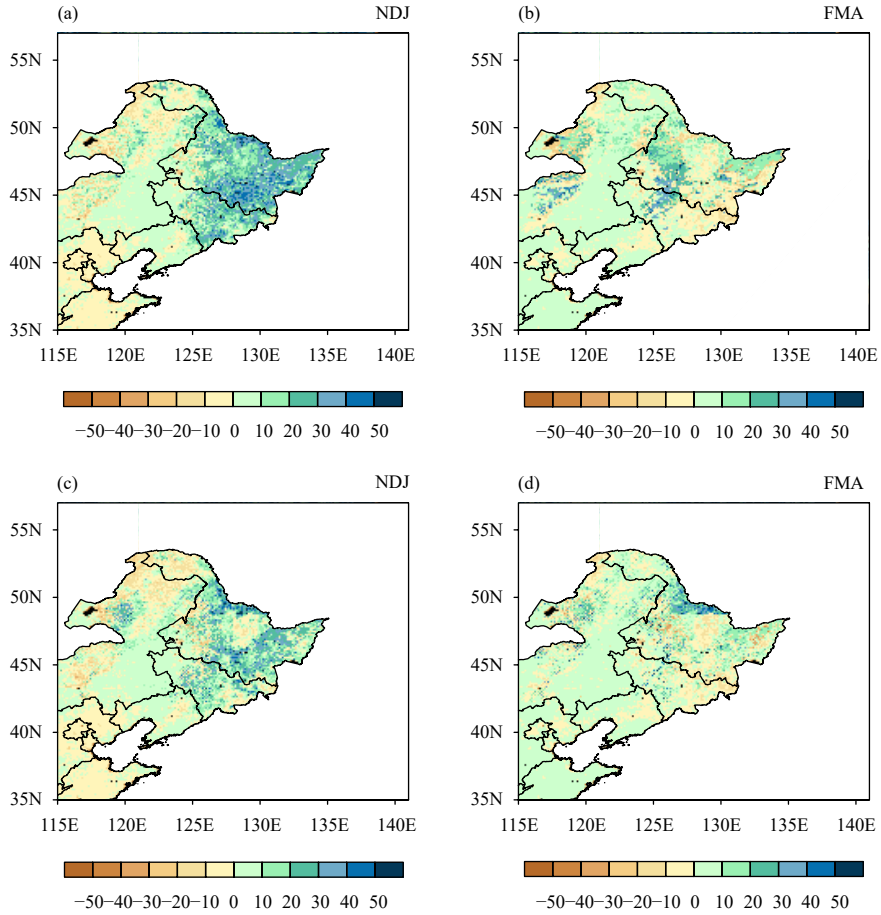

Fig. 7. BIAS distributions of average snow cover fraction (%) during the (a, c) snow accumulation period and (b, d) snowmelt period in northeastern China. (a, b) SCFDA and (c, d) SCFDA_WSD.

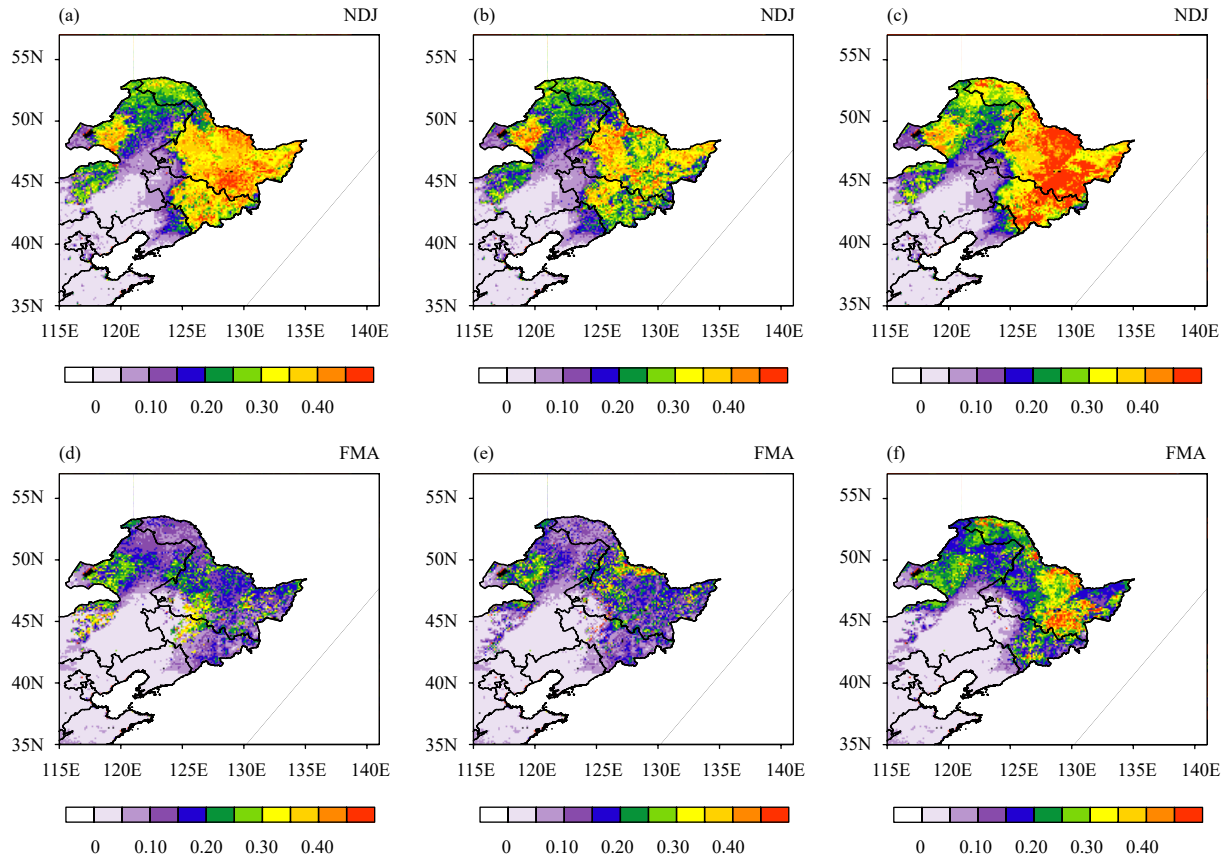

Fig. 8. RMSE distributions of average snow cover fraction during the (a, b, c) snow accumulation period and (d, e, f) snowmelt period in northeastern China. (a, d) SCFDA, (b, e) SCFDA_WSD, and (c, f) Open Loop (OL, simulation).

than that in SCFDA, and SCFDA_WSD successfully improved the monthly SD RMSE from 0.055 m for SCFDA to 0.043 m for SCFDA_WSD; the RMSE decreased by 21.8%, while the correlation coefficient (R) improved from 0.673 for SCFDA to 0.710 for SCFDA_WSD.

4.2.3 *Evaluation against SD observations under different conditions*

The data assimilation performance was evaluated against the SD observations for different stages, land cover types, elevations, and snow depths. The left y axis of Fig. 11 represents the RMSE, and the right y axis represents the number of stations.

Figure 11a shows histograms of the relative RMSE in SCFDA and SCFDA_WSD for each individual month, demonstrating that the SCFDA errors typically started small in November and gradually increased each month to a peak in April. The relative RMSE of SCFDA_WSD was relatively stable. Overall, the SCFDA_WSD achieved significant improvements over SCFDA in terms of SD values during both the snow accumulation and snowmelt periods. The reduced RMSE of the FY-3 snow cover fraction with quality control resulted in a large reduction in errors of simulated SD for all months.

The data assimilation performance was also evaluated against the SD observations for cropland, shrubland, grassland, woodland, mixed land, and forest regions. Figure 11b shows the RMSE histogram for northeastern China from November 2013 to April 2014 for different land cover types. It can be seen that the SCFDA_WSD produced an improvement in SD than the SCFDA for all land cover types. Among the various land cover types, the improvements in woodland and shrubland were the most obvious. The vegetation coverage is the main factor that influences the snow distribution, and the snow cover on woodland and shrubland is scattered. The ability of remote sensing snow products to monitor shredded snow is not sufficient; therefore, SCFDA_WSD plays an important role in areas with low vegetation cover.

Figure 11c shows a histogram of the SD RMSE for the study region from November 2013 to April 2014 for different elevations. For different altitudes, the effect of SCFDA_WSD was basically equivalent. The assimilation of SCFDA_WSD drastically reduced the SD overestimation for all elevations, and the SD RMSE was significantly reduced. The results needed to be further analyzed because samples from higher than 1000 m were

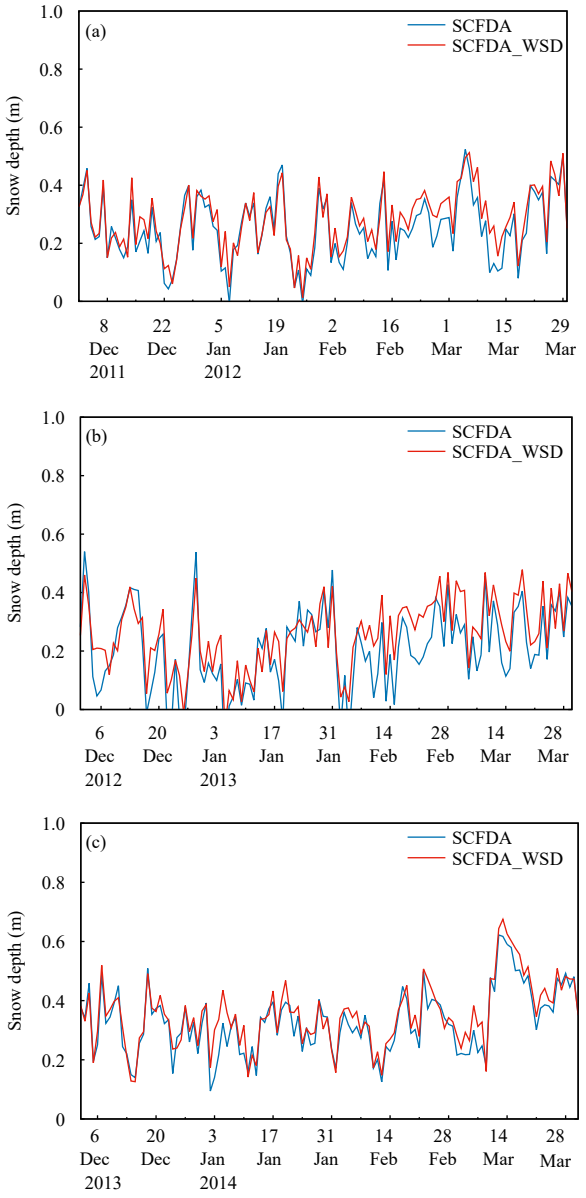

Fig. 9. Time series of the correlation coefficient in Northeast China from December 2011 to March 2014. (a) December 2011 to March 2012, (b) December 2012 to March 2013, and (c) December 2013 to March 2014 .

limited in this study.

Figure 11d shows a histogram of the SD RMSE for northeastern China from November 2013 to April 2014 for different SD ranges. The SCFDA_WSD significantly reduced the RMSE and achieved significantly greater improvements in SD than the SCFDA for all SD ranges. The deeper the SD, the better the effect of the SCFDA_WSD.

Figure 12 shows an SD time series for northeastern China from November 2013 to April 2014 for different land cover types. The data assimilation performance was

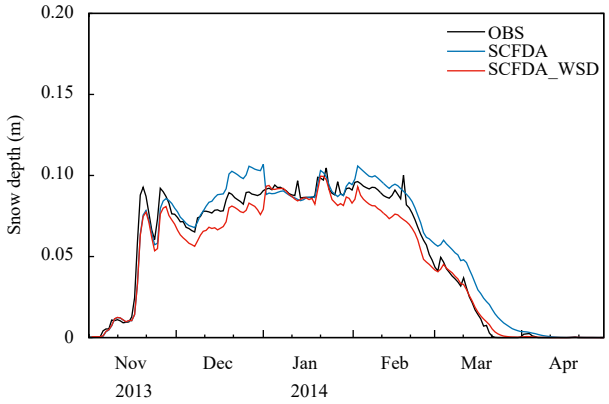

Fig. 10. Time series of regional mean SD in northeastern China from November 2013 to April 2014.

significantly improved for all land cover types. The SCFDA_WSD successfully reduced the SD RMSEs of SCFDA for cropland, forests, grassland, mixed land, shrubland, and woodland (see Table 2 for specific values), respectively. In shrubland (Fig. 12e), where the SD BIAS increased early in January 2014, the SCFDA_WSD also improved, especially after January. Simultaneously, in the end of February 2014, the SD predicted by the SCFDA suddenly increased in the woodland (Fig. 12f), which should have been caused by a sudden increase in the observed snow cover fraction. These SD results were improved by the SCFDA_WSD. Of all land cover types, the improvements in SD for woodland and shrubland were the most obvious throughout the study period, and the SD results in forests were improved in the snow accumulation period.

4.2.4 *Case analysis*

Figure 13 shows the SD time series of Huadian in Jilin Province of China during this period. The SCFDA tended to underestimate the SD, but the SCFDA_WSD effectively produced a snow accumulation curve that was in better agreement with the observations, and the SCFDA_WSD performed very well because of a reduction in the number of erroneous snow cover fraction observations. In addition, the assimilation of the FY-3 snow cover fraction with quality control resulted in a marginal improvement in the snow ablation processes. This case shows that sudden snowfall can be well reflected by the SCFDA_WSD.

5. Conclusions and discussion

5.1 *Conclusions*

To reduce the effects of erroneous observations, which might be caused by cloud cover during the process of as-

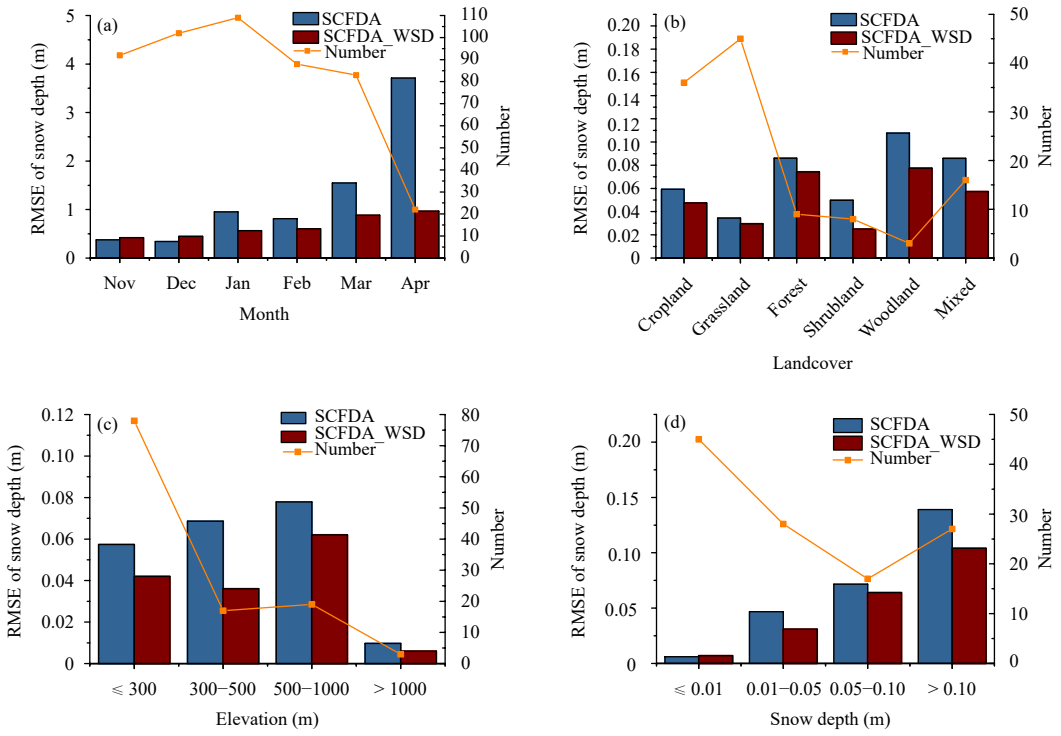

Fig. 11. Histograms of the SD RMSE (SCFDA and SCFDA_WSD) for (a) each individual month, (b) various types of land covers, (c) various elevations, and (d) various SDs. The left *y* axis represents the RMSE, and the right *y* axis represents the number of in-situ SD measurements.

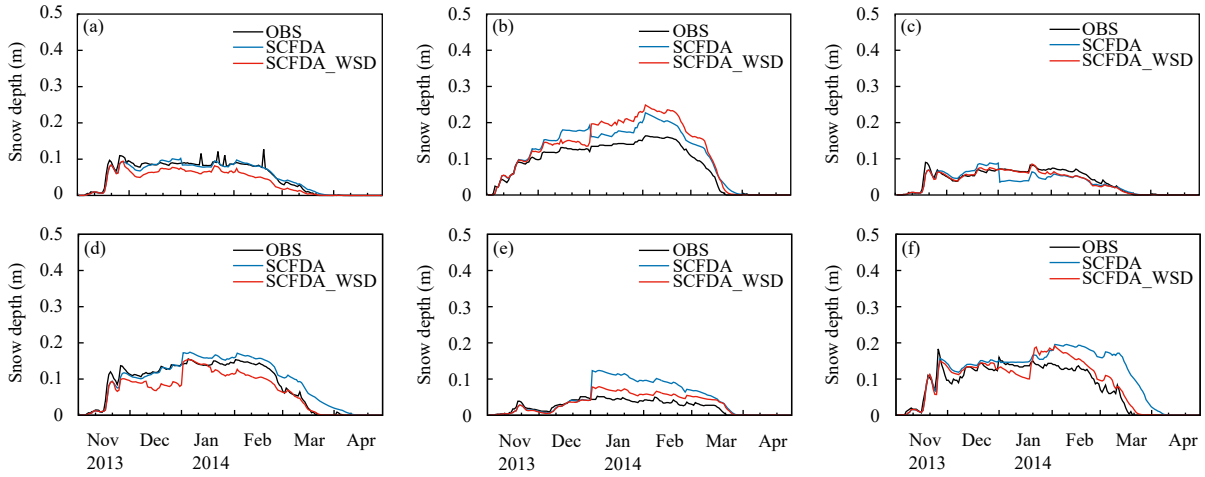

Fig. 12. Time series of mean SD in northeastern China from November 2013 to April 2014 for various land cover types: (a) cropland, (b) forest, (c) grassland, (d) mixed land, (e) shrubland, and (f) woodland .

similating snow cover fraction, an improved approach was proposed in this paper: assimilation of the snow cover fraction with quality control using microwave SD products in northeastern China. The influences of quality control on the snow cover fraction assimilation were analyzed and discussed in this study.

It is concluded that considerable improvements in snow assimilation in northeastern China can be achieved by assimilating the FY-3 satellite-based snow cover fraction products with the proposed quality control. Regarding assimilation of the snow cover fraction with a snow depth constraint (i.e., quality control), the snow cover fraction and SD estimates showed substantial improvements compared to those without the quality control. The method not only performed well for all snow accumulation and snowmelt periods when compared to the observations, but also provided better agreement with the observations during a snowfall event. The SCFDA_WSD

Table 2. Statistics of average SD (m) for different land cover types in northeastern China from November 2013 to April 2014

Land cover	BIAS		RMSE	
	SCFDA	SCFDA_WSD	SCFDA	SCFDA_WSD
Cropland	−0.0011	−0.0141	0.05924	0.04748
Forests	0.0258	0.0318	0.08596	0.07427
Grassland	−0.0052	−0.0034	0.03440	0.02953
Mixed	0.0107	−0.0162	0.08591	0.05723
Shrubland	0.0216	0.0080	0.04979	0.02498
Woodland	0.0310	0.0089	0.10760	0.07743

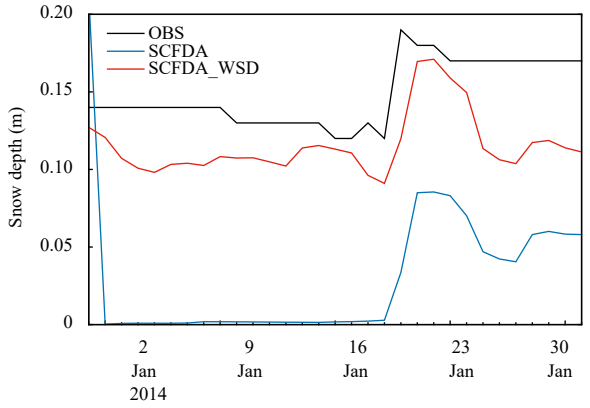

Fig. 13. Time series of assimilated SD and observed data (m) for 19–22 January 2014 in Huadian, Jilin Province of China.

successfully reduced the SD RMSE and increased the correlation coefficient (R).

The SCFDA and SCFDA_WSD errors gradually increased each month, peaking in April, and the relative RMSE of the SCFDA_WSD remained relatively stable. Overall, the SCFDA_WSD produced improved SD estimates over the SCFDA. In addition, the data assimilation performance was evaluated against the SD observations for different stages, land cover types, elevations, and SD ranges. The SCFDA_WSD exhibited significant improvements for all land cover types. The performance improvements in woodland and shrubland were the most obvious. The SD time series for northeastern China from November 2013 to April 2014 for different land cover types showed that the SD values of grassland and shrubland were consistent with the observations, and the SD in forests was better during the snow accumulation period than during the other periods. The SD values in forest and woodland were significantly higher than the observations during the snowmelt period. For different altitudes, the effects of the SCFDA_WSD were basically equivalent. The SCFDA_WSD significantly reduced the SD RMSE and achieved significantly better results than the SCFDA for all SD ranges. The deeper the SD, the better the effect of the SCFDA_WSD.

The focus of this paper was on the assimilation of FY-3 satellite-based snow products in northeastern China. Through quality control of the observations, the influence of the observational errors was reduced during the snow cover fraction assimilation. These results reveal the importance of quality control during snow cover fraction assimilation, which is of great significance for the global use of FY-3 snow cover products. However, this paper focused on only northeastern China and assimilated only one variable—snow cover fraction. In future studies, the assimilation of SD and SWE will be performed and relevant experiments will be further conducted to improve snow and runoff predictions.

5.2 *Discussion*

Figure 12 shows that the SD RMSE of FY-3 snow cover assimilation with quality control (SCFDA_WSD) was less than that of SCFDA for all land cover types. The variability of each station was examined, and it was found that SCFDA_WSD was highly consistent with the observations, so the average RMSE decreased, but the improvement of the average SD was not evident in certain land cover types throughout the snowfall period. The BIAS values in cropland, forests, and mixed land from SCFDA_WSD were not significantly reduced compared to those from SCFDA. The reason might be that cropland had high vegetation coverage, and the snow cover was relatively stable. The quality of the snow cover products was high in stable snow areas, while according to the current threshold, it might have caused excessive quality control, and some real information had been lost. Figure 12b shows that the improvement effect of SCFDA_WSD was obvious at early stage of the snow accumulation period, while the BIAS increased in the late stage of the snow accumulation period. This result was possibly related to the dispersed snow cover at the early stage, but snow cover became gradually stable in the late period in the forest area, and the SCFDA_WSD played an important role in the early snow accumulation period. The effect of SCFDA_WSD on mixed land mainly depended on the proportions of the various land cover types. In addition, the SCFDA results of some cropland, forest, and mixed land sites were significantly different from the observations, although the performance of most stations had been improved. Simultaneously, optimization of the incremental formulas for state variables could be used to further improve the assimilation of snow variables in cropland, forest, and mixed land.

Acknowledgments. The snow depth dataset was provided by the National Meteorological Information Center of the China Meteorological Administration.

Appendix

The FY-3 SD data were evaluated by Ice Mapping System (IMS) snow cover observations to assess the accuracy of the data. IMS Daily Northern Hemisphere Snow and Ice Analysis provided snow and ice-cover maps from February 1997 to October 2019 by the National Snow & Ice Data Center of USA. These maps were derived from a variety of data products, including satellite imagery and *in-situ* data. The data were provided in ASCII text and GeoTIFF formats at three resolutions: 1, 4, and 24 km. IMS snow and ice products depict stable snow cover regions in China with good accuracy, and the annual overall accuracy rate of IMS products is greater than 92% (Liu et al., 2014). The present study used 4-km IMS snow data (http://nsidc.org/data).

Four indices were used to evaluate the FY-3 SD data, including total accuracy (ACC), deviation (BIAS), accuracy (*H*), and false alarm rate (FAR). von Storch and Zwiers (2001), Stevenson (2006), and Wilks (2011) introduced the evaluation method. The calculations were done with Eqs. (A1)–(A4), in which *a*, *b*, *c*, and *d* are the number of pixels that are defined as: "*a*": snow in both the IMS and FY-3 SD products; "*b*": snow-free in the IMS product but snow in the FY-3 product; "*c*": snow in the IMS product but snow-free in the FY-3 product; and "*d*": snow-free in both the IMS and FY-3 products.

$$\mathrm{ACC} = \frac{a+d}{a+b+c+d}, \tag{A1}$$

$$\mathrm{BIAS} = \frac{a+b}{a+c}, \tag{A2}$$

$$H = \frac{a}{a+c}, \tag{A3}$$

$$\mathrm{FAR} = \frac{b}{a+b}. \tag{A4}$$

ACC in Eq. (A1) represents the probability that a pixel is accurately classified, that is, the number of cells that are identical in the IMS product and the FY-3 SD product divided by the total number of pixels. However, this indicator is vulnerable to snow-free pixels and will present a value of 1 when there is no snow in summer. Therefore, an auxiliary discrimination of *H* is needed.

BIAS in Eq. (A2) indicates the ratio of the number of snow pixels detected by the FY-3 product to that detected by the IMS product. If the BIAS is less than 1, the number of pixels detected as snow in the FY-3 product is low. The variable *H* in Eq. (A3) indicates the proportion of snow pixels that account for the correct classification of the FY-3 products from all snow-covered pixels in the IMS product. FAR in Eq. (A4) represents the proportion of snow pixels that have been erroneously classified by the FY-3 product from the total number of snow cells.

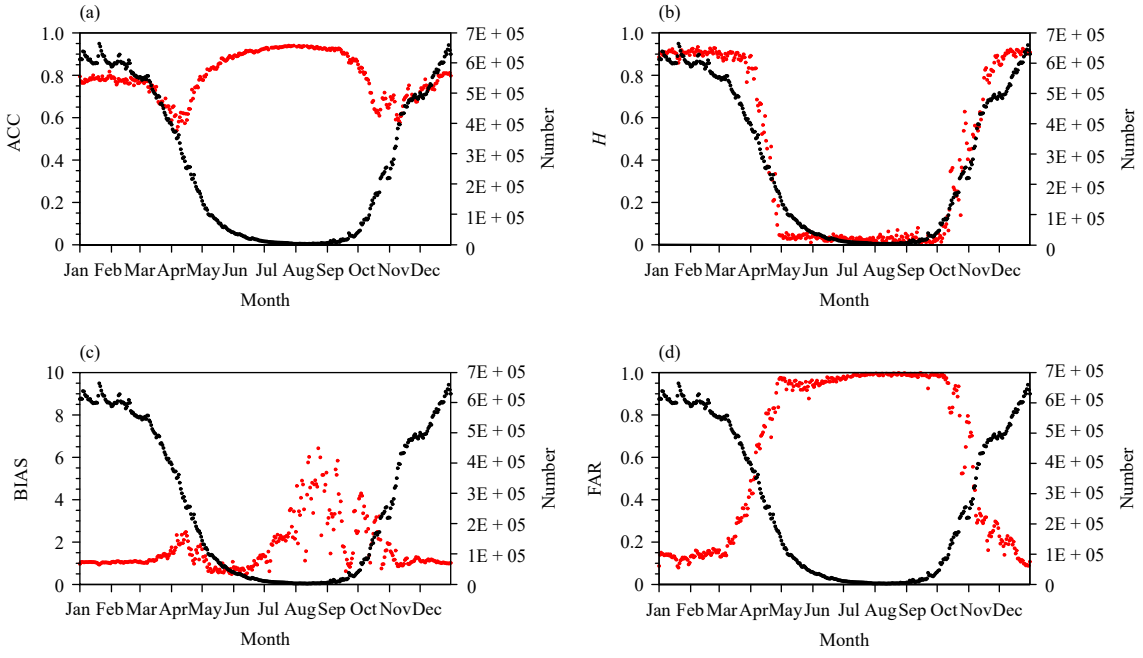

Fig. A1. Comparison between the National Snow & Ice Data Center's Ice Mapping System (IMS) and FY-3 snow products during 2012 and 2014. (a) Total accuracy (ACC), (b) accuracy (*H*), (c) deviation (BIAS), and (d) false alarm rate (FAR). The black "line" in each panel represents the number of snow pixels (corresponding to the right *y* axis) detected by the IMS products, while the red line represents values of each statistical index (corresponding to the left *y* axis).

The FY-3 SD data were evaluated from 2012 to 2014 by using IMS 4-km resolution snow cover data as reference data. The IMS data are snow cover products, and different numbers indicate different land types, where 1, 2, 3, and 4 indicate water, no snow, ice, and snow, respectively. Therefore, FY-3 and IMS are considered to be the same when the following situation occurs: (1) the FY-3 SD is greater than 0 and the IMS grid value equals 4; and (2) the FY-3 SD equals 0 and the IMS grid point value is 2. Likewise, if the FY-3 SD is more than 0 and the IMS value equals 2, or if the FY-3SD is less than 0 and the IMS value is 4, the two products are considered to be different. According to the above rules, the average of the 3-yr time series from 2012 to 2014 (Fig. A1) of the ACC, BIAS, *H*, and FAR indicators were obtained by using Eqs. (A1)–(A4).

In Fig. A1a, the ACC value in northeastern China is consistently high, and it is generally above 0.6 and increases to between 0.8 and 0.9 during the summer, indicating that the FY-3 SD data are consistent with the IMS snow cover data. *H* can be used as an assessment criterion to reduce the effects of snow-free pixels in summer. The value of *H* varied significantly with the season, with a large value during the snow season (approximately 0.9), indicating a high degree of snow consistency in winter (Fig. A1b). During summer, *H* fell to 0. The BIAS in Fig. A1c reflects the ratio of the number of snow-covered pixels detected by the FY-3 SD products to the number detected by the IMS products. The BIAS was found to be nearly 1 from November to March, indicating that the number of snow pixels detected by the two products was identical. At other times, the number of snow pixels detected by FY-3 was slightly higher than that detected by IMS. FAR in Fig. A1d reflects the false-report rate of the FY-3 SD products. FAR was very low during the snow season, almost always remaining at approximately 0.1. However, in summer, the FAR values increased. Figure 12 shows that FY-3 SD data were very consistent with the IMS data during the snow season, and the quality was reliable.

REFERENCES

Andreadis, K. M., and D. P. Lettenmaier, 2006: Assimilating remotely sensed snow observations into a macroscale hydrology model. *Adv. Water Resour.*, **29**, 872–886, doi: 10.1016/j.advwatres.2005.08.004.

Bai, Y. L., X. Li, and X. J. Han, 2011: A review of error problems for land data assimilation systems. *Adv. Earth Sci.*, **26**, 795–804, doi: 10.11867/j.issn.1001-8166.2011.08.0795 . (in Chinese)

Che, T., 2006: Study on passive microwave remote sensing of snow and snow data assimilation method. Ph.D. dissertation, Cold and Arid Regions Environmental and Engineering Research Institute, Chinese Academy of Sciences, Lanzhou, 62 pp. (in Chinese)

Chen, F., 2005: Variability in global land surface energy budgets during 1987–1988 simulated by an off-line land surface model. *Climate Dyn.*, **24**, 667–684, doi: 10.1007/s00382-004-0439-4.

Chen, F., and J. Dudhia, 2001: Coupling an advanced land surface-hydrology model with the Penn State–NCAR MM5 modeling system. Part I: Model implementation and sensitivity. *Mon. Wea. Rev.*, **129**, 569–585, doi: 10.1175/1520-0493(2001)129<0569:CAALSH>2.0.CO;2.

Chen, F., K. Mitchell, J. Schaake, et al., 1996: Modeling of land surface evaporation by four schemes and comparison with FIFE observations. *J. Geophys. Res. Atmos.*, **101**, 7251–7268, doi: 10.1029/95JD02165.

Chen, F., Z. Janjić, and K. Mitchell, 1997: Impact of atmospheric surface-layer parameterizations in the new land-surface scheme of the NCEP mesoscale eta model. *Bound.-Layer Meteor.*, **85**, 391–421, doi: 10.1023/A:1000531001463.

Chen, H. S., Z. B. Sun, and W. J. Zhu, 2003: The effects of Eurasian snow cover anomaly on winter atmospheric general circulation. Part Ⅱ: Model simulation. *Chinese J. Atmos. Sci.*, **27**, 847–860, doi: 10.3878/j.issn.1006-9895.2003.05.06 . (in Chinese)

Clark, M. P., A. G. Slater, A. P. Barrett, et al., 2006: Assimilation of snow covered area information into hydrologic and land-surface models. *Adv. Water Resour.*, **29** , 1209–1221, doi: 10.1016/j.advwatres.2005.10.001.

Crow, W. T., and R. H. Reichle, 2008: Comparison of adaptive filtering techniques for land surface data assimilation. *Water Resour. Res.*, **44**, W08423, doi: 10.1029/2008WR006883.

De Lannoy, G. J. M., R. H. Reichle, K. R. Arsenault, et al., 2012: Multiscale assimilation of advanced microwave scanning radiometer-EOS snow water equivalent and moderate resolution imaging spectroradiometer snow cover fraction observations in northern Colorado. *Water Resour. Res.*, **48**, W01522, doi: 10.1029/2011WR010588.

Dziubanski, D. J., and K. J. Franz, 2016: Assimilation of AMSR-E snow water equivalent data in a spatially-lumped snow model. *J. Hydrol.*, **540** , 26–39, doi: 10.1016/j.jhydrol.2016.05.046.

Evensen, G., 1994: Sequential data assimilation with a nonlinear quasi-geostrophic model using Monte Carlo methods to forecast error statistics. *J. Geophys. Res. Oceans*, **99** , 10,143–10,162, doi: 10.1029/94JC00572.

Evensen, G., 2003: The ensemble Kalman filter: Theoretical formulation and practical implementation. *Ocean Dyn.*, **53**, 343–367, doi: 10.1007/s10236-003-0036-9.

Gao, R., H. L. Zhong, W. J. Dong, et al., 2011: Impact of snow cover and frozen soil in the Tibetan Plateau on summer precipitation in China. *J. Glaciol. Geocryol.*, **33** , 254–260. (in Chinese)

Hall, D. K., and G. A. Riggs, 2007: Accuracy assessment of the MODIS snow products. *Hydrol. Process.*, **21** , 1534–1547, doi: 10.1002/hyp.6715.

Hall, D. K., G. A. Riggs, V. V. Salomonson, et al., 2002: MODIS snow-cover products. *Remote Sens. Environ.*, **83** , 181–194, doi: 10.1016/S0034-4257(02)00095-0.

Hu, Y. M., Y. H. Ding, and F. Liao, 2010: An improvement on

summer regional climate simulation over East China: Importance of data assimilation of soil moisture. *Chinese Sci. Bull.*, **55**, 865–871, doi: 10.1007/s11434-009-0285-1.

Jiang, L. M., P. Wang, L. X. Zhang, et al., 2014: Improvement of snow depth retrieval for FY3B-MWRI in China. *Sci. China Earth Sci.*, **44**, 1278–1292, doi: 10.1007/s11430-013-4798-8.

Koren, V., J. Schaake, K. Mitchell, et al., 1999: A parameterization of snowpack and frozen ground intended for NCEP weather and climate models. *J. Geophys. Res. Atmos.*, **104**, 19569–19585, doi: 10.1029/1999JD900232.

Kumar, S. V., 2015: Assimilation of passive microwave-based soil moisture and snow depth retrievals for drought estimation. *Aerosp. Sci. Technol.*, **45**, 284–293, doi: 10.1016/j.ast.2015.05.021.

Kumar, S. V., C. D. Peters-Lidard, D. Mocko, et al., 2014: Assimilation of remotely sensed soil moisture and snow depth retrievals for drought estimation. *J. Hydrometeor.*, **15**, 2446–2469, doi: 10.1175/JHM-D-13-0132.1.

Kumar, S. V., C. D. Peters-Lidard, K. R. Arsenault, et al., 2015: Quantifying the added value of snow cover area observations in passive microwave snow depth data assimilation. *J. Hydrometeor.*, **16** , 1736–1741, doi: 10.1175/JHM-D-15-0021.1.

Li, H. Y., and J. Wang, 2013: Key research topics and their advances on modeling snow hydrological processes. *J. Glaciol. Geocryol.*, **35**, 430–437, doi: 10.7522/j.issn.1000-0240.2013.0051. (in Chinese)

Li, P. J., and D. S. Mi, 1983: Distribution of snow cover in China. *J. Glaciol. Geocryol.*, **5**, 9–18. (in Chinese)

Lin, P. R., J. F. Wei, Z.-L. Yang, et al., 2016: Snow data assimilation-constrained land initialization improves seasonal temperature prediction. *Geophys. Res. Lett.*, **43**, 11423–11432, doi: 10.1002/2016GL070966.

Liu, X., X. Jin, and C. Q. Ke, 2014: Accuracy evaluation of the IMS snow and ice products in stable snow covers regions in China. *J. Glaciol. Geocryol.*, **36**, 500–507, doi: 10.7522/j.issn.1000-0240.2014.0060.

Liu, X. J., L. M. Jiang, S. L. Wu, et al., 2018: Assessment of methods for passive microwave snow cover mapping using FY-3C/MWRI data in China. *Remote Sens.*, **10** , 524, doi: 10.3390/rs10040524.

Liu, Y. Q., and H. V. Gupta, 2007: Uncertainty in hydrologic modeling: Toward an integrated data assimilation framework. *Water Resour. Res.*, **43**, W07401, doi: 10.1029/2006WR005756.

Liu, Y. Q., C. D. Peters-Lidard, S. Kumar, et al., 2013: Assimilating satellite-based snow depth and snow cover products for improving snow predictions in Alaska. *Adv. Water Resour.*, **54**, 208–227, doi: 10.1016/j.advwatres.2013.02.005.

Mocko, D. M., C. D. Peters-Lidard, S. Kumar, et al., 2012: Changes to drought metrics within the North American Land Data Assimilation System (NLDAS) from the assimilation of soil moisture and snow. AGU Fall Meeting. Available at http://adsabs.harvard.edu/abs/2012AGUFM.H31L.07M.

Pitman, A. J., 2003: The evolution of, and revolution in, land surface schemes designed for climate models. *Int. J. Climatol.*, **23**, 479–510, doi: 10.1002/joc.893.

Qian, Y.-F., Y. Zhang, and Y.-Q. Zheng, 2003: Impacts of the Tibetan Plateau snow anomaly in winter and spring on precipitation in China in spring and summer. *Arid Meteor.*, **21**, 1–7. (in Chinese)

Reichle, R. H., 2008: Data assimilation methods in the Earth sciences. *Adv. Water Resour.*, **31**, 1411–1418, doi: 10.1016/j.advwatres.2008.01.001.

Reichle, R. H., D. B. McLaughlin, and D. Entekhabi, 2002: Hydrologic data assimilation with the ensemble Kalman filter. *Mon. Wea. Rev.*, **130**, 103–114, doi: 10.1175/1520-0493(2002)130<0103:HDAWTE>2.0.CO;2.

Sellers, P. J., R. E. Dickinson, D. A. Randall, et al., 1997: Modeling the exchanges of energy, water, and carbon between continents and the atmosphere. *Science*, **275** , 502–509, doi: 10.1126/science.275.5299.502.

Shi, C. X., S. Zhang, S. Sun, et al., 2018: Effect of improved precipitation CLDAS on snow simulation in China. *Meteor. Mon.*, **44** , 985–997, doi: 10.7519/j.issn.1000-0526.2018.08.001. (in Chinese)

Stevenson, M., 2006: Book review on *Ian T. Jolliffe, David B. Stephenson, Forecast Verification: A Practitioner's Guide in Atmospheric Science, John Wiley and Sons, Chichester (2003), ISBN: 0-471-49759-2. Int. J. Forecasting*, **22** , 403–405, doi: 10.1016/j.ijforecast.2005.11.002.

Stigter, E. E., N. Wanders, T. M. Saloranta, et al., 2017: Assimilation of snow cover and snow depth into a snow model to estimate snow water equivalent and snowmelt runoff in a Himalayan catchment. *Cryosphere*, **11**, 1647–1664, doi: 10.5194/tc-11-1647-2017.

Su, H., Z. L. Yang, G.-Y. Niu, et al., 2008: Enhancing the estimation of continental-scale snow water equivalent by assimilating MODIS snow cover with the ensemble Kalman filter. *J. Geophys. Res. Atmos.*, **113** , D08120, doi: 10.1029/2007JD009232.

Toure, A. M., R. H. Reichle, B. A. Forman, et al., 2018: Assimilation of MODIS snow cover fraction observations into the NASA catchment land surface model. *Remote Sens.*, **10**, 316, doi: 10.3390/rs10020316.

von Storch, H., and F. W. Zwiers, 2001: *Statistical Analysis in Climate Research*. Cambridge University Press, Cambridge, 3–10.

Wang, H. W., C. L. Huang, J. L. Hou, et al., 2016: Estimation of snow depth from multi-source data fusion based on data assimilation algorithm. *Geomatics Inf. Sci. Wuhan Univ.*, **41**, 848–852, doi: 10.13203/j.whugis20140568. (in Chinese)

Wilks, D. S., 2011: *Statistical Methods in the Atmospheric Sciences*. Elsevier/Academic Press, Amsterdam, 380 pp.

Wu., S. L., C. Liu, and J. Chen, 2018: Overview of FY-3 snow monitoring products and applications in remote sensing service. *Aerosp. Shanghai*, **35**, 60–65, doi: 10.19328/j.cnki.1006-1630.2018.02.007. (in Chinese)

Xia Y. L., Z. C. Hao, C. X. Shi, et al., 2019: Regional and global land data assimilation systems: Innovations, challenges, and prospects. *J. Meteor. Res.*, **33**, 159–189, doi: 10.1007/s13351-019-8172-4.

Xiao, L., and T. Che, 2015: Preliminary study on snow feedback to the climate system in the Tibetan Plateau. *Remote Sens. Technol. Appl.*, **30** , 1066–1075, doi: 10.11873/j.issn.1004-0323.2015.6.1066. (in Chinese)

Xu, J. H., and H. Shu, 2016: DEnKF-based assimilation of MODIS-derived snow cover products into common land model considering the model sub-grid heterogeneity. *Geomatics Inf. Sci. Wuhan Univ.*, **41** , 156–162, doi: 10.13203/j.whugis

20140039.

Xu, L. Y., and B. Y. Wu, 2012a: Two physical effects of Eurasian snow cover on the late-spring and early-summer rainfall in South China of 2010. *Chinese J. Atmos. Sci.*, **36** , 271–282, doi: 10.3878/j.issn.1006-9895.2011.11054. (in Chinese)

Xu, L. Y., and B. Y. Wu, 2012b: Relationship between Eurasian snow cover and late-spring and early-summer rainfall in China in 2010. *Plateau Meteor.*, **31**, 706–714. (in Chinese)

Yang, F., H. Lu., K. Yang., et al., 2017: Evaluation of multiple forcing data sets for precipitation and shortwave radiation over major land areas of China. *Hydrol. Earth Syst. Sci.*, **21**, 5805–5821, doi: 10.5194/hess-21-5805-2017.

Yang, K., T. T. Hu, and C. H. Wang, 2017: A numerical study on the relationship between the spring–winter snow cover anomalies over the northern and southern Tibetan Plateau and summer precipitation in East China. *Chinese J. Atmos. Sci.*, **41**, 345–356, doi: 10.3878/j.issn.1006-9895.1604.16119 . (in Chinese)

Yang, Z.-L., 2004: Modeling land surface processes in short-term weather and climate studies. *Observation, Theory and Modeling of Atmospheric Variability*, X. Zhu, X. F. Li, M. Cai, et al., Eds., Singapore, World Scientific, 288–313, doi: 10.1142/9789812791139_0014.

Yatheendradas, S., C. D. Peters Lidard, V. Koren, et al., 2012: Distributed assimilation of satellite-based snow extent for improving simulated streamflow in mountainous, dense forests: An example over the DMIP2 western basins. *Water Resour. Res.*, **48**, W09557, doi: 10.1029/2011WR011347.

Zhang, R. H., R. N. Zhang, and Z. Y. Zuo, 2016: An overview of wintertime snow cover characteristics over China and the impact of Eurasian snow cover on Chinese climate. *J. Appl. Meteor. Sci.*, **27** , 513–526, doi: 10.11898/1001-7313.20160501. (in Chinese)

Zhang, R. N., R. H. Zhang, and Z. Y. Zuo, 2015: Winter snow cover variability over China and its relation to Arctic Oscillation. *Chinese J. Atmos. Sci.*, **39** , 634–642, doi: 10.3878/j.issn.1006-9895.1405.14170. (in Chinese)

Zhang, S., C. X. Shi, X. Liang, et al., 2018: Assessment of FY-3 snow cover product. *Remote Sens. Technol. Appl.*, **33**, 35–46, doi: 10.11873/j.issn.1004-0323.2018.1.0035. (in Chinese)

Zhang, X.-T., X.-D. Huang, T.-G. Liang, et al., 2008: Accuracy analysis for MODIS snow data of MOD10A1 in a pastoral area in northern Xinjiang. *Acta Pratacult. Sinica*, **17**, 110–117, doi: 10.3321/j.issn:1004-5759.2008.02.016 . (in Chinese)

Zhang, Y.-F., T. J. Hoar, Z.-L. Yang, et al., 2014: Assimilation of MODIS snow cover through the data assimilation research testbed and the community land model version 4. *J. Geophys. Res. Atmos.*, **119**, 7091–7103, doi: 10.1002/2013JD021329.

Zhang, Y. H., W. Ren, T. Cao, et al., 2015: Method of snow multi-threshold comprehensive discrimination with FY-3/VIRR data. *Remote Sens. Technol. Appl.*, **30** , 1076–1084, doi: 10.11873/j.issn.1004-0323.2015.6.1076. (in Chinese)

Zuo, Z. Y., and R. H. Zhang, 2012: The anomalies of spring rainfall in China and its relation with tropical pacific SST and Eurasian snow. *Chinese J. Atmos. Sci.*, **36** , 185–194, doi: 10.3878/j.issn.1006-9895.2012.01.14. (in Chinese)

Tech & Copy Editor: Zhirong CHEN

Journal of the Meteorological Society of Japan, Vol. 97, No. 1, pp. 0−0, 2019
DOI:10.2151/jmsj.2019-004

Comparison of Surface Air Temperature between Observation and Reanalysis Data over Eastern China for the Last 100 Years

Siqi ZHANG

Chinese Academy of Meteorological Sciences, China Meteorological Administration, China
Laboratory for Climate Studies, National Climate Center, China Meteorological Administration, China

Guoyu REN

Department of Atmospheric Science, School of Environmental Studies, China University of Geosciences, China
Laboratory for Climate Studies, National Climate Center, China Meteorological Administration, China

Yuyu REN

Laboratory for Climate Studies, National Climate Center, China Meteorological Administration, China

and

Xiubao SUN

Laboratory for Climate Studies, National Climate Center, China Meteorological Administration, China

(Manuscript received 6 May 2018, in final form 10 October 2018)

Abstract

This study aims to improve the understanding of the differences in surface air temperature data between observations and reanalysis since the beginning of the 20th century and addresses the reanalysis data error. The anomaly correlation, standard deviation, and linear trend of temperature during 1909–2010 in Eastern China were analyzed based on the homogenized observation data obtained from 16 stations and two sets of 20th century monthly mean surface air temperature reanalysis data (20CR and ERA20C). The results show that the inter-annual and decadal variabilities were consistent between reanalysis and observations in Eastern China after 1979. The reanalysis data exhibited a large fluctuation during the 1960s. The average 20CR temperature was lower than the observations during 1920–1950. The inter-annual and decadal variability for winter and spring were consistent with the observations. The correlation and standard deviation ratio between the reanalysis and observations demonstrated a high consistency of their inter-annual variability and dispersion. The ERA20C data were generally closer to the observations than the 20CR data for the period 1979–2010. The linear trends of surface air temperature showed clear warming in both reanalysis datasets and the observations but the reanalysis trends were significantly smaller than the observational trends for annual mean temperature and most of the seasonal mean temperatures after the 1950s. Overall, ERA20C was generally closer to the observational temperatures than 20CR during 1909–2010, but this consistency does not necessarily indicate ERA20C's suitability for climate change research because of the systematic bias referenced to the observational data.

Corresponding author: Guoyu Ren, Laboratory for Climate Studies, National Climate Center, China Meteorological Administration, Beijing 100081, China
E-mail: guoyoo@cma.gov.cn, zhangsq@cma.gov.cn
J-stage Advance Published Date: 29 October 2018

©The Author(s) 2019. This is an open access article published by the Meteorological Society of Japan under a Creative Commons Attribution 4.0 International (CC BY 4.0) license.

Keywords observation; reanalysis; Eastern China; temperature; 20th century; inter-comparison

1. Introduction

A series of reanalysis datasets have been developed since the 1990s, such as NCEP–NCAR (Kalnay et al. 1996), NCEP–DOE (Kanamitsu et al. 2002), CFSR (Saha et al. 2010), NASA–MERRA (Rienecker et al. 2011), ERA-40 (Uppala et al. 2005), ERA-Interim (Dee et al. 2011; Uppala et al. 2008), JRA-25 (Onogi et al. 2007), and JRA-55 (Kobayashi et al. 2015). However, the earliest reanalysis product began in 1948 and therefore could not be used in climate change research that focuses on the early 20th century. However, in recent years, the United States and the European Union implemented a series of atmospheric reanalysis projects that span the entire 20th century or even earlier than that. The United States 20CR (Compo et al. 2011) is an outcome of the 20th Century Reanalysis Project from NOAA, and the European ERA20C (Poli et al. 2013) is an outcome of the ERA-CLIM project from ECMWF. The reanalysis data have advantages in terms of coverage in oceanic, polar, and plateau regions and length of time series. However, they also have the disadvantages of incorporating the errors from the numerical prediction model, the assimilation process, and observation system change factors (Bengtsson et al. 2004; Zhao et al. 2010; Thorne and Vose 2010; Zhao et al. 2015; Parker 2016; Lahoz and Schneider 2014; Zhou et al. 2018). To avoid the false trends caused by changes in the observation system and internal incoordination of data, 20CR assimilates surface observations of synoptic pressure, monthly sea surface temperature, and sea ice distribution, whereas ERA20C assimilates observations of surface pressure and surface marine winds only. The surface air temperature is not as reliable as air pressure partly because of the uncertainties associated with the changes in the observational system (Kistler et al. 2001). However, the issue of how to evaluate the potential of reanalysis data over 100 years for climatology and climate change research has not been given sufficient attention because of the lack of high-quality observation data at the regional scale.

In recent years, many scholars have examined the global and regional scale changes and evaluated the applicability of 20CR and ERA20C. Ferguson and Villarini (2012) found that the temperature of 20CR in the central region of the United States was discontinuous from 1940 to 1950, but the temperature of observation data was continuous in the same time period. Fan and Liu (2013) indicated the consistency of climatology in the southern hemisphere between 20CR and the observation data during 1979–2010 but found significant differences from that of HADSLPv2 during 1897–1920. Poli et al. (2016) indicated that the ERA20C ranging from the north to south latitudes within 65° was 1 K colder than the ship observation data at night during 1900–2010. Studies have also focused on China. For example, by comparing with other reanalysis data, Song and Zhou (2012) evaluated 20CR with respect to the East Asian summer monsoon variability and found a higher consistency with other reanalysis data, but it failed to reveal the decadal-scale variation of weakened East Asia summer monsoon since the late 1970s. Liu and Fan (2014) compared surface air temperature between 20CR and observation data from 160 stations in China and found that the correlations were generally better for temperature than for precipitation. Zhou et al. (2018) discussed the main factors influencing regional warming modeling in current reanalysis products. Their results showed that 80 % of the temperature differences between reanalysis and observations could be attributed to station and model-grid elevation differences. The aforementioned studies pointed out the uncertainties of 20CR and ERA20C in different regions during different periods. These may be due to the limited assimilation sources, which produced different results for different periods and regions (Xu et al. 2001). Therefore, it remains necessary at present to evaluate the applicability of the long-term temperature characteristics and linear trends of these two reanalysis datasets in China.

The data inhomogeneity of some observational stations may be caused by the instrumentation, the different periods of observation records, and station relocations. These issues have led to uncertainties in the study of warming during the 20th century. Considering the adjustments for inhomogeneity, there are three main Chinese temperature observation datasets with long time series. Tang et al. (2005, 2009) used the mean values of maximum and minimum temperatures, avoiding the discontinuity caused by using different time observation records, to calculate averages as monthly and annual mean values, but did not account for the inhomogeneity caused by station relocation. Li et al. (2010) used long time series observation data from several neighboring countries, and homogenous

data from the national reference climate stations and basic meteorological stations to establish annual and seasonal mean temperature anomaly sequences from 1900, but the inhomogeneities caused by station relocation were not resolved. Cao et al. (2013) used data from 18 relatively integrated stations in Eastern China and adjusted for the inhomogeneities caused by station relocation to establish the annual average temperature anomaly sequence. It showed that the linear trend of unadjusted surface air temperature was slightly smaller than that of adjusted surface air temperature by ~ 0.23°C/100a from 1909–2010. It means that the inhomogeneous time series appeared to underestimate warming trends during the last 100 years and illustrated the uncertainty of inhomogenization on the assessed linear trend at a 100-year scale. This dataset is considered to be the most suitable and homogenized observation data for use in the temperature change studies at the 100-year scale in Eastern China; however, the urbanization bias from station observations are exaggerated in the data series because of the homogenization procedure and the consideration of observations of only a small number of big cities (Ren et al. 2017).

Because of the uncertainty of reanalysis data in climate change research especially in estimates of linear trends of climatic variables including surface air temperature, there is a need to evaluate the reliability of reanalysis data by comparing with high-quality, long-term observational data. Based on the temperature dataset of Cao et al. (2013), the surface air temperature of two reanalysis datasets from 1909 to 2010 (20CR and ERA20C) were evaluated in the current study. Because there was a larger positive deviation in the linear trend of long-term observation temperature by Cao et al. (2013), the results of Tang et al. (2005, 2009) were also used as a reference for the linear trends. This study is to assess the reliability of the two sets of reanalysis data in estimating long-term trends of surface air temperature. In addition, this study is different from the previous works. First, the 20CR and ERA20C data series from 1909 to 2010 are much longer than those usually used in previous researches; second, we used a new homogenized 100+ year surface air temperature data series to evaluate the applicability of these two reanalysis datasets in the monitoring and detection of long-term temperature change in China, and in particular focused our attention on the long-term trends of temperature. The research findings will provide an indication of the reliability and applicability of the two long-term reanalysis datasets in Eastern China which is important for future climate change research.

2. Data and methods

To compare the observation and reanalysis data, it was necessary to first establish annual and seasonal mean temperature sequences from 20CR and ERA20C in the location of the observation stations. The difference of annual and seasonal mean surface air temperature anomalies between reanalysis data (referred to as REA) and homogenized observation data (referred to as ADJ), and the standard deviations, correlations and linear trends of the annual and seasonal mean surface air temperature of the two reanalysis datasets and ADJ, were then analyzed and compared. In this study, we focused on objectively assessing the applicability of the surface air temperature from the two reanalysis datasets for Eastern China. The monthly mean observation data used in this study were produced by the NMIC/CMA in 2013 (Cao et al. 2013). The data were collected from different sources of long sequence observations, then merged together and quality controlled, using the standard sequence method, partial least-squares regression, and the multiple regression method for interpolation to provide data from missing stations and periods. The extended version of the penalized maximal *F*-test (PMFred) algorithm and the penalized maximal *T*-test (PMTred) algorithm (Wang 2008) were used as the main test methods. In addition, two-phase regression (Easterling and Peterson 1995) and the sliding *T*-test homogenization method were applied as the auxiliary inspection methods, and metadata were used to confirm and correct the discontinuities. The number of observation stations was 4, 12 and 16 before 1900 and in 1909 and 1916, respectively, so we selected 1909–2010 as the research period for observational temperature. There were 12 stations available for use before 1916. The 16 stations under a 1000 m altitude in Eastern China (Fig. 1) were selected in this study because the length of time of observational records was unequal. In the linear trends analysis, we also used the results of Tang et al. (2005, 2009) (henceforth ADJ-T), who used data from a total of 600 and 231 stations in Eastern China after and before 1950, respectively.

The monthly mean temperatures of the two reanalysis datasets, 20CR (monthly mean from 1871 to 2012) and ERA20C (monthly mean from 1900 to 2010) collectively referred to as REA, were derived from NOAA and ECMWF, respectively. The spatial resolution of 20CR is 2.0° × 2.0° and that of ERA20C is 1.5° × 1.5°. The grid box center locations nearest to the observational stations were selected for the comparison

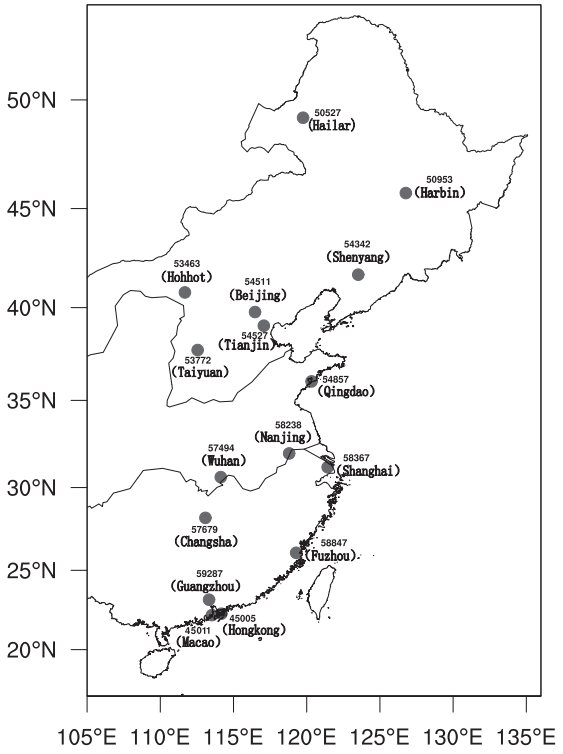

Fig. 1. Distribution of the 16 observation stations in eastern China.

with observation station data. We also selected 1909–2010 as the research period.

The annual mean temperature was calculated from the observation and reanalysis data based on 12 monthly mean values. When calculating the mean temperature sequences of Eastern China, some stations located in close proximity (such as Beijing and Tianjin, Hong Kong, Macao, and Guangzhou) were averaged firstly and then an arithmetic average was calculated between the time series and the other station series. The correlation between ERA20C and ADJ was compared with the correlation between 20CR and ADJ, and the standard deviations and linear trends of REA and ADJ were also compared in the manuscript.

The standard deviation ratio (*SDR*) represents the similarity in standard deviation between REA and ADJ (The overbars indicate mean value):

$$SDR = \frac{\sqrt{\frac{1}{n}\sum_{i=1}^{n}(REA_i - \overline{REA})^2}}{\sqrt{\frac{1}{n}\sum_{i=1}^{n}(ADJ_i - \overline{ADJ})^2}}. \quad (1)$$

The correlation coefficient (R) between REA and ADJ represents the degree of similarity in the annual variability:

$$R = \frac{\sum_{i=1}^{n}(REA_i - \overline{REA})(ADJ_i - \overline{ADJ})}{\sqrt{\sum_{i=1}^{n}(REA_i - \overline{REA})^2}\sqrt{\sum_{i=1}^{n}(ADJ_i - \overline{ADJ})^2}}. \quad (2)$$

A value of *SDR* or R close to 1 reflects a close similarity between REA and ADJ.

The significant correlation coefficient of climate trend (S) represents the quantitative degree of temperature rise and fall under climate change.

$$S = \frac{\sum_{i=1}^{n}(REA_i - \overline{REA})\left(i - \frac{n+1}{2}\right)}{\sqrt{\sum_{i=1}^{n}(REA_i - \overline{REA})^2}\sqrt{\sum_{i=1}^{n}\left(i - \frac{n+1}{2}\right)^2}}. \quad (3)$$

According to the regression theory, the trend value (a) is calculated as follows:

$$\alpha = S\frac{\sqrt{\frac{1}{n}\sum_{i=1}^{n}(REA_i - \overline{REA})^2}}{\sqrt{\frac{1}{n}\sum_{i=1}^{1}\left(i - \frac{n+1}{2}\right)^2}}. \quad (4)$$

3. Comparison of ADJ and REA

3.1 Comparison of average temperatures

The annual and seasonal mean surface air temperature anomalies over Eastern China from the ADJ and REA datasets (Fig. 2) demonstrated that the reanalysis datasets describe the observational temperature characteristics in the inter-annual variation of the 20th century. The temperature of ERA20C was significantly higher than that of ADJ from 1965 to 1975. Furthermore, the annual mean temperature of 20CR was 1°C lower than ADJ in 1920–1950, with a large fluctuation in 1963–1968. The anomaly and variation characteristics for ERA20C were generally closer to ADJ than those of 20CR. The annual mean anomaly characteristics of REA and ADJ were also reflected in the seasonal anomalies; REA was 0.5–1°C lower than ADJ in summer and autumn between 1920 and 1950, and ERA20C was higher than ADJ in winter before the 1930s and lower than ADJ before 1925 in spring. In addition, the annual mean temperature of ERA20C was higher than ADJ during 1965–1975, which was mainly affected by aestival factors. The fluctuation in

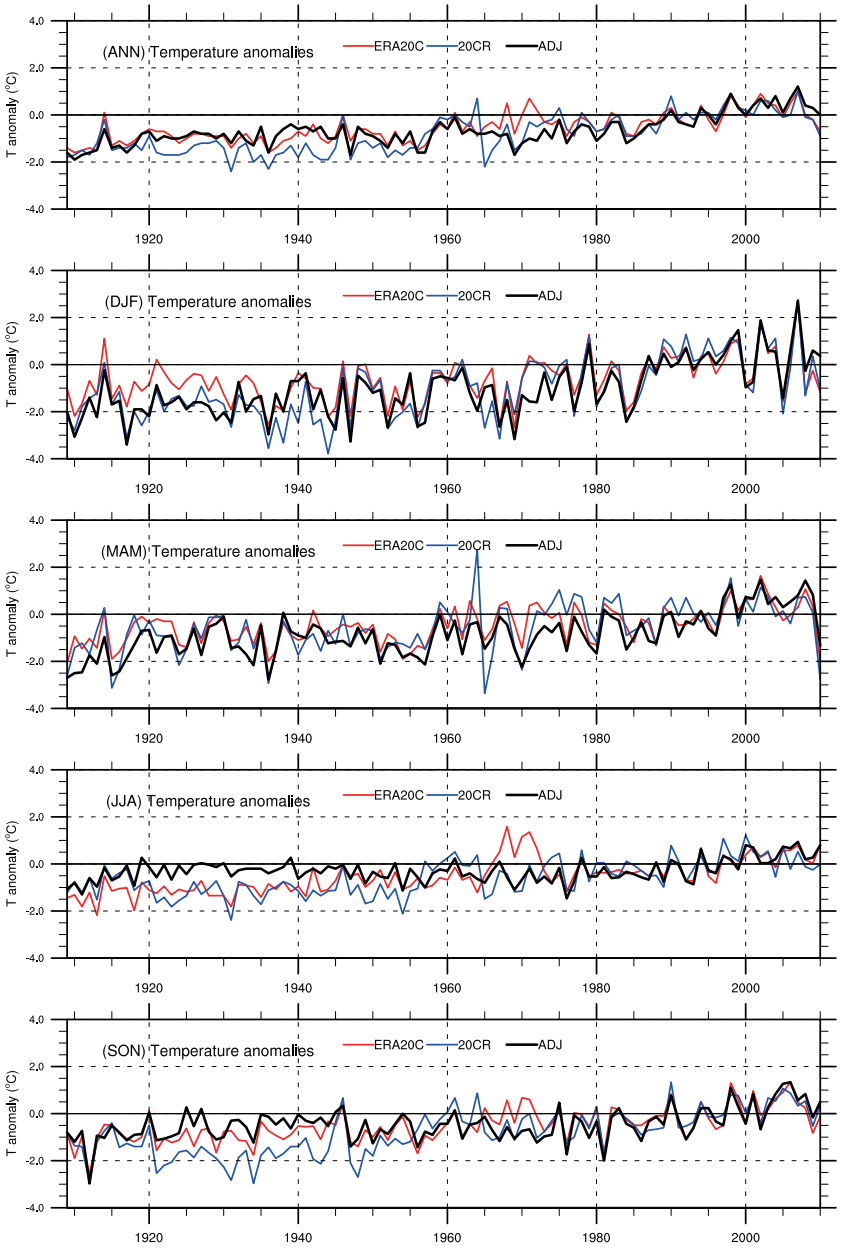

Fig. 2. Annual and seasonal mean surface air temperature anomalies (units: °C) of Eastern China during 1909–2010 derived from observation stations (ADJ) and two reanalysis datasets (ERA20C and 20CR) (ANN, annual; DJF, winter; MAM, spring; JJA, summer; SON, autumn).

20CR during 1963–1968 was mainly affected by the spring temperature.

In order to focus on short-term inter-annual variations, the linear trends of annual and seasonal mean surface air temperature in Eastern China during 1909–2010 were removed from the anomalies series for both ADJ and REA datasets (Fig. 3). It was notable that the annual mean temperature of ERA20C was significantly higher than that of ADJ from 1965 to 1975. This was mainly caused by the higher temperature in JJA and SON. Furthermore, the annual mean temperature of 20CR had a large fluctuation in 1963–1968, which

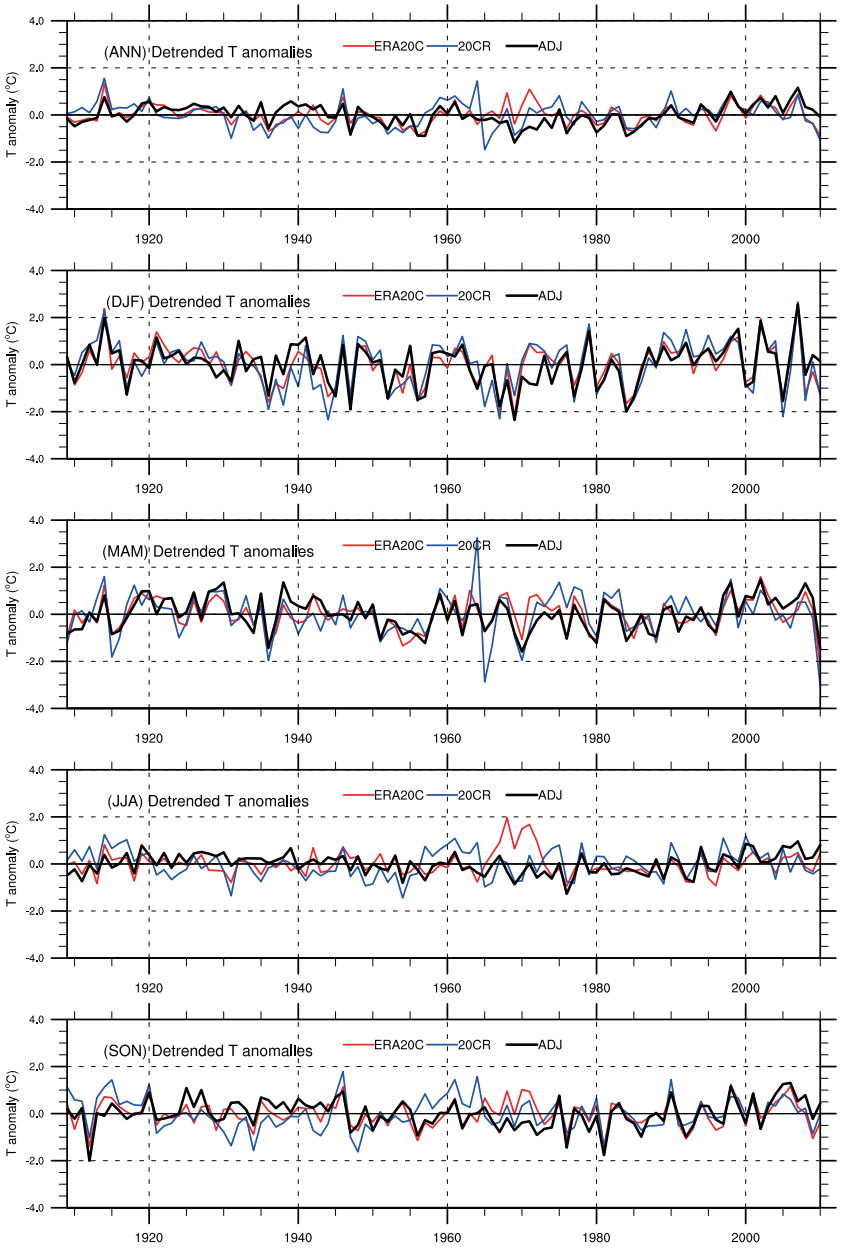

Fig. 3. Annual and seasonal mean surface air temperature anomalies (units: °C) which were removed the trend of Eastern China during 1909–2010 derived from observation stations (ADJ) and two reanalysis datasets (ERA20C and 20CR) (ANN, annual; DJF, winter; MAM, spring; JJA, summer; SON, autumn).

was mainly due to the larger inter-annual variability of temperature in MAM. 20CR was generally higher than that of ADJ from 1955 to 1965 in JJA and SON. Overall, the detrended annual and seasonal mean surface air temperature anomalies showed that the reanalysis datasets could in a larger extent describe the observational temperature characteristics in the inter-annual variation of the 20th century. The correspondence of the reanalysis data series with observations was better in winter and spring than in summer and autumn.

According to the above results, 20CR and ERA20C had a high consistency with ADJ especially after 1975

Table 1. Annual mean surface air temperature of Standard deviation ratio (*SDR*) and correlation coefficient (*R*) over Eastern China derived from observation stations and two reanalysis datasets (ERA20C and 20CR) during the periods 1909–2010, 1951–2010, and 1979–2010 (respective thresholds of 0.19, 0.36, and 0.41 at the 95 % level)

Period	ERA20C		20CR	
	R	*SDR*	*R*	*SDR*
1909–2010	0.81	0.96	0.74	1.28
1951–2010	0.76	0.87	0.74	1.07
1979–2010	0.88	0.85	0.80	0.88

in describing the annual characteristics. However, there were great fluctuations in REA during the 1960s and 1970s, with large differences between 20CR and ADJ before the 1950s. Of the two reanalysis datasets, ERA20C was generally closer to ADJ.

3.2 *Correlation and ratio of standard deviation*

The findings presented in Section 3.1 indicated uncertainties associated with assessing the applicability of the reanalysis datasets. These uncertainties arise as a result of the differences between REA and ADJ at different periods. Therefore, in this section, we compared the similarity of inter-annual variability and standard deviation between REA and ADJ in different periods.

Table 1 shows the *R* values and *SDR* values between annual mean temperature of ERA20C or 20CR and ADJ for the periods 1909–2010, 1951–2010, and 1979–2010. The correlation of REA and ADJ in each period was statistically significant, indicating the similar inter-annual variability to ADJ. The R of ERA20C and ADJ was higher than that of 20CR and ADJ in all three periods (R values were 0.88 and 0.80 respectively in 1979–2010, 0.76 and 0.74 in 1951–2010, and 0.81 and 0.74 in 1909–2010). This shows that ERA20C was closer to ADJ in terms of inter-annual variability. The REA and ADJ temperature SDR shows that the standard deviations of ERA20C were less than ADJ during the three periods. The SDR (1.28 and 1.07) of 20CR and ADJ during 1909–2010 and 1951–2010 were higher than those of ERA20C and ADJ, which indicates that the dispersion of ERA20C was generally lower than ADJ. The dispersion of 20CR was larger than that of ADJ because of the low temperatures before 1950. In order to compare the correlation and standard deviations, a Taylor diagram was used to illustrate the similarity of the annual and seasonal variability, and dispersion derived from

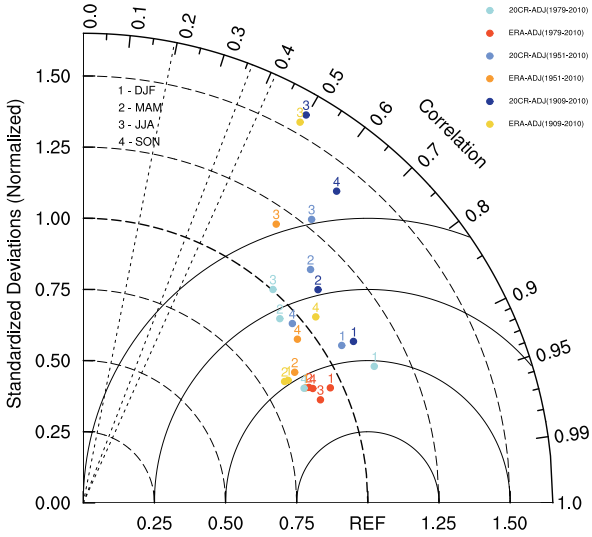

Fig. 4. Taylor diagram of seasonal mean surface air temperature averaged in China derived by reanalysis datasets (ERA20C and 20CR) and observations (ADJ) based on the periods 1909–2010, 1951–2010, and 1979–2010 (DJF, winter; MAM, spring; JJA, summer; SON, autumn).

REA and ADJ during 1909–2010, 1951–2010, and 1979–2010 (Fig. 4). The results demonstrated that the seasonal correlation of ADJ and REA was statistically significant at different times (with respective thresholds of 0.19, 0.36, and 0.41 at the 95 % level). The correlation of REA and ADJ in most of the winter and spring was higher than in summer and autumn, and the consistency of REA and ADJ was greatest for the winter inter-annual variability, with the lowest agreement in summer. The *SDR* from REA and ADJ showed that the seasonal standard deviations of ERA20C were lower than ADJ, except for summer and autumn in 1909–2010 and summer in 1951–2010, with values of 0.8–1.0. The standard deviation of 20CR was consistently higher than ADJ, except for spring and autumn in 1979–2010 and 1951–2010. The greatest bias of standard deviation of REA and ADJ occurred in summer of 1909–2010, indicating poor dispersion of the reanalysis data in summer during this period. Figure 5 shows the spatial distribution of the temperature correlation coefficient (*R*) for 1909–2010, 1951–2010, and 1979–2010 across Eastern China derived from REA and ADJ. The *R* values for all stations were statistically significant at the 95 % level in the three periods except for Nanjing station of 20CR from 1909 to 2010 (*R* of 0.11), indicating the general similarity

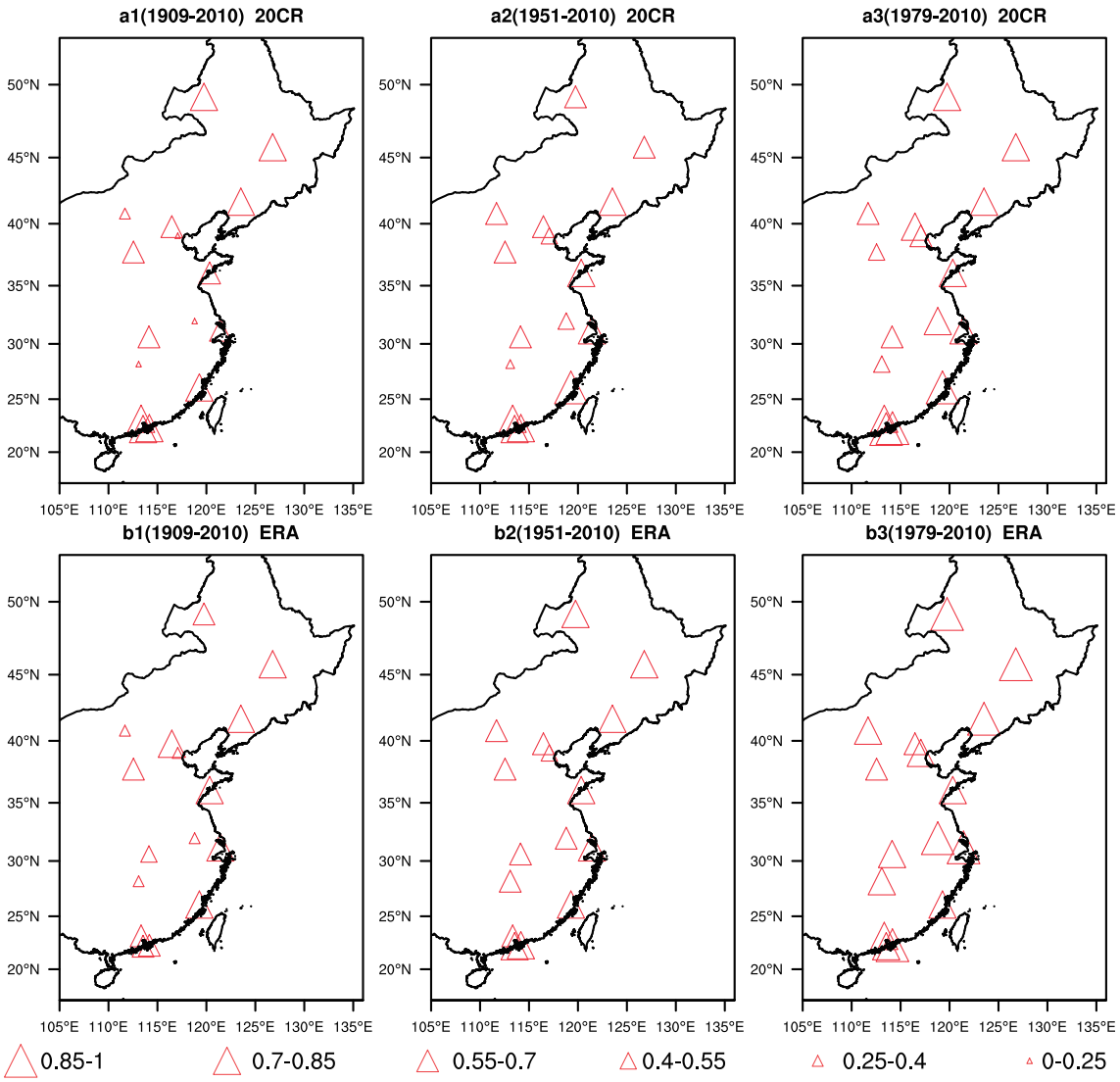

Fig. 5. Spatial distribution of temperature correlation (R) for 1909–2010, 1951–2010, and 1979–2010 over Eastern China based on reanalysis datasets (ERA20C and 20CR) and observations (ADJ).

between REA and ADJ when describing the annual variability characteristics. The R values in Nanjing, Changsha, Tianjin, and Hohhot were lower than in other stations during 1909–2010 and 1951–2010. For example, the R-value of 20CR and ADJ from 1909 to 2010 in Nanjing, Changsha, Tianjin, and Hohhot stations was 0.11, 0.24, 0.25, and 0.35, respectively. During 1951–2010, the Nanjing, Changsha, and Tianjin stations had R values of 0.36, 0.4, and 0.51 between 20CR and ADJ, respectively, which were significantly lower than the other stations in the same period.

Figure 6 shows annual and seasonal mean surface air temperature anomalies (units: °C) of Nanjing, Changsha, Tianjin, and Hohhot during 1909–2010 derived from ADJ and ERA20C and 20CR. The annual mean temperature of REA was lower than ADJ before 1960 at Changsha, Nanjing, and Tianjin. The temperature of Hohhot was lower than ADJ before 1940 and higher in 1960–1980. This may be the main reason for the low correlation between REA and ADJ at the four stations, and it suggests that REA may not be suitable for long-term climate change analyses including the early 20th century data at least at these four stations.

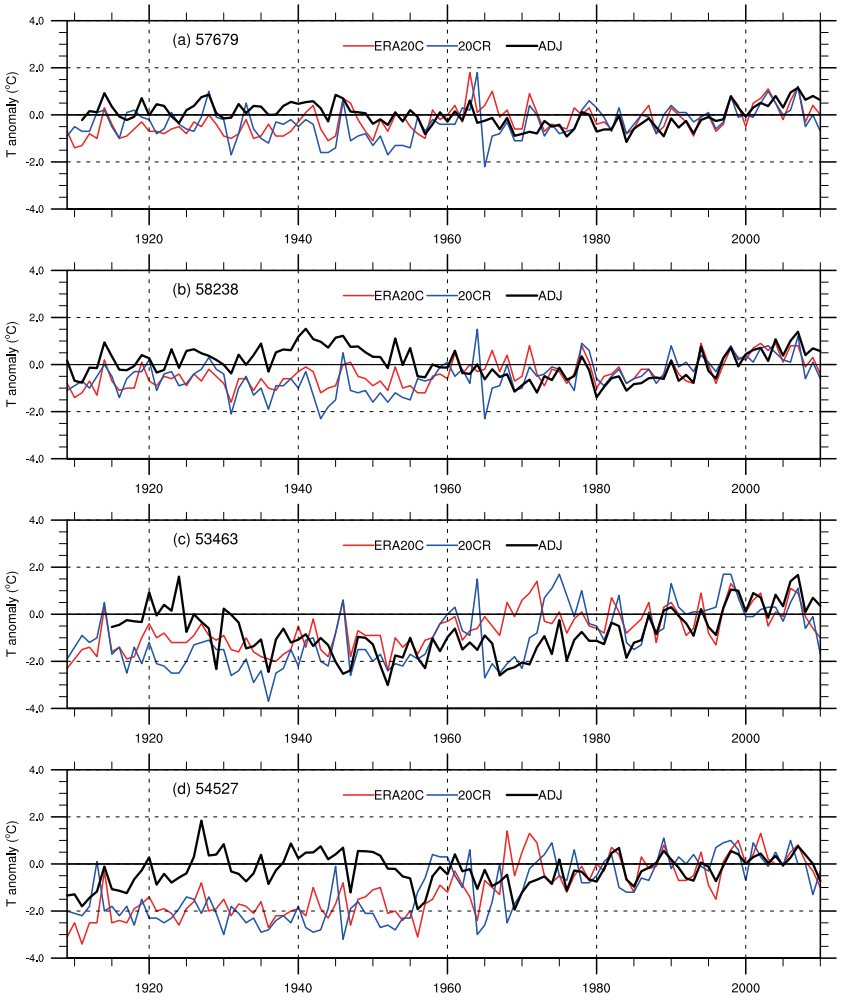

Fig. 6. Annual and seasonal mean surface air temperature anomalies (units: °C) of Nanjing, Changsha, Tianjin, and Hohhot during 1909–2010 derived from ADJ and ERA20C and 20CR (a: Changsha (57679) b: Nanjing (58238) c: Hohhot (53463) d: Tianjin (54527)).

The 20CR assimilates surface observations of synoptic pressure, sea surface temperature and sea ice, whereas ERA20C assimilates observations of surface pressure and surface marine winds only. The difference may have caused the different temperatures between the two reanalysis datasets, and the different levels of uncertainties of the reanalysis data as compared to the ADJ.

Comparison of the REA and ADJ SDR for the spatial distribution of annual average temperature (Fig. 7) indicated that the standard deviations of 20CR were higher than ADJ in North China and East China from 1909 to 2010, including Beijing and Tianjin, with ratios of 1.68 and 1.78, respectively. The standard deviations of 20CR were also higher than that of ADJ in North China, East China and South China stations during 1951–2010. The standard deviations in the north stations were higher than those of ADJ during 1979–2010 except for Hailar and Hohhot, and those in Southern China (except for Macao) were smaller than ADJ. The standard deviations of the annual mean temperature of ERA20C were lower than those of ADJ in the Northeast Inner Mongolia, and southern coastal stations during 1909–2010 and 1951–2010. The main distribution of the standard deviation was higher than ADJ in Northern China during 1979–2010, but smaller in Southern China.

According to the above results, the inter-annual and decadal variability and dispersion were generally

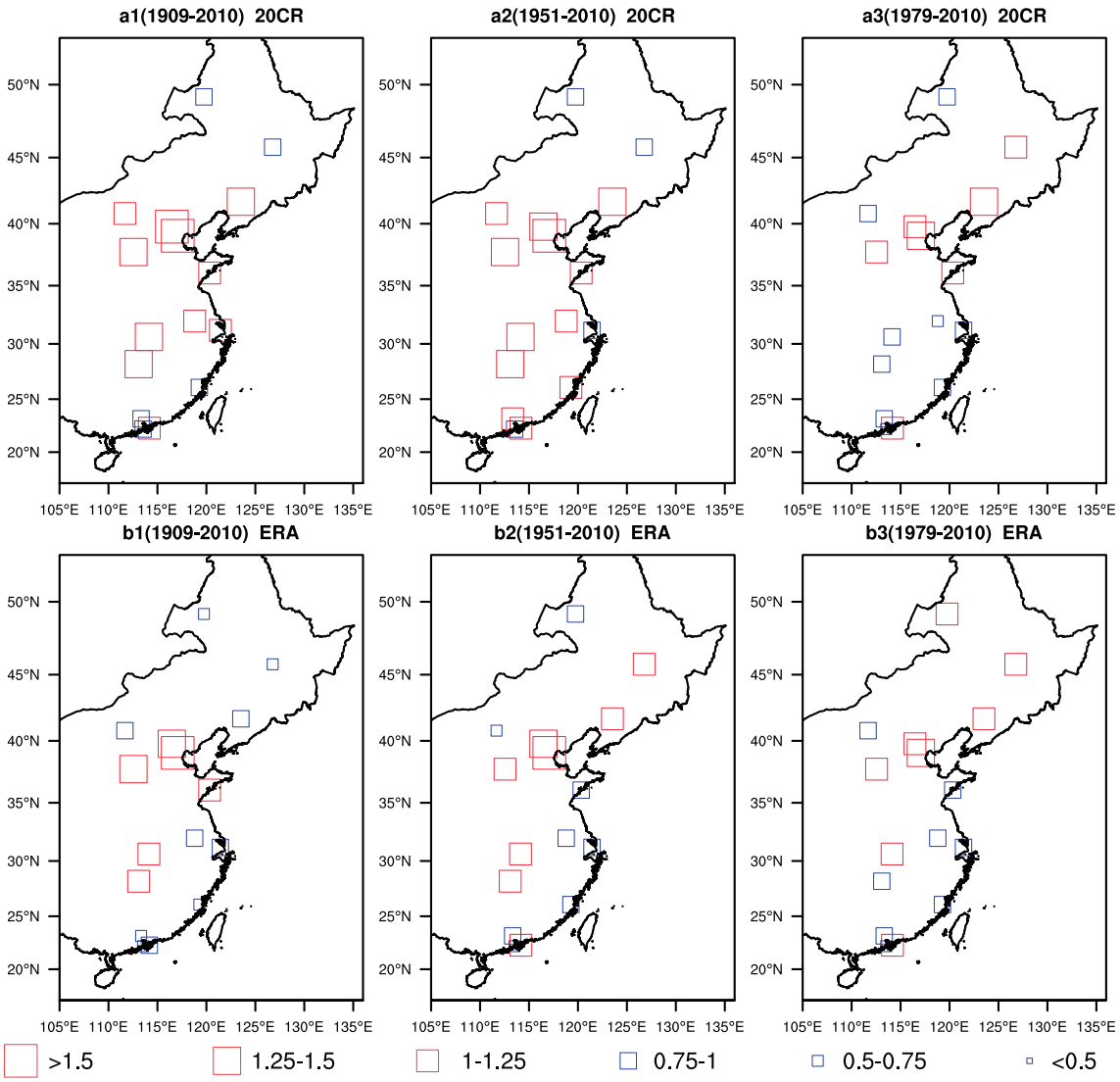

Fig. 7. Spatial distribution of temperature standard deviation ratio (*SDR*) for the periods 1909–2010, 1951–2010, and 1979–2010 over Eastern China based on reanalysis datasets (ERA20C and 20CR) and observations (ADJ).

consistent between REA and ADJ in Eastern China. The *R* values of ADJ with ERA20C were higher than those with 20CR in each time period, and the standard deviations were lower than ADJ. The standard deviations of 20CR were higher than the ADJ in 1909–2010 and 1951–2010. A similar result has also been noted in previous research. Zhou et al 2018 showed that the reanalysis products underestimated the surface air temperature over most of the regions in China. These discrepancies were especially pronounced over the Tibetan Plateau and middle China. In addition, the correlations between the annual surface air temperature anomalies in the reanalysis products and the observations are reasonably strong. The simulated time series of temperature anomalies over Eastern China are depicted most accurately by the reanalysis. ERA20C displays better performance than 20CR. In general, ERA20C was more similar to ADJ than 20CR. The temperature of the 20CR was lower than observation data before 1950, leading to the low similarity in inter-annual variability and the high dispersion. The bias between REA and ADJ was mainly generated in summer and autumn, with minimal deviation in winter.

Table 2. Trend of temperature change for the reanalysis and observation datasets (* indicates that the change was significant at the 95 % level; unit: °C (10 yr)$^{-1}$)

Period		ERA20C	20CR	ADJ	ADJ-T
1909–2010	Annual	0.15*	0.20*	0.15*	0.10*
	Winter	0.14*	0.26*	0.25*	0.17*
	Spring	0.13*	0.17*	0.20*	0.15*
	Summer	0.18*	0.15*	0.06*	0.03*
	Autumn	0.15*	0.23*	0.11*	0.07*
1951–2010	Annual	0.20*	0.24*	0.29*	0.23*
	Winter	0.27*	0.36*	0.43*	0.36*
	Spring	0.20*	0.21*	0.36*	0.25*
	Summer	0.25*	0.19*	0.18*	0.18*
	Autumn	0.28*	0.21*	0.22*	0.20*
1979–2010	Annual	0.26*	0.25*	0.49*	0.44*
	Winter	0.17	0.25*	0.53*	0.41*
	Spring	0.30*	0.08	0.58*	0.53*
	Summer	0.35*	0.20*	0.41*	0.36*
	Autumn	0.28*	0.38*	0.51*	0.46*

3.3 Comparison of the linear trend

Table 2 presents the annual and seasonal linear trends of Eastern China mean temperatures during 1909–2010, 1951–2010, and 1979–2010 derived from ADJ and REA. Because of the large positive deviation of ADJ in reflecting the long-term temperature trend (Cao et al. 2013; Zhao et al. 2014; Wang et al. 2014; Ren et al. 2017), we also referred to the results of Tang et al. (2005, 2009) (ADJ-T) for comparison of the linear trend. The average annual trends of REA, ADJ, and ADJ-T at different periods were statistically significant at the 95 % level. The trend for ADJ was 0.15°C (10 yr)$^{-1}$, which was equal to that of ERA20C and less than the trend of 20CR during 1909–2010, and that of ADJ-T was 0.10°C (10 yr)$^{-1}$, which was less than the trend of REA. During 1951–2010 and 1979–2010, the trends of REA were lower than ADJ, and those of ADJ were higher than ADJ-T. In terms of seasonal mean trends of REA and observations at different periods, ADJ and ADJ-T were statistically significant at the 95 % level in each period. In winter and spring, and most summer and autumn periods, the trends of ADJ were higher than ADJ-T, and seasonal trends of REA during 1909–2010, 1951–2010, and 1979–2010 were significant in summer and autumn. Overall, for most seasons from 1909 to 2010, the trends of 20CR were greater than the observations, and the trends of ERA20C were larger than those of ADJ and ADJ-T for summer and autumn. However, during 1951–2010 and 1979–2010, the trends of the observations were greater than REA.

In order to further compare the annual mean trends of REA and ADJ at different periods, Fig. 8 shows spatial distribution of temperature change of the 16 stations during 1909–2010 1951–2010, and 1979–2010. From 1909 to 2010 (Figs. 6a1–c1), it can be concluded that the warming trends in northern stations were higher than those in southern stations. Moreover, temperature of REA in each station showed increasing trends, and also exceeded a 95 % significance threshold. Except for Nanjing and Changsha, which showed decreasing trends, the annual mean temperature in ADJ significantly increased at most stations. From 1951 to 2010 (Figs. 6a2–c2), the temperatures of REA and ADJ datasets for most stations increased significantly, with 20CR mainly concentrated in the south of Northeast China, ERA20C in the North of the Yangtze River, and an increasing trend in the ADJ dataset at each station during 1909–2010. In the North of the Yangtze River, the ERA20C temperature changes were more similar to those of ADJ, while 20CR and ADJ were closer in the south of the Yangtze River. From 1979 to 2010 (Figs. 6a3–c3), the significant increases of 20CR temperature were mainly distributed in coastal areas, and those for ERA20C were mainly distributed south of the Yangtze River. The increasing trend of ADJ during the recent 30 years was higher than that during 1951–2010. It was also obvious that the trend of REA for 1979–2010 appeared to be smaller than that of ADJ even in north and Northeast China. The linear trends of surface air temperature showed clear warming in both reanalysis

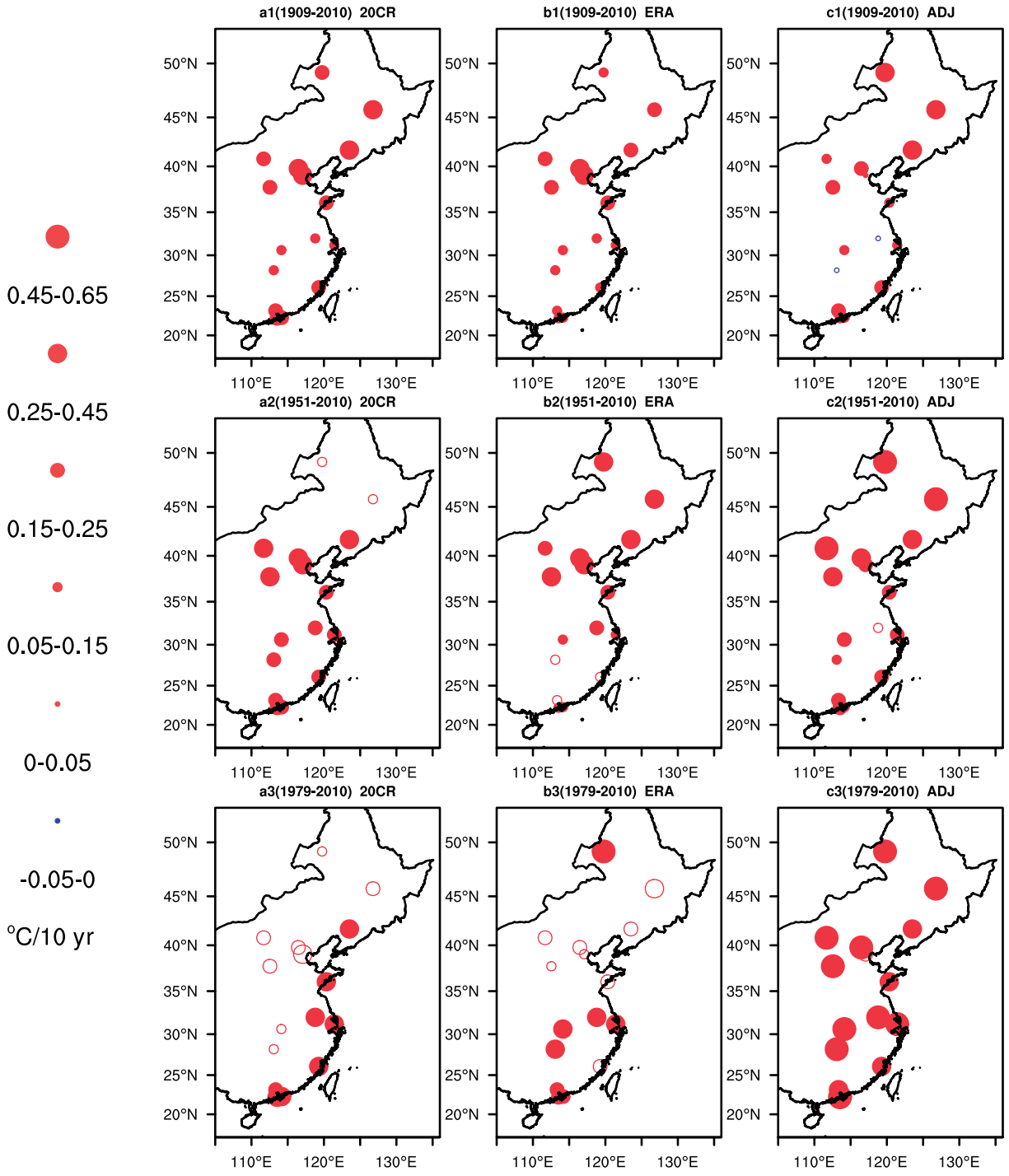

Fig. 8. Spatial distribution of temperature change trends (units: °C (10 yr)$^{-1}$) for the periods 1909–2010, 1951–2010, and 1979–2010 over Eastern China based on reanalysis datasets (ERA20C and 20CR) and observations (ADJ). Solid and empty circles denote that the change is significant or not significant at the 95 % confidence level, respectively.

datasets and the observations from 1979 to 2010 over Eastern China (Zhou et al. 2018).

4. Conclusions and discussion

Based on homogenized observation data from 16 stations in Eastern China and two 20th century monthly mean surface temperature reanalysis datasets (20CR and ERA20C), a preliminary comparison of the anomaly difference, correlation, standard deviation, and linear trend of the temperature data was conducted for the periods 1909–2010, 1951–2010, and 1979–2010. The main findings were as follows:

(1) For ERA20C and 20CR, there was a high consistency with ADJ in annual variation characteristics after 1975. There were large fluctuations of REA during 1960–1970. The differences between 20CR and ADJ were large before the 1950s, and ERA20C was generally closer to ADJ. The annual variation characteristics of REA had a higher agreement with those of ADJ in winter and spring than in summer and autumn.

(2) Most of the stations showed high consistency with ADJ in inter-annual variability and dispersion, but the consistency at Nanjing, Changsha, Tianjin, and Hohhot stations was relatively low. The R values of ERA20C and ADJ were higher than those of 20CR and ADJ in different periods, and the standard deviation of ERA20C was lower than that of ADJ. The standard deviation of 20CR was higher than that of ADJ during 1909–2010 and 1951–2010. In general, ERA20C was closer to ADJ than 20CR. The bias between REA and observation was mainly generated in summer and autumn, with minimal deviation in winter.

(3) The annual mean temperature of REA, ADJ, and ADJ-T increased significantly in different time periods. The annual mean temperature trends of REA were higher than those of ADJ and ADJ-T during 1909–2010 and were lower in 1951–2010 and 1979–2010. The linear trends of ADJ were higher than those of ADJ-T. The temperature trends in most seasons of ADJ and ADJ-T were lower than those of 20CR during 1909–2010. The trend of ERA20C was larger than that of ADJ and ADJ-T for summer and autumn, but smaller for winter and spring. The temperature trends of ADJ and ADJ-T were generally higher than those of REA in 1951–2010 and 1979–2010. In winter and spring, and most periods for autumn and summer, ADJ trends were higher than those of ADJ-T.

The results of the linear trends analysis presented here indicate that annual mean temperature trend of ADJ was higher than previous estimates (Ren et al. 2017). The annual mean temperature change trend in China was generally between 0.08 and 0.12 $(10\ \mathrm{yr})^{-1}$ during 1901–2015 (Wang et al. 1998; Tang et al. 2005, 2009; Li et al. 2010). Ren et al. (2017) suggested that a higher warming rate may be related to urbanization bias in single-station sequences and may also be associated with the use of a low number of stations from cities located in Eastern and central China. Since the middle of the 20th century, the temperature observation records of urban stations and national meteorological station networks have obtained a significant urbanization bias, regardless of whether homogenization corrections were applied (Ren et al. 2008, 2015; Zhao et al. 2009; Zhang et al. 2010; Yang et al. 2011; Wang and Ge 2012; He et al. 2013). This clearly indicates that although the linear trends of REA data may have been more correct than those of the observations for the recent decades, they may have been largely overestimated relative to the real trends based on the urban-bias adjusted observations for the period 1909–2010. It is premature at present to use the REA data for estimating the long-term trends of surface air temperature in regions such as Eastern China.

Correction of urbanization bias is important for studies of long-term surface air temperature changes at individual stations. This paper represents a preliminary comparison of surface air temperatures between observation and reanalysis data over Eastern China for the last 100 years. In future, urban-bias assessment and adjustments must be conducted, and both a larger study area and longer observation period are required to conduct a more detailed comparison and uncertainty study.

Acknowledgments

This study is financed by the National Key Research and Development Program of China (No.2018 YFA0605603), China Natural Science Foundation (CNSF) (Fund No: 41575003), China Meteorological Administration Special Foundation for Climate Change (grant number CCSF201803) and Special Fund for Meteorological Scientific Research in the Public Interest "The 40-year CMA Global Atmospheric Reanalysis (CRA-40): Technique Research and Products" (GYHY 201506002). This work and its contributors (SiQi Zhang, GuoYu Ren, YuYu Ren, XiuBao Sun) were also supported by the UK-China Research & Innovation Partnership Fund through the Met Office Climate Science for Service Partnership (CSSP) China as part of the Newton Fund. We thank LetPub (www.letpub.com) for its linguistic assistance during the preparation of this manuscript.

References

Bengtsson, L., S. Hagemann, and K. I. Hodges, 2004: Can climate trends be calculated from reanalysis data? *J. Geophys. Res.*, **109**, D11111, doi:10.1029/2004JD004536.

Cao, L., P. Zhao, Z. Yan, P. Jones, Y. Zhu, Y. Yu, and G. Tang, 2013: Instrumental temperature series in Eastern and central China back to the nineteenth century. *J. Geophys. Res.*, **118**, 8197–8207.

Compo, G. P., J. S. Whitaker, P. D. Sardeshmukh, N. Matsui, R. J. Allan, X. Yin, B. E. Gleason, R. S. Vose, G. Rutledge, P. Bessemoulin, S. Brönnimann, M. Brunet, R. I. Crouthamel, A. N. Grant, P. Y. Groisman, P. D. Jones, M. C. Kruk, A. C. Kruger, G. J. Marshall, M. Maugeri, H. Y. Mok, Ø. Nordli, T. F. Ross, R. M. Trigo, X. L. Wang, S. D. Woodruff, and S. J. Worley, 2011: The twentieth century reanalysis project. *Quart. J. Roy. Meteor. Soc.*, **137**, 1–28.

Dee, D. P., S. M. Uppala, A. J. Simmons, P. Berrisford, P. Poli, S. Kobayashi, U. Andrae, M. A. Balmaseda, G. Balsamo, P. Bauer, P. Bechtold, A. C. M. Beljaars, L. van de Berg, J. Bidlot, N. Bormann, C. Delsol, R. Dragani, M. Fuentes, A. J. Geer, L. Haimberger, S. B. Healy, H. Hersbach, E. V. Hólm, L. Isaksen, P. Kållberg, M. Köhler, M. Matricardi, A. P. McNally, B. M. Monge-Sanz, J.-J. Morcrette, B.-K. Park, C. Peubey, P. de Rosnay, C. Tavolato, J.-N. Thépaut, and F. Vitart, 2011: The ERA-Interim reanalysis: Configuration and performance of the data assimilation system. *Quart. J. Roy. Meteor. Soc.*, **137**, 553–597.

Easterling, D. R., and T. C. Peterson, 1995: A new method for detecting undocumented discontinuities in climatological time series. *Int. J. Climatol.*, **15**, 369–377.

Fan, K., and H. Liu, 2013: Evaluation of atmospheric circulation in the Southern Hemisphere in 20CRv2. *Atmos. Oceanic Sci. Lett.*, **6**, 337–342.

Ferguson, C. R., and G. Villarini, 2012: Detecting inhomogeneities in the Twentieth Century Reanalysis over the central United States. *J. Geophys. Res.*, **117**, D05123, doi:10.1029/2011JD016988.

He, Y. T., G. S. Jia, Y. H. Hu, and Z. H. Zhou, 2013: Detecting urban warming signals in climate records. *Adv. Atmos. Sci.*, **30**, 1143–1153.

Kalnay, E., M. Kanamitsu, R. Kistler, W. Collins, D. Deaven, L. Gandin, M. Iredell, S. Saha, G. White, J. Woollen, Y. Zhu, M. Chelliah, W. Ebisuzaki, W. Higgin, J. Janowiak, K. C. Mo, C. Ropelewski, J. Wang, A. Leetmaa, R. Reynolds, R. Jenne, and D. Joseph, 1996: The NCEP/NCAR 40-Year Reanalysis Project. *Bull. Amer. Meteor. Soc.*, **77**, 437–471.

Kanamitsu, M., W. Ebisuzaki, J. Woollen, S.-K. Yang, J. J. Hnilo, M. Fiorino, and G. L. Potter, 2002: NCEP–DOE AMIP-II reanalysis (R-2). *Bull. Amer. Meteor. Soc.*, **83**, 1631–1643.

Kistler, R., E. Kalnay, W. Collins, S. Saha, G. White, J. Woollen, M. Chelliah, W. Ebisuzaki, M. Kanamitsu, V. Kousky, H. van den Dool, R. Jenne, and M. Fiorino, 2001: The NCEP–NCAR 50–Year Reanalysis: Monthly means CD–ROM and documentation. *Bull. Amer. Meteor. Soc.*, **82**, 247–267.

Kobayashi, S., Y. Ota, Y. Harada, A. Ebita, M. Moriya, H. Onoda, K. Onogi, H. Kamahori, C. Kobayashi, H. Endo, K. Miyaoka, and K. Takahashi, 2015: The JRA-55 Reanalysis: General specifications and basic characteristics. *J. Meteor. Soc. Japan*, **93**, 5–48.

Lahoz, W. A., and P. Schneider, 2014: Data assimilation: Making sense of Earth observation. *Front. Environ. Sci.*, **2**, 1–28.

Li, Q. X., W. J. Dong, W. Li, X. R. Gao, P. Jones, J. Kenedy, and D. Parker, 2010: Estimate of uncertainties in temperature change of China over the last 100 years. *Chinese Sci. Bull.*, **2010**, 1544–1554 (in Chinese).

Liu, H., and K. Fan, 2014: Eurasia seasonal circulation climatology and variability: Evaluation of 20CR reanalysis data in Eurasia and East China. *Chinese J. Atmos. Sci.*, **38**, 469–483 (in Chinese).

Onogi, K., J. Tsutsui, H. Koide, M. Sakamoto, S. Kobayashi, H. Hatsushika, T. Matsumoto, N. Yamazaki, H. Kamahori, K. Takahashi, S. Kadokura, K. Wada, K. Kato, R. Oyama, T. Ose, N. Mannoji, and R. Taira, 2007: The JRA-25 Reanalysis. *J. Meteor. Soc. Japan*, **85**, 369–432.

Parker, W. S., 2016: Reanalyses and observations: What's the difference? *Bull. Amer. Meteor. Soc.*, **97**, 1565–1572.

Poli, P., H. Hersbach, D. Tan, D. Dee, J.-N. Thépaut, A. Simmons, C. Peubey, P. Laloyaux, T. Komori, P. Berrisford, R. Dragani, Y. Trémolet, E. Hólm, M. Bonavita, L. Isaksen, and M. Fisher, 2013: *The data assimilation system and initial performance evaluation of the ECMWF pilot reanalysis of the 20th-century assimilating surface observations only (ERA-20C)*. *ERA Rep. Ser.*, **14**, ECMWF, 59 pp.

Poli, P., H. Hersbach, D. P. Dee, P. Berrisford, A. J. Simmons, F. Vitart, P. Laloyaux, D. G. H. Tan, C. Peubey, J.-N. Thépaut, Y. Thépaut, E.V. Hólm, M. Bonavita, L. Isaksen, and M. Fisher, 2016: ERA-20C: An atmospheric reanalysis of the 20th century. *J. Climate*, **29**, 4083–4097.

Ren, G., Y. Zhou, Z. Chu, J. Zhou, A. Zhang, J. Guo, and X. Liu, 2008: Urbanization effects on observed surface air temperature trends in North China. *J. Climate*, **21**, 1333–1348.

Ren, G., J. Li, Y. Ren, Z. Chu, A. Zhang, Y. Zhou, L. Zhang, Y. Zhang, and T. Bian, 2015: An integrated procedure to determine a reference station network for evaluating and adjusting urban bias in surface air temperature data. *J. Appl. Meteor. Climatol.*, **54**, 1248–1266.

Ren, G., Y. Ding, and G. Tang, 2017: An overview of mainland China temperature change research. *Acta Meteor. Sinica*, **31**, 3–16.

Rienecker, M. M., M. J. Suarez, R. Gelaro, R. Todling, J. Bacmeister, E. Liu, M. G. Bosilovich, S. D. Schubert, L. Takacs, G.-K. Kim, S. Bloom, J. Chen, D. Collins, A. Conaty, A. da Silva, W. Gu, J. Joiner, R. D. Koster, R. Lucchesi, A. Molod, T. Owens, S. Pawson, P. Pegion, C. R. Redder, R. Reichle, F. R. Robertson, A. G. Ruddick, M. Sienkiewicz, and J. Woollen, 2011: MERRA: NASA's modern-era retrospective analysis for research and applications. *J. Climate*, **24**, 3624–3648.

Saha, S., S. Moorthi, H.-L. Pan, X. Wu, J. Wang, S. Nadiga, P. Tripp, R. Kistler, J. Woollen, D. Behringer, H. Liu, D. Stokes, R. Grumbine, G. Gayno, J. Wang, Y.-T. Hou, H.-y. Chuang, H.-M. H. Juang, J. Sela, M. Iredell, R. Treadon, D. Kleist, P. Van Delst, D. Keyser, J. Derber, M. Ek, J. Meng, H. Wei, R. Yang, S. Lord, H. van den Dool, A. Kumar, W. Wang, C. Long, M. Chelliah, Y. Xue, B. Huang, J.-K. Schemm, W. Ebisuzaki, R. Lin, P. Xie, M. Chen, S. Zhou, W. Higgins, C.-Z. Zou, Q. Liu, Yong Chen, Y. Han, L. Cucurull, R. W. Reynolds, G. Rutledge, and M. Goldberg, 2010: The NCEP Climate Forecast System Reanalysis. *Bull. Amer. Meteor. Soc.*, **91**, 1015–1057.

Song, F., and T. Zhou, 2012: Reliability of the 20CR reanalysis data in measuring the East Asian summer monsoon variability. *Chinese J. Atmos. Sci.*, **36**, 1207–1222 (in Chinese).

Tang, G. L., and G. Ren, 2005: A reanalysis of surface air temperature change of the last 100 years over China. *Climatic. Environ. Res.*, **10**, 791–798.

Tang, G. L., Y. H. Ding, S. W. Wang, G. Ren, H. Liu, and L. Zhang, 2009: Comparative analysis of the time series of surface air temperature over China for the last 100 years. *Adv. Clim. Change Res.*, **5**, 71–78 (in Chinese).

Thorne, P. W., and R. S. Vose, 2010: Reanalyses suitable for characterizing long-term trends. Are they really achievable? *Bull. Amer. Meteor. Soc.*, **91**, 353–361.

Uppala, S. M., P. W. Kållberg, A. J. Simmons, U. Andrae, V. Da Costa Bechtold, M. Fiorino, J. K. Gibson, J. Haseler, A. Hernandez, G. A. Kelly, X. Li, K. Onogi, S. Saarinen, N. Sokka, R. P. Allan, E. Andersson, K. Arpe, M. A. Balmaseda, A. C. M. Beljaars, L. Van De Berg, J. Bidlot, N. Bormann, S. Caires, F. Chevallier, A. Dethof, M. Dragosavac, M. Fisher, M. Fuentes, S. Hagemann, E. Hólm, B. J. Hoskins, L. Isaksen, P. A. E. M. Janssen, R. Jenne, A. P. Mcnally, J.-F. Mahfouf, J.-J. Morcrette, N. A. Rayner, R. W. Saunders, P. Simon, A. Sterl, K. E. Trenberth, A. Untch, D. Vasiljevic, P. Viterbo, and J. Woollen, 2005: The ERA-40 re-analysis. *Quart. J. Roy. Meteor. Soc.*, **131**, 2961–3012.

Uppala, S. M., D. Dee, S. Kobayashi, P. Berrisford, and A. Simmons, 2008: Towards a climate data assimilation system: Status update of ERA-Interim. *ECMWF Newsl.*, **115**, 12–18.

Wang, F., and Q. S. Ge, 2012: Estimation of urbanization bias in observed surface temperature change in China from 1980 to 2009 using satellite land-use data. *Chinese Sci. Bull.*, **57**, 1708–1715.

Wang, J., C. Xu, M. Hu, Q. Li, Z. Yan, P. Zhao, and P. Jones, 2014: A new estimate of the China temperature anomaly series and uncertainty assessment in 1900–2006. *J. Geophys. Res.*, **119**, 1–9.

Wang, S., J. Ye, D. Gong, J. Zhu, and T. Yao, 1998: Construction of mean annual temperature series for the last one hundred years in China. *J. Appl. Meteor. Sci.*, **9**, 392–401 (in Chinese).

Wang, X. L., 2008: Accounting for autocorrelation in detecting mean shifts in climate data series using the penalized maximal *t* or *F* test. *J. Appl. Meteor. Climatol.*, **47**, 2423–2444.

Xu, Y., Y. H. Ding, and Z. Zhao, 2001: Confidence analysis of NCEP/NCAR 50-year global reanalyzed data in climate change research in China. *J. Appl. Meteor. Sci.*, **12**, 337–347 (in Chinese).

Yang, X., Y. Hou, and B. Chen, 2011: Observed surface warming induced by urbanization in East China. *J. Geophys. Res.*, **116**, D14113, doi:10.1029/2010JD015452.

Zhang, A. Y., G. Y. Ren, J. X. Zhou, Z. Y. Chu, Y. Y. Ren, and G. L. Tang, 2010: On the urbanization effect on surface air temperature trends over China. *Acta Meteor. Sinica*, **68**, 957–966 (in Chinese).

Zhao, Z., S. Wang, Y. Luo, and Y. Jiang, 2009: Uncertainty analysis of climate warming during the last 100 years. *Sci. Technol. Rev.*, **27**, 41–48 (in Chinese).

Zhao, T., C. Fu, Z. Ke, and W. Guo, 2010: Global atmosphere reanalysis datasets: Current status and recent advances. *Adv. Earth Sci.*, **25**, 242–254 (in Chinese).

Zhao, T., J. Wang, and A. Dai, 2015: Evaluation of atmospheric precipitable water from reanalysis products using homogenized radiosonde observations over China. *J. Geophys. Res.*, **120**, 10703–10727.

Zhao, P., P. Jones, L. J. Cao, Z. W. Yan, S. Zha, Y. Zhu, Y. Yu, and G. L. Tang, 2014: Trend of surface air temperature in eastern China and associated large-scale climate variability over the last 100 years. *J. Climate*, **27**, 4693–4703.

Zhou, C., Y. He, and K. Wang, 2018: On the suitability of current atmospheric reanalysis for regional warming studies over China. *Atmos. Chem. Phys.*, **18**, 8113–8136.

Bias Correction of Gauge Data and its Effect on Precipitation Climatology over Mainland China

YINGXIAN ZHANG AND YUYU REN

Laboratory for Climate Studies, National Climate Center, China Meteorological Administration, Beijing, China

GUOYU REN

Department of Atmospheric Science, School of Environmental Studies, China University of Geosciences, Wuhan, and Laboratory for Climate Studies, National Climate Center, China Meteorological Administration, Beijing, China

GUOFU WANG

Laboratory for Climate Studies, National Climate Center, China Meteorological Administration, Beijing, China

(Manuscript received 26 February 2019, in final form 5 June 2019)

ABSTRACT

Typical rain gauge measurements have long been recognized to underestimate actual precipitation. Long-term daily precipitation records during 1961–2013 from a dense national network of 2379 gauges were corrected to remove systematic errors caused by trace precipitation, wetting losses, and wind-induced undercatch. The corrected percentage was higher in cold seasons and lower in warm seasons. Both trace precipitation and wetting loss corrections were more important in arid regions than in wet regions. A greater correction percentage for wind-induced error could be found in cold and arid regions, as well as high wind speed areas. Generally, the annual precipitation amounts as well as the annual precipitation intensity increased to varying degrees after bias correction with the maximum percentage being about 35%. More importantly, the bias-corrected snowfall amount as well as the rainstorm amount increased remarkably by percentages of more than 50% and 18%, respectively. Remarkably, the total number of actual rainstorm events during the past 53 years could be 90 days more than the observed rainstorm events in some coastal areas of China. Therefore, the actual amounts of precipitation, snowfall, and intense rainfall were much higher than previously measured over China. Bias correction is thus needed to obtain accurate estimates of precipitation amounts and precipitation intensity.

1. Introduction

Precipitation is the most widely recorded hydroclimatic phenomenon and an essential component of the hydrological cycle. Precipitation observations are obtained from radars, satellites, and rain gauges, with rain gauges having been widely and continuously utilized for centuries around the world. Deficiencies in existing gauge measurements, however, have long been recognized because they usually underestimate the actual precipitation (Kurtyka 1953; Larson 1971; Rasmussen et al. 2012; Nitu et al. 2018). Rain gauge measurements of precipitation suffer from a range of mostly negative biases, especially trace precipitation, wetting losses, evaporation losses, and wind undercatch. Bias correction for precipitation could affect the precipitation climatology and trend, as well as water budget (Ye et al. 2012) and drought assessment (Yao et al. 2018).

Negative biases arise because of the inability to measure the very small amounts of precipitation that are reported as "trace" and ignored when calculating monthly or longer-term totals. Wetting loss occurs when a gauge is emptied into a measuring device to obtain the precipitation total. The small amount left in the gauge (sticking to its sides) is the wetting loss. Overall wetting losses therefore depend on how often the gauge is emptied as

Corresponding author: G. Ren, guoyoo@cma.gov.cn

DOI: 10.1175/JAMC-D-19-0049.1

© 2019 American Meteorological Society. For information regarding reuse of this content and general copyright information, consult the AMS Copyright Policy (www.ametsoc.org/PUBSReuseLicenses).

well as the type of gauge and the type of precipitation. For example, according to the measurements by Aaltonen et al. (1993), the average wetting losses for the Hellmann gauge is 0.14 and 0.1 mm per measurement of rain and snow when the gauge is emptied once, respectively. This is the minimum correction since generally more than one observation was made in a precipitation day. The biases due to trace precipitation are greater in percentage terms at sites where precipitation is predominantly light and the total precipitation is small, for example in polar and cold-desert climates. Like the ''trace''-related bias, wetting losses are greater in percentage terms where precipitation is predominantly light.

Gauges record too little precipitation, especially snow. Surrounding winds are strong because of the deformation of the wind field by the gauge (Folland 1988). The severity of the undercatch depends on the shape of the orifice (Folland 1988) and the exposure of the site, which affects the wind strength. Sevruk and Zahlavova (1994) reported that the average undercatch at a shielded site of Swiss 600 m above sea level was 2% in summer and 7% in winter; at an exposed site, the corresponding losses were 5% and 18%. At high and exposed sites (2000 m above sea level) where winds are strong and snow is more likely to occur, the undercatch reached 25% in summer and even 60% in winter. Besides, 80%–120% correction factors were found in winter over the region north of 40°N (Yang et al. 2005). The errors in the unadjusted shielded measurements were also generally smaller than the unadjusted unshielded measurements, because the shields are designed to reduce the horizontal wind impacting a gauge inside the shield, and thereby reduce the effects of the gauge on the flow around it (Kochendorfer et al. 2017).

However, our understanding of the factors causing undercatch in the shields was not sufficiently well advanced to allow for the optimal shield design and only allowed the development of empirical correction factors (Rasmussen et al. 2012). The Solid Precipitation Intercomparison Experiment (SPICE) was conducted as an internationally coordinated project during 2013–15. SPICE focused on recommendations for adjustments that account for the undercatch of solid precipitation due to gauge exposure, and presented a function of data available at operational sites (Nitu et al. 2018). The winter snowfall in northeast China was generally undervalued due to wind-induced undercatch, and the average of annual wind-induced error was 34.1% during the period of 1960–2009 (Sun et al. 2013). Besides, the wind-induced error obviously resulted in a general overestimation of long-term winter snowfall trend in northeast China, and this is due to the weakening of measured near-surface wind speed (Sun et al. 2013). Scaff et al. (2015) discovered significant inconsistency in the precipitation measurements across the United States and Canada border because of the different instruments and observation methods used. This discontinuity was greater for snowfall than for rainfall, as gauge snowfall observations had large errors in the windy and cold conditions. In addition, Pan et al. (2016) found the bias corrections varied greatly in different eco-climatic regions of western Canada.

Evaporation from the gauge leads to a further negative bias, which is highly dependent on the weather conditions and the site environment. In particular, the surface of the orifice may receive some moisture, which later evaporates without entering the gauge. Water may splash out of the orifice leading to further undercatch, or into it from the ground leading to potential overcatch (Folland 1988). Likewise, snow may blow out of or into the orifice. Tipping-bucket gauges usually underestimate very heavy rain because some precipitation is missed during the bucket-tipping process (Duchon and Biddle 2010). The loss depends on precipitation intensity, and according to Duchon and Biddle (2010), precipitation missed in this way is significant only at intensities exceeding 50 mm h^{-1} and is about 4% in a 75 mm h^{-1} event. In addition, mechanical errors may also affect tipping-bucket gauge measurements (Westra et al. 2014).

Compensation of rain gauge data for systematic biases ideally requires metadata on instrumentation, siting (which affects wind strength), and observing practices. Ren et al. (2003) and Ren and Li (2007) assessed precipitation measurement biases in China using a parallel observational dataset and pointed out great observational bias in the gauge records. Ye et al. (2004) adjusted daily Chinese rain gauge data from 710 stations during 1951–98, which was followed by analysis of the effects of bias correction on precipitation trend (Ding et al. 2007). Based on the adjusted data, new precipitation climatology was also generated. Li et al. (2018) have updated the former results of Ye et al. (2004) at 553 sites in China, and redivided the climate zones of China according to the bias-corrected data. However, precipitation bias correction from the dense national network of 2379 gauges has not yet been conducted so far.

Precipitation is one climatic element that is sensitive to the local environment and topography. A higher-density network can describe the spatial characteristics of precipitation in details. More importantly, the near-surface wind speeds over China have been found to be reduced in recent decades (Ren et al. 2005; Jiang et al. 2009), and this may further complicate the understanding of precipitation bias in this country. Therefore, assessment and adjustment of the precipitation bias for data from the denser network of 2379 stations is urgently

needed. Because the bias-correction method for precipitation could be gauge specific, of course, the uncertainty in corrections is up in the air. In addition, the impact of bias correction on extreme precipitation climatology is still unclear.

The objective of this study is to assess and adjust the precipitation data bias for the 2379 national stations over China. The structure of this study is as follows. In section 2, the dataset and bias-correction methods are introduced. Section 3 presents the results of bias correction. In section 4, we focus on the impact of bias correction on the annual precipitation amount and intensity, and on extreme precipitation climatology. Section 5 discusses the potential uncertainty in snowfall corrections by employing two existing methods for a subset of the observation sites. Conclusions are given in section 6.

2. Data and methods

a. Data

We used measured daily cumulative precipitation amounts, precipitation type (rainfall/snowfall/mixed), daily mean temperature, and daily mean wind speed at 10-m of a dense national network of 2379 stations from 1961 to 2013 provided by the National Meteorological Information Centre (NMIC) of the China Meteorological Administration (CMA). The data have been used in various studies on climate change over China (Ren et al. 2005; Ding et al. 2013; Jiang et al. 2013; Ren et al. 2015a,b; Zhang et al. 2015; Ren et al. 2016). The daily precipitation data were obtained operatively by applying the Chinese standard precipitation gauge (CSPG) for manual observation during 1961–2003, which can measure all types of precipitation. After 2003 tipping-bucket sensors were used for automatic rainfall observation. The most commonly used was the double bucket tipping rainfall sensor. While in winter, the snowfall was measured by weighing precipitation sensor, which can obtain the precipitation amount by weighing without heating the instrument. The information of precipitation type was available in the metadata. The CSPG is a cylinder of galvanized iron with a diameter of 20 cm, and the automatic observation instrument is a tipping-bucket precipitation sensor installed with a water holding device with a diameter of 20 cm. All the gauges were placed 0.7 m above the ground but without wind shelters after 1960. This means wind-induced undercatch was substantial. According to the criterion of surface meteorological observation in China, precipitation was recorded twice a day at 0800 and 2000 [local time (LT) in Beijing], and daily precipitation released by NMIC is the accumulated precipitation amount during one day. Mean wind speed was recorded at 0200, 0800, 1400, and 2000 LT,

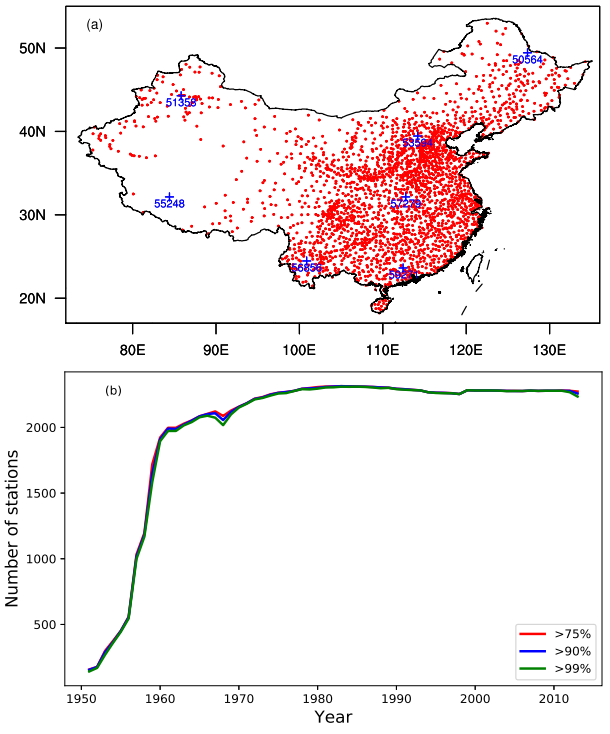

FIG. 1. (a) Distribution of the 2379 CMA national stations (red dots) over mainland China and seven stations with no relocations (blue pluses) chosen to assess the bias correction results, and (b) temporal evolution of the number of available stations with at least 75%, 90%, and 99% valid daily records within each particular year.

and is defined as the mean value during the 2-min period before the hour. The available daily mean wind speed released by NMIC is the average of the mean wind speed at the four individual measurement times. The daily mean temperature released by NMIC is the average value of the temperatures measured at the four time points, the same as the daily mean wind speed.

All the climate data used in this work were subject to quality control by the NMIC including extreme-value and internal consistency checks. This lead to the selection of 2379 CMA national stations having valid records for at least 30 years (Fig. 1a). Figure 1a indicates that more stations were in the southern and southeastern regions of China, while in the northern and northwestern parts the network was sparse. Figure 1b shows the number of available stations year by year with different thresholds for at least 75%, 90%, and 99% valid daily records within each year. The number of stations grew until 1961, when it was maintained at more than 2000. This is one of the reasons why we chose 1961–2013 as the study period.

b. Bias-correction methods

According to Sevruk and Hamon (1984), bias correction for gauge precipitation mainly includes trace

precipitation, wetting losses, evaporation losses, and wind undercatch errors. The general formula for precipitation bias correction was modified as follows (Sevruk and Hamon 1984; Yang et al. 2001; Ye et al. 2004):

$$P_c = K(P_g + \Delta P_w + \Delta P_e + \Delta P_t), \quad (1)$$

where P_c is the corrected precipitation; P_g is measured gauge precipitation; ΔP_w, ΔP_e, and ΔP_t are wetting losses, evaporation losses, and trace precipitation, respectively; and K is the correction coefficient for wind-induced errors, which is defined as 1/CR, and CR is the catch ratios due to wind-induced undercatch.

To determine the systematic biases in gauge measurements for precipitation, a gauge intercomparison study between CSPG and reference gauges was carried out in Urumqi River basin, which is located in northwest China (Yang et al. 1991). According to the intercomparison study, catch ratios due to wind-induced undercatch have been developed for different precipitation types (i.e., snow, rain, and mixed) (Yang et al. 1991; Ye et al. 2004):

$$\mathrm{CR}_s(\text{snow}) = \exp(-0.056W_s) \times 100, \quad (2)$$

$$\mathrm{CR}_r(\text{rain}) = \exp(-0.041W_s) \times 100, \quad \text{and} \quad (3)$$

$$\mathrm{CR}_m(\text{mixed}) = \mathrm{CR}_s - (\mathrm{CR}_s - \mathrm{CR}_r) \times (T_d + 2)/4, \quad (4)$$

where CR_s, CR_r, and CR_m are catch ratios for snow, rainfall, and mixed precipitation, respectively; W_s is the daily 10-m mean wind speed; and T_d is the daily mean temperature. It is noteworthy that the catch ratio for mixed precipitation has a linear relationship with catch ratios for snow and rainfall and daily mean temperature (T_d). The correction factor of wind-induced errors for snowfall in Yang et al. (1991) is more conservative than that in Sun et al. (2013). Therefore, formulas (2)–(4) developed by Yang et al. (1991) were adopted, and the wind-loss correction is defined as 1/CR. Finally, the corrected daily precipitation can be obtained through the following formula (Ye et al. 2004):

$$P_c = \begin{cases} (P_g + \Delta P_w)/\mathrm{CR} \\ \Delta P_t \end{cases}, \quad (5)$$

where P_c is the corrected precipitation; P_g is measured gauge precipitation; ΔP_w is the wetting loss correction; ΔP_t is trace precipitation correction; and CR is the catch ratio of wind-induced undercatch obtained from Eqs. (2)–(4). The upper section in Eq. (5) is for measurable precipitation events, and the one below is for trace precipitation events.

According to the experiments by Yang et al. (1991), the average wetting loss of per observation was 0.23 mm for rainfall measurement, 0.30 for snowfall, and 0.29 mm for mixed precipitation. Therefore, we corrected the wetting losses once for each precipitation day according to the above criteria. For gauge observations in China, a trace event is recorded when precipitation is less than 0.1 mm, which is usually below the measured resolution. Trace precipitations are counted as precipitation days, but treated as zero quantitatively. Two trace precipitation events are sometimes reported in a single trace precipitation day in China. Following Yang et al. (1991) and Ye et al. (2004), to be conservative, we assigned a value of 0.10 mm to a given trace day regardless of the number of the trace events reported in a day.

Wind speed is the most important factor for gauge precipitation catch. To correct wind-induced undercatch, wind speed is required. The data of wind measurements at a standard height of 10 m were available for correction. It has been suggested that gauge exposure should be considered when reducing wind from the standard height to the gauge height (Sevruk 1982). Gauge exposure depends on the average vertical angle of obstacles around the gauge. The relationship between the gauge height and 10 m height wind varies with site exposure, which can be directly measured or estimated by a classification system based on metadata archives (Sevruk 1982). The station metadata are not available for precipitation bias corrections, so site exposure was not accounted for in wind speed estimates at the gauge height. This may introduce some uncertainties in the estimation of gauge catch efficiency. Depending on the different precipitation type (rainfall, snow, and mixed precipitation), the wind-induced undercatch could be different in quantity. It has been documented that for the same wind speed, gauge undercatch of snow is much higher than rain (Larson and Peck 1974; Goodison et al. 1998; Yang et al. 1995, 1998; Ye et al. 2004; Rasmussen et al. 2012; Sun et al. 2013; Nitu et al. 2018).

Though the correction formulas we adopted were determined by an intercomparison experiment between CSPG and reference gauges, uniform bias correction was applied both for CSPG and automatic gauges. Uniform bias correction of wind-induced undercatch was applied both for the manual and the automatic observation instruments, because both gauges had the same diameter and were installed at the same height of 0.7 m without wind shelters. However, the biases are mostly gauge specific, and applying uniform bias correction may lead to some potential uncertainties. The same correction for trace precipitation was used both for manual and automatic gauges, because a precipitation event of less than 0.10 mm is both below the resolution

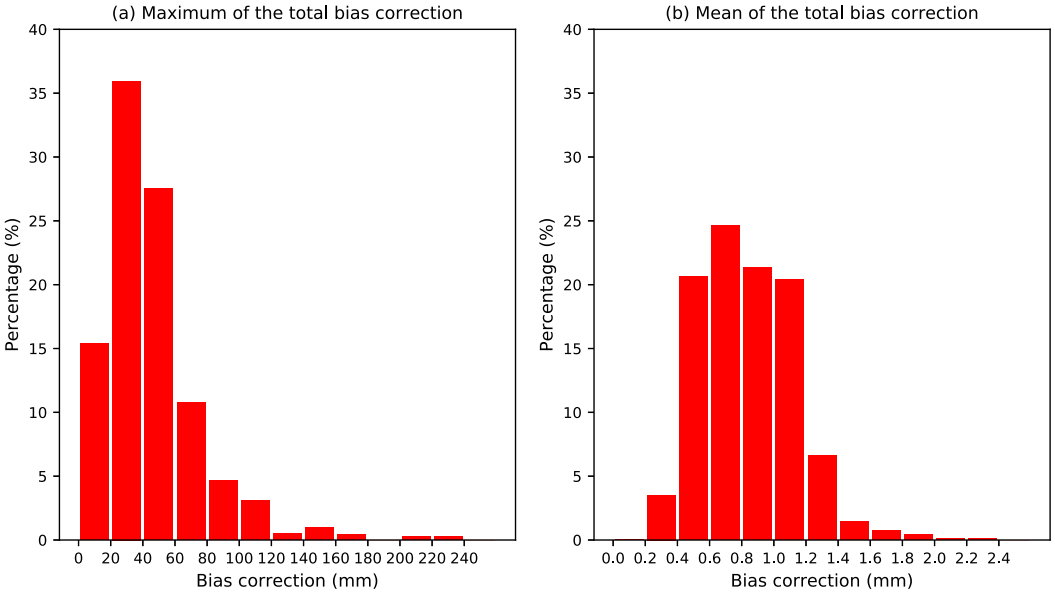

FIG. 2. Frequency distribution of (a) the maximum and (b) mean bias correction for the total correction of daily precipitation in all stations.

of the CSPG and tipping-bucket rainfall sensor. The biases of wetting losses of automatic gauges and CSPG may be slightly different theoretically. But the corresponding intercomparison experiment has not yet been carried out. This is a source of uncertainty for wetting loss correction. We hope to improve this in the future work. Tipping buckets have the unfortunate property of underestimating rainfall in high rain rates, because the collected rainfall would loss during tipping when rain is not being measured during the finite time required for bucket to tip from one side to the other. It is hard to evaluate the undercatch of tipping buckets, so this kind of undercatch was ignored after the beginning of 2003. Evaporation loss is time varying and site dependent, and it is unreasonable to estimate daily evaporation losses at large regional observation networks by using experimental results obtained from a few gauge sites (Ye et al. 2004). Therefore, only trace precipitation, wetting losses, and wind undercatch errors for measured gauge precipitation were corrected in our study.

c. *Statistical analysis methods*

In all following sections, the seasonal or annual bias correction is the total amount of daily correction for each season [December–February (DJF), March–May (MAM), June–August (JJA), September–November (SON)] or a full year, and the corresponding climatology is the average from 1961 to 2013. Annual/seasonal precipitation is the cumulative amount during the corresponding period. The precipitation amount divided by the number of precipitation days is defined as precipitation intensity. The correction percentage is the ratio of the corrected amount to the total measured precipitation. These definitions of precipitation were also applied to snowfall, the units of which refer to liquid equivalents.

Daily measured precipitation between 0.1 and 10.0 mm is defined as light rain. Light rain amounts and intensity are the cumulative amount classified as light rain and the ratio of the total amount of light rain to the number of light rain days. The related definition of rainstorm is the same as that for light rain, but for daily measured precipitation more than 50.0 mm. We used the unadjusted precipitation classification for the adjusted precipitation—in other words, we kept the original classification intact, and evaluated the changes in precipitation based solely on their original classifications.

3. Results of bias correction

By applying the methods described above, we corrected the bias of daily precipitation for the 2379 stations for the period of 1961–2013. Figure 2 illustrates the frequency distribution of the maximum and mean bias correction for all gauges. We found that most stations had a daily precipitation correction of 20–40 mm with the largest correction exceeding 200 mm (Fig. 2a). The most frequent mean correction amount was between 0.6 and 0.8 mm, with the highest value at about 2.2 mm (Fig. 2b).

Seven stations with no relocations and one for each of the seven regions (i.e., northeast, northwest, north, central, southwest, and south China, and Tibet) were

TABLE 1. Locations of 7 representative gauges with no relocations chosen to assess bias correction.

Station ID	50564	51358	53594	55248	56856	57279	59271
Station name	Sunwu	Wulanwusu	Lingqiu	Gaize	Jingdong	Zaoyang	Guangning
Subregion	Northeast	Northwest	North	Tibet	Southwest	Central	South
Climate type	Semihumid	Semiarid	Semihumid	Arid	Humid	Humid	Humid
Latitude	49.43°N	44.28°N	39.45°N	32.15°N	24.47°N	32.15°N	23.63°N
Longitude	127.35°E	85.82°E	114.18°E	84.42°E	100.87°E	112.75°E	112.43°E

chosen to assess the results of bias correction in detail (Fig. 1a and Table 1). The seven stations are located in arid regions (annual precipitation is less than 200 mm), semiarid regions (annual precipitation between 200 and 400 mm), semihumid regions (annual precipitation between 400 and 800 mm), and humid regions (annual precipitation more than 800 mm), respectively (Fig. 3a). In general, the annual bias correction is small for all stations, while the correction percentage is large (between 5% and 25%), both for annual precipitation and daily precipitation intensity (Figs. 3a,b). The lower the annual precipitation/daily precipitation intensity is, the higher the correction proportion. Both Lingqiu and Sunwu stations are located in semihumid regions, but the correction percentage of annual precipitation/daily intensity at Lingqiu station is clearly lower than that at Sunwu station. This is due to the larger proportion of snowfall at Sunwu located in higher latitude than at Lingqiu. The correction percentage of annual precipitation/daily intensity at Lingqiu station is similar to that at Zaoyang station, while the difference of precipitation climatology between them is quite large. The reason is that the snowfall percentage at Lingqiu station (4.7%) is higher than that at Zaoyang station (1.9%).

The features of correction amount/percentage for light rain (Figs. 3c,d) are quite similar to that for unclassified precipitation (Figs. 3a,b). The only caveat is that the difference of amount/percentage among stations for light rain is smaller, compared to that for unclassified precipitation. Due to a lack of heavy precipitation for some of the arid and semiarid stations, the effects of the corrections on rainstorm amount and intensity could not be determined (Figs. 3e,f). It makes sense that rainstorm amount/intensity is much higher in humid-area stations (e.g., Jingdong, Zaoyang, and Guangning). However, the correction percentage of rainstorm intensity in some semihumid areas (e.g., Sunwu) is much higher than that in humid regions (e.g., Zaoyang).

Generally, the frequency of occurrence decreases with precipitation amount for all selected gauges (Fig. 4). After bias correction, the corrected frequency of occurrence increased for most precipitation grades and most stations. The difference of frequency between bias corrected and measured precipitation falls with the increase of precipitation grade. Meanwhile, the frequency gap is larger in arid (e.g., Gaize) and semiarid (e.g., Wulanwusu) regions than semihumid (e.g., Sunwu and Lingqiu) and humid (e.g., Jingdong, Zaoyang, and Guangning) regions. For the same climate type, this gap is larger in colder regions (e.g., Sunwu) than warmer regions (e.g., Lingqiu), due to more snowfall in the colder environment.

To understand the seasonal differences of bias correction, seasonal correction amount and correction percentage for each correction component are also evaluated. Overall, the trace precipitation correction amount differs slightly in the four seasons (Fig. 5). In DJF, MAM, and SON, maximum trace precipitation correction appears in southwest China (including the eastern part of the Tibetan Plateau), the northern part of northwest China, and the western part of northeast China. In JJA, the corrected amount shows the largest values in northwest China. The correction percentage has a quite different spatial and temporal pattern from corrected amount due to different rainfall climatology (Fig. 5). Generally, the correction percentage is higher in DJF and lower in JJA, and the percentage value decreases from northwest to southeast China. Though the absolute magnitude of the trace precipitation correction is not quite large (less than 3.0 mm) across China, the correction percentage is dramatic, especially in the northwestern region of China.

Figure 6 shows that the wetting loss amount in JJA is more than that in DJF. This is due to the number of precipitation days in summer being much more than those in winter over most regions of China. The correction amount exhibits a remarkable seasonal and spatial variation: the maximum value in winter appears in southeast China; in spring another maximum value center arises in southwest China, which becomes obviously prominent in summer; while in autumn, the maximum center begins to shift back to southeast China, which is finally formed in winter. The spatial pattern of correction percentage for wetting loss is similar to that for trace precipitation: the correction percentage is higher in winter, lower in summer, and the percentage value declines from northwest to southeast China. Additionally, except for extremely arid areas in northwest China,

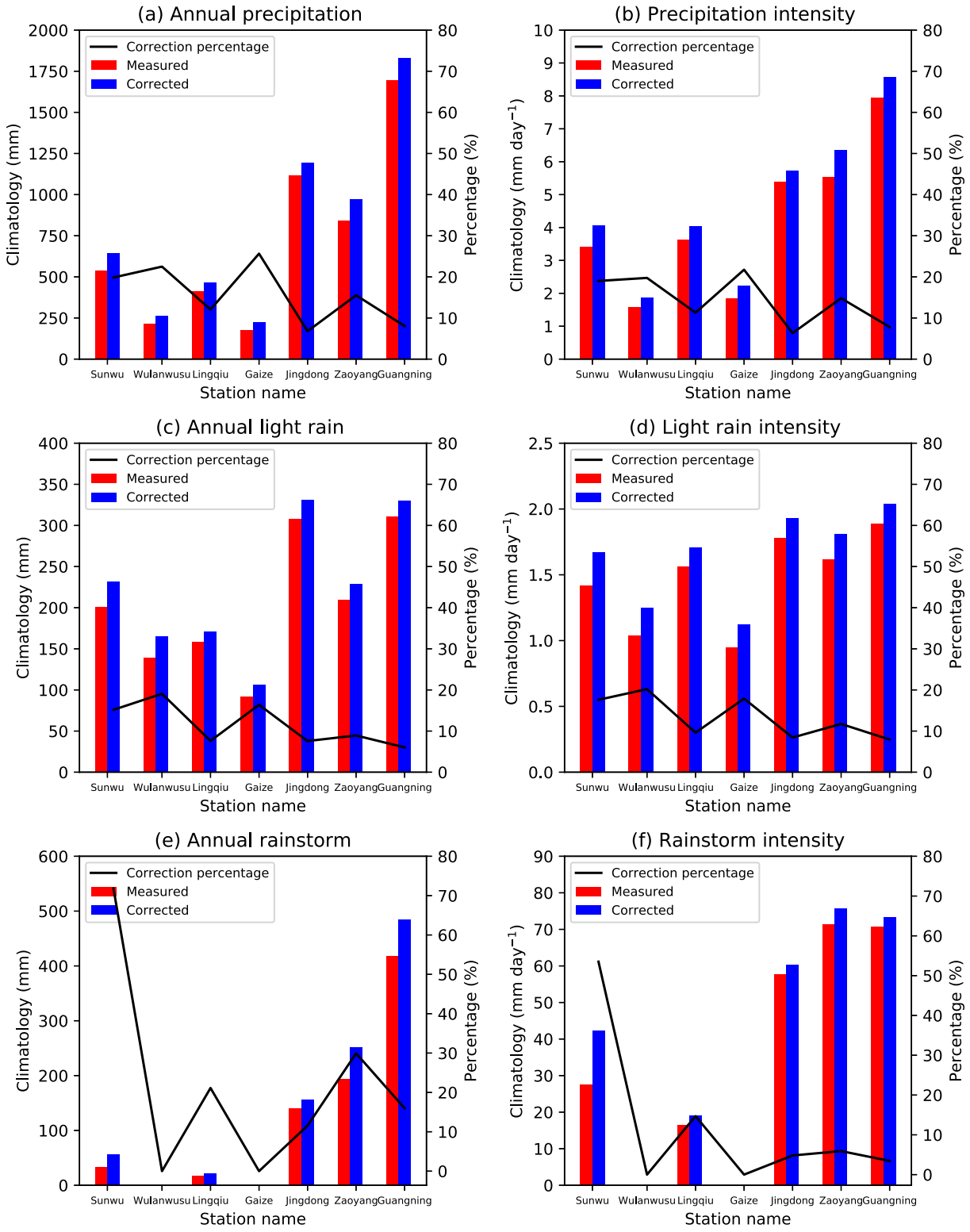

FIG. 3. Measured/corrected climatology and correction percentages for the climatology of (a) annual precipitation (mm), (b) daily precipitation intensity (mm day^{-1}); (c),(d) light rain amount (mm) and intensity (mm day^{-1}), respectively; and (e),(f) rainstorm amount (mm) and intensity (mm day^{-1}), respectively, during the period of 1961–2013 for 7 representative gauges with no relocations.

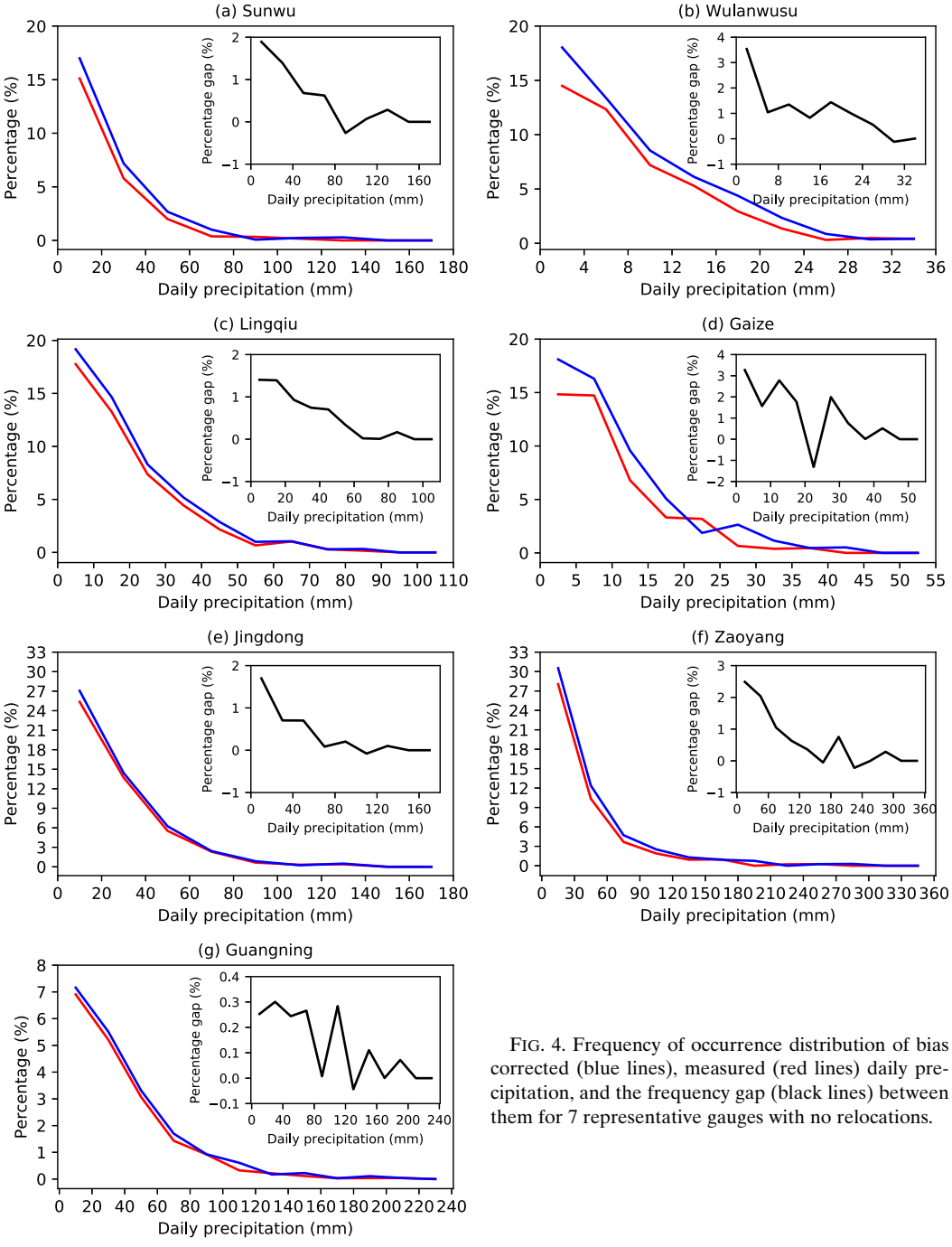

FIG. 4. Frequency of occurrence distribution of bias corrected (blue lines), measured (red lines) daily precipitation, and the frequency gap (black lines) between them for 7 representative gauges with no relocations.

the correction percentage for wetting loss is generally larger than for trace precipitation, indicating that wetting loss correction is more important than trace precipitation correction in most humid regions of China. In extremely arid areas, trace precipitation correction is as important as wetting loss correction.

The correction amount for wind-induced loss is large in wet regions (southeast China) and small in arid regions (northwest China) (Fig. 7). This spatial distribution pattern is quite unambiguous in the dry season (DJF and MAM), which precisely reflects the monsoon rainfall characteristics. In the wet season (JJA and SON), extremely high correction for wind-induced loss is found in coastal regions where typhoons often occur. It is found that large correction percentage for wind-induced undercatch occurs in the Tibetan Plateau, north China,

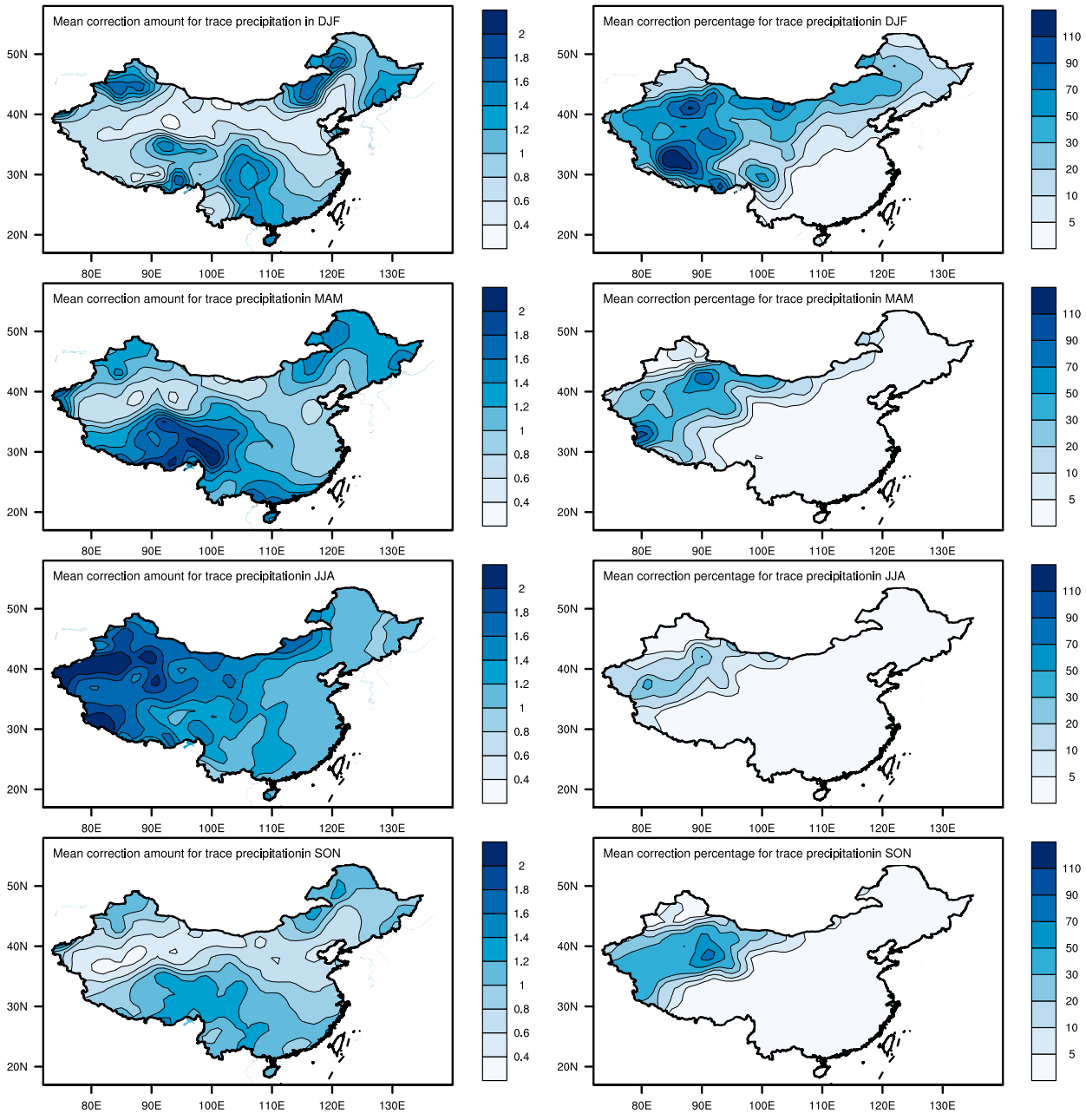

FIG. 5. Mean of seasonal (left) correction amount (mm) and (right) percentage (%) for trace precipitation for 1961–2013 over mainland China.

and northeast China, where winter climate is cold and snowy or dry, and the wind speed is large (Ding et al. 2013). At the same time, the mean correction amount for wind-induced error in period of 1961–2013 was not as large as that during 1951–98 compared to the results of Ye et al. (2004). This is probably due to the gradual reduction of annual mean wind speed on precipitation days over most regions of China (Fig. 8). The significant decline in near-surface wind speed in recent decades has been reported in previous studies (e.g., Ren et al. 2005; Jiang et al. 2009, 2013).

4. Effect of bias correction on precipitation climatology

As shown in Fig. 9, the distribution pattern of bias-corrected annual precipitation is a gradual reduction from southeast to northwest China, which has not changed

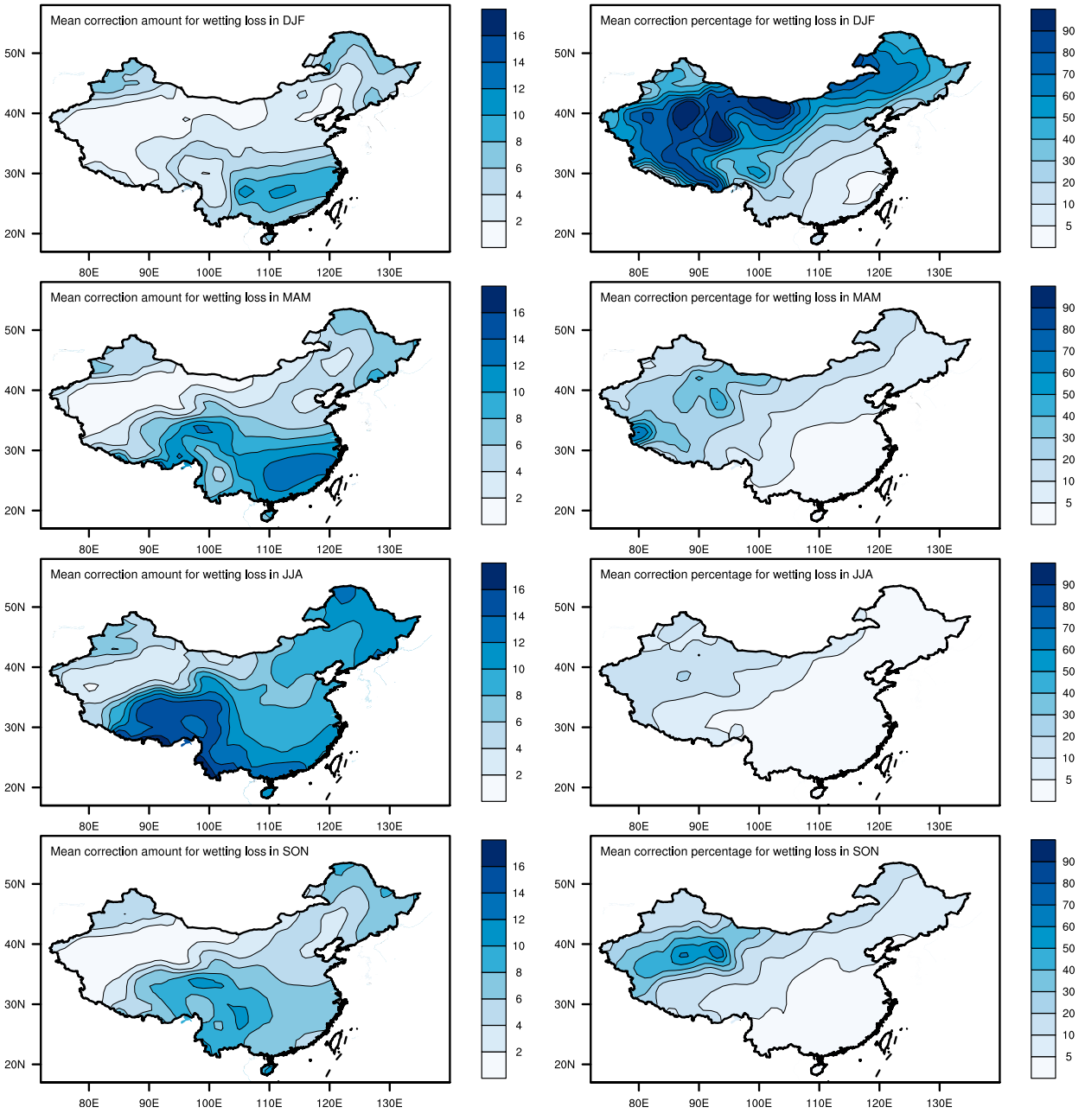

FIG. 6. As in Fig. 5, but for wetting losses.

much compared to that of unadjusted precipitation (figure not shown here). However, annual precipitation increased over China after bias correction to varying degrees. The area with precipitation less than 50 mm is reduced, and the 400, 800, and 1600 mm contours are extended northwestward (Fig. 9b). The spatial pattern of bias-corrected precipitation intensity (Fig. 9c) is quite similar to that of the annual precipitation amount, featured by the heavy precipitation often occurring in southeast China and weak precipitation in arid regions. After bias correction, precipitation intensity increased to varying degrees (Fig. 9d). Figure 9e indicates that the impact of bias correction on precipitation intensity is greatest in dry regions where the corrected precipitation intensity has increased by 35%.

The value of the DJF correction percentage is clearly higher than those of the other three seasons, and the JJA value is the lowest (Fig. 10). This means that bias correction poses a greater influence in the cold and dry season over China. Because the catch ratio of snowfall is

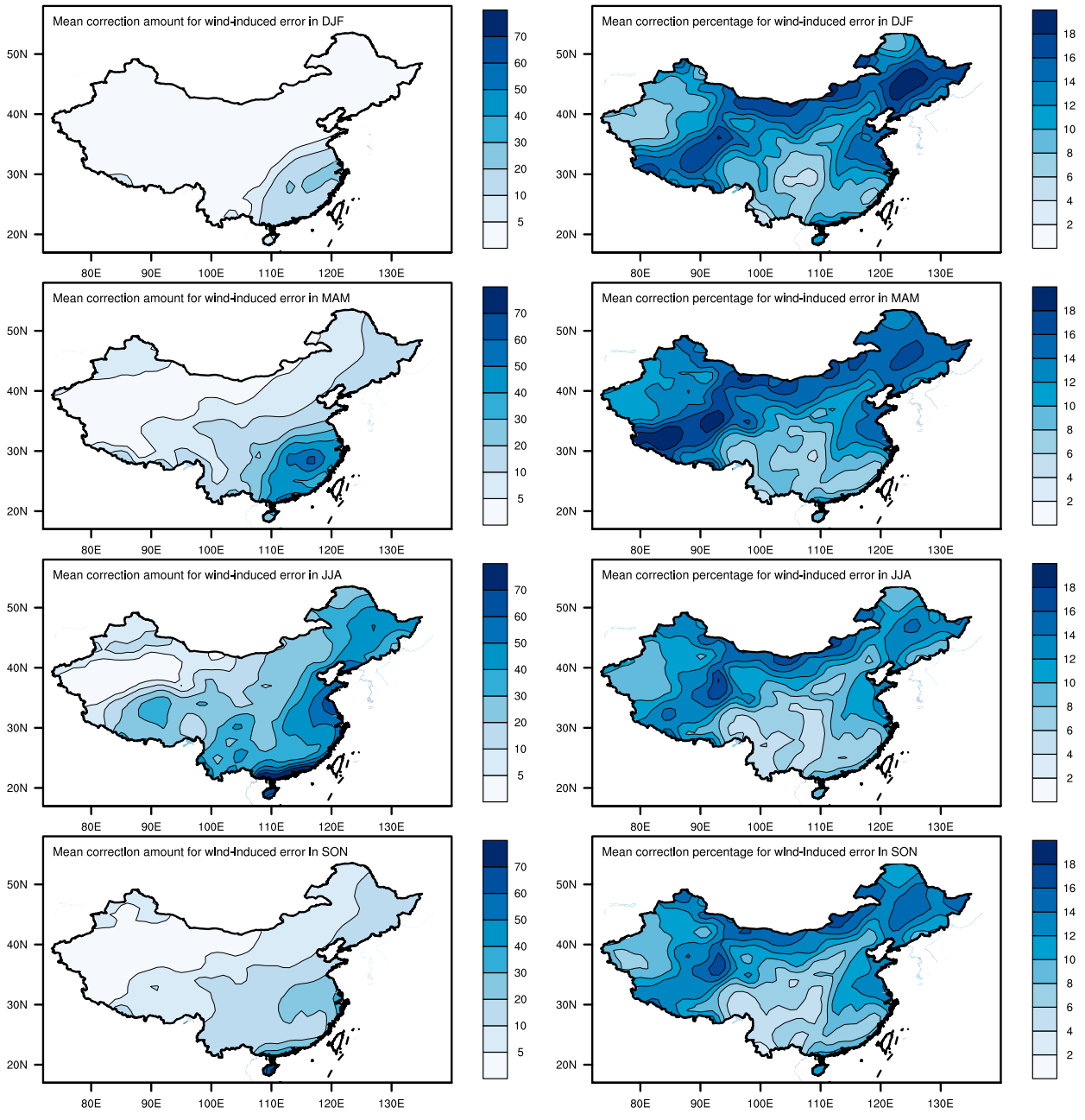

FIG. 7. As in Fig. 5, but for wind-induced undercatch.

less than that of rainfall, the bias correction of precipitation has the greatest impact over northwest and northeast China in winter, with the highest DJF correction percentage reaching more than 80%. The climatology of MAM precipitation shows the highest correction percentage (more than 60%) in the Tibetan region. In summer and autumn, bias correction has a greater influence in arid regions where the highest value is more than 40%.

From Fig. 11, we find that light rain is most likely to occur in southwest China where the annual light rain amount is more than 400 mm. In addition, light rain intensity shows a higher value (more than 2.1 mm day^{-1}) in southeast China and some regions of southwest China. After bias correction, the light rain amount and intensity clearly increased over the whole of China. Figure 11e indicates that the bias correction has the greatest influence on arid regions, and the light rain intensity after bias correction could increase by 40% in some extremely arid regions.

The bias-corrected rainstorm amount and intensity gradually decrease from southeast to northwest China

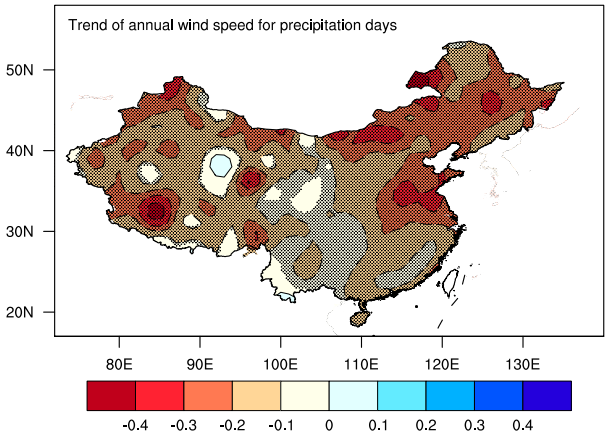

FIG. 8. The per 10 a trend of annual mean wind speed for precipitation days [m s^{-1} (10 yr)$^{-1}$] for 1961–2013 over mainland China, and the regions having significant changes at 0.05 confidence level are stippled.

(Fig. 12). In general, the correction percentage increases gradually from southeast to northwest China, and the correction percentage has larger differences in arid regions than wet regions. The maximum correction percentage could reach as high as 18% in some regions of northwest and northeast China. Though rainstorms are rare in arid regions, the actual amount and intensity of rainstorm events is really higher than the observed value, especially because rainstorms are often accompanied by strong winds. Please note that we used the unadjusted precipitation classification for the adjusted precipitation, so the precipitation events after correction that reached the light rain or rainstorm level were not included in Figs. 11 and 12. Therefore, besides the stronger rainstorm described in Fig. 12e, we should also pay attention to those new emerging rainstorm events due to the correction (Fig. 13). During the period of 1961–2013, the total number of actual rainstorm events could be 90 days more than that of observed rainstorm events (about 500 days) in some coastal areas of China.

The bias correction has a larger influence on snowfall (Fig. 14) than on unclassified precipitation (Fig. 9) and rainfall. This is due to the gauge undercatch of snowfall, which is much higher than rainfall undercatch for the same wind speed. After bias correction, the annual snowfall amount is larger in wet and cold regions (northern part of northwest and northeast China) as well as high-altitude regions (Tibetan Plateau) (Fig. 14a), and the area with more than 10 and 80 mm of annual snowfall is much larger than that derived from measured snowfall data (Fig. 14b). The spatial pattern of bias-corrected snowfall intensity is quite different from that of the snowfall amount (Figs. 14a,c). Stronger snowfall is found in the Yangtze and Huaihe River basins (25°–35°N, 110°–120°E). This is due to the abundant moisture content there, though the annual total snowfall is less than that in the far north (Liu et al. 2012; Zhang et al. 2015). In addition, the corresponding influence of bias correction is much greater in dry and cold regions than that in wet and warm regions (Fig. 14e). The maximum correction percentage of snowfall is up to 50% or more, which is much higher than that of precipitation, including solid state and rainfall.

5. Discussion

Because of the diversity of observational environments and reference gauge types, the bias-correction methods could be different. For example, Sun et al. (2013) developed the correction factors of wind-induced errors for snowfall by comparing parallel observation data from three reference gauges in northeast China during 1992–98, which is presented below:

$$\mathrm{CR}_s(\mathrm{snow}) = \exp(-0.12W_s) \times 100, \qquad (6)$$

where CR_s is catch ratios for snow, and W_s is the daily 10-m mean wind speed. Comparing formula (6) and (2), the functions of wind speed and catch ratio for snow developed by Yang et al. (1991) and Sun et al. (2013) are similar but with different factors (i.e., −0.056 vs −0.12). This indicates the robust relationship between the wind speed and the catch ratios for snow characterized by different coefficients derived from different experiments. Different correction factors may lead to some uncertainties, however. Hence, in this section, we evaluated the uncertainty in different correction methods by applying the two existing correction functions to observed snow events at five stations (ID 50564, 51358, 53594, 55248, and 57279). Two of the seven representative stations (ID 56856 and 59271) were excluded because of no snowfall detected. In the followings, the correction method used in this study is called method I, and the correction method developed by Sun et al. (2013) is called method II.

During the past 53 years, a total of 3614, 2693, 1148, 1664, and 446 snow events were detected at station 50564, 51358, 53594, 55248, and 57279, respectively. For station 50564, the average of corrected daily snowfall is 1.64 and 1.92 mm by employing methods I and II, respectively. The average of corrected snowfall for other 4 stations can also be seen in Table 2. The corrected snowfall by using method II is more than that by method I, which is clear at all selected stations (Table 2). The absolute difference at station 57279 is the largest (i.e., 0.46 mm), while stations 51358 and 53594 register the smallest difference (i.e., 0.13 mm). Figure 15 presents the corrected snowfall by using method I, as well as the

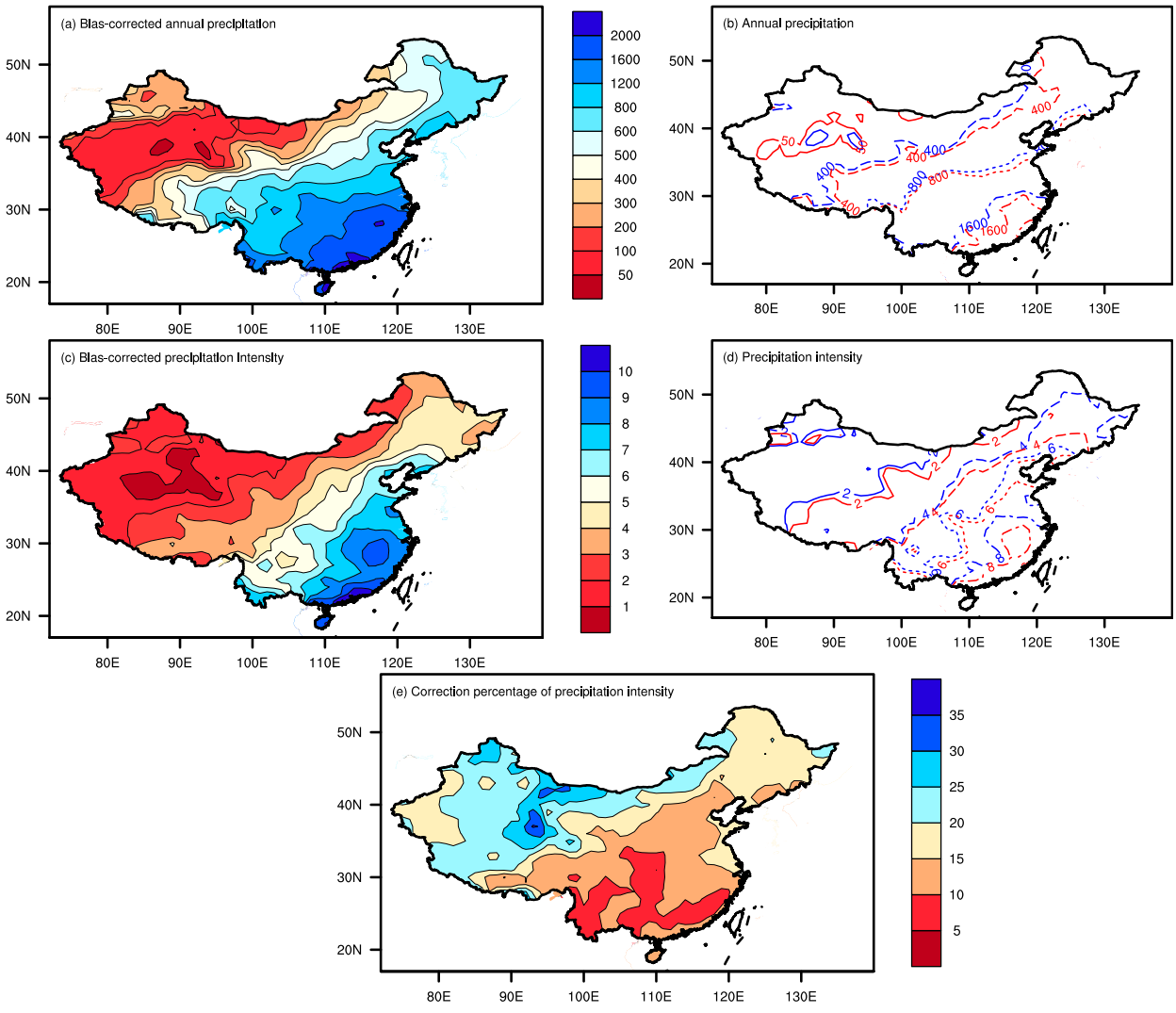

FIG. 9. (a) Climatology of bias corrected annual precipitation (mm), (b) specific contours of annual precipitation (mm), (c) climatology of precipitation intensity (mm day^{-1}), (d) specific contours of precipitation intensity (mm day^{-1}), and (e) correction percentage of precipitation intensity (%) for 1961–2013 over mainland China. Blue (red) lines in (b),(d) represent climatologies with (without) bias correction.

absolute difference between method II and I for each snow event. The absolute difference is quite small in most snow events; however, it reaches 10 mm or more for a few of events at station 50564. Besides, the absolute difference of corrected daily snowfall between method II and I divided by corrected snowfall by applying method I is termed as the relative difference. On average, the smallest relative difference appears at station 51358 (i.e., 5.5%), while station 57279 sees the largest relative difference (i.e., 13.9%). This indicates that the corrected snowfall by using method II is more than that by method I, and the excess is less than 10% in general. Therefore, using different methods for snowfall correction could produce some uncertainty, but the difference of the results using the two methods is less than 10%. Because the data in reference gauge are unavailable for the time being, we are not able to develop new correction method for other precipitation types (i.e., rainfall and mixed precipitation) in this study. Compared with method II, method I developed by Yang et al. (1991) covers a variety of precipitation types (i.e., rainfall, snowfall and mixed). Besides, the correction of wind-induced errors for snowfall in method I is more conservative than that in method II. In view of the above reasons, we adopted the method I in this study.

The corrections for wind-induced undercatch as reported in this study may have other uncertainties of the same magnitude as caused by the applied correction

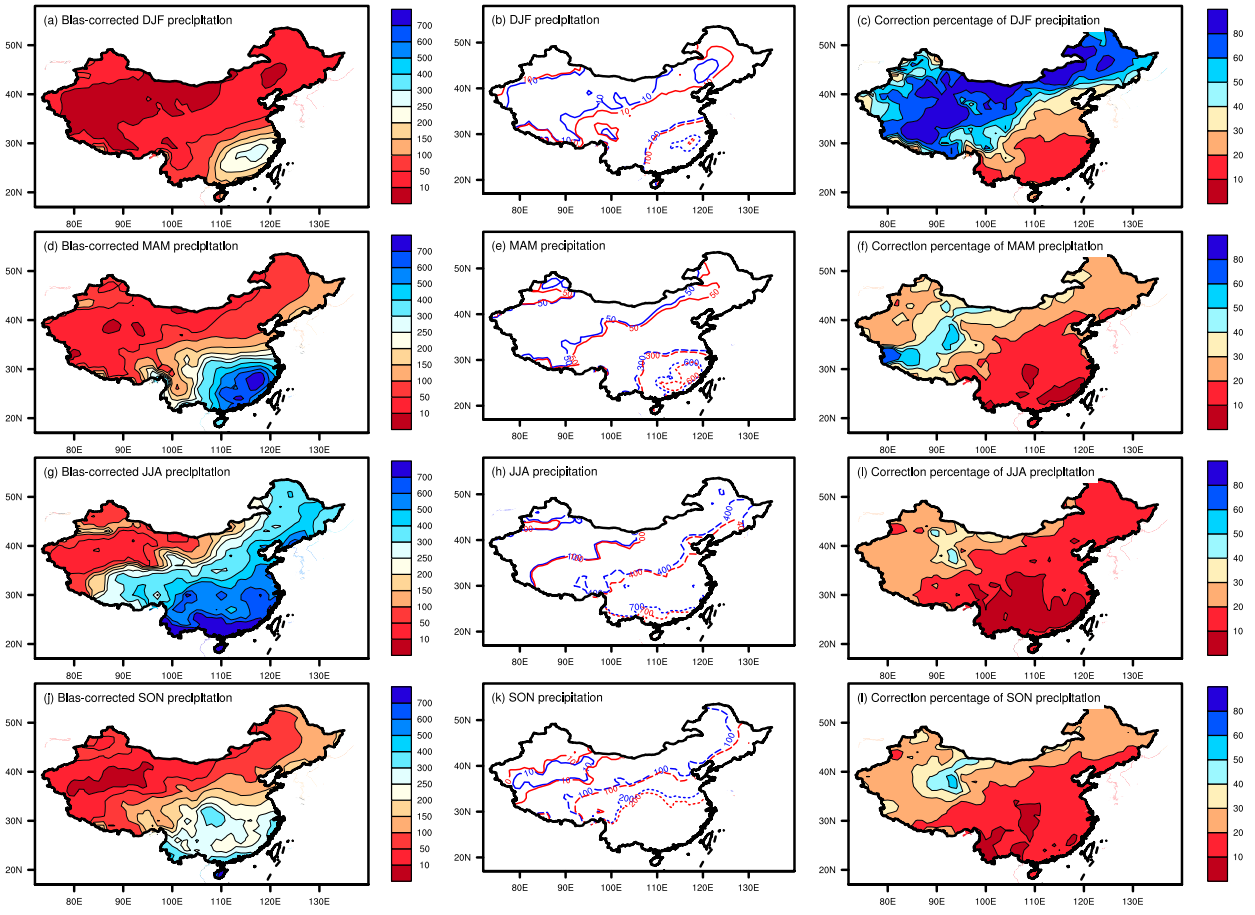

FIG. 10. Climatology of (left) seasonal [(a)–(c) for DJF; (d)–(f) for MAM; (g)–(i) for JJA; (j)–(l) for SON] precipitation after bias correction (mm), (middle) specific contours of seasonal precipitation (mm) with (blue lines) and without (red lines) bias correction, and (right) the corresponding correction percentage (%) for 1961–2013 over mainland China.

method, because wind speed can vary during 24-h period of a day, and the daily mean wind speed in some cases may not represent the simultaneous wind speed with the occurrence of precipitation. Hourly data are preferred, but high-quality hourly precipitation and wind speed data are unavailable at present. Besides, the current methods [e.g., methods developed by Yang et al. (1991) and Sun et al. (2013)] were developed by using daily precipitation data from reference gauges, and the data of hourly reference gauge measurements have not been applied yet for developing correction method. A verification of the effectiveness of the corrections using hourly data should be carried out on the premise of available hourly data and mature methods in the future. One important aim of SPICE is to improve the understanding and reliability of solid precipitation measurements using automatic gauges, and a series of methods for solid precipitation measurement and adjustment in China are being studied by Chinese scientists. In the future, precipitation bias correction in the country will be improved by applying the new methods.

6. Conclusions

Rain gauge estimates of precipitation suffer from a range of biases due to several factors. This results in an underestimate of the actual precipitation. Long-term daily data of precipitation, precipitation type, mean temperature and mean wind speed from 1961 to 2013 at 2379 national stations over China were used to conduct a bias correction for daily gauge records. Trace precipitation, wetting losses, and wind-induced undercatch were estimated for each precipitation day with different precipitation types, namely rainfall, snowfall, and mixed rainfall and snowfall. Based on this, a more reliable daily precipitation dataset was generated, and the influences of bias correction on the climatology of precipitation, snowfall, and extreme precipitation were also analyzed.

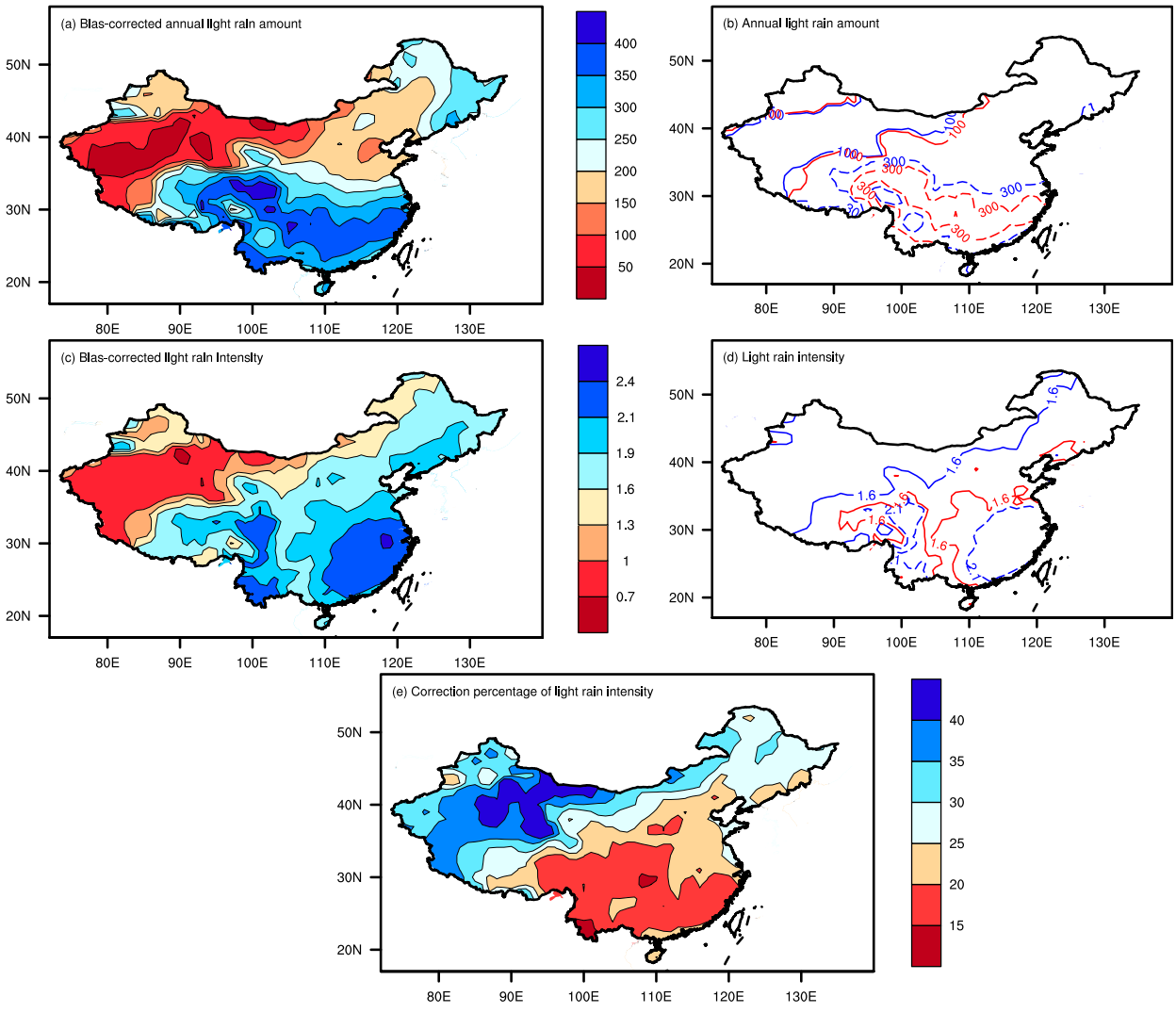

FIG. 11. As in Fig. 9, but for annual light rain.

We found that the corrections of trace precipitation and wetting losses were more important in arid than wet regions. The correction percentage decreased from northwest (e.g., 35% for annual precipitation) to southeast (e.g., 10% for annual precipitation) China, and was higher in cold seasons and lower in warm seasons. Wetting loss correction was greater than trace precipitation in most wet regions, while trace precipitation correction had the equivalent or greater influence than wetting loss correction in extremely arid areas. It is worth noting that, unlike trace precipitation and wetting losses, larger correction percentages for wind-induced error were found in cold or arid regions (the Tibetan Plateau and north and northeast China), as well as in high wind speed areas. The mean correction amount for wind-induced error in period of 1961–2013 was not as large as that during 1951–98 probably due to the gradual reduction of near-surface wind speed on precipitation days over most regions of China.

Generally, the climatology of bias-corrected annual precipitation as well as precipitation intensity increased to varying degrees. The 400, 800, and 1600 mm annual precipitation contours extended northwestward. The correction percentage of both annual precipitation amount and intensity was smallest in south part of China with a minimum percentage value less than 10%, while it was the greatest in arid regions with a maximum percentage value up to 35% or more. In addition, the correction percentage in DJF is clearly higher than that in other seasons due to less precipitation and a higher proportion of snowfall. Gauge undercatch of snowfall is much higher than that of rainfall for the same wind speed, hence the correction percentage of snowfall is overall higher than precipitation (including solid and

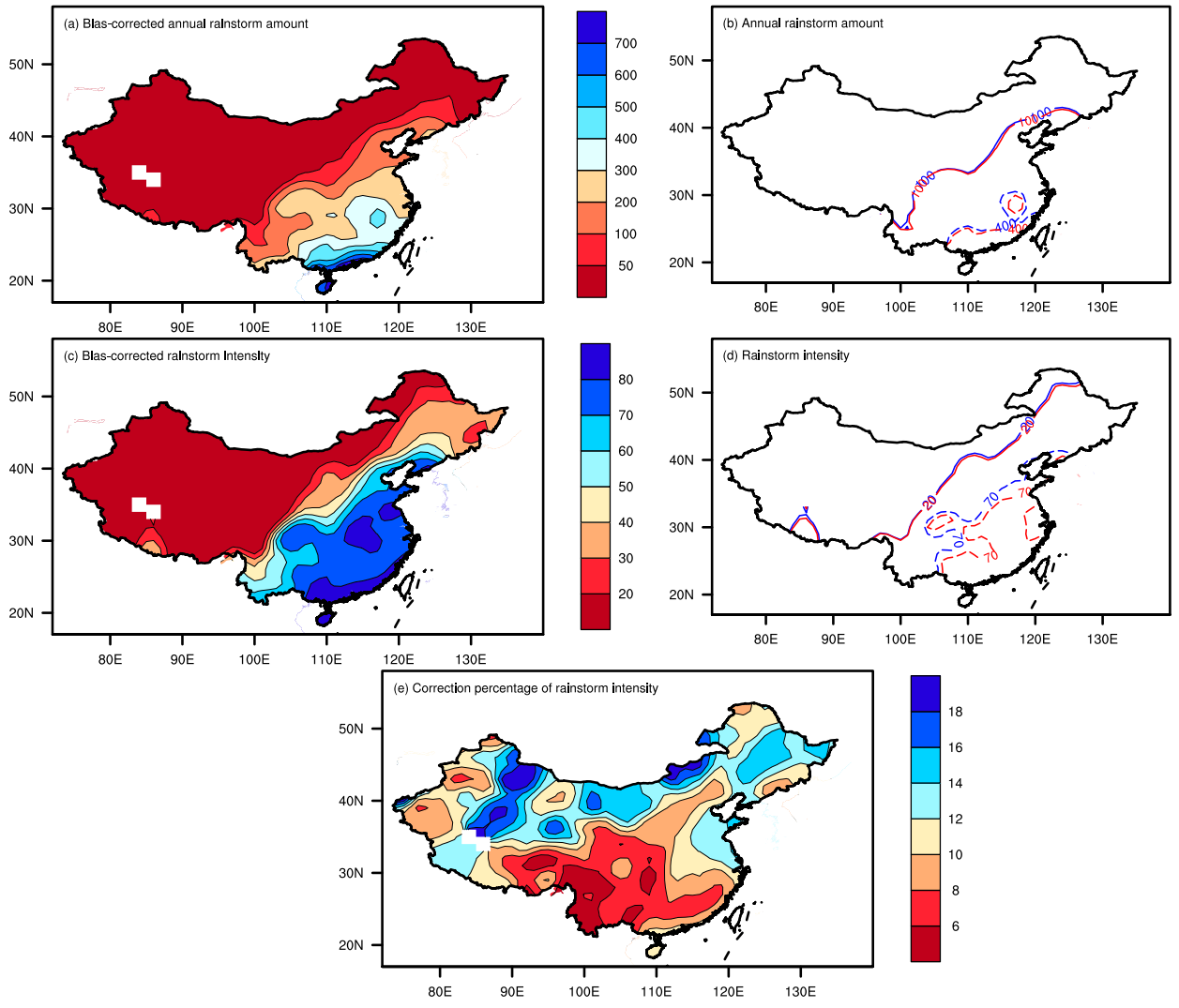

FIG. 12. As in Fig. 9, but for annual rainstorm.

liquid) or rainfall (liquid) with a maximum percentage value up to 50% or more. Due to the bias correction, the correction percentage of light rain intensity increased by more than 40% in extremely arid regions. Though rainstorm events are rare in arid regions, the corrected amount and intensity of rainstorms is higher than the observed value, and the maximum correction percentage for rainstorm intensity could reach 18% or more. Remarkably, the total number of actual rainstorm events during the past 53 years could be 90 days more than the observed rainstorm events (about 500 days) in some coastal areas of China.

Moreover, bearing in mind the results derived from our analysis, it can be concluded that bias correction is truly needed to obtain accurate estimates of precipitation records. Bias-corrected precipitation, especially snowfall, as well as rainstorms increased to different extents. The relative adjustments were greater in cold seasons (10%–80% in DJF) than warm seasons (10%–40% in JJA) and in arid regions (e.g., more than 50% in DJF) than wet areas (e.g., less than 20% in DJF). Therefore, the

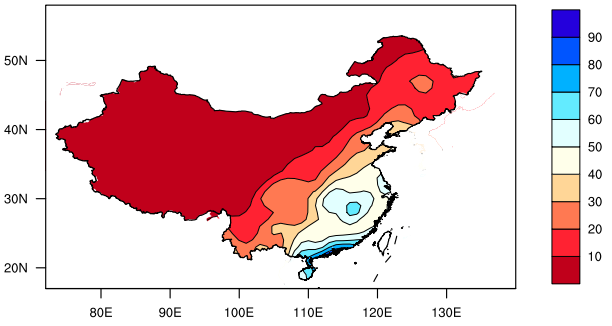

FIG. 13. The total number of increased rainstorm events (days) due to bias correction for 1961–2013 over mainland China.

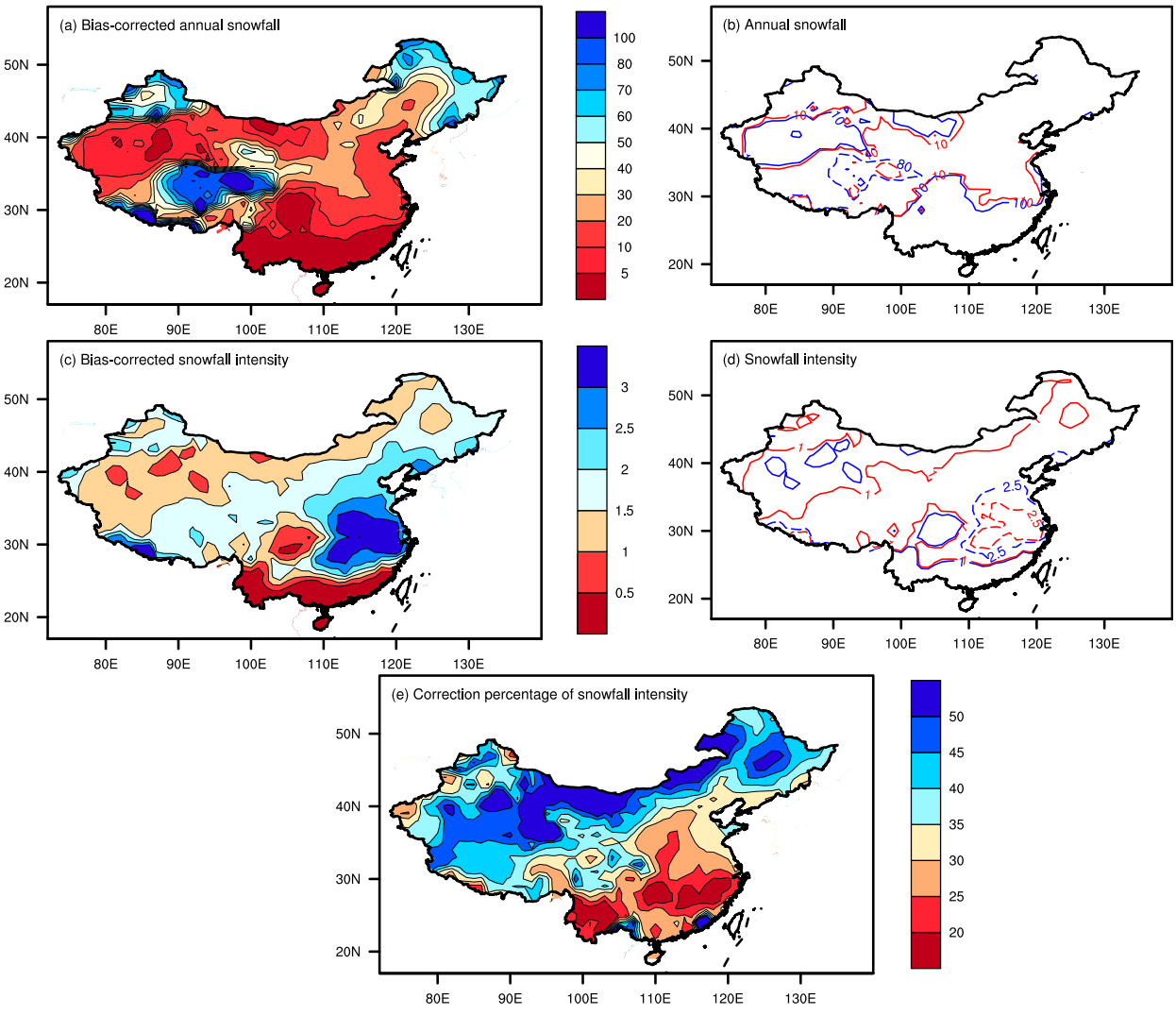

FIG. 14. As in Fig. 9, but for annual snowfall.

corrected daily precipitation data of a high-density observational network will substantially improve the accuracy and reliability of large-scale precipitation analyses over China, including studies and assessments of precipitation climatology and climate variability.

Last but not least, some uncertainties in current study of bias-correction method for precipitation exist. The correction in this study may have been conservative due to the application of a relatively low correction factor and the daily mean near-surface wind speed data. The diversity of observational environments and reference gauge types may have been the other potential causes for the uncertainty of the correction. Further improvements will be achieved in the future when high-quality subdaily data are available and the relevant comparative experiments of precipitation measurement are conducted.

TABLE 2. The average of the corrected snowfall (mm) by two correction methods, and the relative difference between two correction methods (%) for all corrected snow events at five stations.

Station ID		50564	51358	53594	55248	57279
The average of the corrected daily snowfall	Method I	1.64	1.36	1.15	0.85	2.20
	Method II	1.92	1.49	1.28	1.01	2.66
The average of relative difference between two correction methods		11.3%	5.5%	7.1%	9.2%	13.9%

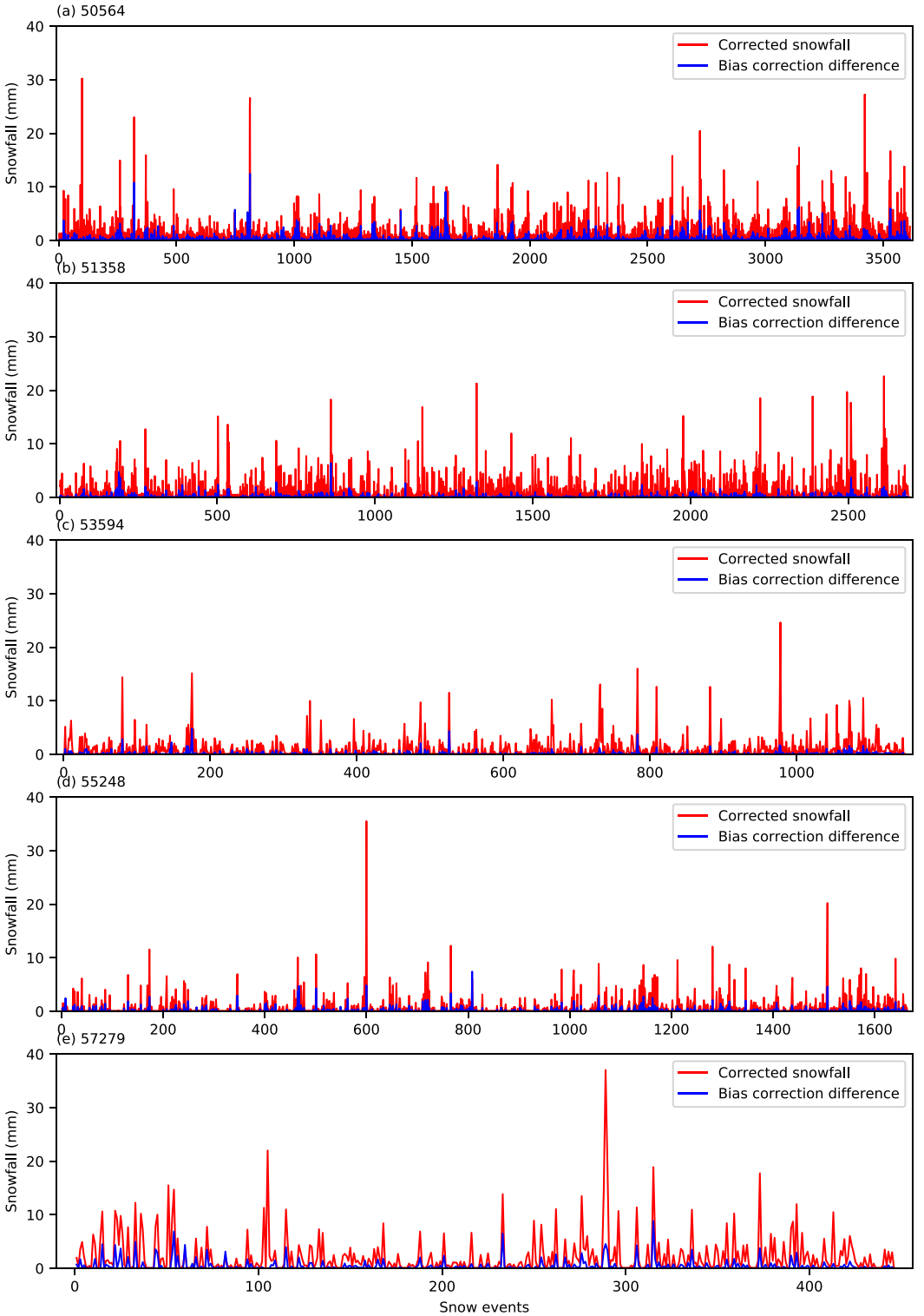

FIG. 15. The corrected snowfall (mm, red lines) by using method I and the absolute difference between two correction methods (mm, blue lines) for each snow event at station (a) 50564, (b) 51358, (c) 53594, (d) 55248, and (e) 57279.

Acknowledgments. We are grateful to the two anonymous reviewers for their valuable comments and helpful advice. This work was sponsored by the National Key Research and Development Program of China (Grants 2016YFA0600301 and 2018YFA0605603), the China Meteorological Administration Special Public Welfare Research Fund (Grant GYHY201406017), and the China Meteorological Administration Special Foundation for Climate Change (Grants CCSF201803 and CCSF201917).

REFERENCES

Aaltonen, A., E. Elomaa, A. Tuominen, and P. Valkovuori, 1993: Measurement of precipitation. *Symposium on Precipitation and Evaporation*, B. Sevruk and M. Lapin, Eds., Slovak Hydrometeorological Institute, 42–46.

Ding, Y., D. Yang, B. Ye, and N. Wang, 2007: Effects of bias correction on precipitation trend over China. *J. Geophys. Res.*, **112**, D13116, https://doi.org/10.1029/2006jd007938.

Ding, Y. H., S. W. Wang, J. Y. Zheng, H. J. Wang, and X. Q. Yang, 2013: *Climate of China* (in Chinese). Science Press, 557 pp.

Duchon, C. E., and C. J. Biddle, 2010: Undercatch of tipping-bucket gauges in high rain rate events. *Adv. Geosci.*, **25**, 11–15, https://doi.org/10.5194/adgeo-25-11-2010.

Folland, C. K., 1988: Numerical models of the raingauge exposure problem, field experiments and an improved collector design. *Quart. J. Roy. Meteor. Soc.*, **114**, 1485–1516, https://doi.org/10.1002/qj.49711448407.

Goodison, B. E., P. Y. T. Louie, and D. Yang, 1998: WMO solid precipitation measurement intercomparison: Final report. WMO Tech. Doc. 872, 212 pp.

Jiang, Y., Y. Luo, and Z. C. Zhao, 2009: Evaluation of wind speeds in China as simulated by global climate models (in Chinese with English abstract). *Acta Meteor. Sin.*, **67**, 923–934, https://doi.org/10.11676/qxxb2009.090.

——, ——, and ——, 2013: Maximum wind speed changes over China. *Acta Meteor. Sin.*, **27**, 63–74, https://doi.org/10.1007/s13351-013-0107-x.

Kochendorfer, J., and Coauthors, 2017: Errors and adjustments for single-Alter shielded and unshielded weighing gauge precipitation measurements from WMO-SPICE. *Hydrol. Earth Syst. Sci.*, **21**, 3525–3542, https://doi.org/10.5194/hess-21-3525-2017.

Kurtyka, J. C., 1953: Precipitation measurements study. Department of Registration and Education and States Water Survey Division, Investigation 20, 163 pp.

Larson, L. W., 1971: Precipitation and its measurement: A state of the art. University of Wyoming Water Resources Research Institute, Water Resource Series 24, 74 pp., http://library.wrds.uwyo.edu/wrs/wrs-24/wrs-24-co.html.

——, and E. L. Peck, 1974: Accuracy of precipitation measurements for hydrologic modeling. *Water Resour. Res.*, **10**, 857–863, https://doi.org/10.1029/WR010i004p00857.

Li, N., Y. Li, and N. Yao, 2018: Bias correction of the observed daily precipitation and redivision of climatic zones in China. *Int. J. Climatol.*, **38**, 3369–3387, https://doi.org/10.1002/joc.5506.

Liu, Y. L., G. Y. Ren, and H. M. Yu, 2012: Climatology of snow in China (in Chinese with English abstract). *Sci. Geogr. Sin.*, **32**, 1176–1185.

Nitu, R., and Coauthors, 2018: WMO Solid Precipitation Intercomparison Experiment (SPICE) (2012–2015). Instruments and Observing Methods Rep. 131, 452 pp., https://library.wmo.int/doc_num.php?explnum_id=5686.

Pan, X. C., and Coauthors, 2016: Bias corrections of precipitation measurements across experimental sites in different ecoclimatic regions of western Canada. *Cryosphere*, **10**, 23–47, https://doi.org/10.5194/tc-2016-122.

Rasmussen, R., and Coauthors, 2012: How well are we measuring snow: The NOAA/FAA/NCAR Winter Precipitation Test Bed. *Bull. Amer. Meteor. Soc.*, **93**, 811–829, https://doi.org/10.1175/BAMS-D-11-00052.1.

Ren, G. Y., J. Guo, M. Z. Xu, Z. Y. Chu, L. Zhang, X. K. Zou, Q. Q. Li, and X. N. Liu, 2005: Climate changes of China's mainland over the past half century (in Chinese with English abstract). *Acta Meteor. Sin.*, **63**, 942–956.

——, Y. J. Zhan, Y. Y. Ren, Y. Chen, T. Wang, Y. J. Liu, and X. B. Sun, 2015a: Spatial and temporal patterns of precipitation variability over mainland China: I: Climatology (in Chinese with English abstract). *Adv. Water Sci.*, **26**, 299–310.

——, Y. Y. Ren, Y. J. Zhan, X. B. Sun, Y. J. Liu, Y. Chen, and T. Wang, 2015b: Spatial and temporal patterns of precipitation variability over mainland China: II: Recent trends (in Chinese with English abstract). *Adv. Water Sci.*, **26**, 451–156.

——, and Coauthors, 2016: Spatial and temporal patterns of precipitation variability over mainland China: III: Causes for recent trends (in Chinese with English abstract). *Adv. Water Sci.*, **27**, 327–348.

Ren, Z. H., and M. Q. Li, 2007: Errors and correction of precipitation measurements in China. *Adv. Atmos. Sci.*, **24**, 449–458, https://doi.org/10.1007/s00376-007-0449-3.

——, G. L. Wang, F. L. Zou, and H. Z. Zhang, 2003: The research of precipitation measurement errors in China (in Chinese with English abstract). *Acta Meteor. Sin.*, **61**, 621–627.

Scaff, L., D. Q. Yang, Y. P. Li, and E. Mekis, 2015: Inconsistency in precipitation measurements across the Alaska–Yukon border. *Cryosphere*, **9**, 2417–2428, https://doi.org/10.5194/tc-9-2417-2015.

Sevruk, B., 1982: Method of correction for systematic error in point precipitation measurement for operational use. WMO Tech. Doc. 589, 91 pp.

——, and W. R. Hamon, 1984: International comparison of national precipitation gauges with a reference pit gauge. WMO Instrument and Observing Methods Rep. 17, 111 pp.

——, and L. Zahlavova, 1994: Classification system of precipitation gauge site exposure: Evaluation and application. *Int. J. Climatol.*, **14**, 681–689, https://doi.org/10.1002/joc.3370140607.

Sun, X. B., G. Y. Ren, Z. H. Ren, and Z. C. Shen, 2013: Effects of wind-induced errors on winter snowfall and its trends (in Chinese with English abstract). *Climatic Environ. Res.*, **18**, 178–186.

Westra, S., and Coauthors, 2014: Future changes to the intensity and frequency of short-duration extreme rainfall. *Rev. Geophys.*, **52**, 522–555, https://doi.org/10.1002/2014RG000464.

Yang, D., Y. F. Shi, E. S. Kang, Y. S. Zhang, and X. Y. Yang, 1991: Results of solid precipitation measurement intercomparison in the Alpine area of Urumqi River Basin. *Chin. Sci. Bull.*, **36**, 1105–1109.

——, and Coauthors, 1995: Accuracy of Tretyakov precipitation gauge: Result of WMO intercomparison. *Hydrol. Processes*, **9**, 877–895, https://doi.org/10.1002/hyp.3360090805.

——, B. E. Goodison, J. R. Metcalfe, V. S. Golubev, R. Bates, T. Pangburn, and C. L. Hanson, 1998: Accuracy of NWS 8 standard nonrecording precipitation gauge: Results and application of WMO intercomparison. *J. Atmos. Oceanic Technol.*, **30**, 57–68, https://doi.org/10.1175/1520-0426(1998)015<0054:AONSNP>2.0.CO;2.

——, and Coauthors, 2001: Compatibility evaluation of national precipitation gauge measurements. *J. Geophys. Res.*, **106**, 1481–1492, https://doi.org/10.1029/2000JD900612.

——, D. Kane, Z. Zhang, D. Legates, and B. Goodison, 2005: Bias-corrections of long-term (1973–2004) daily precipitation data over the northern regions. *Geophys. Res. Lett.*, **32**, L19501, https://doi.org/10.1029/2005GL024057.

Yao, N., Y. Li, N. Li, D. Yang, and O. Ayantobo, 2018: Bias correction of precipitation data and its effects on aridity and drought assessment in China over 1961–2015. *Sci. Total Environ.*, **639**, 1015–1027, https://doi.org/10.1016/j.scitotenv.2018.05.243.

Ye, B., D. Yang, Y. Ding, T. Han, and T. Koike, 2004: A bias corrected precipitation climatology for China. *J. Hydrometeor.*, **5**, 1147–1160, https://doi.org/10.1175/JHM-366.1.

——, ——, and L. Ma, 2012: Effect of precipitation bias-correction on water budget calculation in Upper Yellow River, China. *Environ. Res. Lett.*, **7**, 025201, https://doi.org/10.1088/1748-9326/7/2/025201.

Zhang, Z. F., S. Xi, N. Liu, Y. Yu, S. H. Fan, and M. N. Feng, 2015: Snowfall change characteristics in China from 1961 to 2012 (in Chinese with English abstract). *Ziyuan Kexue*, **37**, 1765–1773, http://www.resci.cn/CN/Y2015/V37/I9/1765.

Received: 18 May 2018 | Revised: 26 October 2018 | Accepted: 3 January 2019 | Published on: 18 March 2019

DOI: 10.1002/qj.3478

RESEARCH ARTICLE

Quarterly Journal of the Royal Meteorological Society RMetS

MJO modulation and its ability to predict boreal summer tropical cyclone genesis over the northwest Pacific in Met Office Hadley Centre and Beijing Climate Center seasonal prediction systems

Chongbo Zhao[1] | Hong-Li Ren[1,2*] | Rosie Eade[3] | Yujie Wu[1] | Jie Wu[1] | Craig MacLachlan[3]

[1]Laboratory for Climate Studies & CMA-NJU Joint Laboratory for Climate Prediction Studies, National Climate Center, China Meteorological Administration, Beijing, China
[2]Department of Atmospheric Science, School of Environmental Studies, China University of Geoscience, Wuhan, China
[3]Met Office Hadley Center, Met Office, Exeter, UK

Correspondence
Hong-Li Ren, Laboratory for Climate Studies, National Climate Center, China Meteorological Administration, Beijing 100081, China
Email: renhl@cma.gov.cn

Funding information
National Key R&D Program of China, 2016YFA0602100. National Natural Science Foundation of China, 41505065.National Basic Research Program of China, 2015CB453203. UK-China Research & Innovation Partnership Fund through the Met Office Climate Science for Service Partnership (CSSP) China.

Many of the current seasonal prediction systems show useful skill in Madden–Julian Oscillation (MJO) prediction but limited skill in forecasting tropical cyclones (TC). Quantifying the influences of MJO on TC in an operational prediction system is therefore useful for prediction purposes. The results in this study show that forecast skill of boreal summer TC genesis potential index (GPI) anomaly by operational seasonal prediction systems in Met Office Hadley Centre (MOHC) and Beijing Climate Center (BCC) are significantly higher than persistence out to four weeks. In the prediction system of MOHC, stronger MJO initial conditions are conducive to better GPI anomaly forecast, and MJO phases 4–7 make for higher GPI anomaly skill at lead 11–20 days. However, the MJO influence on TC forecasting skill is not so significant in BCC's prediction system. Both the prediction systems could reproduce the relationship that there are larger positive GPI anomalies in MJO phases 4–5 and negative ones in MJO phases 8–1 over the South China Sea (SCS) and northwest Pacific (WNP). However, the intensity of MJO effect on GPI is generally underestimated in BCC_CSM1.2, which may be due to the response of inadequate ascending motion and negative outgoing long-wave radiation accompanied by weak MJO over SCS and WNP. In GloSea5, the absolute vorticity, relative humidity, vertical velocity and wind shear terms are relatively closer to ERA-Interim during lead 1–10 days. Considering the intrinsic predictability of the MJO of more than 2 weeks, the forecasted MJO phase information has significant implications for TC genesis prediction on intraseasonal time-scales.

KEYWORDS
Madden–Julian Oscillation, operational seasonal prediction system, tropical cyclone

1 | INTRODUCTION

Tropical cyclones (TCs) are one of the most important weather phenomena due to the significant impacts on mankind with destructive and irreparable loss of life and property in many Asian-Pacific countries (Webster, 2008; Fan and Wang, 2009; Shen *et al.,* 2010). In order to meet the needs of coastal areas, sea shipping and the maritime aviation sector, the timely and highly accurate prediction of tropical cyclones has become a daunting challenge for operational forecast departments. We need to improve forecasting and understanding, with special emphasis on the frequent occurrence times and areas of tropical cyclones.

In recent years, dynamic numerical prediction models have been widely used in improving forecast skill and understanding theoretical mechanisms. Many operational centres have developed and consummated operational prediction systems based on the models for real-time forecasting services. GloSea5 and BCC_CSM1.2 are the seasonal prediction models in the Met Office Hadley Centre and Beijing Climate Center. To guarantee public forecast issuing and warning of extreme events such as tropical cyclones with improved accuracy, timeliness and service, it is important

 © 2019 Royal Meteorological Society

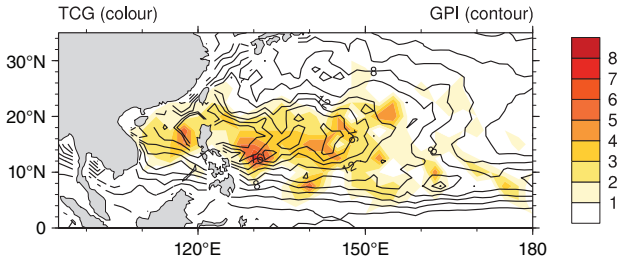

FIGURE 1 Number of TCG (colour) and summer mean GPI (contour) during July–October from 1994 to 2013

to access the reforecast skill in the prediction models in advance.

However, model forecasts have limited application in TC genesis (TCG) forecasting because of uncertainties associated with their forecast biases (Beven, 1999; Schumacher *et al.,* 2009). The TCG is thought to be influenced by a number of different large-scale environmental fields, such as low-level vorticity, vertical wind shear, sea-surface temperature, potential instability and humidity in the middle troposphere. Previous studies also have revealed some consistency between the Madden–Julian Oscillation's (MJO's) modulation of these fields and its modulation of TCs (e.g. Maloney and Hartmann, 2000a; Hall *et al.,* 2001; Bessafi and Wheeler, 2006; Jiang *et al.,* 2012; Wang *et al.,* 2013).

The modulation of northwest Pacific TCs by the MJO has received focused study (Nakazawa, 1988; Liebmann *et al.,* 1994). Many studies demonstrated a link between the enhanced convective phase of the MJO and the increased activity and formation of northwest Pacific TCs (Maloney and Hartmann, 2000b; Kim *et al.,* 2008; Camargo *et al.,* 2009; Vitart, 2009; Satoh *et al.,* 2012). The quantitative estimate of the relative impacts of the different large-scale fields of the MJO for the TC modulation in the reforecast data of operational numerical models needs to be made.

In this article we first assess the TC genesis forecast skill over WNP using the genesis potential index (GPI: Emanuel and Nolan, 2004; Camargo *et al.,* 2009) which is a widely used quantitative diagnosis of the contribution of large-scale factors on TC genesis, then analyse the modulation of TCs by the MJO. We further examine the extent to which the fluctuations in the genesis index associated with the MJO coincide in space and time with observed MJO effects on TC genesis frequency. In addition to improving understanding, these results are potentially useful for future developmental work on TC genesis frequency prediction, as it has been implied that the GPI may be usefully applied to the extended-range output under the precondition of high MJO prediction technique (Leroy and Wheeler, 2008).

The remainder of the article is organized as follows. The datasets used in this article are introduced in section 2.1. In section 2.2 we present the definition of the TC genesis index and describe the construction of the MJO composites. The descriptions of GloSea5 and BCC_CSM1.2 models are given

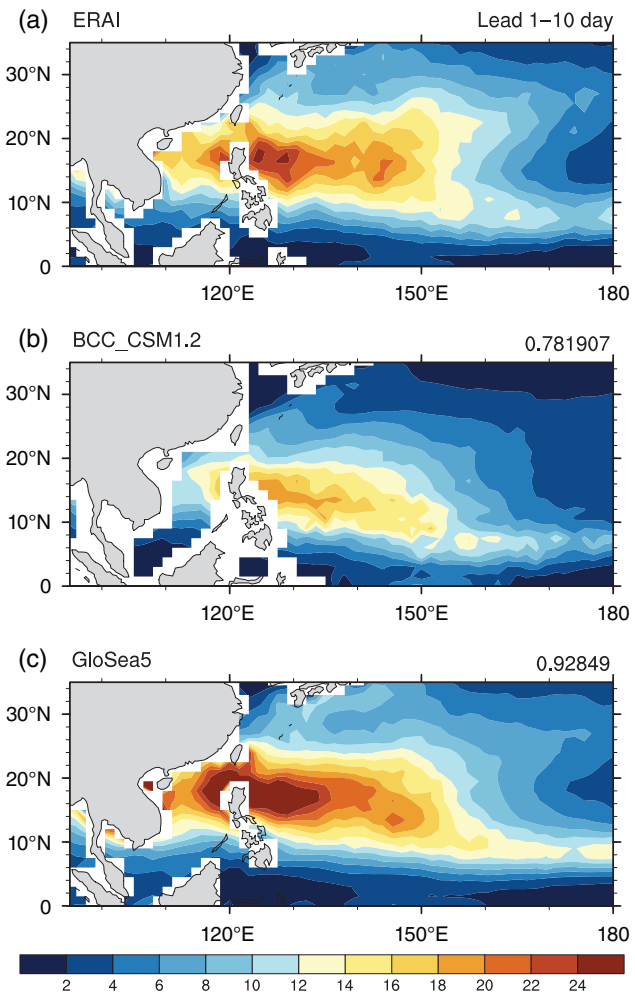

FIGURE 2 Summer mean GPI at lead 1–10 days from (a) ERA-Interim, (b) BCC_CSM1.2 and (c) GloSea5. The pattern correlations between models and ERA-Interim are given at the top-right corner of the panels

in section 2.3. Major analysis results are shown and discussed in section 3. We investigate the impacts of individual GPI terms on the TC genesis climate bias, forecast error and relationship with MJO by models in section 4. Conclusions are given in section 5.

2 | DATA, METHOD AND MODEL

2.1 | Data

The observational data used to verify the TC genesis forecast included the Joint Typhoon Warning Center (JTWC) datasets (available at www.usno.navy.mil/NOOC/nmfc-ph/RSS/jtwc/best_tracks), the daily outgoing long-wave radiation (OLR) from the National Oceanic and Atmospheric Administration (NOAA) (Liebmann and Smith, 1996) and the Optimum Interpolation (OI) Sea-Surface Temperature (SST) V2 dataset by Reynolds *et al.* (2002). For the atmospheric data the European Centre for Medium-range Weather Forecasts (ECMWF) Interim Re-Analysis (ERA-Interim: Dee *et al.,* 2011) was used. The National Climate Center of China Meteorological Administration and Hadley Centre of the Met

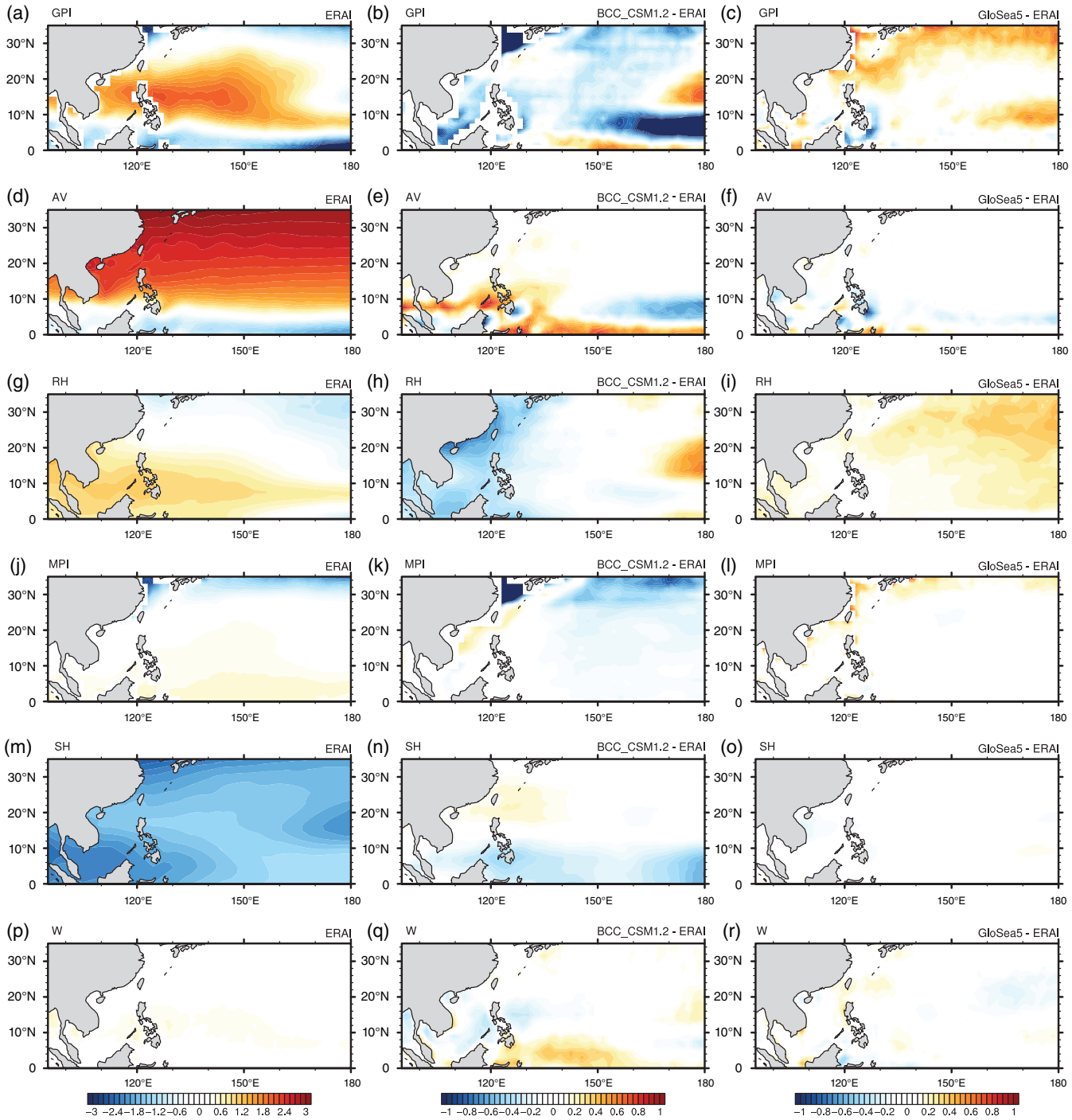

FIGURE 3 The logarithm of summer mean GPI, AV, RH, MPI, SH and W terms from ERA-Interim (a,d,g,j,m,p), difference between BCC_CSM1.2 and ERA-Interim (b,e,h,k,n,q), between GloSea5 and ERA-Interim (c,f,i,l,o,r) during lead 1–10 days

Office have conducted comprehensive seasonal reforecast experiments using BCC_CSM1.2 model (Liu *et al.,* 2017) and GloSea5 (MacLachlan *et al.,* 2015). BCC_CSM1.2 and GloSea5 hindcasts are initialized with National Centers for Environmental Prediction (NCEP) Reanalysis 1 (NCEP-R1: Kalnay *et al.,* 1996) and ERA-Interim, respectively. The original model outputs were converted into standard formatted files, which have 1.5° × 1.5° horizontal resolution and principal isobaric levels. These datasets during the WNP TC season from July to October during 1994–2013 were used.

2.2 | Method

In order to determine the factors that affect the distribution of TC genesis, we used a modified index according to Emanuel and Nolan (2004):

$$GPI' = |10^5\eta|^{3/2}\left(\frac{RH}{50}\right)^3\left(\frac{V_{\text{pot}}}{70}\right)^3 \times (1+0.1V_s)^{-2}\left(\frac{-\omega+0.1}{0.1}\right), \quad (1)$$

where η is the absolute vorticity at 850 hPa (AV; s^{-1}), RH is the relative humidity at 700 hPa (%), V_{pot} is the maximum

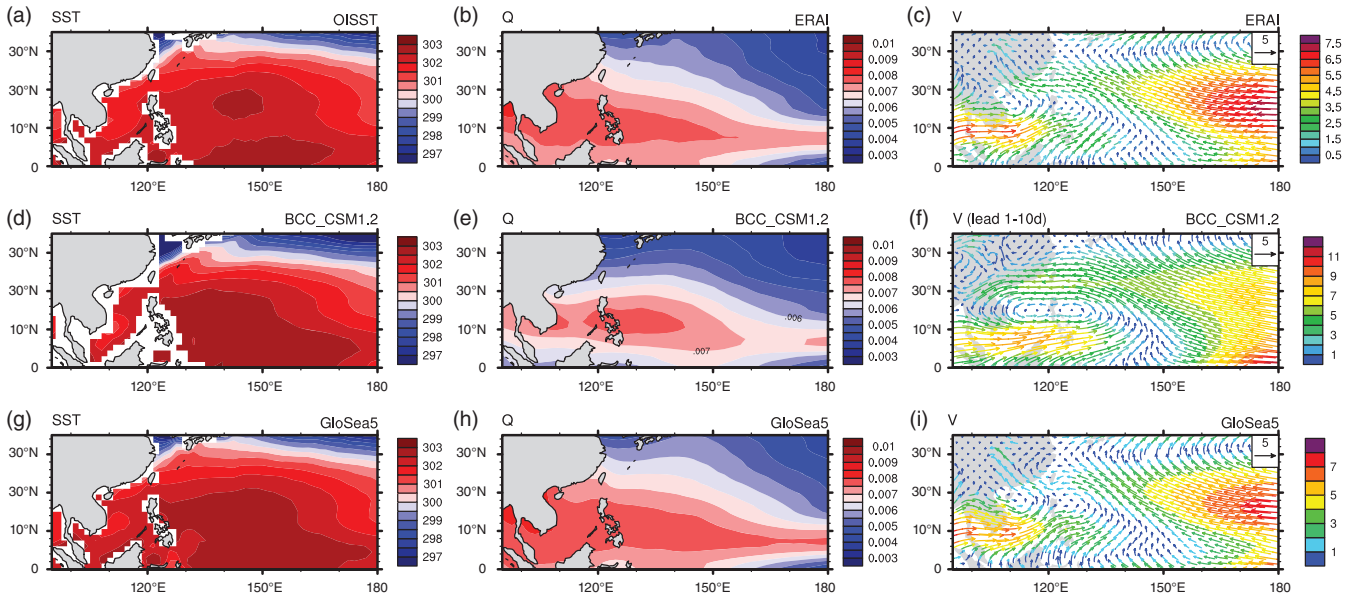

FIGURE 4 Summer mean SST (a,d,g), 700 hPa specific humidity (b,e,h) and 850 hPa wind (c,f,i, vector: 850 hPa wind, colour: absolute value of 850 hPa zonal wind velocity) from (a) OISST, (b,c) ERA-Interim, (d–f) BCC_CSM1.2 and (g–i) GloSea5 during lead 1–10 days

potential intensity (MPI; m/s), Vs is the magnitude of the vertical wind shear between 850 and 200 hPa (SH; m/s), and ω is the vertical wind velocity at 500 hPa (W; Pa/s). This W term in Equation 1 is used for correctly reproducing TC genesis over regions with strong ascending motions, such as the intertropical convergence zone (ITCZ) (Tian *et al.,* 2013). The MPI term is defined in Emanuel (1995) but as modified by Bister and Emanuel (1998):

$$V_{\text{pot}}{}^2 = \frac{C_k T_s}{C_D T_0} (CAPE^* - CAPE^b), \tag{2}$$

where C_k is the exchange coefficient for enthalpy, C_D is the drag coefficient, T_s is the SST (K), and T_0 is the mean outflow temperature (K). *CAPE** is the convective available potential energy (CAPE) of the air lifted from saturation at sea level related to environmental sounding, and $CAPE^b$ is that of the boundary-layer air. To find the relative contribution of five factors (AV, RH, MPI, SH and W) in GPI to the simulation biases, the relative error was calculated in log form (Yokoi *et al.,* 2009).

For MJO composites, we recognized the amplitude and phase of MJO based on real-time multivariate (RMM) MJO indices depicted by Wheeler and Hendon (2004) (hereafter WH04). In this study, we used the same MJO-related spatial structures and variances as WH04. We first calculated intraseasonal anomalies of the observed and predicted data following Lin *et al.* (2008) and Wang *et al.* (2014), then projected the daily data onto these observation-derived spatial structures to get both verification and model hindcast RMM values (Wu *et al.,* 2016).

For a real-time application, a non-filtering method is employed to extract the 10–80-day signal (Hsu *et al.,* 2014). Firstly, the climatologic annual cycle is removed from the raw datasets. Then, a 5-day running mean is used to remove the high-frequency signals. Finally, a 40-day running mean (from day −40 to day 0) is removed from the anomaly field above to remove low-frequency signals longer than 80 days. In this way, the 10–80-day anomaly data are obtained.

2.3 | Models

In this study, we assessed the TCG prediction by two operational seasonal prediction models, namely Beijing Climate Center Climate System Model (BCC_CSM1.2) and the Met Office global coupled model (GloSea5).

BCC_CSM1.2 is a fully-coupled Climate System Model and employed as the current operational model for seasonal prediction in BCC (Wu *et al.,* 2014). The atmospheric component is BCC Atmospheric General Circulation Model (BCC_AGCM2.2) at T106 triangular truncation in the horizontal direction and 40 hybrid sigma/pressure layers in the vertical direction with the top level at 0.5 hPa (Liu *et al.,* 2017). The ocean component is developed by modifying Modular Ocean Model version 4 (MOM4) from NOAA Geophysical Fluid Dynamics Laboratory (GFDL) (Griffies *et al.,* 2005). The sea ice model is GFDL Sea Ice Simulator (SIS; Winton, 2000) and the land model is Atmosphere–Vegetation Interaction Model (BCC_AVIM2; Ji *et al.,* 2008).

GloSea5 (Global Seasonal Forecasting System) is introduced in detail by Williams *et al.* (2015). The atmospheric component is Global Atmosphere 6.0 (GA6.0) at N216 (approximately 60 km in midlatitudes) and N96 (about 130 km) horizontal resolution and 85 vertical levels with the top at 85 km. The ocean component is the Nucleus for European Modelling of the Ocean (NEMO) ocean model Global Ocean 5.0 (GO5.0: Megann *et al.,* 2014). The sea ice model is the Los Alamos Community Ice CodE (CICE) model (GSI6.0: Rae *et al.,* 2015) and the land model is the Joint UK

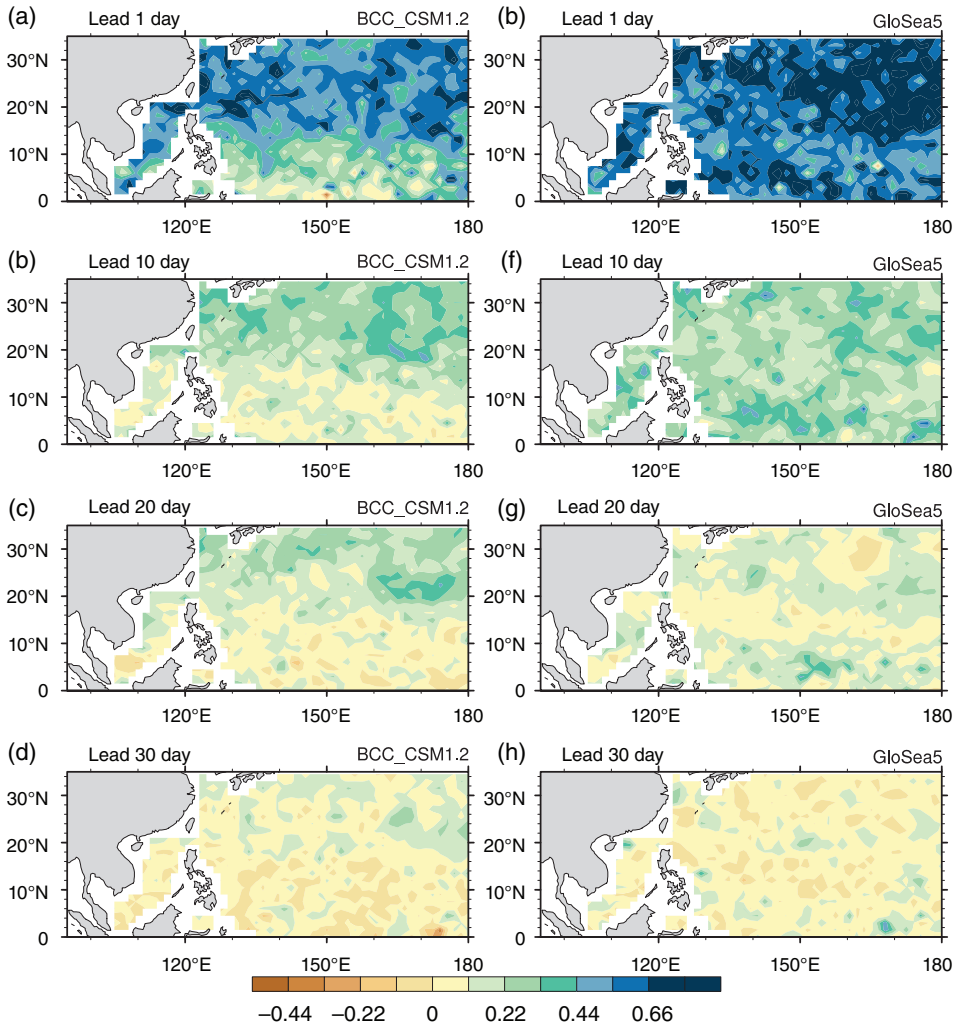

FIGURE 5 Time correlation coefficient (TCC) of the GPI anomaly forecasted by BCC_CSM1.2 (left) and GloSea5 (right) during lead (a,e) 1 day, (b,f) 10 days, (c,g) 20 days and (d,h) 30 days. The green areas are significant at the 0.05 level

Land Environment Simulator (JULES) land surface model Global Land 6.0 (GL6.0; Walters *et al.,* 2017).

The hindcasts were performed on 1st, 9th, 17th and 25th of every month, with three members based on the lagged average forecasting (LAF) method. The forecasts ran on every day from 1 January 1994 and ended with a 60-day integration, and were initialized at 0000 UTC of the first forecast day and 1800, 1200 and 0600 UTC of the previous day, respectively. Each daily hindcast set covered the period from 1994 to 2013, with the same experimental design as the real-time forecast. In this study, we focused on the WNP typhoon season from July to October in the Northern Hemisphere.

3 | GPI FORECAST SKILL IN HINDCASTS

The performance of GloSea5 and BCC_CSM1.2 hindcasts in predicting GPI over the WNP are evaluated in comparison with ERA-Interim reanalysis data. We firstly examine the ability of GloSea5 and BCC_CSM1.2 in reproducing summer mean GPI. Then, we assess the skill of these two models in predicting the GPI anomaly. Finally, the impacts of MJO amplitude and phase on GPI anomaly in the hindcast data are investigated.

3.1 | Evaluation of the summer mean GPI

We select the summer TCs whose genesis locations are over the WNP and whose 1 min maximum sustained surface wind speeds exceed 34 knots based on the JWTC dataset, to calculate the spatial distributions of the total number of TC genesis. The characteristics of the atmosphere and ocean provide favourable conditions for TCG during July–October along the South China Sea to the northwest Pacific. Two large-value centres of the TCG are respectively located on the east and west sides of the Philippines Islands, and the intensity attenuates eastward. Meanwhile, the summer mean GPI is presented in Figure 1, which is consist with the TCG map.

Overall, the pattern of summer mean TCG is reasonably well represented by GPI which are distributed mainly within a band between 5° and 25°N, extending eastward to 160°E, and gradually vanishing to the east of the date-line.

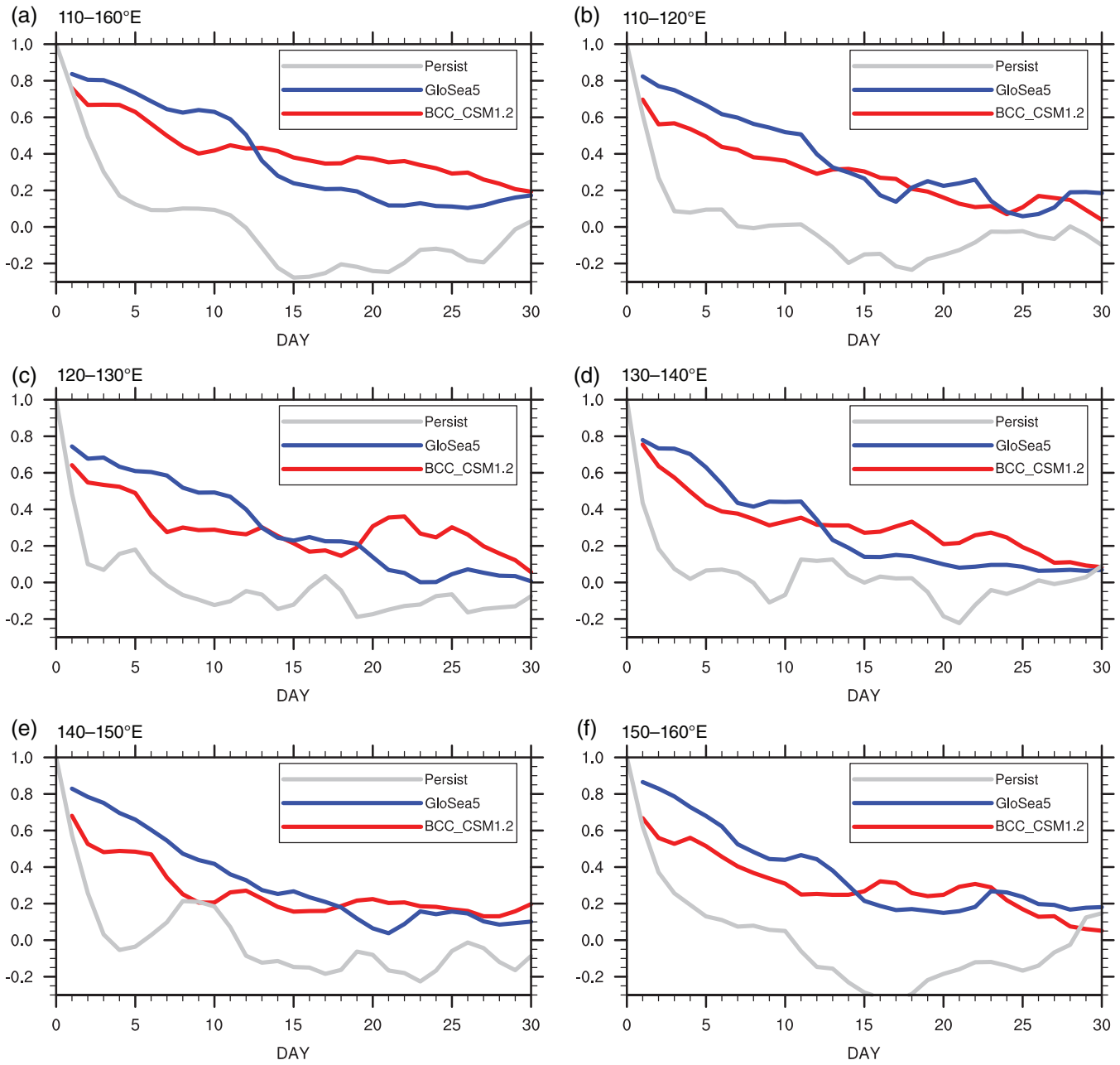

FIGURE 6 Evolution of the GPI anomaly correlation between the models and ERA-Interim as a function of lead time over 10–25°N: (a) 110–160°E, (b) 110–120°E, (c) 120–130°E, (d) 130–140°E, (e) 140–150°E, (f) 150–160°E. The red (blue) line is of BCC_CSM1.2 (GloSea5), and the grey line is the persistence skill of GPI derived with ERA-Interim and OISST data

The spatial structure of GPI in hindcast results at lead 1–10 days resembles the summer mean TCG distribution in the ERA-Interim reanalysis data. Although the main distribution feature of GPI can be well reproduced by GloSea5 and BCC_CSM1.2 (Figure 2), the intensity of the GPI value is underestimated in BCC_CSM1.2 and overestimated in GloSea5.

In order to reveal the causes of the summer mean GPI bias in these two forecast models, Figure 3 shows the patterns of the logarithmic of each component of GPI based on Equation 1. Among these components, RH shows the largest positive error in GloSea5. Hence, excess vapour in the middle troposphere, which favours the formation of cyclones, is the most important contributor to the bias of summer mean GPI in GloSea5 (Figure 3).

However, in BCC_CSM1.2, GPI is relatively low in the area 5–10°N and east of 140°E. In this region it is the AV term that contributes most to the lower GPI. The $-\frac{\partial u}{\partial y}$ component of the AV term is smaller in BCC_CSM1.2 than that in ERA-Interim, leading to the smaller AV term (Figure 4). The maximum potential intensity term is also an important contributor to the negative bias of summer mean GPI on the north side of 30°N. There is a close connection between MPI and SST. In BCC_CSM1.2, summer mean sea-surface temperature is lower than the observations especially around 30°N. The lower sea temperature causes the lower MPI in

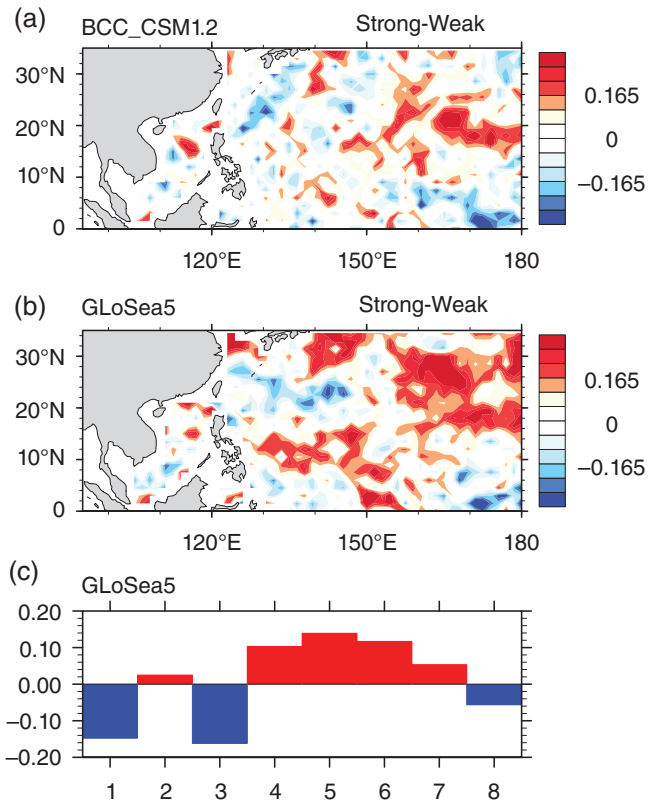

FIGURE 7 TCC difference between GPI derived with strong and weak MJOs in initial conditions in (a) BCC_CSM1.2 and (b) GloSea5 during lead 11–20 days. (c) The bars are TCC difference averaged over 5–20°N, 130–155°E at eight individual MJO phases

BCC_CSM1.2, which is not conducive to the formation of TCs.

3.2 | GPI anomaly forecast skill

In this section, the performances of GloSea5 and BCC_CSM1.2 in predicting the GPI anomaly are analysed. Figure 5 shows the time correlation coefficient (TCC) of the GPI anomaly forecasted by GloSea5 and BCC_CSM1.2 during lead time 1, 10, 20 and 30 days, separately. The green colour filling represents a greater than 0.05 significance level. It can be seen that the forecast skill of summer GPI anomaly drops quickly, with most areas to the south of 15°N not showing significance beyond the 20th day in BCC_CSM1.2. Compared with BCC_CSM1.2, GloSea5 tends to exhibit higher skill in predicting the daily GPI anomaly near the Equator out to 20 days for summer. Similarly, the prediction skill of GPI anomaly averaged over 10–25°N, 110–160°E is relatively high out to a lead time of 2 weeks in GloSea5 (Figure 6). The persistence skill of GPI anomaly falls below 0.1 beyond a lead time of 6 days. Hence, there is improved prediction skill over persistence for GPI anomaly in both these model hindcast sets.

Overall, GloSea5 has a relatively higher prediction skill for GPI anomaly and other terms compared to BCC_CSM1.2 from the first day to two weeks later. This is consistent with the MJO forecast skill in these models (Vitart, 2017). The lower skill may be due to the initialization of BCC_CSM1.2.

3.3 | MJO effect on GPI forecast

The predictability of the MJO could be extended beyond TCs. If the effect of MJO on GPI could be well reproduced, it is indicated that potentially more skilful GPI forecasts could be generated through the relationship between forecasted MJO and GPI anomaly.

Here we first examine this dependence of GPI anomaly on MJO amplitude. To avoid the initialization effect, lead times at 11–20 days are chosen. Figure 7 shows the temporal correlation coefficient (TCC) difference between the cases in which strongest and weakest MJO signal exists in the initial conditions. These two different initial signals have an effect on the prediction of GPI anomaly over 5–20°N, 130–155°E in GloSea5. Especially, the cases initiated at strong MJO phases 4–7, when MJO convection is strong over the eastern Indian Ocean and moving to the northeast, are helpful for TCG prediction.

Next, we further investigate the modulation effect of MJO as a background state on GPI anomaly in the hindcast data to see if the models could capture the observed relationship between them. There are relatively positive GPI signals during MJO phases 4–5 and negative GPI signals during MJO phases 8–1 over the South China Sea (SCS) and WNP in ERA-Interim. Composites of GPI anomaly are also calculated by model MJO phase (Figure 8). The model composites are consistent with those calculated using ERA-Interim reanalysis data. Therefore, we defined the GPI anomaly difference calculated by MJO phases 4–5 minus MJO phases 8–1 to represent the strength of the MJO phase modulation effect on GPI anomaly.

In order to reveal the causes of the MJO phase modulation bias on GPI anomaly in the models, Figure 9 shows distributions of the linearized component variables of GPI anomaly differences calculated by MJO phases 4–5 minus MJO phases 8–1 during lead times 1–10 days. The spatial structure of GPI anomaly during lead times 1–10 days reasonably resembles the ERA-Interim reanalysis data. However, the intensity of the MJO effect on GPI anomaly is generally underestimated in BCC_CSM1.2. The weak responses of AV, RH and W to MJO are the main causes, especially AV and W on both the west and east sides of the Philippines Islands. This may be due to the weak convection in the same region. The weak ascending motion and negative OLR (Figure 10) are accompanied by weak MJO over SCS and WNP in BCC_CSM1.2. Accordingly, the absolute vorticity in the lower troposphere is much weaker. In GloSea5, these terms are larger than those in the BCC_CSM1.2 and closer to the ERA-Interim reanalysis data. It can be inferred that the large-scale dynamical environment changes as the MJO

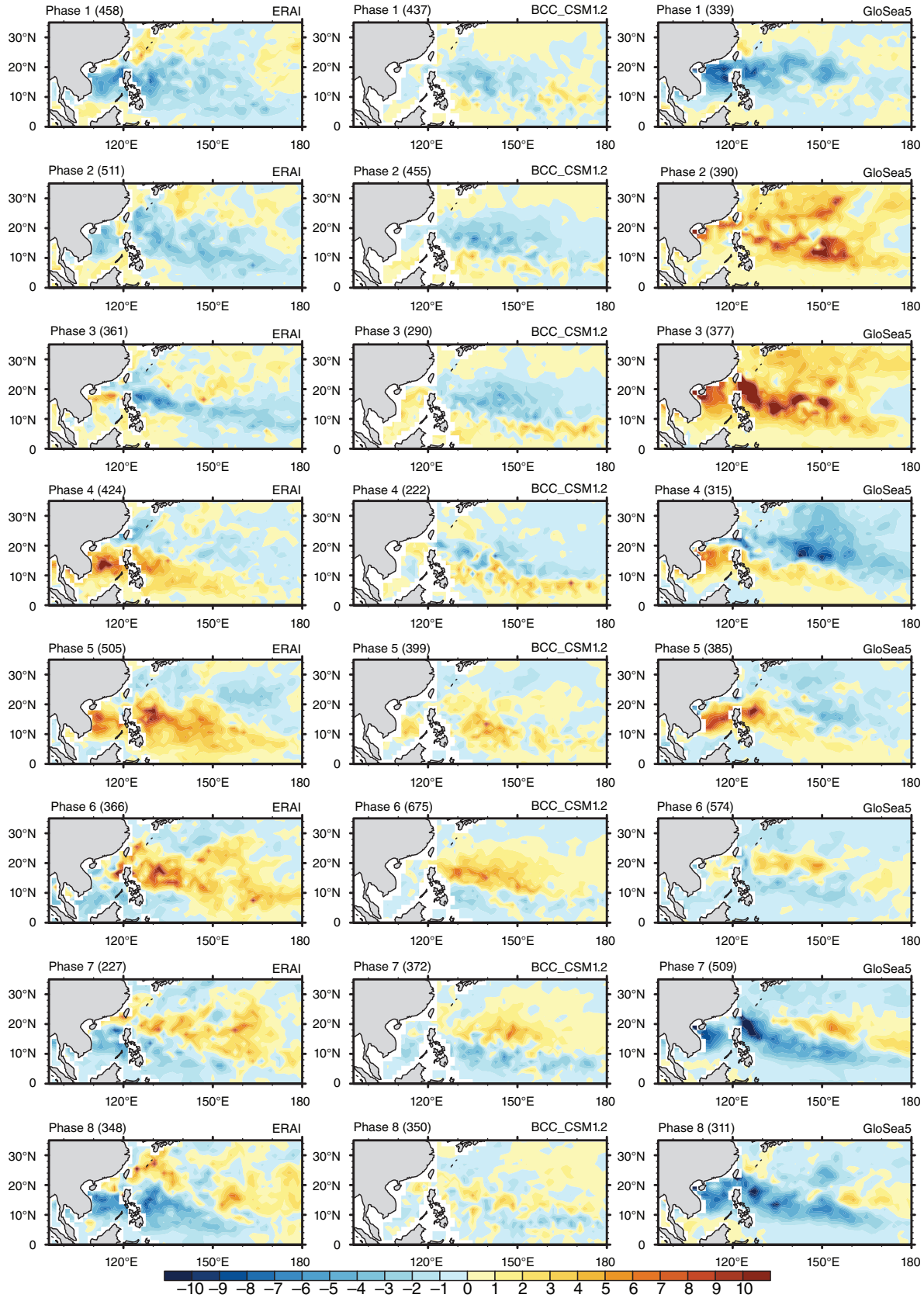

FIGURE 8 Composite of GPI anomalies by eight MJO phases in ERA-Interim (left), BCC_CSM1.2 (mid) and GloSea5 (right) during lead times 1–10 days. The numbers in brackets at the top-left corner of each panel are the numbers of samples used for the composite analysis

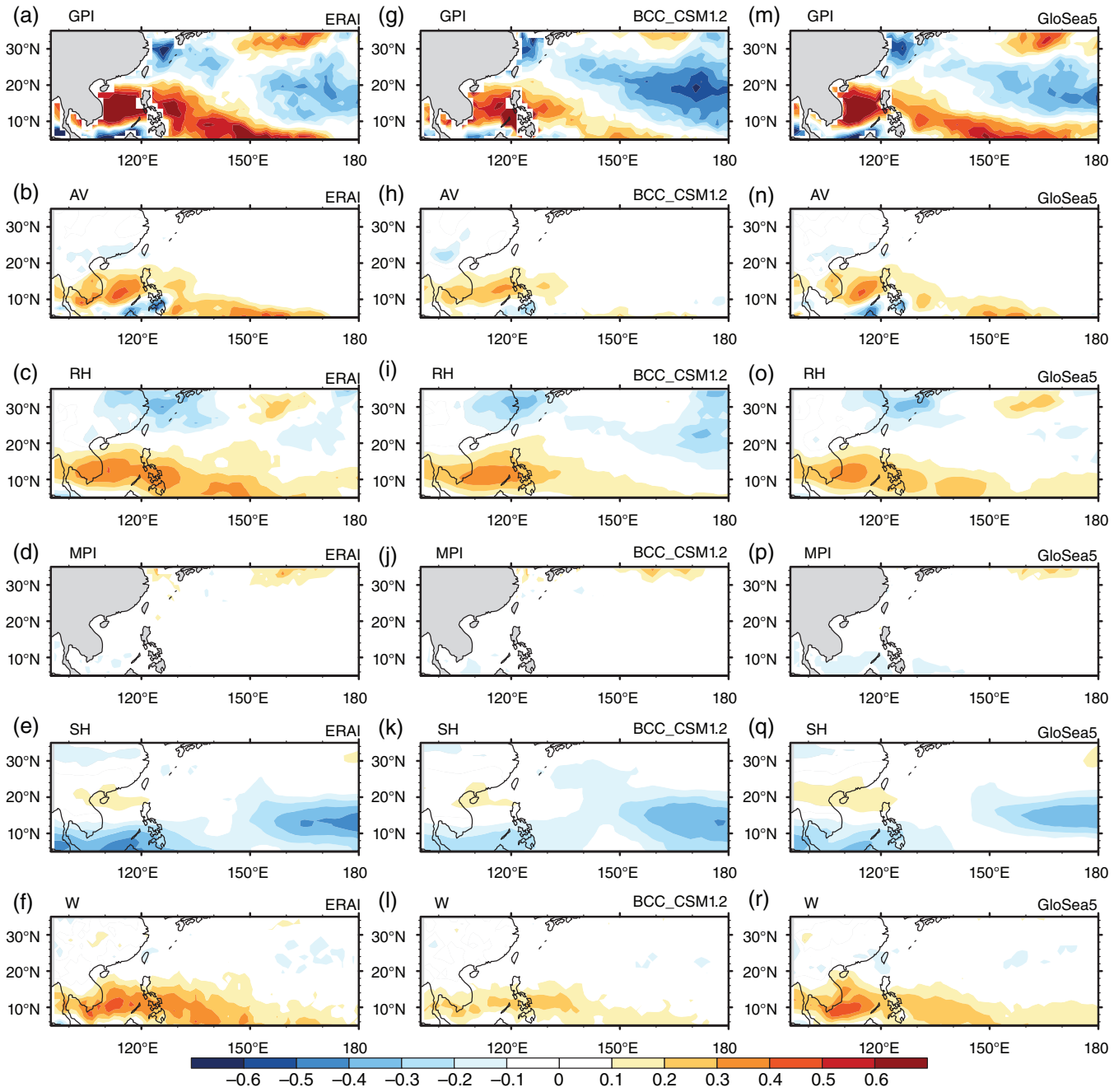

FIGURE 9 Composites of anomaly logarithm of GPI, AV, RH, MPI, SH and W terms by MJO phase 4–5 minus phase 8–1, from ERA-Interim (left), BCC_CSM1.2 (mid) and GloSea5 (right) during lead times 1–10 days

convection propagates, and this plays an important role in the TC genesis.

4 | SUMMARY AND DISCUSSION

4.1 | Summary

The predictability of TCG, and the MJO modulation effect on this, were evaluated using two sets of hindcast data generated from GloSea5 and BCC_CSM1.2 during July–October (JASO) from 1994 to 2013. These were assessed using a variety of indices including the GPI index that has traditionally been used for seasonal and climatological tropical cyclone genesis study, and RMM indices that distinguished the strength and phase of MJO.

Firstly, the results show that summer mean GPI at lead times 1–10 days in GloSea5 and BCC_CSM1.2 can generally reproduce the distribution of TCG. However, the intensity of GPI value is underestimated in BCC_CSM1.2 and overestimated in GloSea5. The patterns of linearized component variables of GPI show that the excess vapour in the middle troposphere, which favours the formation of cyclones, is the most important contributor to the positive error of summer mean GPI in GloSea5. In BCC_CSM1.2, the AV term contributes most to the negative bias of GPI due to the smaller $-\frac{\partial u}{\partial y}$ component and colder SST.

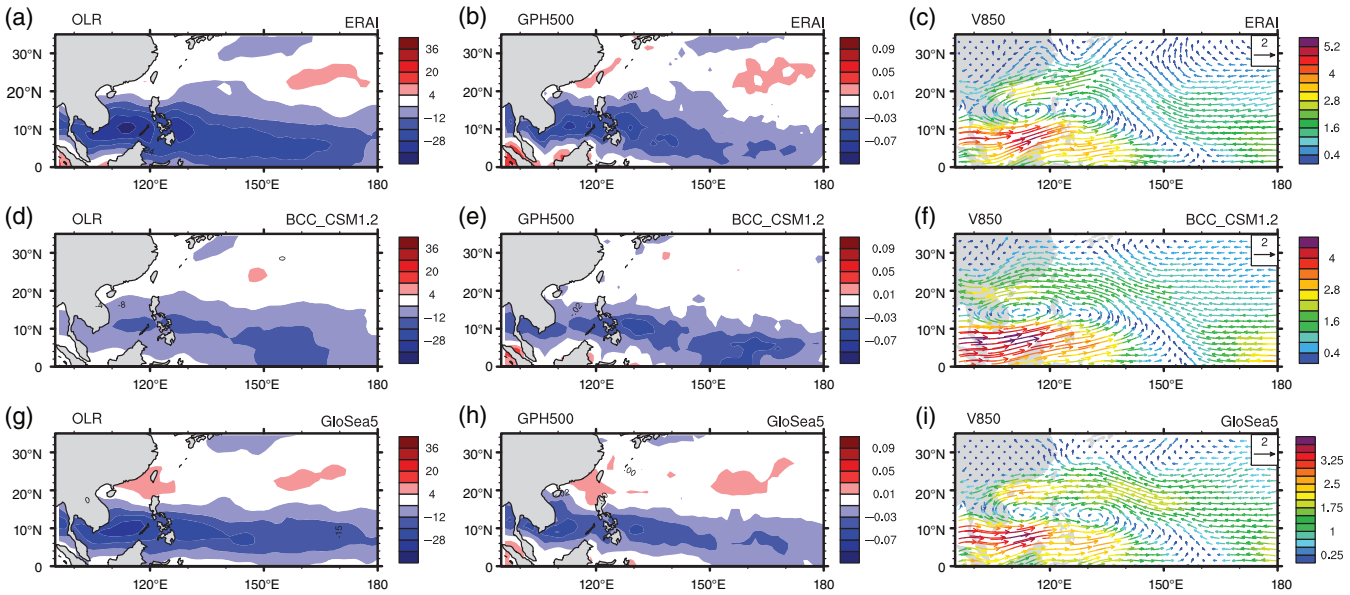

FIGURE 10 Composite OLR (left), 500 hPa geopotential height (mid) and 850 hPa wind (right, vector: 850 hPa wind, colour: absolute value of 850 hPa zonal wind velocity) anomalies by MJO phases 4–5 minus phases 8–1 from (a–c) ERA-Interim, (d–f) BCC_CSM1.2 and (g–i) GloSea5 during lead times 1–10 days

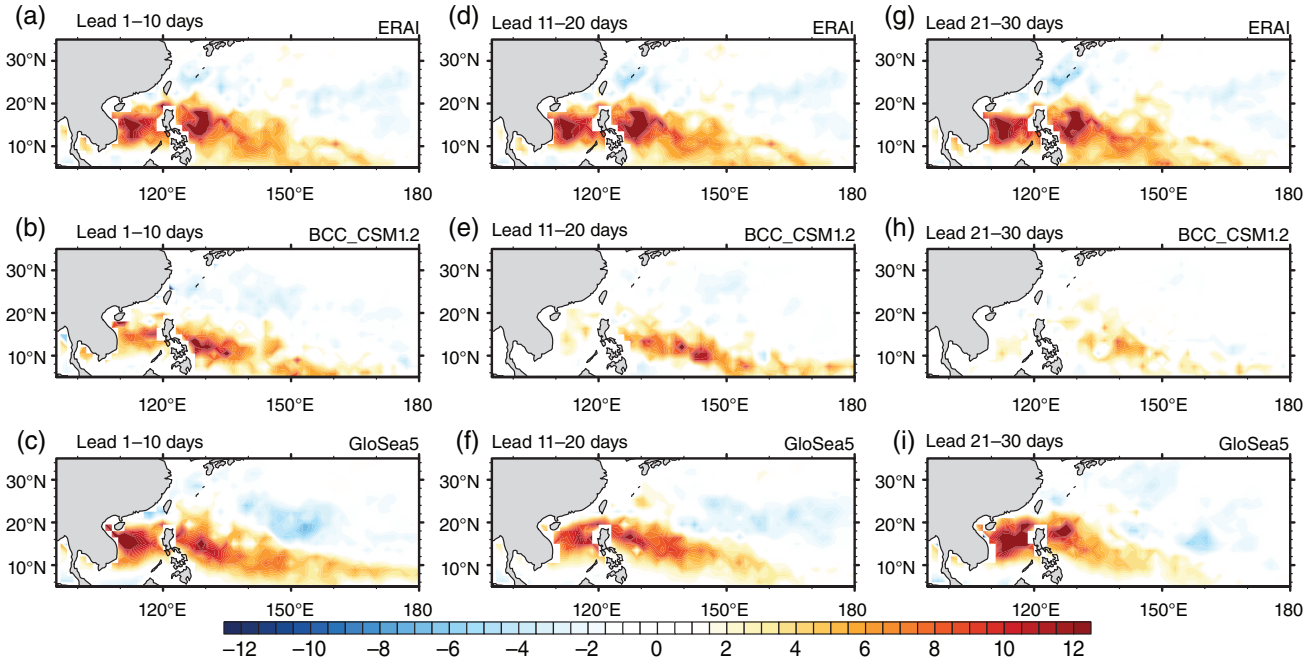

FIGURE 11 Composite GPI anomalies by MJO phases 4–5 minus phases 8–1 derived with ERA-Interim (top), BCC_CSM1.2 (mid) and GloSea5 (bottom) during (a–c) lead 1–10 days, (d–f) lead 11–20 days, and (g-i) lead 21–30 days

Next, the GPI anomaly predicted by GloSea5 and BCC_CSM1.2 shows that the forecast skill of the summer GPI anomaly drops more slowly than for persistence forecasts. Compared with BCC_CSM1.2, GloSea5 tends to exhibit a higher skill in predicting the daily GPI anomaly to the south of 10°N for summer. In both GloSea5 and BCC_CSM1.2 models, the relatively higher GPI anomaly forecast skill can be attributed to the better signal in the circulation terms, but terms related to the convective prediction show lower forecast skill.

Additionally, we use GPI and RMM indices to assess whether these two operational climate models can capture the relationship between MJO and TC genesis. The MJO intensity has a regional effect on GPI hindcast skill from initialization. During lead 11–20 days, the forecasts initiated with stronger MJO signals show higher GPI anomaly skill. Due to the MJO phase effect, better GPI anomaly forecast skill is found during strong MJO phases 4–7 at lead times 11–20 days in GloSea5.

Finally, we further investigate the MJO phase modulation effect on GPI anomaly patterns in the hindcast data. Both models can capture the observed relationship and keep it for 30 days in the models (Figure 11). There are positive GPI signals in MJO phases 4–5 and negative GPI

signals in MJO phases 8–1 over the SCS and WNP. The spatial structure of GPI anomaly during lead times 1–10 days in models reasonably resembles the ERA-Interim reanalysis data. However, the intensity of the MJO effect on GPI anomaly is generally underestimated in BCC_CSM1.2. This may be due to the response of inadequate ascending motion and negative OLR accompanied by weak MJO over SCS and WNP in this model. In GloSea5, these terms are larger than those in BCC_CSM1.2 and closer to the ERA-Interim reanalysis data.

4.2 | Discussion

Many studies have shown that improvements in model initialization and resolution have contributed greatly to advancements in TC prediction (Hendricks *et al.*, 2013; Osuri *et al.,* 2013; Heming, 2016). In the hindcast experiments of this article, the lower GPI forecast skill in BCC_CSM1.2 since the first forecast lead day implies that further improvements in the initialization scheme and reanalysis data choosing may contribute to more skilful GPI forecasts using this model. In the summer mean TCG distribution, the two large-value centres are respectively located on the east and west sides of the Philippines Islands, where the terrain is complex. A better TC prediction also need to depict complex process interactions across spatial scales through the model resolution enhancement.

Besides GPI forecast, the MJO forecast skill could be further improved if a better initial conditions perturbation method and accurate initial conditions are applied, especially at the beginning of the forecast in the BCC model (Ren *et al.,* 2016). It is likely that an improvement in MJO distribution also could be accomplished with a higher model resolution (Inness *et al.,* 2001; Jia *et al.,* 2008; Zhao *et al.,* 2014, 2015). Meanwhile, the convective parametrization determines the basic simulation ability of the model to MJO (Ling *et al.,* 2009; Zhang and Song, 2009). In this study, the OLR responses during different MJO phases in BCC_CSM1.2 is much weaker than that in the observations and GloSea5. The GPI forecast skill could be further improved if more accurate large-convection conditions such as MJO are constructed, especially at the strong MJO phases.

On multi-week time-scales, MJO has previously been shown to be a major driver of TC predictability (Camp *et al.,* 2018). Assessing GloSea5 and BCC_CSM1.2 model hindcasts during boreal summer for the TC genesis potential index (GPI) over WNP, with emphasis on the MJO effect, is conducive to identifying and improving TC forecasts in these models. Our results indicate that the large-scale dynamical environment changes as the MJO convection propagates eastward, and this plays an important role in the typhoon genesis in GloSea5 and BCC_CSM1.2 models. Overall, the forecasting skill of TCG number is far below the prediction skill of MJO. Considering the intrinsic predictability of the MJO of more than 2 weeks, the forecasted MJO phase information has significant implications for TCG prediction on intraseasonal time-scales.

ACKNOWLEDGEMENTS

This work was jointly supported by the National Key Research and Development Program of China (Grant 2016YFA0602102), the National Natural Science Foundation of China (Grant 41505065), the National Basic Research Program of China (Grant 2015CB453203) and the UK-China Research & Innovation Partnership Fund through the Met Office Climate Science for Service Partnership (CSSP) China, as part of the Newton Fund.

ORCID

Chongbo Zhao https://orcid.org/0000-0002-1828-4713
Rosie Eade https://orcid.org/0000-0002-3566-4232

REFERENCES

Bessafi, M. and Wheeler, M.C. (2006) Modulation of south Indian Ocean tropical cyclones by the Madden–Julian Oscillation and convectively coupled equatorial waves. *Monthly Weather Review*, 134, 638–656.

Beven, J.L. (1999) The boguscane: a serious problem with the NCEP medium range forecast model in the Tropics. *Preprints, 23rd Conference on Hurricanes and Tropical Meteorology*. Dallas, TX. American Meteorological Society, 845–848.

Bister, M. and Emanuel, K.A. (1998) Dissipative heating and hurricane intensity. *Meteorology and Atmospheric Physics*, 65, 233–240.

Camargo, S.J., Wheeler, M.C. and Sobel, A.H. (2009) Diagnosis of the MJO modulation of tropical cyclogenesis using an empirical index. *Journal of Atmospheric Sciences*, 66, 3061–3074.

Camp, J., Wheeler, M.C., Hendon, H.H., Gregory, P.A., Marshall, A.G., Tory, K.J., Watkins, A.B., MacLachlan, C. and Kuleshov, Y. (2018) Skilful multiweek tropical cyclone prediction in ACCESS-S1 and the role of the MJO. *Quarterly Journal of the Royal Meteorological Society*, 144, 1337–1351. https://doi.org/10.1002/qj.3260.

Dee, D.P., Uppala, S.M., Simmons, A.J., Berrisford, P., Poli, P., Kobayashi, S., Andrae, U., Balmaseda, M.A., Balsamo, G., Bauer, P., Bechtold, P., Beljaars, A.C.M., van de Berg, L., Bidlot, J., Bormann, N., Delsol, C., Dragani, R., Fuentes, M., Geer, A.J., Haimberger, L., Healy, S.B., Hersbach, H., Hólm, E.V., Isaksen, L., Kållberg, P., Köhler, M., Matricardi, M., McNally, A.P., Monge-Sanz, B.M., Morcrette, J.-J., Park, B.-K., Peubey, C., de Rosnay, P., Tavolato, C., Thépaut, J.-N. and Vitart, F. (2011) The ERA-Interim reanalysis: configuration and performance of the data assimilation system. *Quarterly Journal of the Royal Meteorological Society*, 137, 553–597.

Emanuel, K.A. (1995) The behavior of a simple hurricane model using a convective scheme based on subcloud-layer entropy equilibrium. *Journal of Atmospheric Sciences*, 52, 3960–3968.

Emanuel, K.A. and Nolan, D.S. (2004) Tropical cyclone activity and global climate. *Preprints, 26th Conf. on Hurricanes and Tropical Meteorology*, Miami, FL. American Meteorological Society, 240–241.

Fan, K. and Wang, H.J. (2009) A new approach to forecasting typhoon frequency over the western North Pacific. *Weather and Forecasting*, 24, 974–978.

Griffies, S.M., Gnanadesikan, A., Dixon, K.W., Dunne, J.P., Gerdes, R., Harrison, M.J., Rosati, A., Russell, J.L., Samuels, B.L., Spelman, M.J., Winton, M.a. and Zhang, R. (2005) Formulation of an ocean model for global climate simulations. *Ocean Science*, 1, 45–79.

Hall, J.D., Matthews, A.J. and Karoly, D.J. (2001) The modulation of tropical cyclone activity in the Australian region by the Madden–Julian Oscillation. *Monthly Weather Review*, 129, 2970–2982.

Heming, J.T. (2016) Met Office Unified Model tropical cyclone performance following major changes to the initialization scheme and a model upgrade. *Weather and Forecasting*, 31, 1433–1449.

Hendricks, E.A., Peng, M.S., and Li, T. (2013) Evaluation of multiple dynamic initialization schemes for tropical cyclone prediction. Monthly Weather Review, 141, 4028–4048.

Hsu, P.-C., Li, T., You, L., Gao, J. and Ren, H.-L. (2014) A spatial-temporal projection model for 10–30 day rainfall forecast in south China. *Climate Dynamics*, 44, 1227–1244. https://doi.org/10.1007/s00382-014-22154.

Inness, P.M., Slingo, J.M., Woolnough, S.J., Neale, R.B. and Pope, V.D. (2001) Organization of tropical convection in a GCM with varying vertical resolution: implications for the simulation of the Madden–Julian Oscillation. *Climate Dynamics*, 17, 777–793.

Ji, J., Huang, M. and Li, K. (2008) Prediction of carbon exchanges between China terrestrial ecosystem and atmosphere in 21st century. *Science China (Series D)*, 51, 885–898.

Jia, X.L., Li, C.Y. and Ling, J. (2008) Impacts of the GCM's resolution on the MJO simulation. *Advances in Atmospheric Sciences*, 25, 139–156.

Jiang, X., Zhao, M. and Waliser, D.E. (2012) Modulation of tropical cyclones over the eastern Pacific by the intraseasonal variability simulated in an AGCM. *Journal of Climate*, 25, 6524–6538.

Kalnay, E., Kanamitsu, M., Kistler, R., Collins, W., Deaven, D., Gandin, L., Iredell, M., Saha, S., White, G., Woollen, J., Zhu, Y., Chelliah, M., Ebisuzaki, W., Higgins, W., Janowiak, J., Mo, K.C., Ropelewski, C., Wang, J., Leetmaa, A., Reynolds, R., Jenne, R. and Joseph, D. (1996) The NCEP/NCAR 40-year reanalysis project. *Bulletin of the American Meteorological Society*, 77, 437–472.

Kim, J., Ho, C., Kim, H., Sui, C. and Park, S.K. (2008) Systematic variation of summertime tropical cyclone activity in the western North Pacific in relation to the Madden–Julian Oscillation. *Journal of Climate*, 21, 1171–1191.

Leroy, A. and Wheeler, M.C. (2008) Statistical prediction of weekly tropical cyclone activity in the Southern Hemisphere. *Monthly Weather Review*, 136, 3637–3654.

Liebmann, B., Hendon, H.H. and Glick, J.D. (1994) The relationship between tropical cyclones of the western Pacific and Indian Oceans and the Madden–Julian Oscillation. *Journal of the Meteorological Society of Japan*, 72, 401–412.

Liebmann, B. and Smith, C.A. (1996) Description of a complete (interpolated) outgoing longwave radiation dataset. *Bulletin of the American Meteorological Society*, 77, 1275–1277.

Lin, H., Brunet, G. and Derome, J. (2008) Forecast skill of the Madden–Julian Oscillation in two Canadian atmospheric models. *Monthly Weather Review*, 136, 4130–4149.

Liu, X., Wu, T., Yang, S., Li, T., Jie, W., Zhang, L., Wang, Z., Liang, X., Li, Q., Cheng, Y., Ren, H., Fang, Y. and Nie, S. (2017) MJO prediction using the sub-seasonal to seasonal forecast model of Beijing Climate Center. *Climate Dynamics*, 48, 3283–3307.

Ling, J., Li, C. and Jia, X. (2009) Impacts of cumulus momentum transport on MJO simulation. *Advances in Atmospheric Sciences*, 26, 864–876.

MacLachlan, C., Arribas, A., Peterson, K.A., Maidens, A., Fereday, D., Scaife, A.A., Gordon, M., Vellinga, M., Williams, A., Comer, R.E., Camp, J., Xavier, P. and Madec, G. (2015) Global Seasonal forecast system version 5 (GloSea5): a high-resolution seasonal forecast system. *Quarterly Journal of the Royal Meteorological Society*, 141, 1072–1084.

Maloney, E.D. and Hartmann, D.L. (2000a) Modulation of hurricane activity in the Gulf of Mexico by the Madden–Julian Oscillation. *Science*, 287, 2002–2004.

Maloney, E.D. and Hartmann, D.L. (2000b) Modulation of eastern North Pacific hurricanes by the Madden–Julian Oscillation. *Journal of Climate*, 13, 1451–1460.

Megann, A.P., Storkey, D., Aksenov, Y., Alderson, S., Calvert, D., Graham, T., Hyder, P., Siddorn, J. and Sinha, B. (2014) GO5.0: the joint NERC-Met Office NEMO global ocean model for use in coupled and forced applications. *Geotechnical Model Development*, 7, 1069–1092.

Nakazawa, T. (1988) Tropical super clusters within intraseasonal variations over the western Pacific. *Journal of the Meteorological Society of Japan*, 66, 823–839.

Osuri, K.K., Mohanty, U.C., Routray, A., Mohapatra, M. and Niyogi, D. (2013) Real-time track prediction of tropical cyclones over the north Indian Ocean using the ARW model. *Journal of Applied Meteorology and Climatology*, 52, 2476–2492.

Rae, J.G.L., Hewitt, H.T., Keen, A.B., Ridley, J.K., West, A.E., Harris, C.M., Hunke, E.C. and Walters, D.N. (2015) Development of global sea ice 6.0 CICE configuration for the Met Office global coupled model. *Geoscientific Model Development*, 8, 2221–2230.

Ren, H.L., Zhao, C.B., Cheng, Y.J. and Liu, X.W. (2016) MJO ensemble prediction in BCC-CSM1.1(m) using different initialization schemes. *Atmospheric and Oceanic Science Letters*, 9, 60–65.

Reynolds, R.W., Rayner, N.A., Smith, T.M., Stokes, D.C. and Wang, W. (2002) An improved *in situ* and satellite SST analysis for climate. *Journal of Climate*, 15, 1609–1625.

Satoh, M., Oouchi, K., Nasuno, T., Taniguchi, H., Yamada, Y., Tomita, H., Kodama, C., Kinter, J., Achuthavarier, D., Manganello, J., Cash, B., Jung, T., Palmer, T.N. and Wedi, N. (2012) The Intra-Seasonal Oscillation and its control of tropical cyclones simulated by high-resolution global atmospheric models. *Climate Dynamics*, 39, 2185–2206.

Schumacher, A.B., Demaria, M. and Knaff, J.A. (2009) Objective estimation of the 24-h probability of tropical cyclone formation. *Weather and Forecasting*, 24, 456–471.

Shen, B., Tao, W., Lau, W.K. and Atlas, R. (2010) Predicting tropical cyclogenesis with a global mesoscale model: hierarchical multiscale interactions during the formation of tropical cyclone *Nargis* (2008). *Journal of Geophysical Research*, 115, D14102. https://doi.org/10.1029/2009JD013140.

Tian, F., Zhou, T. and Zhang, L. (2013) Tropical cyclone genesis potential index over the western North Pacific simulated by LASG/IAP AGCM. *Journal of Meteorological Research*, 27(1), 50–62.

Vitart, F. (2009) Impact of the Madden–Julian Oscillation on tropical storms and risk of landfall in the ECMWF forecast system. *Geophysical Research Letters*, 36, L15802. https://doi.org/10.1029/2009GL039089.

Vitart, F. (2017) Madden-Julian Oscillation Prediction and Teleconnections in the S2S Database: MJO prediction and teleconnections in the S2S database. *Quarterly Journal of the Royal Meteorological Society*, 143, 2210–2220.

Walters, D., Brooks, M., Boutle, I., Melvin, T., Stratton, R., Vosper, S., Wells, H., Williams, K., Wood, N., Allen, T., Bushell, A., Copsey, D., Earnshaw, P., Edwards, J., Gross, M., Hardiman, S., Harris, C., Heming, J., Klingaman, N., Xavier, P. (2017) The Met Office Unified Model Global Atmosphere 6.0/6.1 and JULES Global Land 6.0/6.1 configurations. *Geoscientific Model Development*, 10(4), 1487–1520.

Wang, W., Hung, M.P., Weaver, S.J., Kumar, A. and Fu, X. (2014) MJO prediction in the NCEP climate forecast system version 2. *Climate Dynamics*, 42, 2509–2520.

Wang, Y., Song, J.J. and Wu, R.S. (2013) A new insight into the contribution of environmental conditions to tropical cyclone activities. *Acta Meteorologica Sinica*, 27, 344–355.

Webster, P.J. (2008) Myanmar's deadly daffodil. *Nature Geoscience*, 1, 488–490.

Wheeler, M.C. and Hendon, H.H. (2004) An all-season real-time multivariate MJO index: development of an index for monitoring and prediction. *Monthly Weather Review*, 132, 1917–1932.

Williams, K.D., Harris, C.M., Bodas-Salcedo, A., Camp, J., Comer, R.E., Copsey, D., Fereday, D., Graham, T., Hill, R., Hinton, T., Hyder, P., Ineson, S., Masato, G., Milton, S.F., Roberts, M.J., Rowell, D.P., Sanchez, C., Shelly, A., Sinha, B., Walters, D.N., West, A., Woollings, T. and Xavier, P.K. (2015) The Met Office Global Coupled model 2.0 (GC2) configuration. *Geoscientific Model Development*, 8, 1509–1524.

Winton, M. (2000) A reformulated three-layer sea ice model. *Journal of Atmospheric and Oceanic Technology*, 17, 525–531.

Wu, J., Ren, H.L., Zuo, J., Zhao, C., Chen, L. and Li, Q. (2016)) MJO prediction skill, predictability, and teleconnection impacts in the Beijing Climate Center Atmospheric General Circulation Model. *Dynamics of Atmospheres and Oceans*, 75, 78–90.

Wu, T., Song, L., Li, W., Wang, Z., Zhang, H., Xin, X., Zhang, Y., Zhang, L., Li, J., Wu, F., Liu, Y., Zhang, F., Shi, X., Chu, M., Zhang, J., Fang, Y., Wang, F., Lu, Y., Liu, X., Wei, M., Liu, Q., Zhou, W., Dong, M., Zhao, Q., Ji, J., Li, L. and Zhou, M. (2014) An overview of BCC climate system model development and application for climate change studies. *Journal of Meteorological Research*, 28, 34–56.

Yokoi, S., Takayabu, Y.N. and Chan, J.C. (2009) Tropical cyclone genesis frequency over the western North Pacific simulated in medium-resolution coupled general circulation models. *Climate Dynamics*, 33, 665–683.

Zhang, G.J. and Song, X. (2009) Interaction of deep and shallow convection is key to Madden–Julian Oscillation simulation. *Geophysical Research Letters*, 36, 269–277.

Zhao, C., Ren, H., Song, L. and Wu, J. (2015) Madden–Julian Oscillation simulated in BCC climate models. *Dynamics of Atmospheres and Oceans*, 72, 88–101.

Zhao, C., Zhou, T., Song, L. and Ren, H. (2014) The boreal summer intraseasonal oscillation simulated by four Chinese AGCMs participating in the CMIP5 project. *Advances in Atmospheric Sciences*, 31, 1167–1180.

How to cite this article: Zhao C, Ren H-L, Eade R, Wu Y, Wu J, MacLachlan C. MJO modulation and its ability to predict boreal summer tropical cyclone genesis over the northwest Pacific in Met Office Hadley Centre and Beijing Climate Center seasonal prediction systems. *Q J R Meteorol Soc* 2019;145:1089–1101. https://doi.org/10.1002/qj.3478

赵俊虎,王永光,2019. 2018年秋季我国气候异常及成因分析[J]. 气象,45(4):565-576. Zhao J H, Wang Y G, 2019. Features and possible causes for the climatic anomaly in China in autumn 2018[J]. Meteor Mon, 45(4):565-576(in Chinese).

2018年秋季我国气候异常及成因分析*

赵俊虎 王永光

国家气候中心,中国气象局气候研究开放实验室,北京 100081

提 要: 2018年秋季我国气候异常特征总体表现为:气温呈"东高西低"的分布;东部降水呈"南北多、中间少"的分布,其中内蒙古中东部、东北、江南南部和华南大部地区降水异常偏多,而华北至江南北部降水异常偏少,且江南和西南地区降水出现明显的季节内反向分布转变特征。异常成因分析表明,秋季欧亚中高纬度槽脊活动频繁,冷空气活跃,西太平洋副热带高压较常年同期偏强偏西,脊线季节内南北波动较大,西南水汽输送偏强,导致我国东部降水南北多、中间少。进一步研究表明,海温异常是影响2018年秋季我国气候异常的最主要外强迫因子,季节内El Niño由中部型向东部型发展,热带印度洋海温偶极子正位相持续,副热带南印度洋偶极子正位相发展。秋季后期El Niño影响增强,东亚副热带大气环流发生明显的季节内响应。因此,El Niño和印度洋海温的演变及其对东亚环流的影响,加上欧亚中高纬环流异常的季节内调整,二者共同导致了我国南方地区降水出现明显的东西反向的季节内变化。

关键词: 气候异常特征,季节内转折,成因分析,El Niño,印度洋海温

中图分类号: P461 **文献标志码:** A **DOI:** 10.7519/j.issn.1000-0526.2019.04.011

Features and Possible Causes of the Climatic Anomaly in China in Autumn 2018

ZHAO Junhu WANG Yongguang

Laboratory of Climate Studies, National Climate Centre, CMA, Beijing 100081

Abstract: During the autumn of 2018, the surface air temperature was below normal in West China but above normal in East China. And the distribution of precipitation in eastern China was "more in the north and south, less in the middle". The precipitation was above normal in the central and eastern part of Inner Mongolia, Northeast China, the southern part of the south of the Yangtze River and South China, but below normal in the region from North China to the northern part of the south of the Yangtze River. In addition, the precipitation in the south of the Yangtze River and Southwest China showed obvious seasonal reverse distribution characteristics. By analyzing the causes for the climatic anormaly, we found that in autumn, ridge and trough activities in middle and high latitudes of Eurasia were frequent, the cold air was active, the western Pacific subtropical high (WPSH) was stronger and more westward than normal, the ridges of WPSH fluctuated greatly from north to south, and the southwest water vapor transport was stronger, resulting in the abnormal distribution of precipitation in eastern China. Further studies have shown that the sea surface temperature anomaly (SSTA) was the major extermal forcing factor for the climatic anomalies in the autumn of 2018. The El Niño type developed from the central Pacific type (CP) El Niño

* 国家重点研发计划(2018YFC1506005)、国家自然科学基金项目(41875093、41705074和41505061)、中央引导地方科技发展专项(ZY18C12)及陕西省气象局气候监测与预测创新团队项目共同资助

2018年12月26日收稿; 2019年3月21日收修定稿

第一作者:赵俊虎,主要从事短期气候预测研究. Email:zhaojh@cma.gov.cn

通信作者:王永光,主要从事短期气候预测研究. Email:ygwang@cma.gov.cn

to the eastern Pacific type (EP) El Niño. The positive phase of tropical Indian Ocean dipole (TIOD) turned to the positive phase of South Indian Ocean dipole (SIOD). And there was obvious response of the East Asian subtropical atmospheric circulation to the SSTA in the Pacific and Indian Ocean in autumn. Therefore, the evolution of El Niño and the SST in the Indian Ocean and their influence on the East Asia atmospheric circulation, together with the seasonal adjustment of the anomalous circulation in the middle and high latitudes in Eurasia, led to the obvious east-west interseasonal changes of precipitation in southern China.

Key words: climatic anomaly feature, interseasonal change, possible causes, El Niño, Indian Ocean SST

引 言

中国地处东亚季风区,季风气候显著。秋季是夏季风环流向冬季风环流转变的过渡时期。此时,东亚夏季风系统开始南撤,季风槽逐步南移,中高纬度的冷空气活动开始活跃。热带暖湿气流和南下的冷空气在不同地区的交汇造成我国天气和气候的异常,不同强度的冷暖气团在某些区域持续的对峙甚至可以带来一些极端天气和气候事件。同时由于秋季是我国秋收秋种的重要季节,秋季的天气气候异常将对我国粮食生产和人民生活安全造成严重的影响。因此做好秋季气候异常的诊断分析和预测,将有利于认识秋雨发生的科学规律,有助于防灾减灾(鲍媛媛等,2003;白虎志和董文杰,2004;贾小龙等,2008;侯威等,2015;肖科丽等,2015;柳龙生和高拴柱,2018)。

自20世纪90年代以来,我国秋季气温总体处于偏暖的年代际背景下;而秋季降水自21世纪以来进入偏多的时段。近几年秋季我国降水异常偏多(柳艳菊等,2013;王朋岭等,2014;司东等,2015;聂羽等,2016;竺夏英和宋文玲,2017;支蓉等,2018)。2018年秋季,我国气候区域差异大,西部地区总体呈现"冷湿"的特征,东部气温偏高,降水呈"南北多、中间少"的分布特征。在西北地区东部、华北西部、东北地区、江南和华南等地,出现强降水天气过程,部分地区出现洪涝、泥石流等灾害。此外,2018年秋季降水季节内变化显著,9月南方地区呈"东少西多"的分布,而后秋(10—11月)南方地区转为"东多西少"的分布。本文从2018年秋季我国主要气候特点出发,通过诊断分析造成气候异常的大气环流特征和外强迫信号,探讨造成2018年秋季气候异常的可能成因,为今后的气候预测和服务提供参考。

1 资料和方法

本文使用了1961—2018年的中国逐日气温和降水观测资料。数据来源于国家气象信息中心整编的中国地区2400台站观测气候数据集。此外,本文还使用了1961—2018年美国国家环境预报中心和美国国家大气研究中心(NCEP/NCAR)提供的2.5°×2.5°水平分辨率的位势高度场、水平风场、水汽场的逐日再分析资料(Kalnay et al,1996)和美国国家海洋大气局(NOAA)提供的1961—2018年逐月海温资料(Reynolds et al,2007)。文中部分图片出自国家气候中心开发的"气象灾害影响评估系统"及"大气环流交互诊断系统"。

西太平洋副热带高压(以下简称副高)指数、Niño3指数、El Niño Modoki指数(EMI)、热带印度洋海温偶极子指数(TIOD)和副热带南印度洋偶极子指数(SIOD)来自国家气候中心。其中Niño3指数表示5°S～5°N、150°W～90°W区域平均的SSTA。根据Ashok et al(2007),EMI定义为:$(SSTA)_C - 0.5(SSTA)_E - 0.5(SSTA)_W$,其中$(SSTA)_C$、$(SSTA)_E$、$(SSTA)_W$分别表示热带太平洋中部(10°S～10°N、165°E～140°W)、东部(15°S～5°N、110°～70°W)和西部(10°S～20°N、125°～145°E)区域平均的海温距平(Ashok et al,2007;Weng et al,2007;2009)。Niño3指数和EMI分别用于监测东部型和中部型ENSO事件。TIOD定义为热带西印度洋(10°S～10°N、50°～70°E)与热带东南印度洋(10°S～0°、90°～110°E)区域平均海温距平的差值(Saji et al,1999)。SIOD定义为西南印度洋(45°S～30°S、45°～75°E)与东南印度洋(25°S～15°S、80°～100°E)区域平均海温距平的差值(Behera and Yamagata, 2001;晏红明等,2009),*TIOD*

>0℃和 *SIOD*>0℃表示正位相,*TIOD*<0℃和 *SIOD*<0℃表示负位相。文中的气候常年值为1981—2010 年的平均值。

2　2018 年秋季我国主要气候异常特征

2018 年秋季,全国平均气温为 10.0℃,较常年同期(9.9℃)偏高 0.1℃(图 1a)。从空间分布看,气温呈现“东高西低”的分布,内蒙古东部、东北大部、华北南部、黄淮、江淮、江汉、江南大部、华南东南部和西藏大部等地区气温偏高,其中内蒙古东部、黑龙江大部和吉林西北部等地气温较常年同期偏高 1~2℃,局部偏高 2℃以上;而新疆大部、内蒙古西部和中部、西北大部、华北北部、西南大部、华南西部等地气温较常年同期偏低,其中新疆北部局部和西南地区东部局部偏低 1~2℃(图 1b)。季内,由于冷空气活动频繁,华北及内蒙古东部、吉林西部、辽宁南部、山东北部、山西南部、陕西、青海东北部以及江苏等地发生极端日降温事件。

秋季,全国平均降水量为 129.7 mm,较常年同期(119.8 mm)偏多 8.3%(图 2a)。降水空间分布非常不均匀,其中东部地区总体呈现“南北多、中间少”的空间分布,而西部地区总体呈现“南北少、中间多”的空间分布。降水偏多区出现在新疆北部、西北南部、内蒙古中部和东部、东北大部、西南北部和东部局部、江南南部及华南大部等地,尤其是河套地区、内蒙古中东部、东北北部、华南中部至江南南部等地区降水偏多 5 成以上;而华北大部、西北东南部、江汉、江淮大部、西藏南部、西南南部等地降水较常年同期明显偏少,部分地区偏少 8 成至 1 倍(图 2b)。

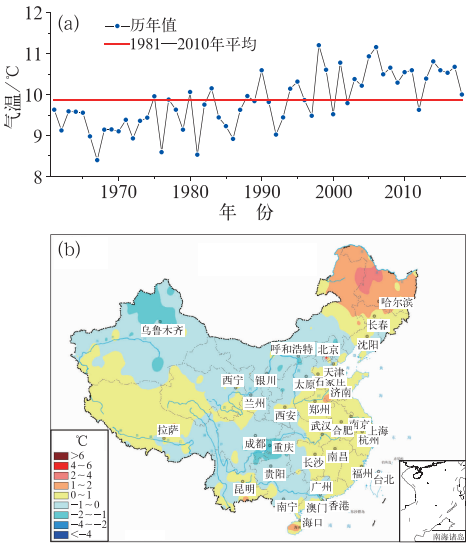

图 1　1961—2018 年秋季全国平均气温历年变化(a)及 2018 年秋季全国气温距平分布(b)

Fig. 1　Time series of autumn mean temperature over China during 1961—2018 (a) and distribution of temperature anomalies in autumn 2018 (b)

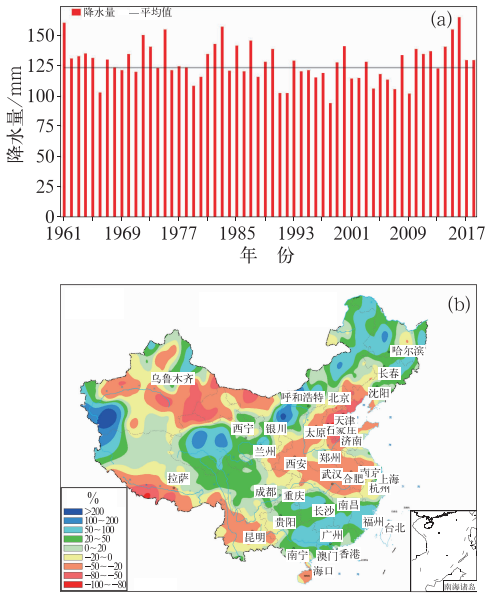

图 2　1961—2018 年秋季全国平均降水量历年变化(a)及 2018 年秋季全国降水距平百分率分布(b)

Fig. 2　Time series of autumn mean rainfall over China during 1961—2018 (a) and distribution of precipitation anomaly percentage in autumn 2018 (b)

从区域特征看,东北地区(黑龙江、吉林、辽宁)平均降水量(119.7 mm)较常年同期(98.2 mm)偏多 21.9%(图 3a)。华北地区(北京、天津、河北和山西)平均降水量(53.8 mm)较常年同期(94.9 mm)偏少 43.3%,为 1998 年以来最少年(图 3b)。南方地区(广东、广西、贵州、湖南、江西、福建)平均降水量(322.0 mm)较常年同期(238.0 mm)偏多 35.3%,为 1983 年以来第五多年(图 3c)。季内,内蒙古、甘肃、青海、宁夏、山东、浙江和江苏等地还出现了极端日降水量事件,其中山东台儿庄(199.4 mm)、内蒙古乌海(133.9 mm)和乌斯太(94.3 mm)、青海甘德(40.1 mm)等站日降水量突破历史极值。

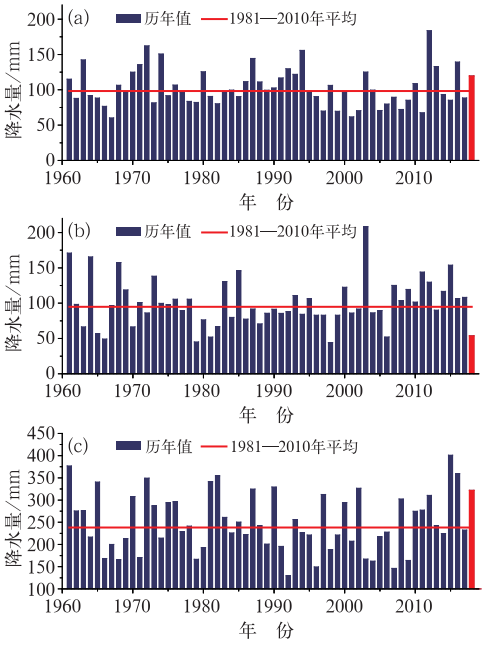

图 3 1961—2018 年秋季东北(a)、华北(b)和南方(c)地区平均降水量历年变化

Fig. 3 Time series of autumn rainfall over Northeast China (a), North China (b) and South China (c) during 1961－2018

从国家气候中心华西秋雨的监测结果来看(表 1),2018 年华西秋雨监测区降水总体较常年偏少 20.1%。其中华西北区(主要包括陕西南部大部、宁夏南部和甘肃南部)秋雨开始日期较常年偏晚 5 d,结束日期偏早 22 d,秋雨期偏短 26 d,累积降水量偏少 67.5%;华西南区(湖北西部、湖南西部、重庆、四川东部、贵州北部以及陕西南部部分地区)秋雨开始日期偏晚 1 d,结束日期偏晚 9 d,秋雨期偏长 8 d,累积降水量偏多 5.4%。

从降水的季节内变化来看,各区域存在明显的季节内转折变化(图 4)。其中长江以南地区,9 月总体表现为“西多东少”的分布特征(图 4a);而10月

表 1 2018 年华西秋雨指数特征

Table 1 Indexes of autumn rainfall over West China in 2018

	开始时间(气候值)	结束时间(气候值)	持续时间(气候值)/d	秋雨量(气候值)/mm
北区	9 月 13 日(9 月 8 日)	9 月 21 日(10 月 13 日)	8(35)	44.3(136.5)
南区	9 月 10 日(9 月 9 日)	11 月 9 日(10 月 31 日)	59(52)	194.3(184.4)
总体	9 月 10 日(8 月 31 日)	11 月 9 日(11 月 1 日)	59(62)	162.0(202.8)

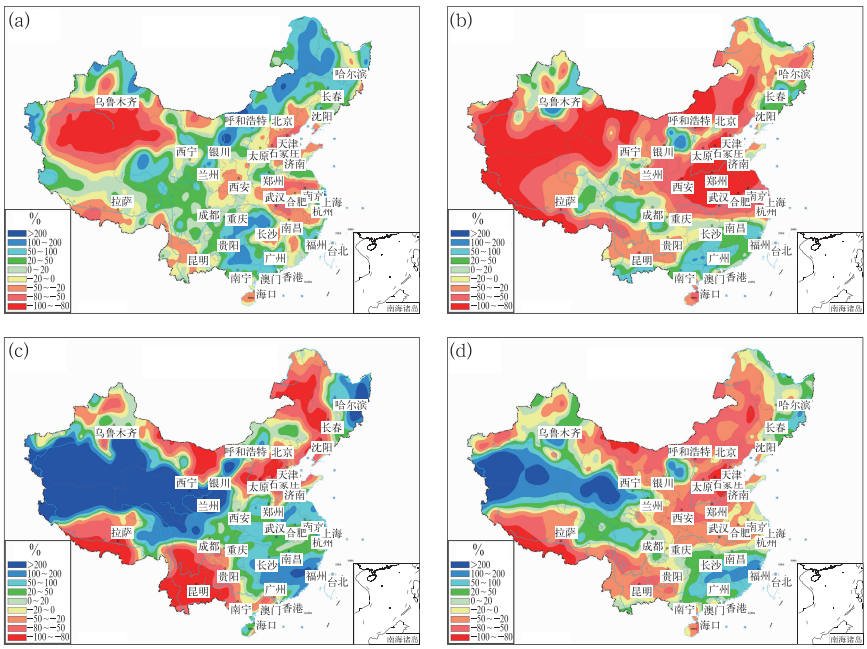

图 4 2018 年秋季逐月全国降水距平百分率分布

(a)9 月,(b)10 月,(c)11 月,(d)10—11 月

Fig. 4 Distribution of precipitation anomaly percentage in 2018

(a) September, (b) October, (c) November and (d) October－November

(图 4b)和 11 月(图 4c)降水异常的空间特征则发生了显著变化,长江以南地区转变为江南多、西南少的东多西少分布特征,尤其是 11 月东多西少分布特征更明显。为了后文的分析,图 4d 给出了 10—11 月的降水距平百分率,中国东部总体表现为南多北少的分布特征,长江以南则为江南多、西南少的东多西少分布特征。

何敏(1984)的研究中将我国秋雨区分成一般秋雨区和明显秋雨区,华西属于明显秋雨区,而长江中下游及其以南的大部分地区属于一般秋雨区。2018 年华西秋雨降水量北区异常偏少,南区接近常年略偏多。而华南至江南的秋雨强度明显强于华西地区,南方 6 省秋季平均降水量较常年同期偏多 35.3%,为 1983 年以来第五多年(图 3c),且季节内空间分布的转变特征较明显,对当地秋收秋种产生显著的不利影响。降水异常空间型的变化伴随着大气环流的调整和次季节尺度大气演变特征。为了突出气候异常特征并使降水成因分析更有针对性,下文将重点分析秋季我国南方地区降水异常偏多及空间分布型转变的原因。

3　气候异常的可能成因

由以上分析可见,2018 年秋季我国的主要气候异常突出表现为:气温总体呈"东高西低"的分布;东部降水呈"南北多、中间少"的分布,其中内蒙古中东部和东北大部、江南南部和华南地区异常偏多,而华北至江淮异常偏少,且南方地区降水异常的空间分布出现显著的季节内转折变化。2018 年秋季我国气候异常的主要原因包括两个方面:大气环流异常是影响气温和降水异常的直接原因,而海温异常则是气候异常的重要外强迫因子。

3.1　大气环流异常特征

大气环流异常是造成我国气候异常的直接原因。从秋季平均的 500 hPa 高度场及距平场上可以看出(图 5a),欧亚中高纬为"两脊一槽",欧洲—乌拉尔山以西为正高度距平,巴尔喀什湖及其以北为低槽控制,贝加尔湖—东亚大部为正高度距平控制,除东北外我国大部分地区处于负高度距平控制区,

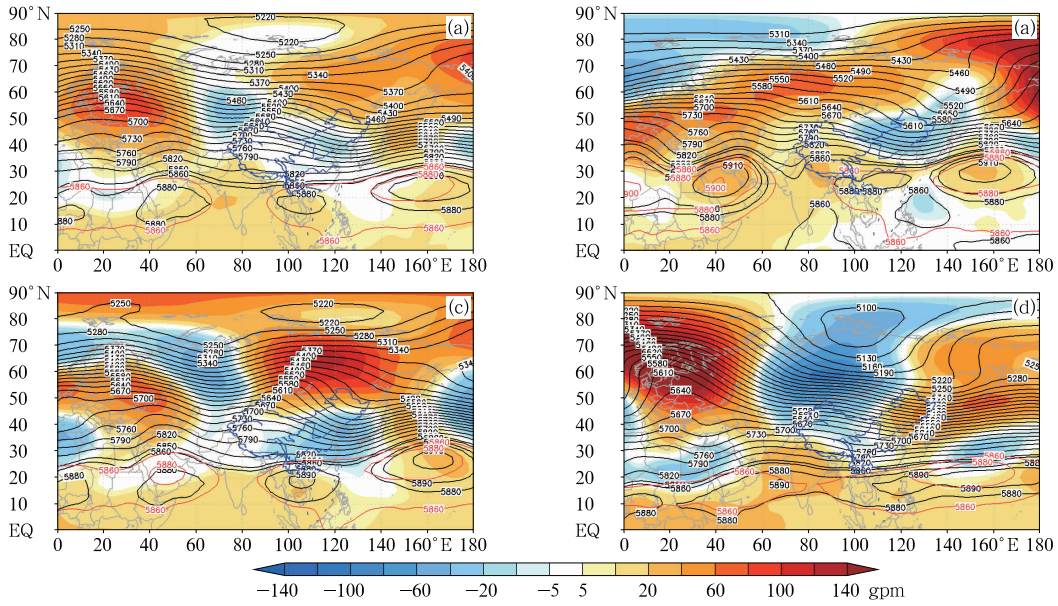

图 5　2018 年秋季 500 hPa 位势高度(等值线,单位:gpm)及距平场(填色)

(a)秋季,(b)9 月,(c)10 月,(d)11 月

(红色线为气候平均的位势高度等值线)

Fig. 5　500 hPa geopotential height (contours, unit: gpm) and anomalies (colored areas) in the autumn of 2018

(a) autumn, (b) September, (c) October, (d) November

(Red contours stand for the climatological mean of geopotential height contours)

从而有利于来自极地和中高纬度地区的冷空气从西北向东南方向扩散。整个秋季共发生了 10 次明显的冷空气过程，较常年同期偏多 2 次，导致我国西部大部分地区气温偏低。对于低纬度地区，副高的主体较气候态偏强偏南，但受到台风活动影响，副高体分为东西两段，西部中心位于南海上空，东部中心位于 130°E 以东的西北太平洋地区。环绕西部副高体的反气旋环流范围较大，且外缘位置明显偏西，从而有利于来自低纬度的西南暖湿水汽向我国南方地区输送，并与西北方南下的冷空气交汇，在西南地区东部、江南和华南这些地区形成明显的水汽通量辐合，有利于南方地区降水偏多。东段副高主体与日本岛以东的高压体相连，引导高压体西侧的南方水汽向北输送至东北地区和内蒙古东部地区，形成明显的水汽通量辐合(图 6a)，造成东北地区和内蒙古东部地区降水明显偏多。

此外，大气环流和水汽输送存在明显的季节内变化。9 月，欧亚中高纬呈“两脊一槽”的分布，乌拉尔山地区和鄂霍次克海为高压脊，而蒙古、我国华北和东北地区为低压槽控制，东亚槽偏弱，副高体位于 20°～30°N，位置略偏北，且分为东西两段，西段副高体位于中国华南至江南地区，菲律宾东部海洋上空为低压槽控制(图 5b)。环绕西部副高体的反气旋控制我国南方地区，从而有利于来自低纬度的暖湿水汽向我国西南地区和华南地区输送，并与西北方南下的冷空气交汇，在两个地区形成明显的水汽通量辐合(图 6b)，有利于西南和华南降水偏多；而江南大部受西北气流控制，降水偏少。

10 月，东亚呈“北高南低”的分布，贝加尔湖及其以东为正高度距平，我国大部分地区为负高度距平。副高形态类似于 9 月，但西段主体位置明显偏南，中心南移至 10°～20°N(图 5c)。菲律宾至孟加拉湾为较强的反气旋距平环流控制(图略)，孟加拉湾的水汽沿着反气旋向我国江南南部和华南地区输送，并与中国东部的冷空气交汇，在江南和华南形成明显的辐合(图 6c)，导致两个地区降水偏多。

11 月，东亚中高纬转为明显的“西低东高”的分布，乌拉尔山以东至贝加尔湖转为较强的负高度

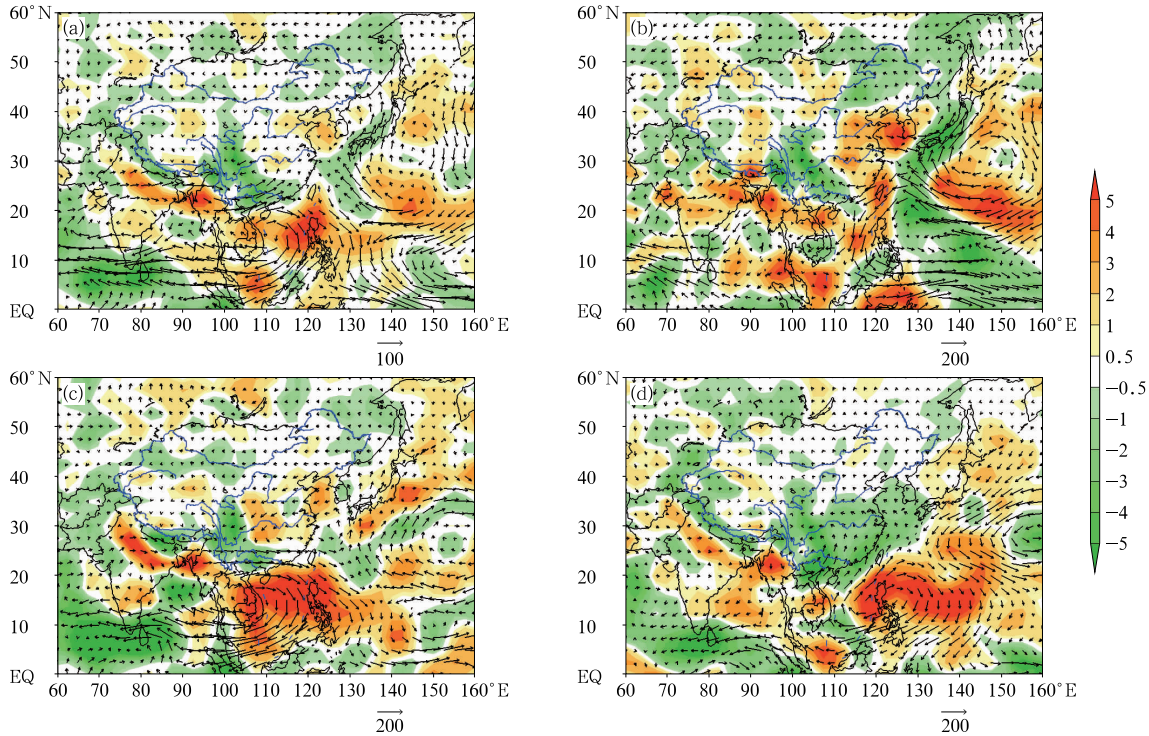

图 6 2018 年秋季对流层整层积分水汽通量(矢量，单位：kg·s^{-1}·m^{-1})
及水汽通量散度距平场(填色，单位：10^{-5} kg·s^{-1}·m^{-2})
(a)秋季，(b)9 月，(c)10 月，(d)11 月

Fig. 6 Anomalies moisture flux integrated from 1000 hPa to 300 hPa (vectors, unit: kg·s^{-1}·m^{-1})
and divergence (colored areas, unit: 10^{-5} kg·s^{-1}·m^{-2}) in 2018
(a) autumn, (b) September, (c) October, (d) November

距平,中国东部至鄂霍次克海转为较强的正高度距平,鄂霍次克海高压脊加强(图 5d)。副高形态较 10 月发生明显变化,强度明显增强,主体位置明显偏南,中心南移至 10°～20°N,连为一体,且异常西伸,西伸脊点最西达到 30°E 以西(图 5d)。菲律宾为较强的反气旋距平环流控制(图略),西南水汽沿着反气旋向我国东南地区输送,华南、江南和江淮地区为明显的水汽辐合区(图 6d),导致我国东南部地区降水异常偏多。

综上可见,2018 年秋季欧亚中高纬度槽脊活动频繁,冷空气活跃,副高偏强偏西,西南水汽输送偏强,导致我国气温"东高西低"的分布,东部降水"南北多、中间少"。且欧亚中高纬环流形势和副高均存在显著的季节内变化,二者共同导致了我国南方地区降水出现明显的东西反向的季节内变化。

3.2　海温

2017 年 10 月开始的拉尼娜(La Niña)事件于 2018 年 4 月结束后,赤道中东太平洋海温缓慢上升,8、9、10、11 月 Niño3.4 区海温指数分别为 0.27、0.38、0.85、0.99℃,8—10 月 3 个月滑动平均为 0.5℃。根据 Ren et al(2018) 制定的《厄尔尼诺/拉尼娜事件监测业务规定》,赤道中东太平洋已经在 9 月进入 El Niño 状态。从 SSTA 的空间演变可见,9 月,赤道中东太平洋暖海温主要位于赤道以北区域,赤道东太平洋赤道以南区域为正常—偏冷海温(图 7a),海温分布更偏向于中部型 El Niño 型;热带印度洋为东冷西暖的海温分布,即TIOD为正位相。

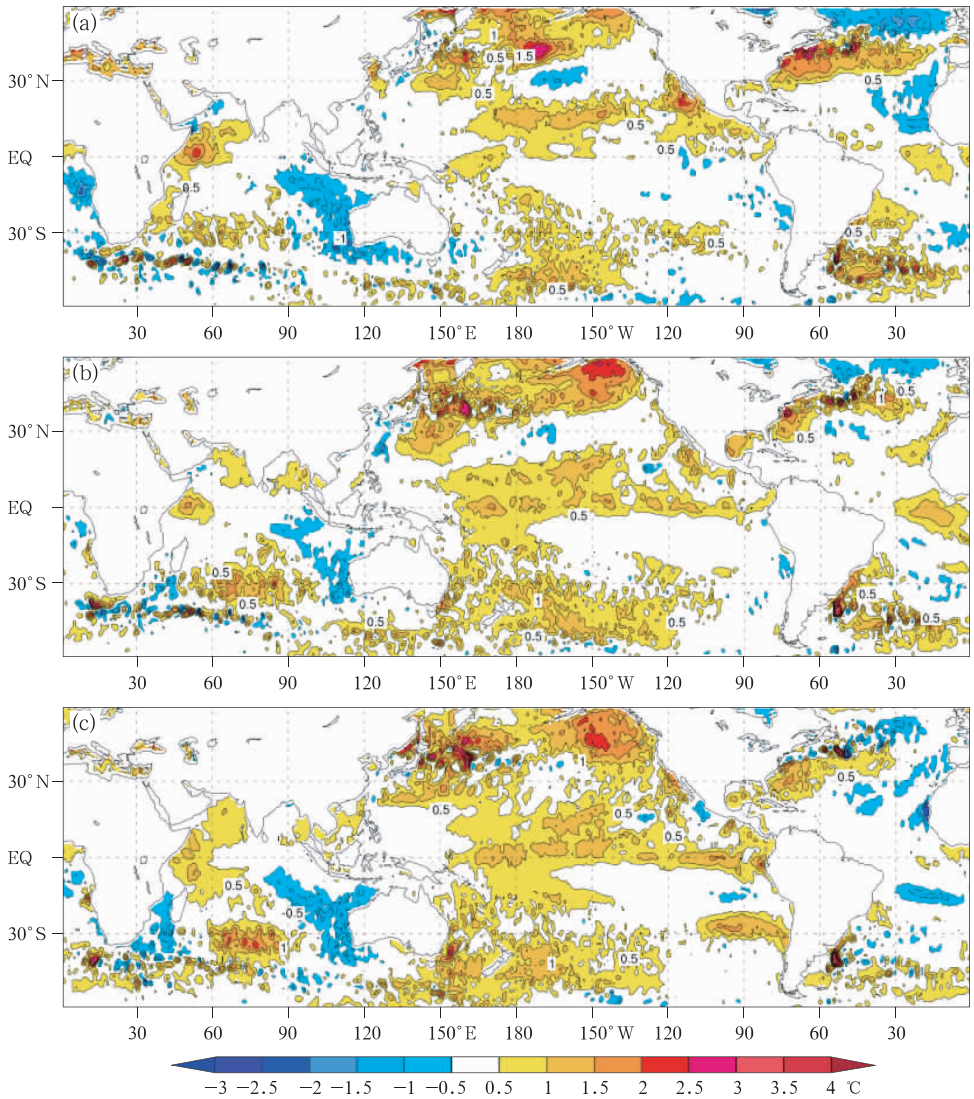

图 7　2018 年 9 月(a)、10 月(b)和 11 月(c)平均海表温度距平

Fig. 7　SST anomalies in September (a), October (b), November (c) of 2018

10 月赤道中太平洋暖海温向东传播，整个赤道中东太平洋均为暖海温，同时 TIOD 正位相减弱，而 SIOD 正位相发展（图 7b）；11 月，整个赤道中东太平洋暖海温进一步发展，中心东移至东太平洋，海温分布更偏向于东部型 El Niño 型，SIOD 正位相也进一步发展（图 7c）。从 2017—2018 年 EMI、Niño3 指数、TIOD 和 SIOD 演变来看，EMI 从 2018 年 4 月转为正值，此后在波动中上升；4—9 月，Niño3 指数明显弱于 EMI，10 和 11 月 Niño3 指数突然分别增加至 0.85 和 0.90℃，且明显高于 EMI；2—9 月，TIOD 维持负位相，SIOD 于 10 月由负转正，11 月达到 0.90℃。

已有研究表明，热带太平洋及印度洋海温异常是影响我国秋季降水的两个重要外强迫因子（谌芸和施能，2003；刘宣飞和袁慧珍，2006a；2006b；贾小龙等，2008；柳艳菊等，2013；顾薇等，2012；韩晋平等，2013；Gu et al，2015；何珊珊等，2015；刘佳等，2015；支蓉等，2018）。通常在 El Niño 年，我国秋季降水容易出现南多北少的异常分布特征。Gu et al（2015）研究发现，热带太平洋东西 SST 差与我国南方秋季降水密切相关，当东太平洋偏暖西太平洋偏冷时，中南半岛至我国东部为显著的偏南风，加强了我国南方的水汽输送和上升运动，导致我国南方地区降水偏多。刘宣飞和袁慧珍（2006b）研究表明，仅有 IOD 发生时，其正位相年使得中国西南地区和黄河流域的秋季降水出现正异常，而当 IOD 与 ENSO 伴随出现时，IOD 正位相年和 El Niño 使得中国西南地区秋季降水正异常区域维持并向东扩展，还使得黄河流域秋季降水转为负异常。从刘宣飞和袁慧珍（2006b）的 IOD 正位相年和 El Niño 联合发生年秋季降水距平百分率合成图与 2018 年秋季降水距平百分率图（图 2b）对比来看，前者降水偏多区域主要位于西南地区东南部至江南西部，而 2018 年降水偏多区域主要位于华南至江南中部，位置有明显的差异。结合中国南方秋季降水季节内转变来看，这一差异可能与赤道中东太平洋和印度洋SSTA的季节内演变有关。2018 年秋季，赤道中东太平洋和印度洋 SSTA 的演变均存在明显的季节内差异，El Niño 由 9 月的中部型向 10—11 月的东部型转变，印度洋秋季 TIOD 正位相维持，10—11 月 SIOD 正位相发展。为了说明这一问题，从 1981—2017 年秋季海温资料中选取四组赤道中东太平洋和印度洋海温异常的组合年。

A 组：9 月 El Niño 中部型和 TIOD 正位相年（$EMI \geqslant 0.5$℃，且 $EMI >$ Niño3 指数，$TIOD > 0$℃：1986、1991、1994 和 2004 年）；B 组：9 月 La Niña 中部型和 TIOD 负位相年（1984、1985、1988、1998、2010 和 2016 年）；C 组：10—11 月 El Niño 东部型和 SIOD 正位相年（Niño3 指数≥0.5℃，且 Niño3 指数$> EMI$，$SIOD > 0$℃：1986、1987、2004 和 2006 年）；D 组：10—11 月 La Niña 和 SIOD 负位相年（1983、1996、1999 和 2007 年）。

从 A 组和 B 组年份我国 9 月降水距平百分率合成图（图略）及二者的差值图（图 9a）可见，9 月 El Niño 中部型和 TIOD 正位相年，我国南方降水呈西南多而江南少的西多东少分布特征（图略），而 La Niña中部型和 TIOD 负位相年，南方降水呈东多西少分布（图略），二者的差值图也显示，西南地区

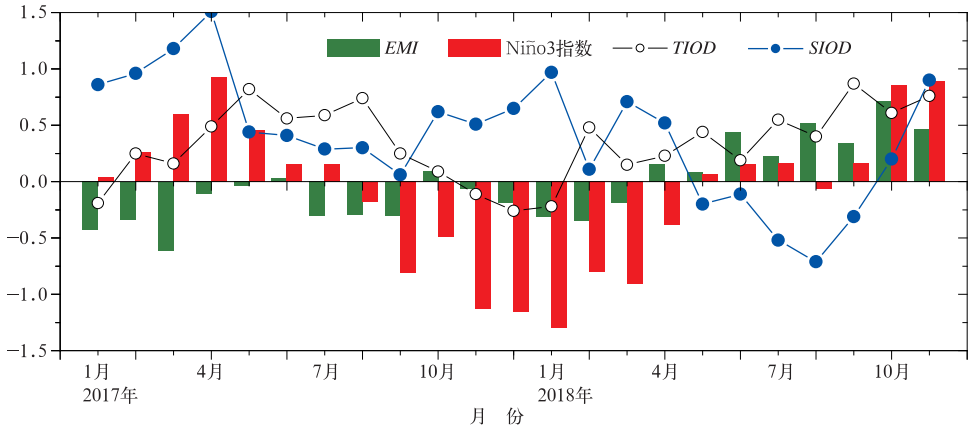

图 8 2017—2018 年 EMI、Niño3 指数、TIOD 和 SIOD（单位：℃）

Fig. 8 Monthly EMI, Niño3, TIOD and SIOD indexes during 2017－2018 (unit: ℃)

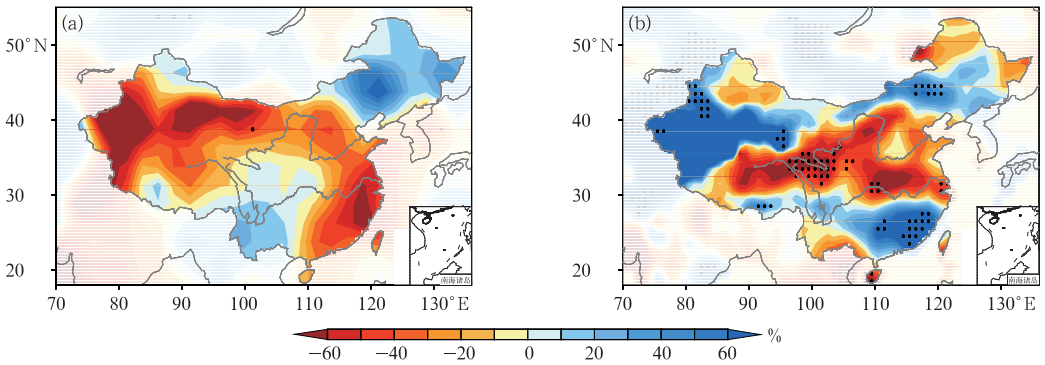

图 9　我国 9 月(a)和 10—11 月(b)降水距平百分率差值

(a)9 月 El Niño 为中部型且 TIOD 正位相年减去 9 月为 La Niña 东部型且 TIOD 负位相年,

(b)10—11 月为 El Niño 东部型且 SIOD 正位相年减去 10—11 月为 La Niña 且 SIOD 负位相年

(黑点为通过 0.05 显著性水平检验区域)

Fig. 9　The difference figures of precipitation anomaly percentage

in (a) September and (b) October−November

(a) years of central Pacific type (CP) El Niño and positive TIOD subtract years

of Eastern Pacific type (EP) El Niño and negtive TIOD in September,

(b) years of EP El Niño and positive SIOD subtract years of La Niña

and negtive SIOD in October−November

(Black dots indicate the area have passed the 0.05 significance level test)

为正差值区,江南至江淮为负差值区(图 9a)。从 9 月降水距平百分率图(图 4a)和图 9a 对比可见,南方降水二者均具有西多东少的分布,但华南地区和东南沿海部分地区有差异,这主要是因为 9 月登陆我国华南的台风较多,造成这些区域降水明显偏多。

从 C 组和 D 组年份我国 10—11 月降水距平百分率合成图(图略)及二者的差值图(图 9b)可见,10—11 月 El Niño 东部型和 SIOD 正位相年,我国东部降水呈南多北少分布,华南北部至江南降水偏多,而江淮至华北降水偏少(图略);而 10—11 月 La Niña 和 SIOD 负位相年,10—11 月我国东部降水分布恰好相反,华南北部至江南降水偏少,而江淮至华北降水偏多(图略),二者的差值图也显示,华南北部至江南为显著正差值区,而江淮至华北为负差值区(图 9b)。从 10—11 月降水距平百分率图(图 4d)和图 9b 对比可见,二者在中东部均具有南多北少的特征,在南方二者也均具有东多西少的分布特征。

从 A 组和 B 组年份 9 月东亚 500 hPa 高度距平场和 850 hPa 风场距平的合成图(图略)及二者的差值图(图 10a)可见,9 月 El Niño 中部型和 TIOD 正位相年,欧亚中高纬呈"两脊一槽"的分布,乌拉尔山地区和鄂霍次克海为高压脊,蒙古、中国华北和东北地区为低压槽控制,副高偏弱位置略偏北,华北为气旋距平,西南地区为西南风和西北风交汇区,江南大部为东北风异常(图略)。这种环流形势与 2018 年 9 月相类似,有利于华北和西南地区降水偏多、江南降水偏少。9 月 La Niña 中部型和 TIOD 负位相年,欧亚中高纬呈"两槽一脊"的分布,乌拉尔山地区和鄂霍次克海为低压槽,乌拉尔山以东至贝加尔湖以东为正高度距平,中国大陆为负高度距平,西北太平洋为正高度距平,副高偏强、位置偏南偏西,华南和江南为南风距平(图略)。这种环流形势有利于华南和江南降水偏多。二者的差值图也显示,贝加尔湖经中国华北至西北太平洋副热带地区为负差值区,江南为东北风距平控制(图 10a)。

从 C 组和 D 组年份 10—11 月东亚 500hPa 高度距平场和 850hPa 风场距平的合成图(图略)及二者的差值图(图 10b)可见,10—11 月 El Niño 东部型年和 SIOD 正位相年,乌拉尔山至鄂霍次克海为负高度距平,中国西部至江南为负高度距平,华北和东北地区为正高度距平,副高偏强偏南且异常西伸,华南至江南地区为西南风异常(图略),这种环流形势与 2018 年 10—11 月较为类似,有利于我国华南和江南降水偏多。10—11 月 La Niña 年和 SIOD 负位相年,东亚环流形势大体上与 El Niño 东部型年和 SIOD正位相年相反,贝加尔湖以西为异常偏强

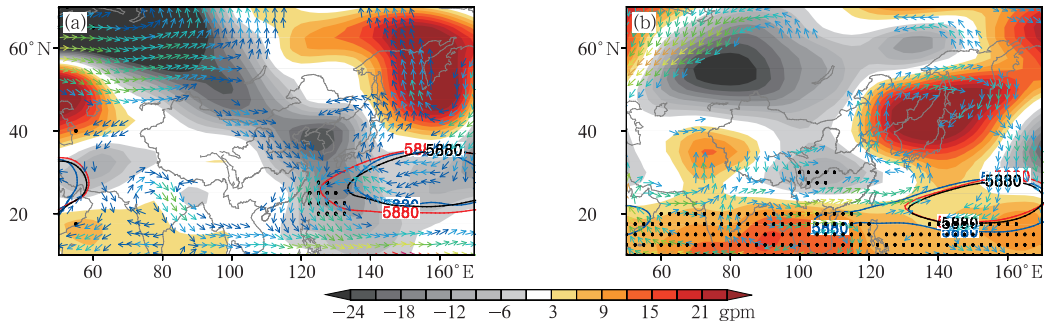

图 10 同图 9，但为 500 hPa 高度场(阴影)和 850 hPa 风场(矢量，单位：m·s^{-1})
(蓝、红和黑线在图 10a/图 10b 中分别表示 A 组/C 组、B 组/D 组和气候平均的 5880 gpm 等值线；
黑点为通过 0.05 显著性水平检验区域)

Fig. 10 Same as Fig. 9, but for 500 hPa geopotential height (contours) and anomalies fields (shadings) and 850 hPa wind anomalies (vectors, unit: m·s^{-1})
(blue, red and black contours stand for the Group A/C, Group B/D and climatological 5880 gpm contours in Fig. 10a/Fig. 10b, respectively; black dots indicate the area have passed the 0.05 significance level test)

的正高度，以东为负高度距平，副高强度和位置接近常年同期，我国华南至河套地区为正高度距平(图略)。南方受正高度距平的控制，降水偏少；而受正高度距平西南侧偏强的水汽输送，我国长江以北地区降水偏多。二者的差值图也显示，巴尔喀什湖至长江流域为显著负差值区，孟加拉湾至西太平洋副热带地区为显著的正差值区，我国南方为西南风距平(图 10b)，即 El Niño 东部型年和 SIOD 正位相年，副高偏强偏西偏南，西南水汽输送偏强，我国南方降水偏多、北方降水偏少；La Niña 年和 SIOD 负位相年，环流和降水则呈相反的分布特征。

4 结论和讨论

(1) 2018 年秋季，全国平均气温为 10.0℃，较常年同期偏高 0.1℃，空间上呈“东高西低”分布；平均降水量为 129.7 mm，较常年同期偏多8.3%，降水空间分布非常不均匀，其中东部地区总体呈现“南北多、中间少”的空间分布，而西部地区总体呈现“南北少、中间多”的空间分布，其中内蒙古中东部、东北、江南中南部和华南大部地区降水异常偏多，而华北至江南北部降水异常偏少，且南方地区降水出现明显的季节内反向变化特征。

(2) 大气环流和水汽输送异常是造成我国气候异常的直接原因。2018 年秋季，欧亚中高纬度槽脊活动频繁，冷空气活跃，副高偏强偏西，西南水汽输送偏强，导致我国气温“东高西低”，东部降水“南北多、中间少”。且欧亚中高纬环流形势和副高均存在显著的季节内变化，二者共同导致了我国南方地区降水出现明显的西南和江南东西反向的季节内变化。

(3) 海温异常是影响 2018 年秋季我国气候异常的最主要的外强迫因子，季节内 El Niño 由中部型向东部型发展，TIOD 正位相维持，10—11 月 SIOD 正位相发展。随着赤道中东太平洋海温和印度洋海温形态的共同转变，秋季后期 El Niño 影响增强，东亚副热带环流显示出清晰的响应，9 月副高偏强偏北，10—11 月副高偏强偏南。因此，El Niño 和印度洋海温的演变及其对东亚环流的影响，加上欧亚中高纬环流异常的季节内调整，二者共同导致了我国南方地区降水出现明显的江南与西南反向的季节内变化。

热带太平洋和印度洋海温异常是影响东亚大气环流的重要因素。袁媛等(2012)、袁媛和晏红明(2012)研究发现，热带大气对不同分布型 El Niño 和 La Niña 事件有不同的响应特征，进而对我国气候造成不同的影响。已有研究探讨过印度洋海温异常尤其是 TIOD 与我国秋季降水的关系(刘宣飞和袁慧珍，2006a；2006b；刘佳等，2015)。一般认为夏、秋季印度洋偶极子均与中国南方秋季降水有很好的正相关关系，同时 ENSO 事件的发生对 TIOD 与中国秋季降水的关系有调制作用，导致 TIOD 与 ENSO 事件联合作用和独立作用时对秋季气候的影响不同。也有研究指出，SIOD 对印太地区及我国

气候具有较大的影响(Behera and Yamagata，2001；Reason，2001；贾小龙和李崇银，2005)。但 SIOD 对我国秋季降水的影响机制还不清晰，需要进一步分析研究。本文通过 2018 年秋季降水异常成因分析发现，ENSO 分布型和印度洋海温模态位相的季节内转变，对我国南方秋季降水空间分布型季节内调整起到了重要的作用，该结论为我国秋季降水预测提供了依据。

参考文献

白虎志，董文杰，2004. 华西秋雨的气候特征及成因分析[J]. 高原气象，23(6)：884-889. Bai H Z，Dong W J，2004. Climate features and formation causes of autumn rain over southwest China[J]. Plateau Meteor，23(6)：884-889(in Chinese).

鲍媛媛，阿布力米提，李峰，等，2003. 2001 年华西秋雨时空分布特点及其成因分析[J]. 应用气象学报，14(2)：215-222. Bao Y Y，Abulimiti，Li F，et al，2003. Space-time distribution and physical mechanisms of autumn rains in west China in 2001[J]. J Appl Meteor Sci，14(2)：215-222(in Chinese).

谌芸，施能，2003. 厄尔尼诺/南方涛动与我国秋季气候异常[J]. 热带气象学报，19(2)：137-146. Chen Y，Shi N，2003. El Nino/ENSO and climatic anomaly in the autumn of China[J]. J Trop Meteor，19(2)：137-146(in Chinese).

顾薇，李维京，陈丽娟，等，2012. 我国秋季降水的年际变化及与热带太平洋海温异常分布的关系[J]. 气候与环境研究，17(4)：467-480. Gu W，Li W J，Chen L J，et al，2012. Interannual variations of autumn precipitation in China and their relations to the distribution of tropical Pacific sea surface temperature[J]. Climatic Environ Res，17(4)：467-480(in Chinese).

韩晋平，张人禾，苏京志，2013. 中国北方秋雨与热带中太平洋海表冷却的关系[J]. 大气科学，37(5)：1059-1071. Han J P，Zhang R H，Su J Z，2013. Relationship between cooling of tropical Pacific sea surface temperature and autumn precipitation in China[J]. Chin J Atmos Sci，37(5)：1059-1071(in Chinese).

何敏，1984. 我国主要秋雨区的分布及长期预报[J]. 气象，10(9)：10-13. He M，1984. Distribution of the main autumn rain area in China and its long-term forecasting[J]. Meteor Mon，10(9)：10-13(in Chinese).

何珊珊，张文君，祁莉，等，2015. 两类厄尔尼诺事件发展年秋季印度洋海温异常特征对比[J]. 气象学报，73(3)：515-528. He S S，Zhang W J，Qi L，et al，2015. Contrasting SST anomalies over the Indian Ocean between the two types of El Niño events during boreal autumn[J]. Acta Meteor Sin，73(3)：515-528(in Chinese).

侯威，邹旭凯，王朋岭，等，2015. 2014 年中国气候概况[J]. 气象，41(4)：480-488. Hou W，Zou X K，Wang P L，et al，2015. Climatic characteristics over China in 2014[J]. Meteor Mon，41(4)：480-488(in Chinese).

贾小龙，李崇银，2005. 南印度洋海温偶极子型振荡及其气候影响[J]. 地球物理学报，48(6)：1238-1249. Jia X L，Li C Y，2005. Dipole oscillation in the southern Indian Ocean and its impacts on climate[J]. Chin J Geophys，48(6)：1238-1249(in Chinese).

贾小龙，张培群，陈丽娟，等，2008. 2007 年我国秋季降水异常的成因分析[J]. 气象，34(4)：86-94. Jia X L，Zhang P Q，Chen L J，et al，2008. Causality analysis of autumn rainfall anomalies in China in 2007[J]. Meteor Mon，34(4)：86-94(in Chinese).

刘佳，马振峰，杨淑群，等，2015. 印度洋偶极子和华西秋雨的关系[J]. 高原气象，34(4)：950-962. Liu J，Ma Z F，Yang S Q，et al，2015. Relationship between Indian Ocean dipole and autumn rainfall in West China[J]. Plateau Meteor，34(4)：950-962(in Chinese).

刘宣飞，袁慧珍，2006a. 印度洋偶极子与中国秋季降水的关系[J]. 南京气象学院学报，29(5)：644-649. Liu X F，Yuan H Z，2006a. Relationship between the Indian Ocean dipole and autumn rainfall in China[J]. J Nanjing Inst Meteor，29(5)：644-649(in Chinese).

刘宣飞，袁慧珍，2006b. ENSO 对印度洋偶极子与中国秋季降水关系的影响[J]. 南京气象学院学报，29(6)：762-768. Liu X F，Yuan H Z，2006b. Effects of ENSO on the relationship between IOD and autumn rainfall in China[J]. J Nanjing Inst Meteor，29(6)：762-768(in Chinese).

柳龙生，高拴柱，2018. 2018 年 9 月大气环流和天气分析[J]. 气象，44(12)：1635-1640. Liu L S，Gao S Z，2018. Analysis of the September 2018 atmospheric circulation and weather[J]. Meteor Mon，44(12)：1635-1640(in Chinese).

柳艳菊，王艳姣，司东，等，2013. 2012 年秋季我国气候异常及成因分析[J]. 气象，39(4)：526-530. Liu Y J，Wang Y J，Si D，et al，2013. Features and possible causes for the climatic anormaly in China in autumn 2012[J]. Meteor Mon，39(4)：526-530(in Chinese).

聂羽，孙冷，李清泉，等，2016. 2015 年秋季我国气候异常及暖湿成因分析[J]. 气象，42(4)：507-513. Nie Y，Sun L，Li Q Q，et al，2016. Possible causes for the warmer and wetter autumn in 2015 in China[J]. Meteor Mon，42(4)：507-513(in Chinese).

司东，邵勰，孙冷，等，2015. 2014 年秋季我国华西地区降水异常的成因分析[J]. 气象，41(4)：508-513. Si D，Shao X，Sun L，et al，2015. Causality analysis of autumn rainfall anomalies in West China 2014[J]. Meteor Mon，41(4)：508-513(in Chinese).

王朋岭，李多，柳艳菊，等，2014. 2013 年秋季东北地区气候异常及成因分析[J]. 气象，40(4)：510-514. Wang P L，Li D，Liu Y J，et al，2014. Study on climate anomaly and possible mechanism over the Northeast China in autumn 2013[J]. Meteor Mon，40(4)：510-514(in Chinese).

肖科丽，赵国令，方建刚，等，2015. 陕西汛期降水年际增量预测新技术研究[J]. 气象，41(3)：328-335. Xiao K L，Zhao G L，Fang J G，et al，2015. Study on interannual increment forecasting approach for rainy season precipitation in Shaanxi[J]. Meteor Mon，41(3)：328-335(in Chinese).

晏红明，李崇银，周文，2009. 南印度洋副热带偶极模在 ENSO 事件中的作用[J]. 地球物理学报，52(10)：2436-2449. Yan H M，

Li C Y, Zhou W, 2009. Influence of subtropical dipole pattern in southern Indian Ocean on ENSO event[J]. Chin J Geophys, 52(10): 2436-2449(in Chinese).

袁媛, 晏红明, 2012. 不同分布型 La Niña 事件及热带大气的响应特征对比[J]. 科学通报, 57(34): 3312-3322. Yuan Y, Yan H M, 2013. Different types of La Niña events and different responses of the tropical atmosphere[J]. Chin Sci Bull, 58(3): 406-415(in Chinese).

袁媛, 杨辉, 李崇银, 2012. 不同分布型厄尔尼诺事件及对中国次年夏季降水的可能影响[J]. 气象学报, 70(3): 467-478. Yuan Y, Yang H, Li C Y, 2012. Study of El Niño events of different types and their potential impact on the following summer precipitation in China[J]. Acta Meteor Sin, 70(3): 467-478(in Chinese).

支蓉, 陈丽娟, 竺夏英, 2018. 2017 年秋季我国北方地区降水异常偏多成因分析[J]. 气象, 44(4): 572-581. Zhi R, Chen L J, Zhu X Y, 2018. Analysis of characteristics and causes of precipitation anomalies over northern China in autumn 2017[J]. Meteor Mon, 44(4): 572-581(in Chinese).

竺夏英, 宋文玲, 2017. 2016 年秋季中国气候特征及其可能成因[J]. 气象, 43(4): 495-500. Zhu X Y, Song W L, 2017. Features of climatic anomalies in China during the fall of 2016 and the possible causes[J]. Meteor Mon, 43(4): 495-500(in Chinese).

Ashok K, Behera S K, Rao S A, et al, 2007. El Niño Modoki and its possible teleconnection[J]. J Geophys Res Oceans, 112(C11): C11007.

Behera S K, Yamagata T, 2001. Subtropical SST dipole events in the southern Indian Ocean[J]. Geophys Res Lett, 28(2): 327-330.

Gu W, Wang L, Li W J, et al, 2015. Influence of the tropical Pacific east-west thermal contrast on the autumn precipitation in South China[J]. Int J Climatol, 35(7): 1543-1555.

Kalnay E, Kanamitsu M, Kistler R, et al, 1996. The NCEP/NCAR 40-year reanalysis project[J]. Bull Amer Meteor Soc, 77(3): 437-472.

Reason C J C, 2001. Subtropical Indian Ocean SST dipole events and southern African rainfall[J]. Geophys Res Lett, 28(11): 2225-2227.

Ren H L, Lu B, Wan J H, et al, 2018. Identification standard for ENSO events and its application to climate monitoring and prediction[J]. J Meteor Res, 32(6): 923-936.

Reynolds R W, Smith T M, Liu C Y, et al, 2007. Daily high-resolution-blended analyses for sea surface temperature[J]. J Climate, 20(22): 5473-5496.

Saji N H, Goswami B N, Vinayachandran P N, et al, 1999. A dipole mode in the tropical Indian Ocean[J]. Nature, 401(6751): 360-363.

Weng H Y, Ashok K, Behera S K, et al, 2007. Impacts of recent El Niño Modoki on dry/wet conditions in the Pacific Rim during boreal summer[J]. Climate Dyn, 29(2/3): 113-129.

Weng H Y, Behera S K, Yamagata T, 2009. Anomalous winter climate conditions in the Pacific rim during recent El Niño Modoki and El Niño events[J]. Climate Dyn, 32(5): 663-674.

Relationship between Tropical Indian Ocean SSTA in Spring and Precipitation of Northeast China in Late Summer

Junhu ZHAO[1,2], Jie ZHOU[3], Kaiguo XIONG[4], and Guolin FENG[2*]

1 *Laboratory for Climate Studies, National Climate Center, China Meteorological Administration, Beijing* 100081
2 *College of Physical Science and Technology, Yangzhou University, Yangzhou* 225002
3 *Chongqing Climate Center, Chongqing Meteorological Service, Chongqing* 401147
4 *Wuhan Regional Climate Center, Wuhan* 430074

(Received March 4, 2019; in final form July 4, 2019)

ABSTRACT

Sea surface temperature anomaly (SSTA) is a major signal for prediction of summer precipitation in East Asia. The relationship between SSTA in the tropical oceans and summer precipitation in East Asia has been documented in many studies. However, the relationship between SSTA and late summer (July–August) precipitation (JAP) over Northeast China (NEC) on the interannual timescale has received little attention. In this study, we examine the relationship between Indian Ocean Basin warming (IOBW) anomalies in spring and the JAP in NEC since the early 1960s. A significant positive correlation is found between the spring IOBW index and JAP over NEC. The positive spring IOBW anomaly is followed by an anomalous anticyclone from Northwest Pacific to the Korean Peninsula. This anomalous anticyclone favors a significantly strong and northward western Pacific subtropical high (WPSH), which facilitates anomalous southerly winds over NEC and the transport of more water vapor into this region. Further analysis indicates that the spring IOBW anomalies have important impacts on the vertical air motion in the tropics and subtropics during the summer. Significant anomalous upward (downward) motion covering Indonesia (Northwest Pacific to the southern Korean Peninsula) occurs when the IOBW is in its positive phase, which favors the northward movement of the WPSH in late summer and more precipitation over NEC in July–August. Modulation of the atmospheric circulation by this mechanism further influences the JAP over NEC.

Key words: Northeast China (NEC), late summer precipitation, interannual, circulation, Indian Ocean Basin warming (IOBW)

Citation: Zhao, J. H., J. Zhou, K. G. Xiong, et al., 2019: Relationship between tropical Indian Ocean SSTA in spring and precipitation of Northeast China in late summer. *J. Meteor. Res.*, **33** (6), 1060–1074, doi: 10.1007/s13351-019-9026-9.

1. Introduction

Northeast China (NEC; 38°–53°N, 118°–135°E) lies on the northeastern boundary of the East Asian summer monsoon (EASM; Sun et al., 2000; Lian et al., 2003; Gao et al., 2014; Han et al., 2018a). Summer is the main season of agricultural growth and concentrated period of precipitation over NEC, and predictions of the spatial distribution of summer floods and droughts are important for agriculture in this region. The weather and climate over NEC are affected by the monsoon circulation systems of the subtropics and the westerly wind belt over the Northern Hemisphere (Sun et al., 2002). In general, the mid- to high-latitude circulation has a dominant influence on the climate over NEC (Wang et al., 2009) and there are distinct sub-seasonal climate features over this region in summer.

The atmospheric circulations affecting the climate of NEC vary greatly over the summer months. In early summer (May–June), the weather and climate over NEC are associated with the activity of the NEC cold vortex and the Okhotsk high (He et al., 2007). However, in late summer (July–August), they are mainly affected by the northeastward movement of the EASM and the western

Supported by the National Key Research and Development Program of China (2018YFA0606301) and National Natural Science Foundation of China (41875093, 41705074, and 41530531).

*Corresponding author: fenggl@cma.gov.cn.

©The Chinese Meteorological Society and Springer-Verlag Berlin Heidelberg 2019

Pacific subtropical high (WPSH), and also influenced by the activity of the Okhotsk high and NEC cold vortex (Sun et al., 1994; Zhao and Feng, 2014; Zhao et al., 2018). The EASM plays a key role in the weather and climate over NEC, and a more powerful EASM leads to more rainfall over NEC on both interannual and decadal timescales (Sun et al., 2003, 2017). Moreover, significant interannual and decadal variations occur in summer precipitation over NEC (Shen et al., 2011).

Zhao et al. (2018) found that the atmospheric circulations that affect early summer precipitation over NEC are different from those that influence late summer precipitation on both interannual and decadal timescales. Han et al. (2015) indicated that a clear shift to less precipitation over NEC during the peak summer months (July–September) occurred from 1999 to 2012 relative to 1984–98. Wang and He (2015) showed that the sea surface temperature anomalies (SSTAs) over the Pacific Ocean, warming over the Caspian Sea and the European Continent, and Arctic sea ice anomalies jointly led to the severe summer drought in northern China in 2014.

SSTA is a main predictor of climate variability over NEC, although multiple factors play a part. The El Niño–Southern Oscillation (ENSO) is the strongest signal in the interannual variability of the atmospheric circulation (Zheng et al., 2006; Zheng and Zhu, 2016; Lin et al., 2018). The occurrence of an ENSO event is an important precursor used to predict interannual climate anomalies in many tropical and subtropical regions, especially for predicting the patterns in the summer rain belt over East China (Shi et al., 2001; Wang and Wu, 2012). However, the influence of ENSO on the variation in precipitation over NEC is intricate, exhibiting large uncertainty (Wang, 2002; Gao and Gao, 2015). There is no remarkable connection between the seasonally averaged precipitation in NEC and ENSO during 1951–2000 (Wu et al., 2003). Gong et al. (2005) reported that there is no direct correlation between ENSO and the summer monsoon over NEC, and that the resulting precipitation anomalies have no significant relation with El Niño events.

The SSTA in the Indian Ocean exerts a crucial influence on the climate variability of the surrounding areas through strong air–sea interactions (Saji et al., 1999; Annamalai, 2010; Huang et al., 2010). The SSTA in the tropical Indian Ocean (TIO) substantially affects the East Asian climate because the TIO is one of the main sources of water vapor for East Asia (Xie et al., 2009; Xu and Fan, 2012). The Indian Ocean Basin warming (IOBW) is the first mode of the variability of sea surface temperatures (SSTs) in the TIO and is closely linked to variations in climate in India and East Asia (Yang et al., 2007; Huang et al., 2016). Huang et al. (2010) showed that the TIO teleconnection with Northwest Pacific has strengthened since the mid 1970s. Qu and Huang (2012) noted that the TIO has exerted an enhanced impact on the South Asian high since the late 1970s. Han et al. (2018b) reported that there has been a close linkage between the March–April SSTs in the TIO and the precipitation over NEC in the following May–June since the late 1980s.

Most of the previously published investigations have considered the evolutionary characteristics of the summer mean rainfall over NEC and/or the relationship between rainfall and SSTs (Bai, 2001; Wu et al., 2003; Wang et al., 2013; Han et al., 2015, 2018b). However, the sub-seasonal variation in summer rainfall in NEC (i.e., the variation in rainfall in early and late summer) has not been considered. The atmospheric circulations and SSTs that affect precipitation over NEC in late summer are significantly different from those in early summer; the EASM and WPSH play a more important role (Zhao et al., 2018). Late summer is the main rainy season in NEC. It is therefore meaningful to study the relationship between the SSTs in the key oceanic regions and late summer precipitation in NEC.

The remainder of this paper is organized as follows. The datasets and methodology are introduced in Section 2. The relationship between the previous winter–spring SSTAs in the TIO and precipitation in late summer of the same year over NEC and the possible mechanisms of this relationship are analyzed in Section 3. A summary and discussion are presented in Section 4.

2. Data and methodology

The monthly average precipitation dataset for 160 stations in China during the time period 1951–2016 was obtained from the China Meteorological Administration. A total of 24 of these stations (Fig. 1a) are located in NEC (38°–53°N, 118°–135°E). The monthly mean circulation data, gridded at a resolution of 2.5° × 2.5°, were obtained from the NCEP/NCAR for the time period 1951–2016 (Kalnay et al., 1996). SST data with a resolution of 2.0° × 2.0° were obtained from the NOAA Extended Reconstructed Sea Surface Temperature version 3b (ERSST.v3b) dataset (Smith et al., 2008). The outgoing longwave radiation (OLR) data were obtained from NOAA for the time period June 1974–December 2013 (Liebmann and Smith, 1996).

The NOAA Niño3.4 index was used to represent the ENSO (https://www.cpc.ncep.noaa.gov/data/indices/sstoi.

indices) for 1951–2016. The IOBW index was defined as the normalized area-averaged SSTA in the TIO (5°S–20°N, 40°–110°E). The WPSH intensity index was defined by the geopotential height at 500 hPa (H_{500}) in the subtropical western Pacific (10°–35°N, 115°–150°E). The WPSH ridge position index was defined as the average latitude of 500-hPa zonal wind (U_{500}) = 0 over 10°–35°N, 115°E–180°, and the NEC south wind (NESW) index was defined as the area-averaged 850-hPa meridional wind (V_{850}) over 32.5°–42.5°N, 120°–130°E (Sun et al., 2003, 2017).

The power spectrum analysis was performed to reveal the periodicity of summer precipitation over NEC. Fast Fourier transformation and bandpass filtering were then employed to decompose the interannual and decadal variations. Correlation analysis and linear regression analysis were implemented to show the connections between the atmospheric circulation and rainfall in NEC. We used Student's t test to check the significance of the correlation and regression analyses. The linear trends were removed before the computations.

3. Results

3.1 *Characteristics of late summer precipitation over NEC*

Figure 1a displays locations of the meteorological stations in NEC; precipitation observations at these stations are used in this study. Figure 1b shows temporal evolution of areal-averaged late summer (July–August) precipitation (JAP) in NEC. There are clear interannual and interdecadal variations in the JAP and there are apparent shifts to more (less) precipitation in the 1960s and mid 1980s (mid 1970s and entire 2000s) over NEC. Figure 1c shows the power spectrum of the JAP. There is a clear interannual (2–4-yr period) and interdecadal (22-yr period) variability during the time period 1951–2016. To focus on the interannual variations, the JAP time series

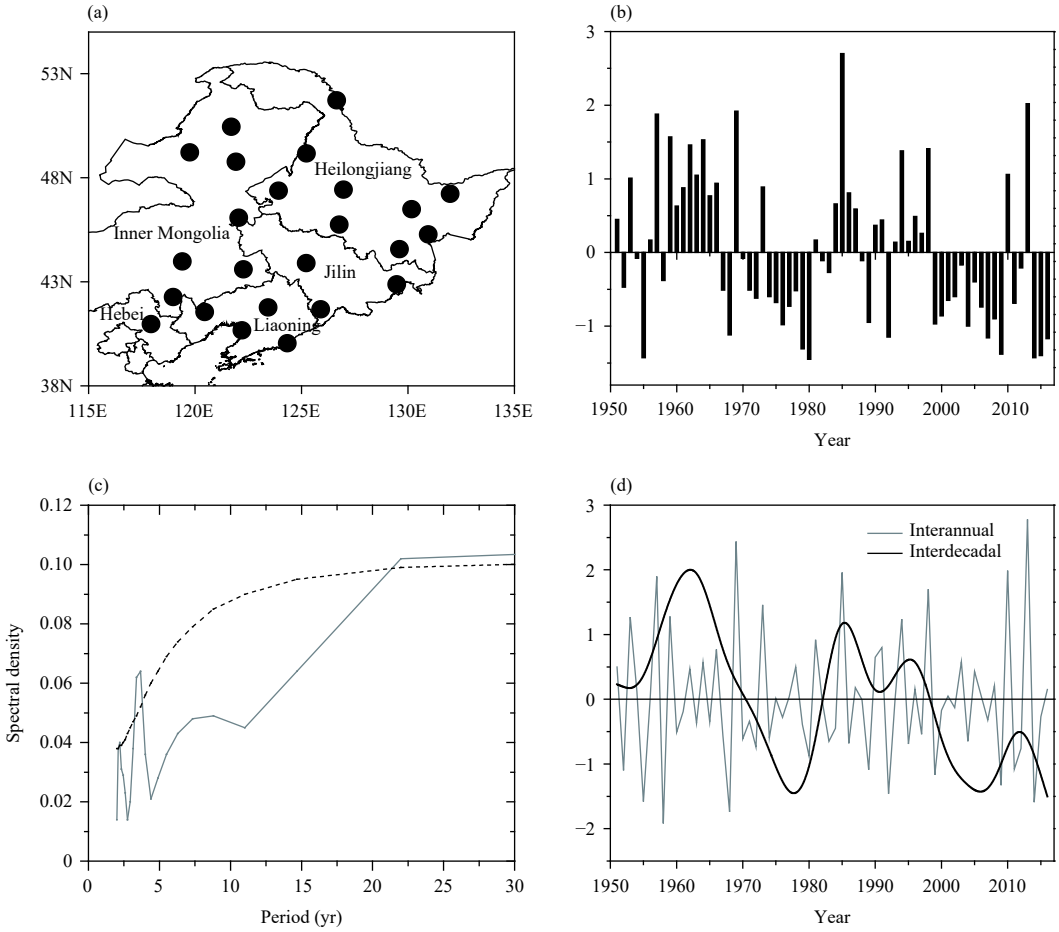

Fig. 1. (a) Locations of meteorological stations in Northeast China (NEC). (b) Standardized time series of the July–August precipitation (JAP) over NEC during the time period 1951–2016. (c) Power spectrum for the JAP. The values above the dotted line show a confidence level of 90% against red noise. (d) Interannual and interdecadal variations in the JAP.

was decomposed into interannual (variation less than 8 yr) and interdecadal (variation longer than 15 yr) components by Fourier decomposition filtering (Fig. 1d). The standard deviations of the interannual and interdecadal components of the JAP were 25.9 and 21.6 mm, respectively. This indicates the necessity of timescale decomposition of the JAP over NEC. To facilitate our analysis of the linkage between the JAP and SSTs on the interannual timescale, all the data were filtered by using a Butterworth 8-yr high-pass filter.

3.2 *Linkage between the JAP over NEC and SSTs*

To investigate the possible linkage between late summer precipitation over NEC and SSTs, Fig. 2 shows the correlation coefficients between the JAP and the SST in the previous winter, spring, and summer during the time period 1961–2016. The data were not filtered before analysis.

The partial correlation map between the JAP and the previous winter (December–February) SST field (Fig. 2a) shows that the SST over the western Pacific warm pool area is significantly negatively correlated to JAP, whereas the SST over the TIO and the central and eastern equatorial Pacific Ocean (CEPO) exhibits statistically insignificant correlations. There is hardly any significant correlation in the spring (March–May) SST field (Fig. 2b). Remarkable negative correlations appear in the TIO in the summer (June–August) SST field (Fig. 2c) and the correlation coefficients over the EPO and North Pacific Ocean are very small, with barely any significant correlation.

To detect whether there is any difference in the rela-

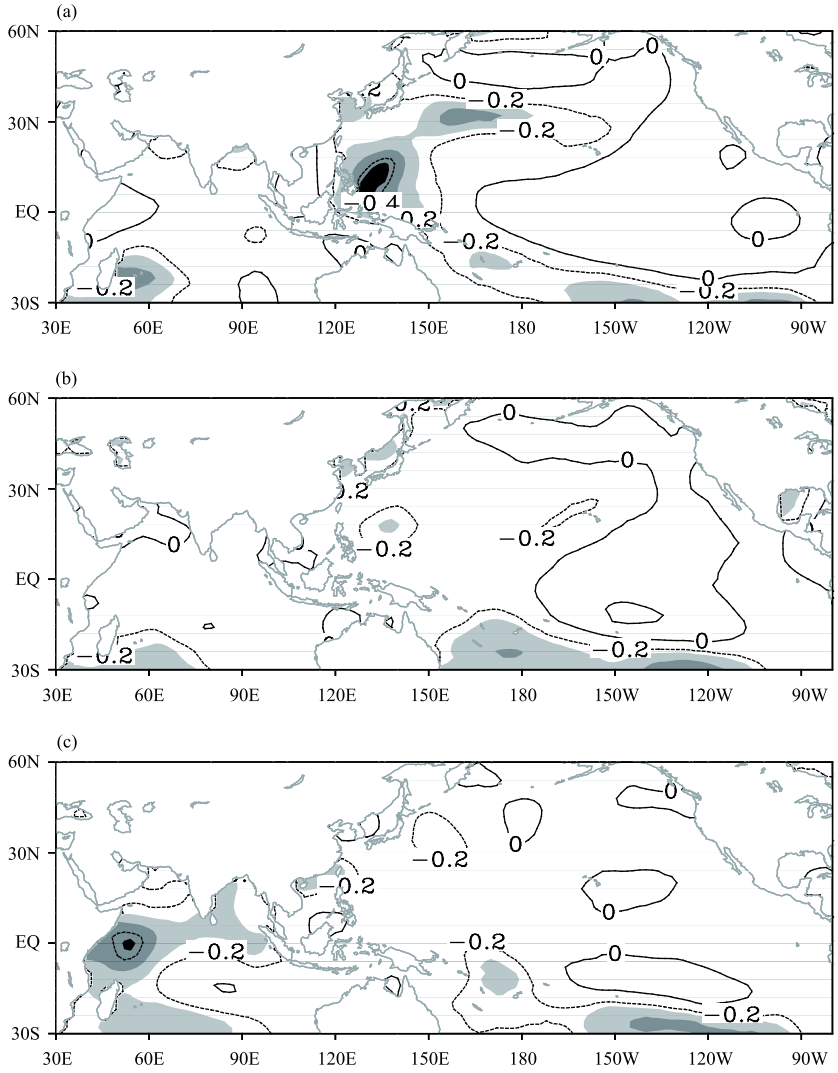

Fig. 2. Correlation coefficients between JAP over NEC and sea surface temperatures (SSTs) in (a) December–January–February, (b) March–April–May, and (c) June–July–August during the time period 1961–2016. Shadings from light to dark indicate values that significantly exceed the 95%, 99%, and 99.9% confidence levels, respectively.

tionship between the JAP over NEC and the SST on interannual and interdecadal timescales, Figs. 3 and 4 present the correlation coefficients between the JAP and SSTs on interannual and interdecadal timescales, respectively.

On the interannual timescale, there are significant positive correlations over the TIO, the CEPO, and the South China Sea (SCS) in the previous winter SST field (Fig. 3a), whereas significant negative correlations are seen over the western Pacific warm pool. The correlations are above the 99.9% confidence level. The same correlation distributions are seen between the JAP and the spring SSTs (Fig. 3b). There are some differences, however. Compared with the correlation distribution in winter, the spatial ranges of significant positive correlations decrease in the CEPO, the significant positive correlation regions in the TIO expand eastward to Northwest Pacific, and the positive correlation fields in the northern TIO become more significant, whereas the correlation coefficients in the western Pacific warm pool area become statistically insignificant. The correlation coefficients in summer (Fig. 3c) are the opposite to those on the winter correlation map. The northern TIO and the CEPO show negative correlations and the western Pacific warm pool shows significant positive correlations.

Figure 4 presents the correlation coefficients on the interdecadal timescale. Positive correlations are seen over Northeast Pacific and negative correlations are located in the Indian Ocean, the western Pacific Ocean, and the Southeast Pacific Ocean in winter (Fig. 4a). Significant negative correlations appear in the Southwest Indian Ocean, the western Pacific warm pool, and east of Australia. The same correlation distributions between the JAP and SSTs occur in both spring (Fig. 4b) and sum-

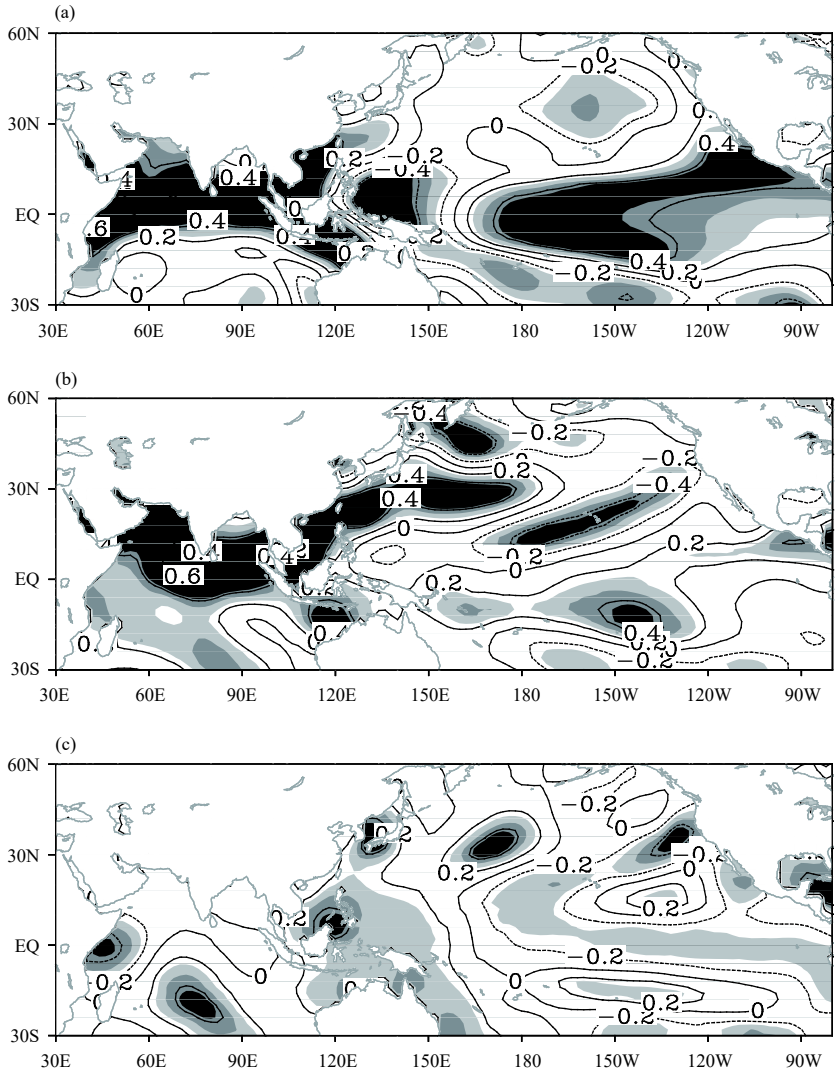

Fig. 3. As in Fig. 2, but for the interannual timescale.

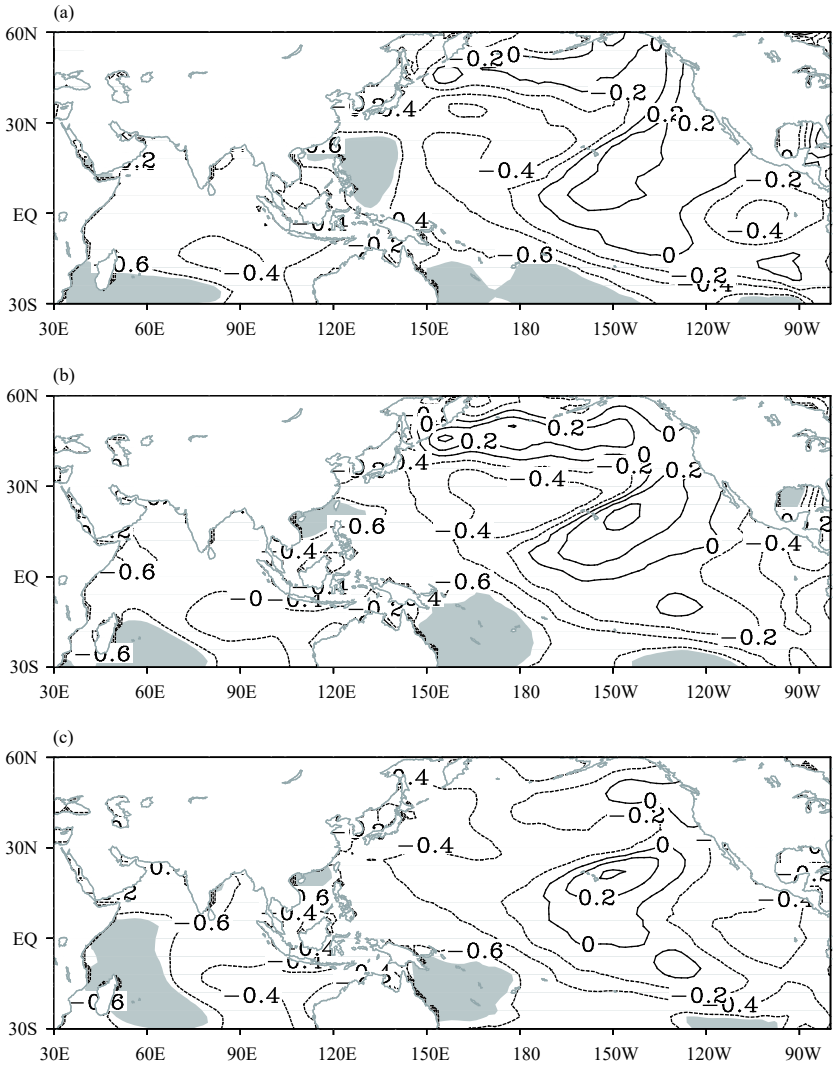

Fig. 4. As in Fig. 2, but for the interdecadal timescale. Shaded areas exceed the 95% confidence level.

mer (Fig. 4c).

The above analyses indicate that the relationship between late summer precipitation in NEC and the SST is most significant on the interannual timescale. The interannual variations of the JAP are closely linked to the interannual variations in the previous winter–spring SSTs in the CEPO and the TIO. NEC experiences more (less) late summer precipitation when the El Niño decays (develops) and the TIO SST warms (cools) during the periods of previous winter to this spring.

It has been documented that El Niño events usually develop in summer or autumn, achieve a maximum value in the subsequent winter, and then decay in spring or summer (Yuan and Yang, 2012). During the autumn and winter with an El Niño episode developing, a Rossby wave over the subtropical East Asia stimulates an anomalous anticyclone near the Philippines via teleconnection, which influences the East Asian climate (Wang and Wu, 2012; Li et al., 2017). The IOBW is the leading mode of variation in SSTs in the TIO. The IOBW starts to develop in winter and achieves a maximum value in the subsequent spring. According to the atmospheric bridge (Klein et al., 1999) or the Indonesian through-flow mechanism (Meyers, 1996), warming appears in the TIO from winter to the subsequent summer during an El Niño developing year in the CEPO. By contrast, during an El Niño decaying summer, the anomalous warming of SSTs weakens in the CEPO. Thus, the continuous anomalous anticyclone near the Philippines and the enhanced WPSH are a response to the persistence of the positive phase of the IOBW. Previous studies have indicated that the IOBW is a delayed response to El Niño events (Xie et al., 2009; Huang et al., 2016). The IOBW usually plays an important relay part in maintaining the effect of El Niño on the East China climate (Yang et al., 2007). Therefore, the impact of the IOBW on late summer pre-

cipitation over NEC lasts longer than that of El Niño events (Fig. 3).

We further analyze the stability of the relationship between the JAP and SSTs on the interannual timescale. It is found that negative correlation exists between the monthly Niño3.4 index and the JAP during 1951–60, and significant positive correlation appears during 1961–2016. The same pattern exists for the correlation coefficients between the monthly IOBW and the JAP. Therefore, the correlation coefficient between the monthly Niño3.4 index and the JAP, and that between the monthly IOBW index and the JAP, are calculated for two different periods: 1951–2016 and 1961–2016. To analyze the variation in the correlation between the Niño3.4 index and the JAP, and that between the IOBW index and the JAP, the lead–lag correlations from the previous January to December (24 months in total) are computed (Fig. 5). It is clear that the correlation coefficients between the Niño3.4 index and the JAP during 1961–2016 are more significant than those during 1951–2016, same for the coefficients between the IOBW index and the JAP. During 1961–2016, there are distinct positive correlation coefficients between the Niño3.4 index and the JAP from previous June to March, and insignificant negative correlations from June to December. The maximum coefficient reaches 0.52 in the previous July. However, in terms of the correlation between the IOBW index and the JAP, a remarkable positive correlation lasts from the previous October to May, especially from January to April, when the coefficient exceeds 0.6. This implies that on the interannual timescale, the impact of the IOBW on the JAP over NEC is more pronounced and prolonged than that of the El Niño event in the following spring.

Figure 6a shows the normalized interannual time series for the March–April IOBW index and the JAP over NEC. It is apparent that the co-variability between the two interannual indices is neither in phase nor out of phase during 1951–60. Specifically, four years are in phase and six years are out of phase. However, the co-variability between them is largely in phase during 1961–2016. During these years, 48 years are in phase and only 8 years are out of phase. The ratio of the same sign (correlation coefficient) between the two indices is 86.0% (0.64) during 1961–2016. The 11-yr sliding correlations between these years are also computed. There is no obvious correlation before 1961, but there are clear positive correlations after 1961 (Fig. 6b). The positive correlation turns insignificant from the late 1970s to the early 1980s. Figure 6a shows that there are only 2 years (1979 and 1983) when the anomalous sign is opposite to that from the late 1970s to early 1980s. This is the main reason why the positive correlation between the JAP and March–April IOBW becomes insignificant from the late 1970s to the early 1980s. This implies that the spring IOBW might have had an intense influence on late summer rainfall in NEC on the interannual timescale after the early 1960s.

A composite analysis is performed to check the consistency of the interannual correlation between the JAP and the SST. The JAP over NEC is arranged in descending order. There are 10 years (arranged from more to less: 2013, 1969, 2010, 1985, 1998, 1973, 1994, 1981, 1991, and 1966) in which the precipitation features above-normal JAP, and 10 years (arranged from less to more: 1968, 2014, 1992, 2009, 1999, 1989, 2011, 1980, 2012, and 1972) in which the precipitation features below-normal JAP. Figure 7a presents a composite map of March–April SSTAs for the above-normal variations of the JAP over NEC and Fig. 7b presents the composite map of March–April SSTAs for the below-normal variations of the JAP over NEC. The most striking feature is

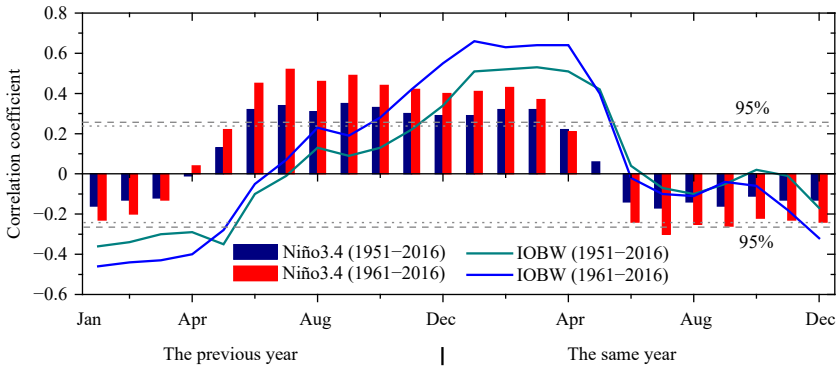

Fig. 5. Lead–lag correlation coefficients between JAP over NEC and the monthly Niño3.4 and Indian Ocean Basin warming (IOBW) indices. Gray dashed (dotted) lines denote the 95% confidence level for 1951–2016 (1961–2016).

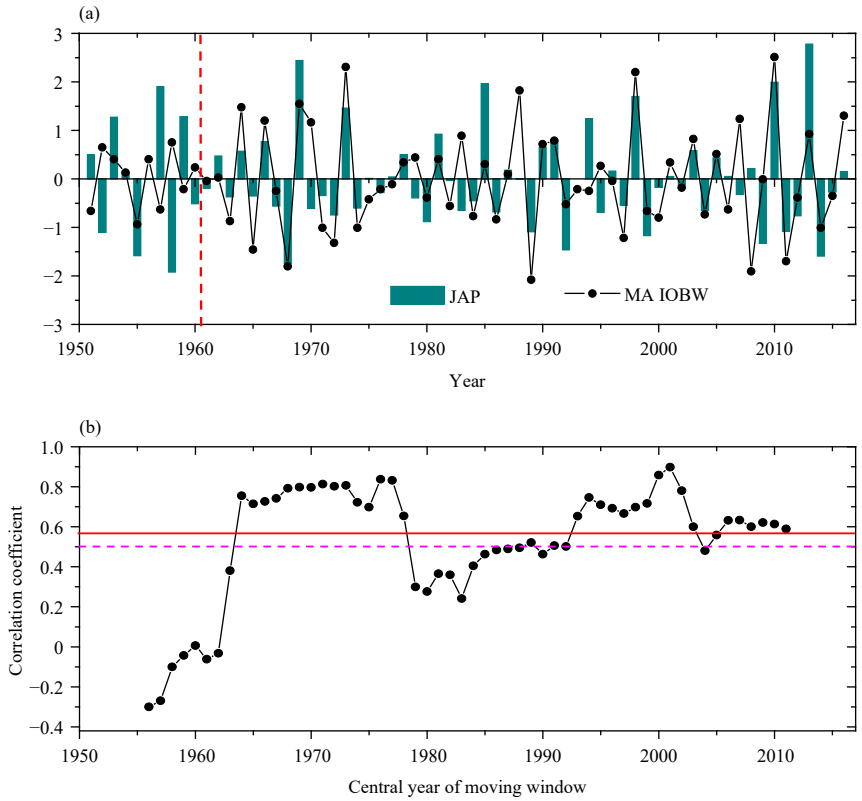

Fig. 6. (a) Interannual time series of the normalized JAP over NEC and the March–April (MA) IOBW index for the time period 1951–2016. The red dotted line indicates that the interannual relationship has changed since this year. (b) The 11-yr-sliding correlation coefficients between JAP and the March–April IOBW index. The dotted line (solid line) denotes the 90% (95%) confidence level.

that significant positive SSTAs are present in the TIO, the subtropical western Pacific Ocean, and the central Pacific Ocean during above-normal JAP years (Fig. 7a). However, the SSTA spatial pattern turns almost opposite during below-normal JAP years. Significant negative SSTAs appear in the TIO (Fig. 7b). The conclusion is in agreement with the preceding correlation analyses (see Figs. 3b, 5, 6).

3.3 *Atmospheric circulation anomalies associated with the March–April IOBW*

To further illustrate the influence of the spring IOBW on the subsequent late summer JAP over NEC after the early 1960s on the interannual timescale, we now examine the atmospheric circulation anomalies associated with the JAP over NEC and the March–April IOBW index. Figure 8 shows the geopotential height anomalies at 500 hPa (H_{500}) and the horizontal wind anomalies at 850 hPa (UV_{850}) in late summer associated with the JAP and the March–April IOBW index from 1961 to 2016. It is clear that when warming SSTAs occur in the TIO (the positive phase of the IOBW), significant positive geopotential height anomalies dominate the western Siberian Plain, South to central China, Northwest Pacific, and the Korean Peninsula, along with weak negative values over Mongolia (Fig. 8b). In addition, the positive JAP anomaly is associated with the analogous abnormal distribution of H_{500} (Fig. 8a). Accordingly, a cyclone and an anticyclone are separately located over Mongolia and Northwest Pacific in the UV_{850} anomalies associated with both the JAP and the March–April IOBW index (Figs. 8c, d). Significant southwesterly wind anomalies extend along East Asia and prevail over NEC, transporting moisture originated from the tropical ocean northward into this region. Thus, it can be seen that the circulation anomalies in connection with the March–April IOBW are basically the same as those associated with the JAP on the interannual timescale.

Water vapor transport is a crucial element of the East Asian monsoon system (Zhou and Yu, 2005). Many investigations have shown that the TIO and the SCS are the main sources of water vapor for rainfall over East China (Li et al., 2014; Yang et al., 2018). We therefore analyze the linkages of the JAP and the March–April IOBW with late summer moisture anomalies. The moisture related to the JAP over NEC is sourced from the TIO and the west-

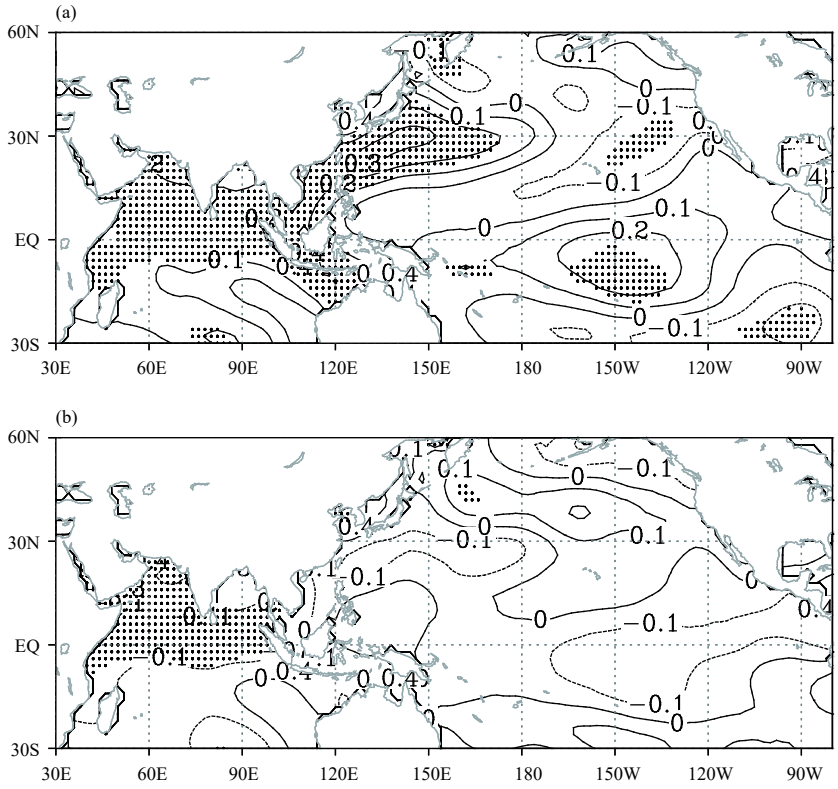

Fig. 7. Composite map of the March–April sea surface temperature anomalies (SSTAs; °C) for the (a) above-normal and (b) below-normal interannual variations of the JAP over NEC. The black dots exceed the 95% confidence level.

ern Pacific through the southern boundary, and from inland Asia across the western boundary (Fig. 9a). The anomalous southwesterly moisture flux that flows over the TIO transports wet and warm air currents northeastward with abundant moisture and then intrudes into NEC, bringing about the rainfall. The strong southeasterly flux on the northern side of the water vapor convergence zone switches to a strong southwesterly flux, which transports moisture into East Asia. The anomalous transport of moisture is overlapped with the northwestward expansion of the WPSH. The peripheral warm and wet southwesterly flow invades NEC, carrying moisture directly from the SCS and the Bay of Bengal. Figures 9c, e present the moisture flux divergence and specific humidity at 925 hPa associated with the interannual JAP anomalies over NEC. Positive JAP is related to the anomalous divergence of moisture from the subtropical western Pacific to the Korean Peninsula and the anomalous convergence of moisture over North China and NEC (Fig. 9c). There are also remarkable increases in the specific humidity in NEC (Fig. 9e). The positive March–April IOBW index shows similar distribution patterns to the JAP for the anomalous moisture flux (Fig. 9b), moisture flux divergence (Fig. 9d), and specific humidity at 925 hPa (Fig. 9f)—that is, the moisture and specific humidity anomalies associated with the March–April IOBW are basically the same as those associated with the JAP, which favor late summer precipitation in NEC on the interannual timescale.

3.4 *Possible mechanisms*

SSTAs show fine seasonal persistence as a result of oceanic "memory," so their effects on climate are often lagged (Chen et al., 2013), and the response of the atmosphere to SSTAs is often delayed. Zhao (1999) indicated that SSTAs in the previous winter–spring can influence the summer circulation over East Asia. The response of the EASM to tropical SSTAs is likely to lag about 2–6 months (Zhao, 1999). Han et al. (2018b) found that the SSTAs in the TIO are potentially persistent. The prominent interannual variability of SSTAs in the tropical oceans can affect the EASM by altering the thermal contrast between the land and sea and through strong sea–air interactions in the tropics. Hence, the spring IOBW anomaly may influence the atmosphere circulation over East Asia and precipitation over NEC in the late summer.

The northward migration of the WPSH and the EASM—together with the NESW, Okhotsk blocking high (OBH), and NEC cold vortex—from mid to high latitudes may influence the weather and climate over

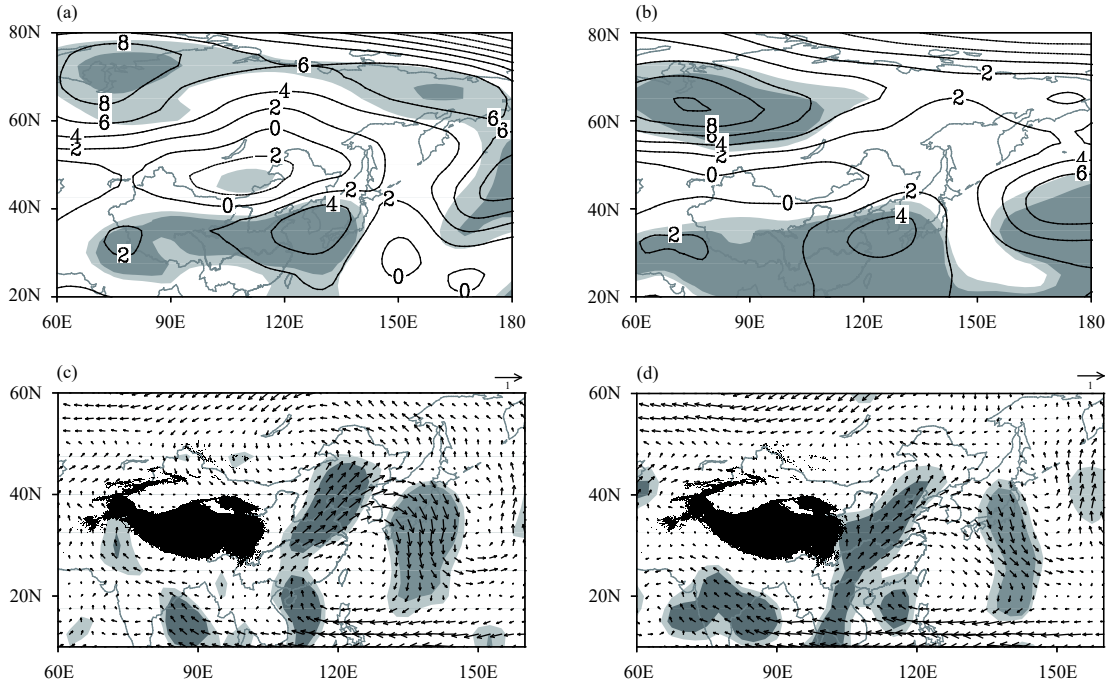

Fig. 8. Linear regression patterns of the late summer H_{500} (gpm) against (a) the JAP index over NEC and (b) March–April IOBW index on the interannual timescale for the time period 1961–2016. The linear regression patterns of the July–August UV_{850} (m s^{-1}) against (c) the JAP and (d) the March–April IOBW index on the interannual timescale for the time period 1961–2016. Light (dark) shaded areas exceed the 95% (99%) confidence level.

NEC in late summer (Shen et al., 2011; Zhao and Feng, 2014; Zhao et al., 2018). The WPSH and NESW have a central role in late summer rainfall. To further validate the interaction between SSTAs in the TIO and the WPSH and NESW, Fig. 10 shows the lead–lag correlations between the March–April IOBW index and the WPSH intensity index, the WPSH ridge point index, and the NESW index from January to December. There are remarkable positive correlations between the March–April IOBW index and the WPSH intensity index from January to September (Fig. 10a). The highest correlation coefficient is about 0.65 in April and August—that is, the warmer the SST in the TIO is from winter to spring, the stronger the WPSH is in the same period and subsequent summer. There is an apparent intraseasonal variation in the correlation coefficients between the March–April IOBW and the WPSH ridge position index (Fig. 10b). The correlation is negative in May–June (the coefficient is about –0.34 in June), but then it increases, changes to positive in July, and then becomes significant in August–October—that is, the warmer the SST in the TIO is from winter to spring, the more favorable the southward movement of the WPSH in May–June and the northward motion in July–August. A positive correlation between the March–April IOBW and the NESW index is present from January to September (Fig. 10c). The correlations are significant in most months except March and May—that is, the warmer the IOBW is from winter to spring, the stronger the NESW is in summer. This condition supports the linkage between the March–April IOBW and the July–August precipitation over NEC.

To clarify the dynamic process linked to the March–April IOBW anomalies, Fig. 11 presents the variability of the OLR and 500-hPa vertical motion (ω) during early and late summer associated with the March–April IOBW index. During early summer, in response to the anomalous positive March–April IOBW, a negative OLR anomaly is located over the TIO and the middle of the northwestern Pacific (from 22° to 32°N), whereas a positive OLR anomaly is located over the tropical western Pacific (between 5°S and 20°N) (Fig. 11a). During late summer, the significant negative OLR anomaly associated with the positive phase of the March–April IOBW is located above the Arabian Sea and southeast of the TIO, and a significant positive OLR anomaly is located above the tropical western Pacific (Fig. 11b). This illustrates that the warming TIO SST in spring may have enhanced convective motion over the TIO and weakened that over the tropical western Pacific, which contributes to the intensification of the ascending motion over the TIO and the descending motion over the tropical western Pacific in summer, especially in late summer. The influ-

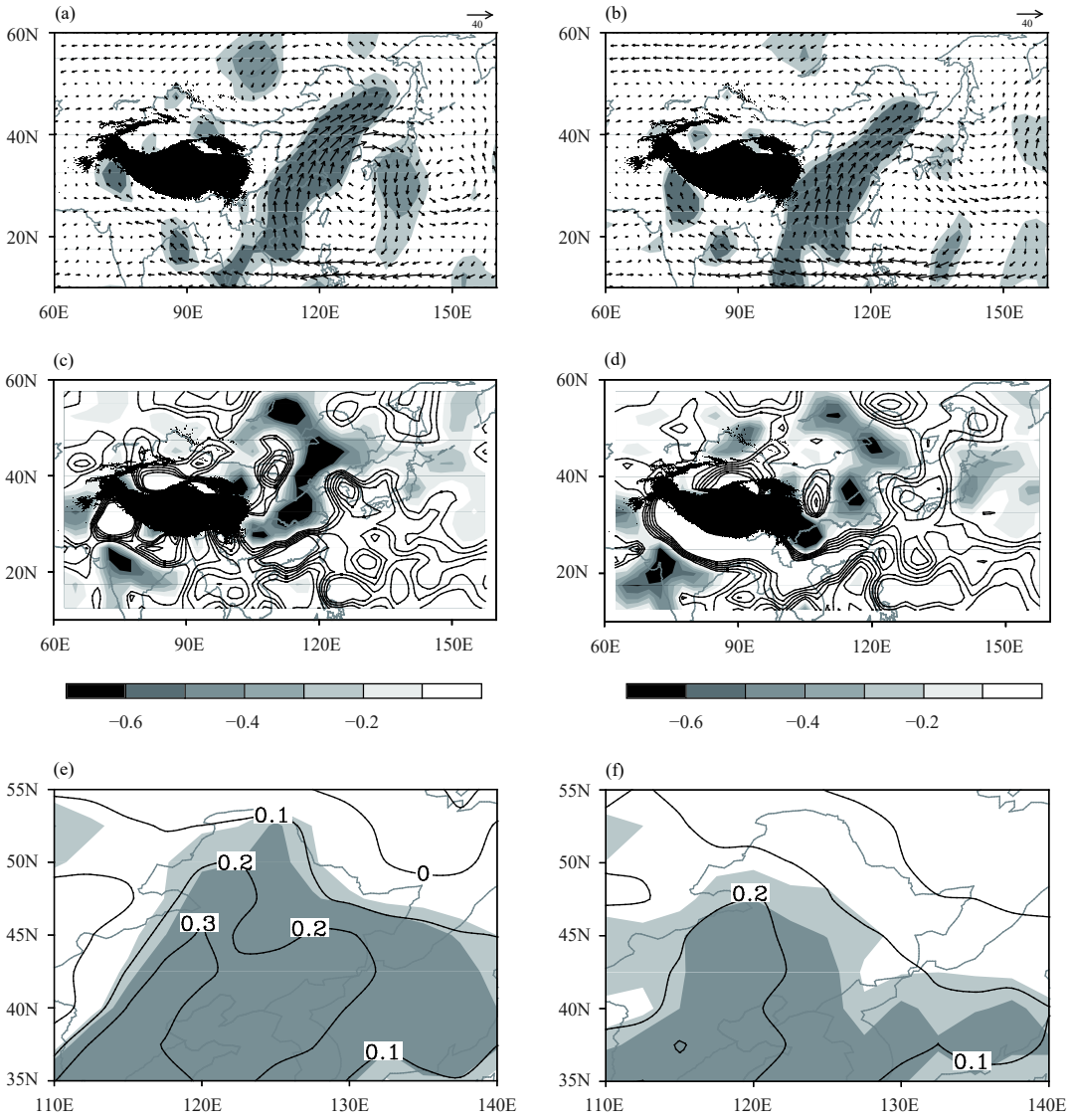

Fig. 9. Linear regressions of the late summer (a) vertically integrated moisture flux (kg m^{-1} s^{-1}), (c) moisture flux divergence (10^{-5} kg m^{-2} s^{-1}), and (e) specific humidity at 925 hPa (g kg^{-1}) against the JAP index over NEC on the interannual timescale for the time period 1961–2016. (b, d, f) are the same as (a, c, e), but against the March–April IOBW index. Shadings in (a, b, e, f) indicate the same as those in Fig. 8.

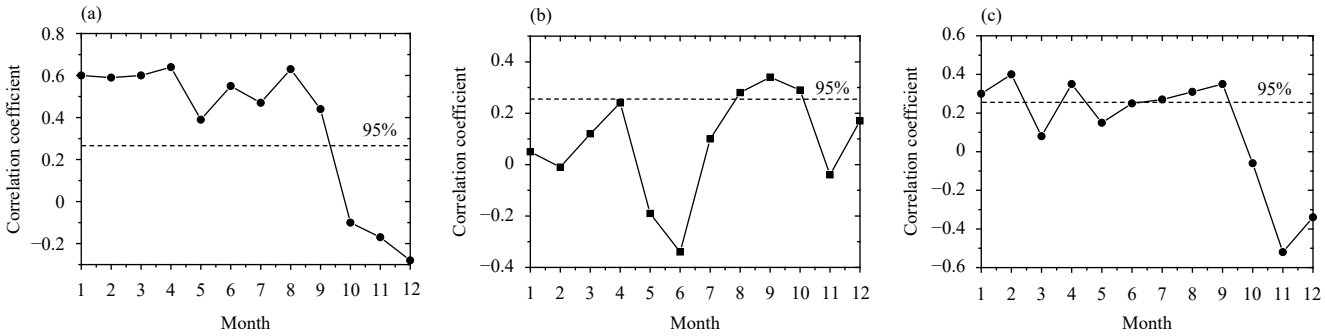

Fig. 10. Lead–lag correlations between the March–April IOBW index and (a) the western Pacific subtropical high (WPSH) intensity index, (b) the WPSH ridge position index, and (c) NEC south wind (NESW) index from January to December. The dotted line indicates the 95% confidence level.

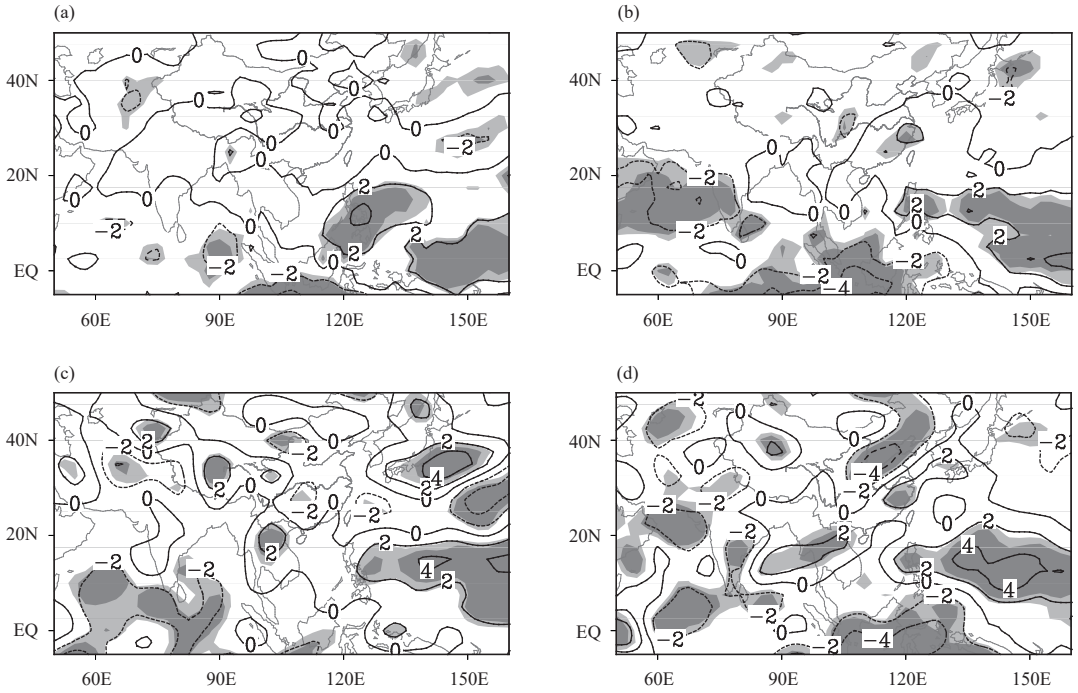

Fig. 11. Linear regression patterns of the March–April IOBW index against the (a) May–June and (b) July–August outgoing longwave radiation (OLR; W m^{-2}). Linear regression patterns of the March–April IOBW index against the (c) May–June and (d) July–August ω at 500 hPa (Pa s^{-1}). Shadings indicate the same as those in Fig. 8.

ence of the March–April IOBW in the mid troposphere is also clear. There is anomalous upward (downward) motion over the TIO (tropical western Pacific from 5° to 20°N) in early summer (Fig. 11c). During late summer, the significant anomalous upward motion moves eastward to Indonesia and the surrounding areas, and the downward motion moves northward to the southern Korean Peninsula (Fig. 11d). The March–April IOBW anomaly therefore has a crucial effect on the vertical movement of the atmospheric circulation in the tropics and subtropics in summer.

The meridional cells are crucial in the relationship between the March–April IOBW and the WPSH. The anomalous Hadley circulation averaged over 120°–130°E associated with the March–April IOBW index shows that anomalous subsidence has controlled the subtropical zone during May–August (Fig. 12), which supplies an important dynamic condition for anomalous rainfall over NEC. In early summer, significant descending motion occurs in the tropics (5°–20°N) and remarkable ascending motion occurs above the subtropical western Pacific (20°–30°N; Fig. 12a). The average position of the WPSH ridge is about 20°N in early summer (Fig. 13a). Therefore, the positive March–April IOBW is favorable for the southward movement of the WPSH in early summer. In late summer, when the March–April IOBW index is in its

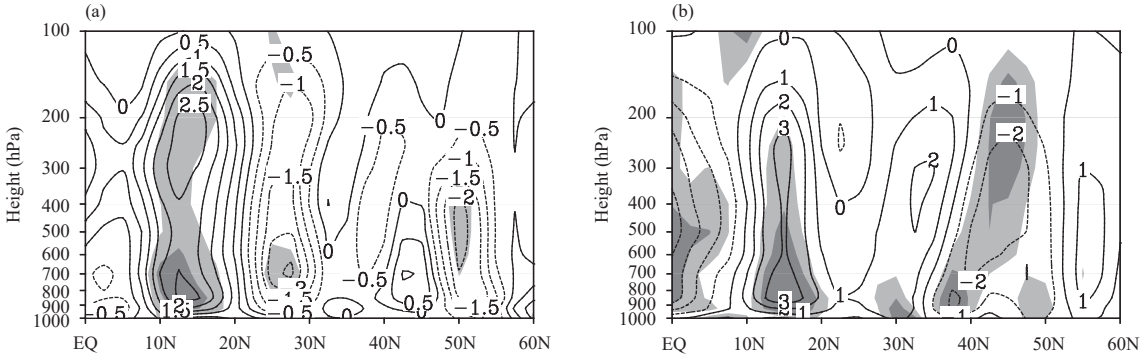

Fig. 12. Linear regression patterns of the March–April IOBW index against the (a) May–June and (b) July–August Hadley circulation averaged over 120°–130°E (ω; Pa s^{-1}). Shadings indicate the same as those in Fig. 8.

positive phase, significant descending motion moves northward to Northwest Pacific (10°–35°N), while ascending motion occurs in the tropical western Pacific Ocean (10°S–5°N) and NEC (Fig. 12b). The average WPSH ridge is located at about 27.5°N in late summer. In addition, NEC is dominated by southwesterly winds (Fig. 13b). Thus, the positive March–April IOBW favors the northward movement of the WPSH in late summer and more rainfall in NEC, consistent with previous studies. Xie et al. (2009) found that an anomalous Kelvin wave led by a positive IOBW anomaly was important to the maintenance and development of the stronger WPSH.

4. Conclusions and discussion

In this paper, we analyzed the linkage between spring SSTAs in the TIO and the following late summer rainfall over NEC on the interannual timescale and the possible associated mechanisms. A strong significant positive linkage between the spring IOBW and the late summer rainfall over NEC has been observed on the interannual timescale since the early 1960s. The impact of the IOBW on late summer precipitation over NEC is more pronounced and prolonged than that of the El Niño event in the previous winter and following spring. The correlation coefficient between the March–April IOBW and late summer precipitation over NEC is 0.64 during 1961–2016. An in-depth analysis has shown that the positive March–April IOBW for 1961–2016 is normally associated with a notable anomalous anticyclone from Northwest Pacific to the Korean Peninsula, which favors a significantly strong and northward WPSH and anomalous southwesterly winds over NEC, bringing more moisture into this region. The March–April IOBW anomaly has a positive influence on the WPSH and NESW through modulation of the atmospheric circulation (e.g., the OLR, vertical motion, and Hadley cells). A significant anomalous upward (downward) motion over Indonesia (Northwest Pacific to the southern Korean Peninsula) occurs when the IOBW is in its positive phase, which favors the northward movement of the WPSH, stronger NESW, abundant water vapor, and more precipitation over NEC in late summer (Fig. 14).

The impact of the tropical oceans on the EASM and precipitation has been explored in many previous studies (Klein et al., 1999; Yuan et al., 2008; Annamalai, 2010; Ren and Jin, 2011; Yuan and Yang, 2012; Chen et al., 2013). The IOBW is the delayed response to El Niño events and acts as a relay function in maintaining the influence of El Niño events on the East Asian climate (Wu and Kirtman, 2004; Yang et al., 2007; Xie et al., 2009;

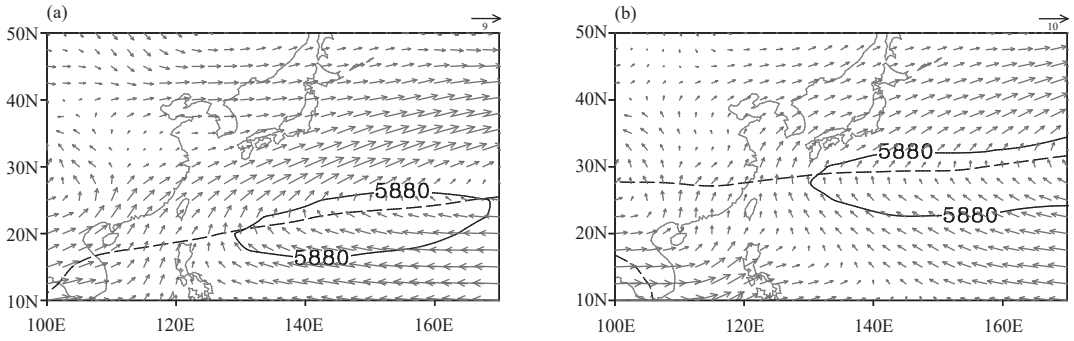

Fig. 13. Climate mean (1981–2010 average) (a) May–June and (b) July–August 850-hPa horizontal wind (m s^{-1}), WPSH (outlined by the 5880 contour line), and the ridge of the WPSH (dashed line).

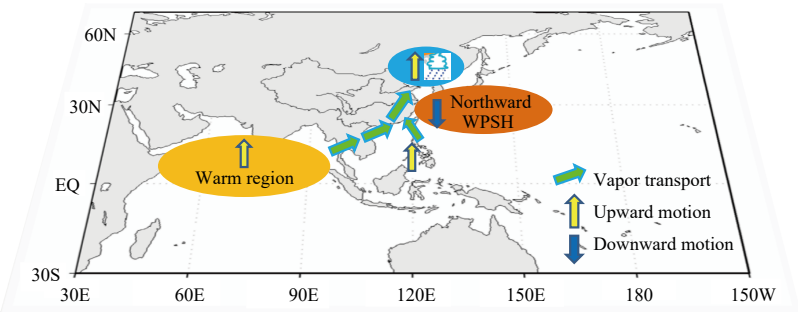

Fig. 14. Schematic diagram showing the relationship between March–April IOBW and the JAP over NEC on the interannual timescale.

Huang et al., 2016). Han et al. (2018b) showed that the early summer rainfall over NEC has been closely linked to the early spring SSTs in the TIO since the late 1980s. The work reported here shows a close interannual relationship between the spring IOBW and the late summer rainfall over NEC since the early 1960s. The impact of the IOBW on late summer precipitation over NEC lasts longer than that of the El Niño event. The linkage between the spring IOBW and the late summer rainfall over NEC may be applied as a helpful clue to short-term predictions of climate.

REFERENCES

Annamalai, H., 2010: Moist dynamical linkage between the equatorial Indian Ocean and the South Asian monsoon trough. *J. Climatol.*, **67**, 589–610, doi: 10.1175/2009JAS2991.1.

Bai, R. H., 2001: Relations between the anomaly of sea surface temperature in the Atlantic and the precipitation in summer over Northeast China. *Marine Sci. Bull.*, **20** , 23–29. (in Chinese)

Chen, L. J., Y. Yuan, M. Z. Yang, et al., 2013: A review of physical mechanisms of the global SSTA impact on EASM. *J. Appl. Meteor. Sci.*, **24** , 521–532, doi: 10.3969/j.issn.1001-7313.2013.05.002. (in Chinese)

Gao, J., and H. Gao, 2015: Relationship between summer precipitation over northeastern China and sea surface temperature in the southeastern Pacific and the possible underlying mechanisms. *Chinese J. Atmos. Sci.*, **39** doi: 10.3878/j.issn.1006-9895.1503.14246. (in Chinese)

Gao, Z. T., Z. Z. Hu, B. Jha, et al., 2014: Variability and predictability of Northeast China climate during 1948–2012. *Climate Dyn.*, **43**, 787–804, doi: 10.1007/s00382-013-1944-0.

Gong, Q., P. X. Wang, H. Y. Wang, et al., 2005: Constitutes and formation cause of inter-decadal and inter-annual variations of summer rainfall anomalies in Northeast China. *J. Nanjing Inst. Meteor.*, **28** , 233–240, doi: 10.3969/j.issn.1674-7097.2005.02.012. (in Chinese)

Han, T. T., H. P. Chen, and H. J. Wang, 2015: Recent changes in summer precipitation in Northeast China and the background circulation. *Int. J. Climatol.*, **35** , 4210–4219, doi: 10.1002/joc.4280.

Han, T. T., S. P. He, X. Hao, et al., 2018a: Recent interdecadal shift in the relationship between Northeast China's winter precipitation and the North Atlantic and Indian Oceans. *Climate Dyn.*, **50**, 1413–1424, doi: 10.1007/s00382-017-3694-x.

Han, T. T., S. P. He, H. J. Wang, et al., 2018b: Enhanced influence of early-spring tropical Indian Ocean SST on the following early-summer precipitation over Northeast China. *Climate Dyn.*, **51**, 4065–4076, doi: 10.1007/s00382-017-3669-y.

He, J. H., Z. W. Wu, Z. H. Jiang, et al., 2007: "Climate effect" of the northeast cold vortex and its influences on Meiyu. *Chinese Sci. Bull.*, **52** , 671–679, doi: 10.1007/s11434-007-0053-z.

Huang, G., K. M. Hu, and S.-P. Xie, 2010: Strengthening of tropical Indian Ocean teleconnection to the Northwest Pacific since the mid-1970s: An atmospheric GCM study. *J. Climate*, **23**, 5294–5304, doi: 10.1175/2010JCLI3577.1.

Huang, G., K. M. Hu., X. Qu, et al., 2016: A review about Indian Ocean basin mode and its impacts on East Asian summer climate. *Chinese J. Atmos. Sci.*, **40** , 121–130, doi: 10.3878/j.issn.1006-9895.1505.15143. (in Chinese)

Kalnay, E., M. Kanamitsu, R. Kistler, et al., 1996: The NCEP/NCAR 40-year reanalysis project. *Bull. Amer. Meteor. Soc.*, **77** , 437–472, doi: 10.1175/1520-0477(1996)077<0437:TNYRP>2.0.CO;2.

Klein, S. A., B. J. Soden, and N. C. Lau, 1999: Remote sea surface temperature variations during ENSO: Evidence for a tropical atmospheric bridge. *J. Climate*, **12** , 917–932, doi: 10.1175/1520-0442(1999)012<0917:RSSTVD>2.0.CO;2.

Li, T., B. Wang, B. Wu, et al., 2017: Theories on formation of an anomalous anticyclone in western North Pacific during El Niño: A review. *J. Meteor. Res.*, **31** , 987–1006, doi: 10.1007/s13351-017-7147-6.

Li, X. Z., W. Zhou, D. L. Chen, et al., 2014: Water vapor transport and moisture budget over eastern China: Remote forcing from the two types of El Niño. *J. Climate*, **27** , 8778–8792, doi: 10.1175/JCLI-D-14-00049.1.

Lian, Y., B. Z. Shen, Z. T. Gao, et al., 2003: The study of the onset criterion and the date of East Asian summer monsoon in Northeast China and its main characteristic analysis. *Acta Meteor. Sinica*, **61** , 548–558, doi: 10.3321/j.issn:0577-6619.2003.05.004. (in Chinese)

Liebmann, B., and C. A. Smith, 1996: Description of a complete (interpolated) outgoing longwave radiation dataset. *Bull. Amer. Meteor. Soc.*, **77**, 1275–1277.

Lin, R. P., F. Zheng, and X. Dong, 2018: ENSO frequency asymmetry and the Pacific decadal oscillation in observations and 19 CMIP5 models. *Adv. Atmos. Sci.*, **35** , 495–506, doi: 10.1007/s00376-017-7133-z.

Meyers, G., 1996: Variation of Indonesian throughflow and the El Niño–Southern Oscillation. *J. Geophys. Res. Oceans*, **101**, 12255–12263, doi: 10.1029/95JC03729.

Qu, X., and G. Huang, 2012: An enhanced influence of tropical Indian Ocean on the South Asia high after the late 1970s. *J. Climate*, **25**, 6930–6941, doi: 10.1175/JCLI-D-11-00696.1.

Ren, H.-L., and F.-F. Jin, 2011: Niño indices for two types of ENSO. *Geophys. Res. Lett.*, **38** , L04704, doi: 10.1029/2010GL046031.

Saji, N. H., B. N. Goswami, P. N. Vinayachandran, et al., 1999: A dipole mode in the tropical Indian Ocean. *Nature*, **401**, 360–363, doi: 10.1038/43854.

Shen, B. Z., Z. D. Lin, R. Y. Lu, et al., 2011: Circulation anomalies associated with interannual variation of early- and late-summer precipitation in Northeast China. *Sci. China Earth Sci.*, **54**, 1095–1104, doi: 10.1007/s11430-011-4173-6.

Shi, N., Y. S. Yang, and H. Chen, 2001: A study on the features of East-China summer rainfall pattern on the multi-time scale in the past 98 years. *Sci. Meteor. Sinica*, **21** , 316–325, doi: 10.3969/j.issn.1009-0827.2001.03.008. (in Chinese)

Smith, T. M., R. W. Reynolds, T. C. Peterson, et al., 2008: Improvements to NOAA's historical merged land–ocean surface temperature analysis (1880–2006). *J. Climate*, **21**, 2283–2296, doi: 10.1175/2007JCLI2100.1.

Sun, L., X. Y. Zheng, and Q. Wang, 1994: The climatological characteristics of northeast cold vortex in China. *Quart. J.*

Appl. Meteor., **5**, 297–303. (in Chinese)

Sun, L., G. An, L. Ding, et al., 2000: A climatic analysis of summer precipitation features and anomaly in Northeast China. *Acta Meteor. Sinica*, **58** , 70–82, doi: 10.3321/j.issn:0577-6619.2000.01.007. (in Chinese)

Sun, L., G. An, Y. Lian, et al., 2002: The unusual characteristics of general circulation in drought and waterlogging years of Northeast China. *Climatic Environ. Res.*, **7** , 102–113, doi: 10.3969/j.issn.1006-9585.2002.01.010. (in Chinese)

Sun, L., G. An, and X. L. Tang, 2003: Relationship between the Northeast Asian summer south wind anomaly and the precipitation in Northeast China. *Chinese J. Atmos. Sci.*, **27**, 425–434, doi: 10.3878/j.issn.1006-9895.2003.03.12 . (in Chinese)

Sun, L., B. Z. Shen, B. Sui, et al., 2017: The influences of East Asian Monsoon on summer precipitation in Northeast China. *Climate Dyn.*, **48** , 1647–1659, doi: 10.1007/s00382-016-3165-9.

Wang, H. J., 2002: The instability of the East Asian summer monsoon–ENSO relations. *Adv. Atmos. Sci.*, **19** , 1–11, doi: 10.1007/s00376-002-0029-5.

Wang, H. J., and S. P. He, 2015: The North China/Northeastern Asia severe summer drought in 2014. *J. Climate*, **28**, 6667–6681, doi: 10.1175/JCLI-D-15-0202.1.

Wang, L., and R. G. Wu, 2012: In-phase transition from the winter monsoon to the summer monsoon over East Asia: Role of the Indian Ocean. *J. Geophys. Res. Atmos.*, **117** , D11112, doi: 10.1029/2012JD017509.

Wang, L., W. Chen, W. Zhou, et al., 2009: Interannual variations of East Asian trough axis at 500 hPa and its association with the East Asian winter monsoon pathway. *J. Climate*, **22**, 600–614, doi: 10.1175/2008JCLI2295.1.

Wang, X. F., J. H. He., and Y. Lian, 2013: Effect of the previous anomalous heat content in the western Pacific warm pool on the summer rainfall over Northeast China. *Acta. Meteor. Sinica*, **71** , 305–317, doi: doi: 10.11676/qxxb2013.024. (in Chinese)

Wu, R. G., and B. P. Kirtman, 2004: Understanding the impacts of the Indian Ocean on ENSO variability in a coupled GCM. *J. Climate*, **17** , 4019–4031, doi: 10.1175/1520-0442(2004)017<4019:UTIOTI>2.0.CO;2.

Wu, R. G., Z. Z. Hu, and B. P. Kirtman, 2003: Evolution of ENSO-related rainfall anomalies in East Asia. *J. Climate*, **16**, 3742–3758, doi: 10.1175/1520-0442(2003)016<3742:EOERAI>2.0.CO;2.

Xie, S.-P., K. M. Hu, J. Hafner, et al., 2009: Indian Ocean capacitor effect on Indo–western Pacific climate during the summer following El Niño. *J. Climate*, **22** , 730–747, doi: 10.1175/2008JCLI2544.1.

Xu, Z. Q., and K. Fan, 2012: Possible process for influences of winter and spring Indian Ocean SST anomalies interannual variability mode on summer rainfall over eastern China. *Chinese J. Atmos. Sci.*, **36**, 879–888, doi: 10.3878/j.issn.1006-9895.2012.11176. (in Chinese)

Yang, J. L., Q. Y. Liu, S.-P. Xie, et al., 2007: Impact of the Indian Ocean SST basin mode on the Asian summer monsoon. *Geophys. Res. Lett.*, **34**, L02708, doi: 10.1029/2006GL028571.

Yang, L., J. H. Zhao, and G. L. Feng, 2018: Characteristics and differences of summertime moisture transport associated with four rainfall patterns over eastern China monsoon region. *Chinese J. Atmos. Sci.*, **42** , 81–95, doi: 10.3878/j.issn.1006-9895.1706.16273. (in Chinese)

Yuan, Y., and S. Yang, 2012: Impacts of different types of El Niño on the East Asian climate: Focus on ENSO cycles. *J. Climate*, **25**, 7702–7722, doi: 10.1175/JCLI-D-11-00576.1.

Yuan, Y., W. Zhou, J. C. L. Chan, et al., 2008: Impacts of the basin-wide Indian Ocean SSTA on the South China Sea summer monsoon onset. *Int. J. Climatol.*, **28** , 1579–1587, doi: 10.1002/joc.1671.

Zhao, J. H., and G. L. Feng, 2014: Reconstruction of conceptual prediction model for the three rainfall patterns in the summer of eastern China under global warming. *Sci. China Earth Sci.*, **57**, 3047–3061, doi: 10.1007/s11430-014-4930-4.

Zhao, J. H., J. Zhou, L. Yang, et al., 2018: Inter-annual and inter-decadal variability of early- and late-summer precipitation over Northeast China and their background circulation. *Int. J. Climatol.*, **38**, 2880–2888, doi: 10.1002/joc.5470.

Zhao, Z. G., 1999: *Drought/Flood and Environment Field of Summer in China*. China Meteorological Press, Beijing, 297 pp. (in Chinese)

Zheng, F., and J. Zhu, 2016: Improved ensemble-mean forecasting of ENSO events by a zero-mean stochastic error model of an intermediate coupled model. *Climate Dyn.*, **47** , 3901–3915, doi: 10.1007/s00382-016-3048-0.

Zheng, F., J. Zhu, R. H. Zhang, et al., 2006: Ensemble hindcasts of SST anomalies in the tropical Pacific using an intermediate coupled model. *Geophys. Res. Lett.*, **33** , L19604, doi: 10.1029/2006GL026994.

Zhou, T. J., and R. C. Yu, 2005: Atmospheric water vapor transport associated with typical anomalous summer rainfall patterns in China. *J. Geophys. Res. Atmos.*, **110** , D08104, doi: 10.1029/2004JD005413.

Tech & Copy Editor: Qi WANG

Theoretical and Applied Climatology (2019) 138:1109–1123
https://doi.org/10.1007/s00704-019-02876-y

ORIGINAL PAPER

Possible causes of the anomalous characteristics of autumn rain in western China in 2017

Jie Zhou[1] · Junhu Zhao[2] · Rong Zhi[2]

Received: 11 September 2018 / Accepted: 16 April 2019 / Published online: 12 May 2019
© Springer-Verlag GmbH Austria, part of Springer Nature 2019

Abstract
We analyzed the anomalous characteristics of autumn rain in western China (ARWC) (26.2–36° N, 101.9–111.8° E) in 2017 and the related large-scale atmospheric circulations based on new monitoring indicators published by the China Meteorological Administration in 2015 and the National Center for Environmental Prediction reanalysis data. We found that the characteristics of autumn rain in the southern (33–36° N, 101.9–111.8° E) and northern (26.2–33° N, 101.9–111.8° E) regions of the monitoring area were different. The onset date of autumn rain in the north (south) of the monitoring area in 2017 was 14 (16) days earlier than in normal years, which is in the 4th (4th) place since 1961. The end of the autumn rain was 5 days later (earlier) than in normal years. The autumn rain period was 54 (63) days long, 19 (11) days longer than in normal years. The autumn rainfall in the north (south) of the monitoring area was 234.1 (322.2) mm, 72.6% (74.4%) higher than that in normal years. The amount of autumn rain in the southern region is in the second place since 1965. The cause of this significantly early onset of the ARWC in 2017 was the advanced transition of the East Asian atmospheric circulation system from a summer pattern to a winter pattern. The westerly jet in the upper troposphere appeared about 10 days earlier than in normal years. The meridional circulation of a west-high and east-low pattern was observed in the mid- and lower troposphere in the mid- and high latitudes of Eurasia. This circulation configuration resulted in an early onset of the ARWC. As a result of the influence of the persistent warming of the Indian Ocean basin-wide mode from spring to summer, the west Pacific subtropical high was extremely strong (the second strongest since 1981) and its westernmost point was greatly extended to the west (the second greatest extension since 1981) during the autumn rain period. The intensity of the moisture flux from the southwest of the western Pacific subtropical high was stronger than usual and the low trough of Lake Baikal was also strong. Cold air from the north and the abundant warm, humid water vapor from the south converged in western China, resulting in more precipitation during the autumn rain period.

1 Introduction

The autumn rain in western China (ARWC) is a special weather phenomenon and mainly occurs in the Weihe river basin, the Hanshui river basin, east Sichuan, and east Yunnan (Gao and Guo 1958; He 1984; Liang 1989). In autumn, cold air from the north interacts with the warm, humid air that stagnates in this area as a result of topographic blocking, which strengthens the front and induces rainfall (Zhang 1941; Bai and Dong 2004). Precipitation is generally greater in autumn than in spring and less than the precipitation in summer, forming a sub-maximum, and leading to remarkable autumn floods (Atmospheric Science Dictionary Editorial Committee 1994). The onset date of ARWC in 2017 was obviously earlier than that in a normal year. In the northern region, the onset date was 14 days earlier than in a normal year, which is in the 4th place since 1961. Also, in the southern region, it was 16 days earlier than in a normal year, which is in the 4th place since 1961. In addition, the total precipitation of ARWC in 2017 was 70% more than that of a normal year (Zhi et al. 2018), which is in the second place since 1965. The maximum

✉ Rong Zhi
z_rongphy@126.com

Jie Zhou
zhoujie1226@126.com

Junhu Zhao
zhaojh@cma.gov.cn

[1] Chongqing Climate Center, Chongqing Meteorological Bureau, Chongqing 401147, China

[2] Laboratory for Climate Studies, National Climate Center, China Meteorological Administration, Beijing 100081, China

precipitation was up to 753.8 mm (Chongqing, Chengkou), which was 143.6 mm more than that in summer. The precipitation at Danjiangkou Station in Hubei was nearly 2 times higher than that of the normal year. Influenced by that, the water level in Danjiangkou reservoir had raised obviously. On September 13th, the water level in Danjiangkou reservoir reached 160.76 m, which was above the record level. Besides, the continuous rain had caused heavy rain floods and geological disasters in Gansu, Shaanxi, Sichuan, Chongqing, Guizhou, Hubei, and Hunan provinces, resulting in enormous losses to local agricultural production and economy (Feng et al. 2018). Our motivation for the present work was to investigate the atmospheric circulation anomalies, as well as the forcing from the sea surface temperature in the context of global warming, and try to determine the possible causes that were responsible for the severe ARWC in 2017.

Prior to the current study, there has already been various research conducted on ARWC. Gao (1958) studied ARWC in the 1950s and showed that the day on which autumn rainfall begins in this region is also the day on which the westerly circulation begins to appear frequently, whereas the end date of ARWC is also the date on which the westerly jet in southern Asia stabilizes in its normal winter position (Gao and Guo 1958). Yuan and Liu (2013) reported that the establishment of the ARWC corresponds to the transition of the East Asian atmospheric circulation from the summer monsoon to the winter monsoon, with a change in wind direction at 850 hPa from southwest to southeast over the south of the middle and lower reaches of the Yangtze River. The end of ARWC is associated with the retreat of the tropical southwest monsoon from the Bay of Bengal (BOB) and the complete establishment of the East Asian winter monsoon, with a change in wind direction from southwest to northeast at 850 hPa over the BOB. Bai and Dong (2004) reported that the west Pacific subtropical high (WPSH), the Indo-Burma trough, and the Lake Baikal low trough are the main systems influencing ARWC. A well-developed Lake Baikal low trough and Indo-Burma trough, and a strengthened WPSH favor more rain over southwest China in autumn. The reverse conditions result in less rain. Wang et al. (2015) showed that the ARWC is more (less) than normal when the sea surface temperature (SST) in the central equatorial Pacific is lower (higher) than usual from summer to autumn, the 500-hPa height field anomaly is positive (negative), the position of the WPSH is westward (eastward), and moisture transport from the South China Sea and the BOB is more (less). Liu and Yuan (2006) found that when the Indian Ocean dipole appears with the El Niño Southern Oscillation; the positive phases of the Indian Ocean dipole and the El Niño maintain the positive anomaly of autumn precipitation in southwestern China.

Possible causes of abnormal ARWC have attracted widespread attention. Bao et al. (2003) analyzed the spatial and temporal characteristics of ARWC in 2001 and its possible mechanisms and found that there was a quasi-stationary trough at 500 hPa near Lake Balkhash, from which short waves were split one by one. The cold air transported by these short waves and the warm, humid air in the southwest of the strong WPSH converged in western China, resulting in continuous rainy days. Liu et al. (2012) analyzed the causes of the abnormal ARWC in 2011 and suggested that the anomalous ARWC was a strong response to the typical La Niña event that began in September 2011. The decadal variation in autumn rain may also be an important cause of the anomalous ARWC. Si et al. (2015) analyzed the causes of precipitation anomalies in western China in autumn 2014 and suggested that the positive precipitation anomaly may have been caused by warming of the tropical Indian Ocean. The dominant factors affecting ARWC therefore vary from year to year, which leads difficulties in the prediction.

However, in previous studies, as the lack of a uniform definition of the indices of ARWC, such as the study area, the onset date, and the end date, the conclusions of previous studies were based on different kinds of definitions of ARWC, which were not universal. We are interested in ARWC of 2017, not only because it showed more typical anomalies in the past half century, but also because of the releasing of the uniform definition of ARWC indices by the Forecasting and Network Division of the CMA. Compared with the previous ARWC indices, the ones that are released by the Forecasting and Network Division of the CMA are relatively uniform at the national and provincial levels, which is more conducive to the monitoring and research work of nationwide ARWC and more universal. Investigating such a severe ARWC in the context of global warming and studying its physical causes will help to improve the understanding of the predictability of ARWC and, hence, to project ARWC events in the future.

2 Data and methods

2.1 Data

The data used in this paper include the following sources:

Daily precipitation data from 373 stations in western China provided by the National Meteorological Information Center of the China Meteorological Administration (CMA).

(1) Atmospheric circulation indexes provided by the National Climate Center of the CMA: the indexes of intensity, area, the westernmost point, and latitudes of the ridge line of the WPSH; the strength index of the

Indo-Burma trough (the accumulation of the product of the grid area and the difference between the geopotential height of each grid at 500 hPa in the area (15–20° N, 80–100° E) and the 5800 geopotential meter); the index of the Lake Baikal trough (Zhao 1999); and the index of the Indian Ocean basin-wide warming (IOBW) (regional average SST anomaly (SSTA) in the area (20° S–20° N, 40–110° E)).

(2) Reanalysis data of the global daily geopotential height field, the wind field (u, v components), and the specific humidity issued by the National Center for Environmental Prediction and the National Center for Atmospheric Research (Kalnay et al. 1996) with a horizontal spatial resolution of 2.5° × 2.5° and a total of 17 isobaric surfaces from 1000 to 10 hPa in the vertical direction.

(3) Monthly SST data with a horizontal spatial resolution of 2° × 2° published by National Oceanic and Atmospheric Administration (Huang et al. 2017).

2.2 Methods

We used the calculation method for water vapor flux reported by Ding (2005). All the data were selected from 1981 to 2017 and the climatological mean was taken as the average of the data from 1981 to 2010.

The Forecasting and Network Division of the CMA released a new monitoring index, the Regulations on the Monitoring of Autumn Rain in Western China (Trial), for ARWC in 2015. This type of rain is mainly distributed in the Weishui river basin, the Hanshui river basin, and eastern Sichuan and Yunnan at (26.2–36° N, 101.9–111.8° E). The administrative areas cover Hubei, Hunan, Chongqing, Sichuan, Guizhou, Shaanxi, Ningxia, and Gansu. Based on the characteristics of the regional climate, the monitoring range of the ARWC can be divided into southern and northern climate zones (Fig. 1). The southern zone includes western Hubei (28 stations), western Hunan (30 stations), Chongqing (34 stations), eastern Sichuan (107 stations), northern Guizhou (60 stations), and parts of southwestern Shaanxi (10 stations), whereas the northern zone includes most parts of southwestern Shaanxi (67 stations), southern Ningxia (five stations), and southern Gansu (32 stations). The main basis for monitoring indicators such as the beginning (end) day of ARWC, the length of the rainy period, and the rainfall is the precipitation conditions of the monitoring stations in these areas. According to the Regulations on the Monitoring of Autumn Rain in Western China (Trial), the definitions of beginning day, end day, and the length of the rainy period in the manuscript are as follows:

(1) The beginning day: Since August 21, when the first rainy season in the region is monitored, the autumn rain in the

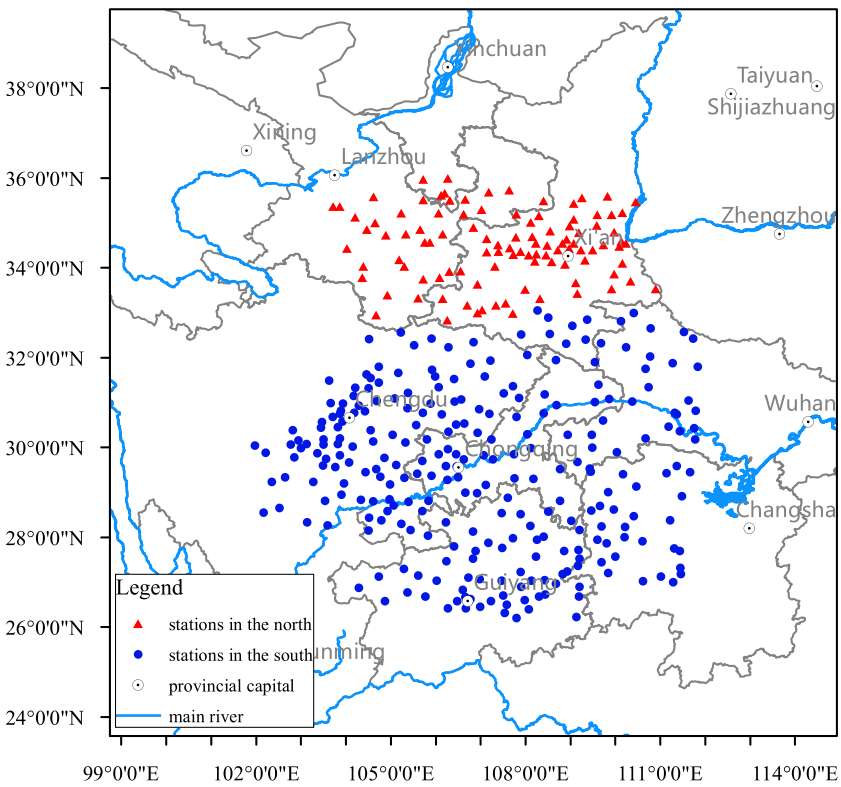

Fig. 1 Map showing the division of the monitoring area into a northern and southern zone and the spatial distribution of monitoring stations used in this study

region will begin, and the beginning day of the first rainy season will be designated as the beginning day of the autumn rain in the region.

(2) The end day: After the beginning of the autumn rain, if there is no more rainy season until October 31, the autumn rain will end, and the end date of the last rainy season will be the end day of the autumn rain in the area.

(3) The length of the autumn rain period: The total number of days between the beginning day and the end day of the autumn rain in the monitoring area is the length of the autumn rain period.

(4) Autumn rainy day: Since August 21, the proportion of stations with daily rainfall equal to or greater than 0.1 mm in the monitoring area is equal to or greater than 50%, then it is called an autumn rain day; otherwise, it is a non-autumn rainy day.

(5) Rainy season: Since August 21, if there are five consecutive autumn rainy days in the monitoring area (one non-autumn rainy day is allowed in the 2nd–4th days), the rainy season will begin and the first autumn rainy day will be designated as the beginning day of the rainy season. If there are five consecutive non-autumn rainy days (one autumn rainy day is allowed in 2nd–4th days), the rainy season ends, and the first non-autumn rainy day is designated as the end day of the rainy season. One or more rainy seasons can occur during autumn rain period.

3 Anomalous characteristics of ARWC in 2017

3.1 Onset (end) date of ARWC in 2017

Table 1 gives an overview of the monitoring of ARWC in 2017. The onset date in the northern area was August 25, 14 days earlier than normal (September 8), which is in the 4th place since 1961. The end date of ARWC was October 18, 5 days later than normal (October 13). The autumn rain period was 54 days, 19 days more than normal (35 days). The onset date in the southern area was August 24, 16 days earlier than normal (September 9), which is in the 4th place since 1961. The end date of ARWC was October 26, 5 days earlier than normal (October 31). The autumn rain period lasted 63 days, 11 days longer than normal (52 days). The onset dates of autumn rain in the northern and southern areas in 2017 were clearly earlier than in normal years. The end date of ARWC in the northern district was later than usual, whereas it was earlier in the southern district. The autumn rain periods in the both the southern and northern areas were longer than usual.

3.2 Temporal and spatial characteristics of ARWC in 2017

3.2.1 Autumn rainfall and average daily precipitation during the autumn rain period

Table 1 shows that the autumn rainfall in the northern part of the monitoring area was 234.1 mm, 72.6% higher than normal (135.6 mm). The autumn rainfall in the southern area was 322.2 mm, 74.4% higher than normal (184.4 mm), the second highest since 1965. The average daily precipitation during the autumn rain period in the northern area was 4.3 mm/day, 0.4 mm/day higher than normal (3.9 mm/day). The average daily precipitation during the autumn rain period in the southern area was 5.1 mm/day, 1.6 mm/day higher than normal (3.5 mm/day).

3.2.2 Characteristics of temporal variation in daily precipitation

Figure 2 shows the variation in daily precipitation in the northern (a) and southern (b) areas during the ARWC from August 21 to November 20, 2017. There were two rainy periods in the two parts of the monitoring area during this period. In the north region, the first rainy period (P1) lasted for 26 days from August 25 to September 20, with a total precipitation of 90.4 mm and an average daily precipitation of 3.5 mm/day. The second rainy period (P2) lasted for only 18 days from 30 September to 18 October, but both the total precipitation (108.2 mm) and the average daily rainfall (6.0 mm/day) were

Table 1 General characteristics of autumn rainfall in western China in 2017.

Region	Period	Onset date	End date	Autumn rain period (days)	Autumn rainfall (mm)	Average daily precipitation during autumn rain period (mm/day)
North	Climatic average	September 8	October 13	35	135.6	3.9
	2017	August 25 (− 14)	October 18 (+ 5)	54 (+ 19)	234.1 (+ 72.6%)	4.3 (+ 0.4)
South	Climatic average	September 9	October 31	52	184.4	3.5
	2017	August 24 (− 16)	October 26 (− 5)	63 (+ 11)	322.2 (+ 74.4%)	5.1 (+ 1.6)

Values in parentheses are deviations and the positive (negative) values for the onset and end date indicate that they are later (earlier) than average

more than those in P1. In the south region, however, the situation was opposite to that in the north. The duration of P1 (18 days) was obviously shorter than that of P2 (38 days), but the average daily precipitation in P1 (8.0 mm/day) was obviously more than that in P2 (4.5 mm/day).

3.2.3 Spatial distribution of rainfall

Figure 2 shows that from August 24 to October 26, 2017, the southern and northern areas were almost in the autumn rain period and that precipitation was significantly higher in the southern area than in the north. The district with the greatest precipitation was at the junction of Chongqing, Sichuan, and Shaanxi (Fig. 3a). The precipitation was 753.8 mm at Chongqing's Chengkou station, 751.8 mm at Sichuan's Wanyuan station, and 711.4 mm at Shaanxi's Zhenba Station, respectively, 1.5 times, 1.2 times, and 1 time more than that in the same period in a normal year (Fig. 3b). There were seven stations with precipitation > 600 mm and 27 stations with precipitation > 500 mm. Figure 3b shows that the overall ARWC in 2017 was higher than that in a normal year and rainfall in the southern area was higher than that in the north. Precipitation at Danjiangkou station in Hubei in 2017 was 516.4 mm, nearly twice more than that in a normal year.

The characteristics of ARWC in the northern and southern parts of the monitoring area were different in 2017. The onset dates of autumn rain in both areas were abnormally early, whereas the end date in the north was 5 days later while the one in the south was 5 days earlier than in normal years. The autumn rain period was longer than normal and the total and mean daily precipitation were both significantly higher than in normal years. The rainfall period in the northern region was mainly from the end of September to the middle of October, while in the southern region, it was mainly from the end of August to the first 10 days of September.

4 Atmospheric circulation and water vapor transport anomalies during ARWC in 2017

The ARWC is a local climate phenomenon in the transitional season (Zhang 1941). The onset of ARWC reflects the adjustment of the East Asian atmospheric circulation system from

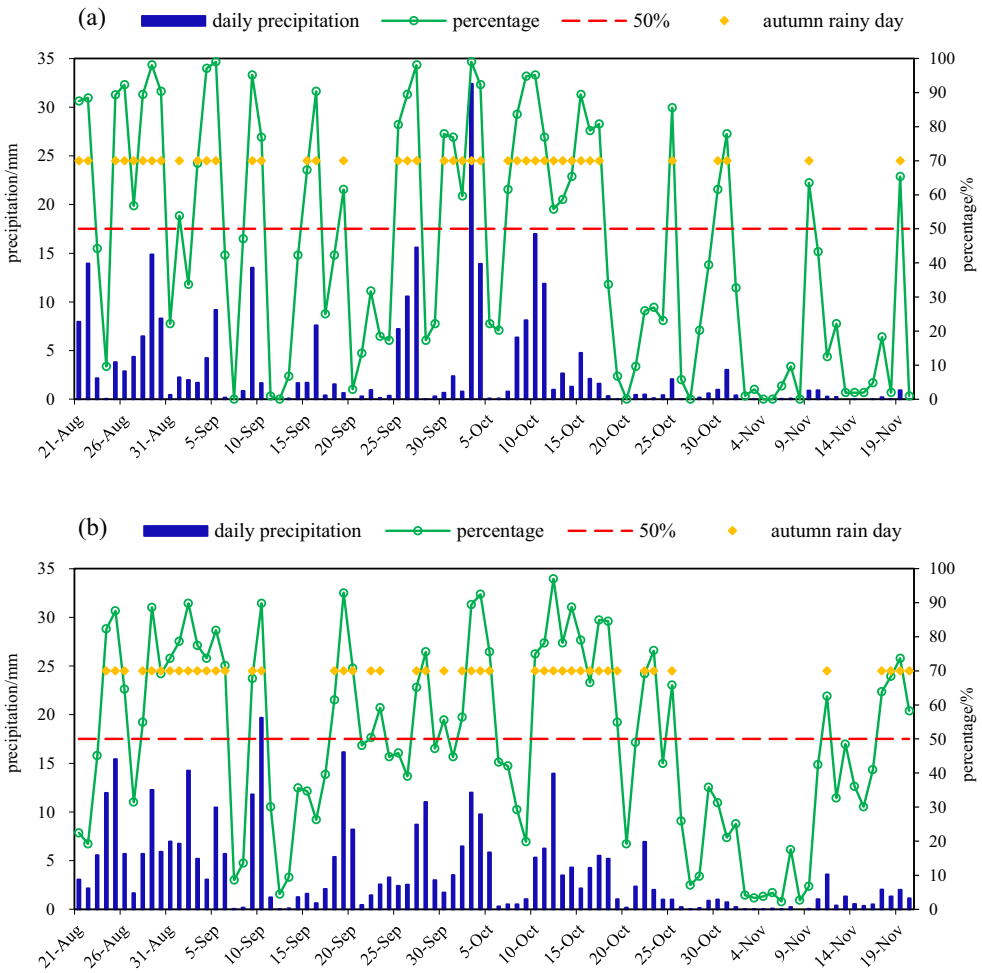

Fig. 2. Variation in daily precipitation from August 21 to November 20, 2017 in western China (**a** north region, **b** south region) (the *y*-axis on the left is daily precipitation of the monitoring area and the *y*-axis on the right is the percentage of stations with daily rainfall equal to or greater than 0.1 mm at total stations. If there is a yellow solid diamond on a certain day, it means that the day is an autumn rainy day.)

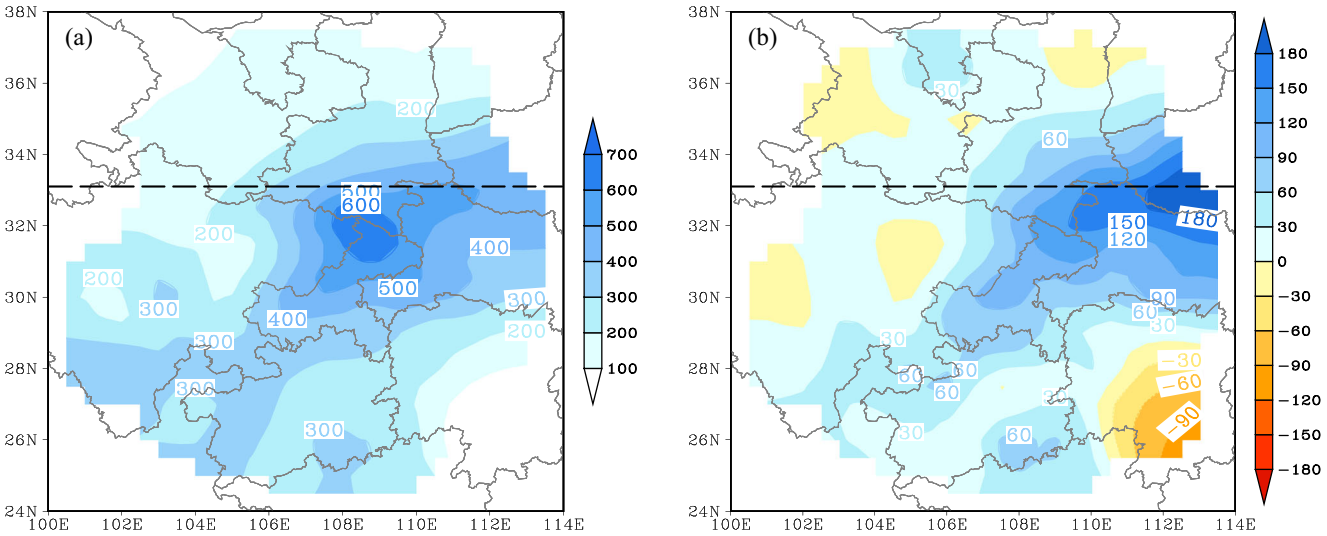

Fig. 3. Spatial distribution of **a** accumulated rainfall from August 21 to November 20, 2017 (units: mm), and **b** percentage in rainfall from August 21 to November 20, 2017 (units: %)

the summer to the winter monsoon circulation system. The onset date of the ARWC in 2017 was especially early as a result of the advanced seasonal adjustment and transformation of the summer and winter circulation systems. It was caused by the mutual interactions of the upper, mid-, and lower tropospheric circulations. The seasonal transition of the atmospheric circulation and the beginning and end of the rainy season in most parts of China are closely related to the north–south movement and changes in intensity of the westerly jet over the East Asian subtropics (Kuang and Zhang 2006; Yang and Zhang 2007). Gao and Guo (1958) reported that the ARWC starts when the easterly circulation over western China disappears and the westerly circulation begins; the autumn rains end when the westerly jet remains stable over western China.

The start date of autumn rain in northern area in 2017 was 14 days earlier than normal, which is in the 4th place since 1961. And the onset date in southern area in 2017 was 16 days earlier than normal, which is also in the 4th place since 1961. According to the criterion of − 0.7 times the standard deviation, we selected the years with onset date earlier than normal in both the northern and southern areas for further study. There were a total of 13 such years (1981, 1982, 1983, 1984, 1985, 1989, 1990, 1991, 1996, 2003, 2004, 2006, and 2007) in the northern area and 11 years (1984, 1988, 1999, 2001, 2003, 2004, 2007, 2008, 2010, 2013, and 2015) in the southern area. The 200-hPa zonal wind was selected and the similarities and differences between 2017 and the historical early years were analyzed. The results for the northern area were clearer than those for the southern area, so the results in the northern area were analyzed. Figure 4 shows the time–latitude profile of the zonal winds at 200 hPa averaged from 100 to 130° E in the years with an early onset of ARWC in the northern area (Fig. 4a), in 2017 (Fig. 4b), and in the earliest years (Fig. 4c–f). The earliest year of ARWC during 1981–2017 is 1981, 1983, 1984, and 2006. In all of the above years, the ARWC began on August 21th. Figure 4a shows that in the years with an early onset of ARWC, the 35-m/s wind speed isoline appeared in late August, 10 days earlier than in normal years (early September). Similar to the situation in the years with an early onset of ARWC, the 35-m/s wind speed isoline began to appear in middle and late August 2017, significantly earlier than usual (Fig. 4b). The intensity of westerly jet in 2017 was significantly stronger than that in the onset early years. Also, the westerly jet anomaly in the earliest years is more significant than that in 2017. The 35-m/s wind speed isoline appeared much earlier in the earliest years than in 2017 (Fig. 4c–f). This indicates that the advanced adjustment of the westerly jet in the upper troposphere at mid- to high latitudes in 2017 provided favorable conditions for the onset of ARWC. Study by Zhang et al. (2018) suggests that the position shift of the EASWJ is affected by the phase variation of Rossby waves propagating northward from South Asia to tropical and subtropical East Asia in August. The Indian Ocean SST anomalies in spring are the most significant forcing signal for the phase variation of Rossby wave propagating from South Asia to tropical and subtropical East Asia (Zhang et al. (2018)). From Fig. 10, it can be seen that the SST of Indian Ocean were continuously warm from spring to summer in 2017, which can procreate Rossby waves. The eastward transmission of Rossby waves further affected the westerly jet jump early in 2017.

Figure 5 shows the pentad evolution of the geopotential height anomaly at 500 hPa and vector wind field at 700 hPa for the mid- and lower troposphere during the autumn rain in 2017. Figure 5a shows that there was a

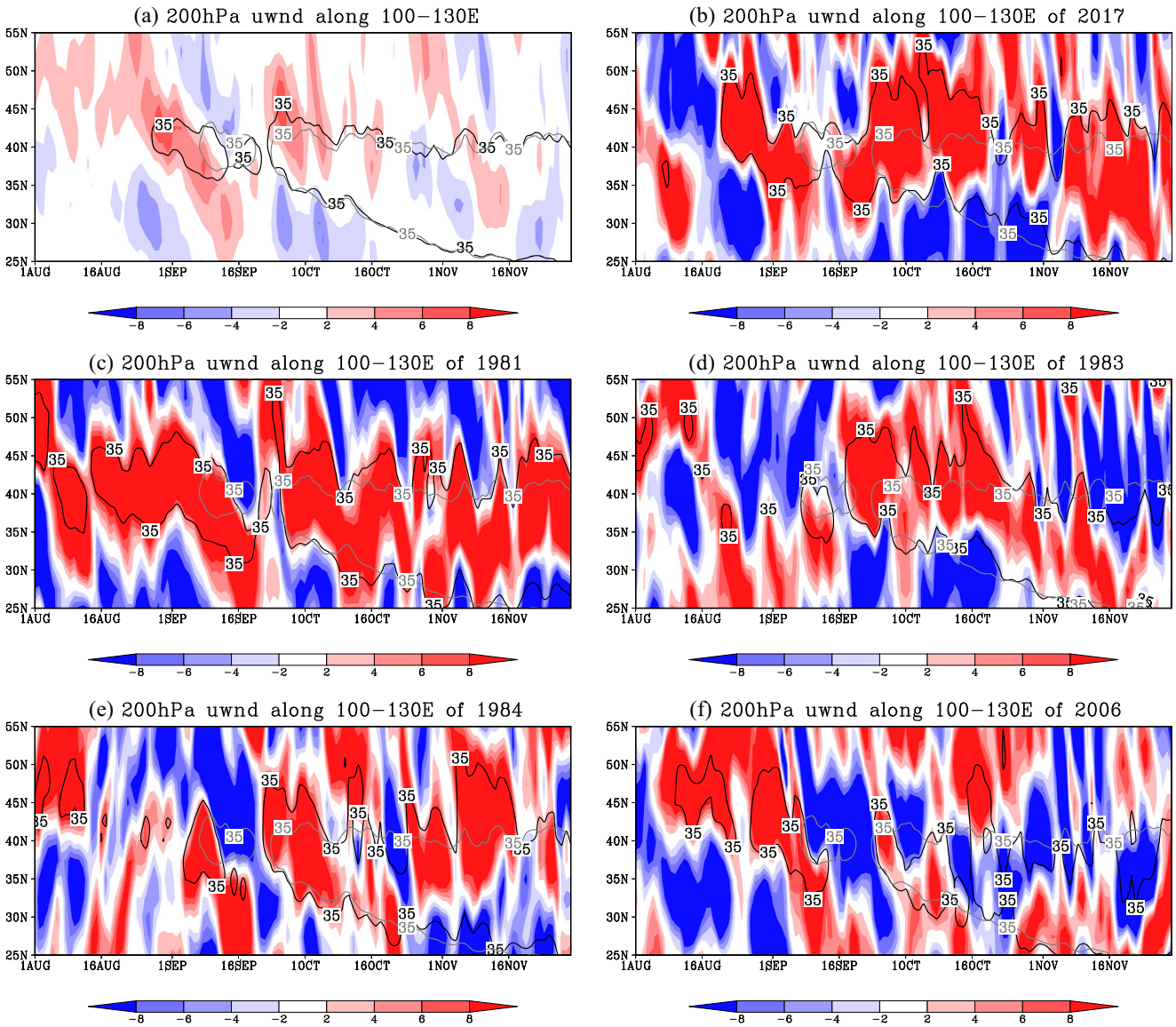

Fig. 4. Time–latitude profile of the zonal winds (unit: m/s) at 200 hPa averaged from 100 to 130° E in the years with an early onset of the ARWC in **a** the northern region, **b** 2017, **c** 1981, **d** 1983, **e** 1984, and **f** 2006. The gray line represents the climatological mean of the 35-m/s contour and the black line represents the mean of the 35-m/s contour in anomalous years

positive geopotential height anomaly and an anomalous anticyclonic circulation over the Ural Mountains in the 47th pentad (August 21–25), together with a negative geopotential height anomaly over Lake Baikal. The meridional circulation in the mid- and high latitudes of Eurasia therefore showed a west-high and east-low pattern, resulting in a flow of cold air down to northern and southwestern China. The WPSH was anomalously strong and to the west, with the western extreme of the WPSH to the west of 100° E. The warm, humid airflow on the southwestern side of the WPSH therefore converged with cold air from the north in southwestern China, resulting in the early onset of ARWC. The evolution of the circulation in the later period shows that the atmospheric circulation was relatively stable in the 48th (Fig. 5b, August 26–31) and 49th pentads (Fig. 5c), September 1–5), which favors the observed convergence and maintenance of ARWC. The Ural blocking high collapsed and the cold air weakened in the 50th pentad, but the subtropical high remained stable, providing the continuous transport of water vapor (Fig. 5d, September 6–10).

The amount of ARWC was abnormally high in 2017 relative to normal years. The autumn rainfall in the north was 234.1 mm, 72.6% higher than normal. The rainfall in the south was 322.2 mm, the second highest since 1965. According to the criterion of 0.8 times the standard deviation, we selected the years with more autumn rainfall (2008, 1999, 2010, 1988, 2007, 1983, 2013, 1989, and

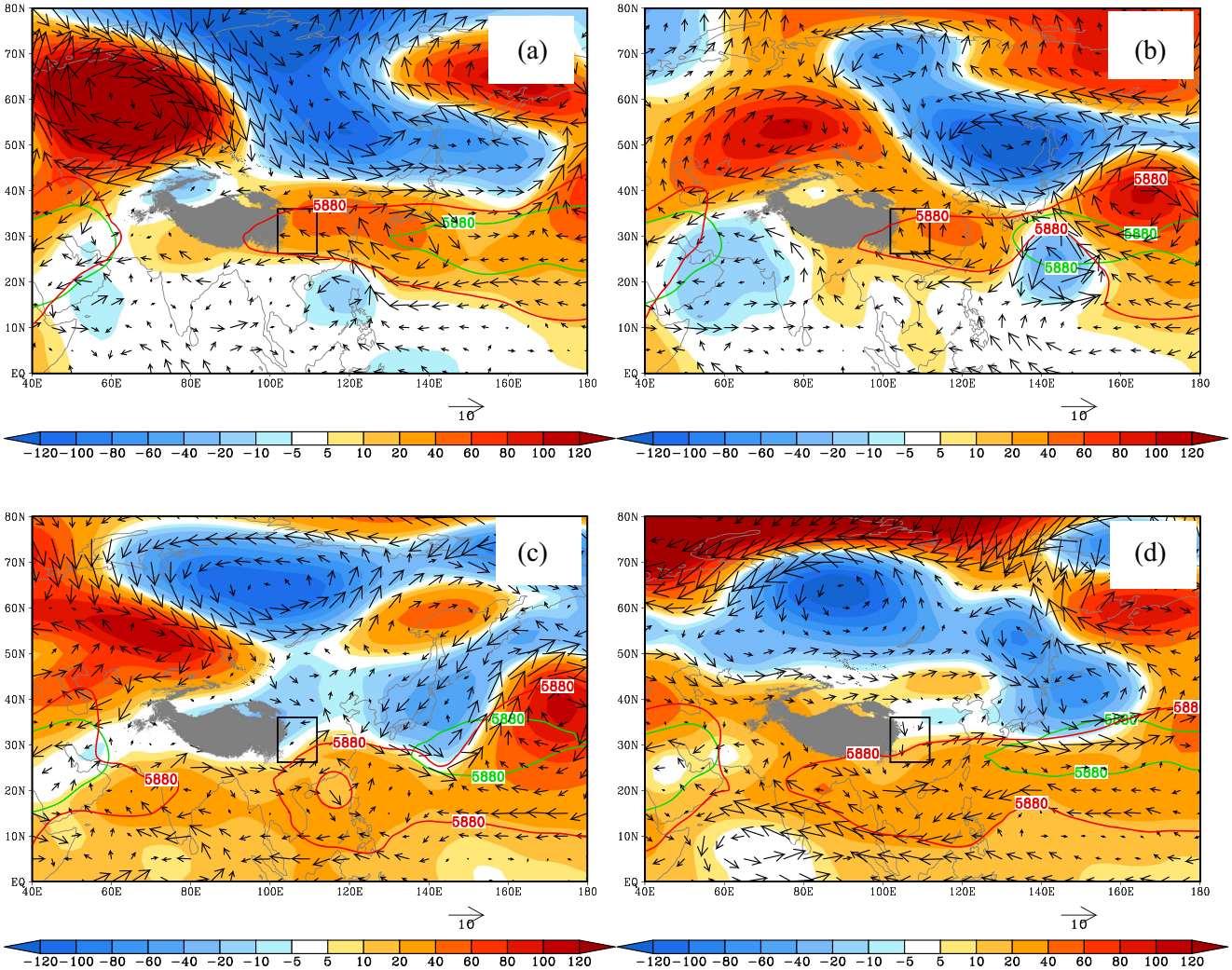

Fig. 5. Spatial distribution of the 500-hPa geopotential height anomaly and the 700-hPa wind anomaly during the ARWC period in 2017: **a** 47th pentad, **b** 48th pentad, **c** 49th pentad, and **d** 50th pentad. The green line represents the climatological mean of the 5800-gpm contour and the red line represents the composed 5800-gpm contour. The black rectangular frame shows the location of western China. The shaded gray areas represent 700 hPa terrain

1982) and those with less rainfall (2009 , 2002, 2006, 1991, 1998, 1992, 1990, 2005, 2012, and 1993) in the southern area, as well as the years with more autumn rainfall (1985, 1981, 1984, 2011, 1983, and 2003) and those with less rain (1998, 1995, 1993, 1987, 2004, 1986, 1990, and 2016 for a total of 8 years) in the northern area. The average circulation in September to October of these years was determined in the southern and northern regions.

Figure 6 shows the geopotential height anomaly at 500 hPa and the wind anomaly at 700 hPa averaged from September to October. In terms of the northern region, the geopotential height anomaly at 500 hPa shows an abnormal "+−+" distribution from high to low latitudes (Fig.6 (a1)) in the years with more autumn rain. At high latitudes, the positive geopotential height anomaly at 500 hPa favors the diffusion of cold air. There is a significant low trough over Lake Balkhash–Baikal at mid-latitudes (Fig. 6(a1)). The positive anomaly in the intensity of the WPSH at 500 hPa is not clear at low latitudes (Fig. 6(a1)), but there is a clear westward extension of the anticyclonic anomalous circulation in the western Pacific to the South China Sea (Fig. 6(a2)). And the westerly wind anomaly in the Indian Ocean at 700 hPa (Fig. 6(a2)) indicates a strong Indo-Burma trough. This configuration of the circulation system results in higher ARWC. In the southern region, there is no obvious difference except the positive geopotential height anomaly in the East China Sea at 500 hPa (Fig. 6(b1)) and the northward wind anomaly from the South China Sea at 700 hPa (Fig. 6(b2)). The results for the northern region are consistent with previous studies (Feng and Guo 1983; Bai and Dong 2004; Wang and Ding 2008) showing that the WPSH, the Indo-Burma trough, and the Lake Baikal low trough were the main systems influencing the ARWC. The reverse conditions result in less autumn rain.

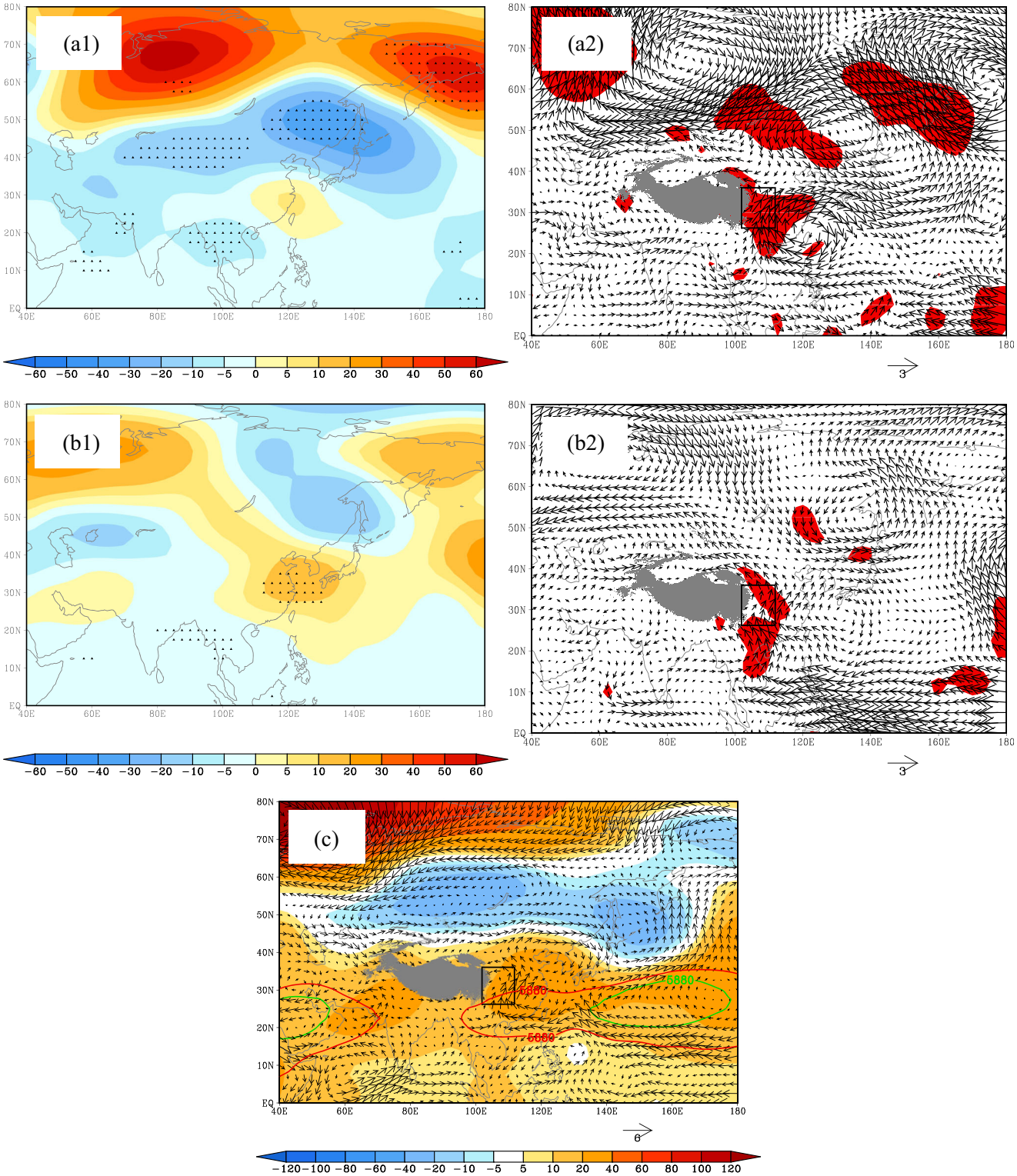

Fig. 6 Composition of the mean 500-hPa geopotential height anomaly (units: gpm) and the mean 700-hPa wind anomaly (units: m s^{-1}) from September to October. (a1) The difference of the 500-hPa geopotential height anomaly between the years with higher autumn rainfall and the years with lower autumn rainfall in the northern region. (a2) The same as (a1), but for the 700-hPa wind anomaly. (b1) The same as (a1), but for the southern region. (b2) The same as (a1), but for the 700-hPa wind anomaly in the southern region. (c) 2017. The green line represents the climatological mean of the 5800-gpm contour and the red line represents the composed 5800-gpm contour. The black rectangular frame shows the location of western China. The shaded gray areas represent 700-hPa terrain. The dotting area in (a1) and (b1) represents the 95% significance level. The red shaded area in (a2) and (b2) represents the 95% significance level

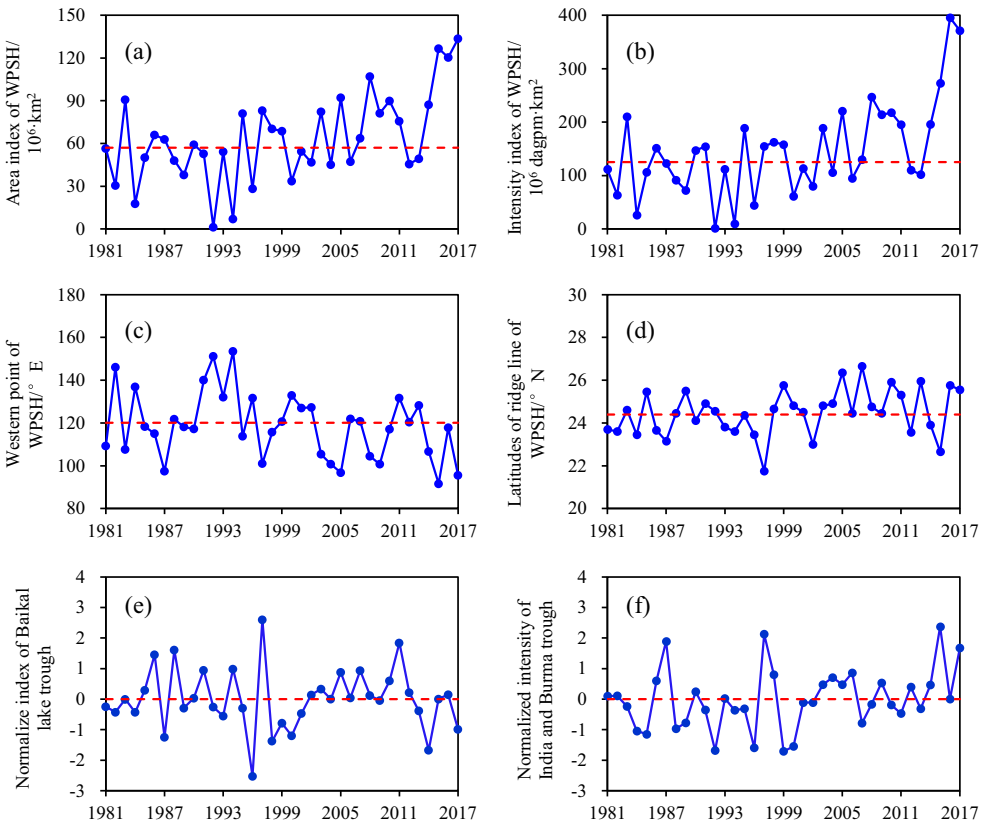

Fig. 7 Variation in the atmospheric circulation indexes averaged from September to October during the time period 1981–2017. **a** Area index of the WPSH, **b** intensity index of the WPSH, **c** index of the westernmost point of the WPSH, **d** index of the latitude of the ridge line of the WPSH, **e** normalized index of the Lake Baikal trough, and **f** normalized index of the Indo-Burma trough. The dotted line in **a**–**d** represents the climatological mean and the dotted line in **e** and **f** represents the zero line

In 2017, the anomalous Lake Baikal trough at 500 hPa and the westward extension of the anticyclonic anomalous circulation in the western Pacific at 700 hPa are consistent with the atmospheric circulation in the northern region. However, the position of the WPSH was significantly westward (Fig. 6(c), Fig. 7c) and its intensity was significantly stronger (Fig. 6(c), Fig. 7b) (the area of the WPSH is the largest since 1981, its intensity and westward point are both in the second place since 1981), which is the main factor that affects the ARWC in 2017. Furthermore, the intensity of the Indo-Burma trough was weak in 2017, which is another obvious difference between 2017 and other years with higher ARWC in history. This also can be found from water vapor transport during the autumn rain period.

Water vapor is a necessary condition for precipitation (Ding and Hu 2003) and anomalies in water vapor transport and the water vapor budget will lead to anomalies in precipitation. The water vapor during the autumn rain period is mainly sourced from the Indian Ocean, the BOB, and the South China Sea–Pacific Ocean (Yuan and Liu 2013; Wang et al. 2015; Zhi et al. 2018). There were two main sources of water vapor in 2017: the South China Sea–West Pacific Ocean and the Indian Ocean and BOB (Fig. 8a). The former source is clearly strong, whereas the latter is weak (Fig. 8b). The entire region of western China was a convergence zone for water vapor in 2017, which favors increased precipitation (Fig. 8c). Figure 8d shows the water vapor budget integrated from the surface to 300 hPa in the northern and southern regions. The water vapor in the northern region mainly flows in from the western and southern boundaries and out from the eastern and northern boundaries. There is a net inflow of water vapor to the northern region. The water vapor budget of the southern region is similar to that of the northern region, except that the inflow of water vapor to the southern area is greater than that in the north. The water vapor source of the ARWC in 2017 was mainly from the South China Sea–Western Pacific Ocean and the source of water vapor from the BOB was weak. The abundant water vapor from the South China Sea–Western Pacific Ocean is the main reason for the increased ARWC in 2017.

5 Influence of Indian Ocean SSTA on the ARWC in 2017

The thermal anomaly over the tropical Indian Ocean has an important role in the difference between the thermal characteristics of the sea and land as the second driving force for the Indian Ocean–Pacific Ocean temperature configuration, the atmospheric circulation, and variations in the

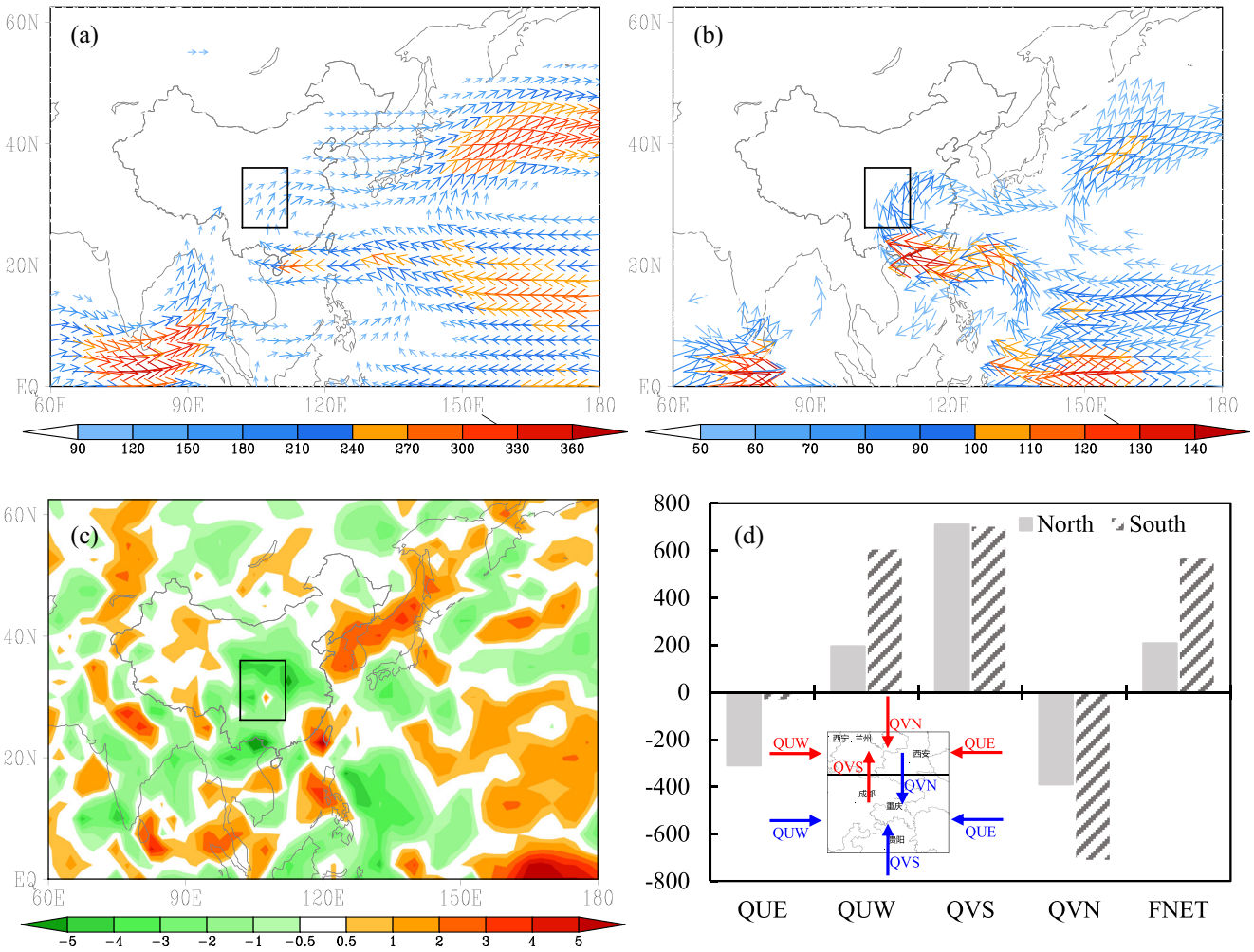

Fig. 8 Anomalous water vapor integrated from the surface to 300 hPa during autumn rain period in western China in 2017. **a** Water vapor transport (units: $kg{\cdot}s^{-1}{\cdot}m^{-1}$), **b** anomalous water vapor transport (units: $kg{\cdot}s^{-1}{\cdot}m^{-1}$), **c** anomalous divergence, and **d** the water vapor budget through the four boundaries of the northern and southern region of western China (QUE, QVS, QUW, and QVN: 10^5 kg s^{-1}) and the regional net water vapor budget (FNET: 10^5 kg s^{-1}). The black rectangular frame shows the location of western China

Asian–Australian monsoon and therefore affects the summer precipitation anomalies in China (Yan et al. 2001; Xiao et al. 2002). The IOBW is the main mode of the SSTAs over the tropical Indian Ocean and is a lagging response to the El Niño event, playing an important part in maintaining the influence of El Niño on the East Asian weather and climate (Yang et al. 2007; Xie et al. 2009; Huang et al. 2016).

The intensity of the WPSH was stronger and its westernmost point was further to the west in autumn 2017 than in normal years. This is the most important reason for the increased ARWC in 2017. Li et al. (2012) reported that the intensity index of the WPSH in summer has a significant negative correlation with the index of its westernmost point, in which a stronger intensity correlates with a more westerly westernmost point. Similarly, we calculated the correlation coefficient between the intensity index of the WPSH and the index of its westernmost point averaged from September to October during 1981–2017. The correlation coefficient was − 0.65 (significant at a = 0.001) and the negative correlation was significant, indicating that the negative correlation between these variables in summer also applies in autumn. We therefore used the intensity index of the WPSH to represent its intensity and its westward extent.

Figure 9 shows the spatial distribution of the correlation coefficient between the intensity index of the WPSH averaged from September to October and the SST from May to August. The SST of the tropical Indian Ocean (20° S–20° N, 40–110° E) from May to August had a significantly positive correlation with the intensity of the WPSH averaged from September and October, indicating that the warm SSTs of the Indian Ocean from May to August favor the enhancement of the WPSH. The SST in the tropical Indian Ocean was in an abnormally warm state from May to August 2017 (Fig. 10), which favored the strengthening

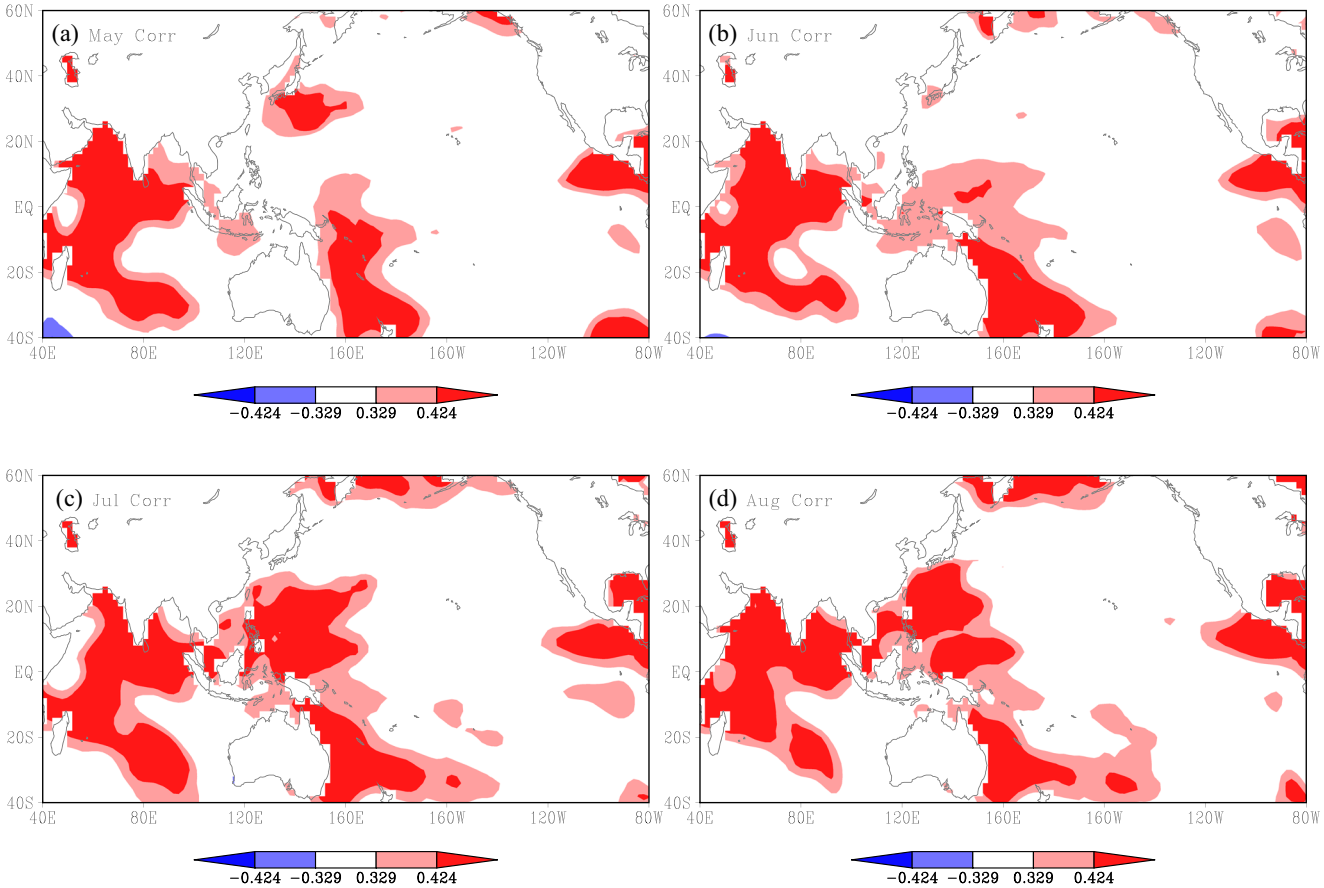

Fig. 9 Spatial distribution of the correlation between the intensity index of the WPSH averaged from September to October and the monthly SSTs during the period 1981–2017: **a** May, **b** June, **c** July, and **d** August. Dark and light shaded areas represent values at the 99 and 95% confidence levels, respectively

of the WPSH. The correlation coefficient between the intensity index of the WPSH averaged from September to October and the IOBW indexes from January to October show a significant positive correlation from May to August (the confidence level reached 99.9%) and the correlation coefficient in July was 0.68 (Fig. 11b). This suggests that when the Indian Ocean SST is warmer in summer, the WPSH tends to be stronger and more to the west in autumn, which favors increased ARWC.

The 500-hPa height field and the 850-hPa wind field averaged from September to October were regressed using the IOBW index averaged from July to August (Fig. 12). Figure 12 shows that there are significant positive anomalies in the 500-hPa geopotential height field in the tropical and subtropical regions, especially in the western Pacific, indicating that the WPSH is clearly more westward and stronger (Fig. 12a). At the 850-hPa wind field, there is a westerly anomaly in the BOB, an anomalous anticyclonic circulation with its center located near the Philippines and a significant southerly anomaly in the South China Sea (Fig. 12b). This circulation configuration is similar to that in the years with increased ARWC and in 2017. This analysis shows that the Indian Ocean SST was warmer from May to August 2017, which increased the intensity of the WPSH and moved its westernmost point further west in September and October. This was the main reason for the significant increase in ARWC in 2017.

6 Discussion and conclusions

ARWC is a special type of weather phenomenon. Anomalies in ARWC have an important influence on the autumn harvest, autumn sowing, and agricultural production. We analyzed the anomalous characteristics and causes of ARWC in 2017 based on the new monitoring indicators published by the Forecasting and Network Division of the CMA in 2015 and National Center for Environmental Prediction reanalysis data. Our conclusions are as follows:

(1) The characteristics of autumn rain in the southern and northern regions of the monitoring area were different. The onset date of autumn rain in the north (south) of the monitoring area in 2017 was 14 (16) days

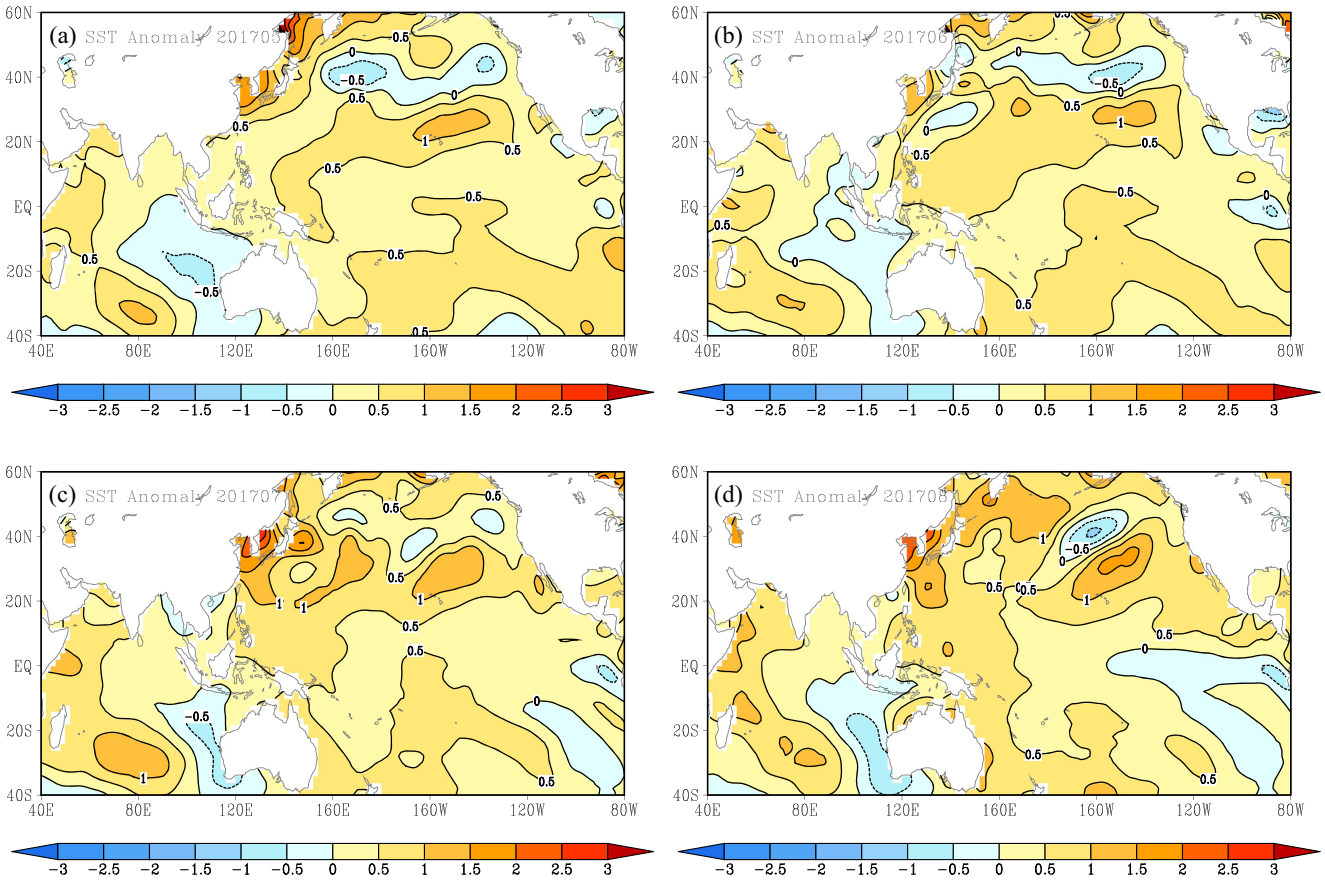

Fig. 10. Spatial distribution of SSTAs in 2017 (units: °C): **a** May, **b** June, **c** July, and **d** August

earlier than in a normal year, which is in the 4th (4th) place since 1961. The end date was 5 days later (earlier). The autumn rain period was 54 (63) days, 19 (11) days longer than in a normal year. The autumn rainfall in the north (south) of the monitoring area was 234.1 (322.2) mm, 72.6% (74.4%) higher than in a normal year. The autumn rainfall in southern region in 2017 is in the second place since 1965.

(2) The advanced transition of the East Asian atmospheric circulation system from the summer to winter pattern resulted in a significantly early onset of the ARWC in 2017. The westerly jet in the upper troposphere appeared about 10 days earlier than in a normal year. The meridional circulation in the mid- and lower troposphere showed a west-high and east-low pattern in the mid- and high latitudes of Eurasia. This circulation configuration resulted in an early onset of the ARWC.

The intensity of the WPSH was influenced by persistent warming of the IOBW from spring to summer and was extremely strong (the second strongest since 1981). Its westernmost point extended far to the west (the second furthest

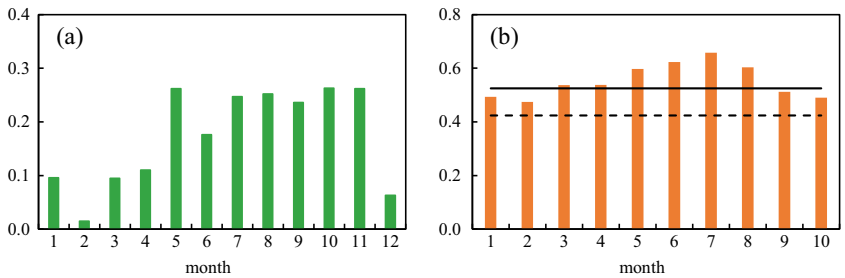

Fig. 11 Variation in **a** the IOBW index from January to December 2017 (units: °C) and **b** the correlation coefficient between the intensity index of the WPSH averaged from September to October and the monthly IOBW index during 1981–2017. The solid line and dotted lines in **b** indicate values at the 99.9 and 99% confidence levels, respectively

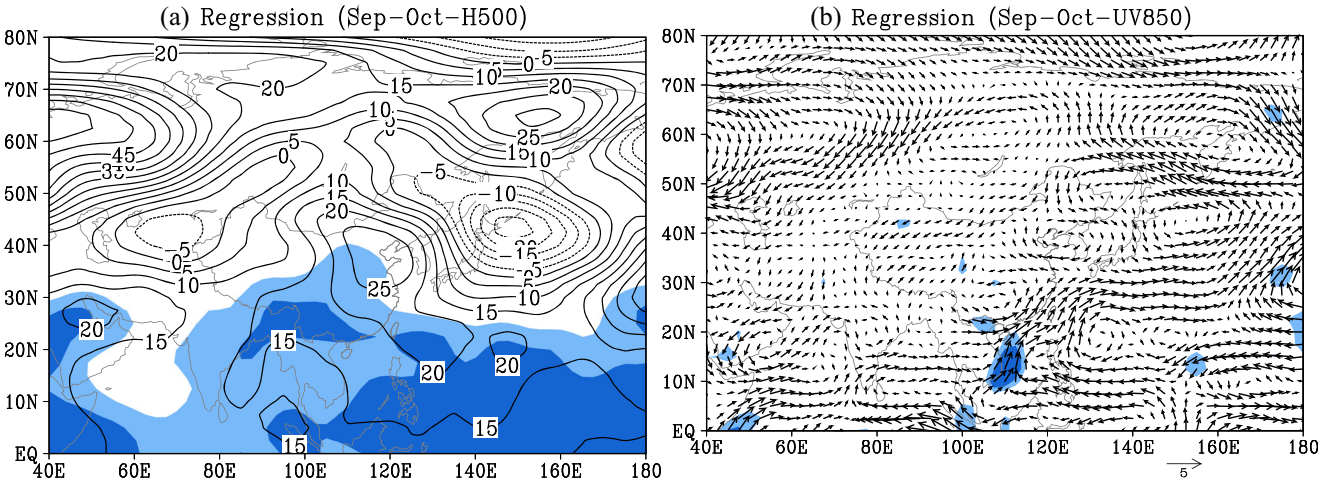

Fig. 12 Spatial distribution of **a** the regressed 500-hPa geopotential height averaged from September to October and **b** the 850-hPa wind field using the IOBW index averaged from July to August. The dark and light shaded areas represent values at the 99 and 95% confidence levels, respectively

extension since 1981) during the autumn rain period. The intensity of the moisture flux from the southwest of the WPSH was stronger than that in normal years and the strength of the low trough of Lake Baikal was also stronger. Cold air from the north and the abundant warm, humid water vapor from the south converged in western China, resulting in more precipitation during autumn rain period.

The characteristics of the autumn rain in the southern and northern regions of the study area were different, so the reasons for the abnormally early onset of the ARWC and the significant increase in precipitation in the autumn rainy season should be different in the two regions. This work analyzed the reasons for the anomalies in the northern region and those in southern region will be analyzed in future work.

Acknowledgments This work was jointly supported by the National Key Research and Development Program of China (2018YFA0606301, 2017YFC1502303), and the National Natural Science Foundations of China (grant numbers: 41875093, 41505061, 41575074, and 41530531).

References

Atmospheric Science Dictionary Editorial Committee (1994) Atmospheric science dictionary. China Meteorological Press, Beijing, p 980 (in Chinese)

Bai HZ, Dong WJ (2004) Climate features and formation causes of autumn rain over southwest China. Plateau Meteorol 23:884–889 (in Chinese)

Bao YY, Abulimiti LF, Wang XW (2003) Space-time distribution and physical mechanisms of autumn rains in west China in 2001. J Appl Meteor Sci 14:215–222 (in Chinese)

Ding YH (2005) Advanced synoptic meteorology. China Meteorological Press, Beijing (in Chinese)

Ding YH, Hu GQ (2003) A study on water vapor budget over china during the 1998 severe flood periods. Acta Meteorologica Sinica 61:129–145 (in Chinese)

Feng LW, Guo QY (1983) The fluctuation of autumn rain in south-west China. Geogr Res 2:74–84 (in Chinese)

Feng AQ, Zeng HL, Yin YZ et al (2018) Climatic characteristics and major meteorological events over china in 2017. Meteor monthly 44:548–555 (in Chinese)

Gao YX (1958) On the high autumn clear weather in China. Acta Meteorologica Sinica 29:23–32 (in Chinese)

Gao YX, Guo QY (1958) On the autumn raining area in China. Acta Meteorologica Sinica 29:42–51 (in Chinese)

He M (1984) Distribution and long-term forecast of major autumn rain regions in China. Meteor Mon 10:10–13 (in Chinese)

Huang G, Hu KM, Qu X et al (2016) A review about Indian Ocean basin mode and its impacts on East Asian summer climate. Chin J Atmos Sci 40:121–130

Huang BY, Thorne PW, Banzon VF, Boyer T, Chepurin G, Lawrimore JH, Menne MJ, Smith TM, Vose RS, Zhang H-M (2017) Extended Reconstructed Sea Surface Temperature (ERSST), Version 5: upgrades, validations and intercomparisons. Journal of Climate 30: 8179–8205. https://doi.org/10.1175/JCLI-D-16-0836.1

Kalnay E et al (1996) The NCEP/NCAR 40-year reanalysis project. Bull Amer Meteor Soc 77:437–470

Kuang XY, Zhang YC (2006) Impact of the position abnormalities of East Asian subtropical westerly jet on summer precipitation in middle-lower reaches of Yangtze River. Plateau Meteorol 25:382–389 (in Chinese)

Li YH, Qing JM, Li Q, Luo WL (2012) Inter-annual and inter-decadal variations of south Asian high in summer and its influences on flood/drought over western southwest China. J Southwest Univ (Natural Science Edition) 34:71–81 (in Chinese)

Liang JH (1989) Spatial and temporal distribution of autumn rain in western China. Scientia Geographica Sinica 9:51–59 (in Chinese)

Liu XF, Yuan HZ (2006) Relationship between the Indian Ocean dipole and autumn rainfall in China. J Nanjing Institute Meteorol 29:644–649 (in Chinese)

Liu YJ, Sun L, Sun CH, Wang ZY, Wang YJ, Yuan Y (2012) Analysis of anomalies of autumn rain in west China in 2011 and its possible mechanism. Meteor monthly 38:456–463 (in Chinese)

Si D, Shao X, Sun L, Wang QY, Li D (2015) Causality analysis of autumn rainfall anomalies in west China 2014. Meteor monthly 41:508–513 (in Chinese)

Wang ZY, Ding YH (2008) Climatic characteristics of rainy seasons in China. Chin J Atmos Sci 32:1–13 (in Chinese)

Wang CX, Ma ZF, Wang JJ, Wang JT (2015) The Characteristics of Huaxi autumn rain and its relationship with sea surface temperatures over the equatorial Pacific. Chin J Atmos Sci 39:643–652. https://doi.org/10.3878/j.issn.1006-9895.1408.14141 (in Chinese)

Xiao ZN, Yan HM, Li CY (2002) The relationship between Indian Ocean SSTA dipole index and the precipitation and temperature over China. J Trop Meteorol 18:335–344 (in Chinese)

Xie SP, Hu KM, Hafner J et al (2009) Indian Ocean capacitor effect on Indo-Western Pacific climate during the summer following El Niño. J Clim 22:730–747

Yan HM, Yan HS, Xie YQ (2001) The SSTA signal characteristic analysis over India Ocean during flood season in China. J Trop Meteorol 17: 109–116 (in Chinese)

Yang LM, Zhang QY (2007) Anomalous perturbation kinetic energy of Rossby wave along East Asian westerly jet and its association with summer rainfall in China. Chin J Atmos Sci 31:586–595 (in Chinese)

Yang JL, Liu QY, Xie SP et al (2007) Impact of the Indian Ocean SST basin mode on the Asian summer monsoon. Geophys Res Lett 34: 02708

Yuan X, Liu XF (2013) Onset-withdrawal dates of autumn persistent rains over western China and the associated autumn to winter evolution of the atmospheric circulation. Acta Meteorologica Sinica 71: 913–924 (in Chinese)

Zhang BK (1941) Climatic regions of Sichuan province. Acta Meteorologica Sinica 1:111–148 (in Chinese)

Zhang QY, Xuan SL, Sun SQ (2018) Anomalous circulation characteristics of intraseasonal variation of East Asian subtropical westerly jet in summer and Precursory Signals. Chin J Atmos Sci 42:935–950. https://doi.org/10.3878/j.issn.1006-9895.1803.18107 (in Chinese)

Zhao ZG (1999) Summer drought and flood in China and its general circulation. China Meteorological Press, Beijing, pp 75–78 (in Chinese)

Zhi R, Chen LJ, Zhu XY (2018) Analysis of characteristics and causes of precipitation anomalies over northern China in autumn 2017. Meteor monthly 44:572–581 (in Chinese)

Publisher's note Springer Nature remains neutral with regard to jurisdictional claims in published maps and institutional affiliations.

Interannual Variability of the Tropical Cyclone Landfall Frequency over the Southern and Northern Regions of East Asia in Autumn

XINGYAN ZHOU

Laboratory for Climate Studies, National Climate Center, China Meteorological Administration, Beijing, China

RIYU LU

LASG, Institute of Atmospheric Physics, Chinese Academy of Sciences, and College of Earth and Planetary Sciences, University of the Chinese Academy of Sciences, Beijing, China

(Manuscript received 22 January 2019, in final form 28 August 2019)

ABSTRACT

This study focused on the interannual variability of tropical cyclone (TC) activity over the western North Pacific in autumn. The results show that the frequencies of TC landfalls in the southern and northern coastal regions of East Asia are roughly independent, implying that they are affected by different factors and should be studied separately. Further analysis indicates that the frequency of TC landfall in the southern region is closely related to El Niño–Southern Oscillation, which affects both the upper- and lower-tropospheric circulation over the western North Pacific and East Asia and induces changes in the steering flow. By contrast, the frequency of TC landfall over the northern region has a close connection with a teleconnection pattern in the upper troposphere over the Eurasian continent, which seems to be triggered by an anomalous Rossby wave source over the North Atlantic. This teleconnection pattern leads to anomalous meridional winds over the western North Pacific and East Asia and induces significant changes in the steering flow.

1. Introduction

Tropical cyclones (TCs), as the worst natural disasters, cause huge human and property losses through strong winds, torrential rainfall, and tidal surges during or after landfall (e.g., Zhang et al. 2009; Park et al. 2011; Corporal-Lodangco et al. 2016). The western North Pacific (WNP) spawns the most TCs of all the ocean basins, accounting for more than one-third of all TCs globally (e.g., Wu and Wang 2004). In addition, East Asia is home to about a quarter of the world's population, with a large percentage living in coastal regions. It is therefore essential to gain a better understanding of the variability of TCs making landfall over East Asia.

The location at which a TC makes landfall is mainly determined by its track. Previous studies have identified three prevailing types of track over the WNP: a straight-moving (or westward-moving) track, a recurving-landfall track, and a recurving-ocean track (e.g., Elsner and Liu 2003; Wu et al. 2005; Camargo et al. 2007a,b; Kim et al. 2011; Colbert et al. 2015; He et al. 2015; Mei and Xie 2016). Straight-moving TCs tend to make landfall in the southern coastal region (the Philippines, Vietnam, and southern China), whereas recurving TCs threaten the northern coastal region (eastern China, the Korean Peninsula, and Japan) or disperse over the ocean without making landfall. Hence the frequency of TC landfall over East Asia can be separated into the two types: those making landfall in the southern coastal region and those making landfall in the northern coastal region, almost corresponding to the TCs with straight-moving and recurving tracks, respectively. The variation in the TC track is significantly influenced by the steering flow (Riehl and Burgner 1950; Chan and Gray 1982; Fiorino and Elsberry 1989; Wu and Emanuel 1995; Wu and Chen 2016).

Interannual variation of TC landfall frequency has great socioeconomic impacts on East Asia. Anomalously high frequency of TC landfall in a particular typhoon season can threaten livelihoods of people in East Asia, especially in the heavily populated coastal areas. Anomalously low frequency of TC landfall, by contrast, may also induce negative effects such as shortage of

Corresponding author: Xingyan Zhou, zhouxingyan@cma.gov.cn

DOI: 10.1175/JCLI-D-19-0057.1

© 2019 American Meteorological Society. For information regarding reuse of this content and general copyright information, consult the AMS Copyright Policy (www.ametsoc.org/PUBSReuseLicenses).

water resources. Therefore, the interannual variation of TC landfall frequency has attracted great attention (e.g., Liu and Chan 2003; Wu et al. 2004; Fudeyasu et al. 2006; Goh and Chan 2010; Zhang et al. 2012; Gao et al. 2018; Wang and Chen 2018).

Sea surface temperature (SST) anomalies can affect the tracks and locations of TC landfalls over the WNP on the interannual time scale. Previous studies have shown that El Niño–Southern Oscillation (ENSO) exerts a great influence on the track and landfall of TCs (Elsner and Liu 2003; Liu and Chan 2003; Wu et al. 2004; Chu 2004; Zhang et al. 2012). According to these studies, during La Niña years, the easterly steering flow over the tropical WNP is enhanced, and TCs tend to be generated farther westward, both favoring a straight track and landfall in South China, the Philippines, and the Malaysian Peninsula. Furthermore, Gao et al. (2018) suggested that SST anomalies in the tropical North Atlantic can also affect the TC landfalls over East Asia: negative SST anomalies in this region favor TC landfalls over Vietnam, China, the Korean Peninsula, and Japan. While these studies focused on the tropical impacts on the interannual variability of TC landfall frequency over East Asia, the extratropical factors affecting TC landfall have been ignored. Whether and how extratropical circulation patterns affect TC landfall over East Asia is one of motivations of this study.

TCs over the WNP are mainly active in summer and autumn. However, TC activities are remarkably different between these two seasons, and there are distinct discrepancies in the mechanisms responsible for the interannual variability of summer and autumn TC activities. Previous studies have identified significant relationships between summer TC activity and Pacific–Japan pattern (Choi et al. 2010; Kim et al. 2012), Antarctic Oscillation (Wang and Fan 2007), and SSTs in the Indian Ocean and tropical Pacific (Liu et al. 2019; Wang and Chen 2018). Due to the significant relationships with tropical circulations and SSTs, summer TC activity can be well predicted (Wang et al. 2013; Camp et al. 2019). As for autumn TCs, Wu et al. (2004) found that the TC landfall activity over the WNP is significantly related to SST anomalies in the equatorial central and eastern Pacific only in autumn, but not in summer. All these previous studies suggested the differences in the interannual variability between summer and autumn, and different physical mechanisms responsible for variability. Therefore, a separate investigation of TC activity in these two seasons may help us gain a better understanding of interannual variability in TC activity over the WNP. In this study, we focus on the interannual variability of autumn TC activity, which has not been well documented compared to summer TCs.

The TC landfalls over the WNP show a wide range of latitudes. As mentioned above, they can be separated into the landfalls in the southern and northern coastal regions, respectively. Are there any differences in the interannual variabilities of TC landfall frequency between southern and northern regions in autumn? If so, do they have different physical mechanisms? These questions are also the motivation of this study.

This paper is organized as follows. Section 2 presents the data and methods. Section 3 describes the interannual variations in TC landfall frequency over the WNP. Section 4 discusses the possible factors responsible for interannual variations in the landfall frequency. Our conclusions are presented in section 5.

2. Data and methods

The monthly horizontal winds are from the National Centers for Environmental Prediction–National Center for Atmospheric Research (NCEP–NCAR) reanalysis dataset for the time period 1958–2014 with a horizontal resolution of 2.5° × 2.5°. The SST data are from the Extended Reconstructed Sea Surface Temperature, version 4 (ERSSTv4), dataset with a horizontal resolution of 2° × 2°. The Niño-3.4 index is defined as the SST anomalies averaged over the region 5°S–5°N, 120°–170°W. We focus on the autumn season, which is defined as September–November (SON).

The TC data are from the Joint Typhoon Warning Center with a 6-hourly interval (www.metoc.navy.mil/jtwc/jtwc.html). We selected tropical storms with a maximum surface wind speed ≥ 34 kt (17 m s^{-1}). Although some of the TC activity might not have been detected before the weather satellite era, it would only slightly affect the results since the majority of the study period is from the 1960s onward. In addition, the choice of tropical storms may lessen the errors possibly arising from the change in TC detection technique (e.g., Wang and Chan 2002).The frequency of occurrence of TCs is counted in each 5° × 5° latitude–longitude grid. The TCs are defined as making landfall if their centers cross the coastline. At the time of landfall, the TCs are required to be of at least tropical storm intensity or higher. The values of TC-related parameters (including the frequency of occurrence, track, and number making landfall) are defined as the sum of each parameter during SON.

3. Interannual variability of the number of TCs making landfall over East Asia during autumn

Figure 1 shows the spatial distribution of the 58-yr mean frequency of occurrence of autumn TCs, which is

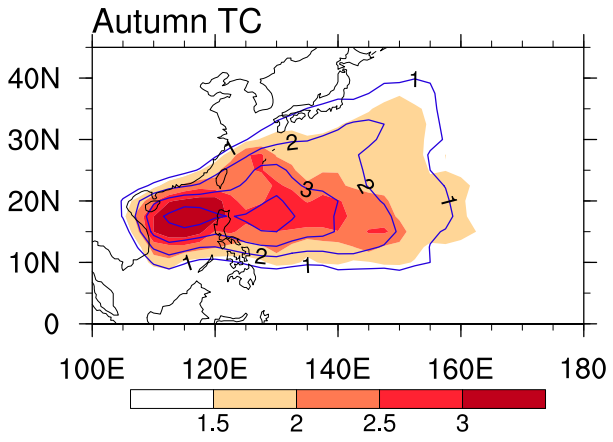

FIG. 1. Climatology (contours) and interannual standard deviation (shading) of the frequency of occurrence of TCs during the time period 1958–2014 in autumn (yr^{-1}).

primarily a reflection of the motion of TCs (e.g., Wu and Wang 2004). TCs mainly appear in the South China Sea (SCS) and tropical WNP, indicating a prevailing track of straight-moving TC. The strongest interannual variability of the frequency of TC occurrence appears over the SCS.

To further illustrate the regional features of the interannual variability of the frequency of occurrence of TCs in autumn, we compared the relationship between the frequency of occurrence of TCs in the SCS, where there is the strongest variability, and other regions. Figure 2a shows the variation in the frequency of occurrence of TCs in autumn averaged over the SCS (10°–22.5°N, 110°–122.5°E), denoted here as the SCS index. The frequency of occurrence of TCs in the SCS shows a decadal variation, with an above-normal frequency of occurrence from the mid-1960s to the mid-1970s and from the mid-1980s to the mid-1990s and a below-normal frequency of occurrence since the mid-1990s. The interannual variability is dominant, however, and, if defined as the residual remaining after removing the 9-yr running mean, explains 85% of the total variance. Therefore, we analyzed the original time series without removing long-term variations.

Figure 2b shows the distribution of correlation coefficients between the SCS index and the frequency of occurrence of TCs on the grids of the WNP. Positive correlations appear in the SCS and extend southeast into the tropical WNP. There is no significant correlation in other regions, with only sporadic regions of negative and weak correlation over the subtropical WNP. This indicates that the TC activity over the SCS has no significant connection with that over the subtropical WNP.

Figure 3 shows the composite TC tracks during the years with anomalously high and low numbers of TCs in the SCS. These years are selected according to the SCS index being higher or lower than one standard deviation. The 9 years with anomalously high number of TCs in the SCS include 1964, 1970, 1973, 1974, 1985, 1986, 1991, 1995, and 1996, and the 9 years with anomalously low number of TCs in the SCS include 1958, 1961, 1963, 1969, 1976, 1997, 2002, 2004, and 2014. As expected, the number of straight-moving TCs during the years with anomalously high number of TCs in the SCS is much greater than that during the years with anomalously low number of TCs.

Table 1 gives mean counts of TCs with straight-moving and recurving tracks averaged over the years with anomalously high and low numbers of TCs in the SCS. A straight-moving (recurving) TC is simply defined as a TC with its extinction latitude lower (higher) than 25°N. Here, the TC extinction latitude is defined as the latitude where a TC's intensity is lower than 34 kt ($17\,m\,s^{-1}$). Although the extinction latitudes do not guarantee whether TCs move straight or recurve, there is a good agreement between the extinction latitudes

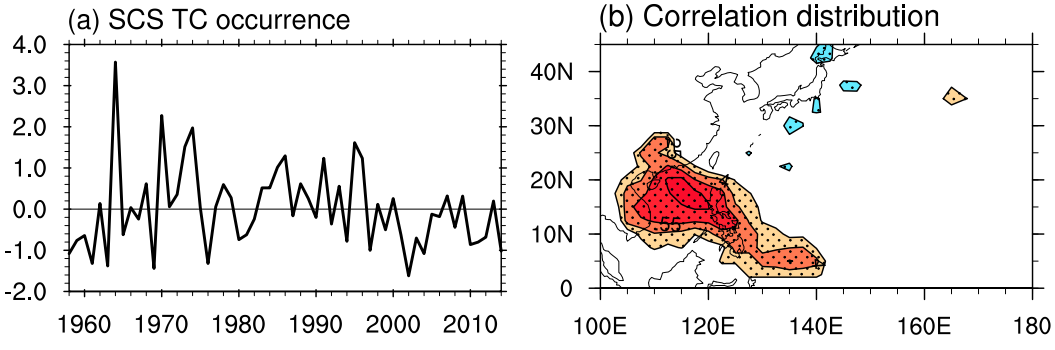

FIG. 2. (a) Normalized frequency of occurrence of TCs averaged over the SCS (10°–22.5°N, 110°–122.5°E) and (b) correlation coefficients between the SCS index and the frequency of occurrence of TCs on the grids of the WNP. Dots denote regions that are significant at the 95% confidence level.

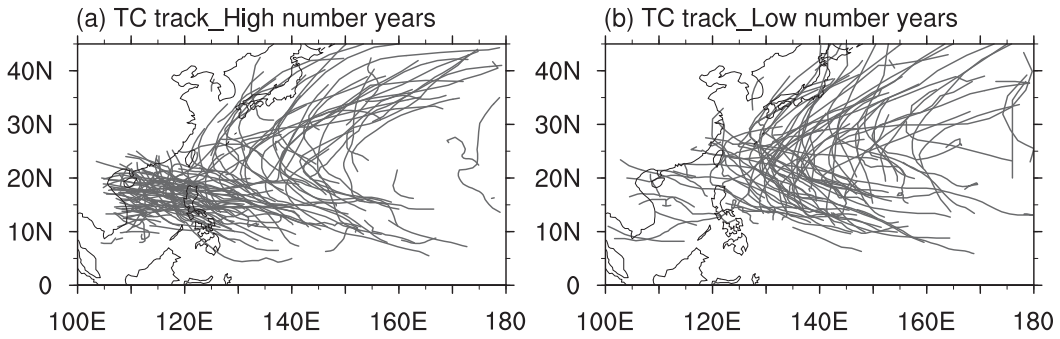

FIG. 3. Composite TC tracks during the years with anomalously (a) high and (b) low numbers of TCs in the SCS.

and tracks. For instance, we have examined all the tracks of 321 TCs whose extinction latitudes are lower than 25°N during the entire analysis period, and we found that about 90% of them show straight-moving tracks (not shown). We also used other latitudes (e.g., 23° or 27°N) as the critical latitude and obtained similar results. The numbers of straight-moving TCs averaged over the years with anomalously high and low numbers of TCs in the SCS are 9.1 and 3.0, respectively, and the difference between them is statistically significant at the 99% confidence level. By contrast, there is no significant difference in the number of recurving TCs between the years with anomalously high and low numbers of TCs in the SCS. This shows that, during the years with anomalously high number of TCs in the SCS, the significant increase in the frequency of straight-moving TCs is not accompanied by a pronounced decrease in the frequency of recurving TCs, suggesting that the frequency of straight-moving TCs is roughly independent of the frequency of recurving TCs. This is consistent with the weak association between the frequency of occurrence of TCs over the SCS and that over the subtropical WNP (Fig. 2b). Considering the close relationship between the track of TCs and the location of landfall, the insignificant link between the frequencies of straight-moving and recurving TC suggests that the numbers of TCs making landfall in the southern and northern regions are mutually independent in autumn.

Figure 4a shows the locations of TC landfall over East Asia in autumn during the time period of 1958–2014. Based on previous studies (e.g., Kim et al. 2008; R. C. Li et al. 2017; Zhou et al. 2018), we divided East Asia into southern and northern regions at the latitude of 25°N, in agreement with the classification criterion of straight-moving and recurving TC tracks. Taiwan Island is excluded from the statistics because roughly the same numbers of straight-moving and recurving TCs affect the island. Figure 4b shows the variations in the frequency of TC landfall in the southern and northern regions. The frequency of landfall in the southern region is usually greater than that in the northern region, consistent with the higher frequency of occurrence of TCs in the tropical WNP relative to the subtropical WNP (Fig. 1). Hereafter, the landfall frequencies in the southern and northern regions are referred to as the south and north TC indices, respectively. These two indices have a weak correlation coefficient (−0.05), implying that the factors influencing the frequencies of autumn landfall in the southern and northern regions are clearly distinct.

4. Possible factors affecting TC landfall in the southern and northern regions

Figure 5 shows the regression of the steering flows with respect to the normalized south and north TC indices. Here, the steering flow is defined as the pressure-weighted mean flow from 850 to 300 hPa (e.g., Holland 1993; He et al. 2015). There are significant easterly anomalies extending from the tropical WNP westward

TABLE 1. Mean counts of TCs with straight-moving and recurving tracks averaged over years with anomalously high and low numbers of TCs in the SCS (yr^{-1}). Two asterisks indicates a difference that is significant at the 99% confidence level.

Variable	No. of straight-moving TCs	No. of recurving TCs
Anomalously high number of TCs in the SCS	9.1	5.3
Anomalously low number of TCs in the SCS	3.0	6.4
Difference	6.1**	−1.1

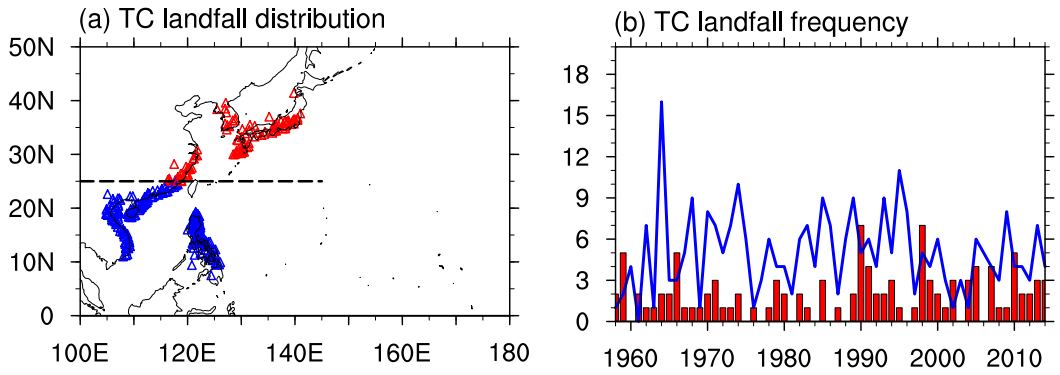

FIG. 4. (a) Locations of landfall of TCs over the WNP and (b) frequencies of landfall of TCs in the southern (blue line) and northern (red bars) regions in autumn during time period 1958–2014. The blue (red) triangles in (a) denote the locations of landfall of TCs in the southern (northern) region.

to southern China and Indochina for the southern landfall frequency. These anomalous steering flows favor a straight-moving track for TCs, which therefore make landfall over the southern region. By contrast, the steering flows associated with the northern landfall frequency are characterized by anomalous southeasterly winds over the extratropical WNP and southwesterly winds over the tropical WNP, which favor a recurving track and TC landfall in the northern region. These steering-flow anomalies can therefore be used to explain the anomalous TC tracks and landfalls for both the southern and northern regions.

To investigate the mechanisms leading to the formation of the anomalous steering flows, we examined the corresponding large-scale circulation anomalies at particular pressure levels. We started with the southern TC landfall. Figure 6 shows the regression of the 300- and 850-hPa horizontal winds with respect to the normalized south TC index. There is an anticyclonic anomaly over eastern China and a cyclonic anomaly to the east of Japan (Fig. 6a), which resemble the steering-flow anomalies over the subtropical and midlatitude WNP (Fig. 5a). The upper-tropospheric wind anomalies show a wave train from East Asia to the North Pacific and North America, with a moderate significance over the North Pacific and North America. At 850 hPa, the wind anomalies are featured by a significant cyclonic anomaly around the SCS, similar to the steering-flow anomalies over the tropical WNP (Fig. 5a). Therefore, both the upper- and lower-tropospheric circulation anomalies contribute to the formation of the easterly steering-flow anomalies extending from the tropical WNP westward to southern China, which favor the landfall of TCs over the southern region. There are also westerly and easterly anomalies in the tropical Pacific at 300 and 850 hPa, respectively, suggesting an enhanced

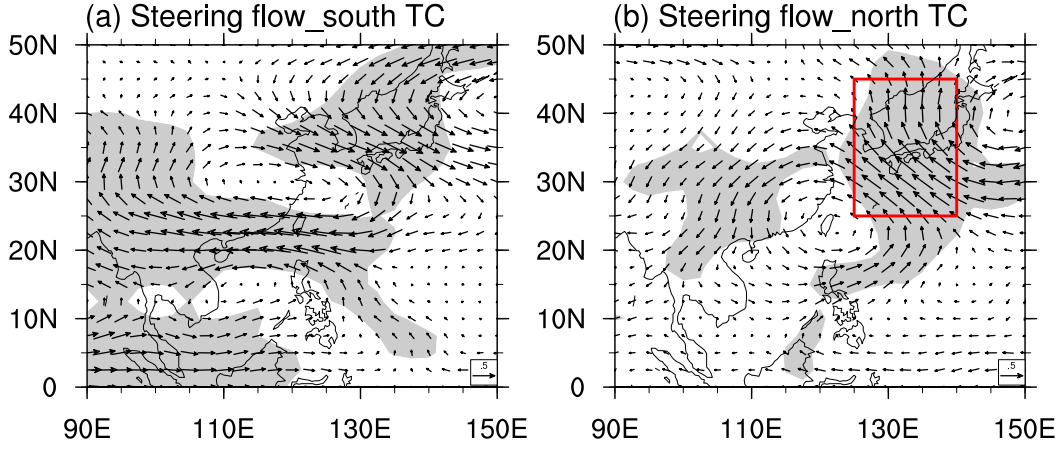

FIG. 5. Regression of the steering flows (vectors; m s^{-1}) with respect to the normalized (a) south and (b) north TC indices during autumn. Shading denotes regions of either the zonal or meridional components that are significant at the 95% confidence level. The red rectangle in (b) represents the defined region of the steering-flow index (SFI).

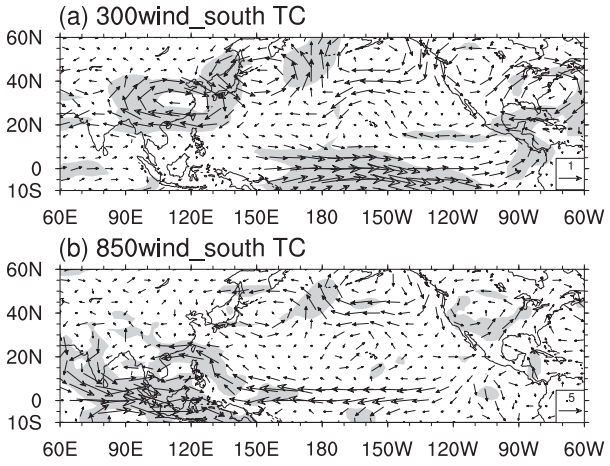

FIG. 6. Regression of the (a) 300- and (b) 850-hPa horizontal winds ($m\,s^{-1}$) with respect to the normalized south TC index during autumn. Shading denotes regions of either zonal or meridional wind anomalies that are significant at the 95% confidence level.

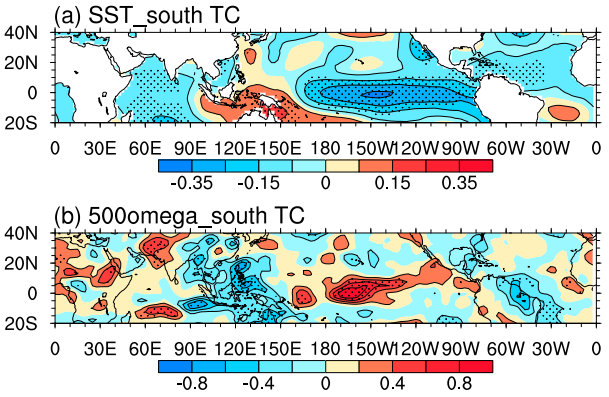

FIG. 7. Regression of (a) the SST (°C) and (b) the 500-hPa omega ($10^{-2}\,m\,s^{-1}$) with respect to the normalized south TC index. The dots denote regions that are significant at the 95% confidence level.

Walker circulation and a possible relationship between the frequency of landfall in the southern region and SST anomalies in the tropical Pacific.

Figure 7 shows the regression of the SST and 500-hPa vertical velocity (omega) onto the normalized south TC index. The SST anomalies in the tropical Pacific show a La Niña pattern with a cold anomaly in the equatorial central and eastern Pacific and a warm anomaly in the western Pacific and Maritime Continent (Fig. 7a). The correlation coefficient between the south TC index and the Niño-3.4 index is −0.37, significant at the 99% confidence level. There are strong ascending anomalies over the tropical western Pacific, including the Maritime Continent and the SCS, and descending anomalies in the equatorial central Pacific (Fig. 7b). These vertical velocity anomalies are in good agreement with the SST anomalies, that is, the positive and negative SST anomalies correspond to the ascending and descending anomalies, respectively. This suggests that the ocean plays an active part in atmosphere–ocean interactions (e.g., Wu et al. 2006; Kumar et al. 2013). Both the SST and vertical velocity anomalies are consistent with the enhanced Walker circulation shown in Fig. 6. There are also negative SST anomalies in the Indian Ocean and tropical North Atlantic. However, there is no significant descending anomaly over these regions, implying that these SST anomalies play a much weaker part in inducing atmospheric anomalies than the Pacific SST anomalies.

The vertical velocity anomalies, which can be considered as a proxy for precipitation and the resultant latent heating anomalies, can also be used to explain the circulation anomalies in remote regions. The heating anomaly over the tropical western Pacific and Maritime Continent, implied by the ascending anomalies, may induce a lower-tropospheric cyclonic anomaly over the SCS, Indochina Peninsula, and the Bay of Bengal as a Rossby wave response to heating (Fig. 6b). This tropical heating anomaly may also be responsible for the upper-tropospheric wave train from East Asia to North America, through a mechanism similar to the formation of the Pacific–Japan or East Asia–Pacific teleconnection pattern in summer (Nitta et al. 1986; Nitta 1987; Huang and Li 1987; Kurihara and Tsuyuki 1987). The response of the extratropical circulation to tropical heating forces may be different between autumn and summer, but specific research on this issue is beyond the scope of this study.

The steering flows associated with the frequency of northern landfall are characterized by anomalous southerlies over the subtropical WNP (Fig. 5b). To further examine the large-scale circulation anomalies associated with these anomalous steering flows, we defined a steering-flow index (SFI) as the normalized meridional component of the steering flow averaged over the region 25°–45°N, 125°–140°E (see the red rectangle in Fig. 5b). The correlation coefficient between this index and the frequency of northern landfall is 0.48, significant at the 99% confidence level, confirming the close link between the steering flow over the WNP and the frequency of northern landfall.

Figure 8 shows the regression of 300-hPa horizontal winds with respect to the normalized SFI. Southerly anomalies appear over the WNP and East Asia and are associated with the anomalous anticyclone centered to the east of Japan and the cyclone centered over central and eastern China. There is also a cyclonic anomaly centered at about 50°E and an anticyclonic anomaly of

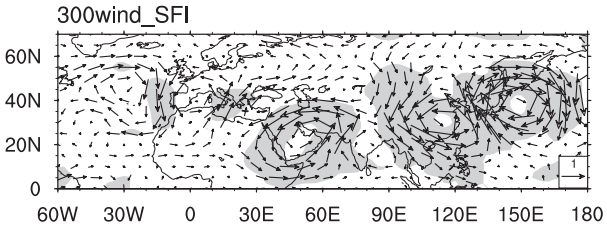

FIG. 8. Regression of the 300-hPa horizontal winds ($m\,s^{-1}$) with respect to the normalized SFI. Shading denotes regions of either zonal or meridional wind anomalies that are significant at the 95% confidence level.

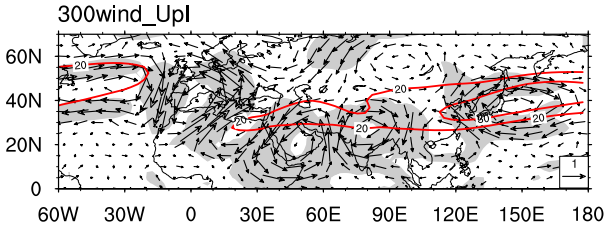

FIG. 9. Regression of the 300-hPa horizontal winds ($m\,s^{-1}$) with respect to the normalized upstream index (UpI), i.e., UpI = $300V_{(10°–25°N,62.5°–67.5°E)} - 300V_{(10°–25°N,27.5°–32.5°E)}$. Red contours represent the climatology of autumn 300-hPa zonal wind ($m\,s^{-1}$). Shading denotes regions of either zonal or meridional wind anomalies that are significant at the 95% confidence level.

relatively weak amplitude located at about 80°E. An anticyclonic anomaly and a cyclonic anomaly appear over the North Atlantic and western Mediterranean, respectively, with a moderate significance level. All these anomalous anticyclones and cyclones appear as a wavelike pattern from the North Atlantic to East Asia.

To further examine this wavelike pattern, we defined an upstream index (UpI) as the difference between 300-hPa meridional winds averaged over two regions, that is, $300V_{(10°–25°N,62.5°–67.5°E)}$ minus $300V_{(10°–25°N,27.5°–32.5°E)}$. The UpI-related 300-hPa horizontal wind anomalies (Fig. 9) are similar to the SFI-related anomalies (Fig. 8). The UpI-related wind anomalies also show a wavelike pattern from the North Atlantic to East Asia. This wave train is roughly aligned along the upper-level westerly jet, represented by the red contour lines in Fig. 9. Rossby waves can propagate eastward along the westerly jets, which act as waveguides according to the theory of Hoskins and Ambrizzi (1993), and previous observational studies, despite for summer situations, have shown a teleconnection pattern along the Asian upper-tropospheric westerly jet (e.g., Lu et al. 2002; Enomoto 2004; Hong and Lu 2016; Hong et al. 2018). Based on these results, we conclude that the upstream wind anomalies affect the downstream steering-flow anomalies and frequency of TC landfall over the northern region through a teleconnection along the westerly jet. This is supported by the significant correlation coefficients between the UpI, SFI, and north TC index (Table 2).

Figure 10 shows the regression of the 300-hPa Rossby wave source with respect to the normalized UpI. The definition of linear Rossby wave source (RWS) refers to Sardeshmukh and Hoskins (1988), that is, $\mathrm{RWS} = -\nabla_H \cdot [\mathbf{u}'_\chi(f+\overline{\zeta})] - \nabla_H \cdot (\overline{\mathbf{u}}_\chi \zeta')$. Here, $\mathbf{u}_\chi = (u_\chi, v_\chi)$ are the divergent wind components, ζ denotes relative vorticity and f is Coriolis parameter. The overbar and the prime denote the climatological mean and the perturbation associated with the upstream index, respectively. The first term on the right-hand side of the equation is the stretching term representing the convergence or divergence of the flow. The second term is the advection term denoting the vorticity advection by the divergent wind. There is a positive and significant RWS anomaly over the mid- to high-latitude North Atlantic, which is the most upstream one among all RWS anomalies. We thus defined the RWS averaged over 50°–65°N, 0°–25°W (see the red rectangle in Fig. 10) as the RWS index (RWSI). This index shows a high correlation with the UpI and is also significantly related to both the SFI and the north TC index (Table 2). In addition to the North Atlantic, there are also other RWS anomalies in the midlatitudes, but they are much weaker. Therefore, we suggest that the RWS over the North Atlantic may trigger the wave train over Eurasia and thus affect the steering flows and frequency of northern landfall. We further analyzed the regression of the stretching and advection terms with respect to the normalized upstream index, and we found that the anomalous RWS is mainly contributed by the stretching term (not shown), suggesting that the RWS is closely linked to the divergence or convergence in the upper troposphere.

We also examined the summertime relationship between the teleconnection pattern along the Asian westerly jet and the frequency of TC landfall in East

TABLE 2. Correlation coefficients among the RWSI (RWS averaged over 50°–65°N, 0°–25°W), the UpI (difference between 300-hPa meridional winds averaged over two regions [$300V_{(10°–25°N,62.5°–67.5°E)}$ minus $300V_{(10°–25°N,27.5°–32.5°E)}$], the SFI (normalized meridional component of the steering flow averaged over 25°–45°N, 125°–140°E), and the north TC index (landfall frequency of the northern region). One asterisk (two asterisks) denotes a correlation coefficient that is significant at the 95% (99%) confidence level.

Index	UpI	SFI	North TC index
RWSI	0.55**	0.31*	0.27*
UpI	—	0.53**	0.34**
SFI	—	—	0.48**

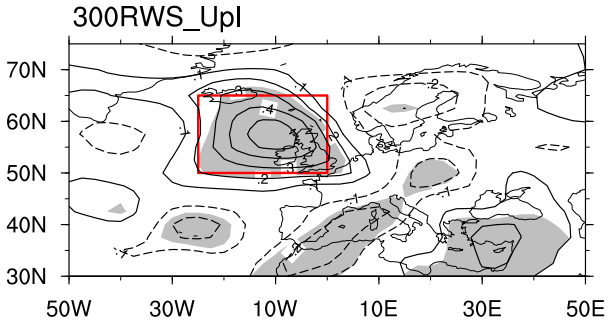

FIG. 10. Regression of the 300-hPa Rossby wave source (10^{-11} s^{-2}) with respect to the normalized UpI. Shading denotes regions that are significant at the 95% confidence level. The red rectangle represents the defined region of RWSI.

Asia and found it to be very weak (not shown). We attribute this difference between summer and autumn to the different latitudes of the Asian jet. The jet is located relatively far to the north in summer and thus the teleconnection pattern along the jet does not change the tropical and subtropical circulations over the WNP.

5. Conclusions and discussion

We investigated the interannual variability of the frequency of TC landfall over East Asia in autumn during the time period of 1958–2014. Our results indicate that the frequencies of TC landfall in the southern and northern coastal regions, which are distinguished by landfall locations to the south and north of 25°N, respectively, are roughly independent. Therefore we separately examined the large-scale circulation anomalies associated with the frequencies of TC landfall in the southern and northern regions and investigated the possible factors affecting these circulation anomalies.

Higher frequency of TC landfalls over the southern region was closely related to the easterly steering-flow anomalies extending from the tropical WNP westward to southern China and Indochina. These anomalous steering flows are part of the wave train from East Asia to North America in the upper troposphere and the cyclonic anomaly over the SCS in the lower troposphere. Furthermore, the increase of TC landfalls over the southern region is also associated with negative SST anomalies in the equatorial central and eastern Pacific and positive SST anomalies over the western Pacific and Maritime Continent, which is consistent with previous studies on the relationship between the ENSO and TC landfalls in the WNP (e.g., Liu and Chan 2003; Wu et al. 2004). Based on the local anomalous SST–vertical velocity relationship, we suggest that these SST anomalies induce strong convective heating over the tropical western Pacific and Maritime Continent and then trigger the easterly steering-flow anomalies over the tropical WNP, which favor more TC landfalls over the southern region.

By contrast, the frequency of TC landfall over the northern region is closely linked to the meridional steering-flow anomalies over the WNP. The steering-flow anomalies are significantly affected by a teleconnection pattern in the upper troposphere roughly along the westerly jet over Eurasia. Further analysis indicates that the anomalous Rossby wave source over the North Atlantic may trigger this teleconnection.

The present results may have an implication for seasonal forecasting of TCs and even rainfall. The predictability of seasonal TC activity mainly comes from slowly evolving climate signals, such as the ENSO and other tropical SST anomalies (e.g., Zhan et al. 2012; Camp et al. 2015; Manganello et al. 2016; Wang et al. 2016; C. Li et al. 2017). Our results indicate that the frequency of TC landfall over the southern region, which is mainly affected by the ENSO, is more predictable than the frequency of landfall over the northern region, which is mainly related to the extratropical circulation. Therefore specific research is required on the predictability of TC landfall in the southern region in autumn. Considering that the TC landfall in the southern region contributes greatly to the amount of autumn rainfall over southern China, Indochina, and the Philippines, the predictability of the landfall in the southern region is an important source of the reliable seasonal prediction of rainfall over these regions. On the other hand, in comparison with the southern region, the vulnerability of the northern region is relatively high due to less opportunity to be hit by a TC. Hence the predictability of TC landfall in the northern region is also of great socioeconomic significance. Currently, most studies on the predictability of TCs in East Asia and the WNP have been for the summer months (e.g., Wang et al. 2013; Bett et al. 2018; Lin et al. 2018), therefore specific research on the predictability of TCs in autumn will help toward a comprehensive understanding of the variability of TCs in the active seasons, as well as improving the prediction of rainfall in autumn.

Acknowledgments. We are grateful to the two anonymous reviewers for their helpful comments that significantly improved the manuscript. This work was supported by the National Natural Science Foundation of China (Grant 41721004).

REFERENCES

Bett, P. E., and Coauthors, 2018: Seasonal forecasts of the summer 2016 Yangtze River basin rainfall. *Adv. Atmos. Sci.*, **35**, 918–926, https://doi.org/10.1007/s00376-018-7210-y.

Camargo, S. J., A. W. Robertson, S. J. Gaffney, P. Smyth, and M. Ghil, 2007a: Cluster analysis of typhoon tracks. Part I: General properties. *J. Climate*, **20**, 3635–3653, https://doi.org/10.1175/JCLI4188.1.

——, ——, ——, ——, and ——, 2007b: Cluster analysis of typhoon tracks. Part II: Large-scale circulation and ENSO. *J. Climate*, **20**, 3654–3676, https://doi.org/10.1175/JCLI4203.1.

Camp, J., M. Roberts, C. MacLachlan, E. Wallace, L. Hermanson, A. Brookshaw, A. Arribas, and A. A. Scaife, 2015: Seasonal forecasting of tropical storms using the Met Office GloSea5 seasonal forecast system. *Quart. J. Roy. Meteor. Soc.*, **141**, 2206–2219, https://doi.org/10.1002/qj.2516.

——, and Coauthors, 2019: The western Pacific subtropical high and tropical cyclone landfall: Seasonal forecasts using the Met Office GloSea5 system. *Quart. J. Roy. Meteor. Soc.*, **145**, 105–116, https://doi.org/10.1002/qj.3407.

Chan, J. C., and W. M. Gray, 1982: Tropical cyclone movement and surrounding flow relationships. *Mon. Wea. Rev.*, **110**, 1354–1374, https://doi.org/10.1175/1520-0493(1982)110<1354:TCMASF>2.0.CO;2.

Choi, K. S., C. C. Wu, and E. J. Cha, 2010: Change of tropical cyclone activity by Pacific-Japan teleconnection pattern in the western North Pacific. *J. Geophys. Res.*, **115**, D19114, https://doi.org/10.1029/2010JD013866.

Chu, P. S., 2004: ENSO and tropical cyclone activity. *Hurricanes and Typhoons: Past, Present, and Potential*, R. J. Murnane and K. B. Liu, Eds., Columbia University Press, 297–332.

Colbert, A. J., B. J. Soden, and B. P. Kirtman, 2015: The impact of natural and anthropogenic climate change on western North Pacific tropical cyclone tracks. *J. Climate*, **28**, 1806–1823, https://doi.org/10.1175/JCLI-D-14-00100.1.

Corporal-Lodangco, I. L., L. M. Leslie, and P. J. Lamb, 2016: Impacts of ENSO on Philippine tropical cyclone activity. *J. Climate*, **29**, 1877–1897, https://doi.org/10.1175/JCLI-D-14-00723.1.

Elsner, J., and K. Liu, 2003: Examining the ENSO-typhoon hypothesis. *Climate Res.*, **25**, 43–54, https://doi.org/10.3354/cr025043.

Enomoto, T., 2004: Interannual variability of the Bonin high associated with the propagation of Rossby waves along the Asian jet. *J. Meteor. Soc. Japan*, **82**, 1019–1034, https://doi.org/10.2151/jmsj.2004.1019.

Fiorino, M., and R. L. Elsberry, 1989: Some aspects of vortex structure related to tropical cyclone motion. *J. Atmos. Sci.*, **46**, 975–990, https://doi.org/10.1175/1520-0469(1989)046<0975:SAOVSR>2.0.CO;2.

Fudeyasu, H., S. Iizuka, and T. Matsuura, 2006: Impact of ENSO on landfall characteristics of tropical cyclones over the western North Pacific during the summer monsoon season. *Geophys. Res. Lett.*, **33**, L21815, https://doi.org/10.1029/2006GL027449.

Gao, S., Z. Chen, and W. Zhang, 2018: Impacts of tropical North Atlantic SST on western North Pacific landfalling tropical cyclones. *J. Climate*, **31**, 853–862, https://doi.org/10.1175/JCLI-D-17-0325.1.

Goh, Z. C. A., and J. C. Chan, 2010: An improved statistical scheme for the prediction of tropical cyclones making landfall in South China. *Wea. Forecasting*, **25**, 587–593, https://doi.org/10.1175/2009WAF2222305.1.

He, H., J. Yang, D. Gong, R. Mao, Y. Wang, and M. Gao, 2015: Decadal changes in tropical cyclone activity over the western North Pacific in the late 1990s. *Climate Dyn.*, **45**, 3317–3329, https://doi.org/10.1007/s00382-015-2541-1.

Holland, G. J., 1993: Tropical cyclone motion [chapter 3]. Global Guide to Tropical Cyclone Forecasting, World Meteorological Organization Tech. Doc. WMO/TD 560, Tropical Cyclone Programme Rep. TCP-31, 337 pp.

Hong, X., and R. Lu, 2016: The meridional displacement of the summer Asian jet, Silk Road Pattern, and tropical SST anomalies. *J. Climate*, **29**, 3753–3766, https://doi.org/10.1175/JCLI-D-15-0541.1.

——, ——, and S. Li, 2018: Asymmetric relationship between the meridional displacement of the Asian westerly jet and the Silk Road Pattern. *Adv. Atmos. Sci.*, **35**, 389–396, https://doi.org/10.1007/s00376-017-6320-2.

Hoskins, B. J., and T. Ambrizzi, 1993: Rossby wave propagation on a realistic longitudinally varying flow. *J. Atmos. Sci.*, **50**, 1661–1671, https://doi.org/10.1175/1520-0469(1993)050<1661:RWPOAR>2.0.CO;2.

Huang, R., and W. Li, 1987: Influence of the heat source anomaly over the tropical western Pacific on the subtropical high over East Asia. *Proc. Int. Conf. on the General Circulation of East Asia*, Chengdu, China, Institute of Atmospheric Physics, Chinese Academy of Sciences, 40–51.

Kim, H., J. Kim, C. Ho, and P. Chu, 2011: Pattern classification of typhoon tracks using the fuzzy *c*-means clustering method. *J. Climate*, **24**, 488–508, https://doi.org/10.1175/2010JCLI3751.1.

Kim, J.-H., C. Ho, H. Kim, C. Sui, and S. K. Park, 2008: Systematic variation of summertime tropical cyclone activity in the western North Pacific in relation to the Madden–Julian oscillation. *J. Climate*, **21**, 1171–1191, https://doi.org/10.1175/2007JCLI1493.1.

Kim, J.-S., R. C. Y. Li, and W. Zhou, 2012: Effects of the Pacific-Japan teleconnection pattern on tropical cyclone activity and extreme precipitation events over the Korean Peninsula. *J. Geophys. Res.*, **117**, D18109, https://doi.org/10.1029/2012JD017677.

Kumar, A., M. Chen, and W. Wang, 2013: Understanding prediction skill of seasonal mean precipitation over the tropics. *J. Climate*, **26**, 5674–5681, https://doi.org/10.1175/JCLI-D-12-00731.1.

Kurihara, K., and T. Tsuyuki, 1987: Development of the barotropic high around Japan and its association with Rossby wave-like propagations over the North Pacific: Analysis of August 1984. *J. Meteor. Soc. Japan*, **65**, 237–246, https://doi.org/10.2151/jmsj1965.65.2_237.

Li, C., R. Lu, and G. Chen, 2017: Promising prediction of the monsoon trough and its implication for tropical cyclone activity over the western North Pacific. *Environ. Res. Lett.*, **12**, 074027, https://doi.org/10.1088/1748-9326/aa71bd.

Li, R. C., W. Zhou, C. M. Shun, and T. C. Lee, 2017: Change in destructiveness of landfalling tropical cyclones over China in recent decades. *J. Climate*, **30**, 3367–3379, https://doi.org/10.1175/JCLI-D-16-0258.1.

Lin, X., C. Li, R. Lu, and A. A. Scaife, 2018: Predictable and unpredictable components of the summer East Asia-Pacific teleconnection pattern. *Adv. Atmos. Sci.*, **35**, 1372–1380, https://doi.org/10.1007/s00376-018-7305-5.

Liu, K. S., and J. C. Chan, 2003: Climatological characteristics and seasonal forecasting of tropical cyclones making landfall along the South China coast. *Mon. Wea. Rev.*, **131**, 1650–1662, https://doi.org/10.1175//2554.1.

Liu, Y., P. Huang, and G. Chen, 2019: Impacts of the combined modes of the tropical Indo-Pacific sea surface temperature anomalies on the tropical cyclone genesis over the western North Pacific. *Int. J. Climatol.*, **39**, 2108–2119, https://doi.org/10.1002/joc.5938.

Lu, R., J. H. Oh, and B. J. Kim, 2002: A teleconnection pattern in upper-level meridional wind over the North African and Eurasian continent in summer. *Tellus*, **54A**, 44–55, https://doi.org/10.1034/j.1600-0870.2002.00248.x.

Manganello, J. V., and Coauthors, 2016: Seasonal forecasts of tropical cyclone activity in a high-atmospheric-resolution coupled prediction system. *J. Climate*, **29**, 1179–1200, https://doi.org/10.1175/JCLI-D-15-0531.1.

Mei, W., and S. P. Xie, 2016: Intensification of landfalling typhoons over the northwest Pacific since the late 1970s. *Nat. Geosci.*, **9**, 753–759, https://doi.org/10.1038/ngeo2792.

Nitta, T., 1987: Convective activities in the tropical western Pacific and their impact on the Northern Hemisphere summer circulation. *J. Meteor. Soc. Japan*, **65**, 373–390, https://doi.org/10.2151/jmsj1965.65.3_373.

——, T. Maruyama, and T. Motoki, 1986: Long-term variations of tropospheric circulations in the western Pacific region as derived from GMS cloud winds. *J. Meteor. Soc. Japan*, **64**, 895–911, https://doi.org/10.2151/jmsj1965.64.6_895.

Park, D. S. R., C. H. Ho, J. H. Kim, and H. S. Kim, 2011: Strong landfall typhoons in Korea and Japan in a recent decade. *J. Geophys. Res.*, **116**, D07105, https://doi.org/10.1029/2010JD014801.

Riehl, H., and N. M. Burgner, 1950: Further studies of the movement and formation of hurricanes and their forecasting. *Bull. Amer. Meteor. Soc.*, **31**, 244–253, https://doi.org/10.1175/1520-0477-31.7.244.

Sardeshmukh, P. D., and B. J. Hoskins, 1988: The generation of global rotational flow by steady idealized tropical divergence. *J. Atmos. Sci.*, **45**, 1228–1251, https://doi.org/10.1175/1520-0469(1988)045<1228:TGOGRF>2.0.CO;2.

Wang, B., and J. C. Chan, 2002: How strong ENSO events affect tropical storm activity over the western North Pacific. *J. Climate*, **15**, 1643–1658, https://doi.org/10.1175/1520-0442(2002)015<1643:HSEEAT>2.0.CO;2.

——, B. Xiang, and J. Y. Lee, 2013: Subtropical high predictability establishes a promising way for monsoon and tropical storm predictions. *Proc. Natl. Acad. Sci. USA*, **110**, 2718–2722, https://doi.org/10.1073/pnas.1214626110.

Wang, C., L. Wang, X. Wang, D. Wang, and L. Wu, 2016: North-south variations of tropical storm genesis locations in the Western Hemisphere. *Geophys. Res. Lett.*, **43**, 11 367–11 374, https://doi.org/10.1002/2016GL071440.

Wang, H. J., and K. Fan, 2007: Relationship between the Antarctic oscillation in the western North Pacific typhoon frequency. *Chin. Sci. Bull.*, **50**, 1251–1257, https://doi.org/10.1007/S11434-007-0040-4.

Wang, L., and G. H. Chen, 2018: Impact of the spring SST gradient between the tropical Indian Ocean and western Pacific on landfalling tropical cyclone frequency in China. *Adv. Atmos. Sci.*, **35**, 682–688, https://doi.org/10.1007/s00376-017-7078-2.

Wu, C., and K. A. Emanuel, 1995: Potential vorticity diagnostics of hurricane movement. Part I: A case study of Hurricane Bob (1991). *Mon. Wea. Rev.*, **123**, 69–92, https://doi.org/10.1175/1520-0493(1995)123<0069:PVDOHM>2.0.CO;2.

Wu, L., and B. Wang, 2004: Assessing impacts of global warming on tropical cyclone tracks. *J. Climate*, **17**, 1686–1698, https://doi.org/10.1175/1520-0442(2004)017<1686:AIOGWO>2.0.CO;2.

——, and X. Chen, 2016: Revisiting the steering principal of tropical cyclone motion in a numerical experiment. *Atmos. Chem. Phys.*, **16**, 14 925–14 936, https://doi.org/10.5194/acp-16-14925-2016.

——, B. Wang, and S. Geng, 2005: Growing typhoon influence on East Asia. *Geophys. Res. Lett.*, **32**, L18703, https://doi.org/10.1029/2005GL022937.

Wu, M. C., W. L. Chang, and W. M. Leung, 2004: Impacts of El Niño–Southern Oscillation events on tropical cyclone landfalling activity in the western North Pacific. *J. Climate*, **17**, 1419–1428, https://doi.org/10.1175/1520-0442(2004)017<1419:IOENOE>2.0.CO;2.

Wu, R., B. P. Kirtman, and K. Pegion, 2006: Local air–sea relationship in observations and model simulations. *J. Climate*, **19**, 4914–4932, https://doi.org/10.1175/JCLI3904.1.

Zhan, R., Y. Wang, and M. Ying, 2012: Seasonal forecasts of tropical cyclone activity over the western North Pacific: A review. *Trop. Cyclone Res. Rev.*, **1**, 307–324, https://doi.org/10.6057/2012TCRR03.07.

Zhang, Q., L. Wu, and Q. Liu, 2009: Tropical cyclone damages in China 1983–2006. *Bull. Amer. Meteor. Soc.*, **90**, 489–495, https://doi.org/10.1175/2008BAMS2631.1.

Zhang, W., H. F. Graf, Y. Leung, and M. Herzog, 2012: Different El Niño types and tropical cyclone landfall in East Asia. *J. Climate*, **25**, 6510–6523, https://doi.org/10.1175/JCLI-D-11-00488.1.

Zhou, X., R. Lu, and G. Chen, 2018: Impact of interannual variation of synoptic disturbances on the tracks and landfalls of tropical cyclones over the western North Pacific. *Adv. Atmos. Sci.*, **35**, 1469–1477, https://doi.org/10.1007/s00376-018-8055-0.

Climate Dynamics (2019) 52:2837–2853
https://doi.org/10.1007/s00382-018-4298-9

Remote forcing of the northern tropical Atlantic SST anomalies on the western North Pacific anomalous anticyclone

Jinqing Zuo[1,2] · Weijing Li[1,2] · Chenghu Sun[2,3] · Hong-Chang Ren[4]

Received: 8 April 2018 / Accepted: 2 June 2018 / Published online: 19 June 2018
© Springer-Verlag GmbH Germany, part of Springer Nature 2018

Abstract
This study uses both observations and numerical modeling experiments to investigate the lead-lag relationship and the associated physical mechanism of the western North Pacific anomalous anticyclone (WNPAC) with sea surface temperature (SST) anomalies over the northern tropical Atlantic (NTA). The results show that the WNPAC from late spring to the middle of autumn has a significant in-phase relationship with the NTA SST anomalies up to two seasons ahead. This relationship reaches a peak when the NTA SST leads by approximately 1–2 months and is nearly independent of the El Niño-Southern Oscillation variability. Diagnosis based on observations and numerical experiments using the Community Atmospheric Model version 5.3 reveals that the NTA warming favors intensified local convection activity during the spring–autumn seasons, causing enhanced low-level convergence and upper-level divergence (i.e., ascending motion) over the NTA and opposite flow anomalies over the central tropical Pacific. The enhanced subsidence over the central tropical Pacific, in turn, triggers an anomalous low-level anticyclone over the western North Pacific. Moreover, the intensity of the anomalous local convection activity that is associated with the NTA SST is closely related to the seasonal migration of the Atlantic intertropical convergence zone (ITCZ). As the Atlantic ITCZ migrates northward, the NTA SST-induced local convection activity extends northward from a narrow band near the equator during early spring to nearly the entire NTA region during the middle of summer, leading to the strongest remote effect of the NTA SST anomalies on the WNPAC during late summer and early autumn.

Keywords SST forcing · Northern tropical Atlantic · WNP anomalous anticyclone · ITCZ

1 Introduction

The western North Pacific (WNP) anomalous anticyclone (WNPAC), which is also referred to as the Philippine Sea anomalous anticyclone, is a large-scale atmospheric circulation system in the low-level troposphere that spans the subtropical Northwest Pacific. The WNPAC strongly affects societal and economic development in East Asia by modulating tropical cyclone activity and monsoon variability (e.g., Wang et al. 2013; Zhang et al. 2017). Therefore, a better understanding of the formation and maintenance mechanism of the WNPAC is of vital importance to the seasonal prediction of East Asian climate variability (He et al. 2001; Xie et al. 2016; Li et al. 2017a).

Over the past few decades, significant effort has been devoted to understand the physical processes and mechanisms that underlie the formation and maintenance of the WNPAC on an interannual timescale (see Li et al. 2017a for a review). Researchers have concluded that the associated

✉ Weijing Li
liwj@cma.gov.cn

✉ Chenghu Sun
sunch@cma.gov.cn

[1] Laboratory for Climate Studies and CMA–NJU Joint Laboratory for Climate Prediction Studies, National Climate Center, China Meteorological Administration, No. 46, Zhongguancun Nandajie, Beijing 100081, China

[2] Collaborative Innovation Center on Forecast and Evaluation of Meteorological Disasters, Nanjing University of Information Science and Technology, Nanjing 210044, China

[3] National Meteorological Information Center, China Meteorological Administration, No. 46, Zhongguancun Nandajie, Beijing 100081, China

[4] National Meteorological Center, China Meteorological Administration, Beijing 10081, China

mechanisms include warm pool ocean–atmosphere interactions (Zhang et al. 1996; Wang et al. 2000, 2013), the Indian Ocean capacitor effect (Xie et al. 2009, 2016), nonlinear interactions between the El Niño-Southern Oscillation (ENSO) and the western Pacific warm pool (Stuecker et al. 2013, 2015), moist enthalpy advection/Rossby-wave modulation (Wu et al. 2017a, b), and central Pacific sea surface temperature (SST) forcing (Wang et al. 2013; Xiang et al. 2013). The east–west SST contrast between the tropical Pacific and Indian Oceans could also affect the WNPAC variability (Terao and Kubota 2005; Chen et al. 2012; Cao et al. 2013).

In addition to the aforementioned mechanisms, increasing evidence suggests the remote forcing of tropical Atlantic SST on the summertime atmospheric variability over the WNP (Lu and Dong 2005; Rong et al. 2010; Hong et al. 2014, 2015; Chen et al. 2015; Chang et al. 2016). Rong et al. (2010) found that warm SST anomalies in the northern tropical Atlantic (NTA) can trigger an eastward Kelvin wave and create easterly anomalies that span from the equatorial Indian Ocean to the western Pacific, which induces an anomalous low-level anticyclone over the WNP during boreal summer. Hong et al. (2014) and Chang et al. (2016) revealed that NTA warming could have induced an anomalous low-level anticyclone over the WNP via a zonally westward-extending overturning circulation over the Pacific–Atlantic Ocean and thereby could have enhanced the relationship of the NTA SST anomalies with the WNP subtropical high during boreal summer after the early 1980s. Hong et al. (2015) further demonstrated that the record-high SST in the tropical Atlantic markedly contributed to the extremely strong WNP subtropical high during July–August 2010. Chen et al. (2015) noted that the effect of the NTA SST on the WNP summer climate tends to be intensified under the background of weakened Atlantic thermohaline circulation.

However, the aforementioned studies that involve the remote forcing of NTA SST anomalies on the WNP climate variability mainly focused on the boreal summer season. During boreal winter, the atmosphere shows strong variability and plays a dominant role in controlling ocean–atmosphere interactions over the North Atlantic on an interannual timescale (Marshall et al. 2001; Xie and Carton 2004; references therein). Questions arise concerning how the relationship between the NTA SST and WNPAC varies over different seasons and the associated mechanisms. Additionally, the interannual variability of the NTA SST is related to both local ocean–atmosphere feedback and remote ENSO forcing (Xie and Carton 2004; Yang et al. 2017). Another question concerns the effect of the ENSO variability on the relationship between the NTA SST and WNPAC. Thus, we are motivated to further understand the lead-lag relationship and the associated physical mechanism between the NTA SST and WNPAC during different seasons.

The remainder of this manuscript is organized as follows. Section 2 describes the datasets, model and experiments that are used in this study. Section 3 presents the lead-lag relationship between the NTA SST and WNPAC during different seasons and its dependence on the ENSO. Section 4 explores the possible mechanisms that are responsible for the NTA–WNP connection, and corresponding model simulations are presented in Sect. 5. Finally, Sect. 6 provides a discussion and summary.

2 Data, model and experiments

2.1 Data and methods

Monthly atmospheric circulation data are obtained from the ERA-Interim dataset (Dee et al. 2011) of the European Centre for Medium-Range Weather Forecasts (ECMWF). The data have a horizontal resolution of $2.5° \times 2.5°$ and are available from 1979 to the present. SST data are obtained from the Met Office Hadley Centre Sea Ice and Sea Surface Temperature (HadISST) dataset; the data have a horizontal resolution of $1° \times 1°$ and are available from 1870 to the present (Rayner et al. 2003). Monthly mean rainfall data, which have a horizontal resolution of $2.5° \times 2.5°$, are obtained from the Climate Prediction Center (CPC) Merged Analysis of Precipitation (CMAP) (Xie and Arkin 1997) for the period from 1979 to the present. The monthly outgoing longwave radiation (OLR) is obtained from the National Oceanic and Atmospheric Administration (NOAA) Interpolated OLR dataset (Liebmann and Smith 1996); the data have a horizontal resolution of $2.5° \times 2.5°$ and are available from June 1974 to the present.

The NTA and NINO3.4 SST indices used in this study are defined as the regionally averaged SST anomalies over EQ–15°N, 70W°–0°E, and 5°S–5°N, 170°–120°W, respectively. Observational analysis is performed for the period 1979–2016, with linear trends removed prior to our analysis. The NTA SST is influenced by the ENSO variability (Klein et al. 1999; Yang et al. 2017), so the effect of the ENSO is removed prior to our analysis by using linear regression with respect to the NINO3.4 SST of the previous November–December–January (NDJ) season unless otherwise stated.

The statistical significance of regression coefficients, correlation coefficients and the ensemble-mean difference of model outputs are determined by a two-tailed Student's t test, while the difference between two correlation coefficients is assessed by using the Fisher z transformation (Fisher 1915). The seasons refer to those in the Northern Hemisphere.

2.2 Model and experimental setup

The model used in this study is the Community Atmospheric Model version 5.3 (CAM5.3), which was developed by the National Center for Atmospheric Research (NCAR). CAM5.3 is coupled to the Community Land Model (CLM version 4.0), and a version with 1.9°-latitude by 2.5°-longitude resolution and 30 vertical levels is used in this study.

One control run (CTL) and two sets of perturbed experiments are conducted. During the control run, the model is forced with a prescribed monthly climatology of SST and sea ice that is obtained from the monthly HadISST dataset and runs continually for 110 years. The first 10 years are discarded as spin up. The initial atmospheric conditions for the perturbed experiments are obtained from the control run; further details regarding the perturbed runs are provided in Sect. 5.

3 Relationship between the NTA SST and WNPAC and its dependence on the ENSO

Simultaneous regressions of the stream function and horizontal wind anomalies at 850 hPa against the NTA SST index in December–January–February (DJF), March–April–May (MAM), June–July–August (JJA) and September–October–November (SON) are computed to examine the relationship between the NTA SST and WNPAC during different seasons, as shown in Fig. 1. During the high-index phase of the NTA SST in DJF, an anomalous cyclone is clearly observed over the subtropical North Atlantic, while the atmospheric circulation anomalies are very weak over the WNP (Fig. 1a). In MAM, a similar atmospheric pattern to that in DJF is observed over the North Atlantic (Fig. 1b). Moreover, an anomalous anticyclone is observed over the central–western North Pacific, while relatively weak anomalous cyclonic flows occur over the eastern North Pacific. The most notable feature observed in JJA is a significant anomalous cyclone over the eastern North Pacific–Atlantic and an anticyclone over the WNP (Fig. 1c), which are clearly weakened in SON (Fig. 1d). The opposite situation is observed during the low-index phase of the NTA SST. Similar circulation patterns are observed over the WNP when the NTA SST index leads by 1 or 2 months, although some differences exist in the amplitude and position of the anomalies (figure not shown).

To clearly demonstrate the seasonal changes in the subtropical atmospheric circulation anomalies associated with the NTA SST, Fig. 2a displays a time-longitude section of the 3-month-running-averaged 10–25°N meridional mean stream function anomalies at 850 hPa regressed against the NTA SST index when leading by 0 months (shaded areas) and 1 month (contoured areas). This figure shows significant anticyclonic flow anomalies over the central–western Pacific and cyclonic anomalies over the eastern Pacific–Atlantic during the spring–autumn seasons in the high-index phase of the NTA SST and vice versa (Fig. 2a). The action center of the flow anomalies over the central–western Pacific is centered in July–August–September (JAS) when the NTA SST index leads by 0 months but shifts slightly eastward and towards the cold season when the NTA SST index leads by 1 month (contoured areas in Fig. 2a). These results indicate that the NTA warming (cooling) favors an intensified (weakened) low-level anticyclone over the central–western Pacific during the spring–autumn seasons, but the associated atmospheric circulation anomalies over this region are very weak during winter.

Lead-lag correlations between the 3-month-running-averaged WNPAC and NTA SST indices are calculated to further quantify the lagged relationship of the WNPAC with the NTA SST (see Fig. 3a, b). Here, the WNPAC index is defined as the regionally averaged stream function at 850 hPa over 10°–25°N, 115°–150°E, where the WNPAC variability is strong (figure not shown). The WNPAC index during the seasons from April–May–June (AMJ) to SON has a significant in-phase relationship with the NTA SST index up to 3–8 months ahead (Fig. 3a). This in-phase relationship peaks when the NTA SST index leads by approximately 1–2 months, and the WNPAC index in July–August–September (JAS) and August–September–October (ASO) has the highest lagged correlation with the NTA SST index (Fig. 3b). Additionally, the significant in-phase relationship of the WNPAC index from AMJ to SON with the NTA SST index dates back to the February–March–April (FMA) season.

The NTA SST anomalies are influenced by the ENSO variability, so the effect of the latter on the relationship between the NTA SST and WNPAC is examined. Figure 3c shows the lead-lag correlations between the 3-month-running-averaged WNPAC and NTA SST indices before removing the effect of the ENSO, and Fig. 3d displays the difference in the lead-lag correlations before and after removing the effect of the ENSO (former minus latter). A comparison of Fig. 3a and c indicates that the pattern of the lead-lag correlations between the WNPAC and NTA SST indices after removing the effect of the ENSO is similar to that observed before removing the effect of the ENSO. The differences in the lead-lag correlations before and after removing the effect of the ENSO are all non-significant at the 95% confidence level (Fig. 3d), suggesting that the effect of the ENSO on the relationship between the WNPAC and NTA SST is limited. This finding is reasonable because the NTA SST index is only partially related to the NINO3.4 SST index, and the correlation between the two indices is less than 0.5 when the former lags the latter over a range of 0–11 months

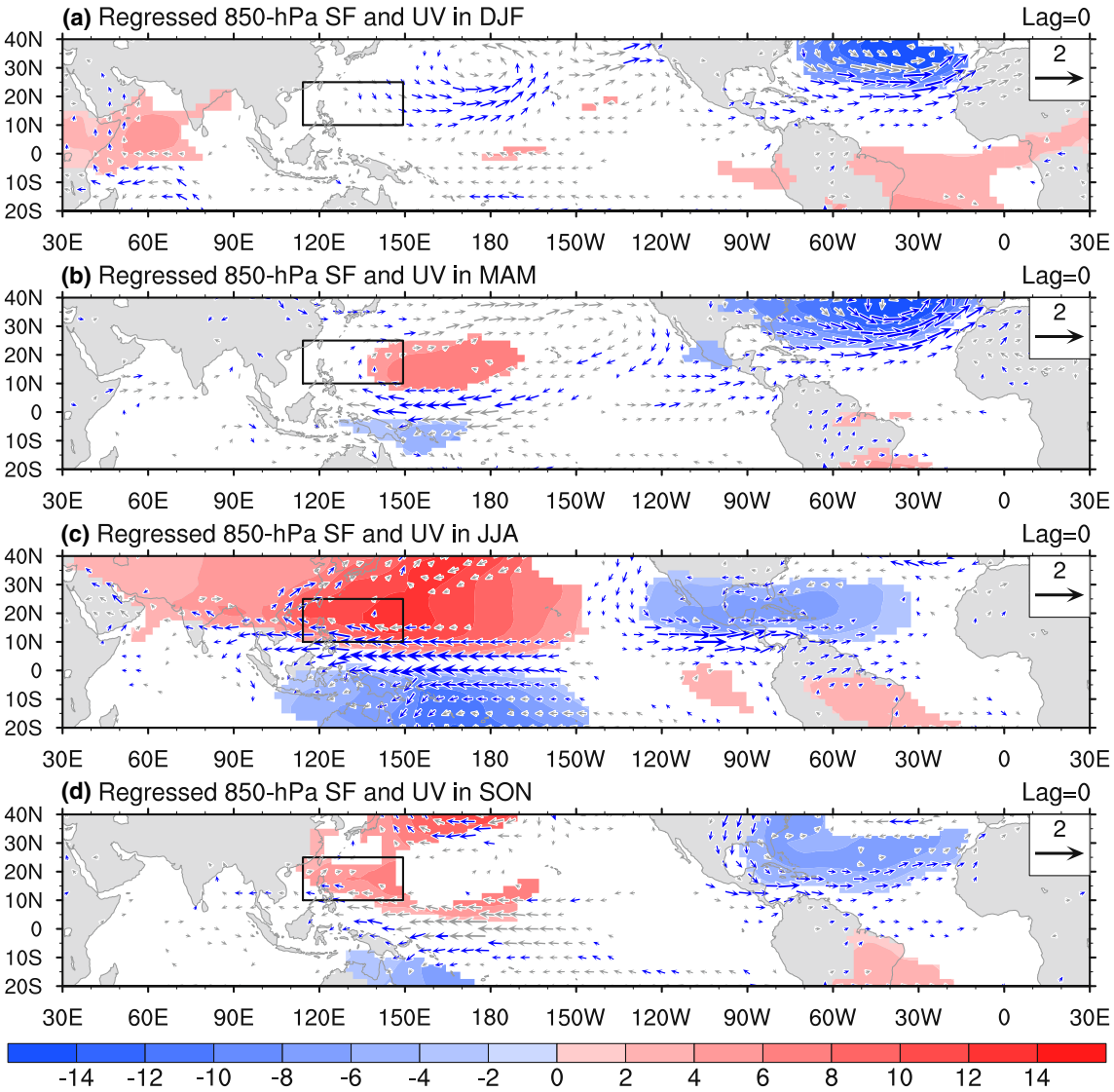

Fig. 1 Simultaneous regressions of the stream function (shaded; unit: 10^5 m^2 s^{-1}) and horizontal wind (vectored; unit: m s^{-1}) anomalies at 850 hPa against the NTA SST index in **a** DJF, **b** MAM, **c** JJA and **d** SON. Only shading (vectoring) with significance at the 95% confidence level is shown (blue). The box indicates the region for defining the regionally averaged WNPAC index

(Fig. 4); this result indicates that the two share no more than 25% of the covariance. In contrast, the NTA SST index has a stronger out-of-phase relationship with the NINO3.4 SST index when the former leads by 8–10 months (Fig. 4), matching the results from Ham et al. (2013), who revealed that the NTA warming (cooling) in FMA can trigger a La Niña (El Niño) event in the following winter via a subtropical teleconnection.

The abovementioned results reveal that the WNPAC from late spring to the middle of autumn has a significant in-phase relationship with the NTA SST variability up to 3–8 months ahead, and this relationship reaches a peak when the latter leads by approximately 1–2 months. Moreover, the WNPAC in late summer and early autumn tends to have the strongest connection to the NTA SST variability, and the earliest signal of the latter in the former could date back to the previous early spring. In contrast, the WNPAC during winter appears to have an insignificant relationship with the NTA SST variability 0–11 months ahead. Although the NTA SST variability is partially influenced by the ENSO (Xie and Carton 2004; Yang et al. 2017), the latter has a limited effect on the relationship between the NTA SST and WNPAC throughout the year.

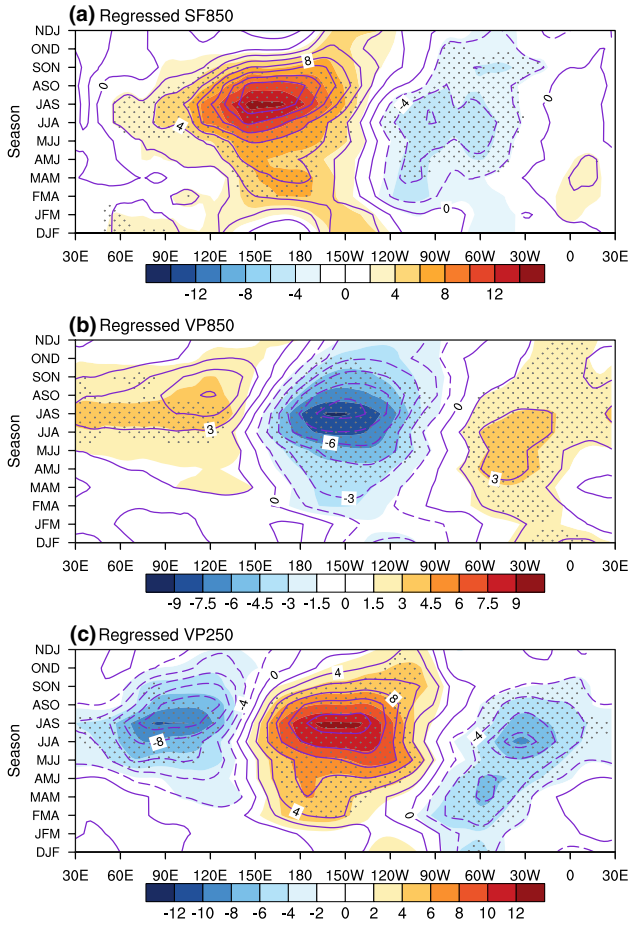

Fig. 2 **a** Time-longitude section of the 3-month-running-averaged 10–25°N meridional mean stream function anomalies (unit: 10^5 m^2 s^{-1}) at 850 hPa regressed against the NTA SST index when leading by 0 months (shaded) and 1 month (contoured), respectively. **b, c** Same as **a** but for the EQ–15°N meridional mean velocity potential anomalies (unit: 10^5 m^2 s^{-1}) at 850 and 250 hPa, respectively. The dots denote significance at the 95% confidence level for the shaded areas

4 Possible mechanism for the NTA–WNP connection

Warm SST anomalies in the tropics generally heat the overlying atmosphere by intensifying local convection activity, which is associated with enhanced low-level convergence and upper-level divergence (i.e., ascending motion) and thus above-average precipitation and below-average OLR anomalies over the heating and vice versa. The characteristics of local convection activity and large-scale atmospheric circulation anomalies associated with the NTA SST are investigated by using observational and reanalysis data to explore how the NTA SST affects the WNPAC variability.

4.1 Anomalous local convection activity

Figure 5 displays the simultaneous regressions of tropical Atlantic SST, precipitation and OLR anomalies against the NTA SST index in DJF, MAM, JJA and SON. The pattern of the regressed SST anomalies in DJF (Fig. 5a) is similar to that in MAM (Fig. 5b), both of which show the maximum anomalies in the eastern North Atlantic. Figure 5a, b also show that significant SST anomalies are mainly confined to the NTA and equatorial Atlantic in DJF and MAM. However, the associated precipitation anomalies are very weak and almost negligible in the tropical Atlantic in DJF (Fig. 5e), whereas significant and positive (negative) precipitation anomalies are observed over the region between the equator and 10°N in the high (low)-index phase of the NTA SST in MAM (Fig. 5f). In JJA and SON, significant SST anomalies span the NTA and extend southward into the southern tropical Atlantic, with the maximum anomalies in the region between 10°N and 20°N and in the equatorial Atlantic (Fig. 5c, d). However, significant precipitation anomalies are observed only over the NTA in JJA (Fig. 5g), and the precipitation anomalies are relatively weak in SON (Fig. 5h).

These results reveal that the simultaneous in-phase relationship between the NTA SST and local precipitation anomalies are statistically significant and strong in MAM and JJA but relatively weak in SON and DJF. Consistent results are obtained from the OLR (Fig. 5i–l) and 500-hPa vertical velocity (referred to as W500 hereafter; Fig. 6) anomalies associated with the NTA SST index. That is, the NTA warming (cooling) is concurrent with negative (positive) OLR anomalies and anomalous ascending (descending) motion over the regions where positive (negative) precipitation anomalies are observed. This finding suggests that warm SST anomalies in the NTA could intensify the local convection activity in MAM and JJA and vice versa.

Lead-lag correlations between the 3-month-running-averaged NTA SST index and precipitation anomalies regionally averaged over EQ–15°N and 10°–50°W are computed to further examine the lead-lag relationship between the NTA SST and the local convection activity (see Fig. 7a, b). The region used to define the local precipitation index is slightly different from that used to define the NTA SST index to exclude the effect of precipitation variability over land. As shown in Fig. 7a, the NTA precipitation index from January–February–March (JFM) to ASO has a significant in-phase relationship with the NTA SST index up to 4–6 months ahead, indicating that the NTA warming (cooling) could intensify (suppress) the local convection activity during these seasons. This in-phase relationship reaches a peak when the NTA SST leads by approximately 1–2 months (Fig. 7b), which is consistent with the relationship between the NTA SST and WNPAC (Fig. 3b).

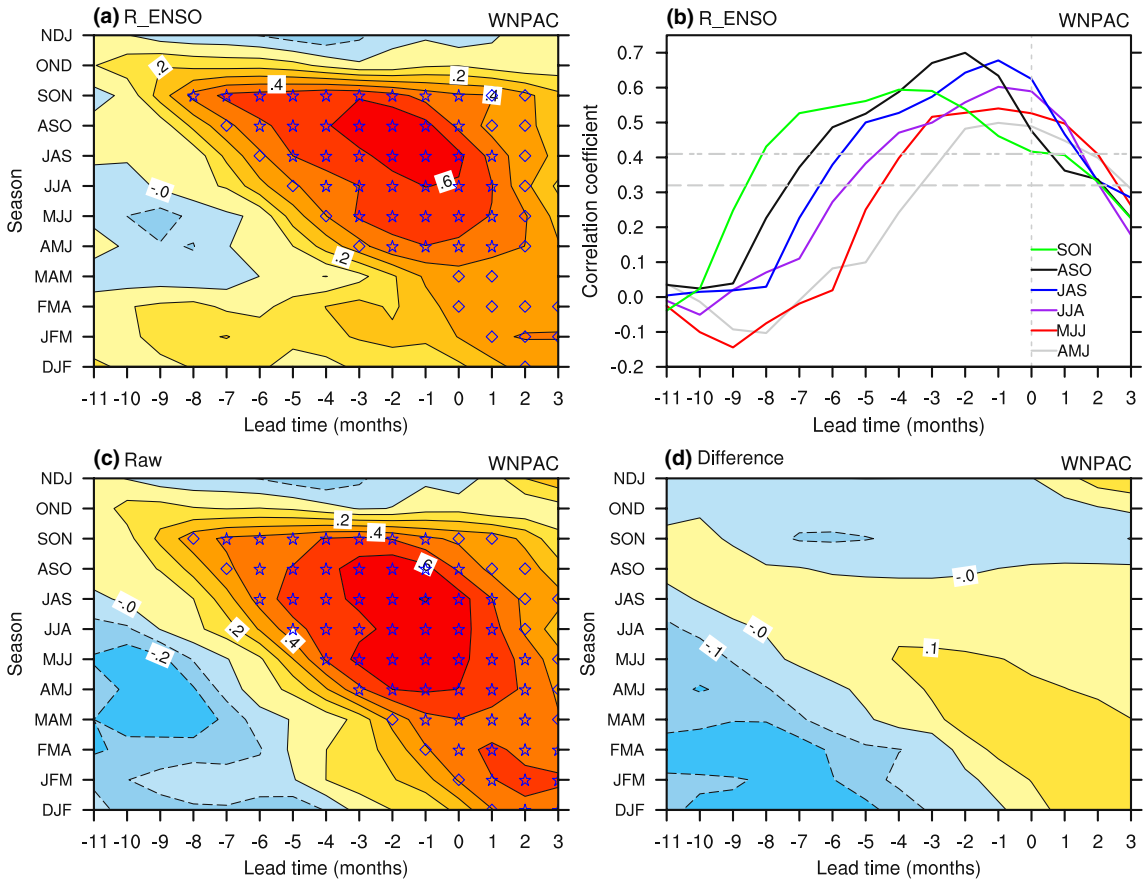

Fig. 3 **a** Lead-lag correlations between the 3-month-running-averaged WNPAC and NTA SST indices after removing the effect of the ENSO. The squares and stars denote significance at the 95 and 99% confidence levels, respectively. The lead time refers to the middle month of the 3-month-running season, and a negative value indicates that the NTA SST is leading. **b** Same as **a** but for the WNPAC from AMJ to SON. The dashed and dashed-dotted lines denote significance at the 95 and 99% confidence levels, respectively. **c** Same as **a** but with the WNPAC and NTA SST indices before removing the effect of the ENSO. **d** Same as **a** but for the difference between **c** and **a** (former minus latter)

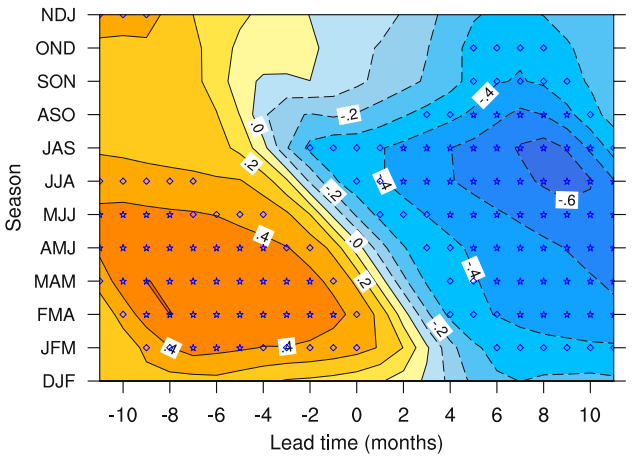

Fig. 4 Lead-lag correlations between the 3-month-running-averaged NTA and NINO3.4 SST indices. The squares and stars denote significance at the 95 and 99% confidence levels, respectively. The lead time refers to the middle month of the 3-month-running season, and a negative value indicates that the NINO3.4 SST is leading

Figure 7a also shows two centers of maximum lagged correlation between the NTA precipitation and SST indices. One is observed in late spring, with a maximum correlation value of approximately 0.74, and the other is observed in the middle of summer, with a maximum correlation value of approximately 0.66. This finding is somewhat different from the lagged correlation of the WNPAC with the NTA SST, which features only one center of maximum correlation in late summer (Fig. 3a). The reason for this difference can be found in the following analysis (see Fig. 8), which is primarily related to the seasonal migration of the Atlantic intertropical convergence zone (ITCZ), where climatological convection activity is strong. That is, as the Atlantic ITCZ migrates northward, the NTA SST-induced local convection activity covers nearly the entire NTA region in summer, leading to a stronger atmospheric circulation response than that associated with the SST-induced local convection activity in spring, which is mainly moored to a narrow band to the north of the equator.

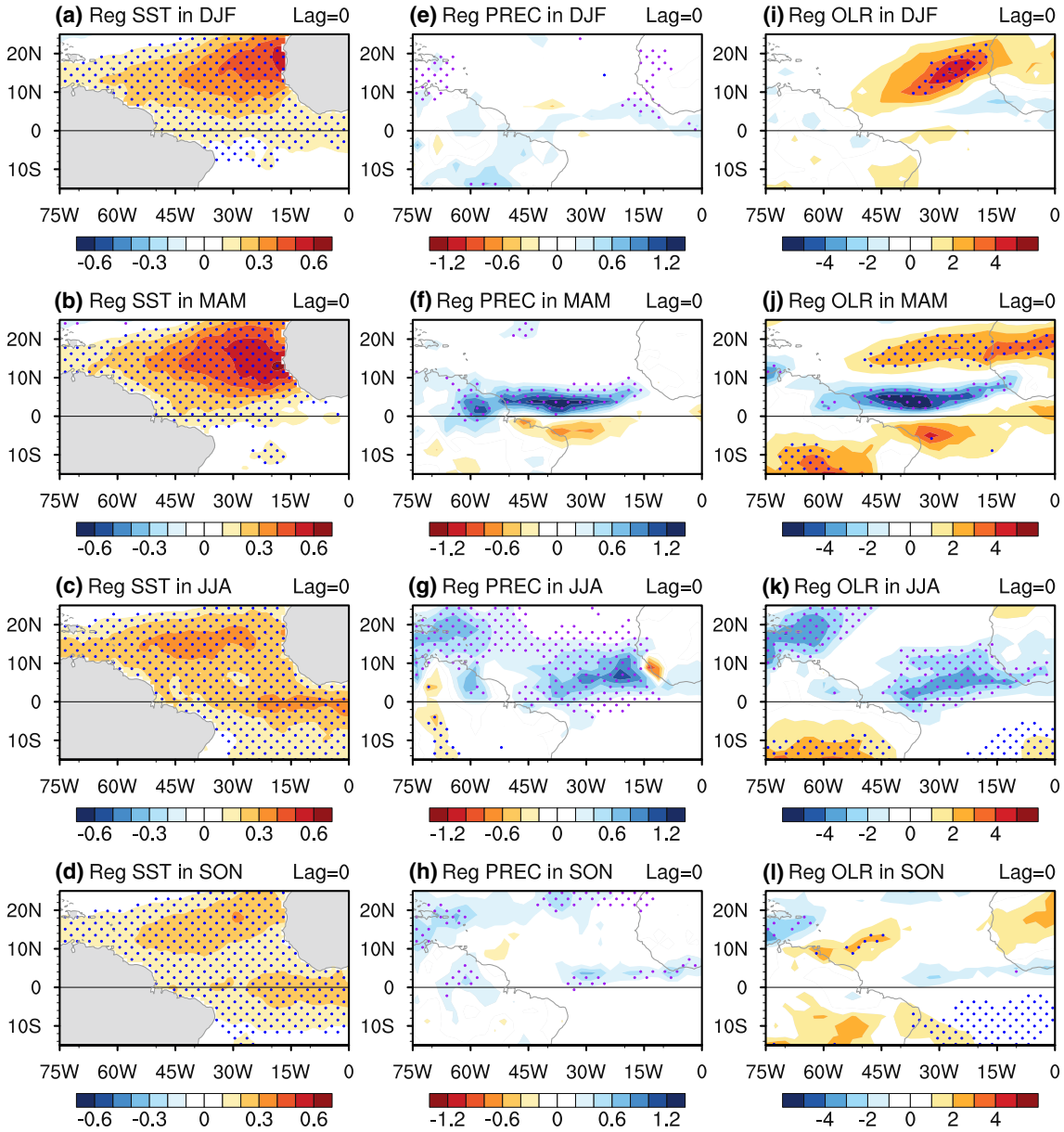

Fig. 5 Simultaneous regressions of the SST anomalies (shaded; unit: K) against the NTA SST index in **a** DJF, **b** MAM, **c** JJA and **d** SON. **e–h, i–l** Same as **a–d** but for the precipitation (unit: mm day^{-1}) and OLR (unit: W m^{-2}) anomalies, respectively. The dots denote significance at the 95% confidence level, and the black line refers to the equator

More evidence for a lead-lag relationship between the NTA SST and local convection activity is provided in Fig. 7c–f, which show lead-lag correlations of the 3-month-running-averaged NTA SST index with the regionally averaged OLR and W500 anomalies. The region used to define the NTA OLR and W500 indices is the same as that used for the precipitation index. A comparison of Fig. 7a, b and c–f shows that consistent results are obtained from the NTA OLR and W500 indices, except that the lagged correlations of these two indices from late winter to early spring with the NTA SST index 0–5 months ahead are relatively weak compared with those for the NTA precipitation index. As shown in the second row of Figs. 5 and 6, this inconsistency is most likely related to the different spatial patterns between the OLR and W500 anomalies and the precipitation anomalies over the NTA region.

Figure 8a–c further display a time-latitude section of the 3-month-running averaged 10°–50°W zonal mean precipitation, OLR and W500 anomalies regressed against the NTA SST index 0 and 1 month ahead. The pattern of the precipitation anomalies regressed against the NTA SST index 0 months ahead (shaded areas in Fig. 8a) resembles that

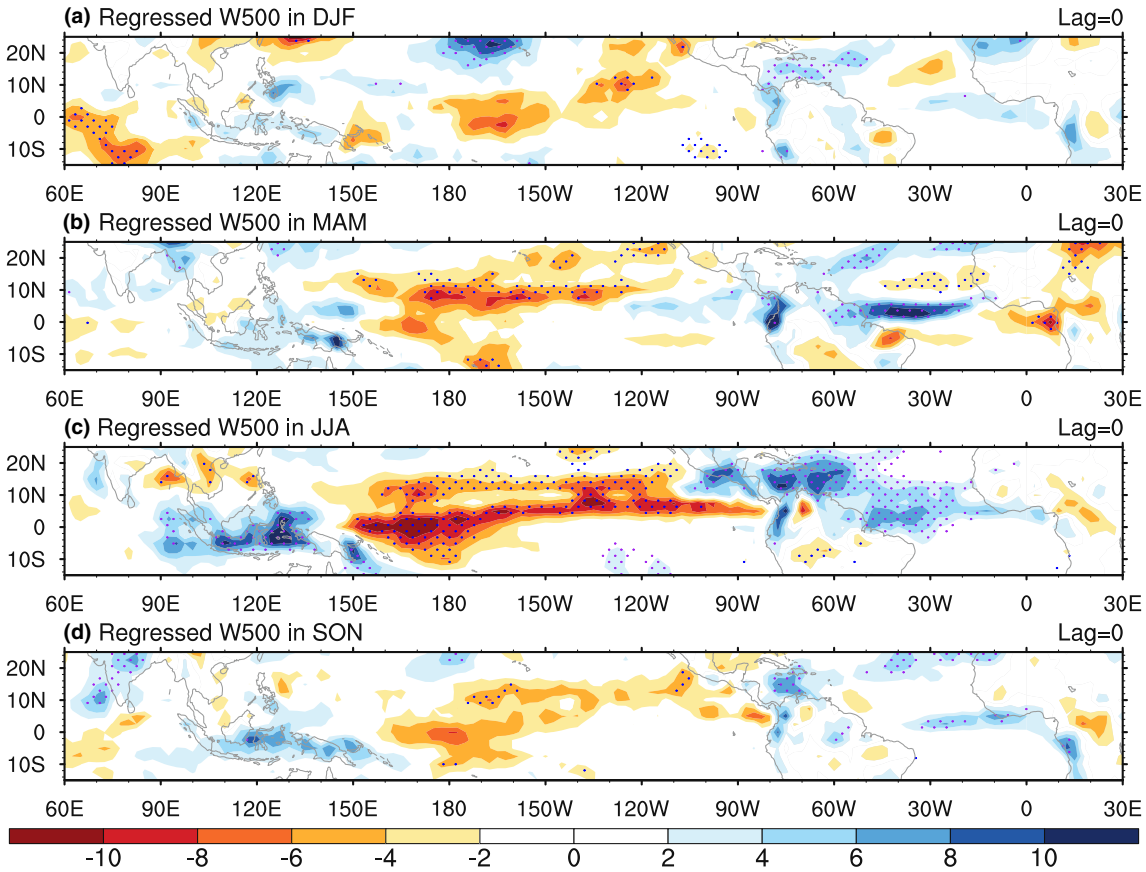

Fig. 6 Same as Fig. 5a–d but for the 500-hPa vertical velocity anomalies (unit: 10^{-3} Pa s^{-1}). Positive values represent ascending motion

for the NTA SST index 1 month ahead (contoured areas in Fig. 8a), and similar results are obtained for the OLR (Fig. 8b) and W500 (Fig. 8c) anomalies. In the high-index phase of the NTA SST during the JFM–MAM seasons, positive precipitation and W500 and negative OLR anomalies are observed in a narrow band between the equator and approximately 10°N, whereas negative W500 and positive OLR anomalies are observed to the north of approximately 10°N and vice versa (Fig. 8a–c). Therefore, this contrast in the anomalous OLR and W500 fields between the areas to the south and north of approximately 10°N weakens the lagged correlation of the regionally averaged OLR and W500 anomalies from late winter to early spring with the NTA SST index 0–5 months ahead.

Nevertheless, seasonal changes in the local precipitation, OLR and W500 anomalies associated with the NTA SST are consistent with the seasonal migration of the Atlantic ITCZ when represented as the climatological mean of precipitation and SST (see Fig. 8d). The intensified (suppressed) local convection activity associated with the NTA warming (cooling) extends northward from spring to summer as the Atlantic ITCZ migrates northward and becomes stronger (Fig. 8). The anomalous convection activity is mainly moored to a narrow band near the equator during spring but spans nearly the entire NTA region during summer. This behavior is consistent with the seasonal changes in the lagged relationship of the WNPAC with the NTA SST, which becomes statistically significant after late spring and reaches a peak in late summer and early autumn (Fig. 3a).

4.2 Large-scale atmospheric circulation anomalies

Figure 9 shows the simultaneous regressions of velocity potential anomalies at 850 and 250 hPa against the NTA SST index in DJF, MAM, JJA and SON. The common feature in these regressions, as shown in Fig. 9, is the anomalous low-level convergence and upper-level divergence over the NTA and opposite anomalies over the central tropical Pacific in the high-index phase of the NTA SST, although the anomalies are relatively weak in DJF and their amplitude becomes stronger from MAM to JJA. The anomalous low-level divergence and upper-level convergence become statistically significant over the central tropical Pacific to the north of the equator in MAM (Fig. 9b) and extend southward and are centered at the equator in JJA (Fig. 9c). Additionally, enhanced low-level convergence and upper-level divergence

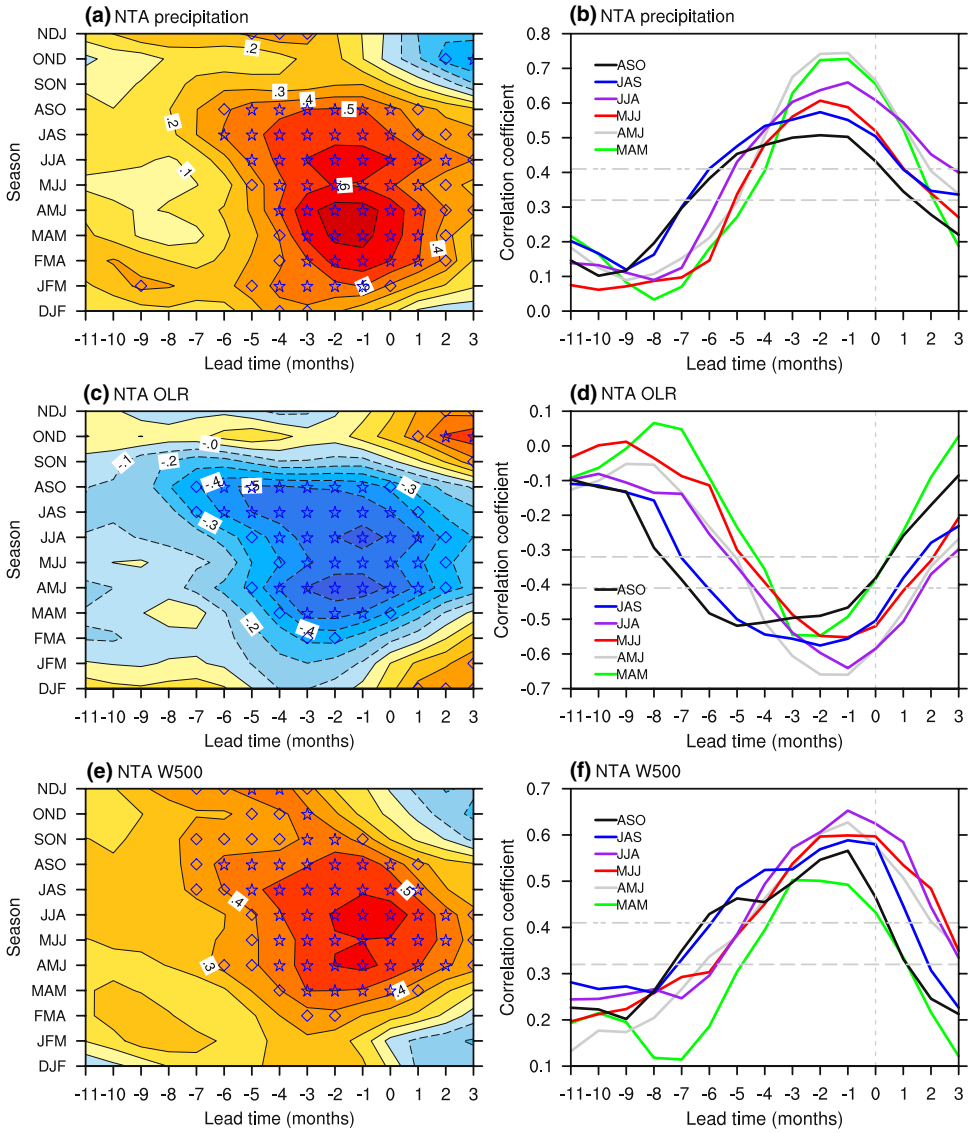

Fig. 7 Same as Fig. 3a–b but for the lead-lag correlations of the NTA SST index with the **a, b** precipitation, **c, d** OLR and **e, f** 500-hPa vertical velocity anomalies regionally averaged over the NTA

are observed over the eastern tropical Indian Ocean–Maritime continent in JJA and SON (Fig. 9c, d). The opposite situation can be observed in the low-index phase of the NTA SST.

Seasonal changes in the tropical divergent flow anomalies associated with the NTA SST are more clearly illustrated in Fig. 2b, c, which display the simultaneous time-longitude section (shaded areas) of the 3-month-running averaged EQ–15°N meridional mean velocity potential anomalies at 850 and 250 hPa regressed against the NTA SST index. In the high-index phase of the NTA SST, anomalous convergent (divergent) flows are observed in the low troposphere over the NTA (central tropical Pacific) during the spring–autumn seasons (Fig. 2b), and opposite anomalies occur in the upper troposphere (Fig. 2c). Over the eastern tropical Indian Ocean–Maritime continent, anomalous low-level convergence and upper-level divergence mainly occur during the summer–autumn seasons. Similar circulation patterns are obtained when the NTA SST index leads by 1 month (contoured areas in Fig. 2b, c), although the action center over the eastern tropical Indian Ocean–Maritime continent shifts toward the cold season as the lead time increases.

A comparison of Figs. 6 and 9 indicates that the anomalous low-level convergence and upper-level divergence are concurrent with anomalous ascending motion over the NTA in the high-index phase of the NTA SST. In contrast, anomalous descending motion is observed over the central tropical Pacific, which is consistent with the anomalous upper-level convergence and low-level divergence over this region. Therefore, the NTA warming appears to be accompanied by an anomalous zonally overturning circulation extending westward from the tropical Atlantic to the central tropical Pacific during the spring–autumn seasons,

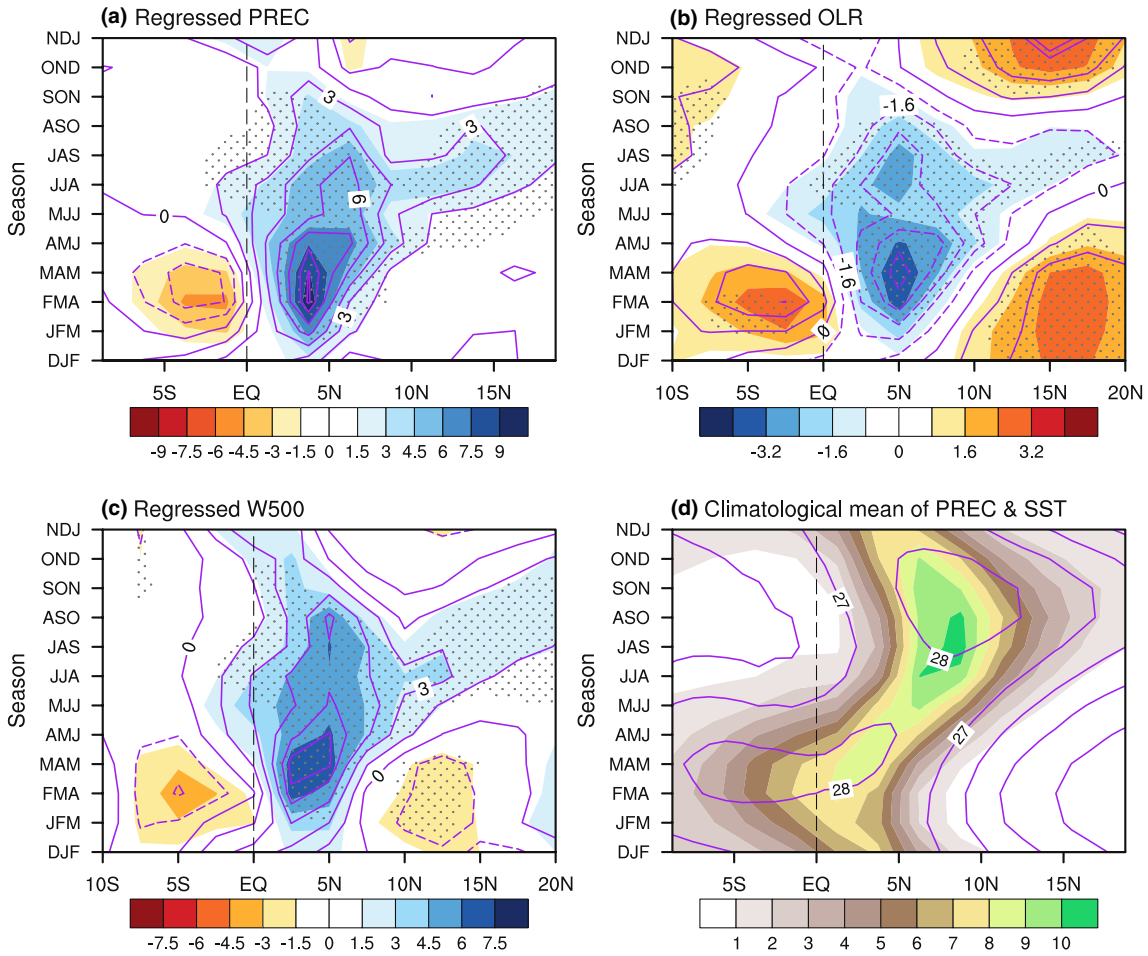

Fig. 8 Time-latitude section of the 3-month-running-averaged 10°–50°W zonal mean precipitation anomalies (shaded; unit: 10^{-1} mm day^{-1}) regressed against the NTA SST index when leading by 0 months (shaded) and 1 month (contoured), respectively. The dots denote significance at the 95% confidence level for the shaded areas, and the black dashed line refers to the equator. **b, c** Same as **a** but for the OLR (unit: W m^{-2}) and 500-hPa vertical velocity (unit: 10^{-3} Pa s^{-1}) anomalies, respectively. **d** Same as **a** but for the climatological mean of the precipitation (shaded; unit: mm day^{-1}) and SST (contoured; unit: °C)

which is associated with anomalous ascending motion over the NTA and opposite anomalies over the central tropical Pacific. The enhanced subsidence over the central tropical Pacific suppresses the local convection activity, which in turn triggers an anomalous low-level anticyclone over the WNP as a Gill-type Rossby-wave response (Gill 1980).

Notably, anomalous descending motion extends westward to the central–western tropical Pacific, whereas anomalous ascending motion are clearly observed over the eastern tropical Indian Ocean–Maritime continent during the summer–autumn seasons (Figs. 2b, c, 6c). Previous studies have shown that intensified convection activity over the Maritime continent could lead to an anomalous low-level anticyclone over the WNP (Lu et al. 2006; Chung et al. 2011). Therefore, the NTA SST-associated anomalous atmospheric circulation and convection activity over the central–western tropical Pacific and Maritime continent favor a stronger WNPAC in late summer and early autumn.

5 Simulations of the forcing mechanism by the CAM5 model

Observational analysis reveals a significant in-phase relationship between the NTA SST and WNPAC during the spring–autumn seasons and a possible mechanism responsible for this linkage. To confirm these observed results, two sets of perturbed experiments are conducted using the CAM5 model forced with SST anomalies over the NTA. The first set includes warm NAT SST perturbed experiments (referred to as WNTA hereafter). In these experiments, monthly SST anomalies are first calculated by regressing against the monthly NTA SST index, and then the SST

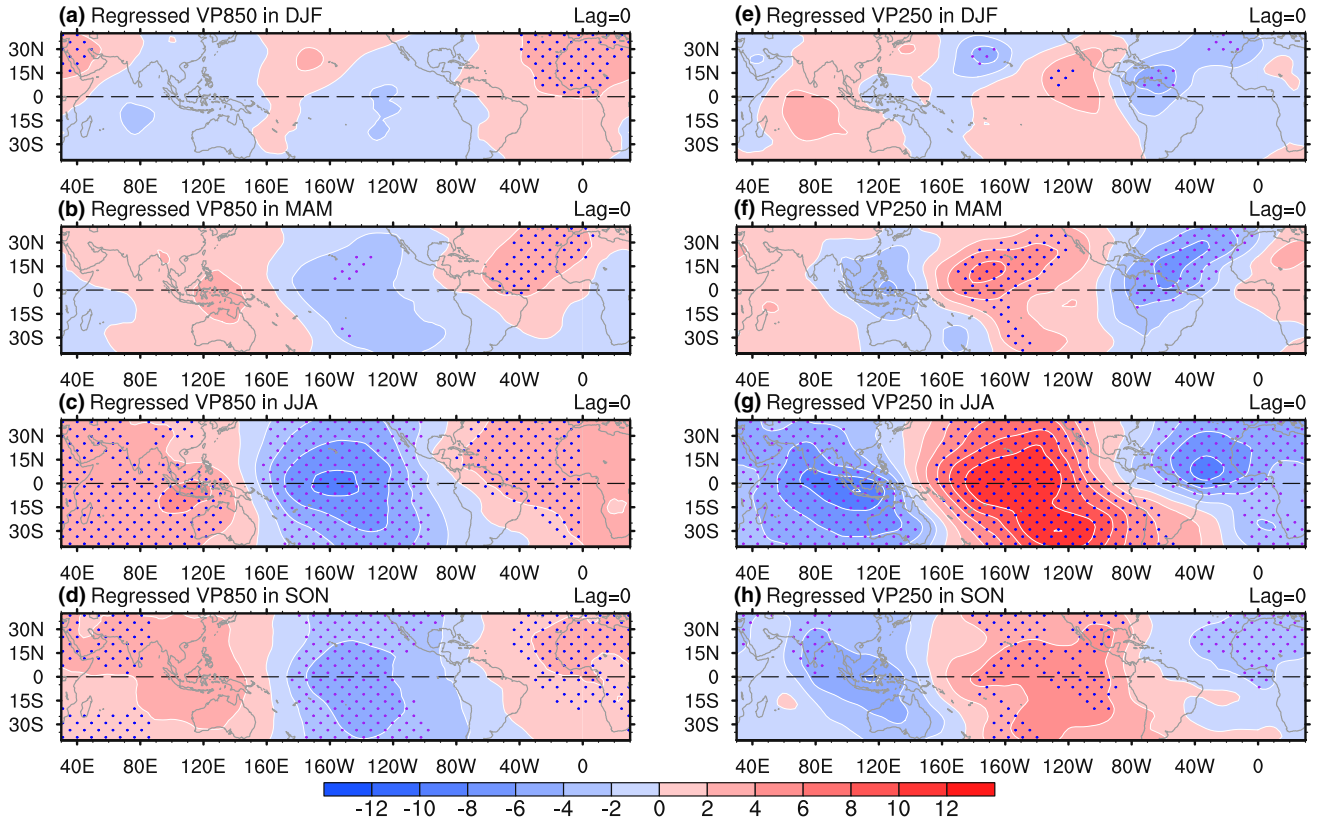

Fig. 9 Simultaneous regressions of the velocity potential anomalies (shaded; unit: 10^5 m^2 s^{-1}) at 850 hPa against the NTA SST index in **a** DJF, **b** MAM, **c** JJA and **d** SON. **e**–**h** Same as **a**–**d** but at 250 hPa. The dots denote significance at the 95% confidence level, and the black dashed line refers to the equator

anomalies are added to the climatological SSTs for the corresponding months in the target region of EQ–15°N and 70 W°–0°E. A 3-month-running average is applied prior to the regression analysis. The second set includes cold NAT SST perturbed experiments (referred to as CNTA hereafter), in which the SST conditions are the same as those in the WNTA experiments except that opposite SST anomalies are added to the climatological SSTs. The perturbed runs are conducted with 100 ensemble members integrated from 1 February with slightly varying atmospheric initial conditions from the control run. Each member runs continually for 2 years, and the first year is discarded as spin up. The ensemble mean of the 100 members is used for analysis. We mainly illustrate the ensemble-mean difference between the WNTA and CNTA experiments (former minus latter) to maximize the signal-to-noise ratio.

Figure 10 shows the ensemble-mean differences of the stream function and horizontal wind anomalies at 850 hPa between the WNTA and CNTA experiments in DJF, MAM, JJA and SON. This figure indicates that the DJF low-level atmospheric circulation responses to the NTA SST forcing are very weak over the WNP (Fig. 10a), which is consistent with the observations (Fig. 1a). In MAM, a significant anticyclone response is observed over the central–western North Pacific (Fig. 10b), with the northward shifting and westward extension of the center compared with the position indicated by the observations (Fig. 1b). In JJA, the atmospheric circulation responses feature a significant anticyclone over the WNP and a cyclone over the eastern North Pacific–Atlantic (Fig. 10c), which resembles the patterns of the observations (Fig. 1c). A similar pattern of atmospheric circulation responses is observed in SON (Fig. 10d), but the simulated anomalous anticyclone over the WNP clearly shifts westward relative to that of the observations over this season (Figs. 1d, 2a). Consistent results are obtained from an analysis of the probability distribution functions (PDFs) of the WNPAC index, which reveal that the PDFs in the WNTA experiments cannot be distinguished from those in the CNTA experiments in DJF (Fig. 11a), while the WNPAC clearly shifts to its high (low)-index phase in the WNTA (CNTA) experiments in JJA (Fig. 11c).

Figure 12a is the time-longitude section of the ensemble-mean difference of the 3-month-running-averaged 10–25°N meridional mean stream function anomalies at 850 hPa between the WNTA and CNTA experiments. A comparison of Figs. 2a and 12a reveals that the pattern of the 850-hPa

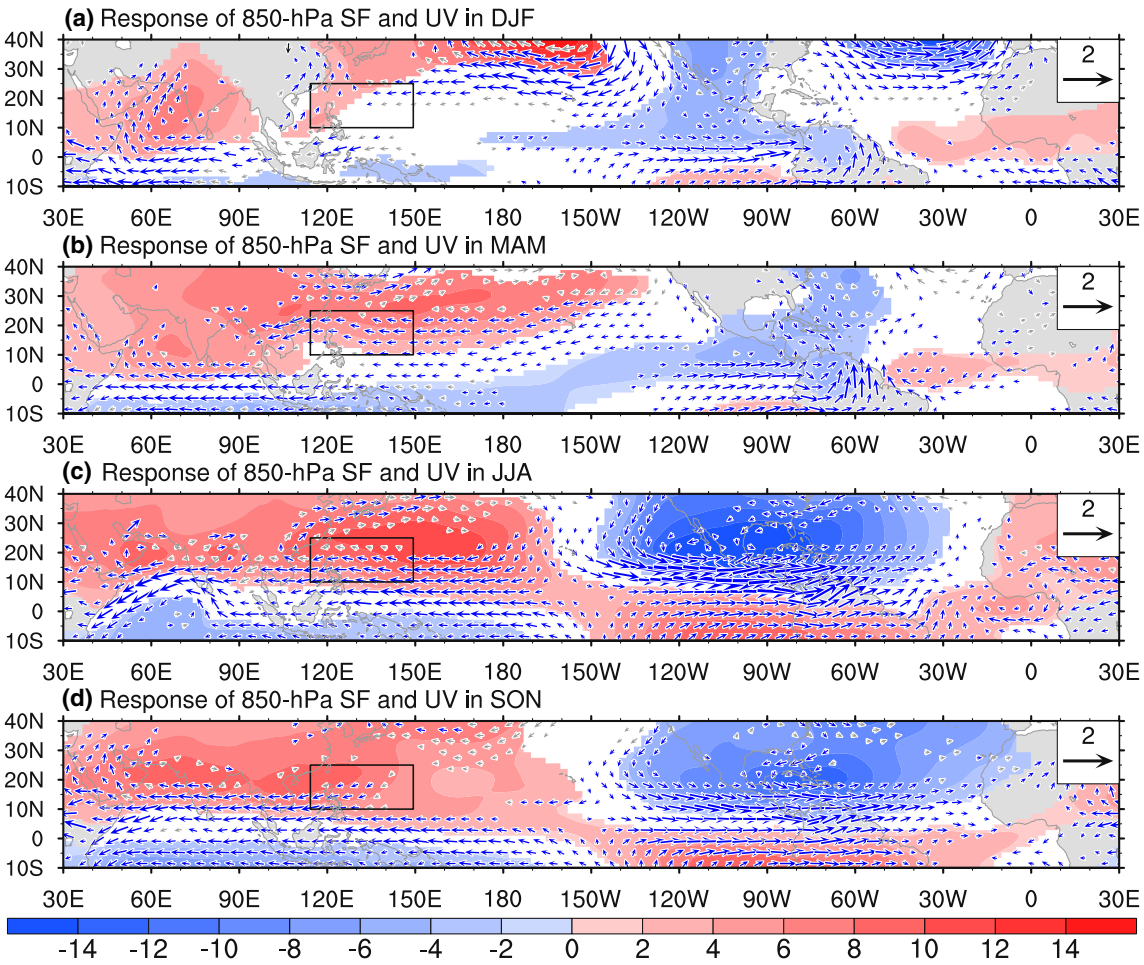

Fig. 10 Same as Fig. 1 but for the ensemble-mean difference between the WNTA and CNTA experiments (former minus latter)

stream function responses in the model resembles that of the observations over the subtropical North Pacific–Atlantic, although there are some differences in the amplitude and position of the action centers. The amplitude of the anticyclone response over the WNP reaches a peak in the middle of summer (Fig. 12a), whereas the observed peak occurs in late summer (Fig. 2a). Furthermore, strong anticyclone responses occur over the subtropical South Asia during the summer–autumn seasons, which are hardly detected in the observations.

Figure 13 further presents the ensemble-mean differences of the velocity potential anomalies at 850 and 250 hPa between the WNTA and CNTA experiments in DJF, MAM, JJA and SON; moreover, Fig. 12b, c show the time-longitude section of the ensemble-mean difference of the 3-month-running-averaged EQ–15°N meridional mean velocity potential anomalies at 850 and 250 hPa. A comparison of Figs. 9 and 13 shows that the patterns of the anomalous low- and upper-level divergent flow responses in the model also resemble those of the observations over the tropical Pacific–Atlantic in all four seasons. That is, the model reproduces the anomalous low-level convergent and upper-level divergent flows over the NTA and opposite anomalies over the central tropical Pacific indicated by the observations. Both the low- and upper-level action centers over the NTA in the model (Fig. 12b, c) extend toward the cold season relative to those indicated by the observations (Fig. 2b, c), which is consistent with the stronger low-level cyclone response over the eastern Pacific–Atlantic in the model (Fig. 12a).

Additionally, Fig. 12 clearly shows that the anomalous low-level cyclone (anticyclone) is located to the west of the anomalous low-level (upper-level) convergence (divergence) in the model. The anomalous low-level cyclone over the eastern Pacific–Atlantic and low-level convergence/upper-level divergence feature a Gill-type Rossby-wave response (Gill 1980) to the NTA SST forcing. The anomalous upper-level convergence and low-level divergence over the central tropical Pacific could suppress the local convection activity, which in turn triggers an anomalous low-level anticyclone over the WNP.

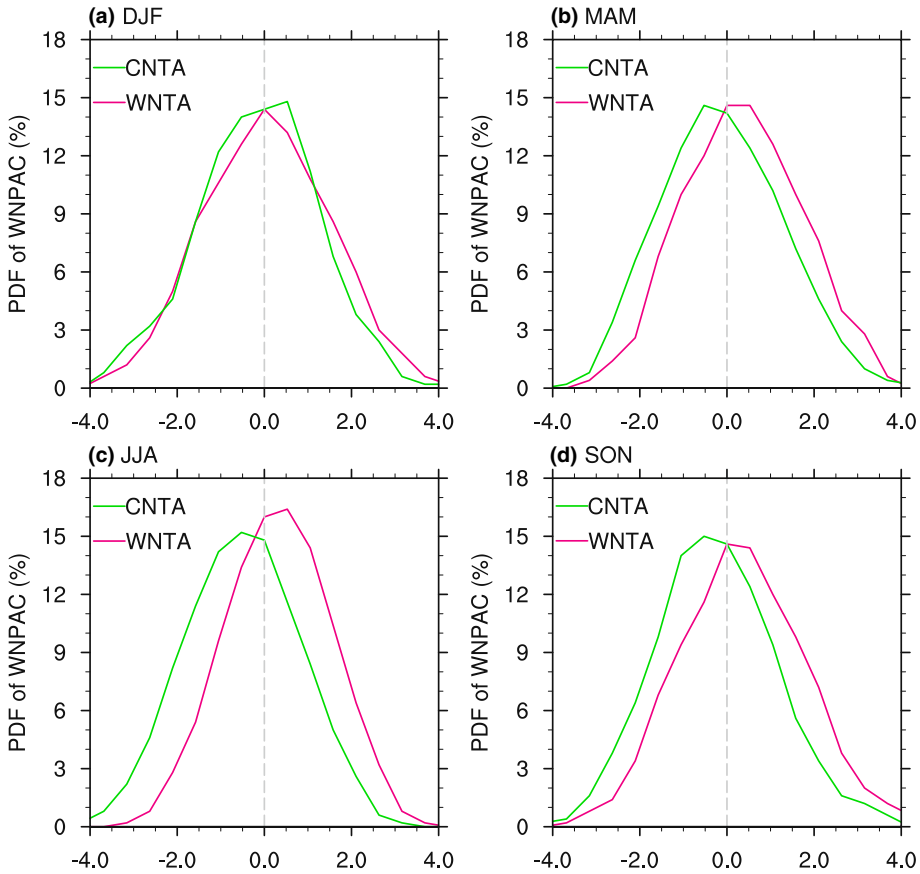

Fig. 11 Probability distribution functions of the WNPAC index for the WNTA (red curve) and CNTA (green curve) experiments in **a** DJF, **b** MAM, **c** JJA and **d** SON

Distinct differences are observed over the tropical Indian Ocean–Maritime continent between the model simulations and observations. The anomalous low- and upper-level divergent flow responses are very weak over these regions in the model (Fig. 12b, c), but anomalous low-level divergence and upper-level convergence are clearly indicated by the observations in the high-index phase of the NTA SST during the summer–autumn seasons (Fig. 2b, c). This difference could be attributed to a lack of ocean–atmosphere interaction in our AMIP-type simulations using an atmospheric model.

Nevertheless, the similarity between the model simulations and observations confirms that the NTA SST anomalies could significantly affect the variability of the summer–autumn WNPAC, while the former has a limited effect on the wintertime WNPAC. This NTA–WNP connection is related to an anomalous zonally overturning circulation spanning from the NTA to the tropical Pacific, which is associated with anomalous low-level convergence and upper-level divergence over the NTA, but the opposite anomalies occur over the central tropical Pacific when the NTA SST anomalies are warmer than normal. Enhanced subsidence over the central tropical Pacific suppresses local convection activity, which in turn triggers an anomalous low-level anticyclone over the WNP as a Gill-type Rossby-wave response (Gill 1980). The opposite situation are observed when the NTA SST anomalies are colder than normal.

6 Conclusions and discussion

The lagged relationship between the WNPAC and the NTA SST variability in different seasons and its dependence on the ENSO variability were investigated in this work. The results showed that the WNPAC from late spring to the middle of autumn has a significant in-phase relationship with the NTA SST variability up to two seasons ahead, and this relationship reaches a peak when the latter leads the former by approximately 1–2 months. Moreover, the WNPAC in late summer and early autumn appears to have the strongest relationship with the NTA SST variability, and the earliest signal of the latter in the former could date back to the previous early spring. In contrast, the WNPAC during winter has an insignificant relationship with the NTA SST variability 0–11 months ahead. Although the NTA SST is partially related to the ENSO variability (Xie and Carton 2004; Yang et al. 2017), the latter has a limited effect on the relationship between the NTA SST and WNPAC throughout the year.

Observational evidence suggests that the NTA–WNP connection is related to an anomalous zonally overturning

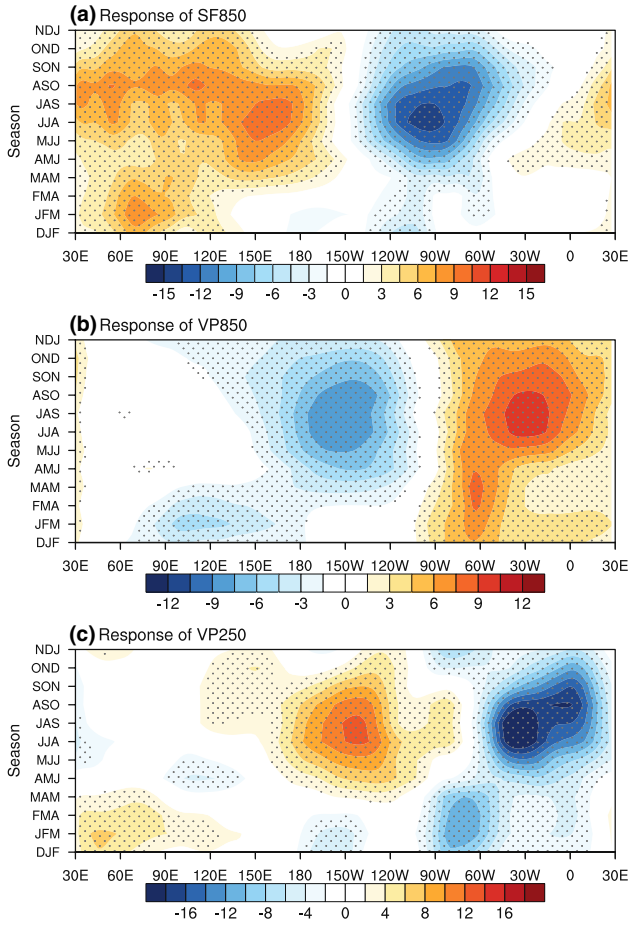

Fig. 12 Same as Fig. 2 but for the ensemble-mean difference between the WNTA and CNTA experiments (former minus latter)

circulation extending westward from the NTA to the tropical Pacific. When the NTA SST anomalies are warmer than normal, enhanced low-level convergence and upper-level divergence are clearly observed over the NTA during the spring–autumn seasons, indicating that the NTA warming could intensify the local convection activity during these seasons. The in-phase relationship between the NTA SST and local convection activity reaches a peak when the former leads the latter by approximately 1–2 months. Moreover, enhanced upper-level convergence and low-level divergence are observed over the central tropical Pacific, which could suppress the local convection activity and in turn trigger an anomalous low-level anticyclone over the WNP as a Rossby-wave response. The opposite situation can be observed when the NTA SST anomalies are colder than normal. These results agree with those of Hong et al. (2014), who suggested that NTA SST anomalies have a significant effect on the WNP subtropical high via an anomalous westward-extending overturning circulation during July–August after the early 1980s.

Moreover, we found that the intensity of local convection activity associated with the NTA SST anomalies is closely related to the seasonal migration of the Atlantic ITCZ. The intensified (suppressed) local convection activity associated with the NTA warming (cooling) is mainly moored to a narrow band near the equator in early spring but extends northward as the Atlantic ITCZ migrates northward and becomes stronger from spring to summer. The in-phase relationship of local convection activity with the NTA SST anomalies exhibits a peak in the middle of summer and then sharply weakens after early autumn. This finding is consistent with the seasonal changes in the relationship between the WNPAC and NTA SST anomalies, which becomes statistically significant in late spring, reaches a peak in late summer and early autumn and then sharply weakens after the middle of autumn. Therefore, a considerable signal associated with the NTA SST anomalies in the WNPAC variability is only detected during the spring–autumn seasons because of the dependence of SST-induced anomalous local convection activity on the seasonal migration of the Atlantic ITCZ. During the winter season, when atmospheric variability is strong and plays a dominant role in controlling ocean–atmosphere interactions over the North Atlantic on an interannual timescale (Marshall et al. 2001; Xie and Carton 2004), anomalous local convection activity associated with the NTA SST is very weak, so the NTA SST barely affects the WNPAC variability.

Finally, a set of numerical experiments was conducted with the CAM5 model forced with SST anomalies over the NTA. Consistent numerical results were obtained for the atmospheric circulation responses over the Pacific–Atlantic region, which confirms that the NTA SST anomalies could exert a significant effect on the WNPAC variability via an anomalous zonally overturning circulation extending westward from the NTA to the tropical Pacific during the spring–autumn seasons. Notably, distinct differences between the model simulations and observations are observed over the tropical Indian Ocean–Maritime continent. Observational evidence shows that the NTA warming tends to be accompanied by enhanced upper-level divergence and low-level convergence over these regions during the summer–autumn seasons, which may intensify the WNPAC (Lu et al. 2006; Chung et al. 2011). However, atmospheric circulation responses over the tropical Indian Ocean–Maritime continent are very weak during the summer–autumn seasons. This feature may be attributed to a lack of ocean–atmosphere interactions in our AMIP-type simulations, which requires further examination but lies beyond the scope of this study.

In this work, we noted that the earliest signal of the NTA SST anomalies in the summer–autumn WNPAC variability could date back to the previous early spring. This result is consistent with the results of Ham et al. (2013),

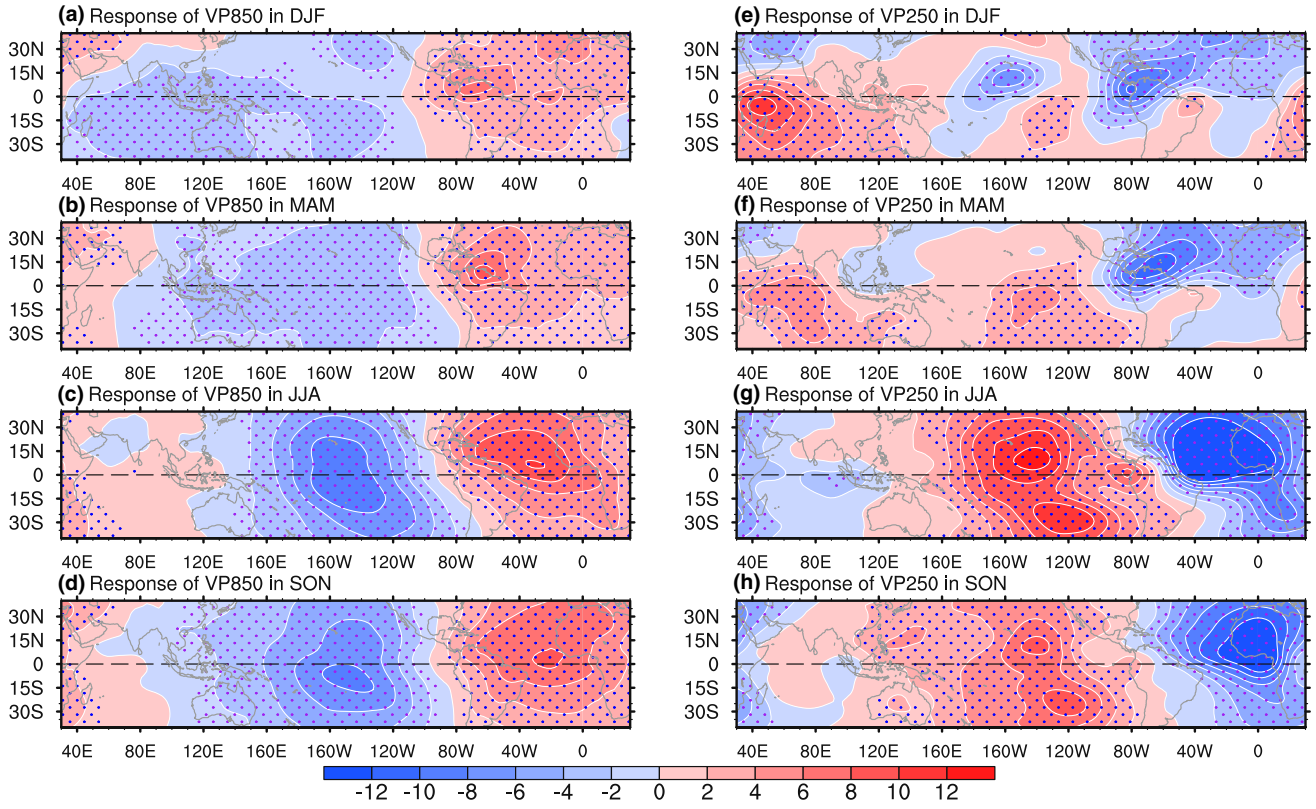

Fig. 13 Same as Fig. 9 but for the ensemble-mean difference between the WNTA and CNTA experiments (former minus latter)

who focused on the impact of early spring NTA warming on the ENSO variability and found that the former can induce an anomalous low-level anticyclone over the WNP, favoring the development of a La Niña event during the following summer–autumn seasons and vice versa. This delayed effect, which could reach two seasons, may be related to the long-lasting persistence of the NTA SST anomalies during these seasons. As shown in Fig. 14, the autocorrelation of the NTA SST index is still significant at the 99% confidence level up to 6 (5) months during spring (summer) both before and after removing the effect of the ENSO. Additionally, ocean–atmosphere interactions over the tropical Pacific may

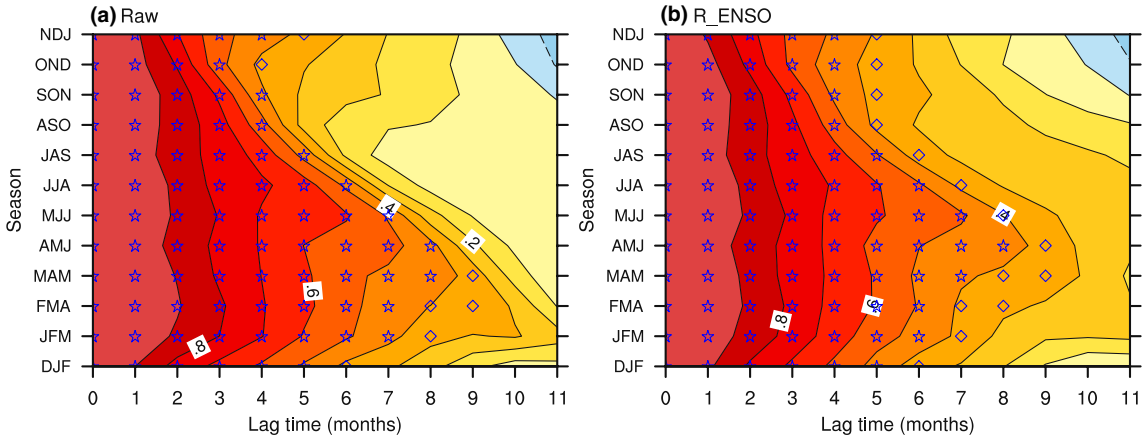

Fig. 14 Autocorrelations of the 3-month-running-averaged NTA SST index **a** before and **b** after removing the effect of the ENSO. The squares and stars denote significance at the 95 and 99% confidence levels, respectively. The lag time refers to the middle month of the 3-month-running season

also play a role in amplifying and relaying the influence of the NTA SST to the Pacific climate variability (Ham et al. 2013; Chen et al. 2015). Ham et al. (2013) highlighted the importance of ocean–atmosphere interactions along the Pacific ITZC for the delayed influence of the early spring NTA SST on the WNPAC and ENSO variability, and Chen et al. (2015) provided a similar mechanism for the simultaneous NTA–WNP connection during summer. Notably, the AMIP-type experiments conducted in this work clearly show direct atmospheric circulation responses to the NTA SST forcing, indicating that the NTA SST can significantly modulate the WNPAC variability without tropical Pacific ocean–atmosphere interactions, which is also supported by the results of Hong et al. (2014, 2015). However, the relative contribution from direct atmospheric circulation responses and tropical Pacific ocean–atmosphere interactions to the NTA–WNP connection still requires further examination by conducting different types of numerical experiment in future works.

The ENSO is recognized as the dominant source of predictability in seasonal–interannual climate prediction over the WNP and East Asia but is usually subject to a persistence barrier during spring (e.g., Webster and Yang 1992; Ren et al. 2016; Tian and Duan 2016). Interestingly, this spring persistence barrier does not apply to the NTA SST (see Fig. 14). Therefore, the long-lasting persistence of the NTA SST and considerable effect of the SST on the WNP large-scale atmospheric circulation may have important implications for the seasonal prediction of WNP tropical cyclone activity (e.g., Huo et al. 2015; Cao et al. 2016; Yu et al. 2016; Gao et al. 2018) and East Asian summer climate (Hong et al. 2015; Ham et al. 2017; Li et al. 2017b; Ren et al. 2017).

Acknowledgements This work is jointly supported by the National Key Research Program and Development of China (2017YFC1502300), the 973 Program of China (2013CB430203), and the China Meteorological Special Program (GYHY201406018). The authors are grateful to the two anonymous reviewers for their insightful comments, which helped us improve the quality of this paper.

References

Cao J, Lu R, Hu J, Wang H (2013) Spring Indian Ocean–western Pacific SST contrast and the East Asian summer rainfall anomaly. Adv Atmos Sci 30:1560–1568. https://doi.org/10.1007/s00376-013-2298-6

Cao X, Chen SF, Chen GH, Wu RG (2016) Intensified impact of northern tropical Atlantic SST on tropical cyclogenesis frequency over the western North Pacific after the late 1980s. Adv Atmos Sci 33:919–930. https://doi.org/10.1007/s00376-016-5206-z

Chang T-C, Hsu H-H, Hong C-C (2016) Enhanced influences of tropical Atlantic SST on WNP–NIO atmosphere–ocean coupling since the early 1980s. J Clim 29:6509–6525. https://doi.org/10.1175/JCLI-D-15-0807.1

Chen W, Park J-K, Dong B, Lu R, Jung WS (2012) The relationship between El Niño and the western North Pacific summer climate in a coupled GCM: role of the transition of El Niño decaying phases. J Geophys Res 117:D12111. https://doi.org/10.1029/2011JD017385

Chen W, Lee J-Y, Lu R, Dong B, Ha K-J (2015) Intensified impact of tropical Atlantic SST on the western North Pacific summer climate under a weakened Atlantic thermohaline circulation. Clim Dyn 45:2033–2046. https://doi.org/10.1007/s00382-014-2454-4

Chung P-H, Sui C-H, Li T (2011) Interannual relationships between the tropical sea surface temperature and summertime subtropical anticyclone over the western North Pacific. J Geophys Res 116:D13111. https://doi.org/10.1029/2010JD015554

Dee DP et al (2011) The ERA-Interim reanalysis: configuration and performance of the data assimilation system. Quart J Roy Meteorol Soc 137:553–597. https://doi.org/10.1002/qj.828

Fisher RA (1915) Frequency distribution of the values of the correlation coefficient in samples of an indefinitely large population. Biometrika 10:507–521

Gao S, Chen Z, Zhang W (2018) Impacts of tropical North Atlantic SST on western North Pacific landfalling tropical cyclones. J Clim 31:853–862. https://doi.org/10.1175/JCLI-D-17-0325.1

Gill AE (1980) Some simple solutions for the heat induced tropical circulation. Q J Meterol Soc 106:447–462. https://doi.org/10.1002/qj.49710644905

Ham Y-G, Kug J-S, Jin F-F (2013) Sea surface temperature in the north tropical Atlantic as a trigger for El Niño/Southern Oscillation events. Nat Geosci 6:112–116. https://doi.org/10.1038/ngeo1686

Ham Y-G, Chikamoto Y, Kug J-S, Kimoto M, Mochizuki T (2017) Tropical Atlantic-Korea teleconnection pattern during boreal summer season. Clim Dyn 49:2649–2664. https://doi.org/10.1007/s00382-016-3474-z

He J, Zhou B, Wen M, Li F (2001) Vertical circulation structure, interannual variation features and variation mechanism of Western pacific subtropical High. Adv Atmos Sci 18:497–510. https://doi.org/10.1007/s00376-001-0040-2

Hong C-C, Chang T-C, Hsu H-H (2014) Enhanced relationship between the tropical Atlantic SST and the summertime western North Pacific subtropical high after the early 1980s. J Geophys Res Atmos 119:3715–3732. https://doi.org/10.1002/2013JD021394

Hong C-C, Lee M-Y, Hsu H-H, Lin N-H, Tsuang B-J (2015) Tropical SST forcing on the anomalous WNP subtropical high during July–August 2010 and the record-high SST in the tropical Atlantic. Clim Dyn 45:633–650. https://doi.org/10.1007/s00382-014-2275-5

Huo L, Guo P, Hameed SN, Jin D (2015) The role of tropical Atlantic SST anomalies in modulating western North Pacific tropical cyclone genesis. Geophys Res Lett 42:2378–2384. https://doi.org/10.1002/2015GL063184

Klein SA, Soden BJ, Lau N-C (1999) Remote sea surface variations during ENSO: evidence for a tropical atmospheric bridge. J Clim 12:917–932. https://doi.org/10.1175/1520-0442(1999)012%3c0917:RSSTVD%3e2.0.CO;2

Li T, Wang B, Wu B, Zhou T, Chang C-P, Zhang R (2017a) Theories on formation of an anomalous anticyclone in western North Pacific during El Niño: A review. J Meteorol Res 31:987–1006. https://doi.org/10.1007/s13351-017-7147-6

Li W, Ren H-C, Zuo J, Ren H-L (2017b) Early summer southern China rainfall variability and its oceanic drivers. Clim Dyn. https://doi.org/10.1007/s00382-017-3898-0

Liebmann B, Smith CA (1996) Description of a complete (interpolated) outgoing longwave radiation dataset. Bull Am Meteorol Soc 77:1275–1277

Lu R, Dong B (2005) Impact of Atlantic sea surface temperature anomalies on the summer climate in the western North Pacific

during 1997–1998. J Geophys Res 110:D16102. https://doi.org/10.1029/2004JD005676
Lu R, Li Y, Dong B (2006) External and internal summer atmospheric variability in the western North Pacific and East Asia. J Meteorol Soc Jpn 84:447–462
Marshall J et al (2001) North Atlantic climate variability: phenomena, impacts and mechanisms. Int J Climatol 21:1863–1898. https://doi.org/10.1002/joc.693
Rayner NA, Parker DE, Horton EB, Folland CK, Alexander LV, Rowell DP, Kent EC, Kaplan A (2003) Global analyses of sea surface temperature, sea ice, and night marine air temperature since the late nineteenth century. J Geophys Res 108:4407. https://doi.org/10.1029/2002JD002670
Ren H-L, Jin F-F, Tian B, Scaife AA (2016) Distinct persistence barriers in two types of ENSO. Geophys Res Lett 43:10973–10979. https://doi.org/10.1002/2016GL071015
Ren H, Zuo J, Li W (2017) Role of the North Atlantic SST anomalies in the 1998 and 2016 summer floods in China. Acta Meteorol Sin (in Chinese) 75:877–893. https://doi.org/10.11676/qxxb2017.063
Rong XY, Zhang RH, Li T (2010) Impacts of Atlantic sea surface temperature anomalies on Indo-East Asian summer monsoon-ENSO relationship. Chin Sci Bull 55:2458–2468. https://doi.org/10.1007/s11434-010-3098-3
Stuecker MF, Timmermann A, Jin F-F, McGregor S, Ren H-L (2013) A combination mode of the annual cycle and the El Niño/Southern Oscillation. Nat Geosci 6:540–544. https://doi.org/10.1038/NGEO1826
Stuecker MF, Jin F-F, Timmermann A, McGregor S (2015) Combination mode dynamics of the anomalous northwest Pacific anticyclone. J Clim 28:1093–1111. https://doi.org/10.1175/JCLI-D-14-00225.1
Terao T, Kubota T (2005) East-west SST contrast over the tropical oceans and the post El Niño western North Pacific summer monsoon. Geophys Res Lett 32:L15706. https://doi.org/10.1029/2005GL023010
Tian B, Duan W (2016) Comparison of the initial errors most likely to cause a spring predictability barrier for two types of El Niño events. Clim Dyn 47:779–792. https://doi.org/10.1007/s00382-015-2870-0
Wang B, Wu R, Fu X (2000) Pacific-East Asia teleconnection: how does ENSO affect East Asian climate? J Clim 13:1517–1536. https://doi.org/10.1175/1520-0442(2000)013%3c1517:PEATHD%3e2.0.CO;2
Wang B, Xiang B, Lee J-Y (2013) Subtropical high predictability establishes a promising way for monsoon and tropical storm predictions. Proc Natl Acad Sci USA 110:2718–2722. https://doi.org/10.1073/pnas.1214626110
Webster J, Yang S (1992) Monsoon and ENSO: Selectively interactive systems. Q J R Meteorol Soc 118:877–926. https://doi.org/10.1002/qj.49711850705
Wu B, Zhou TJ, Li T (2017a) Atmospheric dynamic and thermodynamic processes driving the western North Pacific anomalous anticyclone during El Niño. Part I: maintenance mechanisms. J Clim 30:9621–9635. https://doi.org/10.1175/JCLI-D-16-0489.1
Wu B, Zhou TJ, Li T (2017b) Atmospheric dynamic and thermodynamic processes driving the western North Pacific anomalous anticyclone during El Niño. Part II: formation processes. J Clim 30:9637–9650. https://doi.org/10.1175/JCLI-D-16-0495.1
Xiang B, Wang B, Yu W, Xu S (2013) How can anomalous western North Pacific subtropical high intensify in late summer? Geophys Res Lett 40:2349–2354. https://doi.org/10.1002/grl.50431
Xie P, Arkin PA (1997) Global precipitation: a 17-year monthly analysis based on gauge observations, satellite estimates, and numerical model outputs. Bull Am Meteorol Soc 78:2539–2558
Xie SP, Carton JA (2004) Tropical Atlantic variability: patterns, mechanisms, and impacts. Earth Clim. https://doi.org/10.1029/147GM07
Xie S-P, Hu K, Hafner J, Tokinaga H, Du Y, Huang G, Sampe T (2009) Indian Ocean capacitor effect on Indo-western Pacific climate during the summer following El Niño. J Clim 22:730–747. https://doi.org/10.1175/2008JCLI2544.1
Xie S-P, Kosaka Y, Du Y, Hu K, Chowdary JS, Huang G (2016) Indo-western Pacific ocean capacitor and coherent climate anomalies in post-ENSO summer: a review. Adv Atmos Sci 33:411–432. https://doi.org/10.1007/s00376-015-5192-6
Yang Y, Xie S-P, Wu L, Kosaka Y, Li J (2017) ENSO forced and local variability of North Tropical Atlantic SST model simulations and biases. Clim Dyn. https://doi.org/10.1007/s00382-017-3679-9
Yu J, Li T, Tan Z, Zhu Z (2016) Effects of tropical North Atlantic SST on tropical cyclone genesis in the western North Pacific. Clim Dyn 46:865–877. https://doi.org/10.1007/s00382-015-2618-x
Zhang RH, Sumi A, Kimoto M (1996) Impact of El Niño on the East Asian Monsoon: a diagnostic study of the '86/87 and '91/92 events. J Meteorol Soc Jpn 74:49–62. https://doi.org/10.2151/jmsj1965.74.1_49
Zhang RH, Min Q, Su JZ (2017) Impact of El Niño on atmospheric circulations over East Asia and rainfall in China: role of the anomalous western North Pacific anticyclone. Sci China Earth Sci 60:1124–1132. https://doi.org/10.1007/s11430-016-9026-x

论文编目索引

1. Chen L J，Z S Gong，J Wu and W J Li. 2019：Extremely active tropical cyclone activities over the western North Pacific and South China Sea in summer 2018：Joint effects of decaying La Niña and intraseasonal oscillation. *Journal of Meteorological Research*，33(4)：609-626.
2. Chen L J，Gu W，Li W J. 2019：Why is the East Asian summer monsoon extremely strong in 2018? —Collaborative effects of SST and snow cover anomalies. *Journal of Meteorological Research*，33(4)：593-608.
3. 陈丽娟，顾　薇，龚振淞，等. 2019：影响2018年汛期气候的先兆信号及预测效果评估. 气象，45(4)：553-564.
4. 陈丽娟，赵俊虎，顾　薇，梁　萍，彭京备，等. 2019：汛期我国主要雨季进程成因及预测应用进展. *应用气象学报*，30(4)：385-400.
5. 段居琦，周　骥，黄大鹏，刘绿柳. 2019：基于最大熵模型的中国血吸虫病传播风险评估. *气象科技*，47(3)：520-525.
6. 高　丽，任宏利，郑嘉雯，等. 2019：基于NCEP-GEFS回算资料的我国极端温度变化特征研究. *大气科学学报*，42(1)：58-67.
7. 顾　薇，陈丽娟. 2019：2018年夏季海洋大气特征及对我国气候的影响. 气象，45(1)：126-134.
8. Guo Jun，Guoyu Ren，Mingming Xiong，He Huang. 2019：The spatiotemporal pattern of rainy-season precipitation in the Haihe River basin，North China. *Hydrology*，6，73，doi:10.3390/hydrology6030073.
9. Hao Xiaozhen，Hongli Ren，Wenjun Zhang，et al. 2019：Diagnosing the spatiotemporal diversity of westerly wind events in the tropical Pacific. *Dynamics of Atmospheres and Oceans*，86，90-103.
10. Huang Kai，Ren Hongli，Liu Xiangwen，et al. 2019：Parameter modulation of Madden-Julian Oscillation behaviors in BCC_CSM1.2：The key Role of moisture-shallow convection feedback. *Atmosphere*，10，241. doi:10.3390/atmos10050241.
11. Jia Wenqian，Ren Guoyu，Suonan Kanzhuo，Zhang Panfeng，et al. 2019：Urban Heat Island Effect and Its Cintribution to Observed Temperature Increase at Wuhan Station，Central China. *Journal of Tropical Meteorology*，25(1)：1-12.
12. Li Hongmei，Guoyu Ren，Wanzhi Li，et al. 2019：Diurnal and intra-season variation of warm-season temperature in coastal zone of Qinghai Lake. *Theoretical and Applied Climatology*，DOI:10.1007/s00704-019-02893-x.
13. Weiping Li，Yanwu Zhang，Xueli Shi，et al. 2019：Development of land surface model BCC_AVIM2.0 and its preliminary performance in LS3MIP/CMIP6. *Journal of Meteorological Research*，33(5)：851-869.
14. Li Yan，Guoyu Ren，Qingyuan Wang，et al. 2019：More extreme marine heatwaves in the China Seas during the global warming hiatus. *Environmental Research Letters*，DOI:10.1088/1748-9326/ab28bc.
15. 廖要明，陈德亮，刘秋锋. 2019：中国地气温差时空分布及变化趋势. *气候变化研究进展*，15(4)：374-384.
16. 廖要明，杨文平. 2019：凤县花椒生产气候条件和灾害分析. *中国农学通报*，35(23)：84-90.
17. Liu Jingpeng，Ren Hongli，Li Weijing，Jinqing Zuo. 2019：Diagnosing the leading mode of interdecadal covariability between the Indian Ocean sea surface temperature and summer precipitation in southern China. *Theoretical and Applied Climatology*，135，1295-1306.

18. Liu Yang, Junhu Zhao, Po Hu, Shulin Qu, Guolin Feng. 2019: The Major Interannual Modes of Late-Summer Precipitation over the Northern China Monsoon Region. *Atmosphere-Ocean*, 57(4): 295-306.
19. Liu Yulian, Guoyu Ren, Engyuan Kang, et al. 2019: A significant bias of T_{max} and T_{min} average temperature and its trend. *Journal of Applied Meteorology and Climatology*, DOI:10.1175/JAMC-D-19-0001.1.
20. 刘芸芸，陈丽娟. 2019：2019年春季我国主要气候异常特征及可能成因分析. 气象，45(10)：1483-1493.
21. Lu B, Li H Y, Wu J, et al. 2019: Impact of El Niño and Southern Oscillation on the summer precipitation over Northwest China. *Atmospheric Science Letters*, DOI:10.1002/asl.928.
22. Lu B, Ren H L. 2019: ENSO Features, Dynamics, and Teleconnections to East Asian Climate as Simulated in CAMS-CSM. *Journal of Meteorological Research*, 33(1): 46-65.
23. Yu Nie, Adam Scaife, Ren Hongli, et al. 2019: Stratospheric initial conditions provide seasonal predictability of the North Atlantic and Arctic Oscillations. *Environmental Research letters*, 14,034006.
24. Nie Yu, Hongli Ren, Yang Zhang. 2019: The role of extratropical air-sea interaction in the autumn subseasonal variability of the North Atlantic Oscillation. *Journal of Climate*, 32(22): 7697-7712.
25. Ren Hongli, Adam A. Scaife, Nick Dunstone, et al. 2019: Seasonal predictability of winter ENSO types in operational dynamical model predictions. *Climate Dynamics*, 52(7-8): 3869-3890.
26. Ren Hongli, Yujie Wu, Qing Bao, Jiehua Ma, et al. 2019: The China multi-model ensemble prediction system and its application to flood-season prediction in 2018. *Journal of Meteorological Research*, 33(3): 540-552.
27. Ren Hongli, Jinqing Zuo, Yi Deng. 2019: Statistical predictability of Niño indices for two types of ENSO. *Climate Dynamics*, 52(9-10): 5361-5382.
28. 孙丞虎，崔　童，李维京，等. 2019：动力和统计预测信息融合预测方法及我国夏季降水预测的检测. *地球物理学报*，62(11)：4110-4119.
29. Sun Ying, Hu Ting, Zhang Xuebin, Li Chao, et al. 2019: Contribution of global warming and urbanization to changes in temperature extremes in Eastern China. *Geophysical Research Letters*, 46: 11426-11434.
30. Tian Ben, Hongli Ren, Feifei Jin, Malte F. Stuecker. 2019: Diagnosing the representation and causes of the ENSO persistence barrier in CMIP5 simulations. *Climate Dynamics*, 53(3-4): 2147-2160.
31. Tysa S K, Ren G Y, Qin Y, et al. 2019: Urbanization Effect in Regional Temperature Series Based on a Remote Sensing Classification Scheme of Stations. *Journal of Geophysical Research: Atmospheres*, doi: 10.1029/2019JD030948.
32. Qingyuan Wang, Yan Li, Qingquan Li, et al. 2019: Changes in means and extreme events of sea surface temperature in the East China Seas based on satellite data from 1982 to 2017. *Atmosphere*, 10(140): 1-11.
33. Zheng Wang, Rong Zhi, Yu Wang and Guolin Feng. 2019: Partition of Season Based on Multi-elements and the Decadal Change of Season Duration in China. *Journal of Tropical Meteorology*, 25(3): 385-398.
34. Wei Yuntao, Mu Mu, Hongli Ren. 2019: Conditional nonlinear optimal perturbations of moisture triggering primary MJO initiation. *Geophysical Research Letters*, 46, 3492-3501.
35. Wei Yuntao, Hongli Ren. 2019: Modulation of ENSO on fast and slow MJO modes during boreal winter. *Journal of Climate*, 32(21): 7483-7506.
36. Wen Kangmin, Ren Guoyu, Li Jiao, et al. 2019: Recent surface air temperature change over mainland China based on an urbanization-bias adjusted dataset. *Journal of Climate*, 32: 2691-2705.
37. 伍丽泉，李清泉，丁一汇，等. 2019：BCC_CSM1.1气候模式年代际试验对北极涛动季节回报能力的初步评估. *气候变化研究进展*，15(1)：1-11.

38. Xin Xiaoge, Wei Min, Li Qingquan, et al. 2019: Decadal prediction skill of BCC-CSM1. 1 with different initialization strategies. *Journal of the Meteorological Society of Japan*, 97(3): 1-12.
39. 薛晓颖，任国玉，孙秀宝，等. 2019：中国中小尺度强对流天气气候学特征. *气候与环境研究*，24(2)：199-213.
40. Yang Ping, Ren Guoyu, Hou Wei. 2019: Impact of daytime precipitation duration on urban heat island intensity over Beijing city. *Urban Climate*, 28,100463.
41. 于晓澄，赵俊虎，杨　柳，支　蓉，封国林. 2019：华北雨季开始早晚与大气环流和海温异常的关系. *大气科学*，43(1)：107-118.
42. Naihui Zang, Junhu Zhao, Pengcheng Yan, Guolin Feng. 2019: Interdecadal variations of the temporal and spatial distribution of summer extreme heat in China. *Atmosphere-Ocean*, 57(5): 365-377.
43. 章大全，郑志海，陈丽娟，张培群. 2019：10～30 d 延伸期可预报性与预报方法研究进展. *应用气象学报*，30(4)：416-430.
44. Haoxin Zhang, Weiping Li, Weijing Li. 2019: Influence of late springtime surface sensible heat flux anomalies over the Tibetan and Iranian plateaus on the location of the South Asian High in early summer. *Advances in Atmospheric Sciences*, 36(1): 93-103.
45. Zhang Panfeng, Ren Guoyu, Xu Yan, et al. 2019: Observed changes in extreme temperature over the global land based on a newly developed station daily dataset. *Journal of Climate*, 32: 8489-8509.
46. Shuai Zhang, Chunxiang Shi, Runping Shen, Jie Wu. 2019: Improved assimilation of Fengyun-3 satellite-based snow cover fraction in northeastern China. *Journal of Meteorological Research*, 33(5): 960-975, doi:10.1007/s13351-019-8205-z.
47. Zhang Siqi, Ren Guoyu, Ren Yuyu, Sun Xiubao. 2019: Comparison of Surface Air Temperature between Observation and Reanalysis Data over Eastern China for the Last 100 Years. *Journal of the Meteorological Society of Japan*, 97(1): 1-15.
48. Zhang Y X, Ren Y Y, Ren G Y, et al. 2019: Bias correction of gauge data and its effect on precipitation climatology over mainland China. *Journal of Applied Meteorology and Climatology*, 58:2177-2196.
49. Zhao Chongbo, Hongli Ren, Rosie Eade, et al. 2019: MJO modulation and its ability to predict boreal summer tropical cyclone genesis over the northwest Pacific in Met Office Hadley Centre and Beijing Climate Center seasonal prediction systems. *Quarterly Journal of the Royal Meteorological Society*, 145:1089-1101.
50. 赵俊虎，王永光. 2019：2018 年秋季我国气候异常及成因分析. *气象*，45(4)：565-576.
51. Zhao J H, J Zhou, K G Xiong, G L Feng. 2019: Relationship between Tropical Indian Ocean SSTA in Spring and Precipitation of Northeast China in Late Summer. *Journal of Meteorological Research*, 33(6): 1060-1074.
52. Jie Zhou, Junhu Zhao, Rong Zhi. 2019: Possible Causes of the Anomalous Characteristics of Autumn Rain in Western China in 2017. *Theoretical and Applied Climatology*, 138: 1109-1123.
53. Xingyan Zhou, Riyu Lu. 2019: Interannual Variability of the Tropical Cyclone Landfall Frequency over the Southern and Northern Regions of East Asia in Autumn. *Journal of Climate*, 32, 8677-8686.
54. Zuo Jinqing, Li Weijing, Sun Chenghu, Ren Hongchang. 2019: Remote forcing of the northern tropical Atlantic SST anomalies on the western North Pacific anomalous anticyclone. *Climate Dynamics*, 52:2837-2853.